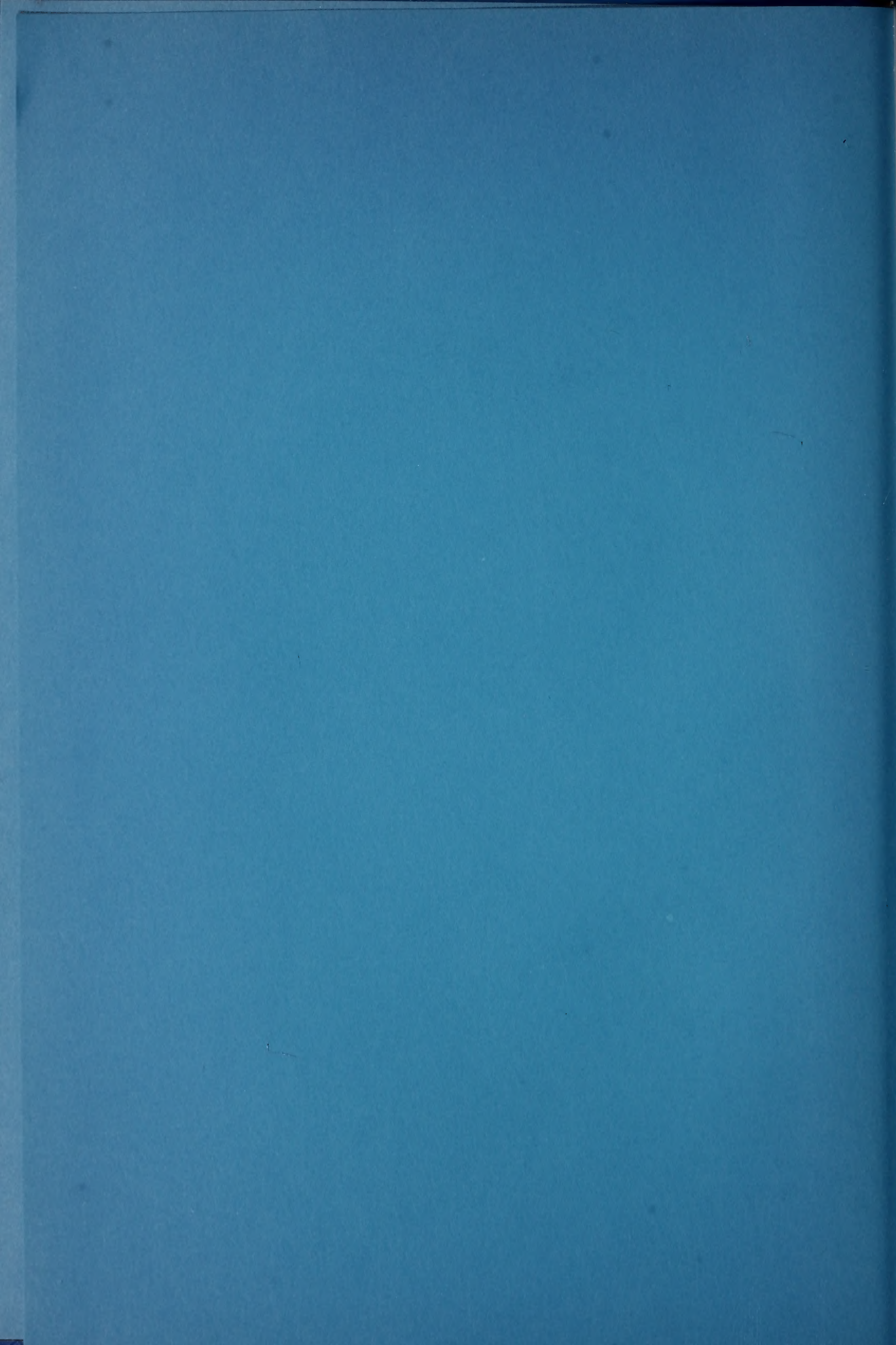


DIRECTOR'S OFFICE

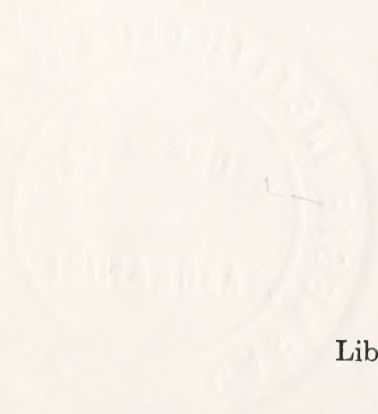


Carnegie Institution

OF WASHINGTON

Year Book 77

1977-1978




Library of Congress Catalog Card Number 3-16716
Port City Press, Inc., Baltimore, Maryland
Issued December 1978

President and Trustees

Contents

Officers and Staff	v
Report of the President	1
Reports of Departments and Special Studies	1
Department of Embryology	3
Hale Observatories	149
Department of Plant Biology	223
Developmental Biology Research Group	365
Department of Terrestrial Magnetism	381
Geophysical Laboratory	629
Administrative Reports	951
Office of Administration	953
Bibliography	955
Report of the Executive Committee	957
Abstract of Minutes of the Eighty-First Meeting of the Board of Trustees	959
Financial Statement	961
Articles of Incorporation	979
By-Laws of the Institution	983
Index of Names	989



Digitized by the Internet Archive
in 2012 with funding from
LYRASIS Members and Sloan Foundation

President and Trustees

PRESIDENT

Philip H. Abelson¹
James D. Ebert²

BOARD OF TRUSTEES

Frank Stanton
Chairman

William C. Greenough
Vice-Chairman

William T. Golden
Secretary

Philip H. Abelson³
Robert O. Anderson
J. Paul Austin
Lewis M. Branscomb
John T. Connor
John Diebold
Michael Ference, Jr.
Carl J. Gilbert
Hanna H. Gray⁴
Crawford H. Greenewalt
Caryl P. Haskins
William R. Hewlett
William McChesney Martin, Jr.
Henry S. Morgan⁵
Franklin D. Murphy³
Walter H. Page
Robert M. Pennoyer
Richard S. Perkins
William M. Roth
Robert C. Seamans, Jr.
Charles H. Townes
Juan T. Trippe
James N. White

Garrison Norton
Charles P. Taft
Trustees Emeriti

¹ Retired June 30, 1978.

² Effective July 1, 1978.

³ Elected May 5, 1978.

⁴ Resigned May 5, 1978.

⁵ Became Trustee Emeritus, May 5, 1978.

Former Presidents and Trustees

PRESIDENTS

Daniel Coit Gilman	1902-1904	John Campbell Merriam	1921-1938
Robert Simpson Woodward	1904-1920	Vannevar Bush	1939-1955
Caryl P. Haskins		1956-1971	

TRUSTEES

Alexander Agassiz	1904-05	Robert A. Lovett	1948-71
Lord Ashby of Brandon	1967-74	Seth Low	1902-16
George J. Baldwin	1925-27	Wayne MacVeagh	1902-07
Thomas Barbour	1934-46	Keith S. McHugh	1950-74
James F. Bell	1935-61	Andrew W. Mellon	1924-37
John S. Billings	1902-13	John Campbell Merriam	1921-38
Robert Woods Bliss	1936-62	Margaret Carnegie Miller	1955-67
Amory H. Bradford	1959-72	Roswell Miller	1933-55
Lindsay Bradford	1940-58	Darius O. Mills	1902-09
Omar N. Bradley	1948-69	S. Weir Mitchell	1902-14
Robert S. Brookings	1910-29	Andrew J. Montague	1907-35
Vannevar Bush	1958-71	William W. Morrow	1902-29
John L. Cadwalader	1903-14	Seeley G. Mudd	1940-68
William W. Campbell	1929-38	William I. Myers	1948-76
John J. Carty	1916-32	William Church Osborn	1927-34
Whitefoord R. Cole	1925-34	James Parmelee	1917-31
Frederic A. Delano	1927-49	Wm. Barclay Parsons	1907-32
Cleveland H. Dodge	1903-23	Stewart Paton	1916-42
William E. Dodge	1902-03	George W. Pepper	1914-19
Charles P. Fenner	1914-24	John J. Pershing	1930-43
Homer L. Ferguson	1927-52	Henning W. Prentis, Jr.	1942-59
Simon Flexner	1910-14	Henry S. Pritchett	1906-36
W. Cameron Forbes	1920-55	Gordon S. Rentschler	1946-48
James Forrestal	1948-49	David Rockefeller	1952-56
William N. Frew	1902-15	Elihu Root	1902-37
Lyman J. Gage	1902-12	Elihu Root, Jr.	1937-67
Walter S. Gifford	1931-66	Julius Rosenwald	1929-31
Cass Gilbert	1924-34	William W. Rubey	1962-74
Frederick H. Gillett	1924-35	Martin A. Ryerson	1908-28
Daniel C. Gilman	1902-08	Henry R. Shepley	1937-62
Patrick E. Haggerty	1974-75	Theobald Smith	1914-34
John Hay	1902-05	John C. Spooner	1902-07
Barklie McKee Henry	1949-66	William Benson Storey	1924-39
Myron T. Herrick	1915-29	Richard P. Strong	1934-48
Abram S. Hewitt	1902-03	William H. Taft	1906-15
Henry L. Higginson	1902-19	William S. Thayer	1929-32
Ethan A. Hitchcock	1902-09	James W. Wadsworth	1932-52
Henry Hitchcock	1902	Charles D. Walcott	1902-27
Herbert Hoover	1920-49	Frederic C. Walcott	1931-48
William Wirt Howe	1903-09	Henry P. Walcott	1910-24
Charles L. Hutchinson	1902-04	Lewis H. Weed	1935-52
Walter A. Jessup	1938-44	William H. Welch	1906-34
Frank B. Jewett	1933-49	Andrew D. White	1902-16
Samuel P. Langley	1904-06	Edward D. White	1902-03
Ernest O. Lawrence	1944-58	Henry White	1913-27
Charles A. Lindbergh	1934-39	George W. Wickersham	1909-36
William Lindsay	1902-09	Robert E. Wilson	1953-64
Henry Cabot Lodge	1914-24	Robert S. Woodward	1905-24
Alfred L. Loomis	1934-73	Carroll D. Wright	1902-08

Under the original charter, from the date of organization until April 28, 1904, the following were *ex officio* members of the Board of Trustees: the President of the United States, the President of the Senate, the Speaker of the House of Representatives, the Secretary of the Smithsonian Institution, and the President of the National Academy of Sciences.

OFFICE OF ADMINISTRATION

1530 P Street, N.W., Washington, D.C. 20005

James D. Ebert *President*

James W. Boise *Bursar; Secretary-Treasurer, Retirement Trust;
Executive Secretary to the Finance Committee*

Sheila McGough *Publications Officer; Editor*

Susan Y. Vasquez *Assistant to the President*

Kenneth R. Henard *Assistant Bursar; Assistant Treasurer,
Retirement Trust*

Joseph M. S. Haraburda *Assistant to the Bursar*

Richard E. Hewitt *Administrative Officer for Services*

Marshall Hornblower *Counsel*

STAFF MEMBERS IN SPECIAL SUBJECT AREAS

Ellis T. Bolton
Roy J. Britten

DISTINGUISHED SERVICE MEMBER IN SPECIAL SUBJECT AREA

Barbara McClintock

RESEARCH ASSOCIATE AT LARGE

Harry E. D. Pollock

Carnegie Institution of Washington adheres in all phases of its operations, including employment and educational programs, to a policy barring discrimination on the basis of race, religion, color, national or ethnic origin, sex, or physical handicap. In its educational programs it admits qualified students as fellows without regard to race, religion, color, national or ethnic origin, sex, or physical handicap to all the rights, privileges, programs, and activities generally accorded or made available to fellows at the Institution. It does not discriminate on the basis of race, religion, color, national or ethnic origin, sex, or physical handicap in administration of its educational policies, admissions policies, fellowship programs, and other Institution-administered programs.

*Carnegie
Institution*

OF WASHINGTON

*Report OF
THE President*

1977-1978

If there is no abiding value in a Beethoven symphony, or a theory of the cosmos, or the tracing of an ancient culture, then the Carnegie Institution of Washington has scant reason for existence. If it is really good that man should look at the stars and should contemplate his great destiny, then it is imperative that in those regions which enjoy the blessings of peace the search for the eternal verities should continue.

Vannevar Bush

THERE HAVE BEEN six presidents of Carnegie Institution before me, six singular individuals whose reports frequently, if not invariably, set out some of the deepest and most enduring truths of science. I have been re-reading their classic essays trying to “see for myself” how the Institution was conceived, as Caryl Haskins wrote in *The Search for Understanding*, as “a wholly new kind of institution in American life—the first to be devoted wholly and completely, in intent and in philosophy, to the ideal of research scholarship over wide fronts of science in its broadest, most unfettered, most completely uncommitted aspects”; and how it was molded to its purpose.

In this endeavor I have been privileged to have before me Caryl Haskins’ and Philip Abelson’s essays appraising the Institution’s role, marking its sixtieth and seventy-fifth anniversaries. They make it abundantly clear that the history of the Institution is not merely the sum of the histories of its several departments but rather of their integration. The differences in form that exist among the departments do not keep them from being united by a common quality: a single-minded dedication to the principle that the Institution’s resources must be devoted to preserving the freedom and the flexibility of gifted, uncommitted investigators. The position of the Institution in world science has altered in the seventy-six years that have elapsed since it was founded; yet the underlying philosophy remains unchanged: to seek out the innovator, to act as a catalyst, and to provide initial support to highly promising but “high risk” ideas.

A New Test

As Abelson wrote, “The Institution has functioned successfully under a wide variety of circumstances. It has adjusted to different economic climates, world wars, and a drastically changing scientific scene.” Unfortunately, in attempting to withstand the vicissitudes of financial stress, our techniques frequently have been costly, not in dollars, but in decreasing our options for fulfilling our mission as it was originally conceived.

We are faced with a quandary. There are now five principal departments in the Institution, each one of the great research centers of the world in its field, all with aggressive, energetic, and wise directors, only two of whom have led their departments longer than five years. Moreover, each department is truly a national resource, a wellspring of exceptionally promising young scientists. Although all of the departments have long and distinguished histories, they have shown themselves to be ever youthful in approach by opening new trails and responding to new opportunities.

Our current income falls substantially short of what is needed to support these departments even in the modest, frequently austere style to which they have become accustomed. But if austerity does indeed engender discipline and stimulate thinking, an overemphasis on austerity can fetter research, especially in those fields in which a rapidly evolving technology places a high premium on equipment.

In his very first annual report, Vannevar Bush had an answer to the then pressing problem of the Institution's decreasing income. He emphasized, properly, that a program of research once entered into need not be carried on unaltered and forever. An institution must have the courage to liquidate as well as the keenness to initiate. As scientific emphasis shifts and as programs are completed—or at least no longer exhibit their pioneering qualities—they must be terminated. In that first report, Bush devoted five pages to “terminations and taperings.” Even so bold and decisive a leader as Bush must have found that section difficult to write, but he did have one significant advantage: several chapters of the Institution's distinguished history were then drawing naturally to a close and their inspiring authors retiring.

Today, happily, we lack the advantage Bush enjoyed. I say “happily” for good reason: during his presidency, Philip Abelson assured the scientific vitality of the departments, which are quietly but surely being reshaped. In 1939 Bush could “trim” the Institution yet continue six productive departments. Today “trimming” is well-nigh impossible. Major surgery would be required to effect the economies necessary to live within our current income. The size of the departments approaches the optimum in every instance. For Astronomy, Embryology, and Plant Biology, the “critical mass” may be slightly smaller than one would ordinarily expect, owing to the cordial relations that exist between these departments and their immediate neighbors, California Institute of Technology, Johns Hopkins, and Stanford University, respectively. The Geophysical Laboratory and Department of Terrestrial Magnetism draw upon the rich and varied resources of Washington and its environs, and are at least to a degree mutually reinforcing.

Further attrition or major surgery would be traumatic. Today we can speak properly of the Institution as being of modest size, participating in

a limited number of carefully chosen fields. Some might argue that this statement would apply if there were only four departments, or even three. However, this extrapolation is seriously flawed. The depletion of reserves would reduce our chances of rapidly exploiting new opportunities. Even more insidious would be the effect of continuing attrition on the Institution's remaining staff members. It is true, as Bush wrote, that "a staff which is over concerned in regard to security is not likely to be fully creative." Yet if we are to continue to attract and hold worthy young scientists, they must be assured that those who are extending the boundaries of knowledge will be free of distractions long enough to make significant contributions. It has been the Institution's policy that terminations would accompany beginnings, that programs reaching a point where they can be carried on better by others would be tapered. This policy must continue—but we must be deeply concerned about the phrase "terminations would accompany beginnings." Further stringent economies would surely render the intellectual climate of the Institution less favorable for "beginnings."

Our continued shrinkage must be reversed. The Institution must go on charting new courses at the frontiers of science and generating distinction in its remarkably effective training programs.

A Further Break with Tradition

The Institution's operating budget for the year 1977–1978 was \$7.8 million. The operating deficit was \$2.1 million, the smallest deficit in the past five years (the operating deficit in 1974 was \$4.8 million). The trend has been salutary, but the rate must be accelerated. Our gains have resulted from both stringent economies and increasing success in securing funds from foundations, individuals, and federal agencies. For example, the \$7.8 million appropriated by the Institution included general support grants and gifts amounting to nearly \$700,000; in addition some \$1.2 million in outside grants to reimburse the direct costs of research were used by the departments in support of specific proposals. The total funding available to the Institution during the year was about \$9 million, of which about \$1.8 million (20 percent) was derived from outside sources.

It follows from our earlier discussion that further stringent economies, short of major changes in the Institution's programs, will have only a marginal effect. Thus, if we are to continue our significant contributions and not merely survive, our support from external sources must be stepped up as rapidly as possible to bring the budget into balance, while a long-range program for doubling the Institution's endowment is developed and implemented. Our task then over the next several years will be to ensure

that from 40 to 50 percent of our annual funding is derived from external sources, both private and public. Our catalogue for 1978-1979 reads, "All salaries of Staff Members and supporting technical and administrative staff are met from Institution funds. Funds from other suitable sources are accepted or administered by the Institution usually for the provision of equipment or for fellowship grants supplementing the Institution's own fellowship fund." This statement of policy reflects a rich and treasured tradition of the Institution. That tradition must now be breached.

This decision, which has been long in coming, was not reached without soul-searching by all of us. My principal concerns are shared by Trustees and Staff Members alike: that our increasing dependence upon external support will reduce the degree of flexibility with which our Staff Members pursue inquiries of their own choice; that our research will be skewed toward questions for which external funding is most readily available; that our autonomy will be reduced; and that our Staff Members' identification with the Institution will be weakened.

We have been proud of our tradition of self-reliance. Yet the hazards implied in these questions do more than hurt our pride; they may gradually and not always subtly erode our ability to determine our own directions. These blows are not softened by the fact that a similar situation has prevailed for nearly thirty years in the nation's great universities where frequently three quarters or more of the annual research budget, including professorial salaries, is provided through short-term grants and contracts.

As one examines the evolution of federal granting programs over three decades, he finds little evidence of a truly comprehensive plan to assure the health of the scientific enterprise. Despite the urgings of many of the nation's most distinguished scholars, of whom Caryl Haskins has been one of the most articulate, little attention has been paid to the crucial need for stability in the support of science.

It must be said, too, that one can discern in few universities a firm policy of seeking primarily those external funds for support of research generated *within* the faculty. All too often universities respond to the expressed needs of the federal agencies; or, to be more accurate, faculty members respond almost as independent entrepreneurs with the nominal blessing of their universities.

Unfortunately, knowing all these pitfalls does not mean that we know how to avoid them. In the years immediately ahead, all of us will have to work together in developing policies to enable our Staff Members to continue charting their own courses in research and to ensure freedom from distraction. One does not wish to belabor the obvious, but some of the salient features of this emerging new policy should be stated at the outset. Every effort must be made to secure funds that are either completely unrestricted or restricted only to a given field or department but with no

additional strings attached. Since many of our more daunting financial problems arise from rapid changes in instrumentation in our several fields, we should emphasize even more strongly our search for funds in support of this highly significant “direct cost” of research. When grants are obtained for specific projects, budgets should include provision for appropriate fractions of the salaries of the scientific and supporting staff engaged in research, along with reimbursement of the Institution’s indirect costs, in accordance with established agency policies.

In short, it is imperative that we intensify our search for funds that will recognize the Institution for what it is: a true national resource. We must continue to argue, not only in the Institution’s behalf but also in behalf of the universities, for the need for institutional grants.

It is my hope, indeed my expectation, that a director would let both the individual and me know in clear, unmistakable terms if he observed, even began to sense, that a Staff Member was warping a proposal solely to fit the guidelines of a particular granting program. I say “*solely* to fit” because it is true that there can be a natural concatenation of interests in a field initiated by a Staff Member and a responsible agency. These interactions, in which the Institution’s leadership can be amplified, should be encouraged. However, the distinctions are subtle, and like others before us we stand in danger of “creeping paralysis” engendered by the severe constraints imposed by some kinds of external funding.

Our change in stance may be troubling to some of our Staff Members who are in the truest sense uncommitted investigators. How often have we heard it said that the Institution buys an investigator’s time and returns it to him as “unconstrained endowment,” to use Caryl Haskins’ term. Can an investigator believe that he is equally “uncommitted” if the Institution “buys” three quarters of his time, with the National Science Foundation or National Institutes of Health “buying” the other quarter? Perhaps the trauma will be lessened if all of us bear in mind that the precious resources conserved as our budgets tend to come more into balance will continue to provide a significant measure of stability as well as high mobility within and between fields, and that our eyes shall ever be on the new, the uncommon, the unconventional idea, and on the highly promising young investigator.

The Kingdom of the Mind

Yet these practical contributions from the work of the Institution, useful and indeed vital as many of them have been over the years of its work, in one sense represent only by-products, mere projecting iceberg-tips, as it were, of the original and continuing vision, indicators only of the seven-eighths submerged.

That seven-eighths, of course, lies in the kingdom of the mind. It lies in that devotion to deeper patterns, that determination to explore the symmetries, the lights and shades of Nature, wherever the search may lead, to which the Institution was originally dedicated and which, undeviatingly, it pursues today.

Caryl P. Haskins

The practical contributions of which Caryl Haskins spoke in *The Search for Understanding* are many and varied, including—to name a few mentioned by him and by Philip Abelson—hybrid corn, radar, geophysical prospecting equipment, improved ceramics, refractories, glass, and cement. We live in an era in which increasing attention is paid to the cost benefit analysis. Measured in dollars, the cumulative benefit to society of the Institution's discoveries is enormous indeed. Yet throughout our history practical considerations have remained of secondary importance. Ours is a "labor of love"—if indeed the word "labor" can be applied at all to the wide-ranging, uninhibited explorations that have characterized the Institution.

Our fundamental research continues to yield practical applications. Hardly a year passes without a discovery that might significantly shape the material basis of our society. Just this year Selwyn Sacks of the *Department of Terrestrial Magnetism* and his colleagues Shigeji Suyehiro, Alan Linde, and J. Arthur Snoke reported on results from specially developed strainmeters with sufficiently high sensitivity over long periods to enable detection and identification of slow earthquakes: seismic events that produce records similar to those from normal earthquakes except that the time scale is considerably longer. Slow earthquakes provide a mechanism for stress redistribution before normal earthquakes. Stress concentration may take place just hours or days before an earthquake, thus helping to set the effective upper limit to the warning period that a specific prediction could provide.

In a series of articles Kiyoshi Suyehiro, Sacks, Linde, and John R. Evans have also reported on their explorations of the oceanic crust and upper mantle in the western Pacific in the vicinity of Japan. This is a favorable area for such studies because of the combination of important tectonic settings with many naturally occurring earthquakes, which provide acoustic "probes" for investigating these structures. Understanding the seismicity and crust-mantle structure of Japan is of considerable practical interest, considering its large population exposed to earthquake hazards.

Clearly, Sacks and his colleagues have not neglected the practical implications of their research; yet earthquake detection is not their primary objective. Their objective is to understand better the complex structure of the Earth's mantle, a goal shared with colleagues both in the Department of Terrestrial Magnetism and in the Geophysical Laboratory.

Physics and Chemistry of the Earth

In this year's report, George Wetherill, director of the Department of Terrestrial Magnetism, has given special emphasis to the Earth's mantle; the mantle was once, in his words, "a somewhat mysterious place from which basalts came, and its properties were visualized as being similarly monotonous in both continental and oceanic regions." The great synthesis in the earth sciences, the concept of plate tectonics, has reshaped our thinking. We know that the surface along which earthquake foci line up define the boundaries of independently moving *plates* of the solid exterior of the Earth; these are laterally extensive slabs of rock, extending downward to a region in which increasing temperature generates a "plasticity"—a "zone of weakness," or asthenosphere, on which the overlying lithospheric plates move. As they move they come into contact, and the different forms these patterns of contact take result in deep-sea trenches, island arcs, mountains, and earthquakes. In his book *Cosmos, Earth, and Man* Preston Cloud wrote, "Thus, as the several plates of Earth's crust try to move past one another, there is no place to go but up, or down, or sideways. Instead of flowing smoothly past one another, however, the plates grind together and stick. When they finally come unstuck they do so with a jolt. The Earth quakes. And man trembles. Thus we have the model of a global framework of rigid surface plates that glide over the plastic asthenosphere beneath and grind against one another along relatively straight, seismically active boundaries to shake and deform Earth's crust. That is plate tectonics."

Special attention has been focused on the mantle in ocean regions, the site of the principal plate tectonic events—those associated with the upwelling basaltic magmas at the mid-ocean ridge and the downgoing solid rock (lithospheric) slabs at oceanic trenches.

Thus Kiyoshi Suyehiro, Sacks, and their colleagues have continued to explore the properties of the downgoing thick slab of oceanic upper mantle in the Japan subduction region east of Japan. Using seismic shear waves, they have confirmed their earlier work based on compressional waves. These investigations show that the lithospheric slab is not uniform, but at least a two-layer model is required to match the seismic data. Work by others had already shown that the horizontally moving oceanic slab has a similar structure, and it is now found that this structure is preserved as the slab is sharply bent and begins its deep descent into the Earth's interior.

Over most of the oceanic region, the moving lithospheric slab overlies the weaker, probably partially melted asthenosphere, characterized by lower seismic velocities. In the subduction zone, the slab plunges *beneath* the asthenosphere, leaving a low-velocity zone above the high-velocity lithospheric slab. Normally this velocity contrast is only a few percent.

However, below a depth of 300 km in the Japan subduction zone, the asthenosphere lying above the downgoing slab has a velocity lower by an additional 10 percent. The dissipation of seismic energy in this zone is anomalously high. Taken together, these data suggest that this zone contains an unusually high proportion of partially melted rock that can yield liquids for the production of volcanic rocks.

Somewhat farther to the north, in the Japan trench, Akira Hasegawa has shown that the plane of high seismicity associated with the downgoing slab is more complex than usual, consisting of two parallel but offset planes. To explain this phenomenon, Linde and Sacks have proposed a rheological model involving consideration of the stress distribution in the slab as it is bent at the onset of subduction and subsequently must be straightened again to produce the straight slab observed at greater depths. This theory also explains aspects of the distribution of earthquakes which could not be understood using earlier models.

Seismology is by no means the only important source of information about the nature of the oceanic mantle, as Wetherill points out. Geochemical and isotopic investigations of volcanic rocks derived from the oceanic mantle can, at least in principle, provide much more detailed information about their mantle source. According to Wetherill the reason that the qualification "in principle" must be added is that the volcanic rocks are erupted on the surface and do not provide direct information about the location of their mantle source. Albrecht Hofmann, William M. White, and David Whitford, in collaboration with several investigators in other laboratories, have addressed this problem. After reviewing isotopic and chemical evidence for the sources of the basalts that erupt at mid-ocean ridges and oceanic islands, they conclude that the evidence favors a layered model with an oceanic asthenosphere depleted in the large ion lithophile or "incompatible" elements, such as potassium, rubidium, strontium, cesium, rare earths, uranium, and thorium, and a heterogeneous deeper mantle containing higher abundances of these elements. The ocean ridge basalts are formed by partial melting of the depleted asthenosphere, whereas the oceanic island volcanic rocks are principally derived by partial melting of the deeper mantle, the material being transported *across* the asthenosphere in plumes that do not mix very much with the asthenospheric material.

These conclusions are supported by three specific studies of volcanic rocks from the Pacific and Indian Oceans: (1) studies of strontium isotope ratios and trace element concentrations in a lava (tholeiite) from Hawaii, reported by Hofmann, Thomas L. Wright, and Mark Feigenson; (2) strontium and neodymium isotopic data and trace element data from the Galápagos (White and Hofmann); and (3) trace element studies on the Ninetyeast Ridge in the Indian Ocean by Whitford and his colleague,

R. A. Duncan, of Oregon State University. Unlike the oceanic ridges that are spreading centers, a ridge like the Ninetyeast is not likely to give rise to earthquakes. Hypotheses for the origin of the Ninetyeast Ridge including, among others, an extinct spreading center, an extinct island arc, and the trace caused by the motion of the oceanic lithospheric plate over a mantle plume or "hot spot," were tested. Again the data require a heterogeneous mantle source. Upon evaluation of the alternatives, the plume hypothesis is favored.

Taken all together, these three studies support the argument for a two-layer model consisting of a depleted asthenosphere overlying a heterogeneous and relatively undepleted deeper mantle. However, demonstration of the uniqueness of this model remains elusive, and there are many detailed chemical and fluid mechanical problems to be satisfactorily understood before it can be considered even moderately well established.

The Institution's studies of the chemistry and physics of the Earth are not confined to the Department of Terrestrial Magnetism, where only a fraction of the staff focuses on the Earth. Indeed, the staff of the *Geophysical Laboratory* devotes itself entirely to the earth sciences: geophysics, geochemistry, and biogeochemistry. This year's report of the Laboratory is dedicated by its director, Hatten Yoder, to the U. S. Geological Survey, which celebrates its 100th anniversary in 1979. Yoder, who has a keen sense of history and a special flair in recounting it, recalls the origins of the Geophysical Laboratory, which grew out of a "physical laboratory" in the Survey. Since then, Geophysical Staff Members have maintained close associations with members of the Survey, who have cooperated in experiments, provided guidance on field excursions, and contributed generously to the activities of the Laboratory. We salute the U. S. Geological Survey on the occasion of its centennial in appreciation of the wisdom of its early leaders and for its continuing support.

Yoder's sense of history (and wry humor) are again expressed when in discussing the impact of one technique, Raman spectroscopy, on the Laboratory's course, he wrote: "In the year in which the international spectroscopic organizations are celebrating the 50th Anniversary of the discovery of the Raman effect, scientists at the Geophysical Laboratory have rejoined the Raman community. The Raman effect was in fact studied at the Laboratory in 1932!"

During the year, Shiv K. Sharma set up a new spectrometer to study the Raman effect using laser excitation. The principal objective in establishing laser-Raman spectroscopy at the Laboratory is to obtain knowledge about the structure of species present in geologically relevant systems. The equipment has been adapted for routine studies of small samples in the crystalline and amorphous states, silicate melts, and aqueous solutions, and for high-pressure studies of samples using the diamond-anvil high-pressure cell.

The availability of the Raman spectrograph quickly opened new vistas as Staff Members not directly concerned became aware of the kinds of information that could be derived from the spectra. Those working on the properties of magma, the theory of melting, and the principles of element partitioning realized that it was essential to understand not only the structure of the crystals but also the structure of the liquid itself derived from melting of the crystals.

One of the purposes of determining the structure of silicate liquids is to provide a theoretical basis for determining the properties of magma—density and viscosity among them, measuring under conditions equivalent to those believed to exist in the Earth or in analogue systems.

In the past it was technically more convenient to study the structure of glass, the quenched silicate liquid, and it was assumed that the structures of the liquid and glass were similar, a view supported by Alexandra Navrotsky's observation of only a small calorimetric heat effect at the glass transition point. Using laser-Raman spectroscopy, Sharma, David Virgo, and Bjørn Mysen compared the structure of the melt with that of glass above the glass transition point. The short-range order in glasses and melts of $\text{Na}_2\text{O} \cdot x\text{SiO}_2$ compositions were indeed found to be similar. In the melts, however, the structure becomes more disordered with increased thermal motions. In glasses of the sodium metasilicate and disilicate compositions, rapid crystallization occurred above the glass transition point, and it became evident that the kinetics of crystallization could be studied by using the Raman effect.

The same investigators tested glasses formed at a series of pressures for structural changes. The Raman spectra of glasses of $\text{NaAlSi}_2\text{O}_6$ composition quenched from 1450° to 1550°C and within a pressure range of 0–40 kbar were examined to evaluate previously inferred changes of Al^{3+} from 4- to 6-fold coordination polyhedra in high-pressure melts. All glasses had a framework structure with Al^{3+} occupying the tetrahedral sites in the three-dimensional network. With increasing pressure, the glass structure became more ordered.

These and other studies of Sharma, Virgo, and Ikuo Kushiro support the view that the structure of glass does not always reflect the structure of the crystals, but it remains to be seen if the structure of the liquid has the same oxygen polyhedra as that of the crystals.

Another approach to tracing liquid trends (and identifying source rocks) is element partitioning between crystals and liquid; and element partitioning between crystals is often used as a geothermometer or geobarometer. Calibration of the partitioning is tedious because many variables must be tested to evaluate their effects before applying the results to natural rocks. For example, Wendy Harrison determined partition coefficients for the rare earth elements samarium and thulium between garnets,

pyroxenes, and hydrous melts at mantle pressures and temperatures. She found that the substitution of rare earth ions into those crystal structures does not obey the thermodynamic laws of dilute solution at low trace element concentrations, as others have noted before, and she suggests that there is probably more than one substitutional site for rare earth elements in the structures. The bulk content of rare earth elements in a mineral phase determines the partition coefficient for any single rare earth between that mineral and melt.

The presence or absence of a gas phase also affects the partitioning, according to Mysen, who noted that the vapor-crystal partition coefficients between H₂O-rich vapor and garnet peridotite minerals increase rapidly from less than 0.05 at 5 kilobars to several hundred at 30 kilobars. From the fractionation of individual rare earth elements by garnet he deduced that H₂O-rich vapor in equilibrium with garnet peridotite in the upper mantle would show significant light rare earth element enrichment. He concluded that metasomatic alteration of rare earth elements in upper mantle rocks is a probable explanation of the heterogeneous distribution of such elements in upper mantle rocks. For example, the apparent contrast between major and trace element distribution patterns found in so-called depleted garnet peridotite nodules in kimberlite can be explained by metasomatism. These important conclusions bear heavily on attempts to relate magmas to specific source rocks by using the rare earth elements as tracers.

A key factor in the understanding of the evolution of igneous rocks is an increasing knowledge of the flow of currents in magma.

The long-popular concept that the layered rocks of gabbroic intrusions are formed by crystal settling has come open to reconsideration in recent years because the supposedly settled plagioclase (feldspar) in some intrusions was evidently less dense than its parental liquid. Neil Irvine has performed experiments to determine whether the mechanics of magmatic currents are such that they may deposit minerals at the floor of an intrusion, even when the minerals should float. He has mapped the flow structure of glycerin currents released into a medium of silicone fluid along the horizontal floor of a small flume. The currents are seen to have a downward component of velocity almost throughout their extent. Relative to fixed reference points, the motion appears as a flow shearing roughly parallel to the forward-sloping top surface of the current; relative to the advancing tip, it resembles the end of a conveyor belt beneath two small vortices. Material is transported forward and down in the fast-moving upper part of the current and is left behind at the floor. He proposes that plagioclase may similarly be left at the floors of gabbroic intrusions by magmatic currents that were dense because they were also charged with mafic minerals, and he suggests that it stays there because the yield

strength of the magma is sufficient to prevent it from floating free. He notes, however, that other plagioclase might occasionally be carried to the roof of the intrusion by local return currents to accumulate as anorthositic rocks.

Evidence for currents in magma is well displayed in the Skaergaard intrusion in East Greenland. During an expedition to the area in 1976, Irvine and Stoesser made detailed maps of some of the remarkable trough-banding structures that occur in the intrusion. They present one of the maps and a section prepared from it, and describe the history of a typical trough. Although there is evidence of local erosion by currents at the bottoms of the troughs, the troughs are essentially constructional features developed between ridgelike mounds of massive ferrodioritic cumulates. The layering in the troughs exhibits distinctive changes in facies between their axes and flanks. Irvine and Stoesser offer a model of current deposition for the layering based on Irvine's flume study, the facies changes being attributed to secondary flow—a phenomenon whereby the fluid moves in a spiral or helicoidal manner in paired or multiply paired cells.

Yoder believes that "The key to understanding how elements concentrate into ore deposits appears to lie within the methods of transport. Determination of the species of an element in the transporting medium may provide the requisite knowledge." He goes on to enumerate the techniques for speciation of an element: solubility measurements, determination of the electrical conductivity of the medium, or observation of Raman spectra of the solution. All these techniques are now being investigated, and the first—solubility measurements—is reported on this year by John Frantz and Robert Popp, who have completed an experimental study of speciation and free energy of aqueous MgCl_2 in the system $\text{MgO-SiO}_2\text{-H}_2\text{O-HCl}$ for the range of conditions 1–2 kbar and $400^\circ\text{--}650^\circ\text{C}$. They conclude that at 2 kbar and temperatures above 550°C , associated MgCl_2 is the dominant magnesium species in the fluid. Their data also suggest that dissociated Mg^{2+} ions dominate at temperatures below 400°C .

The identification of the source of volatiles that act as the transport medium is just as important as characterizing the medium itself. Application of the combined methods of metamorphic petrology, paleontology, and isotope geochemistry by Rumble, Hoering, and Boucot has resulted in the identification of the source and sink for volatiles released during metamorphism of fossiliferous calc-silicate intruded by a quartz monzonite dike. Both mineralogical and isotopic evidence indicate that the dike was permeated and contaminated by CO_2 released by decarbonation of the calc-silicate. Chemical metasomatism accompanying metamorphism consisted of the intergranular diffusion of Ca from the fossiliferous calc-silicate into mica schist and into the dike rock. These observations document the great disparity in effective mobility of CO_2 and Ca during metamorphism:

the diffusion of Ca was limited to a few centimeters adjacent to the fossil bed, whereas CO₂ was able to pervade completely the dike over a distance of several meters.

Another key physical parameter by which to characterize the physics of the earth is the compressibility of minerals in the earth, that is, the change in their volume under pressure. In fact, Yoder believes compressibility may be one of the more important factors.

Ho-Kwang Mao and Peter Bell have designed seventeen megabar-pressure cells, which incorporate combinations of seven basic designs. In addition to high megabar pressure capability, these units—all constructed in the Geophysical Laboratory machine shop—are perhaps more versatile than any high-pressure apparatus previously designed. It is possible to contain a sample under pressure for studies of optical, Raman and infrared spectra, x-ray diffraction, Mössbauer resonance, chemical reaction at external high or low temperatures while at pressure, and electrical resistance. The strain and strength of samples under nonhydrostatic stress can also be measured. The high-pressure cells are thereby being employed for geochemical and geophysical experiments. Recent experiments by Bell and Mao with this apparatus have resulted in the production of a sustained pressure of 1.7 Mbar, the highest internally calibrated static pressure ever achieved. During the same experiments, macroscopic flow in one of the diamond anvils of the megabar-pressure cell was observed, also for the first time, at room temperature. It is now possible to study the behavior of minerals in the earth under conditions corresponding to a depth of approximately 3300 km, a depth beneath the mantle and within the core.

The Interface between the Earth and Astronomic Sciences

As Wetherill wrote, “The center of gravity of this year’s work at DTM lies at the interface between the earth and astronomical sciences: questions about how stars and their associated planets form, and about the extent to which meteors and meteorites are fossil relics of the formation period of our solar system.”

Just as the form of a bird or flower reflects the series of molecular events and interactions during its development, so today’s Earth reflects its past. It seems to have grown by an initial aggregation from a cloud of dust particles, joined subsequently by larger masses.

The Earth is constantly in motion. In his chapter, “Our Restless Earth,” Cloud speaks of this seemingly solid planet being stressed by the gravitational effects of the Sun and Moon, as well as by its internal forces “. . . generated by Earth’s great interior heat machines, fueled by radioactivity

and internal gravitational effects, and lubricated by the universal solvent, water."

Stars, too, probably form in cool clouds of dust and gas. Therefore it is necessary to understand the distribution of dust and gas in the Galaxy and its relationship to regions of star formation if one hopes to understand the circumstances under which these clouds actually collapse to form stars.

It appears likely that stars are not born alone, but rather form in associations from a common cloud with a density $\sim 10^5$ times higher than the average interstellar medium. It also appears likely that the collapse of this cloud to form stars is "triggered" by a shock wave, of which several kinds may be important.

Last year, William Herbst and George Assousa reported the first observational evidence that the shock wave from the explosion of a nearby supernova can trigger star formation. Now, together with Racine and Warner, they offer further observations of the region of star formation for which the evidence for a supernova trigger is strongest, a region including stars of various masses which presumably formed at the same time. It is found that in general the characteristics expected of stars in such a young (3×10^5 years) association are found: circumstellar dust and gas, rapid rotation, and a "turn up" point indicating that the smaller stars of the group are still contracting, that is, they have not yet reached the stable stage at which their luminosity is maintained by thermonuclear reactions in their interiors. However, important discrepancies between the observations and the predictions of current theoretical models are also found. Wetherill concludes, "It seems likely that this primarily indicates the weakness of present theoretical models, and that this association is serving as a natural laboratory in which the predictions of these models can be tested."

Wetherill speaks of the importance of studying regions of star formation in other galaxies because such observations permit tests of theories under various conditions.

Theories of Earth formation, evolution, and structure can be tested by comparing their predictions not only against terrestrial data but against data from the Moon, Mars, Venus, and Mercury. Counting the Moon, there are only five terrestrial planets, and "comparative planetologists" are severely limited. However, the variety of galaxies that can be studied is primarily limited by the rate at which observations can be made rather than by the actual number available for study.

Vera Rubin, W. Kent Ford, Jr., and M. S. Roberts of the National Radio Astronomy Observatory have made a combined neutral hydrogen (radio) and optical investigation of a giant spiral galaxy, NGC 1961, about a factor of ten more massive than our own. This galaxy displays an unusual combination of normal and abnormal characteristics. In composi-

tion and luminosity it appears to be a scaled-up version of an ordinary galaxy, and the velocity of the inner part of its spiral structure seems to represent normal rotation. However the outer part of this galaxy is greatly distorted, large noncircular velocities are found, and a dusty looping structure is observed. Measurement of the colors of the stars in this galaxy supports the idea that a burst of star formation occurred about 200 million years ago and that about 5 percent of the mass of the entire galaxy was involved in this event. Norbert Thonnard, Rubin, and Ford also report measurements on a very small irregular galaxy ($\sim 10^9$ solar masses), which also appears to have experienced a recent burst of star formation. Thus, episodes of star formation are found in galaxies of very different types and are possibly a result of collisions between galaxies.

Wetherill's summary provides a concise statement of some of the problems confronting students of the origin of the Solar System: "Although it is unlikely that an event of this particular kind has occurred in our Galaxy, these measurements show that the rate and temporal uniformity of star formation, and presumably of nucleosynthesis as well, vary greatly from one galaxy to another. Present radiometric chronologies for our Galaxy are based on simple, possibly naive, assumptions about the uniformity of nucleosynthesis. Establishment of reliable nucleosynthetic time scales is essential to an understanding of events in the early history of the solar system. This will require an understanding of the principal facts concerning the evolution of galaxies, especially the rate at which the radioactive isotopes are synthesized by various stellar and galactic processes as a function of time. At present we are a long way from an adequate understanding of these basic principles."

Wetherill has himself paid special attention to the small bodies of the Solar System: comets, asteroids, and the Earth-approaching Apollo-Amor objects and their fragments—meteors and meteorites. Among the interplanetary bodies, the small Earth-crossing bodies known as Apollo objects, and similar "Earth-grazing" Amor objects, are the most likely immediate sources of the meteorites that strike the Earth; they are also the principal cause of cratering on the Moon and terrestrial planets, with the possible exception of Mars. The orbits of these bodies are unstable on a time scale of 10^7 – 10^9 years, and their present population represents a steady state between the derivation of these bodies from some external source, e.g., the asteroid belt, or as the nonvolatile residue of extinct comets. Wetherill has calculated the orbital distribution expected for this steady-state distribution and reports that it agrees with the observed orbits of these bodies. Subject to uncertainties in crater counts and scaling laws, the crater frequencies on the Earth and Moon agree with those calculated from the steady-state distribution. This agreement between observation and theory justifies some confidence in those predictions unverified at present, such

as the age distribution of Apollos, the meteorite yields, and the sources of Apollo objects—information central to questions about the relationship of Apollo-Amor objects to meteorites of various classes.

Astronomy at Hale

There is no better way to begin our review of the year at *Hale Observatories* than with the words of its director, Maarten Schmidt:

In the introduction to last year's Annual Report, retiring Director Horace W. Babcock noted: "The 2.5-meter du Pont Telescope underwent fitting out during the year, with special attention to adjustment of electrical, mechanical, and optical systems, and with much effort devoted to completion of essential auxiliary instrumentation. . . , " and "April 1977 saw the first scientific use of the new telescope. . . ."

This brief factual statement represents the culmination of six and one-half years of intense activity since December 1970, when the Trustees of the Carnegie Institution authorized the construction of a 2.5-meter telescope for the Las Campanas Observatory to be designed by the staff of the Hale Observatories. Babcock guided the entire effort to its successful completion in a remarkably short period of time. That the project is a success, indeed, is best appreciated by inspecting one of the 20×20 in. plates that cover a field of $1.5^\circ \times 1.5^\circ$. The quality of the images is excellent and uniform over the large field. Coupled with the extended periods of good seeing and with the dark sky at Cerro Las Campanas free of city lights, this makes the Irénée du Pont Telescope a most powerful instrument for the study of extended systems, in particular the Magellanic Clouds, and for the conduct of surveys of objects such as variable stars and quasars. The creation and development of the Las Campanas Observatory, started in 1968, and the completion of the 1-meter Swope Telescope and the 2.5-meter du Pont Telescope constitute a lasting tribute to Horace Babcock's tenure as Director of the Hale Observatories.

A question of great moment for many is the role of the Space Telescope now being developed. Will ground-based observatories still be needed? Schmidt answers the question with a resounding YES. After reporting that the Observatories staff has become heavily involved in instrumentation for space astronomy with the award by the National Aeronautics and Space Administration of a preliminary contract for the Wide Field/Planetary Camera of Space Telescope to the California Institute of Technology, the Director addresses himself to the role of the telescope. As he remarks, "photons are scarce." Space Telescope will receive from an object

of magnitude 28 approximately one photon per minute. To form a spectrum, which will allow a determination of the radial velocity, temperature, and chemical composition, at least a few thousand photons have to be collected. Obviously, progress at the very faint magnitudes which only Space Telescope can reach will be slow, and large-scale surveys will be prohibitively time consuming. Space Telescope will achieve results on a shorter time scale in the ultraviolet part of the spectrum, which is inaccessible from the ground. Here its role of complementing optical astronomy will be similar to that of x-ray, infrared, and radio astronomy.

Work conducted by the astronomers at the Hale Observatories continues to be highly diverse, ranging from the solar atmosphere to the smoothness of the Hubble expansion flow; from rings of planets to black holes of billions of solar masses; from metal abundances of stars in dwarf galaxies to clouds in the intergalactic medium.

Black holes have fascinated scientists and laymen alike since the discovery of the x-ray source Cygnus X-1. Since all particles, including photons, are trapped in the black hole, it cannot be seen. For its detection, one has to depend on the effects of its gravity. In the case of Cygnus X-1 the evidence is based on (1) a determination of the mass, around 10 solar masses, (2) the absence of any light emitted by the object, and (3) a theoretical deduction that a dark mass of 10 solar masses has to be a black hole and cannot be a degenerate dwarf or a neutron star.

This year astronomers report the detection at the center of the galaxy M87 of a supermassive, dark object—presumably a black hole with a mass of billions of solar masses. The evidence is based on photometric observations by P. Young, J. A. Westphal, J. Kristian, C. P. Wilson, and F. P. Landauer and on spectroscopic observations by W. L. W. Sargent, A. Boksenberg, K. Shortridge, C. R. Lynds, and F. D. A. Hartwick. The observations show an excess of turbulent motion in the core region of M87 as well as excess light that does not fit any of the standard galaxy models. The investigators believe that these data provide the strongest evidence yet for the existence of a black hole at the center of a galaxy. According to Young, the energy required for the radio and x-ray emission of M87 may be released in the process of accretion by the black hole of gas lost from stars in the galaxy.

When Maarten Schmidt obtained a redshift of around 2 for the quasar 3C9 in 1965, this marked the first observation of Lyman-alpha in an extragalactic object. Two Caltech graduate students immediately recognized the possibility of using quasar spectra to detect the intergalactic medium. James Gunn and Bruce Peterson argued that photons emitted by the quasar at wavelengths below Lyman-alpha would be absorbed and scattered by neutral hydrogen atoms in the intervening intergalactic medium. Gunn and Peterson suspected a small depression in the continuum

of 3C9 below Lyman-alpha and deduced an intergalactic hydrogen density of $6 \times 10^{-11} \text{ cm}^{-3}$. Since little or no depression is seen in spectra of other quasars, this is probably an upper limit.

It now appears that the effect of the intergalactic medium has been observed for the last ten years in the form of certain narrow absorption lines in high-redshift quasars. Some of these absorption lines exhibit redshifts much lower than that of the quasar. Some astronomers feel that the absorbing material is close to, and ejected by, the quasar while others believe that the material is located in intervening galaxies. The nature of these lines has now been studied on the basis of high-resolution spectra of high-redshift quasars obtained over the past few years by Sargent, A. Boksenberg, and co-workers with Boksenberg's Image Photon Counting System at the Anglo-Australian 3.8-meter telescope and the Palomar 5-meter telescope. Typically, around a hundred sharp absorption lines are found, most of them at wavelengths below the Lyman-alpha emission. Analysis, mostly by Sargent and P. Young, shows that virtually all lines longward of Lyman-alpha can be identified as lines of carbon, silicon, magnesium, and iron at a well-defined redshift. Only a small fraction of the absorption lines shortward of Lyman-alpha can be so identified. The investigators then tested a conjecture made by C. R. Lynds in 1970 that all these "unidentified" lines are Lyman-alpha lines. This and further tests have now led to the following hypotheses: (a) The metal-rich absorption line systems are due to intervening galaxies; and (b) Most of the absorption lines shortward of Lyman-alpha lines originate in intergalactic clouds. Hypothesis (a) is strongly supported by last year's findings (*Year Book* 76, p. 163) that the quasar 3C 232 shows absorption lines at the same small redshift as that of the nearby galaxy NGC 3067. Hypothesis (b) is essentially the Gunn-Peterson effect in a new guise, namely, discrete absorption lines. These new developments and insights open broad vistas of new research possibilities involving properties of intergalactic clouds, the distribution of gas and of heavy elements in the halos of galaxies, and other questions.

The most recent determination of the Hubble constant by Sandage and Tammann (*Year Book* 70, p. 417) was based on distance determinations of objects with radial velocities of 5000 km s^{-1} or more. This was done to ensure that the effect of the local supercluster in the Virgo-Coma-Ursa Major region of the sky would be small. As part of a study with A. Yahil and G. A. Tammann to find the motion of the Sun relative to nearby galaxies, Sandage has studied the local expansion field by determining distances to galaxies with very small radial velocities, i.e., less than 400 km s^{-1} . He finds the same value of the Hubble constant, $50 \text{ km s}^{-1} \text{ Mpc}^{-1}$, as the global value derived previously. Hence, even though the local supercluster is on the average five times denser than the global average galaxy

field, its effect is not seen in the small sample of nearby galaxies. A much larger sample of nearby galaxies whose motions are being analyzed by Yahil, Tammann, and Sandage appears to show the same quiet flow.

Closer to home, Charles T. Kowal has continued his series of discoveries of objects in the Solar System. This year he found a unique object, which he has called "Chiron." It has a size of a few hundred kilometers, similar to that of the largest minor planets. But instead of an orbit between Mars and Jupiter like most of the minor planets, Chiron has an orbit between Saturn and Uranus. The nature of the object is likely to be subject to considerable speculation in the future.

The structure of rings around planets can be studied by measuring the brightness of a star or satellite as it gets occulted by the slowly moving planet with its rings. The satellite Iapetus was used for this purpose by G. Neugebauer, K. Matthews, I. Gatley, and S. V. W. Beckwith to obtain information about Saturn's rings. In the case of Uranus the occultation of a 10th magnitude star was used by S. E. Persson, P. D. Nicholson, Matthews, P. M. Goldreich, and Neugebauer. They observed in the infrared at a wavelength of 212μ . Here, the methane absorption bands in the atmosphere of Uranus make the planet very faint, allowing accurate measurements of the occulted star. The observers confirmed the five rings discovered by J. L. Elliot in early 1977 and found at least three new rings.

The Green Earth

Our reach toward the stars has given us a new vision of Earth. We have looked through the camera's eye from space and seen the whole planet in one field of view—floating against the empty blackness beyond like a multicolored oriental lantern. Some lantern! Some view! Mother Earth will never seem the same again. No more can thinking people take this little planet, bounteous and beautiful though it be, as an infinite theater of action and provider of resources for man, yielding new largesse to every demand without limit. Born from the wreckage of stars, compressed to a solid state by the force of its own gravity, mobilized by the heat of gravity and radioactivity, clothed in its filmy garments of air and water by the hot breath of volcanoes, shaped and mineralized by four and a half billion years of crustal evolution, warmed and peopled by the sun, this resilient but finite globe is all our species has to sustain it forever.

Preston Cloud

"Warmed and peopled by the sun." What a beautiful way to illustrate the continuity and interplay of the Institution's studies in astronomy and planetary science, the earth sciences, and biology, interconnections that

"extend throughout the existing global ecosystem and all the way back to the beginning of time on Earth."

Research in the *Department of Plant Biology* is focused on three groups of problems, each one of the major themes of modern plant biology: (1) physiological ecology and photosynthesis, in which studies of photosynthesis at high temperature and of mechanisms of adaptation to high temperature continue to dominate much of the work; (2) the characterization of membranes, not only with respect to photosynthesis but also with respect to photoreceptors for other processes, along with direct studies on known or suspected photoreceptor molecules; (3) the organization of the plant genome. Winslow Briggs, the Department's Director, also stresses that cutting across all the research areas is a dramatic increase in development and exploitation of computer techniques for a wide variety of purposes.

Olle Björkman and his associates have continued their studies of physiological adaptation to high temperature. Björkman, Murray Badger, and Paul Armond completed studies of oleander, a plant with remarkable adaptive capacity, grown at both high and low temperature. They have resolved two distinct adaptive processes: plants grown at low temperature develop a very high photosynthetic capacity, and those grown at high temperature develop a high thermal stability for the photosynthetic machinery. Plants from the cool growth regime do not show a significant difference in the amount of photosynthetic machinery per unit leaf area, level of enzymes involved in carbon metabolism, or capacity for photosynthetic electron transport or photophosphorylation, in comparison with plants on the hot growth regime; nor are there differences in physical restriction of gas exchange. Close examination of the enzymes of carbon fixation, however, revealed that one particular enzyme, fructose-P₂ phosphatase was almost three times as high in activity in the low-temperature-adapted leaves as in the high; this result presented the intriguing possibility that increase in relative activity of a single enzyme could account for the remarkable increase in photosynthetic capacity that accompanies adaptation to low temperature. While there are minor differences in other enzymes, they do not appear sufficient to account for adaptation of the magnitude observed.

Adaptation to high temperatures clearly involved increased thermal stability of the photosynthetic machinery, including both in vivo and in vitro differences in noncyclic electron transport and photophosphorylation and differences in the in vivo heat stability of several enzymes of photosynthetic carbon metabolism. Three enzymes that require light for their activation were especially sensitive to heat inactivation at temperatures at which photosynthesis begins to show thermal inhibition. Since their activation depends upon photosynthetically produced reductant, it is likely

that apparent heat inactivation is related to thermal damage of photosynthetic electron transport, rather than representing a direct effect on these enzymes. Thus, it is most likely the membranes to which one must turn to find an explanation for the way plants become adapted to high temperatures.

Studies on algae and bacteria have shown that adaptation to high temperature involves increasing the degree of saturation of membrane fatty acids such that membrane fluidity at whatever the growth temperature may be is always the same. It is assumed that this increase would maintain the physical integrity of the membranes to higher temperatures. John Raison and Joseph Berry made detailed studies of chloroplast membranes from several sources: high- and low-temperature-adapted oleander and *Atriplex hymenelytra*; *Tidestromia oblongifolia*, a plant which lacks the ability to acclimate to low temperature and can grow only at high temperature; and two *Atriplex* species that fail to acclimate to high temperature. Measurements with membrane probes containing electron spin labels yielded the surprising result that all the membranes were remarkably similar. Differences in fluidity were much smaller than those reported for bacteria or algae grown over such a wide temperature range, and differences in the temperatures for phase transitions of the extracted lipids were negligible. Thus, the mechanisms by which higher plants adapted to high temperatures achieve thermal stability in their membranes are not clear. What is clear, however, is that they do not use exclusively a mechanism involving homeostatic adjustment or membrane lipid fluidity.

The way certain algae can adapt to changes in growth temperature is well illustrated in work by David Fork, Norio Murata, and Naoki Sato. They grew the unusual thermophilic alga, *Synechococcus lividus*, originally collected from hot springs in Yellowstone National Park, Wyoming, either at 38°C or at 55°C (a temperature at which it is perfectly comfortable). They then examined the relative amounts of saturated versus unsaturated fatty acids in the algal membranes. The ratio of total saturated to unsaturated fatty acids was 1.31 for cells grown at 38°C and decreased more than fourfold to 0.31 in cells grown at 55°C. These results are in dramatic contrast with those of Raison and Berry on chloroplast lipids from oleander. Further studies on *Synechococcus*, involving careful measurements of the effects of temperature on several photosynthetic parameters, revealed that the high-temperature phase transition for the membranes was at 43°C for cells grown at the higher temperature, and at about 37°C for cells grown at the lower. The dark reduction of cytochrome *f*, the redistribution of light energy between the two photosystems on a change in the spectral distribution of incident light, and fluorescence in cells with electron transport between the two photosystems inhibited, all showed a sharp change in activation energy near either 43° or 37°.

Michael Blatt, in Winslow Briggs' group, has made substantial progress in understanding at the cellular level the mechanism by which chloroplasts of the filamentous alga *Vaucheria* become trapped in a field of dim blue light. The chloroplasts normally move along distinct longitudinal fibers that are visible under specialized light microscopy. When an area of the cell is irradiated with blue light, the longitudinal organization of the fibers breaks down, and within a few seconds there is formation of a reticulum of fibers with cross bridges forming and breaking continually. Chloroplasts become trapped in this area. Apparently their continued movement depends upon the presence of intact longitudinally oriented fibers. If the blue light is removed, the fibers become reorganized longitudinally within 10 to 15 minutes, and chloroplast movement resumes. The reticulation process invariably precedes chloroplast aggregation.

Blatt has also obtained preliminary evidence on the chemical nature of the fibers. They are stabilized in the light by the *Amanita* toxin, phalloidin, and they become disaggregated by the inhibitor cytochalasin B. Cytochalasin B is known to disrupt filaments of actin, a protein involved not just in muscle contraction but in a large number of motility phenomena including cytoplasmic streaming in algal cells. Phalloidin, on the other hand, is known to stabilize such filaments. It seems likely, therefore, that the fibers visible under light microscopy are cables composed of many actin filaments.

Peter Quail, also in Briggs' laboratory, demonstrated involvement of the pigment phytochrome in enhancing the growth response of corn roots to gravity. A brief exposure to red light causes corn roots to curve downward in response to gravity far more rapidly than dark controls. The potentiation of this response is partially reversed by far red light, but the evidence is consistent with the hypothesis that only a very small proportion of the total phytochrome need absorb red light to saturate the response.

Quail also investigated an odd and fairly widely investigated phenomenon whereby phytochrome, which is transformed by red light to its far red-absorbing form within the cell, becomes pelletable on subsequent extraction under appropriate conditions, whereas it normally would remain soluble. It has thus far proved impossible to determine whether the pigment actually becomes bound to some particulate while still in the cell or becomes bound only upon extraction. Quail, however, was able to show that whatever change occurs in the system which leads to the increase in pelletability in oats, it involves expenditure of metabolic energy. Inhibitors of respiration or of oxidative phosphorylation inhibit the increase, and there is an excellent correlation between decrease in pelletability and decrease in ATP in the tissue. The reaction leading to pelletability has a half time at room temperature of about 2 sec—the earliest reaction

reported to occur on phytochrome phototransformation in the cell. Respiratory inhibitors such as cyanide extend this half time to minutes. Quail, in collaboration with Lee H. Pratt at Vanderbilt University, was also able to obtain preliminary evidence that phytochrome is a phosphorylated protein. The meaning of this phosphorylation is at present unclear, but the finding represents one more step in the characterization of this elusive pigment.

William Thompson together with Michael Murray and Richard Preisler continue to focus on the organization of the higher plant genome, and they report two very different patterns in two relatively closely related plants, the garden pea and the mung bean. The total genome size (amount of DNA per cell) in the pea is almost nine times that in mung bean, and the organization and size of both unique sequences and repetitive ones are quite different (as is the relative proportion of unique to repetitive DNA sequences). No unique sequences were found in pea which were longer than 1200 nucleotide pairs, while three quarters of the unique sequences from mung bean were longer. In fact, in mung bean about half the unique sequences exceeded 6000 nucleotide pairs in length! In pea, almost three quarters of the total DNA was found to be repetitive, and most of the repeated sequences were less than 1000 nucleotide pairs long. By contrast, mung bean had less than half of its DNA present as repeated sequences, and the larger fraction of this repeated DNA was over 1000 nucleotide pairs long. Mung bean DNA extracted from leaves contains a surprisingly high fraction—perhaps over 15 percent—that may be chloroplast DNA. It represents a fraction that behaves as though it were composed of identical repeated sequences present many times per cell. In pea, with its much larger genome, the chloroplast contribution is at most a few percent.

Any hypothesis relating to regulation of transcription in development must somehow take into account the wide divergence of genome organization revealed by these studies. Although the keys to this puzzle are still missing, the resolution of the various components of the genome is increasing dramatically, and the construction and testing of increasingly rigorous hypotheses is becoming a more realistic expectation.

Genes and the Man

I am the family face;
Flesh perishes, I live on
Projecting trait and trace
Through time to times anon,
And leaping from place to place
Over oblivion.

Thomas Hardy

We now turn our gaze to the world inside us—to genes and their controls, to cellular interactions, and to the still largely uncharted realm of morphogenesis.

As Patrick Malone wrote, “In laboratories across the United States and Europe, scientists this summer are performing genetic experiments that could not have been imagined two years ago. They have plucked single genes from human cells, copied them a trillion times in bacterial factories and analyzed them for clues to the nature of human disease. . . .” Fundamental research in the *Department of Embryology* has provided the inspiration and much of the critical information—“a road map”—for such advances.

One of the most provocative discoveries that have been made in the past several years was that eukaryotic genes are interrupted by stretches of DNA that are not expressed in the final gene product. The first of many such discoveries was an intervening sequence located within about half the 28S rRNA genes of *Drosophila melanogaster*. This was discovered by Hogness and his colleagues at Stanford. Igor Dawid found that DNA sequences homologous to this intervening sequence were located in other areas of the *Drosophila* genome as well. In this year’s Report Dawid presents evidence that these intervening sequences are not transcribed; therefore the rRNA genes containing them must be silent. However, many genes for proteins are now known to contain one or more intervening sequence and some of these have been shown to be transcribed. Wahli, working with Dawid, presents evidence that vitellogenin (yolk protein) genes in *Xenopus* have interruptions, and Suzuki and his colleagues have detected an approximately 1000 base pair intervening sequence near the 5’ end of the fibroin gene. In immunoglobulin, globin, and ovalbumin genes the intervening sequences are transcribed into an RNA precursor molecule. Maturation to the functional mRNA requires excision of the extra transcripts and splicing of the ends. The purpose of these intervening sequences remains conjectural and is particularly puzzling in the case of the *Drosophila* rRNA genes, since the intervening sequences appear to inactivate the genes.

The Department’s director, Donald Brown, reminds us that recent innovations in isolating and characterizing genes are responsible for much of the progress reported here. DNA sequencing and restriction enzyme analysis is making possible the localization of the initiation site of very large and complex genes such as rDNA and the fibroin gene. Such detailed information is essential before the control of gene expression can be studied.

In the comparatively simple 5S RNA genes, where the site of transcription initiation is known, Korn has now determined flanking spacer sequences for three different families of 5S DNA, and some interesting sequence homologies have been observed. The prospects are good for

altering these sequences, cloning such mutants, and testing them for 5S RNA synthesis, since Birkenmeier, Brown, and Jordan have shown that an extract of *Xenopus* oocyte nuclei can support 5S RNA synthesis in vitro from added 5S DNA. Although faithful RNA synthesis in vitro has not been obtained using purified fibroin genes or rRNA genes, Reeder's and Suzuki's reports contain accounts of RNA transcription from isolated nuclei or subnuclear fragments. In both systems reinitiation of RNA synthesis appears to occur.

Wahn and Reeder have been examining the components of chromatin from nucleoli of *Xenopus* oocytes. This chromatin is interesting because it contains only ribosomal DNA and therefore represents the first opportunity to analyze proteins associated with a single gene of known function. The major difference between this chromatin and that extracted with the total genomic DNA is the absence of the histone H₁. The presence of this protein has been correlated with contraction of DNA in chromatin. The relationship between the conformation of DNA in chromatin and its function in the living cell is a topic of broad current interest.

An increasing array of glycoproteins have been identified on cell surfaces. Fambrough and his colleagues hope to determine how membranes are assembled and metabolized by careful analysis of the synthesis and degradation of these proteins. The best-studied protein is the acetylcholine receptor on muscle surfaces. In this year's Report Rotundo has extended these studies to acetylcholinesterase, an enzyme located in the plasma membrane and released from cells. Its metabolism resembles that of the acetylcholine receptor enough to suggest that the two may be coordinated. Carbonetto has been studying the incorporation of acetylcholine receptor-like molecules into the plasma membrane of neurons.

These molecules can be studied because they can be measured. They interact specifically with a ligand (α -bungarotoxin) or they have enzymatic activity (acetylcholinesterase). A new and powerful technique for the production of monoclonal antibodies promises to be almost as revolutionary in its applications to cell surface chemistry as recombinant DNA has become for gene studies. Milstein and his colleagues have fused myeloma cells with other antibody-producing cells. The resultant hybrid cells are cloned, and cell lines synthesizing single antibodies can be obtained. Fambrough has begun to use this method to produce cell lines secreting homogeneous antibodies to cell surface molecules that are antigenic. Each probe could be as specific for a surface molecule as α -bungarotoxin is for acetylcholine receptors.

Independent but complementary studies by Pagano and his associates are developing methods to analyze cell surface lipids. Liposomes (lipid vesicles) with different labeled constituents can exchange their components with cell surfaces or fuse entirely to become part of the plasma membrane.

Sandra finds that the exchange reaction labels lipid in the outer leaflet of the plasma membrane. It would be especially useful to have antigenic lipids in the surface to exploit immunochemical methods. Schroit has overcome the problem that most lipids are poor antigens by introducing antigenic phospholipids into cell surfaces by fusion with small unilamellar vesicles. Another approach to probing cell lipids that appears promising is Struck's labeling of cell surface lipids by radioiodination.

Fertilization is one of the most specialized interactions between two cells. S. Ward and his colleagues are analyzing this event in the nematode *C. elegans* by accumulating male sterile mutants. This relatively simple eukaryote is used for genetic studies because of its short life cycle and the ease of accumulating, screening, and storing large numbers of mutants. Eight different genes affecting sperm fertility have been mapped. Mutations are recessive and have produced temperature-sensitive phenotypes. The latter characteristic enables the investigator to define the period of spermatogenesis when the particular gene is being expressed. These mutants are being analyzed microscopically, physiologically, and biochemically.

K. Muller describes a dye that when microinjected into one neuron of the leech diffuses into the cells that are linked to the neuron by synapse. This adds to the variety of substances he has found that can probe the interaction of neurons, either by destroying specifically a given neuron or by labeling them for cytological study. After a nerve is severed, the distal stump plays a role in regeneration of the original precise connections. The leech provides a unique array of identifiable neurons with known function and fully described connections for these studies.

LOSSES

Dean B. Cowie died in November 1977 near his home at Deep Creek Lake, Maryland. Cowie came to DTM in 1939 as a fellow of the National Cancer Institute. His formal training was in nuclear and cosmic ray physics. He took charge of the construction of the Department's cyclotron, which was completed in 1943 and immediately put to use making radioactive materials for war-related medical research. After the war, Cowie joined the newly organized biophysics group at DTM. Most of his subsequent work was done in collaboration with this group, which made use of radioactive tracers to study the complex biochemical mechanisms carried on by growing bacteria. This research was described in two Carnegie publications, *Studies of Biosynthesis in Escherichia coli* (1955) and *Studies in Macromolecular Biosynthesis* (1965). In recent years Cowie had investigated the methods some viruses use to incorporate their genetic material into

the chromosomes of other species. He was also engaged in various studies of bacterial enzymes.

Ernest D. Gardner, associate director of the Carnegie Laboratories of Embryology, University of California at Davis, died in February 1978. He held professorships in the departments of Neurology, Orthopaedic Surgery, and Human Anatomy at the Medical School. Professor Gardner was an authority on malformations of the nervous system. He wrote two widely used textbooks and numerous journal articles. A memorial fund has been established at the Carnegie Laboratories at Davis.

Joseph W. Greig died on October 22, 1977, at the age of 82. Dr. Greig had retired in 1960 after 38 years as a petrologist at Geophysical Laboratory. His research included studies of phase equilibria in mineral systems and investigations of liquid immiscibility in silicate systems. His studies led to the development of low-alumina, low-alkali silica brick and were applied in improving the manufacture of steel. The mineral greigite was named in his honor.

Gordon L. Davis retired June 30 after 37 years as an isotope geochemist at the Geophysical Laboratory. When Dr. Davis came to the Laboratory, he was working on the determination of the radium content of ultramafic rocks and meteorites. His measurements enabled him to demonstrate that previous estimates of the Earth's internal radioactivity and heat production were too high. During World War II Davis put his expertise in trace element geochemistry to use at Geophysical in research on special steels for gun barrels. After the war he embarked on a long-term project for dating rocks and minerals using the rubidium-strontium, potassium-argon, and lead-uranium methods. At the time of his retirement, Davis was still providing precise estimations of the ages of zircons brought up from the Earth's mantle as inclusions in kimberlites.

In the spring of 1978 Igor B. Dawid moved from the Department of Embryology to the National Cancer Institute, but he plans to maintain an active extramural association with the research of the Department. Dr. Dawid's first report as a Carnegie Fellow appeared in *Year Book 62*; it described his studies on "cytoplasmic DNA" of frog eggs. He purified the DNA, accurately determined its amount, and then showed that it was mitochondrial in origin. These experiments led to a series of outstanding studies that helped to establish him as one of the leaders in—and the Department as a center of—molecular studies of eukaryotic cells. Dawid characterized mitochondrial DNA and then the various RNA's transcribed from this small DNA. He was a codiscoverer of gene amplification of ribosomal RNA genes, and he and his colleagues have continued to contribute importantly to structural studies of ribosomal RNA and its genes, first in *Xenopus* and more recently in *Drosophila*. He also assumed a variety of important scientific responsibilities including that of editor-in-chief of

Developmental Biology, the major journal in this field. Such a brief account of Igor Dawid's accomplishments cannot adequately convey the importance of the role he has played in the intellectual growth of the Department of Embryology.

Guido Münch, Staff Member of the Hale Observatories and Professor of Astronomy at the California Institute of Technology, resigned on December 31, 1977, to join the Max-Planck Institut für Astronomie in Heidelberg. When he joined the staff in 1951, Münch was interested primarily in stellar atmospheres, galactic structure, and interstellar matter. More recently, he has done distinguished work on planetary atmospheres. In his new position Münch will be in charge of the West German observatory at Calar Alto in southern Spain.

I must acknowledge with regret the resignation of Hanna H. Gray from the Carnegie Board of Trustees at the meeting of the Board in May. She was named president of the University of Chicago in December 1977 and took office there in July of this year.

Henry S. Morgan also resigned from the Board. I am happy to report, however, that he was promptly named Trustee Emeritus and thus remains "in the fold."

. . . AND GAINS

I am happy to report the election to the Board of Trustees of Philip H. Abelson and Franklin D. Murphy. As former director of the Geophysical Laboratory and former president of the Institution, Dr. Abelson is well known to all of us. Franklin Murphy comes to the Board from Los Angeles, where he is chairman of the board and chief executive officer of the Times Mirror Company. A man of science and academia as well as business, Dr. Murphy was trained as a physician specializing in internal medicine, and served as dean and then chancellor of the School of Medicine at the University of Kansas. He has a strong interest in the arts and is very active in their support.

Nina V. Fedoroff has been appointed a Staff Member in the Department of Embryology. Dr. Fedoroff completed her undergraduate work at Syracuse University and received her Ph.D. at Rockefeller University, where she studied RNA phage. She carried out postdoctoral work in molecular biology at UCLA before joining the Department as a fellow of the National Institutes of Health. Fedoroff produced the first complete sequence for a eukaryotic gene and its flanking spacer regions (that of 5S DNA of *X. laevis*; see *Year Book* 76). Her long-term goal is to describe in molecular terms the transposable elements known from Barbara McClintock's work to affect gene expression in maize.

Samuel Ward joined the Department of Embryology as a Staff Member in September 1977. After taking his Ph.D. from Caltech in 1971, Dr. Ward spent two years at the MRC Laboratory of Molecular Biology at Cambridge, England, where he shared in genetic and developmental studies of the nematode *Caenorhabditis elegans*. He returned to the United States to take up the post of assistant professor of biological chemistry at Harvard Medical School. At Harvard he continued to investigate mutants affecting sensory behavior of nematodes. He is still primarily interested in learning how genes control the morphology of cells. To that end, he is studying fertilization in *C. elegans* by isolating mutants that affect sperm structure and function.

Bjørn Mysen is a recently appointed Staff Member at the Geophysical Laboratory. He studied geology at the University of Oslo in Norway and completed work for a Ph.D. in geochemistry at The Pennsylvania State University. As a Carnegie Corporation Fellow at the Geophysical Laboratory from 1974 to 1977, Dr. Mysen investigated the genesis of igneous rocks by obtaining experimental data on the properties of coexisting silicate melts and crystals under physical conditions of the Earth's crust and upper mantle. He has published results on the solubility of volatiles in silicate melts at high pressure, on phase equilibria of peridotite in the upper mantle, on density and viscosity of melts, and on elements occurring in very low concentrations in rocks.

The following honors were awarded to Staff Members during the past year:

Maarten Schmidt, director of the Hale Observatories, was elected a Foreign Associate of the National Academy of Sciences in April 1978.

Donald D. Brown, director of the Department of Embryology, received the Boris Pregel Award for Research in Biology. The award was presented at the 160th Annual Meeting of the New York Academy of Sciences on December 8, 1977; the citation honored Brown's work in molecular biology and embryology.

Barbara McClintock, Distinguished Service Member of the Institution at Cold Spring Harbor, New York, became the seventh recipient of the Lewis S. Rosenstiel Award for Distinguished Work in Basic Medical Research. The prize, given by Brandeis University, honored McClintock's "imaginative and important contributions to our understanding of chromosome structure, behavior, and function."

Dr. Olle Björkman of the Department of Plant Biology received the Linnaeus Prize in Botany for his contributions in physiological ecology and photosynthetic adaptations. This prize is given only every third year by the Royal Physiographical Society of Sweden; Björkman received the award at Lund on December 2, 1977.

Bjørn O. Mysen of the Geophysical Laboratory was awarded the F. W.

Clarke Medal of the Geochemical Society at the annual meeting of the Geological, Mineralogical, and Geochemical Societies in November 1977. The medal is given to young scientists who have shown excellence in research; Mysen's award was for his paper treating the role of volatiles in silicate melts, published in the *American Journal of Science* in 1976.

James D. Ebert

FACULTY, FELLOWS, AND STUDENTS

1977-1978

DEPARTMENT OF EMBRYOLOGY
Baltimore, Maryland

Gregory Nelson
Shigeru Sakonju

Director

Donald D. Brown

Staff Members

Igor B. Dawid
Douglas M. Fambrough
Kenneth J. Muller
Richard E. Pagano
Ronald H. Reeder
Yoshiaki Suzuki
Samuel Ward

Fellows

Saoko Atsumi
Edward H. Birkenmeier
Peter Botchan
Salvatore T. Carbonetto
Diana Card Linden
Jeffrey Doering
Mark Dworkin
Nina Fedoroff
Elizabeth Godwin
Laurence J. Korn
Eric Long
Steven McKnight
Yasumi Ohshima
Ronald Peterson
Eva Rastl
Richard Rotundo
Alex Sandra
Alan Schroit
Sheryl Scott
Barbara Sollner-Webb
Douglas Struck
Masaaki Tsuda
Yoshihide Tsujimoto
Walter Wahli
Harvey Wahn

Students

Yair Argon
John M. Gardner
Robert A. Hipkind

GEOPHYSICAL LABORATORY
Washington, D.C.

Director

Hatten S. Yoder, Jr.

*Emeritus Carnegie Institution
Distinguished Professor*

Elburt F. Osborn

Emeritus Research Associate

Emanuel G. Zies

Staff Members

Peter M. Bell
Francis R. Boyd, Jr.
Felix Chayes
Gordon L. Davis
David H. Eggler
Larry W. Finger
John D. Frantz
P. Edgar Hare
Thomas C. Hoering
T. Neil Irvine
Ikuo Kushiro
Ho-Kwang Mao
Tsutomu Murase
Bjørn O. Mysen
Douglas Rumble III
David Virgo

Fellows

Nicholas T. Arndt
Nabil Z. Boctor
Marilyn L. F. Estep
John M. Ferry
Anthony A. Finnerty
Wendy J. Harrison
Robert M. Hazen
James D. Hoover
Charles A. Lawson

Robert K. Popp
Joseph L. Ritchey
Shiv K. Sharma
Frank S. Spear
Juergen Trochimczyk
Noreen Tuross
E. Bruce Watson
Richard F. Wendlandt
Takehiko Yagi

Students

Pamela R. Baur
Heather D. Boek
Julia A. Carey
Catherine A. McCammon
Julia D. Pasteris
Marie H. Slezak

HALE OBSERVATORIES Pasadena, California

Director

Horace W. Babcock

Director-Designate

Maarten Schmidt

Associate Director

J. Beverley Oke

Staff Members

Halton C. Arp
Jesse L. Greenstein
James E. Gunn
Robert F. Howard
Jerome Kristian
Robert B. Leighton
Guido Münch
Gerry Neugebauer
S. Eric Persson
George W. Preston
Allan R. Sandage
Wallace L. W. Sargent
Leonard Searle
Stephen A. Shectman
Arthur H. Vaughan
James A. Westphal
Harold Zirin

Staff Associates

Robert J. Brucato
B. Thomas Soifer
Michael W. Werner

Fellows

William M. Adams
Thomas B. Ake III
Gary S. Da Costa
A. Ger de Bruyn
Alan M. Dressler
Thomas R. Geballe
Richard F. Green
Robert C. Kennicutt, Jr.
Barry J. LaBonte
Stefan Mochnecki
Ronald Moore
Jeremy R. Mould
Larry D. Petro
James A. Rose
Anneila I. Sargent
Robert Schommer
Jack W. Sulentic
Althea Wilkinson
Robert J. Zinn

Carnegie-Chilean Fellow

Guido Garay

Student Observers

Steven V. W. Beckwith
Graham Berriman
Kirk D. Borne
France A. Cordova
David J. Diner
Jonathan H. Elias
Boris Gokham
John G. Hoessel
Stephen M. Kent
Daniel Nadeau
William C. Friedhorsky
Jeffrey R. Pier
Douglas M. Rabin
Russell O. Redman
Donald P. Schneider
William L. Sebok
Richard J. Terrile
Richard A. Wade
Howard K.-C. Yee
Peter J. Young

DEPARTMENT OF PLANT
BIOLOGY
Stanford, California

Director

Winslow R. Briggs

Staff Members

Joseph A. Berry
Olle Björkman
Jeanette S. Brown
David C. Fork
Malcolm A. Nobs
William F. Thompson

Emeritus

C. Stacy French
William M. Hiesey

Fellows

Paul A. Armond
Murray R. Badger
Steven J. Britz
Roland Caubergs
John W. Cross
Mary Helen Goldsmith
Aaron Kaplan
Jacob Levitt
Shmuel Malkin
Norio Murata
Michael G. Murray
Peter H. Quail
John K. Raison
Charles E. Rogler
Ulrich Schreiber
Alan J. Stemler
Gijsbert van Ginkel
Larry N. Vanderhoef

Students

Heather S. Belford
Michael R. Blatt
Robert D. Brain
G. James Collatz
Richard Cuellar
Holly Gorton
Marga Höhl
Jeffrey Palmer
Richard Preisler
U. M. Susanne Widell

DEPARTMENT OF
TERRESTRIAL MAGNETISM
Washington, D.C.

Director

George W. Wetherill

Distinguished Service Member

Merle A. Tuve

Emeritus

Scott E. Forbush
Richard B. Roberts

Staff Members

L. Thomas Aldrich
George E. Assousa
Louis Brown
Dean B. Cowie
W. Kent Ford, Jr.
Albrecht W. Hofmann
David E. James
Alan T. Linde
Sundar Rajan
Vera C. Rubin
I. Selwyn Sacks
Fouad Tera
Norbert Thonnard
Kenneth C. Turner

Research Associates

Emilio Filloy
Mordeckai Magaritz
Rambabu P. Ranganayaki
Kiyoshi Suyehiro

Fellows

Charles L. Bennett (trainee)
David Burstein
Gregory S. DeWitt (trainee)
John R. Evans
William D. Heinze
William Herbst
Felix J. Lockman
Douglas O. ReVelle
Stuart J. Weidenschilling
William M. White
David J. Whitford

Reports of Departments and Special Studies

Department of Embryology

Hale Observatories

Department of Plant Biology

Developmental Biology Research Group

Department of Terrestrial Magnetism

Geophysical Laboratory

Department of Embryology

Baltimore, Maryland

Donald D. Brown
Director



Department of Embryology staff, April 1978. *Bottom row, left to right:* Richard Rotundo, Nina Fedoroff, Yasumi Ohshima, Edward Birkenmeier, Eddie Jordan, Igor B. Dawid, Martha Rebert, John Pazdernik, Ronald Reeder, Sheryl Scott, Kenneth Muller. *Second row:* Delores Somerville, Bessie Smith, Yoshiaki Suzuki, Peter Botchan, Sharon Bodmer, Eileen Hogan, Patricia Schmidt, Susan Satchell, Elaine Asch, Harvey Wahn, Richard Grill. *Third row:* Ernestine Flemmings, Alice Mabin, Robert Hipkind, Barbara Thomas, Alex Sandra, Yoshihide Tsujimoto, Masaaki Tsuda, Joyce Patterson, Betty Phebus, Thomas Malooly, Saoko Atsumi, Barbara Sollner-Webb. *Fourth row:* John Gardner, Salvatore Carbonetto, John Wiser, Gregory Nelson, Paul Giza, William Duncan, Sam Ward, Richard Pagano, Donald D. Brown, Walter Wahli, Ronald Peterson, Steven McKnight.

Contents

Introduction	9
Membrane Biogenesis and Glycoprotein Secretion in Excitable Cells	11
Studies on the biosynthesis of acetylcholine receptors	12
Biosynthesis of ACh receptors in vivo	16
Effects of electrical stimulation on the biosynthesis of extrajunctional ACh receptors	17
Chick embryo muscle acetylcholinesterase	18
Relations between the molecular forms of AChE	19
Characterization of the intracellular AChE pool	22
Relationship between acetylcholinesterase secretion and membrane incorporation of ACh receptors	26
A model for AChE release	27
Metabolism and site of insertion of a plasma membrane protein in rapidly growing neurons	29
Construction of continuous cell lines which secrete monoclonal antibodies of predetermined specificity	35
Organization, Dynamics, and Metabolism of Cell Surface Phospholipids	38
Asymmetric insertion of exogenous phospholipids in the cell surface via exchange	39
Immunobiological and immunochemical studies of antigenic phospholipids in mammalian cells	43
Reaction of antibody with trinitrophenylated phosphatidylethanolamine-containing vesicles (Tnp-vesicles)	43
Interaction of Tnp-vesicles with cells	44
Radioiodination of cell surface lipids	50
Analysis of Nematode Fertilization-Defective Mutants	52
Isolation and initial mutant characterization	52
Wild-type and mutant fertilization	54
Wild-type sperm morphology	55
Mutant sperm morphology	56
Initial biochemical characterization of sperm	57
Temperature-sensitive intersex mutant	59
Regeneration in the Nervous System: Formation of Specific Synapses in the Leech	62
Regeneration of the S-interneuron	63
Detection of electrical synapses with Lucifer Yellow dye	63
Regeneration after elimination of target	63
S-cell axonal regeneration in culture	65
Synapses of identified sensory neurons	65
Synapses between a sensory and a motor neuron	65
Regeneration of chemical synapses	68

Specific associations between sensory cells	69
Role of glia in regeneration	70
Structural and Functional Studies of the Fibroin Gene	71
Structure of the fibroin gene	72
Restriction endonuclease mapping of fibroin gene plasmids and description of deletions occurring in its repetitious region	72
Location of a DNA sequence corresponding to the 5' end of mRNA	74
Nucleotide sequence of the region containing the 5' end of fibroin mRNA	74
A 1-kb intervening sequence interrupts the fibroin gene	75
Comparison of the gene organization of "active" and "silent" fibroin genes	80
Precursors of fibroin mRNA	81
Transcription of the cloned fibroin genes in nuclear homogenates	82
Transcription of the fibroin gene by partially purified <i>B. mori</i> RNA polymerase II	85
Studies on Gene Organization in Eukaryotes	85
Ribosomal DNA and related sequences in <i>Drosophila melanogaster</i>	86
Mapping of the rRNA precursor	88
Heteroduplex mapping of cloned rDNA fragments	89
Restriction analysis of spacers from cloned rDNA	91
Are the insertion sequences transcribed in vivo?	92
Non-rDNA insertion-type sequences in <i>Drosophila</i>	93
Isolation and characterization of human ribosomal DNA	93
R-loop mapping of mRNA sites on <i>X. laevis</i> mtDNA	95
The vitellogenin gene in <i>Xenopus laevis</i>	95
Full-length and partial discrete transcripts of vitellogenin mRNA	96
Synthesis of double-stranded cDNA and insertion into hybrid plasmids	99
Characterization of the DNA from pXlvc clones	100
Detection of fragments containing cloned sequences in digests of chromosomal DNA	103
Gene expression in <i>Xenopus laevis</i>	103
Structure and Transcriptional Control of the <i>Xenopus</i> Ribosomal Genes	106
Accurate reinitiation on ribosomal genes in isolated oocyte nuclei	107
Morphology of in vitro transcription	111
Structure of nucleoprotein in the spacer region of ribosomal DNA	112
An inhibitor of ribosomal RNA synthesis in unfertilized eggs	114
Identification and sequencing of transcription initiation sites on <i>X. laevis</i> ribosomal DNA	116
Characterization of the histones on ribosomal genes	119
Mapping the methylation sites in <i>X. laevis</i> rRNA and confirmation of gene order in the transcription unit	121
Insertions and spacers	123
The dual 5S RNA Gene System in <i>Xenopus</i>	124
Nucleotide sequence of three <i>Xenopus borealis</i> 5S ribosomal RNA genes and adjacent control region	124

Sequence of <i>X. borealis</i> somatic 5S DNA	128
Purification and molecular cloning of a third 5S DNA component from <i>Xenopus laevis</i> DNA	130
Deletion analysis of <i>X. laevis</i> 5S DNA	131
A nuclear extract that accurately transcribes 5S RNA genes	136
A variety of 5S RNA genes are transcribed accurately by an extract of oocyte nuclei	139
 The Collection of Human Embryos	 140
Developmental stages in human embryos	140
Development of the nervous system	141
Development of the cardiovascular and urogenital systems	141
 Visitors	 142
 Staff Activities	 142
 Bibliography	 143
 Personnel	 146

INTRODUCTION

In spring 1978 Igor B. Dawid moved to the National Cancer Institute. His first report as a Carnegie fellow appeared in *Year Book 62*, describing studies on "cytoplasmic DNA" of frog eggs. He purified this DNA, accurately determined its amount, and then showed that it was mitochondrial in origin. These experiments led to a series of outstanding studies that helped establish him as one of the leaders in, and this Department as a center of, molecular studies of eukaryotic cells. Dr. Dawid characterized mitochondrial DNA and then the various RNA's transcribed from this small DNA. He was a codiscoverer of gene amplification of ribosomal RNA genes; and he and his colleagues have continued to contribute importantly to structural studies of ribosomal RNA and its genes, first in *Xenopus* and more recently in *Drosophila*. With no apparent reduction in scientific productivity he assumed a variety of important scientific responsibilities including that of editor-in-chief of *Developmental Biology*, the major journal in this field. A brief account of Igor Dawid's accomplishments cannot adequately relate the important role that he has played in the intellectual growth of this Department.

His last report describes new information about intervening sequences in *Drosophila* rDNA. One of the most provocative discoveries in the past several years was that many eukaryotic genes are interrupted by stretches of DNA that are not expressed in the final gene product. The first of many such discoveries was an intervening sequence within about half of the 28S rRNA genes of *Drosophila melanogaster*. This was discovered originally by Hogness and his colleagues at Stanford. Dawid found that DNA sequences homologous to this intervening sequence were located in other areas of the *Drosophila* genome as well. In this report Dawid presents evidence

that these intervening sequences are not transcribed, and therefore the rRNA genes containing them must be silent. However, many genes for proteins are now known to contain one or more intervening sequence, and some of these have been shown to be transcribed. Wahli, working with Dawid, presents evidence that vitellogenin genes in *Xenopus* have interruptions, and Suzuki and his colleagues have detected an approximately 1000 base-pair intervening sequence near the 5' end of the fibroin gene. In immunoglobulin, globin, and ovalbumin genes the intervening sequences are transcribed into an RNA precursor molecule. Maturation to the functional mRNA requires excision of the extra transcripts and splicing of the ends. The purpose of these intervening sequences remains conjectural and is particularly puzzling in the case of the *Drosophila* rRNA genes, since they appear to inactivate the genes.

Recent innovations in isolating and characterizing genes are responsible for much of the progress reported here. DNA sequencing and restriction enzyme analysis is making possible the localization of the initiation site of very large and complex genes such as rDNA (Reeder) and the fibroin gene (Suzuki). This detailed information is essential before the control of gene expression can be studied.

In the comparatively simple 5S RNA genes, where the site of transcription initiation is known, flanking spacer sequences have now been determined for three different families of 5S DNA, and some interesting sequence homologies have been found (Korn). The prospects are good for altering these sequences and then cloning the resulting mutants and testing them for 5S RNA synthesis, since an extract of *Xenopus* oocyte nuclei has been shown to support 5S RNA synthesis in vitro from added 5S DNA (Birkenmeier *et al.*). Although faithful in vitro

RNA synthesis has not been obtained using purified fibroin genes or rRNA genes, Reeder and Suzuki's reports contain accounts of RNA transcription from isolated nuclei or subnuclear fragments. In both systems reinitiation of RNA synthesis appears to occur.

Wahn and Reeder have been examining the components of chromatin from nucleoli of *Xenopus* oocytes. This chromatin is interesting because it contains only ribosomal DNA and therefore represents the first opportunity to analyze proteins associated with a single gene of known function. The major difference between this chromatin and that extracted with the total genomic DNA is the absence of the histone H₁. The presence of this protein has been correlated with contraction of DNA in chromatin. The relationship between the conformation of DNA in chromatin and its function in the living cell is a topic of broad current interest.

An increasing number of glycoproteins have been identified on cell surfaces. Fambrough and his colleagues hope to determine how membranes are assembled and metabolized by careful analysis of the synthesis and degradation of these proteins. The best-studied protein is the acetylcholine receptor on muscle surfaces. In this Report Rotundo has extended their studies to acetylcholinesterase, an enzyme located in the plasma membrane and released from cells. Its metabolism resembles that of the acetylcholine receptor enough to suggest that the two may be coordinated. Carbonetto has been studying the incorporation of acetylcholine receptor-like molecules into the plasma membrane of neurons.

These molecules can be studied because they can be measured. They interact specifically with a ligand (α -bungarotoxin) or they have enzymatic activity (acetylcholinesterase). A new and powerful technique for the production of monoclonal antibodies promises to be as revolutionary in its applications

to cell surface chemistry as recombinant DNA has become for gene studies. Milstein and his colleagues have fused myeloma cells with other antibody-producing cells. The resultant hybrid cells are cloned, and cell lines synthesizing single antibodies can be obtained. Fambrough has begun to use this method to produce cell lines secreting homogeneous antibodies to cell surface molecules. Presumably such probes could be prepared for any surface molecules that are antigenic. Each probe could be as specific for a surface molecule as α -bungarotoxin is for acetylcholine receptors.

In independent but complementary studies, Pagano and his associates are developing methods to analyze cell surface lipids. Liposomes with different labeled constituents can exchange their components with cell surfaces or fuse entirely to become part of the plasma membrane. Sandra finds that the exchange reaction labels lipids in the outer leaflet of the plasma membrane. It would be especially useful to have antigenic lipids in the surface to exploit immunochemical methods. Schroit has overcome the problem that most lipids are poor antigens by introducing antigenic phospholipids into cell surfaces by fusion with small unilamellar vesicles. Another approach to probing cell lipids that appears promising is the labeling of cell surface lipids by radioiodination (Struck).

Fertilization is one of the most specialized interactions between two cells. S. Ward and his colleagues are analyzing this event in the nematode *C. elegans* by accumulating male sterile mutants. This relatively simple eukaryote is used for genetic studies because of its short life cycle and the ease of accumulating, screening, and storing large numbers of mutants. Eight genes affecting sperm fertility have been mapped. Mutations in them are recessive and have produced temperature-sensitive phenotypes. The latter characteristic enables the investi-

gator to define the period of spermatogenesis when a particular gene is being expressed. These mutants are being analyzed microscopically, physiologically, and biochemically.

K. Muller describes a dye which can be microinjected into one neuron of the leech and which then diffuses into those cells that are linked to the neuron by synapse. This adds to the variety of substances he has found that can probe the interaction of neurons, either by destroying specifically a given neuron or by labeling them for cytological study. After a nerve is severed, the distal stump plays a role in regenerating the original precise connections. The leech provides an unique array of identifiable neurons with known function and fully described connections for these studies.

Dr. Nina V. Fedoroff has been appointed a Staff Member. A graduate of Syracuse University, Fedoroff studied RNA phage at Rockefeller University, where she received her Ph.D. She carried out postdoctoral work in molecular biology at UCLA before coming to this Department as a postdoctoral fellow of the National Institutes of Health. Dr. Fedoroff produced the first complete sequence

for an eukaryotic gene and its flanking spacer regions (that of 5S DNA of *X. laevis*; see *Year Book* 76). She has recently become interested in applying her molecular expertise to problems in maize genetics. Her long-term goal is to describe in molecular terms the transposable elements known from Barbara McClintock's work to affect gene expression in maize.

Dr. Ernest D. Gardner, Associate Director of the Carnegie Laboratories of Embryology, University of California at Davis, died in February of this year. He held professorships in the departments of Neurology, Orthopaedic Surgery and Human Anatomy at the Medical School. Dr. Gardner was an authority on malformations of the nervous system and author of two widely used books as well as numerous journal articles. A memorial fund in his honor has been established at the Carnegie Laboratories at Davis.

Grants from the National Institutes of Health supported in part the research programs of Drs. Brown, Dawid, Pagano, Reeder, Suzuki, and Ward. Fambrough's research has benefited from a grant by the Muscular Dystrophy Association.

MEMBRANE BIOGENESIS AND GLYCOPROTEIN SECRETION IN EXCITABLE CELLS

*D. M. Fambrough, S. T. Carbonetto, R. Rotundo, J. M. Gardner,
D. J. Card Linden, and S. Atsumi*

with the technical assistance of D. Somerville, A. Mabin, and W. Duncan

Two of the major features of the development of multicellular organisms are the genesis of cells with different surface specializations and the interaction of these specialized cells via their different (or similar) surfaces. These features of development are prominent in the differentiation of neurons and muscle fibers and in the formation of very specific connections among the neurons and between neurons and muscle. Our research has focused largely upon one such sur-

face specialization of muscle fibers: the acetylcholine receptors. These receptors are glycoprotein molecules which are located in the plasma membrane of the muscle and function as the recognition system for chemical signals from the motor nerves. Acetylcholine receptors appear at a specific time during myogenesis. Interactions between nerve and muscle regulate the number and distribution of receptors. This regulation is effected in part by regulation of receptor

metabolism. In past years we have reported on the number, distribution, and metabolism of acetylcholine receptors. Some new observations on receptor metabolism and its regulation are reported here.

Last year our research program broadened to include the study of two additional membrane glycoproteins: the acetylcholinesterase of skeletal muscle and the α -bungarotoxin-binding glycoprotein (whose function is unknown) of sympathetic ganglion cells. These glycoproteins are involved in cellular processes related to membrane biogenesis: secretion and extension of neurites.

Muscle acetylcholinesterase is a set of enzymes that probably share a common catalytic subunit but are organized in different ways. The term "molecular forms" is used as an unbiased term for the members of the set. Some forms seem to be tightly associated with the plasma membrane and with internal membranes, while other forms are secreted from the myotubes. One form occurs preferentially at neuromuscular junctions and is absent from our cultured chick skeletal muscle. The occurrence of both membrane-bound and secreted forms should facilitate an analysis of the relationship between secretion and membrane biogenesis. Some experiments reported in this Report suggest a tight coupling between secretion and plasma membrane protein production in cultured myotubes.

The α -bungarotoxin-binding protein of chick sympathetic ganglia is distributed fairly uniformly over the surface of cultured sympathetic ganglion cells, including growth cones of cells extending long processes in culture. It has been suggested, mostly on the basis of the behavior of large objects attached to such cell processes, that extension of the processes involved bulk insertion of membrane at the growing tip. We sought to test this suggestion by determining the locus in insertion of the α -bungarotoxin-binding protein into plasma membrane

during neurite outgrowth. Pulse-labeling experiments with cultured sympathetic ganglia indicate that there is little or no preferential insertion of this particular membrane glycoprotein into the tips of growing neuronal processes. The kinetics of biosynthesis and insertion of this glycoprotein into plasma membrane and the kinetics of degradation are somewhat faster than those for the α -bungarotoxin-binding glycoprotein of skeletal muscle (which is the functional ACh receptor in that tissue).

Recently, Milstein and co-workers have perfected a technique for producing continuous cell lines that secrete immunoglobulin molecules of predetermined target specificity. Such cell lines, producing antibody molecules directed against muscle cell surface antigens, would provide a means of identifying individual membrane components other than the ACh receptor and ACh esterase. Using such probes, we could determine whether individual membrane glycoproteins are metabolized at different rates, and we might succeed in identifying which membrane components subserved which functions (a particularly difficult problem to solve by any other means). Some initial results of applying this approach are reported.

STUDIES ON THE BIOSYNTHESIS OF ACETYLCHOLINE RECEPTORS

J. M. Gardner

We have initiated attempts to synthesize ACh receptors in cell-free, *in vitro* protein synthesizing systems. These experiments, if successful, will yield information about the mechanisms involved in membrane glycoprotein synthesis, muscle differentiation, and synapse formation. Preliminary experiments have been directed at the purification of messenger RNA populations from muscle cells in culture and from chick embryo leg muscles. PolyA containing message, total cytoplasmic, and polysomal RNA

preparations have been assayed in a wheat-germ lysate protein synthesis system for the ability to direct muscle cell specific protein synthesis.

Several major problems must be overcome before newly synthesized receptors can be detected in vitro. Since the receptor constitutes less than 0.01% of total muscle protein, it is clear that novel approaches for detecting small amounts of protein made in vitro must be developed. Even highly specific immunoprecipitation of new receptor protein made in vitro would be unlikely to give a detectable signal, because the expected concentration of receptor protein would be below the threshold of sensitivity for this technique. The initial experimental course we have taken is to rely on the ability to detect α -bungarotoxin-binding material made in the cell-free system. The most sophisticated experiment to date consisted of adding purified microsomal membranes obtained from 36-hour-old myoblasts (which had not begun to fuse and undergo the dramatic increase in receptor biosynthesis) to a wheat-germ lysate system. The reaction mixture was supplemented with polyA containing messenger RNA or total cytoplasmic RNA from postfusion myotubes which were very active in ACh receptor biosynthesis. We were unable to detect any synthesis of ACh receptor molecules in vitro. Efforts are now under way to optimize the system for glycoprotein synthesis. We are also attempting to isolate messenger RNA populations enriched for rare sequences, which might serve as better templates for receptor protein synthesis.

In *Year Book 76* we reported that the drug tunicamycin, which blocks the lipid-intermediate pathway of protein glycosylation, inhibits the incorporation of ACh receptors into plasma membrane. The kinetics of this inhibition (see Fig. 14) suggested that the primary effect on ACh receptors was a rapid inhibition of biosynthesis, eventually resulting in de-

pletion of the intracellular pool of newly synthesized receptors. We have extended those observations to provide further evidence that tunicamycin inhibits the assembly of newly synthesized receptor polypeptides into intact receptors, capable of interacting with α -bungarotoxin. Cultures of chick embryo muscle were incubated overnight with unlabeled α -bungarotoxin to block the surface ACh receptors. The muscle cultures were then washed and switched to medium containing ^2H , ^{13}C , ^{15}N -amino acids, tunicamycin (1.0 $\mu\text{g}/\text{ml}$) and unlabeled α -bungarotoxin. Control culture medium was identical except that tunicamycin was not present. The cells were incubated for 6 hours, and the intracellular membranes were isolated, solubilized, and assayed for newly synthesized receptors. For this assay, ^{125}I -labeled α -bungarotoxin was added to the detergent extracts. Aliquots of extract containing iodinated α -bungarotoxin-receptor complexes were subjected to velocity sedimentation to separate the newly synthesized dense receptors from any synthesized before the incubation in medium containing dense amino acid. Under these conditions, the set of intracellular receptors isolated from control cultures is composed of two classes. One class of receptors is rapidly labeled with ^2H , ^{13}C , ^{15}N -amino acids, and serves as precursors to the plasma membrane ACh receptors. Approximately 70% of the receptors in the control intracellular pool belonged to this population. The other receptors, comprising 30% of the intracellular pool in these experiments, are not labeled with dense amino acids and are designated "hidden" receptor sites (which are distinguished from plasma membrane ACh receptors only by their inaccessibility to α -bungarotoxin applied to intact cells). The proportion of dense receptors was reduced by approximately 80% in the tunicamycin-treated cultures.

It must be noted that our assay for new ACh receptors involves ^{125}I -labeled

α -bungarotoxin binding and velocity sedimentation. Any lesion in biosynthesis or assembly of receptor molecules which could lead to failure to generate these binding sites could account for our observations. It is conceivable that the inhibition of production of complete new receptor molecules is a rapid but indirect consequence of tunicamycin action rather than a direct inhibition of receptor glycosylation. However, it seems most likely that glycosylation of receptor protein via the lipid-intermediate pathway plays an essential role in biosynthesis and assembly of functional ACh receptors.

It is generally accepted that plasma membranes of eukaryotic cells are asymmetrically organized with the carbohydrate prosthetic groups, for example, concentrated on the external surface. We sought to discover whether or not the intracellular membranes containing newly synthesized ACh receptors reflected in any way the asymmetry that is established for the receptor as an integral plasma membrane glycoprotein. One approach to investigating the topographical features of intracellular membranes and their proteins is the use of specific affinity labeling reagents, preferably impermeable, to determine the orientation of membrane components. We have used α -bungarotoxin as such a probe in conjunction with the density-shift technique to explore the polarity of organization of newly synthesized receptors in the intracellular membrane fraction. Experiments were performed with chick muscle cultures which had been incubated for 6 hours in the presence of unlabeled α -bungarotoxin to block the surface receptors. The cells were then washed and returned to medium containing dense amino acids and unlabeled α -bungarotoxin for 5 hours. The free α -bungarotoxin was removed and cells were disrupted by homogenization. The homogenate was divided into three fractions for further biochemical analy-

sis. The membranes from one fraction were collected by centrifugation, and the resulting membrane pellet was extracted with detergent solution to solubilize ACh receptors. Incubation of this extract with ^{125}I -labeled α -bungarotoxin and isolation of the toxin-receptor complexes yielded a measurement of the total number of ACh receptor molecules present in the intracellular pool. A second fraction of the homogenate was centrifuged to collect the membranes, which were then resuspended and incubated with ^{125}I -labeled α -bungarotoxin. The membranes were washed thoroughly to remove unbound toxin and the ACh receptors solubilized with detergent. The ^{125}I -labeled α -bungarotoxin-receptor complexes served as a measure of the number of ACh receptor sites which were accessible to α -bungarotoxin in the membrane preparation. The third fraction of the homogenate was incubated with unlabeled α -bungarotoxin and washed to remove unbound toxin, and the ACh receptors were solubilized by detergent extraction. The detergent solution was treated with ^{125}I -labeled α -bungarotoxin and the toxin-receptor complexes were isolated. This fraction was a measure of the ACh receptors in the intracellular membrane preparation which remained unavailable to α -bungarotoxin, probably being oriented with receptor sites toward the lumen of closed membrane vesicles.

Aliquots from each of the three preparations of ^{125}I -labeled α -bungarotoxin-receptor complexes were analyzed by velocity sedimentation in order to determine the distribution and orientation of the newly synthesized (dense) and the hidden (light) ACh receptors. The resulting gradient profiles are shown in Fig. 1. The relative amounts of newly synthesized (dense) receptors and the hidden (light) receptors present in the total intracellular pool are reflected in Fig. 1A. The profile shown in Fig. 1B reflects the proportions of newly synthesized and hidden receptors in the intracellular

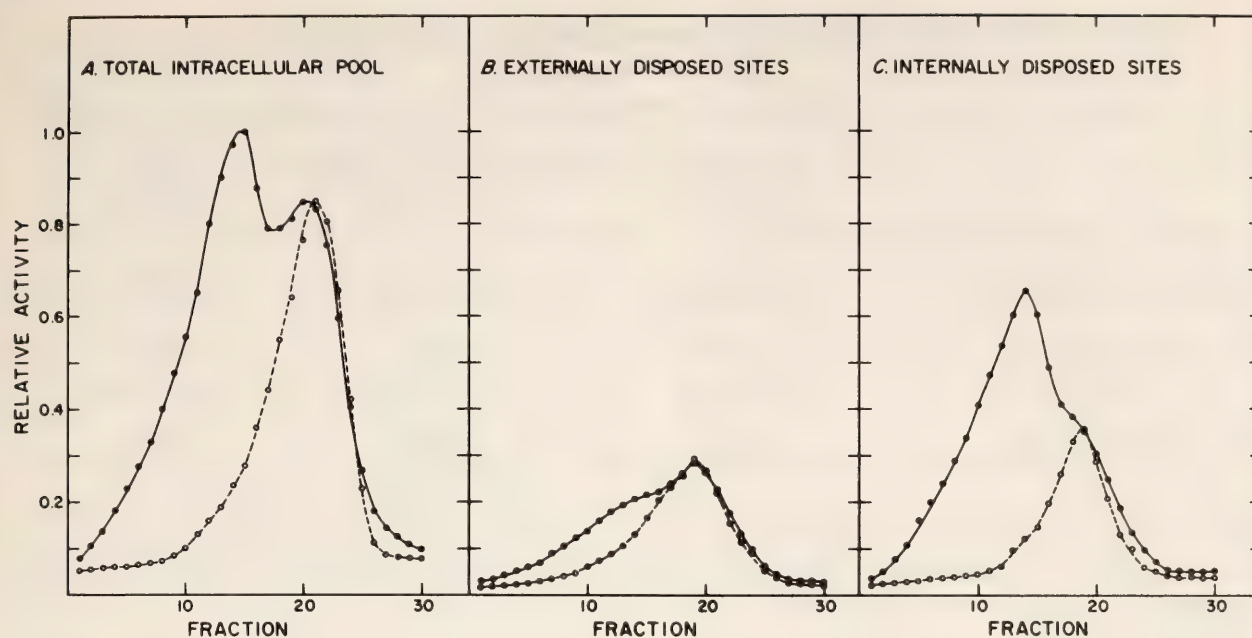


Fig. 1. Sucrose gradient velocity sedimentation profiles of pool receptor distribution as the revealed by application of ^{125}I - α -bungarotoxin. Gradient profiles illustrated here represent the distribution of newly synthesized ^2H , ^{13}C , ^{15}N -labeled and preexisting ^1H , ^{12}C , ^{14}N -labeled acetylcholine receptors in the intracellular pool after reaction with ^{125}I - α -bungarotoxin (\bullet — \bullet). (A) Total number of receptors present in the intracellular pool; (B) externally disposed receptors available to α -bungarotoxin in the original homogenate; (C) internally disposed receptors which were revealed to α -bungarotoxin by detergent solubilization. A marker of ^{131}I - α -bungarotoxin- ^1H , ^{12}C , ^{14}N receptor complexes was mixed with the sample before centrifugation (\circ — \circ), and its position in the gradient is identical to the position of ^{125}I - α -bungarotoxin- ^1H , ^{12}C , ^{14}N receptor complexes present in each fraction of the intracellular pool.

membrane fraction in an orientation allowing accessibility of α -bungarotoxin. The newly synthesized receptors and hidden receptors, which were revealed only by detergent solubilization of the membranes, are shown in Fig. 1C. It is apparent from these profiles that there are differences in the compartmentation of the two classes of receptors (newly synthesized and hidden). Newly synthesized receptors appear to be localized predominantly on the inner faces of closed membrane vesicles in the membrane preparation, while the hidden receptors are present with a greater proportion exposed to the external solution. A quantitative breakdown accounting for these distributions was obtained by computer analysis of the gradient profiles and is shown in Table 1. The total number of internal ACh receptors was about

equally divided between newly synthesized and hidden, in good agreement with previous studies on the kinetics of receptor biosynthesis (*Year Book* 76). The fact that about 80–85% of the newly synthesized ACh receptors are not available for α -bungarotoxin binding even after homogenization and isolation of membranes from muscle cells suggests that these sites are oriented toward the lumen of membrane vesicles. This orientation is consistent with occurrence of newly synthesized receptors in the Golgi apparatus and post-Golgi vesicles as integral membrane proteins with receptor sites facing inward. The transport of such membrane vesicles to the cell surface and fusion with plasma membrane is a reasonable mechanism for exposure of the receptor sites on the external surface of plasma membrane.

TABLE 1. Distribution of Newly Synthesized (dense) and Hidden (light) Receptors in Muscle Homogenate

	Percent of Total Pool*	Percent of Newly Synthesized Receptors†	Percent of Hidden Receptors†
Total intracellular pool (new and hidden sites)	100% (19,700 cpm)	47.5% (9,357 cpm)	52.5% (10,342 cpm)
Externally disposed sites in homogenate	28.5% (5,614 cpm)	27.5% (1,543 cpm)	72.5% (4,070 cpm)
Internally disposed sites in homogenate	65% (12,805 cpm)	67.5% (8,643 cpm)	33.5% (4,289 cpm)

* Numbers in parentheses are the total number of cpm attributable to the ^{125}I - α -bungarotoxin receptor complexes in each fraction of the muscle cell homogenate. The percentages have been normalized to the amount of ^{125}I - α -bungarotoxin receptor complexes present in the total intracellular pool.

† The percentages illustrated here are those derived from the computer analysis of the gradient profiles A, B, and C in Fig. 1. The numbers in parentheses represent the total cpm of ^{125}I - α -bungarotoxin receptor complexes present as ^2H , ^{13}C , ^{15}N -labeled or ^1H , ^{12}C , ^{14}N -labeled receptors in each fraction of the total intracellular pool.

BIOSYNTHESIS OF ACh RECEPTORS IN VIVO

S. Atsumi

In a previous report (*Year Book* 76), the intracellular location of newly synthesized receptors was shown in cultured muscle cells to be the Golgi apparatus. These newly synthesized receptors are transported and incorporated into the plasma membrane after about 3 hours. Cultured muscle cells have ACh-receptors on their entire surface. On the other hand, in vivo most of the ACh-receptors are located at the plasma membrane of the neuromuscular junction (NMJ) and a very few extrajunctional receptors are seen. Cultured muscle cells are comparable to the early embryonic muscle cells, which do not have established neuromuscular junctions. Although it is probable that the fundamental mechanisms of the receptor metabolism are the same in vivo and in vitro, the biosynthesis and transport of ACh receptors may be regulated at certain points by the neuronal component in vivo. Therefore, I have begun a study of the site of biosynthesis

and processing of ACh receptors in recently innervated embryonic chick muscle.

The anterior and posterior latissimus dorsi muscles (ALD and PLD) of the chick embryo are being used. The anterior muscle is a slow muscle and has multiple NMJ's along a single fiber; the posterior is a fast muscle and has only one NJM along a muscle fiber.

First, the concentration of the fixative was determined. Since 2% paraformaldehyde, which was used to fix cultured cells, was low for dissected muscle tissue, 3% paraformaldehyde solution containing 60 mM sucrose was tested and shown to have no significant inhibitory effect on α -bungarotoxin binding with the receptor.

Next, the saturation time of α -bungarotoxin binding with surface receptors was determined. After being fixed and dissected, muscles were incubated in medium containing about 0.1 $\mu\text{g}/\text{ml}$ iodinated α -bungarotoxin. Nonspecific binding was determined by preincubation of the muscle with 10^{-4} M d-tubocurarine and inclusion of this concentration of d-tubocurarine in medium containing α -

bungarotoxin. Then the muscle was thoroughly rinsed and the radioactivity measured in a gamma counter. The saturation time was found to be about 1 hour in ALD from 19-day embryos.

In order to detect internal receptors, surface receptor sites of fixed muscle tissue were blocked with unlabeled α -bungarotoxin and then the muscles were treated with 0.5% saponin for 15 min. Next, internal ACh receptor sites were measured as saponin-revealed binding sites for ^{125}I -labeled α -bungarotoxin. In ALD of 19-day embryos, there were 6–25% as many internal receptors as surface receptors. In light microscope autoradiography of such material only muscle fibers at the periphery of the muscle were heavily labeled. This suggests that saponin at this concentration and incubation time only permeabilizes the plasma membrane of superficial muscle fibers of the muscle. Therefore, the actual number of the internal receptors might be higher than measured so far. The variability in these biochemical results could be explained by an incomplete saponin effect. In the muscle of 11-day embryos, which is very thin compared to that of 19-day embryos, the internal receptor sites were 18–33% of the number of surface sites (Table 2). This is comparable to results in tissue-cultured chick muscle (*Year Book 76*). At this stage, 11 days *in ovo*, the number of NMJ's is still low. Still to be determined is how the amount of internal receptors changes as innervation proceeds.

The saponin-revealed ACh-receptor population was diminished when protein

synthesis was inhibited by puromycin for a period of time before fixation. 1 mg puromycin in phosphate-buffered saline was injected into the yolk sac of 19-day embryos or into 5-day chicks. Since puromycin was injected into thick yolk, the absorption rate appears to vary. In some cases, the saponin-revealed receptor population declined 30–50% after 4–5 hours treatment of puromycin, which is almost comparable to the result with tissue-cultured chick muscle (*Year Book 76*).

To determine the locations of newly synthesized ACh receptors, LM and EM autoradiography is being performed, using ^{125}I -labeled α -bungarotoxin. Although one of the sites of internal receptors was shown to be the Golgi apparatus in cultured muscle cells, this location has not yet been identified in dissected muscles.

EFFECTS OF ELECTRICAL STIMULATION ON THE BIOSYNTHESIS OF EXTRAJUNCTIONAL ACh RECEPTORS

Diana Card Linden

The degradation rates for junctional and extrajunctional ACh receptors of rat skeletal muscles in organ culture were estimated by irreversibly labeling ACh receptors on muscles with radioactive iodinated α -bungarotoxin and measuring the rate of release into the culture medium of mono- and diiodotyrosine, breakdown products of the radioactive α -bungarotoxin. The rates of this proteolytic process yielded average lifetimes of 13 days and 22 hr for ^{125}I - α -bungarotoxin bound to junctional and extrajunctional receptors, respectively, probably reflecting the average lifetimes of the ACh receptors. Varying the denervation period between 5 and 11 days did not affect the estimated degradation rate for extrajunctional receptors in denervated extensor digitorum longus (EDL) muscles. Electrical stimulation in organ culture at 100 Hz for 1 sec was applied

TABLE 2. Saponin-Revealed Specific ^{125}I bungarotoxin Sites Expressed as Percent of Surface Sites (values from two experiments)

Site	Percent
ALD	18, 30
PLD	27, 33

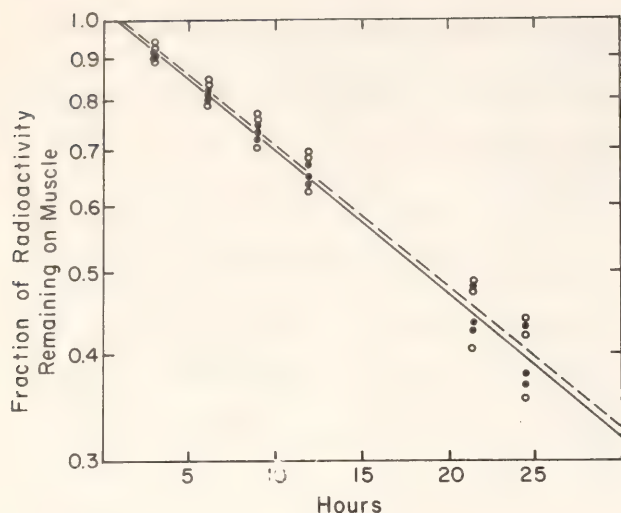


Fig. 2. The effect of electrical stimulation on the loss of radioactivity from 5-day denervated rat EDL muscles maintained in organ culture after labeling ACh receptors with ^{125}I - α -bungarotoxin. On this time scale, loss of radioactivity related to ^{125}I - α -bungarotoxin bound to junctional ACh receptors is negligible, and the label due to ^{125}I - α -bungarotoxin bound to junctional ACh receptors (measured from contralateral innervated muscles) has been subtracted. Closed circles (●—●) represent muscles stimulated at 100 Hz for 1 sec every 80 sec; open circles (○—○) represent unstimulated muscles. The inferred half-life of ACh receptors on stimulated muscles was 18.5 hr, on unstimulated muscles 19 hr. Three stimulated and three control muscles were used in the experiment. All data points for the six muscles are plotted.

every 80 sec for up to 30 hr to produce maximal tetanic tension and had no effect on the apparent degradation rate of receptors in denervated EDL muscles (Fig. 2).

The rate of *de novo* biosynthesis and incorporation of ACh receptors into extrajunctional muscle membrane was measured by determining the rate of appearance of ^2H , ^{13}C , ^{15}N -containing ACh receptors when muscles were cultured in medium containing ^2H , ^{13}C , ^{15}N -amino acids. Cultured denervated EDL and soleus muscles were found to synthesize new receptors for several days in organ culture. Stimulation at 100 Hz for 1 sec every 80 sec, producing visible contraction but not maximal tetanic tension, barely altered the rate of incorporation

of new ACh receptors into extrajunctional plasma membrane of EDL and soleus muscles, even when applied for 5 days (*Year Book 76*). However, supra-maximal stimulation with the same stimulation pattern produced a rapid decline of 10–20% in rate of new receptor production and a corresponding decline in overall protein synthesis. Stimulation beyond 18–24 hours (up to 68 hours) resulted in a selective decrease in new receptor production to about 30% of control rate but no more (Fig. 3). Thus, strong electrical stimulation, producing frequent tetanic contractions, may decrease receptor biosynthesis and thereby contribute to previously reported reduced ACh sensitivity.

CHICK EMBRYO MUSCLE ACETYLCHOLINESTERASE

R. Rotundo

Acetylcholinesterase is an enzyme associated with all cholinergic synapses in the central and peripheral nervous systems. The physiological importance of this molecule lies in its ability to rapidly hydrolyze the neurotransmitter acetylcholine following release from the nerve terminal. This function tells us that the AChE molecules must be oriented with their catalytic sites external to the plasma membranes of the synaptic cleft. The importance of this protein extends far beyond its role as a degradative enzyme for the neurotransmitter. First of all, some AChE is associated with plasma membranes. Its study can yield information regarding the biosynthesis and transport of membrane-associated macromolecules. A second aspect of this particular membrane protein is its existence as a family of molecular forms, several of which may have very specific membrane localizations. This enzyme also exists as a secreted form, thus enabling us to study the relationship between secretion and biogenesis of plasma membrane glycoproteins. Moreover, acetyl-

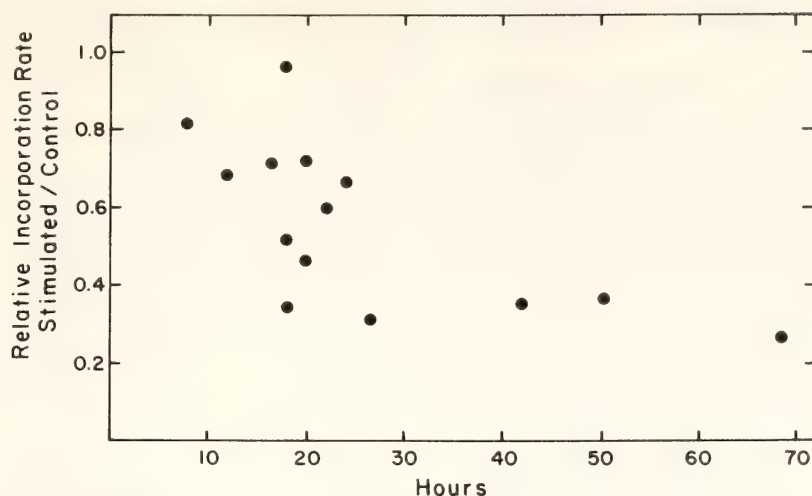


Fig. 3. Effects of electrical stimulation on incorporation of newly synthesized ^2H , ^{13}C , ^{15}N -labeled ACh receptors in denervated muscle in organ culture. These muscles contracted vigorously with full tetanic tension, in response to the electrical stimulation. Relative incorporation rate was measured as the amount of ^2H , ^{13}C , ^{15}N -containing receptors (identified by velocity sedimentation in sucrose gradients) per mg muscle weight in stimulated muscles divided by that measured in nonstimulated muscles cultured for the same time. Incorporation time was 7–9 hr in experiments where stimulation was for 8–18 hr. All longer experiments had incorporation times of 11–12 hr. Each point on the graph represents one experiment, involving two or three stimulated muscles and two or three control, nonstimulated muscles.

cholinesterase is one of a group of proteins present in innervated cells which are, at least in part, under the regulation of the incoming nerves. Studies of the structure, synthesis, transport, and regulation of this enzyme are beginning to yield answers to a number of questions of importance to biologists in general, and to neurobiologists in particular; for example, how are protein components of synapses transported to, and integrated into, their appropriate locations on the membrane?

Relations between the Molecular Forms of AChE

In *Year Book 76* we described the isolation from chick embryo leg muscle of four molecular forms of acetylcholinesterase having sedimentation coefficients of 19.5S, 11.5S, 7S, and 5.4S. In cultures of chick embryo muscle cells, only the 11.5S and 7S forms of the enzyme were present; however, a novel form having a sedimentation coefficient midway between

the two was found to be present only in the culture medium. This novel form is also a true cholinesterase (acetylcholinesterase) and a glycoprotein, and it sediments with an apparent S value of 9. Furthermore, small (<10%) amounts of an additional form having a sedimentation coefficient of 15S are also present in the medium. All of the naturally occurring acetylcholinesterase forms found in embryo leg muscle have a similar K_m for acetylcholine, behave identically in the presence of several specific and non-specific inhibitors of cholinesterases, and share many other biochemical properties. The results suggest that the various forms of the enzyme contain the same catalytic subunit.

Figures 4 and 5 illustrate studies which indicate that the fastest sedimenting form of AChE (19.5S) is composed of smaller subunits, some of which correspond to previously described molecular forms. In the first experiment (Fig. 4), 19.5S AChE was subjected to varying degrees of proteolytic digestion using

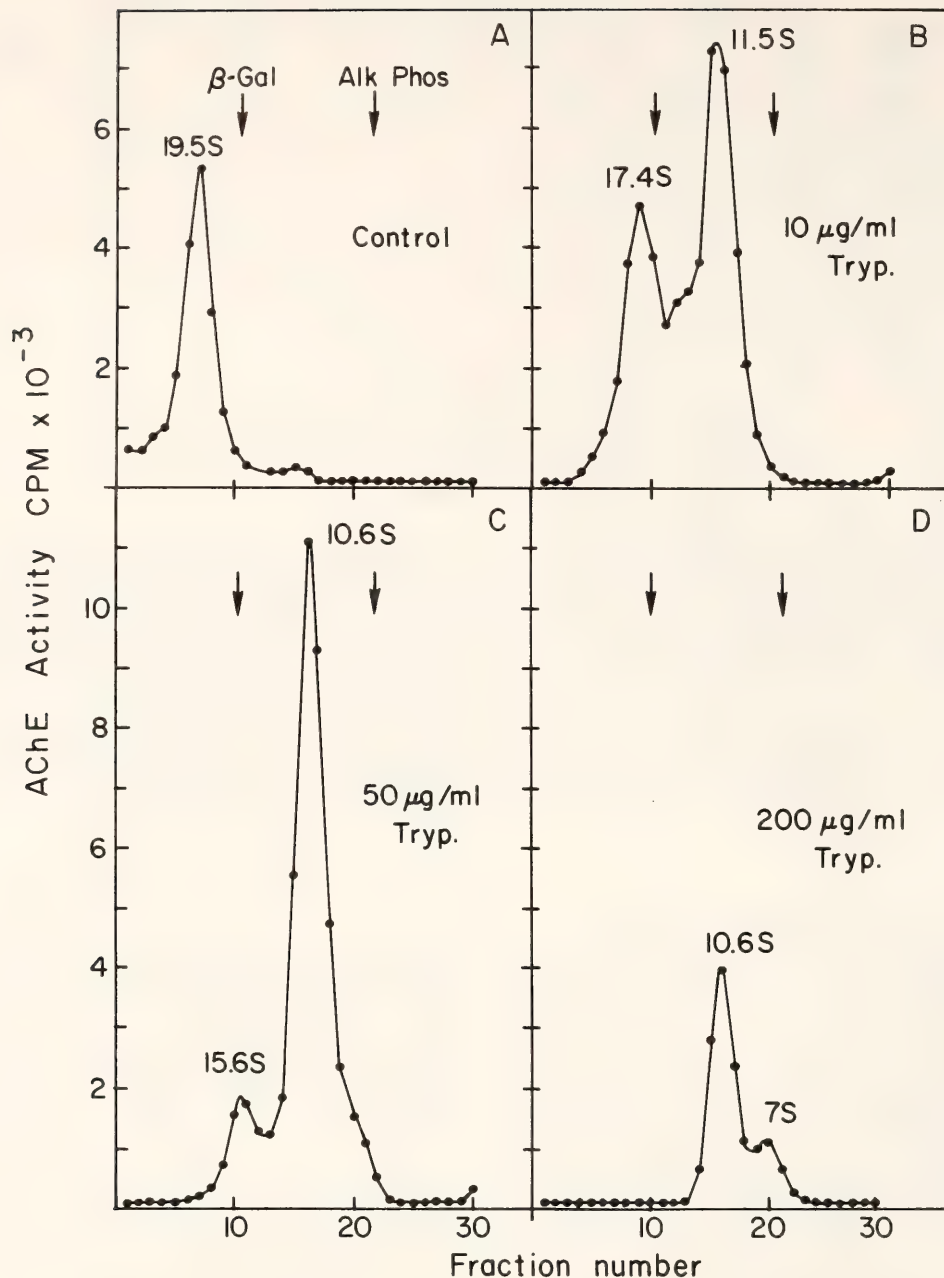


Fig. 4. Effects of trypsin on 19.5S AChE. Acetylcholinesterase was prepared from 16-day-old chick embryo leg muscle by centrifuging 2-ml aliquots of a 1:4 weight/volume homogenate on a 5%–20% sucrose gradient in an SW27 rotor. The pooled fractions containing the 19.5S form were dialyzed against buffer and concentrated using polyethelene glycol 6000. For trypsin treatment incubation mixtures contained 100 μ l 19.5S AChE solution, 625 μ g BSA, and trypsin in a total volume of 200 μ l. Proteolysis was carried out for 30 min. at 37°C. The tubes were then chilled on ice, mixed with 30 μ l enzyme marker solution, and 200 μ l aliquots layered on 5%–20% sucrose gradients. Gradients were centrifuged in an SW50.1 rotor for 12 hours at 39,000 rpm and 4°C. Fractions were collected by puncturing bottom of tube, 20 drops per fraction. (A) Control, no trypsin; (B) 10 μ g/ml trypsin; (C) 50 μ g/ml trypsin; (D) 200 μ g/ml trypsin. Arrows designate the positions of the markers β -galactosidase (16S) and alkaline phosphatase (6.1S).

trypsin, and the resulting forms were examined by velocity sedimentation on linear 5–20% sucrose gradients. Treatment with low concentrations of trypsin (Fig. 4B) converts the 19.5S AChE into

three molecular forms: a 17.4S, the already familiar 11.5S, and an additional form sedimenting midway between the two, possibly the 15.6S form. With increasing proteolysis, the 17.4S and 11.5S

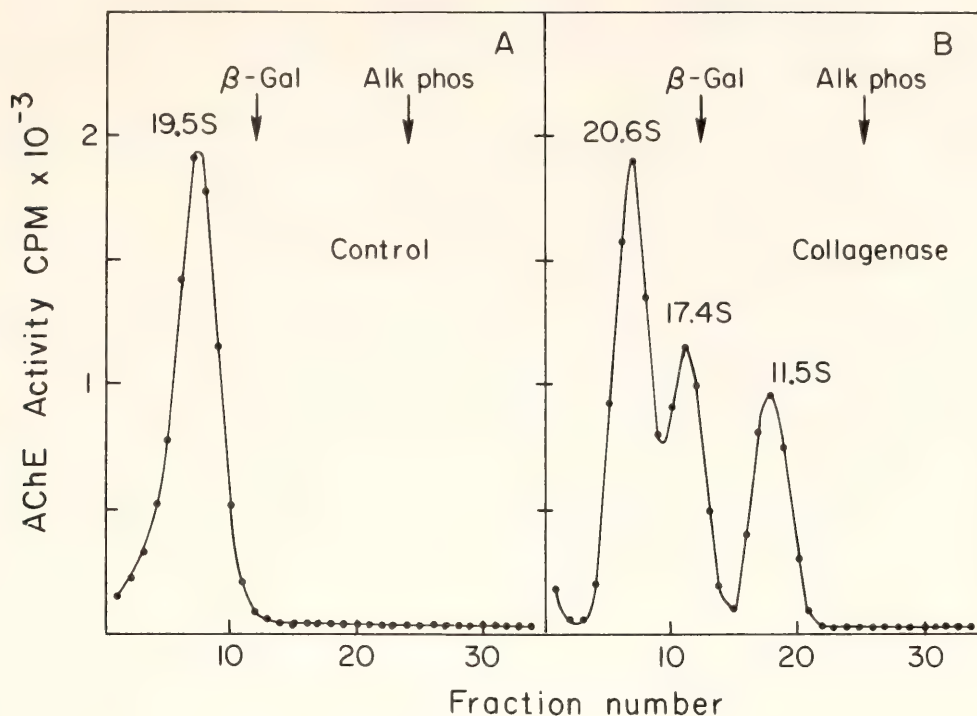


Fig. 5. Treatment of 19.5S AChE with crude collagenase. A 200- μ l aliquot of 19.5S AChE prepared as described in Fig. 4 was mixed with 50 μ l of a Worthington Type IV collagenase solution to give a final concentration of 1.25 mg/ml. No bovine serum albumin was used to protect the AChE from contaminating proteases. After incubation for 2 hours at 37°C the reactants were chilled on ice, mixed with 50 μ l enzyme marker solution, and layered on 5%-20% sucrose gradients as in Fig. 4. Gradients were centrifuged in a SW50.1 rotor for 15 hours at 35,000 rpm. Twenty drop fractions were collected by puncturing bottom of tube. The collagenase stock solution was tested for endogenous esterase activity and found to contain none. (A) Control, incubation in the absence of collagenase; (B) 1.25 mg/ml crude collagenase.

forms completely disappear, leaving only a 15.6S and a 10.6S form (Fig. 4C). Finally, after extensive proteolysis (Fig. 4D) only small amounts of the 10.6S form and a trace of 7S remain.

Treatment of the 19.5S form of AChE with collagenase, on the other hand, yields a somewhat different pattern of molecular forms (Fig. 5). Here the 19.5S enzyme is converted to a novel 20.6S form in addition to the 17.4S and 11.5S forms observed as a result of proteolysis. Since the highest molecular weight forms of AChE from the electrical eel have been shown to be associated with a collagen-like "tail" which is removable by treatment with collagenase, our studies suggest that the 19.5S form of AChE is also associated with a collagen-like macromolecule. The fact that the collagenase has no effect on the 11.5S AChE,

even at high concentrations, strengthens this supposition.

Table 3 summarizes the multiple molecular forms of acetylcholinesterase that we have studied to date. Only the 19.5S, 11.5S, 7.1S and 5.4S are normally found in living tissues. The remainder are forms which have been modified either through proteolysis or collagenase treatment or are found only in tissue culture medium. The observation that treatment of 19.5S AChE with these enzymes results in an array of well-defined molecular forms, several of which are normally found in cells both in vivo and in vitro, suggests that the heaviest form is made up of subunits which include the slower sedimenting forms. We are continuing to investigate the structural relationships between the various molecular forms of this enzyme.

TABLE 3. Summary of AChE Molecular Forms

S Value	Source
20.6	collagenase treatment of 19.5S AChE
19.5	muscle (in vivo), sympathetic ganglia
17.4	product of collagenase or trypsin treatment of 19.5S
15.6	product of collagenase or trypsin treatment of 19.5S
15.0	muscle culture medium
11.5	all tissues examined, serum, product of protease or collagenase treatment of higher forms
10.6	product of protease digestion of 19.5S form
9.0	secreted form found in muscle culture medium
7.1	found in all tissues examined, serum, product of protease treatment of 19.5S form
5.4	found in most tissues, also results from treatment of 7.1S form with DFP, final product of tryptic digestion of 19.5S form

Characterization of the Intracellular AChE Pool

Chick embryo muscle cells grown in culture contain two forms of acetylcholinesterase, the 11.5S and 7.1S, which are present in approximately a 1:4 ratio based on enzyme activity (*Year Book 76*). Also, AChE is secreted by these cells at a rate of 10% of the total cells' contents of AChE activity per hour. When treated with inhibitors or protein synthesis, the cultured muscle cells continue to secrete AChE at the normal rate for approximately 3 hours; after this time the rate drops to zero. This study, as well as several others, indicated that the cells contained an intracellular releasable pool of enzyme equivalent to that secreted over a 3-hour period. The size of this pool appears to be 60% of the total cell contents of AChE rather than the 30% predicted based on the amount of enzyme activity released after inhibition of protein synthesis. The precise reason for this difference is not known, although intracellular degradation of the enzyme and loss of activity during subunit assembly may both play a role.

To determine which molecular forms were present in the intracellular pool, we treated muscle cells in culture with diisopropylfluorophosphate (DFP), an irreversible inhibitor of acetylcholines-

terase. The recovery of the intracellular pool, which consists entirely of newly synthesized AChE molecules, is illustrated in Fig. 6. The levels of AChE rapidly recover at a rate of 20% of total cell contents per hour and reach a plateau between 2 and 3 hours posttreatment, at which time secreted enzyme begins to appear in the medium. The 60% recovery reflects the size of the intracellular pool, for no enzyme activity is detectable on the outer cell membrane at this time. The recovery of the individual AChE forms after DFP treatment (Fig. 7) indicates that both the 7S and the 11.5S forms of the enzyme are present within the cells. The 7S AChE returns at a much higher rate than the 11.5S and may serve as a precursor for this form. The 7S enzyme may also be a precursor of the 9S form found in the medium.

To study the kinetics of depletion of the 7S and 11.5S AChE molecules present in the pool, chick embryo muscle cultures were treated with DFP and allowed to recover for 2 hours prior to the addition of puromycin, an inhibitor of protein synthesis. Following the addition of puromycin, the cells were allowed to secrete AChE for varying lengths of time before analyzing the remaining AChE forms on linear 5–20% sucrose gradients. The results of this experiment

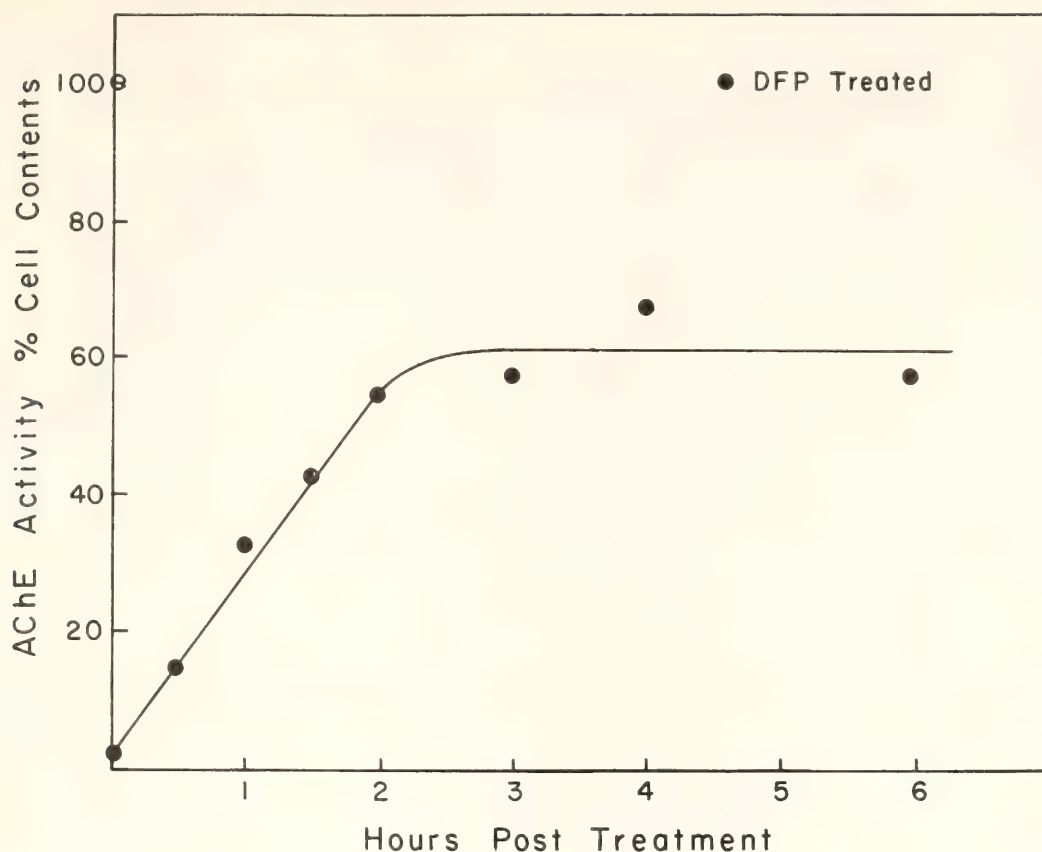


Fig. 6. Recovery of intracellular AChE pool following DFP treatment. Four-day-old chick embryo muscle cultures were washed and treated for 20 minutes with 2×10^{-4} M DFP in Hank's buffered salt solution. Cultures were then washed to remove unreacted DFP, covered with culture medium, and returned to the incubator at 37°C until assayed for AChE activity. Each point is the mean of three cultures, and the standard deviations are less than 10%.

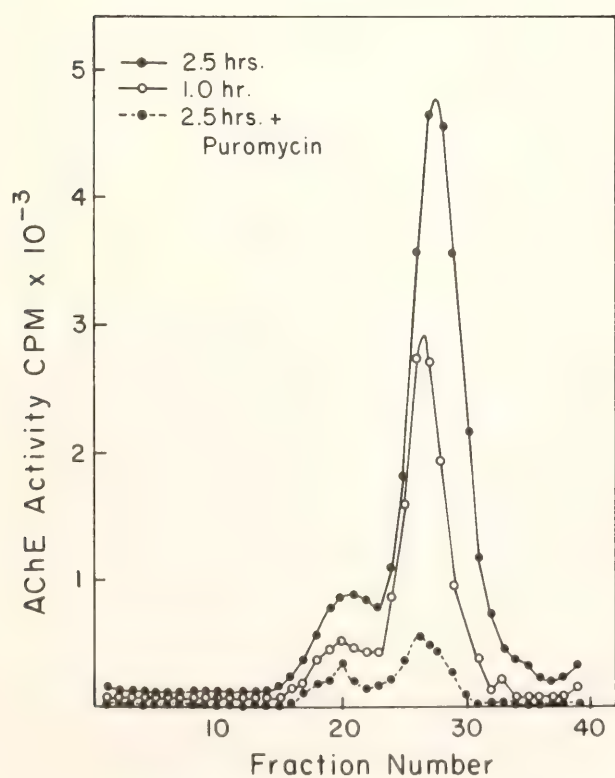


Fig. 7. Recovery of individual molecular forms of AChE in the intracellular enzyme pool following DFP treatment. Five-day-old chick muscle cultures were treated as described in Fig. 6. At the appropriate times, cultures were extracted into 500 μl homogenization medium with Triton X-100, four cultures being pooled for each determination. After centrifugation of the homogenates, 100- μl aliquots of the supernatants were layered on 5%-20% sucrose gradients and centrifuged in an SW50.1 rotor at 4°C , such that the product hours \times rpm² equalled 1.8×10^{10} . The puromycin concentration used was 10 $\mu\text{g}/\text{ml}$.

are shown in Fig. 8. Figure 8A illustrates the molecular forms of AChE present in the cultured cells before (control) and after treatment with DFP (broken line). Following a 2-hour recovery period, total cell AChE had returned to 35% of control levels (60% pool size). When puro-

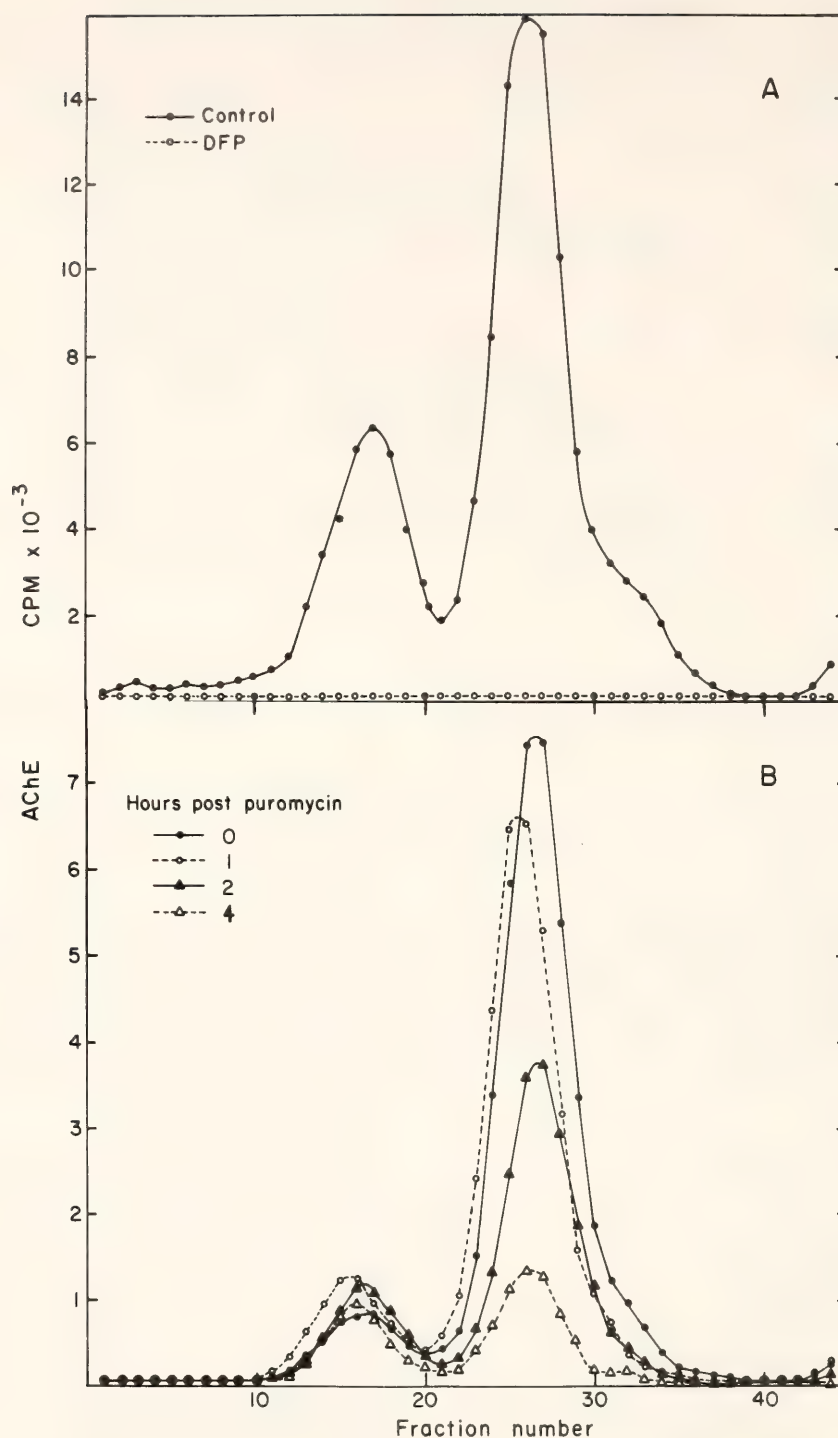


Fig. 8. Depletion of molecular forms of AChE in the intracellular enzyme pool after inhibition of protein synthesis. Seven-day-old chick embryo muscle cultures were used in this experiment, and four cultures were pooled for each gradient. Cultures were treated with DFP as described in Fig. 6 and allowed to recover for 2 hours, at which time $10 \mu\text{g/ml}$ puromycin was added to the experimental cultures. (A) AChE forms in control cultures (untreated) and DFP-treated cultures; (B) AChE forms in cultures containing 2 hours worth of pool AChE and incubated in the presence of $10 \mu\text{g/ml}$ puromycin for 0, 1, 2, or 4 hours to show pool depletion. Enzyme extracts were prepared and analyzed on sucrose gradients as described in Fig. 7.

mycin is added at this time, the kinetics of pool depletion are identical to those in non-DFP-treated muscle cultures.

This decrease can be accounted for entirely by the disappearance of the 7S form of AChE, with essentially no change

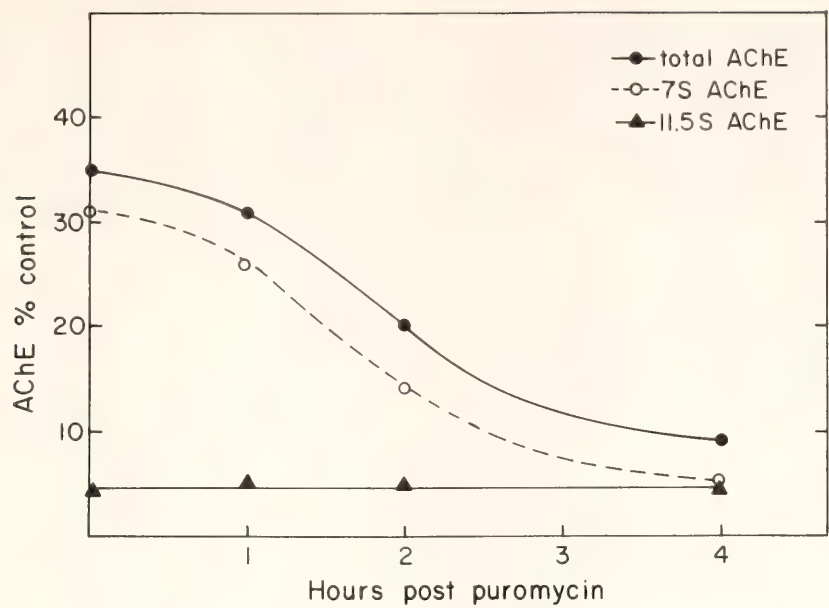


Fig.9. Kinetics of 11.5S and 7S AChE depletion from the intracellular enzyme pool. The values presented in this graph were obtained by summing the areas under the individual peaks in Fig. 8 and dividing by the total AChE activity in the control gradients. Each value is thus expressed in terms of the total amount of AChE activity present in control cultures.

in the levels of 11.5S AChE discernible during this period. The amount of each enzyme form calculated from the curves presented in Figure 8B is presented in Fig. 9 expressed in terms of the total amount of AChE in the cells. This graph shows that the kinetics of 7S AChE depletion is the same as the kinetics for the total AChE pool depletion, suggesting that it is this form which is being se-

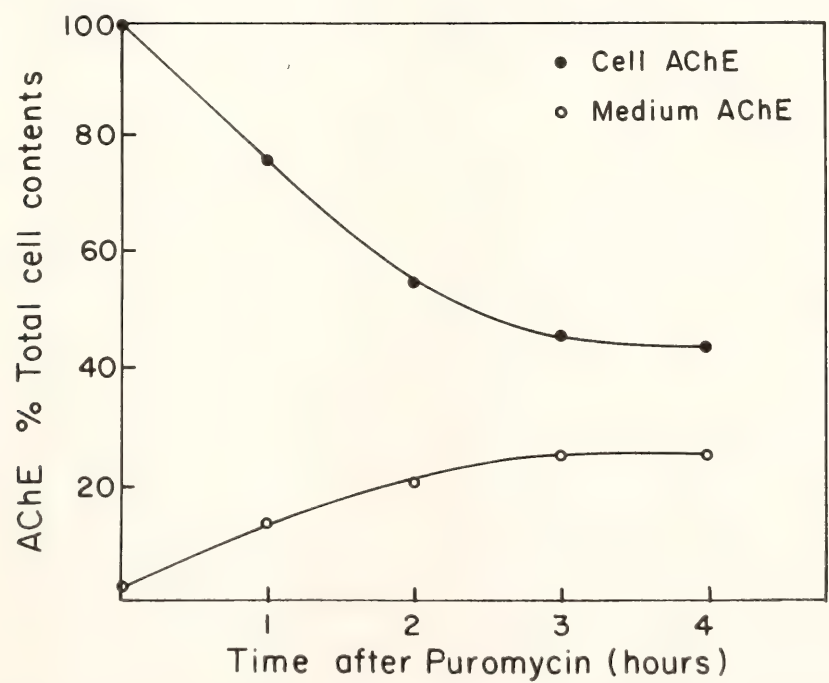


Fig.10. Simultaneous determination of intracellular and secreted AChE following inhibition of protein synthesis. Seven-day-old chick embryo muscle cultures were incubated in the presence of culture medium which had been pretreated to remove endogenous esterase activity and which contained 10 μ g/ml puromycin. At the designated times, both muscle cell activity and the medium AChE activity were determined. The results are expressed in terms of the total AChE activity present in control cells.

creted by the cells. The similarities between the kinetics of pool depletion of AChE in the presence of puromycin and the kinetics of accumulation of AChE in the medium (9S) are illustrated in Fig. 10.

*Relationship between
Acetylcholinesterase Secretion and
Membrane Incorporation of
ACh Receptors*

Our studies of the release of AChE into the medium by cultured chick embryo muscle cells (*Year Book* 76) indicated that the interval between synthesis and secretion of the enzyme was approximately 3 hours, that the cells contained an internal pool of enzyme equivalent to that released over a 3-hour period, and that several kinetic parameters of the release process were essentially identical to those found for the membrane incorporation of newly synthesized ACh receptor molecules. These results led us to examine jointly the kinetics of AChE release and AChR incorporation into muscle plasma membranes and the effects of various pharmacological manipulations upon these processes.

Figure 11 shows the effects of colchicine, an inhibitor of microtubule assembly, on the release of AChE. Colchicine results in only a partial block of AChE release and reaches a maximum effect of about 50% decrease in the rate of secretion compared to controls at concentrations in excess of 3 μ M. Similar experiments measuring the effects of the drug on ACh receptor incorporation show identical results. The reasons for this partial effect are not known, but they do indicate that microtubules are not necessary for AChE secretion into the medium or for AChR incorporation into membranes. Figure 12 illustrates the effects of colchicine and its inactive analogue, lumi-colchicine, on the rate of AChE secretion by cultured muscle cells. Three- μ M colchicine decreases the rate of

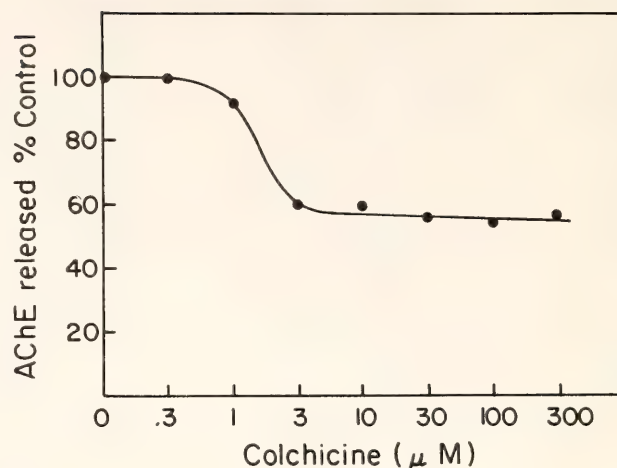


Fig. 11. Effects of colchicine concentration on AChE release. Three-day-old chick muscle cultures were incubated in the presence or absence of colchicine dissolved directly in 1 ml DFP-treated medium and serially diluted to the appropriate concentrations. At the end of the incubation period the medium was removed and assayed for AChE activity. Each point is the mean of four cultures. The incorporation of ACh receptor molecules into muscle plasma membranes was measured in the same cultures (data not shown), and the results were found to be identical to those of AChE.

AChE secretion by about 50–60%, whereas lumi-colchicine, the nondisruptive isomer, has no effect.

In Fig. 13 the effect of 300- μ M colchicine on AChE release and AChR incorporation into muscle membranes are compared. Notice that the relative rates of enzyme release and receptor incorporation are similar in both the control and experimental groups, and that the magnitude of the drug effect is identical. These results support the hypothesis that AChE and AChR molecules are transported together to the plasma membrane.

Another drug that affects AChE and AChR metabolism is tunicamycin. This compound interferes with the glycosylation of glycoproteins by blocking the addition of complex carbohydrates to protein molecules. The results of incubating muscle cells in the presence of 1 μ g/ml tunicamycin are present in Fig. 14, indicating that glycosylation is required for secretion or membrane incorporation of these glycoproteins. Again, the rates

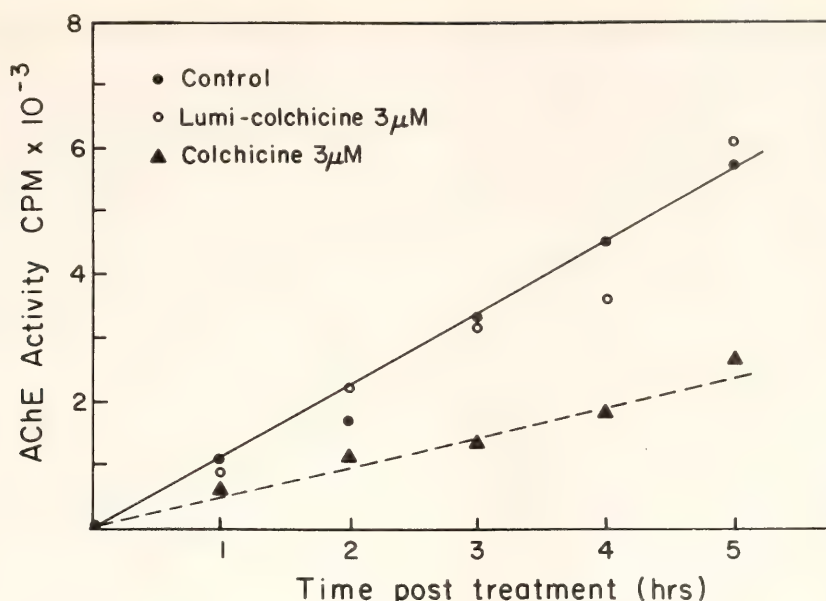


Fig. 12. Effects of colchicine and lumi-colchicine on the rate of AChE release by chick embryo muscle cells in culture. Lumi-colchicine is an analogue of colchicine produced by exposing the drug to UV light, resulting in an isomer which penetrates the cells but does not depolymerize the microtubules. Four-day-old muscle cultures were incubated in the presence of DFP-treated medium either alone or in the presence of 3- μ M colchicine or lumi-colchicine. Four cultures from each group were removed at hourly intervals and their medium subsequently assayed for AChE activity.

of appearance of ACh receptors on the plasma membrane surface and the release of AChE are identical for the control and the experimental groups.

A Model for AChE Release

Depicted in Fig. 15 is a hypothetical model of AChE release based on the Jamieson-Palade model of secretion,

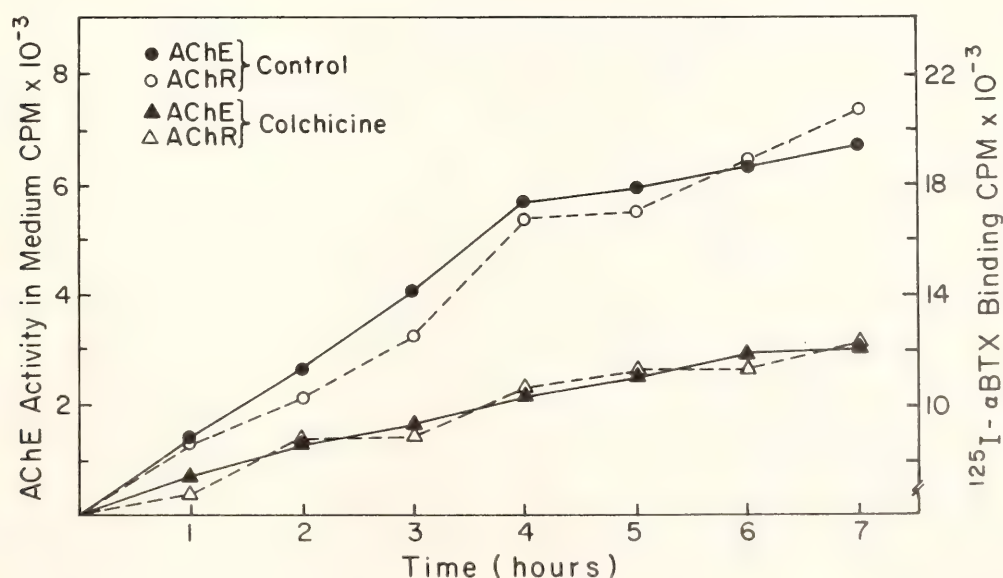


Fig. 13. Effects of colchicine on AChE release and ACh receptor incorporation into muscle plasma membranes. Three-day-old muscle cultures were incubated in unlabeled α -bungarotoxin overnight to saturate all surface ACh receptors. The cultures were then washed and incubated in the presence of DFP-treated medium either with or without 300 μ M colchicine. At hourly intervals four cultures from each group were removed to determine the number of newly incorporated receptor molecules and medium AChE activity.

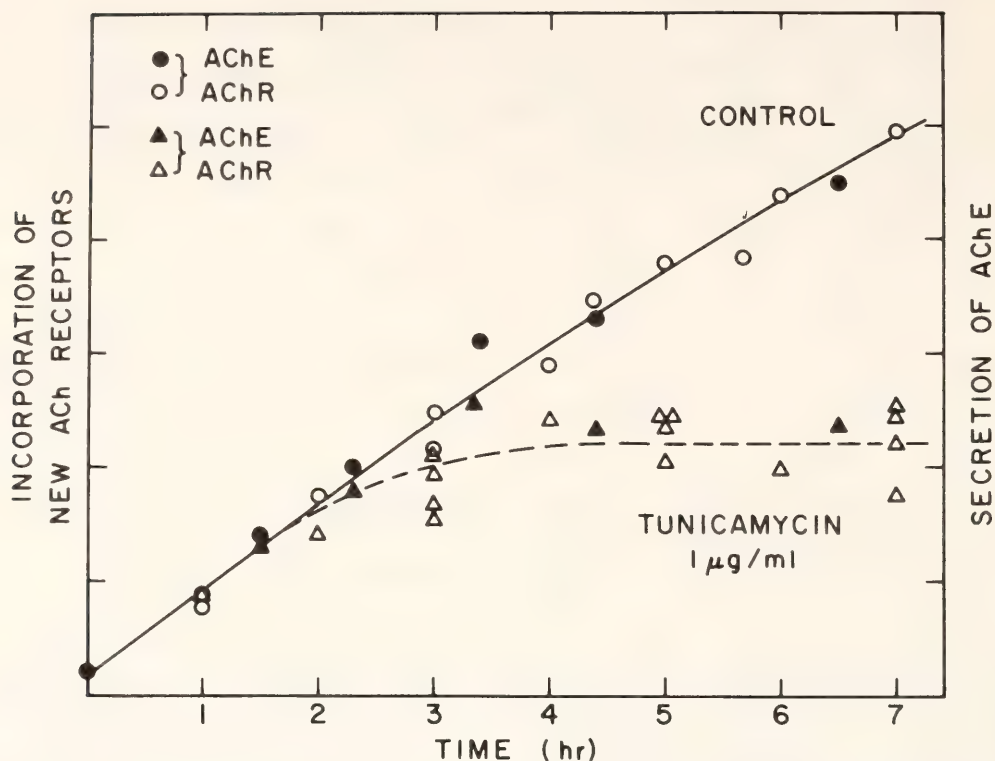


Fig. 14. Effect of tunicamycin ($1 \mu\text{g/ml}$) on secretion of acetylcholinesterase (●, ▲) and on incorporation of new acetylcholine receptors into plasma membranes (○, △). Control rates of secretion (●) and of incorporation (○) were plotted so as to have the same slope. Data from several experiments with different absolute rates are combined, so the ordinates are in units directly proportional to molecules of acetylcholinesterase secreted and new acetylcholine receptor sites appearing after time zero, but the proportionality constants vary slightly from one set of data points to another. In cultures treated continuously from time zero with tunicamycin in complete medium (DFP-treated in the case of secretion experiment) the rates of acetylcholinesterase secretion (▲) and of incorporation of receptors into plasma membrane (△) were not significantly affected until about 3 hours. Each symbol represents the averaged value for 3 to 5 culture dishes. Data from five separate incorporation experiments are plotted, involving four different samples of tunicamycin.

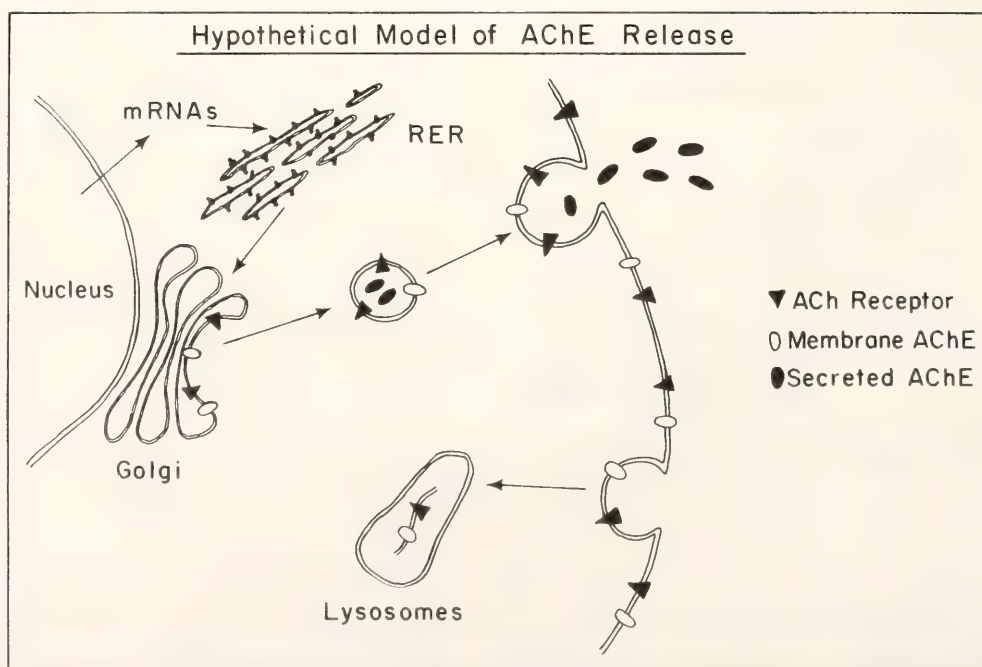


Fig. 15. Hypothetical model of AChE release including biosynthesis and intracellular transport of both the ACh receptor molecule and intracellular AChE.

summarizing our current understanding of the synthesis, transport, and secretion of chick muscle cell acetylcholinesterase together with the information on the biosynthesis and membrane incorporation of ACh receptors reported previously by Devreotes *et al.* (*Year Book 75* and *Year Book 76*). Both molecules are presumably synthesized on rough endoplasmic reticulum (although we have no direct evidence on this matter) followed by rapid translocation to the Golgi apparatus. Following a period in the Golgi apparatus, the molecules are transported to the plasma membrane. This entire process requires about 3 hours for both molecules. The similarities in the kinetics of synthesis and transport of both AChE and ACh receptor molecules suggest that they are transported via a common pathway, thus providing a link between the synthesis and secretion of proteins destined for the extracellular environment, on the one hand, and the synthesis and membrane incorporation of integral membrane proteins, on the other. Whether this proves to be a general mechanism for all such proteins and within all cell types remains to be determined.

METABOLISM AND SITE OF INSERTION OF A PLASMA MEMBRANE PROTEIN IN RAPIDLY GROWING NEURONS

S. T. Carbonetto

Neurons have the unique ability to grow long axonal processes that are specialized to transmit electrical impulses between distant parts of the nervous system. At the tip of each axon, growing neurons form an elaborate structure called a growth cone that moves in amoeboid fashion out from the cell body and can be seen readily on neurons growing in culture (Fig. 16). The structure of growing axons has been studied in a number of laboratories, but little is known about the dynamics of axonal growth. An important aspect of this process is the mechanism by which sur-

face membrane proteins are synthesized, transported to the surface, and eventually degraded; but it is often difficult to study the metabolism of membrane proteins because they are usually only a trace component of the total cell protein and difficult to quantify.

In *Year Book 76* we reported that α -bungarotoxin, a ligand specific for acetylcholine receptors in skeletal muscle, binds selectively to chick sympathetic neurons. Binding of α -bungarotoxin to neurons is saturable and is completely blocked by d-tubocurarine (10^{-4} M). We showed that sympathetic neurons depolarize in response to iontophoretically applied acetylcholine, indicating that they contain acetylcholine receptors in their plasma membranes and that these responses could be blocked by d-tubocurarine. Surprisingly, even at ten times the saturating concentration, α -bungarotoxin had no effect on acetylcholine responses in neurons, and it did not affect the ability of d-tubocurarine to block these same responses. We concluded—and this has since been supported by experiments from other laboratories—that α -bungarotoxin does not bind to acetylcholine receptor sites but to some neuronal membrane protein which we call an α -bungarotoxin receptor.

The α -bungarotoxin receptor is not extracted from the membrane by 1 M NaCl or 1 mM EDTA but is readily extracted by non-ionic detergents (Table 4). α -Bungarotoxin-receptor complexes normally dissociate with a half-time of 3.5 hours at 23°, but in solution they can be cross-linked by glutaraldehyde (0.1%) to form complexes that are stable for several days. Both before and after cross-linking, α -bungarotoxin-receptor complexes sediment in sucrose gradients as a single peak with a sedimentation constant of approximately 11S (compared with 10S for skeletal muscle acetylcholine receptors).

The ability to covalently label the α -bungarotoxin receptor and to assay this



Fig. 16. Scanning electron micrograph of the growing tip of a chick sympathetic neuron in culture. The growth cone at the tip of the axon has a broad, flattened extension called a veil and finer, longer extensions called lamellipodia. Calibration bar is 5μ .

TABLE 4. Efficiency of Extraction of α -Bungarotoxin Receptors by Various Solutions*

Solution	Total Counts Extracted (%)
150 mM NaCl	8.2
150 mM NaCl + 1 mM EDTA	7.8
150 mM NaCl + 1% Triton X-100	65
1 M NaCl	7.2

* Four sets of neuronal cultures (4 plates each) plated at equal cell densities were incubated with 0.1 $\mu\text{g}/\text{ml}$ of ^{125}I - α -bungarotoxin for 1 hr at 37°C . They were then washed thoroughly to remove unbound toxin and treated with 1 ml of a test solution with constant swirling for 1 min. The solution was then removed, centrifuged at $10,000 \times g$ for 5 min and an aliquot of the supernatant counted by scintillation spectrometry. The activity remaining on the plates was solubilized in 1 N NaOH and also counted.

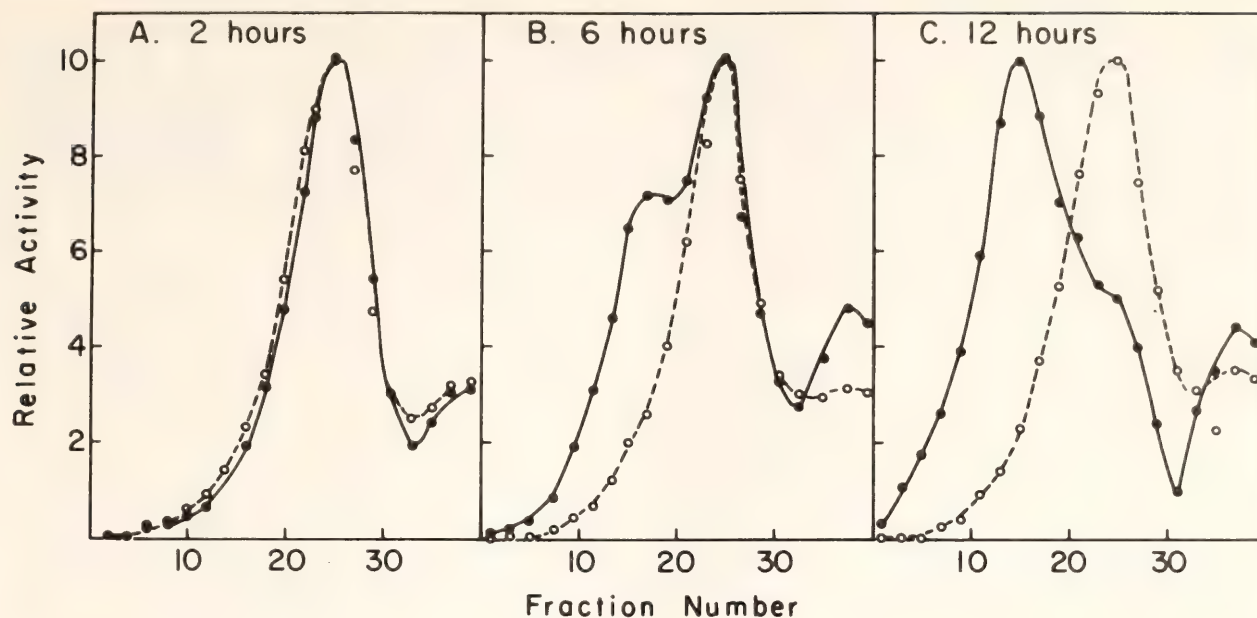


Fig. 17. Sucrose gradient velocity sedimentation profiles of surface receptors appearing during culture of chick sympathetic neurons in medium containing ^2H , ^{13}C , ^{15}N -amino acids (O—O). Gradient profiles illustrated are those from which the data for the 2, 6, and 12 hr time points in Figure 18 were obtained. A marker of ^{131}I - α -bungarotoxin- ^1H , ^{12}C , ^{14}N -receptor complexes (O—O) was mixed with the sample before centrifugation and its position in the gradient is identical to the position of the ^{125}I - α -bungarotoxin- ^1H , ^{12}C , ^{14}N -receptor complexes.

receptor by velocity centrifugation presented an excellent opportunity to study the biosynthesis and degradation of this plasma membrane component of the neurons. We have since been able to accomplish these studies by application of the density-shift technique developed in this laboratory to study the turnover of acetylcholine receptors in muscle. We have grown neurons in "dense" medium (containing ^2H , ^{13}C , ^{15}N -substituted amino acids) for various periods of time. The neurons are labeled with radioactive α -bungarotoxin; the α -bungarotoxin-receptor complexes are detergent-extracted, cross-linked with glutaraldehyde, and then layered on sucrose-deuterium oxide gradients (25–40%) and centrifuged at 48,000 rpm for 48 hours in an SW41 rotor to separate "light" from "dense" receptors. Figure 17 shows several sample gradients demonstrating the appearance of a faster sedimenting peak of newly synthesized receptors in neurons grown in dense medium. The proportion of binding sites in the dense peak increases with longer times in dense me-

dium, and this increase is blocked by the addition of cycloheximide to the medium (Table 5). With this technique we have followed the incorporation of newly synthesized receptors into the plasma membrane (Fig. 18). The curve is approximately linear for the first 10 hours, during which time little degradation of newly synthesized receptors takes place. After 10 hours, degradation of the dense surface pool becomes appreciable, and the incorporation rate becomes noticeably exponential to the extent that it can be fit fairly closely by a first-order exponential curve with a half-time of 7 hours. There is a 2-hour lag before the first newly synthesized receptors appear in the plasma membrane. We have shown that this lag is not due to the time required for amino acid pools in the cell to equilibrate with dense amino acids. Neurons are permitted to synthesize dense receptors for 4 hours, at which time the incorporation rate is maximal and the amino acids should be equilibrated. Cycloheximide at 100 $\mu\text{g}/\text{ml}$, which rapidly blocks protein synthesis,

TABLE 5. Effect of Various Drugs on the Incorporation of Receptors into the Plasma Membrane*

Drug	Incubation Time (hr)	Dense Receptors (% of total surface receptors)	Dense Receptors (% of control)
Control	...	38	...
Cytochalasin B (5 µg/ml)	3	38	100
Colchicine (0.5 µg/ml)	3	34	90
Cycloheximide (100 µg/ml)	8 (continuous)	0	0
Actinomycin D (5µg/ml)	8 (continuous)	38	100

* Neurons were shifted into dense medium for 8 hr and treated with drugs at concentrations and for times shown. Neurons were then incubated with radioactive α -bungarotoxin. Receptors were extracted and analyzed for an increase in density, as described in the text.

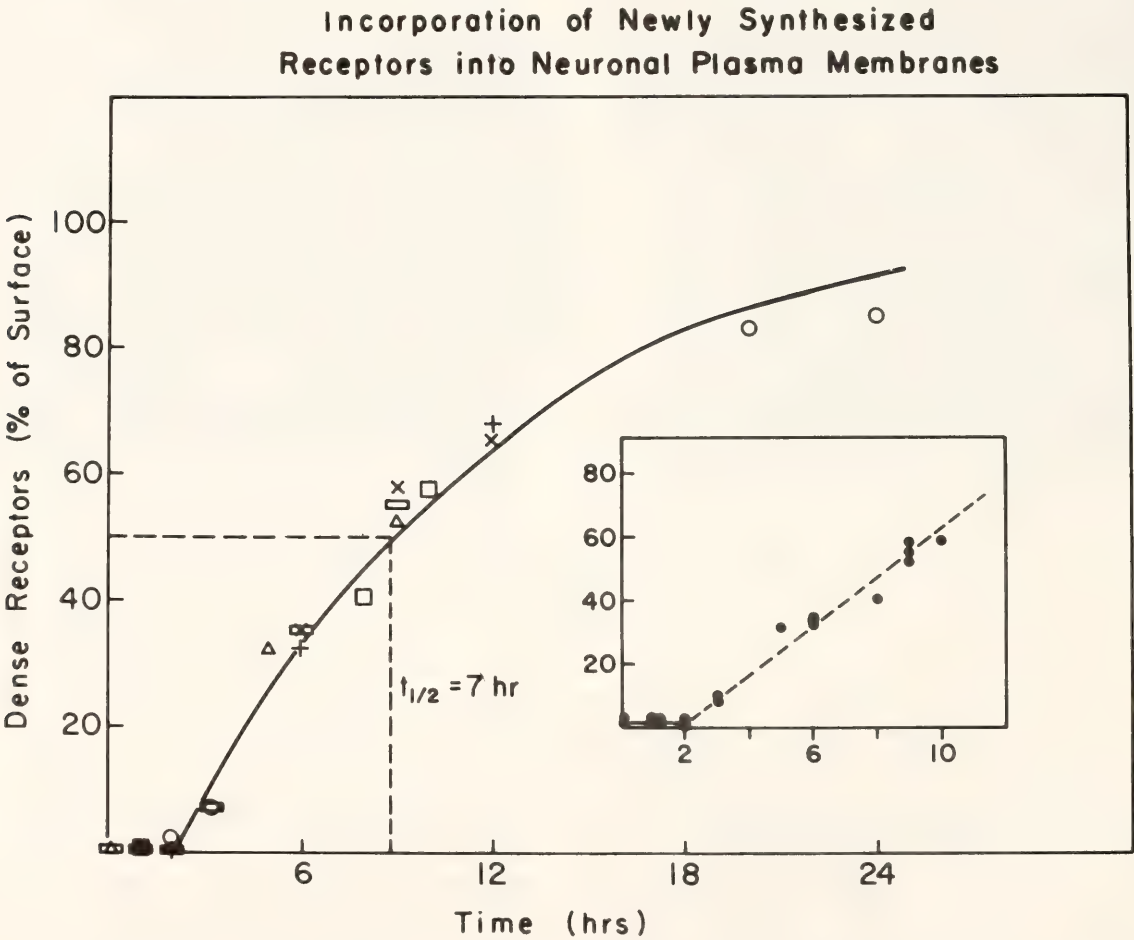


Fig. 18. Kinetics of appearance of newly synthesized, density-shifted receptors in the plasma membranes of chick sympathetic neurons incubated in medium containing ^2H , ^{13}C , ^{15}N -amino acids. Sets of neuronal cultures (usually six plates) plated at equal densities were incubated in medium containing ^2H , ^{13}C , ^{15}N -amino acids for various periods of time. They were then treated with $0.1\text{ }\mu\text{g/ml}$ of ^{125}I - α -bungarotoxin for 1 hour at 37° to saturate the surface receptors and the unbound toxin was washed away. Bungarotoxin-receptor complexes were extracted with 1% Triton, 10 mM Tris, pH 7.8, crosslinked with 0.1% glutaraldehyde, layered on sucrose-deuterium oxide gradients (25–40%) and centrifuged at 38,000 rpm for 48 hours at 13°C . The curve drawn through the data points is a first-order exponential with a half-time of 7 hours. The inset shows that the rate is approximately linear for the first 10 hours of incorporation.

is then added, but receptors continue to appear for 2 hours before incorporation is blocked (Fig. 19). Similar delays in the incorporation of membrane proteins in other systems have been found and are thought to be due to processing of membrane proteins in the rough endoplasmic reticulum (RER) and Golgi apparatus before insertion in the plasma membrane. So far, our efforts to demonstrate an internal precursor pool corresponding to binding sites in the Golgi and RER have met with limited success. Saturating the surface receptors with ^{131}I - α -bungarotoxin, followed by homogenization of the cells and extraction of the homogenate in Triton X-100 reveals a population of receptors that can be labeled with ^{125}I - α -bungarotoxin and is three times greater than the surface population. Only a small fraction of this internal pool, however, would be expected to be precursor to the surface (the

2-hour lag in incorporation would indicate that the internal pool is only about 14% the size of the surface receptor site population). We have had difficulty estimating the size of the metabolically active precursor pool by density shifting because the internal receptors sediment at a slower rate than the surface receptors.

We suggested above that the deviation from linearity seen in the incorporation of newly synthesized receptors into the plasma membrane was due to degradation of receptors. The degradation rate was measured directly by permitting neurons to synthesize a population of dense receptors and then following the disappearance of these receptors from the surface. Measured in this way, the degradation rate is a single exponential with a half-time of 10 hours (Fig. 20). We believe that once internalized, the receptors are degraded, probably by

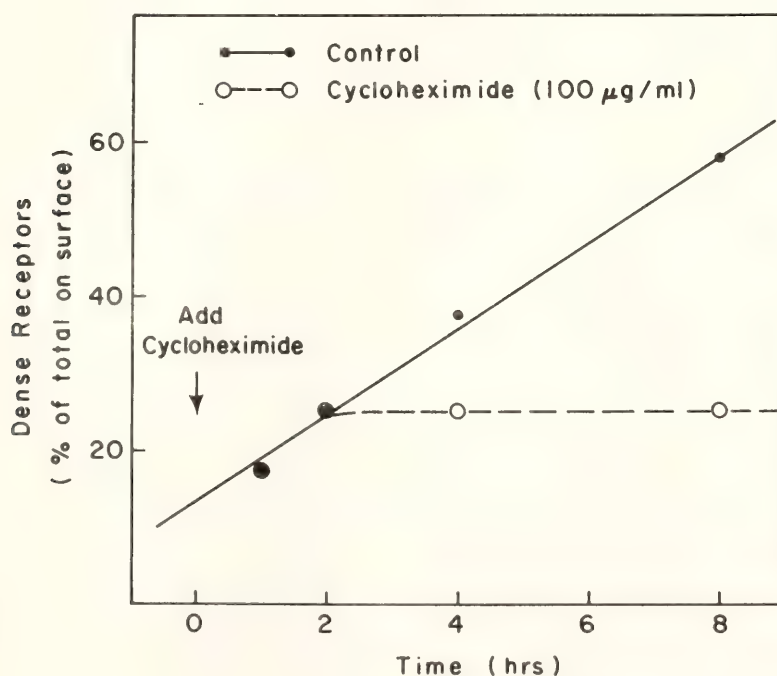


Fig. 19. Kinetics of cycloheximide action on receptor appearance in neuronal plasma membranes. Two sets of neuronal cultures (six plates each) evenly plated were incubated in medium containing ^2H , ^{13}C , ^{15}N -amino acids for 4 hours. At this time ($t = 0$ on the abscissa), cycloheximide $100 \mu\text{g/ml}$ was added to one set of cultures, and incubation in dense medium was continued for up to 8 hours. At $t = 1, 2, 4$, and 8 hours control and cycloheximide-treated cultures were incubated with radioactive α -bungarotoxin, and the amount of dense receptors were assayed.

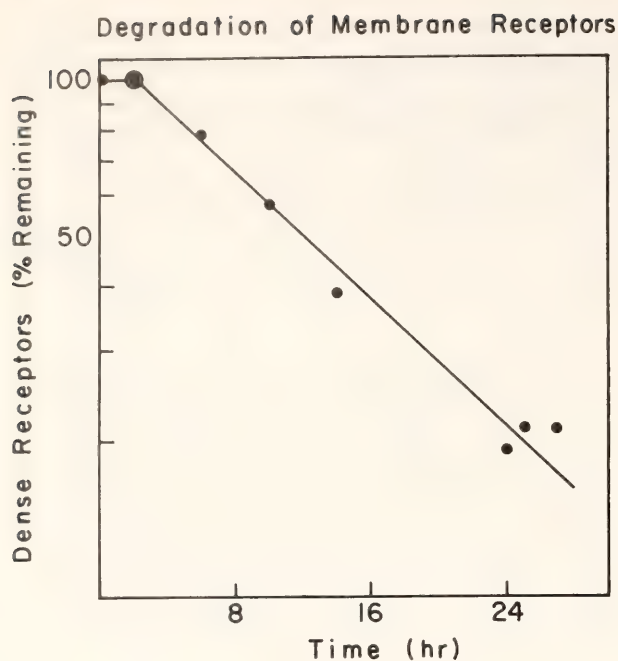


Fig. 20. Kinetics of degradation of receptors in the plasma membranes of chick sympathetic neurons. A set of cultures (six plates) evenly plated was incubated in medium containing ^2H , ^{13}C , ^{15}N -amino acids for 12 hours, at which time approximately 65% of the surface receptors were dense. The cultures were then shifted to medium containing ^1H , ^{12}C , ^{14}N -amino acids ($t = 0$), and at various times thereafter cultures were labeled with ^{125}I - α -bungarotoxin and assayed for the number of dense receptors remaining in the culture.

lysosomal enzymes. This conclusion is supported by the finding that approximately 25% of the ^{125}I - α -bungarotoxin bound to receptors appears in the medium within 10 hours as ^{125}I -iodotyrosine, a proteolytic breakdown product of ^{125}I - α -bungarotoxin.

The difference in the rate of incorporation of receptors (about 7%/hr) and the rate of degradation (about 5%/hr) is reflected in a net increase in the number of α -bungarotoxin receptors in the plasma membrane of neurons during the first 3 days in culture (Fig. 21). We call this period between days 1 and 3 the period of active neuronal growth because during this period growth cones are plentiful and neurons are extending processes at a rate of up to 100 μ per hour. By day 5, growth cones are no longer apparent. It is interesting to note that α -bungarotoxin

receptors decrease at a time when neuronal growth appears to have stopped. This decrease in receptors is not due to cell death, since it can be demonstrated autoradiographically as a decrease in the density of receptors on neurons (Fig. 21B). In future experiments we would like to determine if the loss of α -bungarotoxin receptor is indicative of a general change in the composition of neuronal membranes once they have stopped growing or if it is in some way mediating growth inhibition.

We have done two types of experiments aimed at elucidating the site of this receptor incorporation into the plasma membrane of growing neurons. In the first type we cultured sympathetic ganglia rather than dissociated cells. After several days an extensive axonal outgrowth or "halo" has formed around each ganglion, and by simple dissection we can separate the halo from its ganglion to yield a preparation of pure axons. We have done pulse-labeling experiments with dense amino acids in this preparation and have shown that after several hours in dense medium greater than 10 times more receptors are incorporated into the ganglion than the halo. The rate of incorporation, expressed as percentage of the surface receptor population incorporated per hour is about the same in the ganglion and halo. Thus it appears that at least some membrane components can be incorporated into the surface at sites along the axon and cell body and not just at the growth cone, as has been suggested by others. This conclusion is supported by a second type of experiment in which we monitored the effect of several drugs, most importantly cytochalasin B, that block axonal growth. Cytochalasin B acts very quickly to block growth by disrupting the structure of the growth cone and causing axonal sprouts to retract. However, it has no effect on the rate of new receptor synthesis or incorporation into the surface membrane.

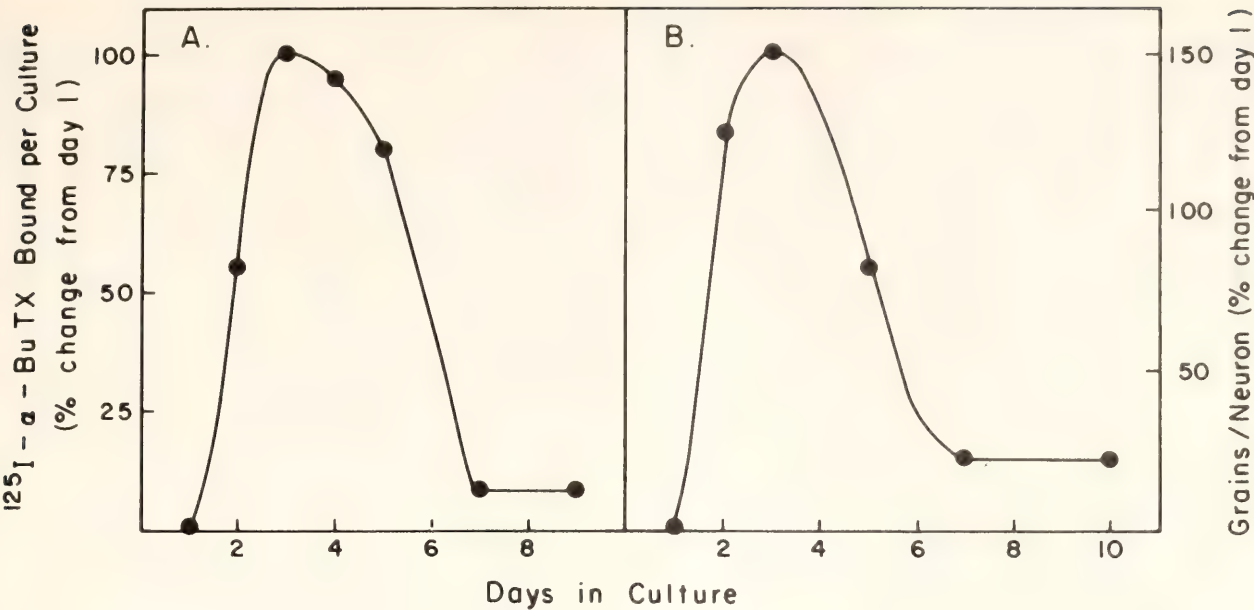


Fig. 21. The number of bungarotoxin receptors in chick sympathetic neurons during time in culture. (A) Neuronal cultures were plated at equal densities and at each time point three plates were incubated with ¹²⁵I-α-bungarotoxin (0.1 μg/ml) with or without d-tubocurarine (10⁻⁴M). The plates were washed of unbound toxin and solubilized in 1% Triton X-100, 10 mM Tris, pH 7.8, and counted. Binding not blocked by d-tubocurarine was less than 10% of control values and was subtracted from controls. (B) Neuron cultures were made and handled as above except that after receptors were saturated with ¹²⁵I-α-bungarotoxin they were fixed in 2% glutaraldehyde, 100 mM cacodylate buffer pH 7.4, dehydrated in alcohols, and coated with Kodak NTB-2 Nuclear Track Emulsion. After 5-7 days, autoradiographs were developed and the number of exposed emulsion grains on neuronal cell bodies counted using a Zeiss compound microscope. Grains over 40 neurons were counted for each time point. Data are plotted relative to day-1 values because this was the earliest time that binding of α-bungarotoxin could be measured without appreciable loss of neurons during washing. The amount of radioactivity specifically bound on day 1 was 3029 cpm in one typical experiment.

CONSTRUCTION OF CONTINUOUS CELL
LINES WHICH SECRETE MONOCLONAL
ANTIBODIES OF PREDETERMINED
SPECIFICITY

D. Fambrough

Cell lines that secrete large quantities of a single species of antibody molecule of known target specificity were first constructed by Kohler and Milstein. Briefly, their technique involved somatic cell hybridization of spleen cells from an immunized mouse with tissue-cultured mouse myeloma cells, followed by selection for vigorously growing hybrids and the screening and cloning of hybrids to obtain the cell lines. In subsequent investigations, Milstein and colleagues have examined many parameters of the technique and have demonstrated its power as a tool for studying minor cell

surface components. Fortuitously, the hybridization preferentially involves recently stimulated spleen cells, so that among the successful hybrid clones an enormously disproportionate number are clones which secrete antibodies directed at the antigens with which the mouse was immunized.

Dr. Milstein generously supplied us with the major myeloma cell line used in his group's studies (P3X63 Ag8, a derivative of MOPC 21) which grows rapidly in suspension culture, lacks the enzyme hypoxanthine-guanine phosphoribosyl transferase, and secretes an IgG1 of unknown target specificity. More recently we obtained from Dr. David Gottlieb a variant of this cell line, which is a nonsecretor but is permissive for secretion of immunoglobulin when hybridized with spleen cells. With the mye-

loma cell line from Dr. Milstein we set out to repeat the original Kohler and Milstein experiments of generating hybrids which secrete anti-sheep red blood cell antibodies. The first two attempts were successful. In each case we obtained hybrids which secreted an anti-sheep red blood cell immunoglobulin. Subcultures of these hybrids secreted sufficient antibody that the culture medium would cause hemagglutination of sheep red blood cells when the medium was diluted 128-fold. In these early fusions and immunological assays, we had the collaboration of Dr. Patricia Gearhart. At this same time, because of her interests, we constructed hybrids which secreted anti-dinitrophenol antibodies and anti-phosphorylcholine antibodies. We isolated six clones from the anti-phosphorylcholine hybrids by micromanipulation of single cells onto feeder layers of primary spleen cells. Dr. Gearhart has grown up large cultures from these clones and is purifying and characterizing the anti-phosphorylcholine antibodies and preparing to do primary sequence work. During the past few months, we have concentrated upon constructing cell lines that produce anti-chick muscle membrane antibodies. It has proved to be relatively easy to generate successful hybrids. The cloning of interesting hybrids has been more difficult, and we have experimented with several strategies.

The following is a description of the immunization and screening procedures we used to obtain the first of these lines. A crude membrane fraction was prepared from 14-day chick embryo leg muscle by homogenization of the muscle masses followed by low-speed centrifugation. The pellet was washed several times by suspension and centrifugation and then suspended in 10 volumes of phosphate-buffered saline. BALB/c mice were injected intraperitoneally with 0.2 ml of the crude membrane suspension. One month later the mice were boosted with freshly prepared membrane suspension

and 3 or 4 days later the mice were bled and the spleens removed. Spleen cells and myeloma cells were hybridized, using polyethylene glycol. The products of each hybridization of the cells from one spleen and a tenth that number of myeloma cells were distributed into 24 culture wells of a Costar culture dish and grown in selective medium for 2 weeks. Vigorous growth was observed in most wells. Conditioned medium (48 hr) from these wells was assayed for mouse anti-chick membrane by incubating a small aliquot of a fresh crude membrane preparation with an aliquot of culture medium, washing the membranes by repeated centrifugation and resuspension, and then incubating these membranes with ^{125}I -labeled goat anti-mouse Fab and washing as before. The bound radioactivity was measured by gamma counting. Some of the results of this test are illustrated in Fig. 22. Hybrid cells from six of the culture wells that tested positive were subcultured and reassayed, and the majority of cells were frozen for later cloning. Culture medium from these subcultures was also tested in a second assay. The medium was placed on live chick muscle cultures maintained at room temperature. After 1 hour the medium was removed and the cultures rinsed thoroughly and then incubated within medium containing ^{125}I -labeled goat anti-mouse Fab. The cultures were then rinsed to remove unbound antibody, and the bound radioactivity was measured by gamma-counting. One of the six hybrid cultures was then cloned by seeding several culture plates at about 0.3 cell per well, growing them for several weeks, and taking the cells from the few positive wells as likely to be clonal in origin. Four out of 10 clones so generated tested strongly positive as secretors of antibody molecules that bound selectively to exposed antigens in cultured chick skeletal muscle. Medium from one of these clones was used to further characterize the assay. Autoradiographs were prepared of

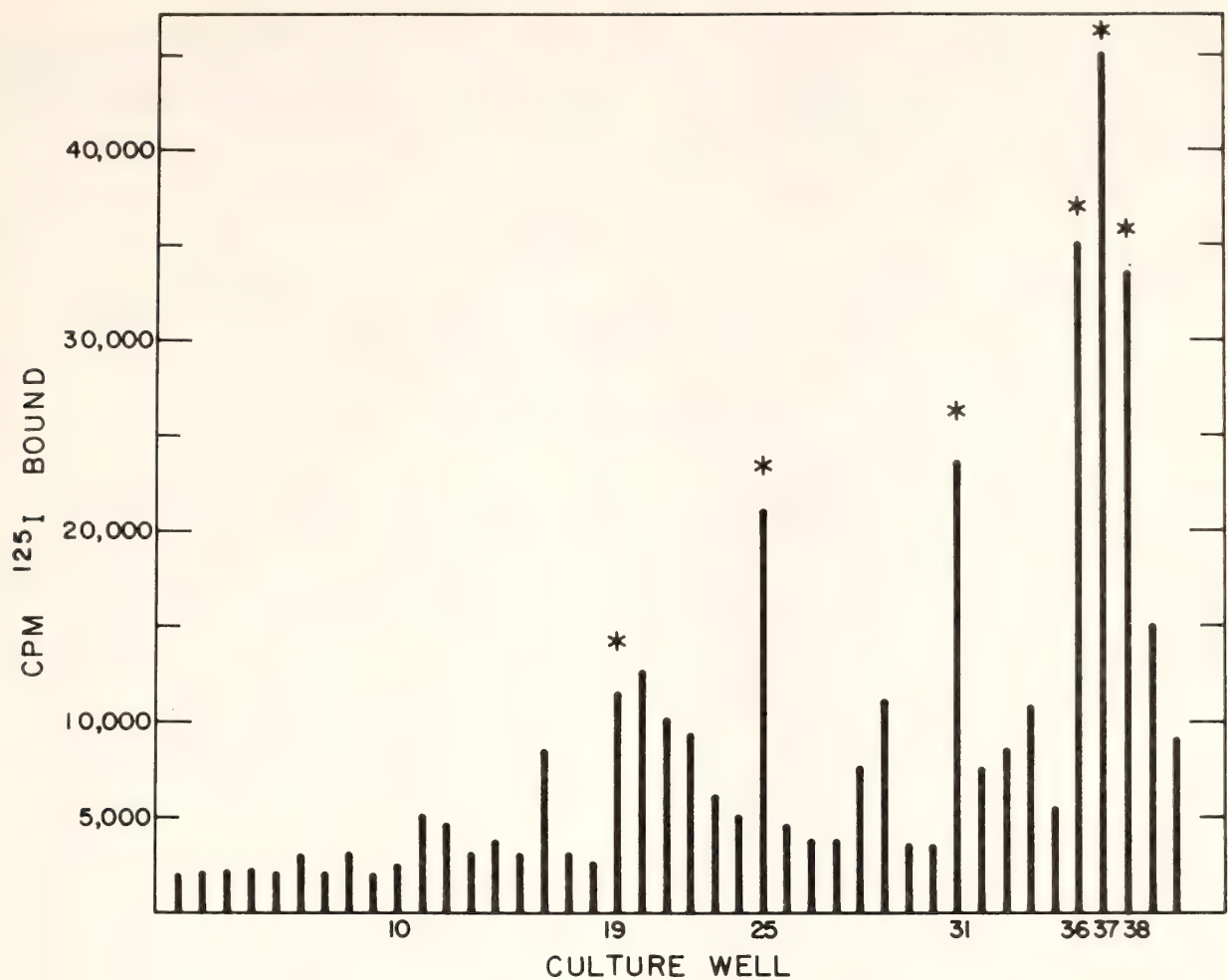


Fig. 22. Assays of culture medium from hybrid cells for anti-chick muscle membrane antibodies. A crude chick muscle membrane preparation was made from 14-day chick embryo leg muscle by repeated homogenization and medium-speed centrifugation. The final pellet was suspended in about 20 volumes of phosphate buffered saline containing 1% bovine serum albumin and 10 mM azide (PBS-BSA). Aliquots of the membrane suspension were incubated with three volumes of culture medium from individual culture wells (48-hr conditioned medium) for 2 hours at 25°C. The incubation mixtures were then centrifuged and the pellets washed twice with PBS-BSA. Each sample was then incubated overnight with ¹²⁵I-labeled goat anti-mouse Fab in PBS-BSA. The membranes were then washed twice to remove unbound iodinated antibody and the bound radioactivity measured by gamma counting. Counts per minute of bound radioactivity for each culture well are plotted in the figure. Duplicate assays gave virtually identical results; the average is plotted. Asterisks above the bars indicate cultures selected for cloning.

chick muscle cultures exposed to the conditioned culture medium and then ¹²⁵I-labeled goat anti-mouse Fab. In these autoradiographs the silver grains were located predominantly over cell-free areas of the collagen substratum, indicating a high concentration of antigen there. This location of the antigen suggests that it is a secretory product of myotubes, possibly related to the formation of basement membrane. The distri-

bution of the target antigen for the monoclonal antibody in different chick tissues and the nature of the antigen are now being examined.

Our research plans are for construction of a large number of antibody-producing cell lines and the use of these antibodies to explore the metabolism of membrane and secretory glycoproteins. Because the antibodies are multi-valent ligands, their interaction with cell surface antigens is

likely to lead to the elimination of the antigen from the plasma membrane. This may provide us with a means of determining the normal *function* of the anti-

genic molecules in the muscle plasma membrane and may thus lead to the further structure-function studies.

ORGANIZATION, DYNAMICS AND METABOLISM OF CELL SURFACE PHOSPHOLIPIDS

*R. E. Pagano, Alexander Sandra, Alan Schroit, and Douglas Struck
with the assistance of E. Asch*

In the last ten to twenty years, our ideas about cellular membranes have undergone a marked change from a point of view in which the lipid component of membranes was considered as a static permeability barrier and as a matrix for the organization of particular membrane proteins, to one in which the membrane lipids are viewed as a fluid dynamic structure in which they and other membrane constituents are capable of undergoing metabolic turnover and of participating in important functions such as cell-cell interactions and cell membrane-genome interactions. The ongoing studies in this laboratory deal with one element of mammalian cell surface membranes, the phospholipids, which are thought by many to be the "simplest" of membrane constituents. We seek to study the metabolism of the lipid constituents on each leaflet of the plasma membrane bilayer and their spatial organization at the cell surface.

It should be noted that while considerable information is now available on the dynamics and metabolism of some membrane proteins, much less is known about the cell surface phospholipids. This is by and large due to the lack of appropriate techniques for studying these processes in intact cells. For example, there are no reagents available which can be used to selectively radiolabel cell surface lipids in a manner analogous to the radiolabeling of cell surface proteins—a technique which has been used so effectively in studying membrane (pro-

tein) turnover. Nor are there immunological probes for any of the major phospholipids, since they are not antigenic. Pulse-chase experiments, in which lipid precursors are fed to cells, suffer from the disadvantage that both lipids in internal pools and cell surface lipids are labeled. Furthermore, the metabolic fate of lipids in such experiments is complicated by the fact that it is difficult to distinguish true *de novo* synthesis from complications arising from base-exchange reactions and acyl transferase activities.

For these reasons and others, we have been developing techniques for the selective insertion of chemically defined, radiolabeled phospholipid molecules and antigenic phospholipid derivatives into the cell surface. Alexander Sandra reports on the use of artificial lipid vesicles (liposomes) as a tool for inserting radioactively labeled phospholipids into the cell surface via an exchange process. This work is particularly significant in that it demonstrates that the exogenous phospholipids are inserted predominantly into the outer leaflet of the plasma membrane bilayer. Thus, in the future this technique will permit us to study the metabolic fate of phospholipids in the outer leaflet of the cell surface membrane, compared to their fate when introduced by vesicle-cell fusion, a process which by definition would result in the addition of exogenous radiolabeled lipids into both leaflets of the plasma membrane bilayer.

In separate studies, Alan Schroit has shown that it is possible to intercalate antigenic phospholipids into the plasma membrane bilayer of cells and has reported on their distribution at the cell surface, using immunochemical methods. We believe that this approach has considerable potential in exploring the dynamics of cell surface phospholipids and providing insight into the possible mechanism(s) of ligand-induced antigen redistribution in eukaryotic cells.

Douglas Struck has examined the use of the radioiodination technique for labeling cell surface lipids and membrane proteins as a potential method of studying their metabolism.

ASYMMETRIC INSERTION OF EXOGENOUS
PHOSPHOLIPIDS IN THE CELL SURFACE
VIA EXCHANGE

A. Sandra

Previous studies from this and other laboratories have demonstrated that artificially generated phospholipid vesicles, or liposomes can interact with living cells in a number of ways. The mechanisms thus far delineated are fusion, endocytosis, stable adsorption, and lipid transfer.

The transfer of lipid molecules between liposomes and cells without cell association of aqueous liposome contents appears to predominate when lipid vesicles whose phospholipids are in a "fluid" phase (i.e., above their gel-liquid crystalline phase transition temperature) are incubated with cells at low temperatures. In the present study, we have examined in detail the mechanisms of this exchange process. Our principal findings are: (1) only lipids from the outer leaflet of the vesicle are transferred to the cell surface, (2) the vesicle lipids which become cell associated are inserted principally into the outer leaflet of the plasma membrane bilayer, and (3) this transfer process is probably a one-for-one process involving exchange of like species of phospholipids between vesicles and cells.

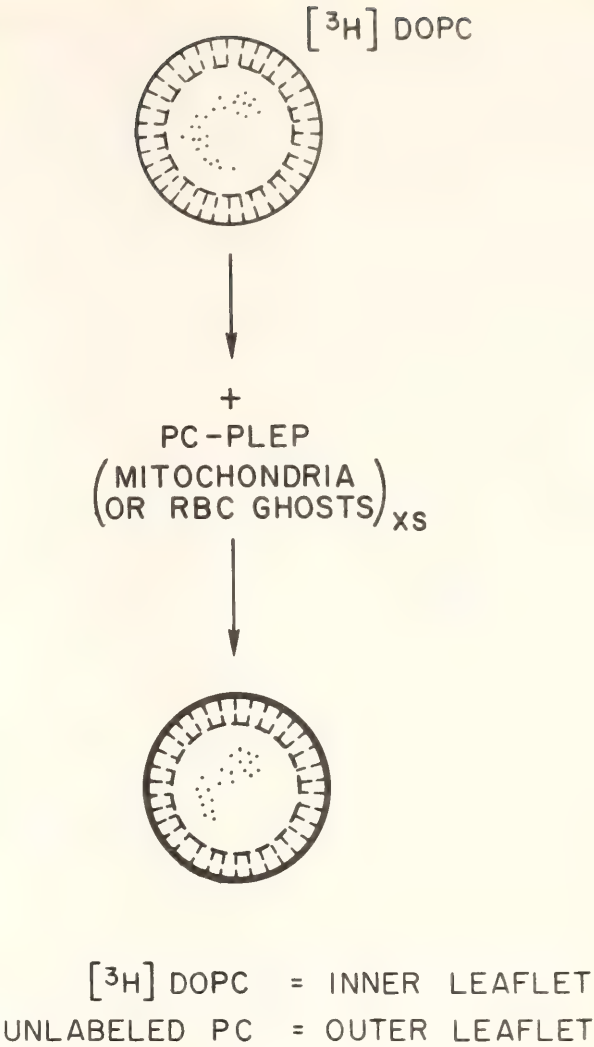


Fig. 23. Strategy for producing isotopically asymmetric vesicles. Unilamellar vesicles generated from [³H] DOPC are incubated at 37°C with phosphatidylcholine-specific phospholipid exchange protein and an excess of unlabeled mitochondria or red blood cell ghosts. The reaction is stopped by separation of donor and acceptor membranes from one another by centrifugation; recovery of asymmetric vesicles is assessed by monitoring a nonexchangeable marker, [¹⁴C] cholesterol oleate, which has been incorporated into the [³H] DOPC vesicles in trace amounts. Complete exchange results in isotopically asymmetric vesicles in which the inner leaflet lipids of the bilayer vesicle are exclusively [³H] DOPC, while the outer leaflet is comprised of unlabeled PC.

In order to further study the lipid transfer mechanism of lipid uptake, isotopically asymmetric phosphatidylcholine vesicles were prepared as depicted schematically in Fig. 23. Unilamellar vesicles prepared from ³H-dioleoyl phos-

phatidylcholine ($[^3\text{H}]$ DOPC) were incubated with an excess of phosphatidylcholine-containing membranes (rat liver mitochondria, human red blood cell ghosts, or multilamellar DOPC vesicles) and phosphatidylcholine-specific phospholipid exchange protein (PLEP). This protein mediates phospholipid exchange between the outer monolayer lipids of the vesicle bilayer and the excess acceptor membranes. In principle, complete exchange results in isotopically asymmetric vesicles in which the inner leaflet lipids of the bilayer vesicle are exclusively $[^3\text{H}]$ DOPC, while the outer leaflet is comprised of unlabeled PC derived from mitochondria, rbc ghosts or multilamellar liposomes.

Isotopically asymmetric vesicles were incubated with Chinese hamster V79 fibroblasts at 2°C , and the cells were subsequently assayed for lipid uptake. We reasoned that for vesicle-cell fusion, adsorption, or endocytosis, lipid uptake would be proportional to the amount of radioactive lipid present in *both* the inner and outer leaflet of the vesicle bilayer; but if an exchange mechanism were operative, lipid uptake by treated cells might only be proportional to the amount of radioactive lipid in the *outer* leaflet of the vesicle bilayer. Indeed, when the uptake of $[^3\text{H}]$ DOPC at 2°C by V79 fibroblasts from isotopically depleted vesicles and the uptake of non-depleted controls were compared, the uptake from depleted vesicles was always substantially less than would be expected on the basis of the percentage of depletion of vesicles. Thus, for example, a 27% reduction in cellular uptake of $[^3\text{H}]$ DOPC was seen when using vesicles depleted by only 12% of their radioactivity. By extrapolation of the data in Fig. 24, we conclude that no cellular uptake would occur at about 60% depletion. The extrapolated value agrees well with the proportion of phospholipid on the outer half of the unilamellar vesicle populations which were used in these

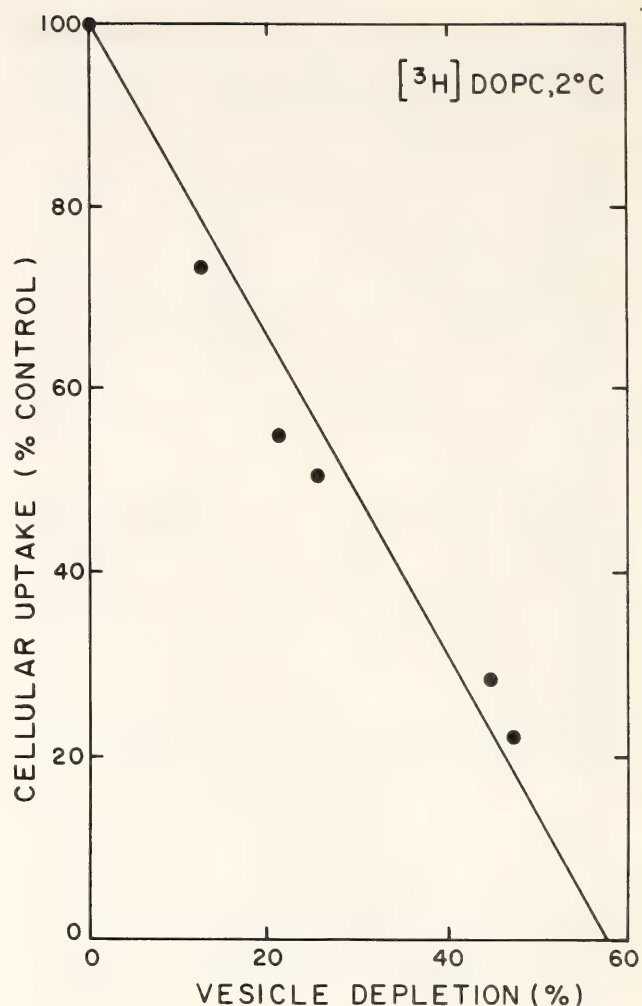


Fig. 24. Cellular uptake of isotopically asymmetric DOPC vesicles. Uptake is plotted against the degree of depletion of the radio-labeled lipid from the vesicles and is normalized to the uptake of uniformly labeled control vesicles.

experiments. This value supports the idea that at 2°C only the outer vesicle monolayer becomes cell-associated with the cell surface, presumably through a lipid exchange or transfer mechanism. Results similar to those shown in Fig. 24 have also been obtained with isotopically asymmetric vesicles generated from ^3H -dioleoyl phosphatidylethanolamine ($[^3\text{H}]$ DOPE) and DOPC. This suggests that the asymmetric exchange is a general process and is not restricted to a particular lipid species.

We have also examined the manner in which the exogenous vesicle phospholipid is inserted into the plasma membrane

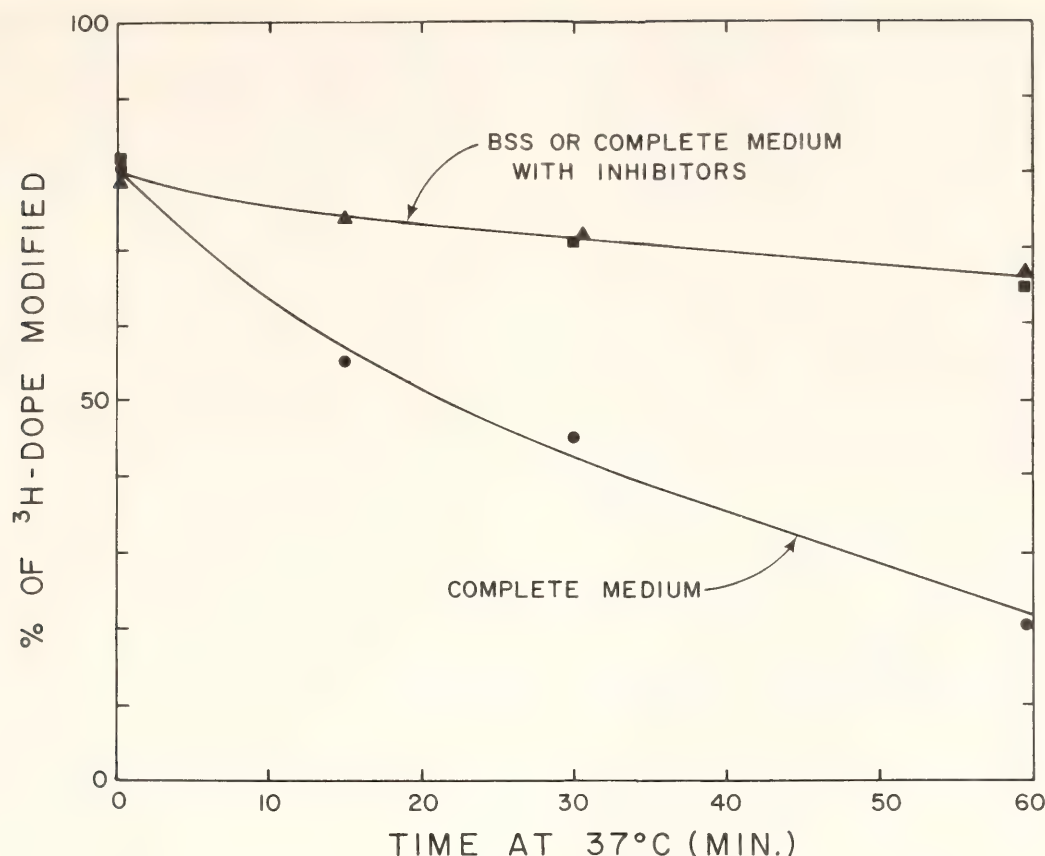


Fig. 25. Asymmetric insertion of exogenous PE into the cell surface. V79 fibroblasts were preincubated with [^3H] DOPE vesicles under exchange conditions, washed, and subsequently incubated at 37°C for varying times in a balanced salt solution. (■—■), complete medium containing 5 mM deoxyglucose plus 50 mM NaN_3 (▲—▲), or complete medium (●—●). At the times indicated, cells were chilled at 2°C , washed, and resuspended in 5 mM TNBS at pH 8.5. The reaction was stopped after 10 min and the cellular lipids extracted and analyzed by TLC. The fraction of [^3H] DOPE which was converted to the Tnp-DOPE derivative provides a measure of the amount of [^3H] PE which is in the outer leaflet of the plasma membrane.

bilayer. Vesicles comprised of DOPC / [^3H] DOPE (4/1) were incubated with cells under "exchange conditions." The washed cells were then incubated with trinitrobenzene sulfonic acid (TNBS) under nonpenetrating conditions in order to determine what fraction of the cell-associated [^3H] DOPE could be derivatized by TNBS (Fig. 25). Immediately after washing the cells free of vesicles, 80–85% of the cell-associated [^3H] DOPE was found to react with TNBS and to be converted to the Tnp-DOPE derivative. This finding demonstrates that the insertion of the exogenous lipid via exchange is predominantly into the outer leaflet of the plasma membrane

bilayer. The proportion of [^3H] DOPE that remains on the exterior leaflet of the plasma membrane decreases with time if the cells are incubated for varying periods at 37°C prior to TNBS labeling (at 2°C). This decrease was about 20%/hr of the cell surface DOPE and was insensitive to metabolic inhibitors (NaN_3 + 2-deoxyglucose), but it could be accelerated by serum. We are uncertain whether the disappearance of [^3H] DOPE from the outer leaflet of the plasma membrane is due to a transbilayer movement of the PE ("flip-flop"), to an endocytotic mechanism (e.g., pinocytosis), or to some other process.

We have determined that the exchange

process between vesicles and cells is a "one-for-one" process in which vesicle and cell lipids are interchanged rather than a net transfer process. Our strategy was as follows. First we determined the amount of cellular PE, x , which is on the external leaflet of the plasma membrane. This was accomplished by growing cells on ^{32}P -orthophosphate (to label the endogenous phospholipids) and subjecting them to derivatization with TNBS. The amount of [^{32}P] PE which was converted to Tnp- ^{32}P PE is x . We then incubated ^{32}P -labeled cells with [^3H] PE containing vesicles under "exchange conditions," and subsequently derivatized the cells with TNBS. If a "one-for-one" exchange process were taking place, we would not expect the *mass* of plasma membrane PE which is converted to Tnp-PE to change, but its *specific ac-*

tivity (^{32}P -cpm/nmol Tnp-PE) should decrease, depending on the extent of exchange. The actual relationship between specific activity of the Tnp-PE and the extent of exchange will be different for a "one-for-one" versus a net transfer exchange process. Experiments were carried out on cells which had been allowed to exchange with vesicles to different extents (Fig. 26). Following the exchange reaction and derivatization of the cells with TNBS, the following were determined: (1) nmol [^3H] PE taken up by the cells, (2) ^{32}P -cpm in Tnp-PE, and (3) nmol Tnp-PE (spectrophotometrically determined). The data in Fig. 26 are seen to be consistent with a "one-for-one" exchange mechanism.

In conclusion, it should be noted that the vesicle-cell lipid exchange phenomenon is highly sensitive to and inhibited

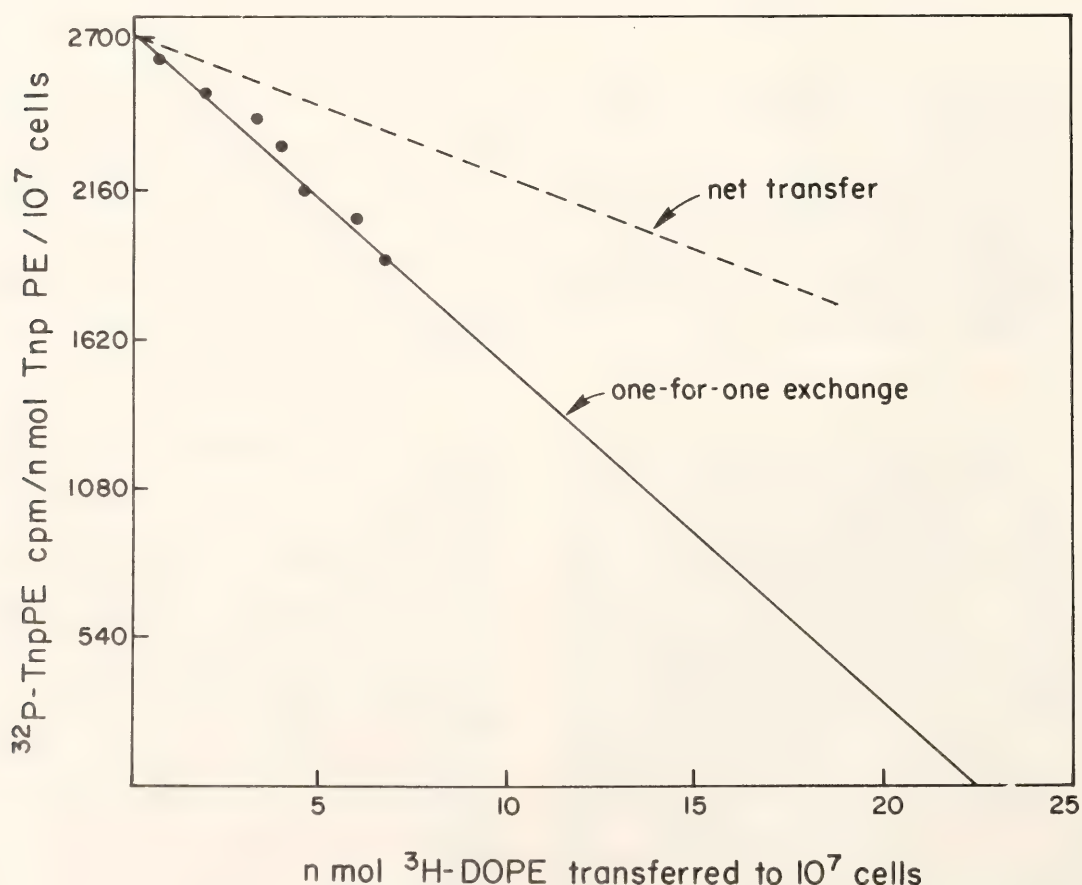


Fig. 26. Test for the mechanism of vesicle-cell lipid exchange. The specific activity of Tnp-PE on the surface of ^{32}P -labeled V79 cells was determined as a function of the degree of incorporation of [^3H] DOPE via exchange. Theoretical curves indicate the expected results for a "one-for-one" vs. a net transfer exchange process (see text).

by brief proteolytic treatments of intact cells. This leads us to speculate that certain cell surface protein moieties may be involved in this phenomenon. Such a possibility is currently under investigation.

IMMUNOBIOLOGICAL AND
IMMUNOCHEMICAL STUDIES OF
ANTIGENIC PHOSPHOLIPIDS IN
MAMMALIAN CELLS

A. Schroit and R. Pagano

The possibility of introducing lipid antigens into the plasma membrane of mammalian cells may provide a means for studying heretofore unexplored biological phenomena. For example, the organization and dynamics of cell surface lipids could be probed using immunological techniques. Moreover, since such phospholipids cannot span the bilayer and are thus presumably free from cytoskeleton-imposed restraints, additional insight into the mechanism(s) of ligand-induced antigen redistribution in eukaryotic cells might also be obtained.

To study these questions, we have explored the possibility of integrating haptenated phospholipids into the plasma

membrane of fibroblasts via transfer from small unilamellar vesicles (liposomes). In this report, we demonstrate that the synthetic phospholipid antigen N-2,4,6 trinitrobenzyl phosphatidylethanolamine (Tnp-PE) can be incorporated into the cell surface. This antigen is able to diffuse freely in the plane of the membrane, consistent with its integration into the plasma membrane bilayer. Moreover, the haptenated lipid undergoes antibody-mediated redistribution in the presence of divalent anti-hapten antibodies.

*Reaction of Antibody with
Trinitrophenylated
Phosphatidylethanolamine-Containing
Vesicles (Tnp-Vesicles)*

The ability of rabbit antibodies prepared against trinitrophenylated bovine serum albumin (anti-Tnp) to react with Tnp-vesicles could be demonstrated by immunodiffusion analysis (Fig. 27). It can be seen that anti-Tnp precipitated the Tnp-vesicles; however, no precipitin lines were detected with nonderivatized vesicles or with the monovalent water-soluble hapten N-2,4,6 trinitrobenzyl-

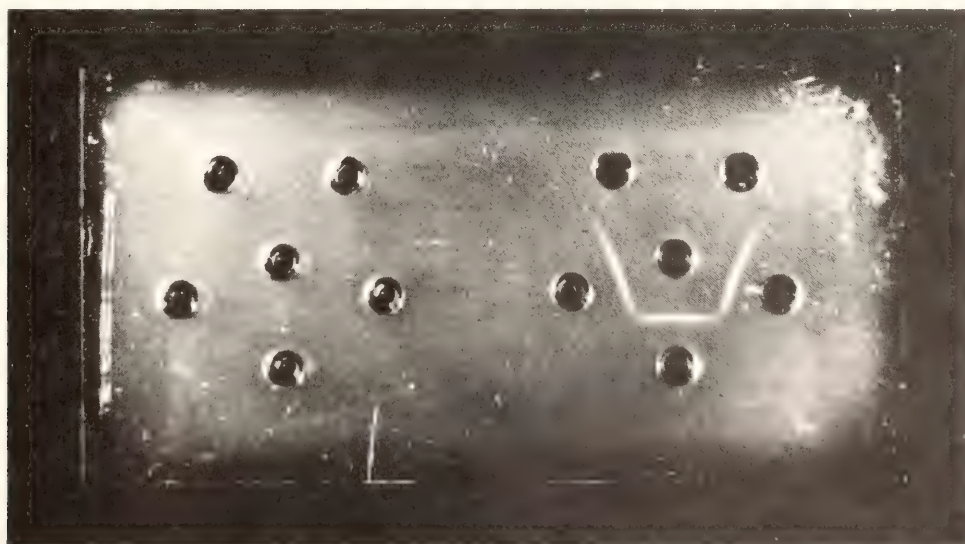


Fig. 27. Immunodiffusion analysis of Tnp-vesicles in 0.75% agar. Peripheral wells: three upper, Tnp-DOPE vesicles (1 mg lipid/ml); lower left, nonderivatized vesicles (1 mg lipid/ml); lower right, Tnp-ethanolamine (0.5 mg/ml). Center wells: left side, 1:10 dilution of anti-Tnp serum; right side, 1:10 dilution of normal rabbit serum.

ethanolamine (Tnp-ethanolamine). Moreover, the precipitin reaction could be completely inhibited by incorporating Tnp ethanolamine into the agar gel (not shown). No precipitation could be seen using pre-immune normal rabbit serum (Fig. 27, right side).

Interaction of Tnp-Vesicles with Cells

We have previously demonstrated (*Year Book 76*) that the mode of interaction of small unilamellar vesicles with mammalian cells in vitro is critically dependent upon the lipid composition of these structures. In particular, it has been noted that phosphatidylcholine vesicles below their gel-liquid crystalline phase transition temperature (T_c) become associated with cells via a stable vesicle-to-cell adsorption rather than by an apparent vesicle-cell fusion mechanism. In order to maximize the possibility that the haptenated phosphatidylethanolamine would be inserted into the plasma membrane bilayer, the present study employed vesicles composed of unsaturated Tnp-dioleoylphosphatidylethanolamine (Tnp-DOPE), dioleoylphosphatidylethanolamine (DOPE) and dioleoylphosphatidylcholine (DOPC) molecules, designated as Tnp-DOPE vesicles. The way in which Tnp-DOPE vesicles interact with cells was determined by incu-

bating V79 fibroblasts with the vesicle suspension for 1 hour at 37°C in the presence or absence of metabolic inhibitors. The results presented in Table 6 demonstrate that significant amounts of all the vesicle components became cell-associated after a 1-hour incubation at 37°C. It is interesting to note that the ratio $\mu\text{gm (DOPE + Tnp-DOPE)}/\mu\text{gm DOPC}$ in the treated cells was nearly identical to the ratio in the applied vesicle suspension. Furthermore, lipid uptake by cells was not substantially inhibited by combined inhibitors of glycolysis and respiration (5 mM NaN_3 + 50 mM deoxyglucose). These results suggest that the Tnp-DOPE vesicles are being taken up as intact structures. This finding is consistent with vesicle-cell fusion, adsorption, endocytosis, or some combination of these processes. However, it would appear that endocytosis can be ruled out as a significant pathway of vesicle uptake in this system, since the presence of metabolic inhibitors during the incubation period reduced uptake by only about 15%.

Several control experiments were carried out in order to rule out the possibility that Tnp-DOPE vesicles were taken up by a stable vesicle-to-cell adsorption. Scanning electron micrographs of V79 cells treated with Tnp-DOPE vesicles failed to reveal any vesi-

TABLE 6. Uptake of Haptenated Phospholipid by V79 Fibroblasts in Suspension

	Uptake ($\mu\text{g}/10^7$ cells)*		
	(Tnp-DOPE + DOPE)	DOPC	(DOPC)
			(Tnp-DOPE + DOPE)
Control	4.5	22.1	0.20
With metabolic inhibitors†	3.4	19.0	0.18

* 10^7 Cells were incubated with 1 mg Tnp-DOPE vesicles composed of 20 mol% ^3H (Tnp-DOPE + DOPE) and 80 mol% ^{14}C -DOPC for 1 hr at 37°C, washed, and assayed for radioactivity. Variation was within $\pm 5\%$.

† Cells were preincubated with 5 mM NaN_3 and 50 mM 2-deoxyglucose for 30 min at 37°C before incubation with vesicles. The metabolic inhibitors were also present during vesicle-cell incubations.

cles or vesicle-like structures adsorbed to the cell surface, although adherent vesicles should be readily visible by this technique (*Year Book* 76). Furthermore, transmission electron micrographs of V79 cells incubated with these vesicles and stained with rabbit anti-Tnp followed by ferritin-conjugated anti-rabbit IgG demonstrated the absence of vesicular structures at the cell surface, which contained large amounts of bound ferritin. In agreement with the lack of ultrastructural evidence for vesicle-cell adsorption, cells incubated with Tnp-DOPE vesicles containing 20 mM CF exhibited a uniform distribution of dye throughout the cell volume (Fig. 28a). In contrast, vesicles composed of the saturated lipids (dipalmitoyl phosphatidylethanolamine, [DPPE]; + Tnp-DPPE + dipalmitoyl phosphatidylcholine, [DPPC]; designated Tnp-DPPE vesicles) preferentially adhered to the cell surface as exhibited by the accumulation of fluorescence at the cell periphery (Fig. 28b). These findings are consistent with our previous observation that vesicles composed of saturated or unsaturated phospholipids preferentially adsorb or fuse with cells, respectively.

Lateral diffusion of Tnp-PE in the plasma membrane. In order to demonstrate that the Tnp-DOPE which becomes cell associated during vesicle-cell incubations is truly intercalated in the plasma membrane, as opposed to possibly surface, we examined the rate of Tnp-PE existing as an adherent antigen at the cell randomization in polykaryons formed between vesicle-treated and latex-labeled cells. Following virus-induced cell-cell fusion, the cells were incubated at 37°C for 0, 5 or 15 minutes, chilled, and subsequently stained at 0°C with appropriate immunofluorescent reagents (Fig. 29). At zero time, the distribution of the antigen on the surface of polykaryons formed from Tnp-DOPE vesicle-treated and bead-labeled cells, was frequently uniform (Fig. 29a), although sometimes a

slight gradient was seen (Fig. 29b). In cells exhibiting a gradient of fluorescence, the marker beads were always distal to the brightest half of the multinucleated cells, consistent with the gradual randomization of antigen in the plasma membrane. At 15 minutes, the distribution of antigen in the polykaryon cell surface was uniform as demonstrated by the uniform ring of fluorescence or random distribution of fluorescent spots over the cell surface, depending on the plane of focus (Fig. 29c,d).

Similar experiments employing Tnp-DPPE vesicles were also carried out. However, in contrast to the rapid randomization of antigen shown in Fig. 29, polykaryons formed between Tnp-DPPE vesicle-treated cells and bead-labeled cells demonstrated no redistribution of antigen over the time course of the experiment. The photomicrographs shown in Fig. 30 demonstrate that the Tnp-DPPE remained confined to one end of cell surface. This might be due to its randomization with intracellular membranes and/or shedding into the external bathing medium. Azide (5 mM), deoxythe heterokaryon, distal to the intravesicle-treated) cells were not fluorescent, whereas mononucleated Tnp-DPPE vesicle-treated (non-bead labeled cells) exhibited an intense ring-like fluorescence. These internal controls demonstrate the inability of cell-associated antigen to be passively transferred between nonfused cells.

The distribution of Tnp-DOPE at the cell surface. The distribution of the exogenously supplied Tnp-DOPE in the plasma membrane of vesicle-treated cells was determined by treating the cells with Tnp antibodies and staining with tetramethylrhodamine-labeled anti-IgG (TMR anti-IgG). It should be emphasized that the antibody treatments were carried out at 0°C to prevent redistribution of the haptenated lipid in the cell surface (see below). Washed Tnp-DOPE vesicle-treated cells were warmed to

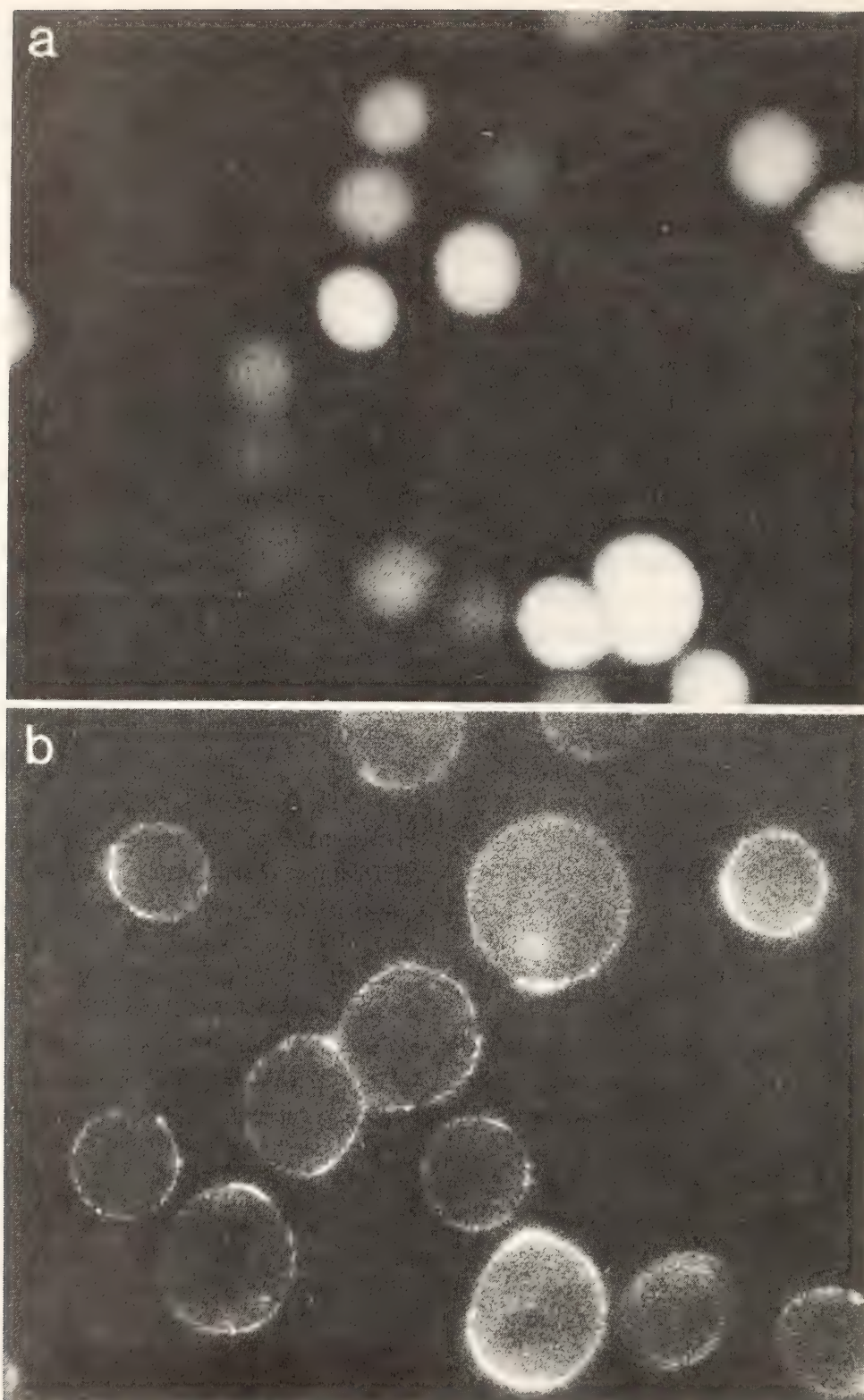


Fig. 28. Fluorescence micrographs of V79 cells treated for 1 hour with CF-containing vesicles. Incubations were with (a) Tnp-DOPE vesicles at 37°C, and (b) Tnp-DPPE vesicles at 2°C.

37°C for 0 or 1 hour prior to treatment with antibodies. The distribution of the cell surface antigen was determined by fluorescence microscopy and revealed a uniform ring fluorescence at each time point (Fig. 31a). This finding suggests

that the haptenated lipid is randomly distributed in the cell surface immediately following vesicle treatments and remains so for up to 1 hour. It should be noted that a slight decrease in the intensity of fluorescence occurred with

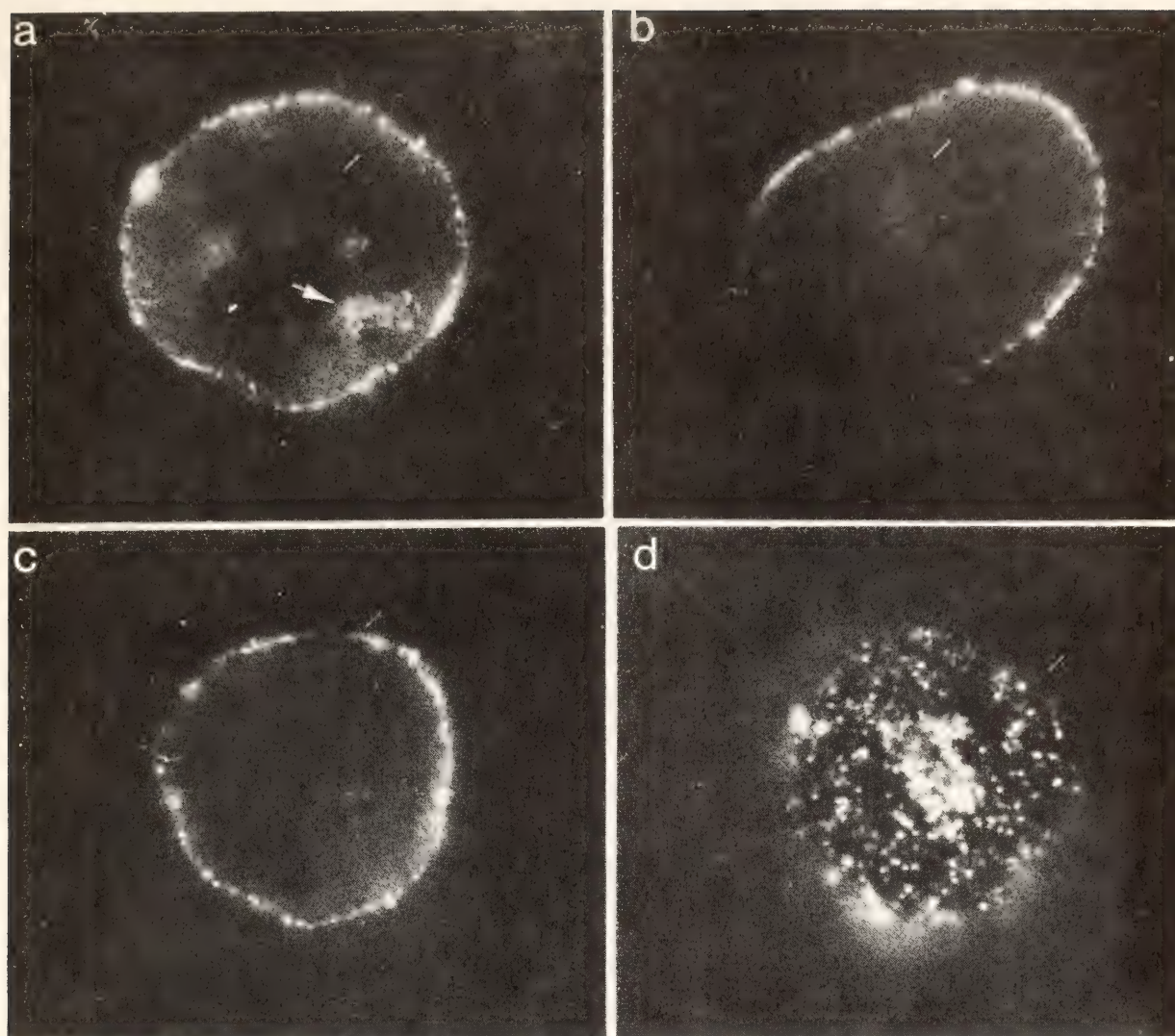


Fig. 29. Fluorescence photomicrographs of polykaryons formed between Tnp-DOPE vesicle-treated and latex-labeled cells. Fused cells were incubated for (a, b) 0 min or (c, d) 5 min at 37°C. The cells were then stained with anti-Tnp and TMR anti-IgG at 0°C. Intracellular light scattering in (a) is due to the presence of ingested latex beads. Photomicrographs (c) and (d) are of the same cell recorded at different focal planes.

time, suggesting that the antigenic lipid was gradually being depleted from the cellular area containing latex beads. As can also be seen in the companion Nomarski and fluorescence micrographs, mononucleated, latex-bearing (but not glucose (50 mM), colchicine (10^{-4} M), and cytochalasin B (15 μ gm/ml) had no apparent effect on the native distribution of the antigen or on the fluorescence intensity at various time intervals.

Antibody-induced reorganization of Tnp-DOPE at the cell surface. Anti-hapten antibodies were observed to reorganize the antigenic lipids at the cell surface upon warming. Washed Tnp-

DOPE vesicle-treated cells were treated with anti-Tnp (at 0°C), washed, warmed to 37°C for 1, 5, 10 or 30 minutes, and stained with TMR anti-IgG at 0°C. At one minute, the uniform ring fluorescence shown in Fig. 31a was observed to break up into an incomplete and spotty fluorescent rim, encircling the cells (Fig. 31b). Further incubation of the cells for 5–10 minutes resulted in many large, patchy aggregates of fluorescence, leaving much of the cell periphery unstained (Fig. 31c,d). Prolonged incubation (30 min) of the cells at 37°C resulted in coalescence of the patches into large, fluorescent clusters which sometimes gave the ap-

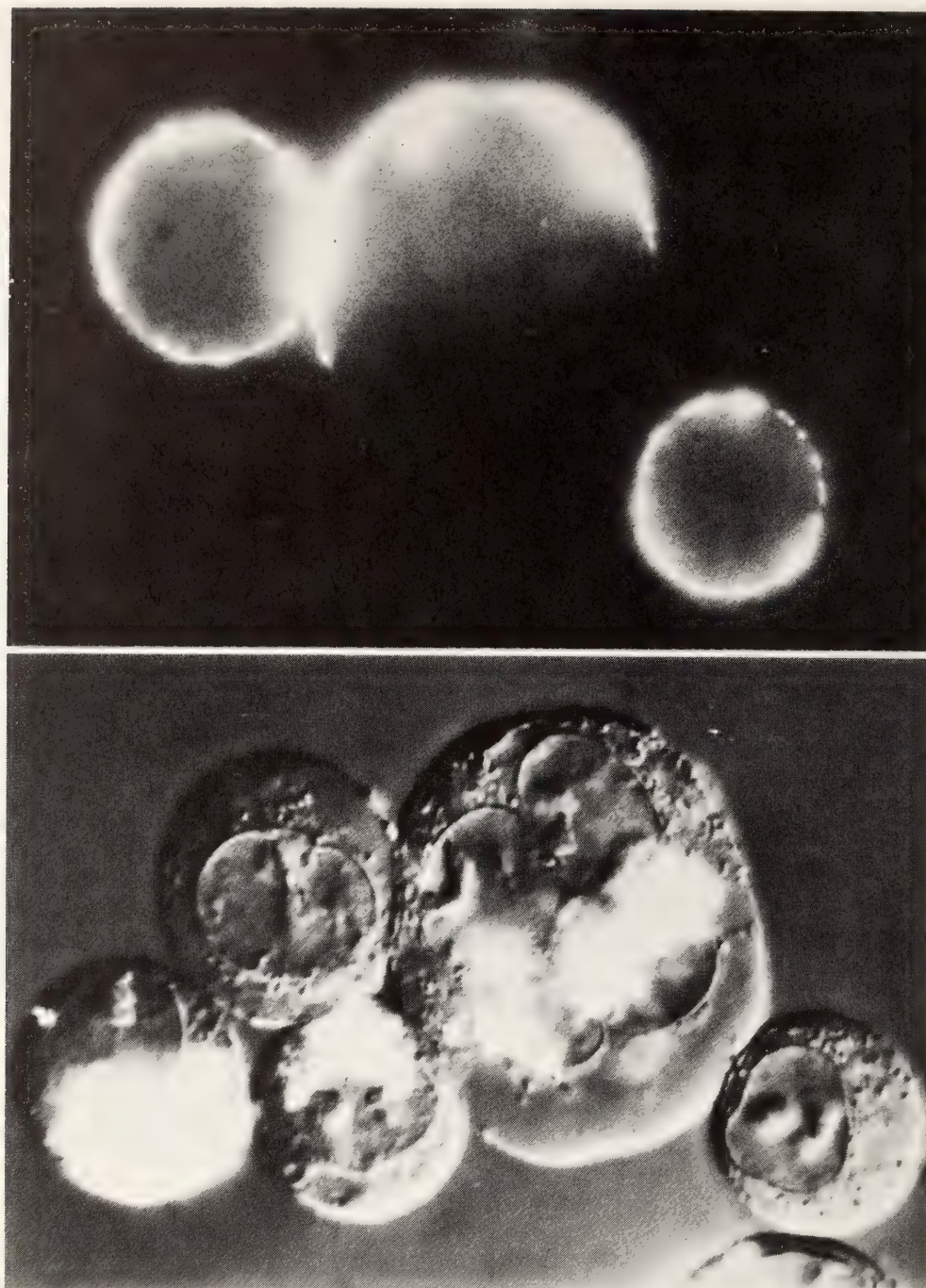


Fig. 30. Fluorescence and Nomarski photomicrographs of polykaryons formed between Tnp-DPPE vesicle-treated and latex-labeled cells. Fused cells were incubated for 15 min at 37°C and stained as described in Fig. 25. Note the absence of fluorescence in nonfused latex-bearing cells. The highly refractile areas in the Nomarski micrographs are due to light scattering from heavily latex-labeled cells.

pearance of a cap-like structure (Fig. 31e). Consistent with other observations of patching of membrane antigens, the redistribution of Tnp-DOPE was not affected by sodium azide (5 mM), deoxyglucose (50 mM), colchicine (10^{-4} M), or cytochalasin B (15 μ g/ml). It should be noted that patched cells could

be restained with anti-Tnp, resulting in fluorescent cells bearing a ring superimposed on the large fluorescent patches (Fig. 31f). Moreover, when patched cells were saturated with nonfluorescent goat anti-rabbit IgG and subsequently stained with anti-Tnp and TMR anti-IgG, only a fluorescent ring was seen.

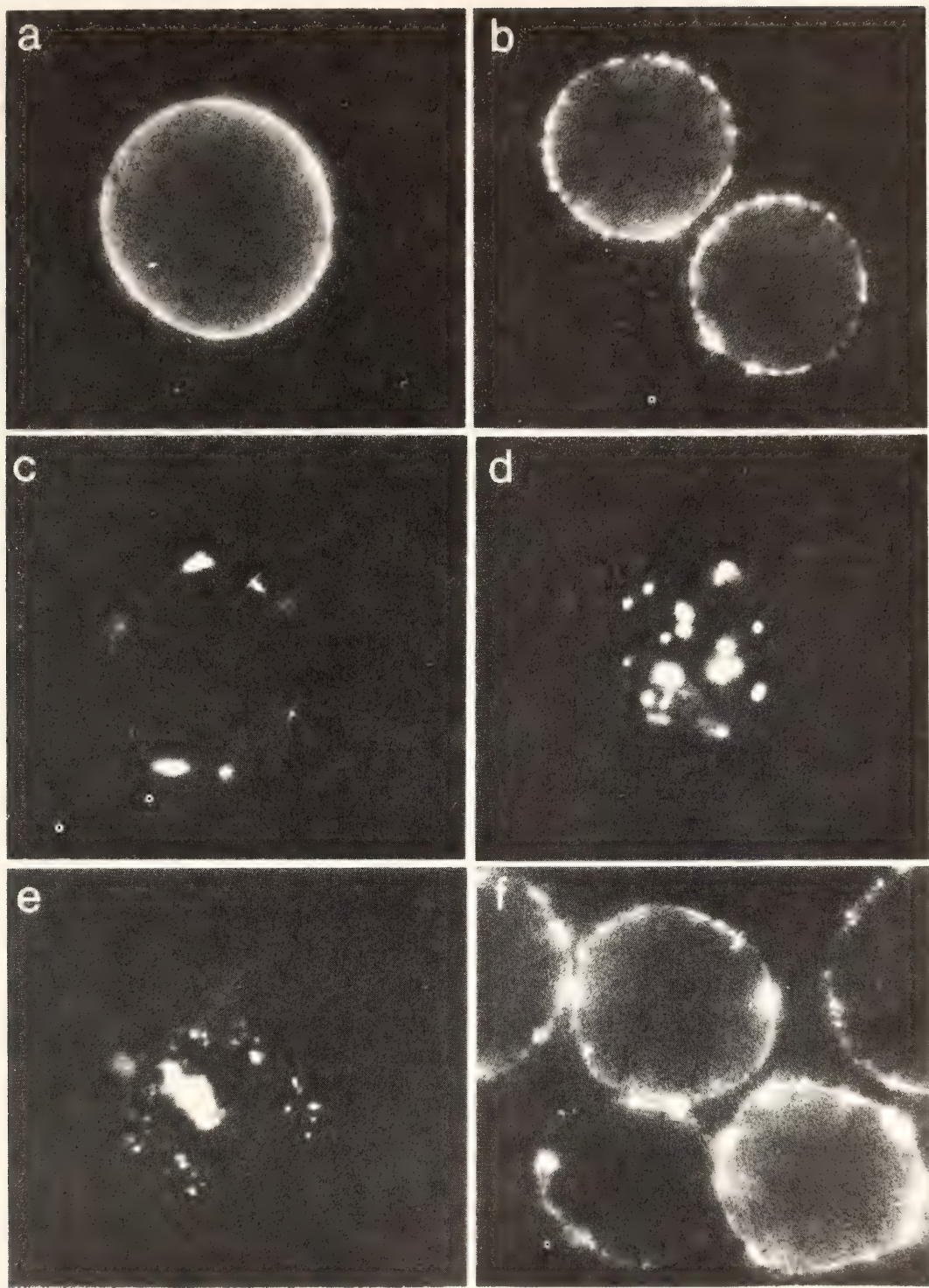


Fig. 31. Antibody-induced redistribution of Tnp-DOPE. Vesicle-treated cells were treated with anti-Tnp for 20 min at 0°C. The cells were then washed, incubated at 37°C for (a), 0, (b) 1, (c, d) 10, or (e) 30 min, and then stained with TMR anti-IgG at 0°C. In (f), patched cells were restained with anti-Tnp and TMR anti-IgG at 0°C. Note both the appearance of patches and ring fluorescence.

These experiments suggest that Tnp-DOPE molecules previously inaccessible to antibody become antibody-accessible after patching.

Studies similar to those described above were also carried out using mono-

valent anti-Tnp Fab fragments in place of divalent anti-Tnp. No patching was observed. However, when cells treated with anti-Tnp Fab and TMR anti-IgG were warmed to 37°C, patching similar to that seen in Fig. 31 was observed.

This demonstrates that patching of the haptenated lipid requires cross-linking by divalent antibodies.

It is difficult to see how a divalent antibody molecule could induce patching by direct cross-linking of the monovalent Tnp-DOPE into an antibody-antigen network.

Experiments are in progress to test the two most likely explanations for this phenomenon. The first is that the integrated phospholipids exist as molecular clusters in the membrane following vesicle-cell fusion and thus act as a multivalent hapten. The second, and more intriguing possibility is that the binding of the antibodies to the haptenated lipids induces a phase separation of the antigenic lipids in the membrane, resulting in a multivalent haptenated entity with the plasma membrane bilayer. The reason for such an antibody-induced phase separation is not obvious, but it might occur as a result of the lateral mobility of the antigen being changed upon antibody binding.

RADIOIODINATION OF CELL SURFACE LIPIDS

D. Struck

The method of enzymatic iodination, using lactoperoxidase-glucose oxidase has permitted a variety of investigations concerning the identification, turnover, and metabolism of the major protein constituents of the plasma membrane of cultured cells. Although a similar technique to specifically label plasma membrane phospholipids has not been described, it has been reported that enzymatic iodination of intact cells also results in significant incorporation of iodine into chloroform-extractable material, presumably lipids. Consequently, we began studies to determine the suitability of this technique for the labeling of plasma membrane phospholipids.

Initial experiments demonstrated that lactoperoxidase-catalyzed iodination of

cultured mouse LM fibroblasts results in the labeling of organic solvent-extractable compounds. Analysis of these products by two-dimensional thin layer chromatography indicated they might include cellular neutral lipids, glycolipids, and phospholipids (Fig. 32). Because of the complexity of this labeling pattern, it was decided that lipid vesicles of known composition would provide a model system for the characterization of the various iodinated species observed with intact cells.

Using dioleoylphosphatidylcholine vesicles, three major ^{125}I -labeled products (corresponding to B, D, and E, Fig. 32) were formed with the complete iodination mixture (^{125}I , lactoperoxidase, glucose oxidase, glucose). The appearance of chloroform-soluble radioactivity was absolutely dependent on the presence of lactoperoxidase, but no such dependence on glucose oxidase or glucose could be demonstrated. When lipid vesicles were omitted, only the major product having a chromatographic mobility similar to that of phosphatidylcholine was eliminated. From this, we concluded that only a portion of the chloroform-soluble radioactivity represents iodinated phospholipid molecules and that lipid iodination, in contrast to protein iodination, proceeds at a maximal rate either in the absence of peroxide or in the presence of low levels of peroxide endogenous to the reaction mixture.

To support our preliminary conclusion that phosphatidylcholine had been iodinated, the radiolabeled species migrating as phosphatidylcholine was purified and subjected to chemical and enzymatic hydrolysis. Mild base hydrolysis in methanolic NaOH gave one major product (85% of the ^{125}I cpm) which had chromatographic properties similar to authentic fatty acid methyl esters. The remainder of the radioactivity was found in free ^{125}I . Hydrolysis of the starting material with phospholipases A, C, and D resulted in major products that were

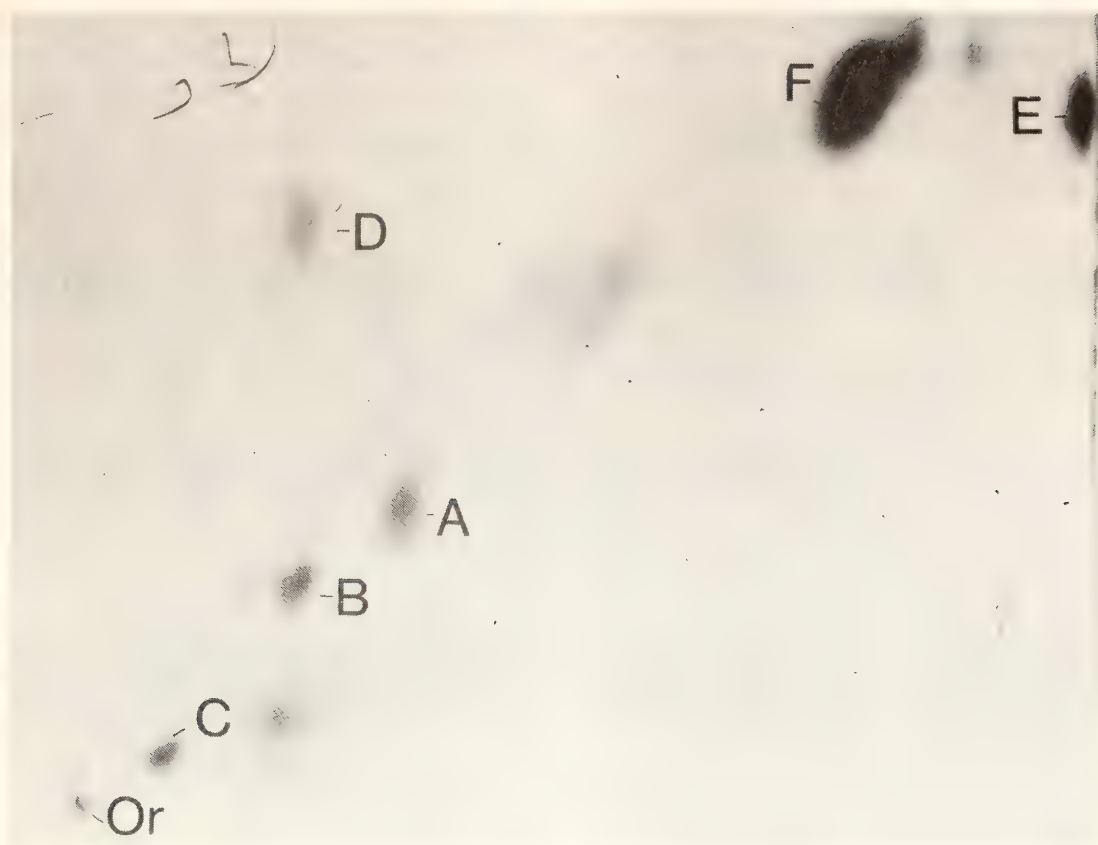


Fig. 32. Autoradiographic analysis of iodinated lipids from cultured mouse LM fibroblasts. Lipids were separated by two-dimensional thin-layer chromatography. *Or*, origin; *A*, phosphatidylethanolamine; *B*, phosphatidylcholine; *C*, sphingomyelin; *D*, free ^{125}I ; *E*, unidentified nonpolar product formed in the absence of cells or lipid (see text); *F*, unidentified nonpolar product.

chromatographically similar to free fatty acid, 1,2-diglyceride, and phosphatidic acid, respectively. In other experiments, it was found that the starting material eluted with authentic dioleoylphosphatidylcholine from DEAE-cellulose and silicic acid and that this radiolabeled species could be quantitatively precipitated with cold acetone in the presence of magnesium. From these results, we conclude that phosphatidylcholine can serve as a substrate for lactoperoxidase-catalyzed iodination and that the majority of the iodine is incorporated into the fatty acyl chains of this phospholipid. Interestingly, using dipalmitoylphosphatidylcholine as the substrate for iodination, qualitatively similar results were obtained, indicating that unsaturation is not required for iodine addition to fatty acids. Similar experiments using other types of phospholipids provided no

evidence for the stable incorporation of iodine into polar head groups of these molecules. Thus enzymatic iodination can be used to label only the acyl chains of membrane phospholipids.

Although the nature of the other chloroform-soluble products formed during iodination of cells or vesicles was not systematically investigated, it is clear that their formation is not dependent upon the presence of added lipid. Furthermore, these products rapidly decompose to free ^{125}I in mildly alkaline solutions during chromatography in basic solvent systems and during storage at -20°C . This complication, when combined with our inability to iodinate the polar portion of phospholipids, precludes the use of enzymatic iodination as a method to study the turnover and metabolism of plasma membrane phospholipids. However, these investigations in-

dicating that caution should be exercised whenever lactoperoxidase-catalyzed iodination is used as a means to label plasma membrane proteins, since the iodinated

lipids and their by-products can give rise to trichloroacetic acid-insoluble ^{125}I and potentially to ^{125}I -containing bands on SDS-polyacrylamide gels.

ANALYSIS OF NEMATODE FERTILIZATION-DEFECTIVE MUTANTS

Samuel Ward and Yair Argon

The development of most differentiated cells includes the attainment of specialized morphology. Many gene products must participate in this morphological differentiation. Some of these will act at the surface membrane of a cell both to control the extension of growth processes and to localize functional molecules such as transport systems, intercellular junctions, and sites of adhesion to other cells. Others will determine the intracellular cytoarchitecture. To understand how these gene products generate cell morphology, one must determine which gene products they are and how they become localized to specific parts of the cell.

We have chosen to approach these problems genetically by studying an organism that allows isolation of a large number of mutants altering the morphology of one type of cell. By analysis of both the morphology and the biochemistry of mutant cells, we hope to discover the biochemical basis for the morphological alterations. It should then be possible to specify the function of the normal gene product in determining the cell's morphology.

The organism we have chosen to study is the soil nematode *Caenorhabditis elegans*. This worm is easily grown in the laboratory on petri plates seeded with bacteria, and its generation time is only $3\frac{1}{2}$ days at 20°C . It is normally a self-fertilizing hermaphrodite, but males can be maintained for genetic crosses. S. Brenner has shown that many kinds of mutants can be isolated and characterized genetically.

The nematode cell we have chosen to study is the sperm. Sperm were chosen because nematode sperm are amoeboid cells with specialized surface structure and specialized morphology and because mutants altering the morphology can be recognized by their sterile phenotype. The hermaphroditic mode of reproduction ensures that most sterile mutations will affect the gametes directly. We have found that the sperm rather than the oocytes is most often defective. Mutants identified as sperm-defective in hermaphrodites have all been sterile as males also. Because males make sperm in large numbers, they provide a source of mutant sperm for isolation and biochemical characterization. One sterile mutation was found with another male phenotype, and this mutant is described in the following report.

Isolation and Initial Mutant Characterization

We have isolated and characterized 13 temperature-sensitive sterile mutants that are fertilization-defective (*fer*). These were isolated by accident (HC1) (Ward and Miwa, 1978), or by screening general temperature-sensitive strains for the sterile phenotype (HC13, HC23, HC24, HC34), or by selecting from the F1 heterozygotes of mutagenized parents those mutants that segregated F2 hermaphrodites that laid unfertilized oocytes. From 1174 F1's screened, nine *ts* mutants were obtained and five were characterized (HC2-HC6).

TABLE 7. Phenotypes of *fer* Mutant Strains

Gene	Strain	16°C		25°C		Sperm
		Progeny	Oocytes	Progeny	Oocytes	
W.t.	N2	285	45	250	24	260
<i>fer-1</i>	HC1	302	17	<1	205	211
	HC13	170	7	<1	170	>200
	HC24	280	50	15	282	290
	HC2	200	...	7	124	252
<i>fer-2</i>	HC3	180	48	2	164	267
<i>fer-3</i>	HC4	164	100	8	180	295
<i>fer-4</i>	HC23	238	64	5	99	~200
<i>fer-5</i>	HC34	108	10	13	90	171
<i>fer-7</i>	HC6	>200	...	2	160	235
?						

The phenotypes of the *fer* mutants we have analyzed in detail are summarized in Table 7. These mutants all accumulate sperm in normal numbers, but the sperm are incapable of fertilizing oocytes. Virtually all the oocytes in mutant hermaphrodites can be fertilized by wild-type male sperm, showing that the sterile phenotypes must be due to defective sperm. Most of the mutants are "leaky" at the restrictive temperature of 25°C (e.g., HC34), and some of the mutants are not fully fertile at the permissive temperature of 16°C (e.g., HC4). At 20°C some are normal and some are sterile (data not shown).

By complementation tests we have assigned the ten mutants listed in Table 7 to eight different fertilization-defective (*fer*) genes. Most of the *fer* genes have been precisely mapped relative to standard morphological markers. All the mutations behave as single loci and are scattered among the autosomes, revealing no unusual linkage relations.

The time of development during which the worms are temperature-sensitive for fertility (TSP) was determined by temperature-shift experiments. All TSP's overlap the time of sperm development in *C. elegans*. Some extend throughout the entire period and others terminate prior to spermiogenesis. Although we have no direct evidence, we presume that

the TSP reflects the time of synthesis or the time of utilization of a gene product that is made temperature-sensitive by a mutation.

All the *fer* mutations obtained so far are recessive: heterozygotes with wild-type are fertile at 25°C. These heterozygotes, however, produce two classes of sperm, one bearing the mutant allele and one bearing the wild-type allele. We have asked whether both types of sperm are equally fertile by measuring the number of zygotes fertilized by each class of sperm after mating by heterozygous males. Table 8 summarizes the results. Two mutations, *fer-7(hc34)* and *fer-4(hc4)*, have reduced fertility of the mutant-bearing sperm. This suggests that there must be expression of the mutated genes late in meiosis because in a heterozygote, both mutant and wild-type sperm have the same heterozygous genotype until after the reductive division of meiosis I. This was further confirmed for HC4/+ by observing two classes of sperm with the SEM. The altered transmission ratio in these two mutants also proves that the mutant phenotype is autonomous to the sperm. That is, the mutant gene product must be made in the sperm itself because the sperm are the only cells to become hemizygous in a heterozygote.

TABLE 8. Transmission Ratio of Mutant Sperm in Heterozygous Males

Male Genotype	Temp. (°C)	Progeny Scored	fer ⁻	P
			fer ⁻ + fer ⁺	
hc1/+	25°	102	0.5 ± .1	0.9
hc3/+	25°	683	0.48 ± .04	0.2
hc34/+	25°	501	0.41 ± .04	<0.001
hc34/+	16°	378	0.51 ± .05	0.9
hc4/+	25°	583	0.34 ± .03	<0.001
hc4/+	16°	440	0.39 ± .04	<0.001

Wild-type and Mutant Fertilization

In order to better understand the fertilization defects in mutant sperm, we have continued studies of normal fertilization. The transparency of the hermaphrodite allows observation of fertilization in live specimens, and the addition of a video camera and a time-lapse video tape recorder to our microscope has allowed a more detailed analysis of the process of fertilization.

In the hermaphrodite, sperm accumulate in the central cavity of the spermatheca and anchor to the surrounding

walls of the spermatheca by their extended pseudopods, as shown in Fig. 33. As an oocyte is pushed into the spermatheca, it is fertilized by the sperm anchored there. Only one sperm fertilizes each oocyte. After fertilization, the oocyte slides into the uterus through the spermathecal valve, which opens to let it pass. Supernumerary sperm carried into the uterus move back through the valve to regain the positions in the walls of the spermatheca.

Previously we showed that male sperm preferentially fertilize the oocytes when mated to hermaphrodites. To understand

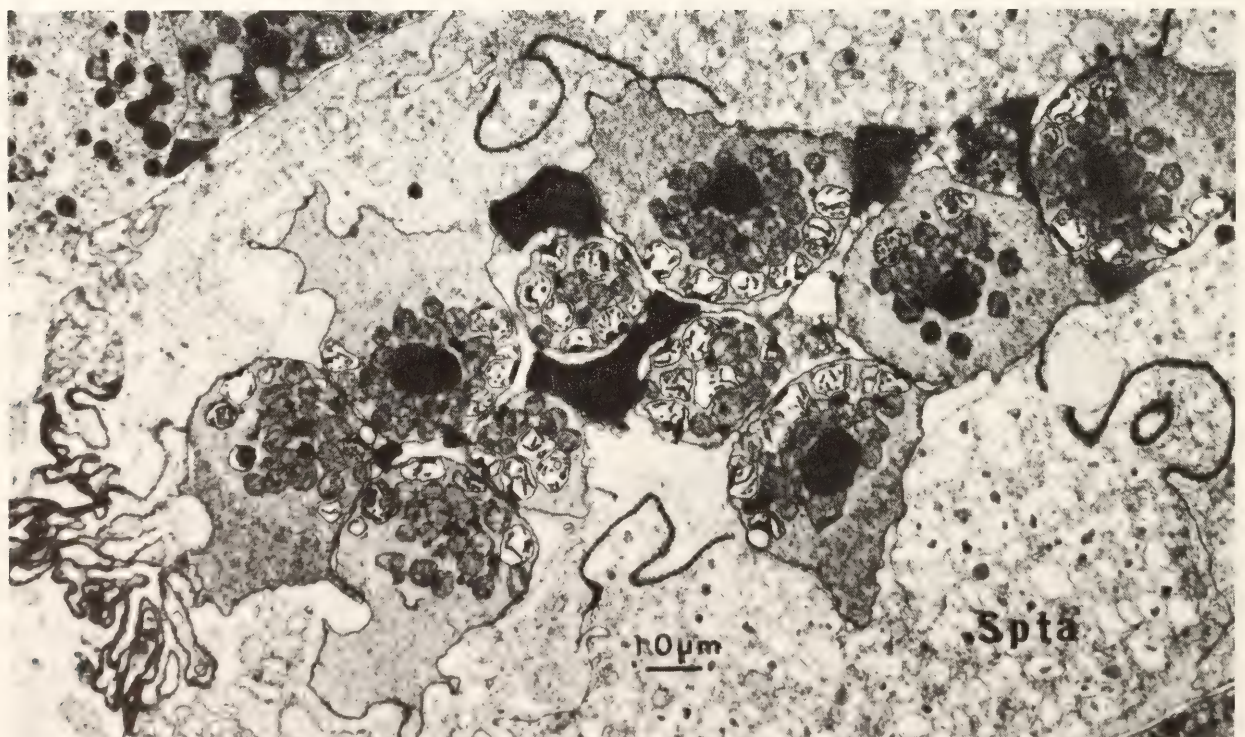


Fig. 33. Wild-type sperm in the spermatheca (Spta).

the basis for this, we identified a fluorescent vital dye that could be used to stain male sperm without altering their fertility. Using dye-labeled males, it was found that the male sperm move up the uterus among the zygotes and do not associate preferentially with the wall of the uterus. They arrive at the spermatheca and appear to anchor themselves to its walls, displacing hermaphrodite sperm to the central cavity. The vital dye, Nile Blue A, is lipid soluble, and it was found that shortly after arrival in the spermatheca, all the dye is transferred from the sperm to the walls of the spermatheca. This makes it impossible to follow the male sperm directly to a fertilization but is consistent with male sperm displacing hermaphrodite sperm by anchoring to the spermatheca.

In the mutant hermaphrodites raised at restrictive temperature, sperm accumulate in the spermatheca normally. They contact oocytes as they pass through the spermatheca, but fertilization fails to take place. The sperm are swept into the uterus by the oocyte and fail to return to the spermatheca. They are eventually expelled as the oocytes are laid. The time required to sweep all the sperm from the spermatheca varies for the different mutants.

Wild-Type Sperm Morphology

C. elegans sperm resemble those found in other nematodes. The sperm are amoeboid cells, devoid of flagella. Figure 33 shows mature *C. elegans* sperm in the spermatheca. They have a pseudopod with a granular cytoplasm which appears to anchor the sperm in the walls of the spermatheca. The cell organelles include an electron opaque nucleus without a nuclear membrane, a paired centriole located in the electron dense cloud surrounding the nucleus (not shown), several mitochondria, and specialized membrane organelles (MO) that fuse with the plasma membrane (see below). There

are no ribosomes or rough endoplasmic reticulum visible and no Golgi apparatus.

The development of the fine structure of *C. elegans* sperm has been described by others, and we have confirmed and extended their results. The membranous organelles begin to form in secondary spermatocytes. They are initially associated with the Golgi complex and appear to arise in conjunction with a membrane-bound filamentous body that contains 70Å filaments. No such filaments are visible in mature sperm. The division of a secondary spermatocyte into two spermatids occurs by division of the cell into three. A middle body, containing all the ribosomes, the rough ER, and the other internal membranes, is split off from the two spermatids by two contractile rings. All these events can be seen in a single longitudinal section through the male gonad because the sperm mature in a linear row.

The spermatids continue morphological maturation with the MO acquiring their electron dense collar and moving from the center of the spermatid to the periphery, where they abut the cell membrane. In young males, the sperm remain arrested at this state; sperm in the oviduct of hermaphrodites prior to entry into the spermatheca are also arrested at this stage. When male sperm are transferred to hermaphrodites or when hermaphrodite sperm enter the spermatheca, they undergo their final maturation. The special membrane vesicles fuse with the plasma membrane, expelling their contents (Fig. 34). In parallel, the sperm extends a pseudopod to the side away from the sites of fusion. In hermaphrodites, this final step in maturation is triggered by transfer of sperm to the uterus, but it can also occur in males if they are allowed to age as virgins. Similar maturation is seen in other nematode sperm, and it can be triggered in vitro in *Ascaris* by addition of extract from the male *vas deferens*.

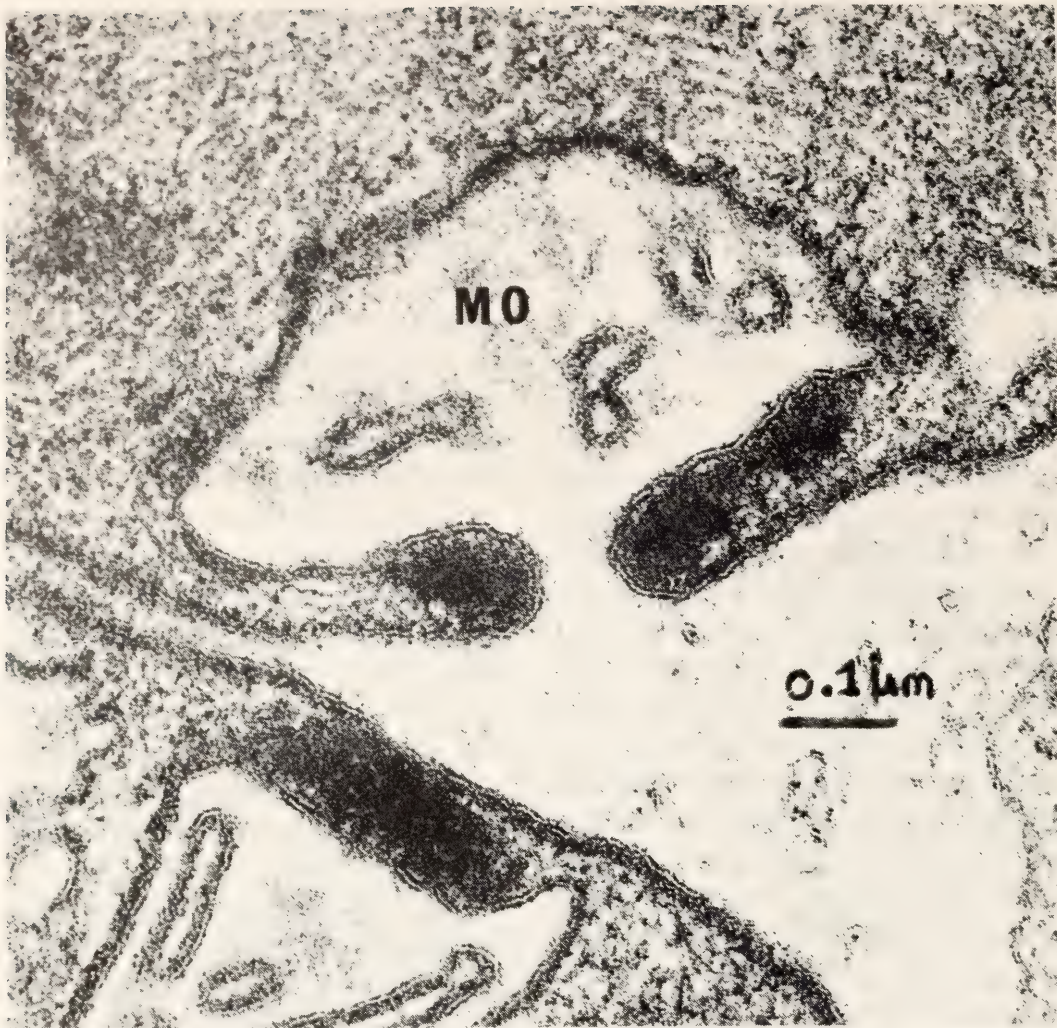


Fig. 34. Membranous organelle (MO) fusion with the plasma membrane in a wild-type sperm.

Mutant Sperm Morphology

Mutations in three of the *fer* genes (*fer-1*, *fer-3*, and *fer-5*) cause production of sperm in which the MO do not fuse with the plasma membrane (Fig. 35). Both hermaphrodite and male sperm have the same defect. The two most different *fer-1* alleles both have the same defect in fusion, showing that this defect is a property of the *fer-1* gene and not just of the specific allele. In addition to the fusion defect, the sperm in these mutants have only rudimentary or no pseudopods. This supports the notion that fusion and pseudopod extension are coupled; perhaps fusion is necessary for pseudopod extension because of alterations in the membrane.

Another fine structural alteration is found in the sperm of the mutant HC4. Large, straight tubules are found surrounding and radiating out from the nucleus (Fig. 36). These have an average diameter of 43 ± 8 nm. This is nearly twice the diameter of ordinary microtubules and is larger than the "macro-tubules" or other large-diameter forms that tubulin can polymerize into. We do not know what subunits make up these tubules. They have not been seen in wild-type sperm and have been seen in only one sperm of another mutant. In spite of the presence of tubules, MO fusion occurs in HC4 sperm, and they extend pseudopods. Both may occur less frequently than in wild-type sperm.



Fig. 35. Membranous organelle in sperm of *fer-1 (hc24)* hermaphrodite grown at 25°C.

Initial Biochemical Characterization of Sperm

Following a procedure developed by M. Klass (personal communication), we have been able to isolate enough sperm to begin biochemical and immunological characterization. *Fer* mutant strains are combined with a *him* mutation that causes 20–25% of the population to be male. Populations of 10^6 synchronized animals can be grown on several large petri plates seeded with concentrated *E. coli*. The males can be isolated by filtration through Nitex nylon filters of appropriate mesh size. The isolated males are squashed between two glass plates to release sperm and the sperm are isolated

from the squash by filtration and centrifugation.

Since the fusion defect might be due to an alteration in membrane phospholipids, we have begun analyzing the phospholipids in sperm, using two-dimensional thin layer chromatography. The major phospholipids in the sperm are phosphatidylcholine, phosphatidylserine, and ethanolamine. There is little sphingomyelin or cardiolipin. Sperm from *fer-1(hc1)* have altered amounts of the amine containing phospholipids and altered amounts of an unknown component that has an *R_f* of 0.9 in two solvent systems. We are working to confirm these results and to identify the un-

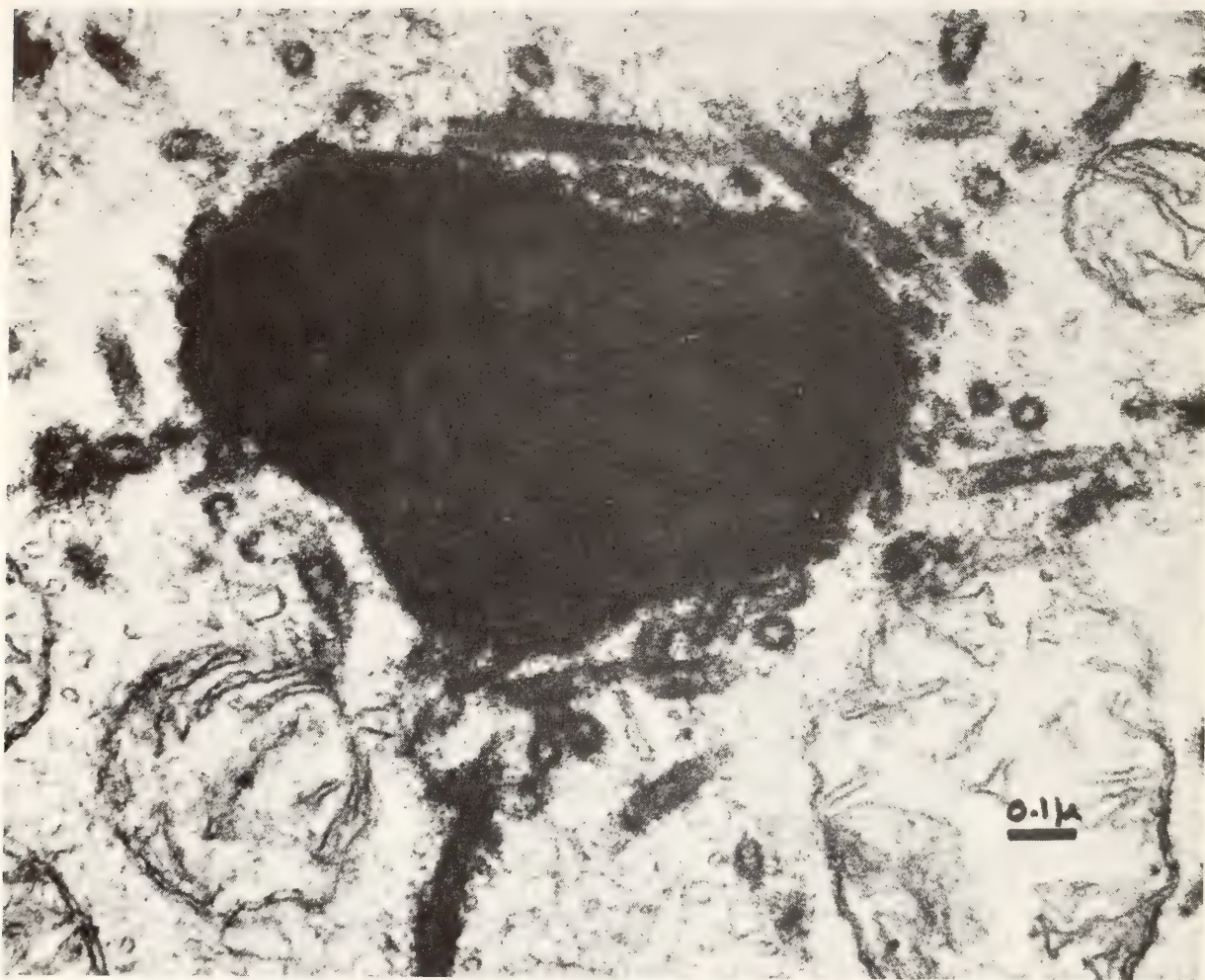


Fig. 36. Large tubules surrounding the nucleus in sperm of a *fer-4(hc4)* male grown at 25°C.

known. It is encouraging to find a biochemical difference between the mutant and wild-type sperm that could be the cause of the fusion defect. In other systems, fusion appears to involve interactions between the lipid portions of two membranes. Studies of mutant sperm proteins are just beginning.

TEMPERATURE-SENSITIVE INTERSEX MUTANT

Gregory Nelson, Kenneth K. Lew,
Samuel Ward

In the course of isolation of fertilization-defective mutants, a strain was isolated which renders hermaphrodites sterile and causes males to develop as intersexual animals. The strain, HC17, is homozygous for the recessive, tem-

perature-sensitive allele *hc17* of the gene *isx-1* (intersex-1), which is located on autosome IV.

We compared the phenotype of this mutant to the wild-type to gain insight into the genetic control of sex determination and gametogenesis in the nematode. Unlike the *fer* mutants described in the previous section, we found that the *isx-1* gene product acts early in gametogenesis. It is necessary for gonad precursor cells in larvae to differentiate properly into gametes and to produce gonadal structures.

HC17 hermaphrodites and males are wild-type at the permissive temperatures of 16°C and 20°C; males mate successfully and hermaphrodites produce many self-progeny. When animals are raised at the restrictive temperature of 25°C, however, they are defective. Figure 37

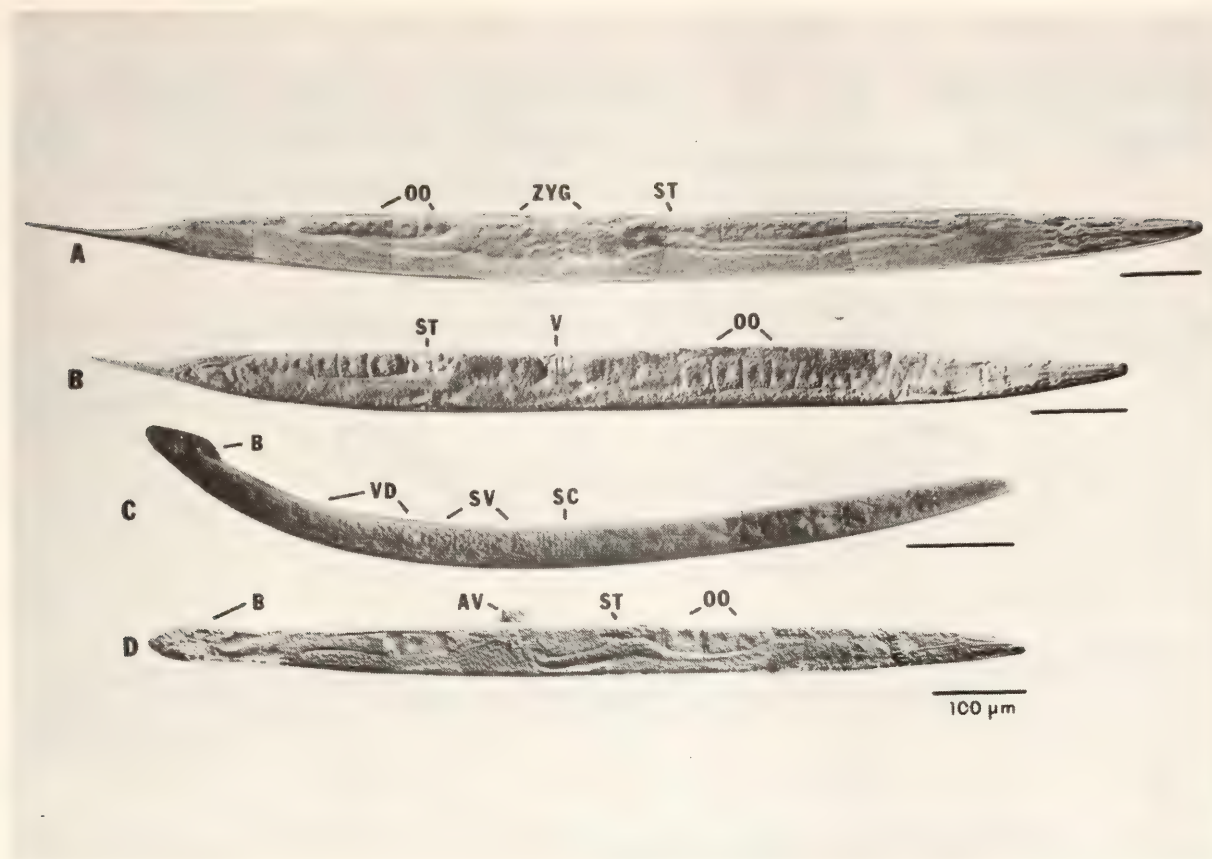


Fig. 37. Light micrographs of HC17 animals raised at 16° (A and C) and 25°C (B and D) photographed with Nomarski optics. Animals with karyotype XX + 5AA develop as hermaphrodites. Permissively grown hermaphrodites (A, subdorsal view) are indistinguishable from wild-type but restrictively grown animals (B, ventral view) produce no sperm and consequently contain no fertilized eggs. Animals with a single X chromosome develop as males at 16°C (C, side view) or intersexes at 25°C (D, subdorsal view). 16° males make only sperm in their J-shaped gonad. Intersexes make no sperm but contain oocytes and often an abortive vulva.

shows the appearance of HC17 animals under the two growth conditions.

Hermaphrodites of HC17 (karyotype XX + 5AA) at 25° make no sperm. Instead, the gonia, which would have normally differentiated into sperm, become oocytes but few of them mature. These oocytes may be fertilized by wild-type male sperm to produce outcross progeny. The presence of exogenous sperm and seminal fluid stimulates the process of oogenesis in mutant hermaphrodites so that a normal number of oocytes are produced. No other defects have been observed in HC17 hermaphrodites. These animals are therefore functionally female and are useful for assessing the fertility of males without the technical complication of self-fertilization.

Since X chromosome number is im-

portant for sex determination in the nematode, triple-X HC17 animals were constructed to test the effect of the additional X chromosome. No significant alterations from the HC17 hermaphrodite phenotype were found other than those of the XXX condition itself.

When karyotypic males (XO + 5AA) of HC17 are raised at 25°C, they develop as intersexes with complex phenotypes. Intersexes lack sperm but often make oocytes and defective gametes. Their gonads vary in morphology but tend to be hermaphroditic. Gametes are sometimes found at ectopic sites in intersex gonads, and occasionally a rudimentary gonad with only a few dozen total cells contains morphologically normal oocytes. These gonadal characteristics are superimposed on animals having mostly male-

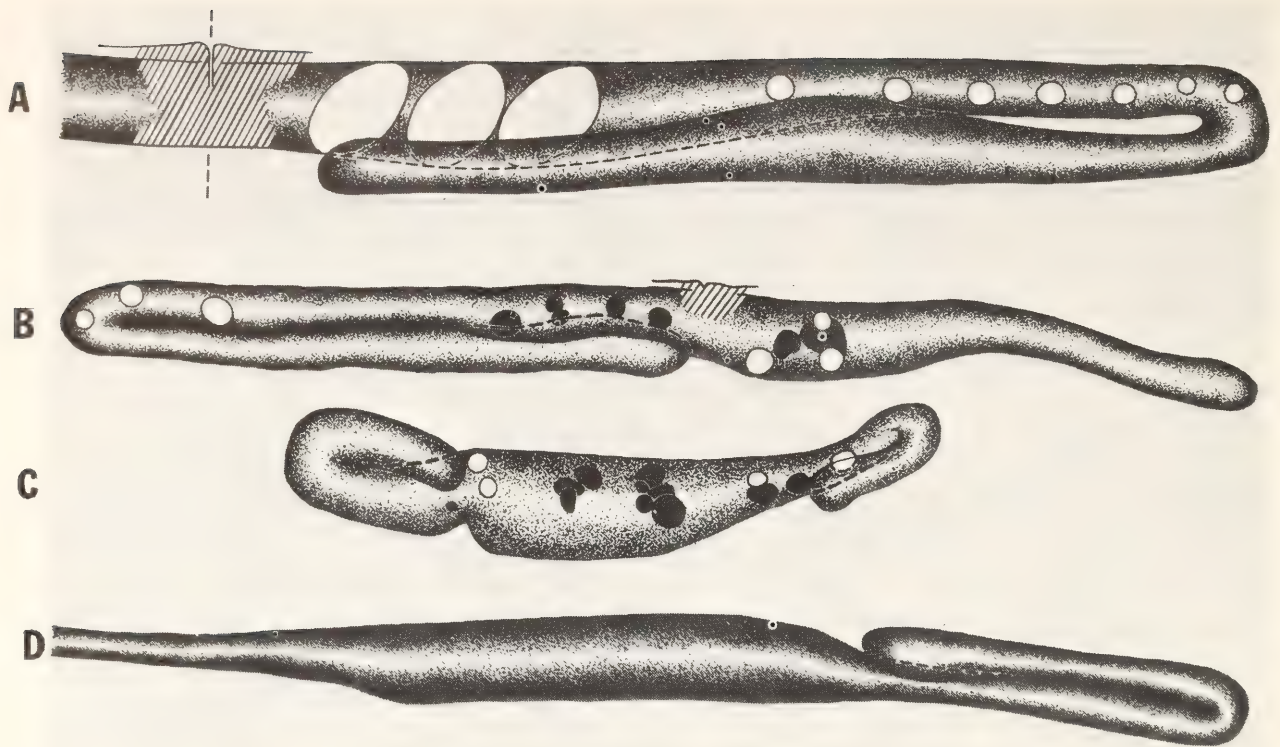


Fig. 38. Drawings of normal hermaphrodite and male gonads and two typical intersex gonads based on camera lucida tracings of feulgen-stained animals. (A) One arm of a wild-type hermaphrodite gonad which is mirror symmetric about a plane indicated by the vertical dashed line. Large open ovals are fertilized eggs. Small open circles are nuclei of oocytes (A-C). The cross-hatched areas in (A) and (B) represent vulva structures, and solid black areas are polyploid defective gametes. (B and C) Two typical intersex gonads; (B) has one hermaphroditic arm and one straight arm whereas (C) is more unusual in structure. (D) The gonad of a wild-type male. Ventral is up and anterior is to the right.

like somatic structures, including sex-specific nervous system and other secondary sexual characteristics (copulatory bursa, spicules, and mating behavior). Figure 38 shows camera lucida tracings of normal hermaphrodite and male gonads along with two typical examples of intersex gonads. The locations and morphological relations of gametes to gonad sheaths suggest that their maturation is not tightly coupled to their location within the gonad and is in large measure cell-autonomous.

Many intersexes possess a vulva, which is the major secondary sexual organ of the hermaphrodite and arises from extra cell divisions of cells that normally proliferate only in hermaphrodites. The presence of vulvas and their morphology correlates with the degree of hermaphroditicity of the underlying

gonad, suggesting an interaction during development. In light of cell lineage and laser microsurgical experiments by other investigators, it seems likely that such a gonad-vulva interaction is indirect, possibly inductive in nature. This is an interesting exception to the pattern of development in *C. elegans*, which is otherwise cell-autonomous and determined by lineage.

isx-1 seems to be a gene whose normal expression is necessary for the production of sperm in animals with one, two, or three X chromosomes. It is also necessary for the proper development of male-like gonads in animals with a single X chromosome. Its primary effects can be traced to the descendants of four primordial gonad cells, two of which give rise to gametes and two of which develop into the gonad sheath. The *isx-1* mutation

reveals that these two pairs of cells respond differently to X chromosome dosage.

Other workers have identified three other autosomal genes that affect sex determination in *C. elegans*: *tra-1*, *tra-2*, and *tra-3*. Mutations in these genes cause XX animals to develop as males but do not affect XO animals. By construction of double mutant strains with alleles of *tra-1*, *tra-2*, and *isx-1* the action of *isx-1* was found to precede the two *tra* genes in gametogenesis. It blocks spermatogenesis at the restrictive tem-

perature. However, no effects of the *isx-1* mutation on the gonad sheath were found in transformed animals with two X chromosomes. This suggests that with respect to gonad sheath development, *isx-1* responds directly to X chromosome dosage and not to the phenotypic sex of transformed individuals. Figure 39 summarizes a proposed logic for how X chromosome number and three autosomal genes may act in the development of gonadal structures and gametes in *C. elegans*.

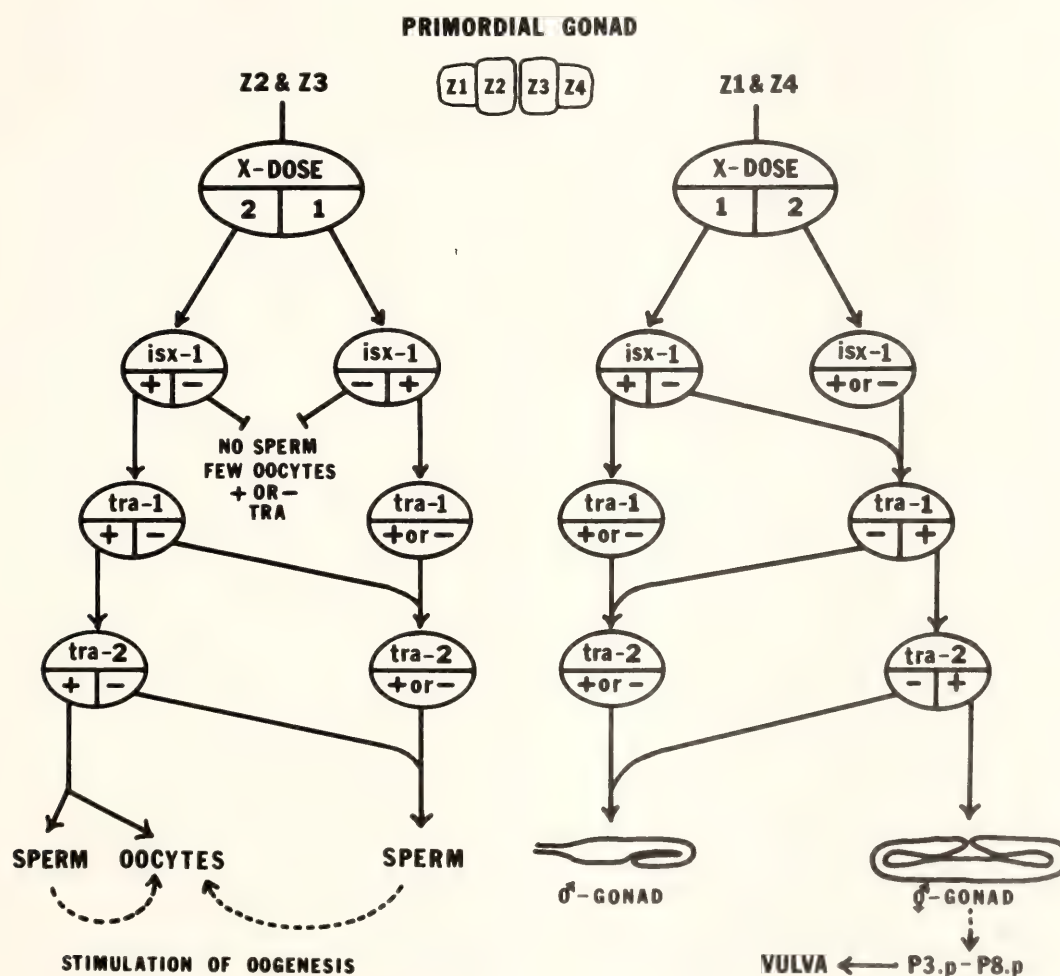


Fig. 39. A model for the logic by which the fate of the gonad is determined. Four variables are considered: X dose and the three genes *isx-1*, *tra-1*, and *tra-2*, each in either an on or an off state. The order of the three genes is based on phenotypes of double homozygotes; all are placed after X dosage upon which their actions depend. Each ellipse in the figure represents a decision, and decisions proceed from top to bottom. Z1 through Z4 are primordial gonad cells present in newly hatched larvae, and P3.p-P8.p are vulva precursor cells. For the 11 cases in which 1 or 2 genes are mutant, 8 have been examined for gonad phenotypes and give the predicted outcome: the three single mutations with X=1 or 2 and the *tra;isx* double mutants with X=2.

REGENERATION IN THE NERVOUS SYSTEM: FORMATION OF SPECIFIC SYNAPSES IN THE LEECH

K. J. Muller, S. T. Carbonetto, S. A. Scott, and B. E. Thomas

In the nervous system the structure of cells is inseparably linked with their functional roles; therefore, the shapes of neurons and their patterns of synaptic connections must be precisely directed during development. Although intrinsic factors play a major role in guiding the initial stages of neuronal growth, interactions between neurons seem to be essential for establishing and maintaining synaptic contacts. In adult vertebrates injured neurons in the central nervous system can restore function by regenerating original connections. However, to show that precisely the same neurons are reconnecting—that is, to study regeneration at the level of single cells—it has been necessary to turn to simpler systems. The nervous system of the leech has been especially useful for this, since it has only 350 neurons in each segmental ganglion and the functions of many of the cells have been identified. The synaptic interactions between these neurons have been found to be surprisingly consistent and are in that sense predictable from one ganglion or animal to the next. It has consequently been possible to show with electrophysiological techniques that individual sensory neurons and interneurons can select their normal postsynaptic contacts from among hundreds of other candidates, forming chemical or electrical synapses. By injecting the enzyme horseradish peroxidase (HRP) into single cells to mark them for subsequent microscopy, we have been able to examine the structure of regenerated neurons and their synapses, trace how they go about finding their normal targets, and ascertain the role the targets play in the stages of regeneration. Two classes of neurons in the leech central nervous system have been

used in these studies. Cells of one class, interneurons called S-cells that make electrical synapses at precise locations in the nerve cord (*Year Book 75*), have been used to follow in detail the stages in regeneration of the synaptic connections (*Year Book 76*). By killing the single cell that is the regenerating neuron's target, we have found that the absence of the target fails to stop the early stages of regeneration. Certain S-interneurons make chemical synapses in addition to electrical synapses at the ends of their axons, and this subclass has provided evidence that a cell's capacity for regeneration may depend upon the types of synapses that it makes. The second class of regenerating neurons we have continued to study is the mechanosensory neurons that are known to make chemical synapses having distinct arrangements and distributions within the ganglion, depending upon the particular cell modality—touch, pressure, or nociceptive (*Year Book 75*). We have sought to characterize the synaptic contacts between individual sensory and motor neurons with the aim of comparing new synapses in structure and distribution to the old. Such a detailing of synaptic contacts requires powerful techniques of computer reconstruction, and we have meanwhile examined the branching patterns and sites of synapses of single regenerated sensory cells. We recently discovered that sensory cells make a set of specific contacts on other sensory cell bodies. By their accessibility to experimental analysis, these associations may help us to determine what properties of cells are used as signposts by growing neurons as they select the targets with which they synapse.

REGENERATION OF THE S-INTERNEURON

*K. J. Muller, S. A. Scott, and B. E. Thomas**Detection of Electrical Synapses
with Lucifer Yellow Dye*

The electrical junctions between S-cells in the leech have been particularly useful for studies of regeneration. This is largely because the synapse that the single S-interneuron in each ganglion makes with its neighbors is midway between ganglia in the bundle of axons called the connective. This location has permitted us to trace precisely the regeneration of the S-cell synapse after the axon of one of the cells has been cut or crushed. However, to demonstrate an electrical junction between two cells, we have had to penetrate both cells with microelectrodes and show that current can pass directly from one cell to the next. One limitation of this technique is that without first testing for coupling between at least hundreds of pairs of cells, one cannot say that a particular connection is the only one a neuron makes. An alternative method is to inject into one cell a small tracer molecule that passes across electrical junctions but not cell membranes, and follow its diffusion into the coupled cell. The dye Procion Yellow has been successfully used for this, but its fluorescence is low and the method unreliable. Walter Stewart of the National Institutes of Health has synthesized and given us a fluorescent naphthalamide dye dubbed Lucifer Yellow (m.w. ~600 daltons), which is about 100 times more fluorescent and considerably more soluble than Procion Yellow. We have found that Lucifer Yellow will pass within minutes from one S-cell to the next but enters no other axons in the connective. By suitably timing fixation of the dye in the tissue, one can detect a discontinuity in the intensity of the stain caused by the slight barrier of the electrical junction. The dye is capable of diffusing into other cells that are synaptically linked to the S-cell, including a

pair of neurons in each ganglion that physiological studies reveal synapse with the S-cell. Because these cells are on the opposite side of the ganglion from the S-cell, the connection had previously escaped notice. With Lucifer Yellow we should be able to confirm the specificity of synaptic regeneration measured with microelectrodes and pinpoint the timing of any uncoupling between the severed distal stump and the target S-neuron.

Regeneration after Elimination of Target

Severed axons in the leech can persist for weeks or months and in some cases can themselves form synaptic connections (see *Year Book* 76). It is therefore insufficient simply to remove the cell's soma to eliminate the distant branches of a cell as possible synaptic targets for regenerating neurons. Recently, techniques have become generally available for injecting a protease into single neurons. The enzyme diffuses throughout the cell within hours or days, eliminating the injected cell from the nervous system without detectably affecting cells that are electrically coupled to the protease-injected cell (Fig. 40). We have injected single S-cells in vivo to determine whether in the absence of a target S-neuron the adjacent S-neuron will sprout as usual after its axon is severed by crushing the connective. If the axon is not crushed, we can learn whether removing the sole input to an axon causes the axon to retract.

On the basis of eight animals examined a month after injection of protease, we find that we can titrate the level of injection to either kill the S-cell soma and its axon, leaving other cells intact, or simply eliminate the soma but not the axon. When the S-cell is killed entirely and the axon of one adjacent S-cell crushed, the neighboring S-cell regenerates in apparently normal fashion along its persistent distal stump toward where

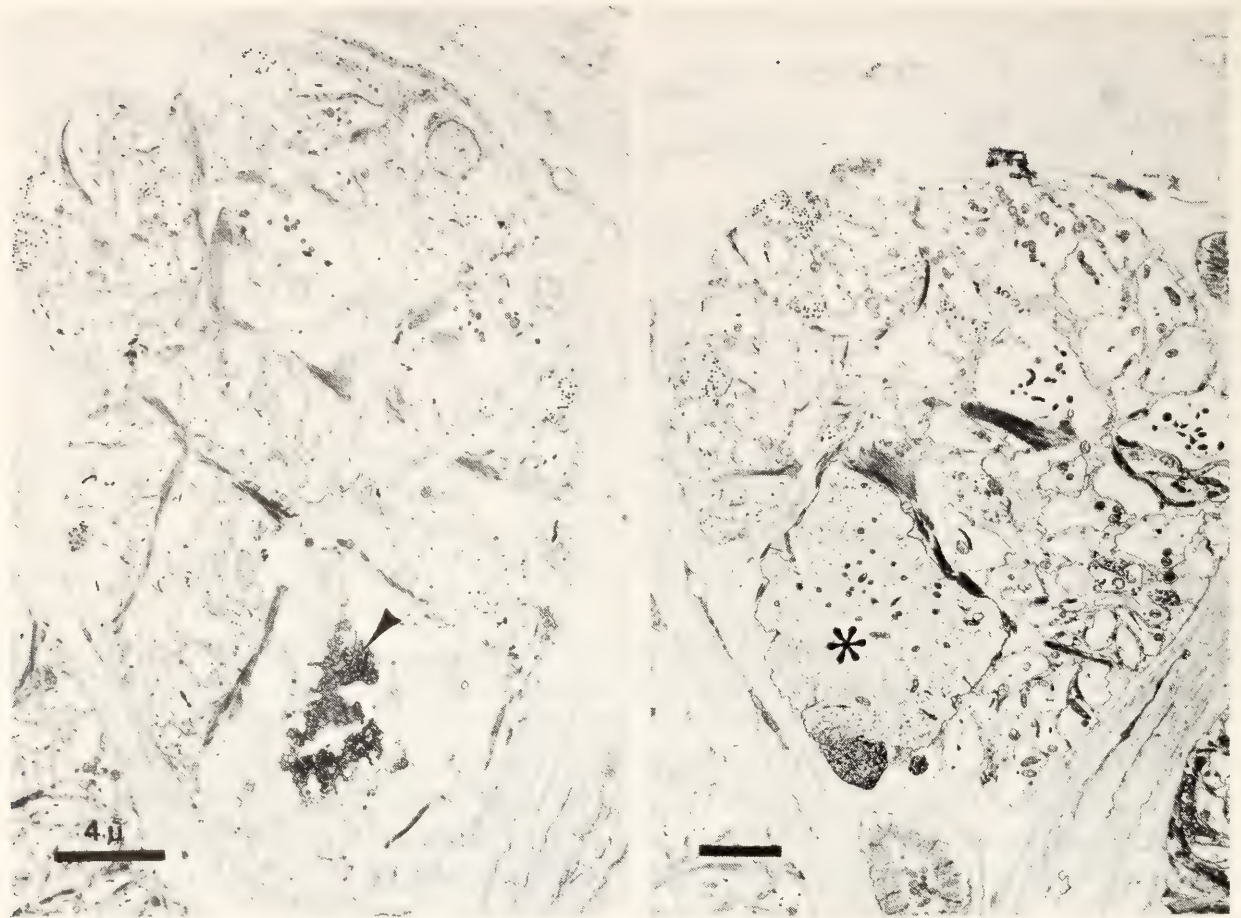


Fig. 40. Pronase injection kills S-cell without affecting the morphology of the adjacent electrically coupled S-cell. At left, arrowhead points to mitochondrial and membranous remnants of axon of S-cell injected with Pronase two days before. The surrounding glial cell has hypertrophied, but other axons look normal. At right, adjacent S-cell axon (*), injected with horseradish peroxidase, has normal morphology even in the immediate vicinity of the Pronase-injected axon.

the target was (Figs. 41 and 42), much as motor neurons have been shown to regenerate to the muscle basement membrane even in the absence of the muscle fiber (*Proc. Nat. Acad. Sci.* 74, 3073-3077, 1977). This result also indicates that the severed stump survives without an electrical junction with the target S-cell. Because we have not yet looked at older preparations, we do not know if the regenerating neuron grows beyond the severed distal stump, or whether it retracts when it finds that the target is missing. No evidence of growth or change has been detected in the uninjured S-cell formerly coupled to the eliminated S-cell, but based on previous findings (e.g., *Year Book* 75), we would expect that plastic

changes might occur at later times. An intriguing result has been obtained with the three preparations, all examined at one month, in which the S-cell was injected with too little protease (measured at the time of injection) to destroy the axon but sufficient that the S-cell soma seemed to be obliterated within the ganglion. In two cases there was no regeneration along the distal stump, although sprouts had crossed the crush; and in the third instance the regenerating sprouts had progressed less than a third as far as normally. We have never before seen such regeneration failures, and they present the possibility that the target may in some fashion be involved in suppressing regeneration.

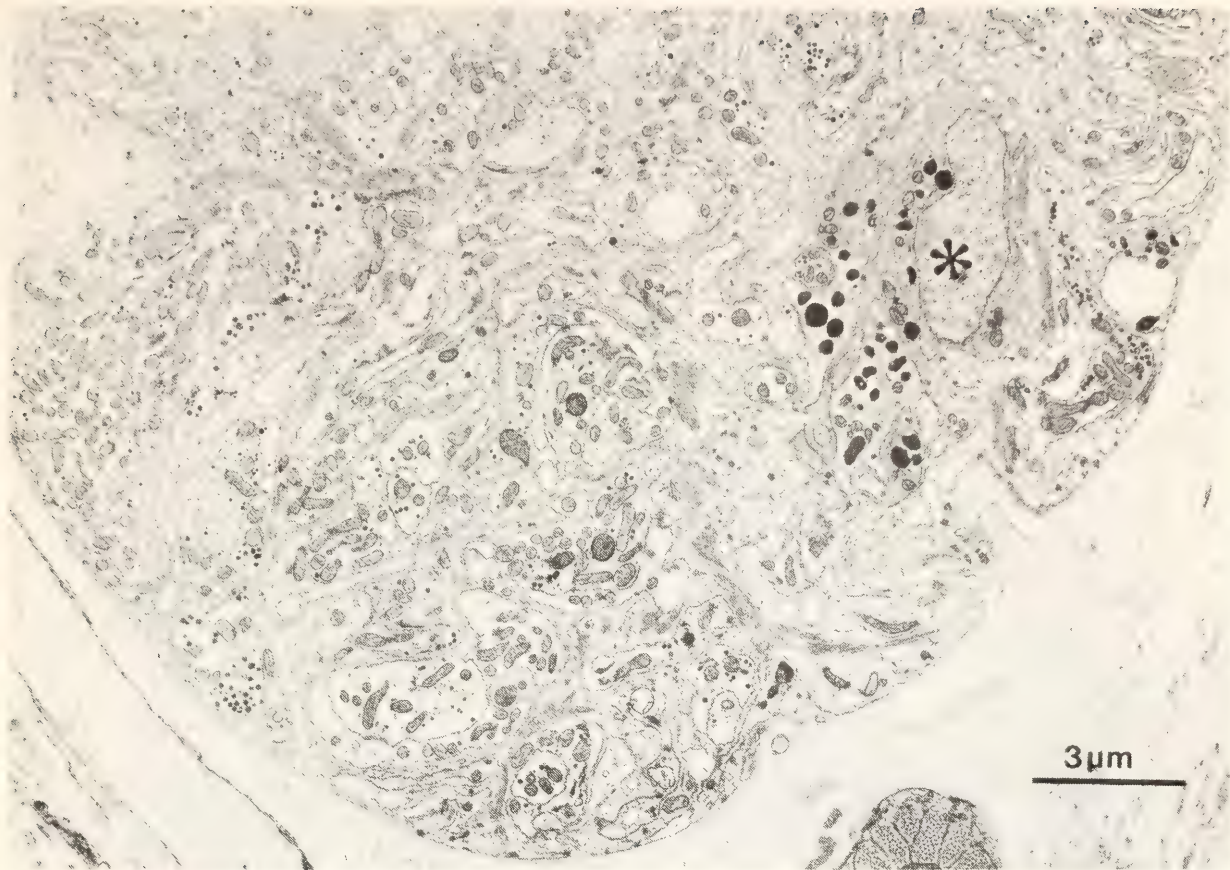


Fig. 41. Region of Faivre's nerve normally occupied by S-cell axon, which in this case was eliminated by in vivo injection of protease 29 days previously. The nucleus of a scavenger cell, possibly associated with the disappearance of the S-axon, is indicated with an asterisk.

S-Cell Axonal Regeneration in Culture

If leech ganglia are maintained in culture for several weeks, many neurons retain the ability to regenerate severed axons and establish interrupted chemical synapses. The electrical synapse of the S-cell is a notable exception, and attempts to obtain S-cell regeneration in culture have reportedly failed. Because of the potential for experimental manipulation in culture, we have continued to seek conditions that might promote S-cell growth. We now have evidence that it is the type of synaptic connection made by the severed axon, rather than cell-type, that determines the ability of the axon to regenerate.

The S-interneuron makes chemical synapses within its ganglion that are typical of chemical synapses in the leech. In the first three and last four or five ganglia, where the connectives are short,

the S-cells send axons the length of the connective into adjacent ganglia where they make both chemical and, apparently, electrical synapses. We have therefore cultured chains of ganglia taken from the extreme ends of the nerve cord, a region not usually examined in culture. In three of six preparations (e.g., Fig. 43) we have obtained morphological evidence for regeneration; no physiology has yet been performed.

SYNAPSES OF IDENTIFIED SENSORY NEURONS

K. J. Muller and B. E. Thomas

Synapses between a Sensory and a Motor Neuron

In the leech, the motoneurons that activate the large longitudinal (L) and annulus erector (AE) musculature re-



Fig. 42. In the same preparation as Fig. 41, the adjacent S-cell's axon was crushed; its severed distal stump persists and provides a pathway for regenerating processes (*R*) marked by HRP. Although the stump is no longer in contact with the killed S-cell, the stump remains healthy looking.

ceive chemical synapses from the pressure (P) and nociceptive (N) sensory neurons in the same ganglia and from sensory neurons whose cell bodies are in adjacent ganglia. Electron microscopic studies have shown that the L and AE motoneurons are postsynaptic within the ganglion and contain few, if any, syn-

aptic vesicles (*Year Book 74*). It is possible, then, to inject a sensory neuron and a motor neuron both with a single marker such as HRP and still distinguish presynaptic and postsynaptic terminals in the electron microscope. To form a picture of the number and distribution of synapses between particular cells, we

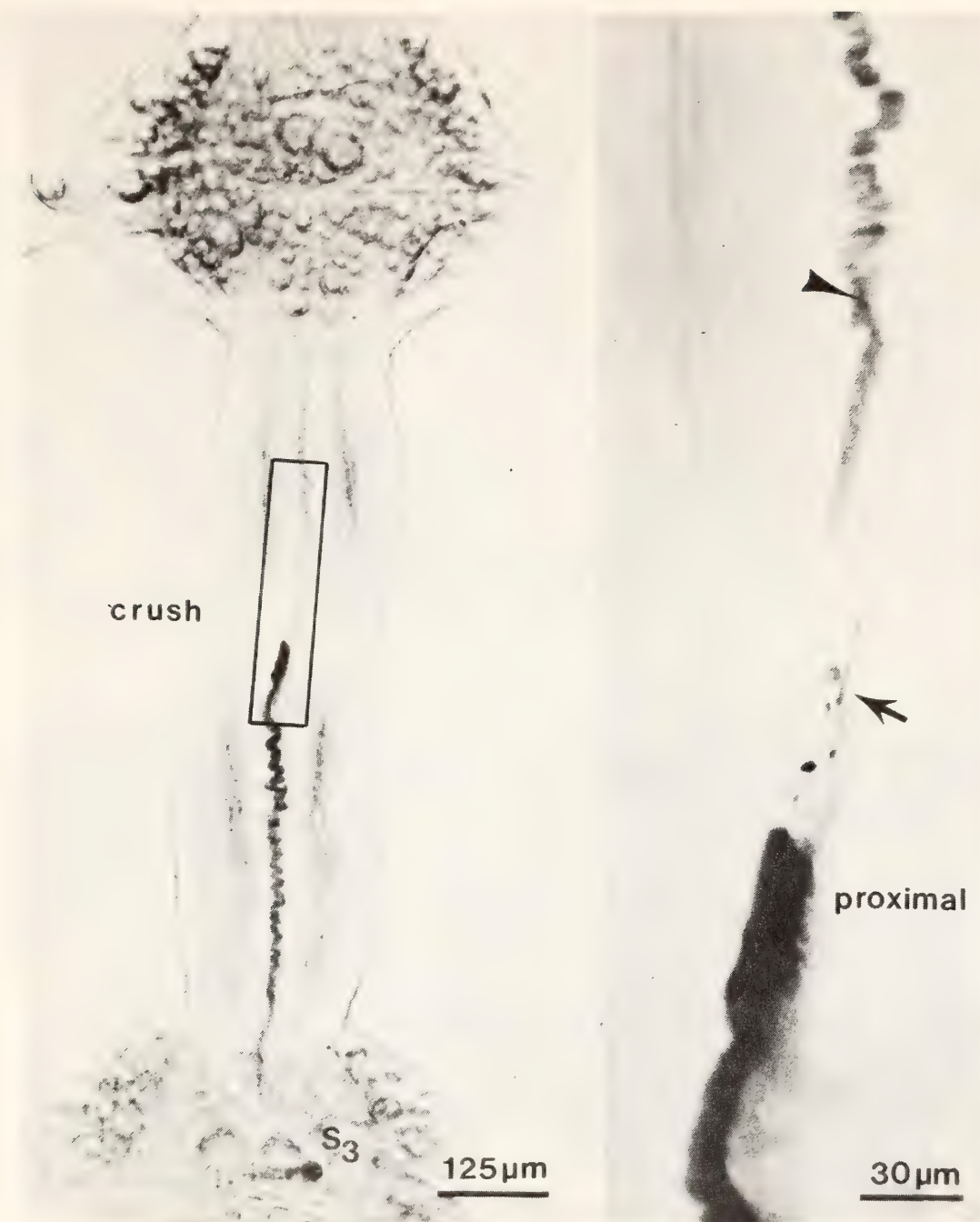


Fig. 43. S-cells in ganglia at the extreme ends of the ventral cord, here ganglia 2 and 3, can regenerate within 2 weeks of removing the ganglia to culture medium and crushing the connective. Before crushing, S₃ projected an axon into ganglion 2, at top. After the axon was severed midway in the connective, it sprouted across the crush (arrow) and could be followed (arrowhead) up to the next ganglion by injecting the soma with HRP. Right-hand panel is enlargement of region of crush, as shown at left.

have been using the computer graphic display facilities at Columbia University in collaboration with Dr. Eduardo Macagno of the Biology Department there. This approach should ultimately allow for a detailed analysis of whether regenerated synapses between particular

neurons are distributed as the normal synapses are, or if synapsing terminals recognize each other and restore function without reference to their original positions within the neuropil.

A pressure sensory and L motor neuron have been stained and largely recon-

structed within a single ganglion from serial thick sections. At the light microscope level it was possible to locate points of apposition between the two cells and confirm them as sites of synaptic contact (Fig. 44). These represent the first chemical synapses seen between functionally identified neurons in the leech. Based on the five synapses found in one region of contact, it seems likely that scores of such synapses occur between one particular pair of cells at distinctive locations within the neuropil. These form the structural basis for the consistently strong connection measured electrophysiologically between the same pair of neurons.

Regeneration of Chemical Synapses

Before an analysis of the distribution of regenerated contacts between two cells is completed, it is useful to know whether single sensory neurons regenerate normal-looking synaptic arbors, or whether the pattern of contacts is likely to be altered. A camera lucida reconstruction of a touch cell arbor, regenerated after crushing more than a year before, indicates that the fine structure of the new synapse is fundamentally like the old but that the secondary processes on which the synapses are located seem shorter than normal (Fig. 45). We are now examining the means by which the touch cell reaches this endpoint and

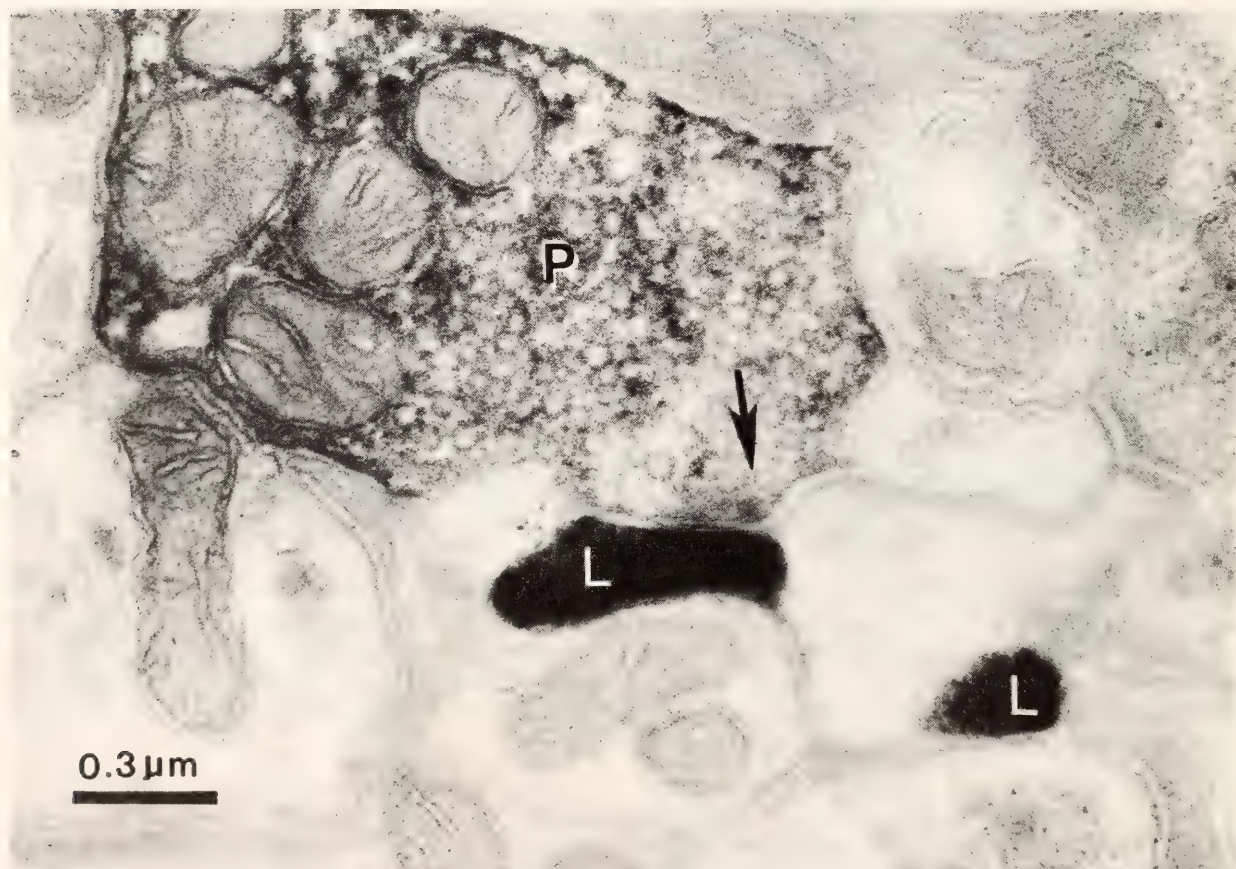


Fig. 44. Synapse of a pressure sensory neuron upon an L motoneuron. In a single ganglion a pressure (P) sensory neuron and an L motoneuron were injected with HRP, the tissue osmicated and embedded for electron microscopy, and serial thick sections cut. The processes of the two cells were traced by Dr. Eduardo Macagno after computer reconstruction, sites of contact noted, and the tissue resectioned for electron microscopy. Sites of presumed synapse were found, as in this case, to be places at which the pressure (P) sensory cell formed a typical chemical synapse (arrow) upon a fine L motoneuron branch.



Fig. 45. Regenerated processes of a touch sensory cell, 14 months after lesion, form a complete synaptic arbor. The stained cell's processes were traced in an adjacent ganglion (outlined) from $8\mu\text{m}$ serial sections embedded in an Epon slab. The thick section containing the region circled was resectioned for electron microscopy (inset), and the stained secondary process was found to contain synaptic vesicles and make synapses, such as that at arrow, on fine branches of unidentified neurons.

whether in the early stages of regeneration, when contact is first made, the synapses are similarly distributed.

SPECIFIC ASSOCIATIONS BETWEEN SENSORY CELLS

K. J. Muller, S. A. Scott, and B. E. Thomas

Leech ganglia are organized into two layers: an outer layer of cell bodies believed to be devoid of synapses and neuron processes, and an inner core called the neuropil where synapses are located. By allowing the horseradish peroxidase

marker to diffuse within N-sensory cells for a day or more, rather than hours, we have discovered that the cells normally envelop specific pressure (P) and Leydig cells with baskets of extremely fine processes (Fig. 46) in their own and in adjacent ganglia. Along the processes are occasional varicosities that might be sites of synapses, but this will require confirmation in the electron microscope. Reports that receptors for exogenous transmitters are collected at spots on the surface of the somata make the possibility of somatic synapses tantalizing. Previous physiological studies were per-

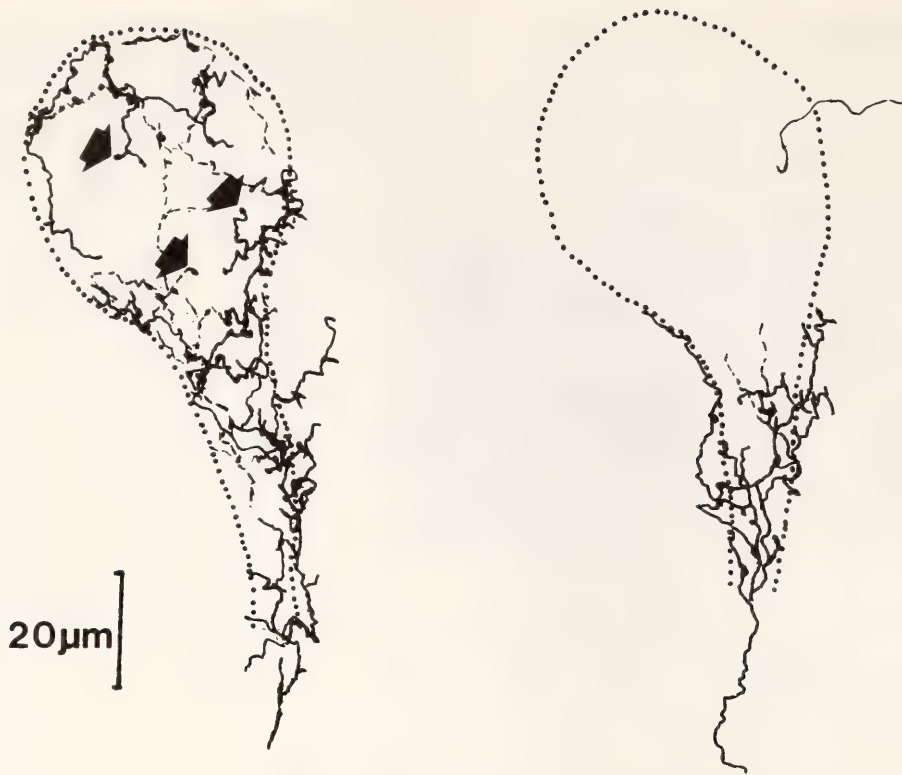


Fig. 46. Fine branches of a nociceptive (N) sensory cell specifically wrap the cell bodies of pressure (P) and Leydig cells. At the left are camera lucida tracings from whole mount of N-cell processes wrapping a medial P-cell soma (dotted outline). Varicosities are visible (arrows) along and at the ends of processes. Electron micrographs confirm that the processes are in direct contact with the cell body. However, when the glial capsule is removed from such a cell (at right), the P-cell sheds the N-cell's processes.

formed on desheathed cell bodies, and we now know the terminals became stripped off when the glial capsule was removed (Fig. 46), while otherwise the processes were in direct contact with the soma. We have observed that the N-cell can regenerate the same wrapping of P-sensory and Leydig cells in culture, but we do not know if such growth will occur in the absence of the enveloping glial sheath.

ROLE OF GLIA IN REGENERATION

K. J. Muller and S. A. Scott

It has been estimated that half the volume of the nervous system consists of nonneuronal cells called glia, which are believed to play a supporting role and may help guide regenerating neurons. In the leech, a single large glial cell ensheathes each of the two lateral connec-

tives; its nucleus lies midway between ganglia. Glial cells are coupled to each other by extensive electrical junctions; and although glial membranes are not electrically excitable, they are permeable to potassium and therefore maintain a large resting potential. When a connective is cut or crushed, each of its glial cells is separated into two portions, one an anucleate piece of glial cell, or stump. In an effort to compare glial regeneration with neuronal regeneration and to determine whether, like severed axon segments, pieces of glial cell can survive once removed from the nucleus, we have begun to examine the fate of the severed glial stump. Single glial cells have been injected with horseradish peroxidase as a marker (Fig. 47). When injected before the cell is injured, the enzyme persists within the severed stump for weeks and shows that the stump survives. Although we do not yet know how glial cells "fill-

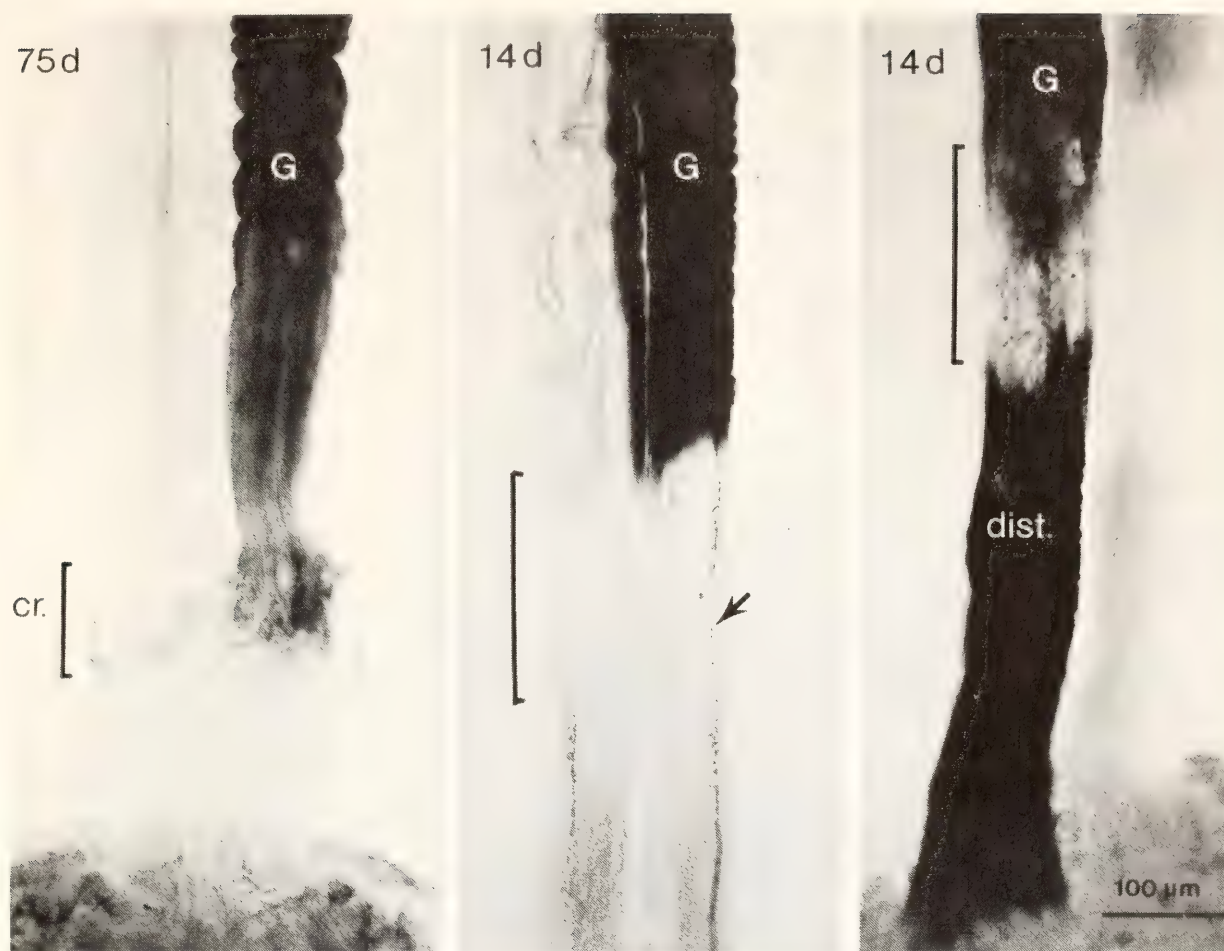


Fig. 47. The fate of the connective glial cell and its severed "stump" after the connective has been crushed. The left-hand panel (75 days) shows that the connective glial cell (G) injected with HRP had not grown posteriorly (lower) beyond the crush (cr., bracket). It is not yet clear if this finding is general, but in similar experiments performed at shorter times in culture (14 days) the glial cell did not grow into the region of crush (middle panel), while the axon of an injected N sensory neuron (arrow) spanned the crush and grew toward the next posterior (lower) ganglion. When the glial cell was injected with HRP before crushing (at right), the marker persisted in both the injected cell and its distal stump. Electron microscopy of such tissue confirms that the HRP is confined to the glial cell and that the cell has a normal appearance even at these late times.

in" regions that have been desheathed, or if they can form electrical synapses with their severed stumps as we have

found for S-cells, it appears that glial regeneration does not occur at the rapid rate seen for neurons.

STRUCTURAL AND FUNCTIONAL STUDIES OF THE FIBROIN GENE

Y. Suzuki, Y. Tsujimoto, Y. Ohshima, M. Tsuda, and P. E. Giza

The fibroin gene with its flanking sequences has been cloned from genomic DNA by the recombinant DNA methodology and is available in mg quantities (*Year Book 76*, p. 63). Using this abundant DNA, we have begun to analyze its

structure. We have located a presumed transcription initiation site on the gene map, and sequenced the DNA surrounding it. DNA regions of about 700 bp near the 5' end of the gene have been sequenced. In other studies a DNA se-

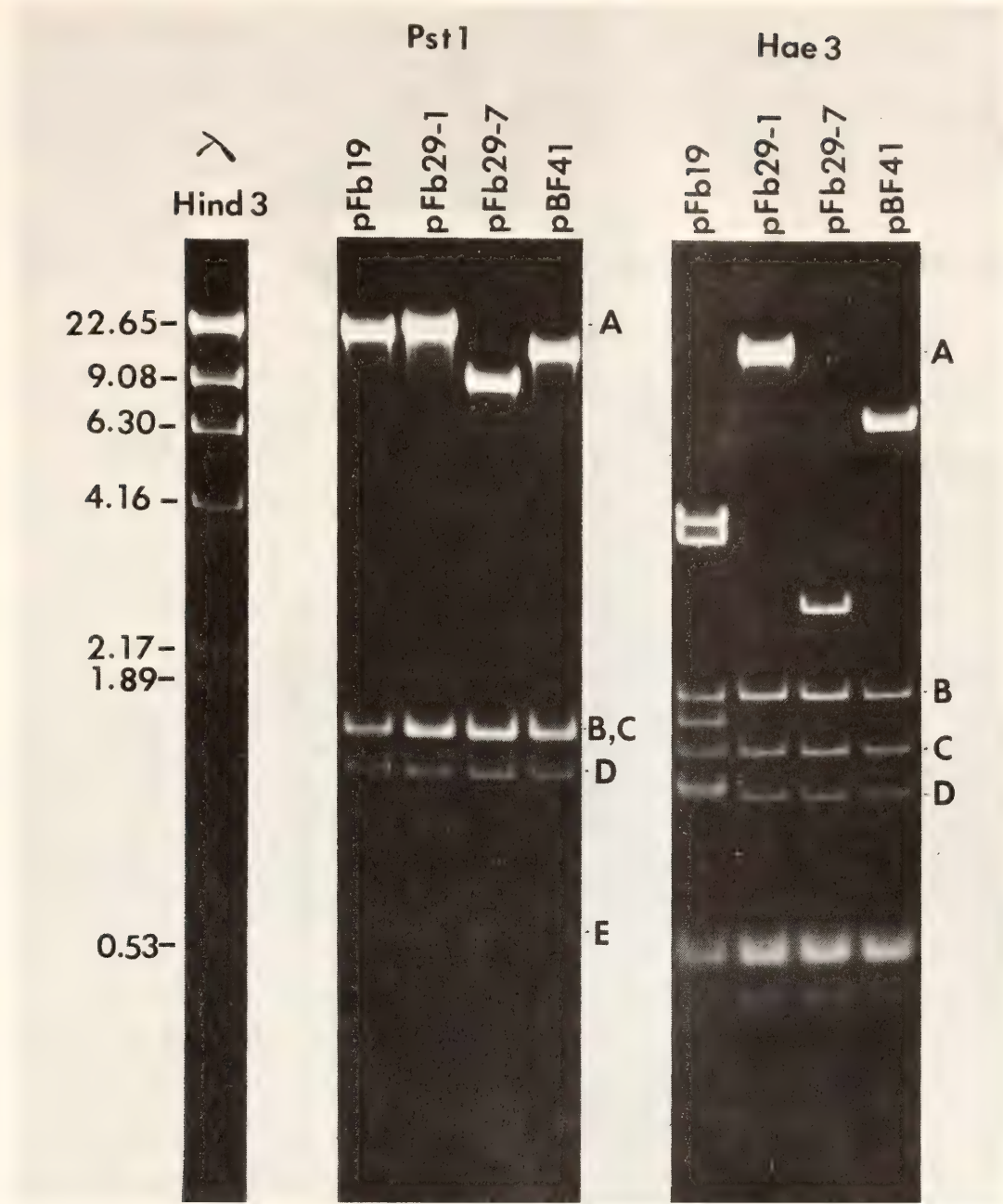


Fig. 49. Electrophoretic patterns of digests of pFb29, pFb19, or pBF41 DNA cleaved with Pst I or Hae III restriction enzymes. Electrophoresis was done in a 1% agarose gel, and the DNA was stained with ethidium bromide. The left lane is a Hind III digest of lambda phage DNA as a size marker. Fragment size (kb) on the left.

only at or near the 5' and 3' ends, giving one large DNA fragment. For convenience, we will call this a core fragment.

From restriction enzyme cleavage of various batches of pFb29 DNA we realized that deletions were occurring very frequently in part of the fibroin gene insert during the cultivation of bacterial cells (*E. coli* K12 HB101, *recA*, *recB*) that possessed the plasmid. The extent of deletion varies from batch to batch. An

example of deletion is shown in Fig. 49. In the Pst I or Hae III digest, the deletion was found only in the core fragment. The seventh batch of pFb29 DNA (pFb29-7) had deleted about 11.8 kb of the gene compared to the original isolate of the plasmid (pFb29-1). It should be noted that other regions of the insert are the same in various batches of DNA. In all batches the deletion is always restricted to the region between the 5' end

of Pst I core and the 3' end of Hae III core fragment of pFb29 (see Fig. 48). This result suggests that the deletion occurs in the repetitious nucleotide sequence characteristic of fibroin gene.

*Location of a DNA Sequence
Corresponding to the
5' End of mRNA*

It is known that about 60% of fibroin mRNA has a capped structure (m^7 -GpppAmpUmpCP) (Yang *et al.*, *Cell* 7, 339, 1976). We have determined that the first G residue from the 5' end of mRNA is located two bases from the first C residue. Thus the structure of the 5' end of fibroin mRNA is m^7 GpppA^m-pUmpCpXpGp.

We have also found that the remaining 40% of mRNA has an unmethylated cap of GpppApPypXpXpGp. This unmethylated cap can be methylated and labeled in vitro with the vaccinia capping enzyme complex in the presence of 3 H-S-adenosyl-methionine. This labeled mRNA was used to locate a DNA sequence corresponding to the 5' end of mRNA on the cloned DNA. The Southern transfer experiments revealed that a sequence corresponding to the 5' end of mRNA is present on Hind III/Hae III "D" fragment of pFb29 DNA. This D fragment is about 0.88 kb long and corresponds to the fragment removed from the 5' end of Hind III core fragment by Hae III (see Fig. 48).

The fine mapping of the 5' end of mRNA within the Hind III/Hae III D fragment of pFb29 DNA was carried out as follows. Hind III/Hae III D fragment was purified and then digested with restriction enzymes Taq I, Hinf I, or Pst I; and the resulting fragments were separated by gel electrophoresis. After recovery of DNA from the gel, DNA fragments were fixed on Millipore filters, and filters were hybridized with mRNA labeled at its cap. The results are shown in Fig. 50. The restriction fragments that

hybridized the radioactive mRNA are denoted by thicker lines, and others that did not bind the mRNA are represented by thinner lines. These results indicate that the DNA sequence corresponding to the 5' end of mRNA is present on a 70-bp region that has a Hinf I site on one end and a Taq I site on the other (Fig. 50).

*Nucleotide Sequence of the Region
Containing the 5' End of
Fibroin mRNA*

The DNA sequence of the fragment described above was determined (Fig. 51). A sequence corresponding to the 5' end of mRNA should be present between the Hinf I site and the nearest Taq I site on Hind III/Hae III D fragment. Since the sequence of the 5' end of mRNA is AUCXG or APyXXG, the corresponding DNA sequence is ATCXG or APyXXg. The sequence ATCAG was found between the Hinf I and the Taq I site and is present in tandem as ATCAGCATCAG. It has not been determined which one corresponds to the true 5' end of mRNA. Since the second ATCAG region was protected from S1 digestion after hybridization with mRNA, we have tentatively assigned it as the 5' end of mRNA.

As described in the next section (Ohshima *et al.*, this volume), the 5' end of the mRNA is a good candidate for the site of initiation of RNA transcription. If so, the sequence preceding this site in the DNA should have signals that control accurate initiation of transcription. The sequence in this region (—118 to —1) is very AT-rich (about 75% AT) and contains clusters of A and T residues (Fig. 51). The sequence from —98 to —118 is the most AT-rich (about 85% AT), the sequence from —7 to —30 immediately preceding the first ATCAG is about 80% AT, and the sequence from —31 to —74 is about 73% AT. On the other hand, the sequence from —75 to —97 is less AT-rich, about 65%, and rather random.

The spacer region from —780 to —500

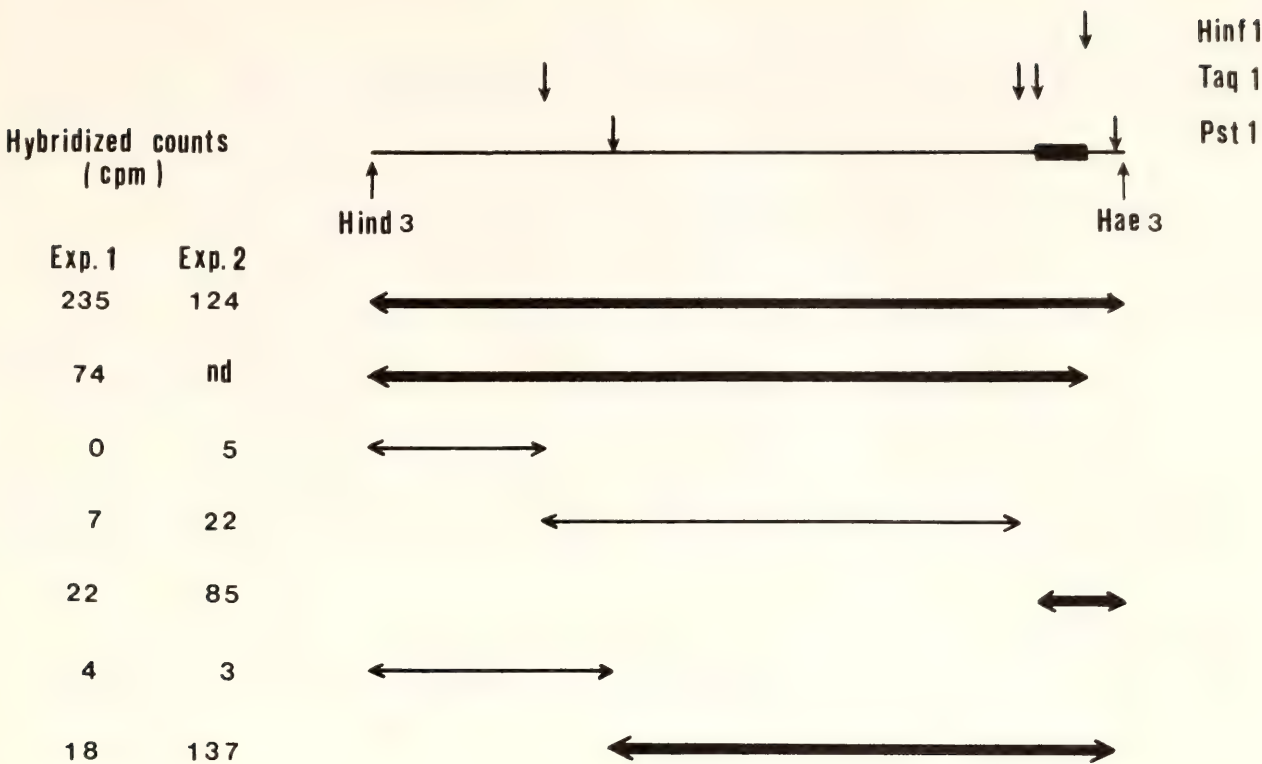


Fig. 50. Hybridization of various restriction fragments derived from the pFb29 Hind III/Hae III D fragment, using mRNA with a radioactive cap at its 5' end. Each fragment was fixed on a Millipore filter and hybridized with mRNA which had been labeled in vitro with a Vaccinia capping enzyme complex in the presence of ³H-S-adenosylmethionine. The results of two hybridization experiments are shown on the left and the summary is shown on the right. The restriction fragments where hybridization was positive are shown by thicker lines and those fragments that did not hybridize with the labeled probe are shown by thinner lines.

from the gene was sequenced (Fig. 51). It was also AT-rich and revealed occasional oligo(dA) and oligo(dT) tracts.

A sequence that could make a good hybrid with the 3' end of *B. mori* 18S rRNA was observed at +50 to +70 within the gene (Fig. 51). In many eukaryotic systems the initiation codon for protein synthesis is found not far from the 5' end of mRNA. However, neither the nucleotide sequence around +500 nor +1200 had the sequence expected for that part of the fibroin gene coding for the peptide structure (see Fig. 51). The expected sequence encoding the repetitious Gly-Ala peptides was found around +1700 bp (Fig. 51). One possible explanation for this unexpectedly long distance, at least 1200 bases, between the 5' end of mRNA and the sequence encoding the repetitious Gly-Ala peptide, is the

presence of an intervening sequence in the fibroin gene that is absent from the mRNA.

A 1-kb Intervening Sequence Interrupts the Fibroin Gene

To test the possibility of an intervening sequence in the fibroin gene, an "R-loop" experiment was carried out. The R-loop between a Bgl I digest of pFb29-7 DNA and mRNA was visualized in the electron microscope. The Bgl I core fragment of pFb29-7 DNA is 4.05 kb long (Fig. 48), and as mentioned above, a deletion had been observed in this core fragment. We observed a single R-loop in this core fragment. A representative photograph is shown in Fig. 52, and a schematic representation of the length measurements are shown in Fig. 54a. The total length of the

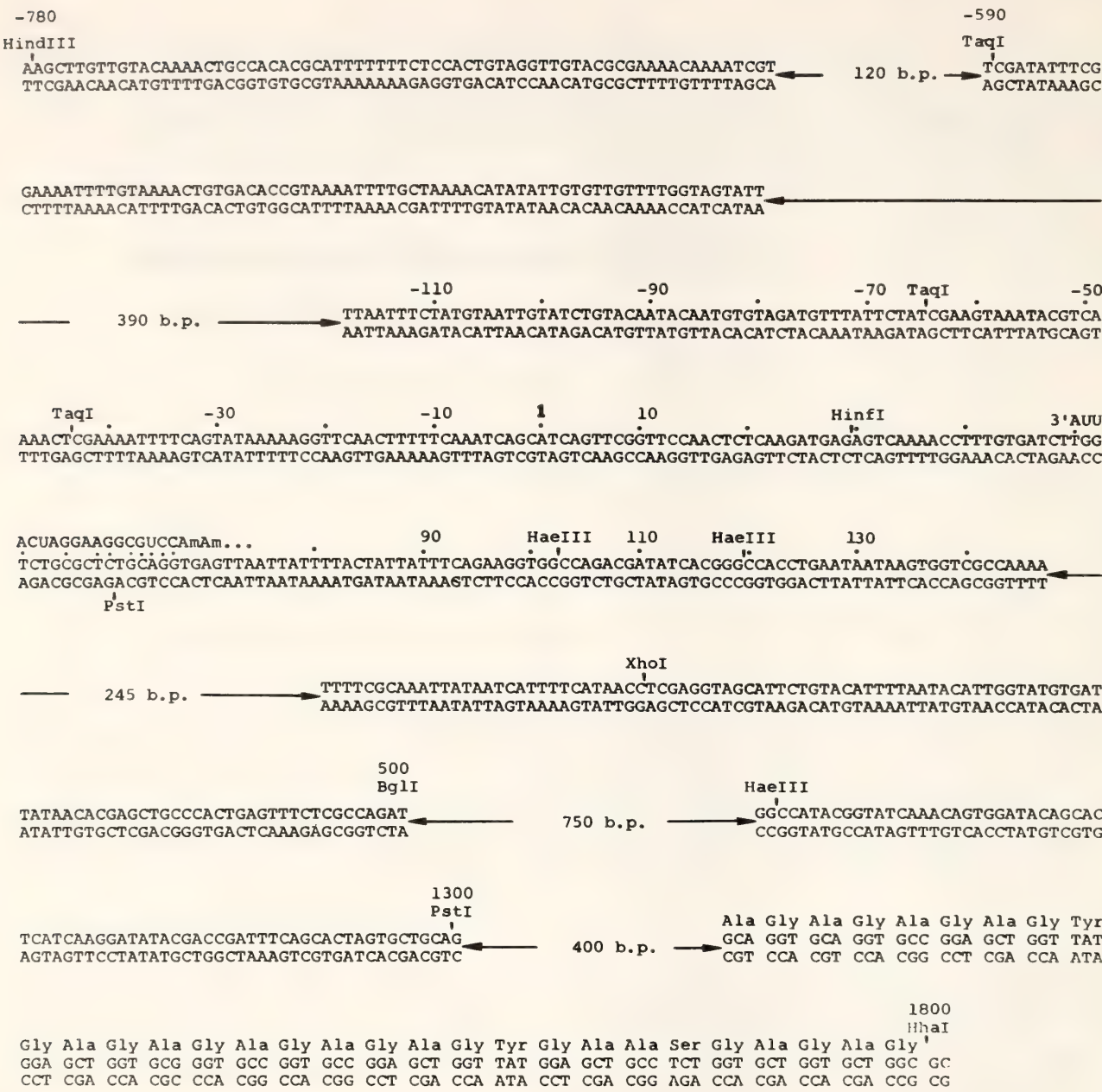


Fig. 51. The nucleotide sequence of some portions of the cloned fibroin DNA. The nucleotide sequence of the region that includes the 5' end of the gene, a region in the middle part of the intervening sequence, and a region encoding the repetitious Gly-Ala peptide are shown. The numbers denote the distance from the 5' end of the gene. The nucleotide sequence of 3' end of 18S RNA (determined by O. Hagenbüchle *et al.*) is also shown above the sequence at about +50 to 70 which can make good hybrid with 3' end of 18S rRNA. At the region coding for the repetitious Gly-Ala peptide, the amino acids are drawn above the nucleotide sequence.

double-stranded region was 4.05kb. In the R-loop, a large loop and occasionally one or more small single-stranded loops were observed. The large loop is due to the deletion observed at a fixed site in the R-loop. The small loops are probably due to branch migration through the repetitious nucleotide sequence of

the fibroin gene. The result of length measurements together with the restriction map of Bgl I shown in Fig. 48 indicates that the shorter arm is toward the 5' end of the gene. Single-stranded whiskers were seen at the 5' and 3' ends of the R-loop. A trivial interpretation is that these whiskers could have arisen by



Fig. 52. Electron micrograph of an R-loop between the Bgl I core fragment of pFb29-7 DNA and fibroin mRNA. The drawing illustrates the molecule with the solid line representing DNA and the dotted line indicating mRNA.

branch migration. Another possibility is that these regions did not hybridize to DNA. One of the whiskers at the 3' end of the R-loop could be poly(A) and part of the mRNA coded by a region of the gene near its 3' end that is not present in the recombinant DNA. As shown above, the sequence corresponding to the 5' end of mRNA is located at about 0.78 kb downstream from the 5' end of the Hind III core, and the sequence to at least 61 bases is present on mRNA. Furthermore, the 5' end of the Bgl I core fragment is 1.28 kb downstream from the 5' end of the Hind III core (Fig. 48). These results suggest that the RNA whisker at the 5' end of the R-loop is complementary to a distant and noncontiguous region beyond

the 5' end of the Bgl I core. To confirm this possibility we prepared another R-loop, using the Hind III digest of pFb29-7 DNA. The Hind III core fragment of pFb29-7 DNA is 4.54 kb long (see Fig. 48) and contains a sequence corresponding to the 5' end of mRNA. In this case, however, we rarely observed an R-loop structure. Indeed, a hybrid of a denatured DNA and mRNA was frequently observed. Representative photographs and their schematic explanations are presented in Fig. 53. The schematic representations and the results of length measurement are shown in Fig. 54b and c. The total length of the double-stranded region of the R-loop is 4.42 ± 0.10 kb (Fig. 54b), which is consistent with the

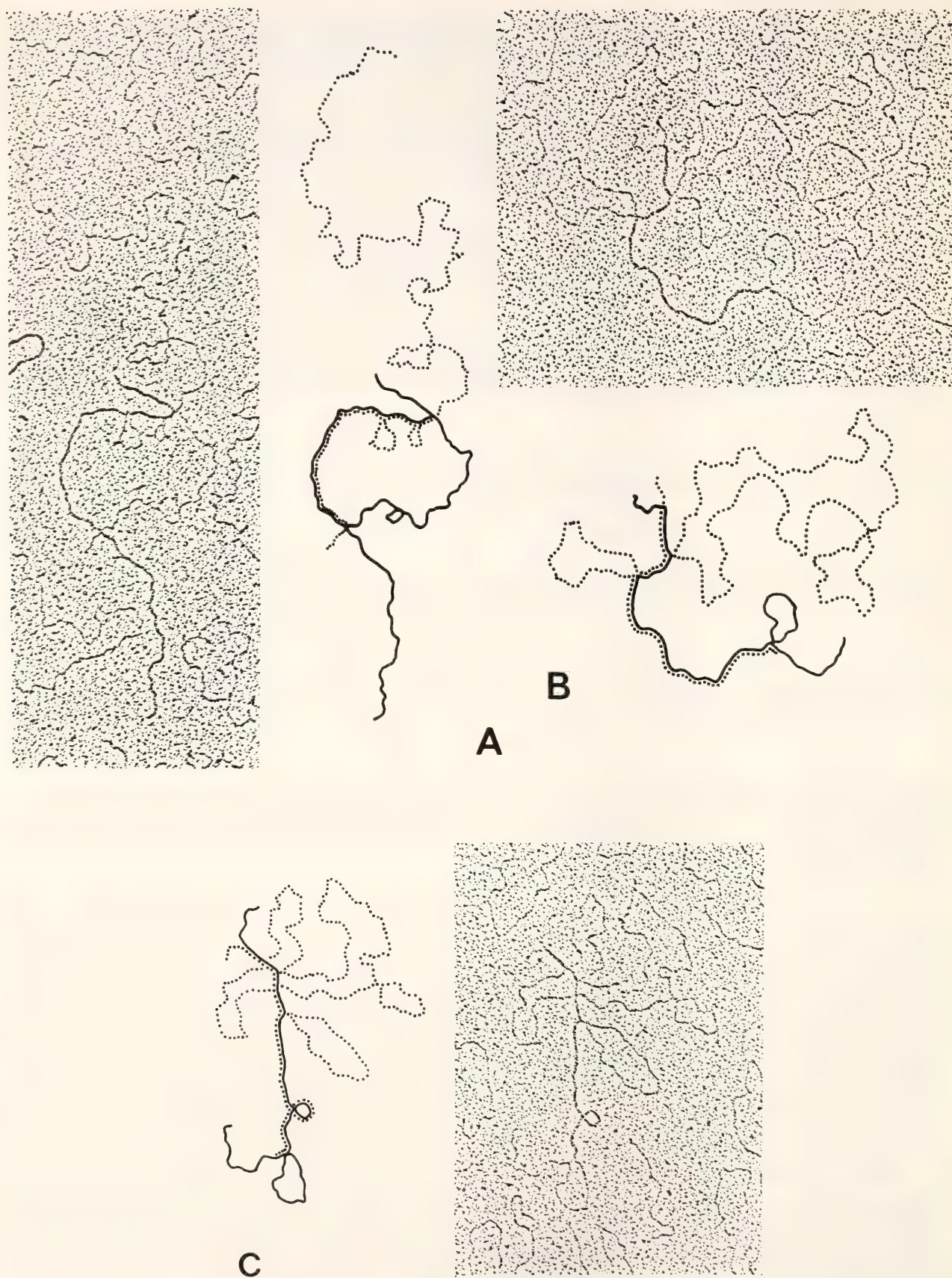


Fig. 53. Electron micrographs of hybrids between Hind III core fragment of pFb29-7 and mRNA. (A) An R-loop between the Hind III core fragment and mRNA. (B) and (C) Hybrids between denatured Hind III core fragment and mRNA. Schematic representations of these molecules are shown with the solid lines representing DNA and the dotted lines representing mRNA.

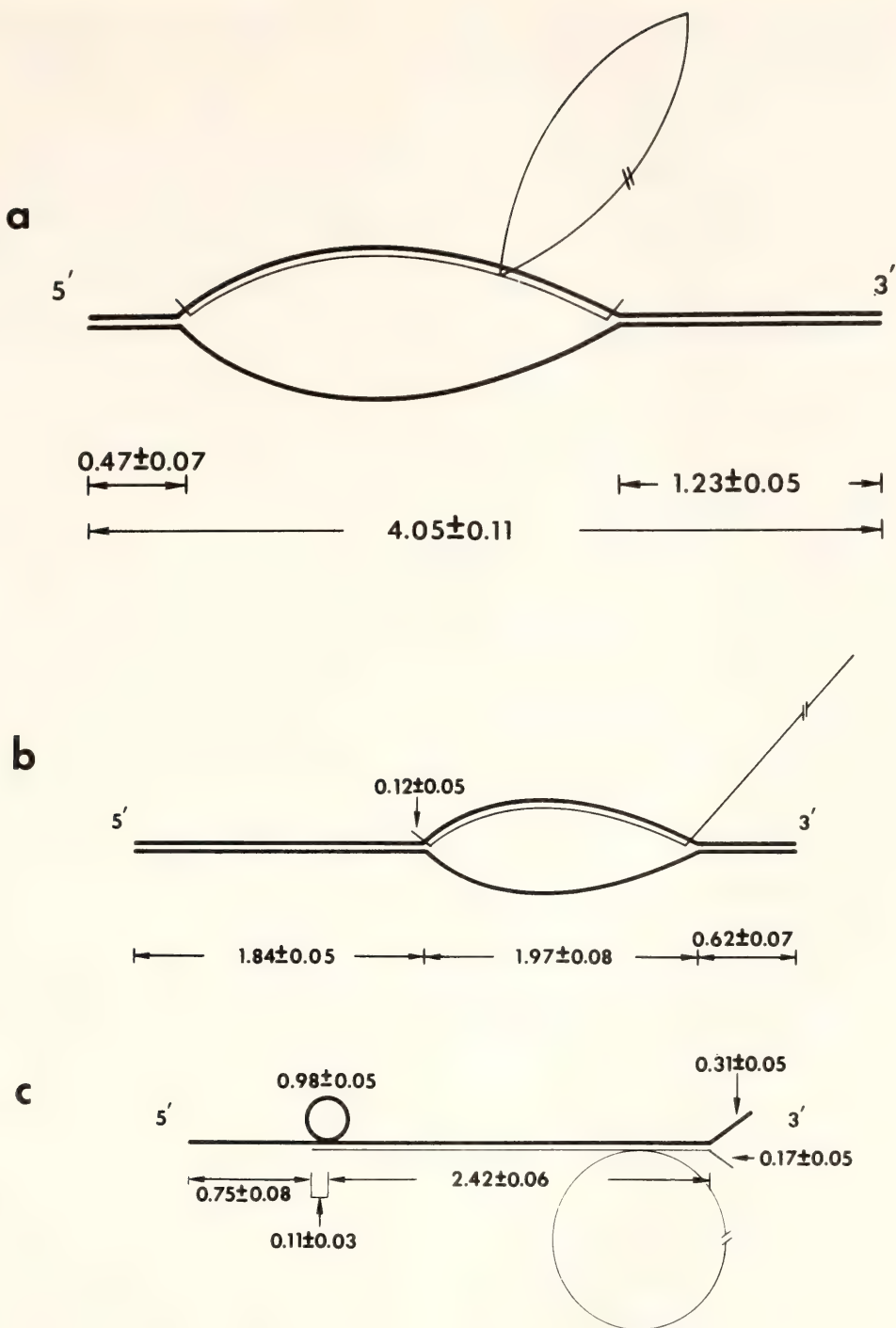


Fig. 54. Drawings of the DNA-RNA hybrids. (a) An R-loop between the Bgl I core fragment of pFb29-7 DNA and mRNA. (b) An R-loop between the Hind III core fragment of pFb29-7 DNA and mRNA. (c) Hybrids between denatured Hind III core fragment of pFb29-7 DNA and mRNA. The length of DNA's and RNA's are given in kilobases. Error limits indicate a standard deviation. The thick lines are DNA and the thin lines are RNA. The number of molecules measured was: (a) 14, (b) 12, (c) 18.

length of the Hind III core fragment. Based on the polarity of R-loop structures formed with the Bgl I core fragment and the restriction map shown in Fig. 48, we can orient the longer arm toward the 5' end of the gene. As described

above, if the sequence of the RNA whisker at the 5' end of the R-loop of the Hind III core fragment comes from the region 0.78 downstream from the 5' end of the Hind III core, the RNA whisker could hybridize with that region of DNA,

and as a result the intervening DNA segment preceding the 5' end of R-loop should be looped out of an RNA-DNA hybrid. This expected structure is seen in a hybrid of a single-stranded DNA of Hind III core and mRNA (Fig. 53b and c). The distance between the 5' end of DNA and the end of DNA loop is 1.84 kb, which is consistent with the length of the longer arm of the Hind III R-loop (Fig. 53a and 54b). The distance between the 5' end of DNA and the 5' end of the DNA-RNA hybrid (0.75 ± 0.08 kb) is consistent with the location of the 5' end of mRNA at 0.78 downstream from the 5' end of the Hind III core. Furthermore, a double-stranded region was observed preceding the DNA loop; its size is about 0.11 ± 0.03 kb, which is equal to the length (0.12 ± 0.05 kb) of the whisker seen at the 5' end of R-loop (Fig. 53a). The length of the longer one of two single-stranded parts at the 3' end of the hybrid molecules (Fig. 53b and c) is about 0.31 ± 0.05 kb, which is also consistent with the length (0.31 kb) of the fragment between the EcoRI site (near the 3' end of DNA) and the 3' end of DNA (Fig. 48). This 0.31-kb region is a part of the pMB9 vector DNA. Thus we conclude that the fibroin gene is interrupted by an intervening sequence of about 1 kb that starts about 110 bp downstream from the 5' end of the mRNA coding part of the gene.

The possibility that this intervening sequence is an artifact derived during the cloning procedure is unlikely because the same restriction fragments containing this region (like Pst I D and Hae III D of pFb29 DNA; see Fig. 48) were also found in digests of independently isolated clones like pFb19 and pBF41 (Fig. 49).

Comparison of the Gene Organization of "Active" and "Silent" Fibroin Genes

The plasmid pFb29 contains an "active" fibroin gene, since it was cloned originally from DNA from posterior silk glands, the tissue that expresses the gene (Ohshima *et al.*, *Proc. Nat. Acad. Sci.*

74, 5363, 1977). The plasmid pBF41 (a gift of J. Morrow) contains a "silent" fibroin gene that was cloned from DNA of pupae in which fibroin gene is not expressed. The comparison of their restriction maps was carried out. Pst I and Hae III digests of pFb29 and pBF41 DNA were fractionated by gel electrophoresis (Fig. 49). Except for their core fragments, all restriction fragments are the same between the two plasmid DNA's. Many other restriction enzymes like EcoRI and Hind III showed the same result (data not shown). The difference between the core fragments in the two plasmids can be explained by the different deletions in the repetitious sequence and different orientation of the cloned genes within the vector DNA. The region that was compared extends to the flanking sequence 5.8 kb distant from the 5' end of the gene. In particular, the DNA sequence of pBF41 from -42 to +101 bp region is identical to the same region of pFb29 (Fig. 51).

As shown in Fig. 48, the Pst I D fragment of pFb29 DNA seems to cover the entire intervening sequence, and the Hae III D fragment covers most of the intervening sequence. These two fragments derived from the two plasmids have the same size (Fig. 49). This result indicates that the intervening sequence is present not only in an active fibroin gene but also in a silent gene. The comparison of restriction patterns by Bgl I, Hind II, and Xho I, which cleave the DNA inside the intervening sequence (see Fig. 48), indicates that at least the nucleotide sequences recognized by these three enzymes and their location in the gene map are conserved in both pFb29-7 and pBF41. In conclusion, these tests were unable to find any difference between the 5' flanking and the intervening sequences of fibroin genes cloned from DNA extracted either from the posterior gland, which expresses the gene in the living animal, or from pupae, which do not express the gene.

PRECURSORS OF FIBROIN mRNA

Y. Ohshima and Y. Suzuki

The fibroin mRNA of *B. mori* has a cap structure, m⁷G(5')ppp(5')A^mpU^mpCp (Yand *et al.*, *Cell* 7, 339, 1976) or G(5')-ppp(5')ApPypXp (Tsujimoto *et al.*, this volume), at the 5' end. Although the mechanisms of formation of these structures in *B. mori* are not known, they could be formed directly at the triphosphate termini of primary transcripts of the fibroin gene by one of the mechanisms for cap formation known in other systems. Therefore, the site on the fibroin gene that corresponds to the 5' end of the fibroin mRNA (the cap site) is a candidate for the initiation site of transcription of the fibroin gene. One of the major interests after the fibroin gene was cloned (*Year Book* 76, p. 63; Ohshima *et al.*, *Proc. Nat. Acad. Sci.* 74, 5363, 1977) has been to determine the real initiation site of transcription. We have undertaken two lines of studies toward this purpose.

We have attempted to study reinitiation of fibroin gene transcription by nuclear fragments obtained from the pos-

terior silk glands of *B. mori*. In order to separate RNA molecules *initiated* in vitro from those only *elongated* in vitro, purine nucleoside triphosphates which have an SH-group linked to the γ -phosphorus (Reeve *et al.*, *Biochem.* 16, 4464, 1977) were used. These triphosphate analogues (γ -S-ATP or γ -S-GTP) can be used for transcription in place of ATP or GTP, but the SH-groups are incorporated only at the 5' ends of the primary transcripts. RNA was made by nuclei in the presence of γ -S-ATP or γ -S-GTP and ³H-CTP, extracted and partially digested in 0.1 N NaOH to an average size of about 200 nucleotides. RNA fragments containing an SH-group (a 5' terminus initiated in vitro) were selected by two cycles of passage through a mercury-agarose column, and hybridized with various DNA fragments from the fibroin gene plasmid pFb19 (Fig. 55). Little or no hybridization was observed around the cap site in the Hind III A fragments, but some hybridization was observed to the Hind III D fragments 1-4 kb upstream from the cap site (with γ -S-ATP) or in the Hind III B fragments (with γ -S-ATP or γ -S-GTP). With γ -S-ATP,

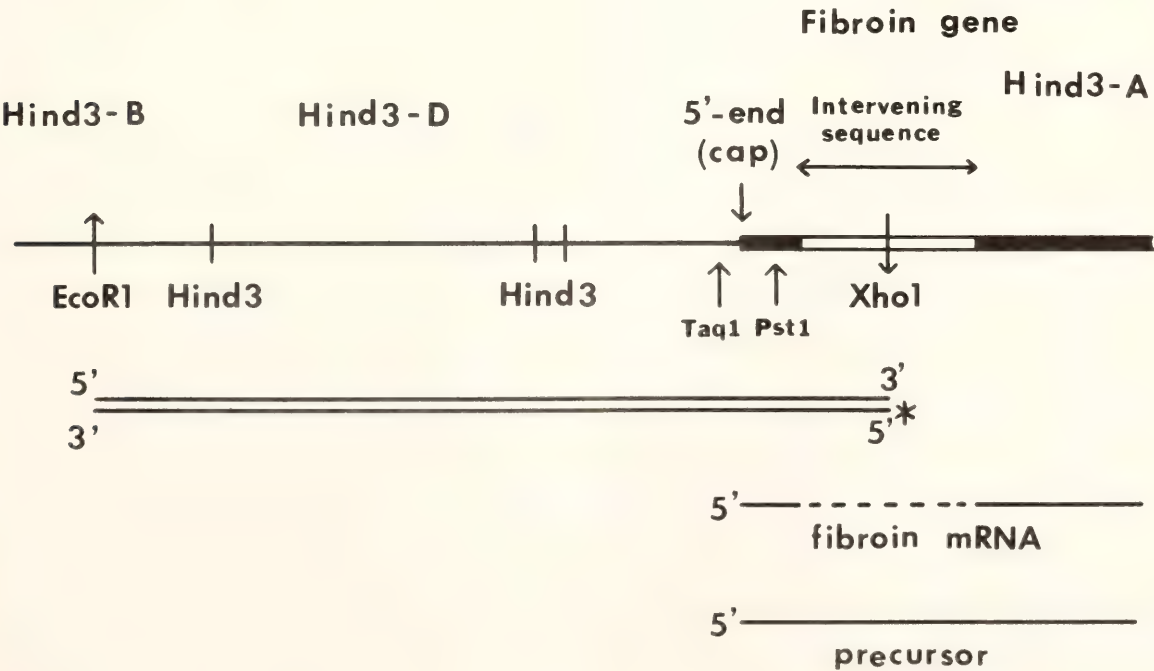


Fig. 55. Detection of a precursor to fibroin mRNA.

the hybridization with the Hind III D fragments was reduced to 2/3–1/2 by the presence of 1 μ g/ml of α -amanitin in the transcription reaction. These results suggested that RNA polymerase form II is responsible for initiation events that might be related to transcription of the fibroin gene, 1–4 kb upstream from the cap site.

To further clarify these possibilities, we have searched for precursors of the fibroin mRNA made in vivo. DNA fragments extending from an XhoI-site about 0.5 kb downstream from the cap site to an EcoRI-site about 6 kb upstream from the cap site were labeled with 32 P only at the 5' end of the XhoI-site (Fig. 55). These DNA fragments were hybridized with nuclear RNA from posterior silk glands under conditions that eliminate DNA reannealing (Casey *et al.*, *Nucleic Acids Res.* 4, 1539, 1977). The annealed products were digested with the single strand-specific nuclease S1. They were then electrophoresed in an alkaline agarose gel and subjected to autoradiography. During this study, an intervening sequence, which is not present in the fibroin mRNA, was found in the fibroin gene near the cap site (Tsujimoto *et al.*, this volume). Since the XhoI-site is in the middle of the intervening sequence, hybridization of the 32 P-XhoI-EcoRI fragments with the fibroin mRNA followed by digestion with S1-nuclease did not produce any labeled band on the gel. On the other hand, when nuclear RNA from posterior silk glands was used, a band about 550 bases long was observed under various conditions of hybridization and digestion with S1. There are TaqI and PstI sites near the cap site (Fig. 55). 32 P-XhoI-TaqI and 32 P-XhoI-PstI fragments were prepared from the 32 P-XhoI-EcoRI fragments and used as specific size markers to locate the 3' end of the protected DNA in the band or the 5' end of the protected RNA, within ± 10 bases from the cap site. When total or nuclear RNA from middle silk glands where fi-

broin synthesis does not take place was used, no radioactive band was observed on the gel. These results show that at least a part of the intervening sequence, which is absent in the fibroin mRNA, is transcribed in posterior gland nuclei. These nuclear transcripts are probably precursor to the fibroin mRNA and are processed by removal of the intervening sequence. The 5' end of the transcript most likely corresponds to the cap site. No precursors initiated upstream of the cap site have been identified. These results strongly support the possibility that the cap site may be the initiation site for fibroin gene transcription.

TRANSCRIPTION OF THE CLONED FIBROIN GENES IN NUCLEAR HOMOGENATES

Y. Suzuki and P. E. Giza

For faithful transcription of fibroin genes in vitro we require two criteria of fidelity. One is the initiation of transcription at the correct site, and the other is strand selectivity. As discussed in a previous section, the cap site is probably the site of initiation. We plan to use γ -S-ATP and γ -S-GTP together with CTP and UTP in the reaction mixture, trap the newly initiated molecules on a mercury-agarose column by affinity, and hybridize the trapped RNA's to various restriction fragments of fibroin gene. For the second criterion we have separated DNA strands of the purified Hind III/EcoRI A fragment of pFb29 or pBF41 (see Fig. 48). This fragment contains most of the mRNA coding sequence and a flanking sequence of about 800 bp adjacent to the 5' end of the gene and lacks about 1% of the mRNA coding sequence at the 3' end. Since the mRNA sequence is about 65% G+U, the coding strand should be 35% G+T and the anticoding strand 65% G+T, which can be easily separated from each other in alkaline CsCl gradient. An example of such a separation is shown in Fig. 56. Hybridization of 3 H-

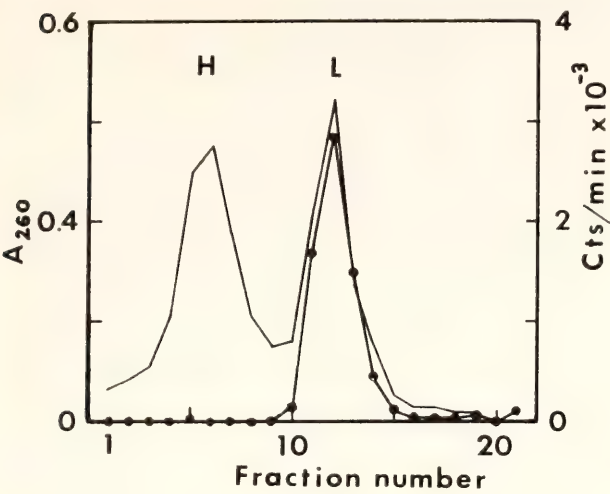


Fig. 56. Strand separation of fibroin gene in an alkaline CsCl gradient. The plasmid pFb29 was digested with Hind III, and the fragment A (see Fig. 48) was purified by agarose gel electrophoresis. About 50 μ g of the A fragment was centrifuged in an alkaline CsCl gradient in a Spinco no. 40 rotor at 35,000 rpm and 20°C for 68 hr. A 1/40 aliquot was used for hybridization with ¹²⁵I-fibroin mRNA. (—), A₂₆₀; (—●—), cts/min.

mRNA with the gradient fractions indicates that the strand separation is almost complete.

A rationale for the use of the cloned fibroin gene in nuclear homogenates is that the homogenates might supply RNA polymerase II, histones and nonhistone

proteins to the exogenous fibroin gene, and transcribe the gene faithfully.

We first tested the germinal vesicles of *Xenopus laevis*, which were known to transcribe the exogenous 5S RNA genes faithfully (Year Book, this volume). But no strand selection of fibroin gene was detected in this system (Table 9). And a low concentration of α -amanitin, known to inhibit fibroin gene transcription (Suzuki *et al.*, *J. Mol. Biol.* 107, 182, 1976) did not effectively inhibit the synthesis of RNA hybridized to the coding strand. We therefore abandoned the use of this system.

We then began to study nuclear homogenates of the posterior silk gland of *B. mori*. This system continues endogenous synthesis of fibroin mRNA (Table 10), which could complicate the analysis of transcripts from an exogenous template. However, the addition of pFB29 gives 10-fold to 25-fold stimulation of fibroin gene transcription (Table 10). An apparent preference for the coding strand selectivity has been observed reproducibly (Table 10). The validity of this observation rests on the assumption that the noncoding strand transcripts do not anneal with endogenous unlabeled

TABLE 9. Nonspecific Transcription of the Fibroin Gene in pFB29 by Various RNA Polymerases

Experimental Systems	Hybridization with		Coding/Noncoding
	Coding Strand	Noncoding Strand	
Exp. 1*: Germinal vesicles of <i>X. laevis</i>	14400 cpm	13600 cpm	1.1
Exp. 2†: Germinal vesicles of <i>X. laevis</i>			
(a) Control	2160	4050	0.53
(b) + α -amanitin 2 μ g/ml	2080	2820	0.74
Exp. 3: <i>E. coli</i> RNA polymerase	18900	16800	1.1
Exp. 4:			
<i>B. mori</i> RNA polymearse I and III	169	206	0.82
<i>B. mori</i> RNA polymerase II	199	147	1.4
Wheat germ RNA polymerase II	1755	518	3.4

* Total RNA synthesized was used for the hybridization.
† Only the RNA trapped on a mercury-agarose column was used for the hybridization.

TABLE 10. Strand-Specific Transcription of the Fibroin Gene by Nuclear Homogenates of the Posterior Silk Gland

Systems*	Hybridization with		Coding/Noncoding	
	Coding strand (³² P cts/min)	Noncoding strand	Apparent	Corrected
<i>Exp. 1</i>				
Psg* endogenous	371	45	8.2	4.2
Psg endogenous +pFb29	9161	45	204	52
<i>Exp. 2</i>				
Msg† endogenous	14	11	(1.3)	(1.1)
Msg endogenous +pFb29	114	260	0.44	0.88
Msg endogenous +pBF41	212	234	0.91	0.65
Psg endogenous	136	40	3.4	1.7
Psg endogenous +pFb29	3219	170	18.9	5.5
Psg endogenous +pBF41	2462	225	10.9	3.0
<i>Exp. 3</i>				
Psg endogenous	158	nd‡	nd	nd
Psg endogenous + α -amanitin 5 μ g/ml	21	nd	nd	nd
Psg endogenous +pFb29	1609	nd	nd	nd
Psg endogenous +pFb29 + α -amanitin 5 μ g/ml	612	nd	nd	nd

* Nuclear homogenate of the posterior silk gland.

† Nuclear homogenate of the middle silk gland.

‡ Not determined.

fibroin mRNA. To monitor this possibility, ³H-RNA that was transcribed from pFb29 by *E. coli* RNA polymerase and showed approximately 1:1 hybridization to coding and noncoding strand (Table 10, exp. 3) was added as an internal standard to the reaction mixture from the beginning. The apparent coding to noncoding ratio in Table 10 was divided by the ratio observed for the internal standard, and the resultant value was shown as the "corrected" coding to noncoding ratio. The corrected ratio shows coding strand preference for both

endogenous and exogenous templates. The coding strand transcripts were inhibited 87% for the endogenous synthesis and 62% for exogenous synthesis by low levels of α -amanitin (Table 10, exp. 3). This L-strand preference was not observed in the nuclear homogenate from the middle silk gland (nonfibroin producer) or the germinal vesicles of *B. mori*. The plasmid pBF41, which contains a fibroin gene derived from pupa DNA, was also active as an exogenous template, and similar strand preference was seen.

TRANSCRIPTION OF THE FIBROIN GENE
BY PARTIALLY PURIFIED *B. mori*
RNA POLYMERASE II
M. Tsuda and Y. Suzuki

The cloned fibroin gene will be a good tool to analyze the regulation of specific gene transcription by reconstituting it with the essential components.

We have partially purified RNA polymerase II from the posterior silk glands of *B. mori* by the fractionation procedure described in Table 11. The overall purification was about 140-fold. The activity was completely sensitive to low concentrations of α -amanitin as predicted for RNA polymerase II but revealed an optimum at 26°C rather than at 37°C. We have tested whether RNA polymerase II

in this fraction has the intrinsic capability of the selective and accurate transcription. As shown in Table 9, experiment 4, the preliminary results show that this RNA polymerase II as well as RNA polymerase I and III transcribes the noncoding strand as effectively as the coding strand of the fibroin gene in pFb29. Wheat-germ RNA polymerase II showed a slight L-strand preference (Table 9, exp. 4), but a meaningful interpretation of this result awaits further study.

Using the initiation and strand selection assays described elsewhere in this Report, we are attempting to reconstruct accurate transcription of the fibroin gene in vitro.

TABLE 11. Solubilization and Partial Purification of RNA Polymerases from the Posterior Silk Glands of *B. mori*

Fraction	Volume (ml)	Protein (mg)	Activity (units)		α -Amanitin Sensitive Activity	
			α -Amanitin Insensitive*	α -Amanitin Sensitive†	Recovery (%)	Specific Activity (units/mg)
0.1 M (NH ₄) ₂ SO ₄ supernatant	215	309	125,900	54,700	100	177 (×1)
(NH ₄) ₂ SO ₄ Ppt fraction	66	210	73,600	43,400	19	107 (×1.2)
DEAE-cellulose			53,000	22,100	40	
Glycerol gradient (10–30%)			10,400	13,100	24	
Pooled fraction	1.5	0.53		13,000		24,500 (×140)

* RNA polymerase I & III of *B. mori* are totally resistant to high concentration of α -amanitin (200 μ g/ml).
† RNA polymerase II is completely inhibited by low concentration of α -amanitin (1 μ g/ml).

STUDIES ON GENE ORGANIZATION IN EUKARYOTES

I. B. Dawid, M. Dworkin, E. O. Long, E. Rastl, and W. Wahli
with the technical assistance of M. Rebbert

In the past year we continued a number of studies reported in previous *Year Books* and initiated some new projects. A more detailed analysis has been carried out on the structure of rDNA in *Drosophila melanogaster*, with particular em-

phasis on the structures of the nontranscribed spacer and the insertion into the 28S RNA gene region. The question whether this insertion is transcribed into RNA was studied. We also cloned a series of DNA molecules derived from regions

outside the ribosomal cluster that carry sequences homologous to the ribosomal insertion.

A second project that continues earlier work is the characterization of poly-(CA)-containing RNA from *Xenopus laevis* mitochondria and the mapping of these RNA molecules on the mtDNA.

Two new projects were begun. We have cloned cDNA copies of vitellogenin mRNA and characterized them in various ways; they are being used to study the structure of the gene within the *Xenopus* genome.

The second new project involves sets of genes that are active in *Xenopus* embryos. Experiments are under way to clone a set of DNA molecules homologous to mRNA's active in one particular embryonic stage and to use these cloned molecules to study the expression of the corresponding genes through development.

A project that was completed in the past year involves the isolation and characterization of human rDNA.

RIBOSOMAL DNA AND RELATED SEQUENCES IN *Drosophila melanogaster*

*E. O. Long and I. B. Dawid,
in collaboration with
P. K. Wellauer**

In *Year Book 76*, pp. 75–77, we reported the cloning of rDNA from *D. melanogaster* and some properties of these molecules. We have characterized further the structure of these rDNA fragments. As reported previously, most cloned fragments are full-length repeating units, since most rDNA repeats in *Drosophila* have a single EcoRI site in the 18S RNA gene. Some rDNA repeats are characterized by an interrupted 28S RNA gene; in our collection of full-length

rDNA clones we find continuous repeats and repeats with insertions of three size classes. The structure of these molecules is shown in Fig. 57. One such map (clone Dmra56) was shown in *Year Book 76*; the current map gives slightly larger distances because of more detailed electron microscopic analysis. Hybridization with labeled restriction fragments and extensive heteroduplex mapping in the electron microscope have shown that the 1-kb and 0.5-kb insertions are homologous in sequence to the right portion of the 5-kb insertions. Because of this homology we classify these molecules as type 1 insertions. As reported in *Year Book 76*, type 1 insertions are present in about 50% of all rDNA repeats on the X chromosome but are rare or entirely absent from Y chromosomal rDNA.

Figure 58 shows the structure of four cloned rDNA fragments that represent only about half of a repeating unit. These clones are the result of the fact that some insertions carry at least one EcoRI site. The sequences interrupting the 28S gene in these repeats have no homology to any part of the 5-kb (type 1) insertion. Therefore, we classify EcoRI restrictable insertions as type 2. One clone, DmrY24, is unusual in that the 28S gene is interrupted at a different position than in all other clones or in all genomic rDNA molecules that we have measured in the electron microscope. We do not know anything about the origin of this particular cloned rDNA fragment.

Figure 59 shows the structure of an unusual rDNA molecule. This structure is explained most easily by assuming the deletion of a segment of rDNA including the entire 18S gene region, although a rearrangement involving the insertion of a portion of a repeat into another repeat is equally possible. This rearrangement is not likely to be a cloning artifact because we found a DNA molecule with a closely similar structure in a sample of uncloned rDNA that had been isolated directly from *Drosophila*.

* Swiss Institute for Experimental Cancer Research, Lausanne, Switzerland.

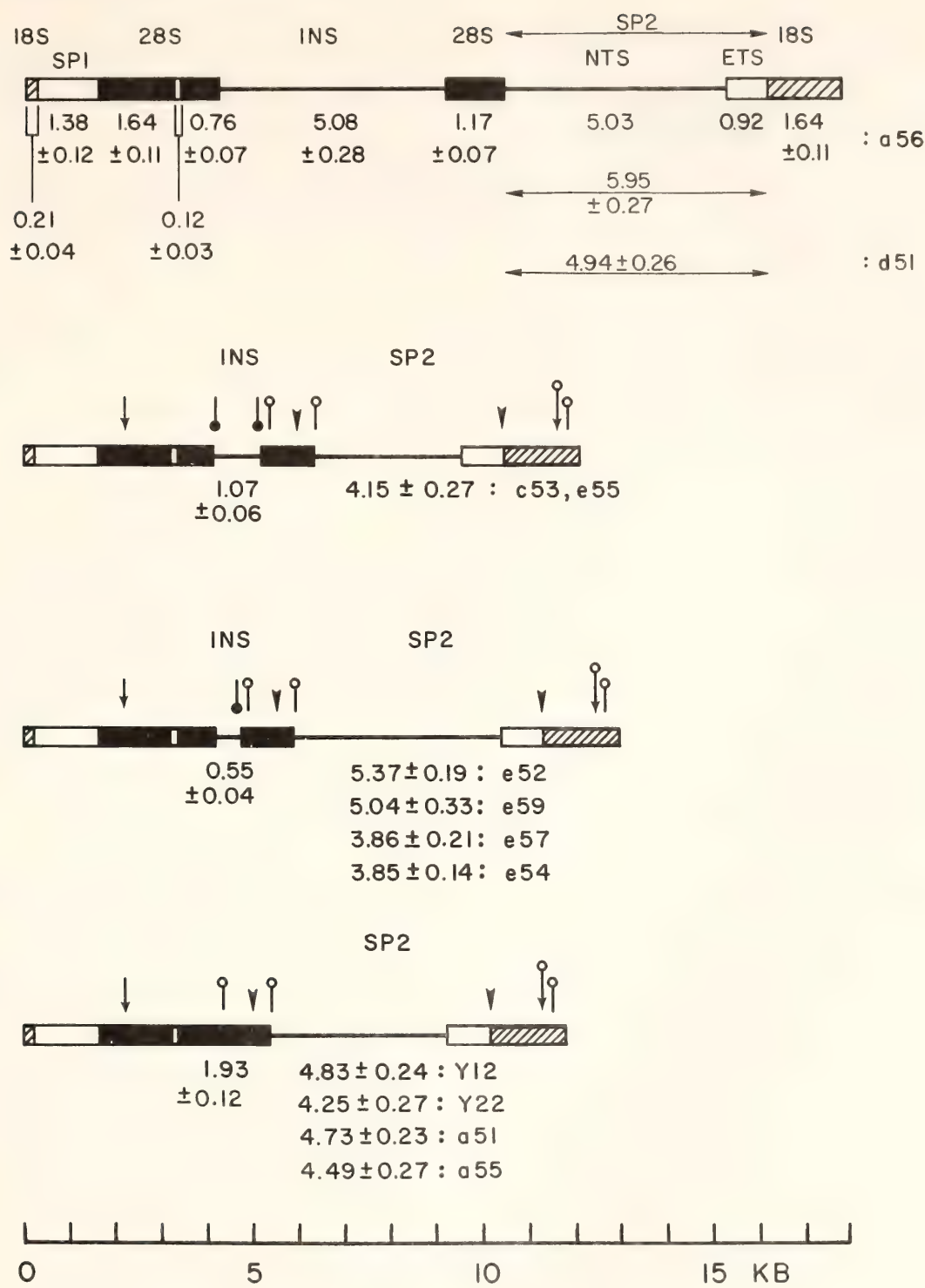


Fig. 57. Maps of cloned rDNA fragments representing full-length repeating units. Each map shows a repeat with one particular size class of insertion. The 28S RNA sequences are shown as heavy bars and the 18S regions as hatched bars. Transcribed spacer regions including the gap in the 28S gene are shown as open bars. Below each region the size with standard deviation is given in kb. At the right end the name of each clone is listed, e.g., a56 standing for Dmra56. In the case of cloned fragments with the same insertion size (or no insertion), different spacer lengths are listed under each other with corresponding clone designations. The lengths of all regions in the molecules are shown at the top (a56); in the lower maps only those regions are labeled that differ in length from the corresponding region in a56. Restriction sites are indicated as follows: ↓ SmaI, † Hind III, ‡ BamHI, ▼ Hae III. Not all Hae III sites are shown as described in the text. The molecules start and end at EcoRI sites.

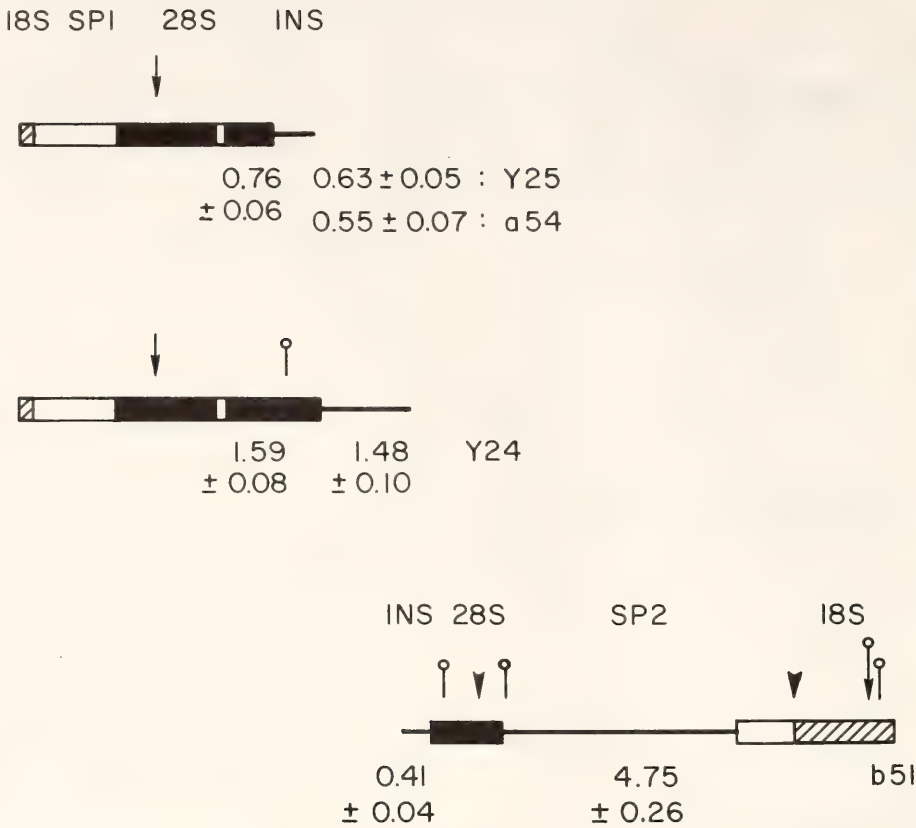


Fig. 58. Maps of cloned EcoRI rDNA fragments of less than repeat size. The meaning of symbols is described in the legend to Fig. 57.

Mapping of the rRNA Precursor

One aspect of the mapping experiments summarized in Figs. 57 to 59 requires further comment. We have mapped the region coding for the rRNA precursor by forming R-loops between large nuclear RNA, isolated from *D. melanogaster* embryos, and restriction fragments of cloned rDNA. Such R-loop molecules

were measured in the electron microscope and allowed us to determine that about 0.92 kb of the spacer is transcribed before the 18S sequence. Figure 60a shows an R-loop obtained with a Hind III fragment (from clone Dmra56) that contains most of the spacer and 18S RNA gene (see Fig. 57). R-loops were also formed with a full repeating unit (clone Y22).

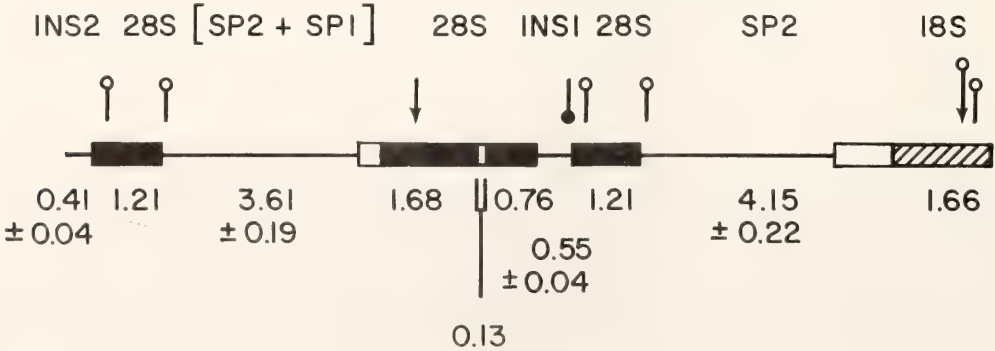


Fig. 59. Map of the cloned rDNA fragment Dmrc52. Symbols are described in legend to Fig. 57. The short arrow below the map designates the position at which a rearrangement occurred. See text for further explanation.

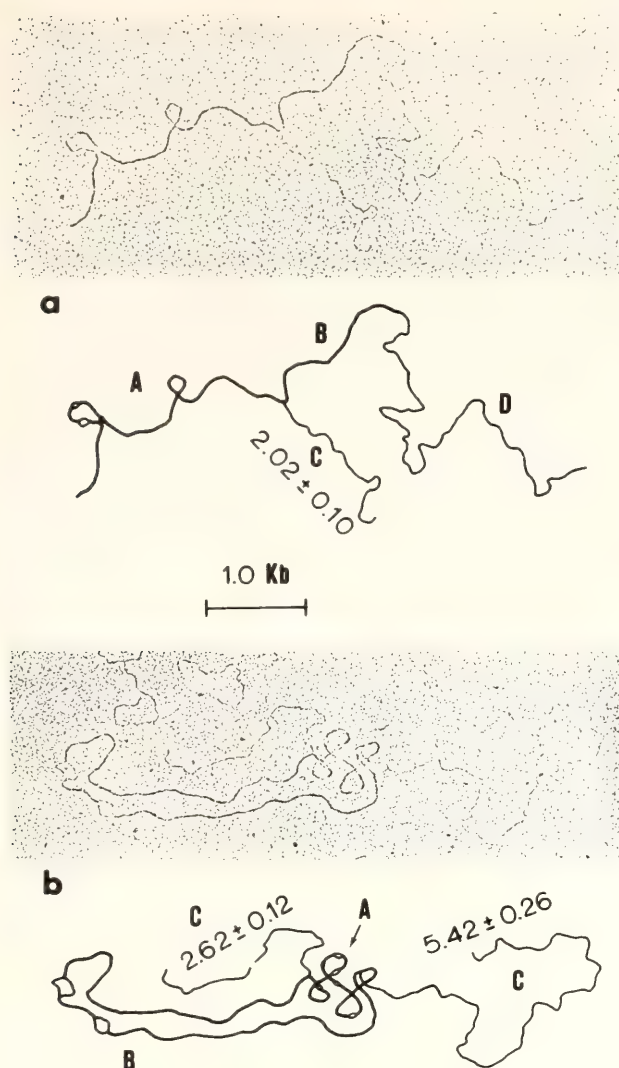


Fig. 60. R-loops between large nuclear RNA (28S) from *D. melanogaster* embryos and restriction fragments of cloned rDNA. Large nuclear RNA from *D. melanogaster* embryos was incubated with rDNA to form R-loops. The resulting molecules were photographed in the electron microscope. Capital letters refer to the nature of the strand(s): A, double-stranded DNA; B, RNA/DNA hybrid; C, single-stranded DNA; D, single-stranded RNA. The size of single-stranded DNA (C) is given in kb+S.D. (a) R-loop molecule with the Hind III fragment of a56 which contains most of the spacer and a large part of the 18S RNA gene (see Fig. 57). The length of the single-stranded branch is based on the measurements of 36 molecules. (b) R-loop formed with the entire rDNA fragment (EcoRI fragment) of Y22 which is a continuous repeating unit (Fig. 57). The rRNA precursor hybridizes to both sides of the DNA molecule, forming a circle.

In the latter case, the rRNA precursor hybridized to both ends of the fragment, forming a circle (Fig. 60b). By adding

the sizes of the two displaced DNA single strands we obtain a value of 8.0 ± 0.29 kb for the length of the rRNA precursor. For comparison, by adding the sizes measured individually for the external transcribed spacer, 18S gene, internal transcribed spacer (Sp1), and the 28S gene we obtain a value of 7.84 ± 0.23 kb. The difference is within the standard deviation of the measurements and need not be real. At this level, the data neither support nor rule out the existence of a short transcribed spacer at the 3' end of the rRNA.

Heteroduplex Mapping of Cloned rDNA Fragments

We compared many of the cloned rDNA fragments by analysis of heteroduplexes in the electron microscope. Homoduplex molecules were examined as a control. In a fraction of these molecules we observed deletion loops in the nontranscribed spacer region. Such loops may arise in homogeneous molecules that are internally repetitive as a result of misalignment of the two strands. The occurrence of these loops suggests that the spacer in *Drosophila* rDNA is internally repetitive. In heteroduplex molecules deletion loops were seen in the spacer as a result of length differences of the various rDNA repeats. Figure 61 shows the position of loops in six pairs of heteroduplexes. Only deletion loops were seen, showing that the shorter spacers are homologous to the longer spacers along their entire length. The position of deletion loops was variable within each pair of cloned rDNA fragments, again suggesting repetitive sequences within the spacer. Loops occurred in insertion and in spacer regions. When two fragments were annealed which had type 1 insertions of different length, a loop formed at a unique position. These measurements show that the shorter insertions of 0.5 and 1 kb are homologous to the rightmost part of the 5-kb insertion. Figure 61f

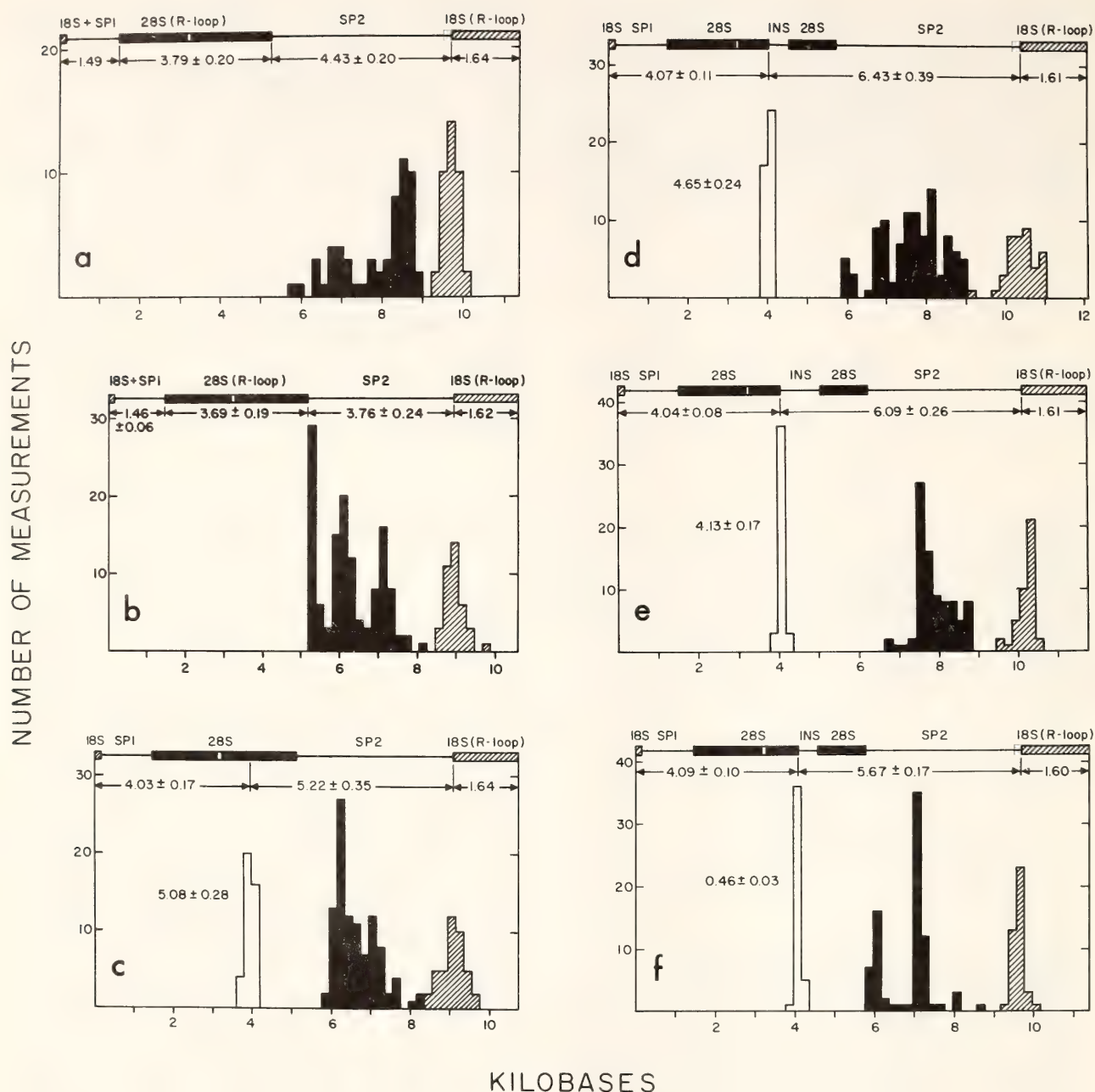


Fig. 61. Histograms of loop positions in heteroduplex molecules between cloned rDNA fragments of different repeat lengths. In each combination of fragments the DNA was annealed first and then R-loops were produced with 18S RNA (see Fig. 57). The positions of the R-loops are shown as hatched regions; loops in the nontranscribed spacer region are shown as solid black regions; loops at the position of the insertion are shown as open regions. At the top of each histogram a map of the duplex is shown, with various regions indicated as in Figure 57. Insertion regions are included in the duplex map only in those cases where both strands have an insertion so that duplex DNA forms in this region. The sizes of the various segments are given with their standard deviations in kb. When insertion loops occur in a heteroduplex, their size is given next to their histogram position. Sizes of loops in the spacer are not listed. Chromosomal origin of clones is listed where known. (a) Dmra51 (X chromosomal, continuous) /Dmra55 (X chromosomal, continuous); (b) DmrY12 (Y chromosomal, continuous) /DmrY22 (Y chromosomal, continuous); (c) Dmra56 (X chromosomal, 5 kb insertion) /DmrY22; (d) Dmra56/Dmre52 (0.5 kb insertion); (e) Dmra56/Dmrc53 (1 kb insertion); (f) Dmre52/Dmre55 (1 kb insertion). We have also examined the following heteroduplexes: Dmra51/Dmrc53; Dmra51/Dmra56; Dmra51/DmrY22; Dmre52/Dmre54 (0.5 kb insertion).

makes the point that the 1-kb insertion is not a duplication of the 0.5-kb insertion as the size relations might suggest. If it were a duplication of the 0.5-kb insertion, the sequence could anneal with the right or left half of the 1-kb insertion, leading to loops with equal frequency at positions 4 and 4.5 kb from the left EcoRI site (origin of the map). In fact, all loops map at 4 kb in a single peak. The 1-kb insertion is not an inverted repeat of the shorter sequence, since no snap-back molecules were seen in these molecules.

The heteroduplex experiments thus lead to the following conclusions. Insertions of type 1 are homologous at their right ends and are not internally repetitive, at least not on a scale that would be visualized by electron microscopy. Non-transcribed spacers are homologous to each other, vary in length, and are internally repetitive. These latter conclusions are supported further by restriction endonuclease mapping reported below.

As shown in *Year Book 76*, the nontranscribed spacers in rDNA derived from the X and the Y chromosome are very similar to each other except for length differences. This conclusion was also supported further by restriction analysis.

Restriction Analysis of Spacers from Cloned rDNA

The spacers of four different rDNA clones were analyzed by restriction endonuclease mapping. Two clones are derived from X chromosome rDNA—one a continuous gene (a55) and the other a gene with a 5-kb insertion (a56). Another clone is derived from the Y chromosome and is an uninterrupted gene (Y22). The fourth clone has a short insertion but its chromosomal origin is not known (e54). Furthermore, clones a56 and e54 have, respectively, the longest and the shortest spacer in our collection of rDNA clones. The Hind III fragments containing the spacer (see Fig. 57) were end-

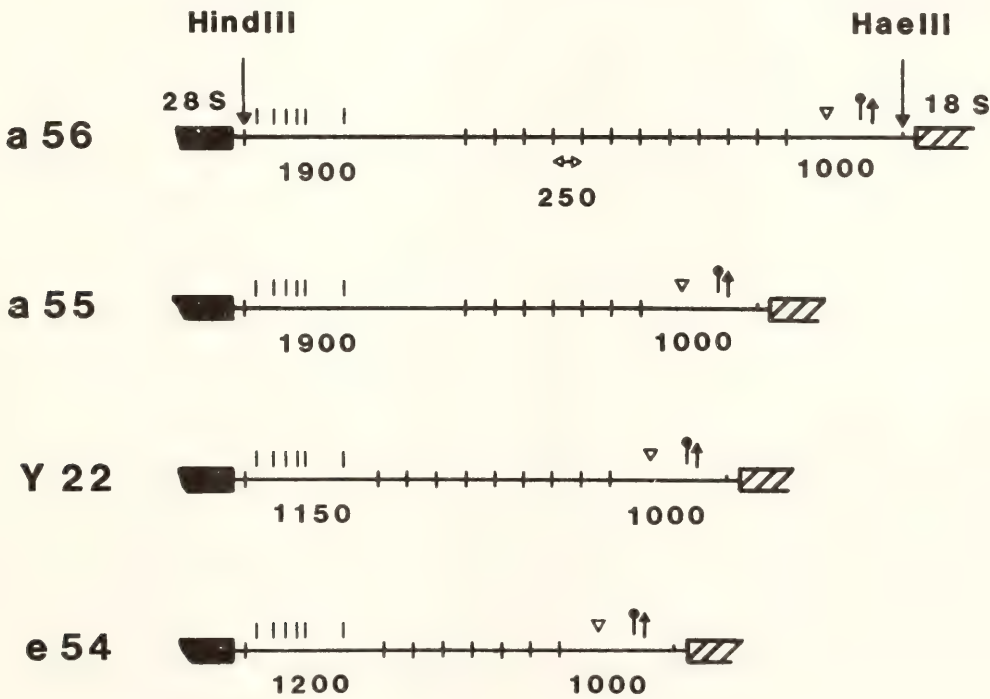


Fig. 62. Restriction map of spacers from cloned *D. melanogaster* rDNA. The sites of restriction by the following endonucleases are indicated as follows. AluI: vertical bar across the horizontal line; the sizes of the AluI fragments are given in bp. EcoRI*: vertical bar above the horizontal line; only the first six EcoRI* sites starting from the Hind III site are shown. There are a few more EcoRI sites throughout the different spacers, but they are not conserved in the different clones. TaqI (▽), Hinf (↑), HhaI (↑). 16 other restriction endonucleases tested did not cut the Hind III-Hae III spacer fragment.

labeled at their 5' ends. After digestion with Hae III, the large spacer fragment, now labeled at one end, was isolated by gel electrophoresis and used for mapping by partial restriction enzyme digestion (Fig. 62). These maps were confirmed and refined by digesting unlabeled spacer fragments with various combinations of restriction enzymes and analyzing the resulting fragments.

The conclusions from this analysis are the following. Spacers are internally repetitive, as shown by the regular 250-bp interval between AluI sites. The number of these repeated elements varies from one gene to another. All clones have a conserved 1.0-kb fragment at the right end of the spacer, generated by AluI-Hae III digestion. Most of this fragment codes for the external transcribed spacer (see above). As evidenced by EcoRI* mapping, a sequence at least 850 bp long is also conserved in all clones at the left end of the spacer. There is no striking difference in the organization and structure of spacers derived from the X or the Y chromosome or from genes with or without an insertion. The spacer heterogeneity between rDNA genes is less extensive in *D. melanogaster* than it is in *Xenopus laevis*.

Are the Insertion Sequences— Transcribed in vivo?

More than half of the ribosomal genes of *D. melanogaster* have an insertion in the 28S RNA coding sequence. We wondered whether these genes are functional. Furthermore, sequences homologous to type 1 insertions are also present in genes outside the nucleolar organizer (see *Year Book* 76, and below). We asked whether these sequences are transcribed. As a first approach to these questions, we tested whether any RNA complementary to type 1 insertion sequences could be found in *D. melanogaster* embryos. The experimental protocol was to hybridize in solution a large excess of total unlabeled

RNA with highly labeled insertion sequences derived from cloned rDNA fragments. Formation of hybrid molecules was tested by digestion with the single-strand-specific nuclease S1. Such liquid hybridizations are quantitative assays and allow the detection of very dilute RNA species, provided that large amounts of total RNA and highly labeled DNA can be used. Embryos were chosen as starting material, crude nuclear and cytoplasmic fractions were prepared, and RNA was isolated from each. RNA was then annealed with restriction fragments corresponding to the insertion region that had been labeled by nick translation. To test that S1-resistant counts which appeared during incubation were not due to DNA reassociation, aliquots were digested with RNase under conditions that destroy hybrids before further digestion with S1. Internal controls were included to show that duplex DNA does resist S1 digestion after the RNase treatment.

These hybridization tests led to the conclusion that no nuclear or cytoplasmic RNA complementary to type 1 insertion sequences was present. The average detection level was 10 RNA molecules per cell. Several control experiments were carried out. First, the kinetics and extent of self-hybridization of the nick-translated probe were determined. This test showed that the insertion probes are able to reassociate and that insertion sequences are not internally repetitive. Second, the RNA preparation was hybridized to a nick-translated fragment derived from the rDNA gene region. Both kinetics and extent of reaction were as expected from reasonable assumptions about rRNA abundance. Third, the integrity of the RNA and DNA was tested by electrophoresis after annealing.

It is known that several thousand rRNA precursor molecules are transcribed in each nucleus of *D. melanogaster* embryos. From the results obtained in our hybridizations it is clear that the

rRNA genes carrying insertions are not transcribed with the frequency of the continuous genes in *Drosophila* embryos. We conclude that interrupted rRNA genes are either not expressed in embryos, expressed in such a way that the insertion sequences are not transcribed, or expressed at a very low level. The third possibility could include relatively frequent transcription of insertions in a few cells. These conclusions suggest that interrupted rRNA genes in *Drosophila* differ from several recently discovered interrupted protein-coding genes in other eukaryotes. In those cases the intervening sequences are transcribed into precursor RNA molecules and are later removed by splicing. In *Drosophila* such a mechanism is not important in a majority of embryo cells and may in fact not occur at all during expression of rDNA genes.

Non-rDNA Insertion-Type Sequences in Drosophila

We reported previously (*Year Book* 75, pp. 78–81) that sequences homologous to the ribosomal insertion occur in the *Drosophila* genome outside the nucleolus organizer. Hybridization experiments *in situ* carried out by M. Lauth in collaboration with us have shown that these sequences are localized in the chromocenter of the *Drosophila* salivary gland chromosome. These sequences are homologous to type 1 insertions. We have looked for, but have not found, any DNA regions outside the rDNA cluster that would be homologous to type 2 insertions. To study in more detail the non-rDNA insertion sequences, we cloned a set of DNA molecules containing such sequences and we are studying 40 such clones. The results to date confirm our earlier conclusion that insertion-type sequences are interspersed with other kinds of DNA sequences not related to insertions. These “flanking” sequences are being studied further. We found one example of a flanking sequence that is represented only

once in the collection of 40 clones; another flanking sequence is represented four times. All four flanking sequences studied so far are represented in multiple copies in the genome. It appears that non-rDNA insertion-type sequences as well as its flanking sequences are representative of the class of middle-repetitive sequences in *Drosophila*.

ISOLATION AND CHARACTERIZATION OF HUMAN RIBOSOMAL DNA

*I. B. Dawid in collaboration with
P. K. Wellauer**

For some time it proved difficult to isolate mammalian rDNA, in particular human rDNA, largely because of the low concentration of this component in the genome. As it turns out, the long repeat length of this DNA is also a complicating factor. Cloning procedures have not been helpful in this case because of the rules against working with human material. Another approach to the study of gene organization, detection of restriction fragments by filter transfer hybridization, is limited because only fragments that contain gene regions can be visualized by hybridization with rRNA while spacer fragments go undetected.

We have isolated rDNA from a sample of about 14 mg of human leucocyte DNA by a series of gradient centrifugation steps. We used high molecular weight starting material with an average size of 50 kb, since the repeat length of the rDNA was expected to be large. After enriching the rDNA in a simple CsCl gradient, we formed R-loops with rRNA and subjected the material to another CsCl gradient. The R-loop hybrid is more dense than unreacted DNA, allowing considerable purification. After removing the RNA from the DNA, we centrifuged the material in a CsCl gradient in the presence of Actinomycin D. At this stage

* Swiss Institute for Experimental Cancer Research, Lausanne, Switzerland.

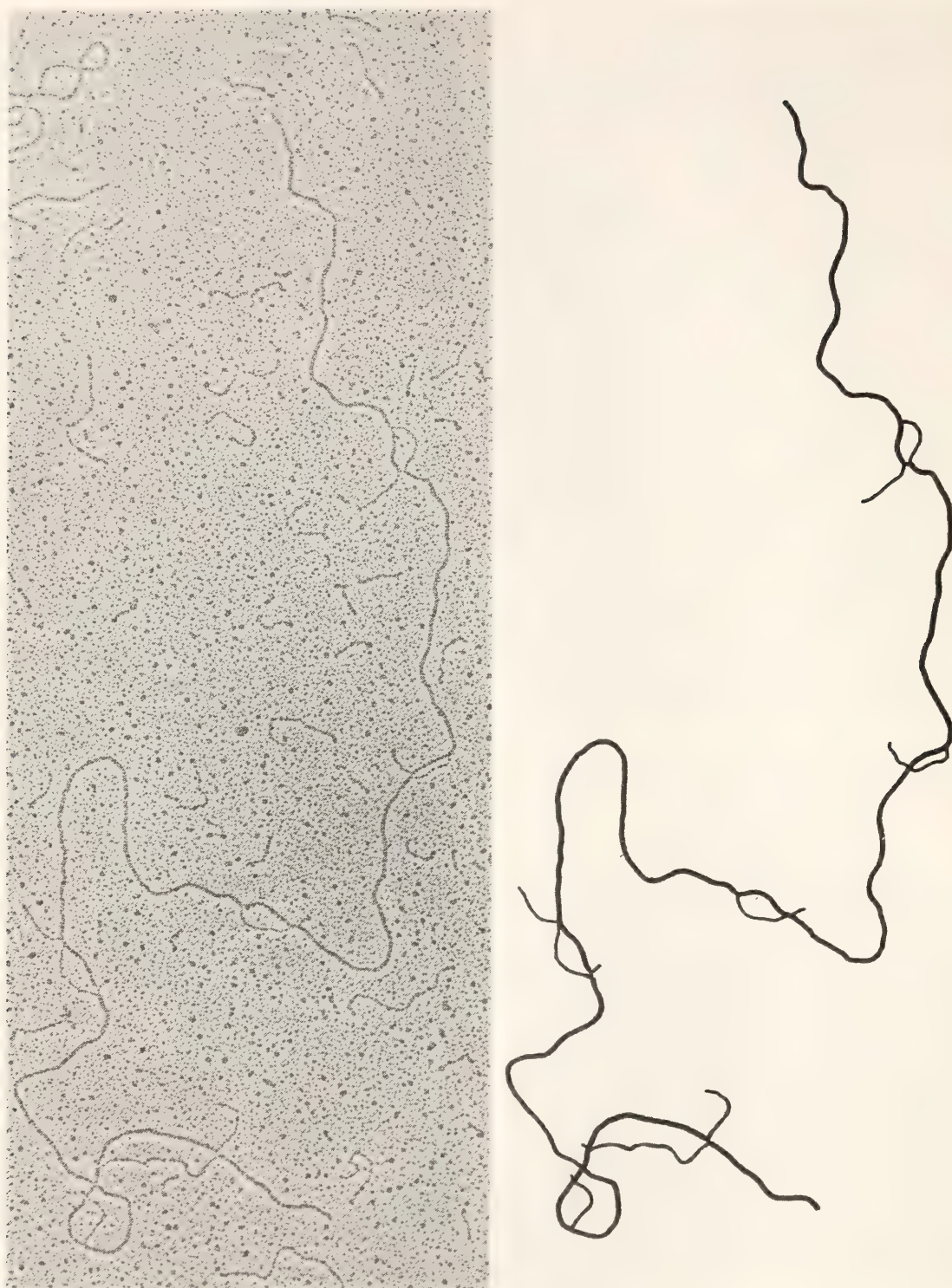


Fig. 63. Electron micrograph and tracing of an mtDNA molecule with R-loops formed by mtRNA. Note that most R-loops have "whiskers," i.e., a portion of the RNA displaced by the DNA, forming a single-strand tail.

we obtained a small yield (5%–10% of theory or about 1 μ g) of essentially pure rDNA, and some partially purified material. The main analysis applied to this material was R-loop mapping in the electron microscope of the regions coding for rRNA, both in intact rDNA and in

rDNA digested with EcoRI. From this work we conclude that the repeat length of human rDNA is 44 kb, very large by comparison to *Xenopus* or *Drosophila* rDNA but similar to mouse rDNA. We found only limited length heterogeneity in this sample of rDNA. The pattern of

rDNA restriction fragments in a sample of HeLa DNA was quite similar to that of the leucocyte DNA, suggesting that human rDNA in general has only limited length heterogeneity. This conclusion is in agreement with studies by other workers.

R-LOOP MAPPING OF mRNA SITES ON *X. laevis* mtDNA

E. Rastl

The mitochondrial (mt) genome of *X. laevis* codes for two rRNA's, a set of tRNA's (at least 21), and an unknown number of mRNA's. In past studies of the mitochondrial genome of *X. laevis*, we have established a restriction map, and have located on it the genes for rRNA's and 4S RNA's and the origin of replication. The two rRNA's are next to each other on the heavy strand of the molecule; tRNA genes are found on both strands, scattered throughout the molecule (see *Year Book* 76, pp. 82-84).

We have recently started to map mRNA sites, using two approaches: (1) electron microscopic mapping of R-loops formed between mtDNA and mtRNA and of hybrids formed between separated strands of the mtDNA and mtRNA, and (2) sizing mtRNA's on denaturing gels and then hybridizing them to various restriction fragments of the mitochondrial genome. In the past year, we obtained sufficient data on R-loop positions to establish a tentative map.

R-loops were formed by hybridizing mtRNA, enriched for poly(A)+ mRNA by chromatography on oligo(dT) cellulose, to full-length mtDNA that had been cut at the Bam HI site. To facilitate this work, we cloned the whole mitochondrial genome in the vector pBR322 by inserting it at its Bam HI site. Figure 63 shows an electron micrograph of a mtDNA molecule with six R-loops. The two R-loops close to the Bam HI site are formed by the two rRNA's that had been added as marker.

Figure 64 shows the histogram obtained by tracing 80 molecules which contained at least two R-loops besides the marker rRNA R-loop(s). This histogram reveals that there are sites for five abundant RNA species and at least two less abundant species (at genome distances 39% and 47%). By tracing individual molecules it becomes clear that there are even more sites which correspond to rare RNA species and so do not show up in the histogram. Also indicated in this histogram are the sites of the 4S RNA genes, most of which seem to "fit" between the mRNA genes, although some map at overlapping positions (especially the two L-strand tRNA sites at position 32% and 39%).

The question whether a certain RNA is coded for by the H-strand or the L-strand of the mtDNA can, in general, not be answered by the R-loop technique. In one case, however, the R-loop pattern indicates that RNA's are transcribed from both strands of the molecule: Fig. 65 shows a case where the R-loop of the small rRNA and the R-loop of another RNA mapping adjacent to it (a "rare" but distinct species) are fused, forming a larger loop. In this case, the "rare" RNA molecule hybridizes to the DNA strand that is displaced by the rRNA. As rRNA is known to be coded by the H-strand, the RNA mapping adjacent to it is coded by the L-strand. To obtain a more general answer to such questions, we have now started to hybridize mtRNA to each of the separated strands of the DNA.

THE VITELLOGENIN GENE IN *Xenopus laevis*

*W. Wahli, in collaboration with G. Ryffel,
T. Wyler, R. Yaggi, and R. Weber**

The estrogen-induced synthesis of vitellogenin, the precursor of the major yolk proteins, in the liver of male frogs represents a favorable system to investi-

* University of Berne, Switzerland.

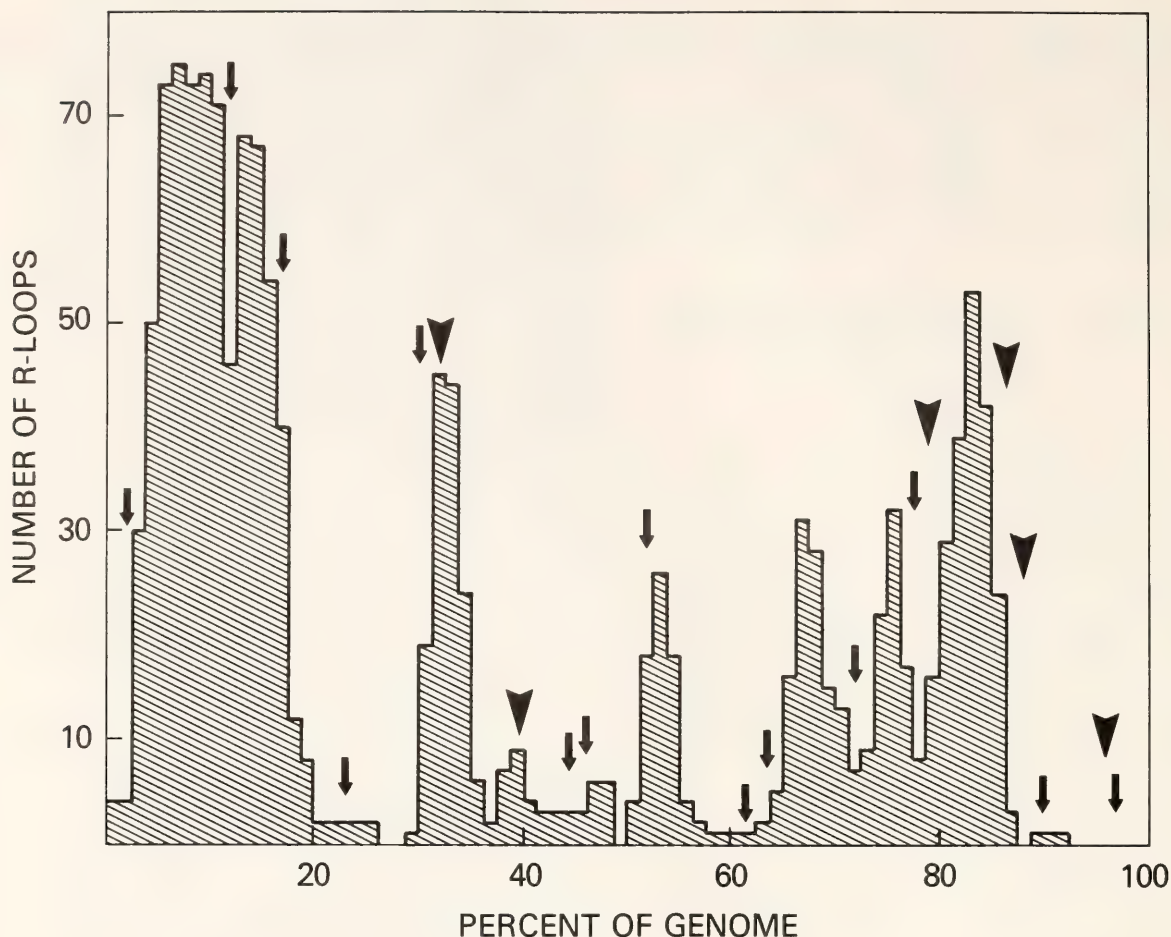


Fig. 64. Histogram of the positions of R-loops on mtDNA. The lengths of the "whiskers" are not included in this histogram. Arrows point to sites of 4S RNA's mapped to the H strand, and arrowheads point to 4S RNA sites mapped to the L strand of mtDNA (see *Year Book 76*, pp. 82-84).

gate several aspects of the hormonal regulation of gene expression in eukaryotic cells. Previously we reported the isolation and characterization of the mRNA coding for vitellogenin and the kinetics of its accumulation in the liver of male *Xenopus* treated with estrogen. Studies on the structural organization of the vitellogenin gene as well as on the transcriptional and posttranscriptional events resulting in functional cytoplasmic vitellogenin mRNA would be greatly facilitated by the availability of gene messenger sequences in high amount and of absolute purity. We report here the enzymatic *in vitro* synthesis of double-stranded DNA copies of vitellogenin mRNA, the construction of hybrid plasmids carrying these sequences, and their use as hybridization probes to identify

the corresponding sequences in chromosomal DNA.

Full-Length and Partial Discrete Transcripts of Vitellogenin mRNA

Intact template mRNA was prepared from the liver of estrogen-treated animals, in which the messenger is the main component of the poly(A)-containing RNA. In cell-free translation systems, this RNA directs the synthesis of polypeptides that are immunoprecipitated by antibodies against vitellogenin. The mRNA has a molecular weight of about 2.1×10^6 , making it particularly challenging to produce long cDNA copies for subsequent use as templates for the synthesis of double-stranded cDNA. Table



Fig. 65. Electron micrograph and tracing of a mtDNA molecule with R-loops. The loops formed by the small rRNA (*A*) and by the RNA mapping next to it (*B*) are fused, leading to a single loop. The double-stranded segments of the R-loops are on opposite strands.

12 and Fig. 66 summarize a series of experiments designed to find reaction conditions for the synthesis of long transcripts in high yields with AMV reverse

transcriptase. Salt concentration, enzyme-to-RNA ratio and, particularly, the incubation temperature are critical factors. Under reaction conditions that gave a

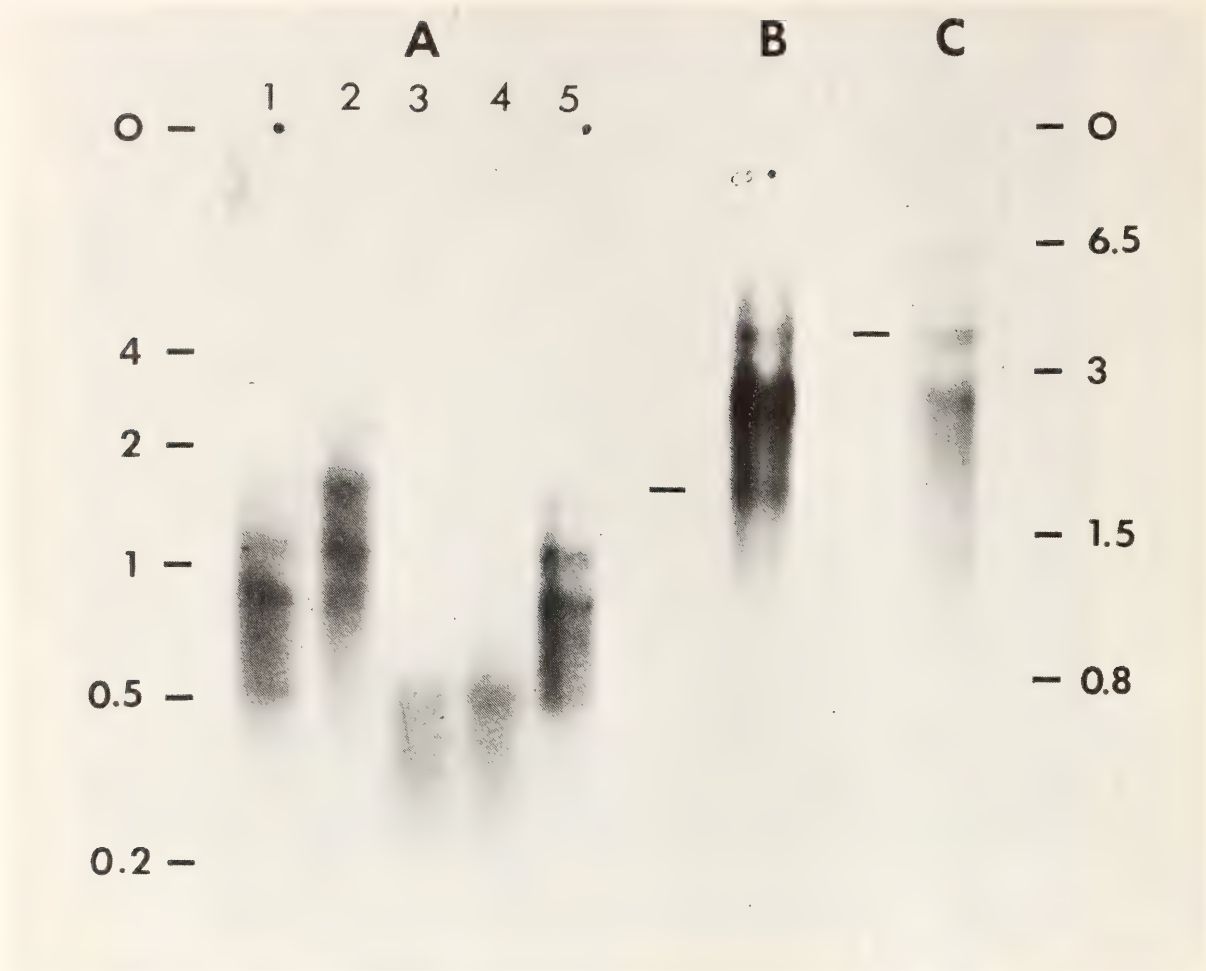


Fig. 66. Length of reverse transcripts of vitellogenin mRNA synthesized under the various conditions given in Table 12, as analyzed by gel electrophoresis. See Table 12 for lane identification. The molecular weight scales are in kb.

yield of cDNA of about 50% of the template RNA (Table 12), we find a prominent band at the upper size limit of the cDNA (Fig. 66c); this band appears to represent full-size vitellogenin cDNA.

In all reaction conditions used, incomplete cDNA products of nonrandom length were observed. Such transcripts might have arisen from starts at specific internal positions. They could also be the

TABLE 12. Reverse Transcription of Vitellogenin mRNA under Various Reaction Conditions

Series	Enzyme/RNA (U/ μ g)	Salt K ⁺ (mM)	Temperature ($^{\circ}$ C)	Time (min)	Yield (%)	Gel Lane in Fig. 66
A	2.5	50	40	120	1.9	A ₃
	2.5	100	40	120	9.6	A ₂
	2.5	150	40	120	7.7	A ₁
	1.1	100	40	120	2.0	A ₄
	2.2	100	40	120	9.4	...
	4.5	100	40	120	6.3	A ₅
B	2.5	100	42	60	22.9	B
C	2.5	75	44	45	39.8	...
	2.5	100	44	45	49.6	C
	2.5	125	44	45	40.3	...

result of premature termination of grown cDNA transcripts at specific points within the mRNA molecules. For example, high temperature, which promotes longer products, probably reduces secondary structure in the mRNA molecules, and allows the enzyme to move farther toward the 5' terminus.

Synthesis of Double-Stranded cDNA and Insertion into Hybrid Plasmids

Single-stranded vitellogenin cDNA was prepared and purified free of mRNA. A small aliquot was analyzed on an alkaline agarose gel (Fig. 67). This cDNA served as template in a reverse transcriptase reaction without addition of an exogenous primer. The products of the

reaction were treated with S1-nuclease to open the terminal hairpin at one end of the double-stranded molecules and to remove any remaining single-stranded regions. The S1-nuclease-resistant products ranged from 0.5 kb to full-size vitellogenin double-stranded transcripts (Fig. 67). This material was sedimented through a neutral sucrose gradient, and short molecules were discarded. Poly(dT) was added to the purified double-stranded cDNA, and the molecules were annealed to pMB9 plasmid molecules that had been elongated with poly(dA) at the EcoRI site. The bacterial strain X1776 was transformed with the recombinant plasmids and tetracycline resistant colonies carrying vitellogenin DNA were identified using colony-hybridization with

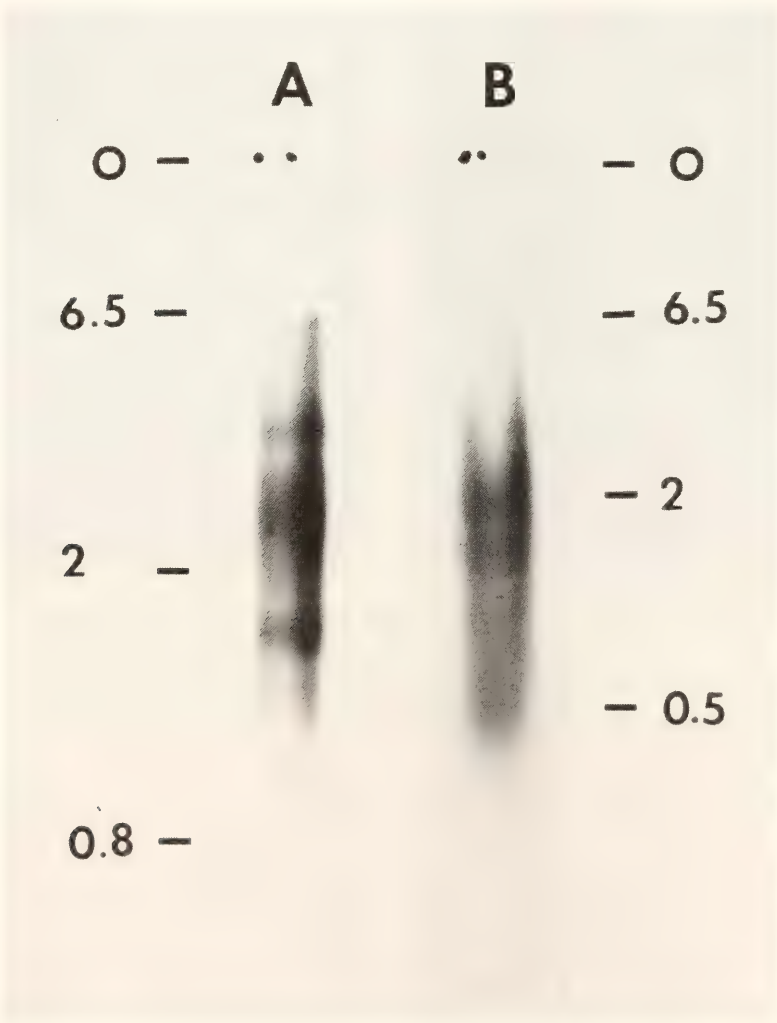


Fig. 67. Gel electrophoretic analysis. (A) Length of the cDNA transcripts used as template for the synthesis of double-stranded cDNA. (B) Length of the double-stranded products derived from the material shown in (A). Molecular weight scales are in kb.

iodine-125-labeled vitellogenin mRNA as probe. The recombinant plasmids from positive colonies were named pXlvc (plasmid-*Xenopus laevis*-vitellogenin-complementary DNA).

Characterization of the DNA from pXlvc Clones

Plasmid DNA from 23 different ¹²⁵I-vitellogenin mRNA positive bacterial clones was prepared for further characterization. The length of the inserted DNA determined by gel electrophoresis is given in Table 13. We mapped the sites of the restriction endonucleases Hind III and EcoRI. The restriction maps were constructed from gel electrophoresis of the digestion products of

each enzyme separately, of both enzymes together, and from hybridizations with ³²P-labeled pMB9 to identify inserted DNA-vector DNA hybrid fragments. Figure 68 shows the electrophoretic pattern of the digestion products of four clones: pXlvc 23, 8, 10, and 19. Cross-hybridization experiments carried out to detect clones containing common inserted DNA sequences were done with ³²P-nick translated EcoRI and Hind III fragments containing no pMB9 sequences from pXlvc 23 and pXlvc 10 (see Fig. 69a and b). Each of the 21 analyzed clones hybridized to either pXlvc 10 or pXlvc 23 (Table 13).

All cloned cDNA molecules are smaller than the mRNA. The positions occupied by the cloned DNA's on the RNA strand

TABLE 13. Length of Inserted DNA and Cross-Hybridization with ³²P-Labeled Restriction Fragments Purified from pXlvc 10 and pXlvc 23

Plasmid	Length of Insert (Kb)	Hybridization with	
		pXlvc 10	pXlvc 23
pMB9	0	—	—
pXlvc 10	2.1	+	—
19	2.3	+	—
23	3.7	—	+
37	1.45	—	+
21	1.5	—	+
18	2.4	—	+
72	1.5	+	—
2	2.0	—	+
13	2.1	+	—
27*	1.2	(+)	—
8	2.6	+	—
12	1.7	—	+
24	1.6	+	—
22	1.75	—	+
34	1.65	—	+
30	2.3	—	+
32	1.5	—	+
73	1.6	+	—
11*	1.1	(+)	—
29	2.1	—	+
20	1.5	—	+
26	1.2	—	+
25	0.96	—	+

* The clones pXlvc 27 and pXlvc 11 do not cross-react with pXlvc 10, but hybridization with iodine-125-labeled RNA and R-loop mapping in the electron microscope showed that they are adjacent to clone pXlvc 10 on the mRNA.



Fig. 68. Gel electrophoresis of four pXlvc clones digested with EcoRI (E-lanes), Hind III (H-lanes), EcoRI + Hind III (D-lanes). Arrows point to weak bands. The first lane in each panel contains marker fragments obtained by digestion of vector pMB9 DNA with Hae III, and the last lane of each panel contains a Hind III digest of phage λ DNA.

were determined by electron microscopy. Heteroduplexes between different clones were also analyzed, and hybridization experiments with labeled fragments were carried out. A further approach was as follows. Purified mRNA was fragmented by mild alkali treatment; and the products of the hydrolysis were fractionated on a poly(U)-Sepharose column into a poly(A)-containing fraction, an oligo(A)-

containing fraction and a poly(A)- and oligo(A)-lacking fraction. As shown earlier, the poly(A)-containing fraction covers the 3' terminal regions of the mRNA molecules; the oligo(A)-containing fraction, a specific internal region located between 2000 and 3000 nucleotides from the 3' terminus; and the poly(A)- and oligo(A)-lacking fraction, the rest of the mRNA molecules (Fig. 69a). The

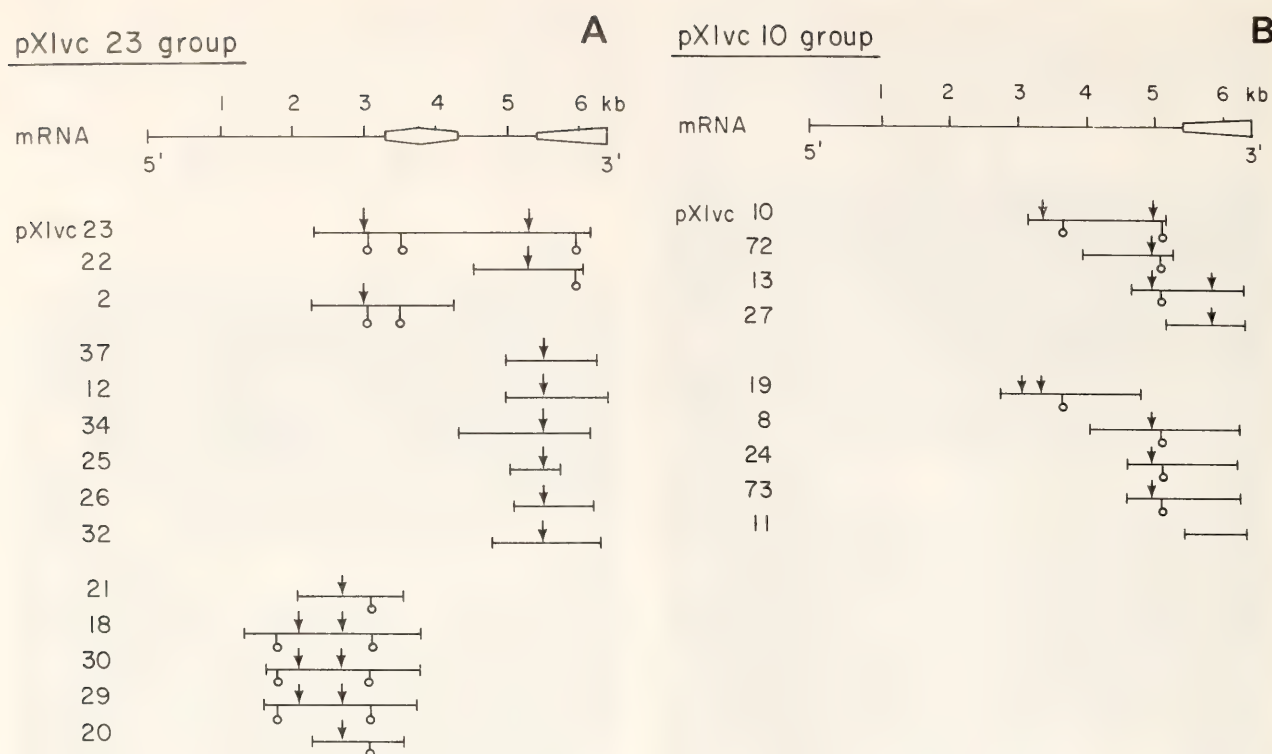


Fig. 69. Map of the pXlvc clones aligned on the mRNA. (A) Clones belonging to the pXlvc 23 group. (B) Clones belonging to the pXlvc 10 group. Arrows indicate Hind III sites; circles, EcoRI sites; quadrilaterals, the poly(A)-containing fraction; and sexagon, the oligo(A)-containing fraction of the fractionated mRNA. These fractions were used as hybridization probes after labeling with iodine-125.

three fractions were labeled with iodine-125 and hybridized to the different pXlvc clones. Figure 69a and b summarizes all these experiments. It gives the cleavage sites for Hind III and EcoRI in the different clones and the location of the clones on the mRNA. The results compelled us to draw the conclusion that the mRNA population used as template for cDNA synthesis contained two types of mRNA molecules with the same length but different sequences. One type, from which the pXlvc 23 group of clones was derived, contains the internal oligo(A) sequence (Fig. 69a). The other type, from which the pXlvc 10 group of clones were generated, does not carry this characteristic internal oligo(A) sequence (Fig. 69b). Clones derived from the same regions of the mRNA (e.g., the 3' terminal part) do not cross-hybridize between these two groups. The two types of mRNA were picked up with about the same frequency in this cloning experi-

ment; this suggests that both are induced by estrogen, since the mRNA population that was cloned appears only after the hormone treatment. In vitro translation experiments should show if both types of mRNA code for egg yolk proteins. From Fig. 69a and b, it is also evident that the cloned DNA within one group (group pXlvc 23 or group pXlvc 10) do not always have the same restriction map at the same position on the mRNA, though cross-hybridization experiments showed that all sequences within each group are closely related. On the basis of these restriction maps, each group must be divided into two subgroups. Melting experiments with heteroduplex molecules have shown that the degree of mismatch between subgroups in either of the two groups is 4–8%. The mRNA population from which the clones were derived was prepared from three animals. Experiments are in progress to determine if the subgroups found in the pXlvc 10 and

pXlvc 23 groups are the result of population polymorphism or the presence of two closely related genes in the same animal.

*Detection of Fragments Containing
Cloned Sequences in Digests of
Chromosomal DNA*

We have used DNA fragments from different pXlvc clones labeled in vitro with ^{32}P as hybridization probes to detect homologous restriction fragments in *Xenopus* erythrocyte DNA. The approach is to digest *Xenopus* DNA with a restriction endonuclease, resolve the digest by electrophoresis in an alkaline agarose gel, transfer the separated fragments onto a nitro-cellulose filter, and hybridize with the ^{32}P probe. After washing, fragments on the filter which have reacted with the probe can be detected as labeled bands by autoradiography. Since these hybridizations are generally carried out at least 20°C below the T_m of a perfect duplex, hybrids between related but nonidentical sequences are expected to yield a signal in this test. To test the stability of hybrids obtained with the pXlvc DNA probes, nitro-cellulose filters carrying Hind III and EcoRI digested DNA were hybridized with a mixture of ^{32}P -labeled pXlvc 10, 23 and 8 DNA at 37°C overnight in 50% formamide, $4 \times \text{SET}$, 0.2% SDS and 1 mg/ml tRNA. Different parts of the filter were washed at 37°C at different salt concentrations (50% formamide, 0.2% SDS and $2 \times \text{SSC}$, or $0.5 \times \text{SSC}$, or $0.1 \times \text{SSC}$, or $0.02 \times \text{SSC}$). In each posthybridization wash a clear pattern is observed (Fig. 70). Yet some of the prominent bands seen in the $2 \times \text{SSC}$ wash completely disappeared in the $0.2 \times \text{SSC}$ wash, while other bands remained stable even in the $0.02 \times \text{SSC}$ wash. This confirmed the presence of both identical sequences and related but different sequences in the genomic DNA. In another experiment, we hybridized members of the two subgroups in both the pXlvc 23 and the pXlvc 10 group to each other, and demonstrated that wash

in $0.2 \times \text{SSC}$ and 50% formamide is sufficient to melt away sequences having as few as 4–8% mismatch. The clone pXlvc 23 contains one Hind III (2.2 kb) and two EcoRI (2.3 kb and 0.48 kb) intragenic fragments. Digestion of *Xenopus* DNA with Hind III or EcoRI should therefore generate the same fragments. Figure 71 shows that none of these fragments could be detected by hybridization with the ^{32}P -labeled pXlvc 23 fragments generated by either of the two restriction enzymes. The posthybridization wash was in $0.2 \times \text{SSC}$ and 50% formamide. Each of the three ^{32}P -labeled probes hybridized to two different fragments of unexpected size which together are much longer than the probe itself. Two simple explanations are possible. The intragenic Hind III and EcoRI sites in pXlvc 23 might not be representative of Hind III and EcoRI sites present in the chromosomal DNA as a result of variation of the sequence of this gene in the *Xenopus* population. However, the high stability of the hybrids formed seems incompatible with the degree of mismatch expected from the observed changes in the position of the different restriction sites. The second explanation is that between the Hind III and EcoRI sites in pXlvc 23, genomic DNA carries stretches of DNA not present in the clone and containing at least one additional Hind III and EcoRI site. The high stability of the hybrids observed indicates perfectly matched sequences between the probe and at least some part of the detected fragment. This fact suggests that the second interpretation is more likely true. The presence of intervening sequences in other eukaryotic genes has been documented, and such interruptions may exist in the vitellogenin gene as well.

GENE EXPRESSION IN *Xenopus laevis*

Mark B. Dworkin

In the past year we initiated a project to study gene activity and regulation in

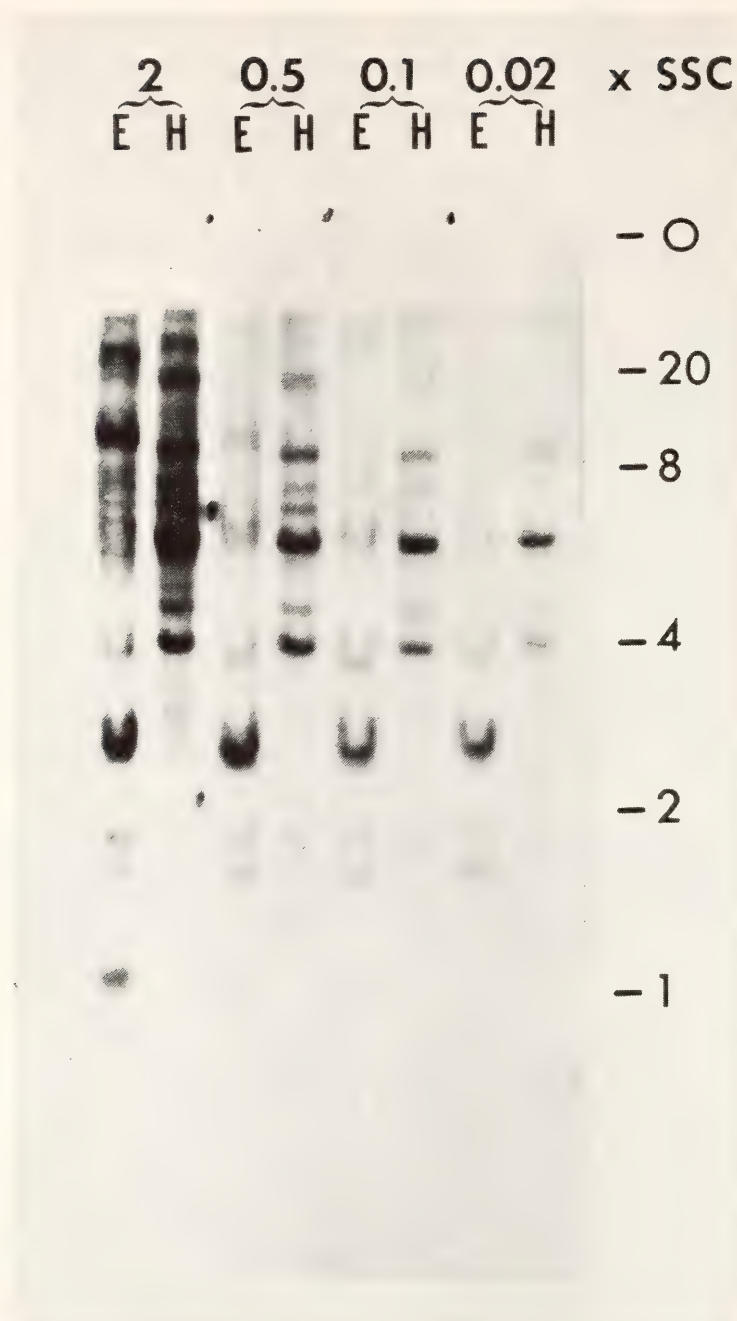


Fig. 70. Restriction patterns of *Xenopus laevis* DNA after digestion with EcoRI (*E*) or Hind III (*H*). Hybridization was with a mixture of ^{32}P -DNA from pXlvc 10, pXlvc 23, and pXlvc 8. The posthybridization wash of different parts of the filter was with 50% formamide, 0.2% SDS, and $2 \times \text{SSC}$, $0.5 \times \text{SSC}$, $0.1 \times \text{SSC}$, or $0.02 \times \text{SSC}$ as indicated. Molecular weight scale in kb.

X. laevis embryos. We are using the recombinant DNA technology to isolate single gene sequences from large populations of gene fragments, and we plan to use these sequences as probes for the presence of particular mRNA's. By studying many fragments simultaneously by filter hybridization we hope to accumulate data from many randomly chosen individual genes. At this stage of

the study we will not be able to identify the protein products of these genes.

We have prepared two libraries of DNA fragments from the *Xenopus* genome. The first library was prepared from 4000-base pair fragments of the genome generated by restricted digestion, joined to the plasmid pMB9 by dA-dT tailing with terminal transferase and amplified in *E. coli*. These clones were

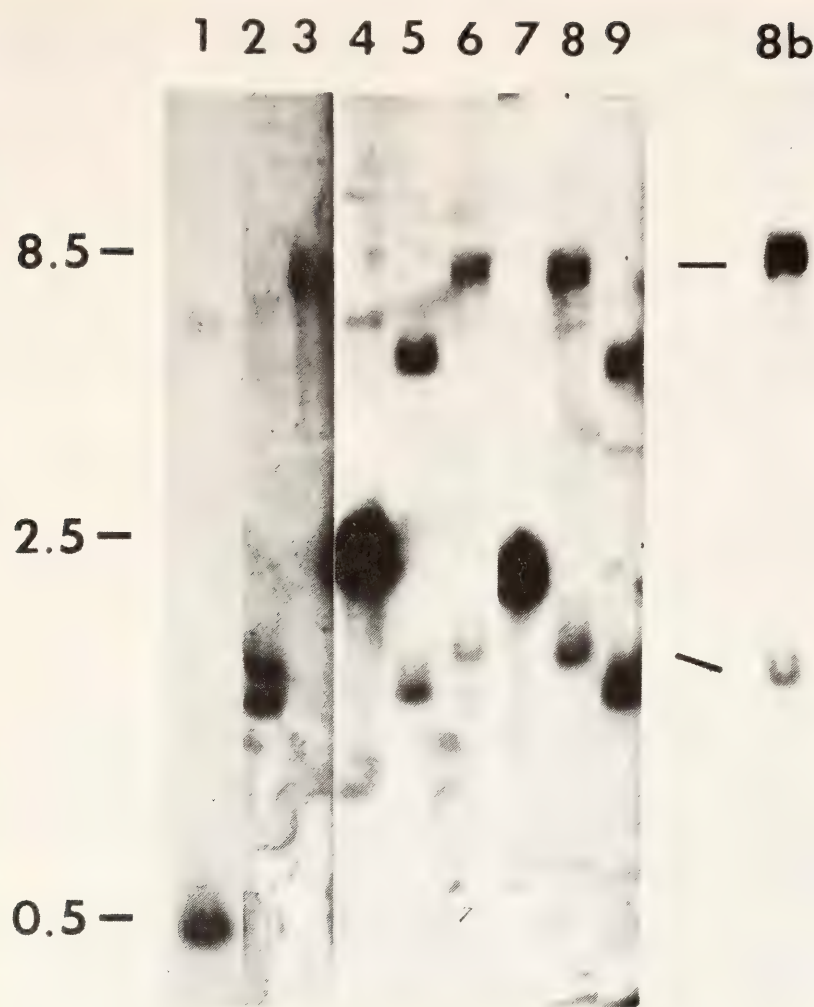


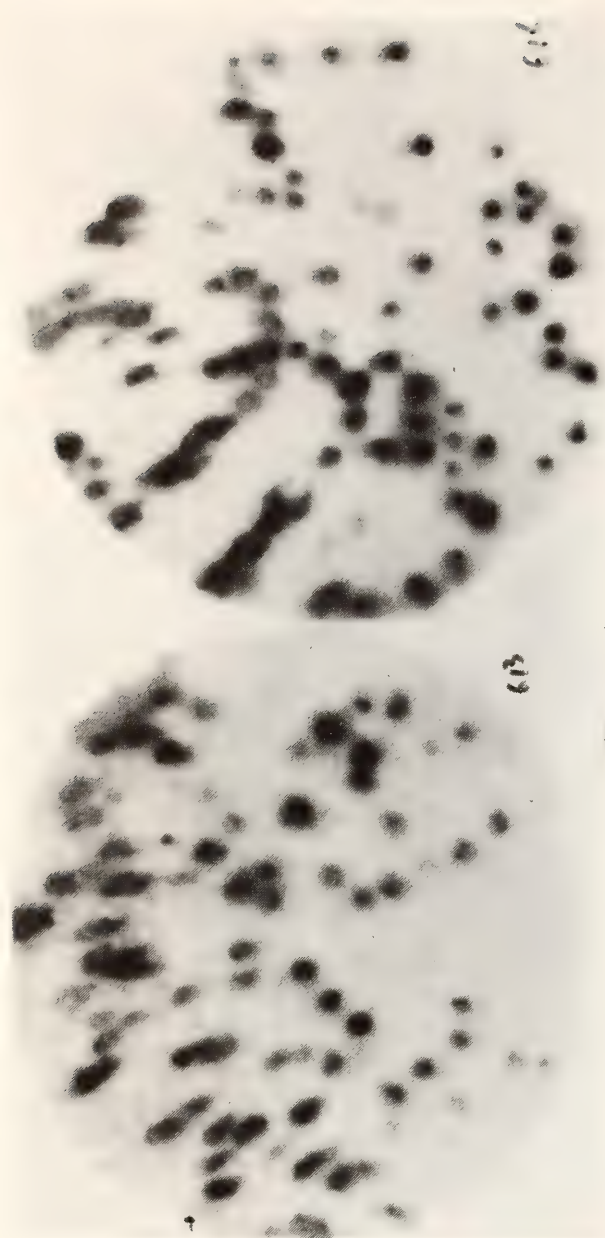
Fig. 71. Detection of DNA fragments containing pXlvc 23 sequences in EcoRI and Hind III digests of *X. laevis* DNA. Lanes 1, 4, and 7 are reconstructions in which pXlvc 23 DNA was mixed with *Drosophila* DNA prior to digestion. The amount of plasmid DNA was equivalent to one copy per haploid *Xenopus* genome in lane 1, and to 10 copies in lanes 4 and 7. In lanes 1 (EcoRI, reconstruction), 2 (EcoRI), and 3 (Hind III), the hybridization probe was the ^{32}P -labeled 0.48-kb intragenic EcoRI fragment. In lanes 4 (EcoRI, reconstruction), 5 (EcoRI), and 6 (Hind III), the hybridization probe was the ^{32}P -labeled 2.3-kb intragenic EcoRI fragment. In lanes 7 (Hind III, reconstruction), 8 (Hind III), and 9 (EcoRI), the hybridization probe was the ^{32}P -labeled 2.2-kb intragenic Hind III fragment. Lane 8b is the same as lane 8 in an experiment where the background between bands was lower.

then searched for fragments that contain active embryonic genes by screening the total library by colony hybridization with ^{125}I -mRNA prepared from stage 32 tadpole polyribosomes. The second library was prepared from double-stranded cDNA copies of stage 32 tadpole polysomal poly(A)⁺ mRNA with reverse transcriptase attached by dA-dT tailing to pMB9 and cloned in *E. coli*.

Figure 72 shows the homologous colony hybridization of the cDNA-gene library against ^{32}P -cDNA prepared from stage

32 tadpole polysomal mRNA. Of interest are the varying intensities of the clones, which may indicate that the library contains clones from various abundance classes of mRNA. This raises the possibility that the intensity of hybridization may allow an estimate of the frequency of the homologous sequence in a population of mRNA.

Poly(A)⁺ RNA has been isolated from polysomes of several different developmental stages as well as from nonpolysomal nuclear and cytoplasmic RNA.



This RNA will be labeled and hybridized against these libraries. From these studies we hope to accumulate data on the synthesis, processing, export, and utilization of these sequences during development in *Xenopus*. Further, the cloned fragments themselves can be isolated and labeled to high specific activity to yield pure probes of specific gene fragments for quantitation of developmentally interesting genes.

Fig. 72. Colony hybridization of cDNA gene library with homologous probe. cDNA was synthesized from stage-32 tadpole polysomal polyA⁺ mRNA using reverse transcriptase. polyA⁺ mRNA was obtained by phenol-CHCl₃ extraction of puromycin-high salt "run-off" polyribosomes followed by oligo(dT)-cellulose chromatography. The cDNA had a modal size of 1000 nucleotides. The final double-stranded product after treatment with S1 nuclease ranged from 500 to 1500 nucleotides. The cDNA genes were tailed with TTP with terminal transferase, hybridized with dATP-tailed pMB9, and used to transform *E. coli* strain HB101. Approximately 2000 transformants were toothpicked onto 6 Whatmann no. 1 filters, grown, and lysed with NaOH on the filters. The filters were hybridized against ³²P-cDNA (average size, 550 nucleotides) prepared from stage-32 tadpole polysomal poly(A)⁺ mRNA, and autoradiographed. Two of the filters are shown above. Many of the clones do not darken the film and contain only background pMB9.

STRUCTURE AND TRANSCRIPTIONAL CONTROL OF THE *Xenopus* RIBOSOMAL GENES

Ronald H. Reeder, Peter Botchan, Robert Hipskind, B. E. H. Maden,
Steven L. McKnight, Barbara Sollner-Webb, and Harvey Wahn
with the assistance of Eileen Hogan

This past year we have made a significant advance toward our long-term goal of understanding how the transcription of ribosomal genes is regulated. For the first time we have been able to obtain extensive and faithful reinitiation of rRNA synthesis in a crude cell-free reaction. This is the first step toward defining the DNA sequences and other molecules that are required for accurate

promoter recognition by the polymerase. Use of this cell-free transcription system has already led to the tentative identification of a substance in unfertilized eggs that acts as an inhibitor of polymerase initiation on ribosomal genes.

In conjunction with the transcription studies, we have continued work on the location of RNA chain initiation sites on rDNA and the nucleotide sequencing

of likely control regions. There appear to be at least two start sites for rRNA chains at the beginning of each gene and both are used *in vivo*. As an aid to sequencing and other studies, extensive restriction maps of the 5' end of the gene have been made, and selected parts of the repeat have been subcloned.

Animal cell genes are complexed *in vivo* with an equal weight of basic histones as well as other proteins of unknown significance. In continuation of our studies of ribosomal gene chromatin we have examined the histones on ribosomal genes for possible secondary modifications. Electrophoresis on high resolution two-dimensional gels has so far failed to reveal any secondary modifications that are not present on the histones of bulk inactive chromatin from somatic cells. The only difference we have detected is that histone H₁ appears to be missing from ribosomal gene chromatin. The absence of H₁ also agrees with the fact that we find rDNA chromatin to be less contracted in length than bulk inactive chromatin.

Secondary modification of ribosomal RNA (as either base or ribose methylation) has long been known to occur, but as yet no function can be ascribed to it. Dr. B. E. H. Maden, on sabbatical from the University of Glasgow, has been using cloned fragments of rDNA to map the location of methylation sites on rRNA. This work continues his long-term interest in rRNA methylation patterns.

ACCURATE REINITIATION ON RIBOSOMAL GENES IN ISOLATED OOCYTE NUCLEI

Robert Hipkind and Ronald H. Reeder

Deciphering the complex of molecular events that regulates ribosomal gene transcription requires the development of an *in vitro* system in which accurate transcription of the ribosomal genes will occur. Early attempts to achieve this goal met with a uniform lack of success.

Addition of partially purified RNA polymerase I to purified DNA (*Year Book 69*, p. 568) or to chromatin (*Year Book 71*, p. 15) resulted in aberrant transcription of both strands of the rDNA and of spacer as well as gene sequences. Examination of rDNA transcription in nuclei isolated from cultured cells revealed that they could elongate already initiated chains to a limited degree but were severely defective in reinitiation of rRNA chains (*Year Book 70*, p. 33). Without chain initiation such nuclei were not useful for study of promoter recognition and other aspects of transcriptional regulation.

A possible solution to this problem was suggested by the experiments of Gurdon and collaborators who have obtained transcription of various DNA's following their injection into the nuclei of oocytes from *X. laevis*. In particular, the injection of 5S DNA (Brown *et al.*, *Year Book 76*, p. 97) was shown to result in highly accurate synthesis of 5S RNA. We reasoned that it might be possible to bring the system one step closer to standard biochemical analysis by isolating oocyte nuclei and studying transcription in nuclear homogenates. Experiments described below show that this approach was successful. Nuclei from mature *Xenopus* oocytes are large, fragile structures that are difficult to isolate by normal nuclear isolation techniques. However, their large size makes it possible to isolate them manually with watchmaker's forceps. Isolation is rapid, and presumably there is a reduced chance for loss of low molecular weight or soluble components of the nucleus. The nuclei are then homogenized, and aliquots of the homogenate are used in transcription reactions as described in the legend to Fig. 73. RNA synthesis has been studied both with and without the addition of purified exogenous rDNA. The time course of RNA synthesis without adding exogenous rDNA is shown in Fig. 73. Synthesis continues for

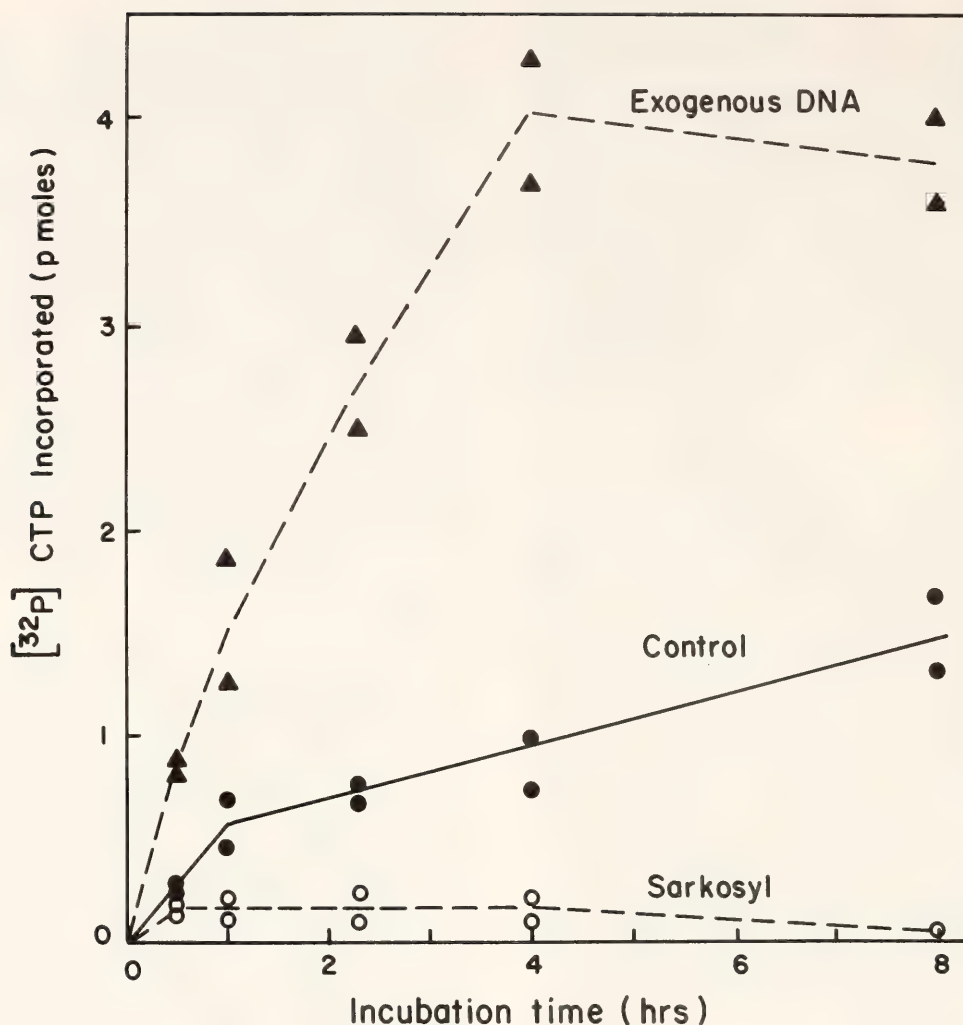


Fig. 73. Time course of RNA synthesis in oocyte nuclear homogenates. Each time point represents a separate reaction which contained 4 homogenized nuclei, 5 mM MgCl_2 , 100 mM KCl, 25 mM Tris pH 8, 1.2 mM dithiothreitol, 10% glycerol, 0.3 mM ATP, UTP and GTP, 2 μCi ^{32}P - α -CTP (350 Ci/mM) plus in some cases 0.5% Sarkosyl or 0.5 μg of cloned rDNA (pXlr14) in a total volume of 5 μl . Reactions were incubated at 20°, stopped by addition of SDS and proteinase K, phenol extracted, and an aliquot precipitated with TCA for scintillation counting. Solid circles, control transcription of endogenous rDNA; open circles, control plus 0.5% Sarkosyl; triangles, control plus 0.5 μg exogenous pXlr14/reaction.

at least 8 hours, and control experiments show that this synthesis is almost exclusively ribosomal RNA synthesis by polymerase I. Calculations show that after 8 hours the reaction has synthesized at least 100 copies of rRNA for each ribosomal gene present. This number alone strongly suggests that rRNA chain reinitiation is occurring in the system. The effect of sarkosyl, a compound that binds free RNA polymerase and blocks initiation, is also shown in Fig. 73. Synthesis proceeds for only 30 minutes and then plateaus. This also agrees with the hy-

pothesis that chain initiation is occurring in the control reaction.

To establish this fact more securely we have made use of a technique recently developed by Dr. R. C. Huang and collaborators. In this procedure the γ -thio-analogs of ATP and GTP are added to the RNA synthesis reaction in place of their normal counterparts. Incorporation of these molecules at the 5' end of new chains results in the presence of a free sulfhydryl group on the 5' terminus. (Molecules incorporated internally in the chain lose the γ (thio)

group.) When the RNA is passed over an agarose column containing covalently bound mercury, the sulfhydryl groups bind to the Hg-agarose and are retained selectively. They can then be eluted with a mercaptan such as dithioerythritol. In this manner, newly initiated RNA can be physically separated from the chain elongation products of RNA polymerase that initiated *in vivo* before the nuclei were isolated.

Figure 74 shows the result of a typical experiment in which RNA was synthesized in the presence of γ -(thio)-ATP and GTP. About 7% of the radioactive RNA bound to Hg-agarose, which suggests that new RNA chains are being initiated in the reaction. One possible problem with this interpretation, however, stems from the fact that nuclear homogenates contain kinases that rapidly exchange the γ (thio) phosphate among all four nucleoside triphosphates. We were worried at the outset that similar enzymes might possibly exchange (thio) phosphates onto preexisting RNA chains, thus confusing the interpretation of Fig. 74. We have done several control experiments demonstrating that γ (thio) phosphate transfer to preexisting RNA chains is not a problem in this system. One of the more definitive controls is shown in Table 14.

In this experiment RNA was synthesized for various short periods, and each aliquot was individually fractionated on Hg-agarose. The bound and the flow-through RNA's from each time point were then separately hybridized to a DNA fragment containing the first 2400 bp of the gene (fragment A, see map in Fig. 75) and another fragment containing almost all of the rest of the gene (fragment B, Fig. 75). We reasoned that if RNA polymerase were reinitiating correctly at the 5' end of the gene, and if the Hg-agarose column were selectively binding those newly initiated molecules, then RNA bound to the column at early time points would hybridize

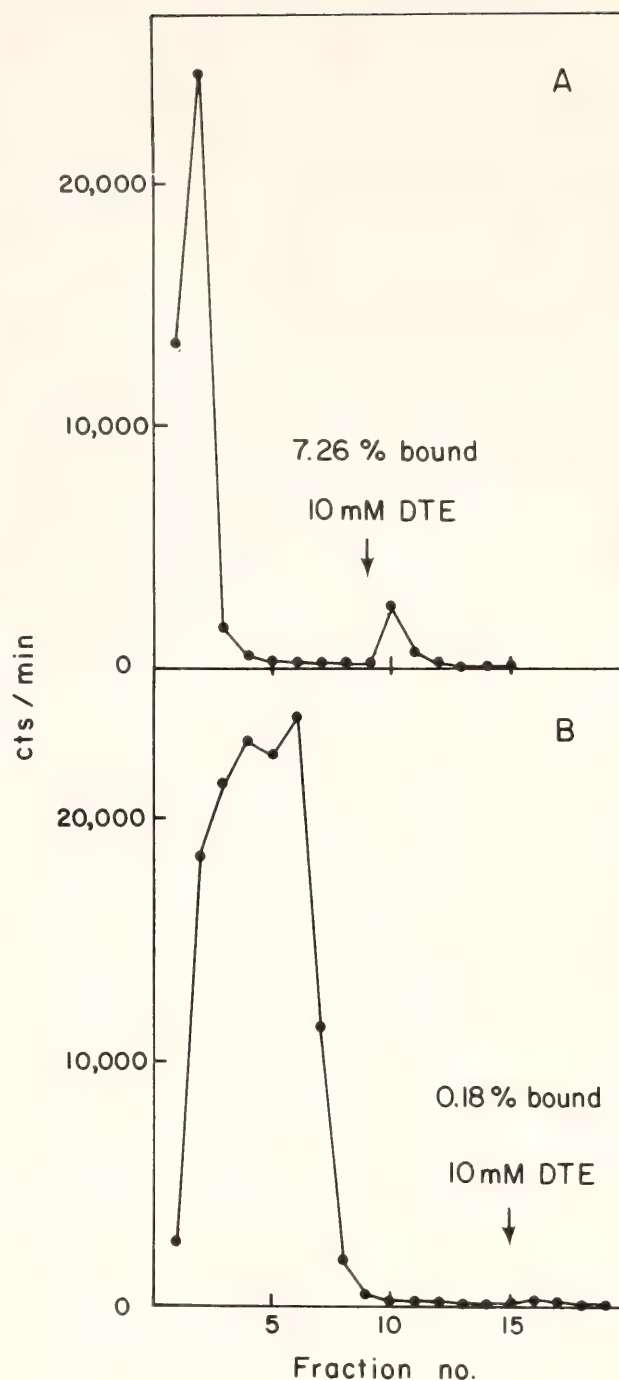


Fig. 74. Binding of γ -thio-initiated RNA to Hg-agarose. RNA was synthesized for 1 hour in two reactions identical to the control reaction described in Fig. 73 except that (1) both reactions were scaled up 20-fold, and (2) in one reaction γ -thio ATP and γ -thio GTP replaced their normal analogues. RNA was first purified by phenol extraction and passage through a G-50 column to remove unincorporated nucleotides, and then ethanol-precipitated. Each sample was redissolved and passed through a column of Hg-agarose. Bound material was eluted with 10 mM dithioerythritol. (A) RNA synthesized in the presence of γ -thio ATP and GTP. (B) Control reaction with normal ATP and GTP.

TABLE 14. Hybridization of in vitro Initiated RNA to Restriction Fragments of rDNA

Incubation Time (min)	RNA Synthesized (cts/min)	RNA Bound to Hg-Agarose (%)	Hybridization of Bound RNA			Hybridization of Flow-Through RNA		
			A	B	A/B	A	B	A/B
7.5	12,600	5.0	150	0	>100	614	2200	.28
15	25,400	8.8	452	32	14	1860	4080	.46
30	57,400	7.0	1390	455	3

selectively to fragment A. At later times, as the chains grew longer, the bound RNA should hybridize more and more with fragment B also.

Table 14 shows that this result was obtained. After 7.5 minutes of synthesis the bound RNA hybridized exclusively to fragment A. At later times the A/B ratio declined more and more. At all times examined, the flow-through RNA hybridized more to fragment B than it did to A. From this and other experiments we conclude that new chains are being initiated and the initiation event is occurring near the 5' end of the gene.

The preceding experiment predicts also the size of the Hg-agarose-bound RNA should grow with time. Electrophoresis of the bound RNA on an acrylamide gel (Fig. 76) shows that the size does grow with time and the growth rate is consistent with the hybridization data shown in Table 14. From Table 14 and Fig. 76 we estimate that the chain growth rate in our system is 3–4 nucleotides/second.

Figure 77 illustrates that the RNA transcribed from the endogenous rDNA hybridizes only to the H strand, the

same strand transcribed in vivo. From all of these results we conclude that the nuclear homogenates are capable of extensive and accurate reinitiation of rRNA synthesis on the endogenous ribosomal genes. In contrast to other transcription systems, therefore, this system has not lost any essential factors needed to complement polymerase I and allow accurate transcription.

The next major question concerns what happens when deproteinized, exogenous rDNA is added to the homogenate. The time course in Fig. 73 also demonstrates that exogenous rDNA is capable of stimulating RNA synthesis. Hybridization to separated strands (Fig. 77) shows, however, that much of this transcription occurs on the noncoding (L) strand and therefore represents aberrant initiation. This aberrant transcription of exogenous rDNA is due to polymerase III (as shown by α -amanitin titration) and occurs only when relatively large amounts of rDNA are added to the reaction. At lower concentrations of exogenous rDNA (10–100-fold excess over the endogenous genes) the system simply ignores the exogenous DNA. Experi-

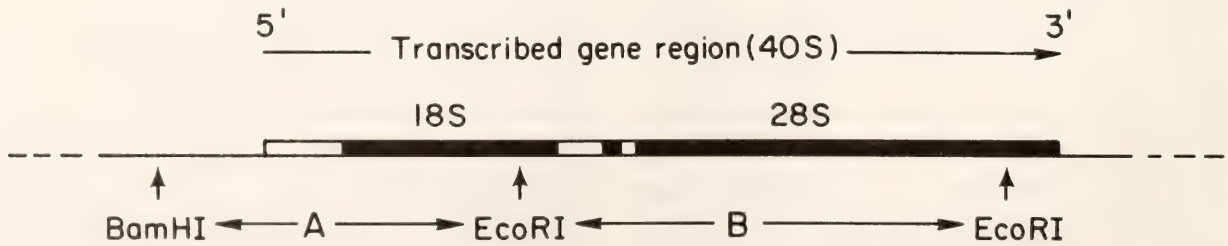


Fig. 75. Map of rDNA showing restriction fragments used for the hybridization experiment described in Table 14.

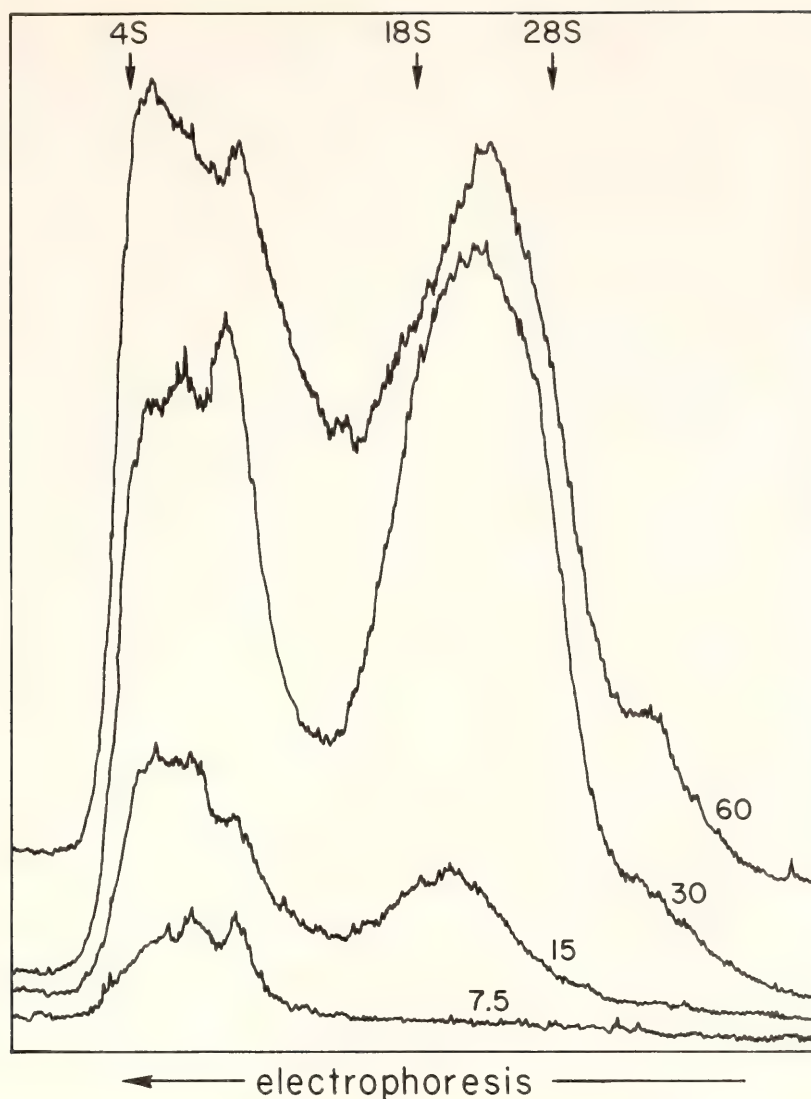


Fig. 76. Size of γ -thio-initiated RNA as a function of reaction time. ^{32}P -labeled RNA was synthesized for various times in the presence of γ -thio ATP and GTP. The RNA that bound to Hg-agarose was isolated and electrophoresed on a 1% agarose gel in 5M urea.

ments are in progress to determine how to make polymerase I transcribe the added rDNA.

MORPHOLOGY OF IN VITRO TRANSCRIPTION

Steven L. McKnight and Robert Hipkind

Some aspects of gene transcription are more clearly revealed by a single good electron micrograph than by months of biochemical experimentation. Since the ribosomal genes of *Xenopus* are singularly good subjects for gene portraiture, we decided to spread some of our in vitro RNA synthesis reactions to look at them.

An example of what we see is shown in Fig. 78. To make this photograph oocyte nuclei were manually isolated, homogenized, and the endogenous ribosomal genes were allowed to synthesize RNA for 5 minutes. As described earlier in this Report, biochemical measurements indicate that accurate RNA chain initiation occurs on the endogenous ribosomal genes in this in vitro reaction. Our measurements also indicated that the average rate of RNA chain growth was about 3–4 nucleotides/second. One would expect, therefore, that after 5 minutes of in vitro synthesis the preinitiated polymerase (bound to the gene before the nucleus was isolated) would have moved



Fig. 77. Hybridization of in vitro synthesized RNA to the separated strands of rDNA. Left, RNA transcribed from the endogenous rDNA in a nuclear homogenate reaction. Right, RNA transcribed from exogenous rDNA added to a similar reaction. H and L refer to the coding and noncoding strands of rDNA, respectively.

only part way down the gene. Newly initiated polymerases should be loaded on behind the old ones, and their density on the gene should reflect the frequency of initiation in vitro.

The electron micrographs (Fig. 78) agree rather well with expectation. Well-defined transcribed and nontranscribed regions are clearly alternating along the DNA fiber. This suggests that after 5 minutes of reaction both initiation and

termination are functioning fairly well. The terminal two thirds of each gene (identified as the end with the longest nascent RNA chains) is closely packed with RNA polymerase molecules at a density similar to that seen in vivo. These presumably represent polymerases that were on the gene when the nucleus was isolated and have now moved part way down the gene. The initial third of each gene also has RNA polymerase molecules with attached RNA fibers, but the polymerases are much more widely spaced. Very likely these polymerases are ones that initiated transcription in vitro. The photographs strongly suggest that in vitro initiation is occurring at a defined point but less frequently than it occurs in the living cell. The micrographs also suggest that the polymerases initiated in vivo have traveled about one third of the gene (about 2500/bp) in 5 minutes. This represents a chain growth rate of about 8 nucleotides/second. This estimate is roughly double the minimum rate estimated biochemically.

The ability to photograph our in vitro reactions adds a valuable dimension to our ability to characterize the components that control ribosomal gene transcription.

STRUCTURE OF NUCLEOPROTEIN IN THE SPACER REGION OF RIBOSOMAL DNA

*Steven L. McKnight, Ronald H. Reeder
and Oscar L. Miller, Jr.**

We would like to know if the structure of active ribosomal gene chromatin is detectably different from nontranscribed, inactive chromatin. One way to approach this question is to examine both types of chromatin by electron microscopy. Several laboratories have reported that inactive chromosome fibers appear as strings of bead-like spheres which measure approximately 100 Å in diameter.

* University of Virginia.

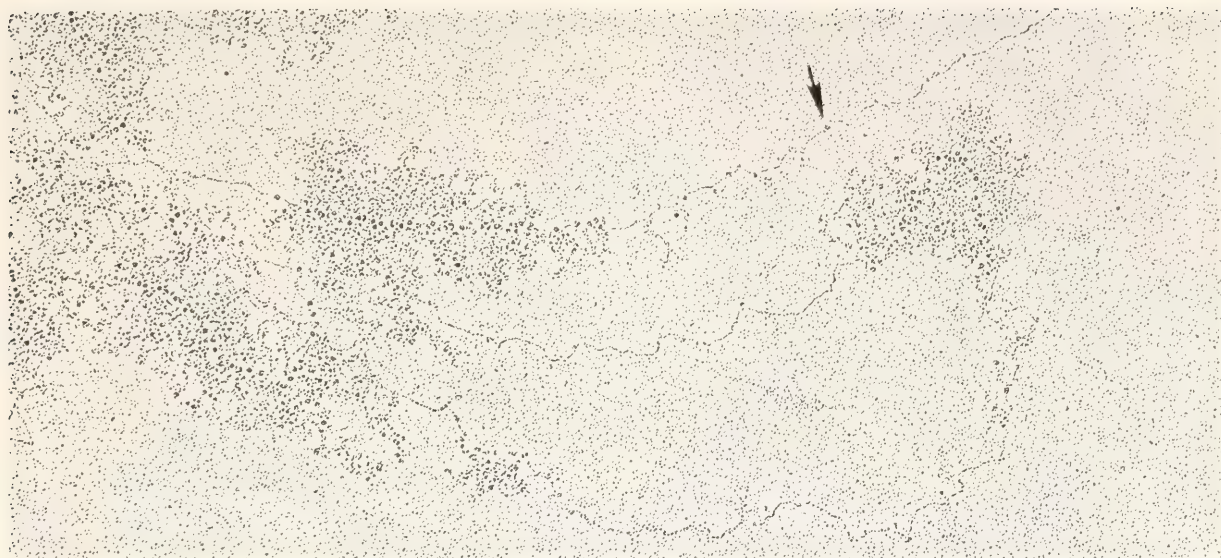


Fig. 78. Electron micrograph of a ribosomal gene after 5 minutes of RNA synthesis in vitro. The arrow indicates the probable site of RNA chain initiation.

These beads, which are termed nucleosomes, contain eight histone molecules complexed with about 200 bp of DNA. Under the hypotonic spreading conditions we employ, inactive *Xenopus* chromatin exhibits a mean nucleosome periodicity of ~ 30 beads/ μm of contour length. Assuming 200 bp of DNA/nucleosome, we estimate there are 6000 bp of DNA/ μm . Since deproteinized B-form DNA contains approximately 3000 bp/ μm , the DNA in inactive *Xenopus* chromatin is contracted about two-fold.

What is the contraction ratio of active ribosomal gene chromatin? Miller and co-workers have previously observed that the mean contour length of the transcribed ribosomal gene region (see Fig. 79) is $2.3 \mu\text{m}$. Since the primary transcription product of this gene (the 40S rRNA precursor) contains 7500 ribonucleotides, this means that each μm of active gene chromatin has ~ 3300 bp of DNA, which represents a contraction ratio of only 1.1 compared to B-form DNA. At present, we do not know whether this low contraction ratio is due to the high density of RNA polymerases on active ribosomal genes or to some other structural feature.

We decided it would also be of interest

to measure the contraction ratio of the nontranscribed spacers between gene regions. This measurement is complicated by the fact that spacer lengths vary from frog to frog, and one frog may have several different spacer length classes in its rDNA. To circumvent this problem, amplified genes from the oocytes of a single frog were spread for microscopy and contour length measurements. The amplified rDNA was then purified from the remainder of the ovary, digested with EcoRI restriction endonuclease, and the distribution of spacer lengths in the rDNA was measured by gel electrophoresis. A comparison of the spacer length measurements by microscopy and by gel electrophoresis is shown in Fig. 80. The amplified rDNA of this particular frog had two predominant spacer sizes. The apparent contraction ratio of both size classes is 1.2—close to B-form DNA and significantly less than that of inactive chromatin.

Amplified nucleoli contain the four nucleosomal histones (H. L. Wahn, this Report), and antihistone antibodies react with spacer chromatin (McKnight and Miller, unpublished) as seen by immunoelectronmicroscopy. Furthermore, beaded structures are seen on spacer

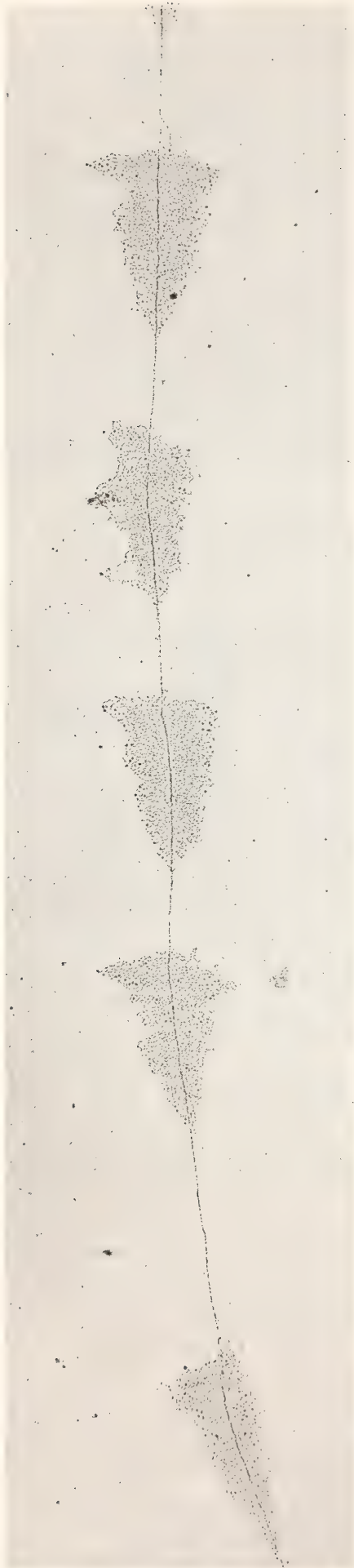
chromatin under certain spreading conditions. These observations suggest that nucleosome cores may be retained on actively transcribed rDNA. We have been unable to find histone H₁ in nucleoli (H. L. Wahn, this Report). This observation is consistent with the increased lability of the beaded structures and may explain the reduced contraction ratio of DNA in ribosomal gene and spacer chromatin. Since nascent transcripts are occasionally observed in the "nontranscribed" spacer, and since spacer and gene chromatin exhibit similarly reduced DNA condensation ratios, we suggest that there may be nothing intrinsic to the structure of spacer chromatin which prevents its transcription. Rather, we suggest that the spacer is not normally transcribed because of efficient RNA polymerase initiation at the 5' end and termination at the 3' end of the DNA complementary to 40S ribosomal RNA precursor molecules.

AN INHIBITOR OF RIBOSOMAL RNA SYNTHESIS IN UNFERTILIZED EGGS

R. H. Reeder

Transcription of rDNA is very low or absent throughout early cleavage in *Xenopus* embryos. Not until the gastrula stage can rRNA synthesis be detected.

Fig. 79. Electron Photomicrograph of amplified ribosomal genes from *Xenopus laevis*. Germinal vesicle plasm from a single oocyte was manually dissected and dispersed in 100 μ l of 0.01 mM borate buffer, pH 9.0. Dispersed chromosomal material was centrifuged through a sucrose cushion containing 10% formaldehyde onto a carbon-coated electron microscope grid. Preparation was rotary-shadowed with platinum metal and examined in the transmission mode on a JEOL-100C electron microscope. Micrograph reveals tandemly repeated "matrix" units separated by fibre-free spacer segments. The chromatin fiber delimited by "matrix" units is interpreted to harbor active ribosomal RNA genes. Fiber-free inter-"matrix" regions are identified as nontranscribed "spacers." Two spacer lengths are observed in this micrograph. Scale bar represents one micrometer.



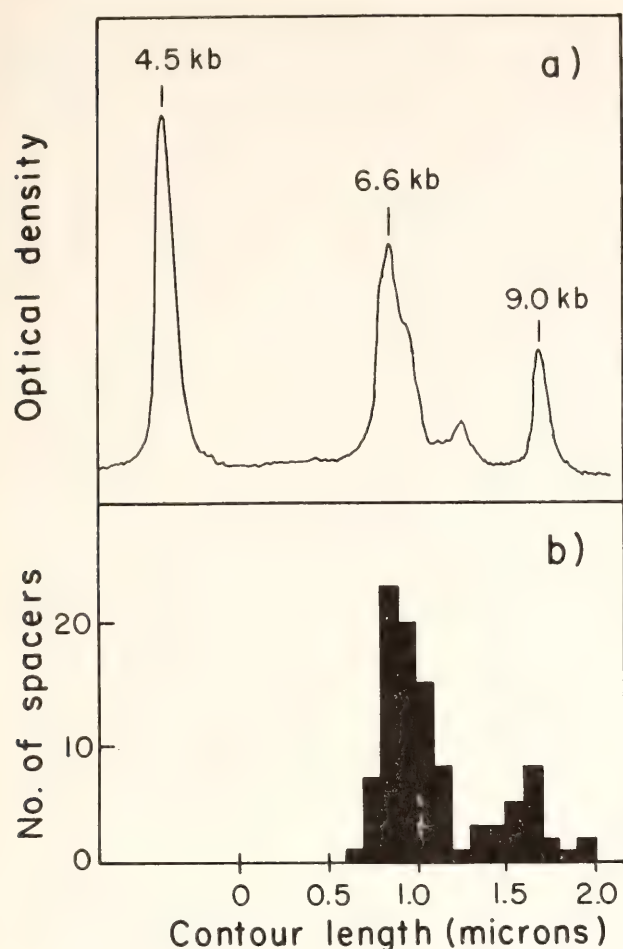


Fig. 80. Contraction ratio of the nontranscribed spacer. (a) Amplified rDNA from a single frog was digested with EcoRI and electrophoresed on a 1% agarose gel. The gel was stained with ethidium bromide and photographed, and the negative was traced with a densitometer. DNA sizes (in kb) were determined by co-electrophoresis of λ -Hind III fragments of known size. The amplified rDNA of this frog yielded the usual 4.5-kb EcoRI fragment that comes from the middle of the gene plus two major classes of EcoRI spacer containing fragments. Allowing for the known amount of gene sequence on each fragment, the 6.6-kb and 9.0-kb fragments contain nontranscribed spacers of 3.6 kb and 6.0 kb, respectively. (b) Amplified ribosomal genes were spread for microscopy from several oocytes of the same frog used in (a). Contour lengths of 98 nontranscribed spacers between active genes were measured and are shown as a histogram. Two major size classes were observed with lengths of about 0.85 and 1.65 microns. Assuming one micron of B form DNA contains 2.94 kb, and further assuming that the two size classes seen in the histogram (b) correspond to the two size classes seen on the agarose gel (a), we calculate contraction ratios of 1.20 and 1.24 for the shorter and longer spacers, respectively.

Gurdon and Brown (*Year Book* 63, p. 504) showed that injection of a nucleus from a neurula cell (active in rRNA synthesis) into an unfertilized egg caused its nucleoli to disappear and rRNA synthesis to stop. These experiments led to the postulate that eggs and cleaving embryos contain a factor that selectively represses rRNA synthesis. Shiokawa and Yamana (*Dev. Biol.* 16, 389, 1967) demonstrated that a substance in cleaving embryos could selectively repress rRNA synthesis when added to dissociated neurula. Laskey *et al.* (*Dev. Biol.* 33, 241, 1973) later showed that a similar repressive substance is present in 0.5 N perchloric acid extracts of eggs but not in similar extracts from neurulae. The substance absorbs to charcoal and behaves like a low molecular weight nucleotide.

Further efforts to purify and characterize this putative repressor have been hampered by the cumbersomeness of the biological assay and the lack of an *in vitro* transcription system that would reinitiate rRNA synthesis with fidelity. Since we now have such a system (described elsewhere in this Report), we decided to use it to continue the search for rDNA transcription control molecules in early development.

A 0.5 N perchloric acid extract of unfertilized eggs was prepared (1 ml packed eggs/2 ml of 0.5 N perchloric acid) as described by Laskey *et al.* The extract was passed through activated charcoal, eluted with 50% ethanol-0.2 N NH_4OH , lyophilized, and redissolved in 0.3 ml of water/initial ml of eggs. The extract was then tested for its effect on rRNA synthesis in homogenized oocyte nuclei. Titration of the extract showed that at a fairly high concentration (1 μl of extract/5 μl reaction) it did depress rRNA synthesis *in vitro*. The question remained whether this depression was due to a nonspecific effect on all transcription or if it was specific for rRNA synthesis.

Both Shiokawa and Yamana and

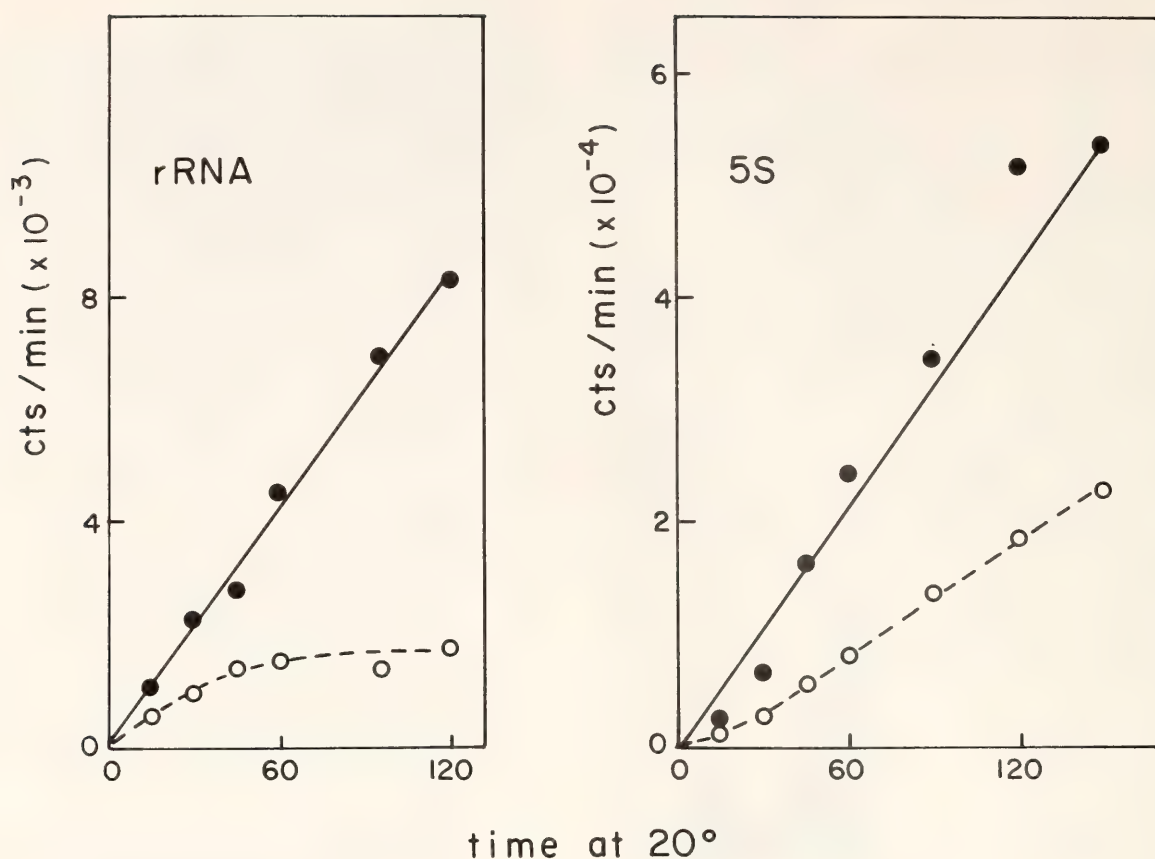


Fig. 81. Effect of an egg extract on the in vitro synthesis of ribosomal RNA and 5S RNA. Unfertilized eggs were extracted with 0.5 N perchloric acid, and the extract was tested for its effect on rRNA and 5S RNA synthesis as described in the text. Solid circles, RNA synthesis in the absence of the extract. Open circles, RNA synthesis in the presence of the extract.

Laskey *et al.*, have reported that the extract has little effect on 4S and 5S RNA synthesis at concentrations that inhibit rRNA. As a control, therefore, we also tested the effect of the extract on 5S gene transcription in vitro. This was done by adding purified 5S DNA to the nuclear homogenate under conditions that Birkenmeier *et al.* (this Report) have shown to support accurate transcription of 5S RNA. The time courses of rRNA and 5S RNA synthesis in the presence and absence of the extract are shown in Fig. 81. Transcription from both templates is inhibited, but the kinetics of inhibition are quite different. The rate of synthesis of 5S RNA is decreased by about 50%. But synthesis at this lower rate is linear for at least 3 hours. This is the effect one would expect if the extract were merely diluting the ^{32}P -CTP specific activity in the re-

action. In contrast, synthesis of rRNA continues for only 45 minutes and then plateaus. This is the expected kinetics if something in the extract were inhibiting the initiation polymerases on rDNA.

We are now in the process of fractionating the extract on various ion exchange columns to purify the inhibitor further.

IDENTIFICATION AND SEQUENCING OF TRANSCRIPTION INITIATION SITES ON *X. laevis* RIBOSOMAL DNA

B. Sollner-Webb and R. H. Reeder

In last year's Report we described a procedure for selectively labeling the 5' polyphosphate termini of rDNA primary transcripts. By hybridizing these labeled termini to restriction fragments of rDNA we were able to establish that transcription initiates near the 5' end of the 40S precursor sequence. We also reported the

somewhat surprising finding that 40S precursor molecules have at least two different termini, as though there were two alternative start sites for the precursor. This year we have mapped the location of these two start sites more finely and have almost completed sequencing of the region where they occur.

As a preliminary aid to sequencing control regions in the rDNA we have subcloned several fragments of the repeating unit and prepared more detailed restriction maps of selected regions. To date all of the subclones have been derived from pXlr14 (see *Year Book 75*, p. 20) and have been inserted into the plasmid pBR322 (or minor derivatives of pBR322). Figure 82 illustrates the sequences that have been subcloned and shows the location of various restriction sites on each. Most of the site mapping

was done by the terminal labeling and the partial digestion method first described in *Year Book 75*, p. 20.

Transcription initiation sites have been mapped by two complementary procedures. The first procedure involves a technique we described last year in which capping enzymes from *Vaccinia* are used to selectively label the polyphosphate termini of primary transcripts. 40S precursor rRNA that was labeled on its 5' end by capping in vitro was hybridized in solution to a series of small restriction fragments covering the 5' end of the gene. It was found that a 200-bp *Sma*I fragment (see Fig. 82) was capable of hybridizing to the 40S termini. Several fragments to either side of this fragment were tested and did not hybridize. After the labeled termini were recovered from the hybrid, they were digested with RNase A and chromatographed on a DEAE column. Two labeled oligonucleotides were recovered (Fig. 83); they coincide in charge to the two major oligonucleotides obtained from the 5' termini of unhybridized 40S rRNA. Therefore, both initiation sites must be located within the 200-bp *Sma*I fragment. When the hybridization is done in RNA excess, the two terminal oligonucleotides are recovered in a 1:1 ratio (data not shown). When DNA is in excess (as is the case in Fig. 83), the larger of the two oligonucleotides is recovered in about 5-fold excess over the smaller one. This is also the ratio in unhybridized 40S rRNA. From this we conclude that the two sites are probably represented once each in the DNA sequence but that initiation at one site is about 5-fold more frequent than at the other site.

As an alternative method for mapping the 5' termini of the 40S molecule, we labeled the ends of the *Sma*I 200-mer with ³²P, hybridized the labeled DNA to an excess of unlabeled 40S RNA, and then digested the hybrid with single-strand-specific S₁ nuclease. The sizes of

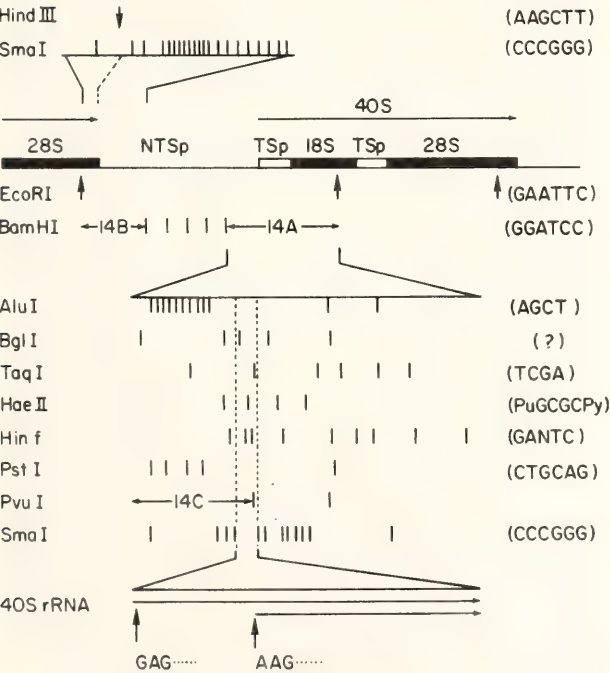


Fig. 82. Structure of *X. laevis* rDNA. 14A, 14B, and 14C designate fragments that have been subcloned in pBR322. Restriction maps are shown for selected regions along with the recognition sequences of the respective enzymes (if known). At the bottom of the figure a 200-bp *Sma*I fragment from 14A is expanded further to show the relative locations of two putative polymerase initiation sites. The tentative sequence of this 200-bp fragment is shown in Fig. 83.

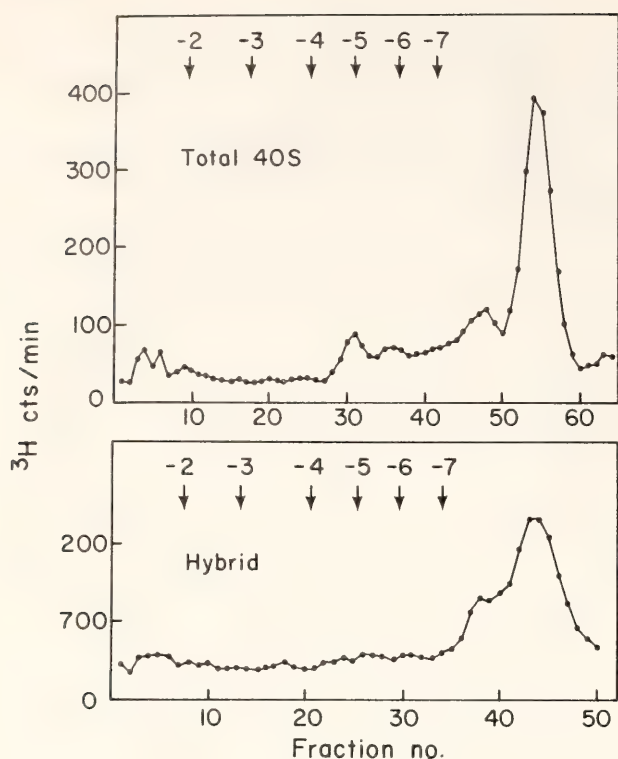


Fig. 83. Oligonucleotides recovered from the 5' ends of 40S precursor rRNA. Top: Unfractionated 40S rRNA was radioactively capped with Vaccinia capping enzymes, digested with RNase A, and the oligonucleotides separated by charge on a DEAE column. Bottom: Capped 40S rRNA was hybridized to an excess of the SmaI 200-mer (map location shown in Fig. 82). The hybrid was recovered, digested with RNase A, and the oligonucleotides fractionated as in the top panel.

the DNA fragments protected by the precursor were then measured by electrophoresis on an acrylamide gel. The results of such experiments are shown diagrammatically in Fig. 82. Two sizes of protected DNA fragments were observed, providing additional support for the notion that there are two separate initiation sites for 40S RNA transcrip-

tion. Both sites appear to be located within the SmaI 200-mer about 75 bp apart.

The SmaI 200-mer has been sequenced by the Maxim and Gilbert procedure. About two thirds of this sequence has been confirmed by labeling the 3' termini with terminal transferase and sequencing from those sites. For comparison with the DNA sequence, we have partial sequence data on the two 5' termini of the 40S precursor. One terminus begins with the sequence pppAAG(Pu)₄₋₈Py, and the other begins pppGAG(Pu)₄₋₈Py. A sequence in the DNA which the G terminus matches is located at the far left-hand end of the SmaI 200-mer. This sequence is GAGAGGAGC and approximately coincides with one of the termini determined by S₁ nuclease protection (Fig. 84). The other S₁-protected terminus is located about 75 bp downstream from the first one. Unfortunately the DNA sequence in this region is still partly ambiguous and will require further work before we can match the RNA terminus and the DNA with certainty.

We have noted before that nucleotide sequences in region D of the nontranscribed spacer can vary from one cloned rDNA repeat to another. But sequence variation in the transcribed gene has never been observed. This conserved sequence boundary is about 200 bp upstream from the nearest site of chain initiation. Figure 82 shows that the repetitive simple sequence in the nontranscribed spacer (as revealed by the regular spacing of AluI sites) stops at nearly the same place that the conserved

GGGGAGAGGAGCCGGCGGCGGCTCTCGGGCCCGCACGACGCCTCCATGCTACGCTTTTTTGGCATGTGCG

GGCAGGAAGGTAGGGGAAGTCCGAACCCTCGAGCGCAGAACGGGCGCCGAAAAAGACCGGCGATTCCCGCC

TCGGTCCCCGGTCTGGGAAGCTCCGCGGTCTGAGTCTCGCTCCCGGCCCGATCGATCTGGCAACCCGCGCCC

Fig. 84. Nucleotide sequence and probable location of transcription initiation sites for 40S rRNA synthesis. The underlined sequences indicate probable initiation sites. About two-thirds of this sequence has been confirmed by two sequencing methods.

sequence boundary is located. Both of these observations suggest that the 200 bp located upstream from the initiation sites may be important for transcriptional control. In any event, they will certainly be sequenced and examined for possible regulatory sites.

Why are there two start sites on these genes? A possible explanation might be that they aid in keeping the gene tightly packed with polymerase, as is clearly seen in electron micrographs of active rDNA.

CHARACTERIZATION OF THE HISTONES ON RIBOSOMAL GENES

H. L. Wahn

The DNA in animal cells is complexed with an equal weight of small basic proteins termed histones. These proteins help neutralize the negatively charged DNA and are probably essential for packaging the exceedingly long DNA thread into the close confines of the cell nucleus. The question remaining is whether the histones have other functions in addition to their structural role in condensing the chromosome. In particular, there has been considerable interest in the possibility that the histones might play a role in the control of gene transcription. If histones are involved in gene control, one might expect that the histones on active genes would in some way be modified or different from the histones on inactive genes. One secondary modification we were especially interested in was acetylation. There is considerable literature describing correlations between increased acetylation of histones and increased gene activity. To date, however, there has been no rigorous test of this hypothesis. In this study we have used the ribosomal gene chromatin isolated as previously described in *Year Book 75*, p. 23, to investigate the above questions. This chromatin is isolated from oocytes actively engaged in ribosomal RNA synthesis. Therefore, an ex-

amination of the basic proteins associated with this transcriptionally active chromatin should allow us to gain insight into these questions.

Ribosomal gene chromatin was isolated, and the basic proteins were extracted with 0.4 N H_2SO_4 , precipitated with ethanol, and then electrophoresed on various high-resolution acrylamide gel systems. As previously reported in *Year Book 76*, p. 91, this chromatin contains proteins that co-electrophoresed with the nucleosomal core histones extracted from somatic tissue culture cells. These proteins were radiolabeled with iodine and subjected to the partial peptide mapping analysis developed by U. K. Laemmli. In all cases the nucleolar histones gave partial peptide maps identical to those of authentic histones (data not shown).

The acid-extracted nucleolar proteins were then subjected to electrophoresis in a two-dimensional acrylamide gel system. Figure 85 shows such a two-dimensional gel in which the proteins were first electrophoresed into an acid-urea gel (separation both by charge and molecular weight) and then into a SDS gel in the second dimension (separation primarily by size). In this experiment the nucleolar proteins were radio-labeled by iodination and then co-electrophoresed with stainable amounts of unlabeled histones from bulk somatic cell chromatin.

Autoradiography of the gel shows that the four nucleosomal histones (H_{2a} , H_{2b} , H_3 and H_4) are all present in the nucleolus. Histone H_1 cannot be detected even after much longer autoradiographic exposures. We believe it is unlikely that H_1 is artificially lost during the nucleolar isolation procedure for these reasons. First, during the Metrizamide gradient step used to purify nucleoli, the nuclei from contaminating follicle cells are found to band just above the nucleoli. These follicle cell nuclei were exposed to the same buffers as the oocyte nucleoli and they have a normal content of H_1 .

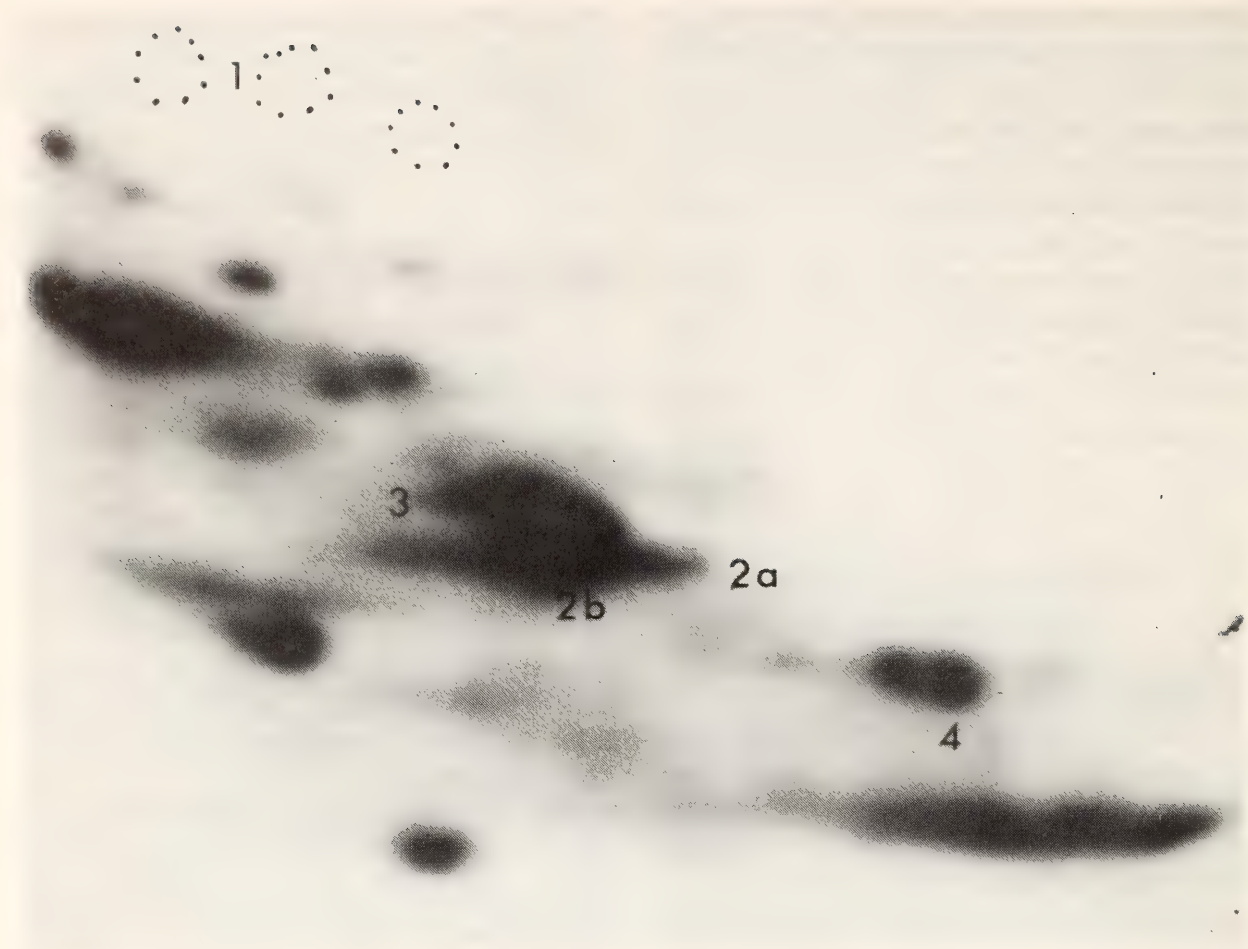


Fig. 85. High resolution electrophoresis of the histones from nucleoli. An acid extract from nucleoli was labeled with ^{125}I and separated by 2-D gel electrophoresis (first dimension, acid urea; second dimension, 5DS).

Second, addition of a variety of protease inhibitors during nucleolar isolation has improved the yield of the nucleosomal histones. However, H_1 is still absent. We believe, therefore, that H_1 is truly absent from nucleolar chromatin. Elsewhere in this Report Dr. S. McKnight describes another line of indirect evidence which agrees with the absence of H_1 on nucleolar chromatin.

In the acid-urea dimension many secondary protein modifications are known to alter the mobility slightly. Thus an acetylation such as those normally found on H_4 or H_3 causes these proteins to migrate slower in the acid-urea dimension. In Fig. 85 histone H_4 is especially well resolved and separates into two spots corresponding to zero and monoacetyl H_4 . These are the same forms

present in bulk inactive chromatin. H_3 is less well resolved but it has no obvious hypermodifications. H_{2a} and H_{2b} also show no apparent modification different from their bulk chromatin counterparts.

This gel also provides proof that the histones on nucleolar chromatin are not contaminants that were adventitiously picked up from the stored pool. Dr. H. Woodland has shown that *Xenopus* oocytes accumulate large pools of histone during oogenesis, but all of the H_4 in this pool is found to be in the form of diacetyl H_4 . Diacetyl H_4 is completely absent from the nucleolar histones.

In summary, we can detect no secondary modifications on the four nucleosomal histones that distinguish them from their counterparts on bulk inactive chromatin. H_1 , however, appears to be com-

pletely absent. As a working hypothesis, therefore, we propose that the only histone modification required for transcriptional activity is the removal of H₁.

MAPPING THE METHYLATION SITES IN *X. laevis* rRNA AND CONFIRMATION OF GENE ORDER IN THE TRANSCRIPTION UNIT

B. E. H. Maden

During ribosomal maturation more than 100 methyl groups are added to the combined 18S, 28S, and 5.8S sequences of vertebrate rRNA's. Methylation is essential for ribosome maturation in HeLa (human) cells, and this is presumably true also for other eukaryotic cells. Detailed information is available on the nucleotide sequences surrounding the methylation sites and the timing of the various methylation reactions during ribosome maturation in several vertebrates including *X. laevis* (Maden *et al.*, *J. Mol. Biol.* 88, 133-164, 1974; Khan *et al.*, *Biochem. J.* 169, 531-542, 1978). However, little is known about the locations of the methylation sites within the overall primary structures of 18S and 28S rRNA. Such information would be of great value for understanding the precise role of methylation in ribosome maturation, as well as the molecular basis of the recognition processes involved in methylation, but progress toward this end has been hampered by the large size of 18S and 28S rRNA and the consequent difficulties of carrying out extensive sequence analysis. We report here the results obtained by an alternative mapping procedure, consisting of preparative hybridization of rRNA to cloned fragments of rDNA, followed by analysis of the hybridized rRNA fragments for the presence of known methylated sequences. An extension of this approach has enabled us to confirm the polarity of transcription in the *X. laevis* ribosomal transcription unit.

The experiments utilized two recombinant plasmids, each containing a part

of the rDNA repeat defined by the cleavage sites for the restriction endonuclease EcoRI. pXlr11 contains a small part of the 18S gene and most of the 28S gene (Fig. 82). pXlr14 contains the remaining large part of the 18S gene and the remaining small part of the 28S gene. Xlr11 and Xlr14 designate the respective rDNA inserts. The inserts also contain transcribed spacer and nontranscribed spacer regions; however, the gene sequences are the focus of interest in the present experiments. Prior to hybridization the inserts were released from the plasmids by digestion with EcoRI.

Figure 86A shows a control fingerprint of *X. laevis* 18S rRNA prepared after *in vivo* methyl labeling. The 18S rRNA contains 40 methyl groups in 34 chemically different T₁ ribonuclease oligonucleotides. Figure 86B shows a fingerprint of methyl-labeled 18S RNA prepared after hybridizing the RNA to Xlr11, trimming the unhybridized region with T₁ ribonuclease, eluting the hybridized RNA and digesting the eluted material with T₁ ribonuclease. Five oligonucleotides are clearly evident in this fingerprint. They were identified (Table 15) by their mobilities and by the results of further digestion procedures. In addition there are two or three weakly labeled oligonucleotides near the origin of the second dimension of the fingerprint (not numbered in Fig. 86B). It is not yet clear whether these represent true

TABLE 15. Methylated Sequences in *Xenopus* 18S rRNA That Hybridize to Xlr11 rDNA

Product*	Sequence
T8	Cm-C-C-G
T30	m ^a ₂ A-m ^a ₂ A-C-C-U-G
T34	(m ^a A,A,C),A,U,G
T48	A-U-U-Am-A-G
T69	... Um-G

* The numbering system and other details of the methylated sequences in *Xenopus* 18S rRNA are given in Khan *et al.*, *Biochem. J.* 169, 531-542, 1978.

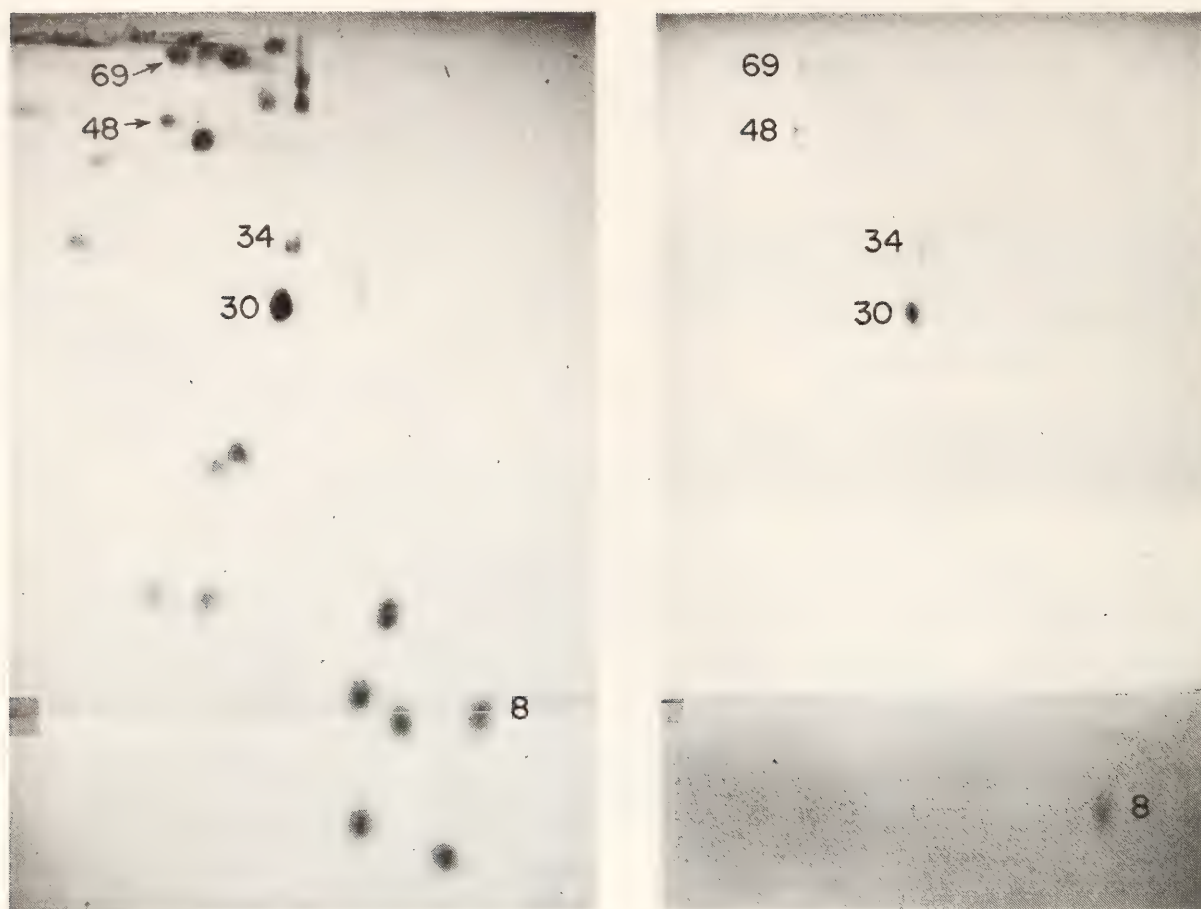


Fig. 86. (A) T_1 ribonuclease fingerprint of *X. laevis* methyl-labeled 18S rRNA. (B) T_1 ribonuclease fingerprint of the region of methyl-labeled 18S rRNA that hybridizes to Xlr11.

hybridization to Xlr11 or contamination. Most of the remaining oligonucleotides in Fig. 86A were present in the fingerprint of the RNA that hybridized to Xlr14, whereas the five products listed in Table 15 were absent from this fingerprint. It is therefore clear that the five methylated oligonucleotides listed in the table are present in the part of 18S rRNA that is encoded within Xlr11, and that most of the other methylated oligonucleotides are present in the region encoded within Xlr14, although there remain two or three oligonucleotides whose assignment is uncertain at the time of writing.

Product T30 contains two adjacent dimethyl-A residues. This product is known to be close to the 3' end of several eukaryotic 18S rRNA's (de Jonge *et al.*, *Nucleic Acids Research* 4, 3655-3663, 1977; Hagenbuschle *et al.*, *Cell* 13, 551-

563, 1978). All recent evidence supports the assignment of the gene order in the ribosomal transcription unit as 5'→18S→28S→3'. The presence of the dimethyl-A sequence in the region of 18S rRNA that hybridizes to Xlr11 strongly supports this polarity assignment. Conclusive evidence that this polarity is correct was obtained from experiments with ^{32}P -labeled 18S RNA. After digestion of 18S RNA with T_1 ribonuclease, the extreme 3' end of the molecule is released as the product A-U-C-A-U-U-A_{OH}. This product was present in the RNA that hybridizes to Xlr11 and absent from the RNA that hybridizes to Xlr14.

It should be possible to extend the mapping of sites of interest within rRNA and ribosomal precursor RNA by preparative hybridization to other restriction endonuclease-derived fragments of rDNA. Such experiments are possible

now that the cleavage sites in rDNA for several restriction endonucleases are known.

INSERTIONS AND SPACERS

Peter Botchan

The ribosomal genes of *Drosophila* and several of the tRNA genes of yeast are known to contain DNA sequences in the midst of the RNA coding regions which either are not expressed in the primary RNA product or else are excised from an internal part of the precursor RNA. These untranslated regions within coding regions are commonly called insertion sequences. A related phenomenon has been reported for mRNA coding genes of various eukaryotes and animal viruses. We wanted to determine whether insertion sequences are necessarily found in *Xenopus* rDNA. Our extensive knowledge of the structure of the rDNA genes of *Xenopus* provides a base from which to look for insertions at this locus.

A second question of interest concerns whether or not rDNA spacer-related sequences are found outside the rDNA locus. A parallel exists in that the insertion found in *Drosophila melanogaster* rDNA is present abundantly outside the nucleolus organizer region, and the insertion probably arose by a transposition of these sequences into the rDNA locus.

A final point of interest concerns the extent of heterogeneity of the ribosomal genes of *Xenopus*. Heterogeneity in the nontranscribed spacer is well documented. The repeating unit can vary in size by 4 kb, all of which can be accounted for by differences in the content of the nontranscribed spacer. However, no variance has been found in the rRNA product itself. We have, therefore, searched for variant rDNA having a different buoyant density than the "major" rDNA class.

Some of the questions we have attempted to examine in this section depend on the ability to detect selectively rare sequences in a very large genome.

This can be accomplished with the use of very high specific activity probes and "blotting" technology originally introduced by Southern. We have found that sequences as small as 200 bp present once per genome can be detected.

To search for possible insertions we have hybridized 18S or 28S rRNA to various restriction fragments spanning the gene and digested the hybrids with single-strand-specific S1 nuclease. The resulting protected DNA fragments are then sized by gel electrophoresis to determine if interruptions exist in the DNA strand. To date we have detected no insertion sequences by this method or by restriction analysis of genomic ribosomal DNA. If any insertions do exist among the 1000 gene copies, our data indicate they would need to be present in fewer than 10% of the copies and then only in the 18S region of the gene.

To search for spacer-related sequences outside the rDNA locus, we have used a technique described in *Year Book 76*. Bulk DNA from a single frog is banded in a CsCl₂ gradient, and DNA from each fraction is digested with EcoRI restriction endonuclease and run on an agarose gel. The DNA is then transferred to a nitrocellulose filter and hybridized with highly radioactive probes made by nick translation of various fragments of cloned rDNA. With this technique we can conclusively state that the *X. laevis* genome has no rDNA spacer-related sequences that are not linked to rRNA genes.

This technique has shown, however, that there are three minor rDNA variants that do not band at the buoyant density position of the main locus. These were first reported last year. Further studies this year show that these variants are present in all frogs and embryos so far tested. Their abnormal buoyant density can probably be explained by a greatly reduced (or entirely absent) nontranscribed spacer. Their possible significance remains unknown.

THE DUAL 5S RNA GENE SYSTEM IN *Xenopus*

D. D. Brown, E. H. Birkenmeier, J. L. Doering, N. V. Fedoroff,
E. Jordan, L. J. Korn, and R. Peterson

The dual 5S RNA gene system in amphibians consists of two (or more) multigene families coding for 5S ribosomal RNA. Although these multigene families are located in the DNA of all cells, somatic cells synthesize only one kind of 5S RNA (somatic type). The 5S RNA genes in all families of 5S DNA appear to be transcribed in oocytes. The 5S DNA's have been characterized in two species of *Xenopus* (*laevis* and *borealis*). Fragments of these multigene families containing the 5S RNA gene and surrounding spacer DNA have been cloned. The nucleotide sequence of one repeating unit of *X. laevis* oocyte 5S RNA (Xlo) was reported in *Year Book 76* (N. Fedoroff). In this report the sequence of a cloned fragment of *X. borealis* oocyte DNA (Xbo) containing three 5S RNA genes is presented (L. Korn). J. Doering has almost completed the sequence of a repeating unit of *X. borealis* somatic specific 5S DNA (Xbs). Its spacer region is markedly different from that of the oocyte 5S DNA's. Of special interest are the sequences that flank the gene and are therefore candidates for control regions. Using a computer program, L. Korn has compared these regions in three *Xenopus* 5S RNA gene families as well as in other genes transcribed by RNA polymerase III. Most of the spacer regions in these multigene families have diverged so that the presence of conserved oligonucleotides suggests a function for these nucleotides.

R. Peterson has discovered a third multigene family of 5S DNA in *X. laevis* genomic DNA. This 5S DNA has been cloned, and preliminary studies suggest that it contains the genes for somatic 5S RNA (Xls). If this is correct, we will have the oocyte and the somatic 5S

DNA's from two species of *Xenopus*. This completes our "systems development," and we can now devote full time to understanding control of gene expression.

Another advance in this project has been the preparation of a nuclear extract from *Xenopus* oocytes that supports accurate 5S RNA synthesis from added 5S DNA (Birkenmeier, Brown, and Jordan). This permits us to assay recombinant DNA molecules containing 5S DNA for transcription of 5S RNA. In addition we have begun to isolate molecules from the nuclear extract that are required for 5S RNA synthesis.

We plan to introduce deletions and base substitutions into various regions of 5S DNA and to determine the effect on 5S RNA synthesis. The first such studies are reported here by N. Fedoroff. She has devised a method for deleting portions of the spacer region of Xlo 5S DNA. She concludes that most (perhaps all) of the AT-rich spacer of Xlo 5S DNA can be deleted without affecting faithful transcription of the 5S RNA gene. Experimental methods are now available to mutate nucleotides so that we can catalogue the sequences responsible for controlling accurate transcription.

NUCLEOTIDE SEQUENCE OF THREE
Xenopus borealis 5S RIBOSOMAL RNA
GENES AND ADJACENT CONTROL REGION

L. J. Korn and D. D. Brown

A cloned fragment of *Xenopus borealis* oocyte 5S DNA (Xbol) containing three 5S ribosomal RNA genes has been sequenced (Fig. 87). Genomic Xbo 5S DNA contains variable numbers of 5S RNA genes in clusters separated by vari-

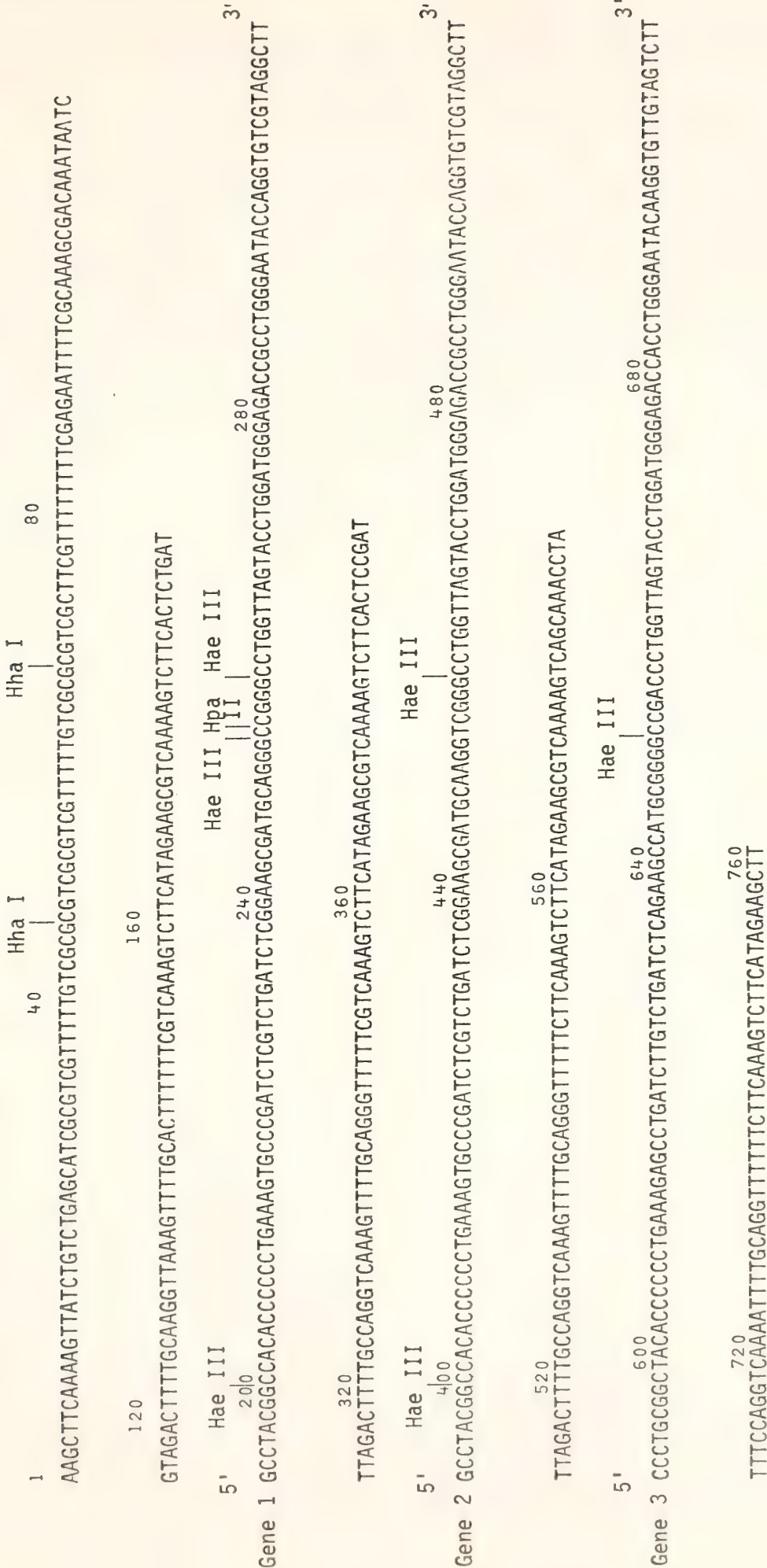


Fig. 87. The nucleotide sequence of Xbol. In this and all subsequent figures only the noncoding strand is shown.

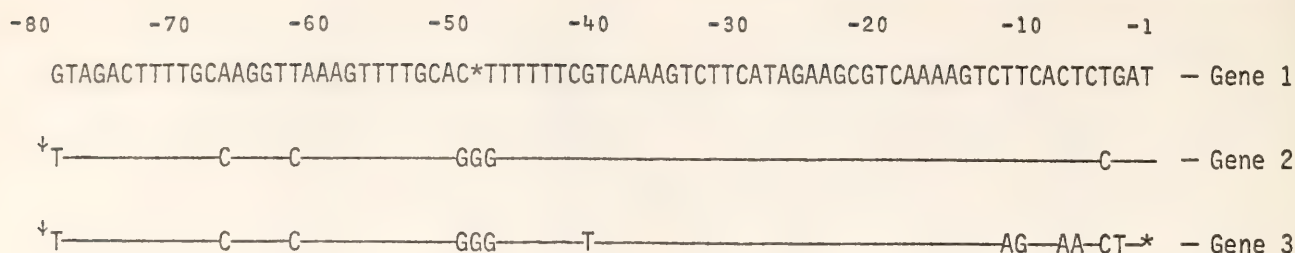


Fig. 88. The nucleotide sequences preceding gene 1, between genes 1 and 2, and between genes 2 and 3. The first sequence is shown in its entirety and only altered bases are shown for the others. The sequences are numbered negatively from the 5' end of the gene. An asterisk between nucleotides indicates a deletion with respect to the second sequence. An arrow is used to indicate the position of the 3' terminal nucleotide of the preceding gene. Note that the two intercistronic sequences (lines 2 and 3) differ in only one base pair between positions -12 and -79, whereas in the first 11 base pairs there are 6 differences.

able length AT-rich spacer DNA. This contrasts with *X. laevis* oocyte 5S DNA (Xlo), which has more regular repeating units each consisting of one gene, one pseudogene, and an AT-rich spacer sequence (see *Year Book 76*). The distance between the Xbo genes within a cluster is about 80 nucleotides. Spacer length heterogeneity in Xbo is due in part to variable numbers of a tandemly repeated 21-nucleotide sequence (CGTCGCGTCGTTTTTGTCGCG), just as varying numbers of a 15-nucleotide repeating sequence are known to account for most of the spacer length heterogeneity in Xlo 5S DNA (see *Year Book 76*). Each 21-nucleotide repeat contains two copies of the hexanucleotide GTCGCG and a cluster of 5 T residues.

The sequence of two of the Xbol genes is very similar to the dominant 5S RNA sequence, whereas 15 of the 120 residues in the third gene are different. This level of sequence divergence is about the same as that found between the gene and "pseudogene" in *X. laevis*; however, the *X. laevis* pseudogene resembles the gene only in its first 100 base pairs (see *Year Book 76*).

In order to make meaningful comparisons between potential promoter and termination sites of the three 5S RNA genes in Xbol, it is necessary to determine whether the genes are transcribed.

To do this, we examined 5S transcription following injection of Xbol into oocyte nuclei (see *Year Book 76*), and after addition of Xbol DNA to an extract of these nuclei (see Fig. 99). All three genes are transcribed. Thus the information to direct initiation and termination of RNA synthesis from each gene is contained within the fragment.

The sequences 12 to 40 nucleotides preceding each of the three Xbol genes are identical (Fig. 88). In contrast, 7 of the first 11 nucleotides preceding the third 5S RNA gene differ from those preceding the first gene. Since all three genes are transcribed, a precise sequence in the 11 bases adjacent to the gene is not essential for initiation of transcription.

The sequences following the three Xbol genes are similar, with the exception of an 8-base deletion after the third gene. This deletion appears not to interfere with transcription termination. The sequences adjacent to the 3' ends of the *X. borealis* oocyte and somatic 5S genes are identical in 12 of 14 nucleotides and contain two T clusters. The corresponding region in Xlo 5S DNA has two similarly spaced T clusters, but the sequence between the T clusters is different.

Nucleic acid sequences flanking several eukaryotic genes that are transcribed by RNA polymerase III were analyzed

	- 70	- 60	- 50	- 40	- 30	- 20	- 10	- 1
Xbo 5S	TTGCAAGGTTAAAGTTTTGCACTTTTTTCGTC AAAGTCTT CAT AGAAGCGTCAAAGTCTT CACTCTGAT							
Xbs 5S	CCTGGCATGGGGAGGAGCTGGGCCGCCCCCA GAAGGCAGCAC AAGGGGAGG AAAAGT CAGCCTTGTGCC							
Xlo 5S	AAAGTTTTCATTTTCATTTTCCACAGTGCCGCT GACA AGTCA AGAAGCCGAAAAGT GCCGCTGTTTCATC							
Adenovirus VA RNA	GGACGCTCTGGCCGGTGAGGCGTGCGCAGTCGTT GACGCTCTAGACC GTGC AAAAG AGAGCCTGATAAGC							
Drosophila 5S	CAGTCTATTT CAGTCTATGGGCATAACTGAATATCAGAGTATAAGG ACACTGTTTAGCCCTCGACTTTC							

Fig. 89. The nucleic acid sequence preceding five eukaryotic genes. For Xlo and Xbo, the dominant sequence of the region was chosen (see *Year Book 76*); the Xbo sequence is the one preceding Xbol gene 2. Position -n is n nucleotides in front of the first nucleotide of the gene. The oligonucleotide analogs of GAC, AGAAG, and AAAAG are shown in boldface. The direct repeat with the lowest probability of occurring by chance is indicated by underlines. The most purine rich region in the 50 nucleotides preceding the gene is overlined.

for common features that may comprise part of the recognition signals for initiation and termination of transcription. In the region preceding the Xlo, Xbo and *X. borealis* somatic (Xbs) (described in this Year Book) 5S ribosomal RNA genes, an extensive sequence homology is seen between 13 to 29 nucleotides before the gene. The hexanucleotides AGAAGC and AAAAGT or slight variants were found at positions -28 to -23 ± 1 and -18 to -13 ± 1, respectively, from the 5' end of the gene in all three sequences (Fig. 89). Moreover, the DNA sequence preceding the virus-associated RNA (VA RNA_I) gene of adenovirus 2 (Pan *et al.*, *J. Biol. Chem.* 252, 9047, 1977) and the *Drosophila* 5S rRNA genes (Tschudi *et al.*, personal communication) also contains oligonucleotides similar to AGAAG and AAAAG, although their position is shifted relative to the gene. In addition the trimer GAC or a close analog is found in all five sequences (Fig. 89). The spacing of the homologous regions is: GAC, then 5 or 6 residues, AGAAG, then 3 to 6 residues, AAAAG, then 13 or 14 residues, transcription initiation (The only exception is the distance be-

tween AAAAG and the *Drosophila* 5S gene.) The degree of matching between these oligonucleotides is seen in Table 16. The probability of these homologies occurring by chance alone is similar to that described for prokaryotic promoters (Gilbert, *RNA Polymerase*, eds. Losick and Chamberlin, Cold Spring Harbor Laboratory, 1976).
A computer program (see *Year Book 76*) was used to scan each of the five 5' flanking sequences for oligonucleotides that appear more than once (direct repeats) and for sequences that are dyad symmetric. The direct repeats least likely to have occurred by chance alone are shown in Fig. 89. The number of direct repeats expected by chance in the 70 nucleotides preceding the gene which are at least as improbable as the one found is tabulated in Table 16. Xbo, Xbs, Xlo, and VA RNA_I have direct repeats that are unlikely to occur by chance alone and are as improbable as the dyad symmetries associated with prokaryotic transcription termination and operator sites (Gilbert in *RNA Polymerase*, Losick and Chamberlin, eds., Cold Spring Harbor Laboratory, 1976). The direct repeat found in the 5'

TABLE 16. Analysis of 5' Flanking Sequences*

	Homology with AAAAG (%)	Homology with AGAAG (%)	Homology with GAC (%)	Best Direct Repeats (no. matches/total length and number expected by chance)		Purine-Rich Regions (no. purines/no. nucleotides and %)	
Xbo 5S	100	100	67	14/15	<0.01	11/14	79
Xbs 5S	100	80	67	10/11	0.05	23/26	88
Xlo 5S	100	100	100	10/10	0.01	11/13	85
Adenovirus VA RNA ₁	100	60	100	14/17	0.05	14/18	78
<i>Drosophila</i> 5S	80	60	67	9/12	0.5	10/12	83

* The nucleic acid sequence preceding the five genes listed was examined for the presence of the oligonucleotides AAAAG, AGAAG, and GAC, for direct repeats, and for a purine-rich region (see Fig. 89). The first three columns show the extent of homology in the 50 nucleotides preceding the gene with the oligonucleotides AAAAG, AGAAG, and GAC. The best direct repeats found by a computer (see *Year Book 76*) are those shown in Fig. 89, and the number of repeated nucleotides divided by the length of the repeat is listed under "Best Direct Repeats." The number of direct repeats expected by chance alone in the 70 nucleotides in front of the gene which are at least as improbable as the one found was determined by Korn *et al.* (see *Year Book 76*), and C. Queen and Korn (*Methods in Enzymology*, in press). The number and percent of purines in the most purine-rich region (Fig. 89) in the 50 nucleotides preceding the gene are tabulated under "Purine-Rich Regions." This region always includes the two pentameric homologies.

flanking region of *Drosophila* 5S DNA is not statistically significant. The probability that the direct repeats present in the five sequences could all have occurred by chance alone is less than 10⁻⁶. In addition to the oligonucleotides AAAAG, AGAAG, and GAC, and a direct repeat, the common features in the region preceding the several genes are: a purine rich region, the absence of dyad symmetry, transcription beginning with a purine, and a pyrimidine residue immediately preceding the first nucleotide of the gene. The termination regions of the Xbo 5S RNA genes and the other eukaryotic genes contain many features in common with prokaryotic termination sites. The terminal portion of the gene is GC-rich and contains a dyad symmetry. The spacer region immediately following the gene is AT-rich, and the noncoding strand contains one or more T clusters.

SEQUENCE OF *X. borealis*
SOMATIC 5S DNA

J. L. Doering and D. D. Brown

The identification and partial characterization of the somatic-type 5S DNA from *X. borealis* (Xbs) has been reported in *Year Book 75* (p. 15) and *Year Book 76* (p. 105). Total frog Xbs is cut by the restriction enzyme Hind III into homogenous 850-base pair fragments, some of which have been cloned. Using the DNA sequencing method of Maxam and Gilbert (*Proc. Nat. Acad. Sci. U.S.A.* 74, 560, 1977), we have determined the nucleotide sequence of 80% of one such cloned repeating unit (Xbsl). There is only one gene sequence in the repeating unit. The nine fragments produced by Hae III digestion of the cloned unit are the same fragments resulting from Hae III + Hind III digestion of



at 34g is C and that XbsI contains A as a base substitution in that position.

In contrast to the oocyte 5S DNA's of *X. laevis* (Xlo) and *X. borealis* (Xbo) (*Year Book* 76, p. 100, and L. Korn, this Report), Xbs has no detectable pseudogene structure and no obvious repetitive simple sequence in the spacer regions. However, like the oocyte 5S DNA's, the Xbs repeating unit can be divided into two regions based on their relative G+C content. The spacer region that extends to a point 39 nucleotides from the 5' end of the gene in the sense of transcription has a G+C content of 68%, which is considerably higher than the remainder of the repeating unit. The finding of two regions of substantially different G+C content confirms the biphasic melting curve for XbsI reported earlier (*Year Book* 75, p. 16).

Since 5S RNA has no known precursor form, the DNA regions immediately adjacent to the gene-coding sequence are logical candidates for transcription control sites. The 39 nucleotides preceding the 5' end of the XbsI gene bear some sequence homologies with the sequences adjacent to the 5' ends of Xlo and Xbo genes (*Year Book* 76, p. 100, and L. Korn, this Report). In the three 5S DNA's studied to date, these flanking sequences are different in G+C content from the contiguous spacer and contain at least one repeated oligonucleotide. The T clusters that characterize the regions adjacent to the 3' ends of Xbo and Xlo 5S RNA genes are also found next to the 3' end of the Xbs gene. This is the only AT-rich region in the entire repeating unit. Since the overall spacer sequences for the various types of 5S DNA have diverged considerably, the small regions contiguous to the genes where the sequences have been conserved may be involved in the control of transcription. A more detailed comparison of the regions adjacent to the 5' and 3' ends of 5S RNA genes is presented by L. Korn (this Report).

PURIFICATION AND MOLECULAR CLONING OF A THIRD 5S DNA COMPONENT FROM *Xenopus laevis* DNA

R. Peterson

Xenopus laevis oocytes synthesize at least three kinds of 5S ribosomal RNA. Only one type, the somatic 5S RNA, is synthesized in somatic cells. The isolation of two families of 5S DNA has been reported (see *Year Book* 76); however, both of these sets of genes are expressed only in growing oocytes. The major class of 5S RNA genes (Xlo) codes for the principal 5S RNA found in oocytes, while the second class of genes (Xlt) accounts for about 10% of the 5S RNA synthesized by oocytes. The relative abundance of each of these two 5S RNA's in oocytes is an approximate reflection of the number of copies of each type of gene present in the genome of *X. laevis*.

Another class of 5S RNA genes from genomic *X. laevis* DNA has now been detected that is less abundant than Xlt 5S DNA. This new class of genes overlaps Xlt DNA when genomic *X. laevis* DNA is banded in an actinomycin D-CsCl₂ density gradient. A second density gradient completely removes Xlo 5S DNA. Digestion of the DNA from fractions containing Xlt 5S DNA with the restriction endonuclease Hind III results in fragments of DNA which can be separated by electrophoresis on a 1.4% agarose gel. Transfer of these DNA fragments to a nitrocellulose filter by the blotting method followed by hybridization of the filter with either ¹²⁵I-labeled 5S RNA or ³²P-labeled nick translated pXbsI DNA and autoradiography revealed a previously undetected 5S RNA fragment that is not derived from Xlo or Xlt DNA (Fig. 91). This new fragment is approximately 900 base pairs long and represents a new class of 5S RNA genes. This fragment has been prepared from embryonic *X. laevis* DNA, extracted from an agarose gel, joined with the plasmid pBR322, and

cloned in *E. coli* strain HB101. Further characterization of this 5S DNA is under way.

DELETION ANALYSIS OF *X. laevis* 5S DNA

N. Fedoroff

The primary sequence of the *Xenopus laevis* oocyte 5S DNA repeating unit was reported and analyzed in some detail in *Year Book 76* (pp. 100–102). The repeating unit, represented schematically in Fig. 92, can be roughly divided into AT-rich and GC-rich halves. The GC-rich half contains the 5S ribosomal RNA gene and appears to comprise a single long duplication. The duplication includes a portion of the gene sequence, and this has been designated the pseudo-gene. The gene is preceded on the 5' side by a GC-rich, relatively nonredundant sequence of 49 nucleotides. Adjacent to this sequence is the AT-rich spacer, which is both internally redundant and variable in length (Fedoroff *et al.*, *Cell* 13, 701, 1978; Miller *et al.*, *Cell* 13, 717, 1978). The objective of the experiments to be described here is to establish whether there are sequences adjacent to the gene on the 5' side which have a promoter function. A procedure has been devised to generate deletion mutants of 5S DNA. A series of deletion mutants has been isolated, and the deletion end points have been mapped in some of them. The ability of the deletion mutants to support transcription of 5S RNA has been assayed by transcription of deletion-bearing plasmids in oocyte nuclei (Brown *et al.*, *Proc. Nat. Acad. Sci. U.S.A.* 74, 2064, 1977).

Deletions were generated by first introducing a bacterial transposable element into the spacer adjoining the 5S rRNA gene and then eliminating it. The transposable element TN9, which carries a readily detectable chloramphenicol-resistance marker, was transposed from the bacteriophage P1 to a bacterial plas-

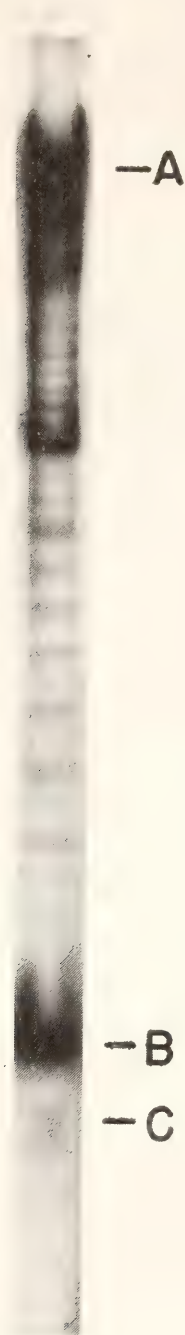


Fig. 91. The localization of a new family of 5S DNA by autoradiography of DNA fragments cleaved with Hind III, electrophoresed on an agarose gel, transferred to nitrocellulose filters and hybridized with radioactive 5S DNA. Genomic DNA of *X. laevis* was centrifuged to equilibrium in an actinomycin-CsCl gradient. A fraction on the light side of main-band DNA was used for digestion. Xlt 5S RNA genes (A) are the major type of 5S RNA genes in this DNA fraction, although a new class of genes (B) and a small amount of Xlo 5S DNA (C) are also present. The numerous minor bands of 5S DNA between A and B are due to Xlt 5S DNA, which is occasionally cut by Hind III. Most of the oocyte-type 5S DNA appears in other fractions of the CsCl gradient.

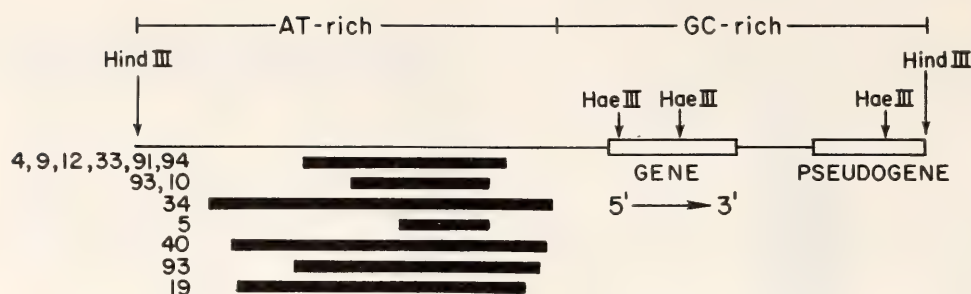


Fig. 92. A diagrammatic representation of the 5S DNA repeating unit from which deletion mutants were derived. The repeating unit in the 5S DNA fragment used to generate deletion mutants is 750 nucleotides in length and typical of 5S DNA repeating units in organization (see *Year Book 76*). The AT-rich internally repetitive spacer is 400 nucleotides long and extends from the Hind III site at the left end of the spacer to within 50 nucleotides of the 5' terminus of the gene sequence. The GC-rich portion of the repeating unit contains the gene and pseudogene sequences and comprises a single long duplication of 174 nucleotides. The bars below the diagram represent the portions of the AT-rich spacer sequence which have been deleted in the 13 mutants mapped so far. The numbers adjacent to each bar designate the individual deletion mutants. The deletion represented by the bar immediately below the diagram has been obtained independently in six different strains; the next deletion has been isolated twice and the remaining deletions have been isolated once each. The largest deletion, observed in strain 34, eliminates all of the spacer except the 70 nucleotides at the left (Hind III) end of the spacer and the 55 nucleotides immediately adjacent to the gene.

mid containing *X. laevis* oocyte 5S DNA. This was accomplished by lysogenizing a bacterial strain (HB101) carrying a 5S DNA-containing recombinant plasmid with a strain of the phage P1 carrying the TN9 transposon. The plasmid population was then isolated and used to transform HB101 to chloramphenicol-resistance. Strains in which transposition of TN9 had inactivated expression of the plasmid's tetracycline-resistance marker were selected for further examination. Such plasmids were thought likely to have TN9 integrated in or near the 5S DNA cloned in the Hind III site located in the promoter region for the tetracycline-resistance genes. We had previously noted that integration of 5S DNA in only one of the two possible orientations permits continued expression of the plasmid's tetracycline-resistance genes, suggesting the existence of a fortuitous promoter sequence for *E. coli* RNA polymerase in the 5S DNA sequence (Fedoroff *et al.*, 1978). Were this true, integration of TN9 in the 5S DNA might yield tetracycline-sensitive strains. A total of 112 chloramphenicol-resistant plasmids were obtained and of these, only

9 were no longer capable of conferring tetracycline-resistance on the host strain. Six of the 9 displayed a low reversion frequency (10^{-9}) to tetracycline-resistance and probably represent integration of the TN9 element into the plasmid genes for tetracycline-resistance. The remaining 3 plasmids reverted to tetracycline-resistance at a much higher frequency (10^{-5} – 10^{-4}). The transposable element in these plasmids had become integrated in the AT-rich spacer of the 5S DNA within 150–200 nucleotides of the gene on the 5' terminal side. The position of integration was estimated from the lengths of the 5S DNA restriction enzyme fragments altered by the integration event.

Virtually every revertant plasmid strain derived by loss of the transposable element from the 5S DNA spacer in such plasmids carried a deletion in the 5S DNA. The high frequency of deletion production was established by selecting independent tetracycline-resistant revertants of the tetracycline-sensitive strains carrying TN9 in the 5S DNA spacer and determining the length of the Hind III 5S DNA fragment con-

tained in the plasmid. Of 120 such plasmids examined, none contained a 5S DNA Hind III fragment of the original length; most had Hind III 5S DNA fragments that were shorter than the original by 10–350 nucleotides. A total of 36 such revertant strains have been analyzed in detail. Of these, 34 contained at least one copy of the 5S DNA from which the TN9 element had been completely deleted, along with portions of the flanking 5S DNA spacer sequences (Fig. 93a). In the remaining two strains, most of the transposable element had been deleted, leaving one of the two terminal insertion sequences (IS1) of the original TN9 element integrated in an otherwise unaltered 5S DNA spacer sequence (Fig. 93b). Most strains contained either a unit length deleted plasmid (14 strains; Fig. 93a), or a double-length plasmid (14 strains), half of which corresponds to the deleted plasmid structure shown in Fig. 93a and the other half of which corresponds to the IS1-containing plasmid structure shown in Fig. 93b. The structure of such plasmid doublets is shown in Fig. 93c. Of the rest, one contained a plasmid that appeared to be a perfect doublet of a deleted plasmid, and the remaining strains contained mixtures of the three types depicted in Fig. 93. Since the plasmid pMB9 contains a single RI site, half-plasmids containing deletions were recovered from EcoRI digests of the doublet type diagrammed in Fig. 93c, religated, and recloned for further analysis of the deletion in the 5S DNA.

All of the deletions were confined to the AT-rich spacer in 5S DNA. It was first established by restriction enzyme analysis that the only fragment whose mobility had been altered by deletion was the large spacer-containing Hind III–Hae III fragment (Fig. 92). The endpoints of the deletions were then determined by DNA sequencing. Since the spacer sequence is known, the deletion endpoints could be determined to the nearest G residue simply by comparing

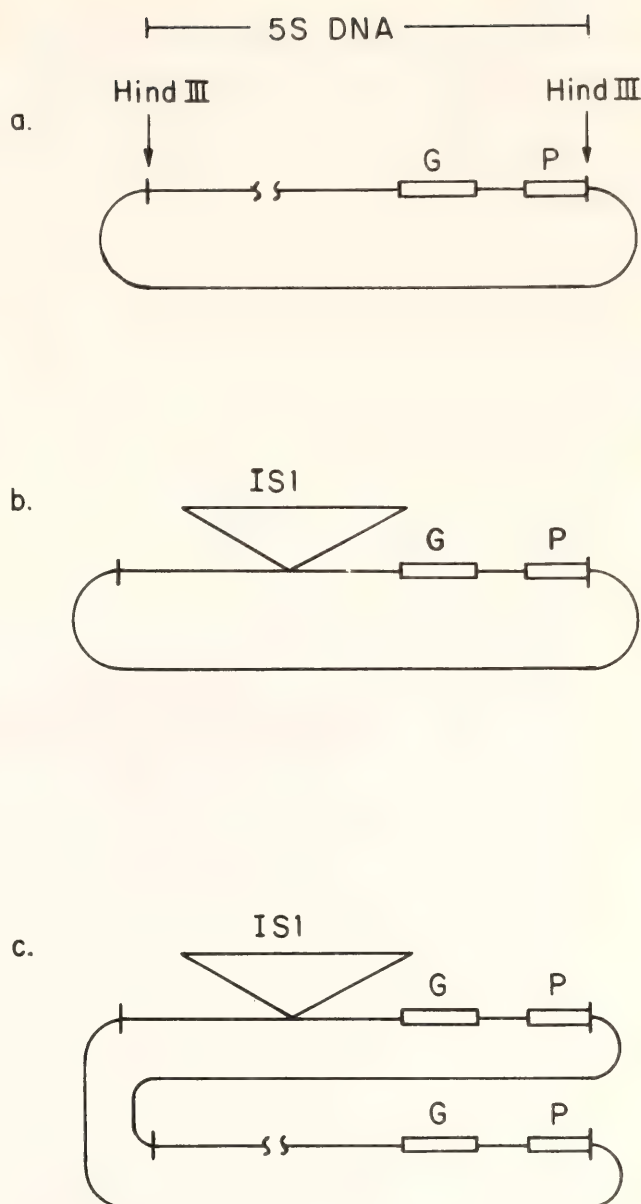


Fig. 93. Structure of revertant plasmids derived from a recombinant plasmid containing 5S DNA and the transposable element TN9. Strains carrying a plasmid (pBR322) in which the original strains arise at a frequency of 10^{-5} – 10^{-4} has integrated in the 5S DNA spacer are chloramphenicol resistant and tetracycline sensitive (see text). Tetracycline-resistant derivatives of the original strains arise at a frequency of 10^{-5} – 10^{-4} . Of the 36 tetracycline-resistant strains whose plasmids have been characterized, 14 had the structure depicted in (a), 2 had the structure shown in (b), 14 had the structure shown in (c), and most of the rest contained various mixtures of the plasmids represented in (a), (b), and (c).

the partial cleavage products terminating at G residues obtained from the initial spacer fragment with those obtained

from the deletion mutants. The portion of the spacer sequence missing in a number of different deletion mutants is represented by the bars in Fig. 92. The longest deletion eliminates about 80% of the AT-rich spacer sequence. The deletion mutant 34 contains only the terminal 70 nucleotides from the left of the AT-rich spacer and the 55-nucleotide sequence immediately adjacent to the 5' terminus of the 5S rRNA gene.

The 5S rRNA gene is transcribable in all of the deletion mutants. This was established by injecting deletion mutant 5S

DNA plasmids into *X. laevis* oocyte nuclei, along with labeled nucleotides, and analyzing the labeled RNA's obtained. Fig. 94 shows the outcome of such an experiment. Each channel of the nondenaturing acrylamide gel contains the RNA extracted from oocytes injected with a different deletion mutant DNA. In the first channel is RNA from oocytes injected with pXlo31; its 5S DNA insertion (Xlo31) has been sequenced, and the gene is known to differ by two nucleotides from the most common gene sequence present in oocyte 5S DNA (Miller *et al.*,

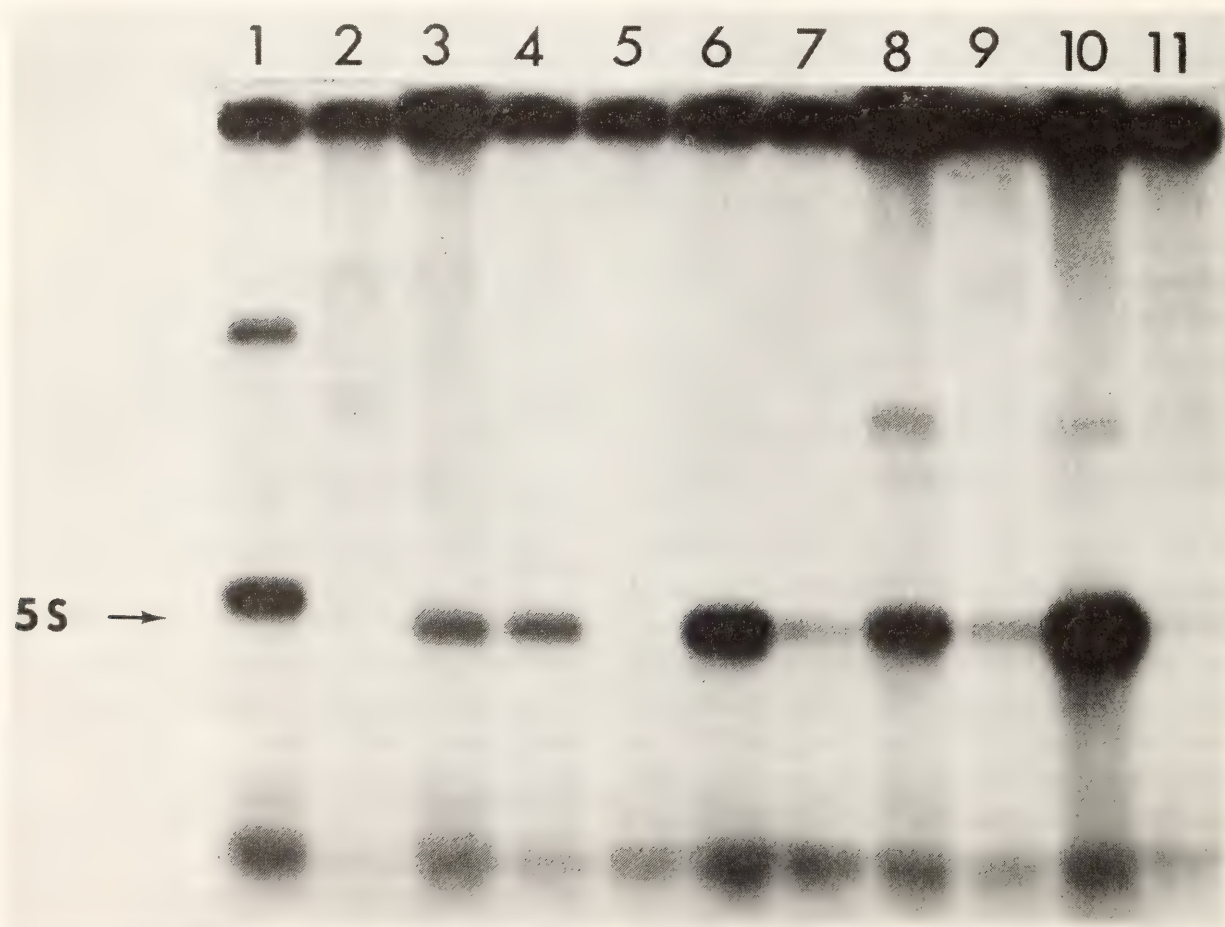


Fig. 94. Transcription in oocyte nuclei of the 5S rRNA gene in mutants having deletions of various sizes. Plasmids containing 5S DNA with spacer deletions of various sizes were injected into oocyte nuclei along with [α - 32 P]-CTP. The labeled RNA was purified and analyzed on a 10% polyacrylamide gel (Brown *et al.*, 1977). The arrow indicates the position of the unlabeled 5S RNA present in each sample. In channel 1 is the RNA extracted from oocytes injected with the plasmid designated pXlo31. In channels 2–10 are the RNA's synthesized in oocytes injected with different deletion mutant DNA's. Channel 12 contains the RNA synthesized in oocytes injected with the plasmid cloning vehicle. The approximate lengths of the deletions in the mutants used in channels 2–10 ranged from 10 to 190 nucleotides. Although two of the mutants (channels 2 and 5) gave no fast-migrating 5S RNA species in this experiment, they did in other experiments. All of the 26 deletion mutants tested so far have yielded the characteristic fast-migrating 5S RNA species associated with the 5S DNA repeating unit from which they were derived.

Cell 13, 717, 1978). Its RNA transcript migrates slightly more slowly than the most common sequence, whose position is indicated by the arrow. Transcripts from the gene carried by the plasmid from which the deletion mutants were derived migrate somewhat faster than the most common 5S RNA sequence (Fig. 94). These variations in electrophoretic mobility appear to be due to secondary structural differences consequent on sequence variations, since these 5S DNA species co-migrate on denaturing polyacrylamide gels. The differences in electrophoretic mobility between the most common 5S RNA synthesized *in vivo* and those transcribed from pXlo31 and from the deletion mutants have been exploited to analyze the quantitative differences observed between samples in Fig. 94. In order to determine whether these variations were attributable to differences between deletion mutants in the efficiency of transcription, labeled RNA precursors were injected along with a mixture of pXlo31 and a given deletion mutant DNA in various proportions. The labeled RNA's were then fractionated on a polyacrylamide gel, and the ratio of the two transcripts determined. It is apparent from the coincidence of the curves in Fig. 95 that a mutant carrying a 325-nucleotide deletion was transcribed at the same rate relative to the gene in pXlo31 as was a deletion mutant missing less than 50 nucleotides, suggesting that the frequency of transcription is unaffected by the size of the deletion.

The results of these studies indicate that the majority of the spacer sequence adjacent to the 5S rRNA gene has no promoter function. Since all of the deletion mutants analyzed in detail so far contain at least the terminal 55 nucleotides immediately adjacent to the 5' terminus of the gene, extragenic promoter-active sequences, if they exist, are likely to be confined to this region. Although there is an additional 70-nucleotide AT-rich spacer sequence in deletion strain 34,

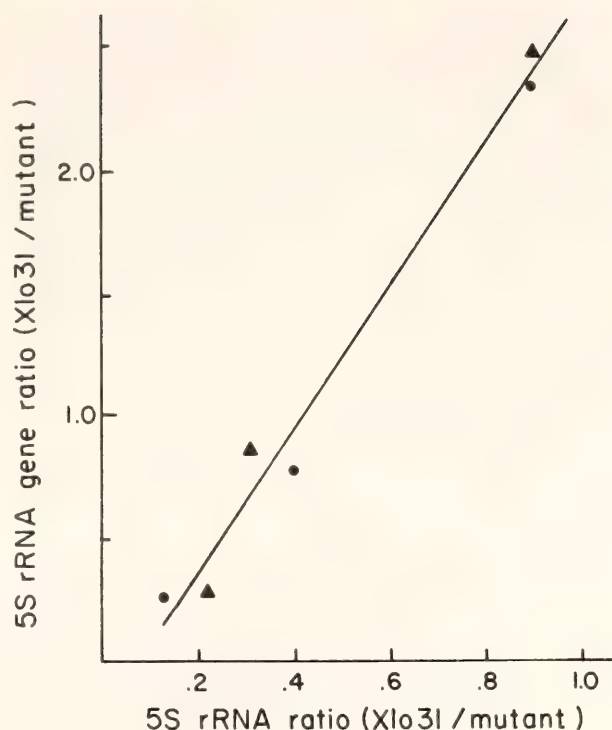


Fig. 95. Relative transcription efficiencies of pXlo31 and deletion mutant DNA's. Labeled RNA was extracted from oocytes injected with a radioactive RNA precursor and a mixture of pXlo31 and the deletion mutant DNA's in different proportions. The RNA was analyzed on a polyacrylamide gel as illustrated in Fig. 94, and the relative amounts of radioactivity were determined in the slowly migrating pXlo31 5S RNA and the fast-migrating deletion mutant 5S RNA transcripts. The gene present in the deletion mutants is transcribed about twice as efficiently as the gene in pXlo31, and the relative rate of transcription does not change with the relative concentration of the two plasmids. The two deletion mutants were missing 325 nucleotides (circles) and about 35 nucleotides (triangles), respectively, from the AT-rich spacer.

which is the most extensive deletion so far characterized, this residual AT-rich spacer sequence is not likely to be critical to gene expression. This follows from the observation that the 5S rRNA gene in the original TN9-bearing plasmid, in which this portion of the AT-rich spacer sequence is removed from the gene by an insertion of more than 3000 nucleotides, is transcribed in oocyte nuclei.

The 73-nucleotide portion of the spacer sequence immediately adjacent to the gene is homologous with the 73-nucleo-

tide sequence separating the 3' terminus of the gene from the 5' terminus of the pseudogene (Fedoroff *et al.*, *Cold Spring Harbor Symp. Quant. Biol.*, in press). Among the 13 nucleotides by which these sequences differ are likely to be some that are responsible for the apparent difference in the transcriptional capacity of gene and pseudogene.

A NUCLEAR EXTRACT THAT ACCURATELY TRANSCRIBES 5S RNA GENES

E. H. Birkenmeier, D. D. Brown, and E. Jordan

Many unsuccessful attempts have been made to reconstruct accurate transcription of 5S DNA in vitro. When RNA polymerase III purified from *Xenopus laevis* oocytes was used to transcribe purified 5S DNA, both strands of DNA were transcribed without evidence of accurate initiation and termination (Parker *et al.*, *Proc. Nat. Acad. Sci. U.S.A.* 74, 44, 1977). Experiments done by Brown and Gurdon showed that purified 5S RNA genes (5S DNA) were accurately transcribed if injected into germinal vesicles (nuclei) of *Xenopus laevis* oocytes (Year Book 76). These results indicated that germinal vesicles contained extra components required for accurate transcription of 5S DNA. In order to identify these components we began manually isolating germinal vesicles (GV's) and fractionating their contents.

Isolated GV's were disrupted by re-pipetting, and the nuclear debris was removed by centrifugation at $500 \times g$ for 10 minutes. The supernatant fluid (GV supernate) contained RNA polymerase activity and was used to transcribe exogenous DNA. Figure 96 shows that 5S RNA was synthesized when *Xenopus laevis* oocyte (Xlo) 5S DNA in recombinant form was added to the GV supernate. The recombinant plasmid used in these experiments (pXlo8) contains four repeating units of Xlo 5S DNA linked to the plasmid pMB9. Inhibition of RNA synthesis by intermediate concentrations of α -amanitin indicated that RNA poly-

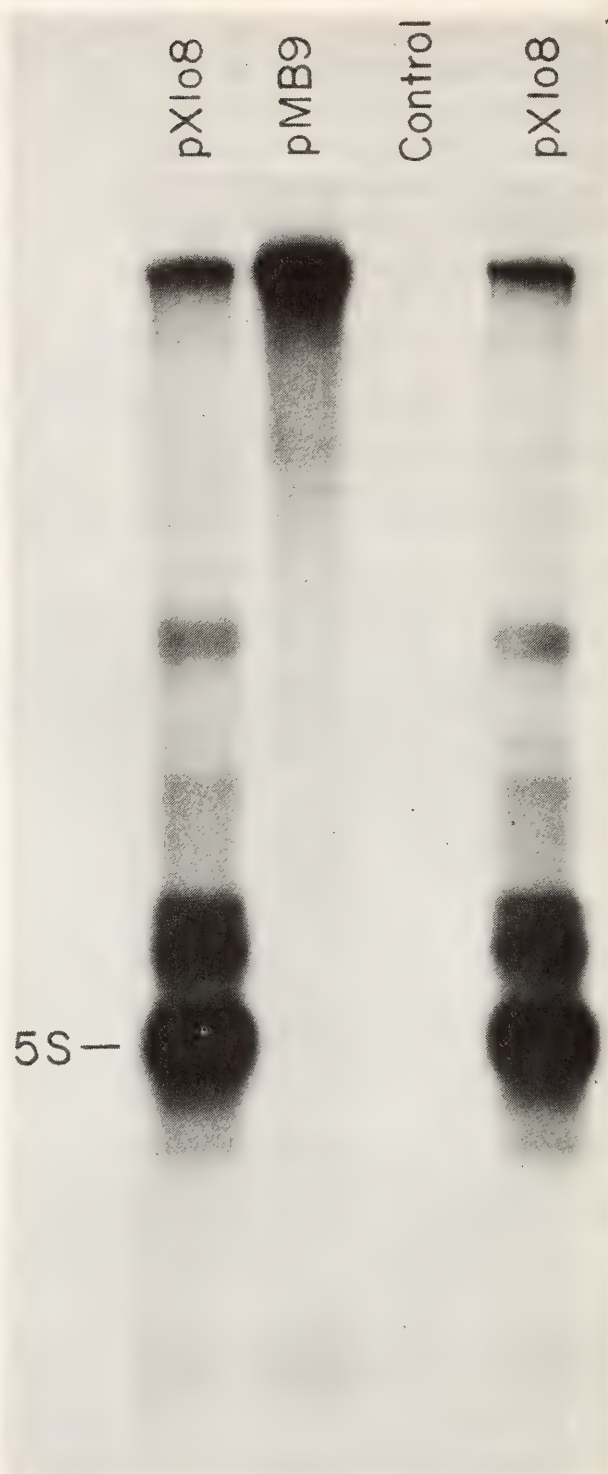


Fig. 96. Autoradiogram of an electropherogram of [32 P]-RNA synthesized by the GV supernate with or without exogenously added DNA. The RNA synthesized in a control reaction in which no exogenous DNA was added was compared to reactions in which either pXlo8 or pMB9 were added. The location of nonradioactive 5S RNA is indicated. The two pXlo8 channels represent duplicate reactions.

merase III was the major enzyme transcribing pXlo8.

When pXlo8 was transcribed in the GV

supernate, 20–40% of the total radioactivity co-migrated with 5S RNA in acrylamide gels. This RNA band was extracted from the gel, digested with RNase T₁, and the oligonucleotides fingerprinted. The fingerprint confirmed that the RNA was Xlo 5S RNA. Hybridization of the total RNA synthesized showed that pMB9 DNA and the spacer regions of Xlo 5S DNA were also transcribed. Thirteen percent of the RNA was plasmid transcripts, and the coding

strand of the 5S DNA was transcribed at a rate 10 to 15 times greater than the noncoding strand. Transcription of the 5S spacer DNA and pMB9 DNA in pXlo8 accounts for the presence of RNA's larger than 5S (Fig. 96).

The fraction of total RNA synthesized that was 5S RNA was strongly affected by MgCl₂ concentration and ionic strength. The RNA synthesized at different MgCl₂ concentrations is shown in Fig. 97. Although the maximum syn-

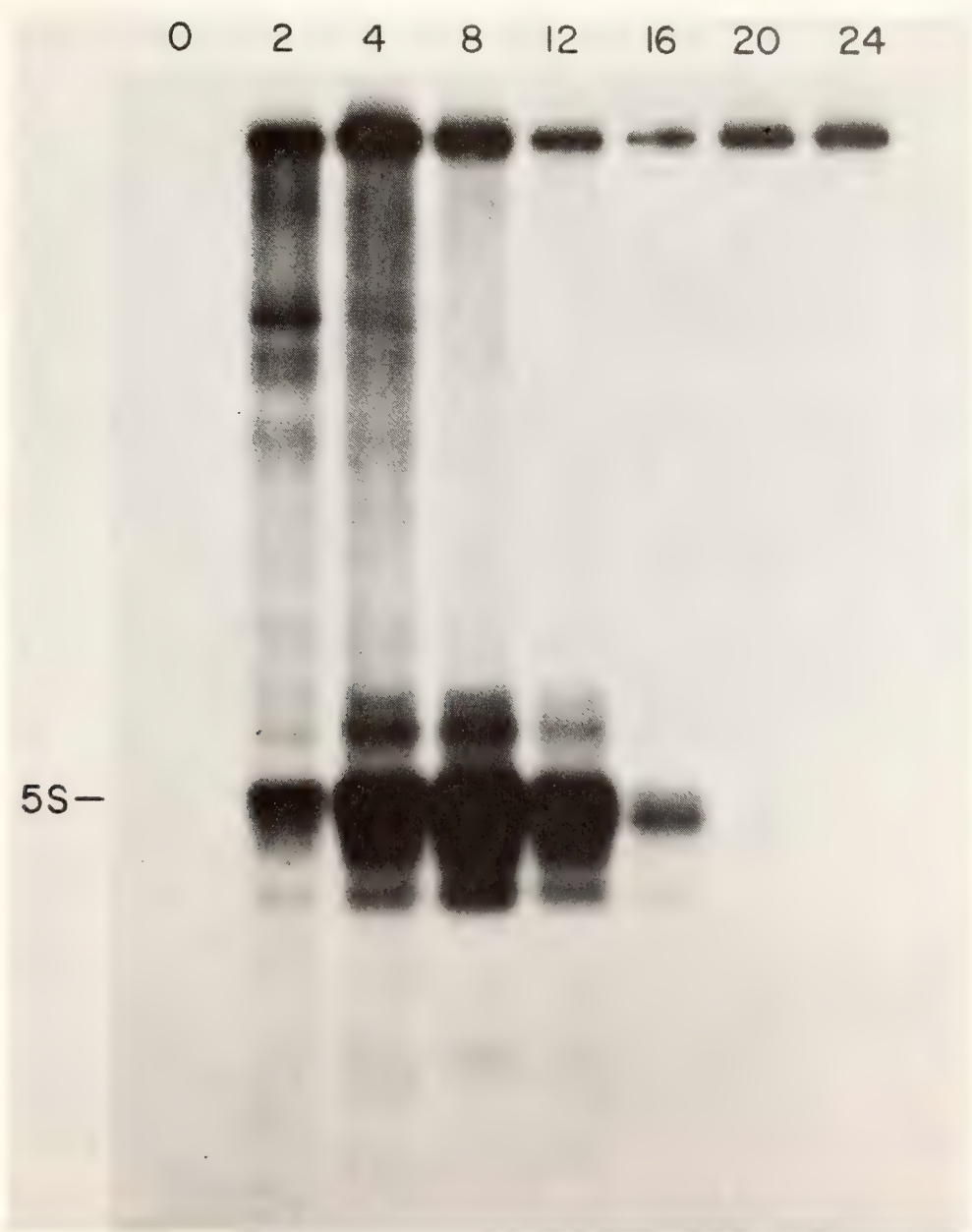


Fig. 97. Autoradiogram of an electropherogram of [³²P]-RNA synthesized with different MgCl₂ concentrations. The species of RNA synthesized at various concentrations of MgCl₂ were examined by electrophoresis of the reaction products in a nondenaturing 10% acrylamide gel. The number above each sample refers to the mM concentration of MgCl₂ in that reaction.

thesis of 5S and total RNA occurred at 8 mM MgCl_2 , the proportion that 5S RNA was of total RNA increased at 12 mM MgCl_2 . Some of the larger species of RNA in the gel were not detected at the MgCl_2 concentrations optimal for 5S RNA synthesis. Similar results were seen with different concentrations of NH_4Cl . Maximum synthesis of 5S and total RNA occurred at 70 mM NH_4Cl . No 5S RNA was synthesized when MnCl_2 replaced MgCl_2 in the GV supernate.

5S RNA synthesis increased as the

number of 5S RNA genes added to the GV supernate increased from 10^8 genes per GV to 10^{10} genes per GV. When more than 10^{11} genes were added per GV, incorporation of radioactivity into total RNA remained unchanged but no 5S RNA was synthesized. At all concentrations of DNA, transcription is inefficient. Less than one 5S RNA molecule is transcribed per 10 genes per hour.

Since adenovirus-2 has at least two genes that are transcribed in vivo by human RNA polymerase III (Weinmann

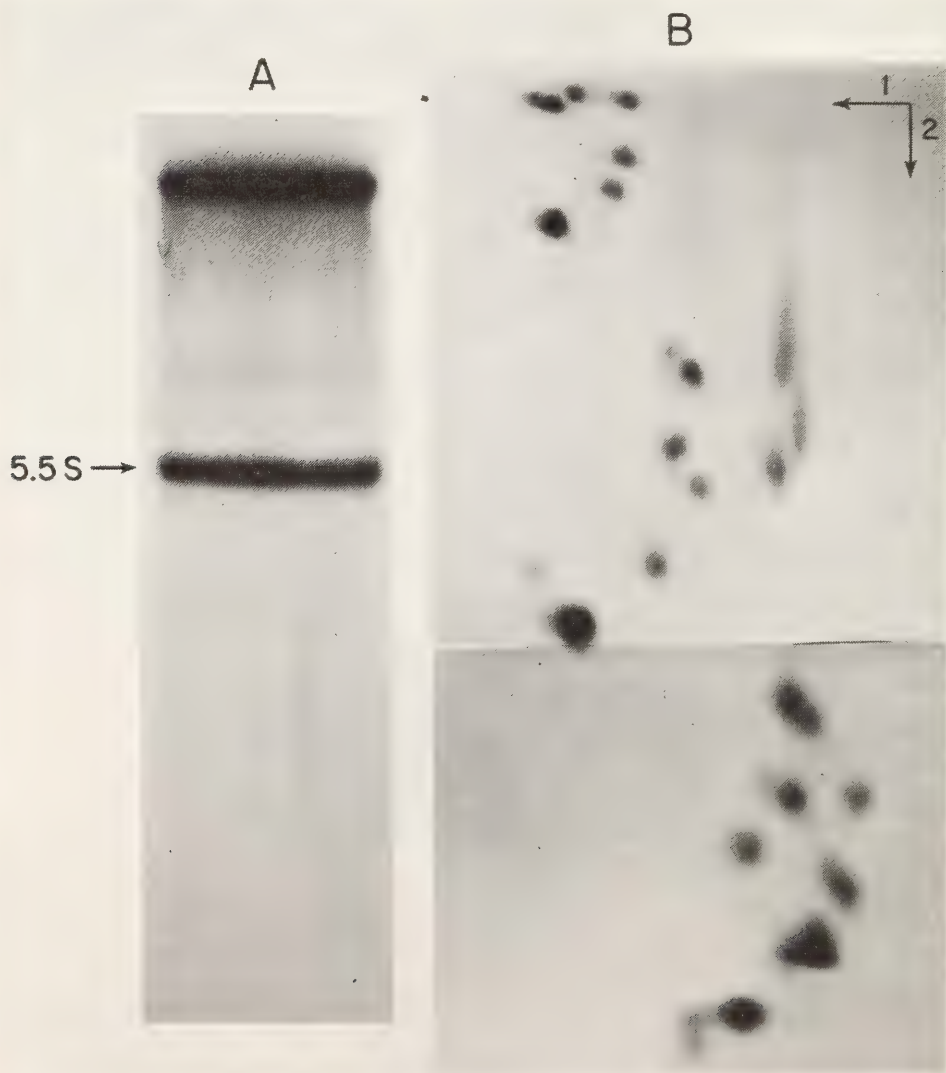


Fig. 98. Autoradiogram of an electropherogram (A) and an oligonucleotide fingerprint (B) of radioactive adenovirus 2-associated RNA_1 . Adenovirus-2 DNA was incubated in the GV supernate reaction using $[\alpha\text{-}^{32}\text{P}]$ GTP as precursor, and the reaction products electrophoresed in a 10% nondenaturing gel (A). The single radioactive RNA band in the gel at 5.5S was eluted and digested with RNase T_1 , and the oligonucleotides were fingerprinted by two-dimensional electrophoresis (B).

et al., *Cell* 7, 557, 1976), adenovirus-2 DNA was used as a template in the GV supernate. Fig. 98A shows that 15% of the total counts were incorporated into one discrete, low molecular weight species of RNA, and its electrophoretic mobility was that predicted for a 5.5S virus-associated (VA) RNA. The fingerprint of this RNA shown in Fig. 98B corresponds to the fingerprint published for VA RNA₁ of adenovirus-2 (Ohe *et al.*, *JBC* 246, 6991, 1971). Fractionation of the GV supernate may allow us to identify which proteins are required for accurate transcription of genes by RNA polymerase III in a wide variety of eukaryotic cells.

A VARIETY OF 5S RNA GENES ARE
TRANSCRIBED ACCURATELY BY AN
EXTRACT OF OOCYTE NUCLEI

D. D. Brown and E. Jordan

Different kinds of plasmids containing 5S DNA have been tested for accurate transcription of 5S RNA in the GV supernate. Fig. 99 shows three such plasmids that are of particular interest. Each contains a 5S DNA insert derived from a different gene family. The inserts from all three of these plasmids have been sequenced (see this Report and *Year Book* 76). pXbsl (*X. borealis* somatic) and pXlo31 (*X. laevis* oocyte) have single 5S

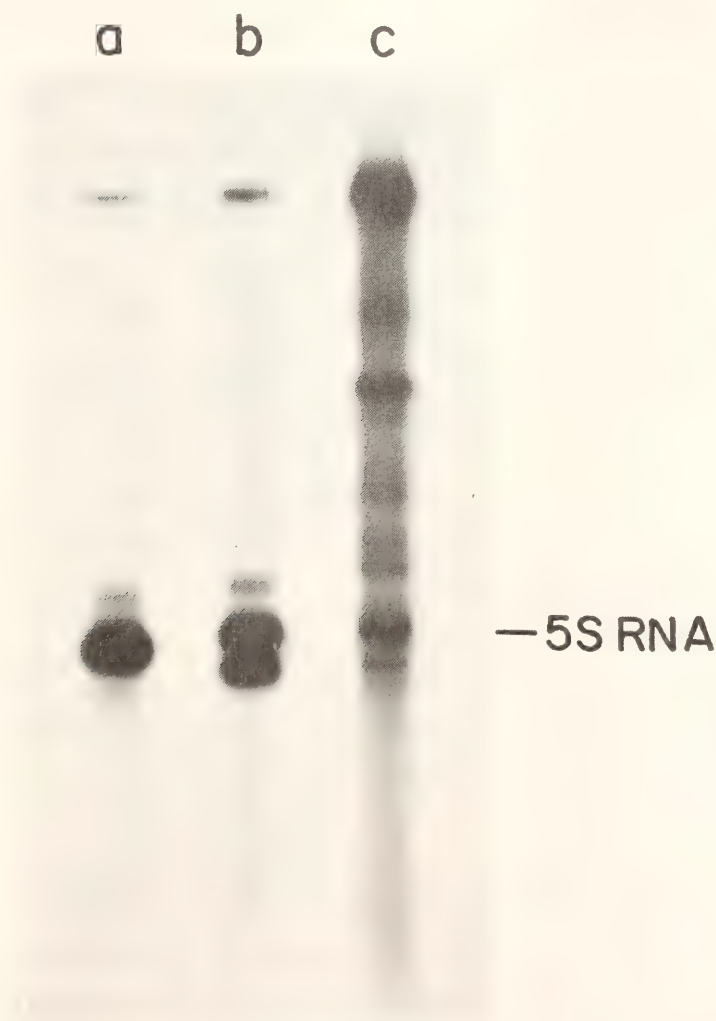


Fig. 99. Autoradiogram of an electropherogram of [³²P]-RNA synthesized by the GV supernate after the addition of three different kinds of 5S DNA. (a) pXbsl; (b) pXbol, and (c) pXlo31.

RNA genes, while pXbol (*X. borealis* oocyte) has three genes. The radioactive RNA's that co-migrate with 5S RNA have the fingerprint expected of their respective 5S RNA genes. The slower migrating RNA from pXbol contains transcripts of gene 1 and gene 3, and the faster moving one is a product of gene 2. Thus, all three 5S RNA genes in pXbol are transcribed in the in vitro system. The recombinant DNA pXbsl is especially efficient in supporting accurate 5S RNA synthesis. The gene comprises 120 of the more than 6000 base pairs in the recombinant DNA molecule; yet 80% of all RNA transcribed from this recombinant DNA is 5S RNA. Transcription from pXlo31 is characteristic of plasmids containing single repeating units of *X. laevis* oocyte 5S DNA. An array of RNA bands is produced, as well as RNA too large to enter these acrylamide gels. A majority of the labeled RNA is plasmid transcripts. However, other experiments show that this apparently inaccurate transcription of pXlo31 is due mainly to improper termination of

transcription, i.e., the RNA polymerase starts synthesis at the correct nucleotide, but it synthesizes past the normal termination site, ending either in the spacer region or beyond the 5S DNA in the plasmid. When more than one Xlo insert is present in a plasmid, a higher proportion of 5S RNA is synthesized than we find with a single repeating unit (compare Figs. 96 and 99). These Xlo-containing plasmids may be useful to assay for termination factors in the GV supernate.

The general usefulness of this in vitro system for supporting accurate transcription of a variety of genes has been pointed out earlier (for example, adenovirus DNA; see Fig. 98). In addition, experiments begun by Dieter Söll of Yale University with our assistance show that tRNA genes of *Drosophila* are transcribed accurately in the *Xenopus* GV supernate. All these genes have in common their dependence on RNA polymerase form III. DNA's normally transcribed by enzyme forms I and II have not been shown to be transcribed accurately in the GV supernate.

THE COLLECTION OF HUMAN EMBRYOS

Ronan O'Rahilly

The embryological collections, both human and comparative, are housed at the University of California, Davis; and all inquiries should be addressed to Professor R. O'Rahilly, Carnegie Laboratories of Embryology, University of California, Davis, California 95616. Some one hundred embryos and fetuses were acquired during the past year.

DEVELOPMENTAL STAGES IN HUMAN EMBRYOS

The revision of stages 10 to 23 is being continued. Considerable difficulty is anticipated in the later stages, and the system of point scores in stages 19 to 23

may need to be reassessed. The tabulation of the timing and sequence of developmental events in staged human embryos is being pursued. An account of the digestive system is in press, and the reproductive and endocrine systems are being studied. A review of "The embryology of movable joints" includes graphs of the major features in the development of the shoulder, elbow, hip, and knee joints in staged human embryos. The computerized catalogue of Carnegie specimens established by Alexander Barry is being extended so as to include other collections, such as that at the University of Michigan, Ann Arbor, and the Hooker-Humphrey collection of the Uni-

versity of Alabama at Birmingham. During the year, Dr. Barry visited both of these institutions to arrange for the staging of their specimens.

DEVELOPMENT OF THE NERVOUS SYSTEM

Studies of the developmental neurobiology of primates continue, but work has been delayed by the untimely death of Ernest Gardner in February 1978. Dr. Gardner was Professor of Neurology, Orthopaedic Surgery, and Human Anatomy at the University of California, Davis, in addition to being Associate Director of the Carnegie Collection, with which he had been connected since 1957.

A chapter on "The developmental anatomy and histology of the human central nervous system" has appeared in the *Handbook of Clinical Neurology*. (See the Bibliography).

An account of "The initial development of the human brain" was presented by R. O'Rahilly and E. Gardner at the Fourth European Congress of Anatomy, Basel, August 1977. Although the general area of the neural plate can be ascertained by stage 7, the first visible indication of the nervous system is the appearance, in certain embryos of stage 8, of the neural groove. The embryonic disc in such specimens is more than 1 mm in length, and the notochordal process is at least 0.3 mm. The neural folds begin to fuse in embryos of 6 to 8 pairs of somites, the fusion is initially at the level of somite 3, and the fusion reaches the rhombencephalon in embryos of 8 to 12 pairs of somites. The closure of the neuropores was found to be less variable than had been anticipated, the rostral closing in specimens of 20 pairs of somites, and the caudal at 25 (or 25 to 27). The interrelationships of the neuromeres, otic primordium, neural crest (rostral, facial, and postotic portions), and somite 1 were also studied. Initially the forebrain consists almost entirely of

diencephalon, but at stages 11 and 12 the telencephalon medium becomes recognizable. At first, it includes the prospective cerebral hemispheres but is a non-paired holosphere (telencephalon impar). Normally the right and left cerebral vesicles appear at stages 14 and 15. Although it is still ignored in the *Nomina anatomica*, a portion of the third ventricle belongs to the telencephalon.

A study of the "Development of the interpeduncular nucleus in the midbrain of rhesus monkey and human" was published by Dr. Nicholas Lenn and colleagues. In the human it was found that the relevant neurons probably underwent their final division between stages 17 and 21, and that the interpeduncular nucleus could first be delineated at stage 23. Great similarity in the timing, rate, and pattern of neuronal differentiation in the nucleus in both rhesus and human was found.

Dr. Ross Tarara, a postgraduate fellow at the Primate Center and the School of Veterinary Medicine, is studying the effect of triamcinolone on the development of the central nervous system in the rhesus monkey. He has been making use of the comparative collection to familiarize himself with the normal development of stages 7 to 17 in the rhesus.

DEVELOPMENT OF THE CARDIOVASCULAR AND UROGENITAL SYSTEMS

Dr. Pieter A. deVries, who has recently joined the group at the Carnegie Laboratories, is studying the early development of the human heart (stages 9 to 11) with particular attention to the truncus arteriosus and also subsequent changes in the outflow tract and aortic arches (stages 12 to 18). In addition, he is investigating the development and involution of the paramesonephric ducts in the male and changes in the mesonephric tubules and the relationship of the testis to the processus vaginalis.

VISITORS

Dr. David B. Meyer (Detroit) visited the collection and continued his studies of the vertebral column as well as the appearance of cervical ribs during early human fetal development.

Visitors to the collection included Professor J. Bossy (Nîmes), Dr. S. G. Driscoll (Boston), Dr. G. M. Hutchins (Baltimore), Professor O. B. Kriens

(Bremen), and Dr. S. J. Robboy (Boston).

The incoming president of the Carnegie Institution, Dr. James D. Ebert, accompanied by Mrs. Ebert, spent two weeks at the Carnegie Laboratories while he was Storer Life Sciences Lecturer at the University. He spoke on "Interacting systems in development" and on "Birth defects: the present and the future."

STAFF ACTIVITIES

During the year staff members participated as chairmen or speakers at the following conferences: Society for Neuroscience; New York Academy of Sciences; Second International Conference on "Molecular Basis of Cell-Cell Interaction"; Batelle Research Center Symposium on "Potential of Liposomes as Drug Carriers"; Gordon Research Conferences on Hormone Action, Biological Regulatory Mechanisms, Nucleic Acids, Developmental Biology, and Animal Cells and Viruses; Symposium on Cholinergic Transmission, American Society for Pharmacology and Experimental Therapeutics; Symposium on Assembly of Organelles and Cell Components, Society of Electron Microscopists; Cold Spring Harbor Symposium on DNA Replication; Conference on "Disorders of Membranes and Receptors," Batelle Institute, Seattle, Washington; Miami University Winter Symposium on Developmental Biology; the Eighth Congress of the International Society for Developmental Biology in Tokyo; Fifth International Congress on Birth Defects, Montreal; Symposium on the Cholinergic Synapse in Czechoslovakia; Symposium on Differentiation, Brussels; International Society for Neurochemistry, Italy.

Lectures were given at Johns Hopkins University, University of Maryland, Cold Spring Harbor Laboratory, Uni-

versity of California at Berkeley, Wayne State University, University of North Carolina, Boston Medical Research Institute, State University of New York at Buffalo and at Stony Brook, University of Tennessee, the Rockefeller University, University of Cincinnati, Merck Sharpe and Dohme Research Laboratories, National Institutes of Health, Yale University, Princeton University, Washington University, University of Missouri, Massachusetts Institute of Technology, California Institute of Technology, University of California at Los Angeles and at San Francisco, Stanford University, University of Nebraska, Columbia University, University of Utah, University of California at San Diego, Salk Institute, Oak Ridge National Laboratories, University of Manitoba, Veterans Administration Hospital in Kansas City, University of Pennsylvania, Hutchinson Cancer Center in Seattle, Baylor University, University of Tokyo, Cancer Institute in Tokyo, the National Institute of Health of Japan, National Institute of Genetics of Japan, Nagoya University, Kyoto University, Osaka University, the Institute for Cancer Research in Philadelphia, New York State University at Albany, the University of Puerto Rico.

Members of the staff served on the Cell Biology Study Section of the Na-

tional Institutes of Health and on editorial boards for the *Journal of Cell Biology*, and *Cell*, and as editor of *Developmental Biology*. A staff member serves as Chairman of the Membrane Biophysics Subgroup of the Biophysical Society. Additional consultant activities include membership on visiting committees for Centre de Genetique Moleculaire of the CNRS at Gif-sur-Yvette, France, Department of Biology (Chairman) and Department of Biochemistry and Molecular Biology at Harvard University and the Roche Institute of Molecular Biology as well as service on the Board of Scientific Counselors of the National Institute of Child Health and Development.

Seminars

The Department offers at least two seminars each week, one of them usually presented by a scientist from outside the Department. This year 35 invited speakers from the Baltimore community participated. The first annual Mini-Symposium was held. The title of the conference was "Nucleic Acid Rearrangements." The four principal speakers were Joseph Gall, Yale University; Fred Alt,

Stanford University; Philip A. Sharpe, Massachusetts Institute of Technology; and Michael Botchan, Cold Spring Harbor Laboratory. In addition to this Symposium the following visiting scientists spoke: V. Chiu, University of Miami; A. Campbell, Glasgow University; U. Siebenlist, Harvard University; N. Kan, University of North Carolina; T. Roberts, Harvard University; A. Infante, Wesleyan University; G-J. Wu, Emory University; R. Roeder, Washington University; S. Adams, National Institutes of Health; L. Bergman, University of Virginia; H. Robertson, Rockefeller University; C. Emerson, University of Virginia; W. Fitch, University of Wisconsin; B. Moss, National Institutes of Health; C. Croce, Wistar Institute; D. Soll, Yale University; J. Zimmerman, University of California, Irvine; O. Hagenbuhle, Yale University; M. Rosenberg, National Institutes of Health; P. Gray, University of Colorado; T. Okada, Kyoto University; J. Prives, Weizmann Institute; S. Clarkson, University of Zurich; H. Westphal, National Institutes of Health; M. Baynes, Northwestern University; E. Wakshull, University of Washington; D. Bogenhagen, Stanford University; E. Yavin, Weizmann Institute.

BIBLIOGRAPHY

- Benbow, R. M., M. R. Krauss, and R. H. Reeder, DNA synthesis in a multigene system from *Xenopus laevis* eggs. *Cell* 13, 307-318, 1978.
- Botchan, P., R. H. Reeder, and I. B. Dawid, Restriction analysis of non-transcribed spacers of *Xenopus laevis* ribosomal DNA. *Cell* 11, 599-607, 1977.
- Botchan, P., see Dawid, I. B.
- Brown, D. D., D. Carroll, and R. D. Brown, The isolation and characterization of a second oocyte 5S DNA from *Xenopus laevis*. *Cell* 12, 1045-1056, 1977.
- Brown, D. D., I. B. Dawid, and R. H. Reeder, *Xenopus borealis* misidentified as *Xenopus mulleri*, *Dev. Biol.* 59, 266-267, 1977.
- Brown, D. D., and N. V. Fedoroff, The dual 5S RNA gene system in *Xenopus*. In *Cell Differentiation and Neoplasia*, G. F. Saunders, ed., Raven Press, New York, pp. 297-303, 1978.
- Brown, D. D., and J. B. Gurdon, Cloned single repeating units of 5S DNA direct accurate transcription of 5S RNA when injected into *Xenopus* oocytes purified genes/recombinant DNA/living oocytes/nuclear injection. *Proc. Nat. Acad. Sci. U.S.A.* 75, 2849-2853, 1978.

- Brown, D. D., see also Fedoroff, N. V., and Miller, J. R.
- Brown, R. D., see Brown, D. D.
- Brownlee, G. G., see Miller, J. R.
- Carbonetto, S., Neuromuscular transmission in dystrophic mice. *J. Neurophys.* 40, 836-843, 1977.
- Carbonetto, S. T., D. M. Fambrough, and K. J. Muller, Non-equivalence of α -bungarotoxin receptors and acetylcholine receptors in chick sympathetic neurons. *Proc. Nat. Acad. Sci. U.S.A.* 75, 1016-1020, 1978.
- Carbonetto, S., and K. J. Muller, A regenerating neuron in the leech can form an electrical synapse on its severed axon segment. *Nature* 267, 450-452, 1977.
- Carbonetto, S., see Muller, K. J.
- Card, D. J., see Devreotes, P. N., and Fambrough, D. M.
- Carroll, D., see Brown, D. D.
- Cartright, D. M., see Miller, R. E.
- Cebra, J., see Ozato, K.
- Dawid, I. B., and P. Botchan. Sequences homomembrane filters: a convenient method using formamide. *Biochim. Biophys. Acta* 477, 191-194, 1977.
- Dawid, I. B., and P. Botchan. Sequences homologous to ribosomal insertions occur in the *Drosophila* genome outside the nucleolus organizer. *Proc. Nat. Acad. Sci. U.S.A.* 74, 4233-4237, 1977.
- Dawid, I. B., and P. K. Wellauer, Ribosomal DNA and related sequences in *Drosophila melanogaster*. *Cold Spring Harbor Symp. Quant. Biol.* 42, 1185-1194, 1978.
- Dawid, I. B., see also Botchan, P., Brown, D. D., Ohi, S., Ramirez, J. L., Upholt, W. B., and Wellauer, P. K.
- Devreotes, P. N., D. J. Card, K. G. Tepperman and D. M. Fambrough, Metabolism of acetylcholine receptors in skeletal muscle. In *Pathogenesis of Human Dystrophies*, L. P. Rowland, ed., Excerpta Medica, Amsterdam, pp. 97-109, 1977.
- Devreotes, P. N., J. M. Gardner and D. M. Fambrough, Kinetics of biosynthesis of acetylcholine receptor and subsequent incorporation into plasma membrane of cultured chick skeletal muscle. *Cell* 10, 365-373, 1977.
- Devreotes, P. N., see Fambrough, D. M.
- Ebert, J. D., see Ozato, K.
- Fambrough, D. M., and P. N. Devreotes, Newly synthesized acetylcholine receptors are located in the Golgi apparatus. *J. Cell Biol.* 76, 237-244, 1978.
- Fambrough, D. M., P. N. Devreotes, and D. J. Card, The synthesis and degradation of acetylcholine receptors. In *Synapses*, G. A. Cottrell and P. N. R. Usherwood, eds., Blackie, Glasgow, pp. 202-236, 1977.
- Fambrough, D. M., P. N. Devreotes, D. J. Card, J. M. Gardner, and K. Tepperman, Metabolism of acetylcholine receptors in skeletal muscle. In *Third Decennial Review Conference: Cell, Tissue and Organ Culture*, K. Stanford, ed., NCI Monograph 48, pp. 277-294, 1978.
- Fambrough, D. M., see also Carbonetto, S. T., and Devreotes, P. N.
- Fedoroff, N. V., and D. D. Brown, The nucleotide sequence of oocyte 5S DNA in *Xenopus laevis*. I. The AT-rich spacer. *Cell* 13, 701-716, 1978.
- Fedoroff, N. V., and D. D. Brown, The nucleotide sequence of the repeating unit in the oocyte 5S ribosomal DNA of *Xenopus laevis*. *Cold Spring Harbor Symp. Quant. Biol.* 42, 1195-1200, 1978.
- Fedoroff, N., P. K. Wellauer, and R. Wall, Intermolecular duplexes in heterogeneous nuclear RNA from HeLa cells. *Cell* 10, 597-610, 1977.
- Fedoroff, N. V., see also Brown, D. D., and Miller, J. R.
- Gardner, E., see O'Rahilly, R.
- Gardner, J. B., see also Devreotes, P. N., and Fambrough, D. M.
- Gurdon, J. B., see Brown, D. D.
- Halfon, N., see Lenn, N. J.
- Huang, L., K. Ozato, and R. E. Pagano, Interactions of phospholipid vesicles with

- murine lymphocytes. I. Vesicle-cell adsorption and fusion as alternate pathways of uptake. In *Membrane Biochemistry*, Crane, Russak & Co., Inc., 1, No. 1/2, pp. 1-25, 1978.
- Huang, L., see Ozato, K.
- Korn, L. J., C. L. Queen, and M. N. Wegman, Computer analysis of nucleic acid regulatory sequences. *Proc. Nat. Acad. Sci. U.S.A.* 74, 4401-4405, 1977.
- Krauss, M. R., see Benbow, R. M.
- Lenn, N. J., N. Halfon, and P. Rakic, Development of the interpeduncular nucleus in the midbrain of Rhesus monkey and human. *Anat. Embryol.* 152, 273-289, 1978.
- Meyer, D. B., The appearance of "cervical ribs" during early human fetal development. *Anat. Rec.* 190, 481, 1978.
- Miller, J. R., E. M. Cartwright, G. G. Brownlee, N. V. Fedoroff, and D. D. Brown, The nucleotide sequence of oocyte 5S DNA in *Xenopus laevis*. II. The GC-rich region. *Cell* 13, 717-725, 1978.
- Miwa, J., see Ward, S.
- Müller, F., see O'Rahilly, R.
- Muller, K. J., and S. T. Carbonetto, Two ways that an electrical connection is re-established in the leech. *Neuroscience Abstracts* 3, 1706 (p. 535), 1977.
- Muller, K. J., see Carbonetto, S.
- Ohi, S., J. L. Ramirez, W. B. Upholt, and I. B. Dawid, Mapping of mitochondrial 5S RNA genes in *Xenopus laevis* by electron microscopy. *J. Mol. Biol.* 121, 1978.
- Ohshima, Y., and Y. Suzuki, Cloning of the silk fibroin gene and its flanking sequences. *Proc. Nat. Acad. Sci. U.S.A.* 74, 5363-5367, 1977.
- Ohshima, Y., see Suzuki, Y.
- O'Rahilly, R., and E. Gardner, The developmental anatomy and histology of the human central nervous system. In *Handbook of Clinical Neurology*, P. J. Vinken and G. W. Bruyn, eds., North-Holland Publishing Co., New York, 30, pp. 15-40, 1977.
- O'Rahilly, R., and E. Gardner, The embryology of movable joints. In *The Joints and Synovial Fluid*, Academic Press, Inc., New York, 10, pp. 49-103, 1978.
- O'Rahilly, R., and E. Gardner, The initial development of the human brain. *Acta Anat.* 99, 353, 1977.
- O'Rahilly, R., and F. Müller, A model of the pancreas to illustrate its development. *Acta Anat.* 100, 380-385, 1978.
- Ozato, K., J. Cebra, and J. D. Ebert, Cell-mediated mitogenic response induced by leukoagglutinin and *lens culinaris* lectin in mouse lymphocytes. *J. Exp. Med.* 146, 779-791, 1977.
- Ozato, K., and J. D. Ebert, Transfer of concanavalin A between responding lymphocytes and syngenic stimulating cells in cell-mediated mitogenic response. *J. Immunol.* 120, 788-795, 1978.
- Ozato, K., L. Huang, and J. D. Ebert, Accelerated calcium ion uptake in murine thymocytes induced by concanavalin A. *J. Cell Physiol.* 93, 153-160, 1977.
- Ozato, K., L. Huang, and R. E. Pagano, Interactions of phospholipid vesicles with murine lymphocytes. II. Correlation between altered surface properties and enhanced proliferative response. In *Membrane Biochemistry*, Crane, Russak & Co., Inc., 1, No. 1/2, pp. 27-42, 1978.
- Ozato, K., Somerville, D., and J. D. Ebert, *Lens culinaris* lectin is a T-cell mitogen: binding inhibition by concanavalin A and phytohemagglutinin-P. *Cellular Immunol.* 36, 65-74, 1978.
- Ozato, K., see Huang, L.
- Pagano, R. E., Liposomes: clinical potential. *Science* 200, 6, 1978.
- Pagano, R. E., A. Sandra, and M. Takeichi, Interactions of phospholipid vesicles with mammalian cells. *Ann. N.Y. Acad. Sci.* 308, 185-199, 1978.
- Pagano, R. E., and J. N. Weinstein, Interactions of liposomes with mammalian cells. *Annu. Rev. Biophys. Bioeng.* 7, 435-468, 1978.
- Pagano, R. E., see also Huang, L., Ozato, K., and Sandra, A.

- Queen, C. L., see Korn, L. J.
- Rakic, P., see Lenn, N. J.
- Ramirez, J. L., and I. B. Dawid, Mapping of mitochondrial DNA in *Xenopus laevis* and *X. borealis*: the positions of ribosomal genes and D-loops. *J. Mol. Biol.* 119, 133-146, 1978.
- Ramirez, J. L., see Ohi, S.
- Reeder, R. H., B. Sollner-Webb, and H. L. Wahn, Sites of transcription initiation *in vivo* on *Xenopus laevis* ribosomal DNA. *Proc. Nat. Acad. Sci. U.S.A.* 74, 5402-5406, 1977.
- Reeder, R. H., see also Benbow, R. M., Botchan, P., and Brown, D. D.
- Sandra, A., and R. E. Pagano, Phospholipid asymmetry in LM cell plasma membrane derivatives: polar head group and acyl chain distributions. *Biochemistry* 17, 332-338, 1978.
- Sandra, A., see Pagano, R. E.
- Sollner-Webb, B., see Reeder, R. H.
- Somerville, D., see Ozato, K.
- Suzuki, Y., Differentiation of the silk gland. . . A model system for the study of differential gene action. In *Results and Problems in Cell Differentiation*, W. Beermann, ed., Springer-Verlag, Berlin/Heidelberg, 8, pp. 1-55, 1977.
- Suzuki, Y., and Y. Ohshima, Isolation and characterization of silk fibroin gene with its flanking sequences. Programme and Abstracts of the Eighth International Congress of the International Society of Developmental Biologists, p. 44, 1977.
- Suzuki, Y., see Ohshima, Y.
- Takeichi, M., see Pagano, R. E.
- Tartof, K. D., see Wellauer, P. K.
- Upholt, W. B., and I. B. Dawid, Mapping of mitochondrial DNA of individual sheep and goats: rapid evolution in the D loop region. *Cell* 11, 571-583, 1977.
- Wahn, H. L., see Reeder, R. H.
- Wall, R., see Fedoroff, N. V.
- Ward, S., Invertebrate neurogenetics. *Annu. Rev. Genet.* 11, 415-450, 1977.
- Ward, S., and J. Miwa, Characterization of temperature-sensitive fertilization-defective mutants of the nematode *Caenorhabditis elegans*. *Genetics* 88, 285-303, 1978.
- Wegman, M. N., see Korn, L. J.
- Weinstein, J. N., see Pagano, R. E.
- Wellauer, P. K., I. B. Dawid, and K. D. Tartof, X and Y chromosomal ribosomal DNA of *Drosophila*: comparison of spacers and insertions. *Cell* 14, 269-278, 1978.
- Wellauer, P. K., see also Dawid, I. B., and Fedoroff, N. V.

PERSONNEL

Year Ended June 30, 1978

(including those whose services ended during the year)

Research Staff

Donald D. Brown, *Director*
 Igor B. Dawid, Biochemistry¹
 Douglas M. Fambrough, Biochemistry
 Kenneth J. Muller, Neurobiology
 Richard E. Pagano, Biophysics
 Ronald H. Reeder, Biochemistry
 Yoshiaki Suzuki, Biochemistry
 Samuel Ward, Biochemistry

¹ To May 5, 1978.

Research Associates (*Extramural*)

Bent G. Böving, Detroit, Michigan
 Robert L. DeHaan, Atlanta, Georgia
 Ernest Gardner,² Davis, California
 Arthur T. Hertig, Boston, Massachusetts
 Irwin R. Konigsberg, Charlottesville, Virginia
 Ronan O'Rahilly, Davis, California
 Elizabeth M. Ramsey, Washington, D.C.

² Died February 21, 1978.

*Postdoctoral Fellows and
Grant-Supported Associates*

Saoko Atsumi, Fellow of Carnegie Institution of Washington
 Edward H. Birkenmeier, U.S. Public Health Service Grant (Brown)
 Peter Botchan, Fellow of the U.S. Public Health Service and Carnegie Institution of Washington
 Salvatore T. Carbonetto, Fellow of the U.S. Public Health Service
 Diana Card Linden, Fellow of Muscular Dystrophy Association of America, Inc.³
 Jeffrey Doering, Fellow of the U.S. Public Health Service⁴ and Carnegie Institution of Washington
 Mark Dworkin, Fellow of Carnegie Institution of Washington⁵
 Nina Fedoroff, Fellow of the U.S. Public Health Service and Carnegie Institution of Washington; U.S. Public Health Service Grant (Brown)
 Elizabeth Godwin, U.S. Public Health Service Grant (Dawid)⁶
 Laurence J. Korn, Fellow of Helen Hay Whitney Foundation and Carnegie Institution of Washington
 Eric Long, Fellow of the Swiss National Fund for Scientific Research⁷
 Steven McKnight, Fellow of Helen Hay Whitney Foundation and Carnegie Institution of Washington
 Yasumi Ohshima, Fellow of Carnegie Institution of Washington
 Ronald Peterson, Fellow of Helen Hay Whitney Foundation and Carnegie Institution of Washington
 Eva Rastl, U.S. Public Health Service Grant (Dawid)⁸
 Richard Rotundo, Fellow of Muscular Dystrophy Association of America, Inc., and Carnegie Institution of Washington
 Alex Sandra, U.S. Public Health Service Grant (Pagano)
 Alan Schroit, U.S. Public Health Service Grant (Pagano)
 Sheryl Scott, Fellow of Carnegie Institution of Washington

Barbara Sollner-Webb, U.S. Public Health Service Grant (Reeder), Fellow of National Institutes of Health and Carnegie Institution of Washington
 Douglas Struck, Fellow of the American Cancer Society and Carnegie Institution of Washington
 Masaaki Tsuda, U.S. Public Health Service Grant (Suzuki)
 Yoshihide Tsujimoto, U.S. Public Health Service Grant (Suzuki)
 Walter Wahli, Fellow of the Swiss National Science Foundation⁹ and Carnegie Institution of Washington
 Harvey Wahn, U.S. Public Health Service Grant (Reeder)

Students

Yair Argon, Graduate, Harvard University
 John M. Gardner, Graduate, Johns Hopkins University
 Robert A. Hipkind, Graduate, Johns Hopkins University
 Gregory Nelson, Graduate, Harvard University
 Shigeru Sakonju, Graduate, Johns Hopkins University

*Visiting Investigators and
Extramural Collaborators*

Robert Benbow, Baltimore, Maryland
 Michael Bustin, Bethesda, Maryland
 Michael Edidin, Baltimore, Maryland
 Patricia Gearhart, Baltimore, Maryland
 John Gurdon, Cambridge, England
 Eduardo Macagno, New York, New York
 B. E. H. Maden, Glasgow, U. K.
 Uel J. McMahan, Boston, Massachusetts
 Brown L. Murr, Baltimore, Maryland
 Cary L. Queen, Ithaca, New York
 Ken Tartof, Philadelphia, Pennsylvania
 Peter Vogt, Tübingen, Germany

Clerical and Technical Staff

Elaine S. Asch, Senior Technician
 James H. Blackwell, Custodian
 Paul Blackwell, Custodian (part-time)
 Sharon Bodmer, Technician
 William H. Duncan, Senior Technician
 Ernestine V. Flemmings, Laboratory Helper
 Paul E. Giza, Technician

³ To December 12, 1977.

⁴ To December 30, 1977.

⁵ To May 5, 1978.

⁶ To November 30, 1977.

⁷ To May 5, 1978.

⁸ To May 5, 1978.

⁹ To May 5, 1978.

Richard D. Grill, Photographer
Virginia Hicks, Laboratory Helper
Mary E. Hogan, Technician
William L. Johnson, Custodian
John E. Jones, Custodian
Eddie Jordan, Senior Technician
Catherine R. Lane, Librarian (part-time)
Alice H. Mabin, Laboratory Helper
Thomas F. Malooly, Business Manager
Jeffrey Mauvais, Technician
Thomas F. Miller, Custodian
Joyce Patterson, Laboratory Helper

John Pazdernik, Building Engineer
Betty Lou Phebus, Bookkeeper
Martha L. Rebbert, Senior Technician¹⁰
Susan D. Satchell, Secretary
Patricia Schmidt, Secretary
Ginny Selby, Secretary (part-time)
Bessie Smith, Laboratory Helper
Delores Somerville, Senior Technician
Barbara Thomas, Technician
John Wiser, Machinist

¹⁰ To May 5, 1978.

Hale Observatories

Operated by Carnegie Institution of Washington
and California Institute of Technology

Pasadena, California

Horace W. Babcock
Director

Maarten Schmidt
Director-Designate

J. Beverley Oke
Associate Director

OBSERVATORY COMMITTEE

Horace W. Babcock, *Chairman*

J. Beverley Oke, *Vice-Chairman*

Halton C. Arp

James E. Gunn

George W. Preston

Allen Sandage

Wallace L. W. Sargent

Maarten Schmidt

Contents

Introduction	153	Globular Clusters	175
Observing Conditions	157	Dynamics of M3	175
Physics of the Sun	158	Radial gradients	175
Mount Wilson observations	158	Infrared studies	176
Solar magnetic fields	158	The Galaxy	176
Solar velocity fields	159	Galactic structure	176
Big Bear Solar Observatory	160	Initial mass function	177
Studies of emerging flux regions	161	Survey for low-metal-abundance stars	177
Prominence rotation	161	Galaxies	177
The $L\alpha/H\alpha$ ratio in solar flares and quasars	162	Globular clusters in M31	177
Ephemeral active regions	162	Spiral structure in M33	178
Coronal holes, the height of the chromosphere, and the origin of spicules	163	Las Campanas survey of southern galaxies	179
Solar System	165	Peculiar galaxies in the southern hemisphere	181
Eclipses of Iapetus	165	Galaxies of bright apparent magnitude and their fainter companions	184
Solar system survey	165	Dwarf spheroidal galaxies	184
The rings of Uranus	166	Nuclei	185
Stellar Spectroscopy	167	Intensity profiles	185
Rotation of B-type stars	167	Supermassive object in the center of M87	185
B-type companion of Antares	167	Dynamics and structure of elliptical galaxies	187
Dwarf novae	167	Velocity dispersion in cD galaxies	187
Variable stars	168	Radio galaxies	187
Flare stars	169	Seyfert galaxies	187
Stellar chromospheres	170	Spectral variability of Seyfert nuclei	189
Lower main sequence	170	Survey of emission-line objects	189
The faint end of the main sequence	170	Clusters of Galaxies	190
M-type stars	170	Compact groups	190
Silicon monoxide in bright infrared objects	171	Structure of clusters	191
A white dwarf-red dwarf eclipsing binary	171	Velocity dispersion in clusters	191
Degenerate stars	172	Radio Sources	191
Interstellar Matter	173	5C2 identification program	191
Molecular hydrogen	173	Quasars and Quasi-Stellar Objects	191
Studies of star formation	173	Nebulosity around PHL 1070	191
Submillimeter heterodyne spectroscopy	174	Near-infrared spectroscopy of quasars	192
Pulsars	175	Surface density of quasars	192
An optical candidate for the binary pulsar 1913+16	175	The Hubble diagram for quasars	193
		Nonuniform radial distribution of quasars	194
		Bright quasar survey	194

Radio emission from optical quasars	194	Instrumentation	199
Quasar absorption lines	194	Mount Wilson aluminizing facilities	199
Quasars near bright galaxies	196	Double spectrograph	199
Observational Cosmology	197	High-speed microdensitometer	200
Properties of the expansion for very		Photon-counting image intensifier	
nearby galaxies just beyond the		system	200
Local Group	197	Infrared photometer	201
Motion of the Local Group relative		Wide field/planetary camera for	
to the metagalaxy	197	Space Telescope	201
Theoretical Studies	198	CCD detectors	201
Gas disks in elliptical galaxies	198	Guest Investigators	202
Cosmological consequences of		LiBe-Deficient F-Type Stars	212
neutral particles	198	Bibliography	212
		Personnel	218

INTRODUCTION

In the introduction to last year's Annual Report, retiring Director Horace W. Babcock noted: "The 2.5-meter du Pont Telescope underwent fitting out during the year, with special attention to adjustment of electrical, mechanical, and optical systems, and with much effort devoted to completion of essential auxiliary instrumentation. . . , " and "April 1977 saw the first scientific use of the new telescope. . . ."

This brief factual statement represents the culmination of six and one-half years of intense activity since December 1970, when the Trustees of the Carnegie Institution authorized the construction of a 2.5-meter telescope for the Las Campanas Observatory, to be designed by the staff of the Hale Observatories. Babcock guided the entire effort to its successful completion in a remarkably short period of time. That the project is a success, indeed, is best appreciated by inspecting one of the 20×20 in. plates that cover a field of $1.5^\circ \times 1.5^\circ$. The quality of the images is excellent and uniform over the large field. Coupled with the extended periods of good seeing and with the dark sky at Cerro Las Campanas free of city lights, this makes the Irénée du Pont Telescope a most powerful instrument for the study of extended systems, in particular the Magellanic Clouds, and for the conduct of surveys of objects such as variable stars and quasars. The creation and development of the Las Campanas Observatory, started in 1968, and the completion of the 1-meter Swope Telescope and the 2.5-meter du Pont Telescope constitute a lasting tribute to Horace Babcock's tenure as Director of the Hale Observatories.

The Observatories staff has become heavily involved in instrumentation for space astronomy with the award by the National Aeronautics and Space Administration of a preliminary contract

for the Wide Field/Planetary Camera of Space Telescope to the California Institute of Technology. Westphal is the Principal Investigator, and general project oversight is in the hands of a team of scientists which includes Gunn and Kristian. Space Telescope will have a 0.1" image size and a low sky brightness. With specially treated charge-coupled silicon detectors, the camera should have a limiting visual magnitude of 28 in half an hour's exposure. In addition, the system will allow observations in the ultraviolet, where the atmosphere inhibits observations from ground-based telescopes.

The question may be asked whether ground-based observatories will still be needed if Space Telescope has such capabilities. The answer (yes!) stems from the fact that photons are scarce. Space Telescope will receive from an object of magnitude 28 approximately one photon per minute. To form a spectrum, which will allow a determination of the radial velocity and of temperature, chemical composition, etc., at least a few thousand photons have to be collected. Obviously, progress at the very faint magnitudes which only Space Telescope can reach will be slow, and large-scale surveys will be prohibitively time consuming. Space Telescope will achieve results on a shorter time scale in the ultraviolet part of the spectrum, which is inaccessible from the ground. Here its role of complementing optical astronomy will be similar to that of x-ray, infrared, and radio astronomy.

The slow arrival rate of photons from faint objects contributes to the fact that astronomy is information limited. Large amounts of data are needed to gain a deep understanding of star formation; of the synthesis of chemical elements; of the formation, structure, and evolution of galaxies, etc. Only a very small fraction of the data needed has been collected as yet. As a consequence, progress in

astronomy as a whole depends on the total collecting power of all telescopes. The contribution of each observatory depends, of course, critically on the ability of its staff in choosing research areas in which observations can have a major impact and in designing and building new instrumentation.

Work done at the Hale Observatories over the past year covered solar system, stellar, and extragalactic astronomy. In the next few paragraphs we summarize some of the results obtained.

Howard has discovered a new global-scale velocity pattern on the sun's surface through application of a new technique to reduce solar magnetograph data collected at Mount Wilson. The size of these features is approximately 1 solar radius. The main component of the velocity is vertical, up to 50 meters per second either way. The pattern may persist for as many as six solar rotations. It probably represents large-scale convective circulation associated with the eruption of magnetic flux at the sun's surface.

Kowal discovered a new type of minor planet with the 1.2-meter Schmidt telescope on Palomar Mountain in November 1977. The object named "Chiron" travels in an elliptical orbit between Saturn and Uranus. Its diameter, estimated at a few hundred kilometers, is similar to that of the larger minor planets such as Ceres, Pallas, Juno, and Vesta. However, its orbit is entirely unlike that of the minor planets, which are mostly located in a belt between Mars and Jupiter. As a consequence, the origin and nature of Chiron is unknown at present.

Persson, Nicholson, Matthews, Goldreich, and Neugebauer have found three or possibly four new rings of the planet Uranus. This was achieved by continuously measuring the brightness of a faint star while the planet was slowly moving across. The observers worked in the infrared, at a wavelength of 2.2μ , where deep methane absorption bands in the

atmosphere of Uranus make the planet very faint. The five rings discovered by Elliot in March 1977 were also seen again.

Preston and S. C. Wolff of the University of Hawaii have completed an analysis of the rotation and other properties of a sample of 256 late B-type stars. Most of the stars show a projected rotation velocity of less than 100 km s^{-1} . The observations favor the hypothesis that early in its evolution off the main sequence, a B-type star suffers complete radial exchange of angular momentum.

Greenstein has completed multichannel spectrophotometry of 465 main-sequence stars. The major effort has been to calibrate the color-magnitude relation for stars fainter than the sun, using stars of known parallax. Metal-poor stars of spectral type G are underluminous by at least 1 magnitude. High-velocity stars of type M do not show this effect. Among the 450 stars for which space motions have been completed, 25 show extreme halo velocities, that is, velocities perpendicular to the Galaxy's plane exceeding 250 km s^{-1} . Rotation velocities around the center of the Galaxy, they have at least 450 km s^{-1} less than ours (corresponding to a retrograde motion of $200\text{--}250 \text{ km s}^{-1}$).

Knapp, Tremaine, and Gunn have completed a rediscussion of the rotation curve and mass models of the Galaxy. They find that a flat rotation curve in the neighborhood of the sun, as observed in essentially all large external systems, is consistent with all 21-cm observations of neutral atomic hydrogen. They derive a value of 110 km s^{-1} for the product AR_0 (considerably lower than the value of 150 km s^{-1} deduced by Schmidt in the early sixties), and propose the following set of structure parameters: $A = 13 \text{ km s}^{-1} \text{ kpc}^{-1}$, $B = -13 \text{ km s}^{-1} \text{ kpc}^{-1}$, $R_0 = 8.5 \text{ kpc}$, $\Theta_0 = 220 \text{ km s}^{-1}$. They state that the rotation curve must be flat out to 100 kpc in order to under-

stand the dynamics of our Galaxy and the Andromeda galaxy.

Gunn and Griffin have concluded their analysis of high-accuracy radial velocities of 111 giants in the globular cluster M3, obtained with their radial-velocity spectrometer at the coudé focus of the Hale Telescope. They found no evidence for binaries on the basis of velocity variations; around 25% of the giants in the field and in galactic clusters show velocity variations. Typical models that fit the observations show less than 1% of the total mass in remnants heavier than 2 solar masses. The mass-to-light ratio for the cluster as a whole is about 3 in solar visual units. There is no evidence for any substantial "missing mass" in globular clusters.

Searle has completed observations designed to map the spatial distribution of globular clusters in the Andromeda galaxy (M31). Metal abundances of clusters within 5 kpc from the center of the galaxy are similar to those found in the same region in our Galaxy. The average metal abundance decreases in both systems out to about 10 kpc with no further systematic change among more remote clusters. However, the outer clusters in M31 have an abundance 3 times greater than those in our Galaxy. It is suggested that in the halo-forming phase some 3 times as much protogalactic gas condensed into stars in M31 as in our Galaxy.

Dr. Roberta Humphreys of the University of Minnesota and Sandage are obtaining the color-magnitude diagram of the 900 brightest stars in the direction of the nearby galaxy M33. A spectroscopic survey to be undertaken soon will allow a separation of the blue and red supergiants in M33 from the many foreground stars belonging to our own Galaxy. Discrete associations of stars show a series of broad spiral patterns in M33. Humphreys and Sandage hope to determine the rate of star formation represented by these associations (for which

the age can be determined) with the amount of gas available (measured from 21-cm data) so as to answer the question: Will M33 be able to maintain its Hubble type Sc, characterized by many resolved stars, or will it soon be forced into an early Hubble type owing to lack of gas?

Zinn has obtained multichannel scanner observations of many of the brightest red giants in the Draco dwarf spheroidal galaxy. He concludes that substantial color differences among these stars, already noticed by Baade and Swope 20 years ago, are due to a range in metal abundance of about a factor of 3. Models that can explain such a variation require that 99% of the original gas cloud that formed the Draco galaxy was lost.

As part of a study with Yahil and Tammann to find the motion of the Sun relative to nearby galaxies, Sandage has studied the local expansion field by determining distances to galaxies with very small radial velocities, that is, less than 400 km s^{-1} . He finds the same value of the Hubble constant, $50 \text{ km s}^{-1} \text{ Mpc}^{-1}$, as the global value derived previously (*Year Book 70*, p. 417) for radial velocities larger than 5000 km s^{-1} . Hence, surprisingly, the effect of the local supercluster, which is on the average five times denser than the global average galaxy field, is not seen in this very small sample of nearby galaxies. The much larger sample of nearby galaxies, whose motion is being analyzed by Yahil, Tammann, and Sandage, appears to show the same quiet flow.

Arp and Sulentic are finishing a three-year study of companion galaxies associated with bright spiral galaxies. They find that a large percentage of Sb and Sc galaxies have physically associated non-equilibrium companions. Studies of redshifts, spectra, and photometry of the companions may elucidate their origin and evolution.

The galaxy M87 became well known in the early fifties when it was identified with one of the brightest radio sources,

Virgo A. The galaxy was also one of the first x-ray sources to be identified with an extragalactic object. This year, attention is called to M87 again, as the claim has been made that its nucleus harbors a massive black hole of billions of solar masses. The evidence rests on photometric and spectroscopic measurements of the central parts of the galaxy. The photometric studies by Young, Westphal, Kristian, C. P. Wilson, and F. P. Landauer, were made with SIT and CCD detectors. They found a central luminosity over the central core out to $10''$. Sargent, Young, Boksenberg, Shortridge, Lynds, and Hartwick obtained spectroscopic measurements which showed a sharp increase of velocity dispersion in the core of the galaxy. The data require that the nucleus of M87 contain a compact mass of $5 \times 10^9 M_{\odot}$ of low luminosity (less than $10^8 L_{\odot}$). The investigators believe that the data provide the strongest evidence yet for the existence of a collapsed supermassive object, presumably a black hole.

De Bruyn reports that many Seyfert class I galaxies show spectral variations in the nuclear region on time scales of a year or less. Variations are strongest in violet light, less in the red parts of the spectrum. The variable continuum has an approximately flat spectrum. Broad emission lines also show variations, in the same sense as those in the continuum. The narrow forbidden [O III] lines at $\lambda\lambda$ 4959, 5007 were steady in intensity.

Green and Schmidt, in continuing the Palomar Bright Quasar Survey, discovered 26 new quasars brighter than $B = 16.5$ in the past year. They conclude from a small, statistically complete part of the survey that the quasar surface density increases by a factor of 8.5 per

magnitude in the range $B = 15.7-18.0$. Such a steep number gradient is incompatible with any local hypothesis in which quasars have a uniform space distribution or are associated with galaxies.

Sargent, Young, and Dr. A. Boksenberg of University College London have analyzed high-resolution spectra of three quasars of high redshift obtained with Boksenberg's Image Photon Counting System at the Anglo-Australian 3.8-meter telescope (*Year Book* 76, p. 162). They were able to identify essentially all the absorption lines longward of the $L\alpha$ emission line, but only a small fraction of those shortward of Lyman α . A cross-correlation study between the regions of spectrum below $L\alpha$ and $L\beta$ emission confirms a suggestion made by C. R. Lynds in 1970 that most of the unidentified lines are single $L\alpha$ lines. Further analysis has also been undertaken of high-resolution observations of PHL 957 (*Year Book* 74, p. 342) and 1225+31 (*Year Book* 75, p. 314) obtained at the 5-meter Hale Telescope on Palomar Mountain. Sargent, Young, Boksenberg, and co-workers conclude that the $L\alpha$ systems are produced by intervening intergalactic gas, and that they are not produced by material ejected from the quasars. They further put forward the hypothesis that the heavy-element absorption redshifts arise in the extended halos of intervening galaxies, while the $L\alpha$ systems are of intergalactic origin. Thus it appears that quasars are finally fulfilling their promise as probes of the Universe: halos of galaxies and intergalactic clouds can now be investigated over a large range of redshifts, allowing studies of their properties and in particular of their evolution.

OBSERVING CONDITIONS

The 2.5-meter Hooker Telescope on Mount Wilson was used for observations on 207 complete nights and 42 partial nights for a total of 2098 observing hours. The mirror was aluminized in May; extensive work on the mirror covers put the telescope out of operation for 14 nights. The 1.5-meter telescope was in regular use. At Mount Wilson, the total rainfall for the year was 1847 mm, and the total snowfall was 470 mm, a 10-year precipitation record.

The 5-meter Hale Telescope on Palomar Mountain was used for a total of 2795 nighttime hours (see Table 1). In addition, 322 hours of daylight or twilight observations were carried out at infrared wavelengths. The Palomar 1.5-meter telescope was in constant use, while the 1.2-meter and 0.46-meter Schmidt telescopes were in regular use except during the light of the moon. Total rainfall

at Palomar was 1612 mm and total snowfall 241 mm. Maximum temperature was 33°C in July; minimum was -4°C in January and February.

Public visitors at the Palomar Observatory totaled 120,000 for the year.

The 2.5-meter du Pont Telescope at the Las Campanas Observatory was used part time in July and August 1977 while undergoing testing and commissioning. The telescope came into full-time operation on October 6, 1977. During the report year, it was used for observations on 267 full nights and 39 partial nights for a total of 2620 observing hours. The 1-meter Swope Telescope was used on 195 nights for a total of 1409 hours. The maximum temperature during the year was 28°C; the minimum, -5°C. Total rainfall amounted to 7 mm; total snowfall was 400 mm.

TABLE 1. Observations With the Hale Telescope

Month	Complete Nights	Partial Nights	Hours of Nighttime Observing
July	30	1	263
August	29	2	251
September	28	2	275
October	29	1	289
November	27	2	314
December	14	7	200
January	11	9	210
February	11	8	169
March	12	4	157
April	12	9	161
May	29	2	264
June	30	0	242
Total	262	47	2795

PHYSICS OF THE SUN

Mount Wilson Observations

Synoptic observations of the sun continue at Mount Wilson under the supervision of Howard. Between June 1, 1977, and May 31, 1978, the following observations were obtained:

Direct photographs	221
H α spectroheliograms, 9-meter focus	386
K2 spectroheliograms, 9-meter focus	387
Full-disk magnetograms	252
Integrated-light magnetic-field measurements	176
Sunspot drawings	272
Sunspot magnetic-field measurements	262

Solar observations were made on 283 days during this period. An unusually wet rainy season resulted in the loss of many days of observing.

The daily full-disk magnetograms, along with sunspot magnetic-field data, are published monthly by the National Oceanic and Atmospheric Administration in *Solar Geophysical Data*. The magnetic synoptic charts are published by the International Astronomical Union in the *Quarterly Bulletin on Solar Activity*. Partial support for these programs and for much of the solar research at Mount Wilson comes from the National Aeronautics and Space Administration, the National Science Foundation, and the Office of Naval Research.

Solar Magnetic Fields

The mean solar magnetic field seen in integrated light has been investigated by Howard in collaboration with Drs. P. H. Scherrer and J. M. Wilcox of the Institute for Plasma Research, Stanford University, and Drs. Kotov and A. B. Severny of the Crimean Astrophysical Observatory. Observations of this inte-

grated-light field have been made at the Crimean Astrophysical Observatory since 1968 and at Mount Wilson since 1970. Although the instruments and observing procedures differ somewhat at the two observatories, the mean magnetic-field results compare well. The polarity of this combined mean field agrees very well throughout the interval with the polarity of the interplanetary magnetic field when a 4½-day lag is introduced to account for the sun-earth distance.

Transequatorial x-ray loops interconnecting an old and a newly born active region were studied by Drs. Z. Švestka, A. S. Krieger, and R. C. Chase of American Science and Engineering, Inc., and Howard. The loop system, seen in soft x-rays, appeared to form by reconnection accomplished 1.5–5 days after the birth of the younger region. Photospheric magnetic-field changes in the young region were followed by brightenings or “sharpenings” of the individual loops. One small solar flare was associated with a magnetic-field change and a resulting loop brightening. Electron temperatures increased from a normal value of about 2.1×10^6 °K to a value in a brightened loop of about 3.1×10^6 °K. Electron densities increased from about 7×10^8 cm⁻³ to about 1.3×10^9 cm⁻³ in a brightened loop. Short-term changes in the magnetic-field configuration of the older region appeared to have no effect on the loop system.

Howard, in collaboration with Z. Švestka of the Space Research Laboratory at Utrecht, investigated transient brightenings of loops interconnecting two active regions seen in soft x-rays. Such brightenings often occur within one or two days after the birth of a new interconnecting loop. These brightenings are clearly associated with the emergence of

new magnetic flux near their footpoints. Enhancements of older loops are triggered by slowly moving disturbances propagating from other centers of activity. Occasionally loop brightenings are associated with flares, but the loop does not brighten as a direct result of the flare. Instead both events seem to result from the emergence of new magnetic flux in the neighborhood. In three events, the loop that later interconnected two active regions was visible long before one of the regions was born. No explanation is currently available for these remarkable observations.

The birthplaces of active regions and x-ray bright points have been investigated by Howard in collaboration with Z. Švestka and F.-Š. Švestka of the Space Research Laboratory at Utrecht. Active regions invariably form at the boundaries of supergranular cells, while the short-lived x-ray bright points, which represent the eruption at the solar surface of a small amount of magnetic flux, form at random locations within the supergranular pattern. The authors suggest that the difference represents a difference in the level of formation of the two features. Active regions are formed deep within the convection zone and are guided in their rise to the surface by the dynamics of the large-scale convection pattern. X-ray bright points evidently represent a shallow phenomenon.

Solar Velocity Fields

The rereduction of the last 10 years or so of Mount Wilson solar magnetograph data continues. The principal result of this program is greatly improved residual velocity data. This is possible because of a new method of handling the background velocity fields that was devised by Howard and Boyden. An improved limb redshift representation was determined. In addition, a global-scale background line-shift effect was discovered and accounted for in the analysis. This effect, the "ears," is corrected

as a background line shift that is linear in $\sin L$, where L is the central meridian distance. It is not yet known whether the ears represent a solar phenomenon or whether they result from some instrumental effect. In past years, this effect has greatly hindered the analysis of large-scale solar velocity fields. The two research results that follow have resulted from analysis of the portion of the archival data that has been reduced so far with the new technique (1974–1977).

Howard has discovered the existence of a global-scale velocity pattern on the solar surface. The size of these features is approximately 1 solar radius. These features are clearly solar features. They rotate at about the photospheric rate, and they are observed on occasion to return for as many as 6 rotations. They may be seen clearly on daily low-resolution residual-velocity plots. A large component of the motion is vertical, because the features can be seen to remain strong as they cross the central meridian at low solar latitudes and they do not change sign at the central meridian. Amplitudes in both directions are of the order of 50 ms^{-1} . Those velocity features that have been identified so far seem to be associated with large complexes of activity. This large-scale pattern differs in an important respect from the well-known granulation and supergranulation patterns. These patterns occupy practically all the surface area of the sun, but the new giant features are only occasionally seen at the 20 ms^{-1} sensitivity of these observations. It seems likely that these features represent a convective circulation pattern of very low order that is associated in some way with the eruption of magnetic flux at the solar surface. Continued research into the nature of these new features is planned.

A second and perhaps related type of large-scale velocity feature has been found by Howard from the rereduced synoptic data. This feature is seen on a superposition of many months of daily

residual-velocity maps. Such an averaged plot washes out longitudinal differences in residual velocities so that large-scale constant-velocity patterns of a few ms^{-1} that do not rotate with the photosphere can be seen. For example, if they were not subtracted out of the signal, the rotation, the limb redshift, and the ears would all be easily visible. The pattern that is seen consists, roughly, of a low-latitude negative (toward the earth) feature in the east and stretching at very low latitudes to the west and two high-latitude positive features symmetric about the equator in the west. The amplitudes of these features are about 5 ms^{-1} . Some limb line shifts may be associated with these features. Studies of such average plots during periods when the earth was at extremes north and south of the plane of the solar equator indicate that these features are equator-centered rather than disk-centered, which is an indication that the origin of the features is solar, not instrumental. A further interesting characteristic of this residual-velocity pattern is that the average patterns before and after the last solar-activity minimum (late 1976) are mirror images of each other about the central meridian: the pattern appeared to reverse itself at minimum. This is a very puzzling phenomenon. Although a complete model has not yet been formulated, Howard believes now that the most likely explanation is that these low-latitude features are indicative of a general upward flow of material at the equator. The east or west preponderance of the flow before and after minimum may be the result of a slight westward or eastward inclination of the nearly vertical flow.

Big Bear Solar Observatory

In 1977, Dr. Alan Patterson assumed the duties of supervisory scientist at Big Bear and took responsibility for all observing programs.

Substantial instrument improvement took place during the year. Particularly

valuable was the introduction of the new reimaging system which produced a smaller image on the 65-cm telescope. Although actually no real improvement in resolution was achieved, the previous focal length of 32 m was so great that the image looked blurry in all but perfect seeing. Now almost all pictures taken with this large telescope look very fine. In addition, there has been a substantial improvement in contrast because an intermediate image is formed which may be better baffled to improve contrast in filters. The spectrograph and videomagnetograph have been brought into regular operation. The universal filter has been brought under computer control. A number of complex programs may be carried out simultaneously with as many as eight cameras operating.

Observational programs turned to active sun phenomena with the return of solar activity. Observations were obtained of some of the large flares in the spring, which brought wide notice. A program of flare spectroscopy was begun and a number of spectra of flares in $\text{H}\alpha$ were obtained through the flash phase. These spectra are particularly valuable because they were made together with slit jaw pictures that tell us exactly what region is being studied. In general, the flare spectra confirm previous results that the impulsive stage of flares is accompanied by extremely broad $\text{H}\alpha$ emission up to 15 \AA wide, whereas most of the flare outside the kernels and the flare in the late stages is only about 1 or 2 \AA wide in $\text{H}\alpha$. Thus the great line widths can be applied only to the emission from the kernels in the impulsive phase.

An extensive program of prominence cinematography and photography was carried out. Results are now under study, but two particularly interesting results were found. In some prominences an interactive region was found where a continuous rotation and motion of material took place while the rest of the prominence was stable and static. In addition,

it was found that erupting prominences far from active regions do not produce optical flares. Zirin has been studying the prominence data to try to understand the necessary and sufficient conditions for the occurrence of prominences.

Coronal holes have been mapped weekly in the helium D3 line. As the magnetic activity has increased during the year, the polar coronal holes have shrunk as the new magnetic field invades the polar regions. However, at this writing, the polar cap holes are still present, covering about 30° of arc at each solar pole.

Other observational programs have investigated spicules and the height of spicules, solar rotation, emerging flux regions, the lifetime of quiet-sun magnetic fields, and the Chapman-Ingersoll effect.

Studies of Emerging Flux Regions

Zirin, Frances Tang, and Arthur Hodges (Caltech undergraduate) have made a study of emerging flux regions—those regions where new sunspot groups emerge. When new sunspots emerge, they are characterized by simple bipolar fields and arched filaments, as found a number of years ago (Weart and Zirin, *Publ. Astron. Soc. Pacific*, 81, 270, 1969). The object of this study was to see what else could be learned about the manner in which the magnetic fields emerge. Emerging flux regions are particularly interesting because these apparently are material and magnetic field fresh from the innards of the sun and should cast light on the whole sunspot phenomenon. In addition, the well-known rapid westward motion of preceding flux has been studied to determine if actually the *p* spot moves forward or if there is simply an expansion of the preceding and following magnetic poles from the central point. Measurements show that during the developing stage of the sunspot group, the *p* spot moves westward with a typical velocity of about 1000 km hr^{-1} , while the following spot moves eastward with a velocity

about one-fifth as great and sometimes not at all. Thus there is a clear asymmetry in the emergence of the flux, which may be thought of as a skewed loop where the lines of force in the preceding part of the sunspot are sloped much more gradually than those in the following part. Unfortunately, no evidence of such particular curvature is seen in the arch filaments that connect the sunspots. It was found also that the appearance of each new sunspot is marked by extremely strong and active arch filaments that disappear as soon as the sunspot appears, that is, as soon as it has a diameter of a few arcseconds or more. It was found also that the satellite spots of the same polarity flock together during the development of the group. This behavior might be produced by the treelike field geometry where the lines of force move closer and closer together as the tree shape emerges from below the surface of the sun. The forward flow of the preceding spots stops as soon as the arch filaments disappear and the region becomes a mature active region. In general, all the development of activity on the sun results from the appearance of these bipolar regions. Once formed, regions do not move about; they may only die out or be cancelled by the appearance of and interaction with other regions. In cases where the polarity of the spots violated the Hale-Nicholson law, or where the magnetic axis was sharply tilted to the equator, there usually was a rapid rotation into a more normal alignment.

Prominence Rotation

Patricia Bornmann, a Caltech undergraduate, continued the study made in previous years by Adams and Tang to produce an extensive catalog of measurements of filaments from many years of Big Bear observations. Her observations simply reduce the scatter of the previous data. It is found that by and large filaments do not show the normal differential rotation, nor do they show rigid body

rotation. They appear somewhere in between. Of course filaments only mirror the rotation of magnetic-field patterns, so the results must be fairly similar.

The $L\alpha/H\alpha$ Ratio in Solar Flares and Quasars

In his study of flare $H\alpha$ emission last year, Zirin was surprised to find that the Lyman α emission as reported by several spacecraft observers does not exceed the $H\alpha$ emission measured on the various Big Bear observations. This resembles Neugebauer's result (Hyland, Becklin, and Neugebauer, *Astrophys. J.*, 220, L73, 1978) that the $L\alpha/H\alpha$ ratio in two quasars in which it was measured was close to unity. Further evidence produced by a literature search showed that in other quasars in which the ratio is not directly measured, indirect ratios indicate that the ratio is of the order of unity. The same is true of a number of flares and even of the solar chromosphere and prominences. A discussion of this interesting result was presented in a paper in *Astrophysical Journal (Letters)* (222, L105, 1978). One would normally expect $L\alpha$ to be brighter than $H\alpha$ because it is more easily excited and is the important resonance line. The proposed explanation is that the $L\alpha$ photons are destroyed by collisional deexcitation as they rattle around the quasar before escaping. Since the optical depth of Balmer α is much less, those photons escape directly.

Zirin proposed that in both flares and quasars the Balmer α and $L\alpha$ are strong energy sinks that play a vital part in the energy balance of the emitting gas. Therefore, neither of them can fluctuate greatly because any great increase in intensity would be accompanied by a rapid decrease in excitation temperature. Furthermore, even under large energy input (by photons in the quasar case and by hard electrons in the flare case) the hydrogen emission temperature does not exceed 20,000°, at which point the black-body intensities of $H\gamma$, $H\alpha$, and $P\alpha$ more

or less show the observed values. Without presenting a definitive solution of the problem, he pointed out that one must consider the energy equilibrium in these sources. It is interesting that the ratio also appears to be near unity in solar prominences that are considerably cooler than either flares or quasars. An extensive calculation of the relative intensity of Balmer lines in flares was made by Barry LaBonte, Caltech graduate student, as part of his thesis work. LaBonte carried out a detailed model calculation using three levels of hydrogen plus a continuum and bombarding a model chromosphere with an electron flux typical of energetic solar flares. It turned out that for a wide range of models (principal difference in the models was in the total energy flux and the hardness of the spectrum of exciting electrons) the $L\alpha/H\alpha$ ratio did not change.

Ephemeral Active Regions

Marsh has carried out a study of ephemeral active regions on films made at the Big Bear Solar Observatory. Ephemeral active regions are very small, bipolar active regions that never reach sunspot size and last only a day. Although they have been known for some time, their importance was first pointed out by Sara Martin and Karen Harvey in 1973. They occur all over the solar disk rather than just in sunspot latitudes and may carry a substantial amount of flux to the surface. Marsh studied the development of individual ephemeral active regions to understand how they grow and what happens to them. He found that the small flares were much more likely to occur if the ephemeral region rose to the surface near some existing magnetic flux. He found two cases in which reconnection between the ephemeral region and the neighboring preexisting flux occurred. Evidence of the reconnection was the appearance of arched fibrils connecting the ephemeral region with the original quiet-sun field. Marsh

pointed out that the appearance of ephemeral regions could play an important role in the movement and diffusion of flux across the surface of the sun. In his model, one pole of the emerging flux is cancelled out by reconnection with the preexisting flux of the opposite sign, and now the other pole of the ephemeral region remains as an element of flux of the same sign as the original field but displaced in distance by the size of the ephemeral region. This process takes about a day and shifts the flux element by about one chromospheric cell. It is frequent enough to play an important role in the diffusion of flux.

*Coronal Holes, the Height of the
Chromosphere, and the
Origin of Spicules*

Coronal holes are regions of the quiet solar atmosphere in which the corona is markedly depleted by the solar wind, so that the density of the corona in these regions is anomalously low by a factor of 2 or 3. *EUV* spectroheliograms from Skylab and from previous space-borne experiments have shown that the chromosphere-corona transition layer is much (2 to 5 times) thicker under coronal holes than in normal quiet regions outside of holes. Thus, the presence of a coronal hole strongly affects the underlying transition layer.

Throughout the June 1973–January 1974 Skylab missions, each of the solar polar caps (latitude $> 60^\circ$) was completely or nearly completely covered by a coronal hole, whereas less than 10% of the solar surface at lower latitudes was covered by coronal holes. From the time of Skylab to the present, He I D3 limb scans from Big Bear Solar Observatory and He I $\lambda 10830$ spectroheliograms from Kitt Peak National Observatory have shown that the polar coronal holes persisted through the intervening minimum in the solar activity cycle, and that the fraction of the area below 60° latitude

occupied by coronal holes has remained less than 10%. Moreover, the configuration of the corona observed in eclipses during the minimum phase of the solar cycle indicates that coronal holes are normally present at the poles during the solar minimum. Therefore, it appears that during solar minimum the average thickness of the chromosphere-corona transition layer in quiet regions at low latitudes is much less than the average thickness of the transition layer in the polar regions.

An important question bearing on the origin of spicules is whether the effect of coronal holes on the chromosphere-corona transition layer extends down into the chromosphere. In quiet regions, the upper chromosphere consists virtually entirely of spicules. Using high-resolution $H\alpha$ filtergrams of the solar limb, obtained by Dr. R. Dunn at Sacramento Peak Observatory in the summer of 1955, Dr. S. Lippincott (*Smithsonian Contr. Astrophys.*, 2, 15, 1957) found that the average height of spicules increased from equator to pole by some 20–30%. The fact that these observations were taken near solar minimum suggests that Lippincott may have been measuring an effect of coronal holes on the underlying chromosphere, that is, that in addition to the transition layer being greatly increased in thickness under coronal holes, the chromosphere may be somewhat (20–30%) extended in height as well.

To test this hypothesis, D. Rabin, Caltech graduate student, and Moore have carried out extensive measurements of the height of the $H\alpha$ chromosphere as a function of latitude and across known polar coronal hole boundaries. The height measurements were derived from 650 microdensitometer scans across the limb on full-disk $H\alpha$ filtergrams from Big Bear Solar Observatory; hole boundaries were located by reference to NRL/Skylab full-disk He II $\lambda 304$ spectroheliograms. The scans covered seven boundaries as well as two quiet regions well

away from the holes. These chromospheric height measurements (1) confirm Lippincott's result by showing a steady increase in average height of about 25% from equator to pole, but (2) show no discontinuity at hole boundaries nor any increase under coronal holes beyond that expected from the latitude trend. Because coronal holes have little influence on the height of the underlying

chromosphere, Rabin and Moore conclude that spicules are not generated by heat conduction or other energy transfer from the corona and are therefore driven from below. The observed increase in height with latitude suggests that the chromospheric magnetic field becomes on average more vertical as the poles are approached, allowing spicules to attain greater heights.

SOLAR SYSTEM

Eclipses of Iapetus

Eclipses of Iapetus by the rings of Saturn occurred in October 1977 and January 1978. Such eclipses provide the chance of investigating the nature both of the rings and of the surface of the satellite itself; measurements at visible or near-infrared wavelengths, which simply see reflected sunlight, give the transparency of the rings, while measurements at 20 μm indicate the thermal emission from the surface of Iapetus. Since the rate of cooling during the eclipse depends on the composition of the surface, this is a useful way of determining gross surface properties.

During October, only one hour's worth of data was obtained because of clouds, but in January 1978 the weather was clear during all the time that Saturn was above the horizon. Data obtained at 2 μm and 20 μm by Neugebauer, Matthews, Gatley, and Beckwith are shown in Fig. 1 (A and B); the measurements of Iapetus were made relative to Titan so that effects of air mass corrections were minimized. The figures show the reflected light (2.2 μm) and emitted light (20 μm) as Iapetus came from the shadow of the disk of Saturn into the shadow of the inner B ring. At UT \sim 8:20, it passed through the shadow of the Cassini division and then entered the shadow of the outer A ring before emerging into the full sunlight.

The 2- μm data have been analyzed by Dr. A. Harris of the Jet Propulsion Laboratory, who is collaborating with the infrared group in these observations and is collating visual and near-infrared observations to study the structure of the rings. The data are consistent with a width of 2000 km and a transmission of 33% for Cassini's division. The analysis of the thermal emission for Iapetus is less straightforward. The rapid changes in the 20- μm flux show that the diffusivity of the surface is low, which implies a very low thermal conductivity. The temperature rise during the passage through the shadow of Cassini's division is, however, too high for any simple one-constituent thermal model of the satellite when related to the incident flux as given by the 2- μm data. This implies that a more sophisticated thermal model is needed. The consequences and limitations of such thermal models are being considered.

Solar System Survey

Kowal has continued his "Solar System Survey" with the Palomar 1.2-meter Schmidt telescope. In spite of extremely bad weather throughout the winter, more than one-third of the ecliptic has been photographed, as well as several fields north and south of the ecliptic. The most interesting result of this program was the discovery, in November 1977, of the ob-

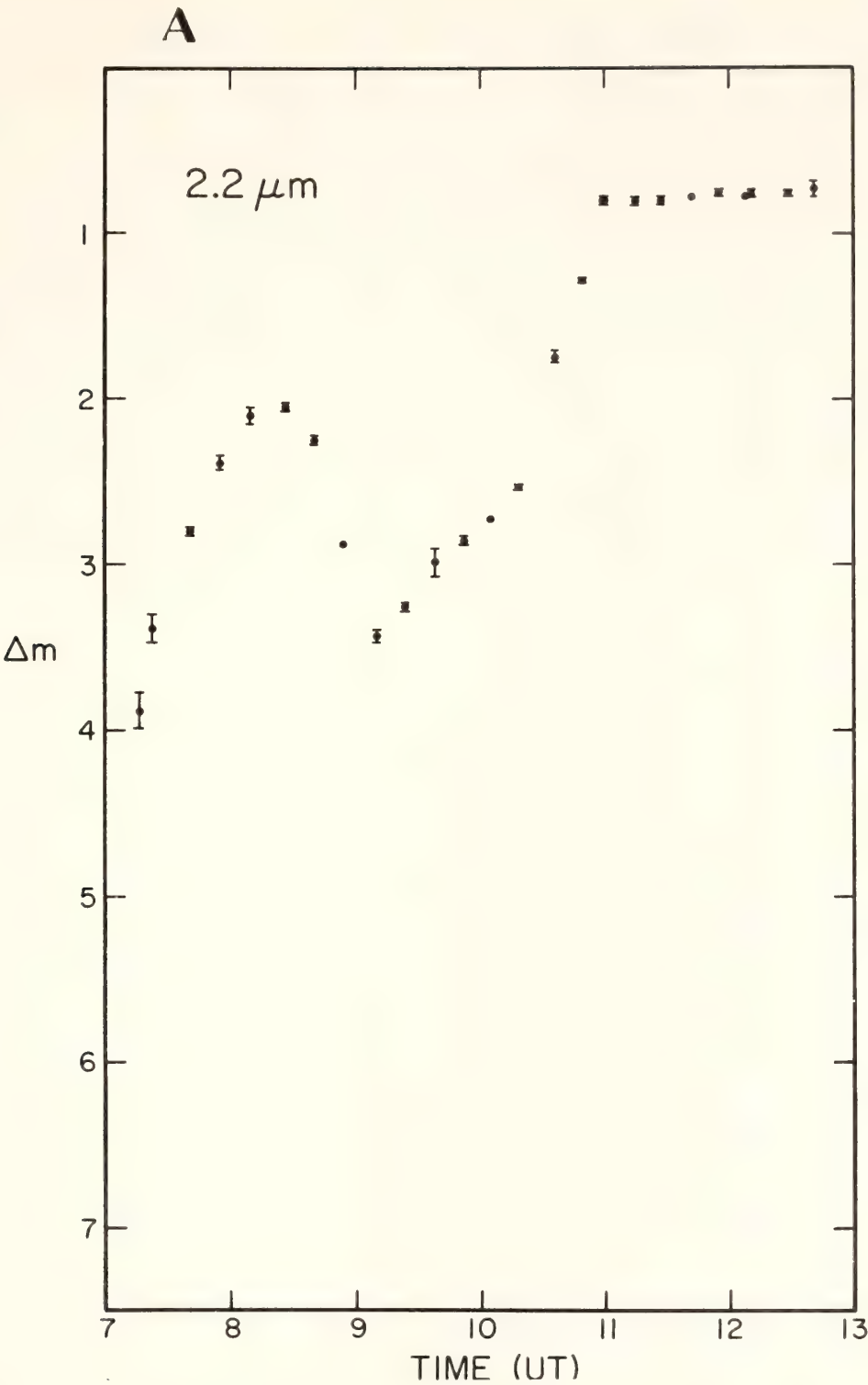


Fig. 1(A). The light curve at 2.2 μm of Iapetus passing through the shadow of Saturn's rings, showing reflected sunlight. Iapetus starts in the shadow of the inner ring, Cassini's division is crossed at around 8:30, and full sunlight is on slightly after 11:00.

ject now named "Chiron." This unique object travels between the orbits of Saturn and Uranus (perihelion distance, 8.5 A.U.; aphelion distance, 18.9 A.U.; inclination, 7°). The diameter of this

object is estimated at a few hundred kilometers. Chiron has technically been classified as a minor planet, but it is too remote from the asteroid belt to have any obvious relation to the asteroids. It

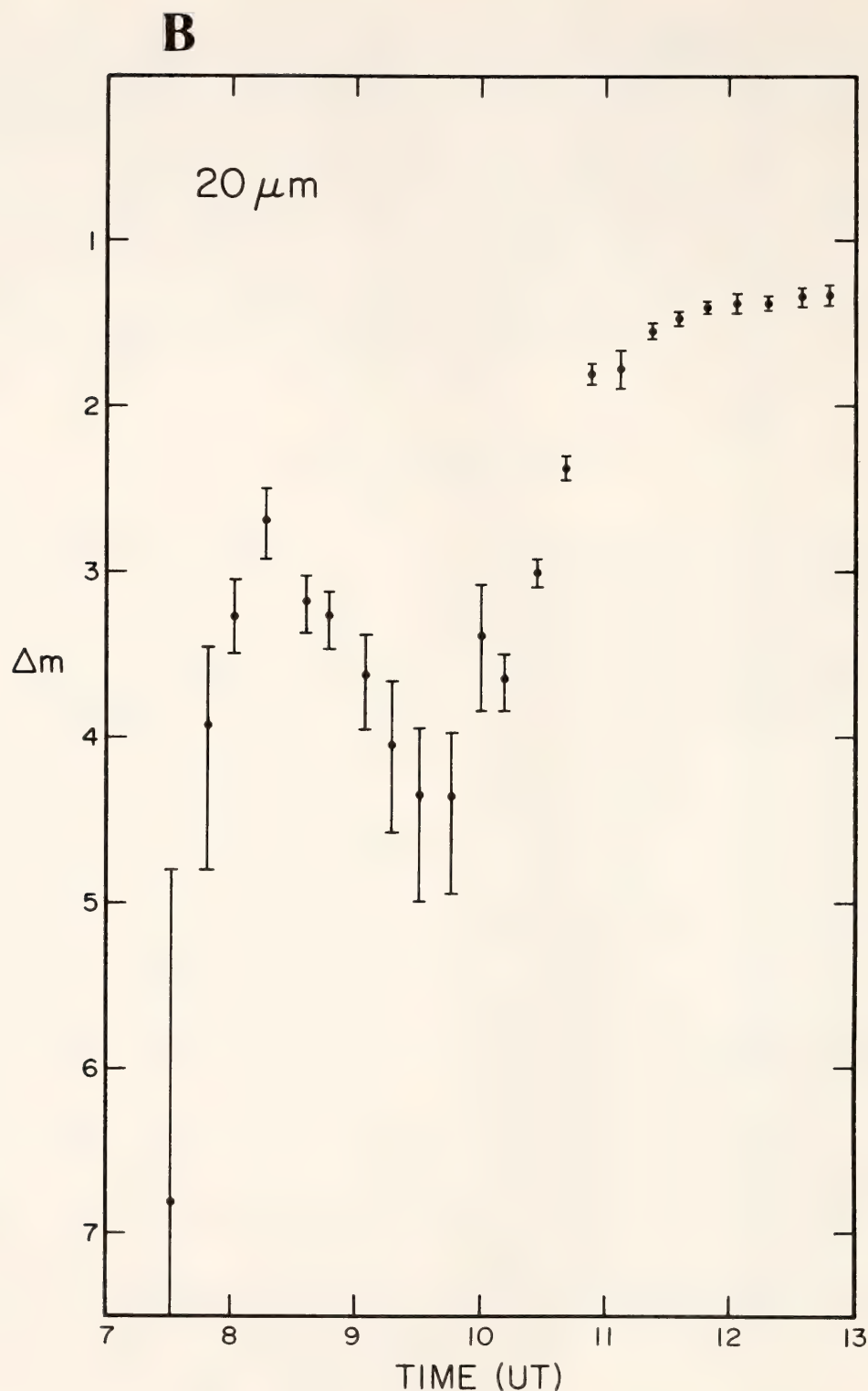


Fig. 1(B). Light curve at 20 μm of Iapetus in the shadow of Saturn's rings. Measurements based on thermal emission from Iapetus; all other conditions same as in Fig. 1(A).

is also much larger than any known comet. The nature and origin of Chiron are unknown. This project is under the general direction of Dr. P. Goldreich and is supported by NASA Grant NGL-05-002-140.

The Rings of Uranus

Three or possibly four new rings of Uranus were found during an occultation of a 10th magnitude star on April 10, 1978. The observations were made with the recently completed InSb detector sys-

tem and infrared photometer at the 2.5-meter du Pont Telescope at Las Campanas. The star was continuously monitored at 2.2μ , where deep methane absorption in Uranus' atmosphere dims the planet by ~ 6 mag. The planet was ~ 10 times fainter than the star, and a signal-to-noise ratio of 6 was achieved in 100 msec. All five rings discovered by J. L. Elliot (Elliot, Dunham, Mink, *Nature*, 267, 328, 1977) in March 1977 were seen again. The new data show that the γ , δ , and η rings are accurately circular and α , β , and 4 have eccentricities $\sim 5 \times 10^{-4}$. The outermost ϵ ring is quite different: its width varies between 20 and 100 km and is linearly dependent on its radius to a

high degree of accuracy. Its optical depth profile has remained essentially unchanged in 13 months, despite the fact that ~ 1100 orbital periods of the ring particles have taken place—and that precession between the inner and outer edges of the ring would be expected to smear out and broaden the ring. A rapidly precessing Keplerian ellipse model fits the radius data; however, more data will be required to test the model. The detection of the new rings was announced by Persson, Nicholson, Matthews, Goldreich, and Neugebauer (*Int. Astron. Union Circ.*, 3215, May 1, 1978). The full results will appear in the *Astronomical Journal*.

STELLAR SPECTROSCOPY

Rotation of B-Type Stars

Preston and Dr. Sidney C. Wolff of the University of Hawaii have completed an analysis of the rotation and other characteristics of a sample of 256 late B-type stars. Approximately half of the stars have $v \sin i < 100 \text{ km s}^{-1}$ and a statistical treatment of the data shows that the distribution of true rotational velocities reaches a maximum in the interval $30 < v < 70 \text{ km s}^{-1}$. The observations favor the hypothesis that early evolution away from the main sequence proceeds with complete radial exchange of angular momentum. Approximately 16% of the nonmagnetic late B-type stars are HgMn stars. The frequency of HgMn stars decreases with increasing rotational velocity from about 70% at $v = 0$ to zero at $v \sim 100 \text{ km s}^{-1}$. The HgMn stars occur throughout the main-sequence band from the zero-age to the terminal-age boundaries. The observations show that HgMn stars are not distinguished from normal ones by their age, duplicity, rotation, or any combination of these characteristics.

B-Type Companion of Antares

Preston and Dr. J. P. Swings of the Institut d'Astrophysique, Liège, have completed a study of the emission nebulosity surrounding the B-type companion of Antares. Measurements of high-resolution spectrograms obtained in excellent seeing conditions indicate that the nebulosity is asymmetrical with characteristic dimensions, probably in excess of $3.5''$. Emission lines due to Fe II, [Ni II], and [Cu II] were detected in addition to the previously recognized lines of Si II and [Fe II]. The electron density and temperature of the nebulosity cannot be determined from the intensities of the blue-violet emission lines because of serious deviations from the statistical distribution of the populations of the metastable levels of Fe II.

Dwarf Novae

Oke is carrying out a program to study a group of dwarf novae and similar kinds of objects. The selected objects, RW Trianguli, U Geminorum, and UX Ursae

Majoris, have periods of several hours and are also eclipsing systems. Two kinds of observations are being pursued. First, multichannel observations are being obtained around the whole cycle. This effectively generates a light curve at every wavelength from 3200 to 10,800 Å and at the same time absolute energy distributions at every phase. Second, the SIT digital spectrograph is being used with its maximum dispersion to obtain spectra around the cycle for velocity studies.

Caltech graduate student Kirk Borne and Oke have analyzed the multichannel spectrophotometric observations of RW Tri. With wavelength coverage from 3200 Å to 1 μ , the composite nature of the spectrum has been discovered and the components separated. The secondary spectrum (previously undetected) is consistent with that of a star of spectral type M1. Reasonable limits on the luminosity yield a value for the distance of 250 ± 100 pc. The dominant source of continuum radiation is identified with an accretion disk. Except for the strong lines of H I and He I in emission, the integrated disk spectrum is of the form $f_\nu = \text{const}$. If the disk radiates isotropically, it emits roughly 10^{33} ergs s⁻¹ longward of 3000 Å. Models for the variation of the integrated disk spectrum with eclipse phase have been constructed and are found to reproduce the data reasonably well. The working models generally represent a disk that radiates everywhere like a blackbody whose projection onto the sky is rectangular and whose temperature varies from 3000°K in the outer regions to 10,000°K in the inner regions, where the projected radius is small. However, the observational evidence clearly indicates that the disk is asymmetric and that more detailed models are needed.

The analysis of the very extensive data for U Gem is being made by Caltech graduate student Richard A. Wade and Oke in collaboration with Dr. B. Paczynski of the Copernicus Astronomical

Center, Warsaw. Analysis of the multichannel observations by Wade has shown that the spectral-energy distribution can be interpreted as the sum of the radiation from a red star of spectral type near M4.5 and a flat radiation component, $f_\nu \approx \text{const}$, which is produced by an accretion disk and a hot spot. The two basic components contribute about equally to the total light near 7200 Å. Digital spectra obtained by Wade with the 1.5-meter reflector at Palomar confirm the presence of the red star in the U Gem system. The multichannel observations also show a secondary eclipse in the near-infrared. This eclipse is presumably caused by the optically thick accretion disk passing in front of the cool red star. The red star appears to be less dense by a factor of 2 than main-sequence stars of similar color. The observations allow the distance modulus of the system to be estimated at 4.4 ± 0.8 mag.

Variable Stars

The novalike magnetic degenerate star VV Puppis was found in January and February 1978 by Greenstein and Oke to be in a "turned-off" state, about 3 mag fainter than usual. In that state, the spectrum of the M-dwarf companion was strong, dominating at $\lambda > 7500$ Å. It brightened and became blue in March 1978. When the bright nova DQ Herculis (1934) was observed during the eclipse of the hot spot, an M-dwarf spectrum was detected at the long wavelength end of the multichannel scan. Both these observations suggest much lower luminosity than the conventional assumed $M = +7.5$ for the accretion disks in old novae and novalike stars at minimum. A routine survey of Lowell blue stars of small motion showed that GD 552 is an intrinsically faint U Gem star (near $M_V = +13$). In this object no red companion was detected, but the bremsstrahlung from the disk was of the same order as the flux from a 9000°K degenerate.

The rapid, small-amplitude variable $-7^{\circ}3007$ has been a difficult object to classify for some time; it has a nearly flat spectrum from 3300 to 10,000 Å, a weak $H\alpha$ emission, and shows shallow Ca II and He II absorption. Almost certainly not degenerate, it may have an accretion disk. The International Ultraviolet Explorer (IUE) satellite observations by Greenstein and Oke were quite unexpected; the continuum flux is only slightly less than in the visible, and a strong P Cygni emission and absorption line of C IV are seen. Lyman α and N V are strong and may show P Cygni emission; Si IV absorption is present. The ultraviolet spectrum may represent a hotter portion of the accretion region, but the P Cygni profiles require ejection or mass loss at over 2000 km s $^{-1}$ outside the region forming the ultraviolet continuum.

The long-period variable R Aquarii has had an interesting history. In 1926 and in 1929–1934 the M-type spectrum was submerged by a blue “companion” studied extensively by Paul Merrill. This secularly variable blue object is not known to be physically distinct from the M giant; both are immersed in a peculiar nebulosity. Taking advantage of a minimum of the long-period variable in September 1977, Greenstein obtained multi-channel and SIT spectra of the star and the inner and outer nebulosity; Gunn obtained an image-tube prime-focus photograph of the nebula. The blue component is seen as a 13th magnitude flat continuum from 5500–3300 Å, with superposed emission lines; the long-period variable dominates at $\lambda > 6500$ Å. The inner nebulosity has a complex spike structure; its outer segments are elliptical. The appearance is that of an explosion some centuries ago, the structure resembling shocks or intersecting shells. Greenstein and Dr. George Wallerstein of the University of Washington are analyzing the complicated emission-line spectrum. If the blue continuum is bremsstrahlung, it has an appreciable Balmer emission continuum

corresponding to high electron temperature. The dominant emission lines near the star are [O III] (especially $\lambda 4363$), H, [Ne III], [S II]; [N II] and [O II] are not very strong; [Fe II] and [Fe III] are seen. Farther out, [N I] becomes quite strong, as does [O II], with [Fe III] visible and, strangely, He II $\lambda 4686$. About 40'' out in the nebula, [O II] and [S II] are strong, although [O III] and He II persist. There are features of both collisional and radiative processes, possibly fossilized ionization, relics of some unusual event. If the star is truly a binary, with the blue component fueled by mass transfer, the observations suggest a past, more violent, possibly nova-like event. If single, then R Aqr, a long-period variable, has ejected a mini-nebula at high excitation. Dr. K. Serkowski of the University of Arizona, during a 1974 minimum, observed high linear polarization of the light with position angle dependent on wavelength.

Flare Stars

The flare star YZ Canis Minoris has been observed during active and quiescent phases. Spectra have been taken by Mochnacki and Schommer, using the Varo-RETICON detector with the Mount Wilson 2.5-meter telescope. The spectral region 5090–5340 Å was covered with an instrumental half-width resolution of 0.5 Å. A spectroscopic flare was observed between 1940 and 2130 hours PST March 28, 1978. Strong emission lines of Mg I (5167, 5173, 5184), Fe I (5270, 5328), and Fe II (5169, 5317) were observed throughout an interval of almost two hours, with a slow decay. The Fe II “ b_3 ” line at 5169 Å had an equivalent width of about 2 Å, twice that of each Mg I “ b ” line. The emission lines were narrow and essentially resolution limited in width (0.5 Å). A spectrum taken at 2057 hours PST March 27, 1978, showed no emission in these lines. Other spectra taken at 2010 hours and 2049 hours PST April 27, 1978, also showed no emission

in the same spectral region. Mochnacki and Schommer are carrying out a detailed analysis to measure radial velocities and the variation of features with respect to time. The discovery of sharp variable emission lines in the yellow part of the spectrum may give new insights into the physics of red-dwarf flare stars.

Stellar Chromospheres

Preston and Vaughan continued the survey, initiated in 1966 by O. C. Wilson, of stellar analogs of the solar activity cycle as revealed by variations in chromospheric H and K line fluxes. The H-K photometer described in *Year Book 76* (p. 134) continues in operation on the Mount Wilson 1.5-meter telescope for this purpose. A first report, in collaboration with Wilson, calibrating this equipment in the H-K photometric system established by Wilson has been published in the *Publications of the Astronomical Society of the Pacific* (90, 267, 1978). In addition to this work, Preston and Vaughan have undertaken a survey of H-K fluxes in some 700 high-velocity and solar-neighborhood main-sequence stars and a similar survey of stars in the Orion Association.

Lower Main Sequence

Mochnacki and Schommer are observing a sample of about 80 K and M dwarfs, using the Varo-RETICON photon-counting detector in the coude spectrograph of the Mount Wilson 2.5-meter telescope. The primary goal is to obtain the spectroscopic-binary frequency of the lower main sequence. Spectral records cover the region 5100–5350 Å at an instrumental resolution of 0.5 Å and a mean sampling pitch of 0.07 Å per pixel. The sample includes (1) K and M dwarfs between 0° and +40° declination, nearer than 10 pc and brighter than $V = 12.0$; and (2) K and M dwarfs between 0° and +40° with proper motions greater than $1''\text{yr}^{-1}$ and with apparent magnitudes brighter than $V = 12.0$. Radial velocities are

being measured, using computer cross-correlation techniques. A spectral reductions program written in FORTRAN for use on the PDP-11/34 of the Caltech Robinson Laboratory has been developed by Mochnacki, with assistance from Schommer, Barbara Zimmerman, and graduate student William Sebok.

The Faint End of the Main Sequence

Multichannel spectrophotometry of 465 main-sequence stars, of which 240 have parallaxes of various qualities, has been completed by Greenstein. The major effort has been to calibrate the HR diagram for stars of the solar neighborhood ($M > +5$) as a function of population type or space motion, using the parallax stars. This allows distances and tangential motions to be determined from the colors; radial velocities are available for only 130 of these, but many are being measured to give full details of the space motion. The complete Lowell Northern Hemisphere catalog of stars to 16.5 pg and motions exceeding $1''\text{yr}^{-1}$ has been completed and provides the luminosity functions of high- and low-velocity stars. The rarity of high-velocity stars at faint M_V is remarkable. The faintest low-velocity star is van Biesbroeck 10, LP619-50, $M_V = +18.8$. For $T > 250\text{ km s}^{-1}$, only five have $M_V > 10.0$, the faintest being at +11.2. Fainter proper-motion stars near 20 mag photographic will be needed to find faint sdM stars. There are 25 stars for which $V_0 < -450\text{ km s}^{-1}$ or $|V_z| > 250\text{ km s}^{-1}$ (i.e., extreme halo velocities) among the 450 stars for which space motions were computed. They are excellent candidates for extreme metal-poor stars and include M stars.

M-Type Stars

Ake has begun work analyzing Greenstein's multichannel observations of the energy distributions and molecular-band strengths of dM and sdM stars to investigate compositional and luminosity differ-

ences among them. Because M-star spectra are heavily blanketed by molecular bands and observations are made in various bandpass modes, care was exercised in locating stable points to represent the energy distribution of these stars. Ake chose four regions at $1/\lambda = 0.95, 1.10, 1.20$, and $2.14 \mu^{-1}$ to give relatively band-free colors as well as provide pseudo-continuum points for measuring band strengths of TiO, CaH, and MgH and the line intensity of Ca I $\lambda 4227$. In addition, a measure at $1.88 \mu^{-1}$ provides a visual magnitude. The three near-infrared points sufficiently avoid both stellar and terrestrial bands, and although the fourth point lies in a banded region, it appears to be the least depressed area from 1.4 to $2.5 \mu^{-1}$, especially for the low-dispersion mode of the multichannel spectrometer. Published dM models by Mould demonstrate that these points do not vary with changes in metallicity and, therefore, effective temperatures and bolometric magnitudes can be determined from them. In a preliminary analysis to calibrate the lower main sequence, Ake used 52 parallax stars with tangential velocities below 100 km s^{-1} and 22 objects of higher velocity to investigate the relationship of color, TiO, and CaH intensity and luminosity with motion. Utilizing recent parallax determinations, the scatter about the main sequence is found to be $\pm 0.5 \text{ mag}$. While a few objects fall more than 1 mag below the main sequence, in general the high-velocity group lies only 0.3 mag below it. Although such a small separation may be due in part to relaxing the criterion for high velocity, many of the newer parallaxes are moving the halo stars closer to the main sequence.

Silicon Monoxide in Bright Infrared Objects

Geballe, collaborating with J. M. Lacy and S. C. Beck of the University of California at Berkeley, has begun a study of the fundamental vibration-rotation band

of silicon monoxide near 8μ in bright infrared objects. This is the longest wavelength molecular band to be observed in extra-solar system objects. Although the earth's atmosphere severely limits the amount of the band that can be observed, even small portions of the band contain SiO lines of a wide variety of excitations and from all isotopic species. Many lines are present in the atmosphere of M stars. For them the analysis is complicated but can lead to values for the line width and column density and can test model atmosphere pressure-temperature relations in the extreme outer parts of the atmosphere about which knowledge is scarce. Measurement of isotopic ratios of silicon and oxygen might allow one to determine a more precise evolutionary state for the star and would test the occurrence of certain nuclear reactions in the stellar interior, as well as the importance of mixing. At present, a study of SiO in VY Canis Majoris, a peculiar M giant or supergiant with a large infrared excess and strong maser emission, is nearing completion. The observations were made with the 2.5-meter du Pont Telescope at Las Campanas. The infrared excess comes from a dust shell, which prevents observation of the atmosphere of the central star at 8μ . However, SiO is present in the surrounding cloud, and the line velocities and profiles show that the cloud is being expelled from the star. Indeed, acceleration is actually observed; transitions of higher vibrational excitation have lower expansion velocities. The stable isotopes ^{29}Si and ^{30}Si are observed to have near-normal abundances relative to ^{28}Si . This probably rules out the star being in an extremely late red-giant stage, but does not settle the question of whether VY CMa and similar objects are protostars or post-main-sequence stars.

A White Dwarf-Red Dwarf Eclipsing Binary

The star PG 1413+01, discovered in the Palomar-Green survey for blue stars

at high galactic latitude, is an eclipsing binary. Observations by Green, Richstone, and Schmidt (*Astrophys. J.*, 224, 892, 1978) show the object to have a period of about $8^h 16^m$ and to resemble the red dwarf-white dwarf binary BD+16°516. The primary is a hot white dwarf with a mass of around $0.7 \pm 0.3 M_{\odot}$. The faint secondary was detected with the multichannel spectrophotometer on the 5-meter Hale Telescope in the red during eclipse and is probably a dwarf of spectral type $M3 \pm 3$. The two components are separated by about $2 R_{\odot}$. Since it is unlikely that the hot white dwarf is heated by accretion, the system has probably been in its present state for less than 10^6 years and may be a post-common-envelope binary.

Degenerate Stars

The dominant composition of degenerate star atmospheres is essentially two-valued—either $H/He > 10^4$ (DA) or $He/H > 10^4$ (DB and some DC). Superposed on this are effects of variations in “trace” elements, for example of metal/dominant element or C/He . The maximum abundance of metals, however, has proved much lower than in the sun, that is, $M/H \lesssim 10^{-5}$ in those few yellow degenerates that showed strong lines of metals. Such a drastic separation of H, He, C, and metals provides insight into the physics of the atmosphere and outer envelope. In addition to initial conditions, the relevant competing mechanisms are gravitational separation of heavy from light elements, radiative-pressure effects on trace elements, convection in either hydrogen- or helium-dominated atmospheres, and accretion. Greenstein has observed numerous candidates among the cooler red degenerates that might show metallic lines, weak or strong. A recent list of 51 additional degenerates (bringing his total lists to 507) includes a spectrophotometric study of 22 red degenerates fainter than $M_V = +15$. This substantial number is to be compared

with the four faint degenerate stars known in 1965 (Eggen and Greenstein, *Astrophys. J.*, 141, 83, 1965) at the beginning of Greenstein’s survey. Nevertheless, the number of known red degenerates is still small and most probably less than that predicted by simple cooling theory. Enough statistical information exists to estimate the “success” probability for a suspected faint, proper-motion star. The reduced proper motion defined as $H = m + 5 \log \mu$ is the selection criterion. Substantially all faint proper-motion stars are degenerate for $H > 15$, for Luyten color-class b, a, f, g . However, at color-class $g-k$, 60% are nondegenerates; at color-class k , with an increased motion limit of $H > 16$, 73% are nondegenerates. Only one color-class m star, with $H = 17.8$, is known to be degenerate. Of the 22 degenerates with predicted $M > +15$, 11 have predicted parallaxes exceeding $0.''025$, but have not been observed trigonometrically. Possible metallic lines in cool degenerates with helium-dominated atmospheres might become so broad as to vanish, because of the large pressure broadening. Multichannel spectrophotometry should detect such broad features. A study of nine red degenerates near $M = +15$ suggests that, if the magnitudes in the continuum are fitted by a quadratic formula, the residuals are $\pm 0.''03$; no convincing broad depressions are seen. The most reasonable but weak features that sometimes exist are Ca II and ultraviolet Fe I. The metal content of this group must be very low; so far only a few strong, metallic-lined red degenerates with obvious lines are known.

A study of a hotter ($\approx 9000^\circ K$), brighter star, Ross 640 (EG 119), DFp, has been made with the International Ultraviolet Explorer (IUE) by Greenstein and Oke. The low-resolution spectrum shows strong, enormously pressure broadened blends of the resonance lines of Mg II and Fe II. These absorptions depress the spectrum so much in the $\lambda\lambda 2000-3000$ region that a failure to de-

tect the cooler, brighter DG, van Maanen 2 (EG 5) may be understood as caused by strong metallic-line blocking. Detection of Mg II and Fe II in the ultraviolet of Ross 640 fits with presence of Ca II and Mg I in the blue. Although the metals may have reasonable abundance ratios, they are low, compared to helium, in this helium-dominated atmosphere. Hotter DA's (27,000 to 12,000°) observed with IUE showed no strong metallic lines from 1200 to 3000 Å. One hot DB (GD

190 = EG 193) showed no unexpected lines on the IUE.

In Greenstein's continued multichannel survey of new possible degenerates, the first high-velocity magnetic star was found, G35-26 (Gr 469). It has Zeeman-resolved H β and possibly He I lines. The energy distribution fitted a star of mixed H and He composition; it is possible that, as in Feige 7 (= Gr 267), the presence of strong magnetic field inhibits the separation of H and He.

INTERSTELLAR MATTER

Molecular Hydrogen

The study of interstellar molecular hydrogen through its 2- μ m emission spectrum was continued by Beckwith, Persson, and Neugebauer with a search for new H₂ emission sources and measurements of the emission from the Orion Molecular Cloud. Thirty-six objects have now been searched and H₂ emission has been seen in nine (seven were discovered through the present search program and two were known previously). Seven of the nine H₂-emission sources are planetary nebulae, one is a T Tauri star, and one is a molecular cloud complex containing young stars and protostars. The propensity for planetary nebulae to exhibit H₂ emission probably indicates that the H₂ is excited by shock waves generated by the ejection of the shell during formation. The detections also show that planetary nebulae contain dense regions of *molecular* gas, a fact not known before these discoveries. Analysis of the properties of the two other H₂ emitters, the Orion nebula and T Tau, also supports the interpretation that H₂ is collisionally excited in the boundary layers of strong shock waves.

The reddening to the H₂ emission in the Orion Molecular Cloud source was determined by measuring the ratio of the

intensities of the 2.12- and 2.42- μ m lines that arise from the same upper level of the $v = 1$ state. The measurements were made at Mauna Kea Observatory where the effects of terrestrial water vapor absorption on the 2.42- μ m line are minimized. The line ratio was calibrated by measuring the same lines in NGC 7027, which is only slightly reddened. The result is that there is ~ 0.8 mag of reddening between 2.12 and 2.42 μ m toward the Orion source. This corresponds to approximately a factor of 40 in intensity of the 2.12- μ m line and roughly the same factor in total H₂ luminosity. The large amount of extinction places the H₂ source close to the BN-KL complex of infrared sources along the line of sight. The energetic requirements favor a shock-wave model for the H₂ emission, and this in turn makes it likely that a violent event, such as a supernova, has gone off deep within the molecular cloud.

Studies of Star Formation

Studies of star formation have been continued by Neugebauer and Werner in conjunction with the Caltech program of airborne far-infrared observations, using the NASA C-141 G.P. Kuiper Observatory. In particular, NGC 7538, a complex region of star formation in Cassiopeia, has been studied extensively.

During airborne observations from the 91-cm airborne telescope, a previously unknown component (now designated NGC 7538 IRS East) was discovered; subsequent ground-based observations found a near-infrared source at this position. Ten-micron slit scans at the 5-meter telescope have shown IRS East to be a point source; the energy distribution of this source is typical of "infrared proto-stars" like the Becklin-Neugebauer object in Orion. Particularly noteworthy in NGC 7538, however, is the fact that two such objects exist only 1' apart; as well as IRS East, there is a protostar-type object, IRS 1. Observationally, IRS 1 appears to be associated with a compact H II region, while IRS East does not. In an effort to discover if this effect can be attributed to self-absorption at radio wavelengths in a very dense "proto-H II region" in IRS East, the intensity of Brackett- γ emission from IRS East was measured. No line emission was detected; clearly, the absence or presence of ionized gas in the vicinity of protostellar objects is simply not understood. One attractive explanation is that the differences between IRS East, the BN object, and IRS 1 can be attributed to the evolutionary state of these objects.

During the measurements of IRS East at 2 μm , it was found that the point source is embedded in an extended region of infrared emission, although there is no hydrogen-line emission from the extended region. The near-infrared color of this extended emission is extremely blue relative to the point source IRS East; the most likely explanation for the origin of the extended emission is that it is reflection nebulosity. Analysis of these data is not yet complete, but the plausi-

bility of the interpretation as reflection nebulosity has been greatly strengthened by the recent discovery that the 2- μm emission from CRL 2688 peaks on the optical-reflection nebula and not on the point source that illuminates the nebula.

Submillimeter Heterodyne Spectroscopy

A program of submillimeter heterodyne spectroscopy from the prime focus of the 5-meter telescope has been continued by Werner and Neugebauer in collaboration with Drs. T. Phillips and P. Huggins of the Bell Telephone Laboratories, using a much-improved receiver system. The (3-2) emission line of ^{12}CO at 870 μm has been mapped with 30" resolution in the central regions of the well-studied W3 and DR21 molecular clouds. In both sources, the (3-2) CO line showed pronounced self-absorption, suggestive of cold foreground gas absorbing the radiation from a warm central component. Self-absorption occurs in a uniform cloud in which the temperature decreases outward and in which there are no large-scale ordered velocities; this phenomenon has been predicted and looked for in CO sources. The fact that it has not been commonly seen in the widely studied CO (1-0) line has sharply reduced the range of fashionable models for molecular clouds; its apparent absence may, however, only reflect the poor angular resolution of the CO receivers previously used. It is, therefore, interesting that self-absorption has been seen in the (3-2) line in both DR-21 and W3; this again indicates how the high-frequency, high-spatial resolution and good pointing capability attained at 870 μm on the 5-meter telescope can lead to important new results in molecular astronomy.

PULSARS

*An Optical Candidate for the Binary
Pulsar 1913+16*

Kristian and Westphal report the detection of a visible object within about 1" of the binary radio pulsar discovered by Hulse and Taylor. The object was originally marginally detected on the SIT slit viewer at the Cassegrain focus

of the Hale Telescope and later confirmed using a CCD at the prime focus. Although quite faint (about 23 mag), it is several magnitudes brighter than published limits on the pulsed visible radiation; if it is to be identified with the pulsar, it is more likely to be the hitherto unseen binary companion.

GLOBULAR CLUSTERS

Dynamics of M3

Gunn and Dr. R. F. Griffin of Cambridge Observatories, England, have completed their analysis of the dynamical state of the globular cluster M3, based on photoelectric radial velocities of 111 giants in the cluster, obtained with their radial-velocity spectrometer at the Hale Telescope coudé. The conclusions are that the mass-to-light ratio is somewhat higher than previously thought for globular clusters, about 3 in solar visual units, consistent with the steeper mass function (logarithmic slope ~ 2 as compared to the ~ 1.35 in the solar neighborhood) demanded by the dynamical data. The velocity distribution in the cluster becomes anisotropic at about 20 pc from the center, at which place the deflection relaxation time is about the age of the universe. One of the most remarkable things that turned up in this study is the complete absence of radial-velocity variations due to binarism; the incidence of variation in the relevant range for field and galactic cluster giants is about 25%, and none are found in M3 (or, for that matter, in any of the other globular clusters in which data have been obtained so far). Limits on the total mass of heavy ($\geq 2 M_{\odot}$) remnants can be placed and for typical models which fit the cluster well are

under 1% of the cluster mass. White dwarfs with masses somewhat greater than the present turnoff mass are probably present in small numbers, though statistical uncertainties in the core luminosity profile limit the accuracy with which their contribution to the total mass can be determined. Population and dynamical M/L 's agree to about 10% with no *ad hoc* additions; there is thus no evidence for any "missing mass" in globular clusters.

Radial Gradients

Globular clusters are generally thought to be chemically homogeneous. However, recent work has shown that some globular clusters, especially those with long relaxation times, possess radial gradients in their integrated colors. The size of these radial color gradients are similar to those found in elliptical galaxies, where they are thought to be a consequence of gradients in the mean metal abundance within the galaxies. The origin of the color gradients in globular clusters is now being investigated by DaCosta. Integrated photometry of a sample of these clusters through apertures of different sizes has been obtained with the 1-meter Swope Telescope at Las Campanas and with the Palomar 1.5-meter telescope. The photometric system

used is that of Zinn (*Year Book* 76, p. 145), and the data will indicate whether or not the clusters also possess metal-abundance gradients. In addition, Da-Costa has used the SIT area photometer attached to the Palomar 1.5-meter telescope to obtain frames of the central region of these clusters. From these data, magnitudes and colors of the stars in the central regions of these clusters will be determined.

Infrared Studies

A program of measuring energy distribution, bolometric luminosities, and $2\text{-}\mu$ CO and H_2O absorption indices for globular-cluster red giants was continued by Persson in collaboration with Drs. J. Cohen (Kitt Peak National Observatory), J. Frogel (Cerro Tololo Inter-american Observatory), M. Aaronson (Steward Observatory), and K. Matthews. Seventy-one stars in ω Centauri

were observed on the du Pont Telescope. The peculiarities of the surface compositions and color-magnitude diagram of the ω Cen stars are evident in the infrared parameters as well. Half of the giant-branch stars observed exhibit strong CO absorption. As is the case for $B - V$ color, the giant branch is wide in $V - K$ at a given bolometric luminosity. Although blanketing in the very carbon-rich stars complicates the interpretation, it appears that a spread in composition (of heavy metals) has been seen and corresponds to the range found for the RR Lyrae variables by Freeman and Rodgers. Stars that lie on the red side of the giant branch in $V - K$ tend to have the largest CO excesses; however, CO increases much more rapidly across the giant branch than it does in going from metal-poor to metal-rich clusters. Possible explanations for this include triple α carbon mixing and primordial CNO/Fe variations.

THE GALAXY

Galactic Structure

S. Knapp of Caltech, Dr. S. D. Tremaine of the Institute of Astronomy, Cambridge, England, and Gunn have recently completed a rediscussion of the rotation curve and mass models of the Galaxy. New data obtained by them at 21-cm wavelength indicate that the much-discussed "cutoff" in the hydrogen distribution at 20 kpc is illusory; in fact, a gas distribution of the form e^{-r/r_0} , with $r_0 \sim 0.4R_0$ from well inside the sun to as far out as one can see (40–60 kpc), is completely consistent with the data. Fitting 21-cm data from inside and outside demands that the rotation curve in the neighborhood of the sun be flat, as is observed in essentially all large external systems, and that the rotation velocity be about 220 km s^{-1} . A new value of 110 km s^{-1} is obtained for AR_0 from the

Weaver-Williams survey data; previous determinations have been in error because of inadequate treatment of turbulent motions in the gas. For a flat rotation curve, $\Theta_0 = 2 AR_0$, which again yields 220 km s^{-1} for Θ_0 . A new set of galactic-structure parameters, $A = 13 \text{ km s}^{-1} \text{ kpc}^{-1}$, $B = -13 \text{ km s}^{-1} \text{ kpc}^{-1}$, $R_0 = 8.5 \text{ kpc}$, $\Theta_0 = 220 \text{ km s}^{-1}$, are suggested. A mass for the Local Group is obtained from consideration of the Galaxy-M31 orbit and is found to be about $3 \times 10^{12} \mathcal{M}_\odot$; thus the Galaxy must extend to 100 kpc with a flat rotation curve. The calculated M/L for the Local Group is about 140, in agreement with that obtained for other, similar external systems by Kirshner and by Gott and Turner. With these parameters, the Galaxy becomes quite typical among large Sbc systems.

Initial Mass Function

An important parameter in studies of galactic evolution is the slope of the initial mass function. It is normally assumed that the value of this parameter for the solar neighborhood applies throughout the Galaxy. However, work by DaCosta (thesis, Australian National University) has shown that there exists considerable variation in the slope of the initial mass function among a small sample of globular clusters in our Galaxy. In an attempt to find the cause of this variation, DaCosta is determining the mass function of other nearby globular clusters from plate material obtained with the 2.5-meter du Pont Telescope at Las Campanas. The wide field and faint limiting magnitude of this telescope make it an ideal instrument for use in this project.

*Survey for
Low-Metal-Abundance Stars*

Preston and Shectman have continued the H-K objective-prism search for low-

metal-abundance stars at high galactic latitudes with the Palomar 46-cm Schmidt. Approximately 800 \square° have been covered to a limiting magnitude of $B \sim 13$ to 14. Slit spectra of 200 candidate objects with weak H and K lines have been obtained with the SIT spectrograph of the 5-meter telescope and the IT spectrograph of the 2.5-meter du Pont Telescope. Preliminary analysis of these spectra has led to the identification of some 40 metal-deficient stars, only one of which may be more metal-deficient than M92. The remainder of the sample consists of a variety of hot stars, peculiar objects, H-K emission stars, and "mistakes." In addition to the metal-deficient candidates, more than 700 A-type stars have been found, the great majority of which are probably halo and old-disk horizontal-branch stars. A program to determine radial velocities, rotational velocities, and metallicities of a sample of these stars has been initiated at the coudé spectrograph of the Mount Wilson 2.5-meter telescope with Shectman's Varo-RETICON detector.

GALAXIES

Globular Clusters in M31

In last year's Report, Searle and Zinn gave an account of their program designed to map the spatial distribution of globular clusters of different metal abundance within the Galaxy (see *Year Book* 75, p. 299 and *Year Book* 76, p. 144). Searle has this year completed observations on a parallel program designed to study the structure of the globular cluster system of M31. Low-resolution spectral scans of the integrated light of 200 clusters in M31 have been obtained. A few of the objects studied turn out to be remote galaxies and nearly 20% of them prove to be young clusters. The remainder appear to be bona fide globular clusters of the Galaxy's spheroidal population.

The metal abundances of these clusters can be obtained from reddening-independent characteristics of their integrated spectra. After setting up an abundance classification by intercomparison with the globular clusters of the Galaxy, Searle finds that for the inner clusters in the two systems (those within 5 kpc of the centers of their parent galaxy) the distribution over abundance is the same in the Galaxy and in M31. An abundance gradient is also present in both systems, being particularly pronounced in the distance range between 3 and 10 kpc. For clusters more remote than 10 kpc, the distribution over abundance is, in both galaxies, independent of galactocentric distance. The average metal abundance of the outer clusters

belonging to M31 is 3 times greater than the average for the Galaxy's outer clusters, but the mathematical form of the abundance distribution for these clusters is the same in both systems—the probability density falls exponentially with increasing metal abundance. These facts appear to be consistent with the picture of halo formation that was outlined by Searle and Zinn in *Year Book* 76 (p. 144) and to suggest that in the halo-forming phase roughly 3 times as much protogalactic gas condensed into stars in M31 as was the case during the similar phase of evolution of the Galaxy. What is novel about this view is the idea that the essential reason that the outer halos of galaxies are metal poor is that fragments located on the outer fringes of the collapsing cloud of protogalactic fragments could lose mass to the intergalactic environment.

The spatial distribution about the center of M31 is very similar for the metal-rich and for the metal-poor subsystems of globular clusters. There is no tendency for the metal-rich clusters to be confined to the galactic disk. This situation appears to be incompatible with the long-held view that metal-rich clusters formed out of gas that had *already* collapsed to the fundamental plane. The implication appears to be that a high degree of chemical enrichment occurred *before* galactic-scale dissipative processes became important.

Near-infrared photometry of 35 clusters in M31 was obtained by Persson and Dr. Jay Frogel of Cerro Tololo Inter-American Observatory on the 5-meter telescope. The $V - K$ colors were corrected for reddening by using a reddening parameter from Searle's spectrophotometric optical measurements. The corrected $(V - K)_0$ colors correlate extremely well with Searle's reddening-free metallicity parameter Q_K . This allows a calibration of Q_K in terms of $[\text{Fe}/\text{H}]$ by use of a $V - K/[\text{Fe}/\text{H}]$ relationship for galactic globular clusters. The M31 clus-

ters range from twice solar to more than 100 times less than solar metal abundance.

Comparison of the M31 infrared data with the colors of early-type galaxies illustrates a problem in stellar population synthesis: galaxies are considerably redder and have stronger CO absorption than even the most metal-rich M31 clusters. The red stars which must therefore be present in the galaxies but not the clusters also contribute strong $2\text{-}\mu$ H_2O absorption. These stars could be members of a super-metal-rich population or are asymptotic giant-branch stars that for some reason are under-represented in the clusters.

Spiral Structure in M33

The highly resolved bright stellar content of the Local Group galaxy M33 [Sc II–III; $(m - M)_v = 24.65$] permits a study of spiral structure unattainable for any other galaxy; the system is so close. The brightest red and blue supergiants are easily identified to $V = 22$ ($M_V \simeq -2.7$), as are H II regions, Cepheids, irregular red and blue supergiants, variables, planetary nebulae, novae, and star clusters. The color-magnitude diagram for the supergiants in M33 has been obtained by Dr. Roberta Humphreys, guest investigator from the University of Minnesota, and Sandage so as to improve the absolute magnitude calibration of the first-ranked red and blue stars, which, together with that of the Cepheids, forms the basis to refine the distance scale beyond the Local Group. To obtain the M33 CM diagram, Humphreys and Sandage have produced a catalog of the bluest and reddest Population I stars brighter than $B \simeq 20$ (complete to $B \simeq 18.5$) by blinking plates that cover the face of M33 in six fields taken in B and V with the Palomar 5-meter reflector in 1955. More recent plates taken with the Kitt Peak 4-meter Mayall Telescope provide a complete coverage of the galaxy on single plates

in each color (but with reduced scale), and the catalog was verified by a second blinking of this new material. Argelander stepscale photometry was used to obtain B and V magnitudes for ~ 300 red stars and ~ 600 blue stars relative to the two photoelectric sequences set up previously (*Astrophys. J.*, 191, 63, 1974). The catalog provides candidates from which Humphreys expects to obtain classification spectra so as to separate the many foreground stars from the M33 supergiants. It is certain that *blue* supergiants exist in M33 to an upper limit at least as bright as $V \simeq 16.6$, but the true limit, which may be as bright as $V \simeq 15.8$ (or $M_v = -8.8$), must be found from the spectroscopic survey, which is the next step. The brightest *red* supergiants may have $V \simeq 16.6$ ($M_v = -8.0$), but again a spectroscopic study to be started by Humphreys in September is required to determine this important upper limit.

The data also clearly show that the youngest stars form a series of broad spiral patterns in M33 that are outlined by discrete associations, similar to those known in the solar neighborhood of the Galactic system. A total of 141 associations have been identified by Humphreys and Sandage, as shown in Fig. 2. Comparison of the spiral patterns traced by these young associations with the distribution of dust and of the H II regions is in progress and is expected to show the spatial positions of the dust relative to the regions of most recent star formation. The color-magnitude diagrams of the individual associations are being determined by Sandage and Humphreys and are expected to show the time distribution of the episodes of star formation over the past 5×10^7 years. Furthermore, the luminosity functions of each association, when summed over the total sample, should permit calculation of the mass budget of the very young Population I component. Comparison with the known present total mass of the H I gas (from 21-cm radio data) should deter-

mine the recycling rate and hence the lifetime of future star formation. Can M33 maintain its present late-Hubble type (many resolved stars) for a long future time, or will it soon become a nearly unresolved earlier Hubble type galaxy with many fewer Population I supergiants?

The survey catalog of the red and blue supergiants, together with large-scale finding charts, is being prepared for publication by Humphreys and Sandage as the first part of their study of spiral structure in M33.

Las Campanas Survey of Southern Galaxies

Accurate Hubble types are still inadequately known for many bright galaxies, especially in the Southern Hemisphere. To improve the situation requires classification plates to be taken with large telescopes of long focal length that provide an adequate plate scale (e.g., $\leq 20'' \text{ mm}^{-1}$). The requirement of large scale is especially important for determining the luminosity classes of spirals and the inner structure of galaxies of all types with high surface brightness.

Classification studies are important for many current problems related to the formation and evolution of galaxies, such as:

1. What is the gas content (e.g., neutral hydrogen from 21-cm observations) of E galaxies compared with S0 and early Sa systems; are there systematic differences in the mean gas density that depend on galaxy type for these very early systems?
2. Are there morphological differences in the S0 galaxies in great clusters compared with S0's in the general field?
3. Are there differences between the early Sa smooth-arm spirals in the great clusters and the many such galaxies found in the general field?
4. Is the distribution of flattening of disks the same for S0's and the early-type spirals, or is there a progression of

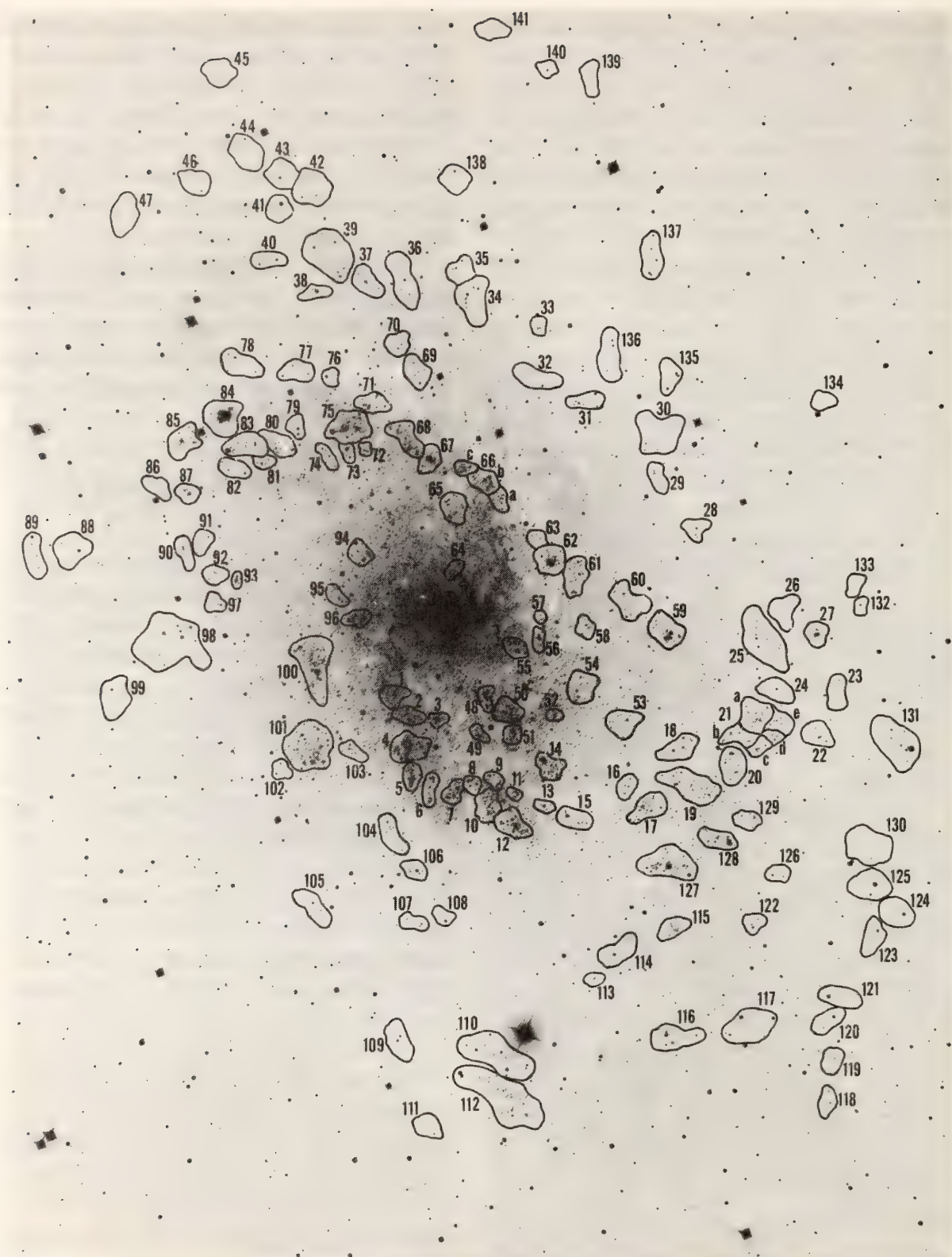


Fig. 2. Associations of blue stars in the galaxy M33, which is in the Local Group. The blue stars were found by blinking blue and red plates taken with the Hale 5-meter reflector. The photograph here is from the Mount Wilson 2.5-meter reflector, so as to show the entire galaxy. The association boundaries enclose the highest concentration of blue supergiants in each clustered area and define the same type of region of coeval star formation as the associations in our own Galaxy. The spiral pattern is clearly outlined by these associations.

increasing flattening as one proceeds from S0 through Sa to the Sc and Sd types?

Questions 2, 3, and 4 are related to the current question of the possible effects that environment (i.e., sweeping out of gas and dust by collision) has in determining the Hubble type at the present epoch, as contrasted to a picture that the type is determined at the time of formation by a variation in the ratio of the initial rate of star formation to the free-fall collapse time from a larger volume. If the latter picture is correct, then the amount of free gas left in the disk immediately after collapse would determine the Hubble type (cf. Sandage, Freeman, and Stokes, *Astrophys. J.*, 160, 831, 1970).

Adequate galaxy classifications are needed to approach these problems. (For example, several current studies of the gas content of "S0" galaxies are erroneous because the catalogued galaxy types are, in fact, in error.) Sufficient plate material exists for only about 70% of the northern Shapley-Ames galaxies from survey programs that have been in progress with the Mount Wilson 2.5-meter Hooker reflector since the 1920's and the Palomar 5-meter Hale Telescope since 1950. Similar data are even less complete for southern galaxies. To study questions of formation and evolution, Sandage, Brucato, and Dressler have begun a galaxy survey with the du Pont 2.5-meter reflector on Las Campanas. The aim is to determine types for all galaxies south of $\delta \simeq +20^\circ$, for which there is no adequate plate material. The first results for 30 southern systems (mostly spirals), obtained from plates taken by Dressler during engineering tests of the du Pont reflector in August 1977, have been published (Dressler and Sandage, *Publ. Astron. Soc. Pacific*, 90, 5, 1978).

A second list containing new types for an additional 153 southern galaxies is being prepared for publication by Sand-

age and Brucato, based on plates taken by Brucato from 1973 to 1978 with the 1-meter Swope reflector and by Sandage during the February 1978 dark run with the du Pont reflector. Examples of the classification plates from the 2.5-meter telescope are shown in Figs. 3 and 4. The scales of the prints are given by the north arrow, which is 60" long. The image size on at least one third of the plates is less than 0.6", which indicates the very high quality of the seeing at Las Campanas and the close tolerance of the du Pont reflector. The exposure times to reach a sky density of 0.7 on the plates taken at the f/7.5 Cassegrain focus were 45 min on 103a-O plates, baked in forming gas (4% mix of H with N₂) for 3 hours at 65°C. Encouraged by these results, a routine classification survey of all bright Shapley-Ames galaxies that can be reached from Las Campanas has been started; it is expected to result in a general photographic atlas at the end of the program.

Peculiar Galaxies in the Southern Hemisphere

Arp and Dr. B. Madore (the latter now at the University of Toronto) have examined more than 40,000 galaxies on the U.K. Schmidt, IIIa-J Southern Survey. They have catalogued positions and descriptions of about 8% of them in the Catalog of Southern Peculiar Galaxies and Associations. One or two more years should see the completion of the southern sky survey and the completion of the Arp-Madore Catalog.

Meanwhile, some of the best examples of interacting galaxies, ring galaxies, and peculiar associations in the Catalog have been investigated by observers in Australia and in Chile. Arp has obtained about 250 spectra with the image-tube spectrograph on the 2.5-meter du Pont. He concentrated on galaxies with interacting companions, but also in collaboration with Miss Jane Few has observed some of the larger ring galaxies. The

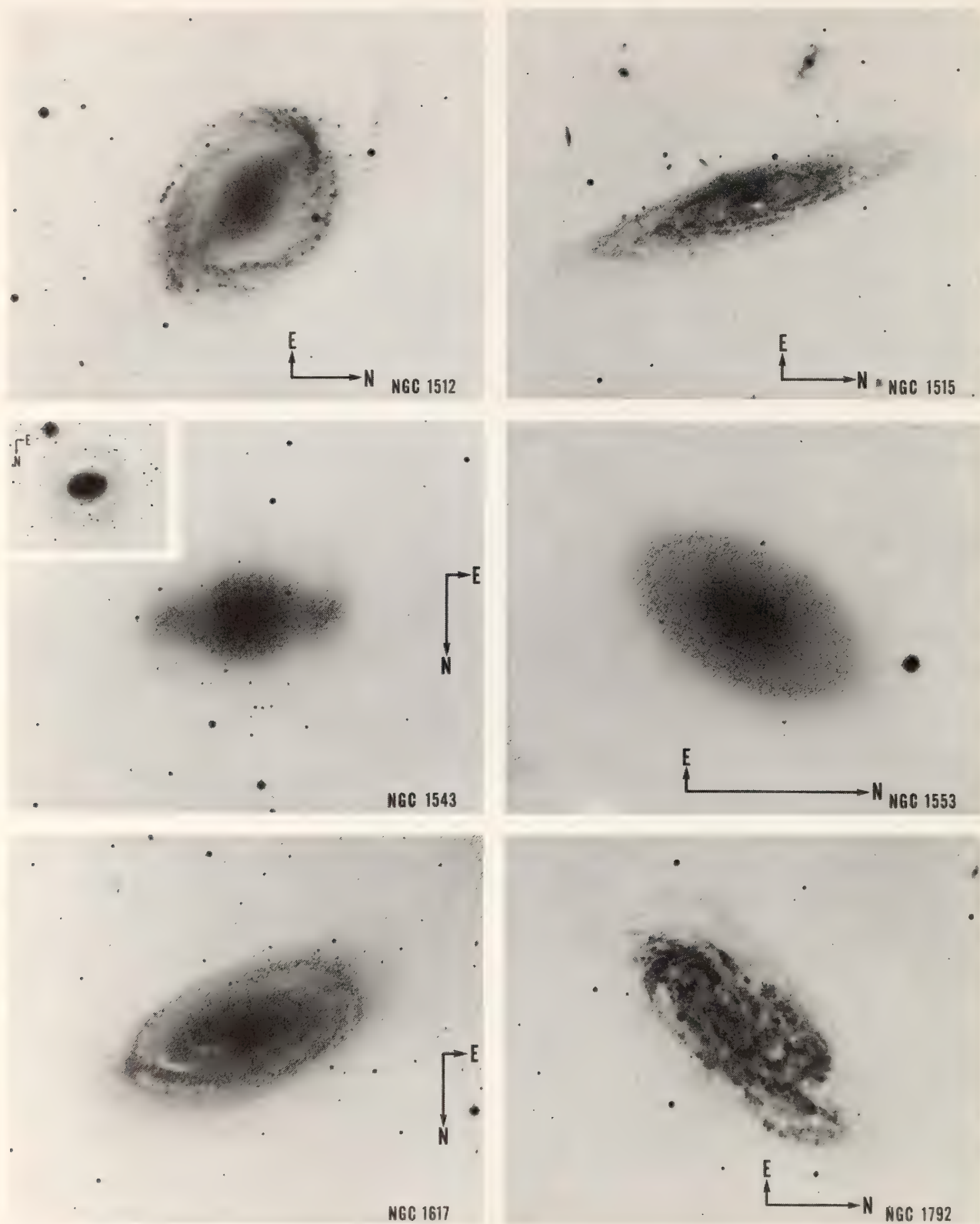


Fig. 3. Representative classification photographs of galaxies taken with the du Pont 2.5-meter reflector at Las Campanas. Scale of the prints is shown by the north arrow, which has a length of 60". Star images on many of the original plates are less than 0.8" in diameter, indicating the excellent quality of the telescope optics and the remarkable phase stability of the atmosphere (the seeing) at the site.

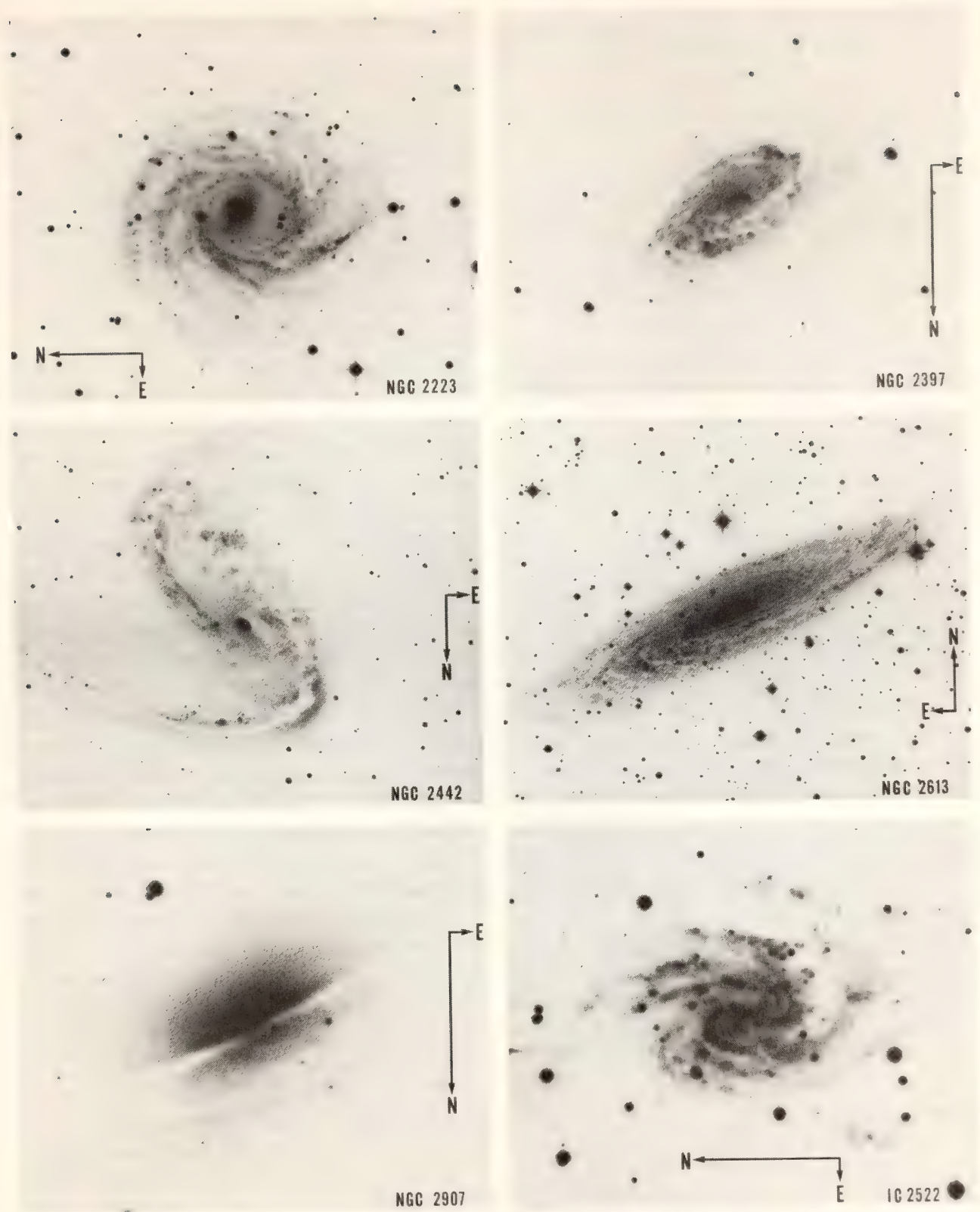


Fig. 4. Same as Fig. 3. The fine detail of the internal dust patterns and the resolution of the stellar content in some of the late-type (Sb, Sc, and Sm types) galaxies photographed in the general survey, of which these photographs are representative, are important aspects in both the current classification studies and the problem of the distances to galaxies.

spectra have now been entirely measured, the last half with the assistance of Louise Lowen. The redshifts and spectral features are currently being collated by Arp. The initial publication will consist of redshifts of central and companion galaxies in various kinds of groups and associations.

*Galaxies of Bright Apparent Magnitude
and Their Fainter Companions*

On August 31, 1978, a three-year study of companion galaxies associated with bright spirals will be ended. The study has been a cooperative project between Arp and Sulentic of the Hale Observatories and Padova University, Italy. The program has been supported by a grant from the Division of International Programs of the National Science Foundation. One paper has been published (*Astrophys. J.*, 220, 47, 1978) in which all interacting double and multiple galaxies were analyzed in 99 galaxy fields and an equal number of control fields. The major result of that paper, that a large percentage of Sb and Sc spirals have physically associated nonequilibrium companions, is now being followed up. The characteristic parameters of these physical associations will be important in determining the answer to the questions of galaxy evolution and origin. If, for example, all the galaxies had been formed at the same time and the companions to the spirals were merely residues of the initial formation, there should be many older, equilibrium-form companions in a variety of orbits around the central spiral. It is difficult to see at this point in the analysis why so many should be disturbed, double- and multiple-interacting systems. Further, it is unlikely that the observed distribution of these systems along the minor axis of the central spiral galaxy could be explained by a conventional picture. Perhaps the most promising solution is the decade-old suggestion of E. Holmberg that the companion galaxies origi-

nate in an ejection process within the central spiral. In order to decide the important question of the origin of these companion galaxies, Sulentic and Arp have compiled spectra and photometry of all the companions. This material will allow analysis of the kinematics and may yield information on the state of evolution of the companions.

Dwarf Spheroidal Galaxies

During the 1950's, Baade, with the assistance of Henrietta Swope, demonstrated that the stellar populations of the dwarf spheroidal galaxies closely resemble those of globular clusters. This was most clearly illustrated by Baade and Swope's work on the color-magnitude diagram of the Draco galaxy (see *Year Book 57*, p. 71), which has motivated many subsequent investigations of these galaxies, including one by Zinn that was completed in the past year.

With the multichannel scanner of the Hale Telescope, Zinn has obtained observations of a large fraction of the brightest red giants in Draco ($M_v \leq -1.4$) in an attempt to understand why Draco's giant branch is wider than the giant branches of most globular clusters in the color-magnitude diagram. These observations confirm the unusual width of Draco's giant branch, for comparisons of the spectral energy distributions of the stars, as measured by the scanner, reveal large star-to-star variations that agree well with the difference between Baade and Swope's measurements of $B - V$. By means of a comparison with Searle and Zinn's observations of globular cluster stars (*Year Book 76*, p. 144), Zinn has derived estimates of the metal abundances of the Draco stars. The variations in the spectral energy distributions of the Draco stars appear to be due to a range in metal abundance of about a factor of 3. For the mean metal abundance of Draco, Zinn obtains a value of $[\text{Fe}/\text{H}] = -1.86$, which is a somewhat larger value than other in-

investigators have found from observations of far fewer stars.

The existence of an abundance range in Draco poses an interesting problem for the theory of the formation of galaxies and clusters from clouds of gas. The mass of Draco, $\sim 10^5 M_\odot$, is similar to the masses of many globular clusters that, with the notable exception of the cluster ω Centauri, have no detectable ranges in metal abundance. Zinn has constructed models that can explain the metal-abundance distribution within Draco if the gas cloud that became Draco lost roughly 99% of its mass through supernova explosions or some other mechanism during its collapse. To explain the uniform compositions of globular stars, these models require that even larger amounts of mass be lost than in the case of Draco, which seems to be incompatible with the fact that the globular clusters have much larger escape velocities than Draco. While this difficulty clearly demonstrates the need for more sophisticated models, it also suggests that further investigations of globular clusters and dwarf spheroidal galaxies may provide demanding tests of such models.

Nuclei

Mochnecki has obtained direct images of the nuclei of a number of bright spiral and Seyfert galaxies, using Oke's CCD detector on the 5-meter telescope with the digital spectrograph serving as a focal reduction camera. He has found the apparent true nucleus of NGC 2903, the center of which contains a group of very bright knots. The nucleus is much redder than the H II regions around it and is prominent in the *I* passband. Several bright Seyferts have been observed in a search for small center barlike features similar to the ones already found in NGC 4736 and NGC 1068. Mochnecki is developing computer programs to analyze isophotal contours and to per-

form image smoothing and interpolation using digital Fourier transforms.

Intensity Profiles

Dressler has completed an analysis of the intensity profiles of several thousand galaxies in 12 rich clusters, taken from his thesis work. Using a Hubble law to parameterize these light distributions, he finds the quantity $(-2.5 \log I_0 - 5 \log a_0)$ to be a well-defined function of galaxy absolute magnitude. As a result the average surface brightness within an isophote of 23.5 *V* mag \square''^{-1} (for example) increases monotonically with increasing absolute magnitude at a rate of Δ surface brightness/ $\Delta M \approx 0.3$ for galaxies with *M* fainter than *M**. For galaxies brighter than *M**, the trend rapidly abates and perhaps reverses. Dressler and Sandage are evaluating the implications and potential applications of these results for the problem of galaxy structure as a function of galaxy mass.

Supermassive Object in the Center of M87

Evidence has been reported for a small, dark mass concentration in the center of M87, an elliptical galaxy in the Virgo cluster that is well known for its jet, as well as for being a radio and x-ray source. Young, Westphal, Kristian, C. P. Wilson, and F. P. Landauer of the Jet Propulsion Laboratory studied the surface brightness distribution of the galaxy, using SIT and CCD detectors. They confirmed earlier reports of a bright, barely resolved central luminosity spike and, in addition, found a less obvious but definite excess of luminosity over the central 10'' core, which is not compatible with standard isothermal dynamical models.

In April 1976, a group consisting of Sargent, A. Boksenberg and K. Shortridge of University College London, C. R. Lynds of Kitt Peak National Observatory, and F. D. A. Hartwick of the

University of Victoria combined to make spectroscopic observations of M87 with Boksenberg's IPCS detector attached to the Cassegrain spectrograph on the KPNO 4-meter telescope. Several spectra were obtained with a slit 102" in length centered on the nucleus of M87 or on a point 102" east or west of the nucleus. Spectra were also obtained of the sky background 1° south of M87. Following the discovery by Kristian, Westphal, and Young of a light spike in the center of M87, these spectra were analyzed by Caltech graduate student Peter Young during the summer of 1977 in order to determine the velocity dispersions σ_v as a function of radius for the stars in M87. Young used the Fourier techniques which had earlier been developed by Sargent, Schechter, Boksenberg, and Shortridge (*Astrophys. J.*, 212, 326, 1977). At the same time, similar observations of the more normal E1 galaxy NGC 3379, which had been obtained by Sargent and Boksenberg at the coudé focus of the Hale Telescope in April 1977, were analyzed by the same method. Both M87 and NGC 3379 showed a slow falloff in σ_v with increasing radius entirely in accord with appropriately chosen King models. However, in M87 the velocity dispersion rose rapidly in the central 10" arc radius in a manner which could not be explained by such a model.

The combined photometric and spectroscopic data were used by both groups of observers to show through model-independent analysis that the nucleus of M87 contains a compact mass of low luminosity, with $M = 5 \times 10^9 M_\odot$, $r < 100$ pc, and $M/L > 60$ (compared with $M/L > 6$ for the rest of the galaxy). The investigators believe that the combined spectroscopic and photometric data on M87 provide the strongest direct evidence yet presented for the existence of a collapsed supermassive object—presumably a black hole—in the center of an active galaxy. All of the existing data are well fitted by a King model

containing a central black hole of 3×10^9 solar masses and a central point luminosity source. While such a model is not uniquely required by the data, it is as plausible as other possible explanations for a very unusual phenomenon. Computations by Young indicate that a nuclear black hole, by consuming mass lost from stars, could plausibly provide the energy for the radio and x-ray output of the galaxy.

In April 1978, Sargent, Boksenberg, and Stuart Arnold (also of University College London) used Boksenberg's speckle camera at the Cassegrain focus of the Hale Telescope in order to try to obtain information on the light distribution of the nucleus of M87 and the brightest knot in the optical jet down to a scale of 1/50", the diffraction limit of the telescope. Preliminary reductions show that the observations were successful and that both the nucleus and the jet of M87 contain very small components; however, at the end of the report year the data had not yet been compared to theoretical models.

In related work, Sargent combined with A. C. S. Readhead, M. C. Cohen, and K.-Y. Lo of the Owens Valley Radio Observatory in order to make VLBI observations of M87 to search for a very small component in the nucleus. Two 8-hour observing sessions were assigned to this project on the JPL Deep Space Network 64-meter dishes at Goldstone and Madrid in May 1978. Preliminary reductions have shown that fringes were obtained, but no information is yet available on the radio structure of M87.

In further work on M87, Sargent, Young, and Boksenberg made spectroscopic observations of the nucleus with the IPCS at the Cassegrain focus of the Hale Telescope in order to try to determine the radial run of velocity dispersion on a scale of 1". This would represent a considerable improvement over the earlier Kitt Peak observations. Owing to technical difficulties, the data have not yet been reduced.

Dynamics and Structure of Elliptical Galaxies

Dr. Paul L. Schechter of the University of Arizona and Gunn have completed observations at 3 Å resolution with the SIT spectrograph at the 5-meter Hale Telescope of 12 relatively nearby elliptical galaxies to measure velocity dispersion and rotation. They confirm Illingworth's recent discovery that ellipticals are in general not rotating as rapidly as their flattening would suggest, the typical ratio of rotation velocity-to-velocity dispersion being less than half that required in simple single-component models such as those of Wilson and of Prendergast and Tomer. During the coming year, models will be constructed in an effort to fit the data; it is clear that either multicomponent models or models with a third integral, or both, will be required. In addition, there is weak evidence that the velocity dispersions are not decreasing with radius, which suggests that the mass-to-light ratios are *increasing*. This is almost certainly required for the elliptical NGC 4278, for which a crude rotation curve is available from 21-cm data in its hydrogen disk.

Schneider and Gunn have completed a photometric and dynamical study of the remarkable system Zw Cl 0257 — 35, the central "galaxy" of which is an amorphous luminous mass containing seven nuclei with elliptical-like colors and spectra. The total mass and luminosity of the system is similar to that of cD galaxies, and the friction estimates, which can be rather carefully done with data of the quality obtained, yield total lifetimes of order 10^9 years; the system may then well be a progenitor of a cD system of the sort that Morgan and collaborators have found in small groups.

Velocity Dispersion in cD Galaxies

Dressler obtained spectra of the envelope of the cD galaxy in A2029 out to

a distance of approximately 100 kpc. The data, acquired on two nights on the Hale 5-meter with the SIT digital spectrograph, have been analyzed, using an SIT data reduction program written by Dressler and a Fourier spectral analysis program by Rose. A preliminary evaluation of the data indicates that the velocity dispersion out to 100 kpc is not decreasing with increasing radius, as constant mass/light ratio models predict, and on the contrary may even be increasing. The aim is to produce a model representing the run of mass/light ratio, using the velocity-dispersion and luminosity profile data.

Radio Galaxies

Yee and Oke have analyzed spectrophotometric observations, obtained with the multichannel spectrometer, of 26 3CR radio galaxies. The spectral characteristics of these objects range from very strong and broad emission line N-galaxies to normal E-type galaxies with only absorption lines. Each spectral energy distribution is decomposed into two components; one component is a normal galaxy spectrum, while the other is a power-law spectrum. Balmer emission-line intensity is well correlated with the power-law luminosity in the optical spectrum, suggesting that photoionization by Lyman continuum photons followed by recombination is the dominating mechanism. In most cases the power-law models derived provide enough ionizing radiation to account for the Balmer-line strengths; in those cases that do not fit, there is some evidence for an additional ultraviolet-radiation source that can provide the ionizing radiation.

Seyfert Galaxies

Oke and Caltech student Tod R. Lauer are in the process of analyzing the emission-line spectrum of Markarian 79, a type I Seyfert with strong Fe II lines.

Observations were made with the digital spectrograph on the 5-meter Hale Telescope. It was assumed that all permitted lines had the same broad profile as $H\beta$, while the forbidden lines had the narrower profile of the [O III] lines. For each section of spectrum, a list of expected lines and their wavelengths was drawn up. The spectrum was then synthesized, using a linear-regression subroutine. The only variables allowed were the individual line intensities. Intensities were determined for nearly 60 lines. Forbidden lines of [O I], [O II], [O III], [S II], [Ne III], [A IV], [Fe VII], [Ca V], and [N II] were measured, as were permitted lines of H I, He I, He II, and Fe II. The analysis of MKN 79 and a similar analysis of I Zw 1 show that the Fe II lines have broad profiles like the Balmer lines. Presumably the Fe II lines are formed in the same gas as the Balmer lines. The electron density in this gas is about 10^9 – 10^{10} cm $^{-3}$. The absence of [Fe II] lines rules out much lower densities.

Oke has obtained a pair of spectra of the BL Lacertae-type object I Zw 187 (1727+5015) taken 2" south of the nucleus. These spectra show a typical elliptical galaxy spectrum with absorption lines. The redshift is 0.055 ± 0.0003 . This object is similar to 3C371 and BL Lacertae in several respects: (1) all objects have extremely weak or absent emission lines, (2) the underlying galaxies are of similar luminosity within a factor of 2.5, (3) the nucleus in all objects is characterized by a power-law spectrum of the form $f_\nu \propto \nu^{-1.6}$, and (4) the luminosity of the power-law component is comparable in all objects except that BL Lac at its brightest is much more luminous than the other two.

De Bruyn and Sargent completed work on a catalog of spectra for 68 Seyfert galaxy nuclei. The data were gathered on a total of 19 nights over a 4½-year period, using the multichannel spectrophotometer on the 5-meter Hale

Telescope. For each of the 68 objects, the absolute spectral energy distribution is given at a resolution of 20 Å in the blue and 40 Å in the red. A total of 270 bands cover the wavelength range from 3140 Å to 10,680 Å. Special attention was paid to the calibration of the spectral scans, using the prime multichannel standards. On the basis of the extensive material available on the standard stars, it was decided not to use the standard HD 84937 to calibrate Seyfert scans, since it is suspected that its absolute calibration is off, with respect to the other standards, by about 0.1 mag. The spectra in the catalog are believed to be accurate to an absolute level of about 0.05 mag. Of the 68 Seyfert galaxies in the catalog, about 50 are of type I, about 15 are of type II, while several objects have an uncertain classification. A start has been made with the interpretation of this large body of data. The emphasis will be on the shape of the continuum and possible correlations between the continuum and the broad and narrow emission lines. It is hoped that this will shed some light on the nature of the different types of Seyfert galaxies and will produce some valuable input to photoionization models of the emission-line region.

To investigate the extent of the emission-line region in Seyfert galaxies, de Bruyn and Sargent continued spectroscopic observations of about 10 Seyfert galaxies with the SIT digital spectrograph at the 5-meter Hale Telescope. A long slit was used positioned at various offsets from the nucleus. It was found, not unexpectedly, that the broad component of the permitted lines in galaxies of type I is always unresolved at the telescope. The narrow forbidden lines, of which the [O III] 4959, 5007 Å lines are invariably the strongest, usually come from a region of several arcseconds across and in some cases can be traced over a sizable part of the galaxy. The width of these forbidden lines outside

the nucleus is less than that of the lines originating in the nucleus in the few cases where this could be established. To investigate whether this gas has been expelled from the nucleus or is due to the effects of nuclear activity on a surrounding disk of gas, 21-cm line observations are planned for several of these galaxies. This is done in collaboration with Dr. E. Meurs of Leiden Observatory.

Spectral Variability of Seyfert Nuclei

It has long been known, from broad-band *UBV* photometry, that the continuous light from the nuclei of Seyfert galaxies is variable in intensity on time scales of months to years. Conclusive evidence has been obtained recently that the broad Balmer emission lines also do vary in intensity, although quantitative data on the line variations are lacking. In an attempt to learn more about these variations, and in particular the relation between the line and continuum variability, de Bruyn continued a program of spectral monitoring with the multi-channel spectrometer of a subset of type I Seyfert galaxies taken from the sample of 68 galaxies described above. The wavelength range and resolution and the diaphragm size of the new spectra are identical to those used for the first-epoch spectra contained in the catalog of 68 objects. Thus far, two or more scans are available for 15 objects. The most extensive data is available for the galaxies NGC 3516 (four scans) and NGC 7469 (five scans). The shortest time span between the observations of a single galaxy is about 6 months. The reduction and analysis of this data is still in progress. However, some very interesting preliminary results are already available. More than half of the galaxies in the program have exhibited large variations in their blue-violet light output with the maximum recorded variation being 1.30 mag. The variations in the red-wavelength region are always

much less than in the blue part of the spectrum. Straightforward subtraction of spectral scans indicates that the variable continuum has an approximately flat spectrum [$\alpha \sim 0$, where α is defined as in (flux density) \propto (frequency) $^\alpha$], which explains the hardening of the overall spectrum during phases of high brightness. Significant variations have also been observed in the intensity of the broad emission lines, in contrast to the strong but narrow [O III] 4959, 5007 Å lines, which were never found to vary. Usually the variations of the line and continuum are in the same sense. The relative changes in the line intensities are considerably less, in general, than those of the blue-violet light around 3500 Å. To give a typical example: between June 1977 and June 1978, the H α intensity of NGC 3516 decreased by 25% while the continuum at 3500 Å decreased by 53% (0.83 mag). In one instance, however, a strong 80% increase of the H α intensity was accompanied by only a modest 15% increase in the blue-violet continuum. Significant variations have also been observed in the intensity of the broad He I, He II, and Fe II multiplet lines, although their relative variations are less well determined because of their intrinsic faintness. From the present limited data it is already evident that a proper documentation of the variability characteristics will require observations to be made at approximately one month intervals. Such an observing program is being considered.

Survey of Emission-Line Objects

Several years ago, the late F. Zwicky examined 1.2-meter Schmidt plates of two fields in the southern extension of the Virgo cluster in order to identify compact galaxies in a systematic way. The objects in these fields constitute a "Ninth List" of compact galaxies, which is being prepared for publication by Sargent and Kowal. Some of the more in-

teresting blue objects in the Ninth List have been observed spectroscopically by Dr. A. W. Rodgers of the Mt. Stromlo Observatory. During 1977–78, objective-prism plates were obtained of both of these fields by the U. K. Schmidt Unit at Siding Spring Observatory in Australia. These plates were scanned by Kowal who produced a list of about 150 emission-line objects. (Practically none of these coincided with the compact objects selected earlier by Zwicky!) In

March 1978, Sargent and Dr. Daniel Kunth of the European Southern Observatory devoted six nights on the Las Campanas 2.5-meter telescope to obtain higher dispersion spectra of Kowal's candidates. They found 19 QSO's with redshifts ranging from $z_{\text{em}} \simeq 2$ up to $z_{\text{em}} = 3.14$ and 10 emission-line galaxies of high excitation. Sargent and Kunth are studying the spectra of four of these galaxies in detail in order to obtain their He/H abundance ratios.

CLUSTERS OF GALAXIES

Compact Groups

Rose is studying the mass-to-light ratios of galaxies in very compact groups similar to Stephan's Quintet. In previous work he found that compact groups are generally surrounded by a looser system of 2–3 additional galaxies. To understand this configuration, he conducted an observational search for evidence of past gravitational encounters between group members, such as would be expected if the groups have been compact during the Hubble time. In particular, a search was made for the presence of diffuse background light in the groups composed of material tidally stripped from the group members in two-body collisions. No evidence of such a diffuse light was found in the two compact groups studied, thus indicating that these systems are transient configurations only occasionally forming within looser groups. N -body simulations of galaxy groups were used to develop a modified virial theorem that could be applied to the compact systems yielding a determination of the overall group mass-to-light ratio. This modified virial theorem was then applied to two compact groups studied in collaboration with J. A. Graham of Cerro Tololo Inter-American Observatory, yielding mass-to-light ratios of 4 and 24.

A program is now underway to measure

M/L for several more compact groups, using radial-velocity data taken with the 5-meter SIT digital spectrograph. Reduction of the two-dimensional digitized spectra to one-dimensional wavelength-calibrated form is accomplished using a reduction system written by Dressler. The radial velocity as well as the internal-velocity dispersion of a galaxy is then found, using a Fourier transform cross-correlation program written by Rose. Altogether the velocities of 15 galaxies in five groups have been obtained. A number of standard galaxies with well-known velocities have also been measured to test the accuracy of the SIT Vidicon and the data-reduction system; an accuracy of $\sim 30 \text{ km s}^{-1}$ has been achieved with data taken at a dispersion of 3 \AA pixel^{-1} . Relative magnitudes for the group members will be determined, using calibrated 1.2-meter Schmidt plates taken by Rose and Da-Costa. They will also use this plate material to look for diffuse light in the compact groups; with the aid of plate-stacking techniques, they hope to work at light levels as faint as $29 \text{ mag } \square''^{-1}$.

Rose and Searle are testing the validity of an alternative model for compact groups in which the initial condition is that of a loose group of galaxies with high M/L massive halos. When a compact configuration forms in the loose

group, the dark halos merge and are left behind in a more extended distribution than the visible galaxies. In this model, a tendency toward equipartition of energy of group members is expected, as evidenced by mass segregation and a lower velocity dispersion for the more massive galaxies. On the other hand, no energy equipartition would occur if compact groups are just transient configurations of low M/L galaxies in loose groups. Hence a differentiation between the two models can be made on the basis of the distribution of velocities and separations of the group members as a function of mass.

Structure of Clusters

Dressler has obtained plates with the du Pont Telescope of approximately 30 rich clusters of galaxies. A light box/viewer has been constructed, which allows (1) the measurement of X - Y positions of galaxies on the plates, (2) evaluation of their morphological types, and (3) estimation of bulge and total brightness by comparison with standard sequences at Hercules and Coma cluster galaxies. These data will be used to com-

pare the proportions and spatial distributions of various galaxy types in a large number of clusters, with the aim of testing models of galaxy differentiation such as the stripping of spirals to form S0's and the production of ellipticals by the encounters and interactions of disk systems.

Velocity Dispersion in Clusters

De Bruyn, Sargent, and Dr. A. C. Readhead of the Caltech radio astronomy group used the SIT spectrograph at the Cassegrain focus of the 5-meter Hale Telescope to take spectra of 16 galaxies in the neighborhood of NGC 6251. This 14-mag elliptical galaxy was recently identified with a giant, 3-Mpc-size, radio source and has an intense collimated jet emanating from its nucleus. NGC 6251 appears to be lying on the outskirts of a medium compact cluster, but no redshift data were available hitherto to ascertain the membership of NGC 6251 to this cluster. If NGC 6251 indeed is a part of this cluster, its velocity dispersion will be an important parameter in the interpretation of the radio-source structure.

RADIO SOURCES

5C2 Identification Program

Deep red and blue plates of the 5C2 survey area, taken last year by de Bruyn with the 1.2-meter Schmidt at Palomar, have been searched for radio-source identifications by Dr. P. Katgert of Leiden Observatory. A total of 85 radio sources were identified, yielding the high gross identification percentage of 36%. To

provide an absolute calibration of the magnitudes of the stellar and galaxy identifications, de Bruyn used the SIT area photometer on the Palomar 1.5-meter telescope to take a series of exposures, in two colors, of several selected fields within the survey area. The fields were selected to contain many stellar and nonstellar objects over a wide range in magnitude.

QUASARS AND QUASI-STELLAR OBJECTS

Nebulosity Around PHL 1070

The quasar PHL 1070, with $z_{\text{em}} = 0.076$, was shown by Kristian (*Astrophys.*

J. [Lett.], 179, L61, 1973) to be surrounded by a faint nebulosity. Drs. Donald C. Morton and T. B. Williams of

Princeton University, in collaboration with Green, measured the spectrum of this nebulosity, using an annular aperture in the multichannel spectrometer on the 5-meter Hale Telescope (*Astrophys. J.*, 219, 381, 1978). They found the spectrum of the light from this nebulosity to be characterized by a red energy distribution with absorption features consistent with those of a normal galaxy at the redshift of the quasar. In this case, the quasar has been shown to be an active galactic nucleus.

Near-Infrared Spectroscopy of Quasars

An extensive program of near-infrared spectroscopy of quasi-stellar sources has been continued by Neugebauer as the logical extension of the multiyear, multi-wavelength broadband study, from 0.3 to 20 μm , of the continua of these sources. In particular, measurements of $\text{H}\alpha$ in PKS 0237-23 in collaboration with Dr. A. R. Hyland of Mt. Stromlo and Siding Spring Observatory, Australia, and Becklin have been analyzed in comparison with visible spectra, and new measurements of $\text{H}\alpha$ and $\text{H}\beta$ in the quasar B2 1225+31 in collaboration with Soifer have been obtained. The latter spectrum has been analyzed in conjunction with optical spectra obtained by Oke. A preliminary analysis indicates that for both quasars $I(\text{H}\alpha)/I(\text{H}\beta) \sim 3-4$, while $I(\text{H}\alpha)/I(\text{L}\alpha) \sim 1$. The recent infrared measurements are of significance in providing two of the three cases where both $\text{L}\alpha$ and $\text{H}\alpha$ have been measured in a single quasar. The $\text{H}\alpha/\text{L}\alpha$ line ratio is much greater than predicted by simple quasar models, where $I(\text{H}\alpha)/I(\text{L}\alpha) = 1/10$, while the $\text{H}\alpha/\text{H}\beta$ line ratio is consistent with simple recombination line theory. The $\text{H}\alpha/\text{L}\alpha$ ratio is quite similar to that previously measured for the quasar 3C273 (Davidsen, Hartig, and Fastie, *Nature*, 269, 203, 1977) and found indirectly for a "composite quasar spectrum" by Baldwin (*Mon. Notic. Roy. Astron. Soc.*, 178, 67P, 1977). The dis-

crepancy has not been understood and is the source of much theoretical work.

A clue to the origin of the discrepancy may be provided by the infrared data of 3C273, which show a bump around 3.5 μm . A possible explanation is that the dust in the line-emitting region absorbs the $\text{Ly}\alpha$, which is resonance scattered; the dust is heated to $\sim 1000^\circ\text{K}$ and reradiates the flux at 3.5 μm . In fact, the observed flux at 3.5 μm is just equal to that predicted to be present in $\text{Ly}\alpha$ on the basis of recombination theory. Calculations indicate that as little as 1 \mathcal{M}_\odot of dust can account for the observed flux.

Surface Density of Quasars

Results for the surface density of radio-quiet quasars in the 8^h QSO survey field of Sandage and Luyten (*Astrophys. J.*, 155, 913, 1969) were reported in *Year Book 76* (p. 160). Sandage has continued the spectrographic survey of the 15^h field and has paid particular attention to the candidates for variability found by Usher in his important and painstaking study of variable statistics over a 25-year period from plates taken of this region (*Astrophys. J.*, 223, 1, 1978). Usher (in his Table 4) lists 27 candidates for variability from the color class I objects in the original catalog (Luyten, Anderson, and Sandage, *Search for Faint Blue Stars*, XLIII, The Observatory, University of Minnesota, 1967), and 7 additional variable candidates from his supplementary blue objects in the 15^h field. Spectra have now been obtained for 20 of the 27 original catalog objects. Of these, 18 are quasars. Hence, Usher's isolation of blue variables over the base line of ~ 25 years, sampled with nine plates, is 90% effective in finding quasars.

Also important is the reverse question of what percentage of the *total* QSO population is isolated by the survey for variables. Analysis of the spectroscopic search statistics now available for the 15^h field shows that the surface density of QSO's in this area to $B \simeq 18.5$ is \sim

1.6 \square° —the same as in the 8^h field reported last year. Hence, over the 42.7 \square° search area of the 1.2-meter Schmidt field, there are 68 expected quasars. Usher's list of candidates for variability totals 34. If 90% of these are QSO's, he has isolated 31 of the total 67 sample, or 45% by his search for variability. Hence, variability to the limits used by Usher is an effective method of isolating the QSO's from the contaminating white dwarfs at this magnitude level.

Dr. Arthur A. Hoag of Lowell Observatory and Sandage continued their search for much fainter emission-line QSO's, using the nonobjective grating technique at the prime focus of the Kitt Peak 4-meter Mayall Telescope, mentioned in *Year Book 76* (p. 161). Plates were completed on IIIa-J and IIIa-F emulsions at a dispersion of 1500 \AA mm^{-1} in Selected Areas 28, 29, 55, 57, 71, 82, 94, 106, 107, and 118 over an area of 1 \square° in each region. The average discovery rate of QSO's to $\langle B \rangle \simeq 20$ is very high at about 12 per square degree. But the incompleteness of the search at the limit of the plate material ($B \simeq 21$) must be substantial and progressive with apparent magnitude. No redshifts greater than $\Delta\lambda/\lambda_0 = 3.5$ were found. The next step is to calibrate the magnitudes in each Selected Area and to determine the incompleteness of the sample before a reliable QSO-growth function of the form $\log N(m) = am + b$ can be established [where $N(m)$ is the number of QSO's per square degree brighter than m , and where a and b are constants]. It is evident from the work of Green and Schmidt that a is substantially and reliably greater than 0.6. This result, known at magnitude limits brighter than $B \sim 18.5$ from the recent large-area survey by Green, when combined with data to this intermediate magnitude level, now apparently holds to $B \simeq 20$. There is, however, evidence that the number then declines rapidly fainter than $B = 21$. (Hoag's observa-

tions are that he could find no new candidates between $B = 21$ and $B = 22$ when the search on IIIa-F plates at 3000 \AA mm^{-1} was carried 1 mag fainter than for the same area searched at 1500 \AA mm^{-1} .) The implications for cosmology of this result and the failure to yet discover redshifts greater than $\Delta\lambda/\lambda_0 \simeq 4$ is still controversial (is it due to selection effects, or is it real?), and the question is likely to hold an important position in all current survey work by all groups for several years to come, as it is central to the question of the redshift (epoch) of galaxy formation in the evolving Friedman Universe.

The Hubble Diagram for Quasars

Many of the newly isolated quasars in the 8^h and 15^h survey fields have small redshifts ($\Delta\lambda/\lambda_0 < 0.3$). These are useful in discussing again the faint limit-line in the redshift-apparent magnitude diagram for quasars. Sandage has combined the new photometric and redshift data for the complete list of radio-quiet QSO's now known in the 8^h and 15^h fields with older data in the literature to show again that no QSO's lie to the right (faintward) of the galaxy ridge line for massive E systems in the Hubble diagram (to within a spread of 2σ in the apparent magnitude coordinate). This, of course, is the requirement if quasars are events in the nuclei of massive E galaxies, because the combined light (central quasar plus underlying galaxy) cannot be fainter than the underlying galaxy taken alone. Although this was one of the original arguments to show that quasars are at their redshift distances and are events in the nuclei of galaxies, it was discounted by proponents of the local school on the grounds of too small an overlap between the quasar and the galaxy redshift distributions. However, data now exist for many low-redshift QSO's, and Sandage considers the test to be considerably more powerful and positive.

Nonuniform Radial Distribution of Quasars

Preliminary results of the Palomar bright quasar survey have yielded a sample of quasars complete to a mean limiting magnitude of $B = 15.7$ over $1434 \square^\circ$. The derived surface density of $0.0034 \square^\circ^{-1}$ was compared by Green and Schmidt (*Astrophys. J. [Lett.]*, 220, L1, 1978) to the surface density at 18th magnitude from work by Braccesi *et al.* (*Astron. Astrophys.*, 5, 264, 1970) and Sandage and Usher (*Year Book* 76, p. 161). The surface density increases very steeply with magnitude, by a factor of 8.5 per magnitude. Or, if the surface density is of the form $\log N(m) = am + b$, then $a = 0.93$. Assuming that redshifts are cosmological, a uniform space distribution would produce a value of a of 0.35–0.40. The corresponding space density evolution is probably somewhat steeper than that derived for quasi-stellar sources with steep radio spectrum by Schmidt (*Astrophys. J. [Lett.]*, 209, L55, 1976). The steep count gradient is a strong argument against any local hypothesis in which quasars have a uniform space distribution. The latter case would yield $a = 0.60$. The derived value of $a = 0.93$ requires in the local hypothesis that the space density increase with distance, approximately as $r^{1.6}$.

Bright Quasar Survey

Schmidt and Green have continued their spectroscopic observations of high-latitude stellar objects selected for ultraviolet excess. In the last year, 780 objects have been observed, leading to the discovery of 26 new quasars with $B < 16.5$. Approximately half the total survey area of $10,000 \square^\circ$ has now had preliminary coverage. Early indications are that the mean redshift of this sample of quasars is lower than that predicted by the luminosity distribution of the 18th magnitude Braccesi sample, implying a luminosity dependence in quasar space density evolution.

Radio Emission from Optical Quasars

Shaffer of National Radio Astronomy Observatory conducted a search for radio emission at 2.7 and 8.1 GHz from six quasars discovered by Green from his survey for ultraviolet excess stellar objects (*Publ. Astron. Soc. Pacific*, 90, 22, 1978). One of the six was detected at a flux density of 0.048 and 0.045 f.u. in the two bandpasses, respectively, while the rest were not detected above a limit of 0.005 f.u. Assuming identical optical luminosity distributions for radio and optically selected quasars, Schmidt (*Astrophys. J.*, 176, 273, 1972) derived a function to predict the fraction of quasars detectable above a given radio flux density limit for an observed optical flux density. That function predicts one out of four of these objects should have been detected above the quoted limit, in satisfactory agreement with the Shaffer result. Further deep radio searches of optically selected quasars are necessary to determine the true form of the function for small values of the ratio of radio-to-optical flux density.

Quasar Absorption Lines

Sargent continued to collaborate with Dr. A. Boksenberg of University College London on high-resolution studies of the absorption lines in QSO's. This year the main work was devoted to an analysis of the spectra of three high-redshift QSO's that had been obtained by Boksenberg, Sargent, and Dr. R. F. Carswell, also of University College London, with Boksenberg's IPCS detector at the Anglo-Australian 4-meter telescope in November 1976. The objects studied were PKS 2126–158 ($z_{\text{em}} = 3.28$), Q0002–422 ($z_{\text{em}} = 2.76$), and Q0453–423 ($z_{\text{em}} = 2.66$). The spectra covered the range $\lambda\lambda 3800$ –5400 at a resolution of 0.8 Å and were analyzed largely by Sargent and graduate student Peter Young. Rigorous criteria were used to produce lists of absorption lines for each object. Thus, 113 lines were found in the spectrum of PKS

2126–158, 80 in Q0002–422, and 77 in Q0453–423. Absorption redshifts of high statistical significance were found at $z_{\text{abs}} = 2.3938, 2.6381, \text{ and } 2.7685$ in PKS 2126–158; at $z_{\text{abs}} = 0.8366, 1.9886, 2.1683, 2.3018, \text{ and } 2.4641$ in Q0002–422; and at $z_{\text{abs}} = 0.7621, 0.9087, 1.1496, 1.1516, 2.2765, \text{ and } 2.3967$ in Q0453–423. These systems identified essentially all the lines longward of the $L\alpha$ emission line in each object; however, only about 15% of the lines shortward of $L\alpha$ were so identified. It was noted that the absorption redshifts found from this excellent material show no tendency to cluster around the emission-line redshift in each object. The data were used to define particular types of absorption systems containing lines of the heavy elements. These types can be used to study the distribution of absorption systems with redshift in a manner which is essentially free from observational selection effects.

In the spectrum of PKS 2126–158, a cross-correlation between the regions of spectrum below $L\alpha$ and $L\beta$ emission showed a strong peak at the $L\alpha/L\beta$ ratio. This peak has the strength to be expected on the hypothesis that $\sim 90\%$ of the lines shortward of $L\alpha$ emission are single $L\alpha$ absorption with their corresponding $L\beta$ buried in the noise. This supports a conjecture made by C. R. Lynds in 1970.

The result that most of the many lines shortward of $L\alpha$ emission are single $L\alpha$ absorptions makes it possible to perform statistical analyses of the distribution of such systems with redshift in individual objects and also to compare such distributions in different QSO's. Accordingly, Sargent, Young, Boksenberg, and D. Tytler, the latter a graduate student at University College London, embarked on such a study of the three QSO's observed at the Anglo-Australian telescope, together with two additional objects that had been observed at Palomar in previous years. These additional QSO's were PHL 957 ($z_{\text{em}} = 2.66$) and B2 1225+31

($z_{\text{em}} = 2.20$). The results of this statistical analysis of the distribution of $L\alpha$ systems make it virtually certain that the absorption lines are produced by intervening intergalactic gas and that they are not produced in material that has been ejected at high speed from the QSO's. This was shown by a variety of tests involving the distribution of the number of lines per unit redshift and the distribution of the equivalent widths of the lines in each object. Perhaps the most compelling argument was provided by a study of the correlation function between pairs of $L\alpha$ absorption redshifts, which is analogous to the correlation function between pairs of galaxies on the plane of the sky as developed by Peebles and his co-workers. Sargent, Young, and their colleagues showed that this correlation function is flat on all scales from 0.3 Mpc up to 300 Mpc when expressed in terms of the appropriate comoving coordinates. This implies that the lines are produced by uniformly distributed material (in terms of the comoving volume) and it would require an extraordinary coincidence for such a distribution to arise by chance in all the five objects studied if the ejection hypothesis for the origin of the lines were true.

As a result of the foregoing high-resolution work, Sargent, Young, Boksenberg, and their co-workers have made the hypothesis that the heavy-element absorption redshifts found in the spectra of QSO's arise in the halos of intervening galaxies, while the $L\alpha$ systems are of intergalactic origin. This opens up the possibility of direct studies of the halos of galaxies and of intergalactic clouds at large redshifts. Such work should eventually lead to new and unexpected insights into the process by which galaxies are formed and into their early evolution.

In further related work, Boksenberg and Sargent returned to the study of PKS 2337–23 ($z_{\text{em}} = 2.22$), which has been the subject of much past work. This object had been found to have a clump

of absorption lines in its spectrum, which Boksenberg and Sargent identified as a clump of C IV $\lambda\lambda 1548, 1550$ doublets at redshifts near $z_{\text{abs}} = 1.65$. The width of this peak in the redshift distribution was $\Delta z_{\text{abs}} \sim 0.07$, which would correspond to an angle of about 1° on the plane of the sky if produced by cosmologically distributed intervening matter. Accordingly, Sargent and Boksenberg requested an objective-prism plate of the region around PKS 0237-23 in order to search for other QSO's within 1° of that object. Fifteen candidate QSO's were found and seven of those were observed at low resolution by Sargent at Palomar and by Boksenberg at the Anglo-Australian telescope in January 1978. Six of the candidates were confirmed to be QSO's, all with redshifts $z_{\text{em}} \gtrsim 2$. In the spectrum of the brightest (18 mag) of these objects, candidate 2A which is 0.4° from PKS 0237-23, Sargent observed apparent absorption features that occur at the same wavelength as the main clumps of lines in PKS 0237-23. This object will be re-observed at higher resolution late in 1978. If it indeed proves to have a clump of absorption redshifts near 1.65, the nature of these redshifts would be put beyond doubt.

Quasars Near Bright Galaxies

In 1976, Arp discovered a group of ultraviolet-excess, stellar-appearing objects near the galaxy NGC 3384. Spectroscopic observations by Arp and Sulentic with the 5-meter SIT spectrograph reveal that eight of these objects are quasars and that six of them have very similar redshifts ($1.1 \leq z \leq 1.3$). The two quasars nearest to N 3384 are aligned exactly across its nucleus and have redshifts of $z = 1.107$ and $z = 1.111$. One interpretation of this result is that the six objects form a cluster of quasars. However, Arp and Sulentic believe that the large physical dimensions of the group at the redshift distance and

the high-velocity dispersion make this explanation unlikely. Arp interprets the alignment of quasars as evidence that they were ejected from the nucleus of NGC 3384. As in other examples of apparent ejection of quasars, which he has discussed in the past, the major part of the quasar redshifts would have to be attributed to a physical mechanism which is not at present understood.

An area of $0.77 \square^\circ$ centered on NGC 3384 was carefully searched for quasar candidates, and all objects found were spectroscopically studied. This study has enabled Arp and Sulentic to determine the density of quasars to $V \approx 20.0$ in this region of the sky. Six quasars were found out of a total of 14 candidates to this magnitude limit. A careful search by Dr. Graziella di Tullio of Osservatorio Astronomico, Padua, Italy, of the entire $20.9 \square^\circ$ field of the Schmidt plate upon which NGC 3384 was located allowed extrapolation of the spectroscopic survey results in order to estimate the average density of quasars over the entire field. The surface density was found to be 7 ± 4 quasar \square°^{-1} to $B = 20.0$, a result in good agreement with previous estimates.

In a spectroscopic study of ultraviolet-excess objects in the vicinity of NGC 1073, Arp and Sulentic have discovered three quasars within $2'$ of this galaxy. The spectra thus far obtained suggest that all three of these objects have very similar redshifts. The survey program near this galaxy was prompted by the reported discovery of a blue-stellar radio source projected on one of the spiral arms of the galaxy. This object was confirmed as a quasar and the two radio-quiet quasars were detected subsequently on a two-color $U - B$ Schmidt plate obtained by Sulentic. Ignoring the radio-detected quasar, the probability that the other two quasars would accidentally appear projected on the disk of NGC 1073 is estimated as one in a thousand. The redshifts of the three quasars are $z = 1.94$, and provisionally $z = 1.89$ and $z = 1.98$. Arp and Sulentic believe that the three qua-

sars are physically associated if these redshifts are confirmed. However, the same arguments against the association being at the redshift distance that applied

for N 3384 also apply here. Arp concludes, as in previous cases of associations of quasars and galaxies, that NGC 1073 has ejected these objects.

OBSERVATIONAL COSMOLOGY

Properties of the Expansion for Very Nearby Galaxies Just Beyond the Local Group

An important question raised by the strong density contrast toward the Virgo Cluster in our local region of space is the effect of the clumpy matter distribution on the expansion rate. If the local supercluster (Virgo-Coma-Ursa Major region in the north galactic polar cap), with its factor of ~ 5 mean density excess, sufficiently perturbs the total gravitational potential field, a large difference is expected between the Hubble expansion field inside the supercluster and the global field (i.e., distances for which $v \geq 5000 \text{ km s}^{-1}$). A study of the *very* local expansion field is possible by determining distances to highly resolved late-type galaxies (isolated or in groups) whose apparent velocities (corrected to the centroid of the Local Group) are less than $\sim 400 \text{ km s}^{-1}$ [i.e., $(m - M) \leq 29.5$], for here the brightest resolved stars will be brighter than $V \simeq 20$. The program to obtain distances to a number of local galaxies was begun by Sandage several years ago (*Year Book* 75, p. 316), primarily using the brightest red and blue stars. The systems currently under study include WLM, NGC 3109, Sextans A, Sextans B, IC 5152, NGC 300, NGC 4214, NGC 4244, and members of the M81/NGC 2403 group.

The preliminary results lead again to the unexpected conclusion that the Hubble flow is uniform (almost noiseless) locally and that the very local value of H_0 is the *same* as the global value of $50 \text{ km s}^{-1} \text{ Mpc}^{-1}$. The new data for the nearby group in the Ursa Major region that includes NGC 4144, 4214, 4244,

4395, 4449, 4736, and IC 4182 (*Year Book* 75, p. 311) shows a resolution of all the involved galaxies to be more difficult than for the M81/NGC 2403 group by 1.0 mag. Hence $(m - M) \simeq 28.7$. Remarkably, this is what it should be if $H_0 = 50 \text{ km s}^{-1} \text{ Mpc}^{-1}$, since the observed velocity of the group is $v_0 = 285 \pm 9 \text{ km s}^{-1}$. The data for other groups (M81/NGC 2403, Sculptor, M101) are similar (see Tammann, *Mon. Notic. Roy. Astron. Soc.*, 35, 50, 1976, for a summary). Hence, the local Hubble diagram of velocity versus distance ties to the Virgo Cluster with no deviation greater than $\sigma = 25 \text{ km s}^{-1}$ (see the Tammann summary), and, remarkably, Virgo ties to the global expansion determined by the great clusters (Coma, Corona Borealis, etc.) to within $\sigma = 25 \text{ km s}^{-1}$, as determined by Visvanathan and Sandage from their analysis of the color-absolute magnitude effect (*Astrophys. J.*, 216, 214, 1977) and by Kormendy (*Astrophys. J.*, 218, 333, 1977) from his analysis of intensity profiles.

Sandage believes that these results pose very severe problems for the local dynamics of the supercluster and provide a strong clue to the nature of the local gravitation field on a scale of 25 Mpc. The work of determining accurate distances to the nearby systems, primarily using the Las Campanas du Pont reflector, is expected to be a major effort in the next several seasons, where all possible distance indicators will be used.

Motion of the Local Group Relative to the Metagalaxy

Related to the problem of the apparent extreme regularity of the local expansion

field and its smooth tie to the global field is the problem of the motion of the Local Group relative to an inertial frame that has relevance to the Universe.

Analysis by Sandage, Tammann, and Yahil of the motions of galaxies in the *Revised Shapley-Ames Catalog* (mentioned in *Year Book* 76, p. 164) has reached a stage of first results, following an analysis of the strong, crucial, and expected Malmquist bias in the *Catalog*. There appears to be no question that the motion of the centroid of the Local Group relative to the 1246 Shapley-Ames galaxies is small (less than 200 km s^{-1}). Yahil's solutions for the residual vector from a pure Hubble flow (as if the field can be described by a simple linear vector field superposed on the regular expansion) are the same to within statistics for E/S0 spirals considered separately. A firm conclusion at the present preliminary state is that the present results, using bright galaxies, cannot be reconciled with the large motion claimed by Rubin and Ford (*Astron. J.*, 81, 719, 1976) or with the supposed detection of an anisotropy of the 3° background

radiation by Smoot, Gorenstein, and Muller (*Phys. Rev. Lett.*, 39, 989, 1977) at the 600 km s^{-1} level. (More complicated motions than a simple superposed linear vector field are now under study by Yahil, Tammann, and Sandage.)

No explanation of the difference between the current result of a quiet Universe and the Rubin and Ford-Smoot *et al.* turbulent case has been found. In view of the urgency of the problem, a better determination of distances to the very local galaxies, and a very accurate tie to the global expansion at the 100 km s^{-1} level at Virgo discussed earlier, would seem to be of vital importance. For, if it could be shown that the velocity field is highly regular to distances corresponding to velocities between zero and $\geq 5000 \text{ km s}^{-1}$, then serious doubt would have to exist as to the reality of an anisotropy of 600 km s^{-1} in the 3°K radiation. It should, however, be noted that Yahil, Tammann, and Sandage emphasize that their analysis of the *Revised Shapley-Ames Catalog* is not complete and that their conclusions, although the result of a long analysis, are not yet final.

THEORETICAL STUDIES

Gas Disks in Elliptical Galaxies

Gunn has completed a theoretical study of the behavior of neutral gaseous disks (such have now been seen in a few systems) in elliptical galaxies. The model involves hydrodynamical interaction of the disk with an ambient very hot medium, such as the Matthews-Baker wind, and eventually shows how a mechanism develops which feeds mass into the galactic nucleus and generates its own wind. The model is of interest primarily as a mechanism for explaining the energetics of emission-line nuclei in ellipticals and as a way to explain how massive objects in nuclei might be "fed" to fuel very violent, energetic activity.

Cosmological Consequences of Neutral Particles

Gunn, together with Drs. B. W. Lee, I. Lerche, and D. N. Schramm of the University of Chicago, and Dr. G. Steigman of Yale University, has investigated the cosmological consequences of the existence of massive, stable neutral particles produced in the early universe. Such particles are predicted to exist in a variety of gauge-theoretic models for the weak interaction. They would interact only weakly, and though they are produced thermally in the early universe and exist in equal numbers with their antiparticles, their present annihilation rates are very slow indeed. If the mass of such

a particle is comparable to that of the proton or a bit larger, the total mass density of such things may well dominate the mass density in the universe. The dynamical properties are studied, and it is shown that this neutral fluid will cluster with ordinary matter but is dissipationless. It is thus an excellent candidate for the "missing mass." It has negligible effect on helium production in the early universe, though it does lead to a large production of deuterium if the overall mean density of the universe is as low as current estimates suggest.

Tremaine and Gunn have also completed a study of the dynamical effects of

light neutral particles; it has been suggested that ordinary neutrinos might have masses of a few eV. In such models, the number density of light particles is comparable to the 3° blackbody photon density. If the mass is greater than about 50 eV, they violate cosmological constraints ($\Omega > 1$). If the mass is greater than about 2 eV, they might well be the dominant form of mass, but such light particles are subject to very strong phase density constraints which prevent their being the "missing mass" in clusters and galactic halos. Thus, they may exist but can have nothing to do with the missing mass problem.

INSTRUMENTATION

Mount Wilson Aluminizing Facilities

A refurbishment of the Mount Wilson vacuum aluminizing facility that had been planned and pursued by Vaughan since 1972 was completed this year, and in May and June 1978 the 2.5-meter mirror and the solar tower mirrors were aluminized successfully. The improvements included the construction of a permanent air-conditioned clean room, housing the system on the ground floor of the Hooker Telescope dome, and complete rebuilding of the vacuum system for the 274-cm aluminizing tank. The new system has a coating cycle time of a little over two hours, of which one hour is the pumpdown time, one hour is used for oxygen plasma cleaning, and about five minutes for coating deposition—as compared with a cycle time of many (≥ 12) hours for the system previously used at Mount Wilson.

Double Spectrograph

Using a grant from the Venture Fund of the California Institute of Technology, Gunn, Oke, and Sargent are designing and building a low-to-moderate-resolution double spectrograph for the 5-meter

Hale Telescope. The spectrograph has a 15-cm collimated beam and can use an unvignetted slit length of up to 50 mm or 125". The spectrograph is unique in that the light is separated by a Dichroic filter just below the slit into two wavelength regions, namely, 3000–3500 Å and 5500–10,000 Å. Light in the two wavelength regions is put through two separate spectrographs. Since each wavelength region covers less than one octave, very efficient antireflection coatings or reflecting surfaces can be used throughout. Cassegrain collimators of a very rigid design are used to keep the instrument compact. Optimum gratings can be used in each spectrograph to further enhance efficiency. The blue spectrograph uses a folded f/1.5 Schmidt camera and can accommodate bulky detectors, provided the light-sensitive element is not more than 1 cm behind the frontmost surface. The red spectrograph is an f/1.0 Schmidt. Since it is anticipated that a CCD detector will be used, it is mounted, along with a field-flattening lens, at the primary focus of the Schmidt. It will be cooled with a controlled LN₂ flow and the camera will be evacuated to itself from the insulating dewar. Many of the

mechanical subassemblies are already built and most of the optics, which are being made by D. Loomis of Custom Optics in Tucson, Arizona, are completed. Both blue and red detectors will be two-dimensional devices, to make use of the large field of view, with digital outputs. A camera controller is being designed and built that will provide the interface to a PDP 11/40 computer which will store, manipulate, and display the spectra.

High-Speed Microdensitometer

With the help of a grant from the National Science Foundation, a large 2-coordinate Mann measuring machine has been converted into a high-speed microdensitometer. Much of the electronics and software has been done by graduate students. The light-measuring device is a thermoelectrically cooled 500-element reticon detector. The reticon array is read out and digitized, the fixed-pattern noise is removed, and the final digitized data are sent to a PDP 11/34 minicomputer for storage on tape or for processing. The readout can take place approximately every 50 msec so that 10,000 measurements are made per second, the maximum rate at which data can be read onto tape. The original optical system, light source, and x and y drives, and encoders, have all been redesigned or replaced. In spite of all these changes, the instrument looks very much as it originally did. All of the construction has been completed and the system is in the final stages of debugging and eliminating of electrical noise.

Photon-Counting Image Intensifier System

This year Sackettman completed the photon-counting image intensifier system for the Las Campanas 2.5-meter Cassegrain spectrograph. The detector is based upon the same magnetically focused Carnegie image tube and transfer lens used when spectra are recorded photographi-

cally. The photographic plate is replaced by a four-stage electrostatic image intensifier, fiber-optically coupled to a solid-state photodiode array. The positions of individual photoelectron events at the input of the Carnegie tube are readily distinguished in the electronic output of the diode array, which is arranged in two rows of 936 diodes each. The two rows of the diode array, which permit simultaneous monitoring of object and sky apertures, are completely scanned every millisecond. The centroid of each photon event is recorded to the nearest $1/4$ -diode in the memory of a minicomputer. The result is a pair of spectra, each 3744 channels long, which represent the accumulated number of photon arrivals along a 29-mm length in the spectrograph focal plane. Along most of this length, the full width at half-maximum resolution of the system is less than four channels. Slow wavelength drifts during the night can be monitored to an accuracy of $1/2$ channel. The computer provides the observer with a display of the sky-subtracted spectrum as the data accumulate, and records the final result on magnetic tape. Irregularities in the channel-to-channel response of the system are removed by dividing by a smooth reference spectrum that is stored in the computer memory. Using this feature, it is possible to obtain continuous spectra that are smooth at the 2% rms level.

Several modifications to the spectrograph permit particularly effective use of this detector system. An electrolytically etched aperture plate provides a wide selection of aperture pairs. A special double-walled magnetic shield prevents the magnetic focus field of the Carnegie tube from interfering with the operation of the electrostatic intensifiers. To align the spectrum on the 750- μ -wide diode array, the rocking block spectrum widener is used in conjunction with a rotating diode-array mounting. With a special software program it is possible to center the spectrum along the entire

length of the diode array to an accuracy of $\pm 15 \mu$.

Installation of the system in Chile, and much of its construction, was carried out by Gary Yanik. The software was developed by Ken Clardy. Special hardware was provided by the Engineering and Shop Group. Financial support was provided by the National Science Foundation through grant AST76-20839.

Infrared Photometer

The infrared photometer and indium antinonide detector system were put into operation on the 2.5-meter du Pont Telescope by Persson and Matthews in October 1977, and the four-channel data system/HP9830 calculator was installed in January 1978. The device has been used to make near-infrared observations of SMC and LMC clusters, globular cluster stars, and galaxies, and was used for the occultation by Uranus' rings in April. It has also been used at optical wavelengths for programs of narrow-band photometry of globular clusters and early-type galaxies.

Wide Field/Planetary Camera for Space Telescope

The National Aeronautics and Space Administration has awarded a preliminary contract for the Wide Field/Planetary Camera of Space Telescope to the California Institute of Technology. Westphal is the Principal Investigator, and general project oversight is in the hands of a team of scientists which includes Kristian and Gunn. Design and construction of the camera will be done by the Jet Propulsion Laboratory. Space Telescope is a 2.4-meter general purpose telescope, to be placed in orbit in 1983. It will be an important complement to ground-based telescopes and orbiting telescopes for measurements on other spectral ranges. Its unique advantages include 0.1" image sizes, which will provide increased signal-to-noise for point

sources and high resolution for extended sources, lower sky brightness, and sensitivity in the ultraviolet. It will be placed in orbit and serviced periodically by astronauts using the Shuttle; they will be able to repair or replace components in orbit or return the entire telescope to the ground for refurbishment and re-launch.

The Wide Field mode of the WFPC will have a 0.1" pixel size to optimize faint object detection; the Planetary Camera mode will have a 0.04" pixels to fully use the high angular resolution on brighter extended objects.

The specially treated CCD detectors used in the camera will have a spectral response from 1150 Å to 11,500 Å, with quantum efficiencies greater than 50% in the visible-red region of the spectrum. The limiting magnitude in a 2000-second exposure will be about $m_v = 28$.

CCD Detectors

In connection with the Wide Field/Planetary Camera project, prototype CCD detectors have been used at the telescope for direct imaging by Westphal, Kristian, Gunn, Hoessel, and Young. These detectors have high quantum efficiency, a broad spectral range (especially in the red), a large dynamic range, and excellent geometric stability. For some classes of problems, such as very faint galaxies, they are near to being the ideal detector. They have supplanted the SIT detectors used earlier by Westphal and Kristian for two-dimensional photometry.

Sargent and graduate student Peter Young were assigned two nights on the Kitt Peak National Observatory 4-meter reflector in May 1978 in order to take part in the program to test the JPL CCD camera which was sent to several observatories. They made several observations to test this device, which had 400×400 elements over a field $1\frac{1}{4} \square'$. The principal programs were (1) a search for globular clusters in the galaxies of the

Coma cluster; these should be at the limit of detection if the accepted distance modulus of the Coma cluster is correct; (2) observations of a field near M87 in order to extend the luminosity function of the system of globular clusters around that galaxy; (3) observations of a field in the center of the Draco dwarf galaxy in order to detect stars on the main se-

quence in that system; (4) short exposures of the centers of two globular clusters which contain bursting x-ray sources in order to study the radial distribution of stars; and (5) observations of the galaxy NGC 6251 in order to confirm a faint optical jet which Kristian, Westphal, and Young may have detected in Palomar observations of this galaxy.

GUEST INVESTIGATORS

Dr. Saul J. Adelman of Boston University used the 2.5-meter telescope at Mount Wilson Observatory to obtain IJa-O and IJa-D coude spectrograms of peculiar A stars. Spectrophotometry of 33 normal B, A, and F stars obtained partially in previous years with the Cassegrain scanner on the 1.5-meter photometric telescope of Palomar Observatory has been published (*Astrophys. J.*, 222, 547-555, 1978). The data was reduced consistent with the Hayes-Latham calibration of Vega. Synthesized $u - b$ and $b - y$ indices were compared with directly observed values. The upper limits on the photometric accuracy are 0.010 and 0.008 mag, respectively. Effective temperatures derived by comparison with metal-line-blanketed model atmospheres agreed well with the recent empirical calibration in terms of *UBV* photometry presented by Code and his associates. Spectrophotometric measurements of Ap stars are being prepared for publication in collaboration with Drs. Diane M. Pyper, University of Wisconsin—Parkside, and Richard E. White, Smith College. For some Ap stars, detailed comparisons have shown that no reasonable matches can be made with $\log g = 3.0$ to 4.5 models. Comparisons of observed colors and those synthesized from the spectrophotometry are being used to help interpret intermediate and broadband photometric observations.

Mr. Gonzalo Alcaino of Santiago, Chile, used the 2.5-meter du Pont Tele-

scope and the 1-meter Swope Telescope at Las Campanas to obtain direct fluxes for his photometric work on globular clusters and on the Magellanic Clouds.

Dr. Lawrence H. Aller of the University of California at Los Angeles, Dr. Stanley J. Czyzak of Ohio State University, and Sheckman engaged in a collaborative program on planetary nebulae. They proposed to measure intensities of rather weak lines in the spectra of gaseous nebulae, which are of prime importance for diagnostic studies. The lines of interest are from C II, C III, C IV, [Fe III], [Fe VI], [Ca V], and He I ions. Spectroscopic observations were begun during the winter quarter, using the spectrometer developed by Sheckman to measure the important transitions of carbon and the other elements in the various stages of ionization. Unfortunately, because of the bad observing conditions during the run in February 1978 (one half of one night), only an extremely limited amount of data was obtained. However, this preliminary data indicates that the Sheckman spectrometer will be extremely useful in measuring the important diagnostic lines.

Earlier work by Aller and Czyzak carried out on the 1.5- and 2.5-meter telescopes on the spectra of ring and ansae in NGC 7009 and on the chemical composition of NGC 6302 have been completed and are in press.

Dr. S. C. Beck, J. Lacy, and C. H. Townes of the University of California

at Berkeley, in collaboration with Geballe, used the 2.5-meter du Pont Telescope at Las Campanas in 1977 to observe Ne II (12.8- μ m) emission from the galactic center with aperture of 7" and spectral resolution corresponding to 36 km s⁻¹. The complicated distribution of gas observed there led them to repeat such measurements with a 3.5" aperture in 1978. These observations resolved many small clouds of ionized gas within the central parsec of the Galaxy. From the velocities of these sources, they obtained an axis of rotation of the gas in this region, which is different from that of the Galaxy as a whole, and derived a mass of $\sim 10^7 M_{\odot}$ within the central parsec. They also studied the distribution of infrared line emission of Ne II, Ar III, and S IV in four southern H II regions. This mapping produced the equivalent of pictures of regions that are embedded in such dense clouds of dust that they cannot be seen in visible light. From these "pictures," they obtained information on the spatial distribution of the ions observed, and from the relative strengths of the lines, the temperatures of the stars that excite the nebulae.

Dr. William D. Benton of the Jet Propulsion Laboratory obtained 172 images of Iapetus during eclipse by the rings of Saturn on October 19, 1977, and January 8, 1978, with the 2.5-meter telescope at Mount Wilson. These images are currently undergoing extensive computer processing at the JPL Image Processing Laboratory. The purpose of the processing is to obtain a light extinction versus ring-location curve and subsequently to derive Saturn ring-plane particle densities.

Professor F. Bertola of the Osservatorio Astronomico, Padova, Italy, has observed the elliptical galaxy NGC 3379 with the SIT-Vidicon spectrograph at the Cassegrain focus of the 5-meter telescope on Palomar Mountain, with the purpose of deriving the rotation curve and the trend of the velocity dispersion. Good signal-to-noise ratio has been obtained

up to 50" from the nucleus at position angle 65°. A preliminary reduction of the data, using the programs developed by Dressler and Rose, shows that the mean internal velocity dispersion in NGC 3379 is 250 km s⁻¹. A complete rotation curve will be available when the beam-bending effect is taken into account. At present, it is possible to state that the maximum velocity of rotation does not exceed the value of 100 km s⁻¹.

Dr. D. E. Blackwell of the University of Oxford used the coudé spectrograph of the 2.5-meter telescope at Mount Wilson to obtain 24 spectra of the stars μ Pegasi, ν Andromedae, δ Trianguli, and δ 5 Pegasi at dispersions of 4.5 and 6.75 Å mm⁻¹. The purpose of this work is to determine the microturbulence in the atmospheres of these stars, using the measures of oscillator strengths of 0.5% accuracy being obtained at Oxford. Measures of equivalent widths from these plates agree well with measures made using the photodiode array attached to the McMath Solar Telescope at Kitt Peak National Observatory.

Dr. Howard E. Bond and Dr. R. Earle Luck of Louisiana State University continued a program of coudé spectroscopy photographically at the 5-meter Hale Telescope on Palomar Mountain and with Shectman's photon-counting spectrometer at the 2.5-meter telescope on Mount Wilson. A program of H α scans of extremely metal poor field, red giants has been started. This demonstrates that globular-cluster-type stars lose mass only during a relatively brief period near the end of their lifetimes as red giants. They hope to determine mass-loss rates as a function of surface temperature from their data, and then use evolutionary calculations to determine the total amount of mass lost during the red-giant phase.

Luck has begun a program of Shectograph scans of 7th–9th magnitude supergiants. Partial material is available for 10 objects at present. The aims of his study are to determine heavy-element

contents of very young stars as a function of distance from the galactic center and to study lithium and carbon-nitrogen oxide abundances as indicators of interior nucleosynthesis and mixing.

During the past year, Dr. E. F. Borra of Université Laval, Québec, Canada, and Dr. J. D. Landstreet, University of Western Ontario, London, Canada, have used the 1.5-meter telescope at Palomar Observatory and the 2.5-meter telescope at Las Campanas Observatory to search for and study magnetic fields in Ap stars and other upper main sequence stars. This work has been carried out using the University of Western Ontario Cassegrain Pockels cell polarimeter with 5 Å interference filters to measure the circular polarization produced in the wings of photospheric Balmer lines by the longitudinal Zeeman effect. Magnetic curves have been obtained in this manner for the known magnetic Ap stars HD 215441 (H. W. Babcock's star, *Astrophys. J.*, 222, 226, 1978), HD 32633, 78 Virginis, CS Virginis, HD 133029, β Coronae Borealis, and 52 Herculis. Fields have been detected in a number of other bright Ap stars. A survey of all Ap stars brighter than $V = 5.0$ mag is almost complete at a level of $\sigma_B \lesssim 200$ gauss. This material is now being analyzed to see what may be determined about the distribution of the field obliquity parameter β and the polar field strength in Ap stars. This program has also led to the recent discovery of strong magnetic fields in a number of helium-rich stars. A field varying up to 3 kG has been found in σ Orionis E, and it seems possible to understand the photometric and spectroscopic variations of this star as an oblique rotator with circumstellar gas trapped in a magnetosphere around the star's magnetic equator (*Astrophys. J. [Lett.]*, in press). Fields have also been found in HD 37017, 37776, 58260, 64740, and 96446. On the average, the observed fields are about a factor of 3 larger than those typically found in classical Ap stars. It seems

clear that these stars are an extension of the classical Ap stars.

Dr. M. M. Dworetzky of University College London has begun a program of high-dispersion coude spectroscopic observations of the Hg-Mn star ι Coronae Borealis with the Mount Wilson 2.5-meter telescope to determine whether or not the line profile asymmetries reported by Smith and Parsons (*Astrophys. J.*, 205, 430, 1976) might be due to a possible binary companion. Plates taken two months apart show definite radial-velocity shifts of some lines that may be due to a cooler spectroscopic companion orbiting the primary.

During May 1978, J. Elias, a graduate student at the California Institute of Technology, used the infrared photometer on the du Pont 2.5-meter Telescope to observe several very young stars embedded in the Ophiuchus dark cloud. Low-resolution (2%) spectrophotometry of several of these objects was obtained between 2.9 and 3.7 microns in order to measure the strength of the water-ice absorption at 3.1 microns and search for other possible features. Two stars that appear to be embedded in infrared reflection nebulae were mapped at 2.2 microns; measurements at other wavelengths were made at selected points in the reflection nebulae. It is expected that the analysis of these data, when completed, should provide information on the scattering and absorption properties of grains in the centers of dense dark clouds.

Dr. Debra M. Elmegreen of Harvard College Observatory obtained *UBVRI* photographs of M51, M101, and M81 with the 1.2-meter Schmidt telescope on Palomar Mountain. The plates will be used to make a quantitative study of the dust distribution in spiral galaxies.

Dr. Neil J. Evans II of the University of Texas collaborated with graduate student Daniel Nadeau of the Caltech infrared group in 5–20 μ m photometry at the 1.5-meter telescope at Mount Wilson. In one project, they observed the stronger sources of a group found by scanning

molecular clouds at $2\ \mu\text{m}$. These molecular clouds form part of a sample of star-forming regions being subjected to a thorough analysis in terms of their physical conditions and energetics. In addition, one of the clouds was scanned simultaneously at 2 and $10\ \mu\text{m}$. Analysis is underway for several of these clouds. In the second project, $5\text{--}20\ \mu\text{m}$ photometry was obtained on an infrared source embedded in the molecular cloud associated with the W44 supernova remnant. This source has an energy distribution similar to that of very young and possibly protostellar objects embedded in other molecular clouds. It may be an example of star formation induced by the supernova remnant. A further study of other infrared objects in clouds near supernova remnants is planned.

Dr. Gilles Fontaine of the University of Montréal has obtained Strömgren photometric data for some 30 nearby white dwarfs with the 1.5- and 2.5-meter telescopes at Mount Wilson. The aim of this program is to gain information about the atmospheric properties of all known nearby white dwarfs and to determine their local luminosity function. Fontaine and Dr. Gérard Vauclair, Caltech visiting research associate from the Observatory of Paris, have also initiated a search for luminosity-variable white dwarfs, using the 1.5-meter telescope at Mount Wilson.

Dr. Tom Gehrels of the University of Arizona Lunar and Planetary Laboratory took plates with the Palomar 1.2-meter Schmidt for a detailed survey of the Following Lagrangian Point of Jupiter. The plates were shipped to Leiden where Drs. C. J. and I. van Houten are processing them as a part of a continuing statistical investigation of Trojan and asteroid populations. A search for Trojans of the earth was made over a $6^\circ \times 18^\circ$ field while guiding for their motion, but none was found.

Dr. Edward H. Geyer of Bonn Observatory obtained plates with the 2.5-meter du Pont Telescope of the globular

clusters ω Centauri and M22. The purpose of the study is to search for eclipsing binaries and intrinsic variables on the main sequence of globular clusters.

Drs. R. E. M. Griffin, R. F. Griffin, and J. Mitton of the Cambridge Observatories, England, continued their work at the coudé spectrograph of the Mount Wilson 2.5-meter telescope. They largely completed the high-resolution coverage of the spectra of Sirius, Vega, and β Geminorum needed for the studies outlined in *Year Book 76* (p. 173). The Griffins also verified, by direct observation of the near-ultraviolet spectrum of the G5 supergiant HD 187299, the existence of a hot companion, which was expected from the large mass function of the spectroscopic orbit, by subtraction of the spectrum of the MK standard G5 Ib star 9 Pegasi. A tolerable approximation to the spectrum of the secondary was recovered over the wavelength region $3700\text{--}4100\ \text{\AA}$.

Gunn and R. F. Griffin were prevented by bad weather, for the third successive year, from adding significantly to their Hyades observations with the radial-velocity spectrometer at the 5-meter coudé. They were, however, able to determine the orbit of van Bueren 117, which is only the second double-lined Hyades spectroscopic binary to have its orbit determined. It yields minimum masses slightly higher than those expected on the basis of the conventional mass-luminosity relationship. A second radial-velocity observing run in May 1978, largely devoted to stars in globular clusters, was more successful. During the year, the new data system referred to in *Year Book 76* (p. 173) was successfully commissioned and proved its value.

The large field provided on the 51×51 cm plates of the 2.5-meter du Pont Telescope has allowed Dr. Eduardo J. Hardy of Université Laval, Québec, to photograph the Fornax galaxy and its six clusters on single exposures. In collaboration with Dr. S. Demers of Laurentian University, Ontario, the clusters and

sections of Fornax itself are being iris-photometered to $V = 20.3$, using the Kunkel and Demers standard sequence. Hardy is taking advantage of the scale and resolution of the du Pont Telescope to study stars close to the center of the rich Small Magellanic Cloud clusters NGC 419 and 416 to determine the nature of these populous clusters, which may turn out to be young objects. Hardy is collaborating with Dr. Jorge Melnick in digitizing and processing calibrated plates taken with the du Pont Telescope at the European Southern Observatory Image Processing Laboratory in Geneva. They are examining over 30 open clusters in the Small Magellanic Cloud, all contained on single du Pont exposures, for a study of the age distribution of the young population.

Dr. Alan W. Harris of the Jet Propulsion Laboratory, Pasadena, observed two eclipses of Iapetus by Saturn's rings on the Mount Wilson 2.5-meter and Palomar 1.5-meter telescopes on October 19, 1977, and January 8, 1978, respectively. Light curves obtained from these events indicate that the rings have normal incidence optical thicknesses of ~ 0.4 and $\gtrsim 1.0$, respectively, for the A and B rings. Considerable radial structure is evident, including a clear indication of Encke's Division. By combining data obtained on both eclipses, it should be possible to refine the ring dimensions to a precision of ~ 100 km. Data reduction is continuing toward that goal.

Dr. Frank Holden of San Jose, California, used the Swope reflector at Las Campanas during the last week of November and early in December for eight nights to measure visual double stars. A bifilar micrometer, on loan from Lick Observatory (by permission of Director D. E. Osterbrock) was fitted at the $f/13.5$ focus. Unfortunately, the weather and the seeing were very poor at this period and it was not possible to make many observations. Nevertheless, more than 50 measures of 30 pairs were obtained. The results have been accepted

for publication in the *Publications of the Astronomical Society of the Pacific*.

Dr. John Huchra of the Harvard-Smithsonian Center for Astrophysics used the Palomar 1.5-meter telescope to initiate a study of highly reddened star clusters embedded in the galactic plane. Coupled with infrared photometry done at Kitt Peak, Terzan 12 was found to be a stellar association rather than a globular cluster.

Huchra, in collaboration with Dr. Marc Aaronson of Steward Observatory, Tucson, used the 2.5-meter Hooker telescope to obtain the optical photometry in a systematic *UBVRJHK* survey of interacting galaxies. This will be used to test theories predicting a very high rate of star formation in such disturbed systems (Larson and Tinsley, *Astrophys. J.*, 219, 46, 1978; Struck-Marcel and Tinsley, *Astrophys. J.*, 221, 562, 1978).

The distribution of H II regions over the face of a galaxy is rather different from one galaxy to the other and is to some extent correlated with the galaxy type. Early-type spiral galaxies, for instance, tend to show H II regions neatly lined up in spiral arms (like "beads on a string"), whereas in late-type spirals the appearance is much more irregular. Since H II regions mark those parts of a galaxy currently engaged in star formation, it is of interest to obtain information on the H II region distribution in a number of galaxies in a more quantitative form. To this end, Drs. V. Icke and F. P. Israel of the California Institute of Technology have started a program of taking calibrated $H\alpha$ plates (Arp's 80-Å filter) of spiral galaxies larger than 4' with the Palomar 1.2-meter Schmidt. The plates will be digitized, and the resulting $H\alpha$ maps will be used to determine the two-point correlation function of the H II-region distribution per galaxy.

Dr. W. Krzeminski of the N. Copernicus Astronomical Center in Warsaw, in close cooperation with Dr. W. C. Priehorsky of Caltech and Dr. S. Topia of the University of Arizona, used the 1.5-

meter telescopes at Mount Wilson and Palomar to study correlated photometric and polarimetric observations of AM Herculis and to search for AM Her-type magnetic binaries. Through simultaneous multicolor photometry and polarimetry of AM Her, they find correlations between polarization, flux, and color in the V and I bands in periodic and non-periodic (i.e., flickering) activity. The primary minimum observed in both bands is accompanied by blueward shift of the $(B - R)$ color and a decrease in the absolute value of the percent circular polarization in the V band. Outside primary minimum, peaks of flickering activity tend to be associated with an increase in the absolute value of the circular polarization and the concurrent reddening of the $(B - R)$ and $(R - I)$ colors. The visual-light curve of AM Her can be explained by a flickering, circularly polarized light source, which is obscured at primary minimum and is redder than the total system color in the $UBVRI$ bands. In the second project, they conducted a circular polarization survey in the V and I bands on about 50 candidate stars among novalike novae, dwarf novae, and R Coronae Borealis-type stars whose optical properties indicated some similarity to already-known magnetic binaries: AM Her, AN Ursae Majoris, and VV Puppis. Multicolor photometry and spectra supplemented polarization data and constrained classification for some stars. The survey yielded negative results; no more magnetic binaries have been found.

The Be-shell star HR 0193 (α Cassiopeiae), used as an infrared standard during its quiescent period from 1964 to 1976, increased significantly in brightness at $2\ \mu\text{m}$ in October 1976. A spectrum taken by Mr. Howard H. Lanning of Mount Wilson Observatory with the varo-reticon system at the coudé focus of the 2.5-meter Mount Wilson telescope in February 1977 exhibited the typical $H\alpha$ emission-line shell features. Additional spectra obtained in July were

noticeably different, represented by a stronger $H\alpha$ emission-line intensity, variations in the separation of the line peaks, and full width at half maximum. Simultaneous IR (J. Elias) and visual spectroscopic observations made on succeeding nights indicated corresponding increases at IR wavelengths. A slight decrease in the $H\alpha$ emission-line intensity, along with a broadening of the central absorption feature, was noted. The IR and spectroscopic variations are presumed to be the result of changes in a circumstellar envelope surrounding the star.

The newly discovered G8 III OBsd eclipsing binary BD-3°5357 and the eclipsing wd-K2V V471 were also observed by Lanning using the varo-reticon. Variations in the $H\alpha$ profiles of both systems have been detected and are represented by changes in intensity and structure during the orbital cycle. The spectra may suggest the presence of circumstellar matter in either or both binaries, or variations due to a heated region on the surface of the cooler component. Investigation of these characteristics is continuing.

Drs. M. S. Longair and J. M. Riley of Mullard Radio Astronomy Observatory, Cavendish Laboratory, England, and Gunn continued their program of deep optical studies of the fields of unidentified radio sources in the 3CR catalog. In the past year, they observed 20 fields, with at least 12 resulting identifications. This sample more or less completes their study of a complete statistical sample of 3CR radio sources.

Longair, Nelson Schuch, a graduate student at the University of Cambridge, England, and Gunn have obtained spectra of 36 galaxies in the supercluster in the field of 5C10. Taking this data in conjunction with some earlier observations, it has been possible to work out the mean velocities of the clusters and their velocity dispersions. It is evident from these results that two and perhaps three of the clusters in this association must be background objects. The three

remaining clusters have similar velocities and probably form a physical association. The overall dimensions of the system are about 20 Mpc. In addition, velocities were found for a number of the radio galaxies in the vicinity of this system. A high-quality IIIa-J plate made with the 1.2-meter Schmidt telescope will be used for optical identifications of the radio sources in the 5C10 survey and for studies of the overall distribution of galaxies in the supercluster field.

Dr. B. F. Madore of the Institute of Astronomy, University of Cambridge, England, used the 1-meter Swope Telescope to secure photographic and photoelectric observations of fields surrounding long-period Cepheids in the Large Magellanic Cloud. These data are being used to study the amount and source of reddening of these rare variables. At the same time, they are being used to delineate the luminosity function responsible for feeding the instability strip at the high-luminosity end.

Dr. D. H. McNamara of the Brigham Young University secured a single-trail spectrogram of the extremely short-period (0.^a039) variable GD 428 with the 5-meter telescope and coudé spectrograph at Palomar Mountain in August 1977. Although the variable at light minimum has the color index of an F0 star, no metal lines other than the *K*-line of calcium were detected. This observation documents an earlier conclusion that all of the short-period dwarf Cepheids with period less than 1.5 hours are metal poor. By combining the radial-velocity data and photometry of the variable, we conclude that its absolute magnitude is $M_{\text{bol}} = 3.1$. It appears to be a post-main-sequence star in the hydrogen shell-burning stage of evolution that has evolved from a Population II zero-age main-sequence star displaced below the Population I main sequence of metal-rich stars. If the evolutionary state has been correctly identified, the age of GD 428 appears to be about $3 \times$

10^9 years—a very young age for such an extremely metal-poor star that was very likely formed in the galactic halo.

High-dispersion plates have been secured of the β Canis Majoris variables BW Vulpeculae and ξ_1 Canis Majoris. The purpose of this investigation is to examine the differences in velocities between the hydrogen line and metal lines as a function of phase.

Drs. Edward P. Ney and B. F. Hatfield continued their search for polarized nebulosities (like the egg nebula in Cygnus). A total of thirty $4^\circ \times 4^\circ$ fields have been photographed through polaroid filters. Some twelve highly polarized nebulosities have been identified. Several of these (e.g., M2-9, LK H $_{\alpha}$ 233, and V380 Orionis) have polarizations exceeding 40%. Ney and Hatfield believe that the polarized nebulosities occur in optically thin dust clouds surrounding very young and very old objects. A catalog with photographs is being prepared for publication. The infrared properties of the polarized nebulosities are being studied at the O'Brien Observatory and the Mt. Lemmon Infrared Observatory.

During three-day observing runs on the 1.5- and 5-meter telescopes in January, Drs. Peter Nisenson and Robert Stachnik of Harvard University obtained data for high-spatial-resolution image reconstruction, using the speckle-imaging technique. Objects observed included several stars resolvable at the diffraction limit of the 5-meter telescope, the Galilean moons of Jupiter, and several single and binary stars used as test and reference objects. The instrument used was an image-intensified film camera. During part of this period, the seeing—particularly at the 5-meter telescope—was extraordinarily poor, frequently worse than $10''$, seriously hampering the observations. The best images, of Betelgeuse and Mira, were digitized and are awaiting processing.

Dr. Peter Pesch of Warner and Swasey Observatory obtained photoelectric *V* and *I* photometry of 51 faint M stars in

the direction of the south galactic pole in September 1977 with the 1-meter reflector at the Las Campanas Observatory. The median $V - I$ (Kron-Mayall system) of the 51 stars is $\sim +2.35$. These observations are included in "A Catalog of Probable Dwarf Stars of Type M3 and Later in the Direction of the South Galactic Pole" by Pesch and N. Sanduleak, which has been submitted for publication to the *Astronomical Journal*.

Dr. Arnold Rots of Radiosterrenwacht Dwingeloo and Radiosterrenwacht Westerbork and Dr. T. R. Cram of the National Radio Astronomy Observatory have obtained deep plates with the 1.2-meter Schmidt telescope on Palomar Mountain to search for low-level optical radiation in areas where neutral hydrogen had been detected. Areas searched were in 21-cm high-velocity clouds, the outer regions of the M81 triplet, and a galaxy in Camelopardalis detected in the 21-cm line.

Dr. W. L. Sanders of New Mexico State University obtained five-color photometry of several hundred Be stars with the 1.5-meter telescope at Mount Wilson. It is expected that the photometric system will allow luminosity classification of the stars.

Dr. Eugene M. Shoemaker and Mrs. Eleanor F. Helin of the California Institute of Technology continued the photographic search program for new planet-crossing asteroids, using the 46-cm Schmidt telescope at Palomar Mountain. A total of 197 independent fields were photographed and reviewed in the interval from June 1, 1977, to May 31, 1978. This sky coverage led to the discovery of four new asteroids, 1977 VA, 1977 VB, 1977 VC, and 1977 RB. One of the two best candidates under consideration for mission exploration/rendezvous is 1977 VA, an Amor asteroid, with a near-earth distance combined with a low inclination of 2.9° . The object 1977 VB is a new Mars-crossing asteroid of high inclination and eccentricity;

1977 VC is a new Phocaea region object, while 1977 RB falls into the Hungaria region of space.

A survey using the 1.2-meter Schmidt was initiated by Shoemaker and Helin to search L_4 and L_5 (libration points) for Trojans of the earth-sun system. Plates were photographed in May in a specific region in a search for these potentially stable objects. Results are not complete at this time, however one new object has been discovered and designated: 1978 JC. Position measurements and orbital computations are currently being carried out on several additional objects.

In addition, a new Hungaria region asteroid, 1978 GB, was discovered on 1.2-meter plates taken by G. Grueff and J. Wall.

Improved estimates of the populations of Apollo, Amor, and Mars-crossing asteroids have been published during the year by Shoemaker and Helin. These estimates have been derived from the discoveries made in their own Palomar survey as well as two other systematic surveys of the sky.

The optical emission from the southwest radio lobe of 3C33, discovered by Dr. Susan M. Simkin of Michigan State University on 1.2-meter Schmidt plates taken the previous year, was confirmed by her on additional plates taken in June. These plates, together with a deep, IIIa-J plate taken by Arp on the 5-meter telescope, show the emission to be very blue. The radio lobe was observed spectroscopically with the Anglo-Australian Telescope, and the optical emission appears to arise from a high-excitation plasma with a redshift very similar to that of 3C33.

The blue jet in the head of the radio galaxy NGC 7385, which was discovered on 1.2-meter Schmidt plates two years ago, was observed with the SIT spectrograph at the 5-meter telescope in December. The object has a strong blue continuum with faint emission lines of [O III] and $H\beta$ superimposed. This jet

appears to be very similar to the optical knots in M87, having the same orientation and absolute magnitude.

In December, the 5-meter SIT spectrograph was used to observe the optical objects associated with the double-lobed radio galaxies 3C98, 3C184, 3C184.1, and 3C218. The spectra are being measured to determine the mass motions of the ionized gas and stars in these galaxies. Preliminary reductions show that the ionized gas in each object is rotating about an axis closely aligned with the object's radio axis. This, combined with earlier observations, strongly suggests that the bilobal nature of classical double radio galaxies is associated with material ejected along the rotation axis of a sizable (2–3 kpc) disk of ionized gas.

Dr. G. A. Tammann of the Basel Observatory has taken with the 1.2-meter Schmidt telescope 24 plates in the *RGU* system of two star fields ("Plaut 2" and around NGC 7006). These plates shall be used within the Basel program to determine the star distribution in different galactic directions by means of improved statistical methods. Five different fields, for which 1.2-meter plates were previously obtained within the same program, have been searched for blue-stellar objects by W. Becker and H. Steppe. A catalog of 1906 such objects has been published (*Astron. Astrophys. Suppl.*, 31, 209, 1978). Preliminary analysis of one of these fields, SA 57, by H. Steppe, M. Véron, and M. P. Véron contains 82 objects within 23° with $B \leq 18.9$ mag and $(B - V) \leq -0.5$ mag. Their steep $\log N(m)$ curve suggests that the majority of these objects are extragalactic (quasars and possibly Seyfert class I nuclei). If this identification is indeed correct, their surface density (down to the magnitude and color limits stated) is ≤ 3.4 per square degree. Further work on these objects is in progress.

Dr. Trinh X. Thuan of the University of Virginia has obtained calibrated fine-grain IIIa-J and 127-04 plates with the

1.2-meter Schmidt telescope on Palomar for most of the poor cD clusters listed by Morgan and his collaborators (*Astrophys. J.*, 199, 545, 1975; *Astrophys. J.*, 211, 309, 1977). These plates are being reduced with the Kitt Peak Interactive Picture Processing System to obtain profiles of the giant ellipticals. Photoelectric photometry for the cD galaxies has also been obtained in order to provide absolute calibration. The plates are also being used for galaxy counts and morphological classification in the poor clusters. Thuan has also obtained IIIa-J Schmidt plates of the Perseus supercluster region (Abell 426, Abell 347, Abell 262, and the NGC 1129, 507, 383, 315, and 68 groups) in order to classify morphologically all galaxies with $m_{pg} < 15.7$ in that region. The morphological classification shall be used to interpret the H I measurements of about 150 galaxies in the Perseus supercluster made at Arecibo.

Dr. Edwin L. Turner of Harvard College Observatory observed 23 very faint field galaxies with the SIT digital spectrograph on the 5-meter telescope. Twenty of the galaxies had $m_v \approx 20$ and were selected in a random (color-independent) way from deep Kitt Peak 4-meter prime-focus plates. Initial data reduction shows three of the 20 to have unexpectedly high redshifts and thus luminosities ($M_B \leq -22.5$) and blue colors ($B - V \leq 0.2$), suggesting stellar population evolution. The remaining 17 appear to be normal ($z \leq 0.2$) field galaxies. Data of this sort are vital to the interpretation of deep galaxy counts and will provide tests of theories of galaxy evolution. Three additional, extremely blue galaxies with $m_v \approx 22.5$ –23.0 were observed; although the continua were well detected, no emission lines were present as hoped. If these galaxies have even moderate redshifts ($z \geq 0.1$), their extremely strong UV continua suggest a spectral type of A or earlier. This work is a collaboration with Gunn and Sargent.

Turner also measured the spectral energy distribution of the stellar nucleus of the peculiar Seyfert galaxy NGC 1275 on several successive nights. Variations in the continuum flux as large as $\sim 20\%$ were observed while a reference A star and NGC 1275's [O III] emission lines remained constant to within $\sim 2\%$. This appears to be the most rapid optical variation reliably established for a galactic nucleus; it is similar to the rapid optical variability of BL Lacertae objects and quasars. The optical polarization of the nucleus of NGC 1275 has also been reported to vary from night to night. The reduction of this data was carried out in collaboration with M. Bruno and M. Geller.

Dr. Roger K. Ulrich of the University of California at Los Angeles and Dr. Gillian Knapp of the Owens Valley Radio Observatory continued using Shectman's pulse-counting spectrometer at the coudé focus of the Mount Wilson 2.5-meter telescope in a survey of Balmer and Na-D line profiles in T Tauri stars. Red-displaced absorption components of the Na-D lines are interpreted as accretions onto the stars. The case of AS 205, in which the absorption-like feature in the Balmer lines is blue-shifted while the Na-D lines are red-shifted, requires further elucidation.

Dr. P. D. Usher of The Pennsylvania State University has commenced with Sandage a collaborative study of selected high-latitude fields, using the Palomar 1.2-meter Schmidt. The purpose is to identify and catalog candidate quasi-stellar objects to $B \sim 20$ mag in the fields that are centered on Kapteyn-selected areas and which cover about 430° of the North and South Polar Caps. The study supplements the ongoing program of selection and photometry being undertaken by Sandage as part of a mapping program of the galactic halo. It will provide a complete intermediate-magnitude catalog that is necessary to bridge the bright-quasar survey being conducted by Dr. A. A. Hoag.

Recent-epoch plates taken with the Palomar 1.2-meter Schmidt will be used to update variability statistics on quasars in the 8^h Sandage-Luyten Survey fields.

The optical remnant of 3C58, which is believed to have been produced by the supernova of 1181 A.D., was found by Dr. Sidney van den Bergh of the University of Toronto on red plates obtained with the Hale 5-meter telescope. Unpublished spectroscopic work by Kirshner shows that this nebulosity has low radial velocity. This appears to be the third case in which a young supernova is embedded in a circumstellar shell.

Van den Bergh has completed a four-year program of searching for optical supernova remnants by blinking matched pairs of $H\alpha$ and [S II] plates obtained with the 1.2-meter Schmidt telescope on Palomar Mountain. The results of this survey are now being published and bring the total number of optically identified supernova remnants up to 29. It is particularly interesting to note that three quarters of the known supernova remnants in the anticenter hemisphere have now been identified. This indicates that the outer parts of the Galaxy are relatively transparent.

Dr. Karl W. Kamper of David Dunlap Observatory and van den Bergh have used seven plates of the optical remnant of Tycho's supernova taken with the Hale Telescope between 1949 and 1977 to study the expansion of the optical remnant of this object. The present expansion time scale for the remnant is found to be 1050 ± 30 years, which is close to the value $\tau(\text{adiabatic}) = 1000$ years that is obtained from a Sedov similarity solution. At an assumed distance of 6 kpc, the *average* expansion velocity of the remnant is $15,600 \text{ km s}^{-1}$.

Van den Bergh and Dr. Elmar B. F. Brosterhus of the Dominion Astrophysical Observatory have initiated a program of photographic and photoelectric photometry of the fields surrounding all known classical Cepheids with periods in excess of 11 days in the Southern

Milky Way. The photographic material for this program is being obtained with the Swope Telescope on Las Campanas and skeleton photoelectric sequences in each field have been obtained at Cerro Tololo. Preliminary indications are that a number of long-period southern Cepheids are probably association members. Follow-up observations of those Cepheids suspected of association membership will be made to improve the calibration of the bright part of the Cepheid period-luminosity-color relation.

LiBe-Deficient F-Type Stars

Drs. Gerard and Sylvie Vauclair of Columbia University have conducted a spectroscopic study of lithium-beryllium-deficient F stars. They have obtained high-dispersion ($\sim 4 \text{ \AA mm}^{-1}$) spectra at the Mount Wilson 2.5-meter coudé spectrograph of the LiBe-deficient stars discovered by Boesgaard. If this LiBe deficiency is due to nuclear destruction, no other anomalies are expected because of the large turbulence required to bring lithium and beryllium from the surface convection zone toward the nuclear destruction region. If the deficiencies are due to microscopic diffusion, then some composition anomalies are expected for other elements as well.

Direct photographs of southern x-ray clusters of galaxies were taken by Dr. N. V. Vidal, Royal Greenwich Observatory, United Kingdom, in March 1978 on the 1-meter Swope Telescope at Las Campanas. A 3° wide-angle field was covered by 14×14 in. plate size. They

are now being used in conjunction with United Kingdom Schmidt telescope plates (Siding Spring, Australia) to classify galaxies in the Hubble-Sandage system. The results will be used to investigate further the correlation found earlier between the percentage of (E + S0) galaxies and cluster x-ray luminosity (Tytler and Vidal, *Mon. Notic. Roy. Astron. Soc.*, 182, 33P, 1978). This correlation may support the mechanism in which S0 and perhaps elliptical galaxies are produced by the interaction of the hot intergalactic medium with spiral galaxies.

During one run of three nights on the 5-meter coudé, Dr. G. Wallerstein of the University of Washington obtained material on four programs: (1) He searched for interstellar lithium in stars found by Lutz (*Astrophys. J. [Lett.]*, 191, L131, 1974) to have strong interstellar neutral potassium lines; no lithium was detected. (2) He obtained three spectrograms of M22-V5 as part of a program to obtain O/Fe ratios in globular-cluster stars. (3) He obtained near-infrared spectra of the long-period variables T Cephei and χ Cygni as part of a program on velocity gradients and discontinuities in long-period variables. (4) He obtained two spectrograms of HM Sagittae, a star that has recently brightened and may be a new planetary nebula with Wolf-Rayet-type central star. A kinematic model of HM Sge, consisting of a central star with extremely broad lines, a planetarylike envelope expanding at about 75 km s^{-1} , and a preexisting quiescent envelope, was presented in *Publ. Astron. Soc. Pacific*, 90, 36, 1978.

BIBLIOGRAPHY

Aaronson, Marc, Jay A. Frogel, and S. Eric Persson, Photometric studies of composite stellar systems, II, Observations of H_2O absorption and the coolest stellar component of E and S0 galaxies, *Astrophys. J.*, 220, 442-448, 1978.

Aaronson, Marc, *see also* Frogel, Jay A.; Har-
toog, M. R.; Persson, S. Eric.

Adams, W. M., and Frances Tang, Differential rotation of short-lived solar filaments, *Sol. Phys.*, 55, 499-504, 1977.

- Arp, Halton, Neighborhoods of galaxies, II, NGC 4151, *Astrophys. J.*, 218, 70–85, 1977.
- Arp, Halton, A compact high-redshift object silhouetted in front of the E galaxy NGC 1199, *Astrophys. J.*, 220, 401–417, 1978.
- Arp, Halton, *see also* Greenstein, Jesse L.; Stocke, John; Sulentic, Jack W.
- Babcock, Horace W., Requirements on ground-based telescopes, in *Optical Telescopes of the Future, Proc. ESO Conference*, pp. 37–41, F. Pacini, W. Richter, and R. N. Wilson, eds., European Southern Observatory, Geneva, 1978.
- Bahcall, Neta A., and Wallace L. W. Sargent, The redshift and optical structure of the x-ray galaxy cluster A478, *Astrophys. J. (Lett.)*, 225, L19–L21, 1977.
- Becklin, Eric E., K. Matthews, G. Neugebauer, and S. P. Willner, Infrared observations of the galactic center, I, Nature of the compact sources, *Astrophys. J.*, 219, 121–128, 1978.
- Becklin, Eric E., K. Matthews, G. Neugebauer, and S. P. Willner, Infrared observations of the galactic center, III, 2.2 micron spectroscopy, *Astrophys. J.*, 220, 831–835, 1978.
- Becklin, Eric E., *see also* Hyland, A. R.; Neugebauer, Gerry; Werner, Michael W.; Wynn-Williams, C. G.
- Beckwith, S., S. E. Persson, and I. Gatley, Detection of molecular hydrogen emission from five planetary nebulae, *Astrophys. J. (Lett.)*, 219, L33–L38, 1978.
- Bergeron, Jacqueline, and James E. Gunn, The extended H I regions around spiral galaxies: a probe for galactic structure and the intergalactic medium, *Astrophys. J.*, 217, 892–902, 1977.
- Black, David C., *see* Greenstein, Jesse L.
- Bohlin, J. David, *see* Moore, Ronald L.
- Boksenberg, A., and Wallace L. W. Sargent, The existence of Ca II absorption lines in the spectrum of the quasar 3C232 due to the galaxy NGC 3067, *Astrophys. J.*, 220, 42–46, 1978.
- Boksenberg, A., A. J. Willis, and L. Searle, Observations of three Wolf-Rayet stars in M33, *Mon. Notic. Roy. Astron. Soc.*, 180, 15p–19p, 1977.
- Boksenberg, A., *see also* Boroson, Todd; Greenstein, Jesse L.; Sargent, Wallace L. W.; Shipman, H. L.; Young, Peter.
- Boroson, Todd, Wallace L. W. Sargent, A. Boksenberg, and R. F. Carswell, New observations of the absorption spectrum of PKS 0237–23 and their implications for the origin of quasar absorption lines, *Astrophys. J.*, 220, 772–782, 1978.
- Boroson, T. A., *see also* Greenstein, Jesse L.
- Borra, Ermanno, and Arthur H. Vaughan, High-resolution polarization observations inside spectral lines of magnetic Ap stars, I, Instrumentation and observations of β Coronae Borealis, *Astrophys. J.*, 216, 357–371, 1977.
- Borra, Ermanno, and Arthur H. Vaughan, High-resolution polarization observations inside the spectral lines of magnetic Ap stars, II, Observations of α^2 Canum Venaticorum, *Astrophys. J.*, 220, 924–930, 1978.
- Burstein, D., *see* Faber, S. M.
- Carswell, R. F., *see* Boroson, Todd.
- Cohen, Judith G., Jay A. Frogel, and S. Eric Persson, Infrared photometry, bolometric magnitudes, and effective temperatures for giants in M3, M13, M92, and M67, *Astrophys. J.*, 222, 165–180, 1978.
- Cowley, A. P., F. D. A. Hartwick, and W. L. W. Sargent, Spectra of giant stars in distant satellites of the galaxy, *Astrophys. J.*, 220, 435–457, 1978.
- de Bruyn, A. G., Radio properties of active nearby spiral galaxies, in *Structure and Properties of Nearby Galaxies, Int. Astron. Union Symp.*, 77, E. M. Berkhysen and R. Wielebinski, eds., D. Reidel Publishing Co., Dordrecht-Holland, pp. 205–219, 1978.
- de Bruyn, A. G., and A. S. Wilson, The radio properties of Seyfert galaxies, *Astron. Astrophys.*, 64, 433–444, 1978.
- Diner, David J., and James A. Westphal, Silicon vidicon imaging of Jupiter: 4100- to 8300-Å absolute reflectivities and limb darkening of spatially resolved regions, *Icarus*, 32, 299–313, 1977.
- di Tullio, Graziella, *see* Sulentic, Jack W.
- Dressler, Alan, Bautz-Morgan classes and the luminosity function for clusters of galaxies, *Astrophys. J.*, 222, 23–28, 1978.
- Dressler, Alan, and Allan Sandage, First results of the Las Campanas survey to classify southern galaxies photographed with the du Pont 2.5 meter reflector, *Publ. Astron. Soc. Pacific*, 90, 5–9, 1978.
- Dressler, Alan, *see also* Faber, S. M.
- Dworetzky, M. M., Howard Lanning, Paul B. Etzel, and Darryl J. Patenaude, BD–3°5357, an unusual eclipsing binary, *Int. Astron. Union Bull. Var. Stars*, 1284, May 26, 1977.
- Dworetzky, M. M., Howard Lanning, Paul B. Etzel, and Darryl J. Patenaude, BD–3°5357: an eclipsing binary with a hot subdwarf component, *Mon. Notic. Roy. Astron. Soc.*, 181, 13P–18P, 1977.
- Elias, H. H., D. J. Ennis, D. Y. Gezari, M. G. Hauser, J. R. Houck, K. Y. Lo, K. Matthews, D. Nadeau, G. Neugebauer, M. W. Werner, and W. E. Westbrook, One-millimeter con-

- tinuum observations of extragalactic objects, *Astrophys. J.*, 220, 25-41, 1978.
- Elias, J., *see also* Huchra, J.
- Ennis, J. H., *see* Elias, J. H.
- Etzel, Paul B., *see* Dworetsky, M. M.
- Faber, S. M., D. Burstein, and A. Dressler, Spectrum of the halo of the CD galaxy in Abell 401^a, *Astron. J.*, 82, 941-946, 1977.
- Frogel, Jay A., S. Eric Persson, Marc Aaronson, and K. Matthews, Photometric studies of composite stellar systems, I, CO and JHK observations of E and S0 galaxies, *Astrophys. J.*, 220, 75-97, 1978.
- Frogel, Jay A., *see also* Aaronson, Marc; Cohen, Judith G.; Persson, S. Eric.
- Gatley, I., *see* Beckwith, S.
- Gezari, D. Y., *see* Elias, J. H.
- Goldreich, P., *see* Persson, S. Eric.
- Gott, J. Richard, III, *see* Thuan, Trinh X.
- Green, Richard F., and Maarten Schmidt, Evidence for nonuniform radial distribution of quasars, *Astrophys. J. (Lett.)*, 220, L1-L4, 1978.
- Green, Richard F., *see also* Morton, D. C.; Shaffer, D. B.
- Greenstein, Jesse L., Astronomical implications of future very large telescopes, in *Optical Telescopes of the Future, Proc. ESO Conference*, pp. 525-535, F. Pacini, W. Richter, and R. N. Wilson, eds., European Southern Observatory, Geneva, 1978.
- Greenstein, Jesse L., Résumé of conference and introduction to panel discussion, in *Optical Telescopes of the Future, Proc. ESO Conference*, pp. 537-542, F. Pacini, W. Richter, and R. N. Wilson, eds., European Southern Observatory, Geneva, 1978.
- Greenstein, Jesse L., The HR diagram, in *The Hertzsprung-Russell Diagram, Int. Astron. Union Symp. 80*, A. G. Davis Philip and D. S. Hayes, eds., D. Reidel Publishing Co., Dordrecht-Holland, pp. 101-116, 1978.
- Greenstein, Jesse L., A high-velocity magnetic degenerate, G35-26, *Publ. Astron. Soc. Pacific*, 90, 303-306, 1978.
- Greenstein, Jesse L., and David C. Black, Report of the Planetary Detection Workshops to the Office of Space Science of the National Aeronautics and Space Administration, Ames Research Center, Moffett Field, January 1977.
- Greenstein, Jesse L., and Barbara A. Zimmerman, VV Puppis, *Int. Astron. Union Circ.*, 3197, March 21, 1978.
- Greenstein, Jesse L., H. C. Arp, and S. Shectman, Blue variables at high galactic latitude, *Publ. Astron. Soc. Pacific*, 89, 741-745, 1977/78.
- Greenstein, Jesse L., M. A. Kazarian, T. Yu. Magakian, and E. Ye. Khachikian, On the distance of R Mon and NGC 2261 (in Russian), *Astron. Circ., USSR, No. 947*, 1-3, 1977.
- Greenstein, Jesse L., M. A. Kazarian, T. Yu. Magakian, and E. Ye. Khachikian, A spectrophotometric study of the cometary nebula NGC 2261 and its nucleus R Mon, in *Flare Stars*, pp. 125-126, L. V. Mirzoyan, ed., Academy of Sciences, Yerevan, U.S.S.R., 1977.
- Greenstein, Jesse L., W. L. W. Sargent, T. A. Boroson, and A. Boksenberg, Velocity curves for broad and sharp components observed in the emission lines from Am Herculis, *Astrophys. J. (Lett.)*, 218, L121-L127, 1977.
- Greenstein, Jesse L., J. B. Oke, D. Richstone, W. F. van Altena, and Hans Steppe, Further degenerate stars, X, *Astrophys. J. (Lett.)*, 218, L21-L25, 1977.
- Greenstein, Jesse L., *see also* Shipman, H. L.
- Gunn, James E., Massive galactic halos, I, Formation and evolution, *Astrophys. J.*, 218, 592-598, 1977.
- Gunn, James E., The nature of the nebulosity around BL Lac objects, *Physica Scripta*, 17, 277-279, 1978.
- Gunn, James E., *see also* Bergeron, Jacqueline; Laing, R. A.
- Hardy, Eduardo, Some integrated photometric properties of the Large Magellanic Cloud, *Publ. Astron. Soc. Pacific*, 90, 132-138, 1978.
- Hartoog, M. R., S. E. Persson, and M. Aaronson, The strength of the 2.3 μ CO band in weak G-band stars, *Publ. Astron. Soc. Pacific*, 89, 660-662, 1977.
- Hartwick, F. D. A., and W. L. W. Sargent, Radial velocities for outlying satellites and their implications for the mass of the galaxy, *Astrophys. J.*, 221, 512-520, 1978.
- Hartwick, F. D. A., *see also* Cowley, A. P.; Sandage, Allan; Sargent, Wallace L. W.; Young, Peter.
- Hauser, M. G., *see* Elias, J. H.; Warner, Michael W.
- Hickson, Paul, The angular size-redshift relation, I, Sizes and shapes of nearby clusters of galaxies, *Astrophys. J.*, 225, 16-23, 1977.
- Hickson, Paul, The angular size-redshift relation, II, Sizes and shapes of nearby clusters of galaxies, *Astrophys. J.*, 225, 964-975, 1977.
- Hoessel, John Greg, Hypersensitization of Kodak red and infrared emulsions, *AAS Photo-Bull.*, 17, 10-11, 1978.
- Hoessel, John Greg, *see also* Huchra, John.
- Houck, J. R., *see* Elias, J. H.; Werner, Michael W.

- Howard, Robert, Large-scale solar magnetic fields, *Annu. Rev. Astron. Astrophys.*, **15**, 153–173, 1977.
- Howard, Robert, Solar cycle, solar rotation, and large-scale circulation, in *Illustrated Glossary for Solar and Solar-Terrestrial Physics*, Vol. 69, pp. 7–12, A. Bruzek and C. J. Durant, eds., D. Reidel Publishing Co., Dordrecht-Holland, 1977.
- Howard, Robert, Solar rotation and large-scale velocity fields, in *Large-Scale Motions of the Sun*, *Proc. Sacramento Peak Observatory Symp.*, pp. 58–76, Sacramento Peak Observatory, Sunspot, New Mexico, 1977.
- Howard, Robert, and Z. Svestka, Development of a complex of activity in the solar corona, *Sol. Phys.*, **54**, 65–105, 1977.
- Howard, Robert, *see also* Svestka, Zdenek.
- Huchra, John, Star formation in blue galaxies, *Astrophys. J.*, **225**, 928–939, 1977.
- Huchra, John, The nature of Markarian galaxies, *Astrophys. J., Suppl. Ser.*, **35**, No. 2, 171–195, 1977.
- Huchra, John, J. Hoessel, and J. Elias, A nearby cluster of galaxies at low galactic latitude, *Astron. J.*, **82**, 671–676, 1977.
- Huggins, P. J., *see* Phillips, T. G.
- Hyland, A. R., E. E. Becklin, and Gerry Neugebauer, The $\text{La}/\text{H}\alpha$ intensity ratio in Pks 0237–23, *Astrophys. J. (Lett.)*, **220**, L73–L75, 1978.
- Katem, Basil, *see* Kristian, Jerome; Sandage, Allan.
- Katz, Jonathan I., *see* Margon, Bruce.
- Kaufman, Michele, and Trinh X. Thuan, Young massive galactic halos at large redshifts, *Astrophys. J.*, **215**, 11–19, 1977.
- Kazarian, M. A., *see* Greenstein, Jesse L.
- Khachikian, E. Ye., *see* Greenstein, Jesse L.
- Kibblewhite, E. J., *see* Laing, R. A.
- Kormendy, John, Brightness distribution in compact and normal galaxies, III, Decomposition of observed profiles into spheroid and disk components, *Astrophys. J.*, **217**, 406–419, 1977.
- Kormendy, John, Brightness distribution in compact and normal galaxies, II, Structure parameters of the spheroidal component, *Astrophys. J.*, **226**, 333–346, 1977.
- Kowal, Charles T., The Perseid comet: Comet Swift-Tuttle, its association with the Perseid meteors and plans to recover it, *Comet News Service, Review Issue*, 78–2, 1–2, 1978.
- Kowal, Charles T., Period comet Kowal (1977f), *Int. Astron. Union Circ.*, **3097**, August 25, 1977.
- Kowal, Charles T., 1977 HB, *Int. Astron. Union Circ.*, **3114**, September 28, 1977; **3223**, May 18, 1978.
- Kowal, Charles T., Slow-moving Object Kowal, 1977 UB, *Int. Astron. Union Circ.*, **3129**, November 4, 1977; **3130**, November 8, 1977; **3134**, November 14, 1977; **3143**, November 28, 1977; **3147**, December 5, 1977.
- Kowal, Charles T., Surprise in the solar system, *The Sciences*, **18**, 12–15, 1978.
- Kowal, Charles T., *see also* Sargent, Wallace L. W.
- Kristian, Jerome, Allan Sandage, and Basil Katem, On the systematic optical identification of the remaining 3C radio sources, II, New data for 50 fields, *Astrophys. J.*, **219**, 803–811, 1978.
- Kristian, Jerome, Allan Sandage, and James A. Westphal, The extension of the Hubble diagram, II, New redshifts and photometry of very distant galaxy clusters, First indication of a deviation of the Hubble diagram from a straight line, *Astrophys. J.*, **221**, 383–394, 1978.
- Kristian, Jerome, *see also* Spinrad, Hyron; Young, Peter J.
- Laing, R. A., M. S. Longair, J. M. Riley, E. J. Kibblewhite, and J. E. Gunn, Investigations of the optical fields of 3CR radio sources to faint limiting magnitudes—II, *Mon. Notic. Roy. Astron. Soc.*, **183**, 457–458, 1978.
- Landauer, Frederick P., *see* Young, Peter J.
- Lanning, Howard, *see* Dworetsky, M. M.
- Leung, Kam-Ching, and Donald P. Schneider, YY Geminorum, I, Photometry and absolute dimensions, *Astron. J.*, **83**, 618–625, 1978.
- Leung, Kam-Ching, and Donald P. Schneider, Evolved contact systems of spectral type A: AU Pup, V535 Ara, and V1073 Cyg, *Astrophys. J.*, **222**, 817–923, 1978.
- Leung, Kam-Ching, and Donald P. Schneider, Evolved contact systems of spectral type O, I, UW Canis Majoris, *Astrophys. J.*, **222**, 924–930, 1978.
- Levine, Randolph H., *see* Svestka, Zdenek.
- Lo, K. Y., *see* Elias, J. H.
- Longair, M. S., *see* Laing, R. A.
- Lynds, C. R., *see* Sargent, Wallace L. W.; Young, Peter J.
- Magakian, T. Yu., *see* Greenstein, Jesse L.
- Margon, Bruce, Jonathan I. Katz, and Larry D. Petro, The nature of Aquila X-1, *Nature*, **271**, 633–634, 1978.
- Marsh, K. A., D3 spicules and the lower chromosphere, *Sol. Phys.*, **57**, 37–48, 1978.

- Matthews, K., *see* Becklin, Eric E.; Elias, J. H.; Frogel, Jay A.; Neugebauer, Gerry; Persson, S. Eric; Wynn-Williams, C. G.
- Melnick, Jorge, and Wallace L. W. Sargent, The radial distribution of morphological types of galaxies in x-ray clusters, *Astrophys. J.*, **215**, 401–407, 1977.
- Miller, William C., Photographic plate fog: An improved method for its correction, *AAS Photo Bull.*, **16**, 3–9, 1977.
- Moore, Ronald L., Frances Tang, J. David Bohlin, and L. Golub, $H\alpha$ macrospicules: identification with *EUV* macrospicules and with flares in x-ray bright points, *Astrophys. J.*, **226**, 286–290, 1977.
- Morton, D. C., T. B. Williams, and Richard F. Green, The spectrum of the halo surrounding the quasar PHL 1070, *Astrophys. J.*, **219**, 381–386, 1978.
- Münch, Guido, J. T. Trauger, and F. L. Roesler, A search for the $H_2(3,0)$, S1 line in the spectrum of Titan, *Astrophys. J.* **216**, 963–966, 1977.
- Münch, Guido, *see also* Trauger, John.
- Nadeau, D., *see* Elias, J. H.
- Neugebauer, Gerry, Infrared observations of Seyfert galaxies and quasars, *Physica Scripta*, **17**, 149–151, 1978.
- Neugebauer, Gerry, Future prospects of infrared observations of active nuclei, *Physica Scripta*, **17**, 325–326, 1978.
- Neugebauer, Gerry, E. E. Becklin, K. Matthews, and C. G. Wynn-Williams, Infrared observations of the galactic center, III, 2.2 μ m spectroscopy, *Astrophys. J.*, **220**, 149–155, 1978.
- Neugebauer, Gerry, *see also* Becklin, Eric E.; Elias, J. H.; Hyland, A. R.; Persson, S. Eric; Phillips, T. G.; Werner, Michael W.; Wynn-Williams, C. G.
- Nicholson, P., *see* Persson, S. Eric.
- Norris, John, and Robert Zinn, The weak G-band effect in M31, M92, NGC 6397, and M15, *Astrophys. J.*, **215**, 74–88, 1977.
- Oke, J. B., Further spectrophotometry of the transient x-ray source A0620–00, *Astrophys. J.*, **217**, 181–185, 1977.
- Oke, J. B., The redshift and other properties of I Zw 1727+5015, *Astrophys. J. (Lett.)*, **219**, L97–L100, 1978.
- Oke, J. B., Seyfert galaxies and quasars, *J. Roy. Astron. Soc. Canada*, **72**, 121–137, 1978.
- Oke, J. B., *see also* Greenstein, Jesse L.; Wade, Richard A.; Wilkinson, Althea.
- Patenaude, Darryl J., *see* Dworetzky, M. M.
- Persson, S. Eric, M. Aaronson, and J. A. Frogel, Broad-band infrared colors and CO and H_2O absorption indices for late-type dwarf stars, *Astron. J.*, **82**, 729–733, 1977.
- Persson, S. Eric, P. Nicholson, K. Matthews, P. Goldreich, and G. Neugebauer, Occultations by Uranian rings, *Int. Astron. Union Circ.*, **3215**, May 1, 1978.
- Persson, S. Eric, *see also* Aaronson, Marc; Beckwith, S.; Cohen, Judith G.; Frogel, Jay A.; Hartoog, M. R.
- Petro, Larry D., *see* Margon, Bruce.
- Phillips, T. G., P. J. Huggins, G. Neugebauer, and M. W. Werner, Detection of submillimeter (870 μ m) CO emission from the Orion molecular cloud, *Astrophys. J. (Lett.)*, **209**, L161–L164, 1977.
- Preston, George W., *see* Swings, Jean Pierre; Vaughan, Arthur H.
- Richstone, D., *see* Greenstein, Jesse L.
- Riley, J. M., *see* Laing, R. A.
- Ritchie, D., *see* Young, Peter J.
- Roesler, F. L., *see* Münch, Guido; Trauger, John.
- Sandage, Allan, Andromeda Galaxy, in *McGraw-Hill Encyclopedia of Science and Technology*, 4th Ed., Vol. 1, p. 423, McGraw-Hill Book Company, New York, 1977.
- Sandage, Allan, Magellanic Clouds, in *McGraw-Hill Encyclopedia of Science and Technology*, 4th Ed., Vol. 8, pp. 14–15, McGraw-Hill Book Company, New York, 1977.
- Sandage, Allan, and F. D. A. Hartwick, The remote halo globular cluster Palomar 5, *Astron. J.*, **82**, 459–464, 1977.
- Sandage, Allan, and Basil Katem, Faint photometry in M15: the intrinsic width of the main sequence, the luminosity function, and the density gradient of faint field stars, *Astrophys. J.*, **215**, 62–73, 1977.
- Sandage, Allan, *see also* Dressler, Alan; Kristian, Jerome; Spinrad, Hyron; Visvanathan, Natarajan; Yahil, Amos.
- Sargent, Anneila I., Molecular clouds and star formation, I, Observations of the Cepheus OB3 molecular cloud, *Astrophys. J.*, **218**, 736–748, 1977.
- Sargent, Wallace L. W., C. T. Kowal, F. D. A. Hartwick, and Sidney van den Bergh, A search for globular clusters in M31, I, The disk and the minor axis, *Astron. J.*, **82**, 947–953, 1977.
- Sargent, Wallace L. W., Peter J. Young, A. Boksenberg, Keith Shortridge, C. R. Lynds, and F. D. A. Hartwick, Dynamical evidence for a central mass concentration in the galaxy M87, *Astrophys. J.*, **221**, 731–744, 1978.
- Sargent, Wallace L. W., *see also* Bahcall, Neta A.; Boksenberg, A.; Boroson, Todd; Cowley,

- A. P.; Greenstein, Jesse L.; Hartwick, F. D. A.; Melnick, Jorge; Young, Peter J.
- Schmidt, Maarten, Optical spectra and redshifts of quasi-stellar radio sources in the NRAO 5-GHz and 4C radio catalogs, *Astrophys. J.*, 217, 318-361, 1977.
- Schmidt, Maarten, Quasars and cosmological evolution, in *The Large-Scale Structure of the Universe*, *Int. Astron. Union Symp.* 79, pp. 289-293, M. S. Longair and J. Einasto, ed., D. Reidel Publishing Co., Dordrecht-Holland, 1978.
- Schmidt, Maarten, The local space density of quasars and active nuclei, *Physica Scripta*, 17, 135-136, 1978.
- Schmidt, Maarten, The cosmological evolution of quasars, *Physica Scripta*, 17, 329-332, 1978.
- Schmidt, Maarten, *see also* Green, Richard F.
- Schneider, Donald P., *see also* Leung, Kam-Ching.
- Searle, Leonard, *see* Boksenberg, A.; Shields, G. A.
- Shaffer, D. B., and R. F. Green, Centimetric radio emission from bright optical quasars, *Publ. Astron. Soc. Pacific*, 90, 22-23, 1978.
- Shectman, S., *see* Greenstein, Jesse L.
- Shields, G. A., and Leonard Searle, The composition gradient across M101, *Astrophys. J.*, 222, 821-832, 1978.
- Shipman, H. L., J. L. Greenstein, and A. Boksenberg, Calcium in the helium white dwarf GD 40, *Astron. J.*, 82, 480-486, 1977.
- Shortridge, Keith, *see* Sargent, Wallace L. W.
- Solodyna, Craig V., *see* Svestka, Zdenek.
- Spinrad, Hyron, James Westphal, Jerome Kristian, and Allan Sandage, Spectroscopy and photometry of the distant radio galaxy 3C343.1, *Astrophys. J. (Lett.)*, 216, L87-L89, 1977.
- Steppe, Hans, *see* Greenstein, Jesse L.
- Stocke, John, and Halton Arp, Two quasars near a peculiar pair of galaxies, *Astrophys. J.*, 219, 367-371, 1978.
- Sulentic, Jack W., Halton C. Arp, and Graziella A. di Tullio, Interacting nonequilibrium systems near bright galaxies, *Astrophys. J.*, 220, 47-61, 1978.
- Svestka, Zdenek, Craig V. Solodyna, Robert Howard, and Randolph H. Levine, Open magnetic fields in active regions, *Sol. Phys.*, 55, 359-369, 1977.
- Svestka, Z., *see also* Howard, Robert.
- Swings, Jean Pierre, and George Preston, The spectrum of the Antares nebula, *Astrophys. J.*, 220, 883-886, 1978.
- Tammann, G. A. *see* Yahil, Amos.
- Tang, Frances, *see* Adams, W. M.; Moore, Ronald L.
- Thuan, Trinh X., and J. Richard Gott, III, The angular momentum of galaxies, *Astrophys. J.*, 216, 194-205, 1977.
- Thuan, Trinh X., *see* Kaufman, Michele.
- Trauger, John, F. L. Roesler, and Guido Münch, A redetermination of the Uranus rotation period, *Astrophys. J.*, 219, 1079-1083, 1978.
- Trauger, John, *see* Münch, Guido.
- van Altena, W. F., *see* Greenstein, Jesse L.
- van den Bergh, Sidney, *see* Sargent, Wallace L. W.
- Vaughan, Arthur H., George W. Preston, and Olin C. Wilson, Flux measurements of Ca II H and K emission, *Publ. Astron. Soc. Pacific*, 90, 267-274, 1978.
- Vaughan, Arthur H., *see also* Borra, Ermanno.
- Visvanathan, Natarajan, and Allan Sandage, The color-absolute magnitude relation for E and S0 galaxies, I, Calibration and tests for universality using Virgo and eight other nearby clusters, *Astrophys. J.*, 216, 214-226, 1977.
- Wade, Richard A., and J. B. Oke, Optical spectrum of HDE 245770 (A0535+26), *Astrophys. J.*, 215, 568-573, 1977.
- Werner, Michael W., E. E. Becklin, and G. Neugebauer, Infrared studies of star formation, *Science*, 197, 723-732, 1977.
- Werner, Michael W., *see also* Elias, J. H.; Phillips, T. G.
- Westbrook, W. E., *see* Elias, J. H.
- Westphal, James A., *see* Diner, David J.; Kristian, Jerome; Spinrad, Hyron; Young, Peter J.
- Wilkinson, Althea, and J. B. Oke, Spectral variations in brightest cluster galaxies, *Astrophys. J.*, 220, 376-389, 1978.
- Williams, T. B., *see* Morton, D. C.
- Willis, A. J., *see* Boksenberg, A.
- Willner, S. P., Infrared observations of the galactic center, II, [Ne II] emission, *Astrophys. J.*, 219, 870-872, 1978.
- Willner, S. P., *see also* Becklin, Eric E.
- Wynn-Williams, C. G., E. E. Becklin, K. Matthews, and G. Neugebauer, Two-micron line emission from the H II region G33.6-0.2, *Mon. Notic. Roy. Astron. Soc.*, 183, 237-244, 1978.
- Wynn-Williams, C. G., *see also* Neugebauer, Gerry.
- Wilson, A. S., *see* deBruyn, A. G.
- Wilson, Christopher P., *see* Young, Peter J.
- Wilson, Olin C., *see* Vaughan, Arthur H.
- Yahil, Amos, G. A. Tammann, and Allan Sandage, The Local Group: the solar motion

- relative to its centroid, *Astrophys. J.*, 225, 903-915, 1977.
- Young, Peter J., Stellar density cusp around a massive black hole, *Astrophys. J.*, 225, 287-295, 1977.
- Young, Peter J., and D. Ritchie, Supernova in faint galaxy, *Int. Astron. Union Circ.*, 3122, October 19, 1977.
- Young, Peter J., W. L. W. Sargent, A. Boksenberg, C. R. Lynds, and F. D. A. Hartwick, Dynamics of the flattened elliptical galaxy NGC 4473, *Astrophys. J.*, 222, 450-455, 1978.
- Young, Peter J., James A. Westphal, Jerome Kristian, Christopher P. Wilson, and Frederick P. Landauer, Photometric evidence for a supermassive object in the nucleus of the galaxy M87, *Astrophys. J.*, 221, 721-730, 1978.
- Young, Peter J., *see also* Sargent, Wallace L. W.
- Zimmerman, Barbara A., *see* Greenstein, Jesse L.
- Zinn, Robert, A spectroscopic survey of the giant branch of M5, *Astrophys. J.*, 218, 96-104, 1977.
- Zinn, Robert, *see also* Norris, John.
- Zirin, Harold, The $L\alpha/H\alpha$ ratio in solar flares, quasars, and the chromosphere, *Astrophys. J. (Lett.)*, 222, L105-L107, 1978.

PERSONNEL

Year Ended June 30, 1978

Ray L. Ballard, Senior Administrative Assistant at the Robinson Laboratory, died on December 7, 1977. He served for 11 years as administrator for the Robinson Laboratory and Palomar Observatory in a modest and efficient way.

Eugene L. Hancock, Senior Night Assistant at Mount Wilson, died on March 2, 1978. Close to retirement, he had been at the Observatory since 1947. He is remembered by many observers for his unstinting support at the 2.5-meter telescope and for his personal qualities.

Research Division

Staff Members

Halton C. Arp
 Horace W. Babcock, *Director*
 Jesse L. Greenstein¹
 James E. Gunn²
 Robert F. Howard
 Jerome Kristian
 Robert B. Leighton³
 Guido Münch^{2, 3, 4}
 Gerry Neugebauer³
 J. Beverley Oke,² *Associate Director*
 S. Eric Persson
 George W. Preston,
Assistant Director, Mount Wilson
 Allan R. Sandage

¹ Lee A. DuBridge Professor of Astrophysics, California Institute of Technology.

² Professor of Astronomy, California Institute of Technology.

³ Professor of Physics, California Institute of Technology.

Wallace L. W. Sargent⁴
 Maarten Schmidt,² *Director-Designate*
 Leonard Searle
 Stephen A. Sheetman
 Arthur H. Vaughan
 James A. Westphal⁵
 Harold Zirin⁶

Members Engaged in Post-Retirement Studies

Alexander Pogo
 Henrietta H. Swope
 Olin C. Wilson

Staff Associates

Robert J. Brucato⁷
 B. Thomas Soifer⁸
 Michael W. Werner⁹

Senior Research Fellows

Alan M. Dressler¹⁰
 Thomas R. Geballe¹⁰

⁴ Professor of Astronomy; Executive Officer for Astronomy, California Institute of Technology.

⁵ Professor of Planetary Science, California Institute of Technology.

⁶ Chief Astronomer of Big Bear Solar Observatory; Professor of Astrophysics, California Institute of Technology.

⁷ Scientific Officer, Las Campanas Observatory.

⁸ Senior Research Fellow, California Institute of Technology.

⁹ Assistant Professor of Physics, California Institute of Technology.

¹⁰ Las Campanas Observatory Fellow.

Ronald Moore⁸
Robert J. Zinn¹⁰

Research Fellows

William M. Adams^{11, 12}
Thomas B. Ake III¹²
Gary S. Da Costa¹³
A. Ger de Bruyn¹³
Richard F. Green¹²
Robert C. Kennicutt, Jr.¹³
Barry J. LaBonte
Stefan Mochnecki¹²
Jeremy R. Mould¹³
Larry D. Petro¹³
James A. Rose¹³
Anneila I. Sargent¹²
Robert Schommer¹²
Jack W. Sulentic
Althea Wilkinson^{12, 14}

Carnegie-Chilean Fellow

Guido Garay

Librarians

Helen Z. Knudsen
Nan W. Schow¹⁵

Senior Research Assistants

Gordon J. Hurford
Grace V. Knox
Charles T. Kowal

Research Assistants

John M. Adkins
John E. Boyden
Ken D. Clardy
Basil N. Katem
Margaret Katz¹⁶
Stephen P. Padilla
Frances Y. C. Tang

Student Observers¹⁷

Steven V. W. Beckwith¹⁸
Graham Berriman
Kirk D. Borne
France A. Cordova
David J. Diner¹⁸
Jonathan H. Elias¹⁸
Boris Gokham
John G. Hoessel
Stephen M. Kent
Daniel Nadeau
William C. Priedhorsky¹⁸
Jeffrey R. Pier
Douglas M. Rabin
Russell O. Redman
Donald P. Schneider
William L. Sebok
Richard J. Terrile¹⁸
Richard A. Wade
Howard K.-C. Yee
Peter J. Young

Photographic Department

John R. Bedke, Photographer

Instrument Design and Construction

David A. Bell,
Electronics Engineering Aide¹⁹
Lawrence E. Blakée, Supervisor,
Electronic Services
Barbara L. Dailey, Draftswoman²⁰
Stephen Doro, Machinist
Earle B. Emery, Senior Research Engineer
Eugene B. Fair, Head Optician²¹
Hannah Fox, Computing Analyst²²
Jerry T. Fridenberg,
Senior Electronics Engineer
C. L. Friswold, Head, Design Group
Robert D. Georgen, Machinist
Richard M. Goeden, Senior Engineer
John G. Golson, Optician²³
Simon Groesz, Electronics Specialist
Fred H. Harris,
Associate Electronics Engineer

¹⁷ Enrolled at California Institute of Technology.

¹⁸ Graduated June 9, 1978.

¹⁹ To April 3, 1978.

²⁰ To March 31, 1978.

²¹ To November 4, 1977.

²² To May 31, 1978.

²³ To June 30, 1978.

¹¹ Fellowship ended September 30, 1977.

¹² Research Fellow, California Institute of Technology.

¹³ Carnegie Fellow.

¹⁴ Fellowship ended October 31, 1977.

¹⁵ Leave of absence.

¹⁶ Sick leave.

Leroy M. Kimoto,
Senior Electronics Specialist²⁴
Erich R. Koch,
Senior Electronics Engineer²⁵
Wilfred H. Leckie, Senior Draftsman²⁶
William H. McLellan, Senior Engineer
Roger L. Minnix, Engineer
Jeff B. Nenow,
Photographic Laboratory Technician
Nancy A. Newton, Illustrator
Frederick G. O'Neil, Shop Foreman
Juan M. Sanchez,
Photographic Laboratory Technician²⁷
Orval A. Smith, Electronics Specialist
Edward H. Snoddy, Designer
Sharon Soltesz, Administrative Secretary²⁸
Douglas Sprague,
Senior Electronics Engineer²⁹
Merle R. Sweet,
Senior Electronics Technician
David F. Thompson,
Senior Technical Assistant
Glenn A. Toennes, Electronics Technician
Felice Woodworth, Illustrator³⁰

Operation and Maintenance

Mount Wilson Observatory and Offices

Richard T. Black, Business Manager
Robert E. Cadman,
Mountain Superintendent
Herman E. Carpentier, Carpenter
Linda Chaffee, Clerk-Typist³¹
Hugh T. Couch, Superintendent,
Buildings and Grounds
Helen S. Czaplicki, Typist-Editor
Bette DeSmet, Secretary
James Frazer, Night Assistant
Hazel M. Fulton, Head Stewardess
Joan Gantz, Assistant Librarian
Thomas S. Gregory, Solar Observer
Robert J. Grosdidier,
Electronics Technician³²
Joseph F. Hacker, Mechanic

Eugene L. Hancock,
Senior Night Assistant³³
Mary Hark, Stewardess
Jeanne M. Knight, Bookkeeper
Howard H. Lanning, Night Assistant
Jose Lopez-Tiana, Purchasing Clerk
Ernest O. Lorenz,
Assistant Mountain Superintendent³⁴
Frank Perez,
Assistant Mountain Superintendent
William D. Qualls, Chauffeur
Delores Sahlin, Typist-Telephone Operator
Glen Sanger, Senior Custodian
Bernard K. Simpier, Electronics Technician
William D. St. John, Chauffeur
Frank Trylko, Custodian³⁵
Larry Webster, Night Assistant
Frederick P. Woodson, Business Manager³⁶
Gary Yanik, Electronics Engineer

Palomar Observatory and Robinson Laboratory

Ranney G. Adams, Night Assistant
Albert R. Andrews,
Maintenance Mechanic³⁷
Bradley N. Bailey,
Night Assistant and Junior Technician³⁸
Ray L. Ballard,
Senior Administrative Assistant³⁹
Jan Adriaan Bruinsma, Painter
Maria J. Bruinsma, Housekeeping Aide
Juan R. Carrasco,
Night Assistant and Mechanic
Lily D. Carrasco, Housekeeping Aide
Rita A. Ewing, Secretary
Liselotte M. Hauck,
Administrative Assistant
Helen Holloway, Administrative Secretary
Dorothy J. Howard,
Administrative Secretary⁴⁰
Willie D. Jones, Custodian
Kevin M. Jordan, Maintenance Mechanic³⁸
Joyce E. Keeble, Secretary⁴¹
Taras Kiceniuk, Mountain Superintendent
J. Luz Lara, Maintenance Mechanic

²⁴ To January 20, 1978.

²⁵ To February 10, 1978.

²⁶ Long term disability.

²⁷ To August 17, 1977.

²⁸ To March 31, 1978.

²⁹ To February 24, 1978.

³⁰ Retired June 30, 1978.

³¹ To January 31, 1978.

³² To February 3, 1978.

³³ Deceased March 2, 1978.

³⁴ To December 31, 1977.

³⁵ Retired September 30, 1977.

³⁶ Retired June 30, 1978.

³⁷ To November 3, 1977.

³⁸ To June 30, 1978.

³⁹ Deceased December 7, 1977.

⁴⁰ To December 2, 1977.

⁴¹ To June 27, 1977.

Isolde Lata, Administrative Secretary
Marilynne J. Rice,
Senior Administrative Secretary
Elsa-Brita Titchenell,
Administrative Secretary
Gary M. Tuton, Senior Night Assistant
Paul Van Ligten, Electrician
Ruth E. Weaver, Administrative Secretary
Larry L. Wickern,
Assistant Superintendent
Larry K. Williams,
Maintenance Mechanic
Dorothy Williams, Cook
Barbara A. Zimmerman,
Computing Analyst⁴²

⁴² Member of the Professional Staff, California Institute of Technology.

Big Bear Solar Observatory

Alberta R. Altman, Secretary
Jack R. Klemroth,
Solar Observing Assistant
Eugene H. Longbrake, Solar Observer
Walter M. Nagao, Custodian
Alan P. Patterson, Superintendent
Owen Phairis, Solar Observing Assistant

Las Campanas Observatory

Maynard Clark,
Senior Electronics Technician
Rhea Goodwin, Secretary
Ljubomir Papic, Mountain Superintendent
Manfred Wagner, Administrative Manager

Department of Plant Biology

Stanford, California

Winslow R. Briggs

Director

Contents

Introduction (Briggs)	227	Temperature dependence of the turnover of P700 in photosynthesis of the blue-green alga <i>Anacystis nidulans</i> (Murata and Fork)	289
Correlation of photosynthetic unit size and density with photosynthetic capacity (Armond and Mooney)	234	Displacement of integral membrane proteins during lipid phase transitions in <i>Anacystis nidulans</i> (Armond and Staehelin)	291
Probing photosynthetic unit sizes of leaves by fluorescence-induction measurements (Malkin, Fork, and Armond)	237	Formation of (proteo)lipid vesicles by means of a French pressure cell (van Ginkel)	294
Chromosomal numbers in <i>Atriplex</i> (Nobs)	240	Composition of isolated P700-chlorophyll-protein complexes and their photoactivity when combined with lipid vesicles or triton micelles (Brown and van Ginkel)	298
Release and refixation of ammonia during photorespiration (Woo, Berry, and Turner)	240	A dynamic binding of HCO_3^- to chloroplast reaction centers in the light (Stemler)	302
The use of isolated whole leaf cells for photosynthesis studies (Collatz and Badger)	245	Bibliographic information retrieval (Brown)	305
The interaction between photosynthesis and ribulose- P_2 concentration—effects of light, CO_2 , and O_2 (Collatz)	248	A centralized laboratory computing system (Ford and Catanzaro)	305
A mechanism for concentrating CO_2 in <i>Chlamydomonas reinhardtii</i> and <i>Anabaena variabilis</i> and its role in photosynthetic CO_2 fixation (Badger, Kaplan, and Berry)	251	Computer analysis of kinetic data (Ford, Catanzaro, and Fork)	307
Thermal acclimation of photosynthesis: effect of growth temperature on photosynthetic characteristics and components of the photosynthetic apparatus in <i>Nerium oleander</i> (Björkman, Badger, and Armond)	262	Perspectives on the evolution of plant DNA (Thompson)	310
The physical properties of membrane lipids in relation to the adaptation of higher plants and algae to contrasting thermal regimes (Raison and Berry)	276	Sequence repetition and interspersion in pea DNA (Murray and Thompson)	316
The lipid and fatty acid composition, electron transport, and light-energy redistribution in the thermophilic blue-green alga <i>Synechococcus lividus</i> grown at 55° and 38°C (Fork, Murata, and Sato)	283	Distribution of nucleotide sequence divergence among families of repetitive sequences in mung bean DNA (Preisler and Thompson)	323
		Higher derivative analysis of thermal denaturation profiles of reassociated repetitive pea DNA (Cuellar, Ford, Briggs, and Thompson)	330
		Blue-light-induced chloroplast aggregation and cortical fiber reticulation in the alga <i>Vaucheria</i> (Blatt and Briggs)	333

Light-enhanced geotropic sensitivity in maize roots: possible involvement of phytochrome (Quail and Briggs)	336	Characterization of light-induced ab- sorbance changes in membrane fractions from corn coleoptiles (Goldsmith and Briggs)	347
ATP and phytochrome pelletability (Quail and Briggs)	339	Biochemical characteristics of solubilized site I auxin-binding protein from <i>Zea mays</i> (Cross and Briggs)	353
In vivo phosphorylation of phytochrome (Quail, Briggs, and Pratt)	342	Effect of inhibitors on light-induced absorbance changes in corn mem- brane fractions (Caubergs, Goldsmith, and Briggs)	356
Some properties of methylene-blue- mediated cytochrome reduction by red light in particulate fractions isolated from homogenates of corn coleoptiles (Widell, Britz, and Briggs)	344	Bibliography	358
		Speeches	359
		Personnel	363

INTRODUCTION

After reading through the many articles that follow, this Director finds himself struck by the inappropriateness of his title. The faculty and fellows of the Department have managed their own research quite well with little evidence of his direction—as the reports themselves will attest. We have had a gifted and articulate group of research fellows who have interacted effectively with our permanent faculty to produce some fine science. Directing this group is a relatively simple task: see to their scientific needs and leave them alone.

The research accomplishments of the Department are revealed in ways other than the articles in this Annual Report. First, there is the large number of invited seminars presented—a substantial number even when one deletes those seminars offered by fellows on a job circuit. Second, there are the many papers presented at professional meetings. This list is somewhat padded, in the current Report, by the occurrence of *two* annual meetings of the American Society of Plant Physiologists during one report year, but is nonetheless still gratifying. Indeed, twelve scientists from the Department attended the most recent meeting, almost all of them presenting their research; the number would have been thirteen, but the Director had to stay home to write this introduction. Yet the accompanying list of publications in reviewed journals is perhaps the best evidence of all—since outside scrutiny always provides the best judgment. One is perhaps justified in inquiring when the faculty and fellows were able to find time to do their research, in view of the amount of time they evidently spent traveling, writing, and talking. The answer to that question can best be found in the following pages.

Both faculty and fellows continue an effective interaction with plant scientists

at Stanford. During the past year, Winslow Briggs joined again with Professor Philip Hanawalt to present a course in photobiology to a group of Stanford undergraduates during the winter quarter. All of the faculty and fellows in the areas of photosynthesis and physiological ecology participated in a graduate photosynthesis seminar during the spring quarter, organized by David Fork and Joseph Berry. And Carnegie faculty continue to be invited as guest lecturers in biology courses at Stanford on all academic levels. In addition, there are now six Stanford graduate students doing their doctoral research under the direction of a Carnegie faculty member.

Despite the broad range of interests shared by members of the Department, several unifying themes will be apparent in the research reports. First, studies of photosynthesis at high temperature and of mechanisms of adaptation to high temperature continue to dominate much of the work in physiological ecology and photosynthesis. Second, the characterization of membranes, not only with respect to photosynthesis but also with respect to photoreceptors for other processes emerges as a closely related theme. Third, direct studies on known or suspected photoreceptor molecules dominate another group of papers. Fourth come several studies dissecting the organization of the higher plant genome. And cutting across all of the research areas is a series of papers dramatically detailing the development and exploitation of computer techniques for a wide variety of purposes.

Olle Björkman and his associates have continued their studies of physiological adaptation to high temperature. *Nerium oleander*, a common shrub from the Middle East which is planted as an ornamental species all over California and can be blissfully neglected by mainte-

nance workers, turned out to have remarkable adaptive capacity, as did *Larrea*, the creosote brush from Death Valley on which they reported last year. For physiological studies of intact leaves, the plants are essentially interchangeable. However, for biochemical and biophysical studies of isolated membrane systems or enzymes, *Larrea* was hardly ideal, since the phenolic compounds that give it its common name make the plant extracts resemble a mixture of tars! Oleander presents no such problem, however, and is therefore a valuable addition to the list of plants which are of great value in temperature adaptation studies.

Björkman, Murray Badger, and Paul Armond completed studies of oleander grown at both high and low temperature. They resolved two distinct adaptive processes: The plants grown at low temperature develop a very high photosynthetic capacity, and those grown at high temperature develop a high thermal stability for the photosynthetic machinery. Plants from the cool growth regime do not show any particularly significant differences in the amount of photosynthetic machinery per unit leaf area, the level of enzymes involved in carbon metabolism, or the capacity for photosynthetic electron transport or photophosphorylation, in comparison with plants from the hot growth regime; nor are there differences in physical restriction of gas exchange. Close examination of the enzymes of carbon fixation, however, revealed that one particular enzyme, fructose- P_2 -phosphatase is almost three times as active in the low-temperature-adapted leaves as in the high, which presents the intriguing possibility that an increase in the relative activity of a single enzyme could account for the remarkable increase in photosynthetic capacity that accompanies adaptation to low temperature. While there are minor differences in activity in other enzymes, they do not appear sufficiently large to account for the degree of adaptation observed.

Adaptation to high temperatures clearly involves increased thermal stability of the photosynthetic machinery, including differences in both in vivo and in vitro noncyclic electron transport and photophosphorylation and in the in vivo heat stability of several enzymes of photosynthetic carbon metabolism. In particular, three enzymes which require light for their activation are especially sensitive to heat inactivation at temperatures at which photosynthesis begins to show thermal inhibition. Since their activation depends upon photosynthetically produced reductant, it is likely that apparent heat inactivation is related to thermal damage of photosynthetic electron transport, rather than representing a direct effect on these enzymes. Thus it is most likely to be the membranes that one must turn to in order to find an explanation for the way plants adapt to high temperatures.

Studies on algae and bacteria have shown that adaptation to high temperature involves an increase in the degree of saturation of membrane fatty acids such that membrane fluidity at any particular growth temperature is always the same. It is assumed that this increase would maintain the physical integrity of the membranes at higher temperatures. John Raison and Joseph Berry made detailed studies of chloroplast membranes from several sources: high- and low-temperature-adapted *Nerium oleander* and *Atriplex hymenelytra*; *Tidestromia oblongifolia*, a plant which lacks the ability to acclimate to low temperature, growing only at high temperature; and two *Atriplex* species which fail to acclimate to high temperature. Measurements with membrane probes containing electron spin labels yielded the surprising result that all of the membranes were remarkably similar. Differences in fluidity were much smaller in the tests than those reported for bacteria or algae grown over such a wide temperature range, and differences in the temperatures for phase transitions of the ex-

tracted lipids were negligible. Thus the mechanisms by which higher plants adapted to high temperatures achieve thermal stability in their membranes are not clear. What is clear, however, is that they do not utilize exclusively a mechanism involving homeostatic adjustment of membrane lipid fluidity.

The way in which certain algae can adapt to changes in growth temperature is well illustrated in work by David Fork, Norio Murata, and Naoki Sato. They grew the unusual thermophilic algae, *Synechococcus lividus*, originally collected from hot springs in Yellowstone National Park, Wyoming, both at 38°C and at 55°C (a temperature at which it is perfectly comfortable). They then examined the relative amounts of saturated versus unsaturated fatty acids in the algal membranes. The ratio of total saturated to total unsaturated fatty acids was 1.31 for cells grown at 38°C and decreased more than four-fold to 0.31 in cells grown at 55°C. These results are in dramatic contrast with those of Raison and Berry on chloroplast lipids from oleander. Further studies on *Synechococcus*, involving careful measurements of the effects of temperature on several photosynthetic parameters, revealed that the high-temperature phase transition for the membranes is at 43°C for cells grown at the higher temperature, and at about 37°C for cells grown at the lower. The dark reduction of cytochrome *f*, the redistribution of light energy between the two photosystems upon a change in the spectral distribution of incident light, and fluorescence in cells with electron transport between the two photosystems inhibited, all showed a sharp change in activation energy near either 43° or 37°, respectively. (The cytochrome *f* studies involved an ingenious interfacing of the spectrophotometric equipment with the computer, a system described in the following reports.)

Murata and Fork also investigated another alga, *Anacystis nidulans*, grown

at two different growth temperatures, 28° and 38°C, and studied the dark reduction or the turnover rate in the light for reaction-center chlorophyll P700. Evidence suggesting phase transitions was obtained at 16° and 6°C in cells grown at 28°C, and at 24° and 10°C in cells grown at 38°C. The upper two temperatures correspond nicely to the temperatures for lipid phase transitions measured directly by Murata and his colleagues in Tokyo; the lower two do not. Thus the origins of the lower temperature points are undetermined but probably do not relate directly to the degree of saturation of fatty acids. In this sense, they are analogous to the results with oleander mentioned above.

Paul Armond and Dr. L. Andrew Staehelin of the University of Colorado were able to look directly at membranes from *Anacystis* cells which had been grown at 38°C, and had then been transferred to lower temperatures for 15 min before fixing for freeze-fracturing and electron microscopy. They obtained clear evidence that a displacement of particles occurs from the center line of the membrane to the outer surfaces when the membrane had been below the phase transition temperature of 24° (see preceding paragraph). Their observations could provide a physical basis for many of the changes observed by Fork and his colleagues in the various photosynthetic parameters with changing temperature.

Interest in pigment-membrane interactions was not restricted to temperature studies just discussed. Gijsbert van Ginkel developed a technique for incorporating reaction-center chlorophyll-protein complex into lipid vesicles, a method which could be used with any of a number of proteins to study protein-lipid interactions. The technique simply involves forcing a lipid-protein suspension through a French pressure cell previously flushed with nitrogen. The result is a suspension of vesicles relatively uniform in size and containing incorporated pigment. Jeanette Brown and van Ginkel

then showed that such preparations demonstrate greatly enhanced proton and oxygen uptake in the light. Both of these reactions had been reported for system I in photosynthesis. Brown and van Ginkel were able to show that these activities are instead simply a function of free chlorophyll in the lipid, and are unrelated to system I. One unexpected consequence of the studies was a clear demonstration of both catalase and superoxide dismutase activities in the reaction-center chlorophyll-protein complexes. These enzymes should be of considerable importance in removing superoxide formed under conditions of imbalance in the production of reducing power and of oxidized receptors.

Studies of photosynthesis this year encompassed more than the work on temperature effects and membrane parameters. Paul Armond and Professor Harold A. Mooney studied the photosynthetic capacity of four desert ephemeral species as a function of their photosynthetic unit size (often defined as the ratio of total chlorophyll to reaction-center chlorophyll). The four species varied almost three-fold in their capacity to fix CO_2 , and it was anticipated that the one with the largest capacity would have the smallest photosynthetic units (i.e., the largest number of reaction centers for processing incoming light, per total chlorophyll). Surprisingly, when reaction-center concentration was assayed by measuring the total amount of P700, this expectation was not borne out. Either the assumption was incorrect, or measuring P700 is not a valid technique for determining the number of functional reaction centers. Shmuel Malkin, Fork, and Armond then applied to the same four species an ingenious technique for determining photosynthetic unit size directly from fluorescence-induction curves. In this study the correlation between unit size and photosynthetic capacity turned out to be excellent. Evidently the amount of P700 measured is not always a valid indicator of reaction-center con-

centration—a result that casts doubt on the validity of a currently accepted method.

Murray Badger, Aaron Kaplan, and Berry continued a study begun earlier on the way two different algae become adapted to a low- CO_2 environment. They had previously shown that the differences between cells of *Chlamydomonas* adapted to high or low CO_2 could not be accounted for by any intrinsic differences in the photosynthetic machinery for fixing carbon, and they postulated that there must be a CO_2 -concentrating system in the cells grown and adapted to low CO_2 . Current studies both with *Chlamydomonas* and with another alga, *Anabaena*, now clearly demonstrate the presence of just such a system for facilitating transport of inorganic carbon into the cells. Indeed, with *Anabaena* the transport of carbon (as bicarbonate) into the cell may achieve concentrations 1000 times higher inside the cell than outside. This transport process is an active one depending upon metabolic energy—although its exact nature remains unclear. The capacity for concentrating CO_2 could be an extremely important parameter in determining the dynamics of algal populations.

Alan Stemler had previously shown that the normal flow of electrons through photosystem II depends upon having bicarbonate bound to the reaction-center complex. This past year he discovered that light can actually prevent such binding in chloroplasts previously depleted of their endogenous bicarbonate. Multiple-flash experiments suggest that bicarbonate cycles and plays some sort of catalytic role. Once it is bound, two flashes are required to remove it and it immediately becomes bound again. Stemler believes that bicarbonate might play a role in facilitating electron transfer from the primary electron acceptor, a hypothesis that appears accessible to experimental test. Thus he continues to make progress in elucidating the events

associated with the first of the two photochemical reactions of photosynthesis—one area of study that has been notoriously resistant to penetration in the past.

Another study related directly to photosynthesis is that carried out by Berry, with Drs. K. C. Woo and Graham Turner, in Australia on the release and refixation of ammonia during the process of photorespiration. Several workers have pointed out that, in addition to CO₂, ammonia may be produced during photorespiration. Berry and his colleagues found that when glycine was fed to isolated spinach leaf mitochondria, equal amounts of ammonia and CO₂ were released. Moreover, they demonstrated that this ammonia is not refixed within the mitochondria. Spinach chloroplasts, on the other hand, readily synthesized glutamine and glutamic acid in the light when they were exposed to the appropriate substrates: 2-oxoglutarate plus ammonia. In a third section of the study they showed that spinach leaf discs, when supplied with ammonia, incorporate the ammonia in a pattern which suggests the transfer of ammonia nitrogen from glutamate and glutamine back into glycine, thus completing the cycle. Apparently, then, by use of this cycling mechanism the plant avoids both the accumulation of toxic amounts of ammonia and a severe loss of ammonia during photorespiration. The fate of the ammonia produced during photorespiration appears to be resolved.

In another photosynthesis study, James Collatz carefully explored the role of ribulose biphosphate, the immediate substrate for carbon dioxide fixation, as a possible factor in limiting the overall rate of photosynthesis. He used both the unicellular alga *Chlamydomonas* and whole leaf cells from spinach, isolated by techniques that he and Murray Badger developed. Collatz determined that when light intensity and carbon dioxide concentration were both high, the concentration of ribulose biphosphate was very low, suggesting ribu-

lose biphosphate as the limiting factor, rather than the enzymatic capacity for carboxylation. Conversely, when carbon dioxide concentration and light intensity were low, and oxygen, which inhibits the carboxylation reaction, was also low, the ribulose biphosphate concentration was very high, suggesting in this case that the enzymatic capacity for carboxylation was limiting. Increasing either the oxygen or the carbon dioxide concentrations, both of which would increase the rate of enzyme turnover (whether by oxygenase or carboxylase activity is immaterial), caused the level of ribulose biphosphate to fall.

Already mentioned are studies by Fork and his colleagues of the kinetics of cytochrome *f* reduction which involved interfacing the spectrophotometric instrumentation with the computer. Glenn Ford and Benny Catanzaro, who have been responsible for the design and execution of the interfacing, present a general description of the entire computer system in this Report. Approaching completion as this Report is written is a microprocessor that can store data from a spectrophotometer and then transmit it to the storage memory of the central minicomputer at a convenient time. This modification represents an important step forward, since now several people will be able to collect spectral information simultaneously on a real time basis, without interfering with each other and without requiring real time access to the computer.

William Thompson, with Michael Murray and Richard Preisler, continue to focus on the organization of the higher plant genome. They report two very different patterns to be found in two closely related plants, the garden pea and mung bean. The total genome size (amount of DNA per cell) in pea is almost nine times that in mung bean, and the organization and size of both unique sequences and repetitive ones are quite different between the two (as is the relative proportion of unique to repetitive

DNA sequences). No unique sequences were found in pea longer than 1200 nucleotide pairs, while three-fourths of the unique sequences from mung bean had a length greater than that. In fact, in mung bean, about half of the unique sequences exceeded 6000 nucleotide pairs in length! In pea, almost three fourths of the total DNA was found to be repetitive, with the bulk of the repeated sequences being fewer than 1000 nucleotide pairs long. By contrast, less than half of the mung bean DNA occurs as repeated sequences, and more than half of this repeated DNA is over 1000 nucleotide pairs long. Mung bean DNA extracted from leaves contains a surprisingly high fraction—possibly more than 15%—which may be chloroplast DNA. This fraction behaves as though it were composed of identical repeated sequences present many times per cell. In pea, with its much larger genome, the chloroplast contribution is at most a few percent.

Any hypothesis relating to regulation of transcription in development must somehow take into account the wide divergence of genome organization revealed by these studies. Although the keys to this puzzle are still missing, the resolution of the various components of the genome is now well under way, and the construction and testing of increasingly rigorous hypotheses is becoming a more realistic expectation. For example, Richard Cuellar, together with Ford, Briggs, and Thompson, has made use of the computer to analyze melting curves for reassociated pea DNA. This is DNA which has been melted so the two strands could separate, and which has then been allowed to become reannealed. Since the repeated-sequence fraction consists of families of sequences that are related but not identical, a fair amount of mismatch occurs during the reannealing process. The question was whether or not one could distinguish discrete components by their characteristic melting behavior. In such experiments the data are normally

plotted as optical density versus temperature, since single-stranded DNA absorbs more light than double-stranded. Cuellar and colleagues digitized melting curves of this sort, using the apparatus designed and built by French, Hart, and Lawrence some years ago (*Year Book* 67, pp. 535–536, 1968), entered the data into the computer, and then did a derivative analysis. If only a single melting component were present, they expected the first derivative curve to appear as a gaussian distribution curve similar to the absorption spectrum for a single absorbing species. If there were several melting components present, all of different stabilities, the first derivative should resemble an absorption spectrum with fine structure in the form of shoulders and peaks. The curve showed just this kind of fine structure; the derivatives could now be handled as though they were absorption spectra. Programs developed for resolving spectra quantitatively and qualitatively into single spectral components, used many years ago by Stacy French, were found to be applicable to the melting curves, as were higher derivative analysis techniques previously used on absorption spectra. A new analytical tool for studying the repeated sequence portion of the genome has thus been made available to the researcher.

Michael Blatt, in Winslow Briggs' group, has made substantial progress in understanding at the cellular level the mechanism by which chloroplasts of the filamentous alga *Vaucheria* become trapped in a field of dim blue light. The chloroplasts normally move along distinct longitudinal fibers which are visible under specialized light microscopy. When an area of the cell is irradiated with blue light, the longitudinal organization of the fibers breaks down, and within a few seconds a reticulum of fibers appears with cross bridges forming and breaking continuously. Chloroplasts become trapped in this network of fibers. Apparently their continued movement depends upon the presence of intact,

longitudinally oriented fibers. If the blue light is removed, the fibers again reorganize longitudinally, within 10 to 15 minutes, and chloroplast movement resumes. The reticulation process invariably precedes chloroplast aggregation.

Blatt has also obtained preliminary evidence on the chemical nature of the fibers. They are stabilized in the light by the *Amanita* toxin, phalloidin, and they become disaggregated by the inhibitor cytochalasin B. Cytochalasin B is known to disrupt filaments of actin, a protein involved not just in muscle contraction but in many other motility phenomena, including cytoplasmic streaming in algal cells. Phalloidin, on the other hand, is known to stabilize such filaments. It seems likely, therefore, that the fibers visible under light microscopy are cables composed of large numbers of actin filaments.

In a continuation of studies begun last year, Susanne Widell, Steven Britz, and Briggs investigated quantitatively the interaction of photoexcited methylene blue with a cytochrome suspected of being involved in many blue-light reactions, possibly including the one mentioned above for the alga *Vaucheria*. The cytochrome has been reported previously as occurring in both corn and pea membrane preparations and in membranes from the pink bread mold *Neurospora*. The influence of methylene blue concentration and of EDTA concentration on the photoreduction of the cytochrome was explored and an action spectrum for the photoprocess obtained. The spectrum indicated that only methylene blue monomers could be participating, despite the presence of a sizable concentration of dimers. Mary Helen Goldsmith and Briggs then used concentrations of EDTA that had been found to be effective in the methylene blue studies in combination with an oxygen-scavenging system to obtain highly reproducible light-induced cytochrome reduction by an endogenous flavoprotein found in the

corn membranes. They also showed that a cytochrome could be reduced by photoexcitation of added riboflavin, and demonstrated that whether the photoreceptor was endogenous flavin, riboflavin, or methylene blue, the same cytochrome was reduced, while other cytochromes present in far greater concentrations were not. Comparison of the various spectra for reduced cytochromes was much facilitated by storing multiple scans of the curves in the computer, averaging and normalizing them, and then subtracting one average from another to determine whether or not any two curves were identical.

Peter Quail, also in Briggs' laboratory, demonstrated the involvement of the pigment phytochrome in enhancing the growth response of corn roots to gravity. A brief exposure to red light causes corn roots to curve downward in response to gravity; the effect is far more rapid than with dark controls. The potentiation of this response is partially reversed by far red light. The evidence is consistent with the hypothesis that only a very small proportion of the total phytochrome need absorb red light to saturate the response.

Quail also investigated an odd and often-studied phenomenon whereby phytochrome that is transformed by red light to its far-red-absorbing form within the cell becomes pelletable on subsequent extraction under appropriate conditions, whereas normally it would remain soluble. It has so far remained unclear whether the pigment becomes bound to some particulate site while still in the cell, or whether it does so only upon extraction. However, Quail was able to show that whatever the nature of the change that leads to the increase in pelletability in oats, it involves an expenditure of metabolic energy. Inhibitors of respiration or of oxidative phosphorylation inhibit the increase; and there is an excellent correlation between decrease in pelletability and decrease in ATP in the tissue. The reaction leading to pellet-

ability has a half-time of about 2 sec at room temperature—the earliest reaction yet reported for phytochrome photo-transformation in the cell. Respiratory inhibitors such as cyanide extend this half-time to minutes. In collaboration with Dr. Lee H. Pratt at Vanderbilt University, Quail was also able to obtain preliminary evidence that phytochrome is a phosphorylated protein. The significance of the phosphorylation is at present uncertain, but the finding represents one more step in the characterization of this elusive pigment.

In other work, John Cross made further progress in the characterization of a membrane protein that binds the plant

growth hormone auxin. He and Briggs report solubilizing this protein by two different techniques and showing that its relative affinity for a series of auxin analogues was similar to the relative affinity of the unsolubilized protein. They report that it has a molecular weight of nearly 80,000 daltons and that it is located primarily in the endoplasmic reticulum.

It is difficult to pick out highlights from the work described so briefly above, and such selection must necessarily be a little arbitrary. Therefore, rather than make the attempt, the author of this Introduction wishes to defer to the following articles. They speak for themselves.

CORRELATION OF PHOTOSYNTHETIC UNIT SIZE AND DENSITY WITH PHOTOSYNTHETIC CAPACITY

Paul A. Armond and Harold A. Mooney

Plants capable of growing in Death Valley have acquired various strategies to cope with the harsh environmental conditions there (Mooney *et al.*, *Year Book* 75, 410–413). While some plants acclimate to the substantial changes in temperature and water availability that take place during the course of a year (Björkman *et al.*, *Year Book* 76, 328–335), others limit their growth to the period of relatively moderate conditions in the winter and early spring. These desert winter annuals are characterized by fast rates of growth, with the interval between germination and flowering being, in many cases, quite short. In this group of plants, one genus, *Camissonia*, had been shown to have very high rates of photosynthesis (Mooney *et al.*, *Year Book* 75, 410–413). A preliminary examination of several other desert ephemeral species indicated, however, that high rates of photosynthesis are not typical of desert annuals.

In the present study, we examined the photosynthetic characteristics of three

desert annuals and a fast-growing herbaceous perennial to determine what factors may contribute to differences in the rates of photosynthesis, and whether any single characteristic or simple combination of characteristics can be used to quickly determine relative photosynthetic capacities (light-saturated CO₂ uptake). In recent years, particular emphasis has been placed on the correlation between photosynthetic capacity and the density of photosynthetic units in a leaf; see, for example, Teeri *et al.*, 1977 (a photosynthetic unit being defined statistically as the number of bulk chlorophyll molecules per reaction center—usually P700, the reaction center of photosystem I). The desert species, plants growing under identical conditions with vastly different rates of photosynthesis, appeared to be an ideal system for testing this proposed correlation.

The species chosen for this study were *Camissonia brevipes* (Onagraceae), *Datura meteloides* (Solanaceae), *Lupinus sparsiflorus* (Fabaceae), and *Perityle*

emoryi (Compositae). The plants were grown under control conditions at a 20°C/15°C day/night temperature regime and a quantum flux density of 70 nEcm⁻² sec⁻¹. Measurements of the response of photosynthesis to light and CO₂ concentration and analysis of certain leaf characteristics were performed on plants before the onset of anthesis.

The responses of photosynthesis to incident light intensity for the four species (Fig. 1) were quite different with respect to both the maximum rates of photosynthesis and the actual light response (curve shape). However, the quantum yields at low incident light intensities (initial slopes of the light-response curves) were similar for all of the species examined. The response of photosynthesis to CO₂ concentration under saturating light intensities (Fig. 2) showed that all four species had similar compensation points and that the rates of photosynthesis were stimulated in all cases by increasing the CO₂ concentration above ambient levels.

Analysis of leaf characteristics (Table 1) revealed that the four species had similar dry weights per area, with the exception of *Camissonia*, which had a value approximately 50% higher. Although the leaves of *Lupinus* had the greatest percentage of leaf dry weight as nitrogen, the *Camissonia* showed the highest concentration of nitrogen on an area basis.

The leaves of the desert species were also analyzed for light absorptance as well as for chlorophyll and P700 content (Table 2). With the exception of *Perityle*, the plants had similar absorptances and chlorophyll densities, and nearly identical chlorophyll *a/b* ratios. In contrast, chlorophyll:P700 ratios (giving an estimate of the photosynthetic unit size) and P700 densities of the leaves (which should show a correlation with photosynthetic capacity) were quite different.

Our criterion for a useful correlation between leaf characteristics and photo-

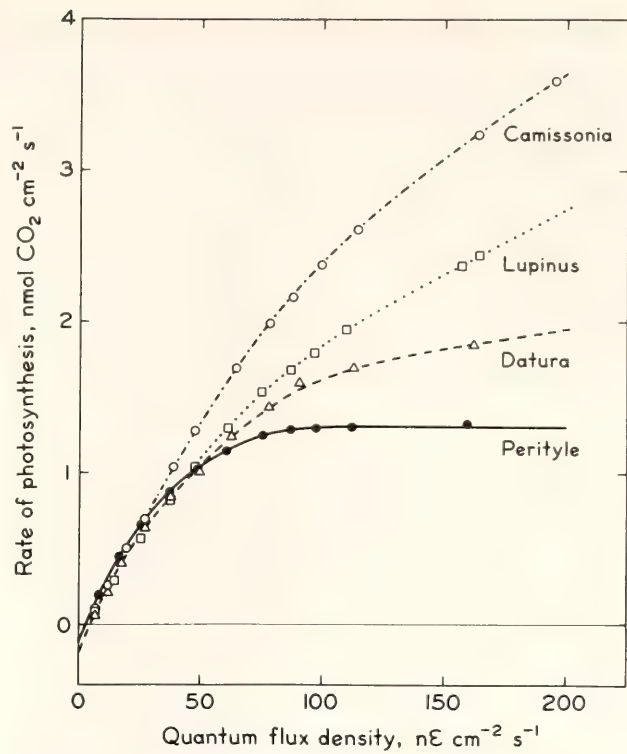


Fig. 1. The response of photosynthesis to light intensity in *C. brevipes*, *D. meteloides*, *L. sparsiflorus*, and *P. emoryi*. Photosynthesis was measured at 20°C in normal air (330 μbar CO₂ 21% O₂).

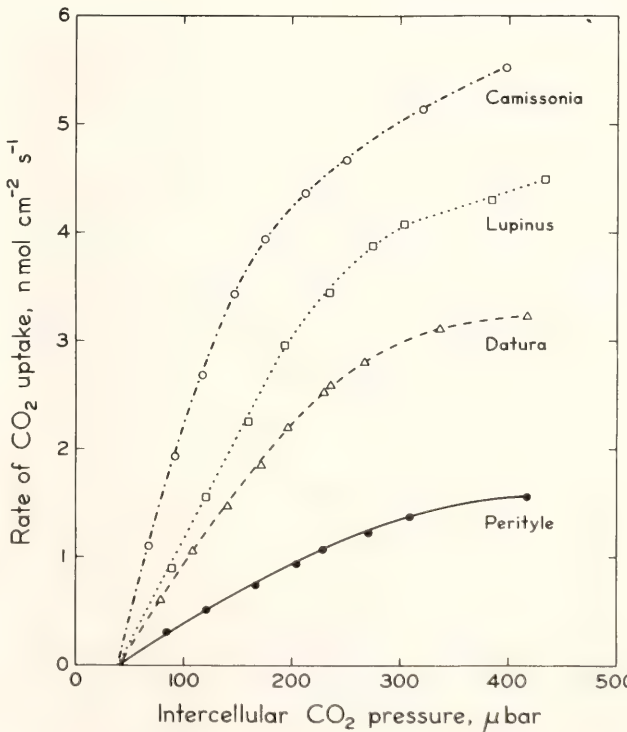


Fig. 2. The response of photosynthesis to CO₂ concentration for the four desert species. Photosynthesis was measured at a leaf temperature of 20°C, 21% O₂ and with a quantum flux density of 180 nE cm⁻² sec⁻¹.

TABLE 1. Leaf Characteristics of *Camissonia brevipes*, *Datura meteloides*, *Lupinus sparsiflorus* and *Perityle emoryi*

Species	mg Fresh Weight per cm ²	mg Dry Weight per cm ²	% Nitrogen	mg Nitrogen per cm ²
<i>C. brevipes</i>	34.19	6.20	3.73	0.2312
<i>L. sparsiflorus</i>	42.68	4.03	4.48	0.1817
<i>D. meteloides</i>	27.64	4.37	2.29	0.1002
<i>P. emoryi</i>	36.14	4.08	2.18	0.0837

synthetic capacity was a simple one, requiring only that the measured parameter order the plants qualitatively with respect to photosynthetic capacity. The similarity of quantum yields, compensation points, and stimulation of photosynthesis by increased CO₂ concentrations indicated that there were no particular aberrations in the photosynthetic apparatus of any of these plants. The analysis of leaf characteristics showed that only leaf nitrogen content expressed on an area basis was positively correlated with the observed photosynthetic capacity (see Fig. 1).

The pigment system analyses gave somewhat unexpected results. Our test of the proposed relationship between photosynthetic unit density and photosynthetic capacity did not demonstrate a good correlation between these two parameters. If P700-determined photosynthetic unit density alone determined photosynthetic capacity, then *Perityle* and *Datura* should have shown nearly

identical photosynthetic rates at any given intensity; the *Lupinus*, with its leaves possessing the greatest density of P700, should have had the highest rate of photosynthesis. *Camissonia* would have been expected to have rates of photosynthesis somewhat greater than those of *Datura* but substantially lower than those of *Lupinus* (see Table 2). These results are not in agreement with the observed photosynthetic characteristics (Fig. 1).

An additional inconsistency between the P700-based photosynthetic unit size measurements and measured photosynthesis appeared in the characteristics of the response curve of photosynthesis to light intensity (Fig. 1). It is generally thought that plants with large numbers of chlorophylls serving each reaction center should reach light saturation at lower light intensities than plants with smaller numbers of chlorophylls per reaction center. If this assumption were true, the *Camissonia*, which was not

TABLE 2. Characteristics of the Pigment Systems of *C. brevipes*, *D. meteloides*, *L. sparsiflorus*, and *P. emoryi*

Species	Leaf Absorptance %(800–700 nm)	µg chl/cm ²	chl a/b	chl/P700 (PSU*)	Pmoles P700/cm ²
<i>C. brevipes</i>	0.82	55	3.80	514	118
<i>L. sparsiflorus</i>	0.82	59	3.85	371	177
<i>D. meteloides</i>	0.86	52	3.74	574	101
<i>P. emoryi</i>	0.76	34	3.80	383	99

* Photosynthetic unit.

light saturated at full sunlight intensity, should have had a much smaller photosynthetic unit size than *Perityle*, which was 90% light saturated at one-quarter sunlight intensity ($50 \text{ nE cm}^{-2} \text{ sec}^{-1}$). The values of photosynthetic unit sizes obtained by P700 measurements (Table 2) do not agree with the observed responses of photosynthesis to light in the four species examined.

The concept of a correlation between photosynthetic unit density and photosynthetic capacity is one which is intuitively appealing. It seems very logical that a greater concentration of photosynthetic "machinery" in a leaf would lead to a greater photosynthetic capacity. The failure of the P700 measurements to

predict photosynthetic capacity accurately could indicate that such measurements are unreliable for determining the number and size of the photosynthetic units actively involved in photosynthesis. This suggestion will be verified in the following paper (Malkin *et al.*, this Report), where a new method for the determination of the number and size of active photosynthetic units in intact leaves is presented.

REFERENCE

- Teeri, J. A., D. T. Patterson, R. S. Aberte, and R. M. Castelberry, *Plant Physiol.* 60, 370-373, 1977.

PROBING PHOTOSYNTHETIC UNIT SIZES OF LEAVES BY FLUORESCENCE-INDUCTION MEASUREMENTS

Shmuel Malkin, David C. Fork, and Paul A. Armond

The rate of photosynthesis and related reactions is often expressed on a chlorophyll basis. Two main factors influence the magnitude of the rate: (1) the rate constant of a limiting step of the enzymatic reactions; (2) the ratio of the number of pigment (chlorophyll) molecules to the number of enzyme molecules involved in that particular step. The rate per chlorophyll (R) can be given simplistically as:

$$R = k \frac{[E]}{[chl]} \quad (1)$$

where k is the rate constant, $[E]$ and $[chl]$ the concentration of the limiting enzyme and chlorophyll, respectively. The rate-limiting step is not defined well under all conditions and could be located in either the CO_2 fixation cycle, the CO_2 supply, or the electron transport chain, depending on the experimental conditions.

Another, perhaps more useful, version

of formula (1) can be given. Multiplying and dividing by the reaction-center concentration $[Rc]$ one obtains:

$$R = k \frac{[E]}{[Rc]} \cdot \frac{[Rc]}{[chl]} = k' \frac{[Rc]}{[chl]} \quad (1a)$$

In (1a) a new rate constant k' is defined in terms of the reaction-center concentration ($k' = k \cdot [E]/[Rc]$). The dependence on the pigment concentration is through the ratio $[Rc]/[chl]$. The reciprocal of this ratio is often called the photosynthetic unit size, and expresses the cooperation of many chlorophyll molecules in the transference of excitation energy to the reaction centers (Emerson and Arnold, 1932; Schmidt and Gaffron, 1971). The photosynthetic unit is an important concept—expressing the actual absorption cross section of the reaction center. It varies among different species and under different environments. An optimal adjustment of the photosynthetic unit would be to match the turn-

over rate of the reaction center (expressed by k') exactly to the influx of quanta to the associated antennae pigments. With too little light the reaction centers will be idle most of the time, implying that their biosynthesis is an unnecessary burden on the cell's economy. With too much light the reaction centers may be photo-inactivated; this consequence also implies a waste of the cell's energy on the synthesis of unnecessary pigments.

In order to study how plants adapt to different conditions (very likely the most important factor would be light intensity), it is important to be able to measure the photosynthetic unit size. A common method is to study the yield of photosynthesis per flash in intact leaves under flashing illumination. This method is time consuming and can be subject to errors arising from losses during the relatively long dark period between flashes (e.g., respiration). Isolating chloroplasts and measuring flash yields of electron transport may be relatively easy, but it suffers from the disadvantage that in many cases the activity of the chloroplasts becomes impaired during preparation, yielding erroneous results.

We have adopted fluorescence-induction measurements as a tool which can yield meaningful results and comparisons between different species. In essence this method is based on the principle of counting the quanta that give rise to the photoreduction of the reaction centers of photosystem II, when the rest of the electron transport chain is blocked by DCMU action. We simply make use of a stoichiometric relation between light and reaction centers, making necessary corrections for the inefficiency of quanta brought about by the progress of the reaction, by the distribution of quanta between the photosystems, and by the inefficiency of the trapping centers. The principles of the method as applied to

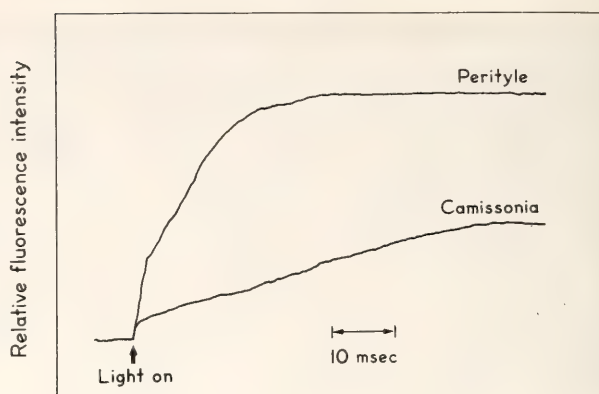


Fig. 3. Fluorescence-induction curves in DCMU-infiltrated *Perityle* (P) and *Camissonia* (C) leaves.

chloroplasts are outlined elsewhere (Malkin and Kok, 1965).

In the present experiments the leaves were soaked with DCMU solution infiltrated through the leaf veins and stomata by evacuation and pressure-restoration treatment. Fluorescence induction (Fig. 3) was measured in an apparatus consisting of fiber optics to deliver actinic irradiation to the leaf surface and fluorescence from the leaf surface to the detector.

To get proper results, the actinic light should be as uniform as possible. The leaves were irradiated with green light for maximal penetration (wavelength ~ 560 nm), and fluorescence at the leaf surface was measured in a wavelength region of high absorbance (~ 680 nm). This technique ensures that the fluorescence that is detected originates mainly from layers at the surface or close to the surface, where the actinic irradiation is approximately uniform. Under such conditions it is possible to prove that:

$$\frac{[Rc]}{[chl]} = (2300 \cdot \epsilon \cdot I \cdot \bar{t}) \cdot \alpha_2 \phi_2 \quad (2)$$

where ϵ is the apparent molar extinction coefficient for the actinic light wavelength (expressed on total chlorophyll basis), I is the incident light intensity expressed in einsteins $\text{cm}^{-2} \text{sec}^{-1}$, and \bar{t} is the average time of fluorescence induction, calculated from the normalized

area above the induction curve; α_2 is the fraction of light channeled to photosystem II and ϕ_2 is the quantum yield of trapping and photochemistry in photosystem II. The term in parentheses can thus be experimentally determined. A value for α_2 must be determined by other methods. Here we assume that α_2 must be 0.5 or close to this value to allow an optimal balance between the two photosystems, as is the case with higher plants. Values of $\alpha_2\phi_2$ measured previously for chloroplasts from different preparations (Malkin and Kok, 1965) were close to 0.5. The term ϕ_2 can be estimated from the ratio of the dark-adapted fluorescence level F_o to the maximal level F_m (Clayton, 1965).

$$\phi_2 \geq 1 - \frac{F_o}{F_m} \tag{3}$$

(The inequality sign is required because a part of F_o may be contributed by

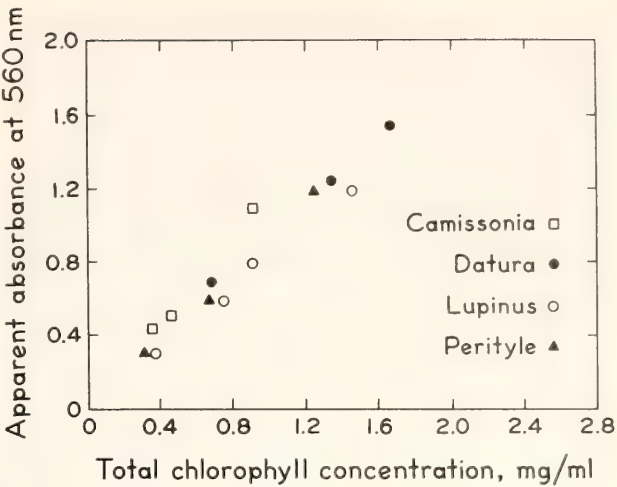


Fig. 4. Light-absorption properties of leaf extracts (1-mm optical path).

irrelevant background, e.g., from photosystem I or from chlorophyll that for some reason does not participate in photosynthesis.)

To find ϵ we assumed that the absorption properties of the leaf and of a thin

TABLE 3. Fluorescence Rate and Photosynthetic Unit Parameters for some Plant Species

Calculation	Species			
	<i>Camissonia brevipes</i>	<i>Lupinus sparsiflorus</i>	<i>Perityle emoryi</i>	<i>Datura meteloides</i>
Ratio F_o/F_m	0.23	0.22	0.21	0.27
ϕ_2 (calc.)	≥ 0.77	≥ 0.78	≥ 0.79	≥ 0.73
α_2 (assumed)	0.5	0.5	0.5	0.5
[RC PSII]/[chl]*	1/215	1/420	1/700	1/780
Rate of CO ₂ fixation per leaf area $\left(\frac{\text{nmoles}}{\text{cm}^2 \text{ sec}}\right)$	6.7†(3.6)	5†(2.45)	1.32	1.96
chlorophyll per leaf area ($\mu\text{g}/\text{cm}^2$)	55	59	34	52
$\frac{\text{Rate of CO}_2 \text{ fixation}}{[\text{chl}]} \text{ (sec}^{-1}\text{)‡}$	0.13†(0.084)	0.094†(0.059)	0.043	0.042
Ratio: $\frac{\text{Rate}/[\text{chl}]}{[\text{Rc}]/[\text{chl}]} = k' \text{ (sec}^{-1}\text{)}$	29 (18)	40 (25)	30	33

* Calculated from the fluorescence-induction curve, assuming lower limits for ϕ_2 .
† Values in parentheses: actual values as measured in the maximal light intensity available. They are clearly not the saturated values. The saturated rates were calculated by hyperbolic linear extrapolation to infinite light intensity (by plotting 1/rate against 1/intensity). Values outside parentheses: calculated by hyperbolic linear extrapolation to infinite light intensity (by plotting 1/rate against 1/intensity).
‡ On mole:mole basis, taking 900 for the average molecular weight of total chlorophyll.

layer of concentrated chloroplast suspension were the same. The ϵ for the latter was estimated by measurements of the absorption for the same actinic wavelength in an integrating sphere (linear Beer-Lambert plots were found for a wide range of chlorophyll concentrations, Fig. 4).

This method was tested on four species of desert plants which give different CO_2 fixation rates versus light intensity. Since their maximal rates in saturating light deviate very markedly from one another (Armond and Mooney, this *Year Book*) it was anticipated that their photosynthetic unit sizes would differ greatly. However, attempts to verify this assumption by assaying P700 in chlorophyll-protein complexes or by chloroplast reactions failed to show any meaningful correlation. This result could be attributed to the poor photochemical activity of the preparations or to the presence of P700 that was not originally associated with photosystem II in vivo.

The results of the fluorescence measurements presented in Table 3 show the predicted correlation and suggest that the variation among these plants stems from widely different photosynthetic unit sizes rather than from different rate constants k' . The last row in the table corresponds to k' in sec^{-1} . This constant shows very little variation (compared to the variations in rate and photosynthetic unit size) and corresponds to a half time in the range of 30 msec.

REFERENCES

- Clayton, R. K., in *Molecular Physics in Photosynthesis*, p. 173, Blaisdell Publishing Company, New York, 1965.
Emerson, R., and W. Arnold, *J. Gen. Physiol.* 16, 191–205, 1932.
Malkin, S., and B. Kok, *Biochim. Biophys. Acta* 126, 413–432, 1966.
Schmid, G. H., and H. Gaffron, *Photochem. Photobiol.* 14, 451–464, 1971.

CHROMOSOMAL NUMBERS IN *Atriplex*

Malcolm A. Nobs

The present report documents the chromosome counts in *Atriplex* that have been accumulated since they were last reported by Nobs (*Year Book* 74, pp. 762–765, 1975). As in the previous report, chromosome numbers have been determined from acetocarmine squashes of pollen mother cells from plants grown

in the experimental gardens of the Carnegie Institution at Stanford, California. Voucher material for each count will be deposited in the Dudley Herbarium, housed in the Herbarium of the California Academy of Sciences, San Francisco. The numbers are presented in Table 4.

RELEASE AND REFIXATION OF AMMONIA DURING PHOTORESPIRATION

K. C. Woo,* Joseph A. Berry, and Graham L. Turner†

Photorespiration is the pathway by which glycolate formed in photosynthesis is metabolized to CO_2 and 3-phosphoglyceric acid. The CO_2 produced in

photorespiration is probably derived from the mitochondrial reaction that catalyzes the conversion of glycine to serine (Kisaki *et al.*, 1971; Bird *et al.*,

TABLE 4. Chromosome Numbers in *Atriplex*

Species	Culture Number	Source	Chromosome Number
<i>A. barclayana</i> (Bentham) Dillrich	8226	Ciudad Constitution, Baja California Sur, Mexico	n = 18 ^{II}
	8228	Bahia De La Paz at Pichilingue Baja California Sur, Mexico	n = 18 ^{II}
<i>A. dimorphostegia</i> Kar. et Kir.	8220	Cornelia Gauhl, Bukhara, U.S.S.R.	n = 36 ^{II}
<i>A. expansa</i> Watson	8241	Colonet, Baja California, Mexico	n = 18 ^{II}
<i>A. flabellum</i> Pge.	8222	Cornelia Gauhl, Tamerlan Mosque, Samarkand, U.S.S.R.	n = 9 ^{II}
<i>A. fominii</i> Iljin	8217	Cornelia Gauhl, U.S.S.R.	n = 18 ^{II}
<i>A. inflata</i> F. Muell.	8180	Barry Osmond, Australia	n = 9 ^{II}
<i>A. julacea</i> Watson	8177	San Quintin, Baja California, Mexico	n = 18 ^{II}
<i>A. leucophylla</i> (Moquin) Dietrich	8164	Bodega Bay, Sonoma County, California	n = 18 ^{II}
<i>A. lentiformis</i> lentiformis (Torr.) Watson	7921	Saratoga Springs, Death Valley, Inyo County, California	n = 9 ^{II}
<i>A. mohavensis</i> (M. E. Jones) Standey	8161	Panamint Valley, Inyo County, California	n = 18 ^{II}
<i>A. mohavensis</i> (M. E. Jones) Standey	8269	7 miles west of Tonopah, Esmeralda County, Nevada	n = 18 ^{II}
<i>A. nummularia</i> Lindl.	8182	Barry Osmond, Australia	n = 18 ^{II}
<i>A. nuttallii</i> var. falcata M. E. Jones	8174	Camby, Modoc County, California	n = 9 ^{II}
<i>A. pentandra</i> ssp. <i>muricata</i> (H and B) Hall and Clements	8237	Villa Insurgentes, Baja California Sur, Mexico	n = 9 ^{II}
<i>A. polycarpa</i> (Torr.) Watson	8239	El Rosario, Baja California, Mexico	2n = 18
<i>A. saccaria</i> Watson	8273	Cameron, Coconino County, Arizona	n = 9 ^{II}
<i>A. suberecta</i> Verdorne	8169	Los Baños, Merced County, California (recent introduction)	n = 9 ^{II}
<i>A. vesacaria</i> Heward	8125	Barry Osmond, Alice Springs, Australia	n = 18 ^{II}
<i>A. watsonii</i> A. Nels	8173	Cabo Colonet, Baja California, Mexico	n = 18 ^{II}
<i>A. wrightii</i> Watson	8231B	Superior, Pinal County, Arizona	n = 9 ^{II}

1972; Canvin *et al.*, 1976; Woo and Osmond, 1976, 1977). The expected stoichiometry of this reaction would require that 2 moles of glycine be converted to 1 mole each of serine, CO₂ and NH₃. This predicts that NH₃ and CO₂ are produced in equivalent amounts during photorespiration. NH₃ should be refixed, since ammonia is not released (Farquhar, personal communication), and would be toxic if it were allowed to accumulate. Reactions that fix ammonia would thus be expected to be linked to photorespira-

tion, and the refixation of photorespiratory ammonia could—at times of active photorespiration—constitute a significant proportion of the total ammonia metabolism in the leaf.

In this report we describe (a) studies of the release of CO₂ and NH₃ by isolated spinach leaf mitochondria during the glycine-to-serine conversion; (b)

* Present address: Dept. of Biology, Queens University, Kingston, Ontario, Canada.

† Present address: CSIRO, Division of Plant Industry, Canberra, Australia.

studies of the fixation of exogenously supplied ammonia by isolated spinach chloroplasts; and (c) studies of the pattern of labeling of amino acids and amide nitrogen from ^{15}N -labeled ammonia in intact spinach leaf discs under photorespiratory conditions. These investigations support the proposal that NH_3 is an important intermediate in photorespiration.

METHODS

Spinach plants were grown as described elsewhere (*Year Book 76*, pp. 307–313). Chloroplasts were isolated according to the methods of Jensen and Bassham (1966). Mitochondria were isolated according to the techniques of Woo and Osmond (1976). CO_2 and NH_3 release by isolated mitochondria were assayed by incubating the mitochondria with appropriately labeled glycine, as described by Woo and Osmond (1976). Labeled CO_2 was recovered by microdiffusion to a glass filter containing NaOH after the incubation medium was brought to pH 4.4 with trichloroacetic acid. Ammonia was then recovered by adjusting the pH of the incubation medium to 11 with sodium borate and microdiffusing the NH_3 to 1N H_2SO_4 . NH_3 was measured by Nesslerization or converted to N_2 for mass spectrometry (Burris, 1972). All experiments with isolated chloroplasts were conducted in Jensen and Bassham's solution (containing 1000 IU/ml of catalase). Experiments with labeled substrates were terminated by adding the chloroplast suspension to four volumes of boiling methanol. Experiments with leaf discs were conducted in 20mM phosphate buffer containing the labeled ammonia. The discs were vacuum-infiltrated by making and releasing the vacuum three times. Treatments were started immediately after vacuum infiltration and terminated by extracting the discs with boiling 80% ethanol. The extracts were separated by ion exchange procedures

into a fraction that contained glutamate and aspartate and a fraction that contained the neutral and basic amino acids and amides. Amide nitrogen was recovered as NH_3 by hydrolysis of the amide with 1N HCl at 100°C for 2 hr, followed by microdiffusion. Trimethyl silyl (TMS) derivatives of amino acid preparations obtained from the extract were prepared for gas chromatography-mass spectrometry essentially as described elsewhere (*Year Book 76*, pp. 307–313). Derivatives of serine, glycine, and glutamate were identified by comparing the gas chromatogram and mass spectra to authentic standards. We were not able to identify a TMS derivative of glutamine, nor did we identify derivatives of several other amino acids detected in the mixture. The ^{15}N enrichment of the TMS derivatives of glycine, serine, and glutamate were determined as described previously (*Year Book 76*, pp. 307–313). Conventional mass spectrometry techniques were used to determine the ^{15}N enrichment of NH_3 derived from deamination experiments or from hydrolysis of amide groups (Burris, 1972).

RESULTS

The first experiments verified that CO_2 and NH_3 were produced at equal rates and in equal final amounts during glycine decarboxylation by isolated spinach leaf mitochondria, as reported by Kisaki *et al.* (1971). In order to verify that the ammonia released was derived from glycine, we provided mitochondria with ^{15}N -labeled glycine and examined the ^{15}N enrichment of the NH_3 released during the incubation. As shown in Table 5, the ^{15}N enrichment of the trapped ammonia is essentially identical to that of the glycine provided. This result clearly shows that the ammonia is derived from glycine deamination accompanying decarboxylation.

Mitochondrial glycine decarboxylation results in reduction of NAD. Woo and Osmond (1976) have shown that the re-

TABLE 5. Release of ¹⁴CO₂ and ¹⁵NH₃ by Spinach Leaf Mitochondria Incubated with ¹⁴C, ¹⁵N-Labeled Glycine

	Release* (μmol mg chl ⁻¹ hr ⁻¹)		Ratio CO ₂ /NH ₃	Enrichment (¹⁵ N atom %)
	CO ₂	NH ₃		
	2.1	2.4	0.9	...
	2.0	2.1	1.0	92.6 (97)
	1.9	1.7	1.1	97.5 (103)
mean	2.0	2.1	1.0	95 (100)

* The rates of the mitochondrial reaction are expressed on a chlorophyll basis by using fumarase activity of the mitochondria and of a sample of the crude extract, in which chlorophyll could also be determined, as an internal standard. Glycine provided (5mM) was 95 atom% enriched in ¹⁵N. Values in parentheses indicate percent relative to the glycine provided.

duction may be linked in vitro either to reduction of exogenously supplied oxaloacetic acid or, through oxidative phosphorylation, to ATP synthesis. Since mitochondria contain glutamate dehydrogenase (Ritenoir *et al.*, 1967), it seems possible that ammonia could be refixed at its site of synthesis in the mitochondrion. We examined the effect of providing 2-oxoglutarate, the α-keto acid substrate for glutamate dehydrogenase, and glutamate, the substrate for glutamine synthetase, on the ratio of CO₂ to NH₃ release. As shown in Table 6, we observed no significant deviation from 1.0. Therefore, the mitochondria did not fix significant ammonia into glutamate or glutamine in the experiments reported here.

Chloroplasts contain glutamine synthetase and glutamine, 2-oxoglutarate amino transferase, which may function in sequence to comprise a cycle for ammonia incorporation into 2-oxoglutarate to form glutamate (Lea and Mifflin, 1974; Mifflin and Lea, 1977). Anderson and Cone (1977) reported glutamine plus 2-oxoglutarate-dependent oxygen evolution by isolated chloroplasts, and Givan (1976) and Mitchell and Stocking (1975) have reported glutamine synthesis by isolated chloroplasts. We also observed 2-oxoglutarate-dependent O₂ evolution by isolated spinach chloroplasts. This activity was not dependent upon added glutamine and was completely inhibited by uncouplers of photophosphorylation. These observations

TABLE 6. Rate and Stoichiometry of CO₂ and NH₃ Release by Isolated Spinach Mitochondria*

Treatment	ADP System μmol mg chl ⁻¹ hr ⁻¹		Ratio CO ₂ /NH ₃	OAA System μmol mg chl ⁻¹ hr ⁻¹		Ratio CO ₂ /NH ₃
	CO ₂	NH ₃		CO ₂	NH ₃	
Control	7.5	7.0	1.1	16	16	1.0
2-oxoglutarate malate	7.3	7.2	1.0	13.6	13.4	1.0
2-oxoglutarate malate glutamate	7.0	7.1	1.0	13.3	13.6	1.0
Glutamate	6.9	7.4	0.9	15.9	17.1	0.9

* The rates of the mitochondrial reaction are expressed on a chlorophyll basis as in Table 5. Either ADP or oxaloacetate (OAA) was provided to consume NADH produced in glycine decarboxylation. All substrates were added at 5mM.

suggested that the chloroplasts might be conducting the complete sequence of ammonia fixation.

To test this possibility we incubated intact spinach chloroplasts with 2-oxoglutarate and $^{15}\text{N-NH}_4\text{Cl}$ (99 atom % ^{15}N). After incubation the amino acids were separated from the incubation mixture, and glutamate was examined for the presence of ^{15}N . The glutamate was found to be $54.8 \pm 1.3\%$ enriched in ^{15}N . This result confirms that intact spinach chloroplasts do fix ammonia into glutamate when provided with 2-oxoglutarate. Mass spectroscopy of the amide nitrogen isolated from the amide fraction of the incubation mixture confirmed that glutamine was probably also labeled. However, because we were unable to analyze glutamine by combined gas chromatography-mass spectroscopy, we cannot be completely sure that it is an intermediate of the pathway of ammonia incorporation. The apparent rate of ammonia incorporation was $5.6 \mu\text{mol mg chl}^{-1} \text{ hr}^{-1}$ in the experiments reported here. It is likely that much higher rates could be obtained in short-term experiments. These results indicate that ammonia fixation can occur in the chloroplasts and that the capacity of the chloroplasts for NH_3 incorporation is probably adequate to account for the refixation of the ammonia released in photorespiration.

If ammonia is released and refixed during photorespiration, we reasoned that this process should cause exogenously supplied ^{15}N from NH_3 to enter the amino acids of the photorespiratory

pathway rapidly. Leaf discs of spinach were infiltrated with $^{15}\text{NH}_4\text{Cl}$ and incubated either in the dark or in the light. The data presented in Table 7 show that glutamate and glutamine (both the α -amino nitrogen and amide nitrogen) became heavily labeled with NH_4Cl . This labeling occurred both in the light and in the dark. Glycine also became heavily labeled with ^{15}N in the light. The relative enrichment after only 1 min in the light is more than twice the enrichment observed after 30 min in the dark. Light would be expected to stimulate photorespiration. Hence, these results suggest that the proposed internal cycling of ammonia does occur.

CONCLUSIONS

Equimolar quantities of NH_3 and CO_2 were released during glycine decarboxylation in isolated mitochondria. This NH_3 was not refixed within the mitochondria in the presence of 2-oxoglutarate and/or glutamate. Chloroplasts isolated from spinach leaves synthesized labeled glutamine and glutamate in the light when supplied with $^{15}\text{NH}_4\text{Cl}$ and ^{14}C -2-oxoglutarate. In illuminated spinach leaf discs supplied with $^{15}\text{NH}_4\text{Cl}$, the pattern of ^{15}N incorporation suggests a transfer of ^{15}N label into glycine from glutamate and glutamine. This evidence suggests that the NH_3 released during photorespiration is refixed and used in the peroxisomal synthesis of glycine during photorespiration.

TABLE 7. Relative Enrichment of Various Nitrogen Fractions Isolated from Spinach Leaf Discs Vacuum-Infiltrated with 10mM $^{15}\text{NH}_4\text{Cl}$.

Treatment	^{15}N (atom %)			
	glycine	glutamate	glutamine- NH_2	amide
30 min dark	5.0	20.9	9.6	17.6
30 min light	23.6	...	55.4	27.8
1 min light	12.3	20.3	21.0	22.4

The integration of the pathway for ammonia reassimilation with the pathway of photorespiration should require that the capacity for NH_3 assimilation exceed that of photorespiration in order for toxic accumulation of NH_3 to be avoided. This requirement leads us to speculate that photorespiration, because it is a large and apparently uncontrolled source of NH_3 , may exert some control over the rate at which ammonia is produced from NO_3^- .

ACKNOWLEDGMENTS

This work was conducted in the Department of Environmental Biology of the Research School of Biological Sciences, Australian National University, Canberra, Australia. J. A. Berry was partially supported by an A.N.U. Visiting Fellowship. Dr. F. J. Bergersen of the Commonwealth Scientific and Industrial Research Organization's Division of Plant Industry kindly assisted with ^{15}N determinations.

REFERENCES

- Anderson, J. W., and J. Done, *Plant Physiol.* 60, 354–359, 1977.
- Bird, I. F., M. J. Cornelius, A. J. Keys, and C. P. Whittingham, *Phytochem.* 11, 1987–1994, 1972.
- Burris, R. H., in *Methods in Enzymology*, Vol. XXIV, part B, A. San Pietro. ed., pp. 415–431, Academic Press, New York, 1972.
- Canvin, D. T., N. D. H. Lloyd, H. Fock, and K. Przybylla, in *CO_2 Metabolism and Plant Productivity*, R. H. Burris and C. C. Black, eds., pp. 161–176, University Park Press, Baltimore, 1976.
- Givan, C. V., *Plant Physiol.* 57, 623–627, 1976.
- Jensen, R. G., and J. A. Bassham, *Proc. Nat. Acad. Sci. U.S.A.* 56, 1095–1101, 1966.
- Kisaki, T., N. Yoshida, and A. Imai, *Plant Cell Physiol.* 12, 275–288, 1971.
- Lea, P. J., and B. J. Mifflin, *Nature* 251, 614–616, 1974.
- Lorimer, G. H., K. C. Woo, J. A. Berry, and C. B. Osmond in *Photosynthesis* 77, D. O. Hall, J. Coombes, and T. W. Goodwin, eds., pp. 311–322, The Biochemical Society, London, 1978.
- Mifflin, B. J., and P. J. Lea, *Annu. Rev. Plant Physiol.* 28, 299–329, 1977.
- Mitchell, C. A., and C. R. Stocking, *Plant Physiol.* 55, 59–63, 1975.
- Ritenoir, G. L., K. W. Joy, J. Bunning, and R. H. Hageman, *Plant Physiol.* 42, 233–237, 1967.
- Woo, K. C., and C. B. Osmond, *Aust. J. Plant Physiol.* 3, 771–785, 1976.
- Woo, K. C., and C. B. Osmond in *Photosynthetic Organelles*, Special issue of *Plant and Cell Physiol.*, pp. 315–323, 1977.

THE USE OF ISOLATED WHOLE LEAF CELLS FOR PHOTOSYNTHESIS STUDIES

G. James Collatz and Murray R. Badger

The measurement of photosynthesis in whole, intact leaves has provided valuable information about how the photosynthetic apparatus functions and how plants respond photosynthetically to environmental conditions. However, this approach requires sophisticated instrumentation for estimating $[\text{CO}_2]$ in the

atmosphere surrounding mesophyll cells. An aqueous system has advantages over a gas-phase system because it is easier to control the levels of CO_2 and O_2 as well as temperature at considerably less expense. Photosynthetic rate can be obtained either by $^{14}\text{CO}_2$ exchange or by O_2 exchange in an O_2 -electrode appa-

ratus. With this system it is relatively easy to determine the photosynthetic rate and to stop metabolism instantly for later analysis of metabolite-pool sizes corresponding to the measured rate of photosynthesis.

The use of isolated, intact chloroplasts capable of CO₂-dependent O₂ evolution has provided an aqueous system for control of experimental variables and constants during simultaneous measurements of photosynthesis and metabolic parameters (e.g., Portis *et al.*, 1977). But it is difficult, if not impossible, to isolate active CO₂-fixing chloroplasts from any but a few species of higher plants (spinach, peas), which limits the usefulness of the technique in the study of plant response and adaptation to diverse environmental conditions. The use of leaf slices in an aqueous system (Jones and Osmond, 1973) is more general in its application to different species but suffers from diffusion and light-distribution problems.

Recently the use of isolated leaf cells for photosynthesis studies has become increasingly popular. The techniques have been developed for a variety of economically important plant species, and have been used to determine the levels of certain intermediates and processes as well as photosynthesis under controlled CO₂, O₂ and light levels (Huber and Edwards, 1975; Servaites and Ogren, 1978; Collatz, this *Year Book*).

We have achieved the isolation of

photosynthetically active leaf cells from several species of higher plants. Leaves of a particular specimen were sliced into approximately 1-mm-wide strips while immersed in 0.4M sorbitol. Slices were then transferred to the maceration medium containing 1% Macerase (Calbiochem), 0.5–0.7M sorbitol, 10mM K₂SO₄, 1mM MgSO₄, 0.5mM KH₂PO₄, 1mM KNO₃, 1% PVP-40, 0.2% methyl cellulose, 0.2% cellobiose, and 50mM MES pH 5.7. The slices were vacuum-infiltrated with the Macerase medium and gently stirred for 1 hr at room temperature. Slices were then rinsed and suspended in a solution containing 0.33M sorbitol, 5mM KNO₃, 2mM Ca(NO₃)₂, 2mM MgCl₂, and 40mM HEPES pH 7.4–7.8.

Cells were released from the slices by gentle stirring in a two-chambered vessel, as described by Rehfeld and Jensen (1973). Cells were then harvested from the suspension medium by centrifugation at about 20*g*. The assay medium was the same as described above for the suspension solution. Photosynthesis was measured as O₂ exchange with a Rank O₂ electrode. During an experiment, cells could be stored in ice, and photosynthetic activity was stable for at least 2 hr. Stirring rate in the O₂-electrode vessel had little effect on the stability of the rates.

Not all species tested yielded high rates of photosynthesis, but Table 8 shows significant rates for several species. The species listed are *Camissonia*

TABLE 8. Photosynthetic Rate of Leaf Cells Isolated from Different Species Expressed on a Per Milligram Chlorophyll and Per Unit Leaf Area Basis

Rate	<i>Spinacea</i>	<i>Heliotropium</i>	<i>Lupinus</i>	<i>Camissonia</i>
CO ₂ -saturated rate*, 25°C	2.25 (1.9)	1.85 (1.7)	1.3 (1.2)	1.6 (1.6)
CO ₂ -saturated rate*, 35°C	3.0 (2.5)	2.78 (2.6)
mg chl cm ²	0.050	0.055	0.055†	0.059†

* Rates are expressed as μmole O₂ mg chl⁻¹ min⁻¹, in parentheses as nmole O₂ cm⁻² s⁻¹.

† From Armond and Mooney, this Report.

brevipes (Onagraceae), *Lupinus sparsiflorus* (Fabaceae), *Spinacea oleraceae* (Chenopodiaceae) and *Heliotropium curvassavicum* (Boraginaceae). The first two species are annuals native to California deserts, while the last is a perennial native to California coastal habitats. Although these rates are about half or less of the CO₂-saturated and light-saturated rates in vivo (e.g., Armond and Mooney, this *Year Book*), they are sufficiently high so that we might expect some similarities between the response of isolated cells and that of intact leaves. This expectation is borne out for spinach by the results shown in Fig. 5.

The CO₂ photosynthetic response by cells in 21% and 3% O₂ at high and low light levels is very similar to the response of intact leaves of C₃ plants in general—that is, under limiting [CO₂], O₂ inhibits both the light-limited and light-saturated rate of photosynthesis; this inhibition is overcome by high [CO₂] (Björkman, *Year Book* 70, pp. 520–526; Ehleringer and Björkman, 1977). The inhibition of the rate by 21% O₂ at 10 μM CO₂ (~300 ppm at 25°C) is about 30% for the high light treatment, while

at low light the inhibition is about 45% in the presence of 21% O₂.

Preliminary studies have also shown the light-saturated photosynthetic temperature response of spinach and *Heliotropium* cells to be similar to that of intact whole leaves (data not shown). Photosynthesis was markedly stimulated by a 10° increase in temperature above 25°C (Table 8).

With cells from these and other species, work is continuing on the nature of photosynthetic response and adaptation to environmental stress.

CONCLUSION

The results reported here indicate that studies with isolated active leaf cells cannot substitute for properly carried out whole-leaf gas-exchange measurements; the latter should be a standard of comparison for determining the relevance of studies on isolated systems to photosynthesis in vivo. The isolated leaf leaves, and the experimental system cells do, however, apparently mimic many of the responses observed in intact offers several advantages for mechanistic studies of the photosynthetic apparatus. We have obtained highly active leaf-cell preparations from several ecologically diverse species, and this may provide a valuable technical approach to the study of photosynthetic adaptation of these and other species.

REFERENCES

- Ehleringer, J., and O. Björkman, *Plant Physiol.* 59, 86–90, 1977.
- Huber, S. C., and G. E. Edwards, *Physiol. Plant.* 351, 203–209, 1975.
- Jones, H. G., and C. B. Osmond, *Aust. J. Biol. Sci.* 26, 15–24, 1973.
- Portis, A. R., C. J. Chon, A. Mosbach, and H. W. Heldt, *Biochim. Biophys. Acta* 189, 207–221, 1969.
- Rehfeld, R. W., and R. G. Jensen, *Plant Physiol.* 52, 17–22, 1973.
- Servaites, J. C., and W. L. Ogren, *Plant Physiol.* 61, 62–67, 1978.

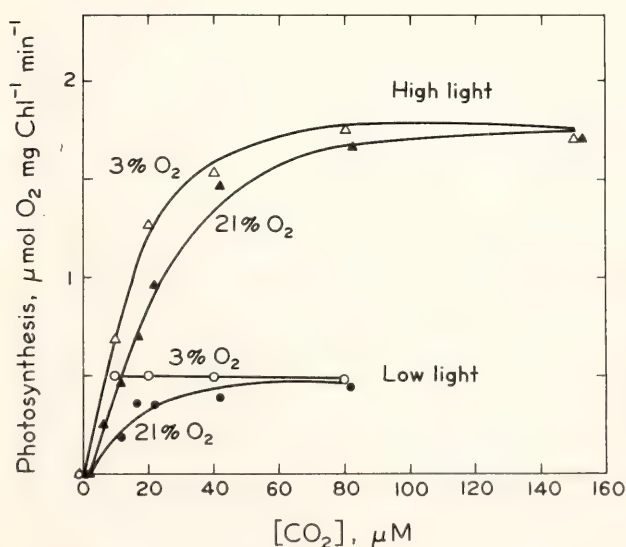


Fig. 5. CO₂ response of photosynthetic oxygen evolution as affected by light and O₂ levels in isolated spinach leaf cells. All rates were measured at 25°C. High light and low light treatments corresponded to 120 and 14 nE cm⁻² sec⁻¹, respectively.

THE INTERACTION BETWEEN PHOTOSYNTHESIS AND RIBULOSE-P₂ CONCENTRATION—EFFECTS OF LIGHT, CO₂, AND O₂

G. James Collatz

The rate of CO₂ uptake (neglecting photorespiratory CO₂ evolution) during steady-state photosynthesis reflects the turnover rate of ribulose 1,5-bisphosphate (Ru-P₂) carboxylase. The rate of reaction catalyzed by this enzyme should be determined by the concentrations of the substrates Ru-P₂ and CO₂ as well as by various effectors. The light response of photosynthesis (and hence of CO₂ fixation) must therefore be a result of an increase in [Ru-P₂] produced from light-generated ATP and NADPH, or activation by effectors, or both. Similarly the photosynthetic CO₂ response curve represents either activation or substrate response or a combination of these. The CO₂ and light-responses of photosynthesis in vivo will reflect these limitations on carboxylation.

Early measurements of Ru-P₂ concentration (symbolized here [Ru-P₂]) made by Wilson and Calvin (1955) showed that exposure of green algae cells to CO₂ in the light resulted in a reduction in [Ru-P₂]. Light-to-dark transitions resulted in a 1000-fold decrease in [Ru-P₂] within 1 min (Calvin and Massini, 1952). Later work also showed that exposure to O₂ caused [Ru-P₂] to fall (Latzko *et al.*, 1971; Atkins *et al.*, 1971). These results are consistent with the interpretation that light intensity affects the production of Ru-P₂ and that CO₂ and O₂ control its consumption. If [Ru-P₂] limits the rate of carboxylation, then factors affecting Ru-P₂ production and consumption will influence the velocity of Ru-P₂ carboxylase and thus the rate of photosynthesis.

A study of the responses of photosynthesis and [Ru-P₂] to light was under-

taken to determine whether the light response of carboxylation in vivo is at least in part a result of control of the rate of the carboxylation reaction by [Ru-P₂].

Work was initiated with the green algae *Chlamydomonas reinhardtii* grown in 5% CO₂ under conditions described elsewhere (Berry *et al.*, *Year Book* 75, pp. 423–432). Photosynthesis was measured as O₂ exchange in an O₂ electrode apparatus at pH 7.0 (50mM HEPES) and the light level was varied with neutral density filters. Samples were drawn into a syringe containing HClO₄ (10% final concentration) after a steady-state rate of O₂ evolution was obtained. The Ru-P₂ concentration was determined according to Latzko and M. Gibbs (1972) with Ru-P₂ carboxylase purified from spinach. Using the same assay approach, similar studies were done on isolated whole-leaf cells from spinach (Collatz and Badger, this *Year Book*). Photosynthesis and [Ru-P₂] increased parallel with increased light in both spinach (Fig. 6) and *Chlamydomonas* (data not shown). This result is consistent with the hypothesis that photosynthesis is regulated at least in part by changes in the [Ru-P₂] as light varies.

In similar experiments at 3% O₂ [Ru-P₂] was higher than at 21% O₂ at all light intensities for both *Chlamydomonas* and spinach cells (data not shown). This observation may account in part for the higher rates of photosynthesis in C₃ plants and high CO₂-grown algae at low [O₂] than at 21%.

The early work of Wilson and Calvin (1955) showing that the presence of CO₂ caused the [Ru-P₂] to fall was inter-

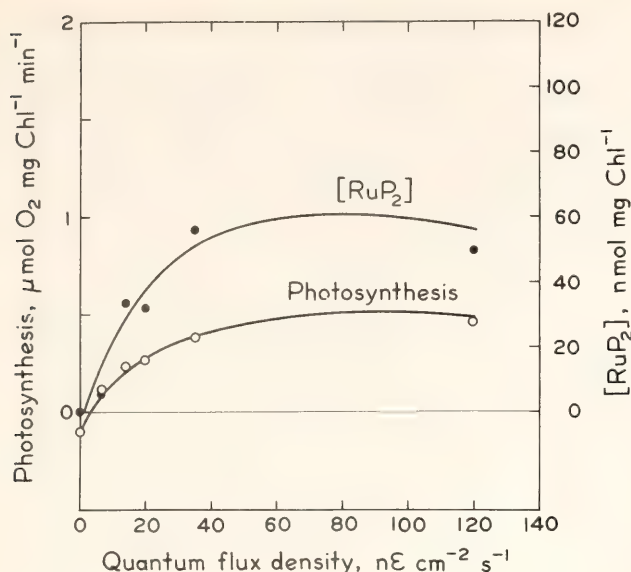


Fig. 6. The response of photosynthesis and Ru-P₂ concentration to quantum flux density in isolated leaf cells of spinach at 25°C, 10 μM CO₂, and 21% O₂.

interpreted as evidence in favor of the hypothesis that Ru-P₂ is the primary acceptor of CO₂ in the photosynthetic carbon reduction cycle. This effect of CO₂ on [Ru-P₂] was studied more closely in spinach leaf cells (Fig. 6) and *Chlamydomonas* (data not shown). As photosynthesis (i.e. consumption of Ru-P₂) increased with higher [CO₂], [Ru-P₂] fell. This drop was most pronounced at CO₂ concentrations below 40 μM. Comparison with Fig. 5, which shows the effect of CO₂ on photosynthesis, indicates that photosynthesis increased to its maximum rate over this range.

At very low levels of carboxylation and oxygenation (low [CO₂] and [O₂]) the [Ru-P₂] reaches a finite value of approximately 100 nmol per mg chl. If Ru-P₂ is produced at a constant rate for a given light intensity, then [Ru-P₂] should tend toward infinity as the consumption rate via carboxylation and oxygenation approaches zero. The data indicate, however, that the rate of production is inhibited at high [Ru-P₂]. Regulation of the maximum [Ru-P₂] may be a result of a limited supply of phosphate or carbon to form Ru-P₂.

At high [CO₂], lowering the light intensity causes a parallel decrease in both photosynthesis and [Ru-P₂] similar to that shown in Fig. 6 (data not shown). The low [Ru-P₂] measured when [CO₂] was high (Fig. 7) indicates that the rate of photosynthesis under these conditions is limited by the capacity of the system to generate Ru-P₂. If [Ru-P₂] could be increased above the levels observed at high CO₂, this interpretation predicts that carboxylation—and thus photosynthesis—would proceed at a faster rate.

The effect of O₂ on the [Ru-P₂] shown in Fig. 7 is probably a result of consumption of Ru-P₂ by the oxygenation of Ru-P₂ catalyzed by Ru-P₂ carboxylase in the presence of 21% O₂. The convergence at high CO₂ of [Ru-P₂] at 3% and 21% O₂ is consistent with the competitive inhibition mechanism for the interaction between CO₂ and O₂. The photosynthesis and [Ru-P₂] responses to CO₂ and O₂ in *Chlamydomonas* (data not shown) were similar to the results shown for spinach cells.

The range of [Ru-P₂] shown in Fig. 7 (0.5–3.0 mM if one assumes 30 μl of chloroplasts volume per mg chlorophyll) lies well above the levels which produce a large response to [Ru-P₂] by the Ru-P₂ carboxylase in vitro. The carboxylase

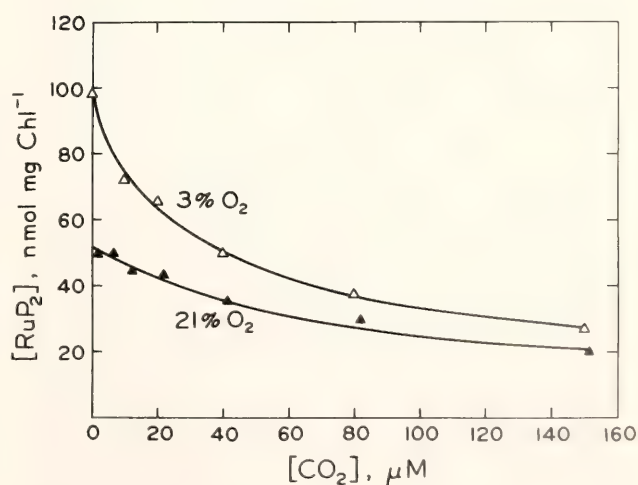


Fig. 7. The dependence of Ru-P₂ concentration on CO₂ concentration at 21% and 3% O₂, 25°C and an incident quantum flux density of 120 nE cm⁻² sec⁻¹.

should be more than 90% saturated at a $[\text{Ru-P}_2]$ more than 10 times the K_M for Ru-P_2 ($K_M = 30\mu\text{M}$ for purified enzyme at saturating CO_2 and 25°C , as determined by Badger and Collatz, *Year Book* 76, pp. 355–361). It may be that a significant portion of the $[\text{Ru-P}_2]$ measured here was bound to the enzyme as enzyme-substrate complexes and that the free $[\text{Ru-P}_2]$ was actually lower and rate limiting.

Carboxylase-active site concentration in spinach chloroplasts has been estimated to be about 4mM (Jensen and Bahr, 1977). At a free $[\text{Ru-P}_2]$ of $30\mu\text{M}$, or the K_M concentration, half of the total active sites are occupied with Ru-P_2 . Consequently the total $[\text{Ru-P}_2]$ (free + bound) is equal to 2.03mM . Assuming the Ru-P_2 concentrations reported here are equal to the sum of bound and free Ru-P_2 , it would require more than 4mM Ru-P_2 for the carboxylase to be saturated with respect to Ru-P_2 .

In order to test whether measured Ru-P_2 concentrations reflect total or free $[\text{Ru-P}_2]$, purified, activated Ru-P_2 carboxylase was incubated with ^{14}C -labeled carboxyribitol bisphosphate (CRP_2) in 12mM NaHCO_3 , 10mM MgCl , 5mM DTT, 50mM HEPPS $\text{pH} = 8.2$. Carboxyribitol bisphosphate is a transition-state analogue of the $\text{Ru-P}_2 + \text{CO}_2$ reaction product and appears to bind very tightly to the active site. This binding is competitive with respect to Ru-P_2 . Under conditions in which all active sites should be occupied by CRP_2 ($[\text{CRP}_2]/[\text{carboxylase}] = 10$, Siegal and Lane, 1972), no CRP_2 could be detected in the HClO_4 precipitate of the enzyme. It follows, then, that the HClO_4 treatment causes bound CRP_2 to be released from the active sites during precipitation. Since this compound binds more tightly to the active site than does Ru-P_2 , it is likely that any bound Ru-P_2 would be released under these conditions. Thus it is concluded that the measured

$[\text{Ru-P}_2]$ reflects the sum of the free-plus-bound species.

Several models have appeared in the literature which couple a single substrate rate equation relating the velocity of carboxylation to $[\text{CO}_2]$ with Fick's Law of diffusion (Lommen *et al.*, 1971; Jones and Slatyer, 1972; Tenhunen *et al.*, 1976). These models attribute deviations from the rectangular hyperbola predicted by the simple rate equation for carboxylation and the CO_2 and light-saturated photosynthetic rate to the resistance to CO_2 diffusion between the intercellular spaces and the chloroplast stroma. The influence of $[\text{CO}_2]$ on $[\text{Ru-P}_2]$ shown here could have a significant effect on the shape of the photosynthetic CO_2 -response curve. Since carboxylation is a two-substrate reaction in which the substrates may bind in random order to the enzyme (Badger and Collatz, *Year Book* 76, pp. 355–361), a simple single-substrate rate equation is clearly an oversimplification of carboxylation kinetics in vivo. The evidence presented here also suggests that the CO_2 -saturated rate of photosynthesis in spinach leaf cells under the conditions reported here does not represent the maximum capacity of the carboxylation reaction (V_{max}) but rather the capacity for regeneration of Ru-P_2 . Models which attempt to separate CO_2 diffusive limitations from carboxylation limitations but do not take into account the variable levels of Ru-P_2 are therefore of questionable value.

Carboxylation kinetics in vivo may be further complicated by light-dependent stromal concentrations of H^+ , Mg^{+2} , and phosphorylated compounds which have been shown to affect the activity of Ru-P_2 carboxylase in vitro (Lorimer *et al.*, 1976; Chu and Bassham, 1975). Jensen and Bahr (1977) have argued that these effectors probably influence the state of activation of Ru-P_2 carboxylase in vivo. Activation and inactivation processes would very likely

affect the shape of photosynthetic CO₂ and light-response curves.

The [Ru-P₂] measured in spinach leaf cells and *Chlamydomonas* shows a CO₂, O₂, and light dependence. The simplest interpretation of the data reported here is that light controls the production of Ru-P₂, whereas CO₂ and O₂ influence its consumption. Since the measured Ru-P₂ levels reflect both free Ru-P₂ and Ru-P₂ bound to the carboxylase, it is likely that the free [Ru-P₂] is at rate-limiting concentrations, particularly under conditions in which Ru-P₂ production is low (low light) or Ru-P₂ consumption is high (21% O₂ or high CO₂).

ACKNOWLEDGMENTS

I gratefully acknowledge the helpful discussions and advice of Drs. M. R. Badger, J. Berry, O. Björkman, G. Farquhar, and A. Kaplan.

REFERENCES

- Atkins, C. A., D. T. Canvin, and H. Fock, in *Photosynthesis and Photorespiration*, M. D. Hatch, C. B. Osmond, and R. O. Slatyer, eds., pp. 497–505, Wiley, New York, 1971.
- Calvin, M., and P. Massini, *Experientia* 8, 445–457, 1952.
- Chu, D. K., and J. A. Bassham, *Plant Physiol.* 55, 720–726, 1975.
- Jensen, R. G., and J. T. Bahr, *Annu. Rev. Plant Physiol.* 28, 379–400, 1977.
- Jones, H. G., and R. O. Slatyer, *Plant Physiol.* 50, 283–288, 1972.
- Latzko, E., and M. Gibbs, *Methods Enzymol.* 24B, pp. 261–268, 1971.
- Latzko, E., L. Laber, and M. Gibbs, in *Photosynthesis and Photorespiration*, M. D. Hatch, C. B. Osmond, and R. O. Slatyer, eds., pp. 196–201, Wiley, New York, 1971.
- Lommen, P., C. Schwintzen, C. Yocum, and D. Gates, *Planta* 98, 195–220, 1971.
- Lorimer, G. H., M. R. Badger, and T. J. Andrews, *Biochemistry* 15, 529–536, 1976.
- Siegel, M. I., and M. D. Lane, *Biochem. Biophys. Res. Commun.* 48, 508–516, 1972.
- Tenhunen, J. D., C. S. Yocum, and D. M. Gates, *Oecologia* 26, 89–100, 1976.
- Wilson, A. T., and M. Calvin, *J. Amer. Chem. Soc.* 77, 5948–5957, 1955.

A MECHANISM FOR CONCENTRATING CO₂ IN *Chlamydomonas reinhardtii* AND *Anabaena variabilis* AND ITS ROLE IN PHOTOSYNTHETIC CO₂ FIXATION

Murray R. Badger, Aaron Kaplan, and Joseph A. Berry

The photosynthetic characteristics of the green alga *Chlamydomonas reinhardtii* suggest that it has an inducible mechanism that dramatically increases the ability of the cells to photosynthesize at low ambient CO₂ concentrations (*Year Book* 75, pp. 423–443). These studies showed that this ability was not the consequence of a change in the biochemical mechanism of CO₂ fixation or in the kinetic constants of the enzyme ribulose-

1,5-bisphosphate (Ru-P₂) carboxylase for CO₂. We suggested that cells adapted to growth at low CO₂ concentrations might have a mechanism for concentrating CO₂ at the site of CO₂ fixation.

It is well known that some algae are able to transport HCO₃⁻ ions actively (Raven, 1970), and we proposed that an active bicarbonate uptake mechanism might be linked with photosynthetic CO₂ assimilation to serve as a CO₂-concent-

trating mechanism. Our concept of how this might work is shown in Fig. 8. CO_2 , the substrate for Ru-P₂ carboxylase, may be formed via the equilibrium catalyzed by carbonic anhydrase from an internal pool of bicarbonate ions. Bicarbonate could be accumulated within the cell by a transport mechanism that may be linked to a metabolically generated electrochemical gradient—for example, a cation gradient. According to Fig. 8, a steady-state internal CO_2 concentration would be established within the cell. It would depend upon: (1) the external CO_2 and HCO_3^- concentrations; (2) the rate of transport of HCO_3^- into the cell; (3) the rate of CO_2 -fixation by Ru-P₂ carboxylase; and (4) the rate of diffusion of CO_2 from the cell to the medium or vice versa. Provided that the rate of HCO_3^- transport at a given external

($\text{CO}_2 + \text{HCO}_3^-$) concentration exceeds the rate of CO_2 fixation by the cell, at that CO_2 concentration, then CO_2 and HCO_3^- will accumulate within the cell until the rates of CO_2 fixation and back diffusion of CO_2 balance the rate of bicarbonate uptake. As a result, the steady-state internal CO_2 concentration would be greater than that outside the cell. Such a mechanism could, in principal, improve the efficiency of CO_2 fixation by stimulating Ru-P₂ carboxylase activity and inhibiting Ru-P₂ oxygenase activity of the alga. This model is consistent with the differences in CO_2 fixation and glycolate formation observed in cells grown under conditions presumed to induce or repress the bicarbonate pump mechanism (Year Book 75, pp. 425–443; Findenegg, 1976).

Direct evidence for the existence of such a concentrating mechanism was obtained from measurements of the concentration of CO_2 within cells of *C. reinhardtii* (Year Book 76, pp. 362–366). These measurements showed that cells adapted to growth at low CO_2 concentrations can accumulate CO_2 internally to a concentration several times higher than that in the surrounding medium. This year we report further studies showing that the production of this CO_2 concentration gradient is dependent upon metabolic energy. In addition, investigations of the kinetics of the bicarbonate transport mechanism of *Anabaena variabilis*, a blue-green alga which also possesses such a CO_2 -concentrating mechanism, are described.

METHODS

Algae were cultured on media bubbled either with air or with air enriched with 3–5% CO_2 . These algae are referred to as low- CO_2 or high- CO_2 cells, respectively. *C. reinhardtii* was grown on HS culture media (Sueoka, 1960), and *Anabaena* was grown on Kratz and Myers C medium (Kratz and Myers, 1955). The methods used to measure the inter-

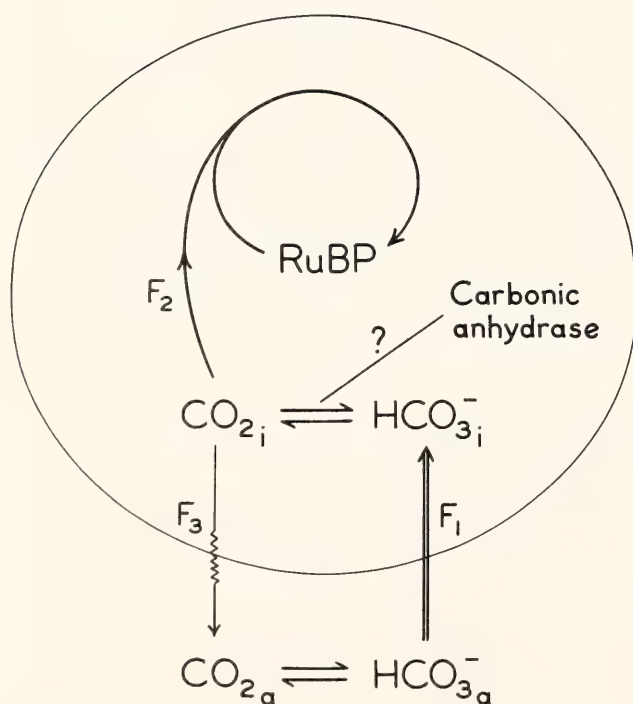


Fig. 8. A simple model showing how an active bicarbonate (HCO_3^-) transport mechanism might act to concentrate CO_2 at the site of carboxylation. F_1 = active HCO_3^- transport flux; F_2 = CO_2 -fixation rate; F_3 = flux rate of the diffusive leak of CO_2 into the medium. At steady state, when $F_1 > F_2$, then $\text{CO}_{2i} > \text{CO}_{2a}$. It is important to note that this scheme depicts a single-compartment system and ignores intracellular compartmentation.

nal inorganic carbon pool are based on the silicon-oil layer centrifugal-filtration technique of Werdan *et al.* (1972). In this technique a layer of silicon oil of appropriate density is used to isolate two aqueous phases in a microcentrifuge tube. The upper phase is the cell incubation medium, while the lower is an alkaline killing solution. Incubations are conducted in the light ($45\text{ nE cm}^{-2}\text{ sec}^{-1}$) and are ended by centrifugation of the cells from the upper phase into the killing solution (in less than 2 sec). This method results in rapid filtration and killing of the cells.

The total volume of water transferred with the cells is determined by incubation and filtration with tritiated water. The proportion of this volume that is extracellular is estimated with a labeled impermeable compound (^{14}C -sorbitol). The difference between these two volumes is assumed to be the intracellular volume—the sorbitol-impermeable space (SIS). In these experiments the SIS was generally 30–40% of the total water volume transferred with the cells. The cell volume, based on cell counts and the SIS or cell dimension, and the chlorophyll parameters of *C. reinhardtii* and *A. variabilis* are shown in Table 9. With the cell volume calibrations this technique may be used to estimate the intracellular concentration of any labeled compound

present during incubation from the quantity of that compound transferred with filtration.

For inorganic carbon determination, $\text{H}^{14}\text{CO}_3^-$ was supplied, and the difference between acid-stable ^{14}C and the total ^{14}C transferred with the cells to the alkaline killing medium was taken as a measure of the inorganic carbon pool. Control experiments showed that this ^{14}C was not produced by decarboxylation of a keto-acid product of CO_2 fixation. Photosynthesis was estimated from the acid-stable ^{14}C .

It is important to know the intracellular pH in order to calculate the equilibrium CO_2 concentration which would correspond to a given intracellular pool of inorganic carbon. This pH was estimated with ^{14}C -dimethyloxazolidinedione (DMO) as a probe. This weak acid will partition between the intracellular and extracellular spaces according to the pH gradient.

Studies with Chlamydomonas

Experiments with *Chlamydomonas* verified the major conclusion reached last year, namely, that the intracellular pool of inorganic carbon ($\text{CO}_2 + \text{HCO}_3^-$) within low- CO_2 -adapted cells—which we predicted should have a CO_2 -concentrating mechanism—accumu-

TABLE 9. Chlorophyll Per Volume of Sorbitol-Impermeable Space (SIS) as Determined by Silicone Oil Filtration, and the Volume Per Cell of *Chlamydomonas reinhardtii* and *Anabaena variabilis* Cells Used in Studies Reported Here

Cell Type	chl/ μl SIS ($\mu\text{g}/\mu\text{l}$)	Internal Cell Volume* (μl)
<i>Chlamydomonas</i>		
low- CO_2 cells	7.69 ± 1.3	$1.44 \pm 0.5 \times 10^{-7}$
high- CO_2 cells	3.5 ± 1.2	$2.7 \pm 0.7 \times 10^{-7}$
<i>Anabaena</i>		
low- CO_2 cells	3.8, 4.75	...
high- CO_2 cells	2.56, 3.12	0.229×10^{-7}

* Determined from μl SIS/ 10^7 cells for *Chlamydomonas*; and from cell dimensions for *Anabaena*.

lates to levels well above that expected by passive distribution alone. Figure 9a shows the measured intracellular concentration of ($\text{CO}_2 + \text{HCO}_3^-$) within illuminated cells of *C. reinhardtii* which were filtrated after incubation for 10 sec with ^{14}C inorganic carbon. The figure also shows the expected internal ($\text{CO}_2 + \text{HCO}_3^-$) concentration assuming completely passive equilibration between the extracellular and intracellular spaces. The ratio of the actual measured concentrations to this lower line is an index of the extent to which the internal pool

exceeds that expected from passive distribution. This ratio is plotted in Fig. 9b (control). It is clear that the measured pool is far larger than would be expected for passive equilibration alone. Werdan *et al.* (1972) showed that inorganic carbon can accumulate within illuminated higher plant chloroplasts according to a pH gradient. Since the pH within the chloroplast was more alkaline than that of the medium and since CO_2 , but not HCO_3^- , can penetrate the inner membrane, an equilibrium that gave equal CO_2 concentrations but unequal HCO_3^-

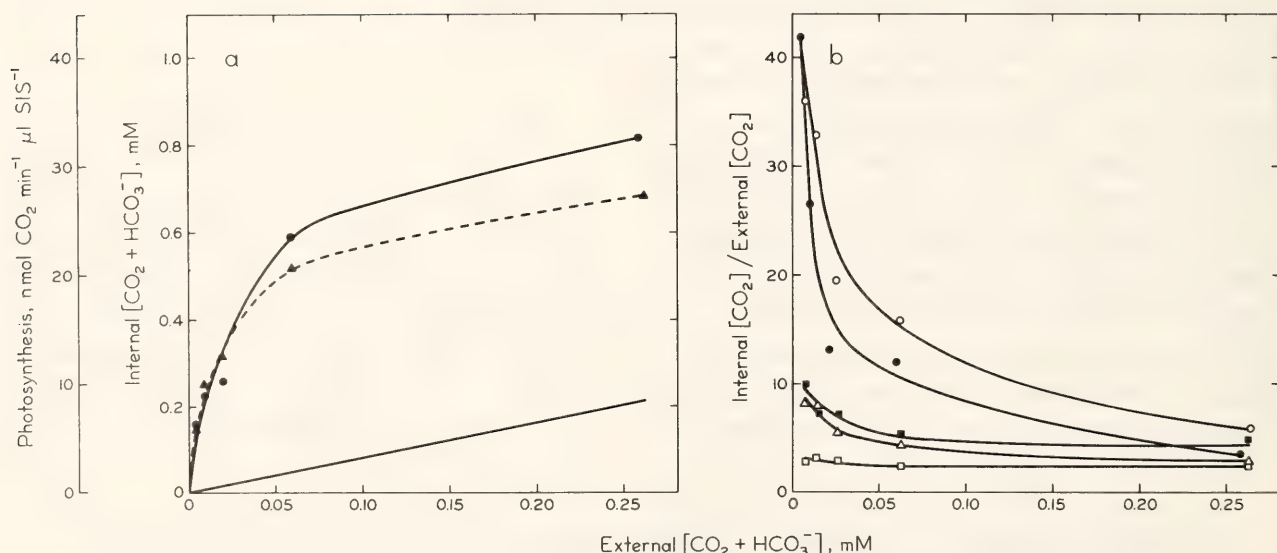


Fig. 9(a). The response of internal [$\text{CO}_2 + \text{HCO}_3^-$] (●--●) and rate of photosynthesis (▲--▲) to external [$\text{CO}_2 + \text{HCO}_3^-$] in low- CO_2 -grown *Chlamydomonas*. Cells were incubated in 25 mM HEPES, pH 7.15, at 25°C. The points are the mean of three 10-sec incubations at each external concentration. Internal pH was 7.08. The lower line represents the internal [$\text{CO}_2 + \text{HCO}_3^-$] that would be expected, assuming passive distribution of inorganic carbon species according to the estimated internal pH. (b) The response of internal [CO_2]/external [CO_2] to external [$\text{CO}_2 + \text{HCO}_3^-$] of low- CO_2 -grown *Chlamydomonas*, with the following treatments: control (●--●); methyl viologen (5mM) (○--○); SF6647 (0.1 μM) (□--□); DCMU (10 μM) (■--■) and FCCP (30 μM) (△--△). Internal ($\text{CO}_2 + \text{HCO}_3^-$) pools were estimated from three 10-sec incubations at each external concentration. Cells were incubated in the light with each inhibitor for 15 sec prior to the addition of $\text{NaH}^{14}\text{CO}_3$ (at time zero). The estimated internal pH's were: Control (7.08); methyl viologen (7.02); DCMU (7.07); FCCP (7.20); SF 6847 (6.92). Internal [CO_2] was calculated from the internal pH and the internal [$\text{CO}_2 + \text{HCO}_3^-$]. External [CO_2] was calculated from the external pH (7.15, 25°C) and [$\text{CO}_2 + \text{HCO}_3^-$]. A pK' of 6.37 (25°C) was assumed for the $\text{HCO}_3^-/\text{CO}_2$ equilibrium.

concentrations on either side of the membrane was established. Measurements of pH conducted with *C. reinhardtii* indicate that the accumulation of ($\text{CO}_2 + \text{HCO}_3^-$) observed here is not a function of pH gradients alone. The measured internal pH was 7.08, while the external pH was 7.15. An internal pH of 8.6 would be required to account for the observed maximal accumulation. If it is assumed that CO_2 and HCO_3^- are in rapid equilibrium, then these results indicate an increase in the free CO_2 concentration within the cell. Photosynthesis (dotted line, Fig. 9a) increases approximately parallel with the intracellular CO_2 concentration. The apparent K_M , expressed in terms of external ($\text{CO}_2 + \text{HCO}_3^-$) concentration, was $35\text{--}40\mu\text{M}$ (or 3.5 to $4.0\mu\text{M}$ expressed on the basis of CO_2 concentration). At this external ($\text{CO}_2 + \text{HCO}_3^-$) concentration the internal CO_2 concentration was $30\text{--}40\mu\text{M}$. This value is approximately ten-fold higher than that of the medium, and is similar to the $K_M(\text{CO}_2)$ of Ru-P₂ carboxylase from *C. reinhardtii*. These results therefore reconcile the large difference in apparent $K_M(\text{CO}_2)$ of the cells and the isolated enzyme.

In interpreting the results it is important to note that the cells were completely depleted of inorganic carbon by preincubation in an illuminated O_2 -electrode chamber prior to incubation with $^{14}\text{HCO}_3^-$. Hence there was very little dilution of the labeled inorganic carbon with unlabeled carbon from the medium or cells. Time-course experiments (Fig. 10) showed no lag in the initial rate of CO_2 -fixation, and the maximal rate of CO_2 -fixation ($27\text{ nmol } \mu\text{L}^{-1} \text{ SIS}^{-1} \text{ min}^{-1}$) corresponds to $258\text{ mole mg chl}^{-1} \text{ hr}^{-1}$, a value comparable to the rates of O_2 -evolution obtained in long-term steady-state experiments. As shown in Fig. 10, the intracellular pool of ($\text{CO}_2 + \text{HCO}_3^-$) in low- CO_2 -grown cells was essentially constant for incubation times from 5 to 80 sec. Thus the time required

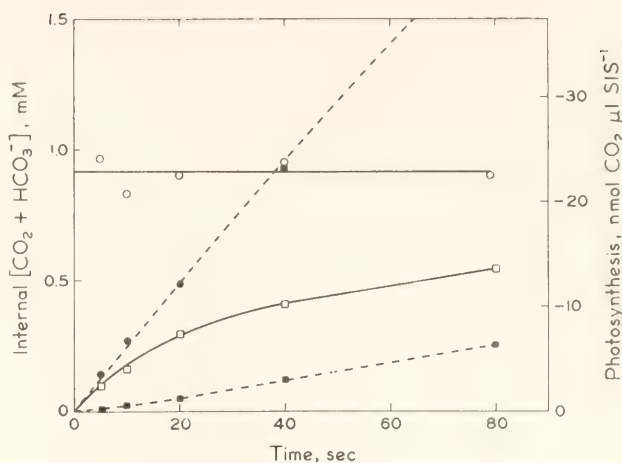


Fig. 10. The change of internal $[\text{CO}_2 + \text{HCO}_3^-]$ (\circ , \square) and total photosynthesis (\bullet , \blacksquare) with time of incubation, for cells grown in high CO_2 (squares) and cells grown in low CO_2 (circles). Incubations were in 25mM HEPES, pH 7.15, 25°C and $100\mu\text{M}$ $\text{NaH}^{14}\text{CO}_3$. Three replicates were run for each time point. Internal pH's were 7.10 (high CO_2) and 7.05 (low CO_2).

to reach steady state was short in relation to the time interval used in these experiments. All of these observations, taken together, indicate that the measurements reported above are representative of steady-state photosynthetic performance of low- CO_2 -grown cells of *C. reinhardtii*.

Results similar to those in Fig. 9a were reported last year. However, we have found that the lot of DMO used in the experiments reported last year contained a labeled contaminant which was accumulated by the cells. As a result, the pH values reported (*Year Book* 76, p. 364, Table 30) are too high. Subsequent lots of ^{14}C -DMO from New England Nuclear give lower values. Control experiments conducted with isolated intact chloroplasts give pH measurements comparable to those reported in the literature. The result of this correction is that the intracellular concentration of CO_2 (calculated on the assumption of rapid equilibrium between CO_2 and HCO_3^-) within cells of *Chlamydomonas* during photosynthesis is actually higher than estimated last year.

It should also be noted that in the experiments reported last year we made several comparisons of high- CO_2 -grown cells to low- CO_2 -grown cells. These comparisons were based on the assumption that there was rapid equilibrium between internal CO_2 and HCO_3^- and that the internal ($\text{CO}_2 + \text{HCO}_3^-$) concentration rapidly reached a steady-state value. Results obtained this year do not support either assumption for high- CO_2 -grown cells. As shown in Fig. 10, there is a continuous accumulation of ($\text{CO}_2 + \text{HCO}_3^-$) within high- CO_2 -grown cells up to 80 sec. The final internal pool is several-fold larger than the external pool, which indicates that these cells have some capacity to transport HCO_3^- . However, the very slow accumulation suggests that the HCO_3^- pool is not in rapid equilibrium with the intracellular pool of CO_2 . If this is the case, then the comparisons made last year (*Year Book* 76, pp. 362-366) of the intracellular pool size in terms of CO_2 between high and low- CO_2 -grown cells are not valid. The slow kinetics of the accumulation and the lack of rapid equilibrium between CO_2 and HCO_3^- may be related to the very low activity of carbonic anhydrase in these cells. We have also observed that low- CO_2 cells, when incubated with the carbonic anhydrase inhibitor ethoxymolamide, become very similar to high- CO_2 -grown cells in the time course of internal pool accumulation and the kinetics of CO_2 -fixation (data not shown). These results suggest that carbonic anhydrase activity is required for the high rate of inorganic carbon transport by low- CO_2 cells as well as for catalyzing the equilibrium between HCO_3^- and CO_2 . Complete details of the role of carbonic anhydrase are not clear.

If the intracellular pool of inorganic carbon demonstrated above is accumulated against a concentration gradient, then some form of energy must be put into the system. It might be expected

that inhibitors of energy transduction would affect the steady-state intracellular pool of low- CO_2 -adapted cells. Experiments were conducted in the same manner as those shown in Fig. 9a, except that an inhibitor was added to the cell suspension 15 sec before addition of labeled inorganic carbon. The ratio of internal CO_2 to external CO_2 was calculated and these ratios are shown in Fig. 9b together with the results of a control experiment. The free-energy gradient is directly proportional to the logarithm of this ratio. As shown, DCMU (dichlorophenylmethylurea), FCCP (carbonylcyanide trifluoromethoxyphenylhydrazone), and SF6847 cause the energy gradient between internal and external CO_2 concentration to fall. These three inhibitors all reduced CO_2 fixation to less than 10% of the control. FCCP and SF6847 are both uncouplers of photophosphorylation. They act by dissipating the proton gradient, while DCMU inhibits photosynthetic electron transport. The effect of these inhibitors on the CO_2 -concentration gradient suggests a critical role for phosphorylation in general and perhaps for photophosphorylation in particular in supplying energy to drive accumulation. Methyl viologen, however, caused a significant increase in the ratio of internal to external CO_2 relative to the control. Methyl viologen does not inhibit photophosphorylation but does inhibit CO_2 fixation by competing with the carbon reduction pathway for reducing equivalents. If CO_2 fixation were inhibited but ATP formation were not, then the intracellular pool of CO_2 might be expected to increase over the control, as was actually observed. With methyl viologen there was nearly complete inhibition of CO_2 fixation, while the inorganic carbon pool was actually stimulated. These studies verify the existence of a CO_2 -concentrating mechanism in cells of *C. reinhardtii*, which appears to be dependent upon photosynthetic energy.

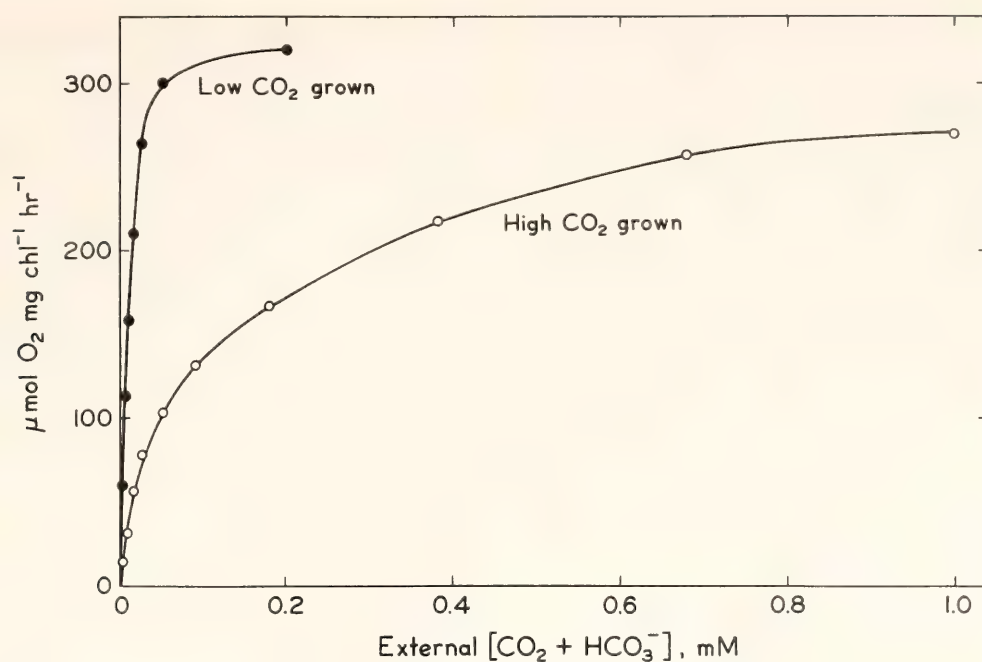


Fig. 11. The steady-state rate of photosynthetic O₂ evolution for both high- and low-CO₂-grown cells of *Anabaena variabilis* in response to external [CO₂ + HCO₃⁻]. Assays were run at 30°C, 50mM HEPES, pH 8.0. The apparent K_M for photosynthesis was 14.2 ± 2 and $86 \pm 12 \mu\text{M}$, and the apparent V_{max} for photosynthesis was 369 and 282 $\mu\text{mol mg chl}^{-1}\text{hr}^{-1}$ for low- and high-CO₂-adapted cells, respectively.

Studies with *Anabaena*

Studies of photosynthesis and glycolate metabolism (Ingle and Colman, 1976) indicated that some blue-green algae might also possess a mechanism for improving their efficiency of CO₂ assimilation. Studies of the CO₂ dependence of photosynthesis of *Anacystis nidulans* (data not shown) and *Anabaena variabilis* (Fig. 11) have confirmed this hypothesis. The apparent K_M (CO₂ + HCO₃⁻) of *A. variabilis* cells which had been grown at low CO₂ was 14 μM at pH 8.0, representing approximately 0.3 μM CO₂. When the cells are grown at high CO₂, the apparent affinity for inorganic carbon is diminished. In either case, this apparent affinity of the whole cell for CO₂ exceeds that of Ru-P₂ carboxylase from *Anabaena*, assayed in vitro (data not shown).

The filamentous cells of *A. variabilis* are very amenable to silicon-oil filtration experiments. Figure 12 shows a time course in which a suspension of low-CO₂-adapted cells was filtered through

the silicon-oil layer at a sequence of times from 5 to 120 sec after addition of 10 μM ¹⁴HCO₃⁻. There is an initial lag in photosynthesis, during which there is an accumulation of inorganic carbon in the internal pool. This pool increases to

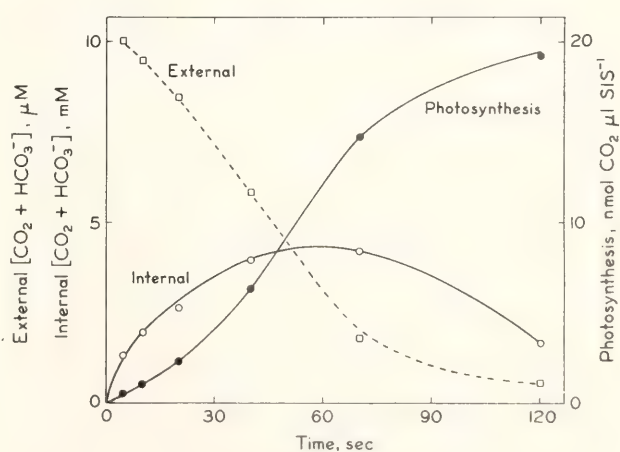


Fig. 12. An incubation time course for low-CO₂-adapted cells of *Anabaena*. Incubation was at 30°C, 25mM HEPES, pH 8.0, 10 μM NaH¹⁴CO₃. Changes in internal [CO₂ + HCO₃⁻], external [CO₂ + HCO₃⁻], and total photosynthesis are shown. There were two replicates for each time point. Maximum internal/external inorganic carbon ratio was over 1000.

a concentration of nearly 4mM, and the pool is so large that it initially exceeds the ^{14}C fixed in photosynthesis. Since the internal pool and photosynthesis are both expressed in units of nmoles carbon per μl SIS, the percentage of ^{14}C in each component can be directly determined from Fig. 12, and the pool can account for as much as 75% or more of the total carbon filtered with the cells after 10 sec incubation. In contrast, the pool of *C. reinhardtii* was generally less than 15%. The very large pool of *A. variabilis* is thus clearly distinct from the products of CO_2 fixation.

Figure 12 also shows that the cells rapidly deplete the concentration of inorganic carbon remaining in the medium. After 120 sec incubation, nearly all the added ^{14}C is fixed into acid-stable products. It can be seen that the internal pool of inorganic carbon plays an active role in this transfer. The flow of carbon appears to proceed initially from the external pool into the internal inorganic carbon pool. As this pool builds up, the rate of fixation of ^{14}C increases. As the external inorganic carbon supply is exhausted, the internal pool begins to be diminished, and the rate of ^{14}C -fixation declines. These characteristics are consistent with the internal acid-unstable ^{14}C 's being a pool of $(\text{CO}_2 + \text{HCO}_3^-)$, which is an intermediate in photosynthetic carbon assimilation for this alga. The maximum accumulation of inorganic carbon within the cells corresponded to a ratio of internal/external concentration in excess of 1000. If this carbon accumulated according to a pH gradient, the cell interior would have to be at least 3 pH units more alkaline than the medium. This pH difference is not found; in fact, the cells are more acid than the medium.

The accumulation of inorganic carbon within cells of *Anabaena* differs in extent and kinetics from that of *Chlamydomonas*. The very slow accumulation time course suggested the possibility that

CO_2 and HCO_3^- in the inorganic carbon pool of *Anabaena* were not in rapid equilibrium. We could detect no evidence of calcium carbonate formation, nor could we detect substantial carbonic anhydrase activity in *Anabaena* cells (data not shown). It seems likely, therefore, that the inorganic carbon pool within these cells is predominantly HCO_3^- , with very little free CO_2 . Since the membranes are permeable to CO_2 and relatively impermeable to HCO_3^- , this suggestion may explain how such a large concentration gradient could be maintained. The slow interconversion of HCO_3^- to CO_2 could be a large part of the "resistance" which prevents inorganic carbon, once accumulated, from escaping to the medium. However, if Ru-P₂ carboxylase of *Anabaena* utilizes CO_2 as its substrate, and if HCO_3^- is not in rapid equilibrium with CO_2 , then the CO_2 concentration available to photosynthetic CO_2 fixation cannot be estimated. Clearly, the internal inorganic carbon pool does support CO_2 fixation. However, the relationship between the intracellular concentration and the requirements of Ru-P₂ carboxylase is not known.

The slow rate of the internal pool accumulation of *Anabaena*, shown in Fig. 12, permits the initial rate of carbon uptake to be estimated. Since the internal $(\text{CO}_2 + \text{HCO}_3^-)$ concentration exceeds the external $(\text{CO}_2 + \text{HCO}_3^-)$ concentration even after 5 sec of incubation, it is likely that there is some back diffusion of CO_2 to the medium. Thus the estimate of the initial influx rate of inorganic carbon would be too low. Nevertheless, this approach provides a useful system for examining the kinetics of the uptake process. Figure 13 shows the initial rate of $(\text{CO}_2 + \text{HCO}_3^-)$ uptake of high- and low- CO_2 -adapted cells of *Anabaena* as a function of external $(\text{CO}_2 + \text{HCO}_3^-)$ concentration. The apparent $K_M(\text{CO}_2 + \text{HCO}_3^-)$ of the uptake process is essentially the same for both cell types; however, the V_{max} of the low- CO_2 -adapted

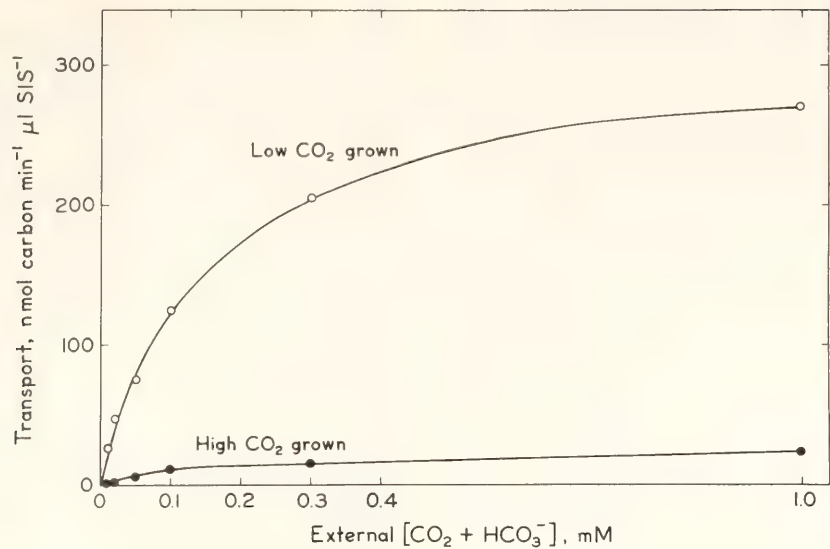


Fig. 13. Initial inorganic carbon transport rates for both high- and low-CO₂-adapted cells as a function of external [CO₂ + HCO₃⁻]. Rates were estimated from the initial slope of (fixed CO₂ + inorganic carbon) accumulation in time-course experiments run at varying external [CO₂ + HCO₃⁻]. Conditions were pH 8.0 and 30°C. The apparent K_M was 141 ± 11 and $166 \pm 22 \mu\text{M}$, and the apparent V_{max} was 3848 and 402 $\mu\text{mol mg chl}^{-1}\text{hr}^{-1}$ for low- and high-CO₂-adapted cells, respectively.

cells is about 10-fold higher than that for the high-CO₂-adapted cells. Expressed on a chlorophyll basis, the rate of transport by low-CO₂ cells appears very large (3840 $\mu\text{mol mg chl}^{-1}\text{hr}^{-1}$). When expressed on a cell surface-area basis, however, the rate is about 350 pmoles cm⁻² sec⁻¹. This rate is not

much higher than rates of HCO₃⁻ transport which have been observed with the giant alga *Chara* (Lucas, 1975). The maximum rate of HCO₃⁻ transport of low-CO₂-adapted cells exceeds the maximum rate of CO₂ fixation by a factor of nearly 10. Figure 14 shows the initial rate of carbon uptake and the steady-

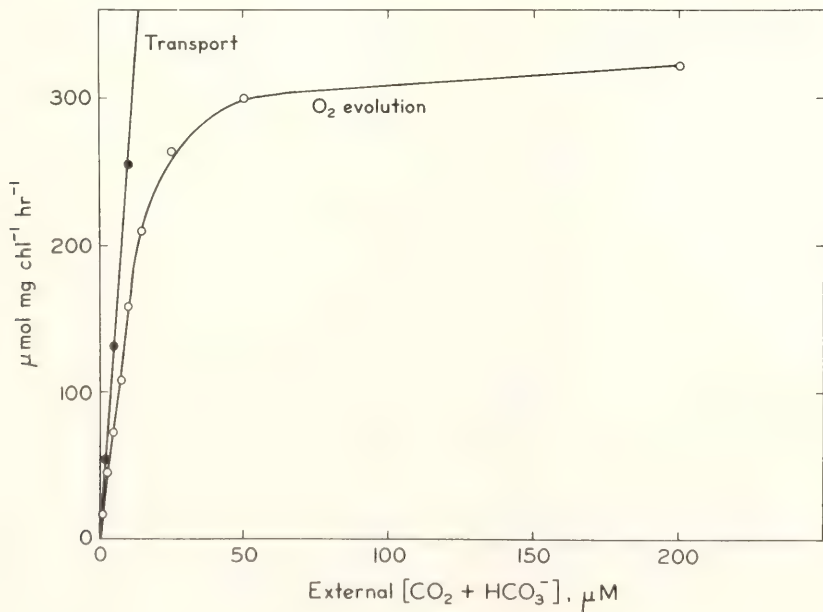


Fig. 14. Initial inorganic transport rates in low-CO₂-adapted cells as a function of external [CO₂ + HCO₃⁻] (from Fig. 13), compared to the response of steady-state O₂-evolution (from Fig. 11).

state rate of photosynthetic oxygen production per mg chl, both as a function of external ($\text{CO}_2 + \text{HCO}_3^-$) concentration. The rate of uptake exceeds the rate of O_2 evolution at all concentrations. It is also clear that photosynthetic O_2 evolution becomes saturated at a ($\text{CO}_2 + \text{HCO}_3^-$) concentration below the K_M of the transport process. Presumably the reason is that the intracellular concentration of inorganic carbon becomes rate saturating at external concentrations in excess of $50\mu\text{M}$. Similar experiments with high- CO_2 -adapted cells support this interpretation. Transport capacity of these cells is much lower (see Fig. 13)—about equal to the capacity for photosynthesis. Thus, as shown in Fig. 15, a higher external ($\text{CO}_2 + \text{HCO}_3^-$) concentration must be provided before the rate of transport approaches the rate required to saturate photosynthesis.

Studies of the effect of inhibitors of energy transduction on the time courses for inorganic carbon uptake were conducted. These studies gave results similar to those presented for *Chlamydomonas*. FCCP and DCMU inhibited both the initial influx rate of inorganic carbon

and the final internal pool size. Methyl viologen did not inhibit the initial uptake rate, but in contrast to *Chlamydomonas*, it had some longer term inhibitory effects on the final pool size.

CONCLUSIONS

These studies with *Anabaena* and *Chlamydomonas* demonstrate the existence of inorganic carbon accumulation within the cells during photosynthesis. This accumulation leads to a concentration of CO_2 available for fixation by Ru-P₂ carboxylase that is far higher within these cells than in the surrounding medium. These experiments confirm our hypothesis that these cells have a CO_2 -concentrating mechanism. Studies with inhibitors show that this CO_2 -concentrating mechanism is an active process requiring ATP. The kinetics of the time course for the internal pool and for photosynthesis in *Anabaena* cells also show that the intracellular inorganic carbon pool is an intermediate in the photosynthetic assimilation of ($\text{CO}_2 + \text{HCO}_3^-$). The estimation of the initial transport rate of inorganic carbon into cells of

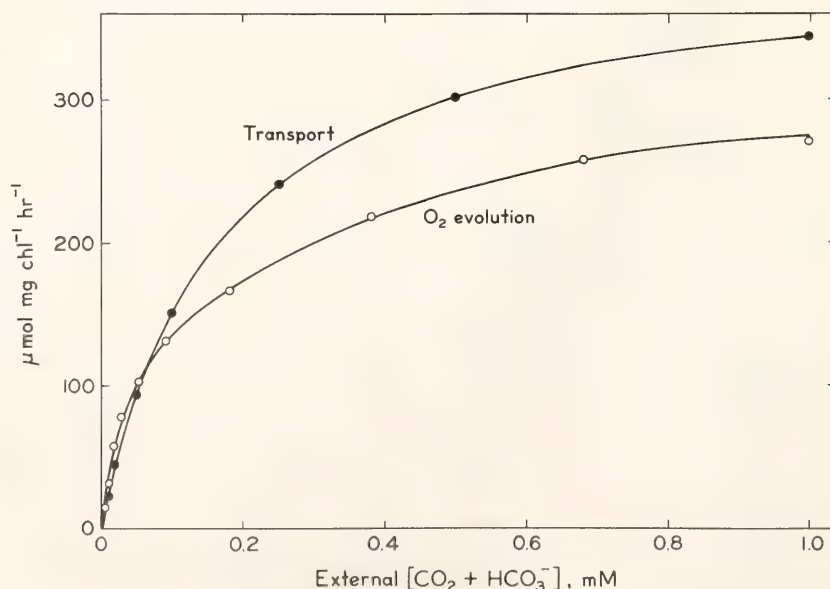


Fig. 15. Initial inorganic carbon transport rates in high- CO_2 -adapted cells as a function of external [$\text{CO}_2 + \text{HCO}_3^-$] (from Fig. 13), compared to the response of steady-state O_2 evolution (from Fig. 11).

Anabaena demonstrates that inorganic carbon transport can be much more rapid than CO_2 fixation, especially at limiting external ($\text{CO}_2 + \text{HCO}_3^-$) concentrations. Taken together, these observations support the proposal in Fig. 8, that the CO_2 -concentrating mechanism is based on an active inorganic carbon (HCO_3^-) transport system.

There are several aspects of the transport mechanism which are not clear. It is presumed that the mechanism is based on a transmembrane carrier for HCO_3^- . We know that this transporter must be located on the cell membrane of *Anabaena*. However, with eukaryotes such as *Chlamydomonas*, the transport system might be located either on the plasma membrane or on the chloroplast membrane. We also do not know how this process might be coupled to energy sources and ionic balances of the cells. For example, if HCO_3^- is taken up and CO_2 is utilized in photosynthesis, then the process would result in the accumulation of OH^- ions which must be excreted or neutralized. The energy for the transport may be provided directly through an ATPase or indirectly through a chemiosmotic gradient. The energy for transport presumably comes from an overall internal metabolic pool, which could otherwise be utilized for CO_2 fixation or growth. The cells obviously obtain some benefit for this energy expenditure on transport—in the form of increased carbon fixation—but the relative energy cost is not known.

The role of carbonic anhydrase in the accumulation mechanism is not clear. It is present in and apparently required by the *Chlamydomonas* system. The induction of carbonic-anhydrase activity seems to parallel the induction of maximum transport capacity in low- CO_2 -adapted cells. However, *Anabaena* appears to function without detectable car-

bonic anhydrase activity. The reason for this difference is not obvious.

The experiments with high- CO_2 -adapted cells of *Chlamydomonas* and *Anabaena* indicate that these cells also have the capacity to accumulate inorganic carbon. However, the capacity of this process is lower than in low- CO_2 -adapted cells. This result suggests that there may not be discrete physiological states, as first presumed, but there may be a continuum of possible states, with the capacity for inorganic carbon uptake increasing as carbon supply decreases. The algae might thus adjust the apparent affinity of the photosynthetic system for carbon to the supply of inorganic carbon available. This could be a very important adaptive mechanism of algae in natural waters. Growth studies (*Year Book* 75, pp. 423–443) indicate that the lower limit for net growth of *Chlamydomonas* is less than 30 ppm CO_2 . This surprising observation leads us to speculate that competition among algal species in the capacity and energetic efficiency of the CO_2 -concentrating mechanism may be an important factor in the dynamics of algal populations.

REFERENCES

- Findenegg, G. R., *Z. Pflanzenphysiol.* 79, 428–447, 1976.
Ingle, R. K., and B. Colman, *Planta* 120, 217–223, 1976.
Kratz, W. A., and J. Myers, *Amer. J. Botany*, 42, 282–287, 1955.
Lucas, W. J., *J. Exp. Bot.* 26, 331–346, 1975.
Raven, J. A., *Biol. Rev.* 45, 167–221, 1970.
Sueoka, N., *Proc. Nat. Acad. Sci. U.S.A.*, 46, 83–89, 1960.
Werdan, K., H. W. Heldt, and G. Geller, *Biochim. Biophys. Acta* 283, 430–441, 1972.

THERMAL ACCLIMATION OF PHOTOSYNTHESIS:
EFFECT OF GROWTH TEMPERATURE ON
PHOTOSYNTHETIC CHARACTERISTICS AND COMPONENTS
OF THE PHOTOSYNTHETIC APPARATUS IN *Nerium oleander*

Olle Björkman, Murray Badger, and Paul A. Armond

For the past six years the Physiological Ecology Group has been engaged in studies of a number of aspects of the adaptation of plants to habitats with contrasting thermal regimes. These studies have ranged from the productive performance and survival of whole plants in the field (*Year Book* 73, pp. 748–767) to photosynthetic characteristics of intact leaves under a series of precisely controlled environments (*Year Book* 74, pp. 743–751; *Year Book* 75, pp. 410–413; pp. 418–421; *Year Book* 76, pp. 328–335) to the molecular bases of thermal adaptation (*Year Book* 74, pp. 751–760; *Year Book* 75, pp. 400–407; *Year Book* 76, pp. 323–327; pp. 335–341; pp. 346–355; pp. 355–361). It is clear from these studies that plants restricted to cool-temperate coastal habitats, such as *Atriplex glabriuscula* (C_3) and *A. sabulosa* (C_4), have much higher capacity for photosynthesis at low temperature ($<25^\circ\text{C}$) than do hot-desert species such as *Tidestromia oblongifolia* (C_4). This higher photosynthetic capacity is unrelated to stomatal conductance or other leaf factors determining CO_2 diffusivity, and reflects instead an increased capacity of one or several as-yet unidentified steps of photosynthesis at the chloroplast level. Conversely, the photosynthetic performance at high temperatures ($>40^\circ\text{C}$) is greatly superior in the hot-desert species. This is largely due to an unusually high thermal stability of the photosynthetic apparatus. Key components showing substantially enhanced thermal stability in the hot-desert species include chloroplast-membrane-bound reactions such as photosystem II-driven

electron transport and photophosphorylation, as well as certain soluble enzymes of photosynthetic carbon metabolism. For example, Ru- P_2 carboxylase, Fru- P_2 aldolase and the “light-activated” enzymes NADP glyceraldehyde 3-P dehydrogenase and Ru-5P kinase have in vivo heat stabilities that are $6^\circ\text{--}10^\circ\text{C}$ higher in *T. oblongifolia* than in *A. sabulosa*, although with the exception of adenylate kinase and the “light-activated” enzymes the thermal stabilities of the enzymes are greater than those of photosystem II-driven electron transport, photophosphorylation, and overall photosynthesis.

It is known that the growth temperature regime may have a pronounced influence on the photosynthetic characteristics of a given species or genotype. In certain instances the changes in photosynthetic characteristics brought about by a change in the growth temperature regime result in a superior performance under the new regime. This phenomenon is often called photosynthetic temperature acclimation. The potential for temperature acclimation may vary considerably among different species in a manner reflecting the temperature regime of their native habitats. In plants from environments exhibiting only a moderate temperature variation during the period of vegetative growth, such as cool-coastal *A. sabulosa* and hot-desert *T. oblongifolia*, the potential for photosynthetic temperature acclimation is very limited. Growth of *A. sabulosa* at 40°C results in a strong reduction in photosynthetic capacity at this temperature in comparison with plants grown at a 16°C regime.

Conversely, the thermophilic *T. oblongifolia* is capable of very high photosynthetic rates at high temperatures when grown under a hot regime, but growing this plant at 20°C or below results in a drastic reduction in photosynthetic capacity at all temperatures. Because of these responses, *A. sabulosa* and *T. oblongifolia* are not well suited for studies of the mechanisms of environmentally induced temperature acclimation of photosynthesis.

A considerably greater acclimation potential is found in evergreen desert species that are subjected to very large seasonal temperature variations. An excellent example of such plants is *Larrea divaricata* from Death Valley, where the mean daily maximum temperature varies by nearly 30°C from winter to summer. Field studies have shown that the temperature dependence of light-saturated photosynthesis varies in concert with these seasonal temperature changes (*Year Book 75*, pp. 410–413; Mooney, Björkman, and Collatz, 1978). Experiments on *L. divaricata* plants grown in the laboratory under a series of controlled temperature regimes (*Year Book 76*, pp. 328–335; Mooney, Björkman, and Collatz, 1978) showed a photosynthetic acclimation response similar to that observed in nature and demonstrated that the observed adaptive responses are primarily the result of changes in intrinsic characteristics of the photosynthetic machinery at the sub-cellular level. Two apparently separate effects of growth temperature could be distinguished. One involves an increased capacity for photosynthesis at low temperature with decreased growth temperature, the other an increased thermal stability with increased growth temperature. Further studies indicated that high growth temperature causes changes in the thylakoid membrane which render the pigment system embedded in this membrane less heat sensitive.

Because of high concentrations of

phenolic compounds in *L. divaricata*, this species does not readily lend itself to quantitative studies on isolated chloroplasts and enzyme preparations. An experimental plant material possessing the same high photosynthetic acclimation potential as *L. divaricata* but without its undesirable characteristics was therefore sought for our continued studies of the mechanism of temperature acclimation.

Nerium oleander L. [Apocynaceae] met the requirements. This C₃ shrub (to 6 meters in height) is native to arid regions of North Africa and Southwest Asia (including the Arabian Peninsula), where it is commonly found along washes. It is widely planted as an ornamental in many parts of the world and is very common in California, where it is extensively grown along highways in many climatic zones ranging from cool coastal to hot desert areas. When supplied with water it is highly successful on the floor of Death Valley, and like *L. divaricata* it remains active throughout the year. Under controlled conditions the same clone is capable of growing over an extremely wide temperature range (10°–46°C).

Because *N. oleander* is easily and rapidly propagated by cuttings, numerous ramets of a single clone can be obtained for experimental purposes. The shape and size of the glabrous leaves make this plant well suited for photosynthetic gas-exchange measurements. Highly active chloroplast and enzyme preparations can be obtained readily and reproducibly with standard methods using simple, conventional extraction media.

METHODS

Propagules originating from an individual of *N. oleander* from local nursery stock were grown in controlled-environment chambers at two temperature regimes, 20°C day/15°C night and 45°C day/32°C night. Light was provided for 14 hr daily by banks of high-intensity

fluorescent lamps giving an average quantum flux density incident on the leaves of $40 \text{ nE cm}^{-2} \text{ sec}^{-1}$. Humidity was kept at 60–75% R.H. Leaf temperature was within $\pm 1^\circ\text{C}$ of air temperature. Root temperatures were 1° to 4°C cooler than air temperatures. The plants were grown in "Turface" (IMC Chemical Group, Inc., Boston, Mass.) and a complete nutrient solution was fed six times daily. All measurements were made on fully exposed 2 to 4 week old leaves which had reached 70% to 100% of full expansion and whose development had been initiated and completed under the indicated temperature regimes.

Photosynthesis measurements were made on single attached leaves, using the gas-exchange system described by Björkman *et al.* (*Year Book 72*, pp. 393–403) with modifications as given by Ehleringer and Björkman (1977) and an experimental procedure similar to that of Mooney, Björkman, and Collatz (1978). Temperature-dependence measurements were also started at the respective daylight growth temperature, and different sets of leaves were used for determinations of photosynthetic temperature-dependence below and above this temperature. Determinations of photosynthetic rates at 20°C were made separately on at least 12 leaves from each of the growth regimes.

Where possible, chloroplasts were isolated and enzymes extracted from leaves whose photosynthetic capacity at 20°C had been determined; when this was not possible, carefully selected leaves of similar age, position, and appearance were used. Chloroplasts were isolated, and photosynthetic electron transport ($\text{H}_2\text{O} \rightarrow \text{methyl viologen}$; $\text{DCIPH}_2 \rightarrow \text{methyl viologen}$) and noncyclic photophosphorylation were determined as described in Table 13 and Fig. 19. Enzymes were extracted and assayed as described by Björkman and Badger (*Year Book 76*, pp. 346–354). To ensure full light activation of these enzymes, activity de-

terminations of Ru-5P kinase, NADP glyceraldehyde-3P dehydrogenase, Fru- P_2 phosphatase, and NADP malate dehydrogenase were made on extracts from leaves that had been kept under a high-intensity illumination for at least 20 min prior to the moment of enzyme extraction. Heat stability in vivo of electron transport and enzymes of carbon metabolism were determined as described last year (*Year Book 76*, pp. 346–354).

RESULTS AND DISCUSSION

Temperature Dependence of Photosynthesis

Figure 16 shows the effect of growth temperature on the temperature dependence of net photosynthesis in intact *N. oleander* leaves. The determinations were made in saturating light, normal air ($330 \mu\text{bar CO}_2$, 21% O_2), and low water-vapor pressure deficit ($<20 \text{ mbar}$). It is clear that the low-temperature-grown plants exhibit considerably higher photosynthetic rates at low temperatures than do the high-temperature-grown plants, and vice versa. For example, the 20°C -grown plants have twice the photosynthetic capacity of the 45°C -grown plants at 20°C , while the 45°C -grown plants have approximately twice the rate of the 20°C -grown plants at 45°C . The rate at 20°C of the 20°C -grown plants is about 95% of the optimum rate. Although 45°C exceeds the optimum temperature for photosynthesis in the 45°C -grown plants in an atmosphere of normal CO_2 and O_2 , the rate is still as much as 85% of optimum.

It is thus evident that *N. oleander* is capable of photosynthetic acclimation over a very wide temperature range; indeed, its acclimation potential may even exceed that of *L. divaricata*. There seems to be little doubt that this potential is an important factor in the ability of the plants to cope with the large seasonal variations in temperature regime that occur in their native habitats, and like-

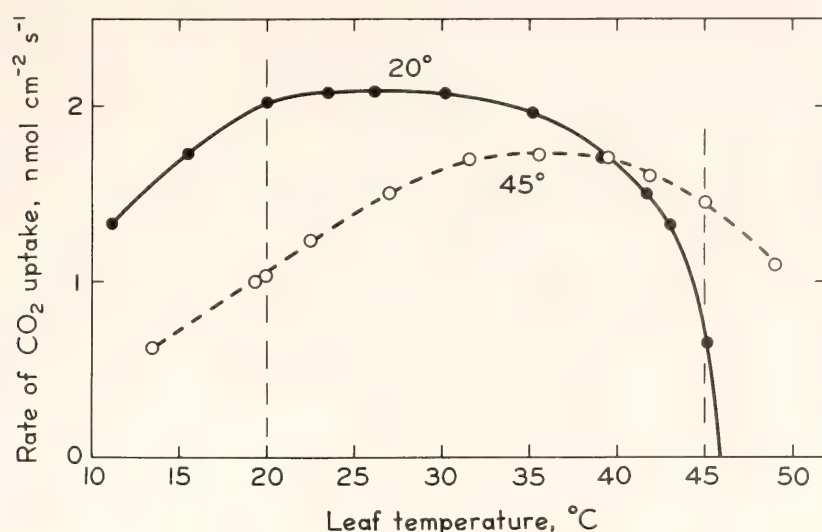


Fig. 16. Temperature dependence of light-saturated net CO₂ uptake in normal air (330 μ bar CO₂, 21% O₂) by intact *N. oleander* leaves grown under two contrasting temperature regimes. The quantum flux density was saturating at all leaf temperatures and ranged from 110 to 175 nE cm⁻² sec⁻¹. CO₂ uptake rates are expressed on a leaf-area basis. The broken vertical bars indicate the two daytime growth temperatures.

wise in the ability of the same clone to succeed in natural or cultural habitats with thermally contrasting climates.

The photosynthetic performance determined in normal air is undoubtedly the most meaningful from an ecological viewpoint. However, since in *N. oleander* and other C₃ plants photosynthesis becomes increasingly CO₂-limited as temperature is increased, the shape of the temperature-dependence curve is strongly influenced by intercellular CO₂ pressure. Analysis of the effect of growth-temperature regime on the intrinsic capacity and thermal stability of the photosynthetic machinery can therefore be best made under conditions of saturating CO₂ pressures. Figure 17 depicts the photosynthetic temperature responses of 20°C-grown and 45°C-grown plants, determined at high intercellular pressures. Determinations of the CO₂ dependence of photosynthesis at a range of temperatures reveal that these high CO₂ pressures were saturating at all measurement temperatures except in the 35°–40°C range for the 20°C-grown plants (data not shown). In this temperature range photosynthetic rates are very high, and

for technical reasons only partially saturating intercellular CO₂ pressures could be obtained. It would seem likely that an even higher, fully saturating CO₂ pressure would tend to increase the maximum photosynthetic rate and to shift the optimum temperature upward by about 3°C. Nevertheless, CO₂ was fully saturating above 40°C and 45° for the 20°C-grown and 45°C-grown plants, respectively, so that the steeply descending parts of the photosynthesis curves at high temperatures were determined under conditions of completely saturating CO₂.

The results shown in Fig. 17 clearly demonstrate that low growth temperature resulted in a large increase in the intrinsic photosynthetic capacity of the leaves. This higher capacity is evident over a wide temperature range but is especially pronounced at moderate and low measurement temperatures. Only at temperatures exceeding 40°C do the 45°C-grown plants become superior to the 20°C-grown plants. This superiority can be attributed entirely to an upward shift in the temperature at which severe thermal inhibition of photosynthesis

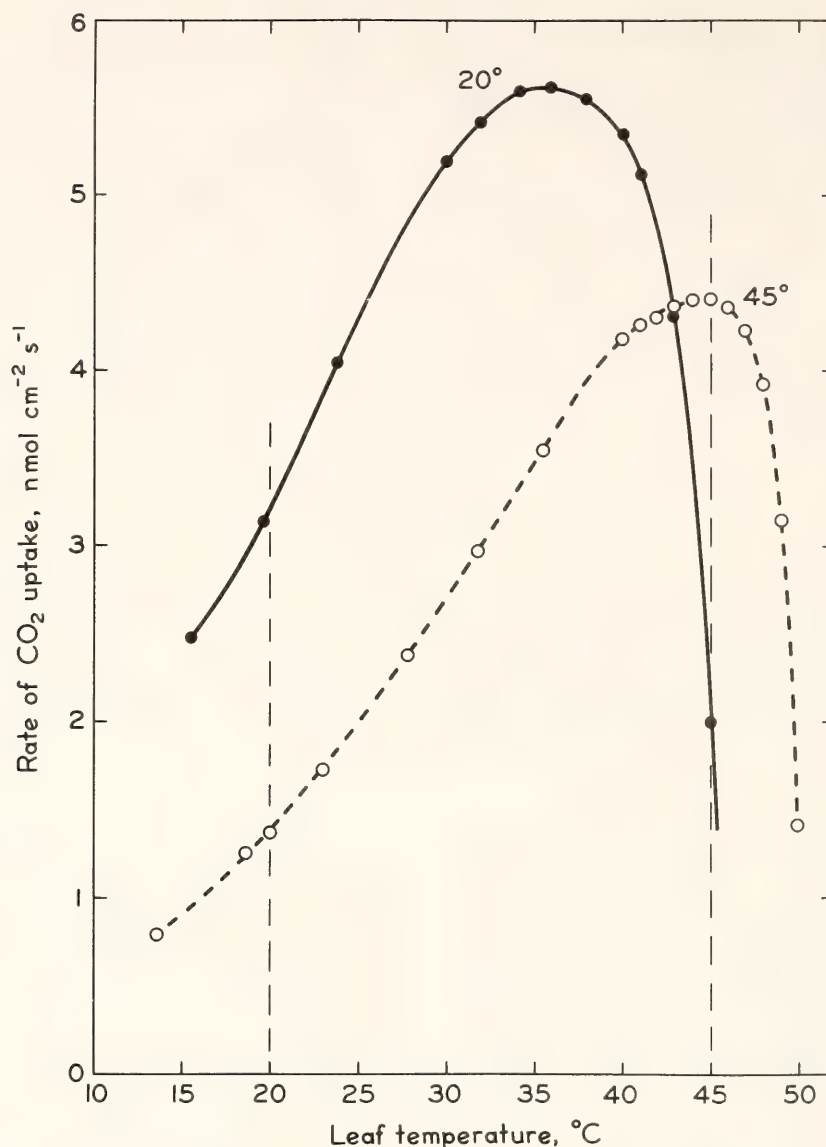


Fig. 17. Temperature dependence of light-saturated net CO₂ uptake at high CO₂ pressures (750–850 μ bar CO₂, 20% O₂) by intact *N. oleander* leaves grown under two contrasting temperature regimes. The quantum flux density was saturating at all leaf temperatures and ranged from 120 to 250 nE cm⁻² sec⁻¹. CO₂ uptake rates are expressed on a leaf-area basis. The broken vertical bars indicate the two daytime growth temperatures.

occurs, indicating an increased stability in temperature-sensitive components of the photosynthetic machinery.

As shown in Table 10, growth temperature affects not only the temperature response of light-saturated photosynthesis; the temperature dependence of the quantum yield for strictly light-limited CO₂ uptake is affected as well. In the 20°C-grown plants the quantum yield remains high and essentially constant up to 40°C, but a marked inhibition can be seen at 45°C. No reduction in the quantum yield could be detected at 45°C in the 45°C-grown plants. In-

stead, an appreciable decline occurred at low temperatures: at 20°C the quantum yield was less than two-thirds of the yield at 40° or 45°C. Nevertheless, the difference in light-saturated photosynthetic capacity at 20°C between low and high temperatures is considerably greater than the difference in quantum yield. It is also noteworthy that the high-temperature inhibition evident at 45°C in the 20°C-grown plants affects the light-saturated photosynthetic capacity to a greater degree than it affects the quantum yield.

It appears that temperature acclima-

TABLE 10. Quantum Yield for Photosynthetic CO₂ Uptake at Rate-Limiting Quantum Flux Densities of Intact Leaves of *Nerium oleander* Grown under Two Contrasting Temperature Regimes*

Measurement Temperature, °C	(A) Grown at 20°C	(B) Grown at 45°C	Ratio A/B
20°	0.070	0.042	1.67
40°	0.074	0.074	1.00
45°	0.058	0.074	0.78

* Determinations were made at 2.5% O₂ and saturating CO₂.

tion in *N. oleander*, as in *L. divaricata*, can be considered to involve two distinct and perhaps unrelated changes: low-temperature acclimation is attributable to the increased capacity of a limiting, temperature-dependent catalytic step; high-temperature acclimation is primarily the result of increased thermal stability in one or several chloroplast components. These two phenomena will therefore be analyzed separately.

Acclimation To Low Temperature

Table 11 shows the mean values of photosynthetic capacity determined at 20°C leaf temperature for 12 plants from each growth regime. Also shown are the mean stomatal conductances and mean intercellular CO₂ pressures, measured at the same time as photosynthesis. In normal air the mean net photosynthetic rate

of the 20°C-grown plants is approximately twice that of the 45°C-grown plants, but rather stomatal conductance is somewhat lower in the 20°C-grown plants. Thus, these plants possess a greatly superior photosynthetic rate in spite of the lower intercellular CO₂ pressure. These results demonstrate unequivocally that stomatal responses play no part in producing the observed differences in photosynthetic capacity between high- and low-temperature-grown plants. The results, obtained at saturating CO₂ pressure, show in addition that these differences are not attributable to other leaf factors influencing the diffusion of CO₂ into the cells. In fact, the difference in photosynthetic rates between the low- and high-temperature-grown plants becomes even more pronounced when any CO₂ limitation of photosynthesis is removed. These results are similar to those

TABLE 11. Light-Saturated Photosynthesis and Stomatal Conductance at 20°C of Intact Leaves of *Nerium oleander* Grown at Two Contrasting Thermal Regimes

Measurement	Grown at 20°C (A)	Grown at 45°C (B)	Ratio A/B
<i>Normal Air (330 μbar CO₂)</i>			
Net photosynthesis, nmol CO ₂ cm ⁻² sec ⁻¹	2.02 ± 0.05	1.04 ± 0.08	1.94
Stomatal conductance (to water vapor transfer), cm sec ⁻¹	0.61 ± 0.02	0.70 ± 0.08	0.87
Intercellular CO ₂ pressure, μbar	205 ± 6	272 ± 5	0.75
<i>Saturating CO₂ (830 μbar CO₂)</i>			
Net photosynthesis, nmol CO ₂ cm ⁻² sec ⁻¹	3.02 ± 0.13	1.17 ± 0.07	2.58
Stomatal conductance (to water vapor transfer), cm sec ⁻¹	0.50 ± 0.03	0.56 ± 0.11	0.89
Intercellular CO ₂ pressure, μbar	600 ± 15	750 ± 30	0.80

TABLE 12. Leaf Specific Weights and Chlorophyll and Protein Contents of *Nerium oleander*, Grown under Two Contrasting Thermal Regimes

Measurement	Grown at 20°C (A)	Grown at 45°C (B)	Ratio A/B
Fresh wt., mg cm ⁻²	44.2±0.9	45.8±1.6	0.97
Dry wt., mg cm ⁻²	12.6±0.3	15.4±0.5	0.82
Chlorophyll (a+b), µg cm ⁻²	76.4±3.8	64.5±1.5	1.19
Soluble protein, mg cm ⁻²	0.668±0.109	0.638±0.067	1.05
Insoluble protein, mg cm ⁻²	0.738±0.036	0.939±0.043	0.79
Total protein, mg cm ⁻²	1.406±0.136	1.647±0.101	0.85

obtained with *L. divaricata* (Mooney, Björkman, and Collatz, 1978).

The possibility was also investigated that the higher photosynthetic capacity of the low-temperature-grown plants was simply a result of a general increase in the amount of photosynthetic machinery per unit leaf area. As shown in Table 12, this is not the case. There were no significant differences in the ratio of fresh weight or soluble leaf protein (mainly enzymes of carbon metabolism) to leaf area. The content of dry matter and insoluble (mainly chloroplast membrane) protein was somewhat lower in the low-temperature-grown plants. On the average, chlorophyll content was higher in the low-temperature-grown plants, but this factor varies considerably and no correlation could be found between chlorophyll content and photosynthetic capacity among leaves from the same growth regime. In any case, the difference in chlorophyll content is much too small to contribute significantly to the difference in photosynthetic capacity between high- and low-temperature-grown plants. Examination of leaf sections under the light microscope also did not show any apparent differences in leaf thickness or gross anatomy between leaves from the two growth regimes.

It was evident that the large differences in photosynthetic capacity between the 20°C-grown and the 45°C-grown plants are not attributable to stomata or other factors determining the diffusion of CO₂ inside the leaf, nor to the overall

content of photosynthetic machinery. Accordingly, an extensive comparative analysis of the activities of a number of component steps of photosynthesis was undertaken. The results are summarized in Table 13. To facilitate comparisons of *in vivo* photosynthetic capacities with the activities of the various reactions obtained with isolated chloroplasts and extracted enzymes, all activities have been expressed on the basis of unit fresh weight of intact leaves.

Coupled whole-chain electron transport (H₂O → methyl viologen) and noncyclic photophosphorylation were determined with isolated chloroplasts at 20°C and saturating light. The rates of these processes are ultimately based on the amount of chloroplast chlorophyll present in the assay system. The average values for whole-chain electron transport were 239 and 212 µmol O₂ mg chl⁻¹ hr⁻¹ for the 20°C-grown and 45°C-grown plants, respectively. Corresponding values for photophosphorylation were 126 and 116 µmol ATP mg chl⁻¹ hr⁻¹. To facilitate comparisons of the activities of the various reactions determined *in vitro*, all activities given in Table 13 are expressed in terms of activity per minute per gram fresh weight of intact leaves. Electron transport and photophosphorylation activities on a chlorophyll basis were converted to a fresh-weight basis, using the average ratio of chlorophyll to fresh weight determined in parallel experiments on leaves similar to those used for

TABLE 13. Comparison of Photosynthetic Capacity at 20°C of Intact Leaves, Photosynthetic Electron Transport and Photophosphorylation Capacities* of Isolated Chloroplasts† and Activities‡ of Enzymes of Photosynthetic Carbon Metabolism in Leaf Extracts of *Nerium oleander*, Grown under Two Contrasting Thermal Regimes

Process	Grown at 20°C (A) (μmol g fresh wt ⁻¹ min ⁻¹)	Grown at 45°C (B)	Ratio A/B
Photosynthetic CO ₂ Uptake at 20°C (saturating CO ₂ pressure and light intensity)	3.88±0.19	1.33±0.05	2.92
Electron transport (H ₂ O→MV) at 20°C	6.42	4.69	1.37
Photophosphorylation (noncyclic) at 20°C	3.11	2.79	1.11
Ru-P ₂ carboxylase activity at 20°C	4.91±0.22	3.29±0.15	1.49
Fru-P ₂ phosphatase	3.64±0.20	1.40±0.24	2.46
Ru-5P kinase	93.3	79.4	1.17
3-Phosphoglycerate kinase	104.0	91.0	1.14
NADP glyceraldehyde-3P dehydrogenase	43.0	42.0	1.02
Fru-P ₂ aldolase	25.7	21.9	1.17
Phosphoglucomutase	9.8	8.3	1.18
Phosphohexose isomerase	10.7	12.4	0.86
NADP malate dehydrogenase	2.07	2.55	0.81
Adenylate kinase	8.9	7.9	1.13

* Whole-chain electron transport was determined polarographically, as described by Armond, Schreiber, and Björkman (*Year Book* 76, p. 337). Photophosphorylation was determined by measuring ADP-dependent pH changes in a weakly buffered (3mM sodium phosphate, pH 6.7) reaction mixture. This was accomplished in an O₂-electrode chamber equipped with a pH electrode.

† Chloroplasts were prepared by grinding leaves with a mortar and pestle in a buffer containing 400mM sorbitol, 100mM sodium tricine (pH 7.8) 50mM sodium ascorbate, 5mM MgCl₂, and 2.5 mg/ml BSA. The homogenate was filtered through two layers of Miracloth and centrifuged at 1000*g* for 10 min. The chloroplasts were resuspended in 10mM NaCl and again centrifuged at 1000*g* for 10 min. The pellet was then resuspended in 400mM sorbitol, 5mM sodium tricine (pH 7.8), 5mM MgCl₂, 5mM sodium ascorbate, 10mM KCl and 5 mg/ml BSA. The final suspension was kept on ice and used for assay of activities.

‡ Enzymes were extracted and assayed as described by Björkman and Badger (*Year Book* 76, pp. 346-354). With the exception of Ru-P₂ carboxylase, all enzyme activities were measured at 30°C.

chloroplast isolation. Photosynthetic rates of intact leaves and enzyme activities, given in Table 13, are based directly on leaf fresh weight.

Although the mean values for electron transport and photophosphorylation on a leaf fresh-weight basis are somewhat higher in the 20°C-grown than in the 45°C-grown plants, these differences are too small to contribute significantly to the difference in photosynthetic capacity. With the exception of Fru-P₂ phosphatase and, to some extent, Ru-P₂ carboxy-

lase, the activities of the enzymes of photosynthetic carbon metabolism are little influenced by the growth-temperature regime and are unlikely to exert a strong limiting influence on overall photosynthetic capacity.

There is much evidence in the literature that Ru-P₂ carboxylase may be an important rate-limiting enzyme in higher plant photosynthesis. Calculations based on the maximum velocity, *K_M*(CO₂), and the temperature dependence of these kinetic properties of *N. oleander* Ru-P₂

carboxylase, and also on the rate, CO_2 and temperature responses of whole-leaf photosynthesis, indicate that the activity of this enzyme may well be limiting photosynthesis in the 20°C-grown plants—especially at temperatures below 30°C. This conclusion applies to both normal and high CO_2 pressures. However, our calculations indicate that it is highly unlikely that Ru-P₂ carboxylase appreciably limits photosynthesis in the 45°C-grown plants at low and moderate temperatures. Although the 45°C-grown plants have a lower level of this enzyme than the 20°C-grown plants, this difference is small in comparison with the difference in photosynthetic capacity. There is no evidence that growth temperature affects the kinetic properties of Ru-P₂ carboxylase, and our determinations showed that the $K_M(\text{CO}_2)$ as well as the activation energy of the isolated enzyme were identical in the 20°C-grown and the 45°C-grown plants. $K_M(\text{CO}_2)$ at 30°C was 19 μM , and the activation energy above 15°C was 15–16 kcal mol⁻¹. These values are similar to those previously reported for other species (e.g., *Year Book* 70, pp. 520–526; *Year Book* 76, pp. 355–361).

Fru-P₂ phosphatase is another Calvin cycle enzyme which has been implicated in the literature to limit photosynthetic CO_2 fixation potentially under certain conditions. Interestingly, this is the only enzyme of those examined here whose activity is affected by growth-temperature regime to a similar extent as photosynthesis. There is evidence that this enzyme requires light for full activation *in vivo*, and we recognize that this could also cause difficulties in determinations of its activity *in vitro*. However, there was no indication that this requirement was a problem in our assay procedure. Our extraction medium contains high concentrations of dithiothreitol and appears to be effective in bringing about rapid and full activation of the enzyme following extraction. In contrast to the

response of other “light-activated” enzymes such as Ru-5P kinase, NADP glyceraldehyde-3P dehydrogenase, and NADP malate dehydrogenase, the treatment of the leaves in light or darkness prior to enzyme extraction did not affect the measured activity of Fru-P₂ phosphatase from low- or high-temperature-grown leaves. As a precaution, the activities reported here were nevertheless measured on extracts from leaves that had been kept in the light sufficiently long to activate fully the three light-activated enzymes mentioned above.

The present results thus show that the Fru-P₂ phosphatase level of *N. oleander* leaves is greatly influenced by growth temperature regime and further suggest that this difference could be primarily responsible for the striking difference in overall photosynthetic capacity between low- and high-temperature-grown plants. Further attempts to elucidate the role of Fru-P₂ phosphatase in temperature acclimation are now being made.

Acclimation To High Temperatures

It is apparent from Figs. 16 and 17 that the relationship between the photosynthetic capacities of the 20°C-grown plants and the 45°C-grown plants is reversed when they are measured at 45°C. At high temperatures a marked superiority of the 45°C-grown plants is observed in photosynthesis at both atmospheric and elevated CO_2 concentrations. This superiority is not caused by a higher stomatal conductance. In both the 20°C-grown and the 45°C-grown plants, stomatal conductance remains high at 45°C leaf temperature (0.6–1.0 cm sec⁻¹). Moreover, the steep decline in photosynthetic rate that occurs at high temperatures is not caused by stomatal closure; indeed, the inhibition of photosynthesis is accompanied by a sharp increase in the intercellular CO_2 pressure.

From the foregoing analysis of photosynthetic capacity at 20°C, it is reasonable to assume that some inhibitory con-

dition is imposed differentially on the photosynthetic apparatus of the 20°C-grown plants at high temperatures, resulting in loss of the photosynthetic superiority that existed at lower temperatures. For the 20°C-grown plants, high-temperature inhibition occurs at temperatures several degrees below the temperatures that inhibit the 45°C-grown plants. This differential thermostability leads to a change in the temperature optimum for CO₂-fixation for the plants grown at the two temperatures. The reasons, then, for the higher photosynthetic capacity of the 45°C-grown plants at 45°C, are best analyzed by determining why the photosynthetic apparatus of the 20°C-grown plants is more sensitive to high-temperature inhibition.

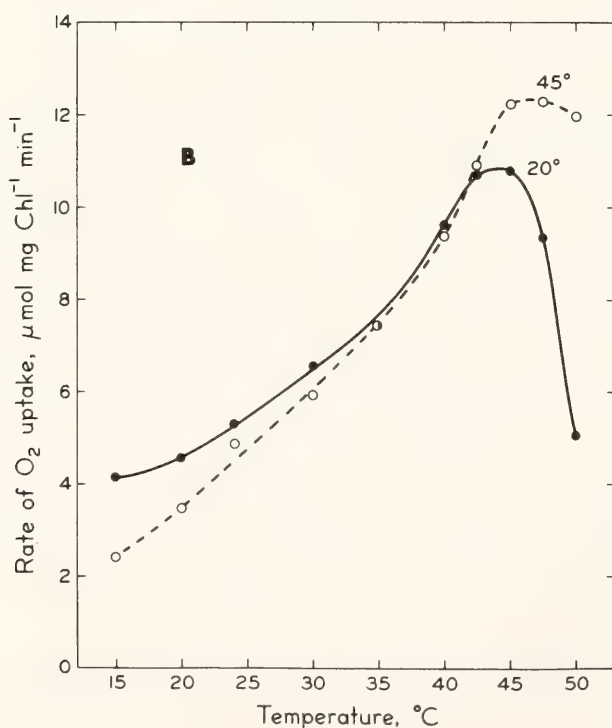
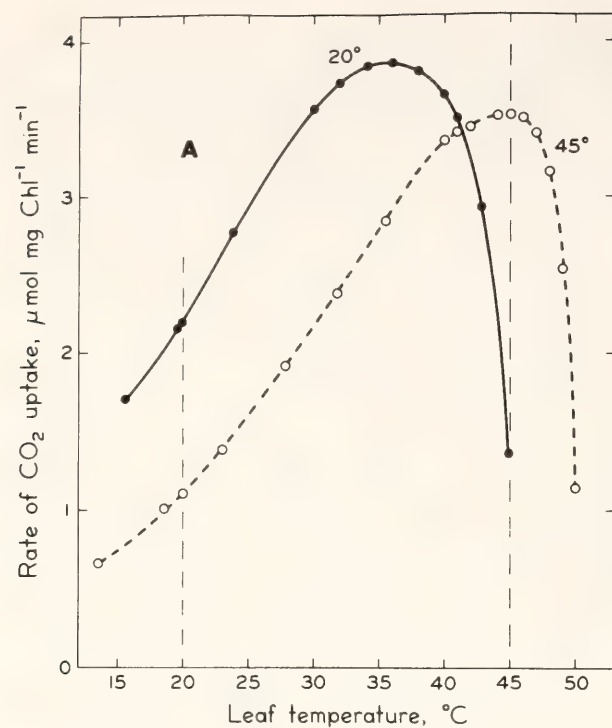
In line with previous studies, we have sought to examine the reasons for differential thermostability through studies of the thermal stability of selected components of the photosynthetic apparatus. In Figs. 16 and 17 the data points for photosynthesis from 15° to 45°C for the 20°C-grown plant and from 15°C to 49.5°C for the 45°C-grown plant represent stable values, in which there did not appear to be any time-dependent change of the rates. The leaves exposed to the inhibitory high temperatures could be returned to lower temperatures with a subsequent restoration of pretreatment rates. Thus, inhibition of photosynthesis up to 45°C in 20°C-grown plants and up to 49.5°C in 45°C-grown plants appears to be reversible. Beyond these two temperatures, a time-dependent irreversible inhibition occurs. Thus, it appears that there is both reversible and irreversible inhibition of the components of the photosynthetic apparatus.

Previous studies on the high-temperature-adapted species *Tidestromia oblongifolia*, the cool-temperature-adapted species *Atriplex sabulosa* (Year Book 75, pp. 400–407), and the desert shrub

Larrea divaricata, acclimated to high and low temperatures (Year Book 76, pp. 335–341), have indicated that photosystem II-driven electron transport and noncyclic photophosphorylation become inhibited at temperatures close to those which irreversibly inhibit both light-saturated photosynthesis and the quantum yield of intact leaves at rate-limiting light intensities. A strong correlation has also been drawn between the inhibition of whole-chain electron transport and the inactivation of certain "light-activated" enzymes requiring reducing power for their activation (Year Book 76, pp. 346–354). Thus, initial studies of high-temperature inhibition have centered on the change in temperature response and thermostability of these temperature-sensitive photosynthetic components.

The temperature dependence of light-saturated whole-chain electron transport ($\text{H}_2\text{O} \rightarrow \text{methyl viologen}$) for chloroplasts isolated from plants grown at 20°C and 45°C is shown in Fig. 18B. These responses can be compared to those of net CO₂ fixation, expressed on a chlorophyll basis, given in Fig. 18A. It is apparent that there are differences in the thermal optima for whole-chain electron transport of the isolated chloroplasts. However, the differences are less distinct than those for CO₂ whole-leaf photosynthesis. These results are similar to those obtained previously with *Larrea divaricata* (Year Book 76, pp. 335–341). The differences in the thermal stability of the chloroplast preparations, however, do correlate closely with the altered high-temperature sensitivity of CO₂-fixation. It is notable that with the chloroplasts from 20°C-grown plants the temperature at which rapid inhibition of whole-chain electron transport begins is close to the temperature which initiates irreversible inhibition of whole-leaf photosynthesis.

To examine further the in vivo stability of chloroplast processes, leaf heat-



treatment experiments were performed. The temperature stabilities of the "light-activated" enzymes NADP glyceraldehyde-3P dehydrogenase, NADP malate dehydrogenase, and Ru-5P kinase were compared with that of whole-chain electron transport, which is thought to supply the reducing power needed to maintain these enzymes in an activated

Fig. 18. Comparison of the temperature dependences of photosynthetic CO_2 uptake by intact leaves (A) and light-saturated whole-chain electron-transport capacity by isolated chloroplasts (B), from *N. oleander*, grown at two contrasting temperature regimes. All rates are expressed on a chlorophyll basis. Conditions for the photosynthesis measurements were the same as those given in Fig. 17. Electron transport was measured polarographically under saturating light with water as the electron donor and methyl viologen as the electron acceptor. The electron transport rates were determined within the first minute following transfer of the isolated chloroplasts, kept at ice-bath temperature, to the reaction vessel, which was kept at the indicated temperatures.

state. The results of these experiments are presented in Fig. 19. As seen previously, photosystem II-driven electron transport and noncyclic photophosphorylation are sensitive to high-temperature inhibition at temperatures close to those at which irreversible inhibition of whole-leaf photosynthesis begins. Photosystem I activity is, by comparison, very heat-stable in both plants. When comparing the sensitivity of the chloroplast functions with that of the "light-activated" enzymes, a somewhat anomalous situation is apparent. For the 45°C-grown plants, these enzymes are inhibited in almost exactly the same manner as whole-chain electron transport and photophosphorylation. This result is consistent with the hypothesis that their state of activation is dependent on the supply of reducing power to ferredoxin. In the 20°C-grown plants, however, inhibition of these enzymes begins at a temperature some 3° to 4°C lower than for the most sensitive chloroplast functions. Within the present concept of the linkage of the light-activated enzymes to electron transport, these data are most easily explained by some degree of reversible inhibition detected in these experiments. Evidence for the occurrence of reversible inhibition *in vivo* is found in both the response of light-saturated CO_2 fixation to temperature and the reversi-

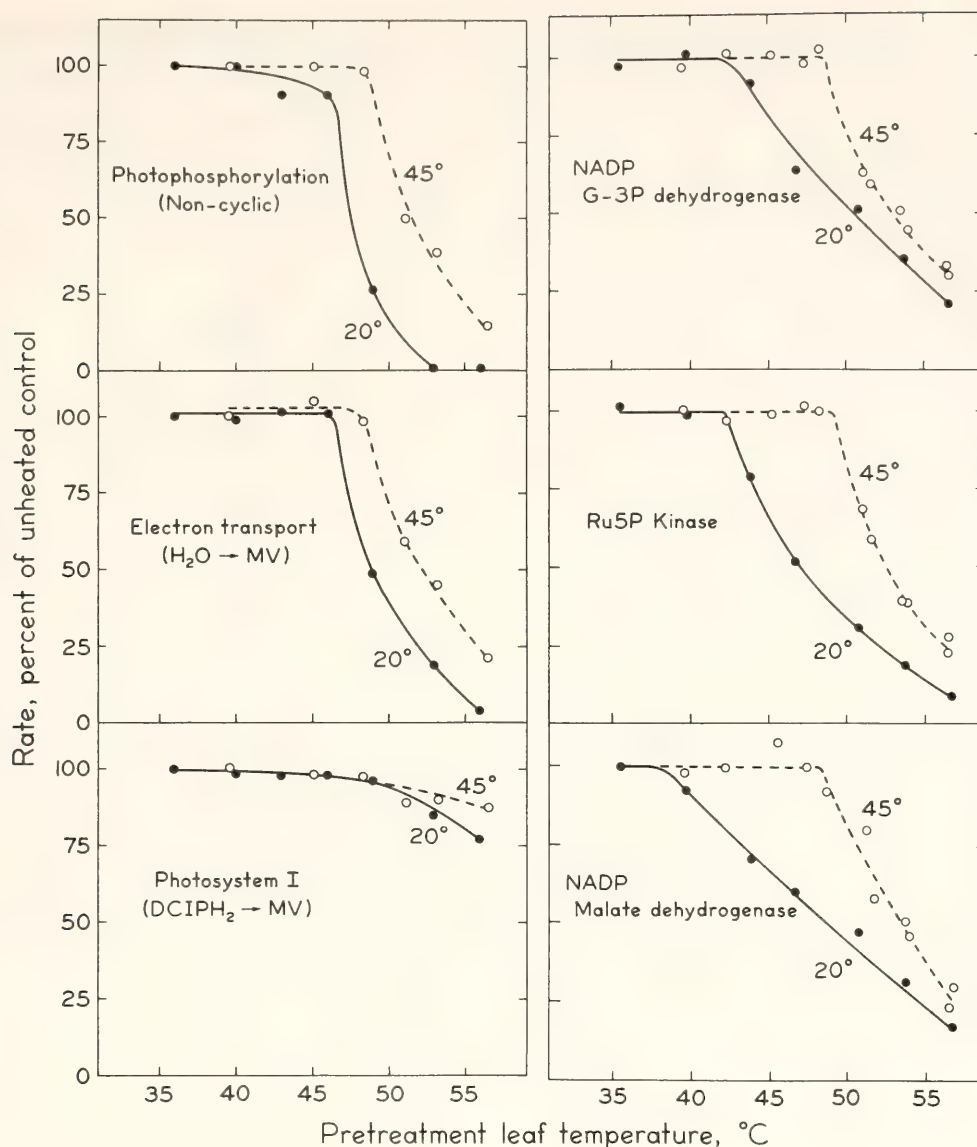


Fig. 19. Effect of pretreatment of *N. oleander* leaves at different leaf temperatures for 10 min, in the light, on the subsequent activities of electron-transport and photophosphorylation by isolated chloroplasts and of three "light-activated" enzymes of photosynthetic carbon metabolism extracted from the leaves. The heat treatments were as described in Table 14. Solid and broken lines depict the responses of 20°C-grown and 45°C-grown plants, respectively. Enzyme activities were determined as described in Table 14. Whole-chain electron transport and photophosphorylation were determined as described in Table 13. Photosystem I activity was determined in the presence of DCMU as the rate of electron flow from ascorbate \rightarrow DCIP \rightarrow methyl viologen (measured as O_2 consumption).

ble inhibition of the quantum yield in the 20°C-grown plants at 45°C (Table 10). The apparent lack of a similar relationship in the 45°C-grown plants might be explained by assuming that irreversible inhibition closely follows the onset of reversible inhibition and that the two effects cannot be resolved in this experimental system.

The *in vivo* thermostability of 10

other soluble enzyme activities associated with both photosynthetic carbon metabolism and respiratory activity have also been examined. The results for all the enzymes studied so far are summarized in Table 14. As was evident from the study of enzyme stability in *T. oblongifolia* and *A. sabulosa* (Year Book 76, pp. 346–354), there are marked differences in the *in vivo* heat stability

TABLE 14. Heat Stability in vivo of Enzymes of Photosynthetic Carbon Metabolism in *Nerium oleander*, Grown under Two Contrasting Thermal Regimes

Enzyme Activity*	Temperature of 10% Inhibition†	
	Grown at 20° C	Grown at 45° C
Ru-P ₂ carboxylase	49.5	56.5
Fru-P ₂ phosphatase	54.0	55.0
Ru-5P kinase	43.0	49.4
3-Phosphoglycerate kinase	50.1	53.7
NADP glyceraldehyde-3P dehydrogenase	43.6	49.2
NAD glyceraldehyde-3P dehydrogenase	45.6	51.5
Phosphoglucomutase	50.2	>56.6
Phosphohexose isomerase	51.0	>56.6
NADP malate dehydrogenase	40.0	49.0
NAD malate dehydrogenase	53.7	>56.6
Adenylate kinase	47.2	49.0
NADP glu-6P dehydrogenase	50.1	51.4
Fru-P ₂ aldolase	48.0	54.5

* Heat treatment of leaves was as described previously (*Year Book 76*, p. 350). Leaves of similar age and position on the plant were detached in the light, weighed, and positioned in a single layer in an illuminated ($125 \text{ nE cm}^{-2} \text{ sec}^{-1}$) and temperature-controlled treatment chamber. The leaves were first kept at a noninhibitory temperature (35°) for at least 10 min to ensure that complete activation of those enzymes requiring light for their activation had been achieved. The temperature was then rapidly raised ($<30 \text{ sec}$) to the desired treatment leaf temperature and kept there for 10 min. Crude extracts were prepared by taking leaves at the end of the treatment period and immediately grinding them in cold extraction buffer with a mortar and pestle. Homogenates were further processed and enzyme activities assayed as described previously (*Year Book 76*, p. 350).

† Determined from heat treatment curves as shown in Fig. 19.

among the different enzymes. Enzyme activities such as NAD malate dehydrogenase, Fru-P₂ phosphatase, phosphohexose isomerase, and phosphoglucomutase are stable at temperatures above 50°C in 20°C -grown plants and 55°C in 45°C -grown plants. Other enzymes such as adenylate kinase and NAD G-3P dehydrogenase become inhibited at considerably lower temperatures. All enzymes studied showed a higher stability in the 45°C -grown than in the 20°C -grown plants. These differences range from slight, such as with Fru-P₂ phosphatase, to quite large, as with Fru-P₂ aldolase. A differential stability of the same enzyme in the same plant genotype acclimated to low and high temperature may indicate changes in the protein. It could, however, also be a consequence of

an alteration in the immediate environment in which the enzyme exists.

Apart from the three "light-activated" enzymes and possibly NAD glyceraldehyde-3P dehydrogenase in the 20°C -grown plants and adenylate kinase in the 45°C -grown plants, the initial inactivation of enzyme activities occurs at temperatures higher than those producing irreversible inhibition of photosynthesis. Thus, of the enzymes studied only the light-activated enzyme activities of NADP glyceraldehyde-3P dehydrogenase, Ru-5P kinase, and NADP malate dehydrogenase appear to be thermally labile in both 20°C - and 45°C -grown plants in a temperature region where these enzymes may be partly responsible for the heat inactivation observed for whole-leaf photosynthesis. However, it

seems likely that the differences in the thermostability of these "light-activated" enzymes produced by acclimation to various temperatures are linked to changes in the thermostability of whole-chain electron transport.

CONCLUSIONS

This study shows that, like *Larrea divaricata*, *N. oleander* has a high potential for environmentally induced photosynthetic acclimation to temperature. Growth under a low temperature regime resulted in a high photosynthetic capacity at low temperature, whereas growth of the same genotype under a very high temperature regime resulted in an increased thermal stability of the photosynthetic machinery. The ability to adjust the photosynthetic characteristics in these ways is undoubtedly an important factor in enabling the plant to cope with very large seasonal variation in temperature within a single habitat as well as to succeed in different habitats with widely diverse climates. In several respects the differences in photosynthetic characteristics between low- and high-temperature-grown *N. oleander* plants approach those found among different species native to cool-temperate and hot-desert habitats. For example, *N. oleander* grown at 45°C possesses the same remarkably high heat stability of its photosynthetic machinery as does the C₄ thermophile *Tidestromia oblongifolia*, although since *N. oleander* is a C₃ plant its photosynthetic rate at normal CO₂ pressures is much lower. Also, 45°C-grown *N. oleander* plants have a CO₂-saturated photosynthetic capacity at low temperatures which is almost as low as in *T. oblongifolia*, while 20°C-grown *N. oleander* plants have a capacity approaching that of the cold-adapted C₄ *Atriplex sabulosa*.

The superior photosynthetic capacity of 20°C-grown compared with 45°C-grown *N. oleander* plants was found to

be unrelated to stomatal or other leaf factors that influence the diffusive transport of CO₂ into the chloroplasts. Neither is the superior photosynthetic capacity attributable to differences in gross leaf anatomy, an increased amount of photosynthetic machinery per leaf area, a general increase in the level of enzymes of photosynthetic carbon metabolism, or the capacity for photosynthetic electron transport or phosphorylation. The higher Ru-P₂ carboxylase activity found in the 20°C-grown plants may, to some extent, contribute to its superior photosynthetic capacity, but the difference in the level of this enzyme is much too small to account for the observed difference in photosynthesis between 20°C-grown and 45°C-grown plants. Fru-P₂ phosphatase is the only component examined so far which is affected by growth temperature to a similar extent as photosynthetic capacity. The possibility that the level of this enzyme is primarily responsible for the striking difference in photosynthetic capacity between low- and high-temperature-grown *N. oleander* (and perhaps other species as well) will be investigated further.

Growth at 45°C resulted in a superior photosynthetic performance at high temperatures. This improvement is primarily due to an increased thermal stability of the photosynthetic machinery. The temperature optimum and the threshold temperature above which CO₂-saturated photosynthesis exhibits a steep decline are shifted upward by 5° to 6°C compared with the 20°C-grown plants. The temperature at which an irreversible heat inactivation begins is also shifted upward to a similar extent. Heat treatment experiments with detached leaves and isolated chloroplasts showed that substantial differences exist between low- and high-temperature-grown materials in the in vivo and in vitro thermal stability of photosystem II-driven electron transport and of noncyclic photophos-

phorylation, and in the in vivo heat stability of several enzymes of photosynthetic carbon metabolism. Of these enzymes, those which require light for their activation were especially sensitive to heat inactivation. The apparently reversible nature of the inactivation of these enzymes in the 20°C-grown plants suggests that it may be linked to the observed inhibition of photosystem II activity, since this would slow the flow of electrons to ferredoxin—whose reduction state is thought to influence the activation of the light-activated enzymes (Wolosiuk and Buchanan, 1977). We cannot at this time exclude the possibility that changes in the properties of Calvin cycle enzymes may be involved in the increased heat tolerance of photosynthesis in high-temperature-grown *N. oleander*, but it seems likely that increased heat stability of photosynthesis is primarily linked to an enhanced stability of the thylakoid membrane.

Previous studies with *Larrea divaricata* indicated that one of the primary events in heat inactivation is decreased efficiency in the transfer of energy between the light-harvesting pigment complexes and the reaction centers, thereby reducing the quantum yield of photosynthesis at limiting light intensities. This mechanism would provide a satisfactory explanation for observed reduction in the quantum yield at high temperatures in low-temperature-grown *N. oleander* leaves. However, it is unlikely that it could also explain the even greater heat

sensitivity of light-saturated photosynthesis. It seems more probable that the photosystem II reaction centers themselves, or a component closely associated with these centers in the thylakoid membrane, is inactivated, although we recognize that a heat-induced loss of membrane integrity or a disruptive change in its conformation may well affect a number of different chloroplast functions simultaneously.

It is a common view that increased thermal stability may be related to an altered lipid composition of the thylakoid membrane. Drs. Raison and Berry have extended their studies of the relationship between chloroplast lipid structure and function to include the possibility that the observed differences in heat stability between low- and high-temperature-grown *N. oleander* leaves are caused by changes in the physical properties of membrane lipids. These observations are discussed in the following article.

REFERENCES

- Armond, P. A., U. Schreiber, and O. Björkman, *Plant Physiol.* 61, 411–415, 1978.
- Ehleringer, J., and O. Björkman, *Plant Physiol.* 59, 86–90, 1977.
- Mooney, H. A., O. Björkman, and G. J. Collatz, *Plant Physiol.* 61, 406–410, 1978.
- Wolosiuk, R. A., and B. B. Buchanan, *Nature* 266, 565–567, 1977.

THE PHYSICAL PROPERTIES OF MEMBRANE LIPIDS IN RELATION TO THE ADAPTATION OF HIGHER PLANTS AND ALGAE TO CONTRASTING THERMAL REGIMES

John K. Raison and Joseph A. Berry

The temperature response of the photosynthetic apparatus of plants adapted to contrasting thermal regimes is, at least in part, related to properties of

the chloroplast membranes. Shenyour *et al.* (1973) and Murata *et al.* (1975) have correlated sharp changes in the apparent activation energy for compon-

ent steps of photosynthetic electron transport with temperature-induced changes in the molecular ordering of the lipid components of the membrane. Percy *et al.* (1976), Schreiber and Berry (1977), and Schreiber and Armond (*Year Book* 76, pp. 341–346) have presented evidence for a high-temperature-induced change in the molecular organization of chloroplast membranes corresponding to the upper limit for thermal stability of the photosynthetic apparatus.

It has long been postulated (Belenradek, 1931) that organisms adapt to changes in growth temperature by altering the fatty acid composition of their lipids. With prokaryotic microorganisms, adaptation to increased growth temperature is correlated with a relative decrease in short-chain, branched-chain, and unsaturated fatty acids, along with an increase in chain length and saturation of the acyl fatty acids (Daron, 1970). One consequence of these adaptive changes is that the viscosity of the lipids of the cell membrane at the growth temperature is held nearly constant in spite of changes in the growth temperature. This capacity has been termed "homeoviscous adaptation" (Sinensky, 1974). For example, Sinensky found that the microviscosity of membrane lipids from *E. coli* cells grown at 43°C was 1.8 poise at 43°C, and lipids from *E. coli* cells grown at 15°C and measured at 15°C had again a viscosity of 1.8 poise. On the other hand, lipids from the cells grown at 43°C and measured at 15°C were much more viscous (15 poise). This compensation to a homeoviscous state at different growth temperatures is accomplished in part by regulation of the fatty acid composition of the lipids formed at the particular growth temperature (McElhaney and Souza, 1976). Changes in the temperature of phase transitions of the lipids are also associated with changes in membrane composition and viscosity (Esser and Souza, 1974; Sinensky, 1974; McElhaney and Souza, 1976).

The lipids of higher plant chloroplasts are in general much more unsaturated and more heterogeneous with respect to both lipid classes and acyl fatty acids than are the lipids of bacteria (Kenyon and Stanier, 1970). There are however, changes in fatty acid composition of higher plant chloroplast lipids with growth temperature which might also bring about compensating changes in viscosity or other physical properties of the lipids (Percy, 1978). Similar differences in lipid composition have been observed among species adapted to contrasting thermal regimes (*Year Book* 75, pp. 400–407). The studies reported here were initiated to examine the extent to which observed modifications of the photosynthetic characteristics of chloroplast membranes at different growth temperatures can be attributed to changes in the physical properties of the lipids with growth temperature.

METHODS

Chloroplasts were isolated from leaves as described (Björkman *et al.*, this *Year Book*), washed twice with 10mM NaCl and resuspended in 0.1M HEPES, 10mM MgCl₂ 0.1mM EDTA, pH 7.9, at approximately 1 mg chlorophyll per ml final concentration. Membranes were obtained from *Synechococcus lividus* by treating the cells with 0.1% lysozyme in 600mM sucrose, 2mM EDTA and 30mM phosphate buffer pH 6.8 for 3 hr at 42°C. After treatment the cells were collected by centrifugation, resuspended in 0.1M HEPES buffer pH 7.9 containing 10mM MgCl₂ and 0.1mM EDTA. The cells were broken by passing them through a French Press at 1000 kg/cm²; unbroken cells were removed by centrifugation for 5 min at 5000 *g*, and membrane fragments were collected by centrifugation at 144,000 *g* for 15 min.

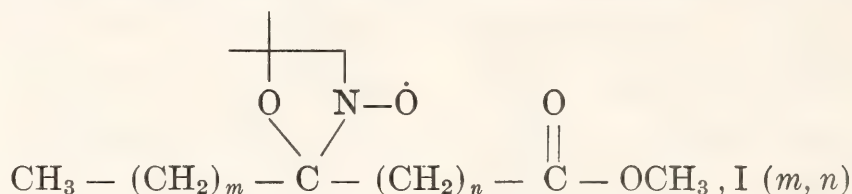
Lipids were extracted from chloroplasts or algae with chloroform:methanol (2:1 v/v) according to the method of Folch *et al.* (1975). Extracts were sepa-

rated into neutral, galactolipid and phospholipid classes by sequential elution from Biosil A with chloroform, acetone, and methanol, respectively. These fractions were verified by TLC.

Liposomes were prepared from the combined galactolipid and phospholipid fractions. These polar lipids were deposited from chloroform onto the surface of a glass tube under N_2 , and residual

solvent was removed under vacuum. The lipid was suspended in 0.1M Tris-HCl buffer pH 7.2 containing EDTA at a concentration of 10–15 mg lipid per ml buffer. The suspension was dispersed by brief sonication.

For electron-spin resonance (esr) spectroscopy, membranes and liposomes were labeled with spin probes having the general structure



The determinants m and n refer to the position of the oxazolidine group relative to the terminal methyl and the carboxymethyl groups, respectively. These were

synthesized by the general procedure of Keana *et al.* (1967). A motion parameter, τ , was calculated for I (6,10) from esr spectra from the relationship

$$\tau = 6.45 \times 10^{-10} [(h_0/h_{-1})^{1/2} + h_0/h_{+1})^{1/2} - 2] W_0$$

where h_{+1} , h_0 and h_{-1} refer to the height of the low-field, mid-field and high-field lines, respectively, and W_0 is the width in gauss of the midfield of the first-derivative esr spectrum. Viscosity of membrane lipids was determined from a calibration curve published by Sinensky (1974) relating τ for I(6,10) to the viscosity of castor oil, in poises, as a function of the temperature. Spectra were recorded on a Varian E112 spectrometer fitted with a temperature-controlled cell housing. The temperature was measured with a copper-constantan thermocouple and was controlled to $\pm 0.05^\circ\text{C}$ by a model TCM 20 temperature control unit (Deltron Pty. Ltd., Sydney, Australia).

Plants were grown in controlled-growth facilities with the diurnal temperature regimes as indicated. *Synechococcus lividus* was grown as described by Fork and Murata (Year Book 76, pp. 222–226).

RESULTS

Plants were grown at temperature regimes which differed by 25°C (day/

night temperatures were either $20^\circ/15^\circ\text{C}$ or $45^\circ/30^\circ\text{C}$). This range of growth temperature is similar to that used in studies with bacteria which showed dramatic modifications of the physical properties of the membrane lipids (Sinensky, 1974; Esser and Souza, 1974). Comparative studies of the photosynthetic characteristics of *Nerium oleander* grown at these contrasting temperature regimes have shown considerable physiological differences between the plants in their thermal stability and their capacity for photosynthesis at low temperature (Björkman *et al.*, this Year Book). These differences are in general similar to those which have been observed in comparative studies of various species native to contrasting thermal regimes (Year Book 75, 400–407) and to those found in *Atriplex lentiformis* (Pearcy *et al.*, 1976) or *Larrea divaricata* (Year Book 76, pp. 335–341) grown at contrasting thermal regimes.

As has been noted, *N. oleander* grown at high temperature is more stable at high temperature than are plants grown at $20^\circ/15^\circ\text{C}$. We have been unable to

detect any evidence for a phase transition affecting the molecular ordering of the lipids or lipid environment of the chloroplasts which corresponds to the threshold for irreversible damage to the photosynthetic apparatus at high temperature. We are therefore attracted to the hypothesis of McElhaney and Souza (1976) that an upper limit exists for membrane lipid fluidity which is compatible with maintenance of a critical structural relationship.

Table 15 presents measurements of the microviscosity of liposomes prepared from polar lipids of *N. oleander* chloroplasts from plants grown at the contrasting temperature regimes. With either preparation there is a considerable change in viscosity with temperature of measurement. At each temperature, the liposomes prepared from the chloroplast lipid of the 45/30 plants are more viscous than the corresponding lipids from 20/15 plants. It is clear, however, that the change in lipid composition with growth temperature is not sufficient to compensate for the large change in viscosity which occurs between 20° and 45°C measurement temperatures. The change in composition does, however, result in partial compensation. By determining the temperature coefficient for lipid viscosity for both preparations (not shown) one can estimate that the difference in viscosity between the lipids of 45/30 and 20/15 plants approximates that

TABLE 15. Microviscosity (η) Measured at 20°, 30° and 45°C of Polar Lipids of Chloroplasts from *N. oleander* Plants Grown Under Contrasting Thermal Regimes

Growth Condition	Microviscosity—Poise		
	$\eta_{(20^{\circ})}$	$\eta_{(30^{\circ})}$	$\eta_{(45^{\circ})}$
20/15	1.83±0.04	1.17±0.02	0.67±0.01
45/30	1.99±0.07	1.53±0.04	0.87±0.02

expected for a change in temperature of 10°C. This modification indicates a partial (10° of 25°) compensation for the change in lipid viscosity at the growth temperatures. If there were some critical minimum viscosity at which the photosynthetic apparatus could no longer be maintained, then the results would imply that 20°/15°-grown plants should reach that limit at a temperature about 10 C degrees lower than would the 45°/30° plants. This hypothesis is consistent with observed differences in thermal stability (see Björkman *et al.*, this *Year Book*, Fig. 17).

One problem with this hypothesis is that the differences observed in partially purified lipids (Table 15) are not as clear in measurements conducted with native membranes of the chloroplast. As shown in Table 16, the chloroplast membranes are far more viscous than the lipids. The basis of this difference is not

TABLE 16. Microviscosity Measured at 20°, 30° and 45°C of Chloroplast Membranes of *Nerium oleander*, *Tidestromia oblongifolia*, and *Spinacea oleracea*

Species		Microviscosity—Poise		
		$\eta_{(20^{\circ})}$	$\eta_{(30^{\circ})}$	$\eta_{(45^{\circ})}$
<i>N. oleander</i>	20/15	8.8±.2	3.5±.1	1.99±.03
	45/30	10.1±.59	3.7±.2	2.00±.02
<i>T. oblongifolia</i>	45/30	>11	4.5	1.86±.02
<i>S. oleraceae</i>	30/15*	6.4±.1	4.0±.1	2.08±.02

* Grown in a greenhouse, diurnal temperature regime approximately 30/15.

known. The results may reflect a true difference in viscosity or may show an artifact brought about by binding of the spin-label probe to protein or neutral lipid components of the native membrane. At 45°C the 20°/15° and 45°/30° chloroplasts have identical viscosity, while the 45°/30° membranes are slightly more viscous than the 20°/15° membranes at 20°C.

The viscosity of chloroplast membranes from spinach (*S. oleracea*), a cool-temperate species, and *Tidestromia oblongifolia*, an obligate thermophilic species native to Death Valley, California, are shown also in Table 16. It is remarkable that the viscosities of these two contrasting species and those of *oleander* grown at contrasting thermal regimes are all very similar—especially at 45°C. If there is any trend, it is for species adapted to or acclimated to low temperature to have a lower temperature coefficient for viscosity and therefore to have chloroplast membranes that are less viscous at low temperature than the contrasting high-temperature-adapted species. The significance of these observations is not clear, and at this time we would prefer to emphasize the absence of any large differences in viscosity among chloroplast membranes of higher plants adapted to contrasting thermal regimes.

A change in the temperature coefficient of the motion parameter τ has also been used to detect the temperature of phase transitions in lipid mixtures (Raison and Chapman, 1976). Two phase transition points, T_f and T_s , are resolved by this technique. The lower point (T_s) has been correlated with the temperature threshold for chilling effects in chilling-sensitive higher plants (Raison and Chapman, 1976), while the upper phase transition (T_f) does not seem to be physiologically important. Studies with bacteria have demonstrated that there are corresponding changes in the lipid viscosity, phase transition temperature,

and fatty acid composition with acclimation to different growth temperatures (Sinensky, 1974; McElhaney and Souza, 1978). Extrapolation of these results to higher plants would suggest that adaptation to high temperature might result in a plant's becoming susceptible to chilling injury at low temperature because of an upward shift in T_s . The temperatures for T_s and T_f , determined for liposomes prepared from plants native to contrasting thermal regimes and grown at different growth temperatures, are shown in Table 17. It is clear that plants which are stable to very high temperature, such as *Atriplex hymenelytra* or *Tidestromia oblongifolia*, do not have an elevated T_s . There was little change with growth temperature in the T_s or T_f of *N. oleander* lipids. Thus, there is no necessary correlation between the temperatures of these phase transitions and the acclimation to high temperature by higher plants. These temperate species are probably subjected to large seasonal and diurnal fluctuations of temperature in their native habitats. It is perhaps not surprising that such species are not chilling sensitive, since such characteristics would probably produce a selective dis-

TABLE 17. Phase Transition Temperatures, T_f and T_s of Chloroplast Lipids of Plants Native To and Grown Under Contrasting Thermal Regimes

Species	Growth Regime	Transition Temperatures (°C)	
		T_f	T_s
<i>Nerium oleander</i>	20/15	34	-1
	45/30	34	-4
<i>Tidestromia oblongifolia</i>	D. V.*	35	-1
<i>Atriplex hymenelytra</i>	D. V.*	27	-1
	20/15	30	3
<i>A. sabulosa</i>	20/15	27	-1
<i>A. glabriuscula</i>	20/15	27	-1

* Leaves collected in early summer from Death Valley, California, 40°/25°C typical diurnal temperature regime.

TABLE 18. The Microviscosity, Measured at 38°C and 55°C, of Polar Lipids and Native Membranes of *Synechococcus lividus* Grown at 38° and 55°C and of *Nerium oleander* Chloroplasts Grown at 20/15

Species	Condition	Microviscosity—Poise			
		Lipids		Membranes	
		$\eta_{(88^{\circ})}$	$\eta_{(55^{\circ})}$	$\eta_{(38^{\circ})}$	$\eta_{(55^{\circ})}$
<i>N. oleander</i>	20/15	1.04	...	2.6	...
<i>S. lividus</i>	38	1.69	1.11	2.5	1.66
	55	1.91	1.07	4.5	2.9

advantage. The presence of chilling susceptibility in some plants remains an enigma. The above results illustrate that it is possible for plants to adapt to high temperature without becoming chilling sensitive.

In the foregoing study we have observed only a very limited natural variation in the properties of lipids from higher plant chloroplasts. In order to extend the scope of our study we have also examined the lipids of the thermophilic blue-green alga *Synechococcus lividus*, which is one of the most extreme examples of adaptation of a photosynthetic organism to high temperature (Meeks and Castenholz, 1971). Analyses of the photosynthetic electron-transport reactions of *S. lividus* cells grown at 55°C (*Year Book 76*, pp. 222–226) suggest that the optimum membrane state for electron-transport reactions occurs over the narrow range from 44° to 53°C. The viscosity of the polar lipids and native membranes of *S. lividus* grown at 55° and 38°C may be compared with analogous measurements of *N. oleander* in Table 18. The viscosity of *N. oleander* lipids measured at 38°C was approximately equal to that of *S. lividus* grown at either temperature and measured at 55°C. It is interesting that at these temperatures both organisms are near their upper limit for thermal stability. This correlation between an absolute viscosity of approximately 1 and the temperature

threshold for thermal stability indicates that this may be the minimum viscosity for functionally stable membranes. At the other extreme, viscosity increases as temperature decreases. *S. lividus* cells undergo an apparent phase transition which for 55°C-grown cells begins at 44°C (*Year Book 76*, pp. 222–226). This temperature is most likely the lower limit for normal function of these membranes. Measurements presented in Table 17 and studies of electron transport reactions of *N. oleander* indicate that the lower limit for normal physiological function is very low—perhaps as low as –1°C. The range between the upper and lower limits imposed by the membrane appears to be much wider in the case of higher plants than for algae. Analysis of the temperature coefficient for viscosity of lipids from different sources does not indicate that the lipids of higher plants change less with temperature. Rather, chloroplast membranes of higher plants apparently remain stable and functional at a higher lipid viscosity than do those of *S. lividus*.

It is of interest that the adaptation of higher plants to contrasting growth regimes differs from the adaptation of this alga and of bacteria. *S. lividus* can grow over a temperature range of at least 17°C; however, as discussed above, cells grown at any one temperature have a fairly narrow range of physiological tolerance to temperature variation. The

range can apparently be modified according to growth temperature—presumably by altering the fatty acid composition. In contrast, the higher plants studied here are either genetically or physiologically adapted to a very large range of growth temperatures and show relatively small change in lipid properties and, presumably, lipid composition in response to growth temperature. The failure of *N. oleander* to achieve complete homeoviscous adaptation to contrasting growth temperatures, reported here, is apparently compensated for by the broad inherent range of thermal stability for plants grown at a given growth temperature. We speculate that this difference in adaptive strategy may be related to the nature of the respective thermal environments of higher plants and algae or bacteria. The temperature of the aqueous environment of bacteria and algae is probably buffered from large seasonal and diurnal changes in temperature. Also, changes in temperature are rather slow in relation to the life span of a particular individual. Higher plants must contend with the probability of large and rapid seasonal and diurnal temperature variations in their native environment. This added constraint may prevent higher plants from achieving complete homeoviscous adaptation, and suggests that additional factors which might enable a membrane to stabilize physiological activity over a wide temperature range may be important in adapting higher plants to the conditions of their native habitats. Very little is known about possible mechanisms for accomplishing this adaptive flexibility. An experimental basis for studying these mechanisms would appear to be a high priority for future research into mechanisms of thermal adaptation in higher plants.

ACKNOWLEDGMENTS

We wish to thank Professor R. Holm and Professor S. Boxer of the Chemistry Department at Stanford University for making the Varian E112 spectrometer available to us. Dr. Paul Armond and Dr. Olle Björkman provided *N. oleander* material for study, and Dr. David Fork provided us with *Synechococcus lividus*.

REFERENCES

- Belehradek, S., *Protoplasma* 12, 406–434, 1931.
- Daron, H. H., *J. Bacteriol.* 101, 145–151, 1970.
- Esser, A. F., and K. A. Souza, *Proc. Nat. Acad. Sci. U.S.A.* 71, 4111–4115, 1974.
- Folch, J., M. Lees, and G. H. Sloane-Stanley, *J. Biol. Chem.* 226, 497–509, 1975.
- Keana, J. F. W., S. B. Keana, and D. Beetham, *J. Am. Chem. Soc.* 89, 3055–3056, 1967.
- Kenyon, C. N., and R. V. Stanier, *Nature* 227, 1164–1166, 1970.
- McElhaney, R. N., and K. A. Souza, *Biochim. Biophys. Acta* 443, 348–359, 1976.
- Meeks, J. C., and R. W. Castenholz, *Arch. Microbiol.* 78, 25–41, 1971.
- Murata, N., J. H. Troughton, and D. C. Fork, *Plant Physiol.* 56, 508–517, 1975.
- Pearcy, R. W., *Plant Physiol.* 61, 484–486, 1978.
- Pearcy, R. W., J. A. Berry, and D. C. Fork, *Plant Physiol.* 59, 873–878, 1976.
- Raison, J. K., and E. A. Chapman, *Aust. J. Plant. Physiol.* 3, 291–299, 1976.
- Schreiber, U., and J. A. Berry, *Planta* 136, 233–239, 1977.
- Shneyour, A., J. K. Raison, and R. Smillie, *Biochim. Biophys. Acta* 292, 152–161, 1973.
- Sinensky, M., *Proc. Nat. Acad. Sci. U.S.A.* 71, 522–525, 1974.

THE LIPID AND FATTY ACID COMPOSITION,
ELECTRON TRANSPORT, AND LIGHT-ENERGY
REDISTRIBUTION IN THE THERMOPHILIC BLUE-GREEN
ALGA *Synechococcus lividus* GROWN AT 55°C AND 38°C

David C. Fork, Norio Murata,* and Naoki Sato*

Last year we used a number of strains of the thermophilic blue-green alga *Synechococcus lividus* having growth temperature optima ranging from around 45° to 65°C for determinations of the temperatures of transition of the physical phase of thylakoid membrane lipids. Comparative physiological studies were initiated on one of these strains that has its growth temperature optimum near 55°C.

This year we continued our studies with the 55°C strain of *Synechococcus* and in addition have adapted it to grow at 38°C. A comparison of the lipid and fatty acid compositions of the two cultures was made. Comparative measurements were also made of the temperature dependence of electron transport and light-energy redistribution between the two pigment systems of photosynthesis, and of the fluorescence in DCMU-treated cells.

S. lividus (strain SY-4) was provided through the courtesy of Dr. Mercedes Edwards of the New York State Department of Health, who isolated it from thermal springs in Yellowstone National Park in Wyoming. This alga has its optimum growth temperature near 55°C (Edwards, personal communication) and was grown in D medium (Sheridan, 1966) following the method of Castenholz (1969, 1970). Young cells growing at 55°C were then transferred and adapted to grow at 38°C. Although the cells grew somewhat more slowly at this temperature than at 55°C, the culture

could be maintained for as long as desired. Cells were grown for at least a week at 38°C before being used for experiments.

Cells grown at the lower temperature were yellow-green compared to the usual blue-green color seen when the cells were grown at 55°C. This contrast is shown in the bottom part of Fig. 20 as the absorbance difference spectrum between the two cultures. The yellow-green color of the 38°C-grown cells appears to be caused by an increased carotenoid content, since the difference spectrum has peaks at 452, 480, and a shoulder near 430 nm. Cells grown at 38°C have less phycobilin pigments than the 55°C cells, as is indicated by the decreased absorption at 618 nm.

Lipids from the two cultures were extracted in a 2:1 v/v chloroform-methanol mixture (Folch *et al.*, 1975) and fractionated by chromatography on thin-layer silica gel (Allen and Good, 1971). Lipids and fatty acids were determined according to methods described by Sato *et al.*, (1978). *S. lividus*, like other blue-green algae, contains four major lipids: mono- and digalactosyldiglyceride, sulfoquinovosyldiglyceride, and phosphatidylglycerol (Sato *et al.*, 1978). Table 19 shows the comparison of the fatty acid composition of the separated lipids of cells grown at 55° and 38°C. This alga, like *A. nidulans*, contained no polyunsaturated fatty acids. Lowering the growth temperature from 55° to 38°C increased the amount of monounsaturated fatty acids 18:1 and 16:1 and decreased the saturated fatty acid 18:0 in the charged lipids sulfoquinovosyldi-

* Current address: Department of Biology, College of General Education, University of Toyko, Komaba, Meguro-ku, Toyko, Japan.

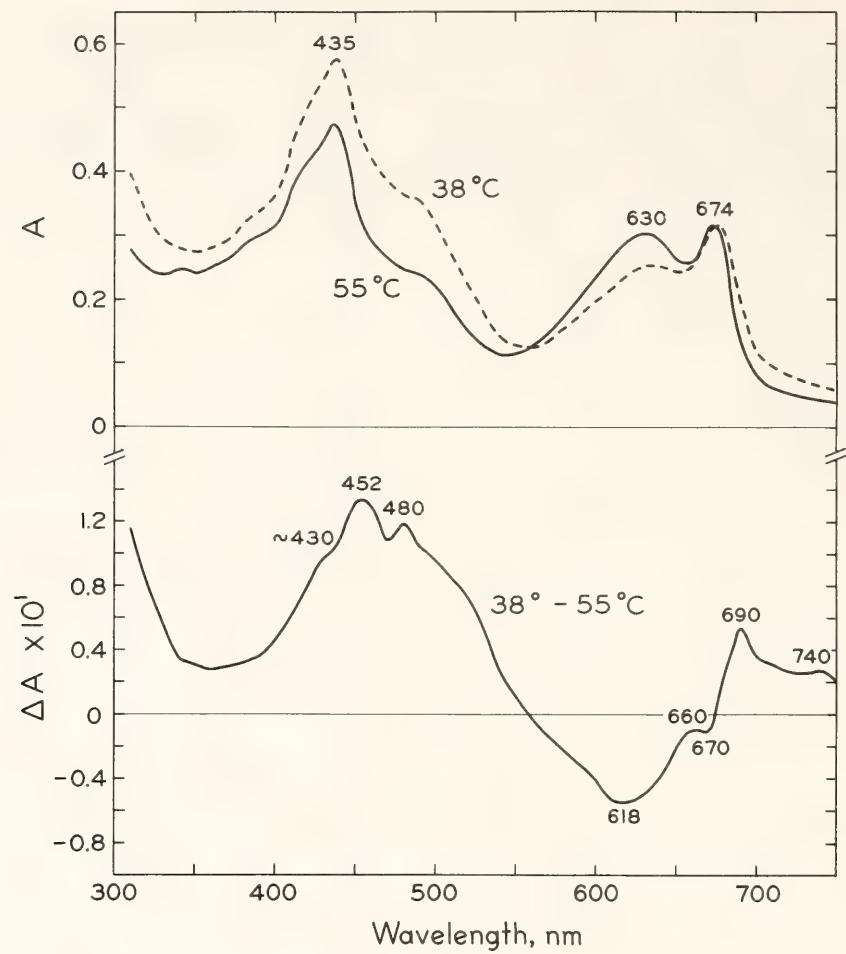


Fig. 20. Absorption spectra of cell suspensions of *Synechococcus lividus* grown at 55°C and 38°C, and the difference absorption spectrum between the two cultures. Absorbance at 674 nm was adjusted to be equal in the two samples.

TABLE 19. Lipid and Fatty Acids Extracted from *Synechococcus lividus* Grown at 55°C and 38°C*

Fatty Acid	Monogalactosyl- diglyceride	Digalactosyl- diglyceride	Sulfoquinovosyl- diglyceride	Phosphatidyl- glycerol	Total
<i>Grown at 55°C</i>					
16:0	50.2	53.3	58.7	55.1	53.8
16:1	14.9	10.2	1.0	4.5	9.6
17:0	0.4	0.5	0.4	0.4	0.5
17:1	0.1	0.0	0.0	0.3	0.0
18:0	21.4	17.7	28.1	21.9	22.3
18:1	13.0	18.2	11.9	17.8	13.8
<i>Grown at 38°C</i>					
16:0	36.4	35.6	59.2	52.6	42.4
16:1	47.3	43.1	10.8	20.2	35.9
17:0	0.2	0.2	0.2	0.4	0.4
17:1	0.5	0.6	0.3	0.4	0.5
18:0	0.5	0.9	0.4	1.8	0.5
18:1	15.2	19.7	29.2	24.6	20.3

* Fatty acid contents expressed as mole percent.

glyceride and phosphatidylglycerol, but it produced no change in the saturated fatty acid 16:0. In the uncharged lipids mono- and digalactosyldiglyceride, lowering the growth temperature produced a decrease of the saturated fatty acids 16:0 and 18:0 and an increase of the unsaturated fatty acid 16:1 while 18:1 remained unchanged. In general the cells grown at the lower temperature produced an increase of the more fluid (unsaturated or short-chained) fatty acids in all of the lipid classes. The ratio of total unsaturated to saturated fatty acid was 0.31 for cells grown at 55°C and increased more than four times to 1.31 for cells grown at 38°C.

Electron transport was followed by measuring the kinetics of the cytochrome *f* change at 420 nm. We reported last year that the kinetics of this change are complex (*Year Book* 76, pp. 222–226). Upon illumination with red light that excited both photosystems of photosynthesis, there was a rapid initial photo-oxidation of cytochrome *f* followed during the illumination period by a partial reduction and finally by a further slow oxidation until a steady-state level of

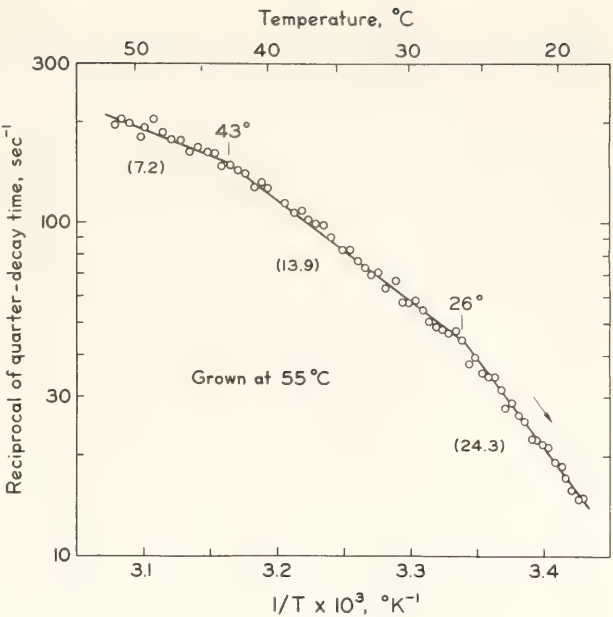


Fig. 21. Arrhenius plot of the transient reduction of cytochrome *f* measured at 420 nm during a period of red actinic illumination of *S. lividus* grown at 55°C. The rates were measured as described in the text. The temperature was changed in the direction shown by the arrow at a rate of about 1°C/min. The values in parentheses are the activation energies in kcal mol⁻¹.

oxidation was attained in the light. Rapid cytochrome reduction occurred when the light was turned off. We saw last year that system II excited by the

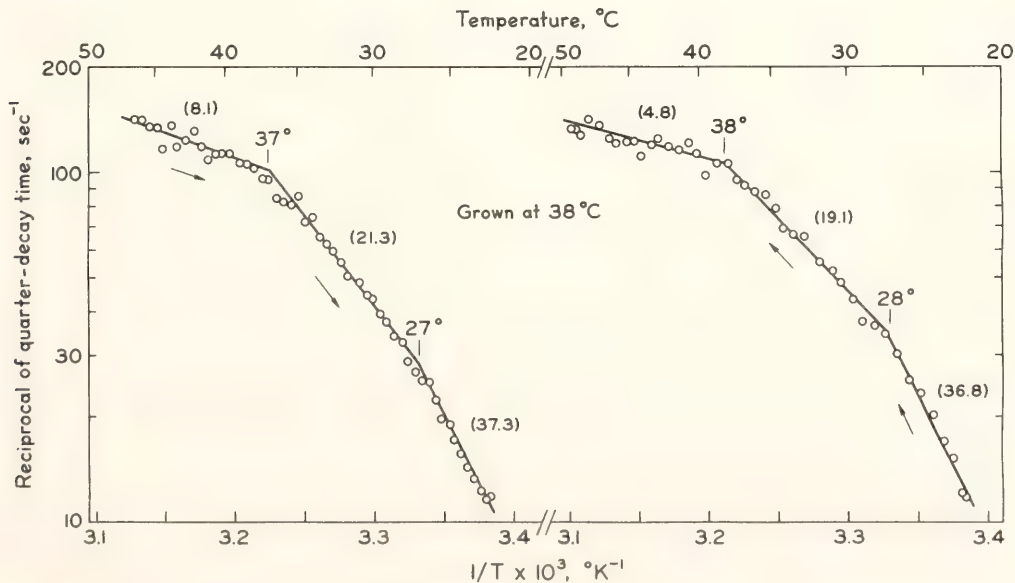


Fig. 22. Arrhenius plot of the transient reduction of cytochrome *f* measured as described in Fig. 21 for cells of *S. lividus* grown at 38°C. The temperature was first decreased and then increased.

red actinic light was responsible for this transient reduction of cytochrome *f* in the light. We measured the transient reduction for both the 55° and the 38°C-grown-cells by determining the reciprocal of the quarter-decay time as a function of the reciprocal of the absolute temperature. For this study we used the system for data acquisition and computer analysis of analogue signals described elsewhere in this *Year Book*. Figures 21 and 22 show the Arrhenius plots for the rate of cytochrome *f* reduction for cells grown at 55° and 38°C.

A discontinuity of the two straight lines can be seen near 43° and 26°C for cells grown at 55°C. For cells grown at 38°C the breaks in the lines occurred near 37° and 27°C. The right side of Fig. 22 shows the reversibility of the effects observed upon cooling the cells. Reheating the cells grown at 38°C again produced breaks at 28° and 38°C, with almost the same activation energies as those seen upon cooling. Although not

shown in Fig. 21, a similar reversibility was noted for the 55°C cells (*Year Book* 76, pp. 222–226).

We also studied the temperature dependence of quantum redistribution between pigment system II and pigment system I. Cells exposed to light preferentially absorbed by system II receive unbalanced excitation of the two systems and would have decreased photosynthesis if it were not for a type of self-regulating mechanism in the thylakoid membranes termed the pigment state 1 to state 2 shift (Bonaventura and Myers, 1969; Murata, 1969, 1970). By this mechanism an alteration of the thylakoid membrane takes place so that some of the excess quanta absorbed by system II are delivered to system I (Murata, 1970). An illustration of the pigment state 1 to state 2 shift observed in the transient kinetics of chlorophyll *a* fluorescence is given in the insert of Fig. 23. Cells were exposed to continuous 600-nm (system II) light, causing some of the

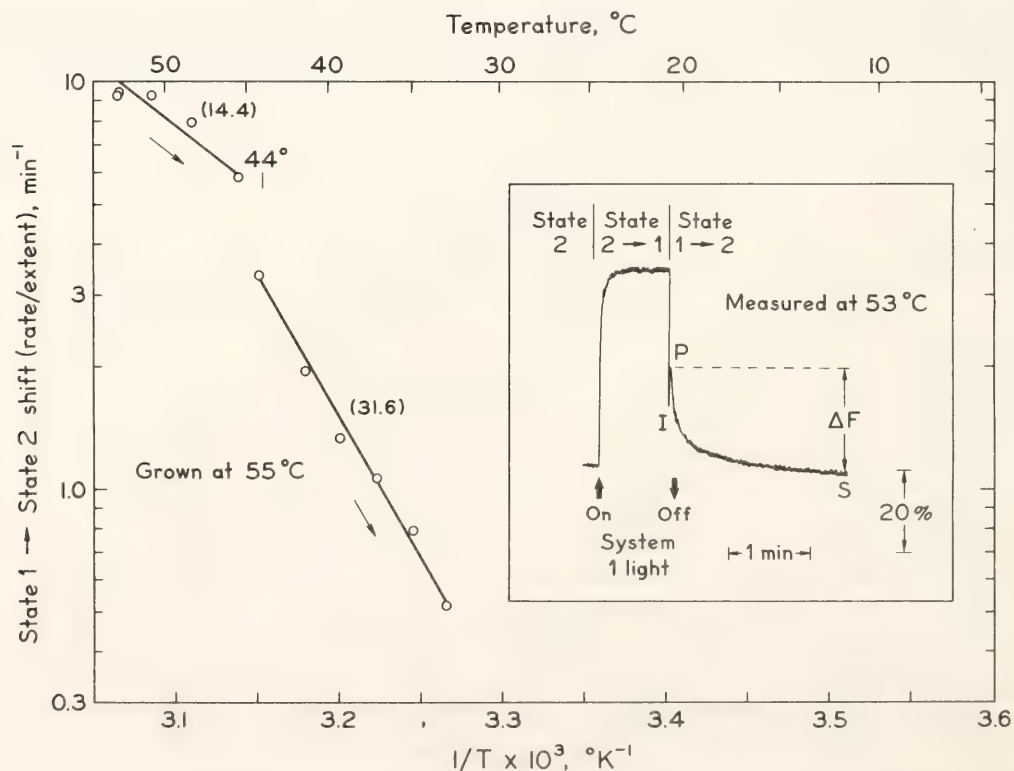


Fig. 23. Arrhenius plot of the state 1 to state 2 shift in *S. lividus* grown at 55°C. The insert shows the time course of the fluorescence transients produced by the state 1 to state 2 shift measured at 53°C with continuous background system II light, as described in the text.

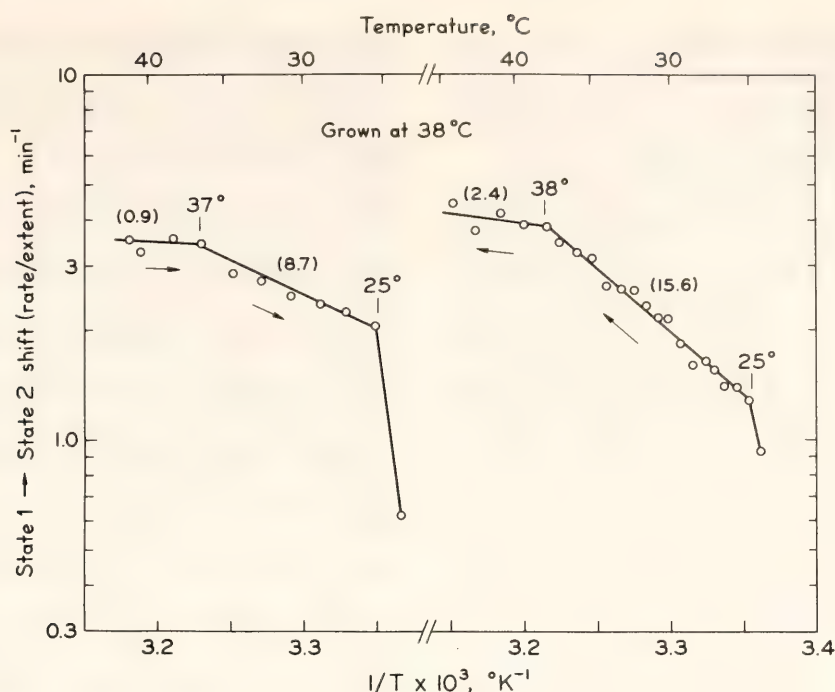


Fig. 24. Arrhenius plot of the shift of state 1 to state 2 in *S. lividus* cells grown at 38°C. The temperature was first decreased and then increased.

excitation to be delivered to system I (state 2). Superimposition, for several minutes, of strong blue light preferentially absorbed by system I caused a reverse quantum redistribution to take place (state 1). Under the strong blue light oxidized forms of electron-transport carriers accumulated, as is seen by the low level (I) of fluorescence yield after the blue light was turned off. Reduction of oxidized intermediates by system II excited by the background light produced the rapid increase in fluorescence yield (I to P). We studied the slow fluorescence decline (P to S) during continued exposure to 600-nm light (pigment state 1 to state 2 shift). The initial rate of the P to S decline was divided by the extent of the fluorescence-yield change (ΔF in the insert) (Murata *et al.*, 1975).

Figure 23 shows the Arrhenius plot of this measure of the rate of the state 1 to state 2 shift for cells grown at 55°C. A clear break can be seen around 44°C. The changes were too small and slow to measure below about 33°C. Figure 24

shows the same experiment done for cells grown at 38°C. Upon decreasing the temperature, a break was seen at 37°C in the Arrhenius plot. Another break may have occurred near 25°C, but only one point was taken in this region since the changes were so small and slow. The effects of temperature on the state changes were reversible. Increasing the temperature of the same sample again produced the break at 38°C and the possible break at 25°C.

We found previously that the appearance of a maximum in the fluorescence-to-temperature curve could be correlated with the occurrence of a transition of the physical phase of membrane lipids (Murata *et al.*, 1975; Murata and Fork, 1975). We made these types of measurements with *S. lividus* grown at 38° and 55°C by exciting chlorophyll *a* fluorescence directly with blue light (435 nm) or indirectly via phycocyanin by using orange light (560 nm). Excitation intensities were kept low (a few hundred ergs $\text{cm}^{-2} \text{sec}^{-1}$) to prevent temperature-dependent pigment state changes such

as those described in Fig. 23 and 24. In addition, DCMU was added to these cells to prevent fluorescence-yield changes produced by electron transport.

Figure 25A shows the fluorescence-versus-temperature curve obtained using phycocyanin excitation. Here maxima appeared at 41° upon decreasing the temperature and at 43°C upon increasing the temperature of 55°C-grown cells. Chlorophyll excitation produced peaks at 40° and 42°C upon decreasing and increasing the temperature, respectively (Fig. 25B). Such distinct features were not seen in the fluorescence-to-temperature curves measured with cells grown at 38°C (C and D), although a peak was seen at 22°C upon decreasing the temperature and near 25°C upon increasing the temperature.

The peaks seen near 40°–43°C in the fluorescence-versus-temperature curves for *S. lividus* grown at 55°C suggest that

the phase transition of the thylakoid membrane lipids takes place at this temperature region and that this phase transition is related to the characteristic points seen at the higher temperature in the cytochrome *f* reaction and the state 1 to state 2 shift. We did not see maxima in the fluorescence-versus-temperature curve in the low-temperature region (25°C) where characteristic discontinuity points for the physiological activities were seen. In the fluorescence-versus-temperature curve for cells grown at 38°C, a maximum (or shoulder) was seen around 25°C with chlorophyll excitation where characteristic discontinuity points for the physiological activities were observed, but no maxima or shoulders were seen around 38°C.

Lowering the growth temperature from 55° to 38°C shifted the high-temperature characteristic point from 43° to 37°C, while the low-temperature char-

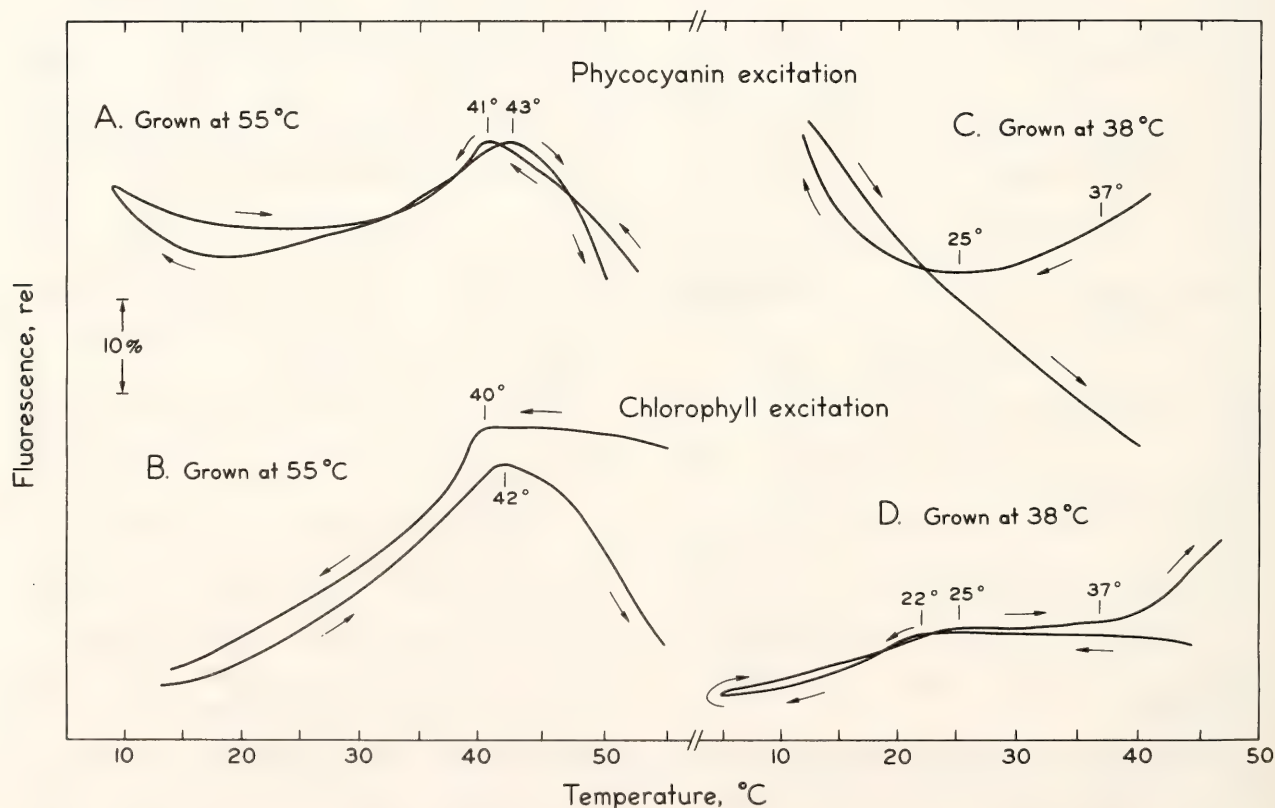


Fig. 25. Temperature dependence of chlorophyll *a* fluorescence in *S. lividus* grown at 55° and 38°C. Chlorophyll fluorescence was excited directly with blue light or indirectly via phycocyanin excitation (yellow-orange light) as described in the text.

acteristic point remained almost constant.

Previous studies with algae such as *A. nidulans*, *Anabaena variabilis*, and *Cyanidium caldarium* have shown that the temperatures at which lipid phase transitions occur depend upon the growth temperature (Murata *et al.*, 1975; Murata and Fork, 1975, 1976; Ono and Murata, 1978; Fork and Murata, 1977). These differences appear to be caused by growth-temperature-dependent changes in the fatty acid composition of the membrane lipids. Sato *et al.* (1978) found that lowering the growth temperature from 38° to 22°C produced an increase in the desaturation of fatty acids in *A. variabilis* and a decrease in the chain length of fatty acids in *A. nidulans*. A three-fold increase in the ratio of unsaturated-to-saturated fatty acids was noted when the temperature of *C. caldarium* was lowered from 55° to 20°C. The lipids of *S. lividus* showed similar striking changes in their fatty acid composition when growth temperatures were lowered from 55° to 38°C. At the lower temperature the more fluid fatty acids increased, and the ratio of unsaturated-to-saturated fatty acids increased four times. These compositional changes in fatty acids would appear to be related to the characteristic points reported in the studies of the temperature dependence of the cytochrome *f* reaction, the state 1 to state 2 shift, and the measurements of chlorophyll *a* fluorescence versus temperature.

REFERENCES

- Allen, C. F., and P. Good, in *Methods in Enzymology*, Vol. XXIII, A. San Pietro, ed., pp. 523–547, Academic Press, New York, 1971.
- Bonaventura, C., and J. Myers, *Biochim. Biophys. Acta* 189, 366–383, 1969.
- Castenholz, R. W., *Schweiz. Z. Hydrol.* 32, 538–551, 1970.
- Castenholz, R. W., *Bact. Rev.* 33, 476–504, 1969.
- Folch, J., M. Lees, and G. H. Sloane-Stanley, *J. Biol. Chem.* 226, 497–509, 1957.
- Fork, D. C., and N. Murata, in *Photosynthetic Organelles: Structure and Function*, S. Miyachi, S. Katoh, Y. Fujita, and K. Shibata, eds., pp. 427–436, Japanese Society of Plant Physiologists, Tokyo, 1977.
- Murata, N., *Biochim. Biophys. Acta* 172, 242–251, 1969.
- Murata, N., *Biochim. Biophys. Acta* 205, 379–389, 1970.
- Murata, N., and D. C. Fork, *Plant Physiol.* 56, 791–796, 1975.
- Murata, N., and D. C. Fork, *Biochim. Biophys. Acta* 461, 365–378, 1976.
- Murata, N., J. H. Troughton, and D. C. Fork, *Plant Physiol.* 56, 508–517, 1975.
- Ono, T., and N. Murata, *Biochim. Biophys. Acta*, in press, 1978.
- Sato, N., N. Murata, Y. Miura, and N. Ueta, *Biochim. Biophys. Acta*, in press, 1978.
- Sheridan, R. P., Ph.D. Thesis, The University of Oregon, Eugene, Oregon, 1966.

TEMPERATURE DEPENDENCE OF THE TURNOVER OF P700 IN PHOTOSYNTHESIS OF THE BLUE-GREEN ALGA

Anacystis nidulans

Norio Murata* and David C. Fork

In our previous studies (Murata *et al.*, 1975; Murata and Fork, *Year Book* 74, 766–776) we investigated the tempera-

ture dependence of photosynthetic activities in the blue-green alga *Anacystis nidulans*, and related them to the transi-

tion of the physical phase of thylakoid membrane lipids. It was shown that the lipid phase transition between the liquid crystalline and the phase-separation states occurred at about 24°C in cells grown at 38°C and at about 13°C in cells grown at 28°C. In the Arrhenius plot of turnover rate of P700 we observed only one break point, around 20°C, for cells grown at 38°C, and near 10°C in cells grown at 28°C. We have recently developed an automatic system that utilizes a computer calculation technique to

measure the dark-reduction kinetics of P700. The system enables us to take a number of points over a wide temperature range (Ford *et al.*, this Report). We reexamined the temperature dependences of the P700 turnover with this measuring system.

The intact cells of *A. nidulans* were suspended in the culture medium and placed in a cuvette whose temperature

* Current address: Dept. of Biol. College of Gen. Education, Univ. of Tokyo, Komaba, Meguro-ku, Tokyo, Japan.

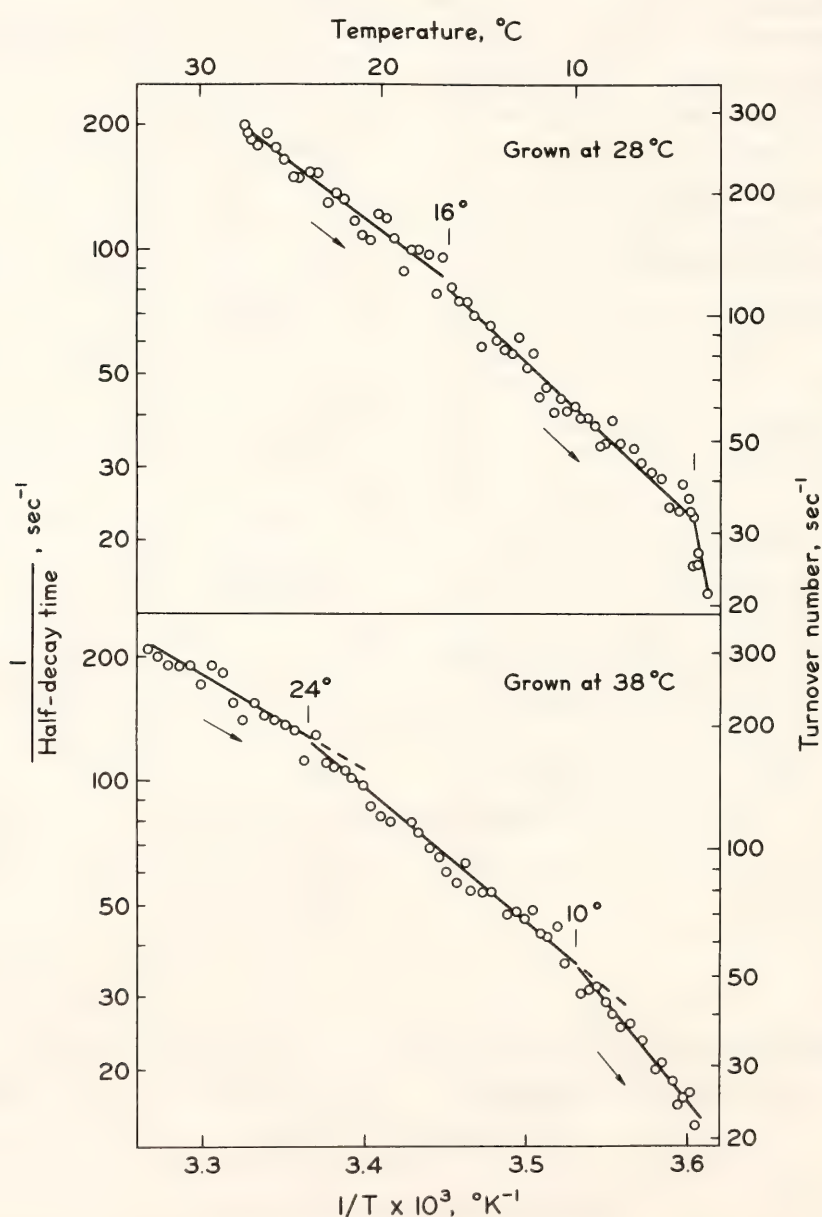


Fig. 26. Arrhenius plot showing the reciprocal of the half-decay time for dark reduction of P700 after turning off the actinic light in *A. nidulans* grown at 28 and 38°C. The turnover rate in the light steady state was calculated from the half-decay time.

was decreased from the growth temperature to almost 0°C at a nearly constant rate of 0.5°C/min. The sample was illuminated with intermittent actinic light with wavelengths from 630 to 750 nm. The light and dark periods of each cycle were 20 and 5 sec, respectively. The light-induced oxidation-reduction reactions of P700 were measured by following the absorbance changes at 435 nm. P700 was oxidized in the light and reduced in the dark. The kinetics of reduction in the dark period after turning off the actinic light was most intensively studied. Semilogarithmic plots of the dark decay kinetics indicated that the reduction was apparently a monomolecular reaction. In this type of reaction kinetics, the reciprocal of the half-decay time is proportional to the turnover rate of P700 in the light period.

Figure 26 shows the Arrhenius plot of the reciprocal of the half-decay time for dark reduction of P700, or the turnover rate of P700 in the light steady state in cells grown at 28° and 38°C. It is clear that in both of the samples the Arrhenius

plot is composed of three straight lines with two break points. In cells grown at 28°C the break points appear at 16° and 6°C, and in cells grown at 38°C the break points were at 24° and 10°C. The characteristic points at 16°C in the 28°C-grown cells and at 24°C in the 38°C-grown cells correspond to the lipid phase transition of thylakoid membrane between the liquid crystalline and the phase separation states, which was elucidated by physical methods (Murata *et al.*, 1975; Murata *et al.*, unpublished results). On the other hand, no such phase transition was observed around 6°C in the 28°C-grown cells or around 10°C in the 38°C-grown cells. The origins of these characteristic break points at the lower temperatures are still under investigation.

REFERENCES

- Murata, N., and D. C. Fork, *Plant Physiol.* 56, 791–796, 1975.
Murata, N., J. Troughton, and D. C. Fork, *Plant Physiol.* 56, 508–517, 1975.

DISPLACEMENT OF INTEGRAL MEMBRANE PROTEINS DURING LIPID PHASE TRANSITIONS IN *Anacystis nidulans*

Paul A. Armond and L. Andrew Staehelin*

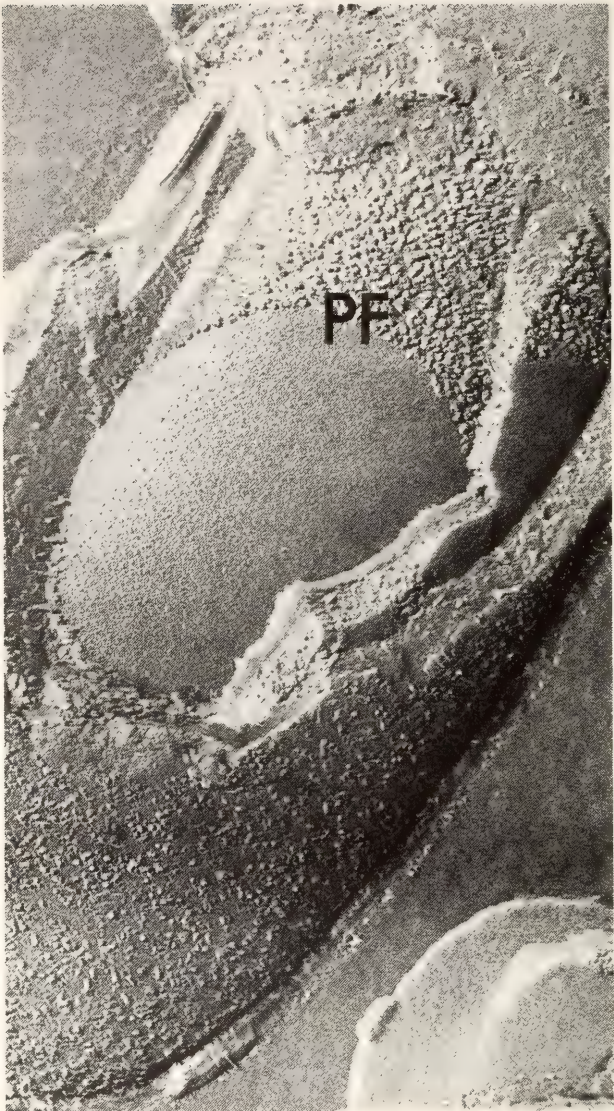
The response of membrane-bound enzymatic activities to temperature has been extensively examined in *Anacystis nidulans* (Year Book 74, pp. 766–776; Year Book 75, pp. 465–472; Murata and Fork, this Year Book). It has been proposed that changes in the slope of Arrhenius plots of such activities are the consequence of changes in the physical state of the membrane lipids. In the present study, we wished to examine the membrane structural alterations that might be associated with the physical

state changes of the lipid constituents.

Anacystis nidulans cells, grown at 38°C, were subjected to 38°C → 21°C, 38°C → 10°C and 38°C → 21°C → 38°C temperature transitions. After the cell suspensions had been equilibrated at their final temperatures for 15 min, sufficient glutaraldehyde for a final concentration of 2% was added to prevent any further structural changes. The

* Department of Molecular, Cellular, and Developmental Biology, University of Colorado, Boulder, Colorado 80302.

Fig. 27. Fracture faces of an *A. nidulans* cell subjected to a 38°C → 21°C temperature transition. The PF face of the thylakoid membranes exhibits a clear delineation between particle-containing regions and particle-free areas (regions of the membrane in which lateral phase separation of the lipid constituents has occurred). Particle-free regions such as this were not observed in control (38°C) cells, or cells which had been returned to the growth temperature following treatment at 21°C (38°C → 21°C → 38°C sample). Magnification: 70,000×.



membranes of control (untreated cells fixed at 38°C) and treated cells were examined by freeze-fracture electron microscopy.

The freeze-fracture preparations of control (38°C) *A. nidulans* exhibited an even distribution of particles on the fracture faces of both the plasma and the thylakoid membranes. In contrast, membranes of cells that had experienced a 38°C → 21°C transition (Fig. 27) showed large particle-free regions on both the thylakoid and the plasma membranes. These regions, presumably pure lipid, became even more extensive in the cell membranes which had experienced the 38°C → 10°C transition. It has been previously reported that such particle-free areas can be the result of either lateral or vertical (normal to the plane of the membrane) displacement of the protein complexes in the membrane. These possibilities are easily distinguished by analysis of the particle den-

sities in the apparently unaffected areas of the membrane. If the redistribution of particles is by lateral movement only, a substantial increase in the particle density of such regions would be antici-

TABLE 20. Density of Particles (per micron²) on *Anacystis nidulans* Plasma and Thylakoid Membranes after Temperature Transition

Temperature	Plasma Membrane		Thylakoid Membrane	
	EF*	PF†	EF	PF
38°C, Control	1572 ± 98	3434 ± 119	703 ± 82	3703 ± 190
38°C → 21°C	1484 ± 101	3853 ± 149	759 ± 156	3804 ± 169
38°C → 10°C	1392 ± 132	3867 ± 148	755 ± 106	4278 ± 235
38°C → 21°C → 38°C	1632 ± 198	3277 ± 251	723 ± 101	3324 ± 257

* Exoplasmic fracture face.
† Protoplasmic fracture face.

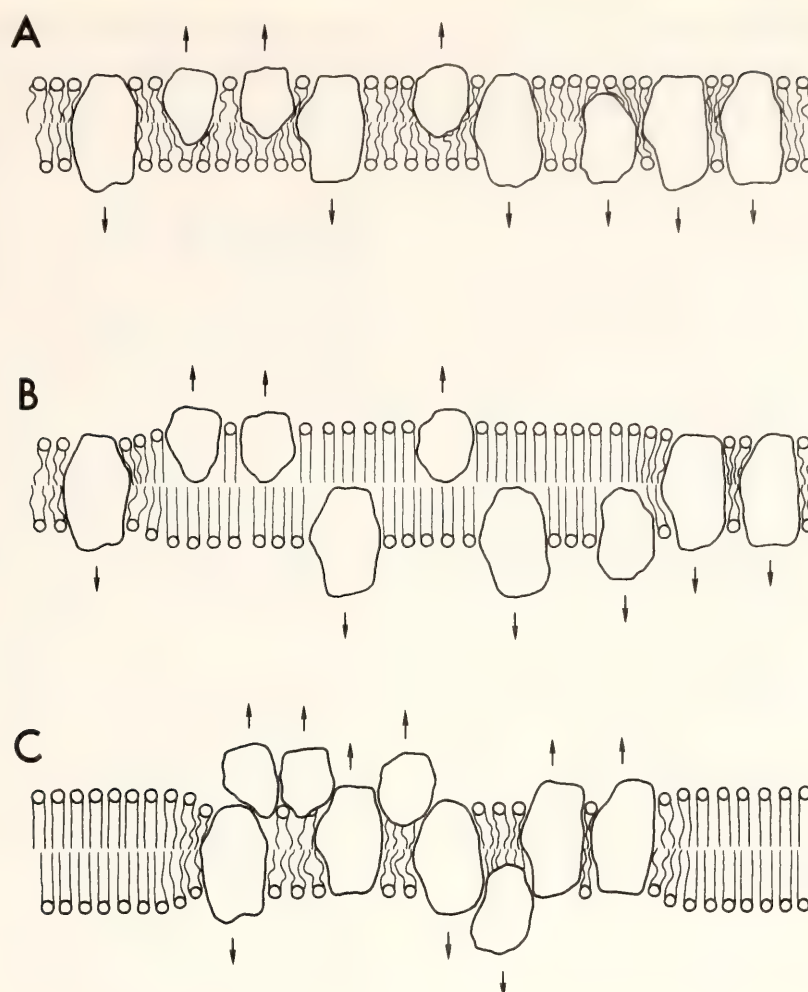


Fig. 28. Model for the vertical displacement of membrane particles in *Anacystis nidulans*. The loss of particles from the fracture plane in the transition from a fluid-phase (A) to a mixed-phase state (B and C) may involve different processes depending upon whether the proteins remain in the less fluid portion of the membrane (B) or laterally migrate to the more fluid region of the membrane. If the proteins remain in their original position, integral membrane proteins that are not transmembranous (B, upper leaflet) could become undetectable at the fracture plane because of the change in bilayer thickness induced by the change of the physical state of the lipids. For such nontransmembranous proteins, approximately the same degree of surface exposure could be maintained. Transmembranous proteins would also require some increase in surface exposure to account for nondetectability at the fracture plane (B, lower leaflet). If the proteins are displaced to a more fluid region of the membrane (C), some proteins might be excluded from the fracture plane by the combined lateral pressure of the proteins and lipids. Integral membrane proteins may also partition between the two fracture faces in a different manner (arrows indicate possible fracture face affinities). The membrane models depicted in B and C are both consistent with areas of the membrane being devoid of particles, without substantial increases in the particle density of the remaining areas.

pated. For the *A. nidulans* cell membranes (Table 20), such increases in particle density are not evident on the EF faces of the plasma and thylakoid membranes and are only marginally observed for the remaining fracture faces. It would appear that the particle redis-

tribution in *A. nidulans* must involve both lateral and vertical displacement of membrane particles.

The loss of particles from the fracture faces in the transition from a fluid (Fig. 28A) to a mixed-phase state (Fig. 28B and C) does not have to be the result of

a complete loss of the protein complexes from the membrane. Exclusion of all the particles from the fracture plane of less fluid regions of the membrane (Fig. 28B) or a maintenance of the number of particles at the fracture plane of fluid regions of the membrane by the exclusion of some particles would be sufficient to explain the observed effect of the fluid-phase to mixed-phase transition on membrane structure. Since both of these possible mechanisms allow for a restoration of normal particle densities upon rewarming of the membranes, as was observed for *A. nidulans* (see Table 20), it is not possible to distinguish between these alternatives at the present time. Such vertical displacement of integral membrane proteins would have important physiological consequences, since protein complexes which were formerly in proximity or direct contact would be-

come separated during the phase transition of the lipids.

ACKNOWLEDGMENTS

The authors would like to thank M. DeWit and T. Giddings for their technical assistance, Dr. D. Fork for providing the cell cultures used in this study, and Dr. J. Berry for his helpful suggestions.

REFERENCES

- Borochoy, H., and M. Shinitzky, *Proc. Nat. Acad. Sci. U.S.A.* **73**, 4526-4530, 1976.
- Jacobs, R. E., B. Hudson, and H. C. Anderson, *Proc. Nat. Acad. Sci. U.S.A.* **72**, 3993-3997, 1975.
- Niedermeyer, W., G. R. Parish, and H. Moor, *Cytobiologie* **13**, 364-379, 1976.

FORMATION OF (PROTEO)LIPID VESICLES BY MEANS OF A FRENCH PRESSURE CELL

Gijsbert van Ginkel

Artificial lipid membranes with closely associated photoreceptor pigment molecules are useful model systems for studying reactions that may occur in biological membranes. Bacteriorhodopsin (Racker and Stoeckenius, 1974; Packer *et al.*, 1977) and bacteriochlorophyll reaction centers (Drachev *et al.*, 1975) have already been incorporated into lipid membranes and photochemical as well as photoelectrical effects observed. Another candidate for such studies is CPI, the chlorophyll *a*-protein complex enriched in P700, from higher plants.

Preliminary experiments with rather fragile black lipid membranes (BLM) suggested that if the protein complexes were first embedded in a lipid phase, subsequent incorporation into a planar

lipid membrane would be facilitated. Therefore, several published procedures for making proteolipid vesicles were investigated, and a new method using a French pressure cell was developed.

The detergents sodium cholate or deoxycholate have often been used to effect recombination of proteins and artificial lipid membranes with restored photochemical activity (Kagawa and Racker, 1971; Jaynes *et al.*, 1975). However, since BLM are unstable in the presence of even low concentrations of detergent, this technique did not seem well suited to our purpose. Other gentle reconstitution procedures which avoid the use of detergents are: (1) incubation of (pigment) proteins and liposomes at room temperature (Eytan *et al.*, 1976);

(2) freezing and thawing of protein-liposome mixtures (Villegas *et al.*, 1977); (3) exposing aqueous mixtures of protein and lipid to sonic oscillation (Racker, 1973).

These procedures were applied to CPI with the lipids egg lecithin or soybean lecithin. Upon combining CPI with lipid, both the absorption (677 to 676 nm) and the fluorescence maxima for chlorophyll in the red spectral region shifted to shorter wavelengths (Fig. 29) and the fluorescence yield increased. These observations suggested that some of the antenna chlorophylls were no longer in as direct contact with P700 as before combining with lipid.

The CPI lipid vesicles showed enhanced photochemical activity for light-induced oxygen uptake and proton uptake in the presence of ascorbate as electron donor. The proton uptake was reversible and oxygen dependent. Since both reactions have been reported for photosystem I (Epel and Neumann, 1973; Fowler and Kok, 1976; Tyszkiewicz *et al.*, 1977), these results initially suggested that reconstituted photosystem I activity had been obtained. That this initial impression was erroneous is discussed elsewhere by Brown and van Ginkel (this Report). Of the three procedures investigated, sonication yielded the highest photochemical activity.

Another technique was suggested by the fact that liposomes can also be formed by pressing lipid suspensions through a syringe. Because the French pressure cell functions in an analogous manner, CPI-lipid mixtures were forced through this instrument. CPI-lipid vesicles were thereby formed and, as can be seen in Table 21, high rates of photochemical activity were observed. The French press procedure consists of the following manipulations.

A chloroform solution of lipid (generally egg or soybean lecithin) is dried in a thin layer inside a round-bottomed glass vessel under a stream of nitrogen.

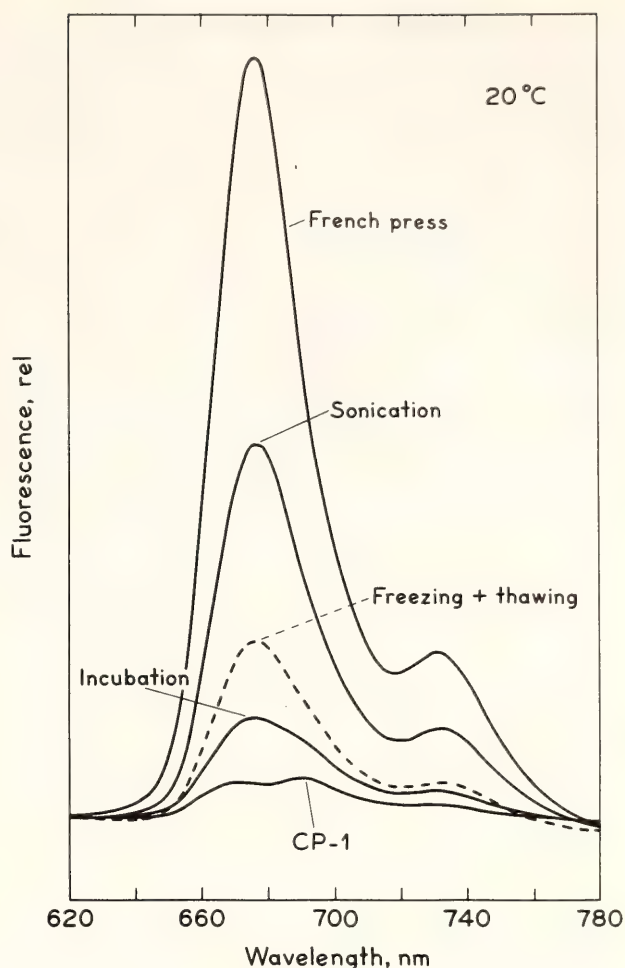


Fig. 29. Fluorescence emission spectra of CPI and CPI lipid vesicles made from the same CPI preparation with different reconstitution procedures. All spectra were measured with the same instrument settings (excitation 438 nm, halfwidth 10 nm, emission halfwidth 3 nm) and the same chlorophyll concentration of about $-5 \mu\text{g chl/ml}$.

One ml of dialyzed CPI ($15\text{--}20 \mu\text{g chl ml}^{-1}$) is added for each 2 or 3 mg of lipid, together with 2 or 3 glass beads (6 mm diameter), and the vessel is shaken for about 2 min at maximum speed on a Vortex mixer. The resulting milky green suspension is forced through a French pressure cell (Aminco 43398 A, flushed with nitrogen before filling) at the maximum available pressure (about 1000 kg cm^{-2}). The effluent is centrifuged for 15–20 min at $45,000g$ to sediment nondispersed lipid, aggregated CPI and larger proteo-lipid vesicles. The supernatant contains a green opalescent

TABLE 21. Photochemical Activities of CPI Lipid Vesicles Obtained by Different Reconstitution Procedures*

Reconstitution Method	O ₂ Uptake ($\mu\text{mol mg chl}^{-1} \text{ min}^{-1}$)	H ⁺ Uptake ($\mu\text{mol mg chl}^{-1} \text{ min}^{-1}$)
CPI without lipid	0.38	0.83
(a) incubation	1.28	2.52
(b) freezing and thawing	1.86	5.12
(c) sonication	3.84	10.50
(d) French pressure cell	6.59	17.50

* The reactions were measured in 2.5mM phosphate buffer pH 7.2 in the presence of 5mM ascorbate. chl α /P700 = 48; 13 $\mu\text{g chl/ml}$; red light with intensity of about 70 W m⁻².

suspension of CPI lipid vesicles, which are very stable and can be stored under nitrogen in the dark on ice for one or two weeks without loss of photochemical activity.

The procedure outlined above can be applied to any aqueous-lipid mixture as a way of obtaining closed lipid vesicles. The following observations indicate that the vesicles are closed: (1) Osmotic shocking of the vesicle suspension yields a floating layer of lipid. (2) When the vesicles are prepared in the presence of 0.2M K₃Fe(CN)₆ or 0.1M mercurochrome (both highly water-soluble compounds) and the nontrapped dye is removed by passing the preparations through a Sephadex column, by dialysis, or by ultrafiltration, a highly colored vesicle preparation is obtained. The trapped dye cannot be removed from the vesicles unless they are osmotically shocked. (3) Negative staining with uranyl-acetate shows closed vesicles in the electron microscope (Fig. 30). Because the French press method, originally developed in this Department for entirely different purposes by Dr. C. S. French, is so rapid, it provides an attractive technique for forming lipid vesicles.

REFERENCES

- Drachev, L. A., A. A. Kondrashin, V. D. Samuilov, and V. P. Skulachev, *FEBS Lett.* 50, 219–221, 1975.
- Epel, B. L., and J. Neumann, *Biochim. Biophys. Acta* 325, 520–529, 1973.
- Eytan, G. D., M. J. Matheson, and E. Racker, *J. Biol. Chem.* 251, 6831–6837, 1976.
- Fowler, C. F., and B. Kok, *Biochim. Biophys. Acta* 423, 510–523, 1976.
- Jaynes, J. M., L. P. Vernon, and S. M. Klein, *Biochim. Biophys. Acta* 408, 240–251, 1975.
- Kagawa, J., and E. Racker, *J. Biol. Chem.* 246, 5477–5488, 1971.
- Packer, L., T. Konishi, and P. Shieh, in *Living Systems as Energy Converters*, pp. 119–134, R. Buvet *et al.*, eds., Elsevier-North Holland Biomedical Press, Amsterdam, 1977.
- Racker, E., *Biochem. Biophys. Res. Commun.* 55, 224–230, 1973.
- Racker, E., and W. Stoeckenius, *J. Biol. Chem.* 249, 662–663, 1974.
- Tyszkiewicz, E., R. Popovic, and E. Roux, *FEBS Lett.* 81, 65–68, 1977.
- Villegas, R., G. M. Villegas, F. V. Barnold, and E. Racker, *Biochem. Biophys. Res. Commun.* 79, 210–217, 1977.

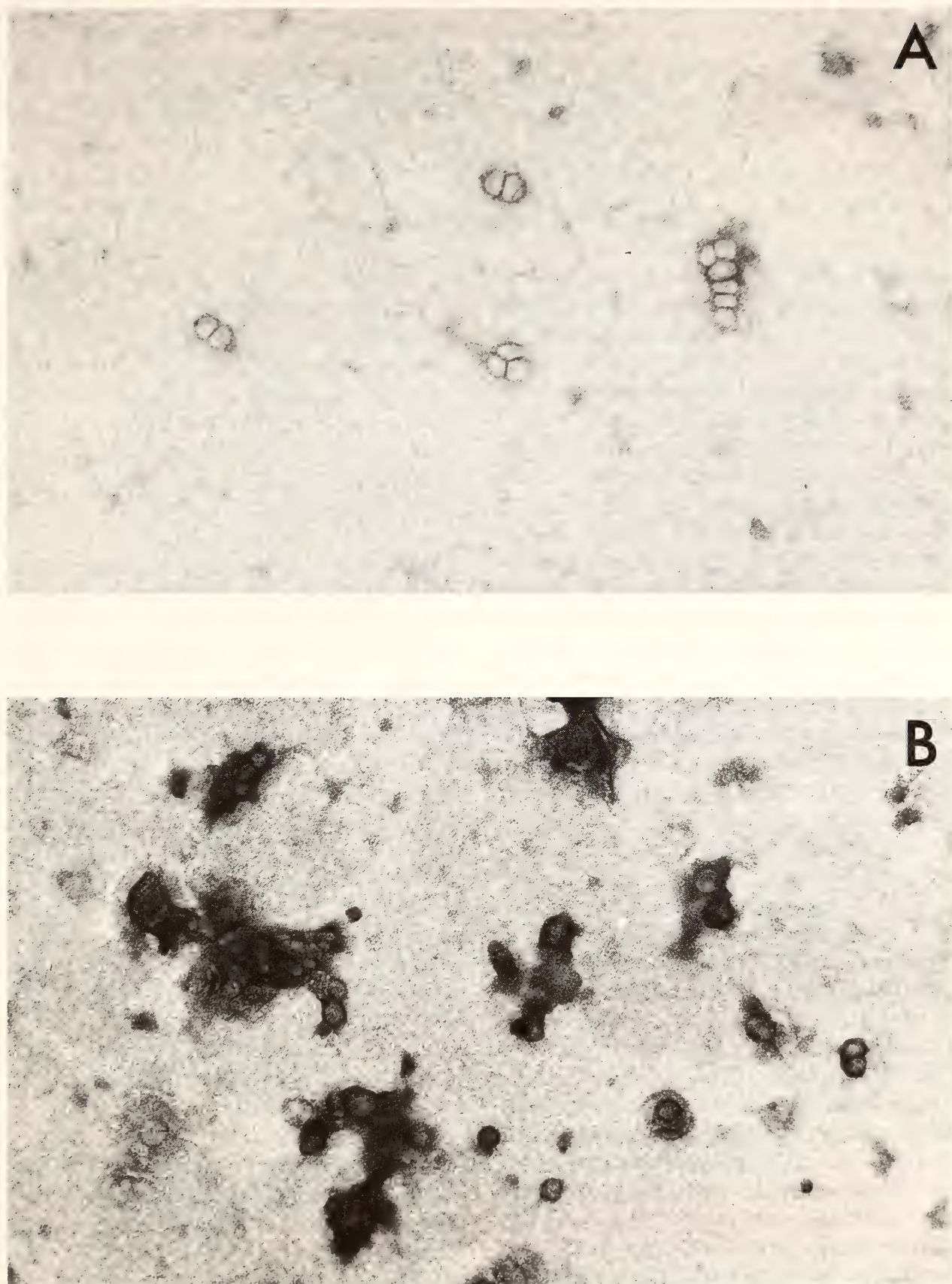


Fig. 30. Electronmicrograph studies of (A) soybean lecithin vesicles and (B) CPI-soybean lecithin vesicles made with the French pressure cell; magnification $40,000\times$, negatively stained with uranyl-acetate. On the basis of light-scattering and filtration experiments the diameter of the vesicles is estimated between 25 and 100 nm. The electronmicrographs were obtained by courtesy of Dr. John M. Mackenzie, Jr.

COMPOSITION OF ISOLATED P700-CHLOROPHYLL-
PROTEIN COMPLEXES AND THEIR PHOTOACTIVITY
WHEN COMBINED WITH LIPID VESICLES
OR TRITON MICELLES

Jeanette S. Brown and Gijsbert van Ginkel

In order to study the mechanism of energy conversion in photosynthesis, we have for several years been investigating the spectroscopic properties of isolated chlorophyll-protein complexes. The most promising of these complexes, CPI,* can be purified by Triton solubilization of chloroplast membranes and hydroxylapatite chromatography according to Shiozawa *et al.* (1974). CPI is highly enriched in the photosystem I reaction-center chlorophyll, P700, and several closely associated electron carriers. In addition, we have recently measured superoxide dismutase (SOD)† and catalase activities in these purified photosystem I protein complexes. We have incorporated these complexes into lipid vesicles and studied their photocatalytic properties.

Composition of CPI Preparations

When Shiozawa *et al.* (1974) described their procedure for isolating CPI, they noted the presence of cytochromes *f* and *b₆* in their preparations. Recently Dr. Tetsuo Hiyama of the Department of Cell Physiology, University of California, Berkeley, measured electron paramagnetic resonance spectra of our CPI preparations at both ambient and cryogenic temperatures and under oxidizing and reducing conditions. He observed signals which in other studies have been correlated with iron-sulfur centers A (Malkin and Bearden, 1971) and B (Evans *et al.*, 1974), an unidentified X (Evans *et al.*, 1975) and plastocyanin,

in addition to the expected reaction-center chlorophyll, P700.

Our own experience (*Year Book* 74, p. 779 and *Year Book* 75, p. 460) as well as the work of others (Bengis and Nelson, 1975; Malkin, 1975) suggested that the cytochromes and plastocyanin are not intimately bound to the isolated P700 complex but can cochromatograph with it. This idea led to a procedure for removing these three components before Triton treatment. Chloroplast fragments were isolated from spinach leaves by blending in 0.15M KCl, 50mM Tris, pH 8 and centrifuging at 5,000*g* for 5 min. After washing several times in 50mM Tris, pH 8.0, the final pellet containing 20–40 mg of chlorophyll was homogenized in about 80 ml of 0.5% digitonin (Sigma Biochemical Co.), 0.15M KCl, 50mM Tris, pH 8.0, and stirred at 20°C for 30 min. This mixture was centrifuged at 45,000*g* for 1 hr at 5°C, and the pellet used for Triton solubilization and CPI isolation. Undoubtedly some P700 is lost to the digitonin supernatant along with nearly all of the cytochromes and plastocyanin, but a reasonable yield of CPI can still be obtained (about 0.4% of the original chlorophyll).

The relatively high rates of oxygen reduction observed when the CPI was combined with lipid vesicles or Triton micelles (described below) prompted us to examine this complex for SOD and catalase activities. Evidence for the presence of both of these enzymes was found in the CPI regardless of a digitonin pretreatment. SOD was assayed by the method of Beauchamp and Fridovich (1971). Elstner and Heupel (1975)

* CPI = P700-chlorophyll α -protein complex.

† SOD = superoxide dismutase.

found about 25–35 units of SOD per mg chl in sugar beet leaves, and the enzyme was enriched to 60–70 units per mg chl in a photosystem I fraction prepared by digitonin treatment and differential centrifugation. Calculated on their basis, we found about 80 units of SOD per mg chl in CPI. This activity was completely inhibited by 1mM KCN, indicating that the enzyme could be the Cu-Zn containing type.

Catalase activity was assayed by adding a few μ l of 1% H_2O_2 to 4 ml of sample in an oxygen-electrode chamber and recording the rate of oxygen evolution. It is generally accepted that catalase originates in peroxisomes (Tolbert, 1971) and is found in chloroplast membranes only as a result of contamination during their isolation. Recently Allen (1977) addressed this problem by very carefully isolating and washing chloroplasts to minimize peroxisomal contamination. He was able to reach a low value for catalase activity of 2–3 μ moles O_2 evolved mg chl⁻¹ min⁻¹, and he considered this value insignificant. We measured activities of only 1–3 μ moles O_2 evolved mg chl⁻¹ min⁻¹ in several CPI preparations, but the important finding was that the specific activity on a chlorophyll basis was always higher in CPI than in the original chloroplast membranes. In one experiment this value rose from 0.3 in washed chloroplasts to 1.1 in the CPI prepared from them, and in another from 0.6 in a French press homogenate to 2.8 in a photosystem I centrifugal fraction. Therefore, we concluded that a com-

ponent with catalase activity is intrinsic in chloroplast membranes as well as SOD activity, and both are located close to the photosystem I reaction-center chlorophyll.

Photoactivity of CPI Combined with Lipid Vesicles or Triton Micelles

When P700-chlorophyll-protein complexes were combined with soybean lecithin in vesicles by the procedure described elsewhere in this Report (van Ginkel), blue shifts in the chlorophyll fluorescence-emission maxima and increases in fluorescence yield were observed as shown in Table 22 and Fig. 29 (in van Ginkel, this Report). The emission maxima at wavelengths very close to the absorption and increase in yield strongly indicate that some of the chlorophyll has become embedded in the lipid phase and therefore absorbs at shorter wavelengths than the remaining pigment still attached to the protein. The extent and rate of P700 photooxidation in the complexes before and after combination with lipid were also compared. Both of these parameters decreased by about 20%, suggesting again that some of the antenna chlorophylls had become dispersed in the lipid phase and could no longer efficiently transfer excitation energy to the reaction centers.

However, because P700 in the proteolipid vesicles was still highly reactive, we next investigated several electron transfer reactions which are believed to function through this photosystem I reaction center in vivo. Two of our initial observations were that light-induced pH changes and O_2 uptake were greatly enhanced in the CPI vesicles compared to CPI alone. The initial rates of these photoreactions with ascorbate, ferrocyanide, and reduced glutathione (GSH) as electron donors are shown in Table 23. The pH measurements were made with a Beckman 3600 digital meter and No. 39030 Ceramic Junction combination electrode immersed in the sample cham-

TABLE 22. Absorption (A) and Fluorescence (F) Maxima of CPI and CPI-Lipid Vesicles. Fluorescence Excitation at 435 nm

Temperature	CPI		CPI-vesicles	
	(A)	(F)	(A)	(F)
20°C	677	685	676	677
–180° (A), –196° (F)	678	696	676	674

TABLE 23. Rates of Light-Induced O_2 -Uptake and ΔpH Shown by Several Chlorophyll-Protein-Lipid-Triton Mixtures with Electron Donors: Ascorbate, Ferrocyanide or Reduced Glutathione (all 5mM)

Mixture	O_2 Uptake (μ moles mg chl ⁻¹ hr ⁻¹)	ΔH^+
<i>Ascorbate</i>		
CPI	14	-41
CPI-lipid vesicles	118	-422
CPI in 0.1% Triton	142	-648
chlorophyll-lipid vesicles	194	-443
<i>Ferrocyanide</i>		
CPI	0	0
CPI-lipid vesicles	16	0.6
CPI in 0.1% Triton	10	0.6
<i>Reduced glutathione</i>		
CPI	3	0.6
CPI-lipid vesicles	28	4.0
CPI in 0.1% Triton	20	5.0

ber of a Clarke-type oxygen electrode. Alternate measurements of pH and O_2 were made with the same sample and red actinic light intensity of 70 W/m². The pH changes were all O_2 dependent and slowly reversible with ascorbate as the electron donor but not with ferrocyanide or GSH.

Subsequently we found that the addition to CPI of Triton X-100 above the critical micelle concentration (0.02%) would also cause an enhancement of the pH change or O_2 uptake (Table 23). One millimolar sodium azide inhibited all of these rates by about 30–50%. When the total pigments of spinach chloroplasts were extracted into organic solvents and a portion added to lecithin, chlorophyll-containing vesicles could be obtained free of any protein or P700. With ascorbate these vesicles also showed high rates of O_2 and H^+ uptake inhibited by azide. If the CPI vesicles were heated to 70°C for 5 min, all photooxidizable P700 was destroyed, but high rates of O_2 and H^+ uptake were still observed (not shown). Therefore, we must conclude that these reactions are caused by lipid-solubilized

chlorophyll (Krasnovsky, 1960; Vernon, 1961) and have little relationship to photosystem I activity in vivo. They are probably also similar to the O_2 consumption by illuminated chlorophyll vesicles reported by Stillwell and Tien (1977).

In addition we investigated another photosystem I reaction, proposed by Shneyour and Avron (1971) and Vernon and Shaw (1972), which involves the light-induced disproportionation of diphenylcarbazone (DPCN). Identical samples containing 2.5mM DPCN were placed in a Perkin-Elmer Spectrophotometer where one of the samples could be illuminated from the side with red light (max. intensity = 200 W/m²). The cuvettes of special design have a path length of 1 cm for the measuring light but only 2 mm for the actinic light. Thus about 0.4 ml of sample can be totally illuminated in the path of the measuring light. The rate of decrease in absorbance of DPCN at 485 nm was recorded. An extinction coefficient of 1.8mM⁻¹ cm⁻¹ at pH 7.8 was used to determine the rate of disproportionation.

The DPCN disproportionation rates of several different chlorophyll-containing samples are shown in Table 24. The differences between the two CPI preparations may reflect varying amounts of aggregation because the first CPI preparation was obviously cloudy at the time of the experiment. However, it appears that incorporation of chlorophyll into lipid or detergent phases enhances its activity; and there is no evidence that P700 is necessary. Recently Gross and Grenier (1978) reported the stimulatory effect of cations on DPCN disproportionation at low-light intensities with a CPI in Triton. Because 7mM KCl can enhance the activity of chlorophyll-lipid mixtures in Triton (Table 24) the conclusion of these authors that cations regulate the energy flow between antenna chlorophylls and the photosystem I reaction centers needs to be reevaluated.

All of the values in Table 24 are more

TABLE 24. Rates of DPCN Disproportionation Shown by Two Different Preparations of CPI and CPI-lipid Vesicles, CPI-Triton Micelles, and Chlorophyll *a* + *b*-lipid- Triton Mixtures

Sample	Activity (mmoles mg chl ⁻¹ hr ⁻¹)
1. CPI	131
CPI* (actinic intensity = 100 W/m ²)	100
CPI-lipid vesicles	135
CPI in 0.1% Triton	399
2. CPI	437
CPI-lipid vesicles	689
3. chlorophyll <i>a</i> + <i>b</i> -lipid vesicles	117
chlorophyll <i>a</i> + <i>b</i> + lipids in 0.1% Triton	175
chlorophyll <i>a</i> + <i>b</i> + lipids in 0.1% Triton, 7mM KCl	205

See text for description of measurement
Actinic light intensity = 200 W/m² except for *.

than one hundred times greater than those reported by either Shneyour and Avron (1971) or Vernon and Shaw (1972)—even without plastocyanin, which they reported to be necessary for the reaction. The most reasonable explanation for all these results is that chlorophyll, dispersed in lipid or detergent, is able to catalyze the photoreduction of O₂ to O₂⁻, and the latter causes the disproportionation. To provide additional support for this hypothesis, we measured the absorption of DPCN at 485 nm before and after the addition of xanthine and xanthine oxidase (an O₂⁻-generating system) and observed a decrease in absorption which indicates that O₂⁻ can indeed induce the disproportionation.

In a preliminary experiment we measured the rate of nitro blue tetrazolium reduction (absorption increase at 560 nm) when a suspension of chlorophyll-lipid vesicles with 0.5mM ascorbate was illuminated with red light (200 W/m²). This experiment was analogous to the

Beauchamp and Fridovich (1971) assay for SOD, but with substitution of the vesicles for the xanthine-xanthine oxidase O₂⁻-generating system. We observed a light-induced rate-of-absorption increase of 0.0186 OD min⁻¹ that decreased to 0.0144 upon the addition of about 200 units of SOD. The results support the hypothesis that O₂⁻ is the key component in many of these chlorophyll-photosensitized reactions and also explains the very high light intensities required to saturate the rates.

That O₂⁻ can be formed under certain conditions in chloroplasts following the photooxidation of P700 is plausible (Allen and Hall, 1974; Epel and Neumann, 1973; Elstner and Kramer, 1973) and the protective effect of SOD likely. However, our results strongly suggest that various treatments can cause some of the antenna chlorophylls to become photoreactive and able to catalyze the formation of O₂⁻ which in turn can cause an apparent but artifactual enhancement of real photosystem I activity.

REFERENCES

Allen, J. F., *FEBS Lett.* 84, 221-224, 1977.
Allen, J. F., and D. O. Hall, *Biochem. Biophys. Res. Comm.* 58, 579-585, 1974.
Beauchamp, C., and I. Fridovich, *Anal. Biochem.* 44, 276-287, 1971.
Bengis, C., and N. Nelson, *J. Biol. Chem.* 250, 2783-2788, 1975.
Elstner, E. F., and R. Kramer, *Biochim. Biophys. Acta* 314, 340-353, 1973.
Elstner, E. F., and A. Heupel, *Planta* 123, 145-154, 1975.
Epel, B. L., and J. Neumann, *Biochim. Biophys. Acta* 325, 520-529, 1973.
Evans, M. C. W., S. G. Reeves, and R. Cammack, *FEBS Lett.* 49, 111-114, 1974.
Evans, M. C. W., C. K. Sihra, J. R. Bolton, and R. Cammack, *Nature* 256, 668-670, 1975.

- Gross, E. L., and J. Grenier, *Arch. Biochem. Biophys.* 187, 387–398, 1978.
- Krasnovsky, A. A., *Annu. Rev. Plant Physiol.* 11, 363–410, 1960.
- Malkin, R., *Arch. Biochem. Biophys.* 169, 77–83, 1975.
- Malkin, R., and A. J. Bearden, *Proc. Nat. Acad. Sci. U.S.A.* 68, 16–19, 1971.
- Shiozawa, J. A., R. S. Alberte, and J. P. Thornber, *Arch. Biochem. Biophys.* 165, 388–397, 1974.
- Shneyour, A., and M. Avron, *Biochim. Biophys. Acta* 253, 412–420, 1971.
- Stillwell, W., and H. T. Tien, *Biochim. Biophys. Acta* 461, 239–252, 1977.
- Tolbert, N. E., *Annu. Rev. Plant Physiol.* 22, 45–74, 1971.
- Vernon, L. P., *Acta Chem. Scand.* 15, 1639–1650, 1961.
- Vernon, L. P., and E. R. Shaw, *Plant Physiol.* 49, 862–863, 1972.

A DYNAMIC BINDING OF HCO_3^- TO CHLOROPLAST REACTION CENTERS IN THE LIGHT

Alan Stemler

Normal rates of electron flow through photosystem II depend on HCO_3^- ions bound to the reaction-center complex (Stemler, 1977). Studies were done to determine the effects of light on the binding of HCO_3^- .

Maize chloroplast fragments were depleted of endogenous HCO_3^- by the method already described (Stemler and Radmer, 1975). When such HCO_3^- -depleted grana are given exogenous HCO_3^- , restoration of oxygen-evolving ability takes place only in the dark (Fig. 31). The control sample (trace A) was illuminated for 30 sec, then given 10mM NaHCO_3 . The chloroplasts were then re-illuminated after a dark period of 2.5 min. As was expected (Stemler, 1977), a ten-fold increase in the rate of oxygen evolution was observed. HCO_3^- given to a dark-adapted sample (trace B) just 10 sec before the first illumination resulted in about 80% recovery. A subsequent dark period of 2.5 min restored full activity. In contrast, if the chloroplasts are illuminated with continuous light for 15 sec before the addition of HCO_3^- (trace C) and continuously thereafter, the grana evolve only slightly more oxygen than do the control (given no HCO_3^-).

Clearly, light prevents HCO_3^- from restoring normal rates of electron flow.

To find out how much light is required to block the effects of added HCO_3^- , chloroplasts were suspended in reaction mixture and dark-adapted for 5 min. The chloroplasts were then given 0–3 strobe-light flashes spaced 1 sec apart. Within 1 sec after the last flash, HCO_3^- was injected (to 10mM) and, 10 sec afterwards, saturating continuous light was applied. Figure 32 shows the percent recovery in oxygen-evolving ability as a function of flash number before HCO_3^- addition. About 80% recovery was observed in samples kept dark. One pre-illumination flash reduced recovery to about 58%. A second preilluminating flash, however, increased the recovery to about 70%. A third flash produced about the same results as the second. What is observed here is the first cycle of an oscillation in recovery based on flash number. The period of the cycle, 2, suggests that the negative charge accumulator on the reducing side of photosystem II, B (Bouges-Bocquet, 1973), is involved. It is proposed that HCO_3^- reactivates photosystem II only when B is in the completely oxidized state, since

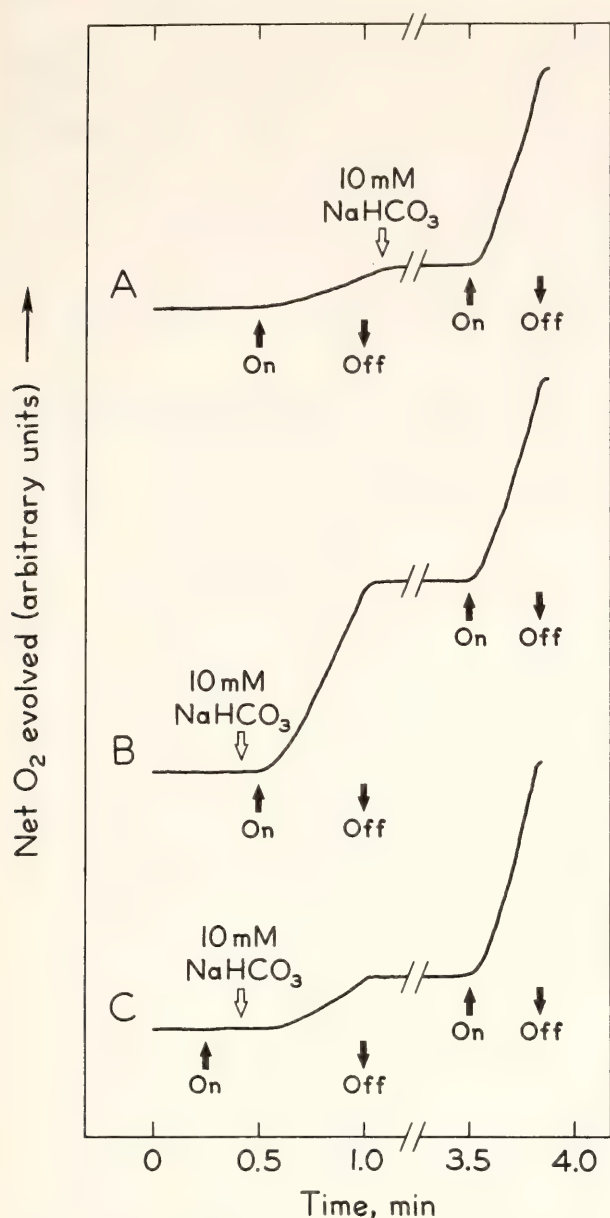


Fig. 31. Restoration of oxygen evolution in the dark with added HCO_3^- . HCO_3^- -depleted chloroplasts ($15 \mu\text{g chl ml}^{-1}$) were suspended in reaction mixture which contained 0.1M sodium phosphate, pH 6.8, 0.175M NaCl, 0.1M sodium formate. $\text{K}_3\text{Fe}(\text{CN})_6$ (final conc. 2mM) was injected into all samples at 0.5 min. Trace A: HCO_3^- was injected in the dark after the first light period. Trace B: HCO_3^- was injected in the dark 15 sec before the first light period. Trace C: HCO_3^- was injected 15 sec after the beginning of the first light period. Temperature: 24°C ; light intensity: $0.2 \mu \text{ einsteins} \cdot \text{cm}^{-2} \cdot \text{sec}^{-1}$.

the concentration of oxidized B varies in the same manner with flash number as does the percent recovery (Bouges-Bocquet, 1973).

Illuminated chloroplast membranes do not normally lose their bound HCO_3^-

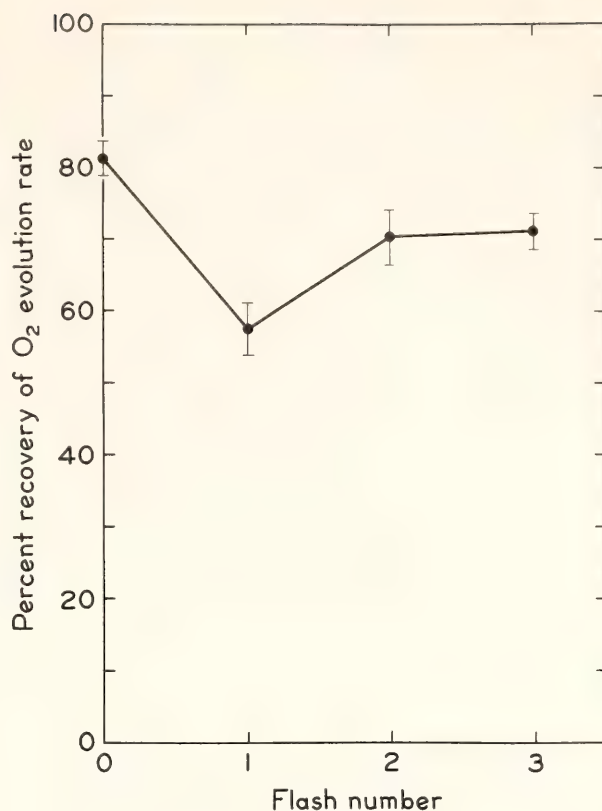


Fig. 32. Restoration of the rate of oxygen evolution as a function of flash number before addition of HCO_3^- . The HCO_3^- -depleted chloroplasts were suspended in the reaction mixture described in Fig. 31 and placed in the chamber of a Clark-type electrode. After 5 min dark adaptation, the grana were subjected to a varying number of light flashes from a strobe lamp. One sec after the last flash, HCO_3^- was injected to a final conc. of 10mM. 10 sec after addition of HCO_3^- , $\text{K}_3\text{Fe}(\text{CN})_6$ was injected (final conc. 2mM) and simultaneously the chloroplasts were illuminated with saturating light. 30 sec later, the light was turned off and the chloroplasts were allowed to reactivate completely in a subsequent 2.5 min dark period. The fully reactivated chloroplasts were given a second period of illumination. The percent recovery is the initial slope of the oxygen trace observed during the first period of continuous light divided by that observed during the second period (after complete recovery) $\times 100$.

while they are evolving oxygen. Under certain circumstances, however, bound HCO_3^- will be lost during illumination. The rate of electron flow will become dependent on exogenous HCO_3^- . The conditions required to induce HCO_3^- dependence in the light are high salt concentrations (0.175M NaCl, 0.1M sodium

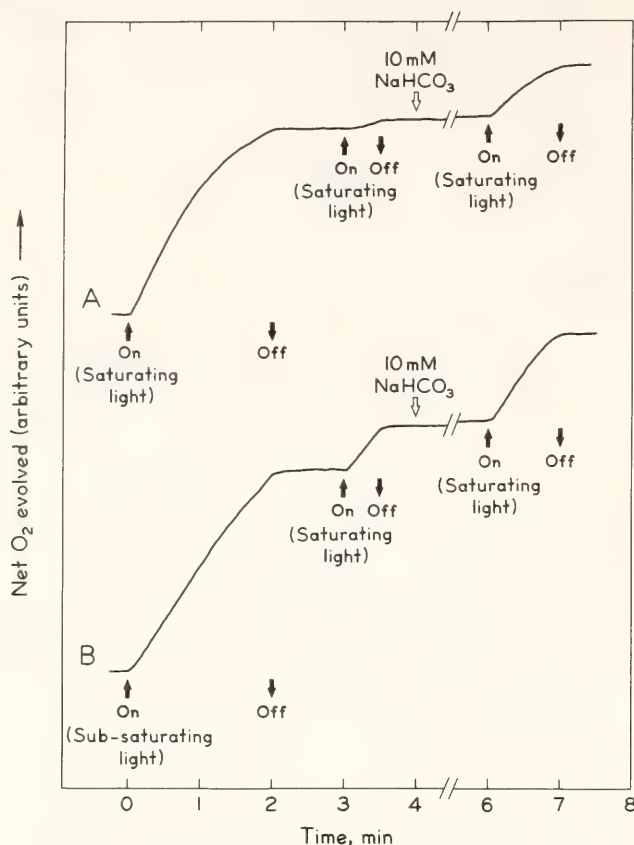


Fig. 33. The capacity of saturating light to increase dependence of oxygen evolution when HCO_3^- is added. Chloroplast fragments not previously HCO_3^- depleted were suspended in reaction mixture containing 0.1M sodium phosphate, pH 7.0, 0.175M NaCl, 0.1M sodium formate and 4mM $\text{K}_3\text{Fe}(\text{CN})_6$. The saturating light intensity was $0.4 \mu \text{ einsteins} \cdot \text{cm}^{-2} \cdot \text{sec}^{-1}$. Sub-saturating light was obtained by passing saturating light through a 5% neutral density filter. Sample A received saturating light throughout. Sample B received subsaturating light during the first 2-min illumination period, and saturating light thereafter.

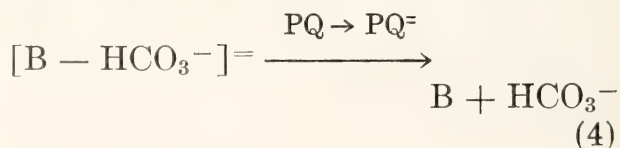
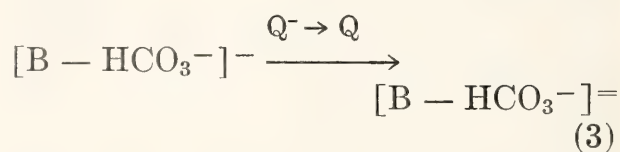
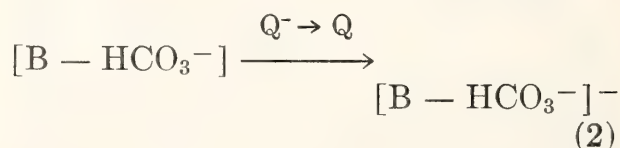
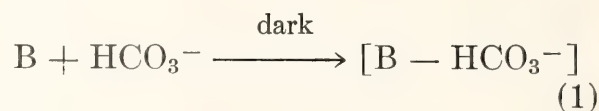
formate) and the presence of a Hill oxidant (Stemler and Govindjee, 1974). A third important requirement is high light intensity. This last requirement is shown by the data in Fig. 33.

Chloroplasts were suspended in reaction mixture that contained high salt concentrations and the electron acceptor ferricyanide. Sample A (Fig. 33) was illuminated with saturating light intensity for 2 min. The rate of oxygen evolution was high at first but declined rapidly as

HCO_3^- was lost from the reaction-center complex. A second period of illumination (3–3.5 min) caused very little oxygen evolution. When HCO_3^- was added to the reaction mixture in a subsequent dark period and the chloroplasts were illuminated a third time (6–7 min), a four-fold increase in oxygen evolution was observed.

Sample B was illuminated for 2 min at a light intensity slightly below saturation. These chloroplasts evolved oxygen linearly with time and little if any dependence on exogenous HCO_3^- developed. This result indicates that it is necessary for photosystem II reaction centers to be turning over at their maximum rate for bound HCO_3^- to escape.

The results reported here suggest that the relationship between the HCO_3^- ligand and the photosystem II reaction center (via the intermediate B) is a dynamic one. The following reactions are proposed:



HCO_3^- forms a complex with B in a "dark" reaction (1). Two molecules of Q^- the acceptor to photosystem II react sequentially with the complex (reactions 2 and 3). When the complex is doubly reduced, electrons are transferred

to plastoquinone (PQ) and the complex is split, yielding B and free HCO_3^- (reaction 4). Normally these two products, B and HCO_3^- , instantly reform a complex (reaction 1). Thus a cyclic process is established in which HCO_3^- plays a "catalytic" role. The reason for the dynamic nature of HCO_3^- binding is not yet known, and further work is required. These studies are described in greater detail elsewhere (Stemler, 1978).

REFERENCES

- Bouges-Bocquet, B., *Biochim. Biophys. Acta* 314, 250–256, 1973.
Stemler, A., and Govindjee, *Plant Cell Physiol.* 15, 533–544, 1974.
Stemler, A., and R. Radmer, *Science* 190, 456–458, 1975.
Stemler, A., *Biochim. Biophys. Acta* 460, 511–522, 1977.
Stemler, A., *Biochim. Biophys. Acta*, in press, 1978.

BIBLIOGRAPHIC INFORMATION RETRIEVAL

J. S. Brown

A computerized bibliographic file of photosynthesis research literature supported by the Department currently contains about 9000 references. The file can be searched by category or author. Categories are listed in a thesaurus that was published in *Year Book* 72, p. 407, and added to in *Year Book* 75, p. 479. A note about the file and another listing of the thesaurus was also published in *Photochemistry and Photobiology* 28, 113–114, 1978.

Beginning in late June 1978 our "Plantbio" file will be continually online and can be searched by anyone having access to Stanford's computer. The Stanford Ballots Library Automation and Information Retrieval System is

supporting the storage costs of keeping the file active, and the Department is responsible for continuing to build it. We urge students of photosynthesis to contact the Associate Director for Library Services, Ballots Center, Encina Commons, Stanford University, Stanford, CA 94305, to obtain instructions for using this bibliography.

Scientists in England may be interested to know that Professor Richard Gregory, Department of Biochemistry, University of Manchester, has a copy of our "Plantbio" file complete up to January 1978. By use of a title-word search program, individual references can be retrieved from this copy.

A CENTRALIZED LABORATORY COMPUTING SYSTEM

Glenn A. Ford and Benny Catanzaro

INTRODUCTION

A centralized computer system designed to aid research at the Department of Plant Biology has been under development for several years. The system we are using, which is within the financial

reach of most research laboratories, has proved extremely versatile in its ability to provide real-time data acquisition from a number of spectrophotometers as well as to allow savings on computations for which this laboratory had previously contracted.

HARDWARE

The focal point of this in-house computer system is a Hewlett-Packard 2116C minicomputer with a core memory of 32,000 16-bit words. Interfaced with the computer is a Hewlett-Packard 7900 dual disk drive, one fixed and one interchangeable cartridge, providing storage for an additional 2.5 million words of on-line, rapidly accessible information.

The system is equipped with three communication terminals: a Teletype ASR-33 running at 10 characters/second and producing a permanent record; a DECwriter LA36 running at 30 characters/second and producing a permanent record; and an ADM-3, a cathode-ray tube terminal operating at 120 characters/second. Additionally, information may be provided to the machine through a high-speed papertape reader (HP2748B).

The data acquisition peripherals consist of one HP91000A analogue data subsystem and two HP12566B microcircuit interface cards. The latter cards provide the system with its capabilities for digital interfacing. Each of these cards permits 16 bits of buffered digital input and output. One of these cards is currently dedicated to a programmable pacer of our design. This pacer subsystem is used to synchronize data collection with external events and to regulate the rate of analogue-to-digital or digital-to-analogue conversion. The digital output of this card provides computer control of the sampling frequency, while the digital input allows the computer to determine the current sampling rate. The output side of the second digital card is wired to a 12-bit digital-to-analogue converter. The remaining four output bits are used as control signals for the pacer system (pace data in, pace data out, wait for trigger, etc.). The input side is interfaced to a curve digitizer allowing for off-line entry of analogue recorder tracings (see *Year Book* 67, 1968).

Analogue-to-digital conversion of up

to eight different channels takes place with 12-bit resolution and can be externally sampled by the pacer subsystem at rates up to 20 KHz. Analog output is achieved with a 12-bit digital-to-analogue converter, as mentioned above. Again the pace of data conversion can be made relatively slow with the pacer subsystem for monitoring via X-Y plotter, or it can be allowed to proceed at maximum speed for monitoring via a storage oscilloscope or other fast device.

A number of cables suitable for either digital or analogue data transmission run from most of the laboratories at the Department and are terminated at a junction box in the computer room, facilitating instrumentation interfacing.

SOFTWARE

Operator control of the computer and its peripheral hardware is achieved through the HP operating system, Real-Time Executive II (RTE-II), and a file management system (BSM). RTE-II provides for foreground/background computing (essentially it enables two programs to reside in computer memory simultaneously). This arrangement allows real-time data acquisition in the foreground and data reduction in the background to proceed concurrently. Multiprogramming (the ability to execute several programs concurrently on a priority basis) is supported by sending out to the disk a program waiting for an input-output operation, and replacing it with another compute-bound job in a matter of milliseconds. The overall advantage of the software operating system is that several researchers may use the system simultaneously and have it appear as though total resources are dedicated to their particular study.

The file management system provides for simplified methods for storing and retrieving complex information such as spectral data as well as simple text-style data on the disk. Additionally,

batch (noninteractive) jobs may be "spooled" to and from the disk under control of this software system. The spooling system assures that incoming jobs are stored on the disk until the computer is free to execute them, and output from an executing program is stored on the disk until the desired printer or other output device is available.

Currently the system supports ALGOL and FORTRAN IV compilers and an Assembler. Also provided is a text editor for ease of modifying program, data, and manuscript text.

We have compiled a library of high-level interactive programs to give the researcher access to computer techniques for data acquisition and data reduction with a minimum knowledge of computer hardware and software concepts. A brief familiarity with a few of the available programs provides him with command of the full program library. Thus he is rapidly in control of most interfaced instrumentation and many data-manipulation routines.

INSTRUMENTATION

Currently a Perkin-Elmer MPF-3L spectrofluorimeter, a Perkin-Elmer 356

dual beam-split beam spectrophotometer, and specialized instrumentation for the study of kinetics are on-line with the computer system. Applications of these computer-enhanced instruments can be found in this and previous reports from the Department. Resources are available for additional interfacing of instruments to provide computer analysis of data.

LIMITATIONS

The major limitation of the system as it now stands is that only one real-time experiment can be conducted at a time. Although background data reduction and foreground data acquisition may proceed concurrently, only one instrument can access computer resources at any one time. This limitation requires completion of one job before another instrument can request data servicing.

The limitation of the present system was anticipated, as it was in part intended to permit us to test the potential utility of such a system and to test some of the proposed interfacing techniques. Software upgrading and hardware enhancements involving low-cost microprocessor buffering are under development to alleviate this limitation.

COMPUTER ANALYSIS OF KINETIC DATA

Glenn A. Ford, Benny Catanzaro, and David C. Fork

To achieve more rapid and accurate data-handling capability we have been using computer analysis methods on analogue signals obtained during measurements of light-induced absorbance or fluorescence changes. We used this data-handling capability as an aid in studying the effects of temperature on photosynthesis at the membrane level.

For this application we needed values for the reciprocal of the rates of various physiological functions as a function of the reciprocal of the absolute tempera-

ture (Arrhenius plot). Arrhenius plots of activities of some membrane-bound enzymes show discontinuities and/or changes of slope of the lines at the temperature of phase transitions (Raison *et al.*, 1971; Linden *et al.*, 1973; and Watson *et al.*, 1975). It is useful in experiments of this type to be able to change the temperature slowly (usually at a rate of about 1°C/min) while giving repeated exposures to actinic light.

Figure 34B is a graphic representation of the type of absorbance change seen

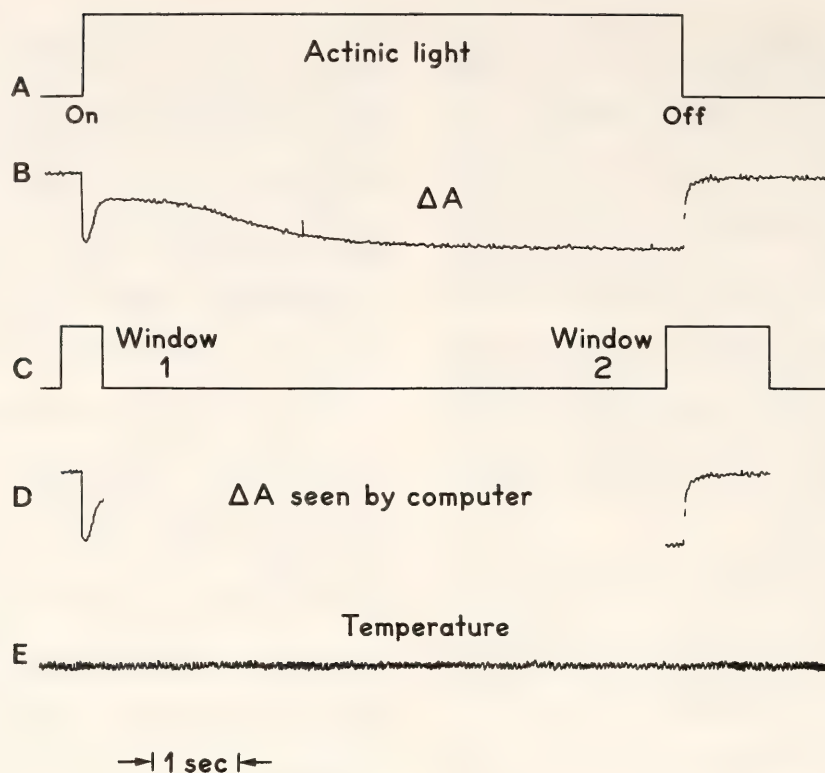


Fig. 34. A diagrammatic presentation of signals produced for computer analysis of the kinetics of light-induced absorbance changes. *A* is the output of the photocell monitoring the actinic lamp; *B* is the full time-course absorption curve provided by the photomultiplier; *C* depicts the square-wave window signals used to limit data acquisition to intervals of interest; *D* is the time-course of the absorbance change as "seen" when the windows are used; and *E* is the output of the thermocouple measuring the cuvette temperature.

in a blue-green alga during measurements of light-induced redox changes of cytochrome *f* (cf. Fig. 11, *Year Book* 76, p. 224). Until recently, kinetic data of this type were obtained with a high-speed oscillographic recorder. Data analysis was done manually at the end of the experiment to obtain the desired rate measurements.

Computer interfacing of this instrumentation has eliminated not only this laborious manual process but also the bias in estimating the rates. In addition, rapid computer analysis allows one to use a single sample to obtain a large number of data points and to observe the course of the experiment while it is in progress.

METHODS

Four channels of data were examined during the experiment: the output of the photomultiplier that provided the ki-

netics of absorption changes (Fig. 34B); the output of a photocell that monitored on/off transitions and intensity of the actinic light (Fig. 34A); the output of a thermocouple that measured the temperature inside the sample cuvette (Fig. 34E); and a "window" signal that functioned to limit computer analysis to areas of interest along the time course of the absorbance change (Fig. 34C, D).

Experiments on electron transport done by measuring light-induced cytochrome *f* oxidation in the thermophilic blue-green alga *Synechococcus lividus* showed that during a period of illumination there was a transient reduction of cytochrome *f* in the light that was produced by excitation of photosystem II (*Year Book* 76, 222–226). This transient reduction was temperature sensitive. To obtain the Arrhenius plot for the effect, we needed values related to the rate of the transient reduction. For this purpose

we measured the time required for the change to decrease by one quarter of its initial magnitude (a in Fig. 34B).

In addition, we wanted to measure the rate of reduction of cytochrome f in the dark after the actinic light was turned off. For these measurements long periods of actinic illumination (8–30 sec) were used so that steady-state conditions of electron transport were attained. Under these conditions, and at favorable temperatures, the half-times for cytochrome f reduction were around 10 msec. Although our instrumentation provided us with a means of accurately measuring rates within $\pm 150 \mu\text{sec}$, we had available a maximum of 1024 data points—a limitation imposed by the software system. Thus, in order to avoid the loss of resolution from spreading the 1024 points over a long period of illumination, we needed a means of using these points only during intervals of interest along a time-course of absorption change. Therefore, a fourth channel was used that monitored the output from two square-wave “electronic windows,” variable in width and distance apart. These windows controlled the system so that data acquisition occurred only when the windows were “open” or in the high state. Since the computer analyzed a much smaller portion of the analogue signal when the windows were used, the analogue-to-digital conversion took place at a much higher frequency, giving increased resolution.

Figure 34D shows the A curve as “seen” by the computer when the 1024 points were restricted to time intervals of interest. Although not shown in Fig. 34, the actinic light and temperature data points were similarly restricted to time portions defined by windows 1 and 2. After coarse adjustment of the windows to coincide with desired portions of the time course of an absorption change, an accurate computer measurement of the window widths was made with a high-resolution calibration program. The

combined width in time of both windows provided information as to the optimum frequency at which A/D conversions should take place to cover the entire set of data with the available points. In addition, a measurement of the width of each window was needed to define the end of the ΔA data representing the transient reduction of cytochrome f in the light (first window) and the beginning of the ΔA data representing the reduction of cytochrome f in the dark (second window). These termination and start values were logged as the point numbers of the 1024-point data array. These values were not successive because a few points were deleted between the sets of data to act as a buffer and ensure validity of analysis.

For computer analysis the first three channels of analogue data were transmitted to the computer via the 91000A analogue data subsystem (Ford and Catanzaro, this Report). With the pacer subsystem each of the channels was converted to an array of digital points equidistant in time as defined by the sampling frequency and such that identically numbered points across each array were coincident in time with each other.

Analysis proceeded by examination of the data points between the limits previously determined by the window settings. For data coming from the light channel, the precise points for the start and finish of actinic illumination and for the average light intensity were required. These values were found by scanning the data array sequentially until a point was located that exceeded a predefined voltage. The number of the point associated with this value was defined as the light-on time (LON). Light intensity was determined as the difference in voltage between the averaged points before and after LON (after discarding sufficient points to ensure that the light signal had attained a stabilized value). The point corresponding to light-off (LOFF) was found by scanning the light channel be-

ginning at the start point of the second window until a value was found that was less than a predefined percentage of the averaged light intensity.

The analysis then focused on the points lying within the two windows, obtained from the ΔA channel transmitting the photomultiplier signal. The absorbance baseline in the dark was obtained by averaging the points before LON. After the maximum ΔA occurring within the first window was found, the rate of a transient OD change in the light could be determined. For example, we wanted to measure the relative rate of cytochrome *f* reduction (absorbance increase) in the light. For this purpose we arbitrarily chose the time required for the change to recover 25% of its maximum negative deflection. This time could readily be found by scanning the points until the chosen magnitude was found and computing the time required to come to this point.

Similarly, the half-time for the decay of the cytochrome *f* change in the dark was found by examining the ΔA points lying within the second window. In this case, a large enough number of points prior to LOFF were averaged to provide the steady-state ΔA obtained during the light. In addition, enough points at the very end of the array were averaged to obtain the dark-absorbance base line. The difference between these two averages constituted the steady-state light-induced absorbance change just before the light was turned off. Scanning the points after LOFF until a value equal to 50% of the steady-state level had been reached and computing the time

elapsed at this point since LOFF provided the half-time of the recovery.

Measurements of temperature during the course of an experiment were provided by averaging the array of points obtained from the thermocouple channel and applying an appropriate conversion equation.

All of these data, along with appropriate reciprocals needed for Arrhenius plots and the time at which each measurement was made, were logged in tabular form by a high-speed communications terminal. At this point the computer was re-initialized and was ready for another round of data acquisition and computation upon command from the instrumentation.

This system has proved to be satisfactory for precise resolution of the kinetics of light-induced absorbance changes. With these methods it has been possible to obtain and plot the results during the course of an experiment. The system is an especially flexible one, able to analyze absorbance changes having very different kinetics. In addition, it is clearly possible to analyze other parameters of photosynthesis, such as fluorescence time-courses.

REFERENCES

- Linden, C. D., K. L. Wright, H. M. McConnell, and C. F. Fox, *Proc. Nat. Acad. Sci. U.S.A.* 70, 2271-2275, 1973.
 Watson, K., E. Bertoli, and D. E. Griffiths, *Biochem. J.* 146, 401-407, 1975.
 Raison, J. K., J. M. Lyons, and W. W. Thompson, *Arch. Biochem. Biophys.* 142, 83-90, 1971.

PERSPECTIVES ON THE EVOLUTION OF PLANT DNA

William F. Thompson

As we continue to study DNA sequence organization we are more and more impressed by the need for an evolutionary

perspective in interpreting the results. In organizing the presentation for this year's Annual Report, therefore, it oc-

curred to me that I should review some of the background for this perspective—particularly for those readers whose principal interests lie in other fields of plant biology.

It is natural for most of us to think of DNA pretty much exclusively in terms of genes and controlling elements. However, if genes and controlling elements actually accounted for all of the DNA in different organisms, we would expect DNA content to be rather directly correlated with organismic complexity. Evolution of more elaborate developmental and physiological processes in more complex organisms should require the evolution of more genes and/or more complex regulatory networks; if most of the DNA in most organisms were functioning in this way, there should be at least an approximate correlation between DNA content and evolutionary sophistication.

Indeed, the minimum DNA content for various major taxa does increase in a more or less regular fashion with increasing complexity (Sparrow *et al.*, 1972). These minimum DNA values might be regarded as indications of the amount that is essential for genes and controlling elements at each level of complexity. However, an even more striking feature of the distribution of DNA contents among organisms is the tremendous range of variation encountered even among those with similar biological complexities. Eukaryotic animals generally contain between 1 and 5 pg of DNA per haploid genome, but the range for salamanders extends up to 100 pg or so and primitive vascular plants may contain as much as 300 pg (Hinegardner, 1976). More advanced vascular plants frequently have much lower genome sizes than psilopsids and ferns, although there is still a nearly 100-fold variation among the angiosperms. Significant differences are seen even within more restricted taxonomic groups such as genera. One well-known example of

intrageneric variation is found in *Vicia*, where DNA contents differ by up to seven-fold even among diploid species with $2n=14$ chromosomes (Chooi, 1971; Bennett and Smith, 1976). On the basis of studies of the life-history features of herbaceous angiosperms with different DNA contents, Bennett (1972) concluded that "nuclear DNA content is not positively correlated either with the amount or the sophistication of genotypic control exercised during development."

In those cases in which information is available, most of the structural genes appear to be composed of single-copy sequences. Thus it is reasonable to ask whether the content of single-copy DNA might not be more directly correlated with organismic complexity. However, examination of the available data for plants (Table 25) and animals (e.g., Davidson *et al.*, 1975) indicates the absence of any clear evolutionary trend even for single-copy DNA. For example, the mung bean has a very low value and the broad bean a very high one, even though the two species are closely related. Thus a wide range of variation exists (even after correction for polyploidy) which would be quite difficult to relate to evolutionary advancement or developmental complexity. Similar discrepancies are observed among animals, as well. For example, both snails and toads have almost as much single-copy DNA as mammals and about 20 times as much as some insects.

Several lines of evidence (reviewed by Britten and Davidson, 1976) also lead to the conclusion that most single-copy DNA sequences are evolving rapidly and are at least relatively free from the constraints of natural selection. Nucleotide substitutions in primate single-copy sequences accumulate at rates consistent with those inferred from studies of the most rapidly changing (selectively unconstrained?) protein sequences, and changes in single-copy

TABLE 25. Total and Single-Copy DNA Contents for Higher Plants

Species	Ploidy, <i>x</i>	Haploid DNA Content*		Single-Copy DNA†		
		NTP × 10 ⁻⁹	REF.	Percent	REF.	NTP × 10 ⁻⁹
1. <i>Vigna radiata</i> (mung bean)	2	0.5	1	70	1	0.4
2. <i>Gossypium hirsutum</i> (cotton)	4	0.8	2	68	2	0.5
3. <i>Glycine max</i> (soybean) embryo DNA	4	1.1	10	60	3	0.7
leaf DNA				39	4	0.4
4. <i>Petroselinum sativum</i> (parsley)	2	1.9	5	30	5	0.6
5. <i>Nicotiana tabacum</i> (tobacco)	4	2.0	11	45	6	0.9
6. <i>Avena sativa</i> (oat)	6	4.3	11	25	7	1.1
7. <i>Pisum sativum</i> (pea)	2	4.8	11	30	8	1.4
8. <i>Hordeum vulgare</i> (barley)	2	5.4	11	30	7	1.6
9. <i>Triticum aestivum</i> (wheat)	6	5.6	11	25	7	1.4
10. <i>Secale cereale</i> (rye)	2	8.6	11	25	7	2.2
11. <i>Vicia faba</i> (broad bean)	2	13.0	11	20	9	2.6

- 1. Murray and Thompson, in preparation
- 2. Walbot and Dure, 1976
- 3. Gurley, 1976
- 4. Goldberg, 1978
- 5. Kiper and Herzfeld, 1978
- 6. Zimmerman and Goldberg, 1977
- 7. Flavell *et al.*, 1977
- 8. Murray and Thompson, submitted for publication
- 9. Taylor and Bendich, personal communication
- 10. Sparrow and Miksche, 1961
- 11. Bennett and Smith, 1976

* Where possible, values for DNA content have been taken from cytophotometric measurements. The genome sizes for mung bean and cotton were estimated from the reassociation kinetics of single-copy sequences.

† Calculated from the indicated values for haploid genome size and percentage of single-copy sequences.

DNA are frequently employed as a kind of “molecular clock” in studies of molecular phylogeny. In both rodent and sea urchin species it is possible to show that the bulk of the single-copy DNA has diverged more rapidly in evolution than have those sequences known to code for messenger RNA (Rosbash *et al.*, 1975; Angerer *et al.*, 1976).

It would appear, therefore, that most single-copy sequences are free to vary quite rapidly in evolution and that the amount of single-copy DNA in a given organism is not an indication of its biological complexity. However, Fig. 35 shows a remarkably consistent relationship between the amount of single-copy DNA and the total genome size in a

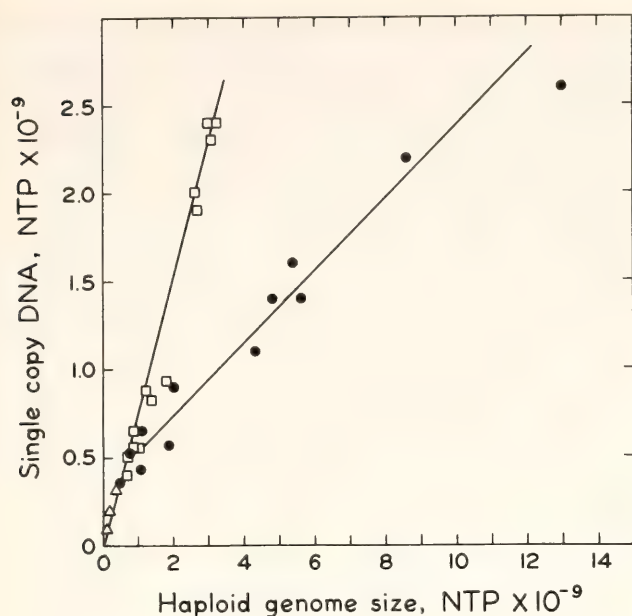


Fig. 35. Single-copy DNA content as a function of total genome size in plants (filled symbols) and animals (open symbols). Data for plants are from Table 25. The majority of the data for animal genomes was taken from Davidson *et al.* (1975). Values for single-copy DNA are based on measurements by techniques, such as S-1 nuclease resistance or optical hyperchromicity, which are not influenced by repetitive sequence interspersion.

variety of plant and animal species. The consistency of this relationship is quite surprising, as is the clear difference between plants and animals which becomes apparent at genome sizes above about 10^9 nucleotide pairs. A working hypothesis might be that increases in total genome size reflect periodic additions of repetitive sequences, while single-copy DNA accumulates by gradual evolutionary divergence of these repeats. According to this hypothesis, base substitutions in the members of a given repeated family would cause the sequences of that family to become more and more different from one another. Eventually the differences would become so great as to prevent cross reactions between different family members under standard *in vitro* reassociation conditions; such sequences would then be recognized operationally as single-copy sequences, able to reassociate only with their exact complements.

Such an analysis suggests that the dif-

ferent slopes of the curves for plants and animals in Fig. 35 might be attributed to a higher rate of repeated-sequence addition to plant than to animal genomes. Given similar rates of sequence divergence by base substitution, more frequent addition of repeats would lead to a higher "steady state" percentage of repetitive DNA. Frequent amplifications might also help to explain the large and variable sizes of plant genomes. Flavell *et al.* (1977) have recently provided direct evidence for relatively frequent amplification and reamplification events in the evolution of the wheat genome. The tandemly repeated sequences expected as the initial result of amplification events might be subject to rapid increases or decreases related to chromosomal events such as unequal crossover (Smith, 1976). However, the many repetitive families whose members are extensively interspersed among other sequences in the genome would be less subject to deletion and would therefore be likely to persist during very long periods of evolution.

This hypothesis suggests that repetitive sequences undergo gradual evolutionary divergence after their original incorporation into the genome. One might therefore expect to find a more or less continuous distribution of pairing precision among reassociated repetitive sequence duplexes. In fact, such duplexes typically do melt over a wide range of temperatures, indicating that large differences in pairing precision exist. More detailed analyses of melting profiles for pea repetitive sequences (Cuellar *et al.*, this *Year Book*) indicate that these broad distributions can be resolved into theoretical thermal denaturation components in much the same way that theoretical kinetic components can be fitted to reassociation data. We recognize that, as in the case of kinetic components, "solutions" generated in this way may be oversimplifications. However, analysis of these melting curves in terms of

discrete theoretical components provides a useful descriptive tool and should greatly facilitate future studies of sequence divergence in complex populations of repeated sequences. We believe such studies will ultimately provide important clues to the evolutionary history of repetitive DNA families.

A related prediction from the "gradual divergence" hypothesis is that the fraction of DNA in a given genome which reassociates with single-copy kinetics should vary inversely with the stringency of reaction conditions chosen for the experiment. As the criterion for recognition of sequence homology is raised (by raising the reassociation temperature, for example), the more divergent repetitive sequences would no longer be able to cross-react with one another. However, they would still be able to react with their exact complements from the opposite DNA strand and would therefore behave as single-copy sequences. The reverse effect, a decrease in the fraction of single-copy sequences, should also be observed as the temperature is lowered—provided that the distribution of repetition precision extends to sufficiently low levels of homology.

Surprisingly little experimental data bearing on this question is available at present, and most of it deals with plant DNA. Bendich and McCarthy (1970) observed that the fraction of wheat DNA reassociating with single-copy kinetics varied from zero to 50% as the stringency of the reaction conditions was increased. Similar results have recently been obtained by Flavell and Smith (1976) for wheat DNA, and by Smith and Flavell (1977) for rye DNA. Bendich and Anderson (1977) showed that the most rapidly renaturing major repetitive components of DNA from four unrelated plant species showed a similar variation depending on reassociation criterion.

A study of mung bean DNA has also indicated that the fraction reassociating

as repetitive sequences is a sensitive function of reassociation conditions (Preisler and Thompson, this Report). In addition, careful analysis of reassociation at a series of temperatures also revealed kinetic heterogeneity in what initially had by conventional analysis (Murray, Preisler, and Thompson, *Year Book* 76, 240–246; Murray and Thompson, unpublished) appeared to be a single, uniform repeated component.

This kinetic heterogeneity seriously complicated our attempts to analyze the pattern of sequence divergence in individual families of mung bean repetitive DNA. Our present experience suggests that future approaches to this problem must recognize that a complex distribution of repetitive families reassociating at different rates is likely to exist in most plant genomes.

Continuing our investigations of sequence organization in the pea genome (Murray and Thompson, this Report), we have carried out much more complete analyses of reassociation kinetics and of the interspersion of repetitive and single-copy sequences. The reassociation kinetics are complex; discrete components cannot be resolved by simple fractionation techniques, and our data are better explained by assuming that repetitive sequences exist in a variety of different frequency classes. Interspersion of repetitive DNA sequences is more extensive than has previously been reported in any organism. The majority of the single-copy sequences appear to be only 300–400 nucleotides long, and we can find no evidence for a significant fraction longer than about 1000 nucleotides. Repetitive sequences therefore seem to be interspersed throughout the entire pea genome at intervals of less than 1000 nucleotides.

The length distribution of repeated sequences, as determined by analysis of the lengths of reassociated repeated sequences resistant to the single-strand-specific nuclease "S1" (Murray, Cuellar,

and Thompson, 1978), was somewhat similar to that for single-copy sequences. The predominant length was on the order of 300–400 nucleotide pairs, although the distribution was quite broad and included a small amount of material several thousand nucleotide pairs long. Since the fraction of single-copy DNA in the pea genome is quite small (about 30% at a standard criterion), we can calculate that many regions of repetitive DNA must be longer than 300–400 nucleotide pairs. Thus we believe that many of the short repetitive sequences in pea DNA must be interspersed with different repeats in a permuted tandem arrangement similar to that which has been demonstrated in wheat DNA (Smith *et al.*, 1976).

Reviewing the available literature and our own findings, we find general support for the view of Hinegardner (1976) that most plant and animal genomes contain large amounts of “secondary” DNA sequences. Secondary DNA would lack any strongly sequence-dependent function and thus would be expected to evolve rapidly. Its evolution would probably reflect many different processes, including amplification, deletion, and transposition events in addition to base substitutions. Transposition events would lead to the widespread interspersion of repeated sequences typical of eukaryotes (Britten and Davidson, 1976). In pea DNA our evidence suggests that transposition has been so extensive that a majority of both repetitive and single-copy sequence elements are now only a few hundred nucleotides long.

The existence of a large amount of secondary DNA that is free to evolve rapidly suggests that the organization and function of higher plant genomes must be studied and understood in an evolutionary as well as a developmental context. We must bear in mind that patterns of sequence repetition and arrangement may arise largely or entirely from stochastic processes rather than by se-

lection for genotypic or phenotypic functions. At the same time, evolution of genotypic functions must proceed in genomes characterized by complex patterns of sequence repetition and interspersion. Since it is logical to suppose that genotypic functions may have evolved to utilize features of these patterns, there may be an intimate relationship between genome organization and function even though most of the DNA may be genotypically inactive at present.

REFERENCES

- Angerer, R. C., E. H. Davidson, and R. J. Britten, *Chromosoma (Berl.)* 56, 213–226, 1976.
- Bendich, A., and R. S. Anderson, *Biochem.* 16, 4655–4663, 1977.
- Bendich, A. J., and B. J. McCarthy, *Genetics* 65, 545–565, 1970.
- Bennett, M. D., *Proc. Royal Soc. London, B181*, 109–135, 1972.
- Bennett, M. D., and J. B. Smith, *Phil. Trans. Royal Soc. London B274*, 227–273, 1976.
- Britten, R. J., and E. H. Davidson, *Fed. Proc.* 35, 2151–2157, 1976.
- Chooi, W. Y., *Genetics*, 68, 195–211, 1971.
- Davidson, E. H., G. A. Galau, R. C. Angerer, and R. J. Britten, *Chromosoma* 51, 253–259, 1975.
- Flavell, R. B., and D. B. Smith, *Heredity* 37, 231–252, 1976.
- Flavell, R. B., J. Rimpau, and D. B. Smith, *Chromosoma (Berl.)* 63, 205–222, 1977.
- Goldberg, R. B., *Biochem. Genetics* 16, 45–68, 1978.
- Gurley, W. B., Ph.D. Thesis, University of Georgia, 1976.
- Hinegardner, R., in *Molecular Evolution*, pp. 179–199, F. J. Ayala, ed., Sinauer Associates, Inc., Sunderland, Mass., 1976.
- Kiper, M., and F. Herzfeld, *Chromosoma (Berl.)* 65, 335–351, 1978.
- Murray, M. G., R. E. Cuellar, and W. F.

- Thompson, *Biochemistry*, in press, 1978.
- Rosbash, M., M. S. Campo., and K. S. Gummerson, *Nature* 258, 682–686, 1975.
- Smith, D. B., and R. B. Flavell, *Biochim. Biophys. Acta* 474, 82–97, 1977.
- Smith, D. B., J. Rimpau, and R. B. Flavell, *Nucleic Acids Res.* 3, 2811–2825, 1976.
- Smith, G. P., *Science* 191, 528–535, 1976.
- Sparrow, A. H., and J. P. Miksche, *Science* 134, 282–283, 1961.
- Sparrow, A. H., H. J. Price, and A. G. Underbrink, *Brookhaven Symposia in Biology* 23, 451–493, 1972.
- Walbot, V., and L. S. Dure, *J. Mol. Biol.* 101, 503–536, 1976.
- Zimmerman, J. L., and R. B. Goldberg, *Chromosoma (Berl.)* 59, 227–252, 1977.

SEQUENCE REPETITION AND INTERSPERSION IN PEA DNA

Michael G. Murray and William F. Thompson

Knowledge of the linear arrangement of repetitive and single-copy sequences in complex eukaryotic organisms is pertinent to understanding the mechanisms involved in evolution of the genome and regulation of transcription. In many animal species as well as the few higher plants that have been studied, short (modal length 300–400 nucleotides) repetitive-sequence elements are interspersed throughout a large fraction of the single-copy sequences at intervals ranging from 800 to several thousand nucleotides (Davidson *et al.*, 1975; Walbot and Goldberg, 1978). While there are a few exceptions in which interspersions can be demonstrated only at much longer intervals (e.g., Crain *et al.*, 1976), the near universal occurrence of the short-period interspersions pattern suggests that it has some functional significance. Britten and Davidson (1969) have postulated that at least some of the repetitive sequences may be involved in coordinate regulation of unlinked genes. It is also possible that much of the observed interspersions reflects the mechanisms by which genomes evolve. The experiments we report here show that the pea genome is an extreme example of short-period interspersions, inasmuch as essentially all of the single-copy se-

quences are less than 1000 nucleotides long.

The pea genome is larger than most eukaryotes that have been examined to date, and 65–70% is composed of repetitive sequences. By comparing the reassociation kinetics of 300-nucleotide-long fragments of either total or isolated single-copy pea DNA with those of radioactively labeled *E. coli* DNA included as an internal kinetic standard, we calculate the kinetic complexity of the pea genome to be 4.5×10^9 nucleotide pairs (Murray *et al.*, 1977a; Murray *et al.*, 1978). This amount of DNA corresponds to 4.6 pg per haploid genome and compares well with chemical estimates of 4.5 pg per 1C pea nucleus (Bennett and Smith, 1976). Thus peas are kinetically as well as functionally diploid. The pea genome is also one of the largest whose reassociation kinetics have yet been analyzed in detail. With the exception of work by Flavell's group on hexaploid wheat (about 6 pg per constituent genome—Smith and Flavell, 1975) and rye (about 9 pg—Smith and Flavell, 1977), most studies have dealt with animals and plants having less than 2–3 pg of DNA on a haploid basis.

The reassociation kinetics of total pea DNA can be adequately described using

only three theoretical second-order components: highly repetitive, moderately repetitive, and single copy. However, the data do not specify a unique solution. The renaturation kinetics of fractions enriched for highly repetitive and moderately repetitive DNA could not be described by any simple combination of theoretical second-order components. Control experiments indicate that this apparent heterogeneity was not a technical artifact resulting from the preferential accumulation of poorly matched or short duplexes in the moderately repetitive fraction. We conclude that the repetitive sequences in peas are present in a continuous distribution of frequency classes ranging from about 100 to over 10,000 copies per haploid genome (Murray *et al.*, 1978).

We have analyzed the interspersion of repetitive and single-copy sequences in the pea genome by measuring HAP binding as a function of fragment length following the techniques and rationale of Graham *et al.*, (1974) (see also Murray *et al.*, 1977a). Preliminary results (Murray *et al.*, 1977a) indicated that most of the single-copy sequences in peas are less than 1000 nucleotides in length. We have since extended the analysis using a larger number of fragment lengths and more discrete size distributions. These improvements were made possible by the use of alkaline agarose electrophoresis (McDonell *et al.*, 1977) rather than sedimentation techniques to prepare different-sized tracers (Hinnebusch *et al.*, 1978).

Figure 36 shows binding to hydroxylapatite as a function of fragment length after incubation to a C_0t value of 50. At this C_0t , most of the repetitive sequences will have renatured but none of the single-copy sequences will be reassociated. Changes in the slope of the binding curve occur at about 400 and 1000 nucleotides. By conventional interpretation (Graham *et al.*, 1974) if one assumes that 4–5% of the tracer is unre-

actable, about 26%, 12% and 8% of the genome would appear to be composed of single-copy sequences with mean lengths of 400, 1000, and 3000 nucleotides, respectively. While C_0t 50 provides a degree of discrimination between repetitive and single-copy sequences comparable to that generally achieved in this type of analysis, the resolution is not sufficient to permit unambiguous conclusions as to the presence of the presumptive 3000-nucleotide class of single-copy sequences.

Since renaturation rate is a function of fragment length (Davidson *et al.*, 1973; Hinnebusch *et al.*, 1978), and since not all 300-nucleotide-long repeats have become reassociated at C_0t 50, some long slowly reassociating repeats could account for all of the increased binding observed above 1000 nucleotides. Such sequences in the tracer DNA's would reassociate more rapidly with increasing fragment length, leading to increases in C_0t 50 binding which would not be related to sequence interspersion. Model experiments in which the binding of reassociated *E. coli* DNA was measured as a function of fragment length indicated that binding will be a strong function of fragment length when reassociation is not essentially complete at the shortest lengths employed (Murray *et al.*, submitted). This problem is aggravated because it is difficult to find a C_0t value that will cleanly discriminate between repetitive and single-copy sequences in a genome as complex as that of peas.

In order to eliminate the complications introduced by such long repetitive sequences, binding was followed after incubation to a C_0t value of 680, a point at which all of the repetitive sequences have become reassociated. However, at this C_0t value we do expect some reassociation of long single-copy sequences. For a fragment length of 1000 nucleotides we calculate that about 30% of the purely single-copy fragments would bind, with the fraction increasing to 50%

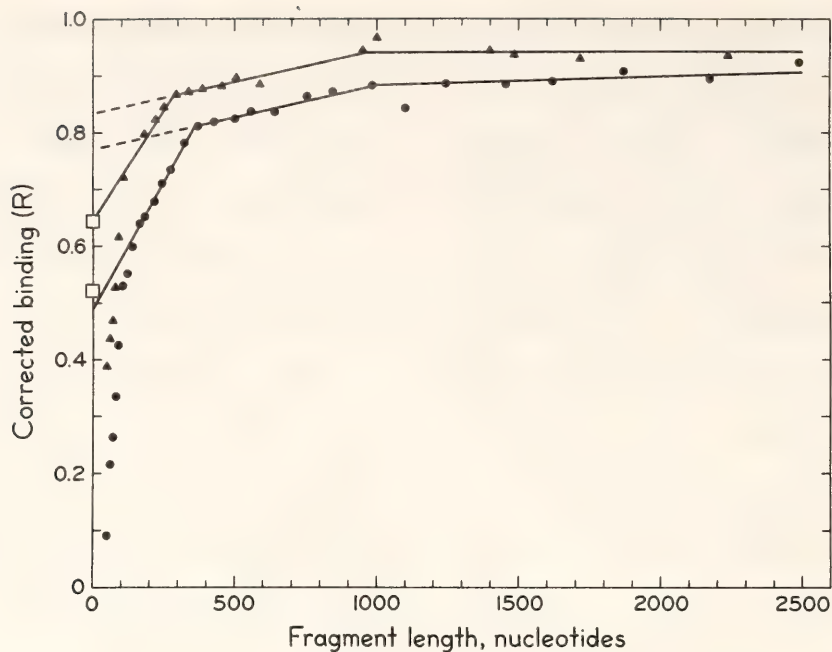


Fig. 36. The fraction of pea DNA fragments containing repetitive elements as a function of fragment length. ^3H -pea DNA fragments labeled in vitro (Murray *et al.*, 1977b) were prepared by alkaline agarose electrophoresis (McDonnell *et al.*, 1977; Murray and Thompson, 1977). Labeled fragments were reassociated with a 2000-fold excess of unlabeled 300-NT-long pea DNA to C_{0t} 50 (circles) or to C_{0t} 680 (triangles). Total HAP binding (B) was corrected to eliminate the effect of "zero time" binding elements (foldback or inverted repeat sequences) by measuring the fraction (Z) of each tracer bound after incubation to C_{0t} 10^{-4} . The fraction bound because of bimolecular reassociation between repeated sequences $R = (B - Z) / (1 - Z)$ was plotted as a function of fragment length. Fragment lengths were determined after incubation to each C_{0t} to take into account thermal degradation. Optical hyperchromicity data were used to provide additional information on the absolute fraction of repetitive sequences. 300-NT fragments of pea DNA were reassociated to C_{0t} 50 or C_{0t} 680 prior to thermal denaturation in a Gilford model 2527 Thermoprogrammer. Thermal denaturation was carried out in 0.12M sodium phosphate (pH 6.8) between 60° and 98°C. The fraction of base-paired nucleotides (squares) was calculated by comparing the hyperchromicity of reassociated DNA with that of long native DNA, allowing for the 2.5% hyperchromic shift observed for single strands under our conditions (Wetmur, 1976).

at 2300 nucleotides. However, we know from the C_{0t} 50 experiments that a maximum of 8% of the genome could consist of single-copy sequences longer than 1000 NT; therefore, we would expect the reassociation of such sequences to contribute less than $(0.08) (0.5 - 0.3) \times 100 = 1.6\%$ additional binding between fragment lengths of 1000 and 2300 nucleotides. The data (upper curve, Fig. 36) show that binding at C_{0t} 680 reaches a constant level of 95% at a fragment length of about 1000 nucleotides; this is close to the maximum binding expected if 4–5% of the tracer is unreactable. Hence the data beyond 1000 NT do not support the existence of any single-copy

sequences greater than this length. By extrapolating these data we calculate that single-copy sequences with mean lengths of 300–400 and 1000 nucleotides account for 19% and 11% of the genome, respectively. Extrapolation of the data between 150 and 300 nucleotides to zero fragment length suggests that 67% (64/95% if 5% of the DNA is considered unreactable) are contained in repetitive sequences at C_{0t} 680. This estimate compares well with the fraction of nucleotides paired, as determined directly by hyperchromicity measurements (Wetmur, 1976; Murray *et al.*, 1978).

In genomes such as peas, where a clean separation of repetitive and single-copy

sequences at a single C_0t value is not possible, it is imperative to consider what effects different patterns of sequence organization might have on the results of binding experiments such as those in Fig. 36. The data for pea DNA fragments at C_0t 50 would normally be interpreted as indicating the presence of single-copy sequences 3000 nucleotides or more in length, and accounting for 8–13% of the DNA. However, the slope of the curve above about 1000 NT could also be explained by the presence of a relatively small fraction of long, slowly reassociating repetitive sequences. Such an effect would not be observed at C_0t 680, where reassociation of even the slower repetitive sequences is much more complete. However, because C_0t 680 is high enough to permit reassociation of any long single-copy sequences which might be present, the binding data at C_0t 50 are required to set reasonable upper estimates for long single-copy sequences.

The foregoing analysis leaves open two important questions. First, while the data do not support the existence of any single-copy sequences longer than 1000 nucleotides, there may be some small fraction of long single-copy sequences present in levels below the limits of detection in the analysis. Moreover, it is impossible to assess the fraction that is unreactable with this approach. Second, binding studies made at one C_0t value do not allow determination of the frequency classes responsible for the observed interspersions. These questions can be addressed by following the reassociation kinetics of long DNA tracers. The reassociation kinetics of 1300-nucleotide-long pea tracer fragments in the presence of excess short unlabeled fragments is shown in Fig. 37A. Seventy-four percent of the long fragments become bound to hydroxylapatite with kinetics suggestive of a single highly repetitive component (10,000 copies per haploid genome). The large increase in the fraction

of the fragments reacting at this rate indicates that a major fraction of the pea genome contains elements of the highly repeated sequence families spaced at intervals of less than 1300 nucleotides. Most of the remaining long tracer becomes reassociated more slowly, but still its rate is some 13 times faster than would be expected for 1300-nucleotide-long single-copy sequences. Again, however, the small amount of reassociation taking place in the single-copy range and the inevitable scatter in the data make it impossible to exclude some small fraction of the genome being composed of long single-copy sequences.

To test further for the presence of long single-copy sequences, 1000-nucleotide fragments that remained unreassociated at a C_0t of 10 were isolated and their reassociation kinetics followed in the presence of excess short unlabeled fragments (Fig. 37B). This fraction should be enriched for long single-copy sequences if they exist. The data have been fitted with three theoretical second-order components, with the constraint that the solution use one component with the reassociation kinetics expected of long single-copy sequences (Pearson *et al.*, 1977). Under this constraint the fit shown in Fig. 37B was obtained, indicating that 6% of the tracer (1% of the genome) might reassociate with single-copy kinetics. However, to obtain any solution including a long single-copy component, the fraction of the tracer assumed to be unreactable had to be fixed. The alternative solutions to the data in Fig. 37B, shown in Table 26, demonstrate that the fraction of long single-copy fitted to the data is a sensitive function of the fraction unreactable that was fixed. A maximum of 15% of the tracer (2.7% of the genome) will fit with single-copy kinetics if the fraction unreactable is fixed at 2%. However, our experience suggests that this unreactable value is too low, and the best solutions to the data do not require the presence of *any* long

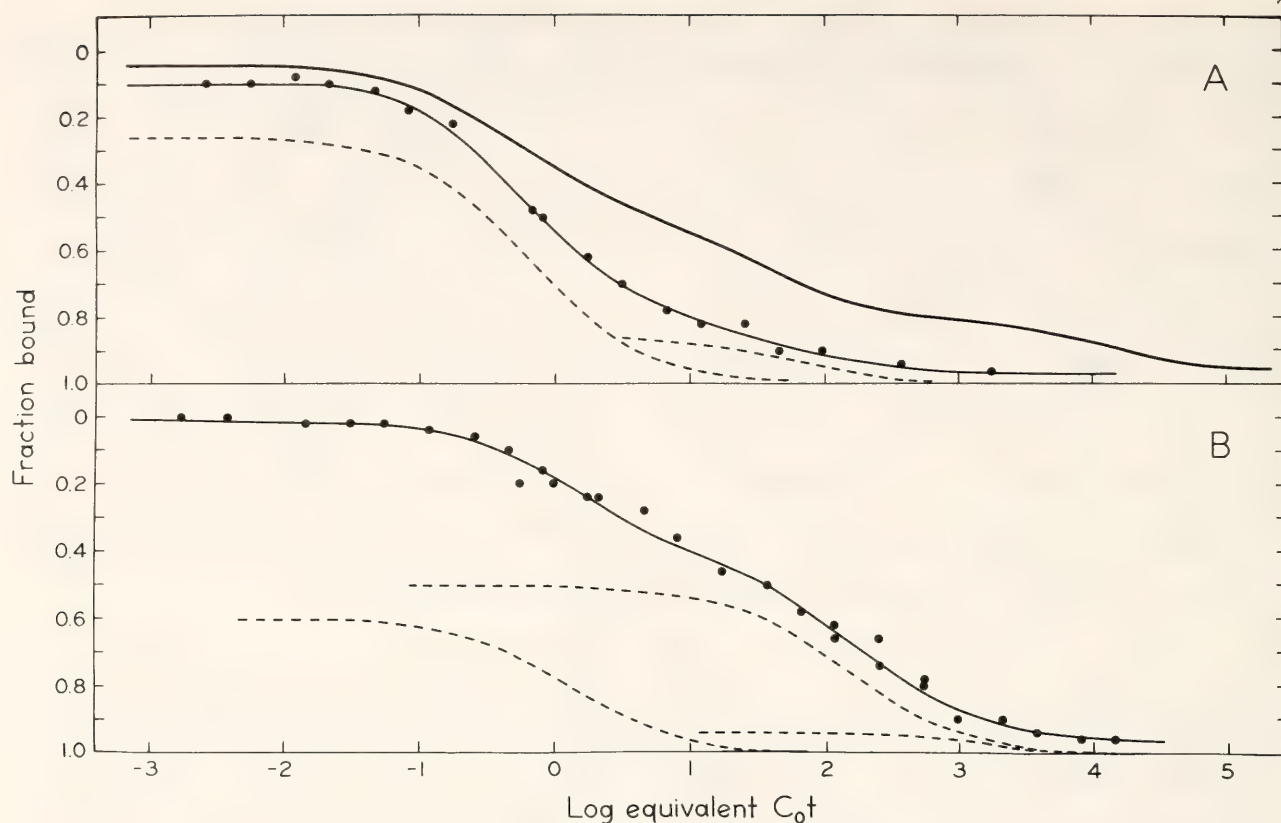


Fig. 37. (A) Reassociation kinetics of 1300-nucleotide-long pea DNA fragments. ^3H -pea DNA fragments were prepared by alkaline agarose electrophoresis and mixed with a 2000-fold excess of 300 NT unlabeled pea DNA and 1% ^{14}C -*E. coli* DNA to serve as an internal rate standard. Samples at various concentrations in 0.4M sodium phosphate (pH 6.8) were heat-denatured and reassociated at 66°C for various times prior to fractionation on HAP in 0.12M sodium phosphate at 60°C . C_0t values have been corrected to the equivalent C_0t values in 0.12 sodium phosphate at 60°C . The upper curve shows the reassociation kinetics of 300-NT pea DNA fragments with each other (Murray *et al.*, 1978). The lower solid line is a least-squares fit to the data for long tracer. The two theoretical second-order components for this solution are indicated by dashed line. Seventy-five percent of the long fragments became reassociated with a rate of 1.05, after correction for viscosity. Fourteen percent of the fragments became reassociated with a rate of 0.12, and 4% of the DNA was unreactable. Similar analysis with 950-NT-long fragments gave comparable results (data not shown). (B) Reassociation kinetics of 1000-nucleotide fragments remaining single stranded at C_0t 10. Fragments were obtained from in vivo-labeled pea DNA by alkaline gel electrophoresis and reassociated in 0.12M sodium phosphate to a C_0t value of 10. Those sequences that did not reassociate (18% of the total) were isolated by HAP chromatography. These slowly reacting fragments were mixed with a 70-fold excess of 300-NT unlabeled pea DNA and 1% ^{14}C -*E. coli* DNA to serve as an internal rate standard. Samples at various concentrations in 1M NaCl, 10mM sodium phosphate, were denatured and reassociated prior to fractionation on HAP. The upper curve is a least-squares solution with three theoretical second-order components (dashed lines). For this fit, a single-copy rate was fixed at 0.0008 (four times the rate of 0.0002 observed for 300-NT fragments) and the unreactable was fixed at 4%. In this model solution, 6% of the tracer, or 1% of the genome, became reassociated with single-copy kinetics. Alternative solutions are given in Table 26.

single-copy DNA. We thus place the maximum reasonable estimate of the fraction of the genome composed of single-copy sequences longer than 1000 nucleotides at 2%, but it may be zero. Such extensive interspersions at such short

lengths has not been demonstrated in any other system.

Additional conclusions may be drawn from Fig. 36 bearing on the question of how such extensive interspersions may have evolved. From Fig. 36 we calculate

TABLE 26. Possible Solutions for the Reassociation Kinetics of 1000-Nucleotide-long Pea Fragments That Remain Single Stranded at *C*₀*t* Value of 10

Solution	Component	Fraction of Tracer	Fraction of Genome*	Normalized Rate†	RMS‡
1	1	.42	.076	.629	.0239
	2	.54	.097	.044	
	unreactable	.03	
2	1	.25	.055	1.820	.0197
	2	.31	.056	.079	
	3	.42	.075	.002	
	unreactable	.02	
3	1	.37	.066	.840	.0229
	2	.45	.081	.009	
	3	.15	.027	.0008 (fix)§	
	unreactable	.02 (fix)§	
4	1	.39	.070	.773	.0233
	2	.47	.085	.007	
	3	.11	.019	.0008 (fix)	
	unreactable	.03 (fix)	
5	1	.40	.070	.720	.0238
	2	.50	.090	.006	
	3	.06	.010	.0008 (fix)	
	unreactable	.04 (fix)	
6	1	.41	.074	.681	.0244
	2	.53	.095	.004	
	3	.006	.001	.0008 (fix)	
	unreactable	.05 (fix)	

* The tracer included 18% of the starting fragments.
† Reassociation rate after normalizing for viscosity, using *E. coli* DNA as an internal rate standard.
‡ Root-mean-square error of the least-squares fit to the data.
§ Solutions 3–6 were constructed by forcing the computer to fit a component with a rate constant of .0008 l sec/mole. This is the rate predicted for single-copy sequences 1200 NT long. Most fragments in the tracer population are less than 1200 NT long, and thus the values in the table are expected to be overestimates of the actual single-copy fraction. These constrained fits required that the fraction unreactable also be fixed, as otherwise the “solutions” included reactions totaling more than 100%, and the “unreactable” fraction became negative.

that there are about 5×10^5 different single-copy sequences in the 1000-nucleotide-length class and about 3×10^6 in the 300–400 nucleotide class. Measurements of the repeat lengths made with S1 nuclease (Murray *et al.*, submitted) indicate that the predominant length of repeated sequences is 300–400 nucleotides (number average). Using this figure, we calculate that there are about 10^7 different repetitive elements. Since

the number of repetitive elements is about three times greater than the number of single-copy elements, we must conclude that much of the pea genome is composed of repetitive elements arranged in regions significantly longer than 300–400 nucleotides. Thus those repeated sequences that are not interspersed with single-copy elements are presumably interspersed with other repeated sequences in permuted tandem arrangements at in-

tervals of 300–400 nucleotides. Since a substantial fraction of the single-copy sequences are also in the 300–400 nucleotide range, single-copy and repeated sequences would appear to have been subject to the same very short interspersal processes during evolution.

While interspersal of repeated sequences of this length with single-copy sequences is commonly observed in other eukaryotes (Davidson *et al.*, 1975; Walbot and Goldberg, 1978), a major class of single-copy sequences 300–400 nucleotides long has been clearly demonstrated before only in rye (Smith and Flavell, 1977). In organisms where repetitive sequences constitute a relatively small fraction of the genome, the principal result of random rearrangement of short (300–400 nucleotide) segments of DNA would be interspersal of single-copy sequences with one another; such interspersal would not be detectable by present techniques. In genomes such as those of peas and rye, however, where repeated sequences constitute a majority of the genome, random rearrangement would be expected to juxtapose single-copy and repeated sequences much more frequently. Such a general process of short segment rearrangement would therefore be expected to produce short single-copy sequences in organisms such as peas that have large amounts of repetitive DNA, but would produce only cryptic rearrangement of single-copy elements in organisms with less-repetitive DNA.

It is apparent from the data in Figs. 36 and 37 that single-copy sequences longer than about 1000 nucleotides do not constitute a readily measurable fraction of the pea genome. Since most structural genes in animals are single-copy sequences (Britten and Davidson, 1976) and the average coding sequence is usually taken to be 1200–1500 nucleotides in length, it would appear that the structural genes in peas must be either significantly smaller than those of animals or

that at least some of the mRNA's must contain repeated sequences. Polysomal mRNA's from peas and other higher plants frequently have lengths greater than 1000 NT (e.g., Key and Silflow, 1975) and the mRNA's in tobacco have been shown to be exclusively single-copy transcripts (Goldberg *et al.*, 1978). One way to resolve this apparent contradiction would be to assume that long mRNA's in higher plants are constructed from shorter sequences by splicing mechanisms similar to those demonstrated in animal systems (e.g., Breathnach *et al.*, 1977). However, it is also quite possible that in organisms with large genomes, such as peas, the coding sequences represent such a small fraction of the genome as to be undetectable in experiments with total DNA. In this context, it should be emphasized that our maximum reasonable estimate (2%) for the fraction of the pea genome composed of single-copy sequences longer than 1000 nucleotides is nearly equivalent to the entire *Drosophila* genome and would contain enough coding capacity for about 70,000 average genes.

REFERENCES

- Bennett, M. D., and J. B. Smith, *Phil. Trans. Royal Soc. Lond. B274*, 227–273, 1976.
- Breathnach, R., J. L. Mandel, and P. Chambon, *Nature (London)* 270, 314–319, 1977.
- Britten, R. J., and E. H. Davidson, *Science* 165, 349–357, 1969.
- Britten, R. J., and E. H. Davidson, *Fed. Proc.* 35, 2151–2157, 1976.
- Crain, W. R., E. H. Davidson, and R. J. Britten, *Chromosoma (Berl.)* 59, 1–12, 1976.
- Davidson, E. H., G. A. Galau, R. C. Angerer, and R. J. Britten, *Chromosoma* 51, 253–259, 1975.
- Davidson, E. H., R. R. Hough, C. S. Amenson, and R. J. Britten, *J. Mol. Biol.* 77, 1–23, 1973.
- Goldberg, R. B., G. Hoschek, J. C. Kam-

- alay, and W. E. Timberlake, *Cell* 14, 121–131, 1978.
- Graham, D. E., B. R. Neufeld, E. H. Davidson, and R. J. Britten, *Cell* 1, 127–137, 1974.
- Hinnebusch, A. G., V. E. Clark, and L. C. Klotz, *Biochemistry* 17, 1521–1529, 1978.
- Key, J. L., and C. S. Silflow, *Plant Physiol.* 56, 364–369, 1975.
- McDonell, M. W., M. N. Simon, and F. W. Studier, *J. Mol. Biol.* 110, 119–146, 1977.
- Murray, M. G., and W. F. Thompson, *Carnegie Inst. Wash. Year Book* 76, 259–262, 1977.
- Murray, M. G., R. S. Preisler, and W. F. Thompson, *Carnegie Inst. Wash. Year Book* 76, 240–246, 1977a.
- Murray, M. G., H. S. Belford, and W. F. Thompson, *Carnegie Inst. Wash. Year Book* 76, 262–267, 1977b.
- Murray, M. G., R. E. Cuellar, and W. F. Thompson, *Biochemistry*, in press, 1978.
- Pearson, W., E. H. Davidson, and R. J. Britten, *Nucleic Acids Research* 4, 1727–1735, 1977.
- Smith, D. B., and R. B. Flavell, *Chromosoma (Berl.)* 50, 223–242, 1975.
- Smith, D. B., and R. B. Flavell, *Biochim. Biophys. Acta* 474, 82–97, 1977.
- Walbot, V., and R. Goldberg, in *Nucleic Acids in Plants*, J. W. Davies and T. Hall, eds. CRC Press, Cleveland, Ohio, in press, 1978.
- Wetmur, J. G., *Annu. Rev. Biochem. Bioeng.* 5, 337–361, 1976.

DISTRIBUTION OF NUCLEOTIDE SEQUENCE DIVERGENCE AMONG FAMILIES OF REPETITIVE SEQUENCES IN MUNG BEAN DNA

Richard S. Preisler and William F. Thompson

INTRODUCTION

One important feature distinguishing the genomes of eukaryotes from those of prokaryotes is the presence in the former of repeated DNA sequences. In general, plant genomes contain a higher proportion of repetitive DNA than do animal genomes (Flavell *et al.*, 1974).

The set of DNA segments containing a particular repeated sequence is called a repeated-sequence *family* (Britten and Kohne, 1968). Most families do not contain identical copies of a sequence; base substitution over the generations results in the gradual divergence of family member sequences. This phenomenon has been demonstrated experimentally by comparing the melting (thermal denaturation) behavior of fragments of native and reassociated DNA. Reassociated duplexes show a lower half-denaturation temperature (T_m) than the perfectly

paired native duplexes. This result indicates that the bulk of repeated sequences forming double-stranded molecules *in vitro* contain regions of divergence, generating mismatched base pairs in the duplexes.

Another observation from these experiments is that reassociated eukaryote DNA melts over a wider range of temperatures than does native DNA. The broad melting transition indicates that not all the duplexes formed between repeated-sequence fragments are equally mismatched. There appears to be a continuum from perfectly paired to highly mismatched reassociated molecules.

Bendich and Anderson (1977) and Bouchard and Swift (1977) have posed the question of whether this broad range of mispairing is caused primarily by different degrees of divergence among the members of each individual family or by

whole families having different average amounts of base substitution. Bendich and Anderson (1977) refer to the first alternative as the *heterogeneous* family model and to the latter possibility as the *homogeneous* family model. In their view, homogeneous family members would be almost equally diverged from each other, so that the broad melting transition of total reassociated repeated sequences would be the summation of sharp melting transitions for individual families. In contrast, heterogeneous family members would show a wide distribution of divergence, so some would form almost perfectly paired duplexes, and others would form highly mismatched molecules. Thus, each heterogeneous family should show a broad melting transition. The evolutionary implications of the homogeneous and heterogeneous family models have been discussed by Bendich and Anderson (1977) and Bouchard and Swift (1977).

It is not possible (at least, without cloning repeat sequences) to isolate individual families and to study their melting behavior. However, there are more indirect experimental approaches to determining whether repeated-sequence families are, on the whole, homogeneous or heterogeneous. One approach used by Bendich and Anderson (1977)—and also in the present work—is to compare the reassociation behavior of repeated DNA at different temperatures.

We have mentioned previously that duplexes with more mismatching have a lower thermal stability. At a particular incubation temperature some complementary fragments will be unable to form stable duplexes because that temperature is above or close to the melting temperature for such duplexes. Therefore, as we raise the incubation temperature toward the native T_m we will lose progressively more of the mismatched duplexes from the pool of reassociating repeated DNA. Bendich and Anderson (1977) showed that in four plant ge-

nomes the fraction of DNA reassociating with repetitive kinetics did indeed drop by a factor of 4 when the incubation temperature was raised from 25° to 5° below the native T_m . At temperatures where repeated sequences are unable to form mismatched duplexes, they will presumably reanneal with their exact complements at a single-copy rate. In fact, Bendich and McCarthy (1970) found an increase in the apparent single-copy fraction of the wheat genome as the incubation temperature was raised.

A heterogeneous family will lose duplexes between its more diverged members out of the pool of reassociating molecules as the melting temperatures of such duplexes are approached. Thus, at higher incubation temperatures, only the less diverged family members can reassociate. Bendich and Anderson (1977) inferred that in the heterogeneous model the effective copy number of each repeated sequence (number of family members reassociating) would decrease as the temperature was increased. Since the measured reassociation rate constant is proportional to the copy number (or the concentration of sequences in total DNA), these authors predicted a decline in rate constant proportional to the decrease in the fraction reassociating, as the native T_m was approached.

A homogeneous family, where all members are about equally diverged, is not expected to lose copies from the reassociating pool until the common melting temperature of its members' duplexes is approached. At this point, the whole family would be lost from the repeat fraction. Thus, Bendich and Anderson (1977) predicted that the effective copy number, measured by the rate constant, should not change with temperature in the homogeneous model.

These inferences from the hypothetical effect of temperature on individual families to the observable behavior at different temperatures of the bulk repeated DNA fraction depend on the condition

that all the families have about the same copy number at the lowest incubation temperature we employ. If this requirement of kinetic uniformity were not met, the rate of the repeated fraction would most likely change with increasing temperature, whether most families were homogeneous or heterogeneous. Even if the families were homogeneous, so that their individual rates did not vary, the loss of some less precisely pairing families at higher temperatures would quite possibly leave a collection of families reassociating with a different mean rate. Conversely, a kinetically diverse set of heterogeneous families might produce a constant bulk rate for the repeat fraction as the temperature was increased.

Bendich and Anderson (1977) analyzed a fast-repeat fraction that appeared to reassociate as a single, kinetically uniform component in total DNA of barley, daffodil, deer fern, and parsley fern. Whereas the fraction of DNA reassociating in this component decreased between 3.6-fold and 4.4-fold over a 20°C temperature increase, the rate constants for the fast repeats dropped only by a factor of between 1.3 and 2.4 for the four species. The authors interpreted the much smaller change in rate as evidence that most of the highly repeated families in these genomes are homogeneous.

A major research objective in our laboratory has been the detailed analysis of genome organization in the garden pea (*Pisum sativum*, cv. Alaska) and the mung bean (*Vigna radiata* (L.) R. Wilcz). We have found a great deal of kinetic diversity in the pea repetitive fraction (Murray *et al.*, 1978; Murray and Thompson, this Report). On the other hand, the reassociation of mung bean repeats at a standard temperature (T_m — 25°C in phosphate buffer), assayed by hydroxylapatite binding, can be described by a single (kinetically uniform) rate component (unpublished data of Michael G. Murray). Thus, we de-

cided that an analysis of mung bean DNA reassociation kinetics at different temperatures might indicate whether the repeated families were predominantly homogeneous or heterogeneous.

METHODS

Our mung bean DNA preparations, total cellular DNA and a repeat-enriched fraction (described below) were isolated from young leaf tissue and sheared to an average fragment length of 300 nucleotides by procedures detailed elsewhere (Murray and Thompson, submitted for publication). Reassociation was monitored spectrophotometrically in the solvent 2.4M tetraethylammonium chloride (TEACl). The T_m of DNA's in this solvent has been shown to be independent of base composition (Melchior and von Hippel, 1973). Therefore, the thermal stability of repeated-sequence duplexes formed in TEACl should be influenced only by their degree of mismatching.

In each experiment we performed, a sample of 300-nucleotide *E. coli* DNA fragments was reassociated in a separate cuvette. Since bacterial DNA is composed of unique sequences that form almost perfectly paired duplexes, this preparation serves as a useful kinetic standard. We measured a 2.5-fold variation in rate constant for *E. coli* DNA and a 10% decrease in the fraction reassociating between 35° and 55°C. These are temperature effects not caused by mismatching and are presumably common to widely different DNA's. Therefore, we have corrected our mung bean reassociation data for variation in the *E. coli* DNA parameters. The *E. coli* reassociation data were also used to estimate collapse hypochromicities (Bendich and Anderson, 1977).

Our kinetic data were analyzed by a least-squares fitting procedure with a computer program supplied by Dr. Eric Davidson and adapted to our computer by Mr. Glenn Ford. This program allowed us to fit the points with up to five

hypothetical kinetic components. The reaction of each component is described by the equation

$$C/C_0 = \frac{1}{(1 + KC_0t)^n},$$

where C is the concentration of nucleotides in DNA that are still in single strands at time t , C_0 is the initial concentration, and K is the rate constant. We used the value $n = 0.44$, derived for reassociations assayed by single-strand S-1 nuclease digestion (Morrow, 1974; Britten and Davidson, 1976). Optical and S-1 kinetics should follow the same form because both techniques measure the fraction of nucleotides that are paired.

RESULTS AND DISCUSSION

The reassociation kinetics of total mung bean DNA at five temperatures, from 35°C (25.3° below the native T_m or $T_{m,n}$) to 55°C ($T_{m,n} - 5.3^\circ\text{C}$), were well described by one repetitive component and one single-copy component. The relative rates of reassociation of mung bean unique sequences and *E. coli* DNA were determined from hydroxylapatite experiments (Murray and Thompson, unpublished results), and the resulting ratio was used to fix the mung bean single-copy rate constant relative to the observed optical *E. coli* rate constant at each temperature. The computer fits yielded values for the fraction of DNA in each component and the rate constant, K , of the repetitive component.

Figure 38 shows that the repetitive fraction decreased 2.1-fold and the relative rate constant for the repeated component increased 2.5-fold over this temperature range. These results would not be predicted by either the homogeneous or the heterogeneous model. The highly stable repeated duplexes formed at 55° comprise 17.1% of the genome and reassociate with a rate constant 5.18 times that of *E. coli* DNA at 55°. Therefore, the rate constant the repeats would show

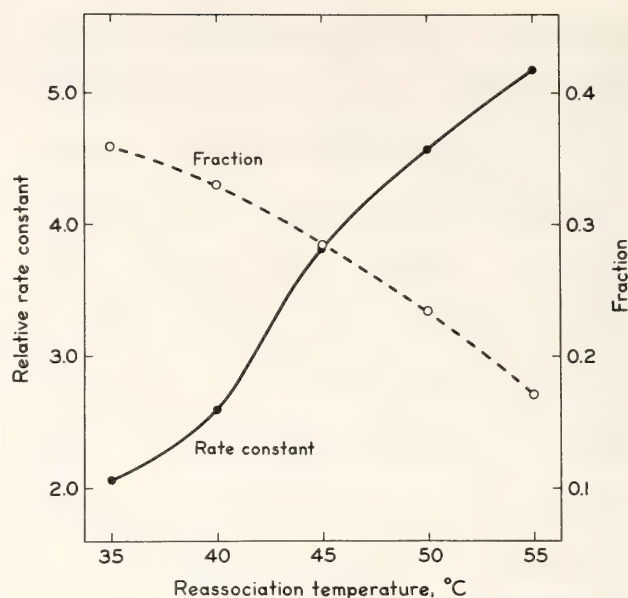


Fig. 38. Fractions and relative rate constants for a single repetitive component fitted to data for total mung bean leaf DNA reassociated in 24M TEACl at different temperatures. Computer analysis was performed as described in the text. *E. coli* DNA was reassociated simultaneously at each temperature. The mung bean data were normalized for a small (10%) decrease in the fraction of *E. coli* DNA able to reassociate at the higher temperatures. Relative rate constants were obtained by dividing the observed rate by the rate for *E. coli* at that temperature and further corrected for mismatch effects, as described by Marsh and McCarthy (1974).

if they reassociated as an isolated fraction is $K(\text{pure}) = 5.18/.171 = 30.3 \times E. coli K(\text{pure})$. $K(\text{pure})$ is inversely proportional to kinetic complexity (G), so that the complexity of the 55° repeats $= G_{E.coli}/30.3 = 4.5 \times 10^6$ nucleotide pairs/ $30.3 = 1.49 \times 10^5$ nucleotide pairs.

Kinetic measurements (Kolodner and Tewari, 1975) have yielded a narrow range of complexities, from 1.35×10^5 to 1.50×10^5 nucleotide pairs for the chloroplast DNA of six higher plants. The two leguminous species examined, garden pea and common bean, had chloroplast genome sizes of 1.44×10^5 and 1.47×10^5 NTP, respectively. Thus, the kinetic complexity of the highly stable repeat fraction from mung beans is almost exactly that expected for chloroplast DNA. In addition, since chloroplast

DNA sequences are mostly unique (Kolodner and Tewari, 1972), they should reassociate extensively at 55°C, and should produce essentially perfect duplexes even at lower temperatures. We have observed a component with a thermal stability equal to that of native DNA in all our melting profiles of re-associated mung bean leaf DNA. The native *T_m* fraction accounts for 15–18% of the total DNA after reassociation at 45°. The mung bean genome is quite small (haploid DNA complement = 0.5 pg) so that it may be reasonable to suppose that chloroplasts could contain 17% of the cellular DNA mass in leaves. No reliable measurements of the amount of chloroplast DNA mass in higher plants have yet appeared in the literature, however, and we recognize that obtaining such information for mung beans will be crucial to our identification of the 55° component.

The putative chloroplast DNA component would account for all the repeats reassociating at 55° but not for the additional reaction at lower temperatures. We attempted to dissect the highly stable from the less stable repeats by fixing the “chloroplast” rate constant, corrected for the temperature effect on *E. coli* reassociation, and asking the computer to fit a second repeated component to the data from each temperature. The parameters obtained from these fits are listed in Table 27. At every temperature except 55°, the computer fitted a second repeat component 6 to 18 times slower than the “chloroplast” component. The fraction of total DNA comprising these slower repeats dropped three-fold from 35° to 50°. Their rate constants exhibited an upward trend, although it was neither as large nor as consistent as that seen in single-repeat component fits.

TABLE 27. Reassociation of Total Mung Bean DNA at Different Temperatures

Reassociation Temperature, T _r (°C)	Fast-Repeat Component		Slow-Repeat Component	
	Fraction*	Relative Rate†	Fraction*	Relative Rate†
<i>Standard Reassociation Data Fit with Two Repeated Components</i>				
55	.17	5.2	...§	...§
50	.21	5.2‡	.07	.66
45	.19	5.2	.16	.80
40	.25	5.2	.16	.29
35	.23	5.2	.21	.40
<i>Temperature-Drop Reassociation Data Fit with One Repeated Component</i>				
55	.17	5.2		
50	.09	2.8		
45	.03	3.8		
40	.02	1.5		

* Fractions obtained by computer analysis have been normalized for a reduction in the fraction of *E. coli* DNA fragments able to reassociate at the higher temperatures. This fraction was 1.0 at 35° and 0.90 at 55°.

† Relative rate constants (*K*_{obs}/*K*_{*E. coli*}) were calculated and corrected for mismatch effects as described for Fig. 38.

‡ The rate constant for these components was fixed at the estimated value for the reassociation of the putative chloroplast DNA (repeat component at 55°C. The 55° repeats had a *K*(corrected) = 5.2 × *K* (*E. coli*). Thus, for the 35°, 40°, 45° and 50°C analyses, the fast-repeat rate was fixed at 5.2 times the corresponding *K* (*E. coli*) at that temperature.

§ The computer failed to fit a slow-repeat component with a rate clearly different from the single-copy rate to the 55° data.

Further experiments were carried out on an isolated fraction of mung bean repetitive DNA. This preparation was isolated from 300-nucleotide fragments by hydroxylapatite chromatography after permitting most of the repeated sequences to reassociate; it comprised 40% of the total DNA. When reassociated as a tracer in excess total DNA it proved to be virtually free of single-copy sequences (unpublished results of Michael G. Murray).

We reassociated this repeat-enriched preparation in the spectrophotometer at 35°, 45°, and 55°C. As shown in Table 28, the fraction of the DNA reassociating in the repeat component was only slightly reduced at 55°C and was actually larger at 45°C than at 35°C. The relative rate constant for this component did not vary by more than 4%. At 55°, the repetitive K (pure) = $14.5/0.526 = 27.6 \times E. coli K$ (pure), yielding a kinetic complexity of 4.5×10^5 nucleotide pairs/ $27.6 = 1.63 \times 10^5$ nucleotide pairs. This value agrees, within 10%, with that for the high-stability repeat complexity measured in total DNA. The fraction of this component is 3.1 times higher in the repeat-enriched DNA than in total DNA and its rate is greater by a factor of 2.8. Since the repeat-enriched preparation represents 40% of total DNA, the concentration of highly re-

peated sequences in this fraction is expected to be $1/0.4 = 2.5$ times greater than in the total genome. We conclude, therefore, that our "chloroplast DNA" was fully recovered in the repeat-enriched fraction.

Besides comparing the reassociation behavior of repeats at different temperatures, we have devised another approach to analyzing the patterns of distribution of mismatching. This method involves allowing the DNA to reassociate to a considerable extent at a temperature close to the native T_m , dropping the temperature by 5 degrees and letting reassociation proceed for the same amount of time, lowering the temperature another 5 degrees, and so on. Only precisely or almost precisely paired duplexes (those which melt around $T_{m,n}$), will form at the highest temperature. At the next step, we should find double strands with a T_m about $T_{m,n} - 5^\circ\text{C}$ reassociating, and so on through the successive steps. Thus we can assay the reannealing of various thermal stability classes of duplexes.

Table 27 shows the results obtained from such a temperature-drop series for total mung bean DNA. The fraction reassociating at 50°C but not at 55° is about one-half as fast as the 55° "chloroplast DNA" fraction. The reactions at 45° and 40°C also were slower than the

TABLE 28. Reassociation of Mung Bean Repeat-Enriched DNA at Different Temperatures

Reassociation Temperature, T_r (°C)	Fraction in Repeated Component*	Relative Rate of Repeated Component†
<i>Standard Reassociation Data</i>		
55	.53	14.5
45	.67	14.7
35	.62	14.2
<i>Temperature-Drop Reassociation Data</i>		
55	.46	13.7
45	.21	6.3
35	.07	3.4

* Fraction (MB, corrected) = Fraction (MB)/Fraction (*E. coli*).

† Rate constants were corrected as described in the legend to Fig. 38.

55° reassociation. We will attempt to interpret these trends in the ensuing discussion.

The marked rate increase with rising temperature that we observed in the repeated fraction of total mung bean DNA defies the predictions of either homogeneous or heterogeneous family model. We have found that although the reassociating repeats appear to be kinetically uniform at any one temperature, a comparison between temperatures shows kinetic diversity. At least 48% (fraction of repeats at 55° C/fraction of repeats at 35°C = 0.17/0.36) of the repeated DNA belongs to a fast well-matched component (putative chloroplast DNA). The rate increase and fraction decrease seen in Fig. 38 can be explained by the loss of slower, more mismatched (lower stability) repeats and the consequent enrichment for the faster, high-stability component as the temperature is raised. This process is also evidenced in the temperature drop experiment by the decreased rate of repeats reassociating at lower temperatures, after the high-stability class has been removed in the 55° step. The smaller changes in repeat fraction and rate seen with repeat-enriched DNA could be explained if some of the slower, more mismatched sequences were lost in the preparation of this fraction, so that "chloroplast DNA" comprised a larger proportion of the total repeats here than in total DNA. If that were the case, then fewer repeated duplexes would be lost at higher temperatures and the average rate for those remaining would not be very different in the repeat-enriched DNA. That there *are* some slower, lower-stability repeats in this preparation is suggested by the results of a 10° temperature drop experiment (see Table 28). The repeated sequences remaining after the 55° fraction has reacted reassociate more slowly, as was the case in total DNA.

Can we determine whether the "non-chloroplast" (presumably nuclear) re-

peat families are homogeneous or heterogeneous? The rate constant fit by the computer for the slow-repeat component, in the presence of a "chloroplast" component of fixed rate, increased 65% from 35° to 50°C (Table 27). Since the trend is not consistent, these results could be interpreted to imply either homogeneous families (constant rate) or the presence of a relatively fast, moderately high-stability subfraction (capable of reassociating at 50°, but not at 55°C) in the slow repeats.

Table 27 shows that the fraction of total DNA reassociating at the "chloroplast" rate decreases from 25% at 40°C to 17% at 55°. Since all chloroplast sequences should form well-matched duplexes, there may be as much as 8% of total DNA in a class of mismatched repeats with a copy number similar to that for the chloroplast genome. More evidence for this proposition comes from comparing the total DNA temperature-drop rates with those for the slow repeats (Table 27). The former values should be average rates for all repeated sequences, slow and fast, in a particular thermal-stability class. The fact that they are several times larger than the slow-repeat rates suggests the presence of faster low-stability repeats. The experiments we have performed cannot characterize the fast mismatched-sequence families as either homogeneous or heterogeneous.

In the case of mung bean DNA, the hidden kinetic diversity was significant enough to produce behavior inconsistent with the predictions of either the homogeneous or the heterogeneous family model. Bendich and Anderson (1977) fitted their data manually rather than by computer analysis, so they would have been more likely to overlook the presence of nonuniform repeat kinetics. A smaller degree of kinetic diversity of the pattern we have observed in mung beans (the presence of a fast, highly stable subcomponent), whether of organellar or nuclear origin, could create

the illusion of a constant repeat reassociation rate as the temperature was increased. Therefore, we are not convinced that the results of Bendich and Anderson from reassociations at different temperatures demonstrate the homogeneity of repeated families.

There is another experimental approach to the question of homogeneity versus heterogeneity which should be valid regardless of the number of rate components because it does not involve any analysis of reassociation kinetics. Thermal stability classes can be isolated from hydroxylapatite by eluting reassociated DNA bound to a column over a temperature gradient. Any duplex will be eluted in the denatured state as its melting temperature is reached. Fractions eluted at different temperatures are allowed to reassociate a second time, and the melting behavior of the duplexes formed is analyzed. Bendich and Anderson (1977) and Bouchard and Swift (1977) found that reassociated thermal fractions from barley and the homosporous fern *Thelypteris normalis*, respectively, remelted over about the same range of temperatures as the original elution steps used to isolate them. These results suggest a considerable degree of family homogeneity in the two species. In our laboratory, a different method of melting profile analysis using higher derivatives has provided evidence for homogeneous repeat families in pea DNA (Cuellar *et al.*, 1978, and this Report).

We are planning to use both high-resolution thermal denaturation and reassociation-kinetic experiments in fur-

ther studies of these isolated thermal fractions. It is our hope that such investigations will ultimately produce a better understanding of the structure and evolution of repeated DNA families.

REFERENCES

- Bendich, A. J., and R. S. Anderson, *Biochem.* 16, 4655-4663, 1977.
 Bendich, A. J., and B. J. McCarthy, *Genetics* 65, 545-565, 1970.
 Bouchard, R. A., and H. Swift, *Chromosoma (Berl.)* 61, 317-333, 1977.
 Britten, R. J., and E. H. Davidson, *Proc. Nat. Acad. Sci. U.S.A.* 73, 415-419, 1976.
 Britten, R. J., and D. E. Kohne, *Science* 161, 529-540, 1968.
 Cuellar, R. E., G. A. Ford, W. R. Briggs, and W. F. Thompson, *Proc. Nat. Acad. Sci. U.S.A.*, 1978, in press.
 Flavell, R. B., M. D. Bennett, J. B. Smith, and D. B. Smith, *Biochem. Genet.* 12, 257-269, 1974.
 Kolodner, R., and K. K. Tewari, *J. Biol. Chem.* 247, 6355-6364, 1972.
 Kolodner, R., and K. K. Tewari, *Biochim. Biophys. Acta* 402, 372-390, 1975.
 Marsh, J. L. and B. J. McCarthy, *Biochem.* 13, 3382-3388, 1974.
 Melchior, W. B., and P. H. von Hippel, *Proc. Nat. Acad. Sci. U.S.A.* 70, 298-302, 1973.
 Morrow, J., Ph.D. Thesis, Stanford University, 1974.
 Murray, M. G., R. E. Cuellar, and W. F. Thompson, *Biochemistry*, in press, 1978.

HIGHER DERIVATIVE ANALYSIS OF THERMAL DENATURATION PROFILES OF REASSOCIATED REPETITIVE PEA DNA

Richard E. Cuellar, Glenn A. Ford, Winslow R. Briggs, and William F. Thompson

Recently, it has been possible to show that reassociated repetitive DNA se-

quences from plants could be fractionated according to thermal stability (by

elution from hydroxylapatite), and each fraction then reassociated again to yield duplexes with thermal stabilities similar to the original fraction from which they were derived (Bendich and Anderson, 1977; Bouchard and Swift, 1977). Such experiments strongly suggested that repetitive sequences existed in "homogeneous" families characterized by a thermal stability indicative of a particular degree of intrafamilial sequence divergence.

Encouraged by these findings, we developed methods of analyzing high-resolution thermal denaturation profiles for the presence of discrete melting components. It was possible to focus on effects of base-pair mismatch alone by melting and reassociating DNA in 2.4M tetraethylammonium chloride (TEACl), which virtually eliminates any effect of base composition on melting behavior (Melchior and von Hippel, 1973). We reasoned that under these conditions the first derivative of the melting curve for a DNA preparation with only a single component of discrete thermal stability should appear Gaussian. First derivatives of melting curves for DNA preparations containing more than one thermal component should show some fine structure analogous to that of a complex absorption spectrum; one should be able to resolve the various thermal components by using curve-fitting techniques developed at this Department (Year Book 67, pp. 535-536, 536-546). In addition, one should be able to analyze these first-derivative curves by using the higher derivative techniques developed by Butler and Hopkins (1970a, 1970b) to resolve individual absorption bands from absorption spectra showing fine structure.

An illustration of the higher-derivative technique applied to pea (*Pisum sativum*) and *Escherichia coli* DNA's is shown in Fig. 39. The curves shown represent actual melting data and manipulations of the data as plotted by the

Hewlett-Packard 2116 C minicomputer interfaced with an x-y plotter. Native DNA, either pea or *E. coli*, behaved nearly identically upon first and fifth derivative analysis. This result is an indication that the TEACl system was working correctly, and that the higher derivative analysis might detect a single component in a melting curve as it could in an absorption spectrum.

The reassociated pea and *E. coli* DNA's, however, behaved quite differently (Fig. 39). The reassociated *E. coli*

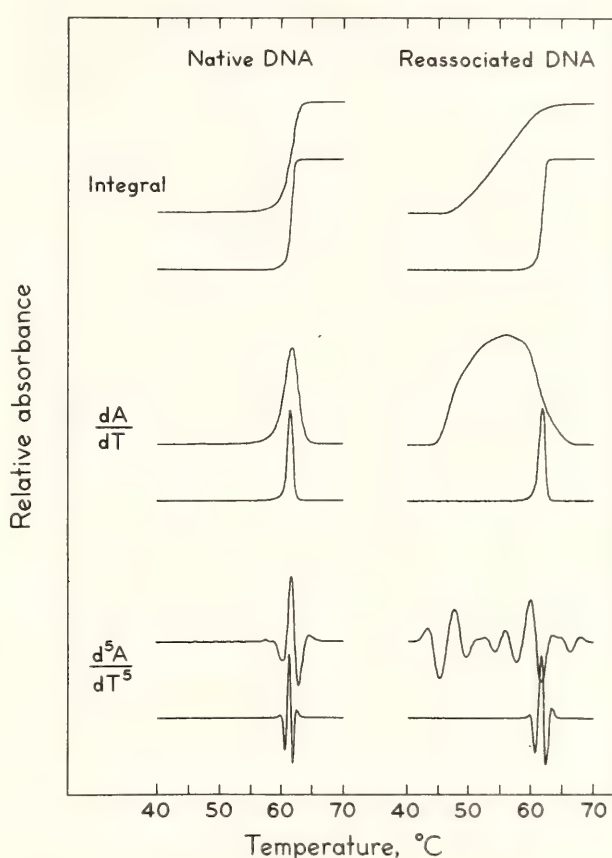


Fig. 39. Comparison of thermal denaturation profiles of pea and *E. coli* DNA's for native (left) and reassociated (right) DNA. For each pair of curves, the upper curve is for pea, and the lower for *E. coli*. DNA's were heated from 45° to 70°C at a rate of 0.25°C/1 min in 2.4M TEACl, pH 7.0. The DNA was then allowed to reassociate to equivalent *Cot* 6 at 45°C and remelted at the same rate, etc. First-derivative (dA/dT) analysis was performed at dx interval = 18, then smoothed three times with a 9-pt averaging procedure. Successive derivatives up to the fifth were performed at dx = 15, 12, 11, 10. All curves are normalized to the same size for clarity.

DNA appeared very much like its corresponding native DNA in that the reassociated *E. coli* had very sharp single first- and fifth-derivative peaks upon analysis. The integral and first-derivative curves of reassociated pea DNA show that melting occurred over a very wide range of temperature, unlike the *E. coli* DNA. The broadening of the reassociated pea melting profile could only be caused by the reaction of divergent but related repetitive sequences to form mismatched duplex molecules with diminished thermal stability. The first-derivative curve shows some asymmetry, which might suggest implicit thermal components but is hardly definitive. However, the fifth derivative yields a great deal of information not found at the integral or first-derivative level. We observe no less than five legitimate peaks in the fifth-derivative curve, which may indicate that at the temperature coincident with a given peak, a certain class of sequences with a characteristic thermal stability is melting rapidly compared to sequences of higher or lower thermal stability.

It has been possible to fit Gaussian components corresponding to the peaks of the fifth-derivative curve to first-derivative melting curves. With the aid of RESOLV (a computer program with curve-fitting capacity; see *Year Book 67*, pp. 536–546) we are able to do this analysis reproducibly for reassociated repetitive pea DNA samples, provided they had been reassociated and melted in precisely the same way. The components observed upon analysis of several independent experiments with reassociated pea DNA are remarkably similar in their modal thermal stabilities. Three major components cluster at $51^{\circ} \pm 1^{\circ}\text{C}$; $55.5^{\circ} \pm 1^{\circ}\text{C}$; and $59.5^{\circ} \pm 1.5^{\circ}\text{C}$. Other

minor components are also observed, but these are more variable between experiments.

We favor the interpretation that the thermal components identified by fifth-derivative analysis and quantitated by RESOLV (*Year Book 67*, pp. 536–546) are representative of groups of distinctive families of repetitive sequence displaying characteristic melting behavior.

The higher derivative analysis we have used allowed us to detect features of thermal-denaturation profiles which could not have been studied otherwise. It represents, to our knowledge, the first successful method for describing complex populations of mismatched reassociated sequences in terms of individual components with characteristic modal temperatures. This approach should provide a powerful tool which should be useful in further studies of repetitive DNA organization and evolution. These studies are appearing in greater detail elsewhere (Cuellar *et al.*, 1978).

REFERENCES

- Bendich, A. J., and R. S. Anderson, *Biochemistry* 16, 4655–4663, 1977.
Bouchard, R. A., and H. Swift, *Chromosoma* 61, 317–333, 1977.
Butler, W. L., and D. W. Hopkins, *Photochem. Photobiol.* 11, 439–450, 1970a.
Butler, W. L., and D. W. Hopkins, *Photochem. Photobiol.* 11, 451–456, 1970b.
Cuellar, R. E., G. A. Ford, W. R. Briggs, and W. F. Thompson, *Proc. Nat. Acad. Sci. U.S.A.*, 1978.
Melchior, W. B., and P. H. Von Hippel, *Proc. Nat. Acad. Sci. U.S.A.*, 70, 298–302, 1973.

BLUE-LIGHT-INDUCED CHLOROPLAST AGGREGATION AND CORTICAL FIBER RETICULATION IN THE ALGA *Vaucheria*

Michael R. Blatt and Winslow R. Briggs

The chloroplasts of many higher plants and some algae undergo subcellular re-distributions in response to directional illumination. These phenomena, collectively referred to as light-induced chloroplast orientation movements, include photoresponses involving light-induced or light-inhibited chloroplast movement, as well as light-induced alterations of chloroplast orientation and conformation (Haupt and Schoenbohm, 1970). These orientation movements reflect both the spatial distribution of incident light within the plant cell and its intensity, and they allow the plant to maximize its photosynthetic potential under less than optimal conditions of illumination while protecting the chloroplast from high, presumably damaging light intensities (Lechowski, 1974).

In all likelihood the sensory transducing mechanism responsible for the light-induced orientation movements is separate from the chloroplast (Haupt and Schoenbohm, 1970). Mechanistically, though, the link between photon absorption and chloroplast movement and orientation remains largely a mystery. Evidence indicates that the light-induced movement of chloroplasts of the alga *Mougeotia* is dependent upon the interactions of an actomyosin system (Wagner *et al.*, 1972). Indeed, Schoenbohm (1975), observing that the number and arrangement of cytoplasmic fibers associated with the chloroplasts of *Mougeotia* are altered coincident with the initiation of the photoresponse, predicted a micro-filament-coupled regulatory function potentiated by light.

A similar situation appears to be the

case in the filamentous alga *Vaucheria sessilis* (Vauch.) D.C. (Xanthophyceae). Point illumination with low-intensity blue light induces the chloroplasts and other organelles which normally stream in the cytoplasm of *V. sessilis* to aggregate in the illuminated region of the algal filament (Fischer-Arnold, 1963). Aggregation is passive, and results from the "trapping" of the organelles as they stream into the blue light. We have observed that aggregation is preceded by and may be dependent upon the localized formation of a cortical fiber reticulum in the light. Figure 40 depicts the normal sequence of events in a dark-adapted algal filament after the onset of actinic blue-light irradiation. The line drawings shown here are tracings taken from a cinematographic recording of aggregation. We employed Nomarski D.I.C. optics to section the algal cell optically and reveal the cortical fibers, 0.5 to 1.0 μm in diameter, which normally are longitudinally oriented within the cell and appear to guide the streaming of organelles. In this film sequence the first signs of the formation of a network or reticulum of cortical fibers are evident within 20 sec on the onset of blue illumination ($t=0$ sec). Chloroplast aggregation, however, did not begin until 10 to 20 sec later (data not shown). Furthermore, reticulum formation is reversible on roughly the same time course as aggregate dispersal, and preliminary spectral and kinetic data (not shown) also point to a strong correlation between the two photoresponses. This sequence of events is regularly repeatable.

It seemed possible that fiber reticula-

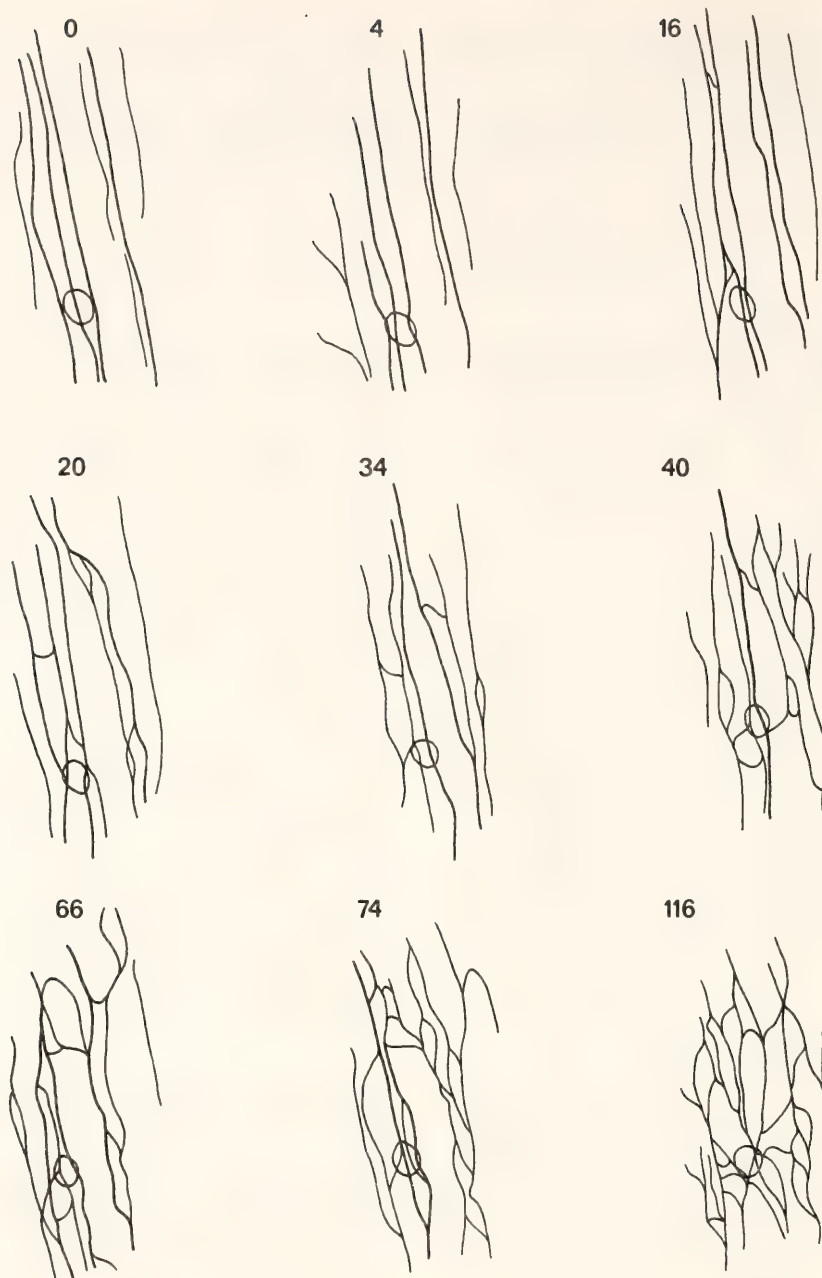


Fig. 40. Tracings of the cortical fibers in a single region of a filament of *V. sessilis* exposed to actinic blue light visible with Nomarski D.I.C. optics. The tracings were made from a time-lapse film of aggregation. The numbers above each tracing refer to the seconds elapsed after the onset of actinic irradiation ($t=0$ seconds). The single circle in each tracing is the outline of a $3\text{-}\mu\text{m}$ diameter chloroplast included as an internal scalar. The lighting necessary for the filming was achieved by combining nonactinic background lighting (wavelengths greater than 560 nm , Corning CS3-66) with the condensed beam from a second light source. The combination was accomplished with a half-silvered mirror (Balzers TF-MT-45) placed beneath the microscope condenser. The actinic beam was first filtered with a 478-nm interference filter (Balzers B-40, HBW 8 nm), and the final beam intensity was approximately $300\text{ ergs cm}^{-2}\text{ sec}^{-1}$. Aggregation, in this instance, began roughly 30 to 40 seconds following the onset of 478-nm illumination. Cortical fiber reticulation, however, can be seen to occur here after as little as 20 seconds of blue light.

tion might be causally related to organellar aggregation in *Vaucheria*. For this reason we investigated the in vivo effects of the *Amanita* toxin, phalloidin,

on light-induced chloroplast accumulation. Wieland and his collaborators (see Wieland, 1976) have found that phalloidin and related phallotoxins bind

tightly but noncovalently (approx. $K_a = 10^8$) to actin in vivo and in vitro. Phalloidin will stabilize F-actin against a variety of harsh chemical and physical treatments which normally depolymerize the actin. Phalloidin will also protect F-actin from the action of the drug cytochalasin B, which is a potent inhibitor of actomyosin-related cell motility processes in both plant and animal systems. In vitro, and in many cases in vivo, cytochalasin B disrupts actin filaments and filament bundles (Goldman *et al.*, 1976). However, protection of actin by phalloidin from the action of cytochalasin is not complete, at least in vitro, and the two drugs may be virtually titrated against one another, resulting in varying degrees of F-actin stability. Surprisingly, phalloidins do not appear to inhibit the normal interactions of actin and myosin.

In preliminary investigations we have found that if *V. sessilis* is exposed to millimolar concentrations of phalloidin, streaming will continue unperturbed, and that subsequent treatment with cytochalasin B is similarly without effect (Fig. 41), although treatment of the algae with cytochalasin in the absence of phalloidin radically alters the appearance of the cortical fibers (not shown) and inhibits streaming (Fig. 41). Furthermore, if dark-adapted phalloidin-treated algal filaments are point-irradiated with low-intensity actinic blue light, neither reticulation nor aggregation occur (not shown). Subsequent treatment of these algae to 50 $\mu\text{g}/\text{ml}$ cytochalasin B, however, will restore light-induced aggregation (not shown).

We suspect the cortical fibers in *Vaucheria* represent large bundles of actin filaments which may participate in generation of the shear force responsible for organellar streaming (Williamson, 1976). Consistent with the observations above, cortical fiber reticulation could then reflect a light-induced development of instability in these microfilament

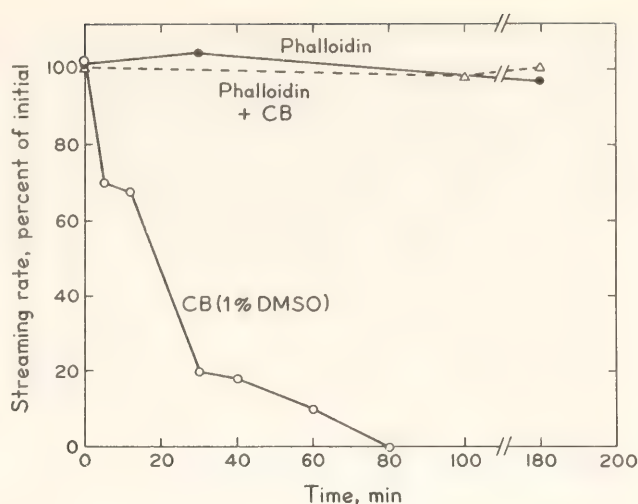


Fig. 41. The influence of 50 $\mu\text{g}/\text{ml}$ cytochalasin B (CB, open circles), phalloidin (closed circles), and 1mM phalloidin plus cytochalasin (triangles) on the rate of streaming in *Vaucheria sessilis*. Cytochalasin B was dissolved in dimethylsulfoxide (DMSO) at a ratio of 5 mg/ml and diluted 100-fold with algal growth medium for use. Phalloidin was dissolved directly in the growth medium. The algae were treated with the drugs by perfusion of media containing cytochalasin or phalloidin under the coverglass on the microscope slide. Measurements of chloroplast streaming rates were made visually with the aid of an ocular micrometer. Each set of points is normalized to the streaming rate of the particular alga prior to drug treatment (the zero time-point), and each point represents the mean of three to five consecutive measurements. Standard errors were never greater than 15% of the mean value. Actual mean initial streaming rates: CB, 15.2 $\mu\text{m}/\text{min}$; phalloidin, 19.2 $\mu\text{m}/\text{min}$; CB plus phalloidin, 19.0 $\mu\text{m}/\text{min}$. For combined treatment of the algae with cytochalasin and phalloidin, the algae were pretreated with the phalloidin-containing medium for 30 min prior to perfusion with the cytochalasin-containing solution. Two-percent DMSO had no measurable effect on the rate of streaming over a 3-hr period (data not shown).

bundles, which would lead to reticulation. Reticulation could in turn disrupt the normal patterns of intracellular motility sufficiently that aggregation ensued. However, further clarification of the processes underlying reticulation and aggregation must await the definitive identification of the cortical fibers in *Vaucheria*.

REFERENCES

- Fischer-Arnold, G., *Protoplasma* 56, 495–520, 1963.
- Goldman, R., T. Pollard, and J. Rosenbaum, in *Cell Motility*, Cold Spring Harbor Laboratory, Cold Spring Harbor, New York, 1976.
- Haupt, W., and E. Schoenbohm, in *Photobiology of Microorganisms*, P. Halldal, ed., pp. 283–307, Wiley Interscience, London, 1970.
- Lechowski, Z., *Acta Soc. Bot. Polon.* 43, 531–540, 1974.
- Schoenbohm, E., *Ber. Deut. Bot. Ges.* 88, 211–224, 1975.
- Wagner, G., W. Haupt, and A. Laux, *Science* 176, 808–809, 1972.
- Wieland, T., in *Molecular Basis of Motility*, L. Heilmeyer and J. Rüegg, eds., pp. 203–213, Springer-Verlag, Berlin, 1976.
- Williamson, R., in *Transport and Transfer Processes in Plants*, pp. 51–58, Academic Press, New York, 1976.

LIGHT-ENHANCED GEOTROPIC SENSITIVITY IN MAIZE ROOTS: POSSIBLE INVOLVEMENT OF PHYTOCHROME

Peter H. Quail and Winslow R. Briggs

It is well established that in the root the geotropic stimulus is perceived by the root cap (see Juniper, 1976, and Wilkins, 1976, for reviews). It has also been reported that light enhances the geotropic sensitivity of roots (Lake and Slack, 1961; Scott and Wilkins, 1969; Pilet, 1973), and there is evidence that the photoreceptor for the enhancement response is likewise located in the root cap (Wilkins and Wain, 1975; Pilet, 1975, 1976). The immunocytochemical demonstration of the presence of high levels of phytochrome in the root cap (Pratt and Coleman, 1971) and its established role in the adhesion of root tips to a negatively charged glass surface (Tanada, 1968; Racusen and Miller, 1972) raises the question of whether or not this pigment might mediate the light-induced increase in geotropic sensitivity. Tepfer and Bonnett (1972) have provided evidence to this effect for *Convolvulus* roots. This is the only documented study of phytochrome involvement in this response, although a preliminary report suggests that a similar situation might exist in maize (McNitt *et al.*, 1974). Maize roots were examined in the present study in an attempt to determine

whether or not phytochrome can mediate the light response in that tissue.

Zea mays L. (WF9 × Bear 38, Bear Hybrid Co., Decatur, Ill.) seeds were soaked for 3 hr in tap water at room temperature and then transferred to 1.5% (w/v) agar in 9-cm plastic petri plates. The seeds were arranged around the perimeter of the plates with the embryo down (flat against the surface of the agar) and toward the center. The plates were wrapped in foil and transferred to the dark for 42 hr at 28°C. Under these conditions the radicle grows horizontally along the top of the agar in radial fashion toward the center of the plate. Routinely at 42 hr from sowing, the emergent radicles were irradiated appropriately, and the plates were inverted and returned to the dark at 28°C.

After 2½ hr more, the roots were rapidly excised from the seed and laid out in the bottom of a petri plate. A shadow graph was immediately made with a photocopier (Fig. 42) and the angle of curvature recorded. A soft foam ring was placed in the petri dish before inversion to act as a "spacer" between the tops of the seeds and the petri plate lid. This held the seeds firmly in place

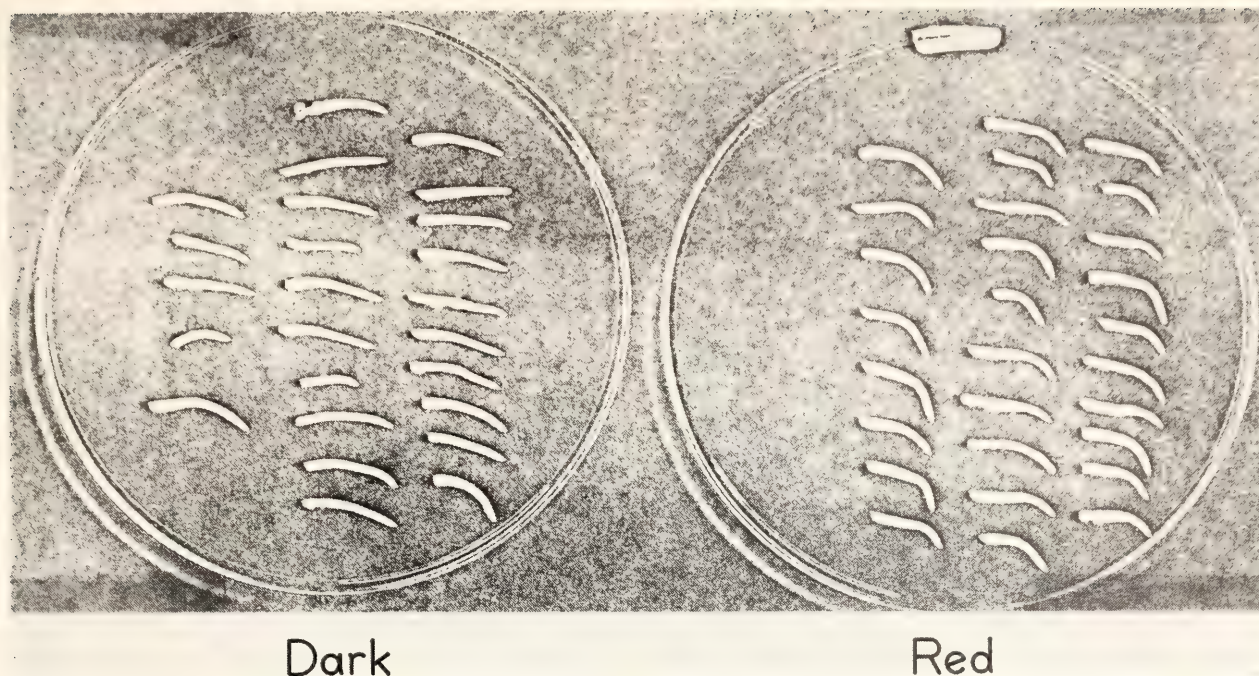


Fig. 42. Geotropic curvature of maize radicles in response to irradiation. *Dark* = dark control; *Red* = red-light-irradiated sample. Seeds were germinated and radicle growth allowed to proceed in darkness for 42 hr at 28°C. At that point the gravitational stimulus was initiated by inversion of the petri plates as described in the text, and 10 nE cm⁻² of 660-nm light was administered in a 10-sec pulse to the irradiated sample. After an additional 2½ hr in the dark at 28°C, the apical root segments were rapidly excised, arranged in petri plates as indicated, and photocopied—leaving the white, reflective cover of the photocopier open to produce a black background. All manipulations up to the point of excision were performed in total darkness. Details of the light source are given in the legend of Fig. 43.

upon inversion while allowing the horizontally grown radicles to experience the gravitational stimulus in the absence of any underlying solid support.

Preliminary experiments showed that light did indeed stimulate the geotropic response in this maize variety (Fig. 42) but that the effect was on the *rate* of curvature rather than on any absolute capacity to perceive gravity. Dark controls responded to gravity as well, but light accelerated the rate of curvature. A period of 2½ hr from the irradiation treatment and the onset of the gravitational stimulus (always initiated simultaneously) was found to maximize the differential between treated and control tissue. Control experiments showed that the direction of irradiation (from above or below the plate) was immaterial; no phototropic component was detected in the response. It was found, however, that

even short exposures to our green safe-light elicited a partial response (cf. Tepfer and Bonnett, 1972; McNitt *et al.*, 1974). Therefore, the experiments reported here were performed in complete darkness (except for the irradiation treatments) up to the point of excision. The number of emergent radicles per plate (= per treatment) ranged from 22 to 31, and each treatment was repeated at least once.

Figure 42 shows a photocopied "shadowgraph" comparing dark control and red-irradiated tissue. Figure 43a shows the dose-response curve for red-light-enhanced curvature. The response threshold appears to lie in the region of 0.1 nE cm⁻² and to saturate at 10 nE cm⁻². This threshold is about four orders of magnitude higher than that reported by Tepfer and Bonnett (1972) for *Convolvulus*. McNitt *et al.* (1974) report that

0.56 nE cm⁻² of 660-nm light is effective in their maize variety.

Figure 43b illustrates the effectiveness of far-red light in reversing the response induced by a dose (10 nE cm⁻²) of red light that is saturating for this response. Three points are apparent: (a) Far-red light does reverse the red-light effect completely down to the level of the far-red control; (b) far-red alone induces a substantial response; and (c) the far-red light dose required for maximum reversal is two orders of magnitude greater than the inductive red dose.

The data indicate that phytochrome does mediate the red-light enhancement of geotropic sensitivity in the present tissue. Moreover, the sensitivity of the response to FR alone as well as to low doses of red light, plus the requirement for high doses of FR to reverse the R effect, are all consistent with the notion that conversion of only a small proportion of the total phytochrome to Pfr saturates the response. The present data do not preclude the possible involvement in this response of other photoreceptors (such as the blue-light photoreceptor).

REFERENCES

- Juniper, B. E., *Annu. Rev. Plant Physiol.* **27**, 385–406, 1976.
 Lake, J. V., and G. Slack, *Nature* **191**, 30–32, 1961.
 McNitt, R. E., L. Glessner, and J. Shen-Miller, *Plant Physiol.* (suppl.) **53**, 46, 1974.
 Pilet, P. E., In *Plant Growth Substances*, Proceedings 8th International Conference, pp. 1104–1110, Hirokawa Publishing Co., Tokyo, Japan, 1974.
 Pilet, P. E., *Physiol. Plant.* **33**, 94–97, 1975.
 Pilet, P. E., *Planta* **130**, 245–249, 1976.
 Pratt, L. H., and R. A. Coleman, *Amer. J. Bot.* **61**, 195–202, 1974.
 Racusen, R., and K. Miller, *Plant Physiol.* **49**, 654–655, 1972.
 Scott, T. K., and M. B. Wilkins, *Planta* **87**, 249–258, 1969.

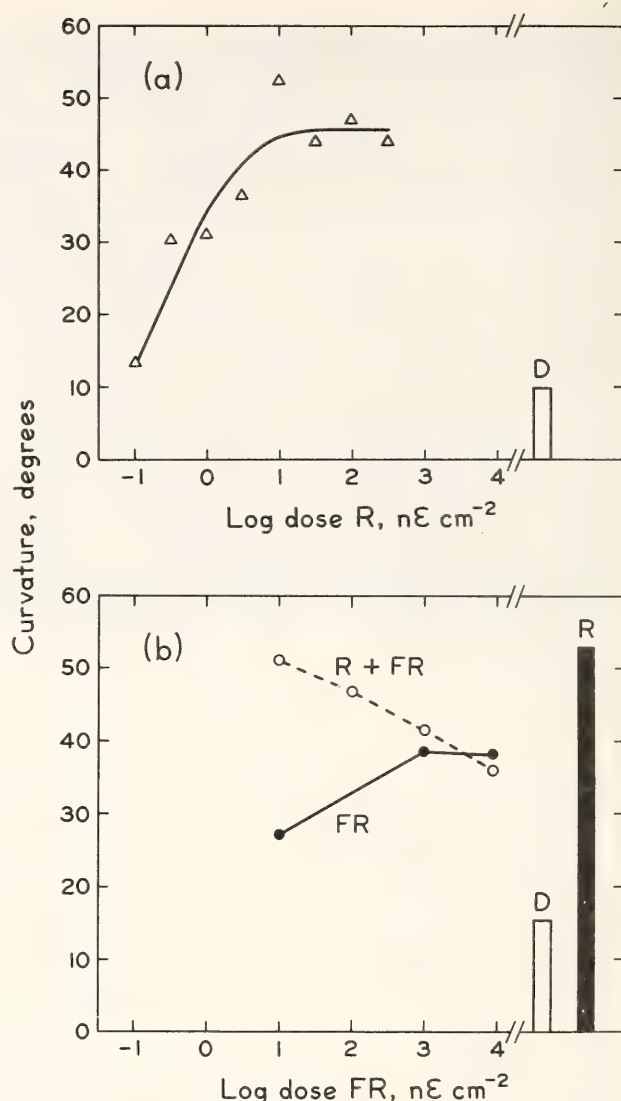


Fig. 43. Geotropic curvature of maize radicles as a function of red (*R*) and far-red (*FR*) light treatments. (a) Curvature in response to increasing doses of red light administered in a 10-sec pulse. *D* = dark control. (b) Curvature in response to increasing doses of far-red light, either alone (solid circles) or following a red pulse of 10 nE cm⁻² (open circles). All irradiations were delivered in 10-sec pulses with no greater than 30 sec darkness between the *R* and *FR* pulses for the *R* + *FR* treatments. *D* = dark control; *R* = sample irradiated with 10 nE cm⁻² of red light only. In all cases the irradiations were administered and the gravitational stimulus initiated simultaneously using 42-hr dark-grown seedlings (see text). After irradiation, the seedlings were returned to the dark for 2½ hr longer before curvature was determined on excised radicles. Irradiations were performed with a rheostat-regulated incandescent lamp filtered through Baird Atomic interference filters: *R* = 660-nm Type B16-A; *FR* = 730-nm Type B16-A. Intensities were determined with a calibrated Epply thermopile.

- Tanada, T., *Proc. Nat. Acad. Sci. U.S.A.* 59, 376-380, 1968.
- Tepfer, D. A., and H. T. Bonnett, *Planta* 106, 311-324, 1972.
- Wilkins, M. B., In *Commentaries in Plant Science*, H. Smith, ed., pp. 171-181, Pergamon Press, Oxford, 1976.
- Wilkins, H., and R. L. Wain, *Planta* 123, 217-222, 1975.

ATP AND PHYTOCHROME PELLETABILITY

Peter H. Quail and Winslow R. Briggs

The level of phytochrome associated with a crude particulate fraction in maize and *Avena* is enhanced 8- to 12-fold by prior irradiation of the intact tissue (Lehmann and Schäfer, 1975; Pratt and Marmé, 1976; Quail, 1978; and Schäfer, 1976) but not by equivalent irradiations of homogenates under appropriate conditions (Pratt and Marmé, 1976; Quail, 1978). In these tissues, therefore, the overall process that leads to such increases in pelletable phytochrome involves one or more steps that are obligatorily intracellular (see Pratt, 1978, for comprehensive discussion). This *in vivo* phase of the phenomenon is initiated upon Pfr formation and requires the continued presence of this form of the pigment to allow the process to run to completion. The reaction will proceed in the dark as long as Pfr remains. There is no requirement for continuous radiant energy input. Premature withdrawal of Pfr by reconversion to Pr immediately terminates the process at the level of pelletability then attained (Lehmann and Schäfer, 1975; Quail, 1978). It is thus possible to induce or terminate the *in vivo* phase of the pelletability response simply by manipulating the form of phytochrome in the cell. Such an approach has been implemented in the present study using the plant material in the growth, irradiation, extraction, and assay procedures described elsewhere (Quail and Briggs, 1978).

Short, high-intensity pulses of red and far-red light have been used to follow,

at room temperature, the kinetics of the *in vivo* dark reaction responsible for irradiation-enhanced phytochrome pelletability. The $t_{1/2}$ for this reaction is 2 sec in air at 25°C, both for *Avena* shoots (Fig. 44) and for maize coleoptiles (data not shown). This is the most rapid Pfr-mediated cellular response so far reported. Anoxia (Fig. 44), NaN_3 (Fig. 45), KCN and p-trifluoromethoxy (carbonyl cyanide) phenylhydrazone reduce the rate (but not the final extent, as shown in Fig. 45) of the reaction by more than an order of magnitude. The rate of the reaction under these conditions is strongly correlated with the inhibitor-induced or anoxia-induced reductions in cellular ATP levels, as determined by the firefly assay (Fig. 46). Likewise, recovery in ATP levels upon withdrawal of the inhibitors is accompanied by a parallel recovery in the rate of the reaction (Quail and Briggs, 1978). The data in Fig. 46 were obtained with the perchlorate procedure for ATP extraction (Strehler, 1968). This method results in an approximately three-fold increase in extractable ATP over the boiling procedure previously used (Quail and Briggs, 1978). Recovery of exogenously supplied ATP is 80-100% with the perchlorate method (H. Gorton, personal communication). The time course of the change in ATP levels under N_2 is qualitatively identical with both extraction methods. Thus, previous conclusions that pelletability is correlated with cellular ATP levels (Quail and

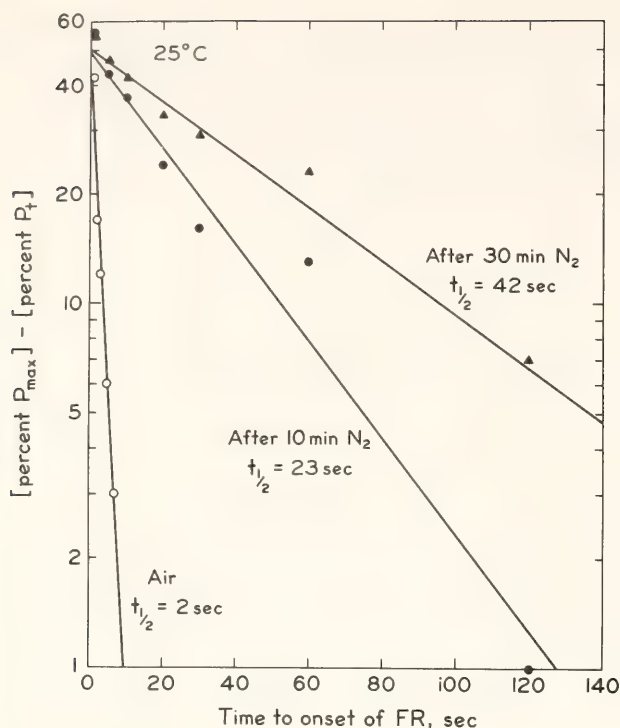


Fig. 44. Semi-logarithmic plot of the time course of the increase in phytochrome pelletability for *Avena* shoots at 25°C as a function of an increasing dark period interposed between 1 sec *R* and 10 sec *FR*. Excised tissue was irradiated as indicated at 25°C, cooled immediately by addition of cold extraction medium on ice, and homogenized. Time zero represents the onset of the 1-sec *R* pulse, so that the first point on the curve is for tissue in which the 10-sec *FR* pulse began immediately at the end of the 1 sec *R* (with no intervening dark period). *R* = 660 nm, Baird Atomic Type B-16A interference filter, 500,000 ergs cm⁻² sec⁻¹; *FR* = Corning Type CSF-69 cut-off filter, 5.4 × 10⁶ ergs cm⁻² sec⁻¹; light source, a 650 W tungsten-halogen lamp. The data are plotted as follows: [%*P*_{max}] = the maximum percent pelletable phytochrome observed for the *R* + *FR* treatment under each of these conditions. [% *P*_{*t*}] = the percent pelletable phytochrome at time *t* on the abscissa. This procedure measures the rate at which pigment molecules are converted from the nonpelletable to the pelletable condition. Tissue maintained in air (open circles); tissue preincubated in a N₂ atmosphere for 10 min (solid circles) or 30 min (triangles) prior to the irradiation cycle.

Briggs, 1978) are unaltered by the findings in Fig. 46. Figure 47 shows the inhibitory effect of NaN₃ on the pelletability response as well as the reversal of this inhibition upon withdrawal of the inhibitor. Cytochalasin B blocks

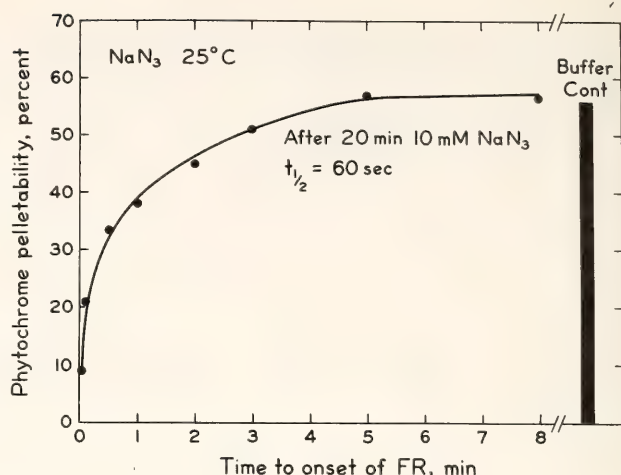


Fig. 45. Phytochrome pelletability in *Avena* as a function of increasing dark period between 1 sec *R* and 10 sec *FR* following prior incubation of excised shoots in 10mM NaN₃ for 20 min in the dark at 25°C. At the end of the incubation the tissue was irradiated at 25°C with 1 sec *R* followed by a variable dark interval (up to 5 min) before the terminal 10 sec *FR* was given. The tissue was then cooled and extracted. The histogram represents tissue incubated at 25°C in buffer for 20 min and then irradiated at the same temperature with 1 sec *R* + 60 sec darkness + 10 sec *FR*. Light source and filters were as for Fig. 44.

cytoplasmic streaming without diminishing the pelletability response to light. Colchicine is likewise without effect.

These data suggest a requirement for phosphorylative energy either directly or indirectly in one or more of the Pfr-dependent intracellular events leading to enhanced phytochrome pelletability. Boeshore and Pratt (1977; and personal communication) have reported that the electrophoretic mobility of pelleted phytochrome on SDS gels is different from that of the nonpelleted pigment. One possible interpretation of the present findings, therefore, is that the intracellular dark reaction responsible for enhanced pelletability represents an ATP-dependent modification of the phytochrome molecule itself, a modification possible only with the Pfr form. It would then be the modified form of the pigment that would possess the capacity to associate with the particulate material. More complicated alternative hypotheses in-

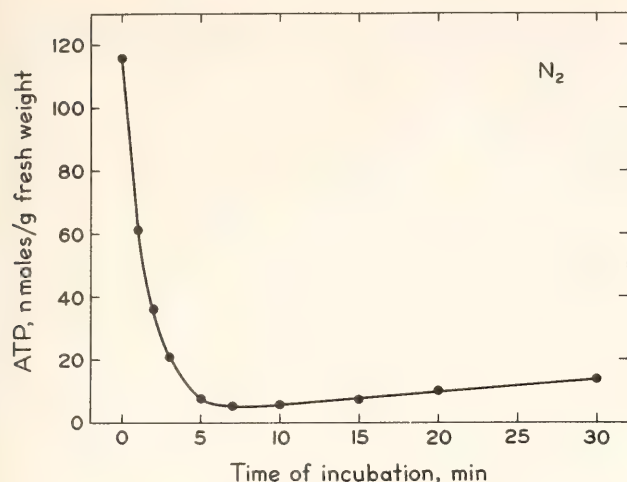


Fig. 46. The effect of anaerobiosis on extractable ATP levels in etiolated *Avena* shoots. Excised shoots (1-g lots) were flushed continuously in the dark at 25°C with a stream of N_2 in a sealed vial for the period indicated. At the end of the incubation period, the vial and tissue were plunged rapidly into liquid N_2 . Four ml of 5% (v/v) perchlorate was pipetted directly into the liquid N_2 in the vial and the latter placed in a -15°C freezer to allow the remainder of the liquid N_2 to evaporate. The tissue and frozen perchlorate were then homogenized directly (without prior thawing) for approximately 1 min with an Ultra-Turrax blender. The homogenate was clarified at 50,000g for 10 min, neutralized with 1N KOH and made up to 10 ml final volume with buffer. The potassium perchlorate precipitate

was allowed to settle, and aliquots of the clear supernatant were removed for immediate assay or frozen overnight at -15°C and then assayed. ATP was determined by the luciferin-luciferase assay (Seitz and Neary, 1976; Strehler, 1968) with commercial ATP as a standard. Firefly lantern extract from Sigma Chemical Co. (St. Louis, Mo.) was reconstituted with water according to manufacturer's instructions, filtered, held on ice for 24 hr to reduce background luminescence, and frozen in aliquots until used. Assays were conducted in a glass-bottomed cuvette designed for vertical light-path spectroscopy. An end-on photomultiplier tube was positioned immediately below the cuvette. The output of the photomultiplier was amplified and recorded on a strip chart recorder. The assay was performed by placing 200 μ l of test solution in the cuvette and rapidly injecting 100 μ l of firefly extract with a syringe while continuously recording the photomultiplier output signal. The peak height of the resulting burst of bioluminescence was the parameter chosen to estimate the ATP present (Seitz and Neary, 1976). Under our conditions of assay, peak height was linearly proportional to the amount of ATP over three orders of magnitude (1-2000 pmoles ATP), and variability between duplicate determinations on the same extract was low (standard error, $\pm 3\%$). All extracts were diluted 50-fold so that the ATP in the diluted aliquots was routinely determined in the range of 5-50 pmoles per assay. A standard of 20 pmoles of ATP freshly diluted from a 100mM frozen stock solution was used to calibrate each experiment.

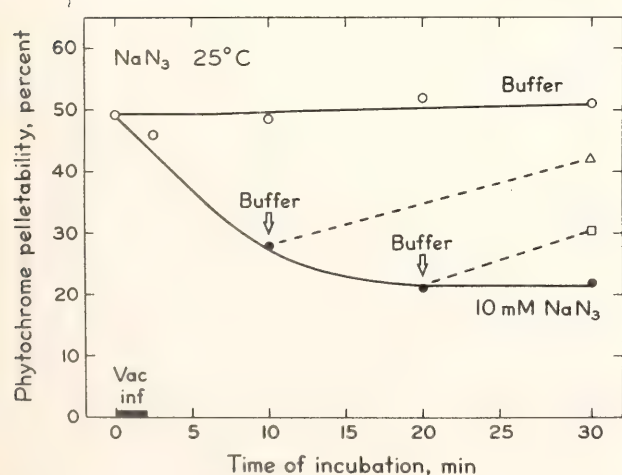


Fig. 47. The effect of prior exposure of excised *Avena* shoots to 10mM NaN_3 on the phytochrome pelletability induced by a standard R/FR irradiation cycle given in vivo. The

tissue was incubated in the dark at 25°C for the periods indicated as described below. At the end of the incubation period a standard irradiation sequence of 1 sec R + 4 sec dark + 10 sec FR was given to each sample at 25°C, prior to cooling and extraction. Two grams of tissue were vacuum-infiltrated (bar, lower left) for 2 min (2×60 sec bursts) in 6 ml of buffer (open circles) or 10mM NaN_3 (closed circles). Air was bubbled through the bathing medium in all samples beginning immediately after the vacuum infiltration and continuing through the remainder of the incubation and irradiation periods. To test for reversal of the NaN_3 inhibition, tissue was preincubated in 10mM NaN_3 for 10 or 20 min as described above, then incubated in buffer (with changes every 5 min) for an additional period before irradiation (triangles, squares). Light source and filters were as for Fig. 44.

volving Pfr-mediated modifications of the binding material via an ATP-dependent mechanism are, however, also compatible with the data. In either case, the question of whether the final binding step follows spontaneously in the cell or is induced artifactually by the preparative procedure remains to be answered (Pratt, 1978; Quail, 1978). This work is presented in detail elsewhere (Quail and Briggs, 1978).

REFERENCES

- Boeshore, M. L., and L. H. Pratt, *Plant Physiol.* 55, 101, 1977.
- Lehmann, U., and E. Schäfer, in *Ann. Europ. Photomorph. Sympos. Abstracts*, H. Smith, ed., pp. 92, Nottingham University Press, Sutton Bonington, 1975.
- Pratt, L. H., *Photochem. Photobiol.* 27, 81–105, 1978.
- Pratt, L. H., and D. Marmé, *Plant Physiol.* 58, 686–692, 1976.
- Quail, P. H., *Photochem. Photobiol.* 27, 147–153, 1978.
- Quail, P. H., and W. R. Briggs, *Plant Physiol.*, in press, 1978.
- Schäfer, E., in *Light and Plant Development*, H. Smith, ed., pp. 45–59, Butterworth, London, 1976.
- Seitz, W. R., and M. P. Neary, in *Methods of Biochemical Analysis*, D. Glick, ed., pp. 161–188, Wiley-Interscience, New York, 1976.
- Strehler, B. L., in *Methods of Biochemical Analysis*, D. Glick, ed., pp. 99–181, Wiley-Interscience, 1968.

IN VIVO PHOSPHORYLATION OF PHYTOCHROME

*Peter H. Quail, Winslow R. Briggs, and Lee H. Pratt**

In vivo-induced phytochrome pelletability appears to involve a Pfr-mediated, ATP-dependent dark process (Quail and Briggs, 1978; and this Report). Moreover, the pelleted molecule exhibits slightly lower mobility on SDS gels than its soluble counterpart (Boeshore and Pratt, 1977; Pratt, 1978) suggesting that the pelleted protein is in some way modified.

In the present study, double labeling in vivo with ^3H -leucine and ^{32}P has been used in conjunction with immunoprecipitation to determine whether direct phosphorylation of the phytochrome protein might be responsible for the pigment's capacity to pellet. SDS gels of immunoprecipitates from prelabeled tissue show significant levels of ^{32}P associated with the 120,000-dalton phytochrome peptide in preparations from both dark and

R/FR (in vivo) irradiated material (Fig. 48; see legend for methods). These data suggest that phytochrome is inherently a phosphorylated protein. Pelleted phytochrome from R/FR-irradiated tissue has twice the $^{32}\text{P}:^3\text{H}$ ratio of the soluble pigment from nonirradiated tissue. However, soluble phytochrome prepared from R/FR-irradiated tissue under nonpelleting conditions (using the same procedures as for nonirradiated material) has a $^{32}\text{P}:^3\text{H}$ ratio indistinguishable from the dark controls. The higher level of ^{32}P associated with pelleted phytochrome would appear to result from differences in the preparative procedures rather than from different initial degrees of phosphorylation. These findings provide no indication, therefore, that the degree of phosphorylation of the phytochrome molecule is responsible for the pigment's capacity to pellet following in vivo irradiations.

* Current address: Department of Biology, Vanderbilt University, Nashville, TN 37235.

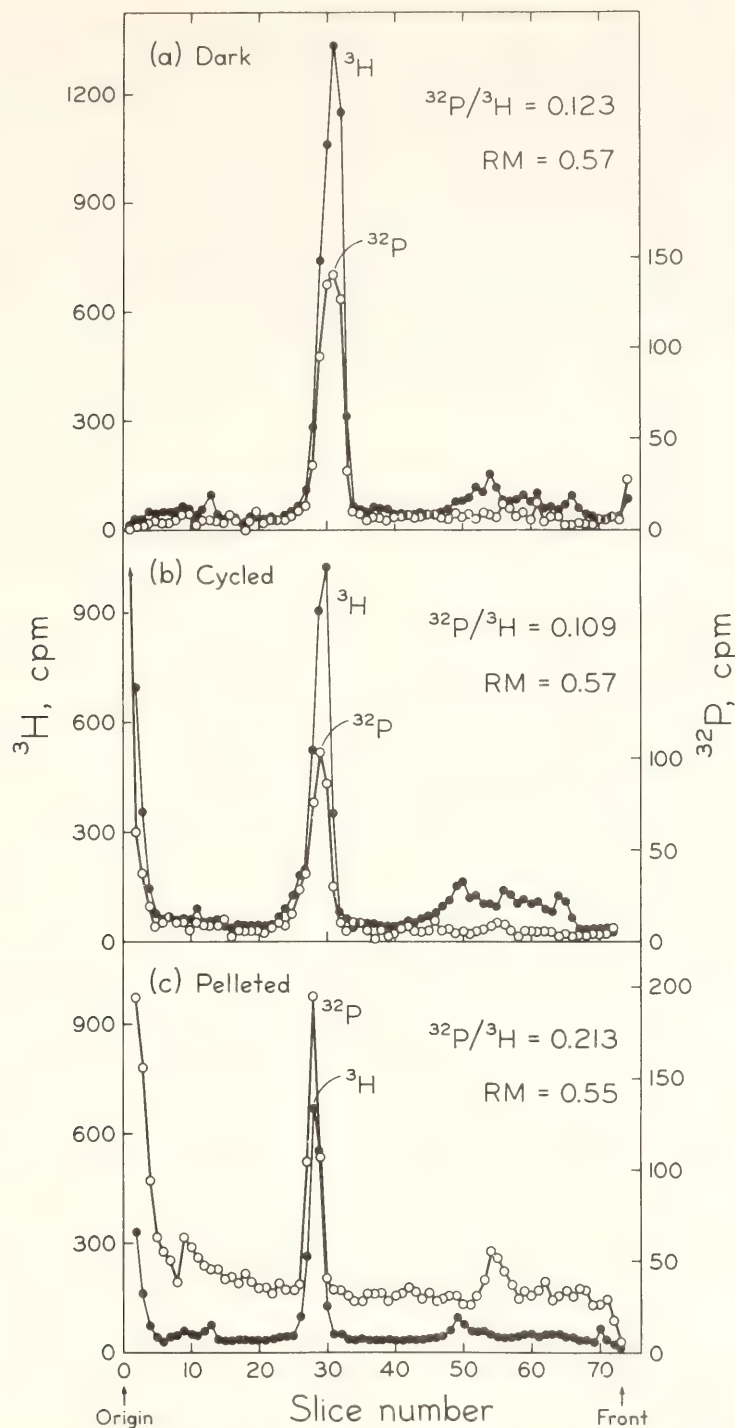


Fig. 48. SDS polyacrylamide gel electrophoresis of phytochrome immunoprecipitates following in vivo labeling. *Avena* (cv. Garry) seedlings were grown for 4 days in the dark at 25°C. On day 3, 750 μCi of ^3H -leucine were applied in 1-2 μl droplets to the coleoptile of the growing shoot. Twenty-four hours later 18-g shoots were harvested and incubated with shaking for 4 hr at 25°C in 15 ml H_2O containing 25 mCi ^{32}P . After rinsing, the tissue was split into three equal lots and treated as follows: (a) *Dark*: nonirradiated tissue was extracted and processed for phytochrome purification to the $(\text{NH}_4)_2\text{SO}_4$ step, following brushite chromatography with the procedure described by Pratt (1973); (b) *Cycled*: tissue was irradiated with 90 sec *R* + 90 sec *FR* at 25°C before extraction and processing as for the dark controls; (c) *Pelleted*: tissue was irradiated as in (b) and extracted in the presence of 20mM Mg^{2+} , and the phytochrome was pelleted as previously described (Quail, 1978). The pellet was resuspended and incubated for 10 min in the presence of 3mM EDTA (causing release of phytochrome from the particulate material), Mg^{2+} was readded (to 20mM), and the particulate material removed by centrifugation. This procedure leaves 80% of the previously pelleted phytochrome

in the supernatant. Phytochrome antiserum was added to all three preparations, and the immunoprecipitates were run on SDS gels as described elsewhere (Pratt, 1978; Kidd *et al.*, 1978). The prominent peak of radioactivity on each gel is the 120,000 phytochrome peptide. $^{32}\text{P}/^3\text{H}$ is the ratio of the total ^{32}P to ^3H counts in the phytochrome band. These totals were computed by integrating the counts under each peak after subtraction of apparent "non-specific" background. The latter represents those numbers of counts that appeared to be relatively constant over several fractions on either side of the peak. This manipulation is of greatest significance in the case of the ^{32}P counts for the pelleted material, where a relatively high level of ^{32}P is spread uniformly across the gel (possibly caused by contaminant RNA carry-over in the procedure). RM = relative mobility of the phytochrome peptide with respect to the heavy IgG band. Note the slightly lower mobility of the pelleted material relative to the dark and cycled phytochrome in agreement with previous observations (Boeshore and Pratt, 1977).

REFERENCES

- Boeshore, M. L., and L. H. Pratt, *Plant Physiol.* 59, 101, 1977.
- Kidd, G. H., R. E. Hunt, M. L. Boeshore, and L. H. Pratt, *Nature*, in press, 1978.
- Pratt, L. H., *Plant Physiol.* 51, 203–209, 1973.
- Pratt, L. H., *Photochem. Photobiol.* 27, 81–105, 1978.
- Pratt, L. H., In *Photochemical and Photobiological Reviews*, Vol. 3, K. C. Smith, ed., in press, Plenum Press, New York.
- Quail, P. H., *Photochem. Photobiol.* 27, 147–153, 1978.
- Quail, P. H., and W. R. Briggs, *Plant Physiol.* in press.

SOME PROPERTIES OF METHYLENE-BLUE-MEDIATED CYTOCHROME REDUCTION BY RED LIGHT IN PARTICULATE FRACTIONS ISOLATED FROM HOMOGENATES OF CORN COLEOPTILES

Susanne Widell, Steven J. Britz, and Winslow R. Briggs

Britz *et al.* (1978; *Year Book* 76, pp. 289–293) have described the reduction of a *b*-type cytochrome by photoexcited methylene blue in particulate fractions from dark-grown corn coleoptiles. The photoexcited methylene blue selectively reduced this cytochrome even in the presence of a large excess of other cytochromes, and the cytochrome became reoxidized in the dark after actinic irradiation. Clearly, it was not exclusively located either in the mitochondria or in the endoplasmic reticulum. Since methylene blue potentiates sensitivity to red light for several reactions that are normally blue-ultraviolet sensitive (see Sagromsky, 1956; and Lang-Feulner and Rau, 1975), and since the action spectrum for photoreduction of a *b*-type

cytochrome in vivo in *Neurospora* mycelium resembles many action spectra for physiological responses to blue and ultraviolet light (Muñoz and Butler, 1975), Britz *et al.* suggested that the *b*-type cytochrome they were studying could be involved in the photoreceptor mechanism in vivo. Goldsmith and Briggs (this Report) have recently shown that the cytochrome reduced by photoexcited methylene blue is spectrally indistinguishable from that reduced either by photoexcited endogenous flavin or by added riboflavin. These results thus strengthen the case for involvement of the cytochrome reduced by photoexcited methylene blue in the normal blue-light photoreception process. The present paper examines some quantitative as-

peets of the methylene blue–cytochrome interaction.

Corn (*Zea mays* L., WF9 × Bear 38) was grown, harvested, homogenized, and fractionated as described previously (Brain *et al.*, 1977). The various particulate fractions obtained after differential centrifugation at 9000, 21,000, and 50,000*g* (designated 9, 21, and 50KP, respectively) were resuspended as described elsewhere (Brain *et al.*, 1977) to yield final protein concentrations of between 2 and 4 mg/ml. The techniques for measuring red-light-induced cytochrome reduction in the presence of methylene blue are described in detail elsewhere (Britz *et al.*, 1978). The results presented below are given as the light-induced absorbance difference between 428 and 410 nm, designated $\Delta(A_{428} - A_{410})$. The maximum change obtainable at saturation for a given variable is designated ΔA_{\max} . The values reported here were reproducible, upon repeated irradiation, to within about 5%.

At a fixed intensity of actinic red light (40 W/m²), increases in the methylene blue concentration up to about 50 μM increased the signal size for the absorbance change, while higher concentrations were somewhat inhibitory. For all three pellets, double reciprocal plots of signal size as a function of methylene blue concentration yielded straight lines. The intercepts and slopes in turn gave values for maximum signal size (ΔA_{\max}), for

the light intensity used, and an apparent Michaelis constant (K_M) for methylene blue. The results are shown in Table 29. Note that for all three fractions, four-fold dilution of the sample leads to a substantial decrease in the apparent K_M . This decrease is probably a function of a decrease in the number of nonspecific sites with high affinity for methylene blue, leading to a higher effective concentration of the dye with respect to the cytochrome. The specific activities for the various fractions are shown in Table 30. Note that the highest specific activity is to be found in the 21KP, despite the fact that the bulk of the mitochondrial cytochromes are located in the 9KP and that the bulk of cytochrome *b*₅ from the endoplasmic reticulum is probably located in the 50KP (Jesaitis *et al.*, 1977; Cross and Briggs, this Report). The increase in specific activity upon dilution is obviously related to the decrease in K_M mentioned above.

The next series of experiments explored the influence of actinic light intensity on signal size. The double-reciprocal plots of signal size as a function of irradiance are shown in Fig. 49. Once again, the intercepts and slopes yield values for maximal signal size and a “ K_M ” for irradiance (expressed in W/m²). The values for the 21KP for three different conditions of methylene blue concentration and protein concentration calculated from the data in Fig.

TABLE 29. Values for $\Delta(A)_{\max}$ and K_M as a Function of Methylene Blue Concentration and Sample Dilution for the Three Fractions*

Fraction	Protein (mg/ml)	$10^3 \times \Delta A_{\max}$	K_M (μM)	Correlation Coefficient
9KP	2.65	2.6	3.0	0.9902
9KP	0.66	1.4	1.6	0.9705
21KP	2.25	10.5	7.6	0.9996
21KP	0.56	3.6	0.4	0.9885
50KP	3.50	10.3	7.2	0.9980
50KP	0.88	4.0	0.4	0.9887

* Values obtained from double-reciprocal plots of signal size against methylene blue concentration. Irradiance throughout was 41 W/m².

TABLE 30. Specific Activity for Cytochrome Reduction Inducible by Red Light in the Presence of Methylene Blue*.

Dilution Factor	Fraction		
	9KP	21KP	50KP
×1	0.98 (21)	4.67 (100)	2.94 (63)
×4	2.12 (33)	6.42 (100)	4.55 (71)

* Calculated from values in Table 29. Numbers in parentheses give values relative to those of the 21KP for a given dilution.

49, are shown in Table 31. Both the diluted sample with 12μM methylene blue and the undiluted sample with 76μM dye are close to saturation with respect to the photosensitizer, and therefore show comparable “*K_M*” values.

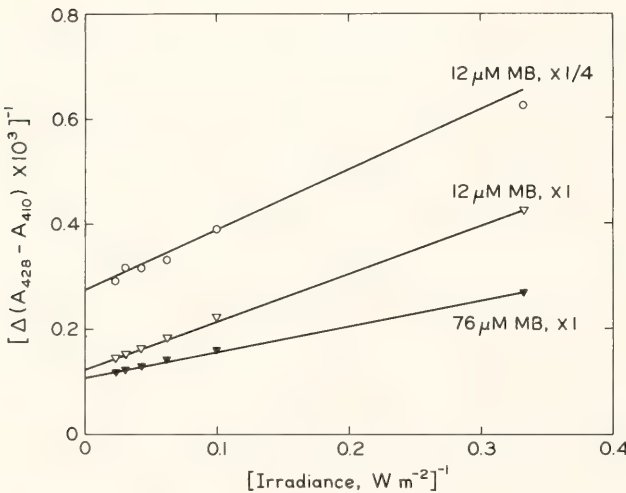


Fig. 49. Double-reciprocal plot of signal size as a function of irradiance for different conditions of sample dilution and methylene blue concentration.

TABLE 31. Values for ΔA_{\max} and “*K_M*” for the 21KP Fraction as a Function of Irradiation under Different Conditions of Methylene Blue Concentration and Sample Dilution*

Methylene Blue Concentration, μM	$10^3 \times A_{\max}$	K_M W/m ²	Correlation Coefficient
76	9.0	3.9	0.9968
12	8.1	7.4	0.9993
12	3.6	3.8	0.9978

* Calculated from the reciprocal plots shown in Fig. 49.

The influence of EDTA concentration on signal size was determined for an undiluted sample with 65μM methylene blue and an irradiance of 20 W/m². Once again, double-reciprocal plots yielded values for ΔA_{\max} and apparent *K_M*. Under these conditions, the *A_{max}* was 9.0×10^{-3} , and the *K_M* 0.32mM, with a correlation coefficient of 0.9241.

The relative spectral sensitivity for the photoreduction was measured between 570 and 700 nm. Monochromatic light was obtained by passing light from a 100 W tungsten-halogen lamp through a Bausch & Lomb monochromator (500 grooves/mm). The methylene blue concentration was 20μM throughout. The intensity at all wavelengths was well below that giving saturation of the absorbance change. The sample was irradiated for 20 sec at each wavelength to assure that it reached steady state, and the measured values corrected for equal incident quanta. The results are shown in Fig. 50. The spectral sensitivity curve matched almost exactly the absorptance spectrum for methylene blue monomers. It had a maximum at 660 nm and only a minor shoulder at 610 nm. It is unlikely that methylene blue dimers participated in any major way in the reaction since they have a much more prominent absorptance peak at 610 nm, and occur in abundance at the methylene blue concentration used for the spectral sensitivity measurements (McKay, 1968).

The system described above provides a convenient method for studying the

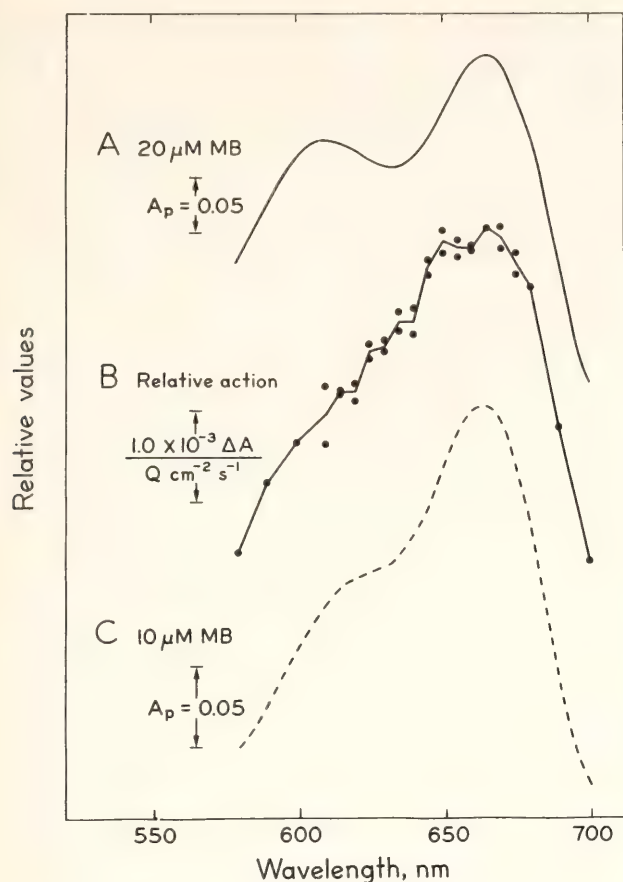


Fig. 50. Comparison of the absorbance spectrum of methylene blue at a concentration at which dimers are present (A) and at a concentration with monomers predominating (C), with the relative spectral-sensitivity curve for cytochrome-photoreduction-mediated methylene blue (B). A_p = Absorbance; Q = quantum flux; MB = methylene blue. ΔA values are for steady-state conditions.

photoinduced reduction of a *b*-type cytochrome, a reaction also induced by photoexcitation of a flavoprotein endogenous

to the membranes or by photoexcitation of added riboflavin (Goldsmith and Briggs, this Report). It has the advantage that actinic and measuring wavelengths are far apart, so that measurements of absorbance changes with the onset of illumination are possible with the use of appropriate filters to protect the photomultiplier from actinic light. As the evidence increases that this *b*-type cytochrome may be involved in photoreception in vivo, further studies of its interaction with several photoreceptor molecules, including methylene blue, should prove very useful.

REFERENCES

- Brain, R. D., J. A. Freeberg, C. V. Weiss, and W. R. Briggs, *Plant Physiol.* 59, 948–952, 1977.
- Britz, S. J., E. Schrott, S. Widell, and W. R. Briggs, *Photochem. Photobiol.* in press, 1978.
- Jesaitis, A. J., P. R. Heners, R. Hertel, and W. R. Briggs, *Plant Physiol.* 59, 941–947, 1977.
- Lang-Feulner, J., and W. Rau, *Photochem. Photobiol.* 21, 179–183, 1975.
- McKay, R. B., in *Cell Structure and its Interpretation*, S. M. McGee-Russell, and K. R. A. Ross, eds., pp. 59–66, Edward Arnold, London, 1968.
- Muñoz, V., and W. L. Butler, *Plant Physiol.* 55, 421–426, 1975.
- Sagromsky, H., *Biol. Zentralblatt* 75, 385–397, 1956.

CHARACTERIZATION OF LIGHT-INDUCED ABSORBANCE CHANGES IN MEMBRANE FRACTIONS FROM CORN COLEOPTILES

Mary Helen M. Goldsmith and Winslow R. Briggs

This laboratory has previously reported on a blue-light-induced reduction of a membrane-bound *b*-type cytochrome in particulate fractions from corn coleoptiles and *Neurospora* mycelium (Brain

et al., 1977). This light response, obtained from membranous fractions isolated by differential centrifugation, is strikingly similar in several respects in the two organisms. A similar particulate

system was also obtained by Galston and Briggs (*Year Book* 76, pp. 293–295) in particulate preparations from etiolated pea seedlings. The photoreceptor for this cytochrome reduction is almost certainly a flavin (Munoz and Butler, 1975). At least in *Neurospora*, the cytochrome which is reduced cannot be assigned exclusively either to mitochondria or to the endoplasmic reticulum. Indeed, in *Neurospora* preparations the distribution of the photoactivity following differential centrifugation coincides closely with that for a known plasma membrane marker enzyme (Brain *et al.*, 1977).

The blue-light-induced cytochrome reduction in corn preparations had proved difficult to study because the signal was not readily obtained and was unstable when it did appear (Brain *et al.*, 1977). However, there were several indications in the literature that the reproducibility and stability problems might be solved. First, Schmidt and Butler (1975), using a solution containing cytochrome *c* and a flavin as a model system, reported that anaerobic conditions greatly stimulated the photoreduction of the cytochrome by FMN. Second, Manabe and Poff (1978) found that the addition of glucose oxidase and its substrate β -D-glucose enhanced the flavin-mediated photoreduction of a cytochrome in a partially purified soluble fraction from *Dictyostelium*. The system required a trace of catalase to remove H_2O_2 produced by the oxidase reaction. The oxidation of glucose to gluconic acid should help to stabilize the oxygen titer at a low value. Third, signals could be obtained from *Neurospora* preparations only when the system was poised at some intermediate redox potential (all cytochromes neither fully oxidized nor fully reduced) whether the measurements were made in vivo (Munoz and Butler, 1975) or in vitro (Brain *et al.*, 1977). Finally, Britz *et al.* (1978) reported that a methylene blue-mediated cytochrome photoreduction in a membrane fraction from corn was strongly

enhanced by increasing the EDTA concentration to 45mM from the 3mM in the buffer normally used to resuspend the membrane preparations. Merkel and Nickerson reported long ago (1954) that EDTA could serve as a source of electrons for reduction of several photoexcited pigments, including both riboflavin and methylene blue.

We have now systematically investigated several of the factors mentioned above to determine their effectiveness in potentiating a stable light-induced cytochrome reduction in corn membranes. The procedure was to optimize one while holding each of the others constant. We report here experiments determining the optimum effective concentrations of glucose, glucose oxidase, and EDTA for the photoreaction. We also report results of preliminary experiments on the effect of temperature on signal size. Additionally, riboflavin can photosensitize the reduction of a cytochrome spectrally identical in the Soret region to that photo-reduced either by the endogenous flavin photoreceptor or by methylene blue, as described by Britz *et al.* (1978). This cytochrome can be spectrally distinguished from the bulk of the cytochromes in the membrane preparations.

Corn seedlings (*Zea mays* L., WF9 \times Bear 38) were germinated and grown in the dark for 4 days at near 100% humidity. The seedlings received 2 hours of red light each night between 2 and 4 a.m. to promote coleoptile growth and suppress mesocotyl growth. The coleoptiles, freed of primary leaves, were harvested onto ice, homogenates were prepared, and the particulate fractions that become pelleted between 9000 and 21,000g (designated 21KP) and between 21,000 and 50,000g (designated 50KP) were collected and resuspended according to the procedures of Brain *et al.* (1977). The only modifications of these procedures were that homogenization was accomplished with an Ultra-Turrax tissue homogenizer and the pellets were re-

suspended in 0.133 ml resuspension buffer without mercaptoethanol, pH 7.0, per gram fresh weight of tissue. Quantitative measurements of flavin concentrations were made with the lumiflavin assay as described by Jesaitis *et al.* (1977). A Perkin-Elmer 356 dual-wavelength spectrophotometer operated in the dual-beam mode was used to measure the signals induced by blue light (light-induced changes in the difference in absorbance between 428 and 410 nm, as described by Brain *et al.*, 1977). Difference spectra were obtained with the Perkin-Elmer in the split-beam mode, and on line with a Hewlett-Packard 2116C computer, as described by Britz *et al.* (1978).

Initially, we added only glucose oxidase (~ 1 mg/ml) and β -D-glucose (~ 8 mg/ml) to our assay mixture. (The glucose oxidase used, Sigma G-6125, was selected because it contained a trace of catalase as a contaminant.) With the enzyme, substrate, and EDTA at a concentration below 10mM, we observed

either no signals at all or, at most, extremely small ones with actinic blue light; however, addition of from 1 to 10 μ M riboflavin to the assay mixture yielded large signals (data not shown). Added riboflavin proved to be active in mediating the photoreduction of the cytochrome only in the presence of the enzyme and its substrate (Table 32, experiment 1).

Glucose oxidase contains FAD that is tightly (but not covalently) bound (Swoboda, 1969). The possibility that the FAD in the enzyme could somehow be functioning as a photoreceptor was therefore investigated. Although glucose oxidase at 1.7 mg/ml contributes about 2 μ M of flavin equivalents (on the basis of the lumiflavin assay) to the reaction mixture, the possibility that this flavin could be functioning as the photosensitizer in the cytochrome reduction appeared remote. Even when the signal no longer increased upon further addition of glucose oxidase (Table 32, experiment

TABLE 32. Role of Glucose Oxidase in Enhancing the Photoreduction of Membrane-Bound Cytochrome

Experiment	Addenda				Response* per mg protein $\Delta(A_{428}-A_{410})$
	EDTA mM	β -D-Glucose mg/ml	Glucose Oxidase mg/ml	Riboflavin μ M	
1	9.8	2.0	0.0
	9.8	5.4	0.0
	8.4	6.4	1.7	5.4	0.0142
2	25	9.1	0.24	...	0.0021
	25	9.1	0.72	...	0.0032
	25	9.1	1.60	...	0.0043
	25	9.1	2.65	...	0.0046
	25	9.1	2.65	1.6	0.014
	25	9.1	2.65	3.2	0.017
	25	9.1	2.65	4.8	0.019
	25	9.1	2.65	6.3	0.020
3	28.8	0.00
	28.8	...	1.15	...	0.004
	28.8	8.3	1.15	...	0.007

* Average of two signals. Variation was less than 5%. Temperatures: Experiment 1, 22°C; Experiment 2, 7°C; Experiment 3, 0°C.

2), addition of riboflavin (to $1.6\mu\text{M}$) brought about a three-fold increase in signal size. Additional riboflavin up to $6.3\mu\text{M}$ brought about additional increase. As mentioned above, obtaining a signal in the presence of $5.4\mu\text{M}$ riboflavin (Table 32, experiment 1) required the presence of the enzyme system. In the absence of its preferred substrate, the enzyme conferred some activity to the system, but the addition of β -D-glucose enhanced the signal (Table 32, experiment 3).

In this system, EDTA presumably donates an electron to the photoexcited flavin, thereby limiting the photodestruction of the photoreceptor (see Schmidt and Butler, 1975). Having determined the optimum conditions for obtaining a signal with an oxygen-scavenging system and added riboflavin, we could now measure the effect of varying EDTA concentration. In the present experiments the optimum concentration of EDTA was reached between 20 and 30mM (Fig. 51). Once we had optimized the EDTA concentration in the presence of riboflavin, the addition of which had permitted us to observe a signal in the first place, we discovered that we could regularly obtain blue-light-induced cytochrome photoreduction even in the absence of exogenously added flavin. The membranes themselves contain sufficient flavin (see Table 33, below) to permit cytochrome reduction at optimal EDTA about one-half as great as that obtained with the addition of $1\mu\text{M}$ riboflavin (Fig. 51). As was the case with the experiments of Brain *et al.* (1977), our initial attempts to obtain a signal had been in the presence of only 3mM EDTA. At this EDTA concentration, the signal obtained with endogenous photoreceptor alone was only about one-third as large ($\Delta A = 0.0002$, Fig. 51) as at the optimal concentration and might easily have passed undetected.

Lowering the assay temperature from 22° to 7°C , with all other factors opti-

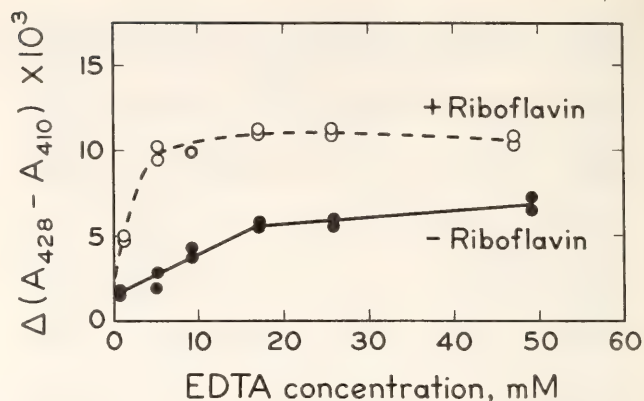


Fig. 51. The absorbance change $\Delta(A_{428} - A_{410})$ as a function of EDTA concentration. A 21KP fraction from corn coleoptiles (7.5-gm fresh weight/ml resuspension buffer) was irradiated with broad-spectrum blue actinic light ($\sim 2 \times 10^4$ ergs $\text{cm}^{-2} \text{sec}^{-1}$), and the resulting signal monitored with a Perkin-Elmer 356 dual wavelength spectrophotometer as described by Brain *et al.* (1977). Increasing amounts of EDTA (from a stock solution of 0.5M in resuspension buffer at pH 7.0) were added to a cuvette initially containing 0.4 ml resuspended 21KP (1.5 mg protein/ml), 9.6 mg/ml β -D-glucose, and 1.33 mg/ml glucose oxidase (Sigma G-6125). The experiment was done both without and with riboflavin added to a final concentration of $1\mu\text{M}$. Solid circles: endogenous flavin only as photoreceptor. Open circles: same plus riboflavin.

mized, appeared to slow down the reoxidation of the photoreduced cytochrome, leading to a still higher steady-state level of reduced cytochrome in the light. This increased level of reduced cytochrome very much improved the accuracy of measurement of signal size on which the assay is based.

Resuspending the membranes in 20 times the usual volume of resuspension buffer and then repelleting (20 min at 21,000g) and again resuspending them did not abolish the signal (Table 33). The washing actually increased the specific activity of the signal while not significantly affecting the flavin/protein ratio (Table 33).

Now that light-mediated cytochrome reduction could be obtained reproducibly either with endogenous flavoprotein of the corn membranes or with externally provided riboflavin, we were able to com-

TABLE 33. The Photoreduction of Membrane-Bound Cytochrome Survives Washing of Membrane Fraction*

Experiment	Signal/mg protein†		Endogenous flavin content μmoles/mg protein × 10 ⁵	
	Washed	Unwashed	Washed	Unwashed
1	0.006	0.003	42	36
2	0.007	0.004	69	55
3	0.007	0.005	51	42

* Glucose oxidase, 1 mg/ml; β-D-glucose, 8 mg/ml; EDTA, 30 mM.

† Average of two signals. Variation less than 5%. Temperature, 0°C.

pare signals induced by blue light in the presence of flavins with those induced by red light when methylene blue was the photosensitizer (Britz *et al.*, 1978). The experiments addressed two questions: First, is the same cytochrome reduced whether endogenous flavin, added riboflavin, or methylene blue is the photoreceptor? And, second, can this cytochrome be spectrally distinguished from the bulk of cytochromes reduced by a strong, nonspecific reducing agent such as dithionite, as had been the case with methylene blue (Britz *et al.*, 1978)?

Using the Perkin-Elmer spectrophotometer in the split-beam mode, on line with the computer system described by Ford and Catanzaro (this Report), we obtained light-minus-dark difference spectra between 405 and 460 nm under three sets of conditions: either (1) blue actinic light and the endogenous flavin only, or (2) blue actinic light and riboflavin in addition (1μM), or (3) red actinic light and methylene blue (20μM). We also obtained for the same membrane preparation dithionite reduced-minus-oxidized difference spectra over the same wavelength range. The details of obtaining these difference spectra, including the methods of averaging and subtracting curves, are discussed elsewhere (Britz *et al.*, 1978).

Regardless of the photosensitizer, whether endogenous flavin, riboflavin, or methylene blue, the difference spectrum

shows a Soret peak at about 429 nm, while the Soret difference peak with dithionite, representing the bulk of the cytochrome in the preparation, was at about 426 nm (Fig. 52). Figure 53 shows that if any one light-minus-dark difference spectrum is subtracted from any other, the result is a straight line across the Soret region. By contrast, subtraction of the dithionite curve from any of the light-minus-dark spectra yields precisely the same negative and positive difference peaks at 421 and 433 nm, respectively. These results provide a sensitive indication that regardless of which of the three photosensitizers is activated, a cytochrome with the same Soret difference maximum is reduced. They also show that the light-induced reduction is highly selective for a cytochrome with this difference maximum, rather than affecting all available cytochromes nonspecifically. Preliminary spectral studies in the alpha-band region support both suggestions, revealing a light-minus-dark difference peak near 558 nm whether the endogenous flavin or riboflavin serves as the photoreceptor. This peak coincides well with the alpha-band difference peak reported by Britz *et al.* (1978), which was obtained with methylene blue as the photoreceptor and red actinic light. Finally, Widell *et al.* (this Report) have shown that the cytochrome reducible by photoexcited methylene blue, like that excited by the endogenous photoreceptor

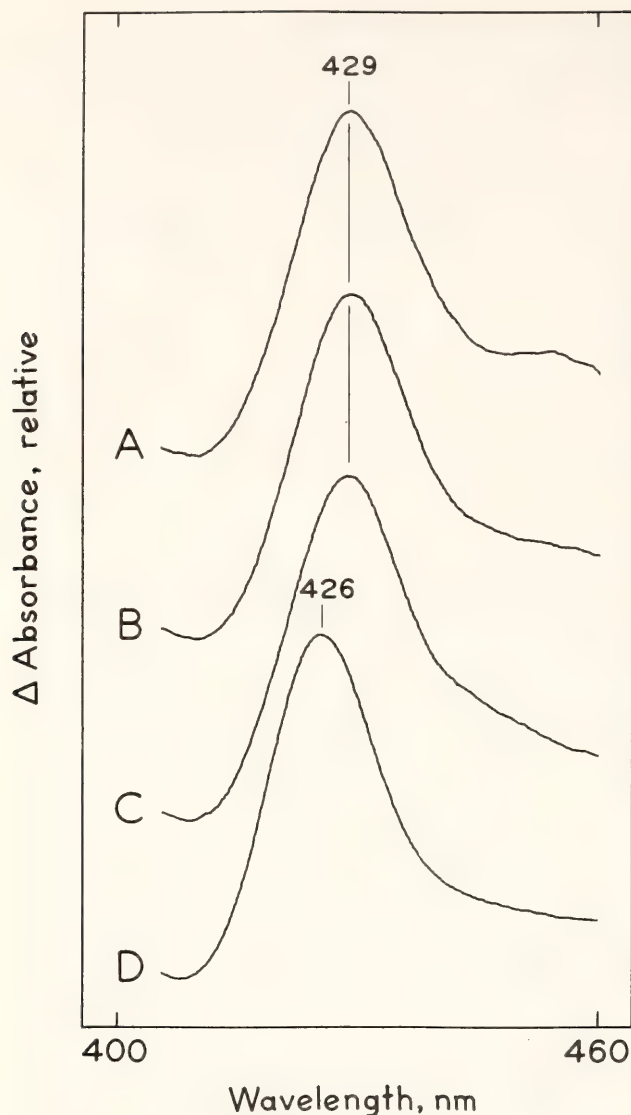


Fig. 52. Comparison of difference spectra induced in the combined 21 and 50KP fractions from corn coleoptiles by actinic light or by dithionite, in the Soret region. Spectra were scanned between 460 and 405 nm with the Perkin-Elmer 356 spectrophotometer in the split beam mode. All samples contained 1.4 mg/ml protein, 20mM EDTA, 8 mg/ml β -D-glucose, and 1 mg/ml glucose oxidase. Riboflavin when present was at a concentration of 1 μ M, methylene blue 20 μ M. Ten difference spectra were averaged for the difference spectrum with the endogenous flavin as photoreceptor (A), and five were averaged for the riboflavin-mediated (B), methylene blue-mediated (C), and dithionite-induced (D) difference spectra. Each of the four averaged curves shown was normalized to the same relative height ($A_{428}-A_{410}$) prior to plotting. The actual absorbance differences between 428 and 410 nm were 0.0013, 0.0037, 0.0049, and 0.022 OD for endogenous flavin, riboflavin, methylene blue, and dithionite, respectively. The Soret difference peak for the bulk of the cytochrome

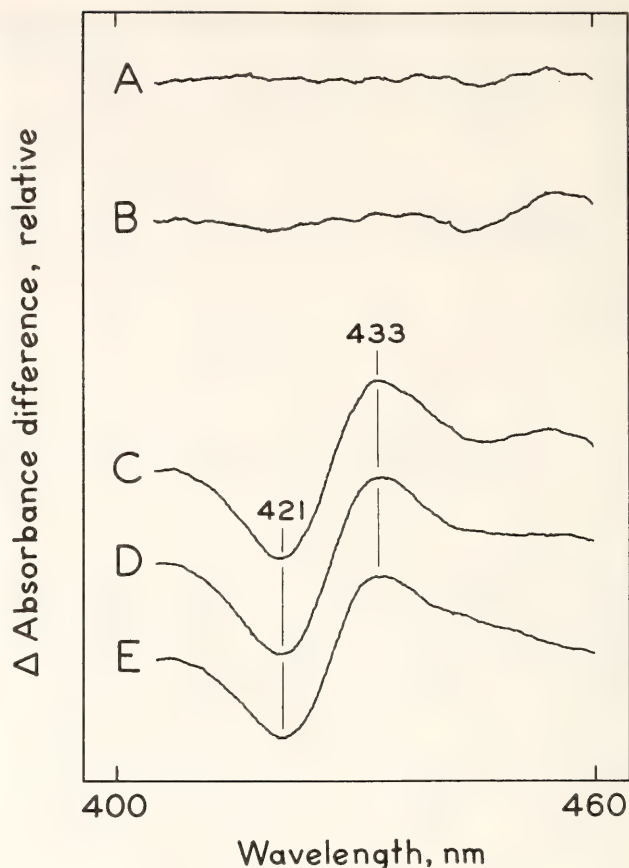


Fig. 53. Curves obtained when one curve in Fig. 52 is subtracted from another curve in Fig. 52. Curve A: curve for riboflavin subtracted from curve for endogenous photoreceptor. Curve B: curve for methylene blue subtracted from curve for endogenous photoreceptor. Curves C, D, and E: dithionite curve subtracted from curves for endogenous photoreceptor, riboflavin, and methylene blue, respectively. The Soret difference peaks for the cytochrome reduced by any of the three photoexcited photosensitizers are indistinguishable, and all differ in the same manner from the Soret difference peak obtained with dithionite as reductant. Subtraction of any curve obtained with one of the three photoreceptors from any other yields a horizontal straight line across the Soret region. Subtraction of the dithionite reduced-minus-oxidized curve from any one of the three light-minus-dark curves yields identical minima and maxima at 421 and 433 nm, respectively.

in the combined 21 and 50 KP membrane fractions clearly lies at a shorter wavelength than those for the cytochrome reduced by the various photoexcited photoreceptors.

in *Neurospora* preparations (Brain *et al.*, 1977), cannot be exclusively located either in mitochondria or in the endoplasmic reticulum. Preliminary differential centrifugation experiments suggest the same conclusion with regard to the endogenous photoactivity reported here—not particularly surprising if the cytochrome reduced by both of these photoreceptors is the same.

REFERENCES

- Brain, R. D., J. A. Freeberg, C. V. Weiss, and W. R. Briggs, *Plant Physiol.* 59, 948–952, 1977.
- Britz, S. J., E. Schrott, S. Widell, and W. R. Briggs, *Photochem. Photobiol.*, in press.
- Jesaitis, A. J., P. R. Heners, R. Hertel, and W. R. Briggs, *Plant Physiol.* 59, 941–947, 1977.
- Manabe, K., and K. L. Poff, *Plant Physiol.*, in press.
- Merkel, J. R., and W. J. Nickerson, *Biochim. Biophys. Acta* 14, 303–311, 1954.
- Muñoz, V., and W. L. Butler, *Plant Physiol.* 55, 421–426, 1975.
- Schmidt, W., and W. L. Butler, *Photochem. Photobiol.* 24, 71–76, 1976.
- Swoboda, B. E. P., *Biochim. Biophys. Acta* 175, 365–379, 1969.

BIOCHEMICAL CHARACTERISTICS OF SOLUBILIZED SITE I AUXIN-BINDING PROTEIN FROM *Zea mays*.

John W. Cross and Winslow R. Briggs

An auxin-binding site (Site I) has been identified in the endoplasmic reticulum membranes of corn coleoptiles by Ray, Hertel, and their colleagues (Ray, 1977; Ray *et al.*, 1977). Although other binding sites have been tentatively identified in the tonoplast (Site II—Dohrmann *et al.*, 1978) and in the plasma-lemma (Site III—Jacobs and Hertel, 1978) membranes of corn, Site I is the only membranous auxin-binding site detected so far with the binding specificity expected for a site of auxin action (Ray *et al.*, 1977). Preliminary reports of auxin-binding sites in the cytosol have also appeared (Ihl, 1976; Wardrop and Polya, 1977), but the data are insufficient to determine their relationship, if any, with auxin action. Moreover, it is possible that these soluble auxin-binding proteins simply represent small microsomal vesicles with Site I activity that were not pelleted in the initial steps of their isolation, as discussed in this report.

To learn more about the auxin-binding components of the corn coleoptile, we have solubilized an auxin-binding pro-

tein from the corn microsomal membranes (which bear all three membranous sites). In last year's Report (Cross *et al.*, 1977) we described the preliminary results of this effort, which was initiated at Stanford by Ulrike Dohrmann and Peter Ray (*Year Book* 75, pp. 395–399). Our first objective this year was to determine whether the protein might bear an ATPase. Such an activity could form the basis of the auxin-induced cellular proton-pump, which is the earliest known effect of this hormone (Jacobs and Ray, 1976). Our results showed that no such ATPase activity is associated with the auxin-binding protein (*Year Book* 76, pp. 299–302; Cross *et al.*, 1978). This result, together with the unsuccessful attempts by several investigators (unpublished) to obtain auxin stimulation of an ATPase *in vitro*, leads us to believe that the auxin-stimulated proton-pump may not be an ATPase. It may instead be the result of the activity of an electron transport chain or other such electrogenic system.

Our next objective has been the characterization of the solubilized binding ac-

tivity, particularly to determine its cellular origin, auxin-binding specificity, and relationship to other cellular components.

Cellular fractionation studies were initiated to determine which of the cellular auxin-binding sites contains this molecule. Homogenized corn tissue was either fractionated by differential sedimentation, or its microsomal membranes

were analyzed by sedimentation to isopycnic equilibrium on sucrose density gradients. Then the resulting fractions were either analyzed for typical marker enzymes or for particulate auxin-binding activity (under conditions which measure only Site I binding), or were extracted to solubilize auxin-binding protein. The resulting distribution of solubilized

TABLE 34. Subcellular Membrane Fractionation (Marker Activity per mg Protein Relative to the Homogenate)

Differential Sedimentation of the Homogenate				
Fraction§	NAA Binding Solubilized	NADH- Cytochrome <i>c</i> Reductase	IDPase	Cytochrome <i>c</i> Oxidase
1. Homogenate	1.00	1.00	1.00	1.00
2. $0.5 \times 10^3 \times g$, 15 min pellet	0.42	0.69	1.92	3.25
3. $9 \times 10^3 \times g$, 15 min pellet	2.41	0.78	0.98	8.59
4. $21 \times 10^3 \times g$, 15 min pellet	6.82	2.08	1.51	1.88
5. $48 \times 10^3 \times g$, 60 min pellet	5.40	2.35	1.52	0.72
6. supernatant	0.49†	0.16‡	1.05	0.

Isopycnic Equilibrium Centrifugation of Microsomal Membranes.

Fraction§	NAA Binding		NADH- Cytochrome <i>c</i> Reductase	IDPase	Cytochrome <i>c</i>
	Solubilized	Native			
1. Total microsomes	1.00	1.00	1.00	1.00	1.00
2. A (15–28% sucrose)	3.45	3.05	3.47	1.36	0.06
3. B (28–33% sucrose)	1.32	1.22	1.05	2.73	0.36
4. C (33–50% sucrose)	0.26	0.30	0.31	1.10	2.99

* The homogenate was sequentially sedimented at the indicated *g*-forces and times. Each pellet was extracted for auxin-binding protein by acetone precipitation and buffer extraction (Cross and Briggs, 1978) or assayed for marker enzymes (Cross and Briggs, 1978).

† This fraction contained 80% of the total homogenate protein and thus 37% of the total auxin-binding activity.

‡ The supernatant has about 20% of this activity. Thus about half of the auxin-binding activity of the supernatant is clearly associated with endoplasmic reticulum fragments not pelleted at this (modest) *g*-force. About 17% of the total binding activity described by Cross and Briggs (1978) is hence unaccounted for. Since the error in measuring NADH-dependent cytochrome *c*-reductase is large, this difference is probably not significant.

§ Microsomes prepared as described by Cross and Briggs (1978) were fractionated on a step gradient into the indicated fractions in the SW27 rotor at 25,000 rpm for 4 hr. The resulting membranous bands were collected, diluted with buffer, and pelleted. These fractions were then assayed for activity as above.

auxin-binding protein (Table 34) resembles that of particulate Site I auxin-binding activity, and the endoplasmic reticulum marker, NADH-dependent cytochrome *c* reductase, rather than the Golgi marker, IDPase or the mitochondrial marker, cytochrome *c* oxidase. Thus, it appears that this protein derives primarily from the endoplasmic reticulum.

If the soluble protein is the same protein as is present in Site I, then it should resemble Site I in auxin-binding specificity. Table 35 shows the relative affinities of Site I and solubilized auxin-binding protein for a series of auxin analogues. The overall patterns of specificity are similar, although the soluble protein has far greater affinity for NAA than does Site I.

We also expect that the solubilized protein should be reduced in its affinity for NAA—but not significantly for IAA—by a low-molecular-weight factor from corn coleoptiles, as is Site I. Our data (not shown) indicate that this is indeed the case. Since the NAA binding affinities of Sites II and III are unaffected by this factor (R. Hertel, personal communication), we can safely conclude that our solubilized protein represents the

active site of binding in the endoplasmic reticulum.

Our data indicate that the binding is due to a single protein of MW \simeq 80,000 (Cross and Briggs, 1978). This same protein is extracted from microsomes by either of two totally different methods (Cross and Briggs, 1978). It has a sulfhydryl group in its active site—as does Site I (Venis, 1977; Cross and Briggs, 1978)—and azide is a competitive inhibitor of auxin binding (unpublished results). This last observation suggests the involvement of a transition element in the active site. Cyanide and carbon monoxide do not affect binding.

These last observations, together with the ER localization of Site I, suggest that this protein could be involved in one of the electron transport systems known to exist there. Since *trans*-cinnamic acid hydroxylase is known to be a component of the endoplasmic reticulum (Benveniste *et al.*, 1978), and since *p*-coumaric acid (its product) serves as a cofactor for the action of IAA-oxidase (Gortner and Kent, 1958), we have examined the interaction of these compounds with the auxin-binding protein, using [¹⁴C]NAA as a probe. Our results indicate that both of these com-

TABLE 35. Relative Affinities of Auxin Binding Sites for IAA and Synthetic Auxins

Analogue	Affinity Relative to IAA	
	Native*	Solubilized†
1. naphthyl-1-acetic acid	5.0	250.
2. naphthyl-2-acetic acid	3.2	80.
3. indole-3-acetic acid	(1.00)	(1.00)
4. indole-3-propionic acid	0.6	6.
5. indole-3-butyric acid	0.4	4.
6. 1-naphthol	0.1	0.6
7. 2,4-dichlorphenoxy acetic acid	0.04	0.12
8. indole-2-carboxylic acid	0.01	0.4
9. benzoic acid	<0.006	0.0005

* Values taken from Ray *et al.* (1977) for intact maize microsomes without added supernatant factor.

† Values taken from Cross and Briggs (1978) for acetone- and buffer-extracted, solubilized protein.

pounds (both non-auxins) can inhibit the binding of NAA to the protein (not shown).

Further experiments are needed to determine whether Site I is indeed associated with an electron transport chain. For instance, does this site have auxin oxidase activity? Or does IAA stimulate the oxidation of other substrates, such as nicotinamide adenine dinucleotides, or intermediates in flavonoid metabolism such as *trans*-cinnamic acid? These questions require further investigation.

REFERENCES

- Benveniste, I., J.-P. Salaün, and F. Durst, *Phytochem.* 17, 359–363, 1978.
- Cross, J. W., and W. R. Briggs, *Plant Physiol.* 62, 152–157, 1978.
- Cross, J. W., W. R. Briggs, U. Dohrmann, and P. M. Ray, *Plant Physiol.* 61, 581–584, 1978.
- Cross, J. W., U. Dohrmann, W. R. Briggs, and P. M. Ray, *Carnegie Inst. Wash. Year Book* 75, 299–302, 1976.
- Dohrmann, U., R. Hertel, and H. Kowalik, *Planta* 140, 97–106, 1978.
- Dohrmann, U., and P. M. Ray, *Carnegie Inst. Wash. Year Book* 75, 395–399, 1976.
- Gortner, W. A., and M. J. Kent, *J. Biol. Chem.* 233, 731–735, 1958.
- Ihl, M., *Planta* 131, 223–228, 1976.
- Jacobs, M., and R. Hertel, *Planta*, in press 1978.
- Jacobs, M., and P. M. Ray, *Plant Physiol.* 58, 203–209, 1976.
- Ray, P. M., *Plant Physiol.* 59, 594–599, 1977.
- Ray, P. M., U. Dohrmann, and R. Hertel, *Plant Physiol.* 60, 585–591, 1977.
- Venis, M. A., *Planta* 134, 145–159, 1977.
- Wardrop, A. J., and G. M. Polya, *Planta* 8, 155–163, 1977.

EFFECTS OF INHIBITORS ON LIGHT-INDUCED ABSORBANCE CHANGES IN CORN MEMBRANE FRACTIONS

Roland J. Caubergs, Mary Helen M. Goldsmith, and Winslow R. Briggs

Goldsmith and Briggs (this Year Book) have described the conditions required to obtain light-induced reduction of a *b*-type cytochrome in membrane fractions from coleoptiles either with or without added riboflavin as photosensitizer. The present article reports further characterization of the system based on experiments with a variety of inhibitors. First, both iodide ion (20mM) which depopulates the triplet state of flavins (Song and Moore, 1968), and phenylacetic acid (30mM) which reacts to form a covalent bond with flavins in the triplet state, effectively inhibit the light-induced reduction. Thus we confirm for

corn the results of Brain *et al.* (*Year Book* 76, pp. 295–299) for *Neurospora* which suggest that the actual photoreceptor is a flavin moiety. Antimycin A (30 μ M) which blocks mitochondrial electron transport from *b* to *c* cytochromes (see Lemberg and Barrett, 1973) had no effect on the reaction; nor did 1mM KCN. Thus the normal mitochondrial electron transport pathway is evidently not involved.

Of special interest, however, are results (Table 36) with salicylhydroxamic acid (SHAM), a known inhibitor of the cyanide-insensitive alternate terminal oxidase pathway in plants (Schonbaum

TABLE 36. Effect of Salicylhydroxamic acid (SHAM) on the flavin-mediated photoreduction of the membrane-bound *b*-type cytochrome.*

Photosensitizer	Concentration SHAM, μ M	Percent Inhibition
Endogenous flavin	10	34
	20	69
	30	80
	40	82
Riboflavin, 3μ M	50	29
	100	39
	300	85
	400	92

* For these experiments, the fraction sedimenting between 21,000 and 50,000 $\times g$ (50 KP) was used. It contains less than 5% of the mitochondria. The $\Delta(A_{428} - A_{410})$ values were: endogenous flavin, 0.0037; 3μ M riboflavin, 0.017. Protein concentrations, 3 mg/ml.

et al., 1971). It strongly inhibited the light reaction with a K_I near 15μ M when endogenous flavin served as photoreceptor and 150μ M with riboflavin as the photosensitizer. The two values are well within the range for the K_I 's of several hydroxamic acid derivatives including SHAM for inhibition of cyanide-insensitive oxygen uptake by mitochondrial preparations (Schonbaum *et al.*, 1971). These results raise questions concerning the relationship between the light-sensitive electron transport system we are studying and the alternate oxidase pathway. Is the effect of the SHAM in the present system completely unrelated to its effects on the alternate oxidase? The alternate pathway is generally considered to be mitochondrial (Solomos, 1977) while the present system does not fractionate with the mitochondria (Goldsmith and Briggs, this *Year Book*). Or, is there some additional alternate oxidase activity in a nonmitochondrial membrane system? Experiments are under way to explore these questions.

REFERENCES

Hemmerich, P., V. Massey, and G. Weber, *Nature* 213, 728-730, 1967.
Lemberg, R. and J. Barrett, *Cytochromes*, Academic Press, London, 1973.
Schonbaum, G. R., W. D. Bonner, Jr., B. T. Storey, and J. T. Bahr, *Plant Physiol.* 47, 124-128, 1971.
Solomos, T., *Annu. Rev. Plant Physiol.* 28, 279-297, 1977.
Song, P.-S. and T. A. Moore, *J. Amer. Chem. Soc.* 90, 6507-6514, 1968.

ERRATUM

Last year the wrong figure was inadvertently submitted by the authors as Fig. 81 in the article by Armond, Schreiber, and Björkman (*Year Book* 76, pp. 335-341). Fig. 54, below, is the one that should have been published. It appears with its proper legend.

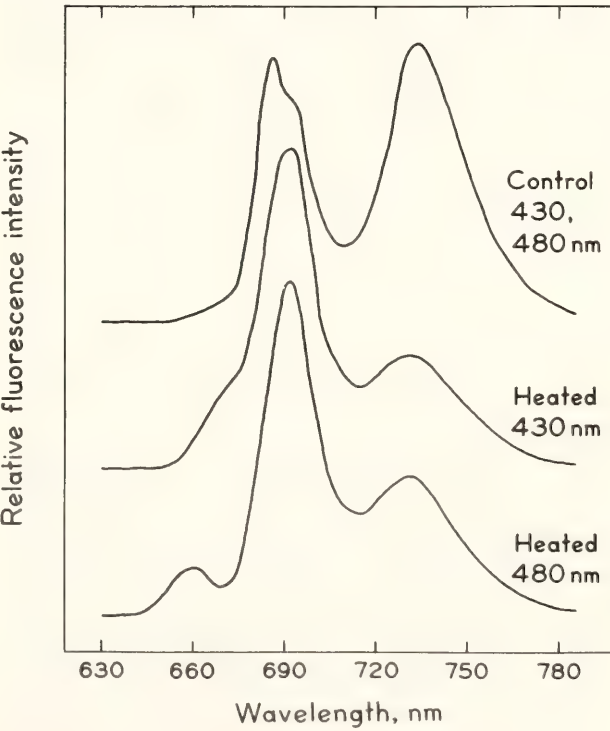


Fig. 54. Chlorophyll fluorescence spectra measured at 77°K for control (unheated) and heated samples of isolated chloroplasts of 32°C-grown *L. divaricata*. Samples labeled "heated" were incubated at 50°C for 5 min prior to freezing in liquid N₂. Spectra were measured in a Perkin-Elmer Fluorescence Spectrophotometer MPF-3L.

BIBLIOGRAPHY

- 608 Armond, P., U. Schreiber, and O. Björkman, Photosynthetic acclimation to temperature in the desert shrub *Larrea divaricata*. II. Light-harvesting efficiency and electron transport. *Plant Physiol.* 61, 411-415, 1978.
- Armond, P., *see* Schreiber, U.
- Avron, M., *see* Schreiber, U.
- 610 Berry, J., and G. Farquhar, The CO₂ concentrating function of C₄ photosynthesis: a biochemical model. In *Photosynthesis 77*, Proceedings of the Fourth International Congress on Photosynthesis, Reading, England, pp. 119-131, D. O. Hall, J. Coombs, T. W. Goodwin, eds., The Biochemical Society, London 1978.
- 619 Berry, J., C. B. Osmond, and G. H. Lorimer, Fixation of ¹⁸O₂ during photorespiration. Kinetic and steady-state studies of the photorespiratory carbon oxidation cycle with intact leaves and isolated chloroplasts of C₃ plants. *Plant Physiol.*, in press, 1978.
- Berry, J., *see* Carey, R.; Ehleringer, J.; Mooney H.; Troughton, J.
- Björkman, O., *see* Armond, P.; Ehleringer, J.; Mooney, H.
- Briggs, W., *see* Britz, S. J.; Cross, J.; Mackenzie, J. Jr.; Quail, P.; Vanderhoef, L.
- 624 Britz, S. J., E. Schrott, S. Widell and W. R. Briggs, Red-light-induced reduction of a particle-associated b-type cytochrome from corn in the presence of methylene blue. *Photochem. Photobiol.*, in press, 1978.
- 633 Britz, S. J., Cytoplasmic streaming in *Physarum*. *Encyclopedia of Plant Physiology*, Vol. V., in press.
- 634 Britz, S. J., Chloroplast and nuclear migration. *Encyclopedia of Plant Physiology*, Vol. V., in press.
- 574 Brown, J., Coupled P700 photooxidation and cytochrome b₆ reduction in a chlorophyll-protein complex. *Photosynthetica* 2, No. 2, 1978.
- 597 Brown, J., Fluorescence spectroscopy of a P700-chlorophyll-protein complex, *Photochem. Photobiol.* 26, 519-526, 1977.
- 604 Cross, J., W. R. Briggs, U. Dohrmann, and P. Ray, Auxin receptors of maize coleoptile membranes do not have ATPase activity. *Plant Physiol.* 61, 581-584, 1978.
- 620 Cross, J. W., and W. R. Briggs, Properties of a solubilized auxin binding protein, from coleoptiles and primary leaves of *Zea mays*. *Plant Physiol.* 62, 152-157, 1978.
- 598 Ehleringer, J., Implications of quantum yield differences on the distributions of C₃ and C₄ grasses. *Oecologia* 31, 255-267, 1978.
- 612 Ehleringer, J., and O. Björkman, Pubescence and leaf spectra characteristics in a desert shrub, *Encelia farinosa*. *Oecologia*, in press, 1978.
- 614 Ehleringer, J., and O. Björkman, A comparison of photosynthetic characteristics of *Encelia* species possessing glabrous pubescent leaves. *Plant Physiol.* in press, 1978.
- Ehleringer, J., *see* Mooney, H.
- Farquhar, G., *see* Berry, J.
- Fork, D., *see* Murata, N.
- 588 Knopf, U., Studies on the bacteriophage PS8 of *Agrobacterium tumefaciens* (Smith and Townsend) Conn.: physico-chemical properties of its DNA. *Microbios* 17, 231-237, 1976.
- 641 Levitt, J., An overview of freezing injury and survival, and its interrelationships to other stresses. In *Plant Cold Hardiness and Freezing Stress*, P. H. Li and A. Sakai, eds., pp. 3-15, Academic Press, New York, 1978.
- Lorimer, G., *see* Berry, J.
- 632 McArthur, J. A., and W. R. Briggs, The effect of red light upon geotropism in pea epixotyls. *Plant Physiol.*, in press, 1978.
- 621 Mackenzie, J. Jr., W. R. Briggs, and L. H. Pratt, Intracellular phytochrome distribution as a function of its molecular form and of its destruction. *Amer. J. Bot.* 65, 671-676, 1978.
- 622 Mackenzie, J. Jr., W. R. Briggs and L. H. Pratt, Phytochrome photo-reversibility: empirical test of the hypothesis that it varies as a conse-

- quence of pigment compartmentalization. *Planta* 141, 129–134, 1978.
- 607 Mooney, H. A., O. Björkman, and G. J. Collatz, Photosynthetic acclimation to temperature in the desert shrub *Larrea divaricata*. I. CO₂ exchange characteristics in intact leaves. *Plant Physiol.* 61, 406–410, 1978.
- 602 Mooney, H. A., J. Ehleringer, and O. Björkman, The energy balance of leaves of the evergreen desert shrub, *Atriplex hymenelytra*. *Oecologia (Berl.)* 29, 301–310, 1977.
- 609 Mooney, H. A., J. H. Troughton, and J. A. Berry, Carbon isotope ratio measurements of succulent plants in Southern Africa. *Oecologia (Berl.)* 30, 295–305, 1977.
- 592 Murata, N., and D. C. Fork, Temperature dependence of chlorophyll *a* fluorescence in lettuce and spinach chloroplasts at subzero temperatures. *Plant Cell Physiol.* 18, 1265–1271, 1977.
- Osmond, C. B., see Berry, J. A.
- Pratt, L. H., see Mackenzie, J., Jr.
- 628 Quail, P. H., and W. R. Briggs, Irradiation-enhanced phytochrome pelletability: requirement for phosphorylative energy in vivo. *Plant Physiol.*, in press, 1978.
- 605 Schreiber, U., and M. Avron, ATP-induced chlorophyll luminescence in isolated spinach chloroplasts. *FEBS Lett.* 82, 159–162, 1977.
- 606 Schreiber, U., and P. A. Armond, Heat-induced changes of chlorophyll fluorescence in isolated chloroplasts and related heat damage at the pigment level. *Biochim. Biophys. Acta* 502, 138–151, 1978.
- Schreiber, U., see Armond, P. A.
- 617 Stein, D. B., and W. F. Thompson, Isolation of DNA from tannin-containing plants. *Plant Sci. Lett.*, in press, 1978.
- 635 Stemler, A., A dynamic interaction between the bicarbonate ligand and photosystem II reaction-center complexes in chloroplasts. *Biochim. Biophys. Acta*, in press, 1978.
- 522 Troughton, J. H., H. A. Mooney, J. A. Berry, and D. Verity, Variable carbon isotope ratios of *Dudleya* species growing in natural environments. *Oecologia (Berl.)* 30, 295–305, 1977.
- Troughton, J. H., see Mooney, H. A.
- 595 Vanderhoef, L. N., and W. R. Briggs, Red-light-inhibited mesocotyl elongation in maize seedlings. I. The auxin hypothesis. *Plant Physiol.* 61, 534–537, 1978.
- Verity, D., see Troughton, J. H.

SPEECHES

- Armond, Paul, and Ulrich Schreiber, Effect of High Temperatures on Photosynthetic Electron Transport Activity and Chlorophyll Fluorescence Characteristics. 4th International Congress on Photosynthesis, Reading, England, September 5, 1977.
- Armond, Paul, Photosynthetic Acclimation to High Temperature in *Larrea divaricata* Cav.: An Analysis of the Response of the Photosynthetic Apparatus to High Temperatures. Department of MCD Biology, University of Colorado, Boulder, Colorado, October 20, 1977.
- Armond, Paul, High-Temperature-Induced Alterations in the Photosynthetic Apparatus of the Desert Shrub *Larrea divaricata* Cav. Biology Department Seminar, University of Utah, Salt Lake City, October 27, 1977.
- Armond, Paul, Investigations of Chloroplast Membrane Structure: A Blend of Morphology and Biochemistry. Plant Science Seminar, University of Utah, Salt Lake City, Utah, October 27, 1977.
- Armond, Paul, Photosynthetic Acclimation to Temperature in the Desert Shrub *Larrea divaricata* Cav.: Analysis of High-Temperature-Induced Alterations of the Photosynthetic Apparatus. Stanford-Carnegie Seminar, Department of Plant Biology, Carnegie Institution of Washington, Stanford, California, November 30, 1977.
- Armond, Paul A., Photosynthetic Acclimation to High Temperatures in *Larrea*

- divaricata*. Seminar, Department of Botany, University of California, Berkeley, California, January 20, 1978.
- Armond, Paul, Photosynthetic Acclimation to High Temperature in *Larrea divaricata* Cav. Seminar at Department of Botany, University of Texas at Austin, Texas, February 21, 1978.
- Armond, Paul, Response of Photosynthetic Electron Transport and Chlorophyll Fluorescence to High Temperature. Seminar, Laboratory of Chemical Dynamics, University of California, Berkeley, California, March 1, 1978.
- Armond, Paul, Photosynthetic Acclimation to High Temperatures: Heat-Induced Alterations of Chloroplast Membranes. Seminar for Botany 221, Department of Botany, University of California at Davis, May 23, 1978.
- Armond, Paul, S. Malkin, D. C. Fork, and H. A. Mooney, General Predictive Value of Pigment System Analysis for Determining Photosynthetic Capacity. American Society of Plant Physiologists meeting, Blacksburg, Virginia, June 28, 1978.
- Badger, Murray R., A. Kaplan, and J. A. Berry, Active Inorganic Carbon Accumulation in *Anabaena variabilis* and Its Relationship to Photosynthesis. American Society of Plant Physiologists meeting, Blacksburg, Virginia, June 29, 1978.
- Belford, H. S., and W. F. Thompson, Comparison of Single Copy DNA Sequences of *Atriplex*. American Society of Plant Physiologists meeting, Madison, Wisconsin, August 17, 1978.
- Belford, H. S., see Murray, M. G.
- Berry, J. A., and G. Farquhar, The CO₂-Concentrating Function of C₄ Photosynthesis; a Biochemical Model. Fourth International Congress on Photosynthesis, Reading, England, September 4-9, 1977.
- Berry, J. A., with G. H. Lorimer, K. C. Woo, and C. B. Osmond, The C₂ Photorespiratory Carbon Oxidation Cycle in Leaves of Higher Plants: Pathway and Consequences. Fourth International Congress on Photosynthesis, Reading, England, September 4-9, 1977.
- Berry, J. A., with K. C. Woo and C. B. Osmond, Photorespiration and the Metabolism of Ammonia. Fourth International Congress on Photosynthesis, Reading, England, September 4-9, 1977.
- Berry, J. A., Isotope Studies on the Pathway of Photorespiration. Stanford-Carnegie Seminar, Department of Plant Biology, Carnegie Institution, Stanford, California, October 5, 1977.
- Berry, Joseph, C₄ Pathway and CO₂-Concentrating Mechanisms. Seminar for Botany 221, University of California, Davis, California, February 21, 1978.
- Berry, Joseph, see Badger, M. R., and Lorimer, G. H.
- Björkman, O., Effect of CO₂ Concentration on Photosynthesis. ERDA Workshop on Environmental Effects of Carbon Dioxide from Fossil Combustion, Miami Beach, March 10, 1977.
- Björkman, O., Photosynthetic Response and Adaptation to Temperature. Seminar, Department of Botany, Oregon State University, Corvallis, Oregon, April 12, 1978.
- Björkman, O., Response of Plants to Future Increase in Atmospheric Carbon Dioxide. Seminar, Department of Biological Sciences, Stanford University, California, April 24, 1978.
- Brain, R. D., D. O. Woodward, and W. R. Briggs, Physiological Correlations to Blue-Light-Induced Cytochrome Reduction in *Neurospora crassa*. American Society of Plant Physiologists meeting, Madison, Wisconsin, August 17, 1978.
- Briggs, W. R., The Search for the Blue-Light Photoreceptor in Higher Plants and Fungi. Seminar, Botany Department, University of Minnesota, St. Paul, Minnesota, October 5, 1977.
- Briggs, W. R., In Search of the Blue-Light Photoreceptor. Seminar, Florida International College, Miami, Florida, January 20, 1978.
- Briggs, W. R., The Photoreceptor Mechanism in Phototropism. II Congresso Latino-Americano do Botanico, Brasilia, Brasil, January 25, 1978.
- Briggs, W. R., In Search of the Blue-Light Photoreceptor. Seminar, Laboratory of Chemical Biodynamics, University of California, Berkeley, February 8, 1978.
- Briggs, W. R., see Brain, R. D., Britz, S. J., Cross, J., Cuellar, R. E., Galston, A. W., and Quail, P. H.
- Britz, S. J., E. Schrott, S. Widell, and W. R. Briggs, Photoreducible Cytochromes in Particulate Fractions of Corn Coleoptiles. American Society of Plant Physiologists

- meeting, Madison, Wisconsin, August 17, 1977.
- Britz, S. J., Inhibitor Studies on the Mechanism of Rhythmic Chloroplast Movement in *Ulva*. IX International Seaweed Symposium, Santa Barbara, California, August 25, 1977.
- Britz, S. J., E. Schrott, S. Widell, and W. R. Briggs, Photoreducible Cytochromes in Particulate Fractions of Corn Coleoptiles. Northeastern Section of American Society of Plant Physiologists meeting, Smith College, Northampton, Massachusetts, May 6, 1978.
- Britz, S. J., E. Schrott, S. Widell, and W. R. Briggs, Photoreducible Cytochromes in Particulate Fractions of Corn Coleoptiles. Sixth Annual Meeting, American Society of Photobiology, University of Vermont, Burlington, Vermont, June 12, 1978.
- Britz, S. J., *see* Galston, A. W.
- Brown, J. S., Fluorescence Spectroscopy of a P700-Chlorophyll-Protein Complex. Symposium on Membrane Bioenergetics, Spetsai, Greece, July 13, 1977.
- Brown, J. S., Spectroscopy of Chlorophyll in vivo. Seminar, Institute of Plant Physiology, Hungarian Academy of Sciences, Szeged, Hungary, July 20, 1977.
- Brown, J. S., Photoreactive Chlorophyll-Protein Complexes Isolated from Nongreen Algae. American Society of Plant Physiologists meeting, Blacksburg, Virginia, June 29, 1978.
- Cross, John W., Solubilized Auxin-Binding Protein and ATPase from Coleoptiles and Primary Leaves of *Zea mays*. International Conference on the Regulation of Developmental Processes in Plants at the Institute for Plant Biochemistry, Academy of Sciences of the G.D.R., Halle am Saale, East Germany, July 9, 1977.
- Cross, John W., Solubilized Auxin-Binding Protein and ATPase from Coleoptiles and Primary Leaves of *Zea mays*. Seminar, Botanical Institute, University of Munich, West Germany, July 14, 1977.
- Cross, John W., Solubilized Auxin-Binding Protein and ATPase from Coleoptiles and Primary Leaves of *Zea mays*. Seminar, Ruhr University, Bochum, West Germany, August 11, 1977.
- Cross, John W., Solubilized Auxin-Binding Protein and ATPase from *Zea mays*. Seminar, Institute for Biology III, University of Freiburg, West Germany, August 2, 1977.
- Cross, John W., Solubilized Auxin-Binding Protein and ATPase from Coleoptiles and Primary Leaves of *Zea mays*. American Society of Plant Physiologists meeting, University of Wisconsin, Madison, Wisconsin, August 18, 1977.
- Cross, John W., and W. R. Briggs, Auxin-Binding Protein Solubilized from Microsomes of *Zea mays*. American Society of Plant Physiologists meeting, Blacksburg, Virginia, June 27, 1978.
- Cuellar, R. E., W. R. Briggs, and W. F. Thompson, Applications of High Resolution Thermal Denaturation Techniques to Reassociated Repetitive DNA Sequences. American Society of Plant Physiologists meeting, Blacksburg, Virginia, June 27, 1978.
- Farquhar, G., *see* Berry, J. A.
- Fork, David C., Photosynthesis and Photophosphorylation. Seminar for Biology 156, Stanford University, Stanford, California, October 10 and 12, 1977.
- Fork, David C., The Effects of Temperature on the Physical Structure of Chloroplast Membranes and Photosynthesis. Seminar for California Botanical Society, Carnegie Institution of Washington, Stanford, California, October 22, 1977.
- Fork, David C., How Temperature Affects the Physical Phase of Thylakoid Membrane Lipids and Photosynthesis. Stanford-Carnegie Seminar, Department of Plant Biology, Carnegie Institution of Washington, Stanford, California, February 1, 1978.
- Fork, David C., Electron Transport in Photosynthesis. Seminar, Carnegie Institution of Washington, Department of Plant Biology, Stanford, California, February 23, 1978.
- Fork, David C., Light Absorption, Migration and Trapping in Photosynthesis; Introduction to Photosystem I. Seminar, Biology 221, Advanced Topics in Plant Physiology, Stanford University, Stanford, California, April 13, 1978.
- Fork, David C., *see* Armond, P.
- Galston, A. W., S. J. Britz, and W. R. Briggs, Photoinduced Spectral Changes in Subcellular Fractions from Etiolated Peas. American Society of Plant Physiologists meeting, Madison, Wisconsin, August 17, 1977.
- Goldsmith, Mary Helen M., A Chemiosmotic

- Hypothesis for Polar Auxin Transport. Stanford-Carnegie Seminar, Department of Plant Biology, Carnegie Institution of Washington, Department of Plant Biology, Stanford, California, April 19, 1978.
- Goldsmith, M. H. M., Informal Discussion: Auxin Transport and the Chemiosmotic Hypothesis. Seminar, Botany Department, University of California, Berkeley, California, May 9, 1978.
- Goldsmith, M. H. M., Twenty-Three Years in the Academic Jungle with Husband and Children. Seminar, Botany Women's Caucus of the University of California, Berkeley, California, May 9, 1978.
- Goldsmith, M. H. M., Polar Transport of Auxin. Seminar, Biology Department, University of Santa Clara, Santa Clara, California, May 12, 1978.
- Goldsmith, M. H. M., A Chemiosmotic Hypothesis for Polar Transport of Auxin. Seminar, Botany Department, University of Washington, Seattle, Washington, May 22, 1978.
- Hannan, G. N., *see* Raison, J. K.
- Kaplan, A., *see* Badger, Murray.
- Levitt, J., An Overview of Freezing Injury and Survival and its Interrelationships to other Stresses. Plant Cold Hardiness Seminar, University of Minnesota, St. Paul, Minnesota, November 2, 1977.
- Levitt, J., Molecular Mechanisms of Low-Temperature Adaptation in Plants. Seminar, Department of Biology, University of Houston, Texas, November 10, 1977.
- Levitt, J., Role of SH and SS Groups in Damage to Biological Systems at Low Water Activities. Stanford-Carnegie Seminar, Department of Plant Biology, Carnegie Institution of Washington, Stanford, California, November 16, 1977.
- Levitt, J., Low Temperature as a Stress Factor in Plants. Seminar, Botany Department, University of California, Davis, California, May 16, 1978.
- Lorimer, G. H., J. A. Berry, G. H. Krause, and C. B. Osmond, Metabolism of [^{18}O] by the Photorespiratory Carbon Oxidation Cycle in Vivo, and Its Significance. American Society of Plant Physiologists Meeting, Madison, Wisconsin, August 17, 1977.
- Malkin, S., Applications of Photoacoustic Spectroscopy in Photosynthesis Research (and other Energy-Converting Photochemical Reactions). Stanford-Carnegie Seminar, Department of Plant Biology, Carnegie Institution of Washington, Stanford, California, May 17, 1978.
- Malkin, S., *see* Armond, P.
- Mooney, H. A., *see* Armond, P.
- Murray, Michael G., R. S. Preisler, and W. F. Thompson, Sequence Organization in Pea DNA. American Society of Plant Physiologists meeting, Madison, Wisconsin, August 17, 1977.
- Murray, M. G., H. S. Belford, W. F. Thompson, Purification and in Vitro Labeling of Plant DNA. American Society of Plant Physiologists meeting, Madison, Wisconsin, August 17, 1977.
- Murray, M. G., DNA Sequence Organization in Peas. Stanford-Carnegie Seminar, Department of Plant Biology, Carnegie Institution of Washington, Stanford, California, March 1, 1978.
- Murray, M. G., and W. F. Thompson, DNA Sequence Organization in Peas and Mung Beans. American Society of Plant Physiologists meeting, Blacksburg, Virginia, June 27, 1978.
- Osmond, C. B., *see* Berry, J. A.
- Preisler, R., *see* Murray, G. M.
- Quail, P., Phytochrome Pelletability: The Role of Mg^{2+} . American Society of Plant Physiologists meeting, Madison, Wisconsin, August 19, 1977.
- Quail, P. H., Phytochrome Pelletability: Requirement for Phosphorylative Energy in Vivo. Seminar, Radiation Biology Laboratory, Smithsonian Institution, Washington, D.C., April 21, 1978.
- Quail, P. H., Phytochrome Pelletability: Requirement for Phosphorylative Energy in Vivo. Seminar, Botany Department, University of Minnesota, St. Paul, Minn., April 27, 1978.
- Quail, P. H., and W. R. Briggs, Phosphorylative Energy Required for Irradiation-Enhanced Phytochrome Pelletability. American Society of Plant Physiologists meeting, Blacksburg, Virginia, June 26, 1978.
- Raison, J. K., Evidence for the Critical Role of Membrane Lipids in Maintaining Cellular Integrity at Low Temperatures. Stanford-Carnegie Seminar, Department of Plant Biology, Stanford, California, April 12, 1978.
- Raison, J. K., The Role of Membrane Lipids in the Adaptation of Plants and Animals to Low Temperatures. Seminar, Palo Alto

- Medical Research Foundation, Palo Alto, California, April 12, 1978.
- Raison, J. K., Biochemical Evidence for Hibernation in Plants: the Role of Membrane Lipids. Seminar, Laboratory of Chemical Dynamics, University of California, Berkeley, California, May 3, 1978.
- Raison, J. K., Biochemical Evidence for Hibernation in Plants: the Role of Membrane Lipids. Seminar, Botany Department, University of California, Davis, May 17, 1978.
- Raison, J. K., The Role of Membranes in the Adaptation of Plants to Low Temperature. Lecture in Botany 221, Stress Physiology, University of California, Davis, California, May 18, 1978.
- Raison, J. K., L. C. Wright, E. Chapman, and G. N. Hannan, Changes in the Structure and Function of Mitochondrial Membranes of Tuber in Relation to Winter Dormancy. American Society of Plant Physiologists meeting, Blacksburg, Virginia, June 26, 1978.
- Schreiber, U., *see* Armond, P. A.
- Schrott, E., *see* Britz, S. J.
- Stemler, A., Photosystem II Activity Depends on Membrane-Bound Bicarbonate. Symposium on Photosynthetic Oxygen Evolution, Tübingen, West Germany, August 31, 1977.
- Stemler, A., Membrane-Bound Bicarbonate and Photosystem II. 4th International Congress on Photosynthesis, Reading, England, September 8, 1977.
- Stemler, A., Two Effects of Bicarbonate Ions on Photosynthetic Light Reaction II. Seminar, Botany Department, University of California, Davis, California, February 1, 1978.
- Thompson, W. F., Genome Organization in Plants and Other Eukaryotes. Presidential Symposium, American Society of Plant Physiologists meeting, Madison, Wisconsin, August 18, 1977.
- Thompson, W. F., Evolutionary Studies Using Nucleic Acid Hybridization. Meeting of California Botanical Society, Carnegie Institution of Washington, Stanford, California, October 22, 1977.
- Thompson, W. F., *see* Belford, H. S., Cuellar, R. E., Murray, M. G.
- van Ginkel, G., Detailed Action Spectra of Photophosphorylation. Seminar, Biophysics Department, Michigan State University, East Lansing, Mich., October 31, 1977.
- van Ginkel, G., Action Spectra of Photophosphorylation: Methods and Results. Seminar, Botany Department, University of Illinois, Urbana, Ill., November 2, 1977.
- van Ginkel, G., Action Spectra of Photophosphorylation. Stanford-Carnegie Seminar, Department of Plant Biology, Stanford, California, January 25, 1978.
- van Ginkel, G., Experiments to Reconstitute Photosystem I. Seminar, Botany Department, University of California, Berkeley, California, May 31, 1978.
- van Ginkel, G., Light-Induced Proton Uptake in Liposomes Containing Photosystem I Reaction Centers. American Society of Plant Physiologists meeting, Blacksburg, Virginia, June 29, 1978.
- Widell, S., *see* Britz, S. J.
- Woo, K. C., *see* Berry, J. A.
- Woodward, D. O., *see* Brain, R. D.
- Wright, L. D., *see* Raison, J. K.

PERSONNEL

Research Staff

Joseph A. Berry
 Olle Björkman
 Winslow R. Briggs, Director
 Jeanette S. Brown
 David C. Fork
 C. Stacy French, Director Emeritus
 William M. Hiesey, Emeritus
 Malcolm A. Nobs
 William F. Thompson

Postdoctoral Fellows

Roland Caubergs, NATO Fellowship, University of Antwerp, Belgium
 Jacob Levitt, Senior Fellow, University of Minnesota, Minneapolis, Minn.

Carnegie Institution of Washington Postdoctoral Fellows

Paul A. Armond
 Murray R. Badger

Steven J. Britz¹
 John W. Cross²
 Mary Helen Goldsmith, Senior Fellow, Yale University
 Aaron Kaplan³
 Shmuel Malkin, Senior Fellow, Weizmann Institute of Science, Israel
 Norio Murata, Senior Fellow, University of Tokyo, Japan⁴
 Michael G. Murray
 Peter H. Quail, Senior Fellow
 John K. Raison, Senior Fellow, CSIRO, Canberra, Australia
 Charles E. Rogler⁵
 Ulrich Schreiber⁶
 Alan J. Stemler
 Gijsbert van Ginkel
 Larry N. Vanderhoef, Senior Fellow, University of Illinois⁷

Students

Heather S. Belford, Graduate, University of Massachusetts, Amherst, Mass.
 Michael R. Blatt, Graduate, Stanford University, Stanford, Calif.
 Robert D. Brain, Graduate, Stanford University, Stanford, Calif.⁸
 G. James Collatz, Graduate, Stanford University, Stanford, Calif.

¹ To August 31, 1977

² To April 1978

³ To January 1978

⁴ July to September 1977

⁵ To July 31, 1977

⁶ To September 30, 1977

⁷ To July 31, 1977

⁸ To September 15, 1977

Richard Cuellar, Graduate, Stanford University, Stanford, Calif.
 Holly Gorton, Graduate, Stanford University, Stanford, Calif.
 Marga Höhl, University of Marburg, Germany
 Jeffrey Palmer, Graduate, Stanford University, Stanford, Calif.
 Richard Preisler, Graduate, Stanford University, Stanford, Calif.
 U. M. Susanne Widell, Graduate, University of Lund, Sweden⁹

Clerical and Technical Staff

Benny Catanzaro, Electronic Technician
 Kirk F. Davies, Technician
 Dorothy Ruth Fischer, Administrative Assistant-Accountant
 Glenn A. Ford, Laboratory Manager
 Edward G. Gausden, Technician
 Steven M. Graff, Laboratory Technician¹⁰
 Karen Griffing, Laboratory Technician¹¹
 Richard W. Hart, Mechanical Engineer
 James Johnson, Technician
 Kathleen Keller, Department Secretary
 Anne E. Kimber, Laboratory Technician
 Fred Lakin, Technical Illustrator
 Frank Nicholson, Senior Technician
 Debra Peters, Laboratory Technician
 Pedro Pulido, Technician
 Ernest Ramos, Technician¹²
 Patricia Sullivan, Laboratory Technician
 Aida Wells, Typist

⁹ To December 31, 1977

¹⁰ To September 2, 1977

¹¹ To January 31, 1978

¹² To May 15, 1978

Developmental Biology Research Group

*Pasadena, California
and Kerckhoff Marine Laboratory,
Corona Del Mar, California*

Roy J. Britten
Senior Research Fellow

Eric H. Davidson
Professor, California Institute of Technology

Contents

Introduction 369

Studies of Nucleic Acid Reassociation Kinetics 370

Sequence Content of the Bithorax Region of the *Drosophila* Genome 370

Complexity of *Drosophila* Egg RNA 370

RNA Synthesis in Sea Urchin Oogenesis 371

Cloned Sea Urchin DNA Complementary to Oocyte RNA. I. CS0088 371

Cloned Sea Urchin DNA Complementary to Oocyte RNA. II. PSC34 372

Repetitive Sequence Transcripts in the Sea Urchin Oocyte 372

Maternal mRNA Localization and Utilization in Sea Urchin Development 373

Sea Urchin Maternal mRNA Sequences Also Synthesized during Embryogenesis 374

Nonmaternal Messenger RNA Sequences in Sea Urchin Embryos 374

Sea Urchin Embryo mRNA Sequences in the Nuclear RNA of Adult Tissues 375

Repetitive Sequence Transcripts in Sea Urchin Nuclear RNA's 375

Repeated Sequences in the Vicinity of Expressed Single Copy Sea Urchin DNA 376

Primary Structure of Repetitive DNA Sequences in the Sea Urchin Genome 376

Selection of Cloned Sea Urchin DNA Coding for mRNA 377

Single Copy DNA Sequence Polymorphism 377

Evolutionary Change in Sea Urchin Repetitive DNA 378

Sequence Organization of Individual Repeated Sequence Families 379

Single Copy DNA Sequence Differences among Related Sea Urchins 379

Staff 380

Publications 380

INTRODUCTION

The work of this group centers on the molecular biology of animal development and includes studies of the regulation of genetic activity, DNA sequence organization and the evolution of DNA sequences, and the evolution of sequence organization. Recombinant DNA clones have become a major tool, while RNA/DNA hybridization and DNA reassociation remain the principal analytical methods. The determination of the DNA sequence of individual repetitive cloned fragments has been initiated. Again this year only short abstracts are included and the report is essentially identical to that in the annual report of the Biology Division of the California Institute of Technology.

Among the most significant of the new information described in the succeeding abstracts are the observations of the expression of particular repetitive sequence families in mature oocyte RNA and rapidly turning over nuclear RNA in the

sea urchin. Using cloned DNA representing each of several families of interspersed repetitive sequences, it was found that there is a highly tissue-specific or stage-specific pattern of transcription. Certain families are highly represented in egg RNA and little represented in nuclear RNA, while others are most highly represented in nuclear RNA at a given stage of development. These specific patterns imply that the transcription of repetitive DNA sequences is functionally important and represents progress toward understanding the roles of nuclear RNA and repetitive DNA sequences.

The work described in the following reports has been supported by:

American Cancer Society
Earle C. Anthony Fellowship
Danforth Fellowship
March of Dimes
McCallum Fund
National Institutes of Health, USPHS
National Science Foundation
Weizmann Fellowship

STUDIES OF NUCLEIC ACID REASSOCIATION KINETICS

Margaret E. Chamberlin, Glenn A. Galau*, Roy J. Britten, Eric H. Davidson

Measurements were made of the kinetics of nucleic acid strand pair reassociation where the complementary strands are of different lengths and are present in different concentrations. Rate constants for the reaction of labeled fragments ("tracer") with excess complementary strands ("driver") were determined, both for driver fragment length greater than tracer fragment length and for the reverse case. Second-order reactions and pseudo-first-order reactions utilizing strand-separated drivers and tracers were studied. The nucleic acids which served for this investigation were $\phi\chi 174$ DNA and RNA, plasmid RSF2124 DNA, and

E. coli DNA. Approximate empirical expressions relating driver and tracer fragment lengths with the observed rate constants were obtained for practical use. In long tracer-short driver reactions the observed rate constant for the tracer reaction increases proportionately with tracer length. In long driver-short tracer reactions the rate of tracer reaction is retarded. The latter result is unexpected and appears to represent a departure from standard interpretations of the renaturation reaction.

* Present address: Department of Biochemistry, University of Georgia, Athens, Georgia.

SEQUENCE CONTENT OF THE BITHORAX REGION OF THE *Drosophila* GENOME

Margaret E. Chamberlin, Eric H. Davidson, Edward B. Lewis

In order to study the DNA of the bithorax region of *Drosophila melanogaster*, we are preparing to hybridize wild-type tracer with DNA isolated from embryos which are homozygously deficient for the bithorax region, and harvest the unhybridized sequences. We have isolated wild-type DNA from *Drosophila* embryos which have been fed on a medium containing ^{13}C , ^{15}N , and ^3H -thymidine (a generous gift of Dr. Robert M. Grainger, University of Virginia). This DNA is significantly denser than the bithorax mutant DNA previously iso-

lated, and thus affords a further purification step by cesium chloride centrifugation. We also plan to end label the tracer DNA with $\gamma\text{-AT}^{32}\text{P}$. Once we have obtained DNA enriched for bithorax sequence we can screen an existing bacteriophage lambda "library" of *Drosophila* DNA sequences, and investigate the positive plaques by *in situ* hybridization to *Drosophila* salivary gland chromosomes. Having thus identified the clones containing bona fide bithorax sequence, we will proceed to examine its sequence content.

COMPLEXITY OF *Drosophila* EGG RNA

Barbara R. Hough-Evans, Eric H. Davidson, Marcelo Jacobs-Lorena*

The eggs of a variety of animals previously examined each contain about 20,000 different kinds of stored "maternal messenger" RNA. We carried out

a similar measurement for an animal with a much smaller genome, using iso-

* Case Western Reserve School of Medicine, Cleveland, Ohio.

lated single copy *Drosophila* DNA tracer, and RNA extracted from ovulated but unfertilized *Drosophila* eggs. From the extent of hybridization of the DNA, and knowing its complexity, it was calculated that the *Drosophila* egg contains only 4000 to 5000 RNA message sequences.

Similar experiments to determine the RNA complexity of several stages of developing *Drosophila* eggs are planned, and will allow us to follow the course of maternal mRNA accumulation through oogenesis.

RNA SYNTHESIS IN SEA URCHIN OOGENESIS

Barbara R. Hough-Evans, Susan G. Ernst, Eric H. Davidson

During the reproductive season, ovaries of the purple sea urchin contain small previtellogenic oocytes and growing vitellogenic oocytes as well as mature eggs. Only previtellogenic oocytes are found in "out of season" ovaries. We extracted nuclear RNA and cytoplasmic RNA from ovaries containing only previtellogenic oocytes, and nuclear RNA from preparations enriched for vitellogenic oocytes. These oocyte RNA's were characterized by hybridization reactions with radioactively labeled single copy sea urchin DNA. A typical nuclear RNA of single copy complexity of about 1.7×10^8 nucleotides of unique sequence was extracted from nuclei of previtellogenic oocytes. These nuclear RNA sequences from young oocytes were found to consist of transcripts of a set of single copy

DNA sequences which significantly overlapped the set which is expressed later in the hnRNA of gastrula stage embryos. The nuclear RNA of vitellogenic oocytes appears to contain a class of more prevalent single copy transcripts that are not, however, the same as the maternal mRNA sequences that are found stored in mature oocytes. This was determined by reacting the vitellogenic oocyte nuclear RNA with a single copy ^3H -DNA fraction enriched for sequences complementary to the maternal single copy sequence set (oDNA). oDNA was also reacted with cytoplasmic RNA of previtellogenic oocytes, and it was found that less than half of the final egg RNA complexity of 37 million nucleotides has been accumulated in the cytoplasm in early stages of sea urchin oogenesis.

CLONED SEA URCHIN DNA COMPLEMENTARY TO OOCYTE RNA. I. CS0088

Terry L. Thomas, Robert C. Angerer, Ze'ev Lev, Robert L. Gimlich, Eric H. Davidson*

We have constructed recombinant bacterial plasmids containing DNA sequences from the sea urchin. Of more than 100 tested, 8 to 12 were shown to contain DNA sequences complementary to oocyte RNA. Several of these cloned DNA sequences have been analyzed in greater detail. In addition, restriction enzyme maps have been generated to show the position of the codogenic regions with respect to restriction fragments containing repetitive and non-

repetitive DNA sequences within the cloned DNA fragment.

The major class of cloned DNA fragments isolated by this approach contained both repetitive and nonrepetitive DNA. This class is typified by the clone designated CS0088. CS0088 is 5800 nucleotides in length. Mapping data place the codogenic region in the terminal third of the cloned fragment. The RNA en-

* Present address: Department of Biology, University of Rochester, Rochester, New York.

coded by this fragment is present at about 6000 copies per oocyte and represents only one strand of the DNA, that is, the transcript is asymmetric. The codogenic region is nonrepetitive and is about 1200 nucleotides in length. Several distinct repetitive sequence elements interspersed with nonrepetitive DNA sequences are located in the remaining two-thirds of the cloned DNA fragment. The transcript is initiated either outside the cloned DNA fragment or within a couple of hundred nucleotides of the fragment terminus.

Of some significance is the isolation of cloned DNA fragments complementary

to nonprevalent maternal RNA. This class of mRNA accounts for about 90% of the different mRNA species present in the oocyte. Like many other known structural genes, these transcripts are encoded by nonrepetitive DNA and are asymmetric. In addition, the RNA encoded by CS0088 is loaded on polysomes by the 16-cell stage of embryogenesis. These data implicate cloned DNA such as CS0088 as bona fide structural genes. As a consequence, these cloned DNA sequences are being employed to investigate a number of interesting aspects of gene expression during sea urchin development.

CLOINED SEA URCHIN DNA COMPLEMENTARY TO OOCYTE RNA. II. PSC34

Amy Shiu Lee, Eric H. Davidson

We have previously described a sea urchin recombinant clone PSC34 which contains three short repeat sequences interspersed with single copy sequences varying from a few hundred to two thousand nucleotides long (Lee *et al.*, 1978). Restriction enzyme fragments from this 7000-nucleotide sea urchin DNA fragment were tested for transcriptional activity. The HhaIA fragment, which is a nonrepetitive sequence and is 2000 nucleotides long, was found to hybridize with mature oocyte RNA. Transcription is asymmetric. From the observed hybridization rates, it can be estimated that there are about 1000 copies of this transcript in the mature oocyte, which is fairly typical of maternal RNA belonging to the single copy sequence set of the oocyte. This sequence also hybridizes to

polysomal RNA isolated from gastrulae, and initial results indicate that it also exists in the cytoplasmic RNA population isolated from sea urchin intestine. The HhaIA sequence can be detected in the hnRNA population from gastrula cells, and is transcribed asymmetrically. There are one to two copies of RNA transcripts of this sequence present in each cell nucleus at the gastrula stage, and one to two copies per cell in the polysomal RNA as well. The orientation of transcription for this sequence has also been determined.

REFERENCE

- Lee, A. S., R. J. Britten, and E. H. Davidson. (1978) *Cold Spring Harbor Symp. Quant. Biol.* 42: pp. 1065-1076.

REPETITIVE SEQUENCE TRANSCRIPTS IN THE SEA URCHIN OOCYTE

Frank Costantini, Richard H. Scheller, Eric H. Davidson

The expression of interspersed repetitive sequences in the RNA of mature sea

urchin oocytes was investigated. ³H-DNA tracers representing short inter-

dispersed repetitive sequences a few hundred nucleotides long, and long repetitive sequences about 2000 nucleotides long, were prepared from genomic DNA of the sea urchin. These tracers were reacted with excess RNA from the mature oocyte. About 80% of the reactable short repeat tracer and 35% of the long repeat tracer hybridized. Therefore most of the repetitive sequence families in the short repeat tracer are represented in oocyte RNA, and transcripts complementary to both strands of many repeat sequences are present. The kinetics of the reaction show that some transcripts are highly prevalent, while others are rare. Nine cloned repetitive sequences were labeled, strand-separated, and reacted with the oocyte RNA. Transcripts of both strands of all nine repeats were found in the RNA. The prevalence of transcripts of the cloned

repeat families varied from about 3000 to 100,000 copies per oocyte. Studies with both cloned and genomic tracers show that transcript prevalence is independent of the genomic reiteration frequency of the transcribed repetitive sequences. Most of the families represented by prevalent transcripts have less than 200 copies per haploid genome. The RNA molecules with which the cloned repeats react are at least 1000 to 2000 nucleotides in length. Other experiments show that a majority of the members of repeat families represented by prevalent transcripts in the oocyte RNA are interspersed among single copy sequence elements in the genome. We are currently attempting to isolate the oocyte repetitive sequence transcripts and examine their sequence organization directly.

MATERNAL mRNA LOCALIZATION AND UTILIZATION IN SEA URCHIN DEVELOPMENT

Susan G. Ernst, Eric H. Davidson

Sea urchin eggs divide into cells equal in size until the fourth division. This unequal division produces the 16-cell stage embryo with three distinguishable cell types. Micromeres, one of the three cell types of defined cell lineage present in 16-cell stage embryos, are responsible for the formation of the primary mesenchyme that produces the embryonic skeleton.

Protein synthesis in early cleavage stages of the sea urchin is coded for by maternal messenger RNA. In this study we are investigating the messenger RNA's found in the 16-cell embryo to determine if there is specific localization of expression of these maternal messenger RNA sequences. The egg contains RNA equal to a sequence complexity of 37 million nucleotides, which is equivalent to about 20,000 structural genes. Hybridization of

cytoplasmic 16-cell embryo RNA with single copy DNA sequences complementary to the complex maternal RNA stored in the egg (oDNA) shows that 100% of the sequences stored in the egg remain in the cytoplasm of the 16-cell embryo. About 73% of the maternal sequences stored in the egg are expressed on polysomes at this early cleavage stage. The RNA from the cytoplasm of isolated micromeres was found to represent the full complexity stored in the egg. Preliminary measurements with oDNA have indicated that these small cells also translate all of these maternal sequences. This is in contrast to the cells of the rest of the embryo which are making proteins from a subset of the stored maternal messenger RNA population.

SEA URCHIN MATERNAL mRNA SEQUENCES ALSO SYNTHESIZED DURING EMBRYOGENESIS

Ze'ev Lev, Eric H. Davidson

Previous work indicates that embryo structural gene transcription accounts for most or all of the polysomal mRNA by gastrula stage. However, the same sequences transcribed in the gastrula are in general also represented in the maternal RNA of the unfertilized egg (Galau *et al.*, 1976, 1977). It appears therefore that at a certain stage between fertilization and gastrulation, transcription of mRNA from genes whose product was already present in the egg is turned on, and the newly synthesized mRNA molecules are added to identical maternal molecules. In more advanced stages the maternal mRNA is degraded and disappears from the cells, so that at the gastrula stage all the mRNA in the cells is in fact newly synthesized. To follow this replacement at the level of a single gene, we are utilizing the recombinant DNA plasmid, designated CS0088, which contains sea urchin sequence complementary to egg RNA.

Hybridization of excess RNA with the

labeled plasmid DNA will indicate the quantity of the specific gene product at various stages, both newly synthesized and maternal. By labeling the mRNA of the embryos, the plasmid probes can be used to detect the appearance of new transcripts of the structural gene. So far, asymmetric transcripts of the putative structural gene included in CS0088 have been found in polysomal RNA from 16-cell embryos, in a quantity of 600 molecules per embryo. This amount is about 20% of their prevalence in unfertilized eggs. Current studies are being done to determine the amount of these transcripts in other stages of sea urchin embryogenesis and in adult tissues.

REFERENCES

- Galau, G. A., W. H. Klein, M. M. Davis, B. J. Wold, R. J. Britten, and E. H. Davidson. (1976) *Cell* 7: 487-505.
Galau, G. A., E. D. Lipson, R. J. Britten, and E. H. Davidson. (1977) *Cell* 10: 415-432.

NONMATERNAL MESSENGER RNA SEQUENCES IN SEA URCHIN EMBRYOS

Barbara J. Wold, Eric H. Davidson

The vast majority of messenger RNA sequences expressed in sea urchin embryos are also present in the maternal RNA of mature oocytes. To detect and quantitate embryo messenger RNA sequences that are not homologous with maternal RNA's, a labeled single copy DNA fraction entirely devoid of oocyte RNA complementary sequences was prepared. This selected DNA, termed null oDNA, was reacted with excess polysomal mRNA from 16-cell, blastula and gastrula embryos. Nonmaternal sequences could not be detected in the

mRNA's from 16-cell and gastrula stage embryos. Mesenchyme blastula mRNA, however, hybridized about 3.6 million nucleotides of null oDNA sequence, which is sufficient to code for approximately 2000 mRNA's of average size. These nonmaternal mRNA's are complex class sequences present on blastula polyosomes at about the same concentration (500 copies per embryo) as are most maternal sequence mRNA's. Thus, a significant number of new, nonmaternal structural genes are expressed in blastula stage embryos.

SEA URCHIN EMBRYO mRNA SEQUENCES IN THE NUCLEAR RNA OF ADULT TISSUES

Barbara J. Wold, William H. Klein, Barbara R. Hough-Evans, Eric H. Davidson

Because the sea urchin displays large differences between embryo and adult tissue messenger RNA sequence sets, it is possible to test the proposition that structural gene sequences are transcribed only in cells where the transcripts are translated. A ^3H -labeled single copy DNA highly enriched for sequences complementary to blastula polysomal messenger RNA was prepared. This selected DNA fraction, referred to as mDNA, represents about 26 million nucleotides of embryo messenger RNA sequence. A maximum of 16% of the blastula sequences are present in coelomocyte and intestine messenger RNA's, while 40% of the blastula sequences are represented in

gastrula mRNA. ^3H -mDNA was hybridized with excess nuclear RNA from coelomocytes, intestine, and gastrula embryos. Within our limits of detection, all mDNA sequences were hybridized by each of the nuclear RNA's. We conclude from this result that virtually all of the blastula mRNA sequences are transcribed in three heterologous tissues in which the transcripts are not utilized as messenger RNA's. The kinetics of hybridization show that the blastula structural gene sequences are present in each nuclear RNA at about the same concentration as are the majority of the complex single copy nuclear transcripts.

REPETITIVE SEQUENCE TRANSCRIPTS IN SEA URCHIN NUCLEAR RNA'S

Richard H. Scheller, Jay W. Ellison, Eric H. Davidson

Nine cloned repetitive sequences were labeled, strand-separated, and individually hybridized with RNA extracted from nuclei of gastrula stage sea urchin embryos and of adult sea urchin intestine cells. The concentration of transcripts complementary to each cloned sequence was measured by RNA excess hybridization kinetics and by a DNA excess titration method. Transcripts of certain of the repeat families are present at over 100 times the concentration of transcripts of other families in each RNA. The set of repetitive sequence families highly represented in intestine nuclear RNA is different from that highly represented in gastrula nuclear RNA. Together with re-

sults obtained with mature oocyte RNA, these findings show that quantitative patterns of repetitive sequence representation in RNA are specific to each cell type. Both strands of all of the nine cloned repeats are represented at some level in all the RNA's studied. Usually though not always the concentrations of transcripts complementary to the two strands of each repeat do not differ by more than a factor of two. The cloned tracers do not react with polysomal messenger RNA, and the nuclear RNA molecules with which they hybridize are many times larger than the repetitive sequences themselves.

REPEATED SEQUENCES IN THE VICINITY OF EXPRESSED SINGLE COPY SEA URCHIN DNA

David M. Anderson, Richard H. Scheller, James W. Posakony, Eric H. Davidson

The studies under way involve an investigation of the relationships between repetitive DNA sequences that occur adjacent to expressed single copy regions in the genome of the sea urchin. Our approach has been to clone long (15 kb) EcoRI DNA fragments, utilizing a lambda vector system. By cloning long fragments, we are assured of being able to study the DNA sequences flanking a given transcribed single copy region. The use of the lambda vector system has provided an efficient cloning vehicle. To date, we have cloned 90% of the sea urchin genome as measured in hybridization reactions utilizing single copy ^3H -DNA driven by DNA extracted from the total clone set.

In order to select individual cloned sequences for detailed study, we have screened the total lambda clone set with several cloned repetitive DNA fragments previously described in Scheller *et al.*

(1977). The repetitive families chosen differ in their representation in the RNA populations of egg, embryonic, and adult tissues. To date, we have selected 10 to 20 different members of three repetitive sequence families. One family is highly represented in intestine nuclear RNA, one in gastrula hnRNA, and one in the total oocyte RNA population. From five members of each of these families, we have obtained 3 to 5 kb fragments which carry the repetitive DNA element used in the initial screening. We are now in the process of identifying those which have adjacent single copy regions that are expressed.

REFERENCE

- Scheller, R. H., T. L. Thomas, A. S. Lee, W. H. Klein, W. D. Niles, R. J. Britten, and E. H. Davidson. (1977) *Science* 196: 197-200.

PRIMARY STRUCTURE OF REPETITIVE DNA SEQUENCES IN THE SEA URCHIN GENOME

James W. Posakony and Eric H. Davidson

The sequencing technique of Maxam and Gilbert (1977) is being used to determine the nucleotide sequence of several members of selected repetitive sequence families in sea urchin DNA.

Plasmid clones of individual repetitive sequence elements (Scheller *et al.*, 1977) were used to screen a "shotgun library" of the sea urchin genome, carried in 15 to 20 kb pieces by the phage vector Charon 4, for fragments containing members of the chosen repetitive sequence families. These individual repetitive se-

quences were isolated from the large Charon 4 inserts by restriction enzyme digestion and gel electrophoresis.

Comparing the nucleotide sequences of several members of several repetitive families will shed considerable light on a number of interesting but heretofore inaccessible problems, such as (1) the internal organization of repetitive sequences, (2) the type and location of the nucleotide substitutions which we observe as sequence divergence within repetitive families, and (3) the nature of the

"boundary" between repetitive sequence elements and other sequences.

The nucleotide sequences of several repetitive plasmid clones (Scheller *et al.*, 1977) have already been determined. Common features include tandem repetitions of simple sequences and regions unusually rich in A-T or G-C base pairs.

REFERENCES

- Maxam, A. M. and W. Gilbert. (1977) *Proc. Nat. Acad. Sci. U.S.A.* 74: 560-564.
- Scheller, R. H., T. L. Thomas, A. S. Lee, W. H. Klein, W. D. Niles, R. J. Britten, and E. H. Davidson. (1977) *Science* 196: 197-200.

SELECTION OF CLONED SEA URCHIN DNA CODING FOR mRNA

Jay W. Ellison and Eric H. Davidson

Our previous studies of structural gene expression during sea urchin development have revealed that the presence on polysomes of certain mRNA's is specific with respect to developmental stage. These studies relied on complexity measurements of mRNA populations, and the conclusions pertain to the rare or "complex" class of mRNA's. We wish to make similar studies of the abundant or "prevalent" class of mRNA's to see if the appearance of these messages is developmentally regulated. This type of investigation is feasible if recombinant DNA clones are available that contain sequences coding for prevalent mRNA's because individual species could then be studied.

This project concerns the isolation of such clones from the sea urchin DNA library of recombinant lambda phage.

The prevalent mRNA probe used to screen the library is in vivo labeled polysomal mRNA from sea urchin blastula. Embryos were grown in phosphate-depleted seawater and labeled with ^{32}P -orthophosphate for 9 hr, which results in mRNA specific activities of about 10^6 to 10^7 cpm/ μg . ^{32}P -RNA extracted from polysome gradients was hybridized to filter-bound DNA from the cloned library, and individual clones were purified by several rounds of screening.

With the use of restriction enzymes the long (15 to 20 kb) sea urchin DNA inserts are being analyzed to confirm the presence of sequences coding for mRNA's. Such sequences could be used as hybridizing probes to study the expression of the respective genes in different sea urchin cell types.

SINGLE COPY DNA SEQUENCE POLYMORPHISM

Roy J. Britten and Richard M. Rohan

Measurements of the differences in average single copy DNA sequence between individual sea urchins have been continued. The thermal stability of duplexes formed between DNA derived from two or more individuals is compared with that for DNA from one individual.

No greater differences have been observed in the single copy DNA sequences

between individuals collected 2000 kilometers apart than between individuals collected from under one boulder off Point Loma, California. The measurements indicate that the two genomes of a diploid individual normally differ about as much as any two genomes present in the population of this sea urchin (*Strongylocentrotus purpuratus*) on the Pacific coast of North America.

The melting temperature for duplexes formed between the single copy DNA sequences of two genomes is about 4° below that for perfect DNA duplexes, indicating a 4% average sequence difference. About one quarter of the single copy DNA sequences appear to differ in about 10% of their nucleotides, while the least divergent quarter of the DNA differs in 1% or less, and the majority of the sequences have intermediate degrees of divergence. If we make the logical assumption that the evolutionary rate of incorporation of base substitutions lead-

ing to polymorphism is the same as that leading to interspecies sequence divergence, we may conclude that much of the polymorphism is due to sequence differences between very ancient versions of single copy sequences in the sea urchin genome. This conclusion is based on measurements summarized below which indicate that the evolutionary rate of change in sea urchin single copy DNA is about 0.25% per million years. Preliminary measurements suggest that mouse single copy DNA polymorphism is much less than that of the sea urchin.

EVOLUTIONARY CHANGE IN SEA URCHIN REPETITIVE DNA

Gordon P. Moore, Roy J. Britten

The frequency of occurrence of particular repetitive sequence families has been estimated in the DNA of the three sea urchin species, *Strongylocentrotus purpuratus*, *Strongylocentrotus franciscanus*, and *Lytechinus pictus*, using individual cloned *S. purpuratus* repetitive sequence elements. Estimates have also been made of frequency changes of many repetitive families by measurement of the reassociation of labeled repetitive DNA fractions with total DNA from other species. In each reciprocal comparison the labeled repetitive sequences reassociate more slowly with DNA of other species than with DNA of the species from which they were prepared. Thus it appears that the dominant repetitive sequence families in each species' DNA are present at lower frequencies in closely related species DNA.

Thermal stability measurements have been made of repetitive DNA fractions from *S. purpuratus* and *S. franciscanus* when reassociated with homologous or heterologous DNA, and indicate that repetitive DNA sequences change more slowly during evolution than single copy

DNA sequences. This supports the concept of a functional role for repetitive DNA.

Measurements of thermal stability have been made of individual *S. purpuratus* cloned repetitive sequences reassociated with *S. franciscanus* DNA or *S. purpuratus* DNA. Most families have changed both in frequency and sequence. Some, however, have changed little in sequence but show great changes in frequency. These frequency differences are therefore not due to divergence and failure of duplex formation under our conditions. We conclude that during evolution member sequences are added or deleted from families of repeated sequences. Repeated sequence families grow or shrink in the DNA of one species and, in general, different families change most rapidly in size in other closely related species DNA. Since families of short interspersed repetitive sequences share in these frequency changes, it appears that some unexpected events of insertion or sequence rearrangement must occur at significant rates during the evolution of the genome.

SEQUENCE ORGANIZATION OF INDIVIDUAL
REPEATED SEQUENCE FAMILIES*William R. Pearson and Roy J. Britten*

The length distribution and sequence organization of four repeated DNA sequence families have been examined in two sea urchin species, using cloned repeated sequence elements and the "Southern blot" hybridization technique. With gel blots of EcoRI-digested *Strongylocentrotus purpuratus* DNA, it was shown that a part of each family is organized in long repetitive regions. In two cases (clones 2034 and 2133) an individual band dominated the gel electrophoresis pattern, indicating that a large fraction of the members of these families is organized in one type of long repeated sequence, possibly a tandem array. For clones 2007 and 2101 most of the hybridization is with a wide distribution of fragment lengths, and thus interspersed sequences make up a majority of these families. With *S. franciscanus* DNA EcoRI gel blots, a reduced level of hybridization was seen as expected from the frequency differences of the repetitive families represented by the clones.

The same cloned repeats were hybridized with gel blots made from reassociated repetitive DNA digested with S1 single strand-specific nuclease, to assay the length distribution of the reassociated repetitive regions containing family members. In the case of one predominantly interspersed family, 2101, a large fraction of the hybridization occurs in two bands at about 300 and 400 nucleotides, supporting the conclusion that interspersed sequences tend to be a given length. Bands also are observed in S1 nuclease digest gel blots for the two families which are dominated by long or tandem repetition. Clone 2133 shows a band at almost the same length as with the EcoRI digest blot, as well as a "ladder" of bands at 2,3,4, and 5 times this length. Thus 2133 may be organized in a long or tandem array which reassociates with regularly spaced partially paired regions, which are often but not always digested by S1 nuclease.

SINGLE COPY DNA SEQUENCE DIFFERENCES
AMONG RELATED SEA URCHINS*Terrence J. Hall, Roy J. Britten*

Most of the single copy DNA sequences of higher organisms do not appear to consist of structural genes, and the sequences change rapidly in evolution. The effect of selection on these changes is not known, but it is considerably less than on changes in average protein sequences. Single copy DNA sequence relationships form a useful baseline for comparison with other evolutionary changes. The measurements reported here represent a significant extension of older work in precision and ability to measure more distant relationships. In a new technique

a series of samples are heated in a solvent (2.4M tetraethyl ammonium chloride) which suppresses the effect of base composition on thermal stability, and the strand-separated DNA is digested with S1 nuclease. With this approach *Strongylocentrotus purpuratus* single copy labeled DNA reassociated with *S. franciscanus* DNA melts 14°C below perfect duplexes, and the reassociation is nearly complete (81%). In previous measurements reassociation proceeded to less than 50% and only about half of this T_m reduction was observed. Similar measure-

ments between *S. purpuratus* single copy labeled DNA and *S. drobachiensis* DNA show a melting temperature about 7°C below perfect duplexes. Considering the effects of the sequence polymorphism of *S. purpuratus* DNA this result is very close to the previous measurements. Thus, as expected, the inclusion of more divergent sequences has a greater effect for the more distantly related pair of

species. When these data are compared with the fossil record, we estimate that single copy DNA sequences have been changing at a rate of about 0.25% per million years in each line, since the last common ancestors of *S. purpuratus* and *S. franciscanus* existed about 15 to 20 million years ago and of *S. purpuratus* and *S. drobachiensis* about 7 million years ago.

STAFF

Senior Research Associate: Roy J. Britten

Professor: Eric H. Davidson

Senior Research Fellows: Barbara R. Hough-Evans, William H. Klein, Amy Shiu Lee

Weizmann Research Fellow: Ze'ev Lev

Research Fellows: David M. Anderson, Robert C. Angerer, Susan G. Ernst, Terrence J. Hall, Gordon P. Moore, William R. Pearson, Terry L. Thomas

Graduate Students: Frank Costantini, Jay

W. Ellison, James W. Posakony, Richard H. Scheller, Barbara J. Wold

Research Staff: Clifford Beall, Peggy R. Bierer, Anita S. Cetta, Margaret E. Chamberlin, Roberta Gerson, Michael Kozlowski, Cary Lai, Patrick E. Leahy, Peter Sin-Yi Lu, James G. Moore, Walter D. Niles, Peter E. Nolan, Jane Rigg, Richard M. Rohan, Linda S. Vock

Laboratory Staff: Robert L. Gimlich, Edward D. Kusby, Robert O. Piehl, Sydne A. Schurmeier

PUBLICATIONS

Britten, R. J., A. Cetta, and E. H. Davidson. (1978) The single copy DNA sequence polymorphism of the sea urchin *S. purpuratus*. *Cell*. Submitted for publication.

Chamberlin, M. E., G. A. Galau, R. J. Britten, and E. H. Davidson. (1978) Studies on nucleic acid reassociation kinetics: V. Effects of disparity in tracer and driver fragment lengths. *Nucleic Acids Res.* In press.

Costantini, F. D., R. H. Scheller, R. J. Britten, and E. H. Davidson. (1978) Repetitive sequence transcripts in the mature sea urchin oocyte. *Cell*. In press.

Hough-Evans, B. R., B. J. Wold, S. G. Ernst, R. J. Britten, and E. H. Davidson. (1977) Appearance and persistence of maternal RNA sequences in sea urchin development. *Devel. Biol.* 60: 258-277.

Klein, W. H., T. L. Thomas, C. Lai, R. H. Scheller, R. J. Britten, and E. H. Davidson. (1978) Characteristics of individual repetitive sequence families in the sea urchin genome studied with cloned repeats. *Cell*. In press.

Leahy, P. S., T. C. Tutschulte, R. J. Britten, and E. H. Davidson. (1978) A large-scale laboratory maintenance system for gravid purple sea urchins (*Strongylocentrotus purpuratus*). *J. Exptl. Zool.* 204: 369-380.

Lee, A. S., R. J. Britten, and E. H. Davidson. (1978) Short period repetitive sequence interspersions in cloned fragments of sea urchin DNA. *Cold Spring Harbor Symp. Quant. Biol.* 42. In press.

Moore, G. P., R. H. Scheller, E. H. Davidson, and R. J. Britten. (1978) Evolutionary change in the repetition frequency of sea urchin DNA sequences. *Cell*. In press.

Scheller, R. H., F. D. Costantini, M. R. Kozlowski, R. J. Britten, and E. H. Davidson. (1978) Specific representation of cloned repetitive DNA sequences in sea urchin RNA's. *Cell*. In press.

Wold, B. J., W. H. Klein, B. R. Hough-Evans, R. J. Britten, and E. H. Davidson. (1978) Sea urchin embryo mRNA sequences expressed in the nuclear RNA of adult tissues. *Cell*. In press.

Department of Terrestrial Magnetism

Washington, District of Columbia

George W. Wetherill
Director

Contents

Introduction	385	Determination of isotopic composition of lithium in meteorites and terrestrial rocks	449
Stars, Planetary Systems, and Galaxies .	393	Petrologic and isotopic constraints on the origin of the Bhola chondrite	453
The formation of stars and planets .	393	Steady state populations of Apollo-Amor objects	456
Supernova-induced star formation .	393	The distribution of orbits of cosmic dust particles detected by Pioneers 8 and 9	471
The newly formed stars in Canis Major R1	395	Relations between Meteors and Meteorites	475
Discovery of an expanding neutral hydrogen shell surrounding the newly discovered supernova remnant in Cygnus	400	Theoretical entry model	475
Dynamics and star formation in the peculiar galaxy NGC 1961: a spiral with a very large mass .	403	Luminous efficiency of meteorites .	478
Galactic neutral hydrogen absorption spectra	405	Identification of meteorites with bright meteors	482
The relationships among HI, galaxy counts, and reddening in the Galaxy	408	Terrestrial microbarograph "air-wave" recordings: the global influx rate of large meteoroids .	490
Radio sources in globular cluster fields	412	Physics and Chemistry of the Earth .	494
Mass loss from T Tauri stars .	414	Velocity structure in the subducting lithosphere: implications from S-wave data	494
Accumulation of the terrestrial planets by the sweeping up of planetesimals	421	An anomalous low-velocity region above the deep earthquakes in the Japan subduction zone . .	505
Extragalactic studies	428	Crust and upper mantle structure of the Japan Sea	511
Rotational properties of spiral galaxies as a function of Hubble type	428	On double Benioff zones in subduction regions	517
Neutral hydrogen observations of a large sample of Sc and Sb galaxies	435	Is the spreading process at mid-ocean ridges episodic? . . .	520
The dwarf galaxy 1346-35	436	Precursors to <i>PKIKP</i> : an earth model discriminant	523
NGC 5506, an x-ray Seyfert galaxy .	441	Structure of the oceanic lithosphere from surface wave observations: North Atlantic .	527
Background fluctuations	443	Strain measurements in the near field of small earthquakes: a preliminary report	537
Acknowledgments	446	Anomalous electrical conductivity structure in central Chile . .	543
Instrument development	446		
A direct image tube camera . . .	446		
A continuum receiver back end . .	446		
Progress on the joint international project for 21-cm observation in the southern hemisphere . .	447		
Interplanetary Matter and Its Interaction with the Earth	449		

Geochemical constraints on mantle models: the case for a layered mantle	548	Origin of the Ninetyeast Ridge: trace element and Sr isotope evidence	909
On the origin of the calc-alkaline volcanics of the central Andes: a revised interpretation . . .	562	Sr isotope geochemistry of calc- alkaline and alkaline lavas from the Sunda arc in Lombok and Sumbawa, Indonesia . .	613
Trace element and Sr isotope abun- dances in recent lavas from Kilauea, Hawaii	590	Separation and isotopic analysis of neodymium	620
Geochemistry of the Galápagos Islands: implications for mantle dynamics and evolution	596	Bibliography	623
		Personnel	625

INTRODUCTION

Faith that the most fundamental truths of nature are elegant in form has had a powerful influence on the development of theoretical physics during this century. It was the sophisticated simplicity of Einstein's gravitational-field equations that convinced him he had found the answer he was seeking. The validity of Einstein's faith has been confirmed by ever more precise tests of these equations against subsequently proposed alternatives. A similar belief led to Dirac's prediction of the world of anti-particles. Time will tell if the identification of fundamental natural symmetries will bring order to the present menagerie of particles found by high-energy physicists and to the more obscure quarks, which seem to explain the variety of the others. However, the theoreticians' faith in his search for order in nature is still strong, and the prospect that it will be further rewarded appears good.

Earth scientists and astronomers have not received this grace. Still, great syntheses of specialized knowledge have been achieved—the recent “plate tectonic revolution” in earth science is a prime example. Here, there was no justification for believing that this is the way the Earth ought to be. Among the four planetary bodies for which we have adequate data (Earth, Moon, Mars, Mercury), only the Earth has moving and subducting lithospheric plates. A plate tectonic world is by no means the only possible world. The synthesis had to be achieved the hard way, through the accumulation of large quantities of data of many kinds and through attempts to relate these raw data to the Earth using physical theory known to be too simple to handle the real complexities of nature. Inevitably, all of these data were inexact and some of the theory either erroneous or puerile. Only after many abortive attempts at

synthesis were geologists, geochemists, and geophysicists able to justify belief in a theory which in rough form seemed evident to bright schoolchildren viewing Africa and South America on a globe of the Earth. Although Occam's razor is often invoked by earth scientists and astronomers, it has proven to be a very dull tool. We know that the fundamental processes of the Earth are complex and that theories can legitimately be faulted on the grounds that they are too simple to have any chance of being true. Unfortunately the number of possibly correct complex theories is infinite.

Observational astronomy clearly shows that the Sun is not the only possible kind of star and that the Galaxy is but one of many varieties. We have not yet seen another solar system, but it is plausible to assume there are many possibilities, that nature has not overlooked these alternatives, and that emphasis on pure thought is not likely to lead us to the truth. Another complication, at once beautiful and frustrating, is that all of these complex problems are linked to one another. Whether or not the Earth's mantle was initially homogeneous or heterogeneous depends on the distribution in size, composition, and velocity of the primitive planetesimals from which it was formed. These smaller bodies are but an adjunct of the poorly understood processes of star formation, which in turn are controlled by the original endowment and subsequent evolution of dust and gas within the Galaxy. Our understanding of the initial conditions and the formation of galaxies is merged at present with the most fundamental unsolved problems of cosmology.

There appears to be no promising alternative but to “labor in the vineyards,” make observations, and carry out experiments and measurements in areas we

feel to be relevant to the most fundamental questions of the Earth, Solar System, Galaxy, and Universe. Progress can be made only by isolation of finite solvable problems, but we must not forget that this isolation is an artifact we have created and not part of the fundamental design of nature. We must also be always trying to understand what it all means.

The studies described in this Report are thus necessarily of this apparently isolated and specialized nature. Nevertheless, the broad scope of the Department's activities should permit both the reader and our scientific investigators to be aware of the interdependence of these various activities and to recognize that they are not ends in themselves but are essential component parts of future scientific revolutions. Earlier hard-won fundamental syntheses can be expressed in simple statements which all people can understand: "The Earth is round," "The Sun is a star," and "The continents move." We too have a faith—that the day will come when these studies, combined with those of the many other laboratories throughout the world, will lead to even more encompassing, simple, profound qualitative truths.

SUMMARY OF CURRENT RESEARCH

New Stars and Galaxies

The center of gravity of this year's work at DTM lies at the interface between the earth and astronomical sciences: questions about how stars and their associated planets form, and about the extent to which meteors and meteorites are fossil relics of the formation period of our solar system. At least until recently, the problem of star formation has been poorly constrained by observation. However, it now appears likely that stars are not born alone but rather form in associations from a common cloud with a density $\sim 10^5$ times higher than the average interstellar medium. It also appears likely that the collapse of this

cloud to form stars is "triggered" by a shock wave, several kinds of which may be important.

Last year, Herbst and Assousa reported the first observational evidence that the shock wave from the explosion of a nearby supernova can provide the necessary trigger. These authors, together with their collaborators, Racine and Warner, now discuss further observations of the region of star formation for which evidence for a supernova trigger is strongest. This region includes stars of various sizes which presumably formed at the same time. The authors found that in general the characteristics expected of stars in such a young (3×10^5 years) association are present: circumstellar dust and gas, rapid rotation, and a "turn up" point indicating that the smaller stars of the group are still contracting (i.e., they have not yet reached the stable stage at which their luminosity is maintained by thermonuclear reactions in their interiors). However, important discrepancies between the observations and the predictions of current theoretical models are also found. It seems likely that this primarily indicates the weakness of present theoretical models and that this association is serving as a natural laboratory in which predictions of these models can be tested.

The newly formed stars in these associations often show blue-shifted absorption features in their spectra. These "T Tauri" spectra are usually interpreted in terms of massive ejection of matter into space during the first few million years of the star's life. Most planets are severely depleted in hydrogen and helium relative to average galactic element abundances. If the Sun went through a T Tauri stage of this kind, this would provide an explanation of how this surplus hydrogen and helium was removed. Weidenschilling has made a theoretical study of the maximum mass that could be removed by this mechanism. He finds that losses of 10% of the

original stellar mass are quite plausible. However, losses approaching 50% are unlikely. Thus it appears difficult to eject a solar nebula as massive as that proposed by some theorists. On the other hand, loss of a "minimal solar nebula" of about 5% of the mass of the Sun seems quite likely.

Stars probably form in cool clouds of dust and gas. Therefore we must first understand the distribution of dust and gas in the Galaxy and its relationship to regions of star formation in order to understand the circumstances under which these clouds actually collapse to form stars and those under which they do not. Two investigations of this kind were made this year, one at 21-cm radio wavelengths (Lockman and Greisen) and the other at optical wavelengths (Burstein and Heiles). Detailed comparison of the 21-cm observations with the predictions of theoretical models provides support for the "density-wave" theory of spiral-arm formation, in which shock compression associated with hydrodynamic instabilities initiates star formation. The luminosity of the bright young stars then "decorates" the spiral-shaped regions of increased density, causing the dense regions to become visible, galactic spiral arms. It is possible that star formation is first initiated in a cloud by these density-wave shocks. The largest stars formed in this way are expected to complete their life cycles in about a million years while still in the cloud. The supernova explosion caused by the gravitational collapse of the interior of the star at the end of its life may then trigger further star formation in the cloud.

Detailed observational studies are needed if we are to understand star formation and the association of new stars with circumstellar disks analogous to the solar nebula from which the solar system formed. Only in the nearby regions of the Galaxy in which stars are presently forming are stars the size of the

Sun bright enough for accurate measurement. However, study of regions of star formation in other galaxies is also of high importance, if only because our view of most of our own Galaxy from inside is obscured by the very dust clouds from which stars are formed. More important, observations of star formation in other galaxies permit tests of theories under various conditions. In recent years "comparative planetology" has been in vogue, whereby theories of Earth formation, evolution, and structure are tested by comparing their predictions not only against terrestrial data, but also against data from the Moon, Mars, Venus, and Mercury. In this way the geologist is liberated from the dilemma, described by Carl Sagan, of "being in the position of a linguistic scholar living on a planet on which only one language is spoken." Counting the Moon, there are only five terrestrial planets, and "comparative planetologists" are thus severely limited. However, the variety of galaxies that can be studied is primarily limited by the rate at which observations can be made rather than by the actual number available for study.

A study of this kind is reported by Rubin, Ford, and M. S. Roberts of the National Radio Astronomy Observatory. A combined neutral hydrogen (radio) and optical investigation was made of a giant spiral galaxy, NGC 1961, about a factor of 10 more massive than our own. This galaxy displays an unusual combination of normal and abnormal characteristics. In composition and luminosity it appears to be a scaled-up version of an ordinary galaxy, and the velocity of the inner part of its spiral structure seems to represent normal rotation. However, the outer part of this galaxy is greatly distorted, large non-circular velocities are found, and a dusty looping structure is observed. Measurements of the colors of the stars in this galaxy support the idea that a burst of

star formation involving about 5% of the mass of the entire galaxy occurred about 200 million years ago. Thonnard, Rubin, and Ford also report measurements on a very small irregular galaxy ($\sim 10^9$ solar masses), which also appears to have experienced a recent burst of star formation. Thus, episodes of star formation are found in galaxies of very different types, and they are possibly results of collisions between galaxies.

Although it is unlikely that an event of this particular kind has occurred in our Galaxy, these measurements show that the rate and temporal uniformity of star formation, and presumably of nucleosynthesis as well, vary greatly from one galaxy to another. Present radiometric chronologies for our Galaxy are based on simple, possibly naive, assumptions about the uniformity of nucleosynthesis. Establishment of reliable nucleosynthetic time scales is essential to an understanding of events in the early history of the solar system. This will require an understanding of the principal facts concerning the evolution of galaxies, especially the rate at which the radioactive isotopes are synthesized by various stellar and galactic processes as a function of time. At present we are a long way from an adequate understanding of these basic principles.

Present observations of galaxies fail to provide a clear idea of so basic a physical property as the total mass of a galaxy. Continuing work of Rubin, Ford, and Thonnard on the rotation of spiral galaxies of different types shows that the orbital velocity of the galactic matter as a function of distance from the galactic center is nearly constant across almost the entire optical disk. If most of the mass were located near the center of the galaxy, orbital velocities would be low near the outer edge of the galaxy, in accordance with Kepler's laws. It has usually been assumed that most of the mass of a galaxy is concentrated near its center. However, these measurements

yield an unexpected result: much of the mass is in the outer portion of the galaxy, perhaps even beyond the optically observable limits of the galaxy. As a consequence, total-galaxy masses must be higher than previously assumed, possibly by a factor of five. Interesting increases in velocity across the spiral arms, a major prediction of the density-wave theory for spiral structure, are also observed.

On a smaller scale, there also appears to be "missing mass" in globular clusters. It is known that stars lose mass as they age, and in densely packed globular clusters the lost gas might be expected to remain in the clusters. Such matter is not seen, however, either in the form of new stars or as neutral hydrogen. Turner, in collaboration with Rood and Goldstein at the National Radio Astronomy Observatory, describes new measurements of radio sources in globular clusters. Several of these show spectral peculiarities not readily explainable. This finding, combined with evidence found by other workers for x-ray sources in globular clusters, suggests that these clusters may contain a new type of object, perhaps a single massive body in the center of the cluster, which could account for the missing gas.

Interplanetary Matter: Apollo-Amor Objects, Meteorites, and Meteors

A direct and detailed record of physical and chemical conditions, events, and processes is available from the small bodies of the solar system: comets, asteroids, and the Earth-approaching Apollo-Amor objects, as well as from their fragments—meteorites and meteors. Studies of these bodies, particularly the meteorites, have provided an enormous wealth of information in the past. The recent discovery in other laboratories of variations in the isotopic composition of many elements in some meteorites shows there is much more to discover and even more to understand.

These isotope anomalies of nuclear origin in meteorites have been found not only in many rare elements but also in two of the most abundant, oxygen and magnesium. They clearly show that the early solar system was heterogeneous and probably contained incompletely mixed contributions of isotopes formed in different stars at different times and by different processes. It is likely that at least some of these isotope anomalies are caused by injection of isotopes from a massive supernova that exploded in the vicinity of the sun 4.5 billion years ago. This supernova may also have triggered the formation of the Sun and solar system, as discussed by Herbst and Assousa. At present there is no consistent explanation of the origin of these anomalies, even though a host of theoretical models are under discussion.

The ratio of the two lithium isotopes, ${}^7\text{Li}$ and ${}^6\text{Li}$, is very sensitive to differences in these models, and could prove important in distinguishing between them. Therefore Brown, Rajan, Roberts, Tera, and Whitford have undertaken an investigation of lithium abundance ratios in meteorites and terrestrial materials. The first results of this study are given in this Report. Earlier attempts to measure lithium isotope ratios were inaccurate because of severe difficulties caused by lithium isotope fractionation in the mass spectrometer. This fractionation has been eliminated by a new technique using the deuteron beam from our Van de Graaff accelerator to produce characteristic nuclear (d, α) reactions in ${}^6\text{Li}$ and ${}^7\text{Li}$. It is found that the ${}^7\text{Li}/{}^6\text{Li}$ ratio in twelve meteoritic samples is indistinguishable from terrestrial lithium at the 1% level. This places restrictions on the extent of any hypothetical widespread high-energy proton bombardment of the early solar system.

A principal problem in the interpretation of evidence from studies of interplanetary bodies is our present uncertainty about the relationships of these

bodies to one another and to their sources. In recent years, considerable attention has been given to the small (1-km-radius) Earth-crossing bodies known as Apollo objects, and to the similar "Earth-grazing" (perihelion < 1.3 A.U.) Amor objects. At present these are the most likely immediate sources of the meteorites, which strike the Earth, and are also the principal cause of cratering on the Moon and terrestrial planets with the possible exception of Mars. The orbits of these bodies are unstable on a time scale of 10^7 – 10^9 years, and their present population represents a steady state between the derivation of these bodies from some external source (i.e., the asteroid belt) or as the nonvolatile residue of extinct comets. In this Report the orbital distribution expected for this steady state distribution is calculated theoretically and is found to agree with the observed orbits of these bodies. Subject to uncertainties in crater counts and scaling laws, the crater frequencies on the Earth and Moon agree with those calculated from the steady state distribution. This agreement between observation and theory justifies some confidence in those predictions unverified at present such as the age distribution of Apollos, meteorite yields, and the sources of Apollo objects. This information is central to understanding the relationship of Apollo-Amor objects to meteorites of various classes.

A series of reports by ReVelle, Rajan, and Wetherill addresses the question of the relationship between meteors—the "shooting stars," most of which burn up in the atmosphere—and the meteorites, which survive passage through the atmosphere. Particular attention is paid to the very bright meteors, "fireballs," which range in mass up to many tons. These contributions include a new theory for the physical processes accompanying the passage of a meteor through the atmosphere. This theory is then combined with observational and laboratory

data on the three meteorites recovered by photographic meteor networks to argue that previous estimates of meteor mass are too high by about a factor of 10. This removes much of the discrepancy between estimates of interplanetary flux of meteorite-size bodies based on meteor data and estimates derived from the lunar seismic network. Previous classified Air Force data on large explosions in the atmosphere are interpreted as being consistent with this result. Finally, it is shown that when these new results are taken into account, about 30% of the bright meteors (fireballs) have properties indistinguishable from those of recovered meteorites; these cannot be weak "dust balls," as maintained by most workers. If these indeed are meteorites, as seems likely, this provides a much larger set of meteorite orbit data to be compared with theoretical models that predict the orbital distribution expected from various hypothetical sources—for example, comets and asteroids.

Physics and Chemistry of the Earth

Twenty years ago detailed geochemical and geophysical studies were primarily directed toward the Earth's crust, its thin (5–50 km) surficial region consisting of rocks of relatively low density. The mantle was a somewhat mysterious place from which basalts came, and its properties were visualized as being similarly monotonous in both continental and oceanic regions. All this has changed since the advent of plate tectonics, and attention has been directed toward understanding the complex structure and chemical heterogeneity of at least the upper several hundred kilometers of the Earth's mantle.

In this year's Report, special attention is given to the mantle in oceanic regions, the place of the principal plate tectonic events—those associated with the upwelling basaltic magmas at the midocean ridge and the downgoing lithospheric slabs at oceanic trenches.

In a series of four reports, Suyehiro, Sacks, Linde, and Evans describe studies of the oceanic crust and upper mantle in the western Pacific in the vicinity of Japan. This is an especially favorable area for such studies because of the combination of important tectonic settings and an abundance of naturally occurring earthquakes, which provide acoustic "probes" for investigating these structures. Understanding the seismicity and crust-mantle structure of Japan is also of considerable practical interest, considering the large population exposed to earthquake hazards there.

This new work includes a further investigation of the downgoing 120-km-thick slab of oceanic upper mantle in the Japan subduction region east of Japan. This study, using seismic shear waves, confirms the earlier work of this group based on compressional waves. These investigations show that the lithospheric slab is not uniform, and that at least a two-layer model is required to match the seismic data. Work elsewhere had already shown that the horizontally moving oceanic slab has a similar structure, and it is now found that this structure is preserved as the slab is sharply bent and begins its deep (more than 700-km) descent into the Earth's interior.

Over most of the oceanic region, the moving lithospheric slab overlies the weaker, probably partially melted asthenosphere, characterized by lower seismic velocities. In the subduction zone, the slab plunges beneath the asthenosphere, leaving a low-velocity zone above the high-velocity lithospheric slab. Normally this velocity contrast is only a few percent. However, below a depth of 300 km in the Japan subduction zone, the asthenosphere lying above the downgoing slab has a velocity which is lower by an additional 10%. The dissipation of seismic energy ($1/Q$) in this zone is anomalously high. Taken together, these data suggest that this zone contains an unusually high proportion of partially

melted rock possibly available for the production of volcanic rocks.

Somewhat farther to the north, in the Japan trench, Hasegawa has shown that the region of high seismicity associated with the downgoing slab (Benioff zone) is more complex than usual, and that it consists of two parallel but offset planes. Linde and Sacks propose a rheological model to explain this phenomenon. This involves consideration of the stress distribution in the slab as it is bent at the onset of subduction and as it subsequently is straightened again to produce the straight slab observed at greater depths. This theory predicts a double Benioff zone, as is observed, and also explains aspects of the distribution of earthquakes that could not be understood using earlier models.

Sacks, Linde, and their collaborators Spottiswoode, McGarr, and Green at the Bernard Price Institute in Johannesburg, South Africa, report the first results of an experiment designed to measure seismic strain in the source region of an earthquake. Normally this must be inferred indirectly from studies of distant earthquakes, and these have led to inconsistencies and ambiguities. In the present experiment, strainmeters as well as higher frequency seismometers have been installed at a depth of 3 km in the source region of earthquakes (up to magnitude 4.0) produced by the nearby mine face of a deep gold mine. These preliminary results show that a step-change in strain is recorded by the strainmeters following a nearby earthquake. Longer period strain changes are also found, which are very similar to the "slow earthquakes" the DTM group has reported in regions of high natural earthquake activity.

Seismology is by no means the only important source of information about the nature of the oceanic mantle. Geochemical and isotopic investigations of volcanic rocks derived from the oceanic mantle can, at least in principle, provide

much more detailed information about their mantle source. The reason that the qualification "in principle" must be added is that the volcanic rocks are erupted on the surface and do not provide direct information about the location of their mantle source. A group of reports by Hofmann, White, and Whitford, in collaboration with several investigators in other laboratories, address this problem. Hofmann, White, and Whitford review various possible models for the sources of the basalts that erupt at midocean ridges and oceanic islands. They conclude that the evidence favors a layered model consisting of (1) an oceanic asthenosphere depleted in the large ion lithophile or "incompatible" elements such as K, Rb, Sr, Cs, rare earths, U, and Th, and (2) a heterogeneous deeper mantle containing higher abundances of these elements. In this model the ocean ridge basalts are formed by partial melting of the depleted asthenosphere, whereas the oceanic island volcanic rocks are principally derived by partial melting of the deeper mantle, the material being transported across the asthenosphere in plumes which mix only slightly with the asthenospheric material.

This general discussion is related to three specific studies of volcanic rocks from the Pacific and Indian Oceans. A study of strontium isotope ratios and trace element concentrations in a particular type of lava (tholeiite) from Hawaii is reported by Hofmann and his collaborators, Wright and Feigenson. They find that the strontium isotope composition of these lavas remains constant as a function of time since eruption, whereas the concentrations of the large ion lithophile elements and the Rb/Sr ratio decrease with time. This can be explained by a partial-melting model in which strontium is retained in decreasing amounts by the mineral clinopyroxene in the unmelted source material. Inasmuch as similar tholeiite lavas are the dominant type of midocean

ridge basalts, these data are interpreted as showing that volcanism with these geochemical properties can produce the observed depletion of the asthenospheric source of the ridge basalts and explain its Rb/Sr and associated $^{87}\text{Sr}/^{86}\text{Sr}$ evolution as well.

White and Hofmann report strontium and neodymium isotopic data and trace element data from the Galápagos. These measurements demonstrate that the mantle source of these rocks is heterogeneous and distinct from the source of midocean ridge basalts. However, it appears that there has been considerable admixture of enriched "plume-type" material and normal depleted oceanic asthenosphere. Although these rocks are from oceanic islands rather than ridges, the data show that depletion in neodymium relative to samarium similar to that found in ridge basalts has occurred. The $^{87}\text{Sr}/^{86}\text{Sr}$ and Rb/Sr data plot on the 1600-million-year "mantle isochron" described by Brooks *et al.* (*Year Book* 75, pp. 176–201), and it is suggested that the Nd/Sm depletion occurred at that time.

Whitford and his collaborator, Duncan of Oregon State University, report trace element studies on the "Ninetyeast Ridge" in the Indian Ocean. Unlike the oceanic ridges that are spreading centers, for the most part earthquakes do not occur along this type of ridge. These authors test various hypotheses for the origin of the ridge including, among others, an extinct spreading center, an extinct island arc, and the trace caused by the motion of the oceanic lithospheric plate over a mantle plume or "hot spot." Again the data require a heterogeneous mantle source. Upon evaluation of the alternatives the plume hypothesis is favored, and it is suggested that the present location of this hot spot is beneath the volcanically active Kerguelen plateau in the southern Indian Ocean, which contains basalts with the highest $^{87}\text{Sr}/^{86}\text{Sr}$ ratios of any found in the Indian Ocean.

Taken together, these three studies support the conclusions of Hofmann, White, and Whitford that a two-layer model consisting of a depleted asthenosphere overlying a heterogeneous and relatively undepleted deeper mantle can explain past results, and that the more obvious alternative models present severe difficulties. However, demonstration of the uniqueness of this model remains elusive, and there are many detailed chemical and fluid mechanical problems to be satisfactorily understood before it can be considered even moderately well established.

James reviews a number of years of work on the origin of volcanic rocks in the central Andes and presents new data bearing on this problem. Like oceanic island-arc volcanoes, the Andean volcanoes are located above a descending plate of oceanic lithosphere. There are characteristic differences, however, between these volcanic rocks and those from island arcs: their $^{87}\text{Sr}/^{86}\text{Sr}$ ratios are distinctly higher (more radiogenic) and they contain higher concentrations of the large ion lithophile elements. Because the magmas that form these rocks must ascend through a continental crust and upper mantle, these differences have often been attributed to derivation from or admixture with this continental material. In principle, this involvement with continental material could be in the form of crustal contamination or could be derived from an ancient undepleted continental lithosphere. Geochemical arguments against crustal contamination were previously advanced and are still thought to be valid. However, oxygen isotope measurements now show that crustal material constitutes a significant portion of the source material for these magmas. This is now interpreted as resulting from incorporation of rather large quantities of eroded continental material in the adjacent oceanic crust and subduction of this material together with oceanic crust and lithosphere. De-

tailed petrological, geochemical, and isotopic arguments are presented to support this model. Thus the differences between Andean and island-arc volcanism are related to the relative proximity of continental platforms. In the Andes the primary subducted material is partly continental in origin. If this process has been common throughout earth history, it has important implications bearing on theories of the evolution of continents and the recycling of continental materials.

Further to the south, in Chile, Aldrich and his collaborators, Bannister, Casaverde, and Triep have been operating a network of magnetometers, which measure the electrical response of the earth to variations in the earth's magnetic field caused by geomagnetic storms. With the use of a model, it is then possible to identify certain aspects of the earth's

conductivity structure in the region. These workers conclude that the conductivity structure in Chile shows no particular relationship to the earthquake-free region north of the array. However, there does appear to be a conductor southwest of the array and possibly a deep conductor under the Andes.

A number of other investigations not summarized above are included in this Report. It may be that some of those not mentioned will ultimately be recognized as the true "highlights" of this year's work. If so, this may not entirely be a consequence of the summarizer's lack of perception. In spite of the valid arguments for well-coordinated, problem-oriented research, there is still an important unpredictable stochastic element in scientific work. There is no *real* way of knowing which particular result will turn out to be the missing piece of a larger puzzle.

STARS, PLANETARY SYSTEMS, AND GALAXIES

THE FORMATION OF STARS AND PLANETS

SUPERNOVA-INDUCED STAR FORMATION

G. E. Assousa and W. Herbst

In *Year Book 76* (Assousa, Herbst, and Turner, pp. 744–753), we described our work on two associations, CMa R1 and Cep OB3, which led us to suggest that supernova explosions are responsible for at least some of the star formation currently going on in the Galaxy. This question is of particular importance to cosmogonists because of the meteoritic evidence (Lee *et al.*, 1976) that "live" Al^{26} was present at the time of formation of the solar system. Since this isotope decays to Mg^{26} with a half-life of only $\sim 7 \times 10^5$ years, the implication is that a source of radioactive Al was present in the vicinity of the proto-solar system at about the time it formed. The

most likely source is a supernova explosion (Schramm, 1978), and it is furthermore likely that this supernova did not occur "by chance" close to the proto-solar system but was itself responsible for inducing the collapse of an interstellar cloud and the subsequent formation of the solar system (e.g., Cameron and Truran, 1977). This scenario, in addition to the expectation that present-day supernovae would also be causing some star formation, lends importance to our observations.

Our "best case" for supernova-induced star formation is the CMa R1 association. Two new studies of that region have recently been completed, and both support our picture. Observations of the newly formed stars by Herbst, Racine, and Warner are described elsewhere in this Report. The other study, by Reynolds and Ogden (1978), reports the dis-

covery of an expanding shell of ionized gas coincident with the CMa R1 emission ring. This complements our discovery of a neutral hydrogen shell and provides additional evidence of an energetic event in CMa OB1.

There remains some controversy over the source of the shell. Blitz (1978) has argued for a stellar wind-driven shell. However, the lack of a plausible source for the wind, the absence of stellar wind-driven shells around other stars, and the presence of a runaway star (probably an escaped member of a binary system in which one star became a supernova) weigh heavily against this hypothesis. The supernova scenario is the only one to provide a simple and comprehensive explanation of the main features of the CMa OB1/R1 region.

Another important observation was reported this year by Wootten (1978). He has discovered a molecular cloud and an embedded protostar associated with the old supernova remnant W44. This seems to be another good example of supernova-induced star formation. Several other supernovae surveyed by Wootten appear to be interacting with molecular clouds, and continued study will probably result in further cases of embedded protostars.

If, as begins to seem likely, supernovae trigger star formation in the Galaxy, one might question their relationship to the well-known spiral pattern of star formation seen in our own and external galaxies. One idea, put forward by Mueller and Arnett (1976) and Gerola and Seiden (1978), is that chains of star-forming regions will be created by successive supernova-star-forming-supernova cycles. These chains will be distorted into spiral patterns by differential galactic rotation and may account for the "spurs" and "feathers" commonly seen in external systems, but they probably do not account for the main spiral arms (see also Rubin, Ford, and Thonnard, this Report).

Another possibility is that the density wave sets up the spiral pattern of dense clouds (forms the clouds?) and the supernovae trigger the star formation. Feathers and spurs can then result from ultraharmonic resonances in the manner described by Shu *et al.* (1973), in spite of the fact that the gas cannot self-shock (Woodward, 1975). This appears to be the situation locally (within 1 kpc of the sun), since we are in a spiral-like feature, but there is no evidence of a density wave (Lin *et al.*, 1978). Other galactic spiral features, beyond the local one, do show evidence of being density-wave induced (see Lockman, this Report). Therefore, we suggest that the Local spiral arm (also known as the Cygnus-Orion arm) is a region of enhanced gas density—probably an ultraharmonic resonance—in which star formation is not triggered by a density-wave shock but by "local" processes, probably mostly supernova explosions.

We conclude that (1) supernovae are responsible for at least some of the star formation presently occurring in the Galaxy, and (2) it is quite possible that they are the major triggering mechanism operating at the solar distance from the galactic center. The meteoritic evidence suggesting that the solar system was formed as a result of a supernova event is, therefore, in agreement with what we know about star formation presently occurring in the vicinity of the sun.

References

- Assousa, G. E., W. Herbst, and K. C. Turner, Supernova-induced star formation, *Carnegie Inst. Wash. Year Book* 76, p. 744, 1977.
- Blitz, L., Star forming molecular clouds towards the galactic anticenter, *Proceedings of the Gregynog Symposium on Massive Molecular Clouds*, P. M. Solomon, ed., Reidel Co., in press, 1978.
- Cameron, A. G. W., and J. W. Truran, The supernova trigger for formation

- of the solar system, *Icarus*, **30**, 447, 1977.
- Gerola, H., and P. E. Seiden, Stochastic star formation and spiral structure of galaxies, *Astrophys. J.*, in press, 1978.
- Lee, T., D. A. Papanastassiou, and G. W. Wasserburg, Demonstration of ^{26}Mg excess in Allende and evidence for ^{26}Al , *Geophys. Res. Lett.*, **3**, 41, 1976.
- Lin, C. C., C. Yuan, and W. W. Roberts, Jr., On the stellar streaming motions and the observational determination of the structure of the Galaxy, *Astron. Astrophys.*, in press, 1978.
- Mueller, M. W., and W. D. Arnett, Propagating star formation and irregular structure in spiral galaxies, *Astrophys. J.*, **210**, 670, 1976.
- Reynolds, R. J., and P. M. Ogden, Fabry-Perot observations of a large expanding gas shell associated with CMa R1 and CMa OB1, *Astrophys. J.*, in press, 1978.
- Schramm, D. N., Supernovae and the formation of the solar system, *Protostars and Planets*, T. Gehrels, ed., Univ. Arizona Press, in press, 1978.
- Shu, F. H., V. Milione, and W. W. Roberts, Nonlinear gaseous density waves and galactic shocks, *Astrophys. J.*, **183**, 819, 1973.
- Woodward, P. R., On the nonlinear time development of gas flow in spiral density waves, *Astrophys. J.*, **195**, 61, 1975.
- Wooten, A., Observations of star formation in dense clouds near supernova remnants, *The Moon and the Planets, Feature Issue on Protostars and Planets*, T. Gehrels, ed., Reidel Co., in press, 1978.

THE NEWLY FORMED STARS IN CANIS MAJOR R1

W. Herbst, R. Racine*, and J. Warner†

We have undertaken a comprehensive optical and infrared study of the 30

* University of Montreal, Montreal, Canada.

† University of Minnesota, Minneapolis, Minnesota.

members of CMa R1 (see Fig. 1) with the aim of determining the physical properties (and thereby the evolutionary status) of these stars. This association is of particular importance because of its location at the edge of an expanding shell of gas which has been identified (see Assousa *et al.*, 1977), as a supernova remnant. A quantity of great interest is the age of the association, since this relates to the formation mechanism, and we discuss this in some detail. The observational data on which this discussion is based have been published in the July 15, 1978, issue of *The Astrophysical Journal*.

Ages of clusters and associations are generally estimated by comparing the locations of the stars on a color-magnitude ($B - V$ vs. V) diagram with isochronal lines determined from theoretical stellar models. To plot the stars on such a diagram we must know the distance to the association and the amount of reddening [$E(B - V)$] and visual extinction (A_V) suffered by each star, as a result of scattering by dust grains along its line of sight. In general, we may write

$$A_V = R \cdot E(B - V).$$

For most regions of the Galaxy, $R = 3.3$ with surprisingly little variation. In dense clouds, however, R is often found to increase (e.g., Herbst, 1977), possibly because the dust grains accrete "mantles" of substances such as CO or H₂O. The uncertainty in R is the major source of difficulty in locating the CMa R1 stars on the color-magnitude diagram.

Since infrared radiation is little affected by interstellar extinction, observations at 1–3.5 micron wavelengths provide a possible means for evaluating R . Care must be exercised, however, since infrared "excesses" may be produced not only by increased values of R but also by additional radiation sources (such as circumstellar dust clouds) close to the stars. It is an unfortunate circumstance that the newly formed stars are both



Fig. 1. An enlargement of the blue print of the Palomar Observatory Sky Survey showing the locations of the members of Canis Major R1. The sole criterion for membership is that a star illuminate a reflection nebula detectable on the Sky Survey print. The authors are grateful to the Hale Observatories for the use of this blue print.

likely to be found in dense clouds and likely to be embedded in circumstellar shells or disks. We have attempted to use spectral differences in the infrared radiation to distinguish between these alternatives for stars in CMa R1 with infrared excesses.

We found ten stars (Nos. 2, 6, 7, 14, 16, 17, 18, 20, 24, and 25) that have excess

radiation at wavelengths 0.9μ and longer probably on account of higher than normal R values. Four of these (Nos. 2, 16, 18, and 20), as well as No. 9, also have spectra characteristic of a circumstellar emission component—either thermal radiation from hot dust (Nos. 9, 16?, 18) or free-free emission from ionized gas (Nos. 2, 20).

There does not seem to be any correlation between a star's location in the association and whether it shows an extinction anomaly. For example, Nos. 16, 17, 18, and 19 form a very tight subgroup. The first three stars show the anomaly, while No. 19 does not. This suggests that the effect occurs in matter quite close to, and perhaps influenced by, the stars. Similar circumstances appear to apply in the Orion nebula, where Breger (1977) reports that less than 10% of the stars show an extinction anomaly.

Figure 2 shows the color-magnitude diagram for the association. We adopt Claria's (1974) value of the distance modulus. This provides a satisfactory fit to the lower envelope of main sequence stars in the association, and confirms Claria's conclusion that CMa OB1 and CMa R1 have a common distance of 1150 pc. The uncertainty in the distance modulus given by Claria is ± 0.3 mag, and that is about the latitude our observations will allow.

There are a number of stars at all luminosities which lie well above the main sequence in Fig. 2. This is true even if extinctions are calculated as $3.3 E(B - V)$. The stars with circumstellar matter (squares in Fig. 2) are particularly striking in this regard. Normally, one interprets deviation from the main sequence at the bright end of a color-magnitude diagram as post-main sequence evolution and deviation at the faint end as pre-main sequence evolution. Deviations over the entire length of the diagram, as seen in Fig. 2, are not readily interpretable in such terms.

What is apparent, however, is that there is a $B - V$ color redder than which no stars are found on the main sequence (the so-called "turn-up" point). This color corresponds to that expected from a star of ~ 6.5 times the mass of the sun. We therefore infer that less massive stars have not yet had time to contract to the main sequence (i.e., to the point where their interiors are hot enough for

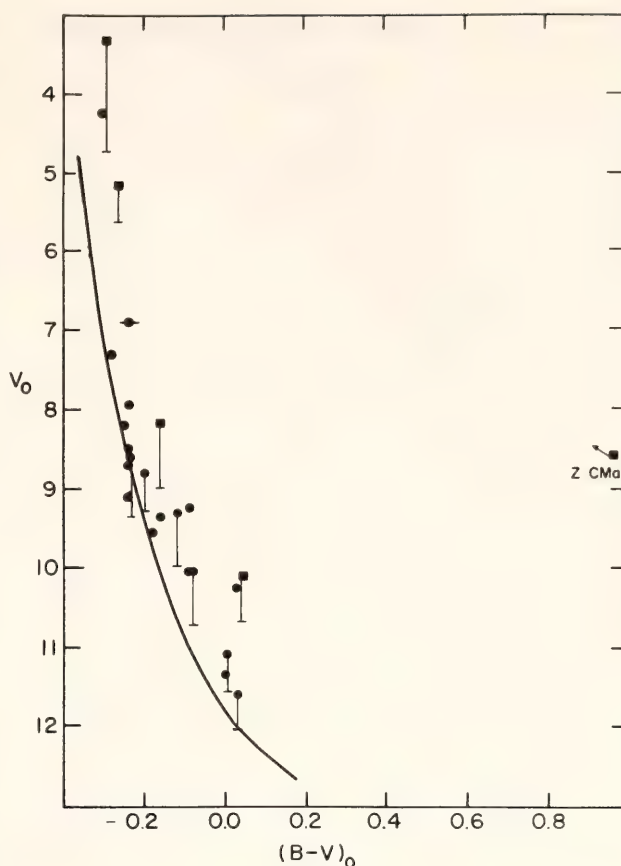


Fig. 2. A color-magnitude diagram for stars in CMa R1. Brightness increases upward and temperature increases to the left. The main sequence (locus of hydrogen-burning stars) is shown as a line, adjusted to the distance of the association. Squares denote stars with infrared excesses indicative of circumstellar matter. Lower limits to the luminosity of stars with large R values are also shown.

hydrogen burning to commence and halt the collapse process). By comparing with theoretical models of collapsing stars, we can estimate an age for the association of $\sim 3 \times 10^5$ years. It should be emphasized that this number is very uncertain, since the isochrones available from current theoretical models do not fit the observations well. This is shown in Fig. 3, where the data have been transformed to the theoretical color-magnitude diagram (in which luminosity is plotted against temperature) and theoretical isochrones from the work of Iben (1965) are given. The apparent conclusions to be drawn from this diagram are that the stars have ages ranging from less than 3×10^5 years to greater than $3 \times$

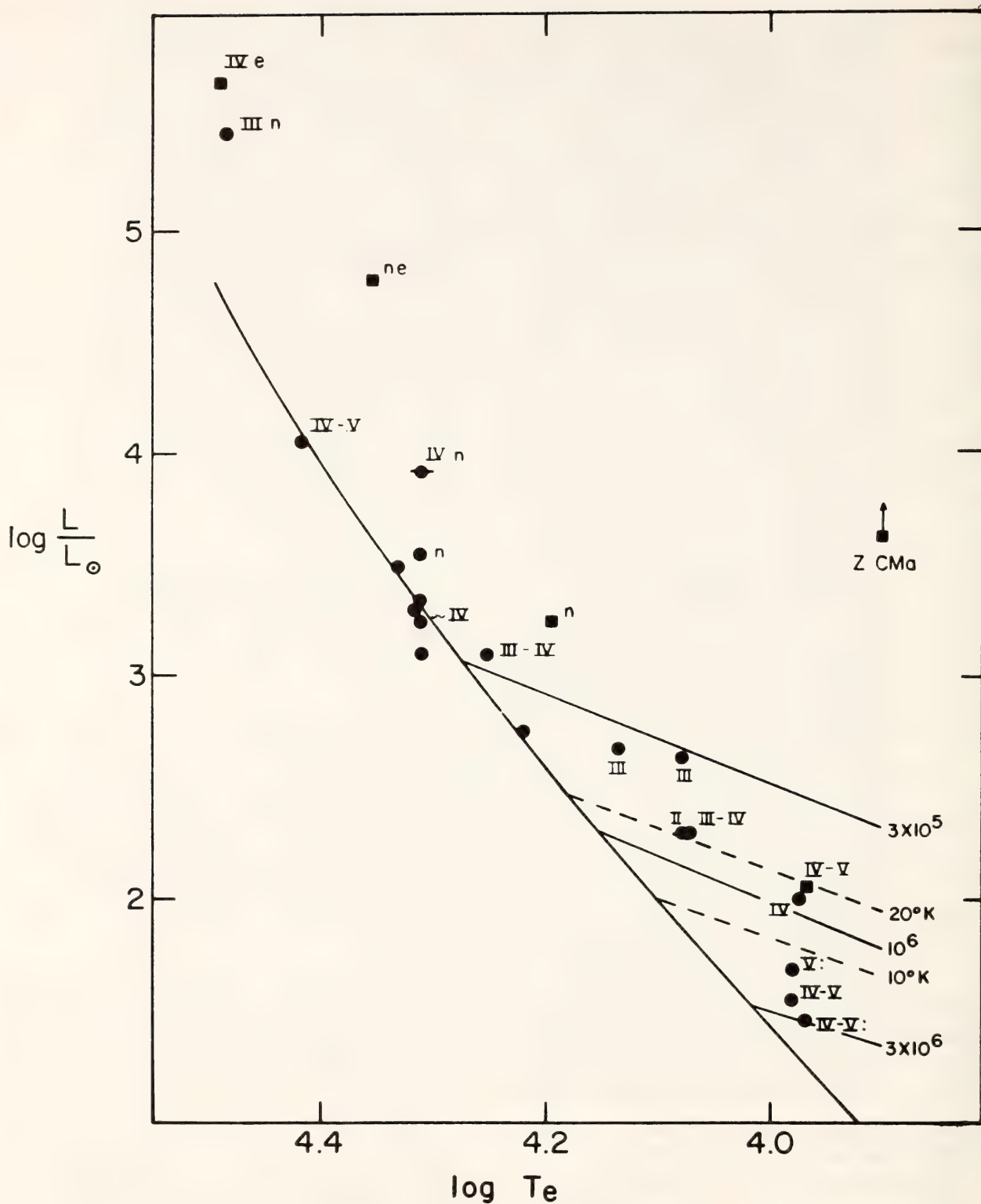


Fig. 3. A theoretical color-magnitude diagram for CMa R1. Isochrones are shown for 3×10^5 , 10^6 , and 3×10^6 years from the work of Iben (1965). The observations are not in good agreement with these isochrones, probably because the theoretical models are not sufficiently accurate representations of real stars.

10^6 years and that the lower mass stars are systematically older. This assumes, however, that the nonrotating, nonmagnetic, isolated stars of Iben's theoretical

model are an accurate representation of reality. This is unlikely for many reasons, and we feel it is prudent to reserve judgment on the mass-dependent forma-

tion time question until more realistic models are available. The turn-up point age, $\sim 3 \times 10^5$ years, is the best estimate we can make at the present time and could well apply to the entire association.

There are five stars (Nos. 2, 5, 16, 20, and 29) that are more massive than those at the turn-up point and should be on the main sequence but are not. Interpreted as pre-main sequence stars, they would have ages an order of magnitude less than those of the main sequence stars, and it seems unlikely that so many stars in CMa R1 would be simultaneously in such a short-lived phase of their evolution. Furthermore, all five are variable stars; and four of the five have strong broadening of their spectral lines, indicating rapid rotation. Only one star not in this group (No. 8) has rotationally broadened lines, and these are only slightly broadened. Nos. 2, 5, and 29 are also known to be binary stars. These facts suggest that duplicity and rapid rotation are mainly responsible for the unusual locations of the stars on the color-magnitude diagram.

A curious correlation between the absence of shell characteristics and the presence of strong rotational line broadening among these five stars may also be understood qualitatively if they are surrounded by optically thick circumstellar disks flattened along the rotation axis. No. 20 is the only one without rotationally broadened lines, but it has the strongest shell characteristics in this sample. In the picture presented here, it is a pole-on object. Nos. 5 and 29 have no shell characteristics, but do have rotationally broadened lines and would represent objects in which the rotation axis is perpendicular to the line of sight. This is certainly true for No. 5, which is an eclipsing binary. Nos. 2 and 16, then, would be examples of intermediate inclination objects exhibiting rotationally broadened lines and "shell" characteristics weaker than in No. 20. We do not

wish to place too much emphasis on this qualitative picture; our point is that rapid rotation and duplicity probably have a large role to play in the observed characteristics of these stars, and attempts to interpret them in terms of models of single, nonrotating stars could be misleading. Further theoretical studies of the evolution of rapidly rotating stars such as those begun by Black and Bodenheimer (1976) will be invaluable. Observationally, it will be an important task to determine the nature of the variability of stars 2, 16, 20, and 29—especially to see if it is periodic.

To summarize, this study has revealed additional evidence of the youthful nature of stars in the CMa R1 association, in particular, (1) stars with circumstellar matter (possibly disks), (2) rapidly rotating stars, and (3) an association turn-up point, suggesting an age of $\sim 3 \times 10^5$ years. Comparison of the observations with theoretical models has not been very successful, and we attribute this to the lack of realistic models—particularly ones that include the effects of rotation. The present study supports the supernova-induced star formation scenario for CMa R1 described by Herbst and Assousa (1977), although it does not permit a more accurate dating of events.

References

- Assousa, G. E., W. Herbst, and K. C. Turner, Supernova-induced star formation, *Carnegie Inst. Wash. Year Book* 76, 744, 1977.
- Black, D. C., and P. Bodenheimer, Evolution of rotating interstellar clouds. II. The collapse of protostars of 1, 2, and 5 M_{\odot} , *Astrophys. J.*, 206, 138, 1976.
- Breger, M., Intracluster dust, circumstellar shells, and the wavelength dependence of polarization in Orion, *Astrophys. J.*, 215, 119, 1977.
- Claria, J. J., A study of the stellar association Canis Major OB1, *Astron. Astrophys.*, 37, 229, 1974.

- Herbst, W., Interstellar extinction in dust clouds, *Carnegie Inst. Wash. Year Book* 76, 742, 1977.
- Herbst, W., and G. E. Assousa, Observational evidence for supernova-induced star formation: CMa R1, *Astrophys. J.*, 217, 473, 1977.
- Iben, I., Stellar evolution. I. The approach to the main sequence, *Astrophys. J.*, 144, 993, 1965.

DISCOVERY OF AN EXPANDING NEUTRAL
HYDROGEN SHELL SURROUNDING THE
NEWLY DISCOVERED SUPERNOVA
REMNANT IN CYGNUS

G. E. Assousa, W. Herbst, and K. Turner

The roles of supernovae as a probe of the interstellar medium (ISM) and as a trigger for star formation have been the primary focal points of the supernova research at the DTM. An understanding of the elegant but complex structure of galactic supernova remnants such as SNR Shajn 147 can shed light on the properties of the cloud and intercloud region within 100 pc from the origin of the SN. In effect the supernova acts as a "night flare," illuminating and interacting with galactic gas and dust. Supernova observations are currently yielding new information as new parts of the electromagnetic spectrum such as x-rays are becoming part of the overall record. Also, in recent years the detection of accreted shells around SNR's has provided additional constraints on our models for both the SNR's and the ISM.

The recent discovery of an old SNR in Cygnus by Gull *et al.* (1977), hereafter referred to as an SNR GKP, prompted us to examine the region surrounding it for evidence of hydrogen-shell formation. The optical filamentary structure seen by them is reminiscent of that seen for Shajn 147 and the Vela SNR (van den Bergh *et al.*, 1973). In fact, it suggests to us that the fragmentary circular filaments may indeed be the profiles of ionized spherical clouds

embedded in a hot interstellar medium (McKee and Ostriker, 1977). The age estimate for the SNR GKP is 3×10^5 years, sufficiently old to have accreted a large HI mass; the remnant appears to be in the isothermal phase of its expansion.

We have examined an $8^\circ \times 8^\circ$ region from the Weaver and Williams Survey (1974) centered at $l = 66.^\circ 0$, $b = 6.^\circ 0$ for the velocity range -30 km/sec to $+47$ km/sec in 5.28 km/sec steps. Four maps shown in Fig. 4 display the sequential evolution of the expanding HI shell as a function of the observed radial velocity as the shell transitions from a disc to a ring configuration (Assousa and Erkes, 1973). The normal confusion with the background galactic hydrogen makes an accurate estimate of the shell-related hydrogen difficult. However, the ring eventually returns to a disc at positive velocities displaying the other (i.e., the receding) side of the shell.

We estimate an expansion velocity for the remnant of the order of 31 ± 3 km/sec centered at $V_{\text{LSR}} = 7 \pm 3$ km/sec. From the Schmidt rotation curve the SNR would have to be at a distance of 870 pc for the maximum estimated velocity (10 km/sec). Gull *et al.* (1977), estimate a distance of 1200. We accept a distance of 1000 pc as a good best estimate.

Preliminary observations of the SNR by Reynolds (1977) in the [OIII] line at $\lambda 5007$ at four regions near the edge and center show emission over 150 km/sec range (-80 km/sec to $+70$ km/sec). This spread in velocity does not reflect the systematic expansion motion of the filamentary structure, as has been shown by Lozinskaya (1976) for the similar case of S147, but reflects the velocity dispersion in the filaments. It is interesting to note that the two sets of velocities become similar for other seemingly older SNR's such as HB 21, which show no filamentary structure (Lozinskaya, 1972; Assousa and Erkes, 1973).

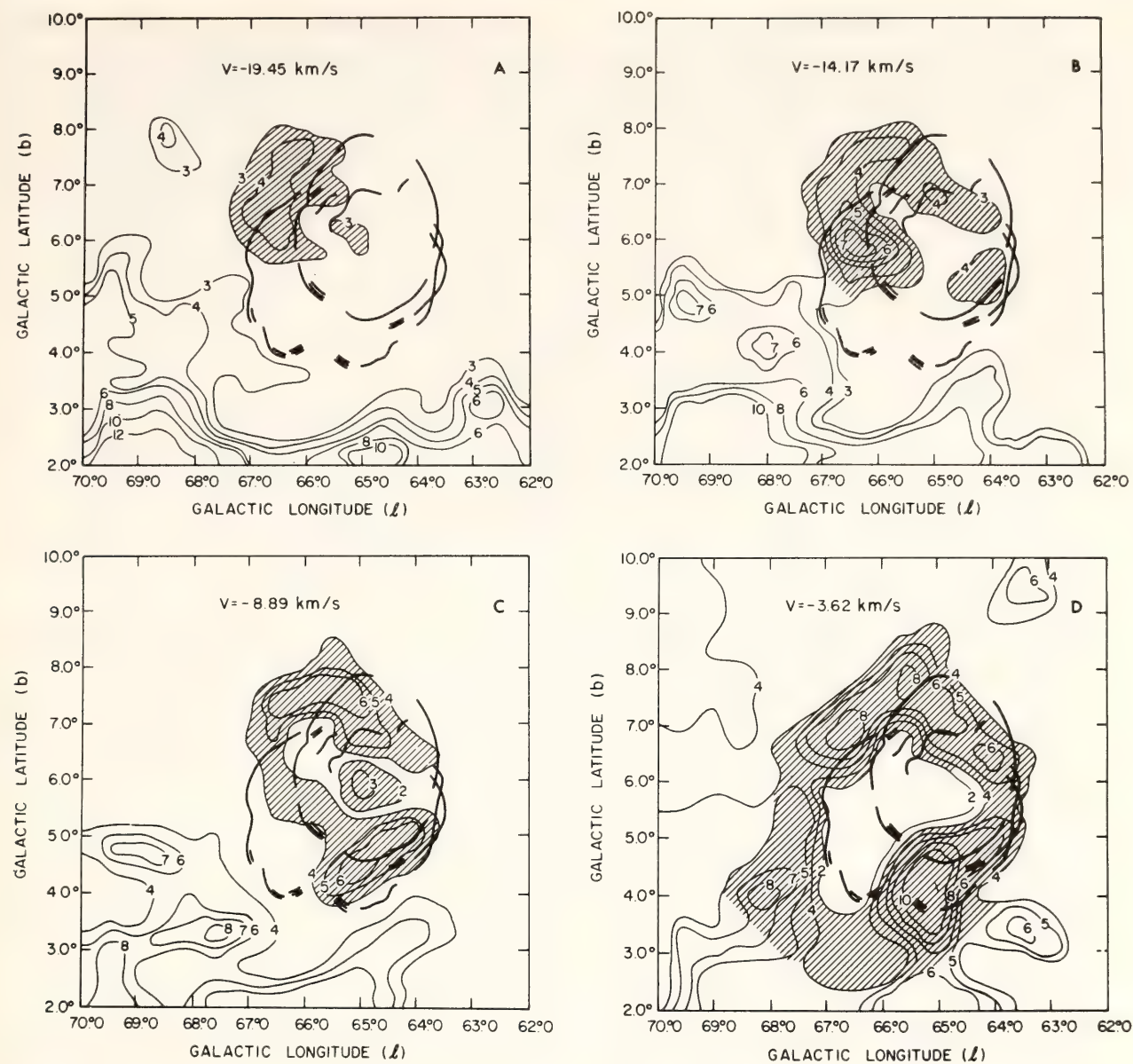


Fig. 4. Four maps of the HI distribution showing the evolution of the disk-ring structure. The contours are in $T_{\text{antenna}} \times \Delta V$ normalized to 1 km/sec. The central velocities of the maps are (A) -19.45 , (B) -14.17 , (C) -8.89 , and (D) -3.62 km/sec. The outline of the optical filaments in the SNR is shown in the dashed line.

In Table 1 we list the basic parameters of the HI shell. We obtain a mass estimate of $2800 M_{\odot}$, based on the directly measured brightness temperature averaged over the shell ($T_b \sim 5^{\circ}\text{K}$), and derive a density of 0.3 cm^{-3} . The resulting initial SN energy suggests a supernova of type II. The age of the SNR is sufficiently old that it may have already initiated star formation. This hypothesis merits investigation, bearing in mind the complex nature of the Cygnus region where the SNR is located.

TABLE 1. The SNR in Cygnus

Distance (est.)	1 kpc
Radius, Inner	26 pc
Radius, Outer	44 pc
n_0	0.32 cm^{-3}
HI Mass*	$2800 M_{\odot}$
E_0	$2.4 \times 10^{50} \text{ erg}$
Age	$4.3 \times 10^5 \text{ yr}$

* HI Mass calculated from an average brightness temperature $T_b = 5^{\circ}\text{K}$ in the fragmentary shell.

References

- Assousa, G. E., and J. W. Erkes, An expanding shell of neutral hydrogen surrounding the supernova remnant HB 21, *Astron. J.*, **78**, 885, 1973.
- Gull, T. R., R. P. Kirshner, and R. A. R. Parker, A new optical supernova remnant in Cygnus, *Astrophys. J. Lett.*, **215**, L69, 1977.
- Lozinskaya, T. A., Investigation of the faint nebula identified with radio source HB 21, *Soviet Astron.*, **16**, 219, 1972.
- Lozinskaya, T. A., Optical observations of supernova remnants: the filamentary nebula S147, *Soviet Astron.*, **20**, 19, 1976.
- McKee, C. F., and J. P. Ostriker, A theory of the interstellar medium: three components regulated by supernova explosions in an inhomogeneous substrate, *Astrophys. J.*, **218**, 148, 1977.
- Reynolds, R., Private communication, 1977.
- van den Bergh, S., A. P. Marcher, and Y. Terzian, An optical atlas of galactic supernova remnants, *Astrophys. J. Suppl. Ser.*, **26**, No. 227, 1973.
- Weaver, H., and D. R. W. Williams, The Berkeley low-latitude survey of neutral hydrogen, *Astron. and Astrophys. Suppl.*, **17**, 1, 1974.

DYNAMICS AND STAR FORMATION IN THE
PECULIAR GALAXY NGC 1961: A SPIRAL
WITH A VERY LARGE MASS

V. C. Rubin, M. S. Roberts*,
and W. K. Ford, Jr.

NGC 1961 (Arp 184) is a pathological spiral galaxy. Although at first glance it appears to be totally distorted outside of the nuclear regions, it can equally

well be described as a generally normal spiral with long, straight, faint outer arms to the north and east of the nucleus, embedded in a confused dusty looping structure to the south and west. A reproduction of NGC 1961 kindly made available by Arp is shown in Fig. 5.

Neutral hydrogen observations with the NRAO 300-ft transit telescope† reveal an extremely broad 21-cm signal, with $\Delta V = 715 \text{ km s}^{-1}$. This is the broadest known velocity width so far detected for a single galaxy. Because the 21-cm signal is spatially extended, it was not known if the observed velocity spread arose in an extended gas cloud or if the velocities arose from an unusually massive rotating galaxy.

Spectra of NGC 1961 were obtained with the Kitt Peak 4-m RC spectrograph plus Carnegie RCA C 33063 image tube at a dispersion of 25 Å/mm , and are shown in Fig. 5. A central velocity of

$V_H = 3965^{+10}_{-50} \text{ km s}^{-1}$ is observed, cor-

responding to $V_o = 4131 \text{ km s}^{-1}$ (corrected to the Local Group) and a distance of 83 Mpc with $H = 50 \text{ km s}^{-1} \text{ Mpc}^{-1}$.

Along both the major and minor axes, the velocities exhibit a surprising degree of symmetry coexistent with some peculiar motions. Ionized gas is leaving the nucleus with a line-of-sight velocity $V = 70 \text{ km s}^{-1}$. Beyond the nucleus, $r > 6 \text{ kpc}$, large-scale asymmetries are observed in the velocities. However, for $r > 6 \text{ kpc}$ out to $r \sim 30 \text{ kpc}$, velocities are generally near 325 km s^{-1} (on the plane of the sky) with respect to the nuclear velocity. Moreover, the velocity pattern is consistent with a normally rotating galaxy. Along the minor axis, evidence for noncircular motions is seen, but only for $r > 30 \text{ kpc}$. If we assume that the region $6 < r < 30 \text{ kpc}$ is partaking of a normal rotation, then in the plane of the galaxy the velocities are near 400 km s^{-1} , larger than any previously known rotational velocities.

* National Radio Astronomy Observatory, Charlottesville, Virginia.

† The National Radio Astronomy Observatory is operated by Associated Universities, Inc., under contract with the National Science Foundation.

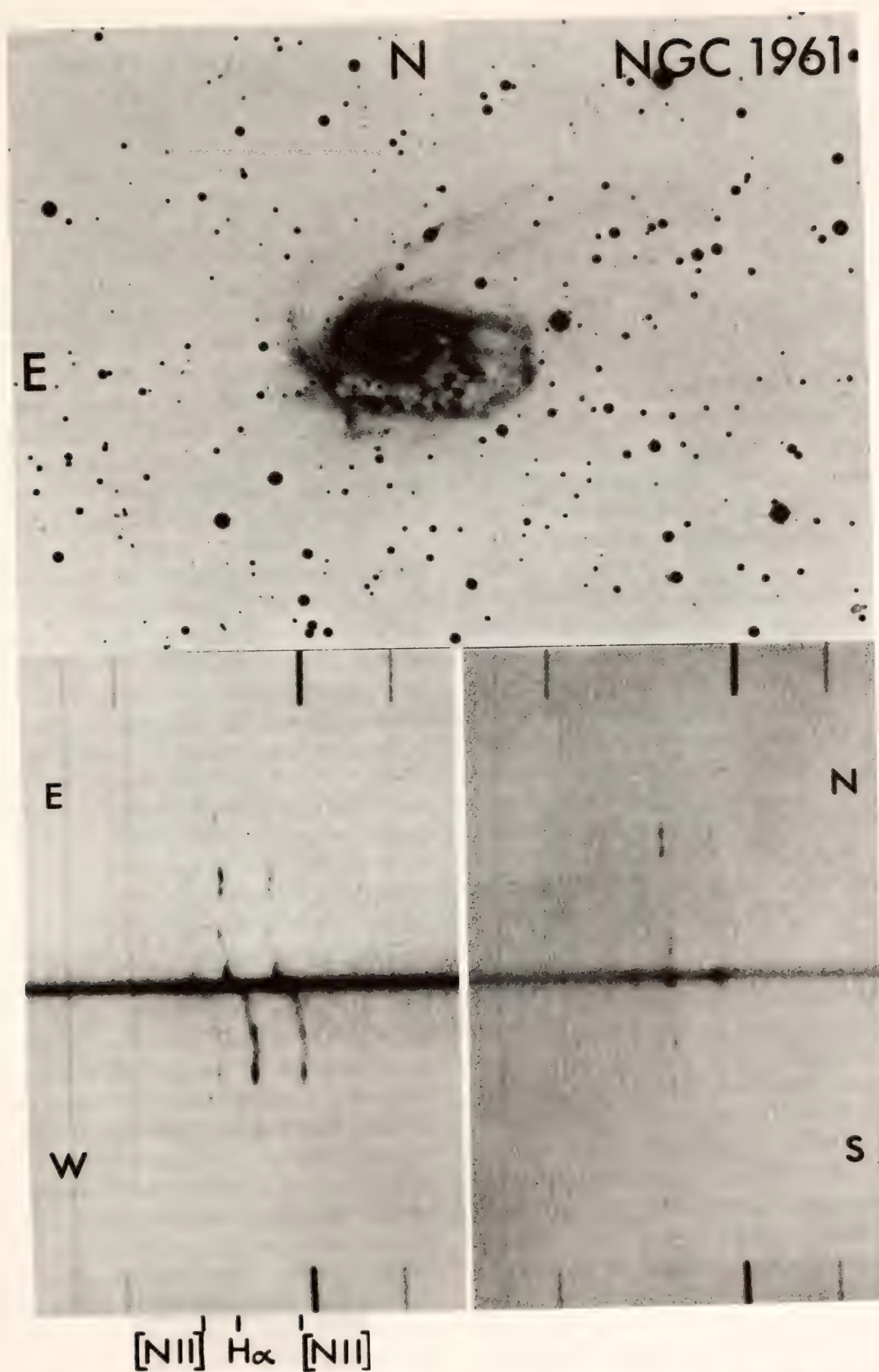


Fig. 5. (top) NGC 1961, from a 200-inch plate kindly made available by Dr. H. Arp. (lower left) Major-axis spectrum, KPNO 4-m RC spectrograph + image tube + H_2 treated + pre-flashed plate. Original dispersion 25 \AA mm^{-1} ; exposure 120 min. (lower right) Minor-axis spectrum; plate details above; exposure 45 min.

NGC 1961 is an enormous galaxy, with a de Vaucouleurs diameter $d = 4'.27 = 102$ kpc and a Holmberg diameter $d = 185$ kpc. For a simple spheroid model, the mass out to the last measured velocity is $M_{36 \text{ kpc}} \sim 1 \times 10^{12} M_{\odot}$, or $M_{90 \text{ kpc}} \sim 3 \times 10^{12} M_{\odot}$ if the rotation curve remains flat out to the limit of the Holmberg radius.

Spiral galaxy masses are generally a few times $10^{11} M_{\odot}$, so NGC 1961 may be an order of magnitude more massive than conventional spirals. Its neutral hydrogen mass is correspondingly large: $M_{\text{HI}} = 1 \times 10^{11}$, also an order of magnitude over normal hydrogen masses. Thus, the ratio of hydrogen mass to total mass is normal, as are also the ratios of hydrogen mass to optical luminosity, and total mass to optical luminosity, $M_B/L \sim 10$.

Beyond $r \sim 30$ kpc the extended outer arms to the north exhibit noncircular velocities, which may indicate that they lie out of the plane of the interior disk. To the south, $r > 30$ kpc, the negative velocities imply that the irregular loopy structure is receding from the nucleus, with $V_{\text{line of sight}} \sim 150 \text{ km s}^{-1}$. Unless the component transverse to the line of sight is significantly larger than this, this velocity is too low for the material to escape from the galaxy.

What are we to make of this curious object? Morphologically, the SW dusty region in NGC 1961 resembles some of the curious structures to which the Burbidges called attention almost 20 years ago (NGC 2444-5, Burbidge and Burbidge, 1959a; PA665, Burbidge and Burbidge, 1959b), although in those systems the predominant galaxy is elliptical or structureless. At that time, the peculiarities were attributed to nuclear explosions or to interactions between the galaxy and the intergalactic medium perhaps involving magnetic lines of force. More recently, Arp (1969) has used NGC 1961 as an example of nuclear ejection to produce spiral arms. In the climate of today's dynamical studies of galaxy evolu-

tion, it is tempting to relate NGC 1961 to a tidal interaction or a galaxy merger. However, NGC 1961 has no nearby bright companions. Moreover, all obscured noncircular velocities are velocities consistent with expulsion from the galaxy, rather than collapse or merger.

One clue to the past history of NGC 1961 comes from its colors [$(B - V)_T^0 = 0.54$, $(V - B)_T^0 = 0.13$; de Vaucouleurs *et al.*, 1976]. These colors place it at the lower envelope of the two-color plot for the peculiar galaxies in the Arp Atlas (1966), in a region containing peculiar interacting galaxies and galaxies with tidal tails but a region unpopulated by single pathological galaxies, peculiar galaxies without tails, or morphologically normal galaxies (Larson and Tinsley, 1978). Galaxy models of Larson and Tinsley indicate that colors like those of NGC 1961 can be the remnants of a burst of star formation 2×10^8 years ago, which involved 5% of the galaxy mass. This region of the two-color plane contains galaxies having the longest time interval since the star formation burst, involving the greatest fraction of galaxy mass. Hence, in NGC 1961 we may be viewing the late stages of a violent dynamical event (perhaps involving a giant spiral galaxy and a companion of more normal galaxy mass), which initiated rapid star formation. The large mass of HI, the large total mass, the peculiar dynamical details, and the anomalous colors are all consistent with a galaxy that earlier formed stars in a burst mode. In the 10^8 years since the burst, only the inner region $r < 3$ kpc will have completed a single revolution about the center; the outer visible region, $r \sim 30$ kpc, will have completed only a fraction ($\sim 1/10$) of a revolution. Such a time scale seems consistent with the regular-irregular overall appearance of NGC 1961. NGC 1961 thus appears to be a galaxy whose abnormal morphology, dynamics, and star formation properties are intricately interwoven. More thorough

studies of the dynamics of other peculiar galaxies may help us to understand the role of dynamical events in the history of star formation and galaxy evolution, for both normal and pathological galaxies.

References

- Arp, H. C., *Atlas of Peculiar Galaxies*, California Institute of Technology, 1966.
- Arp, H. C., On the origin of arms in spiral galaxies, *Sky and Telescope*, **38**, 385, 1969.
- Burbidge, E. M., and G. R. Burbidge, The remarkable extragalactic system NGC 2444-5, *Astrophys. J.*, **130**, 12, 1959a.
- Burbidge, E. M., and G. R. Burbidge, Some interconnected multiple extragalactic nebulae, *Astrophys. J.*, **130**, 23, 1959b.
- de Vaucouleurs, G., A. de Vaucouleurs, and H. G. Corwin, *Second Reference Catalogue of Bright Galaxies*, Univ. of Texas Press, 1976.
- Larson, R. B., and B. M. Tinsley, Star formation rates in normal and peculiar galaxies, *Astrophys. J.*, **219**, 46, 1978.

GALACTIC NEUTRAL HYDROGEN ABSORPTION SPECTRA

*F. J. Lockman and E. W. Greisen**

Stars are thought to form in condensed clouds of cool interstellar gas. By studying the distribution and motions of interstellar clouds we hope to learn about large-scale factors that influence the overall pattern of star formation in the Galaxy. To this end, we have been observing toward selected galactic radio sources and measuring the absorption lines which arise in cool hydrogen clouds along the line of sight. The data discussed here were obtained with the

NRAO spectral-line interferometer and differ from normal spectra in that the interferometer gives information not only on the amplitude of the absorption but also on its phase (i.e., its structure across the source). Here we discuss the distribution of hydrogen clouds along two very different paths through the Galaxy. The first, toward a relatively nearby object, passes through a part of the Galaxy, goes from the solar neighborhood through regions of very active star formation, and on into the inner Galaxy.

NGC 7538

This is a prominent HII region (i.e., a cloud of gas ionized by a newly formed, massive star) near galactic longitude 110° . It is of interest because it lies in a part of the galaxy that has been modeled by Roberts (1972) using nonlinear density-wave theory. Briefly, the density-wave theory postulates that the spiral patterns seen in many galaxies are small perturbations of the stellar distribution, which move as a wave somewhat independent of the rotation of the galaxy (Lin and Shu, 1964). Gas responds to the perturbation by accelerating toward the concentration of stars. If only $\sim 1\%$ of the galaxy's mass is involved in the wave, then the gas response is linear and gas flows are smooth. However, if the mass in the wave rises beyond a certain point the interstellar gas will be accelerated to supersonic velocities and will self-shock. These shocks can enhance the local gas density by an order of magnitude in a thin front extending over a broad region, perhaps initiating collapse of gas into stars to produce the luminous spiral arms we so frequently observe.

In our own Galaxy the kinematic consequences of a density wave may be more observable than other phenomena associated with it. Figure 6 shows the amplitude of the hydrogen absorption spectrum towards NGC 7538 (bottom panel) together with synthetic spectra gener-

* National Radio Astronomy Observatory, Charlottesville, Virginia.

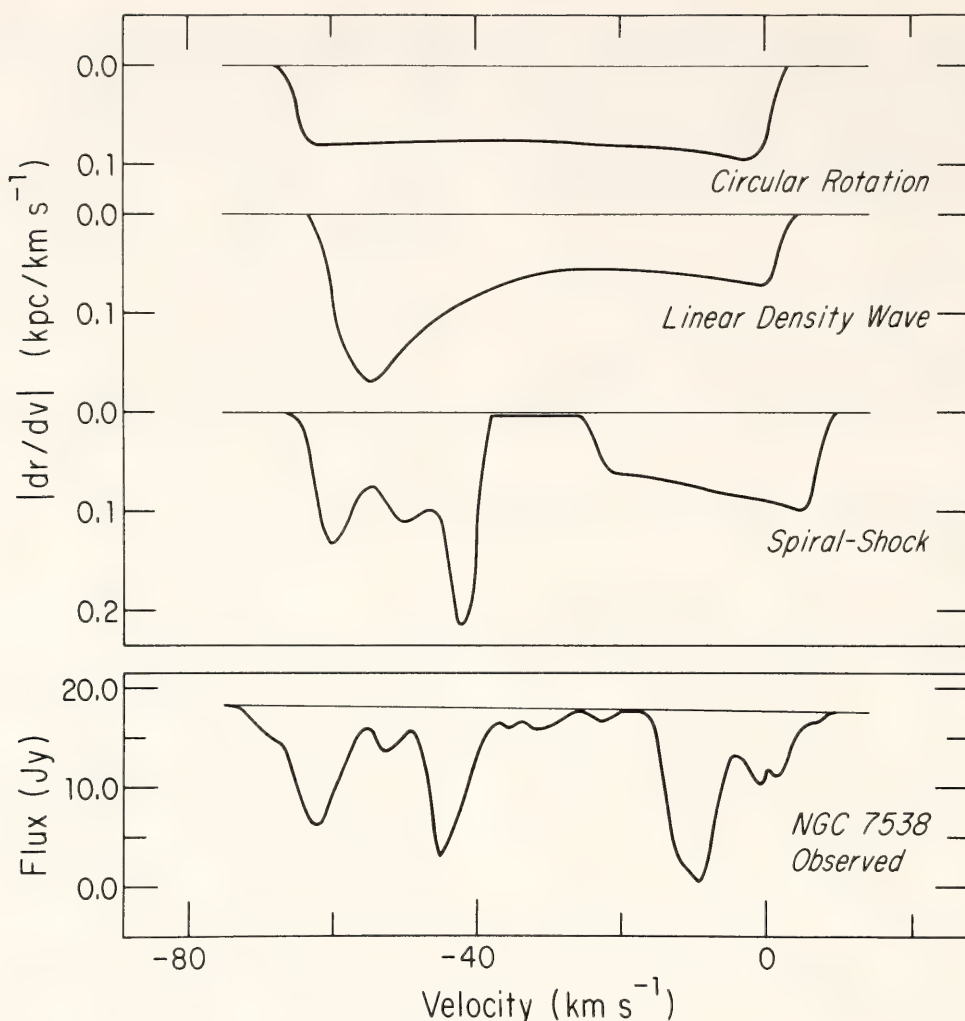


Fig. 6. The neutral hydrogen absorption spectrum toward NGC 7538 (lowest panel), compared with synthetic spectra generated assuming circular galactic rotation, a linear density wave, and a density wave strong enough to cause the gas to shock. The synthetic spectra are proportional to the likelihood of finding absorption at any velocity given a random distribution of clouds.

ated assuming pure circular galactic rotation (i.e., no density wave), a linear density wave, and a wave strong enough to cause shocks in the interstellar hydrogen. These synthetic spectra are directly proportional to the probability of observing absorption in a random distribution of hydrogen clouds along the line of sight. The structure in the shock spectrum is a consequence of the discontinuity of gas flow at the shock: material changes from a velocity of -25 to -45 km/sec over such a short distance that there is virtually no place along the line of sight where gas has a velocity of -30 km/sec , and conse-

quently the probability of observing absorption at this velocity is very low.

It is clear that the shock model kinematics does remarkably well in predicting the presence (and absence) of many important absorption features. In fact, by comparing the NGC 7538 spectrum with spectra obtained against other sources in the vicinity we can show that the main differences between model and observation arise from small localized clouds unconnected with large-scale structure. In particular, the one major absorption line in the NGC 7538 spectrum that is not explicitly produced in the spiral shock model, the line at -10

km/sec, arises in a dust cloud which extends across the nebula and which has been measured in molecular absorption lines (Minn and Greenberg, 1973).

Of course, it could be that the distribution of clouds rather than their kinematics is the source of the structure in the absorption spectrum, but the features of the observed spectrum arise so naturally in the nonlinear gas flow that we feel it is at least the qualitatively cor-

rect description of gas kinematics in this portion of the Galaxy.

W 31

Figure 7 shows the absorption spectrum toward the brightest component of W 31, a very distant HII region located near 10° longitude. The upper panel shows the hydrogen emission profile in this direction, and the lower two

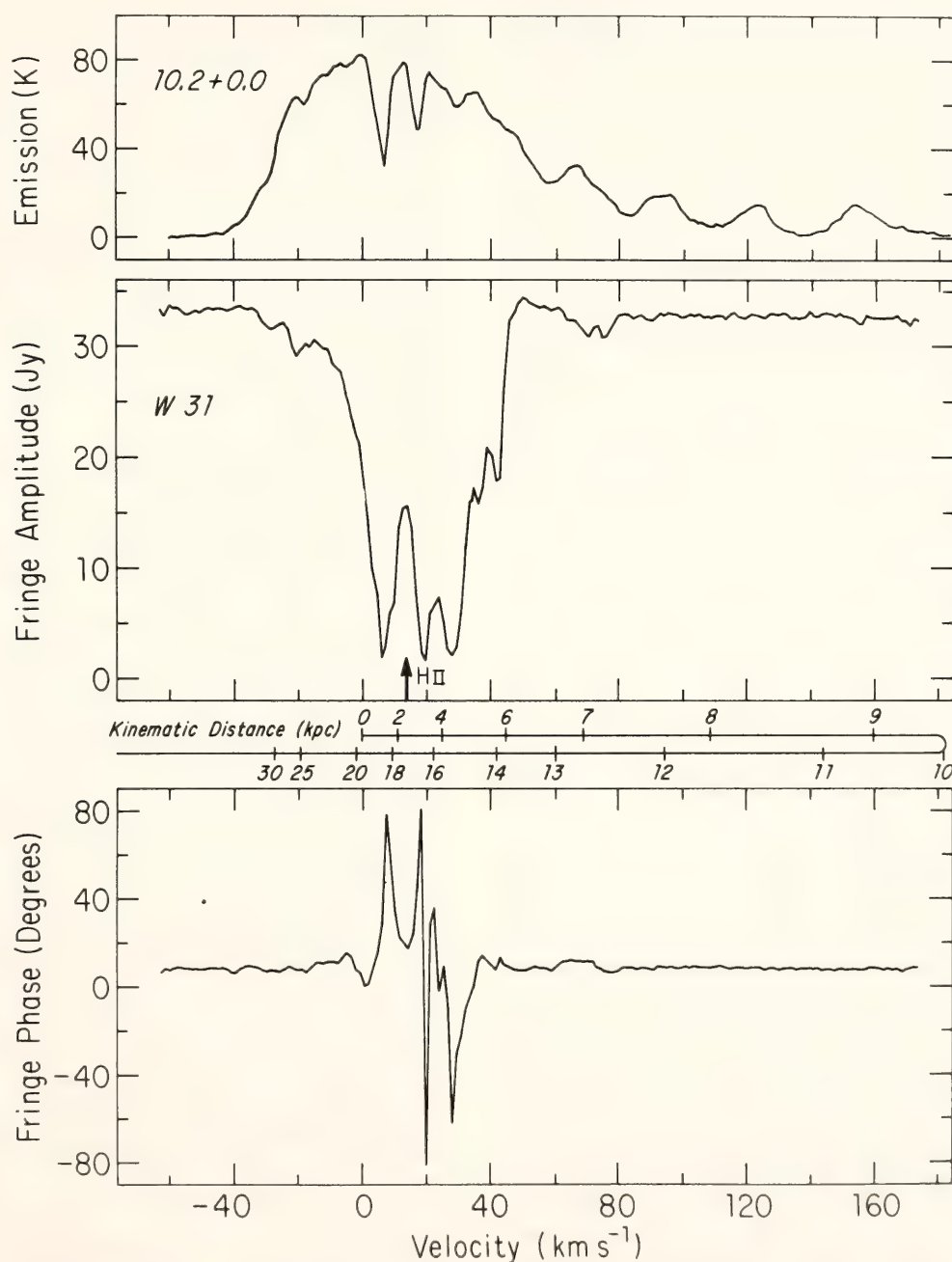


Fig. 7. The amplitude and phase of the neutral hydrogen absorption spectrum toward the brightest component of W 31, together with the hydrogen-emission spectrum seen nearby. Note the almost complete absence of absorption at $V \geq 50$ km/sec despite the presence of hydrogen emission.

panels show the amplitude and phase of the absorption spectrum against the source. Also drawn is a very approximate scale of distance vs. velocity for this direction; the HI region is located some 17 kpc from the sun. The point of interest here is the almost total lack of absorption at $V > 50$ km/sec even though the emission spectrum shows that some hydrogen is present at these velocities. Since the emission profile is roughly proportional to the total amount of atomic hydrogen regardless of its temperature, while the absorption spectrum is a measure only of cool clouds, our data imply that there are few cool clouds with $V > 50$ km/sec. Along this line of sight, material with $V > 50$ km/sec is located less than 4 kpc from the galactic center.

Density-wave models predict that the spiral pattern will not persist to the center of the Galaxy, but will terminate approximately 4 kpc from the galactic center (Lin and Shu, 1964). At the point where the density wave is predicted to terminate we do observe a curious disturbance in the hydrogen (the disturbance is the source of the gas that we see in absorption at negative velocities), and our data show that interior to the postulated inner termination of the density-wave pattern there are few cool hydrogen clouds.

In the solar neighborhood the neutral hydrogen is approximately evenly divided between cool clouds and a hotter intercloud medium (Baker and Burton, 1975); our observations suggest that only $\leq 10\%$ of the atomic hydrogen is in cool clouds in the inner 4 kpc of the Galaxy. In retrospect, this absence of clouds can be seen in some previously published spectra (e.g., some of those in Caswell *et al.*, 1975), but there are also indications from HI and molecular line studies that the inner 4 kpc of the Galaxy is not entirely devoid of clouds—there are simply fewer of them there than elsewhere. This may be the reason for the apparent lack of recent star formation

in this area (Westerhout, 1958): there are few clouds to collapse into stars. It is certainly premature to comment on possible sources of this phenomenon, but it may be that cloud formation is rather inefficient without the large-scale compression provided by a density wave, and when the density wave terminates 4 kpc from the galactic center the percentage of gas in clouds sharply drops.

References

- Baker, P. L., and W. B. Burton, Investigation of low-latitude hydrogen emission in terms of a two-component interstellar gas model, *Astrophys. J.*, **198**, 281–297, 1975.
- Caswell, J. L., J. D. Murray, R. S. Roger, J. D. Cole, and D. J. Cooke, Neutral hydrogen absorption measurements yielding kinematic distances for 42 continuum sources in the galactic plane, *Astron. Astrophys.*, **45**, 239–258, 1975.
- Lin, C. C., and F. H. Shu, On the spiral structure of disk galaxies, *Astrophys. J.*, **140**, 646–655, 1964.
- Minn, Y. K., and J. M. Greenberg, The kinematical distribution of dark clouds surveyed in the 4830 MHz H_2CO line, *Astron. Astrophys.*, **22**, 13–25, 1973.
- Roberts, W. W., Application of the density-wave theory of spiral structure: shock formation along the Perseus arm, *Astrophys. J.*, **173**, 259–283, 1972.
- Westerhout, G., A survey of the continuous radiation from the galactic system at a frequency of 1390 Mc/s, *Bull. Astron. Netherlands*, **14**, 215–260, 1958.

THE RELATIONSHIPS AMONG HI, GALAXY COUNTS, AND REDDENING IN THE GALAXY

*D. Burstein, and C. Heiles**

Knowledge of the distribution of reddening in the Galaxy is necessary not only in measuring the reddening of most

* University of California, Berkeley.

extragalactic objects but also in understanding the large-scale association of gas and dust within our own Galaxy. However, after many attempts to find a reliable method to measure the reddening of extragalactic objects, a generally accepted "best" method has not yet been established.

If the reddening in our Galaxy were evenly distributed in a plane-parallel medium, the cosecant of the angle from the galactic pole ($=90^\circ$) would be directly proportional to the reddening of an extragalactic object. Many previous studies have assumed such a plane-parallel layer. Other studies, influenced by the direct observation that there appears to be little or no reddening at the galactic poles (in contradiction to the assumption of a plane-parallel medium), have inserted a "hole at the pole" in an otherwise plane-parallel reddening distribution. The results of these various studies conflict in several ways, including the value one assumes for the reddening at the poles, and one is unsure whether or not a "smooth" csc-law approximation is the correct one to use.

Despite the use of these smooth-reddening approximations, it is generally acknowledged that the distribution of dust within our Galaxy is irregular. Methods to account for this irregularity have centered on correlating variations in galaxy counts (e.g., Shane and Wirtanen, 1967, = SW) or the HI column density (e.g., Knapp and Kerr, 1974) with variations in reddening. The previous large-scale investigation into the interdependence among HI, galaxy counts, and reddening (Heiles, 1976) concluded that there were no simple relationships among these extinction indicators and produced some unresolved problems.

In this joint investigation, we have examined further the interrelationships among these quantities and are able to resolve many of the problems. Our reddening data come primarily from studies

of colors of 49 globular clusters and 84 RR Lyrae stars; HI column densities come from Heiles (1976) and Heiles and Cleary (1978); galaxy counts come from SW. With these and other data, our analysis shows the following:

1. Some of the discrepancies found by Heiles (1976) were due to subtle biases in his reddening data, which produced spurious latitude dependencies between reddening and HI column densities or galaxy counts. These biases have been removed from the present reddening compilation.

2. The SW galaxy counts should be reasonably reliable indicators of the average extinction in a given general direction. The intrinsic mottling of the surface density of the distribution of galaxies contributes a large percentage of the total error and reduces the accuracy of galaxy counts as a predictor of reddening in a particular direction. Errors in the galaxy counts due to variations in sky and foreground radiation (e.g., zodiacal, galactic) are found to be unimportant, since the original plates examined by SW were not exposed sufficiently long to detect the sky brightness.

3. The gas-to-dust ratio slowly varies with position in the Galaxy and by up to a factor of two from the average. Thus, hydrogen column density alone cannot be used as an accurate predictor of reddening.

4. The galaxy-count data, by themselves, are too noisy to determine the slope of a csc law near the galactic poles and hence the extinction at the galactic poles. The SW counts have been reanalyzed using a new procedure, which is illustrated in Figs. 8 and 9. This method attempts to account for nonrandom variation in the mottling of the galaxy counts, which would most affect their median values at high galactic latitudes. (Since the intent of the following discussion is both to evaluate the csc law from galaxy counts at the galactic poles and to present an accurate equation for

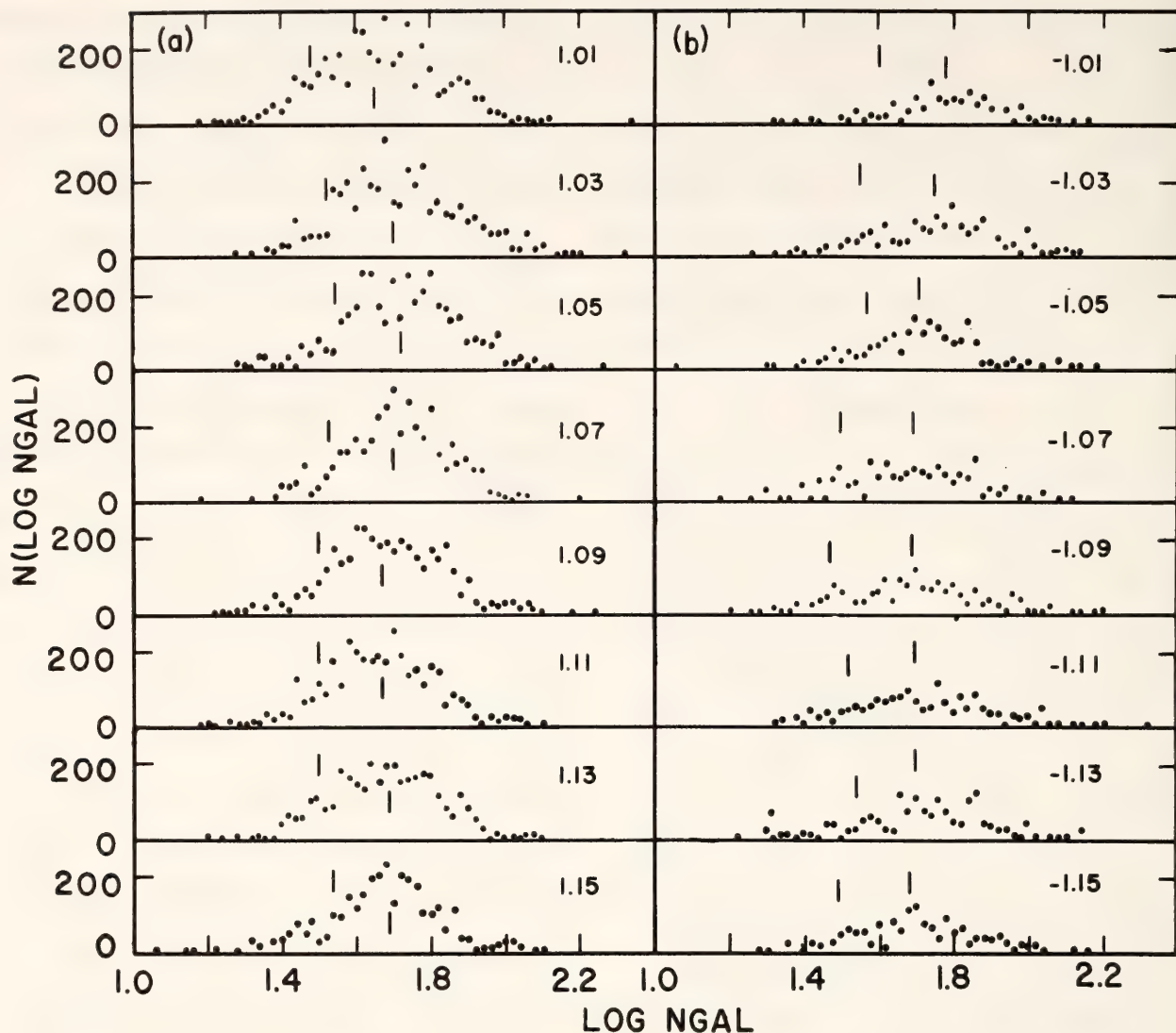


Fig. 8. Histograms for the SW galaxy counts near the galactic poles, plotted as the number of pixels with $\log NGAL$ between N and $N + \Delta N$, versus $\log NGAL$. (a) North Galactic Polar region; (b) South Galactic Polar region. The center of each csc interval is given, and the values of $\log NGAL(C)$ and $\log NGAL(HW)$ are denoted by vertical lines.

the prediction of reddening within our Galaxy, the quantity $E(B - V)$ will be used to denote reddening, N_{HYD} to denote the column hydrogen density, and $\log NGAL$ to denote galaxy counts.) Histograms are plotted in Fig. 8 as $N(\log NGAL)$ (the number of sampled elements with the value $\log NGAL$) versus $\log NGAL$ for intervals of 0.02 in $csc\ b$, from $csc\ |b| = 1.00$ to 1.16. These histograms are noisy, and exhibit a number of different effects which can be understood in terms of statistical fluctuations, galaxy clustering, and variations in the extinction within the latitude bins. To try to compensate for nonrandom clus-

tering in the value of $\log NGAL$ (average), two different averages were taken: (a) a point midway between the half-power points of the central maximum of the histogram [= $\log NGAL(C)$], and (b) the value of $\log NGAL$ at the half-power point toward smaller values [= $\log NGAL(HW)$]. Besides attempting to account for nonrandom clustering in the value of $\log NGAL$ (average), this histogram method also permits a reasonable estimate of the error in $\log NGAL$ (average). Figures 9a and 9b plot $\log NGAL(C)$ (filled circles) and $\log NGAL(HW)$ (open circles) versus $csc\ |b|$ for the North and South galactic

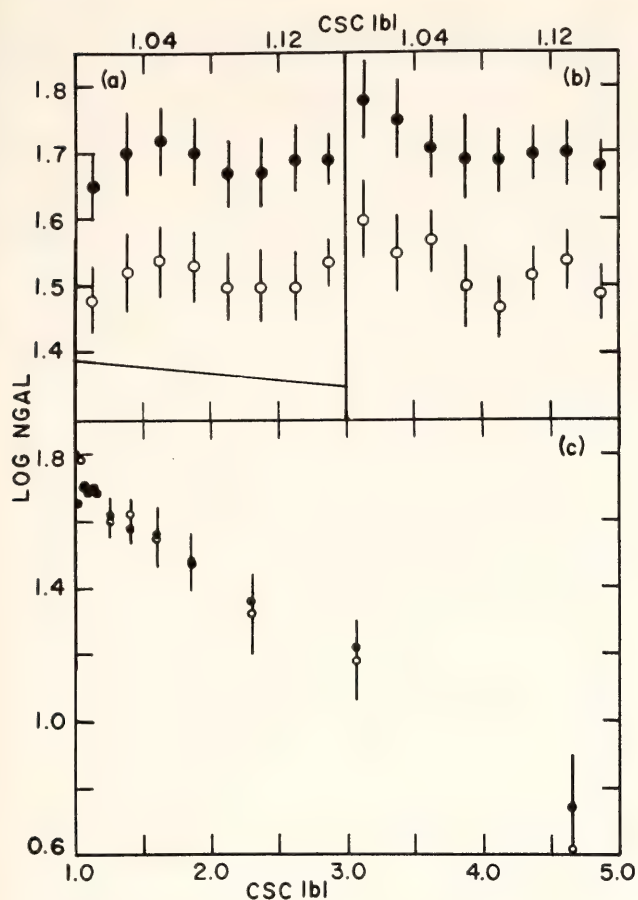


Fig. 9. The average value of $\log NGAL$, as determined by the histogram method, versus $\csc |b|$. (a) NGP region: filled circles are $\log NGAL(C)$, open circles are $\log NGAL(HW)$; a slope corresponding to \csc law extinction coefficient of 0.25 magnitude is given; (b) SGP region: symbols are the same as in (a). The galaxy count data, as evidenced by (a) and (b), are too noisy to be able to discriminate between \csc -law coefficients of 0.00 and 0.25. (c) $\log NGAL(C)$ versus $\csc |b|$ for the SW counts: filled circles have $b \leq -10^\circ$.

poles, respectively. Within the errors, our analysis demonstrates that neither pole shows a statistically significant trend of $\log NGAL$ with $\csc b$ supporting a uniform layer of extinction, with 0.25 magnitude in A_{pg} at $\csc b = 1.00$ (line drawn in Fig. 9a). In fact, the North Galactic Pole data (which is the more complete of the two) actually shows a *decrease* in $\log NGAL$ near $\csc b = 1.00$. For completeness, $\log NGAL(C)$ is plotted versus $\csc |b|$ for the North Galactic Pole (filled circles) with South Galactic Pole (open circles) in Fig. 9c for $\csc |b| \leq 5.0$.

It is evident from Figs. 8 and 9 that

the galaxy count data are too noisy to determine, by themselves, the change in extinction with latitude near the galactic poles. We conclude that all available data, including that from the analysis of galaxy counts, are consistent with there being little or no reddening at the north galactic pole.

5. The use of column hydrogen density and galaxy counts together to predict the reddening should be more accurate than the use of either set of observations alone. Two equations are derived for predicting $E(B - V)$ from $NHYD$ and $\log NGAL$. First,

$$E(B - V) = -0.0372 + 0.357 \times 10^{-3}(NHYD) - 0.346 \times 10^{-4}(R) (NHYD) \quad (1)$$

$\pm .0058 \quad \pm .020 \quad \pm .062$

where R is the residual in Heiles' (1976) contour units (e.g., a residual of 0.1 in $\log NGAL$ has $R = 1.0$) and is mapped as a function of galactic coordinates in Fig. 9 of that paper. $NHYD$ is smoothed in 13 deg^2 averages and is mapped in Heiles (1975). Second,

$$E(B - V) = -0.0171 + 0.399 \times 10^{-3}(NHYD) + 0.140 \times 10^{-6}(NHYD)^2 - 0.126 \times 10^{-3}(NHYD) (\log NGAL) \quad (2)$$

$\pm .0092 \quad \pm .090 \quad \pm .097 \quad \pm .034$

Equation 1 is given since both R and $NHYD$ are mapped in galactic coordinates. However, Equation 2 is the more correct formulation and should be used for $|b| \leq 15^\circ$. $\log NGAL$ at present can only be obtained graphically from SW, and these data must be additionally smoothed to 13 deg^2 . The zero point difference between Equations 1 and 2 is a result of the fact that when $E(B - V) = 0.00$, $NHYD = 100$ and $\log NGAL = 1.8$, and does not represent a real difference between these equations. Whether the non-zero value of hydrogen column

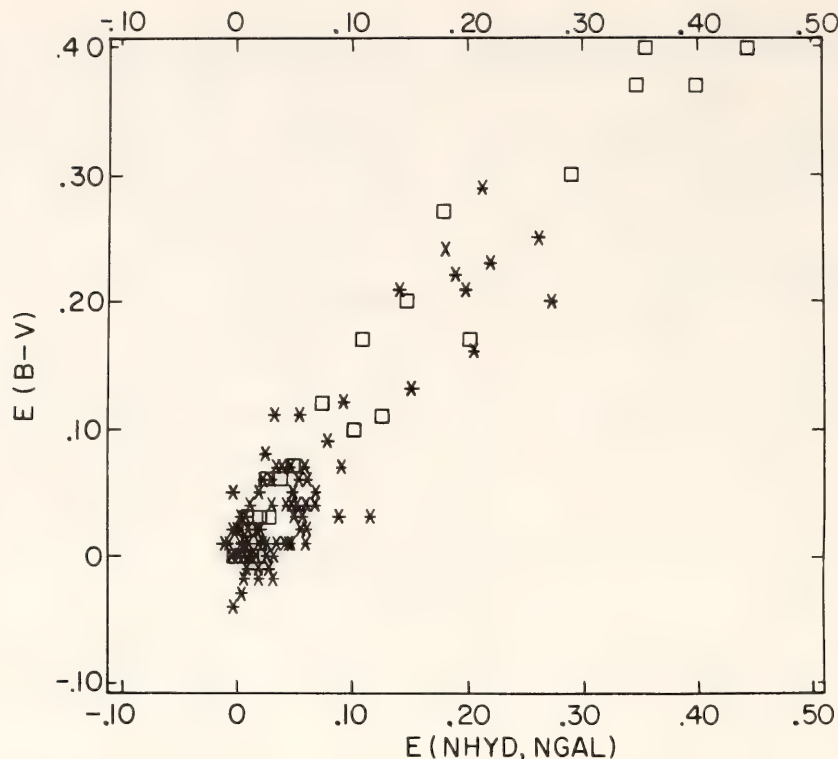


Fig. 10. $E(B - V)$ observed, versus $E(B - V)$ predicted from Equation 2; squares represent globular clusters, stars represent RR Lyrae stars.

density when the reddening = 0.00 is real or not must be further investigated. Figure 10 plots $E(B - V)$ (original) versus $E(B - V)$ (predicted from Equation 2); asterisks are RR Lyrae stars, squares are globular clusters. Both Equations 1 and 2 appear to predict the reddening, $E(B - V)$, to better than 0.03 magnitude.

References

- Heiles, C., An almost complete survey of 21-cm line radiation for $|b| \geq 10^\circ$. III. The interdependence of HI, galaxy counts, reddening and galactic latitude, *Astrophys. J.*, 204, 379, 1976.
- Heiles, C., An almost complete survey of 21-cm line radiation for $|b| \geq 10^\circ$. IV. The HI column density as a function of position in the sky, *Astron. Astrophys. Suppl. Ser.*, 20, 37, 1975.
- Heiles, C., and M. N. Cleary, Preprint on the southern sky survey of 21-cm line radiation, 1978.
- Knapp, G. R., and F. J. Kerr, the galactic gas-to-dust ratio from observations of

eighty-one globular clusters, *Astron. Astrophys.*, 35, 361, 1974.

Shane, C. D., and C. A. Wirtanen, The distribution of galaxies, *Publ. Lick Obs.*, 22, 1, 1967.

RADIO SOURCES IN GLOBULAR CLUSTER FIELDS

R. T. Rood*, K. C. Turner,
and S. J. Goldstein, Jr.*

A long-standing puzzle in the field of stellar evolution is the fate of the mass lost by evolved stars in globular clusters. While it seems inescapable that a very considerable fraction of the initial stellar mass of such objects must return as gas to the interstellar medium, no trace of this gas can be found in these objects, either in the form of newly born stars or as neutral hydrogen.

The possibility that this gas might collapse to form a single massive object in the center of the cluster gained in-

* University of Virginia, Charlottesville, Virginia.

creased interest when several x-ray sources were discovered (e.g., Clark *et al.*, 1975), apparently associated with globular clusters, and several searches for radio sources in the x-ray candidate clusters were made. Several sources were detected in or near some globular clusters, and while there was no obvious association with the x-ray sources, it was suggested that a new class of globular cluster radio sources might exist (cf. Johnson *et al.*, 1977; Terzian and Conklin, 1977).

In July 1977 we conducted a search of several globular clusters using the NRAO Green Bank interferometer at 1394 MHz. Observations at this frequency have the advantage that the clusters can be examined almost out to their tidal radii (the tidal radius is the distance from the cluster where gravitational forces due to the cluster itself and due to our Galaxy would just balance one another), so that there is no *a priori* assumption that the sources will be found in cluster centers. Clusters searched were M53, M3, M92, NGC 6624, NGC 7006, M15, and M2 and included x-ray clusters, x-ray candidates, clusters with previously de-

tected sources, and several comparison clusters.

We detected some but not all of the sources previously reported by other observers, and detected several new ones. Later, in October, the sources were re-observed at 2695 MHz and 8025 MHz to determine spectra and accurate positions. The sources and their characteristics are listed in Table 2.

In a randomly chosen region of sky it would not be unlikely to find a source with 1400-MHz flux comparable to our sources, and indeed seven of the sources have spectral indices near 0.7, not atypical for extragalactic sources. Another five have spectra consistent with thermal sources. Terzian and Conklin (1977) have discussed at some length the possibility that these might be planetary nebulae. On the other hand, it is difficult to see how classical planetary nebulae could have escaped detection in such well-studied objects as these clusters.

Several sources have spectral peculiarities, however; we exhibit some evidence for the variability when our observations are combined with those of other workers. These objects—M3A,

TABLE 2. Characteristics of Observed Sources

Source	Distance from Cluster Center	Flux* 1394	Notes
M53A	11.8	21	Spectrum consistent with extragalactic source
M53B	4.2	14	Spectrum steep, but consistent with extragalactic source
M3A	14.2	33	Spectrum consistent with thermal source
M3B	6.9	97	Spectrum consistent with thermal source
M3C	4.9	34	Spectrum consistent with thermal source
M3D	10.1	<25	Spectrum consistent with thermal source
M92A	12.8	12	Spectrum consistent with thermal source
M92B	7.9	18	Spectrum consistent with thermal source
NGC 6624A	2.2	20	Spectrum consistent with extragalactic source
NGC 6624B	8.3	33	Spectrum consistent with extragalactic source
NGC 7006A	18.0	64	Spectrum consistent with extragalactic source outside tidal radius of cluster
M15A	4.0	48	Spectrum consistent with extragalactic source
M2A	2.0	183	Steep spectrum

* Flux in mJy at 1394 MHz.

M3B, M3C, M3D, M92B, and M2A—all merit further study. If these sources are indeed cluster members, it seems possible that we are dealing with a new class of object, which might help to account for the missing cluster gas.

References

- Clark, G. W., T. H. Markert, and F. K. Li, Observations of variable x-ray sources in globular clusters, *Astrophys. J. (Letters)*, 199, L93, 1975.
- Johnson, H. M., R. C. Catura, P. A. Charles, and P. W. Sanford, Radio and x-ray observations of NGC 1851 and NGC 1904, *Astrophys. J.*, 212, 112, 1977.
- Terzian, T., and E. K. Conklin, Radio sources in the direction of globular clusters, *Astron. J.*, 82, 468, 1977.

MASS LOSS FROM T TAURI STARS

S. J. Weidenschilling

Introduction

T Tauri stars are believed to be in the pre-main sequence (PMS) stage of evolution. A significant fraction of them show blue-shifted absorption features in their spectra. The simplest explanation for these features is that these stars are ejecting matter into space (Kuhi, 1964), although other interpretations are possible (Ulrich, 1976). This is the basis for the concept that the early sun removed the solar nebula by the action of a strong "T Tauri solar wind" (Cameron, 1973, 1977). Kuhi and Forbes (1970) and Ezer and Cameron (1971) modeled PMS evolution with empirical rates of mass loss. Each suggested that the sun lost a substantial fraction of its initial mass during this stage.

There are few observational or theoretical constraints on this phenomenon. Its mechanism is unknown; the ejection does not appear to be a hydrodynamic

expansion, as is the case for the present solar wind (Kuhi, 1964). Not all T Tauri stars appear to be ejecting matter; it is not known whether the phenomenon occurs for all stars at some stage of PMS evolution or is restricted to a particular class or mass range. Quantitative loss rates have been computed for only eight stars (Kuhi, 1964, 1966). Estimates of the total mass loss are based on these rates and theoretical PMS lifetimes.

Williams (1967) suggested that the rate of energy expenditure on mass ejection would always be small compared with a star's luminosity. However, it is not clear from either theory or observation that this condition holds for PMS stars. We can place a stronger constraint on the total mass loss by considering the amount of energy available. Theoretical models of PMS stars (Iben, 1965) show that they do not begin hydrogen burning until they arrive at the main sequence. T Tauri stars derive their energy from gravitational contraction. Regardless of the detailed mechanism, mass loss involves a decrease in the gravitational potential energy of the star, with the transfer of part of that energy to the escaping matter. The amount of mass that can escape is limited by the available energy, as shown below.

Energy Balance of a Contracting Star

A star of mass M and radius R has gravitational potential energy

$$\Gamma = qGM^2/R, \quad (1)$$

where G is the gravitational constant, and q is a factor of order unity. For a polytrope of index n , $q = 3/(5 - n)$. A fully convective star has $n \simeq 3/2$, $q \simeq 6/7$. For radiative energy transfer, $n \simeq 3$, $q \simeq 3/2$.

A change in the star's potential energy is

$$d\Gamma = -\frac{GM}{R} [M dq + 2qdM - qM dR/R]. \quad (2)$$

Suppose that the star ejects a mass element ($-dM$). It gains an amount of energy

$$dE = -CGM/R dm, \quad (3)$$

where $C = (1 + v_\infty^2/v_e^2)$; $v_e = (2GM/R)^{1/2}$ is the escape velocity from the star's surface, and v_∞ the final velocity of the ejected matter. This energy is supplied by a decrease in Γ . The virial theorem requires that half of the change in Γ increase the star's internal energy. If a fraction f of the available energy is used to eject matter, then

$$dE = -f/2 d\Gamma. \quad (4)$$

When $dM < 0$, $d\Gamma$ must be negative, requiring $dR < 0$ and/or $dq > 0$. In a fully convective star, q is constant. Setting $dq = 0$, Equations 2-4 yield

$$\frac{dM}{M} = \eta \frac{dR}{R}, \quad (5)$$

where

$$\eta = \frac{fq}{2(C + fq)}. \quad (6)$$

If f is constant, then

$$\frac{M_2}{M_1} = \left(\frac{R_2}{R_1}\right)^\eta \quad (7)$$

where the subscripts refer to the initial and final values. The semiempirical mass loss rate assumed by Ezer and Cameron (1971) approximates a constant value of f .

When $f \neq 0$, the final mass can be arbitrarily small if the star can contract without limit. Fortunately, the range of R is limited. A collapsing protostar cannot attain hydrostatic equilibrium until its hydrogen has been dissociated and ionized. The gravitational potential energy released during hydrodynamic collapse must be sufficient to accomplish this, setting an upper limit to the radius of a stable PMS star of (Bodenheimer, 1972)

$$R_{1\max} \simeq 50 (M/M_\odot) R_\odot. \quad (8)$$

Radiative losses during collapse will cause R_1 to be smaller. Larson's (1972) models of collapsing protostars produce maximum radii of about $10 R_\odot$ for a wide range of masses.

A star formed in this manner is initially fully convective. It contracts with nearly constant surface temperature, tracing a nearly vertical "Hayashi" track on the H-R diagram. If mass ejection is a property of the convective phase, the radius at the bottom of this track is appropriate for R_2 in Equation 7. In the range $M < 5M_\odot$, Iben's (1965) models have $R_2 \simeq 1.2 (M_2/M_\odot)^{1.8} R_\odot$.

Near the bottom of the Hayashi track, the star begins to develop a radiative core. The surface temperature increases, and the star moves to the left on the H-R diagram. For M in the range of M_\odot to $1.5 M_\odot$, this occurs at nearly constant R , while q increases. If the mass loss is small during this stage, we may set $dR = 0$ in Equation 2, giving

$$\frac{dM}{M} = \frac{-f dq}{C + fq}. \quad (9)$$

For constant f , this gives

$$\frac{M_2}{M_1} = \left[\frac{C + fq_1}{C + fq_2} \right]^{1/f}. \quad (10)$$

In the change from convective to radiative structure, q goes from $6/7$ to $3/2$. The greatest mass loss occurs for $C = f = 1$; this gives $M_2/M_1 = 0.86$. Since mass loss effectively ceases on the main sequence, f should be small at this stage; $f = 0.1$ gives $M_2/M_1 = 0.97$. For solar-type stars, it appears that any significant mass loss is confined to the convective stage. For more massive stars, R and q both change on the radiative track, and the energy balance must be done numerically.

We must still determine an appropriate value of η for use in Equation 5. An absolute upper limit is found by setting $C = f = 1$. This corresponds to a non-luminous star that uses all available energy to eject matter with the minimum

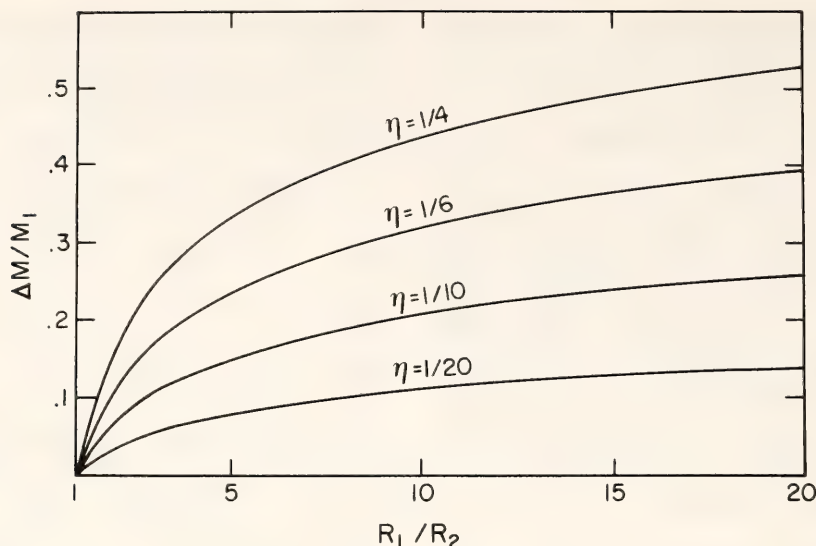


Fig. 11. Fraction of initial mass loss, as a function of the ratio of initial and final stellar radii, according to Equation 7.

energy for escape. When $q = 1$, this case gives $\eta_{\max} = 1/4$. When the rate of energy expenditure on mass ejection equals the luminosity (i.e., $f = 1/2$), then $\eta = 1/6$. Figure 11 shows the fraction of initial mass lost as a function of R_1/R_2 , according to Equation 7. Loss of more than half of the initial mass is effectively impossible. Much lower limits on η and the mass ejected may be set by observations of T Tauri stars, as described below.

Observational Constraints

We may try to determine f directly from observed values of M , R_1 , dM/dt , and luminosity. All of these quantities are poorly known and their determination is complicated by the variability of these stars, but they may at least establish the order of magnitude of f . It is generally assumed, and consistent with Kuhi's (1964) models, that the ejected matter barely escapes ($C = 1$), but we shall consider the more general case.

Let the star's actual luminosity be L_* , which may differ from the observed value, L_{obs} . We define $\dot{E}_o = -GM/R$ dM/dt as the minimum rate at which energy is supplied for mass ejection, and $\dot{E} = C\dot{E}_o$. If L_* is known, and C is as-

sumed to be unity but is actually larger, then it can be shown that f is underestimated by the factor $(C\dot{E}_o + L_*)/(C\dot{E}_o + CL_*)$, and η is overestimated by the factor $[(C+q)\dot{E}_o + L_*]/[(1+q)\dot{E}_o + L_*]$. The assumption that $C = 1$ provides an upper limit to η .

Suppose that a circumstellar cloud is heated by excess energy of the ejected matter (this requires $C > 1$), and that this cloud contributes to L_{obs} . Then $L_{\text{obs}} = L_* + (C-1)\dot{E}_o$, and the true value of f is

$$f = \frac{\dot{E}}{\dot{E} + L_*} = \frac{C\dot{E}_o}{C\dot{E}_o + L_{\text{obs}} - (C-1)\dot{E}_o} = \frac{C\dot{E}_o}{\dot{E}_o + L_{\text{obs}}}, \quad (11)$$

which is C times the value f_o , computed by assuming that $L_* = L_{\text{obs}}$ and $C = 1$. However, the actual value of η is

$$\eta = \frac{Cf_o q}{2(C + Cf_o q)} = \frac{f_o q}{2(1 + f_o q)}, \quad (12)$$

which is the same as that computed by assuming that $L_* = L_{\text{obs}}$ and $C = 1$. Therefore, η is not overestimated by using the observed luminosity if it can be accurately determined, and the quantities which determine \dot{E} can be deduced.

TABLE 3. Properties of T Tauri Stars With Mass Loss

Star	Source*	M/M_{\odot}	R/R_{\odot}	L/L_{\odot}	$-dM/dt$ ($10^{-7} M_{\odot} \text{ yr}^{-1}$)	f ($q=1$)	η	Emission Intensity†
T Tau	K4	0.6	4.65	5.35	0.35	0.026	0.013	2
	IM	2.5	6.2	18.2	0.65	0.042	0.020	
	RSS	2.5	6.2	24.0	0.65	0.032	0.016	
RY Tau	K4	0.9	3.25	3.4	0.31	0.072	0.034	2
	IM	2.7	6.7	33.9	1.32	0.046	0.022	
	RSS	2.25	4.2	16.2	0.52	0.050	0.024	
GW Ori	K4	1.3	8.64	22.1	0.35	0.007	0.0036	2
	IM	3.0	8.22	51.3	0.32	0.007	0.0035	
SU Aur	K6	1.21	5.68	32.3	0.25	0.005	0.0025	1
	IM	2.0	3.6	8.9	0.10	0.019	0.009	
	RSS	1.7	3.0	7.4	0.07	0.016	0.008	
RW Aur	K6	1.16	2.46	5.66	1.11	0.222	0.091	5
	IM	1.5	2.3	4.0	0.97	0.325	0.122	
	RSS	1.5	4.72	7.6	4.08	0.345	0.128	
RU Lup	K4	1.42	2.95	2.63	1.42	0.445	0.154	5
AS 209	K4	0.81	2.94	2.18	0.65	0.202	0.084	4
Lk H α 120	K4	4.1	11.16	68.5	5.85	0.088	0.041	4

* K4 = Kuhi, 1964; K6 = Kuhi, 1966; IM = Imhoff and Mendoza, 1974; RSS = Rydgren, Strom, and Strom, 1976.
† Herbig and Rao, 1972.

Results and Discussion

Table 3 lists properties of those stars for which Kuhi (1964, 1966) computed rates of mass loss. Recent observations over a broader spectral range [Imhoff and Mendoza (IM), 1974; Rydgren, Strom, and Strom (RSS), 1976] yield luminosities that differ from Kuhi's values and imply corresponding changes in R and M . Wherever these sources state L , R , or M , their values are used. Missing values of R and L are computed from the relation (Kuhi, 1964)

$$\log (R/R_{\odot}) = 1/2 \log (L/L_{\odot}) - 2(\log T_e - 3.76). \tag{13}$$

When the effective temperature T_e was not stated, it was derived from the spectral type, using Johnson's (1966) calibration. RSS do not give a spectral type for RW Aur. E. Rydgren (private communication) suggests that it is probably mid- to late-K type; I have assumed it to be K5 for this calculation. For IM and RSS, M was estimated from a star's

position on the H-R diagram with respect to Iben's (1965) theoretical PMS tracks. Kuhi's stated masses are not always consistent with Iben's results. Figure 12 shows the positions of five stars according to IM.

Kuhi's mass-loss rates were calculated from the estimated density and velocity of the ejected matter and the surface area of the star. Therefore, I have scaled Kuhi's values of dM/dt as R^2 for the stellar parameters of IM and RSS (neglecting possible effects of temperature and surface gravity on the calculated rates). Bodenheimer (1972) suggested that upward revisions of L would imply shorter contraction times and smaller total mass losses. However, a change in L generally implies a similar change in surface area, and hence in dM/dt . The value of f is, therefore, not very sensitive to luminosity. Still, all of these stars are variable, and the quoted values of L and dM/dt were generally determined at different times. Kuhi's value of dM/dt for each star is the mean of several de-

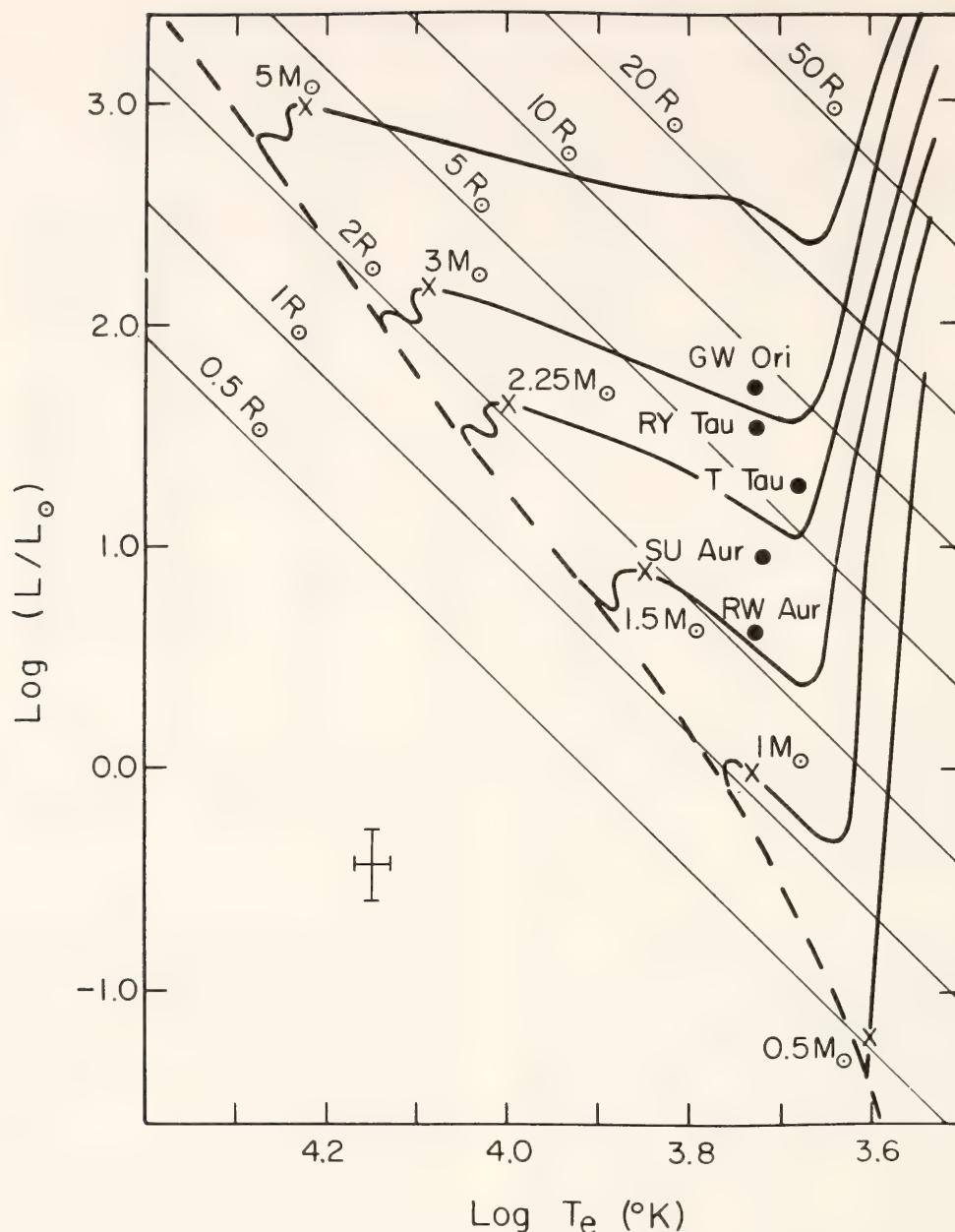


Fig. 12. Positions of five T Tauri stars on the H-R diagram, as determined by Imhoff and Mendoza (1974). "Error bar" is maximum difference from determination by Rydgren *et al.* (1976) for these stars only. Actual uncertainties are presumably much larger. PMS tracks for various masses are from Iben (1965); \times on each track marks the point at which 10% of the star's energy production is due to hydrogen burning. Dashed line: zero-age main sequence.

terminations, which vary by as much as a factor of three. Obviously, all of the listed quantities are very uncertain.

Figure 13 shows the variation of f with Herbig and Rao's (1972) emission-line intensity class. Of the three stars with $f > 0.1$, all are of class 4 or 5. Their high values of f are consistent with their level of activity, but interpretation of their spectra is difficult. Observations of RU Lup allow a wide range of values for

R , L , and M ; any model is complicated by the possibility of a large and variable circumstellar extinction (Gahm *et al.*, 1975). The spectral types of AS 209 and Lk H α 120 are unknown (Herbig and Rao, 1972). RW Aur has an unusually complex spectrum (Gahm, 1970a). Gahm (1970b) reexamined its line profiles, and concluded that Kuhl had overestimated its mass-loss rate by about a factor of two; this would imply $f \simeq 0.15$, $\eta \simeq 0.07$.

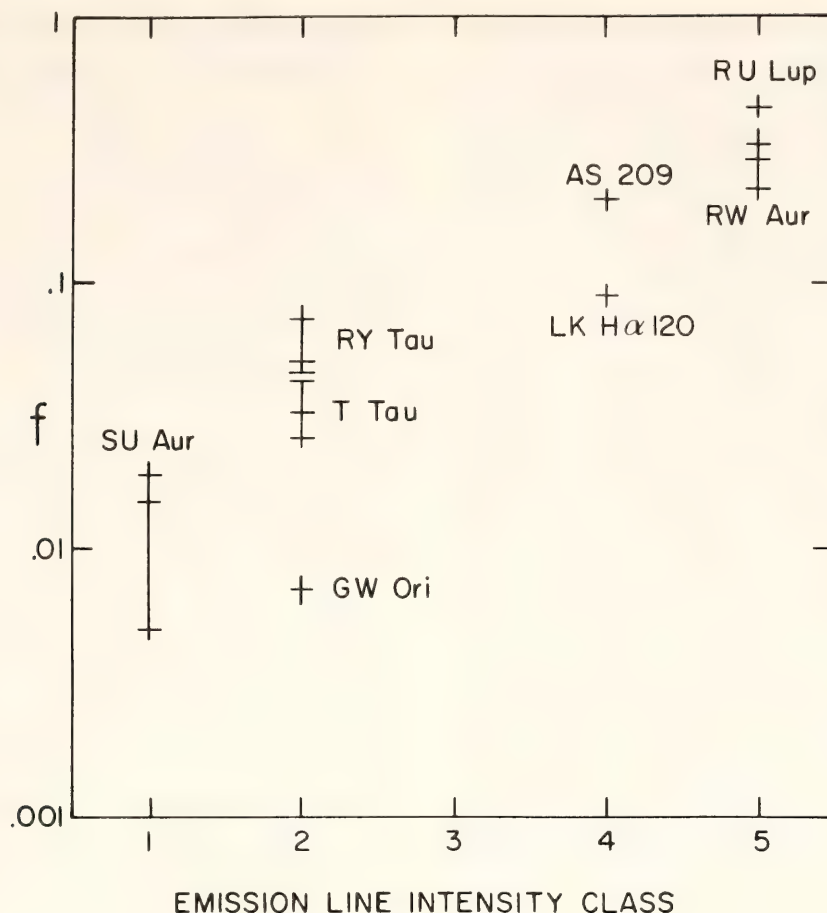


Fig. 13. Log f plotted against Herbig and Rao's emission-line intensity class. Each crossbar is a determination from the sets of parameters given in Table 3.

Similar analyses should be performed for the other stars of classes 4 and 5. These objects, which appear to be the only ones capable of significant mass loss, represent only a small fraction of PMS stars. Herbig and Rao list 36 of class 4, and 12 of class 5, out of a sample of 323 stars. Apparently, Kuhl's selection favored the most-active objects.

If correctly assigned by IM, RW Aur is on the radiative track. In that case, its present level of activity is probably a transient event. If it is of a later spectral type, as suggested by RSS, it would be on the convective track. Its high Li abundance (Zappala, 1972) is consistent with a convective state, since Li destruction would occur nearer the ZAMS. RW Aur has a fainter companion, classed as type M (Herbig, 1962; Joy and Abt, 1974) or K3e (Herbig and Rao, 1972).

If they are coeval, the fainter component should have a lower T_e and smaller mass (probably $0.5\text{--}1.0 M_\odot$). Iben's calculations would imply an age of about 10^6 years for this system, with both components convective.

One is tempted to identify stars of the highest emission-line intensity classes as being fully convective. However, Cohen and Kuhl (1976) report a number of stars that appear to be on convective tracks; several of these are listed by Herbig and Rao as being of classes 1 or 2. It is not known whether any of these stars are losing mass.

Summary

The total amount of mass that may be lost from a PMS star is limited by

the energy released by gravitational contraction, regardless of the mechanism of ejection or its instantaneous rate. For a solar-type star, mass loss on the radiative track will not exceed a few percent. Larger losses are possible on the convective tracks. If the star's radius decreases by a large factor, the fraction of initial mass lost is comparable to the fraction f of available energy expended on ejection. This quantity appears to increase with emission-line intensity; for stars of classes 4 and 5, f may exceed 0.1. However, quantitative estimates of their mass-loss rates are very uncertain because of difficulties in interpreting their spectra. Moreover, these stars represent only a small fraction of PMS objects. Quantitative calculations of mass-loss rates have been performed for only eight stars, more than a decade ago. Such analysis must be extended to a much larger sample, using modern techniques, in order for the concept of a "T Tauri solar wind" to be meaningful.

References

- Bodenheimer, P., Stellar evolution toward the main sequence, *Rep. Progr. Phys.*, **35**, 1, 1972.
- Cameron, A. G. W., Accumulation processes in the primitive solar nebula, *Icarus*, **18**, 407, 1973.
- Cameron, A. G. W., Physics of the primitive solar accretion disk, *Moon and the Planets*, in preparation, 1978.
- Cohen, M., and L. V. Kuhi, Spectrophotometric studies of young stars. I. The Cepheus IV association, *Astrophys. J.*, **210**, 365, 1976.
- Ezer, D., and A. G. W. Cameron, Pre-main sequence stellar evolution with mass loss, *Astrophys. Space Sci.*, **10**, 52, 1971.
- Gahm, G., The spectrum of RW Aurigae, 3250 to 4900 Å, *Astrophys. J.*, **160**, 1117, 1970a.
- Gahm, G., On the mass loss from T Tauri stars, *Astron. Astrophys.*, **8**, 73, 1970b.
- Gahm, G. F., H. L. Nordh, and S. G. Olofsson, The T Tauri star RU Lupi and its circumstellar surrounding, *Icarus*, **24**, 372, 1975.
- Herbig, G., The properties and problems of T Tauri stars and related objects, *Advan. Astron. Astrophys.*, **1**, 47, 1962.
- Herbig, G., and N. K. Rao, Second catalog of emission-line stars of the Orion population, *Astrophys. J.*, **174**, 401, 1972.
- Iben, I., Stellar evolution I. The approach to the main sequence, *Astrophys. J.*, **141**, 993, 1965.
- Imhoff, C., and E. E. Mendoza V., Computed luminosities for T Tauri and related objects, *Rev. Mex. Astron. y Astrofis.*, **1**, 25, 1974.
- Johnson, H. L., Astronomical measurements in the infrared, *Annu. Rev. Astron. Astrophys.*, **4**, 193, 1966.
- Joy, A. H., and H. A. Abt, Spectral types of M dwarf stars, *Astrophys. J. Suppl. Ser.*, **28**, 1, 1974.
- Kuhi, L. V., Mass loss from T Tauri stars, *Astrophys. J.*, **140**, 1409, 1964.
- Kuhi, L. V., Mass loss from T Tauri stars, II, *Astrophys. J.*, **143**, 991, 1966.
- Kuhi, L. V., and J. E. Forbes, The effect of mass loss on a contracting star, *Astrophys. J.*, **159**, 871, 1970.
- Larson, R. B., The evolution of spherical protostars with masses 0.25 to 10 M_{\odot} , *Mon. Notic. Roy. Astron. Soc.*, **157**, 121, 1972.
- Rydgren, A. E., S. E. Strom, and K. M. Strom, The nature of the objects of Joy: a study of the T Tauri phenomenon, *Astrophys. J. Suppl. Ser.*, **30**, 307, 1976.
- Ulrich, R. K., An infall model for the T Tauri phenomenon, *Astrophys. J.*, **210**, 377, 1976.
- Williams, I. P., Maximum mass loss from stars, *Mon. Notic. Roy. Astron. Soc.*, **136**, 341, 1967.
- Zappala, R. R., Lithium abundances of stars in open clusters, *Astrophys. J.*, **172**, 57, 1972.

ACCUMULATION OF THE TERRESTRIAL PLANETS BY THE SWEEPING UP OF PLANETESIMALS

G. W. Wetherill

In *Year Book 76* (pp. 761–792), results of some numerical studies of the growth of the inner planets by the sweep-up of planetesimals were reported. These studies are continuing and further results will be reported at a later time. In the course of this work it was noted that many of the principal results of these numerical investigations could be understood in at least a semiquantitative way from very elementary considerations. These results are given here, as a complement to the work presented earlier, to show that the previous results were not mysterious things “the computer tells me.”

The complete problem of the evolution of a swarm of planetesimals into terrestrial planets is very complex, and at present we are a long way from even a good approximation to a definitive solution. Nevertheless, it is possible to gain some insight into accumulation of planetesimals in a gas-free region by use of simple calculations using methods similar to those of elementary kinetic theory of gases. Results found in this way will also be useful in making starting approximations in more advanced calculations.

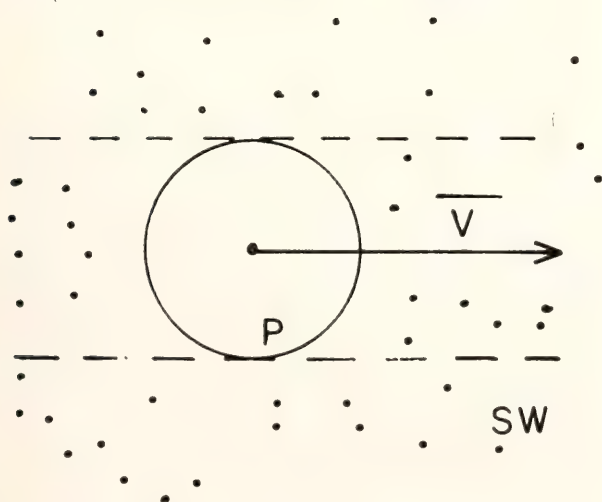


Fig. 14. Schematic representation of an embryo (P) moving at a mean relative velocity \bar{V} through a gas-free swarm (SW).

A. Time Scale of Accumulation

From this elementary point of view, the embryo which is to become the planet can be envisaged as a body of radius R_e moving through a swarm of planetesimals at relative velocity \bar{v} (Fig. 14). The rate of growth of the embryo's radius will be roughly

$$\frac{dR}{dt} = \frac{\rho_{sw}\bar{v}}{4\rho_p} \left(1 + \frac{v_e^2}{\bar{v}^2} \right), \quad (1)$$

where ρ_{sw} = density of the swarm
 ρ_p = density of the planetesimals being accumulated (~ 4 g/cm³)
 v_e = escape velocity of the embryo.

The expression in parentheses represents the enhancement of the effective capture radius of the embryo, as a consequence of its gravitational field.

The density of the planetesimal swarm at the midpoint of growth will be given by the ratio of its mass to its volume. At this stage mutual perturbations by members of the swarm will be small relative to perturbations by the embryo. Referring to Fig. 15, the volume of Earth's swarm will be taken to be a ring with rectangular cross section centered at 1 A.U. and of width 2δ extending midway to the present semimajor axes of Venus and Mars. The height of this volume will be $2a \sin i$ where i is the mean inclination of the bodies in the swarm. Assuming energy equipartition between the three components of velocity,

$$a \sin i \approx \frac{a\bar{v}}{\sqrt{3}v_c}, \quad (2)$$

where v_c = circular Kepler velocity at 1 A.U. (29.8 km/sec). Then

$$\begin{aligned} \rho_{sw} &\approx \frac{\text{Mass of swarm}}{\text{Volume of swarm}} = \\ &= \frac{M_p}{2} \frac{1}{(2\pi a) \left(\frac{2a\bar{v}}{\sqrt{3}v_c} \right) (2\delta)} = \\ &= \frac{\sqrt{3}M_p v_c}{16\pi a^2 \bar{v}} = 3.06 \times 10^{-12} \text{ g/cm}^3 \end{aligned} \quad (3)$$

where M_p is the final mass of the planet, neglecting escape from the swarm during accumulation (see next section).

Substituting Equation 3 into 1,

$$\frac{dR}{dt} = \frac{\sqrt{3}}{64\pi} \frac{M_p v_c}{a^2 \delta \rho_p} \left(1 + \frac{v_e^2}{\bar{v}^2} \right). \quad (4)$$

Equation 4 is independent of \bar{v} , except insofar as it enters into the gravitational cross-section term in parentheses. In order for accumulation to proceed at this stage it is necessary that \bar{v} be large enough that bodies with semimajor axes at $(a + \delta/2)$ have perihelia at least as small as a . The velocity of a low-inclination (i.e., 5°) body in such an orbit with respect to the embryo at 1 A.U. will be 3.1 km/sec. This is a reasonable value to use for \bar{v} , and is the same as the value found by use of Safronov's expression (Safronov, 1972),

$$\Theta \approx 4 = \frac{v_e^2}{2\bar{v}^2}. \quad (5)$$

If lower values of \bar{v} were inserted in Equation 4, larger accumulation rates would be found. However, in this case the use of Equation 4 would not be valid, as the bodies in the swarm would not be "orbitally linked" to the embryo, which dominates the growth at this stage. This term will be used to describe the situation wherein the orbits of the bodies of the swarm are sufficiently strongly coupled by their mutual gravitational perturbations to continue to undergo major changes in their elements on a time scale short compared to 10^8 years.

For small bodies this requires that there be extensive crossing of orbits. Large enough bodies can be linked even when actual intersection of orbits does not take place. The situation opposite to orbital linkage occurs when the system becomes "dead" (i.e. the bodies remain sufficiently distant from one another to lead to nearly stable orbits on this time scale).

It is certainly conceivable that breakdown of linkage may occur, which would lead to a situation in which the rate of accumulation would be controlled not by Equation 4 but by the rate at which bodies would "diffuse" by relatively weak mutual or long-range perturbations into the vicinity of the embryo—in some ways analogous to accumulation of planetesimals in a gaseous medium (Hayashi *et al.*, 1977). This question of maintaining orbital linkage is an important matter, which has not yet been thoroughly addressed in even more sophisticated treatments of planetary accumulation.

Substitution of these numerical values into Equation 4 gives

$$\frac{dR}{dt}_{\text{midpoint}} = 16.7 \text{ cm/yr.} \quad (6)$$

This accumulation rate is seen to be quite low, and if it were concentrated in entirely small particles (which it is not) it could easily be swept away every month or so from one's sidewalk with a broom. At this average rate, the time required for the Earth to complete its growth will be $T_{\text{growth}} = 38$ million years. Similar accumulation time scales of 10^7 to 10^8 years also are found in more complex treatments of this problem. The reason is that the physics is essentially the same—including the assumption of orbital linkage.

B. Distribution of the Initial Swarm

It is obviously necessary that mass, energy, and angular momentum be conserved during the process of accumulating the planetesimal swarm into the planets. If the swarm could be treated entirely as a closed system, the initial values of these quantities would be defined by the masses and orbits of the present planets. However the system is not entirely closed; energy is lost in the form of heat when the planetesimals collide with one another and with the planetary embryos

as they emerge during the later stages of accumulation. Mass, together with associated energy and angular momentum, is lost if members of the swarm are accelerated by perturbations by the embryos into orbits with perihelia beyond Mars, including those accelerated members that escape the solar system in hyperbolic orbits. Angular momentum transfer occurs between the major planets and the terrestrial planets as a consequence of long-range gravitational perturbations. Although these deviations from closed-system behavior cannot be known *a priori* with a high degree of certainty, their values can be estimated. This permits placing some limits on the distribution of mass in the swarm, based on these very general principles.

Expressions for conservation of mass, angular momentum, and energy can be written in the following form:

$$M_{\text{initial}} = \sum_{i=1}^4 M_i + M_{\text{escaped}} \quad (7)$$

$$L_{\text{initial}} = \sum_{i=1}^4 M_i (GM_{\odot})^{1/2} a_i^{1/2} (1-e_i^2)^{1/2} + L_{\text{escaped}} + \Delta L_G \quad (8)$$

$$U_{\text{initial}} = - \sum_{i=1}^4 \frac{GM_{\odot}}{2a_i} + U_{\text{escaped}} + U_{DE} + U_{DP}. \quad (9)$$

The sums $i = 1, 4$ are taken over the present values for the four terrestrial planets, ΔL_G is the angular momentum exchanged between the swarm and the giant planets, U_{DE} is the energy lost as heat in planetesimal-embryo collisions, U_{DP} is the energy lost in planetesimal-planetesimal collisions.

If a fraction f_E of the final mass of the planets escaped, then

$$M_{\text{initial}} = (1+f_E) M_T,$$

where M_T is the present total mass of the terrestrial planets (including the Moon with the Earth).

In the same way:

$$L_{\text{escape}} = f_E L_T \quad (11)$$

and

$$U_{\text{escape}} = f_E U_T, \quad (12)$$

assuming that the initial angular momentum and energies of the bodies that escaped were the same as the rest of the swarm.

The other quantities on the right-hand side of Equations 7, 8, and 9 can be estimated. These estimates will, of course, be model dependent. However, this is equally true of much more complex numerical approaches to the problem of the later stages of accumulation. For a given choice of model parameters (e.g., size distribution and fraction of kinetic energy dissipated in collisions), these simple calculations permit useful estimates of the differences between the initial and final swarms which will be found by numerical calculations employing the same model.

All of the planetesimals must strike the embryo and lose their kinetic energy of relative motion in the process. Using $\bar{v} = 3.1$ km/sec at the midpoint of accumulation, as estimated in the previous section, then

$$U_{DE} \approx \frac{\bar{v}^2}{2} M_T = 5.35 \cdot 10^{38} \text{ erg} \quad (13)$$

(i.e., $\sim 1\%$ of the energy of the present planets).

The energy lost in planetesimal-planetesimal collisions is more model dependent, because most of the energy will be lost in collisions between the smaller members of the swarm and the number of smaller members is dependent on the size distribution of the swarm. One possible model used in the earlier numerical studies is to consider the swarm to consist of large bodies $\sim 10^{24}$ g in mass (440-km radius), each of the bodies being accompanied by a collisional steady state

“retinue” of smaller bodies obeying the power law

$$\frac{dn}{dr} = Cr^{-3.5}. \quad (14)$$

Using the “kinetic theory of gases” approach of the previous section, this size distribution leads to a rate of energy loss per second in the Earth’s zone (Fig. 15) at the midpoint of accumulation:

$$\frac{dU}{dt} = \frac{3}{128} \frac{\bar{v}^3 \alpha M_e^2 (1+f_E)^2 \ln \left(\frac{r_{\max}}{r_{\min}} \right)}{\rho_p \Lambda r_{\max}}, \quad (15)$$

where M_e is the mass of the Earth, Λ is the volume of Earth zone (Fig. 15), α is the fraction of the energy lost in each collision (e.g., 0.5). The result is not sensitive to the value of r_{\min} . Substituting the numerical values defined above and by the earlier calculations, with $r_{\min} = 1$ meter, this gives an energy loss rate of

$$\frac{dU}{dt} = 2.87 \cdot 10^{37} (1+f_E)^2 \text{ erg}/10^6 \text{ years} \quad (16)$$

In the 38-million-year accumulation time calculated as compatible with this choice of parameters, the total energy loss is

$$U_{DP} = 1.09 \cdot 10^{39} (1+f_E)^2 \text{ erg} \quad \text{in Earth's zone.} \quad (17)$$

Since f_E will turn out to $\ll 1$, it represents about a 4% correction to the total energy of the swarm, assuming a similar loss in Venus’ zone. If a larger relative velocity or a size distribution in which

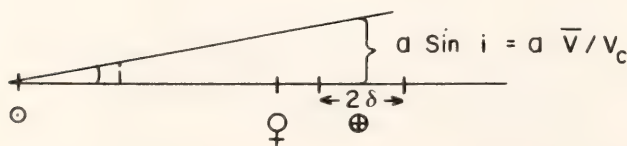


Fig. 15. Illustration of the volume of Earth’s swarm, used in simple calculation. The swarm is considered to be bounded within a circular ring of thickness 2δ centered at Earth’s radius and of height $2a \sin i$.

more of the mass is concentrated in small bodies had been chosen, higher energy losses would be calculated. It will be seen that even these modest energy losses lead to significant restrictions on the distribution of the bodies in the original swarm unless some mechanism exists that permits the swarm to lose angular momentum as well. The difficulties arising therefrom will be only aggravated by larger energy losses.

The remaining quantity to be approximated is ΔL_G , the angular momentum transferred from the terrestrial planet region to the giant planets as a result of secular perturbations. This is difficult to approximate with any degree of certainty, principally because it is not even known when the giant planets formed relative to the terrestrial planets. In addition, the positions of all the planets were probably changing during the time interval of formation of the terrestrial planets, changing both the frequencies and the amplitude of the secular perturbation forcing terms. However, if major condensations existed which gave rise to secular perturbation and forced oscillations similar to those at present some estimate of this angular momentum transfer can be given.

As a consequence of the collisional energy dissipation which resulted in the energy loss terms U_{DE} and U_{DP} , the energies and therefore the semimajor axes of both the planetesimals and the embryos will tend to decrease with time. Since angular momentum will be conserved in these collisions, and since

$$L = (GM_\odot)^{1/2} \sqrt{a(1-e^2)}, \quad (18)$$

a decrease in a requires a decrease in e (i.e., the orbits will tend to become more circular). In the case of the planetesimals, this circularization will be prevented by perturbations of the planetesimals by the embryos, assuming orbital linkage. However, there are no comparable perturbers for the embryos themselves within the system of terrestrial

planets, and one must look to the giant planets if the orbits of the embryos are to remain noncircular. In the present solar system, the root-mean-square eccentricity of the Earth resulting from these perturbations is $\sim .03$, and it varies above and below this value on a time scale of $\sim 10^5$ years. At the midpoint of accumulation of the Earth, the rate at which the Earth's embryo loses energy as a consequence of U_{DE} and U_{DP} will be $\sim \frac{U_{DE} + U_{DP}}{2 \cdot T_{\text{growth}}}$, assuming that the average

semimajor axis of the swarm remains equal to that of the Earth. In other words, some of the energy lost by planetesimal-planetesimal collisions must be supplied by the Earth embryo in the process of maintaining the steady state geocentric velocity of the swarm. The relationship between the energy loss of Earth's embryo and the change in its semimajor axis will be

$$da_E = \frac{-2a_E^2 (1+f_E)^2 dU_E}{GM_\odot M_E} \approx .0013(1+f_E)^2 \text{ A.U.}/10^6 \text{ yr.} \quad (19)$$

$$\frac{1}{L} \frac{dL}{dt} = \frac{1}{2a} \frac{da}{dt}. \quad (20)$$

When combined with the rate of change in semimajor axis given in Equation 19, this relationship leads to the estimate that 2.5% of the Earth's angular momentum will be transferred to the giant planets during the course of its accumulation. The actual value will probably be somewhat less, as the amplitude of the forced oscillations will be decreased by damping during the early, more rapid stages of accumulation.

The observed mass, final angular momentum, and energy of the terrestrial planets, together with the preceding estimates of energy and angular momentum loss during accumulation, can be combined to obtain the initial energy and angular momentum per unit mass of the

swarm by use of Equations 7, 8, and 9 and then dividing by M_{initial} :

$$L_{\text{initial}} = \frac{4.971 \cdot 10^{47} \cdot (1.025)}{1.188 \cdot 10^{28}} = 4.29 \cdot 10^{19} \text{ erg-sec/g} \quad (21)$$

$$U_{\text{initial}} = \frac{-6.219 \cdot 10^{40} \cdot (0.95)}{1.188 \cdot 10^{28}} = -4.97 \cdot 10^{12} \text{ erg/g.} \quad (22)$$

When formulated in this way, the distribution of angular momentum and energy in the initial swarm is expressed in a manner independent of the fraction of the initial mass lost by acceleration out of the terrestrial planet region into Jupiter-crossing. This fraction (f_E) will not be large. The minimum geocentric velocity for a body crossing the orbit of both Jupiter and Earth (in their present orbits) is 8.6 km/sec. Therefore bodies with geocentric velocities of 3 km/sec, as assumed in the preceding calculations, cannot be lost to Jupiter. Only those bodies with geocentric velocities well above the average will have sufficient velocity to become Jupiter-crossing, and only a fraction of such high-velocity bodies will be perturbed into Jupiter-crossing before they impact Earth or Venus. Previously published calculations (Wetherill, 1975, 1977a) show that in the complete absence of dissipation, about 18% of a swarm of objects initially in orbits with low (~ 1 km/sec) geocentric velocity will be accelerated by Earth and Venus perturbations (at their final masses) into Jupiter-crossing. However, because of the absence of dissipation, this swarm was accelerated to a mean geocentric velocity of ~ 12 km/sec, much higher than in the case being discussed here. Furthermore, the smaller embryo masses lead to less acceleration. The results of calculations of accumulation including dissipation discussed elsewhere in this paper lead to escape fractions of 0.3–2%.

The initial values of energy and angu-

lar momentum per unit mass given by Equations 21 and 22 will now be compared with hypothetical initial swarms in order to see what constraints conservation of energy and angular momentum place upon the initial distribution.

For this purpose, initial swarms with semimajor axis distributions

$$\frac{dN}{da} = \rho_s a^n \quad (23)$$

will be considered, in which N is the initial number of bodies per unit area with semimajor axis between a and $a + da$, and the exponential parameter n distinguishes between swarms with different radial density distributions. The total mass, angular momentum, and energy of the swarm will be given by

$$M_t = 2\pi\rho_s \int_{a_1}^{a_2} a^{n+1} da = \frac{\rho_s}{(n+2)} (a_2^{n+2} - a_1^{n+2}) \quad (n \neq -2), \quad (24)$$

$$L_t = 2\pi\rho_s (GM_\odot)^{1/2} \overline{(1-e^2)^{1/2}} \int_{a_1}^{a_2} a^{n+3/2} da = \frac{2\pi(GM_\odot)^{1/2}}{(n+5/2)} \rho_s (1-e^2)^{1/2} (a_2^{n+5/2} - a_1^{n+5/2}) \quad (n \neq -5/2), \quad (25)$$

$$U_t = -\pi GM_\odot \rho_s \int_{a_1}^{a_2} a^n da = -\pi\rho_s \frac{GM_\odot}{(n+1)} (a_2^{n+1} - a_1^{n+1}) \quad (n \neq -1), \quad (26)$$

where a_2 and a_1 are the bounds of the swarm. When n has the values excluded in Equations 24, 25, or 26, the integral in question is given by the substitution: $a^\circ \rightarrow \ln a$ in these equations. Averaging of the initial value of $(1-e^2)^{1/2}$ is permissible, since the initial eccentricities must be low.

Equations 24, 25, and 26 have been numerically evaluated for different swarms, as given in Table 4. The "nomi-

nal" case, corresponding to the estimates of U_{DE} , U_{DP} and ΔL_G given in this section requires the values of L and U given on the fourth line, Table 4C. Comparison with Tables 4A and 4B shows that values of n less than $-1/2$ are excluded: the initial mass density per unit area must be nearly constant, rather than falling off approximately as $a^{-3/2}$, as is the case for the present solar system taken as a whole (Weidenschilling, 1977). Some decrease in surface density with radius ($n \sim -1$) is possible if it is assumed that there is no energy dissipation (first line, Table 4C). This would imply very low relative velocities, which, as discussed before, is not compatible with maintenance of orbital linkage between the embryo and the swarm.

If for some reason the secular perturbations are ineffectual in removing angular momentum (e.g., if the giant planets have not yet formed), then the required values are given in the second line of Table 4C. For all the swarms calculated, the angular momentum is too high at the required energy. In fact, the extreme case—all the mass concentrated at a single radius (0.89 A.U.) corresponding to minimum angular momentum for a given mass—is required to fit both the energy and angular momentum. Therefore, velocities as high as that assumed here in the nominal case, ~ 3 km/sec, require that there be some external mechanism for removing angular momentum from the terrestrial planets during their accumulation, unless the rate of energy dissipation is quite a bit lower than that in the model chosen as an example.

If the dissipation is slightly different from the nominal case (line 3), a good fit is given by the narrow flat distribution ($n=0$) of Table 4B. The differences between the values required may not seem great. The significance of these differences becomes more clear if their consequences are calculated. For example, consider the case where the swarm corre-

TABLE 4. Energy and Momentum Per Unit Mass of Planetesimal Swarms

A. $a_1 = 0.4, a_2 = 1.4$				
n	L (10^{19} ergs sec/g)	U (10^{12} ergs/g)		
-3/2	4.01	-5.91		
-1	4.14	-5.54		
-1/2	4.26	-5.21		
0	4.36	-4.93		
+1/2	4.45	-4.67		
+1	4.54	-4.46		
B. $a_1 = 0.6, a_2 = 1.2$				
n	L (10^{19} ergs sec/g)	U (10^{12} ergs/g)		
-3/2	4.15	-5.23		
-1	4.17	-5.12		
-1/2	4.22	-5.01		
0	4.27	-4.93		
+1/2	4.30	-4.83		
+1	4.33	-4.74		
C. Required values				
L (10^{19} ergs sec/g)	U (10^{12} ergs/g)	Energy Dissipation %	Ang. Mom. Loss %	Remarks
4.18	-5.23	0	0	no orbital linkage
4.18	-4.97	5	0	"no Jupiter"
4.27	-4.92	6	2	good fit to $n=0$ (swarm B)
4.29	-4.97	5	2.5	"nominal" case
4.43	-4.61	12	6	

sponding to $n = -1/2$ in Table 4A is the initial swarm and the nominal losses of energy and angular momentum occurred. If Mercury and Mars turned out to be at their proper mass and orbits, conservation of energy and angular momentum would require that Venus be at 0.63 A.U. (with its present mass) and the Earth at 1.06 A.U. Thus, differences of a few percent in the initial energy and angular momentum will have a large effect on the final positions of the planets.

It is also seen that acceptable swarms do not span the entire range from Mercury's perihelion to Mars' aphelion but must be truncated at the lower end at ~0.4 A.U. and the upper end at ~1.4 A.U. Wider swarms will have too large negative values of energy at the required angular momentum. The form of the terrestrial planet swarm thus is more a band than a broad zone, as discussed by Alfvén and Arrhenius (1976). Another

characteristic of swarms with velocities in the range corresponding to maintenance of orbital linkage and with size distribution containing a steady state population of small bodies, is that the initial mass of Earth's swarm ($a>0.85$) is about twice that of Venus' swarm ($a>0.85$). In order for a swarm of this kind to evolve into the present terrestrial planets, it is then necessary that material originally in Earth's swarm be accumulated by Venus and Mars. This effect will tend to reduce density differences between the terrestrial planets arising from possible initial variation in the chemical composition of the swarm as a function of heliocentric distance.

C. Conclusions

Subject to the validity of the assumptions made in the foregoing calculations and based on these simple considerations, the following are concluded:

(1) If velocities are to be high enough (~ 3 km/sec) to maintain orbital linkage during the principal stages of the embryos' growth, a small but significant (e.g. 5%) loss of energy by planetesimal-planetesimal and planetesimal-embryo collisions will occur for size distributions of the sort considered.

(2) Under these circumstances, some mechanism (i.e., Jupiter perturbations) must exist to transfer angular momentum (in this case 2.5%) out of the terrestrial planet region during the accumulation of these planets if circularization of the embryos' orbits is to be avoided. If circularization occurs, acceleration of the planetesimals by the radial component of the embryos' velocity will be ineffective, relative velocities will drop, and multi-embryo crossing may become unusual, causing further loss of velocity.

(3) Initial swarms spanning the entire range of the present terrestrial planets and with surface density decreasing with distance from the sun are not compatible with these energy and angular momentum calculations. Rather, the swarm must initially occupy a more narrow central band, which spreads during the process of accumulation.

(4) A corollary of (3) is that significant exchange of material must occur between the "feeding zones" of the various terrestrial planets during their accumulation.

In addition to the conclusions listed above, earlier studies of the postaccumulation evolution of Earth's residual swarm (Wetherill, 1977b) show that a significant fraction ($\sim 10\%$) of the swarm is transferred to Mars-crossing, and most of this material will "leak" back to Earth on a time scale of hundreds of millions of years. This same phenomenon should occur during this preceding accumulation stage as well. Its effect will be to impose a long-lived "tail" on the growth of the Earth which, if sufficiently large, will be in conflict with the low crater densities observed

on the lunar maria. This is likely to be a major constraint on such questions as the initial position of Mars' embryo and the collisional lifetime of bodies in the region between Earth and Mars.

References

- Alfvén, H. and G. Arrhenius, *Evolution of the Solar System*, NASA SP-345, 1976.
- Hayashi, C., K. Nakazawa, and I. Adachi, Long-term behavior of planetesimals and the formation of the planets, *Publ. Astron. Soc. Japan*, 29, 163-196, 1977.
- Safronov, V. S., Evolution of the protoplanetary cloud and formation of the Earth and planets, Nauka, Moscow, 1969; translated for NASA and NSF by Israel Program for Scientific Translation, NASA TT F-677, 1972.
- Weidenschilling, S. J., The distribution of mass in the planetary system and solar nebula, *Astrophys. Space Sci.*, 51, 153-158, 1977.
- Wetherill, G. W., Late heavy bombardment of the moon and terrestrial planets, *Proc. 6th Lunar Sci. Conf.*, pp. 1539-1559, Pergamon Press, 1975.
- Wetherill, G. W., Pre-mare cratering and early solar system history, in *Proc. Soviet-American Conf. on Cosmochem. of the Moon and Planets* (1974), pp. 411-424, Nauka, Moscow, 1975; also in NASA SP-370, pp. 553-567, 1977a.
- Wetherill, G. W., Evolution of the earth's planetesimal swarm subsequent to the formation of the earth and moon, in *Proc. 8th Lunar Science Conf.*, 1, pp. 1-16, 1977b.

EXTRAGALACTIC STUDIES

ROTATIONAL PROPERTIES OF SPIRAL GALAXIES AS A FUNCTION OF HUBBLE TYPE

V. C. Rubin, W. K. Ford, Jr., and N. Thonnard

How much mass does the universe contain? Is this mass sufficient by its gravi-

tational attraction to retard or even eventually to halt the Hubble expansion? What fraction of this mass is contained in galaxies? How is the mass of a galaxy related to its morphological type? Of these four fundamental questions, the last two are presently the most amenable to study, and are the ones toward which we have directed our observations.

In a galaxy, the stars and gas are rotating about the nucleus, with velocities which result from the gravitational force field produced by all the matter in the galaxy. If the gravitational force on any mass m at distance r from the center is just balanced by the centrifugal force, then

$$\frac{GmM}{r^2} = \frac{V^2m}{r},$$

where M is the mass of the galaxy and V is the circular velocity of mass m , and G is the gravitational constant. From this we can write

$$M = \frac{V^2r}{G}, \text{ or } V = \sqrt{\frac{GM}{r}}. \tag{1}$$

Thus by determining the rotational velocity V for a region at distance r from the nucleus, the mass M interior to r can be derived. Unfortunately, it is necessary to determine velocities far out in galaxies, where the luminosity is low, in order to get a meaningful measure of the total galaxy mass. Until recently, astronomers had to resort to extrapolations based primarily upon their expectations to infer velocities and masses at large r . In the solar system, where almost all of the mass is in the sun, M (Equation 1) is essentially constant for all r , so the velocities of the planets decrease as $\frac{1}{\sqrt{r}}$ with increasing distance from the sun. Mercury ($r = 0.39$ A.U.) moves with $V = 47.9$ km/sec; Pluto, 100 times farther ($r = 39$ A.U.), moves with a velocity $\frac{1}{\sqrt{100}}$ or 1/10th that of Mercury,

or $V = 4.7$ km/sec. By analogy, astronomers assumed that most of the mass of a galaxy is contained in its luminous bulge and that velocities in the outer regions must hence decrease, with the decrease given by the $\frac{1}{\sqrt{r}}$ law.

The observations which we describe below (Fig. 16) indicate that rotational velocities do not fall for large r , but are nearly flat. This means that M/r is constant (Equation 1); mass is increasing linearly with radius. Thus, total galaxy masses are higher than previously assumed, perhaps by as much as a factor of 5, and much of this mass is located in the outer parts of the galaxy.

The distribution of this mass (i.e., in a halo, in a thin disk, or in a thick disk) is unknown and cannot be determined by our procedure. Its composition is also unknown, although the low luminosity of the outer regions suggests that it is not in stars whose luminosities are as high as a normal stellar population. An increase of galaxy masses by a factor of 5 is still not enough mass to gravitationally halt the Hubble expansion.

In the 52 years since Hubble (1926) introduced his classification sequence for galaxies, few systematic observational programs have attempted to study dynamical properties of galaxies as a function of Hubble type. The constraints have been principally instrumental. Optical rotation curves (e.g., Burbidge and Burbidge, 1975) have furnished valuable dynamical information, but generally only for the inner regions of late-type spirals. Only for a few of the nearest spirals has it been possible to obtain rotation curves extending far out by observing individual HII regions. The analysis of the rotation of M31, based on observations of the emission regions (Rubin and Ford, 1970) made possible by the development of the Carnegie image tube, still represents the most detailed spectroscopic study of an external galaxy. Neutral hydrogen observations

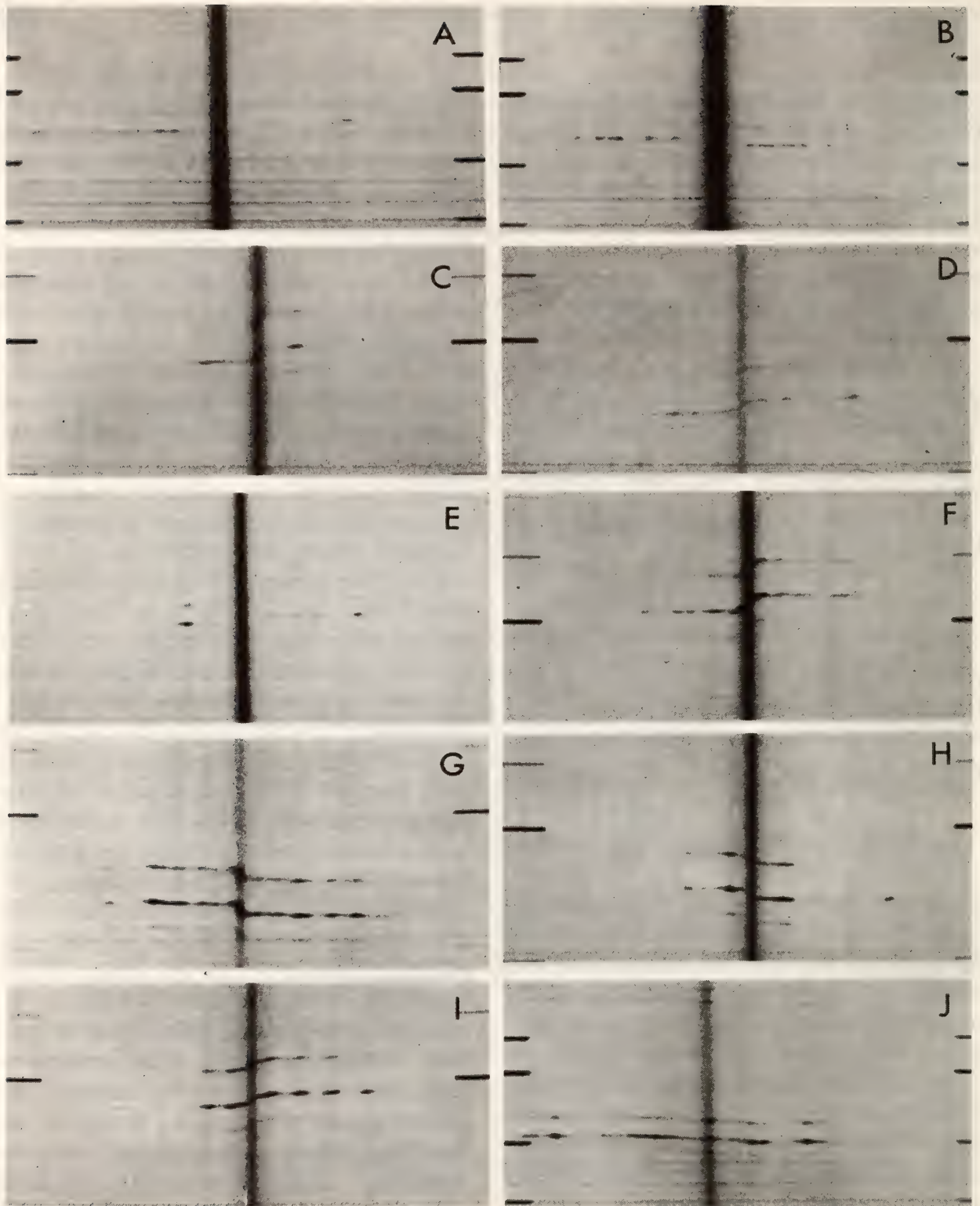


Fig. 16. $H\alpha$ region from high-dispersion major axis spectra for galaxies of a variety of Hubble types, taken with the 4-m RC spectrograph plus Carnegie image tube plus preflashed IIIa-J plate. Plates are (*) H_2 -treated, 25 \AA mm^{-1} , KPNO, or (†) N_2 -baked, 52 \AA mm^{-1} , CTIO. For all spectra, scale perpendicular to the dispersion is $24'' \text{ mm}^{-1}$, and transfer optics are $f/2$. (A) †NGC 3700, Sab-Sb, exp. 150 min. (B) †NGC 3223, Sb, exp. 139 min. (C) *NGC 2590, Sb, exp. 120 min. (D) *NGC 1620, Sbc, exp. 129 min. (E) †NGC 3145, Sbc I, exp. 90 min. (F) *NGC 801, Sbc-Sc, exp. 150 min. (G) *NGC 7541, Sbc-Sc, exp. 114 min. (H) *NGC 7664, Sbc-Sc, exp. 119 min. (I) *NGC 2998, Sc I, exp. 200 min. (J) †NGC 3672, Sc I-II, exp. 120 min. On each spectrum, $H\alpha$ is strongest emission line; $[NII] \lambda 6583$ is at longer λ (up on print). Vertical stripe is continuum from stars in nucleus. Linear extent of spectra varies from a radius of $r = 17.4 \text{ kpc}$ (NGC 2590) to $r = 49 \text{ kpc}$ (NGC 801). Note that velocity is often not constant across emission regions (spiral features) but is lower at inner edge and higher at outer edge, especially apparent in NGC 2998.

have revealed integral properties of gas-rich systems (Roberts, 1975) but with limited spatial resolution. Authors of statistical studies (Holmberg, 1964; Brosche, 1973; Nordsieck, 1973; Roberts, 1975) have struggled with inhomogeneous data and lack of velocities well beyond the "turnover point" in rotation curves.

Available optical instrumentation now permits the detection of emission extending almost across the entire optical disk in early- and late-type spirals. Therefore, we have initiated a program to obtain spectra of spiral galaxies at high velocity resolution and high spatial resolution, to study their rotational properties and masses as a function of Hubble type. Although the program is still in its early stages, the initial results are of great interest. We now have rotational velocities for 10 spirals, Sa through Sc, galaxies of high intrinsic luminosity. The galaxies were chosen with extreme care: to have angular diameters near $3'$ or $4'$ to match the KPNO and CTIO spectrograph slit lengths, to be of high inclination so that uncertainties in inclinations produce little effect on rotational velocities and hence masses, to be of high luminosity as indicated by the widths of their 21-cm profiles (if available), and to have large linear diameters. Three of the galaxies, NGC 3672, NGC 4378, and NGC 7217, have been discussed separately (NGC 3672, Rubin *et al.*, 1977; NGC 4378, Rubin *et al.*, 1978; NGC 7217, Peterson *et al.*, 1978). For all galaxies, distances are determined from the corrected velocities, and we adopt $H = 50 \text{ km s}^{-1} \text{ Mpc}^{-1}$ throughout.

Optical spectra were obtained with the Kitt Peak and Cerro Tololo 4-m spectrographs plus Carnegie image tube, usually at 25 \AA mm^{-1} . Errors in the rotational velocities (measuring errors plus projection uncertainties), are generally less than $\pm 8 \text{ km s}^{-1}$ per point. Reproductions of 10 spectra arranged by HT are shown in Fig. 16. In general, the

emission is measured over 80% of the optical disk. Many striking features can be observed directly from the spectra: (1) *All rotation curves are nearly flat*, with only a slight rise or fall following the initial steep gradient. (2) Secondary velocity undulations occur at positions of spiral features. Rotational velocities are $\sim 20 \text{ km s}^{-1}$ lower on the inner edges of the arms than on the outer edges. This is especially noticeable in NGC 2998, whose velocities are plotted in Fig. 17. (3) The emission across the nucleus is generally strong, and generally exhibits a large velocity gradient, which often continues several kiloparsecs beyond the nucleus. There follows a region of weaker emission with a shallow velocity minimum, beyond which the emission increases in intensity and the velocity rises as the first spiral feature is encountered. (4) Star formation is proceeding vigorously over great distances in a single galaxy. In NGC 801, ionized gas, the signature of young stars and gas, extends to a *radius* of 49 kpc. (5) Nuclear spectra come in a wide variety; emission lines can be narrow with a large velocity gradient (NGC 801), or broad with the entire gradient within the nucleus (NGC 7541). We discuss a few of these results in greater detail.

Several galaxies clearly exhibit an increase in circular velocity across a spiral arm. This is shown, for example, in the spectrum of NGC 2998 (Fig. 16), where the discontinuous emission segments (i.e., regions of spiral features) are not horizontal but slope toward higher velocity at larger nuclear distances. These velocity gradients are shown also in the plot of the rotational velocities in NGC 2998 (Fig. 17). Also of interest is the rather neat symmetry between velocities of the NE and the SW major axis. A remarkable degree of symmetry is seen in all rotation curves.

An increase in rotational velocity across each spiral arm due to streaming motions is a major prediction of the

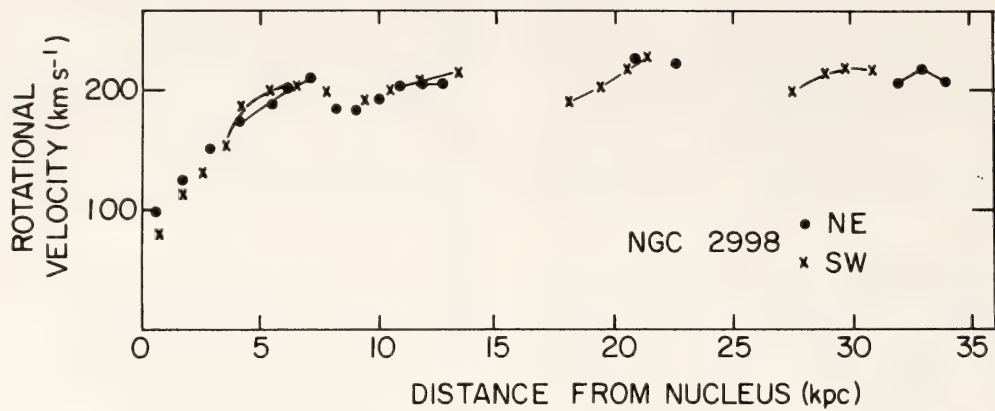


Fig. 17. Rotational velocities in NGC 2998, as a function of distance from center. Velocities for strongest emission regions are connected with lines. Note fairly good velocity agreement between velocities from NE and SW major axes, and positive velocity gradient across each arm.

density-wave theory for spiral structure. Evidence for such an effect from stellar velocities in our Galaxy has been reported (Humphreys, 1976). Any mass concentration from spiral arms will decrease circular velocities on the inner edge of a spiral arm (the presence of mass in the arm will weaken the gravitational force of the interior mass) and increase circular velocities on the outer edge (a stronger interior mass will be felt). However, a velocity gradient $\Delta V \sim 20 \text{ km s}^{-1}$ across an arm, as seen in NGC 2998, requires a density increase by a factor of two in the arms, with little mass between the arms. Such a mass enhancement across an arm does not seem supported by observation, so a simple gravitational explanation of the velocity pattern is not satisfactory. Minimally, streaming motions along the arms appear necessary; such motions arise naturally in the density-wave model.

Typical rotation curves are plotted in Fig. 18; these have been smoothed to eliminate the undulations across the arms. Most notable is the general flatness of the curves. From these results we draw the major conclusion of this work: flat rotation curves are the rule, not the exception, at least for high-luminosity spiral galaxies. A significant fraction of the mass of galaxy is located at large nuclear distances. Roberts and his col-

laborators were the first to call attention to the flatness of rotation curves, based on 21-cm observations of large spirals. More recently, 21-cm observations by Krumm and Salpeter (1976, 1977) have supported this result. Our present sample represents the first optical set for which rotation curves at large nuclear distance are available, and the flatness of the rotation curves seems now well established. These results take on added importance in conjunction with the suggestion of Einasto *et al.* (1974) and Ostriker *et al.* (1974) that galaxies contain massive halos extending to large r . Such models imply that $M \propto r$, which in turn requires that rotational velocities do not fall for large r , just as observed. The observations presented here are thus a necessary but not sufficient condition for massive halos. Mass distributions either from disk models or from spherical models can adequately reproduce the observed velocities, as long as the mass increases linearly with increasing nuclear distance. The choice between spherical or disk models is not constrained by these observations.

For these high-luminosity galaxies, there is a pronounced increase in the maximum circular velocity, V_{max} , with earlier Hubble types (Fig. 19). This correlation has interesting consequences for the mass distribution within these

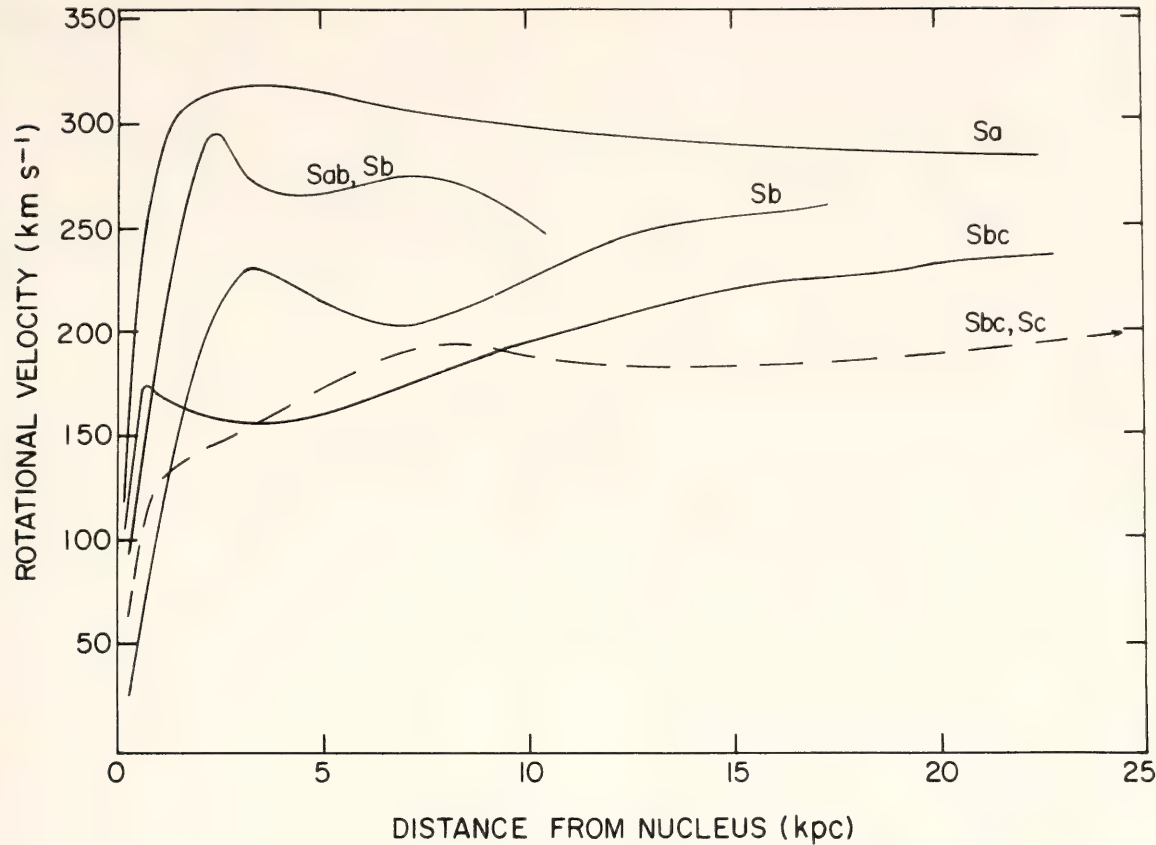


Fig. 18. Rotational velocities for five galaxies, as a function of distance from nucleus. Curves have been smoothed to remove velocity undulations across arms and small differences between major axis velocities on each side of nucleus. Early-type galaxies consistently have higher peak velocities than later types.

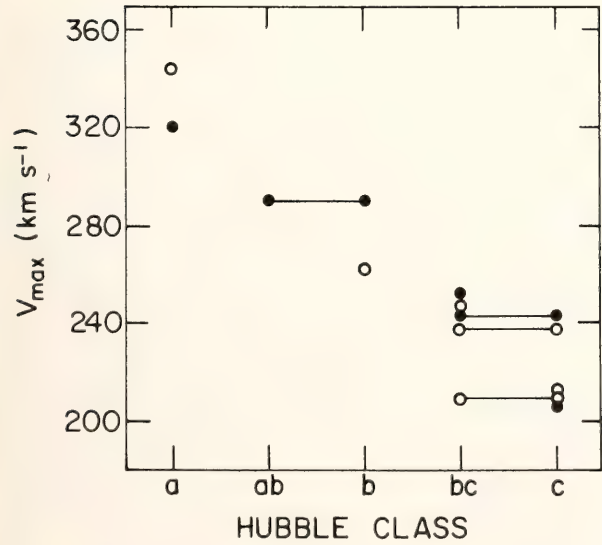


Fig. 19. Maximum rotational velocity in the plane of the galaxy, as a function of Hubble type. Galaxies with two classifications are plotted twice with a connecting line. Open circles denote values of V_{max} which come from the last measured velocity (i.e., rising rotation curves).

galaxies. A flat rotation curve implies that the mass within concentric shells, each of radius Δr , is the same for each ring. The mass contained out to radius r is proportional to $V^2 r$; for constant V , then $M \propto r$. We show in Fig. 20 the integral mass as a function of radius, calculated from thin disk galaxy models. Because total mass varies both with r and V^2 , and because V^2 is correlated with Hubble type (Fig. 20), total mass is a function both of type and of radius. While early-type galaxies have a steeper mass gradient dM/dr (Fig. 20), large late-type galaxies (NGC 801) will have larger total masses than small early types (NGC 4378). For thin-disk models, the surface mass density varies systematically along the Hubble sequence. This is a major result of our study to date.

By choosing to observe galaxies that

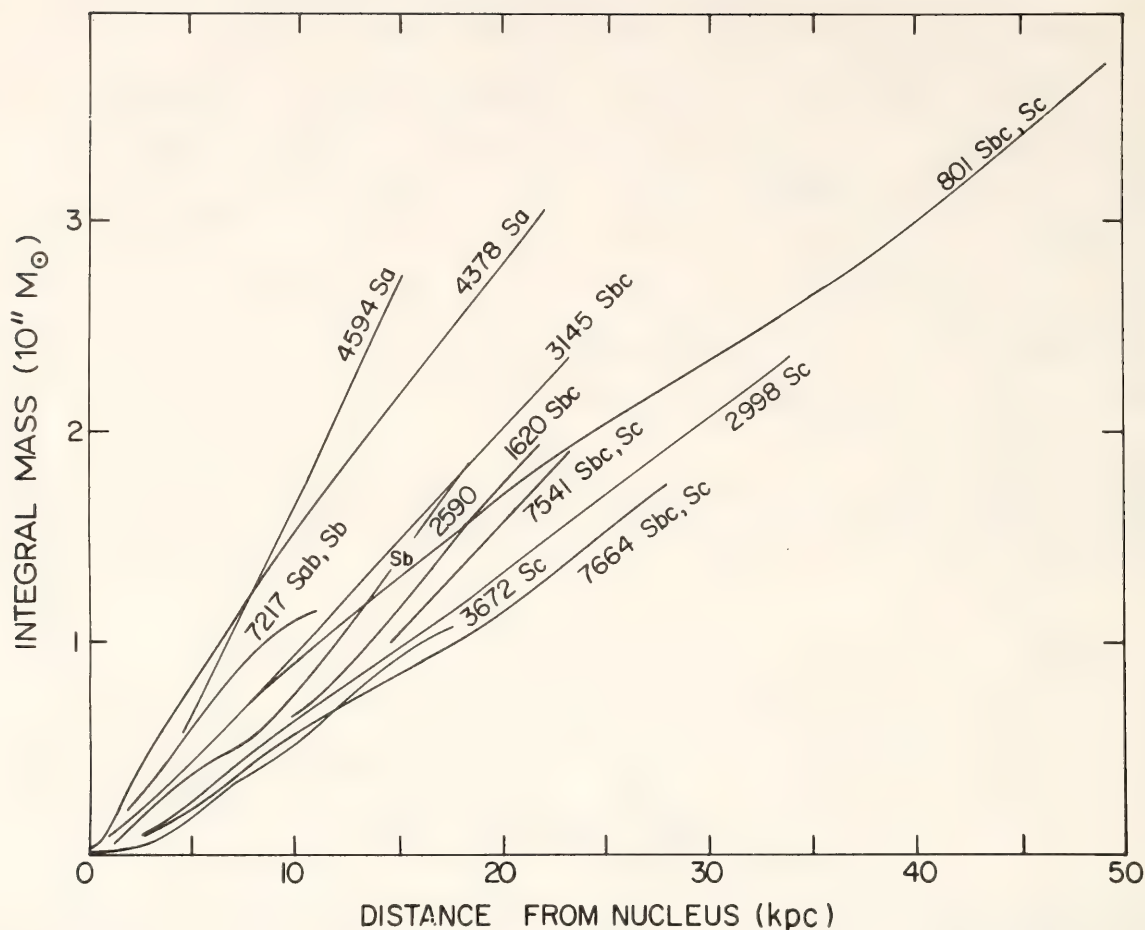


Fig. 20. Integral mass within disk of radius r , as a function of r , for 10 galaxies, Sa through Sc. Linear increase of mass with radius is a consequence of flat rotation curves. Mass gradient, dM/dr , is greater for early types, but total mass is a function of both V^2 and r . Surface mass density decreases systematically with Hubble type.

tend to have high inclinations, we have maximized the accuracy of the rotational velocities and masses. However, we have exacerbated the problems of determining face-on luminosities owing to the very uncertain form for the internal extinction corrections. Regardless of the form for this correction, however, the ratios of the mass to luminosity, M/L , are consistently small, near 5, for this sample of high-luminosity spirals.

There is a weak suggestion that M/L is higher for the earlier galaxies, a result in conflict with the widely quoted result of Roberts (1969) that M/L ratios are constant across the Hubble spiral sequence. For the present, we prefer to keep an open mind on the question of whether M/L varies across the Hubble spiral sequence.

The 21-cm integrated flux densities,

the hydrogen masses, and the hydrogen mass-to-total mass ratios are available for these galaxies from our 21-cm studies. HI constitutes 1% of the mass for our single Sa and Sab, but about 20% of the mass for the Sb and Sc galaxies. No correlation of V_{\max} with radius, or with luminosity, is observed (i.e., no Tully-Fisher, 1977, relation). Galaxies in our sample of the same type and the same V_{\max} have radii which differ by factors of as much as two, and luminosities which differ by factors of three. We presently have no explanation for this contrary result, except to suggest that the normal scatter in the V_{\max} -radius or V_{\max} -luminosity relation is very large in the Sa-Sc domain and may destroy the usefulness of V_{\max} as a luminosity indicator except in a broad statistical sense.

Additional details concerning these

rotation curves and the analysis are to be published elsewhere (Rubin *et al.*, 1978). We intend to extend the study to galaxies of lower luminosity for all Hubble types in order to determine how the properties of high-mass, high-luminosity galaxies differ from those of lower mass and luminosity.

References

- Brosche, P., The manifold of galaxies, Galaxies with known dynamical parameters, *Astron. Astrophys.*, **23**, 259, 1973.
- Burbidge, E. M., and G. R. Burbidge, The masses of galaxies, in *Galaxies and the Universe*, pp. 81–121, A. and M. Sandage, and J. Kristian, eds., Univ. Chicago Press, 1975.
- Einasto, J., A. Kaasik, and E. Saar, Dynamic evidence on massive coronas of galaxies, *Nature*, **250**, 309, 1974.
- Holmberg, E., A study of external galaxies, *Uppsala Astr. Obs. Medd.*, No. 148, 1964.
- Hubble, E., Extra-galactic nebulae, *Astrophys. J.*, **64**, 321, 1926.
- Humphreys, R., Noncircular motions in the Perseus spiral arm, *Astrophys. J.*, **206**, 114, 1976.
- Krumm, N., and E. E. Salpeter, Spatial distribution of neutral hydrogen in Virgo cluster galaxies of early type, *Astrophys. J. Lett.*, **208**, L7, 1976.
- Krumm, N., and E. E. Salpeter, Rotation curves, mass distribution and total masses of some spiral galaxies, *Astron. Astrophys.*, **56**, 465, 1977.
- Nordsieck, K. H., The angular momentum of spiral galaxies. II. Detailed models and correlations for 17 galaxies, *Astrophys. J.*, **184**, 735, 1973.
- Ostriker, J. P., P. J. E. Peebles, and A. Yahil, The size and mass of galaxies, and the mass of the universe, *Astrophys. J. Lett.*, **193**, L1, 1974.
- Peterson, C. J., V. C. Rubin, W. K. Ford, Jr., and M. S. Roberts, Extended rotation curves of high-luminosity spiral galaxies. III. The spiral galaxy NGC 7217, to appear *Astrophys. J.*, Dec., 1978.
- Roberts, M. S., Integral properties of spiral and irregular galaxies, *Astron. J.*, **74**, 859, 1969.
- Roberts, M. S., Radio observations of neutral hydrogen in galaxies, in *Galaxies and the Universe*, pp. 309–357 A. and M. Sandage, and J. Kristian, eds., Univ. Chicago Press, 1975.
- Roberts, M. S., The rotation curves of galaxies, *Comments on Astrophys.*, **VI**, 105, 1976.
- Rubin, V. C., and W. K. Ford, Jr., Rotation of the Andromeda nebula from a spectroscopic survey of emission regions, *Astrophys. J.*, **159**, 379, 1970.
- Rubin, V. C., W. K. Ford, Jr., K. M. Strom, S. E. Strom, and W. Romanishin, Extended rotation curves of high-luminosity spiral galaxies. II. The anemic Sa galaxy NGC 4378, *Astrophys. J.*, **224**, 782, 1978.
- Rubin, V. C., N. Thonnard, and W. K. Ford, Jr., Extended rotation curves of high-luminosity spiral galaxies. I. The angle between the rotation axis of the nucleus and the outer disk of NGC 3672, *Astrophys. J. Lett.*, **217**, L1, 1977.
- Rubin, V. C., W. K. Ford, Jr., and N. Thonnard, Extended rotation curves of high luminosity spiral galaxies. IV. Systematic dynamical properties, Sa→Sc, *Astrophys. J. Lett.*, **225**, L107, 1978.
- Tully, R. B., and J. R. Fisher, A new method of determining distances to galaxies, *Astron. Astrophys.*, **54**, 661, 1977.

NEUTRAL HYDROGEN OBSERVATIONS OF A LARGE SAMPLE OF SC AND SB GALAXIES

N. Thonnard, V. C. Rubin, W. K. Ford, Jr., and M. S. Roberts*

During the study of the isotropy of the Hubble expansion (Rubin *et al.*, 1976; *Year Book* 74, p. 113), it became clear to us that velocities and magnitudes for

* National Radio Astronomy Observatory, Charlottesville, Virginia.

a second sample of nearer galaxies would be valuable in order to examine the motion for the Local Group and to define our co-moving region. A search was made of the entire Palomar Atlas Sky Survey, to produce a Bright Spiral Catalogue consisting of well-defined spiral galaxies with magnitudes generally between 12 and 14. The final catalogue contains about 400 galaxies. As this sample was nearer than the previous ScI sample and the mean angular diameter of the galaxies was larger, photometric magnitudes appeared difficult to obtain. Instead, we decided to study this sample principally in the 21-cm neutral hydrogen line.

Three hundred galaxies from this sample were observed at 21 cm with the NRAO radiotelescopes. Galaxies with declinations $\geq -19^\circ$ were observed with the 300' telescope (10 arc min beam), and those with declination between -19° and -42° were observed with the 140' telescope (21 arc min beam). Also, a set of 20 galaxies, whose angular diameters ranged from 1.5 to 5.0 arc min (the diameter range of the sample), were observed both with the 300' and the 140' telescopes to tie together the integrated flux density scale. For those galaxies with known velocities (less than 25% of the sample), the receivers were tuned to the known velocity and observations were made in both polarizations at a resolution of 10 km s⁻¹ per channel. The remainder were observed at 20 km s⁻¹ per channel resolution, with the receiver back end divided into four sections, each covering a different 10-MHz bandwidth. Hence, it was possible to simultaneously observe from 300 km s⁻¹ to 7,500 km s⁻¹. As it is quite unlikely for an Sc or Sb galaxy brighter than 14th magnitude to have a velocity greater than 7,500 km s⁻¹, and for only a dwarf galaxy fainter than 12th magnitude to have a velocity less than 300 km s⁻¹, all galaxies of interest would be in the observed velocity range.

For 200 galaxies for which we have obtained good signal-to-noise ratio neutral hydrogen velocity profiles, we have determined integrated neutral hydrogen flux densities, velocity widths, and systemic velocities. Analysis of the integral properties of this large sample of Sc and Sb galaxies and comparisons with the previous ScI sample will be undertaken shortly.

The sample has already been a very useful tool in selecting individual galaxies for further detailed study. For example, an interesting subset of the 40 galaxies with velocity widths greater than 400 km s⁻¹ was chosen for detailed optical and resolved 21-cm study. The rotational properties from the optical study are discussed elsewhere in this report.

As there has been considerable recent interest in accurate velocities for large samples of galaxies, we are publishing elsewhere (Thonnard *et al.*, 1978), a list of 200 21-cm velocities for this sample of galaxies; most of the velocities are accurate to within ± 10 km s⁻¹. The analysis of the integral properties will be published separately.

References

- Rubin, V. C., N. Thonnard, W. K. Ford, Jr., and M. S. Roberts, Motion of the galaxy and the Local Group determined from the velocity anisotropy of distant ScI galaxies. II. The analysis for the motion, *Astron. J.*, **81**, 719, 1976.
Thonnard, N., V. C. Rubin, W. K. Ford, Jr., and M. S. Roberts, Radial velocities of spiral galaxies determined from 21-cm neutral hydrogen observations, submitted to *Astron. J.*, 1978.

THE DWARF GALAXY 1346-35

N. Thonnard, V. C. Rubin, and W. K. Ford, Jr.

In trying to understand how galaxies evolve, what their significant properties are, and what effect total mass and mass distribution have on their present rate of star formation, numerous approaches can

be taken. One approach, an example of which is reported elsewhere in this Report, is to study a sample of very massive galaxies to determine their dynamics, composition, and structural properties as a function of distance from the nucleus and as a function of galaxy type. The study of dwarf galaxies provides another approach. In some respects, the properties of dwarf magellanic irregular galaxies are similar to properties of disk regions of giant spiral galaxies such as the solar neighborhood in our own Galaxy. In addition, their space density is large, at least in the vicinity of large gal-

axies. Hence, dwarf galaxies can be found close enough to study with good spatial resolution.

The dwarf irregular galaxy at $13^{\text{h}}46^{\text{m}}.4$ and $-35^{\circ}49'$ was noticed by us while compiling a list of southern high-luminosity spiral galaxies. It is a very faint, low-surface-brightness object on the Palomar Observatory Sky Survey prints. 1346-35 is located on the supergalactic plane and along the projected position of the Magellanic Stream. The only catalogue entry we can find for it is in the 5th volume of Vorontsov-Velyaminov catalogue. Because of the possibility that

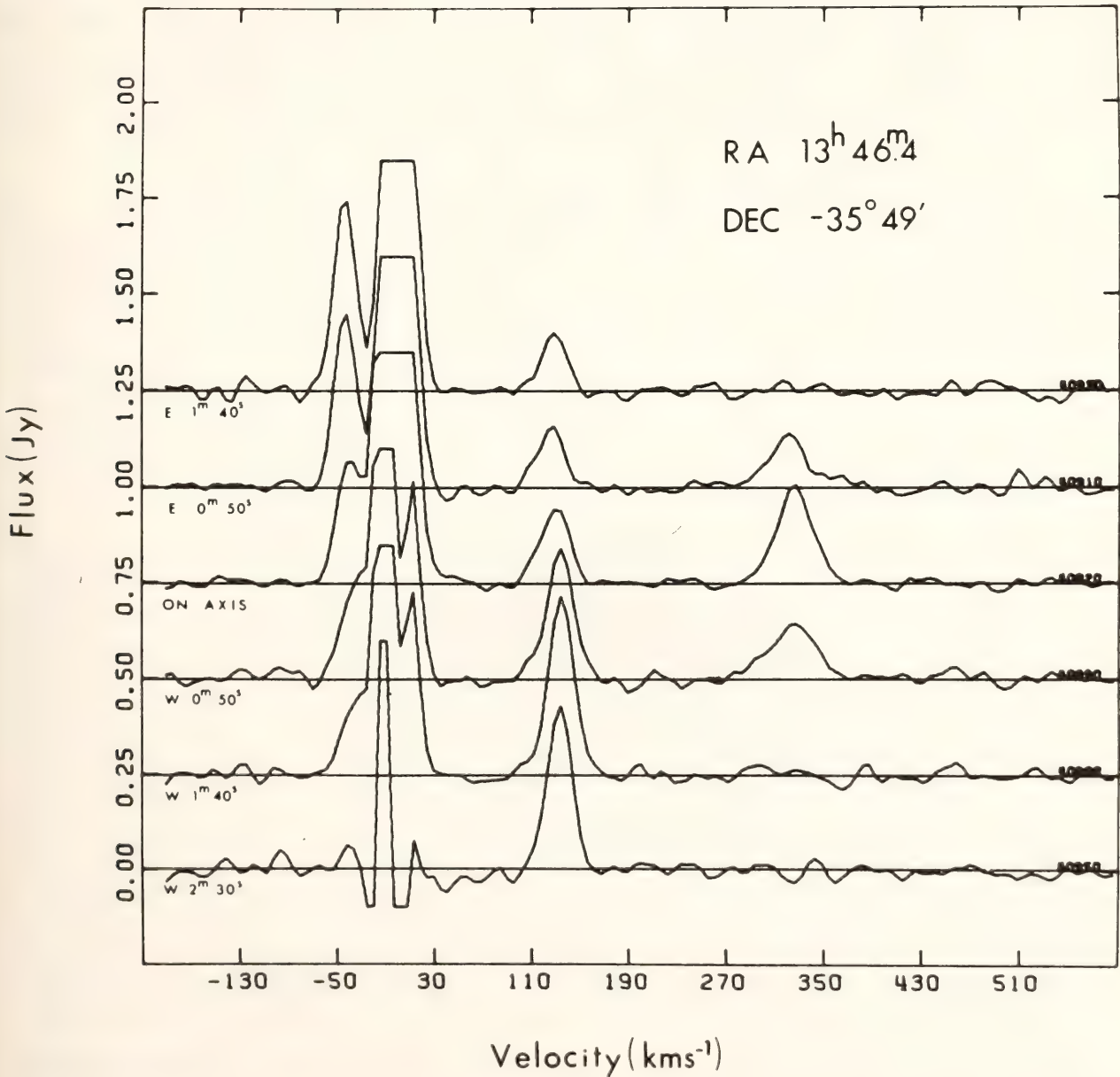


Fig. 21. Neutral hydrogen velocity profiles in the direction of 1346-35.

it is an extremely low mass system, we decided to observe it optically and at 21 cm.

Observations were made with the NRAO 140' radiotelescope (22 arc min HPBW) at the 21-cm neutral hydrogen line. Figure 21 shows the velocity profiles for data taken at half-power beamwidth intervals in the east-west direction on 1346-35. The signal at zero velocity is from HI in our own Galaxy; the signal at 130 km s^{-1} is a large high-velocity cloud discovered by Wannier *et al.* (1972); the signal at 330 km s^{-1} is from 1346-35. Note that there is no signal at the full beamwidth points. From the HPBW signals, we conclude that the HI size is not much larger than 5 arc min, which is the optical size. This is in marked contrast to other dwarf irregulars such as NGC 6822, IC 1613, and

WLM, whose neutral hydrogen diameter is much larger than the optical image.

Figure 22 shows the appearance of the galaxy in the blue-wavelength region, from a plate taken by Barry Lasker at the CTIO 4-m prime focus. Note the numerous HII regions, the largest of which are indicated by the arrows. Very faint spiral structure can be seen in this print; on the ESO blue survey, which goes to considerably fainter surface brightness, the galaxy looks quite axisymmetric, with faint spiral structure also visible. We estimate the van den Bergh luminosity classification as IV-V; the maximum diameter is 4.8 arc min.

Two spectra in the red-wavelength region were taken of 1346-35 with the CTIO 4-m RC spectrograph with a Carnegie image tube at 50 \AA/mm resolution. The position of the slit is shown in Fig.

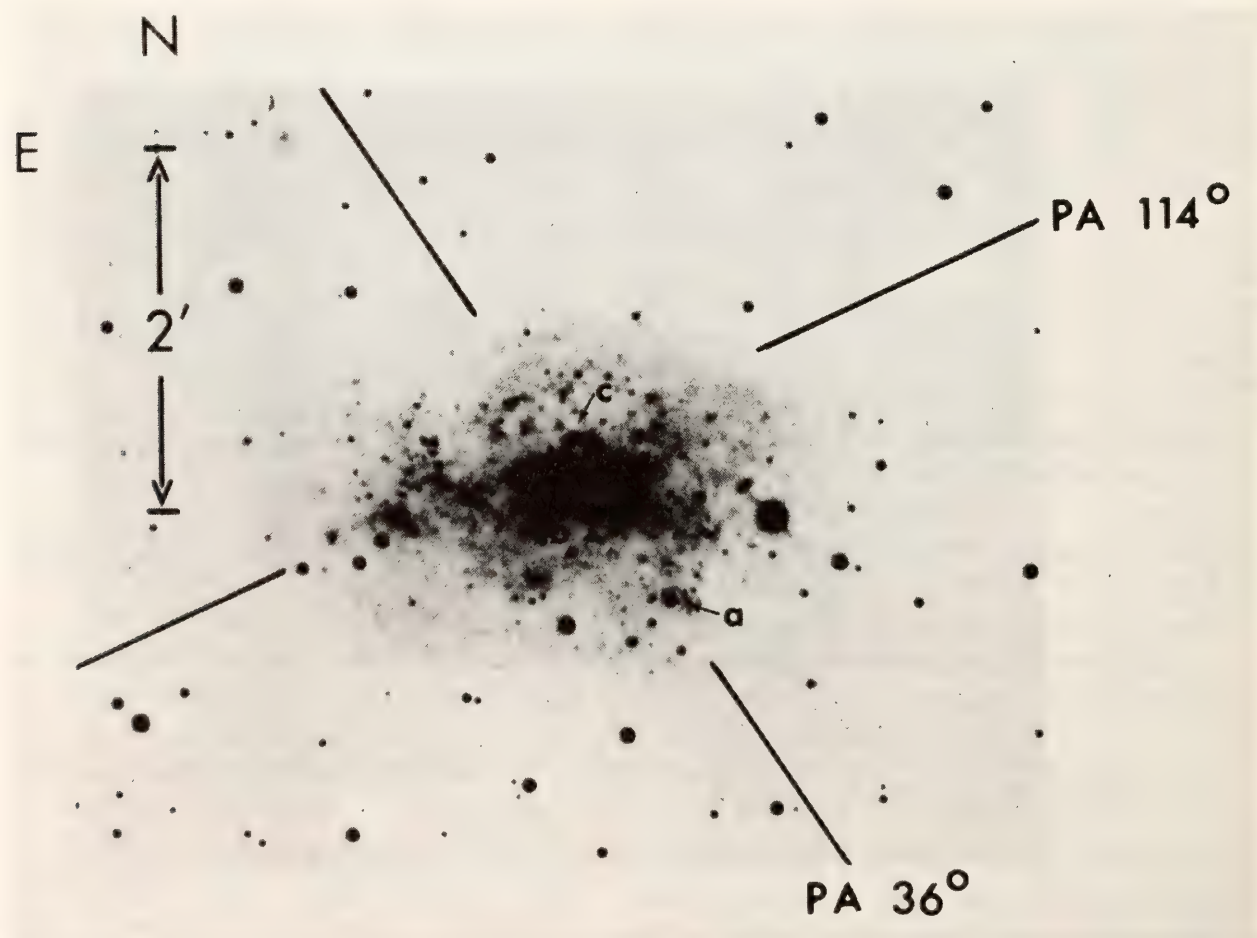


Fig. 22. The dwarf galaxy 1346-35 taken with the CTIO 4-m prime focus camera on N_2 -baked III a-J plate. The position angles of the two spectrograms are indicated, as well as three of the largest HII regions.

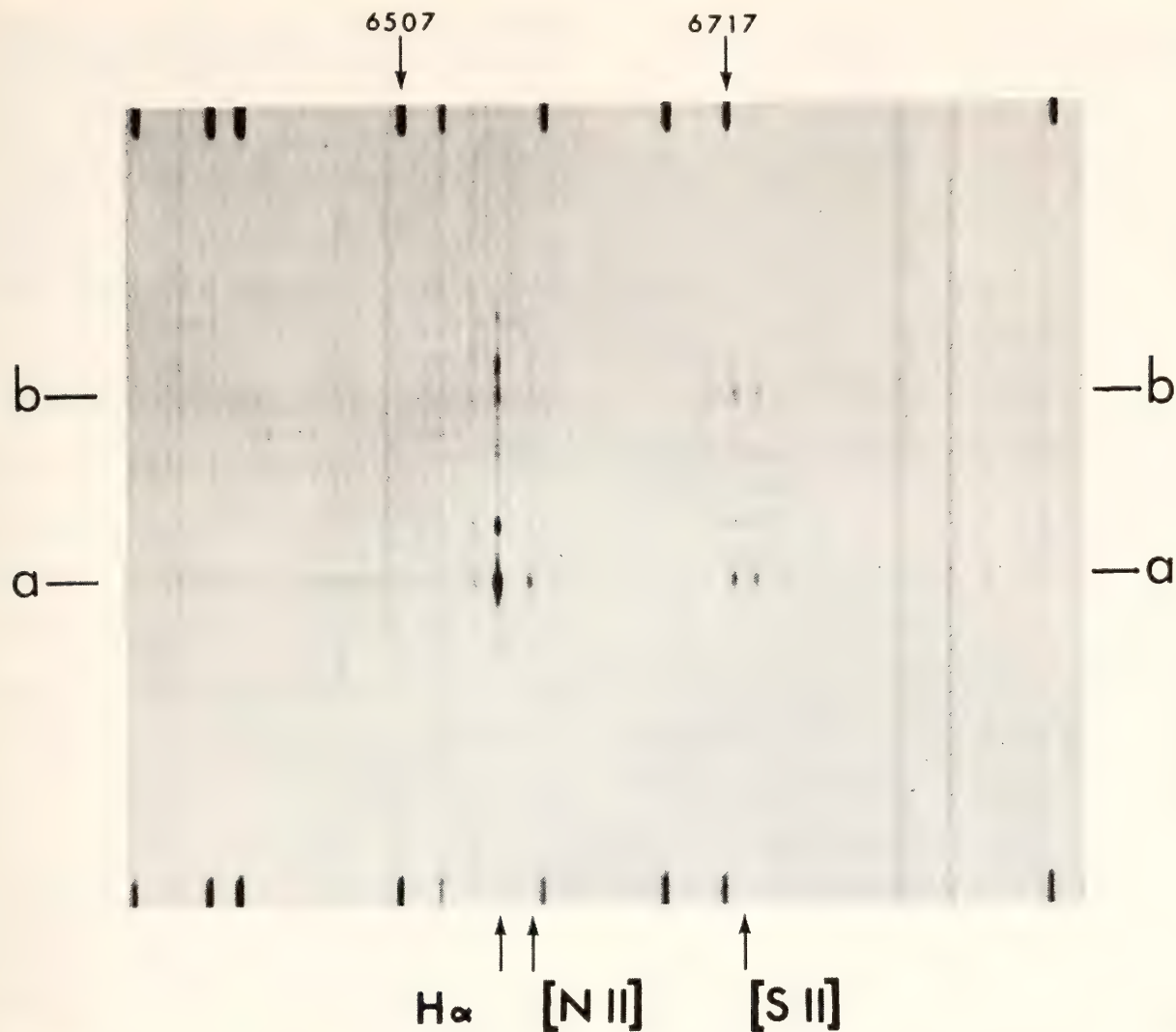


Fig. 23. Spectrum at 36° P.A. taken with the CTIO 4-m RC spectrograph with the Carnegie image tube. Two prominent HII regions are indicated by *a* and *b*.

22. A copy of the spectrum at 36° PA is shown in Fig. 23. Note that at knot *a* the forbidden sulfur lines [SII] are of about the same intensity as the forbidden nitrogen lines [NII], whereas at knot *b* the [SII] lines are brighter than the [NII]. Smith (1975) has shown that for late-type spiral galaxies, the ratio of [NII] to [SII] decreases with increasing distance from the nucleus. From microdensitometer tracings of the plates (C. K. Kumar, 1977), we obtain [NII]/[SII] line intensity ratios for knots *a* and *c* which resemble an ‘inner’ region of a spiral galaxy, and for knot *b* a ratio which resembles the outermost regions. From Fig. 22, though, note that knots *b* and *c* are near the center of 1346-35

while knot *a* is in the outer parts. Significant variations in star-formation properties must take place over a very small spatial scale.

The measured radial velocities for the H α , [NII], and [SII] lines all agree well. The optical velocity with respect to the sun is $319 \pm 8 \text{ km s}^{-1}$ with a slight gradient of $12 \text{ km s}^{-1}/\text{arc min}$ in position angle 36°. The measured H α velocities along the slit are shown in Fig. 24.

Combining the Sandage and Tammann (1974) calibration of linear HII-region size as a function of luminosity class with a luminosity class of IV–V for 1346-35, the measurements of the HII-region angular diameters on the blue plate and

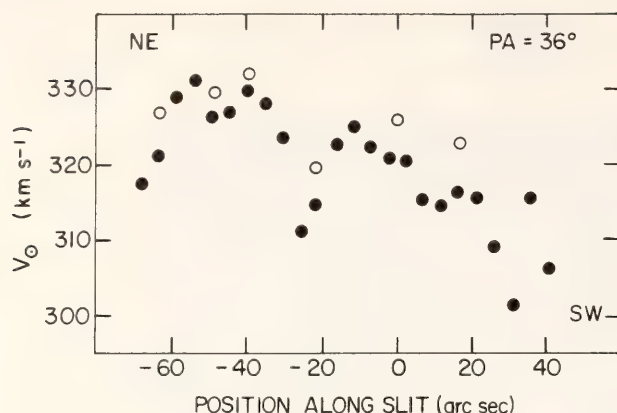


Fig. 24. Measured $H\alpha$ velocities at 36° P.A. The open circles are measurements of the central velocity of prominent knots; the closed dots are velocities of weaker emission.

also on a weak $H\alpha$ plate give a distance of 8.2 ± 0.5 Mpc. However, 1346-35 falls within the NGC 5128 group on the sky, and thus it is likely that it is a member of that group; then the distance is 4.0 Mpc (de Vaucouleurs, 1975). Using an upper limit of 8 Mpc and a lower limit of 4 Mpc for the distance to 1346-35, an apparent blue magnitude of $11^m.7$ (extrapolated from measurements by C. J. Peterson, 1978), a correction for galactic extinction of $0^m.2$, and a total indicated mass computed from the 21-cm profile width, we derive the properties shown in Table 5.

We summarize by noting that 1346-35 is an irregular galaxy, in some respects

similar to the Small Magellanic Cloud if it is a member of the NGC 5128 group, as seems likely. The total mass, hydrogen mass, fractional hydrogen content, and linear size all indicate a dwarf, luminosity class V galaxy. At the 8 Mpc distance, which is indicated by the HII-region sizes, the optical luminosity indicates a more luminous galaxy. In fact, the mass-to-luminosity ratio is near unity, which is low for any galaxy and indicates a very recent burst of star formation. The differences in line-intensity ratio indicate that stellar evolution has progressed at different rates in different parts of the galaxy, not in the regular fashion having the most evolved regions in the center, and that the debris of stellar evolution is not well mixed in the galaxy.

References

- de Vaucouleurs, G., *Nearby Groups of Galaxies, Stars and Stellar Systems, IX*, A. Sandage, M. Sandage, and J. Kristian, eds., Univ. of Chicago Press, p. 557, 1975.
- Kumar, C. K., private communication, 1977.
- Peterson, C. J., private communication, 1978.
- Sandage, A., and G. A. Tammann, Steps towards the Hubble. I, Calibration of

TABLE 5. Observed and Derived Properties for 1346-35

Distance Independent		Distance Dependent		
			$D = 4$ Mpc	$D = 8$ Mpc
V_H (opt)	$319 \pm 8 \text{ km s}^{-1}$	Major Axis	5.6 kpc	11.2 kpc
V_H (21 cm)	$327 \pm 4 \text{ km s}^{-1}$	M_{HI}/M_\odot	1.0×10^8	4.0×10^8
V_0	135 km s^{-1}	M_T/M_\odot	6.7×10^8	1.3×10^9
$\Delta V_{0.25}$ (21 cm)	45 km s^{-1}	M_{HI}/M_T	0.15	0.31
Angular size	$4'.8 \times 3'.5$	M_\odot	-16.5	-18.0
m_{pgC}	$11^m.5 \begin{smallmatrix} +0.3 \\ -0.5 \end{smallmatrix}$	L_\odot	5.6×10^8	2.2×10^9
$\int SdV$	$26.4 \text{ JyK m s}^{-1}$	M_\odot/L_\odot	1.2	0.6
M_{HI}/L_\odot	0.18			

the linear sizes of extragalactic HII regions, *Astrophys. J.*, 190, 525, 1974.

Smith, H. E., Spectrophotometric observation of ionized hydrogen regions in nearby spiral and irregular galaxies, *Astrophys. J.*, 199, 591, 1975.

Wannier, P., G. T. Wrixon, and R. W. Wilson, A survey of positive velocity neutral hydrogen above the galactic plane between $l = 252^\circ$ and $l = 322^\circ$, *Astron. and Astrophys.*, 18, 224, 1972.

NGC 5506, AN X-RAY SEYFERT GALAXY

V. C. Rubin

NGC 5506 is a dust-riddled, almost edge-on late-type galaxy, which has recently been identified as an x-ray galaxy (Ricker *et al.*, 1977). Nuclear spectra by Wilson *et al.* (1976) had shown strong emission lines, including lines of high excitation ([Fe VII]). All lines were characterized as "narrow," that is, ~ 400 km s $^{-1}$ (FWHM). NGC 5506 thus became a galaxy of some significance, for it was the first narrow-line galaxy to be identified as an x-ray source.

A spectrum of NGC 5506 was obtained with the 4-m CTIO RC spectrograph and Carnegie (RCA) image tube, in order to study the dynamical properties of this unique object. Unexpectedly, the spectrum exhibited very broad emission lines (≥ 1500 km s $^{-1}$ total width for both the permitted and forbidden lines; Figs. 25, 26). Thus, NGC 5506 is a Seyfert 2 galaxy, with the spectral features and the semistellar nucleus characteristic of this class. A narrow-emission-line x-ray galaxy has yet to be identified.

It is worthwhile to recall that for the past 20 years radio observations have identified galaxies of exceptional interest by their radio emission—galaxies which optical observers have then studied. Now, x-ray positions have just reached the accuracy where similar identifications of interesting objects will take place.

In the nucleus of a Seyfert galaxy, energetic processes, not yet understood, accelerate discrete gas clouds to velocities of up to thousands of kilometers per second. This nuclear activity is restricted to a small volume with radius typically a few hundred parsecs. At present, the site and size of the x-ray source in NGC 5506 is not known. Resolution of x-ray telescopes is not sufficient to locate the source to better than a galaxy diameter generally, although x-ray observations of some galaxies (NGC 1275, the Seyfert 2 galaxy in the Perseus cluster, for example) can be described by composite point-plus-extended-source models. When it is eventually known how the site of the x-ray source in a Seyfert galaxy is related to the nucleus, then the interaction between the optical and the x-ray phenomenon may become clearer. Ultimately, observations over a broad spectral range, encompassing radio, x-ray, optical, and infrared observations will help specify the source of the Seyfert phenomenon.

The dynamics and mass of NGC 5506 have also been studied from our spectra. Velocities increase to $V \sim 125$ km s $^{-1}$ at $r = 1$ kpc, then remain constant to $r = 6$ kpc, where they again rise to $V \sim 200$ km s $^{-1}$ at 8 kpc. The mass out to 8 kpc is $M_{8.3} = 4 \times 10^{10} M_\odot$. If the rotation curve remains flat to the de Vaucouleurs' radius, $r = 15$ kpc, then $M_{15} = 1 \times 10^{11} M_\odot$. This mass is typical of Seyfert galaxies.

References

- Ricker, G. R., R. G. Dower, J. G. Jernigan, R. E. Doxsey, H. V. Bradt, and H. W. Schnopper, NGC 5506: an X-ray galaxy, preprint, 1977.
- Wilson, A. S., M. V. Penston, R. A. E. Fosbury, and A. Boksenberg, The optical spectrum and morphology of the probable X-ray galaxy NGC 5506, *Mon. Notic. Roy. Astron. Soc.*, 177, 673, 1976.

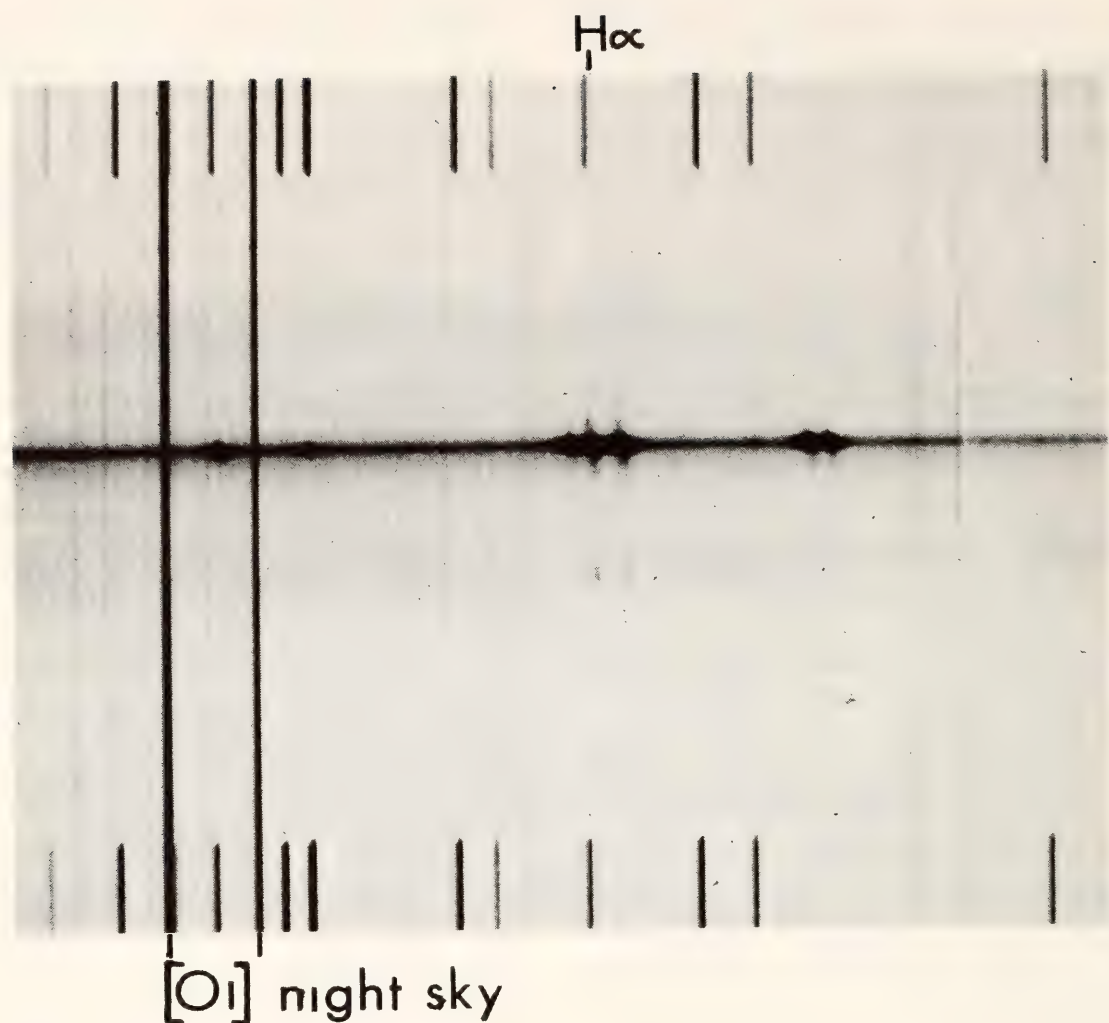


Fig. 25. CTIO 4-m spectrogram of NGC 5506, showing broad nuclear emission lines near $H\alpha$. Lines totally crossing the spectra are emission from the night sky, with $[OI] \lambda\lambda 6300$ and $\lambda 6364$ especially strong. Prominent galaxy lines include $[OI] \lambda\lambda 6300, 6364$, $[NII] \lambda 6548$, $H\alpha$, $[NII] \lambda 6583$, and $[SII] \lambda\lambda 6717, 6731$. Off the nucleus, narrow $H\alpha$, $[NIII]$, and $[SII]$ are seen. Original dispersion 50 \AA mm^{-1} , Carnegie (RCA) C33063 image tube + N_2 -baked + preflashed IIIa-J emulsion, exposure 149 min.

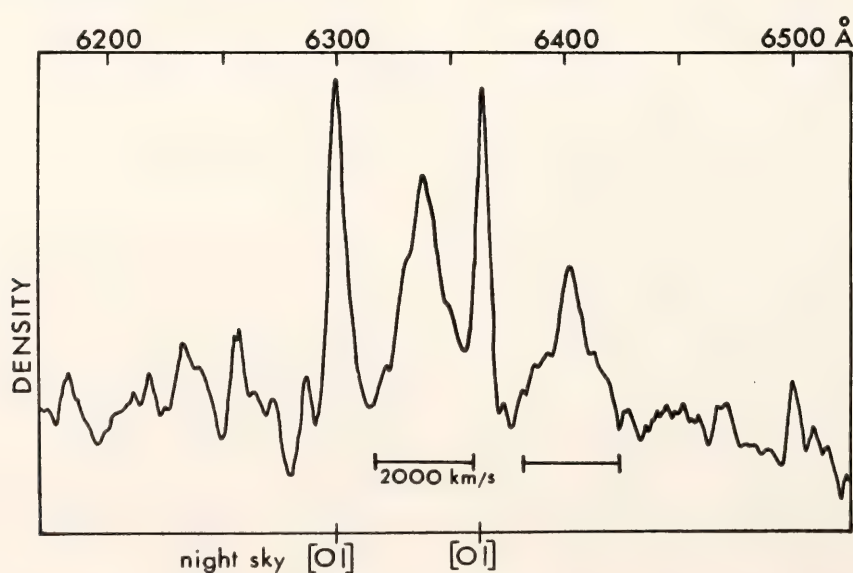


Fig. 26. Densitometer tracing (arbitrary scale) of $[OI]$ region of spectrum, NGC 5506. The night sky lines are more intense than the galaxy lines; the galaxy lines, displaced to the red, are significantly broader.

BACKGROUND FLUCTUATIONS

S. J. Goldstein, Jr.*, K. C. Turner,
and R. T. Rood*

The nature of the most remote, and hence the earliest, parts of the universe we can observe is a topic that has always fascinated humankind. The observations here described were undertaken to push to present-day limits our knowledge of the distribution of radio sources in those very distant times and places where they first could form. In order to do this, two regions were chosen, selected so as to be as free as possible of bright, and hence presumably nearby, radio sources (see Goldstein *et al.*, 1976). These fields, each 1° square, were observed with the NRAO Greenbank interferometer using eight different baselines, for a total integration time of some 10 days. A modeling procedure was then used to remove the effects of sources

brighter than 8 mJy ($= 8 \times 10^{-29}$ watts/m²Hz). Table 6 contains a list of sources so removed from the two fields, and the source positions are illustrated in Figs. 27 and 28. Because the system sensitivity varied

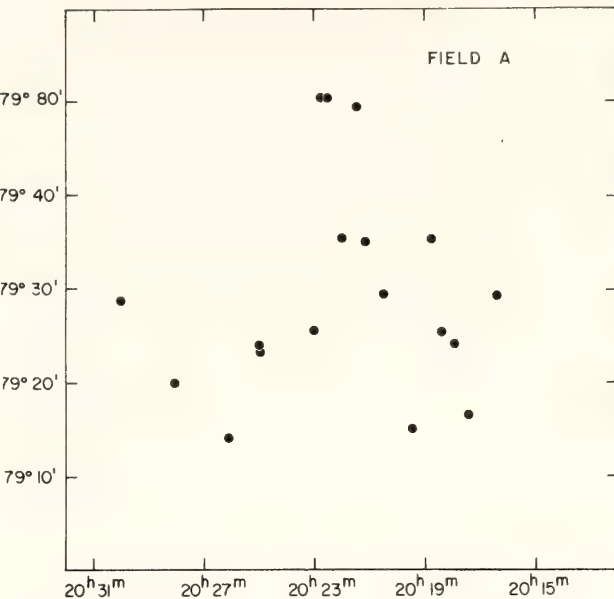


Fig. 27. Sources brighter than 8 mJy in Field A.

TABLE 6. Sources Brighter than 8 mJy Removed from Observed Fields

A Field Sources			B Field Sources		
Right Ascension*	Declination*	Flux (mJy)	Right Ascension*	Declination*	Flux (mJy)
1 20 15 43	79 29 39	26	1 21 23 5	78 43 19	25
2 20 17 47	79 17 1	40	2 21 23 15	78 10 23	46
3 20 18 14	79 24 0	21	3 21 23 22	78 11 21	48
4 20 18 20	79 25 49	13	4 21 26 35	78 13 17	16
5 20 18 27	79 35 19	11	5 21 26 48	78 39 22	11
6 20 19 14	79 15 1	15	6 21 35 22	78 39 3	85
7 20 20 34	79 29 49	8			
8 20 21 19	79 35 16	11			
9 20 21 38	79 49 8	17			
10 20 21 58	79 36 9	14			
11 20 22 31	79 51 25	45			
12 20 22 42	79 51 29	40			
13 20 23 8	79 26 4	14			
14 20 25 3	79 23 13	11			
15 20 25 3	79 23 30	17			
16 20 26 19	79 13 50	39			
17 20 28 12	79 20 1	22			
18 20 30 2	79 27 59	32			

* Right ascension and declination, 1950.0.

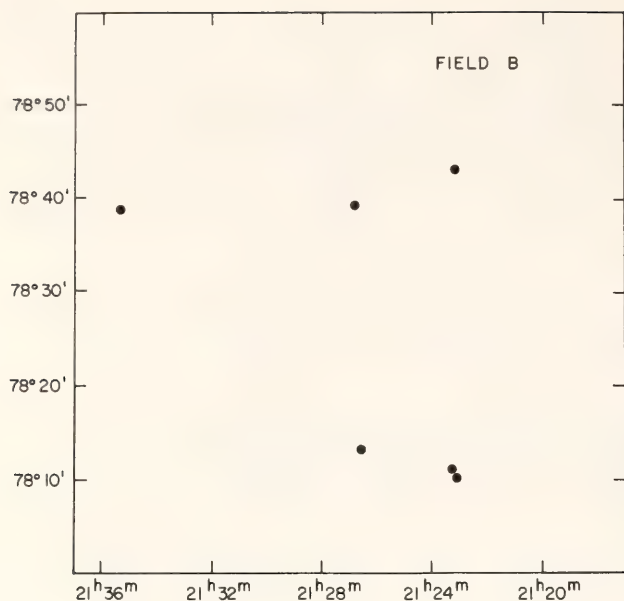


Fig. 28. Sources brighter than 8 mJy in Field B.

with distance from the center of the beam owing to both primary beam shape and delay resolutions, we expect the intensity fluctuations in the map cells due to sources too distant to see individually to also decrease as we move toward the edge of the field. This is the basis for our measurements. Figure 29 shows the relative sensitivity contours over our field of view. The RMS fluctuations were separately determined over the central source and over the area between the border of the diagram and the next inner square. This outer area was taken to represent the fluctuations due to system noise, and the quadratic difference between this and the central-square RMS was taken as being due to distant

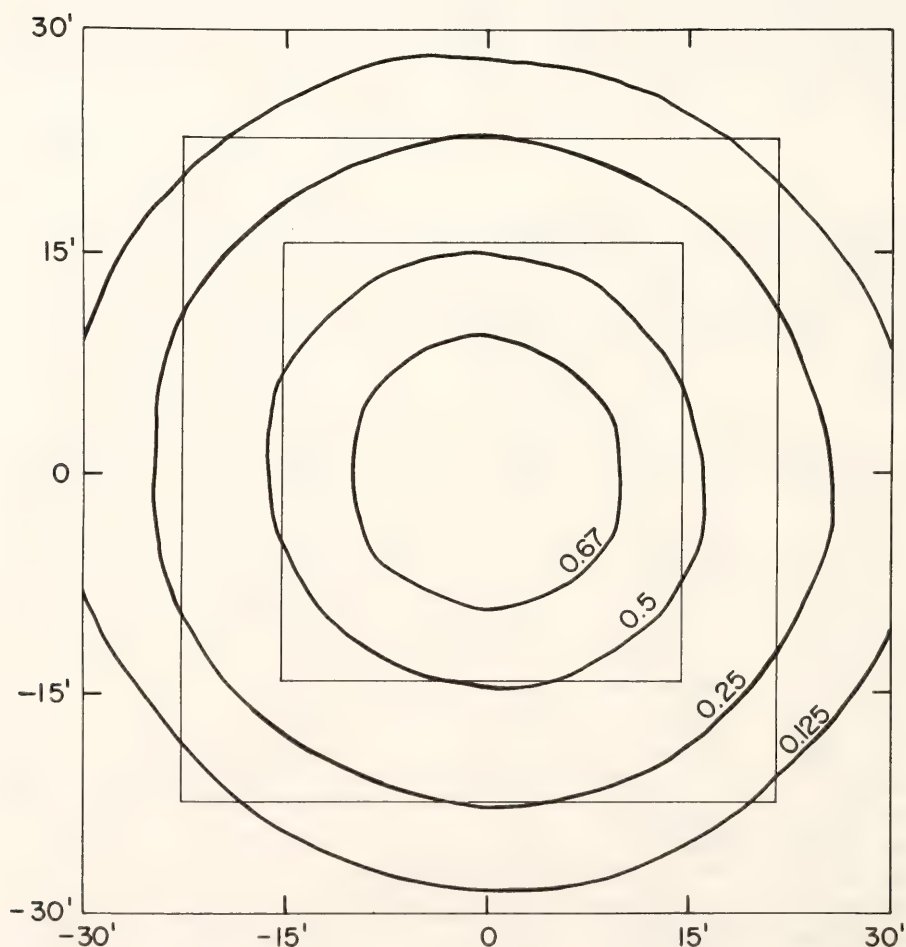


Fig. 29. Relative sensitivity contours over the field of view. The squares are the outer border of the inner area and the inner border of the outer area, as discussed in text.

sources. We obtained 2.7 ± 0.5 mJy and 1.0 ± 0.4 mJy for regions A and B, respectively, over a cell size of $3'$ square. When the cell size used in these calculations was decreased to $45''$ of arc, no excess fluctuations were found, to an accuracy of ± 0.5 mJy. Tests made on the data taken at different baselines indicate that this is basically a signal-to-noise difference in the data sets, and not an effect of source size.

A convenient way to visualize the meaning of these numbers is to introduce the concept of an effective "thickness of the universe." If the volume emissivity of space were characterized by a certain value, which we can try to estimate, how long a path length would be required to encounter enough sources to produce the observed fluctuations? This path length is then our experimental measure of the "thickness of the universe" given our initial model for volume emissivity. If we use Schmidt's estimate (Schmidt, 1972) for the local volume emissivity due to radio galaxies, normal galaxies, and quasars, and ignore cosmological effects and source evolution, which is certainly justified considering the crudeness of our model, we obtain thicknesses for our two fields which are of the order of the Hubble length. That is, our locally observed incidence of radio galaxies, QSO's, and other sources would have to characterize all space in order to produce the observed fluctuations. This is certainly unlikely in all current cosmological models. On the other hand, a volume emissivity obtained by averaging over space out to a redshift of $z = 1$ (Schmidt, 1972) gives a thickness only 10% of the Hubble radius; this seems more reasonable.

Using a volume emissivity estimated over our local supercluster requires a thickness an order of magnitude larger than the supercluster, so we may eliminate that as the source of our fluctuations.

We cannot, however, so simply elimi-

nate our own Galaxy as a source of this variation. Estimates of volume emissivity based on observations of the galactic disk (Baldwin, 1967) produce a thickness of a few kpc. There is no other evidence for galactic continuum structure in this small-scale size, however, and if this is what we are seeing, we must account for the lack of distant QSO's and radio galaxies we would otherwise expect to be there.

A further argument can be made from the anisotropy observed. These two fields are quite different in appearance. Field A contains 18 sources brighter than 8 mJy, while field B contains only six. These sources appear no different than any other extragalactic sources. Now the fluctuations observed in these two fields also stand in roughly this same ratio. It seems very unlikely that our galactic continuum patchiness has adjusted itself to conform to the distribution of very distant objects. It seems more probable that we are seeing here, for the first time, evidence for inhomogeneities on a very large scale in the universe. (We have convinced ourselves that our fluctuations are not artifacts of our source-removal procedure by shifting the model removed slightly in position and intensity from the best-fit parameters and observing that the measured fluctuations do not change appreciably.)

References

- Baldwin, J. E., The non-thermal radio emission from the Galaxy, *I. A. U. Symposium No. 31, Radio Astronomy and the Galactic System*, H. van Woerden, ed., pp. 337-354, Academic Press, London and New York, 1967.
- Goldstein, S. J., Jr., A. P. Marscher, and R. T. Rood, On the aggregate flux of weak point sources at 1404 MHz, *Astrophys. J.*, 210, 321-325, 1976.
- Schmidt, M., Statistical studies of the evolution of extragalactic radio sources, *Astrophys. J.*, 176, 273-287, 289-301, 303-314, 1972.

ACKNOWLEDGMENTS

We thank the Directors of the Cerro Tololo Inter-American Observatory, Kitt Peak National Observatory, Lowell Observatory, and National Radio Astronomy Observatory for observing time. We wish to thank the Office of Naval Research for the continuing use of the lead ballast used in the counterweights of our Derwood telescope (Contract No. 0014-71-C-0211).

INSTRUMENT DEVELOPMENT

A DIRECT IMAGE TUBE CAMERA

W. K. Ford, Jr.

In the course of our astronomical investigations we frequently need rather specialized photographs of galaxies, supernova remnants, planetary nebulae, and other subjects. These are required in preparing our observing programs in order to determine optimum locations and position angles for long-exposure spectroscopic observations. Also, photographs made in the light of a single spectral line isolated by narrow-band interference filters are useful in outlining, for example, the extent of regions in a particular state of ionization. In addition, direct plates of galaxies are often of value in deducing the major scientific objectives of the program. Because of the pressure of observing time and the lack of availability of suitable equipment, these observations are generally difficult to obtain during a limited observing session. For many years we observed at Lowell Observatory with an intensified camera that used one of the early Carnegie image tubes, but we had never upgraded its performance with one of the improved-version Carnegie tubes (RCA type C33063 EP3; see *Year Book* 74, p. 135). Because we have an increasing need for these direct photographs, we have built at DTM a new camera for photographic use at Lowell Observatory.

This camera consists of the image intensifier, permanent magnet, voltage divider, and transfer lens. It is mounted with a dark slide below the DTM guidebox and filter module, and it can be used on either the 42-inch or 72-inch telescope at Lowell Observatory. In collaboration with Dr. Arthur A. Hoag, we are exploring the use of film rather than plates for photometric purposes for recording the intensified images displayed by the image tube. On the basis of our experience thus far, the main problem with this direct camera is in obtaining an image tube with a uniform response in the red region of the spectrum. The blue response in these tubes is usually much more uniform than the red. Because a major advantage of these tubes is their extended red response, we intend to take advantage of both the blue and the red sensitivity for a variety of programs of astrophysical interest. More work will permit us to assess the importance of the nonuniform red response.

A CONTINUUM RECEIVER BACK END

*K. Turner, N. Thonnard, and E. Filloy**

The importance of all sky data can hardly be overemphasized when problems of either local or global scope are to be studied. While the necessity for whole-sky coverage in looking for the anisotropy of the 3-degree background radiation or in studying the Hubble flow is becoming increasingly accepted, this requirement for examining local phenomena may not be so apparent. When we consider, however, that nearby structures in our Galaxy can be expected to subtend large angles, it becomes obvious that data from both hemispheres will be required to obtain a complete picture.

With these facts in mind, astronomers at DTM, at the University of California

* Instituto Argentino de Radioastronomía, Villa Elisa, Argentina.

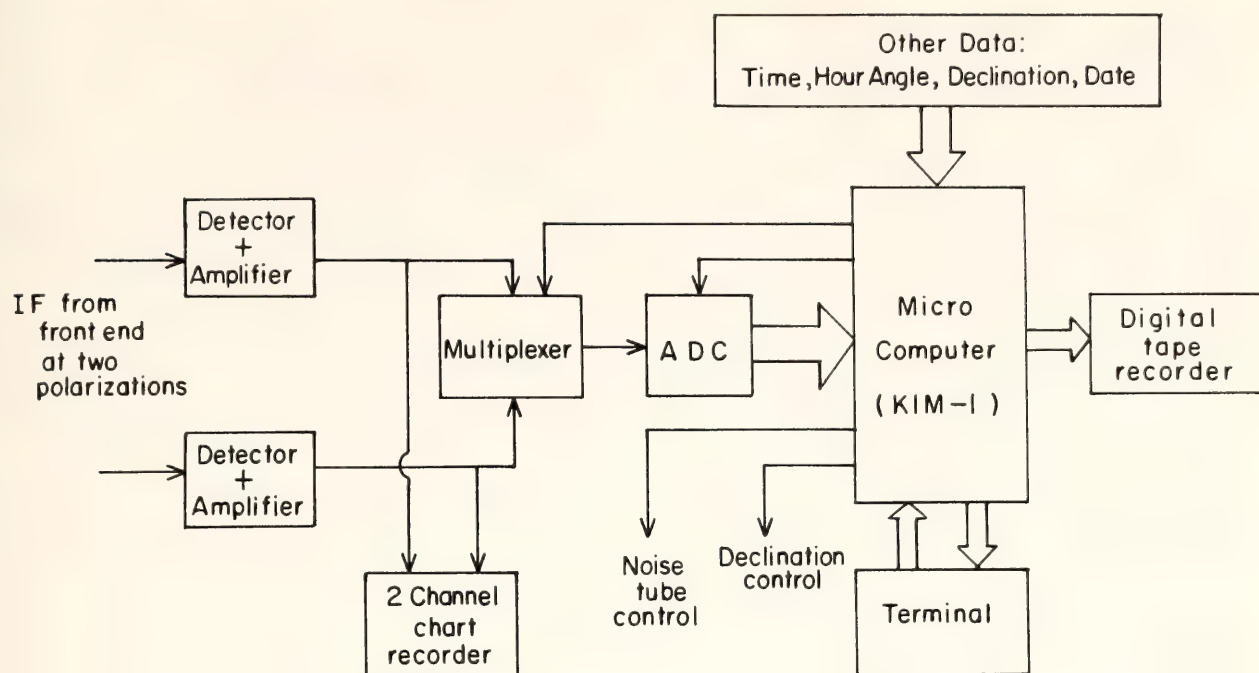


Fig. 30. Back end for the 820 MHz continuum survey receiver.

at Berkeley, and at the Instituto Argentino de Radioastronomía in Argentina, have planned to extend continuum observations at 820 MHz originally made by Berkhuijsen (1972) at Leiden, to cover the whole sky (*Year Book* 74, p. 144). DTM's contribution to the equipment required for this work consists in providing the back-end package. This is the apparatus that controls the receiver as a whole, and records and presents the data in such a way as to be ready for further analysis and reduction. In Fig. 30 is shown a block diagram of the system we have developed.

A set of programs, hand assembled and residing in 1 kilobyte of EPROM, controls the timing, noise-tube calibration, and data conversion for data acquisition, and periodically writes this data in blocks on an IBM-compatible 9-track magnetic tape, together with header information (date, observer codes, etc.).

The system has been designed for both reliability and flexibility, so it should continue to serve usefully in other projects after this one is concluded.

Reference

Berkhuijsen, E. M., A survey of continuum radiation at 820 MHz between declinations -7° and $+85^\circ$. I. Observation and reduction, *Astron. Astrophys. Suppl.*, 5, 263, 1972.

PROGRESS ON THE JOINT INTERNATIONAL PROJECT FOR 21-cm OBSERVATIONS IN THE SOUTHERN HEMISPHERE*

E. T. Ecklund, E. Filloy†, N. Thonnard, and K. C. Turner

Construction of the new 21-cm receiver for the IAR-CIW 100-foot antenna at Parque Pareyra, Argentina, is now approaching completion. Progress was accelerated by the six-month visit of Ing. Emilio Filloy of IAR. Ing. Filloy worked extensively in the simplification of the eventual interfacing of the receiver to the IAR equipment. He also became thoroughly involved in the design of the

* Supported in part by Grant OIP 75 19069 from the National Science Foundation.

† Instituto Argentino de Radioastronomía.

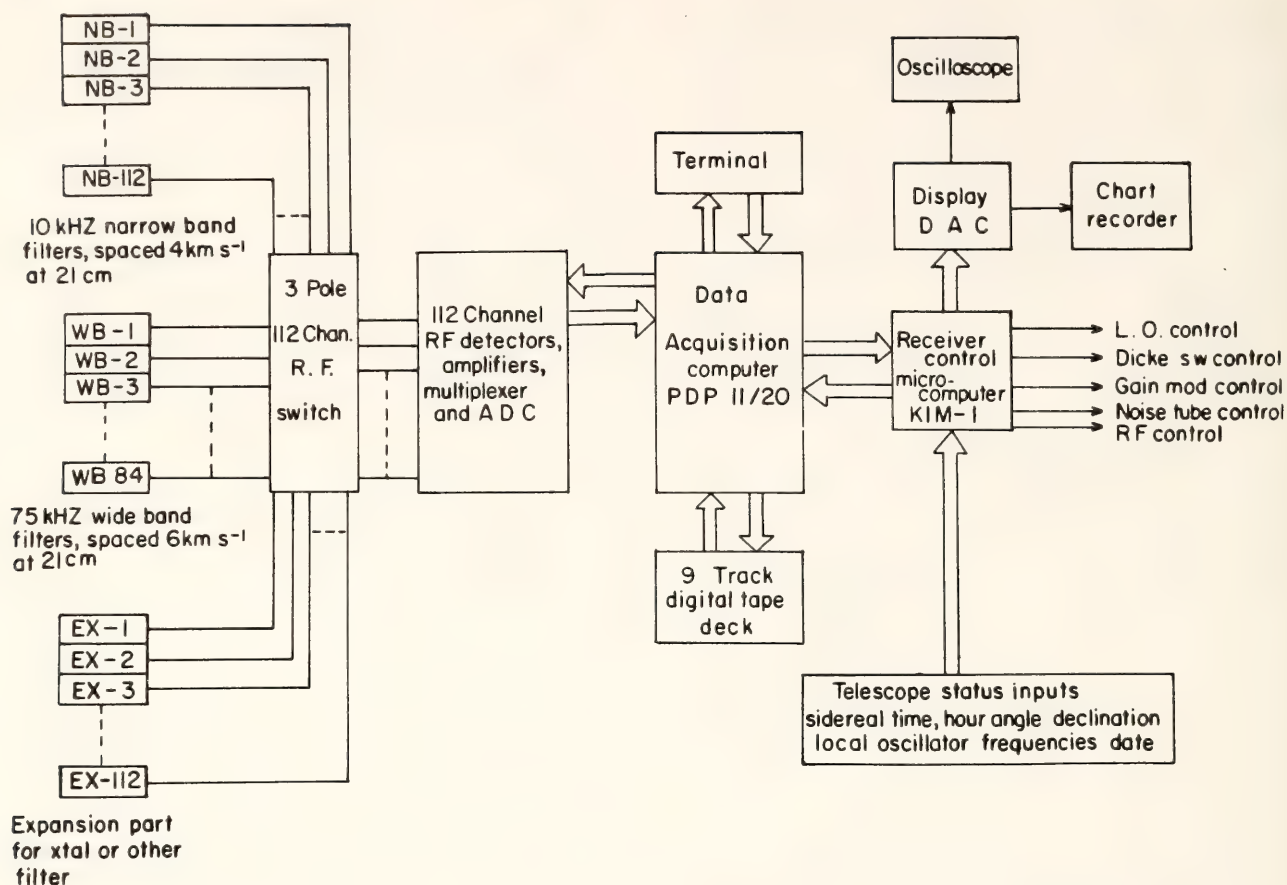


Fig. 31. Back end for the new 21-cm receiver.

digital equipment, which will use a microprocessor to interface the receiver and telescope with the data-acquisition computer.

The receiver front end is nearly complete. All the R.F. components have been mounted inside the front-end box and interconnected with rigid coaxial cable. Considerable attention was paid to the rigidity of the mounting, which will enhance receiver stability while at the same time keeping the components accessible for servicing. All the power

supplies for the front end are also complete. All components for the thermoelectric temperature controller are also finished, so that after mounting of the heat exchanger and the insulation, the front end will be ready for final testing.

The back end is now also essentially complete, awaiting only a small amount of interfacing between the receiver control microcomputer and the outside world and the development of a limited amount of software. A block diagram of the revised back end is shown in Fig. 31.

INTERPLANETARY MATTER AND ITS INTERACTION WITH THE EARTH

DETERMINATION OF ISOTOPIC COMPOSITION OF LITHIUM IN METEORITES AND TERRESTRIAL ROCKS

*L. Brown, R. S. Rajan, R. B. Roberts,
F. Tera, and D. J. Whitford*

In *Year Book 76* (pp. 797–803) we discussed the importance of ascertaining the isotopic composition of lithium in meteorites and described our preliminary work on a new method for determining it, one that avoids the deficiencies inherent in mass spectrometry. During the intervening year the number of isotopically anomalous elements found in a few phases of high-temperature inclusions in carbonaceous chondritic meteorites has increased. This enhances the interest in lithium because its nucleosynthesis is almost certainly different from that of all elements heavier than boron. The intervening year has also seen the first results of our method applied to a sample of meteorites, with results that are from 4 to 6 times more accurate and more numerous than those of any previous determination. Application of this new method, which determines the relative amounts of ${}^7\text{Li}$ and ${}^6\text{Li}$ through deuteron-induced nuclear reactions, has not been without problems, some of which have proved difficult and time-consuming to solve. We shall describe here some important details of the method, the understanding of which grew out of our difficulties, and present the first results attained with it. For a complete description see Brown *et al.* (1978). The instrumental effects can be divided into those that are inherent in the nuclear physics and those that grow out of the extraction chemistry. Those inherent in the nuclear physics that we shall discuss result from target thickness, inhomogeneities of beam and target, and count-rate effects.

The effects of target thickness and homogeneity of target and beam have been the subject of detailed analysis that need not be repeated here except to sketch their nature and solution. The ratio R of ${}^7\text{Li}$ to ${}^6\text{Li}$ counts is a function of both projectile energy E and reaction angle Θ . Errors can occur if $\partial R/\partial E \neq 0$ or $\partial R/\partial \Theta \neq 0$, if targets or beam are nonuniform. Some spread in target thickness is unavoidable but can be deduced from measurements of the spectra. Below 0.9 MeV the cross sections of both ${}^6\text{Li}$ and ${}^7\text{Li}$ reactions are steep functions of energy, examples of the Oppenheimer-Phillips interaction. The ${}^7\text{Li}$ reactions have strong resonances of uncertain spectroscopic nature at deuteron energies 0.36, 0.68, 0.75, 0.98, and 1.8 MeV. The ${}^6\text{Li}(d,\alpha){}^4\text{He}$ reaction is not strongly dependent on energy in the range 1 to 2 MeV, so if a region is to be found where $\partial R/\partial E \simeq 0$, it will have to be there. Higher energies are not practical for the simple arrangement we propose because the thickness of Mylar necessary to remove the elastically scattered deuterons would also remove too much of the ${}^7\text{Li}$ continuum.

Measurements of R as a function of energy disclose a region of about 100 keV width in which $(\partial R/\partial E_d)/R_o = 0.00032 \text{ keV}^{-1}$, where R_o is the ratio measured for very thin targets at $E_d = 1.37 \text{ MeV}$, the beam energy used for these experiments. This can cause errors when measurements are made on targets of various thicknesses; however, it is an effect that is almost exactly compensated by another systematic effect. Spectra differing from the ideal produced by a very thin target will cause errors in the values of counts attributed to ${}^7\text{Li}$. The counts for the four regions of the ${}^7\text{Li}$ continuum are the sums of 10-channel

bands of pulse-height analyzer data. If the α -particles lose energy in passing out of the target, the spectrum will be shifted to lower energies. For a given continuum region this will result in a gain in counts from the high-energy end and a loss from the low-energy end. This effect is of no consequence for ${}^6\text{Li}$, as the entire ${}^6\text{Li}$ line is integrated. Calculation of these effects is straightforward and need not concern us here; the result of target thickness on the counts obtained from the ${}^7\text{Li}$ continuum is, expressed in terms of deuteron energy loss, 0.00035 keV^{-1} . This effect is positive for increasing target thickness, whereas the energy dependence of R produces a negative effect with increasing target thickness. These two sources of systematic error nearly balance.

The value of $\partial R / \partial E$ is not zero, but the use of two detectors placed symmetrically to the right and left of the beam cancels these errors to a high degree. Indeed, assuming the worst possible asymmetry, one can show that $\Delta R / R < 0.001$.

There are many detector pulses in the spectra resulting from low energy particles, many from (d,p) reactions. Owing to their high count rates, these pulses give rise to accidental pile-up pulses (combinations of two or more small pulses to form large ones) that will be counted as data pulses. This source of error was investigated by two methods. Both indicate, however, that if the total count rate is varied so that its square times the total run time is about $3 \times 10^9 \text{ sec}^{-1}$, then the error accruing from this source should be less than 0.2%. In practice this limits the present setup to the examination of samples having 20 ng or more of lithium.

Lithium is extracted using conventional cation-exchange techniques, which are widely used for trace element and isotopic analysis of geological materials. A sample size sufficient to yield about 50 ng of lithium is crushed, dissolved in

a mixture of HF and HClO_4 and evaporated to dryness in a Teflon beaker. The residue is then dissolved in HCl, centrifuged to remove any undissolved residue such as spinel, and then passed through a cation-exchange column. The lithium fraction also contains significant amounts of Na and possibly Sn, Cd, and V, is evaporated to dryness, redissolved, and passed through the column once again. It is again evaporated to dryness and treated with HClO_4 to convert it to LiClO_4 and remove organic residues resulting primarily from the decomposition of the column resin.

This is, of course, standard procedure in trace element chemistry. The organic residues from the columns proved a perplexing problem, one that we were slow to understand. Their presence gave rise to inordinate numbers of (d,p) reactions and an amount of ${}^{14}\text{N}(\text{d},\alpha){}^{12}\text{C}$ that proved too large to ignore. The residues were greatly reduced by careful column techniques and finally removed by a microcolumn.

We have obtained ratios for chondritic and achondritic meteorites and terrestrial rocks. These data are shown in Fig. 33 by their variation from the ratio of a terrestrial standard. The lithium extracted from a piece of the mineral spodumene, furnished by the National Bureau of Standards and designated by them as sample 9a, was taken to be our isotopic standard. All measurements were interspersed with measurements of spodumene. A sufficiently large number of spodumene determinations enable us to plot the results as the histogram shown in Fig. 32. In all cases data were taken until enough counts were obtained to give an error of 1% resulting from counting statistics. Figure 32 shows how the individual runs lie when placed in 1σ bins relative to the mean. The mean deviation of their individual values is 1%. Thus it seems safe to say that any source of error not attributable to counting statistics is no more than about 0.3%. Individual

meteorite datum points generally have errors smaller than 1%, the result of more than one determination at 1%.

It is obvious from the results shown in Fig. 33 that none of the meteorite samples shows a ratio significantly different from our spodumene standard, while there may be a hint of variations in the terrestrial samples. Three determinations of meteoritic lithium were made about 10 years ago. Dews (1966) found various phases of the Bruderheim mete-

orite identical with a terrestrial granite within 1.7%. Krankowsky and Müller (1967) found agreement with terrestrial values within 2% for phases of four meteorites. Balsiger *et al.* (1968) examined five meteorites and reported that their values agreed within 1.75%, although two measurements of the set had values greater than 4% from the mean; they made no comparison with terrestrial standards. Our method is now relatively routine and will allow us to examine a

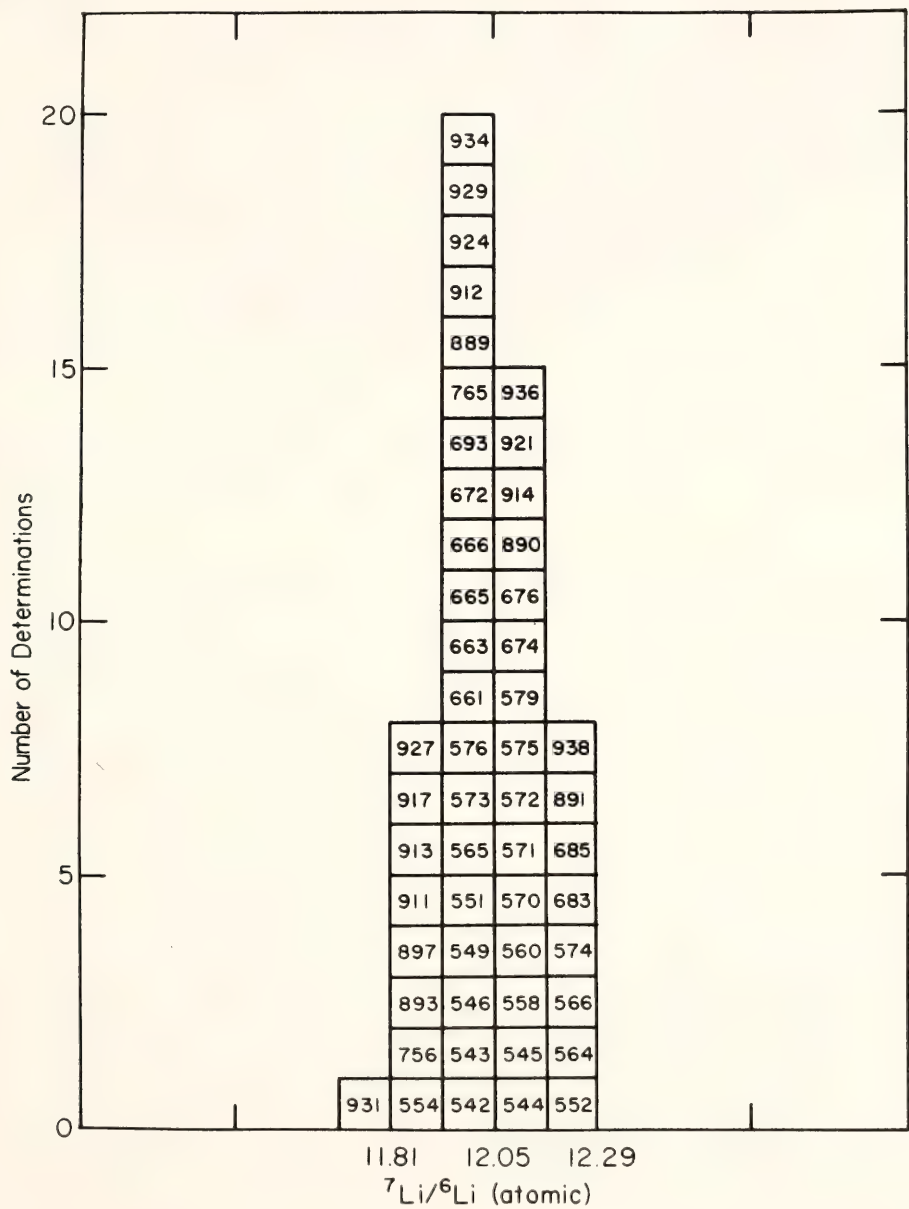


Fig. 32. The distribution of 52 determinations of the ${}^7\text{Li}/{}^6\text{Li}$ ratio for the terrestrial standard of spodumene. Each determination is designated by a block within which is the run number; each one was terminated when it had enough counts to give an error resulting from counting statistics of 1%. The histogram indicates that at this level of accuracy other sources of error are small. The absolute value of the ${}^7\text{Li}/{}^6\text{Li}$ value is probably uncertain by a few percent.

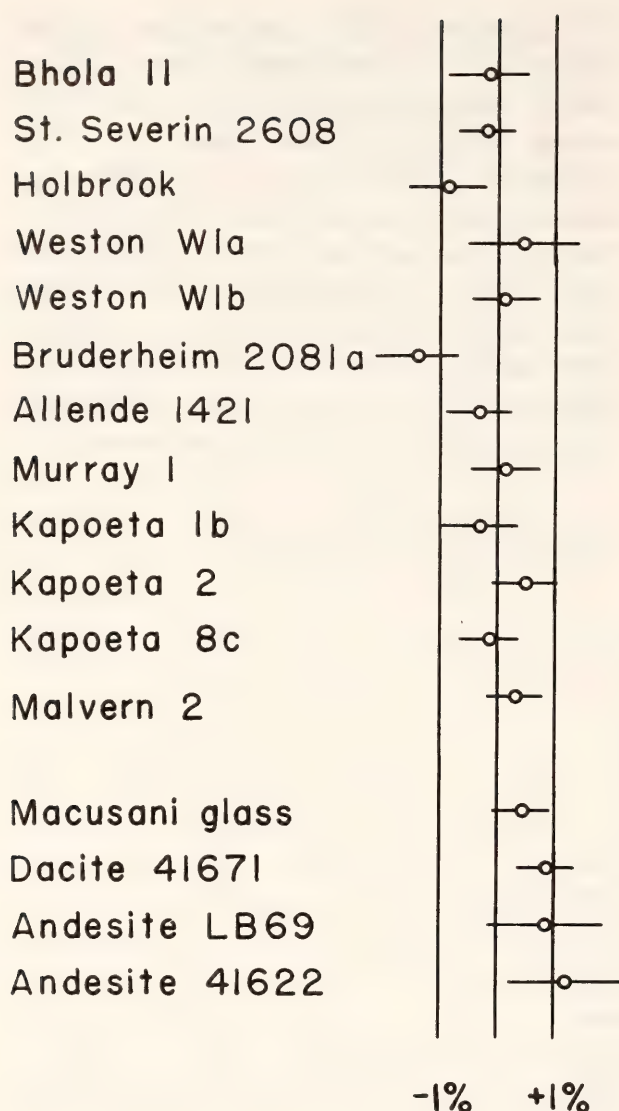


Fig. 33. The deviations of the ${}^7\text{Li}/{}^6\text{Li}$ ratios from the mean value given in Fig. 32 of 12 meteorite and 4 terrestrial samples. In calculating the errors, only counting statistics are considered.

wide variety of material. The discovery or complete absence of anomalous values in a large sample will in either case secure an observational foundation for a matter that has until recently rested on suggestive data. There is also little information about the fractionation of lithium in terrestrial materials, a matter we hope to examine soon.

References

Balsiger, H., J. Geiss, N. Groegler, and A. Wytttenbach, Distribution and isotopic abundance of lithium in stone

meteorites, *Earth Planet. Sci. Lett.*, **5**, 17, 1968.

Brown, L., R. S. Rajan, R. B. Roberts, F. Tera, and D. J. Whitford, A new method for determining the isotopic composition of lithium, *Nuclear Instruments and Methods*, in press, 1978.

Dews, J. R., The isotopic composition of lithium in chondrules, *J. Geophys. Res.*, **71**, 4011, 1966.

Krankowsky, D., and O. Müller, Isotopic composition and abundance of lithium in meteoritic matter, *Geochim. Cosmochim. Acta*, **31**, 1833, 1967.

PETROLOGIC AND ISOTOPIC CONSTRAINTS ON THE ORIGIN OF THE BHOLA CHONDRITE

A. F. Noonan*, R. S. Rajan, J. A. Nelen*, and K. Fredriksson*

Petrologic studies of the Bhola amphoterite show it to be a unique impact breccia containing rounded-to-angular chondritic and igneous clasts, which range in size from submillimeter to at least 1.4 cm across (Fig. 34). Chondritic inclusions vary texturally from fragments with close-packed, well-defined chondrules (LL4) to the more abundant, often shock blackened chondritic inclusions containing relict chondrules (LL5-6), to relatively coarse-grained recrystallized clasts (LL7?). Many of these inclusions were shock altered prior to their incorporation into the meteorite, as indicated by mechanical abrasion, shock blackening, crystal deformation, metal and sulfide veining, and recrystallization of troilite, plagioclase, and chromite. Many of these features are characteristic of known lunar and terrestrial impact breccias. The minerals identified in these chondritic fragments are the primary phases olivine (Fa_{27-30}), plagioclase (An_{10-12}), and pyroxene (Fs_{10-26}),

* Department of Mineral Sciences, Smithsonian Institution, Washington, D.C. 20560.



Fig. 34. Cut surface shows the extreme brecciation of the Bhola stone and angularity of included dark clasts. Arrow indicates the location of the large, K-rich (1.3% K_2O) fragment. Cut surface is approximately 4 cm across.

with minor amounts of augite, tridymite, whitlockite, kamacite, taenite, troilite, chromite, ilmenite, and native copper. In addition to the abundant chondritic xenoliths, unique dark-colored clasts have been found (Fredriksson *et al.*, 1974). These clasts, which range up to 1.4 cm across, are texturally igneous, angular, and contain skeletal olivines (Fa_{28-29}) in finely devitrified glass with up to 4.5% K_2O and 1.5% Na_2O . A typical thin section of the K-rich dark clast is shown in Fig. 35. The potassium enrichment of these clasts is remarkably similar to the dark portion of the Krah-enberg amphoterite (Kempe and Müller, 1969). Our studies imply the existence of new rock types and/or the occurrence of extreme fractionation processes on the parent body of amphoterites.

We have performed ^{40}Ar - ^{39}Ar dating on a sample of the K-rich devitrified

glass clast weighing ~ 10 mg (Rajan, Huneke, Smith, and Wasserburg, unpublished data). The resulting age spectrum is highly anomalous, as shown in Fig. 36. The K-Ar age from the integrated Ar release is 3.65 AE, which is a lower limit to the gas-retention age of the glass. Since the clast contains skeletal and euhedral olivines embedded in the fine-grained K-rich glass, it is possible that ^{39}Ar recoil effects are important. Indeed, Huneke and Smith (1976) were able to produce thermal-release patterns similar to that obtained in Bhola from simulated glass-olivine mixtures. In spite of the recoil problem, it is possible that the nominal plateau around ~ 4.3 AE may have some age significance. In any case, the formation of K-rich Bhola glass took place at ≥ 3.65 AE ago.

The light-colored Bhola host material contains fragments and chondrule sili-

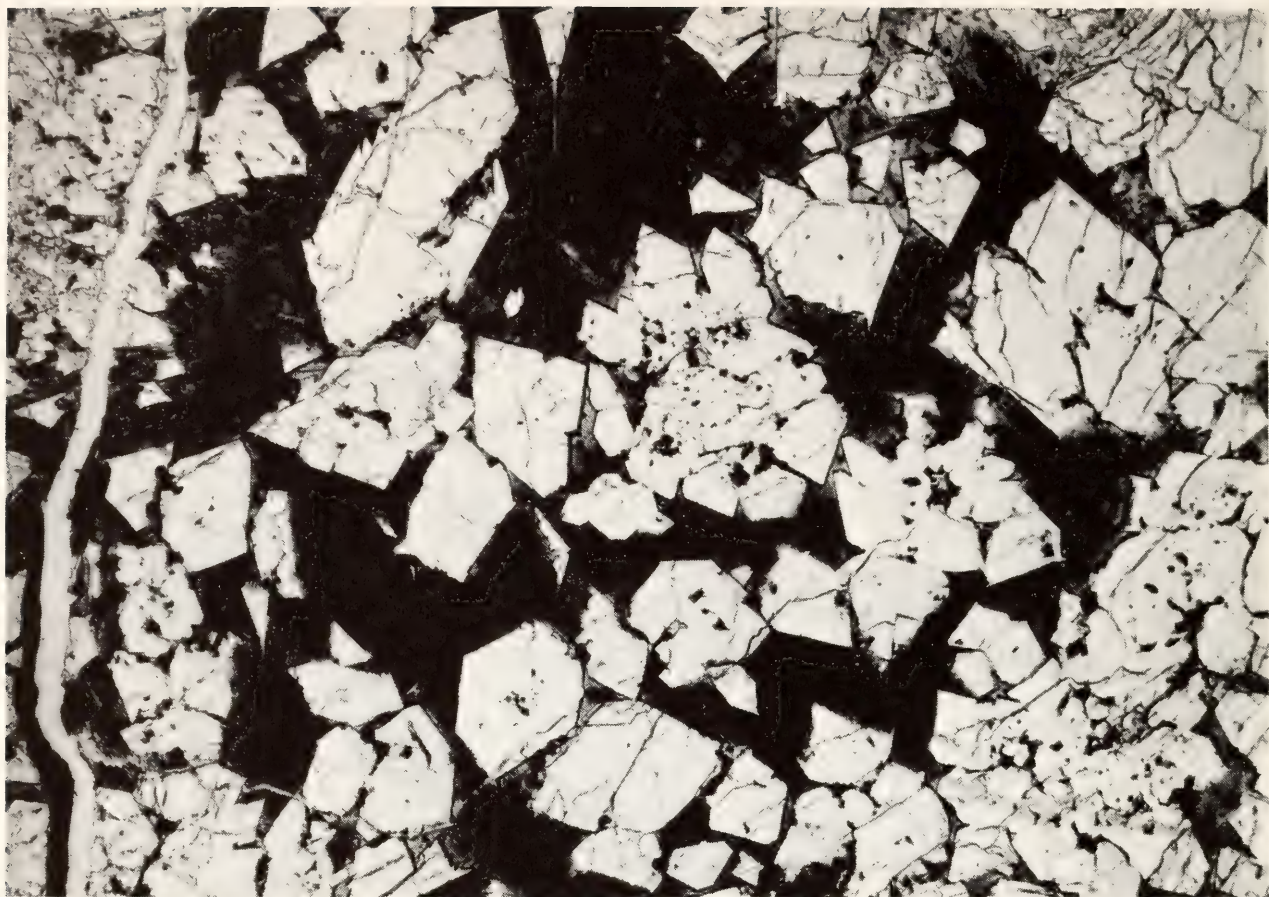


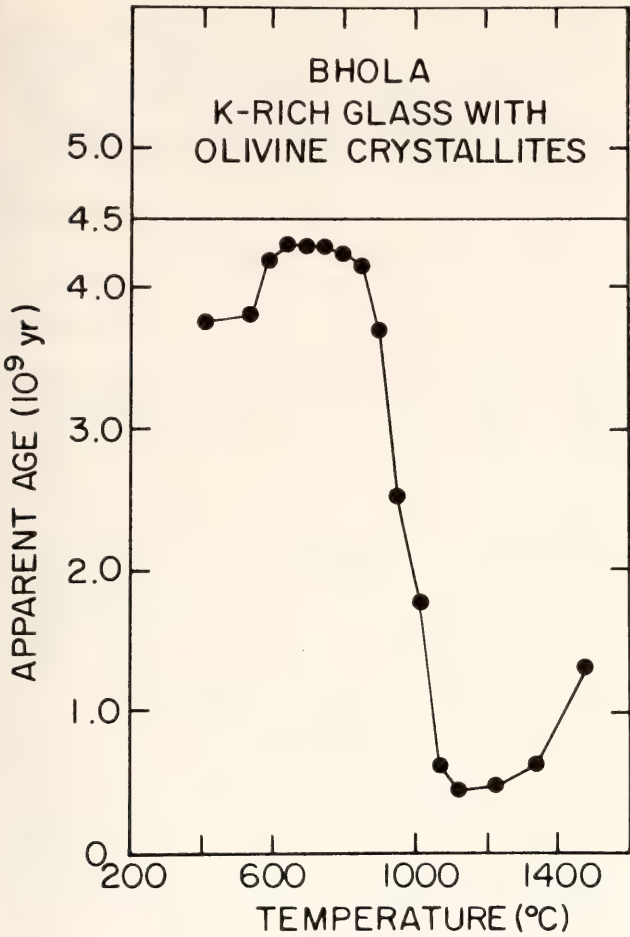
Fig. 35. Photomicrograph of the thin section of the K-rich clast. Igneous texture with olivine phenocrysts in glassy to cryptocrystalline mesostasis can be clearly seen. The field of view is 1.2 mm.

cates which are essentially identical in composition to minerals in the xenoliths. As with other xenolithic chondrites, the host contains less than 10% intact and broken chondrules, the bulk of the matrix silicates apparently being the crushed or fine-grained equivalents of the xenoliths. Fine-grained recrystallized plagioclase appears to be a matrix-bonding material in some parts of Bhola and may account, at least in part, for the white-to-gray matrix coloring. The presence of small amounts of primary glass in the matrix (both fragmental and chondritic), as well as one relatively high iron, matrix olivine crystal (Fa_{18}), shows that there has not been significant thermal metamorphism of the meteorite subsequent to its final agglomeration.

A lithium tetraborate glass bead analysis (Noonan and Nelen, 1976) of ~1 gram of Bhola host material is probably

representative of the major-element chemistry of the bulk meteorite (Table 7). A comparison of the above analysis with that of a coarsely chondritic clast (LL4) suggests that there is no difference in major-element composition between most xenoliths and matrix, with the one important exception of total iron which is attributed to varying amounts of metal in selected samples.

The uniformity in composition of the major silicates in Bhola cannot be attributed to thermal metamorphic equilibration, although this process may in part account for the constant compositions of the silicates in the LL6 clasts. The occurrence of equilibrated silicates in Bhola and other chondrites that contain primitive glassy material (cf. Fredriksson *et al.*, 1975) argues against simple metamorphic equilibration of these chondrites. It is equally apparent that Bhola



and other xenolithic chondrites cannot be assigned a unique petrologic grade using the Van Schmus–Wood classification. On the basis of the various petrologic grades recognized in Bhola, it can be at most classified as an LL4–6 breccia. This is a recurring paradox of the Van Schmus–Wood System, which emphasizes the need for expanding the traditional schemes or establishing a more useful classification.

Fig. 36. Apparent age spectrum obtained from the analysis of a devitrified, K-rich glass clast from the Bhola chondrite. The ages are graphed as a function of extraction temperature, which should better reflect the physical processes yielding the anomalous pattern. The Bhola pattern shows evidence of low-temperature ⁴⁰Ar losses. The apparent age increases to a maximum at 4.30 AE, then decreases precipitously to 0.46 AE. The anomalous pattern is almost certainly due to the recoil transfer of ³⁹Ar into the olivine from surrounding K-rich phases and its retention by the olivine to high temperature.

TABLE 7. Chemical Composition of Components in the Bhola Amphoterite (USNM 1806)

	Bhola* Host	Bhola LL4* Xenolith	Bhola Dark* K-Rich Clast	K-Rich Glass† in Clast	Krahenberg‡ Dark Material
SiO ₂	38.76	38.55	43.66	59.51	41.3
Al ₂ O ₃	2.08	2.08	2.30	8.41	1.59
FeO (all Fe)	24.34	28.73	21.26	10.48	24.52
MgO	24.92	24.00	26.26	5.85	25.0
CaO	1.75	1.73	2.12	8.96	2.02
Na ₂ O	1.04	0.91	0.42	1.63	2.35
K ₂ O	0.09	0.15	1.30	4.34	1.45
TiO ₂	0.15	0.14	0.20	0.44	0.3
P ₂ O ₅	0.17	0.18
MnO	0.46	0.34	0.44	0.27	0.36
Cr ₂ O ₃	0.56	0.60	0.70	...	0.3
C	0.01	0.04

* Measurements made using a lithium tetraborate glass bead technique (see text).

† Measurements are the average of four broad-beam analyses using the ARL-SEMQ electron probe.

‡ Analyses by Kempe and Muller, 1969.

References

- Fredriksson, K., A. Dube, E. Jarosewich, J. A. Nelen, and A. F. Noonan, The Pulsora anomaly: a case against metamorphic equilibration in chondrites, *Contrib. Earth Sci.*, 14, 41–53, 1975.
- Fredriksson, K., A. F. Noonan, and J. A. Nelen, The Bhola Stone—a true polymict breccia?, *Meteoritics*, 9, 338–339, 1974.
- Huneke, J. C., and S. P. Smith, The realities of recoil: ^{39}Ar recoil out of small grains and anomalous age patterns in ^{39}Ar - ^{40}Ar dating, *Proc. 7th Lunar Sci. Conf.* pp. 1987–2008, 1976.
- Kempe, W., O. Müller, The stony meteorite Krahenberg. Its chemical composition and the Rb-Sr age of the light and dark portions, in *Meteorite Research*, pp. 418–428, P. M. Millman, ed., Reidel, Dordrecht, Holland, 1969.
- Noonan, A. F., and J. A. Nelen, A petrographic and mineral chemistry study of the Weston, Connecticut, chondrite, *Meteoritics*, 11, 111–130, 1976.

STEADY STATE POPULATIONS OF APOLLO-AMOR OBJECTS

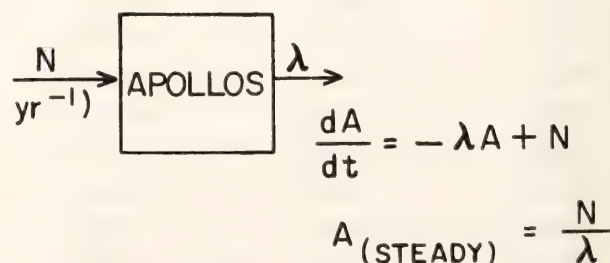
G. W. Wetherill

Introduction

In spite of their small size and number, it is becoming increasingly clear that an understanding of the Earth-approaching interplanetary objects is central to major problems in planetary science. It is almost certain that these bodies are at present the principal cause of 1–100 km diameter craters on the Moon and the terrestrial planets. It is very probable that this has been the case for the last 3×10^9 years or more (Shoemaker, 1977). It is also likely that a large proportion of the meteorites are recent fragments from these bodies (Levin *et al.*, 1976; Wetherill, 1976). There are good reasons to believe that at least many of these objects represent the nonvolatile portions of the nucleus of “extinct”

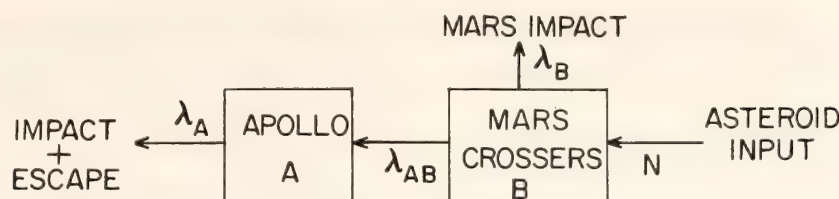
comets, which in active comets is obscured by the coma (Öpik, 1963; Anders and Arnold, 1965; Wetherill, 1976). Certain of these bodies have been identified as relatively accessible sources of raw materials for space construction and manufacturing (O’Leary, 1977).

Because the dynamic lifetime of bodies in planet-crossing orbits is commonly much less than the age of the solar system (Öpik, 1951), the present existence of these bodies requires that there exist a long-lived source which replaces those lost by planetary impact and ejection into heliocentric escape orbits. This leads to the concept that the present population represents at least an approximate steady state balance between injection and removal of Earth-approaching objects. This can be visualized in terms of compartmental models (Fig. 37B) analogous to those useful in physiological modeling and many other applications (e.g., Rabinowitz *et al.*, 1976). Such models and their more complex extensions, to be discussed, predict relationships between the number of bodies in the several compartments and may at least in principle be useful in distinguishing between alternative sources for these bodies. In addition these models may be useful in relating observable quantities to one another (e.g., lunar cratering rate, meteorite flux, and number of Apollos). It is therefore unwise and unnecessary to consider the magni-



SIMPLEST STEADY STATE MODEL

Fig. 37A. Single-compartment model in which Apollo objects are injected as short-period comets and removed by planetary impacts and perturbation into escape orbits.



ÖPIK (1963) STEADY STATE MODEL

Fig. 37B. Two-compartment model in which asteroidal fragments are injected into relatively long-lived Mars-crossing orbits. Some of these objects are perturbed into Earth-crossing (Apollos) and are subsequently removed by impacts and escape.

tudes of such phenomena as independent free parameters. Comparisons of the results of model calculations with observations permit tests of the reliability of our understanding of these phenomena. The measure of reliability learned in this way can then be useful in judging the plausibility of extending these concepts to events in the early solar system that are not subject to such direct observational verification.

The simplest steady state model (Fig. 37A) has a single compartment containing A objects fed by an external source at a rate N objects/yr. The rate at which bodies are removed from the compartment is λA , where λ is the rate constant. In this case the number of bodies in the compartment at time t will be:

$$A(t) = A_0 e^{-\lambda t} + \frac{N}{\lambda} (1 - e^{-\lambda t}), \quad (1)$$

where A_0 is the number of bodies at time $t = 0$. With the passage of time, A approaches the steady state value

$$A \simeq N/\lambda. \quad (2)$$

This simple steady state model was implicitly assumed by Öpik (1963) in discussing the number of Apollos derived from the extinct comets. For example, there is at present one active comet in an Apollo-like orbit, Eneke. If the active lifetime of a comet is taken to be ~ 3000 years (1000 perihelion passages), and the injection rate N is taken to be $1/3000$

yr and λ is estimated to be $\sim 10^{-8} \text{yr}^{-1}$ by the methods of Öpik (1951), then the steady state number of Apollos is found to be 3×10^4 . As Öpik recognized, this is many more than are observed. If Eneke's nucleus of ~ 1 -km diameter is typical of extinct comets, Öpik found it necessary to hypothesize that only a small fraction of comets possess solid nuclei, in order to avoid an "excess of riches."

The opposite problem was encountered when the inner edge of the asteroid belt was considered as the source of Apollos (Fig. 37B), the asteroids being deflected into Earth-crossing orbits by Mars perturbations (Öpik, 1963). Using this model, Öpik showed that the ratio of Mars-crossers to Apollos must be greater than 400. He argued that this is ~ 100 times the observed value, and therefore it seemed unlikely that a major fraction of the Apollo objects could be derived from the asteroid belt. At the time of these earlier calculations, the only mechanism proven to be effective in transferring Mars-crossers into Earth-crossing Apollo orbits was the random accumulation of perturbations following close encounters to Mars. Because the mass and cross section of Mars is small, these perturbations are weak and infrequent. The time required for the major reorientation of the asteroid's orbit from one with perihelion near Mars to one with perihelion near Earth and aphelion near Mars was comparable to the age of the

solar system. In the steady state, this then led to a high ratio of Mars-crossers to Apollos.

As a result of further studies of the dynamics of the asteroid belt carried out in recent years, it is necessary to reconsider these conclusions. In this newer work it was found that long-range perturbations by the major planets, particularly Jupiter, can be more effective than Mars perturbations in transferring asteroidal material into Earth-crossing orbits. The nonlinear interaction of close encounters to Mars with Jupiter perturbations appears to be even more effective. Williams (1969) showed that there exist resonant surfaces in (a, e, i) space for which the amplitudes of the secular forced oscillations in eccentricity reached high values (e.g., ~ 0.4). For favorably placed asteroidal material, this can cause the orbit to become Earth-crossing, either directly or in combination with Mars perturbations. The commensurability resonances with Jupiter (Kirkwood gaps) can have a similar effect (Zimmerman and Wetherill, 1973; Scholl and Froeschlé, 1977). The larger values of eccentricity caused by these mechanisms can also increase the importance of relatively close encounters to Jupiter.

When all these effects are included, the simpler compartmental models (Fig. 37B) lose much of their validity. The secular resonances of Williams can decrease λ_{BA} to $\sim 10^{-8}$ years, and also require inclusion of a comparable value for the inverse process of transferring Earth-crossing material to purely Mars-crossing (Wetherill, 1977a; Wetherill and Williams, 1978). Objects with aphelia beyond ~ 4 A.U. will undergo fluctuations in their perihelion distance, causing them to be Earth-crossing some of the time and Mars-crossing some of the time, without the need for close encounters to Mars. Furthermore the homogeneity of the compartments in Fig. 37B is destroyed by these effects. For example, Mars-crossers with orbital elements near

the values of secular resonance will have much larger probabilities for transfer to Earth-crossing than Mars-crossers far from these resonances.

It would be possible to include these effects in a compartmental model with more compartments. However the algebraic expressions then become so complex that they fail to provide much insight into the processes involved. Furthermore such models will always represent a non-physical idealized homogenization of phenomena which are actually continuously variable. For these reasons, the compartmental approach is not followed further in the present treatment. Instead, approximate methods are used for including these new mechanisms into the Monte Carlo iteration of the Öpik collision formula (Öpik, 1951), as developed by Arnold (1965). This permits the calculation of continuous distributions of orbital elements, which can then be classified at the end into observational categories such as Apollos, Mars-crossers, or Amor objects (perihelion between 1.0 and 1.3 A.U.) insofar as this is a useful thing to do.

Methods of Calculation

Previously published discussions of the orbital evolution of Apollo objects (Wetherill and Williams, 1968) were essentially based on the procedure described by Arnold (1965). In the more recent reconsideration of the importance of Apollo objects as meteorite sources (Wetherill, 1976), only a qualitative discussion of the effects of the secular resonances was included. The present work makes use of the procedure for inclusion of secular resonance subsequently developed for evaluation of asteroidal sources of iron and achondritic meteorites (Wetherill, 1977b; Wetherill and Williams, 1978). This procedure includes the one such resonance likely to be the most effective, ν_6 . The position of this resonance for proper eccentricity $e_0 = 0.1$ is shown in Fig. 38. Its impor-

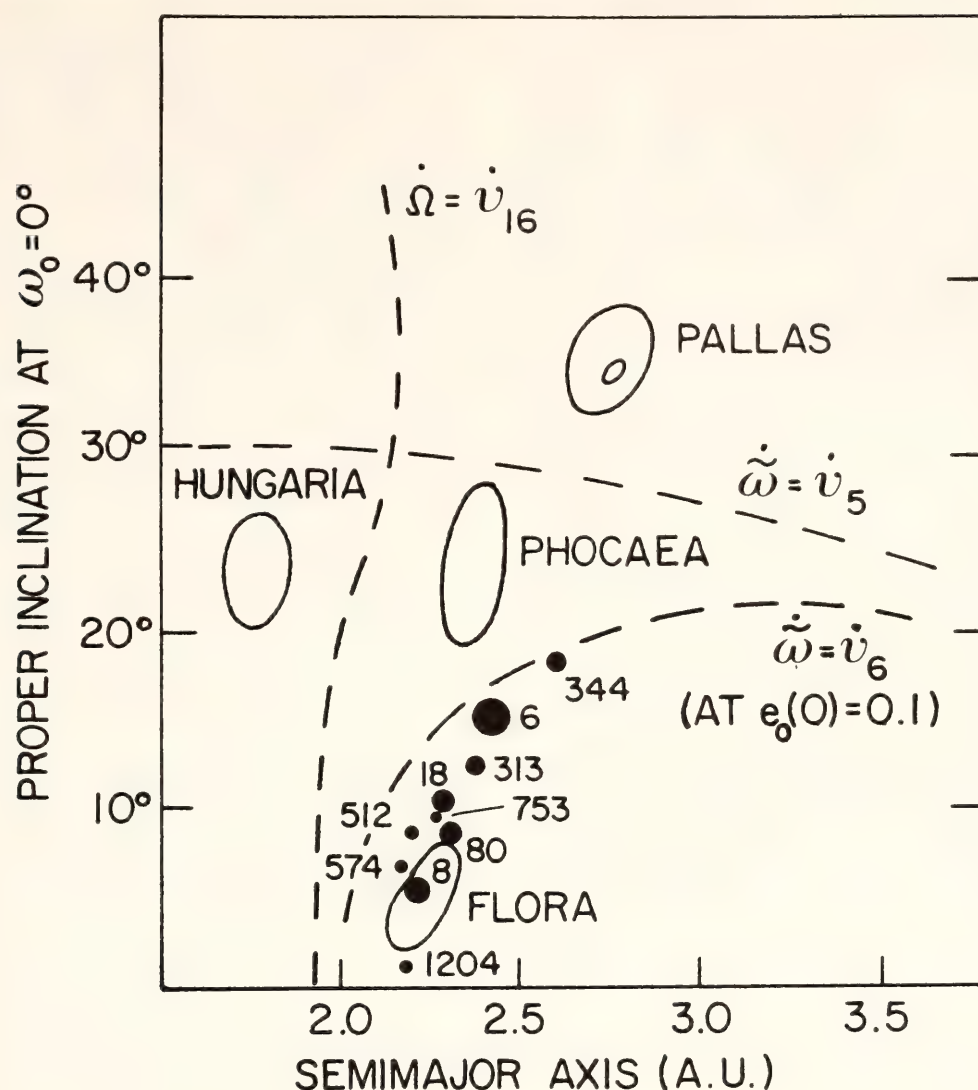


Fig. 38. Position of the ν_5 , ν_6 , and ν_{16} resonances for proper eccentricity of 0.1 (Williams, 1969).

tance results from its proximity to the densely populated region of the asteroid belt with semimajor axes ~ 2.2 – 2.3 A.U. and with inclinations $\leq 10^\circ$. Relatively small (~ 200 m/sec) ejection velocities can cause the semimajor axis of small (e.g., ~ 1 -km diameter) asteroids produced by collisions involving larger asteroids to move closer to the resonant value, increasing the amplitude of their eccentricity oscillations. For injection at a favorable phase of these oscillations, occasional close encounters to Mars will then become possible. The resulting Mars perturbations can random walk the semimajor axis closer to the resonant value, finally resulting in relatively frequent, albeit still shallow, Mars-crossing. This

is the “synergistic” mechanism described earlier (Wetherill, 1974).

In the present work the shallow Mars-crossing orbits resulting from this process are taken as initial orbits, and the subsequent evolution of these orbits is followed. This permits calculation of the number of Apollos, Amors, and lunar craters expected for an assumed injection rate into these initial orbits. The question of the actual injection rate is not yet amenable to a sufficiently quantitative discussion. It is quite possible that this earlier stage of extremely shallow Mars-crossing will turn out to be analogous to the long-lived Mars-crossing “bottle-neck” of Öpik’s theory. However, it is much more difficult to treat because of

uncertainties associated with the distribution of velocities of collision ejecta and the sensitivity of their Mars-encounter probabilities to the tiny details of all the secular terms in eccentricity and inclination for both the asteroidal fragment and Mars.

Another effect that could sometimes be important is that of encounters within ~ 0.5 A.U. of Jupiter. In the original Arnold procedure, encounter perturbations were calculated only for actual crossing orbits. This can lead to a physically unrealistic situation in which Jupiter perturbations have no effect at all until Jupiter's orbit is crossed, at which point the large mass of Jupiter suddenly completely dominates the subsequent orbital evolution. In the real solar system the dominance of Jupiter takes place gradually as the aphelion of the asteroid increases beyond about 4 A.U. In order to avoid a grossly discontinuous approximation, various procedures have been used during the past decade to deal with this problem. All of these are rather crude, inasmuch as no really satisfactory way of handling these relatively distant Jupiter perturbations other than numerical integration is known at present, and this is precluded by prohibitive computing times. On the other hand, comparison of these various schemes and some comparison of these results with actual numerical integration carried out in conjunction with the work on the 2:1 Kirkwood gap (Zimmerman and Wetherill, 1973) argues that an exact treatment may be unimportant. The principal requirement appears to be introduction of stochastic velocity changes near aphelion at more or less the right amplitude and at appropriate time intervals, and that the amplitudes increase and the time intervals decrease with aphelion distance in such a way to smoothly match those found when Jupiter-crossing is reached. In the present work, one of the simpler of these schemes was employed.

This admittedly crude procedure serves the purpose of introducing Jupiter perturbations gradually as the aphelion of Jupiter is approached. The stabilities of Jupiter-grazing orbits calculated according to this scheme are compared with those obtained by numerical integration by Lecar and Franklin (1973) in Fig. 39, and the agreement is seen to be good. Nevertheless, this procedure should not be regarded as being very satisfactory. However, a really good treatment of these Jupiter close-encounter perturbations is probably necessary only in circumstances wherein the orbital evolution is entirely controlled by these perturbations, for example, in orbits similar to those treated by Lecar and Franklin. In the cases considered here, almost any way of treating Jupiter perturbations will bring the semimajor axis occasionally to the ν_6 resonant value when the eccentricity is high enough for the aphelion to lie within 0.65 A.U. of Jupiter. Only a small increase in amplitude of the eccentricity is then required to cause actual Jupiter-crossing followed by ejection from the solar system on a short time scale. In fact, when ν_6 perturbations are included in the calculations, it turns out that the general conclusions of the present investigation are unchanged even if these long-range Jupiter perturbations are totally ignored, although in detail some differences are found. It seems more satisfactory to include these effects in the manner described rather than to ignore them, but in any case it doesn't make much difference. This will be illustrated later by examples.

The calculations reported in the following section are made by envisioning an ensemble of bodies resulting from the injection into the chosen starting orbit of a fixed number of bodies at regular intervals in the past, usually every five million years. At the present time the distribution of the orbital elements of these bodies will be given by the distribution of the present-day survivors of

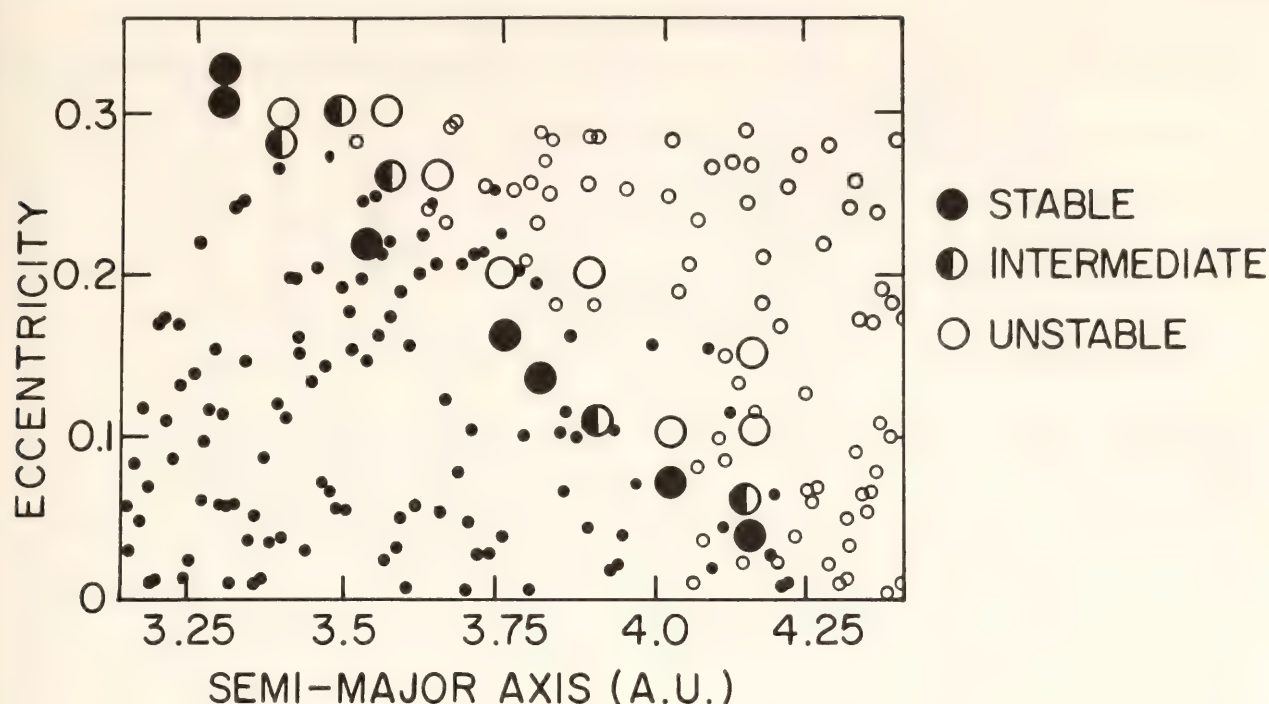


Fig. 39. Comparison between the stability of "Jupiter-grazing" orbits as calculated by Lecar and Franklin (1973) and as calculated in the present work. The small circles are those of Lecar and Franklin; open circles represent initial orbits of bodies eliminated within 2400 years, filled circles, those of bodies surviving for more than 2400 years. Large circles are from the present work. Open circles were stable for more than 2400 years in only $<20\%$ of the cases. Filled circles were stable in $>80\%$ of the cases. Intermediate results were obtained for the half-filled circles.

those bodies injected 1 m.y. ago, 6 m.y. ago, 11 m.y. ago, and so on, back to the formation of the solar system 4500 million years ago. This distribution can be calculated using the usual forward Monte Carlo calculation procedure of Arnold by examining the residual population at 5 m.y. intervals. The contribution of 1-m.y.-old bodies will be represented by the residual population after 1 m.y., 6-m.y.-old bodies by those surviving for 6 m.y., and so forth. These contributions are sorted into bins corresponding to small intervals in semimajor axis, perihelion, aphelion, geocentric velocity, and elongation of the radiant. The contents of these bins are summed at these 5-m.y. intervals during each run, and the summation is continued over the 100 runs comprising the typical Monte Carlo simulation. The procedure described elsewhere (Wetherill, 1975) for properly scoring certain close encounters also as impacts is used to enhance the statistical

reliability of the calculations. This results in each starting orbit effectively being followed 2500 times. Since the lifetime of these bodies prior to impact or ejection from the solar system is typically 100–200 m.y. (i.e., 20–40 5-m.y. intervals), the total content of the "bins" is $\sim 30 \times 2500 \simeq 10^5$, which is adequate to cause the effect of statistical fluctuations to be of very minor importance.

Results of the Calculations

The calculations described above were carried out for the starting orbits listed in Table 8. These include (1) "Mars-grazing" orbits (#1, 2, 3) of the sort expected as collision fragments injected from the inner edge of the asteroid belt, (2) the orbit of the only presently active comet (Encke) in an Apollo-like orbit (Earth-crossing with aphelion well within Jupiter's perihelion distance), and (3) the orbits of hypothetical comets in

TABLE 8. Initial Orbits

Object	<i>a</i>	<i>e</i>	<i>i</i>
1. 1204 Renzia	2.26	.29	2°
2. 313 Chaldaea fragment	2.32	.30	12°
3. Phocaea region fragment	2.20	.25	23°
4. Comet Encke	2.21	.85	12°
5. Hypothetical extinct comet, <i>q</i> = 0.92 A.U.	2.56	.64	5°
6. Hypothetical extinct comet, <i>q</i> = 1.50 A.U.	2.80	.46	6°

orbits similar to that of Encke but with larger perihelia..

Distribution of Apollo and Amor orbits. The populations of Apollo and Amor objects generated by the starting orbits listed in Table 8 are given in Table 9. The numbers are given for a somewhat arbitrary injection rate into these initial orbits of 15 bodies/10⁶ years. If different injection rates are assumed, the numbers will be proportionately higher or lower. The nominal injection rate of 15/10⁶ yr was chosen because use of this rate led to Apollo-Amor populations comparable in number to those observed (Shoemaker, 1977; Wetherill, 1976).

The question remains, whether or not these injection rates actually occur in the real solar system. This question must remain somewhat unresolved at present. If the present existence of the active

comet Encke is assumed to be a probable, rather than an improbable event, then a cometary injection rate of ~100/10⁶ years results, more than an adequate number. Semiquantitative estimates of the injection rate from the inner asteroid belt can be obtained from previous discussions of Apollo (Wetherill, 1976) and meteorite production from this region (Wetherill, 1977b; Wetherill and Williams, 1978). There it was estimated that the number of asteroids >1 km in diameter in adequate proximity to both the ν_6 resonance and Mars aphelion was ~5000. The collision lifetime of these bodies can be estimated to be ~10⁹ years (Wetherill, 1967).

Using this collision lifetime, a steady state production rate of 5/10⁶ years is obtained. If these km-sized collision fragments are ejected with the same ve-

TABLE 9. Steady State Distributions*

Initial Orbit	Amors 1.0< <i>q</i> <1.3	Apollos 1.0< <i>q</i>
1. 1204 Renzia	840	311
2. 313 Chaldaea fragment	1611	661
3. Phocaea region fragment	2181	274
4. Comet Encke	1195	769
5. Extinct comet, <i>q</i> = 0.92	685	233
6. Extinct comet, <i>q</i> = 1.50	495	222
7. Same as 1, no Jupiter encounters	1152	515
8. Same as 1, 1/2 ν_6 amplitudes, and no Jupiter encounters	1457	359
9. Same as 4, no Jupiter encounters	1200	926
Estimated number brighter than <i>V</i> (1, 0) = 18 (Shoemaker, 1977)	600±400	750±300

* Injection rate = 15 objects/million years.

TABLE 10. Objects in "Small Orbits"

Initial Orbit	Fraction of Total $q < 1.0$	
	Apollos $a < 1.0$ %	Aphelion < 1.0 %
1. 1204 Renzia	6.4	3.0
2. 313 Chaldaea fragment	4.5	0.4
3. Phocaea region fragment	4.4	0.4
4. Comet Encke	3.3	1.1
5. Extinct comet, $q = 0.92$	2.1	1.0
6. Extinct comet, $q = 1.50$	2.3	1.9
7. Same as 1, no Jupiter encounters	8.5	4.0
8. Same as 1, $1/2 \nu_6$ amplitudes and no Jupiter encounters	5.7	2.8
9. Same as 4, no Jupiter encounters	6.3	1.0
Observed fraction	8.3	0
	(2 out of 24)	(No Search)

locity distribution assumed previously for meteorite-sized fragments, about 30% will evolve into Apollo-Amor orbits (i.e., $\sim 1.5/10^6$ years). If these numbers are taken at face value, this source appears to be deficient by a factor of ~ 10 . Thus it may be expected that Apollos-Amors are presently derived both from comets and asteroids, but there is reason to believe the cometary component to be the dominant one.

The contribution to the present Apollo-Amor population from very old (more than 2.5×10^9 years in the past) bodies was found to be negligible. Therefore the numbers given in Table 9 represent a good approximation to a steady state. It may be seen that there is no marked difference between the Amor/Apollo ratio expected for cometary and asteroidal sources, except for the high-inclination case No. 3. This is a consequence of the tendency of the ν_6 resonance to rapidly equilibrate the population of these two adjacent regions of the inner solar system. It is likely that the much larger differences predicted for these two sources by earlier work will still be present for the more distant, shallow Mars-crossing populations, but this more diffi-

cult problem has not yet been adequately addressed.

The last three entries in Tables 9 and 10 illustrate the sensitivity of these calculations to the procedures used to include the ν_6 secular resonance and close encounters to Jupiter. Although inclusion of these effects makes some difference, it is not a large difference.

At the present time there is only one comet in an orbit with aphelion well inside the orbit of Jupiter, so it is not possible to say anything much about the distribution of perihelia for extinct comets remaining in orbits of this kind. Prairie Network fireballs of $Q < 4.5$ and of class III (Ceplecha and McCrosky, 1976), almost certainly originally of cometary origin but not associated with a comet at present, have a wide range of perihelia. This suggests that a similar range of extinct comet perihelia will occur unless these weak fireballs have survived long enough to permit significant random walk of their perihelia. Fireballs provide no information concerning perihelia > 1.02 A.U., because Earth-crossing is required for a fireball to be observed. However most short-period comets have perihelia beyond the

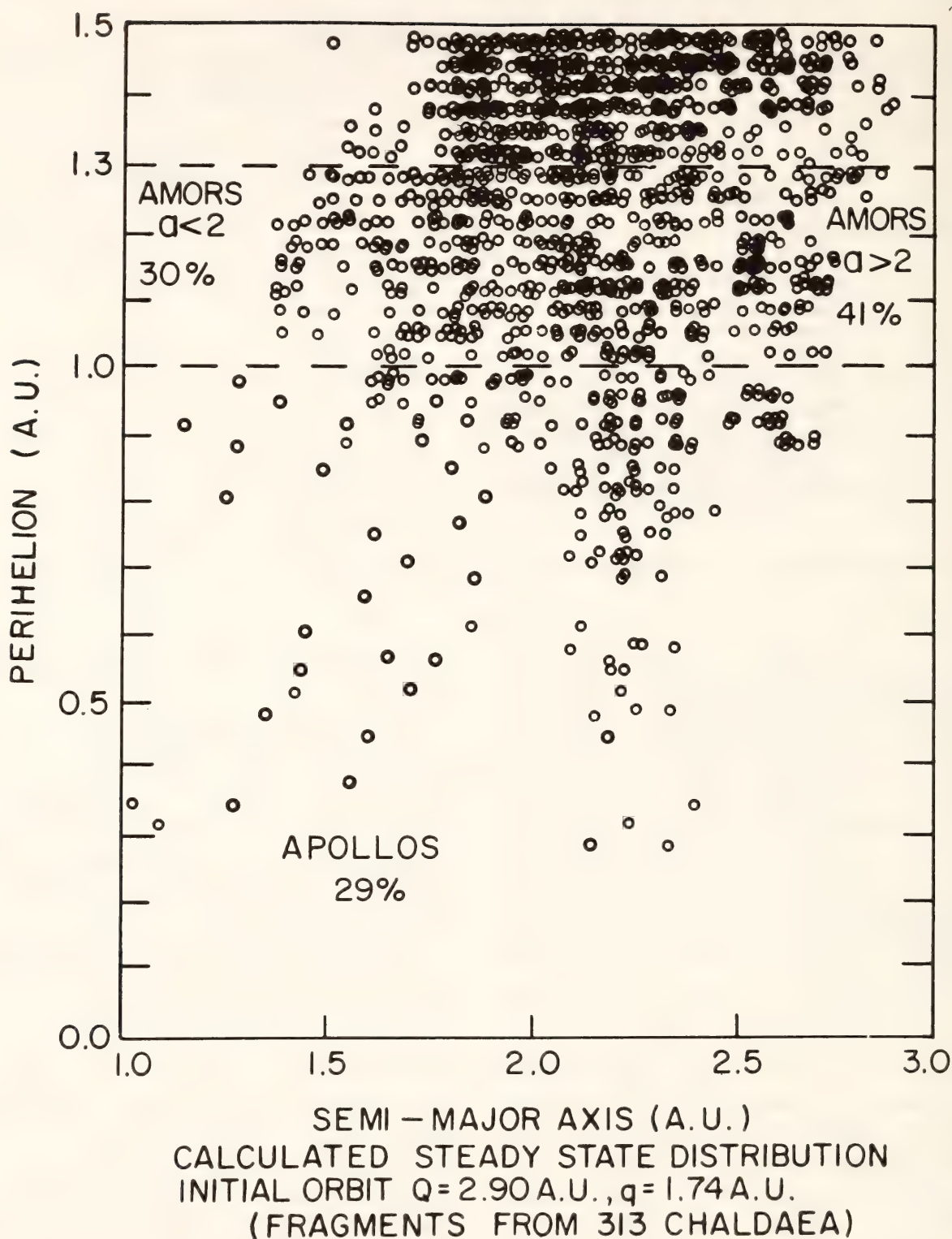


Fig. 40. Steady state distribution calculated for injection of fragment ejected from asteroid 313 Chaldaea. Initial aphelion = 2.90 A.U., initial perihelion = 1.74 A.U. Injection rate = 5 objects/ 10^6 years.

Earth. If the integral effect of the non-gravitational forces that lead to evolution of the comet's aphelion inside Jupiter's orbit (Sekanina, 1969) depend only on the total mass loss and not its rate, then extinct comets with perihelia

beyond 1.0 A.U. should also exist. Table 9 shows that initial Encke-like comets with larger perihelia lead to steady state equilibria with a larger number of Amors relative to Apollos than is the case for Encke. The actual number of Amors and

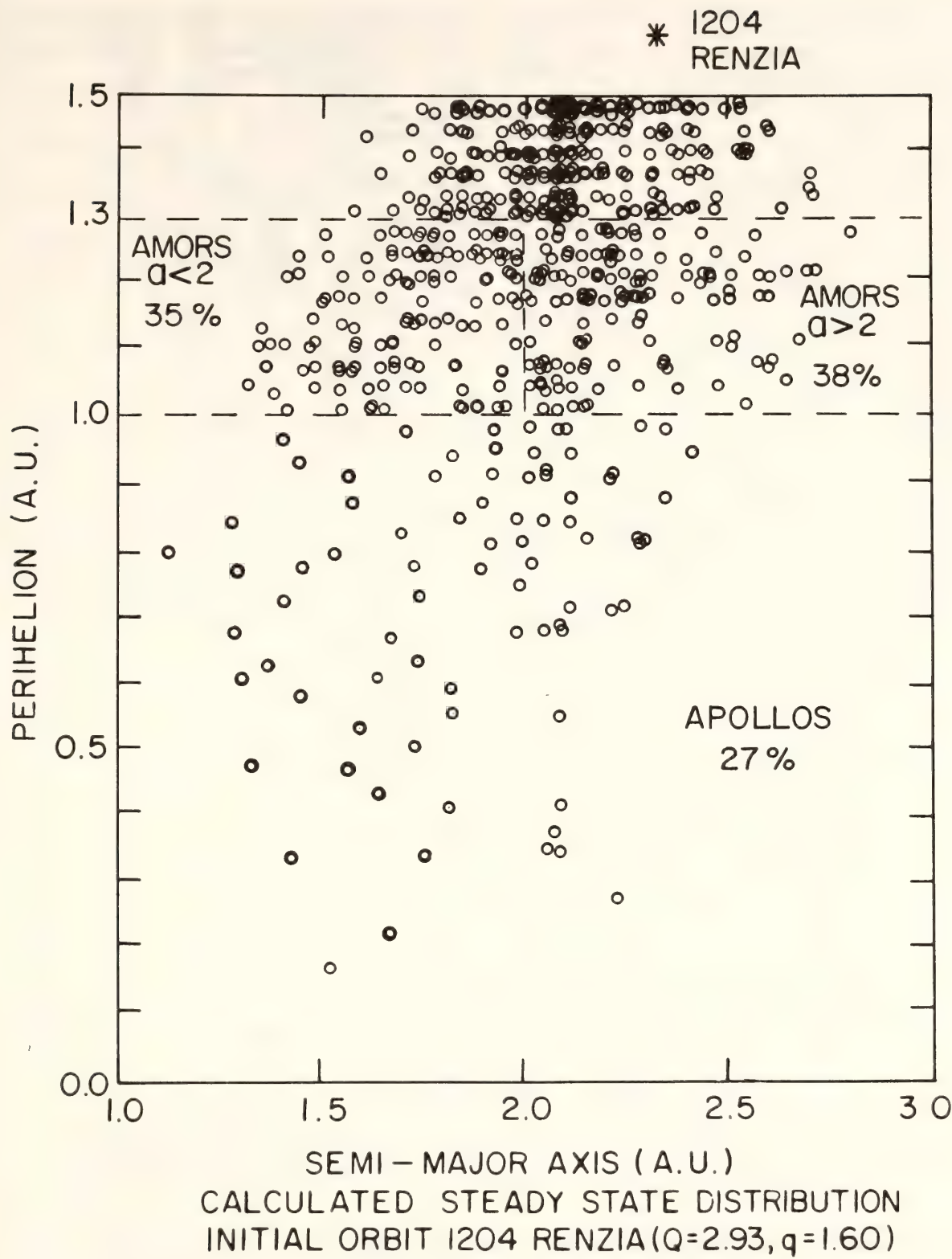


Fig. 41. Steady state distribution calculated for injection of object in initial orbit of 1204 Renzia (aphelion = 2.93 A.U., perihelion = 1.60 A.U.). Injection rate = 5 objects/10⁶ years.

Apollos appear to be nearly the same. A major contribution from these bodies could be a problem, as then both of the possible Apollo-Amor sources (asteroid and comet) will yield steady state Amor/

Apollo ratios of ~ 3 . The resolution of this is not clear as yet. It is possible the actual number of Amors has been underestimated. It is also possible that the integral effect of the nongravitational

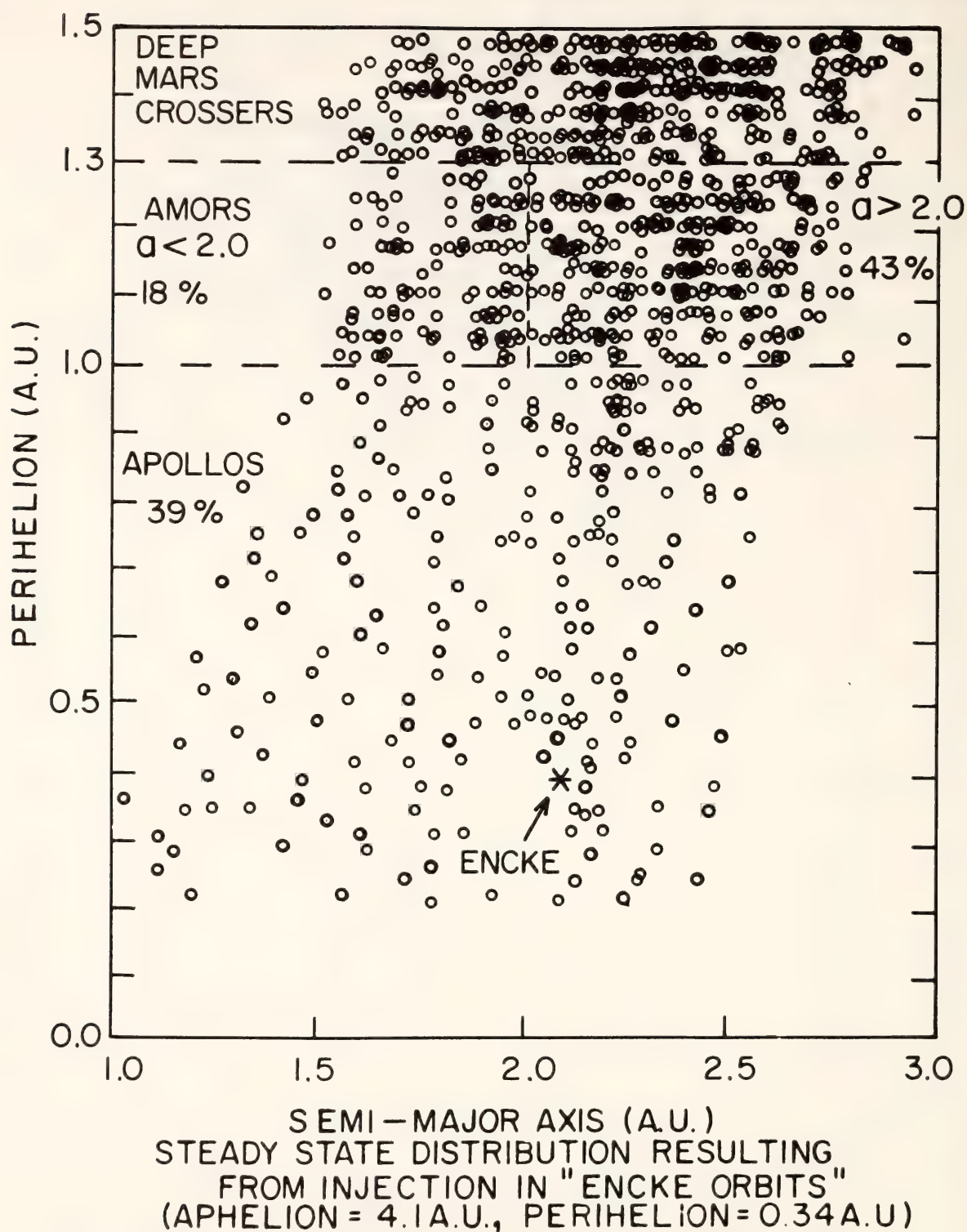


Fig. 42. Steady state distribution calculated for injection of object in initial orbit of short-period Comet Encke (aphelion = 4.1 A.U., perihelion = 0.34 A.U.). Injection rate = 5 objects/ 10^6 years.

forces is greater for comets with small perihelia. For example, the higher solar radiation flux might affect the surface properties of the comet so as to change the lag angle between the subsolar point and the point of maximum emission.

More details of these Apollo-Amor

distributions are given for initial orbits No. 1, 2, and 4 in Figs. 40, 41, and 42. Again it may be seen that very different initial orbits can lead to roughly similar Apollo-Amor distributions. It should be noted that typical orbits in the steady state distribution need not resemble the

initial orbit at all. The initial orbit of Encke is shown on Fig. 42. It lies near the edge of the steady state distribution of objects derived from this initial orbit.

The way this situation arises has been investigated. Soon after injection, the orbits cluster about the initial value. Within ~ 5 million years, the higher semimajor axis portion Apollo region becomes filled and a few Amors appear. After ~ 30 m.y., extensive diffusion of semimajor axis has occurred, and the Apollo region becomes approximately homogeneously filled. At this point the number of Amors and Apollos are comparable, and some of the bodies are in orbits with perihelia beyond 1.3 A.U. With further passage of time, the greater stability of bodies in orbits with perihelia beyond 1 A.U. permits them to accumu-

late more than those in Apollo orbits, and after $\sim 10^8$ years there are about twice as many Amors as Apollos. When the contributions from all of these time intervals are added together, the steady state distribution of Fig. 42 results. In the case of the asteroidal sources (Figs. 40 and 41) the diffusion occurs in the opposite direction—Apollos do not appear in large numbers until after ~ 50 m.y. The Encke initial orbit tends to produce a larger proportion of Amors with >2 A.U. than do the asteroidal sources, and this bears some resemblance to the observed distribution of Amor orbits (Fig. 43). This comparison obviously requires much more attention to observational selection effects and statistical fluctuations, and it is probably premature at the present stage of com-

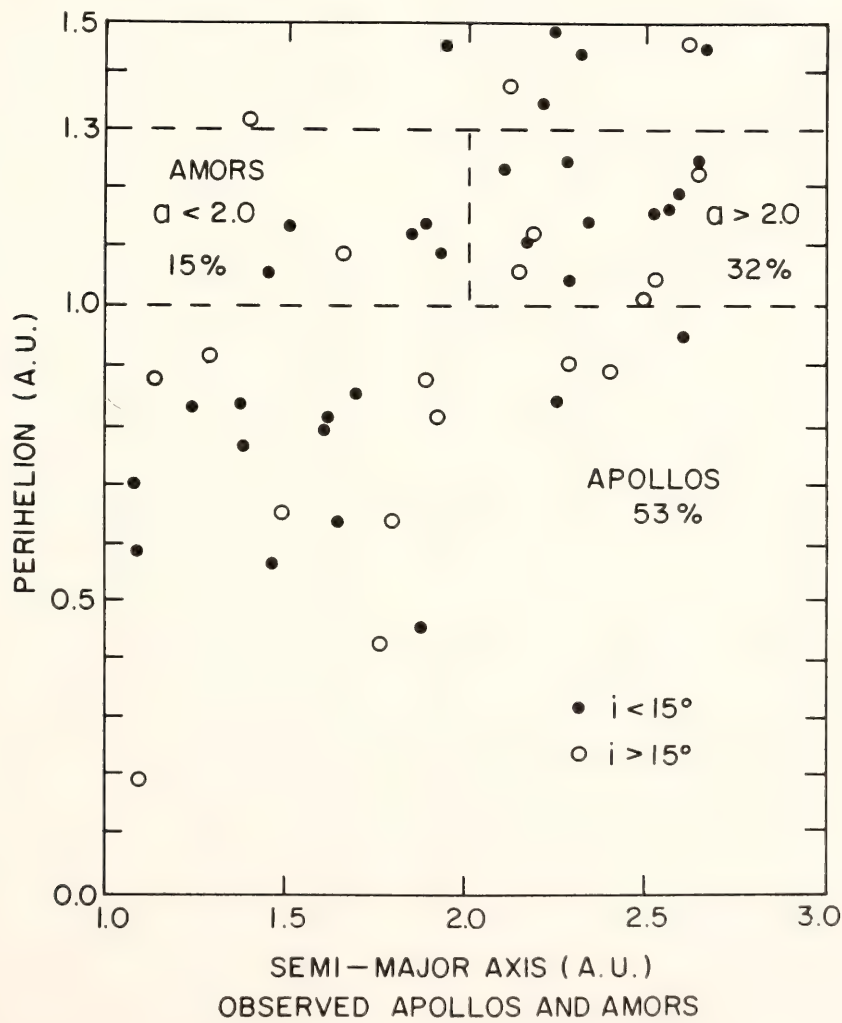


Fig. 43. Observed distribution of Apollo and Amor objects.

pletion of the Apollo-Amor surveys. However, these selection effects are likely to be biased *against* Amors with large semimajor axes, so it is quite likely that these large Amor orbits are even more predominant. This is consistent with the previous conclusion that present evidence favors predominance of cometary sources, but certainly not in a definitive manner.

Occurrence of objects in very small orbits. Typical Apollo and Amor orbits have aphelia in the asteroid belt well beyond Mars, and semimajor axes greater than 1 A.U. However, in recent years two objects (1976AA and 1976UA) have been discovered in much smaller orbits (i.e., with a 1.0 A.U. and aphelion inside the orbit of Mars). It is of interest to inquire whether or not this is to be expected.

The calculated steady state fraction of objects in orbits with a <1.0 A.U. and with aphelion <1.0 A.U. are given in Table 10. It may be seen that orbits of this kind are to be expected. It is also found, in agreement with observation, that about 70% of the orbits with a <1.0 A.U. and with aphelia >1.0 A.U. have aphelia inside the orbit of Mars. A small number of bodies with aphelia inside 1.0 A.U. are also predicted. None has been observed, but no observational search has been made. Considering the small numbers involved, as well as uncertain selection effects, the predicted number of objects in small orbits can be

considered to be in agreement with observation.

Terrestrial and lunar-cratering rates. The steady state orbital distributions described above arise as a consequence of gravitational deflection following close planetary encounters and elimination of objects by planetary impact. The latter process is also responsible for the cratering record on the Moon, Earth, and terrestrial planets. These calculations permit a quantitative discussion of the cratering rate expected to be associated with a given steady state size distribution.

The resulting steady state numbers of Apollo objects required to produce the observed post-mare lunar cratering are given in the next to the last column of Table 11. The results are also given (last column of Table 11) using the terrestrial flux of 2.38×10^{-14} km $^{-2}$ yr $^{-1}$ given by Grieve and Dence (1977) for the Quebec-Labrador area and using the terrestrial scaling law

$$D_c = 1.94 \times 10^{-5} E^{.294}.$$

This scaling law is within $\sim 1\%$ that used by Grieve and Dence (1979).

The calculated lunar values are in good agreement with the observed number of Apollos, and the terrestrial values are about a factor of 3 higher. Use of an average albedo of 0.060 instead of 0.162 will lower the calculated cratering rate by a factor of two, improving the agree-

TABLE 11. Steady State Number of Apollos Required to Match Observed Cratering Rates

Initial Orbit	Velocities (km/sec)			Earth Impacts (%)	Number of Apollos*	
	V	V_M	V_E		A_{Moon}	A_{Earth}
1. 1204 Renzia	15.9	16.1	19.4	7.0	441	1482
2. 313 Chaldaea fragment	18.0	18.2	21.2	5.4	1008	3778
3. Phocaea region fragment	15.7	15.9	19.3	2.5	1119	3673
4. Comet Encke	19.2	19.3	22.2	7.2	804	3163
5. Extinct comet, $q = .92$	15.3	15.5	19.0	3.6	689	2198
6. Extinct comet, $q = 1.50$	19.8	19.9	22.7	2.4	665	2686

* Estimated number (Shoemaker, 1977): 750 ± 300 .

ment for the terrestrial value, but this will not change the ratio of the lunar value to the terrestrial value. Use of the lunar-cratering rate of Neukum *et al.* (1975) will make the discrepancy worse.

The reasons for the discrepancy between lunar and terrestrial results are not clear at present. A similar difference is found by Shoemaker (1977) using the orbital elements of the observed Apollo objects rather than these calculated steady state elements. A smaller difference was found by Grieve and Dence (1979), principally because a higher lunar crater density was used. Therefore most of the discrepancy cannot be attributed to these calculations. Most likely the problem lies in the crater counts and/or the scaling laws. This problem precludes an exact comparison of theory with observation. It can only be said that the calculated number of Apollos required by the somewhat uncertain cratering data is in the range of the number observed.

Concluding Remarks

There is good agreement between the results of these calculations and the observed distribution of Apollos, Amors, and similar bodies in smaller orbits. Agreement with observed terrestrial and lunar crater rates is within the range resulting from uncertainty in the data required to make this calculation. These conclusions are not strongly dependent on the exact way in which the ν_6 resonance or Jupiter encounters are calculated, nor on the relative importance of comets and asteroids as Apollo sources. This provides some measure of confidence in the results of similar calculations for the early solar system.

The principal difference between the observed distribution of Apollo-Amor objects and the calculated steady state distributions presented here is that many high-inclination bodies are observed. This is to a large extent an artifact of the calculation, as only relatively low-

inclination starting orbits were used. This requirement is imposed by the complexities in making such calculations for high inclinations. However, there is no doubt that high-inclination starting orbits will lead to Apollos with inclinations that are high in comparison to those considered here. The observed inclinations are even higher than those observed for typical short-period comets, and the difficulty of obtaining such high-inclination material from the asteroid belt in sufficient quantity has long been recognized (Anders and Arnold, 1965). It is quite possible that the nodal resonance ν_{16} may be important in producing these high inclinations. Because these high-inclination objects will make fewer close encounters to Earth and Venus, the stability of their orbits will be enhanced. Thus a relatively low injection rate may be expected to be capable of sustaining a fairly large steady state population of objects. Whether or not this will work out quantitatively remains to be seen.

The results of these calculations also show that one must be very careful in the use of numerical values of the "half-life" in semiquantitative discussions of these populations. One major effect of the ν_6 resonance is to place a long-lived "tail" on the decrease with time of an initial Earth-crossing population. For typical initial orbits, the number of bodies in Earth-crossing orbit will decrease by a factor of two within $\sim 10^7$ years, and the terrestrial impact rate will decrease by a similar (but not identical) factor. Therefore, in this sense these bodies can be said to have a half-life of $\sim 10^7$ years. However, this rate of decrease will diminish greatly as the transfer of bodies back from Amor and Mars-crossing orbits becomes important, leading to subsequent "half-lives" of $\sim 10^8$ or even $\sim 10^9$ years for the residual population. Furthermore, it was found that an injection rate of ~ 15 objects/ 10^6 years is required to sustain the observed ~ 800 Apollos. Thus after $400/15 \simeq 27$

m.y., half of the Apollos will have been replaced. On the other hand, the median age of a steady state assemblage of Apollos derived from an initial Earth-crossing source (e.g., Encke) will be ~ 200 m.y., and about 35% of the population will be more than 500 m.y. old. This is a consequence of the integral of the long-lived "tail" mentioned above being a large fraction of the total integral. All of these numbers with the dimensions of time are meaningful quantities, but if they are used interchangeably as "half-lives" this can lead to misunderstanding. For example, the high values of the median age cited above show that it would not be improbable for Apollo meteorite sources of cometary origin to experience collisions in the asteroid belt as long ago as 500 m.y., as suggested by some of meteorite ^{39}Ar - ^{40}Ar ages (Turner, 1969; Turner and Cadoğan, 1973; Bogard *et al.*, 1976), even though such times are long compared to $\sim 10^7$ years.

Acknowledgments

I wish to thank J. G. Williams for unpublished results of calculations of the secular resonance amplitudes and for numerous illuminating conversations, as well as E. M. Shoemaker, E. F. Helin, R. A. F. Grieve, and M. R. Dence for very useful discussions of Apollo-Amor objects and their cratering record.

References

- Anders, E., and J. R. Arnold, Age of craters on Mars, *Science*, **149**, 1494–1496, 1965.
- Arnold, J. R., The origin of meteorites as small bodies. II, The model; III, General considerations, *Astrophys. J.*, **141**, 1536–1556, 1965.
- Bogard, D. D., L. Husain, and R. J. Wright, ^{40}Ar - ^{39}Ar dating of collisional events in chondrite parent bodies, *J. Geophys. Res.*, **81**, 5664–5678, 1976.

- Cepilecha, Z., and R. E. McCrosky, Fireball end heights: a diagnostic for the structure of meteoric material, *J. Geophys. Res.*, **81**, 6257–6275, 1976.
- Grieve, R. A. F., and M. R. Dence, The terrestrial cratering record: I and II. In press, *Icarus*, 1979.
- Lecar, M., and F. A. Franklin, On the original distribution of the asteroids I, *Icarus*, **20**, 422–436, 1973.
- Levin, B. J., A. N. Simonenko, and E. Anders, Farmington meteorite: a fragment of an Apollo asteroid?, *Icarus*, **28**, 307–324, 1976.
- Neukum, G., B. König, H. Fechtig, and D. Störzer, Cratering in the earth-moon system: consequences for age determination by crater counting, *Proc. 6th Lunar Sci. Conf.*, **3**, 2597–2620, Pergamon Press, New York, 1975.
- O'Leary, B., Mining the Apollo and Amor asteroids, *Science*, **197**, 363–366, 1977.
- Öpik, E. J., Collision probabilities with the planets and the distribution of interplanetary matter, *Proc. Roy. Irish Acad.*, **54A**, 165–199, 1951.
- Öpik, E. J., Survival of comet nuclei and the asteroids, *Advan. Astron. Astrophys.*, **2**, 219–262, 1963.
- Rabinowitz, M. B., G. W. Wetherill, and J. D. Kopple, Kinetic analysis of lead metabolism in healthy humans, *J. Clin. Invest.*, **58**, 260–270, 1976.
- Scholl, H., and C. Froeschlé, The Kirkwood gaps as an asteroidal source of meteorites, in *Comets, Asteroids, and Meteorites*, A. Delsemme, ed., pp. 293–295, Univ. of Toledo, Ohio, 1977.
- Sekanina, Z., Total gas concentration in atmosphere of the short-period comets and impulsive forces upon their nuclei, *Astron. J.*, **74**, 944–950, 1969.
- Shoemaker, E. M., Astronomically observable crater-forming projectiles, in *Impact and Explosion Cratering*, pp. 617–628, D. J. Roddy, R. O. Pepin, and R. B. Merrill, eds., Pergamon Press, New York, 1977.

Turner, G., Thermal histories of meteorites by the ^{39}Ar - ^{40}Ar method, in *Meteorite Research*, pp. 407-417, P. M. Millman, ed., Reidel, Dordrecht, Holland, 1969.

Turner, G., and P. H. Cadogan, ^{40}Ar - ^{39}Ar chronology of chondrites (abstract), *Meteoritics*, 8, 447-448, 1973.

Wetherill, G. W., Collisions in the asteroid belt, *J. Geophys. Res.*, 72, 2429-2444, 1967.

Wetherill, G. W., Solar system sources of meteorites and large meteoroids, *Ann. Rev. Earth Planet. Sci.*, 2, 303-331, 1974.

Wetherill, G. W., Pre-mare cratering and early solar system history, in *Proc. Soviet-American Conf. on Cosmochem. of the Moon and Planets* (Moscow 1974), pp. 411-424, Nauka, Moscow (also NASA SP-370, pp. 553-567, 1977), 1975.

Wetherill, G. W., Where do the meteorites come from? A reevaluation of the earth-crossing Apollo objects as sources of stone meteorites., *Geochim. Cosmochim. Acta*, 40, 1297-1317, 1976.

Wetherill, G. W., Evolution of the earth's planetesimal swarm subsequent to the formation of the earth and moon., *Proc. 8th Lunar Sci. Conf.*, 1, 1-16, Pergamon Press, New York, 1977a.

Wetherill, G. W., Fragmentation of asteroids and delivery of fragments to earth, in *Proc. of the I.A.U. Colloquium, 39, Relationships between Comets, Minor Planets, and Meteorites*, pp. 283-292, A. H. Delsemme, ed., Lyon, France, 1977b.

Wetherill, G. W., and J. G. Williams, Evaluation of the Apollo asteroids as sources of stone meteorites, *J. Geophys. Res.*, 73, 635-648, 1968.

Wetherill, G. W., and J. G. Williams, Origin of differentiated meteorites, in *Proc. 2nd International Conf. on Origin and Abundance of the Elements*, Paris, 1977, in press, H. De la Roche, ed., Pergamon Press, New York, 1978.

Williams, J. G., Secular perturbations in

the solar system, Ph.D. dissertation, Univ. of California, Los Angeles, 1969. Zimmerman, P.D., and G. W. Wetherill, Asteroidal source of meteorites, *Science*, 182, 51-53, 1973.

THE DISTRIBUTION OF ORBITS OF COSMIC DUST PARTICLES DETECTED BY PIONEERS 8 AND 9

S. J. Weidenschilling

An important clue to the origin of cosmic dust particles is the distribution of their orbital elements. However, most dust-detection experiments have measured only the total flux, while both speed and direction of impact are needed for orbit determination. The most precise data of this type were provided by the Pioneer 8 and 9 spacecraft. These operated in heliocentric orbits near 1 A.U., with sensors scanning the ecliptic plane. For sufficiently energetic impacts, speeds could be determined to about $\pm 15\%$, and directions to $\pm 27^\circ$ (Berg and Gerloff, 1970). We shall consider only these "time of flight" (TOF) events, not the low-energy impacts for which velocities could not be measured.

In eight years of operation, 20 TOF particles were detected. Their nominal orbits and the allowed range of elements were reported by Wolf *et al.* (1976). Five were hyperbolic and are not considered here. Ten were prograde with low inclinations, one had large i , and four were retrograde ($i \simeq 180^\circ$). They were generally characterized by small perihelion distance (q) and large eccentricity (e), with aphelion (Q) near 1 A.U. Rhee *et al.* (1974) classified them by Whipple's (1954) criterion,

$$K = \log_{10} [a(1+e)/(1-e)] - 1 \quad (1)$$

where a = semimajor axis in A.U. K is positive for most periodic comets, and negative for most asteroids. On this basis, most of the particles are "asteroidal." Rhee *et al.* suggested Apollo objects as sources. However, the K -criterion has no

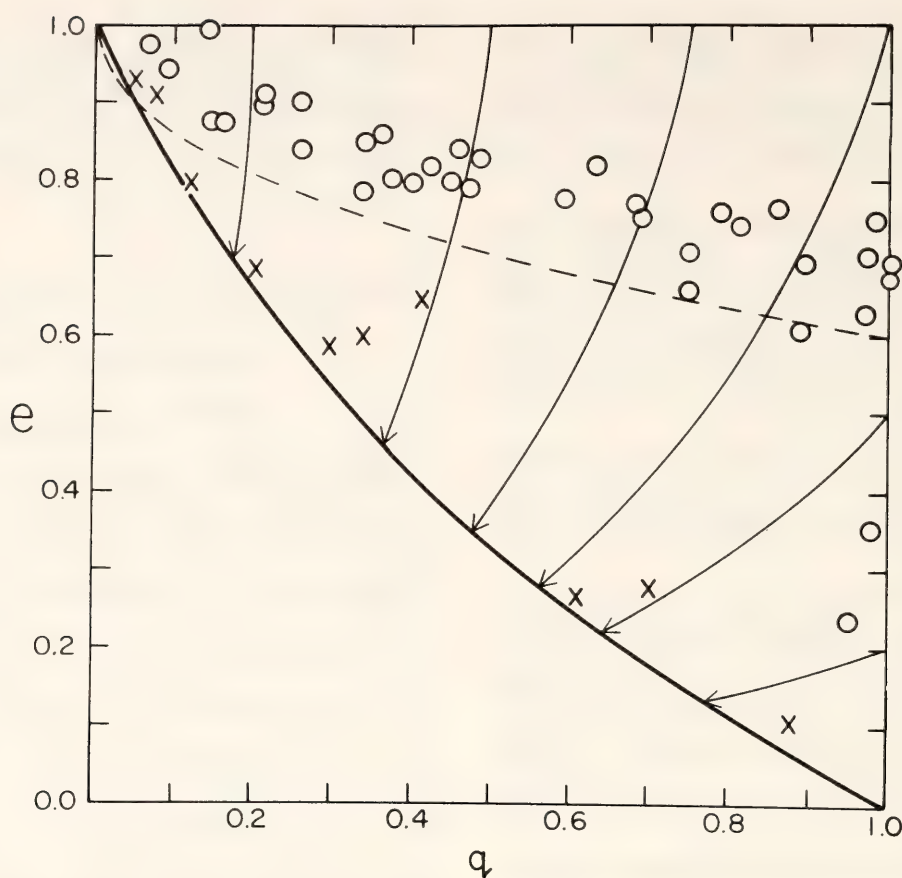


Fig. 44. Eccentricity versus perihelion distance for Pioneer particles with low inclination (crosses), and known meteor streams with $i < 30^\circ$ (circles). Heavy line: $Q = 1$ A.U. Dashed line: $K = 0$. Arrows: Poynting-Robertson evolutionary tracks.

genetic significance; Poynting-Robertson drag can produce such orbits from cometary sources. Figure 44 shows the nominal e and q for 10 low- i particles and the meteor streams with $i < 30^\circ$ listed by Cook (1973). Evolutionary tracks due to P-R drag (Wyatt and Whipple, 1950) are shown. Stream orbits evolve into those typical of TOF particles; in the relevant mass range ($\sim 10^{-11}\text{g}$), this requires $\sim 10^4$ yr. While the present streams are not sources of the detected particles, they typify the distribution of extinct streams which could have produced them.

The TOF particles lack the large aphelia typical of the streams. Particles of this size ($\sim 10^{-4}$ – 10^{-6} times the mass of the faintest detectable meteors) may be missing from the streams, since they are vulnerable to expulsion by radiation pressure. In that case, they may be produced by breakup of larger bodies during

P-R evolution (Kresák, 1976). They also show an apparent excess of small perihelia. Kresák and Kresáková (1976) suggest that this result is spurious because of errors in velocity measurement. Both effects may be present, but the reported distribution of orbits can be explained by consideration of impact probabilities and detector sensitivity.

Consider a spherical target of radius r in a circular orbit at heliocentric distance R . For a particle in an orbit crossing that of the target, the mean impact probability per revolution is (Öpik, 1951)

$$P_i = (r/R)^2 U / (\pi |U_x| \sin i), \quad (2)$$

where U is the magnitude of the particle's velocity relative to the target at impact, and U_x is the radial heliocentric component of that velocity. The formal singularity at U_x or $i \rightarrow 0$ is due to approximations in Öpik's derivation, but

reflects the fact that P_i is greatest when the orbits are most nearly tangent at their intersection. In terms of the particle's orbital elements,

$$U^2 = (1 - \beta)(2 - 1/A) - 2[(1 - \beta)A(1 - e^2)]^{1/2} \cos i + 1 \quad (3)$$

$$U_x^2 = (1 - \beta)(2 - A(1 - e^2) - 1/A), \quad (4)$$

where U and U_x are in units of the target's orbital velocity, $A = a/R$, and β is the ratio of radiation pressure on the particle to solar gravity. Equation 2 implies that impact detection experiments are biased toward orbits with q and Q near the target's orbit ($U_x \rightarrow 0$), and with i near 0° and 180° . (The Pioneer sensor geometry causes additional bias toward these inclinations.) P_i is the impact probability per revolution. For the impact rate, we must divide by the particle's orbital period, $2\pi a^{3/2}[GM_\odot(1 - \beta)]^{-1/2}$, where G = the gravitational constant and M_\odot the solar mass.

The Pioneer data do not allow the distribution of i to be determined. I assume that it can be represented by a mean value which is independent of a and e , and that $\cos i \simeq 1$ for prograde orbits. Then an "impact weight," inversely proportional to the expected impact rate for a given particle, is

$$W_i = (|U_x|/U) A^{3/2} (1 - \beta)^{-1/2}. \quad (5)$$

The TOF orbits, with small A , and with Q near 1 A.U., generally have low values of W_i . This does not explain their apparent excess of small perihelion distances, which may result from the detector characteristics. TOF measurements require impact energies $\gtrsim 1$ erg (Berg and Richardson, 1969). At higher velocities, smaller particles can be detected. If the mass distribution is known and the mass of each impacting particle is measured, each event can be weighted accordingly. Grün *et al.* (1973) report particle masses but do not identify them

by their orbits. When individual masses are unavailable, weights can be assigned statistically, as follows. For a detector with an energy threshold, the smallest detectable mass, m_t , is proportional to U^{-2} . With a mass distribution of the form $N(m) dm \propto m^{-3/2} dm$ (Dohnanyi, 1973), the number of particles with $m > m_t$ is proportional to $m_t^{-1/2}$ or to U . The "detection weight,"

$$W_d = W_i/U, \quad (6)$$

is inversely proportional to the expected rate of *detectable* impacts. W_d is similar in concept to Whipple's (1954) "cosmic weight" for meteors.

Figure 45 shows contours of W_d for $\beta = 0.2$. The expected detection rate is greatest for orbits with small aphelia, and favors those with higher eccentricities. When $\beta < 0.1$, W_d is very large for small values of e , owing to the low impact velocities. Otherwise, the general features are not sensitive to the value of β . Therefore, I have neglected any correlation of β with m . Since the particle densities are unknown, more detailed analysis is not justified. The Pioneer data show good qualitative agreement with the model in spite of its idealizations. The orbital eccentricity of the target has been neglected, and the particles' published values of a and e were used rather than the directly measured velocity components. Still, the model supports the conclusion that the elements reported by Wolf *et al.* for the prograde orbits are generally correct. However, the measured distribution of orbits is severely biased against large aphelia. The lack of such orbits in the sample does not rule out their existence in space or a cometary origin for the detected particles.

A similar calculation for retrograde orbits shows that both impact and detection rates are largest for orbits of low eccentricity and $q \simeq 1$ A.U. However, all four retrograde orbits reported by Wolf *et al.* have $e > 0.8$ and $q < 0.1$

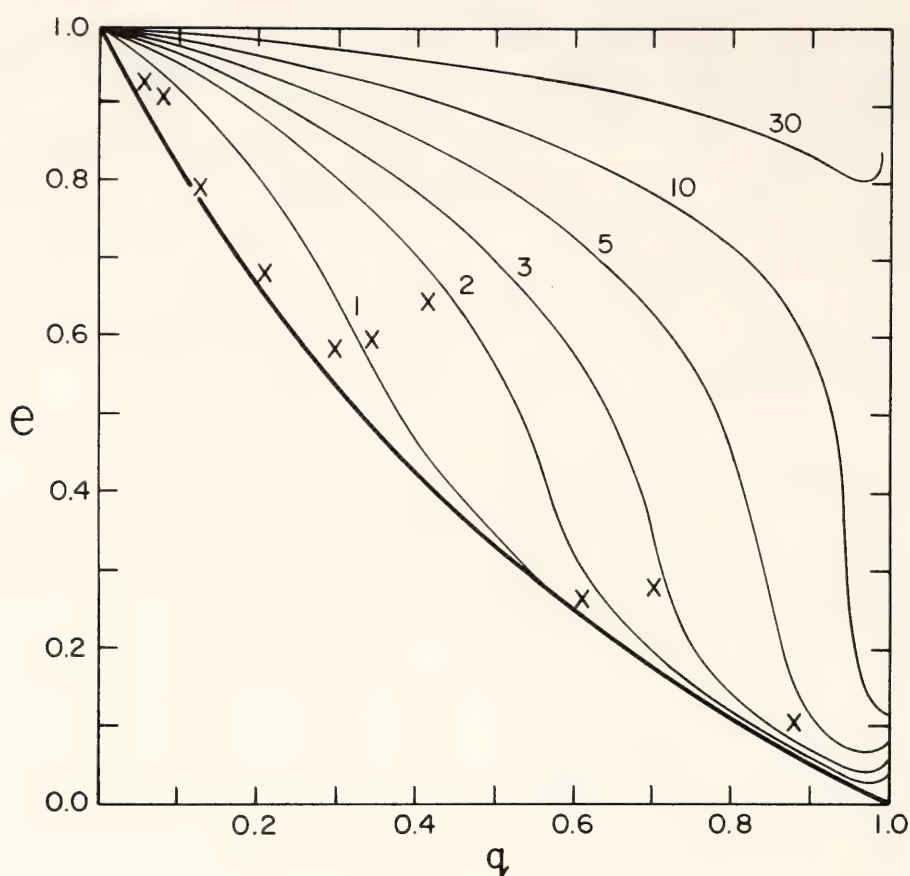


Fig. 45. Contours of detection weight W_d for orbits with low inclination, with $\beta = 0.2$.

A.U. If genuine, they would imply that those particles originated with small q and that there is no population of retrograde particles with larger perihelia. The latter condition is unlikely: evaporation and expulsion by radiation pressure would still require a source at larger heliocentric distance, for example. For orbits of the type reported, with large e and $Q \simeq 1$ A.U., the velocity difference between prograde and retrograde orbits is minimized. An overestimate of the impact velocity could falsely indicate a retrograde orbit. Most probably, the reported retrograde orbits are spurious.

Acknowledgment

I thank R. S. Rajan for bringing this problem to my attention, and for many helpful discussions.

References

- Berg, O. E., and U. Gerloff, Orbital elements of micrometeorites derived from Pioneer 8 measurements, *J. Geophys. Res.*, **75**, 6932, 1970.
- Berg, O. E., and F. F. Richardson, The Pioneer 8 cosmic dust experiment, *Rev. Sci. Instrum.*, **40**, 1333, 1969.
- Cook, A. F., A working list of meteor streams, *NASA SP-319*, 183, 1973.
- Dohnanyi, J., Current evolution of meteoroids, *NASA SP-319*, 363, 1973.
- Grun, E., O. E. Berg, and J. S. Dohnanyi, Reliability of cosmic dust data from Pioneers 8 and 9, *Space Research*, **XIII**, 1057, 1973.
- Kresák, L., Orbital evolution of the dust streams released from comets, *Bull. Astron. Inst. Czech.*, **27**, 35, 1976.
- Kresák, L., and M. Kresáková, A note

- on meteor and micrometeoroid orbits determined from rough velocity data, *Bull. Astron. Inst. Czech.*, 27, 106, 1976.
- Öpik, E. J., Collision probabilities with the planets and the distribution of interplanetary matter, *Proc. Roy. Irish Acad.*, 54A, 165, 1951.
- Rhee, J. W., O. E. Berg, F. F. Richardson, and S. Auer, Origin of fifteen cosmic dust particles intercepted by Pioneer 8 and 9, *Nature*, 252, 555, 1974.
- Whipple, F. L., Photographic meteor orbits and their distribution in space, *Astron. J.*, 59, 201, 1954.
- Wolf, H., J. W. Rhee, and O. E. Berg, Orbital elements of dust particles intercepted by Pioneers 8 and 9, in *Interplanetary Dust and Zodiacal Light*, p. 165, Springer-Verlag, Berlin, 1976.
- Wyatt, S. P., Jr., and F. L. Whipple, The Poynting-Robertson effect on meteor orbits, *Astrophys. J.*, 111, 134, 1950.

RELATIONS BETWEEN METEORS AND METEORITES

THEORETICAL ENTRY MODEL

D. O. ReVelle

Despite the fact that the entry of large meteoroids into the atmosphere can produce some of the most startling and magnificent phenomena known, very few theoretical treatments which might realistically model this complex physiochemical process have been attempted. The classic book by Bronshten (1964) represented a beginning step toward a "modern" treatment of the subject, since the author considered the details of the fluid-meteor interaction rather than the simpler problem of the smaller "shooting stars" and their demise in the upper atmosphere treated previously by Öpik, Levin, and earlier workers. In the work of Baldwin and Sheaffer (1971), a physical theory was advanced which in some ways is similar to the model of ReVelle (1976b, 1978) to be subsequently discussed. The primary differences, how-

ever, are in the inherent methodology (numerical versus analytical approaches) and in the reliability of the radiative portion of the shock-wave energy (which produces ablation of the meteoroid) which was calculated. The model of ReVelle, although it does not consider the fragmentation process, as that of Baldwin and Sheaffer does albeit in an approximate manner, was developed as an improvement over the latter. The extent that this has been achieved is difficult to say in detail. Reasonable agreement with results of other methods is as good a comparison as we now have, considering the uncertainties involved. In this respect, the model to be discussed is in good agreement with results of cosmic ray track analyses of preatmospheric masses of meteorites best exemplified by the well-known Lost City meteorite (Bhandari *et al.*, 1978). The model is also in good agreement with the dynamical-inversion sigma-intersection method of McIntosh (1970b), which was used in an analysis of flight data for the Lost City and Pribram meteorites.

ReVelle (1978) applied the method to the recent Innisfree meteorite and found good agreement with the entry-model results in that case as well.

Consider a meteoroid of mass m and with an entry velocity v entering the atmosphere at an inclination angle Θ with respect to the horizon. Because of the large relative velocity with respect to ambient air molecules, sufficient kinetic energy is available to severely ablate entering meteoroids over a range of velocities and masses. The results of the detailed computations are given in Fig. 46 for the sizes and velocities of interest for chondritic meteoroids similar to Lost City. Although the entry angle is fixed at 45° in this figure, computations made at other angles do not change the ablation loss in a significant manner except perhaps for the case of very shallow entry (small Θ). For such cases, however, the model assumptions eventually

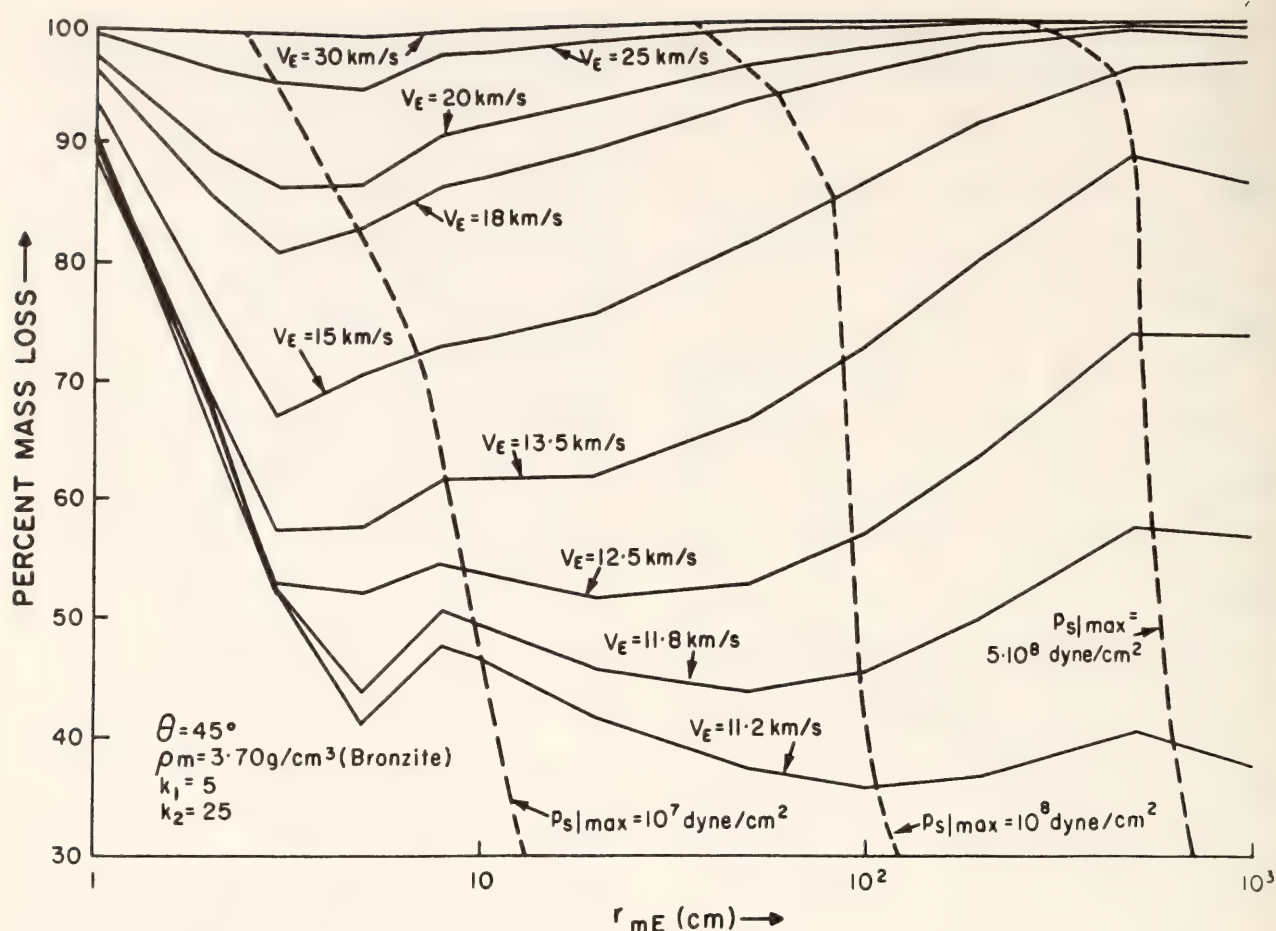


Fig. 46. Percent mass loss versus initial radius, r_{mE} , as a function of entry velocity, V_E , for bronzite chondrites with bulk density, ρ_m , entering at an angle, θ , of 45° from the horizon. The body is assumed to be spherical throughout the entry, which terminates at 3.5 km/sec. The parameters k_1 , and k_2 are constants in the theory, which allows the energy of ablation values to be determined.

break down, so entries for $\theta \leq 10^\circ$ are not considered further. Fortunately, most large meteoroids do not enter at very shallow angles, as can be seen in the Prairie Network fireball data (McCrosky *et al.*, 1976), so this case is not of much concern.

The results clearly indicate that for meteor velocities exceeding ~ 30 km/sec, the expected mass loss is $\geq 97\%$ for masses between ~ 10 g and $\sim 10^{10}$ g. At velocities ~ 11 km/sec, values over this same mass range are more typically $\sim 40\%$ except for the smaller masses less than ~ 1 kg. Also indicated in the figure are lines of constant peak-stagnation pressure, as predicted in the model. According to laboratory studies, meteorite failure due to a uniaxially applied tensile or compressive force for Bronzite chon-

drates occurs at pressures $\geq 2 \cdot 10^8$ to $2 \cdot 10^9$ dynes/cm² (Baldwin and Sheaffer, 1971). If this were the case, the single-body treatment would be a reasonable approximation for those bodies that do not experience such pressure loading during entry. However, all three photographed and recovered meteorites considered in the next section displayed some fragmentation at pressures as low as 10^7 dynes/cm², a value typical of carbonaceous chondrites in terms of compressive induced failure. Thus, whether such break-up effects are due to pressure effects or heat-flux loading (Jones and Kaiser, 1966), or preexisting flaws from prior space collisions, or other causes, cannot now be decided with certainty and in fact may be different for different meteors. In what follows, we assume the

single-body approximation to be reasonable as long as either the number of fragments is small or a size distribution of fragments is produced that has the majority of the mass in a few large pieces.

The uncertainty in the conclusions caused by fragmentation manifests itself in two ways. The first is the effect on the end height of the meteor (end of the luminosity). The second relates to deducing reliably a preatmospheric mass value, to be compared with that obtained by different methods. In order to better appreciate these respective uncertainties we will briefly outline the key features and methodology of the entry model.

The model is based on three key equations—momentum conservation, energy conservation, and a geometrical relation for meteors entering at different angles to the local horizontal. Using an analytic solution of these equations for the special case where σ , the ablation parameter, is a constant, we can immediately determine a generalized iterative result applicable to the realistic case where σ is a free parameter as a function of height, velocity, mass, composition, and other variables. The latter variability of σ for large meteoroids has been predicted by aerodynamicists for many years (Gazley, 1968). It is only recently, however, that the complex physiochemical processes have been understood well enough to obtain reliable values of σ by the lengthy numerical solutions of the aerodynamic equations for flows involving heat transfer with both convective and radiative components. Thus, in essence we assume that the simple ablation theory presented in McIntosh (1970a) is applicable to large meteoroids as long as the predicted variable value of σ to be used is sufficiently accurate. We believe the latter to be correct for the model of ReVelle, although to be sure refinements in the future for other small influences may help clarify certain aspects of the problem.

Having briefly described the single-body model, we next discuss possible effects of fragmentation on our ability to reliably predict the end height and initial mass of a meteorite. In order to determine these quantities with the model, flight data such as velocity versus altitude are first needed for the recovered meteorite. The latter restriction is necessary so that the bulk density of the meteoroid can be input to the model. Flight data are routinely obtained by the photographic fireball networks (Halliday *et al.*, 1978), but for these objects the bulk density is not an *a priori* parameter. For such objects a preatmospheric mass cannot be immediately deduced—rather only the preatmospheric mass-to-area ratio, since it is functionally related to the product of the body radius and bulk density (i.e., neither of these can be determined separately unless one of the two are known via some other independent information). Once a bulk density and flight data are available, the model is initialized at the “top” of the atmosphere (where the drag force balances the body-weight component along the entry such that the deceleration is initially zero) according to the characteristics of the recovered material. Iterative analytic calculation proceeds until the meteor velocity falls below ~ 1 km/sec. Below this velocity various assumptions of the theory are no longer reasonable, but the major part of the ablation has already occurred for velocities ≥ 10 km/sec, so the region below 1 km/sec is not of concern. If a given meteor ceases to be luminous at some velocity > 1 km/sec, the height predicted corresponding to the actual end height is compared for various initial masses. The final mass chosen as the preatmospheric value must satisfy two conditions. Its end height must be lower than that of the actual meteorite by some reasonable amount (see below) and, secondly, the predicted terminal mass must closely approximate the recovered mass of the body. In a sense

these two conditions are related to each other: they are not independent. At present, however, we cannot evaluate their interdependency quantitatively. We proceed with the assumption that fragmentation produces only a relatively minor influence on the entry or else the single-body approach will no longer be a reasonable one.

The reasoning causing the end-height prediction to be lower than that of the actual meteorite is that fragmentation is likely to produce a smaller effective mass-to-area ratio than that of the original single body. If the statistical treatment of Baldwin and Sheaffer (1971) is reasonable (i.e., if break-up into N pieces of equal size, shape, etc., occurs), then the mass-to-area ratio decreases as $N^{1/3}$ relative to the single-body approach, which for $N \leq 10$ is ~ 2 which physically corresponds to an end-height increase of ~ 4.6 to 5.1 km depending on the model atmosphere used in the calculation. Thus, we might expect a reasonable end-height fitting of ≤ 5 km below the observed value for a meteorite which suffered only minor fragmentation during entry for the deduced preatmospheric mass whose terminal value is in reasonable agreement with the recovered mass.

Such fitting has been carried out for the three meteorites considered in the next section. Their reliability is limited with respect to the accuracy of both the entry model and the recovery completeness. It is felt with some certainty that this model is a reasonable approximation to reality for those bodies that do not extensively fragment for whatever reason. Future efforts that more realistically model the fragmentation process would certainly be helpful in evaluating fireballs, which do not appear to behave essentially as single bodies, as discussed later in this Report.

Acknowledgment

The author would like to express his gratitude to Dr. Bruce McIntosh of the

National Research Council of Canada for suggesting the development of the entry model and for encouraging its successful completion. The fellowship provided by the National Research Council of Canada during the course of this work is also greatly appreciated.

LUMINOUS EFFICIENCY OF METEORITES

R. S. Rajan and D. O. ReVelle

Our knowledge of meteor masses in the past has come almost exclusively from the photometric method using the luminous efficiency concept introduced by Öpik. To be sure, meteor radar observations (McKinley, 1961) have contributed valuable information as well. However, for larger meteors, ≥ 1 kg, such data are difficult to obtain because of the rapid recombination rates in the lower atmosphere. Also, the flux rate of large bodies is sufficiently low that few truly large meteoroids have ever been observed by radar methods.

Since we now have light data for three recovered meteorites and confidence in the entry model of ReVelle (1976b, 1978), we decided it would be useful to invert the normal process of integrating the light data during entry to obtain photometric mass and instead solve explicitly for the luminous efficiency in an empirical manner. In Table 12 the entry-model values deduced for these meteorites is presented. In Fig. 47 the light data for these meteorites is displayed. Before discussing the data and its interpretation in terms of luminous efficiency, we will briefly describe the light-generation model considered in this work.

For large meteoroids which penetrate deeply in the atmosphere the process of light generation becomes very complex. Contributions to the observed light can arise from shock-wave radiation, from ablation-products emission, from the remnant processes occurring in the wake behind the meteor, from a precursor ionization "halo" forward of the body,

TABLE 12. Deduced Entry Model Masses of Meteorites

Meteorite	m_{∞}^* (kg)	m_t^* (kg)	V_{∞}^{\dagger} (km/sec)	θ_{\ddagger} (deg)	N§	Predicted Mass Loss (%)
Pribram Cepolecha (1961)	1336	52.9	20.89	43.26	4	96.05
Lost City McCrosky <i>et al.</i> (1976)	52.3	17.1	14.20	38.32	4	67.30
Innisfree Halliday <i>et al.</i> (1978)	14.7	5.05	14.22¶	67.26	9	65.65

* All masses are calculated assuming a spherical shape.
† Observed preatmospheric velocity.
‡ Observed horizontal entry angle.
§ N is the number of recovered fragments.
|| Preatmospheric mass values for Pribram were originally determined in the range 250–3170 kg, with the uncertainty coming primarily from the fact that an additional large fragment (~ 10–100 kg) was suspected, but was not located. We choose the value shown since its terminal mass, m_t , is intermediate to the above estimate and is a reasonable choice on the basis of luminous efficiency calculations and with regard to the observed end height.
¶ The presently accepted value is 14.54 km/sec. The results obtained using this value would differ by only ~ 2% (increase in m_{∞}) over values obtained using the earlier V_{∞} estimate.

from the body surface (especially so at very high or low altitudes), or from other sources. This description is in sharp contrast to the relatively simple process of light generation proposed for smaller meteors which penetrate only into the upper atmosphere (Kovshun, 1977); these are the meteors for which Öpik originally introduced the luminous efficiency concept. Despite the conceptual differences between these two broad mass classes in terms of their ability to generate light, ground-based laboratory measurements have not indicated gross differences in the light produced by either class (Givens and Page, 1971). This seems somewhat surprising, but there are a number of reasons why this may or may not be possible. These include the fact that experiments cannot simulate beyond about 8 km/sec in velocity, but these velocities are about two or more times smaller than those typical of observed deep-penetrating bright meteors (fireballs). Second, at these higher velocities the range of wavelengths generated at a shock-wave source shifts spectrally toward the ultraviolet

(Schneider, 1974) and the photographic plate is not sensitive to such emission. We approach the problem by writing the conservation equation for the rate of change of kinetic energy and assuming that the instantaneous light emission is proportional to it (Romig, 1965).

$$I \propto \frac{d}{dt} \left(\frac{1}{2} m v^2 \right),$$
$$\text{i.e., } \propto \left(\frac{v^2}{2} \frac{dm}{dt} + m v \frac{dv}{dt} \right),$$
$$= \tau_{CF_v} \frac{v^2}{2} \frac{dm}{dt} \left(1 + R_{fa} \right),$$

where I is instantaneous light emission, R_{fa} is inverse ablation efficiency $= \frac{1}{\sigma v^2/2}$, v is meteor velocity, m is meteor mass, τ_{CF_v} is the luminous efficiency with respect to a detector peaked in the visible. Our deduced values of luminous efficiency as a function of velocity for the three photographed meteorites using the above equation is given in Fig. 48, where for $\frac{dm}{dt}$, we have used the

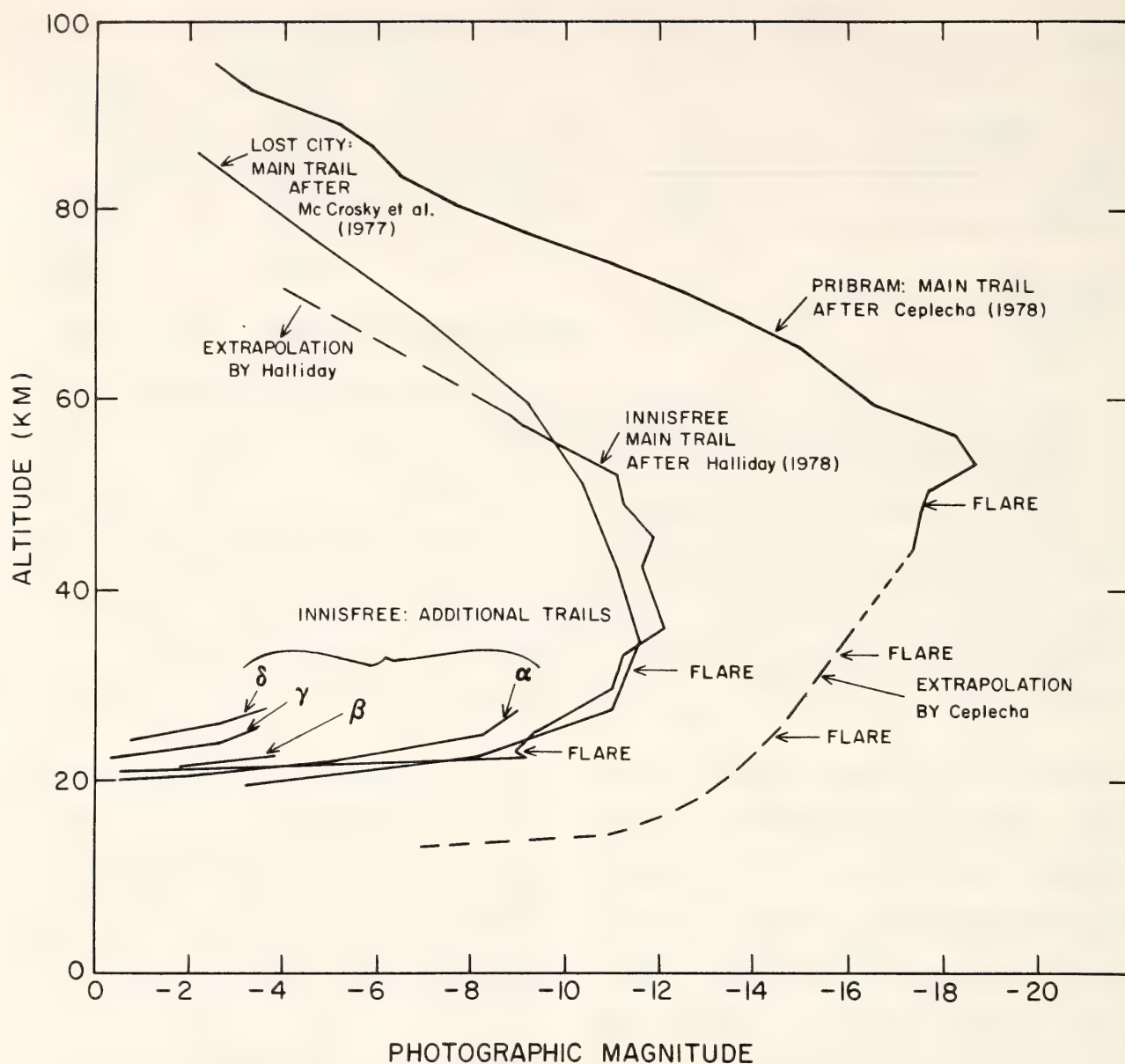


Fig. 47. Photographic magnitude as a function of altitude for the Pribram, Lost City, and Innisfree meteorites, respectively. The symbols α , β , γ , and δ refer to other, less brilliant trails observed for Innisfree. Digital values for the magnitude have kindly been provided by Cepplecha (personal communication, 1978) for Pribram and by Halliday (personal communication, 1978) for Innisfree.

appropriate theoretical mass loss rates, deduced from entry-model results. Further details regarding the calculations can be found in ReVelle and Rajan (1978). Our deduced values of luminous efficiency at velocities corresponding to peak ablation are ~ 0.2 to 0.4% , while typical values used by Cepplecha and McCrosky (1976) are ~ 0.02 to 0.04% .

The standard luminosity equation of Cepplecha and McCrosky (1976) has two

shortcomings. First, it assumes that the deceleration term can be neglected (i.e., $R_{fa} \equiv 0$). It turns out to be quite non-negligible ($\sim 50\%$ to a factor of 2) at velocities ≤ 12 km/sec. Second, the empirical relation used was mostly deduced from simulation experiments done on steel balls with velocities of ≤ 12 km/sec. Consequently, in order to derive the dependence on velocity for chondrites, severe extrapolations and modifications of

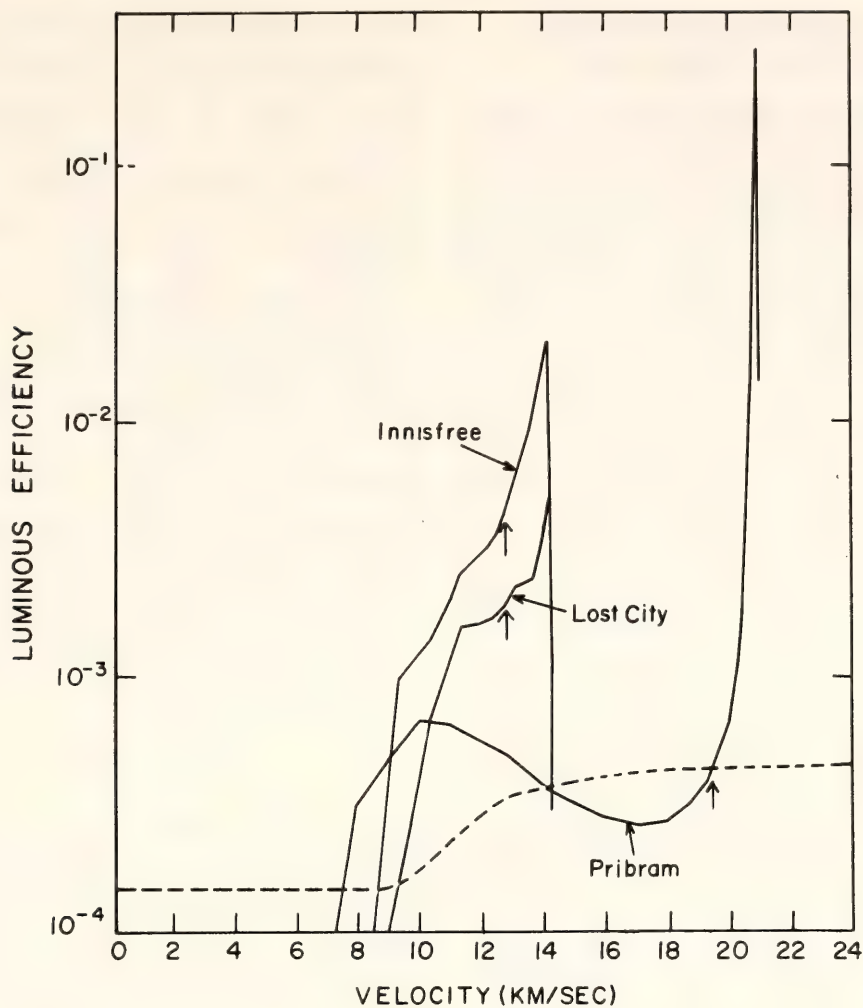


Fig. 48. Luminous efficiency as would be measured by a detector peaked in the visible for the three meteorites in Fig. 47 as a function of the velocity. The dashed line is the empirical luminous efficiency of Ceplecha and McCrosky (1976) for chondritic bodies. The vertical arrow refers to the velocity at which maximum ablation is predicted to occur in the entry model.

the data were needed. Because of the various uncertainties mentioned above, we feel that the final relation deduced by them is quite uncertain and the computed photometric masses for the Prairie Network fireballs do not represent the true preatmospheric masses. Although the additional deceleration term that we have included reduces the discrepancy, the photometric masses still are a factor of 3 to 5 higher compared to those deduced from entry-model results and other methods. The reasons for the discrepancy between luminous efficiency-velocity relationships deduced by us and

those used by Ceplecha and McCrosky (1976) are not totally clear at present. The discrepancy is unlikely to be due to a simple scaling factor, since there are gross differences in the slope of luminous efficiency versus velocity in our results (Fig. 48). Finally, our results are in good agreement both in their absolute value and in the velocity dependence with suitably modified laboratory simulation experiments of Givens and Page (1971). We hope that our work will serve as an impetus for more simulation experiments and possibly to improve theoretical understanding of the processes involved.

IDENTIFICATION OF METEORITES WITH BRIGHT METEORS

G. W. Wetherill, D. O. ReVelle, and R. S. Rajan

Most of our knowledge about the primitive solar system is obtained from chemical, isotopic, and petrographic studies of meteorites. Currently, this detailed information is not matched by a similar understanding of the history of meteorites in the present solar system prior to their recent impacts with the Earth. This gap in our understanding must be closed if we are to make full use of the meteoritic evidence.

During the past decade there has been significant progress in theoretical techniques for tracing the orbital evolution of "stray" solar system bodies: comets, asteroids, Earth-crossing Apollo objects, and meteoritic fragments. However, theory which is not confronted with observation and experiment becomes merely an amusing private game for a few specialists. There is danger that this might prove to be the case in the area of meteorite orbital dynamics. For example, although large-area photographic networks have been in operation for about 20 years, preimpact orbital data have been recorded for only three recovered meteorites.

During the same time period, these networks have photographed thousands of "fireballs"—bright meteors commonly of magnitude -8 or brighter. The most commonly heard opinion is that almost all these fireballs are quite unlike the dense rocks that comprise our meteorite collections. Rather, it is held that the fireballs are fragile "dust-balls," with typical densities of 0.8 g/cm^3 or less.

This view has been recently challenged by Ceplecha and McCrosky (1976). These workers have analyzed data for more than 300 fireballs photographed over a 10-year period by the Smithsonian Astrophysical Observatory's 10^6 km^2 "Prairie Network" in the central United States. The fireballs were classified into

three major groups, on the basis of calculations making use of their end height—the altitude at which the meteor ceases to be visible. The conclusion of this work was that a large fraction of the fireballs are produced by the same type of objects recovered as meteorites.

Although this conclusion is by no means generally accepted at present, from one point of view it seems it must be correct. The three meteorites recovered by these networks were among the brightest and most massive fireballs photographed. However, the observed size distribution of recovered meteorites shows that small meteorites are much more abundant than large ones. The observed distribution law for meteorite mass is of the form

$$dN = C m^{-p} dm, \quad (1)$$

where dN is the number of bodies of mass m in the mass interval dm , and the power-law exponent p lies in the range between 1.7 and 2. For this reason it is to be expected that the three large meteoritic fireballs should be accompanied by many smaller objects of the same kind. Quantitatively, this has the consequence that one third or more of the fireballs should be meteorites. When looked at in this way, the problem appears much simpler and reduces to choosing which ones among the fireballs are most likely to be the meteorites and which ones less likely. Taking this approach, we have extended the work of Ceplecha and McCrosky by using the Prairie Network data in a different way.

Although our overall conclusion will support that of Ceplecha and McCrosky, namely that many of the fireballs are actually meteorites, in detail our results often differ. In this earlier work the mass of the fireballs was estimated from their luminosity. The accompanying report on the luminous efficiency of meteorites argues that this leads to an overestimate of the mass by a factor of 5 to 10. Furthermore, in this earlier treatment, the

end-heights of fireballs with many different characteristics were combined into a single, empirical scaling law relating mass, initial velocity, and entry angle to end height. This is likely to be physically unrealistic because the visible trail of a meteor may end for a number of reasons. The body may be eroded away by ablation as it passes through the atmosphere, it may be disrupted into small fragments by aerodynamic forces, it may be decelerated to velocities too low to produce incandescence, or its brightness may simply fall below the sensitivity threshold of the photographic plates before any of these things.

Rather than attempt to deal with the full set of fireball data, we have concentrated on the low-entry-velocity (<18 km/sec) objects. This greatly reduces difficulties associated with velocity scaling but still includes a major portion of the meteoritic fireballs inasmuch as two of the three recovered fireballs (Lost City and Innisfree) had velocities between 14 and 15 km/sec. Also, rather than develop empirical scaling laws we have made extensive use of the theoretical single-body entry model of Revelle (1978), the validity of which has been tested by comparison with the Lost City and Innisfree observations.

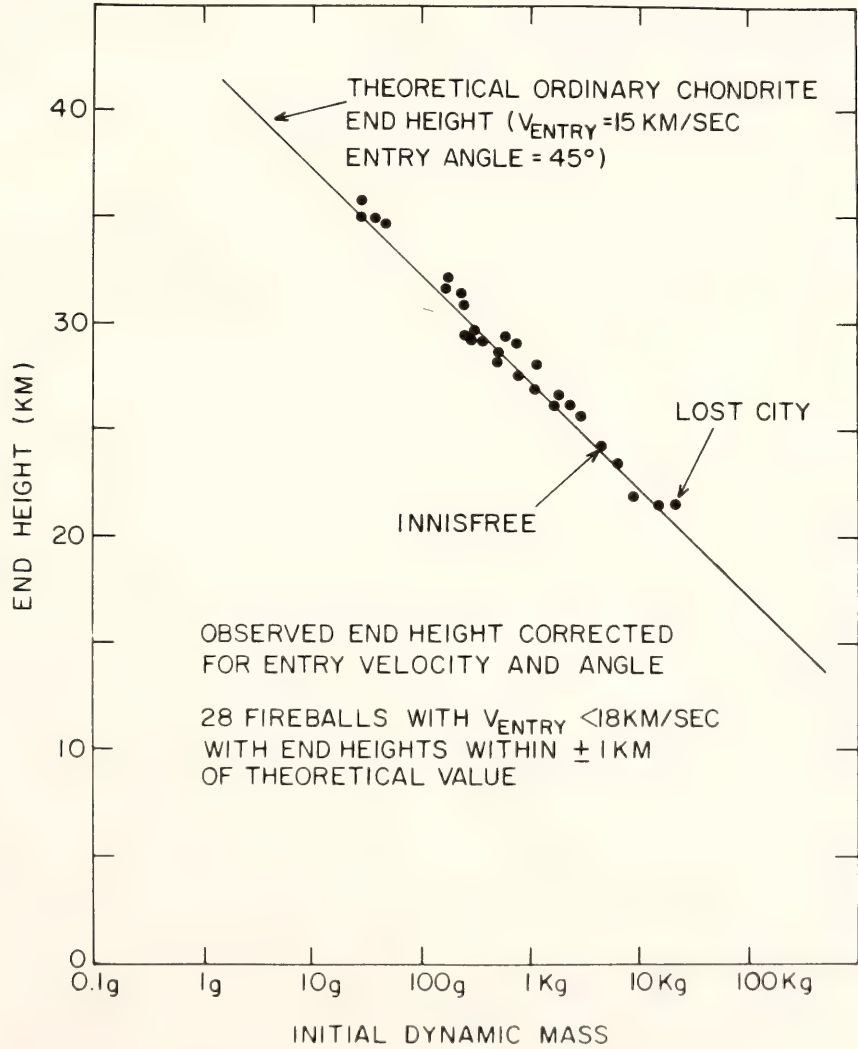


Fig. 49. Comparison of theoretical and observed end height for Lost City, Innisfree, and 26 Prairie Network fireballs ($V_{\text{entry}} < 18$ km/sec), which have end heights within ± 1 km of the theoretical value (scaled to $V_{\text{entry}} = 15$ km/sec), entry angle = 45° .

This theory defines a relationship between the dynamic mass of a meteor (as determined by its deceleration), its entry angle and velocity, and its end height. We have defined the latter quantity dynamically to be the altitude at which the velocity has been decreased to some particular low value, in this case taken to be 6 km/sec. This theoretical end height as a function of mass has been calculated for a nominal entry angle of 45° and nominal entry velocity of 15 km/sec, using laboratory data for the physical properties of ordinary bronzite chondritic meteorites, as shown in Fig. 49. When the observed dynamic masses and end heights of the two recovered low-velocity fireballs, Innisfree and Lost City, are plotted on this same figure, after correction for velocity and entry angle it is found that they lie very near

the theoretical value of the end-height appropriate to their initial dynamic mass. This agreement between the theoretical single-body and observed end heights is a characteristic of these recovered meteorites, in spite of the fact that they did undergo some fragmentation in the atmosphere and hence were not single bodies in the strict sense. This fragmentation is the most likely reason the measured dynamic masses are about a factor of 3 lower than the actual masses, as estimated from the recovered mass and from charged-particle track data. In spite of this complication, this result suggests that such agreement between theoretical and observed end heights, when dynamic masses are used, is a useful criterion for identifying similar ordinary chondrites among the fireballs.

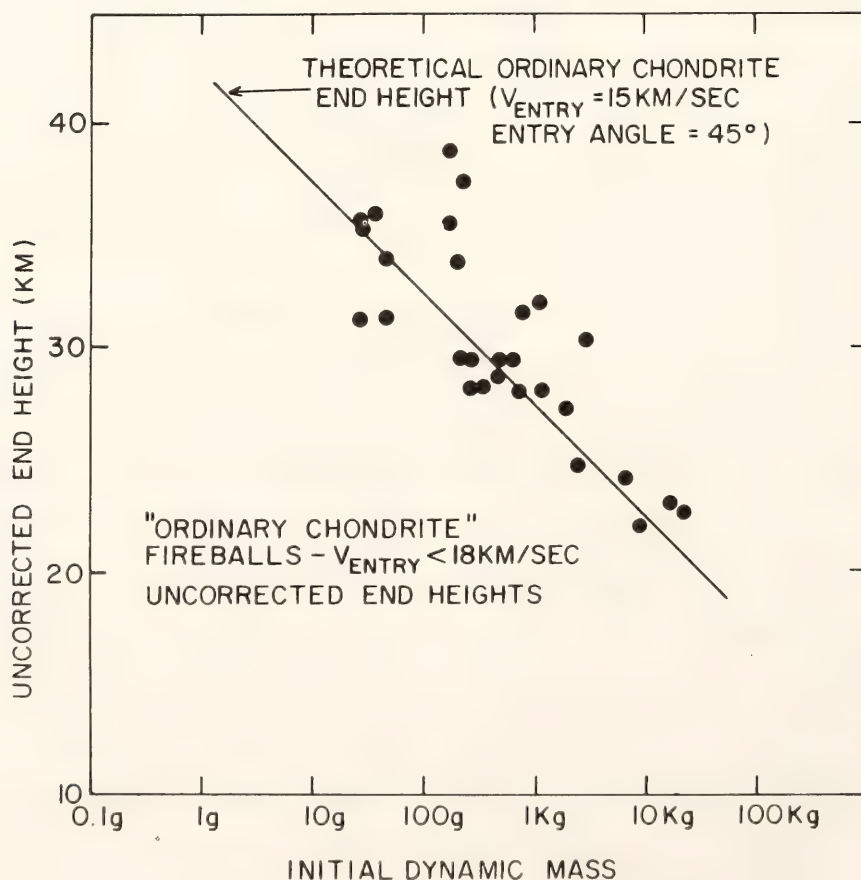


Fig. 50. Same fireballs plotted in Fig. 49, without scaling end height for velocity and entry angle. Scaled end height distribution for all.

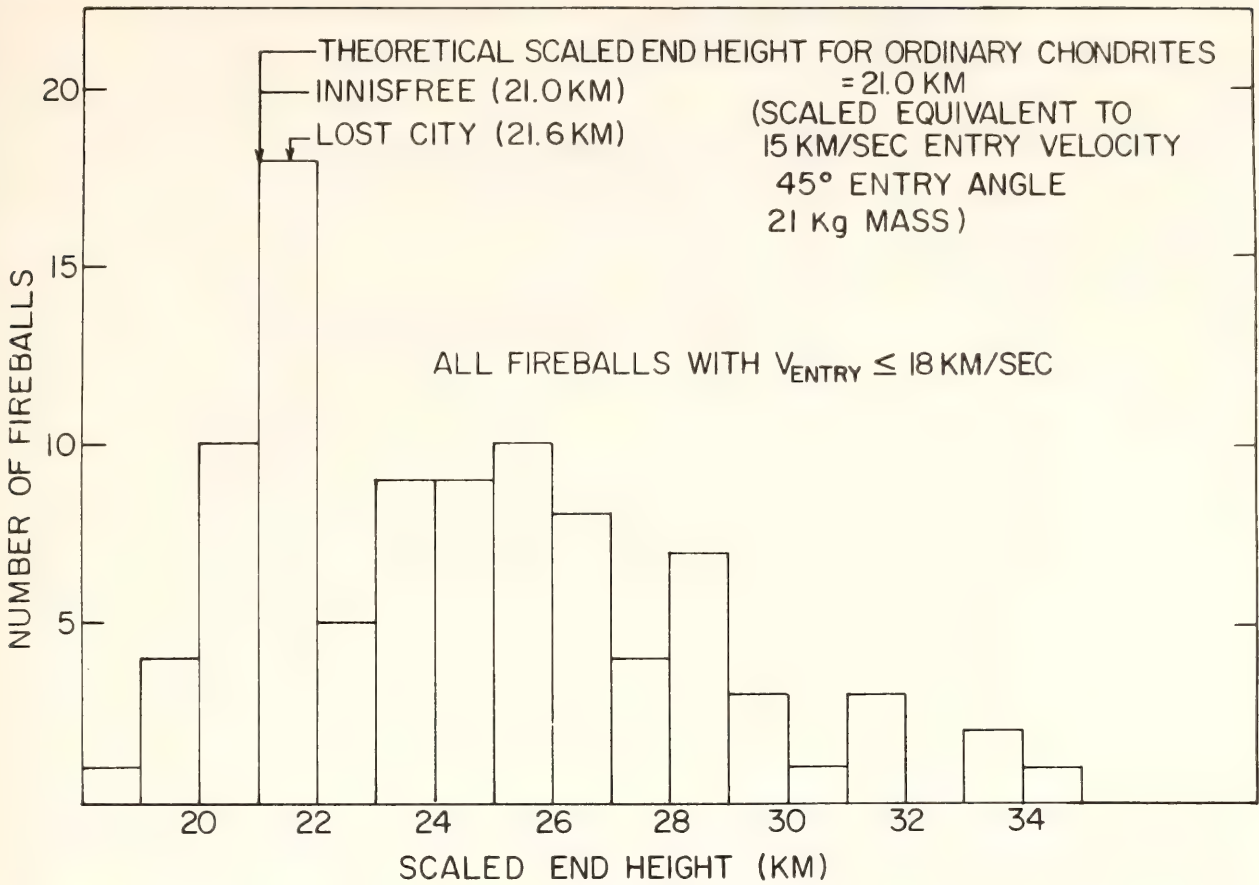


Fig. 51. Prairie Network fireballs with $V_{entry} \leq 18$ km/sec, scaled as in Fig. 49 for entry velocity and angle, and scaled to a dynamic mass of 21 kg. The fireballs falling in the interval 20–22 km are those plotted in Figs. 49 and 50.

The other points on Fig. 49 represent 26 other Prairie Network fireballs, the initial dynamic mass of which has been calculated from deceleration data and corrected for entry angle and entry velocity in accordance with the theory. These fireballs also plot within 1 km of the theoretical line, which is as close as can be expected considering observational errors. The effect of the theoretical correction for entry angle and velocity can be seen by comparison with the uncorrected data (Fig. 50).

In Fig. 51, the theory has been used to scale the end height of these 26 fireballs to a nominal dynamic mass of 21 kg, thus defining the peak centering on the theoretical value of 21 km, which includes the two recovered meteorites as well. Similar calculations have been made for all the remaining low-velocity

(≤ 18 km/sec) Prairie Network fireballs, also shown in Fig. 51. The great majority of these remaining bodies plot well above the theoretical value of 21 km. In almost all these cases, the flight of the meteor ended while still at a velocity above 8 km/sec, in most cases probably due to extensive disruption of the body. For these objects the actual observed end height was used, rather than that corresponding to deceleration to 6 km/sec.

Figure 52 is a similar plot for only those fireballs that were decelerated non-catastrophically to < 8 km/sec and thus survived their peak aerodynamic pressure and principal region of atmospheric ablation. The objects fulfilling these conditions are those most likely to have physically survived entry into the atmosphere. Twenty-three of the 28 members of the peak at 21 ± 1 km are included

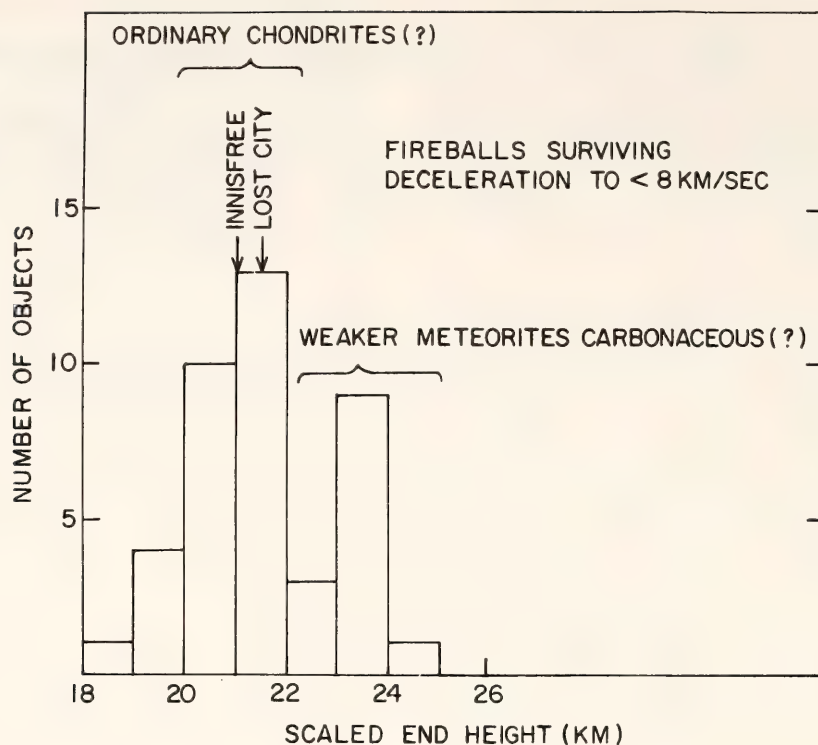


Fig. 52. Scaled end height for fireballs that survived deceleration to <8 km/sec. In addition to objects with scaled end heights in the 21 ± 1 km interval, some fireballs with greater scaled end heights appear to have been safely decelerated.

in this group. Entry data on the remaining members of this peak are not sufficiently complete to define whether or not they also appear to have survived passage through the atmosphere. In addition to those fireballs belonging to the 21-km peak, Fig. 52 contains a number of fireballs with scaled end heights in the range 18–25 km. Some of these may represent scatter from the 21-km peak as a result of observational error. Those in the range 23–25 km probably represent surviving bodies with physical properties differing from those of typical ordinary chondrites such as Lost City and Innisfree.

Figures 53 and 54 show the distribution of the initial and terminal masses of the bodies belonging to the 21-km peak of Fig. 51. The larger members of this group conform to a power law with slope $\sim -5/6$, the theoretical value calculated by Dohnanyi (1969) as the steady state, fragmentation power law exponent. The observed distribution is

deficient at the small mass end, almost certainly as a consequence of failure to photograph fainter fireballs or to eliminate fainter fireballs in the selection of records chosen by McCrosky *et al.* (1977) for reduction.

We now return to the original problem of choosing which of the fireballs are likely to be the ordinary chondrites. The objects in the 21-km peak decelerate and end their atmospheric flight in the same way as the actual recovered ordinary chondrites Innisfree and Lost City, and they also have end heights agreeing with the theoretical value using bronzite chondrite laboratory data. Also, like ordinary chondrites, almost all of them appear to have survived atmospheric entry. Finally, they agree in number with the expected complement of smaller bodies associated with Lost City and Innisfree. It is therefore most plausible to interpret the bodies which constitute the 21-km peak as being the ordinary chondrites, rather than identifying

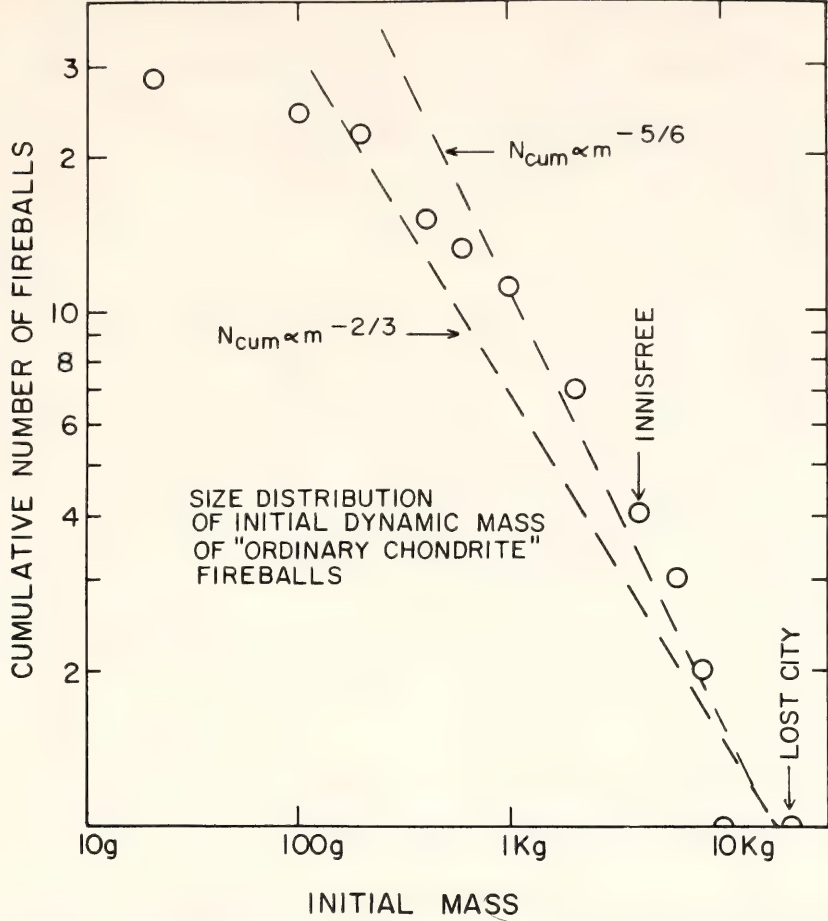


Fig. 53. Cumulative initial dynamic mass distribution of fireballs with scaled end heights of 21 ± 1 km.

fireballs not satisfying these criteria as these meteorites. It is certainly possible that the 21-km peak includes some other meteorites with physical characteristics similar to ordinary chondrites. However, insofar as these observations indicate that these objects survived atmospheric entry, almost all of them should be ordinary chondrites because about 80% of all meteorites observed to fall are of this kind. Many of the objects designated as ordinary chondrites by the criteria of Ceplecha and McCrosky (1976) belong to the 21-km peak, but the grouping of objects by these authors is by no means identical with those in the present study.

If one accepts the identification of the objects in the 21-km peak as ordinary chondrites, it is then possible to investigate the orbital characteristics of the low-velocity component of the terrestrial

flux of these meteorites. One important orbital parameter, which has been emphasized in earlier discussion, is the elongation of the radiant from the anti-apex of Earth's motion. This angle is defined by Fig. 55. Its importance results from the fact that it can be determined with reasonable accuracy (e.g., $\pm 15^\circ$) by visual-observation data obtainable by interviewing persons who happened to witness the fall of a meteorite. Consequently, while there are only three well-determined meteorite orbits, there are many reasonably reliable meteorite radiants (Fig. 56). The principal feature of this distribution is the preponderance of radiants less than 90° compared with the number between 90° and 180° . Previous quantitative calculations (Wetherill 1968, 1969) show that this radiant distribution predicts

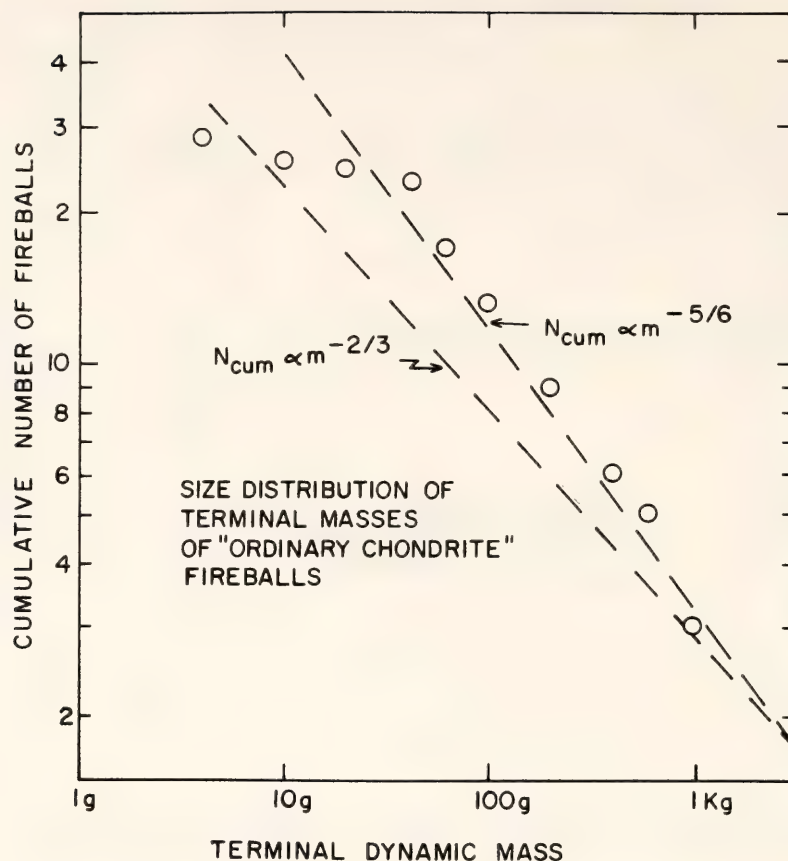


Fig. 54. Terminal dynamic mass distribution of fireballs with scaled end heights of 21 ± 1 km.

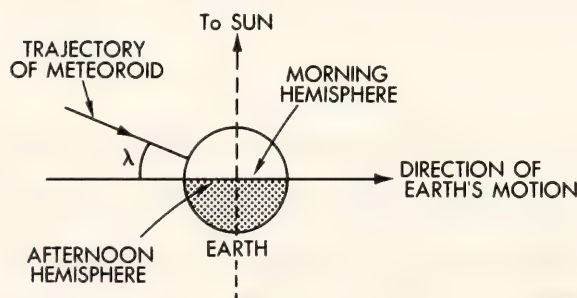


Fig. 55. The angle λ = elongation of radiant from the anti-apex of Earth's motion. Meteoroids with $\lambda < 90^\circ$ predominantly impact Earth in the afternoon hemisphere; those with $\lambda > 90^\circ$ predominantly impact in the morning hemisphere.

the observed $\sim 63\%$ ratio of the frequency of afternoon meteorite falls to morning falls, often attributed to biases of social origin rather than real dynamical circumstances. Although in detail there are statistical fluctuations in the data, the radiant distribution of the

"ordinary chondrite" fireballs identified by the present investigation exhibits a similar excess of radiants $< 90^\circ$ and would therefore also lead to an excess of afternoon falls.

When radiant data is combined with velocities determined by the meteor cameras of the Prairie Network, complete orbital elements can be obtained. Orbital data for our 28 ordinary chondrite fireballs obtained from the calculations of McCrosky *et al.* (1977) were used to obtain Figs. 57 and 58, which show the perihelia and aphelia of these selected fireballs. These are distributed over a wide range, with perihelia tending to concentrate near Earth's orbit at 1.0 A.U. and aphelia in the asteroid belt.

This work must be extended to higher velocities to understand the full distribution of ordinary chondritic orbits. It will also be of value to try to identify more rare meteorite types, such as irons and carbonaceous chondrites among the fire-

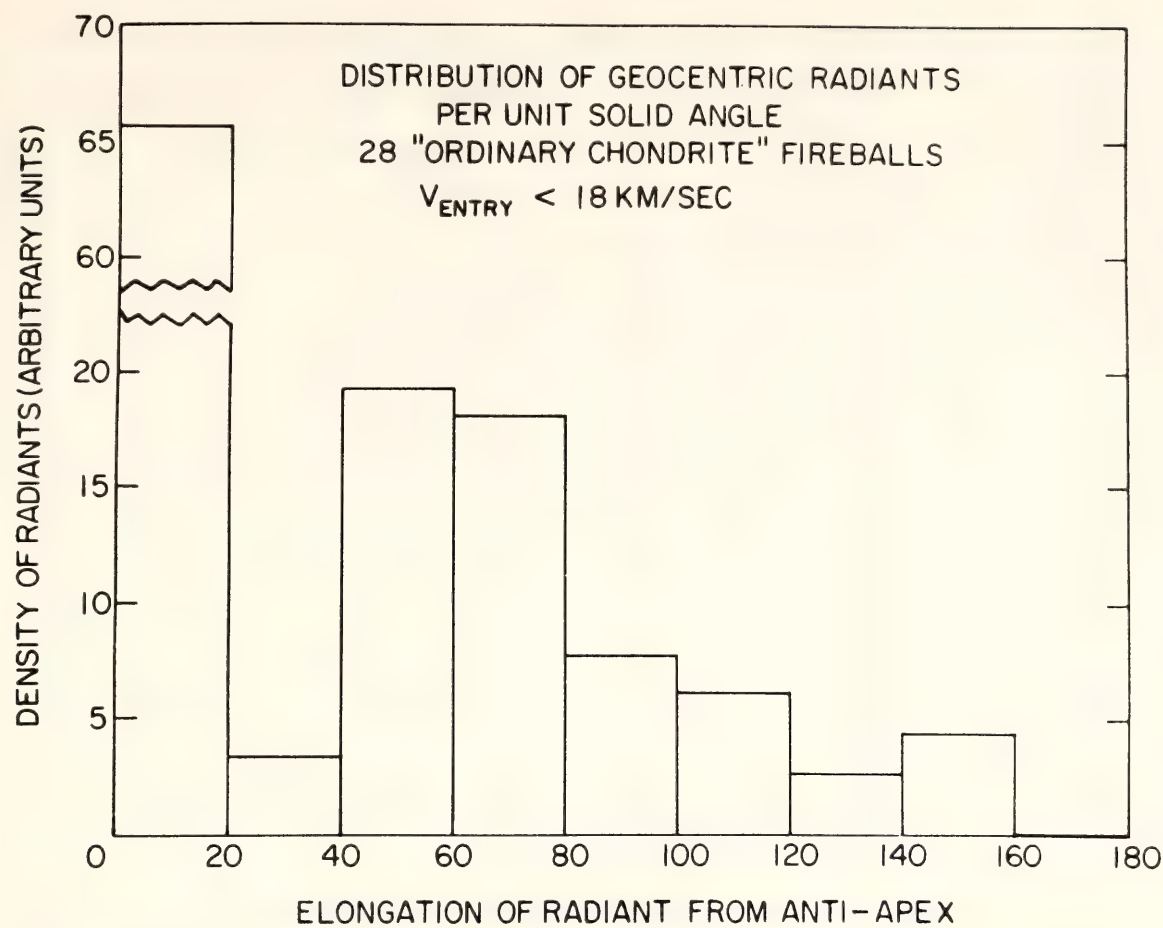


Fig. 56. Distribution of elongation of the radiant for Innisfree, Lost City, and the 26 fireballs with scaled end heights of $21 \pm 1 \text{ km}$.

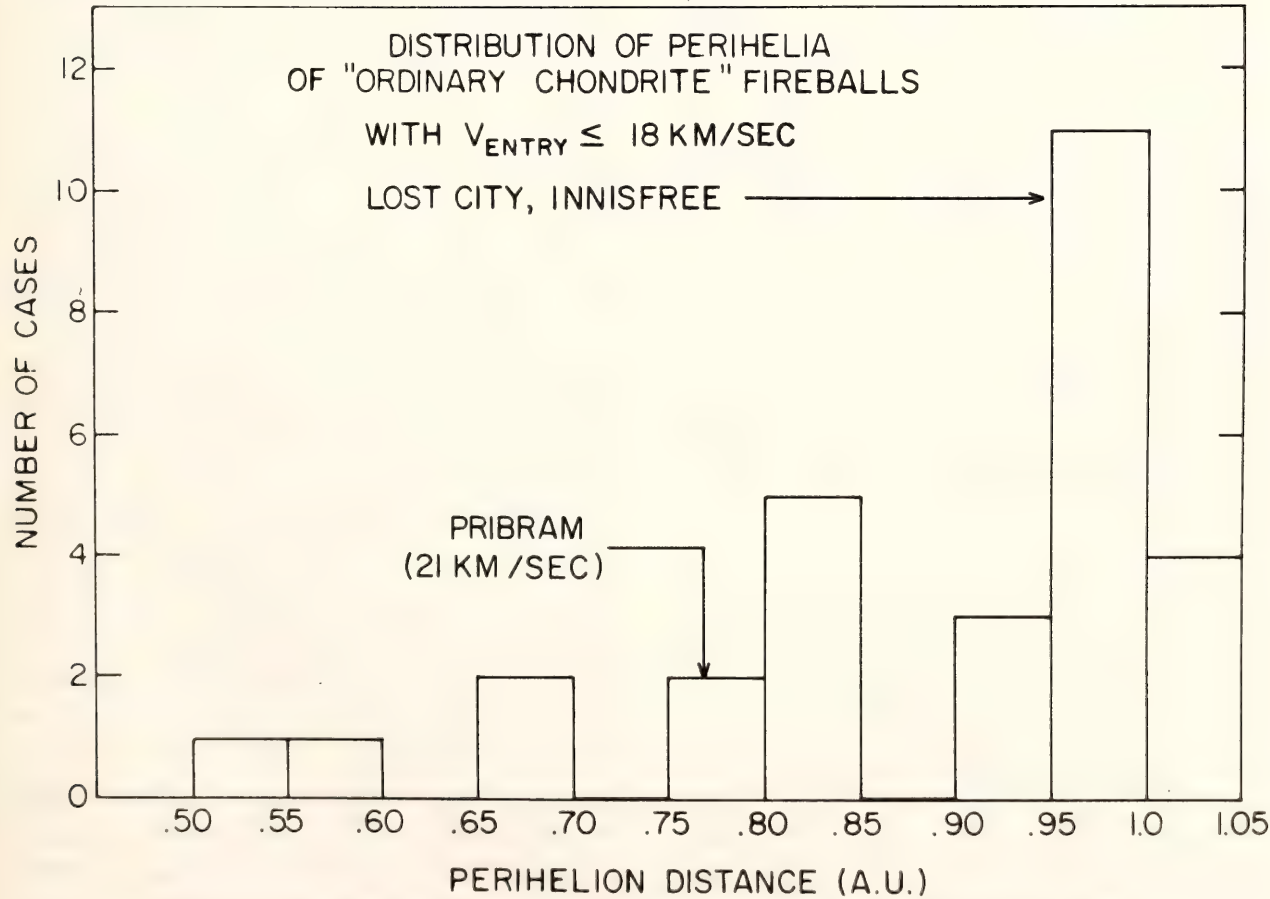


Fig. 57. Distribution of perihelion distances of the 28 fireballs of Fig. 56.

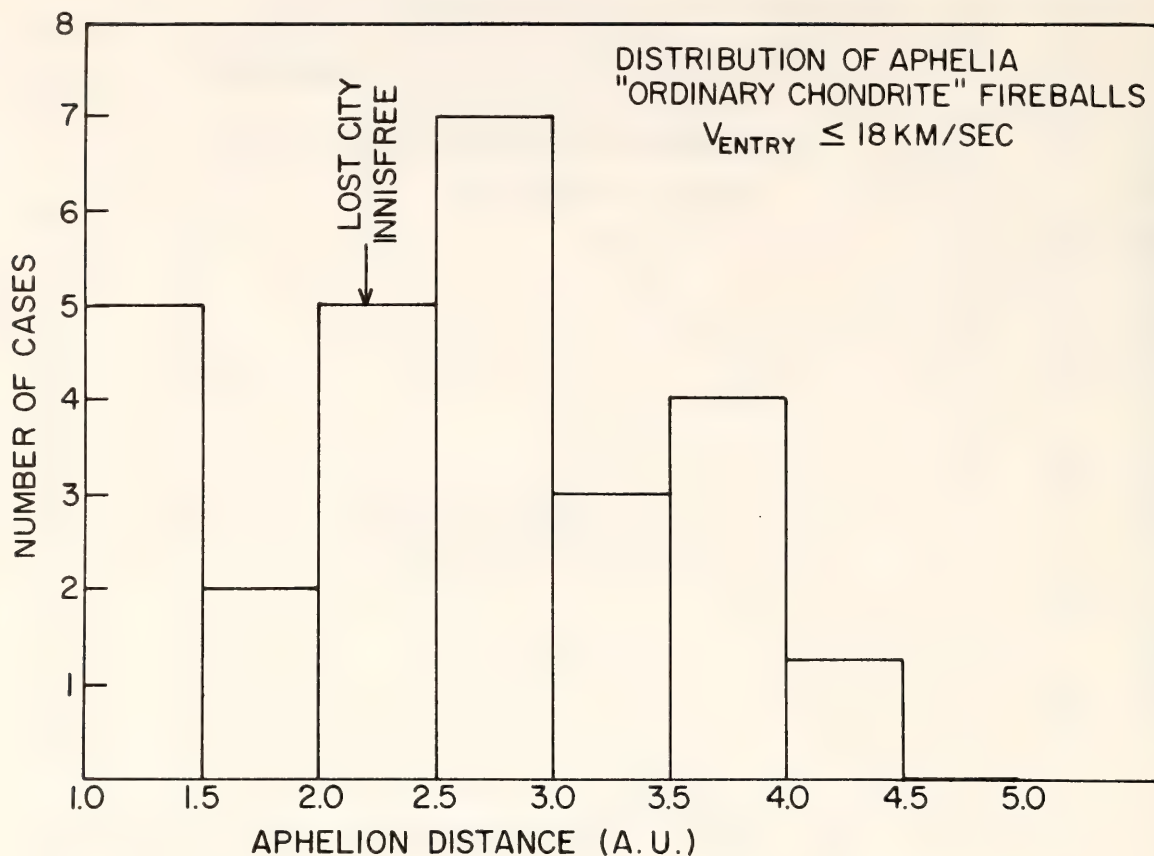


Fig. 58. Distribution of aphelion distance of the 28 fireballs of Fig. 56.

balls. Perhaps some day the fall of a meteorite of these types will be photographed by a fireball network, and the type of "ground truth" which has made the three recovered ordinary chondrites so valuable will be obtained. In the meantime the ordinary chondrite data should be of considerable value in testing the extent these orbital element distributions are compatible with proposed chondrite sources such as the Apollo objects (Wetherill, 1976) or the resonant Kirkwood Gap regions of the asteroid belt (Zimmerman and Wetherill, 1973).

TERRESTRIAL MICROBAROGRAPH
"AIRWAVE" RECORDINGS: THE
GLOBAL INFLUX RATE OF
LARGE METEORIODS

D. O. ReVelle and G. W. Wetherill

Large discrepancies exist between various attempts at determining the global influx rate of large meteoroids

($\geq 10^2$ kg) impacting on the earth and its atmosphere (Shoemaker and Lowery, 1967; McCrosky, 1968; Gault, 1970; Latham *et al.*, 1972; Duennebier and Sutton, 1974; Duennebier *et al.*, 1975; Baggaley, 1978). In an effort to resolve these discrepancies, we have recently obtained a list of the airwave events generated by large meteoroids and recorded during 1960–1974 by the U. S. government network of microbarograph stations designed to monitor distant atmospheric nuclear explosions. These data are summarized in Table 13. If these signals are properly interpreted, they are potentially very useful for inferring the global influx rate of large meteoroids at the earth's orbit. This information is important because of the need to establish a reliable value for the cratering time scale of the inner solar system. This total flux is also a basic constraint on theoretical mechanisms for the production of meteorites (Wetherill, 1974; Chapman, 1976; Wetherill, 1976).

TABLE 13. Summary of Large Meteoroid "Airwave" Data

Event Number	Date	Source Location	Event Origin Time (GMT)	Total Range (mi.)	"Source Energy" (KT TNT equiv.)†
1	11/2/1960	8.8°N,43.4°E	0022	2488	1
2	9/26/1962	30°N,34.5°E	1545	688	10
3	9/27/1962	32.2°N,59.9°E	1529	518	15
4	8/3/1963	50.5°S,24°E	1645	7038	550*
				8590	
5	11/30/1964	18°N,123°W	0310	3243	5*
6	1/3/1965	20.6°N,68°E	2151	2008	.1*
7**	4/1/1965	49°N,117°W	0548	1552	.24-2.4‡
				2173	
8	6/12/1966	51°N,163.5°E	0905	4150	...§
				2750	
				1800	
				3000	
9	1/8/1971	30°N,40°E	1826	8632	3
10	4/14/1972	13°S,78°E	1613	2300	7
				3400	
				4850	
				8000	
				8550	
				2700	

* Indicated as possible meteor.
† 1 KT TNT $\approx 4.2 \cdot 10^{19}$ ergs.
‡ Private communication from E. M. Shoemaker, 1972.
§ Not originally estimated.
** Revelstoke Meteorite.

In order to interpret these records, both a source and a model of propagation through the complex atmospheric medium are needed. The energies listed in Table 13 are those originally deduced for these events by using a nuclear explosion analogy for the source and a quasi-empirical propagation model which relied primarily on wave period (at maximum signal amplitude) as a predictor of source energy as a function of range. If the table supplied to us of the network's percent coverage of the earth as a function of source energy and season is applied to these data, we obtain a meteoroid energy flux of 50.8 KT TNT/year over the whole earth. Converting to CGS units (4.2×10^{19} ergs = 1 KT TNT) and assuming a mean velocity of 20 km/sec in the atmosphere, we deduce that 1×10^9 grams/year is arriving in the

form of large meteoroids (10^6 – 10^{10} g). This value is smaller than that deduced previously using photometry (McCrosky, 1968) and probably represents additional evidence that the photometric masses previously calculated are not indicative of the "true" preatmospheric meteoroid masses.

The numerical values obtained show that there is no obvious discrepancy between flux estimates based on airwave data and by other methods. It will be necessary to further refine the values using different source models and more realistic propagation and attenuation calculations. Among the uncertainties involved in the calculations are primarily the following:

1. The data set available to us has been strongly prefiltered by the removal of other natural sources of atmospheric

waves such as from volcanic eruptions, aurora, and meteorological phenomena. Thus we must rely heavily on the percent coverage values supplied to us and assume that no very large sources have been inadvertently omitted or not detected at all.

2. The source model used to infer meteoroid kinetic energy was assumed to be that of a near-surface nuclear explosion. Various other assumed source configurations, such as point source versus line source models (ReVelle, 1976a, Korobeinikov *et al.*, 1976) and effects of altitude on point source scaling (Korobeinikov, 1973), can lead to different estimates of source energy. On the basis of preliminary calculations, such effects are not expected to produce an order of magnitude variation of the inferred flux. However, it should be appreciated that this is a complex problem, and energy estimates deduced in the future are likely to remain fairly uncertain (Posey and Pierce, 1971; Pierce and Kinney, 1976).

References

- Baggaley, W. J., The size distribution of large meteor bodies, *Bull. Astron. Inst. Czechosl.*, 29, 57-59, 1978.
- Baldwin, B., and Y. Sheaffer, Ablation and breakup of large meteoroids during atmospheric entry, *J. Geophys. Res.*, 76, 4653-4668, 1971.
- Bhandari, N. G., D. Lal, J. R. Arnold, K. Marti, R. S. Rajan, and C. B. Moore, Atmospheric ablation in meteorites: an experimental study of over a hundred meteorites based on observations of cosmic ray tracks, to be submitted to *Icarus*, 1978.
- Bronshten, V. A., Problems of the movement of large meteoritic bodies in the atmosphere, NASA TT-F-247, 1964.
- Cepelcha, Z., Multiple fall of Příbram meteorites photographed, 1, Double-station photographs of the fireball and their relations to the found meteorites, *Bull. Astron. Inst. Czech.*, 12, 21-47, 1961.
- Cepelcha, Z., and R. E. McCrosky, Fireball end heights: a diagnostic for the structure of meteoric material, *J. Geophys. Res.*, 81, 6257-6275, 1976.
- Chapman, C. R., Asteroids as meteorite parent-bodies: the astronomical perspective, *Geochim. Cosmochim. Acta*, 40, 701-719, 1976.
- Dohnanyi, J. W., Collisional model of asteroids and their debris, *J. Geophys. Res.*, 74, 2531-2554, 1969.
- Duennebier, F., J. Dorman, D. Lammlein, G. Latham, and Y. Nakamura, Meteoroid flux from passive seismic experiment data, *Geochim. Cosmochim. Acta, Suppl.* 6, 2, 2417-2426, 1975.
- Duennebier, F., and G. H. Sutton, Meteoroid impacts recorded by the short-period component of Apollo 14 lunar passive seismic station, *J. Geophys. Res.*, 79, 4365-4374, 1974.
- Gault, D., Saturation and equilibrium conditions for impact cratering on the lunar surface: criteria and implications, *Radio Sci.*, 5, 273-291, 1970.
- Gazley, C., Entry deceleration and mass change of an ablating body, in *Reentry and Planetary Entry Physics and Technology*, I, W. H. T. Loh, ed., Springer Verlag, New York, 1968.
- Givens, J. J., and W. A. Page, Ablation and luminosity of artificial meteors, *J. Geophys. Res.*, 76, 1039-1054, 1971.
- Halliday, I., A. T. Blackwell, and A. A. Griffin, The Innisfree meteorite and the Canadian camera network, *J. Roy. Astron. Soc. Canada*, 72, 15-39, 1978.
- Jones, J., and T. R. Kaiser, The effects of thermal radiation, conduction and meteoroid heat capacity on meteoric ablation, *Mon. Notic. Roy. Astron. Soc.*, 133, 411-420, 1966.
- Korobeinikov, V. P., *Problems in the Theory of Point Explosions in Gases*, American Mathematical Society, Providence, Rhode Island, 1973.
- Korobeinikov, V. P., P. I. Chushkin, and

- L. V. Shurshalov, Mathematical model and computation of the Tunguska meteorite explosion, *Acta Astron.*, **3**, 615–622, 1976.
- Kovshun, I. N., A new meteoroid mass scale and meteor emissions at maximum brightness, *Solar System Research*, **11**, 3–8, 1977.
- Latham, G. V., M. Ewing, F. Press, G. Sutton, J. Dorman, Y. Nakamura, N. Toksov, D. Lammlein, and F. Duennebier, Passive seismic experiment, Apollo 16 preliminary scientific report, *NASA SP-315*, Chap. 9, 1972.
- McCrosky, R. E., Distributions of large meteoric bodies, Smithsonian Astrophysical Observatory Special Report 280, 1968.
- McCrosky, R. E., A. Posen, G. Schwartz, and C.-Y. Shao, Lost City meteorite—Its recovery and a comparison with other fireballs, *J. Geophys. Res.*, **76**, 4090–4108, 1976.
- McCrosky, R. E., C.-Y. Shao, and A. Posen, Prairie network fireball data, I. Summary and orbits, Center for Astrophysics Preprint No. 665, submitted to *Meteoritika* (in Russian), 1977.
- McIntosh, B. A., On the end-point height of fireballs, *J. Roy. Astron. Soc. Canada*, **64**, 267–281, 1970a.
- McIntosh, B. A., Meteorite passage through the lower atmosphere: predictions of simple theory, *Meteoritics*, **5**, 210, 1970b.
- McKinley, D. W. R., *Meteor Science and Engineering*, McGraw-Hill Book Co., New York, 1961.
- Pierce, A. D., and W. A. Kinney, Computational techniques for the study of infrasound propagation in the atmosphere—final report, AFGL-TR-76-0056, 1976.
- Posey, J. W., and A. D. Pierce, Estimation of nuclear explosion energies from microbarograph records, *Nature*, **232**, 253, 1971.
- ReVelle, D. O., On meteor generated infrasound, *J. Geophys. Res.*, **81**, 1217–1230, 1976a.
- ReVelle, D. O., Dynamics and thermodynamics of large meteor entry: a quasi-simple ablation model, National Research Council of Canada, SR-76-1, 1976b.
- ReVelle, D. O., A quasi-simple ablation model for large meteorite entry: theory versus observations, submitted to *J. Atmos. Terr. Phys.*, February, 1978.
- ReVelle, D. O., and R. S. Rajan, On the luminous efficiencies of meteorites, to be submitted to *J. Geophys. Res.*, 1978.
- Romig, M. F., Physics of meteor entry, *Amer. Inst. of Aeronautics and Astronautics J.*, **3**, 385–394, 1965.
- Schneider, W., Radiation gas dynamics of planetary entry, *Astronaut. Acta*, **18**, 193–213, 1974.
- Shoemaker, E. M., and C. J. Lowery, Airwaves associated with large fireballs and the frequency distribution of energy of large meteoroids, *Meteoritics*, **3**, 123–124, 1967.
- Wetherill, G. W., Time of fall and origin of stone meteorites, *Science*, **159**, 79–82, 1968.
- Wetherill, G. W., Comments on paper by D. E. Fisher and M. F. Swanson, Frequency distribution of meteorite-earth collisions, *J. Geophys. Res.*, **74**, 4402–4405, 1969.
- Wetherill, G. W., Solar system sources of meteorites and large meteoroids, *Annual Review of Earth and Planetary Sciences*, pp. 303–331, Annual Reviews, Inc., Palo Alto, 1974.
- Wetherill, G. W., Where do the meteorites come from? A re-evaluation of the earth-crossing Apollo objects as sources of chondritic meteorites, *Geochim. Cosmochim. Acta*, **40**, 1297–1317, 1976.
- Zimmerman, P. D., and G. W. Wetherill, Asteroidal source of meteorites, *Science*, **182**, 51–53, 1973.

PHYSICS AND CHEMISTRY OF THE EARTH

VELOCITY STRUCTURE IN THE SUBDUCTING
LITHOSPHERE: IMPLICATIONS FROM
S-WAVE DATA*K. Suyehiro and I. S. Sacks**Introduction*

This paper is a second report on the laterally heterogeneous upper mantle velocity structure in the Japan subduction region using travel-time residual data. The preceding report (Suyehiro and Sacks, *Year Book 76*, pp. 813–822, hereafter referred to as Paper I) discusses the results from *P*-wave travel-time residuals. Those results suggest a two-layer velocity structure in the subducting lithosphere and a *V_p* contrast of $5 \pm 1\%$ across the boundary between subducting lithosphere and overlying asthenosphere (the asthenosphere-lithosphere boundary is hereafter referred to as ALB). In this study, we show similar results from *S*-wave data by comparing

the spatial distribution of the observed travel-time residuals from local deep earthquakes with residuals calculated using a two-dimensional ray tracing method (Jacob, 1970). This method, used also in Paper I, is meaningful only for regions with a high station density such as Japan.

Method and Data

We calculate travel-time residuals for various laterally heterogeneous velocity structures (Fig. 59) and compare those residuals with the observational data. The spatial pattern of calculated travel-time residuals depends essentially on the velocity contrast across ALB (Fig. 59). Observational data, however, are usually contaminated by various effects not related to the laterally heterogeneous structure. Such effects must be taken into account before matching observed with calculated residuals.

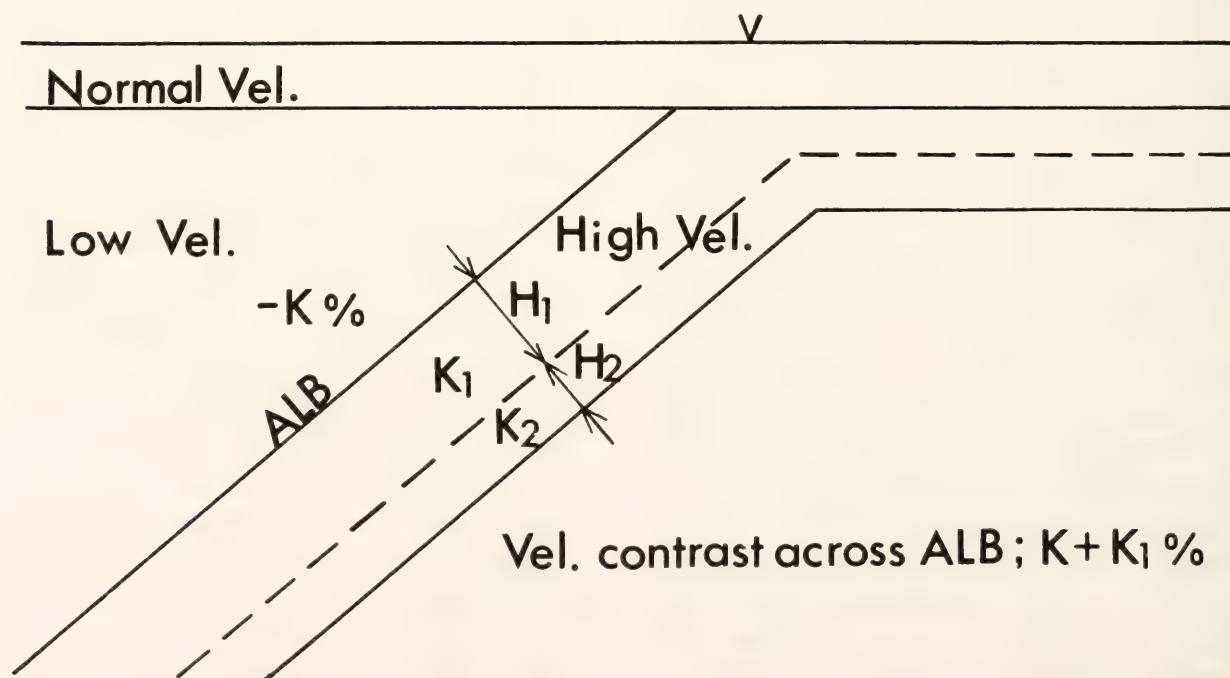


Fig. 59. A model of the upper mantle beneath Japan for ray-tracing calculations. Velocity contrast between the upper and the lower layers inside the slab is K_2 minus K_1 (%) for a two-layer model. Thickness of the crust is fixed at 33 km.

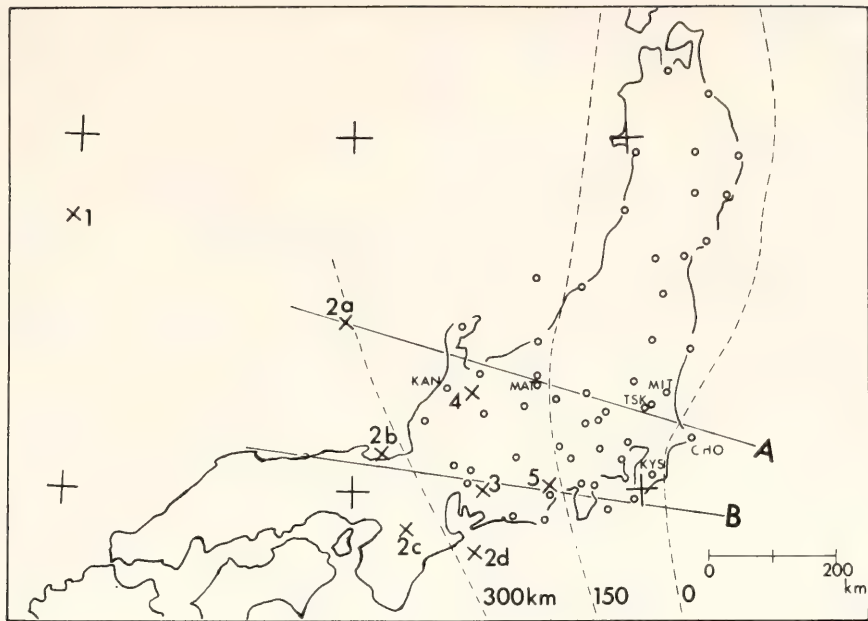


Fig. 60. Map of the Honshu region of Japan. Crosses indicate the mean epicenters of earthquake groups studied. Mean focal depth becomes shallower from region 1 to 5 (550–200 km). Circles show seismic stations in the studied region with station codes that appear elsewhere in the paper identified. Dashed lines indicate contours of the upper boundary of the subducting lithosphere from Yamamizu’s model (1973). Seismicity of the vertical cross sections of profiles A and B are shown in Fig. 61.

Systematic source errors will be minimized by using ISC data (Utsu, 1975; Paper I). Random source errors and reading errors are reduced by calculating mean travel-time residuals. Local crustal effects are evaluated from *P*-wave corrections (Paper I) using the formula $V_p = 1.75 \times V_s$ (Ichikawa and Mochizuki, 1971).

The same earthquakes selected in Paper I are used. Figure 60 shows the mean epicenters of earthquake clusters for which mean travel-time residuals are calculated. We reject data for which the residual varies from the average value by more than 2 sec.

Travel-Time Residual Data

Figures 61 and 62 show mean *S*-wave travel-time residuals (*P*-wave data are also shown) plotted against depth to the upper boundary (Yamamizu, 1973) of the subducting plate (ALB). Stations are selected so that the ray paths from each region are approximately in the dip direction of the subducting lithosphere. A

general feature of the time residuals is that they are approximately constant for stations nearer the source, but become increasingly negative for stations near the trench. As expected, the magnitude of this effect is dependent upon focal depth. As focal depth decreases (region 1–5), we observe the following: (1) the constant residual segment becomes longer, (2) the overall change in residual becomes smaller, and (3) the time residuals become smaller. The model calculations show the same features (Fig. 63).

V_s Contrast Across ALB

We can estimate the *V_s* contrast across ALB using the method described in Paper I whereby the observed data are fitted to calculated residual curves. Because region 2 (focal depth 370 km) contains our best data set, we derive a velocity contrast on the basis of those observations alone and test for consistency with data from the other regions.

The *S*-wave velocity contrast at ALB

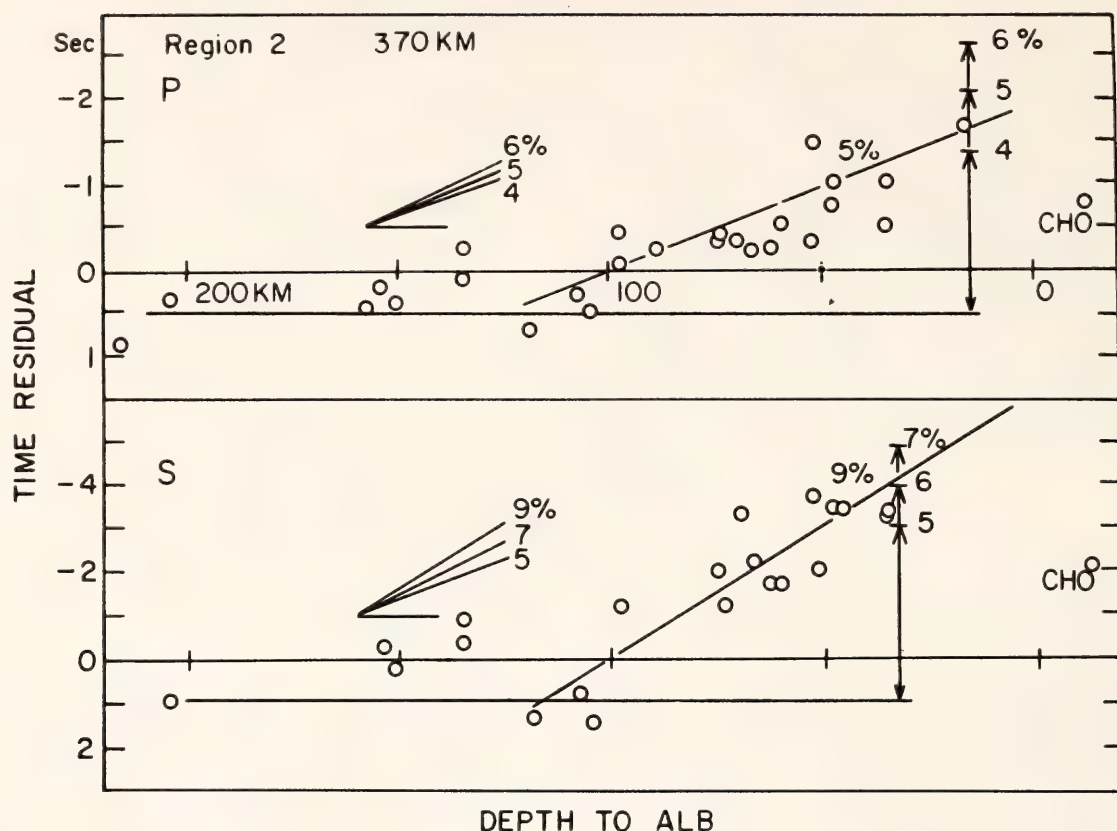


Fig. 61. *P* and *S* travel-time residuals plotted against depth to ALB for region 2. This depth is linearly extrapolated to negative values and approximately indicates epicentral distance on a different scale. Mean values of time residuals from regions with similar focal depths (about 370 km) are plotted. The slopes of BC are 5% for *P* wave and 9% for *S* wave. Differential times of AB and CD, on the other hand, show 4.5% (*P*) and 5.5% (*S*). The travel-time residual segments AB, BC, and CD are defined in Fig. 63.

is $7 \pm 2\%$, as estimated from the time-residual curve shown in Fig. 63. To arrive at this estimate we use both the time difference between segments AB and CD and the slope of BC over the interval 0–120 km depth to ALB. The data from other regions (focal depths 200–550 km) are consistent with a velocity contrast of $7 \pm 2\%$. The *S*-wave velocity contrast is thus slightly larger than the *P*-wave velocity contrast of $5 \pm 1\%$ determined in Paper I.

Implications of V_p and V_s Contrasts

In this section we discuss probable causes of the velocity contrasts ($V_p = 5 \pm 1\%$; $V_s = 7 \pm 2\%$) in terms of temperature and pressure effects and of partial melting in the asthenosphere. In the

absence of partial melting, we have, following Birch (1969),

$$dV = (\partial V / \partial P)_T dP + (\partial V / \partial T)_P dT \quad (1)$$

$$d\rho = (\rho / \kappa_T) dP - a \rho dT, \quad (2)$$

where V is velocity, P is pressure, T is temperature, ρ is density, κ_T is isothermal bulk modulus, and a is volume thermal expansion. Using our velocity contrasts and the laboratory data for forsterite (Anderson *et al.*, 1968), we obtain Fig. 64. The temperature contrast required to explain the velocity contrasts is larger than normally expected (e.g., Hasebe *et al.*, 1970; Toksöz and Bird, 1977). Although the data scatter is such that the temperature contrast could be as little as 600°C, such a thermal contrast would

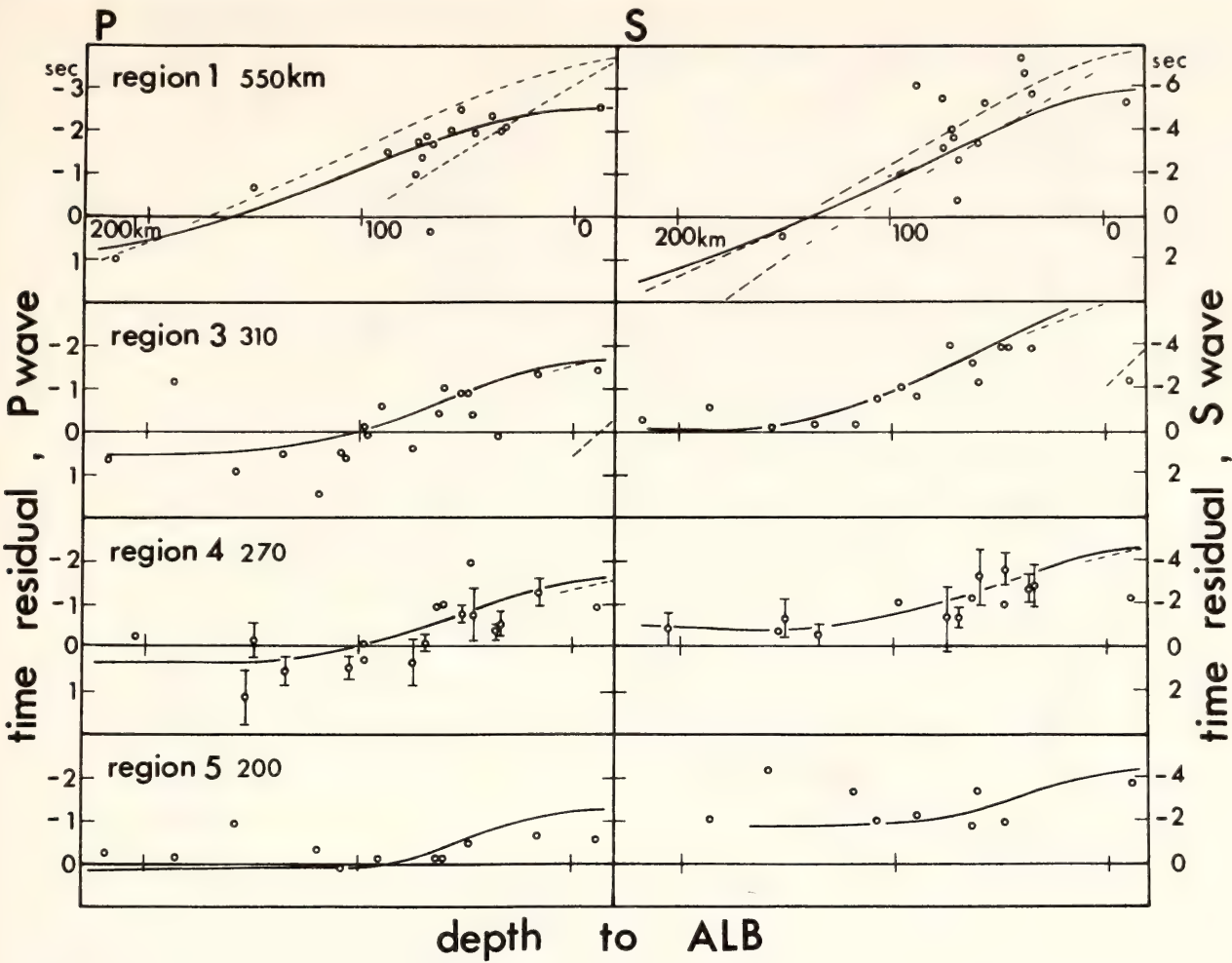


Fig. 62. *P* and *S* travel-time residuals for regions 1, 3, 4, and 5. Station corrections are applied to all the data. Standard deviations are given when each plot represents three or more earthquakes. Note the depth dependence of the data. Solid lines show the fit of the one-layer model obtained for region 2. Dashed lines show the deviation of the two-layer model from the one-layer model.

produce too large a change in density (Segawa and Tomoda, 1976). It is improbable, therefore, that temperature alone can account for the velocity contrasts.

Partial melting would also lower the seismic velocity of the asthenosphere. In this case, the effect on the elastic parameters would be largest in the rigidity, μ , and smaller in the bulk modulus, κ (Hales and Doyle, 1967). If the density remained constant, then $\delta V_p/V_p$ would lie between $2/3$ and $4/9$ of $\delta V_s/V_s$ depending on whether Lamé's constant, λ , or κ remains constant (Hales, 1964). Our result falls within this range but favors the constant- λ model.

is also supported by laboratory data (Mizutani and Kanamori, 1964). The larger change in rigidity can be illustrated by converting the velocity contrast to elastic parameter contrasts using the well-known equations for isotropic elasticity.

$$V_p = \sqrt{(\kappa + 4/3\mu)\rho}, \tag{3}$$

$$V_s = \sqrt{\mu/\rho}. \tag{4}$$

From Equations 3 and 4, we obtain,

$$\delta\mu/\mu = 2\delta V_s/V_s + \delta\rho/\rho \tag{5}$$

$$\delta\kappa/\kappa = (\delta V_p/V_p + 1/2 \cdot \delta\rho/\rho - 2/3/\alpha^2 \cdot \delta\mu/\mu) \cdot 2\alpha^2/(\alpha - 4/3), \tag{6}$$

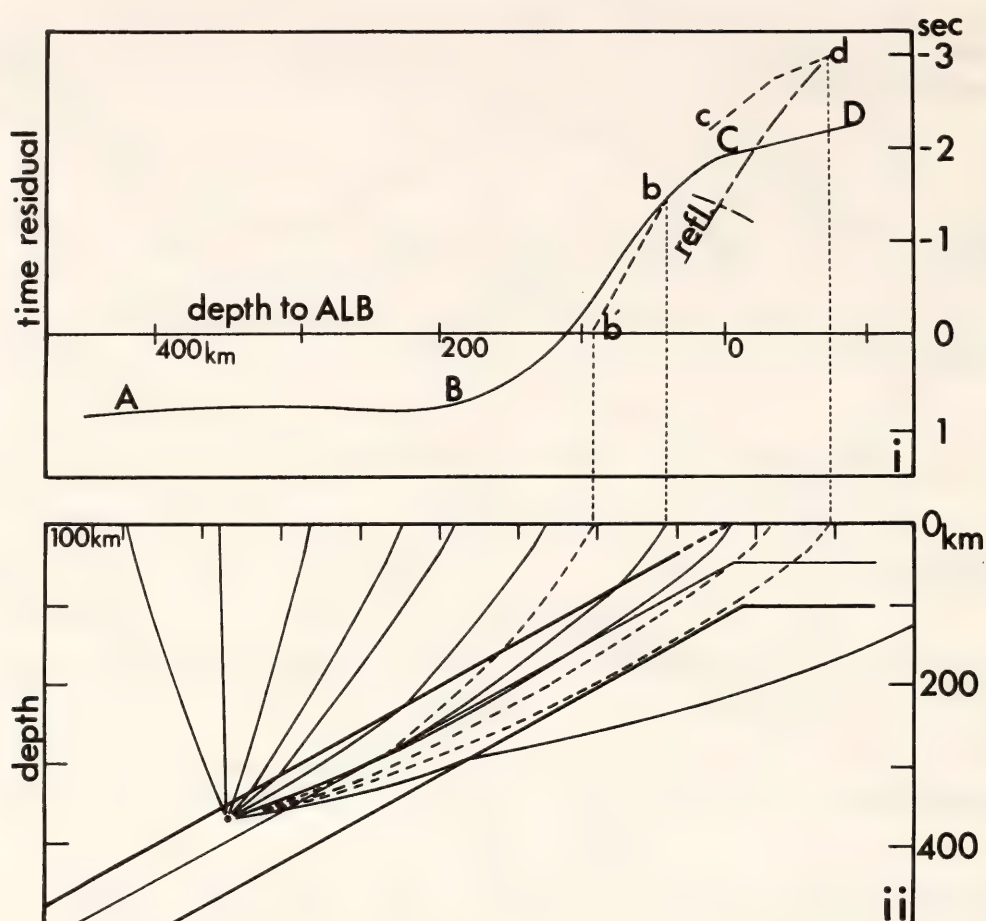


Fig. 63. *P*-wave time residuals for one- and two-layer models from ray-tracing calculations shown with ray paths. The focus is 370 km deep. Velocity contrasts are 5% across ALB ($K = 3\%$, $K_1 = 2\%$) and 1% within the slab ($K_2 = 3\%$: two-layer model). Dashed lines indicate the effect of the faster lower layer for the two-layer model. *AB* is unvarying, as the rays are little affected by the slab. A large change occurs at *BC*, as the rays travel longer paths inside the slab. The slope becomes smaller in *CD* because the rays no longer propagate through the laterally heterogeneous region. Rays beyond *D* penetrate the lower boundary of the high-velocity region surface out to sea and are hence not observed. For a two-layer model, dashed lines show its effect. The upper-layer thickness (H_1) determines *b* and triplication occurs owing to the higher velocity lower layer. Reflection branches from upper and lower boundaries are also shown in lighter dash lines.

where $\alpha = V_p/V_s$. Assuming $\delta\rho/\rho = 0.015$ (Segawa and Tomoda, 1976) and $\alpha = 1.77$ (Utsu, 1969), we can estimate the rigidity and the bulk modulus contrasts. We obtain a variation across ALB of $16 \pm 4\%$ in rigidity as compared to a variation of $9 \pm 6\%$ in bulk modulus, where both elastic parameters are higher in the slab than in the asthenosphere.

An estimation of the melt concentration as deduced from contrasts is not meaningful because of the large uncertainty in the melt-zone geometry, which strongly affects the velocity change

(Anderson, 1977). Although the discussion remains qualitative, we think that both the temperature-pressure effect and partial melting are required to satisfy the data.

Implications of Layered Structure Inside the Subducting Lithosphere

Observations. In Paper I, we have suggested a two-layer velocity structure inside the subducting plate to explain the data at the easternmost station, CHO. Because this station is situated

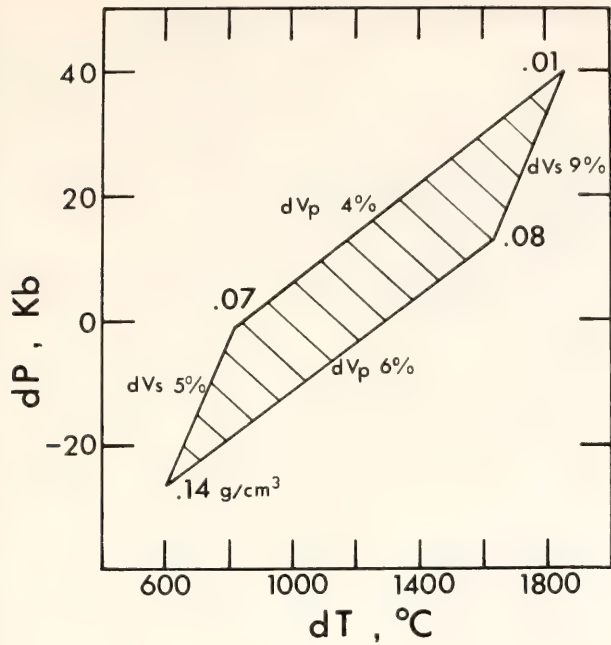


Fig. 64. Relationship between seismic velocity change and temperature, pressure, and density change for forsterite. Data are adapted from O. L. Anderson *et al.* (1968).

nearest the trench, it is most important in delineating the deeper structure inside the subducting plate. For a single-layer slab the data at CHO should show larger negative residuals than other stations and lie on the *CD* curve (Fig. 63). This is, however, not observed for region 2 for either *P* or *S* where, on the average,

arrivals are 1 sec (*P*) or 2 sec (*S*) later than expected from the one-layer model (Figs. 61 and 65).

As a simple one-layer model fails to explain the observed data related to the structure in the deeper portion of the subducting plate, we tested a two-layer velocity structure. Table 14 shows the distinguishing features of a two-layer model. The parameters obtained in Paper I for *P*-wave data also explain the *S*-wave (Fig. 66).

A test of the model is made by examining the varieties of differential time (Fig. 67) residuals as a function of focal depth. These differential residuals are differences between the mean residuals at six stations located about 35 km above the ALB and the residuals at CHO. Fig. 67 also shows the predicted differential travel-time curve from the two-layer model. Note that the deviation from a one-layer model is and should be conspicuous only at around 370-km focal depth. The fit of the curves is moderately good and confirms that a two-layer model is justified. The baseline for *S* waves was shifted 2 sec to give a better fit. Since the station corrections for *S* waves are determined simply from *P* corrections, the *S* correction at CHO may

TABLE 14. Features of Two-Layer Model

	Focal Depth (km)				
	550 (1)*	370 (2)*	210 (3)*	270 (4)*	200 (5)*
Maximum ray penetration†	100 km	50	40	35	25
First arrival‡ at CHO	Early(?)	Late(✓)	O.T.(✓)	O.T.(?)	O.T.(?)
MIT§	Early(?)	O.T.(✓)	O.T.(✓)	O.T.(✓)	O.T.(✓)
Later arrival CHO	L,A	... (✓)	L,A	T,A	T,A
MIT§	L	T(x),L(✓)	T

* Region number.
† Maximum depth of ray penetration inside the slab for rays reaching CHO.
‡ Comparison with one-layer model. O.T.: on-time observations.
§ Also holds for other stations about the same depth to ALB.
|| T: triplication back branch; L: lower boundary reflection; A: ALB reflection; x: not observed. At CHO, our interpretation is that the lower boundary reflection is observed as a first arrival for region 2.

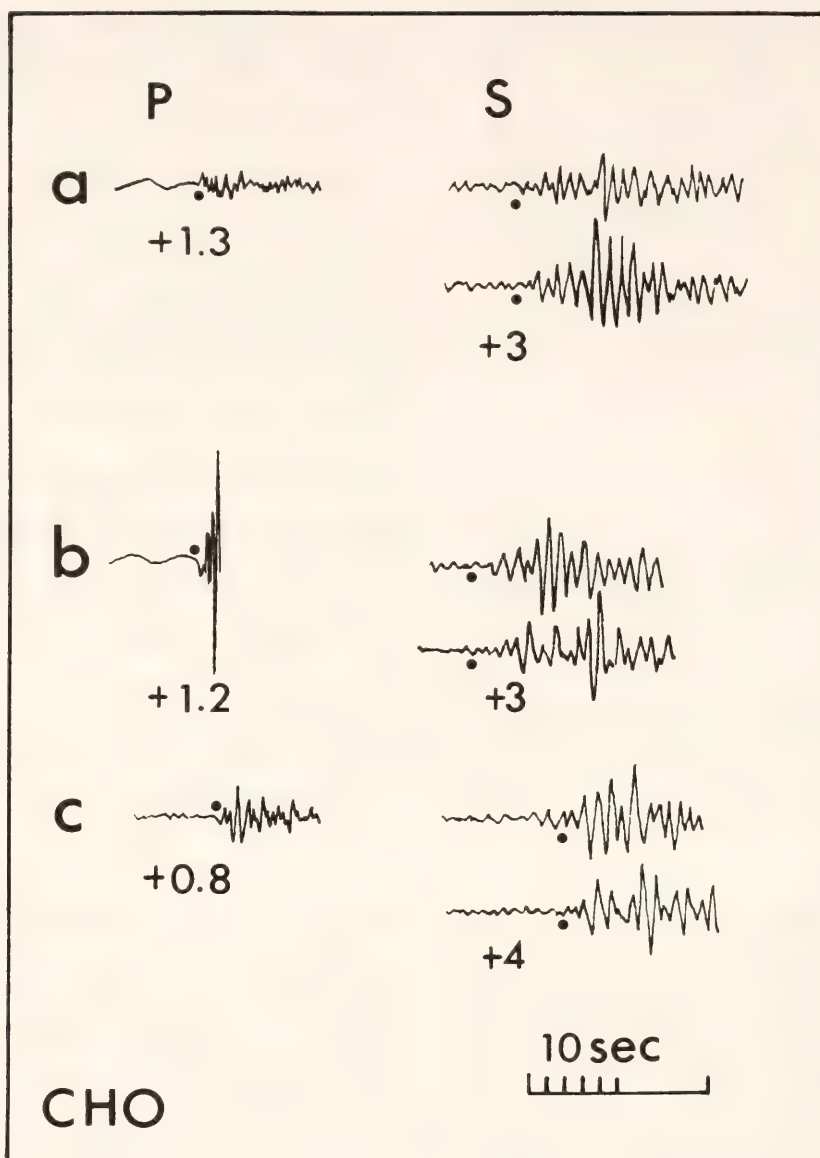


Fig. 65. Seismograms at CHO for three events in region 2. Vertical components are shown for *P* wave and horizontal components (NS, EW) for *S* wave. Dots indicate the arrival times reported in the ISC bulletins. Numbers are the time residuals expected from the one-layer model (-1.7 for *P*, -5.6 for *S*); obtained from 5% (7%) contrast model for *P* (*S*) and indicated in circles, minus the time residuals reported in the ISC bulletins (i.e., deviations from the one-layer model).

require revision. In such a case, shifting the *S* data points for CHO by 2 sec will, in fact, provide better agreement with the *P*-wave data (Fig. 62).

Discussion. Long-range seismic explosion experiments using ocean-bottom seismographs show that the oceanic lithosphere has a two-layer structure (Shimamura and Asada, 1976; Shimamura *et al.*, 1977). We have indicated from travel-time residual data that such a structure may be preserved after subduction. There are, however, quantita-

tative differences in the parameters of our results and of the western Pacific lithosphere (Table 15). Anisotropy, which has not yet been determined in this region, may explain the discrepancy, because the explosion profile from which the oceanic lithosphere structure was obtained is perpendicular to the dip direction of the subducting lithosphere.

We estimate the thickness of the high-velocity (i.e., lithospheric) slab to be about 120 km, based on the assumption that the arrivals at CHO from earth-

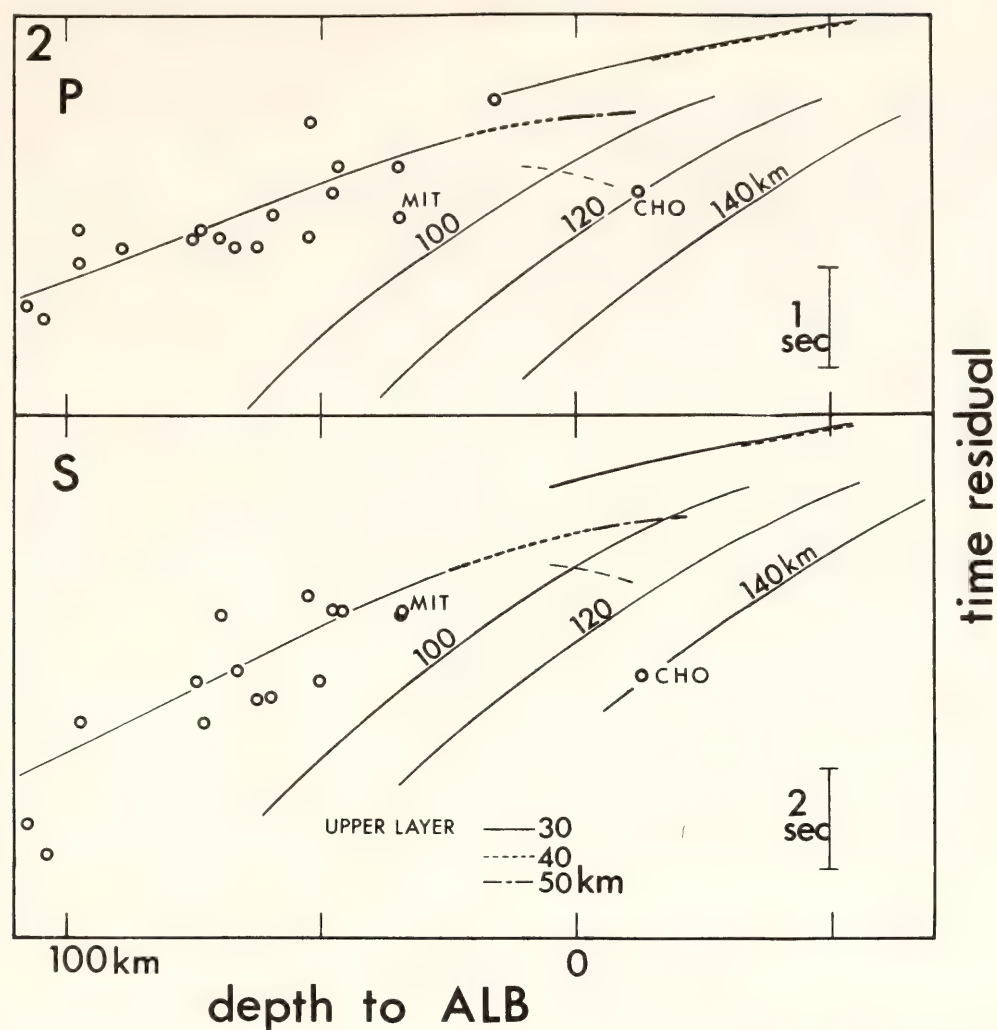


Fig. 66. Two-layer model time residual curves superposed onto data for region 2 (Fig. 59). Numbers on reflection branches indicate total thicknesses of the slab. Dashed lines show the ALB reflection branches. The upper-layer thickness is about 40–50 km for CHO to observe reflection branches first.

quakes in region 2 are wide-angle reflections from the lower boundary. This interpretation is supported by multiple arrivals on the seismograms from stations west of CHO such as MIT. This station is situated sufficiently far from the trench to record both the direct arrival and the wide-angle reflection (Fig. 68).

Conclusions

Using travel-time residuals from local deep earthquakes, we have obtained some quantitative results regarding the laterally heterogeneous upper mantle in the Japan subduction zone. The spatial distribution of the observed residuals is

matched with those from a model calculated by using two-dimensional ray tracing. This method of comparison is similar to the ‘relative’ residuals method (Mitronovas and Isacks, 1971).

In the central Honshu region, the travel-time residuals indicate $5 \pm 1\%$ (P) and $7 \pm 2\%$ (S) velocity contrasts across ALB. This holds, on the average, to the depth of 550 km. It is possible, however, that the amount of the velocity increase inside the slab decreases with depth (Tada, 1972; Hirahara, 1977) or that the asthenosphere on the continent side is laterally inhomogeneous (Noguchi and Okada, 1976), either of which could result in a depth dependence for V_p and

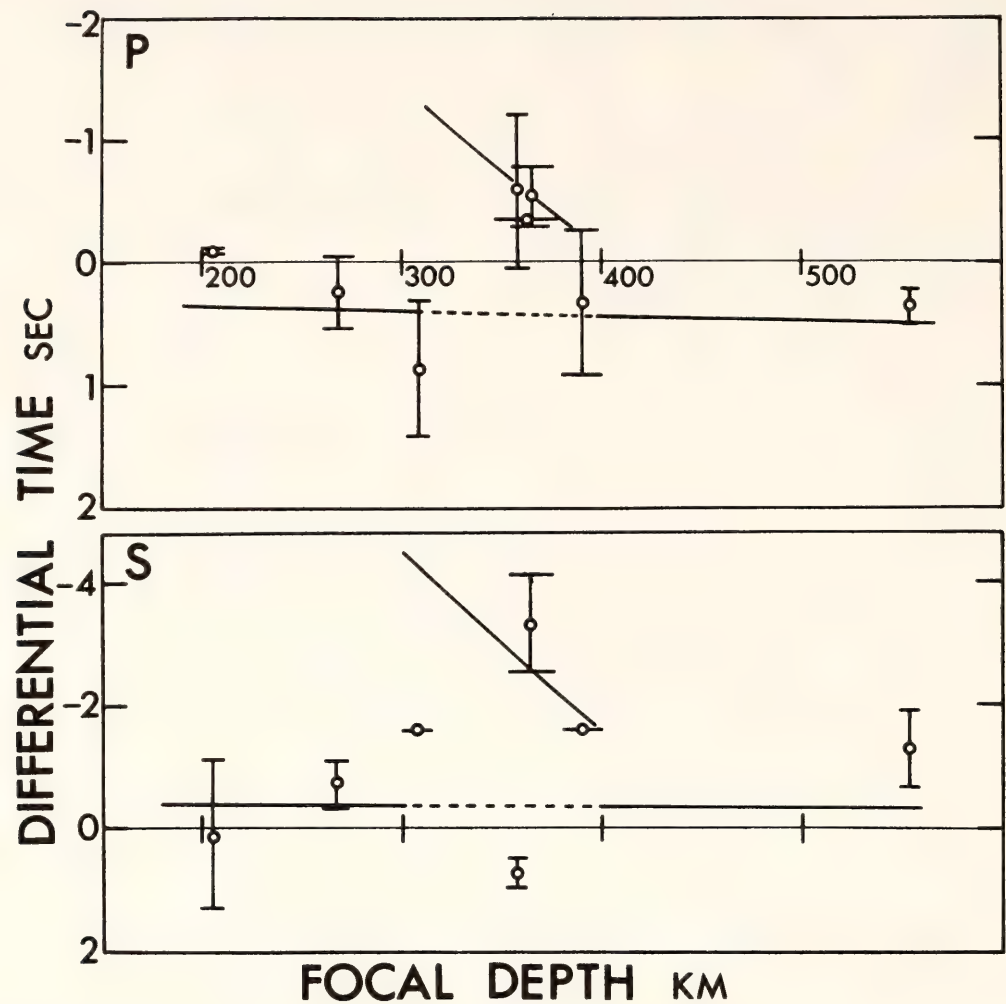


Fig. 67. Time difference between the mean travel-time residual of six stations (KAK, KYS, MIT, MIY, OFU, ONA) located where the depth to ALB is 16–47 km and that of CHO plotted against focal depth. Vertical and horizontal lengths indicate standard deviations of differential time and focal depth of each region, respectively. Solid lines show the calculated differential time for the two-layer model with total thickness of 120 km. Calculations are shifted –2 sec for S wave.

Vs contrast. Our data do not require such a structure but cannot rule it out. From the velocity contrasts we obtained, elastic parameter contrasts are calculated. Our results suggest that rigidity is higher by $16 \pm 4\%$ and bulk modulus by $9 \pm 6\%$ in the subducting lithosphere than in the overlying as-

TABLE 15. Oceanic Lithosphere in the Western Pacific Region

Thickness (km)	Structure (km/sec)		Source
	Vp	Vs	
130*	8.10	4.60	Leeds <i>et al.</i> (1974)
110*	8.10	4.60	Leeds (1975)
80 (50)	8.20	4.6–4.7	Shimamura and Asada (1976)
(20)		4.88	Shimamura <i>et al.</i> (1977)

* Corresponds to 135-m.y. isochron.

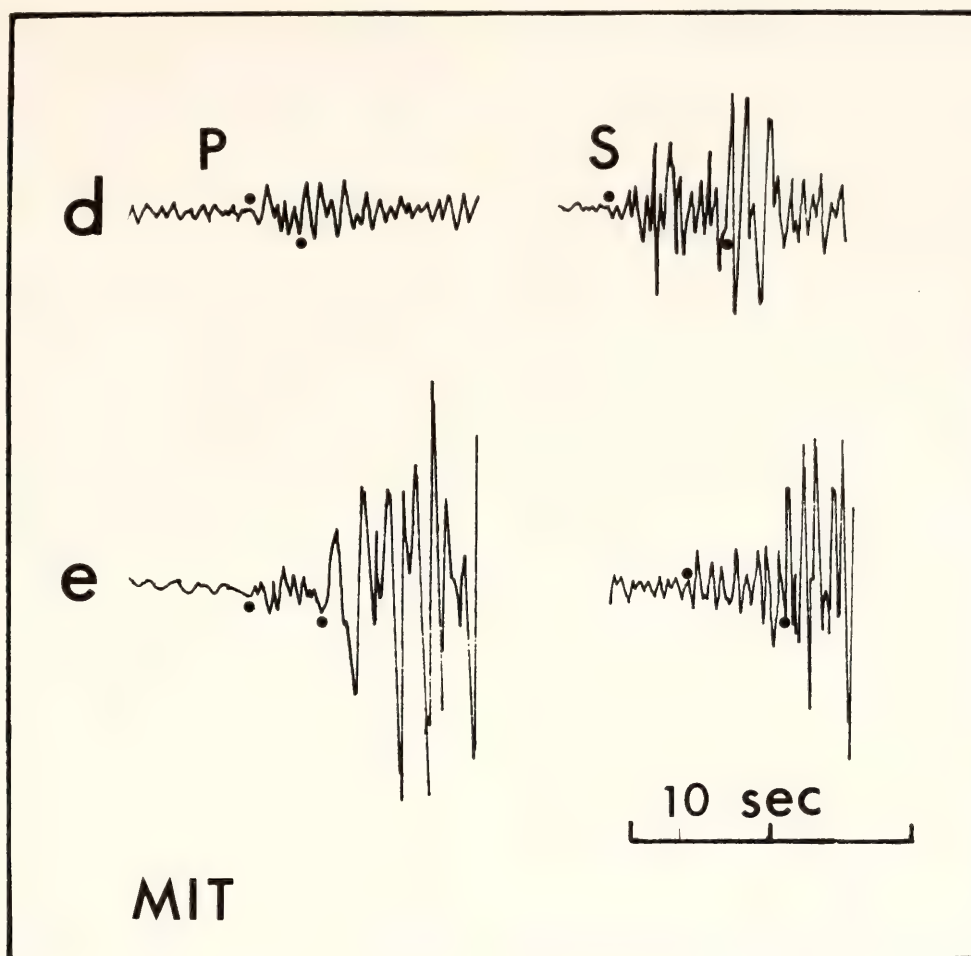


Fig. 68. Seismograms at MIT for two events in the Japan Sea region. Vertical components are shown for *P* wave and EW horizontal components for *S* wave. Note the two arrivals for *P* and *S*. The second arrival could be the wide-angle reflection from the base of the subducting lithosphere, which is the only arrival of CHO (Fig. 65).

thenosphere. It is likely that some mechanism other than the temperature-pressure effect, such as partial melting, is responsible for the calculated velocity contrasts. The relatively larger contrast in rigidity is consistent with the hypothesis of partial melting in the asthenosphere.

Travel-time residual data at the easternmost station, CHO, demand a two-layer model in which the lower layer of the descending lithosphere has a slightly higher (1%) velocity. The data also constrain the total thickness of the high-velocity slab to be about 120 km, which is comparable to results obtained by Leeds (1975) and Leeds *et al.* (1974) for the oceanic lithosphere in the western Pacific.

Acknowledgments

We thank Drs. A. T. Linde and J. A. Snoke for valuable comments and Dr. D. E. James for carefully and critically reading the manuscript. We thank Japan Meteorological Agency for providing the seismograms. This work has been partially supported by the Earth Sciences Section, National Science Foundation, Grant EAR77-13520.

References

- Anderson, D. L., Composition of the mantle and core, *Ann. Rev. Earth Planet. Sci.*, 5, 179–202, 1977.
- Anderson, O. L., E. Schreiber, R. C. Liebermann, and N. Soga, Some elastic constant data on minerals relevant to

- geophysics, *Rev. Geophys.*, 6, 491–524, 1968.
- Birch, F., Density and composition of the upper mantle: first approximation as an olivine layer, in *The Earth's Crust and Upper Mantle*, A.G.U. Monograph 13, pp. 18–36, P. J. Hart, ed., Amer. Geophys. Union, Washington, D.C., 1969.
- Hales, A. L., A look at the mantle, *Geotimes*, 9, No. 1, 9–12, 1964.
- Hales, A. L., and H. A. Doyle, P and S travel time anomalies and their interpretation, *Geophys. J.*, 13, 403–415, 1967.
- Hasebe, K., N. Fujii, and S. Uyeda, Thermal processes under island arcs, *Tectonophysics*, 10, 335–355, 1970.
- Hirahara, K., A large-scale three-dimensional seismic structure under the Japan Islands and the Sea of Japan, *J. Phys. Earth (Tokyo)*, 25, 393–418, 1977.
- Ichikawa, M., and E. Mochizuke, Travel time tables for local earthquakes in and near Japan, *Pap. Meteorol. Geophys.*, 22, 229–290 (in Japanese), 1971.
- Jacob, K. H., Three-dimensional seismic ray tracing in a laterally heterogeneous spherical earth, *J. Geophys. Res.*, 75, 6675–6689, 1970.
- Leeds, A. R., Lithosphere thickness in the western Pacific, *Phys. Earth Planet. Interiors*, 11, 61–64, 1975.
- Leeds, A. R., L. Knopoff, and E. G. Kausel, Variations of upper mantle structure under the Pacific Ocean, *Science*, 186, 141–143, 1974.
- Mitronovas, W., and B. L. Isacks, Seismic velocity anomalies in the upper mantle beneath the Tonga-Kermadec island arc, *J. Geophys. Res.*, 76, 7154–7180, 1971.
- Mizutani, H., and H. Kanamori, Variation of elastic wave velocity and attenuative property near the melting temperature, *J. Phys. Earth*, 12, 43–49, 1964.
- Noguchi, S., and H. Okada, Anomalous seismic wave transmission and the upper mantle structure in and around Hokkaido in *Symposium on Subterranean Structure in and around Hokkaido and its Tectonic Implication*, Hokkaido Univ., Sapporo, 24–43 (in Japanese), 1976.
- Segawa, J., and Y. Tomoda, Gravity measurements near Japan and study of the upper mantle beneath the oceanic trench-marginal sea transitional zones, in *The Geophysics of the Pacific Ocean Basin and its Margin*, A.G.U. Monograph 19, pp. 35–52, G. H. Sutton, M. H. Manghnani and R. Moberly, eds., 1976.
- Shimamura, H., and T. Asada, Apparent velocity measurements on an oceanic lithosphere, *Phys. Earth Planet. Interiors*, 13, 15–22, 1976.
- Shimamura, H., T. Asada, and M. Kumazawa, High shear velocity layer in the upper mantle of the Western Pacific, *Nature*, 269, 680–682, 1977.
- Suyehiro, K., and I. S. Sacks, Velocity structure in the subducting lithosphere, *Carnegie Inst. Wash. Year Book* 76, 813–822, 1977.
- Tada, T., P wave velocity distribution in the downgoing slab, *Jishin*, 27, 125–139 (in Japanese), 1972.
- Toksöz, M. N., and P. Bird, Formation and evolution of marginal basins and continental plateaus, in *Island Arcs, Deep Sea Trenches and Back-Arc Basins*, A.G.U. M. Ewing Series, 1, pp. 379–393, M. Talwani and W. C. Pitman III, eds., Amer. Geophys. Union, Washington, D.C., 1977.
- Utsu, T., Ratio of V_p/V_s in the upper mantle beneath the island arcs of Japan, *Jishin*, 22, 41–53 (in Japanese), 1969.
- Utsu, T., Regional variation of travel-time residuals of P waves from nearby deep earthquakes in Japan and vicinity, *J. Phys. Earth*, 23, 367–380, 1975.
- Yamamizu, F., P travel-time anomaly in Japan as deduced from three-dimensional seismic ray tracing, *Geophys. Bull. Hokkaido Univ.*, 30, 33–56 (in Japanese), 1973.

AN ANOMALOUS LOW-VELOCITY REGION ABOVE THE DEEP EARTHQUAKES IN THE JAPAN SUBDUCTION ZONE

K. Suyehiro and I. S. Sacks

Introduction

Seismic velocities in the asthenosphere overlying the subducting lithosphere in the Japan subduction zone are generally considered to be a few percent lower than the Jeffreys-Bullen standard velocity model (e.g., Utsu, 1967; Kanamori, 1968; Hamada, 1973; Yamamizu, 1973). However, there are indications that the asthenosphere may possess an anomalously low velocity zone (hereafter referred to as ALVZ) in which the velocity variation

is as large as any found in the upper mantle. Noguchi and Okada (1976) suggested a very low velocity zone in the asthenosphere in the northern Hokkaido-Sakhalin region based on *P*-wave travel-time residuals from local deep earthquakes. However, the data they used did not allow separate estimates of the geometry and the velocity of the zone. In this paper, we delineate such a feature in the Japan-USSR region using *P*-wave travel-time residuals from local intermediate and deep earthquakes. We also show that the ALVZ seems to coincide with an extremely low *Q* zone inferred from spectral ratio analyses (Sacks and Okada, 1974).

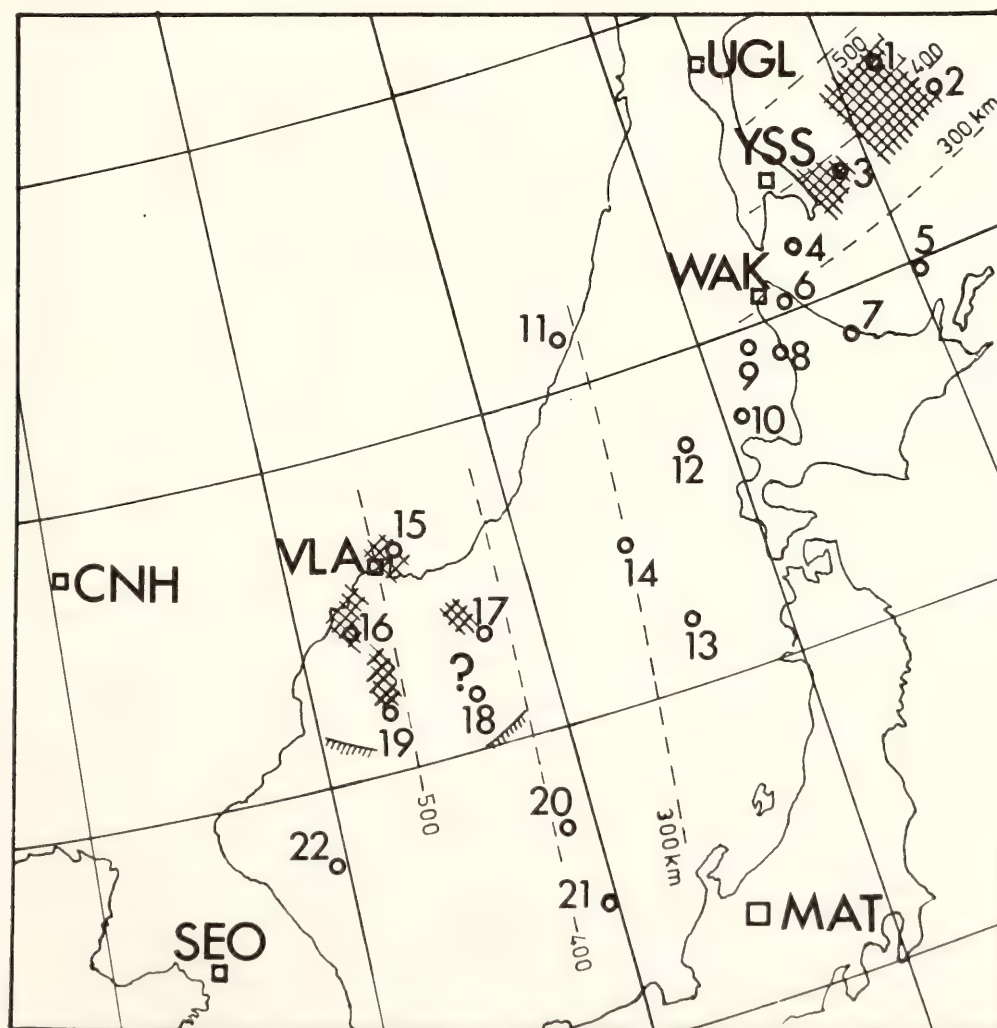


Fig. 69. Map of eastern Asia indicating stations (squares) and mean epicenters of clusters (circles) studied. Benioff zone depth contours are shown in dashed lines. Hatched regions indicate the ALVZ inferred in this study.

Data

From the ISC bulletins, we selected intermediate and deep earthquakes in the Japan-USSR region for which teleseismic data dominated the hypocenter solutions (Table 16, Fig. 69).

Method

To determine uniquely both the physical extent of the anomalous region and the magnitude of the velocity decrease, various epicentral distances, azimuths, and focal depths are covered. After correcting the observed travel-time residuals for location errors or local crustal ef-

fects, these are compared with calculated values. In the calculation, we use a regional velocity model (Suyehiro and Sacks, 1978; Fig. 70) for the data at stations in Japan, since the effect of the dipping high-velocity slab is considerable. Laterally homogeneous model calculations suffice for other stations toward which seismic rays spend negligible amounts of time in the high-velocity slab.

Data Analysis

In order to infer structural anomalies in the asthenosphere from travel-time

TABLE 16. Earthquake Groups and Residuals Used in the Study*

Cluster No.	No. of Earthquakes per Cluster	Lat.°N	Long.°E	Depth(km)	Residuals (sec)		
					YSS	WAK	UGL
1	13	48.09(.13)	146.45(.40)	471(31)	4.4	2.1	3.0
2	6	47.28(.25)	147.10(.37)	366(15)	5.1	4.4	2.5
3	8	46.71(.30)	144.20(.39)	373(12)	5.8	4.1	1.9
4	11	45.81(.22)	142.80(.31)	325(12)	3.3	2.5	2.4
5	1	44.85	145.12	216	1.9	3.3	1.0
6	1	45.14	142.24	271	3.8	N†	1.1
7	1	44.29	143.20	221	0.8	0.5	0.7
8	3	44.46(.03)	141.65(.41)	250(9)	N	N	N
9	2	44.72(.04)	140.99(.26)	259(1)	2.3	2.9	N
10	5	43.74(.06)	140.36(.47)	223(6)	1.6	1.8	0.6
					VLA	CNH‡	SEO
11	2	45.61(.22)	137.03(.19)	359(14)	2.6	...	1.7
12		43.59(.14)	139.16(.04)	241(2)	1.5
13	5	41.00(.14)	137.97(.32)	269(19)	1.7	0.4	...
14	1	42.41	137.20	290	2.1	...	0.9
15	3	43.44(.07)	132.36(.04)	477(7)	6.7	3.9	...
16	9	42.25(.38)	131.05(.12)	545(11)	5.6	2.6	2.8
17	1	41.83	133.82	437	3.8
18	1	40.79	133.35	467	3.4	1.9	...
19	1	40.87	131.49	540	5.3
20	1	38.49	134.52	397	2.5
21	9	37.34(.43)	134.86(.29)	376(10)	1.7	1.9	...
22	2	38.83(.08)	129.88(.34)	544(3)	2.1

* Earthquakes are selected from ISC bulletins for the period 1964–1974. Criteria used are that each earthquake have more than 30 observations which are dominantly from teleseismic stations and that the magnitude be larger than 4.0. Travel-time residuals are given in the form $\Delta T/T$ (%). Numbers in parentheses are standard deviations.

† Negative travel-time residual.

‡ Travel-time data are from Chinese seismological bulletins.

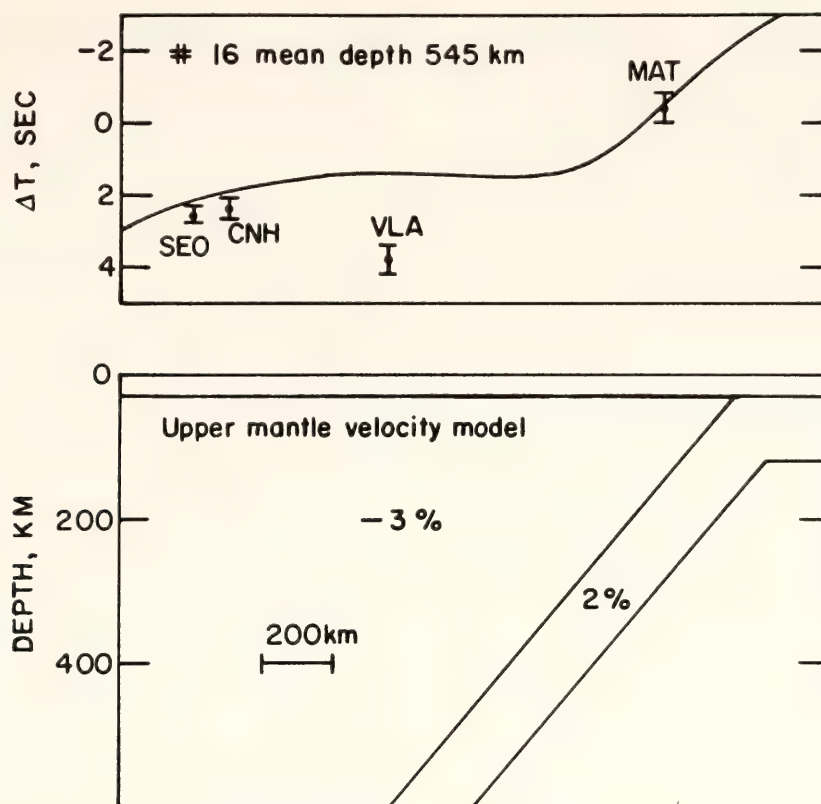


Fig. 70. (Lower) Laterally heterogeneous upper mantle P wave velocity model for Japan subduction region proposed by Suyehiro and Sacks (1978). Velocities are given relative to J.-B. model. (Upper) As an example, travel-time residuals calculated according to this model are shown for the earthquake cluster 16. The observed data show a large departure from the predicted value for VLA. This anomaly is not observed at CNH and SEO, which have depth-error dependence comparable to that of VLA.

residuals, the following sources of error have to be taken into account:

1. Random location errors and reading errors. Mean travel-time residuals for clusters of earthquakes are calculated to reduce these errors; data with large scatter are rejected.

2. Local crustal effects. Utsu's (1975) local station corrections are applied to the residuals at VLA, YSS, WAK, and UGL. For MAT, the value from Suyehiro and Sacks (1978) is used. These corrections are small relative to the observed large positive anomalies.

3. Origin time errors. Relative residuals (e.g., VLA-MAT) eliminate origin time errors. Standard deviations of mean travel-time residuals are reduced considerably by this procedure. These relative residuals are then converted back to absolute residuals by substituting the residual of the standard station with a

calculated value from the model in Fig. 70. MAT is chosen as the standard station for VLA, and UGL for YSS and WAK. It turns out that this procedure does not change the values of the large travel-time residuals significantly (in most cases, residuals are reduced by a few tenths of a second), but it does reduce the scatter of the data. For example, the standard deviation for the cluster 16 (Table 16, Fig. 69) reduces from 0.8 to 0.4 sec. However, large positive residuals at local stations for a few earthquakes were shown to be due to origin time errors. We did not use relative residuals for the nonanomalous residuals ($\Delta T/T < \sim 3\%$), which are used only for the geometrical consideration of ALVZ.

4. Systematic location errors. Location bias for deep earthquakes due to the dipping high-velocity slab is minimized

by using ISC locations, since these are dominated by teleseismic observations (Utsu, 1975). In the following, we check to see whether the large positive anomalies ($\Delta T/T > \sim 4\%$) observed mainly at VLA and YSS (Table 16) could be due to systematic location errors.

4A. VLA data. Consider the data from earthquake cluster 16, which has the largest number of earthquakes. Travel-time residuals at local stations other than VLA are explained by the model in Fig. 70, which was derived from an independent set of data. A horizontal location error ($> \sim 0.5^\circ$) large enough to explain the VLA data is unlikely, since

for a number of azimuths other stations (Fig. 69) with much greater horizontal location error dependence (e.g., MAT, SEO, CNH) do not show anomalies. Of more importance is the depth error, since dT/dZ at VLA is about 0.1 sec/km compared to about 0.03 sec/km for $dT/d\Delta$. (T is the travel time, Z is the depth and Δ is the horizontal distance.) However, dT/dZ values at CNH and SEO are also large (0.06 sec/km and 0.05 sec/km, respectively) and these stations do not show an anomaly (Fig. 70). Therefore if the residual at VLA (2.4 sec) was due to a depth error, the residuals at CNH and SEO would be 1.4 and 1.2 sec. Since the observed residuals at CNH and SEO are both 0.4 sec, it is most likely that the VLA anomaly is mainly due to velocity structure. We expect similar location errors for other earthquake groups because the difference between ISC depths and depths determined using pP - P time are similar for all earthquakes.

4B. YSS data. A similar situation to that above applies. The dT/dZ values at UGL, YSS, and WAK are similar, but UGL does not show anomalies, which suggests that the ALVZ also exists in the northern Hokkaido-Sakhalin region and in the same position relative to the deepest earthquakes.

Results

Geometry of ALVZ. It can be seen from Table 16 that large positive anomalies are observed for earthquakes deeper than 300 km but not for shallower events. Fig. 71, shows the seismic-ray paths to VLA and YSS. From the geometry of the seismic-ray paths studies (Fig. 69 shows the plan and Fig. 71 the vertical section), some limits can be placed on the physical extent of the low-velocity zone. The upper limit of the zone does not extend above 300 km. The zone also does not appear to extend much beyond the toe of the subducted lithosphere, since CNH and SEO show barely significant

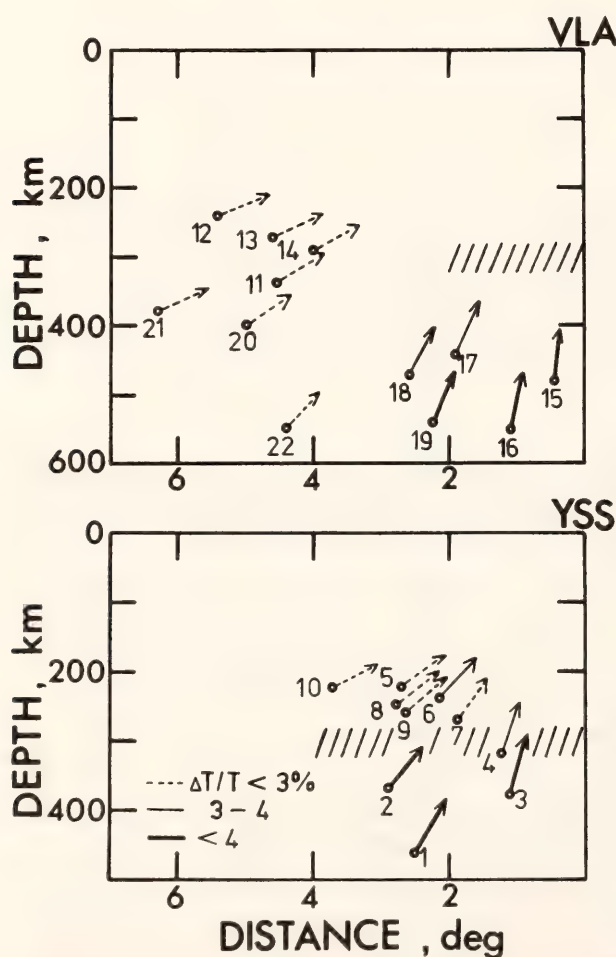


Fig. 71. Seismic ray paths to VLA and YSS are indicated. These provide geometrical constraints on the ALVZ. The ALVZ (indicated by diagonal lines) appears to start at around 300 km depth. The depth constraint is less clear from VLA data. Rays traveling greater distances ($> 4^\circ$ or so) penetrate the high-velocity slab and consequently do not arrive late.

anomalies for the southern group of earthquakes (Fig. 70), and the UGL anomaly for the northern group is less than YSS (Table 16). It was impossible to determine whether this anomalous low-velocity zone exists below the subducted lithosphere as well; we suspect not, however, because its close correlation with the deeper part of the subducted plate suggests that it may be caused by material released from the plate.

Velocity of the ALVZ. The size of the velocity anomaly can be calculated from the time delay and the physical extent of the anomalous region. Assuming that the normal asthenosphere velocity is 3% lower than J.-B., and if the depth range of the ALVZ is 300–500 km for the VLA region and 300–400 km for the YSS region, the velocity in the ALVZ must be 10–15% lower than J.-B. (Fig. 72). Compared with normal asthenosphere therefore, the ALVZ has a 7–12% velocity.

Anelasticity. An anelasticity study in the Japan region (Sacks and Okada, 1974) showed a zone with Q_P values lower than the surrounding asthenosphere for a region above the deepest earthquakes (Fig. 73). The large difference in energy absorption between the region above 500 km and that above 300 km is also apparent from spectral ratio studies of core-reflected shear waves and their surface reflections. Figure 74 shows the ray paths. We compared $sScS$ - ScS for an earthquake at a depth of 544 km with that at a 357-km depth. The spectral ratio $sScS:ScS$ and the travel time from the earthquake to the earth's surface allow us to calculate the average Q value of the region above the earthquake. Between the surface and 300-km depth, the Q_s is 200, whereas between the surface and 500-km depth the Q_s is less than 100. The existence of an anomalously low velocity zone, which also has lower Q than the surrounding asthenosphere, may indicate a region with greater degree of melt.

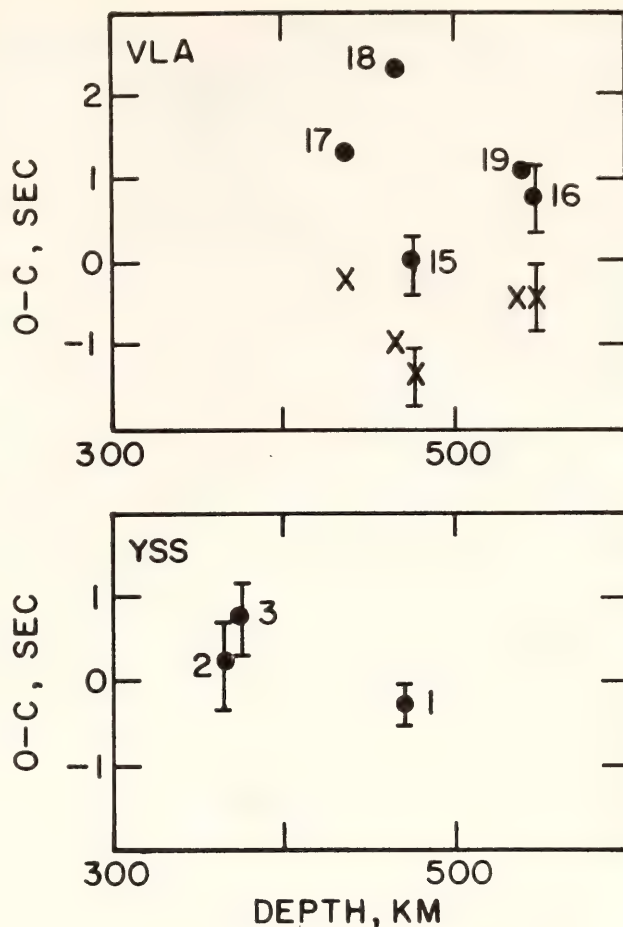


Fig. 72. Travel-time residuals calculated for models with an ALVZ. For the VLA data, an anomalous region between 300 and 500 km is assumed. The observed-calculated time is plotted for various earthquake groups, identified by numbers. Time-velocity models were compared, one 15% lower than J.-B. shown as dots, and one 10% lower shown as crosses. The 15% model gives a mean residual of +1.1 sec and the 10% model gives a -0.6 sec residual, suggesting that the applicable velocity anomaly is about 12%. For the YSS data an anomalous region between 300–400 km is assumed. Dots show the results for three earthquake groups if the anomaly is 15%. The normal asthenosphere is assumed to be 3% lower than J.-B.

Conclusion

To satisfy P -wave travel-time residuals, an anomalously low velocity zone is proposed in the depth below 300 km in the asthenosphere in the Japan subduction zone (Fig. 69). The depth range of the zone seems to match with the low- Q ($Q_p \sim 50$) regions suggested by Sacks and Okada (1974).

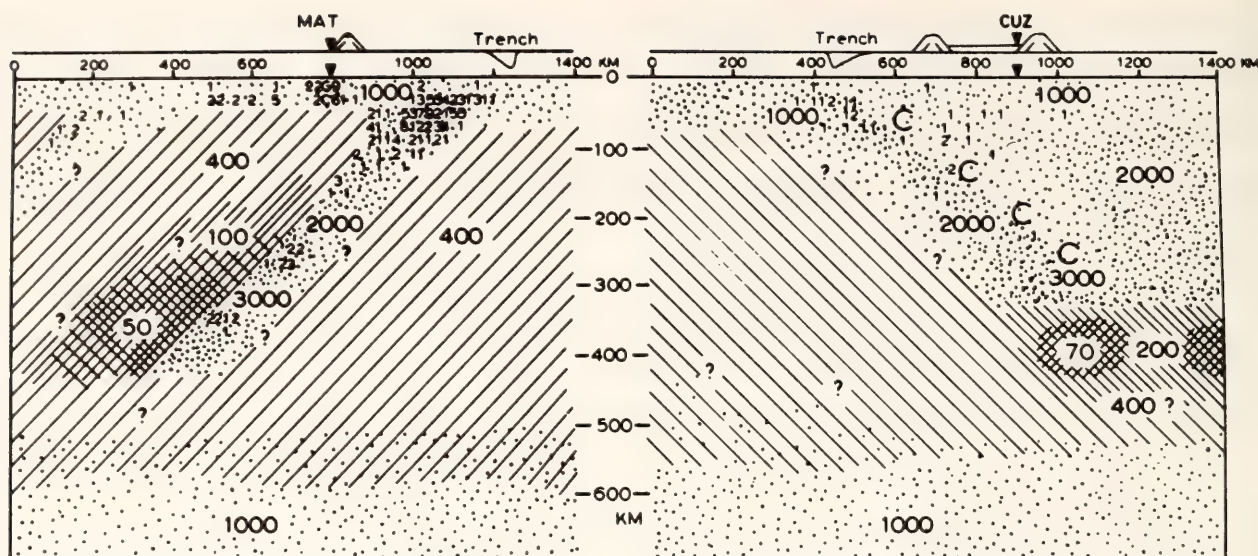


Fig. 73. Q_p structure beneath Japan (left) and South America (right). Low Q values (50–100) are shown cross-hatched. This low- Q region seems to lie in about the same depth range and position relative to the subducted slab as the ALVZ.

References

- Hamada, K., The upper mantle beneath Japan inferred from P travel-time anomalies by means of three-dimensional ray tracing, *J. Phys. Earth*, **21**, 463, 1973.
- Kanamori, H., Travel times to Japanese stations from Longshot and their geophysical implications, *Bull. Earthquake Res. Inst. Tokyo Univ.*, **46**, 841, 1968.
- Noguchi, S., and H. Okada, Anomalous seismic wave transmission and the upper mantle structure in and around Hokkaido, *Symposium on Subterranean Structure in and around Hokkaido and its Tectonic Implications*, Hokkaido Univ., Sapporo, p. 28 (in Japanese), 1976.
- Sacks, I. S., and H. Okada, A comparison of the anelasticity structure beneath western South America and Japan, *Phys. Earth Planet. Interiors*, **9**, 211, 1974.

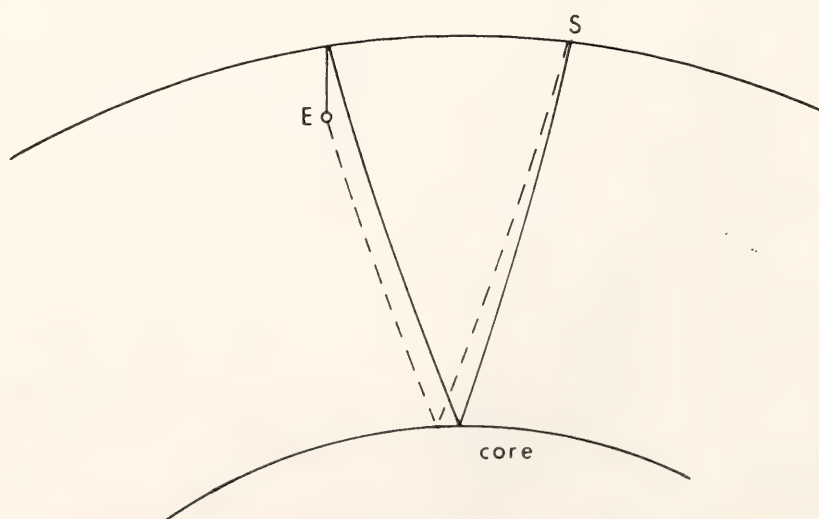


Fig. 74. Ray paths studied to determine Q_p between the earth's surface and the earthquake. E indicates a deep earthquake, S is a seismograph on the surface; the line is the ray path for $sScS$, which is the surface reflection of ScS (shown dashed).

Suyehiro, K., and I. S. Sacks, P and S wave velocity anomalies associated with the subducting lithosphere determined from travel-time residuals in the Japan region, submitted to *Bull. Seismol. Soc. Amer.*, 1978.

Utsu, T., Anomalies in seismic wave velocity and attenuation associated with a deep earthquake zone, 1, *J. Fac. Sci. Hokkaido Univ. Ser. VII*, 3, 1, 1967.

Utsu, T., Regional variation of travel-time residuals of *P* waves from nearby deep earthquakes in Japan and vicinity, *J. Phys. Earth*, 23, 367, 1975.

Yamamizu, F., *P* travel-time anomaly in Japan as deduced from three-dimensional seismic ray tracing, *Geophys. Bull. Hokkaido Univ.*, 30, 33 (in Japanese), 1973.

CRUST AND UPPER MANTLE STRUCTURE OF THE JAPAN SEA

J. R. Evans, K. Suyehiro, and I. S. Sacks

Introduction

The Japan Sea is an important example of a back-arc basin and is a major feature of the subduction system of the western Pacific. The role of such basins in the subduction process is an important question which any comprehensive theory should explain (Uyeda, 1977). Karig (1971) classified the region as an "inactive with high heat flow" basin. Such a prominent feature may well be related to the regional upper mantle velocity structure.

The Japan Sea has been the subject of several seismic refraction experiments (Andreyeva and Udintsev, 1958; Kovylin and Neprochnov, 1965; Kovylin, 1966; Murauchi and Yasui, 1968; Murauchi, 1972), many of which were reviewed by Rikitake *et al.* (1968). The propagation of surface waves across the region was examined by Abe and Kanamori (1970; hereafter referred to as A & K), who determined the group velocities of Love and Rayleigh waves between five earth-

quakes in northern Japan and the WWSSN station in Seoul, Korea (Fig. 75). The group velocities for the oceanic portion of the path were determined by calculating the dispersion due to the "continental" regions using Jeffreys-Bullen model and subtracting this effect from the mixed-path group velocities. On the assumption that a modification of its crustal parameters should affect only the short-period range ($T < 30$ sec), A & K concluded that the ARC-1 model, which fits their observations well in the longer period range (40–80 sec) only, approximates the mantle beneath the Japan Sea (Fig. 76).

ARC-1 differs from typical "average" oceanic models, for example 8099 (Dorman *et al.*, 1960) and CIT 11A (Anderson and Toksöz, 1963), principally in possessing an extremely low shear velocity of 4.23 km/sec between 30-km and 60-km depth, where the "average" models show a 4.6 km/sec lid and have channel velocities of 4.3–4.35 km/sec. However, as the ARC-1 model does not give a uniformly good fit to the Japan Sea data, we have reexamined the analysis incorporating modified crustal parameters as suggested by A & K in order to assess which features of the ARC-1 model are essential.

The features of the crustal structure of the Japan Sea were enumerated by A & K: "The basin has a water layer about 3 km thick, a sedimentary layer 2 to 3 km thick, a lower crust 8 to 12 km thick, and a P_n velocity of 8.1–8.3 km/sec." We note that large sections of the paths examined by A & K traverse the length of the Yamato Bank, an elevated feature associated with a crustal thickness of the order of 20 km (Rikitake *et al.*, 1968). We anticipate, therefore, that the aggregate of the crustal structures sampled by the surface waves should be toward the thicker end of the range quoted by A & K. We have examined records from the DTM broadband station at Matsushiro, Japan, of

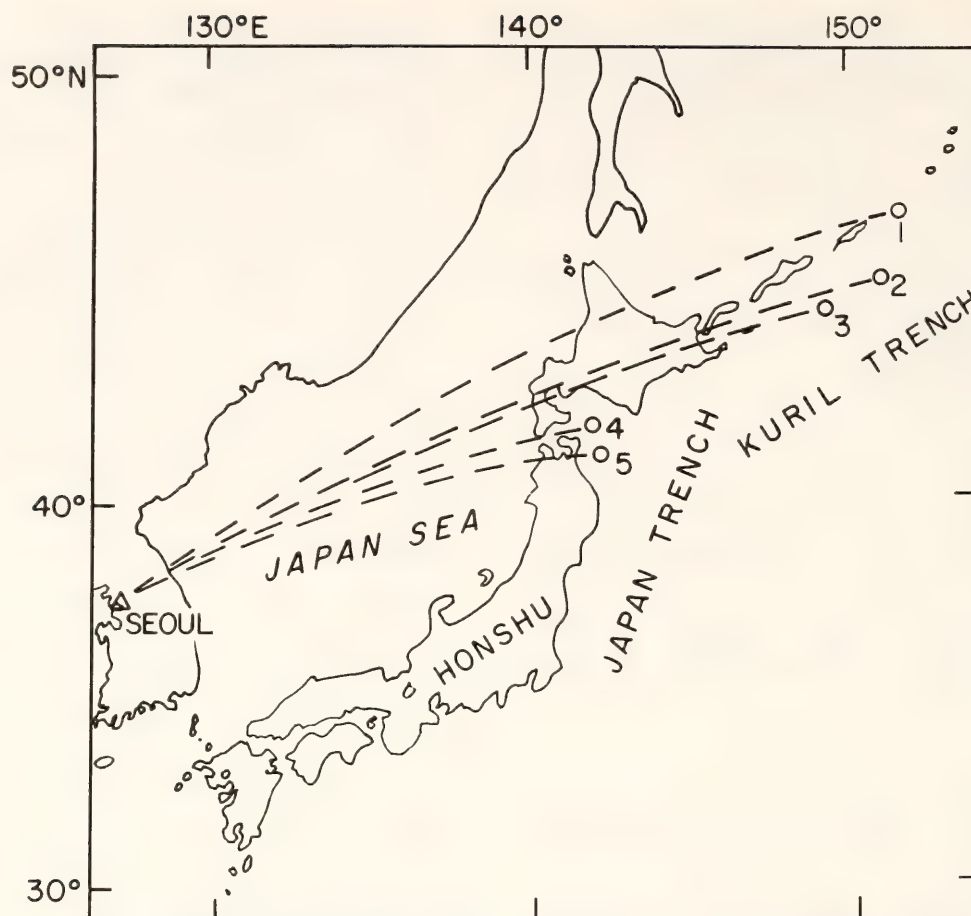


Fig. 75. Map of the Japan Sea region showing epicenters and paths to Seoul used by Abe and Kanamori (1970) (reproduced with permission).

earthquakes near the coast of China and have found dispersion characteristics similar to those of A & K. We therefore adopt their data for the purposes of our analysis.

Computational Technique

Group velocities for fundamental models of Love and Rayleigh waves were calculated using a modification of the method described in detail by Schwab and Knopoff, 1972. Our computations for the velocities of the ARC-1 model agree well with those given by Kanamori and Abe, 1968. However, A & K did not apply any correction for the initial phase of the sources and, since we wish to compare our interpretation with that of A & K, we have not done so either. Applications of this correction would reduce the calculated velocities for Rayleigh waves by

no more than 0.03 km/sec (Knopoff and Schwab, 1968).

Model Studies

A & K suggested two modifications of the ARC-1 crustal model in their interpretation of the Japan Sea data, and the effects of these modifications are shown in Fig. 76. For crustal model A, 3 km of ocean is replaced by unconsolidated sediment (Table 17). Although this preserves a good fit to the long-period data, the fit at short periods, although improved, remains poor, and the model does not agree with the constraints given by refraction data listed earlier. ARC-1B complies with the refraction constraints and provides a moderate fit to the data at all periods. However, Fig. 76 shows that the fit is clearly poorer than ARC-1 in the longer period range. Using ARC-

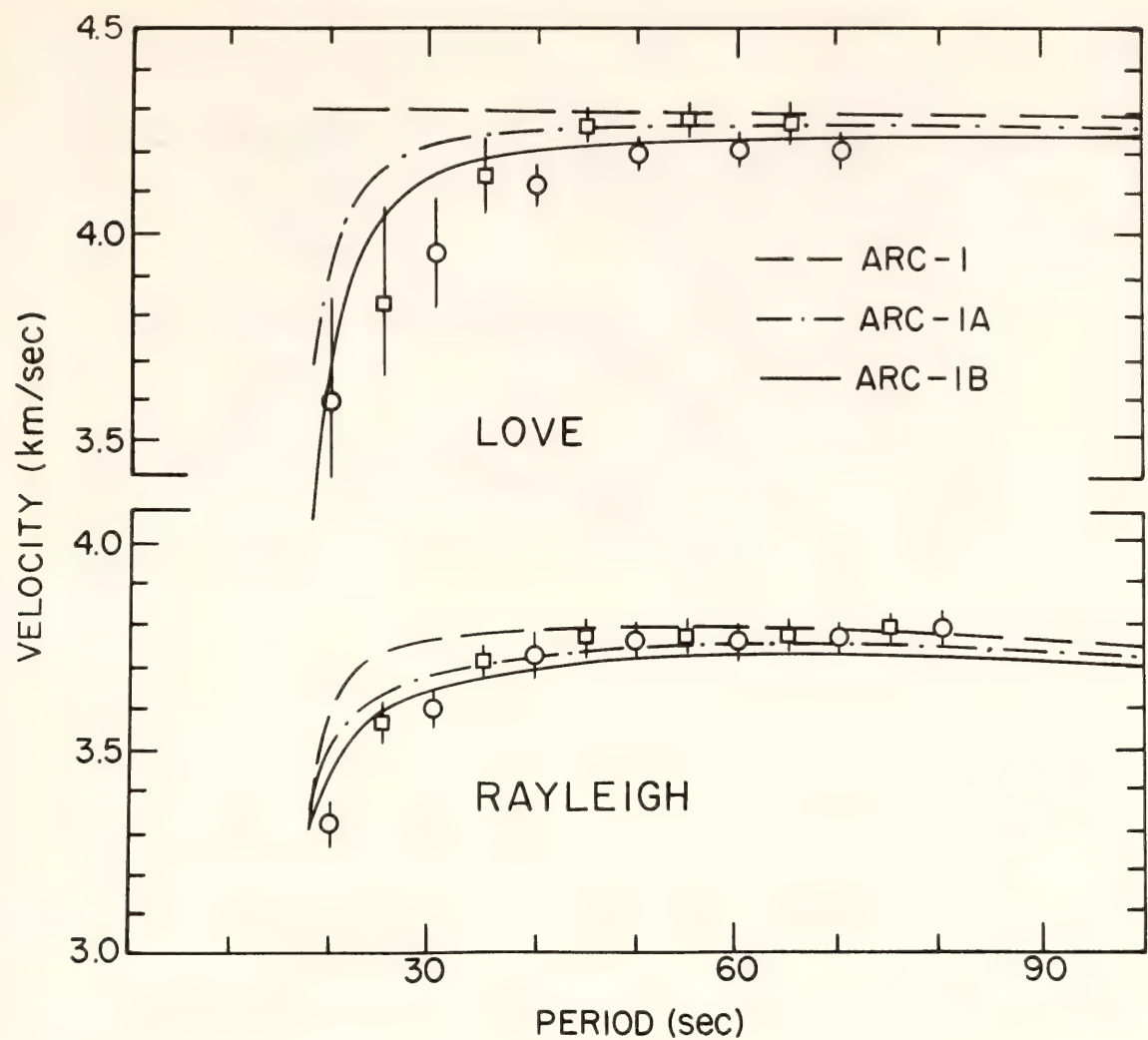


Fig. 76. Surface-wave data for the Japan Sea region and model-dispersion curves for various crustal structures from Abe and Kanamori (1970). Circles show mixed-path dispersion. Squares show pure-path (oceanic) dispersion. The vertical bars represent one standard deviation.

TABLE 17. Crustal Models*

ARC-1	A	B	C	D
0.0 (5)	0.0 (3)	0.0 (3)	0.0 (3)	0.0 (3)
1.0 (1)	1.0 (3)	1.0 (3)	1.0 (1.5) 2.0 (1.5)	1.0 (1.5) 2.0 (1.5)
3.7 (5)	3.7 (5)	3.7 (8)	2.9 (2) 3.5 (3) 3.9 (6)	2.9 (3) 3.36 (3) 3.9 (7)

*Shear velocity values in km/sec; parenthetical values indicate thickness in km.

1B as our standard for comparison, we now look at the effects of modifying various significant parameters of the ARC-1 model (Fig. 77).

Crustal structure. The upper set of

curves shows the effects of modifying crustal structure. We propose two further crustal models (C and D, listed in Table 17) constructed after inspection of the refraction profiles. With a view to satisfying the short-period surface-wave data, a degree of gradient structure is introduced into the sediments and upper crust. Models C and D differ principally in the depth to Moho, and both satisfy the criteria given by A & K. We find that both have a considerable effect on group velocities (~0.1 km/sec) at periods even beyond 100 sec.

Channel velocity. As the second set of curves (channel velocity) shows, similar variations to those due to crustal structure can be obtained within the

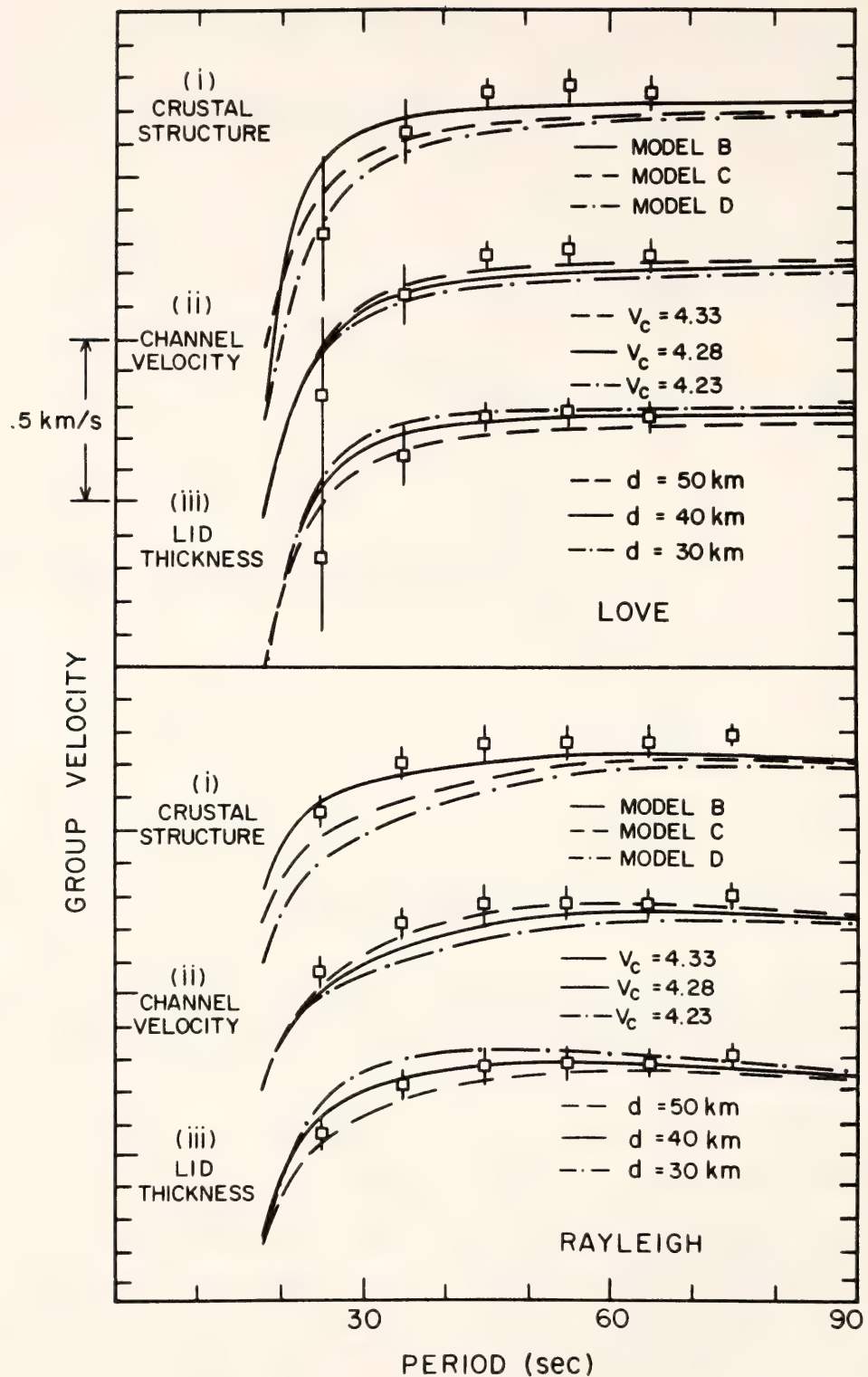


Fig. 77. Effects of varying several parameters of the ARC-1 model. The pure-path data for the Japan Sea (Fig. 76) are included for reference. (i) Effect of crustal structure. The mantle model, ARC-1, is fixed. (ii) Effect of varying shear-wave velocity in the depth range 30–60 km. The crustal model, C, is fixed. (iii) Effect of varying lid thickness. The crustal model, C, and the mantle model, 8099, are fixed.

period range 30–80 sec from changes in the shear-wave velocity in the low-velocity channel at 30–60 km depth. We are only able to distinguish the effects

of crustal structure from those of channel velocity by examination of the period range below 30 sec.

Lid thickness. The last set of curves

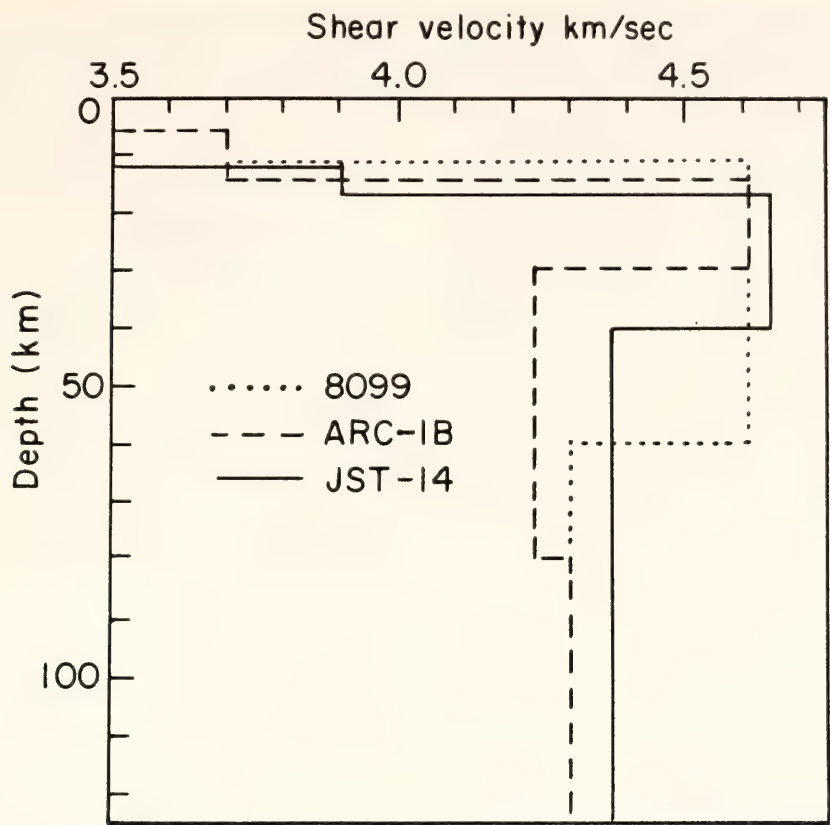


Fig. 78. Shear-velocity structures for 8099, ARC-1B, and JST-14 models. Note the differences in lithospheric thicknesses and velocities in the asthenosphere.

shows the effects of change in lid thickness. It can be seen that there is a trade-off between channel velocity and lid thickness, since increasing the depth to the top of the channel has very similar effects to that of increasing the channel velocity.

Lid velocity. The lid velocity is constrained from observations of P_n velocity of 8.1–8.3 km/sec.

There is a considerable degree of non-uniqueness in the inversion of the available data. Stronger constraints might be obtained either from observation of higher mode surface waves, or (more feasibly) from two-station phase-velocity measurements, or from a considerably larger body of group velocity measurements.

Concluding Remarks

As we have seen, because of the shallow structure each parameter significantly affects the dispersion curves in

TABLE 18. Shear Velocity Models for ARC-1B and JST-14*		
	ARC-1B	JST-14
Crustal Model	B	D
Lid	4.6125 (16)	4.65 (21)
Channel	4.23 (50) 4.30 (140)	4.37 (180)
Mantle Model	8099	8099

*Shear velocity values in km/sec; parenthetical values indicate thickness in km.

overlapping period ranges, and hence all must be taken into account. Our preferred model, JST-14 (Table 18, Figs. 78 and 79) is by no means a unique interpretation, but it fits the surface-wave data better than ARC-1B and also satisfies the constraints of the refraction data. JST-14 does not have the low-velocity channel of the ARC-1 series—indeed the channel velocity of 4.34 km/sec is slightly higher than the channel velocity of the “average” model 8099

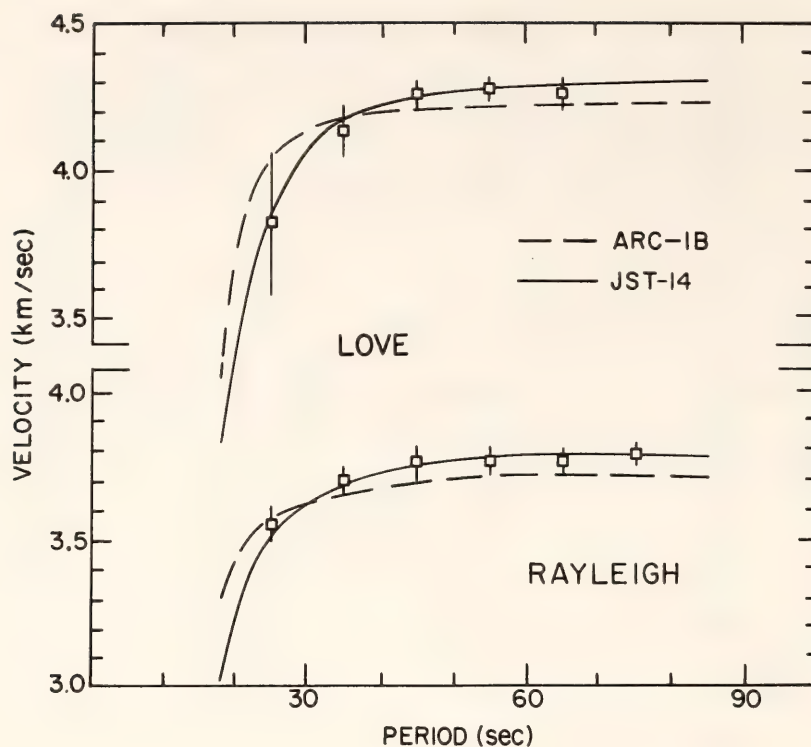


Fig. 79. Surface-wave dispersion curves for ARC-1B model and our preferred JST-14 model.

(4.30 km/sec) (Dorman *et al.*, 1960). This is not achieved at the expense of lid thickness—the depth to the channel is 40 km, against 30 km for ARC-1. The tradeoffs are effected in the crustal layers. We find, therefore, that although the surface-wave data require a shallow (~ 30 –50 km) depth to the top of the low-velocity channel, the data can be satisfied without the unusually low channel velocity of the ARC-1 model.

Acknowledgments

We thank K. Abe and H. Kanamori for their comments on the original manuscript. This work was supported in part by NSF grant #EAR77-13500.

References

- Abe, K., and H. Kanamori, Mantle structure beneath the Japan Sea as revealed by surface waves, *Bull. Earthq. Res. Inst. Tokyo Univ.*, 48, 1011, 1970.
- Anderson, D. L., and M. N. Toksöz, Surface waves on a spherical earth, 1, *J. Geophys. Res.*, 68, 3483, 1963.
- Andreyeva, I. B., and G. B. Udintsev, Bottom structure of the Sea of Japan, from Vityaz expedition data, *Izv. Akad. Nauk SSSR, Ser. Geol.*, 10, 3 (in Russian), 1958.
- Dorman, J., M. Ewing, and J. Oliver, Study of shear velocity distribution in the upper mantle by mantle Rayleigh waves, *Bull. Seismol. Soc. Amer.*, 50, 87, 1960.
- Kanamori, H., and K. Abe, Deep structure of island arcs as revealed by surface waves, *Bull. Earthq. Res. Inst. Tokyo Univ.*, 46, 1001, 1968.
- Karig, D. E., Origin and development of marginal basins in the western Pacific, *J. Geophys. Res.*, 76, 2542, 1971.
- Knopoff, L., and F. A. Schwab, Apparent initial phase of a source of Rayleigh waves, *J. Geophys. Res.*, 73, 755, 1968.
- Kovylin, V. M., Results of seismic studies in the southwest of the Sea of Japan abyssal basin, *Oceanology, Acad. Sci. USSR*, 6, 238, 1966.
- Kovylin, V. M., and Y. P. Neprochnov, Structure of the earth's crust in the deep central part of the Japan Sea,

- according to seismic data, *Izv. Akad. Nauk SSSR, Ser. Geol.*, 4, 10 (in Russian), 1965.
- Murauchi, S., Crustal structure beneath the Japan Sea from seismic prospecting, *Kagaku*, 42 (in Japanese), 1972.
- Murauchi, S., and M. Yasui, Geophysical investigations in the seas around Japan, *Kagaku*, 38 (in Japanese), 1968.
- Rikitake, T., S. Miyamura, I. Tsubokawa, S. Murauchi, S. Uyeda, H. Kuno, and M. Gorai, Geophysical and geological data in and around the Japan Arc, *Can. J. Earth Sci.*, 5, 1101, 1968.
- Schwab, F. A., and L. Knopoff, Fast surface wave and free mode computations, *Methods in Computational Physics*, 11, 87, Academic Press, New York, 1972.
- Uyeda, S., Some basic problems in the trench-arc-back arc system, in *Island Arcs, Deep Trenches, and Back-Arc Basins*, A.G.U. Maurice Ewing Series 1, 1-14, M. Talwani and W. C. Pitman III, eds., 1977.

ON DOUBLE BENIOFF ZONES IN SUBDUCTION REGIONS

A. T. Linde and I. S. Sacks

Introduction

Oceanic lithosphere is consumed by subduction at convergent plate margins. Subduction is characterized by deep seismicity, which usually forms a plane zone (the Benioff zone) that defines the upper boundary of the subducting plate (Figs. 80 and 81). There is no universally accepted model, however, that explains how earthquakes occur at depth. This problem has been compounded by recent detailed and precise seismicity studies, which have demonstrated that the Benioff zone is of complicated structure.

Stauder and Mualchin (1976) observed that intermediate-depth foci in

the Kurile region separate into two types representing either axial compression or axial tension along the dip of the plate. Detailed seismicity studies of the northeastern Japan arc (Hasegawa *et al.*, 1978; Umino and Hasegawa, 1975) show that these two types of earthquakes are separated spatially. In the depth range 70-170 km, there is a plane of compressive (in the dip direction) earthquakes at or near the upper boundary of the descending slab. The tension events occur in a lower, parallel plane with a separation of 30-40 km between the two earthquake zones (Fig. 80).

A similar seismicity pattern in the Aleutians has been reported by Engdahl and Scholz (1977). They propose a model in which these double Benioff zones are interpreted as being due to stresses produced by straightening of the dipping slab after the sharp bending that occurs at shallow depths.

While retaining Engdahl and Scholz's concept of stress due to straightening of the subducting plate, we suggest a different rheology which we believe not only is consistent with the double Benioff zone but also explains the low level of seismicity due to the initial bending process.

The rheological model used by Engdahl and Scholz assumes perfect elasticity for strains less than a yield strain and plastic deformation at greater strains. When the plate bends at the initiation of subduction, all but a relatively thin central arc yields, and tensile (compressive) stresses are produced in the upper (lower) regions of the slab. Because the dip of a Benioff zone is essentially constant with depth, some stress system must straighten the plate. This process results in stress in the slab such that the upper compressive region is separated from a lower tensile region (by ~ 20 km in Engdahl and Scholz's model).

While this model is consistent with the observed double Benioff zones, it also predicts that earthquakes should occur

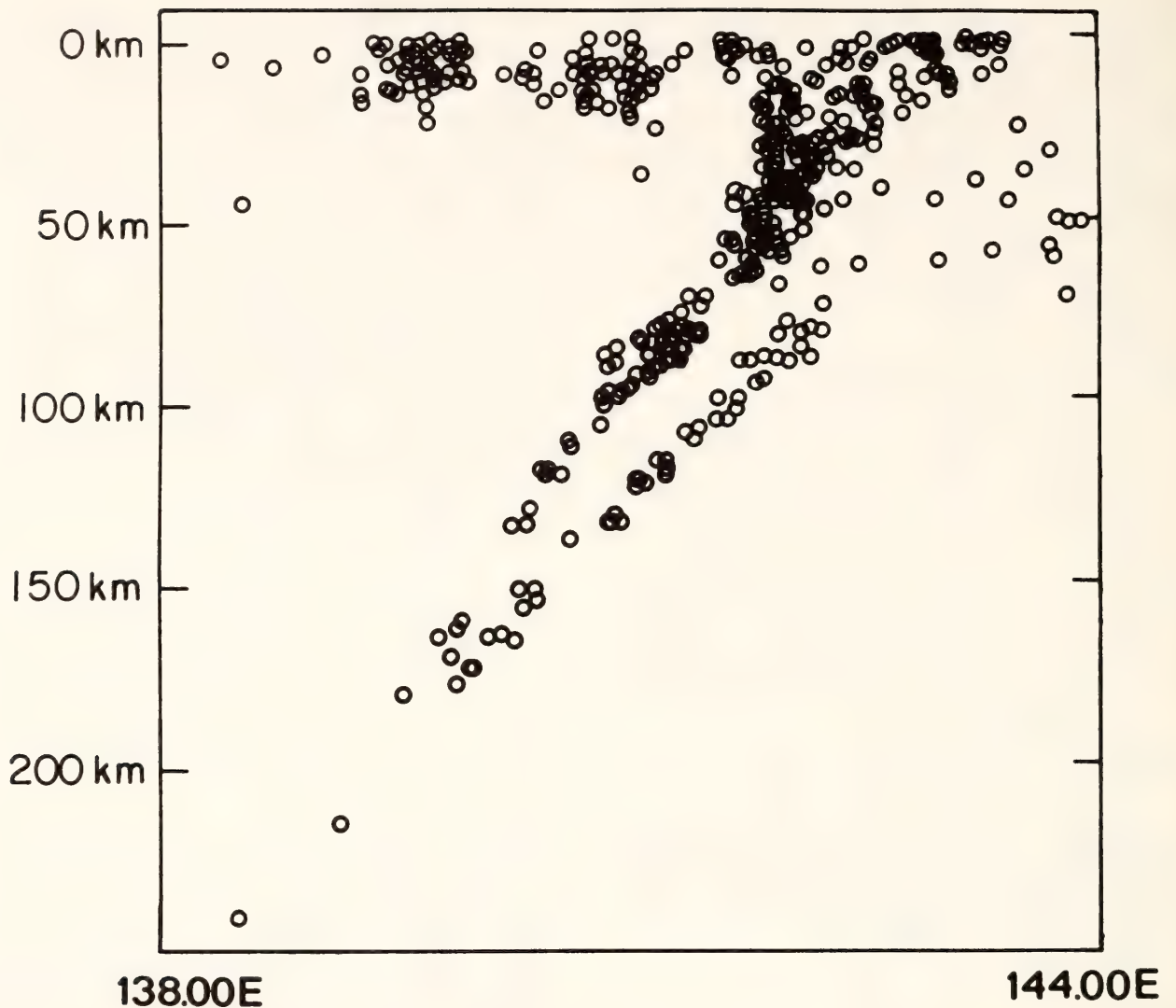


Fig. 80. Seismicity under the northeast Japan arc, from Hasegawa *et al.* (1978). The detailed seismicity from this precision location study shows a clear double Benioff zone. The two planes at depth have different fault-plane solutions, the upper showing down-dip compression and the lower showing down-dip tension.

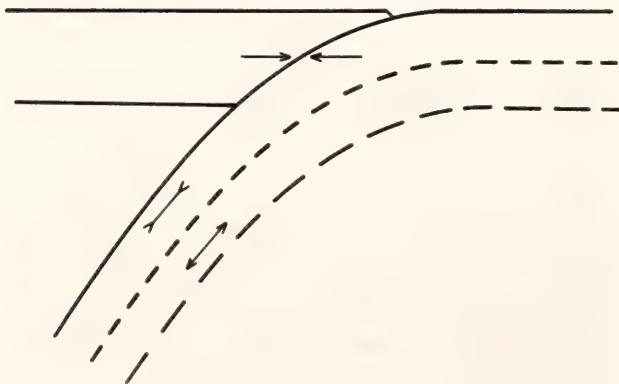


Fig. 81. Schematic illustration of simple model of forces in a subduction zone, as deduced from earthquake fault plane solutions.

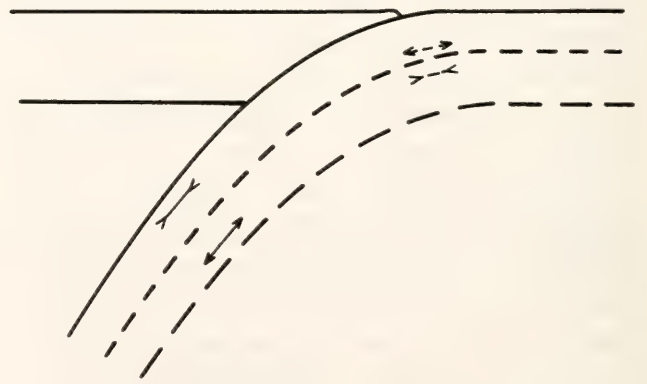


Fig. 82. Forces in the subduction region resulting from the bending model of Engdahl and Scholz.

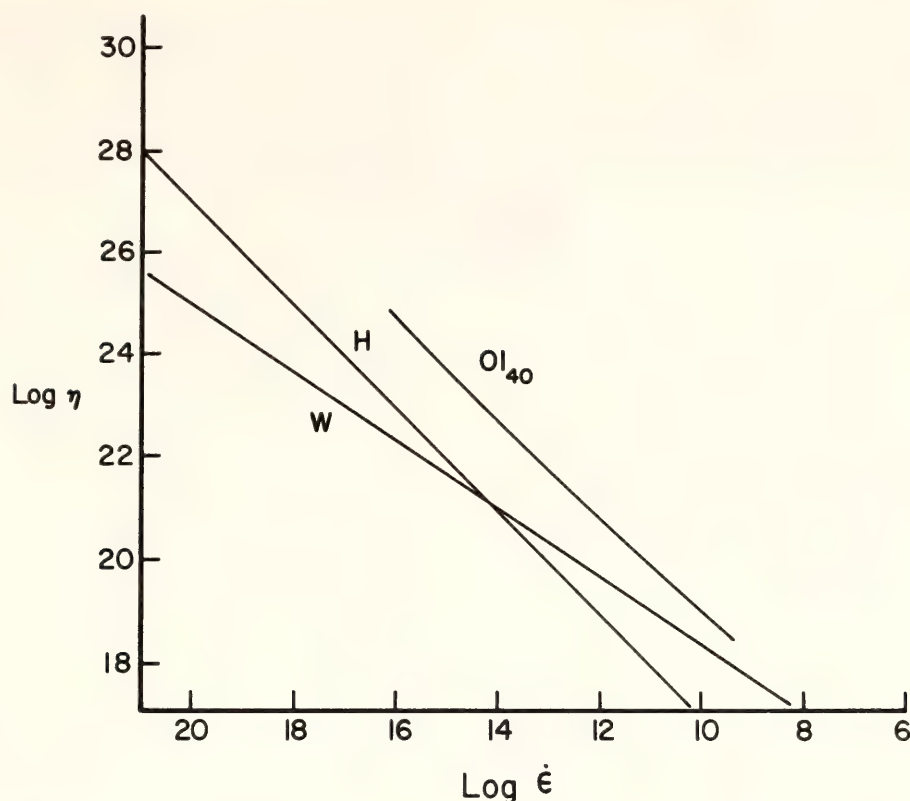


Fig. 83. Viscosity as a function of strain rate. Line *W* is a theoretical calculation from Weertman (1970). *H* shows extrapolated experimental results on Yule marble from Heard (1963). *Ol*₄₀ is the result for olivine at a depth of 40 km from Ashby and Verrall (1977).

in a similar manner in the region where the plate undergoes its initial curvature (Fig. 82). These regions of earthquakes would be tensile in the upper layer and compressive in the lower. Although the model predicts a smaller spatial separation between the two sets, the level of seismicity would be similar to that produced in the straightening process. However, the seismicity in this region is characterized by thrust events in or near the upper layers of the descending lithosphere but little or no seismicity of the type predicted by the model.

Model

We suggest a rheology in which plastic flow occurs such that the viscosity is strain-rate dependent (e.g., Weertman, 1970). Although the model calculations by Weertman are only for temperatures above half the melting temperature, ex-

periments by Heard (1963) indicate that similar behavior occurs at temperatures as low as 25°C (Fig. 83). Ashby and Verrall (1977) show that similar behavior can be expected for olivine in the uppermost mantle.

We further assume that the bending and straightening of the plate are not symmetric (Fig. 84). This is not unreasonable, since the bending is forced by the interaction between the two (strong) lithospheric plates whereas straightening forces are likely to be more spread out. (The seismicity patterns do not constrain this geometry.) Under these assumptions, then, in the bending process we have a relatively high value for strain rate and thus a lower value for viscosity than that resulting from the straightening.

For a lithosphere of thickness 80 km, bent to a radius of curvature of 150 km

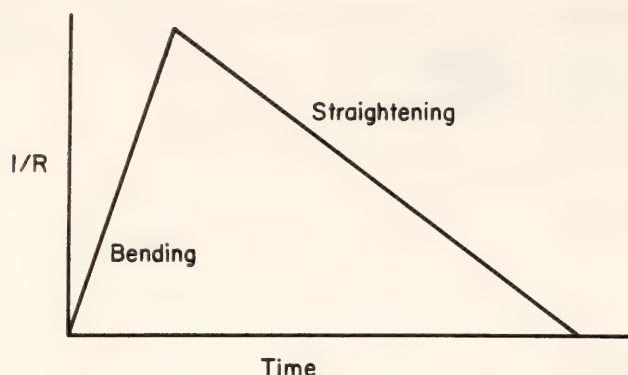


Fig. 84. Curvature of the subducting plate as a function of time. We assume that the bending process occurs more rapidly than the straightening process, since the bending is forced by the interaction with the adjacent nonsubducting lithosphere.

as it travels a distance of 100 km at a velocity of 6 cm/yr, the maximum strain rates are about $10^{-14} \text{ sec}^{-1}$. The corresponding viscosity is 10^{22} dP (Fig. 83), and thus the deformation of the slab is largely by plastic flow. The stress pattern is necessarily similar to that of the model of Engdahl and Scholz, but because of the low viscosity the material may not be capable of producing earthquakes.

As the plate undergoes a more gradual straightening, the strain rate is low and the effective viscosity is high. Thus, there is less supported plastic flow and so fracture can occur. The stress and viscosity patterns are shown in Fig. 85.

Earthquakes can be produced at depths greater than those at which curvature changes occur because of the stresses locked into regions which flow plastically in the first stage because of the high strain rate but which exhibit behavior closer to perfect elasticity thereafter. If internal stresses of order 1 kbar are to persist to depths of 600 km, we require a viscosity of order 10^{25} dP , which is not inconsistent with lithospheric viscosities.

Conclusion

The model proposed here produces a double Benioff zone consistent with observations, but little or no seismicity

(resulting from curvature changes) until the plate straightens (Fig. 81). This agrees with the total seismicity pattern. The problem of providing a mechanism for the straightening process remains.

References

- Ashby, M. F. and R. A. Verrall, Micro-mechanisms of flow and fracture, and their reference to the rheology of the upper mantle, *Phil. Trans. Roy. Soc. London Ser. A*, 288, 59–95, 1977.
- Engdahl, E. R., and C. H. Scholz, A double Benioff zone beneath the Aleutians: an unbending of the lithosphere, *Geophys. Res. Letters*, 4, 473–476, 1977.
- Hasegawa, A., N. Umino, and A. Takagi, Double-planed structure of the deep seismic zone in the northeastern Japan arc, submitted to *Tectonophysics*, 1978.
- Heard, H. C., Effect of large changes in strain rate in the experimental deformation of Yule marble, *J. Geol.*, 2, 162–195, 1963.
- Stauder, W. and L. Mualchin, Fault motion in the large earthquakes of the Kurile-Kamchatka arc and of the Kurile-Hokkaido corner, *J. Geophys. Res.* 81, 297–308, 1976.
- Umino, N., and A. Hasegawa, On the two-layered structure of deep seismic plane in northeastern Japan arc, *Jishin*, 28, 125–139 (in Japanese), 1975.
- Weertman, J., The creep strength of the earth's mantle, *Rev. Geophys. Space Physics*, 8, 145–168, 1970.

IS THE SPREADING PROCESS AT MID-OCEAN RIDGES EPISODIC?

R. Stefansson

Because new oceanic lithosphere is generated at the mid-ocean ridges, the process is in general difficult to monitor. The long-term average spreading rate is reasonably well determined by correlating magnetic lineations on the ocean

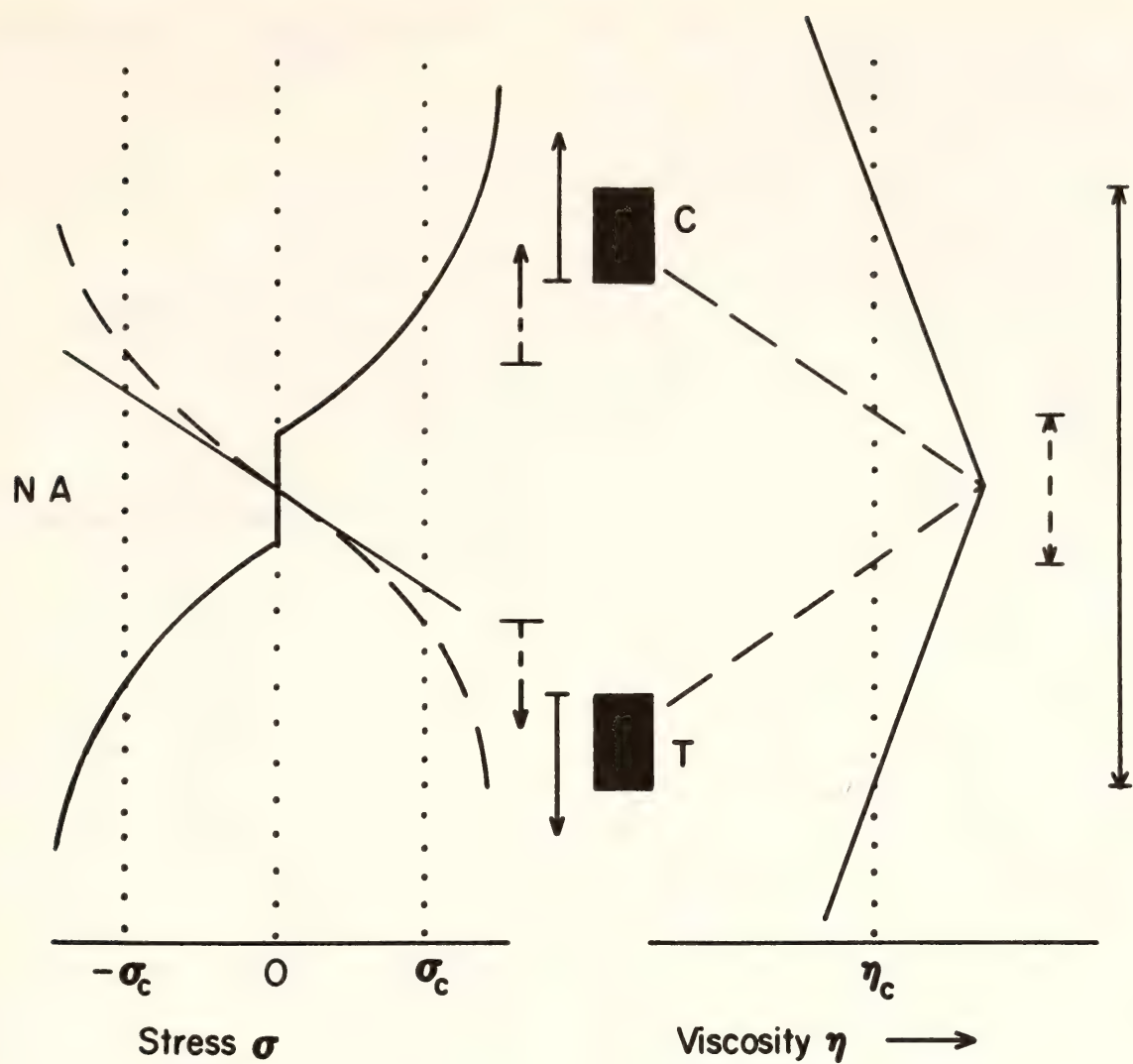


Fig. 85. Variation of viscosity and stress with position across the subducting slab (i.e., with strain rate). In order for an earthquake to result, both the stress and viscosity have to be higher than some threshold value. Broken lines refer to parameters while bending, solid lines during straightening. The arrows indicate regions in the slab where there is sufficient stress (central arrows) and sufficient viscosity (right-hand side arrows) for earthquake occurrence. Only where and if these arrows overlap will there be earthquakes. The large deformation ensures that stresses are above critical for both bending and straightening. In the bending process with its associated high strain rates, however, the resultant viscosity in the region of supercritical stress is below that at which earthquakes can occur.

floor with known reversals of the earth's magnetic field. It is not known, however, whether spreading is continuous or episodic. Iceland straddles the North Atlantic Ridge, and this provides an opportunity to investigate the character of the spreading process in more detail. Geological and historical evidence seem to indicate that episodic rifting occurs in the region with a time interval of hundreds of years. In 1725–1729, major volcanic and seismic activity occurred, and

in 1975 a similar series of tectonic events started in northeastern Iceland. An extensive observational program has been developed to monitor this activity; the program includes the DTM broadband seismic station, which has operated for several years in Akureyri, only 50–100 kms from the active area. A spectacular tectonic event began with a minor volcanic eruption on December 20, 1975 within the Krafla caldera of northeastern Iceland (Figs. 86, 87),



Fig. 86. The currently active zone of the Mid-Atlantic Ridge through Iceland in relation to other parts of the (stippled) ridge, as seismically defined.

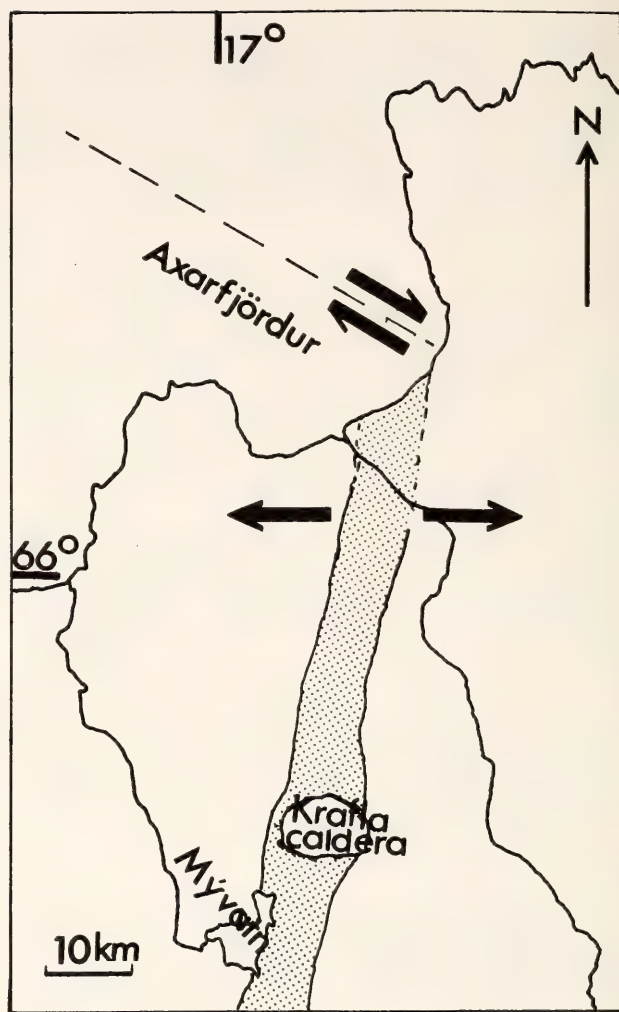


Fig. 87. Enlargement of the area within the frame in Fig. 86 in northeastern Iceland. The shaded area is the fault swarm within which widening of cracks has been observed.

followed by a subsidence of land which far exceeded the erupted volume. In the Krafla area, vertical and horizontal fault movement was close to 1 meter. A day later an intense earthquake swarm began about 30 km north of the caldera, accompanied by widening of cracks and subsidence within the fault swarm; the apparent widening and subsidence were of the order of 1–2 meters each. The activity migrated to the north, toward the junction of the currently active spreading zone and a northwest-trending transform fault. On January 13, 1976, a major earthquake took place on the transform fault near its junction with the ridge,

and its focal mechanism corresponded to right lateral strike slip, as indicated in Fig. 87.

Activity is still going on in the region, with alternating upswelling within the Krafla caldera and horizontal extension (east-west) in the spreading zone, somewhere along a 70-km segment from Lake Mývatn to the junction in Axarfjörður. The total apparent spreading across the indicated zone is now about 2 meters.

More than 100 earthquakes occurring in the period December 1975–January 1976 are being analyzed to determine the variation in source process in time and space.

PRECURSORS TO *PKIKP*: AN EARTH MODEL DISCRIMINANT

J. M. Lock and J. R. Cleary**

Low-amplitude, short-period precursors to the seismic core phase *PKIKP* are commonly observed in the epicentral distance (Δ) range 125° – 141° for earthquakes with magnitudes greater than about 5 m_b . In 1972, Haddon postulated that these precursors were scattered from the core phase *PKP* by small-scale irregularities at or near the core-mantle boundary (CMB). Cleary and Haddon (1972) inferred from this hypothesis that the earliest observable precursor arrivals would correspond to rays *PK(P)* (in the diametral plane containing the source and the receiver), which had been singly scattered on exit from the core at the intersection of the *PKP* caustic and the CMB (i.e., at the core caustic). They showed that a "minimum-time" curve for precursors constructed on this basis from Jeffreys-Bullen (JB) times was in good agreement with published precursor travel time data (see insert to Fig. 88). By the principle of reciprocity in a spherically symmetrical earth, this curve is also valid for rays *P(KP)* singly scattered on entry to the core (Haddon and Cleary, 1973; Doornbos and Vlaar, 1973). Array studies (Haddon and Cleary, 1973; Doornbos and Vlaar, 1973; Doornbos and Husebye, 1972; King *et al.*, 1973a, 1973b; Wright, 1975; Doornbos, 1976; King *et al.*, 1976; Husebye *et al.*, 1976) have demonstrated that the observed features of the precursor wave trains are in good agreement with theoretical expectations based on the scattering hypothesis. The interpretation adequately accounts for the distribution of travel times, slowness, and amplitudes with Δ , variations of amplitude, azimuth,

and slowness along the precursor wave trains, lack of signal coherence across arrays, and variability of observations for different events and recording stations.

Studies of *PKIKP* precursors on the basis of the scattering hypothesis have generally assumed that the precursor train is produced by scattering within an inhomogeneous region above the CMB. Chang and Cleary (1978), in an investigation of precursors to *PKKP* at distances near 60° , demonstrated that these arrivals could not be explained by scattering on entry to or exit from the core, but were consistent with scattering on underside reflection at the CMB. They suggested that both *PKIKP* precursors and the *PKKP* precursors studied by them could be most simply interpreted as signals scattered by irregularities ("bumps") on the CMB. If the scattering occurs at or close to the CMB, differential travel time curves, $t(PKIKP - PK(P))/\Delta$, derived from a velocity-depth model of the earth, should show agreement with those calculated from observed precursor and *PKIKP* onset times. The advantage of using differential times rather than absolute precursor times is that the effects of structure beneath the source and the station, and errors due to mislocation, are thereby minimized. A number of recent earth models were therefore chosen for comparison of their theoretical differential travel times with observational data.

The earth models used were JB (Jeffreys, 1939a, 1939b, from which the JB tables were originally constructed), B1 of Jordan and Anderson (1974), 1066B of Gilbert and Dziewonski (1975), PEM-A of Dziewonski *et al.*, (1975), DI-11 of Derr (1969), "a simple earth model" (SEM) of Wang (1972), and C2 of Anderson and Hart (1976). Excluding model JB, which was based on body-wave observations, each of the models was obtained by generalized inversion procedures and depended on the charac-

* Research School of Earth Sciences, Australian National University, Canberra. (The data used in this study were collected by J. R. Cleary while at the Department of Terrestrial Magnetism on an H. O. Wood Fund grant.)

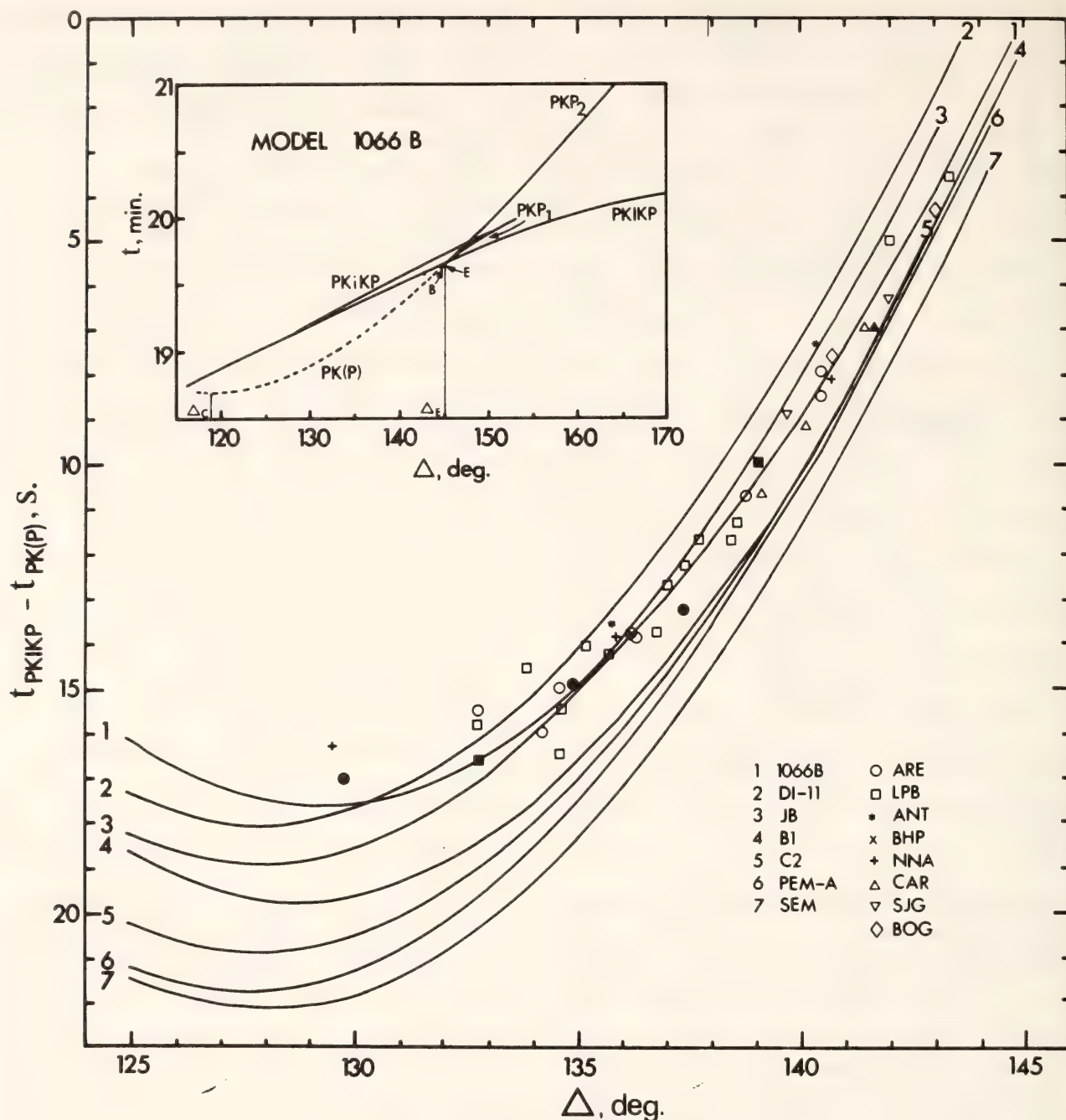


Fig. 88. Differences between $PKIKP$ and earliest precursor times for several models, compared with data from South and Central American stations. The solid symbols correspond to the examples in Fig. 89. Inset: PKP travel time branches and minimum-time precursor curve from model 1066B. Point B is the PKP caustic; point E is the $PKP_2/PKIKP$ intersection. Δ_c is the angular distance between the epicenter and the core caustic.

teristics of the starting model chosen for the inversion, the averaging or smoothing procedure used, and the observational data selected (Gilbert and Dziewonski, 1975). The starting models for B1, DI-11 and SEM were simple, "realistic" models constructed using geophysical arguments, that for C2 was a model based on high-resolution body-wave data, and those

for 1066B and PEM-A were B1 and 1066B, respectively. These starting models were perturbed in order to satisfy observational constraints such as mass and moments of inertia of the earth, free oscillation modes, differential travel times of body waves and surface-wave data.

Differential travel time curves,

$t(PKIKP - PK(P))/\Delta$, were constructed for each model. These were compared with differential travel times calculated from a set of WWSSN short-period, vertical records of *PKIKP* and earliest precursor arrivals at South and Central American stations from 20 earthquakes in the New Guinea region between 1964 and 1971, with times corrected to surface focus. Corrections to surface focus are model dependent, but the differences are not significant for present purposes. Although there is inevitably a subjective element involved in the identification of precursor onsets, on many records the onset was sharp and unambiguous. Some examples of these are shown in Fig. 89. It is apparent from Fig. 88 that 1066B and JB best satisfy the observations, while DI-11, B1, C2, PEM-A and SEM fit the data progressively less well. Each curve in the figure has been terminated at the ray theoretical distance of the caustic point *B* (cf. inset to Fig. 88). *B* is situated no more than a few tenths of a second earlier than the corresponding point on the differential travel time curve. The amplitude of the first core arrival on the records generally increases dramatically at distances beyond about 141° (cf. the example at 141.63° in Fig. 89), suggesting that at these distances the precursor arrival is obscured by a direct phase in the vicinity of the surface caustic.

The relative shapes of the $t(PKIKP - PK(P))/\Delta$ curves for the various models are controlled by two major factors: (1) the position of the PKP_2 branch of the travel-time curve with respect to the *PKIKP* branch, which determines the relative displacements of the curves at the far end of the range, and (2) the angular distance Δ_c between the epicenter and the core caustic. Δ_c is also the epicentral distance at which the minimum-time curve "bottoms" (cf. inset to Fig. 88), so it determines the rate at which the curvature of the differential travel time curve increases with decreasing distance. A third factor, that of the

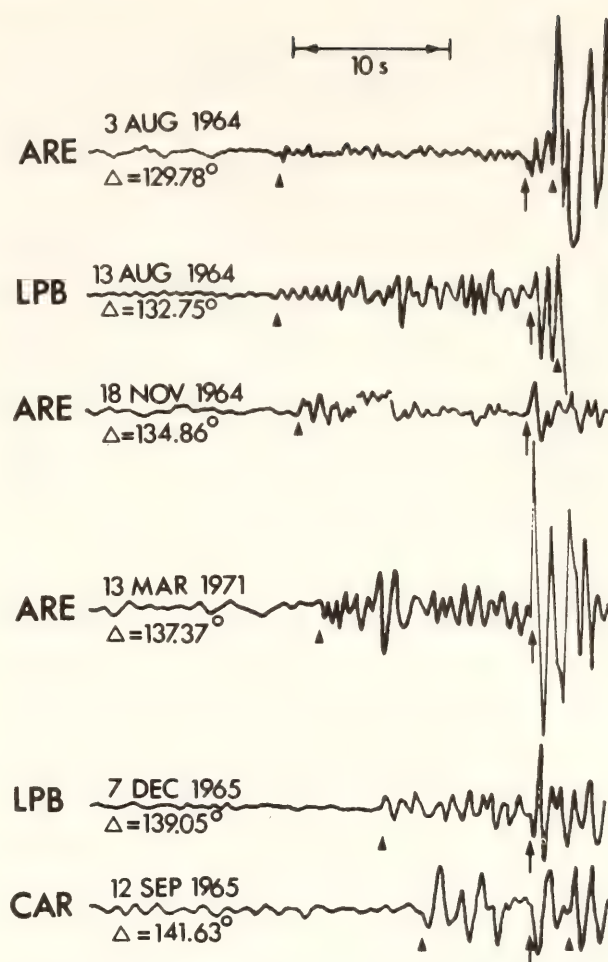


Fig. 89. Some examples of clear precursor arrivals throughout the distance range. Traces are aligned with respect to the *PKIKP* arrivals (indicated by arrows). The arrowheads to the left and right of *PKIKP* indicate the onset of the earliest precursors and of *PKIKP*, respectively.

relative variation of *PKIKP* over the range of interest, is of marginal importance for the models under consideration. The two major factors are indicated for the various models in Table 19, where the distance Δ_E at which PKP_2 crosses *PKIKP* is taken as an adequate representation of factor (1). As indicated in the table, the values calculated from the JB tables differ slightly from those given by the model. It can be seen from Fig. 88 that the larger Δ_E of 1066B relative to JB is compensated for by an increased curvature resulting from a larger Δ_c , and that the two factors combined result in a better fit of this model to the observations at both the longer and shorter distances. Δ_E for DI-11 is too small and for

TABLE 19. Epicentral Distances Δ_E and Δ_c for Various Models

Model	Δ_E (deg.)	Δ_c (deg.)
DI-11	143.80	117.56
JB	144.30	117.39
JB tables	145.00	117.25
1066B	145.00	118.81
C2	145.22	117.25
PEM-A	145.40	117.23
B1	145.40	118.66
SEM	145.75	117.36

SEM is too large. For the other models, Δ_c is too small to compensate for the relatively large values of Δ_E .

We conclude that precursor data can provide a useful additional constraint in earth modeling from seismic data, and that the data used here favor model 1066B. We propose to examine data from other paths to test whether regional differences are significant. We are also investigating the possible effects of irregularities at the CMB on precursor times. It is easy to show that such irregularities would require, if at all, an *increase* in the differential times calculated from models, especially at the shorter distances.

References

Anderson, D. L., and R. S. Hart, An earth model based on free oscillations and body waves, *J. Geophys. Res.*, **81**, 1461–1475, 1976.

Chang, A. C., and J. R. Cleary, Seismic wave scattering near the core-mantle boundary: a new interpretation of precursors to PKP, *Bull. Seismol. Soc. Amer.*, in press, 1978.

Cleary, J. R., and R. A. W. Haddon, A note on the interpretation of precursors to PKP, *Nature*, **240**, 549–551, 1972.

Derr, J. S., Regions of seismic wave scattering in the earth’s mantle and precursors to PKP, *J. Geophys. Res.*, **74**, 5202–5220, 1969.

Doornbos, D. J., Array analysis of PKP phases and their precursors, *Geophys. J. Roy. Astron. Soc.*, **44**, 447–470, 1976.

Doornbos, D. J., and E. S. Husebye, Evidence for seismic wave scattering in the D'' layer, *Phys. Earth Planet. Interiors*, **5**, 387–399, 1972.

Doornbos, D. J., and N. J. Vlaar, Array analysis of precursors to PKIKP in the distance range 128° to 142°, *Nature Phys. Sci.*, **243**, 58–61, 1973.

Dziewonski, A. M., A. L. Hales, and E. R. Lapwood, The origin of short-period precursors to PKP, *Phys. Earth Planet. Interiors*, **10**, 12–48, 1975.

Gilbert, F., and A. M. Dziewonski, Characteristics of lower mantle inhomogeneities from scattered waves, *Phil. Trans. Roy. Soc. London*, **278**, 187–296, 1975.

Haddon, R. A. W., Processing of seismic precursor data, *Trans. Amer. Geophys. Union*, **53**, 600, 1972.

Haddon, R. A. W., and J. R. Cleary, Precursors to PKIKP and seismic wave scattering near the mantle-core boundary, *Phys. Earth Planet. Interiors*, **7**, 495–497, 1973.

Husebye, E. S., D. W. King, and R. A. W. Haddon, Precursors to PKIKP and seismic wave scattering near the mantle-core boundary, *J. Geophys. Res.*, **81**, 1870–1882, 1976.

Jeffreys, H., The times of P, S and SKS, and the velocities of P and S, *Mon. Notic. Roy. Astron. Soc.*, **4**, 498–533, 1939a.

Jeffreys, H., The times of the core waves, *Mon. Notic. Roy. Astron. Soc.*, **4**, 548–561, 1939b.

Jordan, T. H., and D. L. Anderson, Earth structure from free oscillations and travel times, *Geophys. J. Roy. Astron. Soc.*, **36**, 411–459, 1974.

King, D. W., R. A. W. Haddon, and J. R. Cleary, An application of normal mode theory to the retrieval of structural parameters and source mechanisms from seismic spectra, *Earth Planet. Sci. Lett.*, **20**, 353–356, 1973a.

King, D. W., R. A. W. Haddon, and J. R. Cleary, Parametrically simple earth models consistent with geophysical data, *Geophys. J. Roy. Astron. Soc.*, **37**, 157–173, 1973b.

King, D., E. S. Husebye, and R. A. W. Haddon, Internal structure of the earth inferred from free oscillations, *Phys. Earth Planet. Interiors*, **12**, 128–134, 1976.

Wang, C., A simple earth model, *J. Geophys. Res.*, **77**, 4318–4329, 1972.

Wright, C., An earth model based on free oscillations and body waves, *Bull. Seismol. Soc. Amer.*, **65**, 765–786, 1975.

STRUCTURE OF THE OCEANIC LITHOSPHERE FROM SURFACE WAVE OBSERVATIONS: NORTH ATLANTIC

J. R. Evans and I. S. Sacks

Several recent studies have attempted to provide seismological constraints on the processes generating oceanic lithosphere, and have examined the detailed structure of the lithosphere beneath the Pacific. Leeds *et al.* (1974) reported that the high-velocity lithospheric lid increases in thickness with the age of the overlying crust, rapidly for the first 25 m.y. after crustal production but more slowly thereafter. These conclusions were confirmed by Forsyth (1977), Leeds (1975), Schlue and Knopoff (1977), and Burkhard and Jackson (1978), in their studies of the low-velocity channel underlying the lid. Forsyth (1977) showed that the velocities in both lid and channel increased slightly with crustal age, whereas the other studies assumed *a priori* a constant velocity in the lid. It is of interest to determine whether lithospheric structures in other oceanic regions show features similar to those found in the Pacific.

The position of the Carnegie broadband seismograph at Akureyri, Iceland, allows us to examine lithospheric structure in the Atlantic. The station lies on the extension of the great-circle segment

corresponding to the Reykjanes Ridge. Surface waves generated by earthquakes on the ridge travel to the station along paths close to the ridge axis, and the dispersion of these waves can be modelled to estimate the structure near the ridge. Similarly, surface waves generated by earthquakes on the transform faults southwest of Iceland travel along paths nearly parallel to the ridge axis, and can be used to construct models of lithospheric structure as a function of distance from the ridge axis (see Fig. 90). By comparing the models, we can examine the variation of structure with the age of the overlying crust.

The models produced in this study cannot be said to be typical of a given area in an absolute sense. The wave-trains cross Iceland, which shows unusual dispersion characteristics (Trygvasson, 1962), so models derived directly from the observed dispersion of surface waves represent averages of both oceanic and Icelandic structures. However, although none of the models represents the true oceanic structure, they are all similarly biased, and we interpret them in a relative sense. We look for those features that differ markedly between paths lying at different distances from the ridge, and focus on those differences that are robust with respect to variation of our modelling procedure. We demonstrate that in this region of the North Atlantic the lithospheric thickness increases from about 35 km near the ridge axis to about 65 km at the 40-m.y. isochron, while the shear-wave velocity in the lid increases by about 0.2 km/sec. In the following sections, we examine in detail a series of different models and modelling procedures.

Method A

The analogue magnetic tape record for each of the horizontal and vertical components was digitized, and the horizontal records were rotated to provide time series for ground motion parallel

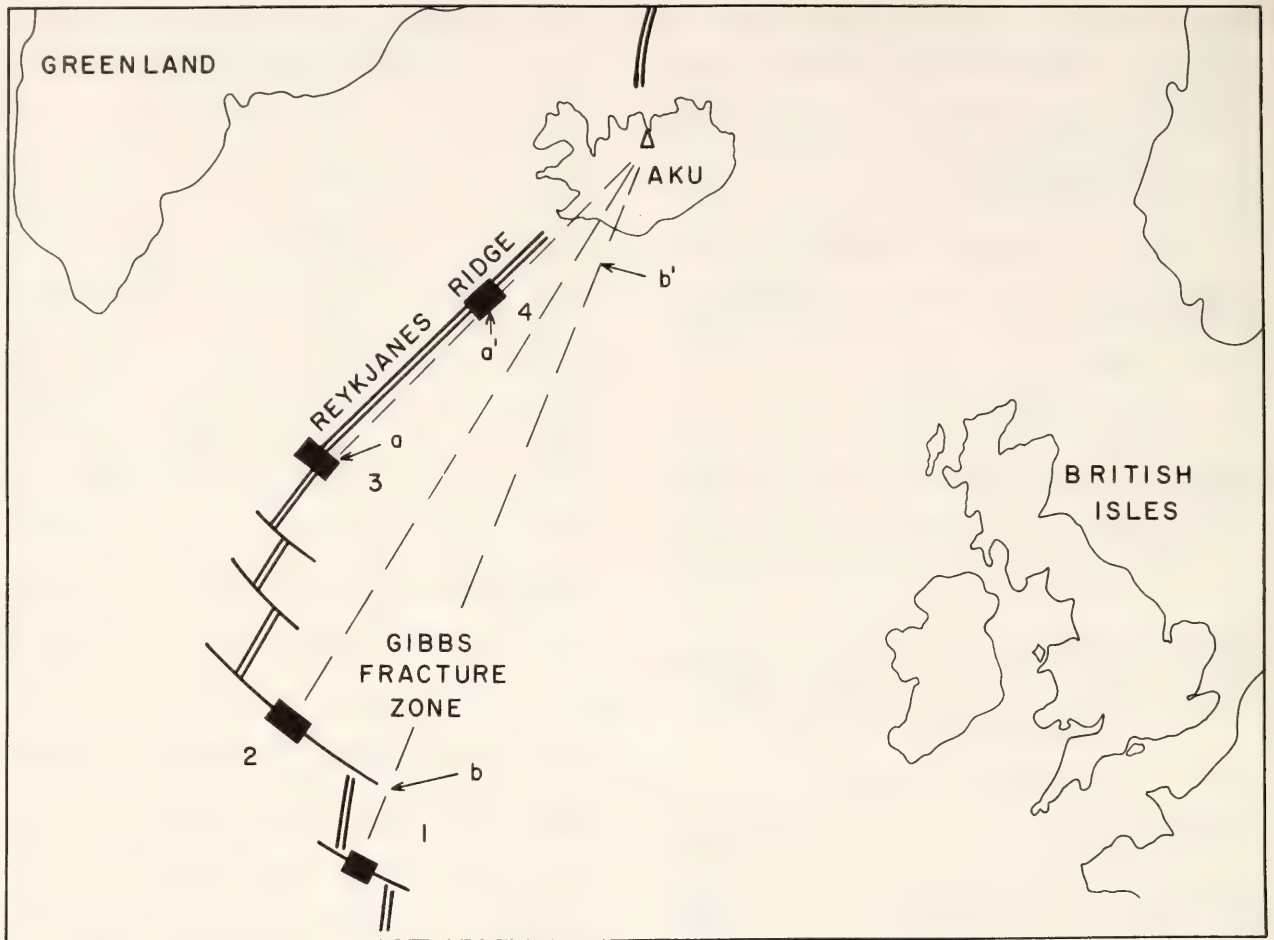


Fig. 90. Map of North Atlantic showing earthquake-source regions, observing station (AKU), and propagation paths. Azimuthal equidistant projection centered on AKU.

and perpendicular to the great circle through the epicenter and station. The records were analyzed using the multiple-filter technique (Dziewonski *et al.*, 1969), modified to incorporate Nyman and Landisman's suggestion (1977) for optimizing resolution in the frequency-time diagram. The frequency-time diagram was contoured at 3-db intervals (or more closely where appropriate) before selecting the maximum corresponding to the dispersion curve.

Theoretical dispersion curves were computed using the algorithms published by Schwab and Knopoff (1972). Neither the quality nor the quantity of data justify the use of a formal inversion technique. Curves were fitted by inspection, occasionally using a single-iteration least-squares inversion.

The epicenters of the earthquakes

studied are listed in Table 20. They fall naturally into four groups, which we consider individually:

Group 1. Good records were obtained from this group and periods up to 100 sec were resolved. We obtained four good Rayleigh-wave records but only one good Love-wave record. We place more importance on fitting the Rayleigh-wave dispersion data than the Love-wave data, not only because more data were obtained but also because the correction introduced for Iceland in the Love-wave data (see below) is larger than that for the Rayleigh-wave data.

The data favor a model with a shear-wave velocity of about 4.5 km/sec immediately underlying the crust and a negative velocity gradient of about .005 km/sec per km over the next 100-km depth. Models with a lid and channel

TABLE 20. Earthquakes Used in This Study*

No.	Date	Time	Lat.	Long.	m_b	Δ_{AKU}
1a	73 Jan 05	01:44:25.8	49.44N	28.23W	5.4	17.1
1b	73 Jul 02	01:04:55.9	49.51N	28.51W	5.0	17.1
1c	77 Feb 11	22:01:36.3	50.65N	30.04W	4.8	16.3
2a	73 Dec 05	17:57:11.3	52.47N	31.55W	4.8	14.9
2b	74 Oct 16	05:36:26.5	52.63N	32.16W	4.8	14.9
2c	74 Oct 16	05:45:11.2	52.63N	32.07W	5.7	14.8
2d	74 Nov 16	19:24:14.5	52.65N	32.00W	5.0	14.8
3a	73 May 19	00:37:23.2	57.53N	33.00W	5.0	10.8
3b	74 Jan 06	10:07:17.1	57.46N	33.65W	4.9	11.0
3c	74 Jan 11	01:59:18.3	57.18N	33.80W	4.5	11.3
3d	74 Jan 01	20:22:22.0	55.33N	35.31W	4.7	13.4
3e	74 Jun 21	08:46:47.6	57.86N	32.69W	4.8	10.4
3f	76 Mar 31	00:01:00.3	58.37N	31.84W	5.1	9.7
3g	76 Mar 31	23:50:00.3	58.39N	31.86W	4.8	9.7
3h	76 Sep 06	09:56:25.6	58.17N	32.17W	4.8	10.0
4a	74 Oct 22	05:06:15.2	62.20N	26.30W	5.0	5.0
4b	74 Oct 22	12:06:12.0	62.20N	26.31W	4.8	5.0

* Locations from ISC Bulletin (where available) or NEIS.

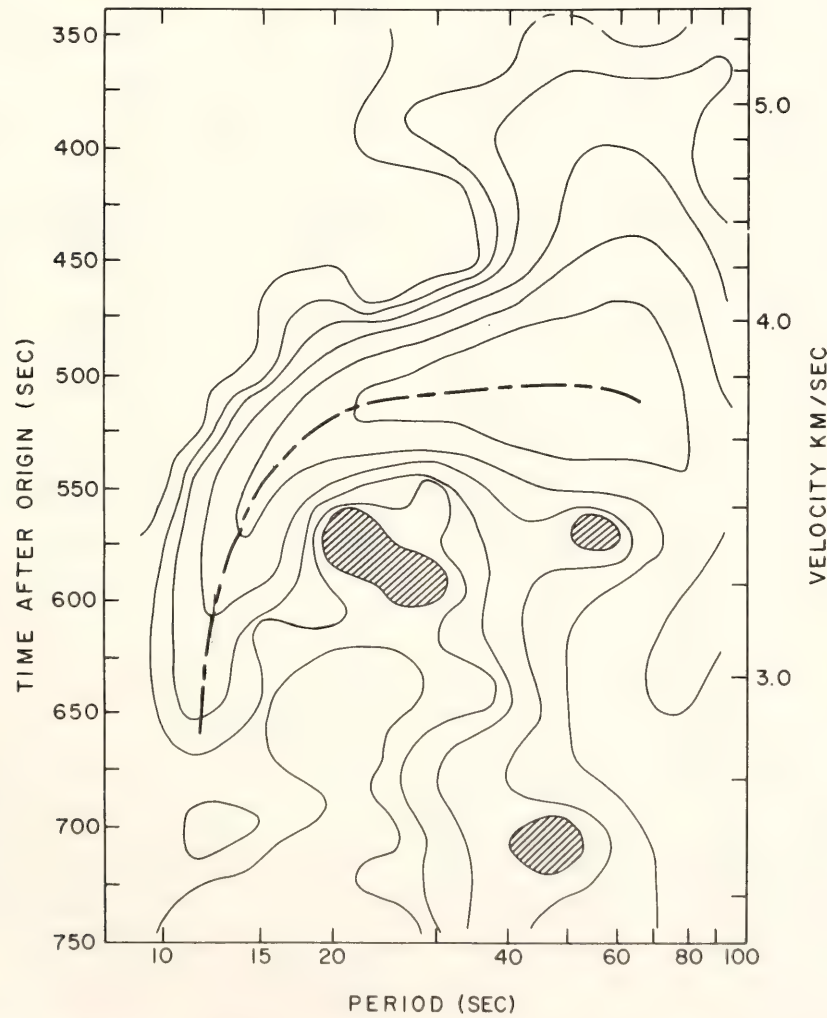


Fig. 91. Multiple-filter display for the vertical component at AKU for earthquake 1a. Contour interval = 5 db.

TABLE 21. Representative Shear-Wave Velocity-Depth Models Constructed in Method A Analysis*

1A			1B			2A			2B			3A			3B		
β	h	d	β	h	d	β	h	d	β	h	d	β	h	d	β	h	d
Water																	
0.0	3.0	0.0	0.0	3.0	0.0	0.0	2.3	0.0	0.0	2.3	0.0	0.0	1.4	0.0	0.0	1.4	0.0
Sediment																	
2.0	1.1	3.0	2.0	1.1	3.0	0.5	0.1	2.3	0.5	0.1	2.3	0.2	0.25	1.4	0.2	0.25	1.4
						1.0	0.2	2.4	1.0	0.2	2.4	1.0	0.2	1.65	1.0	1.0	1.65
						2.0	0.5	2.6	2.0	0.5	2.6	1.5	0.4	1.85	1.5	1.5	1.85
Crust																	
2.8	2.0	4.1	2.8	2.0	4.1	2.8	2.0	3.1	2.8	2.0	3.1	2.8	1.0	2.25	2.8	1.0	2.25
3.75	4.0	6.1	3.75	4.0	6.1	3.75	4.0	5.1	3.75	4.0	5.1	3.2	1.0	3.25	3.2	1.0	3.25
												3.5	1.5	4.25	3.5	1.5	4.25
												3.75	2.0	5.75	3.75	2.0	5.75
Lid																	
4.45	20.0	10.1	4.42	55.0	10.1	4.45	20.0	9.1	4.42	55.0	9.1	3.9	2.0	7.75	3.9	2.0	7.75
4.4	25.0	30.1				4.4	25.0	29.1				4.0	2.0	9.75			
4.3	15.0	55.1				4.3	15.0	54.1				4.1	2.5	11.75	4.0	2.0	9.75
												4.2	5.0	14.25			
												4.15	5.0	19.25	4.15	19.5	11.75
												4.1	13.0	24.25	4.1		
Channel																	
4.2	15.0	70.1	4.12	130.0	65.1	4.2	15.0	69.1	4.12	130.0	64.1	4.0	53.0	37.25	3.9	149.0	31.25
4.15	35.0	85.1				4.15	35.0	84.1				4.1	90.0	90.25	4.3	125.0	180.25
4.2	75.0	120.1				4.2	75.0	119.1				4.3	125.0	180.25			
Sub-channel																	
4.55	260.0	195.1	4.55	260.0	195.1	4.55	260.0	194.1	4.55	260.0	194.1	4.4	125.0	305.25	4.4	125.0	305.25
5.4	250.0	455.1	5.4	250.0	455.1	5.4	250.0	454.1	5.4	250.0	454.1	5.4	250.0	430.25	5.4	250.0	430.25
5.9	150.0	705.1	5.9	150.0	705.1	5.9	150.0	704.1	5.9	150.0	704.1	5.9	150.0	680.25	5.9	150.0	680.25
6.4	∞	855.1	6.4	∞	855.1	6.4	∞	854.1	6.4	∞	854.1	6.4	∞	830.25	6.4	∞	830.25

* The data are insensitive to the minor differences in deep structure, which are included in the models mainly for computation stability. β = shear velocity, km/sec; h = layer thickness, km; d = depth to upper surface of layer, km.

each of constant velocity are, of course, a first approximation to such a negative velocity gradient. We find that it is possible to obtain an acceptable fit to the data with lid velocities of 4.4–4.5 km/sec and lid thicknesses of 50–65 km (i.e., a total lithospheric thickness of 57–72 km). The channel velocity required depends on the model chosen for the lid but can take any value between 4.0 and 4.3 km/sec—higher lid velocities and greater thicknesses give higher channel velocities. Representative examples are shown in Fig. 91 and Table 21. The data are insensitive to details of lower crustal structure, because the water and sediment layers dominate the short-period dispersion. A more complex structure, such as that used for group 3 below, can be introduced into the lower crust without modifying the above conclusions on mantle structure.

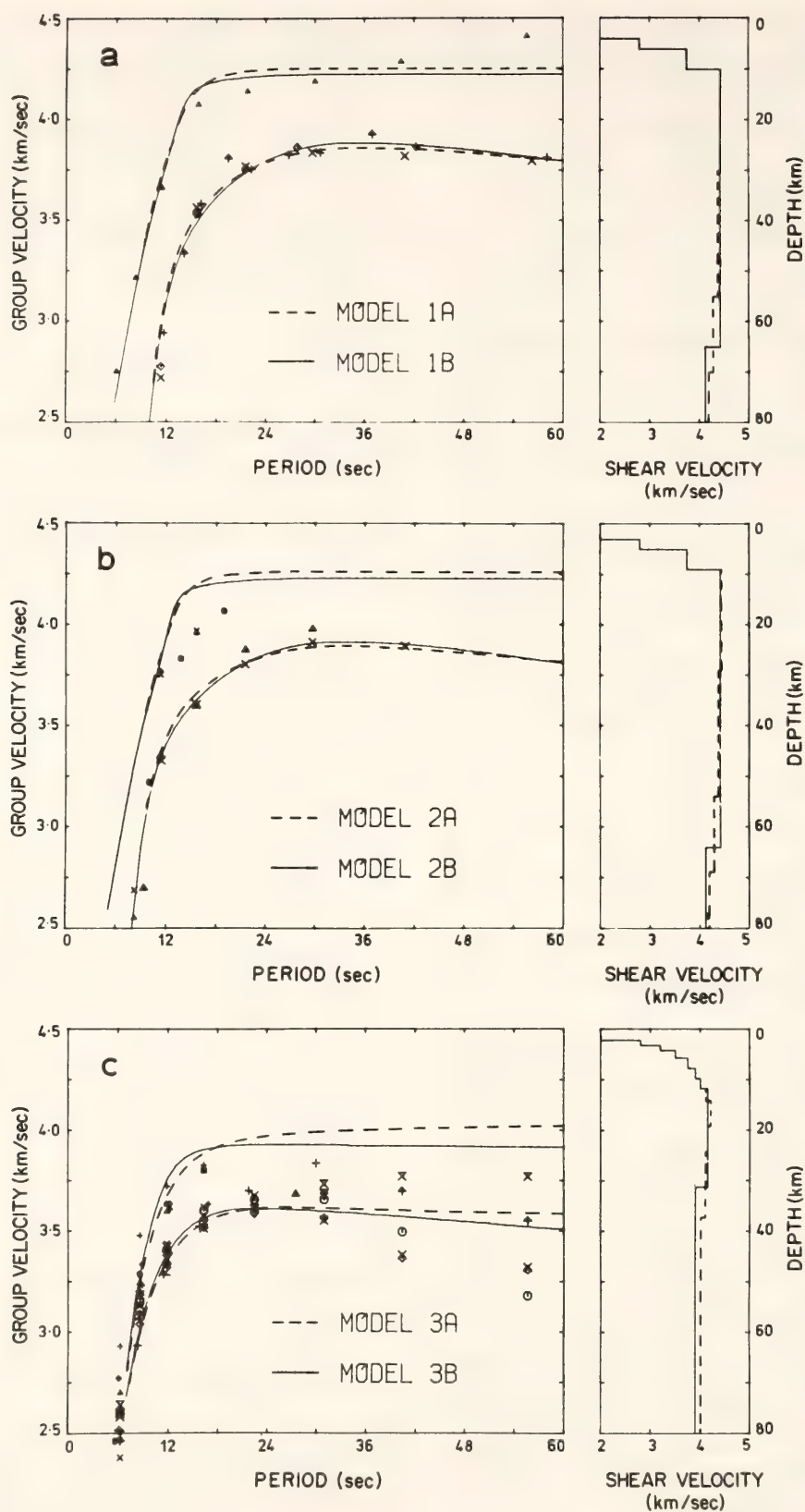
Group 2. Surface-wave records of earthquakes in this region recorded at AKU show signs of interference. They tend to be confused and difficult to interpret. The most reliable determinations are presented in Figure 92b. The Rayleigh-wave data are better than the Love-wave data, and again we place more importance on fitting the Rayleigh-wave dispersion. We found that by changing only the water and sediment layers, almost any model that fitted the group 1 data could be modified to fit the group 2 Rayleigh-wave data. The poorer quality, greater scatter, and smaller range of periods of the group 2 data do not permit the same degree of resolution as do the group 1 data. We conclude that we cannot resolve any differences in mantle structure between the paths for group 1 and group 2 events.

Group 3. Good records were obtained on both vertical and horizontal components, but the horizontal (Love-wave) arrivals were very scattered except in the period range 6–12 sec. The group 3 data show much stronger sensitivity to crustal structure than do the group 1 data, but

are again best modelled with a velocity gradient of negative slope in the mantle. These and simpler models show a poorly developed “lid” of thickness about 20–30 km and shear-wave velocity only 4.1 km/sec, overlying a channel of about 4.0 km/sec, although the channel velocity is poorly constrained.

Method B

The following method was applied by Keen *et al.* (1978) in a recent study of structure in the North Atlantic. The groups of earthquakes that they used correspond to our groups 3 and 4. Assuming that the wavetrains travel along great-circle paths to AKU, then wave-trains from all of these earthquakes travel across the same path between the group 4 epicenters and AKU. By cross-correlating the record of a group 3 earthquake with that of a group 4 earthquake, the dispersion introduced by that part of the path between the group 4 epicenter and AKU can be removed and the multiple-filtering technique described earlier can be applied to the resulting record. This technique is similar to that widely used for phase-velocity determination, where records of the same earthquake from two stations are cross-correlated to give the phase delay introduced by the path between the two stations (Landisman *et al.*, 1969). The advantages of the station-pair method are well known, but when the cross-correlation technique is applied to an earthquake pair it gives a different combination of advantages and disadvantages. At those periods where signal is common to both records, an improvement in signal-to-noise ratio can be obtained, and if the earthquakes have similar source geometries (a reasonable assumption in this study), any source effects are removed. On the other hand, random errors in location are added and only the frequencies present in both records can be analyzed. The principal problem in



applying the method to this study lies in the initial assumption that the surface waves travel along great-circle paths to AKU. As our preceding analysis showed, the ridge structure gives rise to a lateral-

velocity gradient in surface-wave velocities, and wavetrains may well be refracted toward the ridge. The models derived using this method will therefore be representative, not of structure at the

Fig. 92. Observed and theoretical surface-wave dispersion for the regions studied. No correction was made for dispersion introduced by Iceland (Method A). Observed dispersion is indicated in the left-hand section of each subfigure by small symbols (transverse component \doteq Love waves) or large symbols (vertical or radial component = Rayleigh waves). Large and small symbols of the same type are derived from the vertical and transverse components of the same record. The right-hand section of each subfigure shows representative velocity-depth curves, and the solid and dashed curves in the left-hand section are the corresponding computed dispersion curves. In each case, the upper pair of lines is Love-wave dispersion (compare with small symbols), and the lower pair Rayleigh-wave dispersion (compare with large symbols). (a) Data derived directly from observations of group 1 earthquakes. (b) Data derived directly from observations of group 2 earthquakes. (c) Data derived directly from observations of group 3 earthquakes.

ridge axis, but of structure some few kilometers away from it.

We cross-correlated records from each of the group 3 earthquakes with the corresponding records from both of the two group 4 earthquakes. For clarity, the two values of group velocity obtained for each group 3 earthquake were averaged (the differences were typically less than .05 km/sec) and are shown in Figure 93a. Rayleigh waves could be clearly identified to 30 sec, but Love waves only to 12 sec. The model labeled KBFK in the figure gives an excellent fit to the Rayleigh-wave dispersion data presented by Keen *et al.* and is typical of the structures they derive. The model does not fit our data as well as it does theirs. For our data we prefer the second model included in Figure 93a. This model differs from KBFK only slightly in lid structure, but has a channel velocity of 4.2 km/sec instead of 3.9 km/sec. The difference in the two models is significant. The lower velocities in the lid of model KBFK are linked to the low velocity in the channel. The velocity contrast at the bottom of the lid in model KBFK causes Rayleigh-wave phase velocities to be nearly constant in the period range 20–30 sec. Therefore, the group velocity is nearly equal to the phase velocity in this period range, and the characteristic “hump” of the group-velocity dispersion curve is accentuated. The low-channel velocities in the model are revealed by low Love-wave velocities in the period 15–200 sec and by very low Rayleigh-

wave velocities in the period range 50–150 sec. Thus the differences between our model and Keen's *et al.* are based primarily on the determination of Rayleigh-wave velocities at 35 sec period. The studies agree that the thickness of the lid near the ridge axis is about 25 km, and that the lid shear-wave velocity is lower than that generally found in oceanic structures—4.3 or 4.4 km/sec. Representative shear wave velocity-depth models using Method B analysis are shown in Table 22.

The object of our study is to compare the structure near the ridge with that further away from it. The structure that we derived for group 1 paths used wave-trains that crossed Iceland, so we cannot compare this structure directly with the purely oceanic structure we have derived using the cross-correlation technique. Instead, we estimate the true dispersion across the part of the path labelled *b-b'* in Fig. 90 by subtracting the mean travel times for group 4 earthquakes from the mean travel time for group 1 earthquakes at each period. In this way the effects of both Iceland and the southernmost section of the path, which lies close to the ridge axis, may be approximately removed. The remaining path length of 13 degrees is sufficiently long that this approximation is reasonable. The corrected data is shown in Fig. 93b. The lid thicknesses and channel velocities of models fitting these data are similar to those fitting the uncorrected data: 50–65 km and 4.0–4.3 km/sec, respectively; but lid

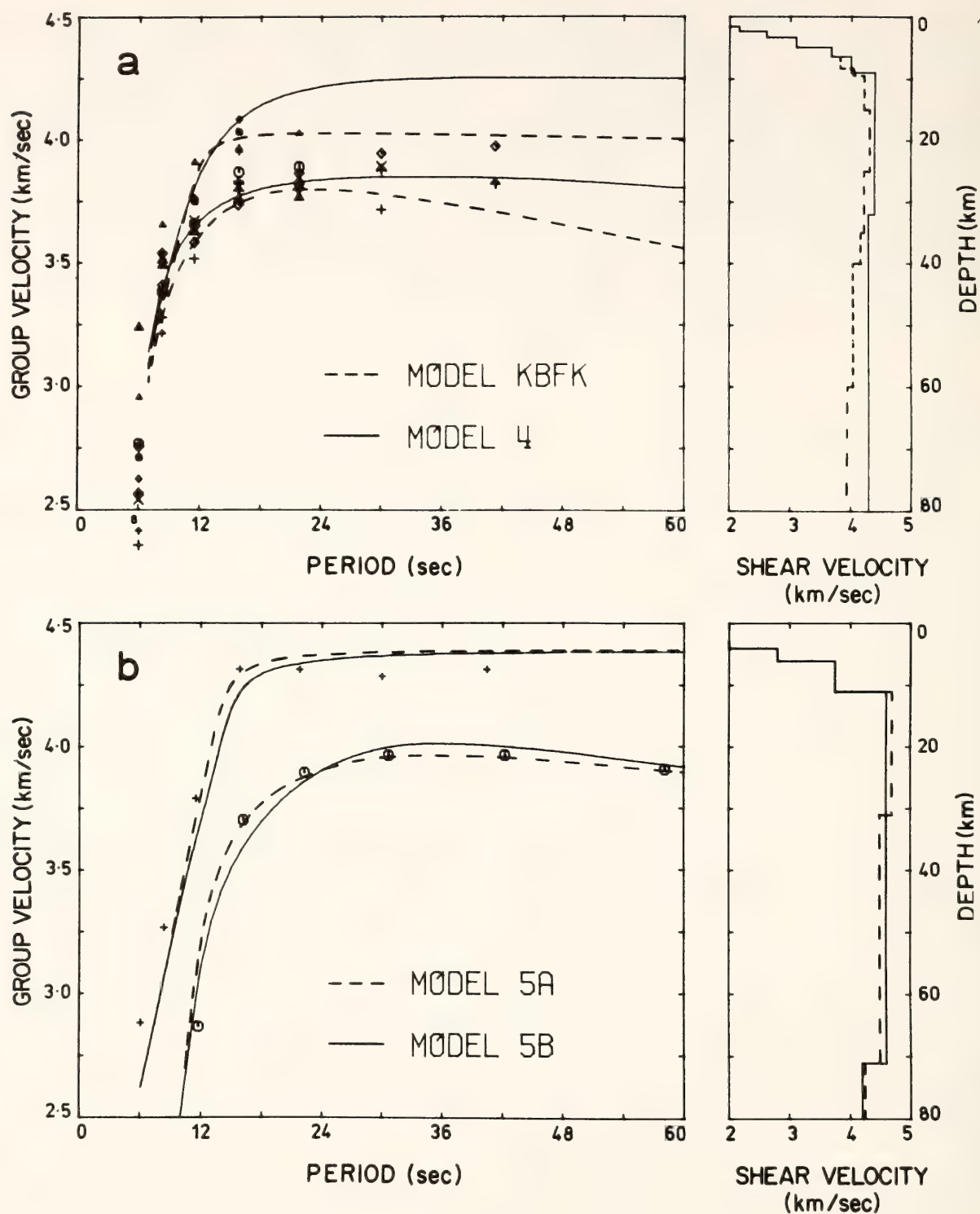


Fig. 93. Observed and theoretical dispersion for the paths $a-a'$ and $b-b'$ indicated on Fig. 90 (Method B). Observed dispersion is indicated in the left-hand section of each subfigure by small symbols (transverse component = Love waves) or large symbols (vertical or radial component = Rayleigh waves). The right-hand section of each subfigure shows representative velocity-depth curves, and the solid and dashed curves in the left-hand section are the corresponding computed dispersion curves. In each case, the upper pair of lines is Love-wave dispersion (compare with small symbols) and the lower pair Rayleigh-wave dispersion (compare with large symbols). (a) Data obtained by cross-correlating records of group 3 earthquakes with those of group 4 earthquakes. (b) Data obtained by subtracting the mean travel times for group 4 earthquakes at each period from the mean travel times for group 1 earthquakes.

TABLE 22. Representative Shear-Wave Velocity-Depth Models Constructed in Method B Analysis*

KBFK			4			5A			5B		
β	h	d	β	h	d	β	h	d	β	h	d
Water											
0.0	1.62	0.0	0.0	1.62	0.0	0.0	3.0	0.0	0.0	3.0	0.0
Sediment											
2.2	0.7	1.62	2.2	0.7	1.62	2.0	1.1	3.0	2.0	1.1	3.0
2.6	1.0	2.32	2.6	1.0	2.32						
Crust											
3.1	1.57	3.31	3.1	1.57	3.31	2.8	2.0	4.1	2.8	2.0	4.1
3.7	1.57	4.88	3.7	1.50	4.88	3.75	4.0	6.1	3.75	4.0	6.1
3.8	1.95	6.45	4.0	2.6	6.38						
4.04	1.15	8.4									
Lid											
4.23	5.45	9.55	4.4	23.0	9.0	4.75	5.0	6.1	4.6	60.0	10.1
4.32	10.0	15.0				4.7	20.0	11.1			
4.23	10.0	25.0				4.5	40.0	31.1			
Channel											
4.18	5.0	35.0	4.3	165.0	32.0	4.25	50.0	71.1	4.2	50.0	71.1
4.05	20.0	40.0				4.3	75.0	121.1	4.3	75.0	121.1
3.95	90.0	60.0									
4.33	50.0	150.0									
Sub-channel											
4.5	50.0	200.0	4.5	50.0	197.0	4.55	260.0	196.1	4.55	260.0	196.1
4.7	50.0	250.0	4.7	50.0	247.0	5.4	250.0	456.1	5.4	250.0	456.1
5.0	∞	300.0	5.0	∞	297.0	5.9	150.0	706.1	5.9	150.0	706.1
						6.4	∞	856.1	6.4	∞	856.1

* The data are insensitive to the differences in deep structure, which are included in the models mainly for computational stability. β = shear-wave velocity, km/sec; h = layer thickness, km; d = depth to upper surface of layer, km.

velocities are higher—typically 4.6 km/sec. Thus, the application of a correction for Iceland has a similar effect on both group 1 and group 3 data—to raise velocities in the lid without altering lid thicknesses or channel velocities.

Discussion

We now compare the different sets of models that we have constructed. We found that the data were not capable of resolving any difference in mantle structure between paths for group 1 and group 2 earthquakes, so we concentrate on the

comparison between group 1 and group 3 paths. Both methods of analysis give lithospheric thicknesses of 30 km for group 1 paths and 65 km for group 3 paths. Although the two methods give different lid velocities for each set of data, both methods give a lid velocity for the group 1 paths about 0.2 km/sec higher than the lid velocity for group 3 paths. The models also suggest that the channel velocity is 0.2 km/sec higher for group 1 paths than for group 3 paths, but neither velocity is well resolved.

To translate the paths into crustal ages, we note that the mean distance of

group 1 paths from the ridge axis is about 400 km, and that that of group 2 paths is about 200 km. Using the angular velocity vector for the Eurasian and North American plates given by Minster and Jordan (1978), we find that the spreading half-rate on the Reykjanes Ridge is about 11 km/my. The group 1 and group 2 paths therefore correspond to average crustal ages of roughly 40 m.y. and 20 m.y., respectively.

Conclusions

The results of this study are summarized in Fig. 94. By examining the dispersion of surface waves travelling along paths nearly parallel to the axis of the Reykjanes Ridge, we model the shear-wave velocity structure in the mantle beneath crust of three differing ages. We find a lid of only 20–30 km

thickness beneath recently produced crust, but a lid of 55–65 km thickness beneath crust about 40 m.y. old. The increase in thickness is coupled with an increase in shear-wave velocity in the lid of about 0.2 km/sec. The structure beneath 20-m.y.-old crust resembles that beneath 40-m.y.-old crust more than that beneath recently produced crust, implying that the thickness of the lithospheric lid increases rapidly within the first 20 m.y. after crustal formation.

References

- Burkhard, N. R., and D. D. Jackson, The shape of the low velocity channel beneath the Pacific, in press, 1978.
 Dziewonski, A., S. Bloch, and M. Landisman, A technique for the analysis of transient seismic signals, *Bull. Seismol. Soc. Amer.*, 59, 427–444, 1969.

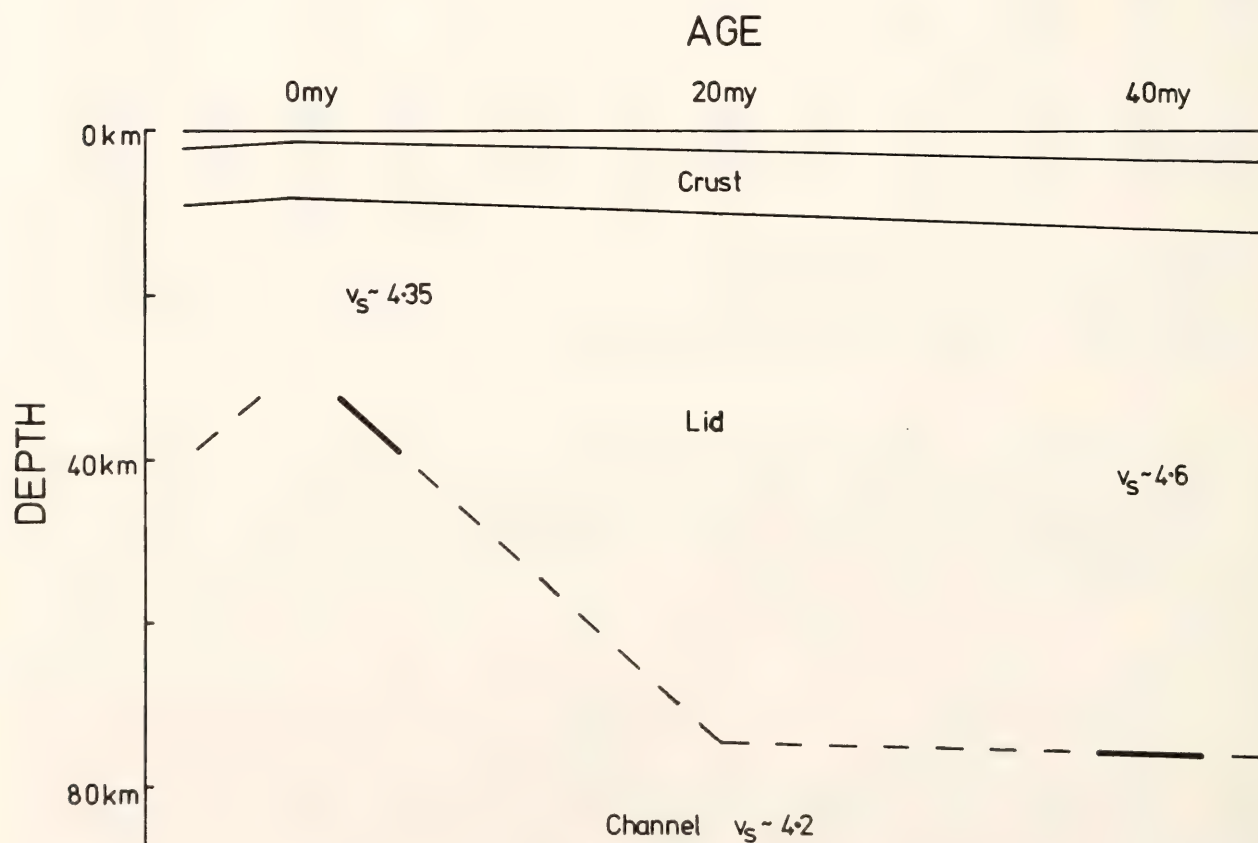


Fig. 94. Sketch showing east-west section through the North Atlantic region determined by this study. With increasing crustal age, ocean and sediment depths increase, while crustal thickness remains constant. The high-velocity lid increases in thickness and velocity especially during the first 20 m.y. after crustal production.

- Forsyth, D. W., The evolution of the upper mantle beneath mid-ocean ridges, *Tectonophysics*, 38, 89–118, 1977.
- Keen, C. E., L. Blinn, A. Fricker, and M. J. Keen, A study of the Reykjanes Ridge by surface waves using an earthquake-pair technique, submitted to *J. Geophys. Res.*, 1978.
- Landisman, M., A. Dziewonski, and Y. Satô, Recent improvements in the analysis of surface wave observations, *Geophys. J. Roy. Astron. Soc.*, 17, 369–403, 1969.
- Leeds, A. R., Lithospheric thickness in the Western Pacific, *Phys. Earth and Planet. Interiors*, 11, 61–64, 1975.
- Leeds, A. R., L. Knopoff, and E. G. Kausel, Variations of upper mantle structure under the Pacific Ocean, *Science*, 186, 141–143, 1974.
- Minster, J. B., and T. H. Jordan, Present day plate motions, in press, 1978.
- Nyman, D. C., and M. Landisman, The display-equalized filter for frequency-time analysis, *Bull. Seismol. Soc. Amer.*, 67, 393–404, 1977.
- Schlue, J. W., and L. Knopoff, Shear wave polarization anisotropy in the Pacific Basin, *Geophys. J. Roy. Astron. Soc.*, 49, 145–165, 1977.
- Schwab, F. A., and L. Knopoff, Fast surface wave and free mode computations, in *Methods in Computational Physics*, 11, 87, Academic Press, New York, 1972.
- Trygvasson, E., Crustal structure of the Iceland region from the dispersion of surface waves, *Bull. Seismol. Soc. Amer.*, 52, 359–388, 1962.

STRAIN MEASUREMENTS IN THE NEAR
FIELD OF SMALL EARTHQUAKES:
A PRELIMINARY REPORT

I. S. Sacks, A. T. Linde, S. M. Spottiswoode*,
A. McGarr*, and R. W. E. Green*

During the past 15 years there have been many studies of earthquake sources

* Bernard Price Institute of Geophysical Research, Johannesburg, South Africa.

in which such parameters as dimensions, displacement, stress release, and radiated energy have been estimated. In general, these studies suffer from two basic limitations: observations are made at distances large compared with the source dimensions of the earthquake, and seismic waves are recorded over a limited frequency range. Although these studies yield some results that are consistent with other observations, there are a number of aspects which indicate that our understanding of earthquake mechanisms is far from complete. For shallow events the calculated stress drops range from less than one bar to hundreds of bars (even within a small geographic region; see, for example, Tucker and Brune, 1973), although the failure strength of the rock is of the order of kilobars. Estimates of seismic efficiency (ratio of radiated energy to released strain energy) are virtually nonexistent, and it is not known how or whether seismic efficiency varies with the frequency of radiated waves (an important but usually neglected consideration when radiation spectra are used to infer source parameters). The temporal distribution of earthquakes in an aftershock sequence presents another problem: after a large earthquake, elastic redistribution of strain, which takes place in a period of seconds, cannot account for the time interval (of the order of hours or days) between subsequent earthquakes in the same region. Rather, some nonelastic changes must occur on a longer time scale than the elastic changes, but we have very little information on the nature of such nonelastic effects.

The deep gold mine of East Rand Proprietary Mines, near Johannesburg, South Africa, provides a unique opportunity to study both near-field and far-field effects of earthquakes. Stresses induced in the rock by the mining operation produce earthquakes as large as magnitude 4. These earthquakes have been the subject of numerous investiga-

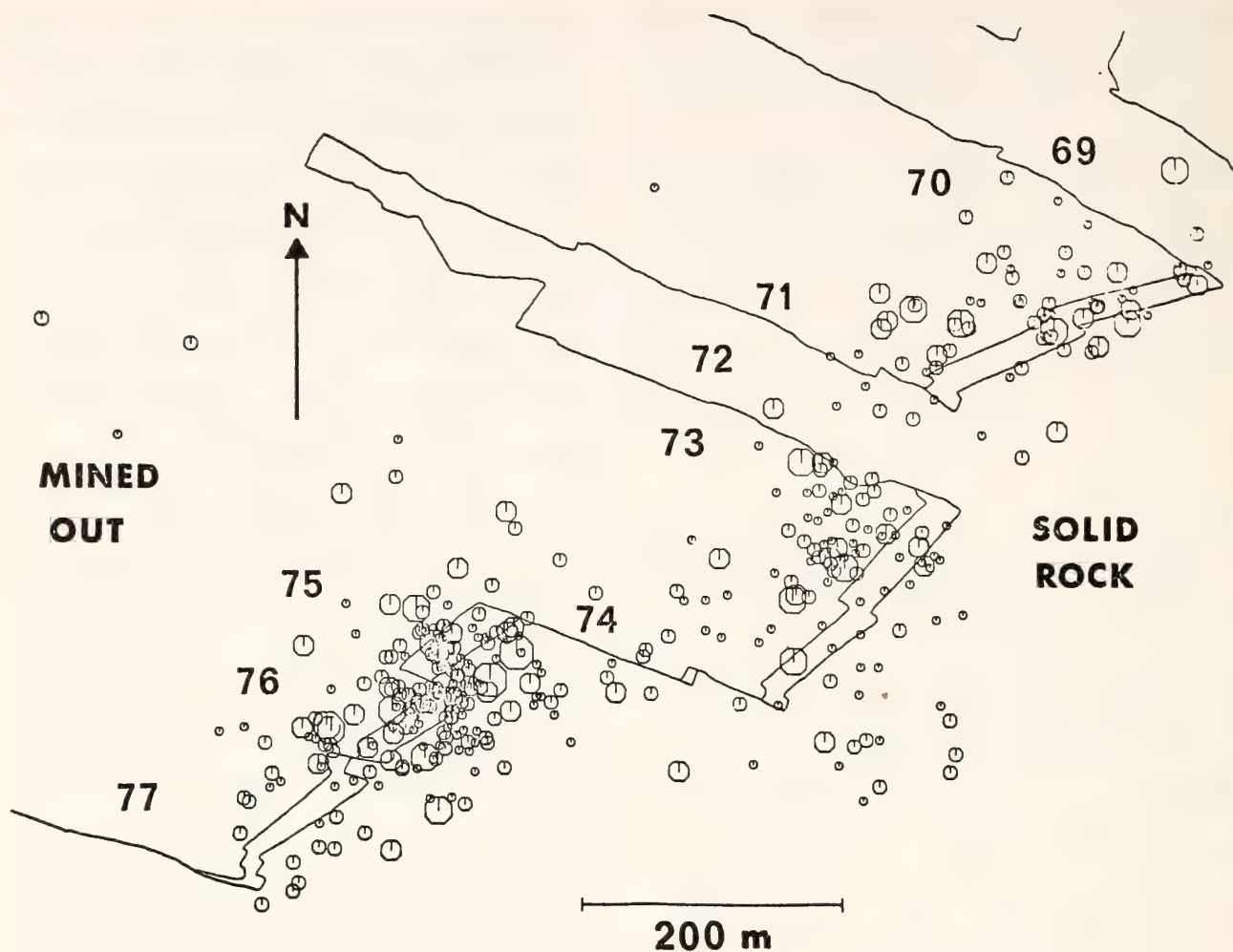


Fig. 95. Plan view of mine showing relation between seismicity and mining geometry. The two contours at the mine face show the advance of the face during the period for which the seismicity is plotted.

tions over the past 30 years and appear to resemble natural earthquakes in all their measured properties. An existing three-dimensional seismograph net gives accurate location data. Figure 95 (from McGarr, *et al.*, 1975) shows the distribution of earthquakes. Damage in the mine provides evidence bearing on the detailed nature of the rupture process. For some events it has been possible to mine into the failed zone and make direct measurements of fault length and displacement.

To gain further information about the behavior of the strained rock, a collaborative experiment between DTM and the Bernard Price Institute of Geophysical Research is now in progress. At a depth of 3.1 km a tunnel, 200 m long, was drilled in advance of the mine face (Fig.

96) so that instruments could be installed nearer the earthquake source region.

Three Sacks-Evertson borehole strainmeters, frequency response 0–10 Hz, (Sacks *et al.*, 1971) were added to the instrument set. The borehole strainmeters provide high-sensitivity data over very long periods, while the other instruments (installed by the BPI) covered the frequency range from 5 Hz to 1 kHz.

In this preliminary report we describe the design and installation of the borehole strainmeter and present some records showing the different types of activity monitored in the mine.

Design and Installation

In previous installations, the strainmeters were placed in vertical boreholes

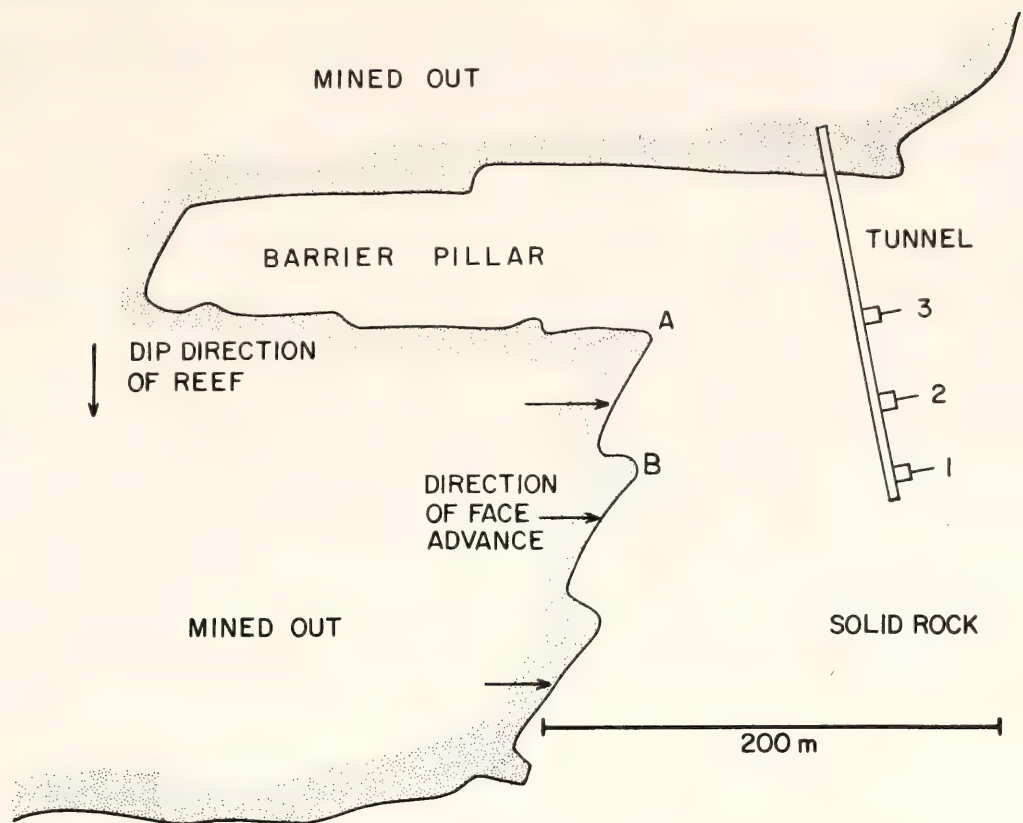


Fig. 96. Plan showing the tunnel and strainmeter locations with respect to the mine face. The tunnel is horizontal at a depth about 3.1 km below the surface. Point A is 100 m below the tunnel; B is about 130 m below the tunnel. By the end of 1977 the mined-out region passed below the tunnel.

drilled from the surface and thus few restrictions were placed on the length (3–4 m) of the instruments. In this experiment tunnel diameter is 2 m, and thus a compact version of the strainmeter had to be developed in which sensitivity would not be sacrificed. Despite the fact that high strains were expected for large, nearby events, the importance of monitoring small inelastic changes to obtain good data from the more numerous smaller events persuaded us to aim for a strain threshold of less than 10^{-10} . This compromise meant that the instruments were driven against their stops by the three largest events. A double-walled instrument (Fig. 97) was designed so that the sensing volume was essentially the total volume of the device. Since the instruments were to be built at the DTM and shipped to South Africa, it was necessary to design the strainmeter so that large temperature variations could be accommodated during transit without

damaging the sensing mechanism. A new recording system was developed to achieve high dynamic range (60 dB) and wide frequency response (0–10 Hz) on FM tape running at 0.15 cm/sec. The physical installation was complicated by two factors in addition to the limited work space. Holes 30 feet long and 6 inches in diameter were drilled from the tunnel, but because of drilling difficulties these were at a small angle (10° – 15°) below horizontal rather than vertical. Also, at 3.1 km depth the rock temperature is $\approx 40^{\circ}\text{C}$, so that the curing time of the expansive cement used to bond the instrument to the rock is much less than at normal room temperature. Laboratory tests showed that at 40° – 45°C the cement chemistry was speeded up about a factor of eight relative to that at about 18°C , the more commonly encountered temperature in surface installations. The setting time (i.e., the

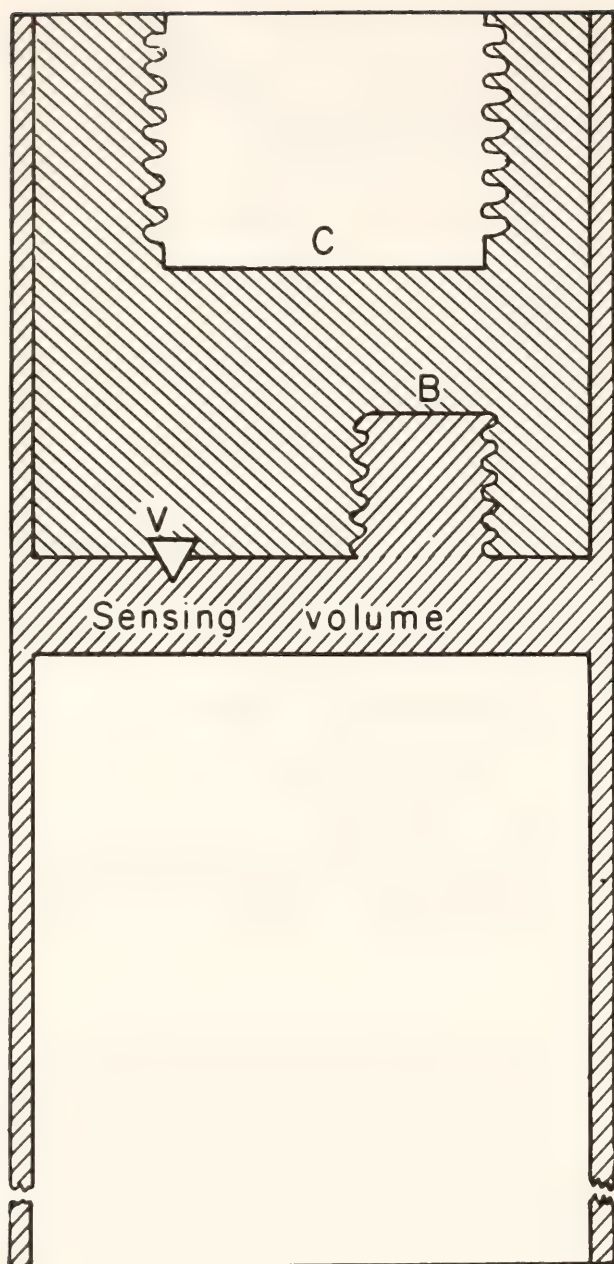


Fig. 97. Schematic illustration of borehole strainmeter. As the instrument is strained, oil in the sensing volume causes the top surface of the bellows *B* to move; the displaced volume is taken up with essentially no back pressure by bellows *C*. The motion of *B* is detected by two separate sensors—a differential transformer and a bender piezoelectric transducer (bimorph). The space above the bellows *B* is also filled with oil. The valve *V* is left open during transport, and temperature-induced volume changes in the oil during the installation are taken up by a compensatory bellows *C*. After installation, the valve is opened periodically to increase the dynamic range.

time after which it is not possible to sink the strainmeter into the cement-filled hole) is 15 min rather than 2 hr, and the

time to achieve maximum expansion of the cement is 1–2 days rather than 1–2 weeks.

Because pumping of the cement results in some separation of sand and cement, the mixture was delivered to the bottom of the hole in a specially designed container with a release mechanism and a pushrod system composed of detachable sections. After removing the emptied container, the strainmeter was thrust to the bottom of the hole using the same pushrod system. This method ensured that the cement contact between strainmeter and rock was complete and voidless. We were able to perform the whole installation procedure in less than 10 min.

Some Observations

Figures 98 and 99 show records of different types of activity recorded. The dynamic range of the strainmeter is increased by periodically opening the valve and recording the change in the active volume in order that the baseline be preserved. A sample valve opening is shown in Fig. 98A. Also in this record a teleseismic event is shown. Coincident with nearby earthquakes, a strain step is observed on the strainmeters. Examples are shown in Figs. 98 and 99. Events with longer time scales are illustrated in Fig. 99. Here we observe a strain change which occurs over a longer time (~ 1 hr). It appears that these events are very similar to slow earthquakes which occur in tectonic settings (Sacks *et al.*, 1977), although results to date are not conclusive.

Figure 99 shows strain changes that occur at blasting time. During the period between April 1977 (Fig. 99a) and November 1977 (Fig. 99b), the instrumental environment underwent a decrease in stress resulting from the advance of the face. The two records show that the response of the rock to the stress change induced by blasting changes in character.

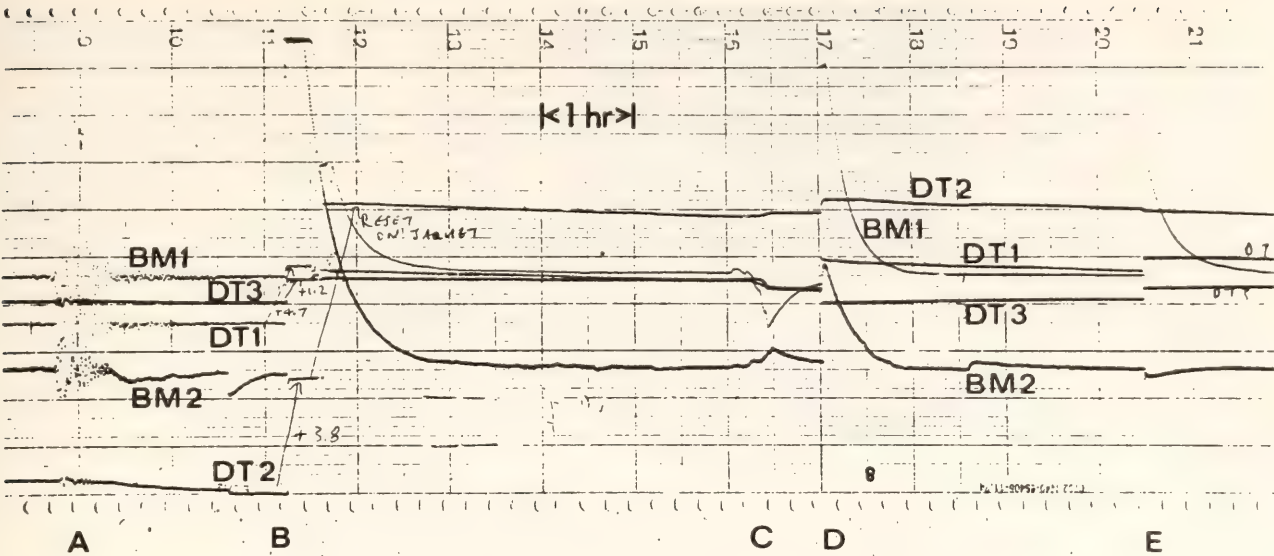


Fig. 98A. Recordings of outputs from differential transformers (DT) and bimorph (BM) of the strainmeters. At A, waves from a distant earthquake are recorded. The valve was opened at B, producing step changes in the DT's and changes in the BM's output which decay with a 25-min time constant. At C are strain changes produced at blasting time. At D and E, earthquakes were recorded.

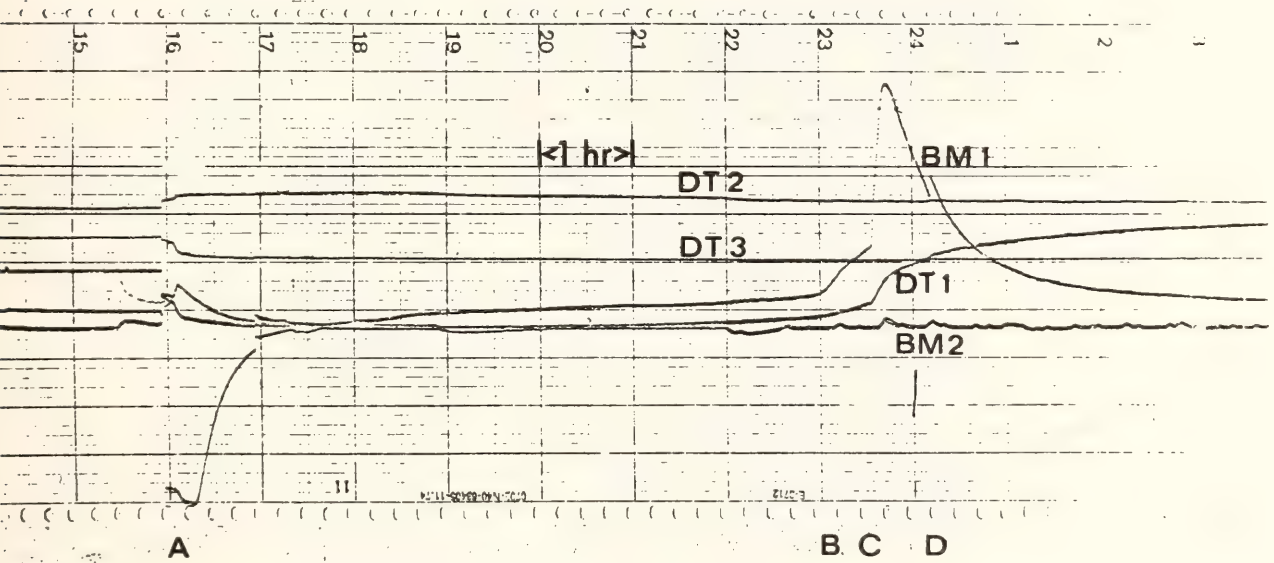


Fig. 98B. A record of the same type as in Fig. 98A. Blasting occurred at A. A slow event was recorded at B followed by a second slow event at C. An earthquake then followed at time D.

When the total stress level is high and the deviatoric stress is low, only a small fraction of the strain change is elastic; most of the readjustment takes place over an interval of an hour or so. Later, when the total stress is reduced but the deviatoric stress is higher, the response is primarily elastic with a small amount of afterstrain. It is not clear at this stage

of the study where the anelastic behavior is taking place. For example, it could be confined to the higher stress region just above and ahead of the face or it might extend to the instrument environment. Anelastic strain in rock under large stress is observed under laboratory conditions (Jaeger and Cook, 1976; Mogi, 1966), and the observation that it ap-

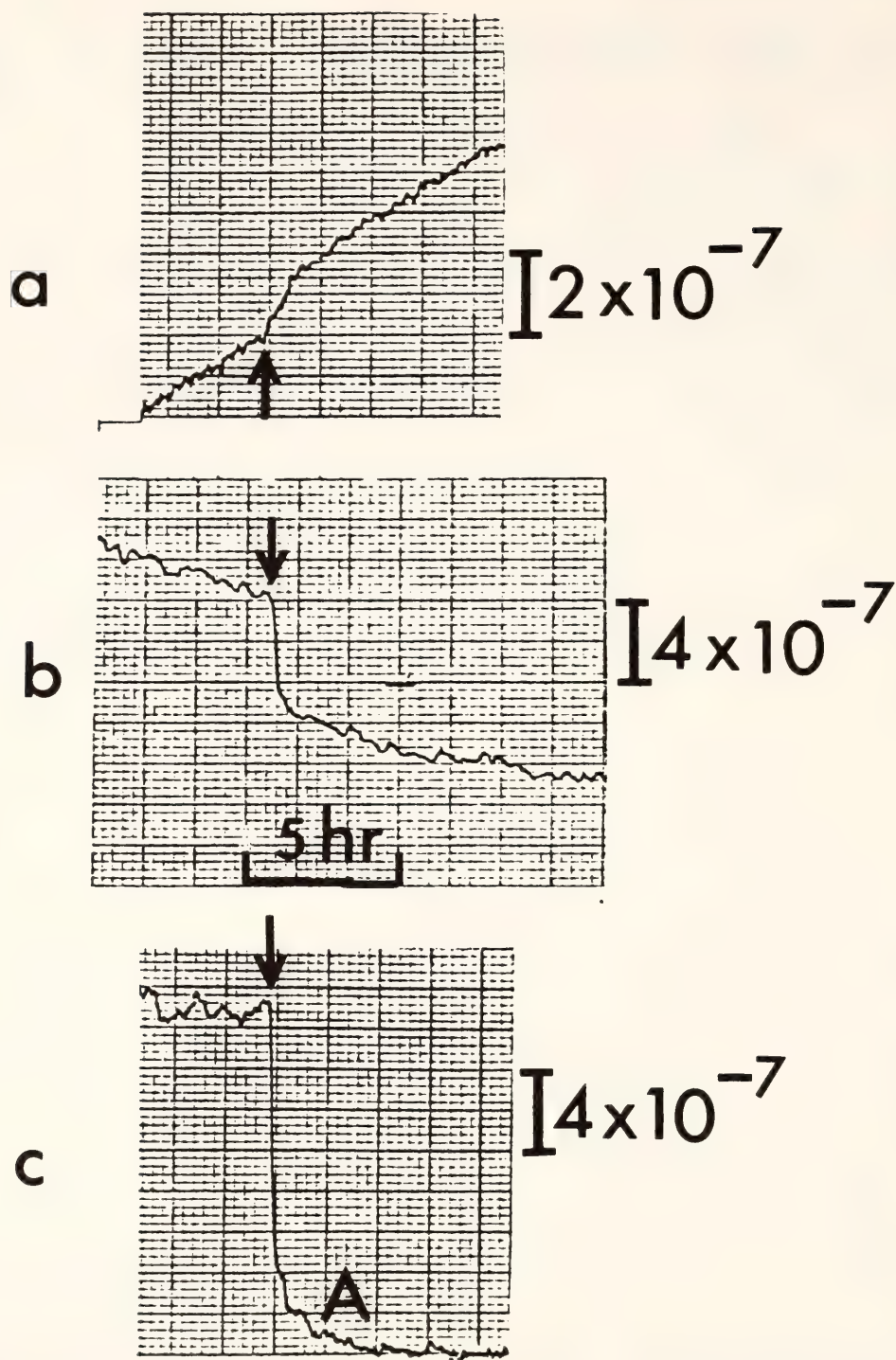


Fig. 99. Strain records at blasting time. Trace *a* was recorded on 7 April, *b* on 11 November, and *c* on 22 November 1977. The arrows indicate blasting time, which lasts for about 5 min. During April, the strain change induced by blasting is gradual, taking about an hour. Later, most of the strain change is coincident with blasting (i.e., elastic). There is, however, still some anelastic behavior (see *A* in trace *c*).

pears to be present in this field situation suggests that this may be a mechanism by which stress redistribution takes place on the long time scales associated with aftershock sequences.

References

- Jaeger, J. C., and N. G. W. Cook, *Fundamentals of Rock Mechanics*, p. 86, Chapman and Hall, London, 1976.

- McGarr, A., S. M. Spottiswoode, and N. C. Gay, Relationship of mine tremors to induced stresses and to rock properties in the focal region, *Bull. Seismol. Soc. Amer.*, 65, 93–112, 1975.
- Mogi, K., Pressure dependence of rock strength and transition from brittle fracture to ductile flow, *Bull. Earth Res. Inst.*, 44, 215–232, 1966.
- Sacks, I. S., S. Suyehiro, D. W. Evertson, and Y. Yamaguchi, Sacks-Evertson strainmeter, its installation in Japan and some preliminary results concerning strain steps, *Pap. Meteorol. Geophys.*, 22, 195–208, 1971.
- Sacks, I. S., S. Suyehiro, A. T. Linde, and J. A. Snoke, Extra seismic redistribution of stress, *Carnegie Inst. Wash. Year Book* 76, 888–896, 1977.
- Tucker, B. E., and J. N. Brune, Seismograms, S-wave spectra, and source parameters for aftershocks of San Fernando earthquake, San Fernando, California, Earthquake of February 9, 1971, vol. III, *Geological and Geophysical Studies*, pp. 69–121 U.S. Dept. of Commerce, 1973.
- zangi and Isacks, 1976; Bonatti *et al.*, 1977). An aseismic region in Chile has as its southern limit the northern limit of our array. This aseismic region is intersected by the Easter Island Volcanic Chain (EIVC), a linear array of volcanic islands and seamounts extending from Easter Island to the coast of Chile. Bonatti *et al.* have discussed the geochemical and geophysical bases for believing in recent (2 m.y. B.P.) simultaneous eruption of volcanoes along the EIVC independent of the age of the sea floor rocks adjacent to them. They suggest that the EIVC is due to a linear convection cell and have labeled it the Easter Island Hot Line. An extension of this line of convection under the continent would also explain the lack of any but the shallowest earthquakes in this region of Chile. The proposed linear mantle convection should also be reflected in an anomalous conductivity structure of the region. It is of some interest to note that a marked change in the geography of the conductivity structure in southern Peru also coincides with the intersection of the continent with the aseismic Nazca Ridge.

ANOMALOUS ELECTRICAL CONDUCTIVITY STRUCTURE IN CENTRAL CHILE

L. T. Aldrich, J. Bannister P.*,
M. Casaverde R.†, and E. G. Triep‡

In previous annual reports, we have given preliminary data from the array of three-component magnetic variometers operated across the Andes in a region between latitudes 30°S and 33°S. The site of the array was chosen because of the existence of a nest of earthquakes in the eastern half of this region at a depth of about 200 km. The nest terminates at the crest of the Andes. Since the operation of the net, the tectonic setting of the region has been the subject of considerable study and speculation (Bara-

A conductivity model of Cox *et al.* (1970), which appears to describe many observations across the margin of deep oceans, places a boundary on the continent between surface material of zero conductivity and material of infinite conductivity at a depth, h . Another layer of conductive material represents the ocean, and terminates at the ocean's edge. This model produces a monotonically decreasing value for Z_P as a function of distance from the ocean edge, the shape of which depends on the depth to the superconductor. Here P is the horizontal field perpendicular to the coastline and Z_P the transfer function between the vertical and horizontal fields for stations on land. Since the coast of Chile lies very nearly in a line parallel to magnetic north, it is expected that Z_H (vertical to NS horizontal) transfer

* Department of Geophysics, University of Chile, Santiago, Chile.

† Instituto Geofísico del Peru, Lima.

‡ Cuyo University, San Juan, Argentina.

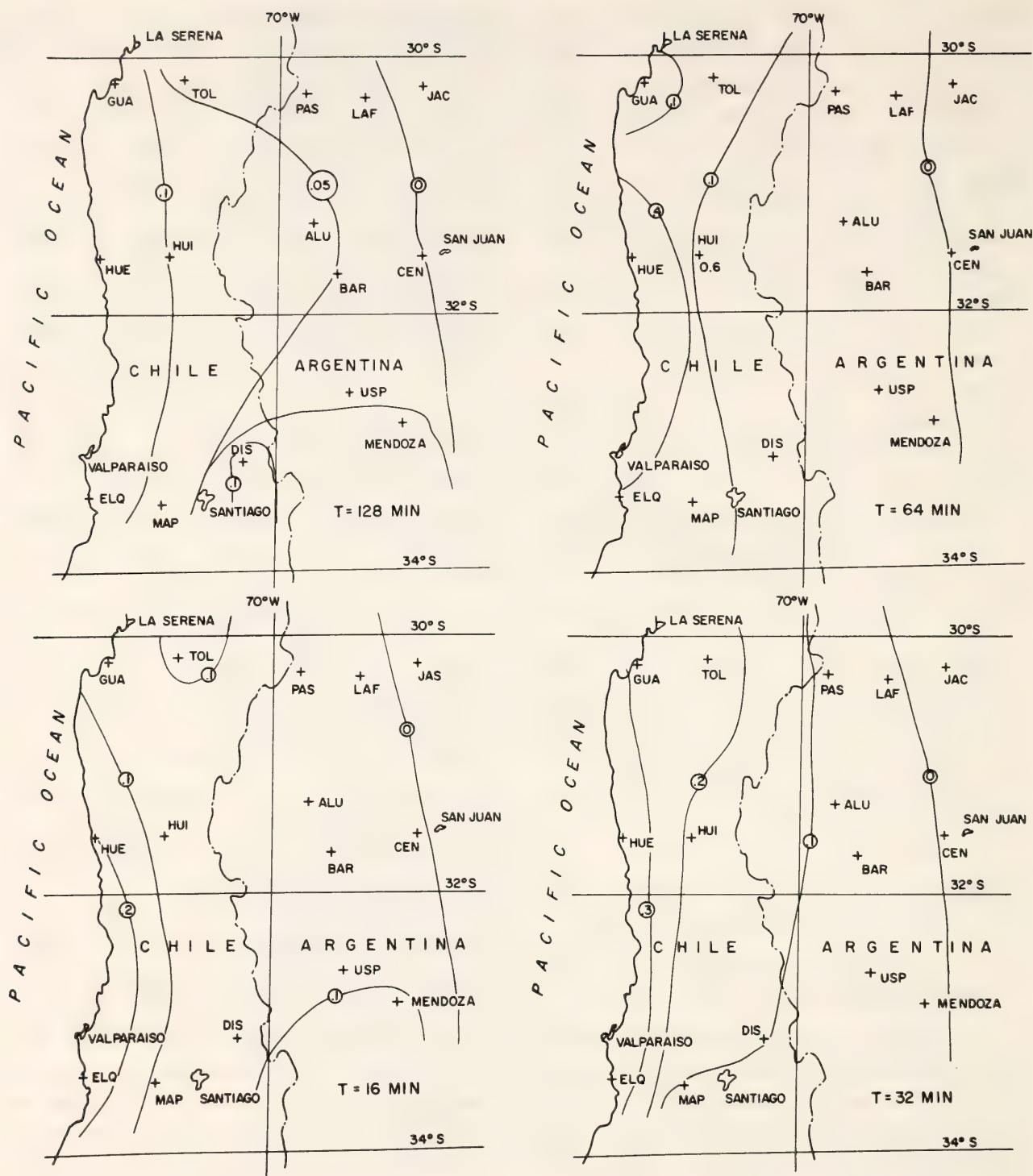


Fig. 100. Contours of Z_H transfer functions for four periods. The alignment, more or less parallel to the coast, is unexpected and is discussed in the text. H is the NS horizontal component, and Z the vertical component of the variation during a nighttime ray May 16, 1972.

functions will be negligible and that Z_D (vertical to EW horizontal) transfer functions will then be due to the structure at the ocean edge. Figure 100 exhibits contours obtained for the transfer functions of the vertical to NS horizontal magnetic field (Z_H) for four periods. If

these contours were due to a conductivity structure just north of the array and perpendicular to the coast, the contours should at least be skewed in a NE-SW direction and be negative. That they are positive and nearly parallel to the coastline (or the trench) would seem to negate

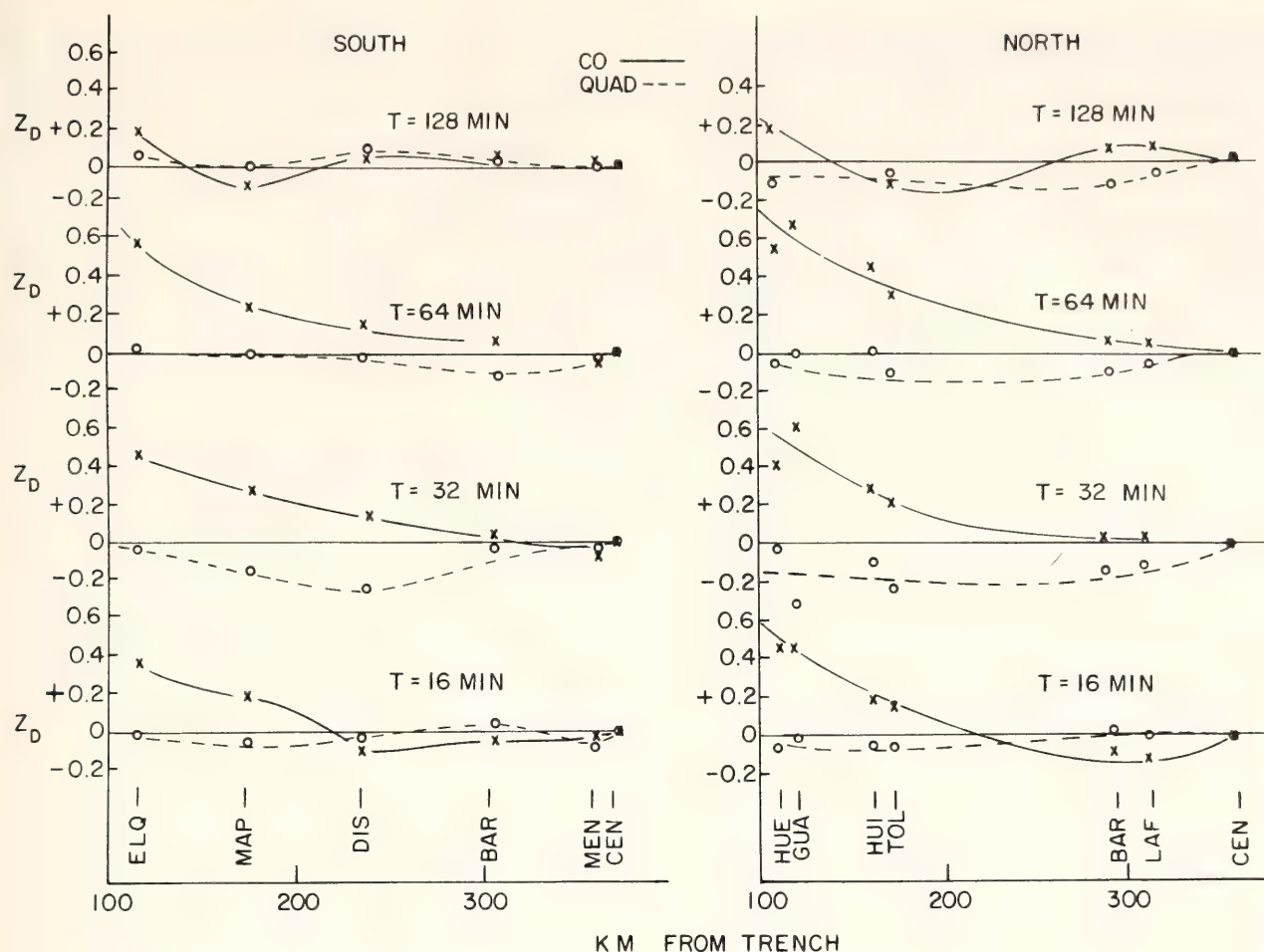


Fig. 101. North and South profiles for Z_D transfer functions for four periods. D is the E-W horizontal component of the variation during magnetic storms. The similarity between the two sets of profiles indicates uniformity of this parameter over the array.

the premise of a conductor close to but north of the array. The conductivity pattern implies that the anomalous vertical field correlated with the N-S variation of the horizontal field must be due to distant conductors with an E-W trend for which the ocean edge provides a return path.

Figure 101 shows plots of the Z_D (E-W horizontal to vertical transfer functions) as a function of distance from the Chilean trench for four periods. The profiles, north and south, both use Barreal (BAR) and Cerro Negro (CEN) in their lines. CEN is used as a station whose vertical component is assumed to be due solely to the magnetic storm. Transfer functions are calculated by subtracting Z (CEN) from Z for all other stations. It is further assumed that H and D at Cerro Negro also represent the storm without local

induction. It will be noted that the two sets of profiles are remarkably similar and therefore indicate uniformity of this relationship over the whole area. It is also seen that the profiles have a much different character at a period of 128 min than at either 64 or 32 min. The amplitude at the coast line of the 128-min period is about 0.3 that at the shorter periods and actually goes negative before becoming slightly positive at the Argentine stations. If one assumes the "normal" model of Cox *et al.*, one may superpose the profile shown for 64 min on the profile for 128 min. Taking the difference between these two (observed—normal) gives an indication of a second and presumably deep conductor east of C. Tololo (TOL) and Maria Pinto (MAP). The profile of the differ-

ence is similar to that found in southern Peru between the ocean and the Eastern Cordillera. For the 128-min period profiles, the absolute value of the transfer function may be in error since it is formed by subtracting Z (CEN) from Z for the various stations. If Z (CEN) has an appreciable component (positive or negative) at this period, the absolute value may be poorly determined. In any case, one cannot obtain the monotonically decreasing curve for Z_D at this period found from the "normal" ocean-edge effect, and a more complex conductivity structure is required.

Another characteristic of both profiles is the increase in magnitude of the quadrature component as the period decreases to 32 min. This is not predicted by the "normal" model and the effect is probably due to the simplicity of the model chosen.

Finally, the data are presented in the form of induction arrows, as described in Schmucker, 1976. These are described by the following equations where

$$Cu = -Z_H(u) \vec{i} - Z_D(u) \vec{j}$$

gives the in-phase arrow and

$$Cv = Z_H(v) \vec{i} - Z_D(v) \vec{j}$$

gives the out-of-phase arrow, and where \vec{i} and \vec{j} are unit vectors toward magnetic north and magnetic east respectively, u indicates an in-phase transfer function, and v a quadrature transfer function. The signs of the terms in the equations above are such that the in-phase arrows point to a region of high internal conductivity. In Fig. 102, we see the progression from mixed directions at 128 min to again a mixed pattern for the arrows for periods of 16 min. This is consistent with the model suggested above of a deep, higher conductivity in the east combined with the ocean step in the structure to the west (128 min pattern), the single-step struc-

ture at 64 and 32 min, and finally a mixed pattern at 16 min. The latter is probably a result of variations in the near-surface conductivity structure, which may be irregular owing to superficial geological features. If the Z_H values are due to a conductor outside the array, the NS component of the vectors should more properly be zero. In this case the arrows of Fig. 102 would point east or west.

In summary, this study has shown that there exists in central Chile an electrical conductivity structure which is complex but which does not in itself suggest any special relationship to the aseismic region north of the array. It rather suggests the existence of a conductor SW of the array and a deep conductor under the Andes. The regular ocean-edge pattern differs markedly from that found in Peru and northern Chile and is more nearly that found in California by Schmucker (1970). For periods of 64 and 32 min, the profiles are sufficiently uniform to apply, for purposes of comparison, to the model of Cox *et al.* used by Schmucker for his study of the ocean edge in California. The values for h for these two periods are shown in Table 23.

These values, except for 32 min on the S profile, are essentially identical to the California results of Schmucker. It is tempting to speculate that perhaps an E-W conductor in the aseismic area could be, in fact, merely a return path for the anomaly found in southern Peru and Bolivia. This would explain the sign of the H - Z transfer functions but not

TABLE 23. Equivalent Depth of a Superconductor for Data of Fig. 101 (after Schmucker, 1970)

Profile	Period (km)	
	64 min	32 min
North	186	146
South	186	213

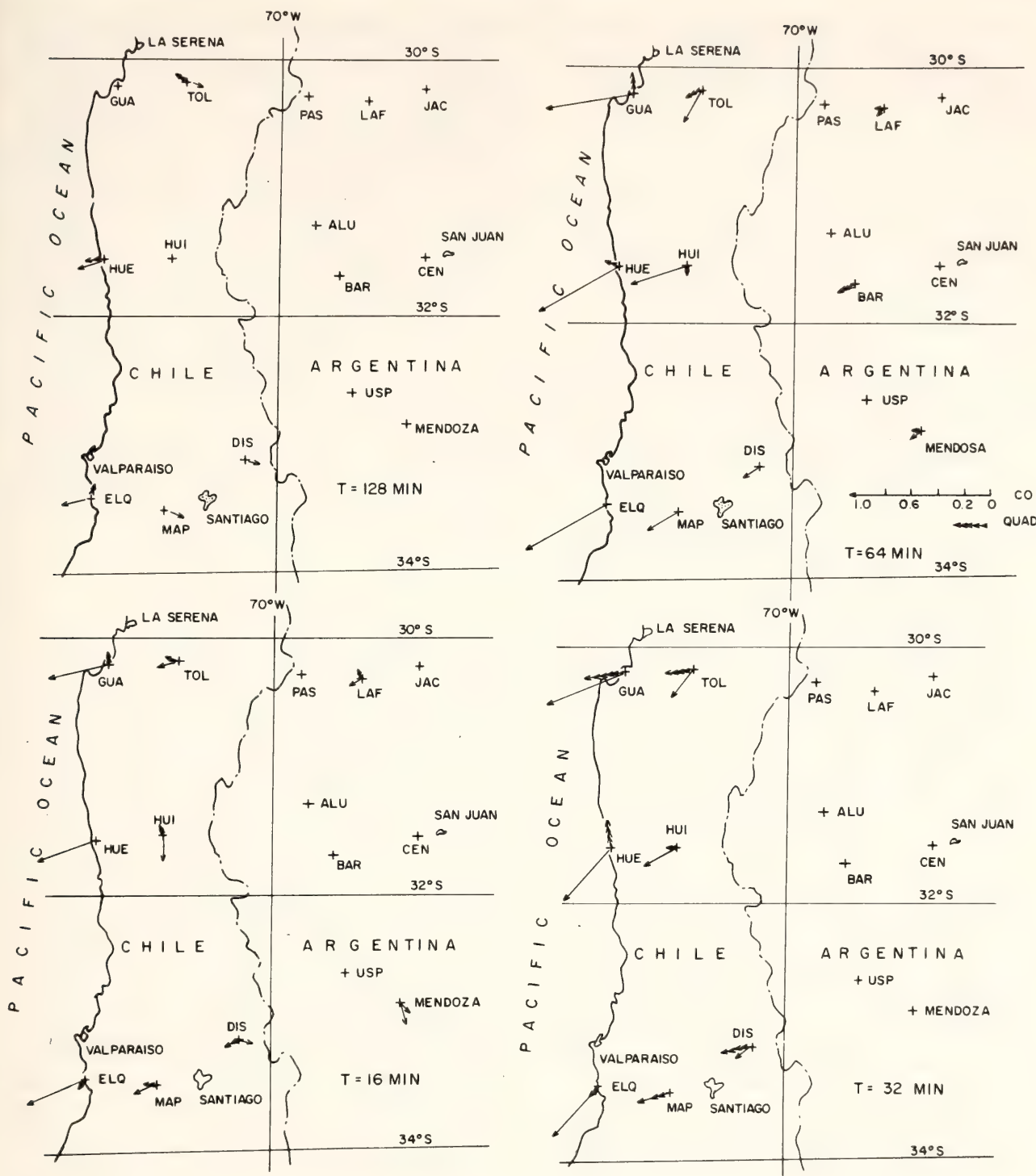


Fig. 102. Induction arrows for four periods. The real parts of Z_D and Z_H are combined to give "real" arrow and quadrature parts are combined to give quad arrows. The sign is chosen to allow the arrow to point to the conductor. Note the difference in direction of the arrows for TOL and MAP at 128 min.

the areal pattern parallel to the coast. Further studies to the north of this array are clearly of interest. Because the induction arrows point to the southwest, it would seem that an extension of the data to the south would be equally fruitful in

adding to the geophysical characterization of the tectonic features of southern Chile. Added stations in Argentina east of longitude 69° are required to verify the suggestion of a deep conductor parallel to the Andean Cordillera.

This work has been partially supported by a grant from the National Science Foundation, Earth Sciences Program.

References

- Barazangi, M., and B. L. Isacks, Spatial distribution of earthquakes and subduction of the Nazca Plate beneath S. America, *Geology*, 4, 686–692, 1976.
- Bonatti, E., C. G. A. Harrison, D. E. Fisher, J. Honnorez, J.-G. Schilling, J. J. Stipp, and M. Zentilli, Easter Volcanic Chain (Southeast Pacific): a mantle hot line, *J. Geophys. Res.*, 82, 2457–2478, 1977.
- Cox, C. S., J. H. Filloux, and J. C. Larsen, in *The Sea*, IV, pp. 637–693, A. Maxwell, ed., Wiley, New York, 1970.
- Schmucker, U., Anomalies of geomagnetic variations in southwestern United States, *Bull. Scripps Inst. of Oceanography*, 13, 1970.

GEOCHEMICAL CONSTRAINTS ON MANTLE MODELS: THE CASE FOR A LAYERED MANTLE

A. W. Hofmann, W. M. White, D. J. Whitford

Ever since Gast's (1960) paper on the difference in isotopic composition and trace element abundances between chondritic meteorites and terrestrial rocks, one of the chief aims of geochemistry has been to investigate the chemistry of the earth's mantle using isotopic analyses of mantle-derived volcanic rocks. One result that has been established is that the mantle is isotopically and chemically heterogeneous. Although this is in itself an important result, it can hardly be regarded as a worthwhile subject of further studies, unless such studies can be expected to lead to some sort of refinement of the structure and distribution of these heterogeneities. At the present time there is still no agreement among geochemists as to what this structure might be. Consequently, the entire body of geochemical evidence has largely been ig-

nored by geophysicists, who have concerned themselves with the kinematics and dynamics of mantle convection (see, for example, the concise yet comprehensive review by Turcotte and Oxburgh, 1978). In this discussion, we will review several simple interpretations of the geochemical data. Some of these have been stated explicitly in the literature, whereas others, especially those related to the "lumpy" mantle, have not been formulated in any detail. We will attempt to assess their relative merits and to draw attention to some aspects of plate kinematics that are well known but have apparently not been considered in previous attempts to interpret the geochemical data.

The Isotopic Data

Surveys of the isotopic data from oceanic basalts have recently been published by Sun and Hanson (1975), Church and Tatsumoto (1975), Tatsumoto (1978), De Paolo and Wasserburg (1977), Brooks *et al.* (1976a), and Hofmann and Hart (1978). Figure 103 is a simplified summary of these results. Ocean floor basalts have comparatively uniform and low $^{87}\text{Sr}/^{86}\text{Sr}$ and $^{206}\text{Pb}/^{204}\text{Pb}$ but high $^{143}\text{Nd}/^{144}\text{Nd}$ ratios, whereas basalts from the oceanic islands (excluding those associated with subduction, namely island arcs) have less uniform and generally higher Sr and Pb ratios and lower Nd ratios. While there is some overlap between the basalts from the two tectonic environments (ocean ridges and isolated volcanoes or midplate volcanic chains), the overall differences are just as clearly quite significant. Hart *et al.* (1972) first pointed out the problems posed by the close geographic proximity of lavas derived from distinctly different mantle sources. By making only the assumption that the earth had initially a uniform isotopic composition (which except for some rare inclusions is true for meteoritic material), one may draw one

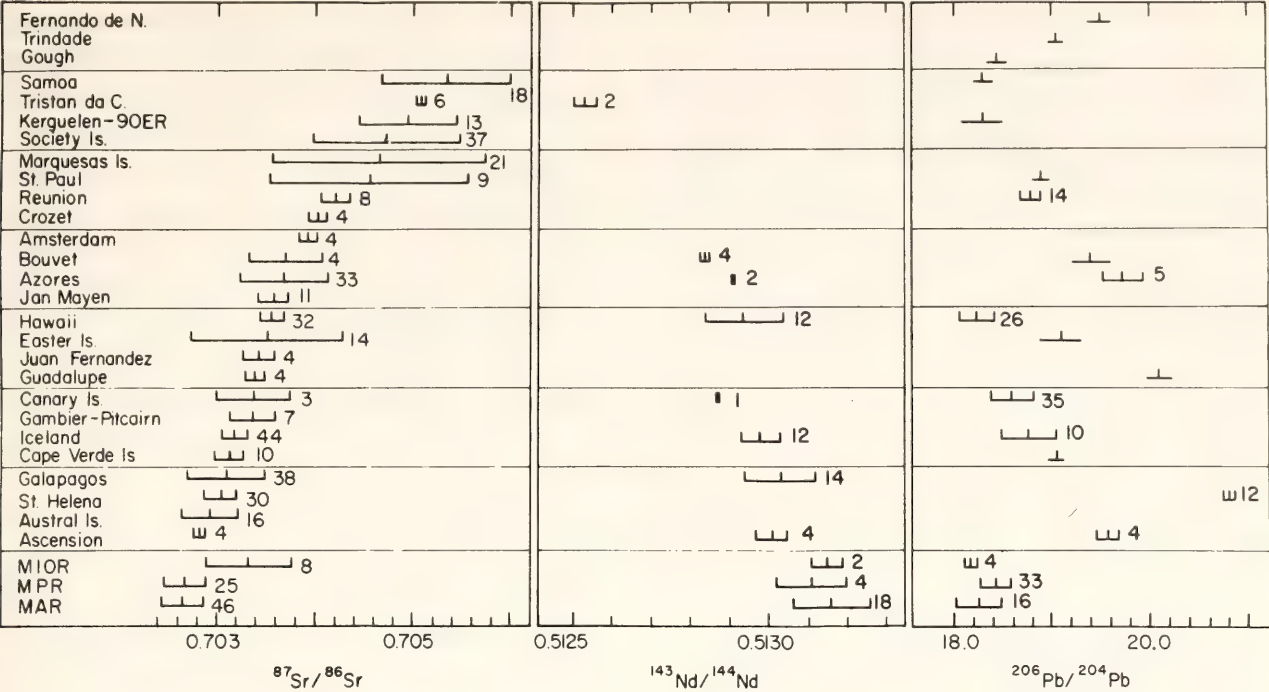


Fig. 103. Isotopic composition of Sr, Nd, and Pb in basalts from midocean ridges and oceanic islands. Island-arc basalts are not included. The names of the islands or island chains are given on the left. MAR, MPR, MIOR stand for Mid-Atlantic Ridge, Mid-Pacific Ridge (including East Pacific Rise, Juan de Fuca, and Gorda Ridge), and Mid-Indian Ocean Ridge. Omitted are data from DSDP drill cores (most of which are older and more altered than ridge samples) and samples from portions of ridges that are obviously (topographically and isotopically) associated with island platforms (i.e., the Reykjanes Ridge and Azores platform). The data bars give the average and the standard deviation for each set of samples. The number of samples is indicated on the right-hand side of each data bar. The tick marks for standard deviation have been omitted for some of the Pb data because these results were taken from the published figure of Sun and Hanson (1975). Data sources are summaries of Brooks *et al.* (1976a), Hofmann and Hart (1975), and Sun and Hanson (1975), and additional published data by Oversby (1972), Sun (1973), Sun and Jahn (1975), Church and Tatsumoto (1975), Sun *et al.* (1975), Tatsumoto (1978), and Vidal and Dosso (1978) for Pb; Gonzales-Ferran *et al.* (1974), Duncan and Compston (1976), White (1977), White and Schilling (1978), Hedge (1978), and the companion reports by Hofmann *et al.*, Whitford and Duncan, and White and Hofmann (this Report) for Sr; De Paolo and Wasserburg (1976 a, b), Richard *et al.* (1976), O'Nions *et al.* (1977), Carlson *et al.* (1978), and White and Hofmann (this Report) for Nd.

firm conclusion: reservoirs with different element ratios—Rb/Sr, U/Pb, Th/Pb, and Sm/Nd—have existed in the mantle for considerable lengths of time. It is also possible to infer these element ratios approximately from observed values of mantle-derived basalts. From these inferred ratios and the half-lives of the parent isotopes, the lifetime of the heterogeneities is found to be on the order of $1 \text{ to } 2 \times 10^9$ years—significantly less than the age of the earth but more than the typical lifetime of a present-day oceanic plate. The same results can be obtained from Pb isotopic ratios alone,

independent of any estimates about U/Pb and Th/Pb ratios in the mantle. The above time estimates have been discussed in more detail, for example by Gast (1969), Church and Tatsumoto (1975), Brooks *et al.* (1976a), Carlson *et al.* (1978). The differences in the parent-daughter element ratios were generated by some episodic or continuous fractionation process. The nature of this process is not known, but it is reasonable to suppose that the formation of a melt or vapor phase and its differential movement relative to the crystalline phases played an important part.

Possible Density Differences

Arguments have been advanced in the literature that the geochemically identifiable mantle reservoirs are also characterized by different major-element chemistry or temperatures, and that different densities could be assigned to the different reservoirs. For example, Anderson (1975) has argued that U- and Th-rich regions in the mantle are characterized by enrichment in the light elements CaO, Al₂O₃, and TiO₂ and are intrinsically less dense than other regions that are richer in MgO, FeO, and SiO₂. O'Hara (1975) has argued that fertile mantle is denser than residual mantle. The terms fertile and residual refer to the composition of solid mantle before and after removal of a melt fraction. Shaw and Jackson (1973) measured densities of fertile and residual mantle xenoliths and came to the opposite conclusion. Boyd and McCallister (1976), after careful consideration of lattice-cell parameters of mantle minerals, decided in favor of O'Hara. Unfortunately, the geochemical indicators of the compositional heterogeneity of the mantle give no direct clues about the major-element composition of the different regions. The problem is made complicated by several factors: (1) An enrichment of light elements does not automatically mean low density. For example, in the upper mantle, the relatively dense phase garnet is enriched in the relatively light element Al. (2) The structure and composition of lower mantle phases are poorly known. (3) A region enriched in K, U, and Th will tend to become hotter than its surroundings. For example, a sphere surrounded by a medium that is maintained at constant temperature will eventually reach a steady state temperature at its center, given by

$$\Delta T(\text{center}) = Hr^2/6K,$$

where ΔT = temperature difference, H = rate of heat production, K = thermal

conductivity, and r = radius of sphere. For a radius of 200 km and present-day chondritic heat production, the temperature difference is about 50°C. Thus, for the radiogenic heat to generate significant density differences, the enriched region must be sufficiently large (on the order of several hundred kilometers or more) and the resulting thermal expansion must not be balanced by intrinsic density differences resulting from unknown differences in major-element composition.

Because of the above-noted uncertainties, we prefer to use the isotopic data only for the purpose of identifying ("fingerprinting"), rather than physically or chemically characterizing the different source reservoirs in the mantle, which are sampled by the basalt extruded on the surface.

Geochemical Models of the Mantle

For the purpose of this discussion, we adopt two conclusions from the preceding sections: (1) The isotopic heterogeneities in the mantle are older than all present-day oceanic plates. (2) Major-element and density heterogeneities cannot be demonstrated from the geochemical data. The models are therefore based primarily on the geographical and temporal pattern of isotopically labeled oceanic volcanism. Using these models we attempt to answer the questions, how large are the heterogeneous regions in the mantle and how are they spatially distributed?

Model I: Local Disequilibrium—Regional Uniformity

In this model, the isotopic heterogeneities exist on a "mineralogical scale," that is, there are isotopic differences between individual mineral grains, but larger volumes of mantle are thought to have uniform composition. Models of this type have become known as "disequilibrium melting" models, because all

the isotopic differences of the extruded basalts are attributed to preferential incorporation of isotopes into the melt from some nonrepresentative portion of the melting mineral assemblage. Disequilibrium melting has been invoked by many authors (e.g., Sigvaldson, 1974; O'Nions and Pankhurst, 1974; Flower *et al.*, 1975; Beswick and Carmichael, 1977). Hofmann and Hart (1978), O'Nions *et al.* (1976), Nelson and Dasch (1976), and White and Schilling (1978) have investigated this model further and have concluded that it is in conflict with the regional isotopic and trace element abundance patterns and with the available (though meager) experimental evidence. Rather than repeat the arguments, we will accept this conclusion for the purpose of the present discussion and therefore reject model I.

Model II: Lumpy Mantle

By *lumpy mantle*, we mean irregular heterogeneities that can be classified by characteristic size. For example, in the model of a veined mantle of Hanson (1977), that size is on the order of meters, whereas the mantle "blobs" envisioned by Schilling (1974, 1975) and by Brooks *et al.* (1976b) are thought to have sizes of tens or hundreds of kilometers. Sleep (1974) described a model using irregular heterogeneities without specifying any lump size. Rather than describing the details of the various models, we classify them into two categories, small lumps and large lumps. In small-lump models the characteristic size of the heterogeneity is much smaller than the size of a volcano ($\ll 10$ km) but much larger than the mineral grain size ($\gg 1$ cm). The important feature of such models is that the isotopic composition of the melt depends on the degree of melting. In this respect, they are quite similar to model I, but the characteristic distances are now chosen to be large enough so that the kinetic objections to

model I are no longer relevant. For example, a good case can be made (Gast, 1968) that oceanic island basalts are generated by smaller degrees of melting than are MOR basalts. Consequently, the island basalt would be derived by preferential melting of the Rb-, U-, Th-, and LREE-enriched portions of the source, which are, in turn, characterized by radiogenic Sr and Pb isotopes and unradiogenic Nd isotopes. In the MOR basalts, the higher degree of melting would lead to a dilution of the melt with material derived from the Rb-, U-, Th-, and LREE-depleted portions of the source rock.

The small-lump model fails to account for the isotopic compositions of many islands where lavas occur that result from different degrees of melting but show no significant differences in their isotopic composition. It is now widely accepted that alkali basalts are formed by much smaller degrees of melting than are tholeiites (Gast, 1968; Green and Ringwood, 1967). Yet, islands have been found where both types of basalt have identical isotopic composition. Iceland is one example (Hart, *et al.* 1973). The Galápagos Islands (see White and Hofmann, this Report) and the Azores (White *et al.* 1976) show the same feature, and the Mauna Ulu sequence of tholeiite eruptions in Hawaii shows a substantial change in the degree of melting with no variation in isotopic composition (see Hofmann, Wright, and Feigenson, this Report). Another objection to the small-lump models is that they fail to explain the excess magma production (over that of normal mid-ocean ridges) and the isotopic composition of on-ridge islands such as Iceland. If island lavas are generated by small degrees of melting with no large-scale differences in the source material, the high rate of magma production leading to a thick crust and the surface emergence of the island seems paradoxical.

In large-lump models, the size of the

mantle heterogeneity is characteristically greater than the size of the volcano but smaller than the distance between oceanic island chains or groups. Thus the lump size may be on the order of tens to hundreds of kilometers. In these models, the isotopic composition of the melt is independent of the degree of melting and is given by the composition of the lump itself.

Large-scale heterogeneities are favored by observations of large-scale variations in the composition of midocean ridge lavas adjacent to oceanic islands. The zone of geochemical transition between Iceland and normal Mid-Atlantic Ridge basalts extends over about 250 km (Hart *et al.*, 1973; Sun *et al.*, 1975) and the equivalent transition zone south of the Azores extends over nearly 1000 km (White and Schilling, 1978). An approximate upper limit might be given by the distance between islands of distinct isotopic composition. For example, Ascension and St. Helena Islands have quite distinct isotopic compositions and are located about 1000 km apart. Two Pacific island and seamount chains, the Austral and Society Islands, are subparallel at a distance of about 400 km and show separate and distinctive isotopic compositions of Sr (Duncan and Compston, 1976). The major objection to the large-lump model is based on the longevity of volcanism associated with some oceanic island or seamount chains. Moreover, the isotopic identity of the basalts has in some cases been shown to be maintained over similarly long times. Examples are the compositions of the Society Islands with a $^{87}\text{Sr}/^{86}\text{Sr} = 0.7047 \pm 0.0008$, and the Austral Islands with $^{87}\text{Sr}/^{86}\text{Sr} = 0.7029 \pm 0.0003$ (Duncan and Compston, 1976; Hedge, 1978). Another example is the Ninetyeast Ridge with $^{87}\text{Sr}/^{86}\text{Sr} = 0.7050 \pm 0.0005$ (see Whitford and Duncan, this Report), a much higher value than is found elsewhere in the Indian Ocean except on Kerguelen-Heard Island, which repre-

sents the present-day continuation of Ninetyeast Ridge volcanism. The duration of volcanism has been shown to be at least 70 m.y. in the case of the Hawaiian-Emperor chain (Clague *et al.*, 1975) and at least 80 m.y. on the Ninetyeast Ridge (Duncan, 1978). Although the documentation of the ages and isotopic composition of island and seamount chains is far from complete, it appears from the above examples that the isotopic variations within one chain are smaller than the differences between chains, even when these chains are in relatively close geographic proximity (such as the Society and Austral Islands). This local uniformity in composition together with the longevity of localized magma production provide very strong arguments against irregularly lumpy source models. For example, if one assumes that the rate of ascent of an island-forming blob is similar to the rate of plate movement in the Pacific, such a blob will rise several hundred kilometers in 10^7 years. The only way in which even a very large blob could produce long-term island volcanism would be for this blob to rise to the base of the lithosphere and to remain there for tens of millions of years without being carried along by the moving lithosphere. Alternatively, a blob rising below a midocean ridge would somehow have to escape being consumed by the process of sea-floor spreading.

If one supposes that the problem of keeping the blob stationary for a sufficiently long time can be solved, one is still faced with the difficulty of how the blob can continue to produce magmas of similar composition. The process of fractional melting is sometimes invoked for extended production of magma from the same batch of source material (e.g., Yoder, 1976, p. 204). However, a fractional melting process would cause a drastic decrease in incompatible-element concentrations as successive melt fractions are removed from the source. Such

concentration decreases are not observed in oceanic basalts. Therefore, the oceanic volcanism must continuously or periodically draw on fresh batches of source material.

In summary, all simple versions of lumpy-mantle models appear to be inconsistent with the longevity of some of the ocean island volcanism. Perhaps the inconsistency is only apparent, but the problem should be addressed by the advocates of this model.

Model III: Layered Mantle

The objections raised to all mantle models involving small-scale or large-scale, irregular inhomogeneities naturally lead to the consideration of a more ordered compositional structure of the mantle. Models involving a layered mantle are intuitively easier to reconcile with the antiquity of the inhomogeneities, the longevity of ocean island volcanism, and the large volume of isotopically identifiable source reservoirs, which nevertheless give rise to volcanism at geographically close surface locations. For sake of simplicity, only two-layer models will be considered.

IIIA: Enriched Asthenosphere-Depleted Deeper Mantle

This model is currently favored by a number of geochemists and geophysicists, for example Kay and Gast (1973), Green and Lieberman (1976), Allègre and Bottinga (1977), and Ito (1977). Large ion lithophile elements, including K, Rb, U, Th, and light REE are thought to be concentrated in the asthenosphere. This enriched asthenosphere is then tapped for the production of oceanic island magmas. The midocean ridge magmas are derived from the upwelling of more depleted deeper mantle material. If some portion of the asthenosphere is partially molten, the melt fraction might be the main reservoir for the incompatible elements. In some versions of the

model (e.g., Green and Lieberman, 1976; Ito, 1977) the enriched reservoir is the uppermost layer of the asthenosphere and the depleted reservoir is the lower part of the asthenosphere. Allègre and Bottinga, on the other hand, propose that the depleted source reservoir for MOR basalts lies in the lower mantle, and they invoke deep-mantle upwelling as the primary mechanism for sea-floor spreading.

Several mechanisms have been proposed for the origin of linear volcanic chains from an enriched asthenosphere. These include (1) propagation of cracks in a lithosphere moving over an aspheric surface (Turcotte and Oxburgh, 1973), (2) propagation of cracks in response to intraplate stress fields, which in turn are caused by forces acting on the plate boundaries and by small-scale secondary convection cells in the asthenosphere (Solomon and Sleep, 1974), (3) propagation of cracks caused by cooling and thickening of the lithosphere with time (Turcotte and Oxburgh, 1976), and (4) shear melting caused by plate motion over the asthenosphere and localization of the melting spot by downwelling of a dense residuum ("gravitational anchor"; see Shaw and Jackson, 1973).

Support for model IIIA is based on a variety of evidence and beliefs: (1) The propagating-fracture mechanism is more acceptable than the plume mechanism (see model IIIB) to many geophysicists as an explanation for linear volcanic chains. (2) There is strong geochemical evidence for upward enrichment of K, U, Th, and light REE in the earth. The crust contains much higher concentrations of these elements than the mantle, and there is also evidence for upward enrichment within the crust. Consequently, it seems reasonable to infer that the same is true within the mantle. In connection with this, it may be important that there is substantial (though certainly not unequivocal) evidence that the upper part of the asthenosphere is

partially molten. This in turn leads to the inference that the partially molten layer is enriched in the incompatible elements because these elements are preferentially partitioned into the melt fraction. (3) The isotopic composition of Sr and Pb from island-arc basalts is almost invariably more radiogenic than the composition of MOR basalts. In this respect, island-arc basalts resemble oceanic island basalts, and because island-arc basalts are known to be derived from the upper mantle, it is reasonable to infer, on the basis of the isotopic composition of Pb and Sr only, that the oceanic islands must also be derived from an upper mantle source. (4) A kind of negative evidence in favor of model IIIA can be found in the failure of the plumes (postulated by Morgan, 1971, in connection with model IIIB) to remain perfectly stationary with time (see Morgan, 1972; Molnar and Atwater, 1973). This might be seen as a failure of the plume model and consequently be viewed as supporting model IIIA.

Arguments against model IIIA are as follows: (1) No suitable mechanism has been proposed in the literature to explain oceanic islands that are located on the midocean ridges (Iceland-type) or have been crossed by midocean ridges (Galápagos type; see also the connection between Kerguelen and the Ninety-east Ridge described by Whitford and Duncan, this Report). Linear volcanic features are associated with these islands as well as with midplate islands of the Hawaiian type, but the proposed mechanisms involving propagating fractures or shear melting are clearly applicable only to the midplate islands. The failure to explain the Iceland-type islands is all the more remarkable in that Morgan (1971) specifically drew attention to the fact that most of his proposed deep-mantle plumes form islands at or near ridges and triple junctions. (2) If one supposes that a physically acceptable mechanism could be found for generating

Iceland-type islands from the upper (or the entire) asthenosphere, an additional difficult question must be answered: Why is the enriched source material not swept off laterally by the movement of the newly formed lithospheric plates? Perhaps the problem can be solved by invoking small-scale convection in the upper asthenosphere as proposed by Ito (1977), but it should be noted that models of two interacting scales of convection proposed by Richter and Parsons (1975) and by McKenzie and Weiss (1975) are not compatible with the geochemical data because in these models both scales of convection affect a single reservoir of material. The isotopic data clearly require a long-term separation of reservoirs. (3) The long lifetime of an enriched asthenospheric reservoir (1 to 2×10^9 years) raises another problem. The depleted material from the deep mantle (or deep asthenosphere) must return to its depth of origin without extensive mixing with the asthenosphere. This return flow is presumably accomplished by subduction of depleted lithosphere. But the locations of ridges and subduction zones are constantly moving with respect to one another. For example, since the time of the initial opening of the Atlantic Ocean, the circum-African ridge system has moved away from Africa, so that the area of the African plate has grown by more than a factor of two. If an enriched asthenosphere now exists under this plate and its expanding margin, this asthenosphere must either have thinned in response to its areal growth, or it must have been replenished by horizontal flow. The only segment of the plate margin where this horizontal flow would not be obstructed by the upwelling of deeper mantle material (which forms the circum-African ridge system) is the northern margin of the plate. The complementary problem is posed by the disappearance of plates, such as the Farallon plate (Atwater, 1970), where the asthenosphere

must either somehow escape laterally across the sinking lithospheric plate or the rising sheet of ocean ridge material or else be subducted into the deeper mantle. A strong tendency toward re-mixing of reservoirs seems an inevitable consequence of the lateral motion of ridges and trenches. This mixing process will affect the mantle at least to the depth from which the ridge material rises. One good measure of the efficiency of this mixing process is the fact that midocean ridge basalts are much more uniform isotopically than are the ocean island basalts as a group. (4) Yet another problem is posed by the ubiquitous transform faults that cause offsets of hundreds of kilometers along midocean ridges. The mantle material ascending at the midocean ridge must be a sheet of no more than about 200-km thickness. It must split into two branches no more than 100 km thick (the thickness of the oceanic lithosphere). If the thickness were greater than that, it would necessarily displace the asthenosphere, which would then no longer be available as a magma source for oceanic islands near the ridge. This comparatively thin sheet ascending from the lower mantle would have to be offset along transform faults, and this offset would have to increase with time. It appears difficult to reconcile the surface pattern of the ridge-transform fault system (which seems to develop primarily to accommodate the requirements of the shapes and movements of surface plates) with a convection mechanism of relatively short segments of thin sheets ascending from the deep mantle.

None of the above-listed arguments seems sufficiently conclusive to rule out model IIIA (two layers with enrichment in the upper layer). Perhaps a mechanism can be devised that will satisfy both the geochemical and the kinematic requirements, but we are not aware of any such model. We suggest that future laboratory and numerical convection ex-

periments include an assessment of the mixing properties. We believe that a comparison of calculated reservoir lifetimes with the geochemically observed lifetime would be a useful test for the validity of the convection model.

IIIB: Depleted Asthenosphere— Enriched Deeper Mantle

This is essentially a variation of Morgan's (1971) model of plumes ascending from the deep mantle. The main difference is the partial or complete isolation of the upper mantle from the lower mantle. This distinction is implicit in Schilling's (1973) version of the model (Morgan envisioned a dispersed return flow toward the lower mantle), which is important to satisfy the geochemical constraints. The essential features are (1) plate accretion occurs at the mid-ocean ridge as a result of upper mantle (asthenosphere) upwelling, (2) oceanic islands are generated by localized upwelling from the deeper mantle, (3) the asthenosphere has been partially depleted in incompatible elements during previous convective cycles, and (4) mixing between the upper and lower mantle has been limited to such an extent that the trace element and isotopic character of the two reservoirs has remained distinct.

Morgan (1971) suggested that the plumes provide the main driving force for plate movement, primarily because most of the plumes are located at or near ridges or triple junctions of ridges, but it might be thought that the plumes merely "pin" the location of the ridges without actually driving the plates. Sun and Hanson (1975) suggested that the oceanic islands are derived from an unspecified depth in a nonconvecting lower mantle. One might explain the mechanism for this by assuming locally enriched, self-heating regions in the lower mantle. It seems difficult to explain long-

lived volcanism (Hawaii-type) in this way, simply because the processes of upward intrusion of such enriched material would remove the heat source. Alternatively, the lower mantle might convect separately, perhaps partly in response to heating from the core. Heating from the base would provide a mechanism for localizing the upward flow (Parmentier *et al.*, 1975) and thereby generating long-lived plumes. Whether the energy source for such a mechanism could be the long-lived isotope ^{40}K in the core has been the subject of considerable speculation and discussion, and is beyond the scope of this contribution.

It is not particularly difficult to construct a two-layer model of this type that satisfies the kinematics of plate tectonics. In fact Morgan's model is quite adequate with the two exceptions mentioned above: (1) the plumes cannot both be stationary with respect to one another and remain near ridges and triple junctions for significant lengths of time, and (2) the upper mantle must convect in such a way that the bulk of its mass remains isolated from the lower mantle. Because subducted plates descend to depths of at least 700 km, the upper mantle convection system must be at least that thick. Plumes can rise through this convecting upper mantle and may be instrumental in pinning the location of accreting plate boundaries. The lower mantle remains less depleted than the upper mantle because a much smaller portion ascends sufficiently close to the surface for the material to be fractionated by the segregation and withdrawal of melt. The upper mantle is depleted by repeated withdrawal of melt and partially replenished by plume additions from the deeper mantle.

A major unsolved problem in this connection is the relatively modest degree of depletion (see also Hanson, 1977). Certainly, a differentiation process of partial melting and subsequent complete removal of the melt would produce a

much more depleted residue than is inferred for the actual source mantle of the midocean ridges. This problem is common to all mantle models discussed in this paper. Perhaps the answer lies in the partial retention of melt, combined with the above-mentioned replenishment.

One feature of midocean ridges, which is much more easily accounted for by broad upwelling of the asthenosphere rather than the rise of thin sheets from the deep mantle, is the occurrence of jumps in the location of ridges, such as have evidently occurred near the Galápagos Islands (Hey and Vogt, 1977). Such jumps would occur in response to the geometric requirements of rigid plates and are accommodated by broad upwelling from underneath. During such a jump, the locus of oceanic island volcanism may be shifted from one side of the ridge crest to the opposite side. This has evidently happened to the Ninetyeast Ridge volcanism in the Indian Ocean, where the fossil trace of volcanism is to the north of the ridge but present-day volcanism is located to the south on Kerguelen (see Whitford and Duncan, this Report). Thus, it seems that although there is a broad connection between hot spots and ridges, their lateral motions are not completely coupled but are locally independent. This local independence is accommodated in the plume model by the opening and passive filling of a new break in the plate surface. In the alternative model (IIIA), special pleading seems to be needed to explain why the ascending sheet should undergo sudden lateral shifts while the asthenospheric hot spot remains quasi-stationary.

The most serious objection to model IIIB is derived from the isotopic compositions of island-arc basalts. The Sr and Pb isotopic compositions of these rocks are almost invariably more radiogenic than are typical midocean ridge basalts. Yet, island-arc volcanism is so closely associated with plate subduction

that there can be little doubt that the source of these rocks lies in the upper mantle, which according to the model should be as unradiogenic as the mid-ocean ridge basalts.

Other geochemical indicators are ambiguous. For example, rare earth abundance patterns of some island-arc tholeiites do show the light rare earth depletion characteristic of midocean ridge basalts. This is also true for other incompatible-element abundances. The depleted character of island-arc basalts has also been stressed by Green (1973). Recently, Nd isotopic data have been published that indicate that the Sr isotopic data may be misleading in this case. $^{143}\text{Nd}/^{144}\text{Nd}$ histograms published by De Paolo and Wasserburg (1977) are somewhat inconclusive, with island-arc data generally being intermediate between midocean ridge and ocean island basalts. However, Hawkesworth *et al.* (1977) compared both Nd and Sr isotopes from Scotia Rise and the nearby South Sandwich Islands (island arc). The $^{87}\text{Sr}/^{86}\text{Sr}$ ratios of island-arc rocks were systematically and substantially higher than those from the rise, but the $^{143}\text{Nd}/^{144}\text{Nd}$ ratios from the two environments were identical within the analytical error.

One possible interpretation of the island-arc isotopic compositions is that they do not primarily reflect the composition of the upper mantle but that of the subducted crust, either through direct melting or volatile transfer. The subducted oceanic crust will consist in part of altered basaltic rocks. Interaction with sea water will tend to increase $^{87}\text{Sr}/^{86}\text{Sr}$ of the rock but will not affect the Nd isotopic composition significantly because of the exceedingly low rare earth concentration of sea water (O'Nions *et al.*, 1977). Involvement of crustal material in island-arc volcanics has recently been demonstrated using oxygen and Sr isotopes (Magaritz *et al.*, 1978), but much more systematic study using Sr, Nd, Pb, and O isotopes is needed to solve

the problem of the island-arc source material in general.

The other objection to the plume model is based on fluid dynamic arguments, which state that plumes are unstable in an internally heated medium, although they can be stable in a base-heated medium with a viscosity that depends on temperature and pressure (Parmentier *et al.*, 1975). This objection seems rather weak in view of the low abundances of radioactive isotopes in the source of mid-ocean ridge basalts. The conclusion of O'Nions *et al.* (1978) that the inferred heat production is insufficient to account for the observed heat flow implies that base heating is necessary for at least some portions of the mantle.

Base heating of the lower mantle by the core has received indirect support from the observations of lateral inhomogeneities in the lowermost mantle (see Snoke and Sacks, *Year Book* 75, pp. 233–239), which can be interpreted as small convection cells of about 150-km diameter. The energy source for core heating might be ^{40}K dissolved in the metallic phase (e.g., Bukowski, 1976). K and Rb removal from the mantle during core formation has also been suggested (Vidal and Dosso, 1978; Hurst, 1978) to explain the early Rb depletion in the mantle relative to chondrites.

A final objection to model IIIB lies in the heterogeneity of the island basalts. This means either that the lower mantle source reservoir is internally more heterogeneous than the upper mantle reservoir or that mixing occurs during the ascent of the plumes.

Summary of the Two-Layer Models

The two-layer model with an enriched asthenosphere is consistent with the Sr isotopic compositions of island arcs and is preferred by those who believe that the history of mantle processes has been one of upward enrichment of radioactive isotopes, which is qualitatively compara-

ble to that seen in the crust. However, several features of oceanic volcanic rocks are difficult to reconcile with such a model. These are the preferred location of oceanic islands near triple junctions and ocean ridges, the long-lived isotopic uniformity of some of the island chains despite considerable isotopic diversity of the islands overall, and the somewhat peculiar kinematic constraints on deep-mantle convection. The constraints are (1) the ascent of thin sheets (< 200 km thick), which are dissected by numerous transform faults with offsets up to several hundred kilometers, (2) the lateral movement with little or no viscous drag on the asthenosphere so that the asthenosphere can somehow continuously supply magma to the triple junctions and the on-ridge islands, and (3) the long-term protection of the asthenosphere from rehomogenizing with deep mantle material despite the constantly changing size of the convection cells ascending from and descending to the deep mantle.

The alternative two-layer model, with a depleted asthenosphere producing mid-ocean ridge basalts and the lower mantle producing oceanic islands, is consistent with isotopic data from oceanic basalts, and there is less difficulty in constructing an explicit model that is consistent with the kinematic constraints of plate movement and island locations. The isotopic composition of Sr and Pb from island-arc volcanics is in apparent conflict with this interpretation, but the relevance of these data is at present open to question because the island-arc Sr and Pb may be derived in part from subducted crust.

Future Research

Geochemical investigation has shown unequivocally that the mantle is isotopically heterogeneous, and that this state has existed for a significant portion of the age of the earth. Almost as firm is the conclusion that the scale of at least some of this heterogeneity is very large—hundreds of kilometers or more. The

future contribution of geochemical research to a more detailed knowledge of mantle structure will most likely be in four different fields: (1) theoretical and experimental investigation of the core composition with emphasis on the possible role of potassium as an energy source, (2) further investigation of the kinetics of melting for a more definitive assessment of model I, (3) more extensive study of the role of seawater and sediment contamination in volcanic rocks, and (4) isotopic “mapping” of ocean floor and ocean islands. Such mapping should give much more detailed information about the ages and isotopic uniformity of island and seamount chains and about the possible distinction between “hot lines” and “hot spots.” With very few exceptions (such as Iceland and Hawaii), the oceanic islands have been studied geochemically and petrologically only in the most cursory fashion. Thus, one is frequently forced to assume that a handful of isotopic measurements yield results that are representative for an entire group of islands. The same is true for most of the major ocean basins. Clearly, both the islands and the ocean floor hold important clues about the compositional structure of the mantle and deserve much more detailed study.

A fifth promising area consists of much more detailed studies of the chemistry of mantle inclusions in oceanic basalts. Isotopic analyses of these inclusions have shown that they are xenoliths rather than cognate. The xenoliths may be expected to contain information on the composition of the lithosphere. Thus, if lower-lithospheric xenoliths could be shown to have oceanic island-type isotope ratios, this result would be evidence in favor of model IIIA. On the other hand, if oceanic mantle xenoliths were found consistently to resemble MOR basalts in their isotopic composition, one would have to conclude that the entire lithosphere consists of depleted material.

This would support model IIIB if one accepts the additional assumption that at least the lower part of the lithosphere is formed by accretion ("freezing out") from the asthenosphere.

References

- Allègre, C. J., and Y. Bottinga, The rising deep crust: an alternative to the hot spot model, *EOS*, 58, 535, 1977.
- Anderson, D. L., Chemical plumes in the mantle, *Geol. Soc. Amer. Bull.*, 86, 1593–1600, 1975.
- Atwater, T., Implications of plate tectonics for Cenozoic tectonic evolution of western North America, *Geol. Soc. Amer. Bull.*, 81, 3513, 1970.
- Beswick, A. E., and I. S. E. Carmichael, Nd isotope variations in basic magmas: a disequilibrium melting model, *Geol. Soc. Amer., Abstracts w. Progr.* 9, 896, 1977.
- Boyd, F. R., and R. H. McCallister, Densities of fertile and sterile garnet peridotites, *Geophys. Res. Lett.*, 3, 509–512, 1976.
- Brooks, C., S. R. Hart, A. W. Hofmann, and D. E. James, Rb-Sr mantle isochrons from oceanic regions, *Earth Planet. Sci. Lett.*, 32, 51–61, 1976a.
- Brooks, C., D. E. James, and S. R. Hart, Ancient lithosphere: its role in young continental volcanism, *Science*, 193, 1086–1094, 1976b.
- Bukowski, M.-S. T., The effect of pressure on the physics and chemistry of potassium, *Geophys. Res. Lett.*, 3, 491–494, 1976.
- Carlson, R. W., J. D. Macdougall, and G. W. Lugmair, Differential Sm/Nd evolution in oceanic basalts, *Geophys. Res. Lett.*, 5, 229–232, 1978.
- Church, S. E., and M. Tatsumoto, Lead isotopic relations in oceanic ridge basalts from the Juan de Fuca—Gorda Ridge area, N. E. Pacific Ocean, *Contrib. Mineral. Petrol.*, 53, 253, 1975.
- Clague, D. A., B. Dalrymple, and R. Moberly, Petrography and K-Ar ages of dredged volcanic rocks from the western Hawaiian Ridge and the southern Emperor seamount chain, *Geol. Soc. Amer. Bull.*, 86, 991–998, 1975.
- DePaolo, D. J., and G. J. Wasserburg, Nd isotopic variations and petrogenetic models, *Geophys. Res. Lett.*, 3, 249–252, 1976a.
- DePaolo, D. J. and G. J. Wasserburg, Inferences about magma sources and mantle structure from variations of $^{143}\text{Nd}/^{144}\text{Nd}$, *Geophys. Res. Lett.*, 3, 743–746, 1976b.
- DePaolo, D. J., and G. J. Wasserburg, The sources of island arcs as indicated by Nd and Sr isotopic studies, *Geophys. Res. Lett.*, 4, 465–468, 1977.
- Duncan, R. A. Geochronology of basalts from the Ninetyeast Ridge and continental dispersion in the eastern Indian Ocean, *J. Volcanol. Geotherm. Res.*, in press, 1978.
- Duncan, R. A., and W. Compston, Sr-isotopic evidence for an old mantle source region for French Polynesian volcanism, *Geology*, 4, 728–732, 1976.
- Flower, M. F. J., H.-U. Schmicke, and R. N. Thompson, Phlogopite stability and the $^{87}\text{Sr}/^{86}\text{Sr}$ step in basalts along the Reykjanes Ridge, *Nature*, 254, 404–406, 1975.
- Gast, P. W., Limitations on the composition of the upper mantle, *Geophys. Res.*, 65, 1287–1297, 1960.
- Gast, P. W., Trace element fractionation and the origin of tholeiitic and alkaline magma types, *Geochim. Cosmochim. Acta*, 32, 1057–1086, 1968.
- Gast, P. W., The isotopic composition of lead from St. Helena and Ascension islands, *Earth Planet. Sci. Lett.*, 5, 353–359, 1969.
- Gonzales-Ferran, O., U. G. Cordani, and M. Halpern, Potassium-argon ages and $^{87}\text{Sr}/^{86}\text{Sr}$ ratios of volcanic rocks from Easter Island, *IAVCEI-Symposium Internacional de Volcanologia. Problemas Volvanologicos, Andinos y Antarticos*, Santiago, Chile, 9–14 September, 1974.

- Green, D. H., Experimental melting studies on a model upper mantle composition at high pressure under water-saturated conditions, *Earth Planet. Sci. Lett.*, 19, 37–53, 1973.
- Green, D. H., and R. C. Liebermann, Phase equilibria and elastic properties of a pyrolite model for the oceanic upper mantle, *Tectonophysics*, 32, 61–92, 1976.
- Green, D. H., and A. E. Ringwood, The genesis of basaltic magmas, *Contrib. Mineral. Petrol.*, 15, 103–190, 1967.
- Hanson, G. N., Evolution of the sub-oceanic mantle, *J. Geol. Soc. (London)*, 134, Pt. 2, 235–254, 1977.
- Hart, S. R., W. E. Glassley, and D. E. Karig, Basalts and sea floor spreading behind the Mariana island arc, *Earth Planet Sci. Lett.*, 15, 12–18, 1972.
- Hart, S. R., J.-G. Schilling, and J. L. Powell, Basalts from Iceland and along the Reykjanes Ridge: Sr isotope geochemistry, *Nature Physical Science*, 246, No. 155, 104–107, 1973.
- Hawkesworth, C. J., R. K. O'Nions, R. J. Pankhurst, P. J. Hamilton, and N. M. Evensen, A geochemical study of island-arc and back-arc tholeiites from the Scotia Sea, *Earth Planet Sci. Lett.*, 36, 253–262, 1977.
- Hedge, C. E., Strontium isotopes in basalts from the Pacific Ocean basin, *Earth Planet Sci. Lett.*, 38, 88–94, 1978.
- Hey, R., and P. Vogt, Spreading center jump and subaxial asthenosphere flow near the Galápagos hotspot, *Tectonophysics*, 37, 41–52, 1977.
- Hofmann, A. W., and S. R. Hart, An assessment of local and regional isotopic equilibrium in the mantle, *Earth Planet Sci. Lett.*, 38, 44–62, 1978.
- Hurst, R. W., Sr evolution in the West Greenland–Labrador craton: a model for early Rb depletion in the mantle, *Geochim. Cosmochim. Acta*, 42, 39–44, 1978.
- Ito, L., Magma genesis in a dynamic mantle, in *Genesis of Metalliferous Ore Deposits in Japan and East Asia*, H. Imai, ed., Tokyo Univ. Press, Tokyo, 1977.
- Kay, R. W., and P. W. Gast, The rare earth content and origin of alkali-rich basalts, *J. Geol.*, 81, 653–682, 1973.
- Magaritz, M., D. J. Whitford, and D. E. James, Oxygen isotopes and the origin of high- $^{87}\text{Sr}/^{86}\text{Sr}$ andesites, *Earth Planet Sci. Lett.*, (in press), 1978.
- McKenzie, D., and N. Weiss, Speculations on the thermal and tectonic history of the earth, *Geophys. J. Roy. Astron. Soc.*, 42, 131–174, 1975.
- Molnar, P., and T. Atwater, Relative motion of hot spots in the mantle, *Nature*, 246, 288–291, 1973.
- Morgan, W. J., Convection plumes in the lower mantle, *Nature*, 230, 42–43, 1971.
- Morgan, W. J., Plate motions and deep mantle convection, *Geol. Soc. Amer., Memoir* 132, 7–22, 1972.
- Nelson, D. O., and E. J. Dasch, Disequilibrium of strontium isotopes between mineral phases of parental rocks during magma-genesis—a discussion, *J. Volc. Geothermal Res.*, 1, 183–191, 1976.
- O'Hara, M. J., Is there an Icelandic mantle plume?, *Nature*, 253, 708–710, 1975.
- O'Nions, R. K., N. M. Evensen, P. J. Hamilton, and S. R. Carter, Melting of the mantle past and present: isotope and trace element evidence, *Phil. Trans. Roy. Soc. London Ser. A.*, 258, 547–559, 1978.
- O'Nions, R. K., P. J. Hamilton, and N. M. Evensen, Variations in $^{143}\text{Nd}/^{144}\text{Nd}$ and $^{87}\text{Sr}/^{86}\text{Sr}$ ratios in oceanic basalts, *Earth Planet. Sci. Lett.*, 34, 13–22, 1977.
- O'Nions, R. K., and R. J. Pankhurst, Petrogenetic significance of isotope and trace element variations in volcanic rocks from the Mid-Atlantic, *Petrology*, 15, 603–634, 1974.
- O'Nions, R. K., R. J. Pankhurst, and K. Grönvold, Nature and development of basalt magma sources beneath Iceland

- and the Reykjanes Ridge, *Petrology*, 17, 315–338, 1976.
- Oversby, V. M., Genetic relations among the volcanic rocks of Réunion: chemical and lead isotopic evidence, *Geochim. Cosmochim. Acta*, 36, 1167–1179, 1972.
- Parmentier, E. M., D. L. Turcotte, and K. E. Torrance, Numerical experiments on the structure of mantle plumes. *J. Geophys. Res.*, 80, 4417–4424, 1975.
- Richard, P., N. Shimizu, and C. J. Allègre, $^{143}\text{Nd}/^{146}\text{Nd}$, a natural tracer: an application to oceanic basalts, *Earth. Planet. Sci. Lett.*, 31, 269–278, 1976.
- Richter, F. M., and B. Parsons, On the interaction of two scales of convection in the mantle, *J. Geophys. Res.*, 80, 2529–2541, 1975.
- Schilling, J.-G., Iceland mantle plume: geochemical evidence along Reykjanes Ridge, *Nature*, 242, 565–571, 1973.
- Schilling, J.-G., Faeroe-Iceland plume: rare-earth evidence, *Earth Planet. Sci. Lett.*, 24, 1–14, 1974.
- Schilling, J.-G., Azores mantle blob: rare-earth evidence. *Earth Planet. Sci. Lett.*, 25, 103–115, 1975.
- Shaw, H. R., and E. D. Jackson, Linear island chains in the Pacific: result of thermal plumes or gravitational anchors?, *J. Geophys. Res.*, 78, 8634–8652, 1973.
- Sigvaldson, G. E., Basalts from the centre of the assumed Icelandic mantle plume, *Petrol*, 15, 497–524, 1974.
- Sleep, N. H., Segregation of magma from a mostly crystalline mush, *Geol. Soc. Amer. Bull.*, 85, 1225–1232, 1974.
- Snoke, J. A., and I. S. Sacks, A model for laterally heterogeneous velocity structure at the base of the mantle, *Carnegie Inst. Wash. Year Book* 75, pp. 233–239, 1976.
- Solomon, S. C., and N. H. Sleep, Some simple physical models for absolute plate motions, *J. Geophys. Res.*, 79, 2557–2567, 1974.
- Sun, S. S., Lead isotope studies of young volcanic rocks from oceanic islands, mid-ocean ridges, and island arcs. Ph. D. Dissertation, Columbia Univ., New York, 1973.
- Sun, S. S., and G. N. Hanson, Evolution of the mantle: geochemical evidence from alkali basalt, *Geology*, 3, 297–302, 1975.
- Sun, S. S., and B. Jahn, Lead and strontium isotopes in post-glacial basalts from Iceland, *Nature*, 255, 527–530, 1975.
- Sun, S. S., M. Tatsumoto, and J.-G. Schilling, Mantle mixing along the Reykjanes Ridge axis: lead isotopic evidence, *Science*, 190, 143–147, 1975.
- Tatsumoto, M., Isotopic composition of lead in oceanic basalt and its implication to mantle evolution, *Earth Planet. Sci. Lett.*, 38, 63–87, 1978.
- Turcotte, D. L., and E. R. Oxburgh, Mid-plate tectonics, *Nature*, 244, 337–339, 1973.
- Turcotte, D. L., and E. R. Oxburgh, Stress accumulation in the lithosphere, *Tectonophysics*, 35, 183–199, 1976.
- Turcotte, D. L., and E. R. Oxburgh, Intra-plate volcanism, *Phil. Trans. Roy. Soc. London Ser. A.*, 288, 561–579, 1978.
- Vidal, P., and L. Dosso, Core formation: catastrophic or continuous? Sr and Pb isotope geochemistry constraints, *Geophys. Res. Lett.*, 5, 169–172, 1978.
- White, W. M., Geochemistry of igneous rocks from the central North Atlantic: the Azores and the Mid-Atlantic Ridge, Ph.D. Dissertation, Univ. of Rhode Island, Kingston, R.I., 1977.
- White, W. M., and J.-G. Schilling, The nature and origin of geochemical variation of mid-Atlantic ridge basalts from the central North Atlantic, *Geochim. Cosmochim. Acta*, in press, 1978.
- White, W. M., J.-G. Schilling, and S. R. Hart, Evidence for the Azores mantle plume from strontium isotope geochemistry of the Central North Atlantic, *Nature*, 263, 659–663, 1976.
- Yoder, H. S., Jr., *Generation of Basaltic*

Magma, Nat. Acad. Sci., Washington, D.C., 1976.

Yuen, D. A., and G. Schubert, Mantle plumes: a boundary layer approach for Newtonian and non-Newtonian temperature-dependent rheologies, *J. Geophys. Res.*, 81, 2499–2510, 1976.

ON THE ORIGIN OF THE CALC-ALKALINE
VOLCANICS OF THE CENTRAL ANDES:
A REVISED INTERPRETATION

David E. James

Introduction

The nature and origin of the calc-alkaline rocks of the central Andean volcanic arc have been subjects of interest and controversy in recent years. Earlier investigations have revealed that while the calc-alkaline rocks of southern Peru and northern Chile are similar in most respects to calc-alkaline rocks of oceanic island arcs, they differ in certain important ways:

1. Andesitic rocks of the central Andes have significantly higher $^{87}\text{Sr}/^{86}\text{Sr}$ ratios (0.705 to 0.708) than do comparable island-arc volcanics (typically, 0.7035 to 0.704).

2. At any given depth to the Benioff zone, Andean volcanics tend to have higher K, Rb, Sr, Ba, and light rare earth element (LREE) concentrations than those observed in comparable island-arc volcanics.

Over the past several years a variety of hypotheses have appeared in the literature to explain the observed differences between Andean and island-arc volcanics:

1. Derivation of the magma from the lower Andean crust rather than from the subduction zone (Pichler and Zeil, 1972).

2. Crustal contamination of a mantle-derived or a subduction-zone-derived magma (Klerkx *et al.*, 1977).

3. Magma derivation from the ancient lithospheric mantle of the South American craton—mantle which could be sig-

nificantly enriched in radiogenic Sr relative to asthenospheric mantle (James *et al.*, 1976).

4. Partial melting of subducted oceanic crust with subsequent rise of magma into overlying mantle to yield andesitic magma (Thorpe *et al.*, 1976). This hypothesis was proposed earlier for island arcs in general by Nicholls and Ringwood (1973).

The genesis of andesite has proven to be one of the more controversial and intractable problems in petrology (e.g., Ringwood, 1975, pp. 245–277). The problem is especially important because it bears upon such major questions as the evolution of continental crust and the possible magmatic recycling of continental material that has been eroded into the ocean basins (Armstrong, 1971). The question as to whether the differences between Andean and island-arc lavas are due to mantle (including subduction zone) processes or to crustal contamination is thus of broad general importance. In particular, if the isotopic and trace element compositional differences between Andean volcanics and those of the island arcs can plausibly be attributed to crustal contamination of otherwise typical calc-alkaline magmas on their way to the surface, those differences are of no value in contributing to our understanding of subduction zone petrogenetic processes; indeed, crustal contamination would effectively mask any such information that might be contained in the original magma compositions. If, on the other hand, the isotopic and trace element character of the Andean lavas can plausibly be shown to reflect the compositional nature of the magmatic source material, then those isotopic and trace element compositions may be of fundamental significance in elucidating petrogenetic processes in subduction zones, particularly as they involve subducted sedimentary material (continental or oceanic).

This paper reports on efforts to syn-

thesize Sr isotopic and trace element data already available for the andesitic volcanics of southern Peru with new analyses of O isotopic compositions in the same rock samples. The results of that synthesis show that the combined data, especially those of oxygen, preclude large-scale crustal contamination as a cause of the observed differences between Andean and island-arc volcanics. The data also demonstrate that the hypotheses of James *et al.* (1976) and Thorpe *et al.* (1976)—hypotheses 3 and 4 above—cannot be wholly correct either. In particular, as reported earlier (Magaritz *et al.*, 1978), Andean volcanics exhibit slightly higher $\delta^{18}\text{O}$ values than do many volcanics of island arcs or other volcanics of known mantle source, thus implying probable sialic involvement at some stage in the genesis of lavas.

The model considered here for the origin of Andean andesite is a variation on the generalized model of calc-alkaline magma genesis proposed first by Nicholls and Ringwood (1973). In that model, subducted oceanic crust undergoes partial melting, rises into and reacts with the overlying mantle to produce melts of calc-alkaline composition (Nicholls, 1975). Studies of a number of volcanic arcs have elaborated on that model by considering melting of oceanic and continental sediments as well as oceanic basaltic crust (e.g., Kay *et al.*, 1978; Magaritz *et al.*, 1978; Kay, 1977; Whitford *et al.*, 1977; Thorpe *et al.*, 1976). Earlier studies, including a quantitative analysis by Gill (1974) demonstrated that derivation of andesitic magma *solely* from subducted oceanic crust cannot be modeled quantitatively for major and minor elements without an appeal to special conditions and processes. Gill concluded, however, that the three-stage model proposed by Nicholls and Ringwood might provide a plausible mechanism for andesite genesis. In any event, it appears that some involvement of subducted material is required to explain

isotopic and trace element compositions of calc-alkaline lavas. Moreover, it is clear that at least for some island arcs (e.g., Aleutians, Banda arc) a significant component of subducted sialic material is necessary to explain isotopic and trace element compositions of the lavas (Armstrong, 1968, 1971; Kay *et al.*, 1978; Whitford *et al.*, 1977; Magaritz *et al.*, 1978).

The isotopic and trace element composition of the central Andean volcanics can plausibly be explained by partial melting at depth of subducted graywacke and altered oceanic basalt, and subsequent reaction of that melt with overlying mantle material to yield andesitic magma. Development of that melting model is heavily dependent upon isotopic compositions which “see through” both partial melting and differentiation processes. Thus, when the isotopic data are combined with other geochemical and geophysical data, the constraints are sufficiently severe that only a rather narrow class of models survives. The conclusion that partial melting of continentally derived sediments is an important part of andesite genesis beneath the central Andes leads to the further conclusion that continental material is being recycled through the subduction zone. Such recycling provides one possible explanation for the differences between continental-arc and island-arc volcanics, for generally only in the continental arcs is mature sialic material available for subduction.

Tectonic Setting and Evidence for Subduction of Continental Sediments

The central Andean orogen is composed of three principal provinces: the western cordillera, comprising the calc-alkaline volcanic arc and situated 150–175 km above the Benioff zone; the eastern cordillera, consisting of crumpled Paleozoic marine sedimentary rocks which have been intruded by magmas of Mesozoic and Cenozoic age; and the

altiplano, a vast intermontaine plateau separating the western and eastern cordilleras. The altiplano stands at an elevation of about 4 km and may be underlain by up to 30 km of continental and marine sedimentary rocks (James, 1971a).

The area of study for this paper is shown in Fig. 104. It lies entirely within the western cordillera of southern Peru. The volcanics are Pliocene to Quaternary in age and constitute the major extrusive units exposed in the region. The central Andes of southern Peru and northern Chile are characterized by abundant Quaternary volcanism. The central Andean volcanic province is bounded both north and south by long volcanically inactive belts that extend as far as Ecuador to the north and southern Chile to the south. The Quaternary volcanics of both Ecuador and southern Chile are similar in most respects to island-arc volcanics and are notably distinct from those of

the central Andes in that they do not exhibit unusually high $^{87}\text{Sr}/^{86}\text{Sr}$ ratios.

Depths to the Benioff zone beneath the western cordillera are shown in plan view in Fig. 104 and in cross section in Fig. 105. In the area of study, as well as in northern Chile, the Benioff zone is well defined, dipping at an angle of about 30° . The crust beneath the western cordillera is extraordinarily thick, attaining about 75 km at its greatest thickness, some 40 km thicker than "normal" continental crust at sea level (James, 1971b). Despite the great crustal thickness, it can be seen in Fig. 105 that the base of the crust beneath the volcanic arc is many tens of kilometers from the subduction plane, a fact that raises serious difficulties for the hypothesis proposed by Klerkx *et al.* (1977) in which sialic material is supposedly added to the base of the crust along the subduction plane. Moreover, the continental lithosphere extends nearly to the subduction zone in

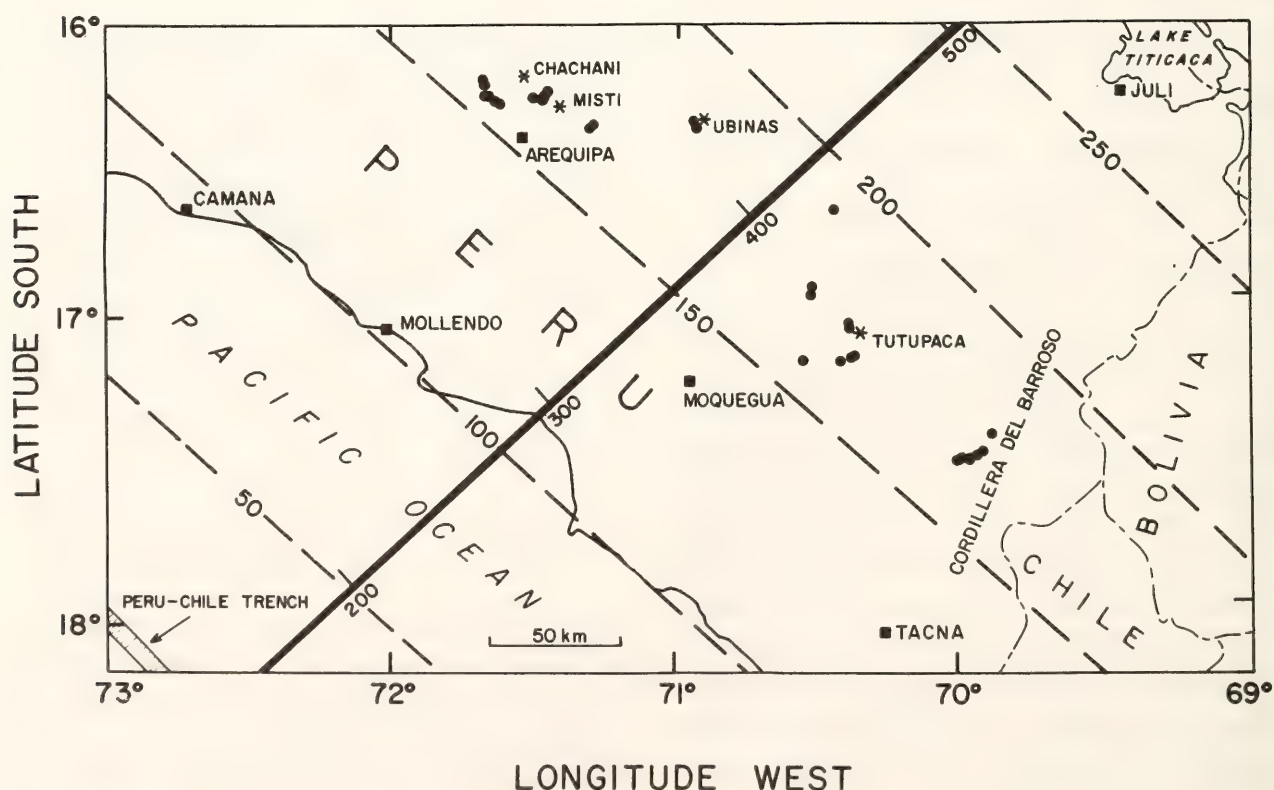


Fig. 104. Map of southern Peru showing sample localities. Kilometer markings along cross-section line (solid black) are keyed to those of Fig. 105. Contours indicating depth to Benioff zone are shown as dashed lines.

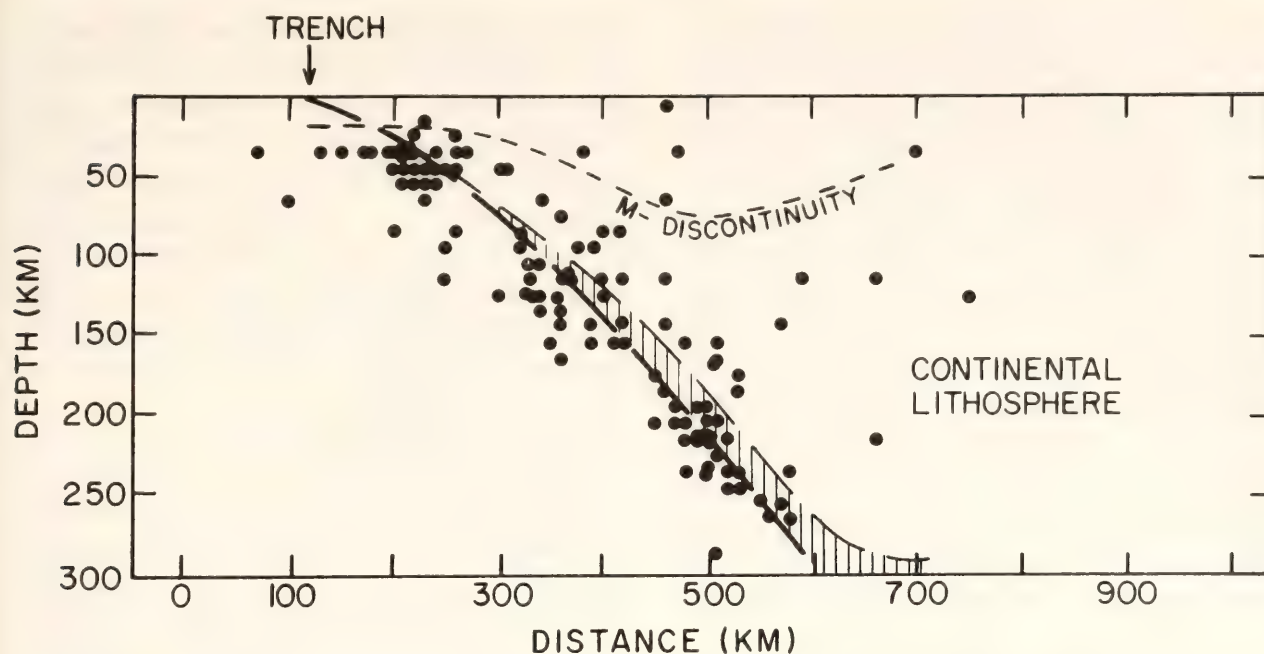


Fig. 105. Schematic cross section through southern Peru showing seismicity and crustal structure. Line of the cross section is perpendicular to the trench and corresponds to the solid black line shown in Fig. 104. Vertical hatching signifies zone of high attenuation sandwiched between the upper boundary of the downgoing plate and the overlying continental lithosphere.

the region of southern Peru (Sacks, 1977).

Subduction rates beneath southern Peru are estimated at about 10 cm/yr (Minster *et al.*, 1974). Despite the comparatively rapid rate of subduction, the Peru-Chile trench off southern Peru is only about 6–7 km deep. Kulm *et al.* (1977) have observed that the morphology and structure of the trench varies with latitude. According to their interpretation, the trench near southern Peru appears to be in an area of transition from accretion to consumption—that is, continental sediments are accumulating on the walls of the trench in the more northerly part of the area but are found in decreasing thickness to the south. Kulm *et al.* interpret this variation as due to a change in the subduction process, with sediments being actively subducted in the south but not in the north. That interpretation is obscured, however, by the fact that although annual rainfall along the coastal regions is directly correlated with the amount of sedimentary fill in the trench (Fisher and Raitt,

1962), those parts of the trench devoid of sediments lie offshore the Atacama Desert, the driest in the world. It may be, therefore, that the *relative* abundance of sedimentary deposits indicates not so much the nature of the subduction process but only the degree to which sedimentary debris shed from the cordillera is being added to the trench.

Regardless of the reason for the latitudinal variation of sediment accumulation on the walls of the trench, it is clear that voluminous detritus, shed from the adjacent Andean volcanoplutonic province, must have been consumed in the trench. This conclusion seems a necessary consequence of the fact that the successive orogenic uplifts that have occurred episodically since late Triassic or early Jurassic time in southern Peru have resulted in the deep erosion of massive volumes of andesitic eruptives and dioritic-to-tonalitic intrusives. The immense volumes of detritus that must have been derived over time from the Andean orogen may in part be found underlying the altiplano, but comparable deposits

are not found to the west of the volcanic arc. Gilluly (1971) noted that offshore the Pacific coast of the United States sediments are less than one-sixth as voluminous as offshore the Atlantic coast, despite the roughly comparable areas tributary to the two regions. He concluded that large volumes of continentally derived sediments have been swept down the subduction zone. Off the west coast of southern Peru the situation is even more discrepant, and no significant sedimentary wedges have been found. From these observations, it appears very likely that continentally derived sediments are being continuously subducted.

Local geology and sample locations. The rocks collected for this study are from southern Peru, generally at elevations in excess of 3000 meters. Sample localities are shown in Fig. 104. The geology of the region has been described in detail elsewhere (LeFèvre, 1973; James *et al.*, 1976; James, 1971a), but a short summary is appropriate for the discussion that follows. I use the same geochemical volcanic groups used by James *et al.* (1976). According to that grouping the volcanics of southern Peru can be divided into the Barroso volcanics and the Arequipa volcanics. In addition, this study includes the Tutupaca volcanics, Ubina volcanics, and the Misti volcanics. The Barroso volcanics are Pliocene-to-Pleistocene in age (Wilson and Garcia, 1962), whereas the other volcanics are probably almost entirely Quaternary. The Tutupaca samples, as shown in Fig. 104, appear to lie within the region of the Barroso volcanics, but they are from a separate cone cutting through the older Barroso volcanics. The Ubina and Misti samples are from young, still active stratovolcanoes.

In general, the more northerly samples (Arequipa, Misti, and Ubina) appear to be slightly fresher petrographically than those from locations further south. This is consistent with water contents meas-

ured in some of the samples, which show the Arequipa volcanics to have 0.25–0.5% H₂O and the Barroso volcanics to have 0.4–0.8% H₂O. None of the samples studied show any appreciable petrographic evidence of alteration. Phenocrysts, almost entirely plagioclase, are clear and unaltered in almost all instances, although there are minor differences from sample to sample.

Analytical Techniques

Rock samples are prepared by removing all cracks, veins, and weathered surfaces, and then crushed, split several times, and finally pulverized in a chrome-steel shatter box. Plagioclase mineral separates are obtained by sieving a disk-milled fraction, washing in water and acetone, and then removing all ground-mass and mafic minerals using a Franz magnetic separator. Separates so obtained are nearly pure plagioclase, although if the sample contains quartz it too will be present. Whole rock powders were made up into fused disks for x-ray fluorescence analysis of Rb, Sr, Ba, and Ni. Estimated accuracy as judged by comparison with values obtained by isotope dilution analysis is $\pm 3\%$ for Rb and Sr and $\pm 15\%$ for Ba. Ni accuracy is estimated to be $\pm 10\%$ or better. REE analyses were done by isotope dilution and have been reported previously by Whitford (*Year Book* 76, pp. 840–844).

Sr isotopic ratios were measured on a computerized six-inch solid-source single-filament mass spectrometer. Analytical precision is at the 95% confidence level. All ratios are normalized to $^{86}\text{Sr}/^{88}\text{Sr} = 0.1194$ and an Eimer and Amend standard SrCO_3 value of 0.70800.

Oxygen isotope analyses were performed using the method of BrF_5 dissolution and collection, as described in detail by Clayton and Mayeda (1963). O isotope ratios were measured on a double-collector machine and corrected for the usual machine and isotope effects (Craig, 1957). Precision of measurement

at 1σ is about 0.02‰ and estimated overall accuracy is $\pm 0.1\%$. All of the apparatus for extraction and measurement of O isotopes is maintained by Drs. T. Hoering and D. Rumble at the Geophysical Laboratory.

Measured $\delta^{18}\text{O}$ values were standardized to an assumed CIT rose quartz standard value of +8.45‰ (Magaritz, oral communication). There is no universally accepted O isotope mineral standard and interlaboratory standards tend to differ by several tenths of a per mill. Consequently, NBS #28 white quartz standard was also run for comparison. If, as has been reported by some, that standard has a $\delta^{18}\text{O} = +10.00\%$, the values reported in this paper would be 0.4 to 0.5‰ higher and CIT rose quartz would have a value of +8.9‰.

Oxygen isotopic ratios are expressed relative to standard mean ocean water (SMOW) by the relationship:

$$\delta^{18}\text{O} (\%) = \left[\frac{(^{18}\text{O}/^{16}\text{O})_{\text{obs}} - (^{18}\text{O}/^{16}\text{O})_{\text{std}}}{(^{18}\text{O}/^{16}\text{O})_{\text{std}}} \right]$$

Weathering. Comparison of whole rock $\sigma^{18}\text{O}$ with those of plagioclase separates shows whole-rock values to be significantly higher in virtually every case (see Magaritz, *et al.*, 1978). This is a surprising result because the rocks are young volcanics exhibiting little or no petrographic evidence of alteration by weathering. Late-stage deuteric or hydrothermal alteration, as evidenced by veining or reaction rims around phenocrysts, is virtually absent. Rock samples with H_2O contents as low as 0.25% show high $\sigma^{18}\text{O}$ relative to their plagioclase phenocrysts.

Use of plagioclase phenocryst separates is motivated by two primary considerations: (1) plagioclase, which appears in large quantity in most of the volcanics, is virtually the only volumetrically significant phenocryst, and (2) feldspars tend to be closest in $\sigma^{18}\text{O}$

to the melt itself (Taylor, 1968, p. 26). Taylor (1968, p. 35) gives a mean $\sigma^{18}\text{O}$ for basaltic plagioclase of +6.2‰, whereas the average for unaltered basalt is +5.9‰. Average $\sigma^{18}\text{O}$ for unaltered andesite ranges between +5.9 and +6.3‰, and the plagioclase phenocrysts of those lavas should be close to or slightly higher than that value.

As volcanics show no evidence of hydrothermal alteration, only low-temperature processes such as isotopic exchange with ground water or weathering should be important. Results on diffusion of oxygen in feldspars (Giletti *et al.*, 1978) would seem to preclude significant low-temperature alteration of feldspar phenocrysts in late Cenozoic lavas. An extrapolation of their results to average surface temperature ($\sim 10^\circ\text{C}$) gives a diffusion coefficient for oxygen in feldspar of $\sim 10^{-28}$. That diffusion coefficient gives a characteristic distance,

$\chi = \sqrt{Dt}$ (Hofmann and Hart, 1978) [where χ = characteristic diffusion distance in cm, t = time in seconds, and D = diffusion coefficient in cm^2/sec] of 1.3×10^{-6} cm in 5×10^6 years. The grain diameter of the separated plagioclase is $1.0\text{--}1.5 \times 10^{-2}$ cm (100–150 mesh), or four orders of magnitude greater than the characteristic diffusion distance even for periods of 5 m.y. Most of the volcanics are much younger. From the above calculations, it is apparent that the plagioclase phenocrysts should remain effectively unequilibrated with meteoric water in any type of low-temperature process. This conclusion is supported by measurements which show no significant correlation of $\delta^{18}\text{O}$ with grain size of phenocrysts. The possibility that phenocrysts and matrix were not in isotopic equilibrium at the time of extrusion is unlikely in view of the fact that $^{87}\text{Sr}/^{86}\text{Sr}$ ratios are similar for both. In one instance, the $^{87}\text{Sr}/^{86}\text{Sr}$ of the plagioclase separate is distinctly higher than that of the whole rock, a discrepancy not yet explained. For that particular sample $\delta^{18}\text{O}$ of the

whole rock and plagioclase separate are virtually identical.

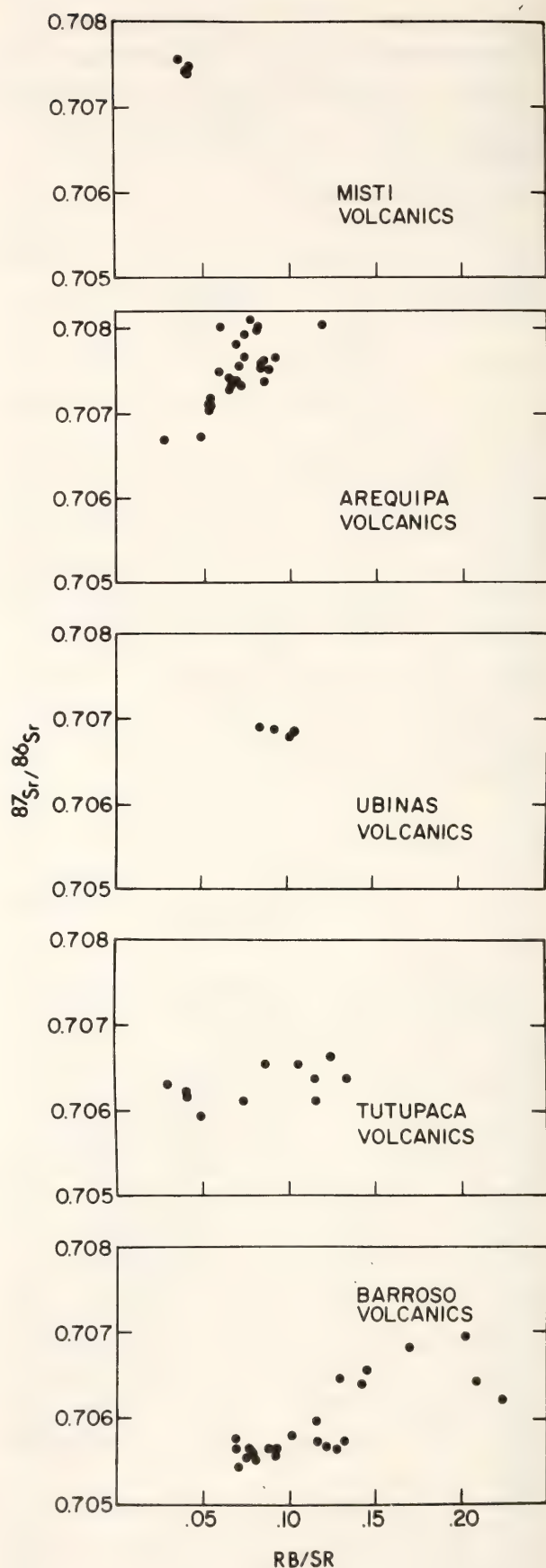
Analytical Results

Analytical results for Sr and O isotope ratios and for K, Rb, Sr, Ba, Cs, Ni, and REE are summarized in Figs. 106–111. The data are grouped by regional geochemical affinity into Barroso, Tutupaca, Ubinas, Arequipa, and Misti volcanics. Broad regional trends of SE to NW character are evident in both trace element and Sr isotopic compositions of the various volcanic groups. Within each volcanic group, however, distinct local geochemical trends are superimposed upon the regional variation. An important exception to both regional and local variations is the O isotopic composition of the lavas. Within the scatter of the data, $\delta^{18}\text{O}$ values exhibit neither regional nor local variations, although a small regional decrease in $\delta^{18}\text{O}$ with increasing $^{87}\text{Sr}/^{86}\text{Sr}$ is possible.

A summary compilation of regional and local geochemical variation is given in the form of end-member compositions in Table 24. Only the local variations for Arequipa and Barroso volcanics are included in Table 24, as those are the only volcanic groups for which a large data set is available.

Sr isotope data. All of the $^{87}\text{Sr}/^{86}\text{Sr}$ ratios reported here are significantly higher than those reported for “normal” oceanic island arc andesites of comparable major-element composition. It is that fact, of course, that has generated most of the controversy over the origin of Andean andesite. It is useful, therefore, to examine the observed variation in $^{87}\text{Sr}/^{86}\text{Sr}$ in terms of other trace element variations.

Sr isotope ratios for the five volcanic series studies are plotted against Rb/Sr ratios in Fig. 106. The Barroso, Tutupaca, and Arequipa volcanics define statistically significant pseudoisochrons of ~ 200–400 m.y. The Ubinas and Misti volcanics do not form sufficient spread



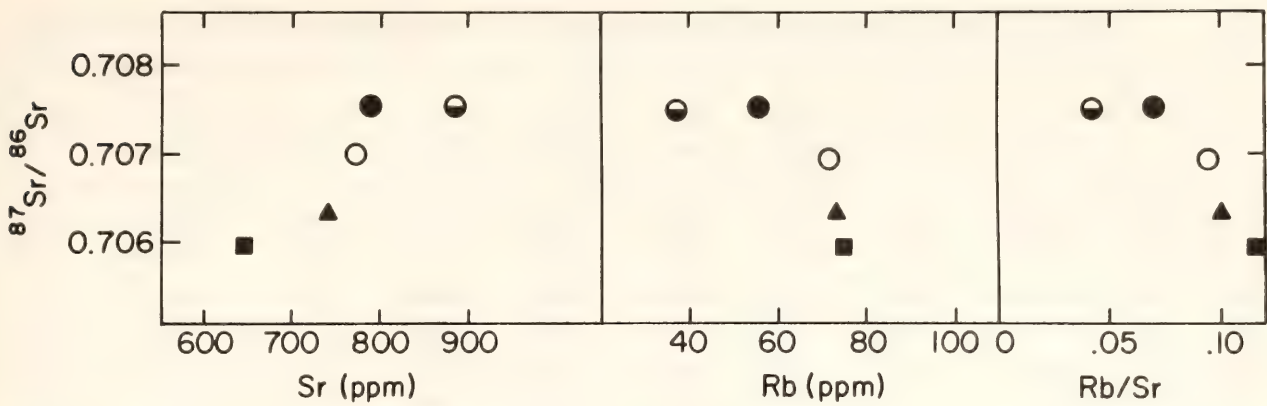


Fig. 107. Average $^{87}\text{Sr}/^{86}\text{Sr}$ ratios for each volcanic group versus average Sr, Rb, and Rb/Sr. Solid circle = Arequipa; semisolid circle = Misti; open circle = Ubinas; triangle = Tutupaca; square = Barroso.

in either Rb/Sr or $^{87}\text{Sr}/^{86}\text{Sr}$ to yield a pseudoisochron. The strong positive correlation between $^{87}\text{Sr}/^{86}\text{Sr}$ and Rb/Sr for the Barroso and Arequipa volcanics, as shown in an earlier paper (James *et al.*, 1976), has been significantly degraded by the inclusion of new data, although reasonably clear pseudoisochrons are still evident.

Since the earlier paper was written, substantially improved regional coverage reveals that there is a rather definite geochemical variation parallel to the arc along which $^{87}\text{Sr}/^{86}\text{Sr}$ ratios *increase* SE to NW and Rb/Sr ratios *decrease* (Sr increases and Rb decreases) producing an apparent negative regional pseudoisochron. That regional trend is shown in Fig. 107 where average $^{87}\text{Sr}/^{86}\text{Sr}$ ratios for each volcanic group are plotted against corresponding Sr, Rb, and Rb/Sr ratios.

The regional trend is in the opposite sense to the local trends within the three volcanic groups for which data are available—Barroso, Tutupaca, and Arequipa. Within those groups, *increasing* $^{87}\text{Sr}/^{86}\text{Sr}$ correlates with *decreasing* Sr and *increasing* Rb. Potash also increases locally with increasing $^{87}\text{Sr}/^{86}\text{Sr}$ but does not increase with increasing $^{87}\text{Sr}/^{86}\text{Sr}$ on a regional scale.

Oxygen isotope data. Average values for measured $\delta^{18}\text{O}$ for the volcanics groups studied are given in Table 24. All

of the $\delta^{18}\text{O}$ values measured for the volcanics of southern Peru are slightly higher than the range of $\delta^{18}\text{O}$ generally associated with volcanics of purely oceanic mantle origin ($+6.0 \pm 0.5\text{‰}$, Taylor, 1968), but they do overlap to some extent the $\delta^{18}\text{O}$ measured for calc-alkaline volcanics of island arcs, where $\delta^{18}\text{O}$ may be as high as $+8.0\text{‰}$ (Taylor, 1968).

Values of $\delta^{18}\text{O}$ for plagioclase phenocryst separates are plotted versus whole-rock $^{87}\text{Sr}/^{86}\text{Sr}$ in Fig. 108. The use of

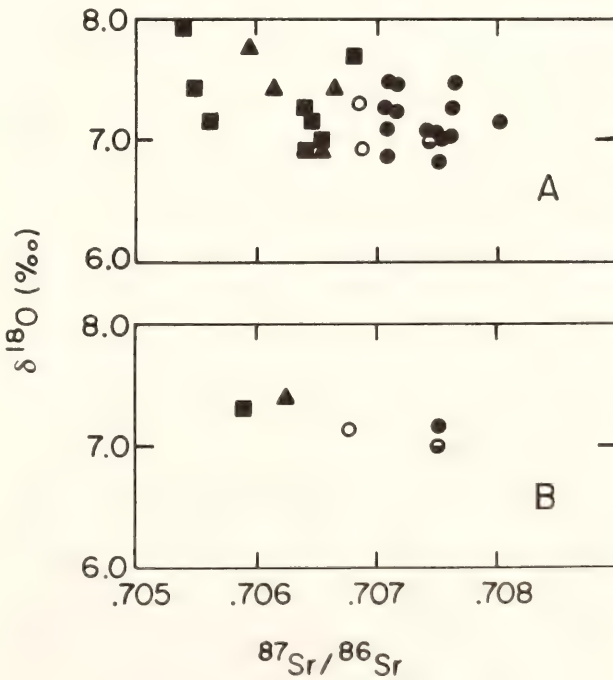


Fig. 108. $\delta^{18}\text{O}$ versus $^{87}\text{Sr}/^{86}\text{Sr}$, (A) for individual plagioclase separates, and (B) averaged by group. Symbols as in Fig. 107.

TABLE 24. End-Member Compositions of Arequipa and Barroso Volcanics and Average

	K (%)	Rb (ppm)	Sr (ppm)	Ba (ppm)	K/Rb	K/Ba	Rb/Sr	K/Sr
Barroso Volcanics	1.6	48	730	580	335	27.6	0.07	21.9
	2.7	108	530	970	250	27.8	0.20	50.9
Arequipa Volcanics	1.6	36	850	620	440	25.8	0.04	18.8
	2.6	79	640	1100	330	23.6	0.12	40.6
Barroso average	2.1	78	630	775	290	27.1	0.12	33.3
Arequipa average (end-pt. averages)	2.1	58	745	860	360	24.4	0.07	24.4
Sunda Arc Andesite	1.5	62	360	420	248	36	0.17	41.7
Franciscan								
Metagraywacke	1.3	60	200	400	217	32.5	0.3	65

whole-rock $^{87}\text{Sr}/^{86}\text{Sr}$ ratios is justified by the fact that there is generally little difference between those ratios and those of the plagioclase phenocrysts.

Measured $\delta^{18}\text{O}$ of the plagioclase separates lie mostly between $+7.0$ and $+7.5\%$. Average $\delta^{18}\text{O}$ is plotted versus average $^{87}\text{Sr}/^{86}\text{Sr}$ in Fig. 108 for the five volcanic groups studied. $\delta^{18}\text{O}$ values show no significant correlation with $^{87}\text{Sr}/^{86}\text{Sr}$, although in general the lower $\delta^{18}\text{O}$ values appear to be associated with higher $^{87}\text{Sr}/^{86}\text{Sr}$ ratios. That trend as well as the reduced scatter in $\delta^{18}\text{O}$ values for the more northerly (higher $^{87}\text{Sr}/^{86}\text{Sr}$) samples probably reflect the younger age and greater freshness of those samples. It is significant, however, that there is no increase in $\delta^{18}\text{O}$ with increasing $^{87}\text{Sr}/^{86}\text{Sr}$, as would be anticipated if the high $^{87}\text{Sr}/^{86}\text{Sr}$ ratios of the lavas were the result of crustal contamination of a mantle-derived magma.

Trace element and REE geochemistry. The most conspicuous aspect of trace element concentrations in the lavas of southern Peru is that in most instances they show a strong correlation with $^{87}\text{Sr}/^{86}\text{Sr}$ ratios. That correlation precludes simple differentiation processes (or those of partial melting) as the major cause of the trace elemental variations

observed. Because Sr isotopic ratios cannot change during differentiation, any variation in isotopic ratios and, by inference, any trace element variation that correlates with changing isotopic composition must be due either to source inhomogeneity or to contamination. It is therefore important to inquire as to the degree of correlation that exists between trace elements and Sr isotopes on both a regional and local level.

Elemental variations in K, Rb, Sr, Ba, $\text{K}_2\text{O}/(\text{K}_2\text{O}+\text{Na}_2\text{O})$ ("k"), and Ce/Yb within the Barroso and Arequipa volcanics are plotted versus $^{87}\text{Sr}/^{86}\text{Sr}$ in Fig. 109. All of these quantities show some correlation with $^{87}\text{Sr}/^{86}\text{Sr}$ ratio and some show remarkably consistent variations. It is thus all the more remarkable that $\delta^{18}\text{O}$ shows no such correlation (see Fig. 108).

It is noteworthy that of all the quantities plotted in Fig. 109, only Sr decreases with increasing $^{87}\text{Sr}/^{86}\text{Sr}$ within a given volcanic group. K, Rb, Ba, "k", and Ce/Yb increase with increasing $^{87}\text{Sr}/^{86}\text{Sr}$. Although it is possible that Sr has been removed by plagioclase fractionation, the general absence of an Eu anomaly (see Whitford, *Year Book* 76) seems to argue against that mechanism.

Trace element variations within the

Compositions of Sunda Arc Andesite* and Franciscan Metagraywacke†

$\frac{K_2O}{(K_2O+Na_2O)}$	Ce (ppm)	Yb (ppm)	$(Ce/Yb)_N$	Ni (ppm)	MgO (%)	SiO ₂ (%)	$^{87}Sr/^{86}Sr$	$\delta^{18}O$ (‰)
0.36	51	1.6	7.6	22	3.7	57	0.7055	+ 7.3
0.45	63	1.3	11.6	33	2.6	63	0.7068	
0.33	42	1.3	7.8	50	3.7	57	0.7071	+ 7.16
0.43	75	1.3	14	20	3.0	59	0.7080	
0.41	57	1.4	9.6	28	3.2	60	0.7062	+ 7.3
0.38	59	1.3	10.9	35	3.4	58	0.7076	+ 7.16
0.34	40.9	2.1	4.64	8	2.9	59.0		
0.31	80	2.8	6.8		2.6	68	0.706-0.710	+12.0

* Whitford, 1975a.
† Bailey *et al.*, 1964; Peterman *et al.*, 1967; Magaritz and Taylor, 1976.

Barroso and Arequipa volcanics are shown as Rb versus Sr, Ba versus K, K/Rb versus K, and K/Ba versus K in Fig. 110. In general, the dispersed ele-

ments K, Rb, and Ba behave coherently, whereas Sr behaves in the opposite sense, decreasing with increasing abundance of the other elements. One exception to the

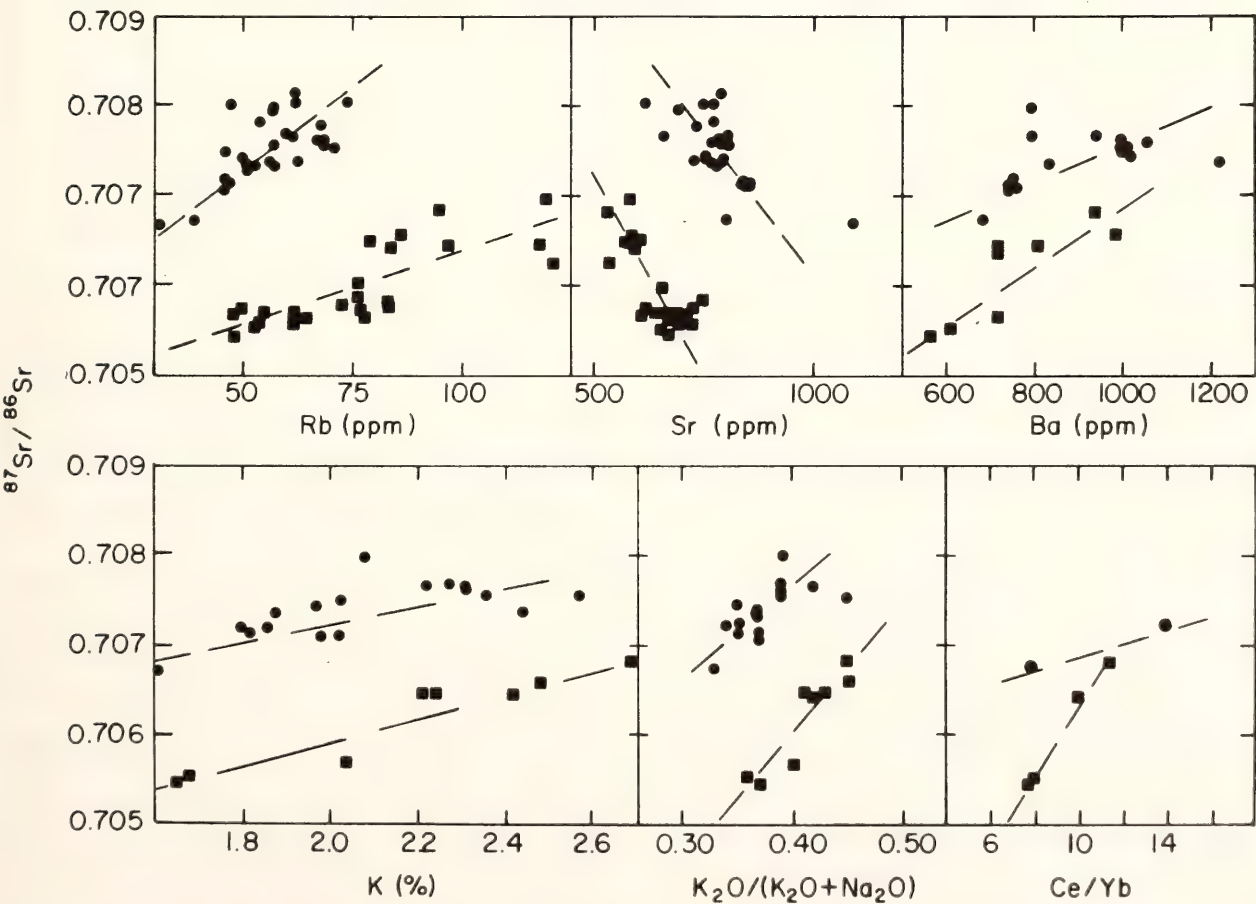


Fig. 109. K, Rb, Sr, Ba, and $K_2O/(K_2O + Na_2O)$ versus $^{87}Sr/^{86}Sr$ within Arequipa and Barroso groups. Symbols as in Fig. 107.

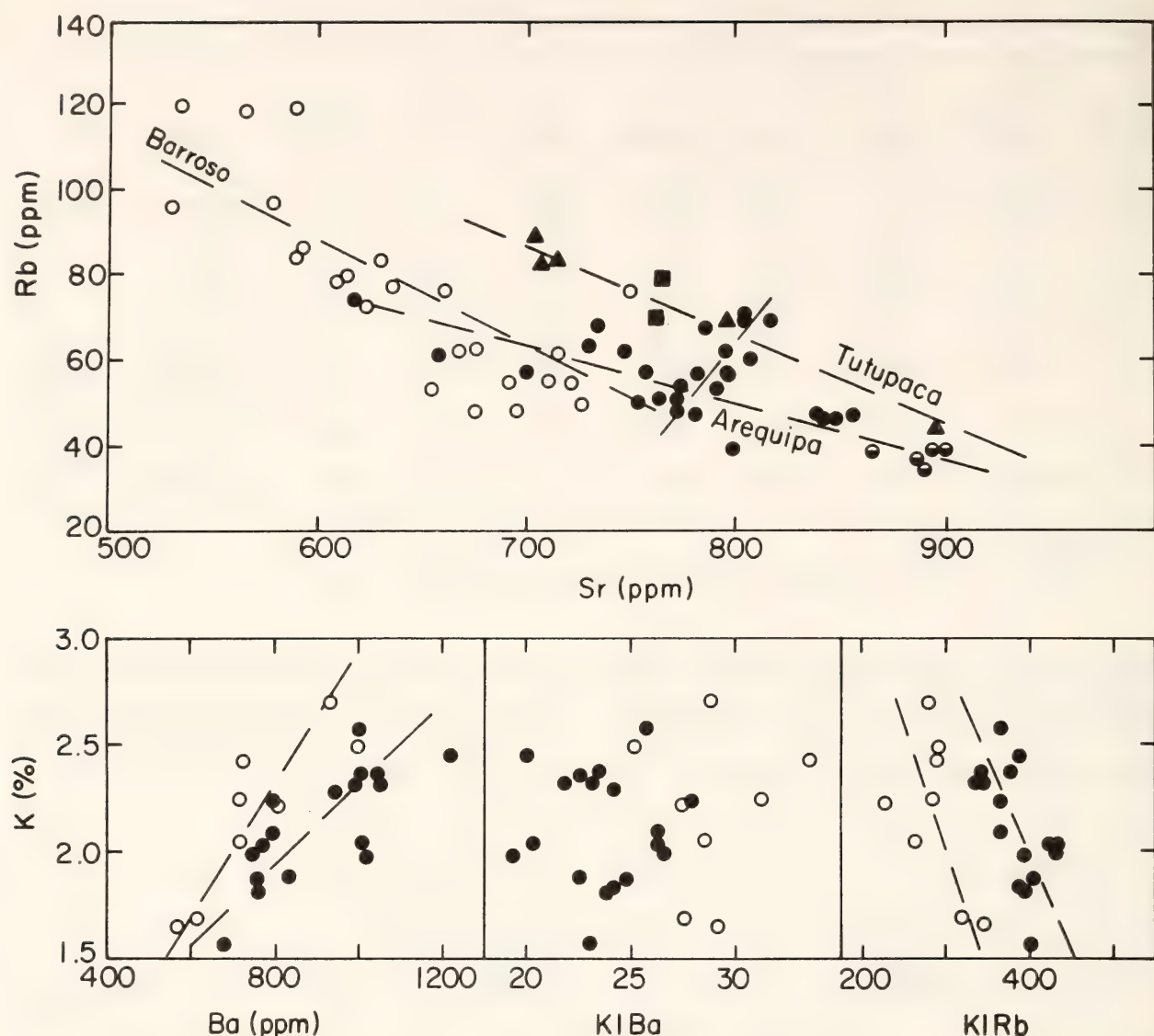


Fig. 110. Rb versus Sr, Ba versus K, K/Rb versus K, and K/Ba versus K for Barroso and Arequipa volcanics. Solid circles = Arequipa; open circles = Barroso.

general pattern is exhibited by Arequipa samples PE46 through PE49 (dashed line with positive slope in Fig. 110), which are significantly enriched in Rb relative to other samples of the Arequipa group but are not correspondingly depleted in Sr.

Regionally averaged Rb and Sr concentrations correlate with $^{87}\text{Sr}/^{86}\text{Sr}$ in an opposite sense to that observed in local variations. It is significant that on a regional basis increasing $^{87}\text{Sr}/^{86}\text{Sr}$ ratios are associated with decreasing Rb/Sr ratios, particularly since the highest Sr isotopic ratios correspond to rocks with very high Sr concentrations (~ 800 – 900

ppm), a fact of some importance when evaluating crustal contamination as a cause of the high $^{87}\text{Sr}/^{86}\text{Sr}$ ratios observed.

Relative to island-arc volcanics (see Table 24), all of the Andean volcanics are greatly enriched in Sr and Ba, somewhat enriched in K and possibly Rb. K/Rb ratios in the Arequipa volcanics are significantly higher than in the Barroso volcanics and are about the same as those of Sunda arc averages (Whitford, 1975a), whereas K/Ba ratios in both Arequipa and Barroso volcanics are significantly lower, reflecting much higher Ba abundances. Rb/Sr ratios of the An-

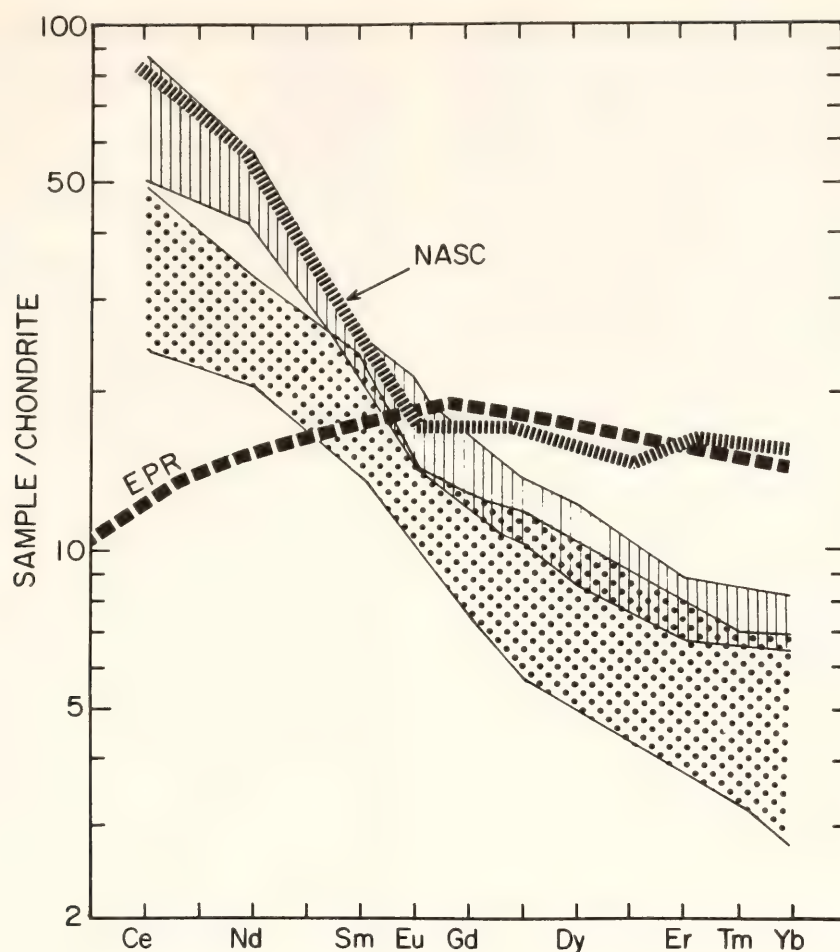


Fig. 111. Chondrite-normalized rare earth element patterns for Arequipa and Barroso volcanics (vertical stripes; from Whitford, *Year Book 76*), compared to data from northern Chile (dots; Thorpe *et al.*, 1976). Data from Nazca plate basalts (EPR; Schilling and Bonatti, 1975) and the North American shale composite (NASC; given by Nance and Taylor, 1976) are shown for comparison.

dean rocks are also somewhat lower than are those of comparable calc-alkaline volcanics of oceanic island arcs.

Rare earth element concentrations have been measured by Whitford (*Year Book 76*) in four Barroso volcanics and in two Arequipa volcanics. The range of concentrations normalized to chondritic values is plotted in Fig. 111. The REE concentrations in the rocks analyzed show a pronounced LREE-enrichment pattern even relative to other central Andean volcanics such as those studied by Thorpe *et al.* (1976) for northern Chile (see Fig. 111). When compared to similar volcanics of the oceanic island arcs, Ce is enriched by 50–300% (60 ppm compared to 40 ppm in Whitford, (1975a) average andesite (see Table 24)

and ~20 ppm in Gill's (1974) "typical" andesite). Slight negative Eu anomalies are present in samples PE144 and PE146 but are otherwise not significant. The flattening of the normalized REE pattern for heavy rare earths is characteristic of these rocks and has been suggested by Whitford to indicate the influence of mantle or basaltic material. The Yb concentrations (1.3 ppm) are about the same as the "typical" andesite of Gill (1.4 ppm) but are slightly lower than in the average andesite of Whitford (2.1 ppm).

Ni analyses and a few Cs determinations have also been done on the rocks. Ni concentration is significantly higher (20–50 ppm) than measured in comparable calc-alkaline rocks of the island arcs

(7–10 ppm; Gill, 1974; Whitford, 1975a) but is typical of Ni concentrations measured elsewhere in the central Andes (Thorpe *et al.*, 1976). The high Ni abundances appear to preclude significant olivine crystallization, as would be required if the lavas were derived by differentiation of basaltic magma. On the other hand, high Ni abundances could reflect the near disappearance of olivine in modified mantle during reaction with the slab melt. The Cs content (0.5–1.1 ppm) of the three Arequipa volcanics for which Cs was determined is significantly lower than that measured in island-arc calc-alkaline rocks where Whitford (1975a) finds typical values of 2–4 ppm. Such low Cs abundances are difficult to explain in terms of any model involving subducted material unless the slab has already been depleted in its more dispersed elements.

End-member compositions. Table 24 summarizes end-member compositions, both local and regional, that characterize the lavas of southern Peru. Model calculations for trace element abundances and isotopic ratios are compared in subsequent sections to those end-member compositions.

Local variations are best seen within the Barroso volcanics and to a lesser extent within the Arequipa volcanics. Considering for the moment only the Barroso volcanics, the geochemical trends related to increasing $^{87}\text{Sr}/^{86}\text{Sr}$ are as follows:

1. Increasing K, Rb, Ba, Ce, Ni(?), Rb/Sr, "k," and Ce/Yb.
2. Decreasing Sr, K/Rb, and Yb.
3. K/Ba roughly constant.

Similar variations characterize the Arequipa volcanics except that Ni variation may be reversed and there is no discernible decrease in Yb with increasing $^{87}\text{Sr}/^{86}\text{Sr}$ ratio.

Average regional trace element concentrations vary with increasing $^{87}\text{Sr}/^{86}\text{Sr}$ in the following fashions:

1. Sr, Ba, Ni, and K/Rb increase.
2. Rb, Rb/Sr, and K/Ba decrease.

3. K, Cs, Yb, MgO, SiO_2 , and Ce/Yb are constant (within experimental and geologic scatter).

Regional variations of Sr, Rb, and K/Rb with respect to $^{87}\text{Sr}/^{86}\text{Sr}$ are in the opposite sense to those observed within each volcanic group. Ba, "k," and possibly Ni behave the same both regionally and locally. Not enough data on REE are available to judge whether the rare earths behave in the same or opposite sense regionally and locally.

Magma Genesis

Statement of problem. The calc-alkaline rocks of the central Andes are distinguished from similar rocks of island arcs by distinctly higher $^{87}\text{Sr}/^{86}\text{Sr}$ ratios and somewhat higher K, Rb, Sr, Ba, Ni, LREE, and $\delta^{18}\text{O}$ at comparable SiO_2 content and depth to Benioff zone. While high trace element abundances may be explained by a number of mechanisms (such as differentiation) that do not necessarily bear directly on magma genesis, high $^{87}\text{Sr}/^{86}\text{Sr}$ ratios and $\delta^{18}\text{O}$ values must be the result of source composition or of contamination.

The case against crustal contamination of a parental magma of "normal" Sr isotopic composition (i.e., $^{87}\text{Sr}/^{86}\text{Sr} < 0.704$) has been reviewed previously by James *et al.* (1976). The crux of the argument against crustal contamination lies in the high Sr concentrations (500–900 ppm) of the eruptives. Those high Sr concentrations require that for a parent magma of low $^{87}\text{Sr}/^{86}\text{Sr}$ either very large amounts of contaminant were assimilated or the contaminant has a high $^{87}\text{Sr}/^{86}\text{Sr}$ ratio (probably > 0.73); however, plots of other trace elements such as Rb, Ba, and LREE against $^{87}\text{Sr}/^{86}\text{Sr}$ ratio (see Fig. 109) reveal systematic variations which would require implausibly high trace element concentrations in any contaminant with $^{87}\text{Sr}/^{86}\text{Sr}$ higher than about 0.715. As the crustal rocks of the Brazilian shield that underlie the central Andes rarely contain more than a few

hundred ppm Sr, even a contaminant with $^{87}\text{Sr}/^{86}\text{Sr}$ ratio as high as 0.715 implies bulk assimilation of at least one part contaminant to one part parent magma. The $\delta^{18}\text{O}$ values reported in this paper preclude such large-scale assimilation unless the contaminant has $\delta^{18}\text{O}$ significantly lower than that generally assumed for old crustal material.

Selective partitioning into the parent magma of trace elements derived from crustal contaminants is improbable because plagioclase, hornblende, mica, and K-feldspar are stable crustal phases. Plagioclase, with a high partition coefficient ($C_{\text{solid}}/C_{\text{melt}}$) for Sr, is on the andesite liquidus so that crustal plagioclase will tend to be a residual phase. In that case the amount of contaminating Sr is not likely to be proportionately much greater than the bulk quantity of contaminant added to the melt. Similar arguments can be made for other trace elements. K is a stoichiometric component in both biotite and K-feldspar and has a partition coefficient of about 1 in hornblende; the partition coefficient for Ba is very large in both biotite and K-feldspar; the partition coefficient for Rb is large (2–3) in biotite and 0.3 to 0.4 in both hornblende and K-feldspar; the partition coefficient for Sr is large in both plagioclase and K-feldspar. The net effect of these partition coefficients is to preclude significant trace element enrichment during partial melting of crustal materials at crustal depths.

Despite compelling arguments against crustal contamination as a cause of high $^{87}\text{Sr}/^{86}\text{Sr}$ ratios, the $\delta^{18}\text{O}$ values require some sialic participation in the magmatic process. If the contamination does not occur in the crust it may occur in the subduction zone. It is therefore appropriate to consider next the implications of the Nicholls and Ringwood model for andesite genesis, and how magma genesis in subduction zones beneath continental margins may differ from that of island arcs.

The most obvious distinction between purely oceanic island arcs and those of the continental margin is the availability of mature sialic crustal material for subduction. Trenches associated with continental margins will receive large amounts of continentally derived detritus which may be swept down the subduction zone. That material, largely graywacke in character, will likely include volcanic and plutonic detritus of the volcanic arc as well as an admixture of mature sialic material of relatively high $^{87}\text{Sr}/^{86}\text{Sr}$ ratio (>0.71). The bulk composition of the graywacke will thus be of high $^{87}\text{Sr}/^{86}\text{Sr}$ and of higher K, Rb, Ba, Sr, and probably $\delta^{18}\text{O}$ than subducted oceanic crust. Although some ocean floor basalt could be involved in Andean subduction zone melting, observed $^{87}\text{Sr}/^{86}\text{Sr}$ ratios of altered basalt (Hart, 1971; Dasch *et al.*, 1973) are not high enough to account for ratios measured in the lavas. Thus, any magma generated in the subduction zone and involving melting (at least in part) of continentally derived graywacke will display important compositional differences, notably in Sr isotopes, from magmas generated by subduction-zone processes involving subducted oceanic crust.

Model assumptions. If graywacke is subducted to 150-km depth and subsequently involved in magma genesis, it will influence isotopic and trace element compositions in fundamentally different ways than will sialic material involved in crustal contamination of mantle-derived magma. This can be shown by considering a mechanism whereby slab-derived magma (in this case, of graywacke rather than oceanic basalt parentage) rises into and equilibrates with overlying mantle material to yield calc-alkaline magma. In such a model, the following processes are important in determining the isotopic and trace element composition of the magma:

1. Preconcentration of trace elements. Major crustal phases that tend to hold

trace elements (i.e., plagioclase, hornblende, and biotite) are unstable at subduction zone depths. Sanidine may be stable but would be the first phase to melt (Stern and Wyllie, 1973). Thus, major residual phases in material of graywacke composition would likely be clinopyroxene, garnet, quartz (coesite), and possible kyanite (Stern and Wyllie, 1978), all of which have relatively low partition coefficients for K, Rb, Sr, Ba, and LREE. Partial melting products of metamorphosed graywacke (granulite) should, therefore, be enriched in K, Rb, Sr, Ba, LREE, H_2O , and SiO_2 . Similar enrichment will occur during melting of subducted oceanic crust, but trace element abundances for comparable degrees of partial melting will generally be lower, though this may not always be the case depending upon the mineral assemblages involved.

2. Mixing and equilibration of a slab-derived melt is with bulk mantle material, not with a mantle-derived melt. Trace element concentrations in the unmodified mantle are so low that the trace element abundances and, in particular, the $^{87}\text{Sr}/^{86}\text{Sr}$ ratios of the modified mantle will be dominated by the slab-derived melt even if the weight proportion of melt is small relative to the mantle material with which it equilibrates. Thus, relatively small amounts of sialic contaminant will have greatly disproportionate effects on the isotopic composition of trace elements such as Sr. For example, if a slab-derived melt of 500 ppm Sr and $^{87}\text{Sr}/^{86}\text{Sr}$ of 0.708 equilibrates with mantle material of 25 ppm Sr and $^{87}\text{Sr}/^{86}\text{Sr}$ of 0.703 in the weight proportion .25 parts melt to 1 part mantle material, the modified mantle will have $^{87}\text{Sr}/^{86}\text{Sr}$ ratio of 0.7072. Regardless of the way the modified mantle undergoes subsequent melting, the melting product will have that $^{87}\text{Sr}/^{86}\text{Sr}$ ratio.

3. Oxygen isotopic composition will be approximately a simple linear function of the bulk proportion of slab-derived

melt to total mantle material with which it equilibrates and of the $\delta^{18}\text{O}$ of the two materials. If graywacke retains a $\delta^{18}\text{O}$ of about +12‰ (SMOW) at depth (Magaritz and Taylor, 1976) and mantle material is +6‰ (SMOW), measured $\delta^{18}\text{O}$ of +7.2‰ in the lavas requires about one part slab to four parts mantle material. Thus, although the trace element abundances and Sr isotopic composition of partial melting products of the modified mantle are dominated by the slab-derived material, the O isotope and bulk chemical composition of the melt is dominated by material of mantle composition.

4. Partial melting of mantle material modified by uprising slab melt will result in trace element abundances that are dependent primarily on the phase proportions, melting relations, and partition coefficients of the modified mantle. Mantle material, even highly modified by the influx of slab-derived melt, will strongly partition trace elements into the magma, so that the degree of enrichment of trace elements in the modified mantle will be reflected in trace element concentrations of the derivative magma.

It is of fundamental importance to recognize that the processes described here are *not* equivalent to magma mixing. In general, the concentrations of trace elements during all phases of partial melting will depend upon the following variables: (1) the concentrations of trace elements in the original solid, (2) the proportions in which crystalline phases are present in the source material, (3) the degree to which those crystalline phases participate in the melting process, (4) the overall degree of partial melting, (5) the type of melting (batch or fractional), and (6) the partition coefficients of the various elements for the phases present.

None of these variables is known, but the major uncertainties lie in the mineralogy and melting relations of both the slab and the modified mantle. In addi-

tion, there is convincing evidence that partition coefficients, poorly determined in many cases, vary not only with temperature and pressure but also with composition of the melt. The partition coefficients I have used here are those compiled by Arth (1976) for various minerals in equilibrium with different melt compositions. Thus, partition coefficients assumed for slab melting may, for the same mineral phases, differ from those assumed for melting of the modified mantle. An extreme example of the compositional dependence of a partition coefficient is for Ni in olivine. Hart and Davis (1978) have shown that the partition coefficient is a function of MgO content of the melt, so that for Andean lavas (MgO = 2.5–3.5%) the partition coefficient may be as high as ~ 35–50.

For K there is the additional complication that it is a stoichiometric component in one or more minor phases such as sanidine or phlogopite that may be present, and is therefore not a true trace element. In such cases the concentrations of K (and probably Rb) will be controlled largely by the degree to which the potassium-bearing phases enter the melt.

Quantitative modeling. The model described above for the generation of calc-alkaline magma can be viewed as involving a three-stage process.

1. Formation of the subducted slab, consisting of oceanic crust and graywacke, that descends down the subduction zone as a Franciscan-like mélange.

2. Melting of that slab mélange at depth.

3. Reaction of slab-derived melt with the overlying mantle wedge to produce calc-alkaline magma.

It remains to consider each of these in turn. The procedure I have followed is to fix the composition of the descending slab material (basalt and graywacke) on the basis of previous studies of such rocks and to treat those compositions as invariant. The relative proportions in

which graywacke and oceanic crust enter the melt and the degree of slab melting are determined by providing a best fit to Sr isotopic ratios and Sr concentrations, the latter of which also depend upon the degree of melting of the modified mantle. With the melting model constrained by the Sr data, it is possible to predict concentrations of other trace elements. Such a procedure is, of course, highly oversimplified and nonunique. It nonetheless seems worthwhile to formulate at least one system of magma genesis that can satisfy some of the more important geochemical variables measured in the lavas.

In the calculations that follow I have made no provision for low-pressure fractionation. The justification for ignoring such fractionation is twofold:

1. Most of the trace element variations correlate closely with variations in $^{87}\text{Sr}/^{86}\text{Sr}$ ratios. As isotopic ratios are invariant during differentiation, it seems likely that the trace element variations are not due primarily to differentiation.

2. The lithosphere beneath the Andean arc extends nearly to the subduction zone (James, 1971b; Sacks, 1977). It is dynamically implausible that crystal mush diapirs formed near the subduction zone could penetrate and rise into that rigid lithospheric mantle of the South American continent.

Composition and melting of subducted slab. Direct information on the composition of subducted materials beneath the central Andes is of course unavailable. It seems likely, however, that eugeosynclinal rocks of the Franciscan mélange of California are characteristic of Andean-type continental margin subduction sequences. Granted this assumption, an estimate can be made of the chemical and mineralogic composition of the slab at depth.

Geologic mapping by Bailey *et al.* (1964) showed that 80% of Franciscan rocks are graywacke or metagraywacke, that 20% are basalts and greenstones,

TABLE 25. Compositional Summary of Rock Types used in Petrogenetic Modelling Calculations.

	Franciscan Metagraywacke	Tonalite*	Andean Intrusive (avg.)	Average Ocean Floor Basalt†	Mantle‡	Modified Mantle
Major Elements						
SiO ₂	68.1	59.1	59.7	49.9	45.2	
TiO ₂	0.24	0.79	0.68	1.4	0.71	
Al ₂ O ₃	13.7	18.2	17.1	16.0	3.5	
Fe ₂ O ₃	1.3	2.3			0.46	
FeO	2.4	3.6	7.52 (as FeO)	9.3 (as FeO)	8.0	
MnO	0.07	0.11	0.15	0.17	0.14	
MgO	2.6	2.5	2.6	8.7	37.5	
CaO	2.6	5.9	6.1	11.3	3.1	
Na ₂ O	3.4	3.8	3.5	2.75	0.6	
K ₂ O	1.6	2.2	2.5	0.27	0.13	
H ₂ O	1.4	0.86	n.d.	
Mode (%)						
qtz	n.d.	13	n.d.			
K-spar		4.5				
Plag		59				
Bt		12.5				
Hb		9				
Opx				47.5	17	18
Cpx					12	55
Oliv					57	5
Gar				47.5	14	14
Phlog						8
Accessories						
		2		5		
Trace Elements (ppm)						
Sr	200	n.d.	445	110	20	100-140
Rb	60		94	1.8	2.5	35-50
Ba	400		526	13	4	140-200
Ni	n.d.		11.6	120	2000	
Ce	n.d.		n.d.	10.3 (est.)	1.7	30-40
Yb	n.d.		n.d.	2.9	0.8	0.75
⁸⁷ Sr/ ⁸⁶ Sr	0.706-0.710		0.7066	0.7040	0.7030	0.7055-0.7068
δ ³⁰ O	+12.0‰		n.d.	+12.0‰	+6.0‰	7.2‰

* Stern and Wyllie, 1975.

† Gill, 1974.

‡ Ringwood, 1966, 1975.

and that cherts and other deep sea sediments constitute only trace amounts of the Franciscan sequence. The composition of the Franciscan formation has been studied by many workers. A summary of those results is given in Table 25. Bailey *et al.* (1964) compiled many major-element analyses of Franciscan graywacke and metagraywacke, and the major-element composition given in Table 25 is for average metagraywacke. Rb, Sr, and $^{87}\text{Sr}/^{86}\text{Sr}$ data for Franciscan graywackes were reported by Peterman *et al.* (1967). Although there is some variation in Rb and Sr concentrations (see Peterman, *et al.*, 1967), the $^{87}\text{Sr}/^{86}\text{Sr}$ ratios tend to be rather consistently within the range 0.706–0.707. Franciscan graywacke and basalts (greenstones) have been studied by Magaritz and Taylor (1976) for O isotopic compositions. They find that most of the samples studied have $\delta^{18}\text{O}$ values in the narrow range +11 to +13‰, averaging +12‰.

Some trace elements such as REE and Ba have not been measured for Franciscan graywacke. Rare earth element concentrations are assumed to be the average of Australian post-Archean sediments (chiefly graywacke), as determined by Nance and Taylor (1976). Rare earth concentrations of those post-Archean sediments are nearly identical to those found for the North American shale composite. Ba is also taken to be the average value for Australian sediments, ~400 ppm (Nance and Taylor, 1976).

It is possible that graywacke of the Andean region could differ in certain important respects from Franciscan graywacke. To a first approximation, the graywacke of the Andean region should consist principally of volcanoplutonic debris that will be dominated by the compositional character of the late cretaceous–early Tertiary igneous rocks. For comparison, therefore, average compositions of Andean batholithic rocks of the Arequipa region are given in Table

25. The Andean intrusives are of roughly the same major-element composition as tonalite used by Stern *et al.* (1975) for experimental studies under hydrous conditions at high temperature and pressure (see Table 25). Studies of that tonalite are important because the rock is close in composition to many graywackes (Wyllie, 1977) and because it is one of the few rocks in the correct compositional range of subducted terrigenous sediments that has been studied at temperatures and pressures similar to those of the deep subduction zone. Trace element and Sr isotopic compositions of the Stern and Wyllie tonalite are taken to be the same as for the average intrusive of the Andean batholith near Arequipa.

Average composition of subducted oceanic basalt is taken from Gill (1974, with references to the sources of the analyses) and summarized in Table 25.

At subduction zone depths of 150 to 175 km, a rock of graywacke composition would probably be granulite and oceanic crust would be quartz eclogite. In general, experimental data on rocks of graywacke (tonalite) composition extend only to pressures of about 30–35 kbar, whereas the depth of magma generation implies pressures of 50–60 kbar. It appears, however, that most of the major phase changes have occurred by 30 kbar (Wyllie, 1977). More serious than the lack of data at higher pressures is the uncertainty over the amount of H_2O present in the slab. To a large measure, the stability of important minor phases such as sanidine and phlogopite is governed by the amount of water present. Studies at 30–35 kbar under water-saturated conditions (~ 20% wt % H_2O) show that sanidine is entirely dissolved in the vapor phase (Fig. 2 in Stern *et al.*, 1975). Under conditions of 5 wt % H_2O , Stern and Wyllie (1978) found no potassic phase present even in the subsolidus assemblage. They concluded that most of the potassium as well as other dispersed elements were

TABLE 26. Mineralogy and Assumed Melting Proportions for Granulite and Modified Mantle

	Granulite (Metagraywacke)	Granulite* (Tonalite + 5% H ₂ O)	Modified Mantle
Subsolidus Mineral Phase Proportions:			
ol	0.05
opx	0.18
cpx	0.40-0.35	0.43	0.55
gar	0.15-0.20	0.13	0.14
phlogopite	0.08
sanidine	0.10
qtz (ct)	0.35	0.27	...
kyanite	...	0.17	...
Phase Melting Proportions (0-20% Melt):			
ol	0.01
opx	0.04
cpx	0.25-0.20	0.29	0.45-0.57
gar	0.00-0.10	0.00	0.20
phlogopite	0.30-0.18
sanidine	0.30-0.40
qtz (ct)	0.45-0.30	0.59	...
kyanite	...	0.12	...

* Granulite of tonalite + 5% H₂O composition from Stern and Wyllie, 1978.

contained in the vapor phase. The mineral assemblage at subsolidus temperatures for both 5 wt % H₂O and H₂O saturation is clinopyroxene, quartz (coesite), garnet, kyanite, and vapor. The relative weight proportions of those minerals present for different degrees of partial melting have been measured by Stern and Wyllie (1978). From those measurements the relative proportions in which the various phases enter the melt can be calculated. The initial mineral proportions in the granulite and the appropriate "eutectic" phase proportions (that is, the proportion in which the different phases enter the melt) for up to 20% partial melting are given in Table 26.

It seems likely that 5 wt % H₂O (~15 volume %) is substantially more than will be present in the subduction zone at 150 km, particularly if water is supposed to exist as a free phase not bound to hydrous minerals. Even in metagraywacke of the Franciscan Formation, total H₂O is typically 3%, and most of that is contained in hydrous phases (Bailey *et al.*, 1964). Free H₂O is probably less

than 1%. One would anticipate, therefore, that at subduction-zone depths free vapor would not exceed about 1% by weight. That conclusion is important in that at lower H₂O contents a potassic phase, probably K-feldspar (sanidine), may be present in significant amounts and kyanite may be largely absent. Anhydrous experiments on rock of diorite (60% SiO₂, 1.3% K) composition by T. H. Green (1970) revealed that significant amounts of K(?)feldspar, here assumed to be sanidine, and no measurable amount of kyanite (≤5%) are present at pressures of 30-35 kbar and temperatures around 900°C. The anhydrous mineral assemblage at those *P-T* conditions is cpx >> qtz (coesite) > gar > K-feldspar. The absence of kyanite may be due to the presence of a comparatively aluminous phase such as sanidine and more aluminous clinopyroxene and garnet. In any event, sanidine may be expected to persist as long as the volume of aqueous phase is small, although it will likely be the first phase to enter the melt.

In the slab melting calculations that follow, I have assumed that sanidine is present in the granulite in proportion sufficient to hold most of the potassium, implying that about 10% sanidine is present. Sanidine has the effect of retaining (i.e., it has large partition coefficients for) some of the dispersed elements such as Rb, Ba, and Sr in addition to K. At comparatively small degrees of partial melting (<20%), this retention of trace elements is an important effect. If sanidine is absent owing to higher concentrations of water in the slab than are assumed here, and if trace element concentrations in the granulite have not been significantly reduced by aqueous fluid transfer away from the slab during its descent, all model calculations of the sort done here will result in greatly excessive trace element abundances in the calc-alkaline magma. I have not included kyanite in the melting calculations principally because its partition coefficients are unknown, although for the elements here considered, the partition coefficients should probably all be low.

Mineralogic compositions and assumed melting proportions for granulite are given in Table 26. Partition coefficients as compiled by Arth (1976) are given in Table 26. Concentrations of trace elements for varying degrees of partial melting are shown in Fig. 112, based on initial trace element abundances given in Table 25. Shown for comparison in Fig. 112 are average trace element concentrations for melting of oceanic crust calculated by Gill (1974) using slightly different partition coefficients than I have used here.

It is probable that at any given temperature the degree of melting of granulite will be greater than the degree of melting of quartz eclogite. Although the temperature of the solidus at 30 kbar under hydrous conditions is nearly the same for basalt as it is for tonalite (Stern and Wyllie, 1973), it is evident that granulite will melt more quickly with

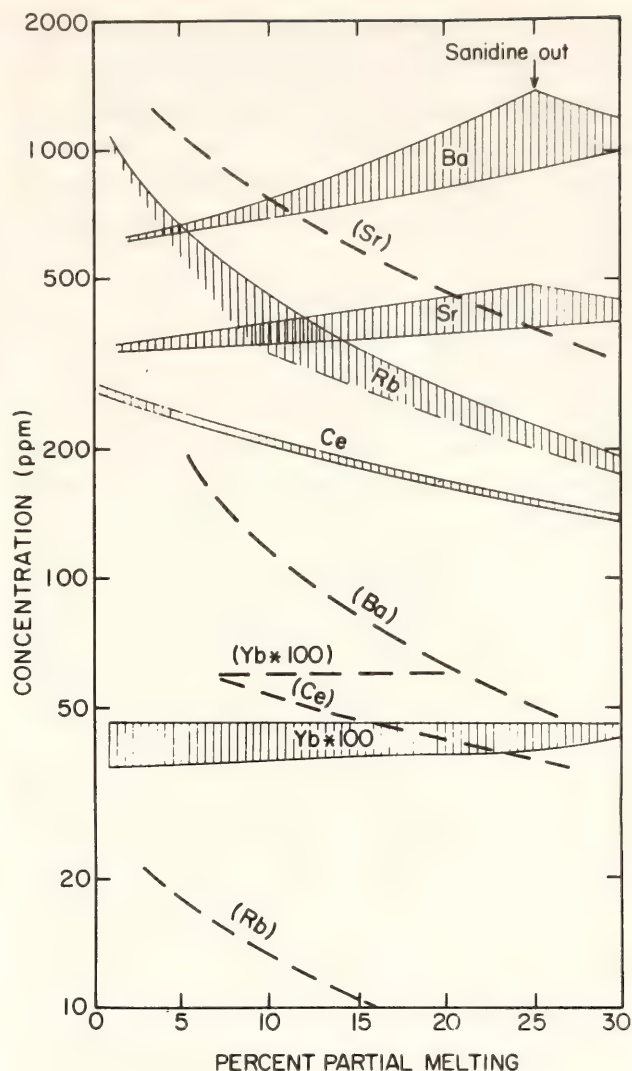


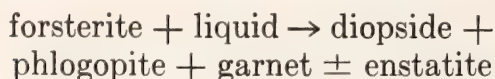
Fig. 112. Trace element concentrations versus degree of partial melting for granulite and oceanic crust (eclogite), the latter from Gill (1974). Partition coefficients used by Gill are not identical to those used for the granulite calculations. Dashed lines with element symbols in parentheses are for eclogite melting. Vertical hatching denotes range of elemental abundances for different granulite mineralogies.

rising temperature than will eclogite because of the greater abundance of early melting phases such as quartz, sanidine, and possibly kyanite in the granulite. From 10 to 20% melting of tonalite with 5% water occurs over the temperature range of about 750°–800°C. In that range of melting, approximately 60% of the melt consists of quartz (see Table 26). If eclogite consists of 50% cpx, 40% garnet, and 10% quartz, and if the minerals melt at about the same rate as in

granulite, for the same temperature interval only about half as much melt will be produced from eclogite (5–10% as opposed to 10–20%). Thus, assuming that effective temperatures remain roughly constant, degrees of partial melting eclogite will typically be about one half those of granulite.

As may be seen in Fig. 112, relatively small degrees of partial melting of eclogite (~10%) will produce Sr concentrations much greater than those of granulite partial melts for similar or greater degrees of partial melting. On the other hand, all other dispersed elements, notably K, Rb, Ba, and LREE, will be much more abundant in granulite partial melt than in partial melts of quartz eclogite for *all* degrees of partial melting. This observation is important, for of the local geochemical variations studied, increases in Sr concentrations are negatively correlated with increasing $^{87}\text{Sr}/^{86}\text{Sr}$ ratios, whereas K, Rb, Ba, and LREE concentrations are positively correlated. This behavior is consistent with the hypothesis that the lavas of lower $^{87}\text{Sr}/^{86}\text{Sr}$ ratios are derived from modified mantle that has received proportionately larger amounts of partial melt from oceanic crust with $^{87}\text{Sr}/^{86}\text{Sr}$ ratios much lower than those of granulite.

Modified mantle melting. Few experimental results are published on the sorts of reactions that may occur between wet rhyolitic melt from the slab and normal peridotitic mantle. From work that is available (e.g., Modreski and Boettcher, 1973; Bravo and O'Hara, 1975; Boettcher *et al.*, 1975) it appears evident that the reaction is approximately the following (assuming no vapor phase is present):

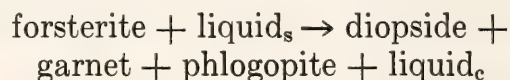


Of particular importance here is the formation of phlogopite and the breakdown of forsterite. Results presented by Boettcher *et al.* (1975) suggest that phlogopite is a very refractory hydrous

mineral, stable at high temperatures and pressures. Melts in equilibrium with a phlogopite-bearing assemblage are typically lower in K than the source material (Boettcher *et al.*, 1975), indicating phlogopite may be a residual phase.

It is evident that the breakdown of forsterite will produce mostly pyroxene, probably as clinopyroxene, since both garnet and phlogopite are low in SiO_2 and would not be favored in reactions involving highly siliceous melts.

Where the modified mantle yields a calc-alkaline magma, the reaction involving forsterite may be



where liquid_s = slab melt and liquid_c = calc-alkaline magma. In the simplest case, where SiO_2 is balanced and assuming 5% forsterite remains, the mineralogy of the modified mantle will be approximately as shown in Table 26: olivine = 0.05, orthopyroxene = 0.15, clinopyroxene = 0.58, garnet = 0.17, and phlogopite = 0.05, with phlogopite varying with amount of K and H_2O in the modified mantle. These mineral proportions are for a subsolidus modified mantle. In actual circumstances, the modified mantle is partially molten and the mineral phases present are residual so that early melting mineral phases will be less abundant than indicated in Table 27 for the subsolidus assemblage.

Of critical importance to the concentration of K and Rb in the calc-alkaline melt is whether phlogopite is a residual phase, as suggested by Boettcher *et al.* (1975). I have assumed here that phlogopite forms in sufficient quantity during reaction to balance the potassium entering the mantle from the slab. If phlogopite is residual, it will control both K and Rb concentrations in the magma, with K entering the melt in proportion to the amount of phlogopite melted. Rb would be controlled by the K/Rb partition coefficient for phlogopite, which has

TABLE 27. Partition Coefficients for Melting of Granulite and Modified Mantle*

Trace Element	Granulite (Dacite-Rhyolite Melt)					Modified Mantle (Basalt-Andesite Melt)				
	cpx	gar	phlog	san	qtz	oliv	opx	cpx	gar	phlog
K	0.037	0.020	0.00	0.00680	0.0140	0.0110	0.0150	...
Rb	0.032	0.0035	(0.940)	(0.340)	0.00	0.00980	0.0220	0.0150	0.0420	(3.00)
Sr	0.516	0.015	0.672	3.87	0.00	0.0140	0.0170	0.120	0.0120	0.810
Ba	0.131	0.017	6.00	6.12	0.00	0.00990	0.0130	0.0130	0.0230	1.09
Ce	0.50	0.350	0.23	0.044	0.00	0.00690	0.0240	0.070	0.0280	0.0340
Yb	1.58	39.90	0.17	0.012	0.00	0.0140	0.0340	0.160	11.50	0.0420

* Arth, 1976.

been measured by Beswick (1973) to be ≈ 3 . Thus, magma generated from modified mantle in which phlogopite is a significant residual phase will have a higher K/Rb ratio than magma generated from modified mantle with little or no residual phlogopite.

Because phlogopite may be a residual phase, it is difficult to treat either K or Rb as trace elements, their abundances depending largely upon the degree to which phlogopite enters the melt (or exists as a residual phase). In the model considered here, however, the K/Rb ratios of the lavas are consistently higher than the calculated K/Rb of the modified mantle, indicating that phlogopite may persist as a residual phase.

Local geochemical variations. Correlation of many trace element abundances with $^{87}\text{Sr}/^{86}\text{Sr}$ ratios is found in most of the lavas of southern Peru but is particularly well displayed in the Barroso volcanics. In the discussion that follows, therefore, only the Barroso volcanics are considered.

Oxygen isotope data show that the proportion of slab-derived melt to mantle material with which it equilibrates remains nearly constant. Despite that fact, the $^{87}\text{Sr}/^{86}\text{Sr}$ ratios within the Barroso volcanics vary over a wide interval. It is evident, therefore, that the slab-derived melt varies either in $^{87}\text{Sr}/^{86}\text{Sr}$ ratio, Sr concentration, or both. One obvious means of achieving that variability

is for the slab-derived melt to consist of differing proportions of granulite partial melt and eclogite partial melt. Thus, larger proportions of eclogite partial melt relative to granulite partial melt will produce modified mantle material of lower $^{87}\text{Sr}/^{86}\text{Sr}$ ratio.

Before examining particular melting models, it is useful to consider the character of mixing relations between a slab-derived melt and mantle peridotite. Figure 113 shows mixing curves between graywacke partial melts and mantle material plotted as functions of $\delta^{18}\text{O}$ and $^{87}\text{Sr}/^{86}\text{Sr}$, where $\delta^{18}\text{O}$ of granulite is assumed equal to 12‰. In general, the Sr concentrations of the slab melt will be 10–40 times those of the peridotite mantle whereas O concentrations will be roughly comparable. The resultant mixing curves will therefore be hyperbolas that are strongly convex downward, reflecting the disparate Sr concentrations of the end members. The range of $\delta^{18}\text{O}$ and $^{87}\text{Sr}/^{86}\text{Sr}$ of the southern Peru volcanics is shown in Fig. 113. The $^{87}\text{Sr}/^{86}\text{Sr}$ variation can be readily modeled over a relatively small range of Sr concentrations by assuming differing proportions of granulite to eclogite end members.

Calculations for differing degrees of partial melting of slab material indicate that $^{87}\text{Sr}/^{86}\text{Sr}$ ratios of the modified mantle can best be satisfied by 20% partial melting of granulite and 10% partial melting of eclogite. At those de-

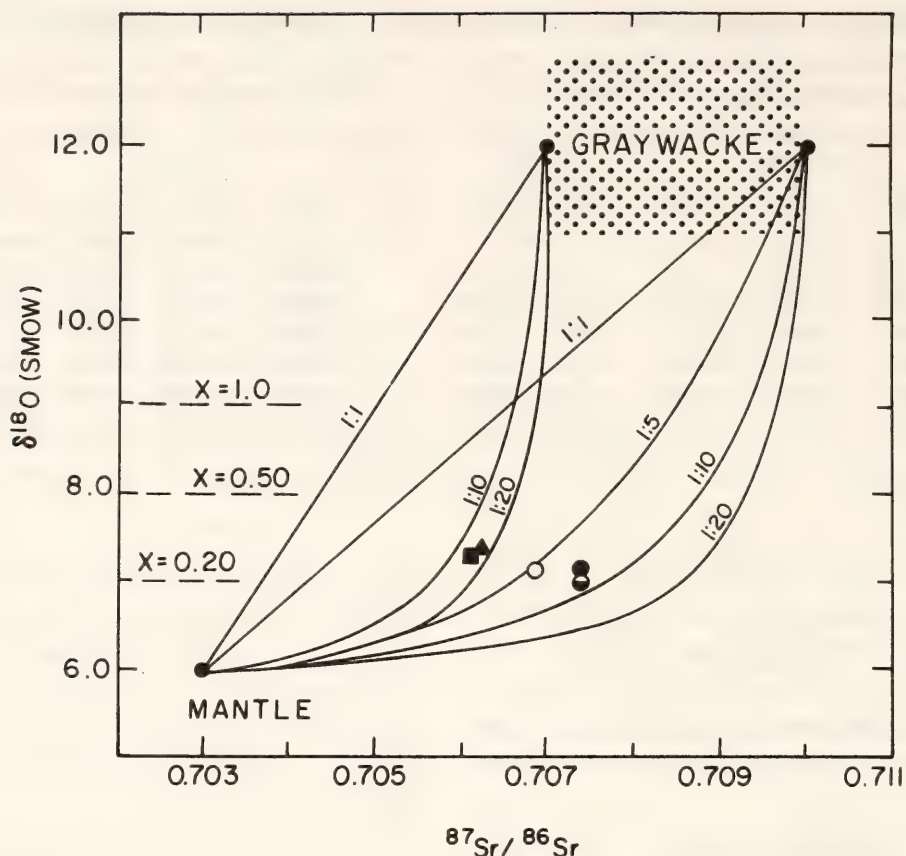


Fig. 113. $\delta^{18}\text{O}$ versus $^{87}\text{Sr}/^{86}\text{Sr}$ mixing curves between partial melt of graywacke isotopic composition and material of mantle isotopic composition. Proportions shown with each curve denote trace element concentration in mantle to trace element concentration in slab-derived melt (i.e., 1:20 signifies 1 ppm Sr in mantle to 20 ppm Sr in melt). X denotes bulk weight proportion of slab-derived melt to 1 part mantle material. Oxygen concentrations assumed equal in the two materials. Approximate range of graywacke compositions shown by dotted pattern.

degrees of melting, Sr concentrations in melts derived from eclogite are significantly higher than in those derived from granulite (see Fig. 112). If granulite is assumed to undergo 20% partial melting and eclogite 10% partial melting, then observed Sr isotopic compositions of the Barroso volcanics imply that for the highest $^{87}\text{Sr}/^{86}\text{Sr}$ ratios the slab-derived melt consists of 90% granulite melting product and 10% eclogite melting product. For the lowest $^{87}\text{Sr}/^{86}\text{Sr}$ ratios the slab-derived melt would consist of 60% granulite melting product and 40% eclogite melting product. In all cases, magma from granulite and eclogite are assumed *not* to be equilibrated with one another prior to rising into overlying mantle.

Sr concentrations for partial melting of modified mantle are shown in Fig. 114. For low $^{87}\text{Sr}/^{86}\text{Sr}$ ratios (60% granulite,

40% eclogite), the degree of melting of modified mantle as determined by observed Sr concentrations (~ 730 ppm) is 10–12%; for high $^{87}\text{Sr}/^{86}\text{Sr}$ ratios (90% granulite, 10% eclogite), the degree of melting based on observed Sr concentrations (~ 530 ppm) is 13–15%. The range of values shown by hatching in Fig. 114 defines the interval between sanidine-bearing granulite and kyanite-bearing granulite with 5 wt % water (Stern and Wyllie, 1978).

Trace element concentrations for melting of modified mantle over the interval 5–20% are plotted in Fig. 115 and compared to concentrations observed in the lavas. Partition coefficients for the trace elements and mineral phases of the modified mantle are given in Table 27. K is taken to be controlled by phlogopite melting and Rb calculated both as a

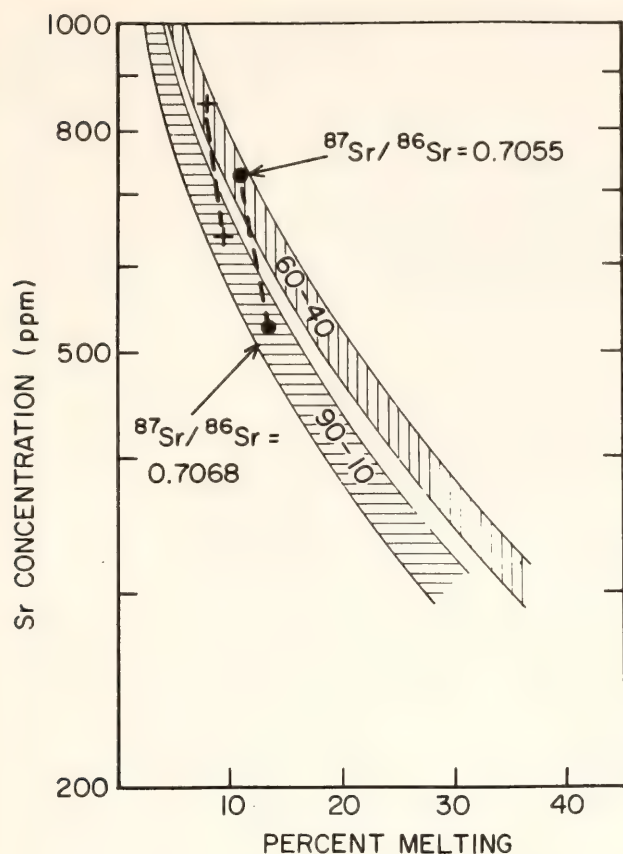


Fig. 114. Sr concentrations in partial melting products of modified mantle for different degrees of granulite and eclogite participation. Range of compositions shown by hatched areas are for different mineralogies and mineralogic melting proportions in granulite. Proportionality 90-10 (60-40) signifies that the slab-derived melt is made up of 90% (60%) partial melt from granulite and 10% (40%) partial melt from eclogite. In all cases, granulite is presumed to undergo 20% partial melting, eclogite to undergo 10% partial melting. The closed circles indicate where the end-member Sr concentrations of the Barroso volcanics intersect the partial melting curves. End-member $^{87}\text{Sr}/^{86}\text{Sr}$ ratios are shown for each point of intersection. Crosses show the concentration-melting curve intersection for Arequipa volcanics. Weight proportion of slab melt to mantle is 1:4.

trace element and according to the proportion of phlogopite melted assuming a K/Rb partition coefficient of 3.

Principal features of the calculated trace element compositions are the following:

1. Calculated LREE (Ce) are much higher than those observed and calculated HREE (Yb) are much lower.

2. Calculated Ba concentrations are very near those of the model.

3. K concentrations require that significant amounts of phlogopite remain as a residual phase. For a K/Rb partition coefficient of 3, that residue results in Rb concentrations that are lower than those observed in the lavas (i.e., calculated K/Rb too high), suggesting that the partition coefficient may not be correct. In any event, calculated K/Rb varies in the correct sense and in roughly the correct proportion, as do observed K/Rb ratios.

The rare earth results are difficult to explain. In the case of Ce, it may be that because its partition coefficient is low for all hypothesized phases (with the exception of possible accessory phases such as apatite), it percolates out of the slab during earlier stages of subduction. The very low levels of Cs measured in the lavas supports the notion that the slab has been depleted in at least some of the more dispersed elements. A more intractable problem is the low concentration of Yb. At the temperatures likely near the subduction zone, garnet is a highly residual phase and will withhold most of the HREE from the melt. I have no explanation for the high Yb observed in the lavas relative to model values, but the problem is a general one for all island arcs and cannot be explained without assuming large-scale melting of garnet or assuming diapiric uprise of a garnet-bearing assemblage to depths where garnet is unstable. It may also be that the assumed HREE partition coefficient for garnet is much too high.

The high observed Ni concentrations (relative to island-arc volcanics) may be due to lesser amounts of olivine in the modified mantle resulting from reaction with a relatively more silicic melt than one derived solely from eclogite. Reduction in olivine will result in a corresponding decrease in the bulk Ni partition coefficient.

Regional geochemical variations. The

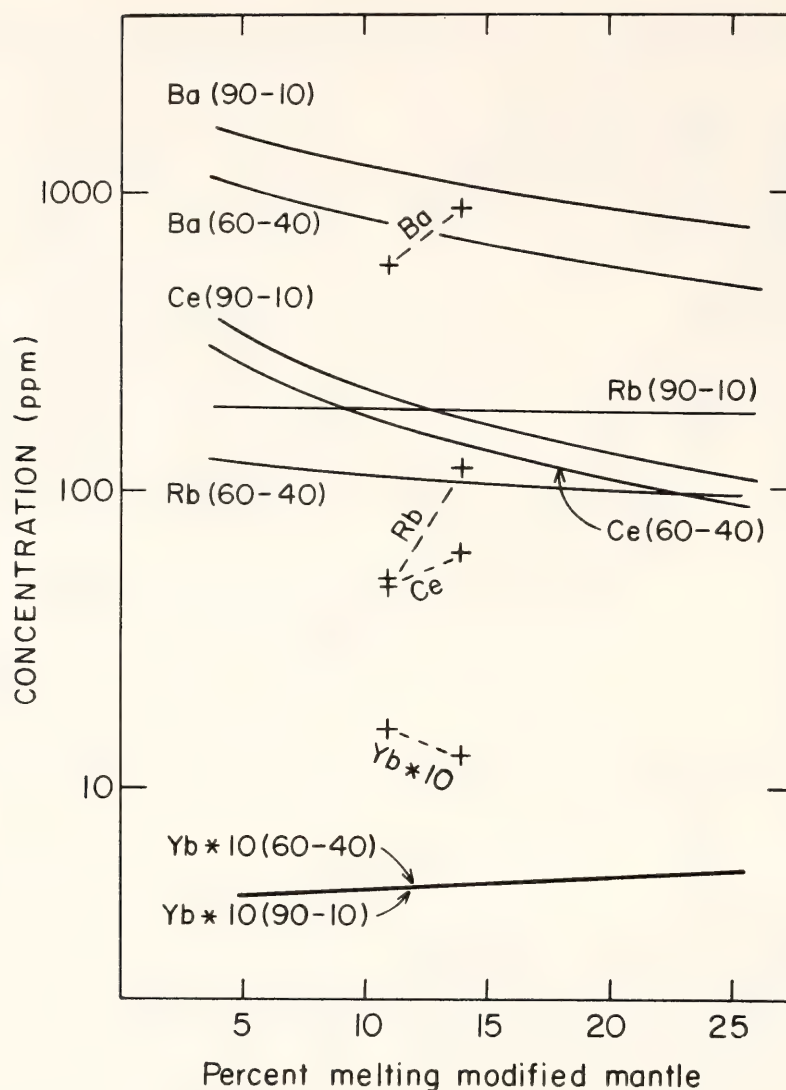


Fig. 115. Ba, Rb, and Ce concentrations over the interval 5-25% melting of modified mantle for the two cases of the Barroso volcanics shown in Fig. 114. As before, granulite is presumed to undergo 20% partial melting and eclogite 10%. Weight proportion of slab melt to unmodified mantle is 1:4. For comparison, crosses connected by dashed lines indicate observed end-member trace element concentrations plotted at the degrees of partial melting implied by Sr in the previous figure.

increase in Sr and Ba concentrations and the increase in K/Rb ratios to the northwest suggest that the overall degree of partial melting of the modified mantle may be decreasing. Independent evidence for this conclusion comes from the fact that there is a general decrease in Quaternary volcanism from southeast to northwest, with Quaternary volcanism ceasing entirely just north of Arequipa.

For similar Sr concentrations of modified mantle source material, concentrations of 650-850 ppm would imply 7-10% partial melting (see Fig. 114). If phlogopite is truly a residual phase,

smaller degrees of melting should result in decreasing Rb for the same K concentrations (K/Rb increases). Ba and LREE should be more concentrated for lower degrees of partial melting.

Higher $^{87}\text{Sr}/^{86}\text{Sr}$ ratios cannot be due to varying degrees of partial melting but may be due either to relatively larger proportions of granulite partial melt or, more probably, to subducted continental sedimentary material with a slightly higher $^{87}\text{Sr}/^{86}\text{Sr}$.

Conclusions. The petrogenetic model proposed in this report can account qualitatively and in some cases quantitatively

for the isotopic and trace element differences observed between late Cenozoic volcanics of the central Andean arc and those of island arcs. Calculations show that compositional characteristics of the central Andean volcanics may be due to subduction and melting of comparatively large amounts of continentally derived sedimentary detritus of graywacke composition.

Trace element and isotopic systematics within the volcanics studied can be partially modeled quantitatively by assuming a petrogenetic system in which both graywacke (granulite) and oceanic basalt (quartz eclogite) melt in varying proportions and then rise into and equilibrate with overlying mantle to produce modified mantle material which yields calc-alkaline magma. The fact that trace element variations observed in the lavas are well correlated with $^{87}\text{Sr}/^{86}\text{Sr}$ ratios indicates that the variations are not due primarily to fractionation.

Oxygen isotope results show that the proportions of slab-derived melt that equilibrate with a given volume of mantle material remain roughly constant at about 20 wt % of the total modified mantle. Of that 20% derived from the slab, 60% is derived from graywacke, 40% from basalt for the low- $^{87}\text{Sr}/^{86}\text{Sr}$ rocks of any given volcanic group; for the high- $^{87}\text{Sr}/^{86}\text{Sr}$ rocks, 90% is derived from graywacke, 10% from basalt. These proportions are for the case in which the degree of partial melting of graywacke is 20%, that of basalt 10%.

The involvement of terrigenous sediments in subduction-zone petrogenesis signifies that continental material is being recycled back into the crust in the central Andes. That recycling of "aged" sialic material may provide a possible explanation for the systematic increase through time of the $^{87}\text{Sr}/^{86}\text{Sr}$ ratios of Andean eruptives (McNutt *et al.*, 1975; James *et al.*, 1976). That is, as the Andean arc evolves and older sialic material is elevated and eroded in the process of

cordilleran development, increasing volumes of radiogenic detritus are shed off the continent and into the trench where they are subsequently subducted and melted, and their trace elements are returned to the continent.

References

- Armstrong, R. L., A model for the evolution of strontium and lead isotopes in a dynamic earth, *Rev. Geophys.*, **6**, 175–199, 1968.
- Armstrong, R. L., Isotopic and chemical constraints on models of magma genesis in volcanic arcs, *Earth Planet. Sci. Lett.*, **12**, 137–142, 1971.
- Arth, J. G., Behavior of trace elements during magmatic processes—a summary of theoretical models and their applications, *J. Res. U. S. Geol. Survey*, **4**, No. 1, 41–47, 1976.
- Bailey, E. H., W. P. Irwin, and D. L. Jones, Franciscan and related rocks, and their significance in the geology of western California, *Calif. Div. Mines Geol. Bull.*, **183**, 177, 1964.
- Beswick, A. E., An experimental study of alkali metal distributions in feldspars and micas, *Geochim. Cosmochim. Acta*, **37**, 183–208, 1973.
- Boettcher, A. L., B. O. Mysen, and P. J. Modreski, Melting in the mantle: phase relationships in natural and synthetic peridotite- H_2O - CO_2 systems at high pressures, in *Physics and Chemistry of the Earth*, **9**, pp. 855–868, L. H. Ahrens, J. B. Dawson, A. R. Duncan, and A. J. Erlank, eds., Oxford, Pergamon, 1975.
- Bravo, M. S., and M. J. O'Hara, Partial melting of phlogopite-bearing synthetic spinel- and garnet-lherzolites, in *Physics and Chemistry of the Earth*, **9**, pp. 845–854, L. H. Ahrens, J. B. Dawson, A. R. Duncan, and A. J. Erlank, eds., Pergamon, Oxford, 1975.
- Clayton, R. N., and T. Mayeda, The use of bromine pentafluoride in the extraction of oxygen from oxides and silicates

- for isotopic analysis, *Geochim. Cosmochim. Acta*, 27, 43–52, 1963.
- Craig, H., Isotopic standards for carbon and oxygen and correction factors for mass-spectrometric analysis of carbon dioxide, *Geochim. Cosmochim. Acta*, 12, 133, 1957.
- Dasch, E. J., C. E. Hedge, and J. Dymond, Effect of sea-water interaction on strontium isotope composition of deep-sea basalts, *Earth Planet. Sci. Lett.*, 19, 177–183, 1973.
- Fischer, R. L., and R. W. Raitt, Topography and structure of the Peru-Chile trench, *Deep Sea Res.*, 9, 423–443, 1962.
- Giletti, B. J., M. P. Semet, and R. A. Yund, Studies in diffusion—III. Oxygen in feldspars: an ion microprobe determination, *Geochim. Cosmochim. Acta*, 42, No. 1, 45–57, 1978.
- Gill, J. B. Role of underthrust oceanic crust in the genesis of a Fijian calc-alkaline suite, *Contrib. Mineral. Petrol.*, 43, 29–45, 1974.
- Gilluly, J., Plate tectonics and magmatic evolution, *Geol. Soc. Amer. Bull.*, 82, 2383–2396, 1971.
- Green, T. H. High pressure experimental studies on the mineralogical constitution of the lower crust, *Phys. Earth Planet. Interiors*, 3, 441–450, 1970.
- Hart, S. R., Dredge basalts: some geochemical aspects, *Trans. Amer. Geophys. Union*, 52, 376, 1971.
- Hart, S. R., and K. E. Davis, Nickel partitioning between olivine and silicate melt, *Earth Planet. Sci. Lett.*, in press, 1978.
- Hofmann, A. W., and S. R. Hart, An assessment of local and regional isotopic equilibrium in the mantle, *Earth Planet. Sci. Lett.*, 38, 44–62, 1978.
- James, D. E., Plate tectonic model for the evolution of the central Andes, *Geol. Soc. Amer. Bull.*, 82, 3325–3346, 1971a.
- James, D. E., Andean crustal and upper mantle structure, *J. Geophys. Res.*, 76, No. 14, 3246–3271, 1971b.
- James, D. E., C. Brooks, and A. Cuyubamba, Andean Cenozoic volcanism: magma genesis in the light of strontium isotopic composition and trace-element geochemistry, *Geol. Soc. Amer. Bull.*, 87, 592–600, 1976.
- Kay, R. W., Geochemical constraints on the origin of Aleutian magmas, in *Island Arcs, Deep Sea Trenches and Back-Arc Basins*, pp. 229–242, M. Talwani and W. C. Pitman, III, eds., Maurice Ewing Series 1, AGU, Washington, D.C., 1977.
- Kay, R. W., S. -S. Sun, and C. -N. Lee -Hu, Pb and Sr isotopes in volcanic rocks from the Aleutian Islands and Pribilof Islands, Alaska, *Geochim. Cosmochim. Acta*, 42, 263–273, 1978.
- Klerkx, J., S. Deutsch, H. Pickler, and W. Zeil, Strontium isotopic composition and trace element data bearing on the origin of Cenozoic volcanic rocks of the central and southern Andes, *J. Volcanology and Geothermal Research*, 2, 49–71, 1977.
- Kulm, L. D., W. J. Schweller, and A. Masias, A preliminary analysis of the subduction process along the Andean continental margin, 6° to 45° S., in *Island Arcs, Deep Sea Trenches and Back-Arc Basins*, pp. 285–301, M. Talwani, and W. C. Pitman, III, eds., Maurice Ewing Series 1, AGU, Washington, D.C., 1977.
- Lefèvre, C., Les caractères magmatiques du volcanisme plio-quaternaire des Andes dans le Sud de Pérou, *Contr. Mineral. and Petrol.*, 41, 259–272, 1973.
- Magaritz, M., and H. P. Taylor, Jr., Oxygen, hydrogen and carbon isotope studies of the Franciscan formation, Coast Ranges, California, *Geochim. Cosmochim. Acta*, 40, 215–234, 1976.
- Magaritz, M., D. J. Whitford, and D. E. James, Oxygen isotopes and the origin of high $^{87}\text{Sr}/^{86}\text{Sr}$ andesites, *Earth Planet. Sci. Lett.*, in press, 1978.
- McNutt, R. H., J. H. Crockett, A. H. Clark, J. C. Caelles, E. Farrar, S. J. Haynes, and M. Zentilli, Initial $^{87}\text{Sr}/$

- ^{86}Sr ratios of plutonic and volcanic rocks of the central Andes between latitudes 26° and 29° south, *Earth Planet. Sci. Lett.*, **27**, 305–313, 1975.
- Minster, J. B., T. H. Jordan, P. Molnar, and E. Haines, Numerical modeling of instantaneous plate tectonics, *Roy. Astron. Soc. Geophys. J.*, **36**, 541–576, 1974.
- Modreski, P. J., and A. L. Boettcher, Phase relationships of phlogopite in the system $\text{K}_2\text{O}-\text{MgO}-\text{CaO}-\text{Al}_2\text{O}_3-\text{SiO}_2-\text{H}_2\text{O}$ to 35 kilobars; A better model for micas in the interior of the earth, *Amer. J. Sci.*, **273**, 385–411, 1973.
- Nance, W. B., and S. R. Taylor, Rare earth element patterns and crustal evolution—I. Australian post-Archean sedimentary rocks, *Geochim. Cosmochim. Acta*, **40**, 1539–1551, 1976.
- Nicholls, I. A., The origin of magmas at convergent plate boundaries, *Bull. Aust. Soc. Explor. Geophys.*, **6**, 75–76, 1975.
- Nicholls, I. A., and A. E. Ringwood, Effect of water on olivine stability in tholeiites and the production of silica-saturated magmas in the island arc environment, *J. Geol.*, **81**, 285–300, 1973.
- Peterman, Z. E., C. E. Hedge, R. G. Coleman, and P. D. Snavely, Jr., $\text{Sr}^{87}/\text{Sr}^{86}$ ratios in some eugeosynclinal sedimentary rocks and their bearing on the origin of granitic magma in orogenic belts, *Earth Planet. Sci. Lett.*, **2**, 433–439, 1967.
- Pichler, H., and W. Zeil, Chilean “andesites”—crustal or mantle derivation?, in *Proceedings of International Upper Mantle Project, Conf. on Solid Earth Problems*, vol. II, 361–371, Buenos Aires, 1972.
- Ringwood, A. E., *Composition and Petrology of the Earth's Mantle*, McGraw-Hill, New York, 1975.
- Sacks, I. S., Interrelationships between volcanism, seismicity, and anelasticity in western South America, *Tectonophysics*, **37**, 131–139, 1977.
- Schilling, J.-G., and E. Bonatti, East Pacific ridge ($2^\circ\text{S}-19^\circ\text{S}$) versus Nazca intraplate volcanism: rare-earth evidence, *Earth Planet. Sci. Lett.*, **25**, 93–102, 1975.
- Stern, C. R., W. L. Huang, and P. J. Wyllie, Basalt-andesite-rhyolite- H_2O crystallization intervals with excess H_2O and H_2O undersaturated liquidus surfaces to 35 kilobars, with implications for magma genesis, *Earth Planet. Sci. Lett.*, **28**, 189–196, 1975.
- Stern, C. R., and P. J. Wyllie, Melting relations of basalt-andesite-rhyolite- H_2O and a pelagic red clay, *Contrib. Mineral. Petrol.*, **42**, 313–323, 1973.
- Stern, C. R., and P. J. Wyllie, Phase compositions through crystallization intervals in basalt-andesite- H_2O at 30 kilobars with implications for subduction zone magmas, submitted to *Amer. Mineral.*, 1978.
- Taylor, H. P., The oxygen isotope geochemistry of igneous rocks, *Contrib. Mineral. Petrol.*, **19**, 1–71, 1968.
- Thorpe, R. S., P. J. Potts, and P. W. Francis, Rare earth data and petrogenesis of andesite from the north Chilean Andes, *Contrib. Mineral. Petrol.*, **54**, 65–78, 1976.
- Whitford, D. J., Geochemistry and petrology of volcanic rocks from the Sunda arc, Indonesia, Ph.D. dissertation, Australian National Univ., Canberra, 1975a.
- Whitford, D. J., Strontium isotopic studies of the volcanic rocks of the Sunda arc, Indonesia, and their petrogenetic implications, *Geochim. Cosmochim. Acta*, **39**, 1287–1302, 1975b.
- Whitford, D. J., Rare earth element abundances in late-Cenozoic lavas from the Peruvian Andes, A preliminary report, *Carnegie Inst. Wash. Year Book* **76**, 840–844, 1977.
- Whitford, D. J., W. Compston, and I. A. Nicholls, Geochemistry of late Cenozoic lavas from eastern Indonesia:

- Role of subducted sediments in petrogenesis, *Geology*, **5**, 571–575, 1977.
- Wilson, J., and W. Garcia, Geologia de los cuadrangulos de Pachia y Palca, *Bol. de la Comision de la Carta Geologica Nacional del Peru*, **2**, No. 4, 1962.
- Wyllie, P. J., Crustal anatexis: an experimental review, *Tectonophysics*, **43**, 41–71, 1977.

TRACE ELEMENT AND SR ISOTOPE
ABUNDANCES IN RECENT LAVAS
FROM KILAUEA, HAWAII

A. W. Hofmann, T. L. Wright,*
and M. Feigenson†

The frequent eruptions of Kilauea offer an unusual opportunity to study the chemical evolution of basaltic magma. Wright, Swanson, and Duffield (1975, hereafter referred to as WSD) have sampled and analyzed in detail the products of a long-lived eruption on the east rift of Kilauea (Mauna Ulu eruption). Using samples collected during 1969–1971, WSD showed that the major variations in composition can be explained by olivine fractionation, but that when the effect of olivine control is removed by normalizing all the compositions to an MgO concentration of 7%, there remain small but significant variations in composition. WSD recognized five variants, the first two of which are nearly indistinguishable from the composition of the 1967–68 summit eruption in Halemaumau. Subsequent variants showed small differences in SiO₂ (0.25%), Al₂O₃ (0.27%), and, in particular, small but systematic decreases in K₂O, TiO₂, and P₂O₅. These variations have been modeled by methods given by Wright and Doherty (1970) and by Wright and Helz (1976) and cannot be explained by

fractional crystallization at either low or high pressure. In this paper we address the question whether they can be explained by a partial melting process. We consider two simple models: (1) varying degree of melting of the same source material, and (2) several source batches of differing incompatible-element content. Isotopic and trace element data are useful in this context, because new source batches may be recognized by their distinct isotopic composition and abundances of incompatible elements. The results show no significant isotopic variations. However, the trace element concentrations decrease systematically with time of eruption, indicating a gradual increase in the degree of melting at the source. At the same time, the Rb/Sr ratios decrease, while Rb/K, Ba/K, and Cs/K remain constant. We interpret this as the result of Sr retention in residual clinopyroxene during tholeiite production, and we believe that this retention mechanism may explain why the mantle source of midocean ridge basalts has a Rb/Sr ratio too low to have produced the observed present-day ⁸⁷Sr/⁸⁶Sr ratios.

Analytical Results

Isotope abundance and isotope dilution analyses were performed using the six-inch-radius mass spectrometer. The analytical errors are approximately ±0.0001 for ⁸⁷Sr/⁸⁶Sr, ±4% for K, and ±2% for Rb, ±1% for Sr and Ba, and ±5% for Cs. The ⁸⁷Sr/⁸⁶Sr values were corrected using the Eimer and Amend SrCO₃ standard value of ⁸⁷Sr/⁸⁶Sr = 0.70800, for which our measured value was 0.70790. The results are given in Table 28. The sample numbers are the same as those given by WSD. Description and locations are also given in that paper.

Our K values are systematically higher by 6–15% than those given by WSD. Such differences in potassium analyses are common when different analytical techniques are employed, and it is not

* U. S. Geological Survey, Reston, Virginia.

† Present address: Princeton University, Department of Geological and Geophysical Sciences, Princeton, New Jersey.

TABLE 28. Sr Isotope Ratios, Trace Element Abundances, and MgO Concentrations

Sample*	Eruption Date*	⁸⁷ Sr/ ⁸⁶ Sr	K ppm	Rb ppm	Cs ppm	Sr ppm	Ba ppm	MgO* %
HM 68-2	1968	0.70354	4586	9.1	0.101	373	127	7.63
HM 68-15	1968	0.70348	4554	9.1	0.094	367	129	7.63
DAS 69-1-3	5/24/69	0.70355	4396	8.5	0.090	355	123	9.14
		0.70351						
DAS 69-78-9	8/18/69	0.70351	4340	8.8	0.095	362	122	9.10
DAS 69-8-1	8/22/69	...	4293	8.6	0.083	364	121	8.97
DAS 70-1213-25	4/9/70	0.70348	4172	8.3	0.081	348	115	8.55
DAS 70-1213-35	5/20/70	0.70360	3796	7.7	0.076	326	107	10.01
DAS 70-1213-41	5/24/70	0.70351	3871	8.0	0.092	330	109	9.57
DAS 70-1213-62	7/9/70	0.70352	3556	7.1	0.086	304	100	12.02
DAS 70-1213-83	9/3/70	0.70344	3683	7.3	0.084	314	103	10.92
DAS 71-1213-127	2/15/71	0.70346	3487	6.9	0.073	303	98	11.33
DAS 71-1213-134	4/12/71	0.70362	3722	7.3	0.068	330	106	8.14
		0.70359						
DAS 71-1213-136	4/19/71	0.70353	3512	7.1	0.072	309	100	10.33
DAS 71-1213-137	4/19/71	0.70358	3373	6.6	0.070	292	93	11.96
		0.70348						
MUI-74-132	1974	0.70345	3527	7.1	0.072	306	99	11.60

* Sample numbers, eruption dates, and MgO values are taken from Wright *et al.* (1975).

our purpose here to investigate the reasons for this problem. Recalibration of our mixed-alkali spike containing ⁴¹K (used for the isotope dilution measurements) with a freshly prepared K-standard solution yielded no significant differences from previously used concentration values. Despite the difference in absolute K concentrations in the two sets of measurements, we emphasize that the trend in K values reported by WSD is confirmed by our new analyses.

Discussion

In order to eliminate the effect of olivine fractionation, we have normalized the trace concentrations to 7.00% MgO content, as was explained by WSD. The measured and normalized Sr concentrations are shown in Fig. 116 as a function of eruption date. It is clear that the normalization procedure results in a substantial reduction of data scatter. This is not surprising because olivine contains no significant amounts of the trace elements analyzed, so that its addition or

subtraction simply dilutes or concentrates the incompatible elements in the melt. The normalization procedure thus clarifies the nearly monotonic decrease in Sr concentration with time of eruption in the parental melt. The other elements analyzed show similar decreases with time.

Another method of removing the effects of fractionation (or cumulus olivine) is to focus attention on ratios of incompatible elements. Figure 117 shows several examples of this with trend lines calculated from linear-regression analyses for the Mauna Ulu eruptions from 1969 to 1971.

These ratios are all remarkably uniform. The total spread about the mean is ±3% for Rb/K, ±14% for Cs/K, ±6% for Rb/Sr, and ±1.8% for Ba/K. We have no good explanation for this anomalously large scatter in Cs/K (which is outside the analytical error), and we speculate that it may be caused by small amounts of Cs contamination of the magma. Such contamination could result from the incorporation of a very

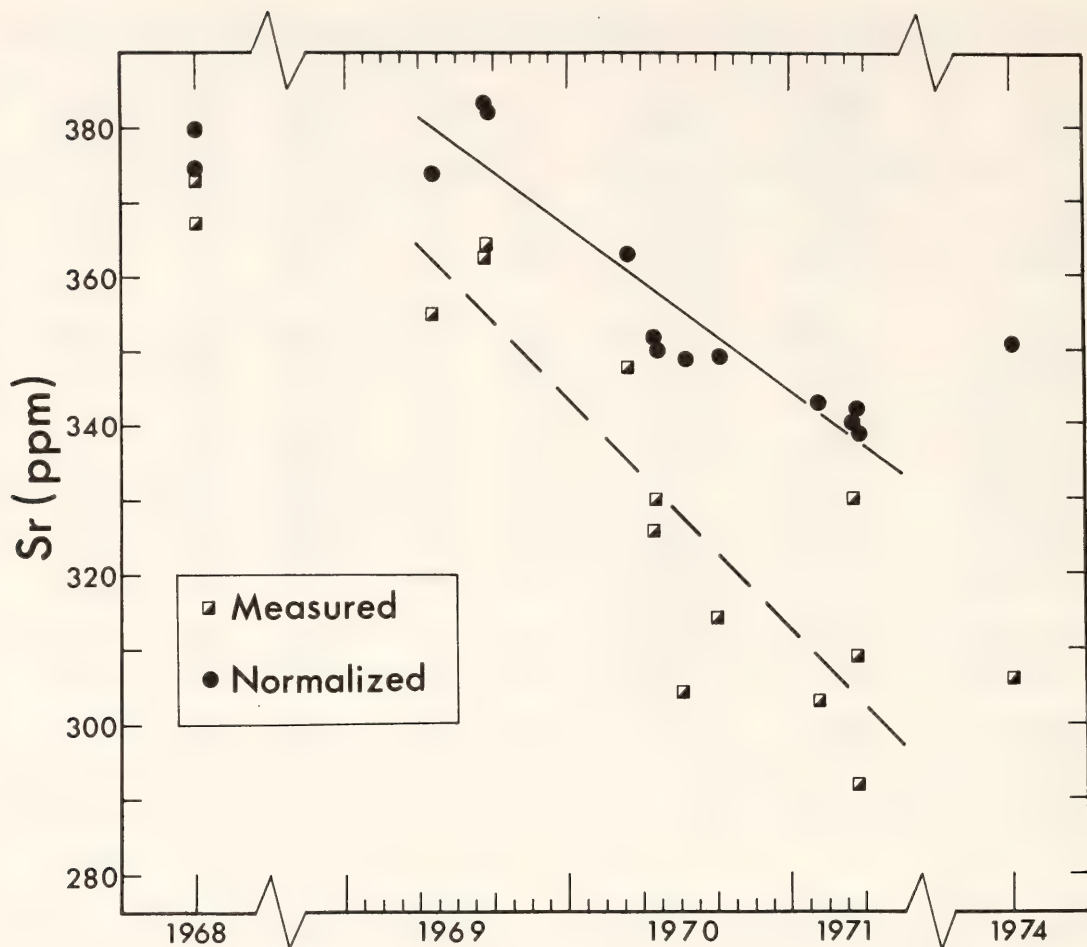


Fig. 116. Sr concentration of Kilauea lavas as a function of eruption date. The normalized values were computed to adjust the composition to an MgO concentration of 7.0% (by removing olivine component; see Wright *et al.*, 1975). The solid lines are linear regressions for the eruptions during the 1969–1971 interval.

small amount of sediment or altered rock into the magma chamber, since Cs is a very sensitive indicator of contamination (Hart, 1969).

None of the element ratios shown in Fig. 117, with the exception of Rb/Sr and Ba/Sr, show any systematic variation with date of eruption, even though all of the element concentrations decrease systematically. Using the type of plot shown in Fig. 117, we find no systematic variations for any of the trace element ratios that do not include Sr. All the ratios that do include Sr vary with time of eruption. This is the result of the fact that Sr concentration decreases less rapidly than the concentrations of the other elements.

The above observations can be used

to set constraints on the petrogenesis of these lavas. For example, we may use the data to test a petrogenetic model recently proposed by Beswick (1976). This involves fractional melting, with phlogopite remaining in the residue. According to Beswick, this process leads to an increase in the Rb/K ratio as more and more melt is removed from the source rock. Clearly, this model is not compatible with our observations because Rb/K remains constant. Another possible mechanism might be some sort of “eclogite” fractionation at depth. However, the crystallization of garnet and pyroxene would result in an increase in the concentrations of incompatible elements, which is the opposite of the observed trends. Other conceivable

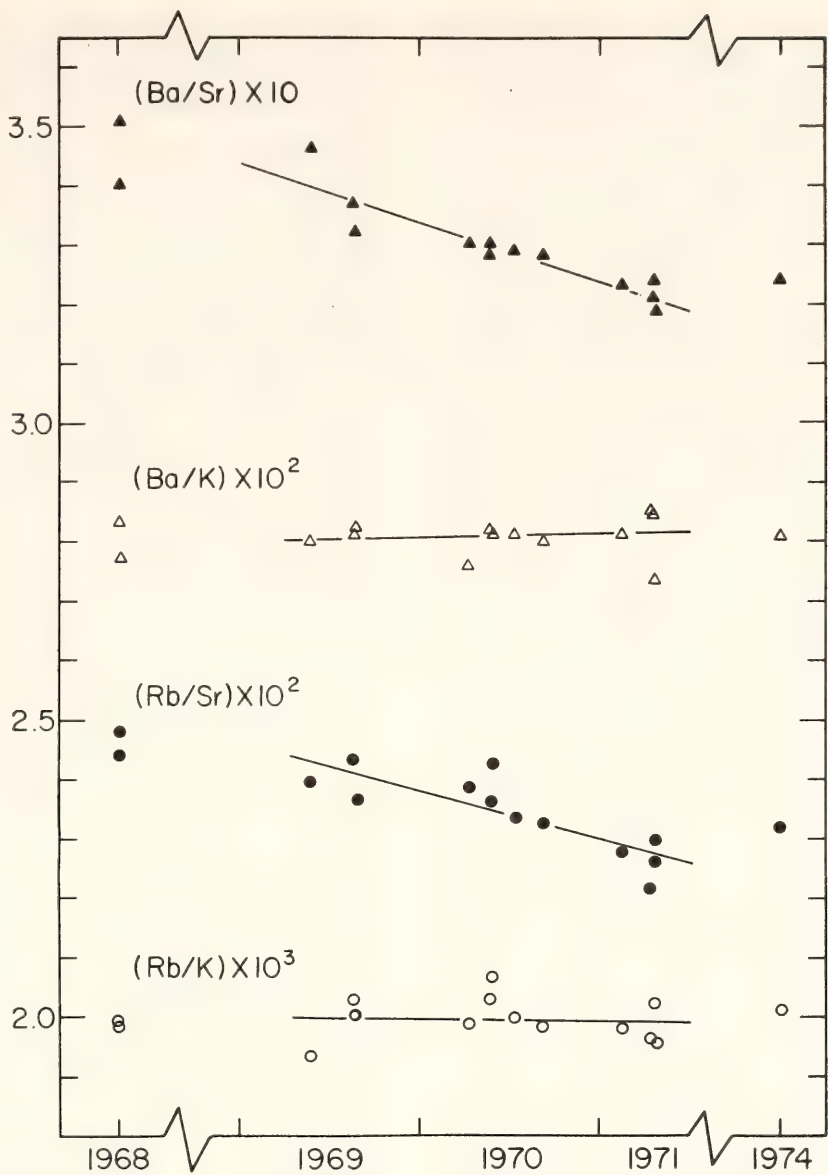


Fig. 117. Ratios of incompatible elements in Kilauea lavas as a function of eruption date. The regression lines are calculated for the 1969–1971 interval only.

mechanisms involving fractional crystallization, for example K-feldspar control, may be compatible with the trace element data presented here but are rejected on other grounds, namely the major-element chemistry presented by WSD and absence of K-feldspars in tholeiites in general.

Because of the failure of all explanations involving fractional crystallization we conclude that the correct explanation must be sought in the melting process. The uniformity of the ⁸⁷Sr/⁸⁶Sr ratios with time indicates that it is not necessary to invoke new batches of source

mantle for each new magma variant. Either all the melts are derived from the same source volume, or the different source batches are isotopically indistinguishable. The concentration decrease of all the incompatible elements is therefore probably caused by a gradual increase in the degree of melting (e.g., Gast, 1968). The simultaneous decrease in the K/Sr, Rb/Sr, and Ba/Sr ratios (while the other element ratios and the isotopic composition remain constant) is most easily explained by the persistence of a residual phase, the partition coefficient of which (relative to the melt) is

significantly greater for Sr than for K, Rb, Cs, and Ba. Clinopyroxene meets all the requirements quite well. There is rather good agreement in the literature that the clinopyroxene liquid partition coefficient K_D for Sr is about 0.1 (ranging from 0.05 to 0.5) whereas K_D is on the order of 10^{-2} to 10^{-3} for K, Rb, Cs, and Ba (Philpotts and Schnetzler, 1970; Shimizu, 1974; Hart and Brooks, 1974). This means that K, Rb, and Cs and Ba will be essentially completely partitioned into the melt ($>99\%$) if the proportion of melt equals the proportion of residual clinopyroxene, and if the other residual phases are olivine, orthopyroxene, and garnet or spinel. On the other hand, approximately 10% of the Sr remains in the clinopyroxene under the same conditions and if $K_D^{\text{cpx}}(\text{Sr}) = 0.1$. Then, as the degree of melting and the melt/clinopyroxene ratio increases, the remaining Sr enters the liquid and the K/Sr, Rb/Sr, Cs/Sr, and Ba/Sr ratios decrease, while simultaneously all the element concentrations decrease. A good quantitative fit of this model to the data is critically dependent on the exact value of the Sr partition coefficient and quite insensitive to the other partition coefficients. The dilution of the trace element concentration indicates a relative increase in the melt fraction of about 20%. This increase in the degree of melting will increase the total amount of Sr in the melt by about 5%, if $K_D(\text{Sr})$ has a constant value of about 0.1. This would change the Ba/Sr ratio by only 5%, rather than 8% as observed. It seems reasonable to suppose that the increase in melt fraction is accompanied by an increase in temperature. For example, according to the experimental data of Sun *et al.* (1974), the partition coefficients for Sr in clinopyroxene are 0.216 at 1150°C and 0.143 at 1170°C. Thus, if at 1150°C the assemblage contains 10% melt and 10% clinopyroxene, 82% of the total Sr will be in the melt. As the temperature increases to 1170°C, the

melt fraction increases to 12%, clinopyroxene decreases to 9%, and 90% of the Sr will be in the melt. This hypothetical example is not unique and is meant only to illustrate the fact that a modest decrease in the partition coefficient is sufficient to give quantitative agreement between model and data.

With the presently available data we are unable to solve the problem uniquely and quantitatively by using the inversion techniques of Minster *et al.* (1977). This is true because the solutions will be very sensitive to the partition coefficient of Sr and its dependence on pressure, temperature, and composition. Unfortunately, to our knowledge, none of the experimental determinations of this partition coefficient in clinopyroxene can be proved to be an equilibrium measurement. Also, we are unable to distinguish between models of batch melting with increasing melt fraction, batch melting of several separate source volumes and fractional melting. The constancy of the $^{87}\text{Sr}/^{86}\text{Sr}$ ratio could mean that there is either only a single source volume or several source volumes identical in isotopic composition.

The main observations made in this paper are (a) the decrease in concentration of the incompatible elements K, Rb, Cs, Sr, and Ba during the course of the Mauna Ulu eruptions, (b) the constant $^{87}\text{Sr}/^{86}\text{Sr}$ ratios, (c) the increase in Sr relative to the other trace elements, and (d) the constant concentration ratios among the elements K, Rb, Cs, and Ba. These features can be explained by a model of partial melting in a mantle consisting of olivine, orthopyroxene, garnet, and clinopyroxene. The degree of melting increases by about 20% during the Mauna Ulu eruptions, and some clinopyroxene remains in the solid residue during this increase. We believe that this model is at least qualitatively unique, although the details of the melting process cannot at present be further specified.

The results bear on two important geochemical questions: (1) What process is responsible for the well-known depletion in incompatible elements and $^{87}\text{Sr}/^{86}\text{Sr}$ of the midocean ridge basalts (and their source mantle)? (2) How was the Rb/Sr ratio in the mantle fractionated to varying degrees in the source materials of ocean island basalts such that these islands now conform roughly to a 1.5-b.y. mantle isochron (see Brooks *et al.*, 1976). A widely held opinion is that oceanic tholeiites are produced by relatively large degrees of melting (on the order of 25%; see for example, Gast, 1968; Green and Ringwood, 1967). Such large degrees of melting would consume most or all of the possible Sr-bearing minerals, so that after withdrawal of the melt the residue would be severely depleted in all incompatible elements with little or no fractionation of Sr relative to Rb. For example, if the proportions of melt and clinopyroxene are 25 and 5%, respectively, and $K_D^{\text{cp}}(\text{Sr}) = 0.2$, then about 96% of the total Sr will be in the melt phase. Model mantle compositions contain typically about 3% CaO and the clinopyroxene contains about 20% CaO (Yoder, 1976; Ringwood, 1969), so that the maximum initial amount of clinopyroxene (assuming all the CaO to be in this phase) is about 15%. Therefore, the assumption of 5% residual clinopyroxene after 25% melting is actually in error on the high side. If the ratio of clinopyroxene to melt fractions were smaller, the residue would be even more severely depleted in Sr (as well as in the more incompatible elements).

The results given in this report demonstrate that such Rb-Sr fractionation does occur during tholeiite production, that clinopyroxene retention is the most likely mechanism, and that the degree of melting is more likely on the order of 10%. Given these conditions, tholeiitic volcanism does indeed appear to be able to generate a moderately depleted mantle reservoir and the variations in Rb/Sr

necessary to account for the observed variations in $^{87}\text{Sr}/^{86}\text{Sr}$.

References

- Beswick, A. E., K and Rb relations in basalts and other mantle derived materials: is phlogopite the key?, *Geochim. Cosmochim. Acta*, 40, 1167–1183, 1976.
- Brooks, C., S. R. Hart, A. W. Hofmann, and D. E. James, Rb-Sr mantle isochrons from oceanic regions, *Earth Planet Sci. Lett.*, 32, 51–61, 1976.
- Gast, P. W., Trace element fractionation and the origin of tholeiitic and alkaline magma types, *Geochim. Cosmochim. Acta*, 32, 1057–1086, 1968.
- Green, D. H., and A. E. Ringwood, The genesis of basaltic magmas, *Contrib. Mineral. Petrol.* 15, 103–190, 1967.
- Hart, S. R., K, Rb, Cs contents and K/Rb, K/Cs ratios of fresh and altered submarine basalts, *Earth Planet. Sci. Lett.*, 6, 295–303, 1969.
- Hart, S. R., and C. Brooks, Clinopyroxene-matrix partitioning of K, Rb, Cs, Sr and Ba, *Geochim. Cosmochim. Acta*, 38, 1799–1806, 1974.
- Minster, J. F., J. B. Minster, M. Treuil, and C. Allègre, Systematic use of trace elements in igneous processes, Part II: Inverse problem of the fractional crystallization process in volcanic suites, *Contrib. Mineral. Petrol.*, 61, 49–77, 1977.
- Philpotts, J. A., and C. C. Schnetzler, Phenocryst-matrix partition coefficients for K, Rb, Sr and Ba, with applications to anorthosite and basalt genesis, *Geochim. Cosmochim. Acta*, 34, 307–322, 1970.
- Ringwood, A. E., Composition and evolution of the upper mantle, in *The Earth's Crust and Upper Mantle*, Amer. Geophys. Union Monograph, 13, 1, P.-J. Hart, ed., 1969.
- Shimizu, N., An experimental study of the partitioning of K, Rb, Cs, Sr, and Ba between clinopyroxene and liquid

- at high pressures, *Geochim. Cosmochim. Acta*, **38**, 1789–1798, 1974.
- Sun, C. O., R. J. Williams, and S. S. Sun, Distribution coefficients of Eu and Sr for plagioclase-liquid and clinopyroxene-liquid equilibria in oceanic ridge basalt: an experimental study, *Geochim. Cosmochim. Acta*, **38**, 1415–1433, 1974.
- Wright, T. L., and P. C. Doherty, a linear programming and least squares computer method for solving petrologic mixing problems. *Bull. Geol. Soc. Amer.*, **81**, 1995–2008, 1970.
- Wright, T. L., and R. T. Helz, Use of mass balance equations to evaluate models of magma genesis: *Geol. Soc. Amer., Abstracts w. Progr.*, **8**, 1176, 1976.
- Wright, T. L., D. A. Swanson, and W. A. Duffield, Chemical compositions of Kilauea east-rift lava, 1968–1971, *J. Petrology*, **16**, 110–133, 1975.
- Yoder, H. S. Jr., *Generation of Basaltic Magma*, Nat. Acad. Sci., Washington, D.C., 1976.

GEOCHEMISTRY OF THE GALÁPAGOS
ISLANDS: IMPLICATIONS FOR MANTLE
DYNAMICS AND EVOLUTION

W. M. White and A. W. Hofmann

Introduction

The Galápagos Islands are of special geochemical interest for several reasons: (1) their proximity to a midocean ridge, the Galápagos Rise, (2) the presence of tholeiitic basalts, permitting a test of the worldwide oceanic mantle isochron of Brooks *et al.* (1976), and (3) the unusually low $^{87}\text{Sr}/^{86}\text{Sr}$ ratios reported by Hedge (1978). We have undertaken a Sr and Nd isotope and trace element study of the Galápagos Islands, the results of which we report here.

The Galápagos archipelago consists of 10 major volcanic islands and numerous islets which emerge from a shallow plateau in the eastern equatorial Pacific (Fig. 118). The archipelago is bounded

on the north by the Galápagos Rise, an active spreading center extending from the East Pacific Rise to the Peru-Chile trench and forming the boundary between the Cocos and Nazca plates. Two aseismic ridges, the Cocos Ridge and the Carnegie Ridge, diverge from the Galápagos Plateau. Morgan (1971) proposed that the Galápagos are the surface manifestation of a deep mantle plume. This interpretation is supported by structural, geophysical, and geochemical evidence (e.g., Johnson *et al.*, 1976; Case *et al.*, 1973; Schilling *et al.*, 1976).

Both tholeiitic and alkali basalts occur in the Galápagos (McBirney and Williams, 1969). Individual islands, however, are usually dominated by a single basalt type, Santa Cruz being the most notable exception. The large western islands of Fernandina and Isabela are tholeiitic and are the youngest and volcanically most active of the group. The oldest exposed lavas in the archipelago are uplifted submarine basalts, which compose all of Espanola and Sante Fe and part of Santa Cruz. K-Ar dates on these lavas vary from 0.74 and 4.2 m.y. (Cox and Dalrymple, 1966; Bailey, 1976). For further background on the geology and petrology of the Galápagos the reader is referred to the thorough study of McBirney and Williams (1969).

Results

Powder splits were kindly provided by A. R. McBirney and C. S. Bow of the Center for Volcanology, University of Oregon. Major element analyses and petrographic descriptions of many of these samples can be found in McBirney and Williams (1969). $^{87}\text{Sr}/^{86}\text{Sr}$ ratios and K, Rb, Cs, Sr, and Ba concentrations were determined using the method described by Hart and Brooks (1974), rare earths by the method of Shimizu (1974), and $^{143}\text{Nd}/^{144}\text{Nd}$ using the method described by Whitford *et al.* (this Report).

The results of the isotopic analyses are reported in Table 29. There is con-

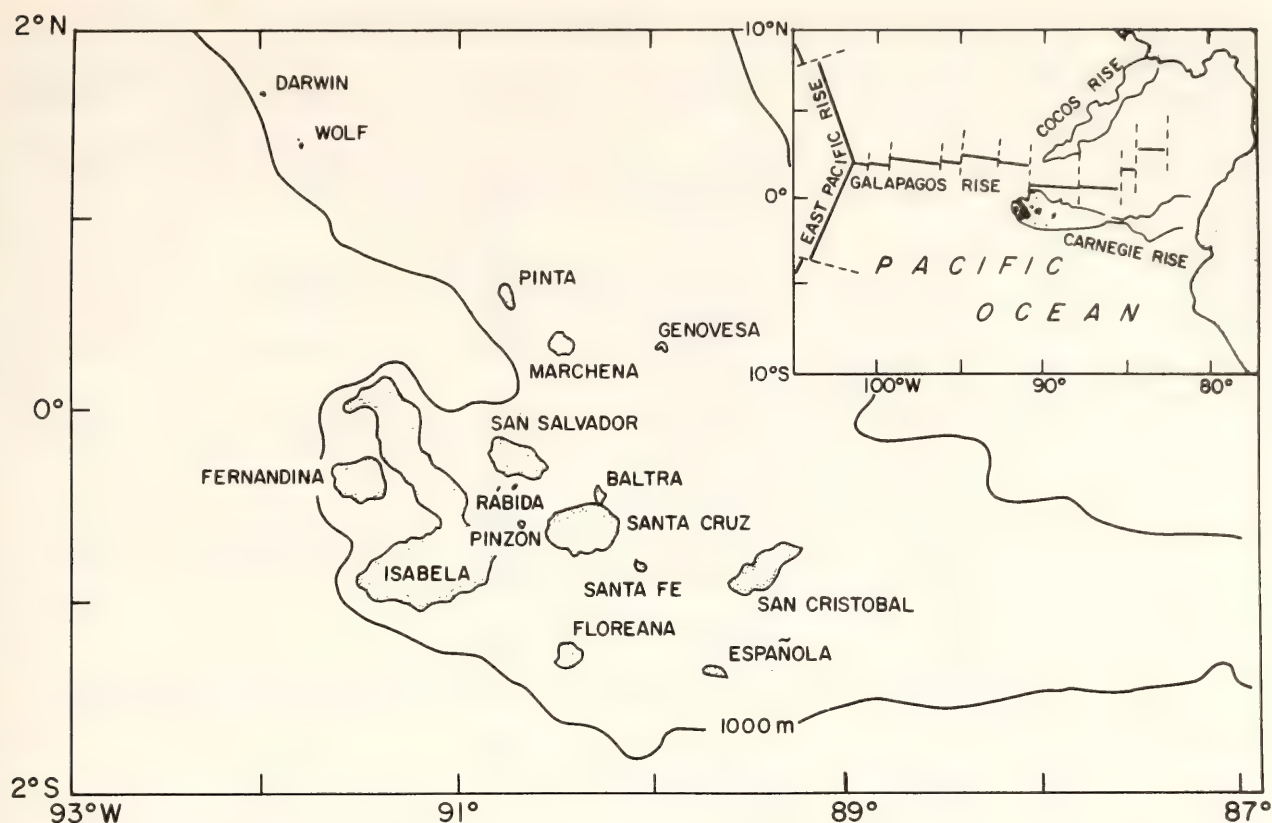


Fig. 118. Map of the Galápagos Islands. The 1000-meter bathymetric contour outlines the Galápagos plateau.

siderable variation in both Sr and Nd isotope ratios: $^{87}\text{Sr}/^{86}\text{Sr}$ ratios range from 0.70263 to 0.70339, and $^{143}\text{Nd}/^{144}\text{Nd}$ from 0.51287 to 0.51315. The range in $^{87}\text{Sr}/^{86}\text{Sr}$ is not unusual compared to those of other island groups, for example Azores (0.7033–0.7052; White *et al.*, 1976), Hawaiian Islands (0.7032–0.7044; O’Nions *et al.*, 1977a), Kerguelen (0.7042–0.7058; Hedge *et al.*, 1973), and Samoa (0.7052 to 0.7065; Hedge *et al.*, 1972). Of these, Nd isotope ratios have been reported only from the Hawaiian Islands, where values range from 0.51307 to 0.51288 (O’Nions *et al.*, 1977a). While the Galápagos as a whole exhibits a wide range in isotope ratios, individual islands tend to be more uniform in isotopic character. Our results are consistent with those of Hedge (1978), although we have failed to find any basalts with $^{87}\text{Sr}/^{86}\text{Sr}$ ratios as low as the value of 0.7024 reported by Hedge. The Nd isotope ratio of a Galápagos basalt reported by De

Paolo and Wasserburg (1976b) falls within the range of our analyses.

De Paolo and Wasserburg (1976b) and O’Nions *et al.* (1977a) showed that there is a negative correlation between $^{87}\text{Sr}/^{86}\text{Sr}$ and $^{143}\text{Nd}/^{144}\text{Nd}$ ratios in oceanic basalts. Figure 119 shows that Nd and Sr isotope ratios in Galápagos basalts scatter about the correlation of previously reported Nd and Sr data (Richard *et al.*, 1976; De Paolo and Wasserburg, 1976b; O’Nions *et al.*, 1977a). As in the case of the Hawaiian data (O’Nions *et al.*, 1977a), however, the correlation in the Galápagos data is not perfect.

One of the most interesting features of our results is the presence on several of the islands of basalts with low $^{87}\text{Sr}/^{86}\text{Sr}$ and high $^{143}\text{Nd}/^{144}\text{Nd}$, ratios similar to those of midocean ridge basalts. Of these, the basalts from Santa Cruz are the most distinctive, in that they have not only the isotopic but also the major-element

TABLE 29. Rb-Sr and Sm-Nd Analytical Results

Island	Sample No.	⁸⁷ Sr/ ⁸⁶ Sr*	Rb/Sr	¹⁴³ Nd/ ¹⁴⁴ Nd†	Sm/Nd
Fernandina	E-42	0.70312±5	0.021	0.512996±30	0.255
	E-87	0.70314±4	0.020		
Isabela	E-56	0.70327±5	0.032	0.513060±40	0.271
	E-63	0.70278±6	0.019		
	E-132	0.70331±4	0.024		
	E-134	0.70327±5	0.016	0.513056±25	
Santa Cruz	E-1	0.70264±4	0.007	0.513090±40	0.309
	SC-64	0.70288±6	0.003		
	SC-78	0.70263±6	0.005		
	SC-100	0.70268±5	0.004		
	SC-151	0.70268±6	0.022	0.513123±40	0.253
	SC-163	0.70267±7	0.004		
	SC-196	0.70399±6	0.004		
San Salvador	E-20	0.70294±6	0.013	0.513119±20	0.278
	E-24	0.70284±5	0.006		
	E-76	0.70286±6	0.008		
Rábida	E-51	0.70302±6	0.042		
Pinzón	E-68b	0.70301±5	0.026		
Pinta	E-4	0.70387±4	0.036	0.512932±40	0.242
	E-8	0.70335±4	0.037	0.512867±30	
Marchena	E-10	0.70278±7	0.004	0.513106±30	0.296
	E-15	0.70276±6	0.019		
San Cristobal	E-103	0.70282±4	0.029	0.513151±30	0.239
Floreana	E-110	0.70366±5	0.081	0.512964±35	0.219
	FL-3	0.70395±6	0.040		
	FL-26	0.70343±6	0.015		
	FL-27	0.70338±5	0.055		
Española	E-102	0.70294±4	0.022		
Santa Fe	E-111	0.70341±4	0.002	0.513090±25	0.331

* ⁸⁷Sr/⁸⁶Sr values are normalized to ⁸⁶Sr/⁸⁸Sr = 0.11940 and are relative to ⁸⁷Sr/⁸⁶Sr = 0.70800 for the E + A Standard. Errors quoted are 2 standard errors of the mean.
† ¹⁴³Nd/¹⁴⁴Nd are normalized to ¹⁴⁶Nd/¹⁴⁴Nd = 0.72190. Two analyses of USGS standard BCR-1 yielded ¹⁴³Nd/¹⁴⁴Nd ratios of 0.512693 ± 15 and 0.512697 ± 35. Errors quoted are 2 standard errors of the mean.

and LIL-element characteristics of mid-ocean ridge basalts. For example, SC-78 has 685 ppm K, 1.04 ppm Rb, 0.013 ppm Cs, 212 ppm Sr, 12.7 ppm Ba, and a slight depletion in light rare earths relative to the intermediate rare earths. This sample is distinguished from mid-ocean ridge basalts only by its higher Sr concentrations. To our knowledge, there are no other reported occurrences

of basalts on oceanic islands this similar to midocean ridge basalts.
The range of LIL-element concentrations from the remaining islands is as follows: K 794–8935 ppm, Rb 0.48–20.01 ppm, Cs 0.006–0.115 ppm, Sr 211–505 ppm, and Ba 25–620 ppm. Representative rare earth patterns are shown in Fig. 120. Rare earth patterns vary from slightly light rare earth depleted in the

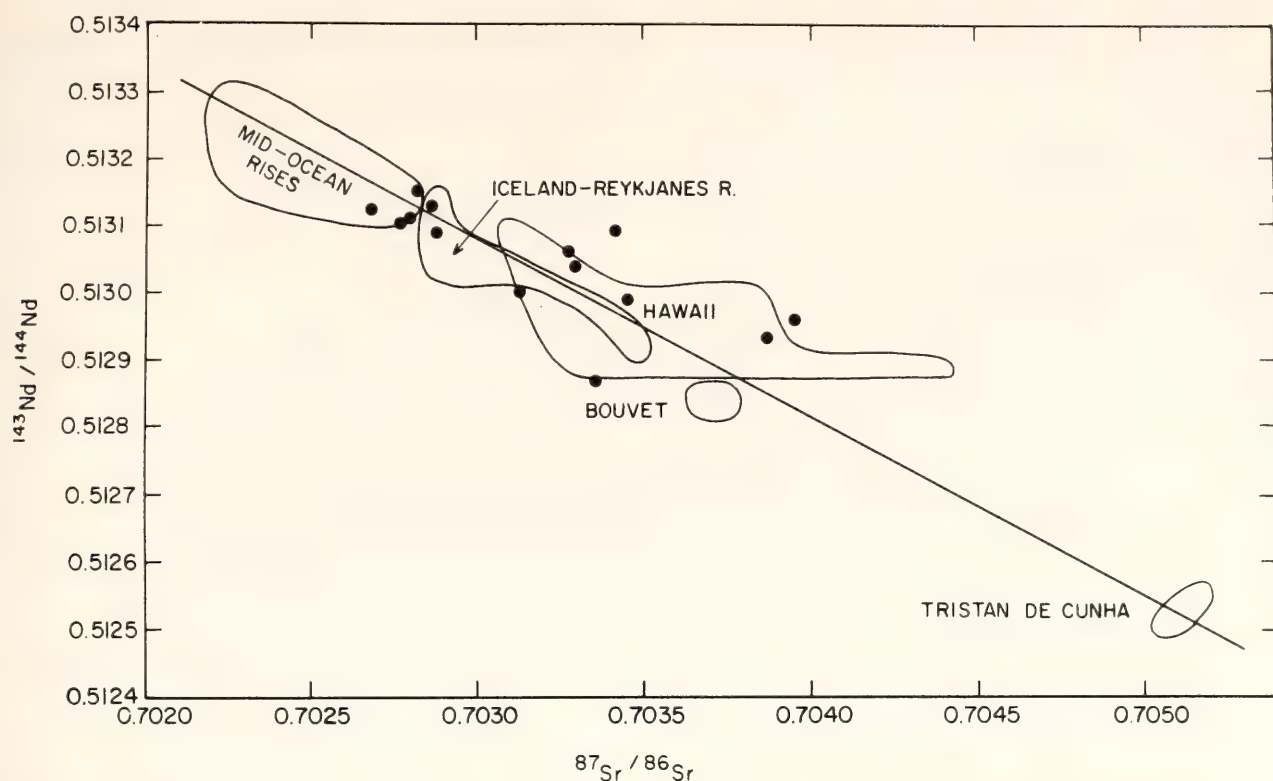


Fig. 119. Variations of $^{143}\text{Nd}/^{144}\text{Nd}$ with $^{87}\text{Sr}/^{86}\text{Sr}$ in Galápagos basalts. Fields of basalts from Tristan de Cunha, Bouvet, Hawaiian Islands, Iceland, and the Reykjanes Ridge, and mid-ocean ridges (O'Nions *et al.*, 1977a; Richard *et al.*, 1976; De Paolo and Wasserburg, 1976b) are also shown.

Santa Cruz tholeiites to moderately and strongly light rare earth enriched. FL-3 exhibits particularly strong light rare earth enrichment but has a nearly flat (chondritic) heavy rare earth pattern. FL-3 is a picritic alkali basalt and also has the highest alkali and alkaline earth concentrations of any basalt we have analyzed from the Galápagos. E-68b exhibits a strong negative Eu anomaly, most probably reflecting extensive plagioclase fractionation. The remaining patterns all have slight positive Eu anomalies. While this could reflect either a systematic error in our Eu determinations or an incorrect chondritic normalization value, positive Eu anomalies are not present in other rare earth patterns determined in this laboratory (e.g., Whitford and Duncan, this Report). It seems most likely, therefore, that the Eu anomalies reflect either source chemistry or peculiarities of magma genesis in this area. A slight positive Eu anomaly also

appears to be characteristic of basalts from the Azores (Flower *et al.*, 1976; White, 1977).

Alkali basalts (defined by their nepheline-normative composition) tend to have higher LIL-element concentrations than tholeiites. This is most apparent on the island of Santa Cruz, where both tholeiites and alkali basalts occur. The recent tholeiites and alkali basalts on this island have the same Sr and Nd isotope ratios, implying that they are derived from the same source. The three recent alkali basalts that we have analyzed have an average of 3664 ppm K, 4.83 ppm Rb, 0.081 ppm Cs, 416 ppm Sr, and 72.8 ppm Ba, while the three recent tholeiites average 708 ppm K, 0.83 ppm Rb, 0.010 ppm Cs, 225 ppm Sr, and 14.6 ppm Ba. There are also clear differences in rare earth patterns between the Santa Cruz tholeiites and alkali basalts (Fig. 120). The tholeiites (e.g., SC-64) have slightly light rare earth-depleted patterns, whereas

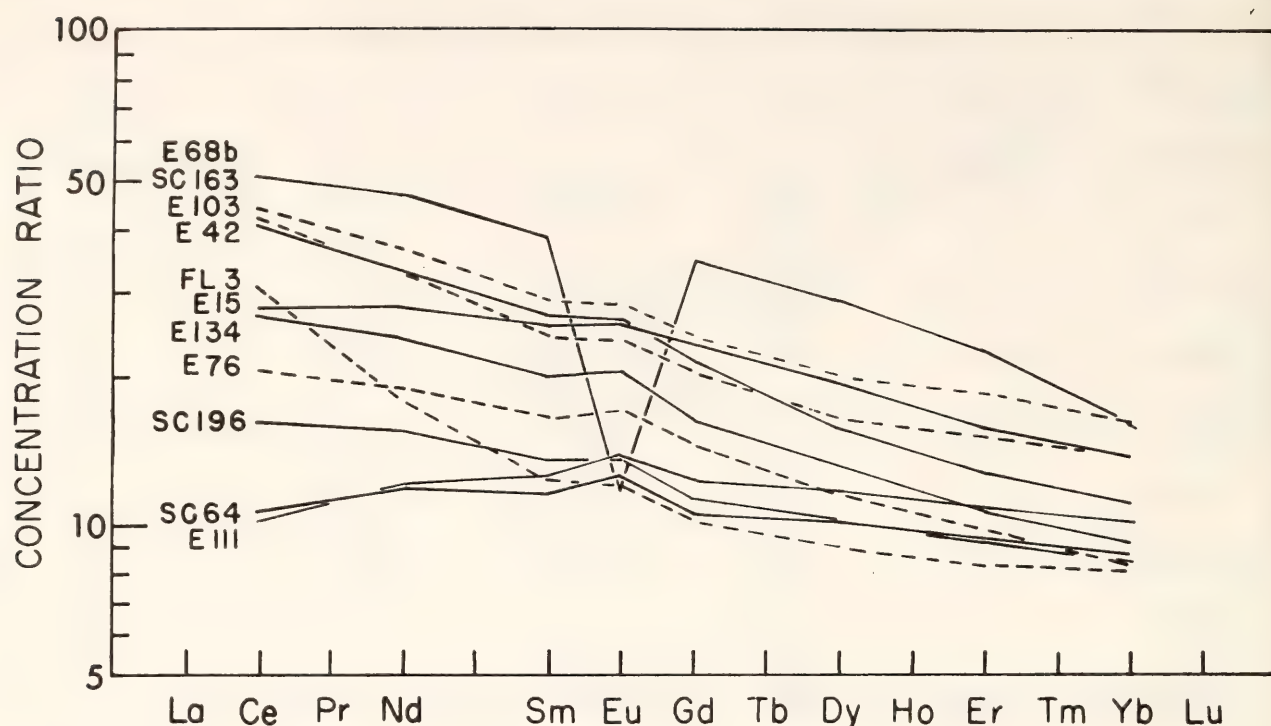


Fig. 120. Chondrite-normalized rare earth abundances in Galápagos basalts. Tholeiites are shown as solid lines, alkali basalts as dashed lines. Chondritic normalization values are from Nakamura (1974).

the alkali basalts (e.g., SC-163) are distinctly light rare earth enriched. Nonetheless, some of the Galápagos alkali basalts have surprisingly low LIL-element concentrations. For example, E-24, an alkali basalt from San Salvador containing 6% normative nepheline (McBirney and Williams, 1969), has only 1190 ppm K, 1.39 ppm Rb, 0.010 ppm Cs, 242 ppm Sr, and 25.3 ppm Ba.

Discussion

Variations in $^{87}\text{Sr}/^{86}\text{Sr}$ ratios in Galápagos basalts fit a simple geographical pattern, and a contour can be drawn that separates those islands having basalts with $^{87}\text{Sr}/^{86}\text{Sr}$ ratios less than 0.7030 from those having basalts with ratios higher than 0.7030 (Fig. 121). The islands with $^{87}\text{Sr}/^{86}\text{Sr}$ ratios lower than 0.7030 all occur in the east-central portion of the Galápagos Plateau, while those islands with higher ratios occur on the western, northern, and southern edges. There are three exceptions to this

pattern: sample E-63 from Isabela, and samples SC-196 and E-111 which are uplifted submarine lavas from the islands of Santa Cruz and Santa Fe.

The uplifted submarine lavas are among the oldest in the archipelago (McBirney and Williams, 1969). SC-196 has been dated at 2.3 m.y. (C. Bow, personal communication). No age is available for E-111, but a similar basalt from the island of Santa Fe has been dated at 2.7 m.y. (Bailey, 1976). Most of the remaining samples we have analyzed, including the remainder from Santa Cruz, are of Brunhes age (less than 0.7 m.y.), and many are probably Holocene. The high $^{87}\text{Sr}/^{86}\text{Sr}$ ratios in SC-196 and E-111 could be due to either secular variation in the magma source of the central Galápagos or posteruptional alteration. The relatively high $^{143}\text{Nd}/^{144}\text{Nd}$ ratio of E-111 (0.51309) suggests that the latter is the more likely possibility. O'Nions *et al.* (1977a, 1977b) have found that submarine alteration of basalts has no detectable effect on Nd isotope ratios,

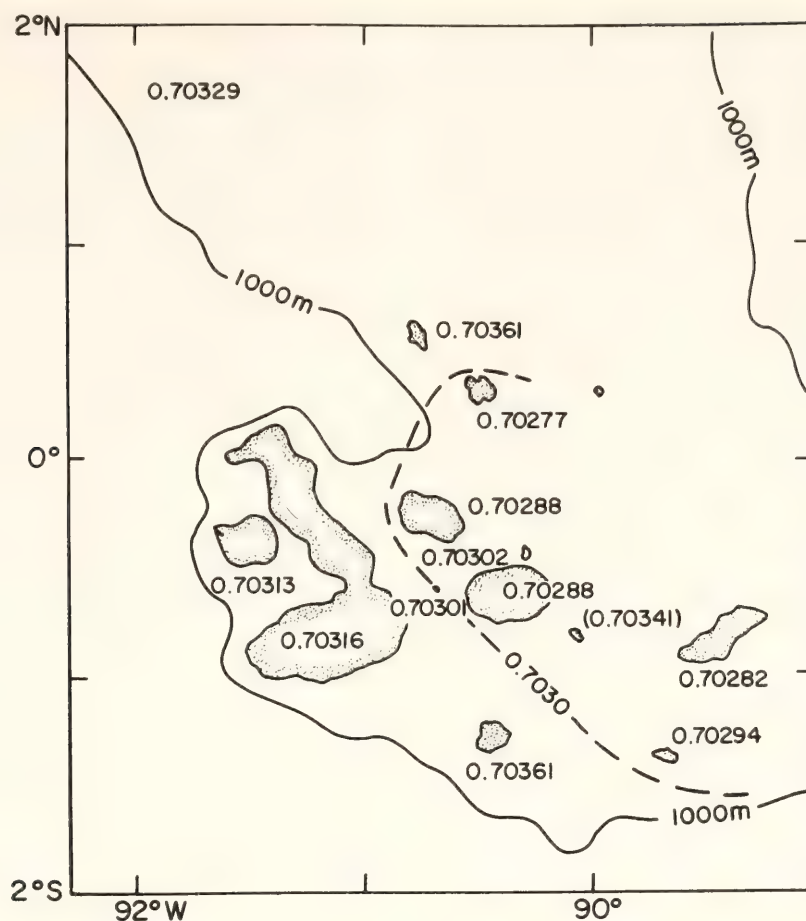


Fig. 121. Geographical variation in $^{87}\text{Sr}/^{86}\text{Sr}$ ratios in Galápagos basalts. The average $^{87}\text{Sr}/^{86}\text{Sr}$ ratio of each island is given. The dashed line separates islands with average $^{87}\text{Sr}/^{86}\text{Sr}$ greater than 0.7030 from islands with average ratios less than 0.7030.

even when $^{87}\text{Sr}/^{86}\text{Sr}$ ratios are increased significantly. The rare earth abundance pattern of E-111 shows light rare earth depletion, and is virtually indistinguishable from the rare earth patterns of the young Santa Cruz tholeiites which have low $^{87}\text{Sr}/^{86}\text{Sr}$ ratios. Thus the combined rare earth and Nd isotope data on E-111 suggests a magma source similar to that of the recent Santa Cruz basalts and that the high $^{87}\text{Sr}/^{86}\text{Sr}$ ratio in this sample is of secondary origin. We presently have no Nd isotope data on SC-196, but it seems likely that the high $^{87}\text{Sr}/^{86}\text{Sr}$ ratio in this sample is also the result of submarine alteration.

The Galápagos archipelago has been proposed as the site of a mantle plume (Morgan, 1971). The high $^{87}\text{Sr}/^{86}\text{Sr}$ and low $^{143}\text{Nd}/^{144}\text{Nd}$ ratios in some of the Galápagos Islands basalts indicate the

presence of a magma source distinct from that of normal midocean ridge basalts. In this respect, our findings are consistent with the presence of a mantle plume beneath the region. Our data do not, however, prove the existence of a plume.

The principal evidence for a mantle plume beneath the Galápagos are the physical and structural features (e.g., Johnson *et al.*, 1976), perhaps the most persuasive of which are the aseismic ridges that diverge from the Galápagos Plateau. To our knowledge, no adequate alternative explanation has been proposed to account for this phenomenon. In view of the physical and structural evidence, and for the reasons outlined by White and Schilling (in press) and Hofmann, White, and Whitford (this Report), we subscribe to the theory that an LIL-element-depleted asthenosphere

is penetrated from below by a "plume" of relatively LIL-element-enriched material.

In support of the mantle plume interpretation, Schilling *et al.* (1976) showed that basalts from the Galápagos Rise become progressively more light rare earth depleted away from the Galápagos Plateau in either direction. Schilling *et al.* (1976) interpreted these gradients as the result of an outward flow of plume material mixing with the LIL-element-depleted asthenosphere. The geographical variation in $^{87}\text{Sr}/^{86}\text{Sr}$ ratios, however, certainly indicates that there is no radial flow of plume material from the center of the archipelago. Schilling (1976) also reached this conclusion and suggested preferential channelling of plume flow along the Galápagos Fracture Zone at 91°N toward the Galápagos Rise. Both Schilling (1976) and Johnson *et al.* (1976) consider the plume to be presently centered beneath the islands of Fernandina and Isabela, which are the largest and volcanically most active islands of the group. The geographical distribution of $^{87}\text{Sr}/^{86}\text{Sr}$ isotope ratios (Fig. 121) would suggest significant plume flow to the north and south of these islands but very little eastward flow.

The possibility of simple binary mixing between magma sources or magmas can be tested by plotting the isotope ratio of one element against the isotope ratio of another element. Assuming that the enrichments of Sr and Nd in the "enriched" end member relative to the "depleted" one are similar, that data should lie along a gentle curve (Langmuir *et al.*, 1978). There is indeed a correlation in Sr and Nd isotope ratios (Fig. 119), but the scatter in the data appears to be too great to be compatible with simple binary mixing. However, if the isotopic composition of either end member is variable, then some scatter would be expected. Normal midocean ridge basalts exhibit limited variability in both $^{87}\text{Sr}/^{86}\text{Sr}$ and $^{143}\text{Nd}/^{144}\text{Nd}$ ratios, and the

other end member, the possible Galápagos mantle plume, may also be somewhat variable in its isotopic character. The possibility of mixing of end members of variable composition cannot be readily tested quantitatively, and thus the question of plume-asthenosphere mixing remains unresolved.

The presence of LIL-element-depleted basalts in the Galápagos is significant. These basalts are apparently derived from a source very similar to that of midocean ridge basalts, presumably the LIL-element-depleted asthenosphere. In this respect these basalts are unique, as almost all other analyzed oceanic island basalts are derived from sources distinctly different from those of midocean ridge basalts. The presence of these basalts may be due to a relatively small ratio of plume material to depleted asthenosphere material available for magma production (Schilling, personal communication). This in turn may be a result of the relatively high asthenosphere upwelling rates implied by high spreading rates in the region. The half-spreading rate of the Galápagos Rise is 3 cm/yr (Hey and Vogt, 1977) compared to half-rates of the order of 1 cm/yr for the northern Mid-Atlantic Ridge.

De Paolo and Wasserburg (1976a, 1976b), Richard *et al.* (1976), O'Nions *et al.* (1977), and Carlson *et al.* (1978) have shown that most oceanic basalts have higher $^{143}\text{Nd}/^{144}\text{Nd}$ ratios than expected in a chondritic reservoir. This is true also of Galápagos Islands basalts, implying that their source has been light rare earth depleted for a considerable portion of their history. If the primitive mantle had a Sm/Nd ratio equal to that of chondrites, then the mantle source of Galápagos basalts must have undergone a fractionation event at some time in the past. The correlation between $^{143}\text{Nd}/^{144}\text{Nd}$ and $^{87}\text{Sr}/^{86}\text{Sr}$ (Fig. 119) in oceanic basalts implies that this fractionation involved partial melting and pref-

erential extraction of Nd and Rb relative to Sm and Sr (O'Nions *et al.*, 1977).

There is a growing body of evidence that large-scale heterogeneities developed within the mantle 1600 to 2000 m.y. ago. Sun and Hanson (1975) found that Pb isotope ratios in oceanic basalts lie along a pseudoisochron with an age of roughly 2000 m.y. Brooks *et al.* (1976) showed that Rb/Sr and $^{87}\text{Sr}/^{86}\text{Sr}$ ratios in oceanic tholeiites lie along a pseudoisochron having a 1600 m.y. age. One of the specific objectives of our study was to test the validity of this Rb-Sr mantle isochron by determining Rb/Sr and $^{87}\text{Sr}/^{86}\text{Sr}$ ratios in Galápagos tholeiites, as data from this island group were not available for consideration by Brooks *et al.* (1976). The average Rb/Sr and $^{87}\text{Sr}/^{86}\text{Sr}$ of 12 Galápagos tholeiites, 0.015 and 0.70298 respectively, falls on the oceanic tholeiite isochron. Our data thus support the results of Brooks *et al.* (1976). (Like Brooks *et al.*, we have excluded alkali basalts from the average because they are probably generated by smaller degrees of melting and their Rb/Sr ratios may be less representative of their source than those of tholeiites. The average Rb/Sr ratio of the Galápagos alkali basalts is higher than the tholeiite average, but there is no systematic difference in $^{87}\text{Sr}/^{86}\text{Sr}$ between the two types. We have also excluded E-51 and E-68b because they appear to have experienced extensive fractional crystallization, and SC-196 and E-111 because of the possibility of seawater contamination discussed earlier.)

While the average Rb/Sr and $^{87}\text{Sr}/^{86}\text{Sr}$ of Galápagos tholeiites fit the 1600 m.y. oceanic mantle isochron, the averages of tholeiites from individual islands also define a younger, local pseudoisochron of 706 ± 106 m.y. (Fig. 122). If the analyses are treated individually, an age of 610 ± 69 m.y. is obtained. Similarly, Brooks *et al.* (1976) found that Rb-Sr data from Samoa and Kerguelen define relatively young local pseudoisochrons

while at the same time averages for these island groups fall on the 1600 m.y. oceanic mantle isochron. The limited amount of Sm-Nd data we presently have is not inconsistent with the local Rb-Sr mantle isochron.

The relationship between the 1600 m.y. whole-mantle isochrons and the younger local isochron may be analogous to the differences that often occur between whole-rock and mineral isochrons (Brooks *et al.*, 1976). If the 1600 m.y. isochron reflects a large-scale mantle event, the 600–700 m.y. isochron may reflect a more local, recent event resulting in local redistribution of Rb and Sr without a net change in the local average Rb/Sr and $^{87}\text{Sr}/^{86}\text{Sr}$ ratios.

Brooks *et al.* (1976) suggested that mantle isochron ages might be an average of many fractionation events, but noted that the simplest interpretation of the approximate concordance of Pb-Pb and Rb-Sr isochrons is that of a single mantle-wide event. It seems plausible to conclude that the mantle process dated is the depletion event (or events) required by the Rb-Sr and Sm-Nd isotope data. O'Nions *et al.* (1977a) and White and Schilling (1978) have argued that this depletion involved partial melting.

If mantle isochrons reflect an episode of vigorous magmatic activity, a complementary record of this event might be found in the crust. Continental crust formation does appear to have been episodic, and one such episode apparently occurred about 1600–1900 m.y. ago (Moorbath, 1977). However, this was neither the most recent nor the most important of such episodes (Moorbath, 1977), and it is unclear why this particular episode should be recorded by isotope ratios in oceanic basalts.

Sun and Hanson (1975) suggested that mantle isochrons reflect a change from whole-mantle convection in the Archean to shallow convection since that time. According to this hypothesis, whole-mantle convection during the Archean

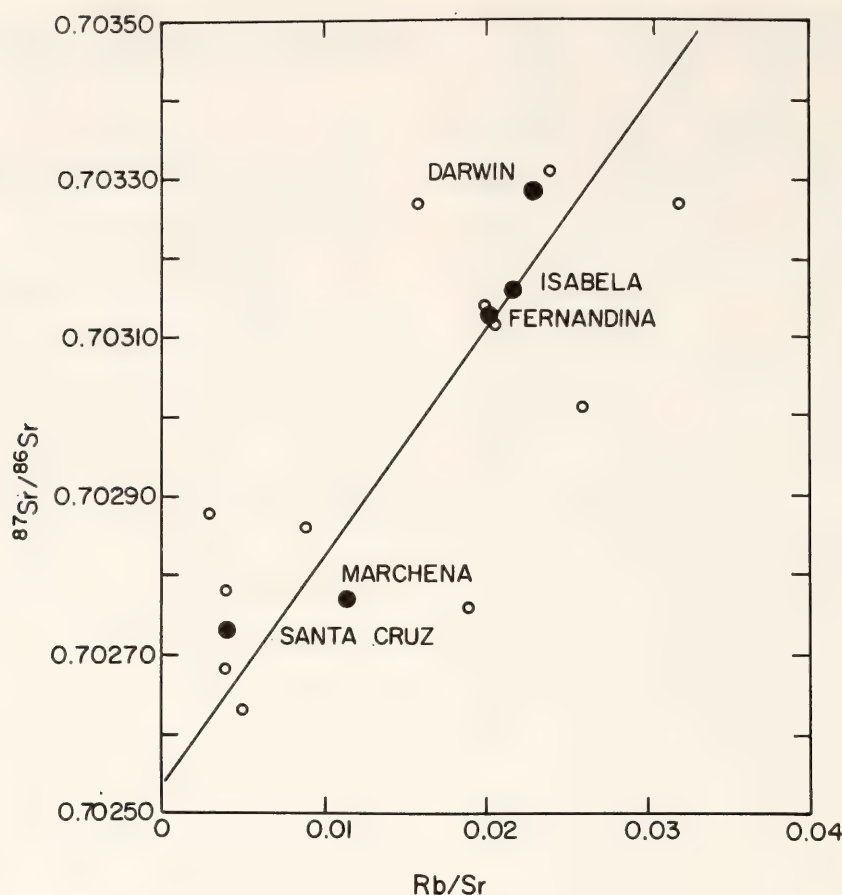


Fig. 122. Variation of $^{87}\text{Sr}/^{86}\text{Sr}$ with Rb/Sr . Open circles are tholeiitic basalts, solid circles are tholeiitic averages for individual islands. The slope of the regression line corresponds to an age of 706 ± 106 m. y.

kept the mantle sufficiently well mixed that isotopic heterogeneities did not develop. Finally, mantle isochrons could date some sort of turnover time of a convecting mantle. If heterogeneities in the mantle result from magma generation and transport, they could only develop in the upper 200 km or so of the mantle. Mantle isochrons could then reflect the last time a portion of the mantle was in this magma-generation region. However, this interpretation is not easily reconciled with the requirement that the mantle be chemically layered (see Hofmann, White, and Whitford, this Report).

The presently available data do not allow us to choose between these various possible interpretations. Our data improve the data base for the Rb-Sr mantle isochron, which presently depends on the averages of a relatively small number of

analyses from only eight tholeiitic islands and island groups. Before the significance of mantle isochrons can be fully understood, additional Pb, Sr, and Nd isotope data from modern oceanic basalts and Archean basalts will be needed.

Summary

1. Variations in $^{87}\text{Sr}/^{86}\text{Sr}$ and $^{143}\text{Nd}/^{144}\text{Nd}$ define a pattern of regional heterogeneity in the mantle beneath the Galápagos: islands with low $^{87}\text{Sr}/^{86}\text{Sr}$ and high $^{143}\text{Nd}/^{144}\text{Nd}$ ratios all occur in the east central portion of the archipelago, while those islands with high $^{87}\text{Sr}/^{86}\text{Sr}$ and low $^{143}\text{Nd}/^{144}\text{Nd}$ ratios are restricted to the western, northern, and southern edges.

2. High $^{87}\text{Sr}/^{86}\text{Sr}$ and low $^{143}\text{Nd}/^{144}\text{Nd}$ ratios in many Galápagos basalts indicate that they are derived from a source

distinct from that of midocean ridge basalts. On the other hand, basalts from some islands, particularly Santa Cruz, are derived from a source indistinguishable from midocean ridge basalts. Our results are consistent with the presence of a mantle plume beneath the Galápagos, but indicate a substantial contribution of magma from the LIL-element-depleted asthenosphere, possibly due to the high rate of asthenosphere upwelling in the region.

3. $^{143}\text{Nd}/^{144}\text{Nd}$ ratios in Galápagos basalts are higher than the ratio expected in a chondritic reservoir, implying that their source has experienced a previous depletion in Nd relative to Sm. The inverse correlation of $^{143}\text{Nd}/^{144}\text{Nd}$ and $^{87}\text{Sr}/^{86}\text{Sr}$ ratios of Galápagos basalts as well as other oceanic basalts implies that this depletion resulted from magma generation.

4. The average Rb/Sr and $^{87}\text{Sr}/^{86}\text{Sr}$ ratios of Galápagos tholeiites fall on the 1600 m.y. oceanic mantle isochron of Brooks *et al.* (1976). This isochron may date the event which resulted in the above mentioned depletion. Average Rb/Sr and $^{87}\text{Sr}/^{86}\text{Sr}$ ratios of individual Galápagos islands also define a local 600–700 m.y. isochron. This younger local isochron may reflect a more recent local event or may simply have resulted from a partial rotation of the 1600 m.y. isochron, as suggested by Brooks *et al.* (1976).

References

- Bailey, K., Potassium-argon ages from the Galápagos Islands, *Science*, **192**, 465–467, 1976.
- Brooks, C., S. R. Hart, A. Hofmann, and D. E. James, Rb-Sr mantle isochrons from oceanic regions, *Earth Planet. Sci. Lett.*, **32**, 51–61, 1976.
- Carlson, R. W., J. D. Macdougall, and G. W. Lugmair, Differential Sm/Nd evolution in oceanic basalts, *Geophys. Res. Lett.*, **5**, 229–232, 1978.
- Case, J. E., S. L. Ryland, T. Simkin, and K. A. Howard, Gravitational evidence for a low density mass beneath the Galápagos Islands, *Science*, **181**, 1040–1042, 1973.
- Cox, A., and B. Dalrymple, Paleomagnetism and potassium-argon ages of some volcanic rocks of the Galápagos Islands, *Nature*, **209**, 776–777, 1966.
- De Paolo, D. J., and G. J. Wasserburg, Nd isotopic variations and petrogenetic models, *Geophys. Res. Lett.*, **3**, 249–252, 1976a.
- De Paolo, D. J., and G. J. Wasserburg, Inferences about magma sources and mantle structure from variations of $^{143}\text{Nd}/^{144}\text{Nd}$, *Geophys. Res. Lett.*, **3**, 743–746, 1976b.
- Flower, M. F. J., H.-U. Schmincke, and H. Bowman, Rare earth and other trace elements in historic Azorean lavas, *J. Volcan. Geotherm. Res.*, **1**, 127–147, 1976.
- Hart, S. R., and C. Brooks, Clinopyroxene-matrix partitioning of K, Rb, Cs, Sr, and Ba, *Geochim. Cosmochim. Acta*, **38**, 1799–1806, 1974.
- Hedge, C. E., Strontium isotopes in basalts from the Pacific Ocean, *Earth Planet. Sci. Lett.*, **38**, 88–94, 1978.
- Hedge, C. E., Z. E. Peterman, and W. R. Dickinson, Petrogenesis of lavas from western Samoa, *Geol. Soc. Amer. Bull.*, **83**, 2709–2714, 1972.
- Hedge, C. E., N. D. Watkins, R. A. Hildreth, and W. P. Doering, $^{87}\text{Sr}/^{86}\text{Sr}$ ratios in basalts from islands in the Indian Ocean, *Earth Planet. Sci. Lett.*, **21**, 29–34, 1973.
- Hey, R., and P. R. Vogt, Spreading center jumps and subaxial asthenosphere flow near the Galápagos hot-spot, *Tectonophysics*, **37**, 41–52, 1977.
- Johnson, G. L., P. R. Vogt, R. Hey, J. Compsic, and A. Lowrie, Morphology and structure of the Galápagos Rise, *Marine Geology*, **21**, 81–120, 1976.
- Langmuir, C. H., R. D. Vocke, G. N. Hanson, and S. R. Hart, A general mixing equation with applications to

- Icelandic basalts. *Earth Planet. Sci. Lett.*, **37**, 380–392, 1978.
- McBirney, A. R., and H. Williams, Geology and Petrology of the Galápagos Islands, in *Geol. Soc. Amer. Mem.* **118**, Geol. Soc. Amer., Boulder, 1969.
- Moorbath, S., Ages, isotopes, and evolution of Precambrian continental crust, *Chem. Geol.*, **20**, 151–187, 1977.
- Morgan, W. J., Convection plumes in the lower mantle, *Nature*, **230**, 42–43, 1971.
- Nakamura, N., Determination of REE, Ba, Fe, Mg, Na and K in carbonaceous and ordinary chondrites, *Geochim. Cosmochim. Acta*, **38**, 757–775, 1974.
- O'Nions, R. K., P. J. Hamilton, and N. M. Evensen, Variations in $^{143}\text{Nd}/^{144}\text{Nd}$ and $^{87}\text{Sr}/^{86}\text{Sr}$ ratios in oceanic basalts, *Earth Planet. Sci. Lett.*, **34**, 13–22, 1977a.
- O'Nions, R. K., N. M. Evensen, P. J. Hamilton, and S. R. Carter, Nd- and Sr-isotope compositions of altered oceanic crust and island arc tholeiites, *EOS: Trans. Amer. Geophys. Union*, **58**, 533, 1977b.
- Richard, P., N. Shimizu, and C. J. Alègre, $^{143}\text{Nd}/^{144}\text{Nd}$, a natural tracer: an application to oceanic basalts. *Earth Planet. Sci. Lett.*, **31**, 269–278, 1976.
- Schilling, J.-G., Galápagos mantle plume: geochemical evidence, *EOS: Trans. Amer. Geophys. Union*, **57**, 343, 1976.
- Schilling, J.-G., R. N. Anderson, and P. Vogt, Rare earth, Fe, and T: variations along the Galápagos spreading center and their relationship to the Galápagos mantle plume, *Nature*, **261**, 108–113, 1976.
- Shimizu, N., An isotope dilution technique for analysis of the rare earth elements, *Carnegie Inst. Wash. Year Book* **73**, 941–943, 1974.
- Sun, S. S., and G. N. Hanson, Evolution of the mantle: geochemical evidence from alkali basalt, *Geology*, **3**, 297–302, 1975.
- White, W. M., *Geochemistry of Igneous Rocks from the Central North Atlantic: the Azores and the Mid-Atlantic Ridge*, Ph.D. dissertation, University of Rhode Island, Kingston, 1977.
- White, W. M., and J.-G. Schilling, The nature and origin of geochemical variations in Mid-Atlantic Ridge basalts from the Central North Atlantic, *Geochim. Cosmochim. Acta*, in press, 1978.
- White, W. M., J.-G. Schilling, and S. R. Hart, Evidence for the Azores mantle plume from strontium isotope geochemistry of the Central North Atlantic, *Nature*, **263**, 659–663, 1976.

ORIGIN OF THE NINETYEAST RIDGE: TRACE ELEMENT AND SR ISOTOPE EVIDENCE

D. J. Whitford and R. A. Duncan*

Introduction

The Indian Ocean provides an interesting natural laboratory in which to study further the geochemical structure of the mantle (Hofmann *et al.*, this Report). From the limited data presently available (Subbarao and Hedge, 1973) there are indications that MORB from this region is characterized by higher $^{87}\text{Sr}/^{86}\text{Sr}$ ratios than that from either the Atlantic or Pacific Oceans (Hart, 1971; White and Bryan, 1977). If this observation can be substantiated (there is some evidence that these high ratios simply reflect secondary alteration: Carlson *et al.*, 1978), particularly with samples well away from oceanic islands and triple junctions, it will provide an important boundary condition as to the degree and scale of homogeneity of the mantle source of MORB and of the homogenizing process itself.

Like other oceans, the Indian Ocean is characterized by linear ridges, most of which are aseismic relative to spreading ridges. One such ridge is the Ninety-

* School of Oceanography, Oregon State University, Corvallis, Oregon 97330.

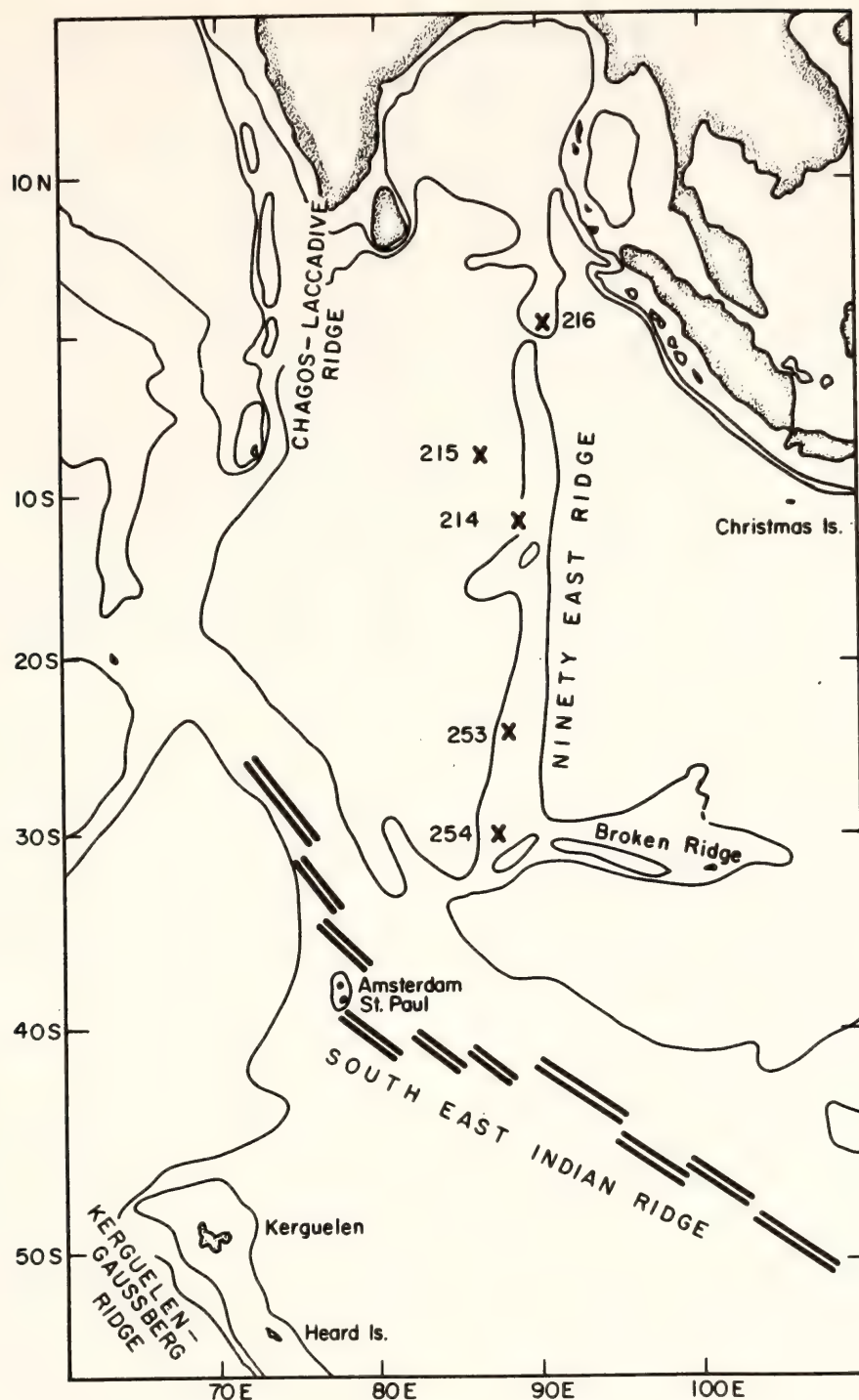


Fig. 123. Regional tectonic framework of the Ninetyeast Ridge in the eastern Indian Ocean. Sampling localities are indicated by DSDP drilling sites.

east Ridge (Fig. 123), located in the eastern Indian Ocean along the 90°E meridian from about 31°S to 9°N . It is elevated about 2 km above the surrounding ocean floor and varies in width from 100 to 200 km. The basaltic basement is now entirely covered with up to 500 m of sediment.

The ridge separates two distinct domains of the Indian Ocean floor. To the west of the ridge, the ocean floor becomes younger to the south. To the east of the ridge, the ocean floor becomes younger to the north (Duncan, 1978). Probably the simplest interpretation of this phenomenon is the location of the Ninetyeast

Ridge on or near a major transform fault. In this regard, it is probably significant that Stein and Okal (1978) have shown that the northern section of the ridge is as seismically active as large transform faults and more active than many spreading ridges. In addition, they showed the ridge to be undergoing significant left-lateral strike slip motion, indicating that the Ninetyeast Ridge represents a site of substantial present-day internal deformation within the Indian plate.

Luyendyk and Rennick (1977) have summarized the numerous theories about the origin of the Ninetyeast Ridge. It has been variously interpreted as a continental fragment, an extinct island arc, a horst structure, a "leaky" transform fault, and a "hot-spot" or plume trace. Drilling has demonstrated that basal sediments overlying the basaltic crust forming the ridge become progressively younger from north to south, and recent K-Ar geochronological studies (Duncan, 1978) have demonstrated a corresponding decrease in age of the underlying basement. Using both palaeomagnetic and geological evidence, Duncan (1978) interpreted these results to indicate that the Ninetyeast Ridge manifests the northward movement of the Indian Plate over a hot-spot at an average rate of $9.4 \pm 0.3 \text{ cm yr}^{-1}$ —a model similar to that proposed by Morgan (1972) and Luyendyk and Rennick (1977) among others.

One point of disagreement among the proponents of the hot-spot models is the present location of the hot-spot that produced the ridge. Luyendyk and Rennick (1977) invoked a complicated model involving two hot-spots—one located beneath Kerguelen and one beneath Amsterdam and St. Paul (Fig. 123). Consistent with this model is Hekinian's (1974) demonstration that lavas from DSDP sites 214 and 216 have geochemical similarities with those from Amsterdam and St. Paul. Duncan (1978) pro-

posed a much simpler model in which the Ninetyeast Ridge has been produced by a single hot-spot now located beneath Heard Island on the Kerguelen plateau in the southern Indian Ocean (Fig. 123).

This report represents an attempt to test further these various models by investigating the trace element and Sr isotope geochemistry of lavas erupted along the ridge. A test of Duncan's (1978) and Luyendyk and Rennick's (1977) models has been made using Sr isotopes. From the limited available data (Hedge *et al.*, 1973), it appears that with respect to Sr, lavas from Kerguelen are the most radiogenic of all island basalts found in the Indian Ocean. On the other hand, lavas from Amsterdam and St. Paul are relatively unradiogenic, and hence the presence only of primary high $^{87}\text{Sr}/^{86}\text{Sr}$ ratios in lavas along the ridge would support Duncan's interpretation. Within the tectonic constraints, the geochemical characterization of lavas from the ridge should also provide clues as to the nature of the underlying mantle source.

Lavas from the Ninetyeast Ridge

Five samples obtained from the Deep Sea Drilling Project (DSDP) have been analyzed. These particular samples were chosen because they have been used by Duncan (1978) in his geochronological study, and all except one (DSDP Site 253) appear to have retained significant age information despite extensive low-temperature alteration. Details of analyzed samples are listed in Table 30.

Lavas drilled from the Ninetyeast Ridge have been described and analyzed in detail (Hekinian, 1974; Thompson *et al.*, 1974; Kempe, 1974; Frey and Sung, 1974). The lavas are dominantly basaltic, although at Site 214 there are a series of oceanic "andesites"—intermediate lavas with SiO_2 concentrations of approximately 55 wt %. The basalts vary from iron-rich tholeiites at Sites 214, 216, and 254 to tholeiites similar to MORB at Site 253. Basalts from Site

TABLE 30. Sr Isotope and Trace Element Results*

DSDP Site		K	Rb	Cs	Ba	Sr	⁸⁷ Sr/ ⁸⁶ Sr ± 2σ	Age (m.y.)
214	TR	13500	34.1	0.49	278	333	0.70492±6	58
	L	15300	41.3	0.52	291	196	0.70493±7	
215	TR	7440	11.2	0.23	276	268	0.70448±6	61
	L	7340	9.5	0.21	327	112	0.70454±10	
216	TR	6230	11.2	0.18	94	143	0.70557±6	81
	L	3240	1.7	0.13	103	86	0.70548±6	
253	TR	1170	1.6	0.052	15	90	0.70554±8	46
	L	880	0.74	0.0018	15	41	0.70666±10	
254	TR	3320	6.0	0.030	88	169	0.70470±8	38
	L	3430	7.2	0.018	82	111	0.70472±11	
MORB		855	0.87	0.012	8.3	103	0.70266	

* All trace element data as ppm. TR = total rock analysis; L = residue after leaching with HCl. Ages and TR K concentrations from Duncan (1978). ⁸⁷Sr/⁸⁶Sr ratios normalized to ⁸⁶Sr/⁸⁸Sr = 0.1194, relative to E & A SrCO₃, ⁸⁷Sr/⁸⁶Sr = 0.70800. MORB data from White and Bryan (1977). Samples: 214-48-1, 147-50; 215-19-2; 216-38-3, 135-138; 253-58-cc, 140-143; 254-35-3, 26-28.

215, which is not located on the crest of the ridge, were compared with MORB by Hekinian (1974), who ascribed the higher alkali abundances as due to secondary alteration. On the other hand, Thompson *et al.* (1974) recognized these basalts as intrinsically more alkaline; this result, together with Duncan's (1978) geochronological information, argues for a genetic relationship between the Site 215 basalt and the Ninetyeast Ridge. The K concentration measured in the analyzed sample from Site 214 indicates that it is probably intermediate rather than basaltic.

The petrological and geochemical work already done clearly demonstrates that the Ninetyeast Ridge is composed primarily of oceanic basalt, which rules out models explaining the ridge as either a continental fragment or an extinct island arc.

Analytical Techniques

We have determined ⁸⁷Sr/⁸⁶Sr ratios, together with LIL-element (K, Rb, Cs, Ba, Sr) and rare earth element (REE) abundances, in the range of lavas from the ridge. Isotope-dilution analytical

techniques had been described by Whitford (*Year Book* 76, p. 841) and Whitford and Jezek (*Year Book* 76, p. 845). In order to test whether the measured ⁸⁷Sr/⁸⁶Sr ratios are the result of alteration and contamination with seawater Sr, samples were also leached in hot 6N HCl for 24 hr and the residue subsequently analyzed in a manner similar to that described by O'Nions and Pankhurst (1976).

Results

Measured LIL-element abundances and ⁸⁷Sr/⁸⁶Sr ratios are listed in Table 30, together with the best estimate of the ages from Duncan (1978) and White and Bryan's (1977) estimate of average MORB from the Atlantic Ocean. Chondrite-normalized REE patterns are shown in Fig. 124.

Except for the basalt from Site 253, all the analyzed lavas have similar geochemical characteristics, although they differ in the degree of their enrichment. In the unleached samples, K, Rb, and Cs range from 3300 to 13,500 ppm, 6 to 34 ppm, and 0.03 to 0.5 ppm, respectively. In the same samples, Ba and Sr

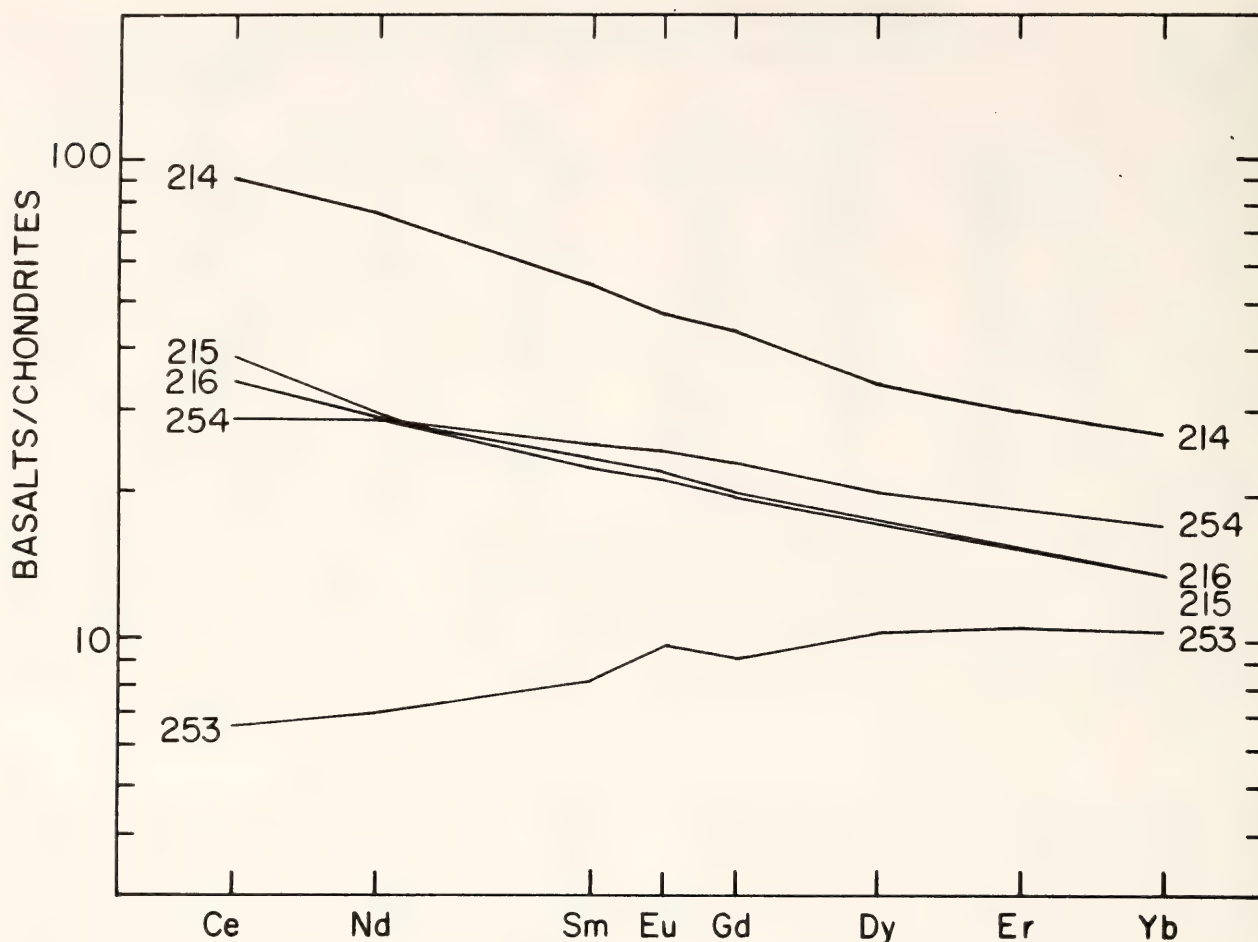


Fig. 124. Chondrite-normalized rare earth element abundance patterns for lavas from the Ninetyeast Ridge. Chondrite values from Nakamura (1974). Samples are denoted by drilling site (see Table 29).

range from 90 to 280 ppm and 170 to 330 ppm, respectively. Except for the basalt from Site 253, the REE show a similar trend of enrichment. The REE patterns are all subparallel, with chondrite-normalized Ce and Yb abundances ranging from approximately 30 to 90 and 15 to 40, respectively. Normalized Ce/Yb ratios range from 1.7 (Site 254) to 3.4 (Site 214). Minor irregularities in chondrite normalized Ce abundances may reflect low-temperature alteration.

Basalt from Site 253 shows many similarities with MORB (Table 30; Fig. 124). It is characteristically depleted in both LIL and light REE. Unlike the other analyzed samples, it shows a (positive) Eu anomaly.

The REE patterns are similar to those reported by Thompson *et al.* (1974) and Frey and Sung (1974) except for basalts

from Site 253. Frey and Sung (1974) reported slightly light REE-enriched patterns from this site, which contrasts with the depleted pattern in Fig. 124. This may reflect primary differences in the lavas or could be a result of a higher degree of alteration in the light REE-enriched rocks.

Except for Sr, there is no consistent relative pattern of trace element gain or loss between leached and unleached samples. For Sr, the leached samples are all depleted by as much as 60%.

Measured $^{87}\text{Sr}/^{86}\text{Sr}$ ratios range from 0.70470 (Site 254) to 0.70557 (Site 216). Using Duncan's (1978) K-Ar ages, calculated initial ratios drop at most by 0.00050 from the measured ratios—a consequence of low ages and low Rb/Sr ratios. From Table 30, it can be seen that in most cases leached and unleached

samples are characterized by essentially the same $^{87}\text{Sr}/^{86}\text{Sr}$ ratios. The similarity between $^{87}\text{Sr}/^{86}\text{Sr}$ ratios in leached and unleached samples suggests that except for the Site 253 basalt the high $^{87}\text{Sr}/^{86}\text{Sr}$ ratios are a primary characteristic and again clearly distinguish these lavas from MORB. Despite its MORB-like trace element characteristics, basalt from Site 253 is characterized by a $^{87}\text{Sr}/^{86}\text{Sr}$ ratio of 0.70554. The leached rock has a considerably higher $^{87}\text{Sr}/^{86}\text{Sr}$ ratio of 0.70666. It is very unlikely that this ratio reflects the primary $^{87}\text{Sr}/^{86}\text{Sr}$ of the lava at the time of its extrusion, especially in light of its MORB-like trace element characteristics. It may be significant that this sample has apparently not retained any K-Ar age information (Duncan, 1978). It seems probable that the sample has been contaminated with seawater Sr ($^{87}\text{Sr}/^{86}\text{Sr} \sim 0.709$) and that this Sr resides in secondary minerals, insoluble in HCl. Hawkesworth *et al.* (1977) noted a similar effect in some basalts from the Scotia Sea. These results emphasize that leaching with HCl may not always reveal the primary isotopic characteristics of rocks that have been subjected to low-grade alteration.

Discussion

Except for the basalt from Site 253, the analyzed lavas do not resemble MORB but show close affinities with oceanic island basalts. This similarity with island basalts argues convincingly against the hypothesis that the Ninetyeast Ridge represents an old spreading center, and the regular age progression (Duncan, 1978) would seem to rule out explanations invoking a leaky transform fault. It seems more likely, therefore, that the Ninetyeast Ridge traces the northward movement of the Indian plate over a hot-spot; this interpretation raises the question of the present location of the hot-spot. The presence of MORB-like basalts from Site 253 may simply reflect the location of the hot-spot

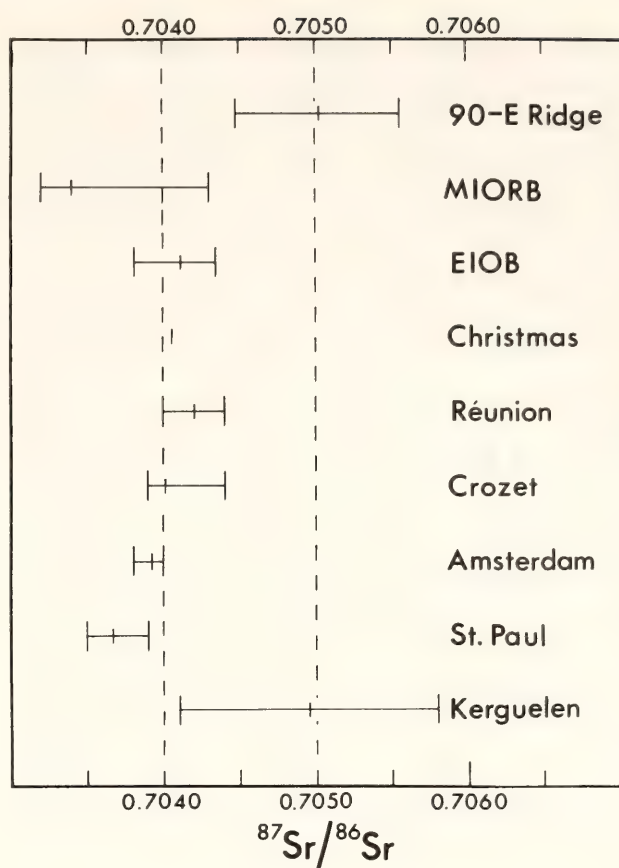


Fig. 125. Comparison of measured $^{87}\text{Sr}/^{86}\text{Sr}$ ratios in basalts from the Ninetyeast Ridge with those from the Mid-Indian Ocean Ridge (MIOB), the eastern Indian Ocean (EIOB) (altered), and various islands in the Indian Ocean. Ranges and average $^{87}\text{Sr}/^{86}\text{Sr}$ ratios are shown. Data sources: Hedge *et al.*, 1973; Subbarao and Hedge, 1973; Whitford, 1975; Whitford (unpublished results).

through much of its history adjacent to a spreading center (Duncan, 1978).

Figure 125 shows the range of $^{87}\text{Sr}/^{86}\text{Sr}$ ratios, together with average compositions measured in basalts from the Indian Ocean. In both average $^{87}\text{Sr}/^{86}\text{Sr}$ ratios and the range of ratios, there is a close similarity between rocks from the Ninetyeast Ridge and those from Kerguelen, the latter of which have been dated from 5–27 m.y. B.P. (Watkins *et al.*, 1974; Lameyre *et al.*, 1976). Therefore, if the Ninetyeast Ridge does represent an older trace of a presently active hot-spot, only that hot-spot which produced the Kerguelen basalts and subsequently migrated southeast relative to Antarctica appears to have the appropri-

ate isotopic characteristics. Although the isotopic data cannot prove this model, it should be noted that the model was originally based on completely independent evidence. We therefore believe that the unusually high $^{87}\text{Sr}/^{86}\text{Sr}$ ratios that characterize both Kerguelen and the Ninetyeast Ridge but no other known samples from the Indian Ocean give strong support to the model.

Like basalts from many oceanic islands, the analyzed lavas from the Ninetyeast Ridge are isotopically heterogeneous. From the results of the leaching experiments, these heterogeneities appear to be primary. The implied differences in source chemistry, therefore, preclude attempts to relate rock-types from different sites by simple fractionation models such as those of Ludden *et al.* (1977) for basalts from Sites 214 and 216.

The implications of these results in terms of the geochemical structure of the mantle have been discussed by Hofmann, Wright, and Feigenson (this Report).

References

- Carlson, R. W., J. D. Macdougall, and G. W. Lugmair, Differential Sm/Nd evolution in oceanic basalts, *Geophys. Res. Lett.*, **5**, 229–232, 1978.
- Duncan, R. A., Geochronology of basalts from the Ninetyeast Ridge and continental dispersion in the eastern Indian Ocean, *J. Volcanol. Geotherm. Res.*, in press, 1978.
- Frey, F. A., and C. M. Sung, Geochemical results for basalts from Sites 253 and 254, in *Initial Reports of the Deep Sea Drilling Project*, **26**, pp. 567–572, T. A. Davies *et al.*, Govt. Printing Office, Washington, D.C., 1974.
- Hart, S. R., K, Rb, Cs, Sr and Ba contents and Sr isotope ratios of ocean floor basalts, *Phil. Trans. Roy. Soc. London Ser. A*, **268**, 573–587, 1971.
- Hawkesworth, C. J., R. K. O'Nions, R. J. Pankhurst, D. J. Hamilton, and N. M. Evensen, A geochemical study of island-arc and back-arc tholeiites from the Scotia Sea, *Earth Planet. Sci. Lett.*, **36**, 253–262, 1977.
- Hedge, C. E., N. D. Watkins, R. A. Hildreth, and W. P. Doering, $^{87}\text{Sr}/^{86}\text{Sr}$ ratios in basalts from islands in the Indian Ocean, *Earth Planet. Sci. Lett.*, **21**, 29–34, 1973.
- Hekinian, R., Petrology of igneous rocks from Leg 22 in the northeastern Indian Ocean, in *Initial Reports of the Deep Sea Drilling Project*, **22**, pp. 413–448, C. C. von der Borch *et al.*, Govt. Printing Office, Washington, D.C., 1974.
- Hofmann, A. W. and S. R. Hart, An assessment of local and regional isotopic equilibrium in the mantle, *Earth Planet. Sci. Lett.*, **38**, 44–62, 1978.
- Kempe, D. R. C., The petrology of the basalts, Leg 26, in *Initial Reports of the Deep Sea Drilling Project*, **26**, pp. 465–504, T. A. Davies *et al.*, Govt. Printing Office, Washington, D.C., 1974.
- Lameyre, J., A. Manot, S. Zimine, J. M. Cantagrel, L. Dosso., and Ph. Vidal, Chronological evolution of the Kerguelen Islands syenite-granite ring complex, *Nature*, **263**, 306–307, 1976.
- Ludden, J. N., G. Thompson, W. B. Bryan, and F. A. Frey, An evaluation of fractional crystallization and the origin of lavas from the 90°E Ridge, eastern Indian Ocean, *Geol. Soc. Amer., Abstr. with Prog.*, **9**, 1077–1078, 1977.
- Luyendyk, B. P., and W. Rennick, Tectonic history of aseismic ridges in the eastern Indian Ocean, *Geol. Soc. Amer. Bull.*, **88**, 1347–1356, 1977.
- Morgan, W. J., Plate motions and deep mantle convection, *Geol. Soc. Amer. Mem.*, **132**, 7–22, 1972.
- Nakamura, N., Determination of REE, Ba, Fe, Mg, Na and K in carbonaceous and ordinary chondrites, *Geochim. Cosmochim. Acta*, **38**, 757–775, 1974.
- O'Nions, R. K., and R. J. Pankhurst, Sr isotope and rare earth element geochemistry of DSDP Leg 37 basalts,

- Earth Planet. Sci. Lett.*, 31, 255–261, 1976.
- Stein, S., and E. A. Okal, Seismicity and tectonics of the Ninetyeast Ridge area: evidence for internal deformation of the Indian Plate, *J. Geophys. Res.*, 83, 2233–2245, 1978.
- Subbarao, K. V., and C. E. Hedge, K, Rb, Sr and $^{87}\text{Sr}/^{86}\text{Sr}$ in rocks from the mid-Indian Oceanic ridge, *Earth Planet. Sci. Lett.*, 18, 223–228, 1973.
- Thompson, G., W. B. Bryan, F. A. Frey, and C. M. Sung, Petrology and geochemistry of basalts and related rocks from Sites 214, 215, 216, DSDP Leg 22, Indian Ocean, in *Initial Reports of the Deep Sea Drilling Project*, 22, pp. 459–468, C. C. von der Borch *et al.*, Govt. Printing Office, Washington, D.C., 1974.
- Watkins, N. D., B. M. Gunn, J. Nougier, and A. K. Bakshi, Kerguelen: continental fragment or oceanic island, *Geol. Soc. Amer. Bull.* 85, 201–212, 1974.
- White, W. M., and W. B. Bryan, Sr isotope, K, Rb, Cs, Sr, Ba and rare-earth geochemistry of basalts from the FAMOUS area, *Geol. Soc. Amer. Bull.*, 88, 571–576, 1977.
- Whitford, D. J., Strontium isotopic studies of the volcanic rocks of the Sunda arc, Indonesia, and their petrogenetic implications, *Geochim. Cosmochim. Acta*, 39, 1287–1302, 1975.
- in potassium and minor elements such as rubidium and strontium with increasing depth, to the underlying Benioff zones. Such regular “K–h” trends have long been recognized in the Sunda arc of Indonesia. However, not all the volcanoes of the Sunda arc follow this compositional trend.
- Quaternary to Recent volcanic centers on the islands of Lombok and Sumbawa lying east of Bali in the Sunda arc (Fig. 126) have erupted several different suites of lavas ranging from a calc-alkaline, basalt-andesite-dacite association on Lombok (Foden, 1978) to undersaturated potassic trachybasalt-trachyandesite and highly undersaturated leucititic suites on Sumbawa (Foden and Varne, submitted for publication). Yet the depths to the Benioff zone underlying these volcanic centers range only between 165 and 190 km, far less than would be expected, based on “K–h” trends elsewhere in the arc.
- Similar departures from regular “K–h” trends are known in other arcs (Arculus and Johnson, 1978). Here we present and discuss some results of a strontium isotope study of volcanic rocks and ultramafic and mafic xenoliths from Lombok and Sumbawa in this little-known sector of the Sunda arc.
- The purpose of this investigation has been (1) to characterize the Sr isotope geochemistry of these lavas and compare them with analyzed lavas from Java and Bali to the west; (2) to attempt to test models explaining the relationships within the range of erupted lavas from individual volcanoes; (3) to examine the relationship between the xenoliths and their host lavas, and the implications for the nature of the mantle source; and (4) to investigate the relationship between spatially and temporally related calc-alkaline and alkaline lavas, whose chemistry appears to bear no simple relationship with the depth to the underlying seismic zone.

SR ISOTOPE GEOCHEMISTRY OF CALC-ALKALINE AND ALKALINE LAVAS FROM THE SUNDA ARC IN LOMBOK AND SUMBAWA, INDONESIA

D. J. Whitford, J. Foden,* and R. Varne*

Introduction

Coeval lavas from island arcs often exhibit trends of progressive enrichment

*Department of Geology, University of Tasmania, Hobart, Tasmania, Australia.

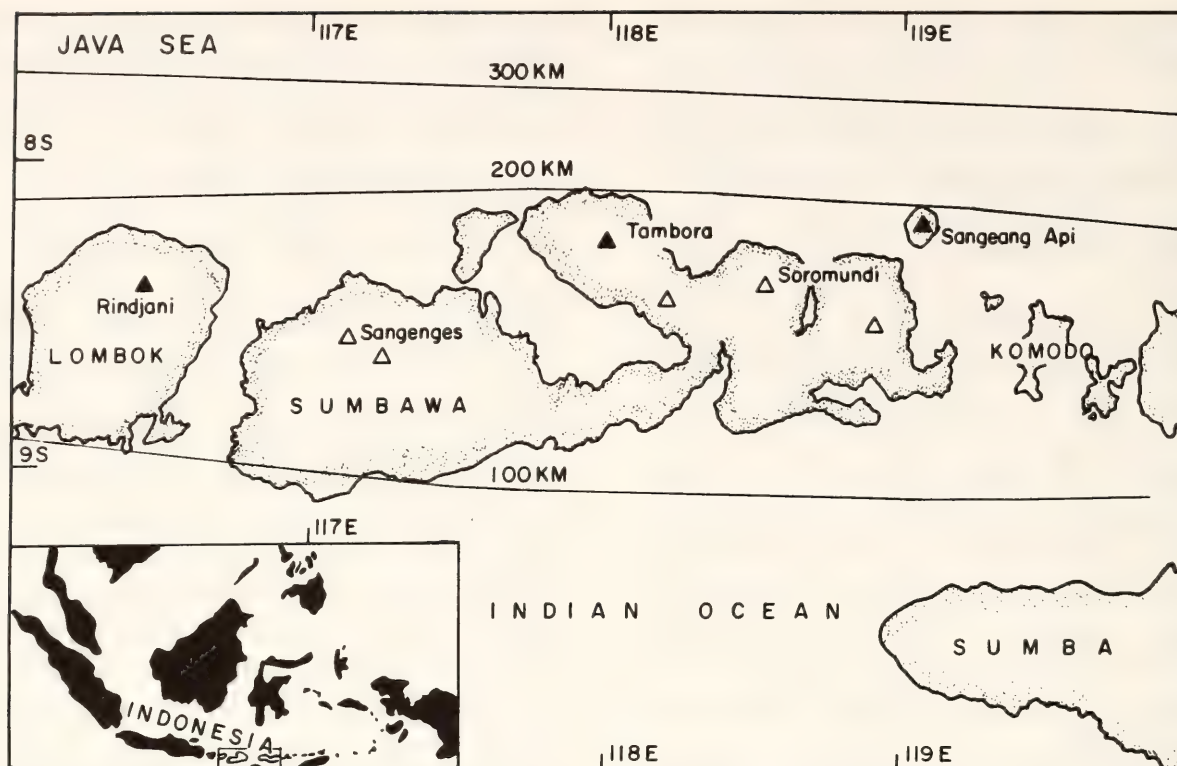


Fig. 126. Location of calc-alkaline and alkaline volcanoes in Lombok and Sumbawa. Solid and open triangles refer to active and extinct volcanoes, respectively. Depth contours (Hamilton, 1974) to the center of the underlying Benioff zone are also shown.

Tectonic Setting

The islands of Lombok and Sumbawa are located in the central sector of the Sunda arc, immediately east of Bali (Fig. 126). The oldest exposed rocks are Miocene, which suggests that the islands themselves are relatively young (Van Bemmelen, 1949; Audley-Charles, 1975; Katili, 1975). The islands are located on the southeastern margin of the Sunda Shelf on the "transitional edge of cratonization" (Curry *et al.*, 1977). The underlying crust, about 20–25 km thick, appears to have a velocity structure transitional between typical oceanic and continental profiles (Curry *et al.*, 1977).

The volcanoes sampled in this study are located over inferred depths to the center of the Benioff seismic zone of 150–200 km (Hamilton, 1974) (Fig. 126). Of the five centers sampled, Rindjani, Tambora (the site in 1815 of perhaps the largest volcanic eruption in historic time), and Sangeang Api are

still active, while Sangenges and Soromundi appear to have become dormant during the Quaternary.

Geochemistry and Petrology

There are marked geochemical differences between the lavas of each of these volcanoes. The lavas range in composition from the calc-alkaline, basalt-andesite-dacite suite of Rindjani, through the nepheline normative, potassic phonolitic tephrites, trachybasalts, and trachyandesites of Tambora and Sangeang Api, to the highly undersaturated leucitites and leucite tephrites of Sangenges and Soromundi. The sequence from calc-alkaline lavas to leucitites is characterized by increasing LIL-element abundances, particularly K, Rb, Sr, Ba, and light REE. K/Rb ratios decrease from 400–500 in the calc-alkaline group to 100–200 in the leucitites. The leucitites tend to be more mafic than the calc-alkaline basalts, having MgO concentra-

tions of 7–10 wt % and atomic Mg/Mg + ΣFe) ratios >0.6.

The calc-alkaline lavas from both Rindjani and Sangenges contain about 2 wt % K₂O at 55% SiO₂ (K₅₅), based on a linear regression of the K₂O-SiO₂ variation diagram. For a depth to Benioff zone (*h*) of 170 km (Fig. 126), that K₂O concentration lies within the K₅₅-*h* field defined by all tholeiitic and calc-alkaline volcanoes from Java and Bali (Whitford and Nicholls, 1976). It may be significant, however, that the K₂O concentrations plot well above the “preferred” K₅₅-*h* trend (Whitford and Nicholls, 1976). The more alkaline lavas plot well above either trend, being located over much shallower Benioff zone depths than those predicted by the results from Java and Bali.

The Sangeang Api volcano is of particular interest because it has erupted a suite of mafic and ultramafic xenoliths. These range in composition from olivine-clinopyroxenite, through amphibole-magnetite-clinopyroxenite, to amphibole-plagioclase-magnetite-clinopyroxene (gabbroic) varieties. Modal analysis of four analyzed xenoliths are listed in Table 31. Some Mg-biotite-rich varieties also occur, and in some cases early-formed olivine can be seen to have reacted with residual liquid, yielding clinopyroxene and Mg-biotite. The most mafic phase recognized in these xenoliths is an Al- and Ti-poor Cr-diopside (Mg/(Mg + Fe²⁺) ~0.9), which occurs in the olivine-clinopyroxene and amphi-

bole-magnetite-clinopyroxene xenoliths. The diopside shows an increasing tendency to react to an Al- and Ti-rich augite in the less mafic xenolith types.

There appears to be a coherent relationship between the bulk compositions of the xenoliths and the compositional trends among the associated lavas, which suggests that the xenoliths may be genetically related to the lavas, perhaps representing cumulates. A TiO₂-MgO variation diagram illustrates the coherent behavior of lavas and xenoliths (Fig. 127). Removal of early high-temperature clinopyroxene low-TiO₂ cumulates apparently produced a trend of TiO₂ enrichment in the early lavas. At lower temperatures and higher oxygen fugacities, crystallization of amphibole and magnetite resulted in an abrupt change in the lava compositions, toward TiO₂ depletion.

Results

Measured ⁸⁷Sr/⁸⁶Sr ratios are listed in Table 32, together with concentrations of SiO₂, K₂O, Rb, and Sr and atomic Mg/(Mg + ΣFe) ratios. The ⁸⁷Sr/⁸⁶Sr ratios are plotted as histograms in Fig. 128. Overall, the lavas define a bimodal distribution with maxima at about 0.7039 and 0.7048.

Analyzed lavas from Rindjani are isotopically indistinguishable from each other with ⁸⁷Sr/⁸⁶Sr ratios ranging from 0.70386 to 0.70402. Lavas from the more alkaline volcanoes are generally more variable in their ⁸⁷Sr/⁸⁶Sr ratios. Analyzed lavas from the nepheline-normative trachybasalt-trachyandesite series from Tambora are characterized by relatively constant, low ratios (0.70385–0.70399), identical to those from Rindjani. On the other hand, not only do geochemically similar lavas from Sangeang Api have higher ⁸⁷Sr/⁸⁶Sr ratios, but also the ratios show a significant decrease from the mafic basalts to the more evolved lavas. The leucitites from Soromundi and that from Sangenges (S19) are also charac-

TABLE 31. Modal Compositions of Xenoliths from Sangeang Api Volcano

	B23	B4	B25x	B8
Olivine	0.35	0.01
Ca-rich Clino- pyroxene	0.62	0.90	0.62	0.26
Amphibole	trace	0.08	0.15	0.20
Biotite	0.02
Ti-Magnetite	trace	0.01	0.14	0.12
Plagioclase	0.09	0.42

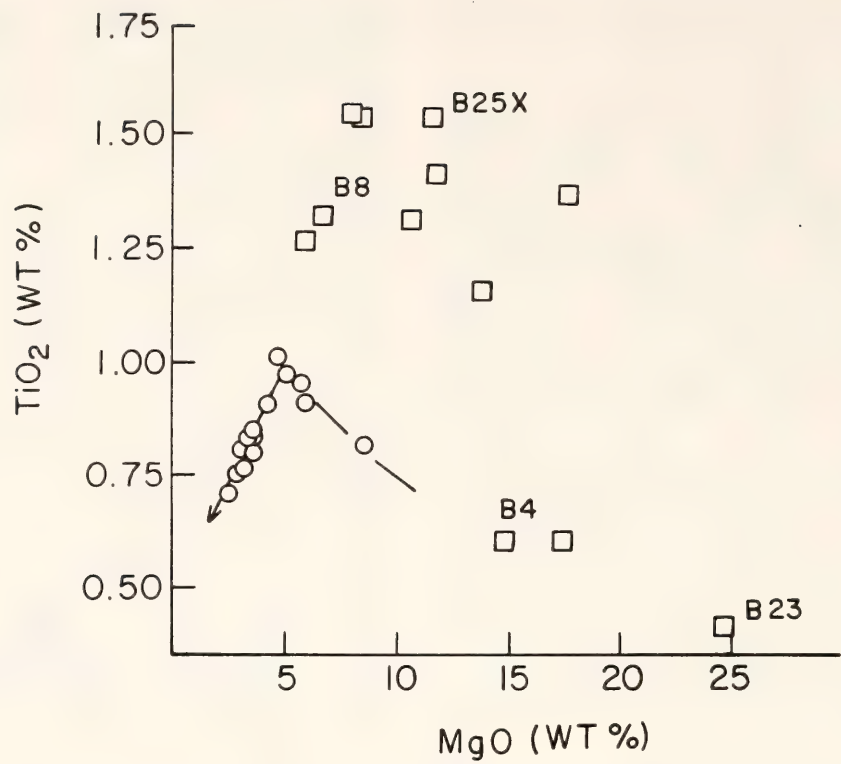


Fig. 127. Plot of TiO_2 (wt %) versus MgO (wt %) for lavas (dots) and associated xenoliths (squares) from Sangeang Api. Sample numbers refer to analyzed xenoliths. The dashed line illustrates the pattern of early Ti enrichment followed by a strong depletion in the more evolved lavas.

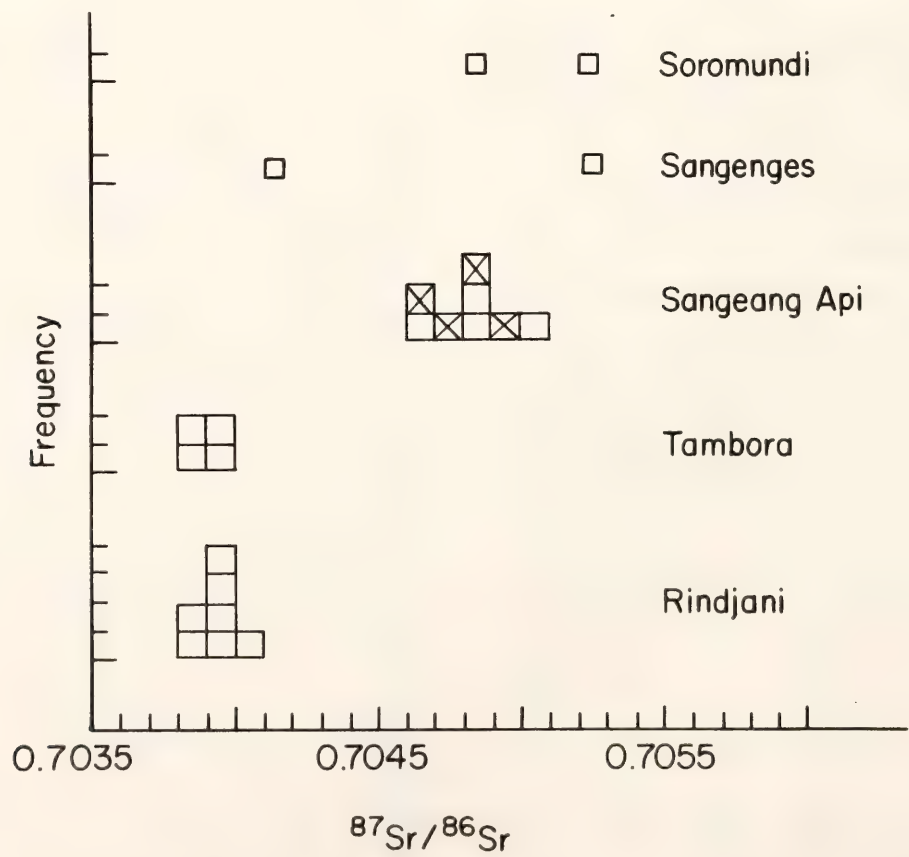


Fig. 128. Histograms showing the frequency distribution of measured $^{87}\text{Sr}/^{86}\text{Sr}$ ratios in lavas from individual volcanoes in Lombok and Sumbawa. Overall, there is a bimodal distribution with maxima at 0.7039 and 0.7048. Xenoliths from Sangeang Api are denoted by X.

TABLE 32. Sr Isotope Results*

	SiO ₂	K ₂ O	Mg No.†	Rb	Sr	Rb/Sr	K/Rb	⁸⁷ Sr/ ⁸⁶ Sr‡	±2σm
Rindjani (A)§									
LB8	48.32	0.90	0.74	21	452	0.046	356	0.70388	±5
41632	50.20	1.21	0.52	20	452	0.044	502	0.70386	±6
41678	52.03	2.00	0.42	51	527	0.096	325	0.70398	±5
41634	52.90	1.37	0.40	30	510	0.058	379	0.70398	±7
41622	55.49	1.60	0.42	35	433	0.080	379	0.70398	±6
LB69	61.82	3.00	0.39	62	403	0.154	401	0.70394	±6
41671	65.58	3.67	0.36	98	293	0.334	311	0.70402	±6
Tambora (B)§									
T17	48.78	2.47	0.52	189	1113	0.169	108	0.70385	±6
T13	51.49	2.89	0.50	86	981	0.087	279	0.70399	±6
T32	55.09	5.03	0.47	132	1036	0.127	316	0.70395	±6
T20	56.10	5.69	0.40	142	923	0.154	332	0.70389	±6
Sangeang Api (B)§									
B43	47.77	1.85	0.64	73	850	0.085	210	0.70500	±5
B25	48.02	2.64	0.46	92	1135	0.081	238	0.70486	±6
B35	50.43	2.75	0.44	84	943	0.089	272	0.70469	±6
B32	53.05	3.56	0.41	112	1010	0.111	264	0.70485	±6
Xenoliths									
B23	45.41	0.10	0.81	5	68	0.073	166	0.70496	±7
B4	50.19	0.05	0.81	5	121	0.041	83	0.70480	±7
B25x	40.48	0.28	0.54	6	221	0.027	387	0.70477	±6
B8	38.31	0.42	0.47	3	1125	0.0027	1162	0.70466	±5
G. Sangenges (B and C)§									
S19 (C)	44.71	4.42	0.56	319	836	0.381	115	0.70529	±6
S28 (B)	50.55	2.21	0.49	61	724	0.084	301	0.70412	±8
Soromundi (C)§									
Si12	47.49	3.32	0.50	114	1511	0.075	242	0.70488	±7
Si9	49.24	4.00	0.41	144	2401	0.059	232	0.70527	±7

* Major and trace element abundances by x-ray fluorescence spectrometry at University of Tasmania—J. Foden, analyst.
† Mg No. = Atomic Mg/(Mg + ΣFe).
‡ All ⁸⁷Sr/⁸⁶Sr ratios normalized to ⁸⁶Sr/⁸⁵Sr = 0.1194 and repeated relative to E & A SrCO₃, ⁸⁷Sr/⁸⁶Sr = 0.70800.
§ Lava types: A = calc-alkaline suite; B = phonolitic tephrite-trachybasalt-trachyandesite suite; C = leucite suite.

terized by high and variable ⁸⁷Sr/⁸⁶Sr ratios (0.70488–0.70529). The less-potassic, nepheline-normative lava S28 from Sangenges has a lower ratio (0.70412). Lavas from Soromundi, Sangenges, and Sangeang Api show an inverse correlation between ⁸⁷Sr/⁸⁶Sr and the ratio K/Rb. Overall there do not appear to be any correlations between major-element and trace element abundances and ⁸⁷Sr/⁸⁶Sr.

⁸⁷Sr/⁸⁶Sr ratios in the four analyzed xenoliths range from 0.70466 to 0.70496. Although there are significant differences in isotopic composition among both the lavas and xenoliths, the ranges in Sr isotopic composition in both groups are identical. Perhaps surprisingly, the most mafic xenoliths are characterized by the highest ⁸⁷Sr/⁸⁶Sr ratios. Although it may be partly a function of the limited number of analyses, ⁸⁷Sr/⁸⁶Sr ratios in the

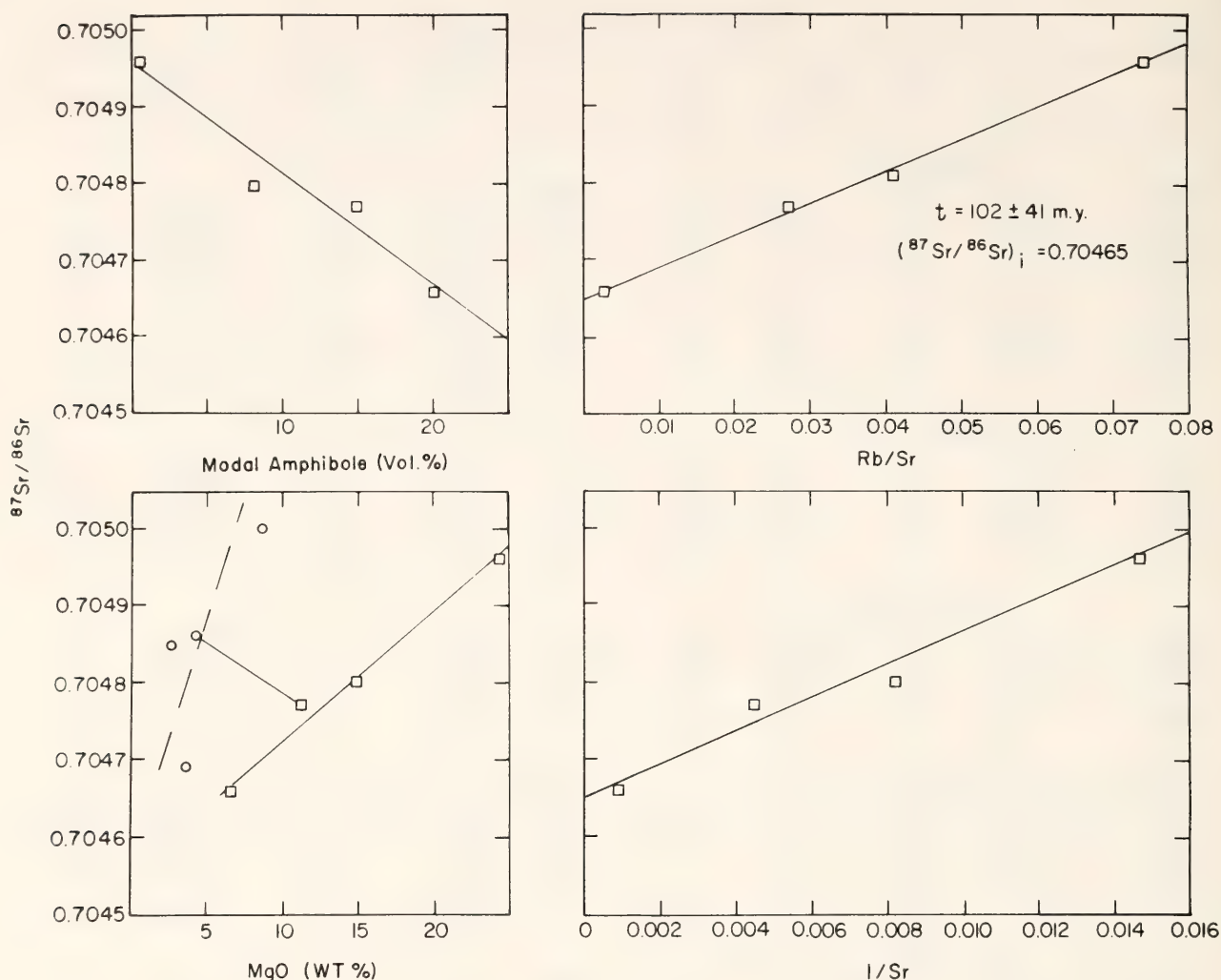


Fig. 129. Variation of $^{87}\text{Sr}/^{86}\text{Sr}$ with the abundance of modal amphibole, Rb/Sr, MgO and $1/\text{Sr}$ in xenoliths from Sangeang Api. MgO contents of associated lavas are also plotted, with a tie-line connecting a xenolith with its host lava.

xenoliths correlate with several petrographic and geochemical variables, including the abundance of modal amphibole, the abundance of MgO, $1/\text{Sr}$ and Rb/Sr (Fig. 129). The correlation between $^{87}\text{Sr}/^{86}\text{Sr}$ and Rb/Sr corresponds to an "age" of approximately 100 m.y. ($\lambda^{87}\text{Rb} = 1.42 \times 10^{-11}\text{yr}^{-1}$) although the error is large (~ 40 m.y.) mainly because of the very small dispersion in $^{87}\text{Sr}/^{86}\text{Sr}$ and uncertainties in the Rb/Sr ratios.

Discussion

The uniformity of $^{87}\text{Sr}/^{86}\text{Sr}$ ratios in lavas from Rindjani and Tambora is compatible with their evolution from

mafic parental liquids by fractional crystallization. The relatively low ratios are also compatible with the observed regional pattern of an eastward decrease in $^{87}\text{Sr}/^{86}\text{Sr}$ in lavas from Java and Bali (Whitford, 1975).

Lavas from the remaining three volcanoes—Sangeang Api, Sangenges, and Soromundi—are characterized by relatively high and variable $^{87}\text{Sr}/^{86}\text{Sr}$ ratios. From Sangeang Api, there is some evidence (Fig. 129) of parallel isotopic behavior between xenoliths and host lavas, which implies a possible genetic relationship. Why there should be significant variations in $^{87}\text{Sr}/^{86}\text{Sr}$ ratios during the evolution of a series of liquids and what may be associated cumulates is not clear,

especially as the most-mafic lavas and xenoliths are both characterized by the most-radiogenic Sr. It is possible that the Cr-diopsides with low Al and Ti and high atomic $\text{Mg}/(\text{Mg} + \text{Fe}^{2+})$ ratios, which occur as megacrysts in the most primitive lava B43 and in some of the olivine-clinopyroxene-rich xenoliths, are of mantle origin. These pyroxenes can be traced into the more Fe-rich amphibole-magnetite xenoliths in various stages of textural and chemical re-equilibration. In this regard, the inverse correlation between $^{87}\text{Sr}/^{86}\text{Sr}$ and the amount of modal amphibole may be significant (Fig. 129).

Although based on limited data, the correlations noted in Fig. 129 suggest that the isotopic variations may reflect mixing or at least a strong mineralogical control over observed $^{87}\text{Sr}/^{86}\text{Sr}$ ratios in the xenoliths. Even if the isochron in Fig. 129 is the result of mixing, the "age" could still have physical significance, perhaps reflecting an enrichment or melting event in the mantle.

The relationship between the alkaline Sumbawan lavas and the subducted lithospheric slab is unclear, but like high-K lavas from other island arcs and active continental margins they are characterized by distinctive "island arc" geochemical features, particularly low concentrations of TiO_2 . Moreover, in some other areas such as Java, the degree of K-enrichment observed in at least some of the alkaline lavas does seem to correlate with the depth to the underlying Benioff zone (Whitford and Nicholls, 1976). In contrast to the Sumbawan rocks, the alkaline lavas from Java are characterized by $^{87}\text{Sr}/^{86}\text{Sr}$ ratios equal to or lower than spatially related calc-alkaline lavas.

Many authors have suggested that the mantle source of highly potassic lavas must be enriched in K and related elements relative to "normal" mantle which serves, for example, as the source of oceanic basalts (Appleton, 1972; Ninkovich

and Hays, 1972; Lloyd and Bailey, 1975; Cox *et al.*, 1976). One possible enrichment mechanism in island-arc regions could be deep dehydration of the crustal component of the subducted lithosphere. Hydrous fluids, possibly derived from the breakdown of hydrated Mg-silicates (Ringwood, 1974), may rise into the overlying mantle wedge, "scavenging" K and related elements during their migration (Ninkovich and Hays, 1972; Best, 1975). Such a process could continue until K-bearing phases such as phlogopite become stable.

One possible explanation of the differences between the alkaline lavas from Java and those from Sumbawa could be the nature and "age" of the mantle source. In the case of Muriah in Java, the Quaternary volcanism may reflect melting of very recently enriched mantle. Compatible with this interpretation are the location of this volcano over great Benioff zone depths and the relatively low $^{87}\text{Sr}/^{86}\text{Sr}$ ratios (Whitford, 1975). On the other hand, the Sumbawan lavas may reflect melting of mantle which has been enriched in the past (perhaps 100 m.y. ago), which would account for both the higher observed $^{87}\text{Sr}/^{86}\text{Sr}$ ratios, together with their anomalous location over too shallow a Benioff zone. A similar model of delayed partial melting of subduction-modified mantle has been proposed by Johnson *et al.* (1978) for some lavas from Papua New Guinea.

Acknowledgments

Fieldwork in Indonesia by J. D. Foden and R. Varne was sponsored by the Indonesian Institute of Sciences (L.I.P.I.) and carried out in collaboration with Dr. Sototo and other staff of the Geology Department, Gadjah Mada University.

Field, travel, and some analytical expenses were met with the aid of research grants from the University of Tasmania and the Australian Research Grants Committee.

References

- Appleton, J. D., Petrogenesis of potassium-rich lavas from the Roccamonfina volcano, Roman Region, Italy, *J. Petrology*, **13**, 425–456, 1972.
- Arculus, R. J., and R. W. Johnson, Criticism of generalized models for the magmatic evolution of arc-trench systems, *Earth Planet. Sci. Lett.*, **39**, 118–126, 1978.
- Audley-Charles, M. G., The Sumba Fracture: a major discontinuity between eastern and western Indonesia, *Tectonophysics*, **26**, 213–228, 1975.
- Best, M. G., Migration of hydrous fluids in the upper mantle and potassium variation in calc-alkalic rocks, *Geology*, **3**, 429–432, 1975.
- Cox, K. G., C. J. Hawkesworth, R. K. O'Nions, and J. D. Appleton, Isotopic evidence for the derivation of some Roman Region volcanics from anomalously enriched mantle, *Contrib. Mineral. Petrol.*, **56**, 173–180, 1976.
- Curry, J. R., G. G. Shor, R. W. Raitt, and M. Henry, Seismic refraction and reflection studies of crustal structure of the eastern Sunda and western Banda arcs, *J. Geophys. Res.*, **82**, 2479–2489, 1977.
- Foden, J. D., Geochemistry and petrology of volcanic rocks from Lombok and Sumbawa, Indonesia, Ph.D. Thesis, Univ. of Tasmania, 1978.
- Foden, J. D., and R. Varne, Potassium-rich lavas from Sumbawa, Lesser Sunda Islands, Indonesia, submitted for publication, 1978.
- Hamilton, W., Earthquake map of the Indonesian region, U. S. Geol. Survey 1:5,000,000 Map I-875-C, 1974.
- Johnson, R. W., D. E. Mackenzie, and I. E. M. Smith, Delayed partial melting of subduction-modified mantle in Papua, New Guinea, *Tectonophysics*, **46**, 197–216, 1978.
- Katili, J. A., Volcanism and plate tectonics in the Indonesian island arcs, *Tectonophysics*, **26**, 165–188, 1975.
- Lloyd, F. E., and D. K. Bailey, Light element metasomatism of the continental mantle: the evidence and the consequences, *Phys. Chem. Earth*, **9**, 389–416, 1975.
- Ninkovich, D., and J. D. Hays, Mediterranean island arcs and origin of high-potash volcanoes, *Earth Planet. Sci. Lett.*, **16**, 331–345, 1972.
- Ringwood, A. E., The petrological evolution of island arc systems, *J. Geol. Soc. Lond.*, **130**, 183–204, 1974.
- Van Bemmelen, R. W., *The Geology of Indonesia*, 2nd ed., **1**, Martinus Nijhoff, The Hague, 1949.
- Whitford, D. J., Strontium isotopic studies of the volcanic rocks of the Sunda arc, Indonesia, and their petrogenetic implications, *Geochim. Cosmochim. Acta*, **39**, 1287–1302, 1975.
- Whitford, D. J., and I. A. Nicholls, Potassium variation in lavas across the Sunda arc in Java and Bali, in *Volcanism in Australasia*, pp. 63–75, R. W. Johnson, ed., Elsevier, Amsterdam, 1976.

SEPARATION AND ISOTOPIC ANALYSIS
OF NEODYMIUM

D. J. Whitford, W. M. White, A. W. Hofmann,
and D. E. James

We report details of a procedure used at Department of Terrestrial Magnetism for the chemical separation and isotopic analysis of Nd from geological materials (see, e.g., White and Hofmann, this Report). The initial REE separation is similar to that described by Shimizu (*Year Book* **73**, pp. 941–943), and the Nd separation is almost identical to that described by Eugster *et al.* (1970) with modifications reported by De Paolo and Wasserburg (1976). The mass spectrometry is similar to that of Shimizu (*ibid.*) and O'Nions *et al.* (1976).

Chemistry

Samples of between 50–200 mg are dissolved in HF and HClO₄ and evaporated

to dryness. After drying down with HCl, the residue is dissolved in 1.5 ml 2.5N HCl, centrifuged in a polyethylene vial, and loaded onto a cation-exchange column. The column consists of 15 ml Bio Rad AG50W x8, 200–400 mesh cation resin conditioned with 2.5N HCl, contained in a 19×1 cm fused quartz cylinder. After washing with 83 ml 2.5N HCl (to the end of the Sr fraction) and then 10 ml 6.2N HCl, a light REE concentrate containing Nd is eluted with 20 ml 6.2N HCl. The Nd concentrate is then evaporated to dryness.

The final separation of Nd is made with a second column consisting of about 1 ml Bio Rad AG50W x8 —400 mesh cation resin conditioned in 0.2M 2 methyl-lactic acid (hereafter referred to as 2mla) adjusted with concentrated NH_4OH to $\text{pH} = 4.6$. The resin is contained in thick-walled 2-mm-diameter precision-bore Pyrex capillary tubing, approximately 35 cm long, beneath a reservoir with about 12 ml capacity. To facilitate both cleaning and changing of resin after each separation, the resin is supported at the base of the column with a disc of filter paper that is held in place with a close-fitting TFE Teflon nipple. The nipple is fitted into a threaded TFE Teflon collar. A similar threaded collar is fitted at the top of the column, and both collars screw into a thick-walled Plexiglas cylinder which serves to maintain a tight seal between the column and the filter paper during the elution. The separation is carried out with an N_2 overpressure of 0.25 kg cm^{-2} . A schematic diagram of the column components is shown in Fig. 130.

The resin for the second column is washed thoroughly prior to use. About 130 ml of resin is placed in a Pyrex column and washed with 2.5l 4N HCl (quartz-distilled). The resin is then back-washed and rinsed with quartz-distilled H_2O until all traces of HCl are removed (yellow in Methyl Orange indicator). 2.5l 2mla (0.4M, $\text{pH} = 4.6$, ad-

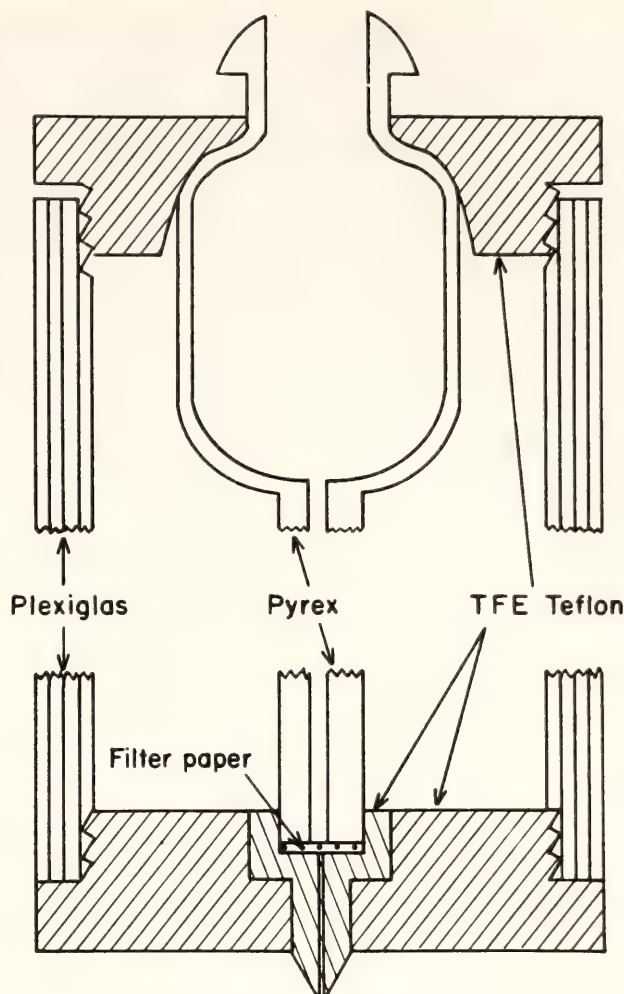


Fig. 130. Schematic configuration of column used for separation of Nd from other REE. A ground-glass seal at the top facilitates the application of N_2 .

justed with NH_4OH) are then passed through. Resin (~ 5 ml) at the top of the column, discolored because of impurities in the 2mla, is removed in H_2O with a clean pipette. 300 ml of H_2O is then passed through the column to remove excess 2mla, leaving the resin in the NH_4^+ form. The upper 30 ml of resin is discarded because of possible Ba contamination, and the remaining resin was stored in H_2O .

2mla solution is prepared from crystalline 2mla (Eastman Kodak Chemicals). The solution is filtered to remove insoluble matter and the pH adjusted with high-purity NH_4OH . For 1l of 0.2M 2mla, this requires approximately 10 ml

NH₄OH. Impurities in the 2mla result in a yellow coloration, which appears to have no effect on the Nd separation.

An aqueous suspension of the resin is loaded into the second column and allowed to settle to a column length of approximately 35 cm. Excess resin and H₂O are removed and approximately 10 ml 0.2M 2mla added and allowed to drain overnight. An N₂ overpressure of 0.25 kg cm⁻² is then applied for 1–2 hours, bringing the total 2mla effluent to about 6–7 ml. 0.2M 2mla and resin in excess of exactly 30 cm are removed with a pipette. In order to remove interstitial 2mla at the very top of the column, 0.15 ml H₂O is added to the column and forced into the resin.

The dried Nd concentrate from the first column is dissolved in minimal 0.1N HCl (~ 0.05 ml), added to the column, and forced into the resin. The use of 0.8N HCl, as described by Eugster *et al.* (1970), appeared to result in fluctuations in the column calibration. Care is taken to load the sample into the top of the resin with a pipette. In order to remove all traces of the sample from the reservoir and upper sections of the capillary, 0.15 ml H₂O is added to the column and forced into the resin. 0.2M 2mla is then added and forced through the column under pressure at a rate of about 2 ml hr⁻¹. Early fractions of the 2mla are used to rinse the top of the column. Nd is collected between 5.5 and 7 ml 2mla. Unlike Eugster *et al.* (1970), we monitor the volume of 2mla added to the column rather than count drops issuing from the column. When temperature and humidity cannot be rigidly controlled, the number of drops per ml 2mla added to the column can vary by as much as 20–25%. Typical REE-elution curves, derived from radioactive tracers, are shown in Fig. 131.

The Nd solution is dried down in an acid-free environment. Exposure to even small amounts of HCl results in the formation of NH₄Cl, which if formed in

large amounts has to be removed in a third “clean-up” column. The dried residue is then treated with HClO₄.

Mass Spectrometry

Isotopic measurements are made using a Nd⁺ beam in a 9-inch, 60° sector, mass spectrometer equipped with an FR41 field control device under computer control. Ion beams are measured with a modified Cary 401 vibrating reed electrometer using a 10¹¹-ohm input resistor. The sample is dissolved in a drop of 2.5N HCl and evaporated onto the side filament of an Re double-filament source and taken to dull-red heat in air for a few seconds. In the mass spectrometer, the current in the center filament is adjusted to obtain a stable ¹⁸⁷Re beam of about 3×10^{-12} Å. Current in the side filament is then increased slowly until a beam of ¹⁴⁴Nd of $7-8 \times 10^{-12}$ Å is attained. Data are taken in blocks of seven mass scans, each scan consisting of three 1-sec integrations on each peak (143, 144, 146) and three 1-sec zero counts taken at mass 140.5. In running the metal Nd⁺ rather than NdO⁺, the only isobaric interference is due to ¹⁴⁴Sm. ¹⁴⁷Sm is routinely monitored with typical beam intensities in the order of 10⁻¹⁵ Å, resulting in corrections to the ¹⁴³Nd/¹⁴⁴Nd ratio of $\leq 0.005\%$. ¹⁴³Nd/¹⁴⁴Nd are normalized to a ¹⁴⁶Nd/¹⁴⁴Nd ratio of 0.7219 (O’Nions *et al.*, 1977). Internal precision within a single run is typically 0.006% (2σ error of the mean) after 100–200 mass scans.

Blanks for the entire procedure have been measured at $< 3 \times 10^{-10}$ g.

References

- De Paolo, D. J., and G. J. Wasserburg, Nd isotopic variations and petrogenetic models, *Geophys. Res. Lett.*, **3**, 249–252, 1976.
- Eugster, O., F. Tera, D. S. Burnett, and G. J. Wasserburg, Isotopic composi-

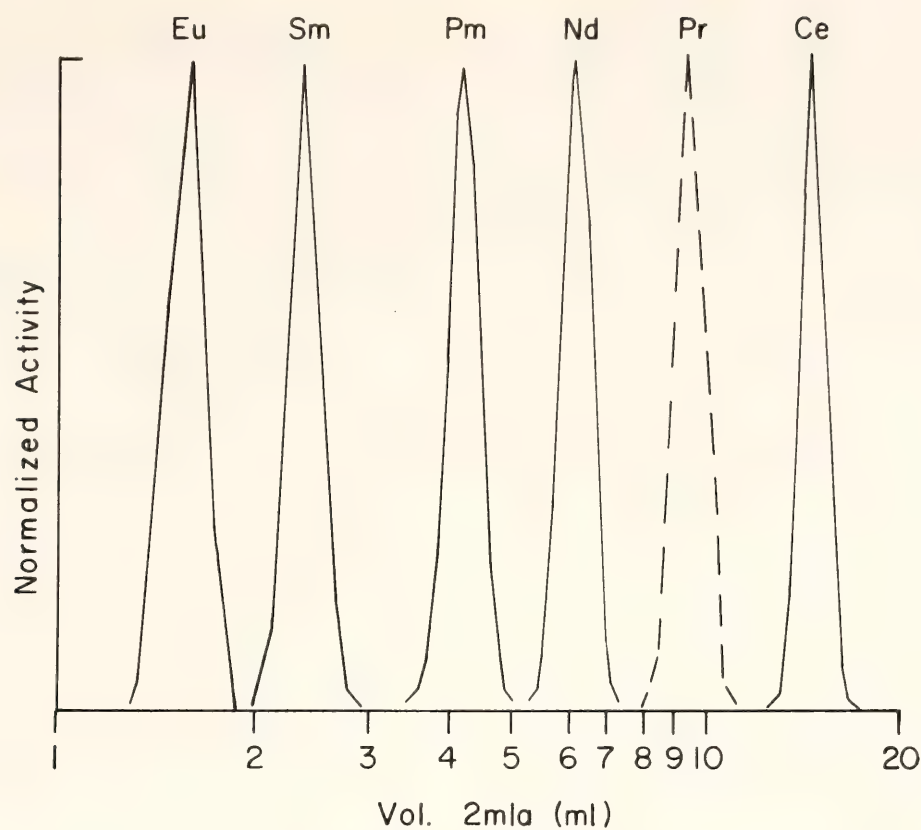


Fig. 131. Elution curves for light REE from 2mla column (see text) derived from radioactive tracers. The Pr elution curve has been interpolated. Nd is collected between 5.5–7 ml 2mla (pH = 4.6).

tion of gadolinium and neutron-capture effects in some meteorites, *J. Geophys. Res.*, **75**, 2753–2768, 1970.
O’Nions, R. K., P. J. Hamilton, and

N. M. Eversen, Variations in $^{143}\text{Nd}/^{144}\text{Nd}$ and $^{87}\text{Sr}/^{86}\text{Sr}$ ratios in oceanic basalts, *Earth Planet. Sci. Lett.*, **34**, 13–22, 1977.

BIBLIOGRAPHY

The publications listed below (except minor publications, such as abstracts) can be obtained at no charge from the Department of Terrestrial Magnetism, 5241 Broad Branch Rd., N. W., Washington, D.C. 20015. When ordering, please give reprint number(s). No reprints are available for titles marked with asterisks.

— Abbott, M. J., *see* Whitford, D. J.
— Aldrich, L. T., *see* Ramirez, J. E., S. J.
4465 Assousa, G. E., W. Herbst, and K. C. Turner, Supernova-induced star formation in Cepheus OB3, *Astrophys. J.*, **218**, L13–L15, 1977.
— Assousa, G. E., *see* Herbst, W.
4466 Bloch, S., and A. W. Hofmann, Magnesium metasomatism during hydrothermal alteration of new oceanic crust, *Geology*, **6**, 275–277, 1978.

— Brown, R. L., *see* Lockman, F. J.
*4467 Brownlee, D. E., R. S. Rajan, and D. A. Tomandl, A chemical and textural comparison between carbonaceous chondrites and interplanetary dust, in *Comets, Asteroids, Meteorites: Interrelations, Evolution and Origin*, pp. 137–140, A. H. Delsemme, ed., The Univ. of Toledo, Toledo, Ohio, 1977.
— Compston, W., *see* Whitford, D. J.
4468 Dodson, M. H., Kinetic processes and thermal history of slowly cooling solids, *Nature*, **259**, 551–553, 1976.
4469 Evans, J. R., K. Suyehiro, and I. S. Sacks, Mantle structure beneath the Japan Sea—a re-examination, *Geophys. Res. Lett.*, **5**, 487–490, 1978.
— Farhat, J., *see* Hurst, R.

- Ford, W. K., Jr., *see* Kinman, T. D., Peterson, C. J., and Rubin, V. C.
- Hart, S. R., *see* Hofmann, A. W.
- Havlen, R. J., *see* Herbst, W.
- 4470 Herbst, W., Extinction law in dust clouds and the young southern cluster NGC 6250: further evidence for high values of R , *Astron. J.*, 82, 902–907, 1977.
- 4471 Herbst, W., Stars in reflection nebulae near the Herbig-Haro objects in the Gum nebula, *Publ. Astron. Soc. Pacific*, 89, 795–796, 1977.
- 4472 Herbst, W., and G. E. Assousa, Observational evidence for supernova-induced star formation: Canis Major R1, *Astrophys. J.*, 217, 473–487, 1977.
- 4473 Herbst, W., and R. J. Havlen, Ara OB1, NGC 6193 and Ara R1: an optical study of a very young southern complex, *Astron. Astrophys. Suppl.* 30, 279–295, 1977.
- 4474 Herbst, W., R. Racine, and H. B. Richer, A luminous carbon star in Canis Major OB1, *Publ. Astron. Soc. Pac.*, 89, 663–667, 1977.
- Herbst, W., *see* Assousa, G. E.
- 4475 Hofmann, A. W., and M. Magaritz, Diffusion of Ca, Sr, Ba, and Co in a basalt melt: implications for the geochemistry of the mantle, *J. Geophys. Res.*, 82, 5432–5440, 1977.
- *4476 Hofmann, A. W., and M. Magaritz, Equilibrium and mixing in a partially molten mantle, in *Magma Genesis, Proc. Amer. Geophys. Union Chapman Conf. on Partial Melting in the Earth's Upper Mantle*, Bull. 96, pp. 37–41, H. J. B. Dick, ed., Portland, Oregon, Dept. of Geol. and Min. Ind., 1977.
- 4477 Hofmann, A. W., and S. R. Hart, An assessment of local and regional isotopic equilibrium in the mantle, *Earth Planet. Sci. Lett.*, 38, 44–62, 1978.
- Hofmann, A. W., *see* Bloch, S., and Magaritz, M.
- *4478 Hurst, R., J. Farhat, and G. W. Wetherill, Very old (>3100 million years) rocks in North America, in *Chemical Evolution of the Early Precambrian*, pp. 25–26, Cyril Ponnampertuma, ed., New York, Academic Press, 1977.
- Husebye, E. S., *see* Sacks, I. S.
- 4479 James, D. E., Subduction of the Nazca plate beneath central Peru, *Geology*, 6, 174–178, 1978.
- 4480 Kinman, T. D., V. C. Rubin, N. Thonnard, W. K. Ford, Jr., and C. J. Peterson, Compact blue-shifted galaxy RMB 56 (1216 + 141), *Astron. J.*, 82, 879–885, 1977.
- 4481 Lockman, F. J., and R. L. Brown, The analysis of radio emission from HII regions: consequences of improper analytic methods, *Astrophys. J.*, 222, 153–164, 1978.
- Lynds, C. R., *see* Rubin, V. C.
- 4482 Magaritz, M., and A. W. Hofmann, Diffusion of Eu and Gd in basalt and obsidian, *Geochim. Cosmochim. Acta*, 42, 847–858, 1978.
- 4483 Magaritz, M., and A. W. Hofmann, Diffusion of Sr, Ba and Na in obsidian, *Geochim. Cosmochim. Acta*, 42, 595–605, 1978.
- Magaritz, M., *see* Hofmann, A. W.
- Nicholls, I. A., *see* Whitford, D. J.
- Okada, H., *see* Snoke, J. A.
- 4484 Peterson, C. J., V. C. Rubin, W. K. Ford, Jr., and N. Thonnard, The velocity field of the barred spiral galaxy NGC 5383, *Astrophys. J.*, 219, 31–45, 1978.
- Peterson, C. J., *see* Kinman, T. D., and Rubin, V. C.
- *4485 Poupeau, G., R. S. Rajan, R. M. Walker, and E. Zinner, The modern and ancient flux of solar wind particles, solar flare particles and micrometeoroids, *Space Research*, XVII, Proc. 19th Plenary Meeting of COSPAR held in Philadelphia, Pennsylvania, pp. 599–604, M. J. Rycroft, ed., New York, Pergamon Press, 1977.
- Racine, R., *see* Herbst, W.
- Rajan, R. S., *see* Brownlee, D. E., and Poupeau, G.
- *4486 Ramirez, J. E., S. J., and L. T. Aldrich, eds., *The Ocean-Continent Transition in SW-Colombia*, Bogotá, Colombia, Instituto Geofísico, Universidad Javeriana, 1977.
- Richer, H. B., *see* Herbst, W.
- 4487 Rubin, V. C., Is there evidence of anisotropy in the expansion of the universe? in *IAU Colloquium No. 37, Red Shifts and Expansion of the Universe*, September 8–9, 1976, pp. 119–140, Paris, Centre National de la Recherche Scientifique, 1977.
- 4488 Rubin, V. C., Is there evidence for anisotropy in the Hubble expansion? *Eighth Texas Symposium on Relativistic Astrophysics* (Boston, December 13–17, 1976), 302, *Ann. N.Y. Acad. Sci.*, pp. 408–421, M. D. Papagiannis, ed., New York Academy of Sciences, New York, 1977.

- 4489 Rubin, V. C., N. Thonnard, and W. K. Ford, Jr., Extended rotation curves of high-luminosity spiral galaxies. I. The angle between the rotation axis of the nucleus and the outer disk of NGC 3672, *Astrophys. J.*, 217, L1-L4, 1977.
- 4490 Rubin, V. C., W. K. Ford, Jr., C. J. Peterson, and C. R. Lynds, A new mapping of the velocity field of NGC 1275, *Astrophys. J. Suppl.*, 37, 235-249, 1978.
- Rubin, V. C., see Kinman, T. D., and Peterson, C. J.
- 4491 Sacks, I. S., J. A. Snoke, and E. S. Husebye, Lithosphere thickness beneath the Baltic shield, *Tectonophysics*, in press, 1978.
- Sacks, I. S., see Evans, J. R., and Snoke, J. A.
- 4492 Snoke, J. A., I. S. Sacks, and H. Okada, Determination of the subducting lithosphere boundary by use of converted phases, *Bull. Seis. Soc. Amer.*, 67, 1051-1060, 1977.
- Snoke, J. A., see Sacks, I. S.
- Suyehiro, K., see Evans, J. R.
- Thonnard, N., see Kinman, T. D., Peterson, C. J., and Rubin, V. C.
- Tomandl, D. A., see Brownlee, D. E.
- Turner, K. C., see Assousa, G. E.
- Walker, R. M., see Poupeau, G.
- 4493 Weidenschilling, S. J., Aerodynamics of solid bodies in the solar nebula, *Mon. Notic. Roy. Astron. Soc.*, 180, 57-70, 1977.
- 4494 Weidenschilling, S. J., The distribution of mass in the planetary system and solar nebula, *Astrophys. Space Sci.*, 51, 153-158, 1977.
- *4495 Weidenschilling, S. J., The solar nebula pressure gradient and its effect on planetesimal motions, in *Comets, Asteroids, Meteorites: Interrelations, Evolution, and Origin*, pp. 541-544, A. H. Delsemme, ed., Univ. Toledo, Toledo, Ohio, 1977.
- 4496 Wetherill, G. W., Evolution of the earth's planetesimal swarm subsequent to the formation of the earth and moon, *Proc. 8th Lunar Sci. Conf.* (Houston, March 14-18, 1977), pp. 1-16, R. B. Merrill, ed., Pergamon Press, New York, 1977.
- *4497 Wetherill, G. W., Fragmentation of asteroids and delivery of fragments to earth, in *Comets, Asteroids, Meteorites: Interrelations, Evolution, and Origin*, pp. 283-290, A. H. Delsemme, ed., Univ. Toledo, Toledo, Ohio, 1977.
- 4498 Wetherill, G. W., The nature of the present interplanetary crater-forming projectiles, in *Impact and Explosion Cratering*, pp. 613-615, D. J. Roddy, R. O. Pepin, and R. B. Merrill, eds., Pergamon Press, New York, 1977.
- *4499 Wetherill, G. W., Accumulation of the terrestrial planets, in *Protostars and Planets*, in press, T. Gehrels, ed., Univ. Arizona Press, Tucson, Arizona, 1978.
- Wetherill, G. W., see Hurst R.
- 4500 Whitford, D. J., W. Compston, I. A. Nicholls, and M. J. Abbott, Geochemistry of late Cenozoic lavas from eastern Indonesia: role of subducted sediments in petrogenesis, *Geology*, 5, 571-575, 1977.
- Zinner, E., see Poupeau, G.

PERSONNEL

Staff Members

L. Thomas Aldrich
George E. Assousa
Louis Brown
Dean B. Cowie¹
Scott E. Forbush, *Emeritus*
W. Kent Ford, Jr.
Albrecht W. Hofmann
David E. James

Alan T. Linde
Sundar Rajan²
Richard B. Roberts, *Emeritus*
Vera C. Rubin
I. Selwyn Sacks
Fouad Tera
Norbert Thonnard
Kenneth C. Turner

George W. Wetherill, *Director*

¹Institut Pasteur, Paris, France. Deceased November 8, 1977.

Distinguished Service Member of Carnegie Institution

Merle A. Tuve

*Research Associates (Staff)*Emilio Filloy³
Mordeckai Magaritz⁴Rambabu P. Ranganayaki⁵
Kiyoshi Suyehiro⁶*Research Associates (Nonresident)*Leonidas Ocola, Instituto
Geofísico del Peru,
Lima, Peru*Carnegie Fellows (Postdoctoral)*David Burstein⁷
John R. Evans
William D. Heinze⁸
William HerbstFelix J. Lockman
Douglas O. ReVelle
Stuart J. Weidenschilling⁹
William M. White
David J. Whitford*Visiting Investigator*Akira Hasegawa¹⁰*Trainee Fellows*Charles L. Bennett¹¹Gregory S. DeWitt¹²*Collaborators*Claude Allégre, University of Paris, Paris,
France
E. Bajaja, Instituto Argentino de Radio-
astronomía, Villa Elisa, Argentina
John Bannister, Universidad de Chile, Santi-
ago, Chile
C. S. Bow, Center for Volcanology, Univer-
sity of Oregon, Eugene, Oregon
M. Bracamonte, Trujillo, Peru
D. E. Brownlee, University of Washington,
Seattle, Washington
B. F. Burke, Massachusetts Institute of Tech-
nology, Cambridge, MassachusettsR. Cabre, S. J., Observatorio San Calixto,
La Paz, Bolivia
Mateo Casaverde, Instituto Geofísico del
Peru, Lima, Peru
R. Colomb, Instituto Argentino de Radio-
astronomía, Villa Elisa, Argentina
G. L. Davis, Geophysical Laboratory, Car-
negie Institution of Washington, Washing-
ton, D.C.
R. A. Duncan, Oregon State University, Cor-
vallis, Oregon
J. W. Erkes, State University of New York,
Albany, New York² From September 1, 1977.³ From August 1, 1977, through January 31, 1978.⁴ Through October 31, 1977.⁵ From May 1, 1978.⁶ Through May 31, 1978.⁷ From December 1, 1977.⁸ From February 1, 1978.⁹ Through May 31, 1978.¹⁰ From June 15, 1978.¹¹ From May 16, 1978.¹² Through July 15, 1977.

- D. W. Evertson, University of Texas at Austin, Texas
- Mark Feigenson, Department of Geological and Geophysical Sciences, Princeton, New Jersey
- J. Foden, University of Tasmania, Hobart, Tasmania
- A. A. Giesecke, Instituto Geofísico del Peru, Lima, Peru
- Nicol Girardin, Institut de Physique du Globe, Paris, France
- S. J. Goldstein, Jr., Department of Astronomy, University of Virginia, Charlottesville, Virginia
- K. Gopalan, Physical Research Laboratory, Navarangpura, Ahmedabad, India
- E. W. Greisen, National Radio Astronomy Observatory, Charlottesville, Virginia
- T. R. Gull, NASA Space Flight Center, Greenbelt, Maryland
- S. R. Hart, Massachusetts Institute of Technology, Cambridge, Massachusetts
- C. Heiles, University of California, Berkeley, California
- D. E. Helsley, University of Hawaii, Honolulu, Hawaii
- P. A. Jezek, Smithsonian Institution, Washington, D.C.
- T. D. Kinman, Kitt Peak National Observatory, Tucson, Arizona
- C. Krishna Kumar, Howard University, Washington, D.C.
- I. Kushi, Geophysical Laboratory, Carnegie Institution of Washington, Washington, D.C.
- B. Lewis, University of Washington, Seattle, Washington
- C. R. Lynds, Kitt Peak National Observatory, Tucson, Arizona
- Y. Motoya, Kamikineusu Seismological Observatory of Sapporo University, Hokkaido, Japan
- T. Murase, Geophysical Laboratory, Carnegie Institution of Washington, Washington, D.C.
- G. Olafsson, Akureyri, Iceland
- C. J. Peterson, Cerro Tololo Interamerican Observatory, La Serena, Chile
- G. Davis Phillips, Dudley Observatory, Albany, New York
- E. Pimental, Cuzco University, Cuzco, Peru
- W. Pöppel, Instituto Argentino de Radioastronomía, Villa Elisa, Argentina
- G. Poupeau, Centre des Faibles Radioactivités, Gif-sur-Yvette, France
- R. Racine, University of Montreal, Montreal, Canada
- J. E. Ramirez, S. J., Instituto Geofísico de los Andes Colombiano, Bogotá, Colombia
- M. S. Roberts, National Radio Astronomy Observatory, Charlottesville, Virginia
- Anibal Rodriguez B., Universidad Nacional de San Agustín, Arequipa, Peru
- R. T. Rood, Department of Astronomy, University of Virginia, Charlottesville, Virginia
- R. H. Sanders, National Radio Astronomy Observatory, Charlottesville, Virginia
- H. Sigtrygsson, Reykjavik, Iceland
- D. Simoni, Arequipa, Peru
- R. Stefansson, Reykjavik, Iceland
- J. Arthur Snoke, Virginia Polytechnical Institute, Blacksburg, Virginia
- K. M. Strom, Kitt Peak National Observatory, Tucson, Arizona
- S. E. Strom, Kitt Peak National Observatory, Tucson, Arizona
- D. A. Tomandl, University of Washington, Seattle, Washington
- F. Volponi, Universidad Nacional de Cuyo, San Juan, Argentina
- J. W. Warner, University of Minnesota, Minneapolis, Minnesota
- J. G. Williams, Jet Propulsion Laboratory, Pasadena, California
- Thomas L. Wright, U. S. Geological Survey, Reston, Virginia
- Y. Yamagishi, Matsushiro Seismological Observatory of Japan, Meteorological Agency, Matsushiro, Japan
- E. Zinner, McDonnell Center for Space Sciences, Washington University, St. Louis, Missouri

Supporting Staff

Gary A. Bors, Maintenance Assistant
Kenneth D. Burrhus, Computer Systems Engineer
Caroline A. Busch, Typist, Fiscal Assistant
Mary K. Coder,¹³ Editorial Assistant
Richard J. Collins, Maintenance Assistant
Gloria J. Counts,¹⁴ Clerk Typist
Dorothy B. Dillin, Librarian
John B. Doak, Electronics Research Specialist
William N. Dove, Office Manager
Everett T. Ecklund, Design Engineer
Maura Fitz-Patrick,¹⁵ Clerk Typist
Esther Gordon, Research Assistant

Bennie Harris, Caretaker
Janet C. Hunt, Secretary
Willis Kilgore, Jr., Caretaker
Niels M. Pedersen, Fiscal Officer
Glenn R. Poe, Electronics Research Specialist
Elliott M. Quade,¹⁶ Assistant Maintenance Foreman
Carl M. Rinehart, Instrument Maker
Michael Seemann, Design Engineer—Mechanical
Milton T. Taylor, Instrument Maker
Marjorie Zeff,¹⁷ Laboratory Technician

¹³ From April 17, 1978.

¹⁴ Through March 17, 1978.

¹⁵ From April 7, 1978.

¹⁶ Through September 30, 1977.

¹⁷ From May 24, 1978.

Geophysical Laboratory

Washington, District of Columbia

Hatten S. Yoder, Jr.

Director

Contents

Director's Commentary and Review . . .	633		
Spectral Mineralogy: Raman	649		
Structure of glasses and melts of $\text{Na}_2\text{O} \cdot x\text{SiO}_2$ ($x = 1,2,3$) composition from Raman spectroscopy (Sharma, Virgo, and Mysen)	649		
Structure of melts along the join $\text{SiO}_2\text{-NaAlSi}_3\text{O}_8$ by Raman spectroscopy (Sharma, Virgo, and Mysen)	652		
Raman study of structure and coordination of Al in $\text{NaAlSi}_3\text{O}_8$ glasses synthesized at high pressure (Sharma, Virgo, and Mysen)	658		
Trimethylsilyl derivatives of silicate minerals and glasses—chromatography and vibrational spectroscopy (Sharma and Hoering)	662		
The coordination of Ge in crystals and melt of GeO_2 composition at low and high pressures by Raman spectroscopy (Sharma, Virgo, and Kushiro)	665		
Properties of Magma	672		
Viscosity change of GeO_2 melt with pressure as a model of SiO_2 melt (Kushiro)	672		
Density and viscosity of hydrous calc-alkalic andesite magma at high pressures (Kushiro)	675		
Element Partitioning	677		
Experimental data bearing on $\text{Eu}^{2+}/\text{Eu}^{3+}$ in silicate melts and crystals (Mysen, Virgo, Hoover, and Sharma).	677		
Rare earth element partitioning between garnets, pyroxenes, and melts at low trace element concentration (Harrison)	682		
Experimental determination of crystal-vapor partition coefficients for rare earth elements to 30 kbar pressure (Mysen)	689		
Phase equilibria and rare earth element partitioning between coexisting immiscible carbonate and silicate liquids and CO_2 vapor in the system $\text{K}_2\text{O-Al}_2\text{O}_3\text{-SiO}_2\text{-CO}_2$ (Wendlandt and Harrison)	695		
The distribution of samarium and thulium between plagioclase and liquid in the systems An-Di and Ab-An-Di at 1300°C (Hoover)	703		
The effect of pressure on the partitioning of nickel between olivine and aluminous silicate melt (Mysen and Kushiro)	706		
Solubility of sulfur in silicate melts as a function of f_{S_2} and silicate bulk composition at high pressures (Mysen and Popp)	709		
Pressure-dependent solubility of calcium in forsterite coexisting with diopside and enstatite (Finnerty and Boyd)	713		
Experimental and Field Petrology	717		
Density current structure and magmatic sedimentation (Irvine)	717		
Structure of the Skaergaard trough bands (Irvine and Stoesser)	725		
Petrologic features of the Skaergaard marginal border group (Hoover)	732		
Melting relations of a new chilled margin sample from the Skaergaard intrusion (Hoover)	739		
Infiltration metasomatism, adcumulus growth, and secondary differentiation in the Muskox intrusion (Irvine)	743		
Phase relations of a kimberlite composition (Eggler and Wendlandt)	751		
Melting phase relations of natural peridotite + CO_2 as a function of degree of partial melting at 15 and 30 kbar (Wendlandt and Mysen)	756		
Nepheline solid solutions in melilite-bearing eruptive rocks and olivine nephelinites (Velde and Yoder)	761		
Liquid immiscibility and the carbonatite-ijolite relationship: preliminary data on the join $\text{NaFe}^{3+}\text{Si}_2\text{O}_6\text{-CaCO}_3$ and related compositions (Verwoerd)	767		
Liquidus relations and Mg-Fe partitioning on part of the system $\text{Mg}_2\text{SiO}_4\text{-Fe}_2\text{SiO}_4\text{-CaMgSi}_2\text{O}_6\text{-CaFeSi}_2\text{O}_6\text{-KAlSi}_3\text{O}_8\text{-SiO}_2$ (Hoover and Irvine)	774		
Change in phase relations in response to change in pressure from 1 atm to 10 kbar for the system $\text{Mg}_2\text{SiO}_4\text{-iron oxide-CaAl}_2\text{Si}_2\text{O}_8\text{-SiO}_2$ (Osborn)	784		
Amphibole stability in a differentiated calc-alkaline magma chamber: an experimental investigation (Ritchey and Eggler)	790		
Preliminary experimental data bearing on the mobility of H_2O in crystalline upper mantle (Mysen, Kushiro, and Fujii)	793		
The role of descending plates in the formation of andesitic melts beneath Island Arcs (Mysen)	797		

Sequence and homogeneity of lavas based on thermal melting models (Yoder)	801	Oxide minerals in Likhobong kimberlite, Lesotho (Boctor and Boyd)	870
Petrogenetic grid for amphibolites from the Post Pond and Ammonoosuc volcanics (Spear)	805	Iron-titanium oxide and sulfide minerals in carbonatite from Jacupiranga, Brazil (Boctor and Svisero)	876
Sodium trioctahedral mica: a possible new rock-forming silicate from the Post Pond volcanics, Vermont (Spear, Hazen and Rumble)	808	Evaluation of sphalerite geobarometry in Bodenmais Ore, Bavaria (Boctor) . .	880
Hydrothermal Solutions and Metasomatism	812	Biogeochemistry	886
An experimental study of complexing and thermodynamic properties of aqueous $MgCl_2$ in the system $MgO-SiO_2-H_2O-HCl$ (Frantz and Popp) .	812	Hydrogen isotope fractionation by cultures of microalgae (Estep and Hoering)	886
The ionization constant of HCl as a function of temperature and pressure (Frantz and Popp)	822	Collagen in fossil bone (Tuross and Hare)	891
Chemical and oxygen isotopic metasomatism of Devonian brachiopods from the sillimanite zone, Mt. Moosilauke, New Hampshire (Rumble, Hoering, and Boucot)	824	Geochronology	895
Spectral Mineralogy: Crystallography . .	830	Zircons from the mantle (Davis) . . .	895
High-pressure phase transitions in FeS , using ^{57}Fe Mössbauer spectroscopy (King, Virgo, and Mao)	830	Age of zircon from a crustal xenolith, Kilbourne Hole, New Mexico (Davis and Grew)	897
Isothermal compression of perovskite-type $MgSiO_3$ (Yagi, Mao, and Bell)	835	Statistical Petrography	898
Effect of iron on the stability and unit-cell parameters of ferromagnesian silicate perovskite (Yagi, Mao, and Bell)	837	The effect of the principal component transformation on closure correlation (Chayes and Trochimezyk) . .	898
Crystal structure and compressibility of MnF_2 to 15 kbar (Hazen, Finger, and Yagi)	841	The effect of rotation on the stability of factor loadings (Trochimezyk and Chayes)	900
Study of lead at high pressure: compressibility and fixed-point transition between the FCC and HCP polymorphs under various degrees of nonhydrostatic stress (Mao and Bell)	842	An algebraic explanation of closure correlation among the coefficients of a principal component (Rosenblatt, Chayes, and Trochimezyk)	901
Relationships between crystal structure and compressibility in oxides and silicates (Hazen and Finger)	848	Status of the project for development of a world data base for igneous petrology (Chayes)	902
Refined occupancy factors for synthetic Mn-Mg pyroxmangite and rhodonite (Finger and Hazen)	850	New Facilities and Techniques	902
Systematic variations of pyroxene absorption spectra with composition (Hazen, Bell, and Mao)	851	Laser-Raman spectroscopy (Sharma) .	902
Luna 24 glass fragments: a study of soil samples recovered from the Russian Luna 24 mission to Mare Crisium (Bell, Mao, and Hazen)	855	Design and varieties of the megabar cell (Mao and Bell)	904
Oxide and Sulfide Mineralogy	866	Static generation of 1.72 megabar pressure (Bell and Mao)	908
Ilmenite association at the Frank Smith kimberlite pipe, South Africa (Boyd and Pasteris)	866	Measurement of chloride ion concentrations in microsamples (Popp, Frantz, Vogel, and Hare)	913
		Problems in the use of evacuated, sealed silica tubes for synthesis of single-phase compositions in the system $FeO-Fe_2O_3-TiO_2$ (Lawson)	917
		Staff Activities	922
		Field Studies	922
		Kimberlite Conference	923
		Conference on Mineral Physics	924
		Petrologists' Club	926
		Washington Crystal Colloquium	927
		Seminar Series	927
		Lectures and Symposia	927
		Bibliography	931
		References Cited	932
		Personnel	948

DIRECTOR'S COMMENTARY AND REVIEW

The Geophysical Laboratory grew out of a "physical laboratory" established within the U.S. Geological Survey. The Survey celebrates its 100th anniversary in 1979, and it is appropriate to recall the events that led to the organization of this Laboratory.

The first Director of the U.S. Geological Survey, Clarence King, and Geologist-in-Charge George F. Becker were well aware of the difficulty of reaching unambiguous solutions to earth problems solely on the basis of limited field observations, without the aid of theory and experiment. Recognizing the need for the application of physics and physical chemistry to geology, in 1880 Becker appointed two physicists, Drs. Carl Barus and William Hallock, to his staff. A physical laboratory was established in 1882, but the project was discontinued during the internal political upheavals of 1892 for lack of appropriations. The need for geophysical measurements remained undiminished, however, and in 1900 Becker was able to re-establish the physical laboratory with Dr. Arthur L. Day as his assistant. Day had studied physics at Yale, where he had been acquainted with J. Willard Gibbs, who worked in the same building. Day had served for four years as an assistant at the Physikalisch-Technische Reichsanstalt in Charlottenburg-Berlin, and there he had obtained experience in high-temperature gas thermometry and a familiarity with high-temperature furnaces. Carl Barus, then a professor at Brown University, visited Berlin and persuaded Day to accept a post with the U.S. Geological Survey.

At the organizational meeting of the newly formed Carnegie Institution of Washington in 1902, an Advisory Committee on Geophysics was formed to assess the need for a laboratory suitable for "occupying the middle ground" between geology and physics. Three geologists (T. C. Chamberlin, C. R. Van

Hise, and C. D. Walcott) and three physicists (R. S. Woodward, Carl Barus, and A. A. Michelson) served on the committee and that year prepared a report recommending the establishment of a central laboratory of geophysics under the auspices of the Carnegie Institution of Washington. In an appendix to the report, Becker outlined the research problems to be investigated and the physical facilities needed. Presumably Day also had a major role in preparing the detailed plans. In the following year the report was further amplified by Van Hise, who widened the scope to include the "vacant ground between geology and physics and geology and chemistry." A more detailed program of investigations of both igneous and metamorphic rocks was then proposed by a group of geologists, physicists, and chemists.

In the meantime the Institution made funds available to Becker and Day for support of their physical laboratory in the U.S. Geological Survey for the years 1904-1906. During this time the Advisory Committee on Geophysics continued to receive recommendations from the directors of European research laboratories, whose views they had solicited, strongly supporting the concept of a central laboratory for the study of the physics and chemistry of the earth. Becoming convinced of the need for such a laboratory, the Trustees of the Institution decided at their December 1905 meeting to appropriate the needed funds. On March 17, 1906, the land for the facility was purchased. Construction of the building took just one year, and the staff moved in towards the end of June 1907.

Day was appointed Director of the new Department on January 1, 1907 but continued to work in the facilities provided by the Geological Survey until July 1, 1907. Becker, then sixty years old, remained a member of the U.S. Geological Survey, but was associated with and

financially supported by the Institution until 1909. His philosophy, still valid today, was set out succinctly in the introduction to the first paper published by the Institution in the then-new fields of geophysics and geochemistry (Day, *et al.*, 1905):

We must patiently begin with the simplest problems that can be devised and, aided by the most perfect appliances known, study them exhaustively before proceeding to more difficult and complex cases.

Throughout the years since, Geophysical Laboratory staff members have maintained close associations with members of the U. S. Geological Survey. Survey scientists have been cooperative in experimental investigations, have provided guidance on field excursions, and have contributed generously to the activities of the Laboratory. The staff of the Geophysical Laboratory salute the U. S. Geological Survey on the occasion of its centennial, in appreciation of the wisdom of its early leaders and for its continuing support.

The steady growth in vitality and achievement of the Geophysical Laboratory over the past seventy years is in itself remarkable. The Laboratory has succeeded by emphasizing leadership in formulating new concepts and pursuing new techniques pertaining to major geological problems. The 1977–1978 session has been a particularly noteworthy year for both new endeavors and progress on age-old problems, as recorded in the following sections.

Spectral Mineralogy: Raman

After the installation of the Raman spectrograph in February 1978, the opportunities for research multiplied rapidly as those staff members not directly involved became aware of the

kinds of information that could be derived from the spectra. Those members working on the properties of magma, the theory of melting, and the principles of element partitioning realized that it was essential to understand not only the structure of the crystals but also the structure of the liquid derived from the melting of the crystals. In the past it was technically more convenient to study the structure of glass—the quenched silicate liquid—and it was assumed that the structures of the liquid and glass were similar. This view was supported by the observation of only a small calorimetric heat effect at the glass transition point (Navrotsky, personal communication). Using laser-Raman spectroscopy, *Sharma, Virgo, and Mysen* compared the structure of the melt with that of glass above the glass transition point. The short-range order in glasses and melts of $\text{Na}_2\text{O} \cdot x\text{SiO}_2$ ($x = 1, 2, 3$) compositions were indeed found to be similar. In the melts, however, the structure becomes more disordered with increased thermal motion. In glasses of the sodium metasilicate and disilicate compositions, rapid crystallization occurs above the glass transition point, and thus it became evident that the Raman effect provided a way to study the kinetics of crystallization.

It was also shown that glasses formed at 1 atm of albite, jadeite, and carnegieite composition ($\text{Al}/\text{Na} = 1$), as well as a glass with Al/Na of 1.42, have three-dimensional network structures. The local ordering varies from β -quartz-type structure in SiO_2 glass to a more open α -cristobalite-type structure in melt of carnegieite composition. No evidence has been found in the Raman spectra for octahedrally coordinated Al^{3+} in these glasses.

The same investigators tested glasses formed at a series of pressures for structural changes. The Raman spectra of glasses of $\text{NaAlSi}_2\text{O}_6$ composition quenched from 1450°–1550°C and within a pressure range of 0–40 kbar were

examined to evaluate previously inferred changes of Al^{3+} from 4- to 6-fold coordination polyhedra in high-pressure melts. All glasses had a framework structure with Al^{3+} occupying the tetrahedral sites in the three-dimensional network. With increasing pressure, the glass structure became more ordered, and the local short-range ordering resembled that of coesite.

Another independent method was chosen by *Sharma and Hoering* to investigate the structure of silicate glasses. They converted known mineral structures and unknown silicate glasses to silicate trimethylsilyl derivatives. Compounds of this class are volatile, are amenable to analysis by gas chromatography and mass spectrometry, and give well-defined spectral bands. After developing improved methods of sample preparation and subsequent gas chromatography, they were able to identify the major bands in the infrared and Raman spectra. The method proved to be of ancillary use for determining their anionic constitution. It is, however, limited to glasses that gel with acids and those that have frameworks with no more than six or seven silicate units.

Of particular importance is the structure of melts of silica itself in the high-pressure region where quartz transforms to stishovite. The principles may be more easily deduced from the analogous material GeO_2 that undergoes a similar transformation at much lower pressures. *Sharma, Virgo, and Kushiro* have shown that in the GeO_2 glasses, quenched over a range of pressures and temperatures where the rutile-type structure is stable at subsolidus temperatures, the local structure closely resembles that of silica glass, having no significant amounts of Ge in 6-fold coordination. It appears that the structure of glass does not always reflect the structure of the crystals, but it remains to be seen if the structure of the liquid has the same oxygen polyhedra as that of the crystals.

Properties of Magma

One of the purposes of determining the structure of silicate liquids is to provide a theoretical basis for understanding the properties of magma, such as viscosity and density. It is essential to gain accurate measurements of these properties under conditions equivalent to those believed to exist in the earth. When those conditions cannot be readily obtained, analogue systems may serve as useful models. Changes in viscosity of a GeO_2 melt and in the density of the quenched melt (glass) with pressure were determined by *Kushiro* as a model of an SiO_2 melt. At 1425°C the viscosity decreases from 6×10^3 poises at 1 atm to 1.2×10^3 poises at 9.5 kbar, and the density of glass increases from 3.62 g/cc at 1 atm to 3.95 g/cc at 18 kbar. These changes may be due to structural changes of the melt, but *Kushiro* believes they are probably not associated with a coordination change of Ge^{4+} .

Kushiro also measured the density and viscosity of a hydrous calc-alkalic andesite melt with about 3 wt % H_2O at pressures between 5 and 15 kbar and at temperatures between 1175° and 1200°C . The density increases from 2.46 g/cm³ at 5 kbar to 2.74 g/cm³ at 15 kbar, and the viscosity varies from 180 poises at 5 kbar to 270 poises at 15 kbar. The results indicate that plagioclase of any composition would sink in hydrous andesitic magma within the crust, and that hydrous andesitic magmas ascend with velocities several times smaller than those of anhydrous basaltic magmas. If they lose H_2O their viscosities increase as much as 50 times, and their ascent velocities suddenly decrease even further, resulting in the formation of an auxiliary magma chamber. If, however, the hydrous andesite magmas retain about 3 wt % H_2O to the surface, they have viscosities of about 200 poises, which is nearly the same as that of basalt lavas, and form extensive andesite lavas of the sort ob-

served in many localities throughout the world.

Element Partitioning

Element partitioning between crystals is often used as a geothermometer or geobarometer, and partitioning between crystals and liquid is useful for identifying source rocks and for tracing liquid trends. Calibration of the partitioning is tedious because a large number of variables must be tested to evaluate their effects before the results can be applied to natural rocks. The europium anomaly, for example, has been especially useful in determining the role of plagioclase (where it is concentrated) in magma fractionation. *Mysen, Virgo, Hoover, and Sharma* used ^{151}Eu Mössbauer spectroscopy to study the influence of T, P, oxygen fugacity, and bulk composition on the redox states of Eu in both liquid and crystals. They chose to investigate compositions in the $\text{CaMgSi}_2\text{O}_6$ - $\text{NaAlSi}_3\text{O}_8$ - $\text{CaAl}_2\text{Si}_2\text{O}_7$ - SiO_2 system at temperatures from 1060° to 1550°C , at P_{O_2} from $10^{-0.68}$ to $10^{-15.8}$ atm, and at total pressures from 1 atm to 30 kbar. To their surprise, no divalent europium was found in any of the compositions investigated within the detection limit of Eu^{2+} (1% Eu^{2+} relative to total amount of Eu). They concluded that previous inferences about the europium anomaly, drawn from the behavior of Eu^{2+} , were not valid. They also pointed out (1) that electron microprobe analysis of Eu may give erroneous results, and (2) that there is a europium loss from silicates by volatilization under experimental conditions with low f_{O_2} .

Harrison has determined partition coefficients for the rare earth elements (REE) samarium and thulium between garnets, pyroxenes and hydrous melts at mantle pressures and temperatures. She found that the substitution of REE ions into those crystal structures does not obey the thermodynamic laws of dilute solution if the trace element concentrations are low (generally <20 ppm in crystal), and suggests that there is

probably more than one substitutional site for REE in the structures. The $D_{\text{Sm}^{\text{pyroxene/liquid}}}$ in synthetic and natural systems also appears to depend on the concentration of other REE in the garnet: the bulk REE content of a mineral phase determines the partition coefficient for any single rare earth between that mineral and melt. On the basis of *Harrison's* results, one must question the assumption that partitioning of REE obeys Henry's Law during crystal fractionation.

In addition to the bulk REE content, the presence or absence of a gas phase also affects the partitioning, according to *Mysen*. He noted that the vapor-crystal partition coefficients between H_2O -rich vapor and garnet peridotite minerals increase rapidly from less than 0.05 at 5 kbar to several hundred at 30 kbar. Furthermore, because of the fractionation of individual rare earth elements by garnet and to a lesser extent by clinopyroxene, it was deduced that H_2O -rich vapor in equilibrium with garnet peridotite in the upper mantle would show significant light-REE enrichment. He concluded that metasomatic alteration of rare earth elements in upper mantle rocks is a probable explanation of heterogeneous distribution of such elements in upper mantle rocks. For example, the apparent contrast between major and trace element distribution patterns found in so-called depleted garnet peridotite nodules in kimberlite may be explained by metasomatism. These important conclusions bear heavily on attempts to relate magmas to specific source rocks by using the rare earth elements as tracers.

The partitioning of REE between two immiscible liquids was studied by *Wendlandt and Harrison* primarily with autoradiographic techniques. A large two-liquid region in the sanidine-potassium carbonate join was found to persist to pressures of at least 20 kbar. Partitioning of REE between the two melts at 20 kbar favors the carbonate melt by a factor of two for the light REE and by a factor of eight for the heavy REE. Partitioning of

REE between CO_2 -vapor and the carbonate melt, and between CO_2 -vapor and the silicate melt at 5 kbar, favors the vapor relative to both melts for the light REE and relative to the silicate melt only for heavy REE. The enrichment of REE in CO_2 vapor is as much as three orders of magnitude greater than in water vapor (see Mysen, above) at comparable pressures. Mantle metasomatism by a CO_2 -rich vapor enriched in light REE may be responsible for the enhanced REE content and light-REE enrichment of carbonatites, potassium-rich silicate magmas, and kimberlites. It is now clear that the vapor phase plays a major role in trace element partitioning.

Hoover has used autoradiography to determine the distribution of two REE, samarium and thulium, between plagioclase and silicate liquid. He has observed that the partitioning is dependent on the amounts of REE in the melt within the concentration ranges observed in natural magmas. It appears, moreover, that Sm may substitute in more sites in intermediate plagioclase (An_{60}) than in anorthite, and indications are that f_{O_2} may affect the site occupancy of REE. Hoover has also shown that REE loss occurs during 1-atm experiments at low f_{O_2} .

Certain trace elements in igneous rocks are occasionally used to indicate the depth of generation of their magma. Nickel, for example, is believed to increase in the liquid with pressure; however, other factors appear to modify the effect. The nickel partition coefficients between forsterite and an aluminosilicate melt of fixed bulk composition were studied, therefore, at 1300°C to 20 kbar by Mysen and Kushiro to evaluate these effects. The value of the forsterite-liquid nickel partition coefficient is lowered from ~ 20 at pressures equal to or less than 15 kbar to < 10 at pressures above 15 kbar. Application of the high-pressure experimental data for Al-rich melts to the partial melting process indicates that the melts would contain about twice as much nickel

as that indicated by the data for the low-pressure experiments. Mysen and Kushiro conclude that data on nickel partitioning obtained at low pressure are not applicable to calculation of the nickel distribution between crystals and melts during partial melting in the upper mantle.

Mysen and Popp determined the solubility of sulfur in silicate melts ($\text{NaAlSi}_3\text{O}_8$ and $\text{CaMgSi}_2\text{O}_6$) as a function of f_{S_2} , P , and T with f_{O_2} controlled with the C- CO - CO_2 buffer and f_{S_2} controlled with the PtS-Pt, Ag_2S -Ag, and Cu_2S -Cu buffers. They found that the sulfur solubility in these melts increases with increasing P , T , and f_{S_2} and with decreasing degree of polymerization of silicate melts. As much as 1.4 wt % S was found in $\text{CaMgSi}_2\text{O}_6$ melt at 30 kbar and 1650°C with the PtS-Pt buffer assemblage. The lowest sulfur solubility was 0.26 wt % in $\text{NaAlSi}_3\text{O}_8$ melt at 15 kbar and 1650°C with the Ag_2S -Ag sulfur buffer assemblage. Mysen and Popp suggest that the f_{S_2} in the source region of basaltic and andesitic melt in the upper mantle is near that of the PtS-Pt buffer assemblage. For this reason primary melts in the upper mantle may contain more than 1 wt % sulfur. Extrusive basalt and andesite contain on the order of 0.1 wt % S. It appears that sulfur is exsolved, most likely as an immiscible liquid, from silicate melts during ascent of the magma. Because of the large values of the sulfide melt-silicate melt partition coefficients for transition metals (> 200), separation of less than 1 wt % sulfide melt will lower the transition metal content (Ni, Cu, and Co) of the silicate melt by more than 50% without significantly affecting its major element composition. Mysen and Popp conclude, therefore, that the transition metal content of basalt and andesite formed by partial melting of peridotite is controlled by the changing sulfur content of the melt resulting from changing pressure and temperature during ascent of the magma.

In spite of all the factors mentioned

above as influencing trace element partitioning, there is still considerable confidence that these factors can be calibrated. The wide range of trace element content in rocks remains a great advantage for characterizing on a fine scale the various modes and conditions, under which rocks are formed. For example, an application by *Finnerty* and *Boyd* of the techniques of element partitioning to rocks formed at high pressures has led to a new geobarometer. The researchers determined the concentration of calcium in forsterite coexisting with diopside and enstatite as a function of both temperature and pressure. Then, by combining this experimental calibration with the diopside-enstatite geothermometer, they estimated pressures of formation for garnet-ilmenite nodules from kimberlite of Lesotho, South Africa; their results are in agreement with pressures obtained from the Al_2O_3 -in-orthopyroxene geobarometer. Because two independent barometers give similar pressure estimates, the inflected geotherm observed by *Boyd* (1973) is probably real—or at the least, it cannot be an artifact of the method of pressure estimation. By means of the olivine barometer, it is now possible to estimate equilibration pressures for ultramafic rocks outside the garnet stability field.

Experimental and Field Petrology

The long-popular concept that the layered rocks of gabbroic intrusions are formed by crystal settling has come in for reconsideration in recent years because the supposedly settled plagioclase in some intrusions (e.g., Skaergaard, Kiglapait) is evidently less dense than its parental liquid. *Irvine* has examined experimentally an alternative possibility—that the mechanics of magmatic currents are such that they may deposit minerals at the floor of an intrusion even when the minerals should float. He has mapped the flow structure of glycerin currents released into a medium of silicone fluid along the horizontal floor of a small flume. The

currents are seen to have a downward component of velocity almost throughout their extent. Relative to fixed reference points, the motion appears as a flow shearing roughly parallel to the forward-sloping top surface of the current; relative to the advancing tip, it resembles the end of a conveyor belt beneath two small vortices. Material is transported forward and down in the fast-moving upper part of the current and is left behind at the floor. *Irvine* proposes that plagioclase may similarly be left at the floors of gabbroic intrusions by magmatic currents that were dense because they were also charged with mafic minerals. He suggests that it stays there because the yield strength of the magma is sufficient to prevent it from floating free, but he notes that other plagioclase might occasionally be carried to the roof of the intrusion by local return currents to accumulate as anorthositic rocks.

Evidence for currents in magma is well displayed in the Skaergaard intrusion in East Greenland. During an expedition to the area in 1976, *Irvine* and *Stoeser* made detailed maps of some of the remarkable trough-banding structures that occur in the intrusion. They present one of the maps and a section prepared from it, and describe the history of a typical trough. Although there is evidence of local erosion by currents at the bottoms of the troughs, the troughs are essentially constructional features developed between ridgelike mounds of massive ferrodioritic cumulates. The layering in the troughs exhibits distinctive changes in facies between their axes and flanks. *Irvine* and *Stoeser* present a model of current deposition for the layering based on the above-described flume study by *Irvine*, and the facies changes are attributed to secondary flow, a phenomenon whereby the fluid moves in a spiral or helicoidal manner in paired or multiply paired cells.

Using rocks collected during several expeditions to the Skaergaard intrusion, *Hoover* has made an electron microprobe study of olivine and plagioclase minerals

from the marginal border group of the body. The general subdivisions and mineralogical trends of the marginal border group recognized by Wager and Deer (1939) and Wager and Brown (1968) have been confirmed and defined in more detail. Hoover discovered additionally that although the marginal border group is essentially a thin equivalent of the layered series of the intrusion, some parts are missing or unusually thick. Plagioclase and olivine variations generally mimic compositions of cumulus minerals in the layered series, but olivine is more iron-rich, possibly because of the different ways that olivine and plagioclase reacted with intercumulus liquid. The parts of the marginal border group that crystallized before the lowest exposed layered-series rocks have mineral compositions not significantly more primitive than those in the layered series; the existence of a large hidden zone is therefore doubtful. Picrite xenoliths, originally thought to be the most primitive differentiates, were probably not formed by fractional crystallization within the intrusion.

Hoover also investigated the melting relationships of a new chilled marginal gabbro from the Skaergaard intrusion. This sample is much more iron-rich than the chilled liquid composition described by Wager (1960). The melting relationships are consistent with the order of appearance and compositions of cumulus minerals in the lower zone of the intrusion and with the compositions of fractionated minerals in the outer part of the marginal border group. The new chilled gabbro sample appears, therefore, to be representative of the parental liquid of the exposed part of the intrusion.

Attention has also been given to post-cumulus crystallization and adcumulus growth in layered intrusions. Irvine used data from the Muskox intrusion, in which layered sequences of cumulates are repeated in a cyclic manner owing to the repeated influx of fresh magma during the primary stage of crystallization differenti-

ation. He shows that certain chemical discontinuities in the cumulates, relating to the regressions in crystallization caused by the introduction of fresh liquid, do not stratigraphically match the modal discontinuities that record these regressions. In some cyclic units, discontinuities in Ni are 5–10 m above the basal contacts of the units and discontinuities in Mg/Fe²⁺ are 10–30 m above. These apparent discrepancies are explained by a model of infiltration metasomatism whereby the chemical discontinuities are shifted upward because of reaction of the cumulus minerals with intercumulus liquid as this liquid is expelled during compaction of the layer pile. Quantitative modelling indicates that some layers were infiltrated by liquid originally trapped several hundred meters below, and Irvine suggests that adcumulus growth in the rocks developed largely because of secondary fractional crystallization of the liquid as it migrated upward.

The shallow, layered intrusions result in general from the crystallization of relatively anhydrous magmas or hydrous magmas where the H₂O is lost during crystallization. Retention of H₂O and CO₂ may result in the production of completely different rock types. Recent emphasis has been on the alkaline rocks whose formation is enhanced by the presence of CO₂ at high pressures. One such rock type is kimberlite, which is of special interest because it contains both hydrous and carbonate-bearing minerals—and occasionally, of course, diamonds. The rock itself is one of those mineral assemblages that are not stable at high pressures, yet its magma is believed to have formed at depths greater than any other known. Egger and Wendlandt have determined the melting relations at 30 and 55 kbar of an average Lesotho kimberlite composition containing 5.2 wt % CO₂ and 0–10 wt % H₂O. For these volatile contents, the solidus temperature of kimberlite is not a function of the volatile composition; compositions of vapor are buffered by reaction with dolomite at 30 kbar and

magnesite at 55 kbar. At 30 kbar garnet is consumed immediately above the solidus, but at 55 kbar it coexists with olivine and two pyroxenes near the liquidus, and the phase-field configuration is consistent with the hypothesis that kimberlite is a product of the beginning of melting of a parental peridotite. Inasmuch as partial melting of peridotite containing CO_2 and H_2O will produce liquids of kimberlite composition at pressures of 50–60 kbar depending on the proportions of those volatile constituents, such liquids may be common in the upper mantle. The rarity of kimberlites as rocks may be attributed, according to Eggler and Wendlandt, to the rarity of tectonic settings conducive to the ascent of the appropriate magma.

In another study *Wendlandt and Mysen* determined the melting relations of a garnet peridotite as a function of the degree of partial melting for CO_2 -saturated and CO_2 -undersaturated conditions at high pressures. They demonstrated that the determination of the proportion of melt by autoradiography can now be extended to systems containing CO_2 vapor through the use of ^{185}W , which does not partition significantly into the crystalline or vapor phases. A principal observation was that the melting behavior of the garnet peridotite is closely modelled by investigations in the appropriate simple systems. The initial partial melt at 15 kbar and 1400°C is tholeiitic, whereas that at 30 kbar and 1200°C is carbonatitic.

Nepheline is one of the common rock-forming minerals in the alkaline rocks. Analyses were made on natural nephelines in feldspar-free assemblages to ascertain how their composition varied with assemblage. *Velde and Yoder* found that nephelines rarely contain more than 4 wt % of excess SiO_2 in solid solution, but they tend to be richer in silica on the sodium-rich side of the Buerger composition, $\text{Na}_3\text{KAl}_4\text{Si}_4\text{O}_{16}$, than on its potassium-rich side. The compositions do not vary consistently, as would be expected

as the assemblage changes from nepheline_{ss} + sanidine \rightarrow nepheline_{ss} + sanidine_{ss} + leucite \rightarrow nepheline_{ss} + leucite \rightarrow nepheline_{ss} + leucite + kalsilite_{ss} \rightarrow nepheline_{ss} + kalsilite_{ss}. It appears that other phases (e.g., biotite) influence the partitioning of K_2O and Na_2O between the common feldspathoids. *Velde and Yoder* also note that nephelines tend to be more potassic in melilite-bearing nephelinites. They suggest that the failure to obtain some nephelinite assemblages in simple experimental systems may be due to the use of pure NaAlSiO_2 , not known in nature, instead of the Buerger composition or an appropriate Ne-Ab solid solution.

Melting relationships of a synthetic mixture consisting of a silicate component approaching ijolite and a calcite-bearing natrocarbonatite component were investigated under 2 kbar pressure by *Verwoerd*. Spectacular immiscibility between carbonate and silicate liquids of this composition was obtained above 800°C . The carbonate liquid (quenched to nyerereite) dissolves less than 2% of the silicate liquid. Various assemblages of hematite, acmite, nepheline, andradite, wollastonite, and calcite were found in equilibrium with these liquids, depending on the bulk composition and temperature. Preliminary results on the acmite-calcite join indicate that these two phases react to form andradite, wollastonite, and nyerereite. The results bear on the genetic problems of the ijolite-carbonatite association, the unusual natrocarbonatite lava of Mt. Oldoinyo Lengai, and mixed carbonate-silicate rocks in alkaline complexes.

Low-temperature liquid immiscibility also occurs in the iron-rich compositions in the join $\text{Mg}_2\text{SiO}_4\text{-Fe}_2\text{SiO}_4\text{-CaMgSi}_2\text{O}_6\text{-CaFeSi}_2\text{O}_6\text{-KAlSi}_3\text{O}_8\text{-SiO}_2$ (Fo-Fa-Di-Hd-Or-Qz). *Hoover and Irvine* have investigated the phase relations of that system at 1 atm, and it appears that in at least the compositions studied, Ca-poor pyroxene and Ca-rich pyroxene are both incompatible with the immiscibility.

Fayalitic olivine crystallizes in place of Ca-poor pyroxene (pigeonite) as the immiscibility region is approached, and ferrobustamite in place of the Ca-rich pyroxene. The partitioning of Mg and Fe between olivine and liquid shifts as the immiscibility region is approached so that the relative enrichment of Fe in the liquid is less pronounced. A close correlation between the structure of the melt (as reflected in the immiscibility) and its crystallization characteristics is indicated. Hoover and Irvine also emphasize the importance of alkalis in the development of trends of silica enrichment in basic magma series.

Fractional crystallization of basaltic magma under oxygen-buffered conditions has been considered by *Osborn* as one means of producing the calcalkaline magma series. He arrived at this conclusion principally from a consideration of courses of crystallization in the system $\text{MgO-FeO-Fe}_2\text{O}_3\text{-SiO}_2$ (MFFS) at a total pressure of 1 atm. Similar studies of the system $\text{MgO-FeO-Fe}_2\text{O}_3\text{-CaAl}_2\text{Si}_2\text{O}_8\text{-SiO}_2$ (MFFAnS), a closer model of basalt and andesite magmas, showed that the same type of crystallization paths occur with An added as a component to MFFS. Studies of MFFAnS at a pressure of 10 kbar by *Osborn* showed that phase relations are indeed markedly different at 10 kbar. At this pressure, fractionation curves of a primary haplobasaltic liquid in equilibrium with Ol, Sp, and Px trend toward higher An and silica contents than that at 1 atm because of Sp and Px precipitation. Owing to the continuous precipitation of Sp, the fractionation paths do not exhibit an abrupt change ("corner") such as is observed at 1 atm when the curves are plotted on a graph of $(\text{FeO} + \text{Fe}_2\text{O}_3)/(\text{FeO} + \text{Fe}_2\text{O}_3 + \text{MgO})$ vs. SiO_2 . Cascades and Paricutin magma series are characterized by curves without a "corner," and *Osborn* suggests that their fractionation may have occurred largely at high pressure (≤ 8 kbar) to produce these magma series. Based on the phase relations at the two pressures, 10 kbar

and 1 atm, *Osborn* postulates that magma series of Santorini, Mashu, and Talasea formed by fractional crystallization first at high pressure and later by further fractionation at low pressure, whereas the magma series of Thingmuli, Galápagos, and Nicaragua apparently formed by fractional crystallization only at low pressure.

Ritchey and Eggler have determined the melting relations of rhyodacite, dacite, and basaltic andesite ash-flow compositions from Crater Lake, Oregon, in an effort to understand the processes leading to bimodal basalt-rhyolite associations. At 1 atm, for f_{O_2} conditions approximating the HM and QFM buffers, magnetite is not a near-liquidus phase for these whole-rock compositions. It appears that *Ritchey and Eggler* disagree, therefore, with *Osborn's* (1959) view that precipitation of magnetite from a parent magma could generate by fractional crystallization the observed ash-flow association. At 2 kbar total pressure, for water-saturated and water-undersaturated conditions, amphibole is stable only at temperatures near the solidi. For this reason *Ritchey and Eggler* argue that amphibole fractionation from a parent magma at pressures believed to exist in a shallow magma chamber cannot be invoked as the genetic process. (This view should be compared to that of T. H. Green and Ringwood [1968], who believe amphibole fractionation is important at very high pressures where amphibole is on or near the liquidus.) The configuration of the amphibole-out curves limits the temperature of the magmas (at 2 kbar) to about 975°C , and relatively high water contents of the melts are implied.

Whether or not amphibole is involved in the generation of calc-alkaline liquids, it is evident from the common explosive eruptions of calc-alkalic magma that volatiles are present. The volatiles may be contained in hydrous minerals prior to melting. Alternatively, the melting may take place because of the migration of water into the site of generation. In the

latter case it is important to know the rate at which water, for example, can migrate through the parental rock. *Mysen, Kushiro, and Fujii* experimentally determined the velocity of migration of nearly pure H₂O in crystalline garnet peridotite in the pressure and temperature ranges 15–30 kbar and 650°–850°C, respectively. The minimum migration rate of H₂O increases at 15 kbar from about 1 mm/hr to about 11 mm/hr with no discernible temperature dependence in the temperature range studied. The migration rate of H₂O was found to be independent of grain size with grains between 40 and 100 μ m across. The determined migration rates for water are so high that, in general, whenever addition of H₂O-rich fluid is required for melting in the upper mantle, the migration rate of H₂O is not the rate-limiting factor. The high rates of H₂O migration and the high solubility of major and trace elements at high pressures and temperatures support the view that metasomatic redistribution of those elements should be commonplace in the upper mantle.

Mysen calculated the REE patterns of peridotite as the result of metasomatism where the source of the metasomatizing fluid was a dehydrating amphibole-bearing eclogite of tholeiitic composition. These rare earth element patterns were considered representative of those in the source rock of partial melts expected to yield andesite in island arcs. Such andesites often show considerable light-REE enrichment, yet experimental results on phase equilibria of H₂O-bearing peridotite indicate that the source rock of andesitic melts is garnet-free peridotite. The REE patterns of metasomatized peridotite show significant light-REE enrichment. This enrichment results from garnet present in the source rock of the metasomatic fluid. The degree of light-REE enrichment increases with increasing garnet content of the source rock. As the result of this light-REE enrichment, partial melts also show light-REE enrichment. In fact, the calculated REE

patterns of 5–10% batch melt from a metasomatically altered peridotite closely resemble the patterns found in island-arc andesite. The resemblance between patterns calculated with this model and those of natural andesite is closer than that between patterns calculated for a garnet peridotite source and those of natural andesite.

The relative uniformity of rare earth and trace element contents in large volumes of a single rock type places constraints on the mode of formation. The manner in which a source rock is partially melted appears to influence not only the homogeneity of the melt produced but also the sequence of magma types intruded or extruded. *Yoder* examined two extreme cases of partial melting wherein (1) heat is supplied externally by a hot, depleted peridotite—the hot-plate process—or (2) the heat is supplied internally by the adiabatic rise of an undepleted peridotite—the diapiric process. In both cases a gradient in composition and temperature results in the melt. In the hot-plate process the gradient results in more parental-like liquids at the base and more daughter-like liquids at the top. In the diapiric process the gradient is reversed, with the more parental-like melt at the top. These deductions indicate that the sequence of magmas intruded or extruded may be dependent on the manner in which heat was supplied for the melting process. *Yoder* appeals to convective mixing to homogenize the melt; however, he suggests that density and thermal constraints may still result in multiple thin convection cells of large horizontal dimensions. He emphasizes the problems inherent in producing large volumes of homogeneous magma such as the Columbia River basalts where limited variation in both major and minor elements is displayed in a volume of 200,000 km³.

Spear has been investigating the phase relations of amphibolites from the Post Pond and Ammonoosuc Volcanics of central New England. This year he has

integrated the results of his study on the phase relations into a petrogenetic grid for amphibolites in the system $\text{Na}_2\text{O}-\text{FeO}-\text{MgO}-\text{CaO}-\text{Al}_2\text{O}_3-\text{SiO}_2-\text{H}_2\text{O}$. The petrogenetic grid is the first to be constructed for amphibolites from this region. The grid provides a basis for evaluating differences in temperature and pressure conditions of metamorphism for different areas based on the mineral assemblages found in amphibolites. Correlation of the geographic distribution of mineral assemblages from west-central New Hampshire and east-central Vermont with the sequence of reactions on the petrogenetic grid reveals that the change in mineral assemblages observed in amphibolites from this region can be explained by a continuous increase in temperature with little or no increase in pressure. A comparison of amphibolite mineral assemblages from central New England with assemblages from other areas of New England and from around the world can be readily made with the grid.

A sodium analogue of the potassium trioctahedral mica biotite has been discovered in the regionally metamorphosed Post Pond Volcanics of Vermont by *Spear, Hazen, and Rumble*. The mineral is an epitaxial intergrowth with K-biotite and talc in cordierite gneisses that also contain gedrite, anthophyllite, quartz, chlorite, plagioclase (An_{10-30}), rutile, and apatite. The Na-biotites are alkali deficient and have higher Si/Al and Mg/Fe relative to coexisting K-biotites. The mineral has not been recognized previously, probably because it occurs in rocks of uncommon chemical composition.

Hydrothermal Solutions and Metasomatism

The key to understanding how elements concentrate into ore deposits appears to be in the methods of transport. Determination of the species of an element in the transporting medium may be the crucial step. The techniques for speciation of an element include solubility measurements, determination of the elec-

trical conductivity of the medium, and observation of the solution's Raman spectra. All three techniques are currently being investigated in the Department. The first of them—solubility measurements—is discussed in this year's Report. *Frantz and Popp* completed an experimental study of speciation and free energy of aqueous MgCl_2 in the system $\text{MgO}-\text{SiO}_2-\text{H}_2\text{O}-\text{HCl}$ for the range of conditions 1–2 kbar and $400^\circ\text{--}650^\circ\text{C}$. They used the Ag-AgCl buffer technique described in *Year Book 76*, which required measurement of total dissolved magnesium and associated HCl in equilibrium with the assemblage talc + quartz + fluid as a function of temperature and pressure. Frantz and Popp concluded that at 2 kbar and temperatures above 550°C , associated MgCl_2 is the dominant magnesium species in the fluid. Their data also suggest that dissociated Mg^{2+} ions dominate at temperatures below 400°C . The data at intermediate temperatures were used to calculate the dissociation constant for MgCl_2° at 2 kbar. Free energy of formation of aqueous MgCl_2° was calculated at 1.0, 1.5, and 2.0 kbar over the temperature range of the experiments. Solubility constants for most of the minerals in the $\text{MgO}-\text{SiO}_2-\text{H}_2\text{O}$ system were calculated.

Experimental studies of this nature involving the Ag-AgCl buffer require knowledge of (1) the dissociation constant of HCl as a function of temperature and pressure, and (2) the imposed concentration of HCl using the chloride buffer in conjunction with an external hydrogen buffer. *Frantz and Popp* refined and expanded the range of these measurements using the assemblage hematite + magnetite + H_2O as the external hydrogen buffer. Data are now available for the range $400^\circ\text{--}700^\circ\text{C}$ at pressures of 1.0, 1.5, and 2.0 kbar.

The identification of the source of volatiles that act as the transport medium is equally as important as characterizing the medium itself. Application of the combined methods of metamorphic

petrology, paleontology, and isotope geochemistry by *Rumble, Hoering, and Boucot* has resulted in the identification of the source and sink for volatiles released during metamorphism of fossiliferous calc-silicate intruded by a quartz monzonite dike. Both mineralogical and isotopic evidence indicate that the dike was permeated and contaminated by CO_2 released by decarbonation of the calc-silicate. Chemical metasomatism accompanying metamorphism consisted of the intergranular diffusion of Ca from the fossiliferous calc-silicate into mica schist and into the dike rock. These observations document the great disparity in effective mobility of CO_2 and Ca during metamorphism: the diffusion of Ca was limited to a few cm adjacent to the fossil bed, whereas CO_2 was able to pervade the dike completely over a distance of several meters.

Spectral Mineralogy: Crystallography

King, Virgo, and Mao have used ^{57}Fe Mössbauer spectroscopy to characterize the structural changes in FeS that occur at high pressure. With increasing pressure, the internal magnetic field associated with the magnetically split absorption pattern shows a sharp break at 34 kbar consistent with the change from a troilite to MnP-type structure. With further increases in pressure the magnetic field intensity systematically decreases, and the magnetic ordering disappears sharply at 67 kbar. Structural details of this high-pressure transition are still unknown. The ^{57}Fe absorption spectra taken at pressures above 67 kbar, however, consist of an absorption doublet with an isomer shift value characteristic of octahedrally coordinated Fe^{3+} . This study highlights the drastically different behavior of iron-sulfur interactions at high and low pressures. Although the magnetic properties of FeS would disappear at great depths (about 200 km) it is interesting to speculate on how such high-pressure behavior, if prevalent in more

complex mineral assemblages at lower pressures, will affect exploration for buried ore deposits using magnetic survey techniques.

The compressibility (change in specific volume of a substance with pressure) of minerals in the earth is, perhaps, one of the most important physical parameters by which to characterize the physics of the earth. Of particular relevance is the compressibility of the newly observed perovskite silicate structures that, it is now known, are dominant mineral phases in the mantle. *Yagi, Mao, and Bell* have succeeded in measuring the compressibility of perovskite of enstatite (MgSiO_3) composition to pressures of 100 kbar by x-ray diffraction measurement with the diamond-anvil high-pressure cell and an improved x-ray monochromator-colimator device. The measurements indicate that a model with a lower mantle of predominantly perovskite composition agrees well with seismic data, and the results are now being assessed to form the basis of a new geophysical model of the mantle.

Examination by x-ray diffraction of products quenched from experiments in the pressure range 0.2–0.5 Mbar by *Yagi, Mao, and Bell* have shown that the site of ferrous ions in silicate perovskites has almost dodecahedral symmetry, a factor that strongly influences stabilization of the perovskite structure and the chemical partitioning of iron at high pressure. This effect is caused by the extremely low crystal-field stabilization of the site of dodecahedral symmetry in comparison to the octahedral site in magnesiowüstite. A single phase of ferromagnesian-silicate perovskite and an assemblage of perovskite and oxides were synthesized from pyroxene and olivine composition, respectively. Measurements of lattice parameters of the perovskite and oxides show a strong partitioning of iron in oxide, thus confirming the theoretical crystal-field analysis. These data indicate the increased role of crystal-field effects on the geochemical behavior of transition

metals in mineral structures at high pressures.

The study of analog systems is usually undertaken because of the advantages of measuring a transition, for example, under more readily obtainable conditions where greater accuracy can be achieved. Stishovite, an SiO_2 polymorph stable only above about 65 kbar, has the rutile structure that appears to be prominent in mantle mineralogy. The compound MnF_2 also has the rutile structure, but at 1 atm. Its study, therefore, can contribute to understanding the behavior of compounds of compositions appropriate to the mantle. The compression and crystal structure of MnF_2 to 15 kbar was studied by *Hazen, Finger, and Yagi*. Compression of this tetragonal compound parallel to a is nearly twice that parallel to c , owing to differences in octahedral linkages parallel and perpendicular to the c axis. A similar 2:1 compression of a to c has been observed for both rutile (TiO_2) and stishovite (SiO_2), and the same explanation is proposed.

Mao and Bell studied the effect of hydrostatic and nonhydrostatic stress on the compressibility and phase transformation of lead at high pressure. Metallic lead was chosen for the experiments because of its low strength and the small volume difference between the low-pressure (fcc—face-centered cubic) and high-pressure (hcp—hexagonal close-packed) phases. *Mao and Bell* employed a special design of the diamond-anvil high-pressure cell in order to obtain x-ray diffraction data on lead in a direction normal to the direction of applied stress. Under hydrostatic pressure, the initial isothermal bulk modulus (K_0) and its pressure derivative (K_0') are found to be 431 kbar and 4.6 for fcc lead, respectively, and 424 kbar and 4.7 for hcp lead. Nonhydrostatic stress results in a broad scattering of data, but does not affect the mean compressibility. On the other hand, the nonhydrostatic stress has a major effect on phase transformation. Whereas the transformation is sharp under hydro-

static conditions, it can be smeared out to a broad 60-kbar, two-phase region at 130 kbar with a shear stress of 5 kbar in fcc lead and 20 kbar in hcp lead. This study is the first experimental evaluation of the contribution of nonhydrostatic stress to thermodynamic equilibrium. The role of shear stress in the earth, which may exceed 1 kbar, may be important in determining the nature of phase transitions in the mantle.

Studies of oxide and silicate crystal structures at high pressure by *Hazen and Finger* have revealed systematic relationships between structure, bulk modulus, and the pressure derivative of bulk modulus. Mineral compression may be modelled as a combination of metal-oxygen bond compression, polyhedral distortion, and changes in angles between polyhedra. In many simple compounds, such as MgO , corundum, garnets, and spinels, bulk compression of the mineral is due entirely to changes in metal-oxygen bond distances; these compounds are generally the least-compressible oxygen-based minerals. In other dense materials, such as pyroxenes and olivines, compression is due to a combination of metal-oxygen bond compression and polyhedral distortion; compressibilities of these compounds are greater than in structures where polyhedral distortions are forbidden. The most compressible oxygen-based minerals are those such as α -quartz, feldspars, and zeolites in which angles between corner-linked polyhedra may contribute to changes in molar volume. Polyhedral linkages are believed by *Hazen and Finger* to be the key to understanding compression of oxides and silicates.

Finger and Hazen have refined the crystal structure and cation occupancies for synthetic Mn-Mg pyroxmangite and rhodonite. The cation occupancies and polyhedral distortions can now be used in a study of quantitative site-preference energies.

Polarized absorption spectra of lunar pyroxenes with varying amounts of major

and minor elements were measured by *Hazen, Bell, and Mao* to determine the effects of compositional variation on absorption features. Major changes in absorption-band positions and intensities with varying iron and calcium content were observed. Most absorption features in pyroxene are due to Fe^{2+} in octahedral coordination, so band intensity is largely a function of iron content. Calcium-rich pyroxenes, in general, have lower band energies than calcium-poor specimens because the larger Ca-bearing sites result in lower crystal-field splitting energies for iron. Lunar pyroxene absorption spectra have additional effects owing to titanium and chromium, but the principal features of the spectra are controlled by major-element chemistry.

A spectral absorption study by *Bell, Mao, and Hazen* of lunar silicate glass fragments returned from the Russian Luna 24 space mission to Mare Crisium has resulted in data that may be critical in the interpretation of telescope spectra of the lunar and planetary surfaces. The laboratory spectra are interpreted to be due to short-range ordering unlike that of any other natural or lunar glasses having octahedrally coordinated Fe^{2+} ions. The process that formed these structures in the glasses appears to be related to the shock-melting of rock that occurred during meteoritic impact on the lunar surface.

Oxide and Sulfide Mineralogy

Ilmenite megacrysts and pyroxene-ilmenite lamellar intergrowths from the Frank Smith mine, South Africa, are believed to be consanguineous because both are distinctively rich in Mg relative to similar megacrysts in other African kimberlites. The ilmenites and associated pyroxene and garnet megacrysts have large ranges in $\text{Mg}/(\text{Mg} + \text{Fe})$ based on the studies of *Boyd and Pasteris*, and the pyroxenes have a range in equilibration temperature of 200°C . These megacrysts are believed to have coexisted in the

mantle with dispersed liquid (kimberlitic?) of variable composition at the time of eruption.

Ilmenite nodules in the Lihobong kimberlite are characterized by complex reaction mantles on their margins, according to *Boctor and Boyd*. For example, Mg is enriched in the outermost zones of the nodules relative to their cores. This enrichment is attributed to reaction with the fluids that produced the reaction mantles. The Mg enrichment in the margins of ilmenite nodules from Lihobong is opposite to that observed in ilmenite from Monastery kimberlite. These two opposite reaction trends seem to be related to variations in the composition of the fluids, temperature, and oxygen fugacity. Perovskite in the Lihobong pipe is enriched in Nb and rare earth elements. This enrichment is attributed to the presence of CO_2 -rich fluids, which provided the complexing agents necessary for concentration of the REE. The abundance of calcite in the groundmass of the Lihobong kimberlite seems to support this interpretation. In addition, two distinct suites of spinel are present in the groundmass of the Lihobong pipe: a Ti-rich suite similar in composition to the titanian ferrian pleonaste in ilmenite reaction mantles; and a suite of titanian chromites. These two suites now appear to be characteristic of many kimberlites.

The relationship between kimberlite and carbonatite remains an open question. Iron-titanium oxide minerals are common to both rock types. A study of the composition of magnetite and ilmenite in the Jacupiranga, Brazil, carbonatite and their comparison with minerals from other carbonatites and kimberlites by *Boctor and Svisero* reveals that the composition of these phases varies from one carbonatite to another, and that they differ markedly from their analogues in kimberlites. Magnetite in carbonatites seems to show more similarity to magnetite from alkaline-rock associations than to spinels in kimberlite. Ilmenite in carbonatite has much higher MnO content than does

primary kimberlitic ilmenite. The Mn enrichment in ilmenite from carbonatite parallels that observed in ilmenites from alkaline rocks and in Mg-depleted secondary ilmenite that is associated with calcite segregations in kimberlite. Sulfides in the Jacupiranga carbonatite crystallized later than the silicate, oxide, and carbonate minerals. The absence of textural evidence supporting sulfide liquid immiscibility at Jacupiranga and the sulfurization of magnetite suggest that the sulfides formed from late-stage sulfur-bearing fluids in the final stages of crystallization of the parent magma.

The sphalerite geobarometer has been widely used to estimate pressures in regionally metamorphosed sulfide ores. It is generally assumed that because of its refractory nature, the equilibrium composition of sphalerite will be preserved during post-metamorphic cooling. *Boctor* evaluated this effect by studying the sphalerite geobarometry in the Fe-Cu-Zn ores from Bodenmais, Bavaria. The pressure estimates for sphalerite coexisting with pyrite and pyrrhotite are in agreement with pressures estimated from the silicate mineral assemblages. Nevertheless, there are indications that post-metamorphic equilibration of sphalerite has taken place. Equilibration of sphalerite was possibly enhanced by the presence of aqueous fluids which also induced retrograde alterations in pyrrhotite and the coexisting silicate minerals. Chalcopyrite-bearing sphalerite displays large variations in FeS content and, consequently, highly variable pressure estimates over a scale of tens of microns within individual crystals. These observations underscore the necessity of an experimental evaluation of the effect of the addition of Cu upon sphalerite-pyrrhotite-pyrite equilibria before applying sphalerite geobarometry to Cu-bearing Zn ores.

Biogeochemistry

Estep and Hoering studied the fractionation of the stable hydrogen isotopes in cultures of microalgae and have dis-

covered several of the biological processes governing the isotope effect when a cell converts water in the medium to organic matter. Information of this kind is necessary for interpreting hydrogen isotope distributions in the organic matter of ancient, sedimentary rocks. Photosynthesis produces a large effect, with the light isotope being fixed more rapidly than the heavy one by a factor of 1.12 to 1.14. Respiration, on the other hand, shows little effect. Hence, organically bonded hydrogen is depleted in the heavy isotope compared to surrounding waters. Marine organisms have a larger isotope effect than fresh-water forms, a fact that may be of importance in determining the source of organic matter in a sedimentary rock. When the microalgae were adapted to grow on the organic substrate glucose, the hydrogen in the cells came from the substrate—not from the water in the medium. Organically bonded hydrogen in a living cell exchanges only slowly with surrounding water. It may be possible, therefore, to delineate the food chains in natural communities. The experiments by *Estep and Hoering* are noteworthy in showing how high-precision, isotope-ratio, mass spectrometry can be applied to biological tracer experiments without the use of artificially enriched isotopes.

Insoluble collagen extracted from fossil bone exhibits only minor differences in amino acid composition and racemization compared to modern bone. A comparison of electrophoresis patterns of pepsin-treated fossil collagen by *Tuross and Hare* reveals extreme differences in the number of high-molecular-weight components. The collagen in fossils is degraded significantly from hydrolysis of the labile peptide bonds, but the material maintains many of its physical properties because of extensive crosslinking present in collagen. Because of the stability of high-molecular-weight components of collagen, it will be possible to follow the early diagenetic changes in fossil bones. The study opens an exciting new venture in vertebrate paleontology.

Geochronology

Kimberlites are known to have erupted through stable Precambrian areas of all the continents except Europe and Antarctica, bringing up the pieces of the mantle and crust gathered during their ascent. The times of eruption are given by the uranium-lead ages of the mantle zircons from the kimberlites because the lead daughter isotopes from the decay of uranium did not accumulate in the zircon crystals until after the sudden cooling at the time of pressure release. *Davis* has measured the times of eruption for some of the many kimberlites that have been discovered in Yakutia, U.S.S.R. Zircon ages lie between 150 m.y. and 450 m.y.—from Silurian to Jurassic times. The ages appear to be in three groups, the two older marking the occurrence of diamond-bearing kimberlites. The youngest kimberlites are barren, as is also the case in South Africa.

The ages of zircons from crustal xenoliths reflect conditions in the crust that are different from those in the mantle. It is possible, therefore, to interpret the discordant ages of these zircons in terms of the origin and subsequent history of the xenolithic source material. Zircon from a crustal xenolith from Kilbourne Hole, New Mexico, was analyzed and the ages calculated by *Davis and Grew*. The effects of incorporation in the host basaltic magma were found to be measurable.

Statistical Petrography

By sampling experiments using the data base of the rock information system RKNFSYS, *Chayes and Trochimczyk* have shown that when the principal component transformation is applied to tables of percentages or other closed data, the interdependence of variance and covariance so characteristic of such data reappears in relations between the coefficients of the lower order principal components; the observed covariance matrix of the coefficients of any lower order component

conforms to the major closure condition about as well as does that of the raw data. *Rosenblatt, Chayes, and Trochimczyk* show that in strictly closed arrays this is the consequence of an algebraic identity. This result, which appears to be new and certainly has not been noted in any previous petrographic application of the transformation, emerges from a broad study of the sampling variation to be anticipated in the application of multivariate statistical techniques to petrographic data.

In another part of that study *Trochimczyk and Chayes* have found that, as measured by observed sampling variances, the coefficients of rotated factors are considerably less stable than are those of unrotated factors; this also has not been previously noted and is in fact rather opposed to what would be anticipated from the scattered references to the subject in the literature.

All existing petrographic data bases, of which that attached to the rock information system RKNFSYS is one of the best, are grossly inadequate with regard to both coverage and information content. International Geological Correlation Project 163 has been established to stimulate and assist in the development of a comprehensive retrospective world data base for igneous petrology. *Chayes* has been assigned the responsibility for designing and modeling the operations of the central office of the organization that will ultimately result from the work of the project.

New Facilities and Techniques

In the year in which the international spectroscopic organizations are celebrating the 50th Anniversary of the discovery of the Raman effect, scientists at the Geophysical Laboratory have rejoined the Raman community. In fact, the Raman effect was studied at the Laboratory in 1932! In the current report year, *Sharma* has set up a new spectrometer to study the Raman effect using laser excitation. The equipment has been adapted for the routine studies of small

samples in the crystalline and amorphous states, silicate melts, and aqueous solutions, and for high-pressure studies of samples using the diamond-anvil, high-pressure cell. The main purpose in establishing laser-Raman spectroscopy at the Laboratory is to obtain knowledge about the structure of species present in geologically relevant systems.

Mao and Bell have designed 17 megabar-pressure cells (MBC) that incorporate combinations of seven basic designs. In addition to high megabar-pressure capability, these units, all constructed in the Geophysical Laboratory machine shop, are perhaps more versatile than any high-pressure apparatus previously designed. It is possible to contain a sample under pressure for studies of optical, Raman, and infrared spectra, x-ray diffraction, Mössbauer resonance, chemical reaction at external high or low temperatures while at pressure, and electrical resistance. The strain and strength of samples under nonhydrostatic stress can also be measured. The high-pressure cells are being employed in these ways for geochemical and geophysical experiments. Recent experiments by *Bell and Mao* with the MBC apparatus have resulted in the production of a sustained pressure of 1.7 Mbar. This pressure is the highest internally-calibrated static pressure ever achieved. During the same experiments, macroscopic flow in one of the diamond anvils of the MBC was observed, also for the first time, at room temperature. It is now possible to study the behavior of minerals in the earth under conditions corresponding to a depth of approxi-

mately 3300 km, a depth beneath the mantle and within the core.

Several new studies of mineral-aqueous solution equilibrium using the Ag-AgCl buffer have been initiated by *Popp, Frantz, Vogel, and Hare*. These investigations, however, require measurement of dissolved chloride ion concentrations in the range 10^{-2} to 10^{-4} molal in micro-volume samples ($1-10 \mu\text{l}$). They developed two new techniques to accomplish such measurements. In the first method, a standard chloride electrode was modified to contain the small sample sizes, and a miniature-reference electrode was developed. The second technique involved modification of the calorimetric flow-cell for chloride ion (*Frantz and Hare, Year Book 72*) and use of standard complexing reagents. Calibration of both techniques resulted in measurements with the required precision and accuracy.

Lawson has found some difficulties in the use of evacuated, sealed silica tubes for the synthesis of single-phase compositions in the system $\text{FeO-Fe}_2\text{O}_3\text{-TiO}_2$. Attempts were made to synthesize compositions along the ilmenite-hematite join, but in all cases the resulting Fe^{3+} - ΣFe ratios were lower than the theoretical Fe^{3+} - ΣFe ratios for the starting compositions. In some runs, small amounts of a magnetite-ulvöspinel solid solution were formed. The main problem with using evacuated, sealed silica tubes, according to *Lawson*, seems to be that there is no direct control of oxygen fugacity, which is of critical importance during synthesis of oxides containing mixed-valence-state cations.

SPECTRAL MINERALOGY: RAMAN

STRUCTURE OF GLASSES AND MELTS OF $\text{Na}_2\text{O} \cdot x\text{SiO}_2$ ($x = 1, 2, 3$) COMPOSITION FROM RAMAN SPECTROSCOPY

S. K. Sharma, D. Virgo, and B. Mysen

It is generally assumed that the network structure of silicate glasses quenched

above the glass transition point reflects the actual melt structure (*Riebling, 1967*). Comparatively few data exist in the literature, however, pertaining to the structure of silicate melts. *Sweet and White (1969)* have compared the infrared reflectance spectra of sodium silicate glasses at room temperature with those of melts above the liquidus temperatures.

They showed that there are few differences between the spectra of glasses and melts in the $\text{Na}_2\text{O}\text{-SiO}_2$ system, although the major peaks are shifted to lower frequencies in the melt spectra because of the increase in average bond lengths. On the other hand, Nukui *et al.* (1978) have shown that the structure of molten SiO_2 is different from that of the glass and that the melt structure cannot be quenched. Vitreous SiO_2 has a closed structure, in which β -quartz-like arrangements predominate over cristobalite arrangements; the melt, however, possesses an open structure with large amounts of cristobalite-like arrangements, and the melt structure becomes more open with further increase in temperature. From laser-Raman spectroscopy, Sharma (1974) has shown that the major species present in the crystalline, glassy, and molten states of hydrated ferric chloride ($\text{FeCl}_3\cdot 6\text{H}_2\text{O}$) are quite different. In crystalline and molten $\text{FeCl}_3\cdot 6\text{H}_2\text{O}$, the major iron molecular species are $\text{Fe}(\text{H}_2\text{O})_4\text{Cl}_2^+$, and FeCl_4^- ions, respectively. Significantly, in the glass the FeCl_4^- ions undergo association to form a polymeric network in which Fe^{3+} ions are octahedrally coordinated.

Because structural differences between melt and glass may be important in explaining certain physical and chemical properties of melts, for example viscosity (Sharma, Virgo, Mysen, this Report), the first Raman spectra of heated silicate glasses and melts are given in this report.

Experimental

Glasses of $\text{Na}_2\text{O}\cdot x\text{SiO}_2$ with $x = 1, 2$ and 3 were samples previously made by the late Dr. J. F. Schairer. Starting materials were dried and heated slightly above their respective melting points and rapidly quenched in a standard 1-atm quenching furnace. The glass samples were crushed and packed into Pt tubes (2.5 mm ID) sealed at one end. Each sample was then held at a temperature $100^\circ\text{--}150^\circ\text{C}$ above the respective melting points and quenched. This latter pro-

cedure was repeated until slit windows near the base of each Pt tube were completely filled with quenched glass. The Pt tubes containing each glass sample were then held vertically and heated in a Pt-Rh (10%) wound furnace. Raman spectra of each sample heated at specific temperatures were taken using equipment described elsewhere (Sharma, this Report).

Results and Discussion

The measured frequencies of bands in the Raman spectra of heated glasses and melts of $\text{Na}_2\text{O}\cdot x\text{SiO}_2$ with $x = 1, 2, 3$ are given in Tables 1, 2, and 3, respectively.

TABLE 1A. Observed Vibrational Frequencies (cm^{-1}) of Heated Glasses and Melt of $\text{Na}_2\text{O}\cdot\text{SiO}_2$ Composition

23°C	989°C	1109°C
~360 vw, bd*	~388 w, bd	
~580 vw, bd		
618 s	~584 m	~558
~732 vw		
849 w		
968 vs	950 s	~948
1056 (Sh)		

TABLE 1B. Observed Vibrational Frequencies (cm^{-1}) of Crystalline $\text{Na}_2\text{O}\cdot\text{SiO}_2$

23°C	574°C
164 s	152
178 m	
212 m	200 w
232 m	
262 m	240 w
300 m	
390 s	384 m
408 (Sh)	
502 w	
544 w	
588 s	578 s
874 m	874 w
968 vs	960 vs
1020 m	1004 (Sh)
1068 m	1056 w

* s, strong; vs, very strong; m, medium; w, weak; vw, very weak; Sh, shoulder; bd, broad.

TABLE 2A. Observed Vibrational Frequencies (cm⁻¹) of Heated Glasses and Melt of Na₂O·2SiO₂ Composition

23°C	408°C	591°C	917°C	1021°C
332 vw, bd*				
572 s	570 s	558 s	568 s	568
~768 vw, bd	~768 vw, bd	~764 vw, bd	760 vw, bd	
946 w	934 w	945 w	934 w	~920
1096 s	1090 s	1088 s	1080 s	1078

TABLE 2B. Observed Vibrational Frequencies (cm⁻¹) of Crystalline Na₂O·2SiO₂

673°C	818°C
122 m	122 w, bd
	232 w, bd
~300 m, bd	~300 m, bd
362 m	~364
508 s	504 s
755 w	
1003 w	
1066 vs	1064 vs

* s, strong; vs, very strong; m, medium; w, weak; vw, very weak; bd, broad.

The data on glasses measured at room temperature are in agreement with those of Brawer and White (1975) for samples of the same composition.

Both Stokes and anti-Stokes components of the Raman spectrum of sodium disilicate (Na₂O·2SiO₂) glass at room temperature and at 591°C as well as molten Na₂O·2SiO₂ at 918°C are shown in Fig. 1.

Generally, the effect of temperature on all three glasses is similar, and there are two main trends. First, there is systematic lowering of frequencies of all vibrational bands owing to weakening and elongation of the Si-O bands associated with thermal expansion. Second, there is an increase in intensity of the Rayleigh tail with increasing temperature that is consistent with increasing disorder of the glass structure.

Above the glass transition temperatures of 443°C and ~550°C for the sodium disilicate and sodium metasilicate com-

positions, respectively, both these glasses begin to devitrify. The results of these devitrifications are shown in Fig. 2 by the presence of sharp Raman lines and the emergence of well-defined lines from the Rayleigh tail. The Raman spectrum of the quenched sodium metasilicate glass, previously held at 574°C for approximately ½ hr (Fig. 2), closely resembles the Raman spectrum of crystalline sodium metasilicate previously reported by Brawer and White (1975). The fact that both these glasses rapidly devitrify indicates that the structural units present in the disordered glass must be very similar to those present in the crystalline state.

In the glass of sodium trisilicate composition there was no indication of crystallization on heating above the glass transition point (~458°C). In this case, the fact that the glass of Na₂O·3SiO₂ composition crystallizes to 3Na₂O·8SiO₂ plus quartz (Schairer and Yoder, *Year Book* 69, pp. 160–163) probably indicates that the network structure and short-range ordering in the glass are quite different from those of 3Na₂O·8SiO₂ crystals.

The Raman spectra of melts for all three compositions (Tables 1, 2, 3) bear close resemblances to those spectra of the heat-treated glasses. A general exception, however, is that the melts have more disordered structures, as indicated by the increase in intensity of the Rayleigh tails (see Fig. 1). The present Raman study, therefore, supports the conclusions reached by Sweet and White (1969) from infrared reflectance study that the structures of glass and melt of the same com-

TABLE 3. Observed Vibrational Frequencies (cm⁻¹) of Heated Glass and Melt of Na₂O·3SiO₂ Composition

23°C	583°C	773°C	933°C
536 s*	530 s	528 m	524 m
~592 (Sh)	~584 (Sh)	~588 (Sh)	
775 w	764 w	~764 w	
950 w (Sh)	940 w (Sh)	~940 w (Sh)	~926 vw
1100 vs	1092 vs	1088 vs	1072 s

* s, strong; vs, very strong; m, medium; w, weak; vw, very weak; Sh, shoulder; bd, broad.

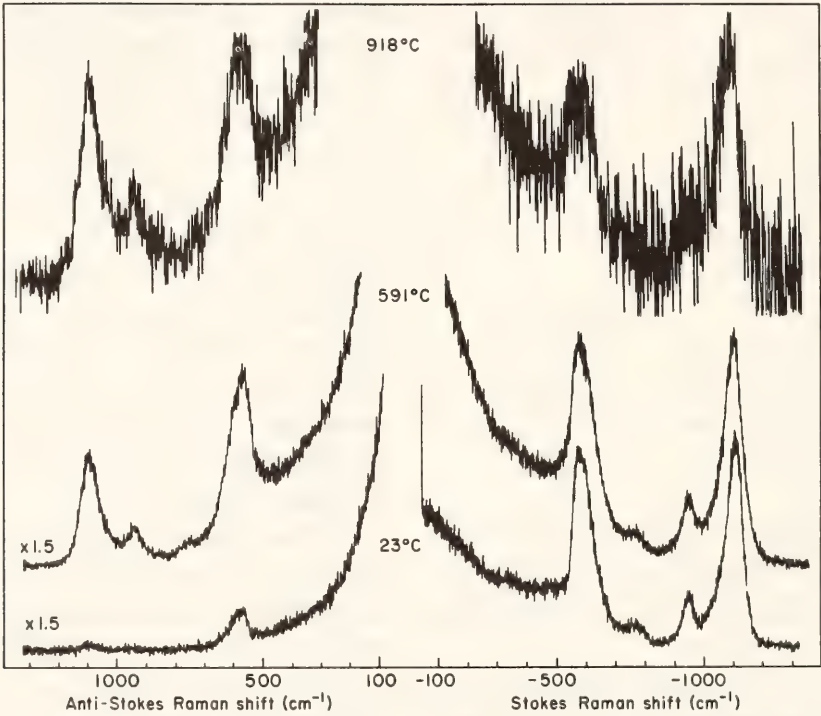


Fig. 1. Raman spectra of glass of Na₂O·2SiO₂ composition heated at room temperature and 591°C and of Na₂O·2SiO₂ melt at 918°C (laser 488.0 nm Ar ion, 200 mw, slit 4 cm⁻¹).

positions are similar. The present study also shows the feasibility of studying the kinetics of crystallization in silicate melts.

STRUCTURE OF MELTS ALONG THE JOIN
SiO₂-NaAlSiO₄
BY RAMAN SPECTROSCOPY

S. K. Sharma, D. Virgo, and B. Mysen

Relationships between the structure and the physical and chemical properties of silicate melts are of fundamental importance in understanding the genesis and

derivation of silicate magmas in the earth's mantle and crust. For melts in the system Na₂O-Al₂O₃-SiO₂, many physical properties such as density refractive index, electrical conductivity, and viscosity have been determined. Furthermore, this system is important in the earth sciences because it includes the subsystem SiO₂-NaAlSiO₄, and knowledge of the melt structures along this latter join will strengthen understanding of the physical and chemical properties of melts of granitic, andesitic, and high-alumina basalt compositions.

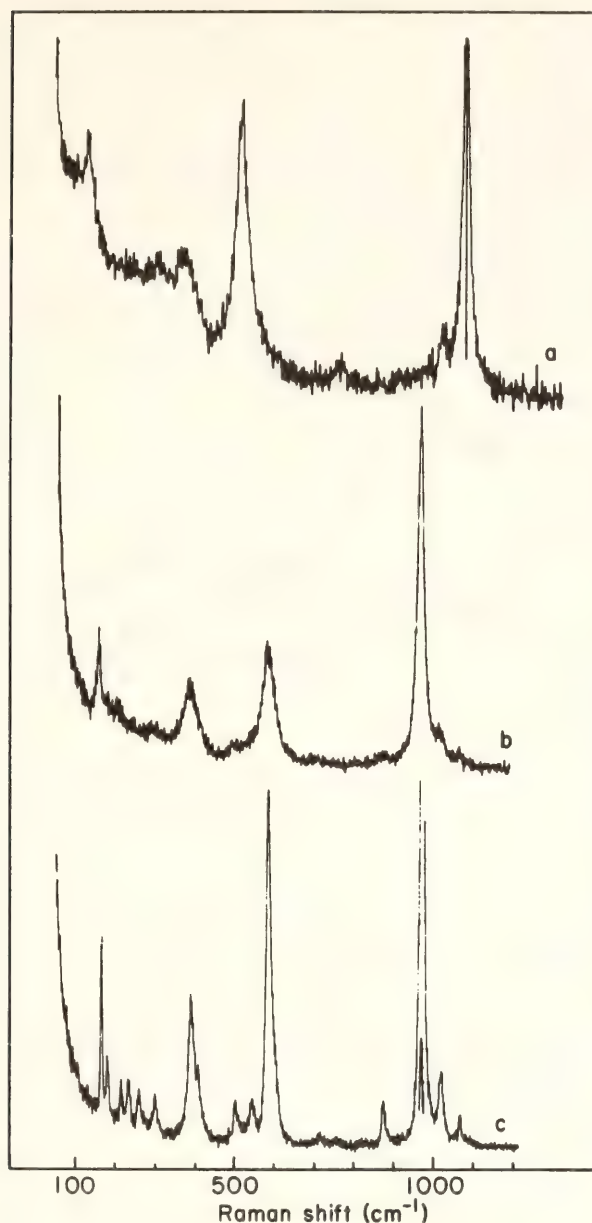


Fig. 2. Raman spectra of (a) glass of $\text{Na}_2\text{O} \cdot 2\text{SiO}_2$ composition at 673°C (b) glass of $\text{Na}_2\text{O} \cdot \text{SiO}_2$ composition at 574°C and (c) quenched glass of $\text{Na}_2\text{O} \cdot \text{SiO}_2$ composition previously heated at $\sim 514^\circ\text{C}$ for 60 min. Experimental conditions as in Fig. 1.

Raman spectroscopy has proved to be a valuable tool for determining the structure of silicate melts and has shown, for example, that the short-range order in SiO_2 glass is best described by a β -quartz model (Hass, 1970; Bates *et al.*, 1974). Brawer and White (1975), in a study of glasses along the join SiO_2 - Na_2O , also demonstrated the usefulness of Raman spectroscopy in determining the local net-

work structure in these chemically more complex glasses. Most important, Brawer and White (1975) were able to demonstrate systematic variations in the ratio of nonbridging-to-bridging oxygens caused by the changing soda content along the Na_2O - SiO_2 join. Furthermore, using the Raman technique to measure the nonbridging-to-bridging oxygen ratio, it has been possible to discriminate between the possible dual roles of elements such as Ti^{4+} , B^{3+} , and Al^{3+} in doped SiO_2 glasses, where such elements might be considered network formers or network modifiers (Kato, 1976a, 1976b).

In this report the structure and coordination of Al^{3+} in some silicate glasses with compositions within the system Na_2O - Al_2O_3 - SiO_2 have been studied using the Raman technique.

Experimental

Glasses with compositions $\text{Na}_2\text{O} \cdot \text{Al}_2\text{O}_3 \cdot x\text{SiO}_2$ where $x = 2$ (carnegieite), $x = 4$ (jadeite), and $x = 6$ (albite) and a glass of composition $\text{Na}_2\text{O} \cdot 1.42\text{Al}_2\text{O}_3 \cdot 5.15\text{SiO}_2$ were prepared from combinations of Johnson-Matthey spec-pure SiO_2 , Al_2O_3 , and reagent-grade Na_2CO_3 . The specific oxide mixtures (~ 250 mg) were ground under acetone for 2 hr and ~ 25 -mg aliquots were loaded into sealed $\text{Pt}_{95}\text{Au}_5$ capsules. Samples were run for 1 hr at temperatures of 1450°C and 1550°C in standard vertical-quench furnaces and subsequently quenched in Hg. Raman spectra were measured on several small chips of each glass (~ 5 mm³) that were free from air bubbles.

The Raman spectra were recorded with a J-Y optical system, holographic grating, double monochromator (HG-2S) using photon-counting detection (Sharma, this Report). The sample was excited with the 488.0-nm line of an Ar^+ ion laser using a laser power of 300–400 m.w. at the sample, with 90° -scattering geometry. The polarization spectra were obtained with the focused exciting beam parallel to the horizontal spectrometer slit and with

the electric vector of the exciting radiation in a vertical orientation. A sheet of polarizer disk in front of an optical scrambler was used to separately record the parallel and perpendicular components of the scattered radiation. More complete experimental details are given by Sharma (this Report).

Results

The Raman spectra of the 1-atm glasses $\text{Na}_2\text{O} \cdot \text{Al}_2\text{O}_3 \cdot x\text{SiO}_2$ with $x = 2, 4$, and 6 referred subsequently in the text as C, J and A, respectively) are shown in Fig. 3. The spectra of the glass $\text{Na}_2\text{O} \cdot 1.42\text{Al}_2\text{O}_3 \cdot 5.15\text{SiO}_2$ (AA) is given in Fig. 4. In Figs. 3 and 4, the spectra in both parallel and perpendicular polarization directions are given for each glass composition. The measured peak positions of the Raman bands are given in Table 4. The spectra are composed of broad bands (factor of 50–100 times greater than that of crystalline phases) and the error in measuring the peak positions is approximately $\pm 5 \text{ cm}^{-1}$.

The Raman spectra of glasses A, J, and AA (Fig. 3) are similar. In the low-frequency region, the spectra show strong Rayleigh tails extending up to 300 cm^{-1} that are generally characteristic of amorphous materials. The strongest Raman peak, which appears at 472 cm^{-1} , has a broad low-frequency shoulder at $\sim 300 \text{ cm}^{-1}$ and a high-frequency shoulder at 580 cm^{-1} . All these bands are strongly polarized (Fig. 3; Table 4). The broad, weak peak at $\sim 800 \text{ cm}^{-1}$ appears to be depolarized. In the $900\text{--}1200\text{-cm}^{-1}$ region, a broad envelope composed of at least two overlapping bands at ~ 1012 and 1108 cm^{-1} is observed. Both these bands show a weak polarization effect. In general, the band shapes and peak positions in glass A are in close agreement with the data reported by Sweet *et al.* (1973) for an albite glass.

The Raman spectra of glass C is distinguished from that of the other glasses examined in this study. The bands

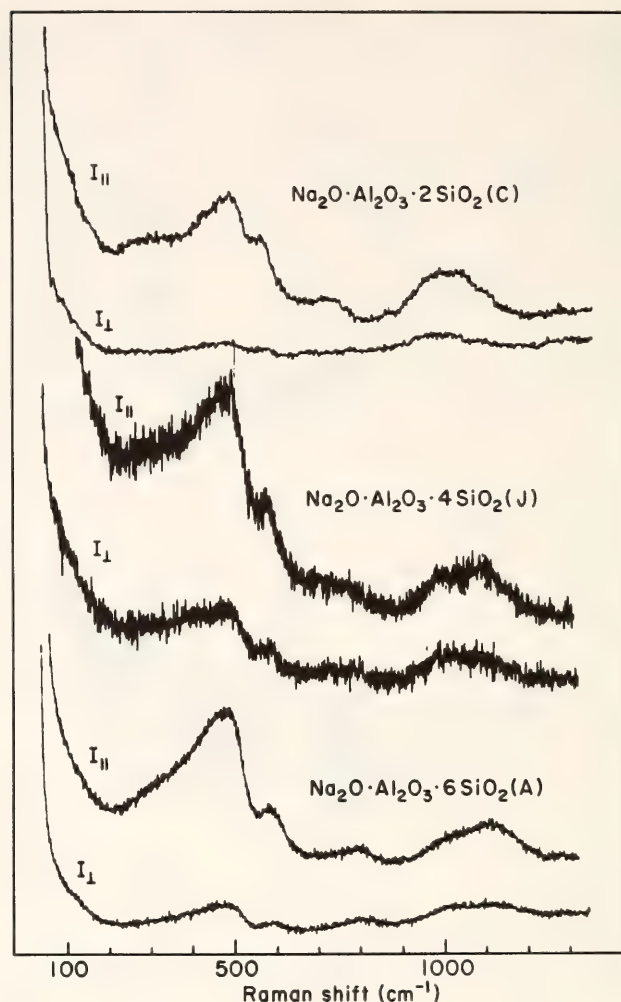


Fig. 3. Raman spectra of soda-aluminosilicate glasses in different polarizations (Slit 10 cm^{-1} , laser 488.0 nm , 300 mw at the sample).

are strongly polarized (Fig. 3) and in the high-frequency region there appears to be only a single band, at 1004 cm^{-1} .

Discussion

The presence of the strong band at 472 cm^{-1} and the weak, broad bands in the $900\text{--}1100 \text{ cm}^{-1}$ region in glasses A and J are characteristic of a three-dimensional network structure as found in vitreous SiO_2 (e.g., Bates *et al.* 1974). The band attributed to the Si-O stretch in the region $900\text{--}1100 \text{ cm}^{-1}$ is shifted to lower frequencies in the aluminosilicate glasses, however, and is only weakly polarized compared to the depolarized bands in fused silica at 1065 and 1200 cm^{-1} . The lowering of the Si-O stretch frequency in

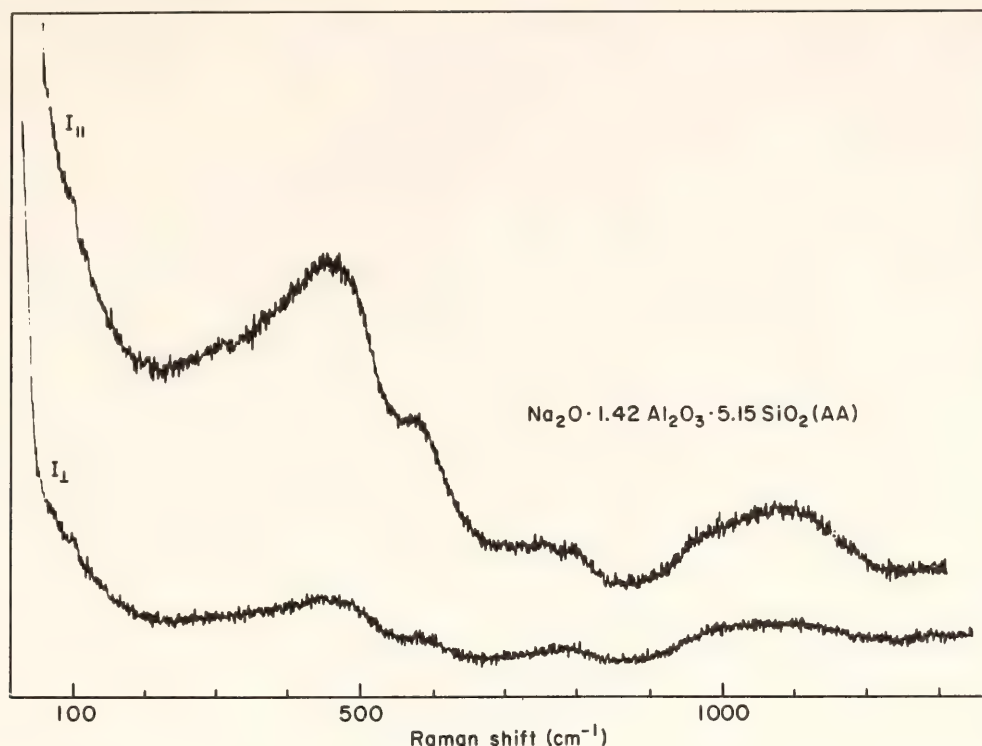


Fig. 4. Raman spectra of $\text{Na}_2\text{O} \cdot 1.42\text{Al}_2\text{O}_3 \cdot 5.15\text{SiO}_2$ (AA) glass in different polarizations. (Slit 10 cm^{-1} , laser 488.0 nm, 300 mw at the sample.)

the aluminosilicate glasses can be attributed to the isomorphous substitution of Al for Si in the glass network. This interpretation is in agreement with Milkey (1960), who investigated the infrared spectra of 57 tectosilicate crystals and found that the frequency of the Si-O absorption peaks shows an irregular but systematic shift to lower frequency as Al/Si increases. In nepheline ($\text{KNa}_3\text{Al}_4\text{Si}_4\text{O}_{16}$), for example, where half of the Si atoms are replaced by Al atoms in the three-dimensional network, Moenke (1974) demonstrated that the infrared spectra is identical to quartz in the 400–500 cm^{-1} region but the 1100 and 800 cm^{-1} bands in crystalline nepheline are shifted to lower frequencies by 100 cm^{-1} . It is apparent, therefore, that the AlO_4 tetrahedra in aluminosilicate crystals are coupled with SiO_4 tetrahedra. In such chemical systems the modes of vibration of SiO_4 and AlO_4 tetrahedra may not be differentiated and thus the material behaves as a “one-mode” system. Such an effect has been observed in simple in-

organic mixed crystals (Chang and Mitra, 1968). It is reasonable to suggest that a similar effect will occur in glasses.

Furthermore, the weak polarization showed by the bands in the 900–1200 cm^{-1} region (Fig. 3) indicates that the structure of the aluminosilicate glasses (A and J compositions) is not *identical* with that of SiO_2 glass in which the short-range ordering closely resembles that of β -quartz (Bates *et al.*, 1974). The weak polarization of the high-frequency peaks indicates that the local symmetry of at least some of the SiO_4 or AlO_4 tetrahedra in the network is lower than that in vitreous SiO_2 .

Additional important structural details of the glasses A and J stem from interpretation of the shoulders at 580 and 572 cm^{-1} , respectively. These features in the Raman spectra probably indicate the presence of a random defect structure involving SiO_4 and AlO_4 tetrahedra with one or two nonbridging oxygens (Koniynendiyk and Stevek, 1976). The absence of the well-defined nonbridging peak at 950 cm^{-1} in these glasses implies that

TABLE 4. Raman Frequencies of Glasses

Specimen label	Composition	Frequencies (cm ⁻¹)					
A-glass	Na ₂ O · Al ₂ O ₃ · 6SiO ₂	~300 w,p*	472s,p	580 (Sh) p	~800 wdp	1012w, wp	1108w, wp
J-glass	Na ₂ O · Al ₂ O ₃ · 4SiO ₂	~300 w,p	472s,p	572 (Sh) p	~744wdp	1000w,wp	1080w,wp
C-glass	Na ₂ O · Al ₂ O ₃ · 2SiO ₂	~272w,p	468s,p	568 (Sh) p	~736wp	1004m,p	
AA-glass	Na ₂ O · 1.42Al ₂ O ₃ · 5.15SiO ₂	...	480s,p	572 (Sh) p	~810wdp	996w,wp	1086w,wp

* w, weak; m, medium; s, strong; p, polarized; dp, depolarized; wp, weakly polarized; (Sh), shoulder.

the defect structure in the aluminosilicate glasses may be of the same order of magnitude as in SiO_2 glass ($\sim 12\%$; Narten 1972).

The glass of carnegieite composition (C) also has a three-dimensional network structure with the vibration mode associated with the Si-O stretching shifted to lower frequencies owing to the increase in Al/Si, as discussed above. Again the absence of a vibration mode associated with nonbridging oxygens and of any additional modes that might be attributed to AlO_6 suggests that the majority of Al^{3+} ions are present in fourfold coordination. The absence of any depolarized band in the spectrum can be attributed to the lower local symmetry of the tetrahedral units in a three-dimensional network compared to SiO_2 glass.

As noted previously, the Raman spectra of the glass AA is similar to that of the glasses of albite and jadeite composition. Noteworthy again is the lack of any spectral features attributable to $(\text{AlO}_6)^{3-}$ groups or to the presence of nonbridging oxygens associated with AlO_6 groups. Thus, it is evident that the majority of Al^{3+} ions are present in fourfold coordination. From a comparison of the greater degree of polarization of the Raman bands in the $900\text{--}1200\text{ cm}^{-1}$ region of the glasses A, J, C, and AA relative to the corresponding bands in SiO_2 glass, it has been suggested that the symmetry of the tetrahedral units is lower in the A, J, C, and AA glasses. The lower symmetry may be consistent with a three-dimensional network structure of these glasses, resembling that of α -quartz or α -cristobalite with Na^+ ions occupying the cavities. From a factor-group frequency analysis for the polymorphs of SiO_2 , it is suggested that α -cristobalite structure would provide a closer match to the observed Raman spectra. Furthermore, because of the different polarization effects (in A, J, and AA, the high-frequency bands are weakly polarized whereas in C the same bands are completely polarized), it is reasonable to

suggest that the network structure of the A, J, and AA glasses may represent mixtures of β -quartz and α -cristobalite structural units, whereas in glass C the average structure is predominately represented by the more open structure of α -cristobalite. Radial distribution studies of a glass of albite composition are consistent with a three-dimensional network structure similar to that of SiO_2 glass. It is of interest to begin to correlate the results of this study with available physical and chemical properties of the same melts. Riebling (1966) has shown that the viscosity decreases and the density increases along the join $\text{SiO}_2\text{--NaAlSiO}_4$. It was originally proposed by Riebling (1966) that these changes were consistent with a change in the glass structure from an SiO_2 glass type to a more open cristobalite-type structure in carnegieite. The interpretation of the present Raman studies are, therefore, in agreement with Riebling's hypothesis. Also, Virgo and Mysen (*Year Book* 76, pp. 400–407; unpublished data) have demonstrated that ferric iron is unstable in albite and jadeite glasses containing $\leq 10\text{ mol } \%$ acmite component and prepared under oxidizing conditions. These results were interpreted by them in terms of a highly polymerized melt structure for those compositions in which the ratio of nonbridging-to-bridging oxygen was small. It is apparent that the present structural studies are consistent with this hypothesis.

Finally, some comments can be made about the question of Al^{3+} coordination for glasses in the system $\text{Na}_2\text{O--Al}_2\text{O}_3\text{--SiO}_2$ with $\text{Al}/\text{Na} \geq 1$. For compositions along the join $\text{SiO}_2\text{--NaAlSiO}_4$, Al^{3+} remains in tetrahedral coordination. The presence of $(\text{AlO}_6)^{3-}$ groups in the melt structure would result in a destruction of the three-dimensional melt structure and an increase in the number of nonbridging oxygen atoms. Such an effect would be revealed in the Raman spectra by the appearance of a band at 950 cm^{-1} , as demonstrated in glasses along the join

SiO₂-Na₂O (Brawer and White 1975; Sharma, Virgo and Mysen, this Report) and by the increase in the intensity of the 950 cm⁻¹ band with addition of small concentrations of Al₂O₃ to the Na₂O·2SiO₂ composition (Brawer and White, 1977). Furthermore, for compositions with Al/Na ≥ 1, it has been shown recently that there is no wavelength shift of AlK α x radiation as a result of increasing Al/Na above 1; this result implies that all Al³⁺ ions remain in fourfold coordination up to Al/Na = 1.5 (Wong and Angell, 1976). The Raman results for the glass composition with Al/Na = 1.42 are consistent with these findings and may, in general, support the hypothesis that AlO₆ octahedra in melts are unstable because of geometrical and energetic considerations, as discussed in detail by Lacey (1963).

RAMAN STUDY OF STRUCTURE AND
COORDINATION OF Al IN NaAlSi₂O₆
GLASSES SYNTHESIZED AT HIGH
PRESSURE

S. K. Sharma, D. Virgo, and B. Mysen

Several recent papers have referred to the relationship between melt structure and important physical and chemical properties of melts at high pressure. Anomalous characteristics of silicate melt properties include: (1) changes in CO₂ solubility in albite melt at high pressure (Mysen, 1976b), (2) changes in Fe³⁺/ΣFe in melts as a function of composition along the NaAlSi₂O₆-NaFeSi₂O₆ join and as a function of pressure for specific compositions along the same join (Virgo and Mysen, *Year Book* 76, pp. 400-407), (3) significant decreases in Ni partitioning between crystals and melt along the NaAlSi₂O₆-MgSi₂O₄ join with increasing pressure (Mysen and Kushiro, this Report), and (4) decreases in the viscosity of jadeite melts with increasing pressure (Kushiro, 1976). In general, the anomalous characteristics noted above have been correlated with a change from 4-fold to

6-fold coordination of Al³⁺ in the melt (Waff, 1975). Such high-pressure cationic coordination changes will be accompanied by a decrease in the degree of polymerization of the melt. To date, however, such structural changes have necessarily been inferred from analogous coordination changes associated with solid-state reactions. In this report, the first Raman spectroscopic studies of quenched high-pressure glasses of NaAlSi₂O₆ composition are presented.

Starting material for the high-pressure runs was a glass of NaAlSi₂O₆ composition (referred to as J-glass) prepared at 1 atm, 1450°C (~250 mg) from an oxide mix of Johnson-Matthey spec-pure SiO₂, Al₂O₃, and reagent-grade Na₂CO₃. The mix of NaAlSi₂O₆ composition was placed in a sealed Pt₉₅-Au₅ capsule and melting was carried out in a vertical quench furnace. The high-pressure experiments were made on aliquots (~10 mg) of the 1-atm glass in the solid-media, high-pressure apparatus (Boyd and England, 1960) at 10, 15, 20, and 30 kbar at 1450°C, and at 40 kbar at 1550°C.

Results

Raman spectra of the J-glass prepared under various pressures are given in Fig. 5. In Fig. 6, the spectra of the glasses prepared at 10 and 20 kbar, but with the electric vector of the scattered light both parallel and perpendicular to the electric vector of the laser beam, are shown. The band positions and their polarization characteristics are listed in Table 5.

It is apparent from Fig. 5 and Table 5 that the unpolarized Raman spectra of the 1-atm and 10-kbar runs show similar characteristics, except that the components of the weak, broad band in the 900-1200 cm⁻¹ region are shifted toward lower frequencies and the strong band at 472 cm⁻¹ is slightly shifted to a higher frequency (~3 cm⁻¹). All the bands in the spectra of the glasses at 10 and 20 kbar are strongly polarized (see Fig. 6). The polarization behavior is in contrast with

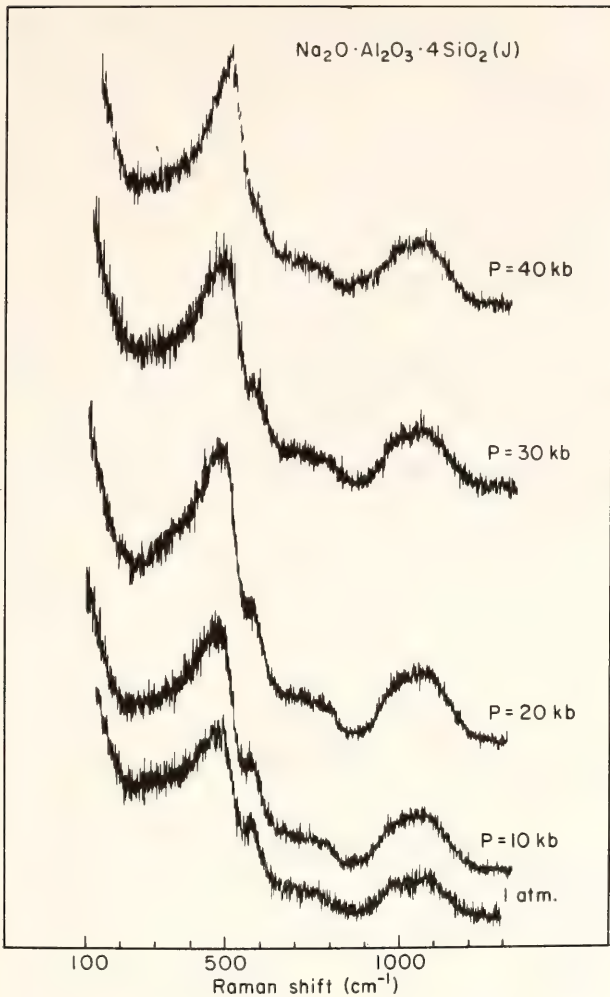


Fig. 5. Raman spectra of NaAlSi₂O₆ glasses synthesized at 1 bar, 10, 15, 20, 30, and 40 kbar (laser 488.0 nm Ar ion, 200 mw, slit 6 cm⁻¹).

the 1-atm J-glass, which shows only weak polarization of the 900–1200 cm⁻¹ band (Sharma, Virgo and Mysen, this Report). In addition to this change in the polarization ratio of the bands in the 900–1200

cm⁻¹ region, the strong band observed at 472 cm⁻¹ in the 1-atm glass is progressively shifted toward higher frequencies with increasing pressure and appears at 496 cm⁻¹ in the 40-kbar run.

In all samples the broad polarized band in the 900–1200 cm⁻¹ region (half-width at half-peak height is 212 cm⁻¹ in the 10-kbar sample) seems to be composed of at least two overlapping peaks. Because of this strong overlap, it is not possible to measure accurately the position of the component peaks of this doublet. Nevertheless it can be established that the positions of component peaks progressively shift to lower frequencies in samples quenched at progressively higher pressures (Table 1). Similar changes were observed in the infrared spectra of a glass of NaAlSi₂O₆ composition (Velde and Kushiro, 1978). No band in the Raman and infrared spectra of the high-pressure J-glasses can be attributed to (AlO₆) groups.

Discussion

As discussed elsewhere (Sharma, Virgo, and Mysen, this Report) the strong band at 475 cm⁻¹ and the broad, weakly polarized band in the 900–1200 cm⁻¹ region in the 1-atm J-glass are characteristics of a three-dimensional network structure. The weak shoulder at 572 cm⁻¹ is probably caused by the presence of defect structure involving a nonbridging oxygen. This follows from a comparison

TABLE 5. Raman Frequencies* of Na₂O·Al₂O₃·4SiO₂ (J-Glass) Prepared at Different Pressures

0.001 kbar	10 kbar	20 kbar	30 kbar	40 kbar
~300, w,bd†	340, w,bd	320, w,bd
472, s,p	475, s,p	478, s,p	480, s,p	496, s,p
572, (Sh),p	572, (Sh),p	568, s,p	564, (Sh)	...
750, w,bd,dp	750, w,bd	760, w,bd	740, w,bd	748, w,bd
1050, w,bd,wp	992, w,bd,p	1008, w,bd,p	996, w,bd,p	984, w,bd,p
1084, w,bd,wp	1050, w,bd,p	1080, w,bd,p	1054, w,bd,p	1056, w,bd,p

* Measurement accuracy is ±10 cm⁻¹ for weak and broad bands and ±4 cm⁻¹ for sharp and strong bands.

† Abbreviations: w, weak; s, strong; bd, broad; p, polarized; dp, depolarized; Sh, shoulder.

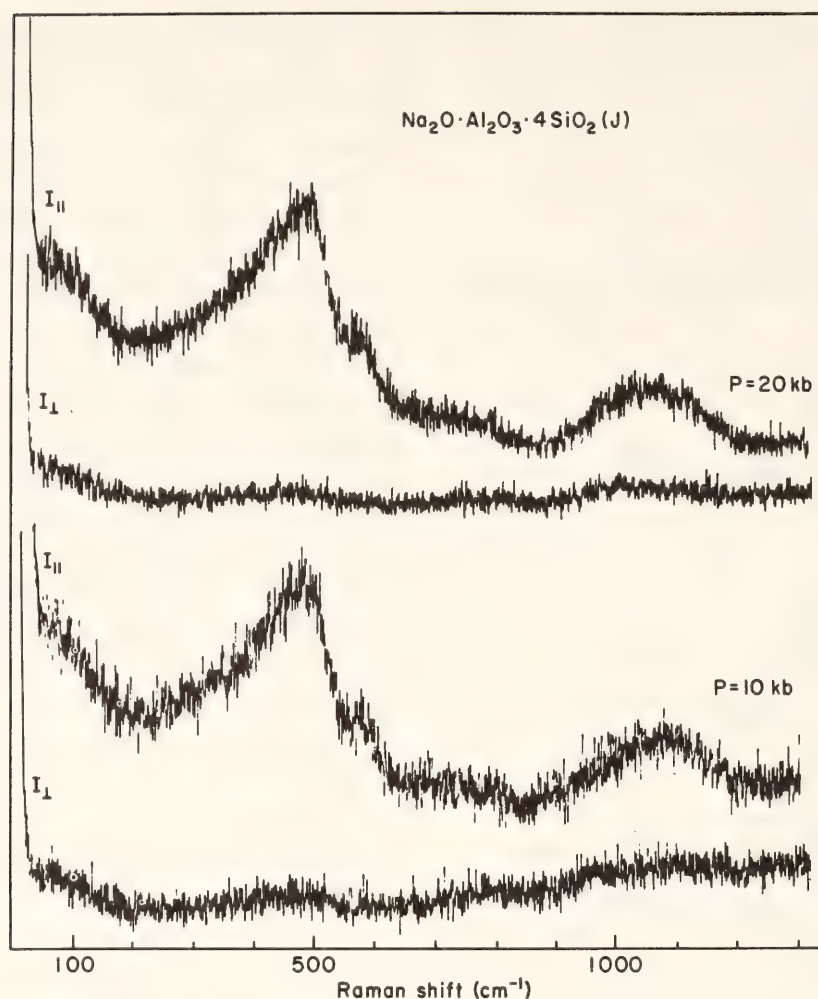


Fig. 6. Polarized Raman spectra of $\text{NaAlSi}_2\text{O}_6$ glasses synthesized at 10 and 20 kbar (laser 488.0 nm Ar ion, 150 mw, slit 6 cm^{-1}).

with the Raman spectra of SiO_2 glass. In SiO_2 glass, however, the bands in 900–1200 cm^{-1} are shifted to higher frequencies and are more depolarized than in the glass of jadeite composition. The shift in position of these high-frequency bands in J-glasses has been attributed to the presence of aluminum in the network (Sharma, Virgo, and Mysen, this Report). In general, then, it appears that the J-glasses have a three-dimensional network comprised of AlO_4 and SiO_4 tetrahedra, with sodium ions present in cavities.

The spectra of the high-pressure J-glasses are in general similar to that of the 1-atm glass; this result implies that the scattering units are the same in all the J-glasses quenched over the range 0.001–40 kbar. But the polarization ratio

of the broad band in the 900–1200 cm^{-1} region is different for the glasses synthesized at pressure (the band is completely polarized) compared to the 1-atm glass where the 900–1200 cm^{-1} band is only weakly polarized. The presence of only highly polarized bands in the Raman spectra of high-pressure J-glasses implies that the local symmetry of $\text{Si}(\text{Al})$ tetrahedra is lower than in SiO_2 glass. A quantitative explanation of the lower local symmetry in terms of the average melt structure is not possible at this time, but some constraints can be suggested. It is generally accepted that the short-range ordering in random network of SiO_2 glass closely resembles that of β -quartz (Wong and Angell, 1976). The SiO_2 polymorphs in which Si has a lower site symmetry are α -quartz, α -cristobalite, tridymite, coesite,

and keatite. Of these polymorphs, coesite has a center of inversion that implies the mutual exclusion of Raman and infrared activity of the vibration modes. A comparison of Raman frequencies observed in the present study with the frequencies observed in the infrared absorption spectra (Velde and Kushiro, 1978) of quenched high-pressure glasses of $\text{NaAlSi}_2\text{O}_6$ composition are found to be noncoincidental. This result implies that the short-range ordering in the network of the high-pressure J-glasses will resemble that of coesite, whereas the short-range ordering in the network of the 1-atmosphere J-glass may resemble that of α -cristobalite (Sharma, Virgo, and Mysen, this Report). This comparison between the structures of glass and crystals does not imply the presence of highly ordered small crystallites but rather the presence of various degrees of local ordering in the random network.

It may be further mentioned that the network structure in the high-pressure J-glasses is more ordered than in the 1-atm glass, as indicated by the sharpness of the band at 496 cm^{-1} in the 40-kbar glass (see Fig. 5). Also, with increasing pres-

sure there is no appreciable increase in the intensity of the 572 cm^{-1} band attributed to defect structure in the network.

It can be inferred from the above discussion that Al^{3+} is predominantly in tetrahedral coordination. This conclusion is in direct contrast to the suggested role of Al^{3+} as a network modifier in jadeite melts at high pressure on the basis of aluminum $K\alpha$ and $K\beta$ wavelength shifts (Velde and Kushiro, 1978). By the latter interpretation, aluminum must leave the network to achieve 6-fold coordination, and in doing so must necessarily be accompanied by an increase in the number of nonbridging oxygens. If this were the case, the high-pressure jadeite spectra could be expected to resemble that of diopside (D-glass, Fig. 7) because both diopside and jadeite crystals have pyroxene chains. In brief, the spectra of the diopside glass made at 1550°C , 1 atm, is similar to that reported by Etchepare (1972), but the spectral resolution in the region $800\text{--}1200\text{ cm}^{-1}$ is more distinct. In general, the glass spectrum of $\text{CaMgSi}_2\text{O}_6$ closely resembles that of crystalline diopside, and the broad peak in the 850--

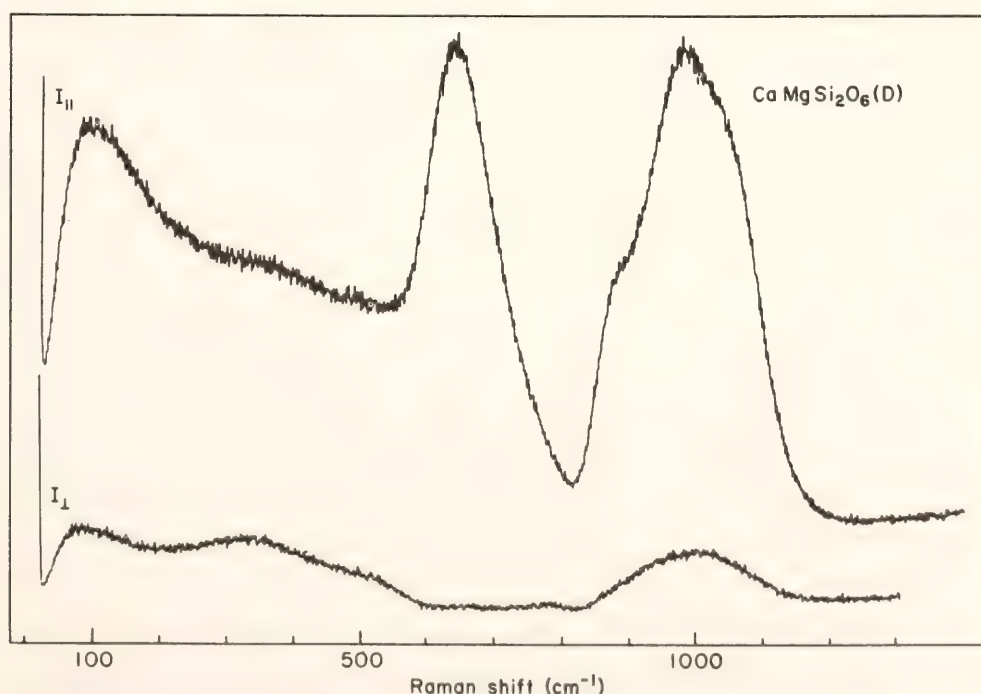


Fig. 7. Polarized Raman spectra of $\text{CaMgSi}_2\text{O}_6$ glass (laser 488.0 nm Ar ion, 350 mw , slit 8 cm^{-1}).

1100 cm^{-1} region is due to Si-O stretching modes at 890, 980, and 1008 cm^{-1} in the silicate chains that consist of two non-bridging and two bridging oxygen atoms. Furthermore, the high-frequency peaks in diopside glass are considerably more intense than in jadeite glasses because of the absence of a three-dimensional network. From the above comparison, it is evident that the spectra of diopside and jadeite glasses at high pressure are distinctly different. Also it can be pointed out that the Si-O stretching modes in glasses of $\text{Na}_2\text{O} \cdot \text{SiO}_2$ composition are represented by peaks at $\sim 950 \text{ cm}^{-1}$ and $\sim 1100 \text{ cm}^{-1}$ corresponding to nonbridging and bridging oxygens, respectively (Brawer and White, 1977). Importantly, the intensity of the 960- cm^{-1} band relative to that of the 1100- cm^{-1} band increases with progressive additions of Al_2O_3 to sodium disilicate glass, thus implying the presence of octahedrally coordinated Al^{3+} . Increases in the intensity of the nonbridging oxygen peak were also observed with the addition of TiO_2 and B_2O_3 to SiO_2 glass (Kato, 1976a). The presence of the analogous band due to nonbridging oxygen is not observed in jadeite spectra at any pressure, and these data reinforce the previous inference that Al^{3+} is in tetrahedral coordination. The results of this study, however, do not

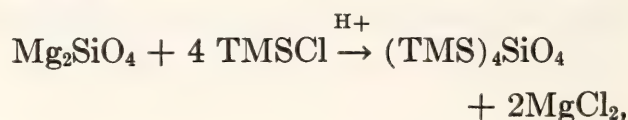
rule out the possibility of a few Al^{3+} ions in 6-fold coordination.

In summary, the Raman spectra of jadeite glass at pressures between 0.001–40 kbar is consistent with a three-dimensional network structure where Al^{3+} occurs predominantly in 4-fold coordination. With increasing pressure, the local symmetry of Si,Al in the network is lowered compared to that in SiO_2 glass, and the glass structure at high pressure may in part resemble that of coesite. It is also suggested that with increasing pressure the network becomes more ordered and the Si,Al polyhedra less distorted.

TRIMETHYLSILYL DERIVATIVES OF SILICATE MINERALS AND GLASSES—CHROMATOGRAPHY AND VIBRATIONAL SPECTROSCOPY

S. K. Sharma and T. C. Hoering

Some silicate minerals and glasses are readily converted into trimethylsilyl (TMS) derivatives by silylation reactions:



where TMS represents the trimethylsilyl group, $(\text{CH}_3)_3\text{Si}$. Figure 8 shows the

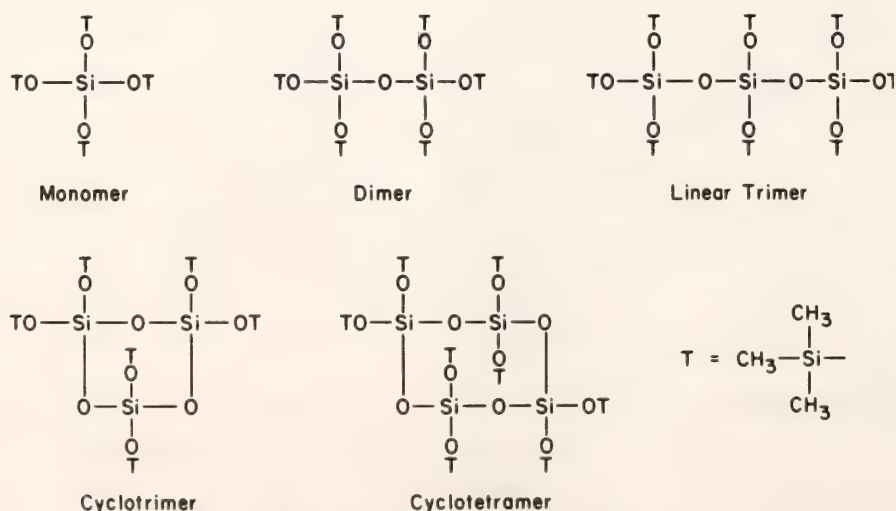


Fig. 8. Schematic structures of trimethylsilyl derivatives of silicate anions.

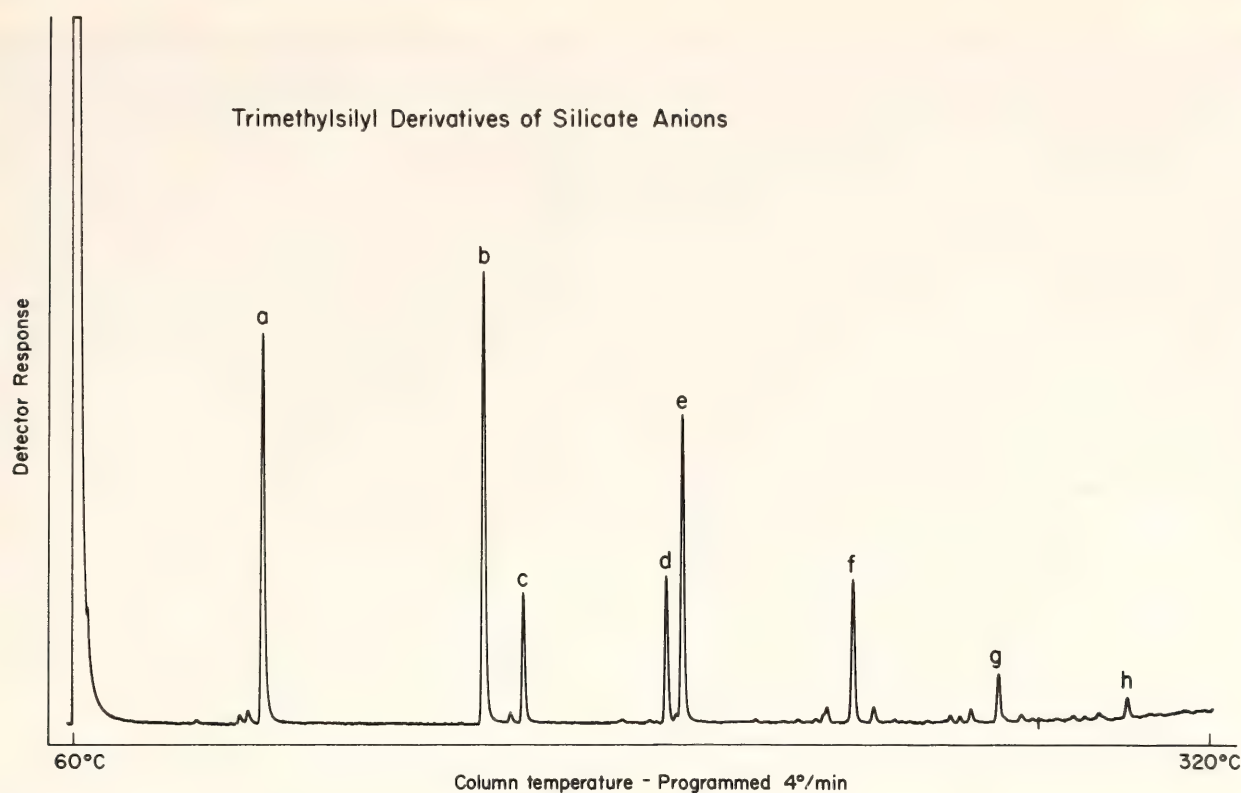


Fig. 9. Gas chromatogram of a synthetic mixture of trimethylsilyl derivatives. The column was 10 ft by 1/8" O.D. and packed with 3% Dexil 300. The column temperature was programmed from 50°C to 320°C at a rate of 4°/min. Helium flow was 30 ml/min. The largest peaks were produced by ~20 μ g of compounds. Identification of the compounds giving rise to the lettered peaks is as follows: (a) monomer, (b) dimer, (c) cyclotrimer, (d) cyclotetramer, (e) linear trimer, (f) linear tetramer, (g) linear pentamer, (h) linear hexamer (?).

molecular structure of typical compounds. The derivatives are chemically inert substances soluble in organic solvents, low melting, and thermally stable. Most important, derivatives with a limited number of silicate units are volatile and amenable to analysis by gas chromatography and mass spectrometry. Figure 9 shows a gas chromatogram for a range of TMS derivatives.

Silylation and chromatography have been used successfully to determine the anionic constitution of silicate minerals and glasses, Portland cements, and metallurgical slags, but there has been a persistent problem. Minerals of known structure have given significant yields of side-products having different silicate structures (Lenz, 1964, 1966; Masson, 1977).

The potential of the TMS method for

studying silicates of petrologic interest has been explored in this work. New techniques for synthesizing the derivatives have been developed and some refinements in the gas chromatographic and mass spectrometric analysis have been made. The infrared and Raman spectra of individual compounds have been measured and assignments made of major bands.

Synthesis of the derivatives can be viewed as occurring in two steps. The first is the exchange of metallic ions in the silicate for hydrogen ions to give the corresponding silicic acid. Thus, the method is presumably limited to silicates that "gel" on acid treatment (Murata, 1943). The second is a reaction of the silicic acid with silylating reagents to block the reactive-acid groups and to yield the stable TMS derivatives. Published methods have

used aqueous hydrochloric acid as the source of hydrogen ions, and this may be a cause of the troublesome artifacts. Free silicic acids participate in rapid and reversible, hydration-dehydration equilibria, and other silicic acids may form in the presence of water before they can be stabilized as TMS derivatives.

Therefore, anhydrous methods for derivative synthesis were developed. In the first method, 10–100 mg of finely ground minerals were reacted with a large excess of trimethylsilyl chloride ($(\text{CH}_3)_3\text{SiCl}$) in hexamethyldisiloxane ($(\text{CH}_3)_3\text{Si-O-Si}(\text{CH}_3)_3$) solvent. Anhydrous methanol saturated with dry hydrogen chloride and Amberlyst-15 ion-exchange resin were added to provide the acidity. After 16 hr reaction, silylation was incomplete and free OH groups were still present in the products. Derivatization was completed by stirring the reaction products with hexamethyldisiloxane in the presence of the ion-exchange resin.

In the second method, the minerals were stirred with a large excess of trimethylsilyl chloride and hexamethyldisilazane ($(\text{CH}_3)_3\text{Si-NH-Si}(\text{CH}_3)_3$) in the solvent hexamethyldisiloxane. Two ml of water was added slowly over a period of several hours by a piston-driven syringe. Water reacts rapidly with the silylating reagents to yield hydrogen chloride and ammonium chloride, which leach the metallic ions from the minerals. The concentration of water in the reaction mixture was always low. Products were isolated and derivatization was completed as in the first method.

When applied to known minerals, the first method gave better yields of purer products. For example, the minerals hemimorphite ($\text{Zn}_4\text{Si}_2\text{O}_7 \cdot (\text{OH})_2 \cdot \text{H}_2\text{O}$), laumontite ($\text{CaAl}_2\text{Si}_4\text{O}_{12} \cdot 4\text{H}_2\text{O}$), and natrolite ($\text{Na}_2\text{Al}_2\text{Si}_3\text{O}_{10} \cdot 2\text{H}_2\text{O}$) gave a 60–80% yield of the dimer, cyclotetramer, and linear trimer respectively, with only a few percent of side products. Optical microscopy and x-ray powder diffractometry of the starting products showed them to be greater than 96% pure.

Gas chromatography of the derivatives on a variety of substrates was performed. The best resolution and peak shape was obtained with Dexil 300, a silicone-carborane polymer that can be temperature programmed up to 400°C. Gas chromatography is limited by the volatility of the TMS derivatives. Chromatograms made with glass columns were the same as those made with metal, indicating no decomposition during analysis.

Mass spectrometry of unknown TMS derivatives gives unique structural information. Electron-impact mass spectra have an easily recognized ion at a mass equal to 15 less than the molecular weight (loss of a methyl group). The general molecular formula can be expressed as

$$(\text{TMS})_{2(n-b)}\text{Si}_n\text{O}_{(3n-b)},$$

where n is the number of silicate tetrahedra and b is the number of silicate rings minus one. A tabulation of molecular weights for a range of TMS-derivatives with varying values of n and b shows that the molecular weight determined by mass spectrometry gives an unambiguous measure of the number of silicon atoms and the number of rings in the silicate portion of the derivatives.

A suite of natural and synthetic minerals was examined by gas chromatography and mass spectrometry. It was verified that only those minerals that gel with acid will produce TMS derivatives. Of these, most give the expected product. The mineral diopside (CaSi_2O_6) was an exception. A monocyclic hexamer was predicted as a product, but the gas chromatogram showed three major constituents, each having a molecular weight of 1170 corresponding to bicyclohexamers. The structures of the three molecules and the cause of the discrepancy is not known.

When minerals containing aluminosilicate chains are subjected to derivatization, the chains are disrupted at the aluminum position. The aluminum is completely removed but the remaining silicate anions remain intact and can be silylated. Lachowski and Glasser (1973)

used this fact to study aluminum-silicon ordering phenomena in high-temperature melilite minerals. The gehlenite specimens examined by these authors gave predominately monomeric and dimeric derivatives. In the present work, a gehlenite from a contact metamorphic deposit in Luna County, New Mexico, was analyzed and found to yield a wider range of linear derivatives with up to five silicate units. Their relative abundances are: monomer 100, dimer 97, linear trimer 34, linear tetramer 22, linear pentamer 6. Considerable ordering of aluminum and silicon tetrahedra is indicated.

A suite of synthetic silicate glasses typical of those used in this Laboratory as starting materials for phase-equilibrium studies were studied by the silylation technique. Only a few gave measurable amounts of TMS derivatives. Either they did not gel with acid or they perhaps had silicate frameworks too large to be soluble in the reaction mixture. Two glasses gave a satisfactory yield of a wide range of TMS derivatives. One had the composition of grossularite, $\text{Ca}_3\text{Al}_2(\text{SiO}_4)_3$; the other corresponded to a 1:1 mixture of diopside ($\text{CaMgSi}_2\text{O}_6$) and calcium Tschermak's molecule, $\text{CaAl}_2\text{SiO}_6$. The cause of this behavior is not known.

Small amounts of pure TMS derivatives were collected by preparative gas chromatography. Raman spectra were measured from 4000 to 100 cm^{-1} on pure liquids or solids. Infrared spectra were measured from 4000 to 400 cm^{-1} on dilute solutions in potassium bromide pellets. For spectral interpretation, bands due to methyl and methyl-silicon vibrations arising from the derivatization groups were identified first. The remaining bands were then assigned to the silicon-to-oxygen vibrations of the silicate framework by comparison with the large bank of spectra of well-characterized organosilicon compounds and silicate minerals obtained from Anderson (1974), Basile *et al.* (1973), Burger *et al.* (1970), Griffith (1969), Kriegsman (1959a, 1959b), and Wright and Hunter (1947). The assign-

ments for linear TMS and cyclo-TMS derivatives are given in Tables 6 and 7. A detailed analysis of the spectra will be published elsewhere. For the purposes of this work, the results show surprisingly little variation of the major bands with increasing chain length of linear derivatives. Some weak bands result in differentiation of linear and cyclic compounds.

Experience to date indicates that the silylation method can be helpful for determining the anionic constitution of selected silicates. The derivitization and chromatographic analysis can be performed on milligram quantities of material. The methods of synthesis developed in this work appear to give a faithful reproduction of the starting silicate structure. Gas chromatography combined with mass spectrometry can disclose structural features of unknown and unexpected silicate anions.

Vibrational spectroscopy, while useful for describing bonds in pure components, may be of limited use for the analysis of mixtures of TMS derivatives. The major spectral bands are not very sensitive to polymer chain size.

The silylation techniques have distinct limitations, being applicable only to silicates with small anions and with metallic ions replaceable by hydrogen ions. A great number of silicates are excluded. The development of new methods for derivitization and the use of liquid chromatography for separation would probably result in extension of the method to a wider range of materials.

THE COORDINATION OF Ge IN CRYSTALS AND MELT OF GeO_2 COMPOSITION AT LOW AND HIGH PRESSURES BY RAMAN SPECTROSCOPY

S. K. Sharma, D. Virgo, and I. Kushiro

It has been suggested that pressure-induced cationic coordination changes may occur in silicate melts (Waff, 1975) and that these changes may result in extensively depolymerized melt struc-

TABLE 6. Raman and Infrared Frequencies (cm^{-1}) of TMS Derivatives

Linear Monomer (liquid)		Linear Dimer (solid)		Linear Trimer (liquid)		Tentative Assignment†
Raman	IR	Raman	IR	Raman	IR	
157 dp (sh)*	n.d.	142 (12.5) (sh)	n.d.	138 dp (15) (sh)	n.d.	ρ SiC_3 δ_{as} SiC_3
165 dp (25)	n.d.	168 (36)	n.d.	167 dp (25)	n.d.	
222 dp, bd (12)	n.d.	210 (12.5)	n.d.	220 dp (13)	n.d.	
232 dp (sh)	n.d.	...	n.d.	...	n.d.	δ
256 (5) (sh)	n.d.	...	n.d.	~260 (sh)	n.d.	
282 (4) (sh)	n.d.	...	n.d.	~280 (3) (sh)	n.d.	
338 (<1)	n.d.	...	n.d.	...	n.d.	ν_s Si-O-Si
...	430 w	
468 (18) p	450 m, bd	457 (12.5)	464 w	453 (15) p	455 w	
...	484 w	ν_s SiC_3
528 (<1)	510 vw	
...	555 w	...	520 m	...	530 (vw)	
600 (2)	596 s	596 (2.5)	596 s	540 (<1)	598 s	ν_s SiC_3
638 (100) p	640 vw	631 (100)	635 vw	602 (5)	...	
...	665 vw	628 (100) p	...	
690 (12) dp, p	688 m	646 (10)	...	ρ_s CH_3
754 bd (5)	756 s	756 (2.5)	756 s	
...	796 w (sh)	759 (3)	758 s	
841 (3.6) dp	848 vs	844 (3.0)	ρ_{as} CH_3
862 (2.5) dp	868 (sh)	865 (1.8) (sh)	844 vs	~842 (3) dp	844 vs	
...	1070 vs (w = 64)	...	868 (sh)	866 (2) sh, dp	868 (sh)	
...	1148 (sh)	...	1076 vs	...	1078 vs	ν_{as} Si-O-Si
~1254 (1.6) p, dp	1252 s	1254 (1.2)	1156 w (sh)	...	1150 w (sh)	
1262 (3) p	1262 (sh)	1266 (2.5)	1252 s	1264 (4) p, dp	1252 s	
1412 (7.5) p	1416 w	1412 (5)	...	1288 (4) p	1285 (sh)	δ_s CH_3
1437 (3) dp	1448 w	1438 (1.2)	1432 w	~1414 (8) dp	1408 w	
...	1636 w, bd	...	1440 w	~1444 (4) dp	1456 w	
2901 (75) p	2904 w	2901 (74)	1650 w, bd	δ_{as} CH_3 H_2O (impurity)
2961 (40) dp	2960 m	2962 (37)	2904 w	2901 (88) p	2900 w	
			2968 m	2961 (40) dp	2960 m	

* p, polarized; dp, depolarized; bd, broad; sh, shoulder; w, weak; vw, very weak; m, medium; s, strong; vs, very strong; and n.d., not determined.

The digits in brackets are relative intensities of Raman bands.

† ν , stretch; δ , deformation; ρ , rocking; s, symmetric; and as, asymmetric.

Measurement accuracy $\pm 2 \text{ cm}^{-1}$ for Raman and $\pm 4 \text{ cm}^{-1}$ for infrared.

TABLE 7. Raman and Infrared Frequencies (cm⁻¹) of Cyclo-TMS Derivatives

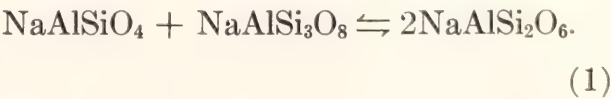
Cyclo-trimer (solid)		Cyclo-tetramer (solid)		Tentative Assignment†
Raman	IR	Raman	IR	
150 (sh)*	n.d.	...	n.d.	
155 (15)	n.d.	152 (11)	n.d.	ρ SiC ₃
181 (13.0)	n.d.	178 (8) sh	n.d.	δ
~230 (8)	n.d.	227 (8)	n.d.	ν _{as} SiC ₃
...	n.d.	296 (<1)	n.d.	
...	n.d.	324 (<1)	n.d.	
430 (3) bd	435 w	447 (6)	...	ν _s Si-O-Si + ring de- formation
...	460 w	...	458 vw	
492 (1.5)	495 w	...	490 vw	ring stretch
587 (31)	ring stretch
...	604 m	601 (sh)	604 m	
629 (100)	630 w	623 (100)	635 w	ν _s SiC ₃
...	688 m	...	688 m	ν _{as} SiC ₃
693 (11) bd	...	693 (7)	705 (sh)	
741 (2.2)	724 (3)	
756 (4.4)	756 s	758 (3)	754 s	ρ _s CH ₃
...	788 m (sh)	
846 (4.4) bd	848 vs	846 (3) bd	848 vs	
871 (2.2) bd	864 (sh)	872 (1.5) bd	868 s (sh)	ρ _{as} CH ₃
...	1056 vs	ring stretch as
...	1072	ring stretch + ν _{as} Si- O-Si
...	1084 vs	
...	1148 (sh)	...	1160 s (sh)	ν _{as} Si-O-Si
1254 (31) (sh)	1256 s	1255 (1.4)	1256 s	
1266 (4)	...	1265 (2)	...	δ _s CH ₃
1361 (1)	(?)
1414 (11.4)	1416 w	1415 (4.4)	1416 w	
1440 (3)	1448 w	1440 (1.4)	1456 w	δ _{as} CH ₃
...	1636 w bd	H ₂ O impurity
2900 (97)	2904 w	2902 (60)	2904 w	ν _s CH ₃
2962 (48)	2960 m	2962 (33)	2960 m	ν _{as} CH ₃

* p, polarized; dp, depolarized; bd, broad; sh, shoulder; w, weak; vw, very weak; m, medium; s, strong; vs, very strong; n.d., not determined.
† ν, stretch; δ, deformation; ρ, rocking; s, symmetric; and as, asymmetric.

tures. Such an effect would have important consequences for understanding the physical and chemical properties of melts. Waff (1975), for example, predicted dramatic decreases in the viscosity of silicate melts with increasing pressure. The basis for Waff's hypothesis stemmed from the well-established cationic coordination changes that occur in crystalline silicate and oxide phases at high pressures.

Experimental data supporting Waff's

position were in fact documented by Kushiro (1976) in his observations of the viscosity decrease in jadeite melts at high pressures. It was inferred that Al switches coordination from 4-fold to 6-fold in the melt, consistent with the subsolidus reaction:



Similar but smaller decreases in viscosity

TABLE 8. Observed Raman Frequencies of Different Modifications of Crystalline GeO₂

Hexagonal* cm ⁻¹		Tetragonal† cm ⁻¹	
120(s) §	E	166(s)	B _{1g}
163(s)	E		
212(w)	A ₁		
246(w)	?		
262(w)	A ₁		
328(w)	E	420(vw)	A ₁ ‡
442(vs)	A ₁		
514(w)	E		
590(w)	E		
699(w) ‡			
856(vw)	E	700(vs)	A _{1g}
876(w)	A ₁		
954(vw)	E		
958(w)	E		
972(w)	E		

* Sample synthesized at 1150°C, 4 ± 2 kbar.
† Sample synthesized at 1150°C, 6 kbar (Kushiro, this Report).
‡ See text.
§ Intensities: vs, very strong; s, strong; w, weak; vw, very weak.

were observed for melts of Na₂Si₃O₇ and K₂MgSi₅O₁₂ compositions (Kushiro, *Year Book* 75, p. 611). In the latter cases, Kushiro suggested that the viscosity changes might be associated with the coordination changes of alkali ions, Mg²⁺, and Si⁴⁺ in the melts. The coordination change of Si⁴⁺ from 4-fold to 6-fold occurs in crystalline SiO₂ (e.g., stishovite) but only at pressures above 80 kbar at 1000°C; however, such a change might occur in a melt at lower pressures.

From an experimental point of view, it is not yet feasible to study SiO₂ melts at pressures in the region of the solid-state transformations coesite ⇌ stishovite. On the other hand, GeO₂ glass at 1 atm is structurally analogous to SiO₂ glass (Wong and Angell, 1976), and in the subsolidus region at temperatures above 1007° ± 10°C GeO₂ undergoes transformation with increasing pressure from an α-quartz (four-coordinated Ge) to a rutile type (six-coordinated Ge) structure (Jackson, 1976). Spectroscopic studies of glasses of GeO₂ composition provide the best available analogue of possible high-pressure changes in the SiO₂ system.

In this study, crystalline and amorphous samples of GeO₂ composition were quenched samples used by Kushiro (this Report) for density and viscosity measurements and preliminary phase equilibrium studies. In the present work, a Raman study has been undertaken to obtain a detailed knowledge of the molecular structure in crystalline and GeO₂ glass. Synthesis conditions of samples studied by the Raman effect are given in Tables 8 and 9.

Results

The Raman spectra of the crystalline hexagonal and tetragonal modifications of GeO₂ are given in Fig. 10, and the observed vibrational frequencies are tabulated in Table 8. Raman spectra of vitreous GeO₂ at 0.001 kbar are plotted in Fig. 11, and the measured frequencies of

TABLE 9. Observed Vibrational Frequencies (cm⁻¹) of Vitreous GeO₂ Synthesized at Different Pressures

1 bar, 1425°C	9.5 kbar, 1425°C	15 kbar, 1650°C	18 kbar, 1700°C
344(s)p*	346(s)p	344(s)p	344(s)p
416(vs)p	420(vs)p	418(vs)p	416(vs)p
520(s)p	520(s)p	520(s)p	520(s)p
856(w)dp	856(w)dp	856(w)dp	862(w)dp
976(w)dp	976(w)dp	962(w)dp	968(vw)dp

* Intensities: vs, very strong; s, strong; w, weak; vw, very weak; p, polarized; dp, depolarized.

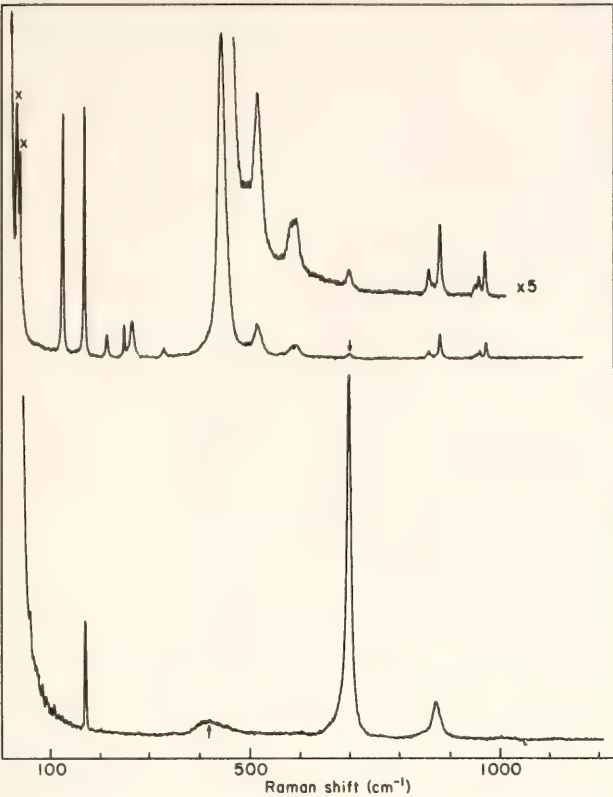


Fig. 10. Raman spectrum of polycrystalline GeO₂ polymorphs with hexagonal (upper) and tetragonal (lower) structures (laser 488.0 nm Ar ion, 400 mw, slit 3 cm⁻¹). x refers to spurious lines.

the bands in spectra of GeO₂ synthesized at various pressures are given in Table 9. In Fig. 12 the spectra of the Na₂O·1.78 GeO₂ glass synthesized at 1 bar are presented. The positions and spectral characteristics of the bands in the spectra of sodium germanate synthesized at 1 bar and 15 kbar are given in Table 10.

The number and symmetry-type of optical frequencies for both GeO₂ polymorphs determined from factor group analysis gives 11 optical modes for tetragonal GeO₂ (space group D_{4h}^{14} , $Z = 2$) of which only four modes are Raman active [$\Gamma = A_{1g}$ (R) + A_{2g} (i.a.) + A_{2u} (IR) + B_{1g} (R) + B_{2g} (R) + $2B_{2u}$ + 3 E_u (IR) + E_g (R)] whereas 16 optical modes are found for hexagonal GeO₂ (space group D_{3d}^4 , $Z = 3$) of which 12 modes are active in the Raman spectrum [$\Gamma = 4A_1$ (R) + $4A_2$ (IR) + 8E (R, IR)]. In the latter case and because of the noncentrosymmetric space

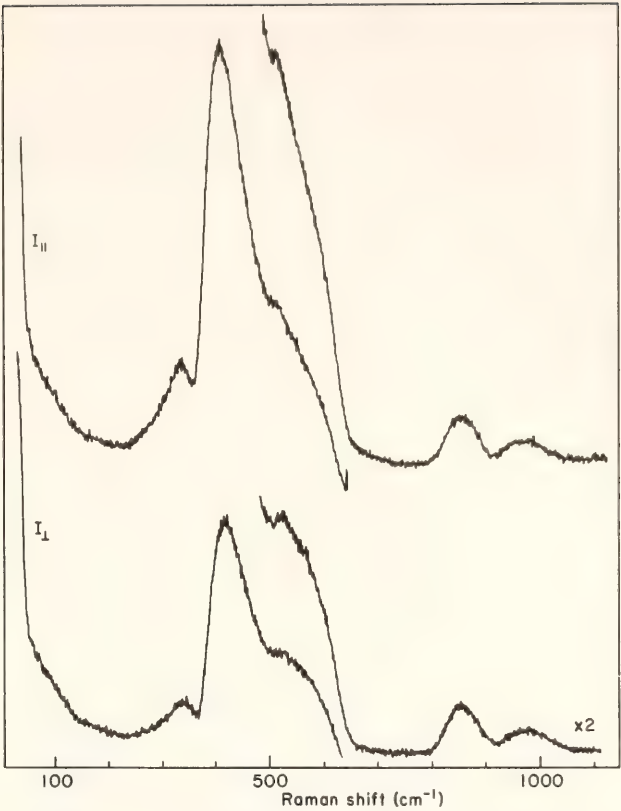


Fig. 11. Raman spectrum of vitreous GeO₂ synthesized at 1425°C, 1 bar, with electric vector || (upper) and ⊥ (lower) to the electric vector of the laser beam. Experimental conditions as in Fig. 10.

group D_{3d}^4 , the E mode will split into transverse (TO) and longitudinal (LO) optic components because of the electric field accompanying the vibrations. Experimental observations of this effect are ideally made in Raman studies of single crystals. In this connection, Scott (1970) has observed and assigned the predicted vibrational modes for both polymorphs

TABLE 10. Observed Vibrational Frequencies (cm⁻¹) of Na₂O·1.78GeO₂ Glass Synthesized at Different Pressures.

1 bar, 1300°C	15 kbar, 1300°C
~100	~100
~300	~300
520(vs)p	520(vs)p
585(sh)p	586(sh)p
784(sh)p	787(sh)p
862(vs)p	862(vs)p

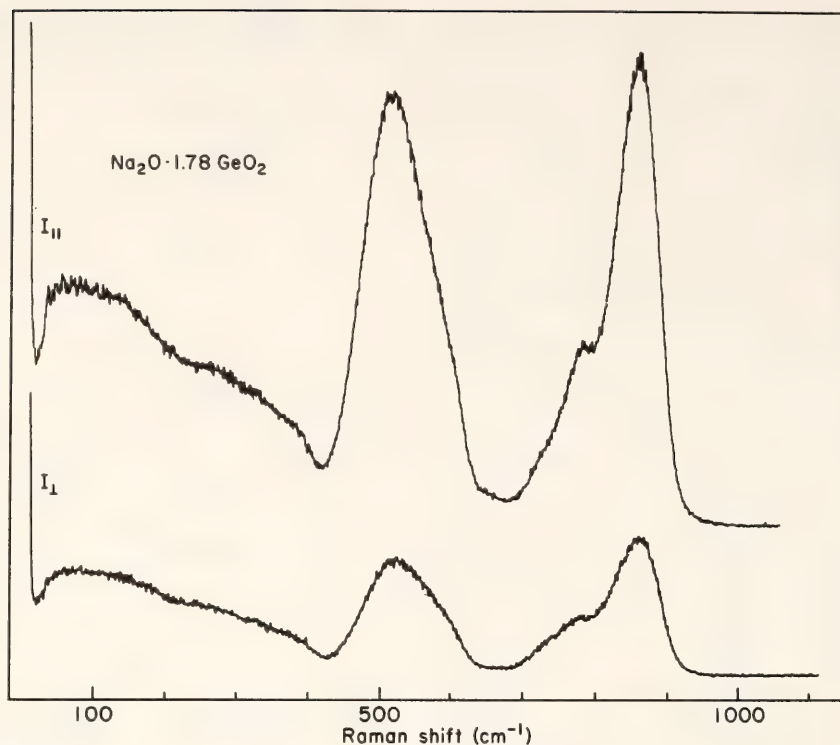


Fig. 12. Raman spectrum of vitreous $\text{Na}_2\text{O} \cdot 1.78 \text{ GeO}_2$ synthesized at 1300°C , 1 bar, with electric vector \parallel (upper) and \perp (lower) to the electric vector of the laser beam (laser 488.0 nm Ar ion, 200 mw, slit 4 cm^{-1}).

using single crystals. Within experimental error, the peak positions of the majority of bands observed in the spectra of polycrystalline GeO_2 crystallized at 1150°C and over the pressure range 4–6 kbar (see Table 8) are in agreement with the work of Scott (1970; see also Wong and Angell, 1976, p. 454) and are, therefore, assigned accordingly. The weak bands at 246 cm^{-1} and 699 cm^{-1} in the Raman spectra of hexagonal GeO_2 were not previously observed in the single-crystal data (Scott, 1970). In the polymorph with rutile-type structure, the strongest Ge-O symmetric stretching mode occurs at 700 cm^{-1} (Table 8). Thus the weak band at 699 cm^{-1} indicates that a small amount of GeO_2 was transformed to the rutile-type structure during quenching. This latter result was also confirmed from x-ray diffraction analyses of this sample. The origin of the band at 246 cm^{-1} is not clear and may be due to the presence of other impurities in the sample.

In the Raman spectrum of the tetragonal GeO_2 the weak, broad band at 420

cm^{-1} can be interpreted only in terms of a small amount of vitreous GeO_2 . The strongest band in vitreous GeO_2 (see below and Table 9) occurs in the region $416\text{--}420 \text{ cm}^{-1}$.

The difference in Ge coordination in rutile and quartz-type GeO_2 results in significantly different Ge-O bond lengths and associated bond energy; thus there is a large difference in the frequency and intensity of the Ge-O symmetric stretching mode at 876 cm^{-1} in hexagonal GeO_2 and 700 cm^{-1} in tetragonal GeO_2 . The low intensity of the symmetric A_1 mode in the spectrum of hexagonal GeO_2 is due to bridging of all the oxygens in the network structure. It should be pointed out that Obukhov-Danisov *et al.* (1960) could not obtain the Raman spectrum of tetragonal GeO_2 from polycrystalline samples.

The Raman spectra of vitreous GeO_2 (Fig. 11) consists of a series of broad bands centered at 344, 418, 520, 856, and 976 cm^{-1} . Polarization data for the individual peaks are given in Table 9. Of

special note is the strongly polarized peak at 418 cm^{-1} , which is compared to the peak at 410 cm^{-1} in vitreous SiO_2 and which can be assigned to "bond-rocking" motion whereby the $\text{Si}(\text{Ge})$ atoms move perpendicularly to the $\text{Si}(\text{Ge})\text{-O-Si}(\text{Ge})$ planes (Hass, 1970). From the band frequencies listed in Table 9, there appear to be no major variations among the glass samples quenched under different pressure-temperature conditions.

The Raman spectra of $\text{Na}_2\text{O}\cdot 1.78\text{GeO}_2$ (Fig. 11; Table 10) are characterized by the appearance of major peaks at 520 cm^{-1} and 862 cm^{-1} and a shoulder at 784 cm^{-1} . In general, it can be expected that the spectra of this material would resemble that of $\text{Na}_2\text{O}\cdot 2\text{SiO}_2$ (Brawer and White, 1975; Sharma, Virgo and Mysen, this Report). Quantitative assignment of the peaks of the $\text{Na}_2\text{O}\cdot 1.78\text{GeO}_2$ glass must await additional studies of glasses with varying Na_2O content and glasses with varying substitution of Si for Ge. By comparing the present spectra with the spectra of $\text{Na}_2\text{O}\cdot x\text{SiO}_2$ compositions, the strong 862-cm^{-1} band can be attributed to stretching motion of the bridging oxygen in chain- and sheet-type structures, whereas the band at 784 cm^{-1} is from the stretching motion of non-bridging oxygens. All bands are strongly polarized consistent with the analogous peaks in sodium disilicate glass.

Discussion

It is well established from the above data that the spectra of the crystalline polymorphs of GeO_2 are consistent with the different coordination polyhedra of Ge determined by x-ray analysis. Furthermore, it is evident from the similarity of the peak positions and intensities and in particular from the strong Raman band at $\sim 420\text{ cm}^{-1}$ and the weak polarized bands at 850 and 956 cm^{-1} that the local ordering in vitreous GeO_2 is similar to that of the hexagonal polymorph of crystalline GeO_2 and consists predo-

minantly of tetrahedrally coordinated GeO_2 units. It is particularly noteworthy that the presence of the anomalous peak at 420 cm^{-1} (Table 9) in crystalline GeO_2 with tetragonal symmetry can reasonably be correlated with the intense peak of vitreous GeO_2 synthesized over the pressure range 1 bar to 18 kbar. This latter result obviously implies that the crystalline material in which Ge is octahedrally coordinated crystallized from a melt in which Ge is totally in tetrahedral coordination.

The presence of significant amounts of Ge in octahedral coordination in the glass would require the presence of a band at $\sim 700\text{ cm}^{-1}$, as observed in tetragonal GeO_2 . In this case a breakdown of the network structure leading to an increase in the number of nonbridging oxygen atoms would be expected. This latter effect occurs in the glass of $\text{Na}_2\text{O}\cdot 1.78\text{GeO}_2$ compositions to satisfy the coordination of the Na ions. It is apparent that there is no peak in the Raman spectra of vitreous GeO_2 at any pressure that could reasonably be assigned to nonbridging oxygens.

The decrease in viscosity in GeO_2 melt with increasing pressure (Kushiro, this Report) cannot be attributed, therefore, to any change in the Ge coordination in melt at pressure-temperature conditions associated with the solid-state transformation from the quartz to rutile-type structures in crystalline GeO_2 . There are, however, more subtle changes in the structure of vitreous and molten SiO_2 . In particular, quenched SiO_2 glass has a more condensed structure in which units resembling β -quartz predominate. Upon melting and with further increases in temperature, the melt structure becomes more open and units resembling the cristobalite structure become increasingly important. This latter effect is nonquenchable (Nukui *et al.*, 1978). Such a change on melting can be associated with an increase in Si-O bond lengths and a more random array of O-Si-O bond angles. Analogous changes in the GeO_2 analogue at 1 atm

can be suggested. In view of the results of this study the effect of pressure on the structure of such melts is obviously speculative at this time. A general increase in the degree of short-range order-

ing on compression leading to a more ordered network structure can be expected. The progressive increase in melt density (Kushiro, this Report), therefore, can be qualitatively rationalized.

PROPERTIES OF MAGMA

VISCOSITY CHANGE OF GeO_2 MELT WITH PRESSURE AS A MODEL OF SiO_2 MELT

I. Kushiro

Recently it has been suggested that melts of jadeite ($\text{NaAlSi}_2\text{O}_6$), albite ($\text{NaAlSi}_3\text{O}_8$), natural basalt, and andesite compositions undergo pressure-induced structural changes that may be partly due to a shifting of Al from 4-fold to 6-fold coordination, comparable to the shifting that occurs with pressure in various Al-bearing crystalline phases (Waff, 1975; Kushiro, 1976; Kushiro *et al.*, 1976; Velde and Kushiro, 1978; Mysen and Virgo, 1978). There is also a possibility that at much higher pressures Si also shifts from 4-fold to 6-fold coordination in silicate melts, as it does in certain phase transitions and breakdown reactions in crystalline silicates—for example, when coesite transforms to stishovite and when enstatite acquires an ilmenite or perovskite structure. If such a shift occurs then the viscosities of SiO_2 melt and other silicate melts would be expected to decrease because the shift is probably associated with the formation of nonbridging oxygens in the melts.

To test this possibility, the change in the viscosity of GeO_2 melt with pressure was determined at 1425°C between 1 atm and 9.5 kbar, and the change in the density of the glass quenched from the melt was determined as a function of pressure of quenching. Melt of GeO_2 composition has a viscosity and a network structure similar to those of SiO_2 melt just above the melting point at 1 atm, but the melting point

of GeO_2 (1116°C) is much lower than that of SiO_2 so that the structural change in its melt might be expected to take place at much lower pressures than in SiO_2 melt. Crystalline GeO_2 transforms from a quartz structure to a rutile structure with increasing pressure at constant temperature. The transition even occurs at 1 atm at $1007^\circ \pm 10^\circ\text{C}$ (Shafer and Roy, 1956) and at pressures lower than 5 kbar near the solidus temperature (about 1180°C) (Jackson, 1976), which is much lower than the pressure for transition of crystalline SiO_2 from coesite to stishovite. Similar relations are also expected for the structural change of GeO_2 and SiO_2 melts (Kushiro, 1977).

In the present studies, the viscosity of GeO_2 melt was first determined at 1 atm in the temperature range $1130^\circ\text{--}1430^\circ\text{C}$ by a falling sphere method similar to that used in the measurements at high pressures. Pt spheres 0.5–1.0 mm in diameter and Pt containers about 8 mm in inner diameter and 15 mm in length were used for the measurements. Glass of highly purified GeO_2 (less than 10^{-5} wt % impurity) was used as starting material. Before a run Pt spheres were placed at the top of a charge of glass that had been melted in the container to get rid of air bubbles. After quenching, the distance the spheres had settled was measured. Viscosity was calculated using the Stokes equation and the Faxen correction for the wall effects.

The results of the measurements are shown in Fig. 13. The viscosity of GeO_2 melt decreases from about 5×10^5 poises at 1130°C to about 6.2×10^3 poises at 1430°C . The present results are compared

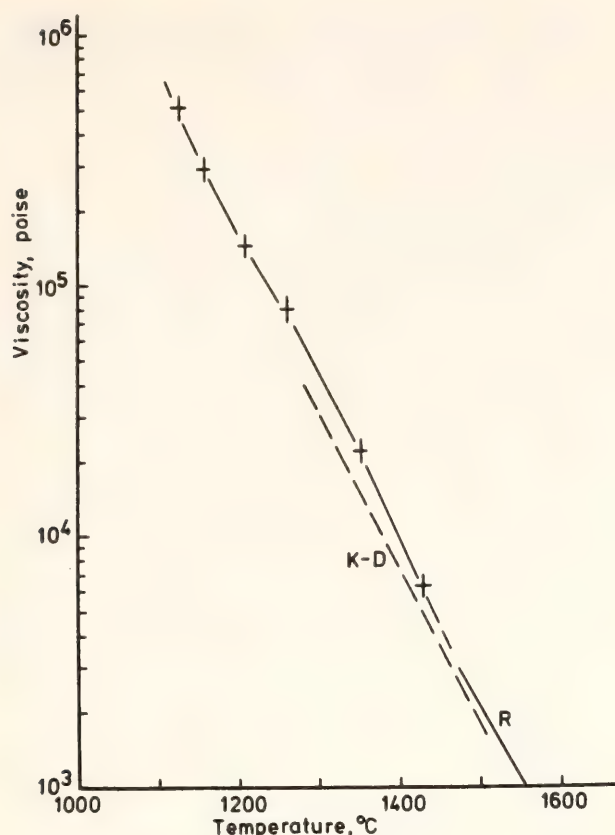


Fig. 13. Viscosity of GeO_2 melt at 1 atm as a function of temperature. Crosses denote the values obtained in the present measurements. Solid line (R) determined by Riebling (1963); dashed line (K-D) determined by Kurkjian and Douglas (1960).

with those obtained by previous investigators who used more sophisticated methods. Riebling (1963) determined the viscosity of GeO_2 melt at temperatures $1470^\circ\text{--}1720^\circ\text{C}$ by means of an improved counterbalanced sphere viscometer. Although the present data were obtained below 1430°C , they define a smooth continuous curve with Riebling's data, as shown in Fig. 13. Viscosity values obtained by Kurkjian and Douglas (1960) with a rotating-cylinder viscometer are slightly lower than those obtained by Riebling and in the present study, but the difference is almost within the uncertainty of the measurements. Such agreement indicates that the present method of using small Pt spheres and Pt containers can give satisfactory viscosity values.

Measurements of viscosity at high pressures were made with a solid-media high-pressure apparatus and the $\frac{3}{4}$ " furnace assemblies designed to provide minimal temperature gradients (Kushiro, 1976). The falling-sphere method was also applied, but it was found that when graphite capsules were used Pt spheres reacted with the GeO_2 melt and Pt-Pt₉₀Rh₁₀ thermocouples were broken at temperatures above 1200°C . These effects apparently resulted from reducing conditions. To avoid them, the GeO_2 glass was sealed in Pt capsules 5 mm in diameter and 12 mm in length, and each capsule was embedded in a small amount of Fe_2O_3 powder inside an AlSiMag sleeve. With this method, Pt spheres did not react with GeO_2 melt at all and the thermocouple did not break. Other procedures are the same as those described in the previous experiments on the $\text{NaAlSi}_2\text{O}_6$ melt and natural basaltic and andesitic melts (Kushiro, 1976; Kushiro *et al.*, 1976).

The high-pressure viscosity measurements were made at 1425°C at pressures of 5, 7, and 9.5 kbar. Above 10 kbar, the solidus of GeO_2 is above 1425°C . As in the 1-atm measurements, the viscosity of the melt was calculated using the Stokes equation and the Faxen correction for the wall effect. In all the runs, two Pt spheres with different diameters were used for the measurements. The difference between the two viscosity values obtained from the two spheres is less than 15%. The results of the measurements are shown in Fig. 14. Each circle in the figure is the average of the two values obtained from two spheres under the same condition. At 5 kbar, two runs with different run durations were made to draw distance-time lines for sinking spheres with fixed diameter. The lines pass near the origin, indicating that the velocity of sinking Pt spheres is constant at least within the run durations (7–15 min). The results of the measurements demonstrate that the viscosity of GeO_2 melt decreases from

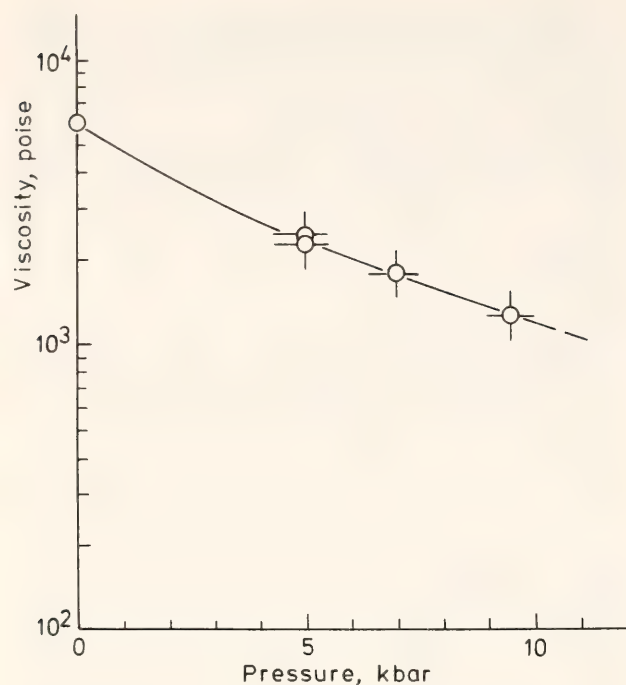


Fig. 14. Viscosity of GeO_2 melt at 1425°C as a function of pressure.

about 6.0×10^3 poises at 1 atm to 1.2×10^3 poises at 9.5 kbar, at 1425°C . The rate of decrease is nearly constant on a logarithmic plot for the pressure range studied. The density of GeO_2 glass quenched at 1 atm and from higher pressures was measured by the method of Berman

(1939). The results are shown in Fig. 15. The values increase from 3.62 ± 0.02 g/cc for glass quenched at 1 atm to 3.95 ± 0.04 for glass made at 18 kbar. This increase is only about 9%, much less than the increase in the density of crystalline GeO_2 in changing from the quartz structure to the rutile structure (47%). Although the density of the glass is not the same as that of the melt, these results indicate that the melt of GeO_2 would also become denser with increasing pressure.

The changes in viscosity of GeO_2 melt and density of the quenched melt could be due to some structural changes of GeO_2 melt with pressure. If a small percentage of the total Ge in the melt changes from 4-fold to 6-fold coordination, the observed viscosity and density changes could be explained. Raman spectroscopy of the quenched glasses, however, does not show any changes in coordination of Ge with pressure (Sharma, Virgo, and Kushiro, this Report); hence it may simply be that the configuration of the GeO_4 tetrahedron or the Ge-O bond length changes with pressure to result in a denser structure. The possibility of a coordination change for Ge and Si at much higher pressures still remains to be tested.

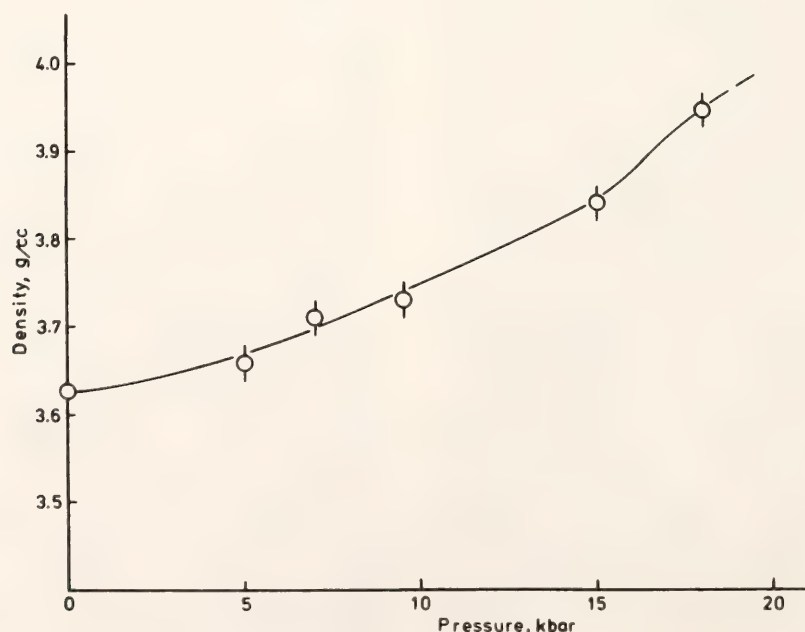


Fig. 15. Density of GeO_2 melt quenched at 1 atm and at high pressures.

DENSITY AND VISCOSITY OF HYDROUS CALC-ALKALIC ANDESITE MAGMA AT HIGH PRESSURES

I. Kushiro

The origin of calc-alkalic andesite magma is one of the current major problems in igneous petrology. Many phase equilibrium studies have been made on calc-alkalic andesites and related synthetic compositions, but very little is known about the physical properties of the magmas, particularly for the depths at which they are generated. Density and viscosity are two important physical properties for understanding the processes of their generation, ascent, and crystallization.

Most calc-alkalic andesite magmas appear to be hydrous, based on both field observations and experimental studies (e.g., Yoder, 1969). Therefore, in the present experiments density and viscosity were measured for a hydrous calc-alkalic andesite melt. The melt contained between 2.86 and 2.98 (± 0.03) wt % H_2O , and the measurements were made at pressures between 10 and 15 kbar and at temperatures between 1175°C and 1200°C. An andesite from Crater Lake, Oregon, was chosen as the starting material. The viscosity of the anhydrous melt of this rock has previously been determined in the pressure range 7.5–20 kbar. One preliminary viscosity measurement was also made previously on this andesite melt with 4 wt % H_2O at 1350°C and at 15 kbar (Kushiro *et al.*, 1976). The temperature of this measurement was too high for natural conditions, however, and the calculated viscosity based on an estimated density has proved also to be unreliable.

The present experimental methods are essentially the same as those used previously (Kushiro *et al.*, 1976; Fujii and Kushiro, *Year Book* 76, pp. 419–424), but sealed Pt capsules were used instead of graphite capsules and glass was used as a starting material rather than powdered rock. When rock powder is used as a

starting material, it takes 1–3 minutes before settling spheres begin to move with constant velocity, even at temperatures more than 100°C above the liquidus. On the other hand, when glass is used such a time lag does not occur, and viscosity and density can be determined by a smaller number of runs.

Spheres of boron nitride (density 2.29 g/cc), chrome diopside (3.33 g/cc), and olivine (3.40 g/cc) were used in the present experiments. In all the runs, the spheres of boron nitride (0.8–1.0 mm in diameter) were placed at the bottom of the capsule, and those of chrome diopside (0.4–0.7 mm in diameter) were placed at the top. Spheres of olivine were also placed at the top in some of the runs. During runs of 8–12 min, the boron nitride spheres float up 2–3 mm, and the chrome diopside and olivine spheres settle 1–4 mm, depending on their diameter. By substituting into the Stokes Law the data from two spheres of different densities that moved with different velocities, two equations are obtained with two unknowns. The unknowns, viscosity and density of the melt, can then be evaluated by solving the equations (Fujii and Kushiro, *Year Book* 76, pp. 419–424).

The H_2O content in the charges ranged from 2.86 to 2.98 wt % (9.4 to 9.8 mol % H_2O), values that are not unreasonable in terms of the H_2O contents of calc-alkalic andesite magmas, at least under the conditions within the crust. The experimental temperatures were 1175°C at 10 kbar and 1200°C at 12.5 and 15 kbar. These values are still 20–50°C higher than the liquidus temperatures of calc-alkalic andesite magmas containing about 3 wt % H_2O . Viscosity was also estimated on the basis of extrapolated density values at 7.5 kbar and 1175°C and 15 kbar and 1225°C.

The results of the measurements of density and viscosity are shown in Figs. 16A and 16B. The density of the melt is 2.57 ± 0.03 g/cc at 10 kbar and 1175°C, 2.69 ± 0.03 g/cc at 12.5 kbar and 1200°C, and 2.74 ± 0.04 g/cc at 15 kbar and

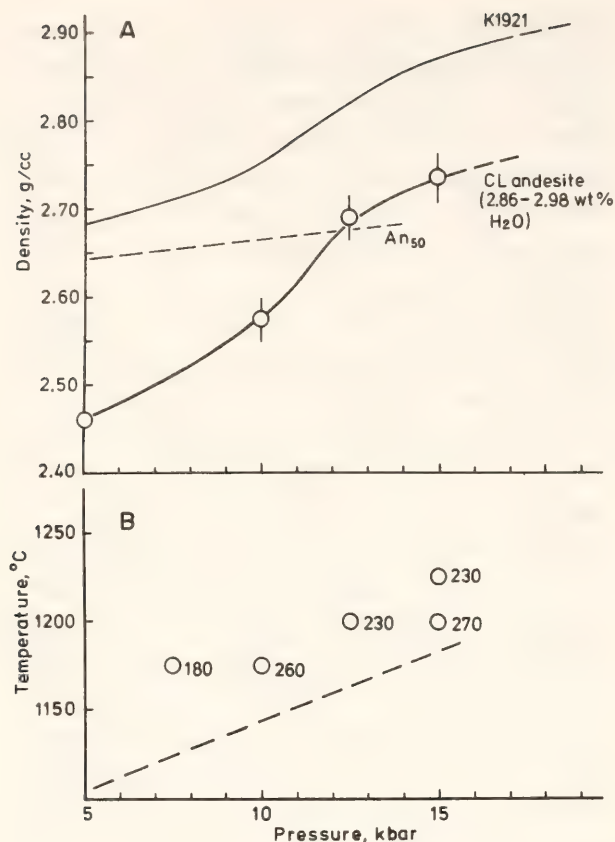


Fig. 16. (A) Density of a hydrous melt of Crater Lake (CL) calc-alkalic andesite (2.86–2.98 wt % H₂O) at 10 kbar and 1175°C, 12.5 kbar and 1200°C, and 15 kbar and 1200°C. The density at 5 kbar at 1175°C is for 2.63 wt % H₂O. Data for the Kilauea 1921 olivine tholeiite are from Fujii and Kushiro (*Year Book* 76, pp. 419–424); the dashed curve represents the density of plagioclase An₅₀. (B) Viscosity of the same hydrous melt. Numbers are values of viscosity in poises. Dashed line shows liquidus temperature of a melt of Mt. Hood andesite with about 3 wt % H₂O, based on Eggler and Burnham (1973) up to 10 kbar. Their data are extrapolated linearly above 10 kbar.

1200°C. The density determined at 5 kbar and 1175°C with a lower H₂O content (2.63 wt %) is 2.46 g/cc. This value is also included in Fig. 16A. The increase in density is 11% from 5 to 15 kbar; the rate of increase is greater between 10 and 12.5 kbar than in other pressure ranges of the experiments.

The viscosity of the melt changes only slightly with pressure, from about 180 poises at 7.5 kbar to 260 poises at 10 kbar, at 1175°C, and from 230 poises at 12.5 kbar to 270 poises at 15 kbar at 1200°C. Although it is not certain whether such

small increases are significant, at least the viscosity does not decrease with increasing pressure within the pressure range studied (7.5–15 kbar). This result is different from those obtained on basaltic and andesitic melts as well as on several synthetic melts under anhydrous conditions. No clear explanation can be given at present for such differences.

The results of the present experiments are applicable to the problems of ascent and crystal fractionation of calc-alkalic andesite magma. For example, andesite magmas containing about 3 wt % H₂O would have viscosities of at least 200–300 poises at depths between 30 and 50 km. Such viscosity values are larger than those of anhydrous basaltic magmas in the same depth range (40–80 poises along the liquidus), but much lower than those of anhydrous andesite melts. The viscosity of the same andesite melt under anhydrous conditions is 3.2×10^3 poises at 7.5 kbar at 1250°C, and 850 poises at 15 kbar at 1350°C (Kushiro *et al.*, 1976). At 1 atm it increases to 5.5×10^3 poises at 1250°C and 1.0×10^4 at 1200°C (Murase, personal communication, 1978). On the basis of these data, hydrous calc-alkalic andesite magmas could ascend with velocities several times smaller than those of anhydrous basaltic magmas in the upper mantle and the lower crust, because the velocity of ascent is inversely proportional to viscosity (Takeuchi *et al.*, 1972). If such hydrous andesite magmas lose some H₂O within the crust, then their viscosity would increase drastically (by as much as a factor of ~50) and their rate of ascent would become very small. Such velocity decrease may result in the formation of magma chambers. The depth of vesiculation depends on the H₂O content of the magma. Andesite magmas with about 3 wt % H₂O begin to vesiculate at depths of about 3 km (Eggler and Burnham, 1973). On the other hand, if hydrous andesite magmas do not lose H₂O on the way to the surface, or if they lose only a part of it but retain, for example, 3 wt % H₂O, their viscosity

is still of the order of 200 poises, which is nearly the same as that of basaltic lavas. Andesitic lavas with such low viscosity will flow with a considerable speed and form flat lava flows. There are many such flat andesite lava flows in the world—for example, the flows of bronzite andesite known as sanukite in northern Shikoku region, western Japan.

The density of an andesite magma containing about 3 wt % H_2O is relatively low (<2.57 g/cc) up to 10 kbar, smaller than that of plagioclase of any composition. Therefore, if plagioclase crystallizes as a near-liquidus phase in calc-alkalic andesite magma containing 3% H_2O at depths less than 30 km, then the plagioclase crystals settle in the magma. At pressures greater than about 12 kbar, however, density of this same magma becomes greater than that of plagioclase more sodic than An_{50} . Anhydrous andesite magmas have higher densities, but the density increase would be less than 4%, based on the specific volume data of melts

in the albite- H_2O system up to 10 kbar (Burnham and Davis, 1971). The density of the Crater Lake anhydrous andesite magma at 10 kbar would therefore be less than 2.67 g/cc, the density of plagioclase An_{50} at 10 kbar. In anhydrous basaltic magma, plagioclase less calcic than An_{90} floats at pressures higher than about 6 kbar (Fujii and Kushiro, *Year Book* 76, pp. 419–424). Floating of plagioclase in basaltic magma has been suggested as a possible mechanism of formation of massif-type anorthosite (Kushiro and Fujii, 1977). The present studies indicate that floating of plagioclase would not occur in hydrous calc-alkalic andesite magma ($\sim 3\%$ H_2O) within the crust, and even in anhydrous andesite magmas, plagioclase more calcic than An_{50} (often found as cores of plagioclase phenocrysts in calc-alkalic andesites) would not float. It is likely, however, that plagioclase of massif-type anorthosite (An_{60-40}) would float in basaltic and basaltic andesite magmas in the deep crust.

ELEMENT PARTITIONING

EXPERIMENTAL DATA BEARING ON $\text{Eu}^{2+}/\text{Eu}^{3+}$ IN SILICATE MELTS AND CRYSTALS

*B. O. Mysen, D. Virgo, J. Hoover,
and S. K. Sharma*

Rare earth elements (REE) are considered important indicators of the processes of formation and evolution of igneous rocks (see Gast, 1968) because of the systematic dependence of their partitioning between phases on the nature of the phases and on atomic number of the individual REE. The europium contents of igneous rocks, however, often deviate from the expected values, as first noted by Towell *et al.* (1965). These authors suggested that such deviations could be explained by some Eu occurring as Eu^{2+} , and that the $\text{Eu}^{2+}/\text{Eu}^{3+}$ of crystals differed from that of coexisting melt. Drake (1975) attempted to calibrate

$D_{\text{Eu}}^{\text{plagioclase-liquid}}$ ($= C_{\text{Eu}}^{\text{plagioclase}}/C_{\text{Eu}}^{\text{liquid}}$) as a function of f_{O_2} and T by combining his data at low f_{O_2} with those of Drake and Weill (1975) obtained in air. Documentation of the presence of Eu^{2+} was not provided, however. Morris and Haskin (1974), Morris *et al.* (1974), and Lauer and Morris (1977) employed electron paramagnetic resonance (EPR) to determine $\text{Eu}^{2+}/\text{Eu}^{3+}$. These authors observed a signal from Eu^{2+} , and used Gd^{3+} as a substitute for Eu^{3+} ; they noted, however, that conversion of the EPR signals from Eu^{2+} and Gd^{3+} to calculate $\text{Eu}^{2+}/\text{Eu}^{3+}$ involved large and uncontrolled uncertainties.

Direct measurement of the $\text{Eu}^{2+}/\text{Eu}^{3+}$ with an independent technique such as ^{151}Eu Mössbauer spectroscopy would provide an independent check on the assumptions necessary in using EPR. Such data can also be used for calibration

of the constant used in calculating $X_{\text{Eu}^{2+}}$ by Morris and Haskin (1974), Morris *et al.* (1974), and Lauer and Morris (1977).

Aside from the important considerations summarized above, Virgo and Mysen (*Year Book 76*, pp. 400–407) and Lauer and Morris (1977) noted that redox states of elements in silicate melts depend on both bulk composition of the melt and pressure, in addition to f_{O_2} . In view of the widespread use of $\text{Eu}^{2+}/\text{Eu}^{3+}$ as an indicator of temperature and oxygen fugacity during crystallization of magma, it was decided that careful determination of the redox ratio as a function of bulk composition, pressure, and oxygen fugacity had to be undertaken.

The present experiments were carried out with compositions in the system $\text{NaAlSi}_2\text{O}_6$ - $\text{CaAl}_2\text{Si}_2\text{O}_8$ - $\text{CaMgSi}_2\text{O}_6$ - SiO_2 . Europium was added as Eu_2O_3 (enriched in ^{151}Eu) in amounts ranging from 0.1 to 3.0 wt %. The europium added was calculated either as Eu^{3+} or as Eu^{2+} in chemical formulae of mineral compositions. The Eu_2O_3 was also added as oxide Eu_2O_3 in addition to the chemical formulae without consideration for stoichiometry. About 200–250 mg of each composition was converted to glass in a vertical quench furnace in air for starting material.

One-atmosphere experiments with controlled f_{O_2} were conducted with about 50-mg samples suspended on a Pt-loop to provide easy exchange of oxygen between the silicate and the gas. The gas used in experiments with controlled f_{O_2} was CO-CO_2 and $\text{H}_2\text{-CO}_2$. Run durations were between 1 and 82 hr. These durations were comparable to those that Morris *et al.* (1974) stated were sufficient to attain equilibrium. Virgo and Mysen (*Year Book 76*, pp. 400–407), in studying varying $\text{Fe}^{3+}/\text{Fe}^{2+}$ in melts of $\text{NaAlSi}_2\text{O}_6$ composition, concluded that run durations on the order of 1 hr were sufficient to attain equilibrium redox ratios for iron in experiments at 1 atm. One experiment with $\text{NaAlSi}_2\text{O}_6$ melt at 30 kbar in a solid-media, high-pressure apparatus (Boyd

and England, 1960) was of 10 min duration—comparable to that used by Virgo and Mysen (*Year Book 76*, pp. 400–407) to attain equilibrium for $\text{Fe}^{3+}/\text{Fe}^{2+}$ under similar physical conditions.

The $\text{Eu}^{2+}/\text{Eu}^{3+}$ was determined by Mössbauer spectroscopy using the 21.6 KeV transition in ^{151}Eu . The source used was 55 mCi anhydrous $^{151}\text{SmF}_3$ encapsulated in a 4-mm-diameter lucite mount (active diameter 2 mm) by hot, high-pressure casting. By this method a source activity of ~ 1750 mCi/cm² was achieved, which is an order of magnitude higher than that of normal Mössbauer sources. In this way the source can be placed within 0.2 mm of the sample, and samples with low Eu_2O_3 contents (~ 0.1 wt %) could be analyzed.

Samples prepared using 96.8% enriched Eu^{151} in Eu_2O_3 were analyzed as powders. Approximately 30 mg of specific samples were packed into holes ($\sim \frac{1}{8}$ " diam) drilled in small pieces of lead sheet. For measurement at 77°K, powdered samples were packed into holes ($\sim \frac{1}{8}$ " diam) drilled in copper discs and with a beryllium backing. In both instances the density of ^{151}Eu in the samples was in the range 1–5 mg $^{151}\text{Eu}_2\text{O}_3$ /cm² and the Mössbauer absorption effect was $\sim 10\%$.

The absorption data were stored in a 1024-channel analyzer using equipment described by Virgo (*Year Book 71*, pp. 607–608). At 77°K, the absorbers were held in a cryostat similar to that described by Virgo and Hafner (1969). The sample chamber was continuously evacuated with an ion-pump during each experiment.

Calibration of the ^{151}Eu absorption as a function of source velocity was based on the spectrum of 0.0025-mm-thick foil of metallic iron generated by a 10 mCi ^{57}Co point source (Huggins *et al.*, *Year Book 74*, pp. 405–410).

Two specific details of the ^{151}Eu Mössbauer resonance experiments should be pointed out. As a consequence of the different $t_{1/2}$ of the 21.64 KeV transition of ^{151}Eu compared with $t_{1/2}$ of ^{57}Fe , the

width of the half-peak height of the ^{151}Eu absorption lines will be at least seven times larger than the absorption lines of ^{57}Fe resonance (line width = 0.097 mm/sec for ^{57}Fe , 0.652 mm/sec for ^{151}Eu). Second, because of the electronic configurations of Eu^{2+} and Eu^{3+} , quadrupole splitting in Eu^{2+} and Eu^{3+} compounds can only arise from the lattice contributions to the electric field gradient and will of necessity be small. In general, such quadrupole splitting will be observed as a slight broadening of the resonance line. Despite the above considerations, chemical isomer shift data for ranges of Eu^{2+} and Eu^{3+} compounds are numerous and, most importantly, show a large separation (~ 15 mm/sec) between Eu^{2+} and Eu^{3+} compounds (Greenwood and Gibb, 1971). Furthermore, it is well established in the literature that ^{151}Eu Mössbauer experiments of compounds containing both valence states of Eu are readily detected in measurements at 298°K. Some exceptions are noted for materials with some degree of metallic character, and for this reason experiments at 77°K were also made.

The ^{151}Eu absorption spectra at 298°K for Eu_2O_3 (enriched) and EuSO_4 are compared in Figs. 17A and 17B. The divalent EuSO_4 was made from EuCl_3 in a Jones reductor as described by Hillebrand *et al.* (1953).

The ^{151}Eu Mössbauer spectra at 298°K of the samples (Figs. 17–19) consist of apparent single absorption peaks that are considerably broadened compared with the natural line width for ^{151}Eu . The absorption spectra for these samples are similar to that of Eu_2O_3 (Fig. 17) and that of a silicate glass synthesized in air previously reported by Taragin and Eisenstein (1970). Isomer shift values for samples listed in Table 11 relative to Eu_2O_3 are in the range 0.1–0.2 mm/sec. The smallest isomer shift of an Eu^{2+} compound relative to Eu_2O_3 is about -10 mm/sec, and thus it follows that more than 99% of the Eu in these samples occurs as Eu^{3+} . (In fact, there is no

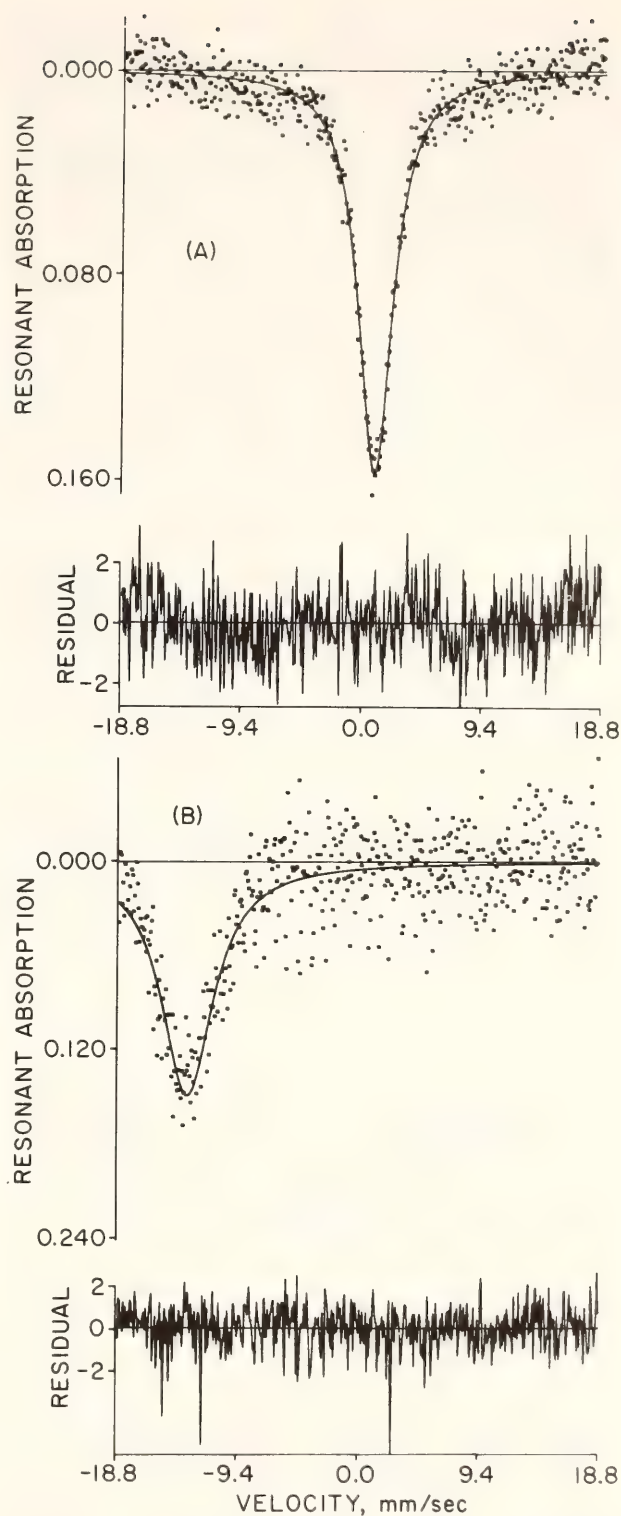


Fig. 17. The ^{151}Eu Mössbauer spectra at 298°K of enriched Eu_2O_3 (upper spectrum) and EuSO_4 (lower spectrum). The absorption data as fitted to a line of Lorentzian line shape (solid line).

evidence for the occurrence of Eu^{2+} within the experimental error.) Similar conclusions are reached for spectra of samples taken at 77°K (Figs. 18A, 18B; Table 11).

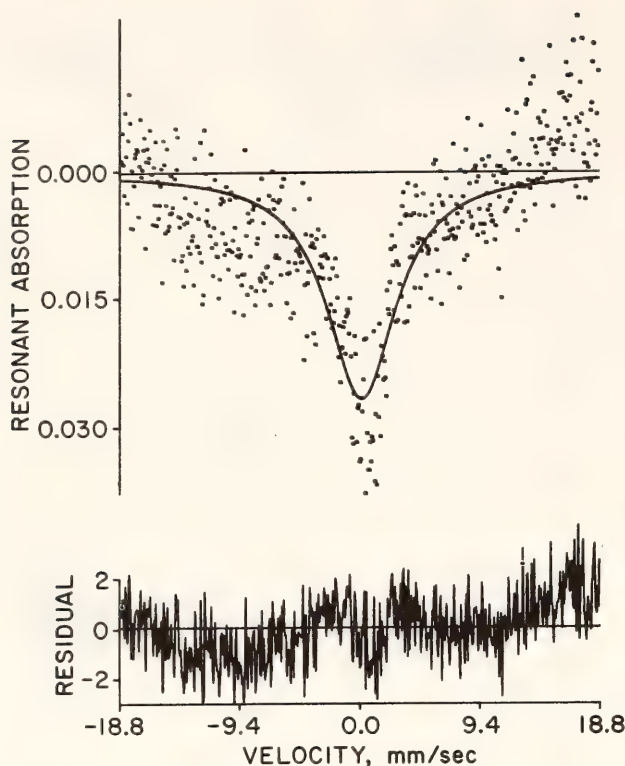


Fig. 18. The ^{151}Eu Mössbauer spectrum at 298°K of glass of MVH An Di 1 composition prepared at 1499°C, $\log f_{\text{O}_2} = -9.1$, 930 min (see Fig. 17 caption).

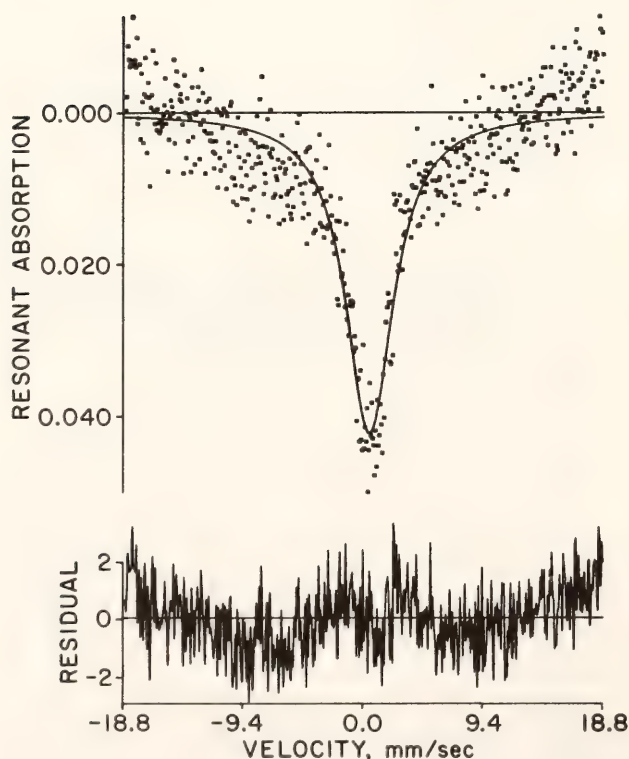


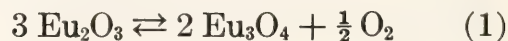
Fig. 19. The ^{151}Eu Mössbauer spectrum at 298°K of crystalline anorthite of MVH An 1 composition prepared at 1200°C, $\log f_{\text{O}_2} = -12.49$, 720 min (see Fig. 17 caption).

TABLE 11. Isomer Shifts of Synthetic Glasses and Minerals

Sample	Isomer Shift* mm/sec.	Measurement °K
EuSO ₄	-13.71	298
MVH An.Di 3	-0.07	298
MVH An.Di 3	~0.01	77
MVH An 1	~0.01	298

* Relative to Eu_2O_3 .

It is concluded, therefore, that less than 2–3% of the total amount of Eu in the systems studied here can occur as EuO over an f_{O_2} range from that of air down to values lower than that of the QIF buffer. It should be noted that the bulk compositions studied included most of these studied by Drake (1975), Morris and Haskins (1974), Morris *et al.* (1974), and Lauer and Morris (1977). Consequently, it is concluded that the proportion of Eu^{2+} in glasses reported by Morris and co-workers is much smaller (by perhaps two orders of magnitude) than suggested by them. So it is likely that the values of correction factors discussed by Morris and Haskins (1974) and Lauer and Morris (1977), as discussed above, are too high by at least two orders of magnitude. This observation is not surprising in light of the thermochemical data by McCarthy (1974), who found that the f_{O_2} for the univariant reaction



is $\sim 10^{-14}$ atm at 1500°C (five orders of magnitude below that of the QIF) and about 10^{-26} atm at 1000°C (14 orders of magnitude below that of the QIF buffer).

The observation that only insignificant amounts of Eu^{2+} can be stabilized in crystals and melts under terrestrial f_{O_2} conditions implies (1) that the europium anomalies found in rocks must be the result of effects other than varying $\text{Eu}^{2+}/\text{Eu}^{3+}$ with f_{O_2} , melt composition, and T , and (2) that the apparent $f_{\text{O}_2} - T$ calibration of $\text{Eu}^{2+}/\text{Eu}^{3+}$ reported by, for

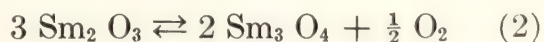
example, Drake (1975), must relate to effects other than stabilization of significant amounts of Eu^{2+} in melt and plagioclase. In fact, Drake (1975) suggested that essentially all Eu occurs as Eu^{2+} in the system An-Ab-Di at the f_{O_2} of the QIF buffer and 1300°C ($f_{\text{O}_2} \sim 10^{-11}$ atm).

As a first attempt toward duplicating the results of Drake (1975), the REE La peaks used in electron microprobe analysis of REE were scanned with the MAC 400 automated electron microprobe at the Geophysical Laboratory to ascertain whether there might be an interference. The REE standards REE2, REE3, and REE4 described by Drake and Weill (1973) and used by Drake (1975) and Drake and Weill (1975) in experimentally determining REE partition coefficients between plagioclase and liquids were used for this purpose. None of these standards contained Eu; yet in the case of REE3 (containing only La, Ce, and Pr) a peak at the position of Eu La corresponding to about 1 wt % Eu_2O_3 (as calibrated against standard REE2) was observed. Thus far the source of this peak remains ambiguous, but it is likely that it affected the analyses of Drake (1975) and Drake and Weill (1975). If so, their electron microprobe analyses of Eu contents of plagioclase and liquid may be incorrect.

After it was established that electron microprobe analysis of Eu could present difficulties, the decision was made to prepare a glass of bulk composition identical to that of liquid coexisting with plagioclase used by Drake (1975) at 1300°C to determine whether Eu^{2+} did in fact occur in this sample (as concluded by Drake, 1975). At the f_{O_2} below that of the QIF buffer ($10^{-12.4}$ atm at 1200°C), no Eu^{2+} was found. Instead, after about 15 hr run duration, europium loss by volatilization was noted from the Mössbauer spectroscopic studies of run products. In fact, after about 4 days' run duration at $f_{\text{O}_2} = 10^{-12.4}$ atm, at least 75% of the europium was lost. Mössbauer studies of coexisting crystals grown for time periods up to 42 hr

revealed only Eu^{3+} with no discernible europium loss. Longer term experiments have not yet been made. In the experiments of Drake (1975), the experimental charges were held for 1 week at 1300°C at f_{O_2} levels down to $10^{-12.5}$ atm after an initial cooling period through the liquidus to facilitate growth of crystals suitable for electron microprobe analysis. It is suggested that because of the much smaller diffusion coefficient of Eu in plagioclase than in melt, anomalously high nonequilibrium contents of Eu were attained in the crystals while Eu volatilized from the melt during the experiment. Consequently, the measured partition coefficient $D_{\text{Eu}}^{\text{plagioclase-liquid}}$ is higher than its equilibrium value. This effect is likely to increase with decreasing f_{O_2} inasmuch as the rate of Eu loss apparently increases with decreasing f_{O_2} . This conclusion is similar to that of Merrill and Wyllie (1973), who studied the effect of Fe loss to noble metal containers on Fe-Mg partitioning between crystals and liquids.

A final potential problem in the experimental studies relating to the europium anomaly is that crystal-liquid partition coefficients for REE's other than Eu may also be f_{O_2} -dependent. In an attempt to resolve this matter, Hoover (this Report) studied Sm partitioning between plagioclase (An_{50}) and liquid in the system An-Ab-Di at 1300°C . It was found that the $D_{\text{Sm}}^{\text{plagioclase-liquid}}$ increased by a factor of 2.5 by lowering f_{O_2} from that of air to $10^{-11.2}$ atm (QIF). This effect was not observed when using pure anorthite rather than an intermediate plagioclase. The presence of Sm^{2+} is not expected in the $f_{\text{O}_2} - T$ range of terrestrial conditions because the f_{O_2} of a univariant reaction such as



is even lower than that of the analogous reaction for Eu (Equation 1). As an alternative to lowered oxidation states it is suggested that a mechanism for formation of defects in the plagioclase structure as a function of f_{O_2} (somewhat analogous to that suggested by Lambe and Schroer,

1976) also exists in the plagioclase formed in these experiments. The presence of the defects affects the activity coefficient of the rare earth element and thus influences its crystal-liquid partition coefficient independently of its oxidation state. In view of the similarity of ionic size and charge of the individual REE elements, qualitatively similar effects may be found for other REE³⁺ such as Eu³⁺. Although the idea is quite speculative at this point, it may be suggested that f_{O_2} -controlled defect substitution of REE in plagioclase may also explain the europium anomalies found in rocks.

Note added in proof. Since the initial writing, the authors have become aware that significant amounts of Eu²⁺, determined from Mössbauer experiments, occurred in glasses synthesized at low f_{O_2} with compositions in the system Di-An-Ab and containing 5 wt % Eu₂O₃ (D. Weill and D. Schroeer, pers. comm., 1978). These latter results can be compared with the present authors' data on bulk compositions that are chemically similar but contain ≤ 1 wt % Eu₂O₃. It is suggested, therefore, that the presence of divalent Eu in silicate systems depends not only on the conditions of f_{O_2} and the structure of the melt and crystalline phases but also on the bulk Eu in the system. In addition, the present authors have confirmed the presence of Eu²⁺ by Mössbauer spectroscopy in EuAl₂Si₂O₈ crystallized at low f_{O_2} from a starting composition Eu₂O₃·2Al₂O₃·5SiO₂ (sample kindly provided by B. Iwasaki).

RARE EARTH ELEMENT PARTITIONING BETWEEN GARNETS, PYROXENES, AND MELTS AT LOW TRACE ELEMENT CONCENTRATION

Wendy J. Harrison*

Rare earth element (REE) abundances in igneous rocks are frequently used to

* Work carried out under a cooperative predoctoral fellowship program of the Geophysical Laboratory and the University of Manchester, Great Britain.

model the origin and evolution of those magmas (e.g., Gast, 1968; Kay and Gast, 1973). The applicability of such an approach is critically dependent on the values of crystal-liquid partition coefficients† used and on the assumption that Henry's Law is obeyed during partial melting and fractional crystallization processes. According to Henry's Law, the coefficients should be independent of the trace element concentration; however, recent experimental work (Mysen, *Year Book* 75, pp. 656–659, *Year Book* 76, pp. 588–594; Wood, *Year Book* 75, pp. 659–662; Harrison, 1977) has shown that the behavior of REE in minerals under pressure and temperature conditions within the mantle deviates from Henry's Law at low dilution (generally < 20 ppm REE in the crystal), and variations in substitution mechanisms have been suggested. In this report, data are presented on the partitioning of REE's between garnets, pyroxene, and hydrous melts at low rare earth concentration.

The partitioning of samarium and thulium has been determined between pyrope and hydrous melt in the binary system Mg₃Al₂Si₃O₁₂-H₂O between grossularite and hydrous melt in the binary system Ca₃Al₂Si₃O₁₂-H₂O, and between diopside and hydrous melt in the binary system CaMgSi₂O₆-H₂O as a function of mineral trace element concentration (0.1 ppm to 10,000 ppm) at 30 kbar and 1300°–1500°C. The partitioning of Sm has also been studied between natural pyrope-rich garnet (from a nodule from kimberlite) and melt under similar pressure and temperature conditions.

Starting materials were glasses produced from oxide mixes at 1 atm, crystalline pyrope grown at 900°C and 30 kbar (in solid-media high-pressure apparatus; Boyd and England, 1960) and grossularite grown at 950°C and 10 kbar (in internally heated gas-media apparatus; Yoder, 1950). The minerals were grown for the

† Partition coefficients $D_i^{a/b}$ are defined as concentration ratios C_i^a/C_i^b where a and b are phases and i is a trace element.

purpose of reversal experiments. Stable and radioactive trace elements were added as dilute acidic chloride solutions. Where concentrations greater than 0.5 wt % Sm and Tm were required, the trace element was added as a high-purity crystalline chloride or nitrate. The glasses were then re-fused at 1 atm, during which process the rare earth salts decompose and the rare earth ions become incorporated in the silicate melt.

All experiments were performed in a solid-media high-pressure apparatus, using the piston-out technique through-out (Boyd and England, 1963). Temperatures were measured using Pt-Pt90Rh10 and W3Re97-W25Re75 thermocouples. No corrections have been applied to the nominal pressures and temperatures quoted. All runs were made using 2-mm-diameter platinum capsules, which were sealed by welding to contain the water added to the starting materials. Run durations ranged from ≥ 12 hr at 1200°C to 2 hr at 1500°C.

The ^{151}Sm and ^{171}Tm contents in the products were determined by autoradiography (Mysen and Seitz, 1975). The liquid that coexists with both garnet and diopside crystals quenches not to a glass but to quench pyroxenes; these appear to retain the trace element content of the liquid (Wood, *Year Book* 75, pp. 659–662). Uncertainties in all figures are $\pm 1\sigma$ and reflect errors due to counting statistics, exposure times of emulsions, and possible element-distribution heterogeneities.

Experimental equilibrium was established on the basis of homogeneity of element distribution, time studies to define the necessary run durations for achieving constant partition coefficients (Fig. 20), and reversal runs. Reversal runs were achieved by mixing crystalline garnet with glass and water. The trace element was added to the glass phase in the system pyrope- H_2O and to the garnet phase in the system grossularite- H_2O during synthesis. Equilibrium partition coefficients are thereby approached from apparent values of D that are less than

the true values for pyrope garnet and melt and from values of D greater than the values for grossular garnet and melt.

Results

Data for the partitioning of samarium and thulium between pyrope, grossularite, diopside, and hydrous melts as a function of crystal trace element concentration are given in Figs. 21–25. It is seen that at rare earth element concentrations greater than about 100 ppm in the minerals, partition coefficients are constant, whereas at lower concentrations they vary, increasing with decreasing concentration. In the Ca-bearing minerals grossularite and diopside another region of constant partition coefficients occurs at rare earth concentrations < 1 ppm.

The crystal rare earth contents at which these changes are observed depend upon the following parameters.

(1) Temperature: for pyrope, $D_{\text{Sm}^{\text{garnet/liquid}}}$ becomes constant at concentrations greater than 12 ppm Sm in garnet at 1300°C ($D_{\text{Sm}} = 0.109 \pm 0.007$), whereas at 1500°C, 100 ppm Sm need to be dissolved in the garnet to achieve constant D_{Sm} ($D_{\text{Sm}} = 0.148 \pm 0.007$).

(2) Rare earth ionic radius: for pyrope at 1300°C, 12 ppm of Sm (ionic radius = 1.17 \AA^*) are required to attain constant D_{Sm} , whereas 80 ppm of Tm (ionic radius = 1.07 \AA) are required to attain constant D_{Tm} ($D_{\text{Tm}} = 0.157 \pm 0.008$) under the same conditions.

(3) Major element composition: D_{Sm} does not become constant until > 500 ppm are held in grossularite ($D_{\text{Sm}^{\text{grossularite/liquid}}} = 0.750 \pm 0.04$ at 1300°C, 30 kbar), whereas only 12 ppm Sm are required to attain constant D_{Sm} in pyrope at the same pressure and temperature. A very low concentration region of constant D_{Sm} is present in the Ca-bearing minerals.

* All ionic radii quoted are for coordination of the rare earth ion with eight oxygens and are taken from the tables of Whittaker and Muntus, 1970.

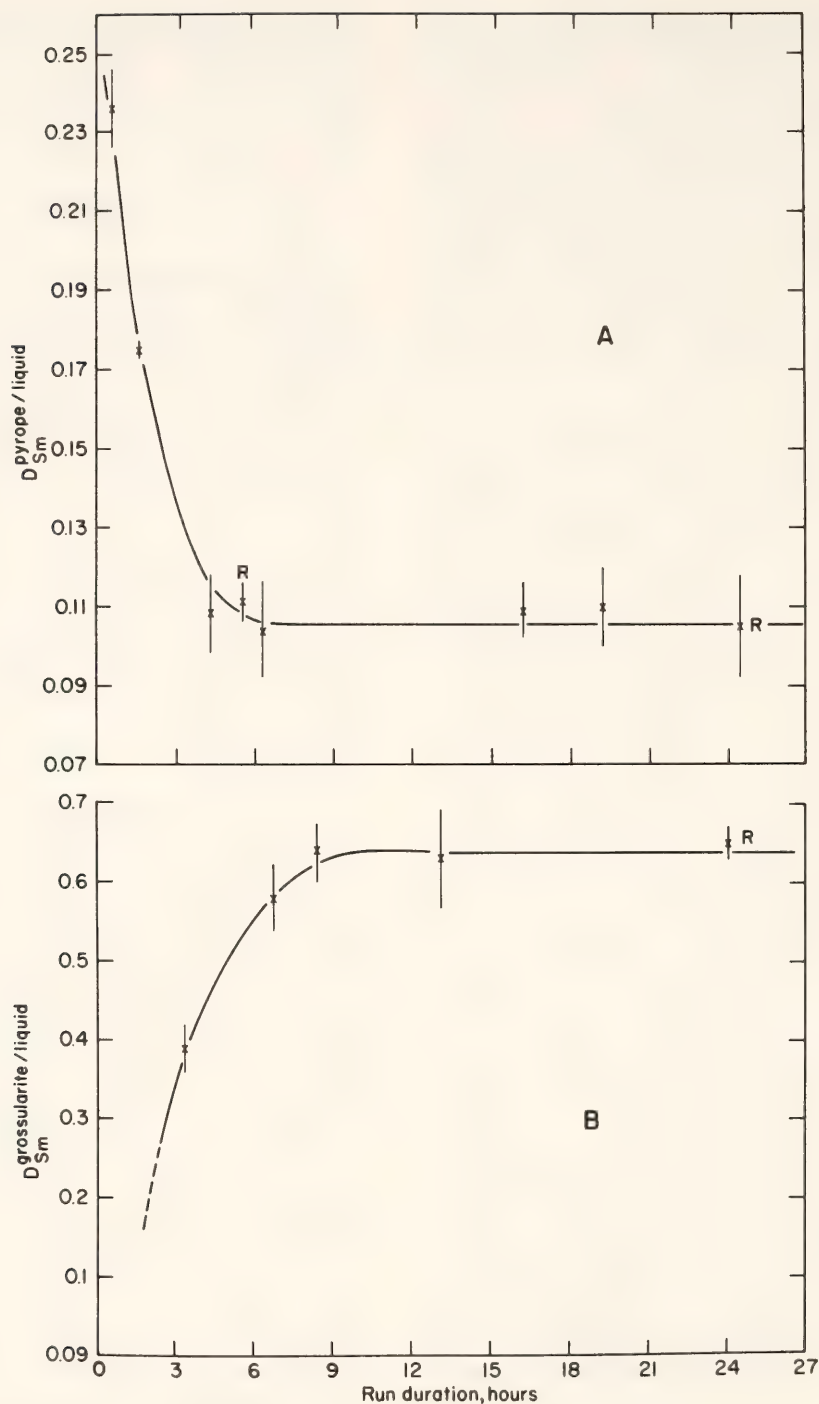


Fig. 20. Partition coefficients for samarium between garnet and melts as a function of run duration. (A) Pyrope and melt at 1300°C, 30 kbar. (B) Grossularite and melt at 1200°C, 30 kbar. R denotes a reversed run. Error bars $\pm 1\sigma$.

Discussion

The variable nature of the relationship of $D_{REE}^{crystal/liquid}$ to REE concentration is a consequence of changing activity coefficients (γ) of rare earth ions in the Henry's Law equation. Mysen (*Year Book* 75, pp. 656–659) has argued that

$\gamma_{REE}^{crystal}$ is more likely to vary than γ_{REE}^{liquid} at low REE concentrations, and thus an explanation of the form of the curves in Figs. 21–25 rests with the substitutional behavior of the REE ion in the crystal structure.

Low-concentration (<1 ppm in crystal) constant D_{REE} is only observed in

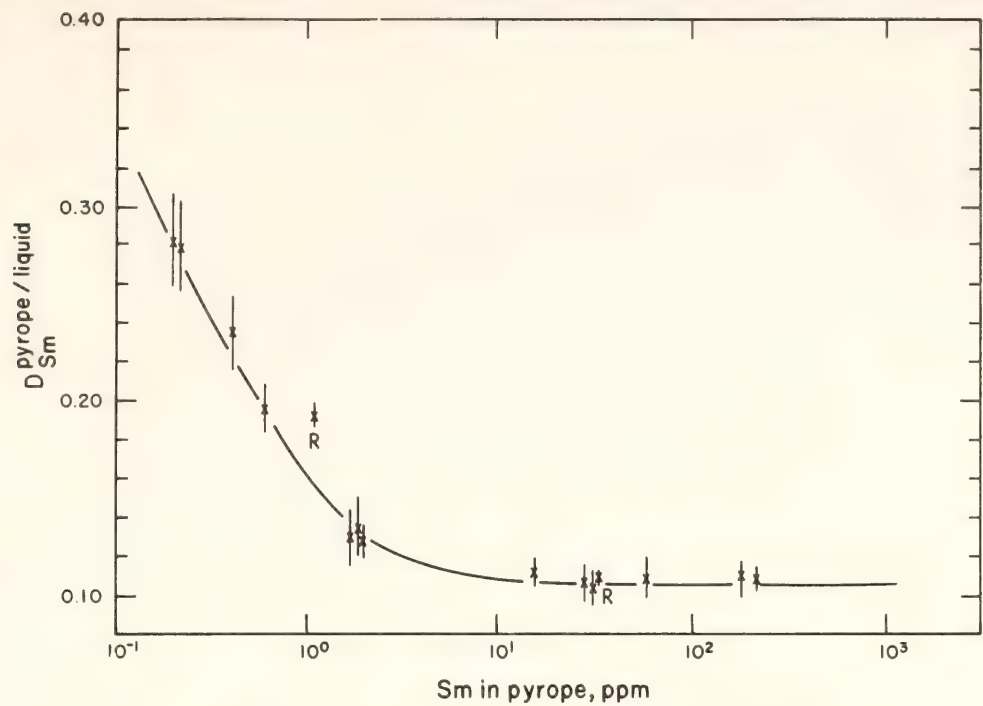


Fig. 21. Partition coefficients for samarium between pyrope and liquid at 30 kbar and 1300°C as a function of samarium content of the garnets (ppm). R denotes a reversed run. Error bars $\pm 1\sigma$.

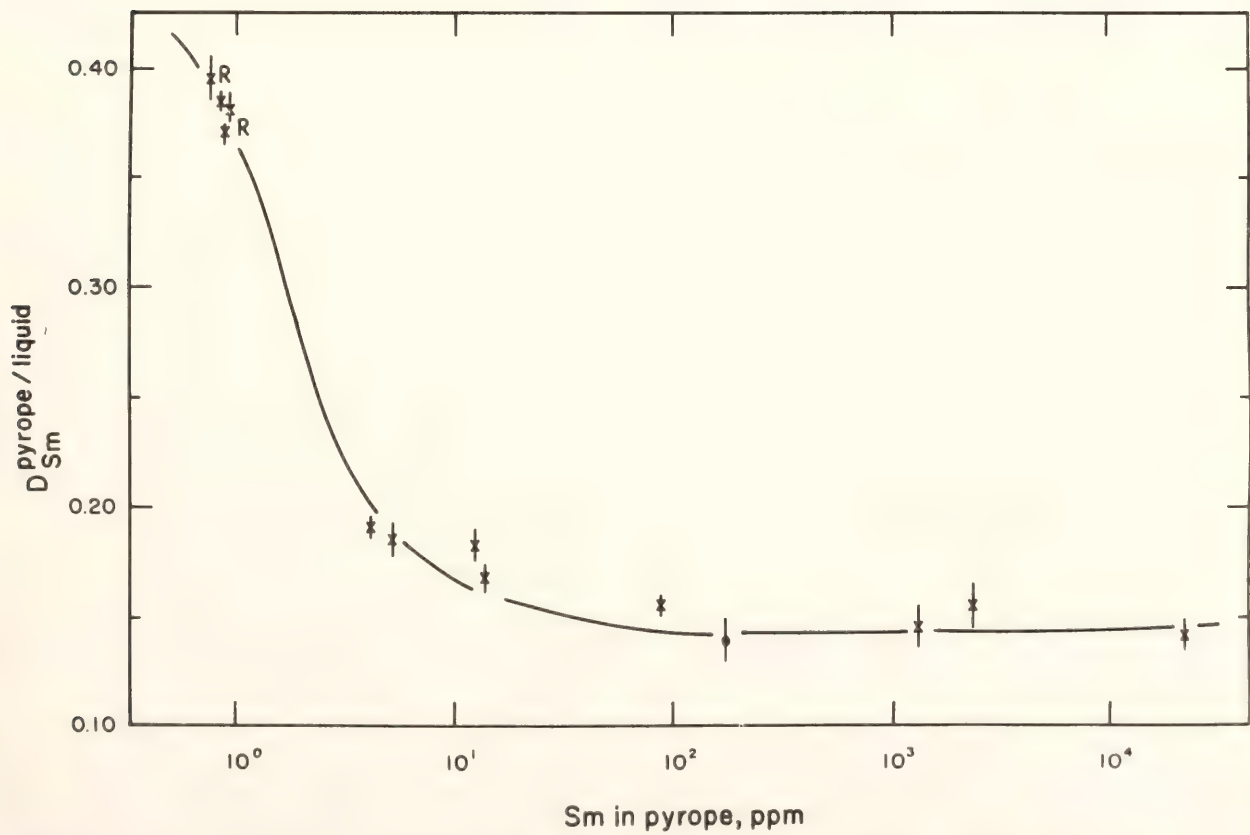


Fig. 22. Partition coefficients for samarium between pyrope and liquid at 30 kbar and 1500°C as a function of samarium content of the garnets (ppm). R denotes a reversed run. Error bars $\pm 1\sigma$. Datum point ϕ is from Wood (1976) for the same system and conditions.

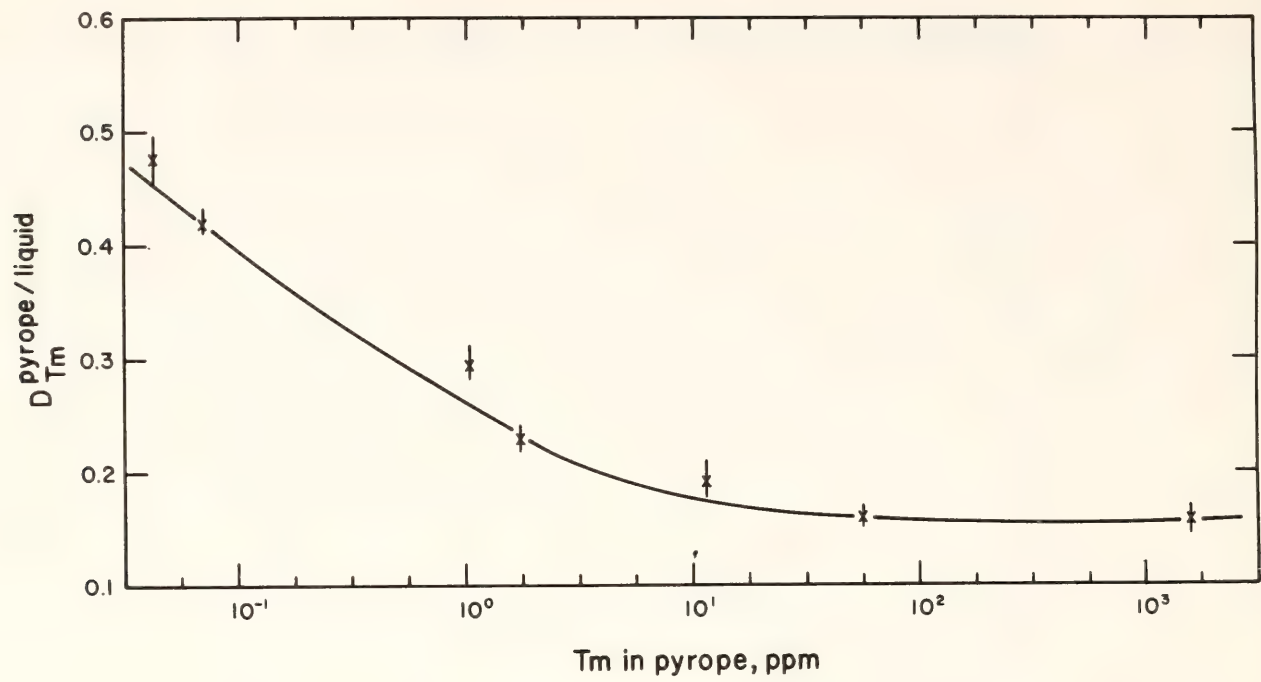


Fig. 23. Partition coefficients for thulium between pyrope and liquid at 30 kbar and 1300°C as a function of thulium content of garnet (ppm). Error bars $\pm 1\sigma$.

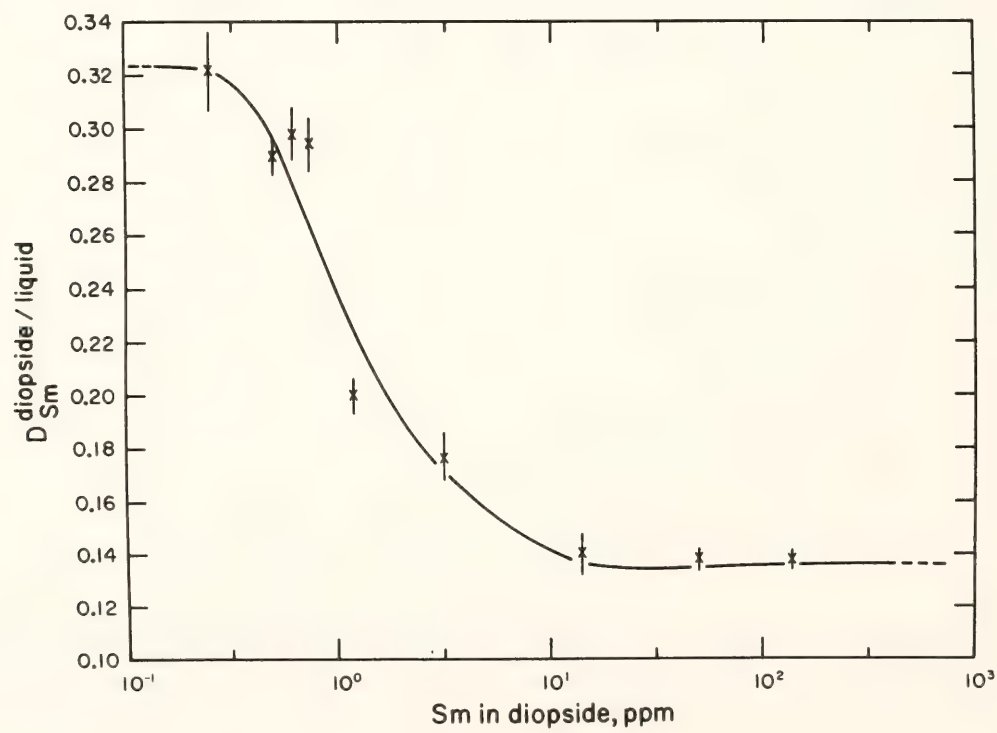


Fig. 24. Partition coefficients for samarium between diopside and liquid at 30 kbar and 1400°C as a function of samarium content of diopside (ppm). Error bars $\pm 1\sigma$.

the Ca-bearing minerals grossularite and diopside. Samarium almost certainly substitutes onto the eight oxygen-coordinated cubic sites in garnets normally occupied by Ca^{2+} , Mg^{2+} , and it is reasonable to assume that the larger Ca^{2+} -bearing

garnet structure ($Ca^{2+} = 1.20 \text{ \AA}$) will accept Sm^{3+} ($Sm^{3+} = 1.17 \text{ \AA}$) more readily than will the Mg^{2+} -bearing garnet lattice ($Mg^{2+} = 0.97 \text{ \AA}$). Thus, the very low concentration constant D_{Sm} region can be attributed to true Henry's Law

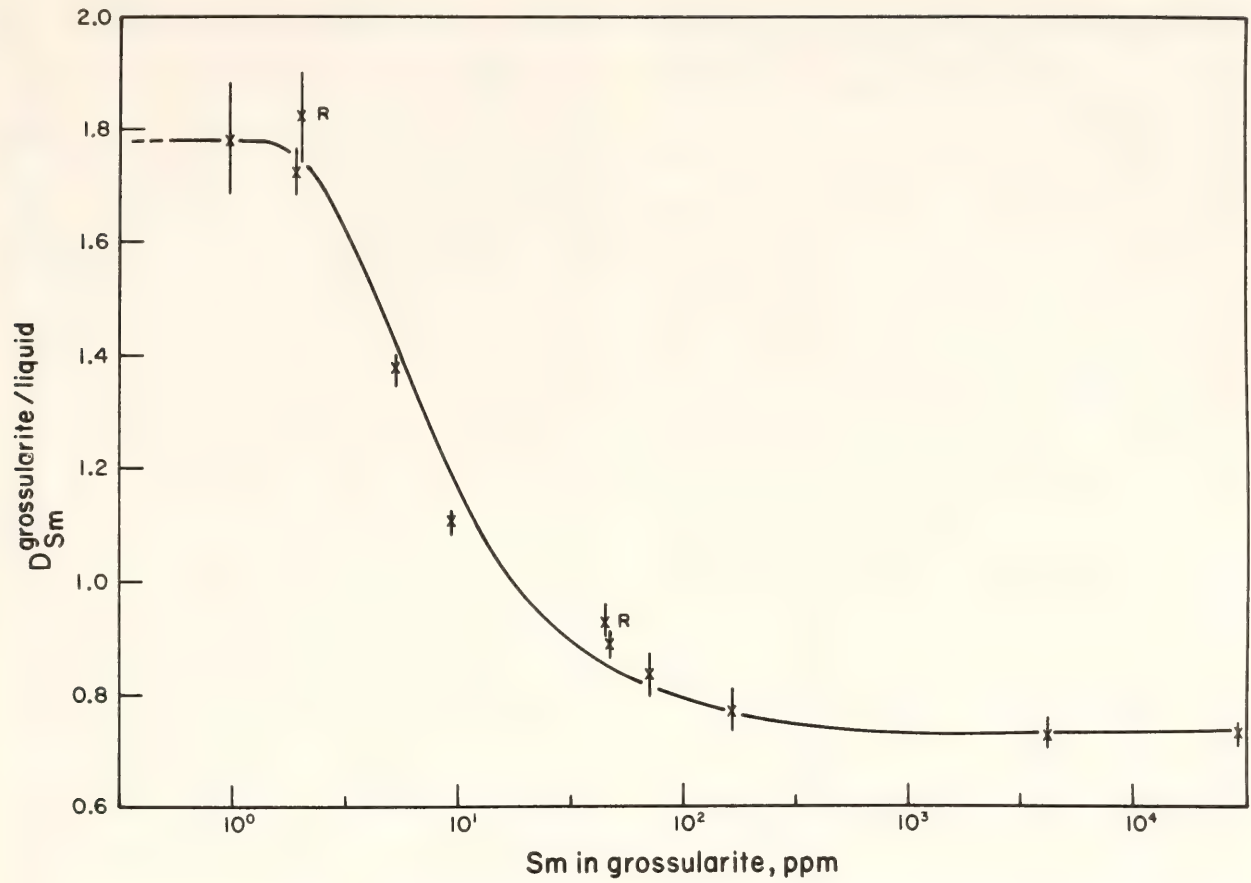


Fig. 25. Partition coefficients for samarium between grossularite and liquid at 30 kbar and 1300°C as a function of samarium content of grossularite (ppm). R denotes a reversed run. Error bars $\pm 1\sigma$.

substitution of samarium into grossularite and diopside. It would be expected that the larger the difference between the size of the host lattice site and the ionic radius of the substituting trace ion, then the lower the concentration of the trace ion that can substitute ideally. Such a relationship would explain the observed differences between the Ca- and Mg-bearing minerals. This same argument has also been used by Lagache and Sabatier (1973) for alkali metals and alkaline earths in feldspars and feldspathoids.

The rare earth concentration region in which D_{REE} is variable is a region over which activity coefficients for REE's in the mineral are changing, probably owing to a change in the substitutional mechanism of the rare earth in the lattice. The suggestion that variable D_{REE} results from the saturation of energetically favorable defect sites in the crystal (Wood, *Year Book* 75, pp. 650–662; Navrotsky,

1978) could explain the solution behavior in this region. Such defects would have to be cation vacancies and interstitial sites generated by REE substitution as growth dislocations; radioisotope transmutation effects can be discounted on the basis of equilibration studies discussed above. In such a model, apparent Henry's Law behavior at high concentration can be explained in terms of substitution onto a normal crystallographic site as discussed above, and low-concentration dilute solution behavior can then be interpreted as a region where the concentration of rare earth ions in the crystal is very small in relation to the concentration of defects. This model cannot account for the necessity that Ca-bearing minerals should contain a higher number of lattice defects than Mg-bearing minerals. Moreover, the rare earth concentration in the crystal at which D_{REE} becomes constant should not vary with different rare earth elements at

a given pressure and temperature because one cation vacancy can only be filled by one rare earth ion. Such constancy, however, is not observed (see Figs. 21 and 23).

The data reported here do not provide strong support either for models involving lattice deformation as a consequence of rare earth substitution (e.g., Iiyama, 1968) or for models of multisite substitution (defects or regular crystallographic sites). A spectroscopic investigation of REE site population in minerals may resolve some of these problems (e.g., Chatelain and Weeks, 1973).

Another aspect of rare earth partitioning behavior that has been investigated is the dependence of $D_{\text{Sm}}^{\text{garnet/liquid}}$ on the concentration of other rare earths in the garnet in addition to Sm; that is, the bulk REE content of a mineral phase determines the partition coefficient of any single rare earth element between that mineral and a melt. Thus, if a sufficiently high concentration of other rare earth elements is present in the mineral, a constant partition coefficient may be attained

for any single REE. This possibility was investigated by adding 80 ppm of La, Dy, Lu, and Cr^{3+} separately to different experimental charges each of which contained 1.852 ppm ^{151}Sm . At 1300°C and 30 kbar, $D_{\text{Sm}}^{\text{pyrope/liquid}}$ for mixes containing 1.852 ppm ^{151}Sm only is 0.235 ± 0.01 . The additional trace element was found, in the cases of La, Dy, and Lu, to lower D_{Sm} to that obtained in the higher concentration region of constant partition coefficients (0.103 ± 0.005). Chromium, on the other hand, did not affect D_{Sm} . Thus, it is concluded that whereas $D_{\text{REE}}^{\text{garnet/liquid}}$ depends upon the total REE content of the garnet, it is independent of the total impurity content. If the total REE content of a phase falls within the variable D_{REE} region, it is inappropriate to assume a constant value of D in petrogenetic modeling.

As a further test of the applicability to natural systems of the low-concentration variable partition coefficients determined in pure synthetic systems, partition coefficients for Sm between a natural

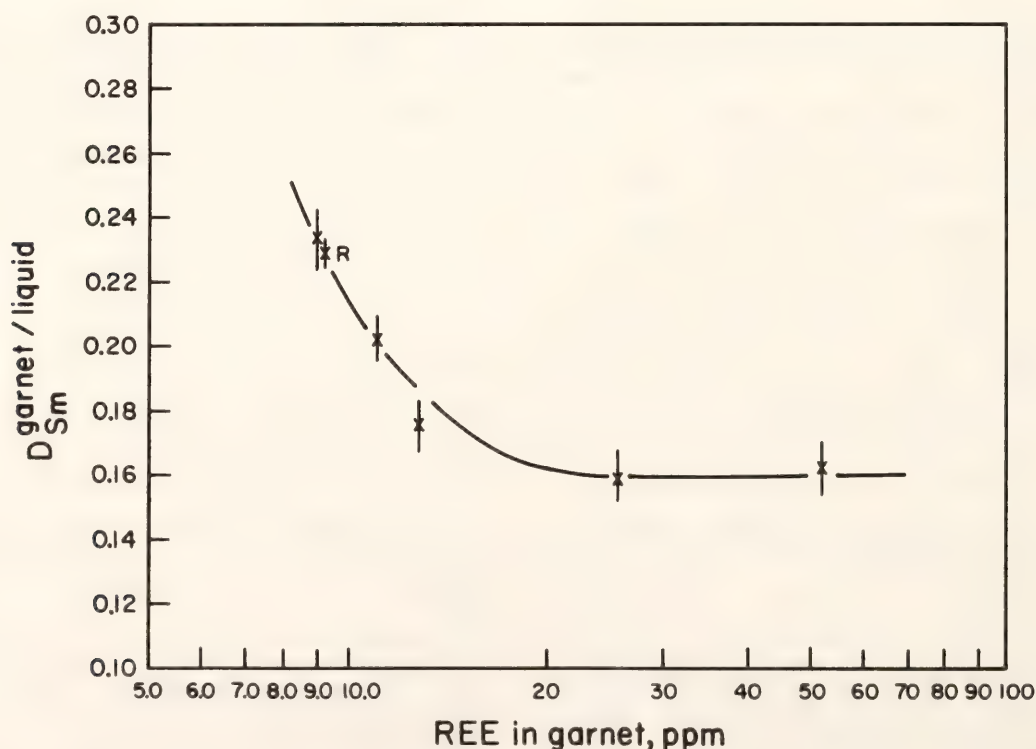


Fig. 26. Partition coefficients for samarium between a natural pyrope garnet (nodule PHN 1925) and silicate liquid at 30 kbar and 1300°C as a function of the REE content of garnet (ppm). Error bars $\pm 1\sigma$. R denotes a reversed run.

pyrope-rich garnet and melt were determined as a function of the REE content of the garnet. The garnet was handpicked from a nodule from kimberlite (PHN 1925, kindly supplied by Dr. F. R. Boyd) that had been previously analyzed for REE by Shimizu (1975). The partitioning data at 30 kbar and 1300°C are given in Fig. 26. The melt contains 10.5 wt % H₂O. It can be seen that D_{Sm} is concentration dependent until ≥ 20 ppm REE is dissolved in the garnet; D_{Sm} falls from 0.234 ± 0.009 with 9 ppm REE in garnet, and to 0.160 ± 0.007 with >20 ppm REE in garnet. Thus, despite the complexities of natural garnet compositions, the principle of variable partition coefficients at low trace element concentrations observed in synthetic systems does apply to natural systems. Such variations should therefore be taken into consideration in petrogenetic modeling. The high-concentration constant D_{Sm} ($D_{Sm} = 0.160 \pm 0.007$ with ≥ 20 ppm REE in garnet) is higher than that determined in the synthetic system pyrope-H₂O for an equivalent concentration of Sm in garnet ($D_{Sm} = 0.110 \pm 0.001$ at 1300°C, 30 kbar). The likely explanations are (1) that the natural garnet is not pure pyrope but has an almandine-grossularite component (garnet analysis given in Table 12), and (2) that the melt with which these garnets coexist is Ti-rich. Titanium is a melt polymeriser and so will probably cause REE crystal-liquid partition coefficients to increase (Watson, 1976).

Conclusions

Variable partition coefficients as a function of rare earth concentration in garnets and pyroxene may be attributed to nonideality of substitutional behavior at low trace element concentrations (1–100 ppm). This nonideality may be a consequence either of multisite substitution or of lattice deformation induced by the substituting rare earth in the crystals. The concentration range over which $D_{REE}^{crystal/liquid}$ varies is of direct geologi-

TABLE 12. Microprobe Analysis of Garnets Synthesized in Experiments on Garnets from Nodule from Kimberlite PHN 1925.

Oxide	% wt
SiO ₂	43.49
TiO ₂	0.25
Al ₂ O ₃	22.56
Cr ₂ O ₃	2.48
FeO*	2.56
MnO	0.34
MgO	26.54
CaO	1.98
Na ₂ O	0.00
Total	100.20
Number of Cations for 12 Oxygens	
Si	2.996
Ti	0.012
Al	1.831
Cr	0.133
Fe*	0.146
Mn	0.018
Mg	2.725
Ca	0.146
Na	0.000
Total	8.007

* Fe denotes sum of Fe²⁺ and Fe³⁺.

cal interest. It has been demonstrated that D_{Sm} is dependent upon the total REE content of the crystalline phase; thus, if the rare earth content of a crystal falls within the region of variable $D_{REE}^{crystal/liquid}$, then the assumption that the partitioning of REE obeys Henry's Law during petrogenetic modeling must be questioned.

EXPERIMENTAL DETERMINATION OF CRYSTAL-VAPOR PARTITION COEFFICIENTS FOR RARE EARTH ELEMENTS TO 30 KBAR PRESSURE

Bjørn O. Mysen

Evidence from volcanic rocks suggests heterogeneous distribution of volatiles in the source regions of partial melts in the upper mantle. Mid-ocean ridge basalts

appear to be essentially H_2O -free, for example (Delaney *et al.*, 1977), whereas island arc magmas contain several percent H_2O (see Anderson, 1975; Muenow *et al.*, 1977). Kimberlite contains large amounts of both CO_2 and H_2O .

A consequence of this heterogeneous distribution is the possibility of migration of these volatiles. Preliminary experimental data of Mysen, Kushiro, and Fujii (this Report) indicate that an H_2O -rich front may infiltrate crystalline mantle materials at the rate of several millimeters per hour at pressures above 15 kbar. Thus, an H_2O -rich phase (as contrasted with H_2O bound in crystalline materials or silicate liquid) may act as a transporting agent of silicate components to the upper mantle, provided that silicate components can dissolve in such fluids.

In view of the importance assigned to knowledge of the trace element contents of parental rocks of partial melts in the upper mantle, an understanding of the processes governing their distribution patterns in upper mantle rocks is needed. Consequently, partition coefficients involving a water-rich vapor and the constituent minerals of garnet peridotite have been determined for representative REE as a function of pressure.

Starting materials for the experiments were synthetic pyrope (ga) and diopside (cpx). All experiments were conducted at 1100°C in the pressure range 5–30 kbar. An internally heated gas-media apparatus (Yoder, 1950) was used at $P \leq 10$ kbar, whereas a solid-media high-pressure apparatus (Boyd and England, 1960) was used at higher pressures. Pressures in the solid-media high-pressure apparatus were corrected by -4% as calibrated against the quartz-coesite transition.

Vapor-crystal partition coefficients were determined by analyzing the crystals and calculating the trace element content of the coexisting vapor by mass balance. Cerium, samarium, and thulium were chosen as representative light, intermediate, and heavy REE, respectively. Analyses were conducted with the beta-

track mapping technique (Mysen and Seitz, 1975) using cerium-141, samarium-151, and thulium-171 as sources of beta particles. Standards for the trace element analyses were $\text{NaAlSi}_3\text{O}_8$ glasses with known amounts of trace element added.

The experiments were conducted with trace element-free crystalline material ($\leq 5 \mu\text{m}$ grain size) that equilibrated with a fluid containing the trace element.* Reversal experiments were done by mixing a split of the crystalline run products with pure H_2O and repeating the experiment. After each forward experiment, individual grains showed homogeneous trace element distributions, and forward and reversal experiments gave results that agreed, within experimental and analytical uncertainty. It is concluded, therefore, that the reported partition coefficients are equilibrium values.

Partition coefficients for olivine-vapor and orthopyroxene-vapor were calculated from REE clinopyroxene-olivine and clinopyroxene-orthopyroxene partition coefficients derived from the data of Mysen (*Year Book* 76, pp. 588–594). The relative uncertainty of the latter data is about 5% (1σ), resulting in an estimated relative uncertainty of about 8% in the calculated vapor-crystal partition coefficients $K_{\text{REE}}^{\text{H}_2\text{O}-\text{Ol}}$ and $K_{\text{REE}}^{\text{H}_2\text{O}-\text{Opx}}$.

A comparison of experimentally determined values for $K_{\text{REE}}^{\text{H}_2\text{O}-\text{crystal}}$ ($=C_{\text{REE}}^{\text{H}_2\text{O}}/C_{\text{REE}}^{\text{crystal}}$) for various garnet peridotite minerals at 20 kbar and 1100°C is shown in Fig. 27. Two features of the data warrant comment. First, with the exception of $K_{\text{Tm}}^{\text{H}_2\text{O}-\text{Ga}}$, the REE are partitioned more strongly into the H_2O -rich vapor relative to the crystalline phases. Second, the partition coefficients vary with the atomic number of the REE.

The pressure dependence of the vapor-crystal partition coefficients has been evaluated for diopside using Sm at 1100°C (Fig. 28). A very strong pressure dependence of the Sm vapor-crystal parti-

* This type of experiment is referred to as a "forward experiment."

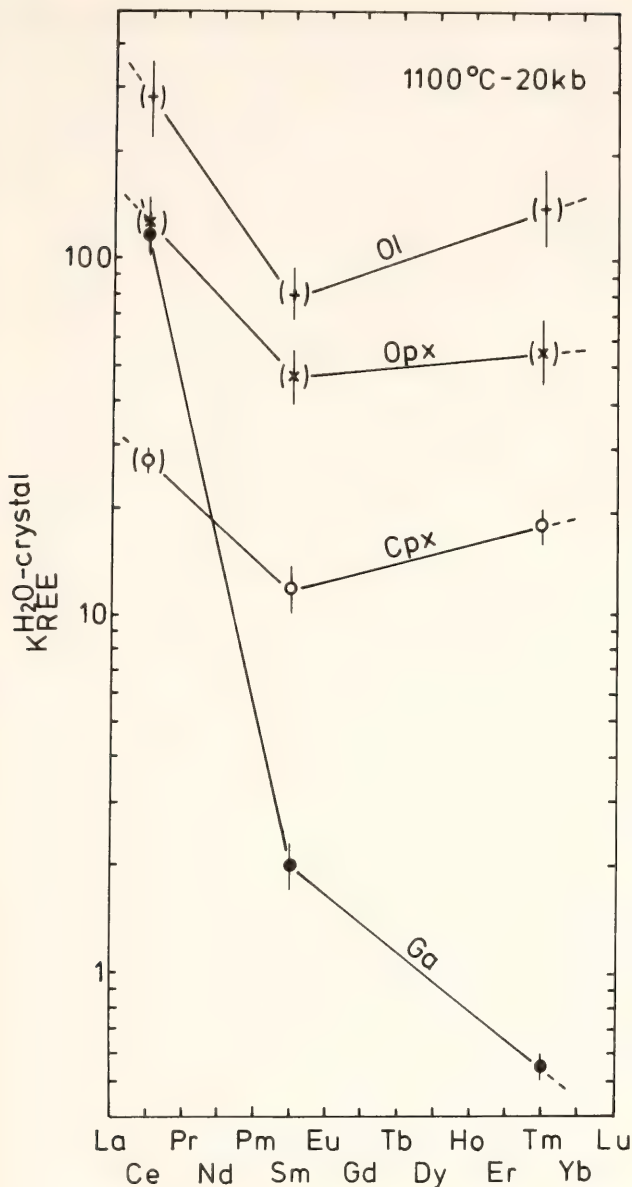


Fig. 27. Vapor-crystal partition coefficients for garnet, clinopyroxene, orthopyroxene, and olivine at 20 kbar and 1100°C. Symbols in parentheses represent calculated partition coefficients. Error bars, $\pm 1 \sigma$.

tion coefficients is evident from the data in Fig. 28. The low-pressure data are comparable to those of Cullers *et al.* (1973) and Zielinski and Frey (1974) at pressures below 5 kbar. There are no other published experimental data with which to compare the present results at pressures corresponding to those of the lower crust and upper mantle.

The data shown in Figs. 27 and 28 may be used to calculate vapor-crystal partition coefficients for other REE and other

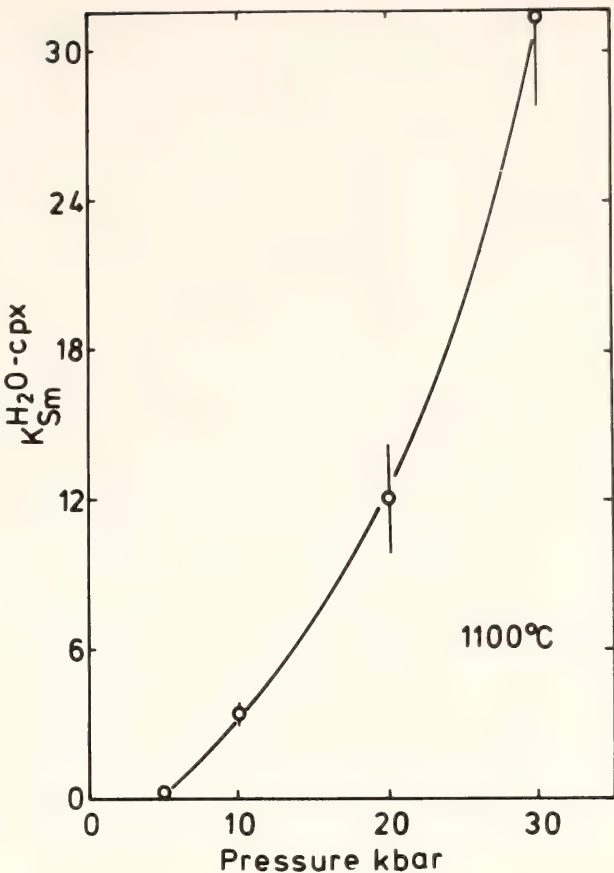


Fig. 28. Vapor-diopside partition coefficients for samarium as a function of pressure at 1100°C. Error bars, $\pm 1 \sigma$.

garnet peridotite minerals provided that the individual REE are not fractionated by the vapor and given that the REE crystal-crystal partition coefficients are available for the minerals and REE in question. Consequently, if two sets of vapor-crystal partition coefficients are known and if one of these sets can also be reproduced by calculation based on the other set, then it can be concluded that the activity coefficients of the REE complexes in the vapor are similar. The results of such an exercise are shown in Table 13, using $K_{\text{Sm}}^{\text{H}_2\text{O-Ga}}$ and the data of Mysen (*Year Book 76*, pp. 588–594) for $K_{\text{REE}}^{\text{Cpx-Ga}}$. The comparison of results shown in Table 13 suggests that the individual REE are not fractionated by H_2O -rich vapor.

On the basis of the above considerations, it is tentatively concluded that the strong positive pressure dependence

TABLE 13. Comparison of Measured and Calculated $K_{\text{REE}}^{\text{H}_2\text{O-diopside}}$ at 1100°C and 20 kbar

	Sm	Tm
Measured	12 ± 1.5	18.5 ± 2.5
Calculated	13 ± 3	21 ± 3

measured for $K_{\text{Sm}}^{\text{H}_2\text{O-diopside}}$ is caused by the increasing solubility of REE in H_2O -rich vapor and that the same pressure dependence is to be expected for other REE and when other minerals are considered. It may be argued that the REE in the vapor may form complexes with cations from the major element silicates. No data are available to test this suggestion. This possibility is therefore not taken into account in the following discussion. It is then possible to calculate all REE vapor-crystal partition coefficients as a function of pressure, provided that the different solubilities of major element components from the different minerals in the vapor are neglected. The neglect of major elements dissolved in the vapor is justified in view of the fact that the mole fraction of H_2O in the fluids is on the order of 0.94–0.98, depending on whether the dissolved silicate components are calculated as oxides or as $\text{CaMgSi}_2\text{O}_6$. It is assumed that this small silicate impurity in the vapor does not significantly affect the REE solubility in the fluid. The results of such calculations are shown in Fig. 29. The 40-kbar curves are based on an extrapolation of $K_{\text{Sm}}^{\text{H}_2\text{O-diopside}}$ to 40 kbar (see Fig. 28). It is evident from the results of these calculations that a water-rich fluid in the upper mantle constitutes a major sink for REE. This observation is further substantiated by the calculated bulk partition coefficients for two model garnet peridotites (Table 14) shown in Fig. 30. The results in this figure demonstrate that the water-rich fluid is strongly enriched in light REE and that the degree of light REE enrichment increases with increasing modal garnet content of the rock. The absolute REE

TABLE 14. Compositions of Garnet Peridotites (wt %)

	GP1	GP1 (16)	GP2
SiO_2	47.6	47.0	47.8
Al_2O_3	2.5	<0.1	5.1
MgO	47.3	52.0	44.5
CaO	2.6	1.0	2.6

Modal Compositions

Ga	10	0.1	20
Cpx	10	4.0	10
Opx	20	22.1	20
Ol	60	73.8	50

*REE Contents**

Ce	1	0.04	1
Sm	1	0.45	1
Tm	1	0.72	1

* Relative to average chondrite (Schmitt *et al.*, 1963, 1964).

abundance of the fluid also increases rapidly with pressure. The bulk partition coefficient involving garnet-free peridotite and water-rich vapor does not vary significantly with atomic number because the vapor-crystal partition coefficients of individual REE for the minerals in such peridotite do not vary significantly with atomic number.

Data supporting an interpretation of metasomatic alteration of peridotite trace element and isotope contents in the mantle prior to transport of the samples of such mantle to the earth's surface by kimberlitic magma have been provided by Ridley and Dawson (1975), Rhodes and Dawson (1975), and Erlank and Shimizu (1977). The REE data of Shimizu (1975) also appear to be best interpreted in terms of metasomatism in the mantle prior to sampling by ascending kimberlite magma.

Boyd and McCallister (1976) suggested that depleted garnet peridotite nodules in kimberlite represent residual crystalline material after partial melting of fertile garnet peridotite. The garnet peridotite nodule 1611 (Nixon and Boyd, 1973) is a

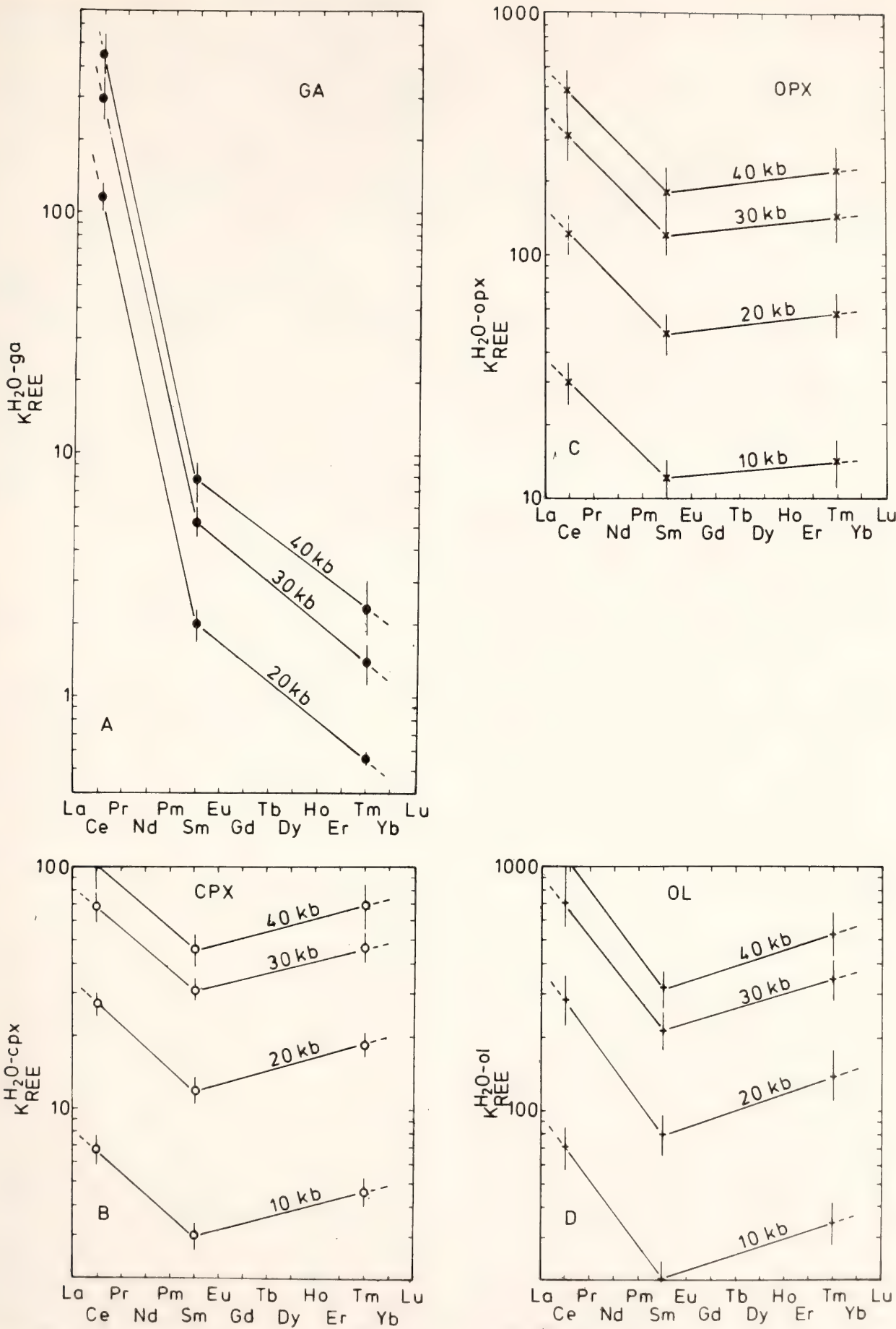


Fig. 29. Pressure dependence of $K_{REE}^{H_2O-crystal}$ at 1100°C for olivine, orthopyroxene, clinopyroxene, and garnet. Error bars, $\pm 1 \sigma$.

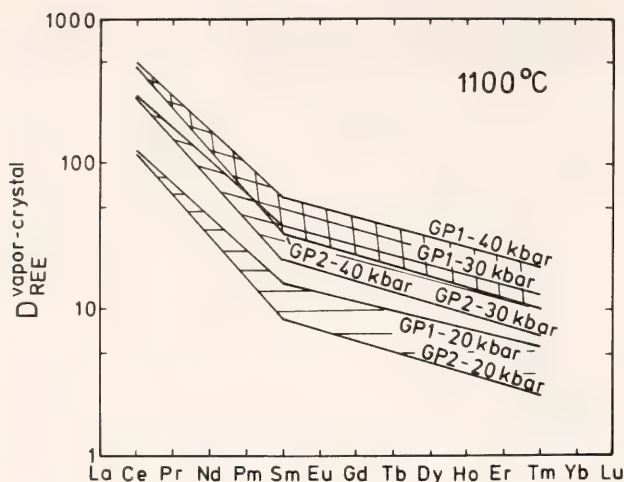
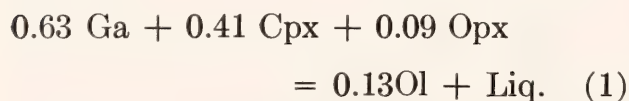


Fig. 30. Bulk partition coefficients, $D_{\text{REE}}^{\text{H}_2\text{O-crystal}}$, for garnet peridotites GP1 and GP2 as a function of pressure at 1100°C. Error bars, $\pm 1 \sigma$.

likely candidate for the fertile mantle material (e.g., Shimizu, 1975). According to Mysen and Kushiro (1977), partial melting of garnet peridotite of a composition similar to that of 1611 is close to the melting behavior observed in simple systems like $\text{CaSiO}_3\text{-MgSiO}_3\text{-Al}_2\text{O}_3\text{-SiO}_2$ (CMAS). By employing the phase-equilibrium data from CMAS (Kushiro and Yoder, *Year Book* 73, pp. 266–269), Mysen (*Year Book* 76, pp. 541–544) showed that the stoichiometry of the equation expressing the melting of garnet peridotite is approximated by the formulation:



The modal composition of the idealized model garnet peridotite, GP1 (Table 14), is similar to that of nodule 1611 (Nixon and Boyd, 1973a). In the following calculations, composition GP1 represents the fertile garnet peridotite. The depleted garnet peridotite is assumed to be generated by partial melting of GP1 until garnet is exhausted (16% melting).

The source of H_2O is considered similar compositionally to undepleted garnet peridotite such as model GP1 because its modal composition is similar to the pre-

sumed undepleted nodule 1611 (Boyd and McCallister, 1976). The amount of H_2O in the upper mantle is not known, but is generally assumed to be on the order of a few tenths of one percent. If such H_2O is bound in crystalline mantle materials, a change in activity of H_2O ($a_{\text{H}_2\text{O}}$) is needed to induce breakdown of the hydrous mineral to release H_2O . This change of $a_{\text{H}_2\text{O}}$ could be the result of increased temperature or introduction of another fluid phase, for example. After release, this H_2O -rich vapor (fluid) then migrates into the surrounding depleted garnet peridotite under near-isothermal and near-isobaric conditions. The concentration of an element i in the metasomatized rock is given by the expression (see Mysen, this Report, for derivation and constraints)

$$R_i^M = R_i^D (1 - Y_v X_M) \\ + \frac{R_i^s X_M Y_v}{D_i^s - X_s (D_i^s - 1)} \quad (2)$$

where the symbols are defined in Table 15. In applying this equation to rocks, X_s is set equal to 0.001, $X_M = 0.002$ and $Y_v = 1$. These values imply that the volume of depleted rock to be metasomatized is half that of the source rock. Inasmuch as the value of Y_v for reasonable mantle conditions is unknown, Y_v is set equal to 1. Values of $Y_v < 1$ and $X_M < 0.002$ will result in lower values of R_i^M . The value of X_s is probably near the minimum for fertile garnet peridotite. Higher values of X_s result in a somewhat higher degree of light-REE enrichment.

The REE abundances of a garnet peridotite source of basalt relative to average chondrite (Schmitt *et al.*, 1963, 1964) may be between 2 and 3. Metasomatic alteration of model garnet peridotite GP1 that has been depleted by 16% partial melting according to the stoichiometry of Equation 1 (the point of exhaustion of garnet) results in a REE pattern like that shown in Fig. 31 ($\text{Ce/Sm} \sim 3$, $\text{Ce/Tm} \sim 10$). The degree of relative light-REE enrichment of

TABLE 15. Definition of Symbols in Equation 2

R_i^s	—Element content of source rock before metasomatism.
R_i^D	—Element content of metasomatized rock before metasomatism.
R_i^M	—Element content of metasomatized rock after metasomatism.
D_i^s & D_i^M	—Bulk partition coefficient of i between crystals and vapor in the source rock and metasomatized rock, respectively.
X_s	—Mass fraction of source rock that is converted to vapor during dehydration.
X_M	—Mass fraction of volatiles in metasomatized rock during metasomatism.
Y_s	—Proportion of fluid left in metasomatized rock after metasomatism.

natural depleted garnet peridotite from kimberlite and associated rocks is quite similar to the calculated results shown in Fig. 31.

In summary, the relative fractionation of REE in nodules of depleted garnet peridotite found in kimberlite and related rocks is closely similar to the REE patterns resulting from metasomatic altera-

tion of rocks that were depleted in their major elements owing to a melting event prior to the metasomatism. The metasomatizing fluid was derived from rocks with composition similar to that of the rocks that became depleted during the partial melting. The absolute REE abundances in natural depleted garnet peridotite rocks cover about an order of magnitude. This wide range may result from variations in the REE contents of the source rock or from variable proportions of fluid in the source rock relative to the altered rock, or both.

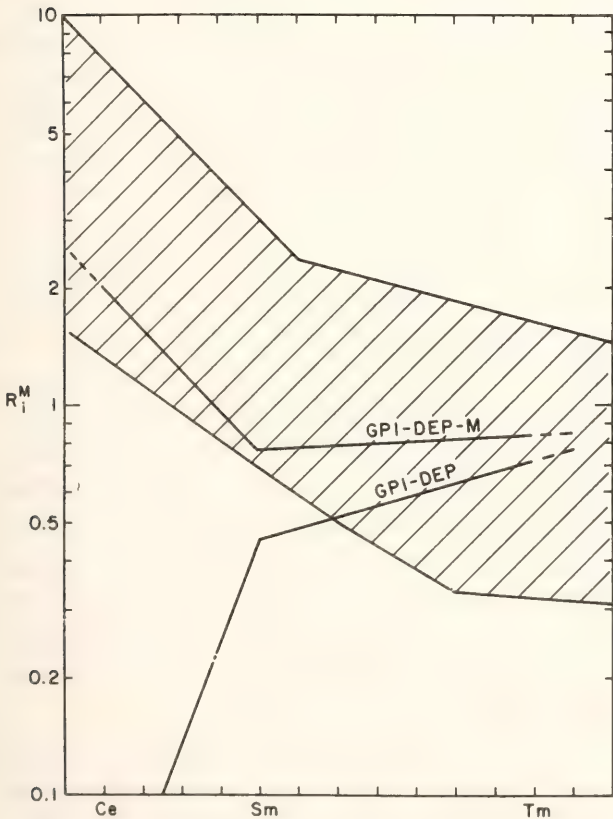


Fig. 31. Rare earth element pattern of metasomatized, depleted garnet peridotite considered most reasonable for the portions of the upper mantle sampled by kimberlite. See text for discussion of variables. Shaded area represents range of REE abundance patterns of depleted garnet peridotite nodules (Shimizu, 1975; Ridley and Dawson, 1975; Mitchell and Carswell, 1976).

PHASE EQUILIBRIA AND RARE EARTH
ELEMENT PARTITIONING BETWEEN
COEXISTING IMMISCIBLE CARBONATE
AND SILICATE LIQUIDS AND CO₂ VAPOR
IN THE SYSTEM K₂O-Al₂O₃-SiO₂-CO₂

Richard F. Wendlandt and Wendy J. Harrison*

Partitioning experiments for rare earth elements (REE's) between H₂O vapor and silicate minerals at high pressures have shown that a metasomatic, H₂O-rich fluid in the mantle may control the REE patterns of mantle-derived magmas (Mysen, 1978*b*). The genesis of magmas with typically high REE contents (e.g., alkali silicate, carbonatite, and kimberlite magmas) that can be related by liquid immiscibility at low pressures (Koster van Groos and Wyllie, 1966; Dawson and

* Work carried out under a cooperative predoctoral fellowship program between the Geophysical Laboratory and the University of Manchester.

Hawthorne, 1973) is enhanced by, if not dependent on, the presence of CO_2 in the magma source region (see Eggler, *Year Book* 73, pp. 215–224; Eggler, 1978; Kushiro, 1975). Because REE's form carbonate complexes (Balashov and Krigman, 1975), it was expected that a CO_2 -rich vapor would be even more REE-enriched than an H_2O vapor. The purpose of these experiments was to investigate the stability of immiscible carbonate and alkali silicate liquids at high pressure and to determine the REE partition coefficients among these immiscible liquids and a CO_2 vapor.

Experimental Method

Starting materials were high sanidine (Sa), prepared by ion exchange of high albite (Orville, 1967) crystallized from glass (Schairer and Bowen, 1955), and reagent-grade potassium carbonate, K_2CO_3 (KC). The hygroscopic nature of K_2CO_3 required that it be dried carefully before preparation of starting mixes. All mixes ($\text{Sa}_{90}\text{KC}_{10}$, $\text{Sa}_{60}\text{KC}_{40}$, and $\text{Sa}_{20}\text{KC}_{80}$ wt %) were subsequently maintained at 120°C and removed from the oven only for the brief periods necessary to load capsules.

All experiments at 20 kbar were carried out in a solid-media high-pressure apparatus (Boyd and England, 1960) using a piston-out technique without correction for friction. Talc-Pyrex furnace assemblies were employed to minimize diffusion of hydrogen into the capsule container. All experiments were conducted in Pt capsules 2 mm or 3 mm in diameter. Nominal pressures quoted in this report are precise to ± 0.5 kbar. Temperatures were measured with Pt-Pt90Rh10 thermocouples and automatically controlled to $\pm 1^\circ\text{C}$ (Hadidiacos, *Year Book* 71, pp. 620–622). No correction was made for the effect of pressure on the emf output of the thermocouple; temperatures are believed to be accurate to $\pm 10^\circ\text{C}$.

Experiments at 5 kbar were carried out

in the internally heated gas-media apparatus (Yoder, 1950). Temperatures were measured with Pt-Pt90Rh10 thermocouples and are precise to $\pm 5^\circ\text{C}$. Nominal pressures are precise to ± 25 bars.

Approximately 1 ppb radioactive tungsten-185 (kindly supplied by Dr. George Cowan of the Los Alamos Scientific Laboratory) was added to portions of the $\text{Sa}_{90}\text{KC}_{10}$ and $\text{Sa}_{60}\text{KC}_{40}$ compositions. Three additional portions of the $\text{Sa}_{60}\text{KC}_{40}$ material were spiked with approximately 203 ± 10 ppm cerium-141, 8.67 ± 0.43 ppm samarium-151, and 94 ± 4.7 ppb thulium-171, respectively.

Liquid-crystal ($D_{\text{W}}^{\text{liquid-crystal}}$) and liquid- CO_2 vapor ($D_{\text{W}}^{\text{liquid-CO}_2 \text{ vapor}}$) partition coefficients for tungsten-185 are in excess of 50 (see Wendlandt and Mysen, this Report); therefore, the wt % of partial melting in the presence of a vapor phase can be determined by relating the ^{185}W concentration in an unknown fraction of melt to the ^{185}W concentration in a completely melted standard (Mysen and Kushiro, 1977). Additionally, the relative proportions of two coexisting liquids, with or without a coexisting vapor phase, can be determined from the relative ^{185}W concentrations in the two liquids. Partitioning of the rare earth element (REE) isotopes between two liquids, in the absence of a vapor, can be used to check the melt portions determined by ^{185}W partitioning. In the presence of a vapor, mass-balance equations for REE's between two liquids can be used to determine vapor-liquid partition coefficients. Trace element concentrations were determined by autoradiography using the method of Mysen and Seitz (1975).

Grain mounts and polished sections were prepared from all runs containing radioactive isotopes. Petrographic determinations of the stable phase assemblage and x-ray confirmations were made immediately upon opening a run capsule because the quenched carbonate liquid hydrates rapidly. Polished sections were prepared under oil.

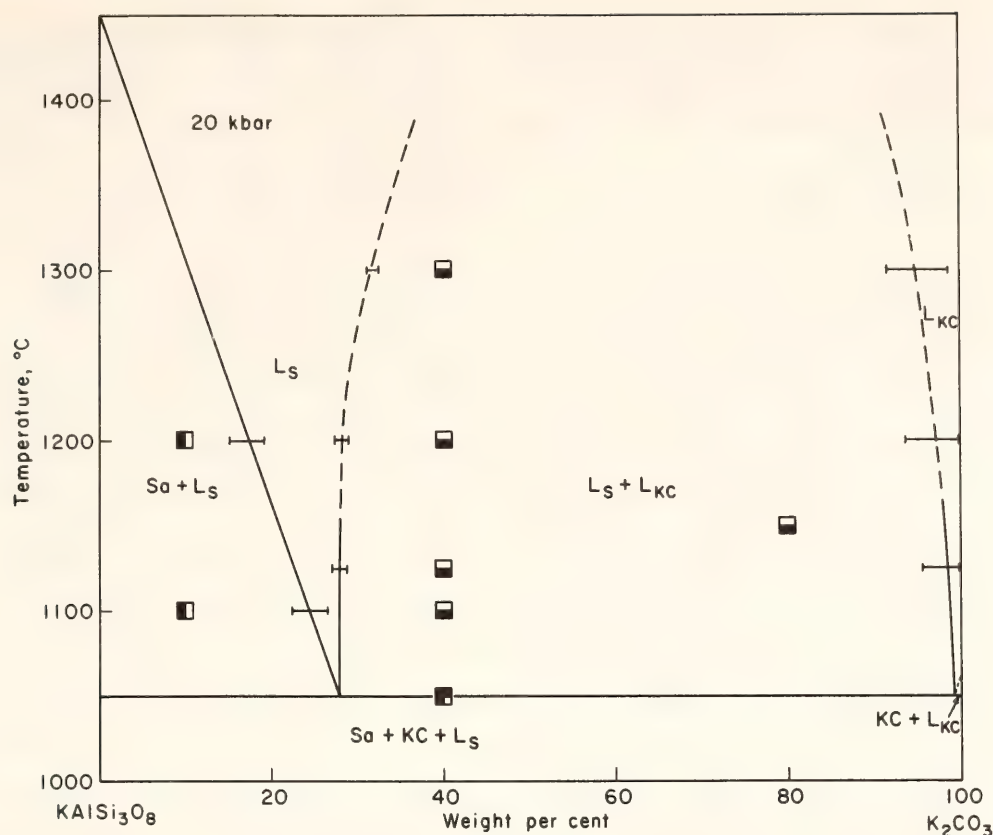


Fig. 32. Melting relations involving coexisting carbonate and silicate melts on the join sanidine-potassium carbonate at 20 kbar. Dashed lines indicate phase field boundaries that are based on presumed carbonate melt compositions. The size of brackets determined by autoradiography includes statistical uncertainty ($\pm 1 \sigma$). Runs are located by boxes. Abbreviations: Sa, sanidine; KC, potassium carbonate; L_s , silicate-rich liquid; L_{KC} , carbonate-rich liquid.

Phase Relations

Melting relations involving coexisting carbonate and silicate melts along the join sanidine-potassium carbonate are presented in Fig. 32 (20 kbar) and Fig. 33 (5 kbar). The relations at both pressures are dominated by the large two-liquid regions that cover more than 60% of the joins at 1200°C. Earlier investigations by Koster van Groos (1975) have revealed immiscible carbonate and silicate melts in the system $\text{NaAlSi}_3\text{O}_8\text{-CaAl}_2\text{Si}_2\text{O}_8\text{-Na}_2\text{CO}_3\text{-H}_2\text{O}$ at 10 kbar. The results of this investigation at 20 kbar represent a substantial extension of the known stability conditions for immiscible liquids.

The melting relations at 20 kbar are more simple than those at 5 kbar because no vapor phase is present, sanidine melts congruently, and the join sanidine-

potassium carbonate is binary within the limits of precision of electron microprobe analyses of quenched silicate melt. The low-temperature limit of the two-liquid region is approximately 1050°C (Fig. 32). This limit is not the solidus for the join; a phase field for $\text{Sa} + \text{KC} + L_s$ (silicate liquid) is inferred at lower temperatures. This lower boundary of the two-liquid region is the only phase-field boundary that was determined at 20 kbar solely by inspection of the stable phase assemblage. All other phase boundaries were determined by partitioning of ^{185}W between sanidine and liquid or between silicate and carbonate liquids. These partitioning data are summarized in Table 16. Because the partitioning data yield only relative proportions of two phases, it is necessary to have an independent fix on the major element composition of one of the phases

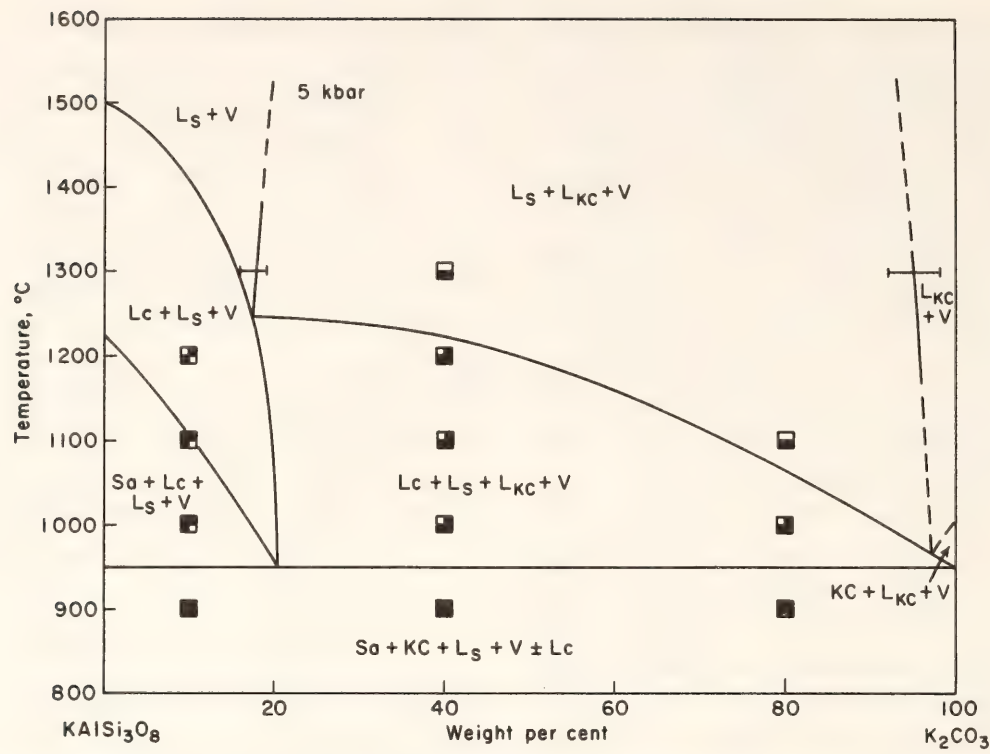


Fig. 33. Melting relations involving coexisting carbonate and silicate melts on the join sanidine-potassium carbonate at 5 kbar. Dashed lines are inferred. The sizes of brackets and abbreviations are defined in Fig. 32; additionally: Lc, leucite; V, vapor.

TABLE 16. Partitioning of ¹⁸⁵W between Carbonate and Silicate Melts in the KAlSi₃O₈-K₂CO₃ System

Bulk Composition (wt %)	P, kbar	T, °C	Melt fractions* (wt %)	D $\frac{\text{carbonate melt}}{\text{silicate melt}}$
Sanidine ₉₀ (K ₂ CO ₃) ₁₀	5	1200	66 ± 1.0 S	—
Sanidine ₉₀ (K ₂ CO ₃) ₁₀	20	1100	41 ± 2.0 S	—
Sanidine ₉₀ (K ₂ CO ₃) ₁₀	20	1200	58 ± 2.0 S	—
Sanidine ₆₀ (K ₂ CO ₃) ₄₀	5	1300	29 ± 1.0 C	16.03 ± 0.77
			71 ± 3.0 S	
Sanidine ₆₀ (K ₂ CO ₃) ₄₀	5	1200	41 ± 1.6 C	29.32 ± 0.97
			59 ± 2.4 S	
Sanidine ₆₀ (K ₂ CO ₃) ₄₀	20	1300	13 ± 0.5 C	17.79 ± 0.89
			87 ± 3.5 S	
Sanidine ₆₀ (K ₂ CO ₃) ₄₀	20	1200	17 ± 0.7 C	19.7 ± 0.55
			83 ± 3.3 S	
Sanidine ₆₀ (K ₂ CO ₃) ₄₀	20	1125	17 ± 0.7 C	18.92 ± 0.89
			83 ± 3.3 S	

* S = silicate melt; C = carbonate melt.

in order to determine the composition of the other. In Fig. 32, it was first assumed that the composition of sanidine was pure KAlSi₃O₈, thus fixing the compositions of the melts in equilibrium with sanidine at 1100° and 1200°C. Second, it was assumed

that the composition of the silicate melt coexisting with a carbonate melt at 1125°C was the same as the composition defined by extrapolating the Sa + L_s surface to the Sa + KC + L_s boundary. Finally, the brackets at 1200°C and 1300°

were determined based on the assumption that the solubility of sanidine component in carbonate melt increases only slightly with increasing temperature. The final assumption is qualitatively substantiated by optical inspection of the relative proportions of carbonate and silicate liquids at 1125°, 1200°C, and 1300°C and is compatible with the data of Koster van Groos and Wyllie (1966) in the system $\text{Na}_2\text{O}-\text{Al}_2\text{O}_3-\text{SiO}_2-\text{CO}_2$. Additionally, $D_{\text{W}}^{\text{carbonate melt-silicate melt}}$ (Table 16) does not change significantly between 1125° and 1300°C; this behavior implies that only slight changes occur in the proportions of the two melts (at the top of the solvus the carbonate melt-silicate melt partition coefficient will approach unity).

Melting relations at 5 kbar (Fig. 33) are complicated by the presence of a vapor for the compositions investigated on the join and by the incongruent melting of sanidine to leucite + liquid (Lindsley, *Year Book* 65, pp. 244-247). (The latter feature results in nonbinary relations on the join.) The low-temperature limit of the two-liquid field is approximately 950°C; the solidus is believed to be only slightly lower because the melting point of K_2CO_3 at 1 atm is 891°C. Leucite coexists with both silicate and carbonate melts over a large temperature interval, particularly when bulk composition is silica-rich. An electron microprobe analysis of the silicate melt coexisting with carbonate melt at 1300°C combined with the proportions of the two melts derived from ^{185}W partition data (Table 16), effectively brackets the miscibility gap at this temperature. Other constraints on the phase relations are derived from the observed equilibrium phase assemblages.

There is ~50% more carbonate component in the silicate melt at 20 kbar than at 5 kbar. Both isobars are characterized by very slight amounts (less than 4 wt %) of dissolved silicates in the carbonate melt. Moreover, the CO_2 -saturated liquidus surface in the system $\text{K}_2\text{O}-\text{Al}_2\text{O}_3-\text{SiO}_2-\text{CO}_2$ does not intersect the

sanidine-potassium carbonate join at 20 kbar, whereas all compositions investigated are CO_2 -saturated at 5 kbar.

Rare Earth Element Partitioning

The partitioning of ^{141}Ce , ^{151}Sm , and ^{171}Tm between the coexisting carbonate and silicate melts was determined at 1200°C and at 5 and 20 kbar. Values for $D_{\text{REE}}^{\text{carbonate melt-silicate melt}}$ are plotted as a function of the rare earth elements in Fig. 34. Relative to the alkali silicate melt, the carbonate melt is enriched 2-3 times in light REE's and approximately eight times in heavy REE's; accordingly, a carbonatite would be expected to have higher total-REE contents and a less pronounced enrichment trend than a conjugate alkalic magma. Such enrichment trends for carbonatites ($\text{La/Lu} \simeq 75$) and alkali syenites ($\text{La/Lu} \simeq 100$) were determined by Haskin *et al.*, (1966).

The partition coefficients for the REE's in the absence of a vapor phase at 20 kbar can also be used to determine the proportions of the two coexisting melts. These calculations are in excellent agreement with the results of the ^{185}W partitioning data (averaging $84 \pm 1.6\%$ silicate melt and $16 \pm 1.6\%$ carbonate melt) at 1200°C. The agreement between the data is confirmation that a free vapor phase does not exist on the join at 20 kbar.

The partition coefficients for REE's between carbonate melt and silicate melt are less at 5 kbar than at 20 kbar (Fig. 34). This difference cannot be attributed directly to the effect of pressure because the melt compositions on the two isobars are different (as discussed above) and because a vapor phase is present at 5 kbar and not at 20 kbar. If the effects of composition are ignored, the partition coefficients at 20 kbar would be expected to be lower than those at 5 kbar (Mysen and Kushiro, 1978). The large composition differences between the systems studied in this report and by Mysen and Kushiro, however, preclude direct comparison. Alternatively, if the effects of composition

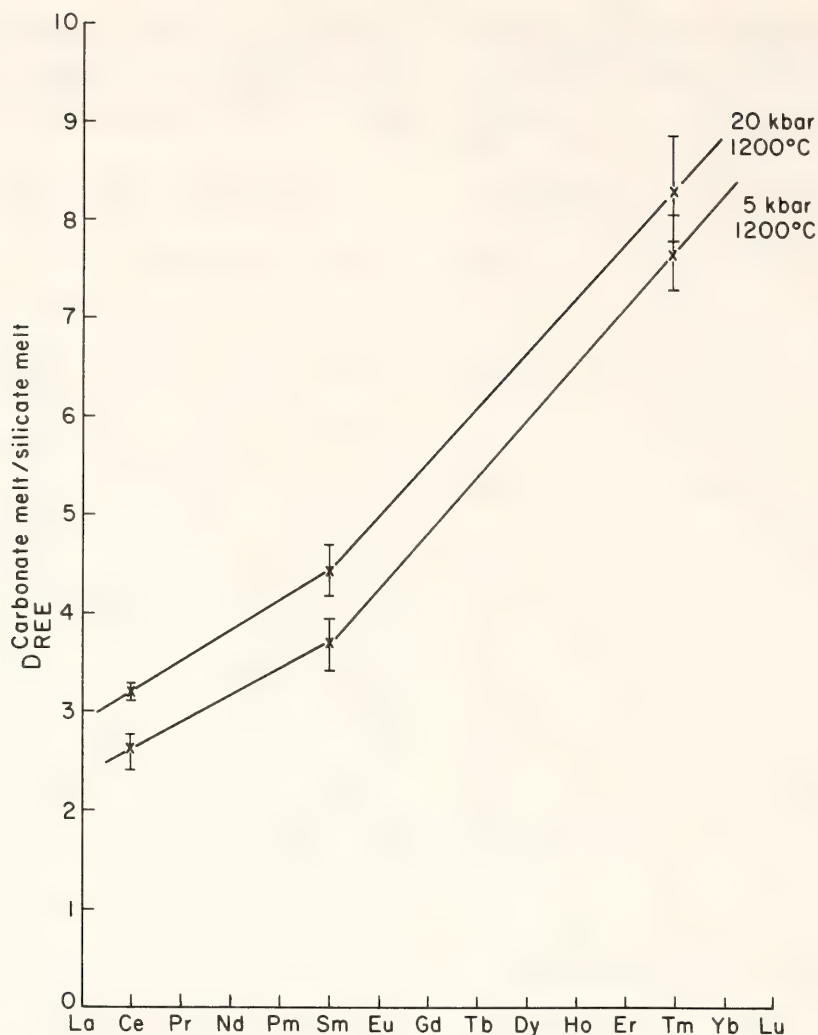


Fig. 34. Partition coefficients for three rare earth elements between coexisting carbonate and silicate melts at 1200°C, 5 kbar and 20 kbar. Error bars = $\pm 1 \sigma$.

are considered independently of pressure, then the increased carbonate content of the silicate melt at 20 kbar would be expected to result in partition coefficients lower than the 5-kbar values as a consequence of REE-carbonate complexes (Balashov and Krigman, 1976). It is apparent that the observed data cannot be reconciled with these predictions. Further experiments are in progress to investigate the influence of a vapor on REE partitioning at 20 kbar, but the phase relations are such that separate evaluation of the relative effects of pressure and composition in this system is impossible.

Mass-balance equations for the REE partitioning data at 5 kbar and 1200°C with the known proportions of melts at

these conditions (^{185}W data, Table 16) cannot be solved satisfactorily. Mass deficiencies are indicated, and these are attributed to the presence of a vapor phase. By assuming that those deficiencies are equal to the REE concentration in the vapor, minimum CO_2 vapor-carbonate liquid and CO_2 vapor-silicate liquid partition coefficients can be calculated, and the silicate melt-normalized rare earth abundances for carbonate melt and vapor can be deduced (Fig. 35). It is apparent that the vapor phase is substantially enriched in light REE's relative to both melts and in heavy REE's relative to the silicate melt.

The high REE contents of the vapor—even higher than the contents of the carbonate melt for ^{141}Ce —suggest that car-

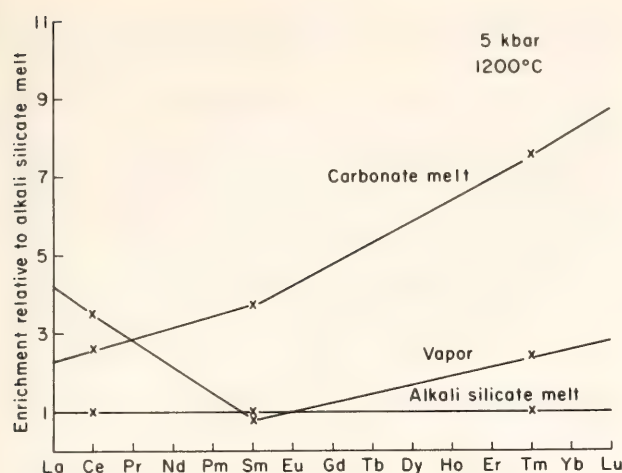


Fig. 35. Enrichment of carbonate melt and CO_2 vapor in REE's relative to a coexisting alkali silicate melt at 1200°C and 5 kbar. Light rare earth elements preferentially enter the vapor phase and heavy rare earth elements enter the carbonate melt.

bonate complexing of REE's by the vapor is almost as efficient as that by the melt. Vapor vesicles up to $30\ \mu\text{m}$ in diameter are observed in the quenched silicate melt. The vesicles are coated with a thin layer of carbonate and are interpreted as being present during run conditions. Extensive solubility of K_2CO_3 in the vapor phase is suggested, but the proportions of vapor and vapor solutes have not yet been determined.

In Fig. 36, $D_{\text{REE}}^{\text{CO}_2 \text{ vapor-carbonate melt}}$ and $D_{\text{REE}}^{\text{CO}_2 \text{ vapor-silicate melt}}$ at 5 kbar and 1200°C are compared with values of $D_{\text{REE}}^{\text{water vapor-silicate melt}}$ at 1075°C and 5 kbar and 20 kbar, which are calculated from water vapor-crystal partition data of Mysen (1978b) and from crystal-liquid data of Mysen (Year Book 76, pp. 588–594). The enrichment of REE's in the CO_2 vapor is approximately two orders of magnitude greater than that in water vapor at comparable pressures! If the effect of pressure on the water vapor-silicate melt partition coefficients is indicative, then the CO_2 vapor-melt partition coefficients for REE's at 20 kbar may be substantially larger.

Values of CO_2 vapor-crystal (olivine, orthopyroxene, and clinopyroxene) parti-

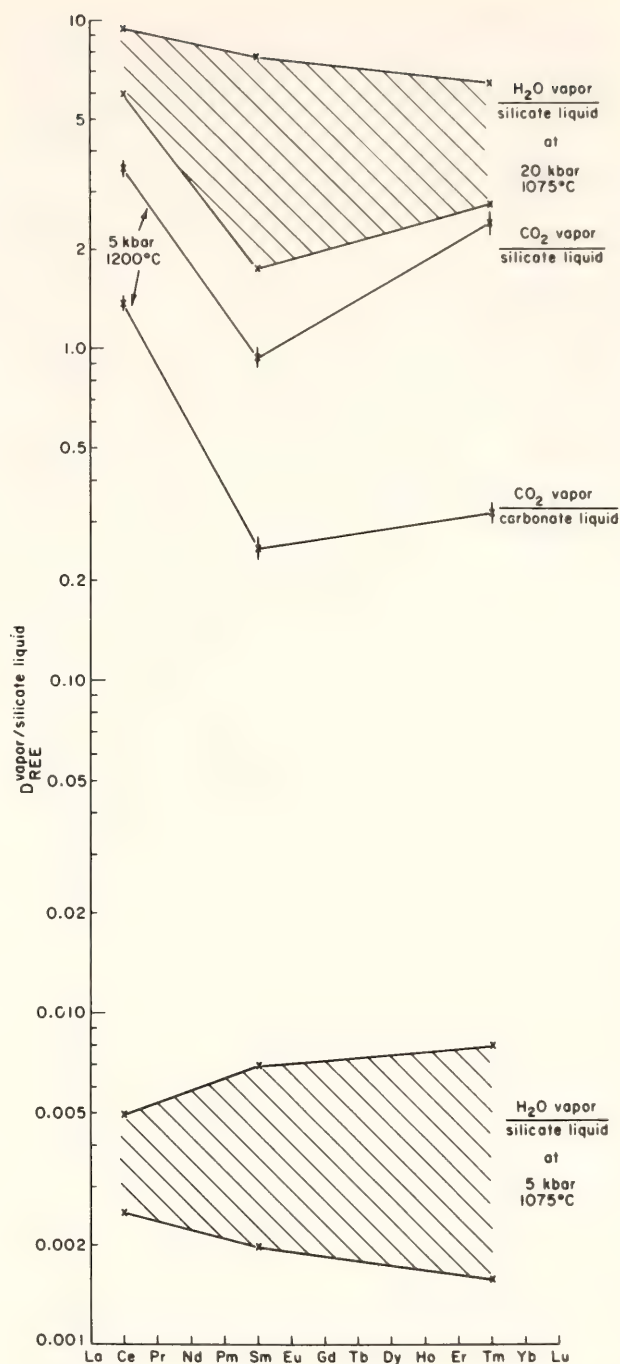


Fig. 36. Partition coefficients for REE's between CO_2 vapor and carbonate melt and CO_2 vapor and alkali silicate melt at 5 kbar and 1200°C . Error bars $\pm 1\sigma$. Also shown are ranges of values for H_2O vapor-silicate liquid partition coefficients at 1075°C , 5 kbar and 20 kbar, calculated from the data of Mysen (1978; Year Book 76, pp. 588–594).

tion coefficients are presented in Fig. 37. These values are calculated from the crystal-silicate melt data of Mysen (Year Book 76, pp. 588–594) and the CO_2 vapor-melt data of this investigation. The data

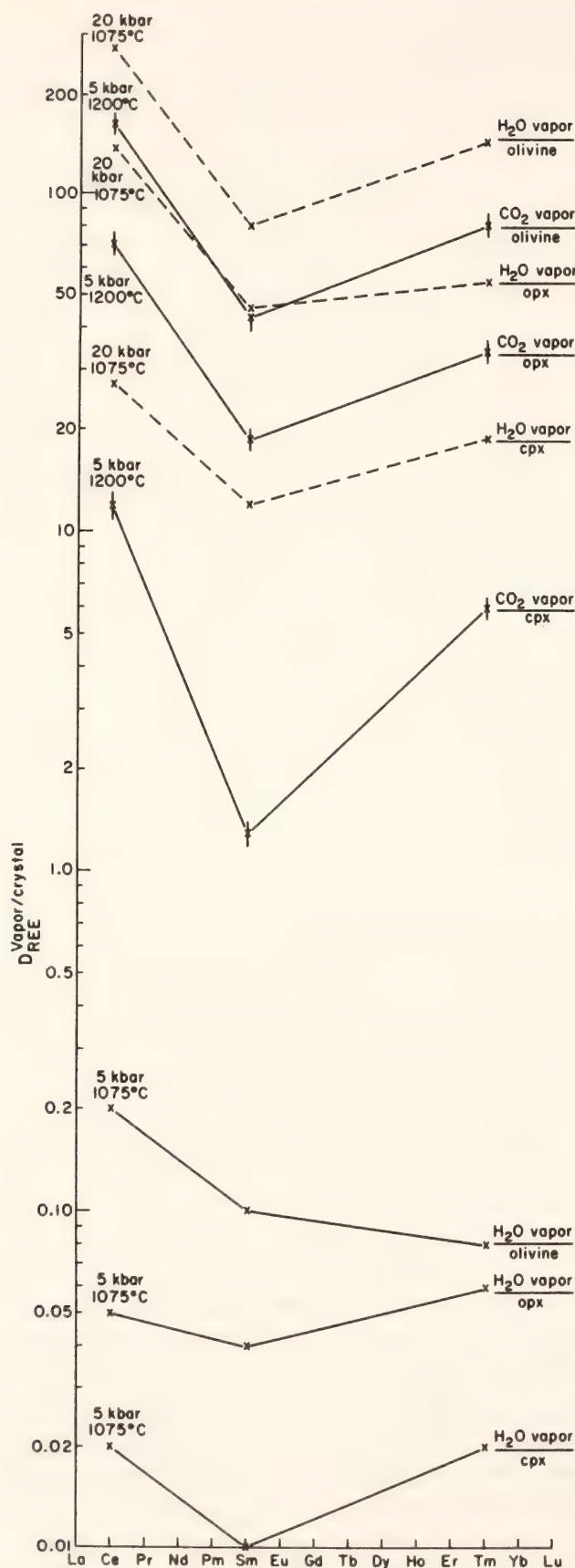


Fig. 37. Partition coefficients for REE's between CO_2 vapor and silicate minerals at 5 kbar and 1200°C , calculated from the data of Mysen (*Year Book 76*, pp. 588–594). Error bars $\pm 1\sigma$. Also shown are H_2O vapor–silicate mineral partition coefficients from data of Mysen (1978) at 1075°C , 5 kbar (solid lines) and 20 kbar (dashed lines).

are subject to restrictions imposed by the dissimilarity of the silicate melt compositions and by the necessity to extrapolate the crystal-melt data of Mysen (*Year Book 76*, pp. 588–594) from 20 kbar and 1075°C to 5 kbar and 1200°C . The latter extrapolation is believed to be valid because the effect of pressure on crystal-melt partition coefficients is small relative to that on water vapor–crystal or water vapor–melt partition coefficients (Mysen, 1978b). Also included in Fig. 37 are REE water vapor–crystal partition coefficients at 1075°C and 5 and 20 kbar (Mysen, 1978b). The CO_2 vapor–crystal partition coefficients for 5 kbar are approximately superimposed on the 20-kbar water vapor–crystal coefficients, again emphasizing the strong tendency for REE's to fractionate into a CO_2 -rich vapor. It is anticipated that this fractionation tendency will be enhanced with increasing pressures.

Discussion

The results of this study are applicable to the origins of alkali silicate and carbonatitic magmas by immiscibility at high pressures, to the REE contents of these magmas and perhaps of kimberlite, and to REE fractionation between CO_2 -rich vapors and melts and peridotite minerals.

Primary carbonatite melts can be derived by partial melting of carbonated mantle peridotite in the pressure range of approximately 25–28 kbar and 1200°C (Eggler, *Year Book 74*, pp. 468–474; Eggler, 1976; Wyllie and Huang, 1975a, 1975b). The carbonatitic melt becomes increasingly silicic with both increasing temperature (Wendlandt and Mysen, this Report) and increasing pressure (Wendlandt, 1977); hence, discrete magmas of variable silicate and carbonate contents are possible. At lower pressures such a magma may intersect a silicate melt–carbonate melt miscibility gap. Progressive separation of the two melt fractions with decreasing pressure and temperature results in a nearly pure carbonate phase at moderate pressures and exsolu-

tion of a vapor phase at lower crustal levels.

Partitioning of REE's between coexisting silicate and carbonate melts favors the carbonate melts, especially for the heavy REE's. When a CO₂ vapor is present, the light REE's are fractionated preferentially into the vapor even more than into the carbonate melt and some two orders of magnitude in excess of the possible contents of a water-rich vapor. The affinity of the REE's for carbonate melt and CO₂-rich vapor is believed to indicate carbonate complexing of the REE's. This affinity has important implications for understanding the genesis of those magma types often characterized by large REE contents and light-REE enrichment, such as carbonatites, alkali-rich basic silicate magmas, and kimberlites. The highly variable REE contents of these magmas could be indicative of variable degrees of melting, variable CO₂/H₂O ratios, and variable total volatile contents in the source region. Mysen (1978) has proposed that mantle metasomatism by a water-rich vapor enriched in light REE's can explain many of the observed REE trends of mantle-derived nodules and magmas. From the present results, it would appear that the presence of a CO₂-component in the vapor should greatly enhance the efficiency of that process.

THE DISTRIBUTION OF SAMARIUM AND THULIUM BETWEEN PLAGIOCLASE AND LIQUID IN THE SYSTEMS An-Di and Ab-An-Di at 1300°C

*James D. Hoover**

Rare earth elements (REE) in igneous rocks and minerals have been considered powerful indicators of the origin and evolution of magmas (Gast, 1968; Kay and Gast, 1973). Such models, however,

depend on reliable estimates of mineral-melt partition coefficients and predictable behavior of REE distribution as a function of intensive variables.

The crystallization and fractionation of plagioclase plays a major role in the evolution of many igneous rocks. In natural systems, partition coefficients for REE between plagioclase and liquid have been sought by measuring REE abundances in phenocryst-matrix pairs from porphyritic volcanic rocks (Philpotts and Schnetzler, 1970; Schnetzler and Philpotts, 1970). Although these results are useful as guidelines, such measurements are of limited value because of a lack of understanding of partition coefficients as a function of intensive and extensive parameters. To this end, several workers (Drake, 1972; Drake and Weill, 1974; Sun *et al.*, 1974) have investigated experimentally the distribution of REE between plagioclase and liquid. In all these studies, Henry's Law behavior was assumed to extend to concentration levels in excess of 0.01 wt %. Recent work by Wood (*Year Book* 75, pp. 659-662), Mysen (*Year Book* 76, pp. 588-594), Mysen (1976a, 1978a), and Harrison (this Report) has demonstrated, however, that REE substitution between garnet, pyroxene, and olivine melts departs from Henry's Law behavior at low concentrations in the range of several ppm to several tens of ppm. The existence of similar deviations in plagioclase melt systems may be of major petrogenetic importance. It was the purpose of this study, therefore, to investigate in the range of natural concentrations the partitioning of two REE's (Sm and Tm) between plagioclase and a haplobasaltic liquid as a function of composition and REE concentration.

Experimental Procedure

A composition on the binary join An-Di (An₅₅Di₄₅ wt ratio) and a ternary composition in the Ab-An-Di system (Ab₆₀-An₃₀Di₁₀ wt ratio) were selected as starting material. About 20% plagioclase

* Work carried out under a cooperative predoctoral fellowship program between the Geophysical Laboratory and the University of Oregon.

crystallizes from both compositions at 1300°C at 1 atm. Starting materials were prepared from synthetic glasses of anorthite, albite, and diopside compositions. Radioactive ^{151}Sm and ^{171}Tm and stable isotopes of Sm and Tm were added as dilute acidic chloride solutions to about 250-mg aliquants of starting mixes. Samples were loaded into $\text{Pt}_{95}\text{Au}_5$ envelopes and suspended in vertical quenching furnaces 100°C above the liquidus for at least one hour to homogenize the mixture. This method yielded a homogeneous glass of the theoretical mix composition (see Murphy, 1977); the homogeneity was verified by electron microprobe analyses. Charges were then quenched, crushed, and returned to the furnace at the experimental temperature, 1300°C. The sodium-free compositions were left at 1300°C for about 4 days and then quenched rapidly in water. In the system Ab-An-Di, difficulty was encountered in growing intermediate plagioclase sufficiently large for β -track analysis. In order to minimize the potential inhomogeneity of crystals that result when melts are cooled through the liquidus to maximize crystal size (cf. Lofgren and Donaldson, 1975), a modified form of the procedure used by Drake (1972) and Murphy (1977) was employed. After homogenization at 1400°C, samples containing an albite component were held at 1300°C for 6–8 hr. The temperature was then rapidly increased to a value just below the liquidus, where it was held for 20 min. The samples were then quenched and returned to the furnace at the experimental temperature. By this procedure most of the abundant small crystals grown at 1300°C were resorbed. The remaining crystals, therefore, provided nuclei on which fewer but larger crystals grew. These charges were also left at 1300°C for about 4 days, then quenched rapidly in water.

Samples containing 100 ppm Sm from both the An-Di and Ab-An-Di systems were also run at $f_{\text{O}_2} = 10^{-11.2}$ (QIF). Oxygen fugacity was controlled by mixtures of CO-CO₂, and run conditions were

the same as those previously described, except that the quenching medium was mercury.

Glass and crystalline run products were analyzed for major elements by the electron microprobe, and individual phases were found to be homogeneous with respect to major elements. Pure anorthite was grown from the $\text{An}_{55}\text{Di}_{45}$ (wt ratio) starting material. A homogeneous plagioclase composition of An_{60} grown from the mixture $\text{Ab}_{60}\text{An}_{30}\text{Di}_{10}$ (wt ratio) agrees with tie-line compositions on the 1300°C equilibrium isothermal section through the system Ab-An-Di, as determined by Murphy (1977). For run durations up to 4 days, sodium loss was negligible within the limits of analytical uncertainty. Samarium and thulium partition coefficients were determined using β -track autoradiography techniques, as described by Mysen and Seitz (1975). Homogeneous distribution of ^{151}Sm and ^{171}Tm in individual crystals was generally observed. The uncertainties shown in Fig. 38 ($\pm 1\sigma$) reflect principally the uncertainties in exposure times, counting errors, and any heterogeneity of Sm and Tm distribution.

Sm Partitioning in the Systems An-Di and Ab-An-Di

Results of Sm partitioning in the systems An-Di and Ab-An-Di are shown in Figs. 38A and 38B. The partition coefficients* of Sm between pure anorthite and liquid was constant ($D_{\text{Sm}}^{\text{plag/liq}} = 0.060 \pm 0.003$) over the range of liquid concentrations from 12 ppm to 1238 ppm Sm, corresponding to $C^s = 0.7$ ppm to 78 ppm Sm in the anorthite crystal (Fig. 38A). For $C^l < 12$ ppm Sm, the

* In the context of this report, D denotes the partition coefficient defined as $D_i = C_i^s/C_i^l$; where C_i^s indicates concentration of i in the crystal and C_i^l the concentration of i in the liquid. The partition coefficient between anorthite and liquid is designated $D^{\text{an/liq}}$, and between intermediate plagioclase and liquid as $D^{\text{plag/liq}}$.

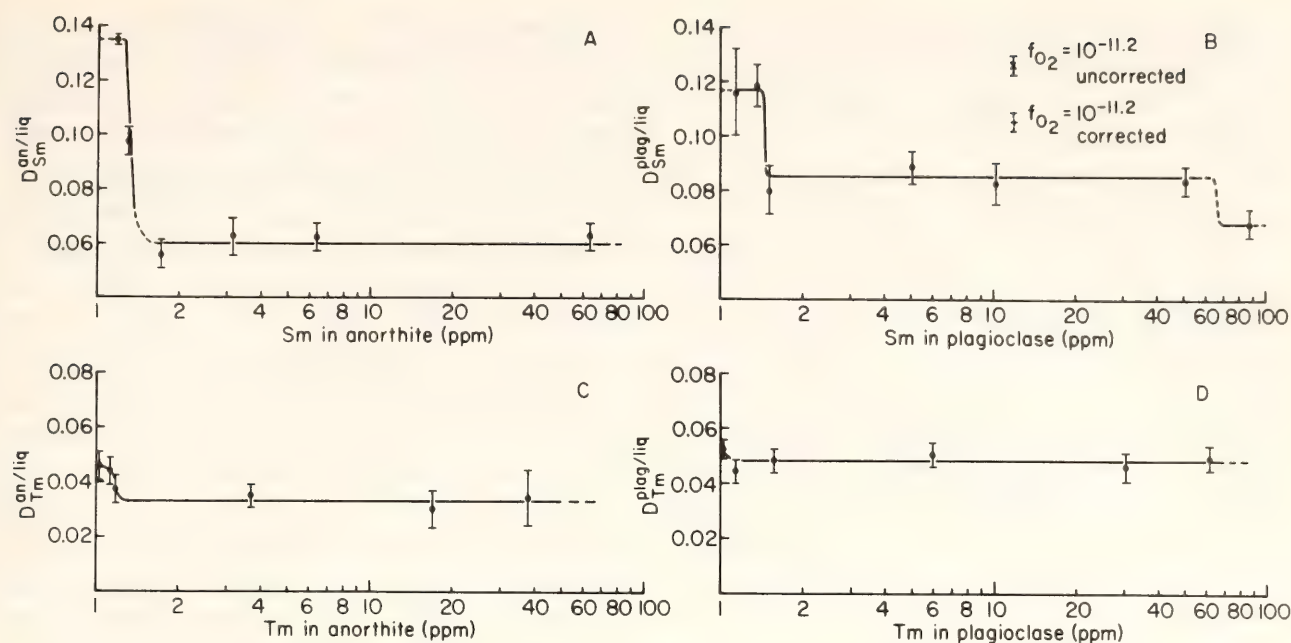


Fig. 38. (A) The distribution coefficient for Sm between anorthite and liquid plotted against the concentration of Sm in anorthite in the system An-Di at 1 atm. (B) The distribution coefficient for Sm between plagioclase An_{60} and liquid, plotted against the concentration of Sm in plagioclase, in the system Ab-An-Di at 1 atm. (C) The distribution coefficient for Tm between anorthite and liquid, plotted against the concentration of Tm in anorthite, in the system An-Di at 1 atm. (D) The distribution coefficient of Tm between plagioclase An_{60} and liquid, plotted against the concentration of Tm in plagioclase, in the system Ab-An-Di at 1 atm.

distribution coefficient increased abruptly to 0.135 ± 0.008 .

The partition coefficients of Sm between the haplobasaltic liquid in the system Ab-An-Di and an intermediate plagioclase (An_{60}) also depend on Sm concentration at low Sm content. At $C^1 = 1342$ ppm Sm (corresponding to $C^s \cong 87$ ppm Sm), D_{Sm} was 0.067 ± 0.005 , similar to the value of $D_{Sm}^{plag/liq}$ between anorthite and the sodium-free liquid. But for melts containing 60-600 ppm Sm ($C^s = 5-51$ ppm), $D_{Sm}^{plag/liq}$ increased to a nearly constant value of about 0.085 ± 0.003 . At $C^1 = 13$ ppm Sm and less ($C^s < 1$ ppm Sm) D_{Sm} further increases to 0.117 ± 0.006 (Fig. 38B).

A single experiment in the system Ab-An-Di with total Sm content equal to 100 ppm and $f_{O_2} = 10^{-11.2}$ (QIF) yielded a $D_{Sm}^{plag/liq} = 0.136$, a value apparently greater than that observed for the same composition done in air. The value is also apparently greater than at concentrations < 13 ppm in air (Fig. 38B). A similar experiment in An-Di system indicated

no marked increase in $D_{Sm}^{an/liq}$. However, a 25% Sm loss—at least in part to the platinum container—occurred during both runs, as indicated by Sm concentrations lower in the resulting glass than in the bulk charge. Because REE loss from the liquid is far greater than from the crystals, the increase in $D_{Sm}^{plag/liq}$ is partially explained. The most important result, however, is that the concentration of Sm in the crystal (An_{60}) for the run at $f_{O_2} = 10^{-11.2}$ was significantly greater than for crystals from experiments in air. In fact, if the liquid prior to Sm loss had the same Sm concentration as the identical run in air, the resulting $D_{Sm}^{plag/liq}$ would still be 0.105, a value greater than that observed in the air experiment but similar to the highest D_{Sm} measured at concentrations < 13 ppm.

Tm Partitioning in the Systems An-Di and Ab-An-Di

Data on thulium partitioning between plagioclase and liquid in the systems

An-Di and Ab-An-Di are given in Figs. 38C and 38D. In the system An-Di, $D_{\text{Tm}}^{\text{an/liq}}$ has a constant value of 0.033 ± 0.003 for C^1 between 11 and 1150 ppm Tm (corresponding to 0.3 ppm and 38 ppm Tm in anorthite) (Fig. 38C).

The partition coefficient increases slightly to 0.049 ± 0.002 in the system Ab-An-Di at nearly all measured liquid concentrations less than 1170 ppm Tm (< 62 ppm Tm in plagioclase). A lowering of C^1 to 1.5 ppm Tm (0.06 ppm Tm in plagioclase), however, increases $D_{\text{Tm}}^{\text{plag/liq}}$ to about 0.053 ± 0.004 .

Discussion

It is observed from these preliminary data that (1) a measurable bulk compositional dependence of $D_{\text{Sm-Tm}}^{\text{plag/liq}}$ is indicated by the differences between $D^{\text{an/liq}}$ and $D^{\text{plag/liq}}$ for both Sm and Tm, (2) Sm may occupy at least three types of sites in the compositionally intermediate plagioclase structure similar to the findings of Iiyama (1968), provided that the activity coefficient of Sm in the liquid does not change with Sm concentration, (3) either thulium does not enter one of these sites or at least one of the sites accommodates Tm more readily than Sm, (4) an imposed low f_{O_2} may affect the nature or number of these sites, and (5) measurable REE loss occurs during experiments in controlled atmospheres.

Because higher values of D_{Sm} and D_{Tm} are observed in the system Ab-An-Di than in the system An-Di above the concentration limit where REE's dissolve in plagioclase according to Henry's Law, the addition of the albite component to the glass or crystal structure results in a relative increase in the number of sites in the crystal reflecting the changes in the ratio of activity coefficients: $\gamma_{\text{REE}}^{\text{crystal}}/\gamma_{\text{REE}}^1$.

Defect sites, however, are inherent to distortions in the plagioclase structure through the replacement of Al by Si and the substitution of Ca by Na (Smith, 1974). The apparent dependence of $D_{\text{REE}}^{\text{plag/liq}}$ on f_{O_2} requires further in-

vestigation but it is supported by observations of Mackey (1966) and may have important ramifications for magmatic systems. The second decrease in $D_{\text{Sm}}^{\text{plag/liq}}$ in the sodium-bearing system at $C^s > 51$ ppm (Fig. 38B) is based on only one data point and must be investigated further. Similarly, no decrease in $D_{\text{Tm}}^{\text{plag/liq}}$ (Fig. 38D) was observed for C^s up to 61 ppm. Further work is being carried out to determine whether $D_{\text{Tm}}^{\text{plag/liq}}$ will indeed decrease at higher concentrations.

The measurable Sm loss for runs at low f_{O_2} is similar to the loss of Eu observed by Mysen and others (this Report). Such REE loss from the liquid phase can seriously affect measured D_{REE} values, as discussed by Mysen and others (this Report), and the nature of the Eu and Sm loss is still under investigation.

THE EFFECT OF PRESSURE ON THE PARTITIONING OF NICKEL BETWEEN OLIVINE AND ALUMINOUS SILICATE MELT

Björn O. Mysen and Ikuo Kushiro

The nickel content of magmas is often considered a sensitive indicator of their petrogenetic history (Gill, 1970; Arndt, *Year Book* 76, pp. 553-557; Frey *et al.*, 1974) because of the large value of the olivine-liquid partition coefficients ($D_{\text{Ni}}^{\text{ol-liq}}$), because of the importance of olivine in the source rock of partial melts in the upper mantle, and because olivine plays a dominant role during fractional crystallization of basaltic magma. If basalts and related magmas are generated in the upper mantle, it is important to understand how crystal-liquid partition coefficients change with pressure. Such dependence may be particularly significant if the structure of silicate melt changes in the pressure range corresponding to magma formation in the upper mantle and magma evolution in the crust. Structural changes of melts at high pressure have been indicated by data on viscosity and density of $\text{NaAlSi}_2\text{O}_6$ melt

to 24 kbar (Kushiro, 1976), by data on solubility of volatiles in melts on the join $\text{NaAlSi}_3\text{O}_8\text{-SiO}_2$ to 30 kbar (Mysen, 1976b), by Mössbauer studies of melts on the join $\text{NaAlSi}_2\text{O}_6\text{-NaFe}^{3+}\text{Si}_2\text{O}_6$ to 40 kbar (Mysen and Virgo, 1978), and by laser Raman spectroscopy of $\text{NaAlSi}_2\text{O}_6$ melts to 40 kbar (Sharma, Virgo and Mysen, this Report).

Crystal-liquid partition coefficients for nickel depend on the bulk composition of the melt (Arndt, *Year Book* 76, pp. 553–557; Hart and Davis, 1978). This bulk compositional dependence has been related to structural changes of the melt as a function of bulk composition (Watson, 1976). It is suggested, therefore, that pressure-induced changes of silicate melts will also result in changes of crystal-liquid partition coefficients. In order to test this possibility, nickel partitioning between forsterite and $\text{NaAlSi}_2\text{O}_6$ -rich melt has been determined as a function of pressure.

In studying the effect of pressure on the partitioning of an element between two phases, it is desirable to minimize the bulk compositional dependence of the two phases on pressure. This condition can be attained by careful selection of compositions on the join $\text{NaAlSi}_2\text{O}_6\text{-Mg}_2\text{SiO}_4$ as studied by Schairer and Yoder (*Year Book* 60, pp. 141–144). Results of reconnaissance experiments at 20 kbar in the $\text{NaAlSi}_2\text{O}_6$ -rich portion of this system reveal that restricted parts of the forsterite liquidus do not change significantly with pressure (Fig. 39). At 1300°C, the forsterite liquidus remains at the same composition within experimental error in the pressure range 0.001–20 kbar. Therefore this was the temperature chosen for these experiments. The compositions of the starting materials ($\text{Fo}_{20}\text{Jd}_{80}$ and $\text{Fe}_{40}\text{Jd}_{60}$ wt %) were chosen to generate large amounts of liquids and small amounts of forsterite. At 1300°C, composition $\text{Fo}_{20}\text{Jd}_{80}$ produces 12–13% crystals and 87–88% liquid, whereas composition $\text{Fo}_{40}\text{Jd}_{60}$ yields 33–36% crystals and 64–67% liquid ($\text{SiO}_2 = 58$ wt %, $\text{Al}_2\text{O}_3 = 23.1$ wt %, $\text{MgO} = 4.9$ wt %, $\text{Na}_2\text{O} = 14.0$ wt %).

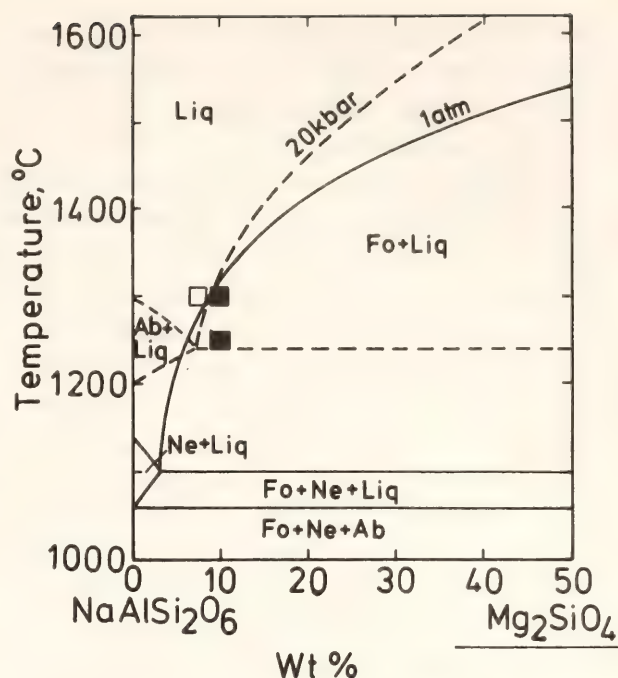


Fig. 39. Phase relations of the $\text{NaAlSi}_2\text{O}_6$ -rich portion of the system $\text{NaAlSi}_2\text{O}_6\text{-Mg}_2\text{SiO}_4$. 1-atm data after Schairer and Yoder (*Year Book* 60, pp. 141–144). Source of 20-kbar data, present work. Open symbol, all liquid. Closed symbols, forsterite + liquid.

The variations of crystal-liquid ratios for a given composition in the pressure interval studied are within experimental uncertainty of determination of the forsterite liquidus boundary. The crystalline phase in all experiments was pure forsterite.

The charges were contained in BN capsules (fired at 1000°C overnight) or in graphite capsules, and then placed inside sealed Pt or $\text{Pt}_{95}\text{Au}_5$ capsules. All experiments at pressures greater than 10 kbar were conducted in the solid-media high-pressure apparatus (Boyd and England, 1960). At pressures below 10 kbar, the internally heated gas-media apparatus (Yoder, 1950) was used. With this technique, no evidence of nickel-loss to the container material was found; nor was metallic nickel detected in the experimental charges by the beta-track maps for ^{63}Ni or by mass-balance calculations.

The nickel partitioning experiments were conducted by adding known amounts of radioactive ^{63}Ni to the starting mate-

rials (forward experiment). For reversal experiments, forsterite doped with known amounts of ^{63}Ni was added to the non-radioactive mixtures.

Nickel analysis was accomplished with the beta-track mapping technique (Mysen and Seitz, 1975) using K-5 nuclear emulsions (supplied by the Ilford Co., England) for recording the beta-activity. With this technique, the nickel contents of the phases could be kept in the natural abundance range. Furthermore, the nickel content of the crystalline phase (forsterite) was kept below the concentration limit at which nickel dissolves in forsterite according to Henry's Law (Mysen, 1978a). The uncertainty of the partition coefficients derived with this technique is 5% or less (1σ). Error bars in the figures represent $\pm 1\sigma$.

In all experiments forsterite crystals grew to a grain size of 15–30 μm at run durations of, with one exception, more than 7 hours. The crystals and glasses were homogeneous within the resolution of the beta-track mapping technique (detection limit: 10% relative variation over about 5 μm distance). As a further test for equilibrium, reversal experiments were carried out at 5 and 20 kbar. The forward experiments were conducted with starting materials where Ni was homogeneously distributed in the charge prior to the experiment, whereas in the reversal experiments all nickel in the starting material was in the forsterite. Forward and reversal experiments gave similar results. It is concluded, therefore, that equilibrium nickel partitioning was attained.

The values of $D_{\text{Ni}}^{\text{ol-liq}}$ are plotted against pressure in Fig. 40. As the pressure is increased from 1 to 5 kbar the value of $D_{\text{Ni}}^{\text{ol-liq}}$ increases from about 20 to about 26. An increase of the pressure to 15 kbar results in the partition coefficient falling to about 20. With a further increase from 15 to 20 kbar, $D_{\text{Ni}}^{\text{ol-liq}}$ decreases from about 20 to less than 10! Inasmuch as there are no bulk compositional changes in this pressure

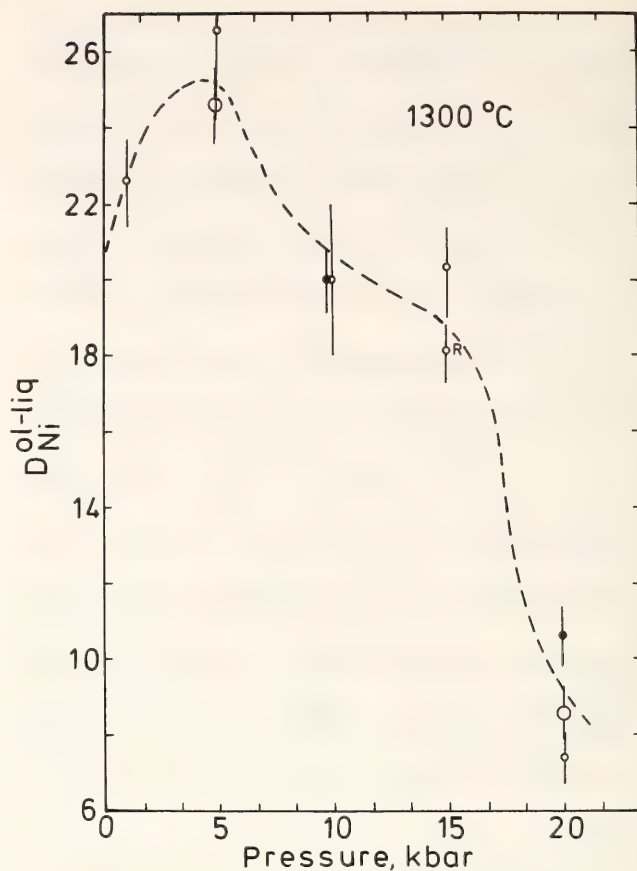


Fig. 40. Partition coefficient, $D_{\text{Ni}}^{\text{ol-liq}}$, as a function of pressure at 1300°C. Open symbols, starting composition Fo₂₀Jd₈₀. Closed symbols, starting composition Fo₄₀Jd₆₀. Enlarged symbols, reversal experiments. Symbol with "R" denotes replicate experiment. Error bars, $\pm 1\sigma$.

range, this decrease in $D_{\text{Ni}}^{\text{ol-liq}}$ indicates a significant change in the structure of the melt coexisting with forsterite in this system.

Sharma, Virgo, and Mysen (this Report) found that NaAlSi₂O₆ melts changed from a structure resembling that of α -cristobalite at low pressure to one best modelled at pressures above about 15 kbar by the structure of coesite. Evidently, this structural change produces a significant change (about 50%) in the activity coefficient of nickel in the melt. The details of the structural role of nickel in three-dimensional aluminum silicate network structure must await further study.

Most magmas are formed by partial melting of an olivine-rich source rock at pressures exceeding 10 kbar. The present results indicate that the use of models of

magma formation based on nickel contents of the magma should be reevaluated. If, for example, 1-atmosphere values of $D_{\text{Ni}}^{\text{crystal-liquid}}$ were used to model partial melting of peridotite in the upper mantle, then the *bulk* partition coefficient of the source rock–melt system would be on the order of 10–12; partial melts from a fertile peridotite source with about 2000 ppm Ni would therefore contain about 200 ppm Ni. However, by employing the high-pressure data on crystal-liquid partition coefficients for nickel, the *bulk* partition coefficient between fertile peridotite upper mantle and partial melt is near 5 (instead of 10–12 from the 1-atm experiments; Mysen, 1978a), and the calculated nickel content of an Al-rich primary partial melt would be 400–500 ppm depending on melting model (instead of about 200 ppm).

These differences in values for transition metal content of primary melts from peridotite in the upper mantle have a bearing on models of andesite formation in island arcs, for example. Andesite in island arcs may contain as much as 200 ppm Ni (DeLong, 1974), but values as high as 400 ppm have not been reported. It must be concluded, therefore, based on experimental data on nickel partition coefficients at high pressure, that fractional crystallization of andesitic melt must have occurred before such melts reached the surface.

SOLUBILITY OF SULFUR IN SILICATE MELTS AS A FUNCTION OF f_{S_2} AND SILICATE BULK COMPOSITION AT HIGH PRESSURES

Bjørn O. Mysen and Robert K. Popp

Transition metals (e.g., Co and Ni) are important indicators of the petrogenetic history of basaltic and related rocks (Gill, 1970; Håkli and Wright, 1967; Frey *et al.*, 1974; Hart and Davis, 1978). Using transition metals for this purpose requires information on which minerals were in equilibrium with the silicate melt during its formation and evolution. Rock-form-

ing silicate minerals typically have crystal-liquid partition coefficients for nickel in a range such that the bulk partition coefficients between typical upper-mantle peridotite and partial melts are on the order of 5 or less (Mysen, 1978a; Hart and Davis, 1978; Mysen and Kushiro, this Report). Primary partial melts of tholeiitic composition from such a peridotite source rock would contain more than 500 ppm Ni. Extensive fractional crystallization of silicate minerals from such a melt (>15% olivine, for example; Mysen, 1978a) is required to bring the nickel content of the melt to the levels found in tholeiite (100–200 ppm). A primary olivine-tholeiite melt will no longer be tholeiite, however, after more than 15% olivine fractional crystallization. On the other hand, separation of a few tenths of a percent sulfide melt would result in a significant reduction of transition metal contents of the silicate melts without appreciably affecting the bulk composition of the melt (Mysen, *Year Book* 76, pp. 545–550).

It is of fundamental importance to understand the solubility behavior of sulfur at high pressure and temperature in order to assess the possibility of separation of immiscible sulfide melt from silicate magma during its ascent to the surface. After the role of sulfur in magmas is understood, the role of transition metals in the petrogenesis of basalts and related rocks can be evaluated. Toward this end, experiments have been conducted to measure sulfur solubilities at high pressures and temperatures with controlled f_{S_2} and f_{O_2} .

High-pressure experiments involving sulfur and silicate melts are cumbersome because sulfur and conventional noble-metal capsules used as sample containers tend to react to form noble-metal sulfides and because sulfide cations (e.g., Fe and Ni) dissolve in both silicate and sulfide melts. The container problem was overcome by placing a fired and cleaned BN capsule (fired at 1000°C overnight and stored at 110°C until use) inside an outer

Pt capsule that was subsequently sealed. The silicate material was mixed thoroughly with graphite (which reacts with oxygen in the capsule to form CO and CO₂) buffer for f_{O_2} control and various noble-metal sulfide buffers for f_{S_2} control. The maximum solubilities of the noble metals in the silicate melts were 0.6, 0.3, and <0.1 wt % for Pt, Cu, and Ag, respectively. Placing this mixture inside the BN capsule eliminates physical contact between the corrosive sulfur buffer assemblage and the noble-metal capsule. With this sample arrangement, equilibrium between the C-O-S gas and the silicate melt is attained in less than 5 min with the temperatures and pressures used here.

This experimental technique works well for buffer combinations of C-CO-CO₂ (f_{O_2}) and Cu₂S/Cu, Ag₂S/Ag, and PtS/Pt (f_{S_2}) with iron-free systems. Consequently, quantitative sulfur solubility determination can be made as a function of f_{S_2} , P , T , f_{O_2} and degree of silica polymerization of the melt.

The sulfide buffers were synthesized from a mixture of elemental sulfur containing ³⁵S and metal with 5–10% excess of metal over that required by stoichiometry. These mixtures were run in evacuated silica tubes for two weeks at 500°C for Cu₂S and Ag₂S, and at 700°C for PtS. The sulfides were checked optically and by x-ray techniques to ensure that the correct phases were made. The buffers were mixed with the graphite (for f_{O_2} buffering) and silicate material and were then subjected to the desired pressure and temperature in a solid-media high-pressure apparatus (Boyd and England, 1960) using the piston-out technique with –4% correction for friction, as calibrated against the quartz/coesite transition. Polished sections of the run products were inspected optically to ensure that both reactants and products of all the buffer materials remained after an experiment. The sulfide buffer assemblage was also analyzed with an energy-dispersive analyzer on a JEOL scanning electron micro-

scope to ascertain the extents of solid solution of sulfide in metal and metal in sulfide. Standards were synthetic Cu₂S, Ag₂S, and PtS. The reactant and products of both f_{S_2} and f_{O_2} buffers remained nearly pure during the experiments, and no corrections for mutual solid solutions were made.

The sulfur contents of the quenched silicate melts were measured with the beta-track mapping technique (Mysen and Seitz, 1975) using ³⁵S as source of beta-particles. Standards were synthetic Cu₂S and Ag₂S.

The solubility of sulfur in CaMgSi₂O₆ melt increases with increasing pressure for a given sulfur buffer assemblage (Fig. 41). It is notable that the rate of increase of sulfur solubility with increasing pressure is less than the rate of increase of solubility of H₂O and CO₂ in similar melt composition and under similar physical conditions (Mysen *et al.*, 1976; Eggler and Rosenhauer, 1978). This difference may be at least partly due to the fact that f_{O_2} of the C-CO-CO₂ buffer increases somewhat with increasing pressure. If the 1-atm f_{O_2} dependence of the sulfur solubility data of Haughton *et al.* (1974) also applies at high pressure, increasing f_{O_2} would result in lowering of

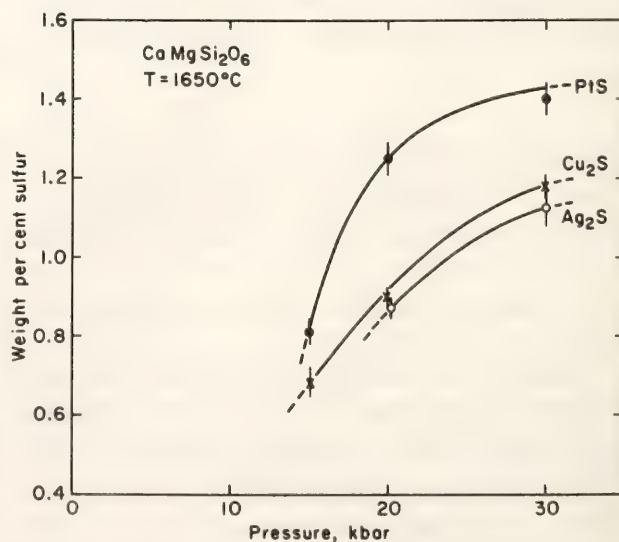


Fig. 41. Solubility of sulfur in CaMgSi₂O₆ melt as a function of pressure and sulfur-buffer assemblage. Cu₂S = Cu₂S-Cu buffer; Ag₂S = Ag₂S-Ag buffer; PtS = PtS-Pt buffer; error bars, $\pm 1 \sigma$.

the sulfur solubility at constant f_{S_2} . The net effect, therefore, is a smaller pressure dependence for sulfur solubility than for the solubility of H_2O and CO_2 .

The three different f_{S_2} buffers were used to monitor the effect of f_{S_2} on sulfur solubility under isothermal and isobaric conditions. The relative calculated values of the buffers are f_{S_2} (PtS-Pt) \gg f_{S_2} (Ag₂S-Ag) $>$ f_{S_2} (Cu₂S-Cu) both at 1 atm (Barton and Skinner, 1967) and at high pressure.* The experimental sulfur solubility determinations indicate slightly higher f_{S_2} with the Cu₂S-Cu than with the Ag₂S-Ag buffer. Although there is no obvious reason for this discrepancy between the expected and the observed relative sulfur solubilities, it should be remembered that for both Ag₂S-Ag and Cu₂S-Cu, extrapolation of f_{S_2} data involves untested assumptions regarding volume changes and thermodynamic similarities (Cp, compressibility, and thermal expansion) between crystals and melts (see above). The sulfur solubility data of CaMgSi₂O₆ (and also NaAlSi₃O₈; see below) melts indicate that some of these assumptions are inappropriate. The inappropriate assumptions, however, cannot be identified from the present data. Alternatively, the higher sulfur solubility with Cu₂S-Cu buffer, compared to the solubility with Ag₂S-Ag buffer, may relate to the small but significant Cu content of the silicate melt. This Cu may result in higher sulfur solubility than if the silicate melt were Cu-free.

Sulfur solubility data for albite melt at 1650°C are shown in Fig. 42. It is clear that for given f_{S_2} and f_{O_2} buffers, the sulfur solubility in albite melt is approximately 50% of that in diopside melt at the same pressure and temperature. As was the case for CaMgSi₂O₆ melt, the sulfur solubility increases with increasing pressures, although at a slower rate than for diopside melt.

* Data for these calculations were taken from French (1966), French and Eugster (1965), Barton and Skinner (1967), Robie *et al.*, (1967), and King *et al.*, (1973).

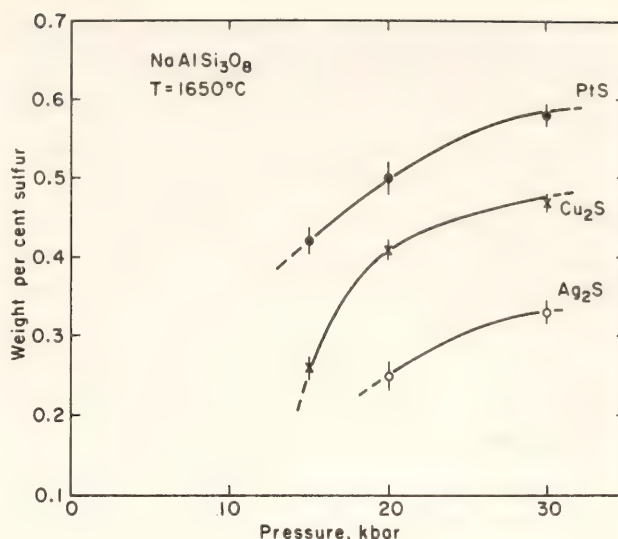


Fig. 42. Solubility of sulfur in NaAlSi₃O₈ melt as a function of pressure and sulfur-buffer assemblage. Symbols as in Fig. 41.

The relative solubility of sulfur as a function of buffer assemblage is the same in albite as in diopside melt (Figs. 41, 42). That is, the solubility increases in the order Ag₂S-Ag, Cu₂S-Cu, and PtS-Pt. As was the case for diopside melt, the solubility is higher with the Cu₂S-Cu buffer than with the Ag₂S-Ag buffer. The temperature dependence of sulfur solubility in albite melt in equilibrium with the Cu₂S-Cu and C-CO-CO₂ buffers at 30 kbar is shown in Fig. 43. The f_{O_2} of the C-CO-CO₂ buffer increases by about four orders

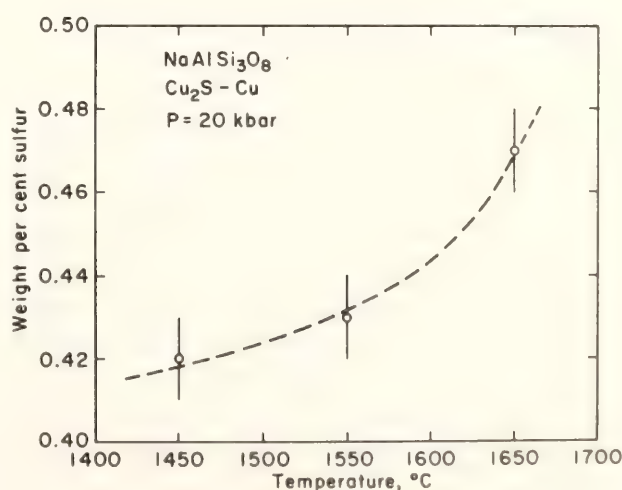
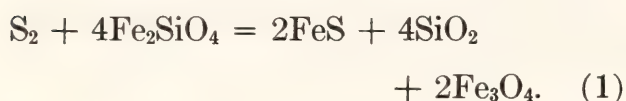


Fig. 43. Sulfur solubility in NaAlSi₃O₈ melt as a function of temperature with Cu₂S-Cu buffer assemblage at 20 kbar pressure.

of magnitude in the temperature range 1450°–1650°C (French, 1966; French and Eugster, 1965); Haughton *et al.*, (1974) found that this change results in a lowering of sulfur solubility at constant f_{S_2} . Sulfur fugacity increases with increasing temperature (King *et al.*, 1973), however, and this effect should increase the sulfur content of the silicate melt. It appears from the data in Fig. 43 that the increasing f_{S_2} with temperature predominates over the effect of temperature on f_{O_2} .

An example of an invariant reaction that buffers both f_{S_2} and f_{O_2} is:



Similar reactions could be written for other Fe-bearing minerals in the upper mantle. No thermodynamic data for other reactions are available, however, and Equation 1 is used as an example. With a correction for the olivine composition ($Fe_{90}Fa_{10}$ rather than Fa_{100}), the f_{S_2} of this buffer reaction is slightly higher than that of the PtS-Pt buffer (Barton and Skinner 1967).

Partial melting of peridotite at about 30 kbar pressure would yield a tholeiitic liquid that contains 600–700 ppm nickel (Mysen, 1978a). This nickel content is about three times higher than that found even in abyssal tholeiite (Frey *et al.*, 1974). Only separation of olivine among the potential liquidus phases can result in significant depletion of Ni in the melt. Mysen (1978a) noted, however, that in view of recent olivine-liquid partitioning data for nickel, 20–25% olivine must separate during a process of perfect fractional crystallization to lower the nickel contents to ~200 ppm. Less-than-perfect fractional crystallization would result in the necessity of even more olivine fractionation. This much olivine fractionation results in a liquid with no resemblance to tholeiite. However, the sulfur solubility in silicate melts is lowered with decreasing pressure. Consider, there-

fore, a partial melt that contains 1–1.5 wt % sulfur at the source (for example, 20-kbar pressure). At 10 kbar, the sulfur solubility in the same melt is at least 50% lower (Figs. 41, 42). The excess sulfur may separate as an immiscible sulfide melt. The silicate melt–Fe-rich sulfide melt partition coefficient for nickel is about 250–300 (Mysen and Kushiro, *Year Book* 75, pp. 678–684). Only about 0.5 wt % immiscible sulfide melt separation is needed to lower the Ni content of a tholeiitic melt from 700 ppm to 150 ppm. It is proposed, therefore, that the nickel contents and probably also other transition metal contents of abyssal tholeiites, are controlled by separation of an immiscible sulfide melt during ascent of the magma from the source toward the surface.

The transition metal content of island arc andesite has played a central role in the discussion of the arcs' petrogenetic history (Taylor *et al.*, 1969; Osborn, 1969b). A partial melt from a spinel peridotite source beneath island arcs would contain perhaps 700–800 ppm Ni (Mysen, 1978a). The same melt is also likely to be saturated with sulfur, which may separate from the andesitic melt during ascent. Values of the sulfide melt–andesite melt partition coefficients are not known, but are likely to be about 500. If the sulfur solubility data for $NaAlSi_3O_8$ melt can be used to model the solubility in andesite melt, such melts would contain 0.3–0.4 wt % at 10 kbar pressure. Inasmuch as the sulfur contents of extrusive rocks typically are reported to be about 0.1 wt % or less (e.g., Moore and Fabbri, 1971), it appears that 0.2–0.3 wt % sulfur must have been separated from the melts during ascent. This amount of sulfur corresponds to 0.5–0.6 wt % (Fe–Ni) sulfide melts. This much sulfide separation would result in the Ni content of the melts being lowered to less than 50 ppm. This value is similar to that often found in island arc andesite (Taylor, 1969; Gill, 1970; Kay, 1977). The major-element composition of the andesite melt would

be essentially unaffected by the process of separation of the immiscible sulfide melt. Other transition metals (Co, Zn, Cu) would also be affected strongly by the separation of sulfide, although no quantitative assessment can be made because of lack of transition metal partition coefficients.

In summary, the sulfur content of partial melts in the upper mantle is likely to be on the order of 1 wt %. Because of the strong positive pressure-dependence of sulfur solubility, most of this sulfur will have separated from the melt by the time it reaches the surface. The separation is likely to be in the form of immiscible sulfide melt. Transition metals show a very strong preference for sulfide melt over silicate melt. Separation of sulfide melts during ascent of magmas is, therefore, likely to control the transition metal content of the silicate melt during their ascent to the surface, as suggested by Shima and Naldrett (1975).

PRESSURE-DEPENDENT SOLUBILITY OF CALCIUM IN FORSTERITE COEXISTING WITH DIOPSIDE AND ENSTATITE

A. A. Finnerly and F. R. Boyd

The only geobarometer thus far found suitable for application to ultramafic rocks is based upon the solubility of Al_2O_3 in orthopyroxene coexisting with garnet (MacGregor, 1974). Its application is subject to an uncertainty caused by compositional effects in complex natural systems, and is limited to pressures greater than those at which pyrope-rich garnet is stable. Alternative barometers that are subject to different uncertainties are desirable for comparison. The solubility of Ca in olivine provides such an alternative and, by obviating the requirement for coexisting garnet, may have application to a much wider variety of ultramafic and mafic rocks and to other pressure conditions. This barometer requires the coexistence of the olivine with both orthopyroxene and clinopyroxene

because the reaction relation between these two pyroxenes fixes the Ca activity in the rock at any particular value of temperature and pressure.

The Ca content of forsterite coexisting with monticellite has been shown to be temperature dependent (Ricker and Osborn, 1954; Warner and Luth, 1973). Simkin and Smith (1970) compared Ca concentrations of natural igneous olivines with crystallization environment, and suggested that variations might be related to differing depths of origin. Experiments in a model (iron-free) garnet lherzolite system (Finnerly, *Year Book* 76, p. 572) showed that increasing temperature increased the solubility of Ca in forsterite, but that increasing pressure decreased such solubility.

Experiments were conducted on a mix in the system $\text{CaO-MgO-Al}_2\text{O}_3\text{-SiO}_2$ (+ minor MnO) to investigate the possible utility of Ca in olivine as a geobarometer. This mix crystallizes to approximately equal proportions of olivine, orthopyroxene, clinopyroxene, and an aluminous phase (garnet, spinel or feldspar). Oxalic acid dihydrate (1 to 10 wt %) was added to promote growth of crystals. The mixture and run procedures were identical to those reported by Finnerly (*Year Book* 76, p. 572), but in these present experiments emphasis was placed on obtaining olivine crystals large enough for accurate analysis of trace Ca. Reversals were attempted by running previously crystallized mixtures containing high-Ca and low-Ca forsterites at 1300°C and 30 kbar for 42 hr, and at 1200°C and 30 kbar for 159 hr. This procedure resulted in a scatter of olivine composition between the two extreme Ca concentrations, with no clearly defined cluster about the value determined in "synthesis" runs. The argument for equilibrium must consequently rest upon the internal consistency of the data obtained from synthesis runs. Presumption of equilibrium in synthesis runs is supported by the agreement between the observed pyroxene compositions and those obtained

in reversal runs by Lindsley and Dixon (1976).

At least four satisfactory electron microprobe analyses of olivine were obtained for each run. Criteria for choosing these analyses were: sum of oxides between 98 and 102 percent, agreement of calculated with theoretical olivine atomic formula, and minimum Ca content (because olivine was always surrounded by high-Ca phases). Consistent Ca concentrations were generally obtained in runs where the maximum olivine grain size was greater than 10 μm . Count time

on each grain was 100 sec on peak, and 50 sec each for background on either side of the peak. In this fashion 3000 to 16,000 counts above background were accumulated for each point analysis. Detection limits were typically below 30 parts per million by weight (ppmw) Ca; standard deviations were usually less than 10% of the amount present. Results are presented in Figs. 44 and 45.

The data plotted in Fig. 44 are preliminary. Isotherms at 1100° and 1300°C suggest an inverse linear correlation between Ca in olivine and pressure. A

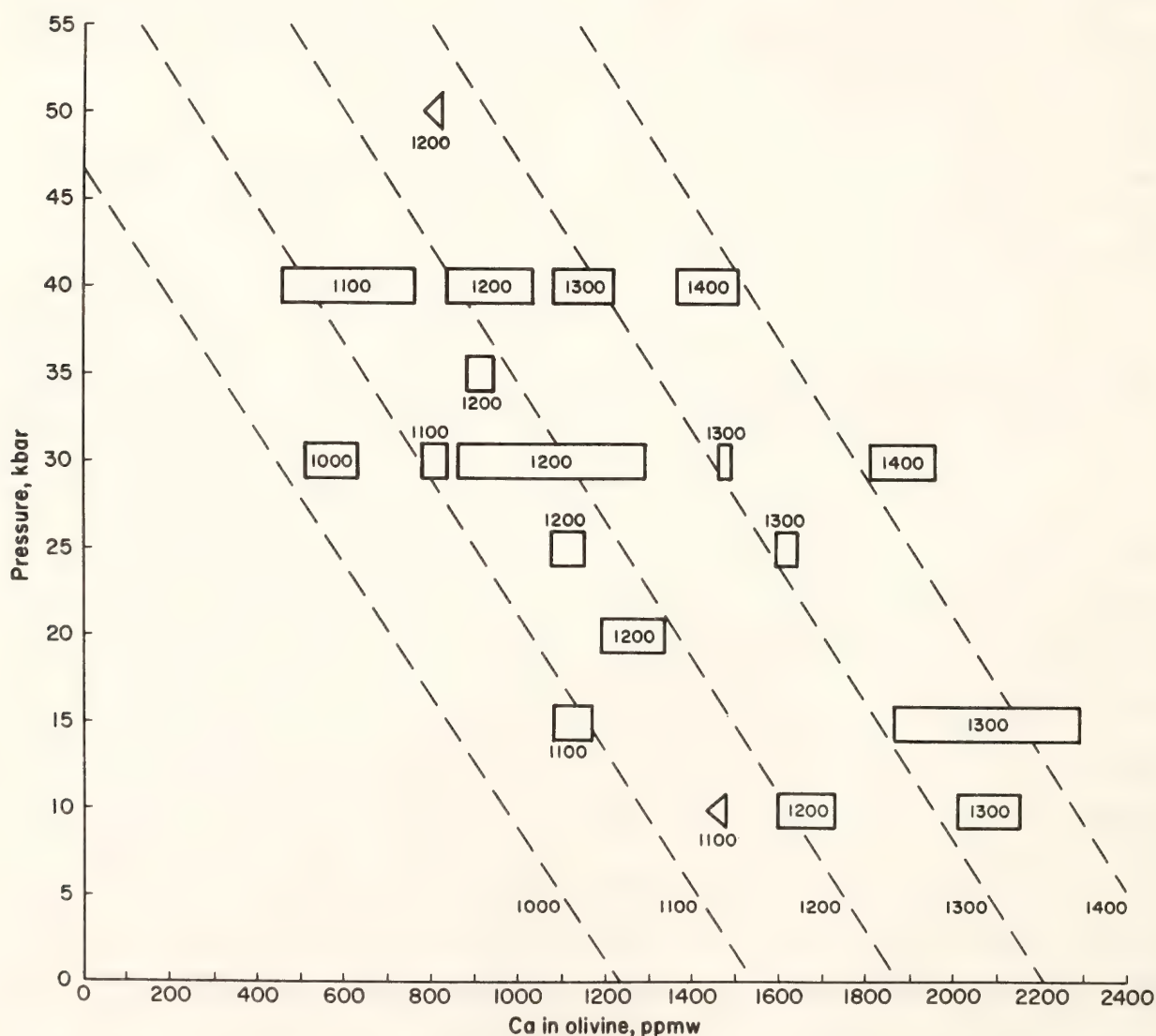


Fig. 44. Pressure-composition projection of data on solubility of Ca in forsterite coexisting with diopside and enstatite. Size of boxes represents 1 standard deviation for analysis of four olivine grains, with ± 1 kbar pressure uncertainty. Triangles represent upper limit of Ca solubility in olivine in runs for which grain size was too small for good analysis. Numbers within the graph refer to temperature ($^{\circ}\text{C}$). The isotherms are dashed because further experiments are expected to require some shifting of their loci.

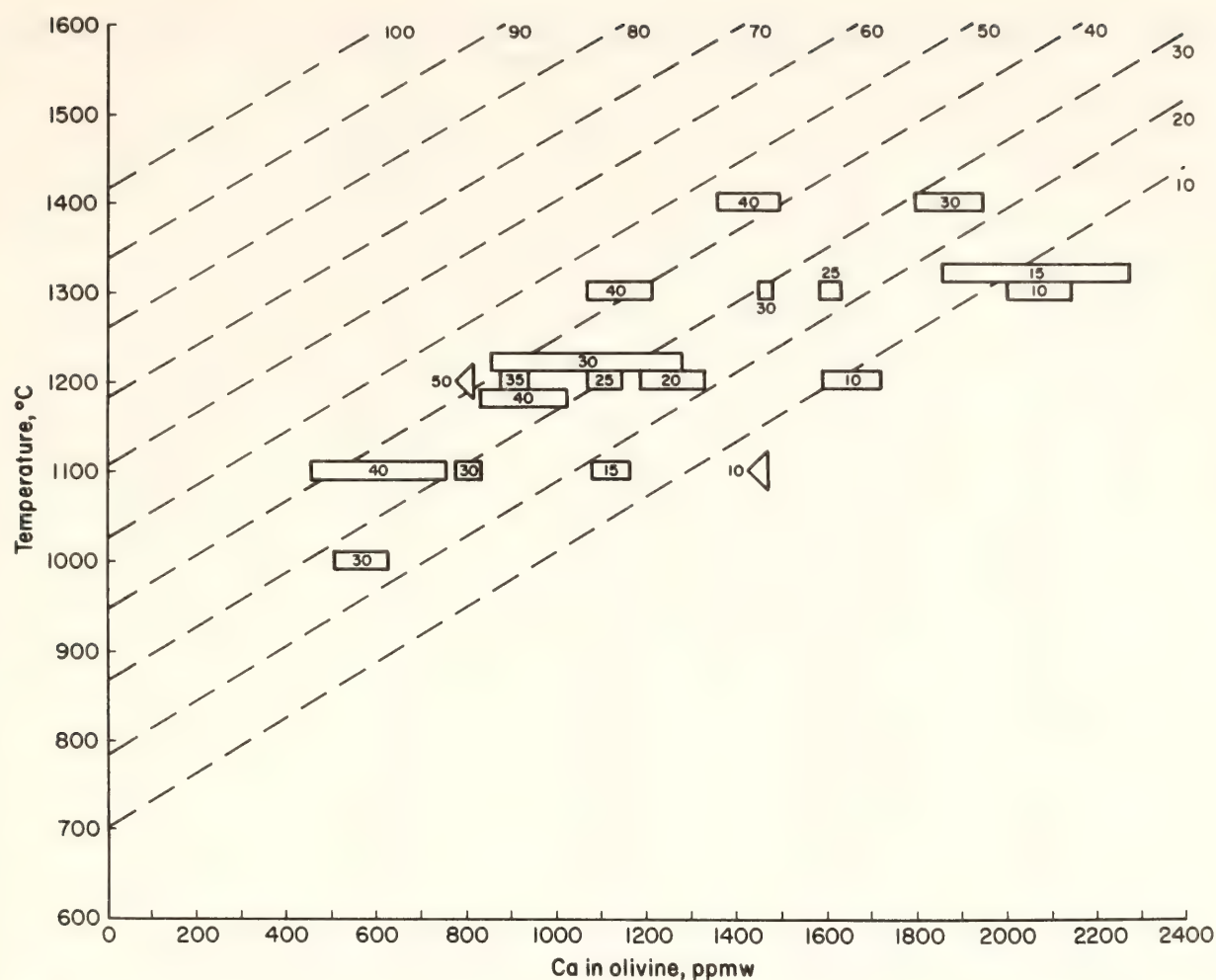


Fig. 45. Temperature-composition projection of data on solubility of Ca in forsterite coexisting with diopside and enstatite. Symbols are the same as for Fig. 44 except that height of symbols represents $\pm 10^\circ\text{C}$ temperature uncertainty. Numbers within the graph refer to pressure (kbar). The isobars are extrapolated from Fig. 44.

curve concave toward the origin could be drawn through the data at 1200°C , but is not required within a 2σ error estimate. The 1200°C isotherm appears to fall closer to the 1100° than the 1300°C isotherm, but the data at 1400°C suggest that spacing of isotherms should be more uniform. There is also some indication that pressure dependence increases at higher temperature, but more data are needed to confirm this observation. The slopes of the isotherms in Fig. 44 are on the order of -26 ppmw Ca/kbar, so that electron microprobe analyses of Ca in olivine coexisting with orthopyroxene and clinopyroxene might be used to estimate pressures of equilibration with a precision of about ± 1 kbar. For the purposes of

illustrating the potential utility of Ca in olivine as a geobarometer, straight and equally spaced isopleths have been drawn through the data in Figs. 44 and 45. The reader is cautioned, however, that further experiments may require the relocation of these isopleths.

The olivine barometer was tested against the pressures estimated for the garnet lherzolite xenoliths from kimberlite in Lesotho, South Africa (Boyd, 1973). For comparative purposes the temperatures were obtained from the 30-kbar diopside-enstatite miscibility gap of Davis and Boyd (1966). New and more accurate analyses for calcium in these olivines were made. In Table 17 and Fig. 46, the pressure estimates are

TABLE 17. Pressure-Temperature Estimates and Ca Contents of Olivines from Garnet Lherzolite Xenoliths in Kimberlite from Lesotho, South Africa

Specimen	Ca in Olivine (ppmw)	<i>T</i> (°C) *	<i>P</i> (kbar) † Al ₂ O ₃ in Opx	<i>P</i> (kbar) Ca in Oliv
PHN 1595	138 (8) ‡	930	41.5	33
PHN 1567	121 (15)	950	42	36
PHN 1592	147 (13)	955	42	36
PHN 1570	141 (11)	965	44	37
M-72	79 (7)	975	44.5	41
PHN 1569	160 (13)	980	44.5	38
PHN 1572	134 (9)	980	44.5	39
PHN 1573	124 (9)	980	44.5	40
PHN 2302A	181 (13)	1015	49	42
PHN 1917	223 (9)	1015	51	40
PHN 1559B	213 (18)	1025	50	42
PHN 2012	176 (7)	1045	49	46
PHN 2011	195 (24)	1050	53	46
PHN 1654	177 (9)	1050	50	47
PHN 2549	198 (6)	1050	52	46
PHN 2001	489 (13)	1240	60	64
PHN 1591	662 (14)	1260	62	55
E-3	643 (10)	1310	61	63
PHN 2573	631 (13)	1345	62.5	68
PHN 1924	568 (4)	1345	62	70
PHN 1925	561 (33)	1356	62	72
PHN 1611	967 (13)	1380	63.5	63
PHN 1610	930 (85)	1390	63.5	62
PHN 1566	946 (32)	1405	65	63
PHN 1596	772 (15)	1415	65	71
PHN 1597	785 (14)	1420	66	71

* Davis and Boyd, 1966.
† Boyd, 1973.
‡ Standard deviations (four-point analyses) are given in parentheses.

compared with those obtained by Boyd (1973) using uncorrected contents of Al₂O₃ in orthopyroxene coexisting with garnet.

Pressures estimated from olivine compositions are within about 10 kbar of those obtained from orthopyroxene compositions. At the present level of development of thermobarometers, this much agreement is encouraging. In both methods of pressure estimation, the nodules are placed in nearly the same relative positions on the fossil geotherm. The data derived from the olivine barometer are more scattered than those obtained from the enstatite barometer, especially for the higher temperature (sheared) xeno-

liths. The analytical precision should yield pressure estimates with ±1-kbar precision. There may be effects of other components on Ca content of olivine that have not yet been experimentally investigated.

It is inferred from the apparent compatibility of these two independent geobarometers that this suite of upper-mantle nodules retains compositions representative of equilibration at high temperatures and pressures. In addition, it can be concluded that the apparent inflection in the fossil geotherm observed by Boyd (1973) is probably real; otherwise it must be an artifact of the diopside-enstatite thermometer. Because the two indepen-

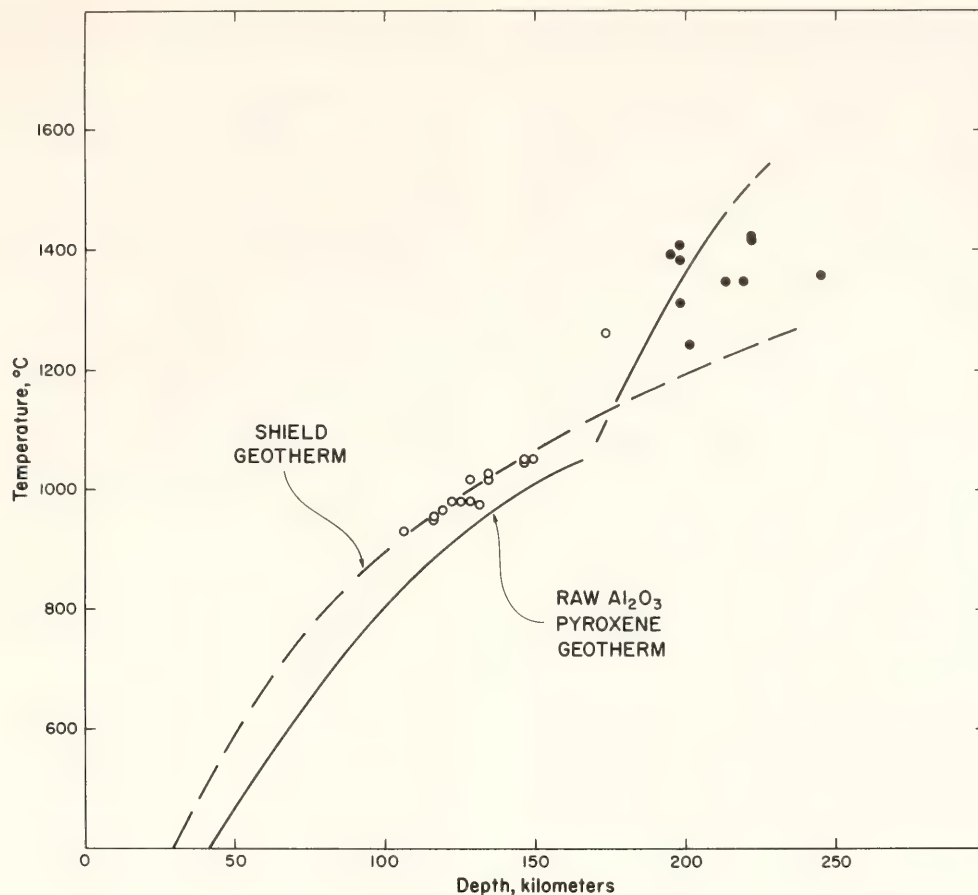


Fig. 46. Temperature-depth estimates for garnet lherzolite xenoliths from kimberlite of Lesotho, South Africa. Temperatures were estimated using the diopside-enstatite miscibility gap at 30 kbar (Davis and Boyd, 1966). Pressures were estimated from solubility of Ca in forsterite coexisting with diopside and enstatite. For reference, the pyroxene geotherm determined by using "raw Al_2O_3 " values for orthopyroxenes (Boyd, 1973), and a shield geotherm (Clark and Ringwood, 1964) are also presented.

dent barometers give similar results, the inflection cannot be an artifact of the enstatite (or olivine) barometer. The solubility of Ca in olivine coexisting with

orthopyroxene and clinopyroxene should be useful as a geobarometer for other ultramafic rocks, most notably those that do not contain garnet.

EXPERIMENTAL AND FIELD PETROLOGY

DENSITY CURRENT STRUCTURE AND MAGMATIC SEDIMENTATION

T. N. Irvine

A longstanding tenet in investigations of layered intrusions is that the layering is essentially formed by crystal settling—that is, by the accumulation of crystals from magmatic liquid in accordance with their individual settling velocities. This

concept became popular particularly through the work of Wager and Deer (1939) and Wager and Brown (1968) on the gabbroic Skaergaard intrusion, in which the rhythmic layering bears remarkable resemblance to bedding in clastic sediments. Many of the Skaergaard layers are vertically graded, with mafic minerals concentrated at their bottoms and plagioclase toward their tops, and so it would appear that the minerals were

sorted on the basis of settling velocities determined principally by the differences between their densities and that of the liquid. There has always been some uneasiness about plagioclase, however, because even from very tenuous early data on the densities of magmatic liquids it was apparent that this mineral is, at the most, only slightly denser than basaltic melts. In fact, Wager and Deer (1939, pp. 282–283, 332) argued that in the late stages of the Skaergaard differentiation, when the liquid became very rich in iron, plagioclase should probably have floated. They believed, however, that it was carried down to the floor of the magma body in convection currents consisting of crystal-liquid suspensions that were denser than the liquid itself by virtue of also being charged with mafic minerals. It was considered that, by the time the floor was reached, the feldspar had become so “entangled” with the mafic minerals that it was carried to the floor with them as they finally settled into layers. Wager and Brown (1968) suggested that some of the convection currents probably resembled turbidity currents in aqueous sedimentary environments.

Several years ago, Bottinga and Weill (1970) made more definite estimates of the densities of the Skaergaard liquid at its various stages of differentiation, and their results supported the Wager and Deer inference that the liquid became denser than the plagioclase that crystallized from it. This relationship has now been confirmed experimentally (T. M. Murase and A. R. McBirney, personal communication, 1975), and Morse (1972) has estimated that the same relationship obtained in the gabbroic Kiglapait intrusion in Labrador. But with these findings, the Wager, Deer, and Brown concept of layer formation has come under question, and the possibility has been raised that Skaergaard-type igneous layering might generally be the result of some very different process relating perhaps to me-

chanisms of crystal nucleation and growth.

The Skaergaard layering, however, is similar as well (especially structurally) to layering in ultramafic cumulates in the Duke Island complex of Alaska (Irvine, 1974), where not only crystals but also rock fragments can be seen to have been transported, sorted, and deposited by magmatic currents and then, in places, eroded and redeposited. Thus, it was considered desirable before abandoning a concept for gabbroic layering that had seemed satisfactory in many respects for many intrusions, to obtain a better understanding of the mechanics of magmatic density currents. The present study was undertaken with a view to testing experimentally the possibility that magmatic currents might deposit minerals at the floor of an intrusion even though the minerals should float. Aqueous density currents have been extensively investigated in relation to engineering and sedimentological problems (Keugelan, 1957, 1958; Middleton, 1966a, 1966b, 1967; Daly and Pracht, 1968; Allen, 1971), but they are generally complicated by turbulence. The present experiments were made with viscous fluids under conditions of laminar flow such as would be expected in magmas.

Experimental Methods

The experiments were performed with a small Plexiglas flume with inner dimensions $1 \times 2 \times 15$ inches. The chamber is completely enclosed except for a 3-inch length of the top at one end, above a part that can be isolated as a lock behind a removable gate. In a typical experiment, the lock is filled with a liquid or liquid-solid suspension denser than the liquid in the main part of the flume. The gate is removed quickly, and the resulting flow is photographed from the side, either with a movie camera or at short intervals with a 35-mm camera equipped with motor drive. The structure of the current is then mapped from the projected

photographic transparencies on the basis of tracer particles included in the fluids. The objective is to define vertical longitudinal flow patterns such as might represent two-dimensional flow in a laterally extensive crystal-liquid suspension flowing as a density current across a floor of layered cumulates at the bottom of an intrusion.

Much of the initial experimenting was devoted to finding combinations of liquids, solids, and tracers suitable to defining flow patterns. Consideration was given to scale modeling magma properties (see Hubbert, 1937), but the uncertainties are large, and ultimately the choice of materials was largely a matter of availability.* In principle, one would like to trace the motion of the liquids, both in the density current from the lock and in the return flow from the main part of the flume, as well as the transport patterns of the solid particles representing crystals. In practice, the tracer particles have to be relatively large in order to be identified and tracked, but it is observed that even if such tracers have neutral buoyancy in the liquid, when they are placed in a suspension of finer, denser particles, they are buoyed up as though they were in denser liquid. Moreover, suspensions containing the percentages of particles thought to occur in magmatic density currents are not transparent. Consequently the only tracers that can consistently be observed are those close to the front wall of the flume, and their motions are strongly affected by the drag of the wall and are not representative of two-dimensional flow.

A workable solution to these problems was achieved by using liquids of different densities and viscosities, with tracers as the only suspended solids. The most in-

formative experiments were made with density currents of glycerin flowing into a medium of silicone fluid. The viscosity and density of the glycerin are comparable to those of a suspension of 20–30 vol % fine glass beads in the silicone fluid. Polystyrene beads, about 0.8 mm in diameter, were used as tracers in the silicone fluid, where they have almost neutral buoyancy (they settle negligible distances in the time period of a typical experiment). No completely satisfactory tracer was found for the glycerin, but useful results were obtained with glass shards, sieved to $-20+28$ mesh size.* The shards are considerably denser than the glycerin but settle slowly because of their irregular shapes. Moreover, the importance of this settling could be qualitatively evaluated through the presence of another type of tracer. It is almost impossible to stir solid particles into glycerin without also introducing small air bubbles, and it was found that many of these bubbles could also be tracked photographically. As will be seen below, their patterns of motion, reflecting their tendency to float, have been profitably compared to those of the glass shards.

In an attempt to overcome wall effects, the tracer particles were introduced along the axis of the flume lock between two temporary baffles that were removed before the gate was opened. This measure was only partly successful because the flow is such that the tracers eventually come to the walls anyway. It was also found, however, that in certain graphs of the flow, the vectors of tracers whose motion was appreciably affected by wall drag can commonly be identified and so can be edited from the graphs.

Results

A first consideration is whether it was realistic to substitute an immiscible

* The flow pattern described below appeared, however, to be characteristic of all the various combinations of fluids tested and can even be recognized in saline aqueous density currents for a brief period after they are released from the lock before they become excessively turbulent.

* The polystyrene beads and glass shards were introduced in two different colors to facilitate their identification and tracking.

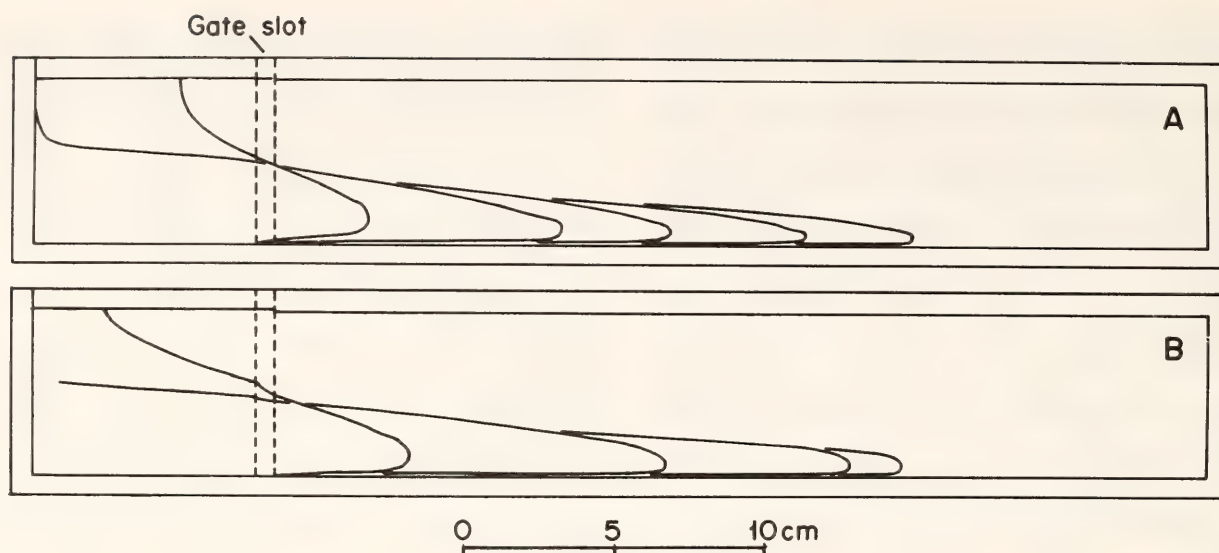


Fig. 47. Profiles of density currents flowing in a medium of silicone fluid, viscosity 350 cs. In (A), the density current is a suspension of about 20 vol % glass shards ($-200+350$ mesh) in the same silicone fluid. In (B), the current consists of glycerin, viscosity about 1100 cs.

liquid (glycerin) for a solid-liquid suspension in making the density currents. Comparative experiments were run, and as far as could be discerned the two types of currents are practically identical. Their bulk properties are comparable, their rates of advance are about the same, and their shapes are closely similar. Both are lobate in plan, and as seen in profile (Fig. 47), the only noticeable difference is that the suspension currents are slightly more tapered and sometimes have a faintly distinguishable head, whereas the glycerin currents are invariably blunt at the front tip. Moreover, after the flow pattern in the glycerin had been determined, it was observed that the same principal elements could be recognized in the suspension currents even though they were not visible consistently enough to be photographed and mapped. Some of these similarities are noted below.

Figure 48 illustrates the motion vectors of tracers in a glycerin current flowing into silicone fluid with the flume horizontal. The vectors represent a time period of about 0.6 sec. It is seen that the appearance of the flow pattern depends strongly on the reference point. In Fig. 48A the motion is plotted relative

to the fixed boundaries of the flume, whereas in Fig. 48B it is referred to a moving point on the floor directly below the front tip of the density current. The latter representation shows which parts of the current are gaining on the tip and which parts are lagging behind, and so defines the internal circulation. Some principal features of Fig. 48A are:

(1) The flow within the density current has a downward component of velocity everywhere but at the front tip. This feature is evident from the motion of unattached air bubbles as well as the glass shards and so is not just a reflection of the tendency of the shards to settle. (In fact, the difference between the motions of the two kinds of tracers is not distinguishable for the time interval involved.) The overall motion in the current appears as a flow shearing roughly parallel to the forward-sloping top surface of the current.

(2) As the glycerin current advances, the silicone fluid is pushed forward and up and then around in a strong return flow that fills the space vacated by the glycerin while turning again to advance with it. This circulation is obviously somewhat constricted by the small vertical dimension of the flume, but the pattern is characteristic of density cur-

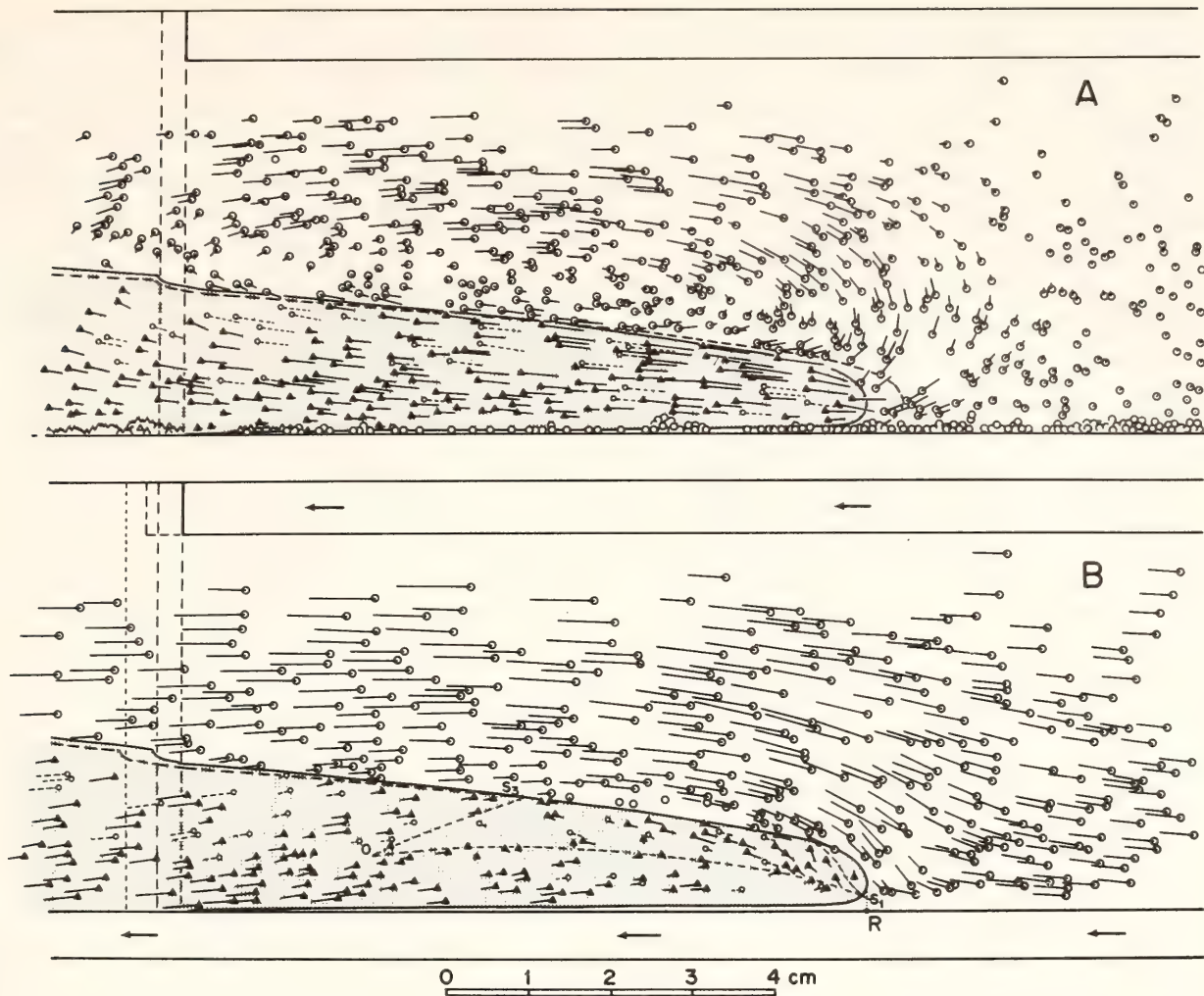


Fig. 48. Motion vectors of tracer particles for a 0.6-sec interval during flow of a density current of glycerin into silicone fluid as in Fig. 47B. The tracers in the silicone fluid are polystyrene beads; those in the glycerin are glass shards (triangles) and air bubbles (circles). In (A) the motion is mapped relative to the floor of the flume; in (B) it is referred to point R moving along the floor directly below the front tip of the current. As many tracers were mapped in (A) as was practicable, but (B) has been edited to eliminate the vectors of particles that were evidently slowed or stopped by the drag of the flume walls.

rents of the type considered here, even when they are produced in flumes with proportionately larger heights (e.g., Daly and Pracht, 1968). It appears that the return flow tends to be "local" because less liquid is then involved and inertial effects are thus minimized.

(3) The density current overrides some of the silicone fluid along the floor. At the end of the experiment, this fluid can be seen gathered in small diapirs that cling to the floor by surface tension and protrude into the glycerin above. More significantly, however, in the illustrated experiment some of the polystyrene beads

were allowed to settle onto the floor before the gate was opened, and those too were overridden by the glycerin. But they were almost undisturbed until they became so immersed in the denser liquid that some finally broke loose and floated upward; the current did not actively erode the unconsolidated floor.

The more important features illustrated by Fig. 48B are that (a) at any given time only a small part of the current, at the top and to the front, is actually gaining on the front tip, and (b) plotted in this way, the return flow appears to sweep up and back over the density current.

Figure 49 shows tracer pathlines plotted from an extended succession of photographs. In A, where their motion is mapped relative to the flume, the glass shards are seen to descend through the current from top to bottom, and air bubbles attached to them follow the same type of path. The trajectories of the free air bubbles eventually flatten and then begin slowly to rise because a stage is reached when their tendency to float compensates, and then exceeds, the effect of downward transport by the flow.

In Fig. 49B, where the tracer pathlines are referred to the tip of the current, various relations are observed. Tracers initially at the top front first advance toward the tip, but descend rapidly and then recede as they near the floor. This type of pathline is observed for free air bubbles as well as glass shards; hence it is evident that the tracers are being carried down and that the circulation in the front of the current somewhat resembles the front end of a conveyor belt. As in Fig. 49A, the paths of the glass shards eventually extend to the floor, whereas those for free air bubbles level off and slowly begin to rise.

Other tracers in Fig. 49B, initially at intermediate distances back of the front tip, have S-shaped pathlines. In such cases, the tracer was at first just to the rear of the part of the current that gains on the front tip (see Fig. 48B). But as the current extended and the velocity of the tip decreased, the "gaining region" expanded backward to include the tracer, and so its pathline changed direction. The tracer then descended below the gaining region, and the pathline direction changed again. Still other tracers were initially either well back of the gaining region or below it, and so they lagged behind the front tip throughout the recorded flow interval.

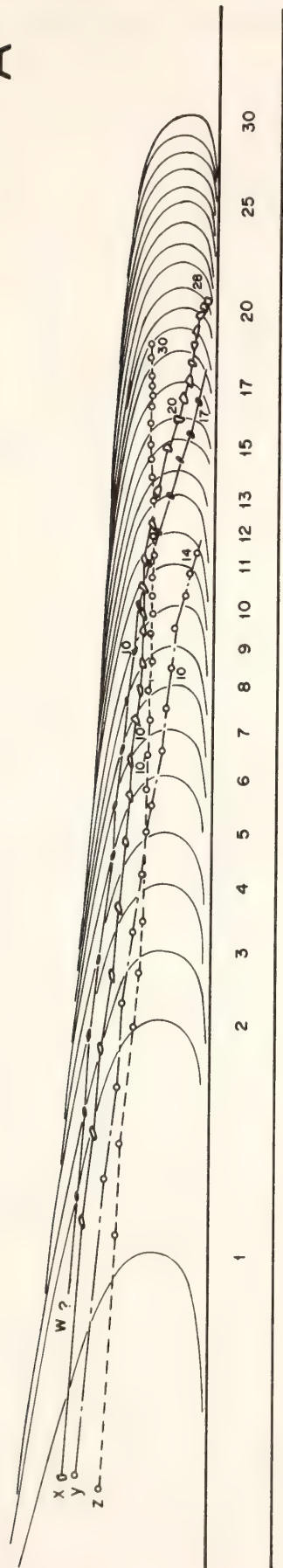
From the above data and observations and from some fundamental rules of fluid flow, complete sets of "instantaneous" streamlines have been constructed for the density current in Figs.

48 and 49. They are shown in Fig. 50. As in the other graphs, the flow pattern appears very different, depending on the reference point. It is emphasized, therefore, that the two diagrams are based on the same data and are drawn to be as compatible as possible. Neither is more correct than the other, and both are necessary to understand the flow. Their differences are simply a matter of viewpoint.

Among the principal features of interest are the points s_1 , s_2 , and s_3 . As represented in Fig. 50B, they are called *stagnation points*, and they are joined by a *dividing streamline* on opposite sides of which the flow rotates in opposite directions. In Fig. 50A, the line $s_1s_2s_3$ is a locus of inflection points on the streamlines, and s_3 might be called a "hinge point" for the top boundary of the density current. The vortices V_1 and V_2 (Fig. 50B) are not readily defined by the present experimental method because the tracer particles rarely enter them, and the definition of V_1 is further complicated in that the density current is lobate in plan. However, vortex V_1 enlarges if the flume is tilted. Also, an analogous vortex is apparently responsible for the slight "head" observed on the currents made from solid-liquid suspensions, and in those currents its motion is readily observed although not easily photographed. Vortex V_2 lies directly above the fastest-moving part of the glycerin current and is essential to the compatibility between the flow of this current and the return flow sweeping back over it.

In Fig. 50B, point o is effectively the origin of the part of the current that gains on the front tip (i.e., $os_1s_2s_3$), and as the density current extends, os_3 shifts backward relative to the materials of the current. Line os_3 is not a dividing streamline, however, even though the streamlines on its opposite sides are directed away from it. It is more a "velocity dividing line" that is distinctive only in that for the instant of time represented in the diagram, it is advancing

A



B

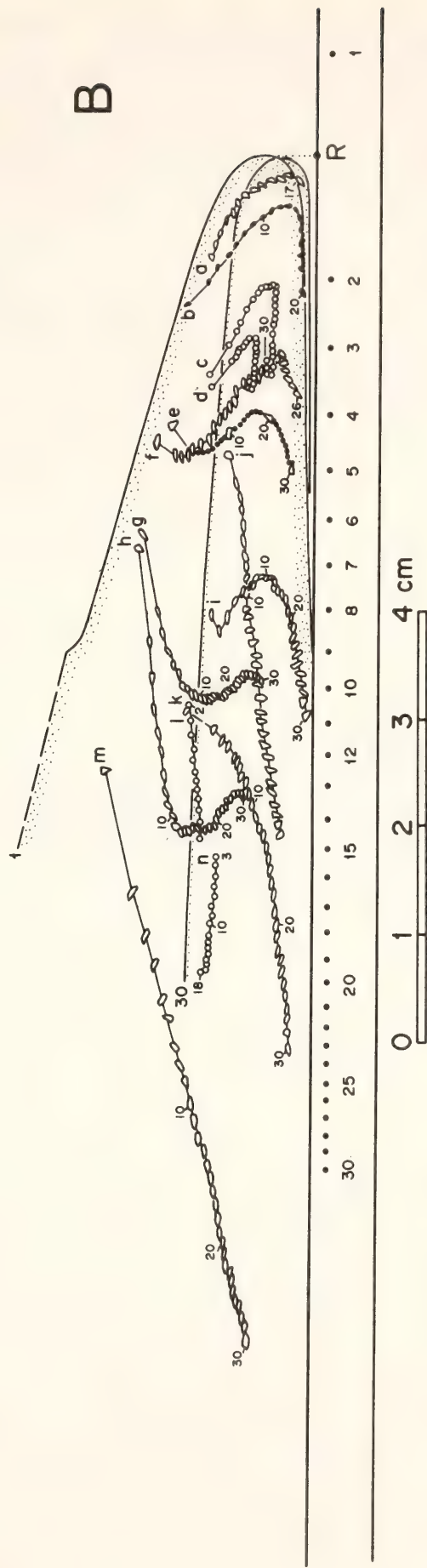


Fig. 49. Pathlines of tracers for the same current as in Fig. 48 through a series of 30 photographs. In (A) the motion is relative to the floor of the flume; in (B) it is referred to the moving point R below the front tip. In (A) tracers w and x are glass shards, y is an unattached air bubble, and z is a bubble that became attached to a glass shard. In (B) tracers c, d, l , and n are air bubbles; the others are glass shards. Current profiles are numbered in (A); the location of a specific point on the flume in successive photographs is indicated in (B).

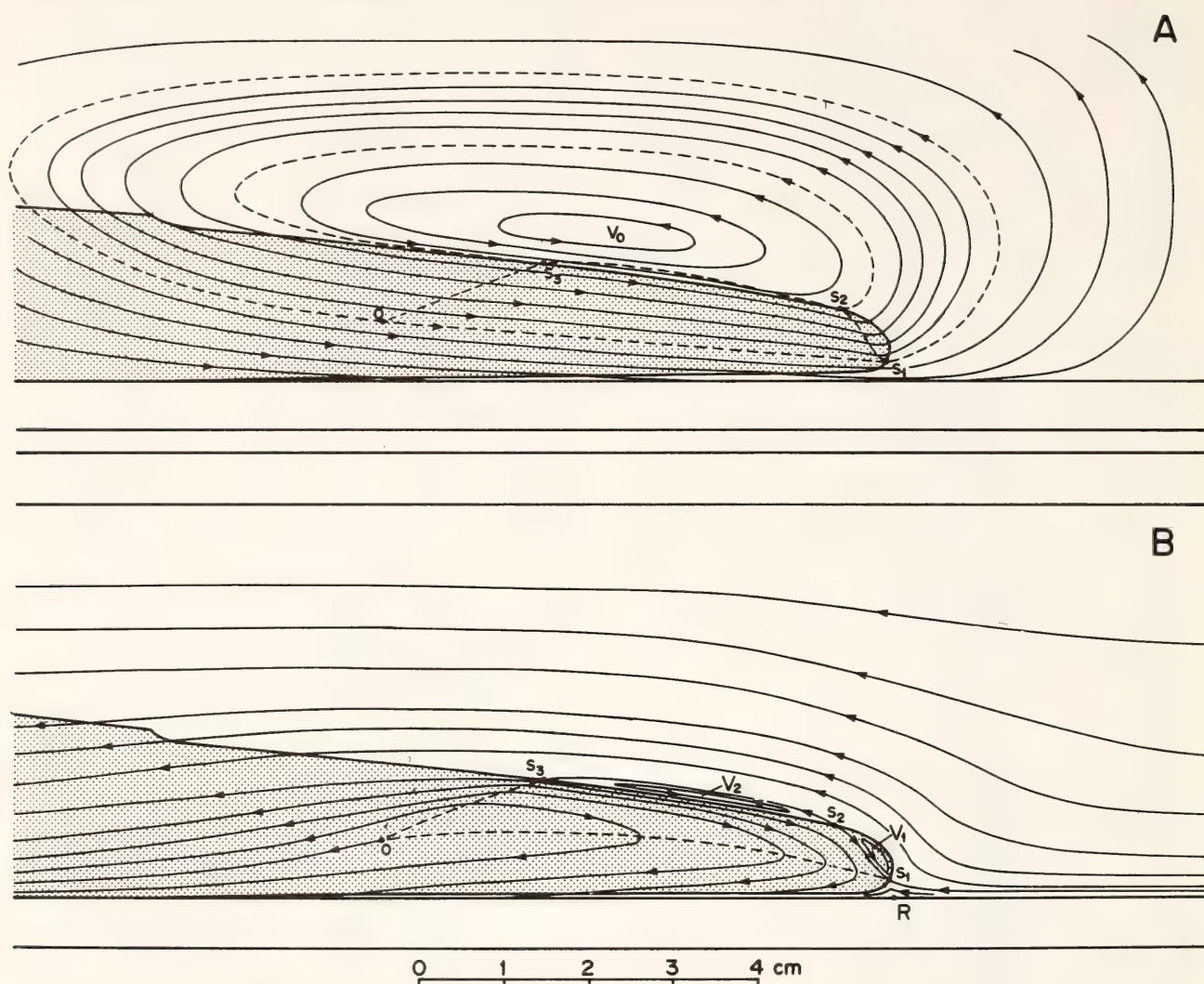


Fig. 50. Streamlines for the current in Fig. 48, plotted relative to the same reference points. The diagrams theoretically depict instantaneous flow patterns. The thicknesses of vortices V_1 and V_2 are slightly exaggerated for clarity of illustration.

at the same rate as the front tip of the current. Considered relative to the tip, however, the flow runs effectively downhill away from os_3 .

The conveyor-belt form of the front part of the current in Fig. 50B is perhaps the most important of all the streamline features. Through this feature, the current is extended by material advancing at the top and then dropping to the floor so as to make way for more material to advance. All streamlines within the glycerin current in Fig. 50B (except those in vortex V_1) must effectively end at the bottom of the current because the glycerin

is moving into a permanent position on the floor and is not just passing through the flume. Consequently, suspended particles are transported downward unless they float up more rapidly.

Applications to Layered Intrusions

The results just described and those of similar experiments appear to have extensive application in relation to igneous processes, but attention is restricted here to problems of plagioclase in layered intrusions. A general implication is that layer formation would seem to be

more a matter of current deposition than crystal settling, although the latter process is obviously involved. As for plagioclase, it no doubt can be transported to the bottom of an intrusion by magmatic currents, and the experiments indicate that it can effectively be deposited close to, if not on, the floor even when it should float. The question thus becomes, will it stay there? One way it might remain at the bottom is by becoming attached, particularly by adhering to mafic minerals. And of course, if it became buried beneath denser cumulates, it would be trapped. The observation that the density current in Fig. 48A did not actively erode the unconsolidated floor of polystyrene beads appears significant in the latter regard.

What may well be a more important factor, however, is that the magma itself has properties that could prevent plagioclase from floating free. It is now well established that magmas are non-Newtonian fluids with substantial yield strengths (Shaw, 1969; Murase and McBirney, 1973), and A. R. McBirney and R. M. Noyes (personal communication, 1976) have pointed out that the buoyant forces causing a crystal to settle or rise must exceed this strength before the crystal will move. In graphs prepared by McBirney and Noyes, it can be seen that a yield strength of less than 5 dynes cm^{-2} would generally be sufficient to retain a typical cumulus plagioclase crystal, even relatively sodic plagioclase in very iron-rich liquid. Measured yield strengths for basic magmas range from 20 to 1200 dynes cm^{-2} .

This is not to say, however, that plagioclase cannot accumulate at the roof of an intrusion. In fact, a possibility suggested by the experiments is that it might sometimes be carried to the roof in large amounts by the *local* return flow from sheetlike density currents descending along large areas of the walls of an intrusion. The degree to which crystals might be directly transferred from a suspension current to its return flow is still un-

certain*, but one can readily imagine a residual cloud of suspended plagioclase from one current becoming the return flow of the next. It would seem that systems of crystal sorting established in this way might be of major importance in the formation of the anorthositic rocks observed in the upper parts of some intrusions (e.g., see Emslie, 1970; Weiblen and Morey, 1976). Such a process is even suggested in the Skaergaard intrusion by the presence of abundant quasi-anorthositic blocks, some of them 100 or more meters on a side, that are now included in the layered series but that were considered by Wager and Brown (1968, p. 76) to be derived from the upper border group of the intrusion.

STRUCTURE OF THE SKAERGAARD TROUGH BANDS

T. N. Irvine and D. B. Stoeser†

Among the many outstanding features of the Skaergaard intrusion described by Wager and Deer (1939) and Wager and Brown (1968), perhaps the most remarkable are the trough-banding structures. These are gently plunging synformal structures distinguished by chutelike axial zones of modally differentiated layers (see Wager and Brown, 1968, Figs. 51–57); the axial zones typically are 10–15 m wide, the layers 3–30 cm thick. Most of the troughs occur in one relatively small stratigraphic interval in the upper part of the intrusion. The rocks in which they are developed are ferrodioritic cumulates of plagioclase, clinopyroxene, olivine, magnetite, and

* It is apparent, however, that a density current tends to "contain itself" by virtue of its flow pattern. In one experiment, it was observed that polystyrene beads were prevented from floating out of a suspension current of glycerin and fine-glass shards into a return flow of clear glycerin by the action of vortex V_2 (Fig. 50B); the beads were dragged down to s_2 before they could escape.

† U.S. Geological Survey, Jeddah, Saudi Arabia.

apatite. Wager and Deer (1939) distinguished 19 major troughs (denoted A to S) in this interval, spread over a distance of about 2.5 km. The most extensively exposed and apparently largest example, trough E, can be traced for about 300 m along strike and more than 100 m stratigraphically. Wager and Deer prepared a map of the area, showing the trace and plunge of each of the major troughs and the maximum dip of layering along its flanks. They observed that the troughs have a slightly radial arrangement converging toward the interior of the intrusion, and they noted that mineral grains at the bottom of the troughs tend to be aligned parallel to the axes. On the basis of these and other features, and a general petrologic analysis of the intrusion, they postulated that the troughs were formed of minerals deposited from convection currents that descended from the walls of the intrusion and flowed across the floor of accumulating layers toward the center of the magma body. The troughs were thought to mark lines of persistent, strong currents and were regarded as a principal indication of the nature of the convection pattern.

Wager and Brown (1968) noted several other minor occurrences of trough-banding scattered elsewhere in the intrusion, and they provided more description and discussion of the main structures. In particular, they mentioned that the main troughs were separated by long mounds of uniform ferrodioritic cumulate, and they suggested that the currents that deposited the layers resembled turbidity currents in aqueous sedimentary environments.

During an expedition to the intrusion in 1976, the present authors made detailed maps of two parts of the main area of troughs. One area, including troughs H, I, J, and K, was mapped at a scale of 1:300 (25 ft in⁻¹); the other, including most of troughs E, F, and G, was done at 1:600 (50 ft in⁻¹). The maps are relatively complete representations of the layering patterns as seen in outcrop, and

they provide unified pictures of many of the features mentioned by Wager, Deer, and Brown. Moreover, as a result of the mapping, several significant additional features have been recognized. Troughs H-J have been especially informative because they can be seen to evolve from a zone of planar layering that is continuous beneath them. The map of their area and a section prepared from it are shown in reduction in Figs. 51 and 52. The apparent history of a typical trough is described below, and a mechanism of current deposition is suggested, based on a flume study described in the preceding article.

Trough Structure and History

Most of the observations to follow carry an implicit assumption that the layering is a stratigraphic feature formed in accordance with the law of superposition. This assumption was justified by Wager and Deer (1939) through mineralogical and chemical evidence that the layered series accumulated from the bottom up. It is also assumed here that, over the relatively short distances that the layering planes can be traced, the planes are time markers. If the layers were indeed deposited by currents, then they presumably become somewhat younger in the direction of flow, but this characteristic cannot be distinguished.

From the mapped relations, the evolution of a typical major trough can be divided into four general stages. The first, which might be called a *prenatal stage*, is represented in the zone of planar layering shown beneath the troughs in Figs. 51 and 52. Despite the continuity of this zone, it includes numerous layers that extend for only short distances beneath the individual troughs, these layers periodically alternating with more extensive ones. Thus it is evident that, through this stage, there were repeated false starts in the process of trough formation.

In the succeeding, *youthful stage*, the trough structure proper was developed.

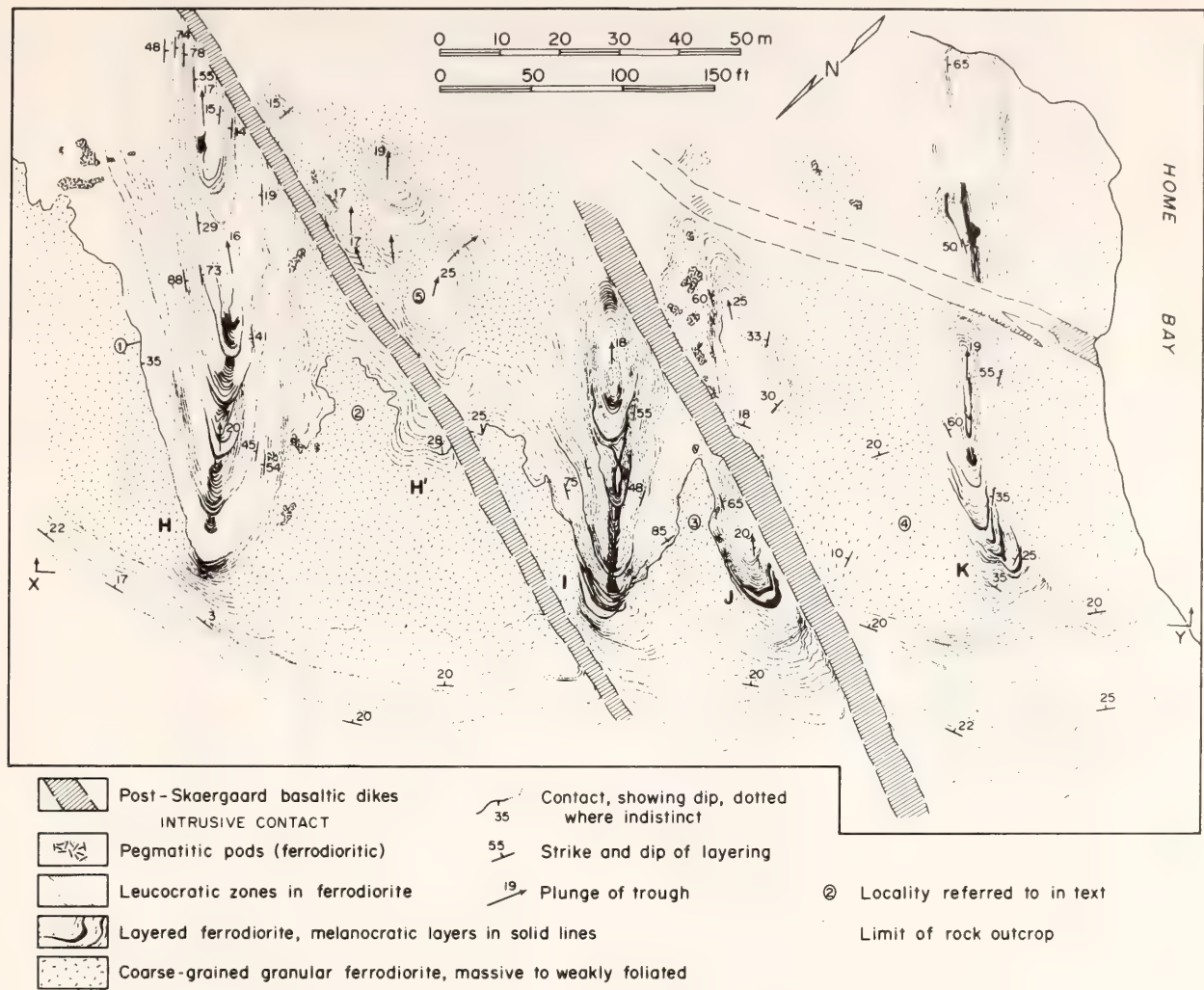


Fig. 51. Map of the Skaergaard trough bands H, H', I, J, and K.

Along the trough axis, this stage typically is represented by only a relatively thin, narrow zone of poorly developed layers exhibiting very little modal differentiation. The main units that were formed are the long mounds or ridges of uniform ferrodiorite mentioned by Wager and Brown as occurring between the troughs (Figs. 52 and 53, localities 2–4). This ferrodiorite is slightly coarser and more granular than that in the axial-zone layers and is perhaps slightly more leucocratic, but the essential minerals are the same. The rock is generally massive—foliation or planar lamination is inconspicuous at best—but this is not an unusual feature among the Skaergaard cumulates. For example, similarly massive ferrodiorite occurs in regular layers alter-

nating with modally graded layers only a few meters below the section considered here (see Wager and Brown, 1967, Pl. VI and Figs. 51–57). The axial-zone layers fade rapidly into the ridgelike mounds with no trace of erosion, and in every case that has been mapped the end of the youthful stage is marked by a layering horizon traceable from the trough axis up over the mounds on either side. In some places this horizon is marked by a thin (~1 cm) magnetite layer (Figs. 51 and 52, locality 1); in others it is simply a sharp transition from massive rock below to layered rock above. From the above combinations of features, it would appear that the troughs took form because the intervening ridges of ferrodiorite were *constructed*. If the law of superposition

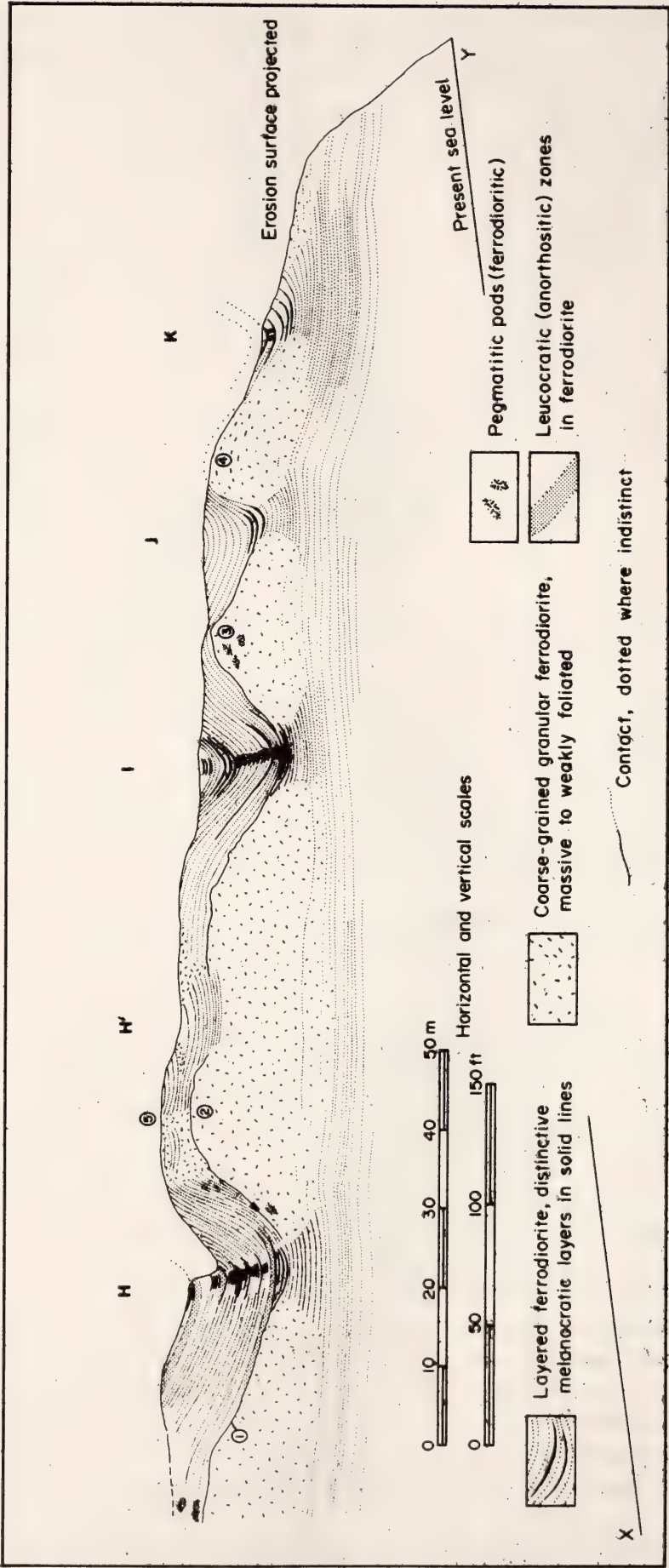


Fig. 52. Cross section of the trough bands in Fig. 51. Basaltic dikes have been eliminated, and the map relations have been projected to an inclined plane normal to the trough axes. The section was then rotated so that the continuous layering at the bottom is approximately horizontal.

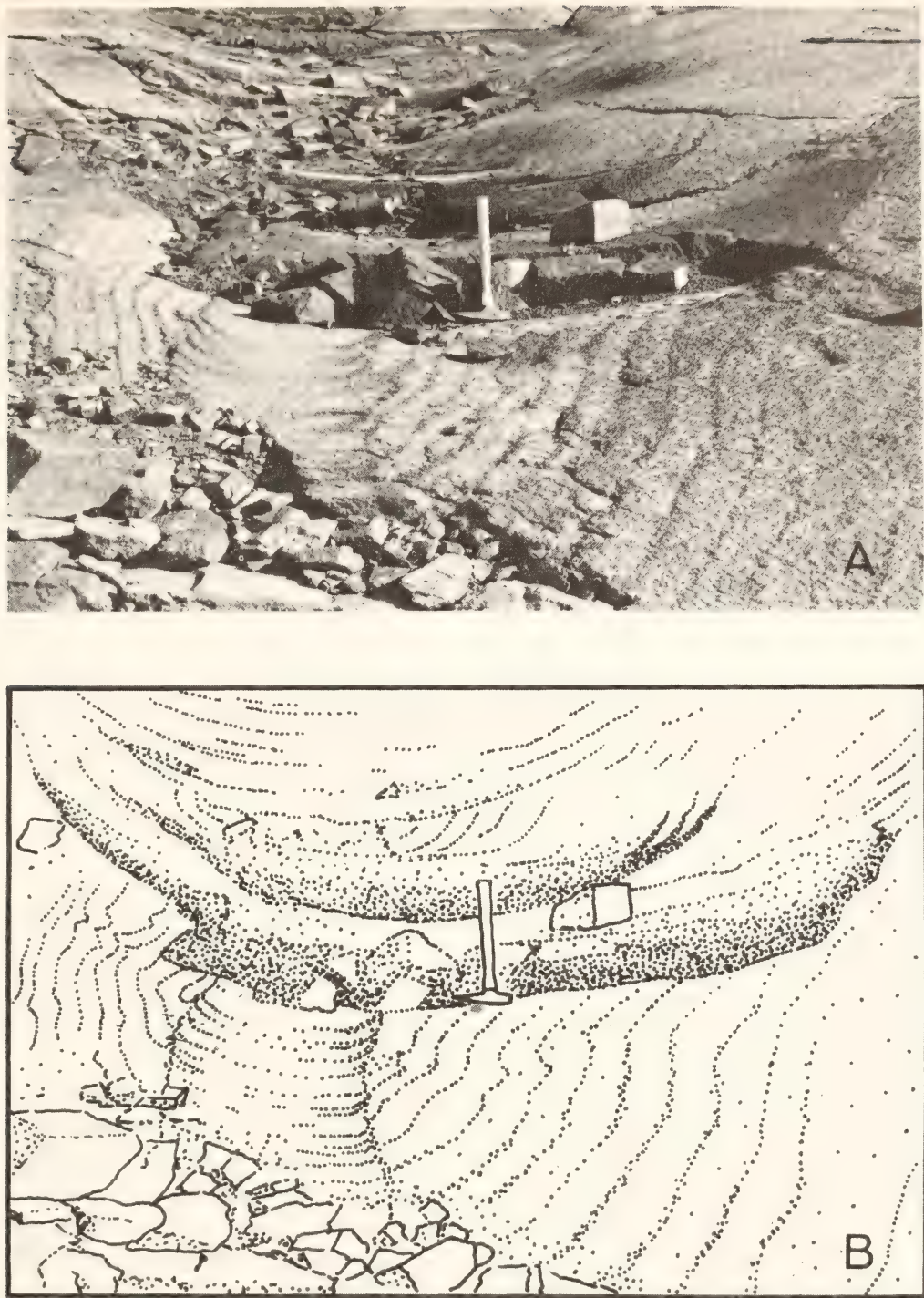


Fig. 53. (A) Photograph of layering relations in the axial zone of trough H. (B) Sketch of the photograph, outlining the main layers. Note the narrow zone of diffuse fine layering immediately along the trough axis and the truncation by the thick melanocratic layers.

was rigorously obeyed during formation of the layering, then the troughs almost certainly were not formed by erosion. The trough history then continues through a *mature stage* during which most of the prominent axial-zone banding or layering was accumulated. Less conspicuous layering was also formed on

the trough flanks, however, above the ridges of massive ferrodiorite. This layering could be described as antiformal, but at the crests of the antiforms it commonly fades or is truncated by small subsidiary troughs that locally overlap, somewhat like linguoid cross beds (Figs. 51 and 52, locality 5). In some cases there were

semiregressions to the youthful stage, and additional massive ferrodiorite was formed. In the major troughs, the mature-stage axial-zone layering is generally highlighted by melanocratic layers with slightly flat-bottomed crescentic cross sections; these dark layers alternate with (and in some cases grade up into) plagioclase-rich layers. The flanking layers are distinctly more feldspathic overall and, in places, even become quasi-anorthositic. This facies change accentuates the trough structure and effectively characterizes it.

In the two areas mapped in detail, the final or *terminal stage* of trough history has been lost through erosion from all but trough E. In this trough, the layering gradually becomes more planar and weakens so that finally it is seen only in the axial zone. The top of the trough is marked by a few extensive, essentially planar layers.

A particularly notable feature in addition to those just described concerns the local structure along the axial zones of troughs H and I (and to some extent K). In the mature-stage parts of these zones, units of alternating, relatively thin, light and dark layers are truncated and, in places, unconformably overlain by thicker, more extensive melanocratic layers that recur in a roughly cyclic way. By analogy with sedimentary rocks, it would appear that the truncation of the thin-layered units was the result of scouring by strong currents that brought in the larger amounts of dense mafic minerals in the thicker dark layers. In addition, the finer layering locally features a pronounced lateral change of facies. Immediately along the trough axis in such places, there is a vertical zone, 30–50 cm wide, within which the layering is much thinner and more diffuse than that on the outside (Fig. 53). The boundaries of this zone typically are enriched in magnetite, and in places along troughs I and K they are so rich in this mineral that they could be mistaken for two vertical magnetite veins or dikes, 5–10 cm wide. These features clearly must be accounted for in

any interpretation of the origin of the troughs.

Mechanism of the Trough Layer Accumulation

Given the case made by Wager, Deer, and Brown for the explanation that the Skaergaard layering was generally formed through current deposition of crystals, it is difficult to refrain from at least attempting to interpret the trough bands on that basis. When the troughs are actually in view, it is even more difficult. The problem with this interpretation is the one discussed in the preceding article on density current structure, namely that the cumulus plagioclase in the Skaergaard layered series was generally less dense than its parental liquid and should have floated. It is considered, however, that the flume study has demonstrated a possible solution to this problem, and the data presented above lead to the view that current deposition is also a plausible explanation of the troughs.

Figure 54 is a schematic illustration of a density current depositing crystals in a trough. The current is supposedly carrying plagioclase but is assumed to be denser than the magma that it is displacing because it is also charged with mafic minerals, these compensating for the low density of the plagioclase. The liquid itself may also be relatively dense because it was cooled and was slightly enriched in iron through crystallization. The assumed form of the current, featuring the bulging head and the sunken upper surface of the body, is based on observations of experimental currents flowing down inclined cylinders. The pattern of streamlines is adapted from the two-dimensional flow patterns described in the accompanying report. Note that the streamlines are referred to the moving tip of the current. The most important feature that has been included, however, is *secondary flow* or *circulation*. This type of circulation is common to currents flowing along channels, particularly channels with rectan-

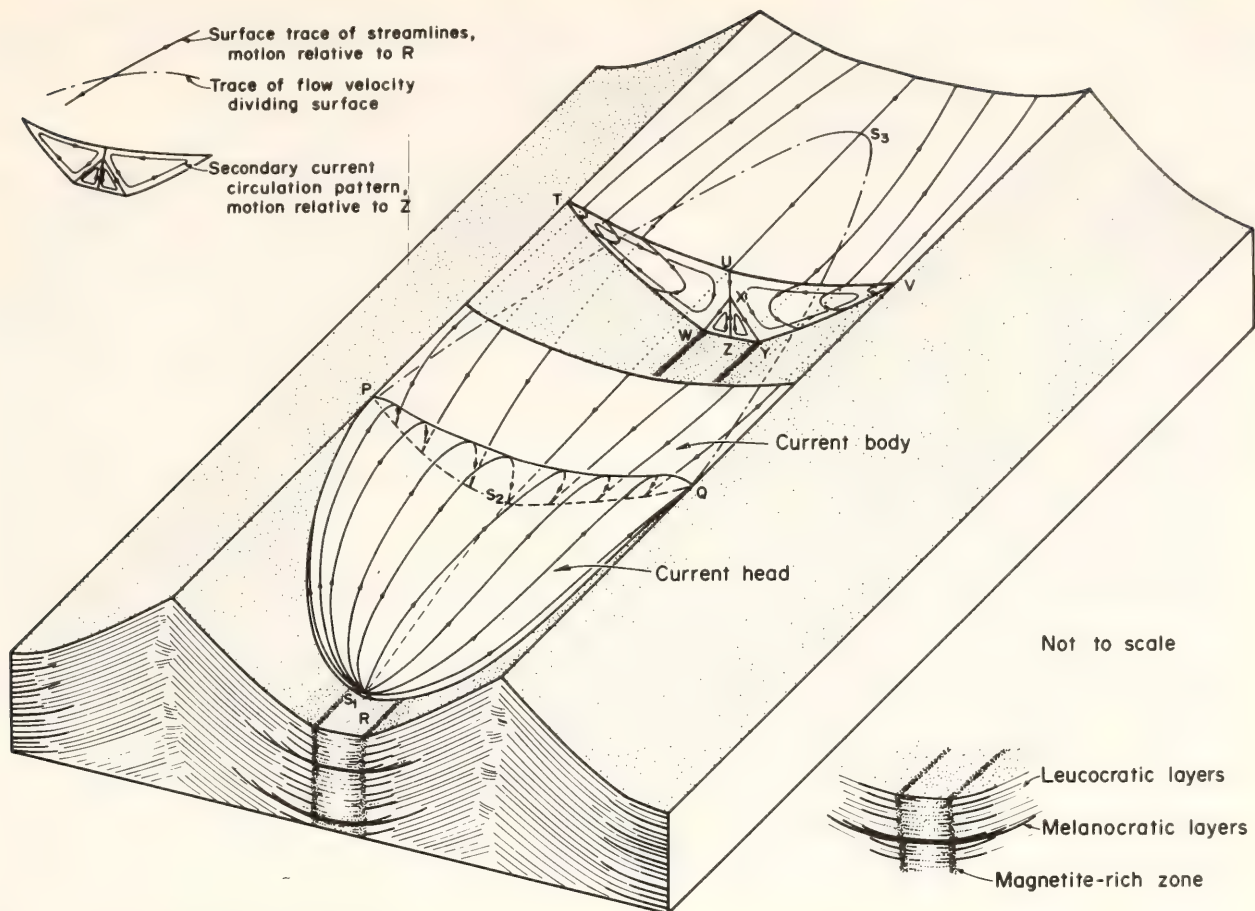


Fig. 54. Schematic diagram illustrating a density current depositing layers in a trough. Only one trough is shown to be occupied, but it is believed that currents commonly flowed down several (if not many) troughs simultaneously. See text for further discussion.

gular, triangular, or trapezohedral cross sections (e.g. Prandtl, 1952). It features a spiral or helicoidal motion in paired (or multiply paired) cells rotating in opposite directions. The possibility that this phenomenon is significant to the present problem is suggested by a comparison of the trough-banding structures with structures in sediments. The ridgelike mounds of ferrodiorite resemble longitudinal dunes, particularly wind-blown sand dunes (e.g., Folk, 1971) but also submarine sand ridges such as occur in the English Channel (Houbolt, 1968). These dune structures are generally believed to have formed because sand was carried up onto their flanks by the secondary circulation in the currents (i.e., the wind or tidal currents) that flowed along the chutes between them.

Only the surface trace of streamlines could be shown in Fig. 54, and the representation is further complicated by the fact that, because the density current is displacing liquid, the main streamlines must end at the bottom surface of the current where the original liquid was removed. Therefore, the inferred pattern of secondary circulation has also been shown separately to illustrate more clearly how such circulation might transport material onto the flanks of the trough. In addition it is seen that, if at times there were two pairs of cells as indicated, the two dividing surfaces between these pairs along which the flow descends to the floor with maximum velocity (as at W and Y) could include the pathlines of the magnetite crystals now contained in the vertical, paired zones of concentrated

magnetite along troughs H, I, and K (Figs. 52, 53). The two contrasting facies of fine layers in Fig. 53 would then represent deposits from the different pairs of cells, the contrast resulting from the differences in the rates of flow and secondary circulation in these pairs.

This interpretation is only preliminary, but it is considered sufficiently reasonable to indicate that the suggested solution to the plagioclase-floating problem is viable. When the major trough structures were formed, the Skaergaard liquid was almost at maximum iron-enrichment—and therefore at maximum density—and the tendency of plagioclase to float should therefore have been practically at a maximum. As for the trough-banding structures themselves, a major question for which no concrete explanation can be offered at present is why the ridges of ferrodiorite were formed in the first place. One possibility is that density currents of the type described here underflowed more general convection currents moving in a different direction. The ferrodiorite ridges might then have been built as a consequence of interference between the two flow systems. Another possibility is that the secondary circulation was initiated when the density currents encountered the break in slope between the walls of the intrusion and its floor. The development of secondary currents along curved boundary surfaces is a well-known phenomenon; helicoidal cells formed in this way are sometimes called Goertler vortices. In the Skaergaard intrusion, the layered series along the walls is generally distinguished by a marginal facies called the crossbedded belt (Wager and Brown, 1968), which exhibits evidence of countless episodes of layer erosion. This erosion might also have been associated with secondary flow, but perhaps by the stage when the main trough-banding structures began to form, the break in slope was not so pronounced or the currents were more gentle, and a new stage of constructional effects was initiated. Field and laboratory testing of these (and other) possibilities is required.

PETROLOGIC FEATURES OF THE SKAERGAARD MARGINAL BORDER GROUP

James D. Hoover*

In their classic study of the Skaergaard intrusion, Wager and Deer (1939) divided the intrusion into a layered series, an upper border group, and a marginal border group (Fig. 55). Systematic chemical and mineralogical variations occur through all three units, and each has zones defined by the order of appearance of minerals and their compositions. On this basis, Wager and Deer (1939) were able to show that the upper border group crystallized from the roof of the intrusion down, the marginal border group crystallized from the walls in, and the layered series accumulated from the bottom up.

Because the marginal border group is believed to have formed from the same fractionating magma as the layered series but largely by *in situ* crystallization against the walls, its study has provided an opportunity to investigate fractional crystallization largely unaffected by gravity-related effects of crystal accumulation. The marginal border group is also the only exposed part of the intrusion where the early crystallization history can be investigated. In this report, new data are presented on the detailed subdivision of the marginal border group and on the compositions of plagioclase and olivine in rock samples collected along 14 traversed sections. The samples were collected during expeditions to the intrusion in 1974 and 1976; the mineral compositions were determined with the electron microprobe.

General Features of the Marginal Border Group

The marginal border group forms the eastern and western sides of the intrusion

* Work carried out under a cooperative predoctoral fellowship program between the Geophysical Laboratory and the University of Oregon.

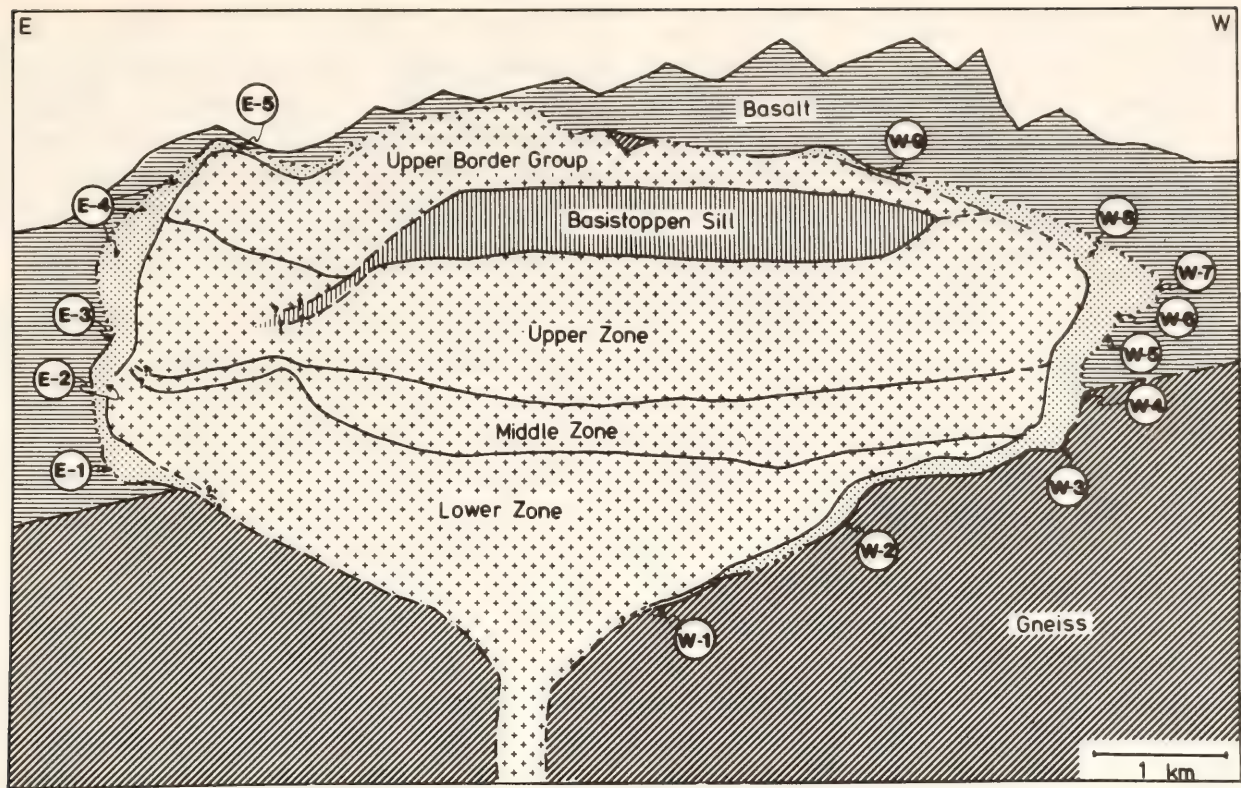


Fig. 55. Schematic east-west cross section of the Skaergaard intrusion made by projecting the mapped relations of the intrusion onto a plane normal to the average regional dip of Eocene basaltic country rock. The circled symbols indicate the locations in the sections of the marginal border group (stippled) sampled in this work.

and is presumed to be continuous around the structurally lower northern end, where a large glacier limits exposure. At the upper (southern) end of the intrusion, the marginal border group merges with the upper border group. Where it is exposed, the marginal border group ranges in width from 70 m to 600 m. Wager and Brown (1967) divided this width into two main parts: an outer “tranquil division”, 50–100 m wide, and an inner “banded division.” The first few meters of the tranquil division commonly consist of fine-grained gabbro that, at least in part, represents chilled liquid (see Hoover, this Report). For the most part, however, the tranquil division is composed of medium-to-coarse-grained olivine gabbro with local sheets and lenses of distinctive rocks called the wavy-pyroxene and perpendicular feldspar rocks (Wager and Brown, 1967).

The banded division is characterized by corrugated layers or bands from a

few centimeters to several meters in thickness, disposed roughly parallel to the intrusion walls. It has been subdivided into a succession of major units equivalent in composition to, but much thinner than, the succession in the layered series. In the layered series, the lowest exposed zone, denoted LZa, consists of cumulates of plagioclase, olivine, and some ilmenite. These minerals are joined by Ca-rich pyroxene in LZb, and by magnetite in LZc. In the middle zone (MZ), olivine disappears with the appearance of pigeonite, but at the base of the first upper-zone unit (UZa) this succession is reversed. Apatite becomes a cumulus phase in UZb, and the pyroxenoid ferrobustamite replaces Ca-rich clinopyroxene in the top-most unit, UZc.

The current investigation has confirmed the presence of equivalents of all these units except UZc in the banded division on the west side of the intrusion. There are no equivalents to LZc or MZ on

the east, however, and part of the unit equivalent to LZb has an anomalous abundance of apatite. The distribution and thickness of the units as defined in the present study are shown in Figs. 56 and 57, where they are symbolized as in the layered series but with asterisks. On the west, the units generally appear at about the same level in the intrusion as the corresponding layered series units, and they tend to thicken upwards, although LZa* and MZ* are major exceptions. On the east, LZa* is especially thick in the structurally lowest sample section.

The Skaergaard intrusion transgresses a major unconformity (Fig. 55), so that the lower parts of the marginal group are in contact with Precambrian gneiss and the upper parts with Eocene basalt and minor Cretaceous sediments. No xenoliths of basalt have been seen, however, and gneiss xenoliths occur in only a few places in the outer part of the tranquil division. Irregular pods, veins, and zones of pegmatitic gabbro—some only a few crystals in size, others several meters in length—occur in abundance throughout the marginal border group. Wager and Deer (1939) regarded these bodies as representing assimilated gneiss, but this interpretation is somewhat doubtful. Few if any of the bodies contain recognizable remnants of gneiss; conversely, most of the gneiss xenoliths that have been seen are not conspicuously pegmatitic.

What are probably the most important inclusions in the marginal border group are subrounded blocks of picrite, which occur in abundance around the northern perimeter of the intrusion. The picrite is a cumulate of olivine and minor chromite with postcumulus pyroxene and plagioclase. Wager and Brown (1967, p. 115) considered it to be the earliest differentiate of the Skaergaard magma, and they thought that the blocks slumped from some higher level in the intrusion. In 1974, however, M. S. Kays discovered an occurrence of similar picrite, apparently in place outside the intrusion and

structurally below it. It seems likely, therefore, that the picrite blocks were carried up by the Skaergaard magma, rather than down, but their exact petrogenetic relationship is still uncertain.

Plagioclase and Olivine Compositions

In Figs. 56 and 57, the sampled sections on the east side of the intrusion are labeled E-1 to E-5, and those on the west W-1 to W-9. Plagioclase compositions are plotted with respect to distance from the intrusion contact in Fig. 56, and olivine compositions are shown similarly in Fig. 57. Mineral variation lines are drawn through the "most calcic compositions" observed for plagioclase, and the "most magnesian compositions" for olivine. The vertical bars represent the ranges of composition determined for each sample. Much of this range for plagioclase is associated with zoning; for olivine, it is mostly grain-to-grain variation. Relations of the most calcic plagioclase to the most magnesian olivine are shown in Fig. 58, in comparison with relationships defined for the layered series by Wager and Brown (1967).

The total observed range for the most calcic plagioclase compositions is from An_{81} to An_{36} . If zoning is considered, this range extends to An_{20} . Compositions generally become more sodic with distance from the contact, as Wager and Deer (1939) observed. In the tranquil division, the most calcic plagioclase compositions range from An_{81} to An_{63} , but values larger than An_{69} are almost without exception exclusive to the gabbro hosting the picrite blocks and to the perpendicular feldspar and patchy pyroxene rocks (Fig. 58). The most calcic compositions in the fine-grained (chilled) contact gabbros are generally An_{66-67} , but some as sodic as An_{62} have been analyzed in complexly zoned grains, and one value of An_{76} was measured. Malløe (1974) reported a value of An_{84} for a "chilled gabbro" collected near section W-5.

The most calcic plagioclase composi-

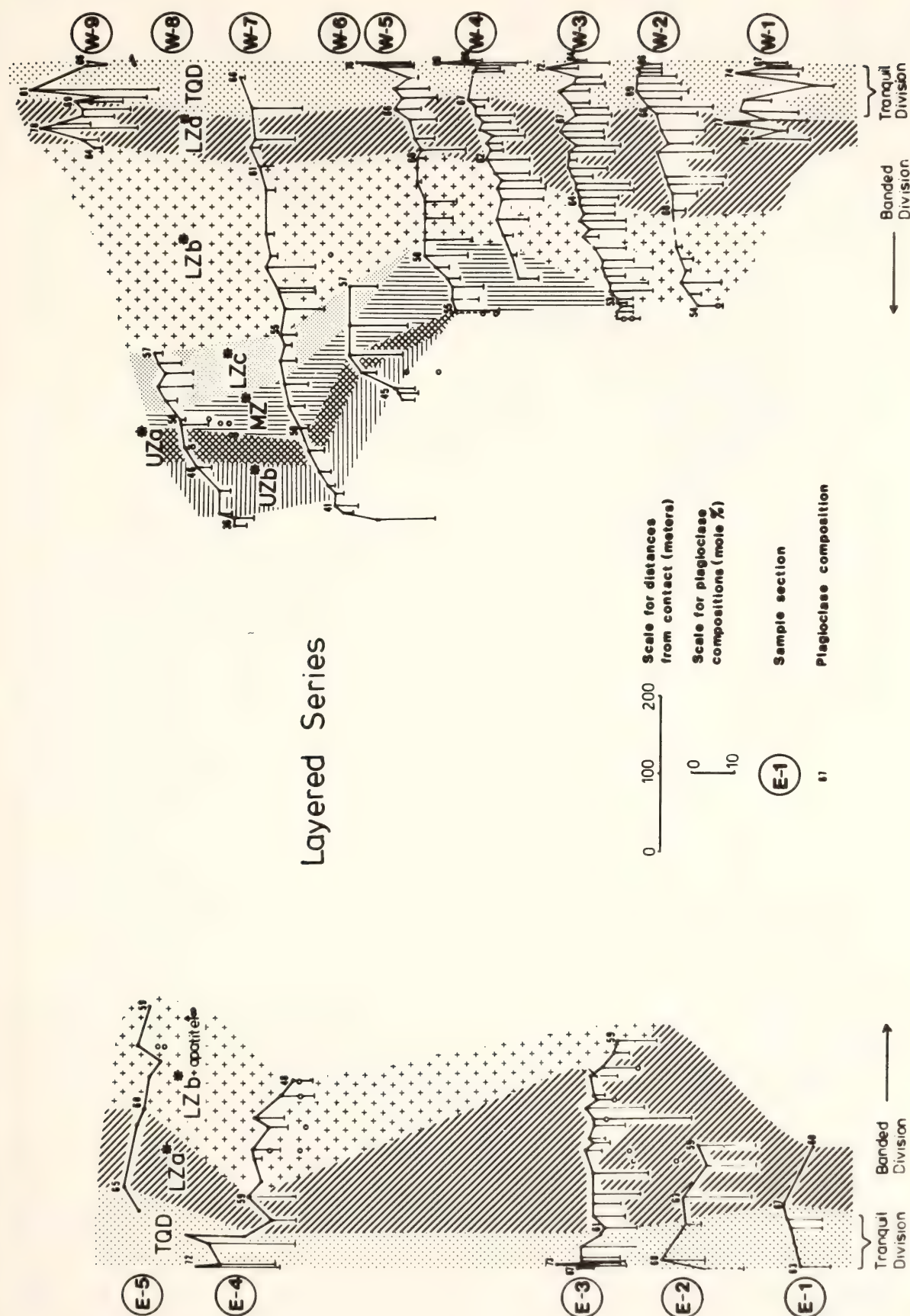


Fig. 56. Plagioclase compositions for sample sections through the marginal border group plotted against distance from the contact, corrected for the dip of the contact. For location of sections, see Fig. 55. Positions of the sections are *relative* stratigraphic heights. Circles denote pegmatitic rocks.

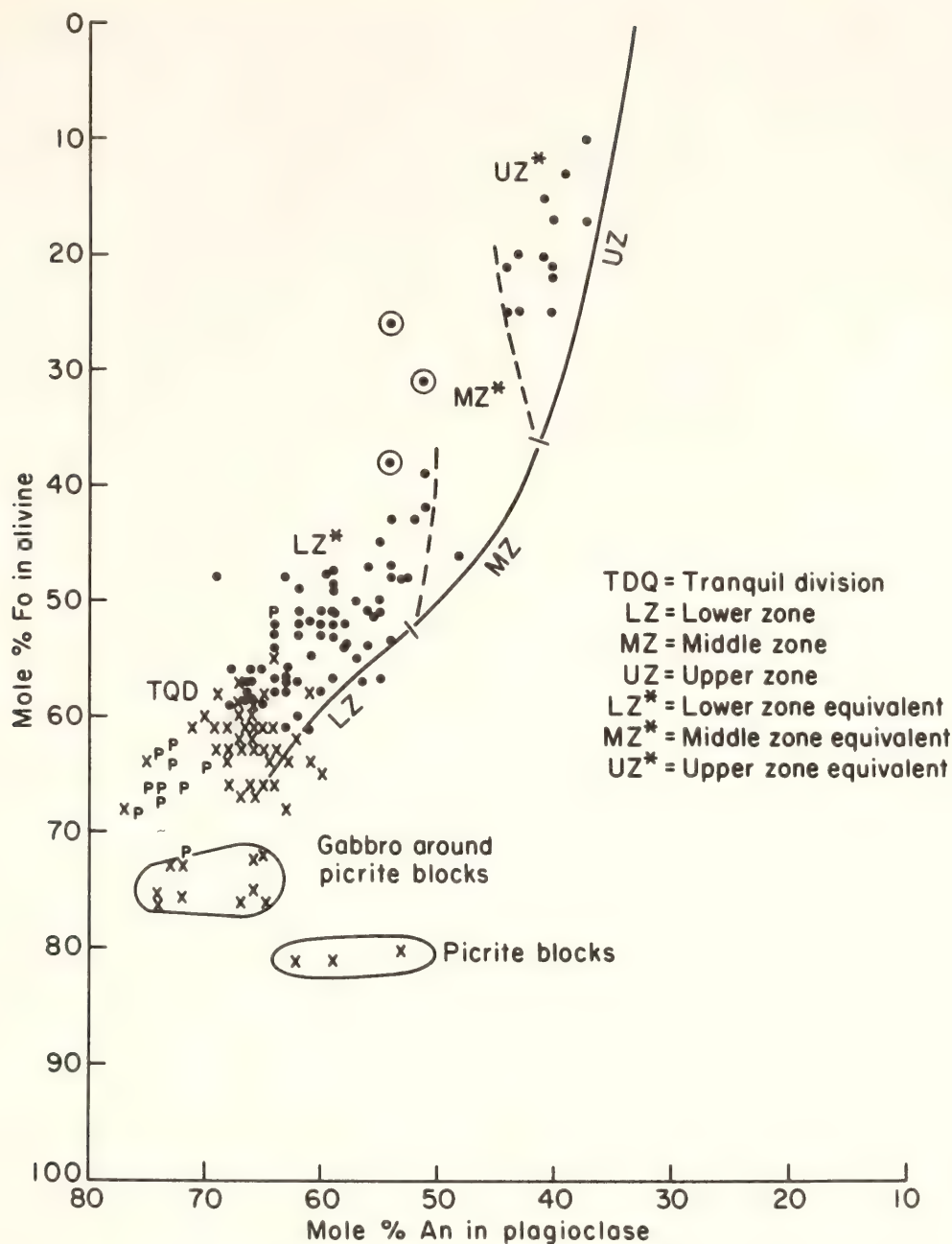


Fig. 58. Plots of the most magnesian olivine compositions (mole % Fo) vs. the most-calcic plagioclase compositions (mole % An) for samples of the marginal border group. Solid circles represent banded-division minerals, crosses (X) represent tranquil-division minerals, letters indicate minerals in perpendicular feldspar and/or wavy pyroxene rock, and circled dots indicate pegmatites. The solid line denotes the trend for the layered-series minerals from Wager and Brown (1967).

tions in rocks from the banded division range from An_{67} to An_{30} , and the ranges in LZ*, MZ*, and UZ* are respectively about the same as those in the LZ, MZ, and UZ of the layered series (Fig. 58). Plagioclase in the pegmatitic gabbros is almost invariably more sodic than that in the rocks adjoining the pegmatite (Fig. 56).

The most magnesian olivines in the common rocks of the marginal border group range from Fo_{72} to Fo_{10} (Fig. 57). The most magnesian composition overall is Fo_{83} (not plotted) analyzed in a sample from a picrite block, and values up to Fo_{76} have been obtained from the gabbro that hosts the picrite (Fig. 58). The most iron-rich olivine that has been analyzed is Fo_8 .

In general, olivine becomes richer in iron with distance from the contact.

In the tranquil division, the most magnesian olivines are characteristically Fo₆₈ to Fo₅₅. Only two exceptions, both Fo₇₂, have been found. Values in the fine-grained, contact gabbros are usually Fo₆₆₋₆₈. The most magnesian compositions in samples from the banded division range from Fo₆₄ to Fo₁₀ (Fig. 58), and on the average are about 6% richer in iron than olivine in the corresponding zone divisions of the layered series.

Discussion

One of the most important results of this study has been to confirm the findings of Wager and Brown (1967) that the marginal border group is indeed a condensed sequence of rocks largely corresponding to those of the layered series. The earliest formed rocks in the exposed part of the intrusion are those in the tranquil division. But inasmuch as olivine and plagioclase in these rocks are only *slightly* more forsteritic and anorthitic than those in the lowest exposed rocks of the layered series, as seen in Fig. 58, there is no evidence of extensive fractional crystallization preceding the formation of the exposed layered series.

An intriguing feature in the plot of olivine vs. plagioclase compositions in Fig. 58 is that points for the common rocks of the marginal border group are displaced from the layered series trend in the direction of iron enrichment. A similar relationship has been observed for the upper border group rocks by Douglas (1961) and Naslund (*Year Book* 75, pp. 640-644). A partial explanation is that the displacement reflects the different ways that olivine and plagioclase reacted with intercumulus liquid. Plagioclase crystals zoned, so their original calcic compositions tended to be preserved in their cores, whereas olivine grains homogenized and are therefore more iron-rich throughout.

In Fig. 58 it is also apparent that al-

though the picrite blocks have exceptionally magnesian olivine, their plagioclase is relatively sodic. Inasmuch as the plagioclase is intercumulus, its composition can be presumed to approximate that in the norm of the intercumulus liquid, whereas most of the plagioclase crystals in the tranquil division are fractionated. The olivine in the picrite, however, is clearly much too magnesian to be derived from the Skaergaard liquid at stages of differentiation represented in the common rocks of the marginal border group, even those of the tranquil division. Either the picrite was fractionated from the Skaergaard liquid at a much earlier, more primitive stage of differentiation, or it was derived from a different magma.

The gabbro around the picrite blocks also has more magnesian olivine, but its plagioclase is about the same as the most calcic compositions in the tranquil division. This relationship can be explained in at least two ways: (1) the gabbro formed from a more primitive liquid than the other marginal border group gabbros, or (2) it is a normal tranquil division rock except that it has exchanged Mg and Fe with olivine from the picrite. No choice can be made between these alternatives at present.

The reason for the relatively calcic plagioclase in the perpendicular feldspar and wavy pyroxene rocks is also uncertain. In view of their texture and distribution (they almost invariably occur only 3-15 m from the contact), it would seem that this feature might be due to undercooling and nonequilibrium crystallization (see Lofgren and Donaldson, 1975). Another possibility is that the rocks formed from a more primitive liquid—perhaps one introduced with the picrite blocks. Wager and Brown (1967, p. 35) considered tranquil-division plagioclase compositions of An₇₇ to An₆₉ to be representative of cumulus plagioclase in the hidden layered series. In the present work, these compositions have been found only in the perpendicular feldspar and wavy pyroxene rocks.

It is interesting to note that plagioclase compositions An_{81} , An_{75} , and An_{78} were observed at distances 37, 80, and 86 m from the contact on section W-9. It was near this section that Wager (1960) collected his preferred chilled margin gabbro, EG4507. This gabbro has a much more primitive composition than a new chilled gabbro sample (Hoover, this Report); the latter appears more nearly representative of the parental liquid of the exposed part of the layered series.

MELTING RELATIONS OF A NEW CHILLED MARGIN SAMPLE FROM THE SKAERGAARD INTRUSION

*James D. Hoover**

In their original study of the Skaergaard intrusion, Wager and Deer (1939) observed that for the first few meters around much of its perimeter the intrusion has a selvage of fine-grained gabbro, which they referred to as the chilled margin. The northern part of the intrusion is in contact with siliceous gneiss, and Wager and Deer (1939) recognized that much of the contact gabbro in this area is extensively contaminated. To the south, however, the country rock is basalt of composition similar to that of the intrusion, and two samples of the chilled margin adjoining this host rock were taken as representing the original Skaergaard liquid. In a subsequent reexamination of the problem, however, Wager (1960) chose a third sample, now well known as EG4507 (Table 18), as being more representative of the first liquid. This sample was especially important in his estimate of the size and composition of the hidden layered series, a part of the intrusion at depth that supposedly embodies the earliest differentiates of the magma. Many additional samples of the

chilled margin were collected during expeditions in 1971, 1974, and 1976. McBirney (1975), in reporting on analyses on one batch of these samples, remarked that although the composition of EG4507 was about average, the fine-grained contact gabbro is highly varied. McBirney preferred to define liquid compositions through melting experiments on the various rocks from the intrusion.

In the present study, which is part of a more extensive investigation of the marginal border group, over 30 additional samples of the fine-grained contact gabbros have been collected, and 21 have been analyzed. Variability similar to that reported by McBirney is observed, but in many cases the rocks can be shown to be contaminated, metasomatized, or to have cumulus minerals. At one particular locality, however, a contact zone of fine-grained gabbro was found that appears to represent a relatively uncontaminated chilled gabbro. This rock is significantly more iron-rich than EG4507, but its composition is appropriate to liquid in equilibrium with the earliest fractionated minerals in the marginal border group.

Description of New Chilled Gabbro

Three samples of the fine-grained gabbro, representing a zone 2.0 m wide adjacent to the south contact of Kraemers Island (Fig. 55) were analyzed and observed to be compositionally uniform. All three samples have an intergranular to subophitic texture, and consist of subhedral to anhedral laths of plagioclase intergrown with augite and pigeonite. Minor amounts of ilmenite, rare interstitial apatite, and traces of secondary biotite are accessory minerals. Minor amounts of olivine in the rock have been replaced by symplectic magnetite and Ca-poor pyroxene. Plagioclase is complexly zoned with a maximum range from An_{50} to An_{82} . Calcium-rich pyroxenes range from augite to subcalcic augite compositions. Analyses of these samples are given in Table 18. The 1-atm melting

* Work carried out under a cooperative predoctoral fellowship program between the Geophysical Laboratory and the University of Oregon.

TABLE 18. Analyses of Chilled Gabbros from the Skaergaard Intrusion

	KT-39†	(KT-39)*	KT-40†	KT-41†	EG4507‡
SiO ₂	49.69	50.10	49.83	49.54	48.08
Al ₂ O ₃	13.21	13.40	13.51	13.68	17.22
Fe ₂ O ₃	1.69	1.77	1.77	1.71	1.32
FeO	11.24	11.81	11.81	11.41	8.44
MgO	6.61	6.54	7.13	7.09	8.62
CaO	10.18	10.09	10.31	10.46	11.38
Na ₂ O	2.37	2.42	2.40	2.46	2.37
K ₂ O	.56	.57	.42	.42	.25
TiO ₂	2.66	2.64	2.65	2.62	1.17
P ₂ O ₅	.22	.22	.22	.24	.10
MnO	.22	.20	.23	.21	.16
H ₂ O±	n.d.	n.d.	n.d.	n.d.	1.06
	98.65	99.76	100.28	99.84	100.17
Q	1.18§	.96	.11	.00	.00
Or	3.43	3.45	2.53	2.53	1.49
Ab	22.01	22.25	21.91	22.51	21.37
An	24.58	24.60	25.27	25.53	35.78
Cpx	20.95	20.16	20.22	20.61	16.23
Opx	21.72	22.44	23.86	21.82	7.75
Ol	.00	.00	.00	.93	14.15
Mt	1.83	1.90	1.88	1.82	1.39
Il	3.83	3.77	3.75	3.72	1.64
Ap	.48	.47	.47	.51	.21
100Mg/(Mg+Fe)	58.6	56.9	58.9	59.8	68.8
100An/(An+Ab)	52.8	52.5	53.6	53.1	62.6

* (KT-39) is an average of six electron microprobe analyses on fused glasses.
† KT-39, KT-40, and KT-41 are whole-rock analyses obtained by x-ray fluorescence.
‡ EG4507 analysis is from Wager and Brown (1967, p. 152).
§ Normative compositions are given as cation norms, Fe³⁺ for KT- samples fixed at 0.15 for normative calculations.

relations of one of them, KT-39, has been determined experimentally under conditions of controlled oxygen fugacity (f_{O_2}).

Experimental Procedure

Starting material for the melting experiments was rock powder that had been prepared in a tungsten carbide mill and further ground under acetone to a maximum grain size of about 10 μ m. Portions of about 50 mg were sintered onto Pt wires (see Naslund, *Year Book* 75, p. 592) by which they were suspended in vertical, gas-mixing quenching furnaces at various temperatures. Oxygen fugacity was controlled by mixtures of CO-CO₂, and the charges were held for at least 24 hr

at various temperatures along the NNO, QFM, and MW buffer curves (Fig. 59).

Results

Along the MW buffer, all three of the crystalline phases olivine (Fo₇₄), plagioclase (An₆₇), and magnetite appear on the liquidus at 1170°C (Fig. 59). On the other two curves at higher f_{O_2} , magnetite is the only liquidus phase appearing at about 1175°C, and it is followed by plagioclase at 1163°C and by olivine at 1154°C. Clinopyroxene is the fourth mineral to crystallize on all three curves, at 1134°C (Fig. 59). Ilmenite was observed in some charges on the NNO buffer, but it could not be detected with enough consistency

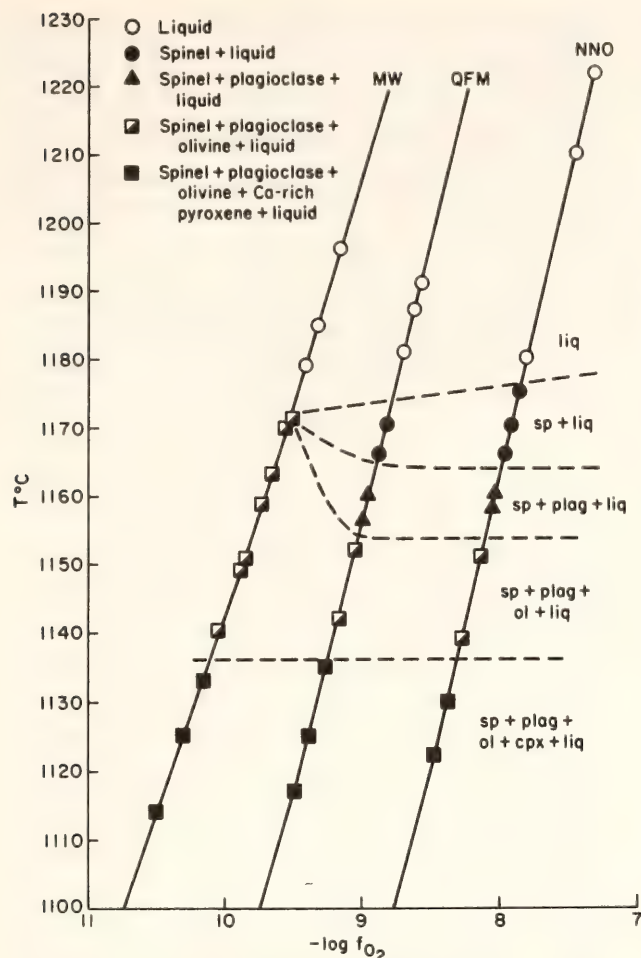


Fig. 59. Phases present for melting relations of KT-39 along the buffer curves magnetite-wüstite (MW), quartz-fayalite-magnetite (QFM), and nickel-nickel oxide (NNO) at 1 atm.

to define its stability limits. The temperature indicated for the beginning of magnetite crystallization on the QFM and NNO buffers is possibly too high because this phase first appears around the platinum hanger wire, where magnetite may have formed from slight iron loss to the platinum and consequent oxidation of the remaining iron in the melt.

Discussion

In the lower zone of the Skaergaard intrusion, crystallization of olivine and plagioclase together with minor amounts of ilmenite preceded the crystallization of Ca-rich clinopyroxene. Essentially the same sequence of crystallization was observed by Tilley, Yoder, and Schairer

(*Year Book 62*, p. 80) and by Biggar (1974) for melting relations of EG4507, although the liquidus temperature was about 1230°C. From the melting relations of KT-39, it is observed that olivine, plagioclase, and spinel are liquidus phases preceding the crystallization of augite along the MW buffer curve about 60°C lower than for EG4507. This order of crystallization is also the same as that observed in the intrusion, and the experimental determination of the conditions of cotectic precipitation of olivine, plagioclase, and spinel is considered a reasonable estimate of the temperature and f_{O_2} (1170°C and $f_{O_2} = 10^{-9.5}$) at the time of emplacement of this liquid.

In the lowest exposed rocks of the layered series, the cumulus minerals have the compositions An_{66} (plagioclase) and Fo_{67} (olivine). A unit in the marginal border group known as the tranquil division (cf. Hoover, this Report) contains the earliest formed cumulates in the exposed parts of the intrusion; they have the compositions An_{66-69} and Fo_{72} . Electron microprobe analyses of the first plagioclase and olivine crystals grown from KT-39 are An_{67} and Fo_{74} , compositions that are remarkably consistent with the earliest cumulus mineral compositions in the layered series and marginal border group.

The composition of KT-39 is strikingly similar to analyses of ferrobasalts from the mid-Atlantic ridge (Bunch and LaBorde, 1976) and the Scottish Hebridean province (Tilley and Muir, 1962), and it is particularly similar to the composition of numerous basalt dikes that occur near and are essentially contemporaneous with the Skaergaard intrusion (Brooks and Nielsen, 1978). Moreover, an initial liquid composition similar to KT-39 is appropriate to the experimentally determined trend of liquid compositions in equilibrium with the cumulus minerals formed in the layered series rocks (McBirney, personal communication).

A few minor features in the tranquil division of the marginal border group, however, are not explained by the crystal-

lization from a parental liquid such as KT-39. Near the intrusion contacts, measured plagioclase compositions are occasionally more calcic (up to An_{77}) than in surrounding gabbros (see Hoover, this Report). Similar compositions are reported by Malløe (1974) as narrow zones surrounding resorbed cores of An_{67} in the hidden zone. Plagioclase is also slightly more calcic (up to An_{78}) and olivine slightly more magnesian (Fo_{76}) in gabbro-hosting picrite blocks in the lower, northern perimeter of the intrusion (Hoover, this Report). Olivine in the picrite blocks also is unusually magnesian (up to Fo_{83}), and these blocks were probably not derived by fractional crystallization within the intrusion (Hoover, this Report). Leeman and Dasch (1978) have noted that $^{87}Sr/^{86}Sr$ in the picrite blocks and in these more calcic plagioclases is more primitive than measured values in other gabbros in the marginal border group. The petrogenetic relationship of these features to the intrusion is not yet clear, but one possibility is that they were formed from a liquid somewhat more primitive than KT-39.

Even greater inconsistencies must be reconciled for EG4507 to be the initial liquid. Largely on the basis of this sample, Wager (1960) and Wager and Brown (1967) estimated that the early differentiates of the magma make up about 70% of the total volume of the intrusion. From these same data, Chayes (1970) has shown that this volume should be even larger, and he suggested that EG4507 may be an unrealistic parental magma if the estimates of the zone compositions are reasonable. The Wager composition also requires over 60% solidification to change the liquid to one compatible with formation of the lower layered series, and the presence of trapped liquid may increase this value to nearly 80% (Brooks and Nielsen, 1978). Because the lowest exposed layered-series rocks have olivine and plagioclase as the only cumulus silicate phases, crystallization of only olivine and plagioclase

after such a large degree of solidification is impossible. Moreover, on the basis of a gravity survey, Blank and Gettings (1973) estimated that the hidden zone probably comprises no more than 10% of the volume of the intrusion. The Fe^{2+}/Mg of EG4507 also requires that the liquid be in equilibrium with olivine (Fo_{84}) much more magnesian than is found anywhere in the intrusion except in the picrite blocks. Finally, Hoover (this Report) has shown that the earliest formed rocks found in the tranquil division of the marginal border group contain plagioclase and olivine only slightly more primitive than in the lowest exposed layered series—further evidence that extensive fractionation of the parental liquid did not occur to form the lower layered series. Conversely, KT-39 is consistent not only with the sequence of minerals crystallized in the Skaergaard intrusion but also with their compositions; therefore, only a small portion of the intrusion is below the lowest exposed layered series.

Both EG4507 and KT-39 are clearly bonafide liquid compositions and both occur as chilled margins, but neither satisfactorily explains *all* the features of the intrusion. Brooks and Nielsen (1978) have shown that dike compositions that occur near the intrusion are similar to the range of compositions deduced for the Skaergaard magmas at various stages of fractionation, and many are similar to the composition of EG4507. This diversity of compositions has been ascribed to a family of magmas modified in lower crustal reservoirs (Goles, in preparation) and is required for the multiple-intrusion models postulated by Moorbath and Welke (1969) for the igneous rocks from Skye, and by Brooks and Nielsen (1978) for the Skaergaard intrusion.

The most probable *primitive* liquid for the Skaergaard intrusion may be an abyssal tholeiite composition like EG4507 (Irvine, *Year Book* 76, pp. 454–461); such a liquid must have contributed in some way to the event or events forming the intrusion but in a manner different

from that suggested by Brooks and Nielsen (1978). Although a composition like KT-39 was undoubtedly not a primitive liquid, it may have been the most probable *primary* liquid initially filling the Skaergaard chamber.

INFILTRATION METASOMATISM, ADCUMULUS GROWTH, AND SECONDARY DIFFERENTIATION IN THE MUSKOX INTRUSION

T. N. Irvine

The formation of cumulates in layered intrusions is commonly envisaged as occurring in two general stages: (1) a primary stage in which the cumulus minerals are fractionated from the main body of magma and accumulated by current deposition and other processes on the floor (and, in some cases, the roof and walls) of the enclosing chamber, and (2) a secondary, postcumulus stage when the fractionated minerals are cemented together by materials crystallized from intercumulus (interstitial) liquid. Discussions of the compositional variations in cumulates and their minerals tend to concentrate on the effects of primary fractionation. Indeed, even the postcumulus materials are commonly treated as being largely formed at the primary stage by a process called adcumulus growth.* In the most widely cited mechanism for this growth, proposed by H. H. Hess (1960) and advocated by Wager (1963), the cumulus crystals continue to grow just beneath the depositional surface from materials supplied from the main body of magma by diffusion through the intercumulus liquid. The intercumulus liquid itself is supposed to be expelled mechanically with the filling of the pore spaces. A mathematical analysis of this process by G. B. Hess (1972) indicated,

* The terminology used here was largely devised by Wager *et al.* (1960) and Wager and Brown (1968). The term postcumulus was originated by Jackson (1967).

however, that diffusion in the liquid was much too slow compared with probable rates of crystal accumulation for the process to be significant. Some other mechanism is apparently involved.

In this report, some compositional relationships in the cumulates of the Muskox intrusion in the Canadian Northwest Territories are described, and a model for their origin is presented that leads to a very different concept of postcumulus crystallization and adcumulus growth.

Cyclic Units and Theoretical Compositional Trends

The Muskox relations of interest involve repeated stratigraphic divisions called cyclic units. Twenty-five such units have been identified, and it has been shown that they formed by primary crystallization differentiation and are repeated because of the repeated influx of fresh magma into the intrusion while the layers were accumulating (Irvine and Smith, 1967). For purposes of background, it is useful to describe the compositional variations that would be expected in hypothetical units like those under consideration, assuming that they formed purely by fractional crystallization and periodic replenishment of the liquid, with no complicating factors. Three cyclic units theoretically formed in this way are shown in Fig. 60. The top unit is the most complete, comprising layers representing three stages of crystallization. Olivine is the main cumulus mineral in the first (dunite) layer; it is joined by clinopyroxene in the second (olivine clinopyroxenite) layer and then by plagioclase in the third (olivine gabbro) layer. This is the crystallization order observed for melts made from the chilled margin of the Muskox intrusion at appropriate oxygen fugacities (Biggar, 1974). Chromite is shown to have precipitated in minor amounts with olivine in the dunite layer but is absent thereafter. Its disappearance would be expected because of a reaction relationship between chromite

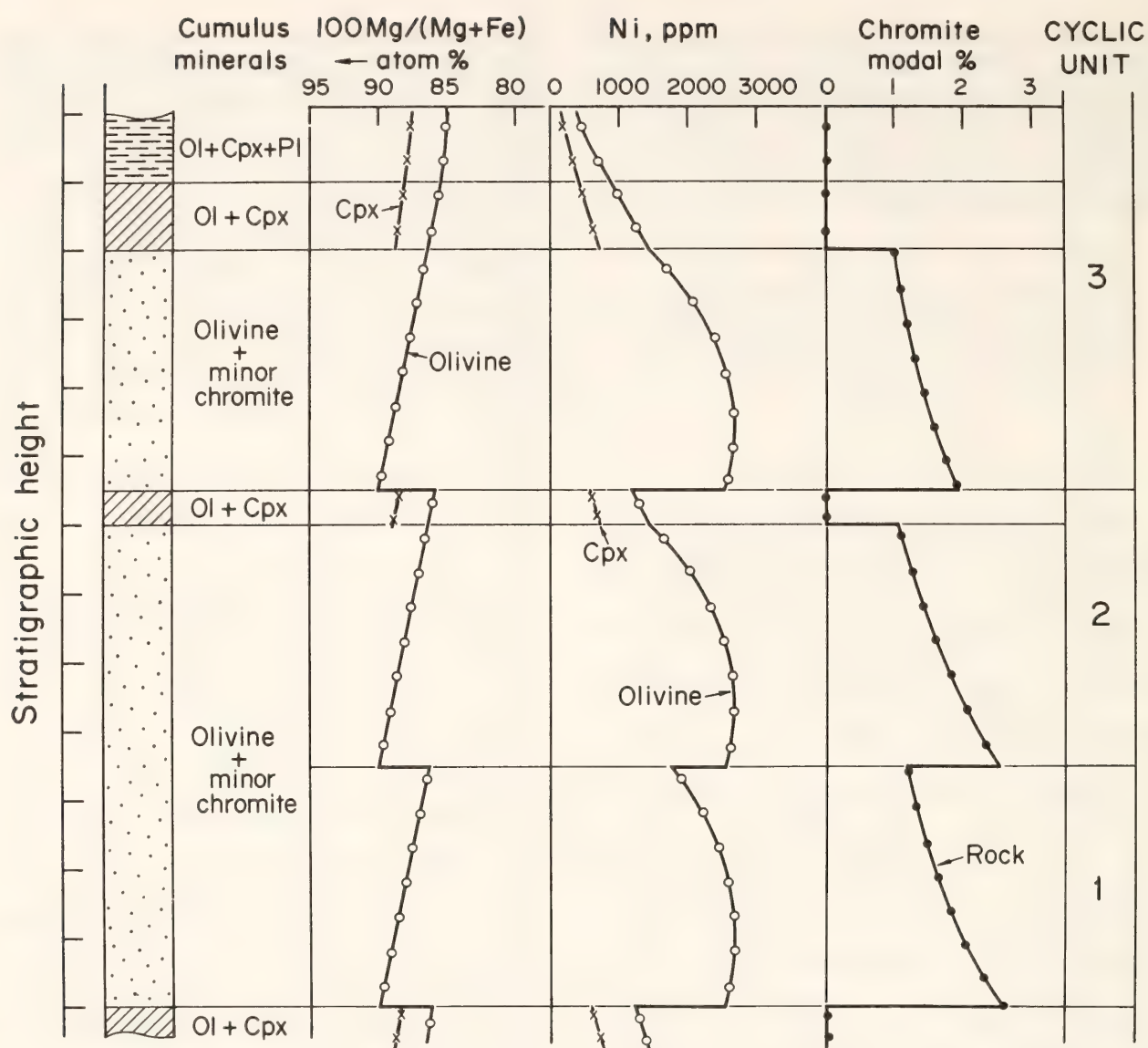


Fig. 60. Hypothetical sequence of three cyclic units analogous to those in the lower part of the Muskox layered series, showing chemical and modal trends that would be expected ideally to develop through fractional crystallization and periodic replenishment of the magmatic liquid.

and clinopyroxene (Bowen, 1928, pp. 279–281; Irvine, 1967; Dickey, Yoder, and Schairer, *Year Book 70*, pp. 118–122). The layer succession could be extended upward to include more stages of crystallization, but more commonly in the Muskox intrusion the crystallization course was interrupted by an influx of fresh liquid before even three stages were completed. Such an event is indicated in the second cyclic unit in Fig. 60, in which no plagioclase was precipitated before the regression to olivine and chromite crystallization, and in the first (bottom) cyclic unit, in which not even clinopyroxene was precipitated.

Two types of primary mineral composition variations are illustrated in Fig. 60, one defined by Mg/Fe, the other by Ni or Ni/(Mg + Fe). The trend of Mg/Fe decrease was calculated by means of a Rayleigh-type fractionation equation (Irvine, *Year Book 76*, pp. 539–541) based on the distribution coefficient $K_D = (\text{Mg/Fe in liquid})/(\text{Mg/Fe in olivine})$, which has an equilibrium value of about 0.3 (Roeder and Emslie, 1970). The trend is practically linear for olivine over the range of 16 wt % crystallization assumed for the dunite layers. The Ni trends were calculated by finite difference methods, based on experimental data for the co-

efficient $D = (\text{Ni in olivine})/(\text{Ni a liquid})$. These trends are convex upward with respect to the concentration of Ni because D increases strongly as the liquid becomes impoverished in olivine (Irvine, *Year Book 73*, p. 307, Fig. 56). At first the effect of increasing D is to maintain high Ni concentrations in the olivine even through the liquid is being depleted, but eventually the liquid becomes so impoverished that the amount of Ni entering olivine must also decline.

Another type of primary differentiation trend is illustrated by chromite abundance, which decreases upward in each of the dunite layers. This type of trend, also observed in several Muskox cyclic units, develops because the olivine-chromite cotectic is curved in such a way that, as the liquid is fractionated round

the curve, less and less chromite is precipitated. Such curvature has been demonstrated in the system $\text{CaO-MgO-Al}_2\text{O}_3\text{-Cr}_2\text{O}_3\text{-SiO}_2$ (Irvine, *Year Book 76*, pp. 539-541).

The key feature represented in Fig. 60, however, is that the discontinuities in the chemical and modal trends associated with the replenishment of the liquid occur at the same stratigraphic levels as the sharp modal changes defining the regressions in crystallization path. Actual relations in the Muskox layered series are locally in marked contrast to this feature.

Observed Compositional Variations in Some Muskox Cyclic Units

Figures 61 and 62 show compositional data from cyclic units 4-7 of the Muskox

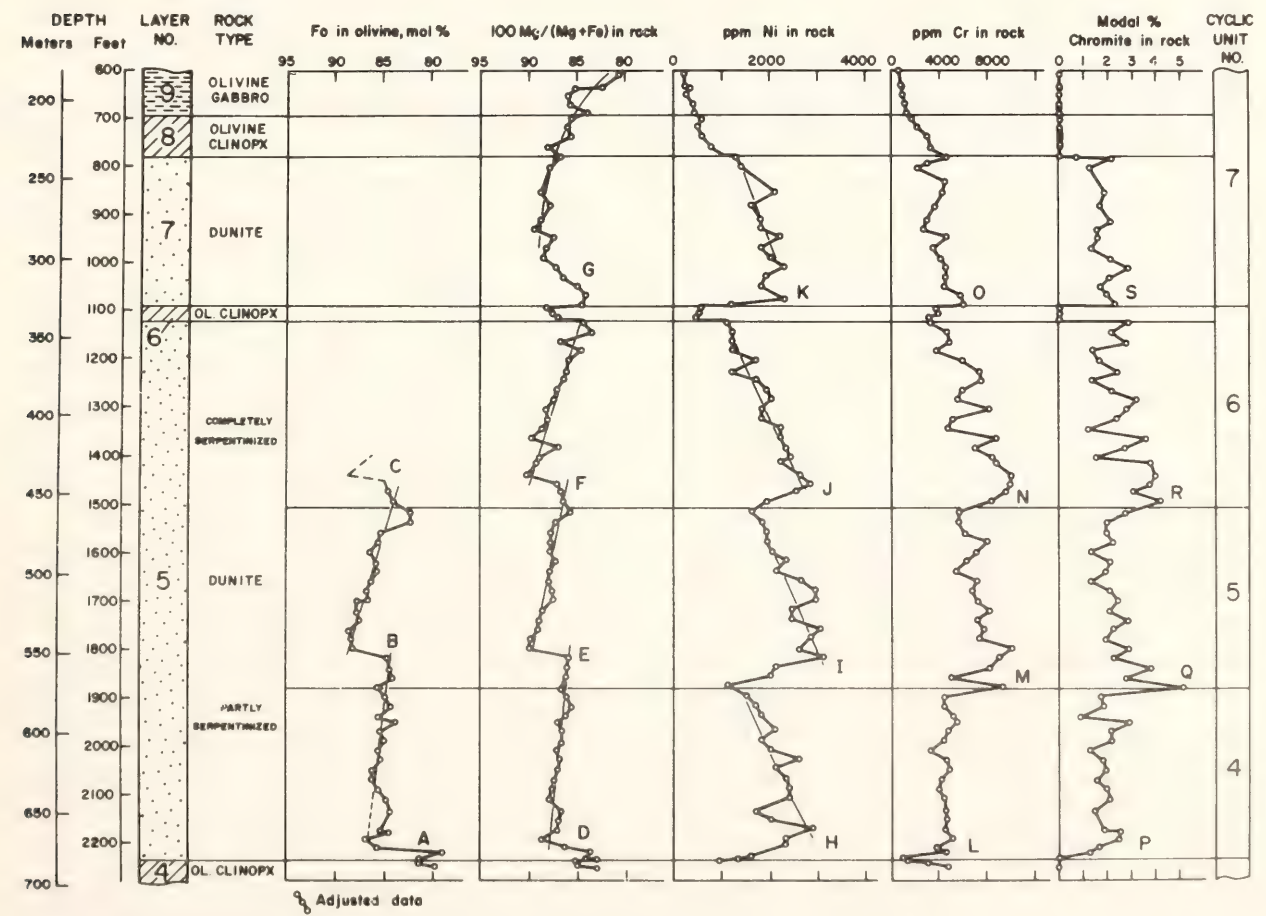


Fig. 61. Mineralogical, chemical, and modal data from the rocks of Muskox cyclic units 4-7 as exposed on the South drill hole. The olivine compositions were determined by the x-ray method of Jambor and Smith (1964); Mg and Fe were determined by x-ray fluorescence, Ni and Cr by emission spectrography, and the chromite abundance by point counting. The cyclic units are defined on the basis of modal discontinuities reflecting regressions in the crystallization order of the magma.

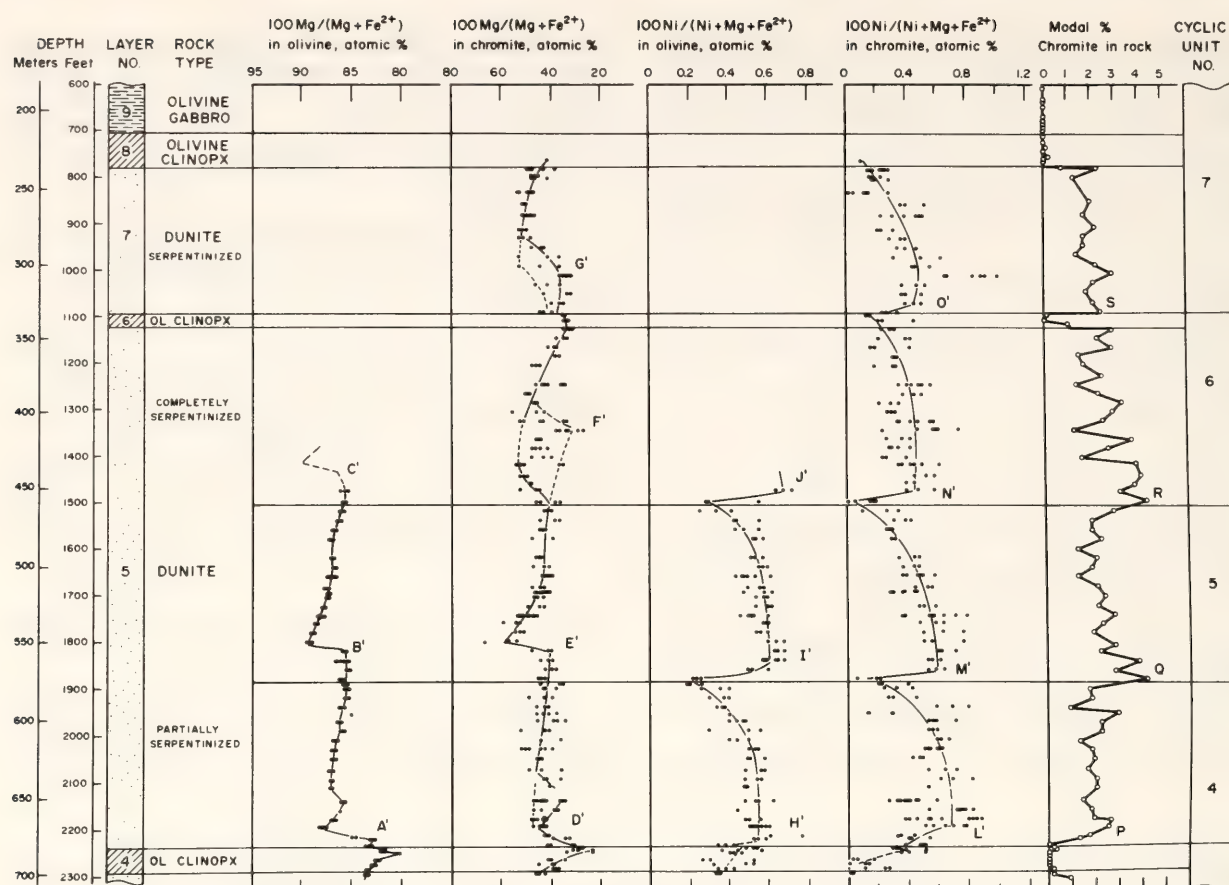


Fig. 62. Electron microprobe data on Mg/Fe and Ni in olivine and chromite in the same section as in Fig. 61. The modal data on chromite are the same as in Fig. 61.

layered series. Each of the units embodies a dunitic layer of olivine-chromite cumulate, 100–120 m thick, exhibiting trends of variation similar to those outlined in Fig. 60. The stratigraphic boundaries of the four units are located on the basis of sharp modal changes. The basal contacts of units 4 and 7 are relatively straightforward; each corresponds to a contact of dunite over pyroxenite, marking a major regression in crystallization order. The basal contacts of units 5 and 6 are more obscure, having dunite both above and below, but in both cases the unit begins with a small but distinct increase in the modal abundance of chromite that also shows in the amount of Cr in the dunite (Fig. 61). Note also that the trends defined by the analyses of olivine in units 4 and 5 are reflected in the whole-rock and chromite compositions, and that these latter compositions show the same types of trends in units 6 and 7 where olivine is completely serpentinized.

Several other minor or “subsidiary” cyclic units may also be represented in the section in Figs. 61 and 62, for example in the whole-rock Mg/Fe profiles for units 4, 6, and 7. It seemed advisable, however, to define a minimum number of units, and as will be seen below, some of the possible subsidiary units may indeed differ in origin from the main units.

Considering first Fig. 61, it is seen that, although the Fo content (or Mg/Fe) of olivine increases sharply near the base of cyclic unit 4 (at A) and then follows a trend of gradual upward decrease like that in the hypothetical model in Fig. 60, the increase does not occur until 6–8 m above the base of the unit. Similar relations occur at the base of unit 5 (at B), only here the sharp increase in Fo does not occur until some 20 m above the contact (see also Fig. 61, A' and B'). The same discrepancies are evident in the whole-rock data on Mg/Fe (at D and E).

The olivine becomes completely ser-

pentinized before an increase in Mg/Fe is defined at the base of unit 6 (at C), but in the whole-rock data (at F) the discontinuity is about 18 m above the defined contact. The increase in Mg/Fe in the lower part of unit 7 (at G) is more gradual, but a maximum is not reached until almost 50 m above the base of the unit.

With regard to the Ni data in Fig. 61, the break in trend at the base of unit 4 (at H) is not closely defined, but certainly a strong increase does not occur until the third sample of dunite, about 10 m up. At the base of unit 5, the high point in chromite (at Q) or Cr (at M) is a low point in Ni (at I). And at the base of unit 6, the high point in chromite (at R) or Cr (at N) is a low point in Ni (at J). At the base of 7, the first dunite sample (near K) is relatively poor in Ni; the next is close to a maximum value.

Similar relations are evident in the electron microprobe data in Fig. 62. The Mg/Fe trends of olivine are essentially identical to those based on x-ray methods in Fig. 60, and similar trends occur in the chromite (although with complications

due to large variations in its composition, especially near “subsidiary” cyclic units at F’ and G’, units 6 and 7). The data for Ni in olivine and chromite exhibit the convex upward profile illustrated in Fig. 60, and more importantly, they show that the first dunite samples at the bases of both units 5 and 6 are indeed poor in Ni. The Ni discontinuities, therefore, are some 3–6 m above the basal contacts.

In summary, then, the chemical breaks are consistently up-section from the modal breaks, and for each contact the difference is 2–4 times larger for the Mg/Fe discontinuity than for the Ni discontinuity.

The Infiltration Metasomatism Model

The proposed explanation of the relations described above involves a process of infiltration metasomatism (Korzhinsky, 1965) whereby the cumulus minerals are changed in composition by reaction with intercumulus liquid migrating upward through the layered series due to compaction effects. The principle of the mechanism is schematically illustrated in Fig. 63. Under the assumed initial condi-

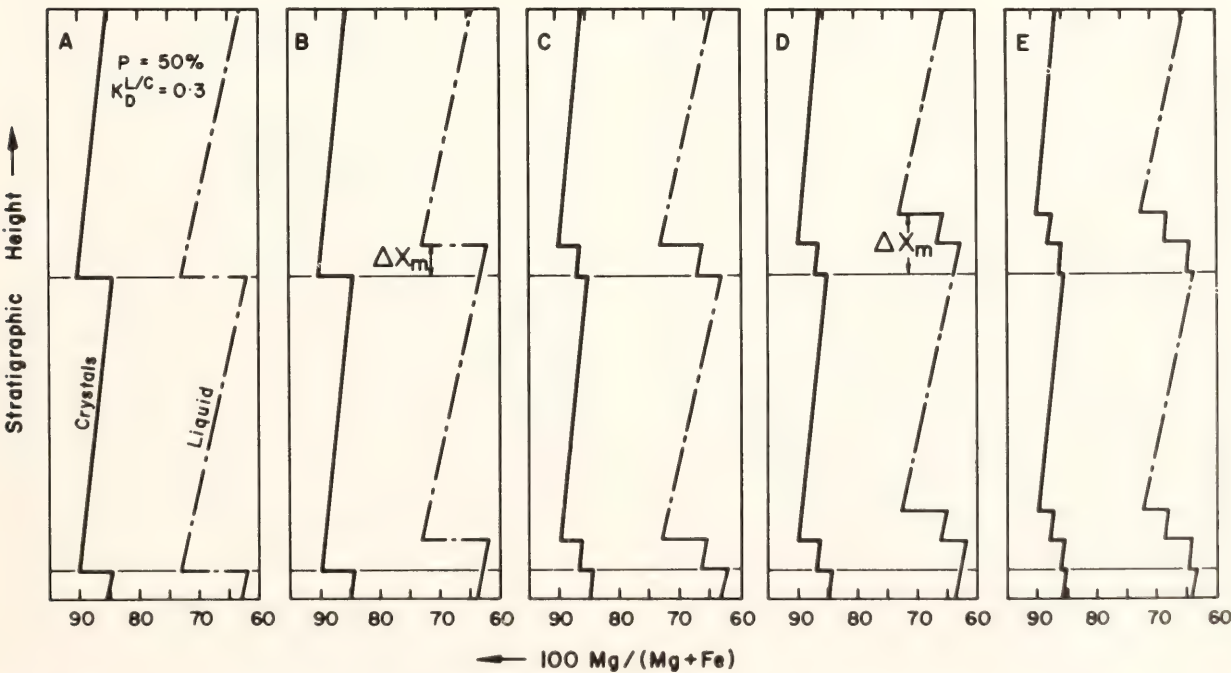


Fig. 63. Schematic illustration of the effect of upward migration of intercumulus liquid on Mg/Fe in cyclic units of olivine cumulates. *P* is porosity; *K_D* is the equilibrium value of (Mg/Fe in the liquid) / (Mg/Fe in the olivine). For explanation, see text.

tions in column A, equal amounts of olivine and interstitial liquid have accumulated in two cyclic units showing upward trends of decreasing Mg/Fe. The phases are in local chemical equilibrium at all stratigraphic levels, in accord with the indicated Mg/Fe distribution coefficient. In B, the liquid has been moved uniformly upward a distance ΔX_m , and the crystals and liquid are now out of equilibrium, especially in the stratigraphic intervals immediately above the basal contacts of the cyclic units. If crystals and liquid then react so that local equilibrium is reestablished, the compositional profiles are modified as in column C. Movement of the liquid another increment ΔX_m gives the relations in D, and repeated equilibration yields the profiles in E. It is seen that the Mg/Fe discontinuities are shifted upward with little change in magnitude.

To be more realistic, this model must be modified in several ways. A principal shortcoming is that the liquid is assumed to have the same content of Mg + Fe as the olivine; consequently the Mg/Fe discontinuity moves very rapidly, practically at the same rate as the liquid itself. With liquid compositions poorer in Mg + Fe, like those estimated for the Muskox intrusion (see below), the discontinuity moves much more slowly than the liquid.

The shape of the discontinuity is modified when it is displaced upward, but if the size of ΔX_m is sufficiently reduced, the incremental steps are effectively smoothed and the discontinuity moves with a relatively sharp, steady-state profile. In effect, there develops a balance between the sharpening of the discontinuity achieved by reducing ΔX_m and the broadening that results from having to move the liquid more increments to cause the same displacement of the discontinuity. For the scale of displacements of interest here, steady-state profiles are obtained at $\Delta X_m \simeq 1$ m.

The main refinement that has been made of the scheme in Fig. 63, in modeling the Muskox relations, is the assumption

that the layers were compacted as they accumulated rather than after the complete section had been built up. The approach has been to assume that there was a "compacting zone" with a steady-state porosity profile, as illustrated in Fig. 64. This profile is defined by the equation $P = P_{min} + kh_{cz}^2$, where P_{min} is a minimum final porosity, h_{cz} is distance measured from the base of the compacting zone, and k is a constant such that $P = P_0$ (the initial porosity) at $h_{cz} = X_{cz}$ (the total or maximum thickness of the compacting zone). The profile is similar to porosity profiles for water-laid sediments compacted by burial (e.g., Baldwin, 1971, Fig. 1B). The objective in the modeling is to find a value for X_{cz} such that the cyclic unit boundaries are infiltrated by enough liquid to cause the observed displacements of the Mg/Fe and Ni discontinuities.

In the computational process, the final form of the layered series is divided into increments having the same content of crystals, and the physical removal of the intercumulus liquid has been simulated in two ways. By one method (Model 1), there is a maximum of mixing of liquid between increments within the constraint that the liquid can move only one increment at a time. In the other (Model 2), there is no mixing from increment to increment. For a given value of X_{cz} , the models give the same displacements of a chemical discontinuity, but they differ in the distance the liquid moves. In Model 1 some liquid moves the full thickness of the compacting zone, whereas in Model 2 the migration distance for all liquid is only a fraction of this thickness. No definite statement can be made as to which model is the more realistic, but they probably represent extremes.

Computational Results

The range of the liquid composition used in modeling the Muskox relations are given in *Year Book* 76, Table 5 (p. 456). A final porosity of 10 vol % was

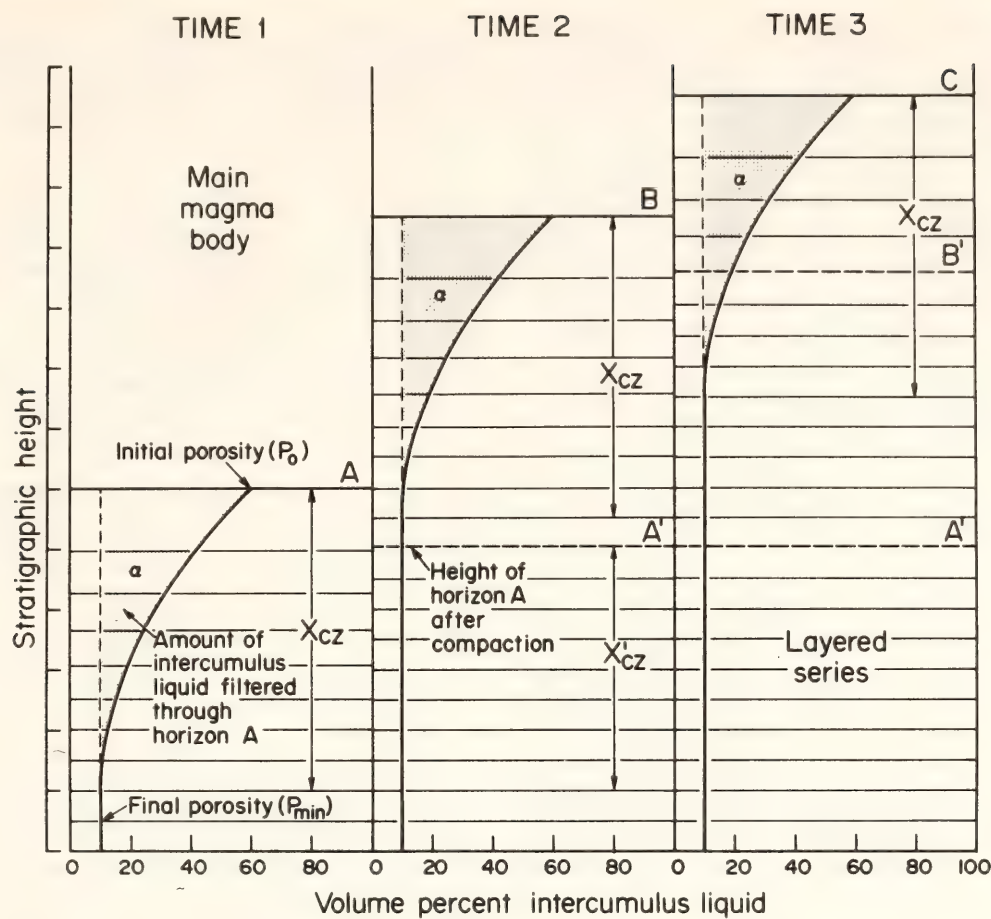


Fig. 64. Steady-state porosity distribution assumed in modeling the accumulation of the Muskox layered series: X_{cz} is the current thickness of the compacting zone; X_{cz}' is the thickness of the same section of cumulates after compaction. By the time horizon A is compacted to A', it is infiltrated by an amount of liquid quantitatively represented by the shaded area α . Similarly for horizons B and C.

used, based on detailed chemical and modal analyses of the rocks in cyclic units 4–7. Initial porosity was estimated to be 60 vol % from the compositions of olivine cumulates in the marginal zones of the intrusion, where intercumulus liquid was largely frozen in place. This value is high compared with usual estimates of cumulate initial porosities (30–50 vol %; Jackson, 1961; Hess, 1960; Wager and Brown, 1968), but it is consistent with the porosity reported for a synthetic olivine cumulate made from basaltic melt in a centrifuge furnace at 500 times the acceleration of gravity (Campbell *et al.*, 1977). Also, if 60 vol % is too large, then the estimated thickness of the compacting zone should be a minimum value, and it is this limit that is of most interest here.

Results of modeling are shown in Fig. 65; values of K_D are indicated. In

columns A and D, the compacting zone has zero thickness: in effect, the pore liquid is eliminated from each increment of cumulate immediately that the increment is deposited. This possibility corresponds to the H. H. Hess (1960) mechanism of adcumulus growth. In such a case, the chemical discontinuities are not displaced from their original positions.

In the other columns, the distance parameters of greatest interest are the thickness of the compacting zone (X_{cz}') and the distance that the intercumulus liquid has migrated (X_m'), both measured in terms of the compacted or *observed* thickness of the layered series. It will be recalled that the values for X_m' from Model 2 (upper part of Fig. 65) are minimum migration distances; those from Model 1 (at the bottom) are maximum values. In comparison with the Muskox

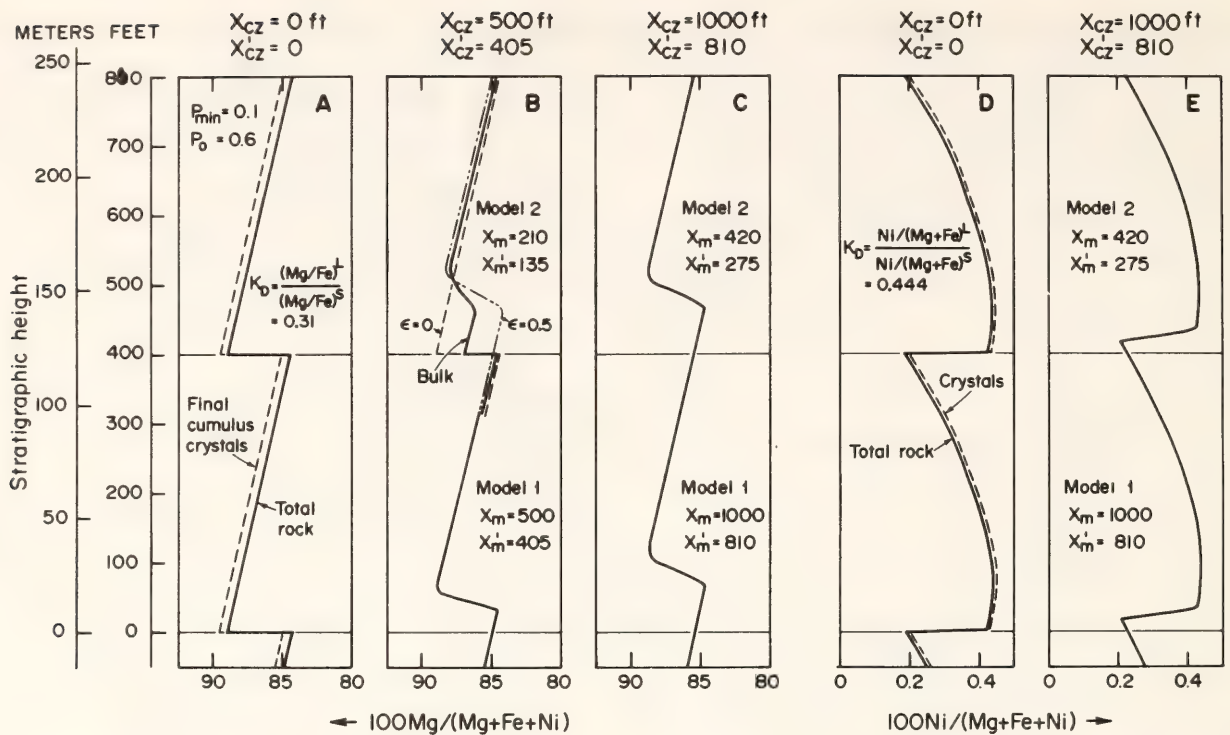


Fig. 65. Compositional profiles calculated by the computer models. X_{cz} is the original thickness of the compacting zone; X_{cz}' is the thickness of the same section after compaction; X_m is the distance that the intercumulus liquid has to migrate, measured on the same basis as X_{cz} ; X_m' is the migration distance measured in terms of the compacted (i.e., the observed) thickness of the layered series. In columns (A) and (D), the cumulate was compacted immediately on accumulation; hence the compositional discontinuities between cyclic units are not displaced. In the other diagrams, the discontinuities are shifted upward. The lower discontinuities are calculated by Model 1 (see text); the upper discontinuities derive from Model 2. The upper part of (B) shows a possible effect of incomplete equilibration of crystals and migrating liquid.

data in Figs. 61 and 62, the computed displacements for $X'_{cz} = 400$ ft (122 m) are just slightly greater than those apparent at the base of cyclic unit 4; those for $X'_{cz} = 800$ ft (244 m) are closely similar to the profiles at the base of units 5 and 6. It is especially notable that the contrast between the displacements for Mg/Fe and $\text{Ni}/(\text{Mg} + \text{Fe})$ is almost identical to the contrast observed in the drill-core sections. This feature is critical evidence that the modeled process is appropriate. The contrast arises because of the relative differences in the contents of $\text{Mg} + \text{Fe}$ and Ni in the liquid and cumulus minerals. The liquid contains about a third as much $\text{Mg} + \text{Fe}$ as the crystals, but only about a tenth as much Ni . Thus, the adjustments that must be made in its Ni content to return it to

equilibrium with the crystals as it passes through a discontinuity are relatively small; hence the Ni content of the olivine is less affected, and the discontinuity moves more slowly.

An additional possibility considered in the modeling is that the crystals and liquid do not completely equilibrate as the liquid moves upward. Results obtained on the assumption that only half of the crystals equilibrate, the remainder being unaffected, are shown at the top of Fig. 65B. The equilibrated crystals have the profile labeled $\epsilon = 0.5$; the others have the profile $\epsilon = 0$, the same as that in Column A. The average profile, labeled "bulk," is intriguing because it has a secondary discontinuity not unlike the subsidiary cyclic units noted above in the Mg/Fe profiles of cyclic units 4, 6, and 7 (Fig.

61). It will be recalled that chromite in these subsidiary units is variable in composition and therefore not equilibrated.

Conclusions

Two immediate conclusions to be drawn from the above results are: (1) the Muskox layered series, while accumulating, was unconsolidated to depths of possibly as much as 250 m below the depositional surface; and (2) intercumulus liquid filtered upward through the cumulate pile for distances of at least 100 m and possibly as much as 250 m. A specific comparison of the compositional profiles for cyclic units 4–7 (Figs. 61 and 62) with the model profiles suggests that, in general, the liquid that infiltrated the base of a Muskox cyclic unit was mostly derived from the underlying unit. Thus, the relatively small Mg/Fe displacement apparent at the base of cyclic unit 4 could largely be effected by liquid rising from the relatively thin unit 3; the larger displacements at the bottoms of units 5, 6, and 7 could be caused by liquid from the thicker units 4, 5, and 6, respectively.

The rocks in cyclic units 4–7 have textures indicative of moderate degrees of adcumulus growth: most are mesocumulates, some are adcumulates. In the light of the modeling, therefore, it would appear that the process of adcumulus growth must have occurred deep in the cumulate pile, extending at times to hundreds of meters below the depositional surface. Also implied is that a principal mechanism in the process was simply compaction of the cumulate pile under its own weight. Moreover, from heat transfer modeling not described here, it is evident that the intercumulus liquid was probably crystallizing most of the time that it was moving upward. In such circumstances, the liquid would be subject to a secondary stage of fractional crystallization, and it seems likely, therefore, that adcumulus mineral growth is principally determined by this type of crystalli-

zation. But if it commonly happens in layered intrusions that as much as 50 vol % intercumulus liquid is continuously returned to the main body of magma by compaction while layers are accumulating (as was assumed on the modeling), then the process must also significantly affect the primary stage of crystal fractionation.

PHASE RELATIONS OF A KIMBERLITE COMPOSITION*

David H. Eggler† and Richard F. Wendlandt‡

In many theories of kimberlite petrogenesis, emphasis is placed upon the role of a magmatic liquid phase. The liquid is generally thought to be derived either by partial melting of a peridotite mantle (Dawson, 1971; Mitchell and Crocket, 1971; Mysen and Boettcher, 1975) or by fractional crystallization of a mafic liquid (O'Hara and Yoder, 1967; MacGregor, 1970).

Phase relations of a kimberlite composition have been examined in order to test the partial melting origin. The following restrictions should be met for the hypothesis to be correct: (1) the composition must have a near-liquidus phase assemblage reflecting equilibration with a peridotite phase assemblage at some pressure, (2) the pressure of equilibration of the near-liquidus phases should be consistent with geobarometric estimates of the depth of origin of kimberlite magma, and (3) the liquidus temperature should not be less than the maximum geotherm temperature of the source region.

Kimberlite composition can be considered to be essentially an oxide composi-

* Study supported by the Earth Sciences Section, National Science Foundation, grants DES 73-00266A01 and EAR 77-15704.

† Now at The Pennsylvania State University, University Park.

‡ Work carried out under a cooperative predoctoral fellowship program between the Geophysical Laboratory and The Pennsylvania State University.

tion plus CO₂ and H₂O. A primary concern in the experimentation program was selection of the oxide composition. Because the number of runs at very high pressures had to be limited (owing to excessive breakage of carbide components), only one refractory composition was chosen. The most useful geothermometry-geobarometry of peridotite nodules in kimberlite has been done on Lesotho kimberlites (Boyd, 1973), so the average composition of Lesotho kimberlite (Gurney and Ebrahim, 1973) was selected. The composition was modified, however, by substitution of CoO for FeO (total Fe as FeO). With this procedure, the intrinsically low f_{H_2} of the solid-media assembly (Eggler, Mysen, and Hoering, *Year Book 73*, pp. 228–232) can be used advantageously to inhibit loss of the transition element to Pt capsules while retaining a divalent transition element in the liquid (Coons *et al.*, 1976). The main effect of the substitution is to increase slightly the solidus and liquidus temperatures (Coons *et al.*, 1976). The CO₂ content of the Lesotho kimberlite (Table 19) was considered to be entirely of mantle origin; its H₂O content was considered to be largely meteoric (Sheppard and Dawson, 1975). Accordingly, an anhydrous starting material was prepared, to which H₂O was added for individual experiments. The starting material was prepared as a finely ground mechanical mixture of titania, cristobalite, CaMgSi₂O₆ glass, magnesia, crystalline leucite, calcite, alumina, crystalline CoSiO₃, Ca₃(PO₄)₂, Cr₂O₃, and Na₂CO₃.

The mixture with H₂O was loaded into 1.8-mm-diameter Pt or Pt5Au capsules, about 5 mm long, that were welded shut. The capsules were run in a vertical position in talc-Pyrex (at 30 kbar) and talc-boron nitride (at 55 kbar) assemblies in solid-media, high-pressure apparatus. At 30 kbar, the piston-out procedure was used with an initial 2-kbar overpressurization. At 55 kbar, the assembly was heated to about 600°C before the piston (supported by floating steel rings) was advanced to

TABLE 19. Compositions of an Average Lesotho Kimberlite and of the Kimberlite Studied

	Lesotho*	Lesotho†	COOKI-7
SiO ₂	33.21	37.88	37.68
TiO ₂	1.97	2.25	2.16
Al ₂ O ₃	4.45	5.08	5.11
Cr ₂ O ₃	0.17	0.19	0.23
Fe ₂ O ₃	6.78	0.00	0.00
FeO	3.43	10.87	0.00
CoO	11.27
MgO	22.78	25.98	25.85
CaO	9.36	10.68	10.62
Na ₂ O	0.19	0.21	0.22
K ₂ O	0.79	0.90	0.91
P ₂ O ₅	0.65	0.74	0.74
CO ₂	4.58	5.22	5.22
H ₂ O	10.70
	99.06	100.00	100.01

* Gurney and Ebrahim, 1973.
† Normalized; Fe recalculated to FeO.

the desired pressure. Nominal pressures are reported. Temperatures, uncorrected for the effect of pressure on emf, were measured with Pt-Pt10Rh thermocouples. Lengths of runs varied from 0.2–22 hr. Phase assemblages were identified with the petrographic microscope. Stable crystalline silicates characteristically appear as euhedra that were unambiguously distinguished from the crystallites to which liquids usually quenched. The criteria of Yoder and Kushiro (1969) for distinguishing stable from quench phlogopite were particularly helpful. Stable dolomite or magnesite was distinguished as relatively clear, inclusion-free grains. No evidence of two-liquid immiscibility was found, and a vapor phase was not detected at supersolidus conditions.

At 30 kbar (Fig. 66), compositions containing less than 0.35 wt % H₂O [$X_{CO_2}^{system} = 0.94$, wt, where $X_{CO_2}^{sys} = CO_2/(CO_2 + H_2O)$ in the volatile portion of the bulk composition] have insufficient H₂O to completely hydrate potential phlogopite in the kimberlite composition (Table 19). Phlogopite therefore coexists in the subsolidus region

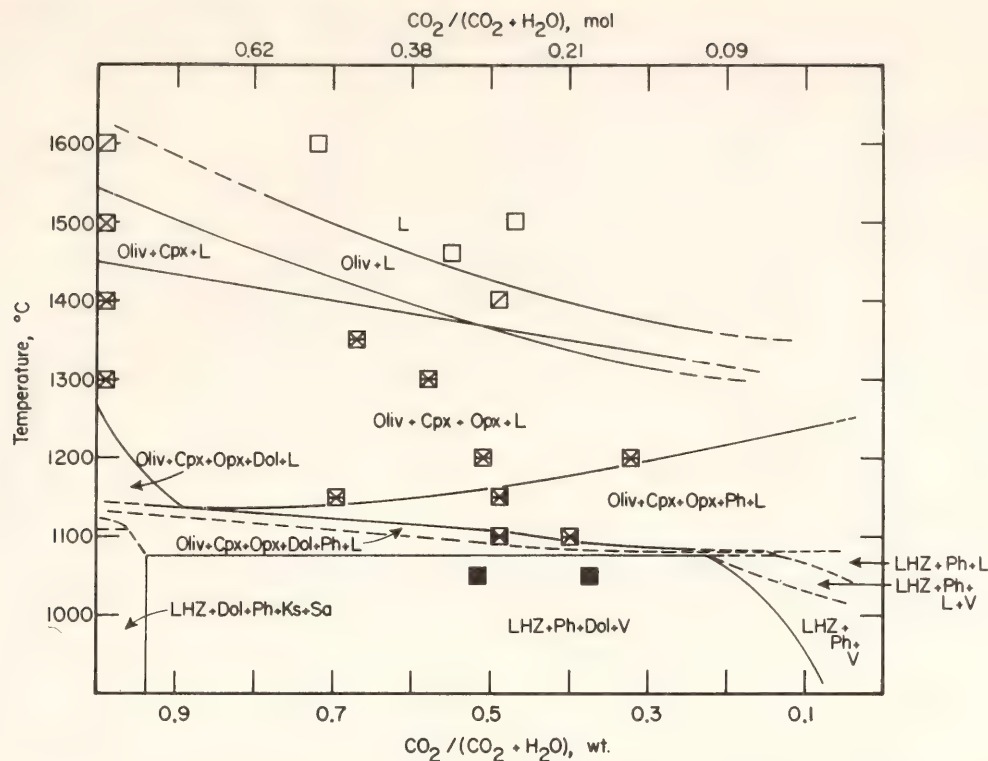


Fig. 66. Phase relations on the join kimberlite + 5.2% CO₂-H₂O at 30 kbar. The kimberlite composition is that in Table 19 with various amounts of H₂O added. LHZ = Oliv + Opx + Cpx + Garnet; Ph = phlogopite; Dol = dolomite; Ks = kalsilite; Sa = sanidine; L = liquid; V = vapor. Some phase fields occurring above the vapor-absent solidus are omitted for clarity. The abscissa is X_{CO₂^{sys}}, not vapor composition.

with its breakdown products, Ks + Sa + Fo, with lherzolite phases (denoted LHZ = Cpx + Opx + Fo + Gar), and with dolomite. Other minor phases may be present, accounting for the TiO₂ and P₂O₅ contents of the kimberlite. For bulk compositions containing more H₂O, there is sufficient H₂O to hydrate the potential phlogopite, and in the subsolidus region, vapor coexists with LHZ + Dol + Ph; because phlogopite does not coexist with its breakdown products, it cannot buffer the vapor composition. To carbonatize the kimberlite composition completely, 16.7% CO₂ is required (calculated from the bulk composition). Because all the compositions studied contained only 5.22 wt % CO₂ (Fig. 66), dolomite coexisted with its breakdown products in all the subsolidus runs, thus buffering the vapor composition except for very low and very high X_{CO₂^{sys}}. The vapor compositions and the decarbonation boundary can be calculated from equilibria in the system

CaO-MgO-SiO₂-CO₂ (Eggler, *Year Book* 76, pp. 428-435). Moreover, because the vapor is buffered, melting of the assemblage LHZ + Ph + Dol + V is isobarically invariant (Eggler, *Year Book* 76, pp. 428-435). The solidus was found to be 1075° ± 25°C at 30 kbar. Garnet is consumed by melting at temperatures immediately above the solidus, but dolomite persists over a small temperature interval and phlogopite over a larger interval. Subsolidus assemblages at 55 kbar (Fig. 67) are similar to those at 30 kbar (Fig. 66). Magnesite (Cm) replaces dolomite as the stable carbonate phase (Kushiro *et al.*, 1975), however, and the decarbonation boundary (between LHZ + Cm + Ph + V and LHZ + Ph + V) is shifted toward H₂O-rich compositions owing to a higher H₂O content of the buffered vapor. Because H₂O-poor compositions were not studied, the relations between supersolidus magnesite and phlogopite are drawn to be consistent

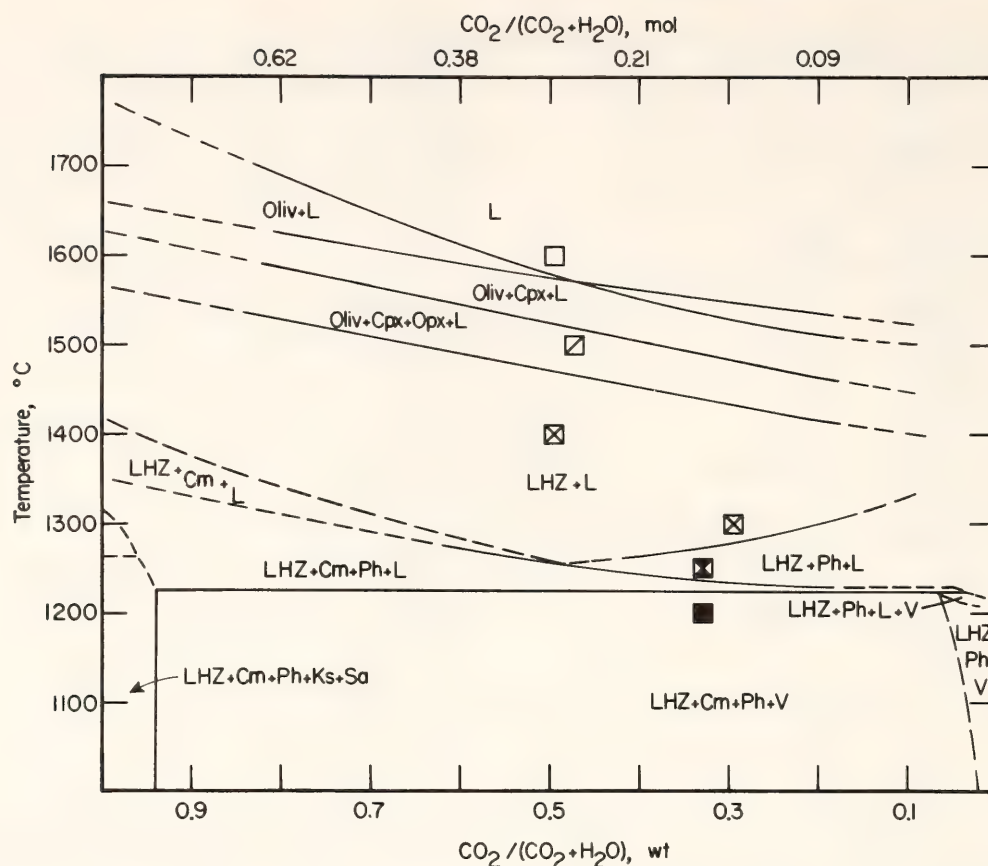


Fig. 67. Phase relations on the join kimberlite + 5.2% $\text{CO}_2\text{-H}_2\text{O}$ at 55 kbar. The kimberlite composition is that in Table 19 with various amounts of H_2O added. Abbreviations as in Fig. 66 and Cm = magnesite. Some phase fields above the vapor-absent solidus have been omitted for clarity.

with the data of Wendlandt (*Year Book* 76, pp. 441–448) on the join $\text{MgCO}_3\text{-KMg}_3\text{AlSi}_3\text{O}_{10}(\text{OH})_2\text{-MgSiO}_3$ from 32.5–50 kbar. The assemblage LHZ + magnesite + Ph + V was found to melt at $1225^\circ \pm 25^\circ\text{C}$. An important discovery in the supersolidus region at 55 kbar was the greatly increased melting range of garnet. For $X_{\text{CO}_2}^{\text{sys}} \simeq 0.5$ (wt), garnet persists for almost 300°C above the solidus and to within 100°C of the liquidus. Liquid thus coexists with LHZ over a wide melting range.

The results at 30 and 55 kbar have been combined in Fig. 68—a $P\text{-}T$ section for one volatile content. The phase fields have been interpolated between 30 and 55 kbar and are slightly extrapolated beyond that range.

The three restrictions listed above for liquid of kimberlite composition to be a primary magma formed by partial melting of a peridotite mantle can now be ex-

amined. The first restriction was that the kimberlite composition must have a near-liquidus phase assemblage reflecting equilibrium with peridotite. At 30 kbar, lherzolite phases (Fo + Opx + Cpx + Gar) are not in equilibrium with liquid except at the solidus of the kimberlite composition (Fig. 66). Liquid of kimberlite composition, therefore, is not likely to be a primary magma at 30 kbar, even if compositional variations other than those studied here are taken into consideration. At 55 kbar, however, lherzolite phases coexist with liquid over a temperature range of $200^\circ\text{--}300^\circ\text{C}$, depending on $X_{\text{CO}_2}^{\text{sys}}$. Inasmuch as the starting material was only an average kimberlite composition, it is remarkable that lherzolite phases were found to coexist near the *liquidus* at 55–60 kbar (Fig. 68) at $X_{\text{CO}_2}^{\text{sys}} \simeq 0.5$ (wt). At 55 kbar, liquids resembling those of kimberlite composition are produced at temperatures ranging

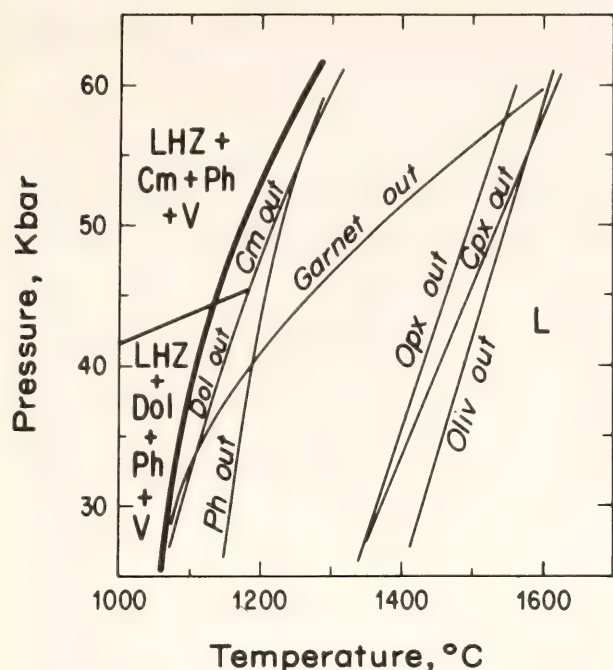


Fig. 68. Phase relations of a kimberlite composition containing 5.0% CO_2 and 5.0% H_2O (wt), interpolated and extrapolated from phase equilibrium data at 30 and 55 kbar (Figs. 66 and 67). The heavy line is the univariant solidus. Abbreviations as in Fig. 66.

from 1250°C, which is near the solidus of the present starting composition, to at least 1500°C, which is near its liquidus. The liquids formed at the lower temperatures are probably slightly more carbonatitic than the bulk composition (Table 19) because they represent the bulk composition minus most of the lherzolite phases.

The other two restrictions were that the ranges of pressure and temperature within which the appropriate phase assemblage exists must be consistent with estimated geotherms. Because the composition investigated is an average Lesotho kimberlite, it is instructive to compare the solidus and liquidus with the pyroxene geotherm that Boyd (1973) determined for nodules in Lesotho pipes (Fig. 69). The inflected limb of that geotherm intersects the solidus for the kimberlite composition at about 53 kbar if the solidus is lowered 50°C to correct for Co substitution as discussed above, and the limb then continues into the

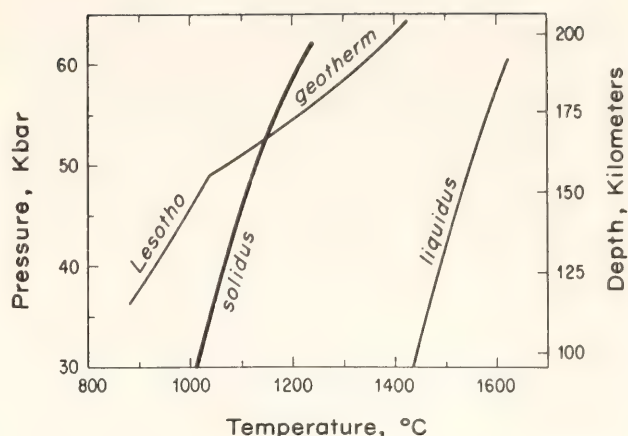


Fig. 69. The solidus and liquidus of a Lesotho kimberlite composition containing 5.0% CO_2 and 5.0% H_2O (wt) (from Fig. 68), with the Lesotho pyroxene paleogeotherm (Boyd, 1973). The solidus has been lowered by 50°C from the position in Fig. 68 to correct for the substitution of CoO for FeO.

melting range. With regard to the kimberlite phase diagram (Fig. 68), temperatures along the inflected geotherm lie in the supersolidus field of Oliv + Opx + Cpx + garnet (\pm magnesite \pm phlogopite) to at least 60 kbar. Liquid compositions in that field are also kimberlitic (see above); hence the pressures and temperatures along the geotherm would appear to be sufficient for the coexistence of a kimberlitic liquid with a peridotitic phase assemblage. It should be noted that, on the basis of REE patterns, kimberlitic liquid has also been proposed to be a partial melt of peridotite (e.g., Mitchell and Brunfelt, 1975).

Boyd (1973) found that calculated equilibration temperatures and pressures of discrete nodules (megacrysts) comprising the assemblage olivine-subcalcic diopside-orthopyroxene-garnet-ilmenite lie along the inflected geotherm. Although megacrysts are usually interpreted as having grown in the presence of a liquid, there is no agreement on the composition of the liquid. The experimental results obtained here are consistent with the suggestion that the liquid is kimberlitic (Dawson and Stephens, 1975; Mitchell and Clarke, 1976; Eggler and McCallum, *Year Book* 75, pp. 538-542).

(It should be noted, however, that ilmenite was not observed in present run products, probably because Co was substituted for Fe.) The experimental results suggest, moreover, that a kimberlitic liquid at pressures less than 60 kbar could also precipitate phlogopite and magnesite. Phlogopite has been identified as a megacryst in kimberlite (Dawson and Smith, 1975), but magnesite megacrysts have not been recognized.

In recent explanations of the inflected limb of the Lesotho geotherm, diapiric flow has been emphasized, whether in the form of an upwelling diapir (Green and Gueguen, 1974), a mantle plume (Parmentier and Turcotte, 1974), or a diapir associated with convective overturn (Boyd, *Year Book* 75, pp. 521–523). If a diapir contained CO₂ and H₂O and if its temperature distribution at depths of 160–200 km resembled the Lesotho geotherm (1150°–1400°C), then it would partially melt (Fig. 69) and the composition of the melt would be kimberlitic. There is, however, no reason to assume that diapirs are confined (or have been confined) to areas of known kimberlites; consequently, there is no reason to assume that liquids produced by melting of diapirs (kimberlites at 160–200 km) are not relatively common *in the mantle*. Thus, the rarity of kimberlite occurrences may be ascribed to the rarity of tectonic settings conducive to their ascent, not to the rarity of the magmas themselves. In fact, there is no reason why kimberlitic magmas should not be present beneath ocean basins as well as continents, provided that the suboceanic mantle contains CO₂ and H₂O (see Delaney *et al.*, 1977). The apparent absence of kimberlites in oceanic settings may be due to tectonic factors; for example, oceanic diapirs can rise high into the asthenosphere, where the partial melt of the diapir would be nephelinitic or basanitic (Eggler, 1978) rather than kimberlitic. Beneath continents, on the other hand, diapiric uprise might be halted near the bottom

of the lithosphere, at depths where the melt is of kimberlitic composition.

MELTING PHASE RELATIONS OF NATURAL PERIDOTITE + CO₂ AS A FUNCTION OF DEGREE OF PARTIAL MELTING AT 15 AND 30 KBAR

Richard F. Wendlandt and Bjørn O. Mysen

Investigations in the system CaO-MgO-SiO₂-CO₂ have emphasized the potential importance of CO₂ and carbonates in the genesis of magmas at high pressures (Eggler, *Year Book* 74, pp. 468–474; Eggler, 1976; Wyllie and Huang, 1975a, 1975b). Although this system is a convenient analogue of a mantle peridotite containing forsterite and two pyroxenes, its applicability to processes of partial melting in the upper mantle is obscured by its compositional simplicity. The purpose of the present study was to test whether melting in natural systems can be effectively modeled by simple systems. The phase relations of a natural garnet lherzolite have been determined as a function of degree of partial melting and pressure for CO₂-saturated and CO₂-undersaturated conditions.

The starting material was a sheared garnet lherzolite nodule, PHN 1611, described by Nixon and Boyd (1973a). The composition of this nodule is considered representative of undepleted peridotite in the upper mantle (for review of data see Mysen and Kushiro, 1977; Mysen and Holloway, 1977). Its melting relations as a function of degree of partial melting at 20 and 35 kbar for volatile-absent and water-undersaturated conditions were published by Mysen and Kushiro (1977).

In the present study, a powdered sample of the nodule (approximately –200 mesh) was dried in air at 600°C for 20 hr to decompose secondary hydrous minerals. About 15 ppb radioactive tungsten-185 (kindly supplied by Dr. George Cowan at the Los Alamos

Scientific Laboratory) was added to the powder. The liquid-crystal and liquid-vapor partition coefficients for this isotope are in excess of 50; so practically all of it enters the melt, relative to crystals and vapor. The degree of melting of the rock can be determined by relating the ^{185}W concentration in a partially melted sample to the ^{185}W concentration in a completely melted sample. The beta activities of both standard and unknowns were recorded on Ilford K-5 nuclear emulsions (supplied by Ilford Co., England) using the technique of Mysen and Seitz (1975) as adapted to this type of problem by Mysen and Kushiro (1977).

The experiments were conducted in a solid-media high pressure apparatus (Boyd and England, 1960) using a piston-out technique with no pressure correction for friction. Pressures are believed to be precise to ± 0.5 kbar. Temperatures were measured with Pt-Pt90Rh10 thermocouples and automatically controlled to $\pm 1^\circ\text{C}$ (Hadidiacos, *Year Book* 71, pp. 620–622). Temperatures were not corrected for the effect of pressure on the emf of the thermocouple and are believed to be accurate to $\pm 10^\circ\text{C}$.

The starting materials were contained in sealed 2-mm Pt95Au5 capsules. Carbon dioxide was added as silver oxalate, $\text{Ag}_2\text{C}_2\text{O}_4$ (Boettcher *et al.*, 1973). Talc-Pyrex furnace assemblies were employed for all the experiments. The Pyrex sleeve ostensibly inhibits migration of water into the sample region, thus decreasing hydrogen diffusion into the capsule. Low hydrogen fugacity retards iron loss to the capsule container and also prevents reduction of CO_2 and concomitant formation of H_2O .

Even with these precautions, iron loss is substantial. Mysen and Kushiro (1977) reported a 20 wt % loss from PHN 1611 at 20 kbar and approximately 1550°C . In the present investigation, experiments at low pressures and low temperatures using small amounts of relatively iron-rich melts were occasionally marked by cap-

sule failure due to Fe-Pt alloying. Run durations had to be minimized (to approximately 90 min at 1400°C) to maintain a coherent capsule. The problem is less serious, however, both at higher temperatures (because the iron content of the melt is then substantially diluted) and at higher pressures (under which the melt is carbonatitic).

The presence of trace amounts of water in the charges is suspected on the basis of the observed melting relations at temperatures immediately above the solidus at both 15 and 30 kbar (see below). The source of this water may be attributed to the presence of absorbed H_2O on the silver oxalate, or, more likely, to the *in situ* generation of H_2O by diffusion of hydrogen into the charge (Eggler, Mysen, and Hoering, *Year Book* 73, pp. 228–232).

The 15-kbar, CO_2 -saturated melting relations of nodule PHN 1611 are shown in Fig. 70 as a function of X_{melt} , wt % partial melting. Three stable phase assemblages were observed: olivine + orthopyroxene + clinopyroxene + liquid + vapor; olivine + orthopyroxene + liquid + vapor; and olivine + liquid + vapor. These phase fields are distinguished by the changes in the slope of the melting curve (Fig. 70). Similar relations for volatile-absent conditions were proposed by O'Hara (1968) and observed by Mysen and Kushiro (1977). The solidus temperature of PHN 1611 + CO_2 at 15 kbar is approximately 1400°C ; the departure of the melting curve to lower temperatures may be attributed to the presence of approximately 0.3–0.4 wt % water, assuming that the melt is entirely due to H_2O generated by reaction between CO_2 and H_2 .

Although the nodule contains 8–10 major components, its melting behavior closely resembles that of a system with fewer components. Clinopyroxene is the first phase to melt out with increasing temperature; it disappears at only slightly above 1400°C and less than 20% melt. The relatively constant temperature of

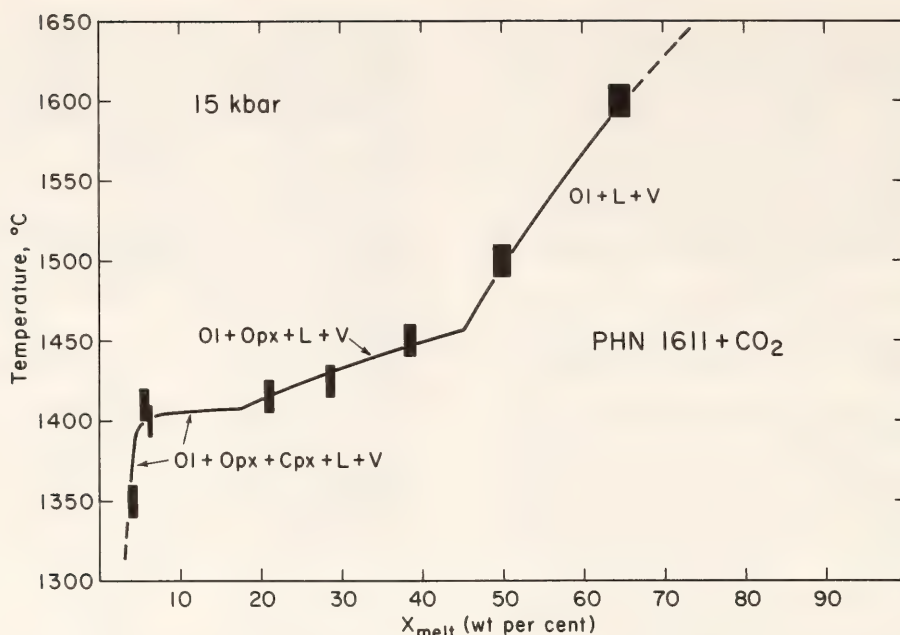
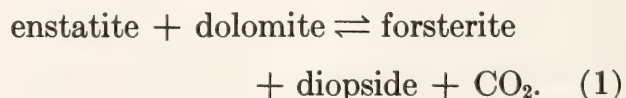


Fig. 70. Melting curve of PHN 1611 + CO₂ at 15 kbar. Size of symbols incorporates uncertainties in temperature ($\pm 10^\circ\text{C}$) and determination of percentage of liquid ($\pm 1\sigma$). Abbreviations: Ol, olivine; Opx, orthopyroxene; Cpx, clinopyroxene; L, liquid; V, vapor.

this initial melting interval is characteristic of isobaric invariant melting behavior that would be observed in the four-component system CaO-MgO-SiO₂-CO₂ when five phases are present. Although Al₂O₃ is significant in amount, an aluminous phase was not observed; the Al₂O₃ in the system is believed to be contained in the aluminous clinopyroxene (Mysen and Kushiro, 1977). The melting interval for the assemblage olivine + orthopyroxene + liquid + vapor commences with the loss of clinopyroxene and is characterized by a distinctly positive slope, implying a greater degree of freedom—possibly approximating isobaric univariant melting behavior (four significant components and four phases). Orthopyroxene is melted at the end of this interval at approximately 1460°C and 45% melt. The melting interval for olivine + liquid + vapor is characterized by an even steeper slope and more degrees of freedom than the lower temperature intervals. The steep slope of the melting interval below 1400°C, attributed to trace amounts of H₂O, may also be a region of isobaric univariant melting behavior (five significant components and five phases).

In Fig. 71, the 30-kbar melting relations for PHN 1611 + CO₂ are presented as a function of X_{melt} . Two isobars have been determined: the first for CO₂-saturated conditions and the second for a total CO₂ content of 5 wt % (CO₂-undersaturated). For the latter conditions, the amount of CO₂ is slightly less than is required to completely carbonate the nodule by the reaction



Consequently, a CO₂ vapor phase is not present during melting.

Major changes occur in the phase relations in going from 15 to 30 kbar. They include the appearance of the highly aluminous phases, garnet and spinel, and the disappearance of clinopyroxene. The 30-kbar phase assemblage can be approximately described in terms of the five components CaO-MgO-Al₂O₃-SiO₂-CO₂ and it is informative to consider the observed assemblage relations for PHN 1611 on this basis.

For conditions of excess CO₂, three stable phase assemblages were observed:

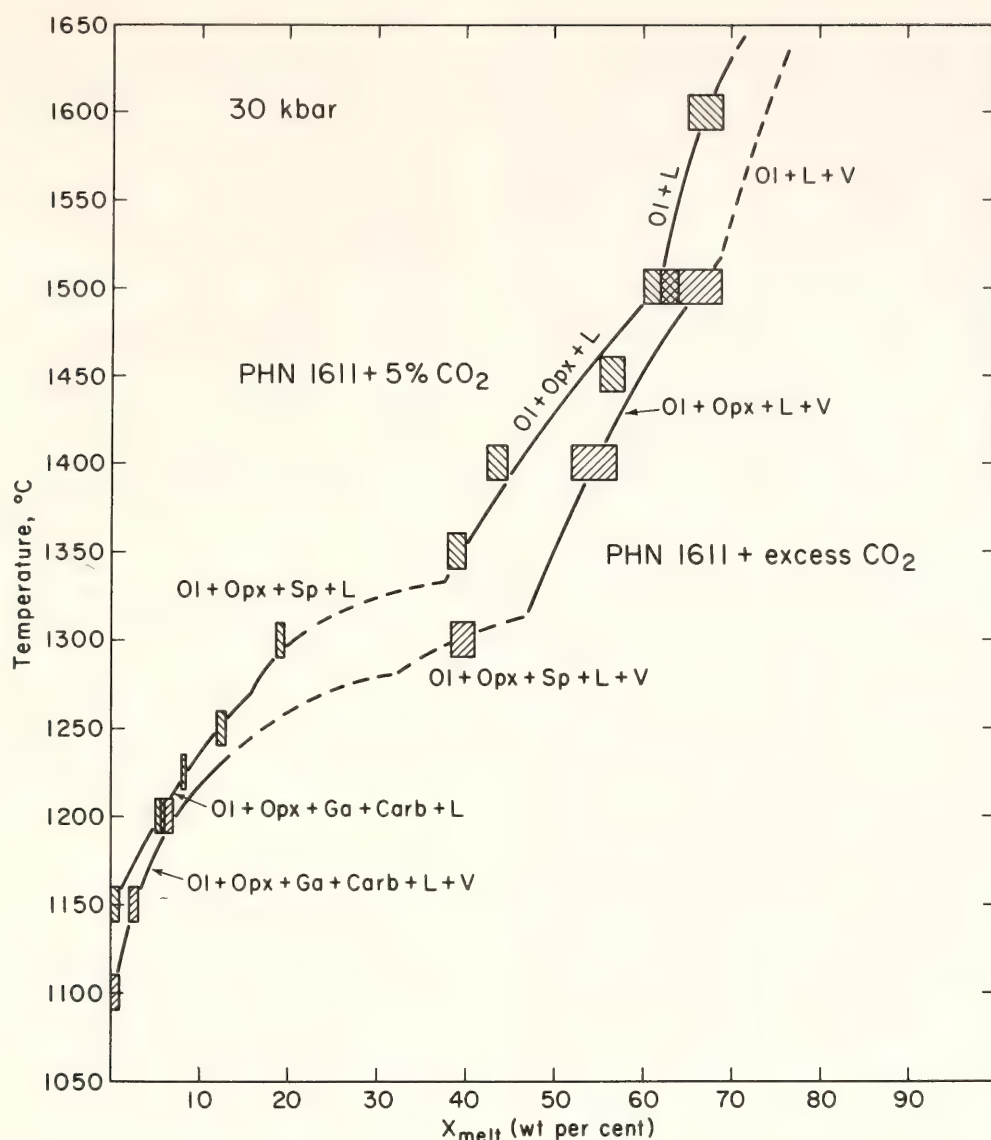


Fig. 71. Melting curves of PHN 1611 + 5% CO₂ (wt) and PHN 1611 + excess CO₂ at 30 kbar. Sizes of symbols are defined in Fig. 70. Dashed lines are inferred. Abbreviations are as in Fig. 70 and Ga, garnet; Sp, spinel; Carb, carbonate solid solution (dolomite).

olivine + orthopyroxene + dolomite + garnet + liquid + vapor; olivine + orthopyroxene + spinel + liquid + vapor; and olivine + orthopyroxene + liquid + vapor. The maximum stability ranges of garnet and carbonate were not closely determined; hence they are shown to have the same limits. The solidus is approximately 1100°C at 30 kbar. The stable assemblage immediately above the solidus, olivine + orthopyroxene + dolomite + garnet + liquid + vapor, has initially a steep melting slope, suggesting melting behavior that is removed from the anticipated isobaric invariancy. This slope

is believed to reflect the presence of trace amounts of water, inasmuch as a temperature increase of more than 100°C results in less than 10% melt. A solidus temperature of approximately 1200°C is believed to be a suitable approximation to the "pure CO₂" solidus and would result in about 50% melt in the interval 100°C above the solidus.

Carbonate occurs as discrete stable grains and as quenched intergranular carbonatitic melt to temperatures of at least 1200°C. At 1300°C, the liquid quench contains approximately equal proportions of carbonate and silicate com-

ponents that are believed to have exsolved during the quench. Spinel is observed at 1300°C and 50% melt, and probably represents an incongruent melting product of garnet. At temperatures above 1300°C, forsterite + orthopyroxene + liquid + vapor coexist over a broad temperature and X_{melt} range. Relative to the 15-kbar results, the stability of orthopyroxene above the solidus is expanded.

In the presence of 5% CO_2 at 30 kbar, the phase assemblages are olivine + orthopyroxene + dolomite + garnet + liquid; olivine + orthopyroxene + spinel + liquid; olivine + orthopyroxene + liquid; and olivine + liquid. Because there is insufficient CO_2 to react all the clinopyroxene by Equation 1, a small (though undetected) interval of olivine + orthopyroxene + clinopyroxene + dolomite + garnet + liquid must exist near the solidus. Again, the steep slope of the initial melting increment is believed to reflect the presence of small amounts of H_2O with attendant divariant melting behavior. A "pure CO_2 " solidus would probably be about 1200°–1250°C. Garnet and carbonate react completely at approximately 1275°C, and spinel is then observed in a small melting interval. As in the presence of excess CO_2 vapor, carbonate occurs as both discrete, stable grains and as the melt quench to approximately 1300°C (20% melt). Carbonate liquid quench is observed at 1350°C (40% melt) but is accompanied by approximately equal amounts of quench silicate liquid that unmixed on the quench. Olivine is the liquidus phase at temperatures in excess of 1500°C.

The melting curve in the presence of a CO_2 -rich vapor phase occurs at lower temperatures. At 1300°C there is a difference of about 30% melt between the two isobars; this difference decreases with increasing temperature. The close proximity of the two curves at lower temperatures may be due to the similar CO_2 contents of both melts at these conditions.

In Fig. 72, the observed variation of $\text{Mg}/(\text{Mg} + \text{Fe})$ with melting for olivine

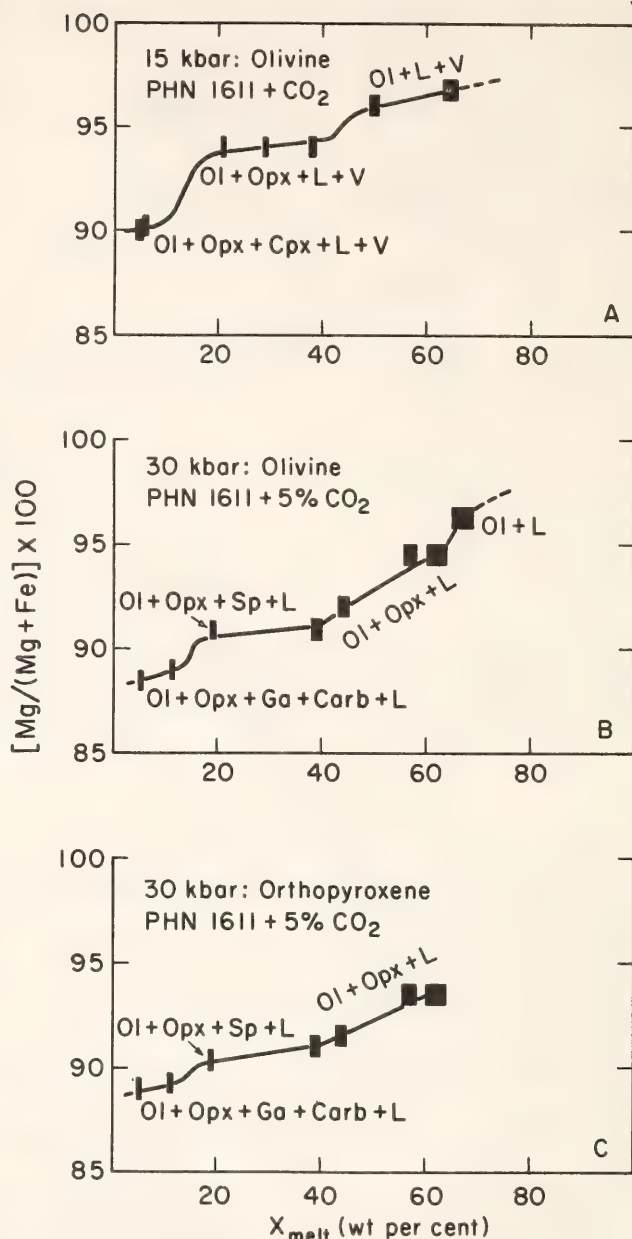


Fig. 72. $\text{Mg}/(\text{Mg} + \text{Fe})$ compositional data as a function of X_{melt} (A) for olivines at 15 kbar, (B) for olivines at 30 kbar, and (C) for orthopyroxenes at 30 kbar. Size of symbols incorporates uncertainties in electron microprobe analyses and % of liquid ($\pm 1\sigma$). Abbreviations as in Figs. 70 and 71.

at 15 and 30 kbar and for orthopyroxene at 30 kbar is illustrated. As a rule, this ratio correlates with the phase relations; it varies only slightly in the intervals of constant mineralogy, but where inflections occur in the melting curve, inflections in the $\text{Mg}/(\text{Mg} + \text{Fe})$ ratio are also observed. In the higher temperature melting intervals where fewer phases are

TABLE 20. Melt Compositions at 15 kbar

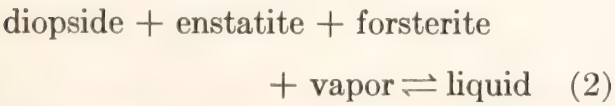
	Melt Temperature			
	1415°C*	1425°C†	1500°C‡	1600°C‡
SiO ₂	51.49	50.11	48.99	45.69
TiO ₂	0.75	0.79	0.50	0.38
Al ₂ O ₃	10.47	10.79	5.56	4.27
Fe ₂ O ₃	n.d.	n.d.	2.80	2.14
FeO	9.87§	10.75§	14.01	11.94
MnO	0.24	0.24	0.18	0.15
MgO	9.08	9.13	20.47	29.28
CaO	9.26	9.11	6.58	5.02
Na ₂ O	0.53	0.67	0.68	0.52
K ₂ O	0.37	0.42	0.28	0.21
NiO	<0.05	<0.05	n.d.	n.d.
Cr ₂ O ₃	0.48	0.49	0.46	0.38
Totals	92.54	92.49	100.00	100.00

* Run no. 482; four analyses.
† Run no. 461; eight analyses.
‡ Calculated using known proportions of melt and olivine compositions.
§ All iron determined as FeO.

present (higher X_{melt}), the Mg/(Mg + Fe) ratios tend to increase somewhat more continuously.

In Table 20, melt compositions at 15 kbar are tabulated. Because of difficulties in quenching the higher temperature liquids, their compositions are calculated. Melt compositions are approximately tholeiitic at temperatures near the solidus, and become picritic at temperatures approaching 1600°C. The melts at 30 kbar could not be analyzed, but they are carbonatitic to at least 20% melt.

The melting behavior of a natural garnet lherzolite is in accord with phase relations observed in the system CaO-MgO-SiO₂-CO₂ (Eggler, *Year Book* 74, pp. 468-474). At 15 kbar, PHN 1611 is believed to melt in the presence of a CO₂-rich vapor by the reaction



at approximately 1400°C. The liquid generated is approximately tholeiitic in

composition. At 30 kbar, melting begins approximately 200°C lower by reactions involving dolomite and perhaps garnet. High-pressure melting relations in the system CaO-MgO-Al₂O₃-SiO₂-CO₂ have not been determined, so the melting reactions cannot be defined. The large decrease in solidus temperatures from 15 to 30 kbar is consistent with the sharp kink in the CO₂-saturated mantle peridotite solidus observed in the system CaO-MgO-SiO₂-CO₂ (Eggler, *Year Book* 74, pp. 468-474, 1976; Wyllie and Huang, 1975a, 1975b). Concurrent with this decrease is an equally dramatic increase in the solubility of CO₂ in the initial melt and the introduction of dolomite as a solidus phase. The generation of carbonatitic magmas at immediately higher pressures is confirmed in the two compositions studied at 30 kbar; carbonatitic magmas persist to approximately 20% melt.

The melting relations at 15 kbar can be interpreted effectively in terms of a reduced number of components (four) whereby five phases melt in an isobaric invariant fashion. Assemblages containing fewer phases are characterized by more degrees of freedom and steeper melting curves. Relations at 30 kbar are less satisfactorily interpreted in terms of a reduced number of components (five) because a small amount of water, believed to be generated *in situ* by hydrogen diffusion, generates a large (100°C) divariant melting interval involving dolomite immediately above the solidus. Nevertheless, relations are sufficiently similar to those in simple systems that the use of the latter in modeling natural conditions is justified.

NEPHELINE SOLID SOLUTIONS IN
MELILITE-BEARING ERUPTIVE ROCKS AND
OLIVINE NEPHELINITES

Danielle Velde and H. S. Yoder, Jr.

Nepheline is an important mineral in undersaturated basic lavas, but prior to development of the electron microprobe

precise determination of its chemical composition was difficult because of the minute size of the crystals. Miyashiro (1951) and Tilley (1952, 1961) analyzed nephelines that were extracted mostly from feldspar-bearing rocks, and they confirmed earlier suggestions of differences in composition between volcanic and plutonic nephelines. Microprobe analyses of nephelines from volcanic rocks free (but for two exceptions) of feldspars give insight into the possible compositions of nepheline in natural and synthetic as-

semblages. The present study is part of a continuing mineralogical investigation of melilite-bearing rocks. The analyses were performed on the automated electron microprobe using the method of Finger and Hadidiacos (*Year Book 71*, p. 598). Very low specimen current (less than $0.02 \mu\text{A}$) was used in order to prevent the loss of alkalis during analysis.

In a study of the $\text{NaAlSi}_3\text{O}_8$ - KAlSi_3O_8 system, Tuttle and Smith (1958) reported extensive solid solution between nepheline and kalsilite at high temperatures. Below

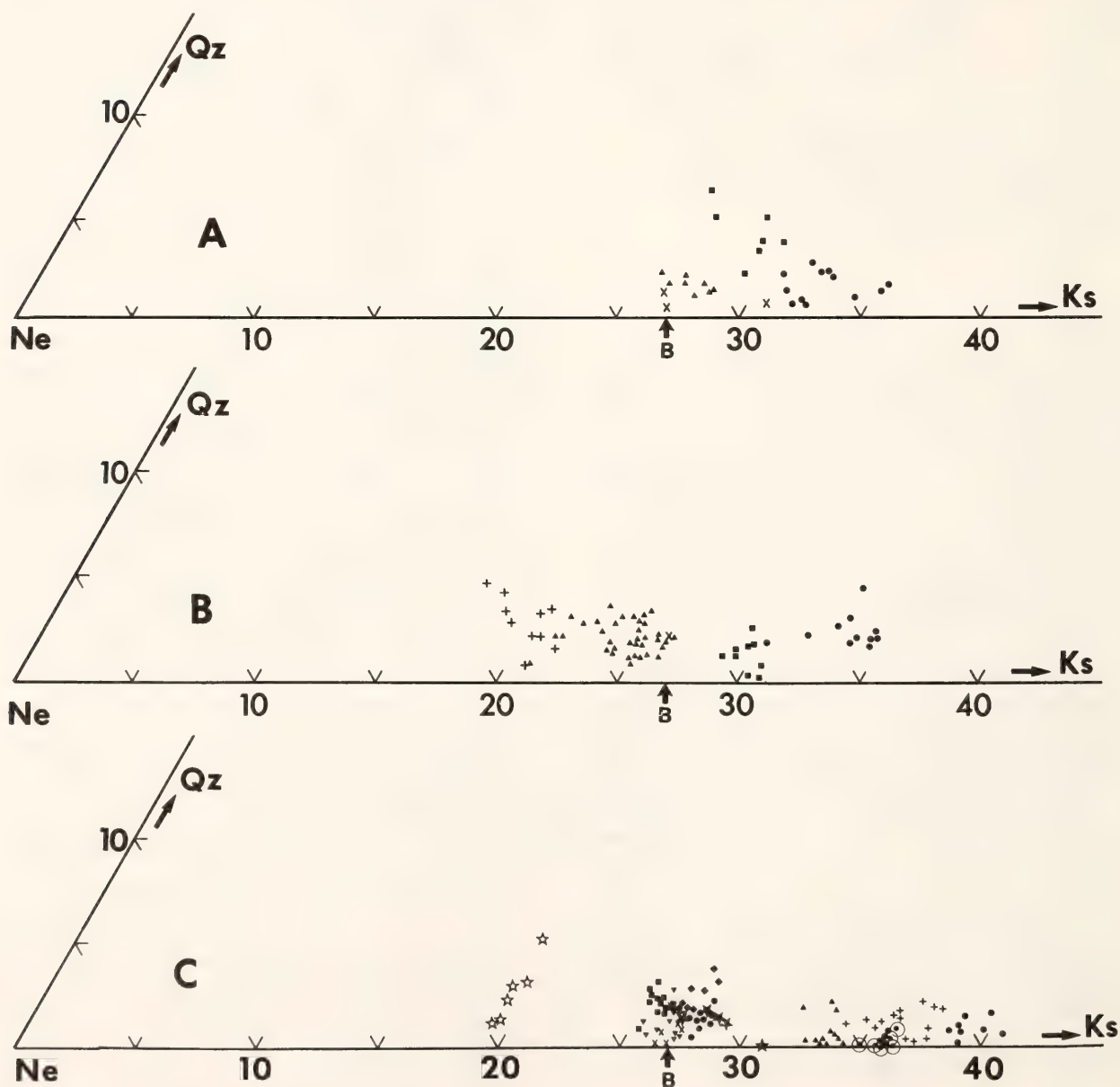


Fig. 73. Composition of nephelines from melilite-bearing eruptive rocks represented in a Ne-Ks-Qz diagram (wt %). (A) Nephelines that coexist with leucite. (B) Nephelines that coexist with sodalite or hauyne. (C) Nephelines without any other feldspathoid. The letter B represents the Buerger composition. The various symbols represent nepheline compositions in individual rock specimens.

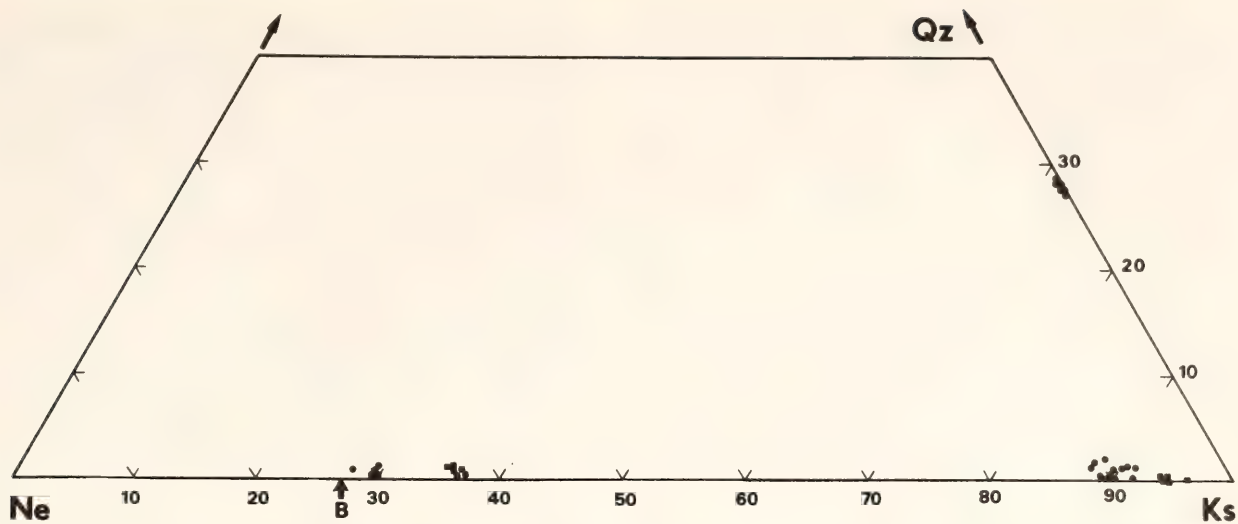


Fig. 74. Composition of nephelines and coexisting kalsilites from a venanzite, San Venanzo, Italy (Y 52; solid circles) and a lava from Villa Senni, Italy (Y 287; solid squares). Leucite is present in both lavas, but has only been analyzed in the venanzite. The letter B represents the Buerger composition.

about 1070°C near Ne₃₀ a solvus evolved, and they believed the limbs become asymptotic to Na₃KAl₄Si₄O₁₆ and essentially pure KAlSiO₄ near 300°C. In a study of the NaAlSiO₄-NaAlSi₃O₈ system, Greig and Barth (1938) placed the maximum solubility of albite in nepheline at about 33 wt %. The limits of solid solution at 700°C in both systems are consistent with those values found by Hamilton and MacKenzie (1960) in the NaAlSiO₄-KAlSiO₄-SiO₂ system at P_{H₂O} = 1 kbar.

Figures 73A, 73B, 73C, and 74 show the range of nepheline compositions found in 22 melilite-bearing eruptive rocks. The nephelines contain 20–39 wt % KAlSiO₄ and the kalsilites contain 84–100 wt % KAlSiO₄. Only rarely do nephelines contain more than 4 wt % excess SiO₂ in solid solution, but they tend to be richer in silica on the sodium side of the Buerger composition Na₃KAl₄Si₄O₁₆ than on the potassium side of that composition. Lime is below the detection limit in kalsilite and less than 1% in nepheline, but the ubiquitous presence of apatite inclusions in nepheline renders the precise determination of CaO difficult. Nepheline may be the only feldspathoid present (Fig. 73C), or it may be accompanied by sodalite or haüyne (Fig. 73B), or by

leucite (Fig. 73A), or kalsilite (Fig. 75), or both (Fig. 74). Feldspar has not been encountered in these or any other melilite-bearing volcanic rocks. The highest K₂O/Na₂O of a nepheline-bearing lava lacking kalsilite and leucite (with or without sodalite or haüyne) is ~0.7, whereas in lavas with higher K₂O/Na₂O nepheline is accompanied by kalsilite, leucite, or both (Figs. 73A and 74), or else kalsilite may be the only feldspathoid present (Fig. 75). Figure 76 relates the kalsilite

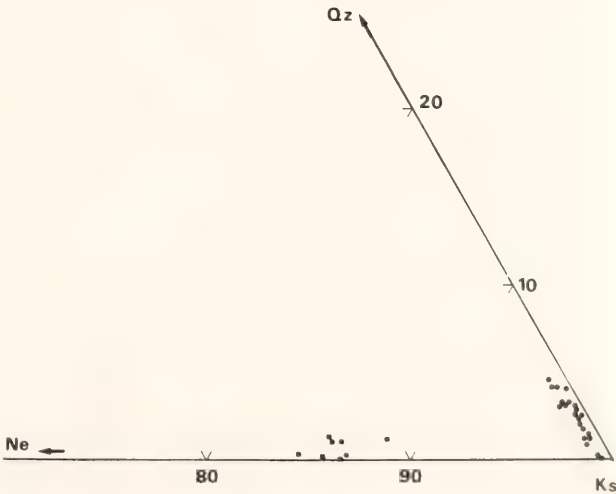


Fig. 75. Composition of kalsilites from two lavas. Solid circles, specimen from Cupaello, Italy; solid squares, melilite-olivine-mica rock from Utah.

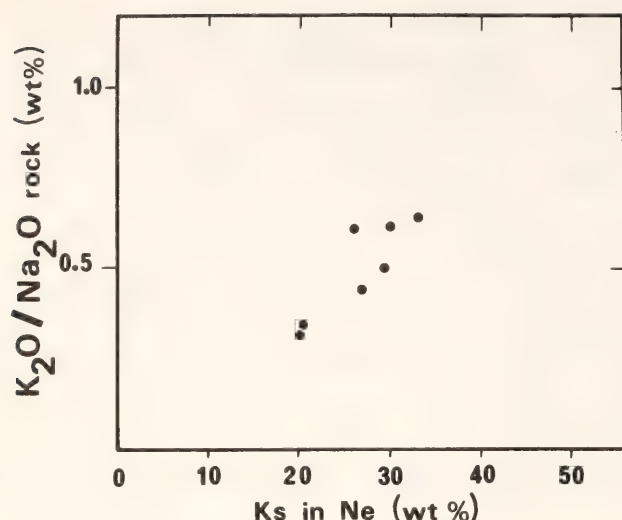


Fig. 76. Variation of the kalsilite content of nepheline with the K_2O/Na_2O ratio of the bulk rock (wt %). Represented are lavas that contain nepheline alone or are accompanied by sodalite or haüyne.

content of nepheline with K_2O/Na_2O in rocks lacking kalsilite and leucite. Although the data are sparse, a positive correlation is indicated, and the most-sodic nephelines are found in the least-potassic rocks.

Assemblages with leucite + kalsilite + nepheline have been found in two speci-

mens. Analyses of nephelines found in a venanzite from the type locality in Italy (Specimen Y 52) plot close to the Buerger composition on the Ne-Ks-Qz diagram (Fig. 74) and are associated with kalsilite Ks_{90} . Leucite has a composition very close to that expected from stoichiometry. The other specimen (Y 287) in which this assemblage has been found is described by Washington (1927, p. 190). It contains contiguous nepheline and kalsilite; leucite is present, and haüyne is infrequent. In Fig. 74, compositions as determined with the electron microprobe for kalsilite and nepheline are plotted (leucite was not analyzed). The kalsilite composition is less sodic than it was in the venanzite because of exsolution of nepheline. Small, oriented blebs of nepheline, qualitatively identified by electron microprobe x-ray scans for K $K\alpha$ and Na $K\alpha$, are common in the kalsilite (Fig. 77). These inclusions can be seen under the microscope in plane-polarized light: their indices of refraction are slightly higher than those of the host kalsilite (as described by Sahama, 1960), but their birefringence and optical orientation are the same. This relationship

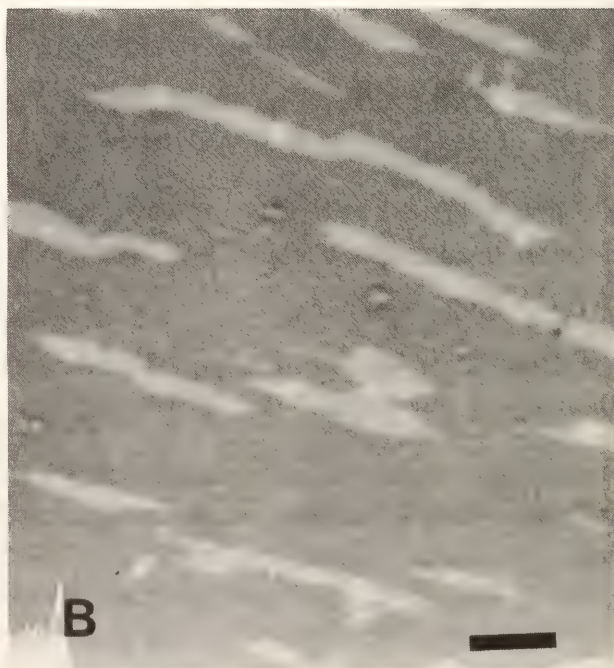
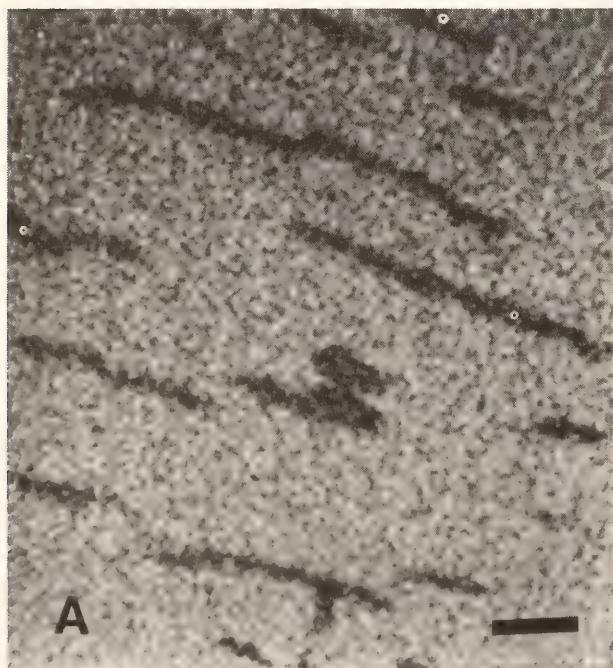


Fig. 77. Kalsilite with nepheline exsolution, Specimen Y 287. Length of bar, $25\mu m$. (A) X-ray scanning image, K- $K\alpha$. (B) Absorbed electrons image; light areas correspond to lower average atomic mass (Na-rich phase) than dark areas (K-rich phase).

indicates that the original sodic kalsilite exsolved nepheline, and that the composition determined by analysis does not correspond to the composition that originally coexisted with the associated nepheline. The composition and amount of the exsolved nepheline could not be ascertained.

Kalsilite also occurs without any accompanying feldspathoid in a rock from Cupaello, Italy, where its presence had previously been reported by Gragnani (1972), and it was found in a melilite-olivine-mica rock from Utah in which sanidine had been alleged to occur (Best *et al.*, 1968). Kalsilite from Cupaello contains less than 1.5% nepheline in solid solution, whereas the kalsilite from Utah contains 10–15% nepheline and no evidence of an exsolved phase. The apparent inconsistency of the potential tie lines joining coexisting phases from the same specimen in Fig. 74 is thereby explained. The relations exhibited are not those expected on the limbs of a solvus; however, it may be assumed that addition of the appropriate amount of exsolved Ne_{ss} would reconstitute the bulk composition of the kalsilite in the Villa Senni specimens to that existing at the high temperature of formation, a temperature no doubt greater than that at which the rock from San Venanzo last equilibrated.

The compositions of nepheline in seven samples of melilite-free olivine nephelinites are plotted in the Ne-Ks-Qz projection, Fig. 78A, 78B, and 78C. In two specimens (Fig. 78A) leucite was found, whereas traces of late crystallizing feldspars were present in two other specimens (Fig. 78C). The differences between the ranges of compositions determined for melilite- and nonmelilite-bearing rocks may be seen by comparing Figs. 73 and 78. The nephelines found in olivine nephelinites are richer in sodium, but also richer in silica than are nephelines found in melilite-bearing rocks; all but three analyses fall on the sodium-rich side of the Buerger composition.

Hamilton and Mackenzie (1960)

among others have noted that nephelines coexisting with feldspar tend to contain excess silica. With two exceptions, the lavas examined in the present study contain no feldspar, and the CIPW norms of olivine nephelinites do not as a rule contain either normative albite or orthoclase. Exceptions to the rule can be expected because the line in the Ne-Ks-Qz projection connecting pure NaAlSiO_4 and leucite, which determines the presence or absence of feldspar in the norm, cuts the boundary of the field of solid solution of nephelines having excess SiO_2 . Consequently, natural nephelines that have compositions on the nepheline-kalsilite join should be found in those lavas with Lc in the norm, not Ab or Or. Comparisons of the data in Figs. 73 and 78 raise at least two questions: (1) Why should nephelines be more potassic in melilite-bearing nephelinites, and (2) Why would nephelines found in extremely undersaturated lavas have compositions within the Ne-Ks-Qz diagram?

In regard to the first question, Fig. 79 is a comparison of the frequency distribution of K_2O in 321 melilite-bearing lavas (Fig. 79A) and 252 ankaratrites and nephelinites (Fig. 79B). The distributions are similar. The melilite-bearing lavas with very high potassium contents are those with high $\text{K}_2\text{O}/\text{Na}_2\text{O}$ and in which a potassic feldspathoid is found coexisting with nepheline. A higher potassium content in melilite-bearing eruptive rocks does not appear to be a plausible explanation for the high potassium content of nepheline, as shown on Fig. 73. In this respect, compositions shown on Fig. 73A should be compared to compositions found on Fig. 78A because nephelines in both cases coexist with leucite. The fact that a sodalite (with a composition very close to that of the end-member) coexists with a nepheline with 25% kalsilite in solid solution in the olivine melilite from Moiliili quarry in Oahu also indicates that in melilite-bearing lavas the nepheline composition does not necessarily reflect the total $\text{K}_2\text{O}/\text{Na}_2\text{O}$ of the rock.

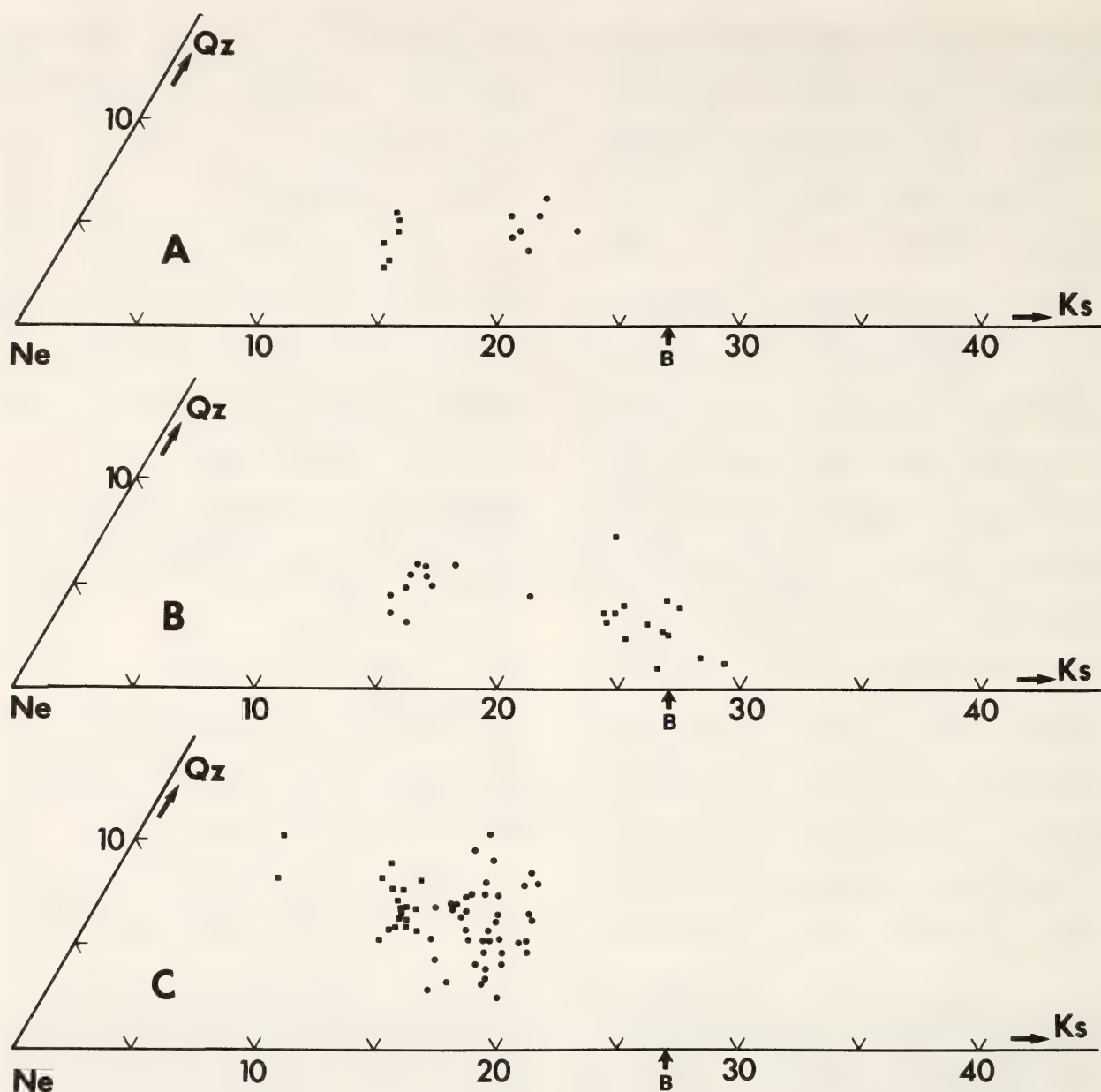


Fig. 78. Composition of nephelines from olivine nephelinites represented in the Ne-Ks-Qz diagram (wt %). Letter B represents Buerger composition. (A) Nephelines that coexist with leucite. (B) Nephelines, no other feldspathoid present. (C) Nephelines coexisting with small amounts of modal feldspar.

The consistency of the potential Ne_{ss} -Lc tie lines in melilite-bearing (Fig. 73A) and melilite-free (Fig. 78A) rocks is complicated by the cross relationship of the Ne_{ss} -Or_{ss} tie lines suggested by the nepheline compositions in Fig. 78C. If the factors resulting in the large variation in composition of those nephelines plotted in Fig. 78C are identified and the conditions of formation of the rocks are characterized, it may be possible to account for the cross relationship. On the

other hand, the overlap of nepheline solid solutions from different assemblages points up the influence additional phases may have on the tie lines referred simply to the Ne-Ks-Ab-Or quadrilateral. The presence of biotite, for example, probably places major constraints on the partitioning of alkalis. It is also important to ascertain how the soda melilite content (norm = nepheline + wollastonite) of the melilite varies with the composition of nepheline after the analytical data

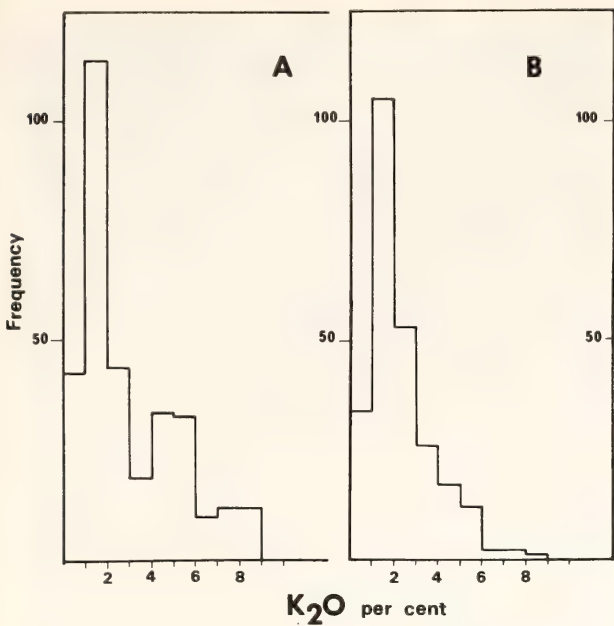


Fig. 79. Frequency distribution of K₂O (wt %). (A) In 321 melilite-bearing eruptive rocks. (B) In 252 ankaratrites and nephelinites.

have been collected on all the coexisting phases.

In regard to the second question, a major difference exists between the bulk chemical composition of olivine nephelinites and melilite-bearing nephelinites: the silica content is higher in olivine nephelinites than in melilite-bearing rocks (Velde and Yoder, *Year Book* 76, p. 480). In one sense, olivine nephelinites are less undersaturated with respect to silica than lavas in which melilite crystallizes. As shown in Figs. 73 and 78, sodic nephelines are also richer in silica than potassic nephelines close to the Buerger composition. It appears that one of the factors controlling the kalsilite content of the nepheline may be the silica content of the lava.

Nephelines on the sodium-rich side of the Buerger composition generally contain excess silica, and those nephelines that correspond to the formula Na₃KAl₄Si₄O₁₆ or are richer in potassium have a composition close to, or on, the nepheline-kalsilite join. This observation seems to be supported by available experimental results. Kushiro and Yoder (*Year Book* 71, p. 415) have shown that the calculated

mode for the starting composition Ne₅₀-Di₅₀ crystallized at 1125°C was similar to the observed mode if the composition of the nepheline was assumed to be a solid solution, Ne₇₁Ab₂₉ (by weight), and not pure Ne. Such a solid solution is in keeping with the fact that the assemblage Ne + Di + Ol is found in the Ne-Di-SiO₂ system but not in the Ne-Di-Ol system. In view of the absence of pure nepheline in these rocks, it appears that the crystallization history of silica-undersaturated nepheline-bearing lavas will not be elucidated in synthetic systems unless the theoretical composition NaAlSiO₄ is replaced by either the Buerger composition or an appropriate Ne-Ab solid solution.

LIQUID IMMISCIBILITY AND THE
CARBONATITE-IJOLITE RELATIONSHIP:
PRELIMINARY DATA ON THE JOIN
NaFe³⁺Si₂O₆-CaCO₃ AND RELATED
COMPOSITIONS

W. J. Verwoerd

Immiscibility of silicate and carbonate magmas at crustal levels has figured prominently in most recent hypotheses on the genesis of the sövite-ijolite association of the alkaline igneous complexes (e.g., Middlemost, 1974; Le Bas, 1977). One reason for invoking this process is that the silicate and carbonate rocks generally occur as discrete units rather than as silicocarbonatites. A small degree of miscibility is indicated, however, in the calcite-bearing ijolites at Rangwa and Usaki in Kenya (Le Bas, 1977) and in some of the so-called hollaite and käsenites of Fen (Brögger, 1921). Similar rocks have been found associated with the Dicker Willem carbonatite in South West Africa.

Experimental verification of silicate-carbonate liquid immiscibility has been limited to systems containing alkali carbonates and aluminosilicates (Koster van Groos and Wyllie, 1966, 1968, 1973; Wendlandt and Harrison, this Report). Such immiscibility has not been en-

countered in melts of calcite and aluminosilicates (Watkinson and Wyllie, 1969, 1971), and Eggler (*Year Book* 74, pp. 468–474) found that at high pressures in the system $\text{CaO-MgO-SiO}_2\text{-CO}_2$, immiscibility plays no part in the derivation of highly silica-undersaturated melts. The alkali carbonates would appear, therefore, to be critical components. Most carbonatites are themselves low in alkalis, but they are commonly surrounded by alkali-rich fenitized aureoles. Moreover, the remarkable natrocarbonatite (Lengait) lava of Mt. Oldoinyo Lengai in Tanzania is unequivocal evidence that at least one natural carbonatite magma was alkali-rich.

An important mineral that has so far been neglected in experimental work on carbonatite systems is pyroxene of the acmite-aegirinaugite series. In the present work, as a first step toward elucidating

the role of this mineral, some exploratory experiments were made on the melting relations of acmite and calcite at 2-kbar pressure. Only tenuous evidence of liquid immiscibility was found, however, and it was recognized that the liquid compositions probably lie far off section. Emphasis was shifted, therefore, to a second, more complex synthetic join, extending between a calcite-bearing natrocarbonate mixture and a silicate mixture simulating ijolite. Experiments on this join, also at 2 kbar, revealed pronounced silicate-carbonatite immiscibility (see Fig. 80) even at temperatures below 900°C . Inasmuch as the two joins form only a small part of a six-component system, overall trends of crystallization and ranges of stability cannot be specified for the liquids and crystalline phases observed, but an important reaction relationship is evident, and some indication of the extent of the

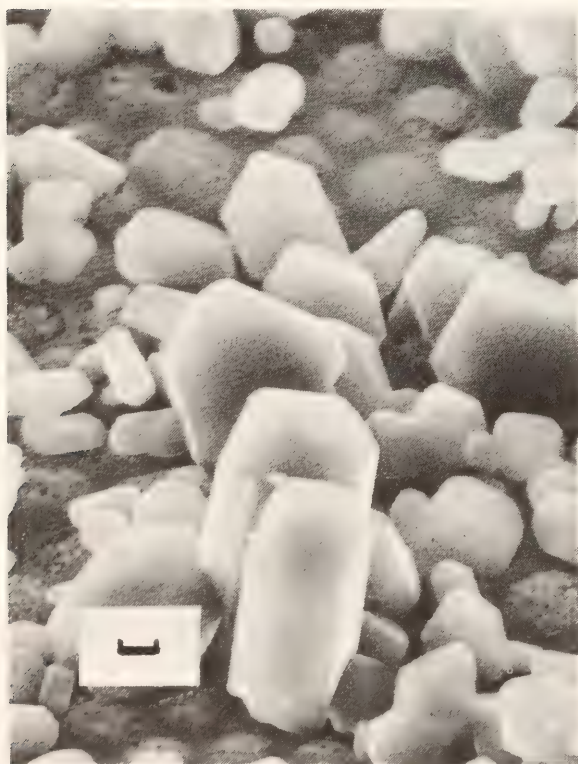


Fig. 80A. Scanning electron micrograph of anhydrous monoclinic Na_2CO_3 crystals deposited in vapor vesicles in silicate glass during quench. Composition of charge 90Ac:10Ce, temperature 1050°C , pressure 2 kbar. Bar scale = $1\ \mu\text{m}$.

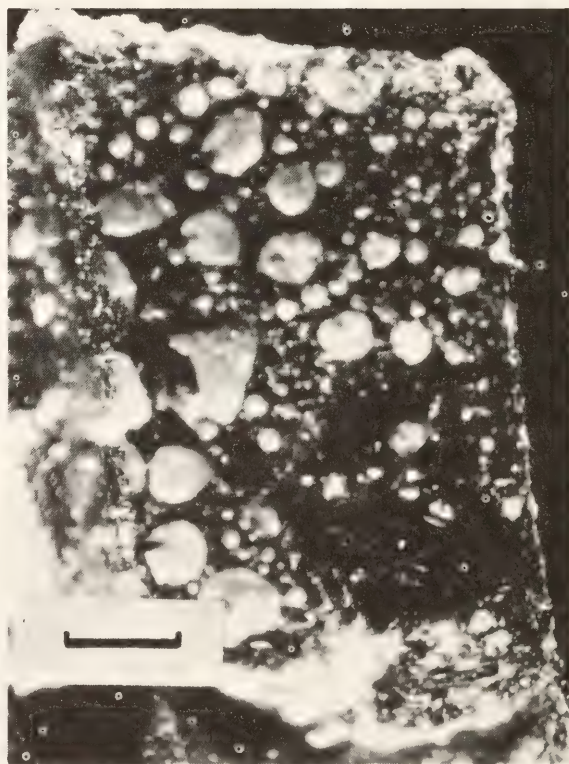


Fig. 80B. Opened capsule showing spherical bodies of nyerereite (quenched carbonate liquid) in black silicate glass, forming an emulsion texture. Each carbonate body has one or more vapor bubbles. Composition is $\text{Silicate}_{90}\text{Carbonate}_{10}$ at 900°C and 2 kbar. Bar scale = 1 mm.

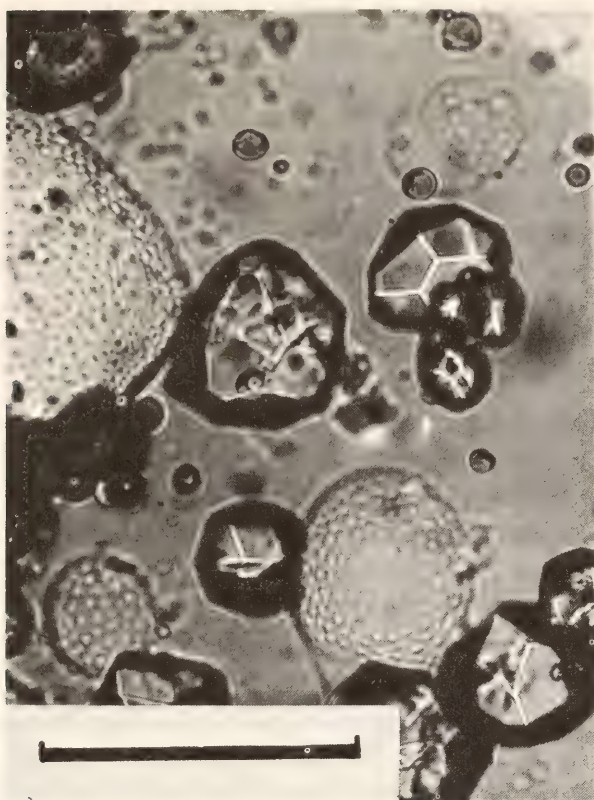


Fig. 80C. Silicate glass with andradite crystals, immiscible carbonate droplets, and dimpled vapor bubbles; the dimpled bubbles should not be confused with emulsion texture. Composition is Silicate₅₀Carbonate₅₀ at 900°C and 2 kbar. Bar scale = 0.1 mm.

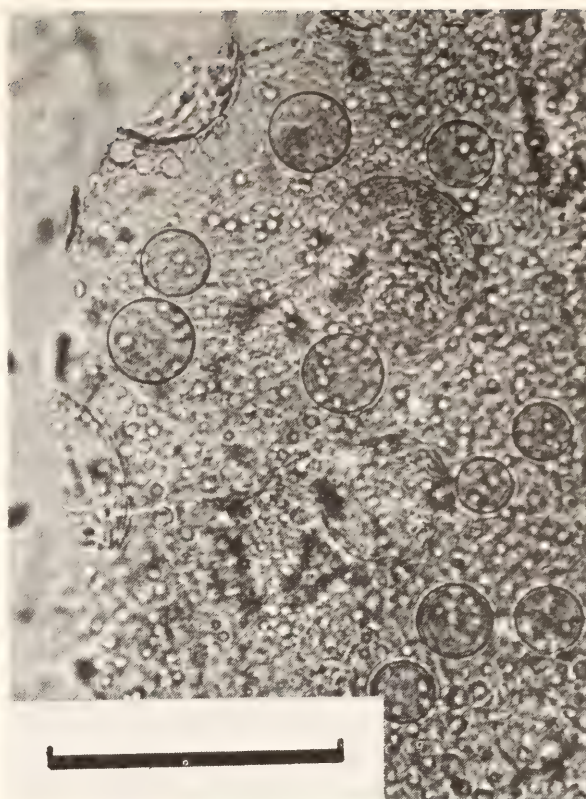


Fig. 80D. Nyerereite (quenched carbonate liquid) riddled with minute globules of silicate glass exsolved during quench crystallization. Perfectly spherical bodies of intermediate size are immiscible blebs of silicate glass, and larger, more vaguely outlined spheres are vapor vesicles. Composition is Silicate₅₀Carbonate₅₀ at 1050°C and 2 kbar. Bar scale = 0.1 mm.

miscibility gap can be deduced from the data obtained.

Experimental Procedure

Starting materials were crystalline mixtures of (1) acmite formed from synthetic acmite glass by heating at 700°C for 3 days, 800°C for 1 day, and 930°C for 32 days; (2) nepheline and sodium disilicate, synthesized some years ago by the late Dr. J. F. Schairer; and (3) reagent grade CaCO₃ and Na₂CO₃. Care was taken to keep these materials dry at all times.

The experiments were run in an internally heated high-pressure apparatus with argon as the pressure medium (Yoder, 1950). In a few initial experiments, the charges were sealed in Pt capsules and PtO₂ was included in an attempt to

maintain the iron in the ferric state and, by the same token, to minimize iron loss to the capsules (Huckenholz and Yoder, *Year Book* 69, p. 182). The PtO₂ reacted with the acmite, however, to form an opaque mass that gave the powder x-ray diffraction pattern of NaPt₃O₄. An alternative buffering reagent, PdO, likewise reacted with calcite to form CaPd₃O₄. In all subsequent experiments, therefore, gold capsules (3 mm in diameter) were used. They absorb almost no iron, so the Fe³⁺/Fe²⁺ and oxygen fugacity of the charge are essentially determined by the compositions of the starting materials. The presence of some Fe²⁺ is indicated by the occurrence of magnetite as a near-liquidus phase in some compositions, but otherwise the phase relations are not obviously affected. Because of the rela-

tively low melting point of gold, the maximum run temperature was 1050°C, but as it turned out, this limitation was not serious. Run durations were 72 hr between 800°C and 1000°C, and 24 hr at 1050°C. From the results, it is clear that these times are adequate to attain equilibrium.

Identification of Phases

Phases were identified primarily by optical examination and x-ray powder diffractometry, and secondarily by electron microprobe analysis and scanning electron microscopy. The silicate liquids generally quenched to glass, and no difficulty was experienced in distinguishing equilibrium crystalline phases in the glass from occasional feathery crystalline growths formed during quenching. The carbonate phases are more problematical, especially at temperatures near the solidus. Nyerereite, $\text{Na}_2\text{Ca}(\text{CO}_3)_2$, was the principal quench product of the carbonate liquids but may also be an equilibrium or primary phase. The natural mineral is stable in air (Fleischer *et al.*, 1975), but the synthetic K-free analogue hydrates within a few hours, yielding a product with a prominent x-ray diffraction peak at 6.10 Å. Cooper *et al.* (1975) identified primary synthetic nyerereite in melting experiments on the system

$\text{Na}_2\text{CO}_3\text{-CaCO}_3$ on the basis that it formed "clear, stubby, prismatic, bubble-included grains" with a characteristic cross-hatch twinning that was not observed in nyerereite crystals that were known to have grown during quenching. In the present study, this distinction could not be made. As seen in basal sections (distinguished by their very low birefringence), the nyerereite crystals commonly show cross-hatch twinning, even in runs made at 1050°C where the crystals were undoubtedly melted. The known quench nyerereite crystals, however, typically occur in complex radial growths, and these growths were observed for all runs in the temperature range 850°–1050°C, which is almost certainly above the melting point of pure nyerereite (817°C at 1 kbar, Cooper *et al.*, 1975). Only in runs at 800°C is the uncertainty considered serious; these runs probably contain stable nyerereite, but there might also be carbonate quenched from liquid in the composition region of the nyerereite sodium carbonate eutectic (see Fig. 81).

Calcite is a prominent phase only on the acmite-calcite join (and only toward the calcite end). It occurs as a granular mosaic, and because the run temperatures are well below its melting temperature, it is considered to be an equilibrium, or primary, phase.

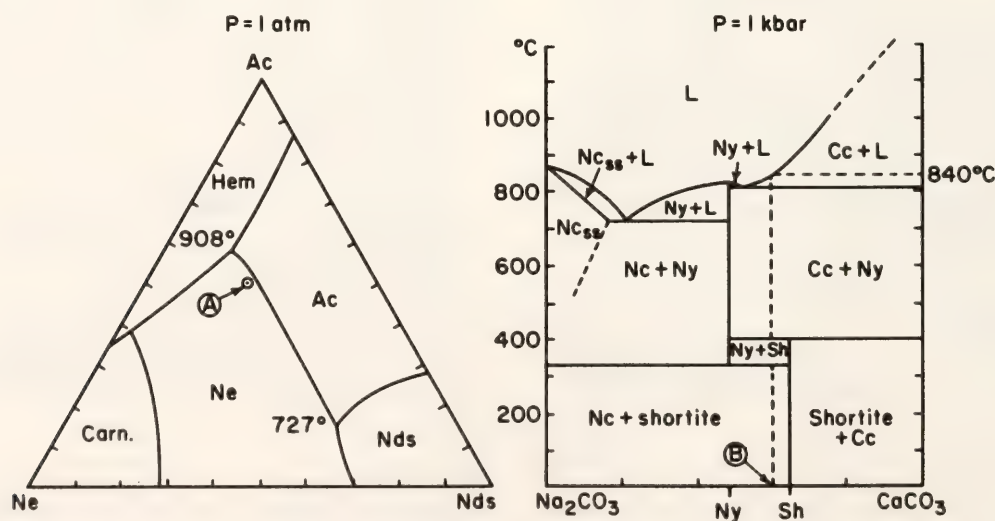


Fig. 81. Phase diagrams applicable to synthetic ijolite (Bailey and Schairer, 1966, p. 127) and natro-carbonatite (Cooper *et al.*, 1975) showing the compositions of starting mixes A and B.

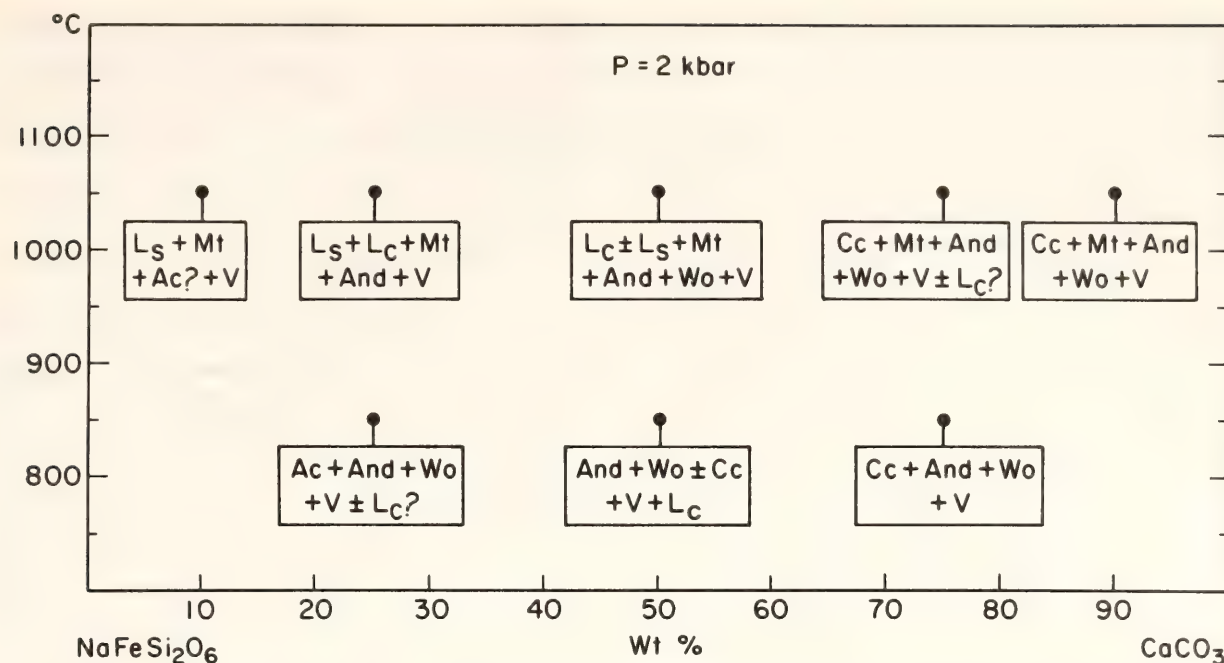


Fig. 82. Phase assemblages encountered in exploratory runs on the acmite-calcite join. L_s = silicate liquid; V = vapor; Hem = hematite; And = andradite; Wo = wollastonite; Cc = calcite.

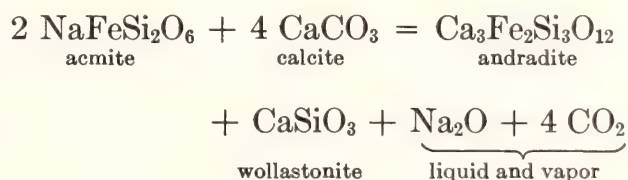
Other primary crystalline phases were acmite, nepheline, andradite, wollastonite, magnetite, and hematite. With the exception of nepheline, their identification was relatively routine after they had been recognized. The nepheline was encountered only as an interstitial phase where no silicate melt was present. Andradite formed on the ijolite-natrocarbonatite join is uniform in composition and showed a maximum Al₂O₃ content of only 1.5 wt %, so there is little solid solution with grossularite.

The presence of a vapor phase, essentially CO₂, was commonly evident by the presence of vesicles, and some capsules were inflated after being run. In charges near the acmite end of the acmite-calcite join, minute crystals of Na₂CO₃ lined the vesicles (Fig. 80A), apparently because of precipitation from the vapor phase.

The NaFe³⁺Si₂O₆-CaCO₃ Join at 2 kbar

Figure 82 shows the phase assemblages that were encountered in the exploratory work on this join. Andradite occurs through the composition range from about

20 to 90 wt % CaCO₃. It coexists with acmite and wollastonite at the silicate end of the join and with calcite and wollastonite at the carbonate end. Magnetite appears in all runs at 1050°C, but is absent at 850°C. The occurrence of andradite and wollastonite indicates a reaction relationship that may be approximately represented:



In the investigated composition closest to the acmite end of the join, the Na₂O probably was largely contained in the silicate melt but must also have occurred in substantial amounts in the vapor, as evidenced by the Na₂CO₃ crystals in the vesicles (Fig. 80A). With increased CaCO₃, it evidently combined with CO₂ and some of the CaCO₃ to form the carbonate melt. Only questionable evidence for coexistence of the silicate and carbonate liquids was found—in the 1050°C run at 25% CaCO₃.

*The Synthetic Ijolite-Natrocarbonatite
Join at 2 kbar*

Bailey and Schairer (1966) found that in the simplified ijolite system, $\text{Na}_2\text{O}-\text{Al}_2\text{O}_3-\text{Fe}_2\text{O}_3-\text{SiO}_2$, any liquid that precipitates acmite must contain excess sodium disilicate. For the present study, a silicate end-member mixture 5Ac:3Ne:2Nds (Fig. 81, composition A) was chosen because it is close to the nepheline-acmite cotectic at a place where the liquidus temperature is only about 880°C at 1 atm, a value that is geologically plausible for the ijolite-carbonatite association. The carbonate end-member composition, 6Cc:4Nc (Fig. 81, composition B), was selected because it melts at a similar temperature (840°C) at 1 kbar (Cooper *et al.*, 1975). The combination of nepheline, acmite, and calcite with excess sodium and CO_2 is particularly relevant to ijolite-carbonatite genesis.

Figure 83 is a provisional phase diagram for the investigated join, based on 27 runs between 800°C and 1050°C . The phase

relations are complicated, and many additional fields remain to be delineated, especially below 900°C . Also, in the lower temperature runs where crystalline phases predominate, there may be minor phases that were not detected. Interest centered on the liquidus phases, however, and these form a logical sequence across the join, although the exact positions of the field boundaries are subject to revision. One field, labeled $L_s \pm L_c + \text{Wo} + \text{V}$, is essential for compatibility between the adjoining fields, but the indicated assemblage has not yet been observed and so the field boundaries are shown by short dashed lines. Narrow, vapor-absent liquid fields should be present at both ends of the join but have been omitted because they have not been investigated.

The liquidus is between 1000° and 1050°C for most compositions on the join, and probably drops below 1000°C at the ends. Magnetite and hematite are on the liquidus near the silicate end of the join, andradite and wollastonite are prominent liquidus phases at intermediate com-

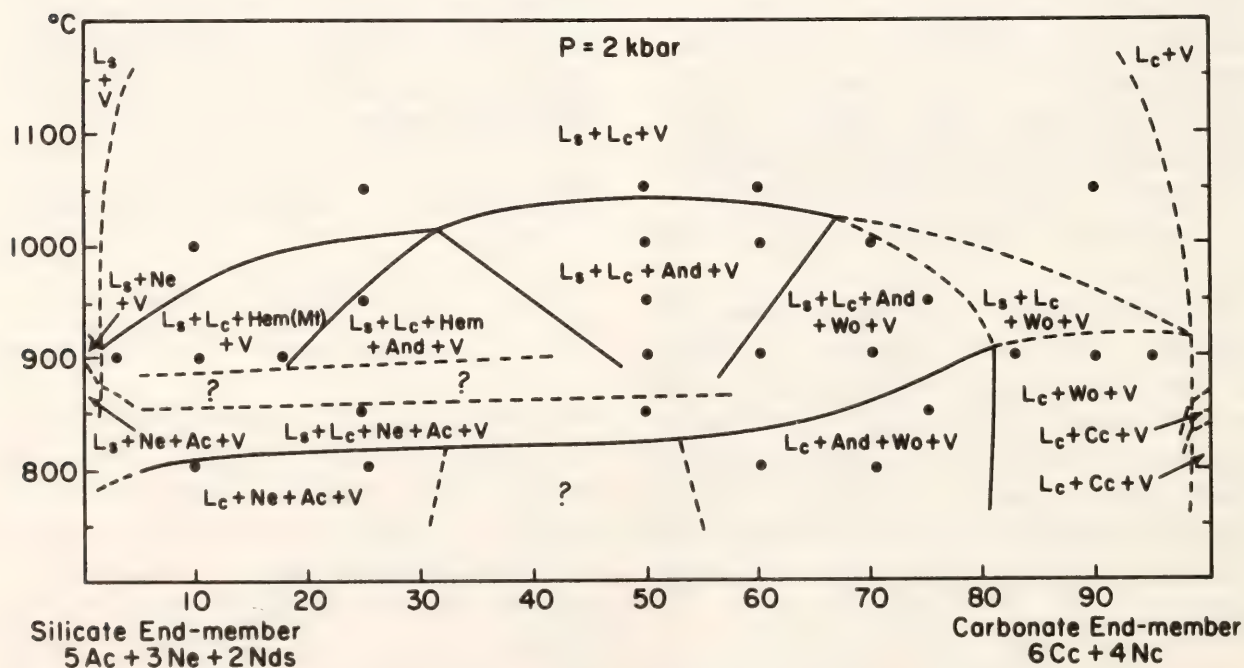


Fig. 83. Provisional phase diagram of the join between synthetic ijolite and calcite-bearing natrocarbonatite at 2 kbar. L_s = silicate liquid; L_c = carbonate liquid; V = vapor; Ne = nepheline; Hem = hematite; Mt = magnetite; And = andradite; Ac = acmite; Wo = wollastonite; Cc = calcite; Ny = nyerereite.

positions, and calcite is probably on the liquidus at the carbonate end, although this is still to be confirmed. The acmite-calcite reaction described above appears also to be applicable to the present join.

The most striking feature of the phase relations, however, is the wide extent of coexisting silicate and carbonate liquids, both above and below the vapor-saturated liquidus. Spectacular liquid immiscibility is evident in many of the charges, on both macroscale (Fig. 80B) and microscale (Fig. 80C). In some cases, droplets of each liquid can be seen scattered through the other; in other cases, the silicate liquid is largely segregated into one or two large globules enveloped by the carbonate liquid. Vesicles are generally seen in both liquids, and at temperatures below the liquidus the same crystalline phases can generally be found in both. Limited solubility of the silicate liquid in the carbonate melt is commonly evident through the presence of a uniform dissemination of minute droplets of silicate glass (average about 1 μ m in diameter) in the quenched nyerereite (Fig. 80D). These small droplets almost certainly

exsolved from the carbonate melt during quenching. By using the electron microprobe with a large beam diameter (30 μ m) and a specimen current of only 0.01 μ A, the quenched carbonate (including the exsolved silicate droplets) was analyzed with only moderate volatilization of sodium. From the result, given in Table 21, it is evident that the melt contained about 0.9 wt % SiO₂, corresponding to about 1.7 wt % of the total silicate end-member composition. Also, the overall composition of the carbonate melt is closely similar to nyerereite, and is comparable to the composition of the natrocarbonatite lava of Mt. Oldoinyo Lengai volcano.

The extent to which carbonate material dissolved in the silicate liquid is not quantitatively established, but two liquids and vapor formed (at 900°C) in a charge containing only 3 wt % of the carbonate end-member, so the solubility is probably no more than 2 wt %. This amount is substantially less than the amounts of 20% and 15–28% observed for carbonate solubility in silicate melts in the systems NaAlSi₃O₈–Na₂CO₃ (Koster van Groos

TABLE 21. Electron Microprobe Analyses of Coexisting Liquids Obtained at 900°C and 2 kbar from a 30% Silicate–70% Carbonate Starting Mixture

	Silicate Glass	Quench Nyerereite (carbonate liquid)	Nyerereite (ideal composition)	Sodium Carbonate Lava Oldoinyo Lengai†
Na ₂ O	17.5	24.3*	30.08	29.53
K ₂ O	7.58
CaO	9.9	26.9	27.21	12.74
Fe ₂ O ₃	12.3	2.2	0	.26
Al ₂ O ₃	10.6	0.1	0	.08
SiO ₂	50.8	0.9	0	trace
CO ₂	n.d.	38.4‡	42.71	31.75
Totals	101.1	92.8	100.00	

* Probably low because of volatilization by the electron beam.
† From Dawson, 1966a, Table IV, analysis 1. Complete analysis shows 0.1 wt % TiO₂, 0.04% MnO, 0.95% BaO, 1.24% SrO, 0.49% MgO, 0.83% P₂O₅, 8.59% H₂O, 2.69% F, 3.86% Cl, and 2.00% SO₃. The original total, less O for F, Cl, and S, was 100.73.
‡ Calculated on the basis of carbonate stoichiometry.

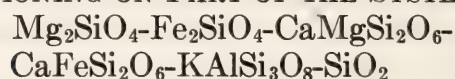
and Wyllie, 1966, 1968) and $\text{KAlSi}_3\text{O}_8\text{-K}_2\text{CO}_3$ (Wendlandt and Harrison, this Report), respectively.

In addition to the 2-kbar experiments represented in Fig. 83, exploratory runs were made on three compositions at 10 kbar to see if the liquid immiscibility is diminished by pressure. All runs were at 1050°C, and it was observed that the liquidus was raised above this temperature, but the extent of the immiscibility appeared to be about the same as at the lower pressure.

Discussion

The occurrence of andradite as a prominent liquidus phase on both of the investigated joins accords with the mineralogy of the ijolite-carbonatite association. Melanite and schorlomite, the two titaniferous varieties of andradite, occur locally in carbonatites, and melanite is the third most important mineral in ijolite. Wollastonite is another common mineral in ijolite and is found in some carbonatites. The mineral assemblages on the synthetic ijolite-natrocarbonatite join are particularly similar to those in the southeastern part of the Oka carbonatite complex (near Montreal, Canada) where Gold (1966, and personal communication, 1978) has demonstrated a progression from sövite through calcite-bearing wollastonite ijolite to wollastonite-melanite ijolite and melanite ijolite. If liquid immiscibility is a common phenomenon in ijolite-carbonatite genesis, then from the present data, acmite would be expected to be rare in the carbonatite facies. The indication that Na_2O or Na_2CO_3 is soluble to a considerable degree in CO_2 -rich vapor may be significant to the origin of the fenitized aureoles around carbonatites. Loss of Na_2CO_3 to such aureoles from a natrocarbonatite magma would be expected to result in precipitation of calcite in the magma.

LIQUIDUS RELATIONS AND Mg-Fe PARTITIONING ON PART OF THE SYSTEM



J. D. Hoover and T. N. Irvine*

It has been observed (*Year Book 74*, pp. 484–500; *Year Book 75*, pp. 597–611) that the liquidus relations of olivine and anorthitic plagioclase at 1 atm are strongly influenced by proximity to regions of liquid immiscibility, an effect that can be theoretically related (at least in part) to thermodynamic nonideality in the melt solution. The present investigation was directed toward assessing the effects of such nonideality on the crystallization relations of olivine and the pyroxenes and on the partitioning of Mg and Fe between these minerals and their parental liquids. Particular attention was given to the region of low-temperature liquid immiscibility discovered by Roedder (1951) on the join $\text{Fe}_2\text{SiO}_4\text{-KAlSi}_3\text{O}_8\text{-SiO}_2$. The observed relations bear on the trends of silica enrichment in tholeiitic and calc-alkaline magmas.

Experimental Method

The investigated compositions lie between the olivine-pyroxene join $\text{Mg}_2\text{SiO}_4\text{-Fe}_2\text{SiO}_4\text{-CaMgSi}_2\text{O}_6\text{-CaFeSi}_2\text{O}_6$ (Fo-Fa-Di-Hd) and a point on the $\text{KAlSi}_3\text{O}_8\text{-SiO}_2$ (Or-Qz) join located at $\text{Or}_{56}\text{Qz}_{44}$ (wt %). The latter composition was originally chosen (*Year Book 74*, p. 492) because it is close to the orthoclase-quartz eutectic and thus represents a simplified rhyolite or granite. Its use has since been continued because the composition line from Fa to $\text{Or}_{56}\text{Qz}_{44}$ passes through the Roedder (1951) low-temperature liquid immiscibility field approximately parallel to the liquid-liquid tie lines at a place

* Research carried out as part of a predoctoral cooperative program with the University of Oregon.

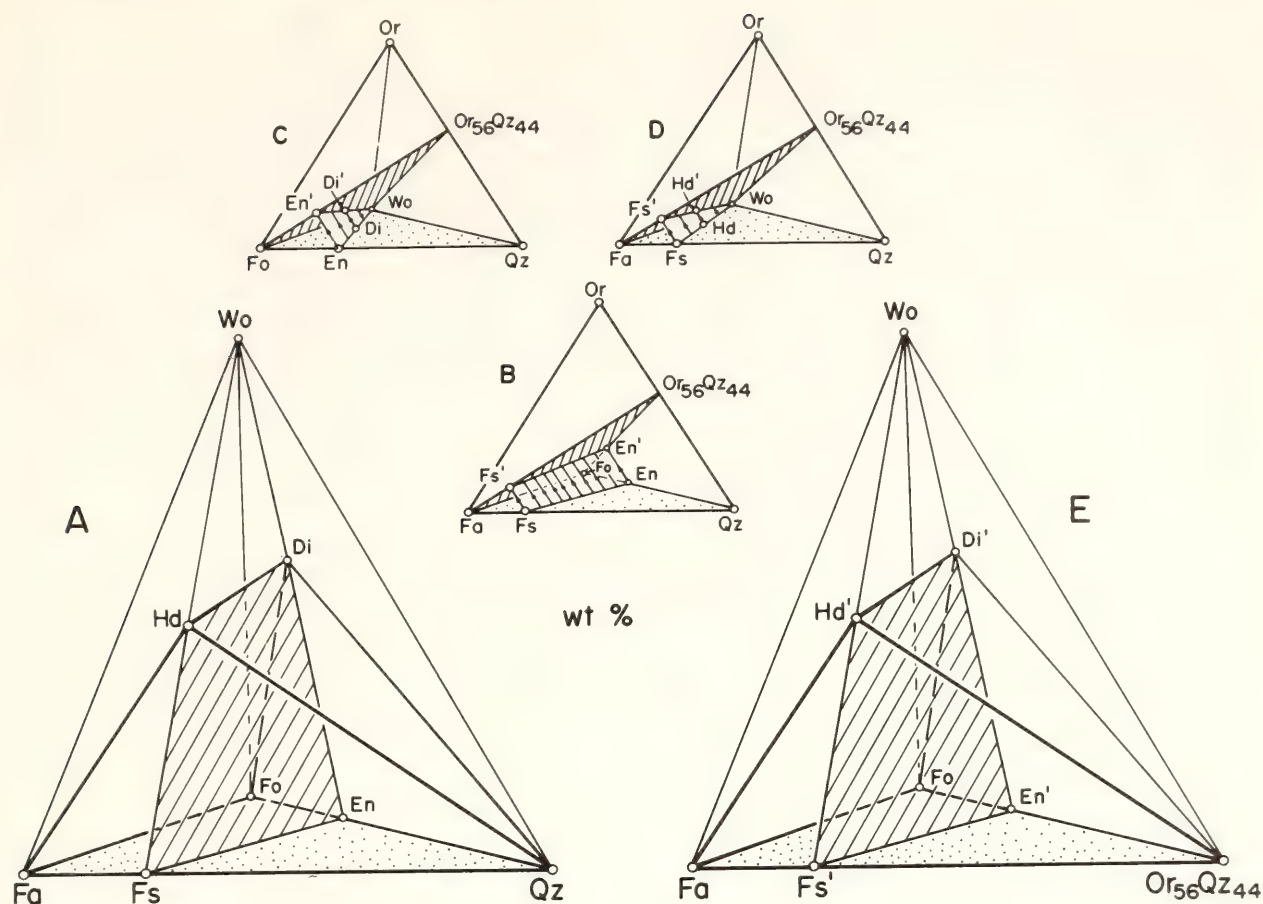


Fig. 84. Projections involved in illustrating relations for the join $\text{Fo-Fa-Di-Hd-Or}_{56}\text{Qz}_{44}$, starting from the quaternary system $\text{Fo-Fa-Wo (CaSiO}_3\text{)-Qz}$. In diagrams (B), (C), and (D), compositions are projected parallel to the Or-Qz join. Arithmetically, this projection is accomplished simply by adding Or and Qz . The pyroxene compositions, being essentially free of $\text{Or (K}_2\text{O)}$, project to the same points in (E) as in (A), but because they are off section, they are denoted by primed symbols.

where the liquid composition separation is close to a maximum. The combination of projections involved in graphically representing the data is shown in Fig. 84. The experimental work was principally concentrated on defining the saturation surface between a Ca-rich pyroxene liquidus volume near the $\text{Di}'\text{-Hd}'$ join in the tetrahedron in Fig. 84E and olivine and Ca-poor pyroxene liquidus volumes that occur toward the $\text{Fo-Fa-Or}_{56}\text{Qz}_{44}$ base. This surface is of interest because most subalkaline basic magmas evolve to a comparable surface including cotectic boundaries for olivine and augitic clinopyroxene and for two pyroxenes.

The data were obtained by melting experiments made in quenching furnaces

in which temperature was controlled to about $\pm 2^\circ\text{C}$ and measured with Pt-Rh thermocouples calibrated to about $\pm 1^\circ\text{C}$. Starting materials were combinations of precrystallized Fo , Fa , and Hd , crystals or glass of Di , and a largely glass mix of $\text{Or}_{56}\text{Qz}_{44}$.* The weighed combinations were mixed by grinding to a grain size of $< 5\ \mu\text{m}$. The usual run time was 20–24 hr, but runs as long as a week were made for some of the more siliceous compositions. Iron-free compositions were melted in

* Melts of this composition are exceptionally viscous, and cannot be fused completely in open crucibles without volatilizing some K_2O . They were, therefore, only partly fused. Residual crystals were mainly corundum and tridymite. (see Schairer and Bowen, 1950).

Pt₉₅Au₅ envelopes in air; those with iron were processed in iron capsules sealed in evacuated silica tubes if the melts could be satisfactorily quenched to glass. If more rapid quenching of the Fe-bearing melts was necessary, the charges were suspended as sintered cakes from the looped ends of thin Pt wires and were melted at controlled oxygen fugacity (f_{O_2}) in an atmosphere of CO and CO₂. In such a case, the melt forms droplets that adhere to the wire loops by surface tension, but iron loss to the thin wire is minimal and quenching in mercury is almost instantaneous (Presnall and Brenner, 1974).

In the iron capsules, f_{O_2} is approximately that imposed by the quartz-fayalite-iron buffer (e.g., Lindsley and Munoz, 1969); therefore, in the gas-mixing runs, CO/CO₂ was adjusted to equivalent values. The glasses of intermediate Mg/Fe typically are greenish, and it has been established by Mössbauer spectroscopy that practically all the iron is Fe²⁺. Glasses of very low Mg/Fe are brownish or brownish yellow, colors that probably indicate the presence of some Fe³⁺. But even in a relatively extreme example in which brown glass contained about 40 wt % FeO, the Fe₂O₃ content was less than 0.4 wt % (D. H. Virgo, personal communication).

Phase compositions were determined by electron microprobe analysis; in fact, in many cases because of the difficulty of optically distinguishing the pyroxenes from one another and from olivine, it was necessary also to use this instrument to substantiate the phase identifications. Only limited x-ray work has been done, principally to identify the Ca-Fe pyroxenoid ferrobustamite. The attainment of equilibrium has been judged mainly from the uniformity of phase compositions and the consistency of the phase relations. The illustrated relations appear satisfactory on this basis but almost no work has been done on melts containing more than 75 wt % Or + Qz because they are so viscous and slow to equilibrate (see Schairer and Bowen, 1955).

Results

Liquidus relations for the bounding joins Fo-Di'-Or₅₆Qz₄₄ and Fa-Hd'-Or₅₆Qz₄₄ are shown in Figs. 85 and 86 in comparison with the systems Fo-Di-Qz and Fa-Hd-Qz. In each case, it is seen that with the addition of Or the joint field of the silica minerals (cristobalite and tridymite) is greatly suppressed and the high-temperature liquid immiscibility associated with it is completely eliminated. A major consequence of these changes, also noted for the system Fo-Fa-An-Or-Qz (*Year Book* 75, p. 605), is that the Or-bearing basic melts can fractionate to residual liquids that are much richer in silica. The exact compositions of the last liquids have not been established, but they are closely limited by relations on the bounding joins. Thus, compared with the lowest-temperature liquid in Fo-Di-Qz, located at a temperature minimum on the diopside-tridymite boundary and containing about 62 wt % SiO₂, the final liquid in Fo-Di-Or-Qz is probably a diopside-enstatite-orthoclase-quartz eutectic melt containing ~79 wt % SiO₂. The difference in the Fe-bearing systems is even more extreme. The last liquid in Fa-Hd-Qz leaves the system on the diopside-ferrobustamite cotectic moving compositionally *away* from Qz; at the point of departure on the Fa-Hd join, the liquid contains about 47 wt % FeO and 40 wt % SiO₂. By contrast, in Fa-Hd-Or-Qz most liquids fractionate toward a fayalite-hedenbergite-orthoclase-quartz eutectic melt that is off-section but near point *j*, estimated to contain only 1–2 wt % FeO and 78 wt % SiO₂.

Another notable feature of the Fo-Di-Or₅₆Qz₄₄ join (Fig. 85A) is the shape of the forsterite field. Along the Fo-Or₅₆Qz₄₄ boundary, forsterite is not succeeded as the liquidus phase by protoenstatite until the melt contains about 70 wt % Or + Qz. But with diopside saturation of the melt, forsterite is succeeded by pigeonite when the melt contains only up to 37% Or + Qz. In addition, the protoenstatite-to-

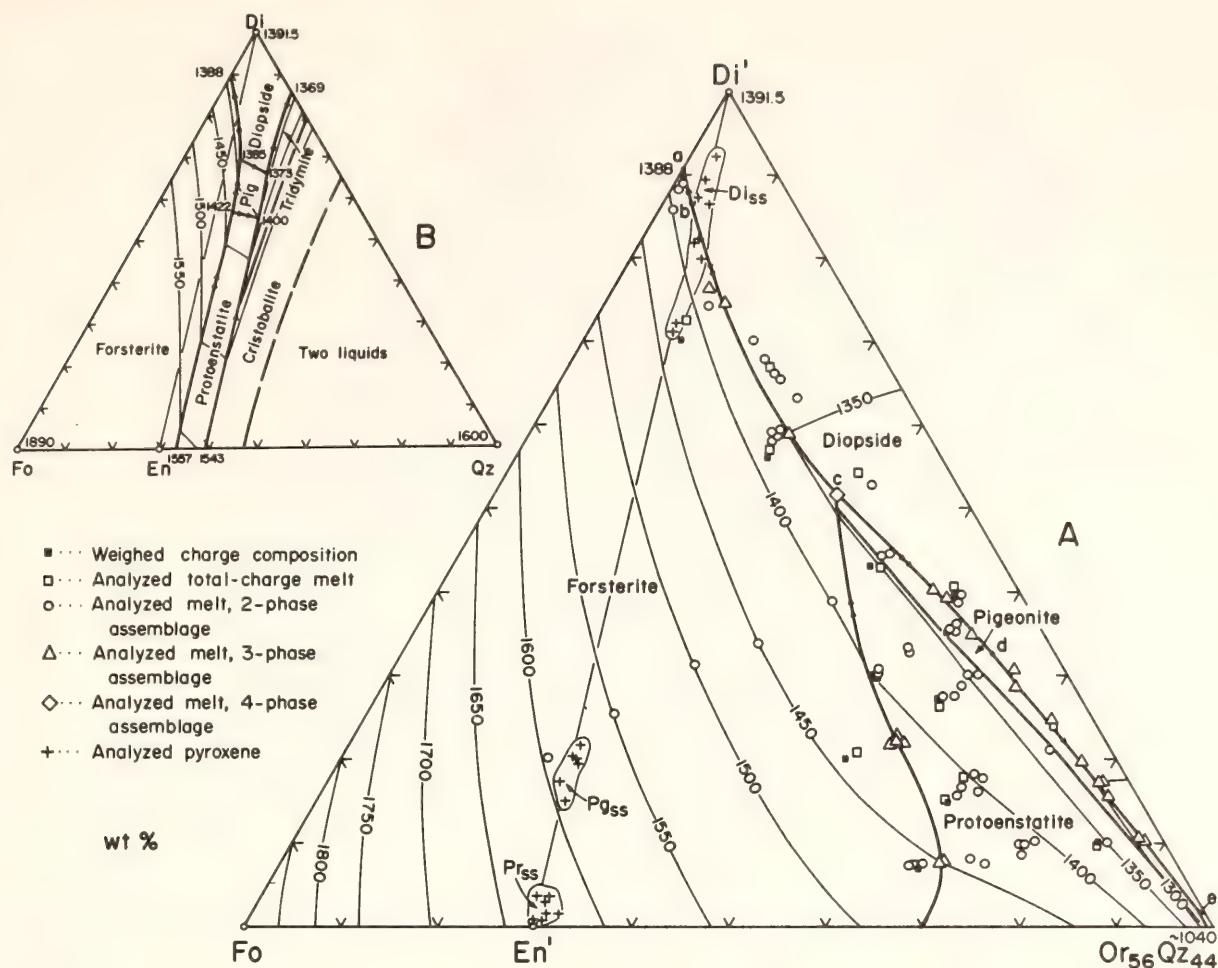


Fig. 85. Liquidus relations for (A) Fo-Di-Or₅₆Qz₄₄ compared with those in (B) Fo-Di-Qz (after Kushiro, 1972; Kushiro and Schairer, *Year Book* 62, pp. 95–103). In (A) relations along Fo-Or₅₆Qz₄₄ are from Schairer (1954); those along Di'-Or₅₆Qz₄₄ are from Schairer and Bowen (1938). Point *b* on the forsterite-diopside boundary is an inferred temperature maximum. Forsterite probably reacts to diopside along all of boundary *a b c*, and indications are that protoenstatite reacts to diopside from *c* to *d* but coprecipitates with it from *d* to *e*.

pigeonite transition occurs in the range 1300°–1340°C. Kushiro (1972) observed the transition between 1422°C and 1400°C on the liquidus of Fo-Di-Qz but showed that it might extend to as low as 1250°C in the subsolidus. The present liquidus surface intersects this lower range.

A principal effect of Hd on Fa-Hd-Or₅₆Qz₄₄ (Fig. 86A) relates to the low-temperature liquid immiscibility. The immiscibility along the boundary of Fa-Or₅₆Qz₄₄ is suppressed by only about 5 wt % Hd, but another field appears at 11–13% Hd and extends slightly across the fayalite-ferrobustamite cotectic. In neither field does the immiscibility occur at more than about 10°C above the liquidus,

however, and although the fields are separate, they undoubtedly represent the same solvus simply reappearing on opposite sides of an interval of metastability (see *Year Book* 75, p. 602, Fig. 58; in fact, the two fields may even be joined stably in some other part of composition space). A point to be emphasized from these relations is that stable low-temperature silicate liquid immiscibility in magmatic systems is a very tenuous feature. Its occurrence is not easily predicted and should not be casually inferred.

Current data on the liquidus relationships of Ca-rich pyroxene and ferrobustamite to olivine and pigeonite are illustrated for the full range of Mg/Fe in

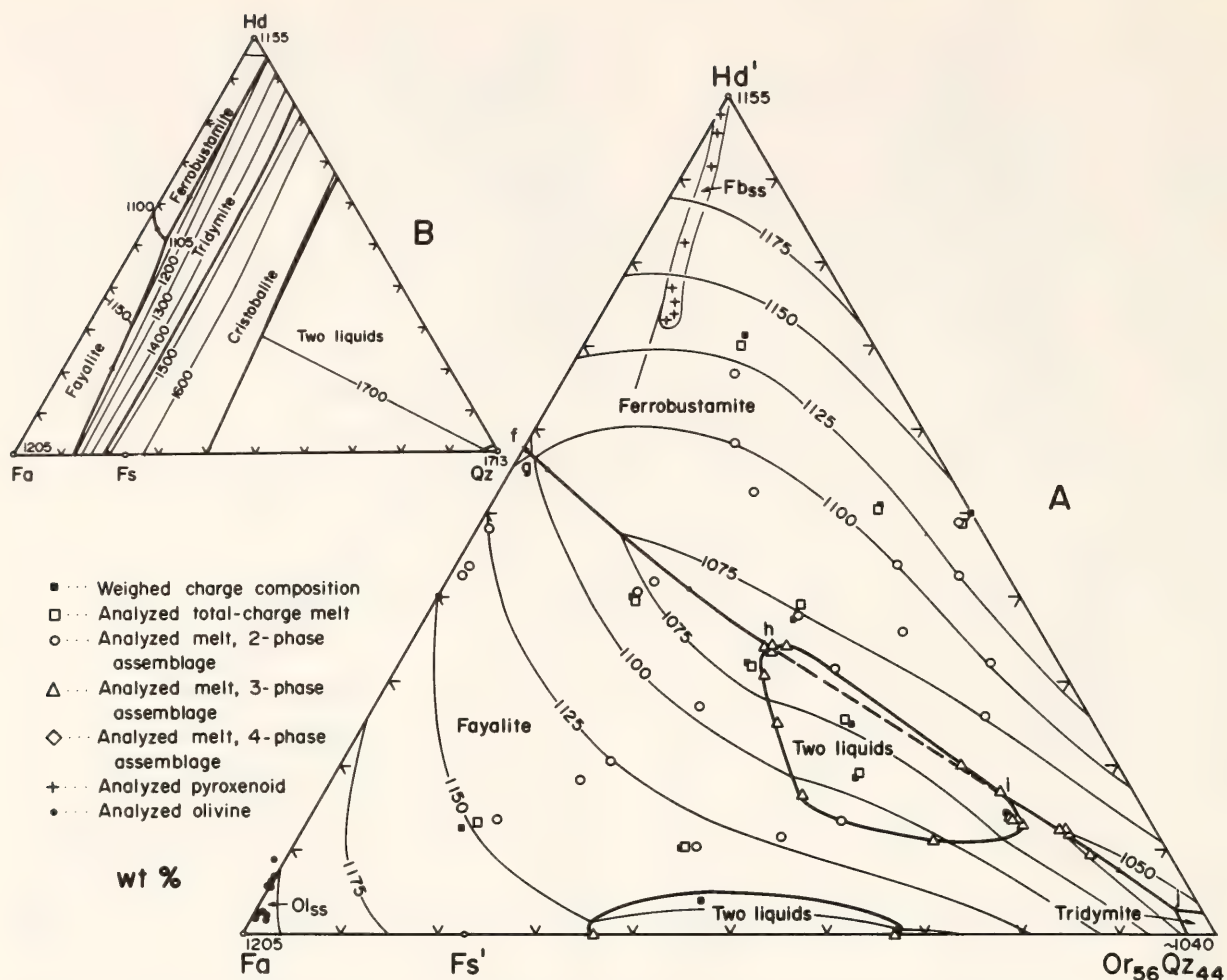


Fig. 86. Liquidus relations for (A) Fa-Hd'-Or₅₆Qz₄₄ compared with those for (B) Fa-Hd-Qz (after Bowen *et al.* 1935; Osborn and Muan, 1960). Relations along Fa-Or₅₆Qz₄₄ are from Roedder (1951); those along Hd'-Or₅₆Qz₄₄ are only approximate.

Figs. 87 and 88. A study of the pyroxene solid solution relations was not planned, but some data are necessary to define liquidus fractionation paths and those that have been obtained are shown in Fig. 89 in comparison with pyroxene solvus relations reported by Ross and Heubner (1975). Data on liquid-solid Mg-Fe partitioning are summarized in Fig. 90. Liquid fractionation paths cannot be defined rigorously, but approximate path traces are shown in Fig. 87B.

In Fig. 89 the solvus from Ross and Heubner (1975) was determined for natural pyroxenes, and the illustrated part is shown only as a frame of reference. Most of the synthetic pyroxenes analyzed herein were formed at temperatures well above the solvus, but the relationships of the few that should lie on it are generally compatible within the uncertainties in-

volved. The main exceptions are some Ca-rich pyroxenes on the Di-En join; they are almost certainly too rich in Ca to have been equilibrated.

The temperature profiles of the Ca-rich pyroxene-ferrobustamite saturation surface in Fig. 88 are similar to those previously defined for an anorthite saturation on the join Fo-Fa-An-Or₅₆Q₄₄ (*Year Book* 75, p. 606, Fig. 60)—the profiles have the sigmoidal form characteristic of a liquidus surface overriding a metastable two-liquid solvus. In the present case, however, the immiscibility actually becomes stable at Mg/(Mg + Fe) less than 0.06 (by wt).

The most interesting liquidus features concern the relationships of the cotectic surface for Ca-rich pyroxene and pigeonite and the fields of ferrobustamite and low-temperature liquid immiscibility

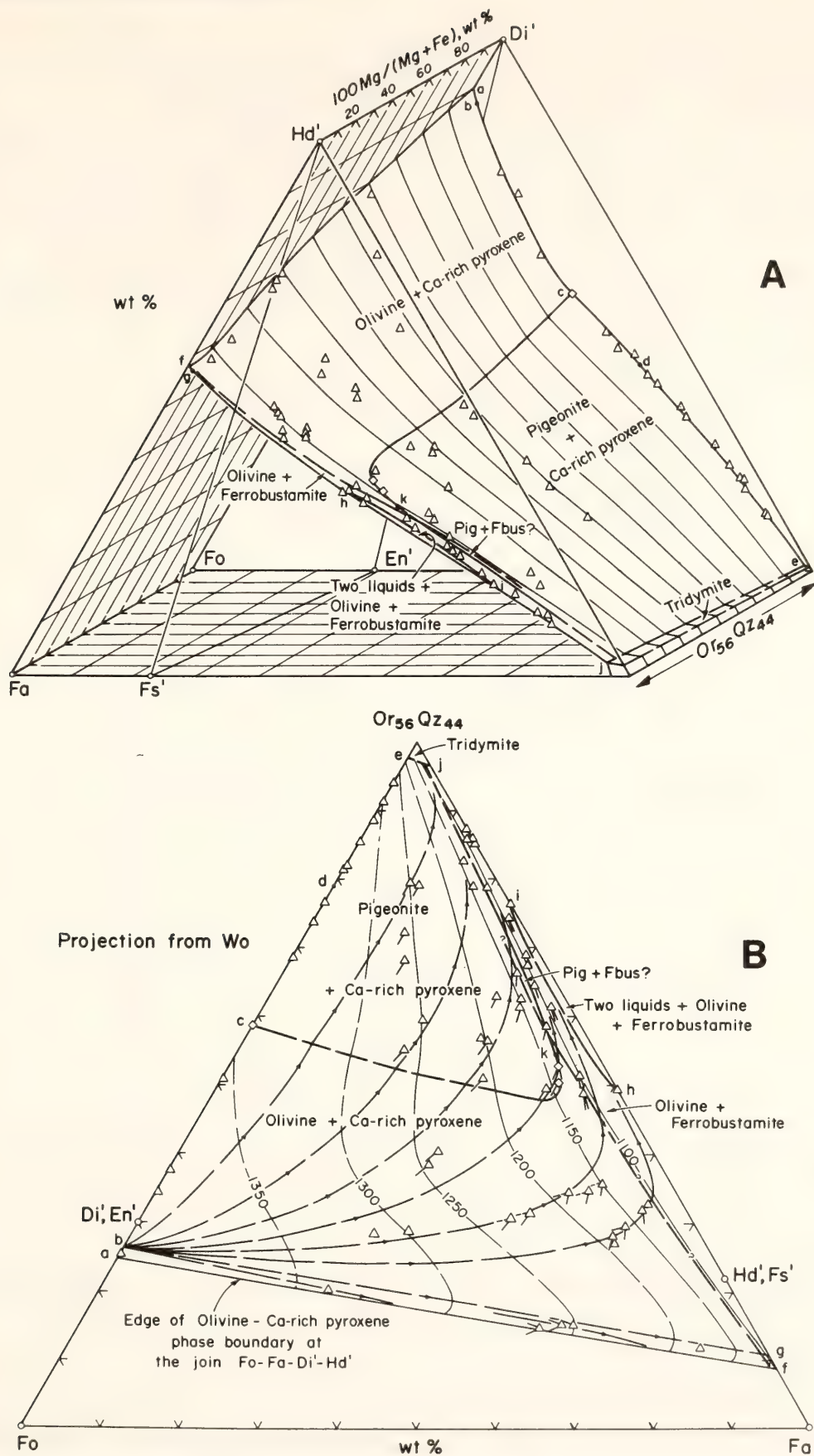


Fig. 87. Ca-rich pyroxene (and pyroxenoid) saturation surface for the join Fo-Fa-Di'-Hd'-Or₅₆Qz₄₄. Points a-e are the same as in Fig. 85A; f-j are the same as in Fig. 86A. In (A) the shifting of the surfaces relative to the olivine and pyroxene joins is evident. The point Or₅₆Qz₄₄ has been "extended" so that compositions can be read from the graph at any Mg/Fe. In (B) the surface is projected from Wo(CaSiO₃), and fractionation path traces are shown. The directions of the fractionation curves are principally dependent on pyroxene-liquid relations, because olivine forms in only minor proportions (at the most). Dashed vectors are estimated from K_D values (Fig. 90).

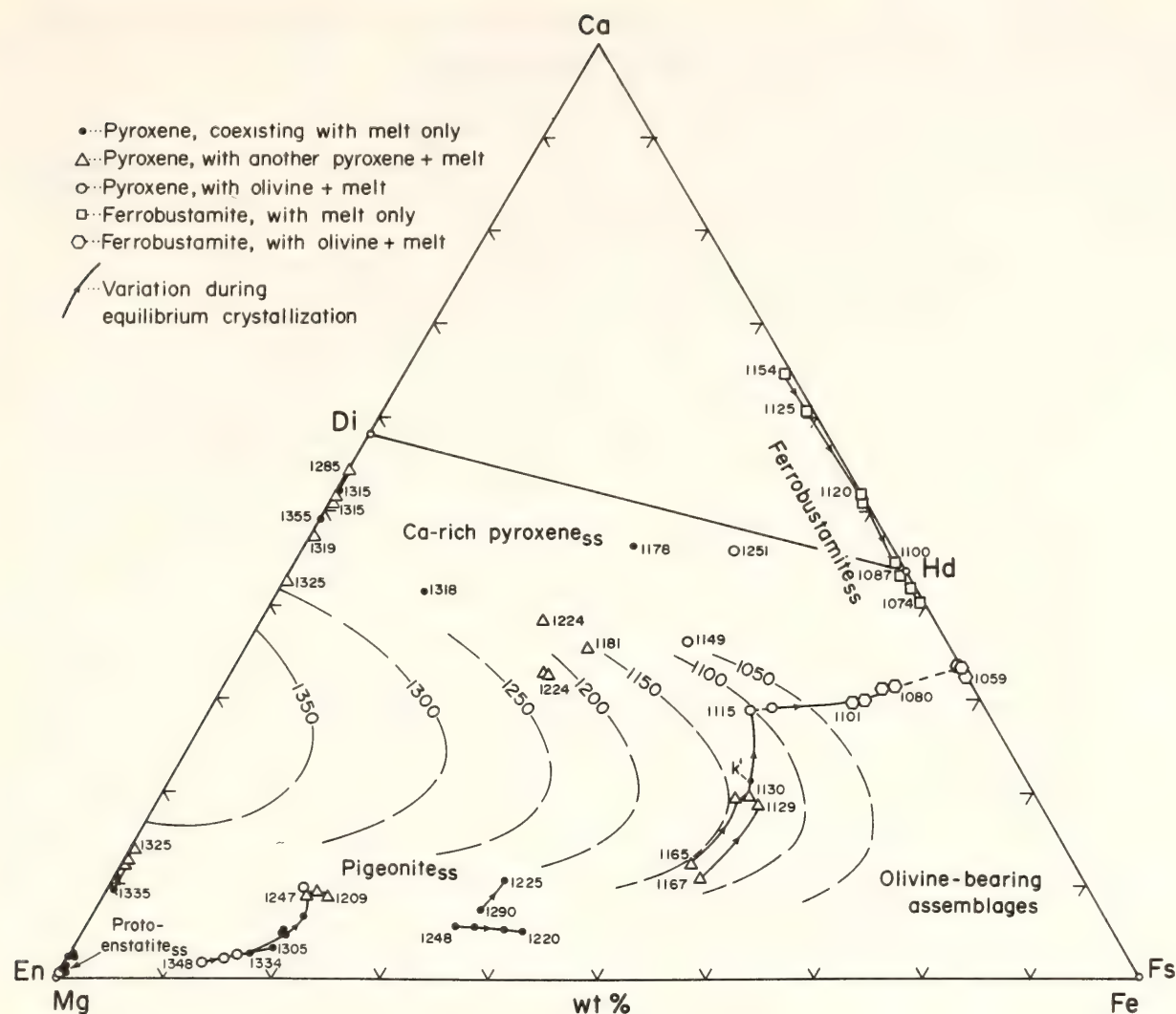


Fig. 89. Measured compositions of pyroxenes coexisting with liquids on or near the join Fo-Fa-Di'-Hd'-Or₆₆Q₂₄₄. The illustrated part of the two-pyroxene solvus is from Ross and Heubner (1976).

pounds. In the present case, the immiscibility occurs only where the pyroxenes are not stable liquidus phases between olivine-rich melts and high-silica melts. It would be premature to suggest that this relationship is a general feature in basic magmas; this might be the case, but more probably the introduction of other constituents such as Fe₂O₃, TiO₂, and P₂O₅ will destroy it. The relationship is, however, further evidence of close but complicated correlations between the structures of silicate melts (as reflected in this case by the immiscibility) and their crystallization characteristics (see also Irvine, *Year Book* 74, pp. 484-492).

In Figs. 87 and 88, point *k* on the edge of the two-pyroxene cotectic is the ap-

proximate composition of the liquid in equilibrium with pyroxene at the crest of the two-pyroxene solvus for the temperatures involved. The pyroxene composition is at about *k'* in Fig. 89. The line of ferrobustamite data points extending from near the solvus to lower Mg/Fe represents pyroxenoid solid solutions crystallized simultaneously with olivine, and the location on the line theoretically is a function of the activity of silica in the melt (see Lindsley and Munoz, 1969).

With regard to the Mg-Fe partitioning data (Fig. 90), it has frequently been observed that equilibrium values for the coefficient $K_D = (\text{Fe/Mg in mineral}) / (\text{Fe/Mg in liquid})$ for olivine and basaltic liquids fall in the range 0.28-0.33, aver-

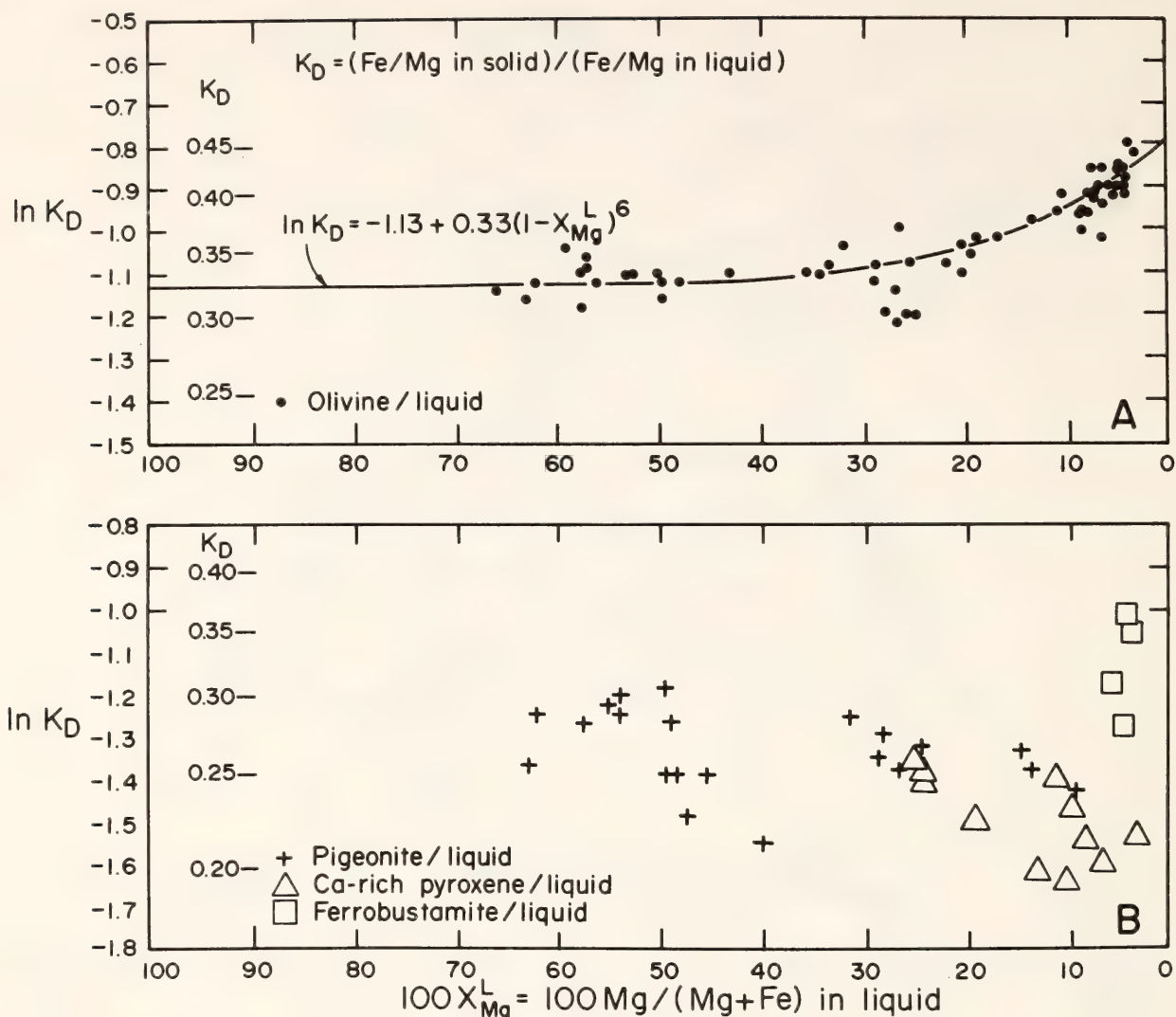


Fig. 90. Variations in Mg/Fe partitioning between olivine and liquid and the pyroxenes and liquid on the join Fo-Fa-Di'-Hd'-Or₅₆Qz₄₄.

aging about 0.30–0.31 (Roeder and Emslie, 1970; O'Hara *et al.*, 1975; Longhi and Walker, 1975; Arndt, *Year Book* 75, pp. 555–562). Values measured for olivine-anorthite cotectic liquids on the join Fo-Fa-An-Or₅₆Qz₄₄ are similar, but they increase to 0.36 at low Mg/Fe in a region just above a metastable two-liquid solvus (*Year Book* 75, p. 607, Fig. 61). The olivine-liquid K_D values from the present study generally range from 0.31 to 0.33, but at Mg/(Mg + Fe) less than 0.2 (by wt) they begin to increase, finally reaching 0.45 near the liquid immiscibility field along the fayalite-ferrobustamite cotectic. The partitioning is dependent on the characteristics of the olivine as well as those of the liquid (and is a

function of temperature as well as composition), but qualitatively at least, much of the increase in K_D can probably be attributed to nonideality in the melt solution associated with the immiscibility. In effect, the Mg-Fe exchange equilibrium is shifting away from iron enrichment of the melt because of the increase in its excess free energy near the two-liquid solvus.

The measured K_D values for pigeonite and liquid generally range from 0.25 to 0.29 with no obvious systematic correlation with melt composition. Values for Ca-rich pyroxene and liquid are mostly 0.19–0.26, whereas those believed to be representative of ferrobustamite and liquid are distinctly higher, 0.31–0.36.

The liquid fractionation curves in Fig.

87B are only *path traces* because the illustrated Ca-rich pyroxene saturation surface is only a section through a five-component system. The pyroxenes and pyroxenoid are all on the Or-poor side of the projection plane; consequently, whenever they crystallize, Or/Qz in the liquid increases and the liquid composition moves off section. The curves, therefore, only indicate the direction of composition variation of liquids as they *pass through* the projected surface. Complete representation would require a series of similar sections at different values of Or/Qz.

The path traces appear, however, to give a reliable qualitative picture of differentiation effects, and that is their intended purpose. Principal features are:

(1) All liquids probably fractionate eventually to a final liquid at the quartz-orthoclase-fayalite-hedenbergite eutectic. As noted previously, this composition probably lies just off the section near *j* in Figs. 87 and 88, in which case the liquid is rhyolitic with some 78 wt % SiO₂ and only about 1–2 wt % FeO.

(2) Liquids on the olivine–Ca-rich pyroxene cotectic at high Mg/Fe (and a given content of Or + Qz) follow paths along which pigeonite succeeds olivine at a relatively early stage and is itself succeeded by fayalite only at a very late stage. With lower Mg/Fe (but the same content of Or + Qz), pigeonite appears later and fayalite olivine earlier, and at very low Mg/Fe there is a narrow corridor along which olivine crystallization is continuous and pigeonite does not form at all.

(3) There is a possibility, most probably obtaining at lower Or/Qz than in the present section, that some liquids will follow paths on which phases appear in the order: olivine + Ca-rich pyroxene; pigeonite + Ca-rich pyroxene; olivine + Ca-rich pyroxene (again); olivine + ferrobustamite; and olivine + ferrobustamite + an immiscible silica-rich liquid that eventually becomes the final liquid. The Skaergaard magma evidently went through exactly this sequence (see Wager

and Brown, 1968; McBirney and Nakamura, *Year Book* 73, pp. 348–352).

A general point that might be emphasized is that the “regression” from pigeonite to fayalitic olivine crystallization can occur in siliceous (acidic) liquids as well as in Fe-rich basic liquids (for example, in the Skaergaard intrusion and the system MgO–FeO–SiO₂; Wager and Deer, 1939; Bowen and Schairer, 1935). This feature is in accord with the mineral content of certain rhyolitic glasses (e.g., Carmichael, 1960).

Petrologic Application

The data presented here together with those for the join Fo–Fa–An–Or₅₆Qz₄₄ (Irvine, *Year Book* 74, pp. 484–500; *Year Book* 75, pp. 597–611) are most relevant to the development of trends of silica enrichment in tholeiitic and calc-alkaline magmas. This type of trend, particularly for the calc-alkaline series, has been a longstanding subject of discussion and has variously been attributed to oxidation, to the effect of H₂O on the crystallization relations of olivine, the pyroxenes, and quartz, and to amphibole fractionation. A concept deriving from the present series of experimental studies (*Year Book* 75, pp. 597–611) is that for silica enrichment to occur the activity of silica must be lower than its levels in melts of Fo, Fa, Di, Hd, An, and Qz. Such lowering is accomplished essentially by suppressing the high-temperature liquid immiscibility that typically separates silica melts from more basic liquids. The joint liquidus field of the silica minerals shrinks simultaneously and the basic liquids can then fractionate to more siliceous compositions. As noted by Irvine (*Year Book* 75, pp. 597–611), this change is *not* effected by oxidation, so if this process is involved it is only an auxiliary, not an essential, factor. The change *is* effected by the addition of H₂O (for example, in the system Fo–Di–Qz–H₂O; Kushiro, 1972), which of course is also essential to amphibole stability. It is well established that calc-alkaline

magmas are generally hydrous, but the quantitative significance of amphibole fractionation in nature is still uncertain (see Ritchey and Eggler on amphibole fractionation, this Report). In the present experimental series it has been demonstrated that, in respects other than amphibole stabilization, the alkalis (specifically K as represented in Or, but also Na in Ab based on analogy to simpler systems) have much the same liquidus effects as H_2O , especially in terms of opening routes of silica enrichment. Thus, given that alkalis occur in substantial quantities in all tholeiitic and calc-alkaline magmas and are essential major constituents in the more siliceous dacitic and rhyolitic types, it seems that their abundance is probably the most critical of all factors in the development of silica-enrichment trends.

CHANGE IN PHASE RELATIONS IN
RESPONSE TO CHANGE IN PRESSURE
FROM 1 atm TO 10 KBAR FOR THE
SYSTEM Mg_2SiO_4 -IRON OXIDE-
 $CaAl_2Si_2O_8$ - SiO_2

E. F. Osborn

Phase relations determined at 1 atm for the system Mg_2SiO_4 -iron oxide- $CaAl_2Si_2O_8$ - SiO_2 (MFAS) have been useful in understanding and illustrating the nature of courses of crystallization of subalkaline basalts under near-surface conditions (Roeder and Osborn, 1966; Osborn, 1969a). Basalts entering the lower crust at a pressure of several kbar may, however, have significantly different courses of crystallization because of the different phase relations that exist at this higher pressure. Studies of the system MFAS at 10 kbar and implications of the results for the origin of volcanic rock series have been discussed by Osborn and Arculus (*Year Book 74*, pp. 504-507) and by Osborn (1976, 1978). Further experimental studies at 10 kbar are described in this report.

In their studies at 1-atm total pressure, Roeder and Osborn (1966) presented diagrams illustrating phase relations at

the constant oxygen partial pressures (P_{O_2}) of $10^{-0.7}$, 10^{-7} , 10^{-9} , and 10^{-11} atm. For the system oxygen-buffered at $10^{-0.7}$ and at 10^{-7} atm, liquidus phase relations were shown to be of the same nature: that is, although the compositions of phases and temperatures at minimum liquidus points are different for the two levels of P_{O_2} , the arrangement of boundary curves and primary phase volumes is similar for the two diagrams. Hence, the P_{O_2} used during runs at constant P_{O_2} is not an important consideration when using the system MFAS as a model within the wide range of $10^{-0.7}$ and 10^{-7} atm, and experiments may, therefore, be made at the high P_{O_2} of $10^{-0.7}$ atm where loss of Fe to the 95Pt-5Au containers is less than at the lower levels of P_{O_2} . To make the most direct comparisons of phase relations at two different total pressures, however, the P_{O_2} should be approximately the same, and for comparison with phase relations at a constant P_{O_2} of $10^{-0.7}$ atm and a total pressure of 1 atm (Fig. 91) a constant P_{O_2} of approximately $10^{-0.7}$ would be desirable for the high-pressure runs.

In a first attempt to determine phase relations for the system MFAS at 10 kbar (Osborn and Arculus, *Year Book 74*, pp. 504-507) a piston press and a hematite-magnetite buffer were used; runs were very short (about 15 min). The results turned out to be inconsistent and unreliable. A close approach to equilibrium was not being obtained, and water content of the charge during the runs was unknown. In current studies a gas apparatus of Yoder (1950) is being used at a pressure of 10 kbar with runs of 4 hr or longer. A charge of about 15 mg is placed in an open-ended 95Pt-5Au tube and equilibrated for a minimum of 24 hr in air at constant temperature. The tube is then sealed by welding and held for 24 hr at 1150° to crystallize the mixture; the capsule is then run at the air-equilibrated temperature at a total pressure of 10 kbar. By this technique, a P_{O_2} of approximately $10^{-0.7}$ is believed to be achieved for the runs. The current studies employ those

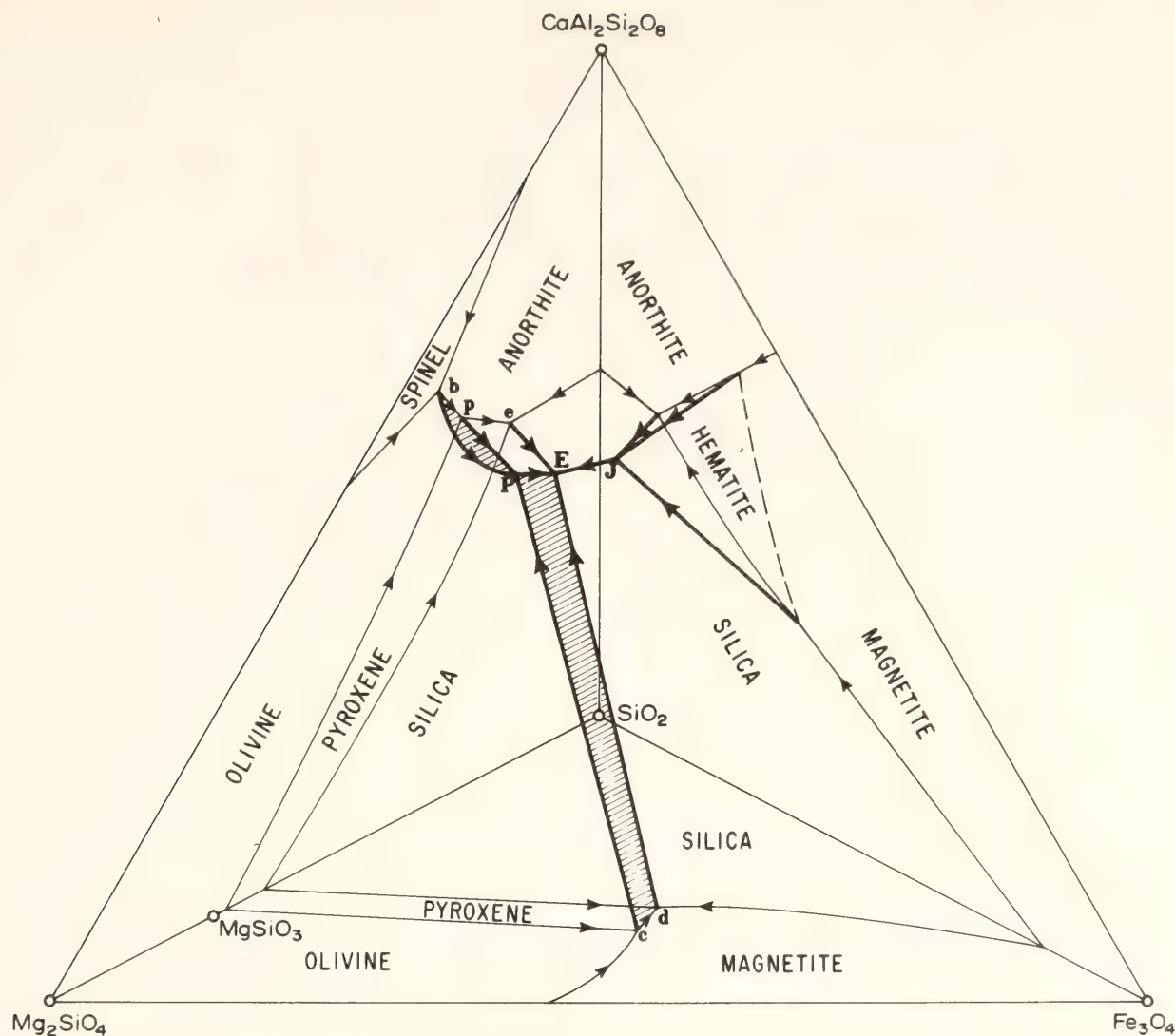


Fig. 91. Tetrahedron representing liquidus phase relations in the $\text{Mg}_2\text{SiO}_4\text{-FeO-Fe}_2\text{O}_3\text{-CaAl}_2\text{Si}_2\text{O}_8\text{-SiO}_2$ system at a constant oxygen partial pressure (P_{O_2}) of $10^{-0.7}$ atm, after Roeder and Osborn (1966). Left face of tetrahedron is after Andersen (1915), base is after Muan and Osborn (1956), and right face is after Roeder and Osborn (1966). Heavy solid lines within the tetrahedron represent liquid compositions in equilibrium with three crystalline phases and a gas phase of $P_{\text{O}_2} = 10^{-0.7}$ atm. Arrows indicate the direction of decreasing temperature. Points P , E , and J are liquid compositions coexisting with four crystalline phases and a gas phase of $P_{\text{O}_2} = 10^{-0.7}$ atm. To improve readability of the diagram, the surface along which olivine and anorthite coexist with liquid and gas, $b\text{-}p\text{-}P$, and the surface along which magnetite and pyroxene coexist with liquid and gas, $P\text{-}E\text{-}d\text{-}c$, have been ruled.

mixtures made and used by Roeder and Osborn (1966) and a series of new mixtures, made as before by four fusions with intermediate crushing to produce homogeneous glasses for starting materials.

Results are illustrated in the preliminary phase diagrams of Figs. 92, 93, and 94. In Fig. 92, modified after Osborn (1976), and in Fig. 93 are shown phase relations along planes of constant iron oxide content within the tetrahedron having as apices $\text{Mg}_2\text{SiO}_4(\text{Fo})$, iron oxide

(calculated as Fe_3O_4), $\text{CaAl}_2\text{Si}_2\text{O}_8(\text{An})$, and SiO_2 , that is, the tetrahedra of Figs. 91 and 94. Dots (Figs. 92 and 93) represent compositions of mixtures lying on or close to the plane and on which liquidus data were obtained at 10 kbar. Temperatures shown are those estimated for piercing points. Data are not sufficiently complete for an estimate of the temperatures of points m'' and s of Fig. 93.

Phase relations within the tetrahedron are sketched in Fig. 94, modified after

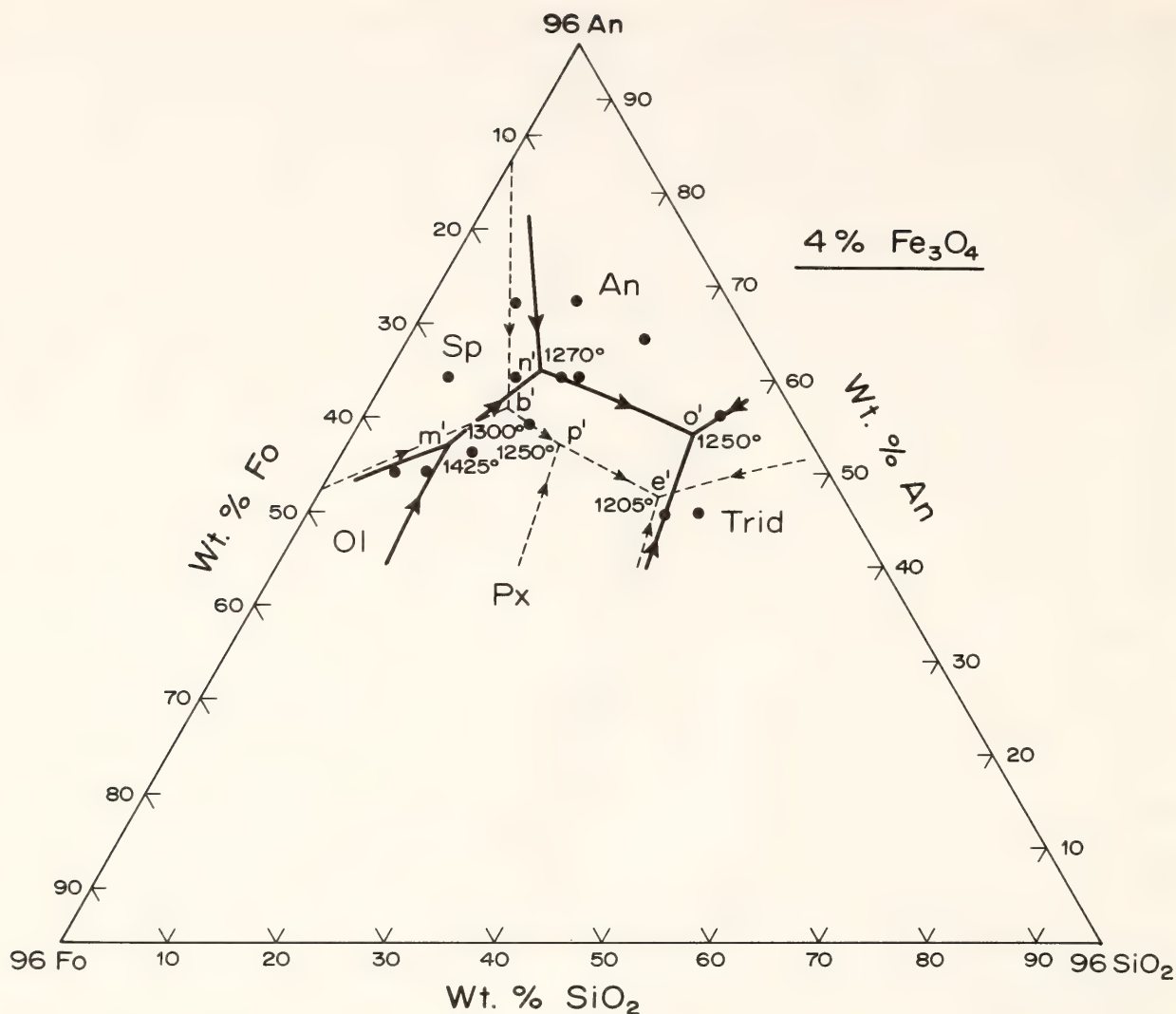


Fig. 92. Sketch (modified after Osborn, 1976) to illustrate liquidus phase relations along a plane through the tetrahedron of Figs. 91 and 94, at a constant Fe_3O_4 content of 4 wt %. Phase relations at 1 atm are shown by dashed lines, and at 10 kbar by solid lines. The dashed lines represent intersections of a 4%- Fe_3O_4 plane, in the tetrahedron of Fig. 91, with the boundary curves and surfaces of that tetrahedron. The points b' , p' , and e' represent points of intersection of the plane with the boundary curves b - P , p - P , and e - E respectively, of Fig. 91. The piercing points m' , n' , and o' represent intersections of the 4%- Fe_3O_4 plane with the boundary curves m - f , n - D , and o - D , respectively, of Fig. 94. Dots represent composition of mixtures studied, all of which contain 4% Fe_3O_4 except for the two points at 45% An that contain 5.5% Fe_3O_4 . Arrows indicate direction of decreasing temperature. Abbreviations: Ol = olivine $[(\text{Mg}, \text{Fe})_2\text{SiO}_4]$; Sp = spinel $[(\text{Mg}, \text{Fe}) (\text{Al}, \text{Fe})_2\text{O}_4]$; An = anorthite $(\text{CaAl}_2\text{Si}_2\text{O}_8)$; Trid = tridymite or cristobalite (SiO_2) ; Px = Mg pyroxene $[(\text{Mg}, \text{Fe}, \text{Ca}, \text{Al}) (\text{Si}, \text{Al})\text{O}_3]$; Fo = Mg_2SiO_4 .

Osborn (1976). Heavy lines represent boundary curves at 10 kbar within the tetrahedron. Light solid lines, after Kushiro (*Year Book 71*, pp. 357–359), represent boundary curves at 10 kbar on the left face. Dashed lines are boundary curves at 1 atm outlining the upper part of the pyroxene primary phase volume, from Fig. 91. The phase relations are shown on a larger scale than the tetrahedron in order to minimize confusion of

lines. The boundary curve m - f (Fig. 94) is a reaction curve along which, with decreasing temperature, olivine dissolves as pyroxene and spinel crystallize. A minimum is believed to occur on m - f , as indicated by the arrows on this boundary curve, but location of the minimum has not been precisely determined. The boundary curve n - D is also a reaction curve, with spinel dissolving as pyroxene and anorthite crystallize. At D at the

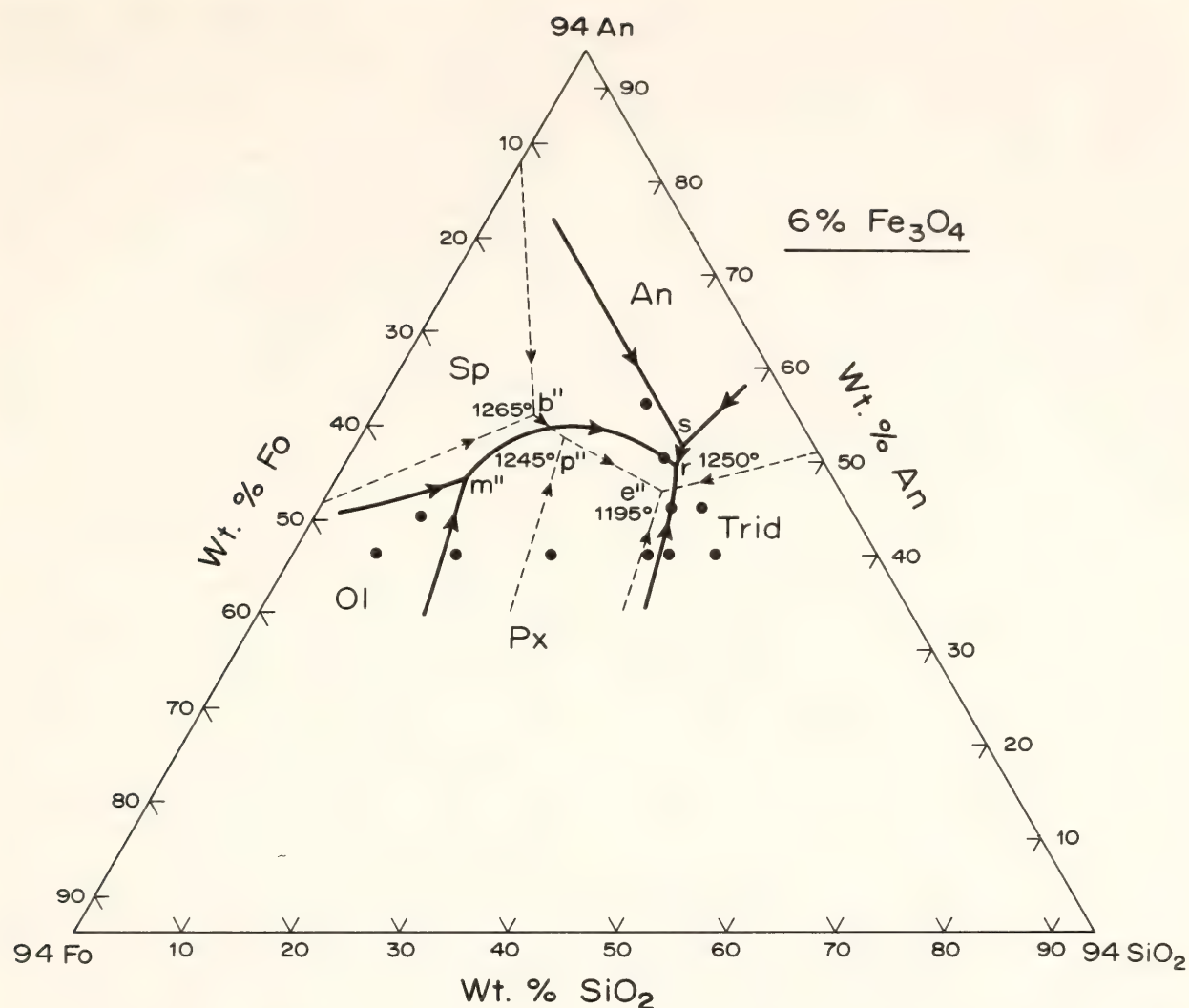


Fig. 93. Sketch to illustrate liquidus phase relations along a plane through the tetrahedron of Figs. 91 and 94 at a constant Fe_3O_4 content of 6 wt %. Phase relations at 1 atm are shown by dashed lines, and at 10 kbar by solid lines. Points b'' , p'' , and e'' represent intersections of the plane with the boundary curves b - P , p - P , and e - E of Fig. 91. Points m'' , r , and s represent intersections of the plane with boundary curves m - F , D - g , and the Sp - An - Trid boundary curve shown as a short, heavy line in Fig. 94. Dots represent compositions of mixtures studied, all of which contain $6 \pm 0.5\%$ Fe_3O_4 . Arrows indicate directions of decreasing temperature. Abbreviations are as in Fig. 92.

liquidus temperature of about 1235° , pyroxene, anorthite, spinel, and silica are in equilibrium with a liquid having approximately the composition $12\text{Mg}_2\text{SiO}_4$, $5\text{Fe}_3\text{O}_4$, $53\text{CaAl}_2\text{Si}_2\text{O}_8$, 30SiO_2 .*

* The liquidus phase relations depicted in Fig. 94 can be treated as quaternary only as a rough approximation because the phases present (except for anorthite and silica) can be represented only approximately in terms of the compounds at the apices of the tetrahedron. The composition of the liquid phase at liquidus temperatures, however, is sufficiently close to that of liquids in the tetrahedron that the diagram can be used as a guide to understanding liquidus phase relations in this very complex system at 10 kbar and constant P_{O_2} of $10^{-0.7}$ atm.

Differences between liquidus phase relations at 1 atm and 10 kbar are well illustrated by the two planes at 4% and 6% Fe_3O_4 (Figs. 92 and 93). In Fig. 92, the large increase in size of the pyroxene field on increasing the pressure from 1 atm to 10 kbar is accompanied by a fundamental change in the compatibility of the phases. At 1 atm, olivine and anorthite coexist along b' - p' (Fig. 92), but at 10 kbar their fields are widely separated. On the other hand, spinel and pyroxene fields do not have a common boundary at 1 atm, but these two phases coexist along m' - n' at 10 kbar. Pyroxene and anorthite coexist at both pressures—along p' - e' at 1

94. The dotted lines $u-u'$ and $v-v'$ indicate the general trends of their fractionation curves. The nature of these crystallization paths can be illustrated by reference to Figs. 92 and 93 and where, for purposes of this discussion, $u-u'$ and $v-v'$ are considered to lie in the planes of Fig. 92 and Fig. 93, respectively. The lines $u-u'$ and $v-v'$ correspond therefore to $m'-n'$ and $m''-r$, respectively. When liquid m' (u of Fig. 94) is fractionally crystallized, spinel and pyroxene precipitate while the liquid composition moves from m' to n' (Fig. 92). At n' , spinel ceases to precipitate as anorthite begins to precipitate, and the liquid composition with decreasing temperature moves along the pyroxene-anorthite surface toward o' , the piercing point of the pyroxene-anorthite-silica boundary curve, $o-D$ of Fig. 94. The liquid composition will then move along $o-D$ toward D (Fig. 94). At D , the four phases pyroxene, anorthite, silica, and spinel will coprecipitate. Liquid v , in contrast to u , has a sufficiently higher iron oxide content that its fractionation curve $v-v'$, (Fig. 94) crosses the spinel-pyroxene boundary surface to $g-D$ and therefore does not intersect the curve $n-D$. Silica appears as a precipitating phase before anorthite, and there is no gap in spinel precipitation. The course of fractional crystallization for v is further illustrated in Fig. 93, where m'' corresponds to v of Fig. 94. During fractional crystallization of haplobasaltic liquid m'' , the liquid composition changes along $m''-r$ as spinel and pyroxene precipitate. At r , silica joins spinel and pyroxene as a precipitating phase. It is seen, therefore, that on fractionally crystallizing either of the haplobasaltic compositions, u or v , at 10 kbar (Fig. 94), the liquid composition changes toward higher SiO_2 and An contents, with spinel and pyroxene as precipitating phases. In the higher iron oxide mixture, however, spinel is a continuing crystallizing phase until a more advanced stage is reached in the fractional crystallization, there being no gap in spinel precipitation.

As illustrated in Figs. 92, 93, and 94, the principal effects of high pressure on these fractionation curves of a haplobasaltic magma are: (a) the composition of the primary haplobasaltic magma formed by partial melting of a haploperidotite is increased in Fo and decreased in SiO_2 ; for example, the liquid composition p' (Fig. 92), in equilibrium with olivine, pyroxene, and anorthite, shifts to liquid composition m' , in equilibrium with olivine, pyroxene, and spinel; (b) spinel and pyroxene become the coprecipitating phases (along $m'-n'$ of Fig. 92 and $m''-r$ of Fig. 93) instead of pyroxene and anorthite (along $p'-e'$ of Fig. 92 and $p''-e''$ of Fig. 93); and (c) the liquid composition during fractionation increases in An, especially during the early stages (the opposite is the case at low pressure).

Because of the great difference between phase relations at the two pressures, an abrupt and significant change in the course of crystallization may occur if a liquid crystallizing at 10 kbar is rapidly moved to a low-pressure region. This effect can be illustrated by examining a liquid composition along the fractionation path $v-v'$ of Fig. 94 ($m''-r$ of Fig. 93). The curve $m''-r$ (along which pyroxene and spinel are precipitating at 10 kbar) is located on the low-pressure phase diagram (dashed lines of Fig. 93), in its first part in the olivine field and in its later part in the anorthite field. If, therefore, the pressure is dropped from 10 kbar to 1 atm during fractionation, either olivine or anorthite will precipitate from the liquid that had been precipitating pyroxene and spinel at 10 kbar. With continuing fractionation at low pressure, if olivine is precipitating, this phase will be joined by pyroxene or anorthite, but olivine will cease precipitating when pyroxene appears. If anorthite is the primary phase precipitating at low pressure, the anorthite will later be joined by olivine or pyroxene, and if olivine is a phase precipitating with anorthite, olivine precipitation will cease when pyroxene begins to precipitate. In either case, the liquid

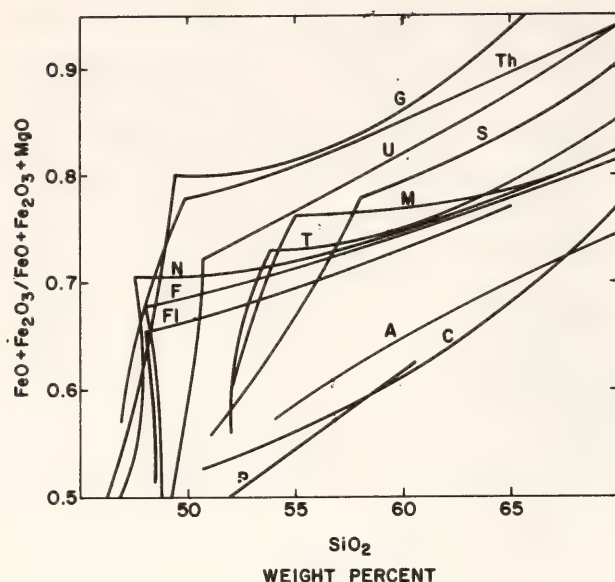


Fig. 95. Curves representing $(\text{FeO} + \text{Fe}_2\text{O}_3)/(\text{FeO} + \text{Fe}_2\text{O}_3 + \text{MgO})$ vs. SiO_2 for volcanic rock suites, after Osborn (1978). Abbreviations used: G = Galápagos Islands (plot of analyses reported by McBirney and Aoki, 1966); Th = Thingmuli volcano, Iceland, after Carmichael (1964); U = Northeast Umnak Island, Aleutian Islands, Alaska (plot of analyses reported by Byers, 1961); S = Santorini volcano, Cyclades, Greece (curve for the Main Series, after Nicholls, 1971); M = Mashu volcano, East Hokkaido, Japan, after Katsui *et al.* (1975); T = Talasea Peninsula, New Britain, Papua New Guinea (plot of analyses reported by Lowder and Carmichael, 1970); N = Nicaragua (plot of analyses reported by Williams, 1952; McBirney and Williams, 1965; Williams and McBirney, 1969; and Ui, 1972); F = Vitu Levu, Fiji (plot of analyses reported by Gill, 1970); FI = Flores Group, Indonesia (plot of analyses reported by Newman van Padang, 1951); A = Aegean (curve for lavas of the western South Aegean Arc, after Nicholls, 1971); C = Cascades, western United States, after Osborn (1959); P = Parícutin volcano, Mexico (plot of analyses reported by Wilcox, 1954; Foshag and Gonzáles, 1956; Tilley, Yoder, and Schairer, *Year Book 65*, pp. 260–269). Analyses for G, U, N, F, FI, and P were taken from the data base of F. Chayes at the Geophysical Laboratory by routine application of his information system, RKNFSYS.

composition moves along the pyroxene-anorthite boundary surface (p'' - e'' of Fig. 93), and spinel, if it reappears, will precipitate only as a late magnetite phase.

Existence of the two distinct types of fractionation curves, high-pressure and low-pressure, may help explain the origin

of composition trends of volcanic suites (Osborn, 1976, 1978). The curves of Fig. 95 (after Osborn, 1978) illustrate $(\text{FeO} + \text{Fe}_2\text{O}_3)/(\text{FeO} + \text{Fe}_2\text{O}_3 + \text{MgO})$ vs. SiO_2 (F/FM vs. SiO_2) for several volcanic rock suites. If we assume that these curves represent the change in F/FM vs. SiO_2 brought about largely by fractional crystallization of basaltic magma, then the composition of the parent magma in terms of F/FM vs. SiO_2 is indicated by the low-silica ends of the curves. For the curves having corners, there is a progression in silica content of the presumed parent magma from about 47% to 52%. In light of the above discussion of Figs. 92, 93, and 94, the higher SiO_2 content for a parent magma may have resulted from significant initial fractionation of the primary magma at high pressure (e.g., 10 kbar). The early, subvertical part of each curve represents fractionation at low pressure without spinel as a precipitating phase, and the corner on each curve represents the beginning of crystallization of magnetite. The three curves without corners (A, C, and P) represent a series of magmas formed by fractional crystallization where high-pressure conditions prevailed to high silica contents.

AMPHIBOLE STABILITY IN A DIFFERENTIATED CALC-ALKALINE MAGMA CHAMBER: AN EXPERIMENTAL INVESTIGATION

Joseph L. Richey* and David H. Egglar

Ash flows associated with the formation of the caldera at Crater Lake, Oregon, provide an opportunity to investigate the processes leading to bimodal basalt-rhyolite associations. The occurrence of the ash flows indicates rapid expulsion from a shallow magma chamber, and the compositions, textures, and modes of the ash flows indicate that the magma was in

* Work carried out under a cooperative predoctoral fellowship program of the Geophysical Laboratory and the University of Oregon.

TABLE 22. Compositions and Modes of Rocks Used in Experiments

Oxide	Basaltic Andesite	Dacite	Rhyodacite
	Wt %		
SiO ₂	54.60	61.65	67.16
TiO ₂	1.07	0.67	0.55
Al ₂ O ₃	18.22	16.30	14.30
Fe ₂ O ₃ *	6.80	4.13	2.93
MnO	0.09	0.08	0.07
MgO	4.15	2.50	0.70
CaO	7.89	4.91	2.27
Na ₂ O	4.17	4.91	5.42
K ₂ O	1.08	1.86	2.72
P ₂ O ₅	0.26	0.14	0.10
H ₂ O ⁺	1.01	2.50	2.92
H ₂ O ⁻	0.17	0.29	0.18
Total†	99.51	99.94	99.32
	Mode (vol %)		
Cpx	5	2	0
Opx	3	3	5
Amph	25	2	1
Plag	25	8	12
Mt	<1	<1	<<1
Glass	42	85	82

* Total Fe as Fe₂O₃.
† Normalized to void-free.

the process of differentiating. The ash-flow deposits are characterized by a lower, crystal-poor zone of rhyodacite composition and an upper, crystal-rich zone of basaltic andesite composition. Pargasitic amphibole and plagioclase are the dominant phenocrysts throughout the ash-flow sequence. There is textural evidence, however (to be discussed below), that at least some of the amphibole is formed by reaction at sub-liquidus temperatures. To clarify the role played by amphibole in the differentiation process, the phase relations of three compositionally distinct samples from the ash flow (Table 22) were determined at 2 kbar total pressure under water-saturated and -undersaturated conditions. A pressure of 2 kbar was considered to approximate the pressure of the chamber. Water-undersaturated conditions were attained through use of a CO₂-H₂O vapor phase, produced by the

breakdown of oxalic acid (e.g., Eggler, 1972); the presence of the vapor phase also facilitated equilibration of the charges. The H₂O produced from the oxalic acid is partitioned between melt and vapor, and it is assumed to mix ideally in the vapor. The CO₂ is strongly partitioned into the vapor, necessitating only a small correction for CO₂ solubility in the melt (Holloway, 1976). Because the fugacity of H₂O can be related to the mole fraction of H₂O in the melt by the thermodynamic data of Burnham and Davis (1974), the amount of oxalic acid that must be added to the capsule to achieve a given concentration of H₂O in the melt can be calculated (Eggler, 1972). In subliquidus runs, where only small amounts of oxalic acid are added (H₂O in melt <~4 wt %), the percentage of glass in the run product must be known in order to calculate the amount of H₂O in the melt (Eggler, 1972).

In this study, the percentages of glass were determined by point-counting the run products. The H_2O contents of the melts are believed to be accurate to ± 0.2 wt %.

Samples were sealed in Pt95Au5 capsules and run in an argon-pressurized, internally heated pressure vessel. Run durations ranged from 5 to 22 hr, depending on run conditions and starting materials. Loss of iron to the capsules, determined by comparing the compositions of glasses quenched from above the liquidus with the bulk compositions (Table 22), was found to be at most 12%, relative. The f_{H_2} intrinsic to the gas apparatus was monitored by runs containing $Fe_2O_3 + H_2O (+H_2)$ or $NiO + H_2O (+H_2)$; the f_{O_2} was bracketed between HM and NNO buffer curves. Incipient oxidation of magnetite grain boundaries in some water-saturated runs on the ash flow samples is suggestive that f_{O_2} conditions were probably closer to the HM buffer, at least when pure H_2O was present.

Phase relations of the ash-flow samples were also determined at 1 atm under f_{O_2} conditions approximating the HM and QFM buffers, using CO_2-H_2 mixing apparatus. The effect of f_{O_2} on silicate liquidus is small, but the stability of magnetite is increased at increased f_{O_2} (Fig. 96). In all rocks, magnetite is not a near-liquidus phase at 1 atm. The orthopyroxene and clinopyroxene boundaries are essentially coincident and are shown as a single curve.

In Fig. 97 the phase relations for the basaltic andesite and dacite are shown as a function of H_2O content at 2 kbar total pressure. Water-saturation at 2 kbar is achieved at about 6.3% H_2O (Burnham and Davis, 1974). At water contents approaching that value in both rocks, the plagioclase-out, orthopyroxene-out, and clinopyroxene-out curves are nearly coincident, and the liquidus are essentially the same. The magnetite-out curve occurs at much lower temperatures. (Although small cubic opaque crystals are present up

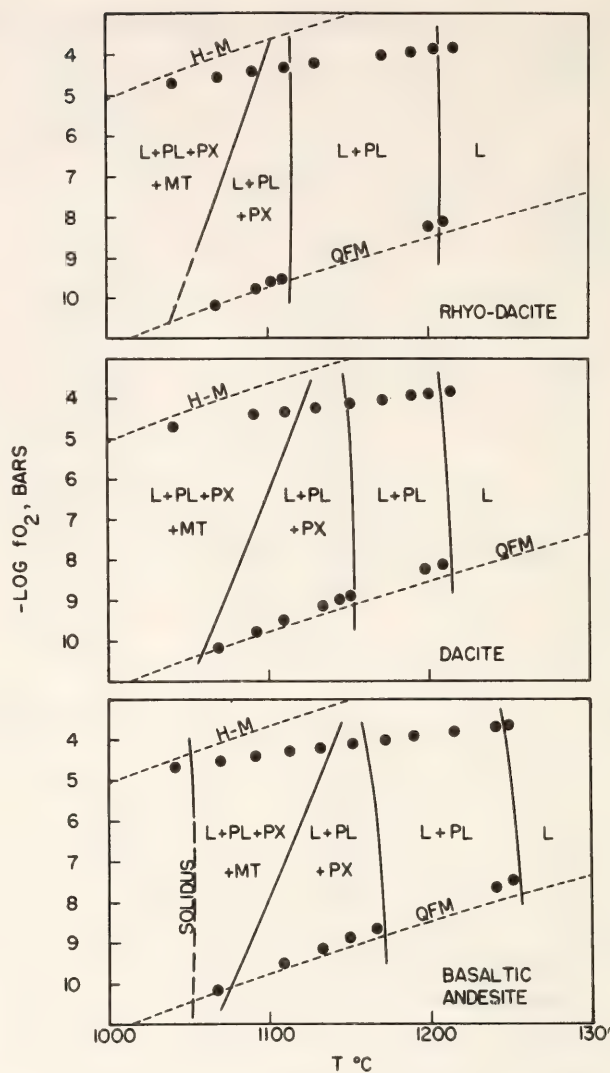


Fig. 96. Phase relations of rock compositions from Crater Lake ash flows as a function of f_{O_2} at 1 atm total pressure. Stability limits are dashed where approximately located. Locations of the HM and QFM buffer curves are shown with short dashes. Phases are: (L) liquid, (PL) plagioclase, (PX) orthopyroxene + clinopyroxene, and (MT) magnetite.

to 1080 $^{\circ}C$ in some runs, these crystals were concentrated near the edges of the charge and are interpreted to be quench products.) Amphibole is stable well below the liquidus in both rocks; the maximum temperature of amphibole stability in the basaltic andesite is about 975 $^{\circ}C$. At that temperature, a minimum H_2O content of 4.2% in the melt is required for amphibole stability. The melting curves at 2 kbar can be extended to higher total pressures, parallel to the analogous melting curves of Eggler (1972) and Eggler and Burnham

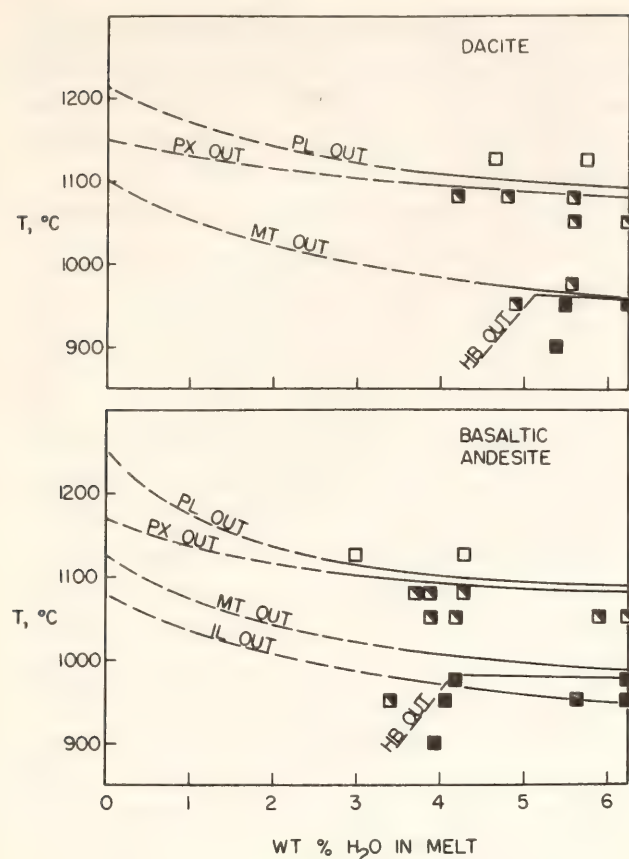


Fig. 97. Phase relations at 2 kbar of rock compositions from Crater Lake ash flows. Liquidi are dashed where approximately located. The H_2O contents of the liquids were calculated (see text). A vapor (CO_2-H_2O) was present in all runs.

(1973). (In those studies, amphibole was also observed to be stable to about $975^\circ C$ at 2 kbar.) Amphibole does not appear on the liquidus of the extended P - T diagram until about 10 kbar, and even then only at H_2O -saturated conditions. Similar configurations of melting curves have been observed for a Paricutin andesite (Eggler, 1972), a Mt. Hood andesite (Eggler and Burnham, 1973), and the Warner basalt (Yoder and Tilley, 1962).

From these data, it is clear that amphibole could not have been a liquidus phase of the basaltic andesite or dacite, at least for the conditions studied, and must have formed by reaction of the liquid with early-formed minerals. This conclusion is consistent with petrography of the rocks: some amphiboles in basaltic andesites near the top of the ash flow at Crater

Lake contain olivine cores, and there are unaltered, euhedral crystals of pargasitic amphibole present in aggregates of crystals of olivine, orthopyroxene, clinopyroxene, and plagioclase; the amphibole crystals are interpreted to have formed by a reaction relationship between the olivine and the liquid. (In none of the rocks examined have amphiboles been observed to break down to aggregates of other minerals, contrary to the hypothesis of Stewart, 1975.) Because amphibole was crystallizing at the time of eruption of the andesite and dacite magmas, the configuration of the amphibole-out curves (Fig. 97) can be used to limit the temperature of those magmas (at 2 kbar) to about $975^\circ C$ and to infer relatively high H_2O contents of the melts. Those conditions can be delimited further by comparison of compositions of phases, including glass, in the rocks with those in the experimental charges (as determined by electron microprobe analysis). A match can be found with products of the run on the basaltic andesite at $975^\circ C$ and 4.2% H_2O .

Phase relations of the dacite and the basaltic andesite are not consistent with hypotheses that they formed by fractionation of parents that contained amphibole, because neither rock has amphibole as a near-liquidus phase at pressures believed to exist in the magma chamber.

PRELIMINARY EXPERIMENTAL DATA BEARING ON THE MOBILITY OF H_2O IN CRYSTALLINE UPPER MANTLE

*Bjørn O. Mysen, Ikuo Kushiro, and
Toshitsugu Fujii**

Magmatic activity involving volatile species (e.g., H_2O , CO_2 , SO_2) is well documented by the occurrence of kimberlite and carbonatite and by the volatile content of glass inclusions in phenocrysts of volcanic rocks from island arcs (Irving

* Address: Geological Institute, University of Tokyo, Hongo, Tokyo 113, Japan.

and Wyllie, 1975; Anderson, 1975; Delaney *et al.*, 1977; Muenow *et al.*, 1977). Recently, material transport by ($\text{H}_2\text{O} + \text{CO}_2$)-rich fluids with resulting metasomatic alteration of mineral assemblages in the upper mantle has been suggested to explain apparent anomalies in major and trace element composition of mantle-derived rocks (Erlank, 1973; Aoki, 1974; Fyfe and McBirney, 1975; Erlank and Shimizu, 1977). In view of the evidence for metasomatism in the Earth's upper mantle, experimental determination of migration rates of volatiles in crystalline peridotite upper mantle is necessary. As a first step toward providing such data, the attempt has been made to measure the migration rate of H_2O as a function of at least some of the variables known to affect migration rates of volatiles through crystalline materials.

Garnet peridotite nodule 1611 (Nixon and Boyd, 1973a) from a Lesotho kimberlite was used as starting material. Grain sizes in the ranges 80–120 μm and 40–60 μm were used. These grain sizes were used to assess uncertainties in extrapolating experimental data obtained with materials in the 50–100 μm range to the grain size of peridotite in the upper mantle (perhaps >1 mm). The starting materials were heated at 1150°C with f_{O_2} buffered at the value of the QFM buffer for 12 hr before use to decompose hydrous minerals (phlogopite and serpentine on grain boundaries; F. R. Boyd, personal communication, 1976). This heat treatment did not alter the anhydrous major mineral assemblage of the sample.

The source of H_2O was synthetic serpentine grown from a finely ground mixture of MgO , SiO_2 (cristobalite), and tritiated H_2O at 450°C and 4 kbar for 5 days. The tritiated serpentine (20–30 mg) was placed under about 200 mg powdered peridotite in a sealed, 5-mm-O.D. gold capsule.

The experiments were carried out in a solid-media high-pressure apparatus (Boyd and England, 1960) using a glass-sleeved, tapered, $\frac{3}{4}$ "-diameter furnace

assembly described by Kushiro (*Year Book* 75, pp. 832–833). With this furnace assembly, the maximum temperature gradient along the 10-mm-long capsules was about 15°C.

Even at high pressure, the peridotite powder is likely to have some porosity. To eliminate such porosity, the samples were annealed for several hours (in some cases for days) prior to initiation of H_2O migration through the peridotite. The annealing process was conducted by subjecting the sample (peridotite + serpentine in the sealed capsule) to 400°–425°C at the pressure of a given experiment.

During the time of annealing a minute amount of tritiated serpentine breaks down. The H_2O thus released is distributed evenly throughout the sample during the annealing and probably combines with peridotite during the high temperature portion of the experiment to form amphibole.

After annealing, the temperature was raised above the breakdown temperature of serpentine, thus releasing H_2O . This H_2O combined with the peridotite minerals to produce rims 1–2 μm wide of amphibole (probably pargasitic hornblende; Mysen and Boettcher, 1975) on the grain boundaries. The H_2O in the amphibole rims contained radioactive ^3H and the distribution of amphibole in the sample after an experiment could be mapped on nuclear emulsions (Mysen and Seitz, 1975). The distance from the serpentine-amphibolitized peridotite interface to the amphibolitized peridotite-dry peridotite front was measured and the velocity of the amphibole replacement front could be calculated. It was found that this replacement velocity was a function of the annealing time when this time was less than several hours and in some experiments less than several days. The minimum annealing time required to eliminate this dependence was therefore determined for the various pressures of the experiments. The minimum run-time needed to reach this state decreases with increasing pressure (Table 23). Annealing

TABLE 23. Minimum Annealing Time as a Function of Pressure to Attain Independence of Migration Rate on Annealing Time

Pressure, kbar	Time, hr
15	40
20	20
30	12

at a higher pressure than that of an experiment was impracticable, however, because the samples tended to crack from expansion of the rock during decompression to the desired pressure.

If the process of amphibolitization of the peridotite results in a negative volume change of the rock, the appearance of amphibole may cause the sample to crack. Under such circumstances, the measured migration rate would probably be controlled by the rate of reaction to form amphibole, and the experimental results could not be applied with confidence to migration of H₂O in the upper mantle. Calculations based on molar-volume data from Burnham *et al.* (1969) and Robie and Waldbaum (1968) lead to the conclusion that a positive volume change (2–3%, relative) occurs during amphibolitization of peridotite and that pore space is not generated in the sample as the result of this volume change. Furthermore, if the replacement velocity were controlled by the amphibole reaction rate, a strong positive temperature dependence of the observed velocity would be expected. As will be further discussed below, there is no significant temperature dependence of this replacement velocity. This supports the contention that the replacement velocity is not controlled by the rate of growth of amphibole.

Finally, because the tracking of H₂O in the samples is based on the formation of amphibole on grain boundaries in the peridotite, the measured velocity is that of replacement, and not necessarily that of the velocity of the front of water. Hofmann (1972), for example, has com-

mented that this velocity will most likely be less than the fluid velocity itself.

The experiments were carried out in the temperature range of 650°–850°C, high enough to ensure the breakdown of all serpentine but low enough to avoid melting of the peridotite. Because small amounts of melt would soak up all available water in the immediate region of melting, the presence of small amounts of melt (1–2%) would appear on the beta-track maps as heavily exposed regions against the surrounding amphibolitized peridotite. It was found, for instance, that at 20 kbar, nodule 1611 begins to melt at 900 ± 10°C. Therefore no experiment was conducted above 850°C.

Runs of various durations were carried out at 20 kbar and 850°C. It can be seen from the data in Fig. 98 that the velocity of the replacement front does not vary with duration of the experiment. This observation, combined with the sharp

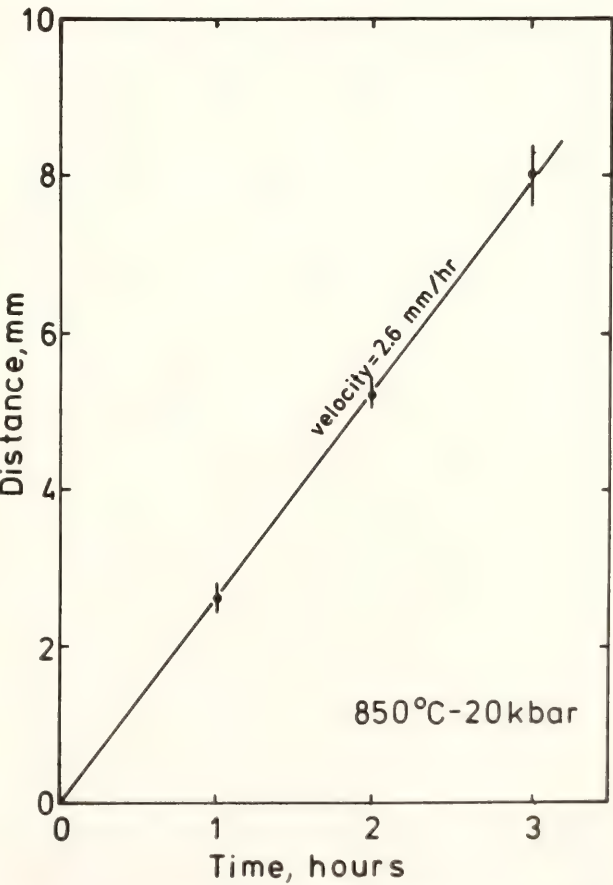


Fig. 98. Thickness of replacement zone at 850°C and 20 kbar as a function of run duration.

amphibolitization front, indicates that the transport mechanism is infiltration (Hofmann, 1972). In infiltration, the fluid and dissolved silicate components move along grain boundaries. The total area of grain surface per unit volume of rock may affect the replacement velocity. The grain size was increased from $\sim 50 \mu\text{m}$ to $\sim 100 \mu\text{m}$ to evaluate this possibility. No effect of grain size was observed in this size range (Fig. 99). It should be emphasized, however, that extrapolation over at least an order of magnitude is necessary to reach the grain size of upper mantle rocks.

The migration rate of the amphibolitization front depends strongly on pressure but appears independent of temperature, at least in the pressure and temperature ranges considered here (Fig. 99). The fugacity of H_2O ($f_{\text{H}_2\text{O}}$) increases rapidly

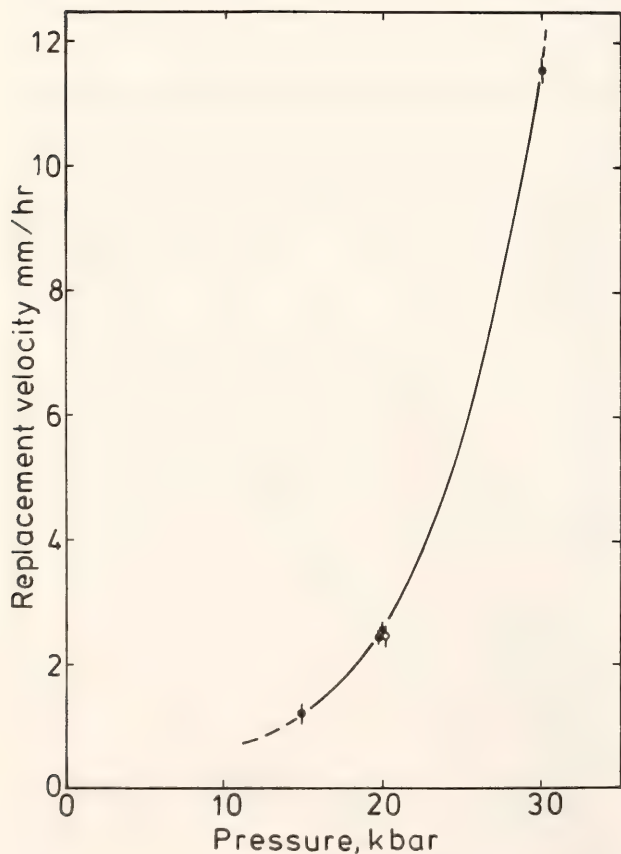


Fig. 99. Replacement velocity as a function of pressure, temperature, and grain size. Closed circles, 850°C ; Open circles, 650°C ; Square, 850°C but with $40\text{--}60 \mu\text{m}$ grain size.

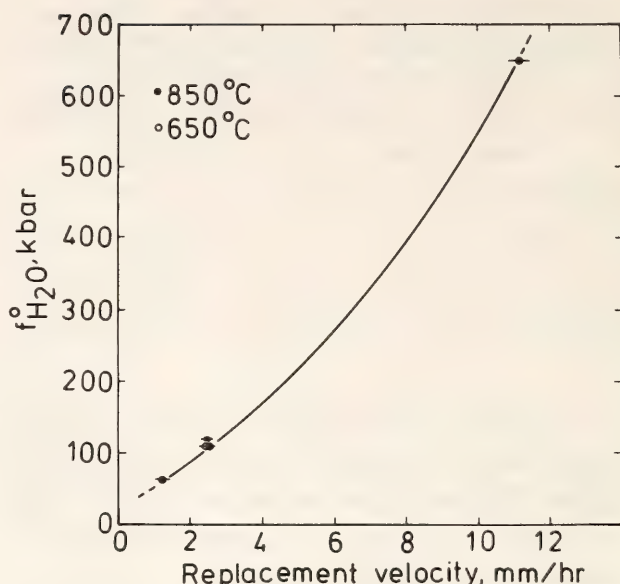


Fig. 100. Replacement velocity as a function of water fugacity ($f_{\text{H}_2\text{O}}$) corresponding to pure H_2O at the pressure and temperature of experiment.

with increasing pressure but is nearly independent of temperature under the physical conditions of these experiments (Sharp, 1962; Burnham *et al.*, 1969; Holloway *et al.*, 1971). Because $f_{\text{H}_2\text{O}}$ may be considered an effective water pressure and because it has been suggested (Hofmann, 1972) that pressure gradients are the driving forces in infiltration metasomatism, the replacement velocity has been plotted against $f_{\text{H}_2\text{O}}$ (Fig. 100). A nearly linear relation between these two variables is observed.

If it is assumed that the above considerations do not seriously alter the migration rate of H_2O , the present data lend support to models involving metasomatic redistribution of elements in the mantle. For example, garnet peridotite nodules found in kimberlites are of two distinct kinds. So-called sheared nodules are typically less depleted in low-temperature fusible components than granular nodules (Boyd, 1973; Nixon and Boyd, 1973). As a result, the garnet and clinopyroxene contents of the depleted nodules are lower than those of the fertile ones. At the same time, the granular nodules appear en-

riched in incompatible trace elements (Erlank and Shimizu, 1977; Shimizu, *Year Book* 73, pp. 954–961) over the sheared nodules. Notably, the sheared nodules appear to have equilibrated at greater depth in the mantle than the granular ones (Boyd, 1973). It is assumed that H₂O is bound in hydrous minerals such as phlogopite. A temperature change may result in phlogopite breaking down, thus releasing H₂O. It is visualized that the released fluid migrates through a zone of sheared peridotite followed by granular peridotite in the mantle. The fluid remains in equilibrium with both rocks during this process. This fluid is likely to dissolve alkalis and other incompatible elements preferentially over transition metals, alumina, and silica. Furthermore, Mysen (this Report) showed that there is no fractionation between individual REE by the fluid itself. Consequently, such a fluid in equilibrium with garnet peridotite bearing an unfractionated REE pattern will be enriched in light REE. The degree of enrichment will increase with increasing garnet content of the sheared peridotite. As such a fluid migrates into neighboring granular peridotite with lower garnet content than the sheared peridotite, the fluid will impose its REE patterns and alkali contents on the rock through which it migrates. At the same time, an REE pattern showing enrichment in the light REE will be developed. Enrichment in Rb in the fluid, for example, would result in enhanced Rb/Sr ratios of depleted granular peridotite compared with sheared peridotite in the upper mantle. Such observations were made by Erlank and Shimizu (1977). Furthermore, the enrichment in Rb over Sr also may result in more rapid growth of ⁸⁷Sr/⁸⁶Sr in granular peridotite than in the less depleted sheared peridotite. It is notable that Erlank and Shimizu (1977) found anomalously high ⁸⁷Sr/⁸⁶Sr in granular nodules containing presumed metasomatically grown phlogopite and K-rich richterite compared with other garnet peridotite

nodules in the Bulfontein pipe, South Africa.

THE ROLE OF DESCENDING PLATES IN THE FORMATION OF ANDESITIC MELTS BENEATH ISLAND ARCS.

Bjørn O. Mysen

Evidence from rocks in island arcs indicates an important role of H₂O in formation and evolution of magmas in such regions (e.g., Anderson, 1975; Muenow *et al.*, 1977). Furthermore, the trace element content of andesitic lavas indicates unusually large enrichments of large lithophile elements (LREE) in the source regions of such melts.

Most models for the formation and evolution of andesitic melts involve an important role of H₂O in affecting phase relations (see Boettcher, 1973, for a summary of these models). It has also been suggested that H₂O may also play a role in governing the trace element contents of andesitic melts (Jakes and Gill, 1970; Fyfe and McBirney, 1975; Kay, 1978).

Helgeson *et al.* (1978) calculated the pressures and temperatures along a descending slab beneath island arcs where dehydration of hydrated rocks of tholeiitic bulk composition might occur. The pressure and temperature ranges given by Helgeson *et al.* (1978) were 25–40 kbar and 400°–600°C, respectively. It should be noted that basalt + H₂O solidi are always at temperatures greater than 600°C to at least 40 kbar pressure (Robertson and Wyllie, 1971; Lambert and Wyllie, 1972; Allen *et al.*, 1975). Consequently, dehydration of the rocks that constitute the upper portions of descending plates would occur at depths ranging from 70 to 120 km without resulting in melting of the slab material. Provided that this fluid can migrate into the overlying peridotitic wedge from the slab itself—as also argued by Jakes and Gill (1970), Fyfe and McBirney (1975), and Kay (1978), and shown experimentally by

Mysen, Kushiro, and Fujii (this Report)—the trace element content of the overlying wedge may be affected. The expected effect on REE patterns of partial melts from a metasomatized peridotitic wedge overlying dehydrating basaltic rocks in the descending plate will be considered here by employing the vapor-crystal partitioning data of Mysen (this Report).

It is necessary first to derive an expression for calculation of element concentrations of the peridotite wedge overlying the descending plate after the metasomatic event. Bulk partition coefficients are defined as follows:

$$D_i^s = \Sigma(P_i^s/K_i^{v/xt}) = \frac{(C_i^{xt})^s}{(C_i^v)^s} \quad (1)$$

$$D_i^M = \Sigma(P_i^M/K_i^{v/xt}) = \frac{(C_i^{xt})^M}{(C_i^v)^s} \quad (2)$$

where P_i^s and P_i^M are modal proportions of phases in source rock (s) and metasomatized rock (M), respectively. The $(C_i^{xt})^s$, $(C_i^v)^s$, etc. are concentrations of element i in crystals and vapor. The partition coefficients,

$$K_i^{v/xt} = \frac{C_i^v}{C_i^{xt}},$$

where C_i^v and C_i^{xt} are weight ratios of element i in vapor and crystal.

From mass balance, for the source rock s the following equation can be derived:

$$(C_i^{xt})^s (1 - X_s) + (C_i^v)^s X_s = R_i^s \quad (3)$$

where X_s is the proportion of s that is converted to fluid. The R_i^s is the total content of element i in rock s .

For the metasomatized rock M the mass balance is:

$$R_i^M = R_i^D (1 - X_M) + (C_i^v)^s X_M, \quad (4)$$

where R_i^D and R_i^M are the concentrations of element i before and after the fluid

entered rock M . The term X_M is the proportion of fluid in rock M . If only a portion of the fluid (Y_v) remains in the metasomatized rock, Equation 4 becomes:

$$(C_i^{xt})^M (1 - Y_v X_M) + (C_i^v)^M Y_v X_M = R_i^M, \quad (5)$$

where $(C_i^{xt})^M$ and $(C_i^v)^M$ are the concentrations of i in crystals and coexisting vapor, respectively.

From Equations 1 and 3 an expression for $(C_i^v)^s$ can be derived:

$$(C_i^v)^s = \frac{R_i^s}{D_i^s - X_s(D_i^s - 1)}. \quad (6)$$

It follows from Equations 4 and 6 that the total content of element i , in metasomatized rock M is:

$$R_i^M = R_i^D (1 - Y_v X_M) + \frac{R_i^s X_M Y_v}{D_i^s - X_s(D_i^s - 1)} \quad (7)$$

TABLE 24. Compositional Data on Eclogite and Garnet-free Peridotite in Model Island Arc Environment

	SP1	GP1	E1	E4
<i>Wt % Oxide</i>				
SiO ₂	47.6	47.6	53.3	50.1
Al ₂ O ₃	2.5	2.5	5.1	12.7
MgO	47.3	47.3	20.8	24.2
CaO	2.6	2.6	20.7	13.0
<i>Modal Compositions</i>				
Ga	...	10.0	20	50
Cpx	10.0	10.0	80	50
Opx	30.1	20.0
Ol	56.4	60.0
Sp*	3.5
<i>REE Contents†</i>				
Ce	1	1	10	10
Sm	1	1	10	10
Tm	1	1	10	10

* Modal spinel evenly divided between Ol and Opx for calculation purposes.

† Relative to average chondrite.

M and vapor can be calculated:

$$(C_i^{xt})^M = \frac{R_i^D(1 - Y_v X_M) + \frac{R_i^s X_M Y_v}{D_i^s - X_s(D_i^s - 1)}}{(1 - Y_v X_M) + \frac{Y_v X_M}{D_i^M}} \quad (8)$$

$$(C_i^v)^s = (C_i^{xt})^M D_i^M \quad (9)$$

A case where spinel peridotite (SP1; see Table 24) overlies a dehydrating slab containing amphibole, clinopyroxene, and garnet is considered. Because $K_{\text{REE}}^{\text{Amph-Cpx}}$ is near 1 (Mysen, *Year Book* 76, pp. 558–564) the vapor-crystal partition coefficients of clinopyroxene and amphibole are nearly the same. Therefore, clinopyroxene + amphibole is considered as one mineral and referred to as Cpx in the following discussion.

Dehydration of an amphibole-rich rock of bulk composition similar to oceanic tholeiite is likely to occur in the pressure range 20–30 kbar, resulting in the rock eclogite. The fluid is considered to be in local equilibrium with both the dehydrating rock of eclogitic mineral assemblage and the peridotite. The amount of released fluid (X_s), the amount of fluid in SP1 after metasomatism (X_M), and the ratio of garnet to clinopyroxene in the eclogite will affect the extent to which the REE pattern of the spinel peridotite overlying the descending plate will be affected. In the following calculations the amount of released water is varied between 0.25 and 1.0 wt %. The amount of fluid in SP1 is also varied between 0.25 and 1.0 wt %, and the modal Ga/(Ga + Cpx) between 0.2 and 0.5 (Table 24). From the view point of modeling bulk compositions of oceanic basalt in CMAS, of the four compositions listed in Table 24, E4 is the most similar to basalt. The slab material is considered to have an unfractionated REE pattern prior to dehydration, with REE abundances equal to ten times that of average chondrite (Schmitt *et al.*, 1963, 1964). Such REE contents are typical for oceanic tholeiite (e.g., Frey *et al.*,

1974). In an open system where H_2O can move freely, the value of Y_v (Equation 7) is less than 1. Lowering of Y_v to values less than 1 would result in a shift of absolute REE abundances of the metasomatized peridotite to lower values. It is assumed, however, that as H_2O migrates into the spinel peridotite and the peridotite begins to melt, all available H_2O will dissolve in the melt. Consequently, the system is effectively closed to H_2O and $Y_v = 1$.

The REE patterns of metasomatized spinel peridotite SP1 are shown in Fig. 101. It can be seen that an increasing proportion of garnet in the source rock results in a slight increase in the relative light-REE enrichment of SP1. A lowering of the proportion of fluid in the source rock (X_s) relative to the proportion of fluid in the metasomatized rock results in a slight increase in light-REE enrichment

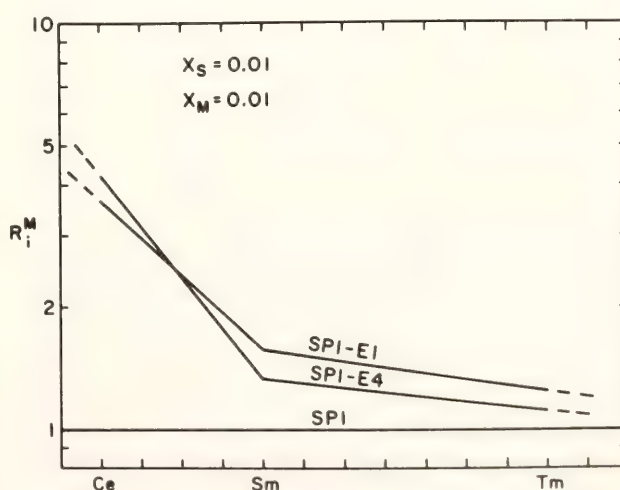


Fig. 101. REE patterns of metasomatized spinel peridotite as a function of garnet content of source rock. In this figure $X_s = 0.01$, $X_M = 0.01$, $Y_v = 1$.

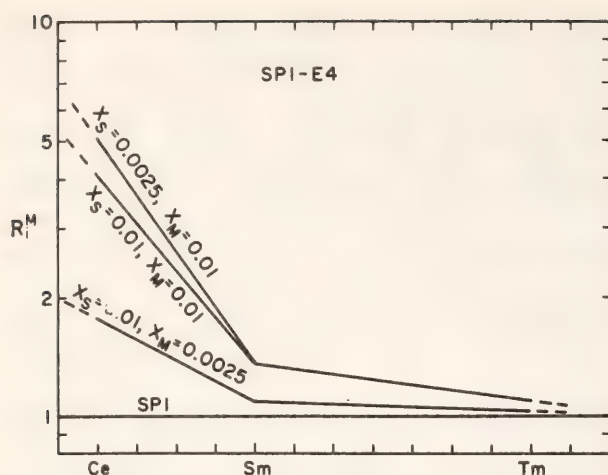
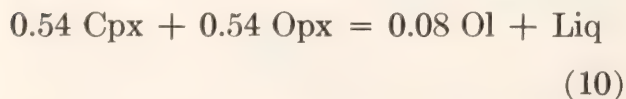


Fig. 102. REE patterns of SP1 after metasomatic alteration by fluid from source rock E4 as a function of proportion of fluid in source rock (X_s) and metasomatized rock (X_M).

of SP1 (Fig. 102). Lowering of X_M results in a more rapid reduction of degree of light-REE enrichment, however (Fig. 102). The latter case would be encountered if the total mass of SP1 exceeds that of the eclogite source, whereas in the former case ($X_s < X_M$) the mass of eclogite source is less than that of SP1 that is metasomatized.

Partial melts of similar major element composition derived from SP1 before and after metasomatism would have different REE patterns. In Fig. 103, the compositions of partial melts from SP1 and GP1 (where GP1 is garnet peridotite of similar bulk composition as SP1) with an unfractionated chondrite-normalized REE pattern equal to unity are compared with the patterns for partial melts derived from metasomatized SP1. The stoichiometry of the equation describing the melting of garnet-free peridotite is based on data of Kushiro (1969) as derived by Mysen (*Year Book 76*, pp. 545–550):



The equation describing melting of garnet peridotite is:

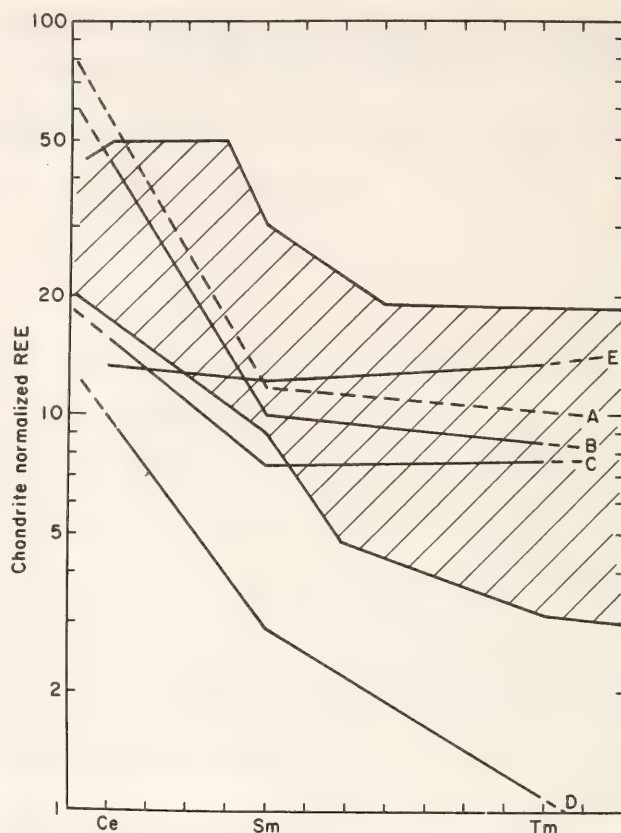
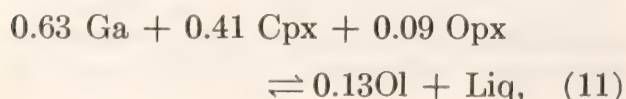


Fig. 103. REE patterns of partial melts from SP1 and GP1 compared with range of REE abundances in island arc andesite (data from: Gill, 1974; Kay, 1977; Yajima *et al.*, 1972; Thorpe *et al.*, 1976). Curve A: 5% accumulated fractional melt from SP1-E4 with $X_s = 0.0025$, $X_M = 0.01$. Curve B: Same as A, but with 10% melt. Curve C: Same as B, but with $X_s = 0.01$, $X_M = 0.0025$. Curve D: 5% partial melt from unaltered GP1. Curve E: 5% partial melt from unaltered SP1.

with crystal-liquid partition coefficients for REE from Mysen (*Year Book 76*, pp. 558–564)*. The liquid compositions are those of an accumulated fractional melt calculated with the formulations of Shaw (1970). The use of a batch-melting model does not significantly affect the results. In

* It should be noted that in this article it was incorrectly stated that Shaw (1970) considered only modal melting, and that his formulations could not be applied to melting of rocks. Shaw (1970) did in fact derive formulations that describe the element distribution between partial melts and coexisting crystals provided that the stoichiometry of the equations describing melting, initial modal compositions of the rock, its trace element content, and crystal-liquid partition coefficients are known.

Fig. 103, 5% and 10% melting ($F = 0.05$ and 0.10 , respectively) are considered.

Metasomatic alteration of the REE contents of spinel peridotite source rock for andesitic melts results in a light-REE enrichment of this rock that is so great that partial melts from such a rock would be more enriched in light REE and also have higher absolute REE abundances than would partial melts from garnet peridotite not metasomatically altered prior to melting (Fig. 103).

The similarity of the calculated patterns and those for andesite in island arcs is striking (Fig. 103). It is concluded, therefore, that metasomatized spinel peridotite that derived its H_2O from dehydration of a descending oceanic plate having an eclogitic mineral assemblage is a likely model for andesitic formation in island arcs. The model leads to agreement between both REE data and information on phase equilibria of wet peridotite under the appropriate pressure conditions.

SEQUENCE AND HOMOGENEITY OF LAVAS BASED ON THERMAL MELTING MODELS

H. S. Yoder, Jr.

The processes by which preexisting rocks are melted in the mantle are probably manifold (Yoder, 1976, pp. 60–61). Each possible process involves specific constraints that may affect the compositional range of liquids produced, the sequence in which the magmas of different composition are moved into or on the crust, and the homogeneity of the magmas. Two extreme and highly simplified cases are analyzed semiquantitatively here to illustrate some of the possible types of constraints that are imposed by the melting process. In the first case heat is conducted from a hot mass depleted of its basaltic constituents into *undepleted* crystalline mantle.* In the second case the heat is obtained internally from an un-

depleted crystalline diapir rising into a *depleted* crystalline mantle (cf. Ramberg, 1972).

Hot-Plate Process

Consider in Fig. 104 a heat source emplaced instantaneously beneath an undepleted peridotite (e.g., Ol + Opx + Cpx + Gr) initially at a temperature appropriate to a continental geotherm, 1100°C . The temperature at the interface, at a depth of 130 km, is maintained at 1800°C . The nature of the heat source is not specified: it could be a sill or diapir of crystalline peridotite completely depleted of its basaltic constituents (e.g., Ol + Opx) and of sufficiently large dimensions and high thermal conductivity to sustain the high temperature at the

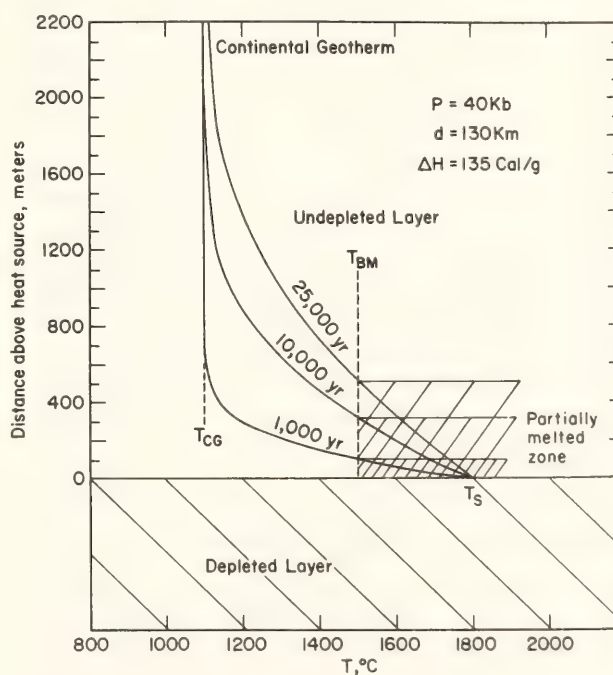


Fig. 104. Hot-plate model of magma generation. Heat is conducted from a hot (1800°C), depleted peridotite to an undepleted garnet peridotite at the temperature on a continental geotherm (1100°C) appropriate for a depth of 130 km. The thickness of the partially molten zone developed after 1,000, 10,000, and 25,000 years is illustrated. Temperature profiles calculated by T. N. Irvine by means of Heat Flow Program IV (Irvine, 1970, p. 1047, equations 27 and 28). The scale of the figure is not adequate to illustrate the abrupt change in slope of the temperature profile at the top of the partially melted layer.

* Compare with Holmes' (1931) hypothesis of refusion of preexisting crustal rocks by heat transfer from a convecting molten mass below.

contact. An inflection in the geotherm such as that proposed by Boyd (1973) would be adequate for developing a magma in an overlying undepleted peridotite because of the implied differential heat flux. The large contrast of temperature, 700°C, between the depleted and undepleted layers may not be wholly realistic; however, it is necessary to choose a heat source with a temperature sufficiently above the beginning of melting for the production of an adequate volume of magma in the absence of volatiles and in a reasonable time period. Because the beginning of melting of anhydrous, undepleted garnet peridotite, T_{BM} , is assumed to be about 1500°C at that pressure, melting will begin at the interface. Based on the behavior of the Fo-Di-Py system at that pressure (Davis and Schairer, *Year Book 64*, p. 124) and that of a natural garnet peridotite (PHN 1611) at 35 kbar (Mysen and Kushiro, 1977), the melting process is essentially invariant. All major crystalline phases persist with liquid at a constant temperature or within a very small temperature interval until about 30% melting is achieved. As heat is transferred from the depleted layer to the undepleted layer, a melt front advances upward with 30% liquid at the leading edge and increasing amounts downward to the interface where about 50% melting is achieved, according to the assumed phase relations.* The higher thermal conductivity

* It is assumed that the heat source of depleted peridotite is static after emplacement even though its density is less than that of the overlying undepleted material at a lower temperature and having a higher initial bulk density. Based on the density data of Boyd and McCallister (1976) for each rock type, 3.30 and 3.39 g cm⁻³ respectively, and the density of liquid basalt at 40 kbar, 3.05 g cm⁻³—an extrapolation of the data of Fujii and Kushiro (*Year Book 76*, p. 423; unpublished data, 1978)—the density of the undepleted peridotite containing 26% liquid would just equal that of depleted peridotite. For this reason the partially melted zone (30–50% liquid) would remain above the hot plate. The consequences of the depleted peridotite and its partially melted border rock rising through an undepleted mantle will be evident after consideration of the second melting model.

in the partially melted zone was neglected. The zone of melting being generated advances 100 m in 1000 years, reaches about 300 m after 10,000 years, and attains half a kilometer after 25,000 years.

Attention is called to two major features that are not strongly dependent on the values assigned to the parameters. There is a thermal gradient through the melt; hence, if there is no mixing, the liquid composition, including the abundances of the trace elements present, would be expected to vary accordingly. Because the composition of the liquid at the top is fixed by the invariant point and that at the bottom is fixed by the high temperature assumed to be constant, the range of magma compositions remains constant; only the volumes change with time. In addition, the higher temperature liquid formed at the more advanced stage of melting is at the *bottom* of the partially melted zone, and the invariant-like liquid is at the top. The large amount of melt at the advancing edge and the heterogeneity of melt are noteworthy and will be discussed further after presentation of a second highly simplified melting model.

Diapiric Process

A popular model (Fig. 105) for the generation of magma involves the special circumstances for initiating a diapir.* If an undepleted garnet peridotite diapir rises in depleted peridotite to a depth where the temperature is equal to the solidus, invariant-like melting of the undepleted garnet peridotite begins. Heat is conserved adiabatically by converting

* There is considerable debate (e.g., O'Hara, 1975) on how an undepleted crystalline mass (density = 3.39 g cm⁻³) will rise through a depleted mantle (density = 3.30 g cm⁻³) based on the density data of Boyd and McCallister (1976). A temperature contrast of 750°C is required just to equalize those densities. After the diapir has reached its solidus temperature, the formation of liquid with a density of about 3.05 g cm⁻³—extrapolated from the data at high pressure of Fujii and Kushiro (*Year Book 76*, p. 423; unpublished data, 1978)—may be adequate for the partially melted undepleted mass to become buoyant.

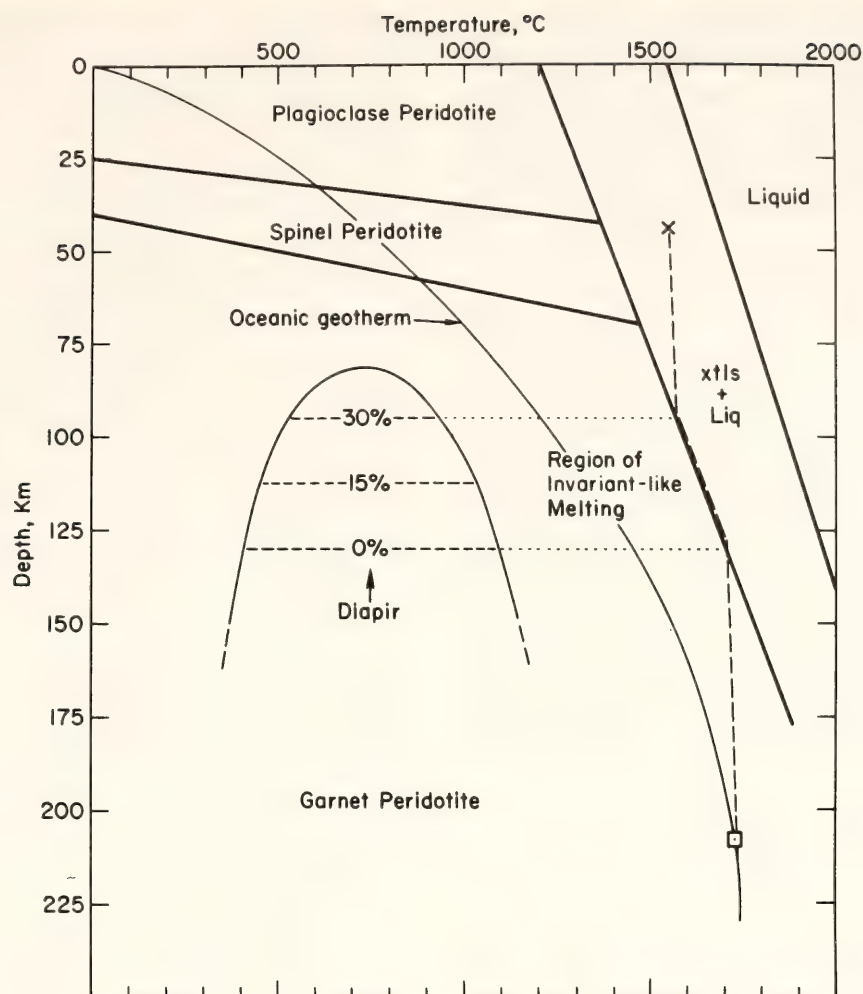


Fig. 105. Diapiric model of magma generation. The diapir of undepleted garnet peridotite rises from about 210 km along an adiabat. At 130 km melting begins and the heat of melting is derived internally. Invariant-like melting is completed after a rise of 35 km where 30% of the rock is melted. That amount of melting is achieved in a minimum of 350,000 years if the rate of rise is 10 cm/yr or a minimum of 3.5 m.y. if the rate of rise is 1 cm/yr. The amount of rise and the time will be greater depending on the heat losses to the environment.

$C_p \Delta T \rightarrow \Delta H_m$. The ΔT is the difference in temperature between that of the solidus and that of the projected adiabat from the point of origin of the diapir. For this model the point of origin is assumed to be on an oceanic geotherm. Heat losses to the environment would be important especially in the time required for the melting event (see below). The amount of melt produced depends directly on the rise of the diapir and the heat losses to the host peridotite. For example, if half of the heat available for melting is lost to the environment then the amount of liquid produced is reduced by about half. In other words, for such heat losses the mass would have to rise twice the distance

to produce the same amount of melting in the absence of heat conduction to the environment. The invariant-like melting is completed at about 30% of the mass and the diapir will have risen 35 km during the melting interval, assuming no heat loss to the environment. (The temperature contrast between the partially molten diapir and its environment is about 375° at this stage.) Further rise would produce additional melting; one major phase will have been consumed and the temperature of the upper portion of the diapir will decrease at a slower rate as the liquid composition changes along a univariant curve, for example.

The principal deductions from Fig. 105

are that the concentrations of the major components of the liquid are roughly the same throughout the interval of 0–30% melting except for variations due to the effect of pressure on the composition and temperature of the invariant point. At shallower depths where melting exceeds 30%, the liquid composition changes at a greater rate. In general, the greater degree of melting is at or close to the *top* of the mass, whereas the smallest degree of melting is at the bottom. If the rate of rise of the diapir were fast, such as 10 cm/yr, it would take a minimum of about 350,000 years to complete the invariant-like stage of melting. At a slower rate of rise of 1 cm/yr, it would take a minimum of 3.5 m.y. to obtain 30% melting. The duration of the melting event would be extended depending on the heat losses to the environment.

Discussion

The contrast is evident between the two models having reversed sequences of melt composition with regard to depth. If liquid is removed from the top, the daughter-like magma (representing the smaller degree of melting) will be intruded or extruded first from the hot-plate model, whereas the more parental-like magma (representing the greater degree of melting) will be first from the diapiric model. It would now appear to be useful to study the sequences of magmas produced in a single thermal event, giving due regard for the fact that perhaps only a fraction of the magma generated is extruded—half, according to Swanson (1972). It may be possible to deduce the heating process from the sequence of magma compositions intruded and extruded.

These two extreme models, and the more complex types that can be simulated, emphasize the problems in understanding the production of large volumes of homogeneous magma (e.g., Columbia River Basalt: 200,000 km³) and the sequences of magmas believed to be related by dif-

ferentiation. It is improbable that large volumes of homogeneous magma will obtain in the light of a Rayleigh-depletion scheme except from an infinite source or by remixing in a subsidiary reservoir. Melting completely a source rock of the appropriate composition only delays dealing with the origin of the source. Fractional melting at an invariant point does indeed yield magma of relatively constant composition (except trace elements); however, the system supplying new source material to a fixed heat source greatly restricts the rate of production.

Because the magmas generated in both of the extreme models have compositional gradients, it is necessary to appeal to thermal convection to mix the magma. The continuity of melt between mineral grains in a partially molten rock is demonstrated in the laboratory by the dramatic increase in electrical conductivity with melting (Presnall *et al.*, 1972; Murase, Kushiro, and Fujii, *Year Book* 76, pp. 416–419). These measurements as well as the observed distribution of glass after quenching a partially molten peridotite (Arndt, 1977) indicate that the rock is permeable; the liquid can therefore convect (and escape) if other conditions are appropriate. In addition, the very low viscosity of basaltic melt at high pressures (Kushiro *et al.*, 1976) is conducive to convective mixing in the source region, and the gradients in temperature and composition would be moderated. The convective cells, however, may be multiple and of limited thickness, as observed in laboratory experiments by Turner and Chen (1974). The conditions required for the complete mixing of a large volume of liquid contained in a partially melted source rock have not yet been ascertained, but the problem is amenable to analysis. The homogenization problem resulting from magma generation in thermal and pressure gradients has many ramifications, and one can expect considerable difficulty in relating the trace element sequence, for example, to a specific differentiation process.

PETROGENETIC GRID FOR AMPHIBOLITES
FROM THE POST POND AND
AMMONOOSUC VOLCANICS

Frank S. Spear

The phase relations of hornblende-bearing amphibolites have been determined in four separate outcrop areas of the Post Pond and Ammonoosuc Volcanics, New Hampshire and Vermont. Each outcrop area is small enough so that all the rocks from a given area experienced the same T and P during metamorphism. The phase relations at each outcrop re-

present a distinct metamorphic facies type for amphibolites. The chemical reactions relating the facies types have been inferred using Schreinemaker's analysis.

The rocks from the Mt. Finish quarry are predominantly leucocratic plagioclase + quartz \pm hornblende \pm garnet \pm chlorite \pm cummingtonite-bearing rocks (Fig. 106A), and all these phases are found in several samples. In some samples both albite and oligoclase are found. No highly aluminous phase has been found in these amphibolites but it is assumed that the Al_2O_3 -saturated phase would be an Al_2SiO_5 polymorph (probably kyanite) at

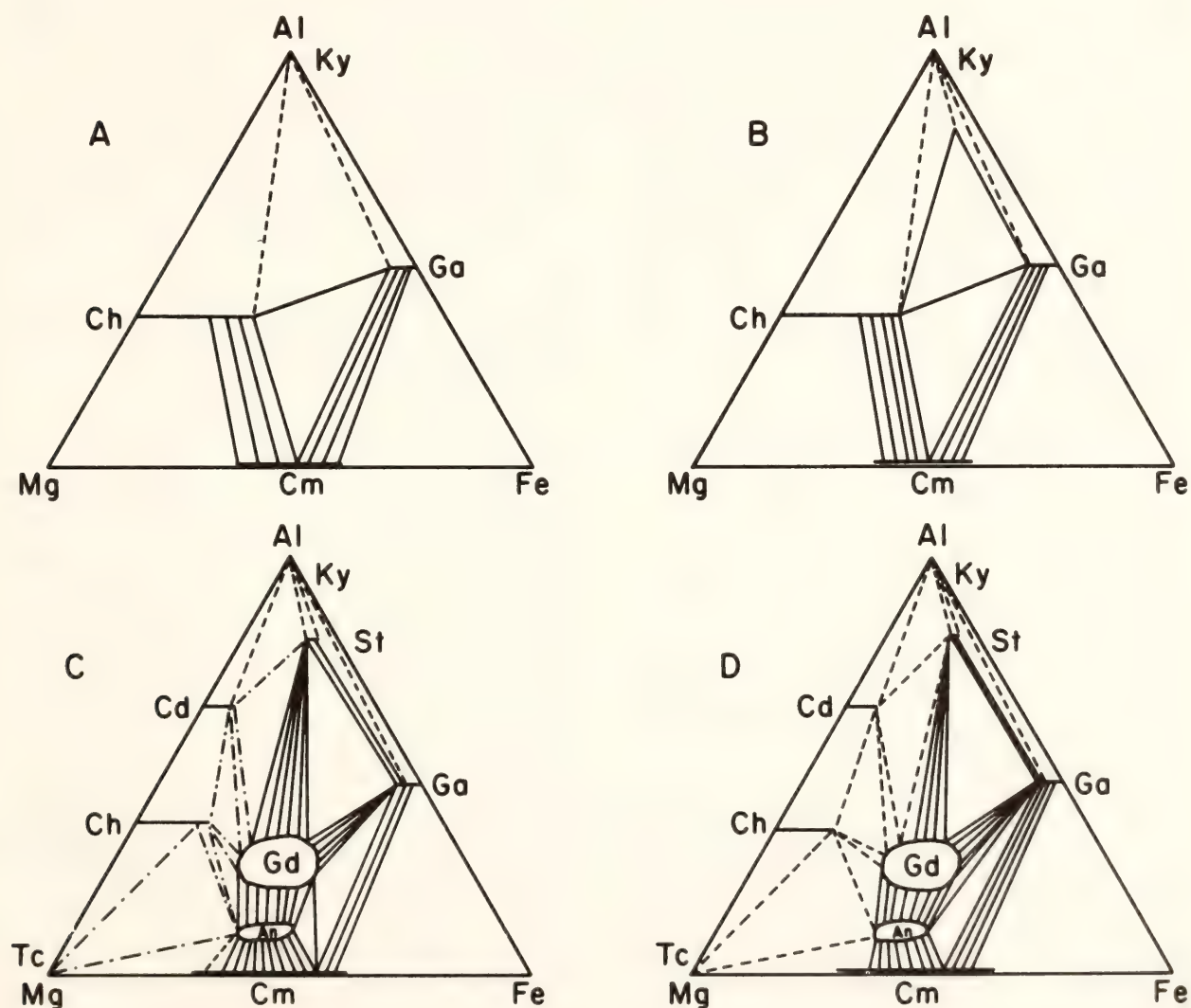
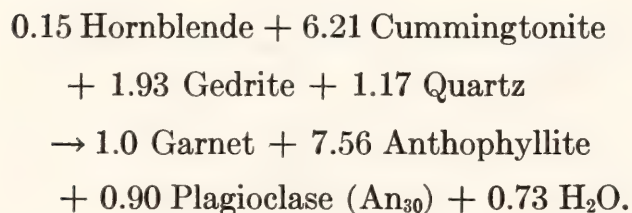


Fig. 106. Generalized phase relations for amphibolites from (A) Mt. Finish quarry, (B) Wilder Dam quarry, (C) Wilnot Mtn., and (D) U.S. Rt. 5. All assemblages are projected from quartz, plagioclase (An_{30}), hornblende, and H_2O . Plotting coordinates are $\text{Al} = (\text{Al} - 1.119\text{Ca} - 1.377\text{Na})/\text{M}$, $\text{Fe} = (\text{Fe} - 1.351\text{Ca} + 0.578\text{Na})/\text{M}$, and $\text{Mg} = (\text{Mg} - 1.217\text{Ca} + 0.522\text{Na})/\text{M}$ where $\text{M} = (\text{Al} + \text{Fe} + \text{Mg} - 3.687\text{Ca} - 0.277\text{Na})$. Heavy lines are observed assemblages, dashed lines are inferred assemblages, dot-dashed lines are observed assemblages without hornblende.

this grade. Staurolite is found in amphibolites approximately 10 km to the north in the Wilder Dam quarry (Fig. 106B). Staurolite may be stable in the Mt. Finish region and not observed owing to the absence of appropriate bulk compositions.

The phase reactions are most completely represented in the Wilmot Mt. area (Fig. 106C) because of the wide range of bulk compositions present. Cordierite, gedrite, and anthophyllite are common in the rocks, and the stable chlorite is Mg-rich. Approximately 2 km to the east, along U.S. Route 5, the phase relations are as displayed in Fig. 106D (see also Spear, *Year Book* 76, pp. 613–619). Here, the stable tie line is anthophyllite-garnet rather than gedrite-cummingtonite as is found in the Wilmot Mt. assemblages. The Mg-rich portion of the diagram is assumed to be identical to that of Wilmot Mt. The reaction between the Wilmot Mt. assemblages (Fig. 106C) and the U.S. Rt. 5 assemblages (Fig. 106) is observed in the field and has been modeled using measured mineral compositions:



The left side of the reaction is more hydrated than the right side, implying that the right side of the reaction (U.S. Rt. 5) is higher metamorphic grade.

There is a large gap in the phase relations between those at the Wilder Dam quarry (Fig. 106B) and Wilmot Mt. (Fig. 106C). The phase relations at Wilmot Mt. differ from those at Wilder Dam in that (1) gedrite, anthophyllite, and cordierite are present, (2) chlorite is more Mg-rich, and (3) the stable tie lines are between gedrite and the more aluminous phases (cordierite and staurolite), rather than between chlorite and garnet. The exact sequence in which gedrite and

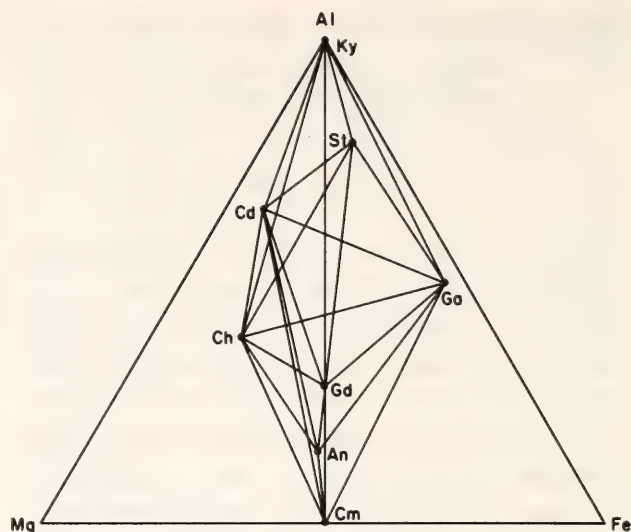


Fig. 107. Generalized mineral compositions used in construction of Schreinemaker net. Mineral compatibilities are indicated by solid lines. Abbreviations are: Ky = kyanite, St = staurolite, Cd = cordierite, Ga = garnet, Ch = chlorite, Gd = gedrite, An = anthophyllite, Cm = cummingtonite. Plotting coordinates are the same as in Fig. 106. All assemblages include quartz, hornblende, and plagioclase (An₃₀). Reactions involving talc have not been considered.

anthophyllite appear, and discontinuous reactions occur, will depend on the specific *P-T* path that a rock experiences.

To explore the possible sequences of discontinuous reactions connecting the Wilder Dam to the Wilmot Mt. assemblages, a Schreinemaker net (Fig. 108) has been constructed using the phase compositions shown in Fig. 107. Several assumptions inferred from the measured phase compositions from Wilmot Mt. (Fig. 106C) have been made about the plotting coordinates of the idealized mineral compositions in Fig. 107: (1) Staurolite is more Mg-rich than coexisting garnet and more Fe-rich than coexisting gedrite, and so it plots inside the three-phase triangles garnet-gedrite-kyanite, garnet-cordierite-kyanite, and garnet-chlorite-kyanite. (2) Anthophyllite is more Mg-rich than coexisting gedrite and cummingtonite; hence it plots within the three-phase triangles chlorite-gedrite-cummingtonite, and cordierite-gedrite-cummingtonite. (3) Gedrite is more Fe-rich than coexisting chlorite and more

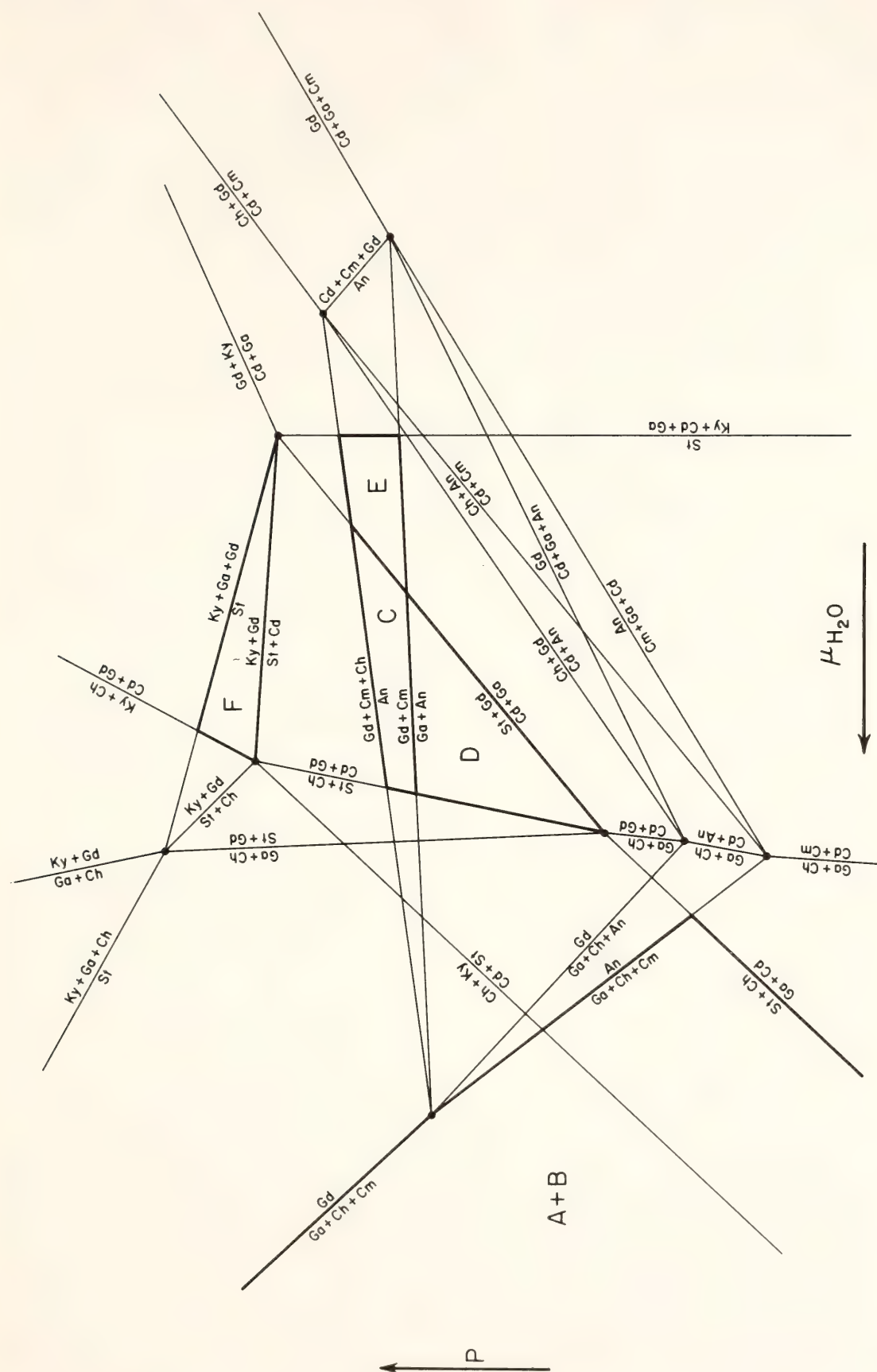


Fig. 108. Generalized P vs. $\mu_{\text{H}_2\text{O}}$ petrogenetic grid for amphibolites in the system Si-Al-Ca-Na-Fe-Mg-H₂O. Some of the reaction slopes have been distorted for clarity in reading but topological relations have been maintained. Heavy lines demarcate regions A + B (Mt. Finish-Wilder Dam), C (Wilmut Mtn.), D (U.S. Rt. 5), E (Stout, 1972), and F (Robinson and Jaffe, 1969). Abbreviations as in Fig. 107. Note that the grid is drawn with $\mu_{\text{H}_2\text{O}}$ increasing from right to left so that T will increase from left to right.

Mg-rich than coexisting garnet, and plots inside the three-phase triangles chlorite-garnet-cummingtonite and chlorite-garnet-anthophyllite.

These assumptions are significant because the chemical reactions responsible for the appearance or disappearance of a phase are dictated by the mineral compositions. It is assumed that kyanite and staurolite do not coexist with anthophyllite or cummingtonite; hence only 12 out of a possible 56 invariant points are stable. Out of these 12, only 9 stable points could be included in an internally consistent net.

The P vs. $\mu_{\text{H}_2\text{O}}$ Schreinemaker's net presented in Fig. 108 was constructed using ΔV of reactions and the stoichiometric coefficients of H_2O in the reactions to determine the slopes. At constant temperature, H_2O is evolved with decreasing $\mu_{\text{H}_2\text{O}}$. Inasmuch as H_2O is evolved with increasing T in a dehydration reaction, the topology of this diagram should be similar to that of a P - T grid.

At values of $\mu_{\text{H}_2\text{O}}$ greater than those bounded by the reactions $\text{Ga} + \text{Ch} + \text{Cm} = \text{An}$ and $\text{Ga} + \text{Ch} + \text{Cm} = \text{Gd}$ and at pressures above those bounded by the reaction $\text{St} + \text{Ch} = \text{Ga} + \text{Cd}$ (region $A + B$), facies types similar to those of the Wilder Dam and Mt. Finish areas are found. The specific facies type cannot be isolated because assemblages involving cordierite are absent. In the region marked C in Fig. 108 is the facies type similar to that found on Wilmot Mt., and the facies type similar to that found at the U.S. Rt. 5 locality is marked with the letter D . It is evident from the diagram that the observed change in mineral facies can be accomplished through a continuous increase in metamorphic grade, starting at low P and a high $\mu_{\text{H}_2\text{O}}$ in the Wilder Dam region and steadily changing these values to the U.S. Rt. 5 locality. The actual P - $\mu_{\text{H}_2\text{O}}$ trajectory will require knowledge of the intermediate phase relations.

It is worth noting that there is only a small P - $\mu_{\text{H}_2\text{O}}$ region where four amphi-

boles (anthophyllite + gedrite + cummingtonite + hornblende) are stable (the long, narrow region bounded by the reactions $\text{Gd} + \text{Cm} + \text{Ch} = \text{An}$, $\text{Gd} + \text{Cm} = \text{Ga} + \text{An}$, and $\text{Cd} + \text{Cm} + \text{Gd} = \text{An}$). This limited stability field, in addition to the fact that four-amphibole assemblages are restricted to a narrow bulk composition range, explains why these assemblages are rare in nature.

Multiple amphibole assemblages reported by Stout (1972) contain the association cordierite + garnet (+ staurolite?) and gedrite + anthophyllite + cummingtonite (+ hornblende?), and hence crystallized at lower $\mu_{\text{H}_2\text{O}}$ (higher T) than the Wilmot Mt. and U.S. Rt. 5 assemblages (Fig. 108, area E). The same conclusion was reached on independent grounds by Spear (*Year Book* 76, p. 619). Amphibole assemblages reported by Robinson and Jaffe (1969, Fig. 12) from the Orange area, New Hampshire and Massachusetts, contain an Al_2SiO_5 polymorph + gedrite + staurolite similar to the facies type in the region marked F in Fig. 108, and are thus representative of higher P than those from Wilmot Mt.

SODIUM TRIOCTAHEDRAL MICA: A POSSIBLE NEW ROCK-FORMING SILICATE FROM THE POST POND VOLCANICS, VERMONT

Frank S. Spear, Robert M. Hazen and Douglas Rumble III

A sodium, trioctahedral, layer silicate intermediate in composition between talc and $\text{Na}_2(\text{Mg,Fe})_6\text{Al}_2\text{Si}_6\text{O}_{20}(\text{OH})_4$ has been discovered in the Post Pond Volcanics, in Vermont. The mineral is similar optically and chemically to biotite but contains an excess of Na over K as the alkali cation. To the authors' knowledge, there are no published reports of a mineral similar in optical, physical, x-ray, or chemical properties and therefore this mineral may be a new rock-forming silicate. Verification of the phase as a new mineral by the International Mineralogical Association is

pending, and in this communication the descriptive name Na-biotite will be used.

Several samples containing Na-biotite were collected from the Ordovician Post Pond Volcanics in the southwest corner of the Mt. Cube Quadrangle, New Hampshire and Vermont. The samples come from the kyanite zone approximately 20 m below the Siluro-Devonian unconformity. The rocks are typically medium grained (average grain size is approximately 0.5 mm) and include the minerals quartz, cordierite, gedrite, anthophyllite, chlorite, talc, Na-biotite, K-biotite, plagioclase (An_{10-30}), rutile, and apatite. The amphiboles (gedrite and anthophyllite) exist as discrete grains and as mutual intergrowths, and some are slightly retrograded to chlorite.

Optical, Physical, and Chemical Properties of Na-Biotite

The Na-biotite was discovered during routine electron microprobe analysis of biotites from the Post Pond Volcanics. In the examples reported here, the Na-biotite is so closely associated with either ordinary K-biotite or talc that it has been possible to determine only gross physical characteristics. Under the petrographic microscope a single biotite-like phase is observed to have the typical "bird's eye maple" extinction characteristic of non-brittle micas. Pleochroism is strong and is similar to K-biotite; α is colorless or pale brown, and β and γ are dark brown. On close examination the color of the Na-biotite can be seen to be slightly lighter than the K-rich biotite; coexisting talc is pale brown. In addition, the extinction of Na-biotite is slightly undulose, whereas the ordinary K-biotite shows no such texture. Indices of refraction for Na-biotite are similar to those of K-biotite: $n_\beta \approx n_\gamma = 1.608 \pm .002$ and $n_\alpha = 1.544 \pm .004$, $\delta \approx 0.06$ and $0^\circ < 2V < 5^\circ$.

Single crystals of Na-biotite are irregular basal cleavage plates of typical mica habit. Twinning is observed in single-crystal photographs with com-

position plane (001) and twin axis $[310]$, as is typical with other biotites. Na-biotite, K-biotite, and talc form epitaxial intergrowths on the (001) plane.

The chemical compositions of coexisting Na- and K-biotites and talc, as determined by electron microprobe analysis, are given in Table 25. The Na- and K-biotites are relatively homogeneous in composition, both within a single grain and from grain to grain. The highest Na_2O content measured in an Na-biotite from this rock is 3.59 wt %, and there appears to be an inverse relation between Na_2O content and K_2O content of the Na-biotites. The Na-biotites are alkali deficient with less than 1.0 alkali cations per formula unit (out of a possible 2.0 based on 22 oxygens) compared with coexisting K-biotite with 1.4–1.5 alkali cations. Na-biotite has a higher Si/Al and Mg/Fe than coexisting K-biotites. Talc coexisting with Na-biotite is relatively high in both Al_2O_3 and Na_2O .

In Figs. 109A and 109B are displayed the composition fields defined by the Na- and K-biotites. There is a clearly defined compositional gap between the Na-biotites (circles) and K-biotites (squares): Na-biotites are lower in Al total, Al^{IV} , $K/(K + Na)$, and $K + Na$ than coexisting K-biotite.

Crystallography

Unit-cell dimensions determined on single crystals with an automated four-circle diffractometer ($MoK\alpha_1$ radiation, $\lambda = 0.70926 \text{ \AA}$) are $a = 5.312(3) \text{ \AA}$, $b = 9.163(5) \text{ \AA}$, $c = 9.825(6) \text{ \AA}$, $\beta = 103.18(6)^\circ$, and $V = 465.6(5) \text{ \AA}^3$. The crystals are monoclinic, diffraction aspect $C2/m$, $Z = 2$. The mica is a 1M polymorph although stacking disorder is present in some specimens. Single-crystal x-ray diffraction photographs reveal neither streaking nor repeat distances greater than 9.5 \AA along c^* . The Na-biotite, therefore, does not appear to be a mixed-layer or alternating-layer structure with talc and Na-biotite layers intermixed on an

TABLE 25. Electron Microprobe Analyses of Na-Biotite and Coexisting K-Biotite and Talc

	Na-Biotite (average of 13 grains)	Na-Biotite with Highest Na ₂ O Content	Range in Na-Biotite Composition (13 grains)	K-Biotite (average of 4 grains)	Talc (average of 2 grains)
<i>Wt % Oxides</i>					
SiO ₂	48.06	46.94	46.29–50.28	39.40	59.43
Al ₂ O ₃	12.69	14.43	11.37–14.43	17.66	2.42
TiO ₂	0.82	.90	0.66–0.97	1.04	0.09
MgO	22.43	21.38	21.38–23.31	19.55	27.49
FeO*	6.91	6.87	6.47–7.39	8.96	3.70
MnO	0.04	0.05	0.01–0.08	0.09	0.03
CaO	0.05	0.02	0.01–0.11	0.07	0.03
Na ₂ O	2.59	3.59	1.78–3.59	0.28	0.29
K ₂ O	0.73	0.62	0.27–1.34	7.37	0.00
Total	94.32	94.79		94.42	93.47
<i>Cations Calculated on the Anhydrous Basis of 22 Oxygens</i>					
Si	6.524	6.360		5.653	7.795
Al	2.031	2.302		2.987	0.373
Ti	0.084	0.091		0.112	0.007
Mg	4.538	4.313		4.180	5.374
Fe	0.784	0.775		1.075	0.404
Mn	0.005	0.004		0.011	0.000
Ca	0.007	0.000		0.011	0.000
Na	0.682	0.942		0.078	0.073
K	0.126	0.103		1.349	0.000
Total	14.781	14.890		15.456	14.025

* All Fe computed as FeO.

ordered 1:1 basis. The question of whether the Na-biotite could be composed of a random mixture of talc and end-member Na-biotite has not yet been resolved.

Powder x-ray diffraction patterns of hand-picked biotites show three distinct peaks in the range 10.4–9.3 Å. Treatment with ethylene glycol had no effect on the positions of these peaks. Similar triplets of peaks appear again in the range 3.42–3.07 Å, 2.56–2.30 Å, and 2.05–1.85 Å and are interpreted as representing the 001, 003, 004, and 005 interplanar spacings of three distinct layer silicates with d_{001} of 10.08 Å, 9.62 Å, and 9.35 Å ($\pm .05$). The 10.08 Å basal spacing compares favorably with those reported by Wones (1963) for synthetic K-biotites,

which have a d_{001} ranging from 10.108–10.166 Å, and with natural K-biotites, which have a d_{001} ranging from 9.99–10.11 Å (Franzini and Schiaffino, 1963). The 9.62 Å interplanar spacing correlates well with the d_{001} spacing obtained from single crystals of Na-biotite of 9.58 Å. The smallest d_{001} of 9.35 Å has been assigned to talc found coexisting with Na- and K-biotite (d_{001} of talc \simeq 9.31 Å).

Discussion

Carman (1974) synthesized three hydrates of Na-phlogopite and found that the least hydrated variety has a maximum thermal stability of 990°C at 2.0 kbar

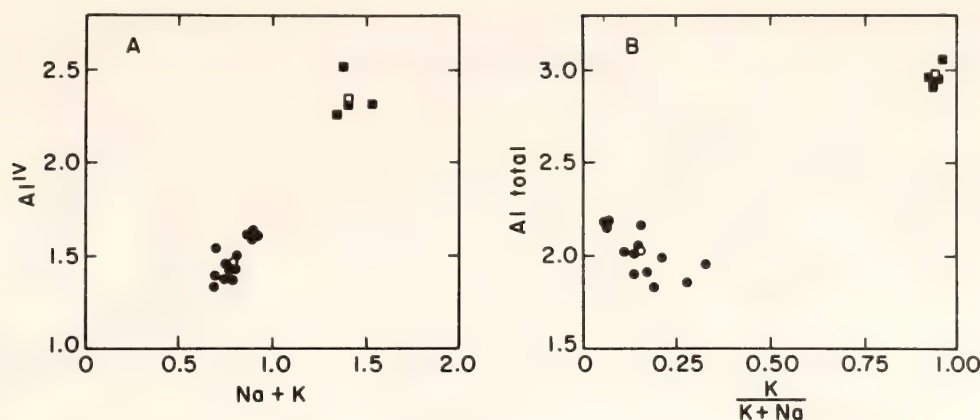


Fig. 109. Compositions of analyzed Na-biotite (circles) and K-biotites (squares). Open symbols are averages.

P_{H_2O} . The natural Na-biotite, however, differs in composition from the sodium phlogopite studied by Carman (1974, Table 6), which has no iron and is not alkali deficient.

The smaller d_{001} of Na-biotite relative to K-biotite can be easily explained from consideration of ionic size: Na is smaller than K, and a mica with Na as the interlayer cation should have a smaller basal spacing than one with K. (Compare 2M muscovite having $d_{001} \approx 19.8$ with 2M paragonite having $d_{001} \approx 19.3$, Burnham and Radoslovich, *Year Book 63*, pp. 232–236; compare also synthetic sodium phlogopite having $d_{001} = 9.9 \text{ \AA}$, Carman, 1974, with synthetic K-phlogopite having $d_{001} = 10.14 \text{ \AA}$, Wones, 1963.) In addition, Na-biotite is alkali deficient relative to K-biotite, a property which also contributes to the smaller d_{001} .

The composition of the natural Na-biotite can be represented in terms of the end members: $Na_2(Mg, Fe)_6Al_2Si_6O_{20}(OH)_4$ (pure Na-biotite)- $K_2(Mg, Fe)_6Al_2Si_6O_{20}(OH)_4$ (K-biotite)- $\square(Mg, Fe)_6Si_8O_{20}(OH)_4$ (talc). There is considerable substitution of the type $Na + Al^{IV} \rightleftharpoons \square + Si^{IV}$ between the hypothetical pure Na-biotite end member and talc as is shown in Fig. 110A. The reason for this extreme alkali deficiency in natural Na-biotite is not clear, but it is suspected that the reported values represent equilibrium alkali contents under metamorphic conditions. If the alkali deficiency were due to

leaching from a more Na-rich phase, one would expect to observe a complete range of alkali contents whereas, in fact, individual grains are relatively homogeneous in composition even where in contact with talc. Moreover, the systematic partitioning of Na, K, and vacancies between Na-biotite, K-biotite, and talc (Fig. 110A) is evidence for the attainment of equilibrium among the alkali cations in these phases and supports the generalized phase relations presented in Fig. 110B.

The presence of Na-biotite in the Post Pond Volcanics can be attributed to the unusual bulk composition. J. B. Thompson (verbal communication, 1976; 1978) speculated on the existence of Na-phlogopite in nature and suggested that natural examples had not yet been found because (1) bulk compositions necessary for the formation of this phase are rare, and (2) Na-phlogopite should weather quickly to vermiculite. The bulk compositions of the samples reported here are unusual in that they contain a moderate amount of Na_2O but very little CaO . Additional CaO would probably stabilize first plagioclase and finally hornblende (these phases are found in metavolcanic rocks only 100 m to the east) rather than Na-biotite. Specimens containing K-biotite + talc but no Na-biotite contain substantially more modal plagioclase (15–30% of An_{15-20}) than specimens containing Na-biotite (0–5%).

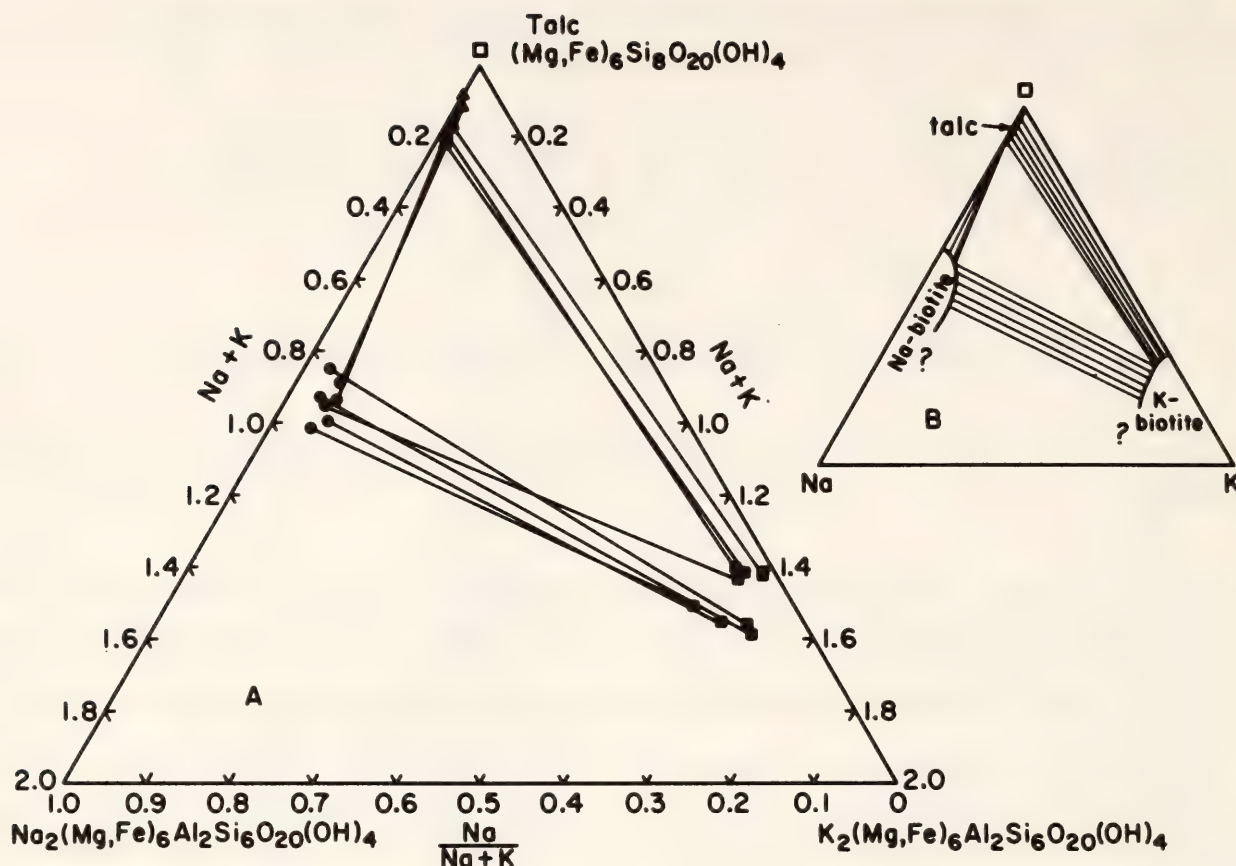


Fig. 110. (A) Compositions of coexisting Na-biotites (circles), K-biotites (squares), and talc (triangles). Tie lines connect coexisting phases. (B) Generalized phase relations for the system shown in (A).

HYDROTHERMAL SOLUTIONS AND METASOMATISM

AN EXPERIMENTAL STUDY OF COMPLEXING AND THERMODYNAMIC PROPERTIES OF AQUEOUS MgCl_2 IN THE SYSTEM $\text{MgO-SiO}_2\text{-H}_2\text{O-HCl}$

John D. Frantz and Robert K. Popp

Two different techniques using the $\text{Ag} + \text{AgCl}$ buffer were used to determine speciation and free energies of magnesium in hydrothermal fluids. Both techniques involve equilibration of the mineral assemblage, talc + quartz, with a chloride-bearing fluid at elevated temperatures and pressures. Details of the techniques are given in Frantz and Popp (*Year Book 76*, pp. 598–601). Subsequent determination of total dissolved magnesium and associated hydrogen chloride (HCl°) that coexisted with the mineral assemblage

provides the necessary information to identify the predominant magnesium species in the fluid and to calculate its free energy.

Experiments were performed using the buffered method with the hematite + magnetite oxygen buffer at temperatures between 450° and 650°C and at pressures of 1000, 1500, and 2000 bars for times ranging from 7 to 20 days. Reversals of equilibrium were performed by using initial solutions both higher and lower in magnesium than the resultant equilibrium concentration. As indicated in Fig. 111, the solutions become very concentrated in magnesium at temperatures below 500°C.

Experiments were run using the unbuffered method at 2000 bars between 400° and 600°C. Initial solutions in the

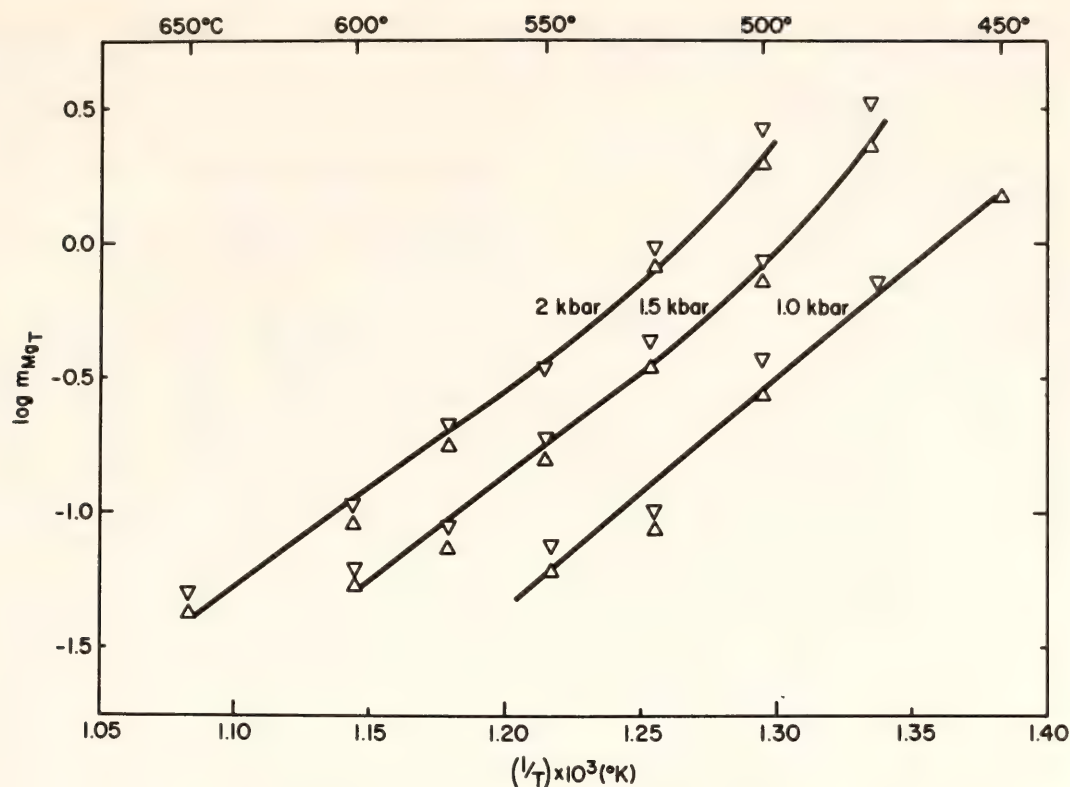


Fig. 111. Results of buffered experiments. The logarithm of the total magnesium concentration measured after quench as a function of temperature ($^{\circ}\text{K}$). The log of the concentration, in molal units, is represented by the apex of each triangle; apices point toward direction of change. Analytical error is $\pm 5\%$ of the concentration.

outer capsule ranged from distilled H_2O to H_2O - MgCl_2 fluids containing 3.6 molar MgCl_2 . Equilibration times were from 18 hr to eight days depending upon temperature.

The concentrations of total magnesium (m_{Mg_t} ; m = molality) and associated hydrogen chloride ($m_{\text{HCl}^{\circ}}$) for the unbuffered experiments are shown in Fig. 112. The concentrations of HCl° were calculated from the concentration of total quench chloride in the inner capsule using the following equation and values of K_{HCl} from Frantz and Popp (this Report):

$$m_{\text{Cl}^-}(25^{\circ}, 1 \text{ atm}) = m_{\text{HCl}^{\circ}}(T_e, P_e) + \sqrt{[m_{\text{HCl}^{\circ}}(T_e, P_e)][K_{\text{HCl}}]} \quad (1)$$

where T_e and P_e represent the experimental temperature and pressure, respectively.

Interpretation of the results of both methods and calculation of the Gibbs free energy of magnesium in hydrothermal

fluids depends upon knowledge of the complexes in which magnesium occurs. At room temperature and pressure, magnesium chloride is a strong electrolyte with magnesium existing primarily as ions (Mg^{2+}). With increasing temperature and decreasing solution density, however, strong electrolytes tend to become weak and appreciable amounts of neutral complexes appear (Franck, 1956a, 1956b; Quist and Marshall, 1968). In solutions containing magnesium chloride, species such as MgCl^+ and MgCl_2° are likely to exist under hydrothermal conditions.

As stated in Frantz and Popp (*Year Book* 76, pp. 598–601), measurement of total magnesium (m_{Mg_t}) in the previous experiments reflects the total concentration of all magnesium species present at the conditions of the runs. If the concentration of MgCl_2° greatly exceeds those of all other species, the relation between total magnesium (Mg_t) and HCl° would be described by the following

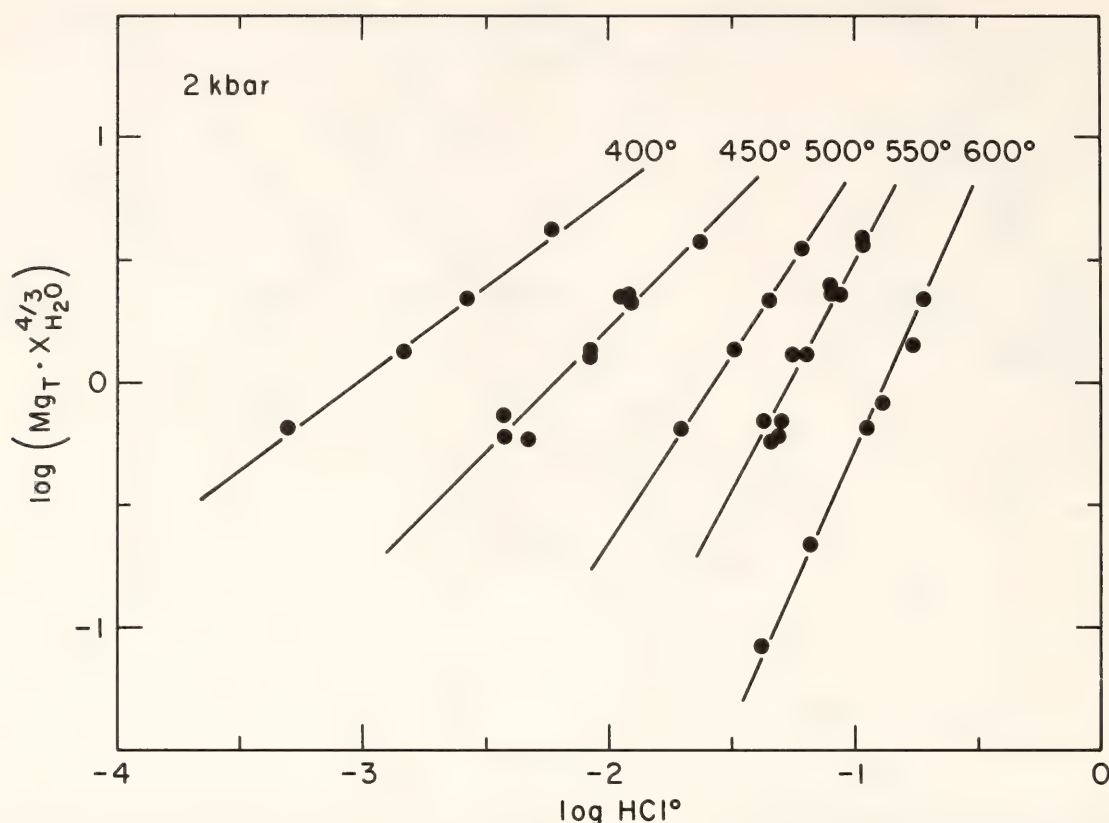
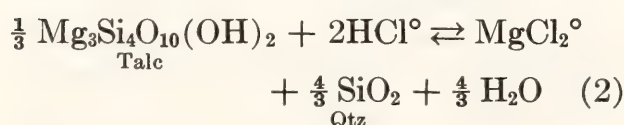


Fig. 112. Results of unbuffered runs. The logarithm of the molality of the total magnesium concentration times the mole-fraction of H_2O to the $4/3$ power as a function of the logarithm of the molality of associated hydrogen chloride (HCl°) at 2000 bars. The lines represent linear least-squares fits to the data. The experimental temperatures ($^\circ\text{C}$) are shown. Errors in measurement are of approximately the same size as the diameters of the solid circles representing the data points.

reaction and equilibrium constant:



and

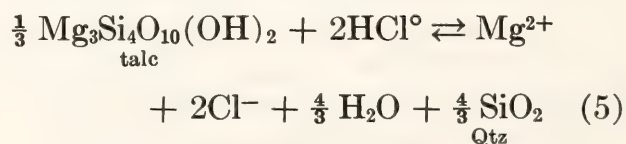
$$K_{TQ} = (m_{\text{MgCl}_2^\circ})(X_{\text{H}_2\text{O}})^{4/3}/(m_{\text{HCl}^\circ})^2 \quad (3)$$

where the activity coefficients are assumed to be unity and the solids are pure phases. If the assumption of MgCl_2° as the predominant magnesium species is correct, then $m_{\text{MgCl}_2^\circ} \simeq m_{\text{Mg}}$, and, therefore, the equilibrium constant (K_{TQ}) should be independent of magnesium and HCl° concentrations and mole fractions of H_2O ; thus

$$\partial \log [m_{\text{Mg}}](X_{\text{H}_2\text{O}})^{4/3} / \partial \log m_{\text{HCl}^\circ} \simeq 2. \quad (4)$$

If the most abundant species is the

Mg^{2+} ion, then the talc + quartz reaction and its equilibrium constant can be written:



and

$$K'_{TQ} = (m_{\text{Mg}^{2+}})(m_{\text{Cl}^-})^2(X_{\text{H}_2\text{O}})^{4/3}/(m_{\text{HCl}^\circ})^2 \quad (6)$$

Because the concentration of magnesium is much greater than any other positive ion, the concentration of chloride ion would be twice that of magnesium ion and:

$$K'_{TQ} \simeq 4(m_{\text{Mg}^{2+}})^3(X_{\text{H}_2\text{O}})^{4/3}/(m_{\text{HCl}^\circ})^2. \quad (7)$$

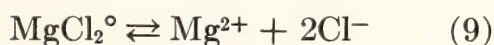
Therefore:

$$\partial \log [(m_{\text{Mg}^{2+}})(X_{\text{H}_2\text{O}})^{4/9}] / \partial \log m_{\text{HCl}^\circ} \simeq 0.67 \quad (8)$$

if Mg^{2+} is the predominant magnesium species.

The experimental results indicate the presence of MgCl_2° as the predominant species at 550° and 600°C at 2000 bars pressure. The equilibrium constant in Equation 3 is independent of concentrations, and the slope of $\log [(m_{\text{Mg}^{2+}})(X_{\text{H}_2\text{O}})^{4/9}]$ as a function of $\log m_{\text{HCl}^\circ}$ (Fig. 112) is 2.05 at 550°C (standard deviation 0.15) and 2.18 at 600°C (standard deviation 0.19). As predicted by Frantz and Popp (*Year Book* 76, pp. 598–601), Mg^{2+} appears to be the dominant species at 400°C. The equilibrium constant in Equation 7 is independent of concentration, and the slope of $\log [(m_{\text{Mg}^{2+}})(X_{\text{H}_2\text{O}})^{4/9}]$ as a function of $\log m_{\text{HCl}^\circ}$ is 0.675 with a standard deviation of 0.013.

The total concentrations of magnesium found at temperatures between 400° and 550°C at 2000 bars would then reflect significant concentrations of both Mg^{2+} and MgCl_2° , and this is reflected by slopes intermediate between 2.0 and 0.67 in Fig. 112. If Mg^{2+} and MgCl_2° are the only significant magnesium species, the following reaction and equilibrium constant can be written (activity coefficients are assumed to equal unity):



and

$$K_{\text{MgCl}_2} = (m_{\text{Mg}^{2+}})(m_{\text{Cl}^-})^2 / m_{\text{MgCl}_2^\circ} \quad (10)$$

Substitution of Equations 10 and 3 into the following mass balance equation for magnesium:

$$m_{\text{Mg}^{2+}} = m_{\text{MgCl}_2^\circ} + m_{\text{Mg}^{2+}} \quad (11)$$

yields an expression relating the concentration of total magnesium to that of

associated hydrogen chloride (HCl°):

$$m_{\text{Mg}^{2+}} = K_{TQ} \frac{(m_{\text{HCl}^\circ})^2}{(X_{\text{H}_2\text{O}})^{4/3}} + \sqrt[3]{\frac{(K_{TQ}K_{\text{MgCl}_2})(m_{\text{HCl}^\circ})^2}{4(X_{\text{H}_2\text{O}})^{4/3}}} \quad (12)$$

Values for K_{TQ} and K_{MgCl_2} were obtained by fitting Equation 12 to the results of the unbuffered runs, using nonlinear regression analysis of total magnesium vs. HCl° with a weighting function equal to one over the square of the total magnesium concentration.

In Fig. 113, the logarithm of K_{MgCl_2} is plotted as a function of the reciprocal of temperature (°Kelvin). A linear least-squares fit yields:

$$\log K_{\text{MgCl}_2} = -17.35 + \frac{13391}{T^\circ\text{K}}, \quad (13)$$

with the standard deviation of the constant equalling 0.2786 and of the slope, 210.25. The dashed lines show an error in $\log K_{\text{MgCl}_2}$ of one standard deviation of the fit. Reliable values for the magnesium chloride dissociation constant could not be obtained above 500°C because of the low concentration of Mg^{2+} in comparison to total magnesium.

The values of the talc-quartz equilibrium constant (K_{TQ} in Equation 3) were calculated for 1000, 1500, and 2000 bars pressure and are shown in Figs. 114 and 115; values for HCl° from the buffer calibrations in Frantz and Popp (this Report) and values for total magnesium from the buffered experiments were used in the calculations. For the experiments done at 2000 bars, the total magnesium concentrations were adjusted for the presence of Mg^{2+} using the dissociation constant of MgCl_2 given in Equation 13. The low-temperature runs at 1000 and 1500 bars have not been corrected for Mg^{2+} . The errors in the HCl° from the buffer calibrations and in the total magnesium analysis were propagated through the calculations and are less than the

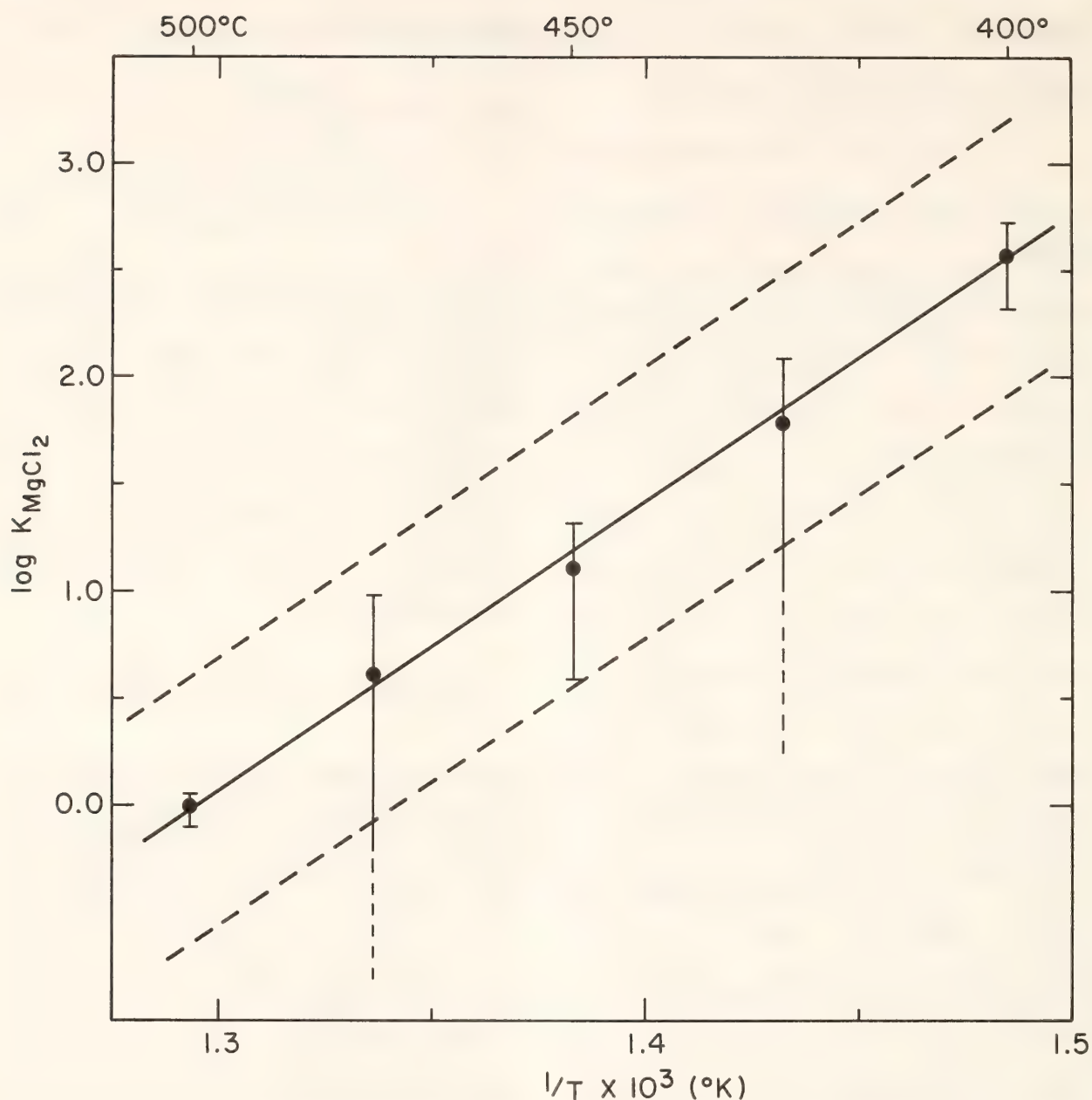


Fig. 113. Logarithm of the dissociation constant of MgCl_2 as a function of the reciprocal of temperature ($^{\circ}\text{K}$) at 2000 bars. Solid line is linear least-squares fit. Dashed lines represent an uncertainty of one standard deviation in this fit.

dimensions of the symbols. Also shown in Fig. 114 are the values of K_{TQ} retrieved from the unbuffered experiments at 2000 bars. The vertical bars for the unbuffered runs represent one standard deviation of the nonlinear regression. The agreement in $\log K_{TQ}$ between the reversed buffered runs and the unbuffered experiments at 500°, 550°, and 600°C indicates that the unbuffered experiments obtained equilibrium. Linear least-squares fits along with the standard deviations of the constants

are plotted in Figs. 114 and 115. Low-temperature experiments at 1000 and 1500 bars that could not be corrected for the presence of Mg^{2+} were not included in the regressions.

The variation in the distribution of the aqueous species in equilibrium with talc and quartz as a function of temperature at 2000 bars pressure was calculated for solutions having a one-molal total magnesium concentration. The results, shown in Fig. 116, were obtained by solving

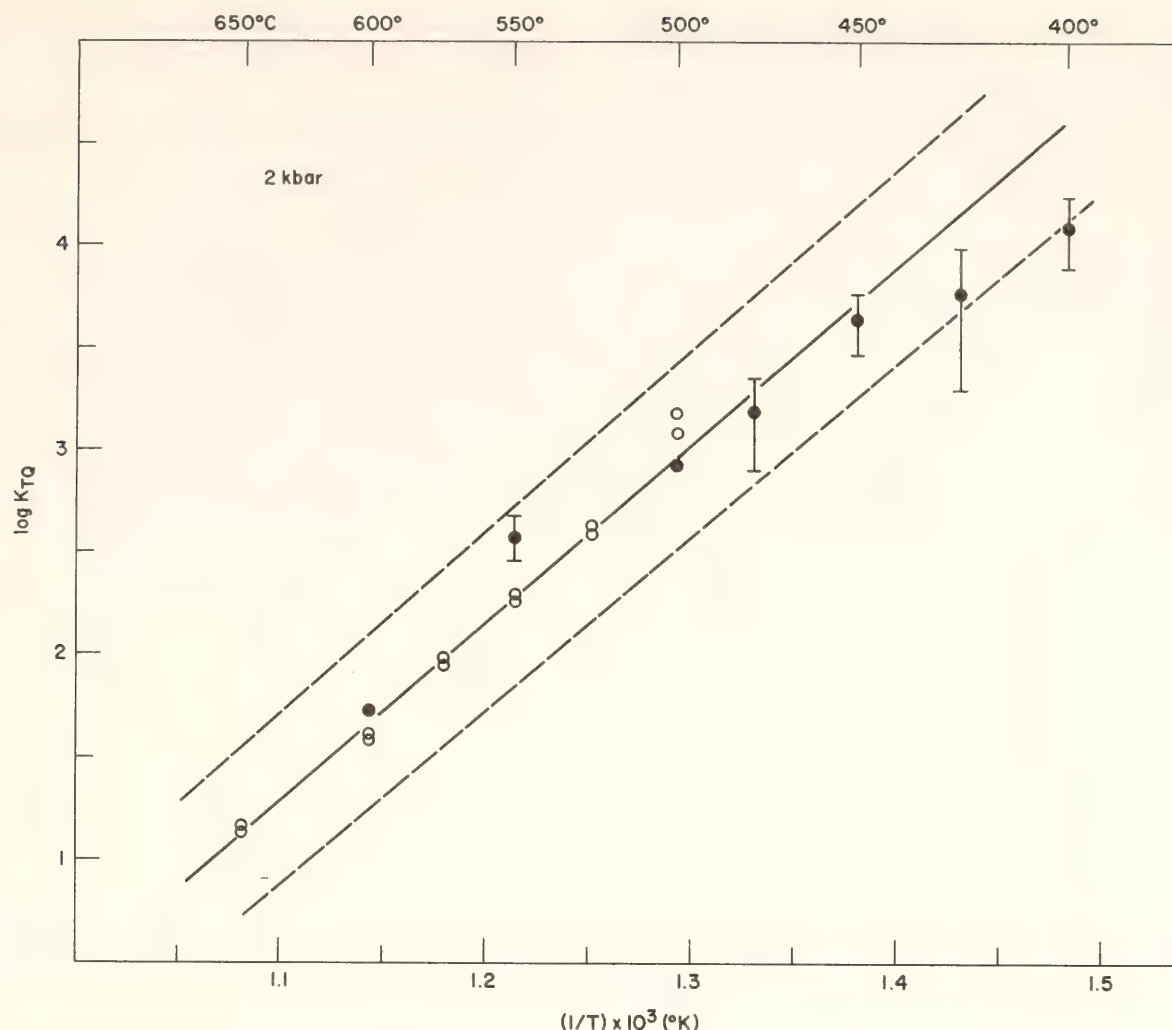


Fig. 114. Logarithm of the equilibrium constant for the talc + quartz reaction (Equation 3, text) as a function of reciprocal temperature (°K) at 2000 bars. Open circles represent buffered runs; solid circles, unbuffered runs. Errors for buffered runs are less than the diameter of the symbols. See text for explanation of errors for unbuffered runs. The solid line represents a linear least-squares fit of all runs (weighted according to their individual errors). Dashed lines represent an error of one standard deviation in the fit.

the following set of equations (the presence of OH⁻ ions is neglected and activity coefficients are assumed to be unity):

$$K_{TQ} = (m_{\text{MgCl}_2^\circ}) (X_{\text{H}_2\text{O}})^{2/3} / (m_{\text{HCl}^\circ})^2$$

$$K_{\text{HCl}} = (m_{\text{H}^+}) (m_{\text{Cl}^-}) / m_{\text{HCl}^\circ}$$

$$K_{\text{MgCl}_2} = (m_{\text{Mg}^{2+}}) (m_{\text{Cl}^-})^2 / m_{\text{MgCl}_2^\circ}$$

$$2(m_{\text{Mg}^{2+}}) + (m_{\text{H}^+}) = m_{\text{Cl}^-}$$

$$m_{\text{Mg}_i} = (m_{\text{MgCl}_2^\circ}) + (m_{\text{Mg}^{2+}}). \quad (14)$$

As previously noted, the concentrations of the ions decrease and those of the associated species increase with increasing

temperature. The maximum in the variation of the hydrogen ion concentration results from the common ion effect of Cl⁻ on the HCl[°] dissociation constant.

Thermodynamic Calculations

At equilibrium the Gibbs free energy of the talc-quartz reaction involving associated magnesium chloride and hydrogen chloride (Equation 2) is:

$$\begin{aligned} \Delta G (\text{reaction}) = 0 = & -\frac{1}{3} G(\text{talc}) \\ & -2G(\text{HCl}^\circ) + G(\text{MgCl}_2) + \frac{4}{3} G(\text{Qtz}) \\ & + \frac{4}{3} G(\text{H}_2\text{O}). \quad (15) \end{aligned}$$

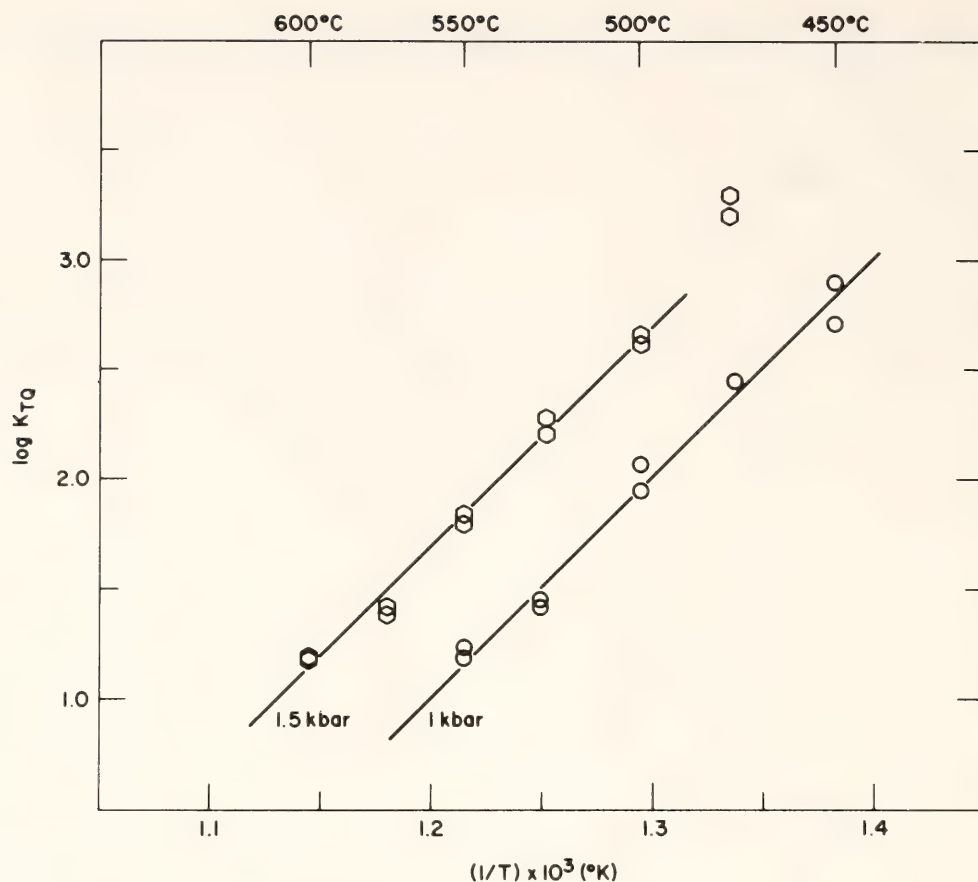


Fig. 115. Logarithm of equilibrium constant for the talc + quartz reaction as a function of reciprocal temperature ($^{\circ}\text{K}$) at 1000 and 1500 bars. Circles represent 1000-bar experiments; hexagons, 1500-bar experiments.

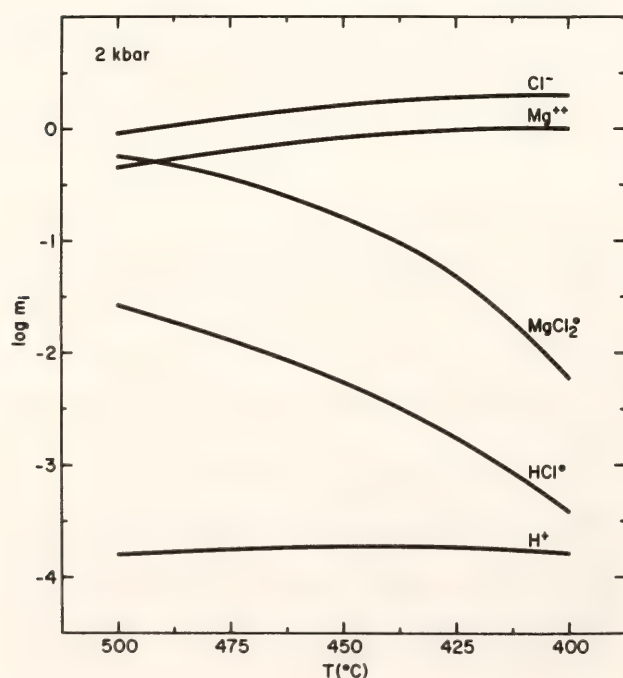


Fig. 116. Variation in the logarithms of the concentrations of the aqueous species in equilibrium with talc + quartz as a function of temperature ($^{\circ}\text{C}$). Total magnesium concentration = 1.0 molal.

The standard states of talc and quartz are assumed to be pure solids at temperature and pressure of interest, that of H_2O to be pure H_2O at temperature and pressure of interest, and those of MgCl_2° and HCl° to be hypothetical one-molal solutions at the temperature and pressure of interest. The difference in the free energies of formation of standard-state one-molal MgCl_2° and HCl° solutions can be calculated from the following (ideal mixing assumed):

$$\begin{aligned} & [G_f^{\circ}(\text{MgCl}_2^{\circ}) - 2G_f^{\circ}(\text{HCl}^{\circ})] \\ &= \Delta G_f^{\circ} - RT \ln [m_{\text{MgCl}_2^{\circ}} \\ & \quad (X_{\text{H}_2\text{O}})^{4/3} / (m_{\text{HCl}^{\circ}})^2] \quad (16) \end{aligned}$$

where:

$$\begin{aligned} \Delta G_f^{\circ} &= \frac{1}{3} G_f^{\circ}(\text{talc}) - \frac{4}{3} G_f^{\circ}(\text{qtz}) \\ & \quad - \frac{4}{3} G_f^{\circ}(\text{H}_2\text{O}). \end{aligned}$$

Standard-state free energies of formation [$G_f^\circ(i)$] refer to free energies of formation of the phases at temperature and pressure from the elements at 25°C and 1 bar. The values obtained using the experimental data shown in Figs. 114 and 115, the thermodynamic data for talc and quartz from Helgeson *et al.* (1978), and the free energy of water calculated from the data of Fisher and Zen (1971), are shown in Fig. 117 for 1000, 1500, and 2000 bars. Least-squares fits yield the following (standard deviations neglecting errors in free energies of the other phases

are given in parentheses):

at 1000 bars from 475° to 575°C,

$$[G_f^\circ(\text{MgCl}_2^\circ) - 2G_f^\circ(\text{HCl}^\circ)]_{\text{kcal}} = -147.98(\pm 2.79) + 0.0763(\pm 0.0036) T^\circ\text{K}; \quad (17)$$

at 1500 bars from 475° to 600°C,

$$[G_f^\circ(\text{MgCl}_2^\circ) - 2G_f^\circ(\text{HCl}^\circ)]_{\text{kcal}} = -146.30(\pm 1.45) + 0.0707(\pm 0.0018) T^\circ\text{K}; \quad (18)$$

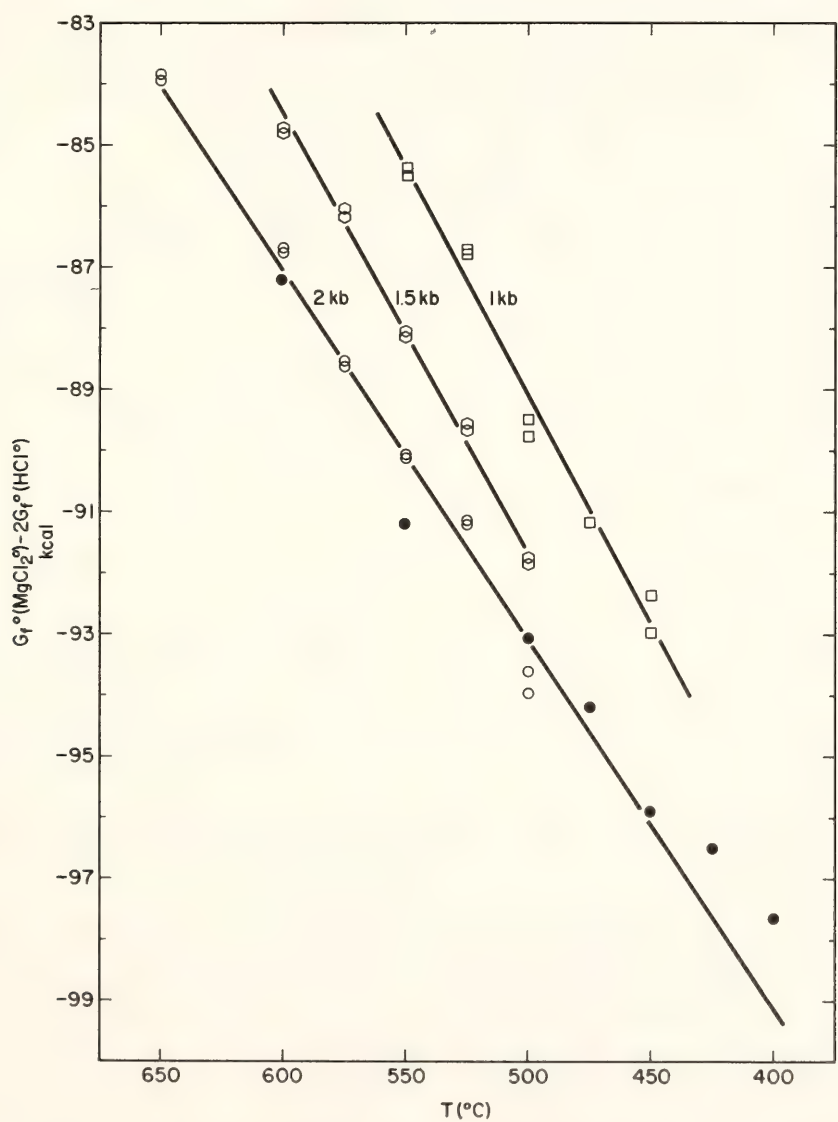


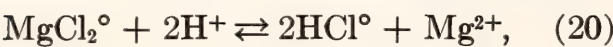
Fig. 117. Difference in Gibbs free energy of formation associated MgCl_2° and HCl° in supercritical fluids. Values represent free energy of formation of aqueous species at T and P from elements at 298°C, 1 bar. Unfilled symbols refer to experiments done with oxygen buffers; filled symbols, those done without oxygen buffers. Squares refer to 1000-bar experiments; hexagons, to 1500-bar experiments; circles, to 2000-bar experiments.

at 2000 bars from 400° to 650°C,

$$[G_f^\circ(\text{MgCl}_2^\circ) - 2G_f^\circ(\text{HCl}^\circ)]_{\text{kcal}} = -139.54(\pm 1.03) + 0.0608(\pm 0.0013) T^\circ\text{K}. \quad (19)$$

The free energy of MgCl_2° alone was not computed because of the large uncertainties in the calculated free energy of HCl° . As seen below, calculation of the solubility constants of other minerals in the $\text{MgO-SiO}_2\text{-H}_2\text{O}$ system only requires the difference in free energy between MgCl_2° and HCl° .

By combining the calculated free energy differences of MgCl_2° and HCl° with the MgCl_2° and HCl dissociation constants, the free energy of magnesium ions can be computed from the following reaction:



according to the following equation:

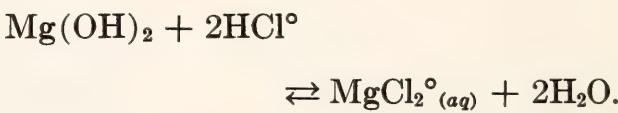
$$[G_f^\circ(\text{Mg}^{2+}) - 2G_f^\circ(\text{H}^+)] = [G_f^\circ(\text{MgCl}_2^\circ) - 2G_f^\circ(\text{HCl}^\circ)] + RT \ln [(K_{\text{HCl}})^2/K_{\text{MgCl}_2}], \quad (21)$$

which yields (at 2000 bars from 400° to 500°C)

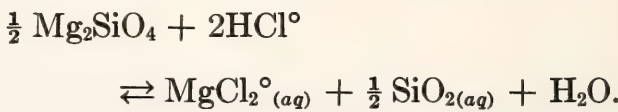
$$[G_f^\circ(\text{Mg}^{2+}) - 2G_f^\circ(\text{H}^+)] = [G_f^\circ(\text{Mg}^{2+})]_{\text{kcal}} = -123.5 + 0.021 T(^\circ\text{K}). \quad (22)$$

If the differences in the free energies of MgCl_2° and HCl° given in Equations 17, 18, and 19, in addition to the thermochemical data summarized in Helgeson *et al.* (1978), water data from Fisher and Zen (1971), and aqueous silica data from Walther and Helgeson (1977) are used, the solubilities of other phases in the system $\text{MgO-SiO}_2\text{-H}_2\text{O-HCl}$ can be calculated. Quartz, talc, forsterite, and brucite are all stable in hydrothermal fluids in the temperature and pressure ranges of the study. In addition, chrysotile is stable in the lower temperature range of the 2000 bar experiments (400° to 440°C). Solubility constants for these phases based on the reactions shown below are given in Table 26.

Brucite:



Forsterite:



Chrysotile:

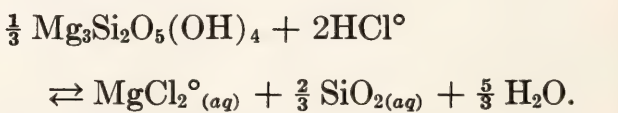


TABLE 26. Equations for Solubility Constants, $\log K = a + b/T^\circ\text{K}$

Mineral	Pressure (bars)	Temperature Range (°C)	a	b
Brucite	1000	475-575	-9.428	10,496
	1500	500-600	-8.831	10,526
	2000	400-650	-6.844	9,235
Forsterite	1000	475-575	-13.123	11,566
	1500	500-600	-11.597	10,958
	2000	400-650	-9.260	9,467
Chrysotile	2000	400-440	-7.258	7,778
Talc	1000	475-575	-12.033	9,372
	1500	500-600	-9.822	8,327
	2000	400-650	-7.385	6,805

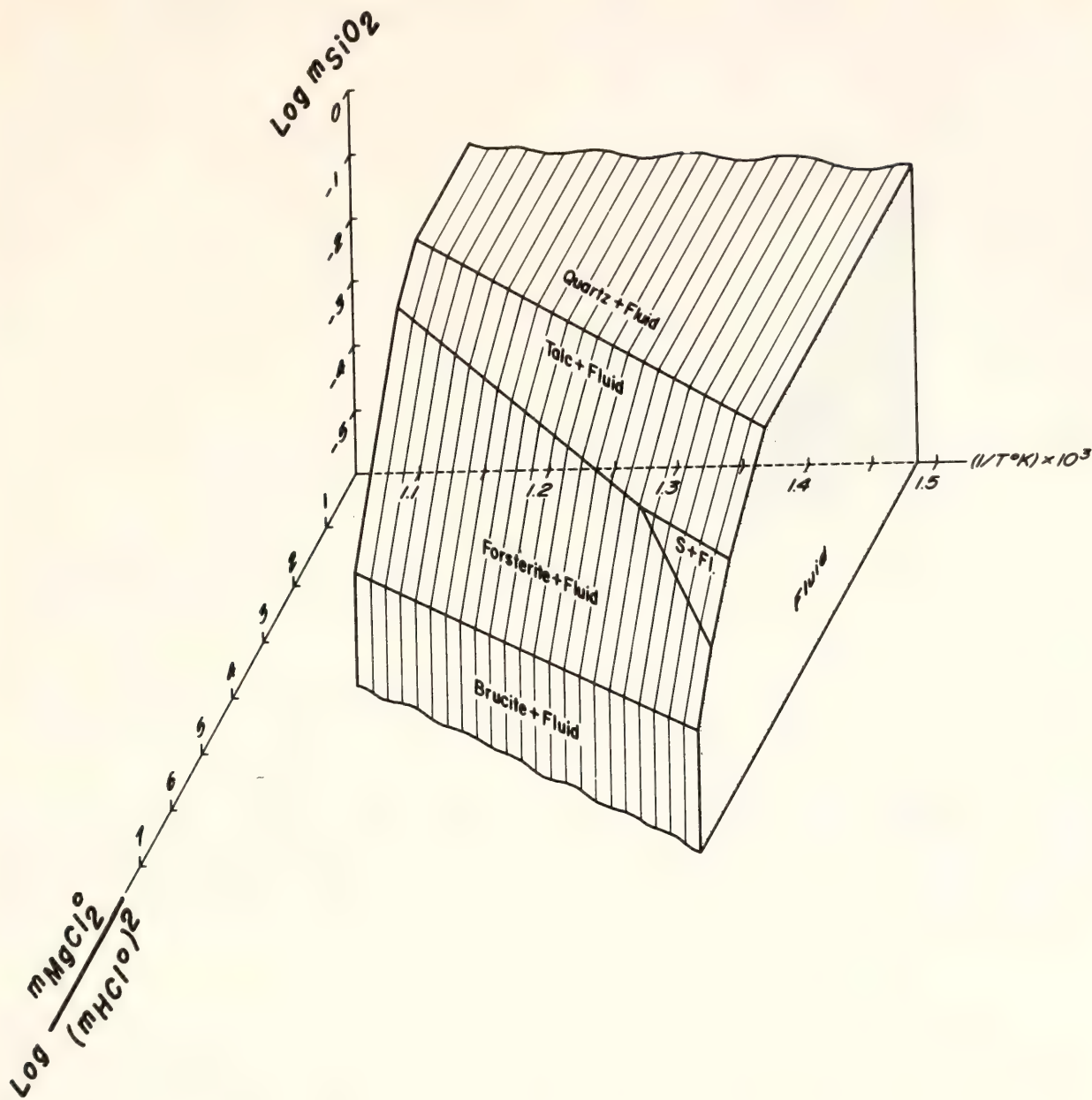
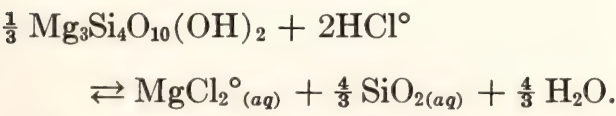


Fig. 118. Mineral solubilities as functions of $\log [m_{\text{MgCl}_2}/(m_{\text{HCl}})^2] - \log m_{\text{H}_4\text{SiO}_4} - 1/T(^{\circ}\text{K})$ at 2000 bars pressure. See text for details.

Talc:



In Fig. 118 the mineral-saturation surfaces are shown in $\log [m_{\text{MgCl}_2}/(m_{\text{HCl}})^2] - \log(m_{\text{SiO}_2}) - 1/T(^{\circ}\text{K})$ space at 2000 bars pressure. Solutions existing within the envelope are undersaturated with respect to the solid phases. Solutions outside are metastable supersaturated fluids.

Conclusions

The usefulness of the $\text{Ag} + \text{AgCl}$ buffer has been extended to the determination of complexing in hydrothermal fluids and the calculation of free energies of aqueous species at lower temperatures than was previously possible. The preceding calculations based on the results of the unbuffered experiments assumed the following: (a) Mg^{2+} and MgCl_2° are the only predominant magnesium species existing

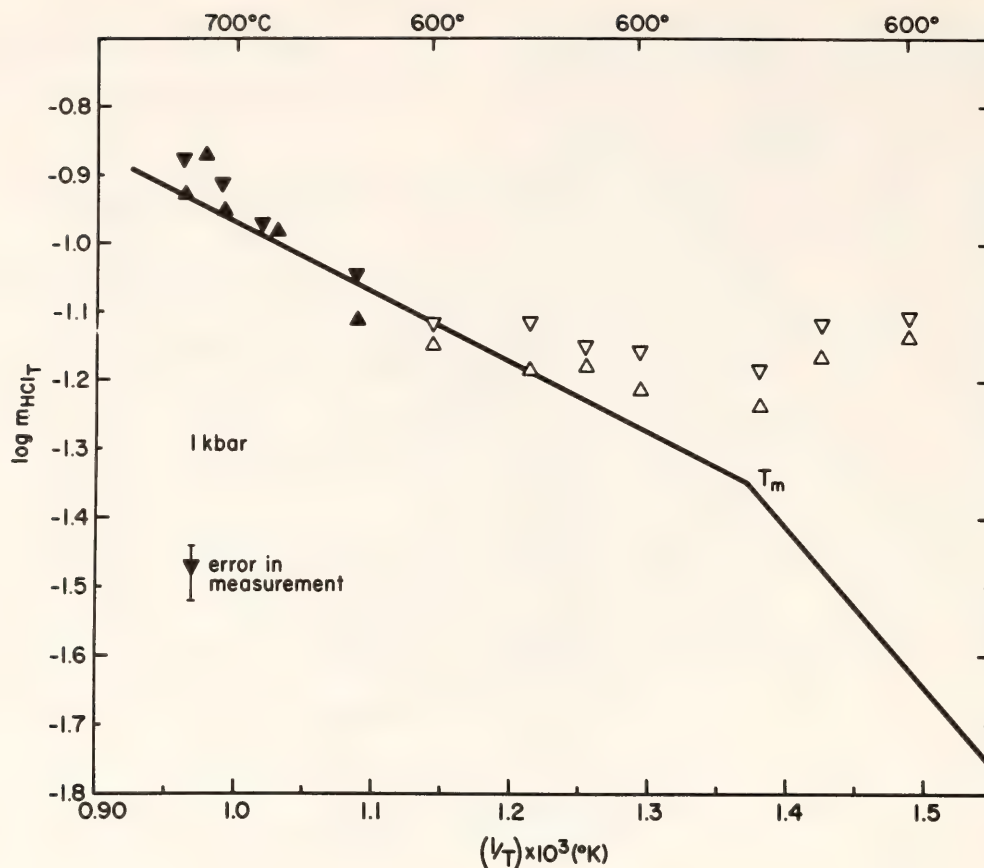


Fig. 119. Logarithm of the molality of total hydrogen chloride as a function of reciprocal temperature ($^\circ\text{K}$) at 1000 bars. Solid triangles refer to data from Chou and Frantz, 1977, error as shown; open triangles refer to experiments reported in the present study, errors approximately represented by size of triangles. The actual measurement is represented by the apex of the triangle. T_m refers to the melting point of AgCl .

in the fluid at the temperature-pressure ranges studied, and (b) the activity coefficients of all aqueous species are unity under the conditions of the experiments. The results of the unbuffered experiments at 550° and 600°C , 2000 bars, are conclusive in showing that MgCl_2 is the predominant magnesium species above 550°C . The independence of the talc-quartz equilibrium constant (Equation 3) with respect to total magnesium concentrations demonstrates that MgCl_2° and H_2O mix nearly ideally. Experiments at 400° strongly indicate that Mg^{2+} is the predominant species. At intermediate temperatures, however, the interpretations are subject to the assumption that Mg^{2+} and MgCl_2 are the only abundant magnesium species. The strong correlation between equilibrium constants obtained from buffered experiments and

those from the regressions of the results of the unbuffered experiments is encouraging. The linearity of the logarithm of the dissociation constant of MgCl_2 with respect to reciprocal temperature (Fig. 113) lends additional credence. It is concluded, however, that complementary studies are needed, using techniques such as electrical conductance and Raman spectroscopy.

With the acquisition of these data, quantitative calculations modeling metasomatic alterations of rocks in the system $\text{MgO-SiO}_2\text{-H}_2\text{O-HCl}$ are possible. By comparing results of calculations using models such as that of Frantz and Mao (1976) with natural systems that have undergone alteration, it will be possible to determine relative magnitudes of the fluxes (and diffusion coefficients) of the components in the intergranular fluid.

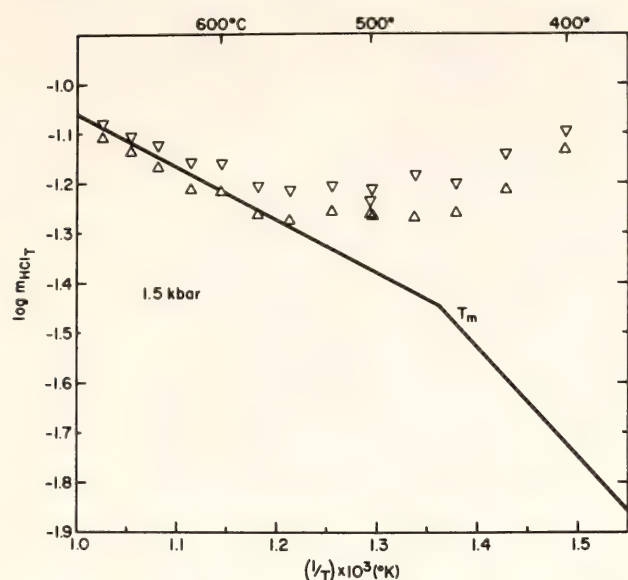


Fig. 120. Logarithm of the molality of total hydrogen chloride as a function of reciprocal temperature ($^{\circ}\text{K}$) at 1500 bars. See text and Fig. 119 for details.

THE IONIZATION CONSTANT OF HCl AS A FUNCTION OF TEMPERATURE AND PRESSURE

J. D. Frantz and R. K. Popp

In the original $\text{Ag} + \text{AgCl}$ buffer calibration experiments, Frantz and Eugster

(1973) obtained values for the dissociation constant of HCl in supercritical fluids at 2000 bars pressure. Chou and Frantz (1977) repeated the experiments. Comparison of these results to the data obtained by conductance measurements (Franck, 1956a) indicates considerable disagreement (approximately one-half log unit). Because experimental mineral-solution studies using the $\text{Ag}-\text{AgCl}$ buffering technique rely heavily on the calibration of the buffer for HCl° (associated hydrogen chloride) and its dissociation constant, additional buffer calibration experiments were undertaken.

Experiments were performed at temperatures between 400° and 700°C at 1000, 1500, and 2000 bars pressure using the hematite + magnetite oxygen buffer. The experimental and analytical techniques were identical to those described in the two papers cited above. The total concentrations of HCl (m_{HCl_t} ; m = molality) measured after quenching by analyzing for chloride ion are shown in Figs. 119–121. As explained in Frantz and Eugster (1973), the chloride measurements for the high-temperature experiments reflect only the concentration of associated hydrogen

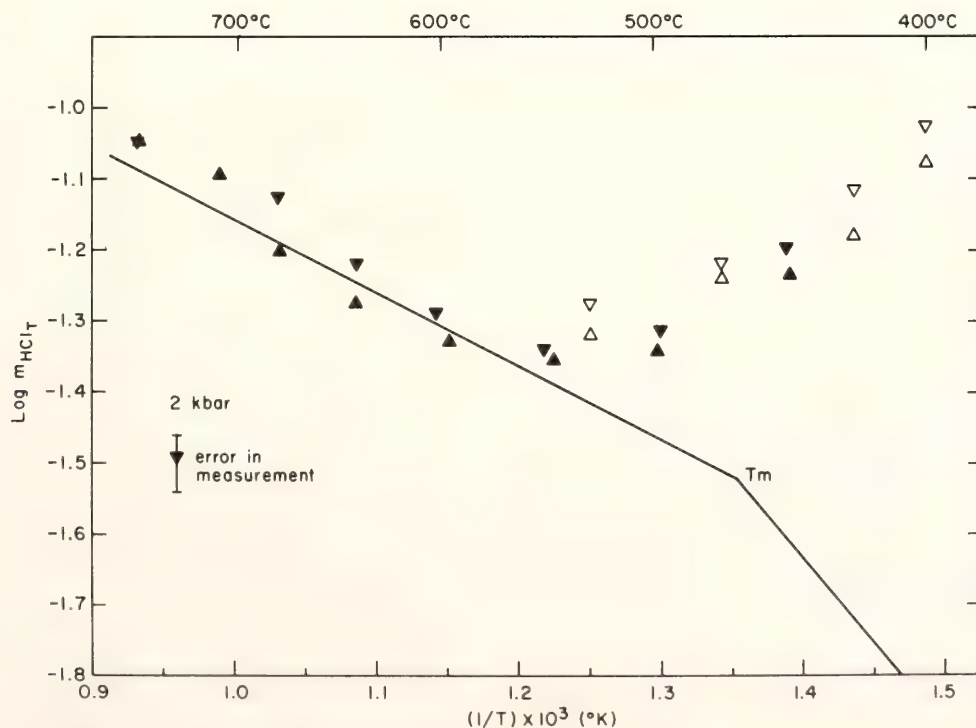


Fig. 121. Logarithm of the molality of total hydrogen chloride as a function of reciprocal temperature ($^{\circ}\text{K}$) at 2000 bars. See text and Fig. 119 for details.

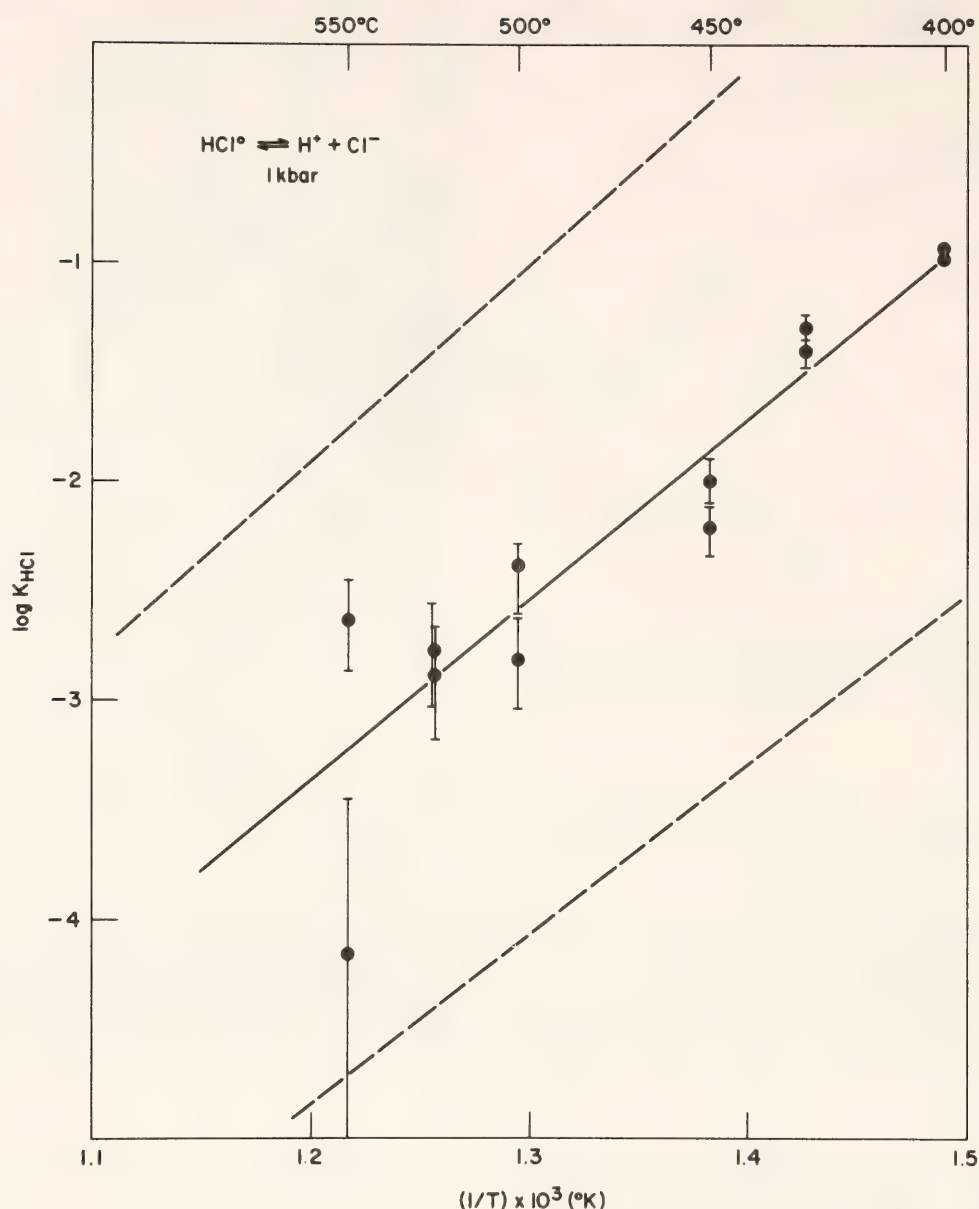


Fig. 122. Logarithm of the dissociation constant of hydrogen chloride as a function of reciprocal temperature ($^{\circ}\text{K}$) at 1000 bars pressure. Error bars represent total analytical error of chloride measurements ($\pm 2\%$ of concentration) propagated through calculations using Equation 6. The solid line represents linear least-squares fit of weighted data; the dashed lines, errors of one standard deviation of the fit.

chloride (HCl°). At lower temperatures, however, dissociated hydrogen chloride becomes increasingly important and its presence is reflected by the upward curvature of $\log m_{\text{HCl}}$, with decreasing temperature in Figs. 119–121. Therefore, at lower temperatures:

$$m_{\text{Cl}^-}(25^{\circ}\text{C}, 1 \text{ atm}) = m_{\text{HCl}^{\circ}}(P_e, T_e) + m_{\text{Cl}^-}(P_e, T_e) \quad (1)$$

where T_e and P_e refer to the experimental temperature and pressure.

A straight line representing $\log m_{\text{HCl}^{\circ}}$ as a function of $(1/T^{\circ}\text{K})$ with a slope obtained from thermochemical calculations has been fit to the data at 1000 and 1500 bars from the higher temperature experiments. At temperatures below the melting temperature of AgCl (T_m), the line representing $\log m_{\text{HCl}^{\circ}}$ is continued, but at a steeper slope. The values of $\log m_{\text{HCl}^{\circ}}$

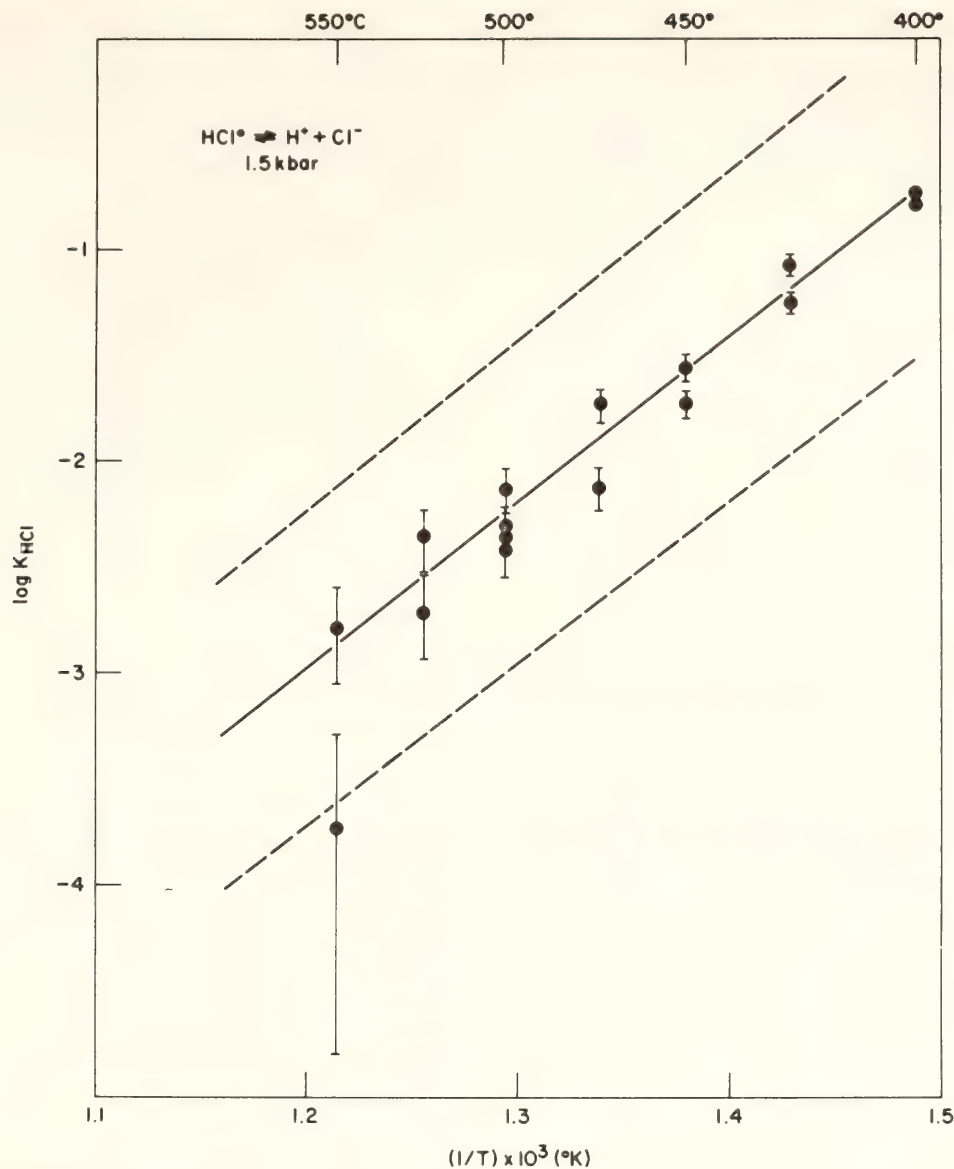


Fig. 123. Logarithm of the dissociation constant of hydrogen chloride as a function of the inverse of the temperature (°K) at 1500 bars. See Fig. 122 for details.

as a function of 1/T above 460°C are given by the following:

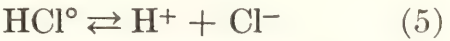
for hematite magnetite at 1000 bars,
 $\log m_{\text{HCl}^\circ} = 0.0453 - 1013.0/T^\circ\text{K}; \quad (2)$

for hematite magnetite at 1500 bars,
 $\log m_{\text{HCl}^\circ} = 0.0057 - 1066.0/T^\circ\text{K}; \quad (3)$

for hematite magnetite at 2000 bars,
 $\log m_{\text{HCl}^\circ} = -0.124 - 1033.0/T^\circ\text{K}. \quad (4)$

Substitution of the mass action expression for the dissociation of HCl° (as-

suming activity coefficients equal to unity)



$$K_{\text{HCl}} = (m_{\text{H}^+})(m_{\text{Cl}^-})/m_{\text{HCl}^\circ}$$

into Equation 1, assuming that $m_{\text{H}^+} \simeq m_{\text{Cl}^-}$, the dissociation constant for HCl° can be calculated using the following expression:

$$K_{\text{HCl}} = (m_{\text{HCl}_2} - m_{\text{HCl}^\circ})^2/m_{\text{HCl}^\circ}. \quad (6)$$

The results of the calculations are shown in Figs. 122–124 for 1000, 1500, and 2000 bars respectively. Least-squares fits weighting the data points as 1/standard

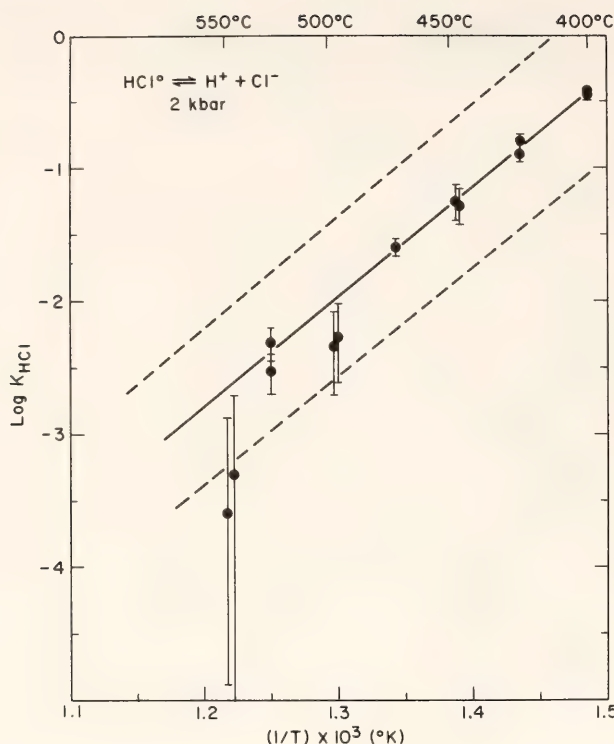


Fig. 124. Logarithm of the dissociation constant of hydrogen chloride as a function of the reciprocal of the temperature ($^{\circ}\text{K}$) at 2000 bars. See Fig. 122 for details.

error yield the following:

$$\begin{aligned} \log K_{\text{HCl}} (1000 \text{ bars}) = \\ -13.49 (\pm 1.14) \\ + 8426.4 (\pm 784)/T^{\circ}\text{K} \quad (7) \end{aligned}$$

$$\begin{aligned} \log K_{\text{HCl}} (1500 \text{ bars}) = \\ -12.34 (\pm 0.564) \\ + 7792.5 (\pm 395)/T^{\circ}\text{K} \quad (8) \end{aligned}$$

$$\begin{aligned} \log K_{\text{HCl}} (2000 \text{ bars}) = \\ -12.85 (\pm 0.447) \\ + 8368.2 (\pm 309)/T^{\circ}\text{K}. \quad (9) \end{aligned}$$

Knowledge of the dissociation constant of HCl over the temperature-pressure range investigated in this study is essential to experimental studies of mineral-solution equilibria in chloride-bearing systems (see Frantz and Popp, this Report).

CHEMICAL AND OXYGEN ISOTOPIC METASOMATISM OF DEVONIAN BRACHIOPODS FROM THE SILLIMANITE ZONE, MT. MOOSILAUKE, NEW HAMPSHIRE

Douglas Rumble III, T. C. Hoering, and
A. J. Boucot

The presence of fossils in metamorphic rocks presents an ideal opportunity to study the metasomatism that accompanies metamorphism because the chemical and isotopic composition of fossils prior to metamorphism is well known (Keith and Weber, 1964). The original composition of the fossils provides a baseline against which metasomatic changes can be measured. In this work, Early Devonian brachiopods from the sillimanite zone are used to assess chemical and oxygen isotopic metasomatism during regional metamorphism.

The fossils are located in the cascades of Beaver Brook on the slopes of Mt. Moosilauke, New Hampshire (Fig. 125). The bed of shells (5–10 cm thick) is the innermost layer within a banded, calc-silicate unit (20–30 cm thick) that is intercalated with gray biotite schist (Fig. 126). Shells are aligned parallel to the bedding of the rock, are thoroughly disarticulated, little sheared, and unbroken. The fossil bed is truncated at the south end of the outcrop by a dike whose mineralogical composition is similar to that of the Kinsman Quartz Monzonite (Fig. 126, see Table 27).

Four genera of Early Devonian brachiopods have been identified, including *Acrospirifer*, *Atrypa*, *Leptocoelia*, and either *Leptostrophia* or *Protoleptostrophia* (Boucot and Rumble, 1978). A high-spired gastropod of unidentifiable genus, similar to *Loxonema*, has also been found. The shells of these organisms are now composed of either quartz and calcite or wollastonite, quartz, and calcite; their impressions are made of grossularite, diopside, clinozoisite, and sphene (Table

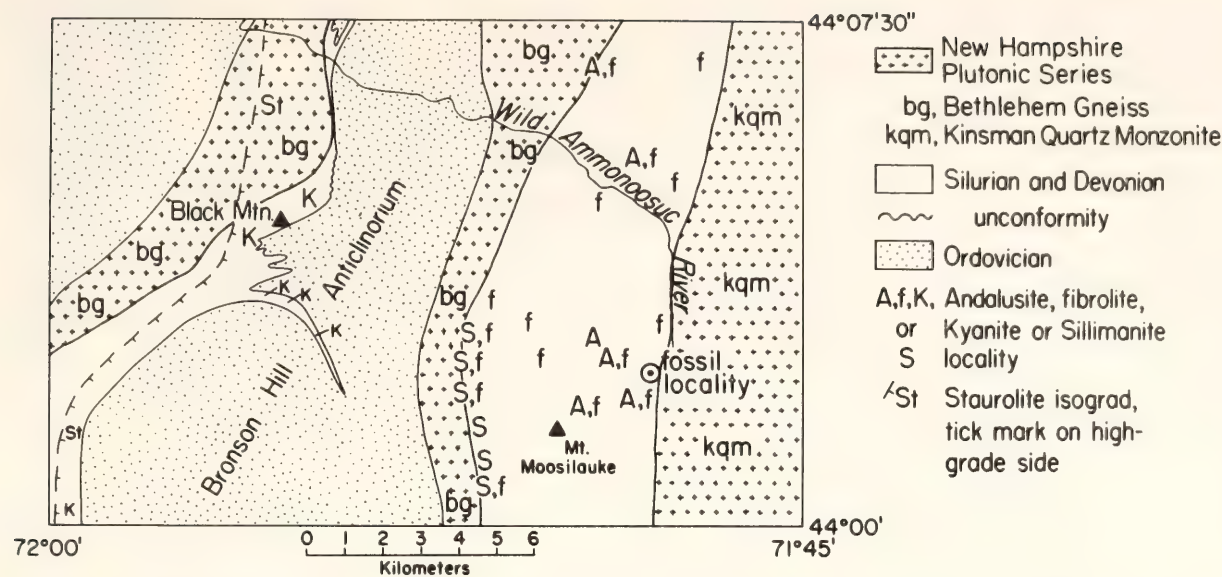


Fig. 125. Geological map of southern half of Mt. Moosilauke 15' quadrangle showing fossil locality and distribution of Al_2SiO_5 polymorphs (after Billings, 1937, and Rumble, 1973).

27). Partial silicification of the shells probably occurred during diagenesis and certainly before metamorphism, for otherwise there would have been no quartz present to react with calcite to produce wollastonite. Because of its premetamorphic age, silicification will not be discussed further.

The approximate P, T conditions of metamorphism may be deduced from the mineralogical data given in Fig. 125. The fossils are located in the outcrop area of regional andalusite and sillimanite, 8 km east of the nearest kyanite occurrences and 3 km east of the outcrop trace of the isobar of the Al_2SiO_5 invariant point (Thompson and Norton, 1968; Rumble, 1973). Metamorphic conditions reached a pressure equal to or less than that of the Al_2SiO_5 invariant point and a temperature exceeding that of the invariant point. Experimental measurements of the coordinates of the invariant point are $P = 3.8$ kbar and $T = 500^{\circ}C$ (Holdaway, 1971). The presence of the main batholith of the Kinsman Quartz Monzonite 200 meters east of the fossils places an upper limit on the temperature reached during

metamorphism. The Kinsman is intrusive into schists of the Littleton Formation and was at least partially molten during emplacement. The Quartz Monzonite is syntectonic and shows no contact aureole or chill zone against its country rocks (Billings, 1937). Thus, it is reasonable to assume that the temperature of the Kinsman during emplacement was similar to that of its metamorphic country rocks. The Kinsman contains quartz-potash feldspar-oligoclase, an assemblage with low melting temperature in rocks of granitic composition. Calculations of Ohmoto and Kerrick (1977) on the coordinates of the minimum melting of granite in the presence of a fluid similar to that at the fossil locality give an upper limit on T of $675^{\circ}C$ at 4 kbar. Rocks at the fossil locality attained $P \leq 3.8$ kbar and $500^{\circ}C < T < 675^{\circ}C$ during metamorphism.

Rocks of the fossil locality were subjected to both chemical and oxygen isotopic metasomatism during metamorphism. Evidence of chemical metasomatism is mineralogical and includes symmetric banding of calc-silicate layers,

TABLE 27. Mineral Assemblages and Oxygen Isotope Composition of Fossil Bed and Contiguous Rocks*

	Fossil Bed		Banded Calc-Silicate				Country Rock Mica Schist	Quartz Monzonite Dike
	Shells	Impressions	Band 1	Band 2	Band 3	Band 4		
Quartz	+14.7‰ [†] (±0.1)	+	+	+	+	+	+	+
Calcite	+	+	+					
Wollastonite	+							
Grossularite		+	+	+				
Diopside		+	+	+	+			
Clinozoisite		+	+	+	+	+		+
Graphite			+			+	+	+
Plagioclase						+		
Hornblende							+	
Biotite							+	+
Ilmenite							+	+
Microcline								
Muscovite								
Sphene		+	+	+	+	+	+	
Pyrrhotite			+	+12.5‰ [†] (±0.3)	+	+	+	+13.0‰ [†] (±0.1)
Whole Rock	+11.8-12.0‰ [‡]					+12.86‰ [†] (±0.1)	+12.2-12.8‰ [‡]	

* Presence of mineral indicated by + mark in tabulation.

† Oxygen isotope composition as δ ¹⁸O_{smow}; number in parenthesis is one standard deviation (‰) of duplicate or triplicate analysis of aliquots of same sample.

‡ Oxygen isotope composition δ ¹⁸O_{smow}; range of values shows variation between different places in same rock type.

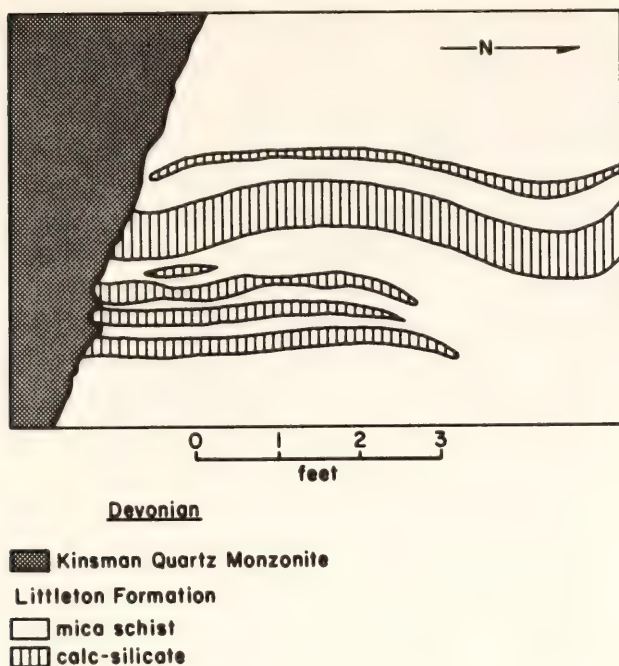
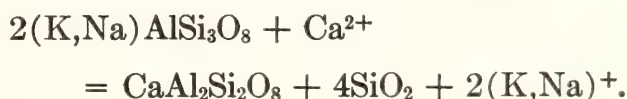


Fig. 126. Sketch map of fossil locality. Fossils have been identified from the thickest calc-silicate layer.

alteration of the margin of the dike where it is in contact with calc-silicate, and the presence of graphite in the dike rock. Each calc-silicate layer contains bands of distinctive mineralogical composition parallel to bedding and arranged symmetrically on either side of the center of the layer. The innermost band, in which fossils are recognized, has the mineralogical composition described above and shown in Table 27; it is separated from biotite schist by the succession of bands listed as numbers 1–4 in Table 27. The chief features of the banding are: (1) the restriction of wollastonite to the innermost band, (2) the presence of calcite in the inner bands, and (3) the successive disappearance of grossularite, diopside, and clinozoisite and the appearance of hornblende and plagioclase in the outer bands. The zoning sequence differs in detail from published accounts of other such banded calc-silicate layers, but the order in which the minerals grossularite, diopside, and clinozoisite disappear passing from the innermost band to biotite schist is identical (see Thompson, 1975). Mineralogical zonation of this kind can be

accounted for, to a first approximation, by the intergranular diffusion of Ca from the calcite-wollastonite core of the calc-silicate layer into biotite schist (Brady, 1977).

Another example of chemical metasomatism is recorded by the mineralogical alteration of the quartz monzonite dike where it is in contact with calc-silicate layers. Unaltered quartz monzonite, in the central part of the dike and near its contacts with biotite schist, consists of quartz-microcline-oligoclase-biotite-muscovite. An alteration zone, 4–5 cm thick, is present in the dike rock wherever it is in contact with calc-silicate. The mineralogical composition of the alteration zone is quartz and anorthite with minor tremolite, sphene, apatite, and clinozoisite. Anorthite is present as a myrmekitic intergrowth with quartz, apparently as a pseudomorph after original microcline and oligoclase. Alteration of the dike was caused by intergranular diffusion of Ca from the calc-silicate into the dike accompanied by the reaction



The presence of graphite in the quartz monzonite dike is important because it, together with the ^{18}O data given below, shows that the dike was permeated by CO_2 evolved from decarbonation of the calc-silicate layers. Graphite is rare as an accessory mineral in plutonic igneous rocks and, where present, is taken as evidence of the contamination of the pluton by its country rock. Graphite will precipitate when CO_2 -rich and aqueous fluids are mixed, provided that the $\text{CO}_2/(\text{H}_2\text{O} + \text{H}_2)$ ratio is 1:1 or greater and that the system f_{O_2} lies within the stability field of graphite (Nockleberg, 1973, p. 509). It is believed that graphite was precipitated when CO_2 , released by decarbonation of the fossil bed, infiltrated the dike and mixed with residual aqueous fluid in the dike rock.

Evidence of oxygen isotopic metasoma-

tism may be seen in the anomalously low ^{18}O content of the shell bed and the anomalously high ^{18}O content of the quartz monzonite. The whole rock oxygen isotopic composition of the fossil shells varies from +11.8 to +12.0 ‰* along the outcrop length of the bed (Table 27). Comparison of these values with those measured on unaltered or silicified Devonian brachiopods shows that the fossils have been depleted by 12 ‰ during metamorphism (Keith and Weber, 1964; Savin and Epstein, 1970). Depletion in ^{18}O content is typical of metamorphosed calc-silicate rocks and takes place because the CO_2 released by decarbonation is enriched in ^{18}O relative to the minerals left behind (Shieh and Taylor, 1969). In contrast to the ^{18}O depletion of the shells, the dike rock with a value of +13.0 ‰ is enriched in ^{18}O relative to normal

plutonic rocks of granitic composition with values of +6 to +10 ‰ (Taylor, 1977). According to Taylor (1977, p. 513) granitic rocks with $\delta^{18}\text{O}$ values greater than +10.0 ‰ "require either derivation from, or exchange with, some type of high- ^{18}O sedimentary rock" Therefore, the ^{18}O data indicate that ^{18}O -rich CO_2 released by decarbonation of the shell bed exchanged oxygen isotopes with the minerals of the dike rock, resulting in fossil shells depleted in ^{18}O and quartz monzonite enriched in ^{18}O .

Application of the combined methods of metamorphic petrology and isotope geochemistry has resulted in the identification of the source and sink for volatiles released during metamorphism. Both mineralogical and oxygen isotopic evidence indicate that the quartz monzonite dike was permeated and contaminated by CO_2 . These observations document the great disparity in effective mobility of CO_2 and Ca during metamorphism: the diffusion of Ca was limited to a few cm adjacent to the fossil bed, whereas CO_2 was able to completely pervade the dike rock over a distance of several meters.

* Oxygen isotopic composition is given as $\delta^{18}\text{O}_{\text{SMOW}} = 1000 \times [(^{18}\text{O}/^{16}\text{O})_x - (^{18}\text{O}/^{16}\text{O})_{\text{SMOW}}] / (^{18}\text{O}/^{16}\text{O})_{\text{SMOW}}$ where "x" refers to an unknown sample and SMOW refers to the standard, Standard Mean Ocean Water (Craig, 1961).

SPECTRAL MINERALOGY: CRYSTALLOGRAPHY

HIGH-PRESSURE PHASE TRANSITIONS IN FeS , USING ^{57}Fe MÖSSBAUER SPECTROSCOPY

H. King, D. Virgo, H. K. Mao

Iron sulphide (FeS) occurs at room pressure and temperature in the troilite crystal structure. Previous workers have shown that it undergoes two phase transitions with increasing pressure. Because both of the higher pressure phases cannot be quenched to room conditions, these transitions appear to be isochemical, polymorphic ones. The first transition occurs at 34 kbar (Pichulo *et al.*, 1976). Although the structure has not been refined, single-crystal diffraction patterns suggest that the new phase is a multiply

twinned, MnP-type structure (King and Prewitt, in preparation). The second transition is to a yet unknown structure type first reported by Taylor and Mao (1970). Data from Pichulo *et al.* (1976) and the present study show that this transition occurs at approximately 67 kbar. Pichulo *et al.* have suggested that there is a 15% volume decrease at this transition.

The present study was undertaken to define further the nature of the structural transformations at high pressure using ^{57}Fe Mössbauer spectroscopic techniques. In general, changes in the physical and chemical properties of iron sulphides as a function of pressure are important because of applications to geomagnetic and palaeomagnetic problems.

Methods

Results and Discussion

The samples used in this study were synthesized from the pure elements using iron enriched in ^{57}Fe and using synthesis techniques previously developed (King and Prewitt, in preparation). The sample had the composition $\text{Fe}_{0.997}\text{S}$ (determined by x-ray powder diffraction, Yund and Hall, 1969) in agreement with those prepared by Horwood *et al.* (1976). In addition, a crystal structure refinement using data collected on a crystal selected from similar material gave results in agreement with the most recent single-crystal study of troilite (Evans, 1970).

The ^{57}Fe Mössbauer experiments were performed on polycrystalline samples in a diamond-anvil high-pressure cell using techniques described by Huggins, Mao, and Virgo (*Year Book* 74, pp. 405–410). Velocities were calibrated by collecting an iron metal spectrum before and after the high-pressure experiments. All isomer shift values quoted here are relative to that of iron metal and are in agreement with a more accurate study by Violet and Pipkorn (1971). A 4:1 methyl-ethyl alcohol mixture was used as the pressure transmitting medium, and pressures were measured using the ruby-fluorescence technique.

The ^{57}Fe Mössbauer spectra of three FeS polymorphs are shown in Fig. 127. At low pressures the spectra consist of six peaks, magnetically split, whereas at high pressure the spectrum is typical of paramagnetic iron and exhibits a small quadrupole splitting. The hyperfine parameters, quadrupole splitting, isomer shift, and internal magnetic field are listed in Table 28. Values of the effective magnetic field and isomer shift are plotted as a function of pressure in Figs. 128 and 129, respectively.

In general, trends in the hyperfine parameters (Table 28; Figs. 128 and 129) indicate that a sharp change in the effective magnetic field occurs around 34 kbar and that a more dramatic change in the ^{57}Fe environment takes place between 52 and 77 kbar. Additional spectra taken at 64 and 69 kbar show that the high-pressure transition is at approximately 67 kbar. Despite the difference in pressure, the high-pressure transition inferred from this study can be correlated with the ^{57}Fe Mössbauer results of Kasper and Drickamer (1968). In this latter case, the ^{57}Fe absorption spectra at 36 kbar consisted of a single broad absorption line with an isomer shift of about 0.29 mm/sec

TABLE 28. Hyperfine Parameters for $\text{Fe}_{0.997}\text{S}$ at 25°C

<i>P</i> , kbar	δ , mm/sec*	<i>H</i> , kOe	2 ϵ , mm/sec§
0.001‡	0.76(3)†	311.6(2)	−0.14(4)
30.	0.73(3)	314.(1)	−0.13(4)
42.	0.71(3)	271(1)	0.30(4)
52.	0.70(3)	259.2(2)	0.30(4)
77.	0.49(2)	...	0.43(1)
142.	0.42(3)	...	0.42(3)

* Relative to iron metal at 1 bar.

† One standard deviation in parenthesis.

‡ The data of 0.001 kbar are in agreement, within one standard deviation, with that determined by Ono *et al.* (1962), Hafner and Kalvius (1966), and Gosselin *et al.* (1976).

§ 2 ϵ = $\frac{1}{2}$ (*V*6 + *V*1 − *V*2 − *V*5) where *V*_{1,2,5,6} refer to the positions of the absorption lines consecutively numbered in Figs. 127, A, B, with line 6 at the largest positive velocity.

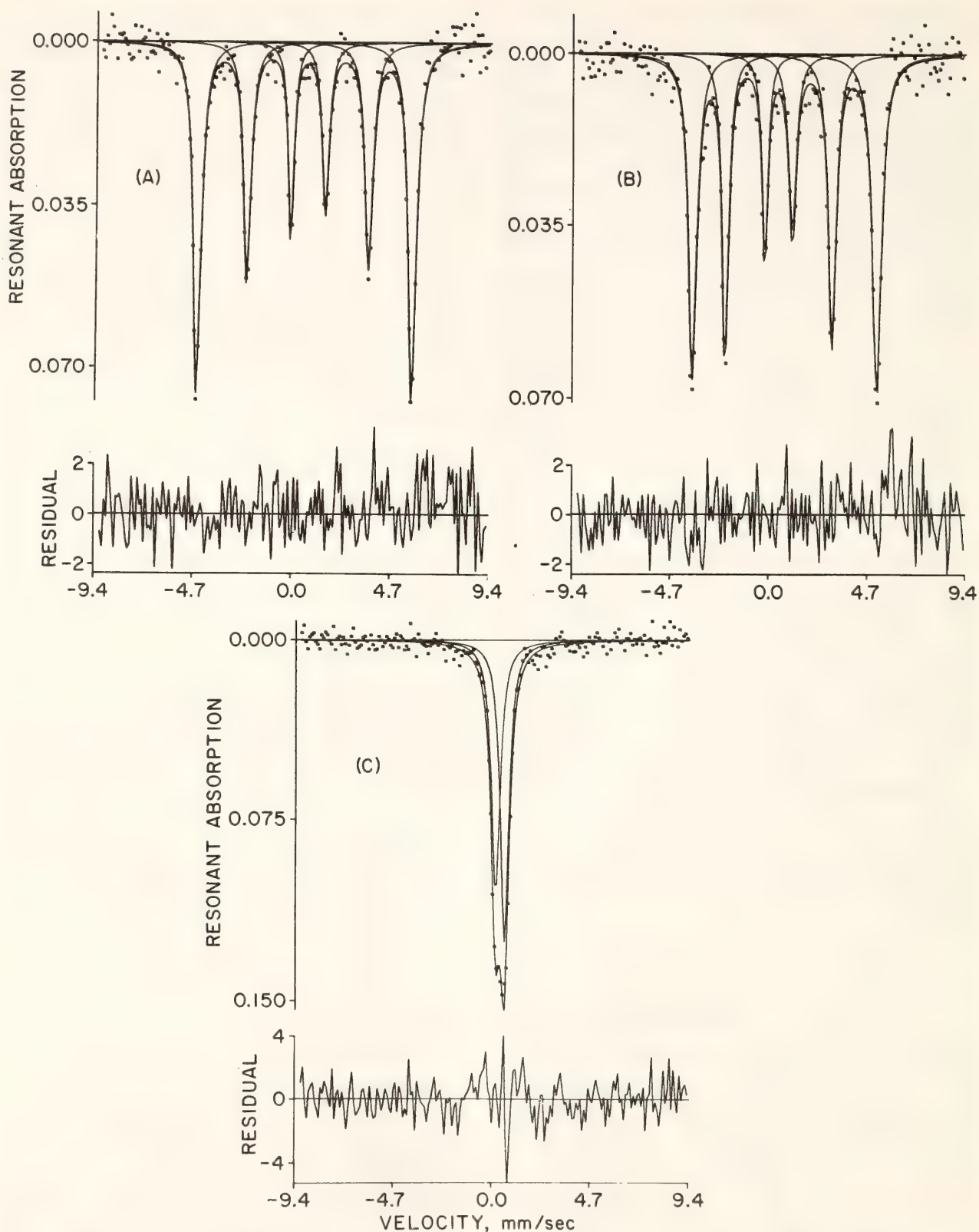


Fig. 127. ^{57}Fe Mössbauer spectra for three FeS polymorphs (solid lines are least-squares fits): (A) the troilite structure at 30 kbar, (B) a high-pressure polymorph with a proposed MnP-type structure at 42 kbar, and (C) a high-pressure polymorph with an unknown structure type at 77 kbar.

relative to Fe metal. In a previous study, however, Kasper and Drickamer (1968) found only one transition in the range 1 bar to 200 kbar; the discrepancy in the transition pressure between the two

studies may result from the use by Kasper and Drickamer of a nonhydrostatic pressure medium and from the high accuracy of the ruby-fluorescence calibration technique used here.

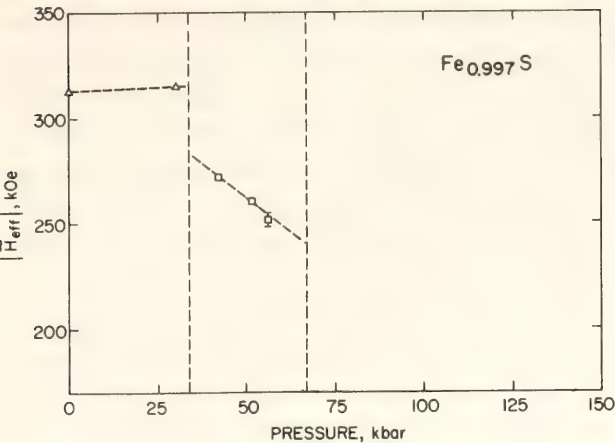


Fig. 128. Mössbauer magnetic hyperfine interactions for Fe_{0.997}S at room temperature. Vertical dashed lines show the structural transformations at 34 and 67 kbar.

A brief discussion of the ⁵⁷Fe hyperfine parameters listed in Table 28 provides further details regarding the high-pressure transitions in FeS.

I. Quadrupole splitting. The FeS spectra below 67 kbar have both quadrupole and magnetic splitting; therefore, the quadrupole splitting is indeterminate without assuming a symmetry for the electric field gradient tensor (Hafner *et al.*, 1967). These assumptions may be questionable for FeS (Townsend *et al.*, 1976). Thus, the 2ε entries in Table 28 for the magnetic spectra reflect some mixture of quadrupole and magnetic interaction. Above 67 kbar, however, 2ε reflects a purely electric quadrupole interaction. There are two important features that can be noted about 2ε for this high-pressure phase. First, its magnitude is small when compared to those of other substances (e.g., Huggins *Year Book* 74, p. 552). Second, its value is invariant for a 70-kbar pressure interval, although the quadrupole splitting usually increases with pressure (Champion *et al.*, 1967; Vaughn and Drickamer, 1967). A zeroth-order approximation for the pressure dependence is that splitting should increase in proportion to 1/*R*³, where *R* is the interatomic distance (Champion *et al.*, 1967). It is suggested, therefore, that this high-pressure phase seems to be relatively incompressible.

II. Internal Magnetic Field. The mag-

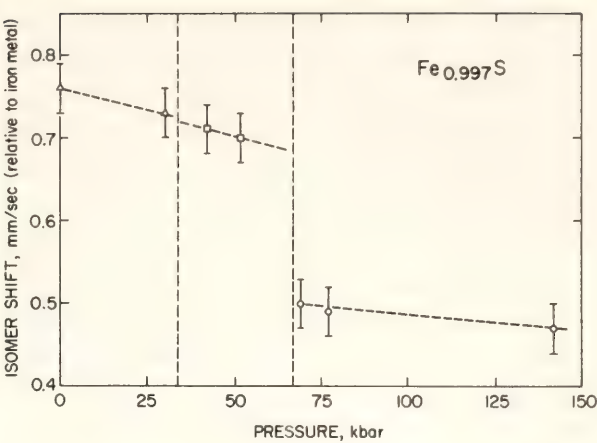


Fig. 129. Mössbauer isomer shift measured on Fe_{0.997}S at room temperature. Vertical dashed lines show the structural transitions at 34 and 67 kbar.

netic field measured by the Mössbauer effect depends on both the magnetic moment of the atom and the magnitude of the magnetic exchange interaction, which is a measure of the energy of ordering. There is some evidence that the latter effect is important in FeS at the 34-kbar transition. Several lines of evidence, namely single-crystal diffraction, electrical conductivity, and DTA, all indicate that the α transition (1 bar and 150°C) is equivalent to the 34-kbar transition (King and Prewitt, 1978). A comparison of the magnetic hyperfine interactions for these transitions, that is, a change from 290 to 250 kOe at the α transition and 314 to 280 kOe at the 34-kbar transition, supports this conclusion. These latter results also suggest that there is a similarity in the magnetic behavior at the transition points. Measurements of magnetic susceptibility and Mössbauer magnetic-hyperfine parameters on FeS at 1 bar show that at the α transition there is a decrease in the exchange interaction but no change in the atom's moment (Horwood *et al.*, 1976; Townsend *et al.*, 1976).

Increasing pressure, however, causes the magnetic field intensity to decrease throughout the MnP-type structure stability field. The decrease in the magnetic field intensity probably reflects a changing Fe-S-Fe geometry because the

exchange interaction can be expected to depend on such geometric details (Benedek, 1963, p. 15). At 67 kbar the magnetic ordering disappears, apparently owing to the change in crystal structure. This high-pressure structural change, however, is not related to the transition to a NiAs-type structure that occurs at the Néel temperature (325°C) at 1 bar. In fact, the latter transition has a positive slope with pressure (3.2 deg/kbar; Anzai and Ozawa, 1974).

III. Isomer Shift. The isomer shift for FeS (Fig. 129) up to 67 kbar follows trends similar to those observed for many substances (Drickamer *et al.*, 1969). These changes can be attributed to changes in the wavefunctions and to changes in the thermal vibration frequency of the absorber atom, the second-order Doppler shift (Greenwood and Gibb, 1971, pp. 50–54). A calculation of the latter effect, however, shows it to be insignificant in this case (-0.002 mm/sec). Two models that have been proposed for the changes in the wavefunctions are expansion of the 3d orbitals (Champion *et al.*, 1967) and electron transfer to the ligands (Huggins, *Year Book* 74, pp. 551–555). The data discussed previously concerning magnetic interactions suggest that the electrons on the

iron are sufficiently localized to contribute to the moment, and for this reason the possibility of electron transfer in FeS up to 67 kbar can be eliminated. Whatever the cause of the changes, the small change in isomer shift shows that they do not produce any significant changes in the bonding.

The data in Fig. 129 show that the 67-kbar transition causes a substantial change in the electron distribution. This result indicates a significant difference between the iron-sulfur interaction at high and low pressure. One way to understand the nature of this high-pressure interaction is to compare the Mössbauer parameters from the high-pressure phase with those from a variety of iron compounds. The isomer shifts and quadrupole splittings for several Group V and VI iron compounds are listed in Table 29. In this table, FeAs has Mössbauer parameters similar to those for high-pressure FeS. The iron in FeAs is in octahedral coordination and is Fe^{3+} . The inference that iron in high-pressure FeS is Fe^{3+} is an entirely unexpected result. Drickamer *et al.* (1969) have found that with increasing pressure Fe^{3+} is often reduced to Fe^{2+} . In addition, Vaughn and Tossell (1973) have suggested that this FeS transition resulted in a change from high-

TABLE 29. Room Pressure Isomer Shift and Quadrupole Splitting for Group V and VI Iron Compounds

	δ mm/sec	2ϵ mm/sec	Reference*		δ mm/sec	2ϵ mm/sec	Reference*
FeP	0.29	0.65	c	FeS	0.76	-0.14	h
FeP ₂	0.09	2.08	g	Fe ₇ S ₈	0.66	...	a
FeAs	0.44	0.49	c	FeS ₂ (P)	0.31	0.61	f
FeAs ₂	0.31	1.68	f	FeS ₂ (M)	0.28	0.51	f
FeSb	0.45	...	b	FeSe	0.61	...	e
FeSb ₂	0.45	1.28	f	Fe ₇ Se ₈	0.67	...	d
				FeSe ₂	0.39	0.58	f
				FeTe ₂	0.47	0.50	f

* References as follows: a, Gosselin *et al.* (1975); b, Ilmenkov *et al.* (1971); c, Maeda and Takashima (1973); d, Ok and Lee (1973); e, Reddy and Chetty (1975); f, Temperley and Leferre (1966); g, Wäppling *et al.* (1971); h, this work.

spin to low-spin iron. None of the low-spin materials listed in Table 29—FeS₂ (pyrite), FeS₂ (marcasite) and FeSe₂—have isomer shifts similar to FeS. Also, high-pressure Mössbauer spectra taken on FeS₂ (pyrite) show that at high pressure there is an even further discrepancy (Vaughn and Drickamer, 1967).

It is clear that a structure determination of the high-pressure phase of FeS above 67 kbar is mandatory. Nevertheless, the isomer shift and quadrupole splitting for iron are similar to Fe³⁺, and therefore at least one conclusion can be reached concerning the electron configuration of iron at high pressure. The major contribution to quadrupole splitting is the asymmetric electric field set up by the d-electrons. A small quadrupole splitting is observed for Fe³⁺ (d⁵), and thus a d⁵ configuration seems likely for the iron in high-pressure FeS. The electron could be transferred to a conduction band, to an iron 4s orbital, or to the sulfur atom. Any of these possibilities would be consistent with the change in isomer shift.

ISOTHERMAL COMPRESSION OF PEROVSKITE-TYPE MgSiO₃

T. Yagi, H. K. Mao, and P. M. Bell

Silicates with perovskite structure are now believed to predominate among the mineral phases in the earth's lower mantle (Liu, 1976; Mao *et al.*, *Year Book* 76, pp. 502–504), but there are no data on the elastic properties of these phases. In this study the isothermal compression curve of MgSiO₃-perovskite is determined from data obtained by high-pressure *in situ* x-ray diffraction measurements.

The MgSiO₃-perovskite was prepared with the laser-heated diamond-anvil high-pressure apparatus (Yagi *et al.*, 1978) at approximately 400 kbar and 1000°C. Quenched samples with dimensions of approximately 100 μm × 20 μm from two experimental runs were held in the sample

chamber of the diamond cell with 4:1 methanol-ethanol as pressure transmitting fluid and with a small crystal of ruby for pressure calibration. Monochromatic MoKα₁ radiation (λ = 0.709261 Å) was collimated so that the x-ray beam incident on the sample had a rectangular cross section of approximately 100 μm × 50 μm. The diffraction line widths on the film are less than 100 μm when the sample-to-film distance is approximately 50 mm. At x-ray power settings of 50 kV and 4 mA, the exposure time was 300 to 400 hr. In this x-ray system two diffraction lines whose 2θ angles differ by 0.2° can be resolved.

In order to determine *d*-values with accuracy in the x-ray cameras used in high-pressure experiments, the sample-to-film distance (including film shrinkage) must be known; normally an internal standard is used to determine this parameter. On the other hand, diluting perovskite with internal standard tends to obscure weak diffraction lines. To resolve the problem, two sets of experiments were made. In the first set, a mixture of MgSiO₃-perovskite, ruby, and MgO internal standard was x-rayed under pressure. By referencing the ruby fluorescence pressure scale and the equation of state of MgO, the sample-to-film distance was determined to within ±20 μm. The *d*-values of six intense diffraction lines of perovskite as a function of pressure were determined. In the second set of experiments, only MgSiO₃-perovskite and ruby were mixed. Films of adequate quality with 24–25 diffraction lines were obtained. The calibrated *d*-values of the six intense lines were used to determine the sample-to-film distance for calculating *d*-values of all diffraction lines. An example of the observed and calculated *d*-values of MgSiO₃-perovskite obtained at 74.5 kbar is summarized in Table 30. The orthorhombic unit cell was refined using 19 lines not affected by overlap. All the observed and calculated *d*-values are in agreement within an error of ±0.15%. Unit-cell dimensions and volume at

TABLE 30. Observed and Calculated d-values of MgSiO₃-Perovskite at $P = 74.5$ kbar and $T = 23^{\circ}\text{C}$

$h\ k\ l$	d_{cal}	d_{obs}	I^*	$h\ k\ l$	d_{cal}	d_{obs}	I^*
0 0 2	3.428	3.402	s	1 2 2	1.836	1.835	mw
1 1 0	3.402			0 0 4	1.714	1.701	s
1 1 1	3.047			2 2 0	1.701		
0 2 0	2.447	2.448	w	2 2 1	1.651	1.649	mw
1 1 2	2.415	2.413	vs	1 2 3	1.575	1.579	w
2 0 0	2.366	2.366	m	1 3 0	1.542	1.543	mw
1 2 0	2.174	2.177	w	1 1 4	1.531	1.522	m
2 1 0	2.130	2.131	mw	2 2 2	1.524		
1 2 1	2.072	2.074	m	1 3 1	1.505	1.503	m
1 0 3	2.058	2.059	w	1 3 2	1.407	1.406	w
2 1 1	2.034	2.035	m	0 2 4	1.404		
0 2 2	1.992	1.991	w	2 0 4	1.388	1.388	w
2 0 2	1.947	1.945	w	3 1 2	1.375	1.376	w
1 1 3	1.897	1.893	w				

* Intensity visually measured.

different pressures are summarized in Table 31 and Fig. 130.

The a -axis is slightly more compressible than the b - or c -axes. With increasing pressure, c/b approaches the ideal ratio for cubic perovskite ($\sqrt{2}$) whereas b/a and c/a depart from the ideal ratios 1 and $\sqrt{2}$, respectively. As a net result, orthorhombic perovskite does not approach the ideal cubic unit cell but is increasingly distorted.

From the volume compression data, one can calculate the isothermal bulk modulus, K_0 , on the basis of Murnaghan, Birch-Murnaghan, or polynomial equations of state. The three equations give practically identical results in this pressure range. With two data points, only the bulk modulus K_0 is calculated. The second

parameter of the equations of state, dK_0/dP , is assumed to be 3 and 6, a range including most solid materials. Fortunately, K_0 is relatively insensitive to the assumption of dK_0/dp . The calculated K_0 ranges from 2.95(2) to 2.83(2) Mbar with the assumed dK_0/dp ranging from 3 to 6. If all possible errors are considered, one can conclude that the isothermal bulk modulus of MgSiO₃-perovskite is 2.9 ± 0.3 Mbar. Liebermann *et al.* (1977) studied the elasticity of Al, Ti, Sn, and Ge compounds with the perovskite structure, and found a correlation between molar volume and bulk modulus. Based on this correlation, it was estimated that the bulk modulus of MgSiO₃-perovskite was 2.5 ± 0.3 Mbar, in agreement with the present results.

TABLE 31. Unit Cell Parameters and Volume of the MgSiO₃-Orthorhombic Perovskite at 23°C

	1 bar	74.5 kbar	84.5 kbar
a (Å)	4.780(1)*	4.732(3)	4.724(3)
b (Å)	4.933(1)	4.895(3)	4.893(3)
c (Å)	6.902(1)	6.855(6)	6.852(8)
\bar{V} (Å ³)	162.75(3)	158.8 (1)	158.4 (2)

* Numbers in parentheses are standard deviations of least-squares fit.

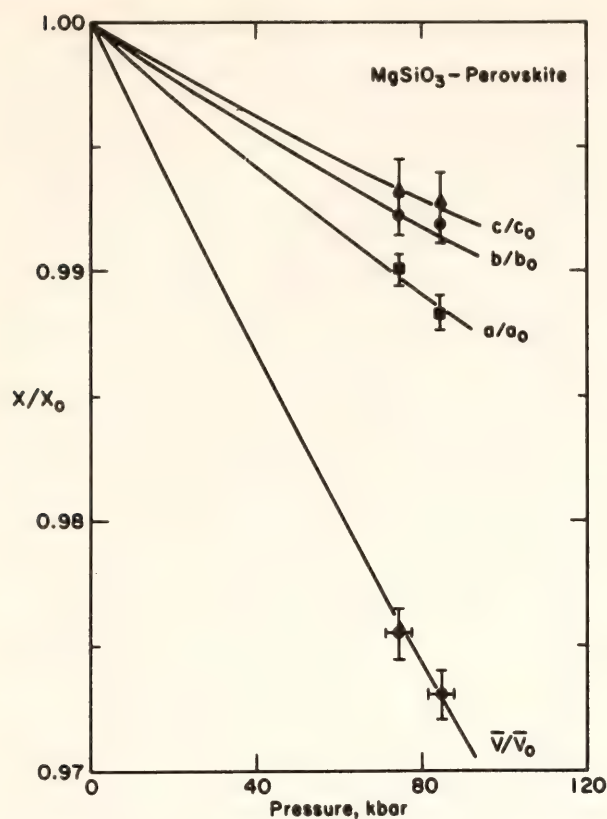


Fig. 130. Isothermal compression of MgSiO_3 -perovskite at 23°C . X in the vertical axis represents the lattice parameter a , b , or c , or the unit-cell volume \bar{V} . The error bars are standard deviations calculated from least-squares fitting of the unit cell.

At one bar, MgSiO_3 -perovskite is approximately 3% denser than the isochemical mixture of periclase and stishovite. For olivine composition, MgSiO_3 -perovskite plus MgO is 2% denser than the component oxides, 2MgO and SiO_2 . Because of the high bulk modulus of MgSiO_3 -perovskite, however, these differences decrease rapidly with increasing pressure and at 300 kbar the difference is only 0.9% for pyroxene and 0.6% for olivine composition. The difference is an order of magnitude smaller than in most other first-order phase transformations such as olivine-spinel. Any minor volume reduction (as low as 2%) of periclase or stishovite due to their high-pressure phase transitions could affect the stability of the MgSiO_3 -perovskite phase. Therefore, it is likely that the MgSiO_3 -perovskite may break down to such mixed oxides at pressures near the core-mantle boundary.

EFFECT OF IRON ON THE STABILITY AND UNIT-CELL PARAMETERS OF FERROMAGNESIAN SILICATE PEROVSKITE

T. Yagi, H. K. Mao, and P. M. Bell

Orthorhombic MgSiO_3 -perovskite has been shown to be a major component in the earth's lower mantle (Liu, 1975; Ito, 1977; Mao *et al.*, *Year Book 76*, pp. 502–504). Most composition models of the mantle conclude that Fe (Fe + Mg) is 0.1–0.2 (Clark and Ringwood, 1964). For a refined earth model, therefore, it is crucial to determine the effect of iron on the behavior of a ferromagnesian silicate perovskite.

Liu (1976) studied the system $(\text{Mg,Fe})_2\text{SiO}_4$ and $(\text{Mg,Fe})\text{SiO}_3$ at 300 kbar. Except when working with pure MgSiO_3 , he always obtained a multiphase product that included perovskite, oxides, and various lower pressure phases, with perovskite in an amount equal to or less than the other phases. The composition of perovskite was uncertain, however, and the results were therefore inconclusive. The purposes of the present study were to synthesize single-phase ferromagnesian perovskite with 10–20% iron, to determine the effect of iron content on the unit-cell parameters of the perovskite, to determine the partitioning of iron between perovskite and ferromagnesian oxide, and to explain the differential partitioning.

Experiments

Synthesis experiments were made with a laser-heated diamond-anvil high-pressure apparatus (Yagi *et al.*, 1978). Starting materials were synthetic olivines and pyroxenes, whose compositions were determined using the electron microprobe. The powdered sample was embedded in the hole of a gasket and a small quantity of ruby as single crystals was placed at the top of the sample. For samples with an iron content less than 10%, 0.5 wt % of finely divided platinum metal (Pt black,

grains 100 Å in size) was mixed for absorption of the YAG laser beam. Pressure was measured by the ruby-fluorescence technique. All the experiments were made at 450 ± 50 kbar and $1000^\circ \pm 300^\circ\text{C}$, and the quenched sample was studied by powder x-ray diffraction technique using $\text{CoK}\alpha$ radiation and a Debye-Scherrer camera 114.6 mm in diameter.

Results

(Mg,Fe)SiO₃ composition. Pyroxene starting materials having the same stoichiometry as perovskite were used to synthesize single-phase perovskite for unit-cell parameter determination. A single phase is necessary because the grain size of the perovskite in a multiphase run product is too small for accurate probe analysis. Pure perovskite-phase was obtained with the composition $(\text{Mg}_{1-x}\text{Fe}_x)\text{SiO}_3$ where $x = 0, 0.1$, and 0.2 . At $x = 0.3$ a mixture of perovskite, magnesiowüstite and stishovite was obtained, possibly indicating that the composition of the three phases will be fixed over a large range of Fe/Mg in an isothermal-isobaric section.

The unit-cell parameters obtained in the present experiments are summarized in Fig. 131. The unit-cell volume of perovskite made from pyroxene increases rapidly with iron content. This result is quite different from that reported by Liu (1976), who observed an almost constant unit cell of perovskite with $x = 0$ – 0.2 . In his experiments, however, the quench product was always a mixture of various phases; therefore, it is likely that partitioning of iron had taken place and the iron content of the perovskite was much lower than that of the starting material.

If one were to make a linear extrapolation of the volume of perovskite with composition based on the present results, the volume of the Fe end-member should be approximately 5% larger than that of

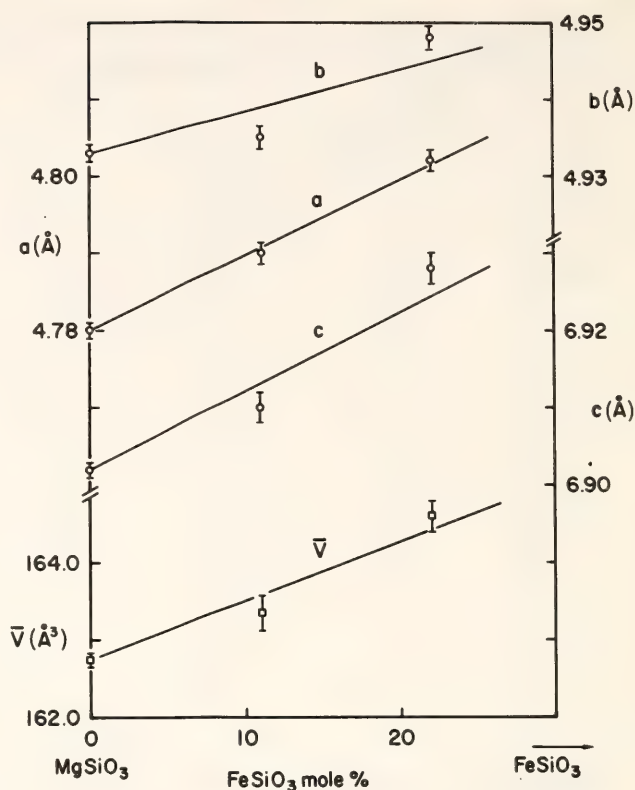


Fig. 131. Change in unit-cell parameters with composition in perovskite-type $(\text{Mg,Fe})\text{SiO}_3$.

the Mg end-member. This relation is similar to that of other Mg-Fe solid solutions such as magnesiowüstite, olivine, and spinel.

(Mg,Fe)₂SiO₄ composition. When the starting material has olivine stoichiometry, the quench product is a mixture of $(\text{Mg,Fe})\text{SiO}_3$ -perovskite and $(\text{Mg,Fe})\text{O}$ -magnesiowüstite. The assemblage is suitable for studying the partitioning of iron between the two phases.

Three compositions of $(\text{Mg}_{1-x}\text{Fe}_x)_2\text{SiO}_4$ with $x = 0, 0.1$, and 0.2 were studied. Pure forsterite produced a perovskite identical to that produced from enstatite and a periclase with ideal unit-cell parameters. The perovskites produced from olivine with $x = 0.1$ or 0.2 , however, have unit cells significantly smaller than those of the equivalent single-phase perovskites synthesized from pyroxene compositions with the same values of x . The coexisting magnesiowüstites, on the other hand, have larger unit cells than the equivalent magnesiowüstite with 10% or

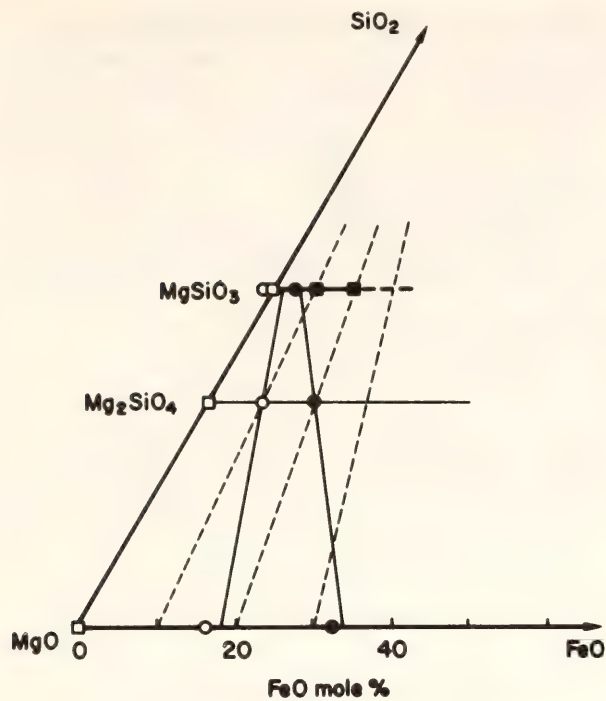


Fig. 132. Phase relations in the system MgO-FeO-SiO₂ at 450 kbar and 1000°C. Open squares, open circles, and solid circles indicate the composition of the starting material (Mg_{1-x}Fe_x)₂SiO₄ and the compositions of the perovskite and magnesiowüstite produced for x = 0, 0.1, and 0.2, respectively. The solid lines connecting them are tie-lines for the two-phase region. Solid squares represent experiments started with pyroxene compositions. Dashed lines indicate constant Fe-Mg ratio.

20% FeO. The iron contents of the two phases can be estimated from the correlations of compositions and unit-cell parameters established above for perovskite and reported by Rosenhauer *et al.* (*Year Book* 75, pp. 513–515) for magnesiowüstite. The results are plotted in Fig. 132, and clearly show strong partitioning of iron in magnesiowüstite.

Crystal-field effects on the stabilization of the perovskite structure. Based on considerations of ionic radii, Ringwood (1975) predicted that the FeSiO₃-perovskite would be stabilized at a lower pressure than would MgSiO₃-perovskite. However, the experimental results indicate an opposite tendency. These experimental results, the destabilization of FeSiO₃ perovskite compared to MgSiO₃, and the concentration of iron in magnesio-

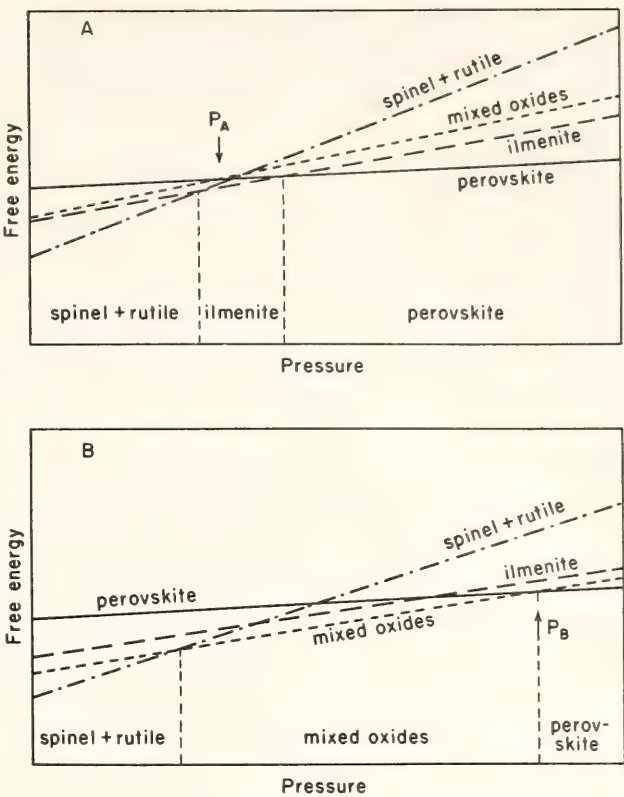


Fig. 133. Schematic diagram of free energy vs. pressure for (A) MgSiO₃ and (B) FeSiO₃.

wüstite, can all be explained by considering the crystal-field effect of ferrous ion in these structures.

Figure 133 is a schematic diagram of free energy vs. pressure for high-pressure phases with MgSiO₃ and FeSiO₃ compositions. In MgSiO₃, transformations occur as follows (in order of increasing pressure): spinel (γ) + rutile → ilmenite → perovskite. The mixed-oxide assemblage has no stable region (Fig. 133A). In contrast, FeSiO₃ transforms from γ + rutile to a mixed-oxide assemblage; no further transitions are known. Perovskite has a smaller volume, however, than the mixed-oxide assemblage, so the oxides may eventually transform into perovskite at higher pressures (Fig. 133B). These differences between MgSiO₃ and FeSiO₃ can be explained by considering the contribution of crystal-field stabilization energy (CFSE) of Fe²⁺ ions in these structures.

The CFSE for Fe²⁺ ions in minerals thought to occur in the mantle has been

TABLE 32. Crystal Field Effects on Fe²⁺ Ion in FeO and Perovskite-type FeSiO₃

	\bar{V} (Å ³ /molecule)	M-O (Å)	Δ (cm ⁻¹)	CFSE (cm ⁻¹)
Perovskite-type FeSiO ₃	41.45*	2.447†	2370	1420
Rock-salt-type FeO	43.47‡	2.162	8820	3530

* Estimated from the systematics between volume and ionic radii in perovskite-type compounds (Yagi *et al.*, 1978).
† Calculated from volume, assuming ideal cubic perovskite structure.
‡ Sum of the volume of FeO and SiO₂ (stishovite).

calculated by Gaffney (1972).^{*} The results for various minerals are summarized by Burns (1976). On the basis of the point-charge model, the following relation gives the crystal-field splitting of 3d electrons:

$$\Delta_{\text{octahedral}} = 2\Delta_{\text{dodecahedral}} \quad (1)$$

In both the spinel and the rock-salt structures, the transition metals are in octahedral sites, but in spinel the sites are slightly distorted and the mean bond lengths are slightly smaller. Considering these factors and Gaffney's (1972) calculations, one can derive the following relation:

$$\Delta_{\text{spinel}} > \Delta_{\text{rock salt}} \geq \Delta_{\text{ilmenite}} \gg \Delta_{\text{perovskite}}.$$

If the free energies in Fig. 133A are modified to account for the contributions of these crystal-field stabilization energies, the results shown in Fig. 133B are obtained.

The pressure for the transition from the mixed-oxide assemblage to perovskite is approximated as follows. The value for crystal-field splitting calculated by Gaffney (1972), $\Delta_{\text{perovskite}} = 2540 \text{ cm}^{-1}$ for an *M-O* distance of 2.414 Å, is used with the relation $\Delta \propto r^{-5} = V^{-5/3}$ and Equation 1. All parameters used for the calculation are summarized in Table 32. The principles are the same as those described by Syono *et al.* (1971). The contribution of

^{*} In the 12-fold coordination site with *O_h* symmetry, CFSE for Fe²⁺ is ($\frac{3}{5}$)Δ instead of ($\frac{2}{5}$)Δ; therefore, the values for perovskite in Tables 4 and 5 of Gaffney (1972) should be revised.

the crystal field stabilization energy to the transition pressure is calculated by the following equation:

$$\Delta P = (\text{CFSE}_{\text{perovskite}} - \text{CFSE}_{\text{rock salt}}) / \Delta V. \quad (2)$$

Using the parameters listed in Table 32 Equation 2 gives $\Delta P = 207 \text{ kbar}$. To make the calculation more precise, the relation

$$\int_P^{P+\Delta P} dV = \Delta \text{CFSE}$$

could be used in place of Equation 2 if data on the compressibility of each phase were available. The Δ*V* term usually decreases with pressure; thus Δ*P* should increase by approximately 30–50%. It should be noted, however, that the above calculation is based on ideal cubic perovskite, and distortion would reduce the CFSE (especially for Fe²⁺) with a consequent reduction of Δ*P*. These last two effects, of opposite sign and similar magnitude, may cancel.

Values for Δ*P* thus calculated give the pressure between *P_A* (transition pressure from mixed oxide to perovskite when there is no effect of CFSE; Fig. 133A) and the real transition pressure from mixed oxides to perovskite, *P_B* (Fig. 133B). Although the pressure *P_A* is unknown, if one assumes that the mixed-oxide assemblage and ilmenite have similar free energies, then *P_A* is close to the pressure of the γ + rutile → ilmenite transition, which is approximately 220 kbar for MgSiO₃. On

the basis of these assumptions, one can estimate that the pressure for the transition from mixed oxides to perovskite in FeSiO_3 is 400–600 kbar.

In Table 32, one can see that crystal-field stabilization energy for Fe^{2+} in the rock salt structure is $252 \text{ cm}^{-1} \text{ mole}^{-1} = 12.5 \text{ kcal mole}^{-1}$ larger than that in the perovskite structure. The large extra energy favors the concentration of iron in magnesiowüstite and the depletion of iron in the coexisting perovskite, as experimentally observed in the present study.

CRYSTAL STRUCTURE AND COMPRESSIBILITY OF MnF_2 TO 15 KBAR

R. M. Hazen, L. W. Finger, and T. Yagi

Manganese difluoride, which has the rutile structure at room conditions, has attracted considerable attention because of its high-pressure-phase transformations (Azzaria and Dache, 1961; Kabalkina and Popova, 1963; Jamieson and Wu, 1977). Transitions in the compressible MnF_2 phase occur at pressures low enough for study in the laboratory, yet may have bearing on possible transitions at very high pressure of the dense SiO_2 polymorph stishovite. As a preliminary step in examining the transition behavior of MnF_2 , the crystal structure of MnF_2 was determined at 1 bar, 10 kbar, and 15 kbar. Each of these pressures is below the first phase transition.

A single crystal of synthetic MnF_2 approximately $100 \times 100 \times 60 \text{ }\mu\text{m}$ was selected for high-pressure study. Unit-cell parameters were determined on a four-circle automated diffractometer using the procedure described by Hamilton (1974) and modified by King and Finger (in preparation), whereby errors in the crystal centering and diffractometer alignment are removed by measuring a reflection in eight different positions. Unit-cell dimensions were refined without geometrical constraint (i.e., as triclinic) to detect any deviation from tetragonal

dimensionality. Parameters to 15 kbar, however, are tetragonal within two estimated standard deviations.

Intensity data at 1 bar were measured using techniques of Finger *et al.* (*Year Book 72*, pp. 694–699). Data were corrected for absorption ($\mu_t = 76.5 \text{ cm}^{-1}$), and the structure was refined to values of R less than 2.0% using a model with anisotropic temperature parameters and a secondary x-ray extinction parameter. The crystal was placed in a diamond cell (Merrill and Bassett, 1974) with 4:1 methanol-ethanol as the pressure-transmitting fluid and small ruby chips for pressure calibration. Intensities were measured at high pressures using techniques of Finger and King (1978) and Hazen and Finger (*Year Book 76*, pp. 655–656). Unit-cell parameters, refined structural parameters, and conditions of refinement are recorded in Table 33.

Compressibilities of a and c unit-cell axes are 4.3×10^{-4} and $2.0 \times 10^{-4} \text{ kbar}^{-1}$, respectively, giving a volume compressibility of $1.06 \times 10^{-3} \text{ kbar}^{-1}$ ($K_0 = 0.94 \text{ Mbar}$). The 2:1 compression ratio of $a:c$ is similar to the behavior of TiO_2 (rutile) observed by Bridgman (1928) and SiO_2 (stishovite) recorded by Sato (1977), although MnF_2 is approximately twice as compressible as either rutile or stishovite.

The structure of rutile-like compounds is tetragonal, space group $P4_2/mnm$, with two atoms in the asymmetric unit: R^{2+} or R^{4+} at $(0, 0, 0)$ and X^{1-} or X^{2-} at $(x, x, 0)$. All R cations are coordinated by six X anions in octahedral groups, and each X anion is surrounded by three R cations. In manganese fluoride the fluorine x parameter changes less than one estimated standard deviation between 1 bar and 15 kbar. The anisotropy of lattice compression in the rutile form of MnF_2 is primarily due to differential compression of Mn-F bonds within the plane normal to the c -axis, the compression is twice that of Mn-F bonds with a large c -axis component. Octahedra are edge-linked in strips parallel to the

TABLE 33. Unit-Cell Parameters, Conditions of Refinement, and Refined Parameters for MnF₂ at High Pressures

Parameter	1 bar	10 kbar	15 kbar	β kbar ⁻¹
a (Å)	4.8730(11)*	4.8509(6)	4.8413(3)	4.3×10^{-4}
c (Å)	3.3101(9)	3.3043(13)	3.3002(5)	2.0×10^{-4}
V (Å ³)	78.60(3)	77.74(4)	77.35(1)	
a/c	1.472	1.468	1.467	
Weighted R † (%)	1.5	1.2	1.5	
R † (%)	1.4	1.3	1.6	
No. of observations	179	32	28	
x_F	0.30496(13)	0.3046(3)	0.3046(5)	
B_{Mn} (Å ²)	0.65(1)	0.74(9)	0.77(12)	
B_F (Å ²)	1.08(1)	1.89(26)	1.62(26)	
r^* ($\times 10^{-6}$)	0.98(8)	0.6(3)	0.3(4)	
Mn-F (Å) [2]§	2.102(1)	2.089(2)	2.086(3)	
Mn-F (Å) [4]	2.132(1)	2.127(2)	2.124(2)	
F-F (Å) [4]	2.688(2)	2.680(4)	2.676(6)	
F-F (Å) [8]	2.994(1)	2.982(1)	2.977(1)	
F-Mn-F (angle in degrees)	101.84(4)	101.9(1)	101.9(1)	

* Numbers in parentheses represent the estimated standard deviation of the last digit presented.
† Weighted $R = [\sum w(F_o - |F_c|)^2 / \sum w F_o^2]^{1/2}$.
‡ $R = \sum |F_o - |F_c|| / \sum F_o$.
§ Numbers in brackets represent bond multiplicities.

c-axis (the least-compressible direction) and corner-linked in the (001) plane, perhaps resulting in the less-rigid configuration and the higher observed compression in this plane.

This study includes the first complete high-pressure structure refinement of a fluoride, and it provides a standard of comparison for bond compression in oxygen-based (Hazen and Prewitt, 1977) and fluorine-based compounds. The predicted value of octahedral Mn-O bond compression cited by Hazen and Prewitt is 1.9×10^{-4} kbar⁻¹, compared to an observed mean Mn-F compressibility of 3.4×10^{-4} kbar⁻¹ in the rutile-type compound. Eight-coordinated Ca in grossularite garnet has a Ca-O compressibility of 2.9×10^{-4} kbar⁻¹ (Hazen and Finger, 1978a) compared to 4.2×10^{-4} kbar⁻¹ for ^{VI}Ca-F bonds in fluorite (Clark, 1966). Metal-fluorine bonds, therefore, appear to be significantly more compressible than corresponding metal-oxygen bonds.

STUDY OF LEAD AT HIGH PRESSURE: COMPRESSIBILITY AND FIXED-POINT TRANSITION BETWEEN THE FCC AND HCP POLYMORPHS UNDER VARIOUS DEGREES OF NONHYDROSTATIC STRESS

H. K. Mao and P. M. Bell

Balchan and Drickamer (1961) first reported a high-pressure phase transition in metallic lead from its increase in electrical resistance; this transition has been widely used as a “fixed point” for high-pressure calibration. Using powder x-ray diffraction, Takahashi *et al.* (1969) determined the transition to be from face-centered cubic (fcc) to hexagonal close-packed (hcp) structure, at a nominal pressure of approximately 130 kbar. The transition appeared to be “smeared” over a pressure range in both the resistance and x-ray studies: although the reaction is univariant and rapid, both phases persisted over a wide pressure range the magnitude of which varied with

different nonhydrostatic stress conditions. These observations and the fact that the volume difference between the polymorphs is small lead to the conclusion that this system is ideal for evaluation of nonhydrostatic stress effects on thermodynamic equilibrium processes at high pressure. Lead is presumed to be weak and to exhibit considerable flow under pressure. The small volume difference of the two polymorphs suggests, however, that relatively minor nonhydrostatic stress affects their free energy and stabilizes a two-phase region that would otherwise be nonexistent.

The experimental measurement of uniform nonhydrostatic stress in a sample of lead requires specialized apparatus that will produce maximum nonhydrostatic stress, yet will minimize pressure gradients and inhomogeneities such as those known to exist in solid-media piston-cylinder and multianvil, high-pressure apparatus. The present experiments were done with the megabar-cell model MBC-N (a design modified after the one of Kinsland and Bassett, 1976; Mao and Bell, this Report) using x-ray diffraction for identification of the hcp and fcc phases and for evaluation of lattice-parameter variation relative to the principal stress direction.

The objects of the present study are: (1) to obtain high-pressure equation of state for fcc and hcp lead under quasi-hydrostatic conditions, (2) to evaluate the effect of nonhydrostatic stress on the equation of state, (3) to determine the effect of nonhydrostatic stress on the transition pressure, and (4) to measure the maximum nonhydrostatic stress in lead.

Isothermal Equation of State of Lead

The lead sample used in all experiments was a pure ingot (99.9999 wt % Pb). For the specific volume measurements, the lead sample was mounted in the megabar-cell model MBC-Y for x-ray diffraction using a 4:1 methanol-ethanol pressure medium hydrostatic to 100 kbar and

known to be quasi-hydrostatic from 100 to 250 kbar, the maximum pressure of these experiments. (Above 100 kbar, the alcohol mixture has a very low shear strength at 25°C, according to measurements by G. Piermarini and S. Block, National Bureau of Standards, personal communication, 1978).

The sample and fluid were held in a gasket of stainless steel (full-hardened T301). Ruby crystals were placed in the fluid for pressure calibration using the ruby-fluorescence technique. The techniques of x-ray and pressure measurement have been described by Mao *et al.* (1978a). Filtered Mo and Ag $K\alpha$ x-radiation were used with 50-mm-radius film cassette in order to obtain d -values for four diffraction lines for fcc phase and 13 lines for hcp phase. The external standard for determining the sample-to-film distance was Mo, Ag, Pb, or V metal.

The results between 67 and 265 kbar are given in Table 34. At pressures below 100 kbar, the volume of fcc Pb shows remarkable agreement with Bridgman's (1945a, 1945b) data. The variation of volume (V/V_0) of the two phases with pressure is plotted in Fig. 134. The curves

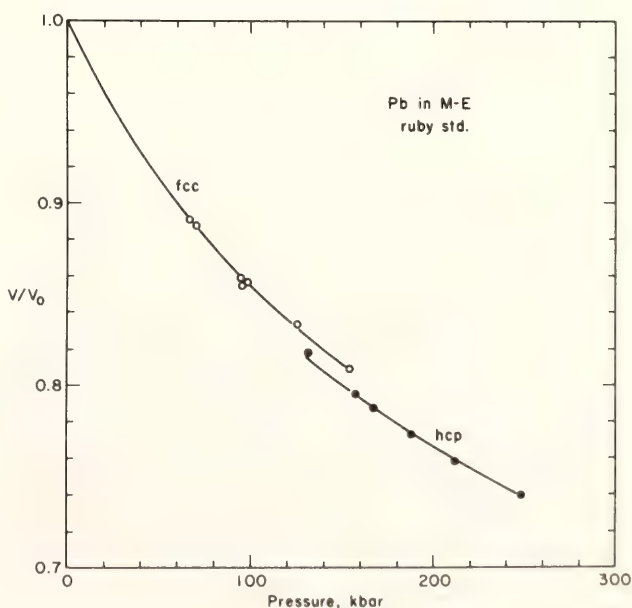


Fig. 134. Isothermal compression of lead in 4:1 methanol-ethanol (M-E) mixture. The pressure is calibrated with ruby R_1 standard. Open circles, fcc lead; solid circles, hcp lead.

TABLE 34. Compression of Lead in Methanol-Ethanol Medium with Ruby Pressure Calibration

Ruby R_1		fcc Pb	hcp Pb			
$\Delta\lambda$, nm	P , kbar	V/V_0^*	V/V_0^\dagger	a , Å ‡	c , Å ‡	c/a
2.42	67	0.890				
2.56	71	0.888				
3.45	95	0.857				
3.46	96	0.855				
3.52	97	0.856				
4.53	126	0.834				
4.74	132	trace	0.818	3.269	5.365	1.641
5.53	154	0.809	trace			
5.65	158		0.796	3.236	5.325	1.646
5.96	166		0.787	3.227	5.295	1.641
5.97	167		0.788	3.227	5.300	1.643
6.72	188		0.773	3.210	5.256	1.638
7.54	211		0.759	3.186	5.237	1.644
9.40	265		0.740	3.161	5.191	1.642

* Estimated uncertainty, 0.003.
† Estimated uncertainty, 0.004.
‡ Estimated uncertainty, 0.2%.

are a least-squares fit using the first-order Murnaghan equation:

$$P = \frac{K_0}{K'_0} [(V/V_0)^{-K'_0} - 1] \tag{1}$$

For fcc Pb,

$$K_0 = 431 \pm 16 \text{ kbar}, K'_0 = 4.6 \pm 0.3$$

For hcp Pb,

$$V_0 = 0.985V_{0_{\text{fcc}}},$$

and

$$K_0 = 424 \pm 25 \text{ kbar}, K'_0 = 4.7 \pm 0.3.$$

It should be noted in Fig. 134 that even using the methanol-ethanol medium there is a two-phase region and that both phases coexist over a range of pressure. Figure 135 is a plot of lattice parameters c and a and the c - a ratio in expanded scale, which shows no change with pressure.

Effect of Shear Strength on Compressibility

Although the change in compressibility of a single substance in a fluid medium

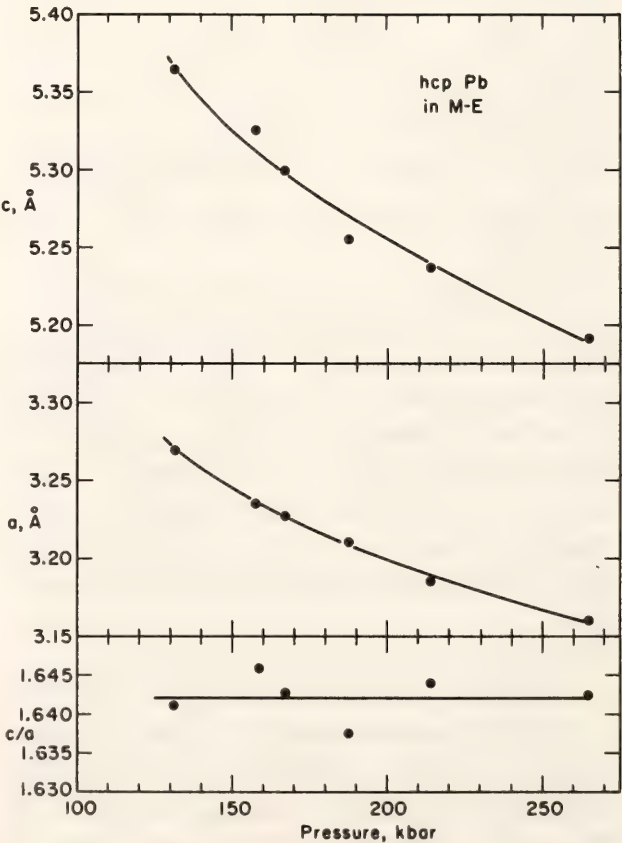


Fig. 135. Change of lattice parameters of the lead with hexagonal-close-packed structure with pressure.

TABLE 35. Compression of Lead with NaCl, Ag, or α -Fe as Solid Pressure Transmitting Medium and Internal Standard

NaCl std		fcc Pb		hcp Pb		
V/V_0^*	P , kbar	V/V_0^*	V/V_0^\dagger	a , Å ‡	c , Å ‡	c/a
0.857	54	0.916				
0.816	80	0.873				
0.783	106	0.851				
0.774	113	0.847				
0.759	128	0.832				
0.716	178		0.788	3.227	5.301	1.643
0.712	185		0.781	3.212	5.303	1.651
0.709	189		0.775	3.209	5.273	1.624
Ag std						
0.920	110	0.847				
0.917	115	0.850				
0.906	137	0.826	trace			
0.903	142	0.818	0.803	3.249	5.326	1.639
0.903	143	0.816	0.814	3.268	5.343	1.635
0.900	148	0.828	0.804	3.256	5.347	1.642
α -Fe std						
0.945	108	0.839				
0.942	118	0.831	0.816	3.264	5.364	1.643
0.938	126	0.830	0.812	3.255	5.370	1.650
0.937	128	0.830	0.816	3.259	5.380	1.651
0.936	131	0.831	0.816	3.262	5.375	1.648
0.933	139	0.825	0.821	3.275	5.359	1.637
0.931	145	0.804	0.797	3.241	5.319	1.641
0.929	151	0.805	0.796	3.239	5.316	1.641
0.927	156	0.808	0.804	3.253	5.321	1.636

* Estimated uncertainty, 0.003.
† Estimated uncertainty, 0.007.
‡ Estimated uncertainty, 0.3%.

with pressure is usually a simple function of pressure, complexities arise for a composite material of two or more substances of differing shear strength. Wilburn and Bassett (1978) demonstrated systematic differences between the measured compressibility of a relatively strong material when immersed in fluid medium and its compressibility in solid medium. The differences were negligible with a weak material such as iron, and greatest with a strong material such as spinel or garnet.

In the present experiments the compressibility of lead mixed with several materials was measured without using a

retaining gasket. The pressure-volume functions of the pressure medium materials were also used for pressure calibration as follows: (A) NaCl (Mao *et al.*, 1978b), (B) Ag (Carter *et al.*, 1971), (C) α -Fe (Mao *et al.*, 1967; Wilburn and Bassett, 1978), and (D) fcc lead as pressure medium and pressure calibrant for hcp lead (Equation 1). Each of these calibration systems is directly or indirectly calibrated with the shock wave equations of state of Cu, Mo, Pd, and Ag determined by Carter, *et al.* (1971).

The above data (A), (B), and (C) are shown in Table 35 and Fig. 136; data (D) are in Table 36 and Fig. 137. Con-

TABLE 36. Compression of Lead Only with fcc-Lead as Internal Standard

fcc Pb std		hcp Pb			
V/V_0^*	P , kbar	V/V_0^\dagger	a , Å ‡	c , Å ‡	c/a
0.853	101	0.848	3.307	5.434	1.643
0.848	106	0.838	3.293	5.411	1.643
0.846	109	0.842	3.303	5.409	1.638
0.844	111	0.833	3.287	5.401	1.643
0.841	114	0.829	3.281	5.392	1.643
0.838	118	0.823	3.274	5.380	1.643
0.836	120	0.827	3.279	5.388	1.643
0.834	122	0.821	3.271	5.377	1.644
0.832	124	0.826	3.282	5.375	1.638
0.829	128	0.823	3.277	5.369	1.638
0.824	135	0.817	3.264	5.371	1.646
0.823	135	0.812	3.267	5.328	1.631
0.821	139	0.812	3.260	5.353	1.642
0.815	147	0.800	3.242	5.331	1.645

* Estimated uncertainty, 0.003.
† Estimated uncertainty, 0.006.
‡ Estimated uncertainty, 0.25%.

siderable scattering of the data points is evident in Figs. 136 and 137 when compared to the results obtained with the methanol-ethanol fluid (Fig. 134); however, the shear strength of lead is suf-

ficiently small to eliminate the existence of a systematic deviation in compressibility. Lead has a shear strength significantly lower than that of α -Fe at low pressure.

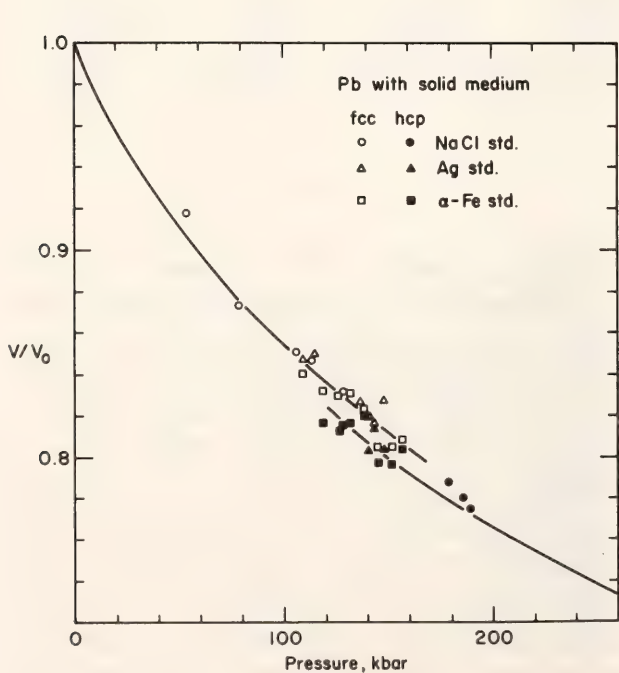


Fig. 136. Isothermal compression of lead in solid medium of NaCl, Ag, or α -Fe. The solid media are also used as pressure standards. The curves are equations of state (Equation 1) obtained in a methanol-ethanol (M-E) medium and are shown for comparison.

Influence of Nonhydrostatic Stress on the Lead “Fixed Point”

The extremely small difference in specific volume between fcc and hcp phases of lead (ΔV is $\sim 1\%$) implies that only a correspondingly small amount of extra free energy is required to stabilize fcc or hcp lead above or below its equilibrium pressure.

$$\Delta F = \int_{P_E}^P \Delta \bar{V} dP,$$

where ΔF is the excess free energy required to stabilize a phase beyond its equilibrium pressure P_E to a pressure P . A relatively small component of nonhydrostatic stress could contribute to the excess free energy and result in a relatively broad two-phase pressure region, even though the strength of lead is low. This factor is important if the phase transition is used as a “fixed-point” pressure calibration in experiments

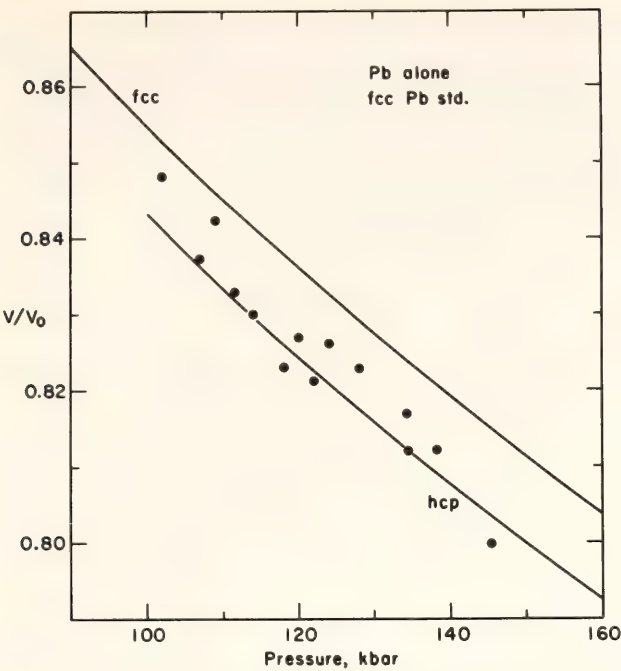


Fig. 137. Compression of hcp lead in the range where fcc and hcp lead coexist. No other medium or standard is added. The curves are equations of state (Equation 1) obtained with M-E medium. The equation of state of fcc lead is used for pressure calibration of the hcp lead.

where the onset of the transition is detected by a change in electrical resistance of the sample. Such a point is usually reproducible with the same apparatus, although a broad two-phase region and a “great metastability” on releasing pressure is usually found (Balchan and Drickamer, 1961). With external calibration, the true two-phase region cannot be distinguished from instrumental hysteresis and change of pressure distribution. In addition, the resistance change at the transition is small (relative to the resistance change of the α - ϵ Fe transition) and, unlike experiments where the sample is observed by x-ray diffraction, a two-phase region may not be well defined in resistance experiments.

In the present study, the metastable coexistence of two phases over a range of pressure is confirmed by x-ray. On the basis of the data listed in Tables 34, 35, and 36 and additional intermittent experiments with short cassette radius (17 mm) and short x-ray exposure (1 day), four points—the first appearance of hcp and

TABLE 37. Transition Pressure (kbar) of fcc — hcp Pb*

	Increasing <i>P</i>		Decreasing <i>P</i>	
	hcp in	fcc out	fcc in	hcp out
Methanol- Ethanol	145	155	140	130
Solid Media	125	160	135	115
Pb alone	110	150	125	100

* Uncertainties, 5 kbar.

disappearance of fcc with increasing pressure, and the first appearance of fcc and disappearance of hcp with decreasing pressure—have been determined with methanol-ethanol pressure medium, solid media, and with lead alone. The increment of pressure is approximately ± 5 –10 kbar. The results are rounded off to 5 kbar and listed in Table 37. The corresponding transition points are different among different media, but they are reproducible (± 5 kbar) with the same medium.

These results demonstrate that the two-phase region is stabilized by shear stress and not by an instrumental factor. Instrumental hysteresis can be ruled out because in each instance the pressure was measured internally. Likewise, reaction kinetics do not play a role, because stabilization of the two-phase region is not time dependent (1–30 days).

It should be emphasized that the effects observed are not caused by pressure gradients or inhomogeneities. A small x-ray collimator was employed to limit the incident beam diameter to 50–80 μ m, within which the ruby-fluorescence measurements showed the maximum gradient to be ± 5 kbar. The volume data also constitute positive evidence that significant inhomogeneities did not exist. The specific volumes of fcc and hcp lead at pressure serve as additional and independent pressure calibrants and can be used to establish that the pressures on the two coexisting phases are equal. Additional evidence comes from the thermodynamic

requirement that the volume difference between the fcc and hcp phases must be positive at equilibrium under hydrostatic conditions. In these experiments the highest value observed for V/V_0 in hcp lead was 0.85 and the lowest in fcc lead was 0.80, a difference considerably larger than the experimental uncertainty (± 0.003). Thus the hcp phase must have persisted below and the fcc above the hydrostatic equilibrium pressure.

This evidence for stabilization of the two-phase region by the nonhydrostatic stress component is also reflected in the results with pressure media of different shear strength. The smallest pressure range of the two-phase region existed with the methanol-ethanol medium. The reproducibility of these results demonstrates that, whereas the "fixed-point" concept of pressure calibration with lead is invalid in the absolute sense, the lead transition is acceptable as a relative calibration point provided that the same pressure medium and experimental apparatus and technique are employed.

Estimation of the Magnitude of Nonhydrostatic Stress

In order to evaluate the magnitude of the nonhydrostatic stress in lead that stabilizes the two-phase region, x-ray diffraction experiments were run with the megabar-cell model MBC-N apparatus (see Mao and Bell, this Report), in which lattice parameters parallel with and normal to the direction of principal stress are measured. Weak gaskets of Be metal or epoxy resin (outer diameter 500 μm) were used to contain a lead sample (less than 100 μm in diameter) in order to produce conditions of maximum nonhydrostatic stress.

The results at 130 kbar indicate that the fcc phase has a shear strength ($\sigma = \sigma_{\text{normal}} - \sigma_{\text{parallel}}$) of less than 5 kbar. Coexisting hcp lead, however, has a maximum shear strength of 20 kbar. The strengths are much less than that of a strong material such as spinel or garnet

at this confining pressure, and are insufficient to introduce a systematic error, as Wilburn and Bassett (1978) observed in spinel and garnet. Nevertheless, the strengths are sufficient to result in a two-phase region stabilized by shear.

Conclusion

The isothermal bulk modulus K_0 and its pressure derivative, K'_0 are determined to be 431 ± 16 kbar and 4.6 ± 0.3 for fcc lead, and 424 ± 25 kbar and 4.7 ± 0.3 for hcp lead, respectively. At 130 kbar, hcp lead can support shear stresses as great as 20 kbar. The small nonhydrostatic stress causes little systematic error in the determination of K_0 and K'_0 when an internal calibration is used. The nonhydrostatic stress causes, however, a wide two-phase region where fcc and hcp lead coexist.

The results have far-reaching implications for the study of the behavior of rocks and minerals under conditions of stress that might be expected in the earth's mantle, and for the study of the general behavior of materials under nonhydrostatic conditions.

RELATIONSHIPS BETWEEN CRYSTAL STRUCTURE AND COMPRESSIBILITY IN OXIDES AND SILICATES

R. M. Hazen and L. W. Finger

Equilibrium distances between atoms in a mineral vary with changes in pressure, resulting in bulk mineral compression. Hazen and Prewitt (1977) demonstrated that compression of metal-oxygen bonds in oxides and silicates may be a simple function of cation charge and polyhedral size. For divalent cations Hazen and Finger (1977) found a linear relationship between polyhedral volume and polyhedral compressibility. Given these simple equations, which enable one to predict metal-oxygen bond distance changes with pressure, it is important to integrate these changes for the entire

crystal structure and relate them to the observed bulk mineral compression.

Recent high-pressure crystal structure studies at this laboratory on pyroxene (Hazen and Finger, *Year Book 76*, 512–515), silicate spinels (Finger, Hazen, and Yagi, *Year Book 76*, 504–505), garnets (Hazen and Finger, 1978a), zircon (Hazen and Finger, 1978b), ruby (Finger and Hazen, 1978), MnF_2 (Hazen, Finger, and Yagi, this Report), SnS_2 (Hazen and Finger, 1978c), phlogopite (Hazen and Finger, 1978d), and analcite (Hazen and Finger, unpublished) provide evidence that in many compounds bulk compression is closely related to polyhedral compression; the key to this relationship is the linkage between polyhedra.

The structures of many simple oxides and silicates share polyhedral edges in three dimensions. If each shared edge between polyhedra is represented as a line segment in space, then all such line segments form a continuous three-dimensional array. In these fully edge-linked structures (including MgO , corundum, spinels, and garnets) any change in molar volume must be accompanied by a change in metal-oxygen bond distances because of the rigid polyhedral linkages. Consequently, the compressibilities of these materials are small because they are similar in magnitude to changes in metal-oxygen bond distances. In MgO and $\alpha\text{-Al}_2\text{O}_3$, for example, compressibilities of the octahedral sites, the only polyhedra, and the bulk mineral are identical. In silicate spinels and garnets, having both silica tetrahedra and larger divalent cation polyhedra, the bulk mineral compressibility is intermediate between compressibilities of these Si^{4+} and R^{2+} sites.

In contrast to the materials described above, such structures as α -quartz, feldspars, and zeolites have primarily corner-linked polyhedra. In framework structures, volume changes may be effected by changes in angles between tetrahedra of the (Al, Si) framework and by alterations of T-O bond lengths. Framework silicates therefore have relatively large bulk com-

pressibilities even though individual tetrahedral units undergo only small volume changes with pressure. It should be noted, however, that bulk compression of feldspars and zeolites is mainly dependent on the predicted compressibilities for large alkali cation polyhedra. If alkali sites are assumed to share edges with the (Al, Si) tetrahedra, then feldspars and zeolites may be treated as fully linked by shared edges, and compressibilities of the bulk minerals should be closely approximated by volume changes of the large cation sites.

Many layer structures, such as SnS_2 and phlogopite, have two-dimensional edge-sharing within octahedral layers but less rigid linkages between layers. In these structures intralayer linear compressibilities are comparable to those of fully linked structures, whereas interlayer linear compressibilities are many times greater.

In other structures (including pyroxenes, olivine, and rutile) all polyhedra have shared edges with some adjacent polyhedra, but a continuous three-dimensional linkage is not obtained. In these materials compression is due to a combination of metal-oxygen compression and polyhedral distortions; the net compression may be greater than that of the component polyhedra. The significant differences between polyhedral linkages of olivines and silicate spinels, for example, lead to the much greater compressibility of the former.

The pressure derivative of the bulk modulus, $K' = (\partial K / \partial P)_T$, may also be related to polyhedral linkages. Compression of metal-oxygen bonds leads to an increase in the repulsion term of the bond energy equal to the externally applied energy of compression. This increase in repulsive energy results in a decrease of compressibility; thus, K' is greater than zero. In fully edge-linked structures, K' of the compound will be the same as the K' associated with metal-oxygen polyhedra (this value is approximately 4 for many dense oxides). In corner-linked

structures, the initial compressibility is large; however, as such materials are compressed, there is a decrease in compressibility due to metal-metal and oxygen-oxygen repulsion as M-O-M angles become smaller. The net K' may be thought of as a sum of the fundamental $K'_{\text{M-O}}$ ($\simeq 4?$), associated with the compression of metal-oxygen bonds in all oxides and silicates, and the distortional or tilting K'_{tilt} , associated with changes in M-O-M angles. The K'_{tilt} is zero in fully edge-linked structures, but is larger for structures with more corner-linked polyhedra. It is possible, therefore, to relate bulk changes in mineral volume to structural changes at the atomic level.

REFINED OCCUPANCY FACTORS FOR SYNTHETIC Mn-Mg PYROXMANGITE AND RHODONITE

L. W. Finger and R. M. Hazen

Cation occupancies in crystals with multiple sites are a sensitive indicator of cooling history for the crystal (e.g., Virgo and Hafner, 1969). Site occupancies can also be used to elucidate crystal chemical constraints on cation ordering and, thus, element partitioning within

and between crystals. The pyroxenoids have several 6- and 7-coordinated cation sites and are ideal minerals for studying the cation partitioning and site preference energies among polyhedra of differing size and shape. The purpose of this study is to report refined occupancy factors for the Mn-Mg positions in synthetic pyroxmangite and rhodonite. These data can be used in a quantitative study of site preference energies.

Pyroxmangite and rhodonite are pyroxenoids with a general formula given by (Ca, Fe, Mn, Mg) SiO_3 . Previous crystal structural work on pyroxmangite, which has a chain repeat of seven units, includes a limited analysis by Liebau (1959), a refinement of the isostructural lunar mineral pyroxferroite by Burnham (1971), and a study by Ohashi and Finger (*Year Book* 74, pp. 545-569). The structure of rhodonite, which has a five-unit chain repeat, was determined by Peacor and Niizeki (1963) and was further refined by Ohashi and Finger (*Year Book* 74, pp. 565-569) and Peacor *et al.* (1978). Synthetic pyroxmangite and rhodonite with composition MnSiO_3 were studied by Narita *et al.* (1977).

Samples for this study were provided by Dr. Jun Ito. In his experiment, a charge

TABLE 38. Unit-Cell and Crystal Data for Synthetic Mn-Mg Pyroxenoids

	Pyroxmangite	Rhodonite
Formula	$\text{Mg}_{0.49}\text{Mn}_{0.51}\text{SiO}_3$	$\text{Mg}_{0.38}\text{Mn}_{0.62}\text{SiO}_3$
Space Group	$C\bar{1}$	$C\bar{1}$
<i>Z</i>	28	20
<i>a</i> (Å)	9.5850(7)	9.649(2)
<i>b</i> (Å)	10.3589(9)	10.389(3)
<i>c</i> (Å)	17.247(2)	12.108(3)
α (degrees)	112.335(7)	108.65(2)
β (degrees)	102.497(7)	102.32(2)
γ (degrees)	83.097(7)	82.95(2)
<i>V</i> (Å ³)	1545.1(2)	1121.6(5)
ρ_x (g/cm ³)	3.488	3.543
μ_l (cm ⁻¹)	35.9	40.4
Crystal size (μm)	70 × 160 × 170	40 × 50 × 160
No. of observations (<i>I</i> > 2σ)	3787	2493
Weighted <i>R</i> (%)	3.8	3.8
<i>R</i> (%)	4.5	4.5

TABLE 39. Refined Positional Parameters and Temperature Factors for Synthetic Mn-Mg Pyroxenoids

Site	Pyroxmangite				Rhodonite			
	<i>x</i>	<i>y</i>	<i>z</i>	<i>B</i> (Å ²)	<i>x</i>	<i>y</i>	<i>z</i>	<i>B</i> (Å ²)
M1*	0.0020(1)	0.0443(1)	0.1050(1)	0.64(2)	0.0021(1)	0.0300(1)	0.1480(1)	0.62(2)
M2	−0.0001(1)	0.1677(1)	0.3113(1)	0.70(3)	0.0012(1)	0.1285(1)	0.4462(1)	0.67(2)
M3	0.0012(1)	0.0672(1)	0.6065(1)	0.70(3)	0.0163(1)	0.2019(1)	0.7327(1)	0.68(2)
M4	0.0144(1)	0.1743(1)	0.8077(1)	0.64(3)	0.0483(1)	0.2652(1)	0.0271(1)	0.85(3)
M5	0.0038(1)	0.2705(1)	0.5096(1)	0.81(2)	−0.0022(1)	0.3442(1)	0.3007(1)	0.92(2)
M6	0.0503(1)	0.2644(1)	0.0170(1)	0.89(3)				
M7	−0.0037(1)	0.3728(1)	0.2116(1)	0.77(2)				
Si1	0.2022(1)	0.4395(1)	0.9374(1)	0.45(2)	0.2050(1)	0.4466(1)	0.9151(1)	0.53(2)
Si2	0.2089(1)	0.3297(1)	0.7522(1)	0.41(2)	0.2112(1)	0.3628(1)	0.6562(1)	0.44(2)
Si3	0.2109(1)	0.5319(1)	0.6630(1)	0.35(2)	0.2136(1)	0.5771(1)	0.5324(1)	0.43(2)
Si4	0.2076(1)	0.4234(1)	0.4684(1)	0.37(2)	0.2113(1)	0.5059(1)	0.2627(1)	0.42(2)
Si5	0.2098(1)	0.6329(1)	0.3799(1)	0.40(2)	0.2085(1)	0.7031(1)	0.1274(1)	0.44(2)
Si6	0.2094(1)	0.5284(1)	0.1878(1)	0.40(2)				
Si7	0.2072(1)	0.7143(1)	0.0911(1)	0.44(2)				
O A1	0.1278(4)	0.0757(3)	0.0265(2)	0.58(5)	0.1254(3)	0.0737(3)	0.0370(3)	0.70(5)
O A2	0.1179(4)	0.1881(3)	0.2262(2)	0.60(5)	0.1171(3)	0.1606(6)	0.3213(3)	0.85(5)
O A3	0.1172(4)	0.9644(4)	0.3099(2)	0.63(5)	0.1153(3)	0.9211(3)	0.4349(3)	0.80(5)
O A4	0.1211(4)	0.0897(3)	0.5209(2)	0.73(5)	0.1196(3)	0.0140(3)	0.7338(3)	0.69(5)
O A5	0.1189(4)	0.8707(4)	0.6073(2)	0.69(5)	0.1239(3)	0.7892(3)	0.8545(3)	0.66(5)
O A6	0.1204(3)	0.9861(3)	0.8076(2)	0.51(5)	0.1020(3)	0.8362(3)	0.1330(3)	0.62(5)
O A7	0.1247(3)	0.7773(4)	0.8981(2)	0.68(5)				
O A8	0.1017(4)	0.8481(4)	0.0949(2)	0.69(5)				
O B1	0.1241(4)	0.3082(4)	0.9309(2)	0.80(5)	0.1252(3)	0.3186(3)	0.9080(3)	0.94(5)
O B2	0.1238(4)	0.1918(3)	0.7238(2)	0.68(5)	0.1232(3)	0.2298(3)	0.6126(3)	0.76(5)
O B3	0.1206(4)	0.6662(4)	0.7124(2)	0.81(6)	0.1225(4)	0.7082(3)	0.5951(3)	0.96(5)
O B4	0.1220(4)	0.2829(4)	0.4236(2)	0.76(5)	0.1200(3)	0.3785(3)	0.1868(3)	0.85(5)
O B5	0.1298(4)	0.7786(4)	0.4208(2)	0.79(5)				
O B6	0.1213(4)	0.3937(4)	0.1295(2)	0.66(5)				
O C1	0.1660(4)	0.4477(4)	0.8412(2)	0.74(5)				
O C2	0.1570(4)	0.4023(4)	0.6811(2)	0.73(5)	0.1710(3)	0.4645(3)	0.7814(3)	0.76(5)
O C3	0.1580(4)	0.4934(4)	0.5612(2)	0.90(6)	0.1599(4)	0.4521(3)	0.5651(3)	1.13(6)
O C4	0.1486(4)	0.5344(4)	0.4201(2)	0.80(5)	0.1620(4)	0.5381(3)	0.3896(3)	0.98(5)
O C5	0.1524(4)	0.5623(3)	0.2767(2)	0.64(5)	0.1580(3)	0.6438(3)	0.2231(3)	0.62(5)
O C6	0.1575(4)	0.6658(4)	0.1619(2)	0.54(5)	0.1477(3)	0.5940(3)	0.9978(3)	0.63(5)
O C7	0.1443(4)	0.5935(3)	0.9986(2)	0.62(5)				

* Atom nomenclature is the same as used by Ohashi and Finger, *Year Book 74*, 564–569.

with composition $\text{Mg}_{0.35}\text{Mn}_{0.65}\text{SiO}_3$ was heated to 1400°C in air, held for three hr, cooled to 1300°C at 25°C/hr , and quenched (Ito, 1972). The run products included pyroxmangite, rhodonite, and various manganese oxides. The compositions of the pyroxenoids were determined by electron microprobe examination. Some crystals were highly zoned; however, the crystals used in the x-ray experiments were chosen to exclude these regions. In addition, only crystals with sharp diffraction maxima and resolution of the $\text{K}\alpha_1$ - $\text{K}\alpha_2$ doublet were used in the x-ray experiments. The unit-cell parameters, based upon the *C*-centered lattice (Ohashi and Finger, *Year Book* 74, pp. 564–569), were measured on the four-circle single-crystal x-ray diffractometer using the techniques of Finger, Hadidiacos, and Ohashi (*Year Book* 72, pp. 694–699).

Single-crystal intensities were measured for a hemisphere of reciprocal space to an angle of 60 degrees for $\text{MoK}\alpha_1$ radiation. The intensity data were corrected for absorption and the crystal structures were refined using the parameters of Ohashi and Finger (*Year Book* 74, pp. 565–569) for starting values. Unit-cell parameters, mineral formulae, and crystal data are listed in Table 38. Each structure was refined to a weighted residual of 3.8% and an unweighted *R*-factor of 4.5%.

The refined positional parameters and

temperature factors for the structures are listed in Table 39. The crystal structure model included occupancy factors for the M-sites (Table 40) constrained to maintain a fixed composition using the method of Finger (*Year Book* 67, pp. 216–217).

The present study, with Mg and Mn as the only divalent cations, is not subject to many of the difficulties in interpretation that arise from the more complicated chemical composition and uncertain temperature of equilibration of natural samples. The major difference in determining site preference between Mg^{2+} and Mn^{2+} is cation size; Shannon and Prewitt (1969) report ionic radii of 0.72 and 0.82 Å for these two cations, respectively. Site distortions will not stabilize either cation because Mg^{2+} (no *d* electrons) and Mn^{2+} (*d*⁵ configuration) have no crystal field-splitting energy.

In rhodonite, the large 7-coordinated M5 site is highly enriched in Mn with Mn/Mg of 7.1, similar to that found by Ohashi and Finger (*Year Book* 74, pp. 565–569); thus, the occupancy of this site does not appear to depend upon bulk chemical composition or thermal history. The M4 site is depleted in Mn in agreement with the results of Peacor *et al.* (1978); but the other sites have Mn occupancies not greatly different from each other or the bulk composition. In pyroxmangite, the large 7-coordinated

TABLE 40. Refined Occupancy Parameters for Octahedral Sites in Synthetic Mn-Mg Pyroxenoids

Site	Pyroxmangite		Rhodonite	
	Mn	Mg	Mn	Mg
M1*	0.516(5)	0.484(5)	0.615(5)	0.385(5)
M2	0.351(6)	0.649(6)	0.687(5)	0.313(5)
M3	0.451(5)	0.549(5)	0.572(5)	0.428(5)
M4	0.452(5)	0.548(6)	0.350(5)	0.650(5)
M5	0.788(5)	0.212(5)	0.876†	0.124
M6	0.253(5)	0.747(5)		
M7	0.777†	0.223		

* Atom nomenclature is the same as used by Ohashi and Finger, *Year Book* 74, 564–569.

† Occupancy factors constrained by chemical composition derived from electron microprobe analysis (see Table 39).

sites M5 and M7 have strong enrichment of Mn, whereas smaller 6-coordinated M2 and M6 are depleted in that element.

The occupancy factors from this study have been determined on phases with a simple composition and a known thermal history; thus, precise site preference energies can now be determined and the details of crystal chemical constraints on compositional limits can be ascertained.

SYSTEMATIC VARIATIONS OF PYROXENE ABSORPTION SPECTRA WITH COMPOSITION.

R. M. Hazen, P. M. Bell, and H. K. Mao

Chemical and structural variations of pyroxenes have received considerable attention owing to the abundance of these phases in terrestrial and extraterrestrial rocks. Many pyroxene compositions may be represented by solid solutions among the end-members enstatite (EN, $\text{Mg}_2\text{Si}_2\text{O}_6$), ferrosilite (FS, $\text{Fe}_2\text{Si}_2\text{O}_6$), diopside (DI, $\text{CaMgSi}_2\text{O}_6$), and hedenbergite (HD, $\text{CaFeSi}_2\text{O}_6$). Physical properties of pyroxenes are frequently plotted on the pyroxene quadrilateral, a compositional plane defined by the four compositions EN-DI-HD-FS; this study includes data on the variation of pyroxene optical absorption spectra as a function of composition within this quadrilateral.

The major features of pyroxene absorption spectra are well known (Burns, 1970; Runciman *et al.*, 1973; Hazen *et al.*, 1978; Goldman and Rossman, 1977). Based on calculated and observed transition energies, prominent absorption bands at 1 and 2 μm as well as several sharp absorption peaks below 700 nm are assigned to crystal field transitions of Fe^{2+} in octahedral coordination. The positions, intensities, and shapes of the absorption features are sensitive to composition because variations in the ratio of Fe:Ca:Mg change the size and distortion of octahedral sites; these changes in turn alter the crystal field of Fe^{2+} . It is important, therefore, to document systematic variations of

pyroxene spectra for compositions within the quadrilateral if understanding of the effects of site distortion on the electronic structure of iron in pyroxene is to be achieved.

Polarized absorption spectra of 15 lunar pyroxene single crystals and a synthetic orthoferrosilite specimen were measured using techniques described by Mao and Bell (1973); details of these spectra as well as pyroxene compositions are recorded by Hazen *et al.*, (1978). These data were combined with those for 20 other previously described pyroxenes (lunar, terrestrial, meteoritic, and synthetic), and variations of the positions of the major 1- and 2- μm bands were plotted on the pyroxene quadrilateral (Figs. 138 and 139). Compositions of these pyroxenes, as projected onto the quadrilateral, are illustrated by points on Fig. 140. Note that several specimens are *metastable* subcalcic augites from lunar samples, whereas other pyroxenes are equilibrated.

The energy represented by the 2- μm band, which is due to spin-allowed crystal field transitions of Fe^{2+} in the larger, more distorted M2 pyroxene octahedral site, decreases with increasing iron and calcium content. The addition of calcium and iron to enstatite increases the size and alters the distortion of the M2 site, thus lowering the transition energy. Of the 36 pyroxenes used to construct Fig. 138, low-calcium specimens have 2- μm bands within 10 nm of the plotted values, whereas augites generally deviate no more than 30 nm from the curves in this figure. Pyroxenes of a given composition may

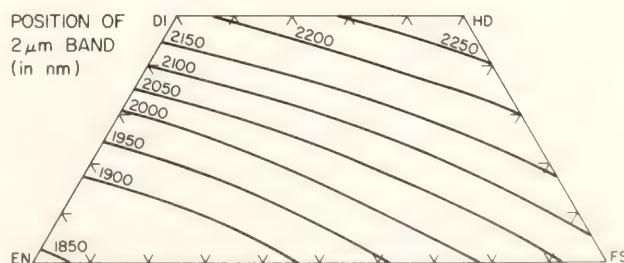


Fig. 138. Position of the 2- μm pyroxene absorption maxima vs. composition, projected on the pyroxene quadrilateral.

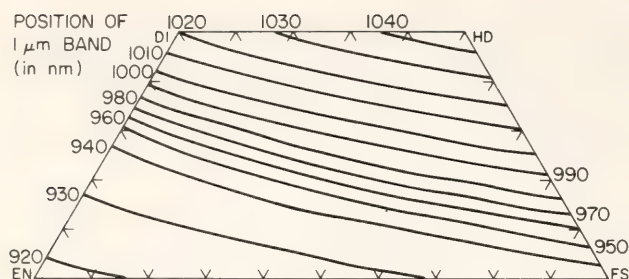


Fig. 139. Position of the 1- μ m pyroxene absorption maxima vs. composition, projected on the pyroxene quadrilateral.

show significant variation in 2- μ m band position, depending on the degree of iron ordering in the M2 site; if iron is significantly ordered into the M2 site then the position should be at a longer wavelength than for a disordered pyroxene of the same composition. Because there is no Fe^{2+} in M2 sites of ideal Ca endmember clinopyroxenes, the 2- μ m band should not be observed for pyroxenes on the join DI-HD.

General trends of the 1- μ m band positional variation vs. composition are similar to those of the 2- μ m band. Positions for orthopyroxene and pigeonite bands agree with the values in Fig. 139 within 2 nm, whereas those of most augites differ by less than 10 nm.

In an octahedral environment ferrous iron (d^6 configuration) has three lower energy (t_{2g}) and two higher (e_g) levels. In a distorted environment these degenerate levels are further split, and the energies of splitting provide information about the

electronic structure of the Fe^{2+} cation. In pyroxenes the 1- μ m band is the result of the transition from the lowest t_{2g} level to the higher e_g level, whereas the 2- μ m band is due to the transition from the lowest t_{2g} level to the lower e_g level (Goldman and Rossman, 1977). The energy between the 1- and 2- μ m bands is therefore equal to the splitting energy of the two e_g levels of Fe^{2+} in the distorted M2 site. The energy of separation between the 1- and 2- μ m bands of pyroxenes has been calculated directly from information in Figs. 138 and 139, and is illustrated in Fig. 141. A line of inflection, very close to the $2V = 0^\circ$ line for pyroxenes, divides the pyroxene quadrilateral into two distinct regions. Low-calcium pyroxenes (below WO_{10}) have 1–2 μ m separation energies that are primarily a function of iron content. Pigeonites and orthopyroxenes with less than FS_{40} show little variation in splitting energy, but between FS_{40} and FS_{100} the energy increases by 7%. Augites display a strikingly different trend in e_g splitting, with separation energy primarily a function of calcium content. The splitting energy decreases by approximately 8% between WO_{15} and WO_{50} , owing to the larger and more regular environment for iron in a calcium-rich M2 site.

The most prominent feature in the visible (400–800 nm) region of the pyroxene spectrum is the sharp peak at 505 nm, the result of a spin-forbidden crystal field transition of Fe^{2+} . The nature of this peak is illustrated on the pyroxene quadrilateral

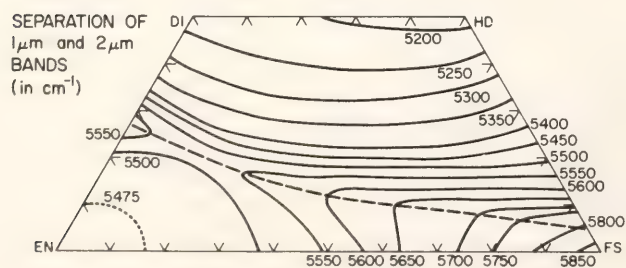


Fig. 140. Nature of the 505-nm peak of pyroxenes. Symbols S, B, and D stand for singlet, broad, and doublet peaks. Dashed lines represent variation of average peak position in nanometers.

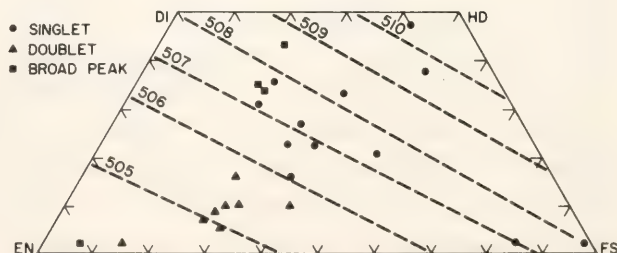


Fig. 141. Difference in energy between the 1- and 2- μ m bands. This difference is related to the distortion of the M2 site.

in Fig. 140. A striking aspect of this plot is that almost all pigeonites and orthopyroxenes have a doublet or broad (4-nm) maximum between 505 and 508 nm, whereas high-calcium pyroxenes have sharp singlets for most specimens. A characteristic significantly distinguishing high-calcium ($C2/c$) and low-calcium ($P2_1/c$) clinopyroxenes from ($Pbca$) orthopyroxenes is the symmetry of the M1 site. There are no symmetry constraints on the M1 site of pigeonites and orthopyroxenes, but the M1 site of clinopyroxene ($C2/c$) has 2-fold symmetry. It is possible that the 505-nm feature is a result of a spin-forbidden transition of Fe^{2+} in M1, and that the splitting of this peak in low-calcium pyroxenes is due to the lower symmetry of the M1 site in those specimens. Note that the position of the 505-nm peak varies systematically across the pyroxene quadrilateral in a way similar to that of the 1- and 2- μm bands.

Positions of the major absorption features at 505 nm, 1 μm , and 2 μm are functions of composition as projected onto the pyroxene quadrilateral, *independent* of pyroxene structure type. There are no apparent "kinks" in curves in the region between low-calcium pyroxenes (pigeonites and orthopyroxenes) and augites. Wavelengths of absorption maxima vary continuously over the quadrilateral, suggesting that octahedral site occupancies, rather than structure type, control the energies of these crystal field effects.

Pyroxene absorption spectra may be complicated by the presence of transition metal cations (other than Fe^{2+}), including Ti^{3+} , Ti^{4+} , Mn^{3+} , Cr^{3+} , and Fe^{3+} , which contribute crystal field and charge-transfer absorption effects. In spite of these complexities, positions of the three major absorption maxima in most pyroxenes are controlled by the major element chemistry. Figures 138–140 can be used, therefore, to identify pyroxene compositions from diffuse reflectance spectra of lunar and other extraterrestrial materials.

LUNA 24 GLASS FRAGMENTS: A STUDY OF SOIL SAMPLES RECOVERED FROM THE RUSSIAN LUNA 24 MISSION TO MARE CRISIUM

P. M. Bell, H. K. Mao and R. M. Hazen

Silicate glasses sampled from the moon's surface have been related to those rock types from the melt portions of which the glasses are quenched. Their compositions have been used to model liquid lines of descent from parental or derivative igneous liquids. However, most lunar glasses are not igneous in origin but were produced by shock processes that accompanied meteorite impacts on the moon's surface. The impact processes have, in many instances, introduced complexities of chemical fractionation, elemental spattering, and other less well understood "shock" effects; thus most lunar glasses may not be appropriate for deducing the liquid descent of lunar igneous rocks. Many glasses are, however, suitable for interpretation of surface processes that occur in the lunar regolith.

Some lunar glasses are true quench products of impact melting and preserve information on redox conditions in the regolith at the instant of quench. Furthermore, the glasses preserve various structural stages of devitrification to rock textures (such as those of rock 14310) by progressive stages of impact (thermal) metamorphism. In this study absorption spectroscopy was used to assess both oxidation state and degree of order of glasses; some glass types were observed for the first time in Luna 24 glass fragments. The spectral data serve an additional purpose in the interpretation of telescope and remote sensing surveys of the moon's surface, because the absorption bands in lunar glasses contribute significantly to the composite soil or regolith absorption (reflectance) spectra. The new data may have critical bearing on the interpretation of telescope data from Mare Crisium.

The Luna 24 Samples

Multiple-grain mounts (several hundred polished grains per mount) were kindly loaned to us by Dr. Larry A. Taylor from his allocation for this study. He selected what he believed to be representative glasses from the Luna 24 samples.

Glass color and composition. The lunar glasses in general, and the Luna 24 glasses in particular, have been classed by petrographers in a system based on color and bulk chemical composition (for example, Norman *et al.*, 1977; Grove and Vaniman, 1977). In the present study it has been determined that there is always a direct relationship between color and spectral properties, but correlation of color alone with chemical composition is often invalid. Clearly there are causes of color changes and darkening other than changes in composition. For example, the brown glasses, "tea-colored" (green-brown) glasses, and green glasses, all sometimes referred to as ferrobasalt, and the Luna 24 green glass, or "low-titanium basalt," all have the same composition. There is more compositional variation (especially for Mg) within the green glasses than between green and brown glasses. Various other glasses, ranging from light green to colorless (spectrally very light green to ultralight green), have been named Fra Mauro basalt and Highlands basalt on the basis of chemical composition.

The relation between color and composition in several Luna 24 glasses can be seen in Tables 41 and 42. The brown glasses are relatively uniform in composition, whereas the green glasses have variable magnesium content (Table 41). The light green and colorless glasses have relatively low iron content. The former are relatively high in titanium and aluminum; the latter, very low in titanium, high in calcium, and very high in aluminum. Other transition elements, such as Mn or Cr, are present in low concentrations (less than 0.5%) and do not affect the color or spectra. Some glasses

appear colored, apparently owing to shock or radiation, which produce darkening effects not related to chemical composition.

Crystal-Field Spectra

The crystal-field spectra of lunar glasses have been correlated in detail with experimental data on crystal-field spectra of synthetic glasses as a function of composition and oxygen fugacity by Bell *et al.* (1976). In Luna 24 glasses, two additional effects that influence the spectra but are not yet correlated experimentally were found. These are structure (development of short-range order) and degree of devitrification. This discussion will examine separately the effects that composition and oxygen fugacity, short-range order, and devitrification have on the spectra.

The absorption spectra were measured with microparticle techniques developed by Mao and Bell (1973). An important parameter in calculation of the absorption coefficient is the grain thickness. The section laboratory at the Johnson Spacecraft Center was unable to state the thickness with accuracy because of the irregularities of their present grain mounts (Mr. John Annestad, personal communication, 1978). The grain thickness could not be accurately measured in this laboratory by micrometer or by other mechanical device. Therefore, a thickness uncertainty of $\pm 5 \mu\text{m}$ and an absorption coefficient uncertainty of $\pm 15\%$ should be applied to all the spectral data in this study.

Spectral Correlation with Oxygen Fugacity and Chemical Composition

The green Luna 24 glasses have normal glass spectra—broad, intense absorption bands caused by octahedrally coordinated Fe^{2+} and a steep apparent absorption edge caused by Ti^{3+} - Ti^{4+} - Fe^{2+} charge-transfer effects (Bell *et al.*, 1976). Representative compositions are given in Tables 41 and

TABLE 41. Electron Microprobe Analysis (wt %) and Optical Absorption Spectral Features of Glass Fragments in Multiple Grain Mount 24077,45

	Brown glass			Tea-colored glass		Green glass			Light green		Colorless glass	
	d	g	b	e	j	a	h	c	f	i		
SiO ₂	46.6	46.5	44.7	44.6	45.7	46.7	47.4	50.2	45.3	45.3		
TiO ₂	1.02	1.00	0.99	1.49	1.00	1.08	0.95	1.96	0.30	0.19		
Al ₂ O ₃	12.1	12.2	13.5	10.7	12.3	11.6	11.1	16.0	25.1	27.4		
Cr ₂ O ₃	0.29	0.30	0.52	0.47	0.45	0.32	0.30	0.04	0.14	0.14		
FeO	20.8	20.8	18.9	19.1	18.8	21.1	19.8	11.9	5.53	5.66		
MgO	6.85	6.86	9.61	12.4	10.9	7.65	7.58	6.49	9.92	6.08		
CaO	12.4	12.3	11.9	10.2	11.3	11.8	11.5	11.6	14.6	15.9		
MnO	0.32	0.33	0.29	0.31	0.45	0.33	0.32	0.16	0.07	0.08		
Total	100.3	100.2	100.4	99.3	100.7	100.6	99.0	98.3	100.9	100.7		
Slope*	18.7	20.8	18.2	16.0	8.3	14.7	10.0	11.1		
λ _{min} , nm	800	820	660	590	590	590	590	625		
λ _{max} , nm	985	985	1040	1080	1080	1080	1090	1100	1080	1080		
α _{max} , cm ⁻¹	192	272	170	205	158	178	148	108	37	33		

* Slope of absorption edge at 20,000 cm⁻¹, in units of cm⁻¹ per 1000 cm⁻¹ wave number.

TABLE 42. Electron Microprobe Analysis (wt %) and Optical Absorption Features of Glass Fragments in Multiple Grain Mounts 24210,48; 24182,48; 24149,49; and 24174,51

	24210, 48				24182, 48				24149, 49				24174, 51			
	Dark brown		Brown glass		Color-less		Color-less		Brown glass		Green glass		Brown glass		Green glass	
	c	a	b	d	c	d	c	e	c	e	a	b	a	b	a	b
SiO ₂	46.4	46.7	46.8	45.0	43.9	45.0	43.9	47.2	47.2	47.8	46.1	46.9	46.1	46.9	46.1	46.9
TiO ₂	0.95	0.96	0.96	0.2	0.00	0.2	0.00	0.99	0.99	1.08	0.15	0.95	0.15	0.95	0.15	0.95
Al ₂ O ₃	11.9	12.0	11.8	27.4	34.6	27.4	34.6	12.0	12.0	11.6	29.2	11.8	29.2	11.8	29.2	11.8
Cr ₂ O ₃	0.25	0.22	0.25	0.09	0.00	0.09	0.00	0.28	0.28	0.21	0.04	0.21	0.04	0.21	0.04	0.21
FeO	19.3	19.5	19.0	3.80	0.46	3.80	0.46	20.6	20.6	20.8	3.21	19.5	3.21	19.5	3.21	19.5
MgO	6.69	6.85	6.93	5.67	0.16	5.67	0.16	7.04	7.04	6.50	3.21	6.70	3.21	6.70	3.21	6.70
CaO	12.2	12.2	12.3	15.7	19.1	15.7	19.1	12.8	12.8	12.4	16.4	12.1	16.4	12.1	16.4	12.1
MnO	0.35	0.33	0.29	0.10	0.01	0.10	0.01	0.32	0.32	0.33	0.09	0.32	0.09	0.32	0.09	0.32
Na ₂ O	0.28	0.28	0.28	0.17	0.48	0.17	0.48	0.66	0.24	0.66	0.24	0.66	0.24
Total	98.3	99.0	98.7	98.2	98.7	98.2	98.7	101.2	101.2	100.6	99.1	98.8	99.1	98.8	99.1	98.8
Slope*	>100	11.5	15.6	0	1.5	0	1.5	1.98	1.98	17.7	9.4	12.0	9.4	12.0	9.4	12.0
λ _{min} , nm	840	800	850	830	830	605	...	590	...	590	...	590
λ _{max} , nm	970	980	970	970	970	1070	...	1040	...	1040	...	1040
α _{max} , cm ⁻¹	141	87	67	181	181	185	...	150	...	150	...	150

* Slope of absorption edge at 20,000 cm⁻¹, in units of cm⁻¹ per 1000 cm⁻¹ wave number.

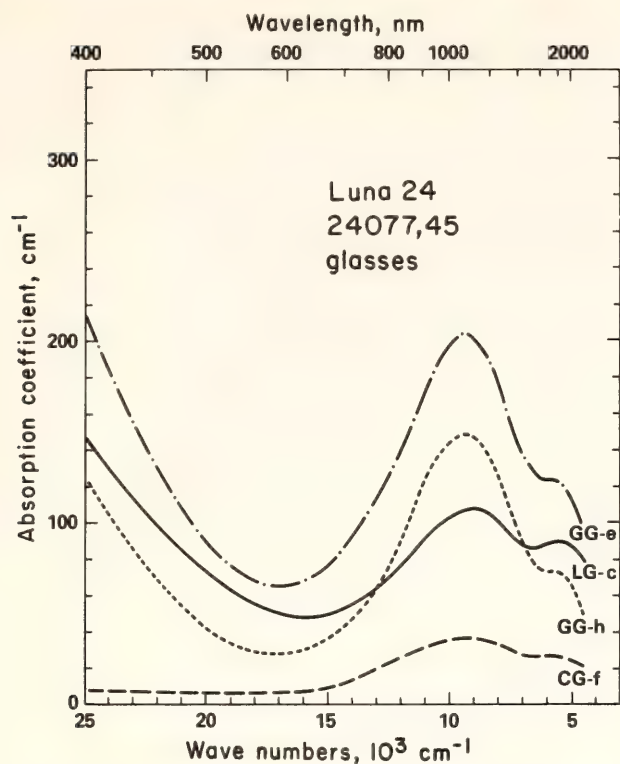


Fig. 142. Optical absorption spectra of glass fragments from Luna 24077,24. GG, green glass; LG, light-green glass; CG, colorless glass. The spectra of the green-to colorless series correlate with the compositions given in Table 42.

42. Figure 142 shows the spectra of a series of four green glasses from sample 24077,45. These glasses have a range of iron concentration (Table 41) that correlates with experimentally observed wavelengths and intensities of the peak maximum of the octahedral Fe^{2+} crystal-field absorption band centered near $1\ \mu\text{m}$ (Fig. 143). The slope at 20,000 wave numbers also correlates with composition when compared with experimental data on the compositional product $\text{FeO} \times \text{TiO}_2$ (in wt %) plotted in Fig. 144. Reference to the plot of TiO_2 (wt %) vs. absorption minimum in Fig. 145 and to the results of Bell *et al.* (1976), who obtained experimental data on spectra and oxygen fugacity of synthetic glasses, indicates that the Luna 24 green glasses are the same as, or slightly more oxidized than, synthetic glasses of the same composition quenched from 1400°C and $\log P_{\text{O}_2} = -9.1$.

The correlations of spectral features of

the Luna 24 green glasses with experimental data are much the same as those obtained with other lunar glasses. Apparently the configurations of iron and titanium sites in Luna 24 green glass are similar to those in all other green and orange (often referred to as "red") lunar glasses studied.

Spectral Correlation with Short-Range Order in Glass

Many of the Luna 24 glasses with deep brown color or brown tone have spectral patterns that have not been reported previously. Figure 146 shows spectra of a brown glass, an intermediate brown-green ("tea-colored") glass, and a normal green glass from section 24077,45. The absorption band at $1\ \mu$ for the brown glass is sharp, and essentially the same as would be obtained with a polycrystalline sample of iron-bearing pyroxene (Hazen, Bell and Mao, this Report). These sharp spectral features are unlike the broad absorption bands of green and orange (red) glasses studied in other lunar samples. In the brown glasses, for example, the band at approximately $1.08\ \mu\text{m}$ in normal glasses is shifted to $0.98\ \mu\text{m}$ and the broad, low-energy shoulder is observed as a distinct band at approximately $2\ \mu\text{m}$. The brown glasses absorb more intensely along the near-ultraviolet edge, and in some cases a small peak is observed at 500 nm. The brown glass spectra correlate with the spectra of lunar pyroxene of augite composition and are attributed to the development of a highly ordered state.

Figure 147 is a photomicrograph of a common Luna 24 brown glass fragment. These glasses are not devitrified on a microscopic scale (to $\times 40,000$, SEM magnification), but they typically contain a few inclusions of plagioclase crystals (nearly pure anorthite on the basis of scanning electron microscope energy-dispersive analysis). The inclusions could have been in the original liquid or could be devitrification products. The grain shown in Fig. 147 shows zones around the

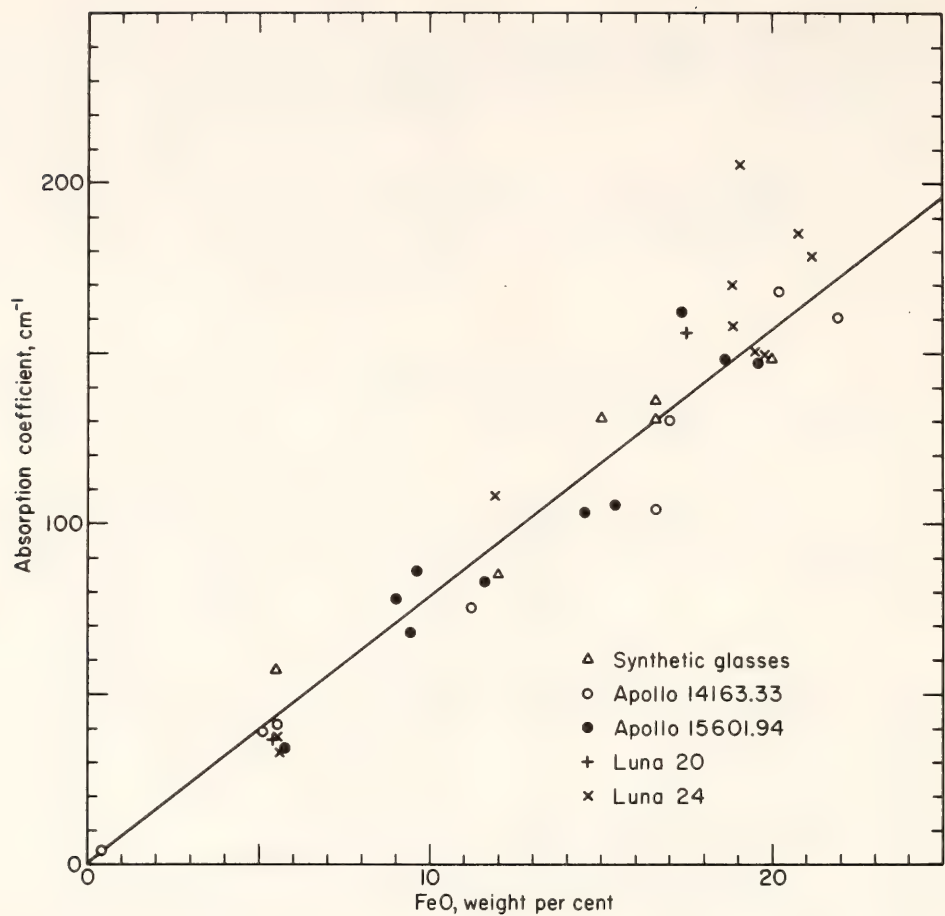


Fig. 143. Intensity of 1- μ m crystal field observation band of glasses vs. FeO content (total Fe expressed as FeO). The symbol x represents the present Luna 24 glasses (brown glasses excluded). All other data are from Bell *et al.* (1976).

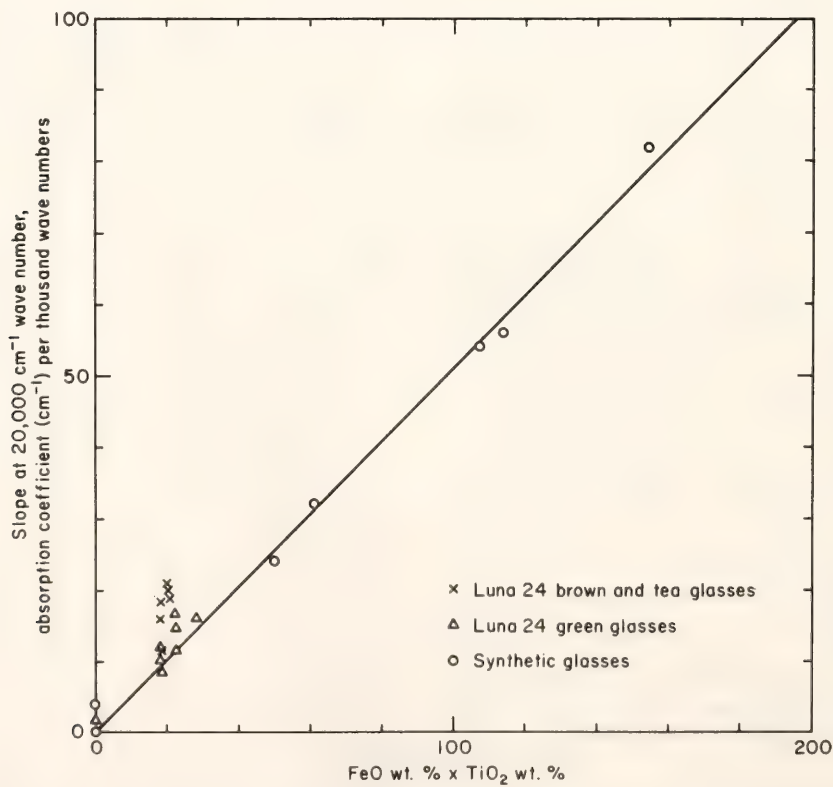


Fig. 144. Slope of absorption edge of glasses at 20,000 cm⁻¹ (500nm) vs. the product of total Fe and total Ti content (expressed as FeO and TiO₂). The data for synthetic glasses are from Bell *et al.* (1976).

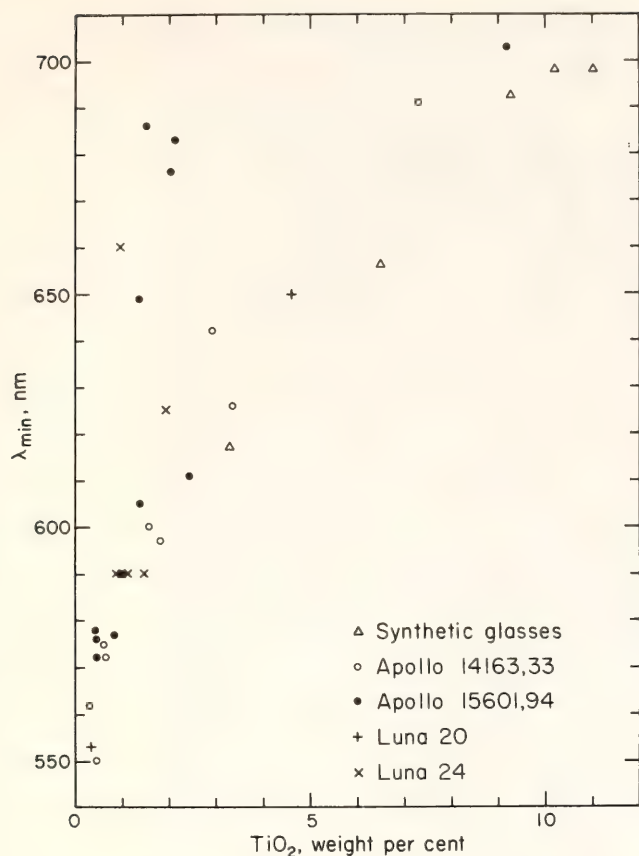


Fig. 145. Position of the absorption minimum of glasses in the visible region vs. TiO_2 content. The present Luna 24 data exclude brown glasses. All other data are from Bell *et al.* (1976).

inclusions that appear to be bleached, but microprobe analysis indicates no compositional gradients. The glass portions of the brown glasses are uniform in composition.

Where extensive submicroscopic devitrification is observed, the intensity of absorption diminishes. The bulk spectra are significantly different from those of the glass portion. (The devitrification products are pyroxene, olivine, plagioclase, and opaque minerals.) The short-range order of the brown glass is an intermediate, distinct stage that apparently occurred before devitrification.

Figure 148 shows a photomicrograph of a brown glass fragment of uniform composition, most of which contains microcrystalline devitrification products. Only the glassy portions (left edge of the grain) give a sharp pyroxene-like absorption spectrum (Fig. 149, 24210,48a). The

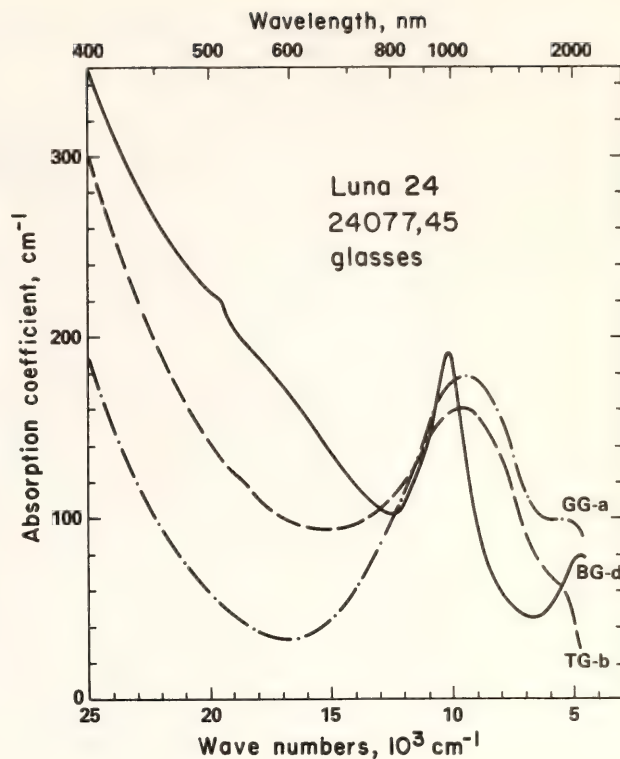


Fig. 146. Optical absorption spectra of glass fragments from Luna 24077,24. GG, green glass; TG, tea-colored (brownish-green) glass; BG, brown glass. Specimens in the green-to-brown series have almost identical compositions, yet different spectra.

devitrified zones (Fig. 149, 24210,48b) give only weak bands and a strong absorption slope into the near-ultraviolet region. The most intense and the sharpest absorption spectrum in Fig. 149 (24149,49c) was obtained from the glassy portions of another brown glass of the same composition that had extensive devitrified portions.

One can conclude from these results that spectral characteristics do not correlate with composition of the brown glasses. This lack of correlation can be seen in Fig. 144, where the brown and "tea-colored" (brownish-green) glasses plot off the composition line. (The Luna 24 glasses are exceptionally low in titanium and their plot is crowded at one end of the diagram, but the brown glasses plot significantly distant from the composition line.)

Assignment of the absorption bands in the brown glasses is important because on



Fig. 147. Photomicrograph of brown glass 24077,45d. The length of the grain is 0.2 mm.

the basis of the observed spectral features these glasses have structural states that were previously unknown: Those grains having sharp pyroxene-like spectra represent a structural state observed for the first time in lunar glass. The grains are otherwise indistinguishable from normal lunar glass. The sharp spectral features indicate, though, that most Fe^{2+} cations are in an M2 pyroxene-like site (Hazen, Bell and Mao, this Report), suggesting that small regions of pyroxene-like chains exist within the glass. These "M2 brown glasses," therefore, possess aspects of both

the glass and the single-crystalline state. Radial distribution x-ray studies are needed to elucidate the structural details of this unusual lunar glass. When and if sufficient material becomes available, index of refraction measurements would be useful in interpreting possible high-pressure shock effects in the glasses. Structural states in glass that are related to the "glass point" (critical Tamann viscosity), devitrification, shocked-glass states ("expanded lattice" crystals), and smectic states can be ruled out in this instance. In effect, the brown glasses, ap-



Fig. 148. Photomicrograph of brown glass 24210,48b. The length of the grain is 0.2 mm.

proximately of basalt composition, exhibit some of the spectral properties of crystalline pyroxenes. Development of M2-like sites suggests that glasses have a high degree of short-range order. When the glasses crystallize or devitrify into a polyphase assemblage, this short-range ordering is altered as the single glass structure is destroyed to re-form as olivine, plagioclase, pyroxene, and opaque-mineral structures.

The proposed assignment of the absorption bands is much the same as those of pyroxenes (Burns and Vaughan, 1975).

The energy-level diagram for d^6 ions (Fe^{2+} ; i.e., the Tanabe-Sugano diagrams by Berkes, 1968) indicates that the fundamental $T_{2g} \rightarrow E_g$ electronic transition is multiply degenerated, and both the ground and excited states undergo crystal-field splitting when the d^6 ion is in a pyroxene-like M2 site (Bancroft and Burns, 1967). The sharp absorption bands at wavelengths near 1 and 2 μm correspond to the transitions ${}^5A_1 \rightarrow {}^5A_1$ and ${}^5A_1 \rightarrow {}^5B_1$ for the selection rules of M2 site symmetry (see Fig. 6 of Bell *et al.*, 1975). By analogy, the fact that both bands occur

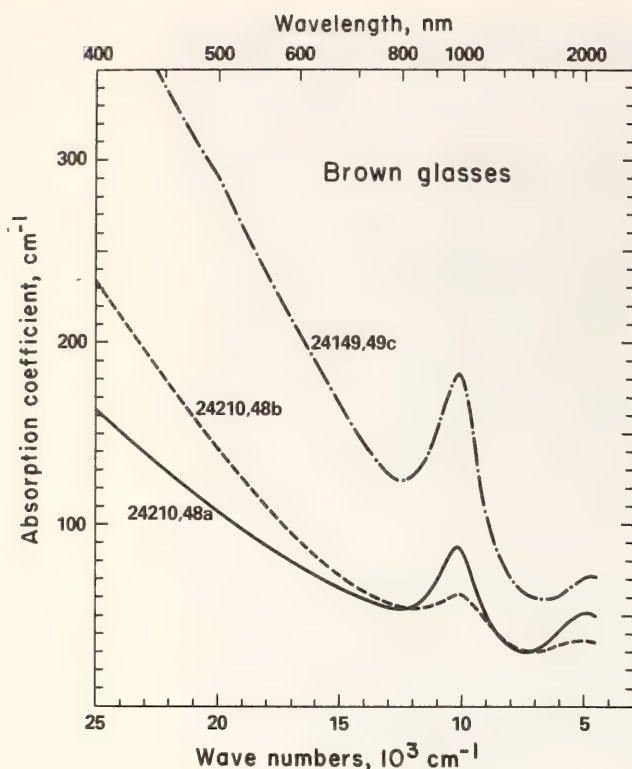


Fig. 149. Optical absorption spectra of three brown glasses with identical chemical compositions.

in the brown glasses suggests that they are the same transitions.

Figure 149 also shows a relatively sharp but weak absorption feature near 500 nm. This feature corresponds with the weak, sharp band observed in lunar pyroxenes (see, for example, Apollo 14 pigeonite spectra of Bell and Mao in Burns and Vaughan, 1975). These bands are assigned as spin-forbidden bands (change of spin multiplicity) of Fe^{2+} in pyroxenes, and are additional confirmation of the existence of octahedrally coordinated Fe^{2+} ions in the brown glasses.

Anorthite Glass Spectra

Glasses of nearly pure anorthite composition comprise a separate set of glasses with distinct spectral characteristics. Some of these glasses have brown and colorless portions with identical composition (Fig. 150), and they should not

be confused with the brown glasses already described. The coloring is not due to the presence of iron or other transition elements, but appears to be due to sub-microscopic devitrification or perhaps to shock effects or radiation damage. The spectrum of the damaged areas appears as a nearly continuous, sloping absorption background in Fig. 151. Also shown in Fig. 151 is the spectrum of a glass fragment of slightly impure anorthite composition (see Table 42). There is a small feature with wavelength near $1\ \mu\text{m}$ that could be caused by Fe^{2+} , but otherwise there is simply a sloping absorption continuum. In both types of anorthite glass, the undamaged or clear zones do not show this absorption background. Absorption effects of this kind in lunar materials have previously been ascribed to metallic coatings on glass or crystals (Bell and Mao, 1977).

Conclusions

The crystal-field spectra of Luna 24 glasses have revealed the effect of several variables: composition, oxygen fugacity, structural state, and degree of devitrification. The last two have been described for the first time in this report.

In summary, spectra of the green glasses are very much like those of other lunar glasses and are thus normal. The iron and titanium concentrations can be deduced directly from spectral data. The Ti^{3+} - Ti^{4+} ratios were compared with those of other lunar glasses and with those of synthetic glasses. The oxygen fugacities of the green glasses vary slightly but cluster about the equivalent value $\log P_{\text{O}_2} = -9.10(\pm 0.05)$ for synthetic glasses of the same composition quenched at 1400°C . Their spectral features are typical of iron-titanium-bearing lunar glasses, and thus their spectral contribution to the soil spectra causes no errors in the interpretation of telescope spectra of the Mare Crisium.

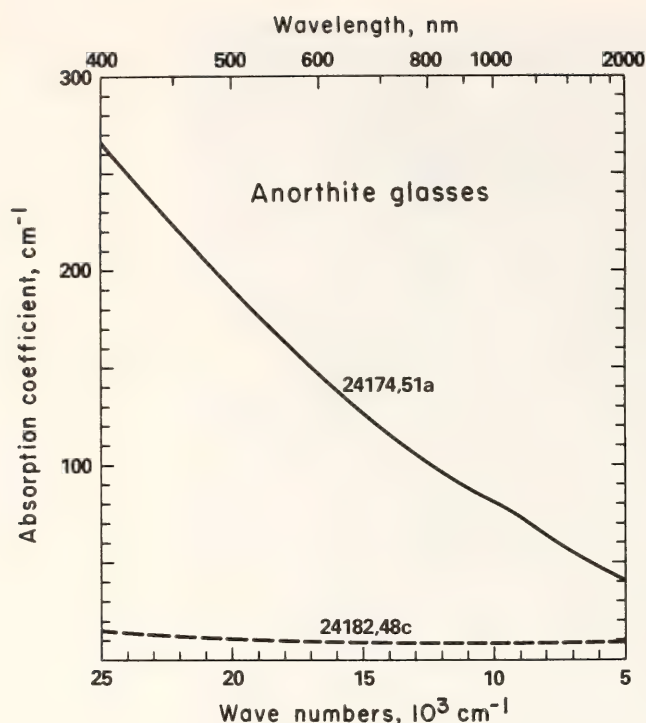


Fig. 150. Photomicrograph of the partially devitrified anorthite glass 24174,51a. The length of the grain is 0.2 mm.

The brown glasses are different. Their spectra appear similar to those of iron-titanium-bearing pyroxenes; yet it has been demonstrated in this study that this appearance is not a true devitrification effect because the glass spectra are essentially those of a single crystal. Where devitrification is observed the product is a polycrystalline basalt. These spectral features vary considerably with the apparent development of order in the glasses,

and they do not correlate well with composition or oxygen fugacity. Fortunately, the spectral features of the brown glasses can be recognized from the present data and should not pose problems of interpretation. Preliminary studies of natural, shocked glasses have not revealed these spectral features, but it would now be desirable to examine a range of terrestrial-impact basalt glasses.

The brown glasses have a degree of



order not previously reported in lunar samples. They are not brown because of composition alone, and thus it would be incorrect to assume that they are a given "basalt" type on the basis of visual observation. It will be important to reassess telescope spectra of Mare Crisium, and the distinct spectral features of the brown glasses should make reassessment possible.

Fig. 151. Optical absorption spectra of the clear anorthite glass 24182,48c and the devitrified anorthite glass 24174,51a.

OXIDE AND SULFIDE MINERALOGY

ILMENITE ASSOCIATION AT THE FRANK SMITH KIMBERLITE PIPE, SOUTH AFRICA

*F. R. Boyd and Jill Dill Pasteris**

Understanding the origin of ilmenite nodules abundant in most kimberlites could provide important insights into the genesis of kimberlite magmas. Ilmenite discrete nodules are most commonly monomineralic but polygranular. In addition, a variety of ilmenite intergrowths with silicates, including host-inclusion combinations, lamellar intergrowths with pyroxenes, and granular intergrowths of various types, have been discovered. A problem that has been especially difficult to resolve is whether the ilmenite discrete nodules formed as high-pressure phenocrysts in kimberlite or protokimberlite magma (Gurney *et al.*, 1977; Mitchell, 1977a; Frick, 1973a) or whether they are accidental mantle inclusions (Boyd and Nixon, 1973, pp. 254–268). It is a further

problem to understand whether or not there is a consanguinity between the ilmenite discrete nodules and the lamellar intergrowths.

Ilmenite discrete nodules and ilmenite-silicate intergrowths are especially abundant in the Frank Smith and associated Weltevreden diatremes of the Republic of South Africa. Previous studies have shown that ilmenites from the Frank Smith mine tend to be rich in MgO in comparison with ilmenites from many other kimberlites (Boyd and Nixon, 1973; Mitchell, 1977a). The Frank Smith ilmenite association is also distinctive in the relative abundance of enstatite-ilmenite lamellar intergrowths and the presence of exotic intergrowths (Meyer *et al.*, 1977; Rawlinson and Dawson, 1977; Clarke *et al.*, 1977). Discrete nodules from Frank Smith, including lamellar intergrowths, differ in texture from those found elsewhere in that they are commonly deformed (Frick, 1973b).

Chemical studies described below are interpreted to indicate that the Frank Smith discrete nodules, including ilmen-

* Department of Geology and Geophysics, Yale University, New Haven, Connecticut 06520.

ites, pyroxenes, garnets, and lamellar intergrowths, are consanguinous. They appear to have crystallized from fractionating liquids prior to kimberlite eruption. The temperature range over which the lamellar intergrowths nucleated and crystallized was $<100^{\circ}\text{C}$. This range is more restricted than that for other discrete nodules.

Compositional Relations

The range in $\text{Mg}/(\text{Mg} + \text{Fe})$ for the Frank Smith ilmenite discrete nodules is 0.376–0.525 after calculation of Fe_2O_3 . There is an apparent positive correlation between calculated Fe_2O_3 (Finger, *Year Book 71*, pp. 600–603) and FeTiO_3 (Fig. 152). Only one nodule was checked in detail for homogeneity, but marginal zoning like that found by Haggerty *et al.* (1977) in Monastery ilmenites was not noted.

The Cr_2O_3 in the Frank Smith discrete ilmenites ranges from <0.03 to 1.18 wt % (Fig. 153A), and there is no correlation with $\text{Mg}/(\text{Mg} + \text{Fe})$. Al_2O_3 contents have the range 0.34–1.75 wt %, with a crude positive correlation with $\text{Mg}/(\text{Mg} + \text{Fe})$ (Fig. 153B). A similar correlation may exist for NiO (Fig. 153C), but there is much scatter. The MnO (0.2–0.3 wt %) does not vary systematically with $\text{Mg}/(\text{Mg} + \text{Fe})$.

Significant SiO_2 was found in all the ilmenites (Fig. 153E), ranging from 0.09–0.34 wt %. The SiO_2 varied from 0.27 to 0.47 wt % in the most Si-rich ilmenite, but inasmuch as all values are higher than for most other ilmenites this variation is more likely due to inhomogeneity than to the presence of submicroscopic inclusions. Ilmenites in nodule suites from Malaita, Solomon Islands, and East Griqualand, South Africa, do not contain significant SiO_2 (unpublished data). These

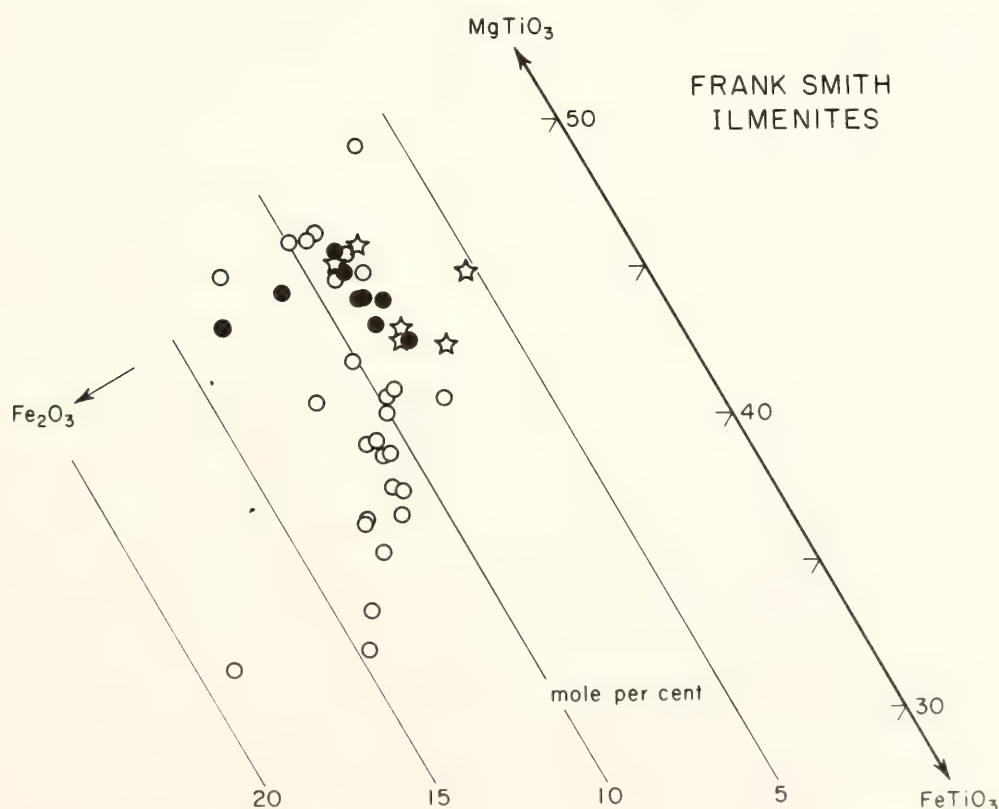


Fig. 152. Ilmenites from the Frank Smith mine plotted in a portion of the ternary MgTiO_3 - FeTiO_3 - Fe_2O_3 . Open circles = ilmenite discrete nodules; solid circles = ilmenite-pyroxene lamellar intergrowths; stars = granular intergrowths, some apparently metasomatic and some of problematic origin. For representative analyses see Boyd (*Year Book 73*, pp. 285–294), Nixon and Boyd (1973d) and Pasteris *et al.* (1978).

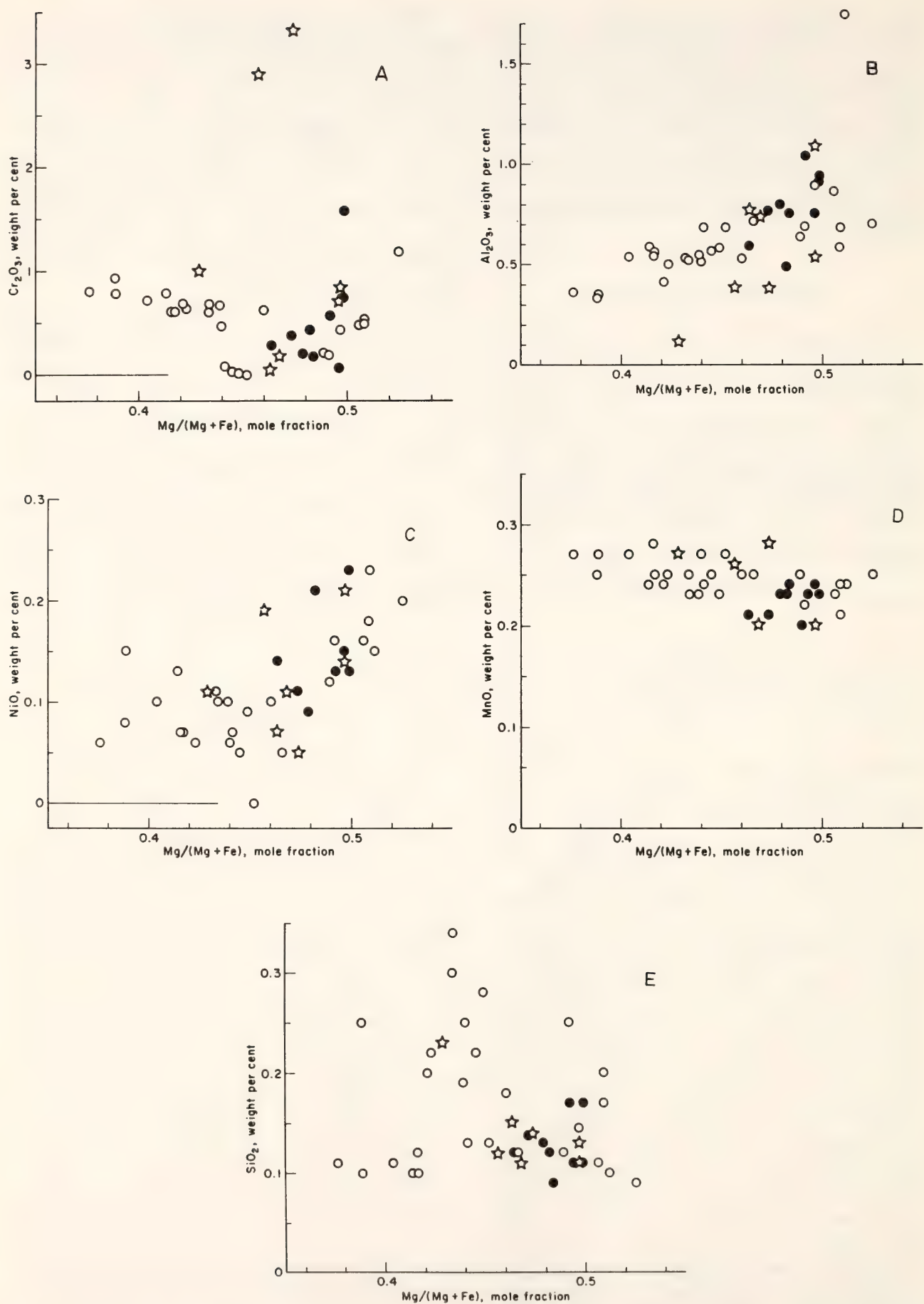


Fig. 153. A-E. Variation of Cr₂O₃, Al₂O₃, NiO, MnO, and SiO₂ with Mg/(Mg + Fe) for Frank Smith ilmenites. See legend of Fig. 152 for explanation of points.

two nodule suites are believed to have originated at shallower depths than the Frank Smith suite (Nixon and Boyd, 1977). Such relations could mean that solution of Si in ilmenite is enhanced by pressure, but the problem may be complex because recent analyses of lunar ilmenites commonly contain values ranging up to 0.1 wt % SiO_2 (Warner *et al.*, 1977).

Six specimens of ilmenite intergrown with garnet or pyroxene in a host-inclusion relationship have mineral compositions that are mainly concordant with those of other Frank Smith discrete nodules and with those found for analogous specimens from northern Lesotho. These relations help to establish the consanguinity of all the discrete nodules.

Two garnet inclusions in ilmenite discrete nodules have TiO_2 in the range 0.5–1.0 wt % and $\text{Cr}_2\text{O}_3 < 0.1$ wt %. These two garnets are slightly more magnesian than comparable specimens from Lesotho, correlating with the fact that Frank Smith ilmenites are more magnesian than ilmenites from many other pipes. Ilmenite inclusions have been found in two bronzite discrete nodules, and one specimen of bronzite included in an ilmenite nodule has been studied. These bronzites have $\text{Mg}/(\text{Mg} + \text{Fe})$ in the range 0.87–0.89; TiO_2 is 0.2–0.3 wt % and Cr_2O_3 is < 0.1 wt %. One sample of diopside included in an ilmenite nodule has a composition very similar to a diopside (PHN 1620A) included in ilmenite from the Solane pipe in northern Lesotho (Nixon and Boyd, 1973b, Table 23).

The ilmenites of the lamellar intergrowths have a much more restricted range in $\text{Mg}/(\text{Mg} + \text{Fe})$ than do the ilmenite discrete nodules (Fig. 152; also Mitchell, 1977a). Analytical data for Fe_2O_3 , MnO , SiO_2 , Cr_2O_3 , and Al_2O_3 in the lamellar ilmenites have no anomalies that would serve to distinguish them from the discrete nodule ilmenites (Figs. 153A–E).

Diopside and enstatite in the Frank Smith lamellar intergrowths are also magnesian. For example, the range in

$\text{Mg}/(\text{Mg} + \text{Fe})$ for five diopsides is 0.868–0.873, compared with 0.824–0.850 for similar specimens from other pipes in southern Africa (Boyd and Nixon, 1973). The Cr_2O_3 in the Frank Smith lamellar pyroxenes is uniformly < 0.2 wt % while TiO_2 is 0.2–0.3 wt % in the enstatites and 0.4–0.5 wt % in the diopsides. The jadeite component in the diopsides is 10–15 mole %.

Discussion

The wide range in $\text{Mg}/(\text{Mg} + \text{Fe})$ of 0.376–0.525 for the Frank Smith ilmenite discrete nodules probably indicates crystallization from liquids of variable composition prior to kimberlite eruption. Garnet and pyroxene discrete nodules from a wide variety of pipes have similar variations (Nixon and Boyd, 1973b; Boyd and Nixon, 1978). Twelve garnet discrete nodules from Frank Smith have the range in $\text{Mg}/(\text{Mg} + \text{Fe})$ of 0.750–0.838, and 20 bronzite nodules have the range 0.876–0.921. It is suggested that these liquids and crystals were mixed during eruption.

The Frank Smith lamellar intergrowths have notably restricted ranges in equilibration temperature as well as in $\text{Mg}/(\text{Mg} + \text{Fe})$. Five diopside intergrowths have $\text{Ca}/(\text{Ca} + \text{Mg})$ of 0.391–0.408, corresponding to a temperature of 1200°C using the solvus of Davis and Boyd (1966) or 1250°C using the solvus of Lindsley and Dixon (1976). The four enstatite intergrowths have $\text{Ca}/(\text{Ca} + \text{Mg})$ of 0.019–0.024 corresponding to a temperature range of 1205°–1280°C using the empirical thermometer of Boyd and Nixon (1973).

The range in equilibration temperature for the lamellar intergrowths of $< 100^\circ\text{C}$ is considerably more restricted than the range of 200°C found for all pyroxene discrete nodules from the Frank Smith pipe (Pasteris *et al.*, 1978).

The circumstances that promote the crystallization of lamellar intergrowths rather than host-inclusion pairs or sepa-

rate crystals are not understood, although Wyatt (1977) has demonstrated that these circumstances are probably igneous. Mitchell (1977a) and Frick (1973b) may well be correct in suggesting that kinetic factors may play a role in the formation of lamellar intergrowths.

The consanguinity of the lamellar intergrowths and the ilmenite discrete nodules is strongly supported by the fact that *both* are distinctively magnesian at the Frank Smith pipe. The hypothesis that all ilmenite, pyroxene, garnet, and possibly olivine discrete nodules from a given pipe are related in origin is difficult to establish in an unequivocal manner. The hypothesis is supported, however, by the fact that the discrete nodules have ranges in composition including $\text{Mg}/(\text{Mg} + \text{Fe})$ that relate them to each other and distinguish them from similar minerals in peridotite and pyroxenite nodules, and by host-inclusion relations of many specimens from a number of kimberlite pipes.

Boyd and Nixon (1973) and Nixon and Boyd (1973b) have proposed that these discrete nodules were crystals in liquid at the time of eruption. Discrete nodules from many kimberlites in southern Africa are characteristically unstrained, but it is clear from the present investigation and the earlier work of Frick (1973b) that the pyroxene-ilmenite lamellar intergrowths and enstatite discrete nodules from Frank Smith are commonly sheared. The presence of deformation textures in the Frank Smith discrete nodule suite certainly weakens, but perhaps does not destroy, the hypothesis that they were crystals in liquid at the time of eruption.

Petrofabric studies have established that the stresses that deformed peridotite and associated nodules from kimberlites were as high as 1 kbar (Nicolas and Ricoult, 1977). The deformation is believed to have occurred immediately prior to eruption, perhaps in the course of conduit formation (Mercier, 1977). In the presence of such high stresses it seems possible that crystals in liquid might be

deformed if the proportion of liquid was small. Moreover, it may be useful to speculate that impact stresses during violent eruption might have produced some of the observed deformation features.

OXIDE MINERALS IN LIQHOBONG KIMBERLITE, LESOTHO

N. Z. Boctor and F. R. Boyd

The physical and chemical changes undergone by kimberlite magma during eruption and crystallization remain puzzling questions. Valuable insights into these changes can be gained by study of the groundmass minerals in kimberlites. A characteristic of these minerals is that they show complex late-stage reactions.

Ilmenite nodules in the hardebank from the South East Blow of the Likhobong kimberlite (see Nixon and Boyd, 1973c) were found in this study to have marginal zones of pronounced enrichment in Mg that are believed to have developed by reaction with fluid. This zoning may be related in origin to the marginal zoning in olivines found by Boyd and Clement (*Year Book* 76, pp. 485–493) in their study of the De Beers kimberlite. Perovskite in the Likhobong kimberlite is markedly enriched in rare earth elements.

Ilmenite

Ilmenite is present in the hardebank as discrete nodules ranging in size from a few mm up to 1.5 cm. Each of the nodules is surrounded by complex reaction mantles similar to those described by Haggerty (1973). Electron microprobe analyses of several ilmenite nodules (Table 43) show that they are rich in Mg and Cr. The MgO content of ilmenite ranges between 10.5 and 21 wt %. The high MgO concentrations are characteristic of the outermost zones adjacent to the reaction mantles in each nodule. Detailed electron microprobe traverses across several of the nodules (e.g., Fig. 154) confirmed this

TABLE 43. Representative Electron Microprobe Analyses of Ilmenite

	2003b nodule		2003b	175		176	
	rim	core	ground-mass ilmenite	rim	core	rim	core
SiO ₂	<0.01	<0.01	<0.01	<0.01	<0.01	<0.01	<0.01
TiO ₂	55.95	52.32	52.12	53.66	52.58	53.09	52.64
Al ₂ O ₃	0.26	0.30	0.34	0.45	0.40	0.60	0.65
Cr ₂ O ₃	1.64	1.54	2.55	2.41	2.36	2.98	3.00
Fe ₂ O ₃	7.85	7.27	11.24	7.76	6.70	7.48	6.91
FeO	14.68	26.62	15.91	16.96	24.98	19.97	23.75
MnO	0.70	0.68	0.66	0.80	0.55	0.65	0.50
MgO	19.59	11.07	16.99	17.10	12.20	15.17	12.92
CaO	<0.01	<0.01	<0.01	<0.01	<0.01	<0.01	0.04
	100.67	99.81	99.81	99.13	99.76	99.99	100.40

observation. Mg enrichment is restricted to a distance between 300 and 500 μm from the margins. Beyond this narrow zone of Mg enrichment, the MgO content of the nodules is almost constant. Within individual nodules, no enrichment of chromium, unlike magnesium, was observed at the margins. When the MgO content in all the ilmenite nodules is plotted against the Cr_2O_3 content, a tendency for increase of Cr content with increase of Mg content is observed in the cores of the nodules, but not in the rims (Fig. 155). A few idiomorphic ilmenite crystals (15–30 μm) are present in the groundmass. Their MgTiO_3 content is

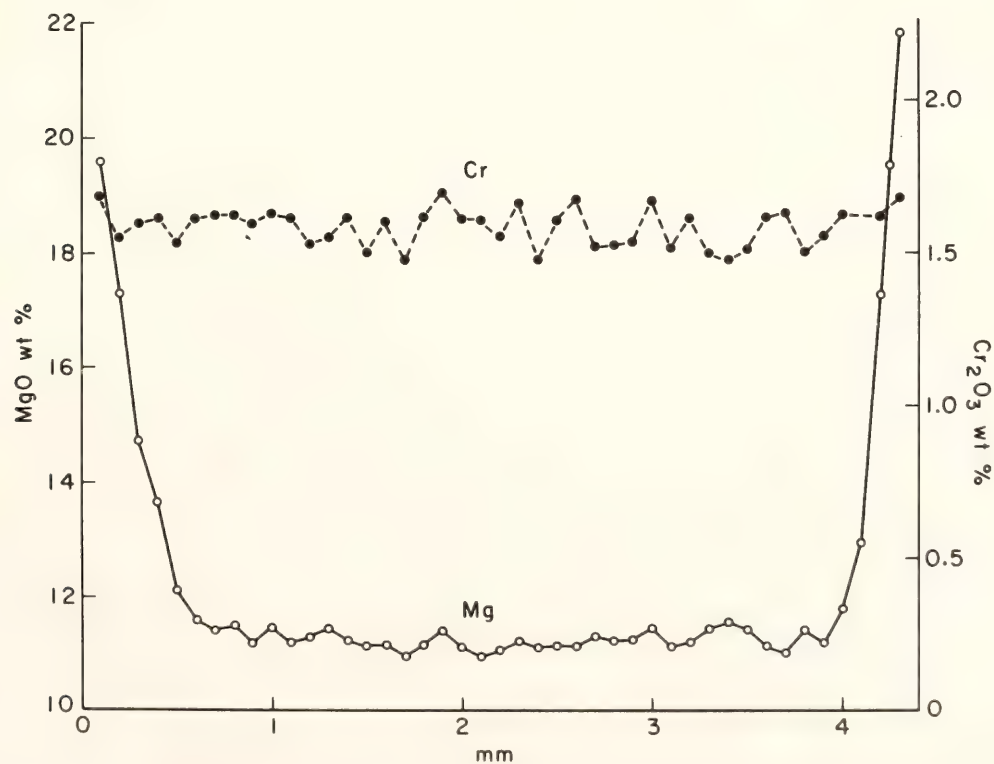


Fig. 154. Microprobe traverse across a discrete ilmenite nodule showing the changes in the MgO and Cr_2O_3 content from rim to core.

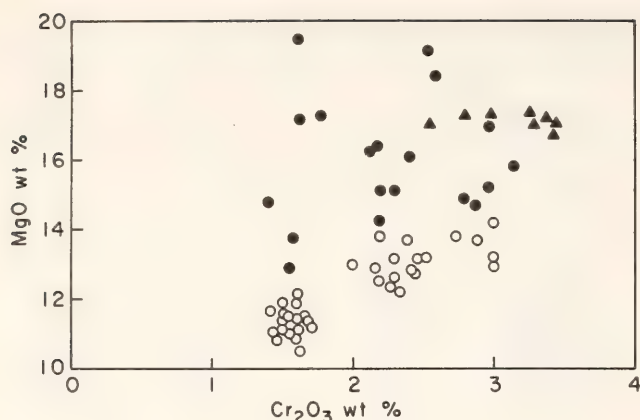


Fig. 155. A plot of the MgO wt % versus the Cr_2O_3 content for discrete ilmenite nodule cores (open circles), for rims (solid circles), and for groundmass ilmenite (solid triangles).

comparable to that of the rims of the ilmenite nodules. Their Fe_2O_3 content, however, is slightly higher than that of the rims (Fig. 156).

Groundmass Spinels

Groundmass spinels are rare in the Lihobong pipe. Two distinct types of spinels were recognized microscopically and by electron microprobe analyses (Table 44; Fig. 157). These are an aluminum-bearing titaniferous chromite and a titanian-ferrian pleonaste, similar in composition to the zone 3 spinel in the reaction mantles on ilmenite nodules described by Haggerty (1973). The titaniferous chromite occurs as euhedral crystals, which appear to be homogeneous in composition and do not show zoning or reaction mantles. The titanian-ferrian pleonaste occurs mostly as subhedral to euhedral crystals that are more common in the groundmass in the vicinity of the reaction mantles on ilmenite nodules. No zoning was observed in titanian-ferrian pleonaste, and it was not found in the

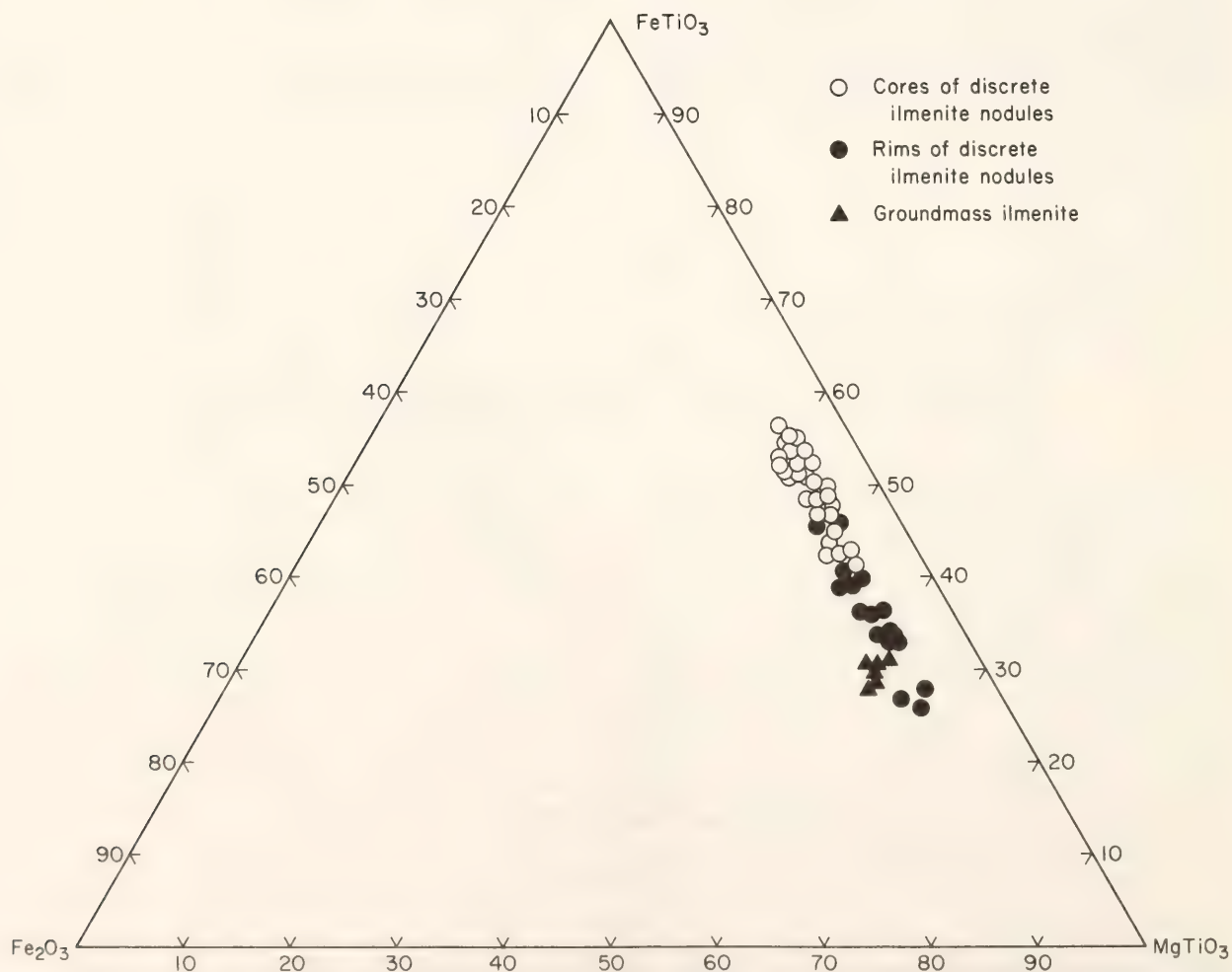


Fig. 156. Composition of discrete ilmenite nodules and groundmass ilmenites in terms of their MgTiO_3 , FeTiO_3 , and Fe_2O_3 content.

TABLE 44. Representative Electron Microprobe Analyses of Spinels

	2003b				173			
	1	2	3	4	1	2	3	4
SiO ₂	0.46	0.70	0.13	0.28	0.18	0.25	0.18	0.33
TiO ₂	20.07	19.54	23.29	19.47	5.74	5.79	6.25	7.71
Al ₂ O ₃	12.37	12.30	9.72	12.53	12.96	13.06	11.58	14.41
Cr ₂ O ₃	1.17	1.04	2.09	0.97	38.74	37.51	37.52	30.44
Fe ₂ O ₃	26.23	26.79	23.71	26.96	10.27	10.31	10.92	14.26
FeO	15.84	15.73	16.58	14.48	17.22	16.67	17.18	14.99
MnO	0.96	1.03	1.09	1.04	0.68	0.70	0.69	0.75
MgO	23.18	23.04	24.03	23.20	13.91	14.06	13.70	16.57
CaO	0.10	0.14	0.11	0.16	0.09	0.11	0.14	0.25
	100.38	100.30	100.69	99.09	99.79	98.46	98.16	99.71

same specimen containing titaniferous chromite. When the chemical analyses of the spinels in the Liqhobong pipe are plotted in the spinel prism (Fig. 157), the two varieties of spinel plot as two separate populations showing markedly different Cr/(Cr + Al) and Ti/(Ti + Cr + Al) ratios. The aluminum-bearing titaniferous chromite analyses plot on the base of the spinel prism, whereas the titanian-ferrian pleonaste analyses plot on its front rectangular face.

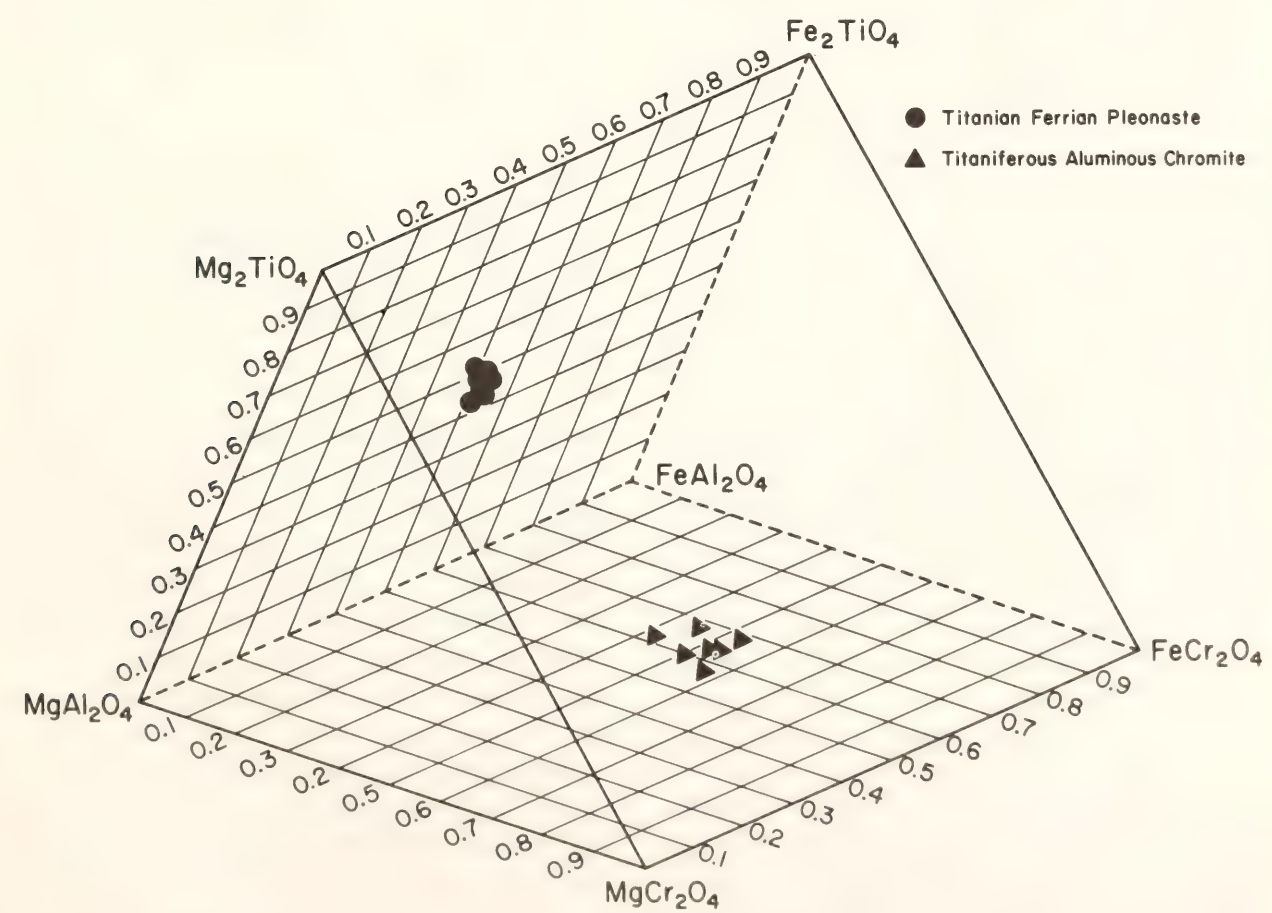


Fig. 157. Groundmass spinel analyses plotted in the spinel prism.

TABLE 45. Representative Electron Microprobe Analyses of Perovskite*

	1	2	3	4	5	6
SiO ₂	0.05	0.01	0.04	0.05	0.04	<0.01
TiO ₂	55.61	55.29	55.45	55.02	55.18	55.82
FeO	1.01	1.06	1.02	1.08	1.27	1.16
MgO	0.50	0.52	0.57	0.51	0.46	0.58
CaO	36.75	37.20	37.52	36.75	36.30	38.26
Na ₂ O	0.63	0.59	0.62	0.74	0.76	0.34
Y ₂ O ₃	0.10	0.07	0.01	0.01	0.07	0.02
La ₂ O ₃	0.89	0.75	0.89	0.77	0.80	0.84
Ce ₂ O ₃	2.13	2.14	2.25	2.42	2.34	1.69
Pr ₂ O ₃	<0.01	<0.01	<0.01	<0.01	<0.01	<0.01
Nd ₂ O ₃	1.41	1.20	1.25	1.30	1.00	0.73
Nb ₂ O ₅	0.66	0.91	0.70	0.71	0.57	0.45
Ta ₂ O ₅	<0.01	<0.01	0.10	0.14	0.07	<0.01
	99.54	99.74	100.43	99.50	99.13	99.90

* ZrO₂ not detected in all analyses.

Perovskite

All the rocks studied from the South East Blow are characterized by the presence of perovskite, which is more abundant than groundmass ilmenite and spinels. Perovskite is Nb-bearing and is rich in rare earth elements. It displays little variation in composition from one sample to another (Table 45). The Nb₂O₅ content of perovskite ranges from 0.45 to 1.02 wt %, and the sum of Pr₂O₅, Nd₂O₃, Ce₂O₃, and La₂O₃ ranges from 3.25 to 5.1 wt %. The FeO content is low (1.0 to 1.3 wt %). Interelement correlations between Ca and REE, Ca and Na, and Ti and Nb (Figs. 158A, 158B, and 158C) show moderate negative correlations which are consistent with the expected isomorphous substitutions in the perovskite structure. The correlation coefficients are -0.57 , -0.51 , and -0.51 for the Ca-REE, Ca-Na, and Ti-Nb pairs respectively.

Discussion

Comparison of the data on the composition of ilmenite in the Lihobong pipe with those reported by Boyd and Nixon (1973) and Mitchell (1973, 1977a) for

other kimberlites seems to support their suggestion that the Mg content of ilmenite from different kimberlites may show wide variation. For example, the Lihobong ilmenite seems to be richer in Mg than the ilmenites from Monastery, Kao, and Arturo de Paiva kimberlites and overlap in composition with those from Premier and Frank Smith.

Zoning in discrete ilmenite nodules in kimberlites seems to be more common than was previously believed. Haggerty *et al.* (1977) reported what they called a "magmatic zoning trend" toward enrichment in MgTiO₃ in discrete nodules from Monastery. They also noted that discrete nodules with closely adhering kimberlite at Monastery have reaction mantles which include ilmenite depleted in MgTiO₃ relative to the nodules. This feature was described as "kimberlite reaction trend" by Haggerty *et al.* (1977). Discrete ilmenite nodules in the Lihobong pipe display complex reaction mantles, but the secondary ilmenite in these mantles is more enriched in Mg relative to the nodules themselves. The Mg enrichment here is attributed to reaction with the late-stage Mg- and Ti-rich fluids that produced the reaction mantles. The limited extent of the zone of Mg enrichment relative to

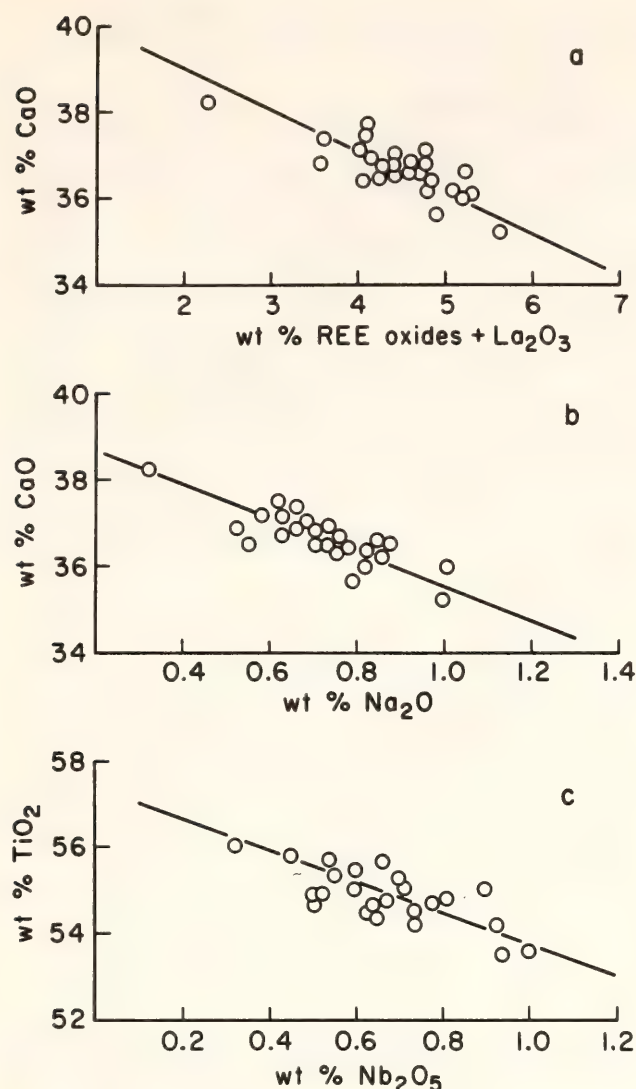


Fig. 158. Interelement correlation in perovskite: (A) correlation between CaO wt % and the sum of the total REE oxides + La₂O₃; (B) correlation between CaO wt % and Na₂O wt %; (C) correlation between TiO₂ wt % and Nb₂O₅ wt %.

nodule size, the fact that Mg content across the major part of the nodules is nearly constant, and the similarity in Mg content between the nodule rims and the idiomorphic groundmass ilmenite all seem to support this interpretation.

Ilmenite mantles in Lihobong kimberlite are enriched in Mg and Ti, contrary to the observation of Haggerty *et al.* (1977) in the discrete nodules at Monastery. A clue to the cause of these two different reaction trends can be found by comparing the composition of the spinels in the two reaction mantles. Reaction

mantles with Mg-rich secondary ilmenite contain spinels of unique composition (Haggerty, 1973) that are remarkably enriched in Mg and Ti, with low-to-moderate Fe₂O₃ content, whereas those with secondary ilmenite depleted in Mg contain titaniferous magnetite. Thus, the two reaction trends may be controlled primarily by the variations in the composition of the fluid that produced the reaction mantles as well as variation in oxygen fugacity and temperature.

The two populations of groundmass spinels observed in Lihobong kimberlite now appear to be characteristic of many kimberlites. The titanian pleonastes are close in composition to the spinels reported by Dawson and Hawthorne (1973) from Benfontein; by Mitchell and Clarke (1976) and Mitchell (1977b) from Penyuk and Kirkland Lake kimberlites, respectively; and by Boctor and Meyer (1977) from Green Mountain, Colorado. These spinels belong to the quaternary system Mg₂TiO₄-Fe₂TiO₄-FeAl₂O₄-MgAl₂O₄ and show trends toward MgFe₂O₄ and Fe₃O₄. The titanian chromites are similar in composition to the titan-magnesium aluminous chromite of Mitchell and Clarke (1976) and are essentially members of the quaternary system FeCr₂O₄-MgCr₂O₄-FeAl₂O₄-MgAl₂O₄.

Perovskite in the Lihobong kimberlite shows Nb content comparable to that given by Mitchell (1972) for kimberlitic perovskite. The rare earth element content of Lihobong perovskite is higher, however, than that previously reported for South African kimberlites (Grantham and Allen, 1960). The enrichment of perovskite in REE can be interpreted as evidence for the presence of CO₂-rich fluids that provided the complexing agents necessary for the concentration of the rare earth elements. The abundance of calcite in many of the samples from Lihobong seems to support this interpretation.

In conclusion, the enrichment or depletion of Mg in the rims of the discrete ilmenite nodules in kimberlite appears to be caused by late-stage reactions between

the nodules and kimberlitic fluids. The Mg enrichment or depletion is probably controlled by variations in the $Mg/(Mg + Fe)$ of the fluids, oxygen fugacity, and temperature. Such variations might also account for the observed reaction rims in kimberlitic olivines (Boyd and Clement, *Year Book* 76, pp. 485–493).

In the Likhobong kimberlite, the presence of Ti-rich spinels in ilmenite reaction mantles and in the groundmass, and the high REE content in perovskite, suggest that the fluid phase was rich in Ti, REE, and CO_2 .

IRON-TITANIUM OXIDE AND SULFIDE MINERALS IN CARBONATITE FROM JACUPIRANGA, BRAZIL

*Nabil Z. Boctor and D. P. Svisero**

In the last few years, there has been a growing interest in the relationship between kimberlite and carbonatite (e.g., Dawson, 1966b; Dawson and Hawthorne, 1973; Gittins *et al.*, 1975). Iron-titanium oxide minerals are common to both rock types. Detailed studies of kimberlitic spinels and ilmenite (Boyd and Nixon, 1973; Haggerty, 1975; Mitchell, 1977a) have provided valuable information on the evolution of kimberlitic magma and the physical-chemical conditions during its emplacement and cooling. Iron-titanium oxide minerals in carbonatites, however, have received less attention than those in kimberlites.

The carbonatite of Jacupiranga, Brazil, forms a small oval body in a large alkaline igneous complex that comprises peridotite, pyroxenite, ijolite, jacupirangite, and fenites. The carbonatite was considered to be a typical sövite (Melcher, 1966), and was therefore selected for study. It is composed of calcite, dolomite, phlogopite with varying amounts of apatite, forsterite, iron-titanium oxides, and accessory sulfide minerals.

Iron-Titanium Oxide Minerals

Iron-titanium oxide minerals in the sövite are represented by magnetite and ilmenite. Magnetite forms crystals ranging in size from a few millimeters to about 1 cm. It commonly contains ovoidal inclusions of calcite, corroded crystals of apatite with calcite rims, or prismatic crystals of phlogopite. Magnetite is either homogeneous or shows exsolution lamellae of ilmenite parallel to its octahedral planes. Exsolved magnetite is less enriched in Mg relative to magnetite that shows no ilmenite exsolutions (Table 46; Fig. 159).

In addition to its presence as exsolution lamellae in magnetite, ilmenite occurs as subhedral crystals enclosed in magnetite or as aggregates of tabular crystals at the interface between magnetite and the carbonate minerals. Mg and Mn are enriched in ilmenite relative to magnetite (Table 46, Figs. 160A, 160B).

Sulfide Minerals

Sulfide minerals are represented by pyrrhotite, chalcopyrite, pyrite, and valleriite (Table 47). Pyrrhotite, chalcopyrite, and pyrite are interstitial between large calcite and dolomite crystals and occasionally form veinlets transecting the carbonate minerals or replacing them along their cleavage planes. Valleriite $[Fe_{1.07}Cu_{0.93}S_2] \cdot 1.526 [Mg_{0.68}Al_{0.32}(OH)_2]^*$ occurs as aggregates of radial crystals at the interfaces between pyrrhotite or chalcopyrite and carbonate minerals or an interstitial phase between pyrrhotite and magnetite. The stability relations of valleriite are not known. Heating experiments on natural valleriite (Yund and Kullerud, 1966) show, however, that it breaks down to chalcopyrite, Al and Mg oxides, and water at temperatures above 450°C. The sulfide minerals in Jacupiranga

* University of São Paulo, São Paulo, Brazil.

* Theoretical formula according to Evans and Allmann, 1968.

TABLE 46. Representative Electron Microprobe Analyses of Magnetite and Ilmenite

	Magnetite			Ilmenite		
	1*	2†	3‡	4§	5§	6
SiO ₂	0.05	0.10	0.03	0.01	0.01	0.01
TiO ₂	0.81	1.88	1.38	55.55	55.18	55.74
Al ₂ O ₃	0.80	0.04	0.30	0.11	0.02	0.13
Cr ₂ O ₃	0.02	0.03	0.04	0.01	0.02	0.03
Fe ₂ O ₃	67.64	64.80	65.06	5.30	4.40	3.69
FeO	22.74	28.53	29.40	21.48	21.04	24.32
MnO	1.21	0.96	0.67	3.40	3.54	3.23
MgO	5.86	3.06	2.24	14.37	13.73	12.61
CaO	0.05	0.01	0.01	0.01	0.01	0.01
	99.18	99.40	99.12	100.22	99.84	99.78

* Analysis 1. Magnetite from phlogopite sövite.
† Analysis 2. Magnetite from olivine sövite.
‡ Analysis 3. Exsolved magnetite in phlogopite sövite.
§ Analyses 4 and 5. Lamellar ilmenite.
|| Analysis 6. Subhedral ilmenite crystal.

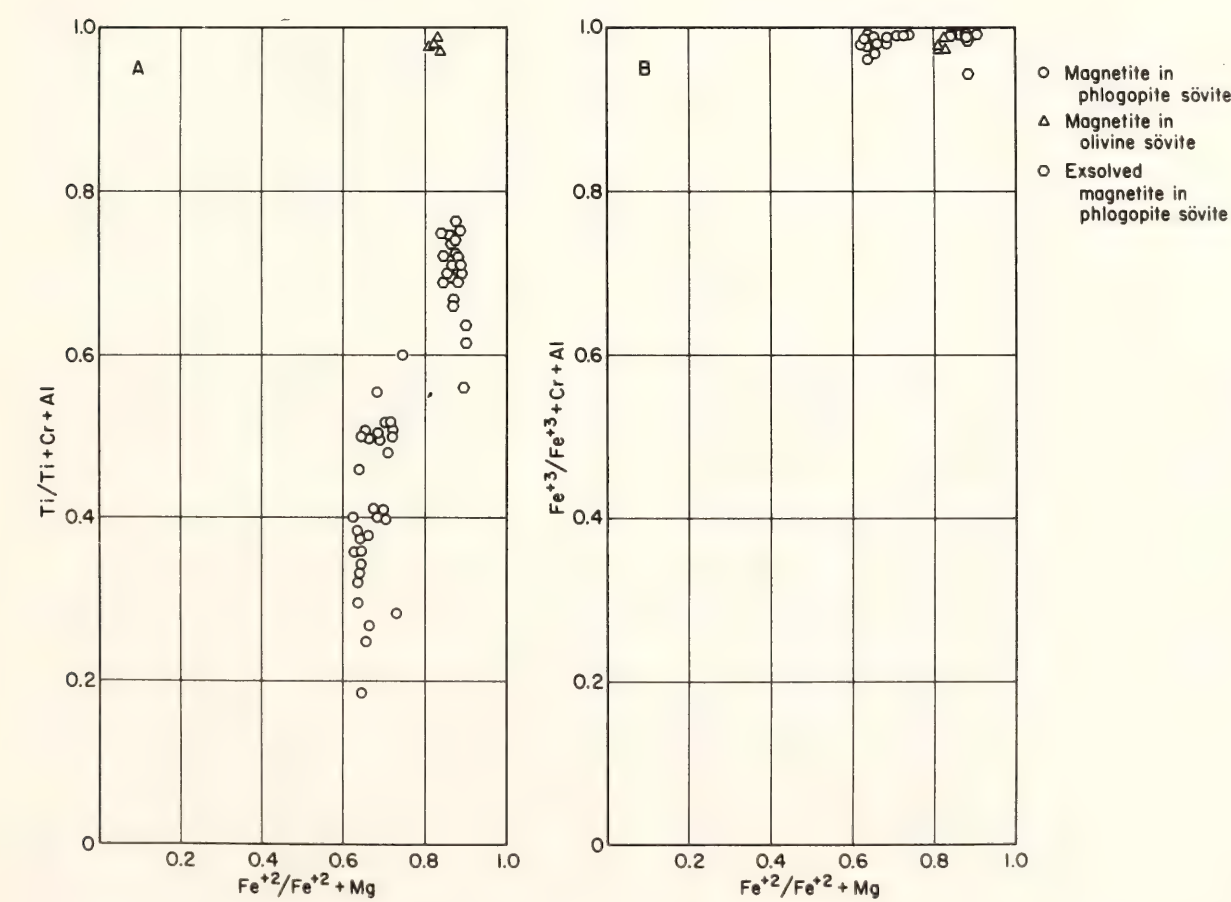


Fig. 159. (A). Plot of $Fe^{2+}/(Fe^{2+} + Mg)$ vs. $Ti/(Ti + Cr + Al)$ in magnetite. (B). Plot of $Fe^{2+}/(Fe^{2+} + Mg)$ vs. $Fe^{3+}/(Fe^{3+} + Cr + Al)$ in magnetite.

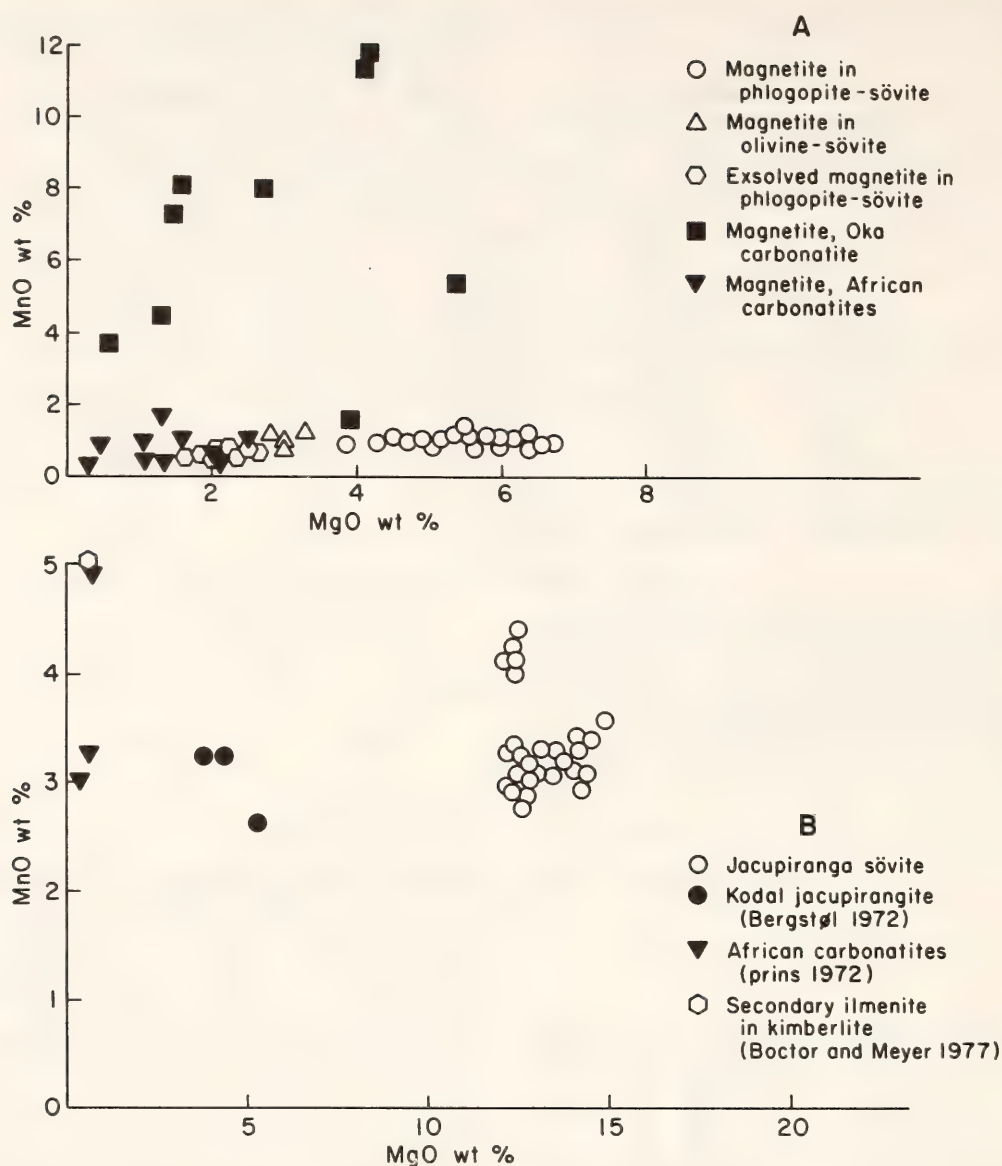


Fig. 160. (A). Plot of MgO wt % vs. MnO wt % in magnetite from Jacupiranga and other carbonatites; Oka carbonatite data after Gold (1966) and McMahon and Haggerty (1976); African carbonatite data after Prins (1972). (B). Plot of MgO wt % vs. MnO wt % in ilmenite from Jacupiranga sövite and other carbonatites and alkaline rocks.

TABLE 47. Representative Electron Microprobe Analyses of Sulfide Minerals

Element *	Pyrrhotite			Chalcopyrite		Valleriite		
Fe	60.49	59.77	60.29	29.76	29.83	23.32	22.92	22.13
Co	0.29	0.23	0.45	0.06	0.05	0.05	0.01	0.04
Cu	<0.01	<0.01	0.01	34.03	34.00	18.04	17.32	19.16
S	39.66	39.81	39.36	35.95	35.73	23.01	23.22	22.55
Mg	11.42	11.57	10.89
Ca	0.01	0.01	0.11
Al	3.54	3.51	4.03
Total	100.44	99.81	100.11	99.80	99.61	79.38	78.54	79.28

* Na and Ni not detected.

sövitite crystallized later than magnetite and form mantles on this mineral or veinlets transecting it. Magnetite has occasionally undergone extensive sulfurization to pyrrhotite and pyrite.

Discussion

Magnetite in Jacupiranga carbonatite belongs mainly to the magnetite-magnesianoferrite solid solution series. It is similar in composition to magnetite from African carbonatite (Prins, 1972), although it does not display zonation with respect to Mg, Ti, and Mn as pronounced as that in the African carbonatites. It differs, however, from magnetite from Oka carbonatite (Gold, 1966; McMahon and Haggerty, 1976, 1977), which belongs to the magnetite-jacobsite solid-solution series and contains up to 12 wt % MnO.

Magnetite from Jacupiranga and other carbonatites differs markedly from spinel phases in kimberlite. Kimberlitic spinels belong either to the system FeCr_2O_4 - MgCr_2O_4 - FeAl_2O_4 - MgAl_2O_4 or to the system Mg_2TiO_4 - Fe_2TiO_4 - FeAl_2O_4 - MgAl_2O_4 and show trends towards magnesianoferrite and magnetite (Haggerty, 1975). Spinel from kimberlitic-carbonatitic dikes (Gittins *et al.*, 1975) are more enriched in Ti, Al, and Mg relative to magnetite from carbonatite and bear more similarity to magnesian titaniferous magnetite in reaction mantles on kimberlitic ilmenite (Boctor and Meyer, 1977; Haggerty *et al.*, 1977) than to magnetite in carbonatite. The only kimberlitic spinel that bears any similarity to magnetite in carbonatite is the Ti-poor magnetite in association with calcite veinlets transecting ilmenite nodules in Green Mountain kimberlite (Boctor and Meyer, 1977) and in Peuyuk kimberlite (Mitchell and Clarke, 1976). In general, however, the data on magnetite from Jacupiranga and other carbonatites show that their chemical composition bears greater similarity to magnetite from alkaline rock associations than to spinels in kimberlites.

Ilmenite in Jacupiranga carbonatite

is a solid solution of MgTiO_3 , FeTiO_3 , MnTiO_3 , and Fe_2O_3 (Figs. 161A, 161B). The Mg content of the ilmenite is much higher than that of ilmenite from other carbonatite and alkaline rocks (Prins, 1972; Bergstøl, 1972; Griffin and Taylor, 1975) but is similar to that of ilmenite in kimberlites. The Mn content of ilmenite from Jacupiranga, however, is much higher and the Cr content significantly lower than that of primary kimberlitic ilmenite. Secondary ilmenite mantles on rutile-ilmenite intergrowths in carbonate-bearing kimberlite (Boctor and Meyer, 1977) may have Mn content as high as that observed in Jacupiranga ilmenite, though it is usually depleted in Mg. The Mn enrichment in ilmenite from Jacupiranga, however, is not as pronounced as that of ilmenite from Oka carbonatite, which may contain up to 50 mole % MnTiO_3 in solid solution (McMahon and Haggerty, 1976).

The partitioning of Mg in favor of ilmenite relative to magnetite in Jacupiranga carbonatite is consistent with the experimental data of Pinckney and Lindsley (1976), who found that in the temperature range 700°–950°C and at oxygen fugacities controlled by FMQ and NNO buffers, Mg is preferentially concentrated in ilmenite. This trend becomes more pronounced with decreasing temperature, regardless of f_{O_2} . Therefore, the Mg-enrichment of ilmenite in magnetite-ilmenite intergrowths from Jacupiranga relative to ilmenite from other carbonatite can be explained in either of two possible ways: either the activity of Mg in the liquid from which the original titanomagnetite solid solution crystallized was high or, after exsolution, the magnetite-ilmenite intergrowths at Jacupiranga equilibrated to lower temperatures than their analogues in other carbonatites. The presence of Fe_2O_3 in solid solution in ilmenite is also consistent with the data of Mazzullo *et al.* (1975) who found that the presence of MnTiO_3 in solid solution in ilmenite increases its $\text{Fe}_2\text{O}_3/\text{FeTiO}_3$.

The sulfide minerals in Jacupiranga

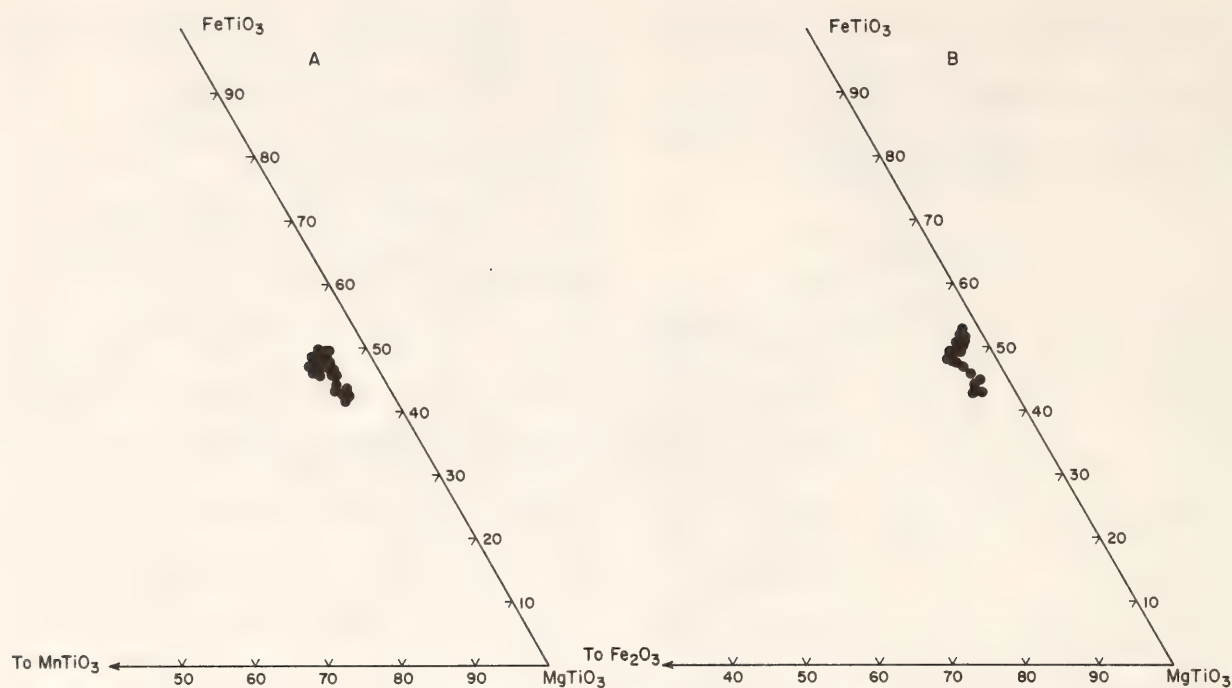


Fig. 161. (A). Composition of ilmenite in terms of MgTiO_3 , MnTiO_3 , and FeTiO_3 end members. (B). Composition of ilmenite in terms of MgTiO_3 , Fe_2O_3 , and FeTiO_3 .

differ from those at Oka in mineralogy and mode of occurrence. The sulfides at Oka, for example, are represented by pyrrhotite that occurs as inclusions in magnetite and shows cobaltian pentlandite exsolutions (8–15 wt % Co; McMahon and Haggerty, 1976). At Jacupiranga, the sulfides appear to have crystallized later than the silicate, carbonate, and oxide minerals and bear some similarity to the sulfide mineral assemblages in Palabora Carbonatite, South Africa (Palabora Mining Company Limited Mine Geological and Mineralogical Staff, 1976). Both carbonatites are characterized by the presence of valleriite and chalcopyrite.

The presence of valleriite in the sulfide mineral assemblage in Jacupiranga carbonatite, the sulfurization of magnetite, and the lack of textural evidence of sulfide liquid immiscibility suggest that the sulfide minerals may have formed by action of late-stage sulfur-bearing fluids in the final stages of crystallization of the parent magma. In this respect, the sulfide minerals in Jacupiranga carbonatite seem to differ from primary sulfide minerals in

kimberlites that appear to have crystallized from immiscible sulfide liquids.

In conclusion, the data on iron-titanium oxide minerals in Jacupiranga carbonatite do not support a genetic relation between carbonatite and kimberlite. The iron-titanium oxide minerals in Jacupiranga and other carbonatites bear more similarity to those from alkaline rock associations than to primary spinels and ilmenite in kimberlites. Sulfide minerals in Jacupiranga carbonatite also seem to have an origin different from that of primary sulfides in kimberlites.

EVALUATION OF SPHALERITE GEOBAROMETRY IN BODENMAIS ORE, BAVARIA

Nabil Z. Boctor

The sulfide deposits near Bodenmais, Bavaria, form an elongated mass in highly metamorphosed migmatitic cordierite-sillimanite gneisses. The metamorphic conditions of the ore and country rocks at Silberberg, Bodenmais, were studied by Schreyer *et al.* (1964). On a more

regional scale, the pelitic and psammitic gneisses in the Lam-Bodenmais area were studied recently by Blümel and Schreyer (1977). Two metamorphic zones in this region were described by Blümel and Schreyer (1977): a sillimanite-K feldspar zone, and a cordierite-K feldspar zone. The temperature and pressure of metamorphism that formed the cordierite-K feldspar zone, the host rock of Bodenmais ore, were estimated by Blümel and Schreyer (1977) as 650°–700°C and 2–3 kbar.

The theoretical principles behind the use of sphalerite as a geobarometer were proposed by Barton and Toulmin (1966). Scott (1973, 1976) calibrated the sphalerite geobarometer experimentally and used it in estimating the metamorphic pressures in regionally metamorphosed sulfide ores. Hutcheon (1978) calculated the P-T-X relations for sphalerite-pyrite-pyrrhotite assemblages and found that the calculated isobars were in agreement with the experimental data of Scott (1973).

The present investigation represents an evaluation of sphalerite geobarometry in Bodenmais ore. The ore seems highly suitable for such a study for several reasons: (1) the assemblage sphalerite-pyrite-pyrrhotite needed for sphalerite geobarometry is well preserved in some specimens, (2) earlier studies by Schreyer *et al.* (1964) suggest that the equilibrium composition of sphalerite has been preserved, and (3) independent estimates of pressure and temperature of metamorphism are available from the study of the silicate mineral assemblages (Blümel and Schreyer, 1977).

Mineralogy

The ore from Silberberg is composed mainly of sphalerite, pyrite, pyrrhotite, and chalcopyrite. Sphalerite occurs as large crystals which may reach up to 1 cm. Where coexisting with pyrite and pyrrhotite, the three phases form inter-

locking crystal aggregates in mutual contact with one another. In many instances, sphalerite coexists with either pyrrhotite or pyrite. Chalcopyrite is abundant in some specimens as large discrete crystals that may enclose smaller sphalerite crystals. Chalcopyrite exsolution in sphalerite are rare. In silicate-rich specimens, pyrrhotite forms a matrix for large cordierite porphyroblasts and is occasionally seen replacing biotite. In some specimens, pyrrhotite is altered to aggregates of marcasite, pyrite, or both, which occasionally show colloform texture. Magnetite is a rare mineral in some specimens; when present, it occurs in contact with the silicates or pyrrhotite but not with sphalerite. Galena is a rare constituent in some specimens.

The ore specimens investigated from Johannestollen area are very rich in Zn-spinel and contain only minor amounts of pyrrhotite, pyrite, and, rarely, sphalerite. Zn spinel forms large, idiomorphic crystals that commonly display biotite rims. In a few instances, discontinuous rims of pyrrhotite are observed on some spinel crystals. Some Zn spinel crystals show exsolution of magnetite.

Optical examination of pyrrhotite in samples from both Silberberg and Johannestollen reveals no intergrowths or alterations. On etching with 50% HI using the technique of Schwarz and Harris (1970), monoclinic pyrrhotite is found to coexist with hexagonal pyrrhotite and pyrite in many specimens. In addition to its occurrence as discrete grains, monoclinic pyrrhotite is commonly observed as rims on hexagonal pyrrhotite, as thin veinlets along cracks, and as irregular domains within hexagonal pyrrhotite crystals.

Mineral Chemistry

The average mole % FeS in sphalerite coexisting with both pyrrhotite and pyrite varies from one sample to another, but lies within a narrow range of 15.8–16.5

TABLE 48. Estimated Pressures from Sphalerite in Different Mineral Assemblages in Silberberg Ore, Bodenmais

Sample no.	Assemblage*	Mole % FeS in sphalerite		P,kbar†	P,kbar‡
		Range	Average		
68919	Sp, py, mpo, hpo	15.35–17.2	16.31 (0.48)§	2.3	1.7
	Sp, py	15.5 –15.98	15.42 (0.60)	3.4	2.7
Bo ₁	Sp, py, mpo, hpo	15.85–16.99	16.65 (0.31)	2.1	1.4
Bo ₂	sp, py, mpo (hpo)	14.92–16.67	15.80 (0.53)	2.9	2.1
	sp, mpo (hpo)	14.97–15.95	15.44 (0.36)	3.5	2.7
Bo ₇	sp, cp	9.63–14.41	13.49 (1.22)	6.1	5.6
Bo ₈	sp, py, hpo, (mpo)	15.72–16.93	16.55 (0.39)	2.2	1.6
	sp, py, cp, hpo (mpo)	12.00–17.20	14.57 (1.50)	4.8	4.0
	sp, hpo, mpo	15.72–16.53	16.2 (0.34)	2.4	1.8
Bo ₁₁	sp, mpo, (hpo)	14.93–16.26	15.35 (0.35)	3.5	2.8

* Abbreviations: sp = sphalerite, py = pyrite, hop = hexagonal pyrrhotite, mpo = monoclinic pyrrhotite. () = minor amounts.
† Pressure estimates from the experimentally determined isobars of Scott (1973, 1976).
‡ Pressure estimates from the calculated isobars of Hutcheon (1978).
§ Standard deviations in parentheses.

mole % FeS (Table 48; Fig. 162). Within individual samples, FeS content in sphalerite associated with pyrrhotite and pyrite varies from grain to grain and within individual grains as well. However, sphalerite in individual samples is essentially homogeneous (standard deviations in FeS mole % are between 0.39 and 0.53). Within individual crystals, the lowest FeS content in sphalerite is frequently observed near grain boundaries at the immediate contact with pyrrhotite.

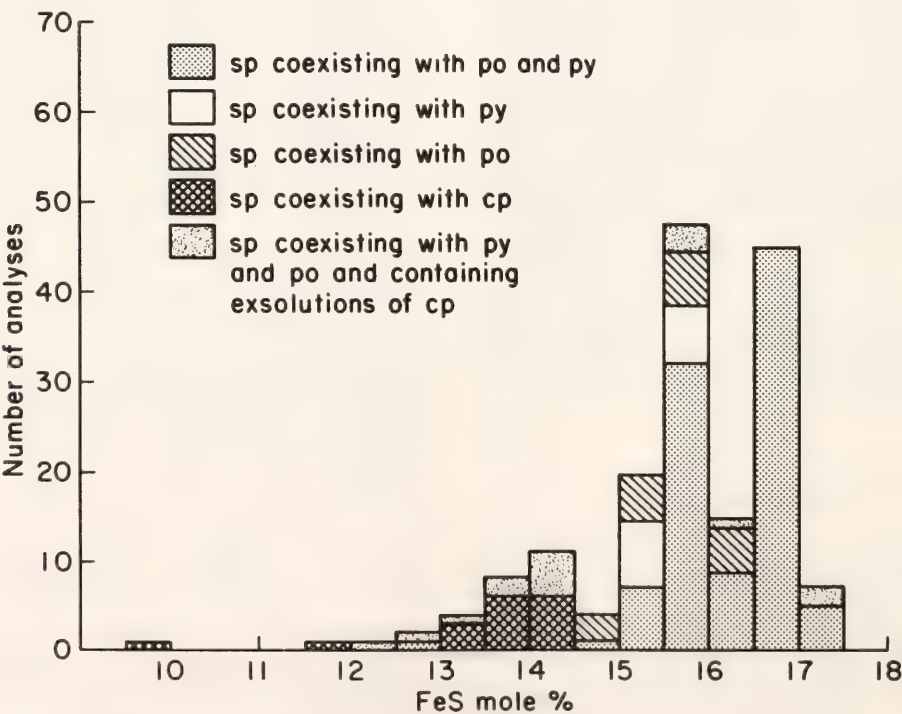


Fig. 162. Frequency distribution of FeS mole % in sphalerite from different mineral assemblages.

Sphalerite in contact with either pyrite or pyrrhotite shows a lower FeS content than sphalerite coexisting with both iron sulfides, even when the two assemblages are separated by a distance of a few millimeters in the same polished section. The mole % FeS in sphalerite coexisting with pyrite ranges between 15.5 and 16.0, whereas that in sphalerite coexisting with pyrrhotite ranges between 15.4 and 16.3.

A large crystal of sphalerite displaying exsolutions of chalcopyrite and showing mutual contacts with pyrrhotite and pyrite was analyzed. Fifteen analyses performed on this crystal show that it is inhomogeneous, having a mole % FeS in the range of 12.0 to 17.2, with an average of 14.6. This heterogeneity is real and cannot be attributed to sampling some of the chalcopyrite exsolutions during the analyses, because the concentration of copper in the 15 sphalerite analyses is low, ranging between 0.03 and 0.38 wt %. Another large sphalerite crystal totally surrounded by chalcopyrite and containing chalcopyrite exsolutions was also analyzed. Pyrrhotite is present a few millimeters from the sphalerite-chalcopyrite assemblage, in direct contact with chalcopyrite but not with sphalerite. The mole % FeS in sphalerite from this specimen ranges between 9.63 and 14.4, with an average of 13.49 for 14 analyses. The Cu content in the analyzed sphalerite is in the range 0.09 to 0.32 wt %. Unfortunately, chalcopyrite-bearing sphalerite coexisting with iron sulfides is rare, and in the few instances in which it was observed (other than those described above) the chalcopyrite exsolutions are fine-grained and evenly distributed in sphalerite. This precludes adequate analysis of the sphalerite host.

In all of the samples analyzed, sphalerite contains minor amounts of MnS and CdS in solid solution. The largest MnS content in sphalerite is 1.8 mole %, whereas the content of CdS does not exceed 0.3 mole %.

The pyrrhotite composition ranges between 46.9 and 48.0 at.% Fe. In speci-

mens with small amounts of monoclinic pyrrhotite, the hexagonal phase is homogeneous, having standard deviations on the order of 0.2 at.% Fe. In specimens where monoclinic pyrrhotite is abundant, the range for pyrrhotite composition reported above can be observed in a single polished section.

Electron microprobe analyses of Zn spinel (Table 49, Fig. 163) show that it is in solid solution of gahnite (56.06 to 72.11 mole %), hercynite (16.56 to 32.71 mole %), and Mg spinel (8.1 to 13.4 mole %). Normalization of the spinel analyses on the basis of 24 cations yields 32 oxygens, which suggests that the iron in the spinel structure is in the divalent state. The Zn-spinel crystals associated with cordierite and mica are compositionally homogeneous. Traverses across spinel crystals showing biotite rims on one side and pyrrhotite rims on the other show strong depletion in Fe and enrichment in zinc towards the contact with pyrrhotite (Fig. 164).

Sphalerite Geobarometry

The mole % FeS in sphalerite coexisting with pyrite and pyrrhotite was used to estimate the pressures from the experimentally determined isobars of Scott (1973, 1976) and from the calculated isobars of Hutcheon (1978). Pressures were also estimated for sphalerite coexisting with either pyrrhotite or pyrite alone and sphalerite in chalcopyrite-bearing assemblages. The temperature of metamorphism at Bodenmais is in the range 650°–700° C (Blümel and Schreyer, 1977). A metamorphic temperature of 650°C was selected for sphalerite geobarometry in this region. Whereas a change in temperature of 50°C may not always be crucial when considering silicate mineral equilibria, it is very critical for sphalerite geobarometry because there is a large change in the slope of the experimentally determined isobars in the temperature range 650°–700°C.

TABLE 49. Representative Electron Microprobe Analyses of Zinc Spinel

	1	2	3	4	5*
MgO	2.88	3.05	2.93	2.84	1.87
Al ₂ O ₃	58.31	58.54	58.42	58.40	58.64
MnO	0.20	0.15	0.19	0.16	0.14
FeO	13.68	13.58	13.39	12.70	7.60
CuO	0.07	0.07	0.02	0.09	0.04
ZnO	24.62	24.79	25.28	25.78	32.02
SO ₂	0.00	0.00	0.05	0.01	0.27
CdO	0.08	0.09	0.00	0.14	0.05
	99.84	100.27	100.28	100.12	100.64
Atomic proportions on the basis of 24 cations					
Mg	1.004	1.059	1.016	0.984	0.652
Al	16.016	16.008	15.992	16.035	16.211
Mn	0.039	0.031	0.039	0.031	0.027
Fe	2.668	2.633	2.602	2.477	1.492
Cu	0.012	0.012	0.004	0.016	0.008
Zn	4.234	4.246	4.336	4.438	5.543
S	0.000	0.000	0.012	0.000	0.059
Cd	0.008	0.008	0.000	0.016	0.008
	32.007	32.000	32.008	32.020	32.164

* Spinel in contact with pyrrhotite.

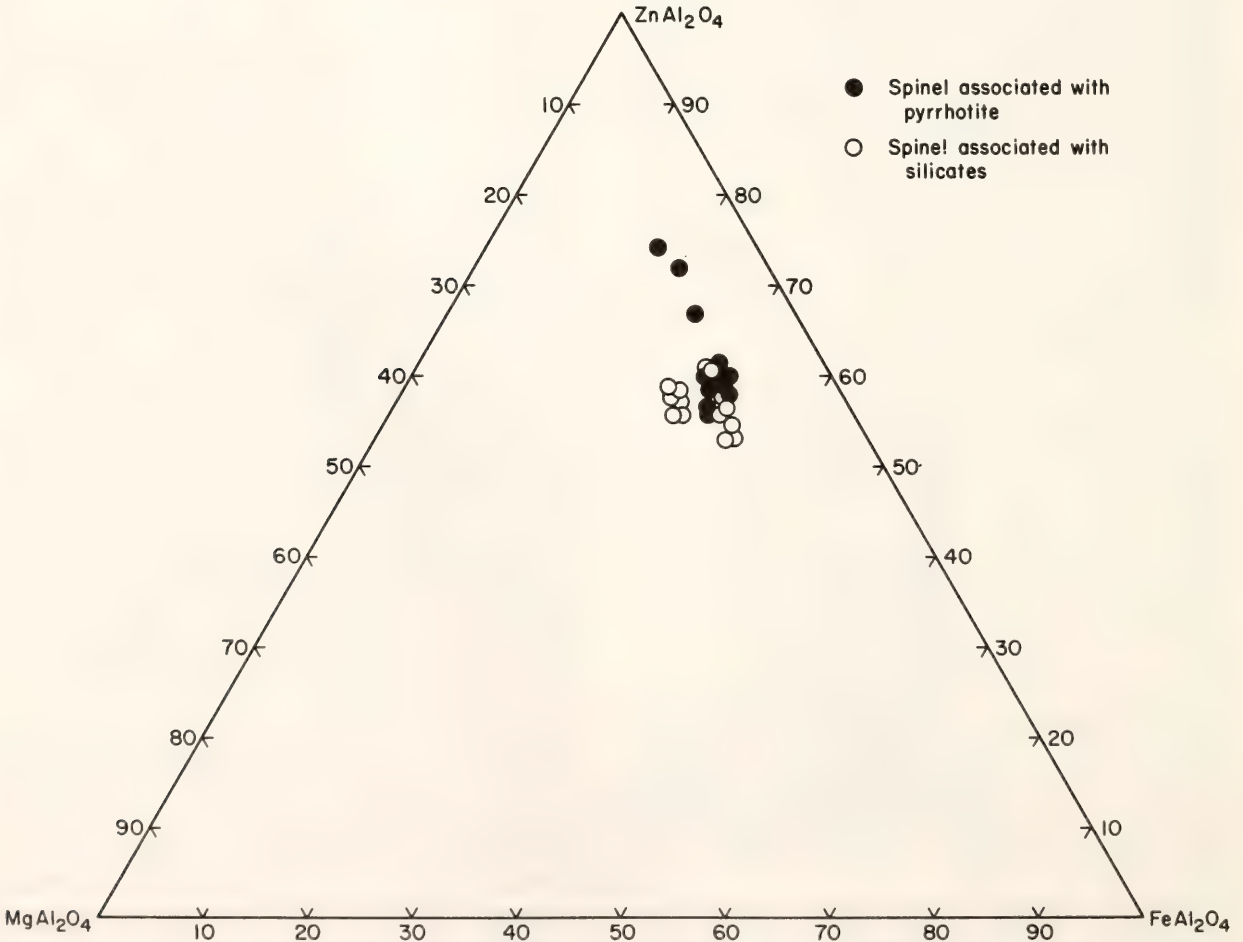


Fig. 163. Composition of Zn spinel in terms of the end members ZnAl₂O₄, FeAl₂O₄, and MgAl₂O₄.

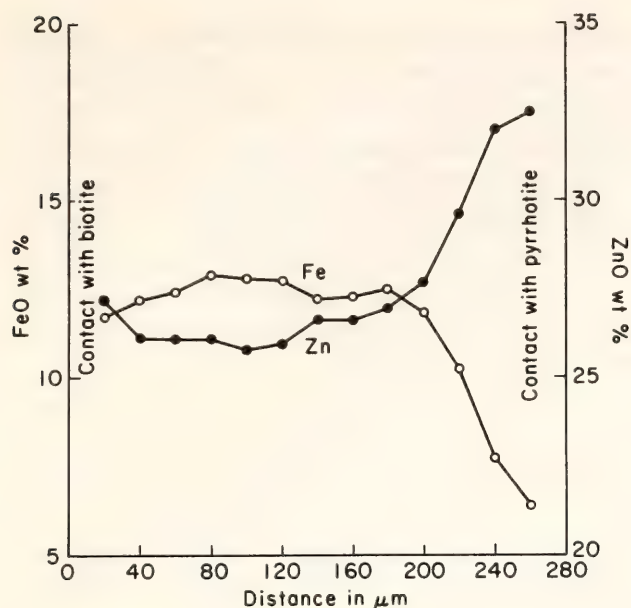


Fig. 164. Electron microprobe traverses showing variation in FeO and ZnO wt % in spinel in contact with pyrrhotite.

The pressures estimated from the data of Scott (1976) for sphalerite coexisting with pyrite and pyrrhotite are in the range 2.1–2.9 kbar, in agreement with the 2–3 kbar pressure of metamorphism determined by Blümel and Schreyer (1977) from the silicate mineral assemblages. The pressure estimated for sphalerite coexisting with pyrite is 3.4 kbar, whereas those determined for sphalerite coexisting with pyrrhotite are 2.4–3.5 kbar.

The average mole % FeS of sphalerite associated with chalcopyrite and pyrrhotite but not in direct contact with the latter yields a pressure of 6.1 kbar. The wide range in mole % FeS for such sphalerite, however, corresponds to a pressure range of from 5 to ~10 kbar. Similarly, the pressures determined for chalcopyrite-bearing sphalerite that coexists with pyrite and pyrrhotite range between 2 and 7.1 kbar, with an average of 4.7 kbar.

Pressures estimated by using the calculated isobars of Hutcheon (1978) are somewhat lower than those estimated from the experimental data of Scott (1973, 1976); however, the two pressure estimates are in reasonable agreement.

Discussion

The application of sphalerite geobarometry to the ores from Bodenmais shows that the pressure estimates vary even in a single specimen and are strongly dependent on the mineral assemblage with which sphalerite coexists.

Although sphalerite coexisting with pyrite and pyrrhotite yields pressures comparable to those estimated from the silicate assemblages, there is evidence to suggest that sphalerite has undergone post-metamorphic equilibration. Sphalerite is frequently depleted in FeS near its contacts with pyrrhotite. Such depletion suggests that equilibration has occurred with pyrrhotite, which is now more sulfur-rich than the pyrrhotite with which sphalerite was in equilibrium at high temperature. If the equilibrium composition of sphalerite coexisting with pyrrhotite was preserved during post-metamorphic cooling, it should have a higher FeS content than sphalerite buffered by the divariant assemblage pyrite-pyrrhotite. At Bodenmais, the FeS content of sphalerite coexisting with pyrrhotite is lower than that of sphalerite associated with pyrrhotite and pyrite. This observation is interpreted as an indication of post-metamorphic change in the composition of sphalerite in response to equilibration with monoclinic pyrrhotite. The formation of monoclinic pyrrhotite involves an increase in the fugacity of sulfur and, consequently, a decrease in a_{FeS} (Scott *et al.*, 1977). The variation in the FeS content of sphalerite coexisting with pyrrhotite is probably a reflection of its equilibration with pyrrhotite of variable composition.

Retrograde alteration of country rocks at Silberberg, Bodenmais, led to the formation of chlorite and muscovite (Schreyer *et al.*, 1964). These alterations involve hydration reactions, which suggest that a fluid phase was present during retrograde metamorphism. Grove *et al.* (1975) and Brown *et al.* (1978) described cases of retrograde recrystallization and reequilibration of sphalerite in the presence

of a chemically active fluid phase. It is possible that the presence of a fluid phase during retrograde alteration at Bodenmais was responsible for equilibration of sphalerite in the ore.

The large variation in FeS content of sphalerite containing chalcopyrite exsolutions and, consequently, the highly variable pressure estimates over a scale of tens of microns within a single crystal

underscore the necessity of an experimental evaluation of the effect of Cu on sphalerite-pyrrhotite-pyrite equilibria. In their reconnaissance study of the chalcopyrite-sphalerite relationship, Wiggins and Craig (1975) found that the solid solubility of ZnS in the intermediate solid solution and of CuS and FeS in sphalerite depend on temperature, sulfur fugacity, and Cu/Fe.

BIOGEOCHEMISTRY

HYDROGEN ISOTOPE FRACTIONATION BY CULTURES OF MICROALGAE

Marilyn F. Estep and T. C. Hoering

Organic substances in plants have large variations in the ratio of stable hydrogen isotopes and generally have concentrations of the heavy isotope lower than those of the associated environmental waters. The limited existing information on the subject has been derived from the analysis of naturally growing material, mainly higher plants, where the causes of the isotope effects are complex and difficult to interpret. In this study, photosynthetic microorganisms have been cultured in the laboratory under controlled conditions. The fractionation of the hydrogen isotopes between the water in the medium and the organically bonded hydrogen in cells has been determined. Some of the biological processes governing hydrogen isotope fractionation have been thereby discovered.

The organic matter in sedimentary rocks is also depleted in the heavy isotope of hydrogen, and there are indications that the isotope ratio of the organic matter reflects its biological source material. This study provides information necessary for interpreting hydrogen isotope phenomena in ancient organic matter.

Research efforts have been focused on two major areas. The first is the development of analytical techniques suitable for routine, precision measurement of hydrogen isotope ratios in organic matter.

The second is the adaptation of well-established microbiological procedures to isotope studies.

Hydrogen has two stable isotopes, ^1H (Protium) and ^2H (Deuterium, D). The atom fraction of the heavy isotope in sea water is 155 parts per million. Analytical results are reported as parts per thousand difference in the D/H ratio as compared to a standard reference material:

$$\delta\text{D} = \left[\frac{(\text{D}/\text{H})_x - (\text{D}/\text{H})_s}{(\text{D}/\text{H})_s} \right] \times 1000$$

where x refers to the unknown sample and s refers to the standard which was Standard Mean Ocean Water (SMOW) distributed by the International Atomic Energy Agency.

The measurement of hydrogen isotope ratios in organic matter consists of three steps: (1) quantitative combustion to water, (2) quantitative reduction of water to hydrogen, and (3) mass spectrometric comparison of the hydrogen with a standard reference gas. The first step is crucial. Quantitative microanalysis of organic hydrogen by combustion is one of the classic problems of analytical chemistry. Although solutions have been found, they are not generally applicable to isotope analysis. Most of the methods use catalysts, which have blanks and memory effects. In this laboratory, samples are combusted in a closed system with pure oxygen. The gases are passed over platinum gauze at 750°C and through a cold

trap by a recycling system. Oxygen and unburned gases are passed through the furnace and cold trap many times to insure quantitative conversion. The water is distilled from the trap into a tube and sealed off. The first attempts used a mercury-filled Toeppler pump for cycling. Samples with organic nitrogen produced erratic results. The combustion of such samples yields oxides of nitrogen and nitric acid that attack mercury and yield hygroscopic mercuric nitrate. Water is absorbed and subsequently exchanged.

A new system, without mercury, was constructed with a diaphragm pump made of stainless steel and Teflon for cycling the gases. The connecting glass tubing and Teflon valves are wrapped with heating tapes to facilitate the transfer of water into the cold trap. This system is used routinely on a variety of organic matter and typically yields δD having a standard deviation of 3.

A third method for analyzing organic matter, based on the procedure of Pepkowitz and Proud (1949), is being evaluated. In this technique, organic matter and metallic magnesium are welded into tubes of pure iron. The tube is heated to 700°C in an evacuated chamber by radio-frequency induction. The organic matter is converted to H_2 and refractory oxides, nitrides, and sulfides of magnesium. At this temperature, the metal tube becomes permeable only to hydrogen gas, which is pumped across a bed of uranium metal at 760°C for purification and then into an evacuated sample bulb. This method eliminates problems of the interaction of water with materials in a combustion system.

There are at present no organic substances to serve as hydrogen isotope reference materials. A suite of materials is being evaluated for this purpose. They are needed to insure the long term reproducibility and precision of organic hydrogen isotope measurements. A second standard reference water is available, Standard Light Antarctic Precipitation (SLAP), which has a well defined isotope

content; $\delta D = -428$. Weighed mixtures of SMOW and SLAP were prepared to provide a set of secondary standards for calibrating the linearity of the mass spectrometer and to provide reference points across the range of δD expected in organic matter.

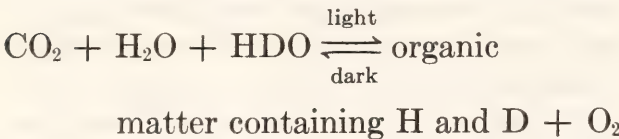
For routine measurements, a set of tertiary working standards of H_2 gas was prepared by mixing commercial tank hydrogen, which has a very low δD , with enriched gas prepared by electrolyzing mixtures of H_2O and D_2O . The gas standards were calibrated against the set of secondary water standards, and a series of seven high-pressure cylinders were prepared having δD in the range of +9 to -339. The working standards were recalibrated periodically and, with one exception, found to remain stable. In one case, the valve on a cylinder developed a leak, and fractionation during sampling occurred.

Axenic cultures of microalgae were obtained from Dr. Chase Van Baalen, Port Aransas Marine Laboratory, University of Texas. Algal cells were grown in batch test-tube cultures in a thermostatically controlled water bath. Continuous light was provided by two banks of two 20-watt cool-white fluorescent bulbs. Cultures were gassed with $1 \pm 0.1\%$ CO_2 in air. The medium used for growing marine microalgae was a defined artificial seawater medium, ASP-2, which was supplemented with vitamin B_{12} (8 $\mu g/l$) (Van Baalen, 1962). Vitamin B_1 (1 mg/l) and sodium metasilicate (300 mg/l) were added to the media used for growing diatoms. Freshwater forms were grown in medium CG-10, a defined mineral-salts medium (Kratz and Myers, 1955). For heterotrophic growth of *Chlorella sorokiniana* strain TX71105R in the dark, glucose or acetate was added to the medium before autoclaving. The pH of the medium was 7.8. The five strains of algae used in these experiments grew at rates of four to seven generations per day.

Algae were transferred from agar slants to liquid media for at least 24 hr prior

to measuring hydrogen isotope fractionation in the light. Fresh medium was then inoculated with these cells, which were incubated until they reached a density of 0.2 to 0.4 mg dry weight per ml of medium. A portion of the water in the medium was reserved, both before and after growth, for isotope analysis. Algae were harvested by centrifugation, washed once with distilled water, recentrifuged, and suspended in 1 ml of water. The preparations were immediately frozen at -70°C . Cells and other plant material were freeze-dried for 48 hr, placed in a drying oven at 100°C overnight, and stored in a dessicator over CaCl_2 until constant weight was reached.

The net chemical reactions for photosynthesis and aerobic respiration in plants can be given by the following equation:



The forward photosynthetic reactions are driven by light, while the reverse respiratory reactions yield chemical energy during periods of darkness. Experiments were designed to determine hydrogen isotope effects in both photosynthesis and respiration.

Isotope effects in photosynthesis were determined by growing microalgae in continuous light, where the forward reaction greatly exceeds the reverse one. The organic matter must obtain its hydrogen from the water, which is present in great excess.

Certain microalgae can be adapted to dispense with photosynthesis. When grown in total darkness with added organic substrates, these plants rely on aerobic respiration for growth. The isotopic composition of the added organic matter becomes another variable in determining the hydrogen isotope effect of respiration. In such cases, it is of interest to know the relative amounts of hydrogen coming from the water and from the substrate.

Table 50 shows results of experiments with microalgae grown photosynthetically. Results are expressed in terms of the fractionation ΔD , where:

$$\Delta\text{D} = \delta\text{D}_{\text{cells}} - \delta\text{D}_{\text{water}}.$$

The standard deviation for a set of experiments with one species was 5. Marine algae fractionated the hydrogen isotopes to a significantly greater extent than did freshwater forms: ΔD of -144 compared with -115 . Experiments with the blue-

TABLE 50. Hydrogen Isotope Fractionation by Microalgae Grown Photosynthetically

Species	Classification	Growth Temperature	ΔD^*
<i>Marine forms†</i>			
<i>Agmenellum quadruplicatum</i> strain PR-6	Coccoid blue-green alga	39°C	-148
<i>Cylindrotheca</i> sp. strain N-1	Pennate diatom	30°C	-140.5
<i>Amphora</i> sp. strain Amph	Pennate diatom	30°C	-142
<i>Freshwater forms</i>			
<i>Chlorella sorokiniana</i> strain TX71105R	Coccoid green alga	39°C	-115
<i>Nostoc</i> sp. strain MAC	Filamentous blue-green alga	39°C	-116

* $\Delta\text{D} = \delta\text{D}_{\text{cells}} - \delta\text{D}_{\text{H}_2\text{O}}$ in medium.
† Algae growing in artificial seawater medium, ASP-2.

green alga *Agmenellum quadruplicatum* showed that fractionation was not sensitive to (1) changing the combined nitrogen in the medium from nitrate to ammonia, (2) increasing the nitrate concentration, (3) lowering the NaCl concentration in the medium from 310 mM to 43 mM, or (4) lowering the growth temperature from 39° to 27.5°C.

Observations on marine and nonmarine species may have geochemical significance. Hoering (*Year Book* 73, p. 590) measured the ΔD between organic fractions and water in contiguous marine and freshwater sediments. He found that the humic acids in freshwater sediments had a ΔD of -60 . In the marine sediments, the corresponding ΔD was -100 . The difference in the ΔD for marine and nonmarine humic acids is the same as for marine and nonmarine microalgae. The results are in agreement with the conclusions reached from studies of stable carbon isotopes and lignin residues in the same sediment samples (Hedges and Parker, 1976); that is, there is little transport of organic matter from the land to the sea.

A dramatic change in ΔD occurred when *Chlorella* was adapted to grow in the dark with glucose or acetate as a sub-

strate. Table 51 and Fig. 165 show that ΔD was dependent on the amount of growth in the dark and in the case of glucose on the δD of the substrate and not of the water. In experiments C and D of Table 51, the δD of the water was intentionally changed by 50 while keeping that of glucose constant. Little effect was noted, indicating that during growth in the dark *Chlorella* obtains most of its organic hydrogen from the glucose with no isotope fractionation. Algae grown on glucose in darkness for 23.5 hr and 0.5 hr of saturating light per day (Experiment E, Table 51) show a marked increase in hydrogen isotope fractionation. Photosynthesis is strongly indicated to be the biological process mediating hydrogen isotope fractionation.

Heterotrophic experiments with acetate are more difficult to interpret. The ΔD of *Chlorella* decreased during growth in the dark on acetate, but increased with increasing growth.

The following experiments were performed to substantiate the conclusion that hydrogen isotope fractionation was a kinetic effect specifically related to photosynthesis and growth, rather than an effect associated with the isotopic exchange of water with organically bonded

TABLE 51. Hydrogen Isotope Effects in *Chlorella sorokiniana**

Substrate (δD)	Conc. of substrate in medium (gm/l)	Cell density at harvest (mg dry wt/ml)	δD H ₂ O	δD cells
Glucose (-18)				
A	1.0	0.20	-52	-84
B	1.0	0.33	-52	-55
C	3.0	0.76	-70	-20
D	3.0	0.72	-21	-14.5
E†	3.0	0.53	-59	-87
Acetate (-150)				
A	1.15‡	0.09	-54	-65
B	2.5	0.23	-63	-103

* Strain TX71105R grown heterotrophically in the dark.

† Cultures were grown in 0.5 hr saturating light and 23.5 hr darkness.

‡ Acetate: NaC₂H₃O₂·3H₂O.

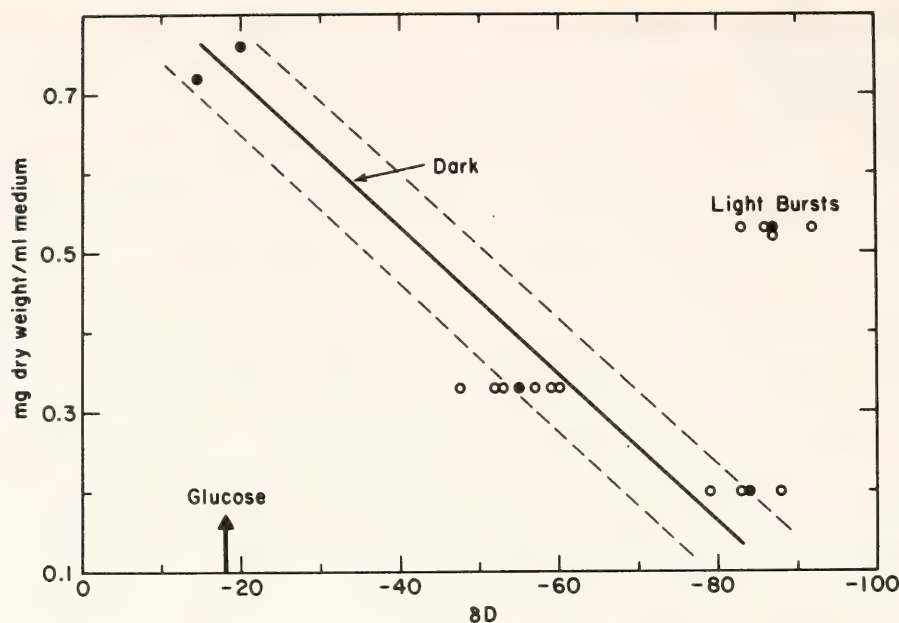


Fig. 165. Hydrogen isotope effects in *Chlorella* grown heterotrophically on glucose. Closed circles represent the average δD of a set of experiments. Open circles represent the δD of individual samples.

hydrogen. Algal cells were grown photosynthetically in a medium with δD of -60 . Then they were centrifuged and resuspended in a medium with δD of $+100$ and incubated in the light and in the dark until harvested. The data in Table 52 shows that after 7 hr in the light, the isotope ratio of the marine, blue-green alga *Agmenellum quadruplicatum* was virtually unchanged. However, the freshwater *Chlorella* showed 7% exchange of its organically bonded hydrogen with the water after 15 min incubation. Cells incubated in the dark behaved similarly. Organic matter bonded in cells exchanges its hydrogens slowly with water in the medium. The observed difference in the rate of exchange may be the basis of the differences observed between marine and nonmarine species.

Several natural plant populations were surveyed to test some of the above relationships. Three mixed phytoplankton samples collected from the Chesapeake Bay near the mouth of the Patuxent River showed a fractionation similar to that of cultures of marine microalgae, $\Delta D = -145$. In addition, leaves from a dogwood tree and three species of mosses were

collected on the grounds of the Geophysical Laboratory once a week for three weeks. The δD of organic hydrogen in leaf tissues was -92 ± 8 ; in the mosses, it was -93 ± 4 . The ground waters of the

TABLE 52. Exchange of Hydrogen Isotopes from Water to Organically Bound Hydrogen in Algae

			δD
<i>Agmenellum quadruplicatum</i>			
Initial water			-60
Heavy water			$+94$
Initial cells			-205
Light incubation	15 min		-205
	1 hr		-203
	3 hr		-211
	5 hr		-203
	7 hr		-200
Dark incubation	7 hr		-214
<i>Chlorella sorokiniana</i>			
Initial water			-66
Heavy water			$+115$
Initial cells			-178
Light incubation	15 min		-156
	3 hr		-152
	5.6 hr		-143
	5.6 hr		-158

area have an average δD of -39 , but the water in plants is enriched in deuterium, having a δD about $+40$ above environmental water. This enrichment is due to isotope effects in evaporation and transpiration. If these effects are accounted for, then the fractionation by terrestrial plants is similar to that seen in cultures of freshwater microalgae. Lichens collected from Wise County, Virginia, and Potter County, Pennsylvania, were analyzed. They seem to be an exception, because they show little isotope fractionation (-10 to -20) from associated environmental waters.

Stable hydrogen isotopes in liver and muscle tissues of laboratory-grown mice were analyzed. Strain C3H mice were obtained as weanlings from the Flow Laboratories, Dublin, Virginia, and grown for one or two months by Dr. Nancy Zeller, University of Maryland, Baltimore, until they were sacrificed. They were fed a constant diet of Purina mouse chow (average $\delta D = -106$) and watered with tap water (average $\delta D = -48$). The organic hydrogen in liver tissue had an average δD of -103 . Muscle tissue had an average δD of -115 . These results correlate with the observations made on cultures of microalgae: the isotope ratio of the food source determines the isotope ratio of a nonphotosynthetic organism.

It is not yet clear which reactions of photosynthesis are responsible for hydrogen isotope fractionation. A pool of reduced nicotinamide adenine dinucleotide phosphate (NADPH) builds up during photosynthesis and is available to the whole cell for biosynthetic reactions. Isotope selectivity is possible. NADPH is required as a reductant in several key reactions of fatty acid and terpenoid syntheses. The hydrogen isotope ratios of both of these lipids have been shown to be even more negative than extracted plant tissue (Hoering, *Year Book 74*, p. 598). Other reactions of photosynthesis involve carbon dioxide fixation and the reactions of the Calvin cycle. Certain

enzymes in this pathway that are involved in the addition of nonexchangeable hydrogens during the biosynthesis of glucose are known to be light activated.

In summary, plants grown under controlled conditions will fractionate hydrogen isotopes reproducibly, facilitating the use of precision isotope ratio mass spectrometry in performing tracer experiments. Some of the major processes that govern hydrogen isotope fractionation have been identified, indicating photosynthesis to be the major process mediating the stable hydrogen isotope ratio in plants.

COLLAGEN IN FOSSIL BONE

Noreen Tuross and P. E. Hare

Collagen is the most abundant protein in vertebrates, accounting for over 95% of the proteins in such calcified tissues as teeth dentin and bone. Bone is of primary interest in the paleontological record and is found in rocks as old as Devonian (400 m.y.) (Colbert, 1955). The amino acid composition of bone collagen from vertebrates of all species is characterized by a glycine content of 33 mol % and the presence of hydroxyproline and hydroxylysine. Species differences are present in the primary sequence of amino acids in the collagen molecule. Under the electron microscope collagen fibrils show a characteristic 640 Å repeat series of striations. Upon solution of the bone in dilute acid an insoluble collagenous pseudomorph or "ghost" remains (Fig. 166).

Previous studies on fossil bone collagen have generally been limited to the study of microstructure by electron microscopy and the determination of amino acid composition and racemization (Wyckoff, 1972; Hare, *Year Book 73*, pp. 576-581). Well-preserved, intact collagen in a fossil was inferred when its amino acid composition closely resembled that of modern bone and the amino acids showed little or no racemization. Qualitatively, a fossil



Fig. 166. Cross section of fragment of modern bone after partial demineralization. Outer rim of hydroxylapatite mineral phase removed by dilute acid leaving a pseudomorph, or "ghost," of insoluble protein collagen.

collagen would also show some physical properties similar to modern bone collagen such as the formation of a pseudomorph or "ghost" of the bone whenever the bone was demineralized in dilute acid. Additionally, the electron microscope has been used to reveal the characteristic repeat pattern of striations (640 \AA) in several fossil bones.

This study reports the first application to fossil bone of a technique developed for isolating intact molecules of collagen from modern bone (Carmichael *et al.*,

1977). The technique can be used to estimate molecular weights, and, therefore, should be useful in determining the extent of degradation of collagen in fossil bone. The first step involves a mild decalcification in ethylenediaminetetraacetic acid (EDTA), followed by treatment with the enzyme pepsin to solubilize the collagen. The final step in the technique is the electrophoresis of the pepsin-solubilized collagen on sodium dodecyl sulfate (SDS) polyacrylamide gels, an extremely sensitive method for separating

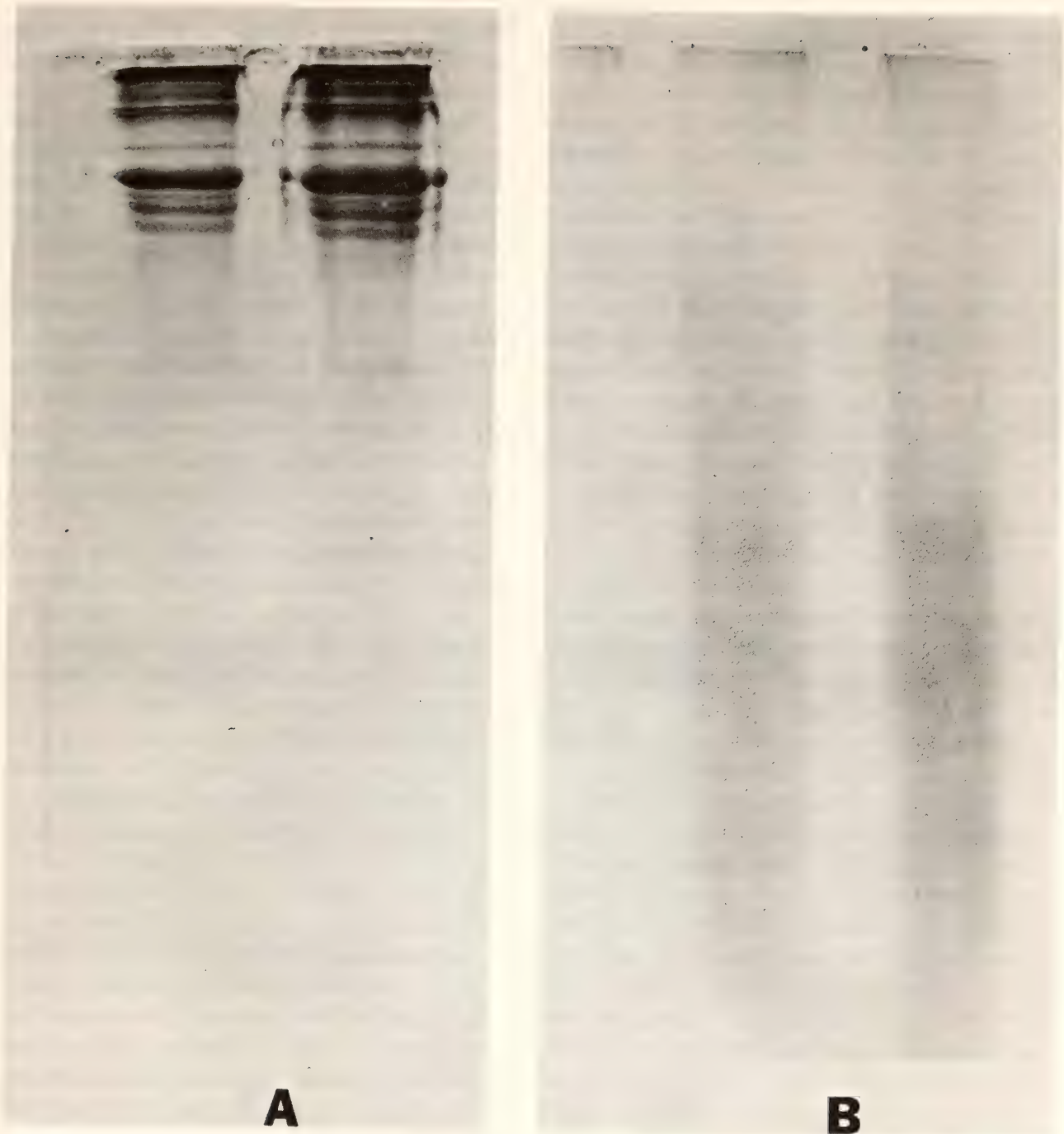


Fig. 167. Gel-electrophoresis patterns on (A) modern and (B) fossil bone collagen. Bone collagen residue is solubilized with enzyme pepsin to yield intact α -chains in modern bone collagen. Also present in modern bone are dimers and trimers of α -chains and some lower molecular weight degradation products. Fossil bone collagen shows no discrete high molecular weight factions.

high-molecular-weight components and estimating actual molecular weights (Furthmayr and Timpl, 1971).

When modern bone is demineralized and the pepsin-solubilized collagen is subjected to electrophoresis, a characteristic pattern of components is produced from the high-molecular-weight components of collagen (Fig. 167). The collagen molecule

consists of a triple helix of three α -chains. The α -chains each consist of over 1000 amino acids and have molecular weights of around 95,000. In those portions of the α -chains involved in the triple helix (excluding 16 amino acids at the N-terminal end and 25 at the C-terminal end) every third amino acid residue is glycine. Hydroxyproline residues are essential for

maintaining the helical structure through interchain hydrogen bonds.

Extensive crosslinking occurs between specific amino acid residues of adjacent α -chains (intramolecular) and adjacent helices (intermolecular) to form fibrils (Tanzer, 1973). Fibrils can be identified in the electron microscope and have been found in fossil bone. The preservation of physical structure, however, does not insure the preservation of intact protein structure. The results of this study suggest that even though the amino acid composition is virtually identical to that found in modern bone collagen, there have been significant changes in the molecular structure of collagen in the fossil bone samples used in this study.

The fossil bones selected for this study were chosen because they contained the most nearly intact collagen of any fossil bones readily available. The first sample, a sabre-toothed tiger femur from the La Brea tar pits, has been radiocarbon-dated at $12,650 \pm 160$ yr *B.P.* (UCLA-1292B) and contains around 4% nitrogen. On demineralization it forms a pseudomorphic "ghost" of the bone fragment and has an amino acid composition nearly identical to that of modern bone. The second sample, a rib bone from an Egyptian mummy less than 3000 years old, also appeared to contain intact collagen from the nitrogen content (3.6%) and amino acid composition. As a control, a modern bovine bone was carried through each step to insure that no degradation was occurring during the sample demineralization step, pepsin solubilization, and subsequent electrophoresis.

The bones were powdered to pass a 200-mesh sieve and demineralized in 0.5M EDTA, pH 7.2 at 4°C. Completeness of demineralization was monitored by atomic absorption spectroscopy. Complete demineralization was presumed when the calcium levels in the EDTA returned to the level of the blank. The demineralized residues were solubilized using pepsin after the procedure of Carmichael *et al.* (1977). The procedure described by

Furthmayr and Timpl (1971) was employed in the SDS polyacrylamide electrophoresis.

The modern bovine bone showed the characteristic collagen bands on a 5% gel (Fig. 167). The α components were resolved, and higher molecular weight dimers and trimers could also be seen. In marked contrast, both fossil bones showed a broad diffuse band, running approximately mid-gel on a 5% gel. There was no indication of the existence of α -chains or higher molecular-weight aggregates in either sample. Preliminary results on three other well-preserved fossil bone collagens show similar broad bands on the electrophoresis gels.

The results suggest that there is a broad range of molecular-weight residues present in the fossil collagen samples. The fossil collagen has apparently undergone degradation that has affected its molecular structure but has not appreciably affected its macrophysical appearance or amino acid composition. It might be expected that selective cleavage (hydrolysis) of labile peptide bonds in the α -chains would yield a wide range of polypeptides with molecular weights up to 95,000 (intact α -chains).

The treatment with pepsin to solubilize collagen may affect the fossil collagen very differently if the fossil collagen had some hydrolyzed peptide bonds within the α -chains. Some of the peptide bonds are known to be very labile and if hydrolyzed during fossilization could provide vulnerable points of attack for the enzyme pepsin.

In intact collagen from modern bone, pepsin degrades the cross-links and releases intact α -chains from the helical structure of collagen. If the α -chains are not completely intact in these fossils the pepsin could further degrade the residues and yield a wide range of molecular-weight fragments.

Some fossil bone collagens may be even more highly cross-linked than modern bone collagens; this condition could prevent normal reaction with pepsin. The

organic matrix of bone contains carbohydrates. The breakdown products of these carbohydrates could interact with amino acid residues in the collagen to increase the cross-linking. Most fossil bone collagens have a slightly yellow to brownish color similar to the color noted in the products of the browning reactions between amino acids and sugars. It seems reasonable that even with some degradation in the α -chains of collagen in fossils, extensive crosslinking prevents the complete degradation and solution of this fossil collagen. Intact residues of substantial molecular weight (40,000 or more) appear to be present, and there seems to be little doubt that significant genetic and evolutionary information remains intact in many fossil collagen residues.

Fossil protein constituents can now be dealt with as intact high-molecular-

weight polypeptides. The primary sequence of amino acids in a protein is species specific, and several differences in amino acid sequences in collagen from different species of living vertebrates have been determined. This study suggests that it is feasible to look for amino acid sequence differences in fossil bone collagens of vertebrate species that have long been extinct. It also suggests a new tool for determining the very early steps in the organic geochemistry of fossil proteins. It should be possible to simulate these changes in modern bone under controlled laboratory conditions and to determine the effects of various environmental parameters. It may be that under unusually anhydrous conditions, collagens in early humanoid and other primate fossils have been preserved well enough to yield significant information on taxonomic affinities and evolution.

GEOCHRONOLOGY

ZIRCONS FROM THE MANTLE

Gordon L. Davis

Zircons from the mantle are carried to the surface in kimberlite magma, along with peridotite nodules, other xenoliths, and occasionally diamonds. The zircon content of kimberlite is so low that samples are recovered only where commercial mining and separating processes are used, or where large volumes of kimberlite are assayed in a prospecting operation. Some kimberlite pipes appear to carry no zircons. Zircons from kimberlites are usually found as single rounded crystals; inclusions within the crystals provide the only clues to the mineral assemblages in which crystallization occurred. Kresten *et al.* (1975) list associations of diopside, diamond, ilmenite, and phlogopite with zircon and indicate that the zircons originate in the upper part of the low-velocity zone. It is usually possible to distinguish by size, shape, and color between mantle zircons and crustal zircons that may have been entrained

during the ascent of the kimberlite. The mantle zircons that have been examined are never euhedral, are much larger than granitic zircons, show no zoning, frequently show well-developed parting, often carry a skin of soft, white ZrO_2 , and have extremely low concentrations of uranium.

No matter how long ago the zircons crystallized, at the ambient temperature of about 1100°C estimated for the nodules lead would be lost by diffusion as rapidly as it was formed by the disintegration of uranium. Lead did not begin to accumulate in the zircons until the temperature dropped shortly before or at the time of eruption of the kimberlite.

In 1976, Davis *et al.* published the first isotope dilution analyses and age measurements for zircons from kimberlites (*Year Book* 75, pp. 821–824). These analyses were made possible by the development of a hydrothermal method of decomposition (Krogh, 1973) and the use of ultrapure reagents (Mattinson, 1972). Additional analyses were presented in the

TABLE 53. ^{206}Pb - ^{238}U Ages, Uranium Contents, and Th-U Ratios of Zircons from the Kimberlites of Yakutia, USSR.

Name and Location†	Age (m.y.)	U (ppm)	Th/U*
"325 Years of Yakutia," Muna	443.2	6.5	0.33
(duplicate)	440.2	6.4	0.30
Druzhba, Middle Olenek	411.5	8.4	0.37
Taezhnaya, Malo-Botuoba	402.8	7.4	0.20
Mir, Malo-Botuoba	361.3	7.7	0.31
Festivalnaya, Daldyn-Alakit	358.1	6.5	0.30
Rassvet, Middle Olenek	344.4	8.1	0.21
Sytykansкая, Daldyn-Alakit	344.1	13.3	0.36
Marichka, Near-Lena	159.3	8.5	0.23
Krisolitovaya, Near-Lena	156.2	18.3	0.46
Irina, Lower Olenek	149.3	21.8	0.40
Beenchime River, Lower Olenek (alluvial)	148.4	38.7	0.25

* Th-U ratios calculated from the ages and the ^{206}Pb content. Decay constants: $^{238}\text{U} = 0.15513 \times 10^{-9} \text{ yr}^{-1}$, $^{232}\text{Th} = 0.49475 \times 10^{-10} \text{ yr}^{-1}$.

† For locations see Fig. 2, p. 12, Sobolev, 1977.

Extended Abstracts of the Second International Kimberlite Conference in 1977 as well as in *Year Book 76* (pp. 631-635). A mixed tracer of ^{205}Pb (Krogh and Davis, *Year Book 74*, pp. 416-417) and ^{235}U has been used since 1976.

Through the courtesy of N. V. Sobolev of the U.S.S.R. Academy of Sciences, zircons from some of the kimberlites of the Yakutian diamond fields were made available for analysis. The results of twelve analyses are given in Table 53 and will be part of a joint report relating the geology and geochronology of the area.

The zircons show no visible or isotopic effects that might be due to chemical alteration or radiation damage, and there are no indications of post-eruption metamorphism. The ages represent the times at which the zircons suddenly became cool enough to accumulate radiogenic lead. These ages are presumed to be the times of eruption of the kimberlites. Diamond-bearing pipes erupted during Silurian and Devonian times; the younger Jurassic kimberlites are barren. The calculated Th-U ratios are characteristic of both granitic and kimberlitic zircons (Ahrens *et al.*, 1967).

The uranium-lead ratios for the samples from Yakutia are plotted on a concordia diagram (See Fig. 168). The points lie close to the curve, the horizontal spread being the result of the correction for common ^{207}Pb on the small amount of ^{207}Pb generated in these low-uranium zircons. The correction on ^{206}Pb is much smaller. It is for this reason that the ages in the table have been calculated from the ^{206}Pb - ^{238}U ratio.

The results obtained from the analyses of zircons from 44 kimberlite occurrences have been generalized (See Table 54). The age intervals should be considered approximate because of the limited number of samples. The ages of the different samples from Yakutia, South Africa, and Brazil indicate that eruptions of kimberlite were not confined to a single period.

The low uranium contents that characterize all of these zircons provide a clue to the range of concentrations of uranium in this source region, if the $U_{\text{zircon}}/U_{\text{liquid}}$ partition coefficient is equal to or greater than 100, as deduced by Kresten (1974). The zircons would then have crystallized in a region of the mantle containing 0.06-0.40 ppm, or less, of uranium.

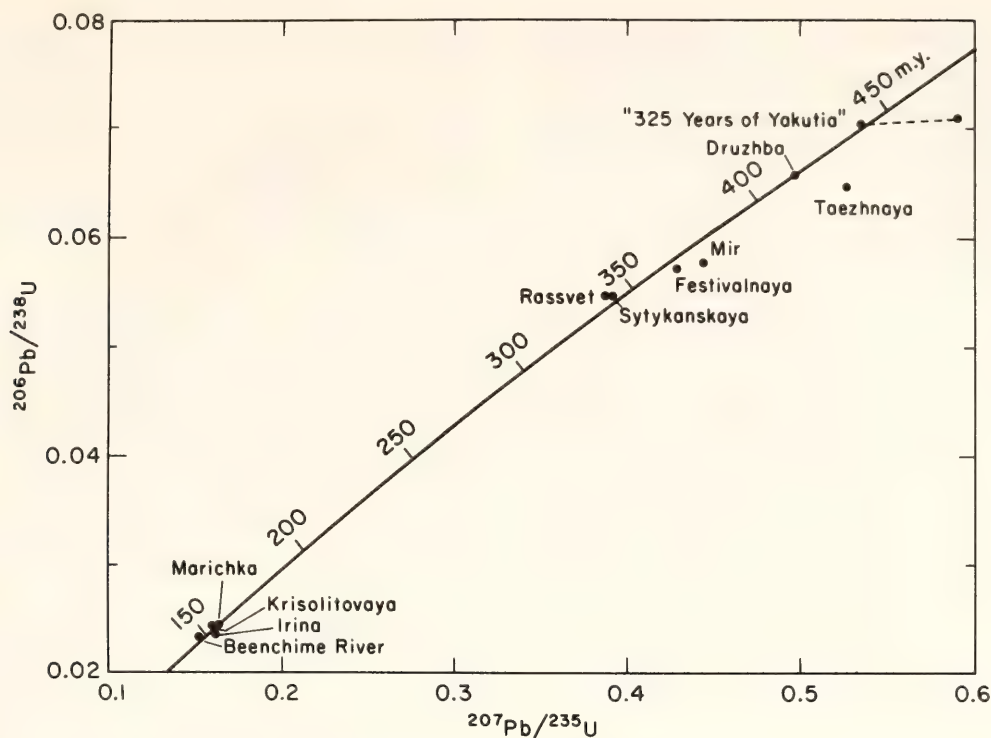


Fig. 168. Concordia diagram for zircons from the kimberlites of Yakutia, U.S.S.R.

TABLE 54. Periods of Kimberlite Eruption based on Zircon Ages

Age (m.y.)	Location	No. of Samples	U (ppm)
443–402	Yakutia, U.S.S.R.	3*	6–8
360–344	Yakutia, U.S.S.R.	4*	6–13
194	So. Africa	1	7
159–148	Yakutia, U.S.S.R.	4	8–18
150	So. Africa	2	12–18
133	Angola	1*	3
120	Brazil	2†	13–30
110–84	Transvaal, So. Africa	14*	6–40
93–80	Brazil	5†	17–30
80–67	Southern Africa	5	12–35
53–40	Tanzania	2*	6–13
34	Solomon Islands	1	5

* From diamond-bearing pipes.
† Possibly diamond-bearing, but information not available.

AGE OF ZIRCON FROM A CRUSTAL
XENOLITH, KILBOURNE HOLE,
NEW MEXICO

Gordon L. Davis and Edward S. Grew*

Xenoliths of feldspathic rocks found in kimberlite, alkali basalt, and other magmatic rocks of deep-seated origin are be-

* Fulbright Scholar, University of Melbourne, Parkville, Victoria, Australia.

lieved to be pieces of the earth's crust plucked by the magmas during their ascent to the earth's surface. Xenoliths are abundant as cores of basaltic bombs at Kilbourne Hole, New Mexico, a maar that formed after extrusion of a Quaternary alkali basalt flow presently exposed in the walls (Hoffer, 1976). Some of these xenoliths are granulites—leucocratic, medium-grained, quartzo-felds-

pathic gneisses that contain sanidine, plagioclase, garnet, prismatic sillimanite, rutile, ilmenite, zircon, and, in some cases, graphite (Padovani and Carter, 1977a, 1977b; Grew, 1977 and in preparation). Such gneisses are usually considered to be products of the recrystallization of pelitic sediments. Glass and a fine-grained orthopyroxene-spinel intergrowth are present in all samples of the quartzofeldspathic gneiss. The glass was formed by partial fusion during incorporation of the xenolith in the basaltic host rock (see also Padovani and Carter, 1977a, 1977b). Some investigators have assumed that the action of the host rock on the xenoliths has not been significant and consider the xenoliths as relatively fresh samples of the earth's crust, from which deductions can be made as to the composition and metamorphic history of the crust along the path of the ascending magma. A study of the compositions of xenolithic ilmenite and sanidine suggests, however, that this may not be valid (Grew, 1977 and in preparation).

A determination of the age of a xenolith by the uranium-lead method could provide information about its history. The only age measurement on a Kilbourne Hole xenolith known to the authors is by Manton and O'Donnell (personal communication, in Padovani and Carter, 1977b), who obtained a 1000 m.y. whole-rock Pb-Pb age.

The present note is an attempt to interpret the U-Pb ages of a zircon sample from a garnet granulite xenolith from Kilbourne Hole, collected in October 1977 during the Second International Kimberlite Conference. The results of the anal-

ysis are:

U	240 ppm
^{206}Pb - ^{238}U age	360 m.y.
^{207}Pb - ^{235}U age	536 m.y.
^{207}Pb - ^{206}Pb age	1375 m.y.

The above concentration of uranium is higher than that in kimberlitic zircons (6–130 ppm, average 24 ppm) and that in zircons from two crustal nodules from Lesotho (62 and 151 ppm, *Year Book* 75, p. 822 and *Year Book* 76, p. 633), and it is near the lower limit of the observed range of uranium content of zircons from granites.

The zircons from the xenolith have rounded forms similar to those shown by Pidgeon and Bowes (1972) for granulitic zircons from Scotland. In addition, examination by scanning electron microscopy shows many micro-facets indicative of a trend toward euhedral forms. The absence of zoning and cores indicates that the zircons either crystallized or recrystallized completely at the time of granulite-facies metamorphism. The ^{207}Pb - ^{206}Pb age of 1375 m.y. is a minimum value for the time of the metamorphism as well as for the time when the source region of the xenolith became cool enough for radiogenic lead to accumulate. No later event was severe enough to completely reset the zircon U-Pb age.

The extreme degree of discordance of the U-Pb ages can be attributed to a major recent episode of lead loss, caused by the thermal action of the basaltic host. The mineralogy of the xenolith may well have been modified during the same episode.

STATISTICAL PETROGRAPHY

THE EFFECT OF THE PRINCIPAL COMPONENT TRANSFORMATION ON CLOSURE CORRELATION

Felix Chayes and Jürgen Trochimczyk

In chemical petrology and particularly in the study of relations among the es-

sential constituents of igneous rocks, the commonest data matrix is a table of proportions or percentages, the so-called closed array. Closed arrays, of course, occur in many other fields of inquiry, and it is now well known that in them there must always be strong negative covari-

ance between variables of large relative variance (Chayes, 1971).

What becomes of this implicit relation between variance and covariance when, as is becoming increasingly common, principal components are calculated from a closed or nearly closed array? The components themselves are orthogonal, and the new variables formed by multiplying each analysis by each component—called “scores” by social scientists—have two properties of immediate interest in this connection: (1) they are uncorrelated, and (2) the sum of their variances is equal to the sum of the variances of the original variables.

In the transformation the total variance of the original array is thus preserved perfectly in the scores, but its covariance disappears from them, so that if a petrographic argument may be rephrased in terms of scores it appears to escape the closure correlation implicit in the raw data. Of course, not only the closure correlation but *all* correlation is eliminated in this fashion.

Having started with familiar variables that may be highly correlated simply because they are members of a closed array, the petrologist who employs this procedure must now deal with variables that are *uncorrelated* simply as a consequence of the transformation to which he has subjected them. In this new context the skills and attitudes developed in generations of graphical analysis of petrographic scatter diagrams are irrelevant. In particular, a conspicuously nonrandom relation between any pair of component scores is not to be interpreted as an indication of some similar relation between the underlying petrochemical variables. Scores are in principle uncorrelated; if in practice their correlation is more than negligible, this is almost certainly a result of computational error or inappropriate sampling (for example, calculating scores for one body of data using components calculated from a different, and differently specified, body of data).

In the passage from a set of percentages to a set of scores, what then becomes of

the relation between variance and covariance that characterizes the closed array? In the course of an experimental study of the sampling variance of the coefficients of the components—the “loadings” of social scientists—we recently stumbled on the answer to this question.

In a strictly closed array, one in which the sum of the variables in each item is the same for all items, it is easily shown (Chayes, 1971, pp. 36–37) that the sum of the covariances of any variable is exactly equal to the variance of the variable, and opposite in sign, i.e.,

$$\sigma_i^2 + \sum_{j \neq i} \sigma_{ij} = 0, \quad (1)$$

where σ_i^2 is a variance and σ_{ij} a covariance. It then follows that

$$\sum_{i=1}^n \sigma_i^2 + \sum_{i=1}^n \sum_{j \neq i}^n \sigma_{ij} = 0, \quad (2)$$

so that the algebraic sum of *all* elements of the covariance matrix of a closed array is zero.

Deviations from Equations 1 and 2 occur if, for example, minor or trace elements are ignored and the raw values for each item are not normalized, so that a small variance attaches to the theoretically constant item-sum. Such deviations are very small, however; the approach to Equation 1 under these conditions is always close enough to assure the existence of pronounced negative correlation between variables of large relative variance.

What we have discovered through sampling experiments is that, even in rather small samples, Equation 2 holds as well for the coefficients of any one of the lower-order principal components as it does for the raw data. The peculiar relation between variance and covariance that characterizes the initial closed array, completely excluded from the scores, thus finds expression in relations between the loadings of each of the lower-order components.

An example is shown in Fig. 169 where, for coefficients of components calculated from random samples of a nine-variable

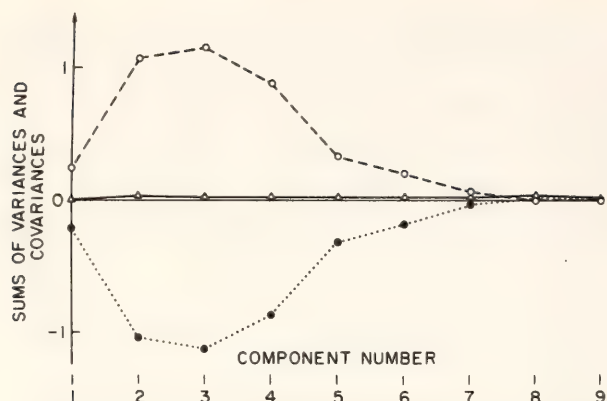


Fig. 169. Total variance (open circles), total covariance (solid circles), and their sum (triangles) for coefficients of scaled components calculated from the covariance matrices of ten random samples drawn from the pooled andesite, dacite, and rhyolite analyses in data base RKOC76. (All analyses with $H_2O > 2\%$ are excluded.)

array, the dashed line connects observed values of the first term of Equation 2, the dotted line those for the second term, and the solid line those for the left side.

The data array in question, extracted from version RKOC76 of the data base attached to the petrographic information system RKNFSYS, consists of analyses of Cenozoic rocks identified in the source references as andesite, dacite, or rhyolite and containing less than 2% of H_2O . Principal components were calculated from the covariance matrices of samples, of ~ 100 items each, drawn simply at random (without replacement) in 10 successive complete scans of a work file containing the 3166 available analyses satisfying these specifications. Variables used included SiO_2 , Al_2O_3 , Fe_2O_3 , FeO , MgO , CaO , K_2O , Na_2O and TiO_2 . The results shown in Fig. 169 are the sums of appropriate elements in the covariance matrix of observed values of the coefficients of each component.

The algebraic compensation of total variance by total covariance of loadings holds for lower-order components whether or not they are computed from standardized data and whether or not they have been normalized after computation. In the present example this compensation

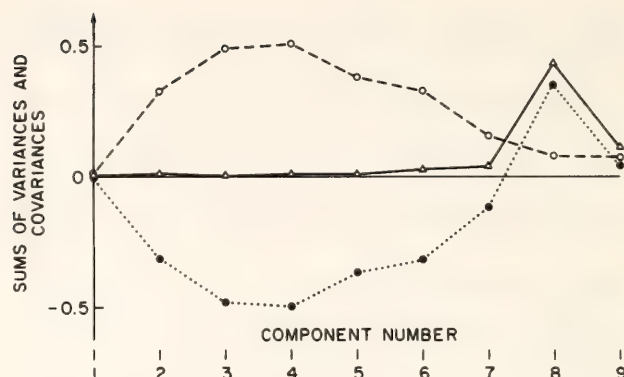


Fig. 170. Variables, symbols, and data as in Fig. 169, but for normalized components.

persists remarkably through the 6th normalized component, is less complete for the 7th, and then fails completely on the 8th and 9th, as shown in Fig. 170.

The moral appears to be that the principal component transformation, although in many respects powerful and appealing, offers no new insight on the vexing problem of appraising the significance of relations between closed variables. Component scores lack information about covariance, and, as shown here, covariances between component loadings are subject to constraints much like those characteristic of the raw data.

THE EFFECT OF ROTATION ON THE STABILITY OF FACTOR LOADINGS

Jürgen Trochimczyk and Felix Chayes

There appears to be theoretical justification for supposing that the loadings of rotated factors should be more stable than those obtained without rotation (see, for example, Kaiser, 1958), but there is little direct evidence bearing on this matter. In order to obtain such information the data array described in the preceding section was used as input to a program prepared by one of us (J. T.) for inclusion in version NTRM of the petrographic information system RKNFSYS.

For every combination of seven of the oxides SiO_2 , Al_2O_3 , Fe_2O_3 , FeO , MgO , CaO , Na_2O , and K_2O , rotated and unrotated

TABLE 55. Sample Variance ($\times 10^4$) in the SiO_2 and MgO Loadings of the First Factor*

Oxide omitted from calculation	Variance ($\times 10^4$) of loading for			
	SiO_2		MgO	
	unrotated	rotated	unrotated	rotated
SiO_2			475	1018
Al_2O_3	142	2092	366	1427
Fe_2O_3	115	1001	379	1615
FeO	106	1118	452	2482
MgO	120	3907		
CaO	116	1522	339	1195
Na_2O	64	1890	383	1656
K_2O	74	743	322	1190
Average value of loading ($\times 10^4$)	−9579	−6491	8563	6444
Loading ($\times 10^4$) computed from entire work file	−9592	−6533	8468	5533

* Each variance based on ten samples, each containing 90–110 analyses. Data as described in text.

factors were calculated from the correlation matrix of the data retrieved in each of ten random sampling scans (sample size, 90–110) of the andesite-dacite-rhyolite work-file. This generates 140 sample estimates of coefficients for each factor in each combination of oxides—a mass of numbers.

The general effect of rotation is nearly always the same, although its intensity varies somewhat, both among coefficients and among factors. When rotated and unrotated factors are calculated from identical sets of samples, the stability of the coefficients of any factor is markedly *less*—i.e., the sampling variance is markedly larger—under rotation. The results shown in Table 55, for the SiO_2 and MgO loadings of the first factor, are quite characteristic.

It is perhaps open to question whether variances obtained in this fashion should themselves be subjected to formal statistical analysis, but such an analysis is hardly necessary. It is obvious from inspection of the table that in these data rotation tends to increase materially the variance of factor loadings. This is not what would be anticipated from the scattered references to the subject in the literature.

AN ALGEBRAIC EXPLANATION OF
CLOSURE CORRELATION AMONG THE
COEFFICIENTS OF A PRINCIPAL
COMPONENT

Joan Rosenblatt, Felix Chayes, and
Jürgen Trochimczyk*

The algebraic compensation of variance and covariance among coefficients of a component described earlier is of obvious concern when principal component analysis is applied to tables of proportions or other closed data. Although this striking property does not seem to have been noted before, it is actually a consequence of definition. For any component (**C**) and its related eigenvalue (λ), for instance,

$$\mathbf{VC} = \lambda \mathbf{C},$$

(1)

where **V** is the initial covariance matrix. **V** is always symmetrical and in closed data is subject to the additional constraint that the sum of each of its rows is zero. Because of these properties, the result of premultiplying both sides of Equation 1 by the unit vector $[1]'$ is

$$0 = \lambda \sum_{j=1}^n c_j$$

(2)

* National Bureau of Standards

where c_j is the j th element of \mathbf{C} . This cannot be true unless either λ or

$$\sum_{j=1}^n c_j$$

is zero, and in nontrivial solutions $\lambda > 0$. Hence

$$\sum_{j=1}^n c_j = 0,$$

which is exactly the form the closure constraint takes in the deviation matrix of the original data. Thus, if the data array \mathbf{X} used in experimentation of the type described earlier is strictly closed—i.e., if the sum of the elements of each observation vector is exactly equal to a constant—then a “data” matrix \mathbf{C} , consisting of successive experimental approximations of any particular component, is also a closed array. Departures from exact closure in \mathbf{X} will surely lead to similar departures in \mathbf{C} , but from Figs. 169 and 170 it is clear that those actually encountered did not destroy the balance of variance and covariance in \mathbf{C} through the first seven components.

STATUS OF THE PROJECT FOR DEVELOPMENT OF A WORLD DATA BASE FOR IGNEOUS PETROLOGY

Felix Chayes

The urgent need for a publicly accessible electronic information system for handling worldwide petrologic data was outlined in *Year Book 76* (see p. 636). At the organizational meeting of International Geological Correlation Project 163 in September 1977, the writer was delegated to provide central administrative facilities, on a pilot scale, for a group seeking to stimulate the development and assist in the construction of such a data

base. During the report year general agreement was reached about the information content of the base, a coding form that will facilitate extraction of this information from the technical literature has been adopted, syntax and vocabulary to be used in transferring data from coding forms to punched cards have been developed, and data accumulation has been initiated.

The principal current assignment of the central facility is to develop software that will provide a convincing demonstration of the feasibility of the project and serve as a prototype of system design that could be modified and adapted for routine operation by an appropriate government data center or, perhaps, the publications office of one of the major earth science professional societies. Four major blocks of software will be required: (1) a program that will read and edit cards prepared in the syntax and vocabulary of the system, detecting and noting formal errors; (2) a program that will generate a listing suitable for direct comparison with the coding form, to facilitate final substantive editing prior to actual inclusion of data in the base; (3) a program that will insert carded information into the base; and (4) a program that will access any specified records of the base, screen the information they contain, and generate cards or card-image files from all data that meet screening specifications.

Preparation of these programs is complicated by the broad spectrum of information to be contained in the base and by the requirement for optimum program portability. Work on steps (1) and (2) is nearing completion, work on step (4) is in progress, and work on step (3) will be essentially a minor extension of certain parts of (1).

NEW FACILITIES AND TECHNIQUES

LASER-RAMAN SPECTROSCOPY

S. K. Sharma

In this report year, a laser-Raman spectrometer has been set up at the Geo-

physical Laboratory for studying the structure of hydrothermal solutions, silicate melts, glasses, and crystals at temperatures and pressures relevant to geological systems.

The value of Raman spectroscopy in studies of the molecular structure of gases, liquids, solids, solutions, and amorphous materials was appreciated soon after the experimental discovery of the effect by Raman (1928). Scientists at the Geophysical Laboratory took part in the historical development of this effect as a research tool as early as 1932 (Hibben, *Year Book* 32, pp. 61–69). With the advent of commercial infrared spectrometers during the 1940's, however, the study of Raman scattering by molecular spectroscopists decreased markedly.

The development of laser sources has led to a renaissance of Raman spectroscopy. Porto and Wood (1962) were the first to report the Raman spectra excited with a laser source. The highly monochromatic, intense, narrow laser line is especially suitable for the study of small samples with accurate control over beam and sample geometry. Furthermore, the determination of depolarization ratios, which in turn may be related to the influence of the surrounding environment on a species, is facilitated by use of a plane-polarized laser beam. With the development of a wide variety of laser sources capable of providing laser radiation of different frequencies, and with advanced optical and electronic instrumentation, Raman spectroscopy has already yielded a wealth of information about the structure of species present in gases, crystals, melts, glasses, and solutions in the fields of physics and chemistry. The Raman technique is also being increasingly used for studying the vibrational spectra of high-pressure polymorphs of solids in the diamond-anvil cell.

The Raman effect is a light-scattering process. When monochromatic light of frequency ν_0 and intensity I_0 illuminates a suitable transparent specimen, the spectrum of scattered light shows, in addition to the Rayleigh line, a weak pattern of lines with shifted frequencies ($\nu_0 \pm \nu'$)—the Raman spectrum. The scattered radiation at ($\nu_0 - \nu'$) is called Stokes radiation and that at ($\nu_0 + \nu'$) is called anti-Stokes radiation. The difference in

frequency between ν_0 of the exciting radiation and ($\nu_0 \pm \nu'$) of the Raman line is independent of the wavelength of the exciting radiation and is characteristic of the vibrational-energy change (or rotational-energy change) of the molecular structural units of the sample. Thus, measurement of $\nu_0 - (\nu_0 \pm \nu') = \pm \nu'$, called the Raman shift, provides information about the molecular-energy levels.

The apparatus installed consists of a Jobin-Yvon Raman spectrometer, "Ramanor HG-2S," equipped with concave, aberration-corrected holographic gratings, a Hamamatsu photomultiplier (R666P) detector mounted in a thermoelectrically cooled (-30°C) r.f.-shielded photomultiplier housing (Product Research model TE177-TS-RF), a Princeton Applied Research photon-counting system (Model 1112), and a strip chart recorder. An Ar^+ ion laser (Spectra Physics Model 164-09) is used as a radiation source. Both blue (488.0 nm) and green (514.4 nm) laser lines are used as the exciting radiation.

For recording the Raman spectra of small ($1 \times 1 \times 2 \text{ mm}^3$) glass samples, liquids, and melts, 90° -scattering geometry was used. To estimate the depolarization ratios of Raman bands, the glass samples were excited with the electric vector of the laser beam vertical, and by recording the observed scattered radiation both perpendicular (I_\perp) and parallel (I_\parallel) to the electric vector of the exciting radiation. The polarization study is achieved by using a polaroid sheet between the collecting lens and the entrance slit. An achromonmatic optical scrambler was placed before the entrance slit to depolarize the scattered light reaching the slit because the diffraction of light from the grating depends on the state of polarization of radiation. The depolarization ratio ($\rho = I_\perp/I_\parallel$) can thus be determined accurately.

The above experimental setup was slightly modified for measuring the Raman spectrum of samples at elevated pressures. A 90° off-axis ellipsoidal mirror system (Adams *et al.*, 1977) is used to collect the

scattered radiation in 0° -scattering geometry. Diamonds exhibiting low fluorescence (Type IIb) have been selected for anvils in the diamond cell. High-pressure Raman studies on glasses and crystals are under way.

For studying the Raman spectra of silicate melts, a furnace wound with Pt₉₀-Rh₁₀ wire operable up to $\sim 1400^\circ\text{C}$ has been constructed, and preliminary results are reported elsewhere (Sharma, Virgo and Mysen, this Report). In this latter study, the 90° -scattering geometry was preserved. The sample was contained in a windowless Pt cell, made from a Pt tube (2.5 mm I.D.) with two slits ($5 \times 0.6 \text{ mm}^2$) at 90° to each other. The high viscosity of silicate melt helped in containing the sample in the "cell." In order to reduce the black-body radiation, the photon counting system was used in "chop mode."

A chopper was used to intercept the beam between the laser and the sample. During illumination of the sample, the signal and background pulse produced in the photomultiplier tube were counted and stored in channel A. During the brief interval of time that the chopper intercepted the laser beam, the detector recorded only the background radiation, which was stored in channel B. The difference (A minus B) then gave a signal free from background. This technique was successful provided the intensity of the signal was \geq background. When the black-body radiation exceeded the signal, however, the signal-to-noise ratio was unsatisfactory. The quality of the spectrum can be improved in future experiments by repetitively scanning the frequency range and storing the digital output from the photon counter in a multi-channel analyzer. In this way, signal-to-noise ratio in the Raman spectrum of the samples at high temperatures ($\geq 900^\circ\text{C}$) will be significantly improved.

Finally, a hydrostatic-liquid optical cell for studying the Raman spectra of aqueous solutions at elevated temperatures ($\sim 700^\circ\text{C}$) and pressures (4 kbar) is

under construction. This cell will be used for studying the structure of species present in hydrothermal systems of geochemical and geophysical interest by laser-Raman spectroscopy.

DESIGN AND VARIETIES OF THE MEGABAR CELL

H. K. Mao and P. M. Bell

Recent research at pressures in the 1–2 megabar range (Bell and Mao, this Report) has been conducted in a new high-pressure apparatus named the MBC (for megabar cell). The MBC is the current result of rapidly changing design technology (see Mao and Bell, *Year Book* 76, pp. 646–650) based on the extraordinary physical properties of single-crystal diamonds. Considerations of cost and availability of diamonds of acceptable quality have made it prudent to employ a small sample volume (of the order of nanoliters) in the experiments. Nonetheless, with the development of microtechniques the MBC has proven to be unusually versatile, and the physical and chemical data obtained with it are remarkably accurate.

Seventeen MBC's have been constructed at the Geophysical Laboratory, incorporating combinations of seven fundamental design variations. Each of the variations is designed to optimize a particular function. Details of these designs and of the design of the lever assembly used to apply force to the cell are described in this report.

All cells and lever assemblies are made of tool steel hardened to Rockwell C 55–60. All bearing surfaces are ground to No. 16 finish. The fitting of each set of piston and cylinder requires individual lapping.

General Design Factors

Alignment of the diamond anvils is critical in operating the MBC. Therefore, one of the primary objectives in design is to achieve precise and stable alignment.

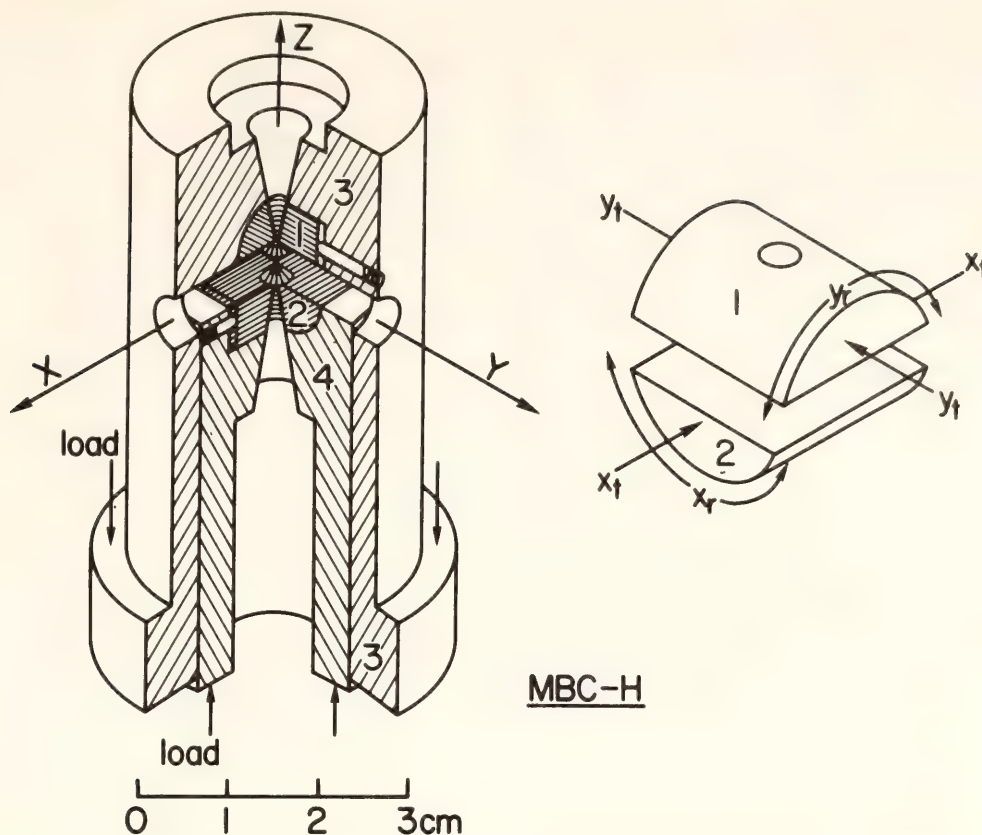


Fig. 171. Left, cut-away view of MBC-H; right, exploded view of rockers: 1, upper rocker; 2, lower rocker; 3, cylinder; 4, piston.

In Fig. 171 the two opposed diamond anvils are seen mounted in a precisely lapped piston and cylinder so that the applied load force will act along the Z -axis. The required tolerance of fit of the piston and cylinder is such that their axes coincide reproducibly to within $5\ \mu\text{m}$. Parts numbered 1 and 2 in Fig. 171 are half-cylinder casts of tungsten carbide with a hole or slot (Fig. 172). The diamonds are centered and then cemented with epoxy resin to the flat surfaces of the half-cylinders; a thin foil of zirconium metal between the half-cylinders cushions the contact of the two hard materials. Parts 1 and 2 fit precisely into the piston and cylinder (parts 3 and 4) where half-cylinder seats have been formed by the spark-erosion technique.

The cutaway view of the MBC in Fig. 171 shows set screws located on the cylindrical axes of half-cylinders 1 and 2, so the half-cylinders can be adjusted for rotation around X and Y directions (X_r , Y_r ,

motion shown in Fig. 171) and translation along X and Y directions (X_t , Y_t , motion shown in Fig. 171). After the half-cylinders with diamonds mounted are set into the MBC, precise adjustments of X_r and Y_r for parallelism and X_t and Y_t for matching of anvils are made under the microscope (see Mao and Bell, *Year Book* 76, p. 646 for description of alignment procedure).

Seven Design Variations of Piston and Cylinder

Model MBC-H. The design shown in Fig. 171 for Model MBC-H is basic in the series in that it provides maximum support of the carbide half-cylinders and the diamond anvils. It is designed for the maximum pressure. The carbide half-cylinders and the piston and cylinder are relieved with small-angle conical holes (20°) for viewing the sample and for transmitting various radiations to the

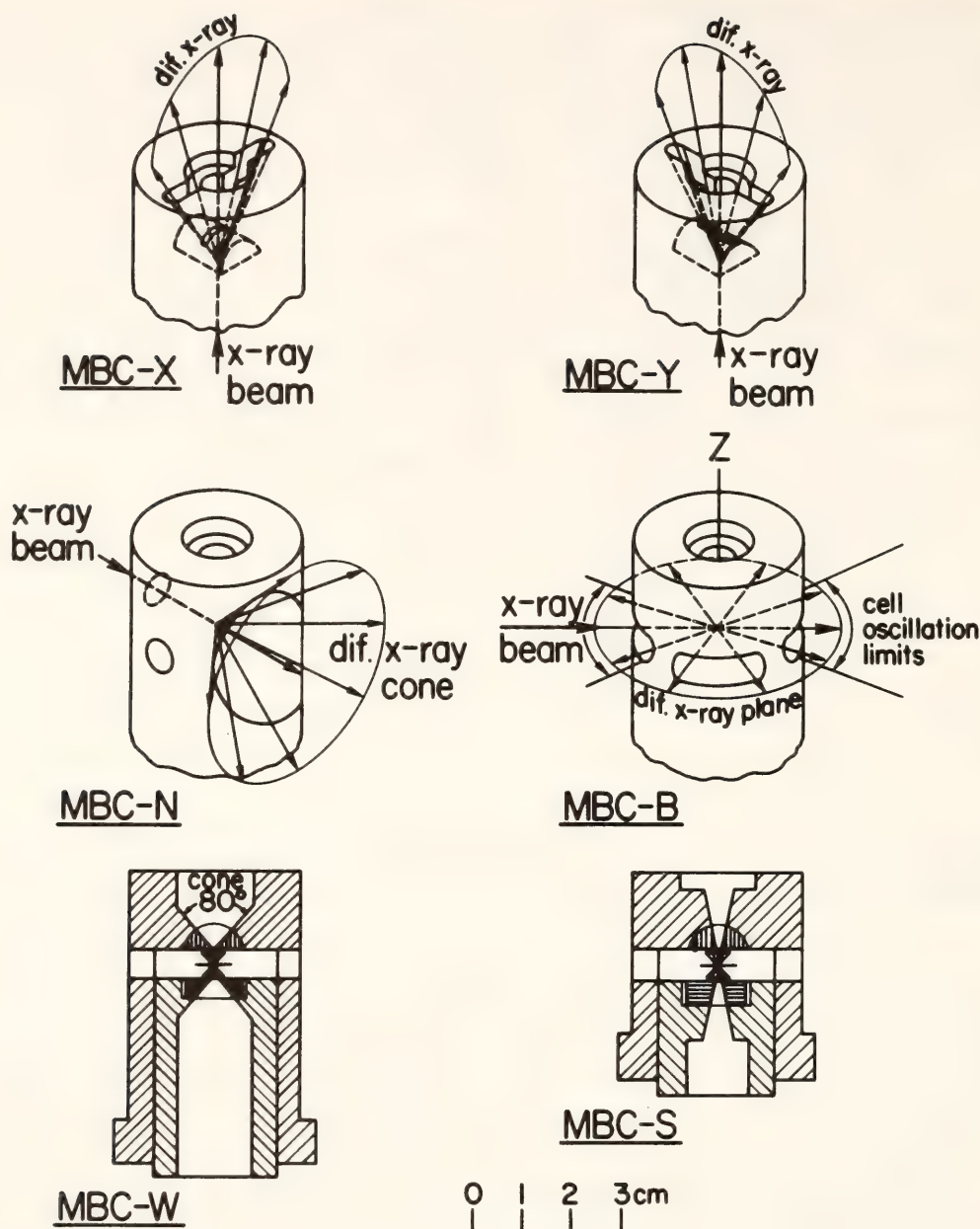


Fig. 172. Six models of MBC (dif = diffracted).

sample. A common feature of all models of the MBC is that the alignment is reproducible even after removing and replacing the piston assembly (lower diamond plus parts 2 and 4). It should be noted that although this model has been successfully tested to 1.7 Mbar (Bell and Mao, this Report), the diamonds can be cracked and broken at very low nominal pressures (less than 10 kbar) if they are incorrectly aligned.

Models MBC-X and MBC-Y. Models MBC-X and MBC-Y (Fig. 172) are

variations of the standard MBC modified for x-ray diffraction studies at high pressure and differ only in the design geometry. The incident x-ray beam is collimated to pass through the cell parallel to the Z-axis (based on a design of Bassett *et al.*, 1967). Slots are located normal (X) or parallel (Y) to the axis of the upper half-cylinder for exit of the diffracted beam, up to 2θ of 40° . X-ray diffraction is limited to the study of lattice planes of a sample within 20° of the uniaxial (Z) load. Under non-hydrostatic conditions

the information obtained from this type of x-ray study is essentially the strain parameter of the sample in the direction normal to Z (Mao *et al.*, 1978a).

Because the x-ray beam can be aligned to pass through the center hole without hitting the sample gasket, a strong metal gasket, such as T301 stainless steel (Rockwell C 42), can be used to confine liquid or solid samples. The strong gasket is necessary for reaching pressures in the megabar range (Mao and Bell, *Year Book* 76, pp. 646–650).

Models MBC-N and MBC-B. Two models, MBC-N and MBC-B, are designed for x-ray diffraction studies where it is required that the incident beam be normal to the Z -axis (Fig. 172). The MBC-N (based on a design by Kinsland and Bassett, 1976) is used for measurement of differential strain in a sample at all angles to the uniaxial (Z) load. The axes of the carbide half-cylinders are positioned 120° apart (rather than 90° as in other MBC), so that an exit cone of 80° ($2\theta = 40^\circ$) can be cut without interfering with the set screws of the half-cylinders.

The MBC-B has four slots cut parallel to the X - Y plane. The cell is employed with a Debye-Scherrer x-ray camera, with the Z -axis coincident with the cylindrical axis of the x-ray film. Oscillation of the cell about Z produces continuous front and back diffraction patterns up to 2θ of 160° . Because the x-ray beam passes only through the tips of the diamond anvils (approximately 0.5 mm thick) instead of the whole thickness of the two diamonds (5 mm) as in the case of MBC-X and MBC-Y, the absorption by the diamonds is minimized, and Cu $K\alpha$ radiation can be used.

In both MBC-N and MBC-B, x rays must also pass through the entire width of the sample gasket. Therefore, non-absorbing gasket such as epoxy or beryllium metal must be used. The strength of the gasket limits the maximum pressure that can be obtained.

Models MBC-W and MBC-S. Studies

of the sample under pressure in the MBC that require the close proximity of an optical lens system can be done with either the MBC-W or MBC-S models (Fig. 172). The MBC-W has a wide cone exit (80°) in the Z direction and the MBC-S has a shortened cylinder. Both models are easily handled on a microscope stage or in apparatus where space or sample distances are limited (as for optical absorption or Raman spectrometry).

Combination of models. Models with combinations of the above features were also constructed. For example, model MBC-XN has an X slot and an N cone; model MBC-YWS has a Y slot, a wide Z cone, and is short. Cutting more slots and openings invariably weakens the support of the diamonds.

Lever Assemblies

Models L1 and L2. The MBC piston and cylinder can be pressed together smoothly by any device that gives a uniform load. For convenience, lever-arm assemblies are used. Figure 173 shows designs of the lever assemblies used to transmit the load to the MBC. The essential difference in the two models is location of the fulcrum (part number 4) and thrust-block (part number 3). The L-2 model is better balanced on a microscope stage, whereas the L-1 is more convenient in applications where the lower surface must be free of obstruction.

It is essential that the plane containing the fulcrum and thrust-block axes is made normal to the Z -axis of the piston and cylinder (part numbers 1 and 2). This condition is satisfied by employing a thrust-block with the thickness adjusted to the vertical dimensions of the diamonds. Torque is applied on part 7, compressing the Belleville springs (part 8) onto the lever arms. The mechanical advantage (B/A) is 5.

Summary of the MBC design

The strongest and most rigid cell is MBC-H, in which a pressure of 1.7 Mbar

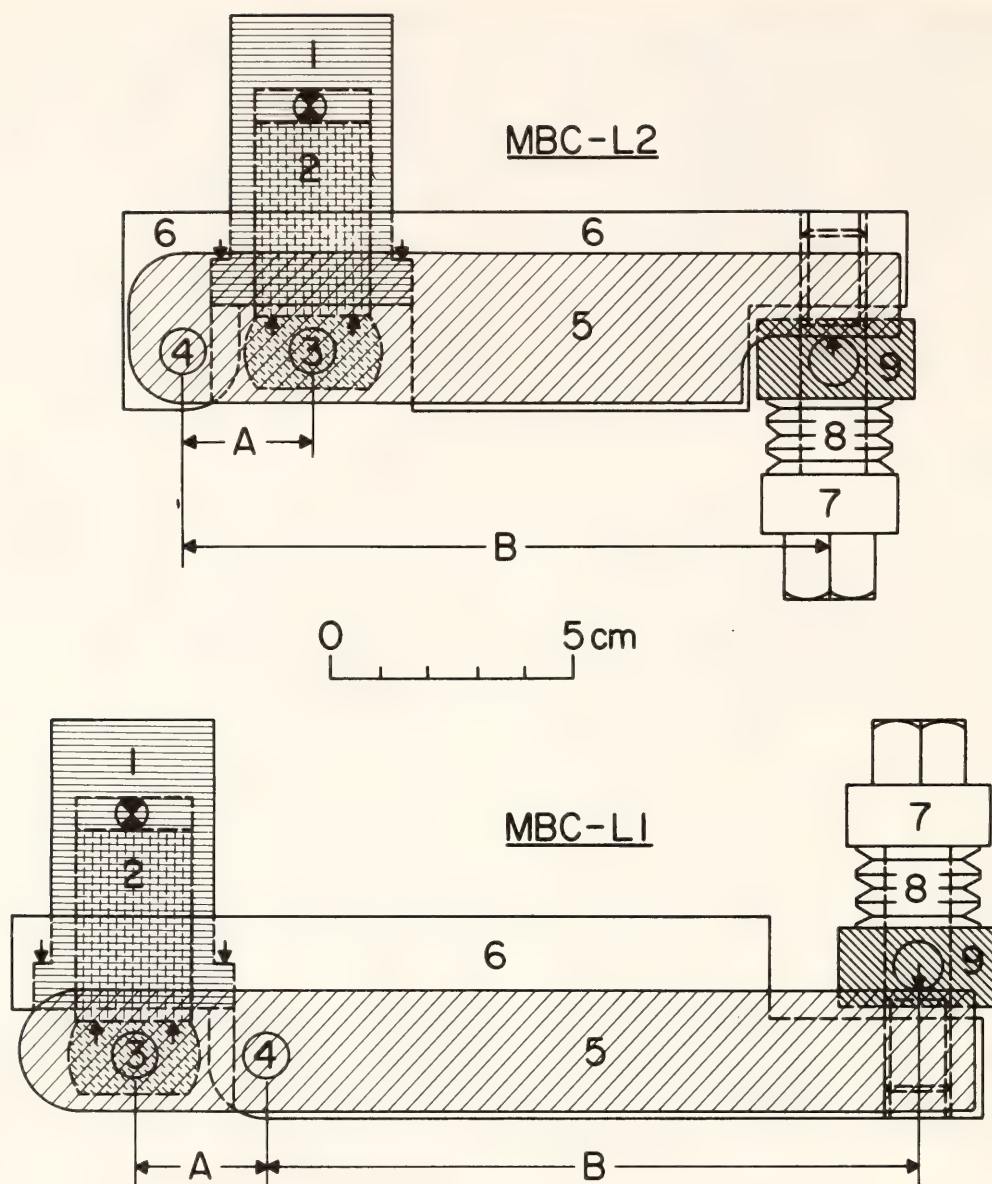


Fig. 173. Lever-arm assembly: 1, cylinder; 2, piston; 3, thrust block; 4, fulcrum; 5, lever arms; 6, main body; 7, bolt; 8, Belleville spring washers; 9, spring holder.

has been reached. The models MBC-X and MBC-Y have been used up to 1 Mbar (Mao *et al.* 1978a; Mao and Bell, 1978). The other models described have so far been tested only to 0.5 Mbar, but a higher pressure range is possible. The designs are optimized for mechanical stability and strength with adaptations for x-ray diffraction requirements. Each of the models has been employed for experiments involving visual observation, optical absorption measurements, laser heating, Mössbauer resonance, Raman and IR spectroscopy, and electrical conductivity

measurements. In all of the models the pressure measurement technique using ruby fluorescence is employed.

STATIC GENERATION OF 1.72 MEGABARS PRESSURE

P. M. Bell and H. K. Mao

The first experiments in which static pressures of 1.72 Mbar were generated at room temperature (25°C) are reported here. Measurements of the pressure were

made directly on ruby crystals in the pressurized medium itself.

In earlier experiments to 1 Mbar, pressure measurements were based on an extension of the National Bureau of Standards ruby R_1 fluorescent pressure calibration scale (Mao and Bell, 1976). More recently, calibration of this extension of the ruby R_1 scale from 0.06 to 1.0 Mbar (Mao *et al.*, 1978*a*) has indicated small positive nonlinearity in the function of wavelength shift of the ruby fluorescent line vs. pressure, but the deviation from the reported pressure at 1 Mbar was within the estimated uncertainty (± 10 percent of pressure). In the present study, pressure was measured using an extension of the known R_1 pressure scale by

$$P \text{ (Mbar)} = 3.808[(\Delta\lambda/694.2 + 1)^5 - 1]$$

where $\Delta\lambda$ (nm) is the wavelength shift of the ruby R_1 fluorescent line between 1 bar and the high pressure.

The apparatus used in these experiments was the diamond-windowed high-pressure cell (Mao and Bell, 1976). The windows were made of 0.3-carat brilliant-cut diamonds whose culet tips were ground flat or beveled to low angles (see

Fig. 174). Diamonds with low-strain birefringence ($2 \text{ to } 10 \times 10^{-5}$) were selected.

The alignment cylinders were cast of tungsten carbide by the Metallurgy Division, General Electric Company. Access ports to the diamond windows were formed in the casting process, except for the cylinders used in experiment 6C1 in which the ports were “drilled” by the electro-etching technique. The alignment cylinders also act as thrust blocks in the pressure cell (*Year Book 74*, p. 402).

High-precision alignment of the diamonds was achieved by measuring pressure gradients at 700 kbar with the fluorescence shift of ruby crystals distributed radially in the cell. Adjustments were made so that these gradients were symmetrical with respect to the center of the diamond culet faces.

The sample assembly consisted of a preindented gasket made of work-hardened stainless steel, on the upper surface of which ruby crystals were imbedded (Fig. 174). During the experiments the ruby R_1 fluorescence line was excited by probing the sample with a He-Cd laser beam focused through the diamond window. The pressure was raised from 700

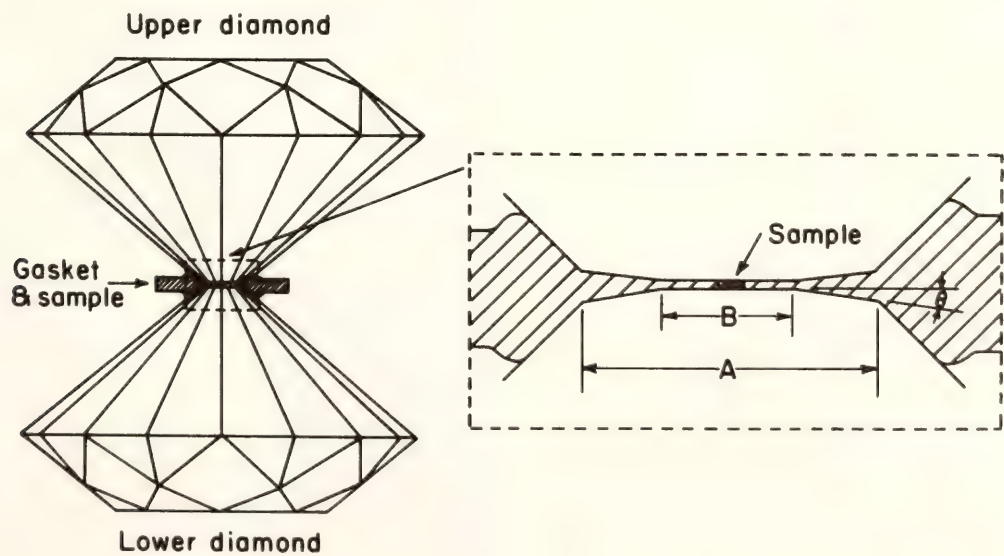


Fig. 174. Sketch of the diamond-windowed high-pressure cell (distance from top surface of upper diamond to bottom surface of lower diamond is approximately 5 mm). Inset: magnified views of cross-section gasket sample assembly. A , outer diameter of bevel; θ , bevel angle; B , flat surface; sample width = $250\mu\text{m}$.

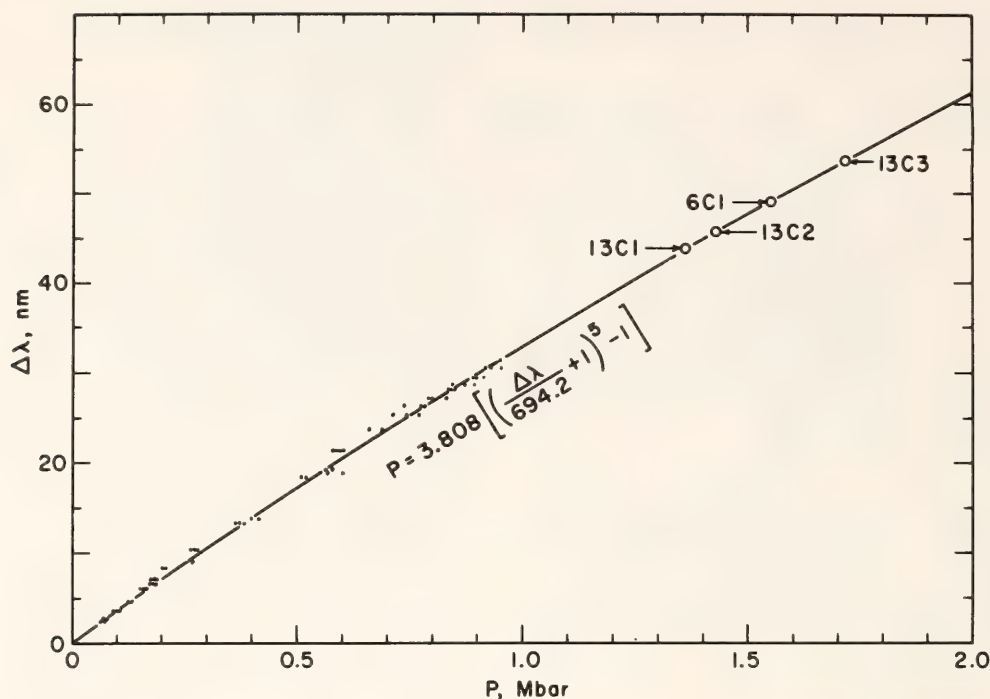
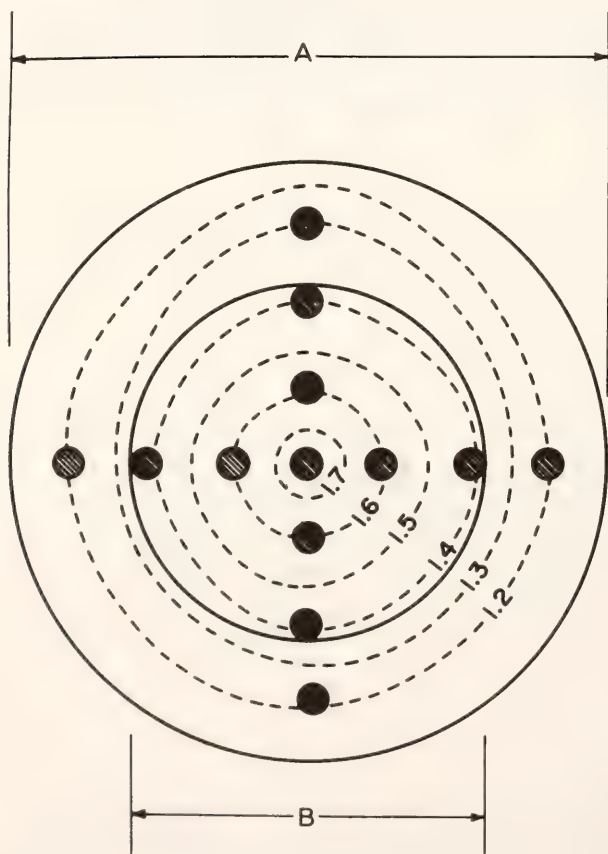


Fig. 175. Plot of the change of the wavelength of the ruby R_1 fluorescent line versus pressure. Solid points are secondary calibration points based on equation-of-state measurements of Cu, Mo, Ag, and Pd from shock-wave data. The solid line is a nonlinear, two-parameter, least-squares fit to the calibration points. Numbered open circles are the maximum pressures measured in the runs of the present study.

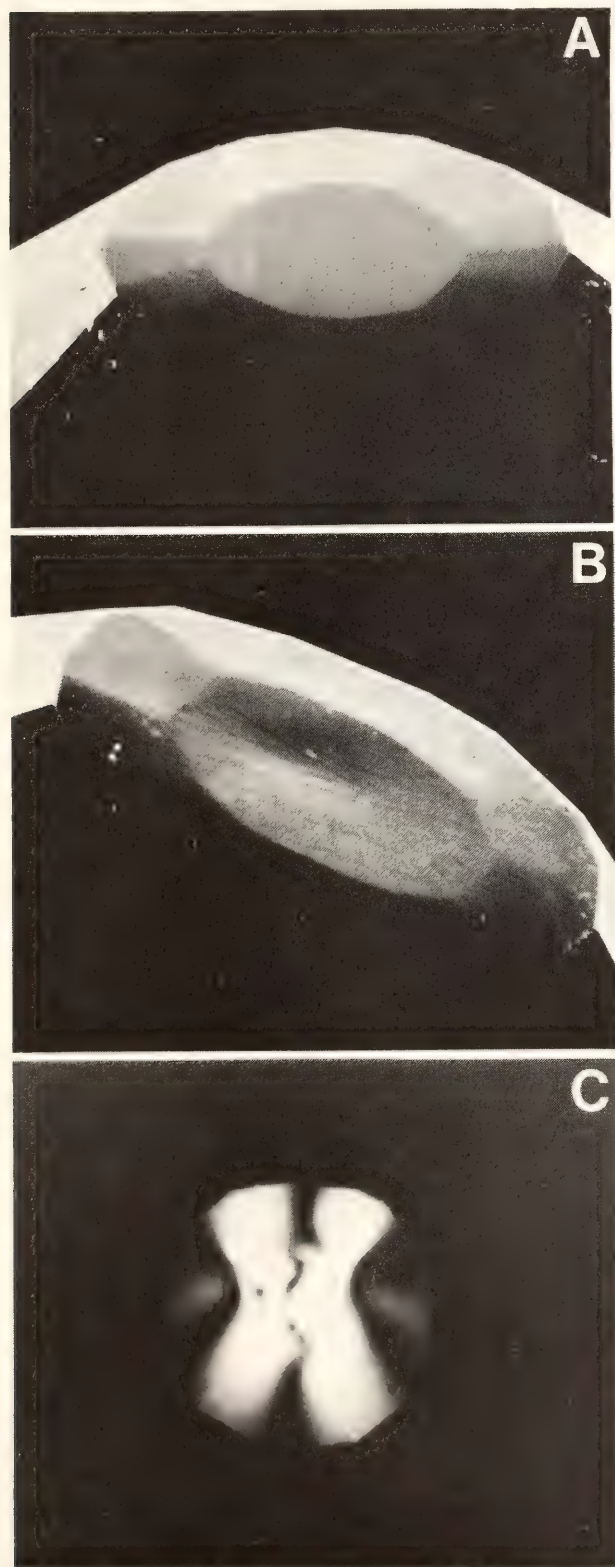


kbar at 25°C (after the alignment described above) to the pressures on the calibration curve indicated by arrows in Fig. 175. Pressures were measured at every 50 to 100-kbar increment in the entire range from 1 bar to the maximum pressure. At the highest pressure, the pressure distribution on the diamond faces was contoured with data from ruby fluorescent measurements at various points, as shown in the example in Fig. 176.

The maximum pressure reading obtained was 1.72 Mbar (the systematic un-

Fig. 176. Pressure contours (units are megabars) on the upper diamond pressure face in experimental run 13C3. Measurements of the ruby R_1 fluorescent line were made at points indicated by the shaded circles (diameter of the He-Cd laser beam). The edges of the bevel are indicated by solid circular lines ($A = 300 \mu\text{m}$; $B = 180 \mu\text{m}$).

certainty in pressure above the calibrated point at 1 Mbar is estimated to be $+20\%$, -10%). At that pressure, a color change was observed at the center of the upper diamond's pressure face (within the 1.7 Mbar contour, Fig. 176) from colorless



to a light shade of brown, possibly suggesting the onset of a phase transformation (discounting possible hysteresis of the presumed transformation) or of deformation. Further applications of force caused no increase in pressure, so the experiment was terminated. The cell was left undisturbed for 18 hours, during which the pressure remained constant at 1.7 Mbar. Pressure was gradually (5 hours) released to 1 bar to avoid possible cracking of the diamonds. The brown coloration persisted until the pressure was reduced to 1.0 Mbar. Between 1.0 and 0.8 Mbar the brown color progressively disappeared, and the diamond pressure face returned to its colorless state below 0.8 Mbar. Examination of the diamonds by microscope upon release of pressure revealed no obvious cracks, but relatively massive flow deformation was observed for the first time at room temperature in the upper diamond along its pressure face in the same region where it had turned brown. The flat *B* area of the upper diamond (Fig. 174) became permanently concave (Figs. 177A, 177B). Also, the strain in the central area of the anvil increased markedly (Fig. 177C). The maximum birefringence increased from the initial 6×10^{-5} to 6×10^{-3} . The lower diamond showed no visual indication of flow or other deformation. Its strain birefringence was unchanged.

In addition to the 1.72 Mbar experi-

Fig. 177. Photomicrographs of flow deformation on upper diamond face in experiment 13C3 after maximum pressure of 1.72 Mbar was reduced to 1 bar (A,B) Scanning electron micrographs (back-scattered electron image) showing (A) undeformed pressure surface on the culet tip of the diamond in a view tilted away from the observer; (B) deformed pressure surface at higher magnification and tilted farther right (oval perspective caused by tilting.) Note bevel and the flow deformation in central portions. (C) Light photomicrograph of diamond under cross polarization viewed normal to plane of pressure face. Interference bands converge toward center, where maximum deformation is observed.

TABLE 56. Orientation, Strain, and Dimensional Parameters of the Diamond Windows

	Run number and diamond window							
	6C1		13C1		13C2		13C3	
	upper*	lower*	upper	lower	upper	lower	upper	lower
Orientation†	(100)	random‡	(510)	(100)	(111)	(111)	(741)	(100)
Maximum strain birefringence ($\times 10^{-6}$)	n.d.	n.d.	10	6	10	2	6	6
A (mm)	0.66	0.66	0.37	0.34	0.26	0.25	0.30	0.29
B (mm)	0.25	0.23	0.15	0.18	0.18
θ (degrees)	2	2	2	0	0	0	2	1
Maximum P (Mbar)	1.55			1.36		1.43		1.72
Damage at maximum P	split	crushed	crushed	chipped§	crushed	chipped§	flowed	none
Damage to carbide seat	cracked	cracked	none	none	none	none	none	none

* Upper diamond mounted on the cylinder; lower diamond mounted on the piston.

† Miller indices of the anvil face.

‡ Not close to (100), (110), or (111).

§ Anvil face slightly chipped from the shock of crushing the other diamond.

ment, Table 56 lists details of experiments in which the maximum pressures were 1.36, 1.43, and 1.55 Mbar. These experiments were terminated because of sudden failure of one of the diamonds in each instance. Although diamond failure appears to be a random process, the fact that one of the diamonds used in the 1.7 Mbar experiments did not flow or fail suggests that it may be possible to generate pressures higher than 1.7 Mbar.

To the best of our knowledge, 1.7 Mbar is the highest sustained static pressure ever measured. This maximum pressure is almost 3.5 times higher than the highest pressures reported by workers employing continuous internal calibration in other laboratories (Piermarini and Block, 1975). The depth in the earth that corresponds to a pressure of 1.7 Mbar is approximate 3000 km and is within the earth's core. The techniques described here are being applied to geophysical problems under conditions simulating those of the core-mantle boundary as well as to a wide range of physical or chemical experiments on the nature of matter.

MEASUREMENT OF CHLORIDE ION CONCENTRATIONS IN MICROSAMPLES

R. K. Popp, J. D. Frantz, G. L. Vogel, and P. E. Hare*

Experimental studies using the Ag-AgCl buffer as a monitor for either hydrogen fugacity (Chou and Eugster, 1976) or for HCl^o concentration (Frantz and Popp, *Year Book* 76, pp. 598-601) require accurate and precise measurement of chloride ion concentrations in micro-volume samples (1-10 μ l). The Buchler chloridometer has proven adequate for samples in which the concentration of Cl⁻ is greater than 0.01 *m* (*m* = molality) (e.g., Frantz and Popp, 1978). This report describes two new techniques for

measurement of Cl⁻ in microsamples in the concentration range 0.01 to 0.0001 *m* chloride.

Chloride Electrode Technique

Vogel and Brown (1978) have recently discussed the adaptation of a commercial solid-state electrode for measurement of fluoride ion in microvolume samples. The method described here is a modification of that technique for chloride ion.

Experimental Procedures. The system requires two modifications to the normal electrode technique: (1) adaptation of the commercial electrode to the small volumes required and (2) construction of a miniature reference electrode.

To accommodate the small samples, an Orion solid-state chloride electrode (Model 94-17) is mounted vertically in an inverted position, and a thin coat of melted red dental wax is applied to the sensing element. The adapter is a nylon disc approximately 13 mm in diameter \times 5 mm, through which a number (up to seven) of 2-mm holes have been drilled (Fig. 178). The adapter is attached to the sensing element by first heating on a hot plate and then pressing onto the dental wax. The wax is removed from the holes using cotton swabs and chloroform.

The configuration of the micro-reference electrode is shown in Fig. 178. The micro-capillary tip is constructed from heavy-walled Pyrex tubing (8 mm O.D., 1.3 mm I.D.) pulled to an inner diameter of 0.10-0.15 mm. A section of this rod is then pulled again to an I.D. of 0.01-0.03 mm to form a tapered end. The micro-capillary tip is inserted into a length of Tygon tubing connected to a tapered glass tube, which was glass-blown to the bottom of a two-neck distillation flask. The flask, tube, and tip assembly is filled with a warm 1.0M KNO₃ solution containing \sim 0.2 wt % agar. The exact agar concentration is determined by the dimensions of the capillary tip: a solution containing too little agar will leak through the tip, whereas one containing too much

* American Dental Association Research Unit, National Bureau of Standards, Washington, D.C. 20234.

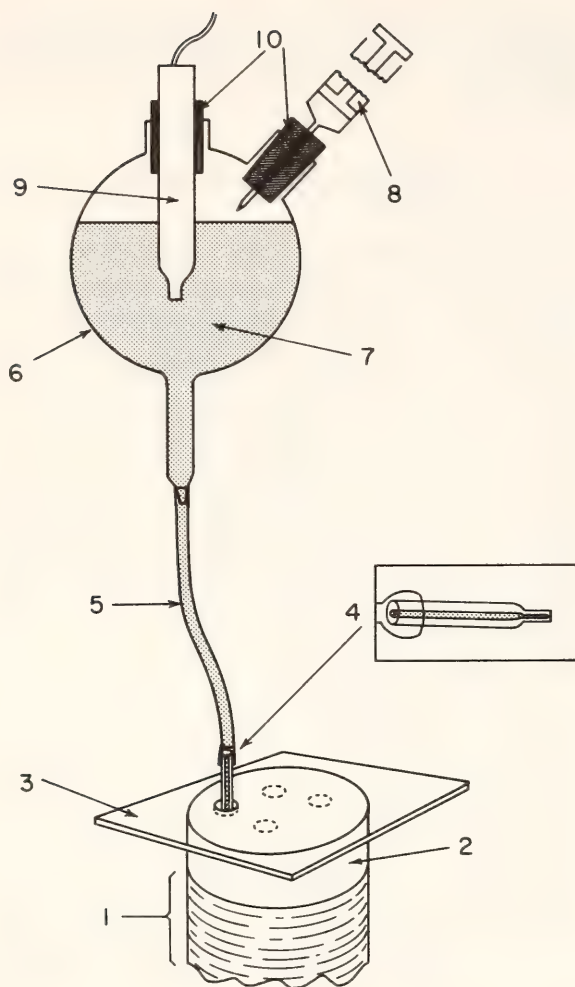


Fig. 178. Configuration of chloride electrode: (1) solid state chloride electrode; (2) nylon adapter; (3) plastic microscope cover slide; (4) micro-capillary tip; (5) Tygon tubing; (6) 2-neck distillation flask with tapered glass tube attached; (7) 1.0 M KNO_3 solution with 0.2% agar; (8) syringe; (9) calomel reference electrode; (10) rubber stoppers.

agar will pull away from the end of the tip and break electrical contact. A syringe inserted through a rubber stopper in one of the necks, however, can be used to pressurize the solution and restore electrical contact. An Orion calomel reference electrode (model 13-639-52) is inserted into the solution by means of a rubber stopper in the second neck of the flask. Finally, both the reference and chloride electrodes are connected to a pH meter or electrometer.

Samples are loaded into the adapter

with an Oxford Micro-Pipetter with disposable plastic tips. The presence of air bubbles at the base of a hole can interfere with the electrical contact, and care is therefore required in pipetting the solution. To retard evaporation, a plastic microscope cover slide with an ~ 1.5 -mm hole is placed over the samples, and the capillary tip is inserted into the sample through the hole. After each measurement, the tip is washed with distilled water and wiped before insertion into a new sample. When all samples in the adapter have been measured, the solutions are removed by inserting absorbent paper into the hole. Each hole is then washed with distilled water and blotted dry before refilling with a new sample.

Results. The electrode assembly with a 4-hole adapter was calibrated with a series of HCl standards ranging in concentration from 0.01 to 0.00012 m . Sample size was 10 μl , but sample sizes as small as 3 μl are feasible (Vogel and Brown, 1978). After the holes were filled with the standards, a period of 10 min was allowed for equilibration.

The results of one calibration are shown in Fig. 179. Measured emf is plotted vs. $\log m_{Cl^-}$ for the range of standards, based on a single measurement of a given standard in a given hole. The numbers above the data points refer to hole numbers. The concentration range for linear response and the slope of the curve (59.0 mV/ $\log m$ unit) agree very well with the manufacturer's performance specifications for the chloride electrode used in the conventional manner for large sample sizes.

A second series of calibration runs was carried out in order to determine the scatter in measurement and to test for systematic differences between holes. The standard deviation for measurements with the same HCl concentration in all four holes increased systematically, from 0.5 mV at $\log m_{Cl^-} = -2.0$, to 1.9 mV at $\log m_{Cl^-} = 3.92$. In addition, small systematic differences on the order of 1 mV were found between holes.

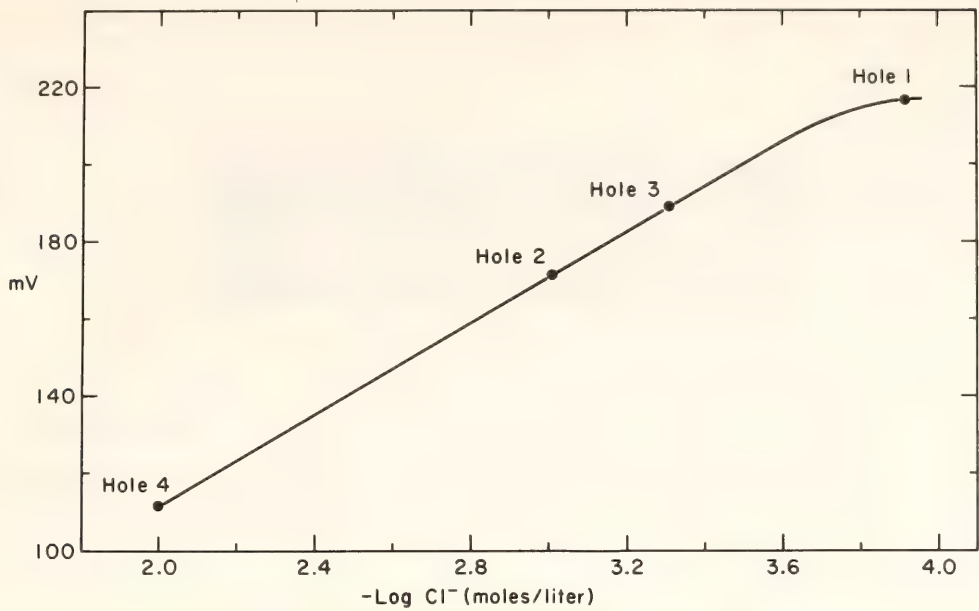


Fig. 179. Results of calibration measurements for the chloride electrode with HCl standards. Numbers refer to hole in which measurement was made.

Flow-Cell Colorimetric Technique

The design and operation of a flow-cell colorimeter for sample sizes in the 1–5 μl range has been discussed by Frantz and Hare (*Year Book 72*, pp. 704–706). A

schematic diagram for the system is shown in Fig. 180. A constant flow of the complexing reagent is pumped through Teflon tubing into a flow colorimeter. Samples are injected into the system from a Dade disposable microliter pipette in-

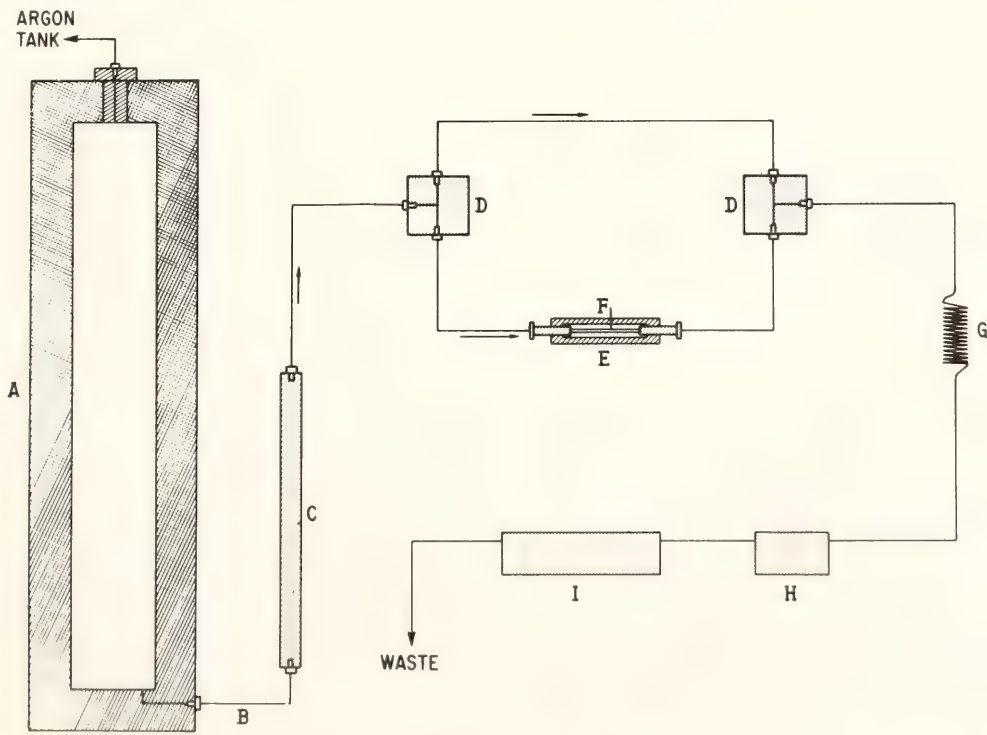


Fig. 180. Schematic diagram of the flow system: (A) Reagent reservoir; (B) Teflon tubing; (C) flow meter; (D) 3-way valve; (E) sample injector; (F) Dade micropipette; (G) 40-foot coil of tubing; (H) 6-mm colorimetric cell; (I) 60-mm colorimetric cell.

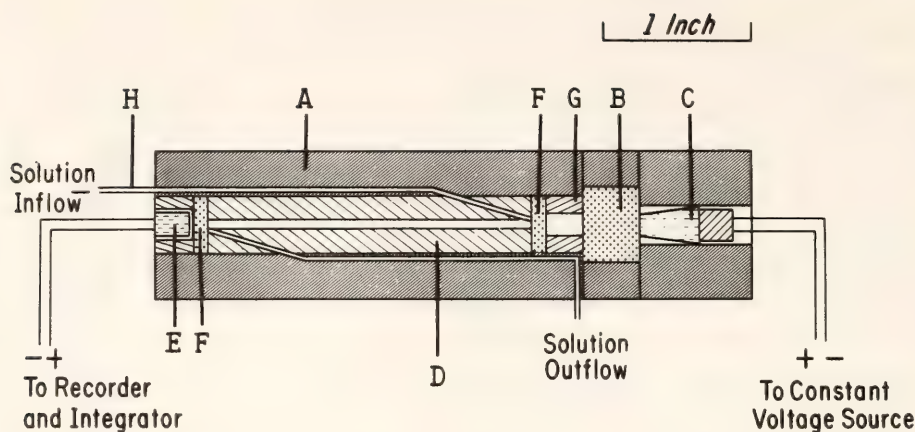
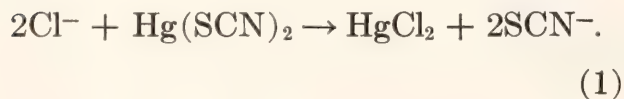


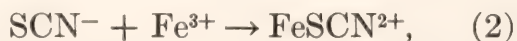
Fig. 181. Schematic diagram of colorimetric cell: (A) Delrin body; (B) interference filter; (C) focusing miniature lamp; (D) black Teflon cylinder, inner surface lined with Teflon tubing; (E) photoconductor cell; (F) clear glass plate; (G) Delrin screw; (H) Teflon tubing.

serted into the stream. During the insertion of a sample, the flow is diverted from the injector by two three-way valves. The sample is mixed with the complexing reagent in a 40-foot coil of tubing before entering the colorimeter. A diagram of the colorimeter itself is shown in Fig. 181. The specifications of all components in the system have been given by Frantz and Hare (*Year Book 72*, pp. 704–706). Output from the photoconductor cell is monitored on a strip chart recorder in parallel with an integrator.

Use of the system for chloride determinations requires only selection of the proper complexing reagent and corresponding interference filter. The standard chloride colorimetric technique utilizes mercuric thiocyanate and ferric nitrate reagents (Gaddy, 1966; Iwasaki *et al.*, 1956). Mercuric thiocyanate reacts with chloride ions to liberate thiocyanate ions:



Thiocyanate ions in turn react with Fe^{3+} ions to form the ferric thiocyanate complex:



which has an absorption maximum at

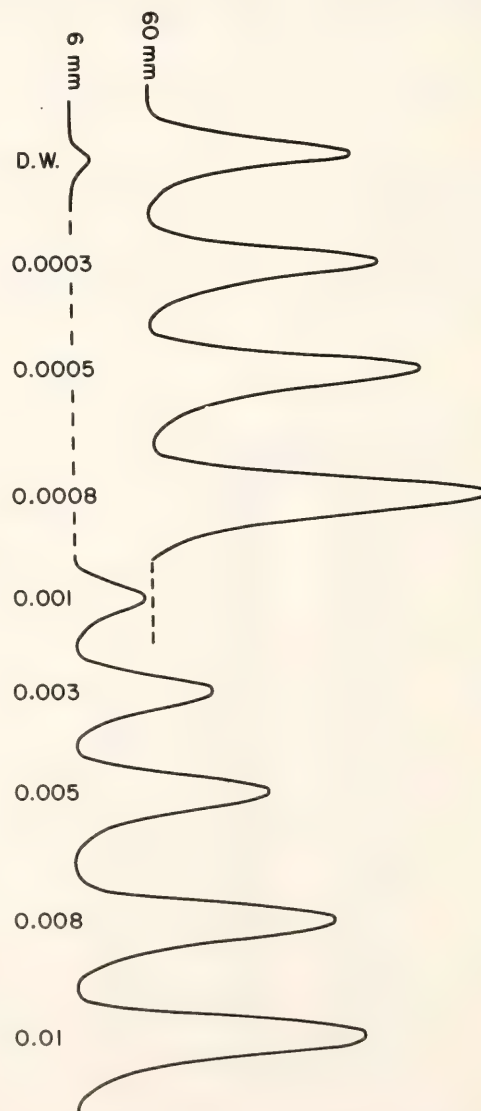


Fig. 182. Strip-chart response to HCl standards. D.W. = distilled water.

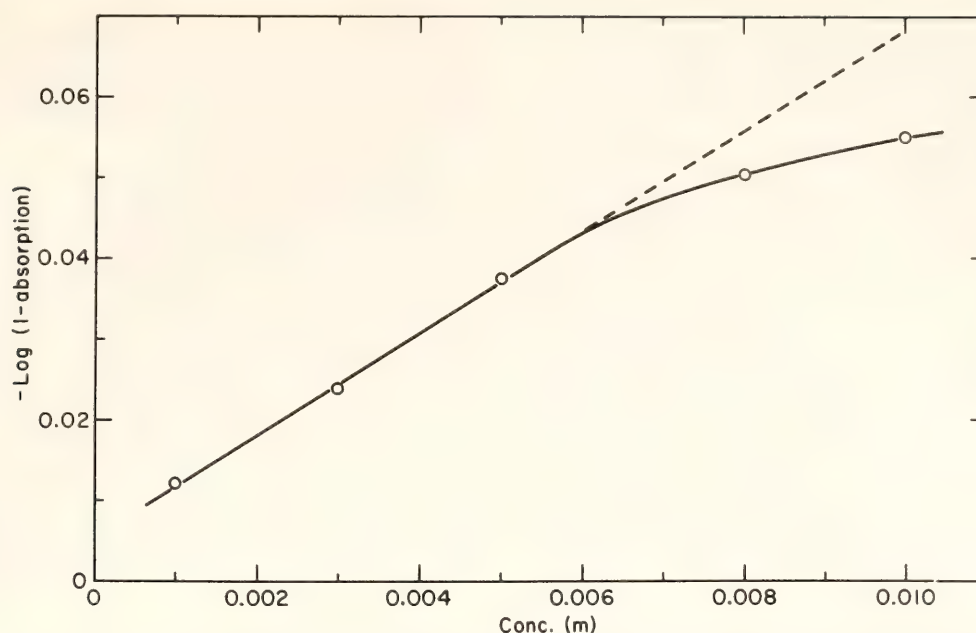


Fig. 183. Plot of absorbance vs. concentration (molality) for HCl standards. Absorbance = $-\log(1 - \text{absorption})$.

480 $m\mu$. Mercuric Thiocyanate Saturated Solution and Ferric Nitrate, 20.2%, both commercially available from Fisher Scientific Co., were premixed in 1:1 volume proportions immediately prior to each series of analyses and added to the reservoir.

Results. The system was calibrated with the same set of HCl standards used to calibrate the chloride electrode. A sample size of 3 μl was used in both 6-mm and 60-mm flow cells with interference filters of $465 (\pm 30)$ $m\mu$. The strip chart response for absorption for a series of standards is shown in Fig. 182. The absorbance for this same series of standards based on the integrator output is shown in Fig. 183. The standard deviation for integrated peak areas is approximately 3% of the total area. Beer's Law of behavior is observed for the lower concentration standards. The range for linear response could be expanded to the higher concentration range by using a smaller sample size, a shorter flow cell, or both.

Conclusions

Both techniques described above extend the range of accurate and precise chloride

measurement to approximately 10^{-4} molal chloride. These improved analytical techniques are required for a study of calcium complexing in the system $\text{CaO-SiO}_2\text{-H}_2\text{O-HCl}$ currently in progress. An analogous study of magnesium complexing using the chloridometer for chloride analyses is given by Frantz and Popp (this Report).

PROBLEMS IN THE USE OF EVACUATED, SEALED SILICA TUBES FOR SYNTHESIS OF SINGLE-PHASE COMPOSITIONS IN THE SYSTEM $\text{FeO-Fe}_2\text{O}_3\text{-TiO}_2$

Charles Lawson*

In the system $\text{FeO-Fe}_2\text{O}_3\text{-TiO}_2$, the role of oxygen fugacity (f_{O_2}) in determining phase compositions for coexisting ilmenite-hematite and magnetite-ulvöspinel solid solutions is well known (Buddington and Lindsley, 1964; Lindsley, *Year Book 61*, pp. 100-106, *Year Book 62*, pp. 60-66, *Year Book 64*, pp. 144-148). Control of

* Work carried out under a cooperative predoctoral fellowship program between the Geophysical Laboratory and Princeton University.

f_{O_2} , therefore, is of utmost importance in experiments designed to study the properties of these phases. One of the most widely used experimental techniques for synthesis of single-phase Fe-Ti oxides (as well as for synthesis experiments in other systems) involves holding the charge in a silica glass tube that has been evacuated and sealed prior to heating (Hoffman, 1975; Lindsley, *Year Book 61*, pp. 100–106; Warner *et al.*, 1972). For this method to be useful in synthesizing single-phase Fe-Ti oxides, all components including oxygen must be present in stoichiometric proportions for the composition of interest before the charge is placed in the silica glass tube. During the experiment, assuming that the glass tube remains sealed, the f_{O_2} is controlled by the phase assemblage in the charge, which in turn depends on the amount of oxygen present initially.

This report presents data on attempts to synthesize single-phase compositions along the ilmenite-hematite solid-solution join. These samples were to be used in experiments designed to delineate the relationship between cation ordering, magnetic properties, and temperature of heat treatment for minerals on this join.

Experimental Methods

Commercially available Fe_2O_3 , TiO_2 , and Fe metal (purity > 99.99%) were used as the starting materials. The Fe_2O_3 and TiO_2 were dried for 1 hr at 800°C and overnight at 1000°C to drive off any absorbed water. The Fe metal was stored in a vacuum desiccator to minimize oxidation. The Fe was analyzed for oxygen by Lindsley using the method described in Turnock *et al.* (1973). The amount of oxygen in the Fe metal was then taken into account when weighing out proportions of Fe and Fe_2O_3 for a given composition. The Fe_2O_3 and TiO_2 were ground under alcohol in an agate mortar for approximately 6 hr, after which the Fe

metal was added and mixed for another hour. This technique was used to try to insure homogeneity but minimize oxidation of the Fe metal.

Approximately 2 g of charge were wrapped in Ag foil and put into the silica tube, and the whole assembly was evacuated to approximately 10^{-3} torr and sealed. Charges were held at 900°C for about 7 days initially, after which they were reground for 1 hr under alcohol and heated at 900°C for another 7 days. The charges were then analyzed using reflected light microscopy, powder x-ray diffraction, electron microprobe, and Mössbauer-effect apparatus.

Results

Eleven compositions along the ilmenite-hematite solid-solution join between $Ilm_{40}Hem_{60}$ and $Ilm_{90}Hem_{10}$ in 5 mole % increments were synthesized using the “evacuated silica tube” method. The quenched charges are porous, sintered aggregates of fine-grained material. Grain size ranges from about 1 μm up to about 10–15 μm , with an average size of about 5 μm . In reflected light, the samples are homogeneous and no exsolution is present. Under plane light, there are patches up to 20 μm across that appear to be single grains. With the polarizers crossed, it is seen that these patches are actually aggregates of finer-grained particles.

Electron microprobe analyses were performed on the larger aggregates (Table 57). Between 5 and 23 spots were analyzed for each composition; the number of spots analyzed was highly variable because some of the more porous samples had very few aggregates of sufficient size to obtain suitable analyses. The amount of ferric iron present was calculated assuming that the phases were stoichiometric, using the method of Carmichael (1967). The analyses are not totally satisfactory because in each case the total wt % is low, even after correcting for

TABLE 57. Comparison of Electron Microprobe Analyses with Theoretical Analyses for Synthetic Ilmenite-Hematite_{ss}

Starting Composi- tions	No. of Spot Anal.	Ave. Measured TiO ₂ (wt%)	Theor.* TiO ₂ (wt%)	Ave.† Recalc. FeO (wt%)	Theor.* FeO (wt%)	Ave.† Recalc. Fe ₂ O ₃ (wt%)	Theor.* Fe ₂ O ₃ (wt%)	Ave. Total (wt%)	Ave. Ilm: Hem	Probe Calc. Fe ³⁺ /ΣFe	Theor.* Fe ³⁺ /ΣFe	Möss- bauer-† Calc. Fe ³⁺ /ΣFe
Ilm ₄₀	14	20.4 (0.7) §	20.42	18.3 (0.7)	18.36	58.2 (0.9)	61.22	97.6 (2.0)	41.2 (0.8)	0.740	0.750	...
Ilm ₄₅	20	23.5 (1.0)	23.03	21.2 (0.9)	20.71	53.3 (1.6)	56.26	98.0 (1.2)	46.9 (1.7)	0.694	0.710	...
Ilm ₅₀	23	25.6 (1.1)	25.65	23.0 (1.0)	23.07	47.1 (1.4)	51.28	96.2 (2.7)	52.1 (1.1)	0.648	0.667	...
Ilm ₅₅	18	28.2 (0.6)	28.29	25.4 (0.5)	25.44	44.4 (1.0)	46.27	98.3 (1.1)	56.0 (0.9)	0.611	0.621	...
Ilm ₆₀	14	30.9 (0.3)	30.94	27.9 (0.3)	27.83	40.2 (0.9)	41.23	99.3 (0.7)	60.6 (0.7)	0.565	0.571	...
Ilm ₆₅	17	33.4 (1.0)	33.61	30.1 (0.8)	30.22	33.0 (1.5)	36.17	96.8 (1.1)	66.9 (1.5)	0.497	0.518	...
Ilm ₇₀	13	36.3 (0.8)	36.29	32.6 (0.8)	32.63	29.8 (1.3)	31.08	98.7 (1.3)	70.9 (1.2)	0.451	0.461	...
Ilm ₇₅	10	37.6 (0.6)	38.98	34.0 (0.8)	35.05	24.5 (1.1)	25.97	96.6 (0.8)	75.5 (1.2)	0.393	0.400	...
Ilm ₈₀	8	41.8 (1.6)	41.69	37.7 (1.4)	37.48	16.7 (1.7)	20.83	96.1 (1.9)	83.4 (1.8)	0.285	0.333	0.267
Ilm ₈₅	5	41.2 (1.2)	44.41	37.2 (1.1)	39.93	16.3 (1.6)	15.66	94.9 (1.0)	83.5 (1.8)	0.283	0.261	0.220
Ilm ₉₀	7	47.1 (1.2)	47.14	42.3 (0.9)	42.93	7.5 (0.8)	10.47	97.4 (1.6)	92.7 (0.9)	0.137	0.182	0.150

* Theoretical wt % and Fe³⁺/ΣFe calculated for the desired starting compositions.
† FeO and Fe₂O₃ wt % calculated from the microprobe analyses using the method of Carmichael (1967).
‡ Fe³⁺/ΣFe calculated from Mössbauer data only for those compositions that are paramagnetic at room temperature (see text).
§ Values in parentheses are standard deviations.

ferric iron* The average total wt % for the various compositions ranges from 94.9% to 99.3%. Several systematic variations in the analyses suggest that the data are at least semiquantitatively significant. First, all compositions, as determined by the microprobe, are more ilmenite-rich than the composition calculated for the starting mixtures, except for the $\text{Ilm}_{85}\dagger$ composition (which is also the composition giving the lowest average total wt % of 94.9%). The calculated $\text{Fe}^{3+}/\Sigma\text{Fe}$ for all these compositions is lower than the theoretical $\text{Fe}^{3+}/\Sigma\text{Fe}$ for the corresponding starting composition. Second, the average TiO_2 wt % measured for every composition except Ilm_{75} and Ilm_{85} is within 0.5 wt % of the theoretical value for the corresponding starting composition.

Determinative curves for estimating composition from powder x-ray diffraction data (Lindsley, *Year Book 62*, pp. 60–66) were also used to check the composition of the charges. Although this method is more qualitative than electron microprobe analysis, the compositions as determined by both methods agree within 2 mole %. Peaks other than those that were assigned to the ilmenite-hematite_{ss} phase were identified in some of the x-ray charts. These peaks were assigned to a magnetite-ulvöspinel_{ss} phase. In all cases, the extra peaks were very small indicating that the magnetite was present in amounts less than 5 vol %.

Room temperature Mössbauer spectra

* Samples were analyzed for SiO_2 , Al_2O_3 , MnO , MgO , CaO , and Cr_2O_3 in addition to TiO_2 and FeO . In no cases were the amounts of minor impurities (SiO_2 and Al_2O_3) large enough to account for the low total weight percentages. Results of electron microprobe analyses on samples synthesized in gas-mixing furnaces, where the grain size of the products ranged from 40 to 90 μm , show in every case a total wt % between 99 and 101 wt %. The low total wt % for samples synthesized in silica tubes may be a function of the small grain size and the resulting porosity of the spot analyzed.

\dagger $\text{Ilm}:\text{Hem}$ compositions (see Table 57) are given in mole %, calculated from oxide wt % determined by electron microprobe analysis.

were obtained on all the compositions. Compositions more hematite-rich than about $\text{Ilm}_{75}\text{Hem}_{25}$ are magnetic (Ishikawa and Akimoto, 1957), resulting in very complex Mössbauer spectra owing to magnetic hyperfine splitting. Compositions more ilmenite-rich than $\text{Ilm}_{75}\text{Hem}_{25}$ are paramagnetic at room temperature. Spectra for these compositions consist of two overlapping doublets owing to the presence of both Fe^{2+} and Fe^{3+} (one doublet for each species; see Fig. 184). Despite the fact that separation of the doublets is not complete, it is possible to determine $\text{Fe}^{3+}/\Sigma\text{Fe}$ from the spectra using constraints of the line parameters (width, or intensity of the peaks, or both). It is desirable to apply as few constraints as possible to minimize the amount of bias introduced into the fit of the spectra. In the fits for the Ilm_{80} , Ilm_{85} , and Ilm_{90} samples, the intensities of the two ferrous peaks are constrained to be equal. Mössbauer spectra of Ilm_{100} specimens have two peaks of equal intensities (Shirane *et al.*, 1962) and this is probably a reasonable constraint for ilmenite-rich phases (D. Virgo, personal communication). The $\text{Fe}^{3+}/\Sigma\text{Fe}$ calculated from the spectra for the Ilm_{80} , Ilm_{85} , and Ilm_{90} samples are all lower than the theoretical $\text{Fe}^{3+}/\Sigma\text{Fe}$ (Table 58). These results are consistent with the results of the electron microprobe analyses (except for the Ilm_{85} microprobe analysis, which has the most uncertainty). It can be seen in Fig. 184 that additional peaks are present on the positive-velocity side of the Ilm_{80} spectra. Although these peaks are too small to be treated quantitatively, their presence is consistent with the presence of a second, magnetic phase in the sample in small amounts ($\sim 5\%$).

Discussion

Examination of the results leads to the conclusion that there is a small amount (probably $\sim 5\%$) of a second phase present in addition to the ilmenite-hematite solid solution. The small extra peaks

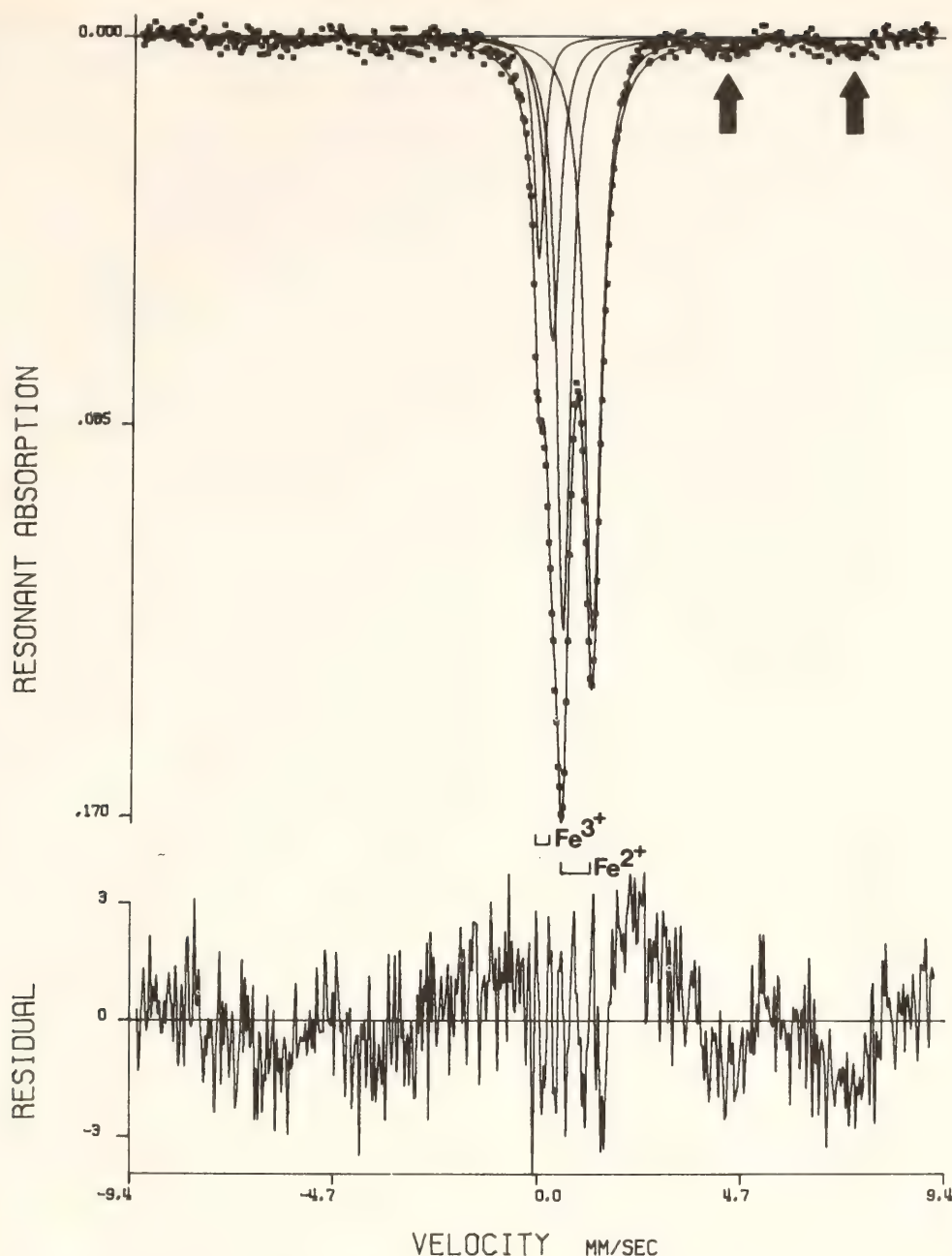


Fig. 184. The $^{57}\text{Mössbauer}$ spectrum at 298°K of the sample with a starting composition of $\text{Ilm}_{80}\text{-Hem}_{20}$. The absorption data were fitted to four lines of Lorentzian shape, as shown in the legend below the spectrum. The two peaks due to the presence of an additional phase are indicated by the arrows (see text for explanation).

on the x-ray charts suggest that the second phase is a magnetite-ulvöspinel solid solution. The additional peaks on the Ilm_{80} Mössbauer spectra can also be explained by the presence of a small amount of a magnetite-ulvöspinel solid solution. The Mössbauer spectrum of pure magnetite consists of two Zeeman splitting patterns (containing six peaks each); one pattern results from iron in the A site

and the other from iron in the B site (Sawatzky *et al.*, 1969). In the negative-velocity region of the spectrum the two patterns can be resolved, whereas in the positive-velocity region the two patterns are superimposed. As a result, the two peaks in the high positive-velocity region are the most intense in the spectrum. In the Mössbauer spectrum of a sample containing only small amounts of mag-

netite, it would be expected that only the two most intense peaks would be easily recognized.

It is not clear what process is responsible for the change from starting material of a given composition on the ilmenite-hematite solid solution join to products having more ilmenite-rich compositions and a small amount ($\sim 5\%$) of magnetite-ulvöspinel. Assuming that the Fe-Ti ratio is constant, then the charge appears to have lost oxygen and is reduced relative to the desired starting composition. One possible explanation is that there was an error in the preparation of the starting materials. If there is any error it must be systematic, because all compositions are reduced relative to the starting composition. The main source of error may be the value used for the oxygen content of the Fe metal. If the Fe metal really contains less oxygen than the value used when calculating proportions of starting materials needed, then the starting material will be reduced relative to the desired starting compositions. Calculations were made assuming the most-reducing situation (i.e., where the Fe metal contains no oxygen). The results indicate that for many compositions this reducing effect is inadequate to account for the $\text{Fe}^{3+}/\Sigma\text{Fe}$ calculated from the microprobe analyses and the Mössbauer

spectra. In particular, the calculations for the Ilm_{80} , Ilm_{85} , and Ilm_{90} samples yield $\text{Fe}^{3+}/\Sigma\text{Fe}$ of 0.309, 0.234, and 0.152, respectively. These compare with $\text{Fe}^{3+}/\Sigma\text{Fe}$ values of 0.267, 0.220, and 0.150, respectively, for Ilm_{80} , Ilm_{85} , and Ilm_{90} calculated from the Mössbauer spectra. Another possible explanation may be related to the lack of direct control on the f_{O_2} imposed on the charge using the evacuated, sealed glass tube method of synthesis. If the glass tube is not a closed system with respect to oxygen, then the bulk composition of the charge will change.

In any event, it is clear that the evacuated, sealed silica glass tube method for synthesis of single-phase ilmenite-hematite minerals yields small amounts of a magnetite-ulvöspinel_{ss} phase. Studies designed to determine the relationship between cation ordering and magnetic properties (using techniques such as the Mössbauer-effect and various magnetic tests) must start with single-phase minerals of known composition. The presence of a small amount of a second phase in such studies can lead to erroneous results. Results of cation ordering and magnetic studies where starting materials are synthesized using the evacuated, sealed silica glass tube method must be interpreted with caution.

STAFF ACTIVITIES

Field Studies

Boyd organized the Second International Kimberlite Conference, held in September 1977, and the associated field trips in Colorado, Wyoming, New Mexico, and Arizona. Participants from the Geophysical Laboratory, in addition to *Boyd*, were *Davis*, *Finnerty*, *Mysen*, and *Wendlandt*. A more detailed account of the conference appears elsewhere in this Report.

Estep collected phytoplankton from Chesapeake Bay in November and from Delaware Bay in June. The hydrogen

isotopic ratios of these samples will be used as a basis for interpreting the isotopic ratios of organic matter in sedimentary rocks.

Finnerty, *Harrison*, *Verwoerd*, and *Wendlandt* joined a field trip in June from The Pennsylvania State University and the University of Massachusetts to the Oka carbonatite complex near Montreal, Canada. The purpose of the trip, in addition to familiarizing the participants with the geology of the complex, was to collect samples for research on opaque phases and micas and on the role of liquid im-

miscibility in carbonate-alkali silicate magma genesis. The trip was organized and led by D. P. Gold of The Pennsylvania State University, and participants included D. H. Eggler and students from that university, S. Haggerty and students from the University of Massachusetts, and A. N. Mariano, Consulting Geologist, from Carlisle, Massachusetts.

Hazen continued pursuing his interest in paleontology by collecting Paleozoic fauna from localities in Montana, Virginia, Pennsylvania, Ohio, and Maryland.

Irvine visited the Stillwater Complex in Montana in August to examine the various layer sequences and chromite deposits in this ultramafic-gabbroic intrusion. During part of the time he was guest of the Johns Manville Company, which has, under the direction of Dr. E. L. Mann, defined a platinum-rich horizon that extends over much of the 30-mile length of the complex.

Popp participated in a field trip in December to the Wichita Mountains, Oklahoma, to examine the structure and igneous rocks of that area. The trip was led by M. C. Gilbert of the Virginia Polytechnic Institute and State University.

Rumble and *Spear* continued their studies of metamorphosed volcanic and sedimentary rocks in west-central New Hampshire and east-central Vermont throughout the summer of 1977. They collected additional samples for petrographic, chemical, paleontological, and isotopic investigations. Results relating to this work are described elsewhere in this Report in articles by *Spear* on the petrology of some of the rocks, by *Spear*, *Hazen*, and *Rumble* on a possibly new silicate mineral (a sodium biotite), and by *Rumble*, *Hoering*, and *Boucot* on some highly metamorphosed fossils.

Van Valkenburg and *Yagi* participated in an eight-day field trip in May on the Colorado River through the Grand Canyon area. The trip covered a distance of 240 miles from Lee's Ferry to Diamond

Creek, and particular attention was given to the great unconformity at the top of the Early Precambrian and its relationship to the contact between the Late Precambrian and Early Cambrian sediments.

Kimberlite Conference

The Second International Kimberlite Conference, September 24 through October 10, 1977, brought 180 earth scientists together for a series of meetings and field trips in four Southwestern states. Among the participants from 16 countries were 24 present and past associates of the Geophysical Laboratory. Staff members F. R. Boyd, G. L. Davis, A. A. Finnerty, B. O. Mysen, and R. Wendlandt all contributed papers.

The conference opened in Little Rock, Arkansas, with a one-day visit to the Prairie Creek kimberlite. This is the only kimberlite in North America that has been commercially exploited for diamonds, and the site is now a state park. The group then flew to Colorado, where they spent two days in the Front Range studying and collecting kimberlites in the State Line district south of Cheyenne, Wyoming.

The conferees then traveled by rafts down the San Juan River through the San Juan Canyon to visit the Mule Ear diatreme on the northern edge of the Navajo reservation. Another three days were spent in field work on the Navajo kimberlites and at a basalt nodule locality in the Puerco Plugs area north of Albuquerque.

The formal scientific sessions were held at Bishop's Lodge, near Santa Fe. In the course of a week over a hundred papers were presented. Among the highlights were the descriptions by Soviet delegates of newly discovered diamondiferous harzburgite nodules from the Udachnaya pipe in Siberia. These strongly depleted peridotites appear to be the host rocks for most natural diamonds, and it now seems probable that diamonds are only ac-

cidental inclusions in kimberlites. After the formal meeting, the group went to Kilbourne Hole, New Mexico, where they collected thousands of pounds of ultramafic nodules. On the next day participants visited Peridot Mesa on the San Carlos Apache Reservation, probably the most spectacular ultramafic nodule locality in the world. After visiting nodule localities at Chino Valley and Williams, Arizona, the group finally dispersed at the Grand Canyon. Discussions at the conference, and the many specimens collected, should stimulate research on kimberlites and upper-mantle rocks for several years.

Conference on Mineral Physics

Relationships between Bonding and Physical Properties of Minerals. Experimental and theoretical investigations into the relationships between interatomic forces and physical properties of minerals are central to current problems in the earth sciences. Effects are fragmented, however, in the sense that relevant research is being conducted by specialists in different disciplines, such as crystallography, spectroscopy, and physical chemistry, with little coordination or cooperation among researchers with different backgrounds and objectives. In the belief that there are many points of common interest involving those interactions between atoms that determine the physical properties of minerals, a conference on mineral physics was held at Airlie House, Warrenton, Virginia, on October 17–19, 1977. Five scientific sessions, as well as informal discussions, afforded maximum interaction among participants with diverse backgrounds.

Eighty scientists from Europe and North America attended the conference, which was convened by C. T. Prewitt (SUNY, Stony Brook) and R. M. Hazen (Geophysical Laboratory). Other Geophysical Laboratory participants were P. M. Bell, L. W. Finger, H. K. Mao, S. K. Sharma, A. Van Valkenburg, D. Virgo,

T. Yagi, and H. S. Yoder, Jr. The conference received generous financial support from the National Science Foundation and the Carnegie Institution of Washington.

Although the most fundamental understanding of the forces between atoms can come only through the use of quantum theory, much useful information has been obtained from the application of empirical models to chemical bonding. The first session was devoted to the successes and failures of this empirical approach, and included lectures on empirical bond valences, electrostatic energy calculations, and electric field gradient calculations. Empirical bond valences (bond strengths) can be used to provide insight into mineral structures. Analytical expressions are used to fit experimental data with curves relating bond strength to bond length, and these curves may in turn be used to predict bond lengths in other structures. When properly applied, Born-Mayer-type electrostatic equations may be used to calculate useful information such as the orientation of water molecules in mineral hydrates. The formal part of this session concluded with a comparison of electric-field gradient and electrostatic energy calculations, and a description of new approaches to calculating electric-field gradients in predominantly ionic crystals.

The second session included presentations on aspects of the electronic structure, geometric structure, stabilities, and cohesive properties of minerals; the lecturers used molecular quantum mechanical models and quantum mechanical methods applicable to bulk solids. Electronic structure calculations for hydrogen-bonded systems may provide accurate dimerization energies and geometries, and are also models for more complex systems. Semi-empirical MO calculations lead to predictions of accurate Si-O-Si angles in two-repeat tetrahedral silicate chains and in the SiO₂ polymorphs. Cluster calculations are also used for prediction of orbital-binding energies measured by

photoelectron and optical spectroscopy for a number of oxide and sulfide minerals. Band-structure calculations on K are in agreement with experimental measurements of the variation of resistivity and compressibility with pressure; results for MgO indicate an increasing band gap with increased pressure. The modified electronic gas method is employed for prediction of bond lengths, bond energies, and compressibilities for alkali halides, MgO and CaO. The role of orbitals in the bonding of second-row tetrahedral oxyanions is smaller than previously believed, although *d* orbital contributions are important in x-ray emission spectra. Approximate MO theory may also be used to explain the effect of various network modifiers upon Si-O bonds in silicate melts.

Electronic and magnetic effects of metal-metal interactions in minerals were the subject of the third session. Magnetic interactions correlate directly with Fe-Fe and Ti-Ti pairs or dimers. The resulting charge-transfer absorption features in the visible region also correlate with metal-metal interactions, and are distinct from other optical spectral features. Charge-transfer transitions in minerals may also result from metal-oxygen interactions. Examples of systematic spectral changes with pressure were described, and interactions were demonstrated to become more intense as interatomic distances are reduced. Charge-transfer effects, and metal-metal and metal-oxygen interactions in general, have a significant effect on the electrical, optical, and magnetic properties of minerals. Recent results were reported on the loss of remnant magnetism of iron sulfide and iron oxide minerals at high pressure.

The geophysicists made their principal contributions in the fourth session. Review papers included experimental techniques used to measure the elastic properties of solids as a function of pressure and temperature, empirical relationships between elastic and other physical properties of minerals, and theoretical equa-

tions of state and bonding in oxides and silicates. Most experimental determinations of single-crystal elastic moduli have been made by ultrasonic techniques with a precision of 0.01% at $P \leq 10$ kbar and $T \leq 1000^\circ\text{C}$ (usually not simultaneously) on specimens of 3–5 mm dimensions. Brillouin-scattering techniques are used for measurements of these moduli on specimens as small as 100 μm with a precision of 1% at pressures up to 50 kbar using a diamond-anvil cell. Volume-compression data are now available from static techniques to 100 kbar in liquid and 300 kbar in solid media and from shock-wave techniques to megabar pressures. Static data in solid media, however, are suspect owing to the presence of nonhydrostatic stress, and uncertainties in the reduction of the shock-wave data tend to offset the increase in pressure range.

Systematic relationships established from empirical data for elastic and crystallographic properties of minerals have proved useful in the construction and interpretation of geophysical models for the elastic velocity and density profiles within the Earth. Such relationships (e.g., Birch's law) are now known to lack universal applicability, and it is important that future work pay closer attention to crystallographic details.

On a theoretical basis, finite strain equations of state provide little insight into bonding in minerals because they are based on arbitrary definitions of strain. Lattice dynamical approaches incorporate the effects of structure and bonding, but need to be extended beyond the two-body rigid-ion model to include noncentral forces known to be present in most minerals. Quantum-mechanical equations of state are the most fundamental, but some approximations are still required to solve the wave equation. Although the quantum-mechanical models may be difficult to apply for nonmetals, they provide guidance for physical parameterization of the atomistic models. Future progress in elasticity studies will require the combined talents and efforts of crystallographers,

solid-state physicists, and quantum chemists, as well as geophysicists.

The fifth session was devoted to aspects of phase transformations, order-disorder processes, and experimental diffraction techniques, which help in understanding bonding in minerals. Perovskites crystallize in more than 30 variant structures characterized by displacements of cations from polyhedral centers and tilting of octahedra. Transformations among these variants may be first or second order, and some are ferroelectric/antiferroelectric transitions. Silicate perovskites are stable high-pressure phases and, therefore, possible mantle minerals; the silicate perovskite structure variants at high pressure are not known, however, nor is it known how physical properties of noncubic perovskites deviate from the ideal cubic form.

Ordering and disordering of aluminosilicates is greatly enhanced by the presence of H_2O , suggesting that H^+ ions may attach bridging oxygens and temporarily break Si-O and Al-O bonds. Arguments of Loewenstein (1954) are insufficient to explain his aluminum-avoidance rule; electrostatic lattice calculations were used to demonstrate that potential energy is minimized in structures with the fewest Al-O-Al bonds.

X-ray diffraction experiments are sensitive to the electron distribution in a crystal and may provide information on bonding. Neutron and high-angle x-ray diffraction data may be used to define atomic nuclei positions and thermal smearing parameters, whereas low-angle x-ray data include nonspherical electron effects such as lone pairs and bonding electrons. Difference electron densities computed from all data may be examined for nonspherical electron effects. Thermal smearing functions also yield information about the dynamics of atomic motion. For rigid groups of atoms in a structure (e.g., CO_3^{2-} or SiO_4^{4-}), thermal motion parameters corresponding to group vibrations may be refined. Mean-square displacements can be changed into a frequency of

vibration for comparison with lattice-mode absorption in the infrared and Raman spectra.

A major objective of the Mineral Physics Conference was to bring together researchers who, though interested in similar problems, had not interacted because of the diversity of their backgrounds. Upon the conclusion of the three-day meeting, participants were more aware of the variety of approaches available for studying bonding in minerals. The success of the Mineral Physics Conference will be measured by the new interdisciplinary approaches that it inspired.

Petrologists' Club

Seven meetings were held during the sixty-seventh year of the Petrologists' Club. The lectures presented were:

"Design and application of hydrothermal solubility experiments," by David Crerar (Princeton University), October 18, 1977.

"Granitoids of Southeastern Australia—The concept of S- and I-types," by A. J. R. White (Pennsylvania State University/Latrobe University), November 22, 1977.

"Compositional heterogeneity of the mantle: isotopic and trace element evidence," by Albrecht Hofmann (Department of Terrestrial Magnetism), December 6, 1977.

"Constraints on the composition of the core of the Earth and its chemical equilibrium with the mantle," by Robin Brett (U.S. Geological Survey), January 17, 1978.

"Minerals at 20,000,000 \times : petrologic problems and potentials," by Peter R. Buseck (Arizona State University), February 14, 1978.

"The nature of silicate melts," by Paul C. Hess (Brown University), March 21, 1978.

"Elasticity and crystallography of phase transformations," by Robert C. Liebermann (State University of New York at Stony Brook), April 25, 1978.

Washington Crystal Colloquium

The Washington Crystal Colloquium, an informal group of crystallographers from the Washington area, met five times during the report year. The following lectures were presented:

"Diterpenoid alkaloids, chemical and structural aspects," by Wilson De Camp (University of Georgia), October 28, 1977.

"RATFOR (Rational Fortran), is it the 'software tool' of the future?" by J. M. Stewart (University of Maryland), December 2, 1977.

"Single-crystal diffraction experiments at high pressure with the miniature diamond cell," by Robert M. Hazen and Larry W. Finger (Geophysical Laboratory), February 10, 1978.

"A mineralogist's view of the 'asbestos' and health problems," by Malcolm Ross (United States Geological Survey), April 14, 1978.

"Biological paracrystallinity," by Albert Hybl (University of Maryland School of Medicine), May 19, 1978.

Seminar Series

The seminar series met twelve times during the report year. The following lectures were presented:

"New petrologic data bearing on the origin of the Vrdefort Structure, South Africa," by W. Schreyer (University of Bochum, Germany), October 13, 1977.

"Reactions among Ca, Mn-carbonates and Ca, Mn-silicates in regionally metamorphic Mn deposits," by T. J. Peters (University of Bern, Switzerland), October 21, 1977.

"Raman spectroscopy at ambient and very high pressures & applications to liquids, glasses and solids," by S. K. Sharma (Geophysical Laboratory), October 27, 1977.

"Parageneses of diamonds in Yakutian kimberlites," by N. V. Sobolev (Novosibirsk, USSR), November 2, 1977.

"Geochemistry of tin," by Gunter Moh

(University of Heidelberg, Germany), November 22, 1977.

"Some aspects of the geochemistry and genesis of granitoids," by Allan White (Pennsylvania State University), November 23, 1977.

"High-resolution TEM: (a) sheet silicates and (b) image calculations," by Peter R. Buseck (Arizona State University), February 15, 1978.

"Subsolidus relations of the Skaergaard pyroxenes studied by analytical electron microscopy," by Nobuo Morimoto (Osaka University, Japan), March 21, 1978.

"The Allende meteorite: fremdlinge and their noble relatives," by Ahmed El Goresy (Max-Planck-Institute für Kernphysik, Heidelberg, Germany), March 23, 1978.

"How alkaline magmatism fits in with plate tectonics," by Wilhelm Verwoerd (University of Stellenbosch, Republic of South Africa), March 30, 1978.

"Synthesis, stability, polarized spectra and structure of Mn^{3+} -andalusites (viridines)," by K. Langer (University of Bonn, Germany), April 7, 1978.

"The system $\text{CaMgSi}_2\text{O}_6$ - $\text{CaAl}_2\text{SiO}_6$ - $\text{CaTiAl}_2\text{O}_6$ - $\text{CaFe}^{3+}\text{AlSiO}_6$, and its significance for Ca-Al-rich inclusions in carbonaceous chondrite," by Kenzo Yagi (Hokkaido University, Japan), June 9, 1978.

Lectures and Symposia

During the report year staff members and fellows presented lectures and participated in symposia and other extracurricular activities:

Bell lectured on high-pressure physics at the Los Alamos Scientific Laboratory, presented a series of lectures on geophysics at the City University of New York (CUNY), Brooklyn, gave the opening address at the meeting of the German Mineralogical Society in Bochum, and attended the 6th AIRAPT International High Pressure Conference at the University of Colorado in Boulder. He served as a member of the NASA Lunar Sample

Planning Team and as Associate Editor of *Journal of Physics and Chemistry of Minerals*.

Boctor attended the 2nd International Kimberlite Conference at Santa Fe, New Mexico, October 3–7, 1977; he presented a paper at the conference and participated in a post-conference field trip.

Boyd served as President, Geological Society of Washington (for 1977), as convenor of the 2nd International Kimberlite Conference, and as a member of the U. S. National Committee for Geochemistry. He gave invited lectures on "Kimberlites and the mantle sample" to the Geological Society of Washington, "The mantle sample from kimberlites" and "Garnet lherzolites" to the U. S. Geological Survey and the University of Northern Arizona at Flagstaff, and "The mantle sample from kimberlites" to the Department of Geology, University of Michigan.

Chayes was named chairman of International Geological Correlation Project 163 at its organization meeting in Bochum, Germany, September 6–8, 1977; he also organized and participated in a symposium on the work of the project, whose mission is to stimulate and assist in the development of a world data base for igneous petrology. The symposium was part of the scientific program of the host society, the Deutsche Mineralogische Gesellschaft. In October he attended the meeting, in Hannover, Germany, of COGEODATA, of whose Task Group on Electronic Data Processing in Igneous Petrology he is chairman. Chayes participated in a conference at Princeton University on "The physics of magmatic processes"; the event was cosponsored by Princeton University and the Geophysical Laboratory in commemoration of the 50th anniversary of N. L. Bowen's lectures at Princeton University. Chayes also was an invited discussant in a symposium on "Appraising peer review," held in Washington, D. C. on February 13, 1978 at the annual meeting of the American Association for the Advancement of Science.

Finger lectured to the Geology Section at the Los Alamos Scientific Laboratory, New Mexico. He attended the 6th AIRAPT International High Pressure Conference at the University of Colorado in Boulder and a tutorial on x-ray diffractometry at the American Crystallographic Association meeting at Norman, Oklahoma. He was reelected Secretary of the Mineralogical Society of America and served as its representative to the 1977 Joint Technical Program Committee of the Geological Society of America. He also spent three weeks in August 1977 as a Guest Investigator at the Max-Planck-Institut für Kernphysik, Heidelberg, Germany.

Finnerty presented lectures on "Thermobarometry in multicomponent systems: determination of mantle geotherms" at the Jet Propulsion Laboratory, March 10, 1978, and at the Department of Earth and Planetary Science, Johns Hopkins University, April 6, 1978.

Frantz lectured on "Determination of aqueous magnesium speciation in the system: $\text{MgO-SiO}_2\text{-H}_2\text{O-HCl}$ " at the American Geophysical Union meeting in San Francisco, December 1977, and on "Theoretical and experimental approaches in interpreting metasomatic activity in the earth's crust" at the Oak Ridge National Laboratory, in January 1978. He also participated in the Gordon Conference on Ore Deposits at Andover, New Hampshire, July 1977.

Hare gave invited lectures at a symposium on peptide sequencing in Montpellier, France, and at a symposium on the Quaternary at the Geological Society of America meeting in Seattle, Washington. He also addressed seminars at Oxford University, England; the University of Maryland, Baltimore; the University of Colorado, Boulder; and the National Institutes of Health, Bethesda, Maryland.

Harrison, Hoover and *Lawson* attended the conference on "The Physics of Magmatic Processes" at Princeton University.

Hazen delivered lectures on high-

pressure crystal chemistry at the 6th AIRAPT International High Pressure Conference, July 1977; at the Department of Geological Sciences, Virginia Polytechnic Institute and State University, Blacksburg, Virginia, May 1978; and at the IBM Thomas J. Watson Research Center, Yorktown Heights, New York, June 1978. He also gave an invited lecture on nineteenth century geological poetry to the Geological Society of Washington, January 1978. Hazen was appointed to the Program Committee of the Mineralogical Society of America, and he served as Secretary of the U.S. National Committee on the History of Geology.

Hoering addressed a seminar at the Department of Chemistry, University of Maryland, April 15, 1978, on "Geochemistry of humic acids."

Irvine lectured on "Chromite precipitation by magma mixing" at the Gordon Conference on Ore Deposits held at Andover, New Hampshire, in July 1977, and he spoke on "Secondary differentiation in layered intrusions" at the N. L. Bowen Memorial Conference on "The physics of magmatic processes" at Princeton University in November 1977. He addressed the Geological Association of Canada at Vancouver in February 1978, and he gave lectures at Bryn Mawr College, Rutgers University, the University of British Columbia, and at the U.S. Geological Survey in Menlo Park, California. Irvine is serving as an Associate Editor of the *Canadian Journal of Earth Sciences*.

Mao gave invited lectures at the 6th AIRAPT International High Pressure Conference, July 25–28, 1977; Tokyo University, Nagoya University, and Osaka University, August 29–September 1, 1977; University of Houston, Texas, December 1, 1977; and the Lawrence Livermore Laboratory, California, December 6, 1977. He also participated in a National Reconstruction Seminar in Taiwan, China, July 30–August 16, 1977.

Mysen lectured on "Physical and chemical properties of silicate melts at

high pressures and temperatures" at the Lunar Science Institute, Houston, Texas, and on "Metasomatism in the upper mantle: experimental evidence to 30 kbar" at the Massachusetts Institute of Technology.

Osborn served as the 1977 Nelson W. Taylor Lecturer in Materials Science at The Pennsylvania State University in September; his two lectures were entitled, "The Mineral Shortage and What Can Be Done About It," and "Can We Be Self-Sufficient in Mineral Resources?" He participated in the symposium "The Future of Science" at DePauw University in October 1977 in connection with the inauguration of R. F. Rosser as 17th president. He presented testimony on Title III of the Surface Mining Control and Reclamation Act of 1977 before the Interior Subcommittee of the House Appropriations Committee, and on H. R. 10859, "National Materials Policy, Research and Organization Act of 1978," before the House Subcommittee on Science, Research and Technology. Osborn served as chairman of the Board of Mineral Resources of the National Research Council. He attended meetings as a member of the Commission on Natural Resources of the National Research Council and as a member of the Materials Advisory Committee, Office of Technology Assessment, Congress of the United States; he chaired the panel on Mineral Accessibility on Federal Lands and the panel on Nonfederal Mineral Accessibility.

Osborn also served on the Geosciences Advisory Panel, Los Alamos Scientific Laboratory, U.S. Department of Energy; the Pennsylvania Science and Engineering Foundation Board (Commonwealth of Pennsylvania, Harrisburg); the Pennsylvania Research Corporation Board of Directors (Pennsylvania State University); the Geisinger Medical Center Board of Directors, Danville, Pennsylvania; the Board of Directors of the Institute for Medical Education and Research at Geisinger Medical Center; the College of

Engineering Advisory Board at the University of California at Berkeley, and the committee of the Dean of the Graduate School, University of California at Berkeley, to evaluate the graduate program of the Department of Materials Science and Mineral Engineering. He served as advisor to the President of the University of Alabama on the University's mineral science and engineering program.

Popp attended the Gordon Research Conference on Inorganic Geochemistry of Ore Deposits at Proctor Academy, Andover, New Hampshire, July 10–15, 1977; and lectured on "Aqueous magnesium speciation in the system $\text{MgO-SiO}_2\text{-H}_2\text{O-HCl}$ " at the Chemistry Division, Oak Ridge National Laboratory, Tennessee, January 10–12, 1978.

Rumble lectured on "Metamorphic petrologists' view of oxygen isotope geochemistry" at the Department of Geological Sciences, Virginia Polytechnic Institute and State University, and on "Devonian brachiopods from the sillimanite zone, Mt. Moosilauke, New Hampshire" at the Geological Society of Washington. He served as chairman of the External Awards Committee of the Mineralogical Society of America and as volunteer "mentor" in planetology, geology, and geochemistry to students in Montgomery County Western Cluster Program for the Gifted.

Trochimczyk attended the organization meeting of International Geological Correlation Project 154 at Orleans, France.

Van Valkenburg lectured on "A window to high-pressure research" at Cornell University before the General Physics Seminar in March 1978 and on "A window to the core of the earth" at the U.S. Geological Survey in Flagstaff, Arizona in May 1978. He also attended the 6th AIRAPT International High Pressure Conference at the University of Colorado in Boulder.

Virgo Attended the 6th AIRAPT International High Pressure Conference at the University of Colorado in Boulder and presented a lecture to the Geological

Society of America at its annual meeting in Seattle, Washington.

Wendlandt attended the 2nd International Kimberlite Conference at Santa Fe, New Mexico, and presented a paper at the Conference.

Yagi lectured on "Physics and chemistry of silicate perovskite" at the Department of Earth and Space Sciences, State University of New York at Stony Brook in May 1978. He also attended the 6th AIRAPT International High Pressure Conference at the University of Colorado in Boulder.

Yoder lectured on "Petrologic constraints on the properties of the upper mantle" at an interdisciplinary seminar at the Lamont-Doherty Observatory of Columbia University. He gave his views on the effects of various methods of melting in the mantle on the composition and sequence of magmas generated at the Lawrence Livermore Laboratory, University of Oregon, Oregon State University, and the University of Michigan. He made the opening address of the Magma Genesis Symposium held in Tokyo in March 1978 in connection with the International Geodynamics Conference. Yoder presented a position paper on "Prospective non-fuel mineral shortages" before the Committee on Science and Public Policy of the National Academy of Sciences in April 1978. In addition, he was the introductory speaker at the symposium on "Experimental mineralogy and crystal growth" held in connection with the 100th anniversary celebration of the Société française de Minéralogie et de Cristallographie at Paris in May 1978. While in France he also spoke before the investigators at the Centre de Recherches Pétrographiques et Géochimiques, Vandœuvre-lès-Nancy. During the year Yoder served as a consultant to the Los Alamos Scientific Laboratory in New Mexico and as editor of the volume *The Evolution of the Igneous Rocks: Fiftieth Anniversary Appraisal* commemorating N. L. Bowen's classic book. The new book is expected to be released by the Princeton University Press in the spring of 1979.

BIBLIOGRAPHY

- Abelson, P. H., Organic matter in the earth's crust, *Ann. Rev. Earth Planet. Sci.*, **6**, 325-351, 1978 (G.L. Paper 1725).
- Arndt, N. T., Ultrabasic magmas and high-degree melting of the mantle, *Contrib. Mineral. Petrol.*, **64**, 205-221, 1977 (G.L. Paper 1726).
- Bell, P. M., and H. K. Mao, Compression experiments on MgO and ruby with the diamond-window pressure cell to 1 megabar, in *High-Pressure Research: Applications in Geophysics*, M. H. Manghnani and S. Akimoto, eds., Academic Press, New York, pp. 509-518, 1977 (G.L. Paper 1720).
- Bell, P. M., *see also* Hazen, R. M.; Mao, H. K.
- Chayes, F., The oceanic basalt-trachyte relation in general and in the Canary Islands, *Amer. Mineral.*, **62**, 666-671, 1977 (G.L. Paper 1710).
- Chayes, F., On ways of making information system software available, *Comput. Geosci.*, **3**, 449-452, 1977 (G.L. Paper 1715).
- Chayes, F., *see also* Trochimczyk, J.
- Chou, I.-M., and J. D. Frantz, Recalibration of Ag + AgCl acid buffer at elevated pressures and temperatures, *Amer. J. Sci.*, **277**, 1067-1072, 1977 (G.L. Paper 1707).
- Eggler, D. H., The effect of CO₂ upon partial melting of peridotite in the system Na₂O-CaO-Al₂O₃-MgO-SiO₂-CO₂ to 35 kb, with an analysis of melting in a peridotite-H₂O-CO₂ system, *Amer. J. Sci.*, **278**, 305-343, 1978 (G.L. Paper 1727).
- Eggler, D. H., and J. R. Holloway, Partial melting of peridotite in the presence of H₂O and CO₂: principles and review, in "Magma Genesis; Proceedings of the American Geophysical Union Chapman Conference on Partial Melting in the Earth's Upper Mantle," *Oreg. Dep. Geol. Miner. Ind. Bull.*, **96**, 15-36, 1977 (G.L. Paper 1723).
- Eggler, D. H., and M. Rosenhauer, Carbon dioxide in silicate melts: II. Solubilities of CO₂ and H₂O in CaMgSi₂O₆ (diopside) liquids and vapors at pressures to 40 kb, *Amer. J. Sci.*, **278**, 64-94, 1978 (G.L. Paper 1721).
- Ferry, J. M., and F. S. Spear, Experimental calibration of the partitioning of Fe and Mg between biotite and garnet, *Contrib. Mineral. Petrol.*, Vol. **66**, No. 2, 1978, pp. 113-117 (G.L. Paper 1735).
- Finger, L. W., and H. King, A revised method of operation of the single-crystal diamond cell and refinement of the structure of NaCl at 32 kbar, *Amer. Mineral.*, **63**, 337-342, 1978 (G.L. Paper 1734).
- Finger, L. W., *see also* Hazen, R. M.; Ohashi, Y.
- Frantz, J. D., *see* Chou, I.-M.
- Hazen, R. M., and L. W. Finger, The crystal structures and compressibilities of layer minerals at high pressure. I. SnS₂, berndtite, *Amer. Mineral.*, **63**, 289-292, 1978 (G.L. Paper 1731).
- Hazen, R. M., and L. W. Finger, The crystal structures and compressibilities of layer minerals at high pressure. II. Phlogopite and chlorite, *Amer. Mineral.*, **63**, 293-296, 1978 (G.L. Paper 1732).
- Hazen, R. M., and L. W. Finger, Crystal structures and compressibilities of pyrope and grossular to 60 kbar, *Amer. Mineral.*, **63**, 297-303, 1978 (G.L. Paper 1733).
- Hazen, R. M., H. K. Mao, and P. M. Bell, Effects of compositional variation on absorption spectra of lunar olivines, *Proc. Eighth Lunar Sci. Conf.*, 1081-1090, 1977 (G.L. Paper 1717).
- Hedges, J. I., The association of organic molecules with clay minerals in aqueous solutions, *Geochim. Cosmochim. Acta*, **41**, 1119-1123, 1977 (G.L. Paper 1712).
- Hedges, J. I., The formation and clay mineral reactions of melanoidins, *Geochim. Cosmochim. Acta*, **42**, 69-76, 1978 (G.L. Paper 1722).
- Hoering, T. C., Olefinic hydrocarbons from Bradford, Pennsylvania, crude oil, *Chem. Geol.*, **20**, 1-8, 1977 (G.L. Paper 1702).
- Holloway, J. R., *see* Eggler, D. H.
- Huckenholz, H. G., *see* Huggins, F. E.
- Huggins, F. E., D. Virgo, and H. G. Huckenholz, Titanium-containing silicate garnets. II. The crystal chemistry of melanites and schorlomite, *Amer. Mineral.*, **62**, 646-665, 1977 (G.L. Paper 1711).
- King, H., *see* Finger, L. W.
- Kushiro, I., *see* Mysen, B. O.
- Mao, H. K., and P. M. Bell, Disproportionation equilibrium in iron-bearing systems at pres-

- tures above 100 kbar with applications to chemistry of the earth's mantle, in *Energetics of Geological Processes*, S. K. Saxena and S. Bhattacharji, eds., Springer-Verlag, New York, pp. 236-249, 1977 (G.L. Paper 1709).
- Mao, H. K., and P. M. Bell, Techniques of electrical conductivity measurement to 300 kbar, in *High-Pressure Research: Applications in Geophysics*, M. H. Manghnani and S. Akimoto, eds., Academic Press, New York, pp. 493-502, 1977 (G.L. Paper 1719).
- Mao, H. K., P. M. Bell, J. W. Shaner, and D. J. Steinberg, Specific volume measurements of Cu, Mo, Pd, and Ag and calibration of the Ruby R_1 fluorescence pressure gauge from 0.06 to 1 Mbar, *J. Appl. Phys.*, June 1978, pp. 3276-3283 (G.L. Paper 1728).
- Mao, H. K., and P. M. Bell, High-pressure physics: sustained static generation of 1.36 to 1.72 megabars: *Science*, 200, 4346, pp. 1145-1147, 1978 (G.L. Paper 1739).
- Mao, H.K., *see also* Hazen, R. M.; Bell, P. M.
- Mysen, B. O., The solubility of H_2O and CO_2 under predicted magma genesis conditions and some petrological and geophysical implications, *Rev. Geophys. Space Phys.*, 15, 351-361, 1977 (G.L. Paper 1714).
- Mysen, B. O., Solubility of volatiles in silicate melts under the pressure and temperature conditions of partial melting in the upper mantle, in "Magma Genesis; Proceedings of the American Geophysical Union Chapman Conference on Partial Melting in the Earth's Upper Mantle," *Oreg. Dep. Geol. Miner. Ind. Bull.*, 96, 1-14, 1977 (G.L. Paper 1718).
- Mysen, B.O., Experimental determination of nickel partition coefficients between liquid, pargasite, and garnet peridotite minerals and concentration limits of behavior according to Henry's Law at high pressure and temperature, *Amer. J. Sci.*, 278, 217-243, 1978 (G.L. Paper 1724).
- Mysen, B.O., Limits of solution of trace elements in minerals according to Henry's Law: review of experimental data, *Geochim Cosmochim. Acta*, 42, 871-885, 1978 (G.L. Paper 1737).
- Mysen, B.O., and I. Kushiro, Compositional variations of coexisting phases with degree of melting of peridotite in the upper mantle, *Amer. Mineral.*, 62, 843-865, 1977 (G.L. Paper 1716).
- Ohashi, Y., and L. W. Finger, The role of octahedral cations in pyroxenoid crystal chemistry. I. Bustamite, wollastonite, and the pectolite-schizolite-serandite series, *Amer. Mineral.*, 63, 274-288, 1978 (G.L. Paper 1729).
- Osborn, E. F., Phase diagrams and refractories, *Amer. Ceram. Soc. Bull.*, 56, 654-659, 1977 (G.L. Paper 1691).
- Osborn, E. F., Origin of calc-alkali magma series of Santorini volcano type in the light of recent experimental phase equilibrium studies, in *Proceedings of the International Congress on Thermal Waters, Geothermal Energy and Volcanism of the Mediterranean Area, Athens, Greece, October 1976*, 3, 154-167, 1976 (G.L. Paper 1750).
- Rosenhauer, M., *see* Eggler, D. H.
- Rumble, D., III, Mineralogy, petrology, and oxygen isotopic geochemistry of the Clough Formation, Black Mountain, western New Hampshire, U.S.A., *J. Petrology*, 19, 317-340, 1978 (G.L. Paper 1738).
- Spear, F. S., *see* Ferry, J. M.
- Trochimczyk, J., and F. Chayes, Sampling variation of principal components, *Math. Geol.*, 9, 497-506, 1977 (G.L. Paper 1713).
- Trochimczyk, J., and F. Chayes, Some properties of principal component scores, *Math. Geol.*, 10, 43-52, 1978 (G.L. Paper 1736).
- Virgo, D., *see* Huggins, F. E.

REFERENCES CITED

- Adams, D. M., S. K. Sharma, and R. Appleby, Spectroscopy at very high pressures. 14: Laser Raman scattering in ultra small samples in a diamond anvil cell, *Appl. Opt.*, 16, 2572-2575, 1977.
- Ahrens, L. H., R. D. Cherry, and A. J. Erlank, Observations on the Th-U relationship in zircons from granitic rocks and from kimberlites? *Geochim. Cosmochim. Acta*, 31, 2379-2387, 1967.
- Allen, J. C., A. L. Boettcher, and G. Marland, Amphiboles in andesites and basalt. I. Stability as a function of P - T - f_{O_2} , *Amer. Mineral.*, 60, 1069-1085, 1975.

- Allen, J. R. L., Mixing at turbidity current heads, and its geological implications, *J. Sediment. Petrology*, **41**, 97-113, 1971.
- Andersen, O., The system anorthite-forsterite-silica, *Amer. J. Sci.*, **39**, 407-454, 1915.
- Anderson, A. T., Some basaltic and andesitic gases, *Rev. Geophys.*, **13**, 37-57, 1975.
- Anderson, D. R., Infrared, Raman and ultraviolet spectroscopy, *Chem. Anal. (N.Y.)*, **41**, 247-286, 1974.
- Anzai, S., and K. Ozawa, Effect of pressure on the Neel and the ferrimagnetic Curie temperatures of $\text{FeSi}_{1+\delta}$, *Phys. Stat. Sol.*, **24**, K31-K34, 1974.
- Aoki, K., Phlogopites and potassic richterites from mica nodules in South African kimberlites, *Contrib. Mineral. Petrol.*, **48**, 1-7, 1974.
- Arndt, N. T., Ultrabasic magmas and high-degree melting of the mantle, *Contrib. Mineral. Petrol.*, **64**, 205-221, 1977.
- Azzaria, L. M., and F. Dacheille, High-pressure polymorphs of manganous fluoride. *J. Phys. Chem.*, **65**, 889-891, 1961.
- Bailey, D. K., and J. F. Schairer, The system $\text{Na}_2\text{O}-\text{Al}_2\text{O}_3-\text{Fe}_2\text{O}_3-\text{SiO}_2$ at 1 atmosphere and the petrogenesis of alkaline rocks, *J. Petrology*, **7**, 114-170, 1966.
- Balashov, Yu. A., and L. D. Krigman, The effects of alkalinity and volatiles on rare-earth separation in magmatic systems, *Geochem. Int.*, **12**, 165-170, 1975.
- Balchan, A. S., and H. G. Drickamer, High-pressure electrical resistance cell, and calibration points above 100 kilobars, *Rev. Sci. Instrum.*, **32**, 308-313, 1961.
- Baldwin, B., Ways of deciphering compacted sediments, *J. Sediment. Petrology*, **41**, 293-301, 1971.
- Bancroft, G. M., and R. G. Burns, Interpretation of the electronic spectra of iron in pyroxenes, *Amer. Mineral.*, **52**, 1278-1287, 1967.
- Barton, P. B., and B. J. Skinner, Sulfide mineral stabilities, in *Geochemistry of Hydrothermal Ore Deposits*, H. L. Barnes, ed., Holt, Rinehart and Winston, Inc., New York, pp. 236-333, 1967.
- Barton, P. B., Jr., and P. Toulmin, III, Phase relations involving sphalerite in the Fe-Zn-S system, *Econ. Geol.*, **61**, 815-849, 1966.
- Basile, L. J., J. R. Ferraro, P. Labonville, and M. C. Wall, A study of force fields for tetrahedral molecules and ions, *Coord. Chem. Rev.*, **11**, 21-69, 1973.
- Bassett, W. A., T. Takahashi, and P. W. Stook, X-ray diffraction and optical observations on crystalline solids up to 300 kbar, *Rev. Sci. Instrum.*, **38**, 37-42, 1967.
- Bates, J. B., R. W. Hendricks, and L. B. Shaffer, Neutron radiation effects and structure of noncrystalline SiO_2 , *J. Chem. Phys.*, **61**, 2421-2432, 1974.
- Bell, P. M., and H. K. Mao, Optical spectra of thin metallic coatings with application to the spectra of lunar soil samples (abstract), in *Lunar Science VIII*, The Lunar Science Institute, Houston, pp. 88-90, 1977.
- Bell, P. M., H. K. Mao, and G. R. Rossman, Absorption spectroscopy of ionic and molecular units in crystals and glasses, in *Infrared and Raman Spectroscopy of Lunar and Terrestrial Minerals*, C. Karr, Jr., ed., Academic Press, New York, pp. 1-38, 1975.
- Bell, P. M., H. K. Mao, and R. A. Weeks, Optical spectra and electron paramagnetic resonance of lunar and synthetic glasses: a study of the effects of controlled atmosphere, composition and temperature, *Proc. Seventh Lunar Sci. Conf., Geochim. Cosmochim. Acta*, Suppl. **7**, Vol. 3, Pergamon Press, New York, pp. 2543-2559, 1976.
- Benedek, G. B., *Magnetic Resonance at High Pressure*, Interscience Publishers, New York, 1963.
- Berkes, J. S., *MRL Monograph No. 2*, Materials Research Laboratory, Pennsylvania State University, University Park, Pennsylvania, 1968.
- Berman, H., A torsion microbalance for the determination of specific gravities of minerals, *Amer. Mineral.*, **24**, 434-440, 1939.
- Bergstøl, S., The Jacupirangite at Kodal, Vestfold, Norway, *Mineral Deposita (Berl.)*, **7**, 233-246, 1972.
- Best, M. G., L. F. Henage, and J. A. S. Adams, Mica peridotite, wyomingite, and associated potassic igneous rocks in northeastern Utah, *Amer. Mineral.*, **53**, 1041-1048, 1968.
- Biggar, G. M., Phase equilibrium studies of chilled margins of some layered intrusions, *Contrib. Mineral. Petrol.*, **46**, 159-167, 1974.
- Billings, M. P., Regional metamorphism of the Littleton-Moosilauke area, New Hampshire, *Geol. Soc. Amer. Bull.*, **48**, 463-566, 1937.
- Blank, H. R., Jr., and M. E. Gettings, Subsurface form and extent of the Skaergaard intrusion, *Eos*, **54**, 507, 1973.
- Blümel, P., and W. Schreyer, Phase relations in pelitic and psamitic gneisses of the sillimanite-potash feldspar and cordierite-potash feldspar zones in the moldanubicum of the Lam-Bodenmais area, Bavaria, *J. Petrology*, **18**, 431-459, 1977.
- Boctor, N. Z., and H. O. A. Meyer, Oxide and sulfide minerals in kimberlite from Green Mountain, Colorado, *Extended Abstracts, Second International Kimberlite Conference*, Santa Fe, New Mexico, 1977.
- Boettcher, A. L., Volcanism and orogenic belts—the origin of andesite, *Tectonophysics*, **17**, 231-244, 1973.
- Boettcher, A. L., B. O. Mysen, and J. C. Allen, Techniques for the control of water fugacity and oxygen fugacity for experimentation in

- solid-media high-pressure apparatus, *J. Geophys. Res.*, **78**, 5898–5901, 1973.
- Bottinga, Y., and D. F. Weill, Densities of liquid silicate systems calculated from partial molar volumes of oxide components, *Amer. J. Sci.*, **269**, 169–182, 1970.
- Boucot, A. J., and D. Rumble III, Devonian brachiopods from the sillimanite zone, Mt. Moosilauke, New Hampshire, *Science*, in press, 1978.
- Bowen, N. L., *The Evolution of the Igneous Rocks*, Princeton University Press, Princeton, N.J., 1928 (reprinted by Dover Publications, Inc., New York, 1956).
- Bowen, N. L., and J. F. Schairer, The system, MgO-FeO-SiO₂, *Amer. J. Sci.*, **29**, 151–217, 1935.
- Bowen, N. L., J. F. Schairer, and E. Posnjak, The system, CaO-FeO-SiO₂, *Amer. J. Sci.*, **26**, 193–284, 1933.
- Boyd, F. R., A pyroxene geotherm, *Geochim. Cosmochim. Acta*, **37**, 2533–2546, 1973.
- Boyd, F. R., and J. L. England, Apparatus for phase-equilibrium measurements at pressures up to 50 kilobars and temperatures up to 1750°C, *J. Geophys. Res.*, **65**, 741–748, 1960.
- Boyd, F. R., and J. L. England, Effect of pressure on the melting of diopside, CaMgSi₂O₆, and albite, NaAlSi₃O₈, in the range up to 50 kb, *J. Geophys. Res.*, **68**, 311–323, 1963.
- Boyd, F. R., and R. H. McCallister, Densities of fertile and sterile garnet peridotites, *Geophys. Res. Lett.*, **3**, 509–512, 1976.
- Boyd, F. R., and P. H. Nixon, Origin of the ilmenite-silicate nodules in kimberlites from Lesotho and South Africa, in *Lesotho Kimberlites*, P. H. Nixon, ed., Lesotho National Development Corporation, Maseru, Lesotho, pp. 149–158, 1973.
- Boyd, F. R., and P. H. Nixon, Ultramafic nodules from the Kimberley pipes, South Africa, *Geochim. Cosmochim. Acta*, in press, 1978.
- Brady, J. B., Metasomatic zones in metamorphic rocks, *Geochim. Cosmochim. Acta*, **41**, 113–125, 1977.
- Brawer, S. A., and W. B. White, Raman spectroscopic investigation of the structure of silicate glasses. I. The binary alkali silicates, *J. Chem. Phys.*, **63**, 2421–2432, 1975.
- Brawer, S. A., and W. B. White, Raman spectroscopic investigation of the structure of silicate glasses. II. Soda-alkali earth-alumina ternary and quaternary glasses, *J. Non-crystall. Solids*, **23**, 261–278, 1977.
- Bridgman, P. W., The linear compressibility of thirteen natural crystals, *Amer. J. Sci.*, **15**, 287–296, 1928.
- Bridgman, P. W., The compression of twenty-one halogen compounds and other simple substances to 100,000 kg/cm², *Proc. Amer. Acad. Arts Sci.*, **76**, 1–7, 1945a.
- Bridgman, P. W., The compression of sixty-one solid substances to 25,000 kg/cm² determined by a new rapid method, *Proc. Amer. Acad. Arts Sci.*, **76**, 9–24, 1945b.
- Brögger, W. C., Die Eruptivgesteine des Kristianigebietes, IV. Das Fengebiet in Telemark, Norwegen, *Nor. Vid. Selsk. Skr. I, Math.-Naturv. kl.*, **9**, 1–408, 1921.
- Brooks, C. K., and T. F. D. Nielsen, Early stages in the differentiation of the Skaergaard magma as revealed by a closely related suite of dike rocks, *Lithos*, **11**, 1–15, 1978.
- Brown, P. E., E. J. Essene, and W. C. Kelly, Sphalerite geobarometry in the Balmat-Edwards district, New York, *Amer. Mineral.*, **63**, 250–257, 1978.
- Buddington, A. F., and D. H. Lindsley, Iron-titanium oxide minerals and synthetic equivalents, *J. Petrology*, **5**, 310–357, 1964.
- Bunch, T. E., and R. LaBorde, Mineralogy and compositions of selected basalts from DSDP leg 34, *Initial Reports of the Deep Sea Drilling Project*, Vol 34, Hart, S. R. et al., eds., U.S. Govt. Printing Office, 1976.
- Burger, H., U. Goetze, and W. Sawodny, Vibrational spectra and force constants of silyl and trimethyl silyl compounds of elements in the Vth group, *Spectrochim. Acta*, **26A**, 671–683, 1970.
- Burnham, C. W., The crystal structure of pyroxferroite from Mare Tranquillitatis, *Proc. Second Lunar Sci. Conf.*, 47–57, 1971.
- Burnham, C. W., and N. F. Davis, The role of H₂O in silicate melts, I, *P-V-T* relations in the system NaAlSi₃O₈-H₂O to 10 kilobars and 1000°C, *Amer. J. Sci.*, **270**, 54–79, 1971.
- Burnham, C. W., and N. F. Davis, The role of H₂O in silicate melts, II, Thermodynamic and phase relations in the system NaAlSi₃O₈-H₂O to 10 kilobars, 700° to 1100°C, *Amer. J. Sci.*, **274**, 902–940, 1974.
- Burnham, C. W., J. R. Holloway, and N. F. Davis, Thermodynamic properties of water to 1,000°C and 10,000 bars, *Geol. Soc. Am. Spec. Pap.*, **132**, 96 pp., 1969.
- Burns, R. G., *Mineralogical Applications of Crystal Field Theory*, Cambridge University Press, Cambridge, 1970.
- Burns, R. G., Partitioning of transition metal in mineral structures of the mantle, in *The Physics and Chemistry of Minerals and Rocks*, R. G. J. Strens, ed., John Wiley and Sons, New York, pp. 556–572, 1976.
- Burns, R. G., and Vaughan, D. J., Polarized electronic spectra, in *Infrared and Raman Spectroscopy of Lunar and Terrestrial Minerals*, C. Karr, Jr., ed., Academic Press, New York, pp. 39–72, 1975.
- Byers, F. M., Volcanic suites, Umnak and Bogoslof Islands, Aleutian Islands, Alaska, *Geol. Soc. Amer. Bull.*, **72**, 93–128, 1961.
- Campbell, I. H., J. M. Dixon, and P. L. Roeder,

- Crystal buoyancy in basaltic liquids and other experiments with a centrifuge furnace, *Eos*, 58, 527, 1977.
- Carman, J. H., Synthetic sodium phlogopite and its two hydrates: stabilities, properties and mineralogic implications, *Amer. Mineral.*, 59, 261-273, 1974.
- Carmichael, I. S. E., The pyroxenes and olivines of some Tertiary acid glasses, *J. Petrology*, 1, 309-336, 1960.
- Carmichael, I. S. E., The petrology of Thingmuli, a Tertiary volcano in eastern Iceland, *J. Petrology*, 5, 435-460, 1964.
- Carmichael, I. S. E., The iron-titanium oxides of salic volcanic rocks and their associated ferromagnesian silicates, *Contrib. Mineral. Petrol.*, 14, 36-64, 1967.
- Carmichael, D. J., C. M. Dodd, and A. Veis, The solubilization of bone and dentin collagens by pepsin, *Biochim. Biophys. Acta*, 491, 177-192, 1977.
- Carter, W. J., S. P. Marsh, J. N. Fritz, and R. G. McQueen, The equation of state of selected materials for high-pressure references, *Nat. Bur. Stand. (U.S.) Spec. Publ.*, 326, 147-158, 1971.
- Champion, A. R., R. W. Vaughn, and H. G. Drickamer, Effect of pressure on the Mössbauer resonance in ionic compounds of iron, *J. Chem. Phys.*, 47, 2583-2590, 1967.
- Chang, I. F., and S. S. Mitra, Application of a modified random-element-iso-displacement model to long-wavelength optic phonons of mixed crystals, *Phys. Rev.*, 172, 924-933, 1968.
- Chatelain, A., and R. A. Weeks, Electron paramagnetic resonance of Fe^{3+} in forsterite (Mg_2SiO_4), *J. Chem. Phys.*, 58, 3722-3726, 1973.
- Chayes, F., On estimating the magnitude of the hidden zone and the compositions of the residual liquids of the Skaergaard layered series, *J. Petrology*, 11, 1-14, 1970.
- Chayes, F., *Ratio Correlation*, University of Chicago Press, 1971.
- Chou, I.-M., and H. P. Eugster, A sensor for hydrogen fugacities at elevated P and T and applications (abstract), *Eos*, 57, 340, 1976.
- Chou, I.-M., and J. D. Frantz, Recalibration of $\text{Ag} + \text{AgCl}$ acid buffer at elevated pressures and temperatures, *Amer. J. Sci.*, 277, 1067-1072, 1977.
- Clark, S. P., Jr., ed., Handbook of physical constants, *Geol. Soc. Amer. Mem.*, 97, 587 pp., 1966.
- Clark, S. P., Jr., and A. E. Ringwood, Density distribution and constitution of the mantle, *Rev. Geophys.*, 2, 35-88, 1964.
- Clarke, D. B., G. G. Pe, R. M. Mackay, K. R. Gill, M. J. O'Hara, and J. A. Gard, A new potassium-iron-nickel sulphide from a nodule in kimberlite, *Earth Planet. Sci. Lett.*, 35, 421-428, 1977.
- Colbert, E. H., *Evolution of the Vertebrates*, John Wiley and Sons, Inc., New York, 1955.
- Coons, W. E., J. R. Holloway, and A. Navrotsky, Co^{2+} as an analogue for Fe^{2+} in high temperature experiments in basaltic systems, *Earth Planet. Sci. Lett.*, 30, 303-308, 1976.
- Cooper, A. F., J. Gittins, and O. F. Tuttle, The system $\text{Na}_2\text{CO}_3\text{-K}_2\text{CO}_3\text{-CaCO}_3$ at 1 kilobar and its significance in carbonatite petrogenesis, *Amer. J. Sci.*, 275, 534-560, 1975.
- Craig, H., Standard for reporting concentrations of deuterium and oxygen-18 in natural waters, *Science*, 133, 1833, 1961.
- Cullers, R. L., L. G. Medaris, and L. A. Haskin, Experimental studies of the distribution of rare earths as trace elements among silicate minerals and water, *Geochim. Cosmochim. Acta*, 37, 1499-1513, 1973.
- Daly, B. J., and W. E. Pracht, Numerical study of density-current surges, *Physics Fluids*, 11, 15-30, 1968.
- Davis, B. T. C., and F. R. Boyd, The join $\text{Mg}_2\text{Si}_2\text{O}_6\text{-CaMgSi}_2\text{O}_6$ at 30 kb pressure and its application to pyroxenes from kimberlite, *J. Geophys. Res.*, 71, 3567-3576, 1966.
- Dawson, J. B., Oldoinyo Lengai—an active volcano with sodium carbonatite lava flows, in *Carbonatites*, O. F. Tuttle and J. Gittens, eds., Interscience Publishers, New York, pp. 155-168, 1966a.
- Dawson, J. B., The kimberlite-carbonatite relationship, *Mineral. Soc. India*, IMA, 1-22, 1966b.
- Dawson, J. B., Advances in kimberlite geology, *Earth Sci. Rev.*, 7, 187-214, 1971.
- Dawson, J. B., and J. B. Hawthorne, Magmatic sedimentation and carbonatitic differentiation in kimberlite sills at Benfontein, South Africa, *J. Geol. Soc. London*, 129, 61-85, 1973.
- Dawson, J. B., and J. V. Smith, Chemistry and origin of phlogopite megacrysts in kimberlite, *Nature*, 253, 336-338, 1975.
- Dawson, J. B., and W. E. Stephens, Statistical classification of garnets from kimberlite and associated xenoliths, *J. Geol.*, 83, 589-607, 1975.
- Day, A. L., E. T. Allen, and J. P. Iddings, *The Isomorphism and Thermal Properties of the Feldspars*, Carnegie Inst. Washington Pub. 31, Washington, D.C., Introduction by G. F. Becker, p. 6, 1905.
- Delaney, J. R., D. Muenow, J. Ganguly, and D. Royce, Anhydrous glass-vapor inclusions from phenocrysts in oceanic tholeiitic pillow basalts (abs.), *Eos*, 58, 530, 1977.
- DeLong, S. E., Distribution of Rb, Sr and Ni in igneous rocks, central and western Aleutian Islands, Alaska, *Geochim. Cosmochim. Acta*, 38, 245-266, 1974.
- Douglas, J. A. V., A further petrological and chemical investigation of the upper part of the Skaergaard intrusion, East Greenland, Part I,

- The Basistoppen Sheet, Part II, The Upper Border Group, Unpubl. D. Ph. Thesis, University of Oxford, 1961.
- Drake, M. J., The distribution of major and trace elements between plagioclase feldspar and magmatic silicate liquid: an experimental study. Ph.D. Dissertation, University of Oregon, 1972.
- Drake, M. J., The oxidation state of europium as an indicator of oxygen fugacity, *Geochim. Cosmochim. Acta*, 39, 55-64, 1975.
- Drake, M. J., and D. F. Weill, New rare earth element standards for electron microprobe analysis, *Chem. Geol.*, 10, 179-181, 1973.
- Drake, M. J., and D. F. Weill, Partition of Sr, Ba, Ca, Y, Eu^{2+} and Eu^{3+} and other REE between plagioclase feldspar and magmatic liquid: an experimental study, *Geochim. Cosmochim. Acta*, 39, 689-712, 1975.
- Drickamer, H. G., S. C. Fung, and G. K. Lewis, Jr., High pressure Mössbauer studies, in *Advances in High Pressure Research*, Vol. 3, R. S. Bradley, ed., Academic Press, New York, 1-39, 1969.
- Eggler, D. H., Water-saturated and undersaturated melting relations in a Parícutin andesite and an estimate of water content in the natural magma, *Contrib. Mineral. Petrol.*, 34, 261-271, 1972.
- Eggler, D. H., Does CO_2 cause partial melting in the low-velocity layer of the mantle? *Geology*, 4, 69-72, 1976.
- Eggler, D. H., The effect of CO_2 upon partial melting of peridotite in the system $\text{Na}_2\text{O}-\text{CaO}-\text{Al}_2\text{O}_3-\text{MgO}-\text{SiO}_2-\text{CO}_2$ to 35 kb, with an analysis of melting in a peridotite- $\text{H}_2\text{O}-\text{CO}_2$ system, *Amer. J. Sci.*, 278, 305-343, 1978.
- Eggler, D. H., and C. W. Burnham, Crystallization and fractionation trends in the system andesite- $\text{H}_2\text{O}-\text{CO}_2$ at pressures to 10 kb, *Geol. Soc. Amer. Bull.*, 84, 2517-2532, 1973.
- Eggler, D. H., and M. Rosenhauer, Carbon dioxide in silicate melts and crystals. II. Solubilities of CO_2 and H_2O in $\text{CaMgSi}_2\text{O}_6$ (diopside) liquids and vapors to 40 kb, *Amer. J. Sci.*, 278, 64-94, 1978.
- Emslie, R. F., The geology of the Michikamau intrusion, *Geol. Surv. Can. Pap.* 68-57, 1970.
- Erlank, A. J., Kimberlite potassic richterite and the distribution of potassium in the upper mantle, *Extended Abstracts, International Kimberlite Conference*, Cape Town, South Africa, pp. 103-106, 1973.
- Erlank, A. J., and N. Shimizu, Strontium and strontium isotope distributions in some kimberlite nodules and minerals, *Extended Abstracts, Second International Kimberlite Conference*, Santa Fe, New Mexico, 1977.
- Etchepare, J., Study by Raman spectroscopy of crystalline and glassy diopside, in *Amorphous Materials*, R. W. Douglas and B. Ellis, ed., John Wiley and Sons, Inc., New York, pp. 337-346, 1972.
- Evans, H. T., Jr., Lunar troilite: crystallography, *Science*, 167, 621-623, 1970.
- Evans, H. T., and R. Allman, The crystal structure and crystal chemistry of vallerite, *Z. Kristallogr.*, 127, 73-93, 1968.
- Finger, L. W., and R. M. Hazen, Crystal structure and compression of ruby to 46 kbar, *J. Appl. Phys.*, in review, 1978.
- Finger, L. W., and H. King, A revised method of operation of the single-crystal diamond cell and the refinement of the structure of NaCl at 32 kbar, *Amer. Mineral.*, 63, 337-342, 1978.
- Fisher, J. R., and E.-A. Zen, Thermodynamic calculations from hydrothermal phase equilibrium data and the free energy of H_2O , *Amer. J. Sci.*, 270, 297-314, 1971.
- Fleischer, M., G. Y. Chao, and A. Kato, New mineral names, *Amer. Mineral.*, 60, 485-489, 1975.
- Folk, R. L., Longitudinal dunes of the northwestern edge of the Simpson Desert, Northern Territory, Australia. Pt. 1: Geomorphology and grain size relationships, *Sedimentology*, 16, 5-54, 1971.
- Foshag, W. F., and J. Gonzáles R., Birth and development of Parícutin volcano, Mexico, *U.S. Geol. Surv. Bull.*, 965-D, 355-489, 1956.
- Franck, E. U., Hochverdichteter Wasserdampf. III. Ionendissoziation von HCl, KOH, and H_2O in überkritischem Wasser, *Z. Phys. Chem. (Frankfurt am Main)*, N.F., 8, 192-206, 1956a.
- Franck, E. U., Hockverdichteter Wasserdampf. I. Elektrolytische Leitfähigkeit in $\text{KCl}-\text{H}_2\text{O}$ -lösungen bis 750°C , *Z. Phys. Chem. (Frankfurt am Main)*, N.F., 8, 92-106, 1956b.
- Frantz, J. D., and H. P. Eugster, Acid-base buffers: use of $\text{Ag} + \text{AgCl}$ in the experimental control of solution equilibria at elevated pressures and temperatures, *Amer. J. Sci.*, 273, 268-286, 1973.
- Frantz, J. D., and H. K. Mao, Bimetasomatism resulting from intergranular diffusion: I. A theoretical model for monomineralic reaction zone sequences, *Amer. J. Sci.*, 276, 817-840, 1976.
- Frantz, J. D., and R. K. Popp, Mineral-solution equilibria: (1) An experimental study of complexing and thermodynamic properties of aqueous MgCl_2 in the system $\text{MgO}-\text{SiO}_2-\text{H}_2\text{O}-\text{HCl}$, *Geochim. Cosmochim. Acta*, in press, 1978.
- Franzini, M., and L. Schiaffino, On the crystal structure of biotites, *Z. Kristallogr.*, 119, 297-309, 1963.
- French, B. M., Some geological implications of equilibrium between graphite and a C-H-O-gas at high temperatures and pressures, *Rev. Geophys.*, 4, 223-253, 1966.
- French, B. M., and H. P. Eugster, Experimental control of oxygen fugacities by graphite-gas

- equilibriums, *J. Geophys. Res.*, **65**, 1529-1539, 1965.
- Frey, F. A., W. B. Bryan, and G. Thompson, Atlantic Ocean floor: geochemistry and petrology of basalts from Legs 2 and 3 of the Deep-Sea Drilling Project, *J. Geophys. Res.*, **79**, 5507-5527, 1974.
- Frick, C., Kimberlitic ilmenites, *Trans. Geol. Soc. S. Afr.*, **76**, 85-94, 1973a.
- Frick, C., Intergrowth of orthopyroxene and ilmenite from Frank Smith Mine, near Barkley West, South Africa, *Trans. Geol. Soc. S. Afr.*, **76**, 195-200, 1973b.
- Furthmayr, H., and R. Timpl, Characterization of collagen peptides by sodium dodecylsulfate-polyacrylamide electrophoresis, *Anal. Biochem.*, **41**, 510-516, 1971.
- Fyfe, W. S., and A. R. McBirney, Subduction and the structure of andesitic volcanic belts, *Amer. J. Sci.*, **275A**, 285-297, 1975.
- Gaddy, R. H., Automated analyses for the characterization of heavy water moderator, in *Automation in Analytical Chemistry*, L. T. Skeggs, ed., Mediad Inc., New York, pp. 210-214, 1966.
- Gaffney, E. S., Crystal field effects in mantle minerals, *Phys. Earth Planet. Interiors*, **6**, 385-390, 1972.
- Gast, P. W., Trace element fractionation and the origin of tholeiitic and alkaline magma types, *Geochim. Cosmochim. Acta*, **32**, 1057-1086, 1968.
- Gill, J. B., Geochemistry of Viti Levu, Fiji, and its evolution as an island arc, *Contrib. Mineral. Petrol.*, **27**, 179-203, 1970.
- Gill, J. B., The role of underthrust oceanic crust in the genesis of a Fijian calc-alkaline rock suite, *Contrib. Mineral. Petrol.*, **43**, 29-45, 1974.
- Gittens, J., R. H. Hewins, and A. F. Laurin, Kimberlitic-carbonatitic dikes of the Saquenay River Valley, Quebec, Canada, *Phys. Chem. Earth*, **9**, 137-148, 1975.
- Gold, D. P., The minerals of the Oka carbonatite and alkaline complex, Oka, Quebec, *Int. Mineral. Ass. Pap. Proc. Gen. Meet. 4th N. D.*, Mineralogical Society of India, India, pp. 109-125, 1966.
- Goldman, D. S., and R. R. Rossman, The spectra of iron in orthopyroxene revisited: the splitting of the ground state, *Amer. Mineral.*, **62**, 151-157, 1977.
- Gosselin, J. R., M. G. Townsend, R. J. Tremblay, and H. H. Webster, Mössbauer investigation of synthetic single crystal monoclinic Fe_7S_8 , *Mater. Res. Bull.*, **10**, 41-50, 1975.
- Gosselin, J. R., M. G. Townsend, R. J. Tremblay, and H. H. Webster, Mössbauer effect in single-crystal Fe_{1-x}S , *J. Solid State Chem.*, **17**, 43-48, 1976.
- Gragnani, R., Le vulcaniti melilititiche di Cu-paello (Rieti), *Rend. Soc. Ital. Mineral. Petrologia*, **28**, 165-189, 1972.
- Grantham, D. R., and J. B. Allen, Kimberlites in Sierra Leone, *Overseas Geol. Miner. Resour.*, **8**, 5-25, 1960.
- Green, H. W., II, and Y. Gueguen, Origin of kimberlite pipes by diapiric upwelling in the upper mantle, *Nature (London)*, **249**, 617-620, 1974.
- Greenwood, N. N., and T. C. Gibb, *Mössbauer Spectroscopy*, Chapman and Hall, London, 1971.
- Greig, J. W., and T. F. W. Barth, The system $\text{Na}_2\text{O} \cdot \text{Al}_2\text{O}_3 \cdot 2\text{SiO}_2$ (nephelite, carnegieite) - $\text{Na}_2\text{O} \cdot \text{Al}_2\text{O}_3 \cdot 6\text{SiO}_2$ (albite), *Amer. J. Sci.*, **35A**, 93-112, 1938.
- Grew, E. S., Blue sillimanite and the origin of crustal xenoliths at Kilbourne Hole, New Mexico, USA, and Bournac, Haute-Loire, France, *Extended Abstracts, Second International Kimberlite Conference*, Santa Fe, New Mexico, 1977.
- Griffin, W. L., and P. N. Taylor, The Fen Damkjernite: petrology of a "central-complex kimberlite," *Phys. Chem. Earth*, **9**, 163-177, 1975.
- Griffith, W. P., Raman studies on rock-forming minerals. Part I. Orthosilicate and cyclosilicates, *J. Chem. Soc. A*, 1372-1377, 1969.
- Grove, D. I., R. A. Binns, F. M. Barrett, and K. G. McQueen, Sphalerite compositions from Western Australian nickel deposits, a guide to equilibria below 300°C, *Econ. Geol.*, **70**, 391-396, 1975.
- Grove, T. L., and D. T. Vaniman, Experimental petrology of very low Ti basalts and origin of Luna 24 ferrobalt (abstract), in *Papers Presented to the Conference on Luna 24*, The Lunar Science Institute, Houston, pp. 68-71, 1977.
- Gurney, J. J., and S. Ebrahim, Chemical compositions of Lesotho kimberlites, in *Lesotho Kimberlites*, P. H. Nixon, ed., Lesotho National Development Corp., Maseru, 1973.
- Gurney, J. J., W. R. O. Jakob, and J. B. Dawson, Megacrysts from the Monastery Mine, *Extended Abstracts, Second International Kimberlite Conference*, Santa Fe, New Mexico, 1977.
- Hafner, S. S., B. J. Evans, and G. M. Kalvius, Second order effects in the hyperfine field of Fe^{57} in troilite (anti-ferrimagnetic FeS), *Solid State Commun.*, **5**, 17-19, 1967.
- Hafner, S., and M. Kalvius, The Mössbauer resonance of Fe^{57} in troilite (FeS) and pyrrhotite ($\text{Fe}_{0.88}\text{S}$), *Z. Kristallogr.*, **123**, 443-458, 1966.
- Haggerty, S. E., Spinels of unique composition associated with ilmenite reaction mantles in the Lihobong kimberlite pipe, Lesotho, in *Lesotho Kimberlites*, P. H. Nixon, ed., Lesotho National Development Corporation, Maseru, Lesotho, pp. 149-158, 1973.
- Haggerty, S. E., The chemistry and genesis of opaque minerals in kimberlites, *Phys. Chem. Earth*, **9**, 295-307, 1975.
- Haggerty, S. E., R. B. Hardie III, and B. M. McMahon, The mineral chemistry of ilmenite no-

- dule associations from the Monastery diatreme, *Extended Abstracts, Second International Kimberlite Conference*, Santa Fe, New Mexico, 1977.
- Häkli, T. A., and T. L. Wright, The fractionation of nickel between olivine and augite as a geothermometer, *Geochim. Cosmochim. Acta*, **31**, 877–884, 1967.
- Hamilton, D. L., and W. S. MacKenzie, Nepheline solid solution in the system $\text{NaAlSiO}_4\text{--KAlSiO}_4\text{--SiO}_2$, *J. Petrology*, **1**, 56–72, 1960.
- Hamilton, W. C., Angle settings for four-circle diffractometers, in *International Tables for X-Ray Crystallography*, Vol. 4, J. A. Ibers and W. C. Hamilton, eds., Kynoch Press, Birmingham, England, pp. 273–284, 1974.
- Harrison, W. J., An experimental study of the partitioning of samarium between garnet and liquid at high pressures (abstract), in *Papers Presented to the International Conference on Experimental Trace Element Geochemistry*, Sedona, Arizona, pp. 41–42, 1977.
- Hart, S. R., and K. Davis, Nickel partitioning between olivine and silicate melt, *Earth Planet. Sci. Lett.*, in press, 1978.
- Haskin, L. A., F. A. Frey, R. A. Schmitt, and R. H. Smith, Meteoritic, solar and terrestrial rare-earth distributions, *Phys. Chem. Earth*, **9**, 869–881, 1966.
- Hass, M., Raman spectra of vitreous silica, germania, and sodium silicate glasses, *J. Phys. Chem. Solids*, **31**, 415–422, 1970.
- Haughton, D. R., P. L. Roeder, and B. J. Skinner, Solubility of sulfur in mafic magmas, *Econ. Geol.*, **69**, 451–467, 1974.
- Hazen, R. M., P. M. Bell, and H. K. Mao, Effects of compositional variation on absorption spectra of lunar pyroxenes, *Proc. Ninth Lunar Sci. Conf.*, in press, 1978.
- Hazen, R. M., and L. W. Finger, Compression models for oxides and silicates (abstract), *Abstr. with Programs (Geol. Soc. Am.)*, **9**, 1008–1009, 1977.
- Hazen, R. M., and L. W. Finger, Crystal structures and compressibilities of pyrope and grossular to 60 kbar, *Amer. Mineral.*, **63**, 297–303, 1978a.
- Hazen, R. M., and L. W. Finger, Crystal structures and compressibilities of layer minerals at high pressures. I. SnS_2 , berndtite, *Amer. Mineral.*, **63**, 289–292, 1978c.
- Hazen, R. M., and L. W. Finger, Crystal structures and compressibilities of zircon at high pressure, *Amer. Mineral.*, **63**, in press, 1978b.
- Hazen, R. M., and L. W. Finger, Crystal structures and compressibilities of layer minerals at high pressures. II. Phlogopite and chlorite, *Amer. Mineral.*, **63**, 293–296, 1978d.
- Hazen, R. M., and C. T. Prewitt, Effects of temperature and pressure on interatomic distances in oxygen-based minerals, *Amer. Mineral.*, **62**, 309–315, 1977.
- Hedges, J. I., and P. L. Parker, Land-derived organic matter in surface sediments from the Gulf of Mexico, *Geochim. Cosmochim. Acta*, **40**, 1019–1029, 1976.
- Helgeson, H. C., J. M. Delaney, and H. W. Nesbitt, Calculation of thermodynamic consequences of dehydration in subducting oceanic crust to 100 kb and 1000°C, *Amer. J. Sci.*, in press, 1978a.
- Hofmann, A., Chromatographic theory of infiltration metasomatism and its application to feldspars, *Amer. J. Sci.*, **272**, 69–90, 1972.
- Holdaway, M. J., Stability of andalusite and the aluminum silicate phase diagram, *Amer. J. Sci.*, **271**, 97–131, 1971.
- Holloway, J. R., Fluids in the evolution of granitic magmas: consequences of finite CO_2 solubility, *Geol. Soc. Amer. Bull.*, **87**, 1513–1518, 1976.
- Holloway, J. R., D. H. Eggler, and N. F. Davis, Analytical expression for calculating the fugacity and free energy of H_2O to 10,000 bars and 1300°C, *Geol. Soc. Am. Bull.*, **82**, 2639–2642, 1971.
- Horwood, H. R., M. G. Townsend, and A. H. Webster, Magnetic susceptibility of single-crystal Fe_{1-x}S , *J. Solid State Chem.*, **17**, 35–42, 1976.
- Houbolt, J. J. H. C., Recent sediments in the Southern Bight of the North Sea, *Geol. en Mijnbouw*, **47**, 245–273, 1968.
- Hubbert, M. K., Theory of scale models as applied to the study of geologic structures, *Geol. Soc. Amer. Bull.*, **48**, 1459–1520, 1937.
- Hutcheon, I., Calculation of metamorphic pressure using sphalerite-pyrrhotite-pyrite equilibrium, *Amer. Mineral.*, **63**, 87–95, 1978.
- Iiyama, J. T., Etude expérimentale de la distribution d'éléments en traces entre deux feldspaths. Feldspath potassique et plagioclase coexistants. I. Distribution de Rb, Cs, Sr et Ba à 600°C, *Bull. Soc. Fr. Mineral. Cristallogr.*, **91**, 130–140, 1968.
- Ilmenkov, G. V., D. N. Nasledov, Y. S. Smetannikova, V. A. Shustrov, and V. K. Yarmarkin, The Mössbauer effect in indium antimonide doped with iron, *Sov. Phys. Solid State*, **12**, 2198–2200, 1971.
- Irvine, T. N., Chromian spinel as a petrogenetic indicator, Part 2, Petrologic applications, *Can. J. Earth Sci.*, **4**, 71–103, 1967.
- Irvine, T. N., Heat transfer during solidification of layered intrusions, I. Sheets and sills, *Can. J. Earth Sci.*, **7**, 1031–1061, 1970.
- Irvine, T. N., Petrology of the Duke Island ultramafic complex, southeastern Alaska, *Geol. Soc. Amer. Mem.*, **138**, 1974.
- Irvine, T. N., and C. H. Smith, The ultramafic rocks of the Muskox intrusion, in *Ultramafic and Related Rocks*, P. J. Wyllie, ed., John Wiley & Sons, Inc., New York, 38–49, 1967.
- Irving, A. J., and P. J. Wyllie, Subsidiary and

- melting relationships for calcite, magnesite, and the join $\text{CaCO}_3\text{-MgCO}_3$ to 36 kilobars, *Geochim. Cosmochim. Acta*, **39**, 35-53, 1975.
- Ishikawa, Y., and S. Akimoto, Magnetic properties of the $\text{FeTiO}_3\text{-Fe}_2\text{O}_3$ solid solution series, *J. Phys. Soc. Jpn.*, **12**, 1083-1098, 1957.
- Ito, E., The absence of oxide mixture in high-pressure phases of Mg-silicates, *Geophys. Res. Lett.*, **4**, 72-74, 1977.
- Ito, J., Rhodonite-pyroxmangite peritectic along the join $\text{MnSiO}_3\text{-MgSiO}_3$ in air, *Amer. Mineral.*, **57**, 865-876, 1972.
- Iwasaki, I., S. Utsumi, K. Hagino, and T. Ozawa, A new spectrophotometric method for the determination of small amounts of chloride using the mercuric thiocyanate method, *Bull. Chem. Soc. Japan*, **29**, 860-864, 1956.
- Jackson, E. D., Primary textures and mineral associations in the ultramafic zone of the Stillwater Complex, Montana, *U.S. Geol. Surv. Prof. Pap.*, **358**, 1961.
- Jackson, E. D., Ultramafic cumulates in the Stillwater, Great Dyke, and Bushveld intrusions, in P. J. Wyllie, ed., *Ultramafic and Related Rocks*, John Wiley & Sons, Inc., New York, 20-38, 1967.
- Jackson, I., Melting of the silica isotypes SiO_2 , FeF_2 and GeO_2 at elevated pressures. *Phys. Earth Planet. Interiors*, **13**, 218-231, 1976.
- Jakes, P., and J. Gill, Rare earth elements and island arc tholeiitic series, *Earth Planet. Sci. Lett.*, **9**, 17-28, 1970.
- Jambor, J., and C. H. Smith, Olivine composition determination with small diameter X-ray powder cameras, *Mineral. Mag.*, **33**, 730-748, 1964.
- Jamieson, J., and A. Y. Wu, A phase transition in NiF_2 at elevated pressures, *J. Appl. Phys.*, **48**, 4573-4575, 1977.
- Kabalkina, S. S., and S. V. Popova, Phase transitions in zinc and manganese fluorides at high pressures and temperatures, *Sov. Phys. Dokl.*, **8**, 1141-1143, 1963.
- Kaiser, H. F., The varimax criterion for analytic rotation in factor analysis, *Psychometrika*, **23**, 187-200, 1958.
- Kasper, H., and H. G. Drickamer, High-pressure Mössbauer resonance studies of compounds of iron with Group V and Group VI elements, *Proc. Nat. Acad. Sci. USA*, **60**, 773-775, 1968.
- Kato, D., Raman spectrometric determination of additive concentration in high-silica-content glasses, *J. Appl. Phys.*, **47**, 2050-2055, 1976a.
- Kato, D., Raman spectrum and refractive index behaviour of Al_2O_3 -added high-silica-content glass. *J. Appl. Phys.*, **47**, 5344-5448, 1976b.
- Katsui, Y., S. Ando, and K. Inaba, Formation and magmatic evolution of Mashu volcano, East Hokkaido, Japan, *J. Fac. Sci. Hokkaido Univ., Ser. 4*, **16**, 533-552, 1975.
- Kay, R. W., Geochemical constraints on the origin of Aleutian magmas, in *Island Arcs, Deep Sea Trenches and Back Arc Basins*, M. Talwani and W. C. Pittman III, eds., American Geophysical Union, Washington, D.C., pp. 229-242, 1977.
- Kay, R. W., The chemical characteristics and origin of Aleutian magnesian andesites, International Geological Congress, Sydney, in press, 1978.
- Kay, R. W., and P. W. Gast, The R.E.E. content and origin of alkali-rich basalts, *J. Geol.*, **81**, 653-682, 1973.
- Keith, M. L., and J. N. Weber, Carbon and oxygen isotopic composition of selected limestones and fossils, *Geochim. Cosmochim. Acta*, **28**, 1787-1816, 1964.
- Keugelan, G. H., An experimental study of the motion of saline water from locks into fresh water channels, *U.S. Nat. Bur. Standards, No. 5168*, 1957.
- Keugelan, G. H., The motion of saline fronts in fresh water: 12th progress report on model laws for density currents, *U.S. Nat. Bur. Standards, No. 5831*, 1958.
- King, H. E., Jr., and E. T. Prewitt, FeS phase transitions at high pressures and temperatures (abstract), *Phys. Chem. Minerals*, in press, 1978.
- Kinsland, G. L., and W. A. Bassett, Modification of the diamond cell for measuring strain and the strength of materials at pressures up to 300 kilobar, *Rev. Sci. Instrum.*, **47**, 130-133, 1976.
- Konijnendijk, W. L., and J. M. Stevels, The structure of borosilicate glasses studied by Raman scattering, *J. Non-crystall. Solids*, **20**, 193-224, 1976.
- Korzhinsky, D. S., The theory of systems with perfectly mobile components and processes of mineral formation, *Amer. J. Sci.*, **263**, 193-205, 1965.
- Koster van Groos, A. F., The effect of high CO_2 pressures on alkalic rocks and its bearing on the formation of alkalic ultrabasic rocks and the associated carbonatites, *Amer. J. Sci.*, **275**, 163-185, 1975.
- Koster van Groos, A. F., and P. J. Wyllie, Liquid immiscibility in the system $\text{Na}_2\text{O-Al}_2\text{O}_3\text{-SiO}_2\text{-CO}_2$ at pressures to 1 kilobar, *Amer. J. Sci.*, **264**, 234-255, 1966.
- Koster van Groos, A. F., and P. J. Wyllie, Liquid immiscibility in the join $\text{NaAlSi}_3\text{O}_8\text{-Na}_2\text{CO}_3\text{-H}_2\text{O}$ and its bearing on the genesis of carbonatites, *Amer. J. Sci.*, **266**, 932-967, 1968.
- Koster van Groos, A., and P. J. Wyllie, Liquid immiscibility in the join $\text{NaAlSi}_3\text{O}_8\text{-CaAl}_2\text{Si}_2\text{O}_8\text{-Na}_2\text{CO}_3\text{-H}_2\text{O}$, *Amer. J. Sci.*, **273**, 465-487, 1973.
- Kratz, W. A., and J. Myers, Nutrition and growth of several blue-green algae, *Amer. J. Botany*, **42**, 282-287, 1955.
- Kresten, P., Uranium in kimberlites and asso-

- ciated rocks, with special reference to Lesotho occurrences, *Lithos*, 7, 171–180, 1974.
- Kresten, P., P. Fels, and G. Berggren, Kimberlitic zircons—a possible aid in prospecting for kimberlites, *Miner. Deposita*, 10, 47–56, 1975.
- Krogh, T. E., A low-contamination method for the hydrothermal decomposition of zircon and extraction of U and Pb for isotopic age determination, *Geochim. Cosmochim. Acta*, 37, 485–494, 1973.
- Kriegsmann, H., The vibrational spectra and structure of hexamethyl cyclotrisiloxane and hexamethyl cyclotrisilaxane, *Z. Anorg. Allg. Chem.* 298, 223–231, 1959a.
- Kriegsmann, H., The vibrational spectra of higher dimethyl polysiloxane rings and the structure of octamethyl cyclotetrasiloxane, *Z. Anorg. Allg. Chem.*, 298, 231–240, 1959b.
- Kurkjian, C. R., and R. W. Douglas, in *Phys. Chem. Glasses*, 1, 19–21, 1960.
- Kushiro, I., The system forsterite-diopside-silica with and without water at high pressures, *Amer. J. Sci.*, 267A, 269–294, 1969.
- Kushiro, I., Determination of liquidus relations in synthetic silicate systems with electron probe analysis: The system forsterite-diopside-silica at 1 atmosphere, *Amer. Mineral.* 57, 1260–1271, 1972.
- Kushiro, I., On the nature of silicate melt and its significance in magma genesis: regularities in the shift of the liquidus boundaries involving olivine, pyroxene, and silica minerals, *Amer. J. Sci.*, 275, 411–431, 1975.
- Kushiro, I., Changes in viscosity and structure of melt of $\text{NaAlSi}_2\text{O}_6$ composition at high pressures, *J. Geophys. Res.*, 81, 6347–6350, 1976.
- Kushiro, I., Phase transformation in silicate melts under upper mantle conditions, in *High Pressure Research, Applications in Geophysics*, Academic Press, Inc., New York, San Francisco, London, 25–37, 1977.
- Kushiro, I., and T. Fujii, Flotation of plagioclase in magma at high pressures and its bearing on the origin of anorthosite, *Proc. Japan Acad.* 53, Ser. B, 262–266, 1977.
- Kushiro, I., H. Satake, and S. Akimoto, Carbonate-silicate reactions at high pressures and possible presence of dolomite and magnesite in the upper mantle, *Earth Planet. Sci. Lett.*, 28, 116–120, 1975.
- Kushiro, I., H. S. Yoder, Jr., and B. O. Mysen, Viscosities of basalt and andesite melts at high pressures, *J. Geophys. Res.* 81, 6351–6356, 1976.
- Lacey, E. D., Aluminum in glasses and in melts, *Phys. Chem. Glasses*, 4, 234–238, 1963.
- Lachowski, E. E., and F. P. Glasser, Application of gas chromatography to mineral chemistry: aluminum and silicon ordering in melilites, *Mineral. Mag.*, 39, 412–419, 1973.
- Lagache, M., and G. Sabatier, Distribution des éléments Na, K, Rb et Cs à l'état de trace entre feldspaths alcalins et solutions hydrothermales à 650°C, 1 kbar: données expérimentales et interprétation thermodynamique, *Geochim. Cosmochim. Acta*, 37, 2617–2640, 1973.
- Lambe, R. L., and D. Schroer, Mössbauer studies of oxygen stabilized Eu^{2+} in CaF_2 , *Phys. Rev. Lett.*, 56, 45–48, 1976.
- Lambert, I. B., and P. J. Wyllie, Melting of gabbro (quartz eclogite) with excess water to 35 kilobars, with geological applications, *J. Geol.*, 80, 693–708, 1972.
- Lauer, H. V., and R. V. Morris, Redox equilibria of multivalent ions in silicate glasses, *J. Amer. Ceram. Soc.*, 60, 443–451, 1977.
- Le Bas, M. J., *Carbonatite-Nephelinite Volcanism: An African Case History*, Wiley, London, 1977.
- Leeman, W. P., and E. J. Dasch, Strontium, lead, and oxygen isotopic investigation of the Skaergaard intrusion, East Greenland, *Earth Planet. Sci. Lett.*, in press, 1978.
- Lenz, C. W., Silicate minerals as sources of trimethylsilyl silicates and silicate structure analysis of sodium silicate solutions, *Inorg. Chem.*, 3, 574–579, 1964.
- Lenz, C. W., The silicate structure analysis of hydrated Portland cement paste, *Highw. Res. Board Spec. Rep.* 90, 1966.
- Liebau, F., Über die Kristallstruktur des Pyroxmangits $(\text{Mn, Fe, Ca, Mg})\text{SiO}_3$, *Acta Crystallogr.*, 12, 177–181, 1959.
- Liebermann, R. C., L. E. A. Jones, and A. E. Ringwood, Elasticity of aluminite, titanate, stannate and germanate compounds with the perovskite structure, *Phys. Earth Planet. Interiors*, 14, 165–178, 1977.
- Lindsley, D. H., and Munoz, J. L., Subsolidus relations along the join hedenbergite-ferrosilite, *Amer. J. Sci.*, Schairer Volume, 267A, 295–324, 1969.
- Lindsley, D. H., and S. A. Dixon, Diopside-enstatite equilibria at 850° to 1400°C, 5 to 35 kb, *Amer. J. Sci.*, 276, 1285–1301, 1976.
- Liu, L., Orthorhombic perovskite phases observed in olivine, pyroxene, and garnet at high pressures and temperatures, *Phys. Earth Planet. Interiors*, 11, 289–298, 1976.
- Liu, L. G., Post-oxide phases of forsterite and enstatite, *Geophys. Res. Lett.*, 2, 417–419, 1975.
- Loewenstein, W., The distribution of aluminum in the tetrahedra of silicates and aluminates, *Amer. Mineral.*, 39, 92–96, 1954.
- Lofgren, G. E., and C. H. Donaldson, Curved branching crystals and differentiation in comb-layered rocks, *Contrib. Mineral. Petrol.*, 49, 309–319, 1975.
- Longhi, J., and D. Walker, Fe-Mg distribution between olivine and lunar basaltic liquids (abstract), *Eos*, 56, 471, 1975.
- Lowder, G. G., and I. S. E. Carmichael, The volcanoes and caldera of Talasea, New Britain:

- geology and petrology, *Geol. Soc. Amer. Bull.*, **81**, 17–38, 1970.
- Maeda, Y., and Y. Takashima, Mössbauer studies of solid solution systems of Fe(P, As), (Fe, Co) P, (Fe, Mn) P and (Fe, W) P, *J. Inorg. Nucl. Chem.*, **35**, 1219–1225, 1973.
- Malløe, S., Crystallization relationships of the Skaergaard intrusion, East Greenland, Ph.D. dissertation, University of Chicago, 1974.
- Mao, H. K., and P. M. Bell, Polarized crystal-field spectra of micro particles of the moon, *Am. Soc. Test. Mater. Spec. Tech. Publ.*, **539**, 100–119, 1973.
- Mao, H. K., and P. M. Bell, High-pressure physics: the 1-megabar mark on the ruby R_1 static pressure scale, *Science*, **191**, 851–852, 1976.
- Mao, H. K., and P. M. Bell, Equations of state of MgO and ϵ -Fe under static pressure conditions, *J. Geophys. Res.*, in press, 1978.
- Mao, H. K., W. A. Bassett, and T. Takahashi, Effect of pressure on crystal structure and lattice parameters of iron up to 300 kbar, *J. Appl. Phys.*, **38**, 272–276, 1967.
- Mao, H. K., P. M. Bell, J. Shaner, and D. Steinberg, Specific volume measurements of Cu, Mo, Pd, and Ag, and calibration of the ruby R_1 fluorescence pressure gauge from 0.06 to 1 Mbar, *J. Appl. Phys.*, **49**, 3276–3283, 1978a.
- Mao, H. K., P. M. Bell, J. Shaner, and D. Steinberg, A system of pressure calibration for the range 0.05–1.0 Mbar based on shock wave equations of state for Cu, Mo, Pd, and Ag, in *Proceedings of the Sixth AIRAPT International High Pressure Conference*, in press, 1978b.
- Masson, C. R., Anionic constitution of glass-forming melts, *J. Non-Cryst. Solids*, **25**, 3–41, 1977.
- Mattinson, J. M., Preparation of hydrofluoric, hydrochloric and nitric acids at ultralow lead levels, *Anal. Chem.*, **44**, 1715–1716, 1972.
- Mazzullo, L. J., S. A. Dixon, and D. H. Lindsay, T-FO₂ relationships in Mn-bearing compositions, *Geol. Soc. Amer., Abstracts with Programs*, **7**, 1192, 1975.
- MacGregor, I. D., A hypothesis for the origin of kimberlite, *Mineral. Soc. Amer. Spec. Paper* **3**, 51–62, 1970.
- MacGregor, I. D., The system MgO-Al₂O₃-SiO₂: solubility of Al₂O₃ in enstatite for spinel and garnet peridotite compositions, *Am. Mineral.*, **59**, 110–119, 1974.
- Mackey, J. H., H. L. Smith, and A. Halperin, Optical studies in x-irradiated high purity sodium silicate glasses, *J. Phys. Chem. Solids*, **27**, 1759–1772, 1966.
- McBirney, A. R., Differentiation of the Skaergaard intrusion, *Nature (London)*, **253**, 691–694, 1975.
- McBirney, A. R., and K. Aoki, Petrology of the Galápagos Islands, in *The Galápagos; Proceedings of the Symposia of the Galápagos International Scientific Project*, R. I. Bowman, ed., University of California Press, Berkeley and Los Angeles, pp. 71–77, 1966.
- McBirney, A. R., and H. Williams, Volcanic history of Nicaragua, *Univ. Calif. Publ. Geol. Sci.*, **55**, 65 pp., 1965.
- McCarthy, G. J., Oxygen fugacity-temperature diagram for the Eu-O system, *J. Amer. Ceram. Soc.*, **57**, 502, 1974.
- McMahon, B. M., and S. E. Haggerty, Oka carbonatite-complex oxide mineral zoning in mantle petrogenesis, *Geol. Soc. Amer., Abstracts with Programs*, **8**, 1006, 1976.
- McMahon, B. M., and S. E. Haggerty, The Oka carbonatite composition and the role of immiscible silicate liquids, *Extended Abstracts, Second International Kimberlite Conference*, Santa Fe, New Mexico, 1977.
- Melcher, G. C., The carbonatite of Jacupiranga, Sao Paulo, Brazil, in *Carbonatites*, O. F. Tuttle and J. Gittins, eds., John Wiley and Sons, New York, 169–181, 1966.
- Mercier, J. C., Peridotite xenoliths and the dynamics of kimberlite intrusion, *Extended Abstracts, Second International Kimberlite Conference*, Santa Fe, New Mexico, 1977.
- Merrill, R. B., and P. J. Wyllie, Absorption of iron by platinum capsules in high-pressure rock melting experiments, *Amer. Mineral.*, **58**, 16–20, 1973.
- Merrill, L., and W. A. Bassett, Miniature diamond anvil pressure cell for single-crystal X-ray diffraction studies, *Rev. Sci. Instrum.*, **45**, 290–294, 1974.
- Meyer, H. O. A., H-M. Tsai, and J. J. Gurney, Enstatite xenocryst containing coexisting Cr-poor and Cr-rich garnet, Weltevreden Floors, South Africa, *Extended Abstracts, Second International Kimberlite Conference*, Santa Fe, New Mexico, 1977.
- Middlemost, E. A. K., Petrogenetic model for the origin of carbonatites, *Lithos*, **7**, 275–278, 1974.
- Middleton, G. V., Experiments on density and turbidity currents: I. Motion of the head, *Can. J. Earth Sci.*, **3**, 523–546, 1966a.
- Middleton, G. V., Experiments on density and turbidity currents. II. Uniform flow of density currents, *Can. J. Earth Sci.*, **3**, 627–637, 1966b.
- Middleton, G. V., Experiments on density and turbidity currents, III. Deposition of sediment, *Can. J. Earth Sci.*, **4**, 475–505, 1967.
- Milkey, R. G., Infrared spectra of some tectosilicates, *Amer. Mineral.*, **45**, 990–1007, 1960.
- Mitchell, R. H., Composition of perovskite in kimberlite, *Amer. Mineral.*, **57**, 1748–1753, 1972.
- Mitchell, R. H., Magnesian ilmenite and its role in kimberlite petrogenesis, *J. Geol.*, **81**, 301–311, 1973.
- Mitchell, R. H., Geochemistry of magnesian

- ilménites from kimberlites from South Africa and Lesotho, *Lithos*, 10, 29–37, 1977a.
- Mitchell, R. H., Mineralogy of the Tunraq kimberlite, Somerset Island, N.W.T., Canada, *Extended Abstracts, Second International Kimberlite Conference*, Santa Fe, New Mexico, 1977b.
- Mitchell, R. H., and A. O. Brunfelt, Rare earth element geochemistry of kimberlite, *Phys. Chem. Earth*, 9, 671–686, 1975.
- Mitchell, R. H., and D. A. Carswell, Lanthanum samarium and ytterbium abundances in some southern African garnet lherzolites, *Earth Planet. Sci. Lett.*, 31, 175–178, 1976.
- Mitchell, R. H., and D. B. Clarke, Oxide and sulphide mineralogy of the Peuyuk kimberlite, Somerset Island, N.W.T., Canada, *Contrib. Mineral. Petrol.*, 56, 157–172, 1976.
- Mitchell, R. H., and J. H. Crocket, The isotopic composition of strontium in some South African kimberlites, *Contrib. Mineral. Petrol.*, 30, 277–290, 1971.
- Miyashiro, A., The ranges of chemical composition in nepheline and their petrogenetic significance, *Geochim. Cosmochim. Acta*, 1, 278–283, 1951.
- Moenke, H. H. W., in *Infrared Spectra of Minerals*, V. C. Farmer, ed., Mineralogical Soc. London, ch. 16, pp. 365–382, 1974.
- Moorbath, S., and H. Welke, Lead isotope studies on igneous rocks from the Isle of Skye, northwest Scotland, *Earth Planet. Sci. Lett.*, 5, 217, 1969.
- Moore, J. G., and B. P. Fabbi, An estimate of the juvenile sulfur content of basalt, *Contrib. Mineral. Petrol.*, 33, 118–127, 1971.
- Morris, R. V., and L. A. Haskin, EPR measurement of the effect of glass composition on the oxidation state of europium, *Geochim. Cosmochim. Acta*, 38, 1415–1445, 1974.
- Morris, R. V., L. A. Haskin, G. M. Biggar, and M. J. O'Hara, Measurements of the effect of temperature and partial pressure of oxygen on the oxidation states of europium in silicate glasses, *Geochim. Cosmochim. Acta*, 38, 1447–1459, 1974.
- Morse, S. A., The feldspar/magma density paradox, The Nain Anorthosite Project, Labrador: Field Report 1972, *Univ. Mass. Geol. Dept. Contrib. No. 11*, 113–116, 1972.
- Muan, A., and E. F. Osborn, Phase equilibria at liquidus temperatures in the system $\text{MgO-FeO-Fe}_2\text{O}_3\text{-SiO}_2$, *J. Amer. Ceram. Soc.*, 39, 121–140, 1956.
- Muenow, D., J. R. Delaney, A. Meijer, and N. Liu, Water-rich glass-vapor inclusions in phenocrysts from tholeiitic pillow basalt rims in the Marianas back arc basin (abstract), *Eos*, 58, 530, 1977.
- Murase, T., and A. R. McBirney, Properties of some common igneous rocks and their melts at high temperatures, *Geol. Soc. Amer. Bull.*, 84, 3563–3592, 1973.
- Murata, K. J., Internal structure of silicate minerals that gelatinize with acid, *Amer. Mineral.*, 28, 545–562, 1943.
- Murphy, W. M., An experimental study of solid-liquid equilibria in the albite-anorthite-diopside system, M.S. Thesis, University of Oregon, 1977.
- Mysen, B. O., Partitioning of samarium and nickel between olivine, orthopyroxene and liquid; preliminary data at 20 kbar and 1025°C, *Earth Planet. Sci. Lett.*, 31, 1–7, 1976a.
- Mysen, B. O., The role of volatiles in silicate melts: solubility of carbon dioxide and water in feldspar, pyroxene and feldspathoid melts to 30 kbar and 1625°C, *Amer. J. Sci.*, 276, 969–996, 1976b.
- Mysen, B. O., Experimental determination of nickel partition coefficients between liquid, pargasite, and garnet peridotite minerals and concentration limits of behavior according to Henry's law at high pressure and temperature, *Amer. J. Sci.*, 278, 217–243, 1978a.
- Mysen, B. O., Trace element partitioning between garnet peridotite minerals and water-rich vapor: experimental data from 5 to 30 kbar, *Amer. Mineral.*, in press, 1978b.
- Mysen, B. O., and A. L. Boettcher, Melting of a hydrous mantle: I. Phase relations of natural peridotite at high pressures and temperatures with controlled activities of water, carbon dioxide, and hydrogen, *J. Petrology*, 16, 520–548, 1975.
- Mysen, B. O., and J. R. Holloway, Experimental determination of rare earth fractionation patterns in partial melts from peridotite in the upper mantle, *Earth Planet. Sci. Lett.*, 34, 231–237, 1977.
- Mysen, B. O., and I. Kushiro, Compositional variations of coexisting phases with degree of melting of peridotite in the upper mantle, *Amer. Mineral.*, 62, 843–865, 1977.
- Mysen, B. O., and I. Kushiro, Pressure-dependence of nickel partitioning between forsterite and aluminous silicate melts, *Earth Planet. Sci. Lett.*, in press, 1978.
- Mysen, B. O., and M. G. Seitz, Trace element partitioning determined by beta-track mapping—an experimental study using carbon and samarium as examples, *J. Geophys. Res.*, 80, 2627–2635, 1975.
- Mysen, B. O., and D. Virgo, Influence of pressure, temperature and bulk composition on melt structures in the system $\text{NaAlSi}_3\text{O}_8\text{-NaFe}^{3+}\text{Si}_2\text{O}_6$, *Amer. J. Sci.*, in press, 1978.
- Mysen, B. O., D. H. Eggler, M. G. Seitz, and J. R. Holloway, Carbon dioxide in silicate melts and crystals. Part I. Solubility measurements, *Amer. J. Sci.*, 276, 455–479, 1976.
- Narita, H., K. Koto, and N. Morimoto, The crystal structures of MnSiO_3 polymorphs

- (rhodonite- and pyroxmangite-type), *Mineral. J.*, **8**, 329–342, 1977.
- Narten, A. J., Diffraction pattern and structure of noncrystalline BeF_2 and SiO_2 at 25°C , *J. Chem. Phys.*, **56**, 1905, 1972.
- Navrotsky, A., Thermodynamics of element partitioning: (1) Systematics of transition metals in crystalline and molten silicates and (2) Defect chemistry and “the Henry’s Law problem,” *Geochim. Cosmochim. Acta*, in press, 1978.
- Neumann van Padang, M., *Catalogue of the Active Volcanoes of the World, Part 1, Indonesia*, International Volcanological Association, Naples, pp. 161–213, 1951.
- Nicholls, I. A., Petrology of Santorini volcano, Cyclades, Greece, *J. Petrology*, **12**, 67–119, 1971.
- Nicolas, A., and D. Ricoult, Estimates of stress and recovery conditions in various types of mantle peridotites, *Extended Abstracts, Second International Kimberlite Conference*, Santa Fe, New Mexico, 1977.
- Nixon, P. H., and F. R. Boyd, Petrogenesis of the granular and sheared ultrabasic nodule suite in kimberlites, in *Lesotho Kimberlites*, P. H. Nixon, ed., Lesotho National Development Corporation, Maseru, Lesotho, pp. 48–56, 1973a.
- Nixon, P. H., and F. R. Boyd, The discrete nodule association in kimberlites from northern Lesotho, in *Lesotho Kimberlites*, P. H. Nixon, ed., Lesotho National Development Corporation, Maseru, Lesotho, pp. 67–75, 1973b.
- Nixon, P. H., and F. R. Boyd, The Lihobong intrusion and kimberlitic olivine composition, in *Lesotho Kimberlites*, P. H. Nixon, ed., Lesotho National Development Corporation, Maseru, Lesotho, pp. 141–148, 1973c.
- Nixon, P. H., and F. R. Boyd, Discrete nodules (megacrysts) and lamellar intergrowths in Frank Smith kimberlite pipe, *Extended Abstracts, International Conference on Kimberlites*, Rondebosch, South Africa, 1973d.
- Nixon, P. H., and F. R. Boyd, Garnet-bearing ultrabasic and discrete nodules suites from Malaita, Solomon Islands, S.W. Pacific, and their bearing on an oceanic geotherm, *Extended Abstracts, Second International Kimberlite Conference*, Santa Fe, New Mexico, 1977.
- Nockleberg, W. J., CO_2 as a source of oxygen in the metasomatism of carbonates, *Amer. J. Sci.*, **273**, 498–514, 1973.
- Norman, M., R. A. Coish, and L. A. Taylor, Glass chemistry and magma evolution at Mare Crisium (abstract), in *Papers Presented to the Conference on Luna 24*, The Lunar Science Institute, Houston, pp. 136–138, 1977.
- Nukui, A., H. Tagai, H. Morikawa, and S. Iwai, Structural study of molten silica by an x-ray radial distribution analysis, *J. Amer. Ceram. Soc.*, **61**, 174–176, 1978.
- Obukhov-Danisov, V. V., N. N. Sobolev, and V. P. Cheremisinov, Vibrational spectra for germanium dioxide modifications, *Opt. Spektrosk.*, **8**, 505–510, 1960.
- O’Hara, M. J., The bearing of phase equilibria studies in synthetic and natural systems on the origin and evolution of basic and ultrabasic rocks, *Earth Sci. Rev.*, **4**, 69–133, 1968.
- O’Hara, M. J., Is there an Icelandic mantle plume? *Nature*, **253**, 708–710, 1975.
- O’Hara, M. J., and H. S. Yoder, Jr., Formation and fractionation of basic magmas at high pressures, *Scot. J. Geol.*, **3**, 67–117, 1967.
- O’Hara, M. J., M. J. Saunders, and E. L. P. Mercy, Garnet peridotite primary ultrabasic magma and eclogite; interpretation of upper mantle processes in kimberlite, *Phys. Chem. Earth*, **9**, 571–604, 1975.
- Ohmoto, H., and D. Kerrick, Devolatilization equilibria in graphitic systems, *Amer. J. Sci.*, **277**, 1013–1044, 1977.
- Ok, H. N., and S. W. Lee, Mössbauer study of Fe_7Se_8 , *Phys. Rev.*, **138**, 4267–4269, 1973.
- Ono, K., A. Ito, and E. Hirahara, Mössbauer study of hyperfine field, quadrupole interaction, and isomer shift of Fe^{57} in $\text{FeS}_{1.00}$, $\text{FeS}_{1.05}$ and $\text{FeS}_{1.07}$, *J. Phys. Soc. Japan*, **17**, 1615–1620, 1962.
- Orville, P. M., Unit-cell parameters of the microcline–low albite and the sanidine–high albite solid solution series, *Amer. Mineral.*, **52**, 55–86, 1967.
- Osborn, E. F., Role of oxygen pressure in the crystallization and differentiation of basaltic magma, *Amer. J. Sci.*, **257**, 609–647, 1959.
- Osborn, E. F., The complementariness of orogenic andesite and alpine peridotite, *Geochim. Cosmochim. Acta*, **33**, 307–324, 1969a.
- Osborn, E. F., Genetic significance of V and Ni contents of andesites: Comments on a paper by Taylor, Kay, White, Duncan and Ewart, *Geochim. Cosmochim. Acta*, **33**, 1553–1554, 1969b.
- Osborn, E. F., Origin of calc-alkali magma series of Santorini volcano type in the light of recent experimental phase equilibrium studies, in *Proc. Int. Congr. on Thermal Waters, Geothermal Energy and Volcanism of the Mediterranean Area*, Athens, Greece, October 1976, **3**, 154–167, 1976.
- Osborn, E. F., The reaction principle, in *The Evolution of Igneous Rocks (Fiftieth Anniversary Appraisal)*, H. S. Yoder, Jr., ed., Princeton University Press, Princeton, New Jersey, ch. v, in press, 1978.
- Osborn, E. F., and A. Muan, The system $\text{CaO}-\text{FeO}-\text{SiO}_2$, Phase equilibrium diagrams of oxide systems, *Amer. Ceram. Soc.*, plate 7, 1960.
- Padovani, E. R., and J. L. Carter, Granulite facies xenoliths from Kilbourne Hole Maar, New Mexico, and their bearing on deep crys-

- tal evolution, *Extended Abstracts, Second International Kimberlite Conference*, Santa Fe, New Mexico, 1977a.
- Padovani, E. R., and J. L. Carter, Aspects of the deep crustal evolution beneath south-central New Mexico, in "The Earth's Crust," J. G. Heacock, ed., *Geophys. Monogr. Am. Geophys. Union*, 20, 19-55, 1977b.
- Palabora Mining Company Limited Mine Geological and Mineralogical Staff, The geology and economic deposit of copper, iron and vermiculite in the Palabora igneous complex: a brief review, *Econ. Geol.*, 71, 177-192, 1976.
- Parmentier, E. M., and D. L. Turcotte, An explanation of the pyroxene geotherm based on plume convection in the upper mantle, *Earth Planet. Sci. Lett.*, 24, 209-212, 1974.
- Pasteris, J. D., F. R. Boyd, and P. H. Nixon, The Frank Smith ilmenite association, *Proceedings of the Second International Kimberlite Conference*, in press, 1978.
- Peacor, D., and N. Niizeki, The determination and refinement of the crystal structure of rhodonite, (Mn, Ca)SiO₃, *Z. Kristallogr.*, 119, 98-116, 1963.
- Peacor, D., E. Essene, P. Brown, and G. Winter, The crystal chemistry and petrogenesis of a magnesian rhodonite, *Amer. Mineral.*, 63, in press, 1978.
- Pepkowitz, L. P., and E. R. Proud, Determination of hydrogen—a universal gasometric micromethod, *Anal. Chem.*, 21, 1000-1003, 1949.
- Pichulo, R. O., J. S. Weaver, and T. Takahashi, Experimental study of high pressure polymorphism in FeS (abstract), *Meteoritics*, 11, 351, 1976.
- Pidgeon, R. T., and D. R. Bowes, Zircon U-Pb ages of granulites from the central region of the Lewisian, northwestern Scotland, *Geol. Mag.*, 109, 247-258, 1972.
- Piermarini, G. J., and S. Block, An ultrahigh pressure diamond-anvil cell and several semiconductor phase transition pressures in relation to the fixed point pressure scale, *Rev. Sci. Instrum.*, 46, 973-979, 1975.
- Pinckney, L. R., and D. H. Lindsley, Effects of magnesium on iron-titanium oxides, *Geol. Soc. Amer., Abstracts with Programs*, 8, 1051, 1976.
- Philpotts, J. A., and C. C. Schnetzler, Phenocryst-matrix partition coefficients for K, Rb, Sr, and Ba, with applications to anorthosite and basalt genesis, *Geochim. Cosmochim. Acta*, 34, 307-322, 1970.
- Prandtl, L., *Essentials of Fluid Dynamics*, Blackie, London, 1952.
- Presnall, D. C., and N. L. Brenner, A method for studying iron silicate liquids under reducing conditions with negligible iron loss, *Geochim. Cosmochim. Acta*, 38, 1785-1788, 1974.
- Presnall, D. C., C. L. Simmons, and H. Porath, Changes in electrical conductivity of a synthetic basalt during melting, *J. Geophys. Res.*, 77, 5665-5672, 1972.
- Prins, P., Composition of magnetite from carbonatites, *Lithos*, 5, 227-240, 1972.
- Proto, S. P. S., and D. L. Wood, Ruby optical maser as a Raman source, *J. Opt. Soc. Amer.*, 52, 251-252, 1962.
- Quist, A. S., and W. L. Marshall, Electrical conductances of aqueous sodium chloride solutions from 0° to 800° and at pressures to 4000 bars, *J. Phys. Chem.*, 72, 684-703, 1968.
- Raman, C. V., A new radiation, *Indian J. Phys.*, 2, 387-398, 1928.
- Ramberg, H., Mantle diapirism and its tectonic and magmatic consequences, *Phys. Earth Planet. Interiors*, 5, 45-60, 1972.
- Rawlinson, P. J., and J. B. Dawson, A quench orthopyroxene-ilmenite xenolith from kimberlite—evidence for Ti-rich liquid in the upper mantle, *Extended Abstracts, Second International Kimberlite Conference*, Santa Fe, New Mexico, 1977.
- Reddy, K. V., S. C. Chetty, Mössbauer studies on the Fe-Se system, *Phys. Status Solidi*, A32, 585-592, 1975.
- Rhodes, J. M., and J. B. Dawson, Major and trace element geochemistry of peridotite inclusions from the Lashaine volcano, Tanzania, *Phys. Chem. Earth*, 9, 545-559, 1975.
- Ricker, R. W., and E. F. Osborn, Additional phase equilibrium data for the system CaO-MgO-SiO₂, *J. Am. Ceram. Soc.*, 37, 133-139, 1954.
- Ridley, W. I., and J. B. Dawson, Lithophile trace element data bearing on the origin of peridotite xenoliths, ankaramite and carbonatite from Lashaine volcano, Tanzania, *Phys. Chem. Earth*, 9, 559-571, 1975.
- Riebling, E. F., Structure of molten oxides. I. Viscosity of GeO₂, and binary germanates containing Li₂O, Na₂O, K₂O and Rb₂O, *J. Chem. Phys.*, 39, 1889-1895, 1963.
- Riebling, E. F., Structure of sodium aluminosilicate melts containing at least 50 mole % SiO₂ at 1500°C, *J. Chem. Phys.*, 44, 2857-2865, 1966.
- Riebling, E. F., Structural similarities between a glass and its melt, *J. Amer. Ceram. Soc.*, 51, 143-149, 1967.
- Ringwood, A. E., *Composition and Petrology of the Earth's Mantle*, McGraw-Hill, New York, pp. 450-451, 1975.
- Robertson, J. K., and P. J. Wyllie, Rock-water systems, with special reference to the water-deficient region, *Amer. J. Sci.*, 271, 252-278, 1971.
- Robie, R. A., P. M. Bethke, and K. M. Beardsley, Selected x-ray crystallographic data, molar volumes, and densities of minerals and related substances, *U.S. Geol. Surv. Bull.*, 1248, 1967.

- Robie, R. A., and D. R. Waldbaum, Thermodynamic properties of minerals and related substances at 298.15°K (25.0°C) and one atmosphere (1.013 bars) pressure and at higher temperatures, *U.S. Geol. Surv. Bull.*, 1259, 1968.
- Robinson, P. R., and H. W. Jaffe, Chemographic exploration of amphibole assemblages from central Massachusetts and southwestern New Hampshire, *Mineral. Soc. Amer. Sp. Pap.*, 2, 251-274, 1969.
- Roedder, E., Low-temperature liquid immiscibility in the system K_2O - FeO - Al_2O_3 - SiO_2 , *Amer. Mineral.*, 36, 282-286, 1951.
- Roeder, P. L., and R. F. Emslie, Olivine-liquid equilibrium, *Contrib. Mineral. Petrol.*, 29, 275-289, 1970.
- Roeder, P. L., and E. F. Osborn, Experimental data for the system MgO - FeO - Fe_2O_3 - $CaAl_2Si_2O_8$ - SiO_2 and their petrologic implications, *Amer. J. Sci.*, 264, 428-480, 1966.
- Ross, M., and J. S. Heubner, A pyroxene geothermometer based on composition-temperature relationships of naturally occurring orthopyroxene, pigeonite, and augite, *Int. Conf. on Geothermometry and Geobarometry, Extended Abstracts*, The Pennsylvania State University, 1975.
- Rumble, D., III, Andalusite, kyanite, and sillimanite from the Mt. Moosilauke region, New Hampshire, *Geol. Soc. Amer. Bull.*, 84, 2423-2430, 1973.
- Runciman, W. A., D. Sengupta, and M. Marshall, The polarized spectra of iron in silicates. Enstatite, *Amer. Mineral.*, 58, 444-450, 1973.
- Sahama, Th. G., Kalsilite in the lavas of Mt. Nyiragongo (Belgian Congo), *J. Petrology*, 1, 146-171, 1960.
- Sato, Y., Pressure-volume relationship of stishovite under hydrostatic compression, *Earth Planet. Sci. Lett.*, 34, 307-312, 1977.
- Savin, S. M., and S. Epstein, The oxygen isotopic composition of coarse-grained sedimentary rocks and minerals, *Geochim. Cosmochim. Acta*, 34, 323-329, 1970.
- Sawatzky, G. A., F. van der Woude, and A. H. Morrish, Recoilless-fraction ratios for ^{57}Fe in octahedral and tetrahedral sites of a spinel and a garnet, *Phys. Rev.*, 183, 383-386, 1969.
- Schairer, J. F., The system K_2O - MgO - Al_2O_3 - SiO_2 : I. Results of quenching experiments on four joins in the tetrahedron cordierite-forsterite-leucite-silica and on the join cordierite-mullite-potash feldspar, *J. Amer. Ceram. Soc.*, 37, 501-533, 1954.
- Schairer, J. F., and N. L. Bowen, The system, leucite-diopside-silica, *Amer. J. Sci.*, 35A, 289-309, 1938.
- Schairer, J. F., and N. L. Bowen, The system K_2O - Al_2O_3 - SiO_2 , *Amer. J. Sci.*, 253, 681-746, 1955.
- Schmitt, R. A., R. H. Smith, J. E. Lasch, A. W. Mosen, D. A. Olehy, and J. Vasilevski, Abundances of fourteen rare-earth elements, scandium and yttrium in meteoric and terrestrial matter, *Geochim. Cosmochim. Acta*, 27, 577-622, 1963.
- Schmitt, R. A., R. H. Smith, and D. A. Olehy, Rare-earth, yttrium and scandium abundances in meteoric and terrestrial matter, II, *Geochim. Cosmochim. Acta*, 28, 67-86, 1964.
- Schnetzler, C. C., and J. A. Philpotts, Partition coefficients of rare earth elements between igneous matrix material and rock-forming mineral phenocrysts—II, *Geochim. Cosmochim. Acta*, 34, 331-340, 1970.
- Schreyer, W., G. Kullerud, and P. Ramdohr, Metamorphic conditions of ore and country rock of the Bodenmais, Bavaria sulfide deposit, *Neues Jahrb. Mineral. Abh.*, 101, 1-26, 1964.
- Schwarcz, E. J., and D. C. Harris, Phases in natural pyrrhotite and the effect of heating on their magnetic properties and composition, *Geomagnetism Geoelectricity J.*, 22, 463-470, 1970.
- Scott, J. F., Raman spectra of GeO_2 , *Phys. Rev. B*, 1, 3488-3493, 1970.
- Scott, S. D., Experimental calibration of the sphalerite geobarometer, *Econ. Geol.*, 68, 466-474, 1973.
- Scott, S. D., Application of the sphalerite geobarometer to regionally metamorphosed terrains, *Amer. Mineral.*, 61, 661-670, 1976.
- Scott, S. D., R. A. Both, and S. A. Kissin, Sulfide petrology of the Broken Hill Region, New South Wales, *Econ. Geol.*, 72, 1410-1425, 1977.
- Shafer, E. C., and R. Roy, The system GeO_2 - SiO_2 , Tenth technical report on U.S. Army Signal Corps Contract DA36-039, SC. 63099, 1956.
- Shannon, R. D., and C. T. Prewitt, Effective ionic radii in oxides and fluorides, *Acta Crystallogr.*, B25, 925-946, 1969.
- Sharma, S. K., Raman study of ferric chloride hexahydrate and ferric chloride hexadehydrate in crystalline, molten and glassy states, *J. Non-crystall. Solids*, 15, 83-95, 1974.
- Sharp, W. E., The thermodynamic properties for water in the range -10° to $1000^\circ C$ and 1 to 250,000 bars, *ECRL-7118, Chemistry, UC-4, TID-4500*, Lawrence Radiation Laboratory, University of California, Livermore, 51 pp., 1962.
- Shaw, D. M., Trace element fractionation during anatexis, *Geochim. Cosmochim. Acta*, 34, 237-243, 1970.
- Shaw, H. R., Rheology of basalt in the melting range, *J. Petrology*, 10, 510-535, 1969.
- Sheppard, S. M. F., and J. B. Dawson, Hydrogen, carbon and oxygen isotope studies of megacryst and matrix minerals from Lesothoan and South African kimberlites, *Phys. Chem. Earth*, 9, 747-764, 1975.

- Shieh, Y. N., and H. P. Taylor, Jr., Oxygen and carbon isotope studies of contact metamorphism of carbonate rocks, *J. Petrology*, 10, 307-331, 1969.
- Shima, H., and A. J. Naldrett, Solubility of sulfur in ultramafic melt and the relevance of the system Fe-S-O, *Econ. Geol.*, 70, 960-967, 1975.
- Shimizu, N., Rare earth elements in garnets and clinopyroxenes from garnet lherzolite inclusions in kimberlites, *Earth Planet. Sci. Lett.*, 25, 26-32, 1975.
- Shirane, G., D. E. Cox, W. J. Takei, and S. L. Ruby, A study of the magnetic properties of the FeTiO_3 - $\alpha\text{Fe}_2\text{O}_3$ system by neutron diffraction and the Mössbauer effect, *J. Phys. Soc. Jpn.*, 17, 1598-1611, 1962.
- Simkin, T., and J. V. Smith, Minor-element distribution in olivine, *J. Geol.*, 78, 304-325, 1970.
- Smith, J. V., *Feldspar Minerals*, Vol. 1, Springer-Verlag, New York, 1974.
- Sobolev, N. V., *Deep-seated Inclusions in Kimberlites and the Problem of the Composition of the Upper Mantle*, translated from the Russian by David A. Brown, English translation edited by F. R. Boyd, American Geophysical Union, Washington, D.C., 1977.
- Stewart, D. C., Crystal clots in calc-alkaline andesites as breakdown products of high-Al amphiboles, *Contrib. Mineral. Petrol.*, 53, 195-204, 1975.
- Stout, J. H., Phase petrology and mineral chemistry of coexisting amphiboles from Telemark, Norway, *J. Petrology*, 13, 99-145, 1972.
- Sun, C. O., R. J. Williams, and S. S. Sun, Distribution coefficients of Eu and Sr for plagioclase-liquid and clinopyroxene-liquid equilibria in oceanic ridge basalt: an experimental study, *Geochim. Cosmochim. Acta*, 38, 1415-1433, 1974.
- Swanson, D. A., Magma supply rate at Kilauea Volcano, 1952-1971, *Science*, 175, 169-170, 1972.
- Sweet, J. R., and W. B. White, Study of sodium silicate glasses and liquids by infra-red reflectance spectroscopy, *Phys. Chem. Glasses*, 10, 246-251, 1969.
- Sweet, J. R., W. B. White, E. W. White, and R. Roy, Structural and mineral investigations of lunar glasses and terrestrial glasses by Raman spectroscopy, *Proc. Fourth Lunar Sci. Conf. Geochim. Cosmochim. Acta supp.* 4, 1, 389-396, 1973.
- Syono, Y., M. Tokonami, and Y. Matsui, Crystal field effect on the olivine-spinel transition, *Phys. Earth Planet. Interiors*, 4, 347-352, 1971.
- Takahashi, T., H. K. Mao, and W. A. Bassett, Lead: x-ray diffraction study of a high-pressure polymorph, *Science*, 165, 1352-1353, 1969.
- Takeuchi, H., N. Fujii, and M. Kikuchi, Mechanism of magma ascent (in Japanese), *Jishin*, 25, 266-268, 1972.
- Tanzer, Marvin L., Cross-linking of collagen, *Science*, 180, 561-566, 1973.
- Taragin, M. E., and J. C. Eisenstein, Mössbauer study of europium in glass, *Phys. Rev. B*, 2, 3490-3494, 1970.
- Taylor, H. P., Jr., Water/rock interactions and the origin of H_2O in granitic batholiths, *J. Geol. Soc. London*, 133, 509-558, 1977.
- Taylor, L. A., and H. K. Mao, A high-pressure polymorph of troilite, FeS , *Science*, 170, 850-851, 1970.
- Taylor, S. R., Trace-element chemistry of andesites and associated calc-alkaline rocks, in "Proceedings of the Andesite Conference," A. R. McBirney, ed., *Oreg. Dep. Geol. Miner. Ind. Bull.*, 65, 43-63, 1969.
- Taylor, S. R., M. Kaye, A. J. R. White, A. R. Duncan, and A. Ewart, Genetic significance of Co, Cr, Ni, Sc and V content of andesites, *Geochim. Cosmochim. Acta*, 33, 275-286, 1969.
- Temperley, A. A., and H. W. Leferre, The Mössbauer effect in marcasite structure iron compounds, *J. Phys. Chem. Solids*, 27, 85-92, 1966.
- Thompson, A. B., Calc-silicate diffusion zones between marble and pelitic schist, *J. Petrology*, 16, 314-346, 1975.
- Thompson, J. B., Jr., Biopyroboles and polyso-matic series, *Amer. Mineral.*, 63, 239-249, 1978.
- Thompson, J. B., Jr., and S. A. Norton, Paleozoic regional metamorphism in New England and adjacent areas, in *Studies of Appalachian Geology*, E-an Zen *et al.*, eds., John Wiley and Sons, Inc., New York, pp. 203-218, 1968.
- Thorpe, R. S., P. J. Potts, and P. W. Francis, Rare earth data and petrogenesis of andesite from the North Chilean Andes, *Contrib. Mineral. Petrol.*, 54, 65-78, 1976.
- Tilley, C. E., *Nepheline Parageneses*, Sir Douglas Mawson Anniversary Volume, University of Adelaide, 167-177, 1952.
- Tilley, C. E., The nepheline rocks of the Port Herald Hills, Southern Nyasaland, *Overseas Geol. Miner. Resour.*, 8, 255-259, 1961.
- Tilley, C. E., and I. D. Muir, The Hebridean Plateau magma type, *Edinburgh Geol. Soc. Trans.*, 19, 208-215, 1962.
- Towell, D. G., J. W. Winchester, and R. V. Spurr, Rare earth distributions in some rocks and associated minerals of the batholith of Southern California, *J. Geophys. Res.*, 70, 3485-3496, 1965.
- Townsend, M. G., J. R. Gosselin, R. J. Tremblay, and A. H. Webster, Semi-conductor to metal transition in FeS , *J. Physique*, 37, C4-11, 1976.
- Turner, J. S., and C. F. Chen, Two-dimensional effects in double-diffusive correction, *J. Fluid Mech.*, 63, 577-592, 1974.
- Turnock, A. C., D. H. Lindsley, and J. E. Grover, Synthesis and unit cell parameters of Ca-Mg-

- Fe pyroxenes, *Amer. Mineral.*, 58, 50-59, 1973.
- Tuttle, O. F., and J. V. Smith, The nepheline-kalsilite system. II. Phase relations, *Amer. J. Sci.*, 256, 571-589, 1958.
- Ui, T., Recent volcanism in Masaya-Granada area, Nicaragua, *Bull. Volcanol.*, 36, 174-190, 1972.
- Van Baalen, C., Studies on marine blue-green algae, *Bot. Mar.*, 4, 129-139, 1962.
- Vaughn, D. J., and J. A. Tossell, Magnetic transitions observed in sulfide minerals at elevated pressures and their geophysical significance, *Science*, 179, 375-377, 1973.
- Vaughn, R. W., and H. G. Drickamer, Effect of pressure on the Mössbauer resonance in ferrocene and pyrite, *J. Chem. Phys.*, 47, 468-472, 1967.
- Velde, B., and I. Kushiro, Structure of sodium aluminosilicate melts quenched at high pressure; infrared and aluminum K-radiation data, *Earth Planet. Sci. Lett.*, 40, 137-140, 1978.
- Violet, C. E., and D. N. Pipkorn, Mössbauer line positions and hyperfine interactions in α iron, *J. Appl. Phys.*, 11, 4339-4342, 1971.
- Virgo, D., and S. S. Hafner, Fe^{2+} -Mg disorder in heated orthopyroxenes, *Mineral. Soc. Amer. Spec. Pap.*, 2, 67-87, 1969.
- Vogel, G. L., and W. E. Brown, Modification of solid state electrodes for microliter volumes, *Anal. Chem.*, in press, 1978.
- Waff, H. S., Pressure-induced coordination changes in magmatic liquids, *Geophys. Res. Lett.*, 2, 193-196, 1975.
- Wager, L. R., The major element variation of the Layered Series of the Skaergaard intrusion and re-estimation of the average composition of the Hidden Layered Series and of the successive residual magmas, *J. Petrology*, 1, 364-398, 1960.
- Wager, L. R., The mechanism of adcumulus growth in the layered series of the Skaergaard intrusion, *Mineral. Soc. Amer., Spec. Paper* 1, 1-19, 1963.
- Wager, L. R., and G. M. Brown, *Layered Igneous Rocks*, Oliver and Boyd, Ltd., Edinburgh, 1968.
- Wager, L. R., G. M. Brown, and W. J. Wadsworth, Types of igneous cumulates, *J. Petrology*, 1, 73-85, 1960.
- Wager, L. R., and W. A. Deer, Geological investigations in East Greenland, Pt. III, The petrology of the Skaergaard intrusion, Kangerdluqssuaq, East Greenland, *Medd. Groenl.*, 105, No. 4, 1939 (reissued 1962).
- Walther, J. V., and H. C. Helgeson, Calculation of the thermodynamic properties of aqueous silica and the solubility of quartz and its polymorphs at high pressures and temperatures, *Amer. J. Sci.*, 277, 1315-1351, 1977.
- Wäppling, R., L. Häggström, S. Rundgrist, and E. Karlsson, Mössbauer study of phosphides containing iron, *J. Solid State Chem.*, 3, 276-292, 1971.
- Warner, B. N., P. N. Shive, J. L. Allen, and C. Terry, A study of the hematite-ilmenite series by the Mössbauer effect, *J. Geomagn. Geoelectr.*, 24, 353-367, 1972.
- Warner, R. D., K. Keil, and G. J. Taylor, Coarse-grained basalt 71597: a product of partial olivine accumulation, *Proc. Eighth Lunar Sci. Conf.*, 1429-1442, 1977.
- Warner, R. D., and W. C. Luth, Two-phase data for the join monticellite (CaMgSiO_4)-forsterite (Mg_2SiO_4): experimental results and numerical analysis, *Amer. Mineral.*, 58, 998-1008, 1973.
- Washington, H. S., The Italite locality of Villa Senni, *Amer. J. Sci.*, 14, 173-198, 1927.
- Watkinson, D. H., and P. J. Wyllie, Phase equilibrium studies bearing on the limestone-assimilation hypothesis, *Bull. Geol. Soc. Amer.*, 80, 1565-1576, 1969.
- Watkinson, D. H., and P. J. Wyllie, Experimental study of the composition join NaAlSiO_4 - CaCO_3 - H_2O and the genesis of alkalic rock-carbonatite complexes, *J. Petrology*, 12, 357-378, 1971.
- Watson, E. B., Two-liquid partition coefficients: experimental data and geochemical implications, *Contrib. Mineral. Petrol.*, 56, 119-134, 1976.
- Weiblen, P. W., and G. L. Morey, The Duluth complex—a petrologic and tectonic summary, *Proc. 48th Annu. Mtg., Minnesota Sect., Amer. Inst. Min. Eng.*, 72-95, 1975.
- Wendlandt, R. F., The system K_2O - MgO - Al_2O_3 - SiO_2 - H_2O - CO_2 : phase relations of the joins $\text{Ph-H}_2\text{O-CO}_2$ and Ph-En-Mag at high temperatures and high pressures and applications to the genesis of alkalic magmas, *Extended Abstracts, Second International Kimberlite Conference*, Santa Fe, New Mexico, 1977.
- Whittaker, E. J. W., and R. Muntus, Ionic radii for use in geochemistry, *Geochim. Cosmochim. Acta*, 34, 945-956, 1970.
- Wiggins, L. B., and J. R. Craig, A reconnaissance investigation of chalcopyrite-sphalerite relationships in the Cu, Fe-Zn-S systems (abstract), *Geol. Soc. Amer. Abstracts with Programs*, 7, 1327, 1975.
- Wilburn, D. R., and W. A. Bassett, Hydrostatic compression of iron and related compounds: an overview, *Amer. Mineral.*, 63, in press, 1978.
- Wilcox, R. E., Petrology of Parícutin volcano, Mexico, *U.S. Geol. Surv. Bull.*, 965-C, 281-353, 1954.
- Williams, H., The great eruption of Coseguina, Nicaragua, in 1835 with notes on the Nicaraguan volcanic chain, *Univ. Calif. Publ. Geol. Sci.*, 29, 21-46, 1952.
- Williams, H., and A. R. McBirney, Volcanic

- history of Honduras, *Univ. Calif. Publ. Geol. Sci.*, 85, 101 pp., 1969.
- Wones, D. R., Physical properties of synthetic biotites on the join phlogopite-annite, *Amer. Mineral.*, 48, 1300-1321, 1963.
- Wong, J. and C. A. Angell, *Glass structure by spectroscopy*, Marcel Dekker, Inc., New York, 1976.
- Wright, N., and M. J. Hunter, Organosilicon polymers. III. Infrared spectra of methylpolysiloxanes, *J. Chem. Soc.*, 69, 803-809, 1947.
- Wyatt, B. A., The melting and crystallization behavior of a natural clinopyroxene-ilmenite intergrowth, *Contrib. Mineral. Petrol.*, 61, 1-9, 1977.
- Wyckoff, R. W. G., *The Biochemistry of Animal Fossils*, Sciencetechnica (Publishers) Ltd., Bristol, United Kingdom, 1972.
- Wyllie, P. J., and W. L. Huang, Influence of mantle CO₂ in the generation of carbonatites and kimberlites, *Nature (London)*, 257, 297-299, 1975a.
- Wyllie, P. J., and W. L. Huang, Peridotite, kimberlite, and carbonatite explained in the system CaO-MgO-SiO₂-CO₂, *Geology*, 3, 621-624, 1975b.
- Yagi, T., H. K. Mao, and P. M. Bell, Structure and crystal chemistry of perovskite-type MgSiO₃, *Phys. Chem. Minerals*, in press, 1978.
- Yajima, T., H. Higuchi, and H. Nagasawa, Variations of rare earth concentrations in pigeonitic and hypersthenic rock series from Izu-Hakone region, Japan, *Contrib. Mineral. Petrol.*, 35, 235-245, 1972.
- Yoder, H. S., Jr., High-low quartz inversion up to 10,000 bars, *Trans. Amer. Geophys. Union*, 31, 827-835, 1950.
- Yoder, H. S., Jr., Calcalkalic andesites: experimental data bearing on the origin of their assumed characteristics, *Oreg. Dep. Geol. Miner. Ind. Bull.*, 65, 77-89, 1969.
- Yoder, H. S., Jr., *Generation of Basaltic Magma*, National Academy of Sciences, Washington, D.C., 1976.
- Yoder, H. S., Jr., and I. Kushiro, Melting of a hydrous phase: phlogopite, *Amer. J. Sci.*, Schairer Vol., 267A, 558-582, 1969.
- Yoder, H. S., Jr., and C. E. Tilley, Origin of basaltic magmas: an experimental study of natural and synthetic rock systems, *J. Petrology*, 3, 342-532, 1962.
- Yund, R. A., and H. T. Hall, Hexagonal and monoclinic pyrrhotites, *Econ. Geol.*, 64, 420-423, 1969.
- Yund, R. A., and G. Kullerud, Thermal stability of assemblages in the Cu-Fe-system, *J. Petrology*, 7, 458-488, 1966.
- Zielinski, R. A., and F. A. Frey, An experimental study of the partitioning of a rare earth element (Gd) in the system diopside-vapor, *Geochim. Cosmochim. Acta*, 38, 545-565, 1974.

PERSONNEL

Scientific Staff

Director: H. S. Yoder, Jr., *Petrologist*

Emeritus Research Associate: E. G. Zies, *Chemist*

Emeritus Distinguished Professor, CIW: E. F. Osborn, *Petrologist*

Systematic Petrologist: F. Chayes

Petrologists: F. R. Boyd, Jr., D. H. Eggler,¹ T. N. Irvine, I. Kushiro,² D. Rumble III

Physical Chemists: J. D. Frantz, T. C. Hoering

Geophysicists: P. M. Bell, H. K. Mao

Organic Geochemist: P. E. Hare

Crystallographer: L. W. Finger

Isotope Geochemist: G. L. Davis³

Solid State Geochemist: D. Virgo

Geochemist: B. O. Mysen⁴

Volcanologist: T. Murase⁵

Postdoctoral Research Associates: R. M. Hazen, Harvard University;⁶ J. Trochimczyk, University of Mainz, Germany;⁷ E. B. Watson, Massachusetts Institute of Technology;⁸ T. Yagi, University of Tokyo⁴

Postdoctoral Fellows: N. T. Arndt, University of Toronto;⁹ N. Z. Boctor, Purdue University;¹⁰ Marilyn L. F. Estep, Marine Science Institute, University of Texas at Port Aransas;⁴ J. M. Ferry, Harvard University;¹¹ A. A. Finnerty, University of California at Los Angeles; R. K. Popp, Virginia Polytechnic Institute and State University; S. K. Sharma, University of Leicester, England;¹⁰ F. S. Spear, University of California at Los Angeles; R. F. Wendlandt, Pennsylvania State University¹²

Predoctoral Fellows: Wendy J. Harrison, University of Manchester, England;¹⁰ J. D. Hoover, University of Oregon;¹⁰ C. A. Lawson, Princeton University;¹⁰ J. L. Ritchey, University of Oregon;¹³ Noreen Tuross, Bryn Mawr College;¹⁴ R. F. Wendlandt, Pennsylvania State University¹⁵

Fellowship Trainees: Pamela R. Baur, University of Connecticut;¹⁶ Heather D. Boek, Duke University;¹⁷ Julia A. Carey, Duke University;¹⁷ Catherine A. McCammon, Massachusetts Institute of Technology;¹³ Julia D. Pasteris, Yale University;¹⁸ Marie H. Slezak, Oberlin College;¹³ Noreen Tuross, Bryn Mawr College¹⁹

Guest Investigators: J. Benson, Stanford University; B. Burton, State University of New York at Stony Brook; J. M. Ferry, Arizona State University; J. Friel, Lehigh University; H. King, State University of New York at Stony Brook; R. Koseluk, Temple University; A. R. McBirney, University of Oregon; G. H. Miller, University of Colorado; J. Myers, Johns Hopkins University; M. Nasrallah, American University, Cairo, Egypt; Alexandra Navrotsky, Arizona State University; Saki Olsen, Johns Hopkins University; Marie H. Slezak, Oberlin College; S. Steinhórrsson, University of Iceland; R. G. J. Strens, University of Newcastle upon Tyne, England; G. C. Ulmer, Temple University; A. Van Valkenburg, U.S. Bureau of Mines (retired); Danielle Velde, University of Paris, France; W. J. Verwoerd, University of Stellenbosch, South Africa; D. W. Von Endt, Smithsonian Institution; B. Wyatt, Anglo American Corporation of South Africa, Ltd.

Operating and Maintenance Staff

Executive Officer: A. D. Singer

Editor and Librarian: Dolores M. Thomas

Stenographers: Majorie E. Imlay, Mabel B. Mattingly

Typist-Accounting Clerk: Barbara B. Jones

Typist-Clerks: Joan F. Facchina,²⁰ Julie Furth,²¹ Gloria J. Proctor²²

Clerk and Technician: H. J. Lutz

Electronics Technicians: D. J. George, C. G. Hadidiacos

Shop Foreman and Instrument Maker: C. A. Batten

Laboratory Technician and Instrument Maker: G. E. Speicher

Instrument Makers: C. Brown, L. S. Carter,²³ J. W. Schwartz

Building Engineer: H. L. Moore

Custodian and Painter: M. Ferguson

Custodian and Thin-Section Technician: D. Ratliff, Jr.

Custodian and Mechanic: L. B. Patrick

¹ Appointment terminated August 31, 1977, to accept position as Associate Professor of Petrology, Pennsylvania State University.

² Appointment from April 1, 1978; on leave of absence at University of Tokyo, July 1, 1977 through March 31, 1978.

³ Retired June 30, 1978.

⁴ Appointment from July 1, 1977.

⁵ Temporary appointment from April 1, 1978.

⁶ Appointment terminated June 30, 1978, to accept position as Temporary Staff Member (Experimental Mineralogist).

⁷ Appointment terminated January 15, 1978, to return to Germany.

⁸ Appointment terminated August 31, 1977, to accept position as Assistant Professor of Geology, Rensselaer Polytechnic Institute, Troy, N. Y.

⁹ Appointment terminated August 31, 1977, to accept Postdoctoral Fellowship at Department of Geology, University of Montreal, Canada.

¹⁰ Appointment from September 1, 1977.

¹¹ Appointment terminated August 31, 1977, to accept position as Assistant Professor of Geology, Arizona State University, Tempe.

¹² Appointment from January 1, 1978.

¹³ Appointment terminated August 5, 1977.

¹⁴ Appointment terminated August 12, 1977.

¹⁵ Appointment terminated December 31, 1977.

¹⁶ Appointment from May 30, 1978.

¹⁷ Appointment from May 15, 1978.

¹⁸ Appointment from June 12, 1978.

¹⁹ Appointment from May 10, 1978.

²⁰ Appointment from January 3, 1978.

²¹ Temporary appointment from July 7 through August 5, 1977.

²² Temporary appointment from September 27 through October 7, 1977.

²³ Temporary appointment from July 1, 1977 through June 30, 1978.

Administrative Reports

Office of Administration

1530 P Street, N.W.
Washington, D.C. 20005

OFFICE OF THE PRESIDENT

Philip H. Abelson, *President*¹
Dorothy D. Blaska, *Acting Assistant to the President*²
Franklin H. Portugal, *Historian*³
Susan Y. Vasquez, *Secretary*
Marjorie H. Walburn, *Assistant to the President*⁴

OFFICE OF THE BURSAR

James W. Boise, *Bursar*
Denise L. Daniels, *Secretary*⁵
Mary G. Hedger, *Administrative Assistant*
Kenneth R. Henard, *Assistant Bursar*
Joseph M. S. Haraburda, *Assistant to the Bursar*
Sherman L. E. Johnson, *Payroll Supervisor*
Arnold J. Pryor, *Computer Operations Supervisor*
Terry L. Stahl, *Accountant*
Julia G. Thompson, *Secretary*⁶

PUBLICATIONS OFFICE

Sheila McGough, *Editor, Publications Officer*
Ray L. Bowers, *Assistant Editor*
Courtland Lewis, *Assistant Editor*

ADMINISTRATIVE OFFICE

Richard E. Hewitt, *Administrative Officer for Services*
Lloyd H. Allen, *Custodian*
Don A. Brooks, *Custodian*
Yvonne Daniels, *Secretary*⁷
Catherine A. Pool, *Secretary*⁸
Julia G. Thompson, *Secretary*⁹

¹ Retired June 30, 1978.

² From February 1, 1978, to May 17, 1978.

³ From September 1, 1977.

⁴ Retired February 17, 1978.

⁵ To April 27, 1978.

⁶ From April 26, 1978.

⁷ To September 23, 1977.

⁸ From May 12, 1978, to June 30, 1978.

⁹ From September 12, 1977, to April 25, 1978.

Bibliography

July 1, 1977–June 30, 1978

PUBLICATIONS OF THE INSTITUTION

Carnegie Institution of Washington Year Book 76. viii + 67 + 947 pages, 467 figures. December 1977.

Ceramics for the Archaeologist, Publication 609, by Anna O. Shepard. xxvi + 414 pages, 59 figures. Reprint. September 1977.

Drosophila Guide: Introduction to the Genetics and Cytology of Drosophila melanogaster, by M. Demerec and B. P. Kaufmann. ii + 45 pages, 14 figures. Reprint. April 1978.

Notes from a Ceramic Laboratory, by Anna O. Shepard with H. B. Gottlieb, E. W. Andrews, and H. E. D. Pollock, v + 100 pages, 11 figures. Collection of four previously published essays. October 1977.

Carnegie Institution of Washington Catalogue 1978–1979. 79 pages, 20 figures.

Carnegie Institution of Washington Newsletter. Issued in November 1977, February and June 1978.

PUBLICATIONS BY THE PRESIDENT OF THE INSTITUTION

Philip H. Abelson

Organic matter in the Earth's crust, *Amer. Rev. Earth Planet. Sci.*, 6, 325–351, 1978.

The new dimension, *Wilson Qtrly.*, 2, 65–73, 1978.

Energy II: Use Conservation and Supply, P. H. Abelson and Allen L. Hammond, eds., American Association for the Advancement of Science, 1978.

Health Care Regulation, Economics, Ethics, Practice, P. H. Abelson, ed., American Association for the Advancement of Science, 1978.

Editorials in Science

197: The Tris controversy, p. 113, July 8, 1977; Control of automobile emissions, p. 517, August 5, 1977; Recombinant DNA, p. 721, August 19, 1977; Energy and climate, p. 941, September 2, 1977; The Voyager missions, p. 1039, September 9, 1977; Coercion of medical schools, p. 1137, September 16, 1977; Commission on federal paperwork, p. 1237, September 23, 1977; Public opinion and energy use, p. 1325, September 30, 1977.

198: The leadership of the Geological Survey, p. 11, October 7, 1977; How much more oil? p. 451, November 4, 1977.

199: Recombinant DNA legislation, p. 135, January 13, 1978; Intercountry energy comparison, p. 605, February 10, 1978; Policy for energy, p. 1034, March 10, 1978.

200: Energy and development, p. 133, April 14, 1978; The federal regulatory machine, p. 487, May 5, 1978; Employment opportunities for scientists, p. 609, May 12, 1978; A view of health research and care, p. 845, May 26, 1978; Obsolete instrumentation at universities, p. 1111, June 9, 1978; Scientists and world needs, p. 1341, June 23, 1978.

Report of the Executive Committee

To the Trustees of the Carnegie Institution of Washington

In accordance with the provisions of the By-Laws, the Executive Committee submits this report to the Annual Meeting of the Board of Trustees.

During the fiscal year ending June 30, 1978, the Executive Committee held three meetings. Printed accounts of these meetings have been or will be mailed to each Trustee.

The estimate of expenditures for the fiscal year beginning July 1, 1978, has been reviewed by the Executive Committee.

Two vacancies exist in the membership of the Board of Trustees resulting from the resignations of Hanna H. Gray and Henry S. Morgan.

The terms of office of all Committee Chairmen and the following members of Committees expire on May 5, 1978:

Executive Committee

Michael Ference, Jr.
Crawford H. Greenewalt
Robert M. Pennoyer
Richard S. Perkins

Finance Committee

William McChesney Martin, Jr.
Robert M. Pennoyer
Richard S. Perkins

Nominating Committee

Hanna H. Gray

Auditing Committee

Crawford H. Greenewalt
Robert C. Seamans, Jr.

William C. Greenough, *Chairman*

May 5, 1978

Abstract of Minutes

of the Eighty-First Meeting of the Board of Trustees

The annual meeting of the Board of Trustees was held in the Board Room of the Administration Building on Friday, May 5, 1978. The meeting was called to order by Chairman Frank Stanton.

The following Trustees were present: Robert O. Anderson, Lewis M. Branscomb, John T. Connor, John Diebold, Michael Ference, Jr., Carl J. Gilbert, William T. Golden, Crawford H. Greenewalt, Caryl P. Haskins, William R. Hewlett, William McChesney Martin, Jr., Robert M. Pennoyer, Richard S. Perkins, Robert C. Seamans, Jr., Frank Stanton, Charles H. Townes, Juan T. Trippe, and James N. White. Garrison Norton, Trustee Emeritus, Philip H. Abelson, President, James D. Ebert, President-elect, James W. Boise, Bursar, and Marshall Hornblower, Counsel, were also in attendance.

The minutes of the Eightieth Meeting were approved.

The resignations of Hanna H. Gray and Henry S. Morgan were accepted with regret. Mr. Morgan was designated Trustee Emeritus.

The reports of the Executive Committee, the Finance Committee, the Employee Benefits Committee, and the Auditing Committee were accepted. On the recommendation of the latter, it was resolved that Arthur Andersen & Co. be re-appointed as public accountants for the fiscal year beginning July 1, 1978.

On the recommendation of the Nominating Committee, Philip H. Abelson and Franklin D. Murphy were elected members of the Board of Trustees.

The following were elected for one-year terms: William C. Greenough, as Chairman of the Executive Committee; Richard S. Perkins, as Chairman of the Finance Committee; Juan T. Trippe, as Chairman of the Auditing Committee; John Diebold, as Chairman of the Nominating Committee; and Carl J. Gilbert, as Chairman of the Employee Benefits Committee.

Vacancies in Standing Committees, with terms ending in 1981, were filled as follows: J. Paul Austin, Crawford H. Greenewalt, and Robert M. Pennoyer were elected members of the Executive Committee; William McChesney Martin, Jr., Robert M. Pennoyer, and Richard S. Perkins were elected members of the Finance Committee; Crawford H. Greenewalt and Robert C. Seamans, Jr., were elected members of the Auditing Committee; and William M. Roth was elected a member of the Nominating Committee. In addition, John T. Connor was elected a member of the Executive Committee for the unexpired term ending in 1980.

The annual report of the President was accepted.

To provide for the operation of the Institution for the fiscal year beginning July 1, 1978, and upon recommendation of the Executive Committee, the sum of \$8,318,400 was appropriated.

Financial Statement

for the year ended June 30, 1978

CARNEGIE INSTITUTION OF WASHINGTON
TEN-YEAR FINANCIAL SUMMARY, 1969-1978
(All Figures are Thousands of Dollars)

	<i>Total</i> 1969-1978	1978 ³	1977 ³	1976 ³	1975 ³	1974 ³	1973	1972	1971	1970	1969
<i>Receipts</i>											
Interest and dividends	\$40,230	\$ 5,019	\$ 4,675	\$ 3,958	\$ 3,295	\$ 3,356	\$ 3,647	\$ 3,863	\$ 4,127	\$ 4,077	\$ 4,213
Other	1,004	80	338	126	83	60	58	65	90	45	59
Restricted grants, expended ¹	6,948	1,544	1,077	772	447	484	554	470	517	517	566
Total	<u>\$48,182</u>	<u>\$ 6,643</u>	<u>\$ 6,090</u>	<u>\$ 4,856</u>	<u>\$ 3,825</u>	<u>\$ 3,900</u>	<u>\$ 4,259</u>	<u>\$ 4,398</u>	<u>\$ 4,734</u>	<u>\$ 4,639</u>	<u>\$ 4,838</u>
<i>Expenditures</i>											
Terrestrial Magnetism	\$10,087	\$ 1,106	\$ 1,209	\$ 1,046	\$ 1,188	\$ 1,025	\$ 1,022	\$ 937	\$ 909	\$ 801	\$ 844
Mount Wilson Observatory	10,389	1,168	1,204	1,085	1,027	1,051	1,016	992	930	1,154	762
Las Campanas Observatory	13,629	700	1,056	1,753	2,138	2,572	2,559	1,075	1,184	466	126
Geophysical Laboratory	9,558	1,202	1,162	1,032	1,136	964	984	770	779	768	761
Embryology	7,492	818	900	816	851	791	718	699	668	613	618
Plant Biology	5,079	530	636	620	1,270	673	330	271	252	244	253
Genetics Research Units	752	22	23	22	24	70	65	68	165	151	142
Research Projects, etc.	676	85	92	89	51	98	29	22	61	63	86
Office of Administration	5,406	602	577	500	571	520	592	583	559	469	433
General publications	729	78	59	66	78	57	79	58	98	111	45
Consulting fees, insurance, taxes	1,157	216	226	158	134	95	62	67	75	44	80
Employee benefits, special	934	145	117	102	81	89	97	78	77	71	77
Financial advisory, services	1,633	265	238	205	213	199	195	108	66	70	74
Restricted grants ¹	6,948	1,544	1,077	772	447	484	554	470	517	517	566
Total ²	<u>\$74,469</u>	<u>\$ 8,481</u>	<u>\$ 8,576</u>	<u>\$ 8,266</u>	<u>\$ 9,209</u>	<u>\$ 8,688</u>	<u>\$ 8,302</u>	<u>\$ 6,198</u>	<u>\$ 6,340</u>	<u>\$ 5,542</u>	<u>\$ 4,867</u>
Restricted grants, unexpended ¹		\$ 777	\$ 95	\$ 430	\$ 368	\$ 21	(\$ 10)	(\$ 26)	(\$ 34)	(\$ 80)	\$ 32
Gifts received		637	241	41	146	330	377	354	611	5	66
Total market value of investments		84,136	89,287	92,215	93,719	98,200	124,770	128,826	113,042	89,000	109,262

SEE FOOTNOTES 1, 2, 3 ATTACHED.

CARNEGIE INSTITUTION OF WASHINGTON
FOOTNOTES TO THE TEN-YEAR FINANCIAL SUMMARY, 1969-1978

¹ Restricted grants are funds received from Federal Agencies, Foundations, etc., in support of specific proposals for scientific research and educational programs.

Many restricted grants received are for the entire grant period which may not coincide with the Institution's fiscal year. Accordingly, the Ten-Year Financial Summary lists separately the portions of the grants expended and unexpended within the fiscal year.

During the report period, significant grants were received from Carnegie Corporation of New York, Max C. Fleischmann Foundation, Andrew W. Mellon Foundation, Alfred P. Sloan Foundation, National Aeronautics & Space Administration, National Science Foundation, Office of Naval Research, and Public Health Service.

²The Institution capitalizes expenditures for land, buildings, telescopes and other significant equipment, and construction projects in progress. Expenditures for other equipment are charged to current operations as incurred, and the cost of such equipment is not capitalized. The Institution follows the policy of not depreciating its buildings, telescopes and significant equipment.

Included in the Expenditures of Appropriated Funds are purchases of capitalized equipment as follows:

1978	\$ 56,526
1977	316,607
1976	2,133,374
1975	2,806,042
1974	2,048,947
1973	3,078,426
1972	11,987
1971	370,566
1970	371,023
1969	<u>424,637</u>
TOTAL	<u>\$11,618,135</u>

During the report period, significant items of capitalized equipment were:

100" Irene duPont Telescope	\$7,881,348
Plant Biology Building Annex	952,767
60" Palomar Telescope	800,800
40" Swope Telescope	541,115
Mount Wilson Observatory	
Building Annex	261,395

³ In 1974, the financial statements of the Institution were prepared on the accrual basis of accounting. In prior years, the Institution used the cash receipts and disbursements basis of accounting. The purpose of this change was to conform with Audit Guides of the American Institute of Certified Public Accountants which recommend accrual basis accounting for nonprofit institutions. The differences in the financial data on the accrual basis and on the former cash basis are not material.

ARTHUR ANDERSEN & Co.

1666 K STREET, N. W.
WASHINGTON, D. C. 20006
WRITER'S DIRECT DIAL NUMBER

202/862-3100

August 18, 1978

REPORT OF INDEPENDENT PUBLIC ACCOUNTANTS

To the Auditing Committee of
Carnegie Institution of Washington:

We have examined the statement of assets, liabilities and funds of CARNEGIE INSTITUTION OF WASHINGTON (a nonprofit corporation chartered by Act of the United States Congress) as of June 30, 1978 and 1977, the related summary statement of changes in funds for the year ended June 30, 1978, and the supporting exhibits and schedules, all of which are set forth on the fourteen immediately following pages. Our examinations were made in accordance with generally accepted auditing standards and, accordingly, included such tests of the accounting records and such other auditing procedures as we considered necessary in the circumstances.

In our opinion, the financial statements and supporting exhibits and schedules referred to above present fairly the assets, liabilities and funds of Carnegie Institution of Washington as of June 30, 1978 and 1977, and the changes in funds for the year ended June 30, 1978, in conformity with generally accepted accounting principles consistently applied.

Arthur Andersen & Co

CARNEGIE INSTITUTION OF WASHINGTON
SUMMARY OF SIGNIFICANT ACCOUNTING POLICIES

Basis of Accounting

The financial statements of the Institution are prepared on the accrual basis of accounting. The Institution follows a policy of reporting all commitments outstanding at year-end as liabilities for financial statement purposes.

Land, Buildings and Equipment

The Institution capitalizes expenditures for land, buildings, telescopes and other significant equipment, and construction projects in progress. Expenditures for other equipment are charged to current operations as incurred, and the cost of such equipment is not capitalized. The Institution follows the policy of not depreciating its buildings, telescopes and significant equipment.

Retirement Plan

The Institution has a noncontributory money purchase retirement plan in which all United States personnel are eligible to participate. Voluntary contributions may also be made by employees. Actuarially determined contributions are funded currently by the Institution, and there are no unfunded past service costs. The total contributions made by the Institution were \$553,851 in 1978 and \$502,395 in 1977. Benefits under the plan upon retirement are dependent upon the investment performance of the Institution's Retirement Trust. After four years' participation, benefits are fully vested.

CARNEGIE INSTITUTION OF WASHINGTON
STATEMENT OF ASSETS, LIABILITIES AND FUNDS
JUNE 30, 1978 AND 1977

ASSETS

	1978	1977
Cash	\$ 452,151	\$ 141,929
Accrued interest receivable	537,327	576,630
Grants receivable	1,426,050	784,208
Advances	15,282	19,985
Investments (cost),* Schedule 3:		
United States Government	2,626,600	4,747,271
Corporate debt securities	31,192,775	27,591,708
Loan and Collateral Pledge Agreement	200,000	—
Corporate stocks — preferred	150,000	2,153,596
Corporate stocks — common	<u>43,910,629</u>	<u>44,860,380</u>
Total investments	<u>78,080,004</u>	<u>79,352,955</u>
Land	899,138	884,749
Buildings	4,816,816	4,818,239
Equipment	<u>10,221,752</u>	<u>10,197,244</u>
Total assets	<u>\$96,448,520</u>	<u>\$96,775,939</u>

LIABILITIES AND FUNDS

Appropriated funds:

Accounts payable and accrued expenses —		
Operating Fund	\$ 645,008	\$ 466,362
Restricted Grants	<u>67,202</u>	<u>85,012</u>
Total liabilities	<u>712,210</u>	<u>551,374</u>
Operating Fund, Exhibit 1	1,593,352	1,326,871
Restricted Grants, Exhibit 2	1,705,901	928,600
Unappropriated Funds, Exhibit 3	76,499,351	78,068,862
Plant Fund	<u>15,937,706</u>	<u>15,900,232</u>
Total liabilities and funds	<u>\$96,448,520</u>	<u>\$96,775,939</u>

*Approximate market value on June 30, 1978: \$84,135,709

CARNEGIE INSTITUTION OF WASHINGTON
SUMMARY STATEMENT OF CHANGES IN FUNDS
FOR THE YEAR ENDED JUNE 30, 1978

	<u>Appropriated Funds</u>		<u>Unappropriated</u>	<u>Plant</u>	
	<u>Operating</u>	<u>Restricted</u>	<u>Funds</u>	<u>Fund</u>	<u>Total</u>
	<u>(Exhibit 1)</u>	<u>(Exhibit 2)</u>	<u>(Exhibit 3)</u>		
Balance, July 1, 1976	<u>\$1,326,871</u>	<u>\$ 928,600</u>	<u>\$78,068,862</u>	<u>\$15,900,232</u>	<u>\$96,224,565</u>
<i>Additions</i>					
Realized capital loss, net	—	—	(101,813)	—	(101,813)
Investment income					
Interest	—	—	2,499,208	—	2,499,208
Dividends	—	—	2,520,251	—	2,520,251
Gifts	—	—	637,139	—	637,139
Other income	—	—	79,534	—	79,534
Land, buildings and equipment					
Current year capitalized ...	—	—	—	56,526	56,526
Prior years Retirements, Net	—	—	—	(19,052)	(19,052)
Appropriations					
Budget	7,188,830	—	(7,188,830)	—	—
Bush Gift	15,000	—	(15,000)	—	—
Restricted Grants	—	<u>2,321,658</u>	—	—	<u>2,321,658</u>
	<u>7,203,830</u>	<u>2,321,658</u>	<u>(1,569,511)</u>	<u>37,474</u>	<u>7,993,451</u>
<i>Deductions</i>					
Expenditures	<u>6,937,349</u>	<u>1,544,357</u>	—	—	<u>8,481,706</u>
Net change during period	<u>266,481</u>	<u>777,301</u>	<u>(1,569,511)</u>	<u>37,474</u>	<u>(488,255)</u>
Balance, June 30, 1978	<u>\$1,593,352</u>	<u>\$1,705,901</u>	<u>\$76,499,351</u>	<u>\$15,937,706</u>	<u>\$95,736,310</u>

CARNEGIE INSTITUTION OF WASHINGTON

EXHIBIT 1

APPROPRIATED FUNDS

CHANGES IN OPERATING FUND

FOR THE YEAR ENDED JUNE 30, 1978

Balance, July 1, 1977		\$1,326,871
-----------------------------	--	-------------

Appropriations

Budget, July 1, 1977, to June 30, 1978	\$7,188,830	
Bush Gift	<u>15,000</u>	<u>7,203,830</u>

Total available for expenditures		8,530,701
--	--	-----------

Expenditures

Salaries	\$3,435,664
Fringe benefits	666,427
Payroll taxes	210,616
Retiree benefits	126,774
Building maintenance	426,452
Educational and research supplies	440,637
Equipment	321,010
Administrative	304,271
Financial advisory services	265,636
Fellowship grants	218,476
Insurance	193,397
Travel	167,386
Publications	113,785
Consulting fees	57,608
Awards	41,247
Commissary	39,130
Shop	26,192
Rent	21,364
Entertainment	20,310
Taxes	5,876
Fellowship travel	<u>5,236</u>
	7,107,494

Less reimbursement of indirect costs by restricted grants	<u>(226,671)</u>	6,880,823
--	------------------	-----------

Transfers to Plant Fund

Land	14,389	
Telescope (improvements)	<u>42,137</u>	<u>56,526</u>

Total expenditures		<u>6,937,349</u>
--------------------------	--	------------------

Balance, June 30, 1978		<u>\$1,593,352</u>
------------------------------	--	--------------------

CARNEGIE INSTITUTION OF WASHINGTON

EXHIBIT 2

APPROPRIATED FUNDS

CHANGES IN RESTRICTED GRANTS

FOR THE YEAR ENDED JUNE 30, 1978

	<i>Balance July 1, 1977</i>	<i>Grants</i>	<i>Expenditures</i>		<i>Balance June 30, 1978</i>
			<i>Salaries</i>	<i>Other</i>	
American Cancer Society	\$ —	\$ 1,000	\$ —	\$ 80	\$ 920
Carnegie Corporation of New York	1,960	80,000	—	81,960	—
Max C. Fleischmann Foundation	22,186	—	—	22,186	—
The Andrew W. Mellon Foundation	200,000	400,000	36,992	161,903	401,105
Muscular Dystrophy Association	6,535	23,788	—	21,932	8,391
National Academy of Sciences	34,165	—	—	19,190	14,975
National Aeronautics & Space Administration	49,642	104,000	40,003	40,475	73,164
National Science Foundation	366,068	627,324	123,641	351,387	518,364
Office of Naval Research	6,996	24,750	17,000	5,560	9,186
Plant Biology — Book Fund	—	100	—	100	—
Public Health Service .	217,965	425,197	132,700	344,336	166,126
Research Corporation	—	1,999	—	1,999	—
Alfred P. Sloan Foundation	—	600,000	29,407	68,552	502,041
Whitehall Foundation	21,500	—	—	18,246	3,254
Helen Hay Whitney Foundation	<u>1,583</u>	<u>33,500</u>	<u>—</u>	<u>26,708</u>	<u>8,375</u>
Total	<u>\$928,600</u>	<u>\$2,321,658</u>	<u>\$379,743</u>	<u>\$1,164,614</u>	<u>\$1,705,901</u>

CARNEGIE INSTITUTION OF WASHINGTON
CHANGES IN UNAPPROPRIATED FUNDS
FOR THE YEAR ENDED JUNE 30, 1978

EXHIBIT 3

	Balance July 1, 1977	Investment Income	Gifts and Other Income	Realized Capital Loss, net	Appropriations	Transfers	Balance June 30, 1978
<i>Endowment Fund</i>							
Andrew Carnegie	\$22,000,000	\$	\$	\$	\$	\$	\$22,000,000
Sybil & William T. Golden	—	—	25,000	—	—	—	25,000
William R. Hewlett	—	—	443,250	—	—	—	443,250
Realized Capital Gains	36,372,705	—	—	76,011	—	—	36,296,694
<i>Unrestricted Capital Funds</i>							
Carnegie Corporation	10,000,000	—	—	—	—	—	10,000,000
Carnegie Futures	127,027	—	4,125	—	—	—	131,152
Vannevar Bush	100,000	—	—	—	—	—	100,000
Realized Capital Gains	8,143,460	—	—	24,202	2,090,475	—	6,028,783
<i>Working Capital Fund</i>							
Income	25,181	4,943,907	—	—	5,048,620	79,532	—
Sales	—	—	—	—	—	—	—
Assets	—	—	26,322	—	—	(26,322)	—
Optical Services	—	—	2,771	—	—	(2,771)	—
Royalties	—	—	30,466	—	—	(30,466)	—
Rent	—	—	6,054	—	—	(6,054)	—
Refunds	—	—	1,919	—	—	(1,919)	—
University of Toronto	—	—	12,000	—	—	(12,000)	—
<i>Special Funds</i>							
Ira S. & Mary Bowen	—	5,022	112,639	117	—	—	117,544
Bush Gift	34,712	2,178	—	44	15,000	—	21,846
Colburn	249,384	15,498	—	313	14,169	—	250,400
Hale Relief	6,776	422	2	8	55	—	7,137
Harkavy	12,054	677	—	14	619	—	12,098
Lundmark	48,601	2,521	—	51	2,306	—	48,765
Morgenroth	40,906	1,817	—	37	1,662	—	41,024
Moseley Astronomy	108,138	5,903	—	119	2,702	—	111,220
Special Instrumentation	113,180	5,626	—	114	—	—	118,692
Special Opportunities	17,858	2,715	52,125	113	—	—	72,585
Wood	668,880	33,173	—	670	28,222	—	673,161
Total	\$78,068,862	\$5,019,459	\$716,673	\$101,813	\$7,203,830	\$	\$76,499,351

CARNEGIE INSTITUTION OF WASHINGTON
APPROPRIATED FUNDS
BUDGET SUMMARY OF OPERATING FUND
FOR THE YEAR ENDED JUNE 30, 1978

SCHEDULE 1

	<i>Unexpended Appropriations July 1, 1977</i>	<i>Appropriations</i>	<i>Transfers and Allotments</i>	<i>Total Expenditures</i>	<i>Unexpended Appropriations June 30, 1978</i>
Terrestrial Magnetism	\$ 4,221	\$1,131,117	\$ (28,192)	\$1,105,723	\$ 1,423
Mount Wilson Observatory	—	1,076,521	149,665	1,168,197	57,989
Las Campanas Observatory	—	734,000	(29,630)	700,128	4,242
Geophysical Laboratory	17,927	1,124,037	77,216	1,202,243	16,937
Embryology	44,300	802,464	(29,213)	817,551	—
Plant Biology	17	479,491	50,502	530,010	—
Genetics Research Unit	—	23,500	(1,915)	21,585	—
Research Projects, etc.	83,511	97,500	(3,868)	85,196	91,947
Office of Administration	—	626,400	(24,593)	601,807	—
General publications	750	65,000	12,403	78,153	—
Consulting fees, insurance, taxes	—	261,500	(45,845)	215,655	—
Retiree benefits	74,640	110,000	58,437	126,077	117,000
Employee benefits, special	—	22,300	(2,912)	19,388	—
Financial advisory services	—	300,000	(34,364)	265,636	—
Contingent operating fund	—	350,000	(350,000)	—	—
Unallocated appropriations	<u>1,101,505</u>	<u>—</u>	<u>202,309</u>	<u>—</u>	<u>1,303,814</u>
Total	<u>\$1,326,871</u>	<u>\$7,203,830</u>	<u>\$ —</u>	<u>\$6,937,349</u>	<u>\$1,593,352</u>

CARNEGIE INSTITUTION OF WASHINGTON
SCHEDULE 2 SUMMARY OF INVESTMENT TRANSACTIONS
FOR THE YEAR ENDED JUNE 30, 1978

Cash awaiting investment, June 30, 1977 \$ 309

Sales and Redemptions

	<i>Cost</i>	<i>Capital Loss (Net)</i>
Bonds	\$102,548,865	\$ (166,834)
Preferred stocks	2,153,596	(283,462)
Common stocks	<u>13,279,767</u>	<u>348,483</u>
	117,982,228	(101,813)

Total sales and redemptions	117,880,415
Gifts of securities at fair market value	573,288
Cash transferred to Operating Fund	<u>(1,713,087)</u>
Total	116,740,925

Acquisitions

Bonds	104,029,261
Loan and Collateral Pledge Agreement	200,000
Preferred stocks	150,000
Common stocks	<u>12,330,025</u>
Total acquisitions	<u>116,709,286</u>

Cash awaiting investment, June 30, 1978 \$ 31,639

CARNEGIE INSTITUTION OF WASHINGTON

SCHEDULE 3

INVESTMENTS, JUNE 30, 1978

<i>Description</i>	<i>Par</i>	<i>Cost</i>	<i>Approximate Market</i>
United States Government Securities			
Federal Home Loan Banks, Cons., 7.30s, 1983	\$ 600,000	\$ 599,625	\$ 564,750
Federal Home Loan Banks, Cons., 7.60s, 1987	600,000	605,062	554,250
Federal National Mortgage Association, 7.25s, 1985	600,000	594,938	548,250
Twelve Federal Land Banks, Cons., 7.35s, 1997	655,000	627,191	566,575
United States of America Treasury Notes, 7.375s, 1981	200,000	<u>199,784</u>	<u>194,186</u>
Total United States Government Securities		<u>2,626,600</u>	<u>2,428,011</u>
Corporate Debt Securities			
Alcan Aluminum Corporation, Prom. Note, 4.75s, 1984	414,000	414,000	359,145
Aluminum Company of Canada, Ltd., S.F. Deb., 9.50s, 1995	500,000	517,267	485,000
American Express Credit Corp., Prom. Note, 7.50s, 1978	125,000	125,000	125,000
American Hoechst Corp., Note, 5.75s, 1986	604,000	604,000	533,030
American International Group, Inc., Conv. Sub. Deb., 4s, 1997	175,000	147,125	168,000
Atlantic Richfield, Co., Demand Note	346,000	346,000	346,000
Australia (Commonwealth of), 9.125s, 1993	500,000	498,125	496,875
Bank of America, CTF of Dep., 7.50s, 1978	1,000,000	1,000,049	1,000,049
Bell Telephone Co. of Pennsylvania, Deb., 9.625s, 2014	150,000	168,000	158,625
Boeing Co., Note, 6.375s, 1986	480,000	480,000	428,400
Chesapeake & Potomac Tel. Co. of Va., Deb., 9.25s, 2015	155,000	162,406	157,713
Churchill Falls (Labrador) Corp., Ltd., 1st Mtg. Series A, 7.75s, 2007	778,000	778,000	637,960
CITIBANK, CTF of Dep., 7.50s, 1978	2,000,000	2,000,098	2,000,098
C.I.T. Financial Corp., Prom. Note, 7.55s, 1978	575,000	575,000	575,000
Columbia Broadcasting System, Inc., Prom. Note, 5.50s, 1991	600,000	600,000	492,000
Commonwealth Edison Co., 1st Mtg., 8.125s, 36th Series, 2007	400,000	400,000	362,500
Consolidated Edison Co. of New York, Inc., 1st & Ref. Mtg., 5s, 1987	2,000	1,532	1,498
Crown Zellerbach Corp., Prom. Note, 4.625s, 1981	100,000	100,000	92,500

CARNEGIE INSTITUTION OF WASHINGTON
INVESTMENTS, JUNE 30, 1978

<i>Description</i>	<i>Par</i>	<i>Cost</i>	<i>Approximate Market</i>
Corporate Debt Securities — Continued			
Digital Equipment, Conv. Sub. Deb., 4.50s, 2002	350,000	350,000	348,250
Federated Department Stores, Inc., Demand Note	313,000	313,000	313,000
First International Bancshares, S.F. Deb., 9.75s, 1999	200,000	221,500	207,500
Ford Motor Credit Co., Medium Term Note, 9.25s, 1981	285,000	291,413	290,344
Four Corners Pipe Line Co., Sec. Note, 5s, 1982	27,000	27,000	26,325
General Electric Co., Demand Note	89,000	89,000	89,000
General Electric Credit Corp., Note, 8.60s, 1985	500,000	500,500	490,625
General Electric Credit Corp., Prom. Note, 7.55s, 1978	215,000	215,000	215,000
General Motors Acceptance Corp., Deb., 8.25s, 2006	250,000	250,625	230,000
General Motors Acceptance Corp., Prom. Note, 7.50s 1978	2,000,000	2,000,000	2,000,000
General Motors Acceptance Corp., 8s, 2002	500,000	489,375	447,500
General Motors Acceptance Corp., Demand Note	163,000	163,000	163,000
GNMA, Pool #14728, 7.50s, 2007	699,710	628,646	618,369
GNMA, Pool #16544, 7.50s, 2007	638,148	613,129	563,963
GNMA, Pool #16944, 7.50s, 2007	485,475	461,505	429,039
Gould Inc., Conv., 5s, 1987	375,000	482,025	439,219
IAC Ltd., Sec. Note, Series Z, 5.25s, 1982	750,000	750,000	622,500
Indiana Bell Telephone Co., Inc., 8.125s, 2017	500,000	495,000	460,000
Inter-American Development Bank, Note, 8.25s, 1985	500,000	502,500	482,500
International Bank for Reconstruction and Development, Note, 8.15s, 1985	400,000	400,000	384,000
International Bank for Reconstruction and Development, Note, 8.35s, 1980	285,000	284,664	282,150
Kaiser Aluminum & Chemical Corp., 1st Mtg., 5.50s, 1987	145,000	145,000	117,088
Kraft Inc., 7.60s, 2007	500,000	484,375	460,000
K Mart Corp., Prom. Note, 4.875s, 1983	396,667	396,667	350,058
Manufacturers Hanover Corp., 8.125s, 2007	1,000,000	998,750	900,000

CARNEGIE INSTITUTION OF WASHINGTON
INVESTMENTS, JUNE 30, 1978

<i>Description</i>	<i>Par</i>	<i>Cost</i>	<i>Approximate Market</i>
Corporate Debt Securities — <i>Continued</i>			
Mercantile Stores Co., Inc., 8.70s, 1995	478,000	478,000	455,295
Michigan Bell Telephone Company, 9.60s, 2008	800,000	893,000	847,000
Mountain States Tel. & Tel. Co., Deb., 8.625s, 2018	200,000	193,250	190,750
N C R Corp., Conv. Sub. Deb., 6s, 1995	450,000	428,625	434,250
New York Telephone Co., 7.875s, 2017	500,000	488,750	442,500
Pacific Gas & Electric Co., 1st & Ref. Mtg., 9s, 2001	1,000	1,036	966
Pacific Gas & Electric Co., 1st & Ref. Mtg., 9.375s, 2011	500,000	497,725	496,875
Public Service Electric & Gas Co., 1st & Ref. Mtg., 8.45s, 2006	500,000	494,875	462,500
Quebec Hydro-Electric Commission, S.F., Deb., 5s, 1988	571,000	561,008	421,113
Quebec Hydro-Electric Commission, 9.25s, 1995	500,000	504,126	473,750
Revlon, Inc., Note, 8.45s, 1985	500,000	501,375	500,000
Sears, Roebuck Acceptance Corp., 8.375s, 1986	400,000	399,200	388,500
Sears, Roebuck Acceptance Corp., Prom. Note, 7.65s, 1978	325,000	325,000	325,000
Sears, Roebuck & Co., 7.875s, 2007	500,000	491,875	451,875
Shell Funding Corp., Collat. Tr. Series B, 4.75s, 1985	455,000	455,000	395,850
South Central Bell Telephone Co., Deb., 8.25s, 2015	250,000	250,937	229,375
Tenneco Corp., Demand Note	102,000	102,000	102,000
Texas (Republic of) Corp., 9.375s, 2001	500,000	528,495	504,375
United Air Lines, Inc., Note, 5s, 1984	420,000	420,000	367,500
United States Steel Credit Corp., Prom. Note, 7.55s, 1978	510,000	510,000	510,000
U. T. Credit Corp., S.F. Note, 8.25s, 2002	600,000	600,000	547,500
Westinghouse Credit Corp., Prom. Note, 7.60s, 1978	1,200,000	1,200,000	1,200,000
Woolworth (F. W.) Company, Prom. Note, 5s, 1981	399,222	399,222	352,313
Total Corporate Debt Securities		<u>31,192,775</u>	<u>29,448,110</u>

CARNEGIE INSTITUTION OF WASHINGTON
INVESTMENTS, JUNE 30, 1978

<i>Description</i>	<i>Shares</i>	<i>Cost</i>	<i>Approximate Market</i>
Corporate Debt Securities — Continued			
Loan and Collateral Pledge Agreement			
James D. & Alma C. Ebert (non-interest bearing loan to president secured by real estate)	200,000	200,000	200,000
Corporate Stocks — preferred			
Burlington Northern Inc., CVT PFD, 2.85	3,000	150,000	121,500
Corporate Stocks — common			
Allied Stores Corp.	10,000	241,674	227,500
American Home Products Corp.	14,025	485,482	397,959
American International Group, Inc.	7,500	278,750	322,500
American International Reinsurance Co.	2,000	84,250	90,000
American Standard Inc.	10,000	246,297	418,750
American Telephone & Telegraph Co.	29,209	1,845,199	1,748,889
AMP Incorporated	28,000	724,769	903,000
Automatic Data Processing, Inc.	2,500	34,003	76,875
Avnet, Inc.	20,000	369,500	337,500
Avon Products, Inc.	19,000	923,448	1,009,376
Baxter Travenol Laboratories, Inc.	8,000	248,380	339,000
Big Three Industries	9,000	281,928	324,000
Boeing Co.	13,000	230,471	687,375
Bristol-Myers Co.	16,000	537,000	574,000
Cameron Iron Works, Inc.	2,400	69,750	100,800
Capital Holding Corp.	22,000	488,823	503,250
Caterpillar Tractor Co.	7,250	298,378	405,094
Central Telephone & Utilities Corp.	40,000	596,512	967,746
Charles River Breeding Laboratories, Inc.	1,500	59,154	31,500
Chemed Corp.	2,000	67,681	56,000
Chesebrough-Pond's, Inc.	10,000	186,583	245,000
Citicorp.	15,000	268,929	350,625
Clark Equipment Co.	6,500	244,668	216,938
Coca-Cola Company (The)	10,000	80,228	417,500
Colt Industries, Inc.	5,000	246,675	267,500
Consolidated Edison Company of New York, Inc.	19,000	445,477	437,000
Consolidated Foods Corp.	17,500	435,288	444,063
Continental Corp.	11,600	293,361	295,800
Continental Group, Inc.	10,500	350,807	311,063
Continental Illinois Corp.	11,600	302,346	327,700
CPC International, Inc.	6,500	303,098	324,188
Cross (A. T.) Co.	3,000	89,250	81,750
Crum & Forster	12,000	387,219	415,500
Cummins Engine Co., Inc.	7,351	354,586	271,068
Data General Corporation	1,000	31,168	54,125
Denny's, Inc.	6,500	158,720	209,625

CARNEGIE INSTITUTION OF WASHINGTON

INVESTMENTS, JUNE 30, 1978

<i>Description</i>	<i>Shares</i>	<i>Cost</i>	<i>Approximate Market</i>
Corporate Stocks — common — Continued			
Dominion Bankshares Corp.	14,000	220,500	220,500
Dover Corporation	11,500	415,595	511,750
Dow Chemical Company (The)	8,015	237,176	197,369
du Pont (E. I.) de Nemours & Co.	2,822	342,241	316,064
Eastman Kodak Company	6,510	134,683	347,471
Eckerd (Jack) Corp.	10,500	262,730	280,875
Engelhard Minerals & Chemical Corp.	7,500	263,350	162,188
Exxon Corporation	36,040	643,219	1,581,256
Farmers Group, Inc.	30,000	650,875	772,500
First Charter Financial Corporation	18,000	311,773	288,000
First Kentucky National Corp.	10,500	307,375	288,750
Fleming Cosmetics, Inc.	13,000	208,945	264,875
General Electric Co.	15,000	290,867	757,500
General Motors Corporation	19,124	476,259	1,135,487
General Telephone & Electronics Corp.	18,000	566,825	515,250
General Tire & Rubber Company (The)	9,996	217,471	252,399
Gilbert Associates, Inc.	2,300	84,944	66,700
Gillette Company	14,000	365,255	400,750
Goodyear Tire & Rubber Co. (The)	20,050	279,854	338,344
Great Western Financial Corp.	11,000	271,155	305,250
Gulf Oil Corp.	15,000	427,688	348,750
Halliburton Company	7,900	410,507	506,588
Harland (John H.) Co.	2,500	65,068	65,938
Hewlett-Packard Co.	6,150	453,875	498,150
Honeywell, Inc.	4,000	178,300	222,500
Household Finance Corp.	22,100	441,810	428,188
Houston Industries, Inc.	7,200	223,900	221,400
Illinois Power Company	14,000	360,864	339,500
INA Corporation	18,000	811,302	758,250
INCO Limited	11,500	368,385	188,313
Interco, Incorporated	14,550	634,074	625,650
International Business Machines Corp.	15,530	995,471	3,995,093
International Paper Company	5,000	213,750	198,125
International Telephone & Telegraph Corp.	12,500	359,043	379,688
Interpace Corp.	3,750	52,018	81,563
Kaiser Aluminum & Chemical Corporation	12,535	391,658	402,687
Levi Strauss & Co.	4,000	104,500	133,000
Mallory (P. R.) & Co. Inc.	12,000	417,012	375,000
Malone & Hyde, Inc.	16,500	395,198	470,250
Marathon Oil Co.	7,500	420,465	326,250
McCormick & Co., Inc.	18,400	321,388	266,800
Merck & Co., Inc.	12,000	210,518	666,000
Minnesota Mining & Manufacturing Company	8,015	404,350	440,825
Monsanto Company	4,000	386,732	205,000
Moore McCormack Resources, Inc.	7,500	235,767	245,625
Motorola, Inc.	6,000	218,910	276,000
NALCO Chemical Co.	5,000	147,525	147,500
National Gypsum Co.	24,500	416,025	425,688
Norfolk & Western Ry. Co.	12,650	367,314	316,250
Norris Industries, Inc.	16,000	380,378	352,000
Northwest Industries, Inc.	5,500	293,213	352,000

CARNEGIE INSTITUTION OF WASHINGTON
INVESTMENTS, JUNE 30, 1978

<i>Description</i>	<i>Shares</i>	<i>Cost</i>	<i>Approximate Market</i>
Corporate Stocks — common — <i>Continued</i>			
Ocean Drilling & Exploration Co.	1,000	42,100	39,000
Pepsi Company, Inc.	10,000	215,086	297,500
Petrie Stores Corporation	2,000	68,391	87,000
Pfizer, Inc.	10,000	273,878	335,000
Phelps Dodge Corporation	6,000	254,400	123,000
Pittston Company (The)	10,200	365,900	234,600
Potlatch Corporation	16,500	331,258	490,875
Procter & Gamble Company (The)	8,012	743,408	689,032
Public Service Co. of Indiana, Inc.	13,000	341,350	347,750
Quaker Oats Co.	13,000	293,100	321,750
Ralston Purina Co.	22,500	329,053	360,000
Revco D. S., Inc.	25,000	501,140	603,125
Reynolds (R. J.) Industries, Inc.	6,000	356,500	342,750
Royal Dutch Petroleum Co.	13,100	669,823	769,626
Safeway Stores, Inc.	9,500	409,924	383,563
Schlumberger Ltd.	16,000	420,663	1,334,000
Sears, Roebuck and Co.	12,024	649,382	278,055
Security Pacific Bank	15,000	407,875	459,375
Southern Co.	12,000	203,043	193,500
Squibb Corporation	15,600	607,910	542,100
Standard Oil Co. of California	22,500	894,189	897,188
Tandy Corp.	3,000	117,420	133,125
Tenneco, Inc.	28,000	1,005,080	857,500
Texas Gas Transmission Corp.	18,600	833,724	848,625
Time Inc.	6,500	235,790	266,500
Transway International Corp.	14,500	328,263	384,250
Travelers Corp. (The)	14,500	445,512	507,500
UAL, Inc.	10,000	280,275	295,000
Union Camp Corp.	6,000	264,714	253,500
Union Carbide Corp.	10,000	627,500	380,000
Union Pacific Corp.	6,050	269,376	269,981
United States Steel Corp.	7,500	341,250	197,813
United Technologies Corp.	16,666	573,054	706,222
West Point-Pepperell, Inc.	7,500	262,346	256,875
Total Corporate Stocks — common		<u>43,910,629</u>	<u>51,938,088</u>
Total Investments		<u>\$78,080,004</u>	<u>\$84,135,709</u>

Articles of Incorporation

Fifty-eighth Congress of the United States of America;

At the Second Session,

Begun and held at the City of Washington on Monday, the seventh day of December, one thousand nine hundred and three.

AN ACT

To incorporate the Carnegie Institution of Washington.

Be it enacted by the Senate and House of Representatives of the United States of America in Congress assembled, That the persons following, being persons who are now trustees of the Carnegie Institution, namely, Alexander Agassiz, John S. Billings, John L. Cadwalader, Cleveland H. Dodge, William N. Frew, Lyman J. Gage, Daniel C. Gilman, John Hay, Henry L. Higginson, William Wirt Howe, Charles L. Hutchinson, Samuel P. Langley, William Lindsay, Seth Low, Wayne MacVeagh, Darius O. Mills, S. Weir Mitchell, William W. Morrow, Ethan A. Hitchcock, Elihu Root, John C. Spooner, Andrew D. White, Charles D. Walcott, Carroll D. Wright, their associates and successors, duly chosen, are hereby incorporated and declared to be a body corporate by the name of the Carnegie Institution of Washington and by that name shall be known and have perpetual succession, with the powers, limitations, and restrictions herein contained.

SEC. 2. That the objects of the corporation shall be to encourage, in the broadest and most liberal manner, investigation, research, and discovery, and the application of knowledge to the improvement of mankind; and in particular—

(a) To conduct, endow, and assist investigation in any department of science, literature, or art, and to this end to cooperate with governments, universities, colleges, technical schools, learned societies, and individuals.

(b) To appoint committees of experts to direct special lines of research.

(c) To publish and distribute documents.

(d) To conduct lectures, hold meetings, and acquire and maintain a library.

(e) To purchase such property, real or personal, and construct such building or buildings as may be necessary to carry on the work of the corporation.

(f) In general, to do and perform all things necessary to promote the objects of the institution, with full power, however, to the trustees hereinafter appointed and their successors from time to time to modify the conditions and regulations under which the work shall be carried on, so as to secure the application of the funds in the manner best adapted to the conditions of the time, provided that the objects of the corporation shall at all times be among the foregoing or kindred thereto.

SEC. 3. That the direction and management of the affairs of the corporation and the control and disposal of its property and funds shall be vested in a board of trustees, twenty-two in number, to be composed of the following individuals: Alexander Agassiz, John S. Billings, John L. Cadwalader, Cleveland H. Dodge, William N. Frew, Lyman J. Gage, Daniel C. Gilman, John Hay, Henry L. Higginson, William Wirt Howe, Charles L. Hutchinson, Samuel P. Langley, William Lindsay, Seth Low, Wayne MacVeagh, Darius O. Mills, S. Weir Mitchell, William W. Morrow, Ethan A. Hitchcock, Elihu Root, John C. Spooner, Andrew D. White, Charles D. Walcott, Carroll D. Wright, who shall constitute the first board of trustees. The board of trustees shall have power from time to time to increase its membership to not more than twenty-seven members. Vacancies occasioned by death, resignation, or otherwise shall be filled by the remaining trustees in such manner as the by-laws shall prescribe; and the persons so elected shall thereupon become trustees and also members of the said corporation. The principal place of business of the said corporation shall be the city of Washington, in the District of Columbia.

SEC. 4. That such board of trustees shall be entitled to take, hold and administer the securities, funds, and property so transferred by said Andrew Carnegie to the trustees of the Carnegie Institution and such other funds or property as may at any time be given, devised, or bequeathed to them, or to such corporation, for the purposes of the trust; and with full power from time to time to adopt a common seal, to appoint such officers, members of the board of trustees or otherwise, and such employees as may be deemed necessary in carrying on the business of the corporation, at such salaries or with such remuneration as they may deem proper; and with full power to adopt by-laws from time to time and such rules or regulations as may be necessary to secure the safe and convenient transaction of the business of the corporation; and with full power and discretion to deal with and expend the income of the corporation in such manner as in their judgment will best promote the objects herein set forth and in general to have and use all powers and authority necessary to promote such objects and carry out the purposes of the donor. The said trustees shall have further power from time

to time to hold as investments the securities hereinabove referred to so transferred by Andrew Carnegie, and any property which has been or may be transferred to them or such corporation by Andrew Carnegie or by any other person, persons, or corporation, and to invest any sums or amounts from time to time in such securities and in such form and manner as are permitted to trustees or to charitable or literary corporations for investment, according to the laws of the States of New York, Pennsylvania, or Massachusetts, or in such securities as are authorized for investment by the said deed of trust so executed by Andrew Carnegie, or by any deed of gift or last will and testament to be hereafter made or executed.

SEC. 5. That the said corporation may take and hold any additional donations, grants, devises, or bequests which may be made in further support of the purposes of the said corporation, and may include in the expenses thereof the personal expenses which the trustees may incur in attending meetings or otherwise in carrying out the business of the trust, but the services of the trustees as such shall be gratuitous.

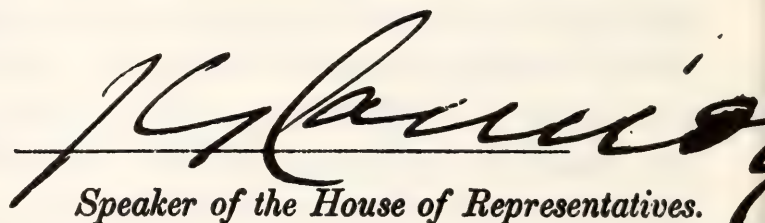
SEC. 6. That as soon as may be possible after the passage of this Act a meeting of the trustees hereinbefore named shall be called by Daniel C. Gilman, John S. Billings, Charles D. Walcott, S. Weir Mitchell, John Hay, Elihu Root, and Carroll D. Wright, or any four of them, at the city of Washington, in the District of Columbia, by notice served in person or by mail addressed to each trustee at his place of residence; and the said trustees, or a majority thereof, being assembled, shall organize and proceed to adopt by-laws, to elect officers and appoint committees, and generally to organize the said corporation; and said trustees herein named, on behalf of the corporation hereby incorporated, shall thereupon receive, take over, and enter into possession, custody, and management of all property, real or personal, of the corporation heretofore known as the Carnegie Institution, incorporated, as hereinbefore set forth under "An Act to establish a Code of Law for the District of Columbia, January fourth, nineteen hundred and two," and to all its rights, contracts, claims, and property of any kind or nature; and the several officers of such corporation, or any other person having charge of any of the securities, funds, real or personal, books or property thereof, shall, on demand, deliver the same to the said trustees appointed by this Act or to the persons appointed by them to receive the same; and the trustees of the existing corporation and the trustees herein named shall and may take such other steps as shall be necessary to carry out the purposes of this Act.

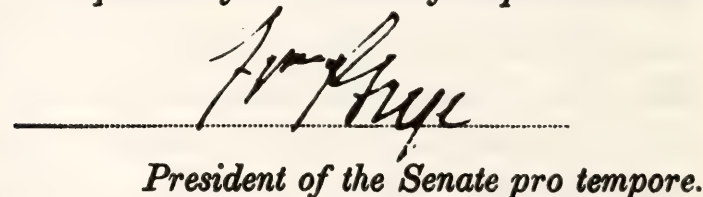
SEC. 7. That the rights of the creditors of the said existing corporation known as the Carnegie Institution shall not in any manner be impaired by the

passage of this Act, or the transfer of the property hereinbefore mentioned, nor shall any liability or obligation for the payment of any sums due or to become due, or any claim or demand, in any manner or for any cause existing against the said existing corporation, be released or impaired; but such corporation hereby incorporated is declared to succeed to the obligations and liabilities and to be held liable to pay and discharge all of the debts, liabilities, and contracts of the said corporation so existing to the same effect as if such new corporation had itself incurred the obligation or liability to pay such debt or damages, and no such action or proceeding before any court or tribunal shall be deemed to have abated or been discontinued by reason of the passage of this Act.

SEC. 8. That Congress may from time to time alter, repeal, or modify this Act of incorporation, but no contract or individual right made or acquired shall thereby be divested or impaired.

SEC. 9. That this Act shall take effect immediately.


Speaker of the House of Representatives.


President of the Senate pro tempore.

Approved,

April 28, 1904.

Theodore Roosevelt

By-Laws of the Institution

Adopted December 13, 1904. Amended December 13, 1910, December 13, 1912, December 10, 1937, December 15, 1939, December 13, 1940, December 18, 1942, December 12, 1947, December 10, 1954, October 24, 1957, May 8, 1959, May 13, 1960, May 10, 1963, May 15, 1964, March 6, 1967, May 3, 1968, May 14, 1971, August 31, 1972, May 9, 1974, and April 30, 1976.

ARTICLE I

The Trustees

1. The Board of Trustees shall consist of twenty-four members with power to increase its membership to not more than twenty-seven members. The Trustees shall hold office continuously and not for a stated term.

2. In case any Trustee shall fail to attend three successive annual meetings of the Board he shall thereupon cease to be a Trustee.

3. No Trustee shall receive any compensation for his services as such.

4. All vacancies in the Board of Trustees shall be filled by the Trustees by ballot at an annual meeting, but no person shall be declared elected unless he receives the votes of two-thirds of the Trustees present.

5. If, at any time during an emergency period, there be no surviving Trustee capable of acting, the President, the Director of each existing Department, and the Executive Officer, or such of them as shall then be surviving and capable of acting, shall constitute a Board of Trustees *pro tem*, with full powers under the provisions of the Articles of Incorporation and these By-Laws. Should neither the President, nor any such Director, nor the Executive Officer be capable of acting, the senior surviving Staff Member of each existing Department shall be a Trustee *pro tem* with full powers of a Trustee under the Articles of Incorporation and these By-Laws. It shall be incumbent on the Trustees *pro tem* to reconstitute the Board with permanent members within a reasonable time after the emergency has passed, at which time the Trustees *pro tem* shall cease to hold office. A list of Staff Member seniority, as designated annually by the President, shall be kept in the Institution's records.

6. A Trustee who resigns after having served at least five years and having reached age seventy shall be eligible for designation by the Board as a Trustee Emeritus. A Trustee Emeritus shall be entitled to attend the annual meeting of the Board but shall have no vote and shall not be counted for purposes of ascertaining the presence of a quorum. A Trustee Emeritus may be invited to serve in an advisory capacity on any committee of the Board of Trustees except the Executive Committee.

ARTICLE II

Officers of the Board

1. The officers of the Board shall be a Chairman of the Board, a Vice-Chairman, and a Secretary, who shall be elected by the Trustees, from the members of the Board, by ballot to serve for a term of three years. All vacancies shall be filled by the Board for the unexpired term; provided, however, that the Executive Committee shall have power to fill a vacancy in the office of Secretary to serve until the next meeting of the Board of Trustees.

2. The Chairman shall preside at all meetings and shall have the usual powers of a presiding officer.

3. The Vice-Chairman, in the absence or disability of the Chairman, shall perform the duties of the Chairman.

4. The Secretary shall issue notices of meetings of the Board, record its transactions, and conduct that part of the correspondence relating to the Board and to his duties.

ARTICLE III

Executive Administration

The President

1. There shall be a President who shall be elected by ballot by, and hold office during the pleasure of, the Board, who shall be the chief executive officer of the Institution. The President, subject to the control of the Board and the Executive Committee, shall have general charge of all matters of administration and supervision of all arrangements for research and other work undertaken by the Institution or with its funds. He shall prepare and submit to the Board of Trustees and to the Executive Committee plans and suggestions for the work of the Institution, shall conduct its general correspondence and the correspondence with applicants for grants and with the special advisers of the Committee, and shall present his recommendations in each case to the Executive Committee for decision. All proposals and requests for grants shall be referred to the President for consideration and report. He shall have power to remove, appoint, and, within the scope of funds made available by the Trustees, provide for compensation of subordinate employees and to fix the compensation of such employees within the limits of a maximum rate of compensation to be established from time to time by the Executive Committee. He shall be *ex officio* a member of the Executive Committee.

2. He shall be the legal custodian of the seal and of all property of the Institution whose custody is not otherwise provided for. He shall sign and execute on behalf of the corporation all contracts and instruments necessary in authorized administrative and research matters and affix the corporate seal thereto when necessary, and may delegate the performance of such acts and other administrative duties in his absence to the Executive Officer. He may execute all other contracts, deeds, and instruments on behalf of the corporation and affix the seal thereto when expressly authorized by the Board of Trustees or Executive Committee. He may, within the limits of his own authorization, delegate to the Executive Officer authority to act as custodian of and affix the corporate seal. He shall be responsible for the expenditure and disbursement of all funds of the Institution in accordance with the directions of the Board and of the Executive Committee, and shall keep accurate accounts of all receipts and disbursements. Following approval by the Executive Committee he shall transmit to the Board of Trustees before its annual meeting a written report of the operations and business of the Institution for the preceding fiscal year with his recommendations for work and appropriations for the succeeding fiscal year.

3. He shall attend all meetings of the Board of Trustees.

4. There shall be an officer designated Executive Officer who shall be appointed by and hold office at the pleasure of the President, subject to the approval of the Executive Committee. His duties shall be to assist and act for the President as the latter may duly authorize and direct.

5. The President shall retire from office at the end of the fiscal year in which he becomes sixty-five years of age.

ARTICLE IV

Meetings and Voting

1. The annual meeting of the Board of Trustees shall be held in the City of Washington, in the District of Columbia, in May of each year on a date fixed by the Executive Committee, or at such other time or such other place as may be designated by the Executive Committee, or if not so designated prior to May 1 of such year, by the

Chairman of the Board of Trustees, or if he is absent or is unable or refuses to act, by any Trustee with the written consent of the majority of the Trustees then holding office.

2. Special meetings of the Board of Trustees may be called, and the time and place of meeting designated, by the Chairman, or by the Executive Committee, or by any Trustee with the written consent of the majority of the Trustees then holding office. Upon the written request of seven members of the Board, the Chairman shall call a special meeting.

3. Notices of meetings shall be given ten days prior to the date thereof. Notice may be given to any Trustee personally, or by mail or by telegram sent to the usual address of such Trustee. Notices of adjourned meetings need not be given except when the adjournment is for ten days or more.

4. The presence of a majority of the Trustees holding office shall constitute a quorum for the transaction of business at any meeting. An act of the majority of the Trustees present at a meeting at which a quorum is present shall be the act of the Board except as otherwise provided in these By-Laws. If, at a duly called meeting, less than a quorum is present, a majority of those present may adjourn the meeting from time to time until a quorum is present. Trustees present at a duly called or held meeting at which a quorum is present may continue to do business until adjournment notwithstanding the withdrawal of enough Trustees to leave less than a quorum.

5. The transactions of any meeting, however called and noticed, shall be as valid as though carried out at a meeting duly held after regular call and notice, if a quorum is present and if, either before or after the meeting, each of the Trustees not present in person signs a written waiver of notice, or consent to the holding of such meeting, or approval of the minutes thereof. All such waivers, consents, or approvals shall be filed with the corporate records or made a part of the minutes of the meeting.

6. Any action which, under law or these By-Laws, is authorized to be taken at a meeting of the Board of Trustees may be taken without a meeting if authorized in a document or documents in writing signed by all the Trustees then holding office and filed with the Secretary.

7. During an emergency period the term "Trustees holding office" shall, for purposes of this Article, mean the surviving members of the Board who have not been rendered incapable of acting for any reason including difficulty of transportation to a place of meeting or of communication with other surviving members of the Board.

ARTICLE V

Committees

1. There shall be the following Standing Committees, viz. an Executive Committee, a Finance Committee, an Auditing Committee, a Nominating Committee, and an Employee Benefits Committee.

2. All vacancies in the Standing Committees shall be filled by the Board of Trustees at the next annual meeting of the Board and may be filled at a special meeting of the Board. A vacancy in the Executive Committee and, upon request of the remaining members of any other Standing Committee, a vacancy in such other Committee may be filled by the Executive Committee by temporary appointment to serve until the next meeting of the Board.

3. The terms of all officers and of all members of Committees, as provided for herein, shall continue until their successors are elected or appointed.

Executive Committee

4. The Executive Committee shall consist of the Chairman, Vice-Chairman, and Secretary of the Board of Trustees, the President of the Institution *ex officio*, and, in addition, not less than five or more than eight Trustees to be elected by the Board by ballot for a term of three years, who shall be eligible for re-election. Any member elected

to fill a vacancy shall serve for the remainder of his predecessor's term. The presence of four members of the Committee shall constitute a quorum for the transaction of business at any meeting.

5. The Executive Committee shall, when the Board is not in session and has not given specific directions, have general control of the administration of the affairs of the corporation and general supervision of all arrangements for administration, research, and other matters undertaken or promoted by the Institution. It shall also submit to the Board of Trustees a printed or typewritten report of each of its meetings, and at the annual meeting shall submit to the Board a report for publication.

6. The Executive Committee shall have power to authorize the purchase, sale, exchange, or transfer of real estate.

Finance Committee

7. The Finance Committee shall consist of not less than five and not more than six members to be elected by the Board of Trustees by ballot for a term of three years, who shall be eligible for re-election. The presence of three members of the Committee shall constitute a quorum for the transaction of business at any meeting.

8. The Finance Committee shall have custody of the securities of the Institution and general charge of its investments and invested funds and shall care for and dispose of the same subject to the directions of the Board of Trustees. It shall have power to authorize the purchase, sale, exchange, or transfer of securities and to delegate this power. So long as the Institution is the trustee under any retirement or other benefit plan for the staff members and employees of the Institution, it shall be responsible for supervision of matters relating to investments thereunder and for the appointment or removal of any investment manager or advisor. It shall also be responsible for reviewing the financial status and arrangements of any employee benefit plan for which the Institution is not the trustee and for appointment or removal of any plan trustee or insurance carrier. It shall consider and recommend to the Board from time to time such measures as in its opinion will promote the financial interests of the Institution and improve the management of investments under any retirement or other benefit plan. The Committee shall make a report at the annual meeting of the Board.

Auditing Committee

9. The Auditing Committee shall consist of three members to be elected by the Board of Trustees by ballot for a term of three years.

10. Before each annual meeting of the Board of Trustees, the Auditing Committee shall cause the accounts of the Institution for the preceding fiscal year to be audited by public accountants. The accountants shall report to the Committee, and the Committee shall present said report at the ensuing annual meeting of the Board with such recommendations as the Committee may deem appropriate.

Nominating Committee

11. The Nominating Committee shall consist of the Chairman of the Board of Trustees *ex officio* and, in addition, three Trustees to be elected by the Board by ballot for a term of three years, who shall not be eligible for re-election until after the lapse of one year. Any member elected to fill a vacancy shall serve for the remainder of his predecessor's term, provided that of the Nominating Committee first elected after adoption of this By-Law one member shall serve for one year, one member shall serve for two years, and one member shall serve for three years, the Committee to determine the respective terms by lot.

12. Sixty days prior to an annual meeting of the Board the Nominating Committee shall notify the Trustees by mail of the vacancies to be filled in membership of the Board. Each Trustee may submit nominations for such vacancies. Nominations so submitted shall be considered by the Nominating Committee, and ten days prior to the annual meeting the Nominating Committee shall submit to members of the Board by mail a list of the persons so nominated, with its recommendations for filling existing vacancies on the Board and its Standing Committees. No other nominations shall be received by the Board at the annual meeting except with the unanimous consent of the Trustees present.

Employee Benefits Committee

13. The Employee Benefits Committee shall consist of three members to be elected by the Board of Trustees by ballot for a term of three years, who shall be eligible for re-election and the Chairman of the Finance Committee *ex officio*. Any member elected to fill a vacancy shall serve for the remainder of his predecessor's term.

14. The Employee Benefits Committee shall, subject to the directions of the Board of Trustees, be responsible for supervision of the activities of the administrator or administrators of any retirement or other benefit plan for staff members and employees of the Institution, except that any matter relating to investments or to the appointment or removal of any trustee or insurance carrier under any such plan shall be the responsibility of the Finance Committee. It shall receive reports from the administrator or administrators of the employee benefit plans with respect to administration, benefit structure, operation, and funding. It shall consider and recommend to the Board from time to time such measures as in its opinion will improve such plans and the administration thereof. The Committee shall submit a report to the Board at the annual meeting of the Board.

ARTICLE VI

Financial Administration

1. No expenditure shall be authorized or made except in pursuance of a previous appropriation by the Board of Trustees, or as provided in Article V, paragraph 8, hereof.

2. The fiscal year of the Institution shall commence on the first day of July in each year.

3. The Executive Committee shall submit to the annual meeting of the Board a full statement of the finances and work of the Institution for the preceding fiscal year and a detailed estimate of the expenditures of the succeeding fiscal year.

4. The Board of Trustees, at the annual meeting in each year, shall make general appropriations for the ensuing fiscal year; but nothing contained herein shall prevent the Board of Trustees from making special appropriations at any meeting.

5. The Executive Committee shall have general charge and control of all appropriations made by the Board. Following the annual meeting, the Executive Committee may allocate these appropriations for the succeeding fiscal year. The Committee shall have full authority to reallocate available funds, as needed, and to transfer balances.

6. The securities of the Institution and evidences of property, and funds invested and to be invested, shall be deposited in such safe depository or in the custody of such trust company and under such safeguards as the Finance Committee shall designate, subject to directions of the Board of Trustees. Income of the Institution available for expenditure shall be deposited in such banks or depositories as may from time to time be designated by the Executive Committee.

7. Any trust company entrusted with the custody of securities by the Finance Committee may, by resolution of the Board of Trustees, be made Fiscal Agent of the Institution, upon an agreed compensation, for the transaction of the business coming within the authority of the Finance Committee.

8. The property of the Institution is irrevocably dedicated to charitable purposes, and in the event of dissolution its property shall be used for and distributed to those charitable purposes as are specified by the Congress of the United States in the Articles of Incorporation, Public Law No. 260, approved April 28, 1904, as the same may be amended from time to time.

ARTICLE VII

Amendment of By-Laws

1. These By-Laws may be amended at any annual or special meeting of the Board of Trustees by a two-thirds vote of the members present, provided written notice of the proposed amendment shall have been served personally upon, or mailed to the usual address of, each member of the Board twenty days prior to the meeting.

Index of Names

- Aaronson, M., 176, 206
 publications, 212
 Abe, K., 511, 512, 513, 516
 Abelson, P. H., v, 953, 959
 publications, 931
 Adams, W. M., 34, 161, 219
 publications, 212
 Adelman, S. J., 202
 Ake, T. B., III, 34, 170, 171, 219
 Alcaino, G., 202
 Aldrich, L. T., 35, 393, 625
 publications, 623
 studies, 543–548
 Allégre, C., 553, 676
 Allen, J. F., 299
 Aller, L. H., 202
 Anderson, D. M., 380
 studies, 376
 Anderson, R. O., v, 959
 Angerer, R. C., 380
 studies, 371–372
 Argon, Y., 33, 147
 studies, 52–58
 Armond, P. A., 22, 35, 228, 229, 230, 240, 247,
 277, 282, 357, 363
 publications, 358, 359, 360
 studies, 234–237, 237–240, 262–276, 291–294
 Arndt, N. T., 33, 706, 707, 782, 933, 948
 publications, 931
 Arnold, J. R., 458
 Arnold, S., 186
 Arp, H. C., 34, 149, 155, 181, 196–197, 209, 218,
 402, 403, 404
 publications, 213
 Asch, E. S., 4, 38, 147
 Assousa, G. E., 16, 35, 386, 389, 395, 399, 625
 publications, 623
 studies, 393–395, 400–402
 Atsumi, S., 33, 4, 147
 studies, 11–12
 Austin, J. P., v, 959
 Avron, M., 300, 301, 358
- Baade, W. A., 155, 184
 Babcock, H. W., 34, 149, 153, 204, 218
 publications, 213
 Badger, M. R., 22, 35, 228, 230, 231, 248, 250, 251,
 264, 363
 publications, 360
 studies, 245–247, 251–261, 262–276
- Bajaja, E., 626
 Ballard, R. L., 218, 220
 Balsiger, H., 451
 Bannister, J., 393, 626
 studies, 543–548
 Barry, A., 140–141
 Barus, C., 633
 Bassham, J. A., 242, 250
 Baur, P. R., 34, 949
 Beck, S. C., 171, 202–203
 Becker, G. F., 633
 Becker, W., 210
 Becklin, E., 174, 192, 213
 Beckwith, S. V. W., 21, 34, 164, 173, 219
 publications, 213
 Belford, H. S., 35, 364
 publications, 360
 Bell, P. M., 15, 33, 644, 645, 646, 649, 924, 927,
 933, 938, 941, 948
 publications, 931
 studies, 835–837, 837–841, 842–848, 853–855,
 855–866, 904–908, 908–913
 Benbow, R., 147
 publications, 143
 Bendich, A. J., 314, 323, 324, 325, 330, 331
 Bennett, C. L., 35, 626
 Bennett, M. D., 311
 Benton, W. D., 203
 Benson, J., 949
 Bergersen, F. J., 245
 Berriman, G., 34, 219
 Berry, J. A., 23, 227, 228, 229, 230, 231, 245, 248,
 250, 276, 294, 363
 publications, 358, 360
 studies, 240–245, 251–261, 276–282
 Bertola, F., 203
 Birkenmeier, E. H., 27, 33, 4, 9, 116, 147
 studies, 124, 136–139
 Björkman, O., 22, 31, 227, 228, 234, 247, 250, 263,
 264, 268, 277, 278, 282, 357, 363
 publications, 358, 360
 studies, 262–276
 Blackwell, D. E., 203
 Blatt, M. R., 24, 35, 232, 233, 364
 studies, 333–336
 Blitz, L., 394
 Block, S., 843, 913, 944
 Boctor, N. Z., 33, 646, 647, 928, 948
 studies, 870–876, 876–880, 880–886
 Bodenheimer, P., 415, 417

- Bodmer, S., 4, 147
 Boek, H. D., 34, 949
 Boise, J. W., vii, 953, 959
 Boksenberg, A., 19, 20, 156, 185-186, 186, 194, 195-196, 213
 Bolton, E. T., vii
 Bond, H. E., 203
 Borne, K. D., 34, 168, 219
 Bornmann, P., 161
 Borra, E. F., 204, 213
 Botchan, P., 33, 4, 143, 147
 publications, 143
 studies, 106-107, 123
 Boucot, A. J., 14, 644, 923, 934
 studies, 826-830
 Böving, B. G., 146
 Bow, C. S., 626
 Bowen, N. L., 928, 929, 934, 945
 Boxer, S., 282
 Boyd, F. R. Jr., 33, 638, 646, 678, 682, 689, 690, 692, 694, 696, 707, 710, 752, 755, 756, 757, 794, 796, 797, 802, 922, 923, 928, 934, 943, 944, 948
 studies, 713-717, 866-870, 870-876
 Boyden, J. E., 159
 Bracamonte, M., 626
 Brain, R. D., 35, 345, 347, 348, 349, 350, 352, 356, 364
 publications, 360
 Branscomb, L. M., v, 959
 Brenner, S., 52
 Brett, R., 926
 Briggs, W. R., 22, 24, 35, 223, 227, 232, 233, 234, 330-332, 363
 report of the Director, Department of Plant Biology, 223-364
 publications, 358, 360
 studies, 333-336, 336-339, 339-342, 342-344, 344-347, 347-353, 353-356, 356-357
 Britten, R. J., vii, 311, 315, 316, 322, 323, 365, 374, 376, 380
 report of the Developmental Biology Research Group, 365-380
 publications, 380
 studies, 370, 377-378, 378, 379, 379-380
 Britz, S. J., 35, 233, 344, 348, 349, 351, 364
 publications, 358, 360, 361
 studies, 344-347
 Brooks, C., 594, 595, 596, 603, 605
 Brosterhus, E. B. F., 211
 Brown, D. D., 26, 27, 31, 33, 4, 11, 107, 115, 131, 134, 146
 report of the Director, Department of Embryology 3-148
 publications, 143
 studies, 124, 124-128, 128-130, 136-139, 139-140
 Brown, G. M., 639, 717, 718, 725-738, 742, 743, 749, 783, 947
 Brown, J. S., 229-230, 295, 363
 publications, 358, 361
 studies, 298-302, 305
 Brown, L., 35, 389, 449, 625
 publications, 623
 studies, 449-452
 Brownlee, D. E., 626
 publications, 623
 Brucato, R. J., 34, 181, 218
 Bruno, M., 211
 Burbidge, E. M., 404, 429
 Burbidge, G. R., 404, 429
 Burke, B. F., 626
 Burstein, D., 35, 387, 626
 studies, 408-412
 Burton, B., 949
 Buseck, P. R., 926, 927
 Bush, Vannevar, 3, 4, 5
 Bustin, M., 147
 Cabre, R., 626
 Calvin, M., 248
 Carbonetto, S. T., 27, 33, 4, 10, 147
 publications, 144
 studies, 11-12, 29-35, 62
 Card Linden, D. J., 33, 147
 publications, 144
 studies, 11-12, 17-18
 Carey, J. A., 34, 949
 Carswell, R. F., 194, 213
 Casaverde, M., 393, 626
 studies, 543-548
 Castenholz, R. W., 283
 Catanzaro, B., 231, 305-307, 307-310, 351, 364
 Caubergs, R., 35, 363
 studies, 356-357
 Ceplecha, Z., 463, 480, 481, 482, 487
 Chamberlin, M. E., 380
 publications, 380
 studies, 370
 Chamberlin, T. C., 633
 Chase, R. C., 158
 Chayes, F., 33, 648, 742, 928, 935, 948
 publications, 931
 studies, 898-900, 900-901, 901-902, 902
 Clardy, K. D., 201, 219
 Claria, J. J., 397
 Cleary, J. R., 523-527
 Clement, C. R., 870, 876
 Cloud, P., 9, 15, 21
 Cohen, J. G., 176, 213
 Cohen, M. C., 186
 Collatz, G. J., 35, 231, 246, 248, 263, 264, 268, 364
 studies, 245-247, 248-251
 Colomb, R., 626
 Connor, J. T., v, 959
 Cordova, F. A., 34, 219
 Costantini, F., 380
 publications, 380
 studies, 372-373
 Cowan, G., 696, 756
 Cowie, D. B., 28, 35, 625
 Cox, C. S., 543, 544, 546
 Cram, T. R., 209
 Crerar, D., 926

- Cross, J. W., 35, 234, 345, 364
 publications, 358, 361
 studies, 353-356
- Cuellar, R., 35, 232, 313, 314, 330, 332, 364
 publications, 361
 studies, 330-332
- Curry, J. R., 614
- Czyzak, S. J., 202
- Da Costa, G. S., 34, 175, 177, 190, 219
- Davidson, E. H., 311, 315, 316, 317, 322, 325, 365, 380
 publications, 380
 studies, 370, 370-371, 371, 371-372, 372, 372-373, 373, 374, 375, 376, 376-377, 377
- Davis, G. L., 29, 33, 577, 626, 648, 922, 923, 948
 studies, 895-897, 897-898
- Dawid, I. B., 26, 29, 30, 33, 4, 9, 11, 146
 publications, 144
 studies, 85-86, 86-93, 93-95
- Day, A. L., 633, 634
- de Bruyn, A. G., 34, 156, 188, 189, 191, 219
 publications, 213
- Deer, W. A., 639, 717, 718, 725-739, 783, 947
- De Camp, W., 927
- DeHaan, R. L., 146
- Demers, S., 205
- Dence, M. R., 468, 469, 470
- deVries, P. A., 141
- Devreotes, P., 29, 144
- DeWit, M., 294
- DeWitt, G. S., 35, 626
- Dickey, J. S., 744
- Diner, D. J., 34, 219
 publications, 213
- di Tullio, G., 196, 213
- Diebold, J., v, 959
- Doering, J., 33, 147
 studies, 124, 128-130
- Dohrmann, U., 353
- Drake, M. J., 677, 680-681, 703, 704, 936
- Dressler, A. M., 34, 181, 185, 187, 190, 191, 203, 218
 publications, 213
- Duffield, W. A., 590
- Duncan, R. A., 11, 392, 552, 554, 599, 626
 studies, 606-612
- Duncan, W. H., 4, 11, 147
- Dworetzky, M. M., 204, 213
- Dworkin, M., 33, 147
 studies, 85-86, 103-106
- Ebert, J. D., v, vii, 142, 959
 Report of the President, 1-35
 publications, 144
- Ecklund, E. T., 447, 628
 studies, 447-448
- Edidin, M., 147
- Edwards, M., 283
- Eggler, D. H., 33, 639, 641, 676, 696, 702, 710, 756, 757, 761, 768, 784, 923, 936, 942, 948
 publications, 931
 studies, 751-756, 790-793
- Ehleringer, J., 247, 264, 358
- El Goresy, A., 927
- Elias, J. H., 34, 204, 207, 219
 publications, 213-214
- Elliot, J. L., 21, 154, 167
- Ellison, J. W., 380
 studies, 375, 377
- Elmegreen, D. M., 204
- Engdahl, E. R., 517, 520
- Erkes, J. W., 400, 626
- Ernst, S. G., 380
 publications, 380
 studies, 371, 373
- Estep, M. L. F., 33, 647, 922, 948
 studies, 886-891
- Evans, J. R., 35, 390, 626
 publications, 623
 studies, 511-517, 527-537
- Evans, N. J., II, 204-205
- Evertson, D. W., 627
- Fambrough, D. M., 27, 33, 10, 11, 146
 publications, 144
 studies, 11-12, 35-38
- Farquhar, G., 251, 358, 361
- Fedoroff, N., 30, 33, 4, 11, 147
 publications, 144
 studies, 124, 131-136
- Feigenson, M., 10, 391, 627
 studies, 590-596
- Ference, M., Jr., v, 957, 959
- Ferry, J. M., 33, 948, 949
 publications, 931
- Few, J., 181
- Fillooy, E., 35, 447, 626
 studies, 446-447, 447-448
- Finger, L. W., 33, 645, 762, 867, 924, 927, 928, 936, 938, 948
 publications, 931
 studies, 841-842, 848-850, 850-853
- Finnerty, A. A., 33, 638, 922, 923, 928, 948
 studies, 713-717
- Flavell, R. B., 313, 314, 316, 322, 323
- Flemmings, E. V., 4, 147
- Ford, G. A., 231, 232, 290, 305-307, 307-310, 325, 330-332, 351, 364
- Foden, J., 613, 626
 studies, 613-620
- Fontaine, G., 205
- Forbush, S. E., 35, 625
- Ford, W. K., Jr., 16, 17, 35, 198, 387, 388, 395, 625
 publications, 624
 studies, 402-405, 428-435, 435-436, 436-441, 446
- Fork, D. C., 23, 227, 229, 230, 231, 278, 282, 287, 289, 291, 294, 363
 publications, 358, 361
 studies, 237-240, 283-289, 289-291, 307-310
- Forsyth, D. W., 527
- Frantz, J. D., 14, 33, 643, 649, 928, 936, 948
 publications, 931
 studies, 812-822, 823-826, 913-917

- Fredriksson, K., 452
 French, C. S., 35, 232, 296, 363
 Friel, J., 949
 Frogel, J., 176, 177, 214
 Fujii, T., 642, 675, 677, 793, 798, 802, 804

 Gaffney, E. S., 840
 Gahm, G., 418
 Galau, G. A., 370, 374, 380
 Galston, A. W., 348, 361
 Garay, G., 34, 219
 Gardner, E. D., 29, 11, 141, 146
 publications, 144
 Gardner, J. M., 33, 4, 147
 publications, 144
 studies, 11-12, 12-16
 Gatley, I., 21, 164, 214
 Gearhart, P., 36, 147
 Geballe, T. R., 34, 171, 203, 218
 Gehrels, T., 205
 Geller, M., 211
 Geyer, E. H., 205
 Gibbs, J. W., 633
 Giddings, T., 294
 Giesecke, A. A., 627
 Gilbert, C. J., v, 959
 Gilbert, M. C., 923
 Gilbert, W., 376
 Gimlich, R. L., 371, 372, 380
 Girardin, N., 627
 Giza, P. E., 4, 71, 82, 147
 Godwin, E., 33, 147
 Gokham, B., 34, 219
 Gold, D. P., 923, 937
 Golden, W. T., v, 959
 Goldreich, P. M., 21, 154, 166, 167, 214
 Goldsmith, M. H., 35, 233, 344, 347, 357, 364
 publications, 361-362
 studies, 347-353, 356-357
 Goldstein, S. J., 388, 443, 627
 studies, 412-414, 443-445
 Gopalan, K., 627
 Gorton, H., 35, 339, 364
 Gottlieb, D., 35
 Graham, J. A., 190
 Grainger, R. M., 370
 Gray, H. H., v, 30, 957, 959
 Green, R. F., 34, 156, 172, 192, 193, 194, 219
 publications, 214
 Green, R. W. E., 391, 537
 Green, T. H., 641
 Greenewalt, C. H., v, 957, 959
 Greenough, W. C., v, 957, 959
 Greenstein, J. L., 34, 154, 168, 169, 170, 172, 173, 218
 publications, 214
 Gregory, R., 305
 Greig, J. W., 29
 Greisen, E. W., 387, 627
 studies, 405-408
 Grenier, J., 300
 Grew, E. S., 648, 897, 898

 Grieve, R. A. F., 468, 469, 470
 Griffin, R. E. M., 205
 Griffin, R. F., 155, 175, 205
 Grill, R. D., 4, 148
 Gross, E. L., 300
 Grueff, G., 209
 Gull, T. R., 627
 Gunn, J. E., 19, 34, 149, 153, 154, 155, 169, 175, 176, 187, 198, 199, 201, 202, 205, 207, 210, 218
 publications, 214
 Gurdon, J., 107, 115, 136, 147
 publications, 144

 Hadidiacos, C., 620, 757, 762, 850, 949
 Haggerty, S. E., 870, 872, 874, 875, 876, 878, 879, 880, 923, 937, 941
 Hall, T. J., 380
 studies, 379-380
 Hallock, W., 633
 Hanawalt, P., 227
 Hancock, E. L., 218, 220
 Haraburda, J. M. S., vii, 953
 Hardy, E. J., 205, 206, 214
 Hare, P. E., 33, 647, 649, 928, 948
 studies, 891-895, 913-917
 Harris, A., 164, 206
 Harrison, W. J., 12, 33, 636, 637, 703, 767, 774, 922, 928, 938, 949
 studies, 682-689, 695-703
 Hart, S. R., 548, 551, 552, 567, 575, 577, 592, 594, 596, 606, 627
 publications, 624
 Hartwick, F. D. A., 19, 156, 185, 186, 214
 Harvey, K., 162
 Hasegawa, A., 10, 391, 626
 Haskins, C., v, 3, 6, 7, 8, 959
 Hatfield, B. F., 208
 Hazen, R. M., 33, 643, 645, 646, 923, 924, 927, 928, 929, 936, 938, 948
 publications, 931
 studies, 808-812, 841-842, 848-850, 850-853, 853-855, 855-866
 Hedges, J. I., 931
 Heiles, C., 387, 409, 627
 studies, 408-412
 Heinze, W. D., 35, 626
 Helin, E. F., 209
 Helsley, D. E., 627
 Hennard, K. R., vii, 953
 Herbig, G., 418, 419
 Herbst, W., 16, 35, 386, 389, 393, 399, 626
 publications, 624
 studies, 393-395, 395-400, 400-402
 Hertel, R., 353, 355
 Hertig, A. T., 146
 Hess, P. C., 926
 Hewitt, R. E., vii, 953
 Hewlett, W. R., v, 959
 Hiesey, W. M., 35, 363
 Hipkind, R. A., 33, 4, 147
 studies, 106-107, 107-111, 111-112
 Hiyama, T., 298

- Hoag, A. A., 193, 211, 446
 Hodges, A., 161
 Hoering, T. C., 14, 33, 635, 644, 647, 752, 757, 889, 891, 923, 929, 948
 publications, 931
 studies, 662-665, 826-830, 886-891
 Hoessel, J. G., 34, 201, 219
 publications, 214
 Hofmann, A. W., 10, 35, 391, 392, 567, 625, 926, 938
 publications, 624
 studies, 548-562, 590-596, 596-606, 620-623
 Hogan, M. E., 4, 106, 148
 Hogness, D., 26, 9
 Höhl, M., 35, 364
 Holden, F., 206
 Holm, R., 282
 Holmberg, E., 184
 Hoover, J. D., 33, 636, 637, 638-639, 640-641, 928, 949
 studies, 677-689, 703-706, 732-739, 739-743, 774-784
 Hornblower, M., vii, 959
 Hough-Evans, B. R., 380
 publications, 380
 studies, 370-371, 371, 375
 Howard, R. F., 34, 154, 158, 159, 160, 218
 publications, 215
 Huang, R. C., 108
 Huchra, J., 206, 215
 Huckenholz, H. G., 769, 931
 Huggins, F. E., 831, 833, 834, 931
 Huggins, P. J., 174, 215
 Humphreys, R., 155, 178, 179
 Hybl, A., 927
 Hyland, A. R., 192, 215

 Iben, I., 397, 398, 414, 417, 418, 419
 Icke, V., 206
 Imhoff, C., 417, 418
 Irvine, T. N., 13, 14, 33, 638, 639, 640, 641, 801, 923, 929, 938, 948
 studies, 717-725, 743-751, 774-784
 Israel, F. P., 206
 Iwasaki, B., 682

 Jacobs, M., 353
 Jacobs-Lorena, M., 370, 371
 James, D. E., 35, 392, 503, 564, 566, 574, 586, 625
 publications, 624
 studies, 562-590, 620-623
 Jensen, R. G., 242, 246, 250
 Jezek, P. A., 627
 Jordan, E., 27, 4, 124, 136, 139, 148

 Kamper, K. W., 211
 Kanamori, H., 511, 512, 513, 516
 Kaplan, A., 35, 230, 251, 364
 publications, 362
 studies, 251-261
 Katgert, P., 191
 Keen, C. E., 531, 533

 Kennicutt, R. C. Jr., 34, 219
 Kent, S. M., 34, 219
 King, C., 633
 King, H., 644, 841, 939, 949
 publications, 931, 936
 studies, 830-835
 Kinman, T. D., 627
 publications, 624
 Klass, M., 57
 Klein, W. H., 376, 377, 380
 publications, 380
 studies, 375
 Knapp, G., 211
 Knapp, S., 154, 176
 Kohler, G., 35, 36
 Kohne, D. E., 323
 Koningsberg, I. R., 146
 Kormendy, J., 197, 215
 Korn, L. J., 26, 33, 9, 130, 147
 publications, 145
 studies, 124, 124-128
 Koseluk, R., 949
 Koslowski, M., 380
 Kowal, C. T., 21, 154, 164-166, 189-190, 219
 publications, 215
 Krieger, A. S., 158
 Krishna, C., 627
 Kristian, J., 19, 34, 153, 156, 175, 185, 186, 191, 201, 202, 218
 publications, 215
 Krogh T. E., 895, 896, 940
 Krzeminski, W., 206
 Kushiro, I., 12, 33, 627, 635, 637, 642, 658, 659, 661, 694, 696, 699, 709, 712, 752, 753, 756, 757, 758, 767, 777, 786, 788, 798, 800, 804, 940, 942, 947, 948
 publications, 931
 studies, 665-672, 672-674, 675-677, 706-709, 793-797
 Kuhi, L. V., 414, 416, 417, 418, 419
 Kunth, D., 190

 LaBonte, B. J., 34, 162, 219
 Lacy, J. M., 171, 202, 203
 Laemmli, U. K., 119
 Landauer, F. P., 19, 156, 185, 215
 Landstreet, J. D., 204
 Langer, K., 927
 Lanning, H. H., 207, 215, 220
 Larson, R. B., 404, 415
 Lasker, B., 438
 Lauer, T. R., 187, 188
 Lauth, M., 93
 Lawson, C. A., 33, 649, 928, 949
 studies, 917-922
 Leahy, P. M., 380
 Lee, A. S., 376, 377, 380
 publications, 380
 studies, 372
 Lee, B. W., 198
 Leighton, R. B., 34, 218
 Lenn, N. J., 141, 145

- Lerche, I., 198
 Lev, Z., 380
 studies, 371–372, 374
 Levitt, J., 35, 363
 publications, 358, 362
 Lew, K. K., 58
 Lewis, B., 627
 Lewis, E. B., 370
 Lieberman, R. C., 926, 940
 Linde, A. T., 8, 10, 35, 390, 391, 503, 625
 studies, 517–520, 537–543
 Lindsley, D. H., 699, 714, 776, 781, 869, 879, 917,
 920, 934, 946
 Lippincott, S., 163, 164
 Lo, K.-Y., 186, 215
 Lock, J. M., 523
 Lockman, F. J., 35, 387, 394, 626
 publications, 624
 studies, 405–408
 Long, E. O., 33, 147
 studies, 85–86, 86–93
 Longair, M. S., 207, 215
 Loomis, D., 200
 Lorimer, G. H., 358, 362
 Lowen, L., 184
 Luck, R. E., 203, 204
 Luyendyk, B. P., 608
 Luyten, W. J., 192, 211
 Lynds, C. R., 19, 20, 156, 185, 186, 195, 215, 627
 publications, 624

 Mabin, A. H., 4, 11, 148
 Macagno, E., 67, 68, 147
 Mackenzie, J., Jr., 358
 Maden, B. E. H., 147
 studies, 106–107, 121–123
 Madore, B. F., 181, 208
 Magaritz, M., 35, 563, 567, 576, 579, 626
 publications, 624
 Malkin, S., 35, 230, 237, 238, 239, 298, 364
 publications, 362
 studies, 237–240
 Malone, P., 26
 Malooly, T. F., 4, 148
 Mann, E. L., 923
 Mao, H. K., 15, 33, 644, 645, 646, 649, 924, 929,
 933, 936, 938, 941, 946, 948
 publications, 931
 studies, 830–835, 835–837, 837–841, 842–848,
 853–855, 855–866, 904–908, 908–913
 Mariano, A. N., 923
 Marsh, K. A., 162, 215
 Martin, S., 162
 Martin, W. M., Jr., v, 957, 959
 Matthews, K., 21, 154, 164, 167, 176, 201
 publications, 216
 Maxam, A. M., 376
 McArthur, J. A., 358
 McBirney, A. R., 718, 725, 739, 741, 783, 790,
 794, 797, 937, 941, 942, 947, 949
 McCammon, C. A., 34, 949
 McClintock, B., vii, 30, 31, 11

 McCrosky, R. E., 463, 476, 480, 481, 482, 486,
 487, 488, 490, 491
 McElhaney, R. N., 277, 279, 280
 McGarr, A., 391, 537, 538
 McGough, S., vii, 953
 McIntosh, B., 475, 477, 478
 McKnight, S. L., 33, 4, 120, 147
 studies, 106–107, 111–112, 112–114
 McMahan, U. J., 147
 McNamara, D. H., 208
 Melnick, J., 206, 216
 Merrill, P., 169
 Meurs, E., 189
 Meyer, D. B., 142, 145
 Michelson, A. A., 633
 Miller, G. H., 949
 Miller, O. L., Jr., 112, 113
 Miller, W. C., 216
 Milstein, C., 27, 10, 12, 35, 36
 Mitton, J., 205
 Mochnecki, S., 34, 169, 170, 185, 219
 Moh, G., 927
 Mooney, H. A., 230, 234, 240, 247, 263, 264, 268,
 359, 362
 Moore, G. P., 380
 publications, 380
 studies, 378
 Moore, R. L., 34, 163, 164, 219
 publications, 216
 Morgan, H. S., v, 30, 957, 959
 Morgan, W. J., 554, 555, 556, 596, 601, 608
 Morimoto, N., 927
 Morrow, J., 80
 Morton, D. C., 191, 216
 Motoya, Y., 627
 Mould, J. R., 34, 171, 219
 Muller, K. J., 28, 33, 4, 11, 146
 publications, 145
 studies, 62, 63–65, 65–69, 69–70, 71–72
 Münch, G., 30, 34, 218
 publications, 216
 Murase, T., 33, 627, 676, 718, 725, 804, 942, 948
 Murata, N., 23, 35, 229, 276, 278, 286, 287, 289,
 291, 364
 publications, 359
 studies, 283–289, 289–291
 Murphy, F. D., v, 30, 959
 Murr, B. L., 147
 Murray, M. G., 25, 35, 231, 314, 316, 317, 325,
 328, 364
 publications, 362
 studies, 316–322
 Myers, J., 949
 Mysen, B. O., 12, 13, 31, 32, 33, 634, 636, 637,
 640, 642, 695, 696, 699, 701, 702, 703, 704, 706,
 751, 752, 904, 922, 923, 929, 940, 942, 948
 publications, 931, 933
 studies, 649–652, 652–658, 658–662, 677–689,
 689–695, 706–709, 709–713, 756–761, 793–797,
 797–801

- Nadeau, D., 34, 219
 publications, 216
 Naslund, H. R., 738, 740
 Nasrallah, M., 949
 Navrotsky, A., 12, 634, 949
 Nelen, J. A., 452
 Nelson, G., 33, 4, 147
 studies, 58–61
 Neugebauer, G., 21, 34, 154, 162, 164, 167, 173,
 174, 192, 218
 publications, 216
 Ney, E. P., 208
 Nicholson, P. D., 21, 154, 167
 publications, 216
 Nisenson, P., 208
 Nobs, M. A., 363
 studies, 240
 Noonan, A. F., 452
 Norton, G., v, 959
 Noyes, R. M., 725
- Ocola, L., 626
 Ogden, P. M., 393, 394
 Ohashi, Y., 850, 851, 931
 Ohshima, Y., 33, 4, 74, 147
 publications, 145
 studies, 71–72, 81–82
 Oke, J. B., 34, 149, 167, 168, 169, 172–173, 185,
 187, 188, 192, 199, 218
 publications, 216
 Olafsson, G., 627
 Olsen, S., 949
 O'Nions, R. K., 551, 557, 597, 602, 603, 620
 Opik, E. J., 456, 458, 459, 475, 479
 O'Rahilly, R., 146
 publications, 145
 studies, 140–142
 Osborn, E. F., 33, 641, 712, 713, 929, 942, 943,
 944, 945, 948
 publications, 931
 studies, 784–790
 Osterbrock, D. E., 206
- Paczynski, B., 168
 Pagano, R. E., 27, 33, 4, 10, 11, 146
 publications, 145
 studies, 38–39, 43–50
 Page, W. H., v
 Palmer, J., 35, 364
 Pasteris, J. D., 34, 646, 944, 949
 studies, 866–870
 Patterson, A., 160, 221
 Patterson, J., 4, 148
 Pazdernik, J., 4, 148
 Pearson, W. R., 380
 studies, 379
 Pennoyer, R. M., v, 957, 959
 Perkins, R. S., v, 957, 959
 Persson, S. E., 21, 34, 154, 167, 173, 176, 177,
 201, 218
 publications, 216
 Peters, T. J., 927
- Peterson, B., 19
 Peterson, C. J., 627
 publications, 624
 Peterson R., 33, 4, 147
 studies, 124, 130–131
 Pesch, P., 208, 209
 Petro, L. D., 34, 219
 publications, 216
 Phebus, B. L., 4, 148
 Phillips, G. D., 627
 Phillips, T. G., 174, 216
 Pichulo, R. O., 830, 944
 Pier, J. R., 34, 219
 Piermarini, G., 843, 913, 944
 Pimental, E., 627
 Pogo, A., 218
 Popp, R. K., 14, 34, 637, 643, 649, 923, 930, 936,
 948
 studies, 709–713, 812–822, 823–826, 913–917
 Pöppel, W., 627
 Pollock, H. E. D., vii
 Posakony, J. W., 380
 studies, 376, 376–377
 Poupeau, G., 627
 publications, 624
 Pratt, L. H., 25, 234, 339, 342, 359
 Preisler, R., 25, 35, 231, 314, 364
 publications, 362
 studies, 323–330
 Preston, G. W., 34, 149, 154, 167, 170, 177, 218
 publications, 216
 Prewitt, C. T., 924, 938, 939, 945
 Priedhorsky, W. C., 34, 206, 219
 Pyper, D. M., 202
- Quail, P. H., 24, 25, 35, 233, 234, 364
 publications, 359, 362
 studies, 336–339, 339–342, 342–344
 Queen, C. L., 128, 147
 publications, 146
- Rabin, D. M., 34, 163, 164, 219
 Racine, R., 16, 386, 393, 627
 publications, 624
 studies, 395–400
 Raison, J. K., 23, 35, 228, 229, 276, 280, 307, 364
 publications, 362, 363
 studies, 276–282
 Rajan, S., 35, 389, 453, 474, 625
 publications, 624
 studies, 449–452, 452–456, 478–481, 482–490
 Ramirez, J. E., 627
 publications, 624
 Ramsey, E. M., 146
 Ranganayaki, R. P., 35, 626
 Rastl, E., 33, 147
 studies, 85–86, 95
 Ray, P. M., 353
 Readhead, A. C. S., 186, 191
 Rebbert, M. L., 4, 85, 148
 Redman, R. O., 34, 219

- Reeder, R. H., 27, 33, 4, 9, 10, 11, 146
 publications, 146
 studies, 106-107, 107-111, 112-114, 114-116, 116-119
- Rennick, W., 608
- ReVelle, D. O., 35, 389, 475, 626
 studies, 475-478, 478-481, 482-490, 490-493
- Reynolds, R. J., 393, 394
- Riebling, E. F., 649, 657, 673
- Riley, J. M., 207, 216
- Ringwood, A. E., 641, 839
- Ritchey, J. L., 34, 641, 784, 949
 studies, 790-793
- Roberts, M. S., 16, 387, 432, 434, 627
 studies, 402-405, 435-436
- Roberts, R. B., 35, 389, 625
 studies, 449-452
- Rodgers, A. W., 190
- Rodriguez B., A., 627
- Rogler, C. E., 35, 364
- Rohan, R. M., 380
 studies, 377-378
- Rood, R. T., 388, 627
 studies, 412-414, 443-445
- Rose, J. A., 34, 187, 190, 191, 203, 219
- Rosenblatt, J., 648, 901, 902
- Rosenhauer, M., 839, 931
- Ross, M., 927
- Roth, W. M., v, 959
- Rots, A., 209
- Rotundo, R., 33, 4, 10, 147
 studies, 11-12, 18-29
- Rubin, V. V., 16, 17, 35, 198, 387, 388, 395, 431, 435, 625
 publications, 624
 studies, 402-405, 428-435, 435-436, 436-441, 441
- Rydgren, A. E., 417, 418
- Ryffel, G., 95
- Rumble, D., III, 14, 33, 643, 644, 923, 930, 948
 publications, 931, 934
 studies, 808-812, 826-830
- Sacks, I. S., 8, 9, 10, 35, 390, 391, 506, 509, 538, 540, 557, 577, 625
 publications, 625
 studies, 494-504, 505-511, 511-517, 517-520, 527-537, 537-543
- Sagan, C., 387
- Sakonju, S., 33, 147
- Sandage, A. R., 20, 21, 34, 149, 155, 178-179, 181, 185, 192, 193, 194, 197, 198, 211, 218, 439
 publications, 216
- Sanders, R. H., 627
- Sanders, W. L., 209
- Sandra, A., 28, 33, 4, 10, 147
 publications, 146
 studies, 38-39, 39-43
- Sargent, A. I., 34, 219
 publications, 216
- Sargent, W. L. W., 19, 20, 34, 149, 156, 185, 186, 186, 188, 189, 190, 191, 194, 195, 196, 199, 210, 218
 publications, 216
- Satchell, S. D., 4, 148
- Sato, N., 23, 229, 283
- Schairer, J. F., 650, 651, 696, 707, 741, 744, 772, 775, 776, 777, 783, 790, 802, 933, 945
- Schechter, P. L., 186, 187
- Scheller, R. H., 376, 377, 380
 publications, 380
 studies, 372-373, 375-376
- Scherrer, P. H., 158
- Schilling, J.-G., 596, 601, 602, 603
- Schmidt, M., 18, 19, 31, 34, 149, 154, 156, 172, 193, 194, 218, 445
 report of the Director, Hale Observatories, 149-221
 publications, 217
- Schmidt, P., 4, 148
- Schneider, D. P., 34, 187, 219
 publications, 217
- Schoenbohm, E., 333, 357
- Scholz, C. H., 517, 520
- Schommer, R., 34, 169, 170, 219
- Schramm, D. N., 198
- Schreiber, U., 35, 277, 357, 364
 publications, 359, 363
- Schreyer, W., 927
- Schroit, A., 28, 33, 10, 147
 studies, 38-39, 43-50
- Scott, S. A., 33, 4, 147
 studies, 62, 63-65, 69-70, 71-72
- Schuch, N., 207
- Seamans, R. C., Jr., v, 957, 959
- Searle, L., 34, 155, 177, 178, 184, 190, 191, 218
 publications, 217
- Sebok, W. L., 34, 170, 219
- Serkowski, K., 169
- Severny, A. B., 158
- Sharma, S. K., 11, 12, 34, 634, 635, 636, 648, 649, 653, 707, 708, 924, 927, 945, 948
 publications, 932
 studies, 649-652, 652-658, 658-662, 662-665, 665-672, 677-689, 902-904
- Shaffer, D. B., 194, 217
- Sheetman, S. A., 34, 177, 200, 202, 203, 211, 218
 publications, 217
- Shimizu, N., 797, 936, 946
- Shiozawa, J. A., 298
- Shoemaker, E. M., 209
- Shortridge, K., 19, 156, 185, 186, 217
- Sigtrygsson, H., 627
- Simkin, S., 209
- Simoni, D., 627
- Sinensky, N., 277, 278, 280
- Snoke, J. A., 8, 503, 557, 627
 publications, 625
- Slezak, M. H., 34, 949
- Smith, B., 4, 148
- Smith, D. B., 311, 313, 314, 316, 322
- Sobolev, N. V., 927, 943, 946
- Soifer, B. T., 34, 218

- Söll, D., 140
 Sollner-Webb, B., 33, 4, 147
 publications, 146
 studies, 106–107, 116–119
 Somerville, D., 4, 11, 146, 148
 Souza, K. A., 277, 278, 279, 280
 Spear, F. S., 34, 642, 643, 923, 948
 publications, 931
 studies, 805–808, 808–812
 Spottiswoode, S. M., 391, 537
 Stachnik, R., 208
 Staehelin, L. A., 229, 291
 Stanton, F., v, 959
 Stefansson, R., 627
 studies, 520–522
 Steigman, G., 198
 Steinhórrsson, S., 949
 Steppe, H., 210, 217
 Stemler, A. J., 35, 230, 302, 305, 364
 publications, 359, 363
 studies, 302–305
 Stern, C. R., 576, 579, 580, 581
 Stewart, J. M., 927
 Stewart, W., 63
 Stoesser, D. B., 14, 638, 725
 Strens, R. G. J., 949
 Strom, K. M., 627
 Strom, S. E., 417, 627
 Struck, D., 28, 33, 10, 147
 studies, 38–39, 50–52
 Sulentic, J. W., 34, 155, 184, 196, 197, 219
 publications, 217
 Suyehiro, K., 8, 9, 35, 390, 506, 626
 publications, 625
 studies, 494–504, 505–511, 511–517
 Suyehiro, S., 8, 543
 Suzuki, Y., 26, 27, 33, 4, 9, 10, 11, 146
 publications, 146
 studies, 71–72, 72–80, 81–82, 82–84, 85
 Svestka, F. S., 159
 Svestka, Z., 158, 159, 217
 Svisero, D. P., 876
 Swanson, D. A., 590
 Swings, J. P., 167, 217
 Swope, H. H., 155, 184, 218
- Taft, J. N., v
 Tammann, G. A., 20, 21, 155, 197, 198, 210, 439
 publications, 217
 Tang, F. Y. C., 161, 217, 219
 Tarara, N., 141
 Tartof, K. D., 147
 publications, 146
 Teeri, J. A., 234
 Tera, F., 35, 389, 625
 studies, 449–452
 Terrile, R. J., 34, 219
 Terzian, T., 413
 Thomas, B. E., 4, 62, 63, 65, 69, 148
 Thomas, T. L., 376, 377, 380
 publications, 380
 studies, 371–372
- Thompson, J. B., 811
 Thompson, W. F., 25, 231, 232, 314, 325, 363
 publications, 359, 363
 studies, 310–316, 316–322, 323–330, 330–332
 Thonnard, N., 17, 35, 388, 395, 436, 625
 publications, 625
 studies, 428–435, 435–436, 436–441, 446–447,
 447–448
 Thuan, T. X., 210, 217
 Tilley, C. E., 741, 762, 790, 793, 946, 948
 Tomandl, D. A., 627
 publications, 625
 Topia, S., 206
 Townes, C. H., v, 202, 203, 959
 Tremaine, S. D., 154, 176, 199
 Triep, E. G., 393, 543
 Trippe, J. T., v, 959
 Trochimczyk, J., 34, 648, 930, 948
 publications, 931
 studies, 898–900, 900–901, 901–902
 Troughton, J. H., 359
 Tsuda, M., 33, 4, 147
 studies, 71–72, 85
 Tsujimoto, Y., 33, 4, 81, 147
 studies, 71–72, 72–80
 Turner, E. L., 210, 211
 Turner, G. L., 231, 240
 Turner, K. C., 35, 388, 393, 625
 publications, 625
 studies, 400–402, 412–414, 443–445, 446–447,
 447–448
 Tuross, N., 34, 647, 949
 studies, 891–895
 Tuve, M. A., 35, 626
 Tytler, D., 195, 212
- Ulmer, G. C., 949
 Ulrich, R. K., 211
 Usher, P. D., 192, 193, 194, 211
- Van Baalen, C., 887
 van den Bergh, S., 211, 217, 400
 Vanderhoef, L. N., 35, 364
 publications, 359
 van Ginkel, G., 35, 229, 230, 295, 299, 364
 publications, 363
 studies, 294–296, 298–302
 Van Hise, C. R., 633
 van Houten, C. J., 205
 van Houten, I., 205
 Van Valkenburg, A., 923, 924, 930, 949
 Varne, R., 613
 studies, 613–620
 Vasquez, S. Y., vii
 Vaclair, G., 205, 212
 Vaclair, S., 212
 Vaughan, A. H., 34, 170, 199, 218
 publications, 217
 Velde, D., 640, 659, 661, 947, 949
 studies, 761–767
 Véron, M., 210

- Verwoerd, W. J., 640, 922, 927, 949
studies, 767-784
- Vidal, N. V., 212
- Virgo, D., 12, 33, 634, 635, 636, 644, 657, 707, 708,
776, 850, 904, 920, 924, 930, 942, 947, 948
publications, 931
studies, 649-652, 652-658, 658-662, 665-672,
677-689, 830-835
- Visvanathan, N., 197, 217
- Vogel, G. L., 649, 913
- Vogt, P., 147
- Volponi, F., 627
- Von Endt, D. W., 949
- Wade, R. A., 34, 168, 219
publications, 217
- Waff, H. S., 665, 667, 672
- Wager, L. R., 639, 717, 718, 725, 742, 743, 749,
783, 947
- Wahli, W., 26, 33, 4, 9, 147
studies, 85-86, 95-103
- Wahn, H. L., 27, 33, 4, 10, 113, 114, 147
publications, 146
studies, 106-107, 119
- Walcott, C. D., 633
- Wall, J., 209
- Wallerstein, G., 169, 212
- Ward, S., 28, 30, 33, 4, 10, 11, 146
publications, 146
studies, 52-58, 58-61
- Warner, J. W., 16, 386, 393, 627
studies, 395-400
- Watson, E. B., 34, 948
- Weber, R., 95
- Weidenschilling, S. J., 35, 386, 426, 626
publications, 625
studies, 414-420, 471-475
- Weill, D. F., 681, 682, 703, 718
- Wellauer, P. K., 86, 93, 146
- Wendlandt, R. F., 636, 637, 639, 640, 702, 767,
774, 922, 923, 930, 947, 948, 949
studies, 695-703, 751-756, 756-761
- Werdan, K., 253, 254
- Werner, M. W., 34, 173, 174, 218
publications, 217
- Westphal, J. A., 19, 34, 153, 156, 175, 185, 186,
201, 202, 218
publications, 217
- Wetherill, G. W., 9, 10, 15, 16, 17, 35, 381, 389,
425, 490, 625
report of the Director, Department of Ter-
restrial Magnetism, 381-628
publications, 625
studies, 421-428, 456-471, 482-490, 490-493
- White, A. J. R., 926, 927
- White, J. N., v, 959
- White, R. E., 202
- White, W. M., 10, 35, 391, 392, 606, 626
studies, 548-562, 596-606, 620-623
- Whitford, D. J., 10, 35, 389, 392, 554, 566, 570,
573, 574, 596, 599, 601, 604, 626
publications, 625
studies, 449-452, 548-562, 606-612, 613-620,
620-623
- Widell, U. M. S., 35, 233, 351, 364
publications, 363
studies, 344-347
- Wieland, T., 334-335
- Wilcox, J. M., 158
- Wilkinson, A., 34, 219
publications, 217
- Williams, J. G., 470, 627
- Williams, T. B., 191, 217
- Wilson, A. T., 248
- Wilson, C. P., 19, 156, 185, 217
- Wilson, O. C., 170, 187, 218
- Wiser, J., 4, 148
- Wold, B. J., 374, 380
publications, 380
studies, 374, 375
- Wolff, S. C., 154, 167
- Woo, K. C., 231, 240-245, 363
- Wood, B. J., 682, 683, 685, 687, 703
- Woodland, H., 120
- Wooten, A., 394
- Wright, T. L., 10, 391, 590, 627
studies, 590-596
- Wyatt, B., 949
- Wyler, T., 95
- Wyllie, P. J., 576, 579, 580, 581
- Yaggi, R., 95
- Yagi, K., 927
- Yagi, T., 34, 644, 645, 849, 923, 924, 930, 948
studies, 835-837, 837-841, 841-842
- Yahil, A., 21, 155, 198
publications, 217
- Yamagishi, Y., 627
- Yanik, G., 201, 220
- Yee, H. K.-C., 34, 187, 219
- Yoder, H. S. Jr., 11, 14, 15, 33, 552, 595, 629, 640,
642, 651, 675, 682, 690, 696, 707, 741, 744, 751,
752, 769, 788, 790, 793, 924, 930, 940, 948
report of the Director, Geophysical Labora-
tory, 629-949
studies, 761-767, 801-804
- Young, P. J., 19, 20, 34, 156, 185, 186, 194, 195,
201, 218, 219
- Zeller, N., 891
- Zies, E. G., 33, 948
- Zimmerman, B., 170, 218, 221
- Zinn, R. J., 34, 155, 176, 177, 178, 184, 185, 219
publications, 218
- Zinner, E., 627
publications, 625
- Zirin, H., 34, 161, 162, 218
publications, 218

